Edited by Jürgen Popp, Valery V. Tuchin,
Arthur Chiou, and Stefan H. Heinemann

WILEY-VCH

Handbook of Biophotonics

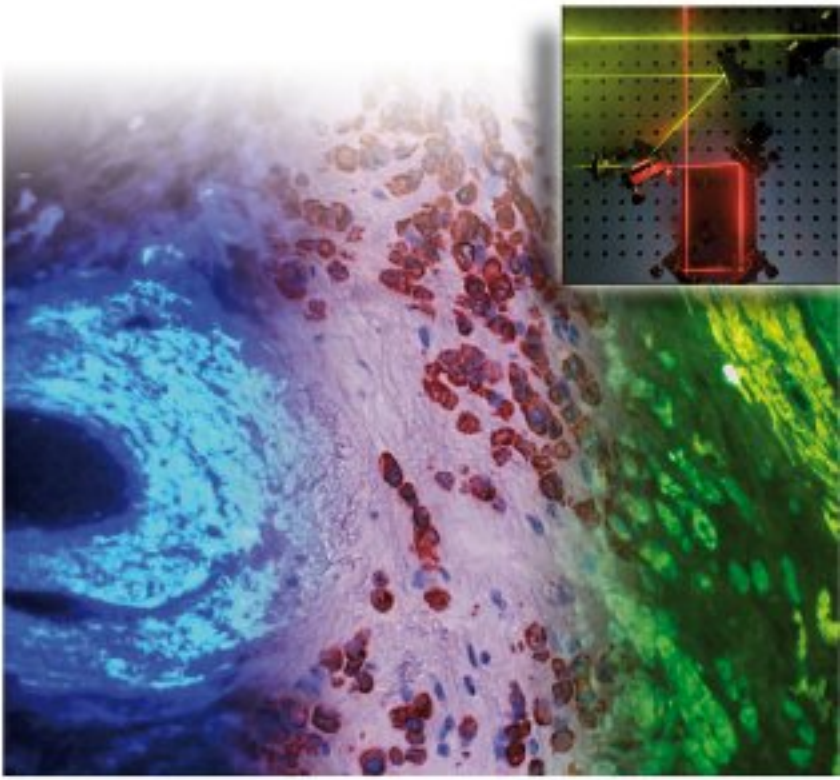

1
Introduction to Biophotonics

Marion Jürgens, Thomas Mayerhöfer, and Jürgen Popp

1.1
Definition of and General Introduction to Biophotonics

1.1.1
Definition

Biophotonics is an emerging multidisciplinary research area, embracing all light-based technologies applied to the life sciences and medicine. The expression itself is the combination of the Greek syllables "*bios*" standing for life and "*phos*" standing for light. Photonics is the technical term for all methodologies and technologies utilizing light over the whole spectrum from ultraviolet through the visible and the infrared to the terahertz region, and its interaction with any matter (Figure 1.1).

Beyond this definition, biophotonics is a scientific discipline of remarkable societal importance. For hundreds of years, researchers have utilized light-based systems to explore the biological basics of life. After the invention of the light microscope dating back to the seventeenth century and the systematic improvements introduced by Carl Zeiss, Ernst Abbé and Otto Schott in Jena in the nineteenth century, it became an essential tool in the life sciences and medicine and had a crucial influence on the work of biologists of this time, such as Ernst Haeckel. Since then, its importance has grown even stronger. Today, ultrahigh resolving microscopes enable us to observe cellular structures smaller than 20 nm across and their functions, and thus to study diseases right at their origin. We also benefit greatly from photonic technologies in medical practice – in fact both in diagnosis and in therapy of diseases. For example, laser scalpels have become routine tools which reduce the expense of many surgeries, sometimes even down to an ambulant intervention ("keyhole surgery"). Due to novel photonic technologies such as fluorescence endoscopy and photodynamic therapy (PDT), some types of cancer can be recognized much earlier and treated more gently than several years before. In ophthalmology, optical coherence tomography (OCT) has become the gold standard for detecting morphological changes in the eye by adding the third dimension, helping to obtain high-resolution 3D images of the retina and diagnose prevalent diseases such as glaucoma and macular degeneration.

Handbook of Biophotonics. Vol.1: Basics and Techniques, First Edition.
Edited by Jürgen Popp, Valery V. Tuchin, Arthur Chiou, and Stefan H. Heinemann.

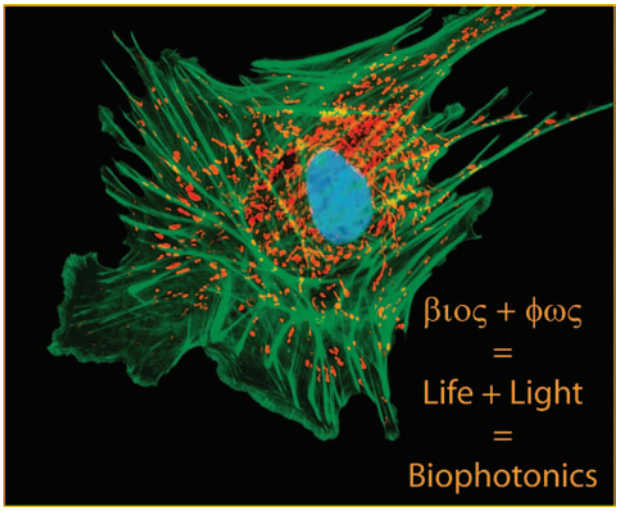

Figure 1.1 Shedding light on life: biophotonics utilizes light-based technologies for applications in medicine and the life sciences (fluorescence image: PCO AG).

The widespread use of biophotonic systems and methods is also reflected in economic terms. Regarding market shares as well as growth rates, biophotonics belongs to the most important sectors of the global photonics market [1, 2].

1.1.2 Visions Connected with Biophotonics Research

The controlled use of light has already revolutionized life in many respects (Figure 1.2). There is high hope that light as a tool will provide further breakthroughs in the life sciences and medicine, and also in closely related topics and subjects such as nutrition, the environment and well-being in general. A current example from the field of medicine is a novel approach for the early recognition of Alzheimer's disease, which so far is considered incurable. In the next few years, fluorescence imaging could provide reliable early recognition and help to verify novel therapeutic approaches which aim at an early intervention in the future [3]. Basically, light allows us to explore cellular structures and functions rapidly and with utmost sensitivity and precision. At the same time, light allows us to manipulate tissues and cellular structures without damaging them. These features make light a unique tool for the whole range of modern medicine:

1) **Understanding diseases on a molecular level:** Light helps to explore fundamental life processes on a cellular and molecular level, and thus to develop novel, targeted therapies.
2) **Early recognition of diseases:** Light allows us to recognize changes on the cellular scale as early signs of diseases, even long before manifest symptoms occur. The earlier is the diagnosis, the better are the chances of healing.
3) **Targeted treatment of diseases:** Light measures and cures in a careful manner, paving the way towards minimally invasive medicine.

Figure 1.2 Visions connected with biophotonics (photographs: LMU Munich/BIZ, World of Medicine AG, Fraunhofer IZM).

4) **Preventing diseases:** Light can measure a multitude of health-relevant parameters, including endogenous parameters such as genetic dispositions and physiological conditions, and also exogenous parameters such as pathogens in air, water, and food. This helps to monitor the health state of individuals and possible harmful influences, which is an important prerequisite to prevent diseases.

Thus the term "biophotonics" covers a wide spectrum of biomedical questions from understanding life processes to prevention, early recognition, and therapy of diseases. Attention should be paid to an alternative use of the term as a complement to the term "biomedical optics." In that context, the field of biophotonics only covers applications of photonics in the life sciences and fundamental biomedical research such as the investigation of cellular processes, whereas the field of biomedical optics covers the clinical applications of light in diagnostics and therapy. This distinction seems to have evolved historically, as the term "photonics" was only coined about 50 years ago, when light-based technologies were already well established in medicine. In this book, the term "biophotonics" is used for both mentioned areas. Furthermore, it reaches into the fields of environmental, food and pharmaceutical analysis and thus even applies to the fields of process control and security applications. The authors consider this definition more conclusive, more purposeful and more forward-looking, as it provides a holistic perspective. This approach advances a likewise holistic, modern health care, and particularly the groundbreaking paradigm change from the treatment of diseases towards health maintenance. Moreover, the close linking of diagnosis, therapy, preventive and follow-up care paves the way towards

personalized medicine. This promises major benefits not only for individual patients, but also for society as a whole: Personalized, targeted therapies can help significantly in limiting health-care costs, and thus in facing the challenges associated with population aging and the consequent increase in age-related diseases.

1.1.3 Why Photons?

What makes light an ideal tool in medicine and the life sciences? A multitude of favorable properties of light and light-related technologies:

1) **Spatial scale: six orders of magnitude:** Light as a tool helps to observe and manipulate objects on a scale from several nanometers to centimeters (Figure 1.3). This opens up a whole range of biomedical applications, reaching from the detection and manipulation of macromolecules to subcellular manipulation and macroscopic diagnosis and surgery of tissue. This is a huge advantage, as novel diagnostic options that work in single cells can be directly adapted to the inspection of cellular networks and tissues. In clinical diagnostics, values can be integrated optically using arbitrary volumes.
2) **Time scale: from 10^{-15} to 10^{6} s:** Using the ultrashort light pulses of femtosecond lasers, extremely fast processes can be analyzed or manipulated with the required high precision in time. On the other hand, light sources are stable enough for long-term monitoring of structures and processes, even covering several days. The repeated application of short light pulses also allows the monitoring of changes in fast processes over long time periods. Photonics is the only available technology to cover this immense time scale.
3) **Multiple functionality:** Optical technologies allow the determination of very different features of molecules, cells, and tissue:
   a) Morphological features [e.g., by measuring reflection, transmission (absorption), and scattering]
   b) Chemical features and their changes (using spectroscopy, e.g., Raman and fluorescence)
   c) Mechanical features (using optical trapping and holography)
   d) Movement (using, e.g., Doppler spectroscopy and dynamic light scattering measurements).
4) **Compatibility:** Optical methods can be combined smoothly with one another. This applies to different diagnostic methods, and also to combinations of diagnostic and therapeutic methods. Moreover, measurements can similarly

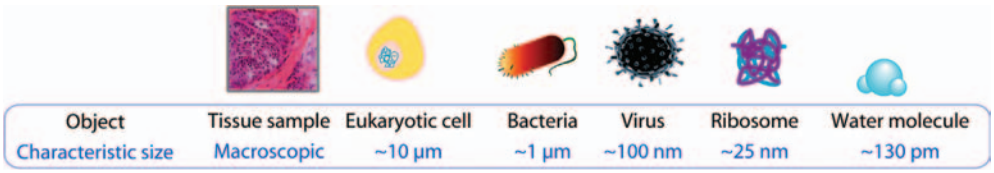

Figure 1.3 Characteristic size of selected objects of biomedical interest.

be performed in the spatial and temporal domain. This wide compatibility facilitates a multitude of feedback-controlled therapies on the microscopic and macroscopic scales. Optical methods can also be combined with non-optical methods and with other advanced technologies such as nanotechnology (e.g., nanoparticles, optically activatable nanocapsules, optical nanostructures) and microsystem technology (e.g., integrated microoptics, microfluidics).

5) **Practicability:** Apart from their fundamental properties, optical technologies also offer important practical advantages. Among them are contactless application, even in therapy, and the easy transmission of energy and signals using light conductors. The application of light has no or only minor side effects and thus enjoys wide acceptance among patients. Moreover, optoelectronic compounds have become increasingly compact and inexpensive to produce (e.g., laser diodes), which allows the development of reasonably priced systems. The mentioned properties and advantages are unequaled by any other biomedical tools, be they ultrasound, X-ray, or magnetic and nuclear medical technologies. Like no other technology, photonics is suited as cross-sectional technology to master a broad variety of biomedical challenges.

1.1.4 Fields of Application and Technology

The scientific discipline covers a broad range of applications and technologies (Figure 1.4). The following overview cannot provide a complete list of them, but

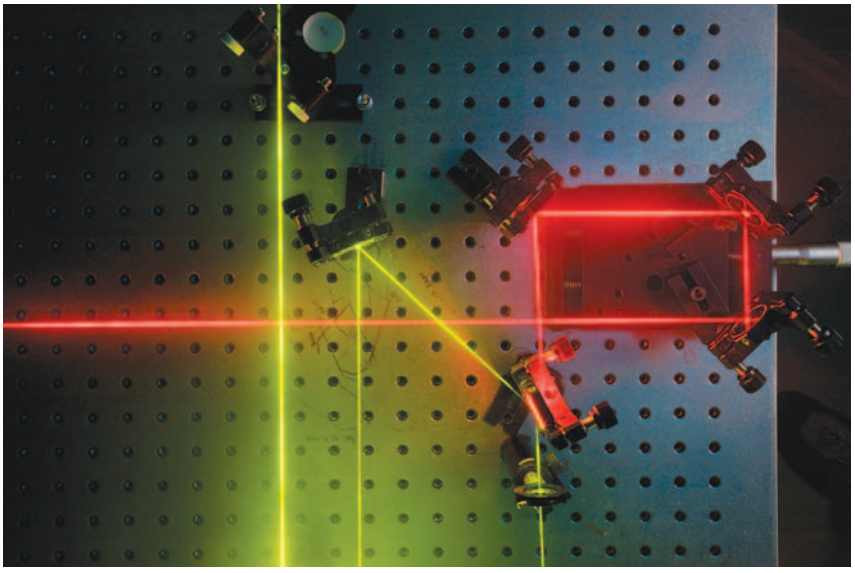

Figure 1.4 Light measures fast, gently, and with high precision, and thus holds unique potential for medical applications. This includes both medical practice and fundamental research in the life sciences (photograph: IPHT Jena).

is rather intended as a first map for readers who are new to this field. The emerging discipline covers a growing multitude of technologies and applications; moreover, many applications in medicine and the life sciences require the combined use of different technologies.

Important Fields of Application

Fundamental biomedical research: Cell biology, molecular biology: understanding of life processes, and also the origin and genesis of diseases, on a cellular and molecular level.
Pharmacological research: Drug development, for example, target evaluation, high-throughput screening (HTS) and/or high-content screening (HCS) of drug candidates, drug delivery.
Laboratory tests, point of care (POC) diagnostics: Analysis of body liquids, for example, in allergology, immunology, hematology, cardiology, epidemiology, endocrinology, medical microbiology; Optical sensing, for example, optical oximetry.
Clinical diagnostics, therapy control, and therapy: (Methods in clinical routine or testing): see Table 1.1.
Regenerative medicine: Stem cell research, tissue engineering, transfection of genetic material.
Environmental monitoring, food safety: On-site testing and monitoring of harmful compounds in air, water, and food, for example, pathogens, fine dust, pollen, chemicals.
Process control: Controlling composition and quality of pharmaceuticals, nutrition and cosmetics.
Security applications: Detection of harmful biological and chemical substances and weapons.

Important Methods and Technologies

Spectroscopy

- Absorption (THz, microwaves, IR, UV–Vis).
- Emission (all fluorescence methods: one-photon/multi-photon fluorescence, FRET, FRAP, FLIM, FLIP).
- Elastic and inelastic light scattering (e.g., Rayleigh, Raman, CARS, SRS, SERS, TERS, Mie, LIDAR).

Light Microscopy

- Fluorescence microscopy (observing autofluorescence or using fluorescence labels, e.g., proteins), including sub-diffraction techniques (optical nano-

scopy, e.g., STED, NSOM, PALM/STORM, structured illumination) and 3D imaging techniques (e.g., confocal and multi-photon excitation microscopy).
- Raman Microscopy (CARS, SRS, TERS).
- Other contrast methods, for example, phase contrast microscopy, digital holographic microscopy (DHM).

Multimodal Approaches, Molecular Imaging

- Combinations of molecular techniques, for example, spectroscopy, and imaging techniques, for example, microscopy. Spectroscopy can provide molecular information for each spot of a microscopic image to deliver multidimensional images of the examined cells or tissues. This allows visualization of cellular functions and following of molecular process in living organisms without perturbing them.
- Other multimodal approaches also include combinations with nonphotonic technologies, for example, PET imaging and PCR assays.

Chip-Based Analysis

- Biochips for POC diagnostics ("lab-on-a-chip").

Therapeutic Methods

- PDT, controlled release of bioactive agents, Laser-in-situ Keratomileusis (LASIK), low-level laser therapy (LLLT), laser-induced thermotherapy (LITT).

Optical Micromanipulation

- Optical tweezers, optical stretcher, laser catapulting, cell sorting and cell positioning.

Optical Components

- Innovative light sources and detectors, optics and optical devices for biophotonics, e.g., ultrafast lasers, adaptive optics, fiber endoscopes.

Enabling Technologies (Not Photonics Based, Yet Preliminary)

- For example, micro- and nanofluidics, nanoparticles, biochemistry (evaluation of targets, development of markers), data modeling (image analysis, chemometrics), data management (user-oriented GUI, handling massive amounts of data, integrating information from multiple channels), system integration.

Table 1.1 Important fields of application in clinical diagnostics, therapy control, and therapy.

Medical discipline	Field of application	Examples
Cardiology, angiology	Intracoronary diagnostics Microcirculation Imaging laser surgery of atrial fibrillation Varicose vein treatment	Imaging of atherosclerotic plaques
Dentistry	Dental diagnosis	Caries, stress/cracks, pulp vitality, periodontal disease
	Dental laser surgery (restoration, prosthetics)	Endodontic therapy, ablation of soft and hard tissue and of restorative materials
Dermatology	Skin diagnosis (structural and functional imaging)	Melanoma and nonmelanoma skin cancers, actinic keratosis, skin injuries, tissue vasculature, atopic dermatitis, acne, psoriasis. Age-related skin conditions, evaluation of transdermal processes (e.g., drug and agent delivery)
	Skin therapy	Photonic therapy, photodynamic therapy, and surgery of above-mentioned diseases
Gastroenterology	Endoscopy and optical imaging PDT of Barrett's esophagus	Laryngoscopy
Laboratory medicine	Pathogen detection	Detecting and identifying pathogens and host response in case of sepsis
Oncology	Tissue-based cancer diagnostics	Tumor detection, staging and grading based on visual inspection and molecular analysis of biopsies
	In vivo cancer diagnostics	Endoscopic detection of tumors
	Intraoperative cancer diagnostics	Tumor border delineation
	PDT	
Ophthalmology	Structural and functional ocular imaging	Retinal angiography and structural imaging, corneal surface
	Eye as diagnostic window to the body	Early recognition of Alzheimer's disease
	Ocular laser therapy	Corneal (refractive eye) surgery, retinal surgery, for example, treatment of glaucoma, AMD, and cataract
Urology	Endoscopic diagnosis	Ureteroscopy, prostatectomy
	Minimally invasive surgery	Removal of benign hyperplasia, strictures, and renal calculi

1.1.5 Societal Relevance of Biophotonics

1.1.5.1 Fighting Prevalent and Severe Diseases

The motivation of biophotonics research is most often the battle against the most prevalent and severe diseases of mankind. As an example, many research studies in Germany are currently focusing on diseases such as cancer, cardiovascular diseases, eye disorders and infections [4]. For comparison purposes, Figure 1.5 lists the leading causes of death as published by the World Health Organization (WHO) [5].

In order to ensure a sustainable and capable health care, the role of biophotonics will probably grow even more in the next decades. The reason is the ongoing demographic change in industrialized countries, which is about to confront their health care systems with their greatest challenges. The case numbers of age-related diseases such as dementia, cardiovascular diseases, and loss of sight are expected to rise sharply in the coming decades. At the same time, the financial resources of public health care systems will probably stagnate and thus not keep pace with the expected increase in costs for treatment and nursing care. Here, biophotonics can meet urgent needs: Early, targeted, and gentle interventions could attenuate or even avoid diseases and thus improve the quality of people's lives, especially for the elderly. This would also help savings of therapeutic costs and economic follow-up costs. The dimensions of the above-mentioned effects are estimated by a number of forecasts and studies:

1) **Demographic change in industrialized countries:** All developed countries are facing rapid demographic changes towards an aging society. A key figure for health care systems is the "elderly dependent ratio" (EDR), indicating the number of people aged 65 years or above, expressed as a percentage of people of working age (Figure 1.6). According to a forecast by the United Nations [6], the EDR is expected to increase from currently about 23% to 45% by 2050 in developed regions. Here, the group of working age is defined as those aged from 15 to 64 years. Although even in the Western world the pace and extent of this aging process differ significantly, the trend itself holds true worldwide. As a consequence, considerably fewer people of working age will be available to fulfill the intergenerational contract and help bear health expenses in a solidarity-based system. Extreme pressure on the public health care system is expected, for example, in Germany. Here, the number of people aged 80 years or above will probably more than double from 2007 to 2050. At the same time, the group of people of working age (here 20–64 years) will probably decrease by nearly one-third. Whereas today about three people of working age correspond to one elderly person, this ratio will shrink to 1.6 : 1 by 2050 [7].
2) **Growing case numbers of age-related diseases:** As the described demographic change stems not only from an improved health care but also from other effects (e.g., decreasing birth rates), one cannot conclude that people will age healthier

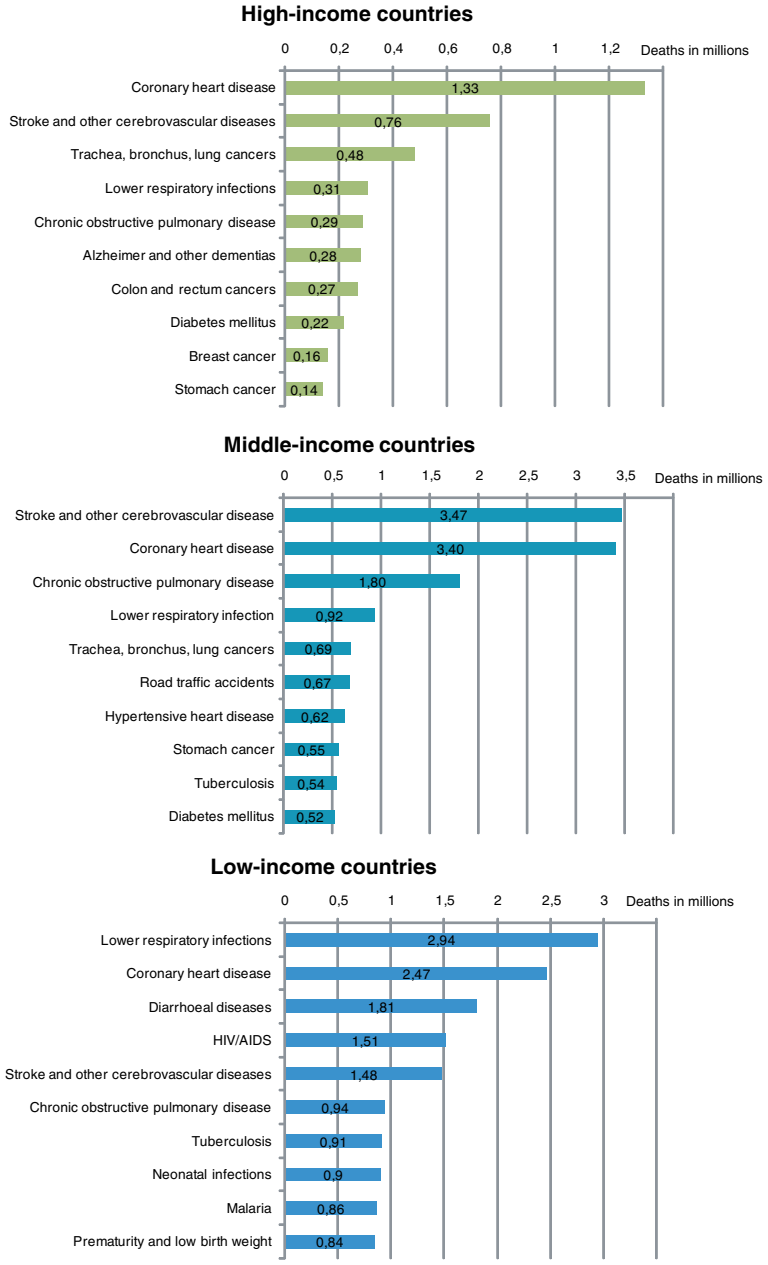

Figure 1.5 The 10 leading causes of death by broad income group (2004). Low-, middle- and high-income categories as defined by the World Bank; countries grouped based on their 2004 gross national income [5].

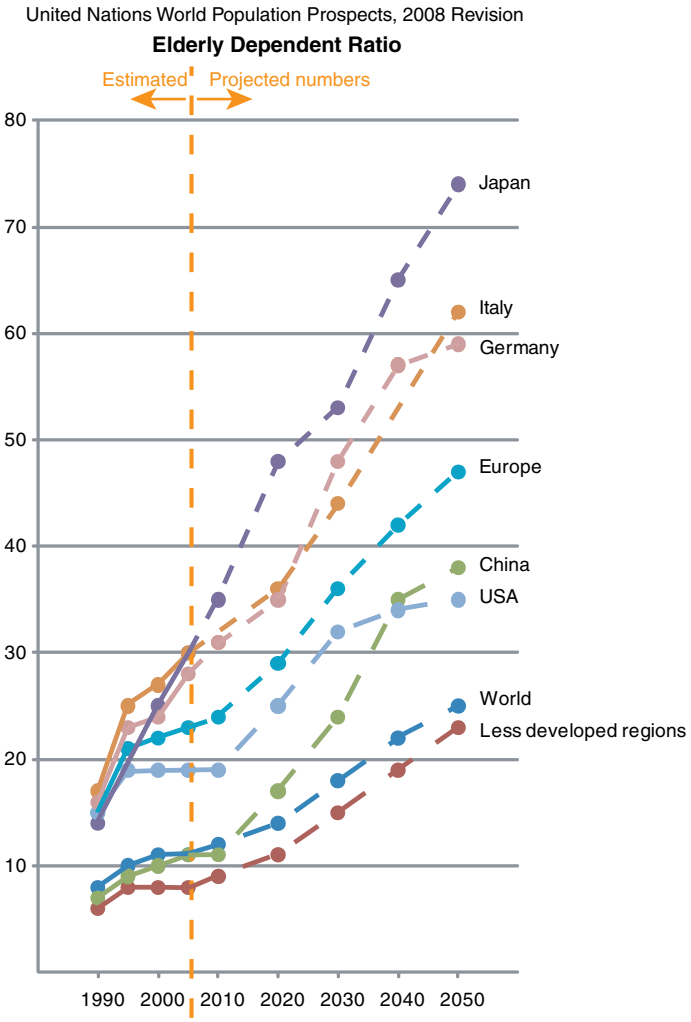

Figure 1.6 Elderly dependent ratio of selected countries and regions: estimated values 1995–2005 and values for a medium projection scenario 2010–2050 [6].

than today. In fact, age-related diseases, and also chronic and lifestyle-related diseases, are expected to become more prevalent in industrial countries. A recent study predicted the expected case numbers of selected widespread diseases in Germany for the years 2030 and 2050, based on current case numbers and the expected demographic development [7] (Figure 1.7). According to this study, the number of patients suffering from dementia as related to the total population will more than double by 2050. The same holds true for the number of patients suffering from age-related macular degeneration (AMD), which is the most prevalent cause of sight of loss in elderly people. Likewise,

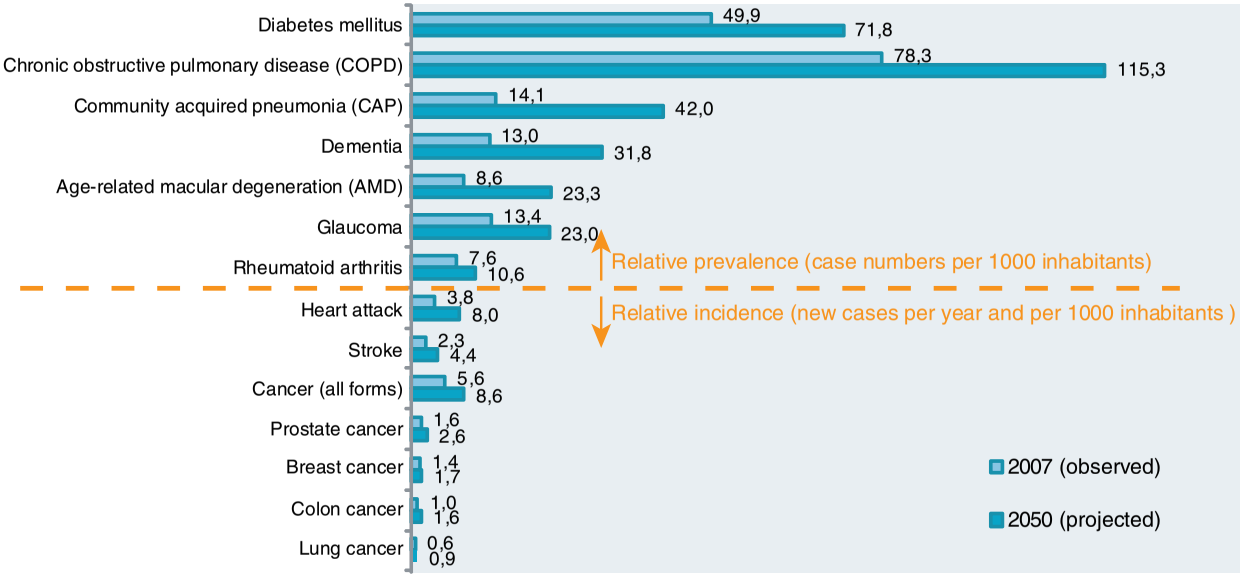

Figure 1.7 Case numbers of selected, widespread and/or severe diseases in Germany, expressed as a percentage of the total population, current as of 2007 and prognosis for 2050 [7].

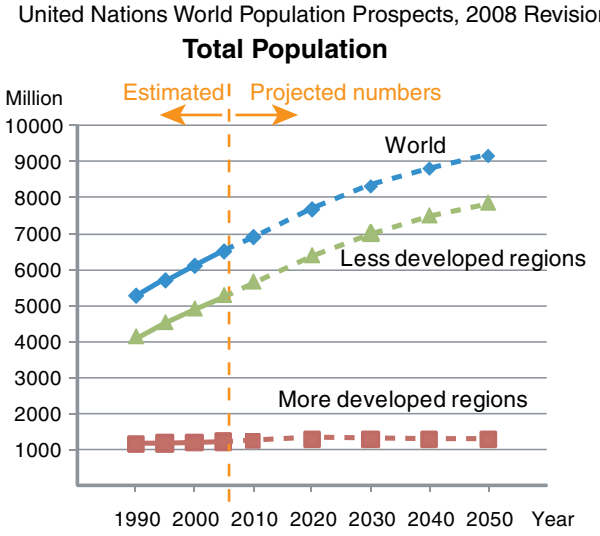

Figure 1.8 Development of world population: estimated values 1995–2005 and medium projection value 2010–2050 [6].

the relative incidence of heart attacks and stroke cases will about double, and the relative incidence of community-acquired pneumonia (CAP) will even be threefold higher than today.

3) **Increasing spendings on health care:** Health care spendings represent a substantial portion of the gross domestic product (GDP) in developed countries. In many European countries, total expenditure amounts to about 10% of the GDP [8]. In the US, the total expenditure on healthcare reached 16% in 2007 [8] and is expected to rise to 20% by 2020 [9]. The study cited above expects that the expenditure on benefits in German health care will more than triple per inhabitant of working age, from €320 in 2000 to €1078 by 2050 [7].

1.1.5.2 Unmet Medical Needs in Third World Countries

The demographic development is also expected to impose major burdens on medical care in Third World countries, as the population will probably continue to grow rapidly in the foreseeable future. The United Nations expects the world population to exceed 7 billion in 2012 and to reach 9.2 billion by 2050 in a medium projection case [6] (Figure 1.8). If this development is not accompanied by a corresponding economic growth, the quality of life will decrease further for many individuals. In the health care sector, this development can only be stopped or even reversed by major breakthroughs towards cost-effective medical procedures that possibly could be applied even in the absence of a physician. Particular attention must be paid to the fast and reliable identification of life-threatening infections in order to prevent their unimpeded propagation. Here, optical technologies might contribute greatly to sustainable health care.

Theses on Future Trends in Health Care, Especially in Developed Countries

- The aging societies will generally experience growing case numbers of diseases, even in the case of a shrinking population. This particularly affects age-related diseases such as neurodegenerative, cardiovascular and eye diseases, and also cancer.
- People's expectations for their own health state will grow, especially in the elderly. Healthy aging is desired; the tolerance towards age-related handicaps will decrease.
- A paradigm change will occur from disease treatment towards health maintenance. Systems and methods for preventive monitoring of the health state, and here especially self-monitoring solutions, will be strongly demanded.
- Due to increasing worldwide traveling activities and urbanization in Third World countries, the risk of pandemics is growing. Fast and easy-to-use screening methods for infectious diseases will be required to counter this.
- Antibiotic-resistant germs ("hospital germs") will occur to a greater extent, including multi-resistant germs.
- The requirements on medical treatments will grow. Patients will expect them to be less invasive, highly efficient and precise.
- Medical treatments will become more personalized. This includes gene and stem cell therapies, and also individual medications (active ingredients, dosage).
- Financial resources in public health care will not grow proportionally to the expected performance and benefit.

1.1.6 Economic Impact of Biophotonics

Market analyses have identified biophotonics among the most important growth segments of the worldwide photonics market [1, 2, 9, 10]. However, quantification of the market situation suffers from several peculiarities. First, the existing studies start from different definitions of the term "biophotonics," which entails different considerations of products and product classes. Growth prognoses are especially complicated as the biophotonics market is fairly young and features many technologies in an early stage of commercialization. Effects such as the development of new markets and the replacement of existing technologies can hardly be estimated.

A market study published by the German Federal Ministry of Education and Research [1] estimated the world market for biophotonics products to be worth about €19 billion in 2005; at about 10%, a significant growth rate was expected for the following years. When excluding the area of ophthalmic optics (spectacle and contact lenses, which are not biophotonic products according to the definition used in this book), the biophotonics market is worth about €10 billion. This includes medical therapeutic systems, "systems for *in vivo* and *in vitro* diagnostics, and

optical systems for the life sciences and for drug discovery. Lee *et al.* estimated the biophotonics market to be worth $53–63 billion in 2004 [10]. However, this study included not only photonic technologies but also technologies such as X-ray, PET and ultrasound.

As typical of the photonics sector, small and medium-sized enterprises (SMEs) are driving the market to a significant extent. Only a few major enterprises appear alongside hundreds of SMEs [2]. Typically, biophotonics is only one of several areas of business in these companies.

1.2
Worldwide Research Activities in Biophotonics

1.2.1
Biophotonics – a Cross-Disciplinary Science

Biophotonics is a highly cross-disciplinary science and bundles knowledge from a wide range of scientific disciplines (Figure 1.9), including, but not restricted to:

- optics and photonics (e.g., optical components and systems)
- cell biology and molecular biology (e.g., handling and examination of cells and tissues)
- physics and physical chemistry (e.g., molecular spectroscopy)
- biochemistry (e.g., development/verification of markers and labels)

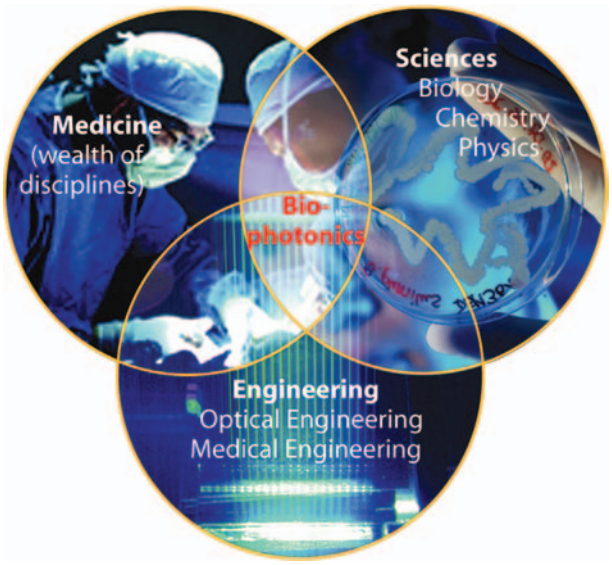

Figure 1.9 Biophotonics bundles knowledge from a wide range of scientific disciplines.

- bioinformatics (e.g., data handling and presentation)
- a wealth of medical disciplines.

Biophotonics research is driven by numerous research groups at university hospitals, universities, and other research institutions, and also through corporate R&D. However, optical solutions for medicine and the life sciences rarely develop from the isolated work of a single research group or company. Many tasks require intense communication, networking and collaboration of experts from the mentioned areas, for example, in the course of collaborative research projects. As many governments have recognized biophotonics as a scientific discipline of high economic and societal importance, they have established national funding programs which have driven such collaborations significantly. At the same time, the number of research groups working in the field has grown remarkably throughout the world. The number of institutes which have established a main area of their research in the field has increased strongly in recent years and is still growing. With extensive funding, the US has even set up a National Research Center on Biophotonics.

However, many indicators show that the interdisciplinary dialog and cooperation still need further improvement. Experts believe that especially the communication between developers and users of biophotonic solutions must be considerably intensified [9, 11, 12]. According to a survey among German biophotonics companies, this communication gap between developers and users is the most important bottleneck to further advances in the field (Figure 1.10).

From our observations, one consequence of this communication gap is that biophotonics research generally remains too much technology driven. To overcome this, technologists should become more aware of important, yet unmet medical needs: Which important diseases cannot be diagnosed or treated adequately yet? On the other hand, more medical doctors and life scientists should become acquainted with the latest optical technologies in order to recognize their value and potential use

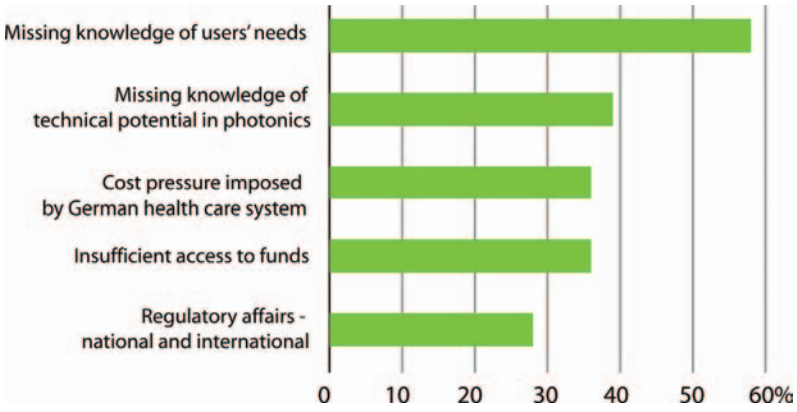

Figure 1.10 Barriers to innovation in biophotonics, as mentioned in a survey among German companies involved in the field [11].

for their specific application. Ideally, users and developers of biophotonic solutions should jointly evaluate which technologies promise the greatest benefit in selected applications, and collaborate on rapid implementations. This would ensure that applications drive the development of technologies and devices (technology "pull") rather than "pushing" technologies into applications. Although of course this interdisciplinary dialog already takes place in many collaborations and informal networks, it can also be amplified further by cross-disciplinary conferences and workshops, such as the International Congress on Biophotonics (ICOB). Furthermore, interdisciplinary efforts should also include suitable education. In academia, foresighted planning would include special lectures in master studies, or even completely new courses of study that cover both photonics and medical topics in such a way that students learn both languages right from the start. Fortunately, several dedicated summer schools for graduates have already been established, including the International Graduate Summer School on Biophotonics (Ven, Denmark), the Nano-Biophotonics Summer School (US) and the Biophotonics and Imaging Graduate Summer School (BIGSS (Ireland)).

1.2.2 Scientific Landscape

1.2.2.1 International Conferences

A number of recurring conferences are dedicated to the field of biophotonics or biomedical optics. Some of the most important among them are organized by the optical societies SPIE and OSA. Moreover, biophotonic methods and applications are showcased at numerous other meetings with related or overlapping topics, some of them focusing on specialist topics such as spectroscopy, microscopy, or therapeutic laser applications. Selected, important conferences include the following:

- SPIE conferences, particularly Photonics West (US; subconference BIOS – Biomedical Optics), Photonics Europe (Brussels, Belgium; subconference Biophotonics)
- OSA conferences, particularly BIOMED, Biomedical Optics (US)
- EOS conferences (EOSAM, Paris, France; subconference Biophotonics – Advanced Trapping and Optofluidics in Life Science)
- ECBO (European Conferences on Biomedical Optics) (Munich, Germany; joint SPIE–OSA conference)
- APS (American Physical Society) annual meeting
- CLEO/QELS – Conference on Lasers and Electro Optics
- Biophotonics and Imaging Conference (BioPIC) (Meath, Ireland)
- IEEE (Institute of Electrical and Electronics Engineers) conferences
- BMES (Biomedical Engineering Society) annual meeting
- ICOB (International Congress on Biophotonics)
- Frontiers in Neurophotonics
- OWLS (Optics Within the Life Sciences)
- APBP (Asian and Pacific Rim Symposium on Biophotonics)

- International Symposium on Topical Problems of Biophotonics
- International Conference on Laser Applications in Life Sciences (LALS)
- International Conference on Photonics and Imaging in Biology and Medicine
- Medical Laser Applications
- International Photodynamic Association meeting
- European Society for Photobiology meeting
- European Platform for Photodynamic Medicine.

1.2.2.2 **Scientific and Trade Journals**

To date, there are two peer-reviewed scientific journals that are fully dedicated to the field of biophotonics: the *Journal of Biophotonics* published by Wiley-Blackwell and the *Journal of Biomedical Optics* published by SPIE. Moreover, biophotonic methods and applications are published in numerous journals with related or overlapping topics. Some of the peer-reviewed journals attracting the most readership among biophotonics researchers are listed below. The data were collected by polling approximately 120 scientists, students, industry researchers, and other participants at the first International Congress on Biophotonics in 2008.

- *Journal of Biophotonics*
- *Journal of Biomedical Optics*
- *Applied Optics*
- *Biophysical Journal*
- *Nature Photonics*
- *Nature*
- *Optics Express*
- *Optics Letters*
- *Physical Review Letters*
- *Proceedings of the National Academy of Sciences of the Unites States of America*
- *Science*
- *Journal of Innovative Optical Health Sciences*.

There are also a number of trade journals that publish news in the field, upcoming events, interviews with scientists, information about new instruments, and other materials related to biophotonics. Specialized titles on biophotonics include *BioOptics World*, *Biophotonics International* (both US) and *BioPhotonik* (Germany).

1.2.2.3 **Networks and Funding Programs**

All over the world, many governments have recognized the economic, scientific, and social importance of biophotonics. Their funding programs (Table 1.2) are stimulating further advances in the field, but also strengthen the pressure of competition between research institutions, regions, and countries. The vast majority of funds are provided for infrastructure (e.g., research centers; see table entries for the US and Singapore), and for research projects to ensure the fast transfer of scientific findings into products and services (see the entry for Germany). Additionally, networking and knowledge management activities are also supported, as in the case of the European

Table 1.2 Worldwide initiatives and funding programs on biophotonics, data retrieved in 2008 (without claiming to be complete) [9].

Country	Project name	Main focus	Budget
The Netherlands	IOP Photonic Devices for Health and Medicine	Imaging techniques, cancer diagnosis, molecular imaging, Raman spectroscopy, optical coherence technology, breath analysis, fluorescence microscopy, SPECT	€25 million
Germany	BMBF Forschungsschwerpunkt Biophotonik	• Optical imaging for medical research and diagnostics, optical POC testing and on-site monitoring • Improved understanding, detection, and treatment of widespread diseases such as cancer, neurodegenerative, dermal, and cardiovascular diseases • Rapid detection of environmental quality, for example, germs in air and water; fine dust in air • Technology focus: microscopy (live cell, 3D, high-resolution), spectroscopy, fluorescence, molecular imaging	~€100 million (2002–2010)
Scotland	SUPA	• Spectral imaging • Optical manipulation of molecules and cells • *In vivo* sensing and imaging • Multi-planar imaging microscope • Micron-sized sources and nanooptics with single-photon (quantum dot) sources and detectors	~£14 million (first 5 years)
Ireland	NBIPI	• Molecular imaging • Live cell and histology imaging • 3D reconstruction and stereology • Small animal *in vivo* imaging • Human diagnostic imaging • Numerical and computational image analysis	€30 million for 2007–2010

(*Continued*)

Table 1.2 (*Continued*)

Country	Project name	Main focus	Budget
USA	NSF Center for Biophotonics	• Bioimaging • Cellular and molecular biophotonics • Medical biophotonics • Education and human resource development • Knowledge transfer	$52 million for the first 10 years (2002–2012)
USA	Biophotonics for Life	• Create and foster a global consortium • Develop a worldwide network • Develop a strategic roadmap	Initially $1.5 million
Japan	Large-scale R&D projects initiated by the Ministry of Economy, Trade and Industry (METI), the Ministry of Education, Culture, Sports, Science, and Technology (MEXT), and the Ministry of Health, Labor, and Welfare (MHLW)	Molecular imaging research program: • Imaging equipment for early detection of lifestyle-related diseases • Molecule imaging equipment for malignant tumor therapy support Knowledge cluster initiative (e.g., Hamamatsu Optronics Cluster): • Next-generation imaging devices, which feature a dynamic range of previously unattainable width and smart imaging, permitting efficient acquisition of only the necessary image information • Highly functional microscope systems, endoscope systems, and surgery support systems • Camera device for high-energy rays used in nondestructive inspection and X-ray CT	~€20.5 million for 5 years (start: 2005)

Canada	Biophotonics Initiative in the framework of the Network of Excellence, Canadian Institute for Photonic Innovations (CIPI)	Biophotonics as one of three main focal areas: • CellLab: the living cell as a laboratory • Advanced photonic technologies on a chip for single-cell analysis • Two-photon excitation photodynamic therapy • Integration of digital micro-mirror devices with confocal macroscopy for improved genetic microarray reading and tissue imaging • Biophotonic systems using high-resolution and diversity imaging • Improved femtosecond laser-based approaches for cellular imaging in live tissue	Can$4.2 million for fiscal year 2006–2007
Australia	Research Network for Fluorescence Applications	• Development of time-resolved fluorescence instrumentation for ultrasensitive microbial screening • Laser-based biochemical assays to instantly recognize heart attack • Extraction of commercially significant fluorescent proteins native to Australian reef corals • Specific microorganisms in complex environments such as industrial waste using high-level multiplex fluorescent probes	A$2 million (2004–2009)
Australia	Center for Biophotonics and Laser Science (at the University of Queensland)	• Fundamentals of light–matter interactions • Biological imaging and sensing • Biological spectroscopy and devices • Laser manipulation • Biomedical and clinical applications	?
Taiwan	Institute of Biophotonics, National Yang Ming University	?	?

(*Continued*)

Table 1.2 (*Continued*)

Country	Project name	Main focus	Budget
Singapore	Biomedical Sciences (BMS), Biopolis Initiative	Institute of Bioengineering and Nanotechnology: • Nanobiotechnology • Delivery of drugs • Proteins and genes • Tissue engineering • Artificial organs and implants • Medical devices • Biological and biomedical imaging Bioimaging Consortium (SBIC) • Coordinated national program of imaging research • Identification and consolidation of the various bioimaging capabilities across research institutes, universities and hospitals • Fostering closer collaboration in bioimaging among researchers and medical practitioners. Technology platforms (used to support research in areas such as cancer, metabolic medicine, and regenerative medicine): • Optical imaging • Image processing and management • Small animal imaging with magnetic resonance • Development of chemical/biological probes	Biopolis 2003–2006: ~$570 million (infrastructure only), ~$600 million venture capital (via Agency for Science, Technology and Research – A*STAR) $4 million
China	Laser manipulation	Optical brain imaging and neuroinformatics • Optical molecular imaging and systems biology • Digital life and biomedical informatics • Optical probes and nanobiophotonics • Multimodal biomedical imaging and tissue optics	?

Network of Excellence (NoE) Photonics4Life and the worldwide network Biophotonics4Life (see also Section 1.3 below).

1.2.3 Current Research Trends and Future Goals

Here we want to emphasize a selection of important areas where biophotonics promises major progress in the near future. Many of the current research activities in biophotonics can be summarized with the following global trends:

Current Global Trends in Biophotonics

- From microscopy of fixed (dead) cells towards video-rate nanoscopy of processes in and between living cells in 3D
- From structural imaging (morphology) towards molecular and functional imaging
- From two-dimensional towards multidimensional imaging
- Seamless imaging from the level of the entire body down to the subcellular and molecular level
- From biopsy and *ex vivo* examination towards minimally-invasive or non-invasive *in vivo* diagnostics
- From laboratory analysis towards rapid testing (POC tests or even home self-tests)
- Closer alliance of diagnosis and therapy (e.g., intraoperative diagnosis, feedback-controlled therapies, combined diagnostic–therapeutic laser systems).

1.2.3.1 Photonic Methods for Biomedical Research

Today, a wide range of microscopic and spectroscopic methods allow the detailed examination of physiological processes in cells and cellular networks and thus have paved the way for molecular cell research (Table 1.3). The investigation of cellular communication, or in more general the investigation of life processes on a cellular or even subcellular level, is a prerequisite for a fundamental understanding of the origin and progression of diseases. This understanding could open up new avenues of curing diseases right at their point of origin. For these scientific questions, fluorescence methods have become indispensable tools. Especially fluorescence microscopy has provided us with novel, manifold insights into the building blocks of the human body. However, until recently such studies were restricted to the examination of fixed, that is, dead cells and thus could only deliver snapshots. Moreover, with lateral resolutions of above 200 nm, many important cellular components were not resolved sufficiently (see Figure 1.3). In contrast, a true understanding of signaling processes, cellular communication or transport processes requires the observation of living cells and cell aggregates, namely three-dimensional, real-time imaging with improved penetration depth and at resolutions down to a few nanometers in all spatial directions. A major breakthrough was the introduction of stimulated emission depletion (STED) microscopy, a few years ago. This technology allows the mapping

Table 1.3 Photonic methods for health research and cellular and molecular biology: important fields of current research.

Application	Optical technology
Investigation of biomolecular interactions (e.g., receptor–ligand, receptor–drug), elucidation of biomolecular modes of action, analysis of signal cascades, identification of specific cellular states	Fluorescence spectroscopy: • Spectrally resolved, temporally resolved (FLIM) • FRET • Ultrahigh resolving in space (STED, structured illumination, dSTORM; two-photon) • Fluorescence correlation spectroscopy (FCS) Raman spectroscopy: • Linear, spectrally resolved • Coherent anti-Stokes Raman scattering (CARS) • Stimulated Stokes–Raman scattering (SRS) • Tip-enhanced Raman scattering (TERS)
Identification of specific receptors and antigens and their mapping on cell surfaces	TIRFS, surface enhanced Raman spectroscopy (SERS)
Cell mapping, distribution of metabolic products in cells	Raman spectroscopy, CARS, fluorescence
Characterization of extracellular matrix	Second harmonic generation (SHG), third harmonic generation (THG)
Analysis of mechanic properties of cells	(Multifocal) optical tweezers, holography
"Cell surgery," membrane perforation, "optical knockout"	Pico- and femtosecond lasers ("two-photon or multi-photon surgery")
Separation of defined histological areas	Laser microdissection

of cellular structures with a lateral resolution of a few nanometers. The technique uses the nonlinear de-excitation of fluorescent dyes to narrow the size of the excitation spot. Unfortunately, this requires high laser intensities and thus might induce photobleaching and damage living cells. Resolution on the nanoscale is also provided by single-molecule microscopic techniques such as PALM (photoactivated localization microscopy) and STORM (stochastic optical reconstruction microscopy). Here, special fluorescence dyes are used that can be switched on and off optically and reversibly, which allows their localization as single molecules. Nevertheless, improvements in order to leverage nanoscopy for widespread use in biochemical laboratories, or even in clinical environments, are still necessary. This includes the development of novel fluorescent labels. Here, novel fluorescent proteins will probably play a major role, as they allow photostable and highly specific labeling. Further innovations are also required on the hardware side for the examination of living cells, including concepts for their handling [13], novel short-pulse lasers for non-damaging excitation,

fast detection methods and innovative software and data management in order to handle the enormous amount of data associated with 3D and video-rate imaging.

Dynamic processes in and within cells can particularly be observed using special fluorescence methods such as FLIM (fluorescence lifetime imaging) and FRET (Förster resonance energy transfer). Both methods can also be carried out in a spatially resolved mode and thus can be used for imaging. Even more detailed insights down to the molecular level are provided by the Raman-based CARS (coherent anti-Stokes Raman scattering) microscopy, SRS (Stimulated Raman Scattering), and fluorescence correlation spectrometry (FCS). All these methods are fairly demanding in technical respects and therefore are not yet used extensively, but are in the process of being commercialized. In contrast, two-photon microscopy is already widespread. With gentle illumination of the sample and comparably high penetration depth, this technology is ideally suited for the spatial imaging of living cellular structures and is already being used in clinical *in vivo* diagnostics (Figure 1.11). As an alternative to fluorescence microscopy, marker-free technologies such as DHM and phase contrast microscopy are being developed further.

Optical methods allow not only the observation but also the active micromanipulation of cellular processes. An important example is the breeding of cell lines for biotechnical production of pharmaceutically active substances [13]. Today, many drugs are based on biomolecules such as hormones, enzymes, growth and coagulation factors, antibodies, and vaccines. To an increasing extent, these substances are produced using microorganisms and cell lines that have to be optimized beforehand through genetic modification to suit the target substance. In practice, the selection and subsequent sorting of living cells from cultures can be performed using so-called optical tweezers that hold or move microparticles with the help of a laser beam that is coupled into the microscope and focused onto the object. Another application is the exact dissection of selected cell areas from tissues using ultrashort laser pulses (laser dissection, laser catapulting, "cell surgery"). This technology is

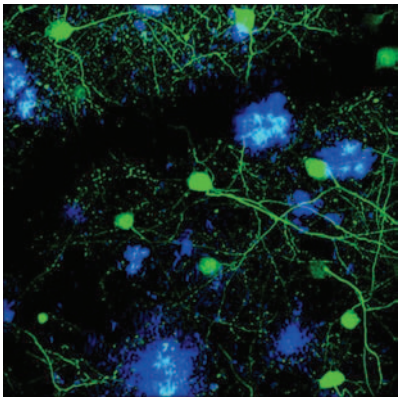

Figure 1.11 Two-photon microscopy reveals cellular and molecular structures *in vivo*: amyloid plaques (blue) between the neurons of transgene Alzheimer's mice (image: Zentrum für Neuropathologie, LMU München).

already used in clinical tissue pathology, for example, for a precise diagnosis and prognosis of cancer. For this purpose, selected areas are cut out from the tumorous tissue and submitted to molecular diagnosis using microarrays or polymerase chain reaction (PCR). In addition, optical micromanipulation is also employed as a tool in regenerative medical applications, including cartilage growth and transplantation, new methods of wound treatment, and the transfection of genetic material into single cells. In order to integrate the described micromanipulation technologies smoothly into laboratory and clinical routines, system manufacturers are currently working on integrated platforms for microscopic imaging and cellular, or even subcellular, manipulation.

Fluorescence methods are also of great importance in pharmaceutical drug discovery. Today, the drug libraries of large pharmaceutical companies contain millions of substances. Their number is growing further, due to genomic analyses which deliver more and more drug targets for novel therapies. During the drug discovery process, the potential effectiveness of drug candidates has to be tested in the laboratory. Here, fluorescence methods are used for HTS of thousands of candidates per day, and also for HCS [13]. This helps to reduce costs and analysis times drastically compared with other methods.

1.2.3.2 **Photonic Methods for Point-of-Care Diagnostics**

For an improved early recognition or even prevention of diseases or for therapy monitoring, the further spread of low-cost, easy-to-handle test systems for the fast examination of readily obtainable samples such as body fluids would be highly beneficial. Such POC devices could facilitate routine examinations of patients and risk groups directly at the doctor's practice (Table 1.4). Technically, this application is covered by chip-based systems that work on a molecular level: Selected proteins, DNA, or small biomolecules are detected as biomarkers, that is, as a precursor or an early sign of a possible disease, or quantified to monitor the progress of a therapy. Crucial success factors for novel POC devices are the sensitivity, selectivity, and robustness of detection, but also the cost per information, the time elapsed from sample collection to result, and the possibility of acquiring several parameters in parallel. Here optical technologies offer a unique potential, as described previously in Section 1.1.3. This is also reflected by their widespread use in comparable diagnostic

Table 1.4 Photonic methods for POC diagnostics: important fields of current research.

Application	Optical technology
Detection and identification of pathogens (bacteria, viruses)	Fluorescence measurements, in combination with antigens
Identification of metabolic products and biomarkers, analysis of the composition of cells, tissues, and body fluids	Fluorescence measurements (spectral and temporal domain), Raman spectroscopy
Analysis of morphological abnormalities (with sub-microscopic resolution)	Light-scattering microscopy

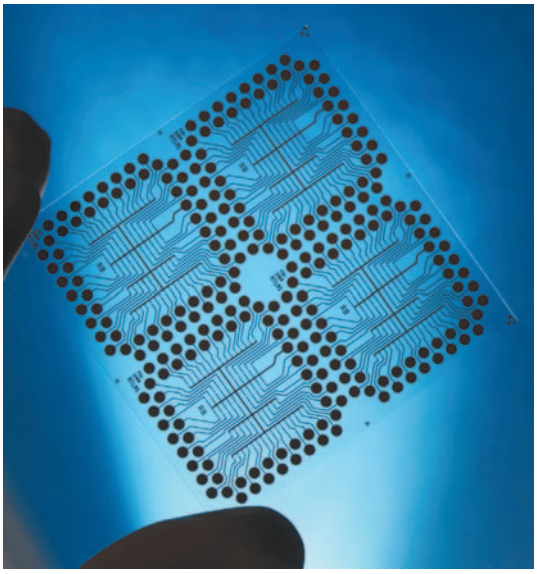

Figure 1.12 This electro-photonic biochip for POC can simultaneously screen for up to 40 different biomolecules such as DNA or proteins (photograph: IPHT Jena).

applications performed in the laboratory. However, existing systems that work on a macroscopic scale cannot be miniaturized arbitrarily as, for example, many optical detection paradigms such as absorbance and fluorescence suffer at smaller geometries. In many cases, new principles that are only effective on the microscale must be implemented. A current approach is also the combination of electrochemical and photonic detection (electro-photonic biochip, Figure 1.12). Microfluidics also plays an important role, as it permits the handling of liquids (e.g., dosage, mixture, separation) in extremely small amounts. Especially sample preparation and manipulation can be automated and miniaturized in this way. This is one of the key factors for a device that can be handled easily and possibly even by untrained persons, for example, in patient self-testing. Most often, sample preparation is the most critical and difficult analysis step, especially with complex samples or samples with complex optical behavior such as blood. The combination of microfluidic and optical technologies results in a so-called optofluidic system.

An important area of application of molecular-based POC devices is the detection of risk factors for cardiovascular diseases. Medical research has revealed a number of relevant biomarkers, including certain protein fragments, proteins and enzymes [14]. For the analysis of single biomarkers, for example, C-reactive protein (CRP), compact, fast immunoassays have already been introduced on the market. However, a fast test that detects several biomarkers in parallel would deliver more significant results (see, e.g., www.labonfoil.eu). The implementation of such multiplex assays ranks among the most important research topics in the field of optical POC testing. For this purpose, multichannel readers for fluorescence lifetime measurements and spectroscopic methods such as SERS (surface-enhanced Raman

spectroscopy) are currently being investigated, among other methods. For fluorescence methods, stable fluorescence labels must be developed that bind to the desired biomarkers with high selectivity. Here, so-called quantum dots hold great promise [14]. In addition to POC solutions, systems for patient self-testing have considerable market potential. Generally, they must meet even higher requirements concerning cost and reliability and therefore will need more time to succeed in the market compared with systems for the doctor's practice. Here, remarkable potential lies also in the field of wellness and health maintenance. Portable systems might help to adjust physical training by monitoring physiological parameters during sports activities, and to control nutrition by monitoring selected blood parameters such as triglycerides, cholesterol and γ-glutamyl transpeptidase (γ-GT) values.

An urgent, yet largely unmet, medical need is the fast identification of pathogens in the case of sepsis. Despite all hygiene efforts, about 150 people per day die from sepsis in German hospitals alone [15]. In order to avoid mortal cases, the time for pathogen identification must be reduced from currently about 36 h to about 30 min after onset of sepsis. Here, optical cell-based diagnostics (readout of spectral signatures) promises a considerable gain of time compared with conventional culture-based methods. Not only must the pathogen be reliably identified but also resistances and host responses must be determined.

1.2.3.3 **Photonic Methods for Clinical Imaging**

Clinical imaging delivers images of the human body (or parts and function thereof) for clinical purposes, especially for the diagnosis of diseases, but also for prognosis, follow-up, and therapy control. In addition to widespread methods such as positron emission tomography (PET) and magnetic resonance tomography (MRT), optical methods have become increasingly important (Table 1.5). Technically, this includes a broad range of methods that deliver two- or multi-dimensional images of tissue

Table 1.5 Photonic methods for clinical imaging: important fields of current research.

Application	Optical technology
Early detection of tumors	One- and two-photon fluorescence spectroscopy, possibly together with endoscopy
Intraoperative recognition of tumor borders	Fluorescence and Raman spectroscopy, with surgical microscopes/endoscopes
Detection and quantification of (hidden) caries	(Red excitation) fluorescence, terahertz spectroscopy, CARS, OCT
Structural examination of the ocular fundus	OCT
Determination of plaques in blood vessels	Endoluminal OCT
Microscopic characterization of dermal changes	OCT, two-photon microscopy, confocal reflection spectroscopy
Monitoring of biomarkers, metabolic products, pharmaceutical agents, and so on for control of therapy and progression	Fluorescence and Raman spectroscopy

surfaces or from within the body. Preferably, the optical window in biological tissue is used, which lies in the near-infrared (NIR) region (700–900 nm). The most important optical technologies for clinical imaging are endoscopy, OCT, microscopy and spectroscopy, and also combinations of them (so-called multimodal approaches). In the sense of patient-friendly diagnostics, especially noninvasive and minimally invasive technologies are advanced. As biopsies cannot be avoided in all cases, the imaging of tissue samples remains an important field of research, however.

In addition to the well-established structural (or morphological) imaging, current research also tends towards functional and molecular imaging. While functional imaging seeks to explore, for example, changes in metabolism, blood flow, and regional chemical composition, molecular imaging aims at the visualization of biological processes in living organisms on a cellular and molecular level. Especially molecular imaging is expected to revolutionize clinical diagnostics, as this method can trace pathological changes in the body already on a molecular scale – and thus possibly long before the first perceptible symptoms occur. It is known that some types of cancer can lead to the production of modified proteins as soon as 10 years before they develop into a solid, palpable tumor. This offers the opportunity to detect and influence abnormally changed cells before they turn into malignant tumor cells. Similar latency is presumed for neurodegenerative diseases such as Alzheimer's disease, which currently can only be diagnosed safely at an advanced stage when the brain is already severely damaged. Furthermore, the understanding and targeted treatment of widespread skin diseases such as neurodermatitis and actinic keratosis might be improved due to molecular imaging. For these purposes, multi-photon imaging is already deployed in clinical environments. Endoscopic molecular imaging also allows a sensitive and gentle intraoperative diagnosis. Further improvements in diagnostic imaging are needed, especially with respect to selectivity. Possible approaches are the development of new fluorescent labels, but also the further development of label-free methods. Although optical imaging methods are already well established in oncology and ophthalmology, great demand exists also in cardiology and in the area of neurodegenerative diseases.

In the field of cancer diagnostics, current biophotonics research seeks to expand the existing methods in three directions:

1) **Early recognition:** The recognition of cancer at the earliest possible stage remains one of the most important aims in modern health care. As an example, cancer organizations estimate that the number of mortal cases due to colon cancer (the most prevalent form of cancer, e.g., in Germany) might be reduced by about half if screening was performed consistently. Today, tumors can only be visualized by radiography at a size of about 100 million cells or more. Here, the method of fluorescence endoscopy holds great promise: Current research gives rise to the hope that soon small tumors of about 1 mm diameter (1 million cells) or even smaller might be differentiated safely from healthy tissue. Fluorescence endoscopy is already used to detect tumors of the bladder and brain, and is currently being extended to permit highly specific detection of tumors in other organs (e.g., colon, lung) [16]. Typically 5-aminolevulinic acid (5-ALA) is administered to

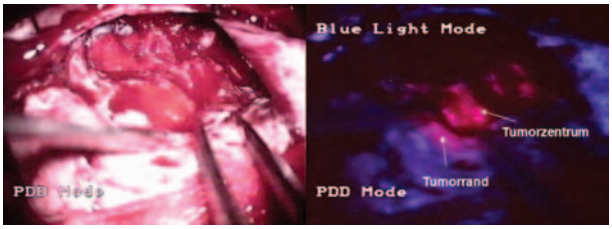

Figure 1.13 Fluorescence endoscopy using 5-ALA provides a much clearer picture of this malignant brain tumor than classical whitelight endoscopy. Especially the infiltrating borders (purple) can be better distinguished from healthy tissue. *Tumorzentrum*, center of tumor; *Tumorrand*, tumor border (source: LMU Munich, LIFE Center, Laser-Forschungslabor).

the patient ahead of the examination, which induces increased generation and accumulation of a fluorescent dye in possibly existing tumor cells (Figure 1.13). The future perspective is to intervene at a much earlier stage of tumorigenesis and to recognize the very first tumor precursors. However, this requires the development of novel, highly specific fluorescent probes that bind to known tumor markers such as TKTL-1 [17]. At present, peptide and nanoparticulate probes are being investigated for this purpose. As the development of such probes is comparably extensive, marker-free technologies such as autofluorescence, Raman spectroscopy and CARS are also advanced further.

2) **Closer linkage of diagnosis and therapy:** At present, fluorescence endoscopy enables the surgeon to recognize the exact borders of tumorous lesions in internal organs and thus to perform surgery in a highly precise and gentle mode. In the future, small tumors might even be removed easily during endoscopic examination using an endoscope that is equipped for laser-induced, thermal, or photodynamic destruction of the detected tumor [16].
3) **Improved grading and individual therapy recommendations:** Today, optical technologies offer important improvements for the histological examination of tissue samples. Although pathologists can answer the question "cancer – yes or no?" safely after microscopic inspection of tissue slices, unfortunately their prognosis of the course of disease often remains vague. Many experts are convinced that multimodal tumor diagnostics can fundamentally change this. By refining classical morphological diagnostics and combining it with molecular methods, for example, optical spectroscopy and biomolecular assays, a better grading and prognosis might become possible, which would permit individual therapy recommendations.

In the field of ophthalmology, OCT has become the gold standard for detecting morphological changes in the eye over the last 20 years. In contrast to fundus imaging, OCT allows one to visualize also deeper layers below the surface, opening the third dimension and allowing, for example, macular thickness measurements. Thereby a multitude of different eye diseases can be diagnosed, such as pigment epithelial detachment (PED) and the diagnosis of glaucoma in a non-invasive and fast way [9]. On the other hand, many age-related diseases such as cardiovascular diseases, diabetes,

Figure 1.14 Laser fibers have paved the way towards minimally invasive medicine (Photograph: World of Medicine AG, Berlin).

and neurodegenerative diseases might be diagnosed at an early stage and in a gentle manner by utilizing the eye as a "diagnostic window to the body". Here, suitable techniques for the measurement of morphological and functional parameters, for example, autofluorescence and fluorescence lifetime measurements, are currently being advanced towards clinical systems. Again, multimodal approaches seem favorable – especially combinations of OCT with fluorescence methods.

1.2.3.4 **Photonic Methods for Therapeutic Applications**

At present, laser radiation is routinely used for the targeted treatment of tissues. For this purpose, the radiation can be conducted through optical fibers and adjusted for a highly precise local application (Figure 1.14). Different effects can be achieved by adjusting wavelength, intensity, and duration of radiation. The most common application (Table 1.6) lies in ophthalmology (e.g., refractive surgery), followed by applications in dermatology (e.g., PDT) and surgery. More optical procedures for clinical use are currently being developed, including the use of ultrashort laser pulses

Table 1.6 Photonic methods for therapeutic applications: important fields of current research.

Application	Optical technology
Precision surgery (e.g., cornea)	Excimer lasers, femtosecond lasers
Selective therapies, restricted to abnormal cells	PDT, (pulsed) lasers with optical feedback
Treatments on a molecular scale (gene switching, activation of molecules)	Pulsed lasers combined with optical switches, nanoparticles
Novel antimicrobial strategies	PDT and combined methods

for precision surgery of the eye, brain, and nerves, and therapeutic lasers for dentistry. Furthermore, closer diagnostic feedback will fundamentally change and enrich medical interventions, as indicated above. They will become even more precise and gentle (due to, e.g., intraoperative *in vivo* diagnostics), but also develop into personalized therapies (due to, e.g., multimodal tumor diagnostics). Moreover, novel methods such as the optical selection of living cells from tissues or cultures and their examination and manipulation will provide new perspectives for regenerative medicine (see Section 1.2.3.1).

1.2.3.5 Photonics in Pharmaceutics, Bioanalysis, and Environmental Research

As described in Section 1.2.3.2, optical POC devices can match urgent analytical needs in the fields of environmental analysis, food analysis, and drug safety. This includes agricultural applications such as prevention or stemming of animal and plant epidemics. In addition, wellness applications can be assumed to gain further importance, for example, the evaluation of blood values (lactose, antioxidant agents) to determine the level of fitness and to control the success of exercises and also the evaluation of stress levels. Another important contribution of biophotonics to this field is the development of optical systems for the continuous monitoring of the quality of air, water, soil, food, pharmaceuticals, and cosmetics with respect to quality and possible contamination. Already introduced on the market are online monitoring systems for pollen and for germs in air (Figure 1.15). Current research includes the fast detection of germs in potable water [18] and an improved detection method for fine dust in air, which might even help to trace individual sources of pollution [19]. Furthermore, security applications have become more and more important over recent years, comprising the detection of harmful biological and chemical substances (pathogens, toxins, explosives, etc.) and weapons. Last but not least, the search for new biomarkers and the screening for new pharmaceutics via optical high-throughput and content screening belong to this group of applications, which will be covered in more detail in volume III of this handbook.

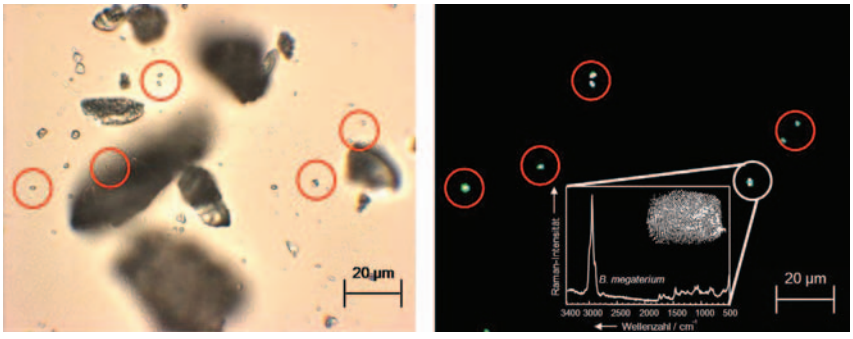

Figure 1.15 Fast on-site monitoring of bacteria: a combination of fluorescence analysis and Raman spectroscopy allows reliable identification down to the strain within a few minutes (Images: Jena Univ., Institute of Physical Chemistry).

1.3
The Biophotonics4Life Worldwide Consortium

Gabriela Lee, Dennis L. Matthews, Jürgen Popp, and Brian C. Wilson

1.3.1
Mission and Purpose of the Biophotonics4Life Worldwide Consortium

The Biophotonics4Life (BP4Life) Worldwide Consortium is a network of biophotonics researchers, educators, companies, and end-users from 20 nodes or regional "hot spots" of activity in many countries around the world. The mission of BP4Life is to spearhead activities that better harness global talent and resources in biophotonics and then focus these on fundamental discovery and innovation in order to meet major challenges in health care and other biotechnology needs. Examples of how this will work include: providing end-users with access to the very best possible technologies and expertise instead of just that available in their region; providing end-users with team-based, multi-institutional, even multi-national solutions; providing quality assessment of biophotonics techniques and educational materials – basically, letting the research community create its own standards; fostering worldwide community participation in a web-based knowledge bank known as http://www.biophotonicsworld.org (see later under BP4Life activities); having medical experts define the "grand challenges" in their specialty, followed by worldwide community brainstorming to create solutions; engaging private industry regionally and globally to create products based on innovations and needs defined by a worldwide community of researchers and end-users; providing students of all levels with access to webinars and blogs to learn from experts within the field of biophotonics; and many more ideas to come from our global social network of scientists, corporations, and end-users.

1.3.2
History and Organization of the Consortium

BP4Life was itself founded as a partnership between the UC Davis Center for Biophotonics Science and Technology (CBST), the Canadian Institute for Photonic Innovations (CIPI) and a European Network of Excellence called Photonics4Life. These are major centers or networks of researchers in North America and Europe. CBST (http://cbst.ucdavis.edu) consists of nine participating institutions, more than 10 affiliated foreign and domestic universities, and numerous industry partners all focused on developing and deploying photon-based technologies for grand challenges in the biosciences and medicine. The CIPI (www.cipi.ulaval.ca) is headquartered at the University of Laval, Quebec, but spans nearly all of Canada. Its participants focus on many different projects, from novel fiber-optic systems for biomedicine to optical biosensors to advanced light-based therapeutics. Photonics4Life (www.photonics4life.eu) is a European Network of Excellence which is funded by the European Commission (EC) and coordinated from the Institute of Photonic

Technologies (Jena, Germany). The network bundles the forces of 13 research partners from 10 EC Member States, in addition to associated partners and local cluster partners. It aims at providing a coherent framework for the strongly fragmented field of biophotonics in Europe and has the important goal of bridging the gap between different disciplines working in the field. The founding Co-Chairs of the BP4Life Consortium are the current Director of CBST, Dennis L. Matthews of UC Davis and Lawrence Livermore National Laboratory, the CIPI Biophotonics Program Leader, Brian C. Wilson of the University of Toronto, and Photonics4Life Coordinator, Jürgen Popp of the University of Jena and Institute of Photonics Technology. All three researchers have been pioneers and leaders in the field of biophotonics and are joined by many other researchers and students from their respective programs, centers, and networks. Ms. Gabriela Lee, who is also a co-author on this section and one of the knowledge transfer officers at CBST, serves as the BP4Life Coordinator, managing all of the activities of the Consortium and its Node Leaders and their assistants. The Co-Chairs and Coordinator meet virtually via monthly web conferences and in person at major biophotonics events, together with the Node Leaders from major centers of research throughout the world. These meetings discuss how to support the Consortium, define its roles, and improve the content and utility of the web portal (http://www.biophotonicsworld.org), in addition to focusing on regional and global opportunities for the application of biophotonics.

1.3.3
Node Leaders for the Consortium

The 20 current nodes (more are being developed as we write) are shown in Table 1.7. The rationale for the choice of nodes is largely geographic, so as to ensure that every region globally has good representation. The primary purpose of the nodes is to assemble information about "who is doing what and where" within their region, basically to function like a local chapter of special interest in the field of biophotonics and its applications. Table 1.7 also names the current Node Leaders or co-leaders if the responsibilities are shared. These individuals were chosen because of their expertise in the field of biophotonics and also their ability to access and assemble resources and lead programs. Currently their roles and responsibilities are to:

- represent BP4Life at a local/country/node level
- participate in monthly teleconferences among node leaders and Chairs
- discuss upcoming activities such as webinars and conferences
- make suggestions for continuously improving the www.biophotonicsworld.org website
- pass along opportunities for collaboration and funding
- communicate any other biophotonics-related items of interest
- identify other biophotonics researchers and companies in their region
- present webinars on their fields of research
- promote the field of biophotonics and communicate the potential that photonics technologies have in health care, research, agriculture, biometrics, and so on.

Table 1.7 BP4Life Nodes and Node Leaders.

Node no.	Node	Node Leaders
1	US West	Bruce Tromberg Steven Jacques
2	US Central	Lihong Wang Stephen Boppart
3	US East	Gary Tearney
4	Canada	Brian Wilson Yves de Koninck
5	Mexico/Argentina/Chile	Oscar Martinez
6	Brazil	Vanderlei Bagnato
7	North-West Europe	Tia Keyes Kishan Dholakia
8	Europe/Photonics4Life	Jürgen Popp
9	Southern Europe	Francesco Pavone Turgut Durduran
10	Benelux	H.J.C.M. Sterenborg
11	Scandinavia	Peter E. Andersen Stefan Andersson-Engels
12	Central/Eastern Europe	Gert von Bally
13	Israel	Israel Gannot
14	Russia	Valery Tuchin
15	Taiwan	Arthur Chiou
16	Singapore	Colin Sheppard Zhiwei Huang
17	Hong Kong	Jianan Qu
18	China	Quingming Luo Sailing He
19	Korea	Woong Shik Ahn
20	Australia/New Zealand	Halina Rubinzstein-Dunlop David Sampson

1.3.4
Current Activities of the BP4Life Consortium

The Consortium's Chairs and node leaders coordinate the activities listed below, which benefit faculty, students, and other members of the biophotonics community. Most of these activities and programs are implemented via the www.biophotonics-world.org portal.

1) Research opportunities:
   a) Collaborative projects.
   b) Exchange opportunities for students, faculty, researchers, and so on to spend time in another laboratory (in the same or different country); funding opportunities for exchange programs.

   c) Webinars delivered live via the Internet and recorded for offline use.
   d) Information sharing on how biophotonics is funded in each region.
   e) Focus on medical needs that may have biophotonics-based solutions.
2) Education opportunities:
   a) Curricula for different educational levels, from beginners to advanced.
   b) Courses.
   c) Review articles.
   d) Other resources (computer codes, movies, tutorials, etc.).
3) Knowledge transfer:
   a) Overview of activities and biophotonics strengths and resources (equipment, skills, and capabilities) for each node.
   b) Brokering knowledge of needs and biophotonics tools.
   c) Information sharing on companies active in biophotonics in each region.
   d) Current and developing biophotonics industry clusters.
   e) News: local, regional, national, international.
4) Industry participation:
   a) Membership.
   b) White papers.
   c) Advertising.
5) Roadmapping to guide research and development, commercialization, and policy in applications of photonics-enabled technologies to medicine and the life sciences.

The Chairs and Node Leaders meet via web conferences once per month, and in person 2–3 times per year, during existing conferences, and discuss the Consortium's activities. For example, the Consortium's leaders met in January 2010, during the Photonics West Conference, in April 2010, during Photonics Europe, and will meet again in Quebec, Canada, in September 2010, during the BiophotonicsWeek series of events. Many of the BP4Life Node Leaders will be active participants in the 2nd International Congress on Biophotonics (part of BiophotonicsWeek), where they will update the roadmaps of biophotonics generated during the first Congress, and generate new content for this year's areas of focus: biophotonics in neurosciences, infectious diseases, and point-of-care, and drug discovery and development.

Perhaps one of the most important activities of the Consortium is to chart and monitor trends in how much biophotonics research funding is being provided in different areas of the world. We illustrate a very preliminary (and not yet validated) example of this in Figure 1.16. As we accumulate more data, these will be updated and published on the web portal, but it serves to illustrate that many regions are beginning to provide substantial research funding for the field, albeit far short of the actual revenues being generated by the biophotonics industry marketplace [10].

1.3.5
Medical Fellows

One of the many important recommendations of the Node Leaders has been the creation of voluntary positions known as Medical Fellows. These are physicians who

Figure 1.16 Government funding levels in 2009 for biophotonics research for three different regions of the world: North/South America, Europe, and Asia/Australia/New Zealand. These are lowest level estimates based on a partial survey of researchers in a given region, but the arrows indicate the trends, either constant or increasing support.

help our Consortium members understand medical needs that could, in particular, benefit from biophotonics devices or methods. The Medical Fellows are asked to address the Consortium regularly through webinars and blogs to help create lists of medical challenges. They are also encouraged to be early adopters of any new technology created and, if applicable, to assist or even lead clinical trials. The identities of the Medical Fellows will be changing regularly and can be viewed on the www.biophotonicsworld.org portal.

1.3.6
Anticipated Role of Industry

The Consortium is still determining the role(s) for biophotonics industry players, but it is planned to be substantial. Clearly, just as with Medical Fellows, it will be important for industry to voice their needs and challenges through webinars and blogs so that Consortium members can provide assistance. We would also anticipate that private companies will be interested in knowing who is doing what type of research and has what type of technology in their immediate region. We also believe that the web portal will be an excellent place for industry to advertise positions and, of course, their products. We are also considering an entrepreneur-in-readiness program, whereby CEOs could advertise their availability to lead startup companies that may be the outcome of research technology applied to medical needs and leading to medical devices.

1.3.7
Potential Future Activities of the Consortium

Our vision for the BP4Life Consortium is that it will grow into a thriving and productive science and technology social network that will be the knowledge source

for the field of biophotonics. It will also become the forum to discuss end-user needs and further where industry finds its new technologies and employees and vets its products. Ultimately, it has potential to become a "self-assembling" model for how science, industry, students and end-users can convene and network on a global basis.

References

1 Mayer, A. (2007) *Optische Technologien – Wirtschaftliche Bedeutung in Deutschland*, German Federal Ministry of Education and Research (BMBF), Bonn/Berlin.

2 Mayer, A. (2007) *Photonics in Europe – Economic Impact*, European Technology Platform Photonics21, Düsseldorf.

3 German Biophotonics Research Program (2010) Alzheimer-Krankheit: Früherkennung künftig per Augenscan? Press release of the German Biophotonics Research Program, March 2010.

4 Jürgens, M. and Popp, J. (2008) Biophotonik in Deutschland: Trends und Perspektiven. *BioPhotonik*, **1**, 22–26.

5 World Health Organization (2008) Fact Sheet No. 310: The Top Ten Causes of Death. WHO, Geneva, November 2008.

6 United Nations Department of Economic and Social Affairs Population Division (2009) World Population Prospects: The 2008 Revision. United Nations, New York.

7 Beske, F., Katalinic, A., Peters, E., and Pritzkuleit., R. (2009) *Morbiditätsprognose 2050. Ausgewählte Krankheiten für Deutschland, Brandenburg und Schleswig-Holstein*, vol. 114, Schriftenreihe/Fritz Beske Institut für Gesundheits-System-Forschung Kiel, Kiel.

8 Organisation for Economic Co-operation and Development (OECD) (2009) OECD Health Data 2009. OECD, Paris, November 2009.

9 European Technology Platform Photonics21 (2010) Lighting the Way Ahead: Photonics21 Strategic Research Agenda. European Technology Platform Photonics21, Düsseldorf.

10 Lee, G., Chu, K., Conroy, L., Fix, L., Lui, G., and Truesdell, C. (2007) A study of biophotonics: market segments, size and growth. *Opt. Photonik*, **2**, 30–35.

11 Deloitte Consulting GmbH (2005). Biophotonik in Deutschland – Wohin geht die Reise? Technology Report. Deloitte Consulting, Hannover.

12 Editorial (2007). The next big thing? *Nature Photonics*, **1**, 485.

13 Jürgens, M., Popp, J., Uhl, R., and Krüger, S. (2008) Examining and sorting – new device concepts for the microscopy of living cells. *Photonik Int.*, **2**, 24–27.

14 Jürgens, M., Popp, J., Engel, A., and Vielsack, C. (2008) Bright nanocrystals for medical diagnostics. *Photonik Int.*, **1**, 94–97.

15 Brunkhorst, F.M. (2006) Epidemiologie, Ökonomie und Praxis – Ergebnisse der deutschen Prävalenzstudie des Kompetenznetzwerkes Sepsis (SepNet). *AINS*, **41**, 43–44.

16 Jürgens, M. and Popp, J. (2009) Optische molekulare Bildgebung für die medizinische Diagnostik. *BioPhotonik*, **1**, 30–33.

17 Liedtke, S., Popp, J., Schönborn, K.-H., and Schubert, P. (2008) Fluorescence diagnosis of cancer. *Photonik Int.*, **1**, 98–101.

18 Friedberger, A. and Homann, C. (2009) Mikrobiologischer Trinkwassertest in weniger als einer Stunde. *Opt. Photonik*, **1**, 28–31.

19 Jürgens, M., Rösch, P., Keller, F., and Popp, J. (2009) Feinstaub: Verursachern auf der Spur. *Nachr. Chem.*, **3**, 326–327.

2
Short Introduction to Atomic and Molecular Configuration

Dirk Bender, Leticia González, and Stefanie Gräfe

In this chapter, we introduce the basic ideas and concepts of computational chemistry. We have tried to avoid using equations as much as possible; however, for better understanding, we provide some mathematical expressions. For the mathematically more interested reader, literature is cited where derivations and exact expressions can be found. We start with some basic ideas of quantum mechanics, as much as will be needed in the following. Next, we introduce some model systems frequently used in spectroscopy, and illustrate fundamental approximations used for chemical applications. We conclude by describing quantum chemical methods used for calculating the electronic structure of molecules.

2.1
Introduction

Today, we are aware of the fact that molecules (and atoms) can only be described properly on the foundations of quantum mechanics. Historically, however, chemists (and also alchemists) for a long time did not know of the existence of chemical bonds. What was known was that substances can be transformed into each other, thereby changing their properties – nowadays we call this a *chemical reaction*. In the beginning, a more phenomenological approach led to the idea that all substances consist of small building blocks – *atoms*. These atoms are stuck together by *chemical bonds*.

Later, physicists started to experiment with atoms. At the beginning of the twentieth century, the *electron* was discovered. It was found that atoms are not the smallest possible units but that they consist of building blocks. For chemical purposes, the most relevant units are the negatively charged electrons which surround in a classical picture a heavy positive charge – the *nucleus*. Very soon it was clear that the number of electrons that each atom possesses can be used to classify them in the so-called periodic system of the elements. By this means, a categorization of different atoms was put on a more quantitative footing. Each

Handbook of Biophotonics. Vol.1: Basics and Techniques, First Edition.
Edited by Jürgen Popp, Valery V. Tuchin, Arthur Chiou, and Stefan H. Heinemann.

element has a certain atomic number, that is, a certain number of electrons equals to the atomic number.

Subsequently, chemists realized that the chemical bonds that hold the atoms together are composed in most cases of *two electrons*. A picture of a molecule built up by atoms connected by bars should exactly symbolize this: each stick contains two electrons representing a chemical bond. This very intuitive picture is able to explain many properties and reactivity of the molecules but does not suffice to describe the molecule or chemical substance more quantitatively. For this purpose, a quantum mechanical description is required.

The basic difficulty in this quantum mechanical description is that many-body problems (more than three particles) cannot be solved exactly. However, atoms and molecules are intrinsically many-body problems with many electrons (according to the atomic number) involved. To describe the realm of chemistry, we are therefore left to seek approximations and numerical solutions, which unfortunately can be computationally very demanding.

2.2 Basics of Quantum Mechanics

Physicists assumed for a very long time that light is an (electromagnetic) wave. Huygens showed that from a light source, light spreads out circularly – the same behavior can be observed on throwing a stone into water. However, in contradiction to classical physics, Planck showed in 1900 that light cannot have all energies but only discrete values occur, all separated by a very small constant number h, nowadays known as *Planck's constant*. This constant takes the value 6.634×10^{-34} Js – a very tiny number indeed. Despite being small, this means that the energies are not continuous but *quantized* (discrete). To exemplify this fact, let us take a lamp with a rotary switch with which we can dim the light. By turning the switch we can obtain all possible values of brightness of the lamp. This is *not*, however, what we find in the quantum world: the energy is *quantized*, that is, we find only discrete values of energy (Figure 2.1). This is similar to what we would have with an electric fan – we can only access speeds 1, 2, and 3 but nothing in between. The *quantum numbers* (speeds 1, 2, 3 in the fan example) indicate on which energy level we are situated. The lowest level indicates the ground state, the others are excited states. Planck described the connection between the frequency of the light radiation ν and its energy E by the equation

$$E = h\nu. \tag{2.1}$$

By explaining the photoelectric effect in 1905, Einstein could demonstrate that light consists of tiny particles, called *photons*. This discovery caused a serious dilemma: is light a wave or a particle? The solution to this problem was to assign both – wave *and* particle character – to the light. This we call the *wave–particle duality*. De Broglie was able to establish a direct connection between the particle and the wave character of the light with the equation

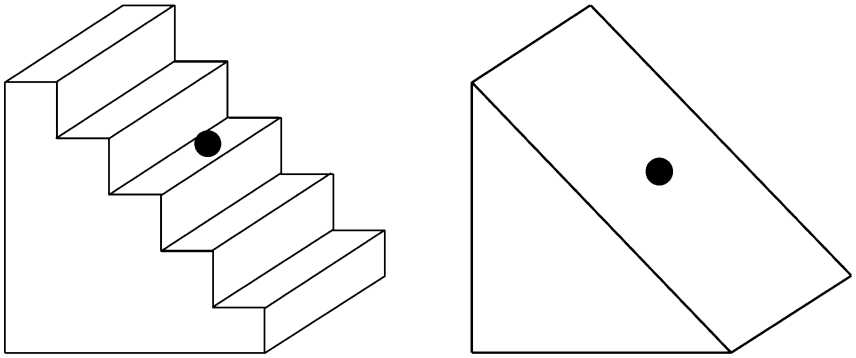

Figure 2.1 Quantization of the energy. The ball in (a) can have only discrete potential energies, represented by the steps. The ball in (b) can have *any* energy on the plane; this is the macroscopic behavior.

$$\lambda = \frac{h}{p} \tag{2.2}$$

where the wavelength λ refers to the wave character, the momentum p to the particle character of the photon, and h is again Planck's constant. De Broglie stated that his simple equation should be universally valid, applying to *all* particles: electrons, nuclei, atoms, and even macroscopic "particles" such as humans. (Due to the macroscopic size and weight of humans, the "wave character" does not affect much every day life, however.) In 1925, Davisson and Germer demonstrated that the electron also possesses wave character. Nowadays, the wave character of larger particles, even as large as the fullerenes, has also been proven. Inspired by all these new discoveries, Heisenberg and Schrödinger formulated their equations to describe a new form of mechanics, applicable to such microscopic particles: *the quantum mechanics*.

In quantum mechanics, the keynote to memorize is the following: *everything we want to know about a system is incorporated in its wavefunction* Ψ. Hence, whether we are interested in spectra, geometries, or other properties of a molecule, all we need to know is its state or its state vector – the wavefunction Ψ. The only problem is that calculating the wavefunction Ψ is very difficult and except for a few examples it is not possible to obtain Ψ exactly. Calculating the wavefunction and extracting its molecular properties by approximated methods is the aim of computational chemistry.

2.2.1
Wavefunctions and Operators

Let us first become more familiar with the concept of a wavefunction and describe some of its properties. The wavefunction Ψ is typically a complex function which depends on all spatial coordinates of all particles in the system, and on the time. For N

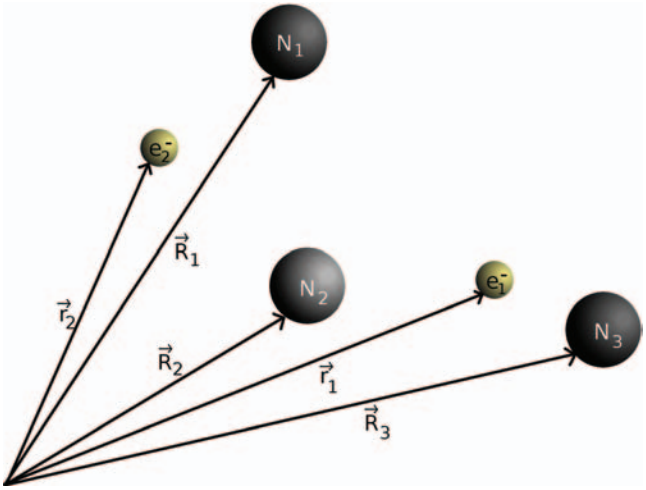

Figure 2.2 Visualization of the coordinates of two electrons (e^-, $\vec{r}_1, \vec{r}_2$) and three nuclei (N, $\vec{R}_1, \vec{R}_2, \vec{R}_3$).

electrons and M nuclei we therefore write $\Psi(\vec{r}_1, \vec{r}_2, \vec{r}_3 \ldots \vec{r}_N, \vec{R}_1, \vec{R}_2 \ldots \vec{R}_M, t)$. We denote all electronic coordinates with lowercase letters, $\vec{r}_1, \vec{r}_2 \ldots \vec{r}_N$, and the coordinates of the nuclei with capital letters, $\vec{R}_1, \vec{R}_2 \ldots \vec{R}_M$. The distances r_i, R_j we are referring to are on the sub-nanometer scale. Typical interatomic distances are $\sim 0.1\,\text{nm}$ (or $10^{-10}\,\text{m} = 1$ Å). Figure 2.2 displays the definition of coordinates of a sample system of two electrons and three nuclei.

The Probability Density

The value $|\Psi|^2 = \Psi^*\Psi$ is called the probability density; Ψ^* is the complex conjugate of Ψ. In the one-dimensional case, the value $|\Psi(x)|^2 \mathrm{d}x$ is proportional to the probability of finding the particle described by Ψ in the interval $x \ldots x + \mathrm{d}x$. Because Ψ and $c\Psi$ describe for any complex number c the same state, it is possible to normalize the wavefunction, that is, to find a factor c such the integral

$$\int_{-\infty}^{\infty} |c\Psi|^2 \mathrm{d}x \tag{2.3}$$

gives 1. If we include this factor in Ψ, we can interpret $|\Psi(x)|^2 \mathrm{d}x$ directly as the probability of finding the particle in the interval $x \ldots x + \mathrm{d}x$.

In the three-dimensional case, the probability of finding the particle at the position $\vec{r}$ in the infinitesimal volume element $\mathrm{d}V$ (see Figure 2.3) is proportional to (or after normalization equal to) $|\Psi(\vec{r})|^2 \mathrm{dV}$.

Although it is not intuitive to visualize the wavefunction itself as it is normally complex, one very important interpretation suggested by Bohr is based on its absolute

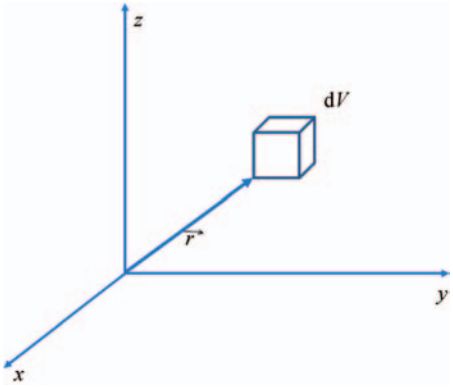

Figure 2.3 In a three-dimensional space, the probability of finding the particle described by Ψ at position $\vec{r}$ in the infinitesimal volume $dV = dxdydz$ is proportional to $|\Psi|^2 dV$.

squared, $\left|\Psi\left(\vec{r}_i, \vec{R}_j\right)\right|^2$, the so-called *probability density* ρ. The probability density gives a measure of the probability of finding a particle at the position in a small given volume (see Figure 2.3). The larger the number, the higher is the probability that the particle is there. Small values denote a low probability of finding the particle. The concept of probability density means that we have to bid farewell to the picture that we know exactly where a particle is: in the quantum world, we can only state where the highest probability of the particle position is. This probability is represented by the probability density ρ. Figure 2.4 shows an arbitrary function $\Psi(\vec{r}_1)$ for one electron depending on the coordinate $\vec{r}_1$, and its probability density $\rho(\vec{r}_1) = |\Psi(\vec{r}_1)|^2$. Here, for example, the probability of finding the particle is highest around $r = -2$ and $r = +2$, while the probability is zero at three values of $\vec{r}$. These zeros in the probability ρ are exactly the roots (nodes) of the wavefunction $\Psi(\vec{r}_1)$. By convention, the probability of finding a particle anywhere in space is 100% or, mathematically speaking: the probability density $\rho(r)$ is normalized to 1. Figure 2.4 clearly illustrates that quantum mechanics offers a more statistical description with probabilities than classical mechanics.

One fundamental implication of quantum mechanics is the Heisenberg *uncertainty principle*. In brief, it says that it is not possible to determine simultaneously the exact position and the exact velocity (or the momentum) of a particle. Although there is no one-to-one correspondence to the classical world, we can exemplify this with a runner on a racetrack: we can at one time either determine the position where he/she is *or* the speed he/she has at that moment. In the macroscopic world, we can measure both; in the quantum world, we can determine both properties at the same time only with a certain accuracy. It is important to stress that this incapability has nothing to do with the measuring devices but with the quantum system itself: the accuracy with which we can measure the position $\vec{r}$ immediately limits the accuracy with which the momentum $\vec{p}$ can be measured see (Figure 2.5). Figure 2.5d shows two probabilities with the same coordinate but with different "precision": the more narrow the distribution is, the more accurately the position can be determined. When, for example, the coordinate r is fairly accurately known, then the distribution

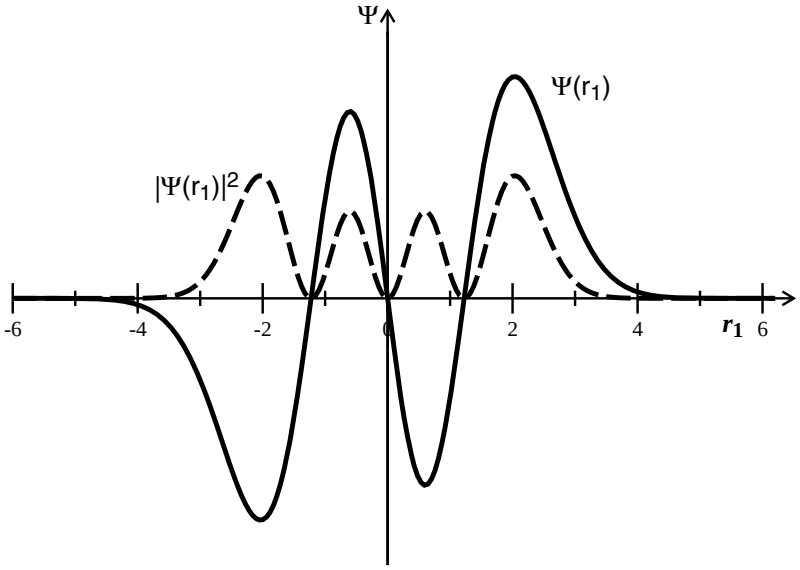

Figure 2.4 A wavefunction $\Psi(\vec{r}_1)$ depending on one electronic coordinate $(\vec{r}_1)$ and the corresponding probability density $|\Psi(\vec{r}_1)|^2$ (dashed line). The probability of finding the electron is zero on several values of $\vec{r}_1$, whereas it is most probable to find the electron around $r_1 = -2$ or $r_1 = +2$.

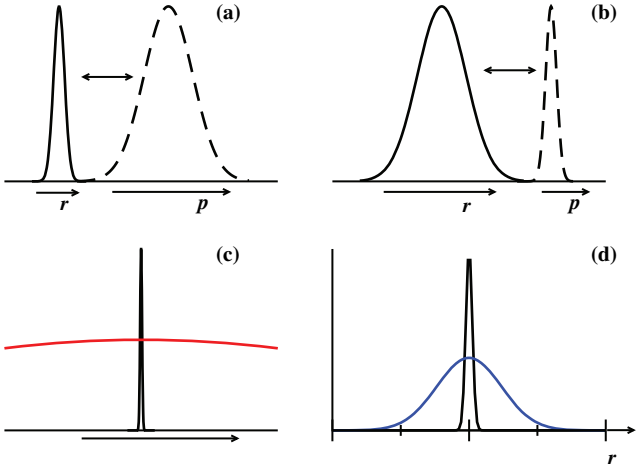

Figure 2.5 Visualization of the uncertainty principle. (a) A narrow distribution (solid line) in coordinate representation has a smeared momentum distribution. (b) Vice versa: a narrow momentum distribution has a smeared coordinate representation. (c) In the limit of a very precise distribution of one property, no information about the other property can be obtained. (d) Two distributions with the same value of coordinate but with a different width.

of the momentum p (the velocity) is smeared (Figure 2.5a), and vice versa (Figure 2.5b). In the limit of a highly accurately known coordinate (or momentum) distribution, virtually no information of the other respective property can be gathered (Figure 2.5c). Mathematically, the uncertainty relation is expressed by the inequality

$$\Delta x \cdot \Delta p \geq h/2. \tag{2.4}$$

The product of uncertainties of coordinate and momentum is always larger than (or equal to) Planck's constant divided by 2. Other properties of the wavefunction $\Psi(\vec{r}_i, \vec{R}_j)$ can be found in quantum mechanics textbooks (see, for example, [1–4]). We will restrict ourselves here to the necessary properties to deal with basic theoretical chemistry.

As we stated before, all necessary information on any system is in its wavefunction. In addition to the probability interpretation, how do we extract this desired information? For this purpose, we introduce the concept of a mathematical operator, represented by $\hat{A}$ (we will denote all operators in this chapter by the "hat" ^). The operator $\hat{A}$ can represent different physical properties; it can be, for example, the momentum operator $\hat{\vec{p}}$, the operator of coordinate $\hat{\vec{r}}$, or the operator of energy $\hat{H}$. Mathematically, they can have different forms: it can be a derivation, an integral, or just a multiplication. Generally, when an operator $\hat{A}$ *acts* on a wavefunction Ψ, it might modify the function and yield another function, which we call, for example, Φ:

$$\hat{A}\Psi = \Phi. \tag{2.5}$$

This can be visualized by thinking of an example function, say $\Psi = f(x) = x^2$. If the operator is a derivative, $\mathrm{d}/\mathrm{d}x$, we evaluate the derivative of $f(x)$ and obtain the new function $\Phi = f'(x)$:

$$\hat{A} = \frac{\mathrm{d}}{\mathrm{d}x} \qquad \Psi = f(x) = x^2$$

$$\hat{A}\Psi = \frac{\mathrm{d}}{\mathrm{d}x} x^2 = 2 \cdot x = \Phi.$$

The desired information about an observable A can be extracted by calculating from the operator $\hat{A}$ the *expectation value* $\langle \hat{A} \rangle$, which represents the mean value that one obtains in an experimental measurement. Mathematically, the expectation value $\langle \hat{A} \rangle$ is calculated by acting the operator on the wavefunction, subsequently multiplying by the complex conjugate of the wavefunction, and integrating over the space. This yields a number which is the mean value that one would obtain by an experimental measurement:

$$\int \Psi^*(\vec{r})\, \hat{A}\, \Psi(\vec{r}) \mathrm{d}V = \langle \hat{A} \rangle. \tag{2.6}$$

Let us assume we are interested in the momentum that a particle has. For this, we act the momentum operator $\hat{\vec{p}}$ on the wavefunction Ψ and evaluate the integral. The number we obtain is the momentum expectation value $\langle \hat{\vec{p}} \rangle$ – or the average

momentum we would measure in an experiment. The same holds if we are interested in the position (or the energy) of the system – we then evaluate the coordinate expectation value $\langle\hat{\vec{r}}\rangle$ (or the energy expectation value $\langle\hat{H}\rangle$).

In some special cases, the action of an operator $\hat{A}$ on a function Ψ yields the wavefunction itself, just multiplied by a factor, some number a[1)]:

$$\hat{A}\Psi = a\Psi. \tag{2.7}$$

We call such equations, where an operator acting on a function does not change the function but just multiplies it by some number a, an *eigenvalue equation*. One of the most famous examples for such an eigenvalue equation is the *time-independent Schrödinger equation*:

$$\hat{H}\Psi = E\Psi. \tag{2.8}$$

We see that this equation is an eigenvalue equation for the energy, defined by the energy operator $\hat{H}$, which is called the *Hamilton operator* of a system. The action of the Hamilton operator $\hat{H}$ on the wavefunction yields the wavefunction itself and a value E, which is the energy of the system. This is the central equation for calculating the energy of a molecule and, as we will see later, also for obtaining the wavefunction itself.

The Hamilton operator $\hat{H}$ consists of two terms: the *kinetic energy operator* $\hat{T}$ and the *potential energy operator* $\hat{V}$ (which describes in many cases the electrostatic interaction between the particles):

$$\hat{H} = \hat{T} + \hat{V}. \tag{2.9}$$

The Hamilton operator (or the Hamiltonian) has to be specified for each problem we want to solve. For a molecule, the kinetic energy operator $\hat{T}$ contains the kinetic energy of the electrons and of the nuclei. The potential energy operator $\hat{V}$ has the nuclear–nuclear repulsion (all nuclei are positively charged), electron–electron repulsion (all electrons are negatively charged), and the nuclear–electron attraction. In total, $\hat{H}$ can be written as

$$\hat{H} = \hat{T}_{\text{el}} + \hat{T}_{\text{nuc}} + \hat{V}_{\text{el–nuc}} + \hat{V}_{\text{nuc–nuc}} + \hat{V}_{\text{el–el}}. \tag{2.10}$$

As we see immediately, the actual form of the Hamilton operator $\hat{H}$ depends on the system: how many electrons, how many nuclei are we dealing with? Which charge do the nuclei have? How far are the nuclei apart? ...

At this point, we know that the fundamental equation (the Schrödinger equation) can describe microscopic particles but unfortunately, except for a few model systems, this equation cannot be solved exactly at all. In the following, we will describe these model systems, as they are of special importance.

1) In most cases a is not just a number, but a physical quantity, characterized by a *value* and a *unit*.

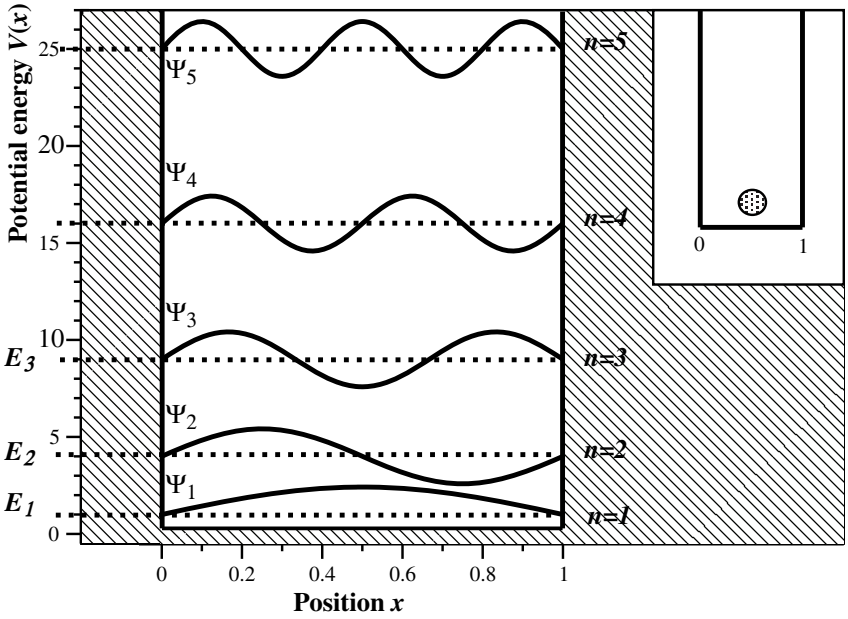

Figure 2.6 The quantum mechanical particle in a box model with infinitely high walls. Wavefunctions and energies are shown, depending on the quantum number *n*.

2.2.2 Particle in a Box

One of the model systems which can be solved exactly is the "particle in a box" (see Figure 2.6). Assuming infinitely high walls on both sides, we can set up the Hamilton operator for this system, which is just the kinetic part since the potential contribution is zero inside the box and infinite outside the wall.

Particle in a Box

We have a box of length L. A particle with mass m is confined between the two walls at $x = 0$ an $x = L$. Inside the well, the potential is zero, but rises abruptly to infinity at the walls. Defining the potential as

$$V = \begin{cases} 0 & 0 \leq x \leq L \\ \infty & \text{else} \end{cases} \tag{2.11}$$

the total Hamiltonian becomes

$$\hat{H} = -\frac{\hbar^2}{2m}\frac{\mathrm{d}^2}{\mathrm{d}x^2} + V. \tag{2.12}$$

Inside the box we have a free particle. The Schrödinger equation is

$$-\frac{\hbar^2}{2m}\frac{\mathrm{d}^2\Psi}{\mathrm{d}x^2} = E\Psi. \tag{2.13}$$

The wavefunction must vanish on both ends of the box. With these boundary conditions, we obtain the energy eigenvalues:

$$E_n = \frac{\hbar^2\pi^2 n^2}{2mL^2} \tag{2.14}$$

and after normalization the wavefunction is

$$\Psi_n(x) = \sqrt{\frac{2}{L}}\sin\frac{n\pi}{L}x \tag{2.15}$$

with the quantum number $n = 1, 2, 3, \ldots$.

The probability of finding the particle outside the box is therefore zero. Solving the Schrödinger equation (see Box), we obtain the solutions and energies depicted in Figure 2.6. Note that the probability of finding the particle directly on the wall is also zero. With increasing quantum number, the number of nodes increases (the number of nodes is one less than the quantum number) and, therefore, with increasing quantum number also the nodes come closer to each other. In the limit of very high quantum number, the probability is more or less equally distributed in the box – as we would expect it intuitively: classically, the probability of finding the particle somewhere in the box should be everywhere the same. This extrapolation to high quantum numbers reaching the classical values and probabilities is called *Bohr's correspondence principle*.

The energy spacing (the energies are quantized) is not equal: it grows with increasing quantum number. Another special feature is that there is no state with zero energy. Even for the lowest possible state ($n = 1$), there is an associated energy.

Let us next consider a small extension to this model. Assume that the walls are not infinitely high, but have a height V_0 (Figure 2.7). Now the situation is peculiar: taking a closer look at the tails of the wavefunctions, we can see that the probability of finding the particle on the wall is *not* zero any longer but there is a small probability of finding the particle *outside the wall*. How far the particle may enter the wall depends on its mass. For electrons, this is very probable, and electrons can reach far into the walls (this is an important property to describe processes on surfaces of electrodes in batteries, for example). For protons this is still probable, but for almost all heavier systems this effect is negligible.

Another difference to observe in Figure 2.7 is in the energies: above the wall, the energies are truly continuous – the particle can have all possible energies. We say, for energies below the wall height ($E < V_0$), the particle is bound, whereas for the opposite case the particle is unbound – or free.

We can further extend this model and put a small potential barrier in the middle of the box (Figure 2.8). If we locate the particle initially on one side of the barrier, there is a small probability (again depending on the mass of the particle) of finding it after

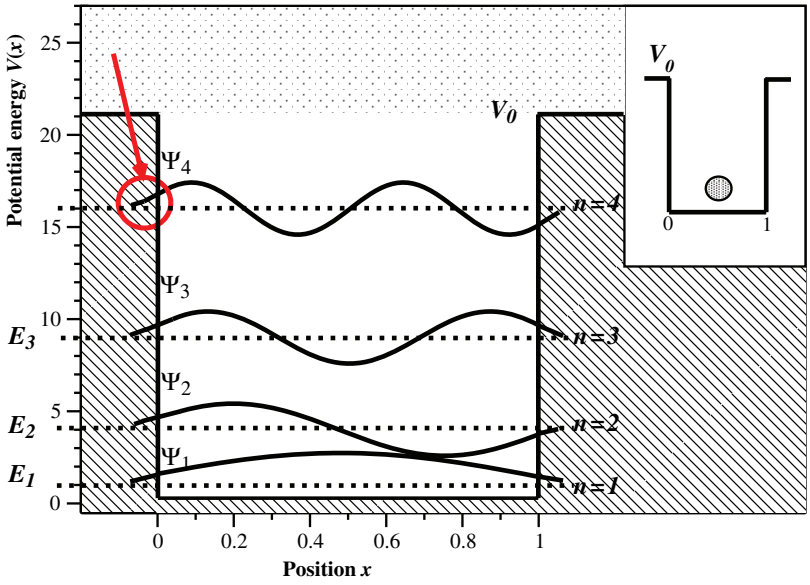

Figure 2.7 The quantum mechanical particle in a well model with finite high walls. Wavefunctions and energies are shown, depending on the quantum number *n*. Note that the wavefunctions here enter the wall. Energies above the potential well are continuous – only four levels are bound in this example.

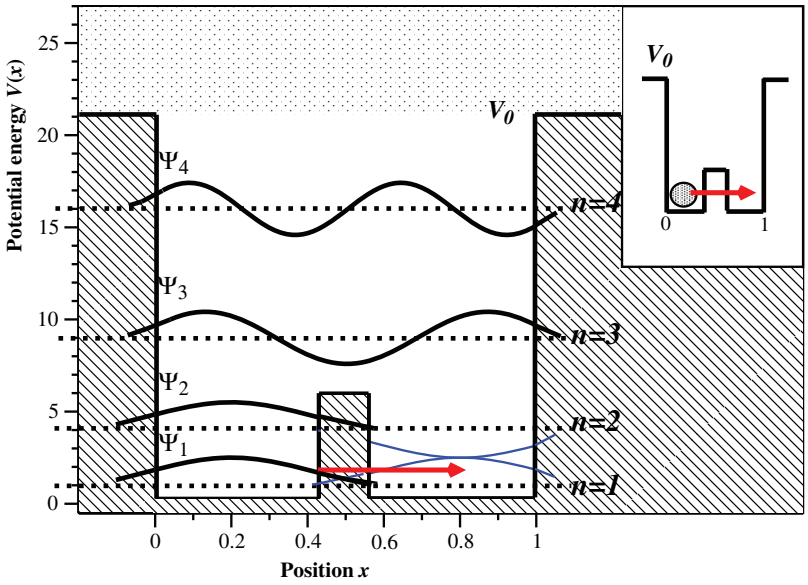

Figure 2.8 Same as before, particle in a potential well, now with a small barrier inside the well. There is a probability that the particle, initially located on the left-hand side of the potential barrier, will tunnel to the right-hand side.

some time on the *other side* of the barrier – also due to the non-zero tail of the wavefunction. This process is called *tunneling*. Although tunneling may sound rather exotic, it plays an important role in, for example, vibrational spectroscopy; the tunneling time can even be measured experimentally by analyzing the spectral linewidth.

2.2.3 Harmonic Oscillator – Vibrations

The *harmonic oscillator* is another very important model system which can be solved exactly. The harmonic oscillator serves in classical mechanics to describe the potential energy of springs or the pendulum motion: on deflecting a pendulum to one side, it will swing back (oscillate) exactly to the same height on the other side and back (in the absence of friction). Classically, any deflection is possible – quantum mechanically not.

The One-Dimensional Harmonic Oscillator

The problem of a one-dimensional harmonic oscillator is described by the following potential energy:

$$\hat{V} = \frac{k}{2}x^2 \tag{2.16}$$

where the constant k in the classical interpretation describes the strength of the spring (force constant). The Hamiltonian is then

$$\begin{aligned}\hat{H} &= \hat{T} + \hat{V} \\ &= -\frac{\hbar^2}{2m}\frac{\mathrm{d}^2}{\mathrm{d}x^2} + \frac{k}{2}x^2\end{aligned} \tag{2.17}$$

where x is the displacement from equilibrium. The Schrödinger equation is

$$-\frac{\hbar^2}{2m}\frac{\mathrm{d}^2\Psi(x)}{\mathrm{d}x^2} + \frac{k}{2}x^2\Psi(x) = E\Psi(x). \tag{2.18}$$

After some steps we obtain the solutions

$$E_n = h\nu\left(n + \frac{1}{2}\right) \tag{2.19}$$

$$\Psi_n(x) = \frac{1}{\sqrt{2^n n!}}\sqrt[4]{\frac{4\pi m\nu}{h}}\exp\left(-\frac{2\pi^2 m\nu}{h}\mathrm{x}^2\right)H_n\left(2\pi\sqrt{\frac{\mathrm{m}\nu}{\mathrm{h}}}\mathrm{x}\right) \tag{2.20}$$

with the quantum number $n = 0, 1, 2, \ldots$ and the frequency $\nu = \frac{1}{2\pi}\sqrt{\frac{k}{m}}$. The H_n are the so-called *Hermite polynomials*.

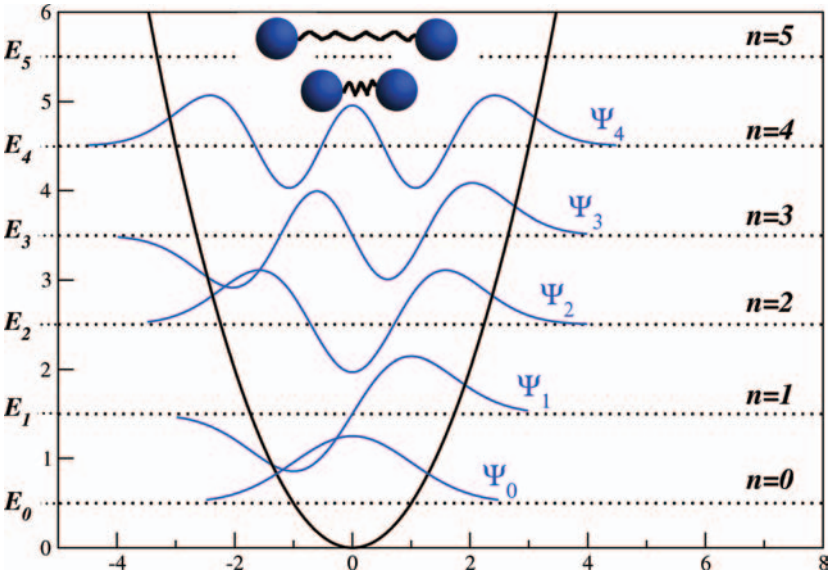

Figure 2.9 The quantum mechanical harmonic oscillator with its wavefunctions (blue) and energies (dotted), depending on the quantum number *n*. The black curve is the potential energy.

Solving the Schrödinger equation for the harmonic oscillator (see Box) will give the wavefunctions and energies shown in Figure 2.9. Although at first glance the probabilities may look similar to those of the particle in a box, there is one very important difference here: the energies are quantized but *equally spaced*.

The quantum mechanical harmonic oscillator serves as a model system to describe chemical bonds: a chemical bond can to some approximation be expressed by two atoms held together by a spring (the bond). Pushing the atoms closer together increases the potential, as the spring is squeezed. Stretching the bond also increases the potential, as now the spring is stretched. There is a certain distance where the potential is lowest: this is the *equilibrium internuclear distance*. The strength of a spring represents the bond strength (see Figure 2.10). The harmonic oscillator therefore serves in spectroscopy as a model to analyze vibrational spectra – the excitation of vibrational motion between atoms. It works reasonably well as a model system for small deviations from equilibrium but becomes poor for larger deviations (and therefore larger quantum numbers). The reason for this poor description for larger quantum numbers is that the description of atoms held together by a spring is not adequate for long, stretched bonds: it is intuitive that a bond may break if the atoms are pulled too far apart. Such a situation is not contemplated in the harmonic oscillator and is better described by an anharmonic one – or a *Morse potential* (see Figure 2.11). However, we will not discuss details of this potential and its solutions here.

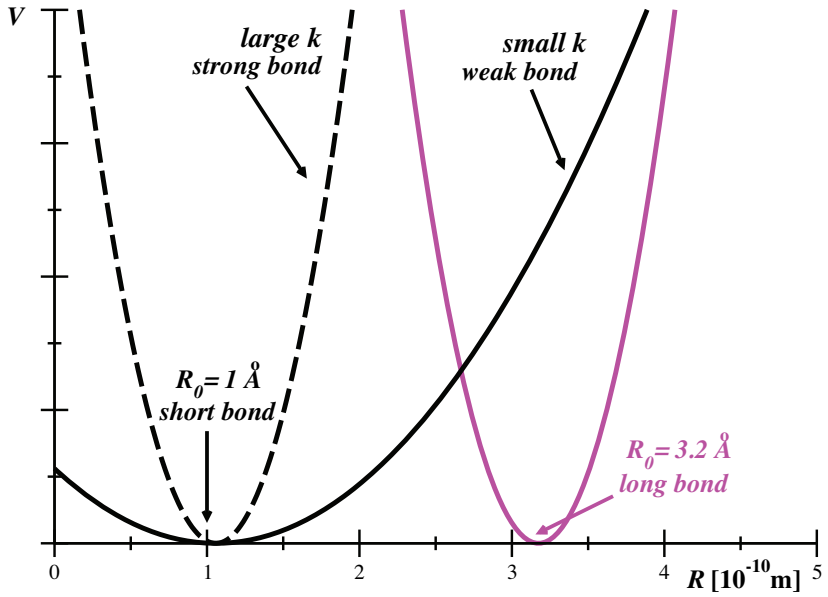

Figure 2.10 Quadratic (harmonic) potential describing the stretching of a bond. The figure visualizes the effect of the equilibrium internuclear distance R_0 and the bond strength k, parameters describing a chemical bond.

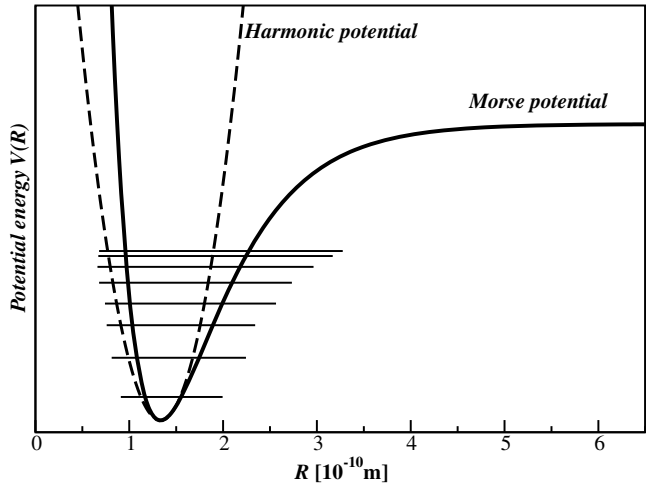

Figure 2.11 Morse potential and harmonic potential describing the stretching of a bond. For small deviations from equilibrium, the harmonic potential describes the vibration reasonably well, whereas it becomes a poor model for larger deflection.

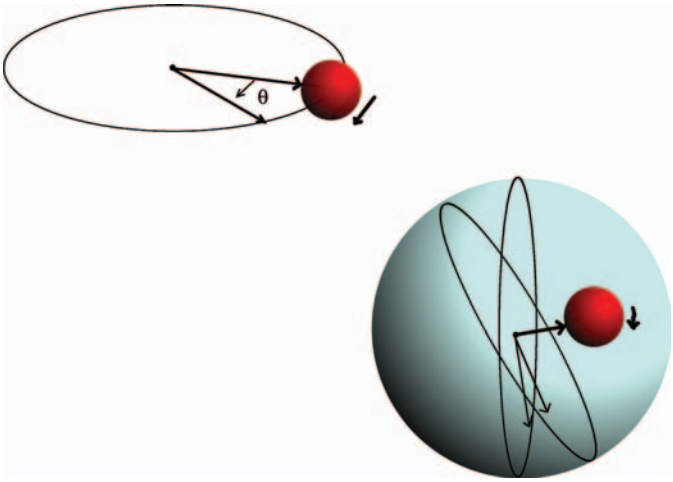

Figure 2.12 Particle on a ring and particle on a sphere as model systems for rotational motion.

2.2.4
Particle on a Sphere, Rigid Rotor – Rotations

The *rigid rotor* is used to describe rotational motion. It is a special case of the model system of a particle on a ring (or on a sphere). For visualization, imagine a carousel or a gyroscope, as shown in Figure 2.12.`

Particle on a Sphere

The Schrödinger equation for a three-dimensional rotation – or the motion of a particle with mass m on a sphere with radius r – is

$$-\frac{\hbar^2}{2mr^2}\left\{\frac{1}{\sin^2\theta}\frac{\partial^2\Psi(\theta,\phi)}{\partial\phi^2}+\frac{1}{\sin\theta}\frac{\partial}{\partial\theta}\left[\sin\theta\frac{\partial\Psi(\theta,\phi)}{\partial\theta}\right]\right\}=E\Psi(\theta,\phi) \tag{2.21}$$

where θ and ϕ are the inclination and azimuth – the two angles from the spherical coordinate system.

The solution involves two quantum numbers:

$$l=0,1,2,\ldots \tag{2.22}$$

and

$$m_l=-l,-l+1,\ldots,l-1,l. \tag{2.23}$$

The energy depends only on the quantum number l:

$$E = l(l+1)\frac{\hbar^2}{2mr^2}. \tag{2.24}$$

The normalized wavefunctions are called *spherical harmonics* – denoted Y_{lm_l}. They depend on both quantum numbers l and m_l.

The quantum mechanical solutions of this problem (see Box) are represented by a class of functions, the so-called *spherical harmonics*, often denoted Y_{l,m_l}, which depend on *two* quantum numbers, l and m_l. The quantum number l counts as $l = 0, 1, 2, \ldots$; for a given value of l, m_l can assume the values $-l, -(l+1), \ldots, -1, 0, 1, \ldots, l-1, l$. For $l = 0$, there is only one value of m_l, namely $m_l = 0$. The spherical harmonic Y_{00} is a sphere, commonly denoted an *s*-function. For $l = 1$, m_l can assume three values, $m_l = -1, 0, 1$, and we are dealing with three functions, the *p*-functions. In a coordinate system, these dumb-bell-type functions are oriented along the three axes, x, y, z. For $l = 2$, there are five values for m_l, $-2, -1, 0, 1, 2$, the *d*-functions. All these functions are displayed in Figure 2.13.

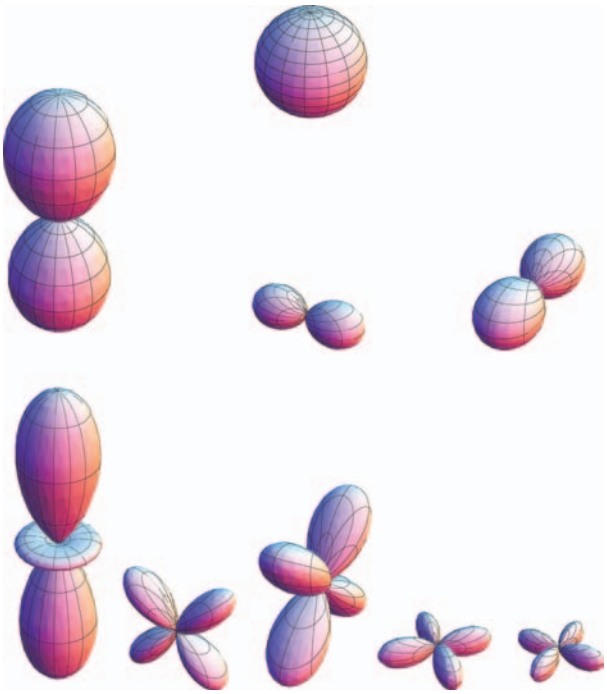

Figure 2.13 The spherical harmonics, the solutions of a particle on a sphere model. The top one is the Y_{00} (the one for $l = 0$), the next row shows the three functions for $l = 1$, and the bottom row the five for $l = 2$. Note that the spherical harmonics are complex-valued functions. Therefore, real-valued linear combinations are shown here.

We will meet these functions again in the following subsections. The energies increase quadratically with l. The rigid rotor is a special case of the particle on a sphere model. The functions and energies of the rigid rotor show the same behavior as discussed before. The rigid rotor is commonly used as a model system in rotational spectroscopy, where the quantum numbers are typically denoted j, m_j instead of l, m_l.

2.2.5 The Hydrogen Atom

The lightest of all atoms, the hydrogen atom, consisting of one proton and one electron, is the only one which can be calculated exactly. Its Hamilton operator can be decomposed into two parts: a radial part, describing the distance r of the electron to the nucleus, and an angular part, which is described by the particle on a sphere model. The solution of the radial part is an exponential function, $\exp(-\zeta r)$, multiplied by a polynomial, the *Laguerre polynomial*. The radial part has a dependence on the quantum number n, and its energies increase with $1/n^2$. (This dependence of the energy on the quantum number n had earlier been found empirically by Rydberg.) Above $V = 0$, there is again a continuum of states for the electron.

The Hydrogen Atom

The wavefunctions of the hydrogen atom are products of a radial part and the spherical harmonics:

$$\Psi_{nlm_l} = R_{nl}(r)\, Y_{lm_l}(\theta, \phi). \tag{2.25}$$

Therefore, they depend on *three* quantum numbers: n, l, m_l. These quantum numbers can take the following values:

$$\begin{aligned} &n = 1, 2, 3 \ldots && \text{(principal or main quantum number)} \\ &l = 0, 1, 2, \ldots, (n-1) && \text{(angular momentum quantum number)} \\ &m_l = -l, \ldots, 0, \ldots, l && \text{(magnetic quantum number).} \end{aligned} \tag{2.26}$$

The radial part R_{nl} of the wavefunction contains the so-called *associated Laguerre polynomials* L:

$$R_{nl}(r) = N \exp\left(-\frac{r}{a_0 n}\right)\left(\frac{2r}{a_0 n}\right)^l L_{n-l-1}^{(2l+1)}\left(\frac{2r}{a_0 n}\right) \tag{2.27}$$

where N is the normalization factor and a_0 is the Bohr radius.

The energy is related to the principal quantum number n:

$$E_n = -\frac{m e_0^4}{2\hbar^2 (4\pi\varepsilon_0)^2}\,\frac{1}{n^2}. \tag{2.28}$$

Each energy level is n^2-fold degenerate.

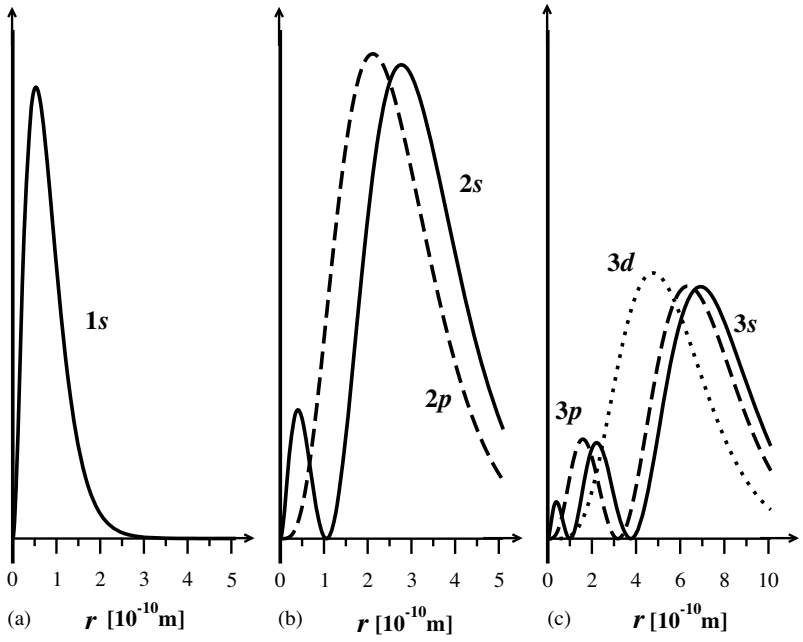

Figure 2.14 The radial part of the atomic orbitals of the hydrogen atom, sorted by the quantum number *n*. (a) $n = 1$; (b) $n = 2$; (c) $n = 3$.

The total state of the electron is given by the product of the radial part and the spherical harmonics, and therefore depends on *three* quantum numbers: n, l, m_l. The quantum numbers take the values $n = 1, 2, 3, \ldots; l = 0, 1, 2, \ldots, (n-1)$; $m_l = -l, \ldots, 0, \ldots, l$. The resulting solutions are labeled according to these quantum numbers, giving 1 *s* ($n = 1,\ l = 0,\ m_l = 0$), 2 *s* ($n = 2,\ l = 0,\ m_l = 0$), three times 2 *p* ($n = 2,\ l = 1,\ m_l = -1, 0, +1$), 3 *s* ($n = 3,\ l = 0,\ m_l = 0$), three times 3 *p* ($n = 3,\ l = 1,\ m_l = -1, 0, +1$), five times 3 *d* ($n = 3,\ l = 2,\ m_l = -2, -1, 0, +1, +2$), and so on. These functions are the *atomic orbitals* of the hydrogen atom. The radial dependence is depicted in Figure 2.14; for the angular dependence, we refer to Figure 2.13. In Figure 2.14 the orbitals are sorted by the quantum number *n*, which is also called the main quantum number. Often, it is also referred to as a *shell*. The first shell includes all orbitals with $n = 1$, which is the 1*s* orbital only. The second shell, $n = 2$, includes the 2 *s* and the 2 *p* orbitals. Each atomic orbital offers space for up to two electrons of different spin.

An orbital without electrons inside is empty or unoccupied; orbitals containing one or two electrons are called singly and doubly occupied orbitals, respectively. The electronic ground state of the hydrogen atom contains just one electron in the orbital with the lowest energy – the 1 *s* orbital.

Heavier atoms with more electrons have more occupied atomic orbitals, thereby occupying first the 1 *s* orbital twice (this would be the case for the helium atom), and subsequently the 2 *s* and 2 *p* orbitals, and so on. As every atomic orbital may contain

two electrons, the first shell (with only the 1*s* orbital) offers space for two electrons, the second shell with the 2*s* and three 2*p* orbitals has space for eight electrons, and so on. Remember that atoms with more than one electron cannot be exactly calculated any longer, and thus some approximations are required.

2.3 Approximations

We have seen in the previous subsections that the Schrödinger equation (Equation 2.8) can only be solved for a few problems and the simplest atom, the hydrogen atom. For all other atoms or even molecules, the Schrödinger equation cannot be solved exactly. Although we know the form of the Hamilton operator $\hat{H}$ (defined by the molecule in which we are interested), we do not know either the wavefunction Ψ or the energies E. Because we are interested in both, we are left with making some approximations to obtain these quantities.

2.3.1 Variational Principle

As we have seen, in order to calculate the energy E of a system (from the energy expectation value, see Equation 2.6), one has to know the wavefunction Ψ describing the system. As we do not know the wavefunction, we may guess it, using a test wavefunction $\tilde{\Psi}$. Of course, when choosing just any guess wavefunction, we will obtain just some arbitrary energy of our system.

However, here the *variational principle* comes to help: it states that the true and exact wavefunction yields the lowest energy. Or, differently formulated: if we have obtained by variation the lowest possible energy, then the corresponding wavefunction is the exact wavefunction Ψ. No other test-wavefunction can possibly yield a lower energy than the exact wavefunction. This can be expressed as

$$\left\langle \hat{H} \right\rangle = \left\langle \tilde{\Psi} \middle| \hat{H} \middle| \tilde{\Psi} \right\rangle \geq \left\langle \Psi \middle| \hat{H} \middle| \Psi \right\rangle = E_0 \tag{2.29}$$

where E_0 is the true ground-state energy of the system. In practice, we start with a test wavefunction $\tilde{\Psi}$, calculate the corresponding energy expectation value $\left\langle \hat{H} \right\rangle$, and vary the test function iteratively until the energy does not decrease any more (upon definition of a threshold value that determines the accuracy). Depending on the choice of the test wavefunction, the variational wavefunction will more or less well describe the exact wavefunction.

2.3.2 Perturbation Theory

A second avenue to find approximations to the wavefunction is the so-called *perturbation theory*. The starting point here is that if we cannot solve the system exactly at least a similar problem can be solved and taken as a reference. Then, we

declare any deviance from the reference system as a *perturbation*. By taking higher and higher orders of corrections, we approach the exact solution to our system. The order of correction that we consider is called the order of the perturbation.

We start by solving the Schrödinger equation for the reference system, obtaining the wavefunctions $\Psi^{(0)}$ and energies $E^{(0)}$. The superscript (0) denotes the reference system. Then, we calculate the contribution of perturbation – this will give an additional energy $E^{\text{pert},(1)}$ and an additional part to the wavefunction, $\Psi^{\text{pert},(1)}$. We now have a new wavefunction consisting of the reference part $\Psi^{(0)}$, and the contribution of the perturbation, $\Psi^{\text{pert},(1)}$, and correspondingly, the same for the energy, $E^{(0)}$ and $E^{\text{pert},(1)}$. We can then use the new wavefunctions to calculate the next higher order of the perturbation, $\Psi^{\text{pert},(2)}$, and so on. In principle, if all orders of perturbation are included, we would obtain the exact solution. In practice, one normally does not go to higher than the fourth order of perturbation. It is fair to mention that perturbation theory only works if the reference system is reasonably similar to the exact one. If this is not the case, the problem might arise that higher order corrections do not converge to the exact solution or, even worse, that they diverge.

2.3.3
Born–Oppenheimer Approximation

The Born–Oppenheimer approximation is the most basic approximation underlying all quantum chemical calculations for molecules. We recall that for molecules, the total wavefunction $\Psi(r_i, R_j)$ depends on both the electronic and nuclear coordinates. Within the Born–Oppenheimer approximation, one separates the nuclear motion from the electronic motion:

$$\Psi(r_i, R_j) \approx \psi^{\text{el}}(r_i, \bar{R})\chi^{\text{nuc}}(R_j). \tag{2.30}$$

Now $\bar{R}$ is no longer a variable, but a parameter which we can fix beforehand. As the nuclei are at least 1823 times heavier (depending on the atom) than the electron, they do not move as fast as the electrons, and therefore the separation into an electronic and a nuclear part is reasonable. Equation 2.30 says that we separate the total wavefunction Ψ into two parts: one which describes the state of the electrons ψ^{el} for a fixed nuclear geometry $\bar{R}$, and another which describes the nuclear part χ. This separation automatically implies that we shall be dealing with *two* Schrödinger equations, one for the electrons, and one for the nuclei:

$$\hat{H}_{\text{el}}\psi_{\text{el}} = E_{\text{el}}\psi_{\text{el}} \tag{2.31}$$

and

$$\hat{H}_{\text{nuc}}\chi_{\text{nuc}} = E_{\text{nuc}}\,\chi_{\text{nuc}}. \tag{2.32}$$

Figure 2.15 visualizes the two systems which we are now considering. The *electronic Schrödinger equation* is of particular interest for quantum chemistry. The *nuclear Schrödinger equation* is relevant for vibrational spectroscopy and reaction dynamics. We will concentrate here only on the former one. Note that as the

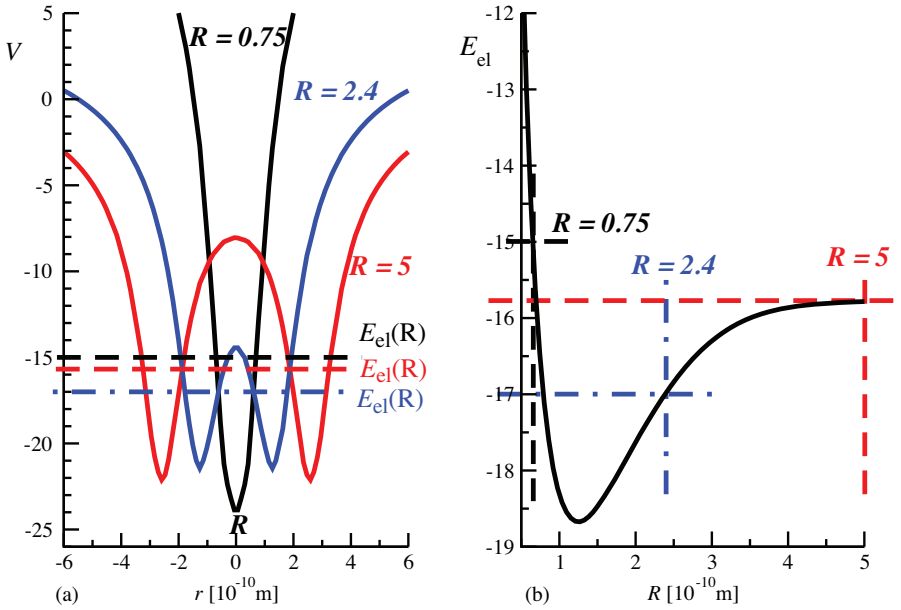

Figure 2.15 Visualization of the Born–Oppenheimer equation and its implications. Panel (a) shows that varying the nuclear geometry leads to different electronic wavefunctions ψ^{el}, the energies $E_{el}(\bar{R})$ of which correspond to the potential energy curves shown in (b). (b) Potential energy curves and nuclear motion on these curves.

electronic part depends parametrically on R ($\bar{R}$), also the energies E_{el} depend on the nuclear geometry $\bar{R}$. We therefore write $E_{el}(\bar{R})$ – these energies are the potential energy curves (or potential energy surfaces PESs). In general, these energies are potential energy hypersurfaces depending on $3M-6$ degrees of freedom, where M is the number of atoms in the system. Such PESs are evaluated by solving the electronic Schrödinger equation for single points at a particular nuclear configuration. Because these PESs are a direct consequence of the Born–Oppenheimer or adiabatic approximation, the resulting PESs are also called adiabatic potentials. As the energies of the electronic system depend on the geometry, we can find a point where the energy is lowest – this is the most stable geometry – the *equilibrium geometry*. This is one of the important pieces of information that we want to know about the system! Often, there are different possible geometries but the one with the lowest energy is the most stable and therefore the most probable geometry of the molecule. This is of particular interest when looking at chemical reactions, but also for protein and enzyme structures. The concept of a PES is fundamental to chemistry, since it allows us to understand chemical reactions. For large molecules, however, one does not compute a total hypersurface in all degrees of freedom. Normally, it is sufficient to find critical points, such as minima and saddle points of first order (associated with the chemical concept of a transition state), which correspond to optimal structures that define the most important regions of the PES that the system can visit in a particular chemical reaction (e.g., reactants, intermediates, and products). The

optimization of such points can be routinely performed at different levels of theory, i.e. with different levels of approximation (see Section 2.5 and 2.7).

We just mention that the second equation, the nuclear Schrödinger equation (Equation 2.32), is of special importance for the motion (dynamics) of the nuclei in a molecule (e.g., to analyze and calculate vibrational and rotational motion). The calculated vibrational spectra (infrared and Raman spectra) help to characterize a substance (see Chapter 3).

The Born–Oppenheimer or adiabatic approximation is usually a good approximation, provided that two (or more) solutions of the electronic Schrödinger equation (Equation 2.31) are energetically far from each other. At points where two states are close or even cross, the Born–Oppenheimer approximation breaks down, and nonadiabatic corrections, which are far off the scope of this introductory chapter, need to be evaluated.

The next section deals with methods to obtain solutions of the electronic Schrödinger equation (Equation 2.31).

2.3.4
Linear Combination of Atomic Orbitals

So far, we have intuitively seen how chemical bonds are constructed. But which conditions have to be fulfilled to obtain stable molecules? One very simple rule is based on the stability of a fully completed shell: the most fundamental way to construct stable molecules is to ensure that every atom in the molecule has a fully occupied shell. Recall Section 2.2.5, where we have seen that each atomic orbital offers space for up to two electrons, and that the first shell (with the 1*s* orbital), and the second shell (including the 2*s* and 2*p* orbitals) offers space for two or eight electrons, respectively: the rule now simply states that atoms in the first row (hydrogen and helium) are especially stable, if they contain two electrons. For helium, being the second element in the periodic system of the elements, and therefore possessing two electrons, this is already the case – helium does not need any other atom to reach a completed shell. In fact, helium does not make any stable molecule with any other atom, or with itself. We say that helium is chemically inert. For hydrogen, the situation is different. We have seen that it has only one electron, and therefore it needs one more electron to complete the shell. This is why it forms a molecule, consisting of two hydrogen atoms, each contributing with one electron. The two electrons form the chemical bond and are shared by the two hydrogen atoms.

Looking at the other atoms of the periodic system of the elements, this rule explains why all noble gases, such as helium, neon, argon, krypton, and xenon (all found in the last column of the periodic system of elements), do not form molecules or chemical bonds with other atoms: they all already have a full shell. Hence they all are chemically inert.

All other atoms do not have a completed outer shell and therefore need to form chemical bonds with other atoms to reach an octet, sharing the electron pairs of the chemical bond with their neighbors. Molecules in which all atoms have a completed shell (always including the shared electrons into the count of outer electrons) are

Figure 2.16 Formation of a chemical bond in hydrochloric acid, H–Cl. The hydrogen atom contributes one electron and the chlorine atom seven electrons, all indicated by the dots (left-hand side). The bond is formed by two electrons shared by both atoms, middle part. Two electrons forming an electron pair (two dots) are replaced by a bar, right-hand part.

especially stable. Molecules in which this is not the case are typically highly reactive – such as radicals, where at least one orbital is occupied by only one electron. Radicals try to form other molecules where the full shell rule is fulfilled, and are therefore highly reactive.

Consider as an example the chlorine atom (Cl) (number 17 in the periodic system of the elements, column number 7) with seven outer valence electrons; it needs one more electron to complete the outer shell. Therefore, chlorine forms bonds with, for example, the hydrogen atom (with one electron), creating the H–Cl (hydrochloric acid) molecule, where the hydrogen and the chlorine share one electron pair. In the molecule Hydrogen has again two electrons, and chlorine is surrounded by eight electrons (see Figure 2.16).

This also applies for larger molecules, such as CH_4: the carbon atom (C) (number 6, column 4) has four outer electrons, and the four hydrogen contribute one electron each. Together they form the methane molecule, in which each hydrogen is surrounded by two electrons and the carbon atom by eight molecules, yielding a full shell for all atoms (see Figure 2.17).

2.4
Solving the Electronic Schrödinger Equation

Methods which solve the electronic Schrödinger equation without including empirical parameters are called *ab initio* methods. *Ab initio* methods are restricted to small and medium size molecules, as they need substantial computer power. We introduce the different *ab initio* methods in Sections 2.5 and 2.7. In contrast, semiempirical methods contain empirical parameters that might have been derived from experiment or parameterized from *ab initio* information. In general, in the semiempirical methods several calculation steps are omitted and, to compensate for these errors,

Figure 2.17 Formation of chemical bonds in methane, CH_4. Each hydrogen atom contributes one electron and the carbon atom four electrons, all indicated by the dots (left-hand side). The bond is formed by two electrons shared by both atoms, middle part. Two electrons forming an electron pair (two dots) are replaced by a bar, right-hand part.

other values are parameterized. Semiempirical methods are valuable for larger molecules, say around 100–1000 atoms, and are discussed in more detail in Section 2.9.

So far, we have separated the nuclear motion from the electronic motion. However, we are still dealing with the coordinates of all N electrons. It would be highly convenient if we could describe each electron separately, for example, in the following form:

$$\begin{aligned}\psi^{\mathrm{el}}(\vec{r}_1, \vec{r}_2, \vec{r}_3, \ldots, \vec{r}_N) &= u_1(\vec{r}_1) \cdot u_2(\vec{r}_2) \cdot u_3(\vec{r}_3) \ldots u_N(\vec{r}_N) \\ &= u_1(1) \cdot u_2(2) \cdot u_3(3) \ldots u_N(N).\end{aligned} \tag{2.33}$$

The above form is called the *Hartree ansatz*. In general, this is not a good approach as it violates some basic principles of quantum mechanics: first the indistinguishability of identical particles. We can imagine this principle by a swarm of mosquitoes: as all mosquitoes look the same when looking at a cloud of them we cannot trace the motion of one particular insect. Quantum mechanics goes one step further: even if there are only two mosquitoes, we are not able to distinguish them. However, Equation 2.33 assumes that we know exactly which is electron 1 and it is located in $\vec{r}_1$, and so on. The second principle that is violated is the *Pauli principle*: when interchanging two particles, the state has to change its sign (it has to be antisymmetric). Let us exemplify this by means of a battery: on changing the two poles, the current runs in the opposite direction – the direction changes its sign. Writing the wavefunction as a Hartree product violates both the indistinguishability and the Pauli principle.

A better approach is to write the wavefunction as a *Slater determinant*, which, for two electrons, has the following form:

$$\psi^{\mathrm{el}}(\vec{r}_1, \vec{r}_2) = \frac{1}{\sqrt{2}} \begin{vmatrix} u_1(\vec{r}_1) & u_2(\vec{r}_1) \\ u_1(\vec{r}_2) & u_2(\vec{r}_2) \end{vmatrix} \tag{2.34}$$

$$= \frac{1}{\sqrt{2}} [u_1(1)u_2(2) - u_2(1)u_1(2)]. \tag{2.35}$$

Now it can be easily seen that changing the numbering of the electrons will invert the sign of $\psi^{\mathrm{el}}(\vec{r}_1, \vec{r}_2)$ and, simultaneously, the electrons are indistinguishable, since each of the electrons can be at $\vec{r}_1$ and $\vec{r}_2$. What are the functions $u_i(j)$? They are the so-called *spin orbitals*, wavefunctions consisting of a spin part and a spatial wavefunction. The spin also appears when throwing a baseball – in addition to the forward direction which you targeted, the ball additionally has an intrinsic rotation around itself. Similarly, we can understand the spin of an electron – however, as we have seen already with the energies, the spin cannot have all values, but it is restricted to two values, which we call *up* and *down*, or mark by arrows, $\uparrow, \downarrow$. The total spin of the system is then just the sum of the individual spins of the electrons. By writing the wavefunction ψ^{el} as a Slater determinant, it is an antisymmetric combination of individual functions and the spin of each electron. Now we are in the position to ask: What is the energy of ψ^{el}, written as a Slater determinant?

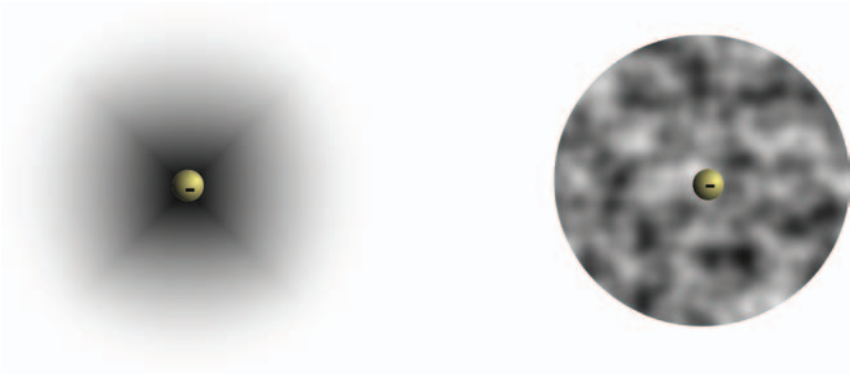

Figure 2.18 Schematic diagrams contrasting the average potential that an electron feels with the explicit interaction.

2.5 The Hartree–Fock Method

With the Hartree–Fock method, the energy and a wavefunction being represented by a Slater determinant can be calculated. Recalling the explicit form of the Hamilton operator (Equation 2.10), the term of the electron–electron repulsion term prevents us from solving the Schrödinger equation. The other terms in the Hamilton operator – the kinetic energy and the electron–nuclear attraction – depend only on one electron (for all but each individually). However, the electron–electron repulsion depends on at least two electrons repelling each other. We therefore can expect that the energy of the wavefunction also depends partially on one electron, and partially on two electrons.

This is indeed what we find. One part $\hat{h}$ depends on one-electron terms (and this N times for all N electrons). The second part gives the two-electron parts, the Coulomb term J, and the exchange term K. The former is the electrostatic repulsion between the electrons, and the latter arises from the explicit form of the wavefunction as a Slater determinant.

Calculating the energy of a single Slater determinant – using the variational principle – leads to the Hartree–Fock equations:

$$\hat{f}^{\mathrm{HF}} u_i = \varepsilon_i u_i \tag{2.36}$$

where $\hat{f}^{\mathrm{HF}}$ is the Hartree–Fock operator, consisting of the above-mentioned one-electron operators $\hat{h}$, and the Coulomb and exchange operators $\hat{J}$ and $\hat{K}$, respectively, and ε_i is the orbital energy. Note the formal similarity to the Schrödinger equation.[2)]

One important approximation used here is that the electron–electron interaction is only accounted for in an average way: each electron moves in the average potential of all other electrons (Figure 2.18). As an example in every-day life, imagine you are

2) Despite this formal similarity, the Hartree–Fock equations are *no* eigenvalue equations, because the Hartree–Fock operator depends on all of the u_i.

walking into a perfume shop: people shopping inside test different fragrances. As soon as you have entered into the shop, you will not be able to distinguish the different smells any longer. This is how in the Hartree–Fock method the electron–electron interaction is described. The approximation is quite fair, however, coming back to the perfume example: when you walk around the shop you will approach a person who has tested an unpleasant smell. You try to avoid him/her and do not approach further. This also happens similarly to the electrons – they try to avoid each other and not come closer. This is the so-called *dynamic electron correlation* and it is not accounted for within the Hartree–Fock approximation. The Hartree–Fock equations have to be solved iteratively. One starts with a trial spin-orbital $\tilde{u}_i$, calculates the energy, modifies the trial function, re-calculates the energy, and so on until the energy does not change any longer (upon the predefined threshold value). Then we have reached *self-consistency*. The Hartree–Fock method is therefore often called the Hartree–Fock self-consistent field (HF-SCF) method. The variational principle thereby ensures that the spin-orbital giving the lowest energy will be closest to the true solution. Recall that when applying the variational principle we can never obtain energies lower than the true energy.

The energies ε_i of each spin orbital can be interpreted according to *Koopmans' theorem*: The orbital energies ε_i are the negative value of the ionization energy – the energy which is necessary to remove one electron from the molecule or, in different terms, to ionize the molecule.

In practice, we do not vary the orbitals themselves in every iteration step – this is computationally too demanding – but represent them by a set of *basis functions*:

$$u_i = \sum_j c_j \varphi_j. \tag{2.37}$$

The orbital u_i is expressed by a sum of known, predefined functions φ_j, the *basis set*. Then, we keep the known functions and vary only the coefficients c_j, the weight of each basis function. The variational principle also applies when using the basis set expression instead of the wavefunction itself. Now, by variation of the coefficients c_j, we need to find the lowest possible energy. Varying only numbers instead of the wavefunction is much faster. Therefore, in computational chemistry, we mainly work with basis sets.

2.6 Basis Sets

As shown above, every function (every orbital) can be expressed as a sum of basis functions. The idea is to represent the molecular orbitals as a sum of basis functions which can be, for example, atomic orbitals. If the sum is up to infinity, the expression in Equation 2.37 would be exact, and we would have a complete basis; the (extrapolated) energy is called the energy in the *basis set limit*. Calculating with infinities is

always challenging. Truncating the summation leads to additional error, the basis set truncation error.

It is intuitive to see that the largest possible basis leads to most exact results. On the other side, the larger the basis, the more computational effort we have to do. We therefore have to find some compromise concerning the basis set size. In what follows, we will introduce the most common basis sets and provide some explanations.

2.6.1
Slater Versus Gaussian Functions

A common discrimination of basis functions is between Slater and Gaussian functions. Both functions are used in computational chemistry; we will use the acronyms STO for Slater-type orbitals and GTO for Gaussian-type orbitals. The two different types have mathematically different expressions. The STOs are exponential functions:

$$\varphi^{\mathrm{STO}}(r) \propto \mathrm{e}^{-\zeta r} \tag{2.38}$$

as they occur in the analytical solutions of the hydrogen atom. The GTOs are of the form

$$\varphi^{\mathrm{GTO}}(r) \propto \mathrm{e}^{-\zeta r^2}. \tag{2.39}$$

The STO and GTO functions are centered around $r = 0$, the position of the nucleus. The factor ζ occurring in the exponent is called the *orbital coefficient* as it describes the spatial extent of the function (of the orbital). Large values of ζ describe compact functions, whereas small values of ζ yield functions which are spread over space and are more diffuse. Figure 2.19 demonstrates the behavior of GTOs for different values of ζ. Comparing the STO and GTO functions, they show similar behavior but differ in some important details. As already mentioned, Slater functions

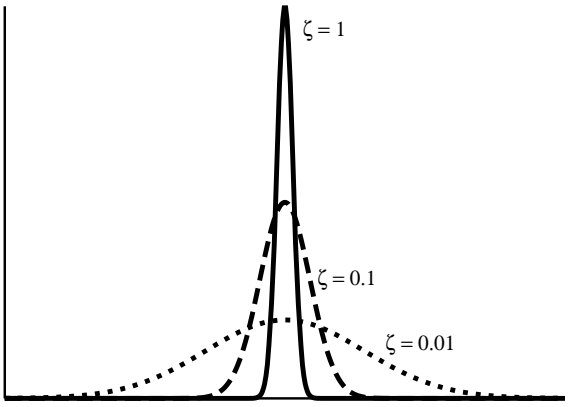

Figure 2.19 Gauss functions (GTOs) for different values of the orbital coefficient ζ. Large values of ζ yields compact functions, whereas small values produce diffuse functions.

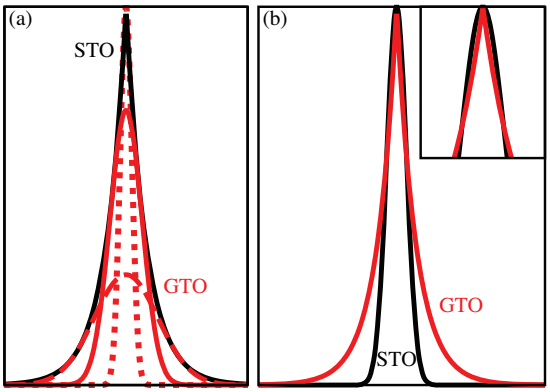

Figure 2.20 (a) Slater function (STO) being represented by 3 Gauss functions (GTOs); (b) Quantitative difference between GTO and STO.

are analytical solutions of the hydrogen atom, meaning that they should be a good starting point to describe other atoms also. Since we are interested in basis functions representing atomic functions that we would like to combine to form molecular orbitals, Slater functions should be very well suited. This is indeed the case. However, they are computationally difficult to handle.

In contrast, GTOs are not functions representing solutions to any atomic problem, but they are computationally much easier to handle. The aforementioned two-electron integrals are faster to calculate using GTOs. Additionally, we can represent any STO by a clever combination of GTOs. Figure 2.20a demonstrates how a Slater function can be approximated by three GTOs. Figure 2.20b illustrates the qualitative difference between STOs and GTOs. The Slater functions have a cusp around the position of the nuclei and fall off less rapidly than the GTOs. Despite the fact that we need more GTOs to represent one STO, most quantum chemical programs use Gaussian functions due to faster processing. If not indicated differently, we will from now on concentrate on Gaussian basis functions.

2.6.2 Number of Basis Functions

Recall that the basis set is constructed from a certain number of atomic orbitals φ_j. How many functions do we need to include? The smallest number of basis functions possible to describe an atom is called a *minimum basis*. For the hydrogen and the helium atoms, this simply corresponds to a single *s* orbital. The atoms in the second row, starting from lithium to neon, are represented by two *s* functions, and three *p* functions. We need two *s* functions, as one *s* function is needed to describe the inner 1*s* orbital, and the other one to represent the valence 2*s* orbital.

The next step in complexity would be just to double the number of basis functions from the minimum basis. Such a basis is called a double zeta (DZ) basis. The zeta originates from the orbital exponent ζ which we have introduced before. In practice,

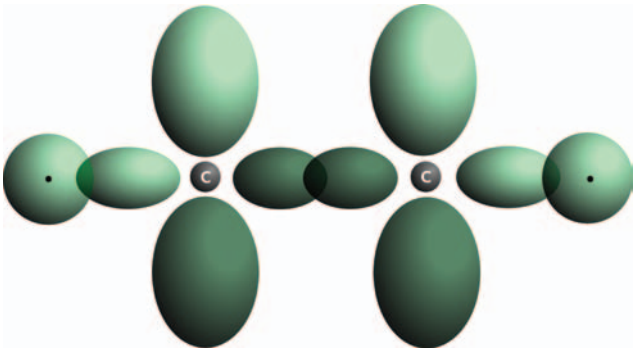

Figure 2.21 Molecule with two different bond types (σ and π) including *p* orbitals. The two different bonds may have different spatial distributions.

this means for the elements hydrogen and helium each is now described by two *s* functions, and for the elements lithium to neon by four *s* and six *p* functions. Such a basis is already much better suited to represent an atom. Why is this the case? We exemplify this by a simple example, illustrated in Figure 2.21. This molecule has two different C−C bond types with two different neighbors. Most probably the spatial distribution of electrons in each of the neighbors is different. By using only one set of *p* functions, as done in the minimum basis, we have to make a compromise between the two different bonds, resulting in an average value for the orbital exponent ζ. In doubling the number of functions, we account for two different bonding types, allowing two different values of ζ, and enable a better (and more individual) description of the two different bonds. Naturally, this leads to much more realistic wavefunctions and energies closer to the experimental value.

Nothing prevents us from tripling the minimum basis, thereby creating a triple zeta (TZ) basis, or quadrupling (QZ), or even quintupling (5Z) the minimum basis. In practice, however, a 5Z basis is in most cases too expensive.

By multiplying all basis functions, we create a huge basis set. In order to describe chemical bonds, we especially need to describe the outer electrons (the valence electrons) properly. Therefore, instead of multiplying the complete minimum basis, we can solely multiply the basis functions for the outer electrons. Such a multiplication of a chopped basis is called a *split valence basis*. They are denoted VDZ (for a basis where the valence basis set is doubled), VTZ (denoting a tripling of the valence basis set), VQZ, and so on.

Very often, we need to add *polarization functions*. As the name indicates, polarization functions contribute with higher angular momentum, thereby polarizing other functions. A *p* function polarizes an *s* function, a *d* function polarizes a *p* function, and so on. Typically, adding polarization functions improves the description of chemical bonds. Also, polarization functions allow for a certain degree of asymmetry of the bond. This is important to describe bonds where the two atoms are not the same. Adding a set of polarization functions (that is, *p* orbitals to the hydrogen atom and *d* orbitals to the heavier atoms) is commonly denoted DZP (double zeta plus polarization) basis, and analogously one can have TZP, QZP basis set, and so on.

2.6.3
Contracted Basis Sets

The disadvantage of basis sets is very often that the inner electrons make the largest contribution to the total energy. Applying the variational principle, we are iterating to achieve the lowest possible energy. This, in turn, means that many basis functions are used to describe the core with the inner electrons properly, as they make the largest contribution to the energy, as shown in Figure 2.22a. However, we are interested in describing the chemical bond as accurate as possible, implying that the valence electrons have to be represented properly. Unfortunately, describing the outer electrons accurately does not change as much in the total energy as representing the inner electrons properly (see Figure 2.22b). By taking a large basis, we can account for both types of electrons, the inner and the valence electrons. This, however, is computationally inefficient. A common solution to this problem is to contract basis sets: a certain number of functions describing the core (the inner electrons) are combined into one function describing the whole core. Often, three, four, or six basis functions are combined into one. The rest of the basis set is used to describe the chemically more relevant valence electrons. In common quantum chemical programs, we find already a pre-built variety of contracted basis sets. A well-known class was introduced by John Pople and co-workers. In the following we describe some of the most common Pople types of basis sets.

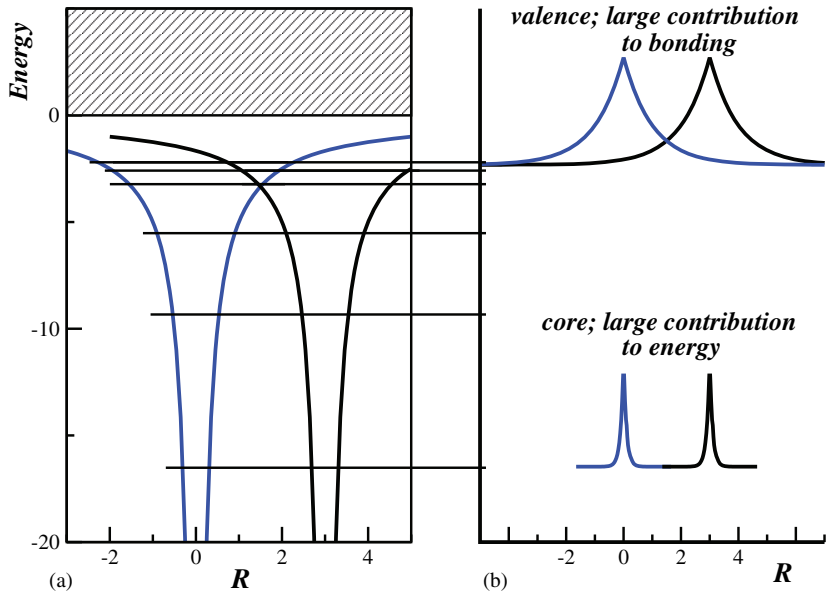

Figure 2.22 Inner electrons make the largest contribution to the energy, but are not so important in describing the chemical bond, and vice versa. (a) Energetic picture; (b) the wavefunctions.

STO-nG basis sets represent a minimum basis set of one Slater orbital (STO) consisting of *n* Gaussian orbitals (GTO). The exponents of the Gaussians are fitted to describe an STO. The best known member of this class is the STO-3G basis set, where one Slater orbital is described by three Gaussian orbitals. As an example of the hydrogen atom, out of three *s* GTO functions, one STO function is constructed. Similarly, for any element between lithium and neon, out of six *s* functions and three *p* functions, two *s* functions and one *p* function are constructed to describe the 1*s*, 2*s*, and 2*p* orbitals.

The *k-nlmG* class of basis functions consist of Gaussian functions split by the valence shell, which we call "split valence." The coding by the letters representing numbers can be interpreted as follows. The letter *k* denotes how many Gaussians functions are contracted to one core orbital. The *nlm* codings contains several pieces of information. First, when only two numbers are present, this indicates a double split valence, whereas three numbers indicate a triple split valence. Then, the numbers themselves specify the contraction scheme.

A common basis set of this type is the *3-21G basis set*. This is a split valence basis set. Here, out of three functions, one core function is constructed, whereas for the inner valence two basis functions are contracted to one function and the outer valence is not contracted, consisting of one basis function. Similarly, the common *6-31G basis set* can be interpreted as follows. The core is constructed from six orbitals, the inner valence from three orbitals, and the outer valence is again uncontracted. Although both the 3-21G and the 6-31G basis sets result in the same number of basis functions, the 6-31G basis set typically performs better, as more functions (called primitives) are used to construct this basis set. Another representative of this class of basis sets is the *6-311G basis set*, being a triple split valence basis set. The core again consists of six functions contracted to one, the inner valence is contracted from three functions, and additionally there are two more valence functions being not contracted.

If additionally diffuse functions (*s* or *p* orbitals with a very small orbital coefficient ζ) are present, these are typically marked by adding a $+$ or $++$ before the letter G. One $+$ indicates a set of diffuse functions on the heavy atoms, whereas $++$ denotes diffuse functions on both the heavy functions and the hydrogen atom. Adding polarization functions is denoted by a * or **, where analogously one * indicates a set of polarization functions on the heavy atoms, whereas ** denotes polarization functions on the hydrogen also. Often, we find explicit notation where the specific functions are written, that is, 6-31G** is equivalent to 6-31G(d,p). The largest standard basis of this style is the 6-311$++$G(2df,2pd), a triple split valence basis with a set of diffuse *s* and *p* functions on the heavy atoms and the hydrogen, two *d* and one *f* polarization functions on the heavy atoms, and two *p* and one *d* polarization function on the hydrogen atom.

A different class of contracted basis sets is the so-called *correlation consistent* basis sets developed by Dunning and co-workers, denoted cc-pVDZ, cc-pVTZ, cc-pVQZ, cc-pV5Z, and so on. They have the advantage that they build a sequence of basis sets where each step of increasing the basis size converges to the basis set limit. For this reason, they are slightly more expensive than the counterparts of

Pople. In the sequence of these functions, always one more function is added, thereby increasing the basis set size in a stepwise manner. As an example, let us consider the sequence from cc-pVDZ, cc-pVTZ to cc-pVQZ: while the smallest basis cc-pVDZ from this sequence consists of 3*s*, 2*p*, and 1*d* orbital for the heavy atoms (we will omit the explicit form for the hydrogen atoms, which is always one function and one polarization function less than the heavy atom), the basis for the next larger basis, cc-pVTZ, has one more function of each type, therefore consisting of 4*s*, 3*p*, 2*d*, and as a new function with higher angular momentum: 1*f* function. Correspondingly, the cc-pVQZ basis has 5*s*, 4*p*, 3*d*, 2*f* and 1*g* function, and so on. The functions can be augmented by additional diffuse functions, which is denoted by the prefix *aug-*.

Of course, for special tasks, self-made basis sets can be constructed. However, there are some general rules to obey which we cannot mention here. Instead, we refer the interested reader to the computational chemistry literature [1–4].

2.7 Electron Correlation

Assuming a complete basis set, the calculated energies with the Hartree–Fock–procedure still do not agree fully with the experimentally measured values. In the ideal case, we obtain up to 99% of the experimentally exact energy – but the chemistry often is very well hidden in the remaining 1%. Which contributions are behind this 1% (or more)?

This 1% (or more) is the so-called *electron correlation*. The electron correlation energy is commonly defined by the difference between the exact energy and the Hartree–Fock energy in the limit of a complete basis set:

$$E_{\text{corr}} = E^{\text{exact}} - E_0^{\text{HF}}. \tag{2.40}$$

This energy is the sum of different contributions, which can be grouped into two different types of electron correlation:

1) **Dynamic electron correlation:** We recall that in the Hartree–Fock method, we made the explicit assumption that an electron moves in the average potential of all other electrons. This does not correspond to reality since the electrons try to avoid each other due to their charges – they do not come close but swerve, as sketched in Figure 2.23. There is a reduced probability of finding an electron in the close neighborhood of another electron. This implies that the dynamics of each electron are not independent of the motion of the other electrons but is correlated with the dynamics of all other electron.
2) **Static electron correlation:** Unfortunately, there is no common definition of static electron correlation; we therefore try to approach its meaning by exemplifying typical occurrences. Static electron correlation occurs close to degeneracy or, generally, when several electronic configurations are important. We often

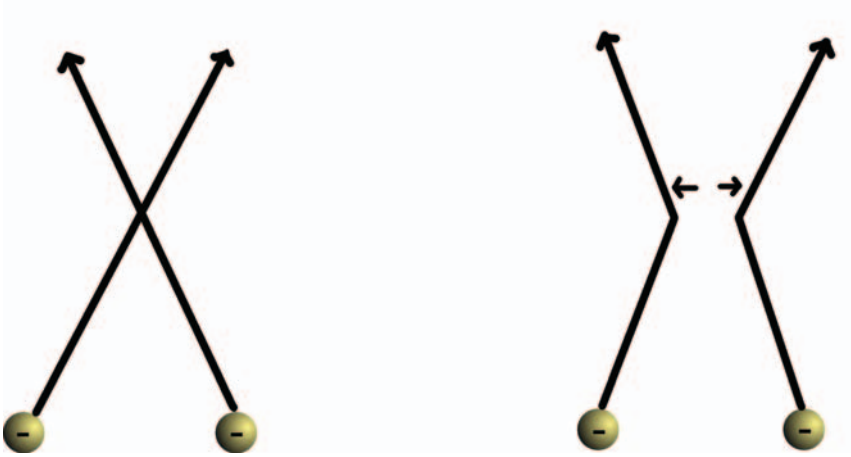

Figure 2.23 Dynamic electron correlation: Electronic motion is not independent of the motion of all other electrons but depends explicitly on the motion of the other electrons, thereby avoiding each other.

encounter static electron correlation, for example, when transition metals are involved, as there are many electronic energies lying close together, or in homolytic dissociation. The reason for the latter might not be so obvious, hence we would like to address this problem briefly.

For simplicity, let us imagine the hydrogen molecule, which consists of two nuclei and two electrons. Applying a single Slater determinant with a minimal basis of two spin orbitals in the Hartree–Fock method, we obtain different contributions describing the hydrogen–hydrogen bond, as depicted in Figure 2.24. As a result of a Hartree–Fock calculation, we obtain four wavefunctions. Two of them are of ionic character, meaning that the two electrons are located around one nucleus (formally negatively charged) whereas the other one has no electrons (formally positively charged). The other two wavefunctions are of covalent character, where each nucleus has one electron around it. This is an appropriate description for the bond around the equilibrium internuclear distance.

However, how is the bond described in the limit of infinite internuclear distance? For homolytic dissociation, the system should be described by two (infinitely) separated hydrogen atoms, having one electron each. Hence, in the dissociation limit, the wavefunction has 100% pure covalent character. Then it is clear that the character of the bond changes during dissociation: whereas it is 50% covalent and 50% ionic around the equilibrium internuclear distance, it is 100% covalent and 0% ionic at large internuclear distances. Unfortunately, this change of the character of the wavefunction cannot be described by the Hartree–Fock method, which uses one determinant only. This error in the Hartree–Fock description is known as static correlation and requires more than one determinant.

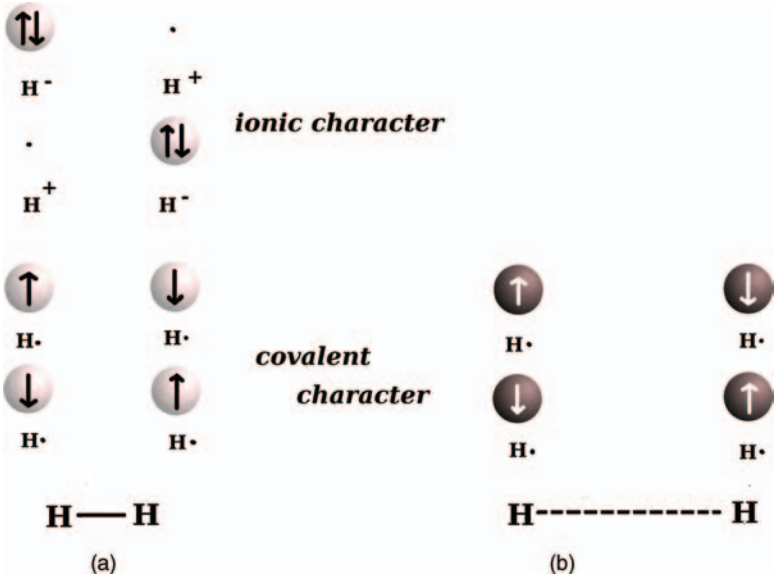

Figure 2.24 (a) Hartree–Fock wavefunction describing the hydrogen molecule around its equilibrium internuclear distance. The bond has 50% ionic (both electrons on one nucleus) and 50% covalent character (each nucleus has one electron). Part (b) shows that in the limit of infinite internuclear distance (dissociation limit), the wavefunction should be exclusively described as covalent.

In order to describe such problems where several electronic configurations or other determinants are important, quantum chemical methods including (static or dynamic) electron correlations have to be employed.

The lack of additional determinants in Hartree–Fock calculations results in the following errors:

- The bond energies for stretched bonds are too high. This is crucial for transition states, which often are described by stretching and breaking/making of different bonds. Consequentially, the energies of transition states are typically too high at the Hartree–Fock level of theory.
- As the energies increase too rapidly on stretching the bonds slightly, it often appears that the minimum on the potential energy surface is at too short internuclear distances and the curvature is too strong. This is important for vibrations, which are for this reason too high.
- The opposite is true for complexes involving metals or for charge-transfer systems. Here, within the Hartree–Fock approach the ionic character during dissociation is correctly described but the equilibrium distance is too long.

In general, the main sources of error in quantum chemical calculations are (a) insufficient treatment of electron correlation and (b) a limited basis set. (Minor errors are due to relativistic and non-Born–Oppenheimer effects.) We have introduced the different forms of electron correlation, namely dynamic and static electron

correlation. As a next step, we introduce quantum chemical methods accounting for electron correlation in the calculation.

2.7.1 Configuration Interaction

The conceptually easiest method to recover electron correlation is the so-called *configuration interaction* (CI) method. As we have seen before, a description of the wavefunction by only one Slater determinant is not capable of incorporating electron correlation effects. The next logical step is to include more determinants (more configurations) in the wavefunction. If we include all of the possible ones, this is called a full-CI wavefunction:

$$\Phi^{\text{full-CI}} = \sum_{i}^{\infty} a_i \psi_i^{\text{el}} \tag{2.41}$$

$$= a_0 \psi_{\text{HF}}^{\text{el}} + a_1 \psi_1^{\text{el}} + a_2 \psi_2^{\text{el}} + \cdots . \tag{2.42}$$

The different determinants ψ_i^{el} are the different configurations. What is the physical meaning of these configurations? Figure 2.25 sketches different determinants occurring in Equation 2.42. The different configurations can be categorized by their excitation level. Whereas the Hartree–Fock determinant corresponds to the ground-state configuration where no electron is excited, there are different configurations which can be classified as single excitations, as double excitations, and so on. We can see immediately that the number of configurations of a system contributing to, for instance, single excitations depends on the size of the chosen basis, as the electrons sitting in the occupied orbitals can be excited to all virtual orbitals. The number of virtual orbitals, in turn, depends on the basis set size. Including all possible excitations (full-CI) within the chosen basis leads to an exact wavefunction including the full electron correlation.

The problem of including all possible configurations in a sufficiently large basis lies at hand: except for very small systems, accounting for all possible configurations

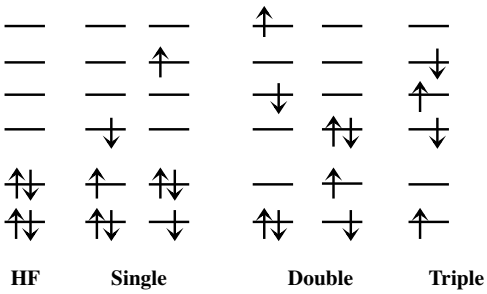

Figure 2.25 Different configurations contributing to the full-CI wavefunction. The configurations can be categorized according to their excitation level as single, double, triple, and so on excitations.

is computationally too expensive, if not even impossible. For typical systems, we can analyze the importance of the particular excitation. On doing so, it was found that double excitations provide the most important contribution to the electron correlation energy, much more important than single or triple excitations. In order to reduce computational effort, truncated CI methods have been implemented. Single configuration interaction (CIS) means that in addition to the Hartree–Fock determinant wavefunction, all kinds of single excitations contribute. Analogously, for double configuration interaction (CID), the Hartree–Fock wavefunction and all different kinds of double excitations contribute. In the CISD method, the Hartree–Fock determinant, single and double excitation contribute. Not considering all excitations but just excitations up to a certain level reduces the computational effort substantially, but introduces a different problem: the calculations are not size consistent (Figure 2.26).

Size-consistent calculations are calculations where the relative errors scale proportionally to the size of the system. Consider a molecule consisting of two atoms; a size-consistent calculation (e.g., HF or full-CI) yields a certain energy. Now we double the system size, that is, treating four atoms, where two are building one molecule, and we separate the two molecular entities. In the limit of infinite separation of the monomer units, there would be no interactions between these subunits, and the system's energy would be just twice the energy of the single molecule, as to be expected. Non-size-consistent calculations, such as the truncated-CI methods (e.g., CISD), would yield an energy for the two molecules different from the correct value of twice the one-molecule energy. Even worse: in the limit of very large systems, as the energy does not scale with the system size, the correlation energy is not recovered at all any longer. The reason for this deficiency lies in the truncation itself: consider a hydrogen molecule with two electrons being described by CISD calculations. For a chosen basis (for simplicity let it be even the minimal basis of one *s* function on each nucleus), the wavefunction contains besides the Hartree–Fock part all single and double excitations. On adding a second hydrogen molecule at large

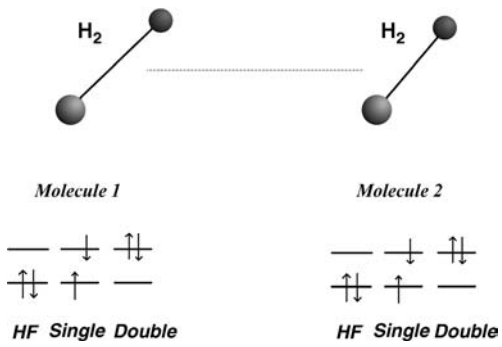

Figure 2.26 Visualization of the size consistency problem using two hydrogen molecules as an example. Each hydrogen molecule has two electrons and can therefore be maximally doubly excited. Two hydrogen molecules, being both doubly excited, correspond to a quadruply excited system.

distances to our calculation, the second hydrogen molecule can be described by the same excitations, the Hartree–Fock determinant, as well as all single and double excitations. However, as each of the two hydrogen molecules can have double excitations, this would correspond to all four electrons (two on each molecule) to be excited – this is formally a quadruple excitation, which is not included in the CISD series, as we truncate after double excitation and explicitly omit triple, quadruple, and all higher excitations. Therefore, on doubling the system size, the degree to which electron correlation is accounted for shrinks and the description becomes worse for larger systems. The problem of size consistency has led to a reduced disposal of truncated-CI methods. Instead, the conceptually similar *coupled cluster* methods, the subject of the next subsection, have gained in importance.

2.7.2 Coupled Cluster Method

The message of the last subsection is that in order to permit electron correlation in the calculation, we need to include different configurations in the wavefunction. However, a full-CI calculation (being size consistent) is for most of the systems not possible, and truncating the series of configurations causes size-consistency errors. Within the coupled cluster (CC) approximation, the concept of expanding the wavefunction to higher excitations is retained, while the problem of the size consistency is eliminated. The ansatz for a CC wavefunction is to introduce the CC operator e^{T} so that

$$\Phi^{\mathrm{CC}} = \mathrm{e}^{\hat{T}}\psi_{\mathrm{HF}}^{\mathrm{el}}. \tag{2.43}$$

As in the case of full-CI, a full-CC calculation is exact but computationally not feasible. The truncated-CC wavefunctions are similarly built according to the level of excitation in which they are truncated. For instance, CCSD indicates the inclusion of single and double excitations.

Recall that the problem of the size inconsistency occurred because higher excitations were omitted. The CC wavefunction accounts for the contribution of higher excitation by approximating their contribution from lower excitations: the probabilities (the coefficients) with which the lower excitations appear are used to describe the probabilities in which the higher excitations would occur. Consider as an example the CCSD method; here we include single and double excitations. Remember the example of the hydrogen dimer for the CISD method: we stated that we did not account for the quadruple excitations which caused the size inconsistency. Within the CCSD method, we also account for the quadruple excitations approximately by describing the quadruple excitations as products of double excitations. Although not including the quadruple excitations explicitly, we approximate their contribution to be about the product of the corresponding double excitations. By doing so, the CC method is size consistent.

The CC theory is probably the most accurate method to compute electronic energies to date, but it is also one of the most expensive.

2.7.3 Multi-Configurational Self-Consistent Field Theory

In chemistry, we often encounter situations where not only one configuration is important and contributes to approximately 99% of the energy. Typical examples are molecules where chemists draw mesomeric structures – structures where different charge distributions play a role. One of the textbook examples is the ozone molecule, O_3, which can exist as a zwitterionic structure or a biradical structure (Figure 2.27). In the case of ozone, the wavefunction has approximately 60% zwitterionic character and about 40% biradical character. It is straightforward to see that we introduce large errors if we consider only the zwitterionic character as the Hartree–Fock approach would do. We therefore need a theoretical description in which we account for different configurations. The *multi-configurational self-consistent field* (MCSCF) method is such a theory: in a conceptually similar manner to the CI method, the total wavefunction is likewise written as a linear combination of different configurations (see Equation 2.42), but with the important difference that the coefficients from which the configurations (the molecular orbitals) are built are also varied. Choosing the hydrogen molecule as an example, we are dealing with two configurations, as shown in Figure 2.28. Note that the single excitation does not contribute for symmetry reasons. These configurations correspond to the Hartree–Fock ground state (a) and a doubly excited configuration (b). In analogy with the CI approach, the MCSCF wavefunction for this case is written as

$$\Phi^{\mathrm{MCSCF}} = a_A \psi_A^{\mathrm{el}} + a_B \psi_B^{\mathrm{el}} \tag{2.44}$$

$$\psi_A^{\mathrm{el}} = \sum_i b_{iA} \varphi_i \qquad \psi_B^{\mathrm{el}} = \sum_i b_{iB} \varphi_i \tag{2.45}$$

where the φ_i are basis functions. Then, the coefficients a_A, a_B, b_{iA}, b_{iB} are varied until self-consistency is reached. However, in general, the problem is to know of which configurations have to be chosen. One very common approach is the complete active space self-consistent field (CASSCF) method. Here, the choice of configurations is made by defining a so-called active space, consisting of n electrons and m orbitals ($[n,m]$-CASSCF). Inside this active space, a full-CI is performed. Figure 2.29 visualizes a typical partitioning of a set of orbitals (wavefunctions) into active and inactive spaces. The active space consists of the relevant occupied and unoccupied (virtual) orbitals; typically, the highest occupied molecular orbital (HOMO), in addition to the lowest unoccupied molecular orbital (LUMO), should be at least contained in the active space. As inside the active space a full-CI is calculated, the size of the

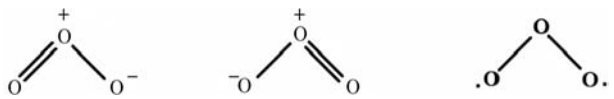

Figure 2.27 Different mesomeric structures of ozone. The first two structures are zwitterionic, whereas the last structure has biradical character.

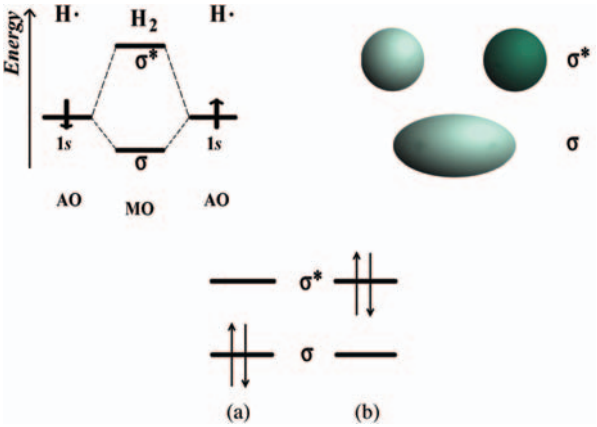

Figure 2.28 Two configurations in the hydrogen molecule: (a) is the Hartree–Fock ground state and (b) is a doubly excited configuration.

active space cannot be large. The biggest CASSCF calculations up to date contain 18 electrons/orbitals.

The main disadvantage with the CASSCF method is that it can lead to an "unbalanced" description: as electron correlation is only accounted for in the active space and not, for example, the inactive core electrons. Further, the CASSCF method tends to overestimate the biradical character of chemical compounds.

2.7.4
Møller–Plesset Perturbation Theory

Recall that the idea behind perturbation theory is that the problem to be handled differs only slightly from a known problem. Then the Hamiltonian operator can be defined as the sum of two parts, a reference Hamiltonian $\hat{H}^{(0)}$ and a perturbation $\hat{H}'$.

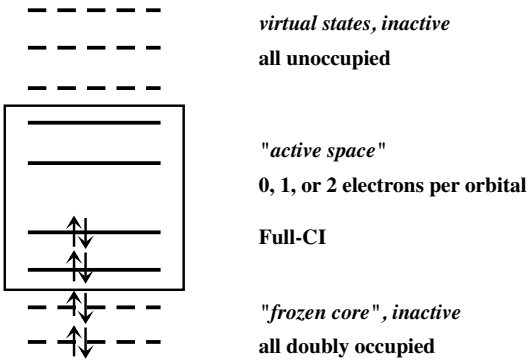

Figure 2.29 Partitioning of the orbitals into active and inactive spaces. The inactive spaces are either doubly occupied (frozen core) or empty (virtual). Inside the active space, the orbitals are either singly, doubly or not occupied, and a full-CI is performed.

The perturbation has to be small compared with the reference Hamiltonian. The n solutions of $\hat{H}^{(0)}$ are assumed to be known and given. In 1934, Møller and Plesset [5] proposed to partition the Hamiltonian operator such that the unperturbed Hamiltonian is $\hat{f}$, the Fock operator defined in Equation 2.36. With this definition of $\hat{H}^{(0)}$, the zeroth-order energy $E^{(0)}$ is the sum of the energies ε_i.

The perturbation $\hat{H}'$ is the difference between $\hat{H}$ and $\hat{H}^{(0)}$, that is, everything in the electron–electron interaction which has not been accounted for by the smeared Hartree–Fock average potential of all other electrons.

In this so-called Møller–Plesset or MP partition, one can realize that the Hartree–Fock energy already corresponds to the zeroth- and first-order corrections. Hence it is just the second-order correction that allows an estimate of the correlation energy. The essence of the MP2 method is then to calculate the energy correction for the ground state. A detailed analysis shows that the second-order correction to the energy in the MP2 theory involves all possible double excitations.

MP2 typically accounts for 80–90% of the correlation energy, and as it is computationally highly efficient, it is a popular *ab initio* method for including electron correlation. It should be noted that although not variational, the MPn perturbation method is size consistent. Beyond MP2, the only MPn methods implemented in standard codes are MP3 and MP4. Whereas MP3 is very often divergent, MP4 can be very accurate, recovering up to 98% of the correlation energy, but of course at a higher computational cost than MP2.

2.8 Density Functional Theory

The electronic wavefunction has been the central key to quantum chemistry so far. If ψ – or a good approximation to it – is known, all information about our target system can be calculated. This approach, however, has a series of disadvantages. First, this wavefunction is very complicated. It depends on $4N$ variables (three spatial and one spin coordinate) and its complexity grows with increasing number of electrons. Second, there is no observable for the wavefunction which can be easily probed experimentally. On the other hand, one can consider the electron density or, strictly, $\rho(r)$, the probability density, that we introduced at the beginning. We will follow the common practice of calling it electron density.

The electron density ρ depends on three spatial coordinates regardless of how many electrons our system includes; moreover, it can be measured via X-ray experiments. But is the electron density sufficient to obtain the energy and all the other properties of interest? The first hint about this is that the expectation value of a (multiplicative) operator $\hat{A}$ can be calculated analogously using the electron density.

Furthermore, the electron density has the following interesting properties:

- Integrating the electron density gives the number of electrons.
- The cusps of the density match the positions of the nuclei.
- The density at the nucleus position contains information about the nuclear charge.

Hence it seems that the electron density provides all information to set up the system-specific Hamiltonian and to determine all molecular properties. Therefore, it is the electron density which is used in density functional theory (DFT).

2.8.1 The Hohenberg–Kohn Theorems

DFT is based on two basic pillars, the two *Hohenberg–Kohn theorems*, which are exposed in the following.

The first Hohenberg–Kohn theorem [6] provides a proof that the electron density can be used in quantum chemistry calculations instead of the wavefunction. It states that the electron density is uniquely determined by the external potential, that is, the electron–nuclear interaction potential. In other words, it means that the ground-state electron density uniquely specifies the external potential or that there is a one-to-one correspondence between the external potential and the electron density.

A semantic note is in order here. A *function* is an instruction on how to obtain a number from a set of variables (e.g., coordinates). A *functional* is in this context an instruction on how to obtain a number from a function which itself depends on variables; it is a "function of a function". To denote functionals depending on a function, square brackets, $F[f]$, will be used instead of parentheses, $f(x)$.

The ground-state energy E_0 is a unique functional of the ground-state density ρ_0 and so are its individual parts. Hence we can write

$$E[\rho_0] = T[\rho_0] + E_{\text{el}-\text{el}}[\rho_0] + E_{\text{el}-\text{nuc}}[\rho_0]. \tag{2.46}$$

We can split this expression into parts which depend on the actual system determined by the external potential – that is, the potential of the electron–nuclei interaction $E_{\text{el}-\text{nuc}}[\rho_0]$ – and those which are universal, meaning that the form of the functional is independent of the actual system:

$$E[\rho_0] = \underbrace{E_{\text{el}-\text{nuc}}[\rho_0]}_{\text{system dependent}} + \underbrace{T[\rho_0] + E_{\text{el}-\text{el}}[\rho_0]}_{\text{system independent}}. \tag{2.47}$$

The system-independent parts can be gathered in the *Hohenberg–Kohn functional* $F_{\text{HK}}[\rho_0]$:

$$E[\rho_0] = E_{\text{el}-\text{nuc}}[\rho_0] + F_{\text{HK}}[\rho_0]. \tag{2.48}$$

This functional $F_{\text{HK}}[\rho_0]$ can be considered as the holy grail of DFT. Knowledge of it would allow us to solve exactly the Schrödinger equation. Also, since this is a universal functional, this would be valid for all systems, independent of the number of atoms or electrons. Unfortunately, the explicit form of $F_{\text{HK}}[\rho_0]$ lies completely in the dark. In an effort to simplify the problem, F_{HK} is divided into parts:

$$\begin{aligned} F_{\text{HK}}[\rho_0] &= T[\rho_0] + E_{\text{el}-\text{el}}[\rho_0] \\ &= \underbrace{T[\rho_0]}_{\text{unknown}} + \underbrace{J[\rho_0]}_{\text{known}} + \underbrace{E_{\text{ncl}}[\rho_0]}_{\text{unknown}} \end{aligned} \tag{2.49}$$

where $J[\rho_0]$ is the classical Coulomb part and $E_{\mathrm{ncl}}[\rho_0]$ represents the non-classical contribution to the electron–electron interaction. This includes self-interaction and correlation.

Finding explicit expressions for the yet unknown parts of the Hohenberg–Kohn functional represents the major challenge in DFT.

Up to now it has been demonstrated that the ground-state density suffices to obtain all properties of interest. But how one can be sure that a given density is the ground-state density we are looking for? Fortunately, the second Hohenberg–Kohn theorem provides a way. This theorem is nothing else than the variational principle for densities. In plain words, it states that $F_{\mathrm{HK}}[\tilde{\rho}]$ – with an arbitrary test density $\tilde{\rho}$ – delivers the lowest energy if, and only if, the input density is the true ground-state density ρ_0, that is,

$$E_0[\tilde{\rho}] = \langle \tilde{\psi} | \hat{H} | \tilde{\psi} \rangle \geq \langle \psi | \hat{H} | \psi \rangle = E_0[\rho_0] \tag{2.50}$$

with the equals sign valid only if $\tilde{\rho} = \rho_0$. A consequence of this variational principle is that DFT is formally only a ground-state theory.

2.8.2 The Kohn–Sham Approach

The main problem with DFT (besides the unknown Hohenberg–Kohn functional) is related to the way in which the density is expressed to put the theory to work. Kohn and Sham [7] proposed to replace the density ρ of the *full-interacting* electron system with the density ρ_{KS} of a reference system of *non-interacting* quasi-particles with $\rho = \rho_{\mathrm{KS}}$. For this system we can write a Hamiltonian $\hat{H}_{\mathrm{KS}}$ analogously to what we did for the Schrödinger equation earlier. Since this Hamiltonian does not contain any electron–electron interactions, the Slater determinant is the exact wavefunction for the system and its kinetic energy can be calculated.

The spin orbitals in the latter determinant are the so-called *Kohn–Sham orbitals* u_i^{KS} and are one-particle wavefunctions which satisfy, in analogy with the Hartree–Fock Equation 2.36, the *Kohn–Sham equations*:

$$\hat{f}^{\mathrm{KS}} u_i^{\mathrm{KS}} = \varepsilon_i u_i^{\mathrm{KS}} \tag{2.51}$$

with the Kohn–Sham operator

$$\hat{f}^{\mathrm{KS}} = \hat{T}_{\mathrm{KS}} + \hat{V}_{\mathrm{KS}} \tag{2.52}$$

which resembles the Fock operator. Due to this similarity, one can solve the Kohn–Sham equations using the same algorithms as in the Hartree–Fock theory, that is, the same self-consistent field approach. Note that the Kohn–Sham orbitals u_i^{KS} are *not* the same as the Hartree–Fock orbitals u_i^{HF}, as we require the Kohn–Sham density to be the same as the ground-state density of our real target system ρ_0.

Of course, the kinetic energy of the non-interacting system T_{KS} is not equal to the true kinetic energy T of our real target system. Keeping this in mind, the functional $F_{\mathrm{HK}}[\rho]$ can be written split into the following parts:

$$F_{HK}[\rho] = T_{KS}[\rho] + J[\rho] + E_{XC}[\rho] \tag{2.53}$$

with the so called exchange-correlation functional

$$\begin{aligned} E_{XC} &= (T[\rho] - T_{KS}[\rho]) + (E_{el-el}[\rho] - J[\rho]) \\ &= (T[\rho] - T_{KS}[\rho]) + E_{ncl}[\rho]. \end{aligned} \tag{2.54}$$

The residual part of the true kinetic energy is added to the non-classical electrostatic contributions. In this way, the exchange-correlation functional contains everything that is unknown. Often this functional is split into an exchange part and a correlation part:

$$E_{XC}[\rho] = E_X[\rho] + E_C[\rho] \tag{2.55}$$

both of which are approximated independently.

The remaining quest is to obtain the exchange-correlation functionals. The explicit form of the functionals is often very complicated because they are developed in a more or less systematic way using empirical models[3)].

The corresponding correlation functionals have even more complicated analytical forms and therefore they will not be explicitly written here. Currently the most popular are hybrid functionals such as B3LYP with three optimized parameters [8].

2.8.2.1 **Advantages**

DFT is able to consider electron correlation at the computational cost of Hartree–Fock. In most cases, it delivers reliable molecular geometries, good values for H-bond distances and good values for binding energies (hybrid functionals). The DFT method is universally applicable (i.e., for the solid state, surfaces, and molecules and for all elements). At the same accuracy, it is more efficient than correlated Hartree–Fock methods.

2.8.2.2 **Disadvantages**

The main disadvantage of DFT is that, unlike wavefunction-based methods that are hierarchical, there is no systematic way to improve the accuracy of the DFT results. It is not necessarily true that larger basis sets deliver better energies or better properties. Due to the variational principle (second Hohenberg–Kohn theorem) DFT can only describe the ground state; however, as will be shown in Section 2.8.3, an extension to treat electronic excited states is possible.

2.8.3
Time-Dependent Density Functional Theory

DFT is formally a ground-state theory. To describe the interaction with time-dependent potentials such as electric or magnetic fields and to extract

3) In this sense DFT is not a clean *ab initio* method, but more a semiempirical method.

information such as excitation energies or (resonance) Raman spectra, it has to be extended to the so-called time-dependent density functional theory (TDDFT). The concepts and computational foundations of TDDFT are analogous to those of the pure DFT.

The formal foundation of TDDFT is the Runge–Gross theorem [9]. It shows that, for a given initial wavefunction, there is a unique one-to-one relation between the time-dependent external potential of a system and its time-dependent density. Unlike DFT, there is (unfortunately) no general variational principle in time-dependent quantum mechanics.

The Runge–Gross theorem was originally derived for electrons moving in an external field.

Two external potentials differing only by an additive time-dependent, spatially independent function, $c(t)$, give rise to the same electronic density. The Runge–Gross theorem [9] shows that there is a unique mapping from an external potential to the electronic density. The proof is done in the following steps:

1) It is shown that two external potentials differing by more than an additive constant generate different current densities. This is done via the expansion of the external potential in a Taylor series about a given time.
2) Using the continuity equation, it is then shown that for finite systems, different current densities correspond to different electron densities.

For a given interaction potential, the Runge–Gross theorem shows that the external potential uniquely determines the density. The Kohn–Sham approach chooses the density of the interacting system as that of the non-interacting one for all times. The wavefunction of a non-interacting system can be represented as a Slater determinant and the kinetic energy of the non-interacting system can be expressed exactly in terms of those orbitals. The problem is therefore to find a potential, denoted $V_{\mathrm{KS}}(\vec{r}, t)$, that sets up a non-interacting Hamiltonian, $\hat{H}_{\mathrm{KS}}$, which in turn specifies a determinantal wavefunction which is constructed in terms of a set of orbitals and generates a time-dependent density $\rho_{\mathrm{KS}}(\vec{r}, t)$ such that ρ_{KS} is equal to the density of the interacting system at all times.

The problem of obtaining approximations to the Kohn–Sham potential is challenging. Analogously to DFT, the time-dependent Kohn–Sham potential is decomposed to extract the external potential of the system, the time-dependent Coulomb interaction and the exchange-correlation potential.

Linear response TDDFT can be used if the external perturbation is small. That means that it does not completely destroy the ground-state structure of the system. In this case one can analyze the linear response of the system. This is a great advantage as, to first order, the variation of the system will depend only on the ground-state wavefunction so that we can simply use all the properties of DFT. Consider a small time-dependent external perturbation $\delta V^{\mathrm{ext}}(t)$. Looking at the linear response of the density, one can obtain an equation from which it is possible to derive the excitation energies of the system, as these are simply the poles of the response function.

2.9 Semiempirical Methods

Semiempirical methods come into play when molecules cannot be calculated *ab initio* any longer due to computational insufficiencies, i.e. the system is too big. For all semiempirical methods, we can summarize the following general properties:

- Use of a minimal basis, typically STOs are applied.
- Explicit consideration of the outer valence electrons only; the inner electrons are modeled by changing the effective nuclear charge acting on the outer electrons.
- Compared with the Hartree–Fock approximation, several types of integrals involving the electron–electron interaction are neglected. This is a consequence of the so-called *zero differential overlap* (ZDO) approximation.
- To compensate for the errors made by the approximations above, several other integrals are parameterized.

The particular semiempirical methods differ on the one hand in the types of integrals being neglected, and on the other hand in the parameters chosen to represent the remaining integrals.

Some semiempirical methods, such as the method proposed by Hückel and the Pariser–Parr–Pople (PPP) method, can treat only a subset of the valence electrons orthogonal to the molecular plane – the p_π electrons (see Figure 2.30). Other methods are able to treat all valence electrons of different atoms. Especially the Hückel method provides a fundamental qualitative understanding of organic compounds containing conjugated (alternating) π-electrons. Although making crude approximations such as neglecting the overlap of orbitals between different atoms and ignoring interactions between atoms that are not bonded to each other, it qualitatively predicts excitation energies between electronic states and stabilization energies correctly. The Hamiltonian is not specified as its corresponding energy expectation value is never calculated directly but just parameters are added. Let us consider an example of a simple model system consisting of a certain number of electrons and nuclei. The energy expectation values (Equation 2.6) are *all* set to the same value α if they describe contributions from one atom *A* only, and set to a second value β if they describe interactions between two neighboring atoms *A* and *B*. Otherwise, the integrals are set to zero:

$$\int \phi_A^* \hat{H} \phi_A \mathrm{d}V = \alpha \tag{2.56}$$

$$\int \phi_A^* \hat{H} \phi_B \mathrm{d}V = \beta \qquad \text{if } A \text{ and } B \text{ neighbors} \tag{2.57}$$

$$\int \phi_A^* \hat{H} \phi_B \mathrm{d}V = 0 \qquad \text{if } A \text{ and } B \text{ not neighbors.} \tag{2.58}$$

The parameters α and β are chosen such that the resulting energies match experiments. From the above equations, it is clear that the Hamilton operator does not have

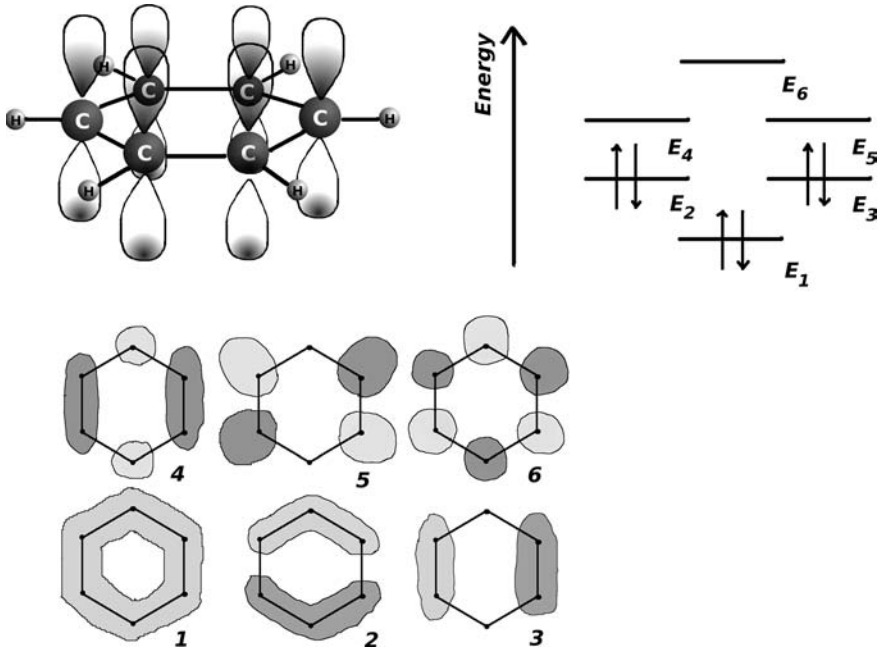

Figure 2.30 Visualization of p_π electrons (in the orbitals above and below the molecular plane) within the Hückel picture and resulting π-bond combinations using the benzene molecule (C_6H_6) as an example. There are six different combinations, corresponding to six different molecular orbitals. As for the simple systems, the higher the number of nodes (nodal planes), the higher is the energy of the system. Molecular orbitals 2 and 3, and also 4 and 5, have the same number of nodal planes (one and two, respectively) and have the same energies ($E_2 = E_3$ and $E_4 = E_5$).

to be specified, as the integrals are anyway never calculated and just the parameters are considered. Later, Roald Hoffmann, extended the Hückel method to include more than just π-electrons. This *extended Hückel method* was and still is extremely successful in elucidating reaction mechanisms in chemistry (e.g., the Woodward–-Hoffmann rules).

As already mentioned, there are several semiempirical methods that can be distinguished according to the integrals neglected and parameterized. We will not specify these approximations in detail. Instead, we mention two of the most commonly used semiempirical methods – the AM1 and the PM3 methods developed by Dewar and co-workers. Here, too, we are dealing with energy expectation values and a minimal basis. Minimal basis means that for most of the light atoms with which we are dealing, only *s* and *p* orbitals are included. From combinatorics, we can easily understand that different electron–electron interaction integrals have to be parameterized, depending on whether both electron are in *s* orbitals or in *p* orbitals, or each in different orbitals. It is also clear that these parameters differ for different atoms. All together, at least 12 parameters for each atom have to be considered.

The advantage of the semiempirical methods is that larger systems with up to a few thousand atoms can be calculated. As the parameters for the integrals are typically averaged or fitted to match known species, semiempirical methods provide good results for molecules or groups of similar molecules that have been considered during the fitting procedure. Known problems for all semiempirical methods are that weakly bound systems (e.g., including van der Waals interactions) are very poorly described. Further, molecules including metal atoms are not well described. Additionally, other more specific problems arise. We refer the interested reader to more specific literature here [10].

2.10 Force Field Methods

The last type of method that we introduce here is *not* a quantum chemical method. We neither have a Hamilton operator, nor a wavefunction, nor an electron density in these methods. Instead, the method is based on classical mechanics; therefore, it is often called *molecular mechanics* (MM) method. Simply speaking, within the *force field methods*, the atoms in a molecule are held together by bonds which are described by potentials V representing bending, stretching, torsion, and so on. Then, the total potential is minimized (mathematically, this is performed by calculating the derivative: in classical mechanics, the derivative of the potential is the force, hence the name of this method). With the force field method, equilibrium geometries and relative energies can be obtained. The absolute values of the energy obtained within the MM methods are meaningless; the most obvious reason is the neglect of kinetic energy. However, on comparing different possible arrangements of atoms in a molecule, the energy differences (the relative energies between the possible isomers) can be considered to find the one lowest in energy (the most stable one). Using force field methods, systems with more than 10 000 atoms (and therefore biologically relevant systems such as small proteins and enzymes) can be calculated.

In more detail, the total potential is given by the sum of different potentials, describing stretching, bending, out-of-plane bending, torsion, cross-terms, van der Waals interactions, and electrostatic interactions:

$$V_{\text{tot}} = V_{\text{stretch}} + V_{\text{bend}} + V_{\text{out-of-plane bend}} + V_{\text{torsion}} + V_{\text{cross}} + V_{\text{van der Waals}} + V_{\text{electrostatic}}. \tag{2.59}$$

The total potential gives the force field acting on the atoms. For all individual potentials, there are analytic expressions and parameterized values. Take as an example the stretching of a bond: the potential energy is described by a harmonic potential (parabola), $k \cdot (R - R_0)$ (see Section 2.2.3), As parameters, the equilibrium internuclear distance R_0 (where the potential energy is zero), and a constant k describing the strength of the bond (the inclination of the parabola) are fitted (see Figure 2.10).

Similar expressions and parameterizations can be found for all the other potentials. The basic idea here is that atoms in molecules often behave very similarly; considering the C−H bond as an example, we find values for the equilibrium bond length varying between 0.6 and 1.1 Å, and vibrational frequencies also in a similar range. Further diversifying into C−H bonds, where the carbon atom is bonded to three, two, or one more atoms, will yield even closer values for these subclasses. Therefore, atom "types" are classified (71 different atom types), representing atoms and their subclasses. For these atom types, the parameters used for the potentials describing a chemical bond are listed.

The information that we can obtain with the force field methods, in addition to the aforementioned equilibrium geometries and the relative energies, is very accurate values for the heat of formation, dipole moments, gas-phase entropies, and vibrational frequencies. It is clear that the results of the MM method are most accurate for common molecules where parameter sets are available.

As an extension to this section, we would like to mention that hybrid methods between molecular mechanical and quantum mechanical methods exist. These *QM/MM methods* are applied to chemical reactions, enzymes, solvent effects, and so on – or generally to larger systems, where one small part of the whole system is of special importance (such as the active center of an enzyme). QM/MM methods treat the large system with MM methods, whereas the small, important part is calculated with quantum mechanical methods. This partitioning allows for efficient treatment of such systems; the trick, however, is to couple these two methods efficiently.

References

1 Levine, I.N. (1999) *Quantum Chemistry*, Prentice Hall, Englewood Cliffs, NJ.

2 Atkins, P.W. and Friedman, R. (2004) *Molecular Quantum Mechanics*, 4th edn, Oxford University Press, Oxford.

3 Jensen, F. (2006) *Introduction to Computational Chemistry*, 2nd edn, John Wiley & Sons, Ltd., Chichester.

4 Koch, W. and Holthausen, M. (2002) *A Chemist's Guide to Density Functional Theory*, 2nd edn, Wiley-VCH, Weinheim.

5 Møller, C. and Plesset, M.S. (1934) Note on an approximation treatment for many-electron systems. *Phys. Rev.*, **46** (7), 618–622.

6 Hohenberg, P. and Kohn, W. (1964) Inhomogeneous electron gas. *Phys. Rev.*, **136** (3B), B864–B871.

7 Kohn, W. and Sham, L.J. (1965) Self-consistent equations including exchange and correlation effects. *Phys. Rev.*, **140**, A1133–A1138.

8 Becke, A.D. (1993) A new mixing of Hartree–Fock and local density-functional theories. *J. Chem. Phys.*, **98** (2), 1372–1377.

9 Runge, E. and Gross, E.K.U. (1984) Density-functional theory for time-dependent systems. *Phys. Rev. Lett.*, **52** (12), 997.

10 Segal, G.A. (1977) *Semiempirical Methods of Electronic Structure Calculation*, Plenum Publishing Corp., New York.

3
Light–Matter Interaction

Michael Schmitt, Thomas Mayerhöfer, and Jürgen Popp

3.1
Electrical Properties of Matter

Biophotonics deals with the interaction of light with biological systems such as cells, tissue which consist of molecules such as lipids, DNA, amino acids, and so on. This chapter aims to provide a basic description of the physical foundation of the manifold interplay (e.g., absorption, emission, scattering, reflection, diffraction, dispersion) between light and matter. Light can exhibit properties of both waves and particles, a phenomenon known as wave particle dualism. Here, the description of light as electromagnetic waves is mostly employed to describe light–matter interaction. Thus, electromagnetic radiation is a wave-like perturbation recurring periodically over a certain distance called the wavelength. Light waves are described as oscillating electric (E) and magnetic fields (B) being perpendicular to each other. Matter, for example molecules, consists of positively charged nuclei held together by negatively charged electrons. In a very simple theory, matter can be described as an aggregation of oscillating nucleus–electron dipoles. On an atomic scale, light–matter interactions are governed by the quantum mechanical nature of matter and light, but many are adequately explained by the interactions of classical electromagnetic radiation with charged particles, that is, nucleus–electron dipoles. That means that when an electric field is applied to matter it causes the charges to move. Thus the interaction of electromagnetic radiation with matter can polarize matter and induce molecular dipole moments. In other words, positive and negative charges are driven in opposite directions and the matter acquires a frequency-dependent electric polarization. Since the electric polarization of molecules induced by electromagnetic radiation (light) is one of the central quantities for understanding light–matter interactions, this chapter presents an introduction to the electric properties of matter.

Detailed descriptions of electromagnetism and the electric properties of matter can be found in [1–4].

Handbook of Biophotonics. Vol.1: Basics and Techniques, First Edition.
Edited by Jürgen Popp, Valery V. Tuchin, Arthur Chiou, and Stefan H. Heinemann.

3.1.1 Polar Molecules

To understand light–matter interactions, it is necessary to obtain a basic understanding of both the nature of light and the structure of matter. This section aims at presenting the reader with an introduction to the properties of matter that determine the way in which matter interacts with light.

Assuming that matter appears homogeneous to light (this supposes that any inhomogeneities, which are always present since there is always a scale in which matter is discontinuous, albeit on the scale of molecules and atoms, are much smaller than the wavelength of light; since the wavelength of light has not yet been introduced we will come back to this point at a later stage), the mode of interaction is determined by its properties on an atomic and molecular scale.

Assuming that matter is generally composed of molecules (as we are nearly exclusively interested in biological matter, this assumption is generally true), it is the structure and the atomic composition of these molecules, and also their mutual alignment, that are vital for further discussion. The most frequent atoms in organic matter are carbon, hydrogen, oxygen, and nitrogen. As described in Chapter 2, the different atoms share common electron pairs in molecules, which leads to chemical bonding between these atoms. If the atoms that share an electron pair are chemically identical, for example, two carbon atoms, the common electron pair is usually located between both atoms, on average symmetrically. This is no longer true if two chemically different atoms share an electron pair, for example, a carbon and an oxygen atom. In this particular example, the common electron pair is displaced towards the oxygen, meaning that the electrons have a higher sojourn probability close to the oxygen compared with the carbon. The oxygen is therefore said to have a higher electronegativity, a property that quantifies the attraction of the common electrons. Important for the following discussion is that because the common electron pair is on average closer to the oxygen than to the carbon, a dipole exists. Such a dipole is quantified by the size of the dipole moment, μ, which is given by the product of the charge difference Q and the distance l between the negative and the positive charges (see Figure 3.1):[1)]

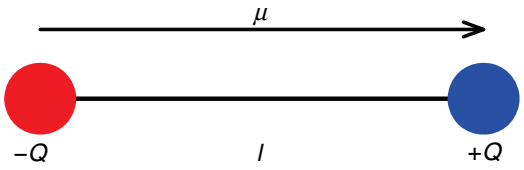

Figure 3.1 A dipole is characterized by two charges $+Q$ and $-Q$ at a distance l.

1) Note that μ and l are vector quantities. Keeping this in mind, vector notation is dropped from now on if not mentioned explicitly.

$$\mu = Q \cdot l. \tag{3.1}$$

A molecule with such a permanent dipole moment is also said to be a polar molecule. Molecules without a permanent dipole moment can nevertheless also adopt a (temporary) dipole moment if an electrical field interacts with them, since this field can either distort the electron distribution around the molecule or dislocate the cores of the atoms, or both. The dipole moment that is generated by the distortion or dislocation is called an induced dipole moment, μ_{ind}. For comparably small strengths of the electric field, this dipole moment is proportional to the electric field, E. The proportionality constant, α, is called the polarizability of the molecule:[2)]

$$\mu_{ind} = \alpha \cdot E. \tag{3.2}$$

By its nature μ_{ind} is a microscopic quantity. The corresponding macroscopic quantity is the so-called polarization, P, which is the average electrical dipole moment per unit volume of a sample or material (the "density of the dipole moments").

3.1.2 Induced Dipole moments by External Electrical Fields

To obtain a more elaborate understanding of the polarization and the macroscopic situation, it is instructive to discuss the properties of a plate capacitor. A plate capacitor consists of two metallic plates with a surface area A and a distance between them d, which have a different potential U by feeding a voltage. As a consequence, an electrical field E results given by (Figure 3.2)

$$E = \frac{U}{d}. \tag{3.3}$$

One of the plates is depleted of electrons and carries a positive charge Q, whereas the other plate is enriched with electrons and carries a negative charge $-Q$. If we divide the charge Q by the area of the plates, we obtain the electric surface density $\sigma = Q/A$, which we also obtain by definition if we multiply the electric field by the permittivity of vacuum, ε_0:

$$\sigma = \frac{Q}{A} = \varepsilon_0 \cdot E. \tag{3.4}$$

Another characteristic property of a plate capacitor is its capacity, C:

$$C = \frac{Q}{U}. \tag{3.5}$$

If matter is placed between the plates, the electric fields acts on it and induces dipole moments. The capacity depends on the material in the volume which is enclosed by the plates (see Figure 3.3). The dipole moments introduce surface

2) Note that α represents a third-rank tensor. Keeping this in mind, tensor notation is dropped from now on if not mentioned explicitly.

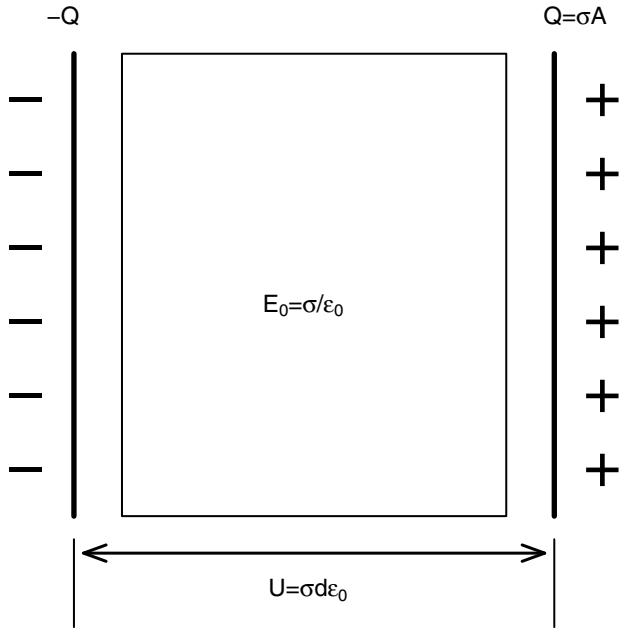

Figure 3.2 Plate capacitor.

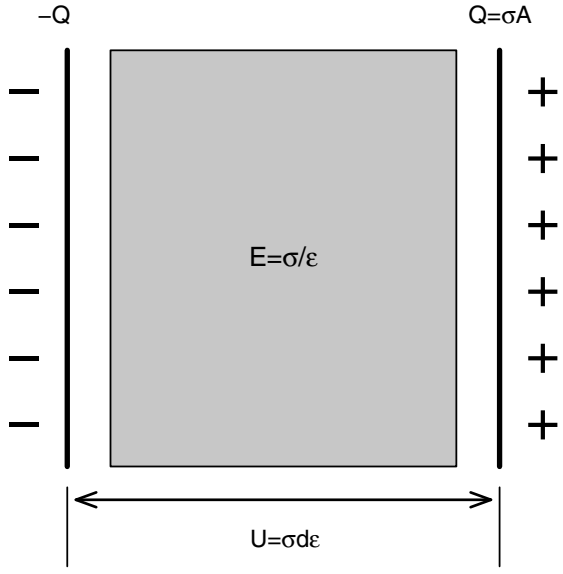

Figure 3.3 Plate capacitor filled with a material characterized by a dielectric constant ε.

charges which partly compensate the charges on the plates. If the voltage is kept constant, the charge Q and with it the surface density σ increase. From Equation 3.5, it follows that C increases.

The ratio between the capacity of an empty capacitor, C_V, and the capacity with a material between the plates, C_M, defines a new quantity called the relative dielectric constant, ε_r:

$$\frac{C_M}{C_V} = \frac{\varepsilon}{\varepsilon_0} = \varepsilon_r \tag{3.6}$$

which, when multiplied by the permittivity of vacuum, ε_0, gives the dielectric constant ε, both being macroscopic properties of a material.

How can these results be explained and what is happening on a microscopic scale? The material that is brought into the capacitor consists of atoms and molecules or molecular entities. The electric field within the capacitor exerts forces on the molecules, which on the one hand try to orient dipoles if a permanent dipole moment is present and/or on the other hand induce dipoles within the material parallel to field lines. Whereas in the volume of the material the charges neutralize each other since positive and negative charges are adjacent to each other (Figure 3.4), the surface of the material neighboring the negatively charged plate is positively charged and vice versa, leading to partial neutralization of the charges on the plates. If the capacitor is not separated from the voltage source, the source consequently increases the charge of the plates compensating the surface charge of the material inserted into the capacitor. The relation between the polarization P and the electric field E depending on the relative dielectric constant is found to be

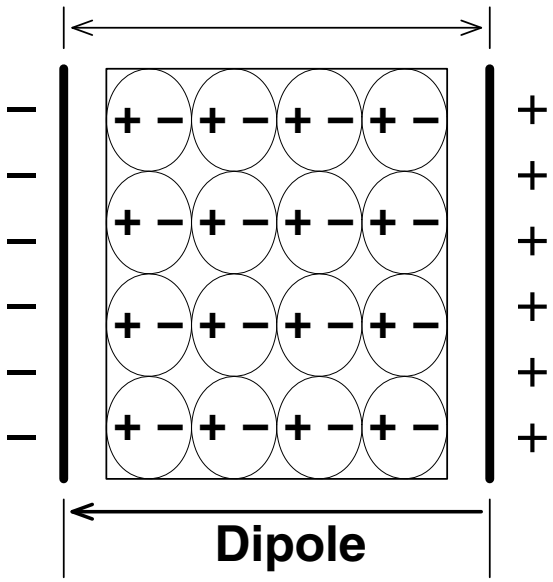

Figure 3.4 Plate capacitor filled with a material: microscopic picture.

$$P = \underbrace{(\varepsilon_r - 1)}_{\chi_{el}} \varepsilon_0 E \tag{3.7}$$

where the quantity χ_{el} is referred to as the electric susceptibility, which can be seen as the receptivity of the electric field strength of the particular material of interest. By employing P and E a new field quantity D can be defined, which is given by

$$D = \varepsilon_0 E + P = \varepsilon_0 \varepsilon_r E = \varepsilon E. \tag{3.8}$$

D is called the electric flux density and, in contrast to E, is not defined by the potential drop over distance, but by the charge per unit surface area.

Anisotropic Materials

For anisotropic materials (anisotropy: dependence of the properties on direction), χ_{el} becomes a so-called tensor (a 3×3 matrix) χ_{el}. This is due to the fact that both P and E are vector quantities, $\vec{P} = \chi_{el}\varepsilon_0 \vec{E}$, and the direction of $\vec{P}$ is only in isotropic materials always parallel to the field $\vec{E}$, which induces the polarization, whereas in case of anisotropy, χ_{el} accounts for both a change of length and a change of direction. In anisotropic materials, also the direction of the electric field $\vec{E}$ and the electric flux density $\vec{D}$ differ in general. Consequently, the dielectric constant also becomes a tensor.

3.2 Classical Dispersion Theory

It is well known that the interaction of light[3)] with matter depends strongly on the frequency (i.e., color) of light. Hence the general form of the polarization and with it the dielectric constant depend on the frequency of the applied electric field. In other words, the dielectric constant is constant only for a given frequency. Otherwise, the dielectric constant is transformed into a dielectric function, which reflects the fact that at certain frequencies matter is more strongly polarized than at others. The overall trend is that matter is more strongly polarized at lower frequencies than for higher frequencies as there are several mechanisms which introduce polarization in matter. Some of these, such as the displacement of atoms, need more time than the displacement of the relatively light electrons. However, there exist certain frequencies, called eigenfrequencies, at which the polarization can be extraordinarily large. These results can be understood to a first approximation by applying a comparably simple model, where we assume that an applied electric field displaces charges, for example, the electrons from the

3) Note that light refers to electromagnetic radiation of any frequency (or wavelength), whether visible or not.

nucleus of an atom, and there exists a restoring force, which is the attracting force between two opposite charges. A modification of the model, where we introduce a third force, which is proportional to the speed of the electron and leads to damping, allows us to describe quantitatively the variation of the dielectric constant with frequency, which is very important to understand the frequency (i.e., color) dependence of light–matter interactions discussed in the following sections.

More complex models for the dielectric function can be found in [2–4].

Employing the plate capacitor from Section 3.1.2, we could also apply an alternating voltage instead of direct voltage (in fact, we did not make any statement about that in Section 3.1.2). Would that leave the response of a medium inside the capacitor, that is, the polarization of the material, unchanged or would we detect differences that probably could depend on the number of voltage direction changes per unit time (i.e., the frequency)? Indeed, the response of the medium to an electric field applied to it depends critically on the frequency if it is an alternating field. This phenomenon is called dispersion.

What happens on the microscopic level if the voltage and therefore the electric field change their direction? Since the permanent dipoles orient themselves according to the applied electric field of the plate-type capacitor, they have to reorient with every directional change of the field. One can easily imagine that such a reorientation is not instantaneous, but takes some time to be completed. In fact, there exists an upper limit of frequency above which it is no longer possible for the dipoles to follow the electric field changes. Therefore, the orientation of permanent dipoles no longer takes place and adds to the polarization. This frequency limit depends on the material. Usually, a rotation happens within picoseconds. Therefore, the frequency limit usually lies within the microwave region, that is, around 10^{11} Hz.

As already mentioned, there are two kinds of induced polarizations; one is due to dislocations of the cores (distortion polarization), whereas the other is caused by distortions of the electron shell (electronic polarization). It is easy to imagine that the much heavier cores are more inert compared with the lightweight electrons. As a consequence, the electrons are able to follow the electric field changes up to much higher frequencies than the cores. In fact, distortion polarization is no longer able to contribute beyond the infrared (IR) region (10^{14} Hz), whereas the electronic polarization usually ceases to exist somewhere in the ultraviolet (UV) region, well above 10^{15} Hz. (see Figure 3.5).

In the following, these findings will be quantified by assuming a comparably simple atomic picture known as Lorentz atom (see Figure 3.6).

The atomic core is

- positively charged
- non-mobile (heavy, fixed within the crystal lattice)
- with the center of charge at $x = 0$.

For the electrons the following assumptions are made:

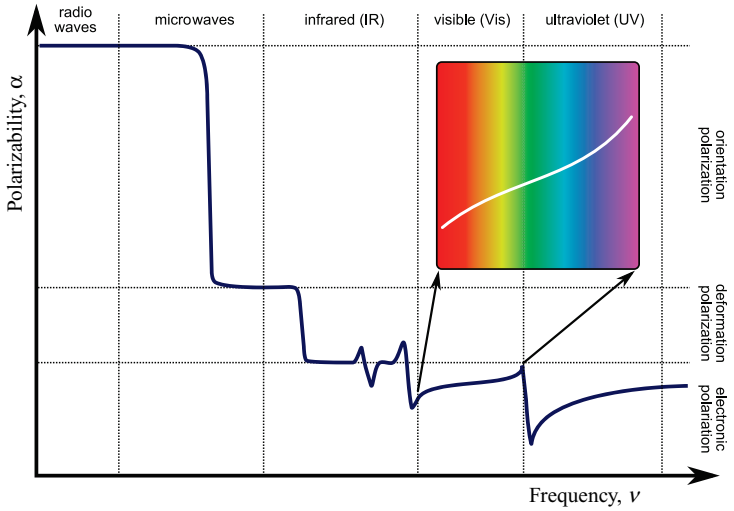

Figure 3.5 Changes of the polarizability α with frequency (adapted from [1]).

- lightweight (mass = m_e)
- elastically bound by a massless spring with spring constant k
- equilibrium position x_{eq} at $x = 0$
- carrying out a damped movement, that is, after removing the force, which led to the acceleration of the electrons (i.e., the electric field), with the movement decreasing and finally ending.

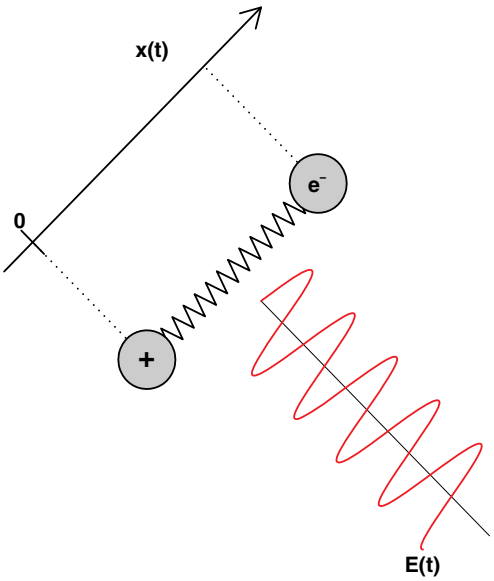

Figure 3.6 Illustration of the Lorentz atom.

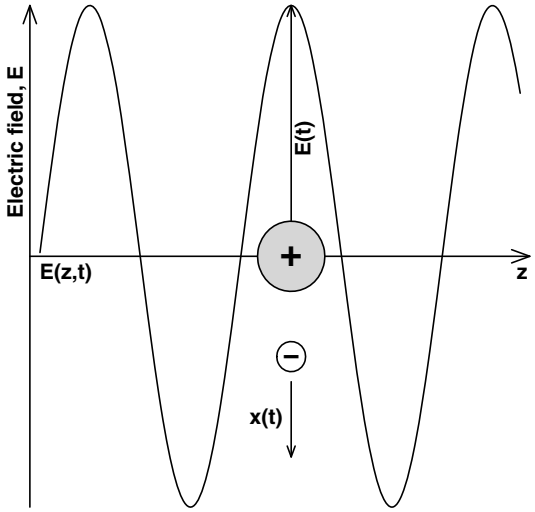

Figure 3.7 An oscillating electric field $E(t)$ induces an oscillating dipole.

Without an applied field, the centers of the negative and the positive charges coincide. Therefore, the dipole moment is zero. If a field constant in time is applied, the electrons are displaced relative to their position in the absence of an external field. As a consequence, the centers of the positive and negative charges no longer coincide and a static dipole moment is induced.

If we now assume that a time-dependent electric field $E(t) = E_0 \cos(2\pi\nu t)$ interacts with the atom, where ν is the frequency[4)] and t the time, then the electron starts to oscillate with frequency ν around its equilibrium position ($x = 0$), that is, the position of the electron becomes time dependent: $x(t) = x_0 \cos(2\pi\nu t)$. As a consequence, an oscillating dipole $\mu(t) = -e \cdot x(t)$ results, where e is the charge of the electron (see Figure 3.7). However, an oscillating dipole corresponds to an accelerated charge and therefore an electromagnetic wave will be emitted.

The forces acting on an electron are due to

- the electric field $E(t) = E_0 \cos(2\pi\nu t)$, which drives the electron away from its equilibrium position by a force $F_E = -e \cdot E(t)$ (driving force)
- the "spring," which tries to push the electron back to its equilibrium position with a force that is proportional to the deflection $x(t)$ from the equilibrium position ($x = 0$): $F_x = -k \cdot x(t)$ (restoring force).

According to Newton's second law, the sum of all forces acting on a body (in this case the electron) is equal to the body's mass m multiplied by its acceleration a, which is the second derivative of the position [in this case the displacement from the equilibrium position $x(t)$] with respect to time t: $a = d^2x(t)/dt^2$. If we put this together, it results in the following equation of motion:

4) Very often instead of the frequency ν the angular frequency $\omega = 2\pi\nu$ is used.

$$m_e \frac{d^2x(t)}{dt^2} = F_E(t) + F_x(t) = -e \cdot E(t) - k \cdot x(t) \tag{3.9}$$

where m_e represents the electron mass. In this equation, both the function $x(t)$and one of its derivatives (in this case the second derivative) is present. We write Equation 3.9 in the following form, where we have divided the left- and right-hand sides by m_e and where all terms containing $x(t)$ are on the left-hand side:

$$\frac{d^2x(t)}{dt^2} + \frac{k}{m_e} \cdot x(t) = -\frac{e}{m_e} \cdot E(t). \tag{3.10}$$

Before solving Equation 3.10 it is instructive to solve the somewhat simpler problem of the vibration of the electron without being forced by the external electric field $E(t)$. In this particular case Equation 3.10 reduces to the simplest possible form:

$$\frac{d^2x(t)}{dt^2} + \frac{k}{m_e} \cdot x(t) = 0. \tag{3.11}$$

What does the solution for $x(t)$ looks like? We see from Equation 3.11 that the sum of the function $x(t)$ multiplied by k/m_e and its second derivative must be zero. Consequently, $x(t)$ and its second derivative differ only in a constant $\omega_0^2 = k/m_e$ such that

$$\frac{d^2x(t)}{dt^2} = -\omega_0^2 \cdot x(t). \tag{3.12}$$

This equation is fulfilled if $x(t)$ equals, for example, $x_0 \sin(\omega_0 t)$, since $d\sin(\omega_0 t)/dt = \omega_0 \cos(\omega_0 t)$ and $d^2\sin(\omega_0 t)/dt^2 = -\omega_0^2 \sin(\omega_0 t)$. Therefore, without external force, the electron carries out vibrations with angular frequency ω_0, which is called its eigenfrequency. The eigenfrequency depends only on the spring constant k, which is a measure of the bond strength and consequently depends on the material, and the electron mass m_e. From this result, we can already suspect that the interaction of the electron with an external field is especially strong if this external field varies also with ω_0. This brings us back to Equation 3.10. Mathematically, Equation 3.10 is an inhomogeneous differential equation, in contrast to Equation 3.11, which is the related homogeneous differential equation. To solve Equation 3.10, we assume that the inhomogeneous differential equation has also a solution of the form $x(t) = x_0 \cos(\omega t)$, like its homogeneous counterpart. Setting $x(t) = x_0 \cos(\omega t)$ in Equation 3.10, we obtain

$$-\omega^2 \cdot x_0 \cos(\omega t) + \frac{k}{m_e} x_0 \cos(\omega t) = \frac{-e}{m_e} \cdot E_0 \cos(\omega t) \tag{3.13}$$

and after dividing by $\cos(\omega t)$ and solving for x_0 we have

$$x_0 = \frac{-e \cdot E_0}{\left(\frac{k}{m_e} - \omega^2\right) m_e}. \tag{3.14}$$

Using ${\omega_0}^2 = k/m_e$, we finally obtain

$$x_0 = \frac{-e \cdot E_0}{\left(\omega_0^2 - \omega^2\right) m_e} \tag{3.15}$$

After some consideration, it can be recognized that Equation 3.15 must be an unphysical result since the displacement $x(t)$ becomes infinite if the frequency ω of the external field approaches the eigenfrequency ω_0 of the electron. This is a consequence of having neglected damping of the vibration of the electron. For damping, we assume an additional force F_{damp}, which is proportional to the velocity of the electron $\mathrm{d}x(t)/\mathrm{d}t$ with a proportionality constant $-\Gamma$, so that $F_{\text{damp}} = -\Gamma \cdot \mathrm{d}x(t)/\mathrm{d}t$. Accordingly, the equation of motion Equation 3.10 becomes

$$\frac{\mathrm{d}^2x(t)}{\mathrm{d}t^2} + \frac{\Gamma}{m_e} \cdot \frac{\mathrm{d}x(t)}{\mathrm{d}t} + \frac{k}{m_e} \cdot x(t) = -\frac{e}{m_e} \cdot E(t). \tag{3.16}$$

We are now looking for a function $x(t)$ which differs from its first and second derivative only by a constant factor. This excludes sine and cosine functions and we have to rely on an exponential function of the form $x(t) = x_0 \exp(i\omega t)$, where i is the imaginary unit with $i^2 = -1$.[5)]

Setting $x(t) = x_0 \cdot \exp(i\omega t)$ in Equation 3.16, we obtain

$$-\omega^2 \cdot x_0 \exp(i\omega t) + \frac{\Gamma}{m_e}\omega \cdot i \cdot x_0 \exp(i\omega t) + \frac{k}{m_e} \cdot x_0 \exp(i\omega t) = -\frac{e \cdot E_0 \cdot \exp(i\omega t)}{m_e}. \tag{3.17}$$

Setting $\Gamma/m_e = \gamma$ and recapitulating that $k/m_e = {\omega_0}^2$, we obtain after some algebraic manipulation the solution

$$x_0 = -\frac{e}{m_e} \frac{1}{\omega_0^2 - \omega^2 + i\gamma\omega} E_0. \tag{3.18}$$

Through the forced oscillation of the electron with charge $Q = -e$, a microscopic dipole moment is induced. The macroscopic polarization, which is the sum of the induced dipole moments per unit volume, is then given by the product of electron charge, microscopic deflection, and the number of oscillators per unit volume N:

$$P(t) = -e \cdot x(t) \cdot N = \frac{Ne^2}{m_e} \frac{1}{\omega_0^2 - \omega^2 + i\gamma\omega} E(t). \tag{3.19}$$

If we compare this result with Equation 3.7, we find that

$$(\varepsilon_r - 1)\varepsilon_0 = \frac{Ne^2}{m_e} \frac{1}{\omega_0^2 - \omega^2 + i\gamma\omega} \tag{3.20}$$

and consequently

5) The function $x(t) = x_0 \exp(i\omega t)$ is also a potential solution of Equation 3.12, which is a consequence of Euler's equation $\exp(i\omega t) = \cos(\omega t) + i\sin(\omega t)$ and the fact that any linear combination of solutions of a differential equation again generates a solution to this equation. The exponential function is often preferred, especially because multiplication and division are very easily carried out. Therefore, time-dependent electric fields $E(t) = E_0 \cos(2\pi\nu t)$ are also often written as an exponential function: $E(t) = E_0 \exp(i \cdot 2\pi\nu t)$. One has to keep in mind, however, that the real electric field is then represented by the real part $\mathrm{Re}[E(t) = E_0 \exp(i \cdot 2\pi\nu t)] = E_0 \cos(2\pi\nu t)$.

$$\varepsilon_r(\omega) = 1 + \frac{Ne^2}{\varepsilon_0 m_e} \frac{1}{\omega_0^2 - \omega^2 + i\gamma\omega}. \tag{3.21}$$

The obvious conclusion is that the relative dielectric constant depends on the frequency and should henceforth better be called dielectric function. According to Equation 3.21, the dielectric function $\varepsilon_r(\omega)$ consists of a real part $\varepsilon_{r,1}(\omega)$ and an imaginary part $\varepsilon_{r,2}(\omega)$: $\varepsilon_r(\omega) = \varepsilon_{r,1}(\omega) + i \cdot \varepsilon_{r,2}(\omega)$. If we separate these two parts in Equation 3.21, we obtain

$$\begin{aligned} \varepsilon_{r,1}(\omega) &= 1 + \frac{Ne^2}{\varepsilon_0 m_e} \frac{\omega_0^2 - \omega^2}{\left(\omega_0^2 - \omega^2\right)^2 + \gamma^2\omega^2} \\ \varepsilon_{r,2}(\omega) &= \frac{Ne^2}{\varepsilon_0 m_e} \frac{-\gamma\omega}{\left(\omega_0^2 - \omega^2\right)^2 + \gamma^2\omega^2}. \end{aligned} \tag{3.22}$$

The resulting functions are displayed in Figure 3.8. $\varepsilon_{r,1}$ is unity at frequencies high compared with the eigenfrequency ω_0, which was set to $1600\,\mathrm{cm}^{-1}$ ($\tilde{\nu} = 1/\lambda = \nu = \omega/2\pi\omega$, where $\tilde{\nu}$ is the wavenumber, λ the wavelength, ν the frequency, and ω the angular frequency), then decreases until it reaches a minimum close to the eigenfrequency before it increases steeply. After a maximum it reaches

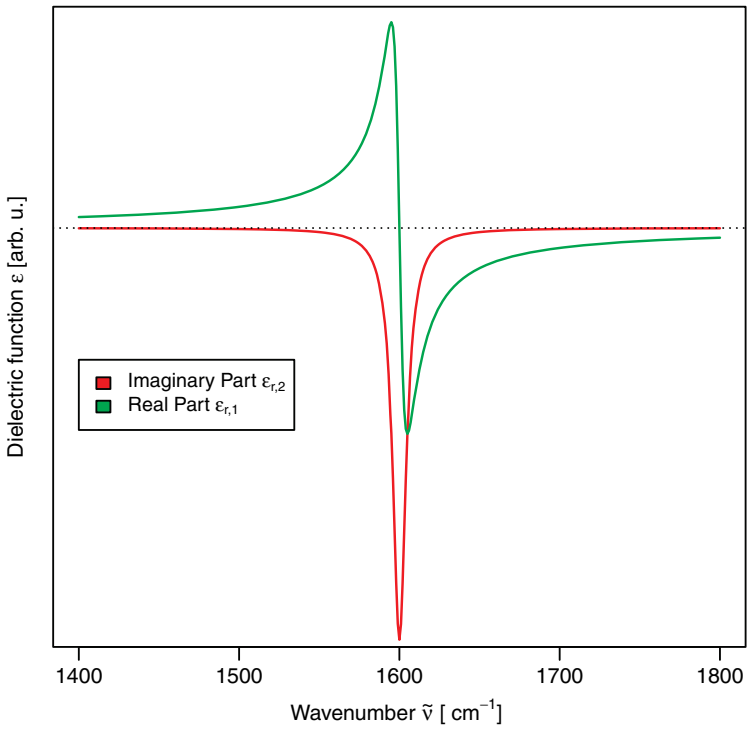

Figure 3.8 Dependence of the real $\varepsilon_{r,1}$ and the imaginary part $\varepsilon_{r,2}$ of the dielectric function for $\omega_0 = 1600\,\mathrm{cm}^{-1}$ and $\gamma = 10$.

a nearly constant value for low frequencies, which is higher than its nearly constant value at high frequencies. $\varepsilon_{r,2}$, on the other hand, is close to zero for frequencies well below and above the eigenfrequency, at which it reaches its maximum. This frequency dependence of the dielectric function will be very important for understanding or explaining the different light–matter interaction phenomena such as absorption (see Section 3.4) and its dependence on the light frequency, that is, color.

3.3
Electromagnetic Waves in Matter

In the preceding section, it has been shown that the interaction of electromagnetic radiation with matter can polarize matter and induce on an atomic scale a dipole moment or a macroscopic polarization in the molecular ensemble. Furthermore, we have seen that the general form of the polarization depends on the frequency of the applied field: radiofrequency radiation (10 GHz) leads to an alignment of polar molecules according to the external electric field, that is, a reorientation of the complete molecules (orientation polarization) takes place. The same is true for the electrons, which can follow the changing electric field much more easily due to their low mass. However, higher frequencies lead to a distortion polarization of the electrons (induced electric dipole moment), since molecules exhibiting a permanent dipole cannot follow such rapidly oscillating fields any longer. The induced dipole moment oscillates with the same frequency as the exciting oscillating electric field. Since the oscillating induced dipole moment is nothing else than an oscillating charge, matter radiates light of the same frequency. This is in total analogy with a Hertzian dipole acting as a broadcasting and receiving antenna which is based on the radiation of electromagnetic waves from a dipole. In an antenna, electrons are driven by a generator to the top or the bottom, respectively. This generates a charge distribution similar to a dipole.

Hence the interplay of molecules with light, in particular with visible light which polarizes molecules, leads to the emission of a secondary radiation of the same frequency as the polarizing field. This section aims to describe the physical foundation of the generation of this secondary radiation, that is, how the induced polarization acts as a source of the radiation of a secondary electromagnetic field. In doing so, a set of equations known as Maxwell's equations are needed. These equations relate the electric and magnetic fields that constitute electromagnetic waves. Here we examine how Maxwell's equations describe the generation of this secondary radiation. This approach results in so-called wave equations, which, when solved, lead to sinusoidal functions containing the frequency and the wavelength as variables and providing the amplitude of the electromagnetic waves.

The major difference between waves in vacuum and waves in matter is that the speed in matter is reduced by a factor n, which is called the refractive index, and is usually given by the square root of the dielectric function. As the dielectric

function is dependent on frequency, the same is valid for the refractive index. The frequency dependence of the refractive index is the basis to describe quantitatively the absorption of light, as will be shown in the next section.

For the less mathematically inclined reader, this section can be skipped. Interested readers are referred to [2, 3].

The aim of this section is the calculation of the electromagnetic wave which is caused by the oscillating electric dipole density $\vec{P}$ distributed in matter. In the following we have to introduce the fields in vector form. In a field, at least in the case of such fields as we are interested in, each position in space is assigned a vector. For example, in case of the electric field $\vec{E}$ is explained by the force that acts on a charge. The amount of the vector is proportional to the magnitude of the force and its direction is oriented parallel to that of the force. Since we are dealing with a three-dimensional space, each vector can be split into its x, y, and z components; for example, in the case of $\vec{E}$ these are E_x, E_y, and,E_z each being a scalar quantity. Therefore, the calculation with vectors can be easily traced back to calculations with scalars, except that we have to carry out three calculations per vector. In the following we give the equations for both the component and the short vector form.

Since electromagnetic radiation (light) consists of electric and magnetic fields, oriented perpendicular to each other, we also have to introduce the magnetic field $\vec{B}$ (historically referred to as magnetic induction). However, since the force induced by the magnetic field of an electromagnetic wave on charged particles is much smaller than that induced by the electric field, it can be neglected for most light–matter interaction phenomena. This means that we will not explain $\vec{B}$ in detail, since it will be eliminated from the equations below and will not be of importance for the majority of light–matter interaction phenomena treated within this book.[6)]

The starting point of this calculation is the Maxwell equations in differential form. The physical meaning of these equations will also be explained in detail:

1) The source of the electric flux density is charges (the field lines begin at positive and end at negative charges). These charges, which are represented by the charge density $\rho = Q/V$, where V is a unit volume, cause the existence of the electric flux density and the electric field, the latter being the origin of the force that acts on other charges.

$$\vec{\nabla} \cdot \vec{D} = \frac{\partial D_x}{\partial x} + \frac{\partial D_y}{\partial y} + \frac{\partial D_z}{\partial z} = \rho. \tag{3.23}$$

2) Unlike with electric fields, there are no sources of the magnetic field (a magnetic monopole, the magnetic equivalent of a charge, has not been observed so far; if a magnet is separated between its south and north poles, two magnets, each with its own south and north poles, result). Also, unlike electric fields, magnetic field

6) However, the magnetic field component is of importance for the interaction of polarized light with chiral molecules such as proteins and amino acids, which will be treated in Section 3.10.

lines are closed loops without beginning or end.

$$\vec{\nabla} \cdot \vec{B} = \frac{\partial B_x}{\partial x} + \frac{\partial B_y}{\partial y} + \frac{\partial B_z}{\partial z} = 0. \tag{3.24}$$

3) **Law of induction:** Every change of the magnetic induction in time leads to a response and a related change in the shape of the electric field. In particular, the electric field tends to oppose the changes of the magnetic field.

$$\begin{aligned}
\left(\frac{\partial E_z}{\partial y} - \frac{\partial E_y}{\partial z}\right) &= -\frac{\partial B_x}{\partial t} \\
\left(\frac{\partial E_x}{\partial z} - \frac{\partial E_z}{\partial x}\right) &= -\frac{\partial B_y}{\partial t} \\
\left(\frac{\partial E_y}{\partial x} - \frac{\partial E_x}{\partial y}\right) &= -\frac{\partial B_z}{\partial t} \\
\vec{\nabla} \times \vec{E} &= -\frac{\partial \vec{B}}{\partial t}.
\end{aligned} \tag{3.25}$$

4) Magnetic fields can be generated in two ways, either by an electrical current or by a changing electromagnetic field. If we assume that there are no free charges moving inside the medium, the following equation results:

$$\begin{aligned}
&\left(\frac{\partial B_z}{\partial y} - \frac{\partial B_y}{\partial z}\right) = \mu_0 \frac{\partial D_x}{\partial t}, \left(\frac{\partial B_x}{\partial z} - \frac{\partial B_z}{\partial x}\right) = \mu_0 \frac{\partial D_y}{\partial t}, \left(\frac{\partial B_y}{\partial x} - \frac{\partial B_x}{\partial y}\right) = \mu_0 \frac{\partial D_z}{\partial t} \\
&\vec{\nabla} \times \vec{B} = \mu_0 \frac{\partial \vec{D}}{\partial t}
\end{aligned} \tag{3.26}$$

where μ_0 represents the permeability of free space and is therefore the magnetic counterpart of ε_0.

Together with the so-called constitutive relations or material equations, one of which we already know (Equation 3.8), and the second, which is already implicitly contained in Equation 3.26, the Maxwell relations establish a system of equations the solution of which eventually leads to the concept of electromagnetic waves. To derive the wave equation, we differentiate first the left- and the right-hand side of Equation 3.26 with respect to time

$$\vec{\nabla} \times \frac{\partial \vec{B}}{\partial t} = \mu_0 \frac{\partial^2 \vec{D}}{\partial t^2} \tag{3.27}$$

and subsequently employ Equation 3.25 to replace $\partial\vec{B}/\partial t$. This yields

$$-\vec{\nabla}\times\vec{\nabla}\times\vec{E}=\mu_0\frac{\partial^2\vec{D}}{\partial t^2} \tag{3.28}$$

in which we replace $\vec{D}$ by using Equation 3.8[7)]

$$\begin{aligned}&\frac{\partial^2 E}{\partial x^2}+\frac{\partial^2 E}{\partial y^2}+\frac{\partial^2 E}{\partial z^2}-\varepsilon_r\varepsilon_0\mu_0\frac{\partial^2 E}{\partial t^2}=0\\&\Delta\vec{E}-\varepsilon_r\varepsilon_0\mu_0\frac{\partial^2\vec{E}}{\partial t^2}=0.\end{aligned} \tag{3.29}$$

For one dimension (e.g., the electric field travels along the z-direction and, additionally, has only a component in the x-direction), Equation 3.29 reduces to

$$\frac{\partial^2 E_x}{\partial z^2}-\varepsilon_r\,\varepsilon_0\mu_0\frac{\partial^2 E_x}{\partial t^2}=0. \tag{3.30}$$

Equations which link the second derivative of a quantity with respect to position with the second derivative of the same quantity with respect to time are called wave equations, since their solutions have wave character. A wave equation for a wave traveling in the z-direction with only an x-component is usually of the form

$$\frac{\partial^2 E_x}{\partial z^2}-\frac{1}{\upsilon^2}\frac{\partial^2 E_x}{\partial t^2}=0 \tag{3.31}$$

where υ represents the speed of the wave (the phase velocity) inside the medium. Therefore, we find that the velocity υ of an electromagnetic wave inside a medium is generally given by

$$\upsilon=\frac{1}{\sqrt{\varepsilon_r\varepsilon_0\mu_0}}=c\frac{1}{\sqrt{\varepsilon_r}} \tag{3.32}$$

since, if we had made the same derivatization for a wave in vacuum (no free charges, therefore $\vec{\nabla}\cdot\vec{D}=0$), we would have found that $\upsilon=1/\sqrt{\varepsilon_0\mu_0}=c$, where c is consequently the speed of light in vacuum. Therefore, the influence of the medium and its polarization is to decrease the velocity of the wave by a factor $\sqrt{\varepsilon_r}$, which, as we will see later, corresponds to the refractive index n inside the medium.

The simplest solution of the wave equation (Equation 3.29) is the plane wave given by

$$\vec{E}(\vec{r},t)=\vec{E}_0\cos(\omega t-\vec{k}\cdot\vec{r}+\varphi). \tag{3.33}$$

This plane wave, the form of which is depicted in Figure 3.9, moves in the direction of the wavevector $\vec{k}$; φ represents the phase of the wave and is employed to adapt the plane wave to certain initial or boundary conditions. If we feed Equation 3.33 into Equation 3.30, assuming thereby that the wave travels in the z-direction ($\vec{k}$ has

7) Here, also the identity: $\vec{\nabla}\times\vec{\nabla}\times\vec{E}=\vec{\nabla}\cdot(\vec{\nabla}\cdot\vec{E})-(\vec{\nabla}\cdot\vec{\nabla})\vec{E}$ with $\vec{\nabla}\cdot\vec{E}=0$ (for nonconducting matter where ρ vanishes) and $\vec{\nabla}\cdot\vec{\nabla}=\Delta=\partial^2/\partial x^2+\partial^2/\partial y^2+\partial^2/\partial z^2$ has been used.

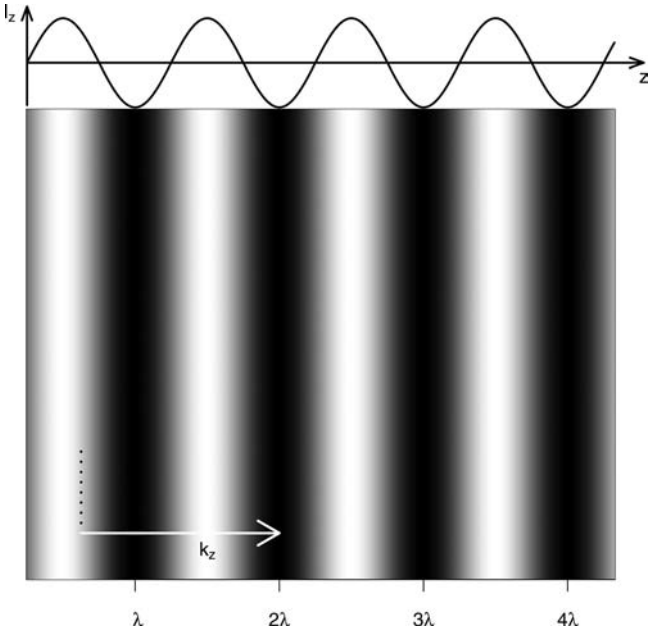

Figure 3.9 Plane wave traveling along $\vec{k}$.

a component only in the z-direction and is therefore given by $\vec{k} = (0, 0, k_z)^T$ and, additionally, that the electric field has a component only in the x-direction, that is, $E_0 = E_{0,x}$. Therefore, $E_x(z,t) = E_{0,x} \cdot \cos(\omega t - k_z \cdot z + \varphi)$ and

$$\begin{aligned} &\frac{\partial^2 E_x(z,t)}{\partial z^2} - \varepsilon_r \varepsilon_0 \mu_0 \frac{\partial^2 E_x(z,t)}{\partial t^2} = 0 \\ &-k_z^2 E_x(z,t) + \varepsilon_r \varepsilon_0 \mu_0 E_x(z,t) \omega^2 = 0 \\ &k_z^2 = \varepsilon_r \frac{\omega^2}{c^2} = n^2 \frac{\omega^2}{c^2} \\ &k_z = n \frac{\omega}{c} \end{aligned} \tag{3.34}$$

which is the dispersion relation for light inside matter with n being the refractive index. In Figure 3.9, the distance between two maxima or minima is the wavelength λ. Considering that the angular frequency $\omega = 2\pi \cdot \nu = 2\pi c/\lambda$, one obtains for the relation between wavevector and wavelength the following equation:

$$k_z = n \frac{2\pi}{\lambda}. \tag{3.35}$$

Since the refractive index is a dimensionless quantity and the dimension of the wavelength is length, the dimension of the wavevector is that of an inverse length, for

example, the number of maxima of the wave per unit length. Traditionally, one "counts" the number of maxima per centimeter, leading to the dimension cm^{-1} for the wavevector, which is especially popular among vibrational spectroscopists (also called wavenumber if the directional property is less important for the problem at hand). For deriving the relations above, we have implicitly also assumed that the medium of interest is microscopically and macroscopically isotropic, meaning that for light traveling through the medium in an arbitrary direction ε_r always remains the same. If this is not the case, ε_r becomes a tensor, as already mentioned in Section 3.1.2. In anisotropic materials, the dispersion relations become much more complex and generally two different refractive indices exist, depending on the direction of the light wave and its polarization. This important term will be explained in Section 3.5.3. The next section focuses on the very important quantity refractive index and its significance for the description of light absorption.

3.4 Absorption of Light

The simplest form of microscopy, bright field microscopy, relies on white light absorption changes of the microscopic sample. White light is composed of various wavelengths. If we see them separately, they appear as colors, and each color has a different wavelength. Substances appear colored because they absorb (i.e., filter out) some wavelengths and reflect or transmit others out of the broad white light spectrum. A very prominent example commonly used in histology where white light absorption changes are utilized for medical diagnosis is H&E (hematoxylin and eosin) staining. The following image displays such an H&E image of a breast cancer tissue section:

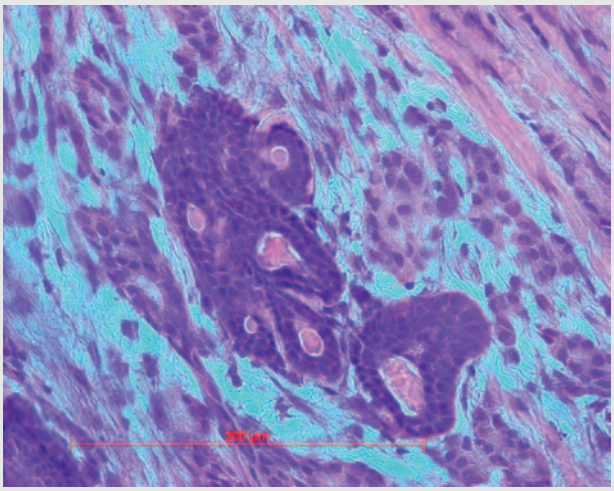

Here, the blue dye hematoxylin is applied to color basophilic structures, which are usually the ones containing nucleic acids, such as the cell nucleus, whereas eosin is used to color eosinophilic structures, which are generally composed of intracellular or extracellular protein, bright pink.

Thus, absorption of electromagnetic radiation is the way in which the energy of electromagnetic radiation is taken up by matter. This section combines all the topics treated in the preceding sections to characterize the very important phenomena of light absorption.

In the preceding sections, it has been shown that light traveling through matter induces oscillating dipoles. These vibrations of the electrons against the core or vibrations of one atom against another are usually damped, as we learnt in Section 3.2, which means on the one hand that vibrations forced by radiation at an eigenfrequency finally end when the excitation is removed, and on the other hand that the amplitude will not reach infinite values. The reason for the damping is energy dissipation, which means that the exciting radiation looses intensity while traveling through the medium, that is, absorption takes place. In addition to scattering, which will be discussed later, absorption is one reason for a medium not to be transparent. The damping manifests itself in the dielectric function by an additional imaginary part. Due to the relation between dielectric function and refractive index function through the wave equation, the refractive index also becomes a complex property where the imaginary part is responsible for the absorption of light. At the same time, the wavenumber of the wave, which is linearly dependent on the refractive index, also becomes a complex number. As a consequence, the relation describing the amplitude of the wave as a function of time and place, can be split up in two parts, one of which is dependent only on the place. This latter part is an exponential function and is the reason for an exponential decay of the intensity of a wave in an absorbing medium, which is known as the Lambert–Beer law. The absorption index is especially high in the vicinity of an eigenfrequency and tends to decrease rapidly when the frequency is increased or decreased. In contrast, the refractive index decreases when the eigenfrequency is approached from higher frequencies, whereas it increases steeply at the eigenfrequency. After reaching a maximum, it decreases again until the next eigenfrequency. This decrease between two eigenfrequencies is called normal dispersion. Local changes in the absorption index cause contrast in a sample, which can be exploited to investigate the sample under a bright field microscope. Corresponding changes in the refractive index allow one to investigate a sample with a dark field, phase contrast, or differential interference contrast microscope. They are also exploited in optical coherence tomography (OCT).

As further reading for this section, two books [5, 6] are recommended.

In Section 3.2, we have already touched upon the fact that the dielectric function (or the individual components of the dielectric tensor function in the case of anisotropic media) consists of a real and an imaginary part, $\varepsilon_r(\omega) = \varepsilon_{r,1}(\omega) + i\varepsilon_{r,2}(\omega)$, as a result

of damping of the vibrations of electrons against the core (or, equivalently, the vibrations of atoms against each other). The question that we want to tackle in this section is "how does the damping act upon a light wave passing through the medium?" Since $\varepsilon_r = n^2$ (for cubic or isotropic media), the refractive index also becomes a complex function: $n = \mathrm{n} + i\kappa$. For diluted media such as gases, where the refractive index is close to unity, the refractive index can be calculated from Equation 3.21

$$
\begin{aligned}
&(\varepsilon_r - 1) = (n^2 - 1) = (n+1)(n-1) \cong 2(n-1) \\
&(n-1) \cong \frac{1}{2}[\varepsilon(\omega) - 1] = \frac{e^2 N}{2\varepsilon_0 m} \frac{1}{\omega_0^2 - \omega^2 + i\gamma\omega} \\
&\mathrm{n} = 1 + \frac{e^2 N}{2\varepsilon_0 m} \frac{\omega_0^2 - \omega^2}{\left(\omega_0^2 - \omega^2\right)^2 + \gamma^2\omega^2} \\
&\kappa = \frac{e^2 N}{2\varepsilon_0 m} \frac{-\gamma\omega}{\left(\omega_0^2 - \omega^2\right)^2 + \gamma^2\omega^2}.
\end{aligned}
\tag{3.36}
$$

The corresponding frequency dependence of the real part n and imaginary part κ of the refractive index are displayed in Figure 3.10 (compare the changes in the dielectric function displayed in Section 3.2). The real part of the refractive index n starts for small frequencies $\omega \to 0$ at $n_0 = 1 + e^2 N / 2\varepsilon_0 m\omega_0^2$ and increases for higher frequencies. Only in direct vicinity of the eigenfrequency ω_0 does n decrease. For high frequencies $\omega \gg \omega_0$, n approaches 1. For diluted media such as gases which are considered here, to simplify matters the imaginary part κ is always negative

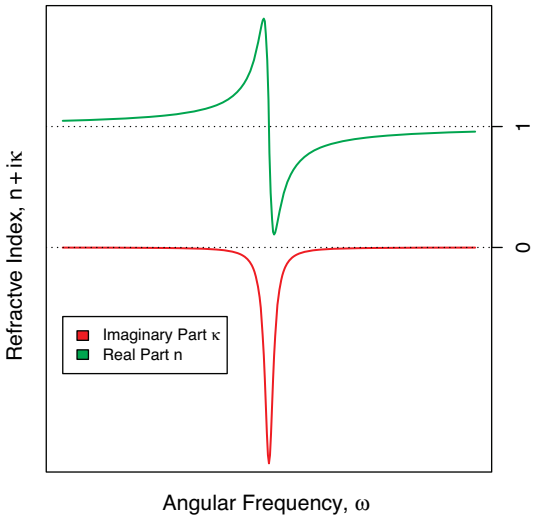

Figure 3.10 Dependence of the refractive indices and absorption in the vicinity of an eigenfrequency.

(further below dense matter will also be considered). In general, κ is very small and differs from 0 only in close vicinity to the eigenfrequency ω_0. The frequency dependence of κ exhibits a Lorentzian lineshape.

To understand the relevance of the complex refractive index, we use the result of Equation 3.34, $k_z = n \cdot \omega/c$, in combination with the exponential notation of the electric wave $\vec{E}(\vec{r}, t) = E_x(z, t) = E_{0,x} \cdot \exp[i(\omega t - k_z \cdot z)]$:

$$\begin{aligned} k_z = n\frac{\omega}{c} &= \frac{\omega}{c}(\mathrm{n} + i\kappa) \\ E_x(z,t) &= E_{0,x} \cdot \exp[i(\omega t - k_z \cdot z)] \\ &= E_{0,x} \cdot \exp\left\{ i\left[\omega t - \frac{\omega}{c}(\mathrm{n} + i\kappa) \cdot z\right]\right\} \\ &= E_{0,x} \cdot \exp\left[i\left(\omega t - \frac{\omega}{c}\mathrm{n} \cdot z - \frac{\omega}{c} i\kappa \cdot z\right)\right] \\ &= E_{0,x} \cdot \exp\left(\frac{\omega}{c}\kappa \cdot z\right) \cdot \exp\left[i\left(\omega t - \frac{\omega}{c}\mathrm{n} \cdot z\right)\right]. \end{aligned} \tag{3.37}$$

It can be seen that the electric field $E_x(z, t)$ exhibits a rapidly oscillating contribution whose wavelength is determined by the real part n of the refractive index. However, the initial amplitude of the wave $E_{0,x}$ will decrease exponentially with increasing travel distance along the z-direction because the factor $\exp[(\omega/c)\kappa \cdot z]$ is real and $\kappa < 0$ (see Figure 3.10). Hence κ is called the absorption index, since it causes the wave to weaken as a consequence of the damping of the vibrations inside the medium. As the light intensity I is given by E^2, it follows that also the intensity is weakened as the wave travels along the z-direction:

$$I(z) = I_0 \exp\left(\frac{2\omega}{c}\kappa \cdot z\right) = I_0 \exp(-a \cdot z) \tag{3.38}$$

where a is the extinction coefficient

$$a = \frac{e^2 N}{\varepsilon_0 mc} \frac{\gamma\omega^2}{\left(\omega_0^2 - \omega^2\right)^2 + \gamma^2\omega^2}. \tag{3.39}$$

Equation 3.38 is known as the Lambert–Beer law. The absorption A is then given by[8)]

$$A = 1 - \frac{I(z)}{I_0} = \exp(a \cdot z). \tag{3.40}$$

8) Note that fairly often in the literature also a quantity named absorbance or extinction A is referred to, which is given by $A = a \cdot z$. Since the terms are also not consistently used in the literature (the terms absorption and absorbance, for example, are switched), one has to deduce from the context what is actually meant.

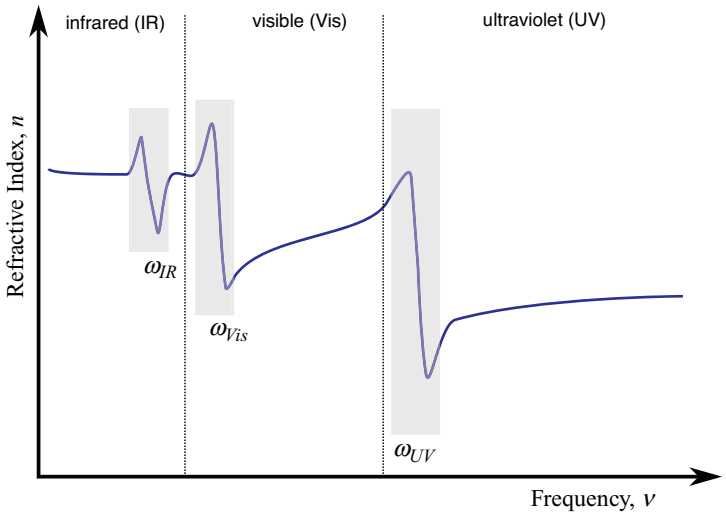

Figure 3.11 Schematic diagram displaying the frequency dependence of the real part of the refractive index for eigenfrequencies in the IR (ω_{IR}) and UV–Vis regions (ω_{UV} and ω_{Vis}). Abnormal dispersion ($dn/d\lambda > 0$) can be only found close to an eigenfrequency. In these regions of abnormal dispersion, absorption also takes place (adapted from [4]).

The absorption index and also the extinction coefficient are both macroscopic quantities. To relate the properties of single atoms or molecules, the number of atoms or molecules N per unit volume can be extracted from the extinction coefficient according to $a = \sigma \cdot N$, were σ represents the separated cross-section. Equation 3.40 then reads

$$I(z) = I_0 \exp(-\sigma \cdot N \cdot z). \tag{3.41}$$

Equation 3.41 remains valid in the case of solutions. Instead of using the number of entities N per unit volume, usually concentrations c in moles per liter ($\mathrm{mol\,l^{-1}}$) are introduced (1 mol corresponds to 6.0225×10^{23} entities). The equivalent to Equation 3.40 then reads

$$I(z) = I_0 \exp(-\alpha_\omega \cdot c \cdot z) \tag{3.42}$$

where $-\alpha_\omega$ is the molar natural extinction coefficient.[9)]

So far, it has been assumed that the refractive index n is close to unity, for which its frequency dependence can be expressed by Equation 3.36 (see also Figure 3.10). For dense media, the most significant difference from Equation 3.36 is that the maximum of the absorption index is slightly shifted from the eigenfrequency ω_0 towards higher wavenumbers and the band is no longer symmetric around ω_0. Figure 3.11 displays the frequency dependence of the real part of the refractive index n for the case of different eigenfrequencies. It can be seen that in the spectral ranges

9) The Lambert-Beer law is often written in the form: $I(z) = I_0 10^{-\epsilon \cdot c \cdot z}$ where ϵ is the molar decadic extinction or absorption coefficient. ϵ and α_ω are related to each other by: $\epsilon = \alpha_\omega / \ln 10 = \alpha_\omega / 2.302$. The molar decadic absorption coefficient ϵ must not be confused with the dielectric function ε.

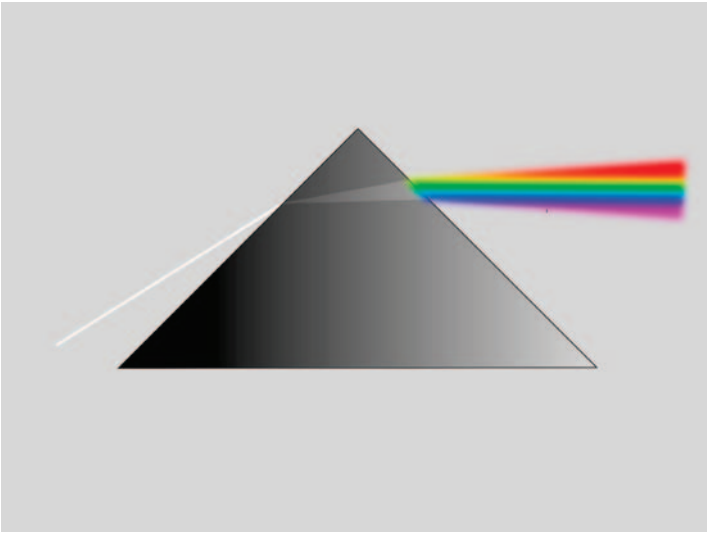

Figure 3.12 Normal dispersion: white light refracted by a prism is split up into its components as the refractive index increases with frequency.

where absorption is close to zero (i.e., outside hatched areas of Figure 3.11), the refractive index increases with increasing frequency, and as a consequence blue light is refracted more strongly than red light (see also Figure 3.12). These areas with $dn/d\omega > 0$ or $dn/d\lambda < 0$ are called areas of "normal dispersion." Only in the close vicinity of the eigenfrequencies where the imaginary part of the refractive index κ (absorption index) differs from zero does $dn/d\lambda > 0$ apply. In these areas of "abnormal dispersion," electromagnetic waves are absorbed. The resonances in the IR region are determined by molecular vibrations whereas those in the UV–Vis range result from electronic absorption. IR absorption is treated in detail in Section 3.8 and UV–Vis spectroscopy is covered in Section 3.9.

Equation 3.37 is also fundamental for the understanding of some of the most important contrast modalities in conventional microscopy, namely bright field, dark field, phase contrast and differential interference contrast microscopy (Figure 3.13).

Bright field microscopy is the simplest and most basic light microscopy method and is based on the absorption of light within the microscopic specimen. Here, the sample is illuminated from below with white light and the sample becomes visible because it is contrasted from its environment by its color or by its lack of color. Such an object is called an amplitude object because its recognizability is based on amplitude variations of the light wave. In other words, an object keeping the phase of an incoming wave constant and retarding the amplitude is called an amplitude object (see the left side of Figure 3.13). Decreasing an amplitude contrast by different light transmissions is directly visible. Unfortunately, the differences in the absorption index are comparably low for most biological samples, resulting in a low contrast. Therefore, bright field microscopy is not practical for transparent and thin objects since these objects absorb no light. This means that most cell compartments are not

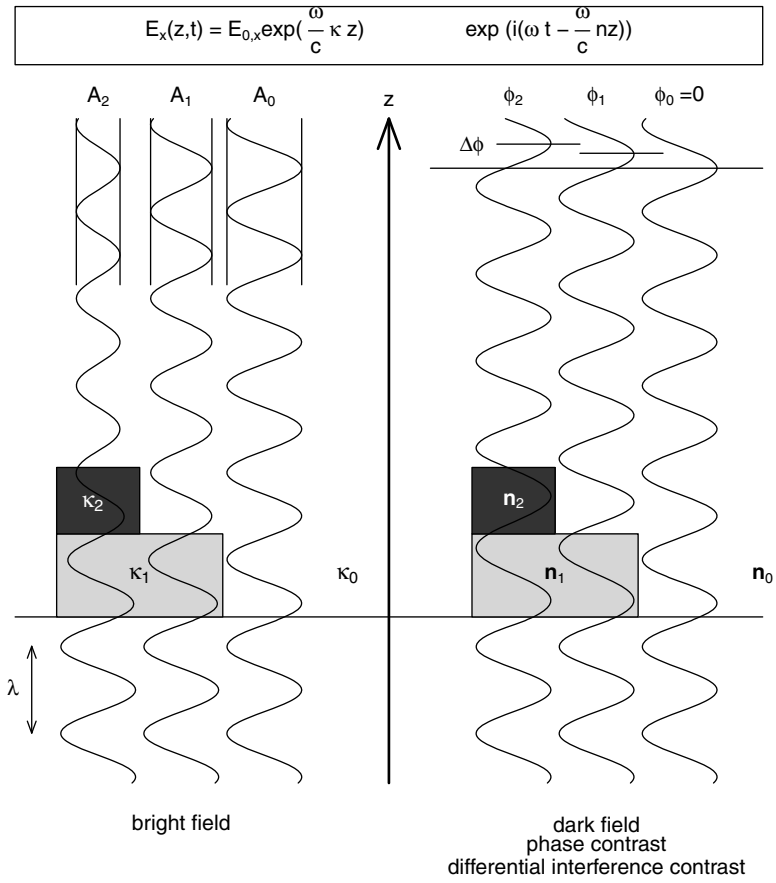

Figure 3.13 Significance of absorption and dispersion for light microscopy.

amplitude objects. Practically, the contrast can be increased by bright field staining (chemical contrasting), where the samples are stained with dyes to visualize and mark certain cell and tissue structures. Most dyes are selectively accumulated within cells due to special chemical or physical properties. Bright field staining is commonly used to dye histological cross-sections such as H&E stain for morphological inspection of biopsy specimens to identify malignant changes or Gram staining to differentiate bacterial species into two large groups based on the chemical and physical properties of their cell walls. Most bright field dyes require cell fixation prior to staining in order to be able to work with high dye concentrations, which is why the investigation of living cells becomes difficult.

In addition to chemical contrasting light microscopy with instrumental contrast enhancement (optical contrasting) such as dark field, phase contrast, and differential interference contrast (DIC) microscopy is possible. Dark field microscopy, which also requires transparent samples, utilizes light refracted at phase boundaries, that is, between structures with different refractive indices to visualize phase boundaries.

This is achieved by illuminating the sample with special microscopic condenser units in such a way that without a specimen the light rays do not arrive at the microscope objective, that is, the field of view is dark, whereas with a specimen the light rays will be refracted at sample edges and arrive at the microscope objective, that is, bright sample edges are seen on a dark background. The reason for light being refracted is the inhomogeneities of the sample leading to an inhomogeneous refractive index (see also Section 3.5).

An inhomogeneous distribution of the refractive index also leads to a phase change of the light waves, which travel through areas of the sample with different refractive indices. Many cell organelles exhibit different refractive indices and therefore diffract light beams differently, leading to a phase shift compared with an undisturbed reference beam. Such specimens are called phase objects (see the right side of Figure 3.13). Phase objects are not visible in the bright field. Phase contrast visualizes these phase shifts by converting them into amplitude differences. In this way, light passing through the sample and which is phase shifted is combined with a reference beam [i.e., unshifted (undeviated) light passing through or around the sample] in such a way that the resulting wave interference reveals the phase structure of the sample. This is achieved by introducing a phase plate, which introduces a phase difference between the sample and reference beam to produce interference between these two beams such that an amplitude-modulated wave results where the phase shift induced by the specimen appears as an intensity variation.

DIC microscopy works by separating a polarized light source (see Section 3.5) into two beams which take slightly different paths through the sample. Where the lengths of each optical path (i.e., the product of refractive index and geometric pathlength) differ, the beams interfere when they are recombined after leaving the sample.

Figure 3.14 shows some microscopic images of biological specimens summarizing the different contrast mechanisms which are based on absorption and dispersion.

OCT is also based on inhomogeneities of the refractive index in biological samples such as tissue. OCT is a method in which light is used to measure distances in a highly scattering medium such as tissue where the scattering of light (see Section 3.12) is due to changes in the refractive index within the tissue because of cell membranes or organelles. OCT contrast is achieved by utilizing the interference between backscattered light and a reference beam. As shown above, interference between two light waves occurs only when the two waves have a well-defined phase relation within a certain region. In contrast to light microscopy, OCT uses light with longer wavelengths than visible light, namely near-IR light. In addition, the light used is coherent, which means that all waves emitted from the light source have the same phase (see Section 3.7). This coherence becomes partly lost when the light is scattered inside the sample. For OCT, only the part of the light which is ballistically backscattered (i.e., unscattered or coherently scattered) is detected and evaluated. This means that ballistic scattered light propagates in the direction of the incoming light and therefore travels the shortest path and carries the maximum information on the internal structure of the tissue. A displacement of the reference beam produces the pathlength difference between the light reflected from the reference mirror and the backscattered ballistic light from the scattering sample, generating an

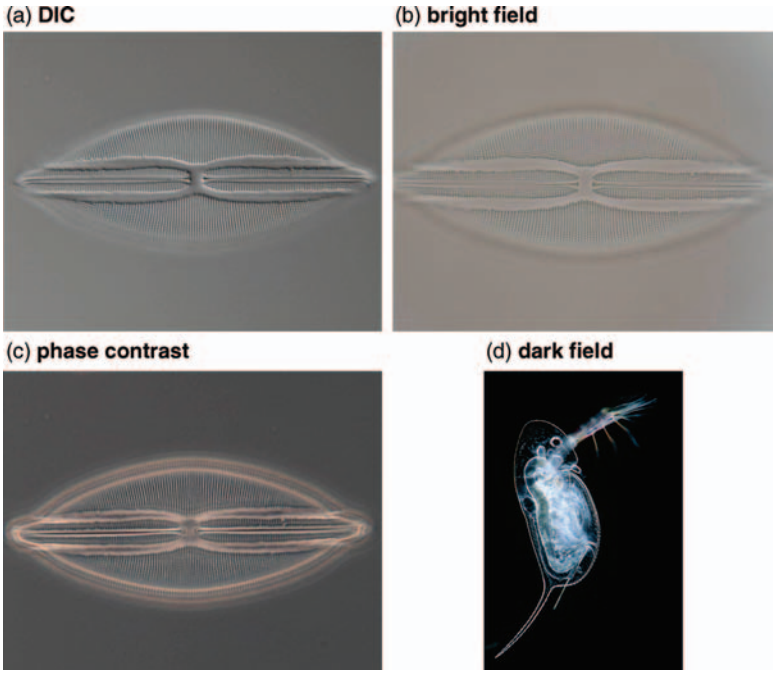

Figure 3.14 Comparison of the different contrast modalities based on absorption and dispersion. Bright field, phase contrast, and differential interference contrast images of the diatom *Navicula lyra*. Dark field image of a water flea *Daphnia* sp. (images courtesy of Carl Zeiss MicroImaging GmbH, Jena).

interference pattern containing information about the refractive index variation of the tissue, which thus provides an optical image. OCT allows the non-coherent part of the scattered light, which usually carries little information about the sample under investigation, to be suppressed.

3.5 Reflection and Transmission

In the previous section, it was detailed how absorption originates and how useful it can be to determine this quantity. Unfortunately, absorption cannot be measured directly. Instead, absorption can be determined by measuring transmission (the quantity of light that remains after light has traveled through the sample) and reflection (the part of light that is sent back without entering the sample). Absorption is then the remaining part which is neither reflected nor transmitted (if the sample is inhomogeneous, which most biological materials are, scattering may also have to be taken into account; see Section 3.12). As a further

consequence, for example, microscopes can be operated in either the transmission or reflection mode.

When a light wave hits a smooth interface that separates two media with different dielectric properties, part of the light is unable to penetrate the interface and is reflected back into the medium from which the light wave was approaching the interface. If the incidence of the light is not perpendicular to the interface, the angle of incidence, which is measured from the perpendicular, has the same magnitude as the angle of reflectance. The part of the light, which is reflected, depends on the angle of incidence, on the dielectric functions of both media, and on the polarization direction. The other part of the light wave permeates the interface and travels through the second medium, while its intensity may decrease due to absorption. The quantity of both parts can be calculated from the boundary conditions, which state that an electric field tangential to the interface remains unchanged whereas the perpendicular part is either decreased or increased depending on whether the dielectric constant of the second medium is larger or smaller than that of the first medium. To calculate the quantities, it is of advantage to calculate separately the cases where the electric field vector is either perpendicular or parallel to the plane of incidence, which is defined by the incoming, reflected, and transmitted beams. From the results of the calculation we find that if the dielectric constant of the first medium is smaller than that of the second medium, the reflectance of perpendicular polarized light increases monotonically with increasing angle of incidence, whereas the reflectance of parallel polarized incoming light is zero (minimum if the second medium is absorptive) at a certain angle of incidence. Both reach the value of unity when the angle of incidence reaches its maximum value of 90°. If the dielectric constant of the first medium is larger than that of the second medium, the principal behavior of the reflectance is the same except that it reaches unity at an angle of incidence smaller than 90°. This is called total reflection. If the second medium is absorptive, the total reflection is weakened. This effect is called attenuated total reflection (ATR); it is very sensitive and is exploited in a number of different microscopic and spectroscopic methods. If the interface between two media is not smooth, part of the light is not reflected in one particular direction but scattered in all directions. This is called diffuse reflection. The higher the surface roughness is, the higher becomes the proportion of diffusely reflected light. The interpretation of diffuse reflectance spectra is not straightforward. Spectra also become more complicated if the simple optical model isotropic medium/interface/isotropic medium is not applicable. One possibility is that the second medium has such a small thickness and such a low absorption that light is able to reach its back side, which is then again an interface. This means that part of the light leaves the medium, whereas another part of the light is reflected and travels backwards. While traveling backwards it interferes with the forward traveling light. Depending on the thickness, this generates regular minima and maxima in spectra. If the second medium is anisotropic, light absorption and reflection depend on the orientation of the medium. In the case of inhomogeneous media, absorption and reflection depend strongly on the size of the inhomogeneities relative to the

wavelength of light. In the latter case, scattering may not be negligible, which is another optical quantity in addition to absorption that can provide most useful insights into the nature of biological matter.

A full description of reflection and transmission of light can be found in [6–9].

In vacuum (and also in optically isotropic media such as glass or cubic crystals but not generally in isotropic materials), each electromagnetic wave is purely transversal. This means that the electric field vector (and also the magnetic field vector) is always oriented perpendicular to the direction of the wave (to the wavevector). For illustration, let us assume that an electromagnetic wave is traveling along the z-direction. Therefore, the electric field vector $\vec{E}$ is confined to the $x-y$ plane

$$\vec{E} = \begin{pmatrix} E_x \\ E_y \\ 0 \end{pmatrix}. \tag{3.43}$$

If the electromagnetic wave has its origin in a conventional light source (see Chapter 4), then all possible directions of the $\vec{E}$ vector in the $x-y$ plane will be realized, as illustrated in the Figure 3.15. Such light is said to be unpolarized or naturally polarized. With the help of so-called (linear) polarizers, it is possible to extract a single polarization direction. Such a polarizer can consist, for example, of a wire grid that is embedded in a transparent material, which can be a polymer. In the example above, the resulting wave is polarized along the y-axis. Therefore, the resulting electric field vector has only one component, E_y, and is said to be linearly polarized in the y-direction

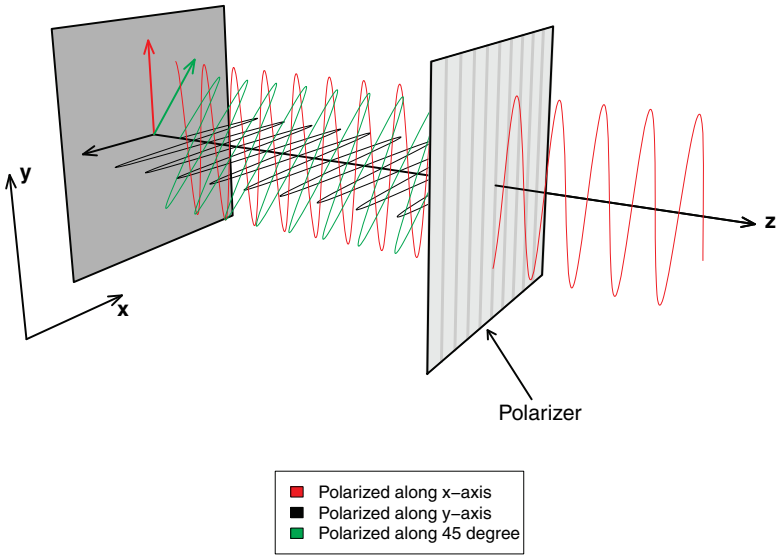

Figure 3.15 A linear polarizer acts on unpolarized light resulting in linearly polarized light.

$$\vec{E} = \begin{pmatrix} 0 \\ E_y \\ 0 \end{pmatrix}. \tag{3.44}$$

The superposition of two linearly polarized waves of the same wavelength with mutually perpendicular polarization directions, which are traveling in the same direction and have the same amplitudes E_0 and phases, always leads to unpolarized waves since the superposition of two electromagnetic waves is purely additive. If the amplitudes are not equal, elliptically polarized light results. On the other hand, we are allowed to split unpolarized waves into two linearly polarized waves, the linear combination of which again produces the unpolarized wave. This is of great importance, for example, for the calculation of reflection and transmission: if the light wave does not come in perpendicular to an interface, light that is polarized parallel to the plane of incidence behaves differently from that which is polarized perpendicular to that plane. Further, linearly polarized light usually experiences different refractive indices and is absorbed differently when traveling through anisotropic materials depending on their orientation.

To obtain information about the molecular structure, the resonance frequencies of a medium (a sample) can be studied, by measuring either the transmission or the reflection. From both of these the dielectric function in which this information is contained can be regained. If we denote the intensity of the incident light I_0, as was done in the previous section, the conservation of energy leads to the following relation:

$$I_0 = I_R + I_T + I_A \tag{3.45}$$

where I_R, I_T and I_A are the intensity of the reflected, the transmitted, and the absorbed light, respectively (see Figure 3.16). If we divide these quantities by I_0 we obtain

$$1 = \frac{I_0}{I_0} = \frac{I_R}{I_0} + \frac{I_T}{I_0} + \frac{I_A}{I_0} = R + T + A \tag{3.46}$$

by which the quantities reflection R, transmission T, and absorption A are defined. If we rearrange Equation 3.46, we obtain

$$1 - R - T = A \tag{3.47}$$

which shows that we have actually disregarded reflection in Equation 3.40 as is often done in the literature. Since, as we will see, reflection is especially strong in spectral regions with strong absorption, this can lead to considerable errors. For Equation 3.45, we have implicitly assumed that the medium of interest is homogeneous. In the case of samples where this assumption is incorrect, scattering also has to be taken into account. We will come back to scattering in Sections 3.12 and 3.13.

Figure 3.17 illustrates the optical model of reflection and refraction. We assume a plane wave $\vec{E}_e = \vec{E}_{0,e}\cos(\omega t - \vec{k}_e \cdot \vec{r})$ that is incident from a medium 0 with a refractive index n_0 (usually air, therefore $n_0 \approx 1$) under an incidence angle α_e on to an interface that separates the incidence medium from medium 1 (usually the sample) with an in

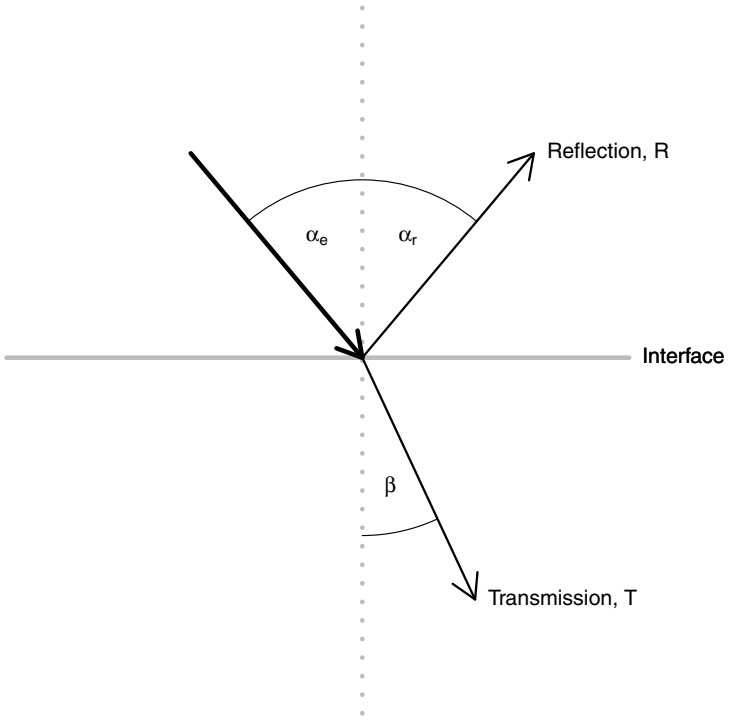

Figure 3.16 Reflection and transmission.

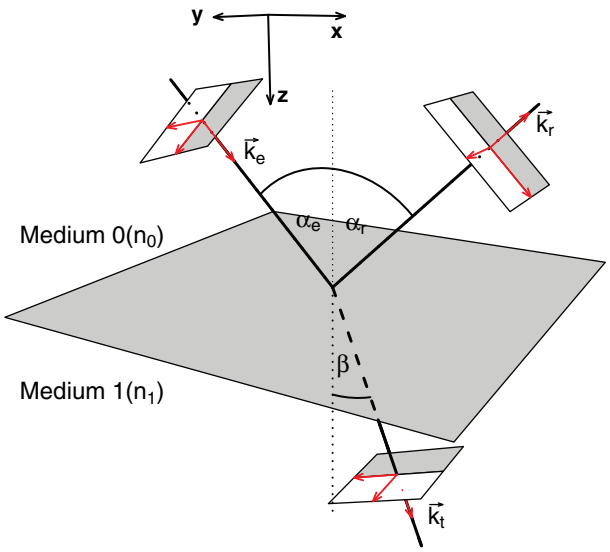

Figure 3.17 Reflection and refraction at a single interface.

general complex refractive index $n_1 = \mathrm{n}_1 + i\kappa_1$. The interface is perfectly smooth and the media are assumed to be so-called semi-infinite media (in practice, this means that the extent of medium 1 along the z-direction is large enough that the wave is not again reflected and refracted at the back side of the sample, since this considerably complicates the situation; we come back to this problem later). We choose a coordinate system in such a way that the interface is lying in the $x-y$ plane, whereas the plane of incidence is the $x-z$ plane. The wavevector $\vec{k}_\mathrm{e}$ therefore has components along both the x and z directions according to

$$\vec{k}_\mathrm{e} = n_0 \frac{\omega}{c} \begin{pmatrix} \sin\alpha_\mathrm{e} \\ 0 \\ \cos\alpha_\mathrm{e} \end{pmatrix}. \tag{3.48}$$

At the interface, the incident, the reflected, and the refracted (transmitted) waves must at all times have the same phase, that is, if the incident wave has a maximum of the amplitude at the interface, the same holds for the reflected and the refracted waves. As a consequence, it can be derived from

$$\begin{aligned} \vec{E}_\mathrm{e} &= \vec{E}_{0,\mathrm{e}} \cos\left(\omega t - \vec{k}_\mathrm{e} \cdot \vec{r}\right) \\ \vec{E}_\mathrm{r} &= \vec{E}_{0,\mathrm{r}} \cos\left(\omega t - \vec{k}_\mathrm{r} \cdot \vec{r}\right) \\ \vec{E}_\mathrm{t} &= \vec{E}_{0,\mathrm{t}} \cos\left(\omega t - \vec{k}_\mathrm{t} \cdot \vec{r}\right) \end{aligned} \tag{3.49}$$

that the following condition must be valid:

$$\vec{k}_\mathrm{e} = \vec{k}_\mathrm{t} = \vec{k}_\mathrm{r}. \tag{3.50}$$

Therefore, the y-component of all three vectors is zero and all lie in the plane of incidence. Accordingly, $\vec{k}_\mathrm{r}$ and $\vec{k}_\mathrm{t}$ are given by

$$\vec{k}_\mathrm{r} = n_0 \frac{\omega}{c} \begin{pmatrix} \sin\alpha_\mathrm{r} \\ 0 \\ -\cos\alpha_\mathrm{r} \end{pmatrix}, \; \vec{k}_\mathrm{t} = n_1 \frac{\omega}{c} \begin{pmatrix} \sin\beta \\ 0 \\ -\cos\beta \end{pmatrix} \tag{3.51}$$

where β is the angle of refraction. As a consequence, from Equations 3.48 and 3.51 the so-called Snell's law can be derived focusing on the x-components

$$\begin{aligned} \sin\alpha_\mathrm{e} &= \sin\alpha_\mathrm{r} \\ \sin\alpha_\mathrm{e} &= \frac{n_1}{n_0} \sin\beta. \end{aligned} \tag{3.52}$$

Therefore, the angle of incidence equals the angle of reflection: $\alpha_\mathrm{e} = \alpha_\mathrm{r}$. As already mentioned, in media that can be characterized by a single refractive index, the electric fields are perpendicular to the wavevector.

Due to the so-called boundary conditions, the relations are simplified if we consider two cases separately (see below). In the first case, the electric field vector is oriented perpendicular to the plane of incidence and therefore has only a component $E_{\mathrm{e},y}$ in the y-direction tangential to the interface (often this case is called

"transverse electric"). In the second case, the electric field has components in both the x- and z-directions and is given by

$$\vec{E}_{\mathrm{e}} = E_{\mathrm{e}} \begin{pmatrix} \cos\alpha_{\mathrm{r}} \\ 0 \\ \sin\alpha_{\mathrm{r}} \end{pmatrix}. \tag{3.53}$$

As a consequence, it possesses one component $E_{\mathrm{e},x}$ that is also tangential to the interface and a second component $E_{\mathrm{e},z}$ that is oriented perpendicular to the interface (often this case is called "transverse magnetic" in the literature). The electric fields are accompanied by magnetic fields $\vec{B}$. Employing Equation 3.25 and inserting a plane wave of the form $\vec{E} = \vec{E}_0 \cos\left(\omega t - \vec{k}\cdot\vec{r}\right)$, one obtains for the magnetic field $\vec{B}$ the following relation:

$$\begin{gathered} \vec{k} \times \vec{E} = \frac{\vec{B}}{\mu_0} \\ \begin{pmatrix} k_y E_z - k_z E_y \\ k_z E_x - k_x E_z \\ k_x E_y - k_y E_x \end{pmatrix} = \begin{pmatrix} -k_z E_y \\ k_z E_x - k_x E_z \\ k_x E_y \end{pmatrix} = \frac{1}{\mu_0} \begin{pmatrix} B_x \\ B_y \\ B_z \end{pmatrix} \end{gathered} \tag{3.54}$$

since $k_y = 0$. According to the boundary conditions, the tangential component of the electric field remains unchanged:

$$E_x(\text{medium } 0) = E_x(\text{medium } 1),\ E_y(\text{medium } 0) = E_y(\text{medium } 1). \tag{3.55}$$

Similar relations apply to magnetic fields. Again, the tangential components are not altered:

$$B_x(\text{medium } 0) = B_x(\text{medium } 1),\ B_y(\text{medium } 0) = B_y(\text{medium } 1). \tag{3.56}$$

Case I: Electric field polarized perpendicular to the plane of incidence

In medium 0, the existing electric fields are those of the incident and reflected waves. Therefore, their sum must be equal to the field of the transmitted wave

$$E_y(\text{medium}0) = E_y(\text{medium}1) \rightarrow E_{\mathrm{e},y} + E_{\mathrm{r},y} = E_{\mathrm{t},y.} \tag{3.57}$$

An equivalent relation can also be derived for the x-components of the magnetic fields

$$B_{\mathrm{e},x} + B_{\mathrm{r},x} = B_{\mathrm{t},x}. \tag{3.58}$$

Employing Equation 3.54 together with Equations 3.48 and 3.51 to replace the components of $\vec{k}$ (see Equation 3.54), we obtain

$$E_{\mathrm{e},y}\cos\alpha - E_{\mathrm{r},y}\cos\alpha = E_{\mathrm{t},y} n_1 \cos\beta \tag{3.59}$$

using $\alpha_e = \alpha_t = \alpha$. Solving Equation 3.59 for $E_{\mathrm{r},y}$ and $E_{\mathrm{t},y}$ in terms of $E_{\mathrm{e},y}$, we find that

$$E_{r,\gamma} = \frac{\cos\alpha - n_1\cos\beta}{\cos\alpha + n_1\cos\beta} E_{e,\gamma}$$
$$E_{t,\gamma} = \frac{2\cos\alpha}{\cos\alpha + n_1\cos\beta} E_{e,\gamma}. \tag{3.60}$$

The next step is to replace the complex angle β. To that end, we employ Snell's law, $\sin\alpha = n_1 \sin\beta$ ($n_0 = 1$); taking into account that $\sin^2\beta + \cos^2\beta = 1$ and, therefore, $\cos\beta = \sqrt{1-\sin^2\beta} = \sqrt{1-\frac{1}{n_1^2}\sin^2\alpha}$, we obtain

$$E_{r,\gamma} = \frac{\cos\alpha - \sqrt{n_1^2 - \sin^2\alpha}}{\cos\alpha + \sqrt{n_1^2 - \sin^2\alpha}} E_{e,\gamma}$$
$$E_{t,\gamma} = \frac{2\cos\alpha}{\cos\alpha + \sqrt{n_1^2 - \sin^2\alpha}} E_{e,\gamma}. \tag{3.61}$$

The ratios $E_{r,\gamma}/E_{e,\gamma}$ and $E_{t,\gamma}/E_{e,\gamma}$ are the reflection and the transmission coefficients r_γ and t_γ, respectively. To indicate the polarization relative to the plane of incidence, it is common to denote them as t_s (from the German "*senkrecht*") and r_t.

Case II: Electric field polarized parallel to the plane of incidence:

Again the tangential components of the electric and the magnetic field vectors $\vec{E}$ and $\vec{B}$ must be continuous at the interface. These components are $E_{i,x} = E_{i,p}\cos\vartheta$ (Equation 3.53) and $\mu_0 B_{i,\gamma} = -\cos\vartheta \cdot E_{i,x} - \sin\vartheta \cdot E_{i,z} = E_{i,p}$, wherein $i = e,\ r,\ t$ and ϑ stands either for α or β. Therefore, we obtain the following equations

$$E_{e,p}\cos\alpha + E_{r,p}\cos\alpha = E_{t,p}\cos\beta$$
$$B_{e,p} + B_{r,p} = B_{t,p}. \tag{3.62}$$

Solving Equation 3.59 for $E_{r,p}$ and $E_{t,p}$ in terms of $E_{e,p}$, we find that

$$E_{r,p} = \frac{\cos\beta - n_1\cos\alpha}{\cos\beta + n_1\cos\alpha} E_{e,p}$$
$$E_{t,p} = \frac{2\cos\alpha}{\cos\beta + n_1\cos\alpha} E_{e,p}. \tag{3.63}$$

After replacing the complex angle β $\left[\cos\beta = \sqrt{1-\sin^2\beta} = \sqrt{1-(1/n_1)\sin^2\alpha}\right]$, we obtain

$$E_{r,p} = \frac{\sqrt{n_1^2 - \sin^2\alpha} - n_1\cos\alpha}{\sqrt{n_1^2 - \sin^2\alpha} - n_1\cos\alpha} E_{e,p}$$
$$E_{t,p} = \frac{2\cos\alpha}{\sqrt{n_1^2 - \sin^2\alpha} - n_1\cos\alpha} E_{e,p}. \tag{3.64}$$

The ratios $E_{r,p}/E_{e,p}$ and $E_{t,p}/E_{e,p}$ are the reflection and the transmission coefficient r_p and t_p, respectively.

Equations 3.58 and 3.63 are known as the Fresnel equations. From the reflection and transmission coefficients, we obtain the reflectance and transmittance by considering the time-averaged energy flow through the interface. To that end, we have to invoke the so-called Poynting vector $\vec{S}$, which is given by

$$\vec{S} = \frac{\vec{k}}{2\omega}\left|\vec{E}\right|^2 \tag{3.65}$$

provided that the media are nonmagnetic ($\mu = 1$). Its magnitude is simply the intensity of the plane wave. The reflectance is then given by the intensity I_r of the reflected wave in the direction perpendicular to the interface (the z-direction) divided by the intensity of the incident wave I_0:

$$R_i = \frac{I_{r,i}}{I_0} = \frac{S_{z,r,i}}{S_{z,e,i}}, \quad i = s,\ p. \tag{3.66}$$

In case of transmission the component of the wavevector in the z-direction is different. Therefore the transmission is not simply the square of the value of the transmittance coefficients but obtained as

$$T_i = \frac{I_{t,i}}{I_0} = \frac{S_{z,t,i}}{S_{z,e,i}} = \frac{\sqrt{n_1^2 - \sin^2\alpha}}{\cos\alpha}|t_i|^2, \quad i = s, p. \tag{3.67}$$

Figure 3.18 shows the dependence of the reflectance on the angle of incidence for $n_0 = 1$ and $n_1 = 2$. At $\alpha = 0^\circ$ (normal incidence), the polarization of R_p has only a component parallel to the interface, as has R_s. Therefore, $R_s = R_p$. With increasing angle of incidence, R_s increases monotonically, whereas R_p possesses not only a minimum at 63°, but actually reaches zero. This angle is called the Brewster angle. After the Brewster angle, R_p also increases monotonically and reaches unity together with R_s at 90°, which actually simply means that the wave is traveling parallel to the interface and therefore reflection no longer occurs.

If we allow the medium to be absorptive, then the reflectance at normal incidence increases with increasing absorption index κ (see Figure 3.19). R_s is still a monotonically increasing function of the angle of incidence and R_p still shows a minimum, at which, however, R_p no longer reaches zero. This minimum shifts with increasing absorption index to higher angles of incidence.

An important peculiarity occurs if the refractive index of the incidence medium is higher than that of the exit medium. In this case, Equations 3.61 and 3.64 have to be modified to allow for a refractive index of the incidence medium that does not equal unity

$$\begin{aligned} r_s &= \frac{n_0\cos\alpha - \sqrt{n_1^2 - \sin^2\alpha}}{n_0\cos\alpha + \sqrt{n_1^2 - \sin^2\alpha}} r_p \\ E_{t,p} &= \frac{2\cos\alpha}{\sqrt{n_1^2 - \sin^2\alpha} - n_1\cos\alpha} E_{e,p}. \end{aligned} \tag{3.68}$$

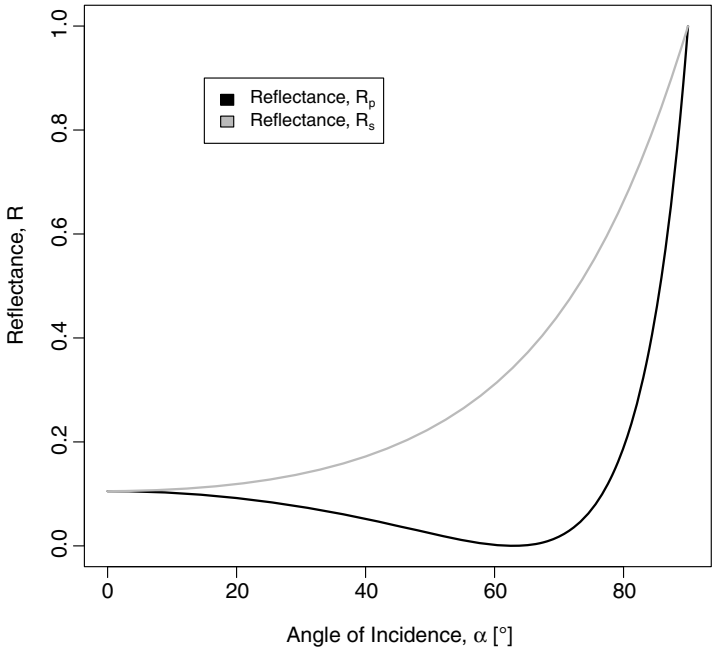

Figure 3.18 Dependence of the reflectance of the angle of incidence.

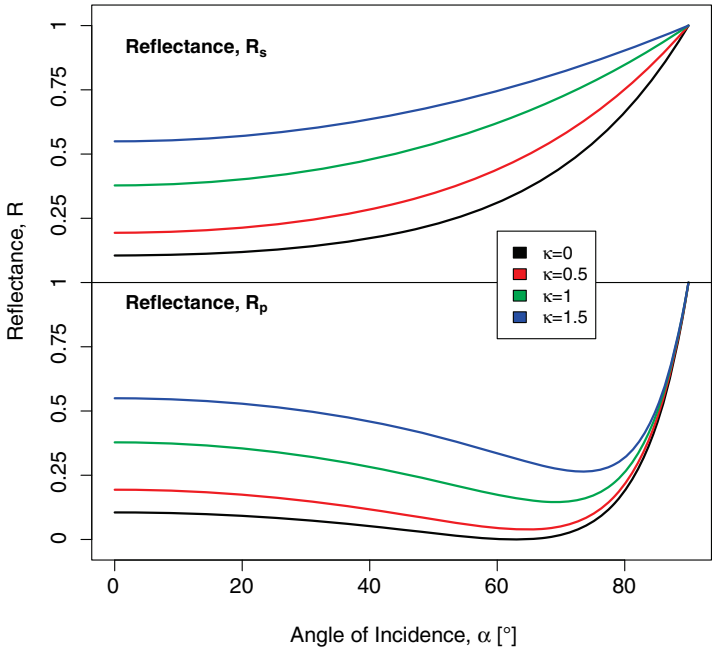

Figure 3.19 Variation of the reflectance with increase in absorption.

If we now set, for example, $n_0 = 3$ and keep $n_1 = 2$, the reflectance reaches unity already at 41°. The reason for this is comparably simple. As long as $n_0 < n_1$ holds, it follows from Equation 3.52 that $\alpha > \beta$. If this is inverted ($n_1 < n_0$) the consequence is that $\alpha < \beta$. The maximum β that can exist, however, is $\beta = 90°$. Based on Equation 3.52, the corresponding α_c is given by

$$\alpha_c = \arcsin\left(\frac{n_1}{n_0}\right) \tag{3.69}$$

and is called the critical angle. If the angle of incidence is chosen above the critical angle $\alpha > \alpha_c$, no energy is transferred into medium 1. As a consequence, the reflectance must reach unity independent of the incoming light's polarization. Again as a consequence, the transmittance must be zero (note that so far we have assumed that n_1 is real!) Despite the fact that no energy is transferred into the second medium, the wave nevertheless penetrates the interface; however, since cosβ is a purely imaginary quantity, the wave decays exponentially. Such a wave is called evanescent. The penetration distance is in the order of several wavelengths except close to the critical angle.

It is instructive to investigate what happens if the medium with the lower refractive index is absorptive. As can be seen from Figure 3.20, even an absorption index as low as $\kappa = 0.06$ has a strong influence on the reflectance and considerably weakens it. This phenomenon, ATR (see earlier), constitutes the basis of a number of different

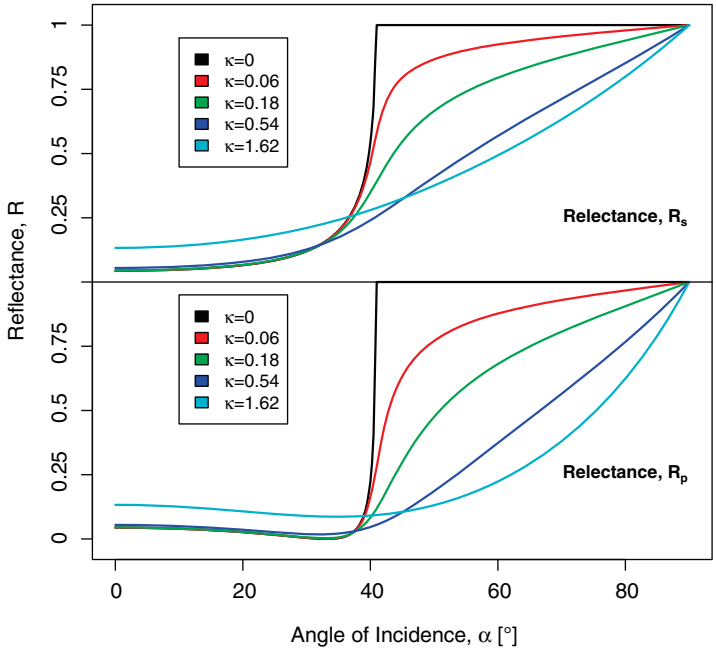

Figure 3.20 Reflectance from a medium that has a lower refractive index than the incidence medium.

spectroscopy and microscopy methods. If the medium is not absorptive, but inhomogeneous, total reflection may also become attenuated, since inhomogeneities close to the interface may distort the evanescent field. As a consequence of this distortion, a wave may be emitted, which receives its energy from the evanescent wave, leading to the attenuation of the total reflection. This phenomenon is called evanescent wave scattering.

It must be emphasized that so far we have treated the simplest optical model that one can think of (for example, we have assumed the media to be semi-infinite, characterized by a scalar dielectric function, homogeneous, etc.). If we remove one or more of the conditions of the model, the situation becomes considerably more complicated. Even taking into account that in the case of biological matter nearly all of the complications are present, we will abstain from treating the theory in detail. Instead, we will describe the effects, with some exceptions, in only a qualitative manner.

3.5.1
Diffuse Reflection

Diffuse reflection occurs whenever the interface is not perfectly smooth and is uneven or granular or possesses holes (see Figure 3.21). Part of the light is then scattered in all directions. As a consequence, the measured specular reflection is smaller, which can often be corrected by applying a factor to the measured spectrum. The larger the diffusely reflected portion of light is, however, the more problematic is

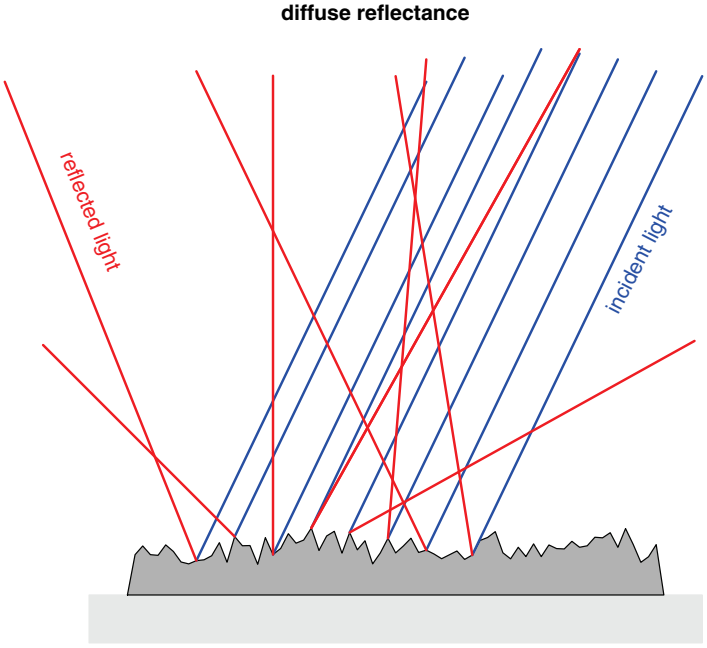

Figure 3.21 Illustration of diffuse reflectance.

such a simple correction. In the extreme case of a powdered sample, all of the light is diffusely reflected. Using a so-called integrating sphere (often also called Ulbricht sphere), which collects the light that is spread over the whole hemisphere, spectra can also be recorded. An interpretation of such spectra, however, is not straightforward. One possibility to evaluate such spectra quantitatively is to employ the so-called Kubelka–Munk theory or one of its various forms, which assumes that scattering is dominant compared with absorption (and compared with specular reflection). It requires a powder that is evenly spread in a surplus of a nonabsorbing powder, for example, KBr. Due to many simplifying assumptions, the results are usually of comparably poor quality.

3.5.2
Layered Media

If a medium cannot be considered as semi-infinite, it must be treated as a layer. A simple realization of this situation is a glass plate. In the spectral region where absorption is weak, the light that is transmitted through the first surface reaches the back side of the sample. Assuming that the sample surfaces are smooth and that it has a uniform thickness, part of the transmitted light is reflected back to the first surface where again a portion is reflected. Depending of the wavelength of the light and the thickness of the sample, interference peaks occur, that is, the reflectance shows periodically, as a function of both wavelength and layer thickness, minima and maxima caused by destructive and constructive interference since in the equations for transmission and reflection a phase factor occurs, which is given by

$$\exp\left(-i\frac{2\pi}{\lambda}n_1\cos\beta\right). \tag{3.70}$$

The underlying physical principle is the principle of superposition of waves (in this case, the waves traveling forwards and backwards inside the sample), which states that the resulting displacement at a point is equal to the vector sum of displacements of all waves present. Exact equations to interpret the resulting spectra quantitatively are somewhat cumbersome, but have been derived for an arbitrary number of layers and even for anisotropic media.

3.5.3
Anisotropic Media

A characteristic feature of biological tissues is that they consist of both amorphous and well-ordered crystalline regions. Typical examples are collagen fiber bundles, which consist of bundles of fibrils. In most cases these crystalline regions form anisotropic media.

Whereas in isotropic media, for example, the electric flux density and the electric field are vectors with equal direction which can be related to each other by a scalar factor (the dielectric function), this is no longer true for anisotropic media. As a consequence, the dielectric function becomes a 3×3 tensor function. In general, the

wave Equation 3.29 becomes much more complex and its solutions indicate that depending on the polarization of the wave and its direction, two different refractive indices exist. Consequently, a wave upon entering an anisotropic medium generally decomposes into two waves with mutual perpendicular polarization directions and traveling with different velocities. This behavior can be exploited in a manifold of optical techniques to detect changes in tissues which change into malignant forms.

From general experience, it seems that anisotropic media are somehow exotic whereas isotropy is what is usually encountered. Indeed, most of the volume of the universe is made up of isotropic media, that is, vacuum, gases, and liquids. The last state of matter, however, has at least one class of liquids that already belong to anisotropic media, namely liquid crystals. In the case of solid matter, which also includes soft matter such as biological material, anisotropy nearly always plays a role. In almost all kinds of solid matter ordered regions exist, which are in most cases anisotropic. Even if these ordered regions are randomly oriented and form a macroscopically isotropic medium, the anisotropy of the ordered regions makes the properties of such a medium differ from those of an original isotropic medium such as a cubic crystal. Unfortunately, the relationships can become complicated and it is far beyond the scope of this book to give an exhaustive introduction to optics and anisotropy. Nevertheless, the reader should be able to grasp some basic aspects after reading this section.

In an anisotropic medium, the polarization $\vec{P}$ is in general not parallel to the electric field $\vec{E}$ that causes it. As a consequence, the dependence between electric field $\vec{E}$ and dielectric displacement $\vec{D}$ must in general be written as

$$\begin{pmatrix} D_x \\ D_y \\ D_z \end{pmatrix} = \begin{pmatrix} \varepsilon_{xx} & \varepsilon_{xy} & \varepsilon_{xz} \\ \varepsilon_{yx} & \varepsilon_{yy} & \varepsilon_{yz} \\ \varepsilon_{zx} & \varepsilon_{zy} & \varepsilon_{zz} \end{pmatrix} \begin{pmatrix} E_x \\ E_y \\ E_z \end{pmatrix}. \tag{3.71}$$

The tensor generally consists of nine independent components. In the absence of optical activity, however, the tensor possesses only six independent components, since $\varepsilon_{ji} = \varepsilon_{ij}$ and the tensor is symmetric. Since the tensor transforms one vector into another, it can be seen as being fixed within a medium or a region of order to which it belongs. Usually the ordered region or the medium as a whole (e.g., a crystal) has a certain symmetry which can simplify the tensor considerably. To illustrate this, let us assume that the medium of interest has a mirror plane and perpendicular to the plane an axis of rotation. If we align the x, y, z coordinate system in such a way that the axes of the coordinate system are all parallel and perpendicular to the axis of rotation and the mirror plane, then the tensor takes on the diagonal form:

$$\begin{pmatrix} D_x \\ D_y \\ D_z \end{pmatrix} = \begin{pmatrix} \varepsilon_x & 0 & 0 \\ 0 & \varepsilon_y & 0 \\ 0 & 0 & \varepsilon_z \end{pmatrix} \begin{pmatrix} E_x \\ E_y \\ E_z \end{pmatrix}. \tag{3.72}$$

Now we can distinguish the following three cases:

1) The medium is of cubic symmetry; this means that $\varepsilon_x = \varepsilon_y = \varepsilon_z$ and the tensor reduces to a scalar. This is the case that we have discussed in detail in the preceding sections.

2) The medium is of hexagonal, trigonal, or tetragonal symmetry and the axis of rotation is oriented along the z-axis. Accordingly, $\varepsilon_x = \varepsilon_y$ and the tensor has only two independent components, ε_x and ε_z. The medium is then said to be optically uniaxial. As a consequence, each wave entering the medium is split into two waves with mutually perpendicular polarization directions and two different traveling speeds. One wave, which is called the ordinary wave, experiences a refractive index n_o, which is given by $n_o = \sqrt{\varepsilon_x} = \sqrt{\varepsilon_y}$. The other wave is called the extraordinary wave, and its refractive index n_e depends on the angle ϑ between the direction of the wave and the z-axis, which is called the optical axis

$$n_e = \sqrt{\frac{\varepsilon_x \varepsilon_y}{\varepsilon_x \sin^2\vartheta + \varepsilon_z \cos^2\vartheta}}. \tag{3.73}$$

3) The medium is of orthogonal, monoclinic, or triclinic symmetry. These are the optically biaxial media, since now two axes exist which, when the waves travel along them, behave like isotropic media. For a general direction, each wave is still split into two waves with mutually perpendicular oriented polarization directions. However, unlike in the uniaxial case, both waves are now extraordinary in the sense that the refractive indices generally depend on all elements of the dielectric tensor. The case of biaxial media can be further subdivided according to their symmetry:
   a) **Orthogonal media:** The dielectric tensor takes on the diagonal form whenever an incoming wave is aligned with one of the symmetry axes or, in case of crystals equivalently, with one of its crystal axes, and is polarized along another principal axis of the tensor. The principal axes of the tensor are independent of frequency (The principal axes of the tensor are those belonging to the coordinate system in which it takes on the diagonal form.) The refractive indices can be stated to depend on the three diagonal elements $\varepsilon_x = \varepsilon_y = \varepsilon_z$.
   b) **Monoclinic media:** Only one of the principal axes of the tensor is fixed; the orientations of the other principal axes depend on the frequency of the incoming wave. Usually the y-axis is chosen as the fixed axis. Accordingly, the refractive indices depend on one diagonal element ε_y and the elements ε_{xx}, ε_{xz}, ε_{zz}.
   c) **Triclinic symmetry:** The orientations of all principal axes of the tensor depend on the frequency of the incoming wave. As a consequence, the refractive indices depend on all six tensor elements ε_{xx}, ε_{xy}, ε_{yy}, ε_{yz}, ε_{xz}, ε_{zz}.

      For general directions inside biaxial media, the two refractive indices are obtained by solving the following equation:

$$\left| \begin{pmatrix} \varepsilon_{XX} - n^2 & \varepsilon_{XY} & \varepsilon_{XZ} \\ \varepsilon_{YX} & \varepsilon_{YY} - n^2 & \varepsilon_{YZ} \\ \varepsilon_{ZX} & \varepsilon_{ZY} & \varepsilon_{ZZ} \end{pmatrix} \right| = 0 \tag{3.74}$$

      where X, Y, Z is an external coordinate system (i.e., the coordinate system is not fixed inside the medium and is some kind of laboratory coordinate system, where the light wave is traveling along the Z-axis).

The derivation of reflection from and transmission through anisotropic media follows the procedure outlined in this section. The complexity increases with decreasing symmetry. Especially for monoclinic and triclinic symmetry, the solutions can no longer be given in closed form even in the case of normal incidence. The most important consequence of anisotropy is that upon reflection from and transmission through an anisotropic medium, a linearly polarized wave generally decomposes into two waves, which are mutually orthogonally polarized and each of which has a different speed. Therefore, a linear polarized wave becomes in general elliptically polarized inside the anisotropic medium (see Figure 3.22). Due to the boundary conditions at the interface, it is usually nearly impossible to determine the component of the dielectric tensor that is oriented perpendicular to the interface (consider, e.g., a uniaxial medium with the optical axis perpendicular to its surface) even for parallel polarized light and large angles of incidence. Exact solutions for the reflectance and transmittance can be found in the literature even for layered samples consisting of anisotropic layers.

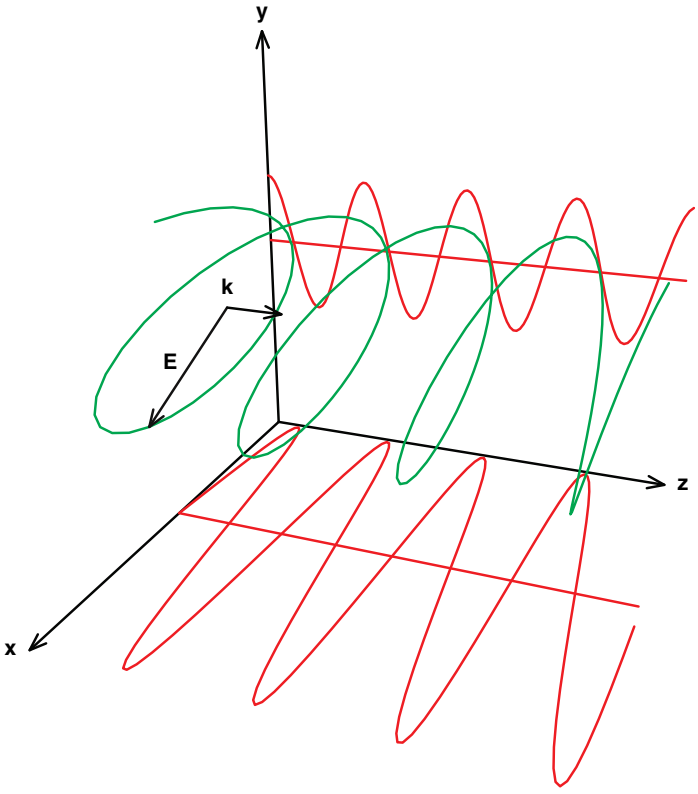

Figure 3.22 Illustration of elliptically polarized light.

3.5.4 Inhomogeneous Media

The simplest case is given by spheres in a matrix or a mixture of two kinds of spheres. The general problem consists in finding the appropriate optical constants (either the dielectric function or the refractive index) that optically characterizes the medium. This is possible only if the inclusions or the particles can be considered small compared with the wavelength (usually smaller than one-tenth of the wavelength). In principle, there are two different approaches. The first consists in constructing an averaged dielectric function starting from calculations of the local electric field (a simple average with the volumes as weighting factors does not work in this case!), for example, the so-called Lorentz–Lorentz relation. The second approach consists in averaging the refractive indices according to

$$\langle n \rangle = \sum_i f_i n_i \tag{3.75}$$

where n_i represent the refractive indices of the individual materials and f_i the part of the volume that is occupied by the medium i inside the sample. Both approaches have their merits and their drawbacks, so that it is not possible to decide *a priori* which method should be used for a problem at hand.

If particles or ordered regions in a heterogeneous sample are large compared with the wavelength, then the reflectance has to be averaged directly according to

$$\begin{aligned} \langle R \rangle &= \sum_i f_i R_i \\ \langle T \rangle &= \sum_i f_i T_i \end{aligned} \tag{3.76}$$

where R_i and T_i are the reflectances and transmittance of the corresponding homogeneous media.

The same applies to samples that consist of one sort of particles or ordered regions if the ordered regions are anisotropic. If the ordered regions are randomly oriented, the resulting medium is optically isotropic. If the ordered regions are small compared with the wavelength, the medium can be characterized by an averaged refractive index or an averaged dielectric function. As a consequence, such a medium no longer converts linear polarized light into elliptically polarized light. Such a conversion, however, still takes place if the medium consists of large ordered regions. This can be easily verified with, for example, a microscope. If linear polarized light is used and a second polarizer oriented perpendicular to the first is employed, usually no light should be transmitted. However, since the ordered regions are large enough to be optically resolved in the microscope, they convert linear polarized into elliptically polarized light, the ellipticity depending on the dielectric tensor and the orientation of the ordered region.

In addition to the discussed deviations from the simple optical model of two semi-infinite media separated by a smooth interface, numerous further deviations are possible, for example, a quasi-continuous change of the refractive index, a

non-homogeneous layer thickness, and so on. Fairly often such aberrations lead to changes in the spectra such as band shifts and intensity and shape changes, which can easily lead to the conclusion that the sample has different properties on a molecular level compared with a reference sample. Therefore, if a spectrum is to be interpreted quantitatively, it is important to model correctly the "optical influences" in order to obtain and interpret the optical constants with regard to the molecular level.

3.6
Nonlinear Optics

3.6.1
Nonlinear Polarization

The recent progress in the development of high-intensity ultrashort lasers (see Section 3.7) made it possible to utilize nonlinear optical phenomena in microscopy to create a higher microscopic/imaging contrast. Nonlinear microscopy methods have been successfully applied for the investigation of biological samples and have revolutionized many areas of biophotonics research. Nonlinear microscopy spans a multitude of different technologies from, for example, multi-photon fluorescence microscopy to label-free methods such as the generation of the second or third harmonics and also coherent anti-Stokes Raman scattering (CARS) microscopy. The application of these nonlinear microscopy techniques opened up exciting new possibilities for studying important biomedical processes. This section aims to provide a general introduction to the basic physical principles of nonlinear light–matter interaction phenomena.

So far we have only considered the case where the polarization responds linearly to the electric field, which is the case for normal light intensities. Here an incoming electromagnetic wave induces a dipole oscillating at the same frequency ω as the exciting wave. This oscillating dipole acts as a source for the emission of a secondary wave with frequency ω, that is, it must radiate and produce light with a frequency equal to the oscillation frequency. Such linear light–matter interactions are characterized by a linear dependence between the signal intensity and the irradiating light intensity and by the fact that no new frequencies are generated in a linear regime. This linear regime has been described in Section 3.2 by a harmonic approximation where the displacement of an electron attached to a spring from its equilibrium position is considered to be small. This harmonic representation is expressed by employing Hook's law, which states that the displacement of a spring is directly proportional to the applied force. In the equilibrium the external force of the electromagnetic wave is balanced by the force of the spring. It is well known that Hook's law is no longer valid when a

large force or displacement is applied to the spring. A large oscillating force acting on the electron spring corresponds to large electric fields and thus to high light intensities. Hence for high light intensities, the electron movement becomes nonlinear and has to be described by an anharmonic potential. As a consequence, the emitted light is no longer identical with the incident light and new frequencies are generated. On illumination of matter with intense light, the polarization of a molecule is no longer linearly proportional to the applied electric field and we have to consider the polarization by a power series expansion in the applied electric field resulting in a nonlinear polarization.

The interested reader is referred to [3, 10–12] for further details.

The mathematical description of the nonlinearity between polarization $\vec{P}(t)$ and electric field strength $\vec{E}(t)$ is expressed by a power series:

$$\vec{P}(t)/\varepsilon_0 = \chi^{(1)} \cdot \vec{E}(t) + \chi^{(2)} : \vec{E}(t) \cdot \vec{E}(t) + \chi^{(3)} \vdots \vec{E}(t) \cdot \vec{E}(t) \cdot \vec{E}(t) + \ldots \qquad (3.77)$$

in which $\chi^{(i)}$ are $i+1$ rank susceptibility tensors, that is, $\chi^{(1)}$ is the linear susceptibility whereas the higher order terms $\chi^{(2)}$ (second-order susceptibility), $\chi^{(3)}$ (third-order susceptibility), and so on are the nonlinear susceptibilities. Since $|\chi^{(1)}| \gg |\chi^{(2)}| \gg |\chi^{(3)}|$, nonlinear polarization effects can be seen only for or high field strengths. The magnitude of the nonlinear susceptibility depends on the nature and symmetry of the matter and is a measure of the size of the nonlinear restoring force during the distortion of the electron cloud by the incoming light wave.

Under the assumption of a power series expansion in just one dimension (neglecting the tensor characteristics of the susceptibility and vector characteristics of the field strength), the polarization can be written as

$$P(t)/\varepsilon_0 = \chi^{(1)} \cdot E(t) + \chi^{(2)} \cdot E(t) \cdot E(t) + \chi^{(3)} \cdot E(t) \cdot E(t) \cdot E(t) + \cdots . \qquad (3.78)$$

Now we can separate the polarization $P(t)$ into a linear part $P_{\text{lin}}(t)$ and a nonlinear part $P_{\text{NL}}(t)$:

$$\begin{aligned} P_{\text{lin}}(t) &= \chi^{(1)} \cdot E(t) \\ P_{\text{NL}}(t) &= \chi^{(2)} E^2(t) + \chi^{(3)} E^3(t) + \cdots . \end{aligned} \qquad (3.79)$$

In the following we will discuss the consequences of the nonlinear polarization $P_{\text{NL}}(t)$ in light–matter interaction. We will start with a simple example and calculate the polarization with a plane wave approach, that is, inserting $E(t) = E_0 \cos \omega t$ into Equation 3.78 resulting in

$$|P(t)| = \varepsilon_0 \cdot \chi^{(1)} E_0 \cos(\omega t) + \varepsilon_0 \cdot \chi^{(2)} E_0^2 \cos^2(\omega t) + \varepsilon_0 \cdot \chi^{(3)} E_0^3 \cos^3(\omega t) + \cdots . \qquad (3.80)$$

By employing the trigonometric relations

$$\begin{aligned}\cos^2\alpha &= \frac{1}{2}(1+\cos 2\alpha)\\ \cos^3\alpha &= \frac{1}{4}(3\cos\alpha+\cos 3\alpha)\end{aligned} \tag{3.81}$$

the polarization can be rewritten as

$$\begin{aligned}|P(t)| = \varepsilon_0\chi^{(1)}E_0\cos(\omega t) + \frac{1}{2}\varepsilon_0\chi^{(2)}E_0^2[1+\cos(2\omega t)]\\ + \frac{1}{4}\varepsilon_0\chi^{(3)}E_0^3[3\cos(\omega t)+\cos(3\omega t)] + \ldots.\end{aligned} \tag{3.82}$$

It can be seen that the nonlinear terms in the expansion series of the polarization lead to polarization terms vibrating at different frequencies:

- $\chi^{(2)}$ induces a term oscillating with twice the frequency of the incoming wave 2ω and a temporally constant term called optical rectification.
- $\chi^{(3)}$ results among other terms in a polarization oscillating with the triple frequency 3ω.

In Section 3.3, we have seen that employing the linear polarization $\vec{P}_{\text{lin}}$ in $\vec{D} = \varepsilon_0\vec{E} + \vec{P}_{\text{lin}} = \varepsilon_0\varepsilon_r\vec{E} = \varepsilon\vec{E}$ as source term within the Maxwell equations leads to the irradiation of an electromagnetic wave of frequency ω. By following the same derivation as outlined in Section 3.3 (see Equations 3.23–3.26) and using the relation $\vec{D} = \varepsilon_0\vec{E} + \vec{P}_{\text{lin}} + \vec{P}_{\text{NL}} = \varepsilon_0\varepsilon_r\vec{E} = \varepsilon\vec{E}$ results in a nonlinear wave equation:

$$\frac{\partial^2\vec{E}}{\partial^2 z} - \left[\chi^{(1)}+1\right]\varepsilon_0\mu_0\frac{\partial^2\vec{E}}{\partial t^2} = \mu_0\frac{\partial^2\vec{P}_{\text{NL}}}{\partial t^2}. \tag{3.83}$$

Now we assume a medium where we have to consider only the lowest order nonlinearity, that is, $\chi^{(2)}$:

- For small electric field strength E, we can neglect P_{NL}. Thus we obtain the undisturbed propagation of an electromagnetic wave $E(z,t) = E_0\exp(i\omega t - ikz)$ according to its dispersion relation with the refractive index $n_0 = \sqrt{\chi^{(1)}+1}$ (see 3.4 + 3.6.3).
- However, if we increase the field strength $\vec{E}$, we have to consider the term $\mu_0\cdot\partial^2\vec{P}_{\text{NL}}/\partial t^2$ within the nonlinear wave Equation 3.83. If we choose a plane wave approach, $E(z,t) = E_0\exp(i\omega t - ikz)$, and assume that the field envelope E_0 varies slowly with z, we obtain

$$\mu_0\frac{\partial^2\vec{P}_{\text{NL}}}{\partial t^2} = \varepsilon_0\mu_0\chi^{(2)}\omega^2E_0^2[\exp(i2\omega t - i2kz)]. \tag{3.84}$$

The right side of Equation 3.84 contains a term oscillating with frequency 2ω. This term is responsible for the generation of light with a double frequency (half wavelength), which is called second harmonic generation (SHG) (see also

Section 3.6.2). Within the photon picture, one photon of frequency 2ω is generated from two photons of frequency ω.[10)]

Generally, the different frequency contributions of the nonlinear polarization will lead to an emission of electromagnetic waves with exactly these frequencies. The dipole moments induced under the influence of an incoming electromagnetic wave act as sources of new electromagnetic waves whose frequency spectrum is determined by that of $\vec{P} = \vec{P}_{\mathrm{lin}} + \vec{P}_{\mathrm{NL}}$.

Now we want to examine the frequency spectrum of the polarization induced by two plane waves with frequencies ω_1 and ω_2, that is

$$\text{wave 1}: \; E_1(z,t) = E_1^0 \cos(\omega_1 t - k_1 z)$$

$$\text{wave 2}: \; E_2(z,t) = E_2^0 \cos(\omega_2 t - k_2 z).$$

Superposition of both waves E_1 and E_2 in the medium and considering only the polarization at the lowest nonlinear order results in

$$P(t)/\varepsilon_0 = \chi^{(1)}(E_1 + E_2) + \chi^{(2)}(E_1 + E_2)^2 + \cdots . \tag{3.85}$$

The linear contribution of the polarization $P_{\mathrm{lin}}(t)/\varepsilon_0 = \chi^{(1)} E_1 + \chi^{(1)} E_2$ leads to two waves which will propagate independently of each other in the medium, that is, the two waves possess different propagation velocities. Now we want to evaluate the nonlinear part of the polarization, $P_{\mathrm{NL}}(t)/\varepsilon_0 = \chi^{(2)}(E_1^2 + 2E_1E_2 + E_2^2)$. By inserting the fields $E_1(z,t)$ and $E_2(z,t)$ and employing common trigonometric relations, the nonlinear polarization can be expressed by

10) Light shows the properties both of waves (electromagnetic waves) and of particles (photons). To understand its nature completely, both concepts are needed. According to the duality principle developed by de Broglie in 1923, electromagnetic radiation is both

- a current of particles named photons, which carry a measurable momentum, and
- a vibration (wave), which is a disturbance propagating in space and time carrying energy with it.

Both concepts are simultaneously needed, since it is not possible to explain all properties of light with only one model. According to de Broglie, photons have corresponding to their momentum an energy characteristic for their spectral range and the equivalent wave are characterized by

- the speed of light c, which is characteristic for all electromagnetic waves in vacuum and is given by approximately $3 \times 10^8\,\mathrm{m\,s^{-1}}$,
- the frequency ν ($\mathrm{Hz} = \mathrm{s^{-1}}$), and
- wavelength λ (m).

Between momentum p and frequency or wavelength and between energy and frequency or wavelength, the following relations hold:

$$p = \frac{h}{\lambda} = \frac{h\nu}{c}$$

$$E = h\nu = h\frac{c}{\lambda}$$

where h is the quantum of action according to Planck. Depending on the frequency of the radiation, the properties of either a wave or a particle dominate in light–matter interaction. However, in the frequency range in which we are most interested in this book, we can mostly focus on the wave properties, as these will allow us to understand most phenomena of light interaction with biological matter.

$$P_{NL}(t) = \frac{1}{2}\chi^{(2)} \cdot \begin{pmatrix} (E_1^0)^2\cos[2(\omega_1 t - k_1 z)] + \\ (E_2^0)^2\cos[2(\omega_2 t - k_2 z)] + \\ 2 \cdot E_1^0 E_2^0\{\cos[(\omega_1 + \omega_2)t - (k_1 + k_2)z]\} \\ 2 \cdot E_1^0 E_2^0\{\cos[(\omega_1 - \omega_2)t - (k_1 - k_2)z]\} \\ (E_1^0)^2 + (E_2^0)^2 \end{pmatrix} \begin{matrix} \rightarrow P_{2\omega_1}\ \text{SHG of}\ \omega_1 \\ \rightarrow P_{2\omega_2}\ \text{SHG of}\ \omega_2 \\ \rightarrow \text{Sum frequency}\ \omega_1 + \omega_2 \\ \rightarrow \text{Difference frequency}\ \omega_1 - \omega_2 \\ \rightarrow \text{Optical rectification.} \end{matrix}$$

Thus, already the first nonlinear term of the polarization leads to the emission of five different frequencies. In the next section we will see that which of these new frequency contributions is generated within the nonlinear medium with high efficiency depends on the so-called phase matching condition.

3.6.2 $\chi^{(2)}$ Processes

$\chi^{(2)}$ processes that are of significance to biophotonics are SHG (also called frequency doubling), sum frequency generation, difference frequency generation, and optical parametric generation. However, not all matter can support these kinds of nonlinear optical effects. In particular for susceptibilities of even order, such as for $\chi^{(2)}$, a very important symmetry relationship is valid: for materials possessing a center of inversion the even order susceptibilities are identically zero. This is the case for all gases, liquids, and amorphous solids. $\chi^{(2)}$ processes can be induced only in materials without inversion symmetry, such as optically anisotropic, that is, birefringence systems (see Section 3.5.3) or at the surface of a material where the inversion symmetry is always broken.

Thus, for example, SHG microscopy can be used to highlight the spatial distribution of highly ordered non-centrosymmetric structures. Collagen is the most prominent protein structure in mammalian tissue that is characterized by these prerequisites for efficient SHG. Generally, during the development of various diseases, collagen structures underlie alterations which are readily detectable by means of SHG imaging. SHG allows one to image selectively the distribution of ordered collagen.

Furthermore, $\chi^{(2)}$ processes and also many other nonlinear processes require phase matching to be efficient. Essentially this means that a proper phase relationship between the interacting waves (for optimum nonlinear frequency conversion) is maintained along the propagation direction. For phase-matched SHG, this means that a macroscopic frequency-doubled wave can be formed if the fundamental and frequency-doubled wave propagate with the same phase velocity, that is, the refractive index at the fundamental ω has to match the refractive index at the second harmonic 2ω: $n(\omega) = n(2\omega)$. This phase matching condition for $\chi^{(2)}$ processes can only be achieved in birefringence materials.

For this subsection, for further descriptions of $\chi^{(2)}$ processes [10, 13] can be used.

Let us assume that we have an isotropic medium with a center of inversion (e.g., cubic crystal or gas). If we apply an electric field in one direction, for example $+y$, the induced polarization also points in the same direction, that is, in the $+y$ direction. The application of an electric field in the opposite direction, that is, the $-y$ direction, has to lead to a polarization also pointing in the $-y$ direction. A crystal or a gas with inversion symmetry is isotropic and looks the same from all sides. This means that the respective forward and backward directions around the individual atoms are the same, that is, the material properties such as $\chi^{(1)}$ and $\chi^{(2)}$ must not be changed by space inversion, for example, $\chi^{(1)}(x,y,z) = \chi^{(1)}(-x,-y,-z)$ and $\chi^{(2)}(x,y,z) = \chi^{(2)}(-x,-y,-z)$ (see Figure 3.23).

Hence for linear polarization it follows that

$$+y \text{ direction} : P_{\text{lin}} = \chi^{(1)} E(t) \tag{3.86}$$

$$-y \text{ direction} : P_{\text{lin}} = \chi^{(1)}[-E(t)] \tag{3.87}$$

which is consistent. However, on changing the y direction from $+$ to $-$, a discrepancy for the second-order nonlinear polarization arises:

$$+y \text{ direction} : P_{\text{NL}} = \chi^{(2)} E^2(t) \tag{3.87a}$$

$$-y \text{ direction} : -P_{\text{NL}} = \chi^{(2)}[-E(t)]^2. \tag{3.87b}$$

Equation 3.87b can be only fulfilled if

- $\chi^{(2)}$ depends on the field direction ($+/-y$), which is impossible due to the center of inversion, that is, isotropic material.
- $E(t) = 0$, which represents a trivial case with no meaning for optics.
- $\chi^{(2)} = 0$.

This example shows that the second-order polarization vanishes in materials with inversion symmetry. The second-order polarization can only be induced in media without a center of inversion. Exceptions are surfaces or interfaces where the

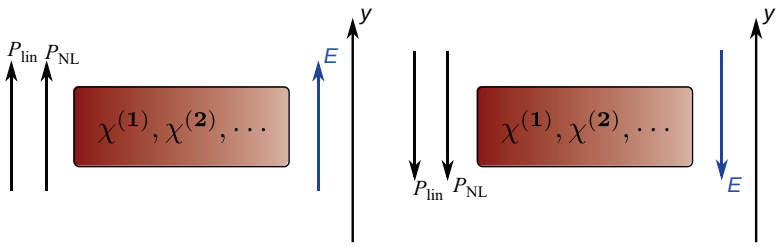

(a) Case1: *E* field in *y* direction (b) Case 2: *E* field in −*y* direction

Figure 3.23 Illustration of vanishing $\chi^{(2)}$ for materials with center of inversion.

inversion symmetry is always broken. In general, second-order nonlinear effects (and all even-order nonlinear processes) can only be induced in materials without a symmetry center, surfaces, interfaces, or places where the symmetry is broken.

In the previous section, we have seen that the interaction of two waves with frequencies ω_1 and ω_2 leads to a second-order polarization which can oscillate at different frequencies and therefore can act as a source for the irradiation of electromagnetic waves with these different frequencies. According to these frequencies, the most important $\chi^{(2)}$ processes for biophotonics are (see also Figure 3.24):

- SHG, also called frequency doubling
- sum frequency generation
- difference frequency generation
- optical parametric generation.

Optical parametric generation (see Figure 3.24) is a special $\chi^{(2)}$ process where an incident photon of energy $\hbar\omega_1$ (called pump) is divided into two photons (called signal and idler) such that the sum of their energies $\hbar\omega_2 + \hbar\omega_3$ is equivalent to the incident photon energy $\hbar\omega_1$. More details about this process can be found further below.

These $\chi^{(2)}$ processes can be induced in materials where $\chi^{(2)} \neq 0$. However, the efficiency of a $\chi^{(2)}$ processes depends on the so-called phase matching condition. In the following, we attempt to explain this important phenomenon of nonlinear processes, phase matching condition, for the example of SHG.

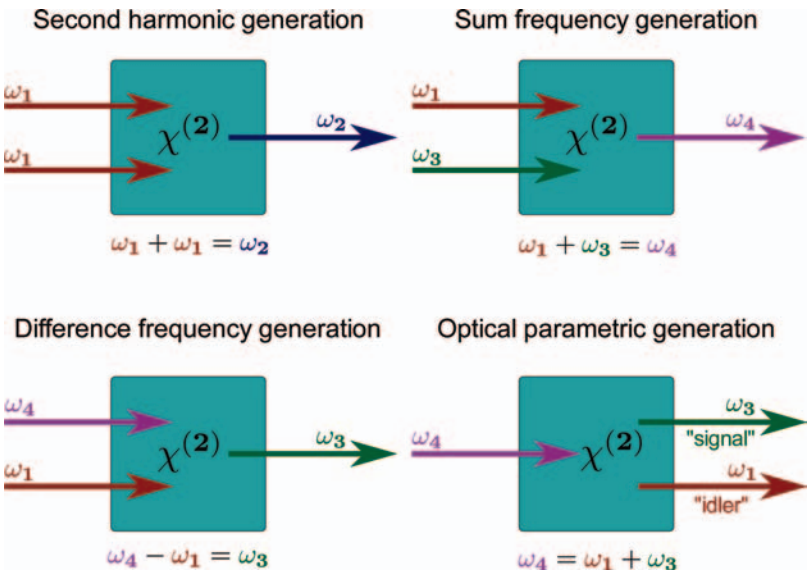

Figure 3.24 Illustration of important $\chi^{(2)}$ processes.

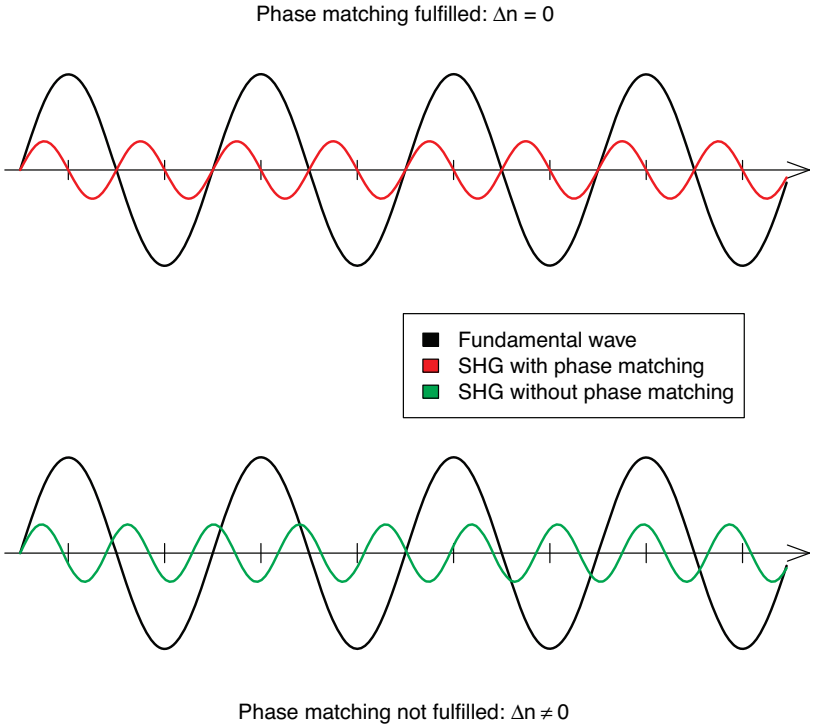

Figure 3.25 Illustration of phase-matching condition.

The incoming wave of frequency ω propagates through the $\chi^{(2)}$ medium with the phase velocity $\upsilon_{\mathrm{ph}}(\omega) = c/n(\omega)$ and generates light with the frequency 2ω anywhere in the medium. Due to dispersion, SHG light possesses a different phase velocity $\upsilon_{\mathrm{Ph}}(2\omega) = c/n(2\omega)$ than the fundamental wave. In order for a macroscopic frequency-doubled wave to build up, the fundamental and frequency-doubled wave have to propagate with the same phase velocity, that is, $n(\omega)$ must be equal to $n(2\omega)$ (see Figure 3.25).

Light at 2ω generated at the beginning of the material initially constructively interferes with light further inside the material, therefore increasing the overall intensity at 2ω. However, after a certain distance, l_{Ph} = coherence length, the light generation takes place out-of-phase and the SHG intensity decreases. The SHG intensity varies as a function of the propagating distance z within the material

$$I_{2\omega}(z) \sim \mathrm{sinc}^2\left(\frac{\pi z}{l_{Ph}}\right) \cdot z^2 \text{ with } l_{Ph} = \frac{\lambda_0}{2(n(\omega) - n(2\omega))}. \tag{3.88}$$

The sinc function is defined by $\mathrm{sinc}\,(x) = \sin x/x$ and has its maximum for $x = 0 : \mathrm{sinc}(0) = 1$. This means that in order to generate SHG light at 2ω efficiently, it has to be guaranteed that the SHG generation proceeds with phase matching, that

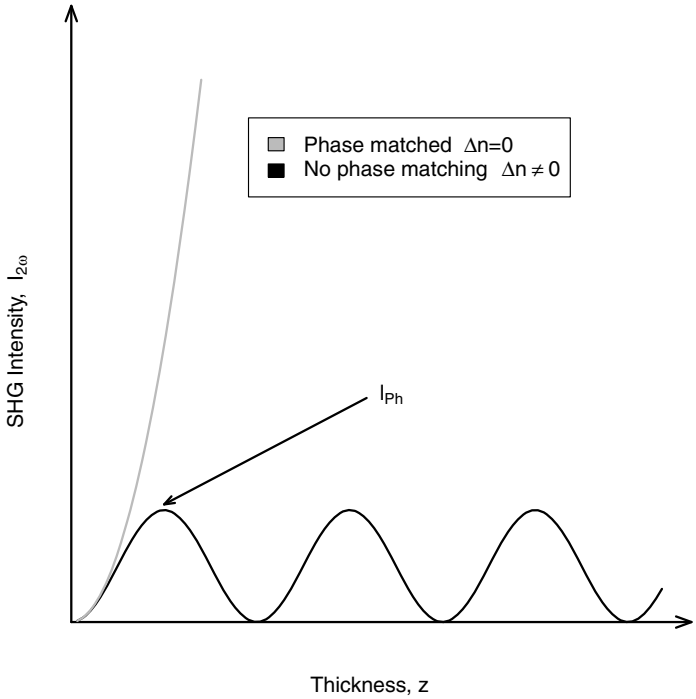

Figure 3.26 SHG intensity $I_{2\omega}$ as a function or material thickness for phase-matched ($\Delta n = 0$) and non-phase-matched ($\Delta n \neq 0$) conditions.

is, $\Delta n = n(\omega) - n(2\omega) = 0$ or $n(\omega) = n(2\omega)$. Figure 3.26 shows the SHG intensity as a function of the material thickness z for phase-matched and non-phase-matched conditions. It can be seen that if phase matching is fulfilled ($\Delta n = 0$), the SHG intensity increases quadratically with z. For non-phase-matched conditions ($\Delta n \neq 0$), the SHG intensity oscillates with the coherence length, $2l_{\mathrm{Ph}}$.

The phase matching condition $n(\omega) = n(2\omega)$ can be also seen as photon momentum conservation, that is, the momentum $\vec{k}$ of two photons of frequency ω("two red photons in") must be equal to the momentum $\vec{k}$ of one photon of frequency 2ω ("one blue photon out"):

$$\vec{k}(\omega) + \vec{k}(\omega) = \vec{k}(2\omega). \tag{3.89}$$

Equation 3.89 can be derived from Equation 3.35 by employing the phase matching condition $n(\omega) = n(2\omega)$. However, we have seen in Section 3.4 that normal dispersion prevents $n(\omega) = n(2\omega)$ from ever happening (see also Figure 3.27), hence special materials are needed to ensure phase matching. In Section 3.5.3 we learned that a wave, upon entering an anisotropic medium, decomposes into two waves with mutual perpendicular polarization directions and traveling with different velocities. In particular it is interesting to induce the $\chi^{(2)}$ processes depicted in Figure 3.24 for optically uniaxial crystals exhibiting two polarization directions:

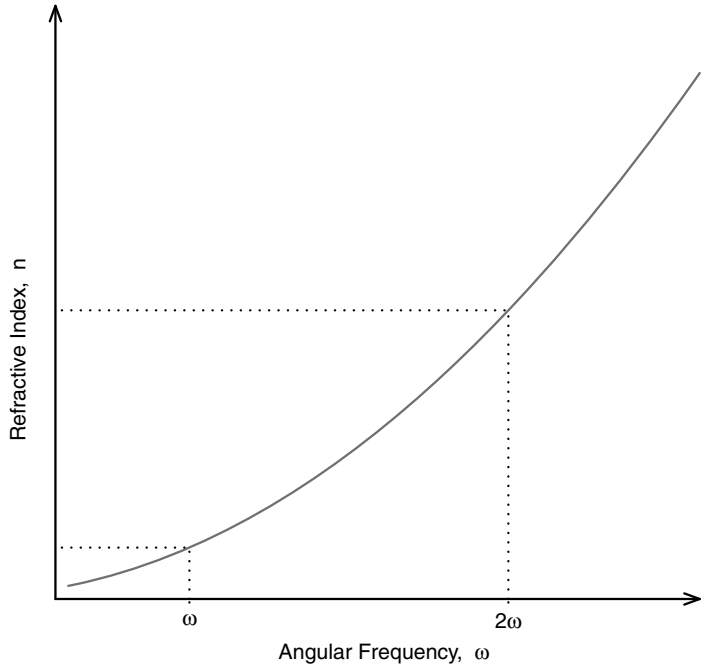

Figure 3.27 Normal dispersion curve.

- ordinary wave experiencing a refractive index n_o and obeying Snell's law (see Equation 3.52)
- extraordinary wave with a refractive index n_e depending on the angle ϑ between the direction of the wave and the z-axis, which is called the optical axis (see Equation 3.73).

Thus, uniaxial crystals can be used to ensure phase matching if for a wavelength λ and a certain direction ϑ the extraordinary refractive index $n_e(2\omega)$ for the SHG wave is equal to the ordinary one $n_o(\omega)$ for the fundamental wave. This means that for a fundamental wave with a propagation direction ϑ the phase matching condition for an SHG process $n_o(\omega) = n_e(2\omega)$ is achieved and a macroscopic SHG wave of frequency 2ω can build up (see Figure 3.28).

Since n_e depends on the propagation angle ϑ (see Figure 3.28a), by rotating the optical uniaxial crystal we can tune the phase matching condition precisely by moving the blue dispersion curve in Figure 3.28 up and down relative to the red curve. The phase matching conditions for the other $\chi^{(2)}$ processes depicted in Figure 3.24 are

- sum frequency generation: $k_4(\omega_4) = k_1(\omega_1) + k_3(\omega_3)$
- Difference frequency generation: $k_3(\omega_3) = k_4(\omega_4) - k_1(\omega_1)$
- Optical parametric generation: $k_4(\omega_4) = k_1(\omega_1) + k_3(\omega_3) = k_{\text{idler}} + k_{\text{signal}}$.

Technically relevant uniaxial crystals with large $\chi^{(2)}$-values are as follows:

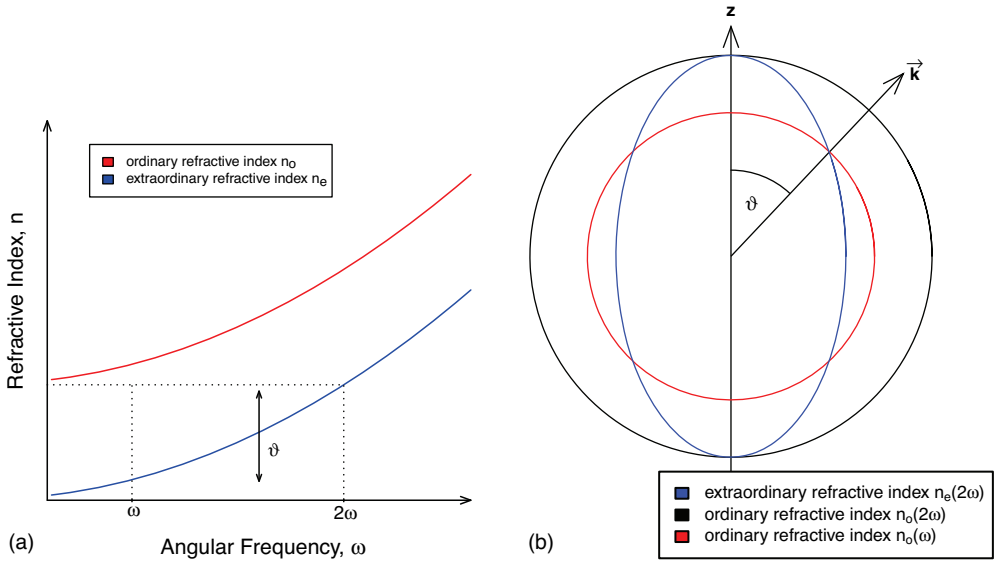

Figure 3.28 Phase matching in an optical uniaxial crystal. (a) Refractive index, ellipsoid, n_0 and $n_e(\theta)$ (adapted from [14]).

- KDP: potassium dihydrogenphosphate ($K_2H_2PO_4$)
- KD*P: potassium dideuteriumphosphate ($K_2D_2PO_4$)
- ADP: ammonium dihydrogenphosphate
- $LiNbO_3$: lithium niobate
- BBO: β-barium borate
- $AgGaS_2$: silver thiogallate.

These crystals can be used to induce all the $\chi^{(2)}$ frequency conversion processes sketched in Figure 3.24. By selecting the appropriate input beam or beams and by adjusting the required phase matching condition, a selective enhancement of one particular process is achieved. For optical parametric generation, a pump photon is divided into two photons by interaction with the crystal, that is, light with ordinary and extraordinary polarizations is generated. The ordinary polarized light is called the signal and the extraordinary light is called idler. The wavelength of signal and idler pulses is determined by the phase matching condition, which is changed by the angle ϑ between the pump light and the optical axis z of the crystal. Hence the wavelength of the signal and idler waves can be tuned by varying ϑ, that is, changing the phase matching condition. The signal and idler light can subsequently be frequency doubled or used for sum and difference frequency generation. Hence a wide range of different frequencies (wavelengths) can be generated by the above-mentioned $\chi^{(2)}$ frequency conversion crystals.

3.6.3 $\chi^{(3)}$ Processes

$\chi^{(3)}$ processes that are of particular relevance for biophotonics are two-photon absorption and the nonlinear Raman techniques stimulated Raman scattering (SRS) and CARS. $\chi^{(3)}$ phenomena, in contrast to $\chi^{(2)}$ processes, can be induced in all materials. As for $\chi^{(2)}$ processes, energy and momentum conservation (phase matching) must be also fulfilled for $\chi^{(3)}$ phenomena. In the following, we focus in particular on two-photon absorption, which is a consequence of the nonlinear refractive index (CARS and SRS will be treated in detail in Section 3.13). For sufficiently high intensities I, the refractive index contains, in addition to the linear dispersion term $n_0(\omega)$, also a nonlinear term $n_2(\omega)$, that is, $n(\omega, I) = n_0(\omega) + n_2(\omega)I$. The intensity-dependent refractive index $n_2(\omega)$ is determined by $\chi^{(3)}$ and is also a complex function like the linear dispersion term $n_0(\omega)$. The imaginary part of the nonlinear refractive index describes the two-photon absorption, which depends linearly on intensity. The real part of $n_2(\omega)$ is responsible for the nonlinear optical effects of self-focusing and self-phase modulation.

This section provides a general introduction to $\chi^{(3)}$ processes. The interested reader is referred to [10, 13].

Equation 3.82 reveals that the third-order polarization $P^{(3)}(t)$, that is, the terms of the power series expansion of the polarization depending on $\chi^{(3)}$ can be written as

$$\begin{aligned} \left|P^{(3)}(t)\right| &= \frac{1}{4}\varepsilon_0\chi^{(3)}E_0^3[3\cos(\omega t) + \cos(3\omega t)] \\ &= \frac{3}{4}\varepsilon_0\chi^{(3)}E_0^3\cos(\omega t) + \frac{1}{4}\varepsilon_0\chi^{(3)}E_0^3\cos(3\omega t). \end{aligned} \tag{3.90}$$

Then the third-order nonlinear wave equation appears as (see Section 3.6.1)

$$\mu_0\frac{\partial^2\vec{P}^{(3)}}{\partial t^2} = \frac{9}{8}\varepsilon_0\mu_0\chi^{(3)}\omega^2E_0^3\exp(i3\omega t - i3kz) + \frac{3}{8}\varepsilon_0\chi^{(3)}\omega^2E_0^3\exp(i\omega t - ikz). \tag{3.91}$$

Here the first part describes the third harmonic generation (THG) in analogy with the second harmonic generation (SHG) discussed above (see also Equation 3.84). However, in the following we focus on the second term of the right-hand side of Equation 3.91, which leads to an intensity-dependent refractive index. For the derivation of the intensity-dependent refractive index, we consider exclusively the terms of the polarization (see Equation 3.82) oscillating on ω:

$$\begin{aligned} |P(t)| &= \varepsilon_0\chi^{(1)}E_0\cos(\omega t) + \frac{3}{4}\varepsilon_0\chi^{(3)}E_0^3\cos(\omega t) \\ &= \varepsilon_0E_0\cos(\omega t)\left[\chi^{(1)} + \frac{3}{4}\chi^{(3)}E_0^2\right]. \end{aligned} \tag{3.92}$$

Now we follow the same procedure as outlined in Section 3.3 (Equations 3.23 – 3.30). This involves differentiation of the left- and right-hand sides of the Maxwell Equation 3.26 with respect to time, employing Maxwell Equation 3.25 to replace $\partial\vec{B}/\partial t$, replacing $\vec{D}$ by using $\vec{D} = \varepsilon_0\varepsilon_r\vec{E}$ and using Maxwell Equation 3.23 taking into account that for nonconducting materials $\rho = 0$, resulting in the following equation:

$$\Delta\vec{E} = \mu_0 \frac{\partial^2 \vec{D}}{\partial t^2} \tag{3.93}$$

Now we replace $\vec{D}$ by $\vec{D} = \varepsilon_0\vec{E} + \vec{P}$

$$\Delta\vec{E} = \mu_0 \left(\varepsilon_0 \frac{\partial^2 \vec{E}}{\partial t^2} + \frac{\partial^2 \vec{P}}{\partial t^2} \right) \tag{3.94}$$

and employ for the polarization Equation 3.92

$$\Delta\vec{E} = \mu_0\varepsilon_0 \left\{ 1 + \left[\chi^{(1)} + \frac{3}{4}\chi^{(3)} E_0^2 \right] \right\} \frac{\partial^2 \vec{E}}{\partial t^2}. \tag{3.95}$$

In Section 3.3 we have seen that equations where the second derivative of a quantity with respect to position is linked to its second derivative with respect to time have wave character. Thus Equation 3.95 is a wave equation with a velocity υ given by (see also Equation 3.31)

$$\upsilon = \frac{1}{\sqrt{1 + \chi^{(1)} + \frac{3}{4}\chi^{(3)} E_0^2}} \cdot c \tag{3.96}$$

where we used the relation $c = 1/\sqrt{\varepsilon_0\mu_0}$. From Equation 3.3, we know that the velocity of an electromagnetic wave inside a medium is given by $\upsilon = c/n$. Therefore, when considering the third-order nonlinear term of the polarization oscillating with frequency ω (see Equation 3.92), the refractive index n yields

$$n = \sqrt{1 + \chi^{(1)} + \frac{3}{4}\chi^{(3)} E_0^2}. \tag{3.97}$$

With $\chi^{(1)} = \varepsilon_r - 1$ and $n_0 = \sqrt{\varepsilon_r}$, it follows that the linear refractive index is given by $n_0^2 = \chi(\omega) + 1$. Hence we obtain for the refractive index n (Equation 3.97)

$$n = \sqrt{n_0^2 + \frac{3}{4}\chi^{(3)} E_0^2}. \tag{3.98}$$

Expanding the square root to first order yields

$$n = n_0 + \frac{\frac{3}{4}\chi^{(3)} E_0^2}{2n_0}. \tag{3.99}$$

The light intensity of a plane wave with linear polarization $E(t) = E_0 \cos \omega t$ is given by

$$I = \frac{1}{2}\varepsilon_0 n_0 c|E_0|^2. \tag{3.100}$$

Hence inserting Equation 3.100 into Equation 3.99 yields

$$n(\omega, I) = n_0 + \frac{3\chi^{(3)}}{4n_0^2\varepsilon_0 c} \cdot I. \tag{3.101}$$

Equation 3.101 shows that for sufficiently high intensities the refractive index contains, in addition to the linear dispersion term $n_0(\omega)$, also a nonlinear part $n_2(\omega)I$ that cannot be neglected:

$$n(\omega, I) = n_0(\omega) + n_2(\omega) \cdot I \quad \text{with} \quad n_2(\omega) = \frac{3\chi^{(3)}}{4n_0^2\varepsilon_0 c}. \tag{3.102}$$

If other higher order nonlinear polarization terms of odd order are also considered, the refractive index can be expressed by

$$n(\omega, I) = n_0(\omega) + n_2(\omega) \cdot I + n_3(\omega)I^2 + \cdots. \tag{3.103}$$

The linear refractive index n_0 refers to $\chi^{(1)}$ and is independent of the intensity. The nonlinear refractive indices n_2 and n_3 are related to $\chi^{(3)}$ and $\chi^{(5)}$, respectively, and depend on the incident intensity.

In the following, the influence of the nonlinear refractive index on light–matter interaction leading to important processes, the optical Kerr effect and two-photon absorption, will be discussed in more detail.

3.6.3.1 Optical Kerr Effect

Let us assume the interaction of a laser beam with a Gaussian intensity profile along the y-axis of sufficiently high intensity with a $\chi^{(3)}$) medium (see Figure 3.29).

The spatial intensity distribution of a Gaussian laser beam leads to a spatial variation of the refractive index over the beam profile within the medium. At the beam edges, where the light intensity is low, the refractive index is small. However, at the center of the light beam, where the intensity is highest, the refractive index is much larger than at the edges. This effect that an intense light pulse, when traveling in a medium, induces a varying refractive index of the medium is called the optical Kerr effect. The larger refractive index in the center as compared with the edges of the light beam leads to retardation of the light propagation. In other words, the wavefront is bent and delayed substantially in the center part of the wavefront, which means that the laser beam is being focused (see Figure 3.29). This phenomenon where a medium, whose refractive index increases with the electric field intensity, acts as a focusing lens for an electromagnetic wave is called Kerr-induced self-focusing. Self-focusing is often observed when radiation generated by femtosecond lasers (see Section 3.7) propagates through many solids, liquids, and gases.

A second effect that has its origin in the nonlinear refractive index is self-phase modulation. As we will see in Section 3.7, ultrashort laser pulses exhibit a broad frequency spectrum. We have seen above that the optical Kerr effect induces a varying

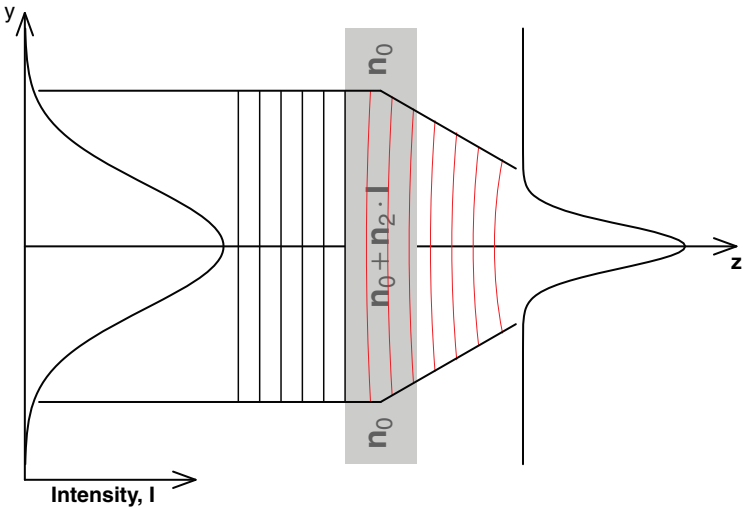

Figure 3.29 Illustration of Kerr-induced self-focusing: spatial intensity profile of a pulse traveling through a $\chi^{(3)}$ medium (adapted from [4]).

spatial refractive index distribution within a medium through which the ultrashort pulse is traveling. This variation in refractive index will produce a phase shift in the pulse, leading to a change of the pulse's frequency spectrum. The nonlinearity of the refractive index acts via the wavenumber $k = 2\pi n/\lambda$ on the phase of the light pulses. The field distribution of a Gaussian light pulse at position z in the medium can be expressed by

$$E(z,t) = E_0(t)\cos(-\varphi[t,z]) \quad \text{with} \quad \varphi[t,z] = -\omega_0 t + k \cdot z. \tag{3.104}$$

With $k = 2\pi n/\lambda$ and the intensity-dependent nonlinear refractive index $n = n_0 + n_2 \cdot I$, it follows for the phase:

$$\varphi[t,z] = -\omega_0 t + \left[\frac{2\pi n_2 I(t)}{\lambda_0} + \frac{2\pi n_0}{\lambda_0}\right] \cdot z. \tag{3.105}$$

This phase $\varphi[t,z]$ results in an instantaneous frequency $\omega(t)$:

$$\omega(t) = -\frac{\partial\varphi[t,z]}{\partial t} = \omega_0 - \frac{2\pi n_2 z}{\lambda_0} \cdot \frac{\partial I(t)}{\partial t} \tag{3.106}$$

leading to a frequency shift of

$$\delta\omega(t) = \omega(t) - \omega_0 = -\frac{2\pi n_2 z}{\lambda_0} \cdot \frac{\partial I(t)}{\partial t}. \tag{3.107}$$

Equation 3.107 shows that for the leading edge of the pulse ($\partial I/\partial t > 0$), the frequency is shifted to lower frequencies ("redder" wavelengths) whereas for the trailing edge of the pulse ($\partial I/\partial t < 0$), the frequency shifts to higher frequencies ("bluer") (see Figure 3.30). Hence the spectral profile of the pulse is increased. Such

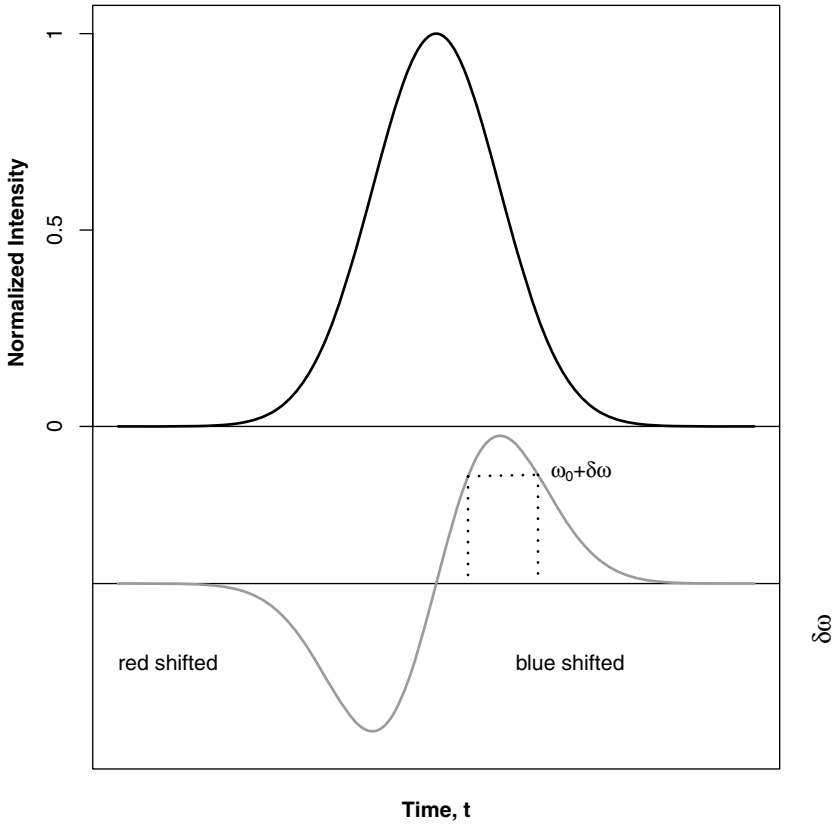

Figure 3.30 Illustration of self-phase modulation (SPM): the temporal intensity profile of the pulse is shown. Ultrashort laser pulse (top) traveling through a $\chi^{(3)}$ medium experiences a frequency shift $\delta\omega(t)$ because of SPM: the front of the pulse is shifted to lower frequencies whereas the back shifts to higher frequencies. The frequency shift within the center of the pulse is almost linear (adapted from [4]).

a generation of new frequencies by the optical Kerr effect is called self-phase modulation (SPM). The extra frequencies generated by the SPM broaden the spectrum of the pulse symmetrically. This spectral broadening is often utilized for the generation of ultrashort laser pulses or so-called coherent white light continua, which are very important for the realization of innovative nonlinear microscopic approaches discussed throughout this book.

3.6.3.2 **Two-Photon Absorption**

In Sections 3.2 and 3.4, it has been shown that the susceptibility and also the refractive index are complex quantities. This is also the case, of course, for the nonlinear susceptibilities and refractive indices. This means that $\chi^{(3)}$ and also the nonlinear refractive index can be separated into real and imaginary parts:

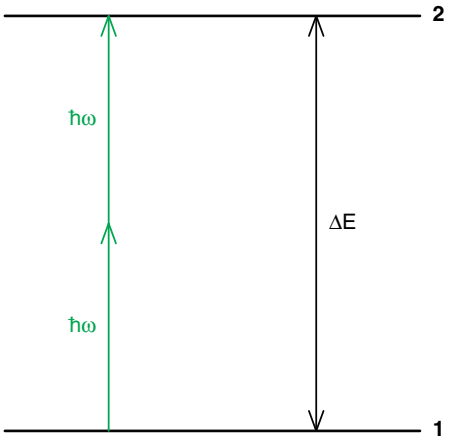

Figure 3.31 Illustration of two-photon absorption.

$$\chi^{(3)} = \chi_R^{(3)} + i\chi_I^{(3)}. \tag{3.108}$$

The real part of the third-order nonlinear susceptibility $\chi_R^{(3)}$ is responsible for the optical Kerr effect described above whereas the imaginary part $\chi_I^{(3)}$ is responsible for the two-photon absorption, which will be discussed in the following.

Two-photon absorption describes the simultaneous absorption of two photons by molecules to reach an excited state.[11)] Thereby the energies of the involved lower, 1, and upper, 2, molecular states are equal to the sum of the energies of the two photons: $\Delta E = E_2 - E_1 = 2 \cdot \hbar\omega$ (see Figure 3.31). Two-photon absorption is several orders of magnitude weaker than linear absorption.

The light attenuation for a two-photon absorption as the wave travels along the z-direction can be expressed by (see Equation 3.38 for one-photon absorption)

$$\frac{dI}{dz} = -\alpha_{2\omega} I^2 \tag{3.109}$$

where $\alpha_{2\omega}$ is the two-photon absorption coefficient

11) Section 3.4 reports the classical description of light absorption where we have seen that the imaginary part of the refractive index κ (called absorption index) causes an electromagnetic wave to weaken as a consequence of the damping of the vibrations of electrons against the core inside the medium. This description was based on the simple atomic picture known as the Lorentz atom. However, quantum mechanics associates with molecules discrete quantized energy levels (see Chapter 2). Later, in Sections 3.8 and 3.9, it will be shown that if the quantum energy of a photon matches the energy gap between two energy levels, the photon can elevate the molecular system from a lower to a higher state, that is, the transition between two molecular states is induced by the absorption of a photon.

$$\alpha_{2\omega} = \frac{3\omega\chi_I^{(3)}}{2\varepsilon_0 c^2 n_0^2(\omega)}. \tag{3.110}$$

In general, the simultaneous absorption of more than one photon is called multi-photon absorption. Thereby the imaginary parts of the nonlinear refractive indices n_2, $n_3, \ldots$ (see Equation 3.103), which depend on the nonlinear susceptibilities of odd order, are responsible for these multi-photon absorption processes, that is, for example, a three-photon absorption is described by the imaginary part of $\chi^{(5)}$. Since multi-photon processes require high excitation intensities, pulsed laser sources with high peak powers, such as femtosecond titanium–sapphire lasers (see Section 3.7), are required. The possibility of exploiting multi-photon absorption in multi-photon microscopy has attracted a great deal of interest across all fields of biophotonics. As we will see throughout this book, multi-photon microscopy has evolved from a photonic novelty into an indispensable tool in biological and biomedical research.

3.6.3.3 Other $\chi^{(3)}$ Processes

In addition to the optical Kerr effect and two-photon absorption, many other $\chi^{(3)}$ processes exist. This can be easily seen by analyzing the third-order polarization $P^{(3)}$ induced in a $\chi^{(3)}$ medium by three plane waves with the frequencies ω_1, ω_2, and ω_3:

$$\begin{aligned} P^{(3)}(t)/\varepsilon_0 &= \chi^{(3)}[E_1(t) + E_2(t) + E_3(t)]^3 \\ &= \chi^{(3)}\Big[E_1(t)^3 + E_2(t)^3 + E_3(t)^3 \\ &\quad + 3E_1(t)E_2(t)^2 + 3E_1(t)E_3(t)^2 + 3E_1(t)^2E_2(t) + 3E_1(t)^2E_3(t) \\ &\quad + 6E_1(t)E_2(t)E_3(t) + 3E_2(t)E_3(t)^2 + 3E_2(t)^2E_3(t)]. \end{aligned} \tag{3.111}$$

If we insert the three plane wave equations

$$\begin{aligned} E_1(t) &= E_1^0 \cos\omega_1 t, \\ E_2(t) &= E_2^0 \cos\omega_2 t, \\ E_3(t) &= E_3^0 \cos\omega_3 t \end{aligned}$$

and apply common trigonometric relations, the third-order polarization can be expressed by

$$\begin{aligned} P(t)^{(3)}/\varepsilon_0 = {} & P(\omega_1) + P(\omega_2) + P(\omega_3) \\ & + P(3\omega_1) + P(3\omega_2) - P(3\omega_3) \\ & + P(\omega_1 + \omega_2 + \omega_3) + P(\omega_1 + \omega_2 - \omega_3) \\ & + P(\omega_1 + \omega_3 - \omega_2) + P(\omega_2 + \omega_3 - \omega_1) \\ & + P(2\omega_2 \pm \omega_1) + P(2\omega_3 \pm \omega_1) + P(2\omega_1 \pm \omega_2) \\ & + P(2\omega_1 \pm \omega_3) + P(2\omega_3 \pm \omega_2) + P(2\omega_2 \pm \omega_3) \end{aligned} \tag{3.112}$$

with

$$
\begin{aligned}
P(\omega_1) &= \chi^{(3)}\left(\frac{3}{4}(E_1^0)^2+\frac{3}{2}(E_2^0)^2+\frac{3}{2}(E_3^0)^2\right)E_1^0\cos\omega_1 t\\
P(\omega_2) &= \chi^{(3)}\left(\frac{3}{4}(E_2^0)^2+\frac{3}{2}(E_1^0)^2+\frac{3}{2}(E_3^0)^2\right)E_2^0\cos\omega_2 t\\
P(\omega_3) &= \chi^{(3)}\left(\frac{3}{4}(E_3^0)^2+\frac{3}{2}(E_1^0)^2+\frac{3}{2}(E_2^0)^2\right)E_3^0\cos\omega_3 t\\
P(3\omega_1) &= \frac{1}{4}\chi^{(3)}(E_1^0)^3\cos 3\omega_1 t\\
P(3\omega_2) &= \frac{1}{4}\chi^{(3)}(E_2^0)^3\cos 3\omega_2 t\\
P(3\omega_3) &= \frac{1}{4}\chi^{(3)}(E_3^0)^3\cos 3\omega_3 t\\
P(\omega_1+\omega_2+\omega_3) &= \frac{6}{4}\chi^{(3)}E_1^0E_2^0E_3^0\cos(\omega_1+\omega_2+\omega_3)t\\
P(\omega_1+\omega_2-\omega_3) &= \frac{6}{4}\chi^{(3)}E_1^0E_2^0E_3^0\cos(\omega_1+\omega_2-\omega_3)t\\
P(\omega_1+\omega_3-\omega_2) &= \frac{6}{4}\chi^{(3)}E_1^0E_2^0E_3^0\cos(\omega_1+\omega_3-\omega_2)t\\
P(\omega_2+\omega_3-\omega_1) &= \frac{6}{4}\chi^{(3)}E_1^0E_2^0E_3^0\cos(\omega_2+\omega_3-\omega_1)t\\
P(2\omega_2\pm\omega_1) &= \frac{3}{4}\chi^{(3)}(E_2^0)^2E_1^0\cos(2\omega_2\pm\omega_1)t\\
P(2\omega_3\pm\omega_1) &= \frac{3}{4}\chi^{(3)}(E_3^0)^2E_1^0\cos(2\omega_3\pm\omega_1)t\\
P(2\omega_1\pm\omega_2) &= \frac{3}{4}\chi^{(3)}(E_1^0)^2E_2^0\cos(2\omega_1\pm\omega_2)t\\
P(2\omega_1\pm\omega_3) &= \frac{3}{4}\chi^{(3)}(E_1^0)^2E_3^0\cos(2\omega_1\pm\omega_3)t\\
P(2\omega_3\pm\omega_2) &= \frac{3}{4}\chi^{(3)}(E_3^0)^2E_2^0\cos(2\omega_3\pm\omega_2)t\\
P(2\omega_2\pm\omega_3) &= \frac{3}{4}\chi^{(3)}(E_2^0)^2E_3^0\cos(2\omega_2\pm\omega_3)t\,.
\end{aligned}
\tag{3.113}
$$

It can be seen that many different frequencies can be generated by $\chi^{(3)}$ processes. It is important to note that these processes can be induced in all materials since for $\chi^{(3)}$

phenomena no symmetry restrictions have to be fulfilled. However, the efficiency of these $\chi^{(3)}$ processes depends on the different phase matching conditions for every single frequency component. In Section 3.11 we will discuss with SRS and CARS two other important $\chi^{(3)}$ process for biophotonics.

3.7 Lasers

Modern biophotonic research is unthinkable without lasers. In particular, the development of ultrashort laser pulse sources revolutionized the microscopy sector by utilizing nonlinear optical phenomena as described in Section 3.6. These ultrashort lasers allow a moderate amount of energy to be generated within an extremely short time scale (pico- or femtoseconds). These ultrashort laser pulses can be focused down to generate extremely high light intensities.

The laser (light amplification by stimulated emission of radiation) is based on a process called stimulated emission, which occurs only in materials (so-called active media or gain media) that have quantum states in which a state with higher energy can become much more populated than a corresponding lower energy state. In this way, the emission occurs in a coordinated way in many atoms or molecules. Lasers are usually classified according to the nature of the active medium, that is, the medium that gives rise to the amplification of radiation by stimulated emission (gas, liquid, solid, photonic crystal, fiber).

This section aims to provide a short introduction to the basic principles of lasers with special emphasis on the generation of ultrashort laser pulses. Detailed information can be found in [14–16].

A laser is an apparatus which emits light by a process called stimulated emission. What renders the light of a laser so extraordinary is its unique properties:

1) Light from a laser is usually nearly monochromatic, which means that it has a very narrow wavelength spectrum, in contrast to white light or so-called blackbody radiation, which always consists of a very broad spectrum.
2) Laser light consists of a very narrow beam with a low beam divergence, meaning that the beam has a minimal tendency to spread while traveling through a (non-scattering) medium.
3) Laser light can reach a very high spectral energy density, which renders it a very valuable tool to investigate intrinsically weak processes such as Ramam scattering (see Section 3.13).
4) The individual waves possess a high temporal and spatial coherence, meaning that they are in-phase (see Figure 3.32) when they are emitted and even after some time due to their narrow wavelength spectrum. The propagation distance from a laser where the emitted wave maintains coherence, that is, a well-defined

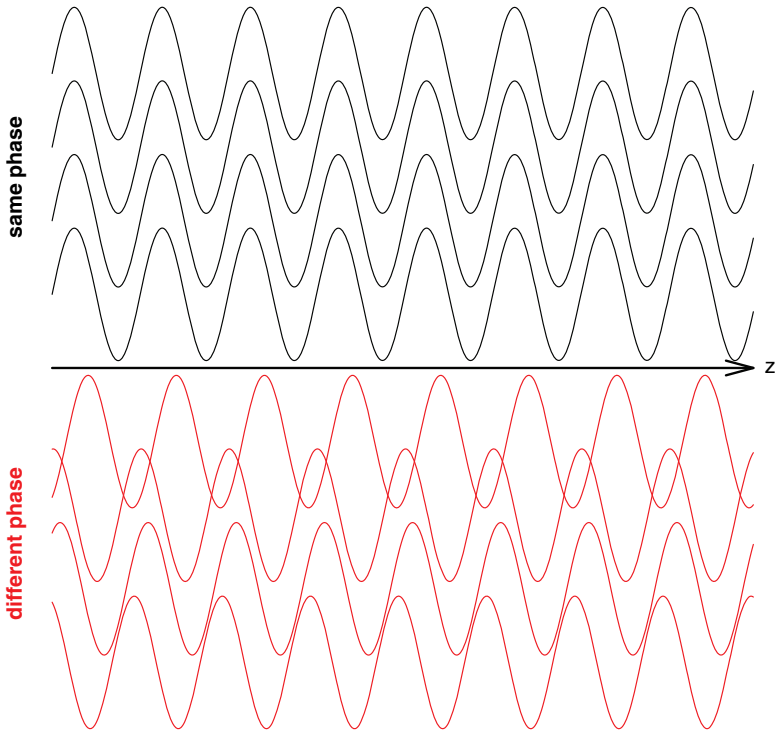

Figure 3.32 Sine waves that possess the same as compared with sine waves with different phase.

phase relation, is called coherence length. Within the coherence length the emitted light waves can interfere with each other.

To understand the lasing principle, it is necessary to investigate the connection between the processes absorption, induced emission, and spontaneous emission (note that absorption is always induced, therefore this is omitted from the term). Figure 3.33 illustrates these processes. In the case of absorption, a photon induces an atom or a molecule to step up from a ground state 1 to an excited state 2 (note that the photon must be of the same energy as the difference between the states 1 and 2, that is, $\Delta E = E_2 - E_1 = h\nu$). If the molecule is already in an excited state, there are two possibilities: either another photon of the same energy induces the molecule to fall back to the ground state by emitting a second photon, or the emission of a photon can be spontaneous. The spontaneous process is therefore obviously not dependent on the spectral energy density ρ of the electromagnetic field (see Figure 3.33) at the place where the molecule is sited. N_1 and N_2 represent the population density (of atoms or molecules) in the energy states 1 and 2 and B_{12}, B_{21}, and A_{21} are the so-called Einstein coefficients, which are a probability measure of the particular transition.

The precondition for laser activity is a population inversion: in thermodynamic equilibrium, the ground or energetically lower state is stronger occupied than its

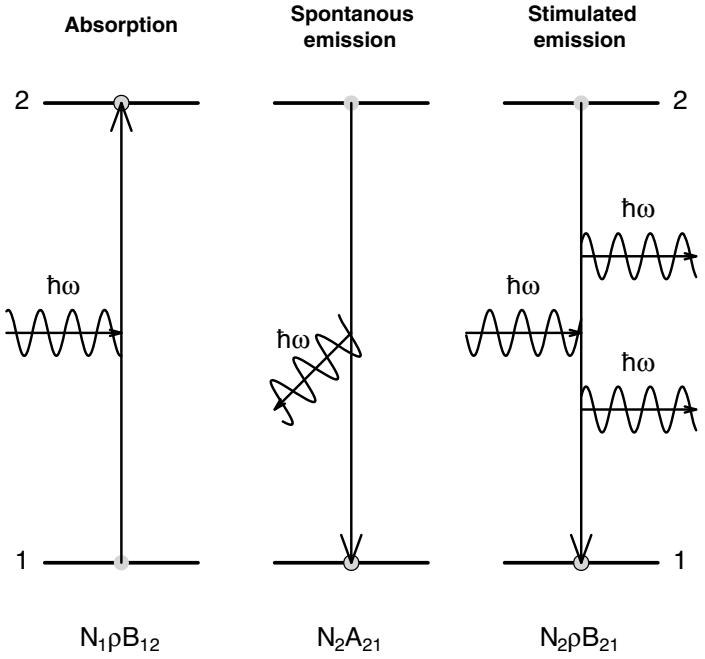

Figure 3.33 Illustration of absorption and induced and spontaneous emission.

energetically higher pendant according to Boltzmann if the degree of degeneracy g_i equals unity:

$$\frac{N_1}{N_2} = \frac{g_1}{g_2}\frac{\exp\left(-\frac{E_1}{kT}\right)}{\exp\left(-\frac{E_2}{kT}\right)} = \frac{g_1}{g_2}\exp\left(-\frac{\Delta E}{kT}\right) = \frac{g_1}{g_2}\exp\left(-\frac{h\nu}{kT}\right) \tag{3.114}$$

where, k denotes Boltzmann's constant and T represents the thermodynamic temperature. The energy difference between states 1 and 2 equals the photon energy $h\nu$. A laser is possible only if a population inversion can be caused by a pumping process so that the population of an excited state is higher than that of a ground state. This cannot be realized by optical pumping within two-state systems. Instead, a system with at least three or four states is necessary (see Figure 3.34). In the system displayed in Figure 3.34, the time constant A_{32} for a change from state 3 to 2 is much higher than that for a change from state 3 to the ground state 0 A_{30}. Therefore, most entities will use the right path. As, on the other hand, the transition from state 2 to 1 is slow, an inversion of the population will be established. If it is possible to preserve this inversion, then a continuous beam will be permanently intensified (continuous wave operation). Otherwise, an intensification can be achieved for only a short time, resulting in a pulsed operation mode which will also sometimes be desirable (e.g., for ablation of material).

To obtain as strong an inversion as possible, it is of advantage if state 2 in the system displayed in Figure 3.34 is depopulated only by induced emission and not by

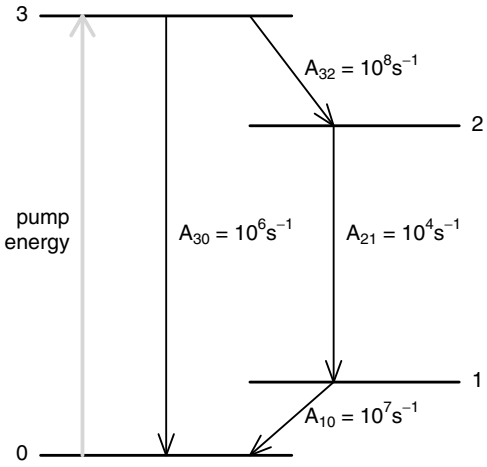

Figure 3.34 Four-state energy level diagram to achieve population inversion.

spontaneous emission or nonradiative processes. On the other hand, it is desirable if N_1 remains small, meaning that state 1 should be depopulated as fast as possible.

Most lasers are composed of the following three components: (1) an active medium (gain medium), (2) a means to deliver energy to the gain medium (energy medium), and (3) a highly reflecting optical cavity (resonator). The active medium is placed inside the resonator, which consists of a tube of length L with two highly reflecting mirrors at each end (see Figure 3.35). The resonator forms a standing wave cavity resonator for light waves. The resonator modes of a laser are characterized by radiation patterns which are reproduced on every round-trip of light in the resonator cavity. Two types of resonator modes exist: (1) longitudinal modes and (2) transverse modes. Longitudinal modes are axial standing waves and correspond to the wavelength of the wave. The frequency distance between two adjacent longitudinal modes q and $q+1$ (axial mode distance) is given by $\Delta\nu = c/2L$. Transverse modes are modes

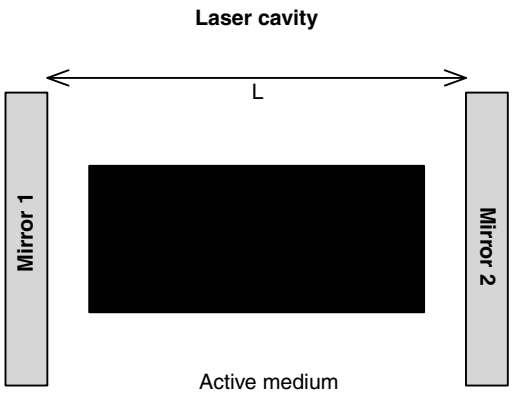

Figure 3.35 Active medium and resonator.

vibrating perpendicular to the long laser axis and are expressed by TEM_{mnq} where m and n are the number of nodes in the two directions perpendicular to the longitudinal optical axis and q is the longitudinal mode number. This means that for every transverse mode many longitudinal modes can exist. Transverse modes are determined by the geometry of the laser resonator. The TEM_{00} mode, for example, exhibits a Gaussian beam shape with its maximum intensity in the center of the beam. This TEM_{00} mode can be selected by placing an appropriately sized aperture in the laser cavity.

The lowest frequency ($q = 1$) is called the fundamental frequency. In the case of a laser it is not desirable that the power is distributed over all possible frequencies. Instead, the laser resonator is designed in such a way that the radiation energy will be concentrated in only a few modes (ideally only one, Figure 3.36), whereas the energy distributed by the gain medium to other modes will not be reflected but transmitted to the outside.

The energy pump, which consists of either an electric current or light of different frequency (pump laser), induces the stimulated emission inside the active medium. The resulting light bounces back and forth many times between the two mirrors and is increasingly (exponentially) amplified during the bouncing until saturation sets in and a certain equilibrium state is established. As one of the mirrors is partially transparent ($R > 99\%$), part of the light leaves the resonator and constitutes the laser beam. As certain losses occur within the resonator, for example, by absorption, scattering by imperfections within the active medium, and of course through the

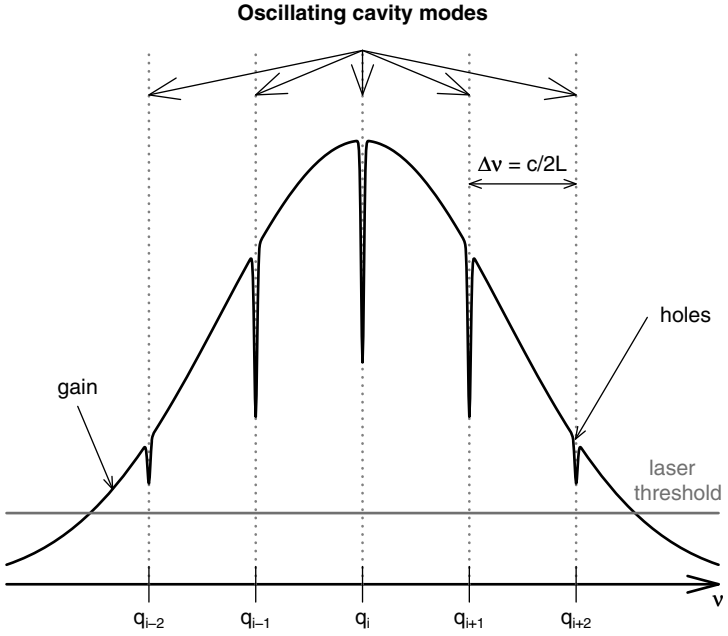

Figure 3.36 A laser cavity resonator restricts the number of oscillations to a few around discrete resonance frequencies (adapted from [14]).

leaving radiation, a minimum pump power is necessary to induce the laser, which is called the lasing threshold (see Figure 3.36).

Depending on the nature of the medium, certain types of lasers can be distinguished. In gas lasers, gases form the active medium, for example, the helium–neon laser, which emits at a variety of wavelengths of which the 633 nm line is very common, and the carbon dioxide laser, which is very efficient at the IR wavelengths 9.6 and 10.6 μm. Also fairly often employed, for example in Raman spectroscopy, is the argon ion laser with its most commonly used lines at 458, 488, and 514.5 nm.

Chemical lasers are powered by chemical reactions, for example, excimer lasers. Excimer lasers usually generate UV light and are therefore used for the photolithographic step in the production of microchips. Examples are the fluorine laser (emitting wavelength 157 nm), the argon fluoride laser (193 nm), and the krypton fluoride laser (248 nm).

Solid-state lasers involve a crystalline or glassy host doped with ions, for example, the ruby laser, which consists of corundum (crystalline Al_2O_3) doped with 0.05–0.1% chromium oxide (Cr_2O_3), which contributes the actual active ion. Another well-known dopant, neodynium, which is usually employed in yttrium-containing hosts such as yttrium aluminum garnet (YAG, $Y_3Al_5O_{12}$), constitutes high power lasers (Nd:YAG) in the NIR spectral region at 1064 nm, which is also often used in its frequency-doubled form at 532 nm. Also the titanium-doped sapphire laser should be mentioned, the frequency of which is highly tunable between 650 and 1100 nm, which is often-used in spectroscopy, especially as ultrashort pulses can be generated (see below). The advantage of solid state lasers is a much higher inversion density due to the higher material density compared with gases. As a consequence, the output power per unit volume is generally much higher, but requires efficient cooling as heat is generated by unconverted pump power. A solution to this problem is to use fiber lasers, in which the host medium consists of glass, which is drawn into fibers. A characteristic of fiber lasers is that the exciting light can be guided through long gain regions and an advantageous surface area-to-volume ratio is achieved, which easily allows efficient cooling. Another type of solid-state laser is semiconductor lasers, for example, laser diodes. They are often used to pump other lasers due to their high efficiency and due to the broad wavelength region that they cover (about 375–1800 nm).

Other types of lasers are photonic crystal lasers (consisting of well-ordered nanostructures leading to mode confinement), free electron lasers (widely tunable and with high output but with high cost and space considerations, hence not standard laboratory equipment), and also dye lasers in which organic dyes are employed as active media.

For more details concerning laser types, see Chapter 4.

3.7.1 Mode Locking

As outlined in Section 3.6, for inducing nonlinear optical effects [e.g., multi-photon absorption, SHG, THG, CARS, SRS (see Section 3.6)], pulsed lasers with high peak intensities are required. An ultrashort pulse of light is a laser pulse whose time duration τ_p is in the order of femtoseconds (10^{-15} s). Such pulses are characterized by

a broadband optical spectrum determined by the inverse pulse length τ_p. Ultrashort pulses are created by mode-locked oscillators.

In the following we briefly introduce the mode-locking technique used to generate ultrashort light pulses. A laser cavity playing the role of a frequency selector as described above allows oscillations in only a very few narrow-frequency domains and therefore cannot deliver ultrashort laser pulses. In other words, a laser operating in its free multimode regime oscillates simultaneously over all the longitudinal modes for which the gain is greater than the cavity losses. Lasers in a free-running regime produce waves with a mixture of longitudinal modes with a random mode-to-mode phase relationship. Since each longitudinal mode oscillates independently of the other modes, the output intensity of a laser operating in its free multimode regime is a chaotic sequence of fluctuations (see the upper part of Figure 3.37). Hence the intensity output of a free multimode regime laser results from the interference of longitudinal modes with random phase relationships. However, if it would be possible to lock the phases of the oscillating longitudinal modes, that is, to establish a fixed phase relationship the laser output would consist of a periodic sequence of pulses. In other words, the constructive interference of longitudinal modes generates

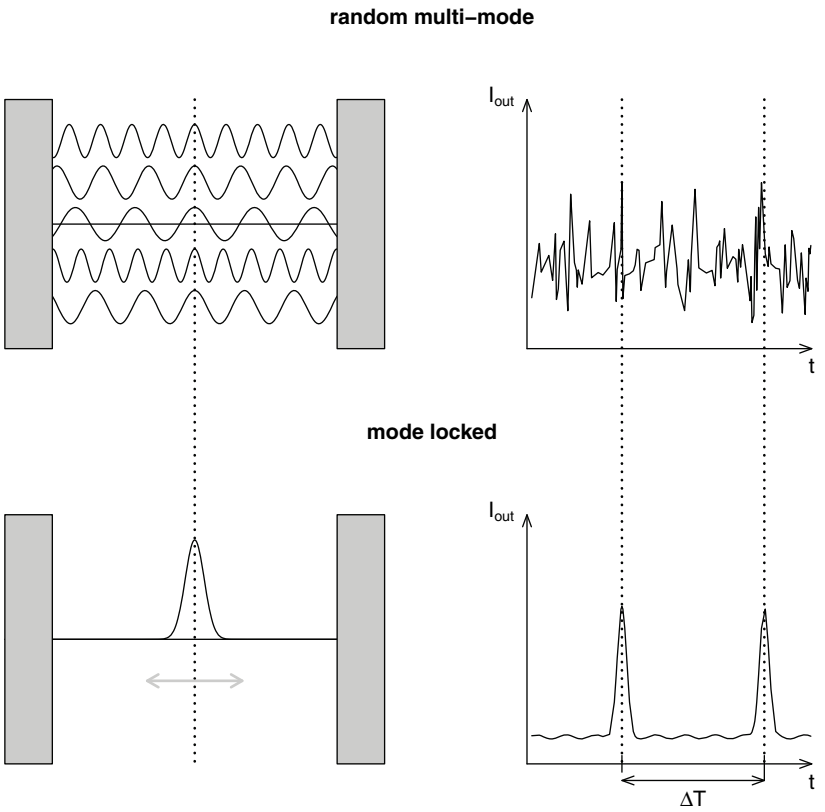

Figure 3.37 Illustration of the mode-locking principle (adapted from [16]).

a wave packet which oscillates back and forth within the laser cavity. This means that the laser beam consists of a periodic series of pulses with a repetition time $T = 2L/c$ (see the lower part of Figure 3.37). The width of the pulses (pulse duration $\Delta\tau_p$) depends on the number of modes N contributing to the wavepacket, that is, the number of phase-locked longitudinal modes: $\Delta\tau_p \sim N$. Pulses which are generated with identical initial phases are called Fourier transform limited. Figure 3.37 depicts schematically the mode locking principle to generate short laser pulses.

Now the question arises of how to produce mode locking, that is, a fixed phase relationship between the oscillating longitudinal modes. One method to achieve mode locking is to introduce a nonlinear medium inside the cavity, which is able to promote stronger intensities inside the cavity. By doing so, initial intensity maxima of a laser running in a free multimode regime (see Figure 3.37) will grow much stronger at the expense of less intense temporal features because of the competition within the gain medium. Eventually the situation arises where all the cavity energy is concentrated in a single pulse. However, the selection of a single starting intensity maximum in the time domain is totally equivalent to establishing a fixed phase relationship between the oscillating longitudinal modes in the frequency domain. In other words, the introduction of a nonlinear medium promoting stronger intensity starts mode locking out of normal intensity fluctuations. This means that one starting intensity fluctuation is slightly more intense than the others and is promoted by the nonlinear medium and therefore reduces its losses.

One of the most successful schemes of mode locking is Kerr lens mode locking (KLM). This scheme, which is also called self-mode locking, is based on the optical Kerr effect (self-focusing), which was described in Section 3.6.3. Here, the laser medium acts as a Kerr medium, that is, high-intensity light is focused differently to low-intensity light due to the intensity-dependent nonlinear refractive index. That means that the active laser medium decreases the losses of the initially stronger intensity peaks of the laser cavity by behaving like a lens (see Figure 3.38). Hence strong intensity maxima of the laser cavity are much more strongly focused than the weaker ones, for which focusing is negligible, and the transverse laser wave structure with respect to its intensity is modified. By carefully inserting an aperture or a slit in the laser cavity, the differences between the losses undergone by the weak intensities and those undergone by the intensity maxima can be increased. Most of the stronger intensity maxima can pass through the aperture whereas the weak intensity maxima are blocked.

This KLM principle exists in the most successful femtosecond laser in biophotonics, the titanium–sapphire (Ti:sapphire) laser. The active lasing medium consists of a sapphire crystal (Al_2O_3) which is doped with titanium atoms. The Ti:sapphire lasers are pumped by other lasers with a wavelength around 500 nm. The Ti:sapphire laser emit red and NIR light. Figure 3.39 depicts the configuration of a KLM Ti:sapphire laser.

Such KLM Ti:sapphire lasers routinely generate pulses of less than 100 fs at a repetition rate of 80 MHz with an average power of 1W. This corresponds to peak powers of close to 100 kW, which allows a great variety of nonlinear effects to be induced. Hence the KLM Ti:sapphire laser has become the most important light source for nonlinear microscopy in biophotonics.

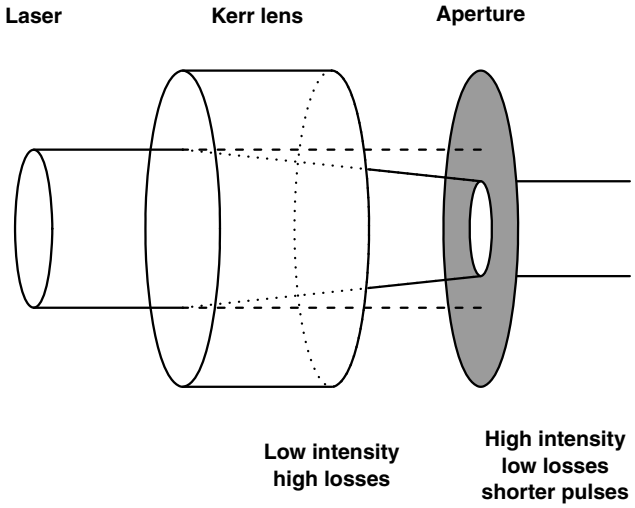

Figure 3.38 Illustration of the Kerr lens mode locking principle.

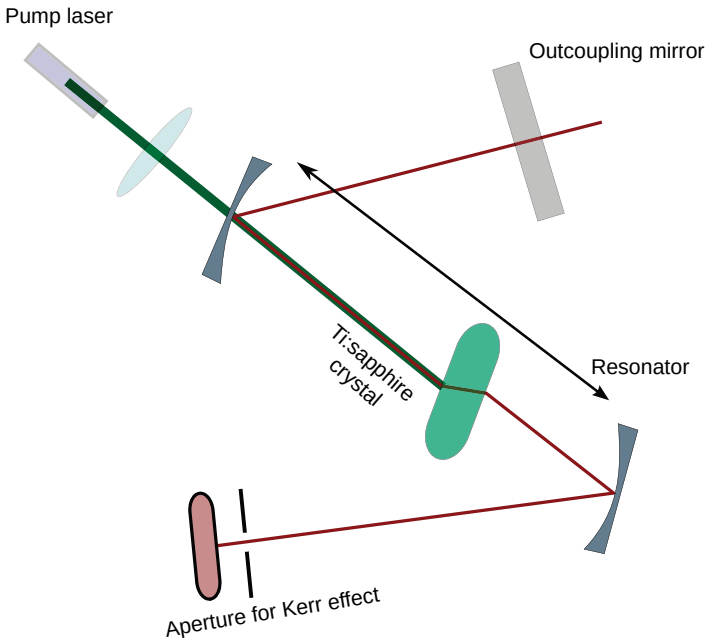

Figure 3.39 Cavity design of a KLM Ti:sapphire laser.

3.8 Infrared Spectroscopy

In Chapter 2, it was shown that for the description of molecular systems quantum effects need to be considered. This means that the energy of a microscopic system is quantized, that is, divided into well-defined energy portions. Molecules exhibit certain movement patterns, that is, the molecular degrees of freedom can be classified into translation, rotation, and vibration. The energy of all these degrees of freedom is quantized. Likewise, the electron energy in a molecule is quantized.

This section deals with molecular vibrations. A polyatomic molecule exhibits a multitude of vibrations. Of interest are the so-called normal mode vibrations. These vibrational motions differ from each other by different atomic displacements. One can differentiate between pure stretching (chemical bonds are stretched or compressed) and pure bending (bond angles are changed) vibrations, and mixed forms exhibiting both stretching and contraction of chemical bonds and extension and reduction of the bond angles. The easiest way to describe such a vibration is by approximating or describing the chemical bond as atoms held together by a spring. The vibrational frequency then depends on the atomic mass and the spring force constant. The atoms move during a vibrational period towards or away from each other. This movement is repeated periodically and can be easily described by a harmonic oscillator. A harmonic oscillator is a system performing periodic vibrations about its equilibrium position where the restoring force F is direct proportional to the displacement. According to quantum theory, the vibrational energy is also quantized. Light with the appropriate frequency can be absorbed by the ensemble of vibrating molecules, promoting them from the vibrational ground state into the first excited vibrational state. The light frequencies required to excite vibrational absorptions directly covers the spectral range from 2.5 to 1 mm or, in spectroscopic wavenumber units, from 400 to 4000 cm^{-1}. This frequency range is also called the mid-infrared (MIR) region.

Since the number and type of vibrations depend directly on the atoms present in the molecule and in particular how these atoms are chemically bonded to each other, IR absorption spectra can be considered as a molecular fingerprint of the molecules existing in a biological sample. Moreover, the energy of the vibrational transition depends on the chemical environment in which the molecules are embedded. Therefore, vibrational spectroscopy provides a key to learning about the molecular environment in which the molecules are located. However, the application of IR absorption spectroscopy or microscopy in biophotonics is often hindered by the presence of water, since water exhibits broad IR absorption bands, causing a large background.

This section provides a general introduction to IR absorption spectroscopy. A complete detailed description of IR absorption and IR spectroscopy is given in [5].

The energy of a molecule consists of translational energy (the center of gravity of the molecule moves), rotational energy (the molecule rotates around the center of

gravity), vibrational energy (the distances of the atoms vary), and electronic energy (electrons are in excited states). In this section we focus on the vibrations of a molecule, which are usually excited in the IR spectral range. This range extends from about 10 to 12 800 cm^{-1}, a unit which is the inverse of the wavelength and is generally preferred in IR (and in Raman) spectroscopy. In microns this range is from 1000 to 0.78 μm. Generally, the IR spectral range is further divided into the parts near-infrared (NIR, 4000–12 800 cm^{-1}), mid-infrared (MIR, 400−4000 cm^{-1}) and far-infrared (FIR, also called the terahertz regime, 10−400 cm^{-1}).

A polyatomic molecule exhibits a multitude of vibrations. However, of interest are the so called normal mode vibrations. Normal modes describe collective, independent, and synchronous vibrational displacements (motions) of atoms or groups of atoms within molecules. Since the normal modes of a molecular system are independent of each other, that is, they do not couple with each other, they can be excited without exciting another normal mode. A nonlinear N-atomic molecule exhibits $3N-6$ normal modes. This can be easily understood by analyzing the different molecular degrees of freedom, namely translation, rotation, and vibration. If we consider a molecule consisting of N atoms, the N atoms could move independently through the space by varying one of its three coordinates (x, y, and z) if they are not connected via chemical bonds. This independent motion would result in $3N$ translational degrees of freedom. However, the atoms in a molecule cannot move independently through the space but only the whole molecule as an entity. Hence the motion of the molecule through the space can be described by the three directions in space x, y, and z. Therefore, these three degrees of freedom describe the translational motion of the whole molecule in space from the the entirety of motions, that is, of the $3N$ degrees of freedom, only $3N-3$ remain. By taking into account that a molecule can rotate along the three axes of the coordinate system, we need to subtract three more degrees of freedom for the rotational motion. Of the original $3N$ degrees of freedom, only $3N-6$ remain.[12] These remaining degrees of freedom can be assigned to the vibrational degrees of freedom (displacements of the atoms against each other), that is, the normal modes of the molecule. The four normal modes of CO_2 are shown in Figure 3.40. These vibrational motions differ from each other by different atomic displacements. One can differentiate between pure stretching (chemical bonds are stretched or compressed) and pure bending (bond angles are changed) vibrations, and mixed forms exhibiting both stretching and contraction of chemical bonds and extension or reduction of the bond angles.

The easiest way to describe such a vibration is by approximating or describing the chemical bond as atoms hold together by a spring. In this view, we consider the atoms as mathematical points with masses that are connected by massless springs. These springs represent the bonds between the atoms. The vibrational frequency then depends on the atomic mass and the spring force constant. The atoms move during a

12) For nonlinear molecules, three coordinates are needed to describe their orientation in space. However, for linear molecules, two coordinates are sufficient since the moment of inertia for rotation around the molecular axis is vanishingly small (i.e., rotation only takes place around the two axes perpendicular to the molecular axis). This means that three or two degrees of freedom which remain after subtracting the three translational degrees of freedom belong to the rotation of the molecule.

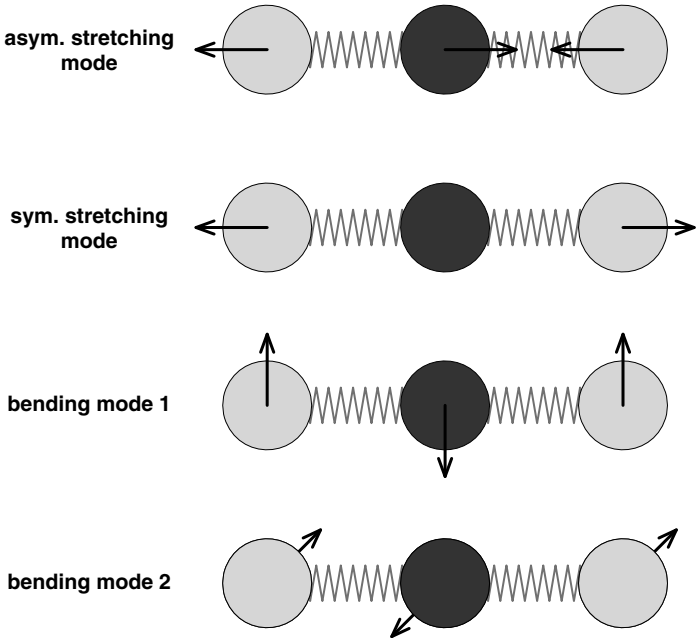

Figure 3.40 Four normal modes of CO_2. The atoms move along the arrows. These vibrational motions exhibit different vibrational frequencies and can be excited independently, bending mode 1 and 2 are identical but mutual perpendicular motions.

vibrational period towards or away from each other. This movement is repeated periodically and can be easily described by a harmonic oscillator. In the following we examine the resulting equations for a harmonic oscillator for the simplest case of a diatomic molecule (see Figure 3.41a).

Classically, the potential energy of a molecule depends on the distance R between the nuclei. A good approximation of this curve, at least around the equilibrium distance R_0, is given by a parabola which is represented by the equation $V = (1/2)k(R-R_0)^2 = (1/2)kx^2$, where $R-R_0 = x$ is the displacement from the

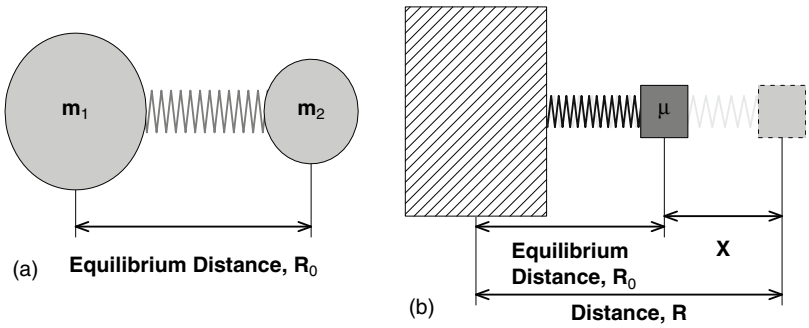

Figure 3.41 Illustration of the replacement of the molecule by an equivalent spring pendulum.

equilibrium position, k is the force constant, and V is the potential energy. Such a relation is the consequence of assuming a restoring force, which is proportional to $x = R - R_0$ with proportionality constant k, given by $F = -\mathrm{d}V/\mathrm{d}R = -k(R - R_0) = -kx$. It can be shown that the vibration of a diatomic molecule with two masses m_1 and m_2 is equivalent to that of a so-called reduced mass μ in a spring pendulum (see Figure 3.41b), with the reduced mass given by

$$\mu = \frac{m_1 \cdot m_2}{m_1 + m_2}. \tag{3.115}$$

Note that if one mass is much smaller than the other, than the small mass is to a good approximation the reduced mass. As a consequence, if H atoms are involved in a vibration, nearly exclusively these move, whereas the rest of the molecule remains stationary.

If we assume that the displacements from the equilibrium position of the spring is small, the force that tries to push or pull the mass is proportional to the displacement $x(t)$ from the equilibrium position ($x = 0$), $F_x(t) = -k \cdot x(t)$, where k is again the force (or the spring) constant. The situation is now equivalent to that of an electron bound to a nucleus which we treated in Section 3.2. Applying Newton's law, $F = \mu \cdot \mathrm{d}^2x/\mathrm{d}t^2$, we arrive at an equation similar to Equation 3.11:

$$\frac{\mathrm{d}^2x}{\mathrm{d}t^2} + \frac{k}{\mu} \cdot x(t) = 0 \tag{3.116}$$

where we have just replaced the mass of the electron m_e by the reduced mass μ. As a consequence, $x(t)$ and its second derivative again differ only in a constant ω_0:

$$\frac{\mathrm{d}^2x}{\mathrm{d}t^2} = -\omega_0^2 \cdot x(t) \tag{3.117}$$

with the solutions $x_0 \cdot \sin(\omega_0 t)$, and the only difference that the constant ω_0 is now given by $\omega_0 = \sqrt{k/\mu}$. This also shows that the dispersion relation that we derived in Section 3.2 for an electronic excitation still holds true in the IR spectral range in spite of the completely different nature of the excitation (see also Figure 3.11).

As ω_0 is directly proportional to the square root of the force constant k and indirectly proportional to the square root of the reduced mass μ, we can expect that the wavenumber of a particular vibration will rise if we increase the bond strength while keeping the masses constant or will decrease if the masses are increased while the bond strength remains constant. This finding is exemplarily illustrated in the following:

- In carbon monoxide, the oxygen and the carbon atoms are strongly bound by a partial triple bond. As a diatomic molecule it has only one vibration which can be found in the MIR region at 2143 cm^{-1}. In the case of a more weakly bound C = O double bond in $R_1R_2C = O$, as can be found, for example, in aldehydes (R_1 = H, R_2 = alkyl or aryl) or ketones (R_1/R_2 = alkyl/aryl), the wavenumber is downshifted to 1600–2000 cm^{-1}. A further downshift can be noticed for alcohols (R–OH) or ethers (R_1–O–R_2), where the C–O vibration appears between 1000 and 1200 cm^{-1} depending on the molecular groups R.

- C−H vibrations can usually be found between 2800 and 3000 cm^{-1} in alkanes, whereas in the deuterated species the C−D vibration usually shows up around 2100 cm^{-1} since the reduced mass has been almost doubled due to the atomic mass of the deuterium atom being double that of the hydrogen atom.

As biological matter consists nearly exclusively of comparably light atoms such as H, C, N, O, S, and so on, the fundamental vibrations of tissue can be found nearly exclusively in the MIR region with the stretching vibrations involving the movement of an H atom having the highest wavenumbers. A higher force is necessary to lengthen or shorten a spring than to bend it, and the same is valid for molecular vibrations. Accordingly, bending vibrations can be found at lower wavenumbers than their corresponding counterparts.

In Section 2.2.3, it was shown that according to quantum theory the vibrational energy of a molecule cannot be continuous but quantized. This means that the energy of a harmonic oscillator can only amount to

$$E_v = \left(v + \frac{1}{2}\right)\hbar \cdot \omega_0 \tag{3.118}$$

where v is the quantum number of the harmonic vibration, $\hbar$ is Planck's constant devided by 2π and ω_0 is the classically derived vibrational frequency (see above). This quantum harmonic oscillator can be symbolized by horizontal lines inside the parabolic harmonic potential (see Figure 3.42a). It can be seen that the energy levels form a uniform ladder with a spacing of $\hbar\omega_0$. Furthermore, the vibrating quantum

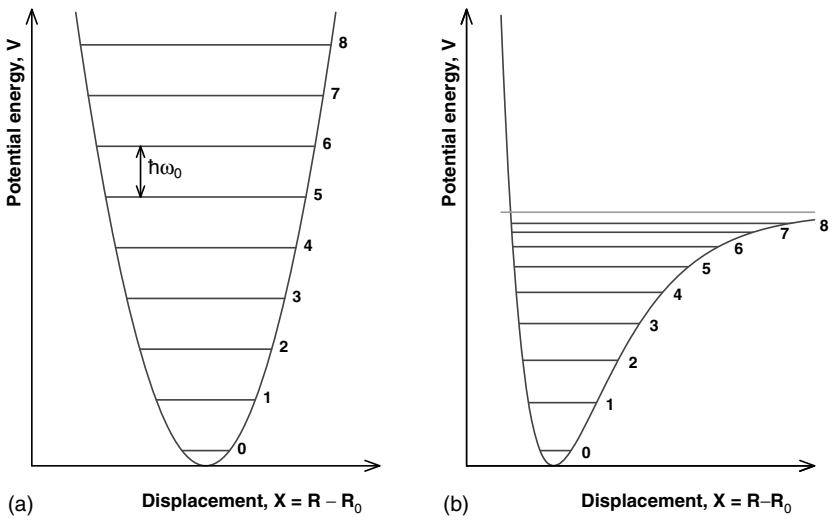

Figure 3.42 Comparison between (a) harmonic and (b) anharmonic oscillator. The anharmonic oscillator considers the fact that molecules can dissociate for high vibrational energies. Whereas for the harmonic oscillator the energy distance between the vibrational levels is constant, the corresponding energy difference decreases for the anharmonic oscillator with increasing energy until a continuum is reached where dissociation takes place.

mechanical system possesses a zero point energy of $^1/_2\hbar\omega_0$ because the smallest allowed value of v is 0. This means that molecules are always vibrating and are never at "rest."

Since normal modes can be excited independently (they are decoupled), every normal mode q is a harmonic oscillator independent of the rest of the molecule:

$$E_{q\mathrm{v}} = \left(\mathrm{v}_q + \frac{1}{2}\right)\hbar\omega_{0,q} \tag{3.119}$$

where v_q is the vibrational quantum number of the normal mode q, $\omega_{0,q} = \sqrt{k_q/\mu_q}$ is the vibrational frequency of the normal mode q with μ_q the effective mass of the vibration, that is, a measure of the mass which is moved during the vibration, and k_q is the force constant of the normal mode. Hence the total vibrational energy E_{vib} of polyatomic molecule is

$$E_{\mathrm{vib}} = \sum_{q=1}^{3N-6\ (\text{or } 3N-5)} \left(\mathrm{v}_q + \frac{1}{2}\right)\hbar\omega_{0,q}. \tag{3.120}$$

A normal mode q is excited when the molecule absorbs a quantum of energy $E = \hbar\omega_{0,q}$ corresponding to the normal mode's frequency $\omega_{0,q}$. It follows from the Boltzmann distribution (see Equation 3.114) that at room temperature most molecules will be in their vibrational ground state initially, that is, the vibrational quantum numbers of all normal modes v_q equals 0. Hence IR light in resonance with a particular normal mode (i.e., of frequency $\hbar\omega_{0,q}$) can be absorbed by the ensemble of vibrating molecules, promoting them from the vibrational ground state ($\mathrm{v}_q = 0$) into the first excited vibrational state ($\mathrm{v}_q = 1$).[13] During the course of the absorption process, only the amplitude of the normal mode out of equilibrium position changes while the vibrational frequency $\omega_{0,q}$ remains constant.

The absorption of IR radiation with the appropriate frequency promoting the molecule from its vibrational ground state into the first excited vibrational molecular state decreases the transmitted intensity with respect to the incident intensity (see also Section 3.4). A plot of the transmitted intensity versus the radiation frequency yields an IR absorbance spectrum. Figure 3.43 displays a typical IR absorbance spectrum of an organic molecule, propionamide.

As the molecules become more complex, so do their vibrational patterns, and vibrations (normal modes) often involve change of both the distance and angles. However, some of the vibrations are constrained on single molecular bonds or functional groups (localized vibrations) whereas other vibrations involve the complete molecule. The localized modes consist of valence (stretching), bending,

13) It can be shown in quantum mechanics that for the model of a harmonic oscillator the absorption of a photon can increase the vibrational quantum number only by one. That means that the so-called specific vibrational selection rule for the absorption of radiation by a molecular vibration for the model of a quantum mechanical harmonic oscillator can be expressed by $\Delta\mathrm{v}_q = 1$. This selection rule can be derived from an analysis of the expression for the transition dipole moment (see Equation 3.121) and the properties of integrals over harmonic oscillator wavefunctions (see Chapter 2).

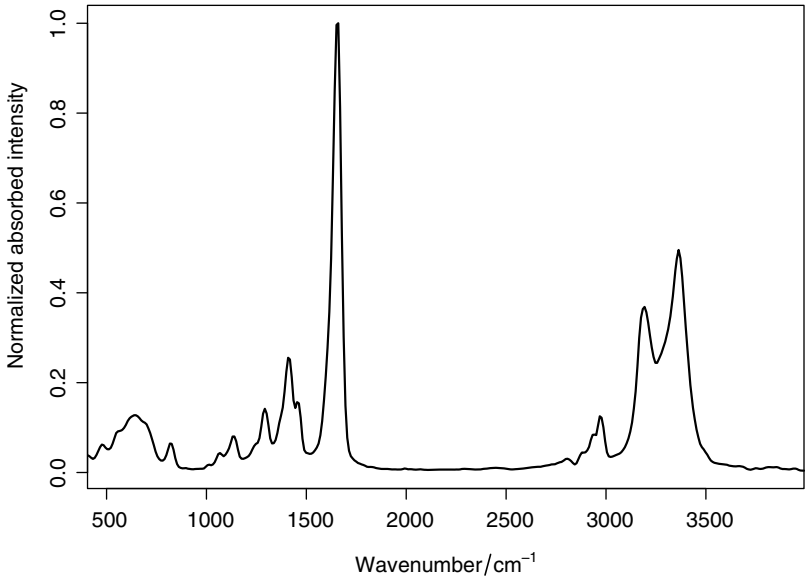

Figure 3.43 IR absorbance spectrum of propionamide.

rocking, twisting or wagging vibrations. Many of these localized normal modes can be used to identify functional groups such as $-C\equiv N-$, $-C\equiv C-$, $-C=C-$, and $-C=O-$. In complex molecules with atoms having mostly comparable masses such as the C, N, and O atoms in organic molecules, many vibrations involve not only some atoms but usually the complete backbone of the molecule. These backbone or skeletal motions lead to IR absorptions between 600 and 1500 cm^{-1}; this wavenumber range shows a more complex pattern the more complex the backbone of a molecule is. It is therefore a characteristic of the molecule and this range is called the fingerprint region. Thus, an IR spectrum can be divided into two regions: (1) above 1500 cm^{-1} absorption bands due to functional groups are present whereas (2) the wavenumber region below 1500 cm^{-1} is dominated by the presence of many absorption bands characterizing the complete molecular entity. The latter region is called the fingerprint area since it is characteristic of a particular molecule. This fingerprint region can be used to identify molecules.

In the solid state, free rotations and translations are not possible and the corresponding movements of the molecule as a whole, for example in a crystal lattice, constitute a third class of vibrations, the so-called lattice vibrations. Therefore, in the solid state all $3N$ degrees of freedom of a molecule are vibrations. As the interactions between molecules are usually much smaller than the interactions between atoms which lead to covalent bonding, the force constants for lattice vibrations are usually very small, so that the lattice vibrations can be found in the FIR spectral region. Therefore, especially in the FIR region, the more complex

organic molecules display interesting spectral patterns, especially if the interactions consist of intermolecular hydrogen bonding. The corresponding vibrational modes most probably are very sensitive to the intra- and intermolecular structure and should therefore also provide a fingerprint of the molecule like the backbone vibrations in the MIR region, but with emphasis on the conformational state of the molecule and interactions with the environment.

In addition to the transition from the vibrational ground state to the first excited vibrational state (fundamental transition), direct absorption processes into the second, third, or even higher vibrational states can also take place, but with much lower probability than the fundamental transition. These higher transitions are called overtones. The energy required to excite overtones lies mostly in the NIR region. The selection rule for a quantum mechanical harmonic oscillator ($\Delta v = \pm 1$) forbids the presence of overtones. However, the harmonic oscillator model, which is based on the parabolic potential energy curve, is a good approximation only around the equilibrium position. This means that for small displacements from the equilibrium position, which is true for small vibrational quantum numbers, the harmonic oscillator model is well suited to describe a vibrational absorption process. However, for large displacements, that is, for high vibrational states, the model of the harmonic oscillator model (parabolic potential) is problematic since it is impossible to put an arbitrary amount of energy into the system without destroying the molecule. However, it is well known that chemical bonds can break, that is, dissociate, or molecules can fall apart if they are heated too much. To allow for dissociation to take place, the harmonic oscillator model has been refined as the anharmonic oscillator model, which takes into account the fact that molecules at high vibrational energies dissociate, that is, the spring between the atoms breaks. Here, the vibrational motion becomes anharmonic in such a way that the restoring force F is no longer linearly related to the displacement, $x = R - R_0$. Whereas for the harmonic oscillator the energy difference between quantized vibrational states is always the same (see Figure 3.42b) this difference for the anharmonic oscillator decreases with increasing energy till one reaches a continuum where all vibrational states have almost the same energy (see right side of Figure 3.42). Anharmonicity accounts for the appearance of weak overtone absorptions in the NIR. That means when two quanta are absorbed the first overtone is excited, and so on to higher overtones (see Figure 3.42a). Since the spacing between the energy levels in an anaharmonic oscillator decreases with increasing vibrational quantum numbers, the first overtone appears at a wavenumber position slightly lower than twice that of the fundamental transition. Excitation of the higher overtones involves progressively less and less additional energy and eventually leads to dissociation of the molecule, when reaching the continuum where the atoms of the molecule can leave the molecules' force field. The anharmonic oscillator also accounts for so-called combination bands, which can occur at frequencies that correspond to a sum or a difference of the fundamental frequencies of two different normal mode frequencies. These bands, just as overtones, are comparably weak.

As molecules and especially biomolecules can be almost arbitrarily complex and consist of a large number of atoms (e.g., for proteins up to 10 000 and more), the

number of possible vibrations can be high. Accordingly, it is obvious that already comparably small molecules have a large number of different vibrations, which should render a spectrum very complicated. Fortunately, for a number of reasons the number of bands displayed in an IR spectrum is in many cases much smaller than the number of vibrations (i.e., $3N-6$ or $3N-5$). Unfortunately, the former is in general not true for biomolecules, but even if the number of bands is high, valuable information can nevertheless be gained. Since the frequencies of the vibrations depend on the geometry of the molecules and the masses of the atoms, whereas the intensity depends on the partial charges of the atoms, vibrational spectroscopy is very sensitive to structural changes of molecules and how and with what composition they form aggregates such as cells and tissue. Generally, not all vibrations cause a band in an IR spectrum. Since IR light is nothing else than a change of the electric field at the location of a molecule, a requirement for a vibration to be excited by IR light is that during the vibration the dipole moment of a molecule is changed. In other words, the change of the electric field needs to affect negative charges differently to positive charges so that the distance between the centers of the negative and the positive charges in a molecule changes. One consequence is that in a highly symmetric molecule such as benzene, usually only a few of the totality of vibrations are IR active.

Figure 3.44 displays two normal modes of benzene. Only the vibration illustrated in Figure 3.44b changes the dipole moment of the benzene molecule during the course of the vibration, that is, this vibration gives rise to an oscillating dipole and can therefore be excited by the absorption of an IR photon. The normal mode shown in Figure 3.44a does not lead to an oscillating dipole as it is impossible to excite this vibration through a direct IR absorption process.

Without going into all the details, which is impossible within this book, the following is true in general: the more complex a molecule is, the lower its symmetry

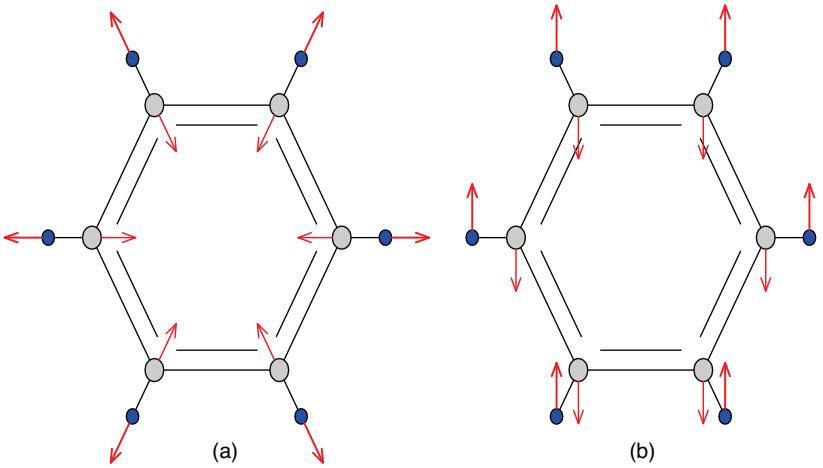

Figure 3.44 Two vibrational modes of benzene. The vibration illustrated in (a) is IR inactive as no dipole moment change occurs during the vibration.

usually is, which eventually renders all vibrations IR active. In many cases it is therefore very difficult, if not impossible, to reach the ultimate goal for every vibrational spectroscopist (the same is also true in Raman spectroscopy), namely to assign to each band in a spectrum a particular molecular vibration. Even if this ultimate goal cannot be achieved, vibrational spectroscopy is nevertheless an invaluable tool. Assuming that a spectrum of a pure substance was taken, a first inspection of it usually gives general hints about the class of substance, such as whether it is an aliphatic compound consisting only of single bonds between C atoms or if double bonds are present, which means that the compound is an alkene or an aromatic compound. Additional bands can reveal the presence of functional groups such as −OH and C=O groups, which have characteristic bands in distinct spectral ranges clearly separated from the C−C bands or C−H bands of pure hydrocarbons. This allows us to determine whether the compound is, for example, an alcohol, an organic acid, or an amine. This further enables us to distinguish proteins from fat as the former consists of amino acids and the latter of aliphatic or olefinic acids esterified to glycerol. It is even possible to distinguish the different amino acids and therefore different proteins as they consist of different quantities of amino acids. This example and other complex compounds, however, push IR spectroscopy and vibrational spectroscopy in general to their limits as the differences in the spectra become very subtle and eventually unrecognizable by visual inspection. To proceed and to permit the interpretation of spectra in such cases, usually different chemometric methods such as multivariate calibration, pattern recognition, cluster analysis, and multivariate curve resolution are employed. Such methods even allow the detection of the subtle changes in composition that healthy tissue undergoes when changing to precancerous and cancerous tissue.

In Section 3.13, it will be shown that there does not always need to be a direct absorption of radiation to promote a vibrational transition. Vibrational transitions can also take place via an inelastic light scattering process called Raman scattering. The two vibrational spectroscopic methods, Raman and IR absorption spectroscopy, are complementary methods based on two different light–matter interaction phenomenam thus exhibiting different selection rules. As has been shown above, selection rules determine which vibration of a molecule can be excited by what method. In the case of IR absorption, one photon directly promotes the molecule into a higher vibrational state whereas in the Raman scattering process two photons are involved. In Section 3.13, it will be demonstrated that in order for a molecular vibration to be Raman active, the polarizability α has to change during the vibration so that a molecular vibration can be promoted via an inelastic scattering process into a higher vibrational state. The benzene vibration displayed in Figure 3.44 which is IR inactive can be excited via a Raman scattering process, nicely demonstrating the complementarity of Raman and IR spectroscopy.

The important role of vibrational spectroscopy and in particular Raman spectroscopy in biophotonics (Raman spectroscopy, in contrast to IR spectroscopy, can be applied in aqueous environments) can be found in Section 3.13, where a detailed introduction to Raman spectroscopy is given.

3.9
UV–Vis Spectroscopy

Section 3.4 provided a classical introduction to the absorption of light. It was shown that the contrast in bright field microscopy is based on white light absorption changes of colored substances. This section aims to characterize the molecular origin of the absorption of visible and UV light by molecules based on quantized electron energies in molecules.

In the UV–Vis spectral range, the comparably high energy of the photons is able to excite electrons, which successively and in pairs fill up the energy levels of atoms or molecules, to higher energy states. Usually, the energy of the photons is only sufficient to excite those electrons which are in the highest occupied states (so-called valence electrons) to the lowest unoccupied states unaffected by being involved in bonding or not. Especially electrons involved in double bonding between C atoms can have low excitation energies, in particular if there is more than one double bond and the double and single bonds alternate. Then the excitation wavelength is shifted further to the red the more alternating single and double bonds are present in the molecule. Functional groups involving heteroatoms such as O, N, and S, which have free electron pairs (valence electrons that are not involved in bonding), can not only lead to a further red shift of excitation wavelengths but also cause intensification of the absorption. The intensity of an absorption in the UV–Vis is influenced by rules from quantum mechanics. Accordingly, the transition from a certain energy level to another may usually be forbidden or only "weakly" allowed due to a certain structural distortion of a molecule which breaks the rules. Such transitions are nevertheless weak and can be several orders of magnitude less intense than allowed transitions. An example of such a weakly allowed transition is the so-called $d{-}d$ transition in transition metal atoms such as Cu, Fe, and Ni, which renders many or their compounds colored. Electronic transition can be localized on an atom or a molecule but photons can also induce transitions of electrons from molecules to other molecules or to ions. Such charge transfers are often very strong transitions and play important roles in photochemistry and photobiology. In complex molecules, it is often a small part named a chromophore that is responsible for the color. Nevertheless, if the chromophore is separated from the rest of the molecule the properties of a mixture may be different from those of the compound due to interactions that may be due to secondary and ternary structure.

This section aims to present a short introduction to UV–Vis spectroscopy. Detailed information can be found in [17–20].

The UV–Vis spectral range can be subdivided into three different parts, namely the visible ranging from wavelengths of 700 to 400 nm, the near-UV covering the range from 400 to 200 nm, and the far-UV or vacuum UV extending from 200 down to 10 nm. Due to the higher energy of light in this spectral wavelength range, it is

possible to excite electrons from their ground state to higher energy levels. To understand the electronic excitations completely it would be necessary to have a detailed knowledge of quantum theory and bonding theories. As we cannot cover this topic fully here, we will just give a very general introduction and subsequently focus on different examples which are important in the context of this book.

In Chapter 2, it was shown that the quantum mechanical description of molecules allows only certain energy states of an electron. These quantized molecular energy states are described by many-electron wavefunctions. These many-electron wavefunctions are commonly approximated by an antisymmetrized product (Slater determinant) of one-electron wavefunctions called molecular orbitals (MOs). In other words, electronic states can be approximated by a single electronic configuration which is commonly displayed by a molecular orbital diagram where the MOs are represented by horizontal lines. The MOs are filled with electrons obeying the Pauli exclusion principle (the maximum number of electrons occupying an MO is two with opposite spins) and Hund's rule of maximum multiplicity (if there are several MOs with equal energy, the electrons fill one MO at a time). In a molecular orbital diagram (representing a single electronic configuration), the highest occupied molecular orbital is called HOMO and the lowest unoccupied molecular orbital LUMO.

MOs are most commonly represented as a linear combination of atomic orbitals. By doing so, bonding MOs result when the atomic orbitals enhance each other in the region of the nuclei. In contrast, antibonding MOs are formed when the atomic orbitals cancel each other in the region between the nuclei. Bonding MOs have lower energies than antibonding MOs. MOs are classified according to their symmetry: bonding MOs which are symmetrical with respect to rotation around the molecular axis are called σ-orbitals. The corresponding antibonding σ*-orbital is defined by a nodal plane within the molecular axis. A π-orbital results from the overlap of two lobes of one atomic orbital with the two lobes of the other atomic orbital. In addition to bonding and antibonding MOs, nonbonding molecular orbitals (n) also exist. These orbitals contain lone pairs of electrons which do not participate in bonding atoms together since they are unshared. They are localized on just a single atom. Nonbonding electrons usually possess higher energies than bonding orbitals.

The interaction of a molecule with light can promote an electron from an occupied MO into an empty MO. The electrons in single bonds, that is, σ-MOs, have the lowest energies and can be excited by light with wavelengths ranging between 120 and 130 nm into a σ*-MO. The π-bonds can be excited at about 170 nm into the π*-level when they are isolated. However, when the single and double bonds alternate and form so-called conjugate systems, the excitation wavelength depends on the extent of the system and can rise into the visible and NIR regions as in the case of, for example, β-carotene (see Figure 3.45).

The excitation energy can also or additionally be lowered if certain functional groups with nonbonding molecular orbitals are added to the molecule, such as $-$OH, $-$OR, and $-NH_2$, where the unshared electrons n are located on O and N, respectively. Here, another type of transition is possible involving the unshared (nonbonding) electron pairs n, which can also be excited into higher energy levels that belong to the molecule. As the unshared electron pairs are usually in energy levels

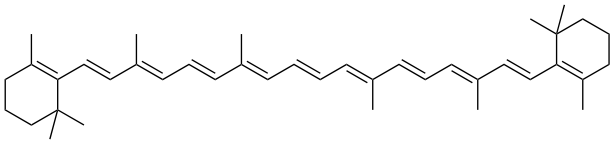

Figure 3.45 The large system of alternating single and double bonds in β-carotene.

with higher energy than electrons involved in σ-bonds or even in π-bonds, the energy required to transfer them into the unoccupied energy levels σ* and π* is usually smaller and varies in a broad range from about 200 to 665 nm. Figure 3.46 illustrates a $\pi \rightarrow \pi^*$ and an $n \rightarrow \pi^*$ transition by the respective boundary surfaces of the corresponding MOs displaying their spatial representation.

An overview of the different electronic transitions possible in organic molecules is given in Figure 3.47. This shows that the absorption of a photon can be attributed to

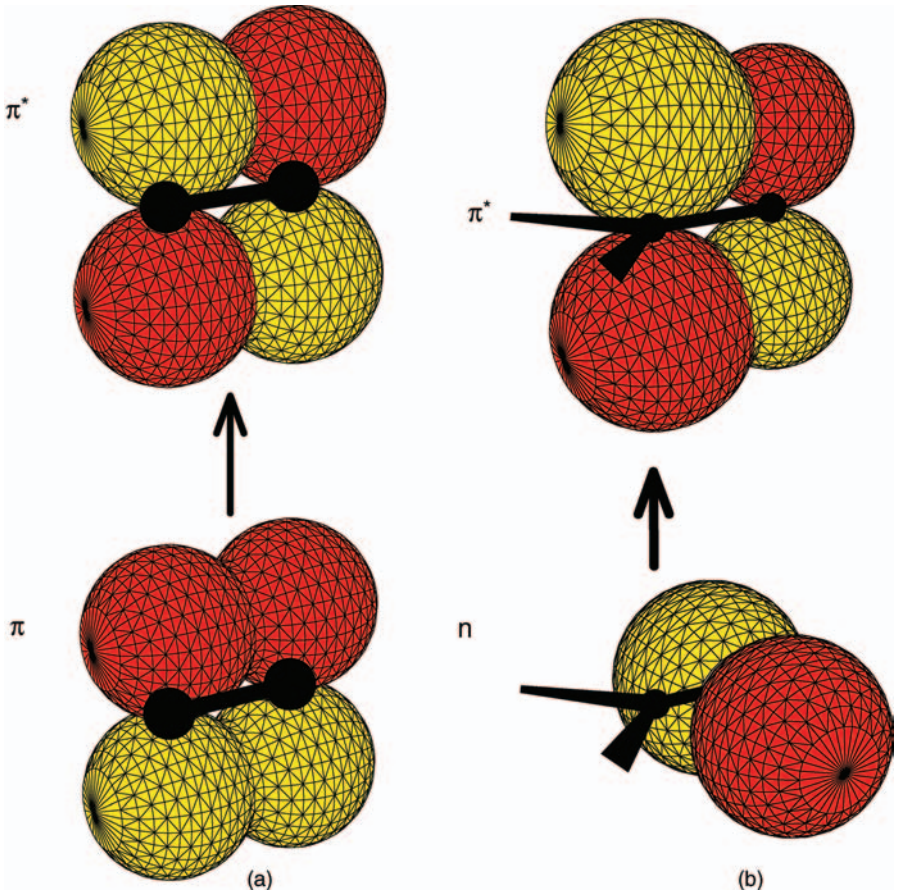

Figure 3.46 Illustration of the $\pi \rightarrow \pi^*$ and the $n \rightarrow \pi^*$ excitation with the boundary surfaces of the respective MOs (adapted from [18]).

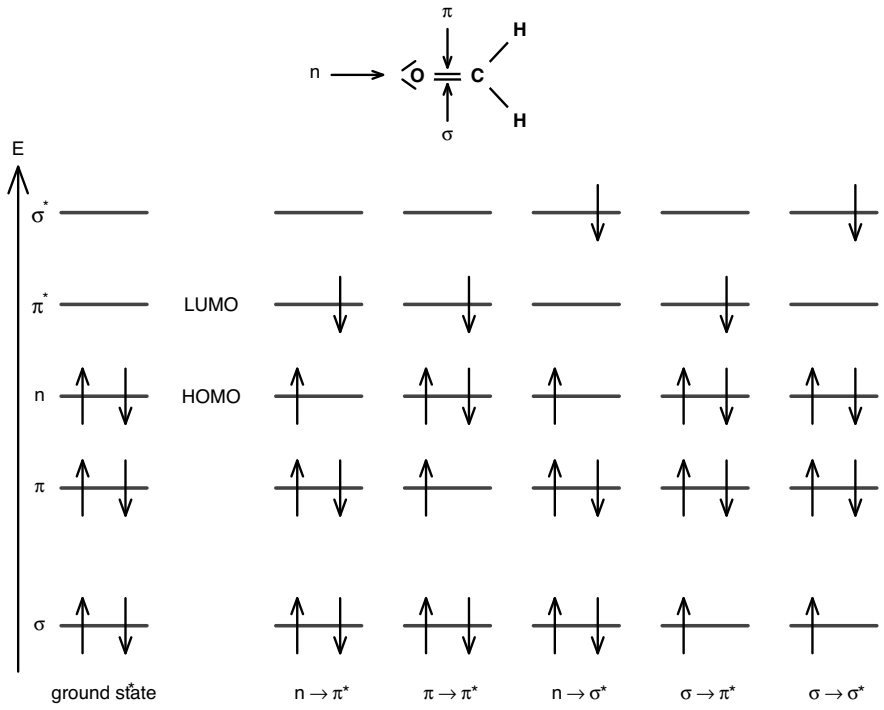

Figure 3.47 Overview of the electronic transitions in molecules exemplified with formaldehyde (H_2CO). Each horizontal line symbolizes a molecular orbital and each arrow an electron and its spin. HOMO stands for highest occupied molecular orbital and LUMO for lowest unoccupied molecular orbital. The order of excitation energy is mostly given by $(\sigma \rightarrow \sigma^*) > (\sigma \rightarrow \pi^*) > (n \rightarrow \sigma^*) > (\pi \rightarrow \pi^*) > (n \rightarrow \pi^*)$ (adapted from [17]).

certain electrons in a molecule or to certain electrons of characteristic functional groups of molecules. These moieties or parts of molecules which are responsible for the absorption of UV–Vis light are called chromophores.

The qualitative MO model also applies to metal complexes of the *d*-block elements, which play an important role in biology as natural chromophores, for example, chlorophyll and heme. In the free metals, all *d* atomic orbitals share the same energy. This degeneracy is lifted once the atom is surrounded by ligands (molecules) in complexes. The differences in energy are nevertheless small, and therefore visible light is generally able to excite a $d-d$ transition, which is the reason why many of the transition metal compounds are colored. Apart from $d-d$ transitions, the spectra of transition metal complexes also contain (1) bands from transitions localized in the ligands, called ligand-centered transitions between bonding and antibonding ligand-centered MOs, and (2) charge-transfer bands. In the latter case, an electron is transferred either from a bonding ligand-centered MO to an antibonding metal-centered MO (LMCT = ligand-to-metal charge transfer) or from a nonbonding metal-centered MO to an antibonding ligand centered MO (MLCT = metal-to-ligand charge transfer).

The MO diagrams allow the classification of electronic transitions and electronically excited configurations. The ground state of most molecules (i.e., closed-shell systems where all electrons are spin paired) has a total spin $S = 0$. The total spin S of a number of electrons is defined as the sum of the spin quantum numbers of the electrons involved. Usually an electronic state is specified by its spin multiplicity, which is defined as $2S + 1$. Thus, the ground state of a molecule has a spin multiplicity of 1, which is referred to as the ground state singlet state or S_0. However, as stated above, electronic excitation can promote an electron to an orbital of higher energy, resulting in excited electronic states. For such excited electronic states, usually two spin configurations exist: if the excited electron, for example a π^*-electron, and the residual electron, for example an n-electron, in the case of an $n \rightarrow \pi^*$ transition have opposite spins, the excited state has a spin multiplicity of 1 and is a singlet excited state. However, if the two electrons have parallel spins, the excited state has a spin multiplicity of 3 and is referred to as an excited triplet state. The excited singlet states are labeled S_1, S_2, and so on and the corresponding excited triplet states are denoted T_1, T_2, and so on depending on the underlying electronic transition, that is, excited electronic configuration (see Figure 3.48).

In order to visualize the energetic properties of a molecule – corresponding to the experimental UV–Vis absorption spectrum – instead of the molecular orbital diagram a Jablonski diagram is used (see Figure 3.49). In a Jablonski diagram, the electronic states of a molecule and the transitions between them are depicted. According to Hund's law the excited triplet states are always lower in energy than the corresponding excited singlet states of the same electronic configuration.

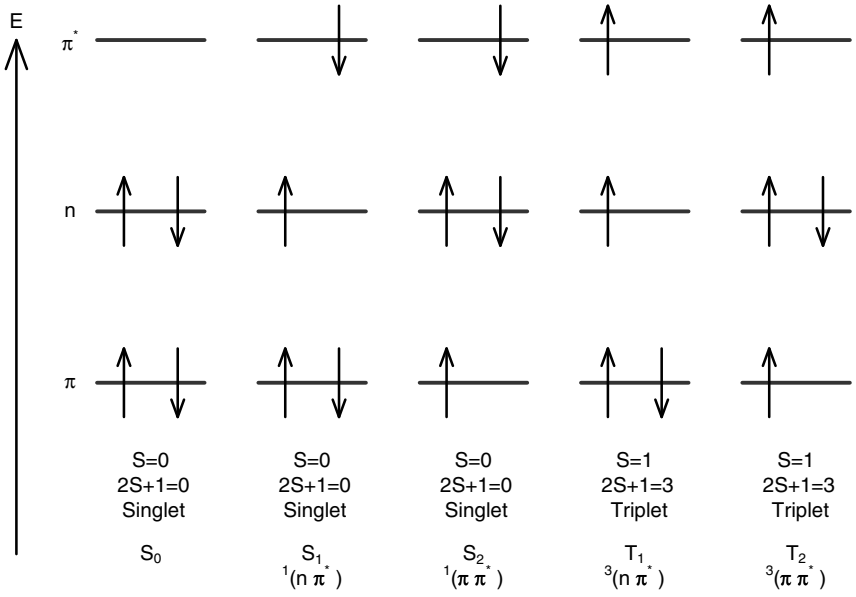

Figure 3.48 Ground and excited state electronic configurations and their spin multiplicity (adapted from [20]).

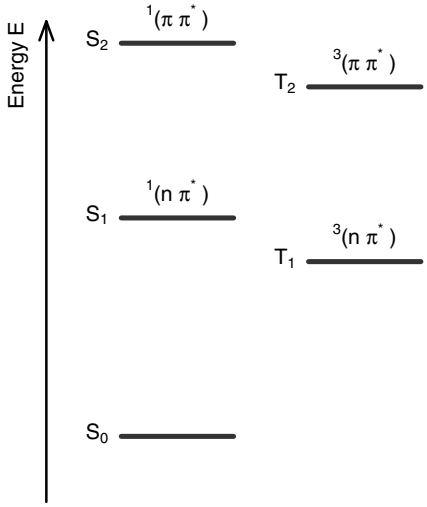

Figure 3.49 Energy state diagram (adapted from [20]).

3.9.1 Electronic Selection Rules

Electronic transitions between the energy levels in molecules are subject to certain constraints which are expressed by selection rules. When an oscillating electromagnetic field of appropriate energy interacts with a molecule, this molecule can be promoted from the ground state S_0 to a higher excited electronic state.

When an electronic transition occurs, the absorbing molecule undergoes an electric dipole transition and the intensity I of the electronic absorption is directly proportional to the square of the modulus of the transition dipole moment μ_{fi}:[14)]

14) The intensity of an absorption process (optical dipole transition) can be expressed by Fermi's golden rule, which is a way to express the transition rate $W_{i\to f}$ (probability of transition per unit time) between two quantum states ψ_i and ψ_f due to a perturbation $\hat{V}$:

$$W_{fi} = \frac{2\pi}{\hbar}\left|\int_{-\infty}^{\infty}\psi_f^*\,\hat{V}\,\psi_i \mathrm{d}x\mathrm{d}y\mathrm{d}z\right|^2 \rho$$

where ψ_i is the initial state and ψ_f the final state; ρ represents the density of final states. The integral within Fermi's golden rule is called matrix element in quantum mechanics and is very often expressed in "bracket" notation:

$$\int_{-\infty}^{\infty}\psi_f^*\,\hat{V}\,\psi_i \mathrm{d}x\mathrm{d}y\mathrm{d}z = \langle\psi_f|\,\hat{V}\,|\psi_i\rangle.$$

The intensity of a transition is proportional to $W_{i\to f}$ and therefore also to the square of the modulus of the perturbation matrix element $\left|\langle\psi_f|\hat{V}|\psi_i\rangle\right|^2$. For an electronic absorption process, the perturbation can be identified as the electric dipole moment interacting with the electric field of the incoming electromagnetic wave $E(t)$. Hence the perturbation can be expressed by

$$\hat{V}(t) = E(t)\cdot\hat{\mu}$$

$$I \sim |\mu_{fi}|^2 = |\langle \psi_f | \hat{\mu} | \psi_i \rangle|^2 \tag{3.121}$$

where ψ_i is the initial state, ψ_f the final state and $\hat{\mu}$ the dipole moment operator. The transition dipole moment arises due to the displacement of electron density during the electronic excitation. From Equation 3.121, it can be seen that the absorption intensity is theoretically determined by the transition dipole moment. As has been shown in Section 3.4, the absorption is experimentally determined by recording the transmittance, which is defined as $T = I(z)/I_0$, where $I(z)$ is the light intensity after it has passed through the sample and I_0 is the initial light intensity. The transmittance is expressed by the Lambert–Beer law (see Footnote 9 page 108):

$$T(\lambda) = \frac{I(z)}{I_0} = 10^{-(\epsilon(\lambda) \cdot zc)} \tag{3.122}$$

which expresses a logarithmic dependence between the transmittance of light T through a substance and the product of the molar absorption coefficient $\epsilon(\lambda)$, the concentration of absorbing molecules c, and the pathlength z that the molecule travels through the material. The absorbance A is defined as

$$A(\lambda) = \epsilon(\lambda) \cdot zc. \tag{3.123}$$

Usually, a plot of $\epsilon(\lambda)$ against the wavelength λ is called an absorption spectrum and the absorption maximum of a certain substance is characterized by its maximum value of ϵ_{max} ($l\,mol^{-1}\,cm^{-1}$).

The explicit treatment of optical dipole transitions by means of perturbation theory yields a relation between the integral of an absorption band of a transition of frequency ν_{fi} and the transition dipole moment:

$$\int \epsilon(\nu) d\nu = \frac{\pi \nu_{fi} N_L |\mu_{fi}|^2}{3\varepsilon_0 \hbar c} \tag{3.124}$$

which is a direct link between an experimentally measurable quantity $\int \epsilon(\nu) d\nu$ and a theoretical computable quantity μ_{fi}. Another useful way of expressing the absorption intensity is the introduction of the dimensionless oscillator strength f_o of a transition of frequency ν_{fi}:

$$f_o = \left(\frac{4\pi m_e \nu_{fi}}{3e^2\hbar}\right) |\mu_{fi}|^2. \tag{3.125}$$

The relation between the oscillator strength f_o and the integrated absorption $\int \epsilon(\nu) d\nu$ can be obtained by combining Equations 3.124 and 3.125:

$$f_o = \left(\frac{4m_e c\varepsilon_0}{N_L e^2}\right) \int \epsilon(\nu) d\nu \tag{3.126}$$

which can be expressed more practically as

$$f_o = 6.257 \cdot 10^{-19} \cdot \left(\frac{\int \epsilon(\nu) d\nu}{m^2 mol^{-1} \cdot s^{-1}}\right). \tag{3.127}$$

Hence the oscillator strength of a molecular transition can be determined experimentally from absorbance band intensities. Allowed dipole transitions are

characterized by an oscillator strength of $f_o \approx 1$ whereas for forbidden transitions $f_o \ll 1$.

In the following we evaluate the transition dipole moment μ_{fi} in more detail to obtain a deeper physical insight into the nature of electronic absorption transitions. As has been shown in Chapter 2, the total molecular wavefunction of a molecule can be divided into a nuclear $|\chi_v\rangle$ and an electronic component $|\psi_{el}\rangle$. This assumption is based on the Born–Oppenheimer approximation, which states that the electronic and nuclear motions within a molecule can be separated because the nuclear motion is usually much slower than the electron motion. As a consequence, the total energy of a molecule is made up of its electronic energy E_{el} and vibrational energy E_v discussed in Section 3.8. Hence the absorption of UV–V is light by molecules results in a combined electronic and vibrational transition, that is, both the electronic and vibrational states change. Such transitions are named vibronic transitions. The application of the Born–Oppenheimer approximation to express the transition dipole moment of a vibronic transition $|\psi_{el}\chi_v\rangle \rightarrow |\psi_{el'}\chi_{v'}\rangle$, that is, from the vibrational level χ_v in the electronic ground state ψ_{el} to the vibrational level $\chi_{v'}$ in the excited state $\psi_{el'}$ results in

$$\mu_{fi} = \langle\psi_f|\hat{\mu}|\psi_i\rangle \approx \langle\psi_{el'}\chi_{v'}|\hat{\mu}|\psi_{el}\chi_v\rangle = \langle\chi_{v'}\langle\psi_{el'}|\hat{\mu}|\psi_{el}\rangle\chi_v\rangle. \tag{3.128}$$

The electronic transition dipole moment, $\bar{\mu}_{\psi_{el'}\psi_{el}} = \langle\psi_{el'}|\hat{\mu}|\psi_{el}\rangle$, is assumed to be independent of small nuclear displacements (Condon approximation) and evaluated for the equilibrium nuclear geometry, that is, $\bar{\mu}_{\psi_{el'}\psi_{el}} \approx \bar{\mu}^{(0)}_{\psi_{el'}\psi_{el}}$. Thus, for the transition dipole moment it follows that

$$\mu_{fi} = \bar{\mu}^{(0)}_{\psi_{el'}\psi_{el}}\langle\chi_{v'}|\chi_v\rangle. \tag{3.129}$$

The electronic transition dipole moment at the equilibrium nuclear geometry, $\bar{\mu}^{(0)}_{\psi_{el'}\psi_{el}}$, is a measure of the degree of electron density redistribution during the electronic transition. The overlap integral $S_{v'v} = \langle\chi_v|\chi_{v'}\rangle$ is called the Franck–Condon integral and represents the degree of similarity of the nuclear configurations between vibrational wavefunctions of the initial and final states. Hence the intensity of a vibronic transition is directly proportional to the square modulus of the Franck–Condon integral, which is called the Franck–Condon factor: $|S_{v'v}|^2$. This is the quantum mechanical basis for the Franck–Condon principle, which is a rule to interpret electronic absorption spectra and their vibronic structure. The basis of this principle is that electronic transitions happen on a time scale ($\sim 10^{-16}$ s) that is significantly shorter than the vibrational period ($\sim 10^{-13}$ s) of a molecule and therefore the distance at which they occur can be assumed to be fixed during the transition. As a consequence, electronic transitions are vertical transitions. Hence transitions between vibrational levels in the lower v and upper electronic states v′ will be most intense when the two vibrational states have similar internuclear separations, that is, when the Franck–Condon overlap integral is greatest. This principle is illustrated in Figure 3.50 for a diatomic molecule.

The potential energy curves for a diatomic molecule can be expressed by Morse curves together with its quantized vibrational energy levels (see Section 3.8). Each

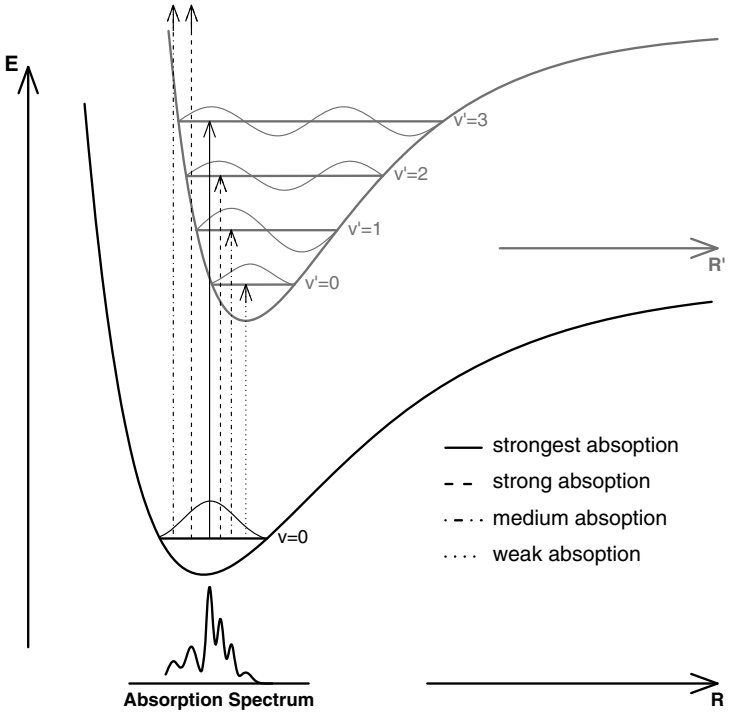

Figure 3.50 Illustration of the Franck–Condon principle (adapted from [19]).

vibrational level is expressed by its wavefunction or by its square modulus, which corresponds to the probability distribution of internuclear distances. At room temperature most molecules will be in the vibrational ground state ($v = 0$) of the electronic ground state ψ_{el} from where the absorption process starts. For the ground state vibrational level $v = 0$ the molecule spends most of the time at its equilibrium configuration. Thus, the most likely vibronic transition from $v = 0$ within the electronic ground state ψ_{el} at the equilibrium nuclear configuration to a vibrational level v' of the excited electronic state $\psi_{el'}$ corresponds to a transition for which the Franck–Condon factor $S_{v'v} = \langle \chi_{v'} | \chi_v \rangle$ is maximal, that is, where the vibrational wavefunctions for the ground and excited electronic states have a large overlap. In Figure 3.50 this corresponds to the $v = 0$ to $v' = 3$ transition. Other transitions from $v = 0$ away from the equilibrium nuclear configuration to vibrational levels v' of the electronic excited state will also occur, but with lower probability as shown in Figure 3.50. The resulting absorption spectrum and its vibronic structure is also shown in Figure 3.50.

The vibronic fine structure of absorption spectra of polyatomic molecules is more complex due to the larger number of vibrations (see Section 3.8). These vibrations, which lead to a vibronic structure in the absorption spectra of polyatomic molecules, are called Franck–Condon active modes. These are usually vibrations whose

equilibrium position is most greatly changed by the electronic transition. For example, during an $n\pi^*$ absorption of a ketone or an aldehyde the C=O stretch vibration is excited, that is, Franck–Condon active. However, very often the absorption spectra of organic molecules appear broad and featureless since the spectra are broadened by solvent interactions.

Now we have seen that the Franck–Condon factors determine the intensity of vibronic transitions. However, electronic transitions are only allowed if the electronic transition dipole moment $\bar{\mu}^{(0)}_{\psi_{el'}\psi_{el}}$ (see Equation 3.129) does not vanish. In practice, the integral itself does not need to be calculated to determine selection rules: it is sufficient to know if its value is not zero and the transition is allowed. This can be done with the help of molecular symmetry (group theory), which allows the analysis of integrals of the form of the electronic transition dipole moment $\langle\psi_{el}|\hat{\mu}|\psi_{el'}\rangle$ with respect to whether they vanish or not. Such a symmetry analysis leads to the orbital symmetry selection rules. It would go beyond the scope of this book to discuss the role of molecular symmetry in identifying vanishing electronic dipole matrix elements, that is, symmetry-forbidden transitions. In the following, the symmetry selection rules for the electronic transitions with which we shall be most concerned in biophotonics will be given. For organic molecules these are in particular $\pi\pi^*$ and $n\pi^*$ transitions. According to symmetry selection rules, $\pi\pi^*$ transitions are mostly allowed and $n\pi^*$ transitions are forbidden. However, in practice, $n\pi^*$ transitions are weakly allowed since the molecular symmetry is often distorted by molecular vibrations, that is, vibrations cause deviations from ideal molecular symmetry. These structural distortions can change a symmetry-forbidden transition into a weakly allowed transition. However, the different symmetry selection rules for these two transitions manifest themselves in the corresponding absorption coefficients. While the symmetry-allowed $\pi\pi^*$ transition is characterized by large absorption coefficients of 10^3-10^5 l mol^{-1} cm^{-1}, $n\pi^*$ transitions exhibit much weaker absorbance coefficients of 1–10^2 l mol^{-1} cm^{-1}.

We have learned above that $d-d$ transitions in metal complexes are very often the reason why many of the transition metal compounds are colored. However, for complexes with a center of inversion, $d-d$-transitions are symmetry forbidden. They can nevertheless be observed with small extinction coefficients since the ligands around the metal very often distort the perfect symmetry or vibrations remove the inversion symmetry. Other absorption processes within metal complexes have been identified above as charge-transfer transitions. These charge-transfer transitions are characterized by large electronic transition dipole moments.

Another selection rule is called the spin selection rule. It is especially impossible for light to alter the spin of an electronic state, that is, $\Delta S = 0$. This rule is a consequence of quantum mechanics. It is therefore also a forbidden transition to change a singlet state into a triplet state. Such a change can strictly speaking not be induced by light. However, spin-forbidden transitions can be weakly allowed by spin–orbit coupling, which is an interaction of the electron spin with the electron's motion. As a consequence of spin–orbit coupling, singlet and triplet states become mixed, making the spin selection rule no longer strictly applicable. Spin–orbit coupling is especially large for molecules containing heavy atoms.

We will come back to electronic transitions when we discuss fluorescence emission in Section 3.11.

3.10
Polarimetry, Optical Rotatory Dispersion, Circular Dichroism

Polarimetry, optical rotatory dispersion (ORD), and circular dichroism (CD) are based on a different response of chiral media to right- and left-circularly polarized light. Light is said to be circularly polarized if the polarization direction describes a circle around the direction of travel while the amplitude remains constant. On looking against the source of circular polarized light, the polarization direction rotates either clockwise or counterclockwise. A typical example of such a chiral medium is a solution of a molecule having a C atom with four different substituents. Such a molecule has two different forms, which are called enantiomers, one of which is the mirror image of the other. If the solution contains only one enantiomer, or one enantiomer in excess, then this medium is said to be optically active. As a consequence, it will rotate the tip of the *E*-vector of linearly polarized light in one direction, whereas if there is an excess of the other enantiomer, the *E*-vector is rotated in the opposite direction, and either light with right- or left-handed circular polarization will travel faster than the other form. If the rotation of the *E*-vector for linearly polarized light is measured at a fixed frequency, this method is called polarimetry. On the other hand, if the rotation is recorded as a function of the wavelength, then this method is named ORD.

Since a change in the refractive indices is always accompanied by a corresponding change in the absorption indices, there will always be a range in the spectrum of optically active media where the absorption indices are different for right- and left-circularly polarized light. Consequently, one form will be more strongly absorbed than the other. This effect is called CD.

Optical activity measurements are of great importance, since they are capable of determining the molecular stereochemistry of molecules in solution or even *in vivo*. An understanding of chirality is of the utmost importance in life since Nature itself is chiral. A lot of naturally occurring substances such as amino acids, terpenes, carbohydrates, and alkaloids are often enantiopure or at least enantioenriched, that is, one of the enantiomers predominates over the other. The occurrence of chirality in Nature usually results in totally different effects of the two enantiomers on cells, that is, only one enantiomer leads to the correct response in a living organism. As a consequence, normally only one enantiomer of a given drug has the desired activity. Hence understanding chirality is extremely important, for example, for the development of therapeutic drugs.

This section aims at a short introduction to the concept of polarimetry, ORD, and CD. The interested reader is referred to [6, 21].

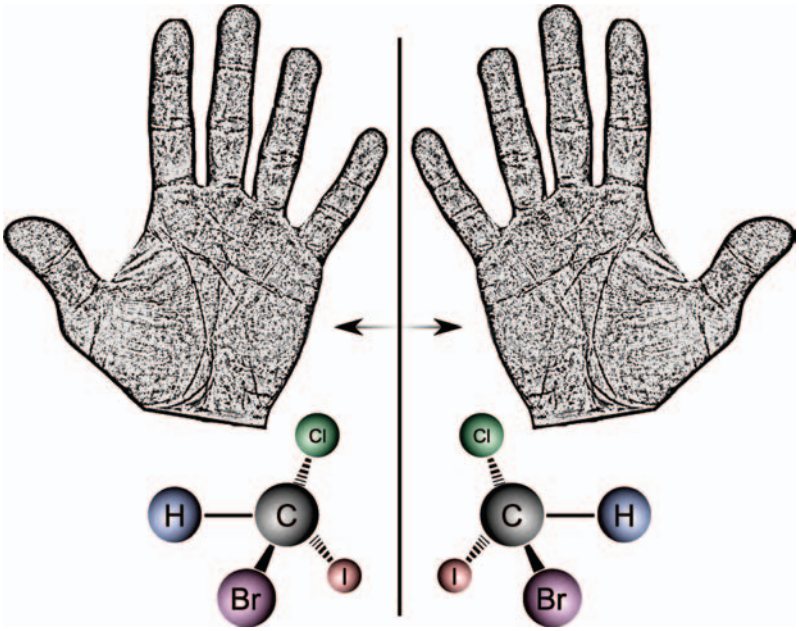

Figure 3.51 Two enantiomers.

3.10.1 Polarimetry

Polarimetry, optical rotation, and circular birefringence are based on the rotation of the *E*-vector of linearly polarized light at a fixed wavelength. The reason for the rotation lies in differences in the refractive index for circularly polarized light: $n_R \neq n_L$.[15] Such differences can be based on, for example, the presence of chiral molecules in a solution. Chirality or handedness can be best explained by employing the hands: the left hand is a mirror image of the right hand and even if one of the hands could be freely rotated in three dimensions it is impossible by an arbitrary series of rotations around different axes to superimpose the left hand on the right and vice versa. The same is true for chiral molecules. The two forms of a chiral molecule are called enantiomers (see Figure 3.51). If both forms are present in a solvent in

15) Circularly polarized light can be described as linearly polarized light where the direction of polarization is not fixed, for example, to the *x*-direction, but describes a circle in the plane perpendicular to the direction of propagation. Circularly polarized waves can also be described as a superposition of two waves that are mutually orthogonally polarized to each other. They also have the same wavelength and direction; however, they differ by 90° in phase, meaning that one wave has its maximum field strength when the field strength of the other wave is zero and vice versa. Looking against the source of the two superimposed waves, one can "see" the electrical vector rotating either clockwise or counterclockwise. The former is referred to as right (R) and the latter as left (L). Inversely linearly polarized light can be described a superposition of left and right circularly polarized light.

equal amounts, this solution is termed "optically inactive" as the *E*-vector of linearly polarized light is neither rotated to the left nor to the right. It needs one of the enantiomers to be present in excess to render the solution optically active. The observed rotation angle α_{obs} of the tip of the electric vector depends on the excess of one of the components, its total concentration c in the solution, and the length of the sample tube z.

The incoming linearly polarized light beam experiences in chiral materials different refractive indices for its left and right circular components. However, if $n_R \neq n_L$ then one component travels faster than the other (i.e., the phasing of left or right rotating component of exiting light beam is shifted while the absolute *E*-field vectors do not change) and finally, after leaving the sample tube, the addition of the components results again in linearly polarized light, but having a polarization direction that is rotated by an angle α_{obs} compared with the incoming polarization. This angle is given by

$$\alpha_{obs} = [\alpha]_\lambda^T \cdot z \cdot c \tag{3.130}$$

where $[\alpha]_\lambda^T$ is the specific angle of rotation characteristic of an optically active substance at a certain wavelength λ and at a certain temperature T. The molar rotation $[\Phi]_\lambda^T$, which is important for the ORD, is defined as

$$[\Phi]_\lambda^T = \frac{[\alpha]_\lambda^T \cdot M}{100} = \frac{\alpha_{obs} \cdot M}{100 \cdot z \cdot c} \tag{3.131}$$

where M is the relative molar mass.

3.10.2 Optical Rotatory Dispersion (ORD)

In ORD, the molar rotation $[\Phi]_\lambda^T$ is investigated as a function of the wavelength. If a compound does not absorb in the investigated wavelength range, a typical ORD spectrum is displayed as in Figure 3.52. Obviously, the ORD spectra of two enantiomers are not symmetric with the line $[\Phi]_\lambda^T = 0$. The reason for this observation is that the refractive indices for right- and left-circularly polarized light change differently with wavelength (i.e., the rotatory dispersion is proportional to the refractive index difference).

In the region of an absorption band, the indices both for right- and left-circularly polarized light show abnormal dispersion, with two possible developments of the molar rotation. For increasing wavelengths the molar rotation first becomes strongly negative, then increases, and crosses zero ORD for the wavelength of the absorption maximum. After reaching a maximum, the molar rotation finally decreases and approaches values close to zero. In the second case, the ORD develops as a mirror image (see Figure 3.53). This behavior of ORD spectra in the wavelength regions of an electronic absorption is called the Cotton effect after the French physicist Aimé Cotton, who discovered this effect in 1895. The Cotton effect is called positive if the ORD decreases with increasing wavelength, otherwise it is called negative.

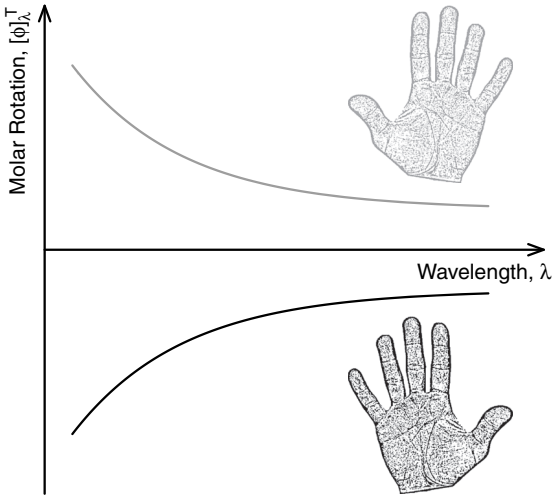

Figure 3.52 Typical ORD spectra for molecules showing no absorption band in the investigated wavelength region.

Quantitative theoretical correlations between molecular structure and ORD (Cotton effect) are difficult, if not impossible, to derive. Therefore, the investigations are mostly empirical. However, empirical investigations within this area have become important; for example, ORD has been successfully applied for constitution elucidation such as to find the position of carbonyl groups in complex optically active molecules.

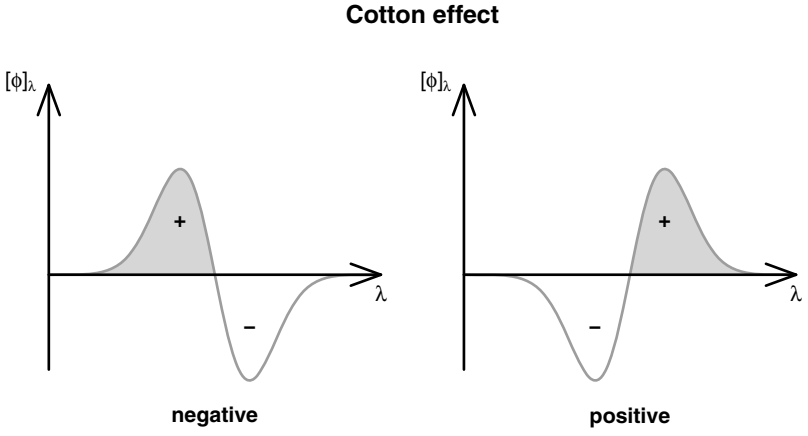

Figure 3.53 Positive and negative Cotton effect for a wavelength region of an absorption.

3.10.3
Circular Dichroism (CD)

As has been shown in Section 3.4, abnormal dispersion results from an absorption of electromagnetic waves, that is, in the close vicinity of an absorption the imaginary part of the refractive index (absorption index) differs from zero. Hence enantiomeric molecules exhibit, in addition to different refractive indices for left- and right-circularly polarized light, also different absorption indices for left- and right-circularly polarized light. Therefore, the extinction coefficients ϵ_L and ϵ_R are also different: $\Delta\epsilon = \epsilon_L - \epsilon_R$. However, compared with ϵ_L or ϵ_R, $\Delta\epsilon$ is rather small and lies in the range 10^{-3}–10^{-6}. Depending on the wavelength, the difference in absorbance for right- and left-circularly polarized light, $\Delta A(\lambda)$, is therefore given by

$$\Delta A(\lambda) = \Delta\epsilon(\lambda) \cdot z \cdot c = A_L(\lambda) - A_R(\lambda). \tag{3.132}$$

For pure ORD bands, left- and right-circularly polarized components have different velocities while traveling through the sample and combine with each other again to give linearly polarized light, but with a rotated plane of rotation. However, for a CD band one component of the circularly polarized light also becomes weaker due to stronger absorption. As a result, the amplitudes of left- and right-circularly polarized light are different, leading to elliptically polarized light. To quantify the ellipticity, the ratio between the short and the long elliptical axes is defined as tangent of an angle ϕ, the so-called ellipticity: $\tan\phi = b/a$ with $a = E_R + E_L$ and $b = |E_R - E_L|$ (see Figure 3.54). The specific ellipticity is then given by

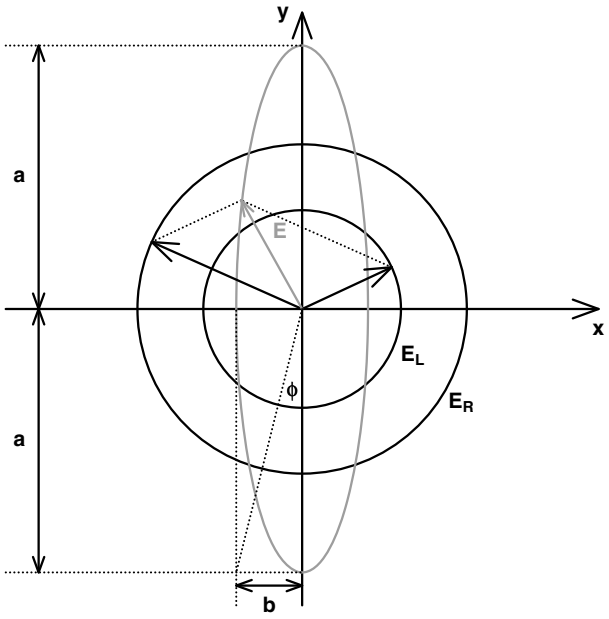

Figure 3.54 Definition of the ellipticity ϕ.

$$[\phi]_\lambda^T = \frac{\phi_{obs}}{z \cdot c} \tag{3.133}$$

where ϕ_{obs} is the experimentally determined ellipticity. Finally, as was the case for ORD, a molar ellipticity can be defined as

$$[\theta]_\lambda^T = [\phi]_\lambda^T \cdot \frac{M}{100}. \tag{3.134}$$

The peak height of CD bands can either be displayed as an absorption difference $\Delta\varepsilon$ or, equivalently, as molar ellipticity $[\theta]_\lambda^T$. Molar ellipticity and CD can be interconverted by the following relation:

$$[\theta]_\lambda^T = 3300 \cdot \Delta\epsilon. \tag{3.135}$$

For an electronic transition to be CD active, the product of the electronic transition moment $\mu_{el} = \langle\psi_f|\hat{\mu}_{el}|\psi_i\rangle$ (see Equation 3.121) and magnetic transition moment $\mu_{mag} = \langle\psi_f|\hat{\mu}_{mag}|\psi_i\rangle$ must be different from zero: $\mu_{el} \cdot \mu_{mag} \neq 0$. Here $\hat{\mu}_{el}$ and $\hat{\mu}_{mag}$ are operators for the electric and magnetic dipole, respectively. The electronic transition moment μ_{el} corresponds to a linear displacement of electrons upon transition from a ground state ψ_i into an excited state ψ_f. μ_{mag} is the magnetic transition moment and corresponds to a radial displacement of electrons upon excited state transition. Therefore, the scalar product $\mu_{el} \cdot \mu_{mag}$ is characterized by a helical electron displacement. Depending on the chirality of the helix, preferably more right- or left-circularly polarized light will be absorbed, respectively. A typical example of the application of CD is the determination of the relative quantities of the α-helix, β-strand, and random coil in proteins.

Of course, CD can also occur in the IR spectral region and is then often called vibrational circular dichroism (VCD). The advantage in this spectral region is that there is no electronic chromophore necessary and that an IR absorption spectrum (see Section 3.8) contains more characteristic absorption bands, making the identification of the stereo isomer easier.

3.11 Fluorescence

Fluorescence is the emission of light by molecules that have absorbed light of shorter wavelength. Fluorescence spectroscopy and in particular fluorescence microscopy have emerged as the most important technology in biophotonics since they allow a multitude of questions in the life sciences and medicine to be resolved. The detection of fluorescence instead of the weak absorption changes of white light in optical microscopy offers several advantages: the detection of fluorescence is virtually background free and extremely sensitive, so that even single molecules can be investigated. Fluorescence in biophotonics is generally used as a way of tracking biological molecules by means of the fluorescence emission. Its unique sensitivity, specificity, and versatility make fluorescence an

ideal diagnostic tool in biological and biomedical research. In fluorescence microscopy, naturally occurring autofluorescent biomolecules or introduced fluorescence labels selectively attached to another biomolecule such as a protein or nucleic acid or to certain cellular structures of interest are used. In particular, the selective fluorescence labeling allows for localization of a target within a cell or the identification of specific biostructures. Furthermore, elaborate fluorescence techniques such as FRET (Förster resonance energy transfer), FRAP (fluorescence recovery after photobleaching), FLIM (fluorescence lifetime imaging microscopy), and so on that allow the analysis of complex processes in biological specimens have been developed. More recently, the breakthrough from fluorescence microscopy to fluorescence nanoscopy was achieved by utilizing saturated optical transitions. Fluorescence nanoscopy paves the way for new, exciting insights into cellular processes. This section aims at providing insights into the underlying molecular processes and into basic theoretical concepts of fluorescence spectroscopy/microscopy.

A comprehensive introduction to fluorescence is given in [17, 19, 22], and the emerging concepts of fluorescence nanoscopy are described in [23–26].

3.11.1
The Fate of Electronically Excited States

In Section 3.9 it was shown that certain chromophores within molecules are able to absorb light, promoting the molecule into an electronically excited state. However, excited electronic states are usually energetically unstable and short-lived; what short means will be discussed later. Fluorescence is one pathway for a molecule to relax from an excited electronic state back to the ground state (nonexcited state). However, fluorescence is only one of numerous processes that can occur subsequent to an electronic absorption. These processes are usually represented in a Jablonski energy level diagram. A simple Jablonski diagram for an organic molecule is depicted in Figure 3.55.

The different electronic states together with their vibrational levels are plotted as horizontal lines. The processes taking place after absorption can be classified into radiative and radiationless (nonradiative) transitions. Radiative processes which involve the emission of light while the molecule relaxes back to the ground state are depicted as solid arrows pointing downwards, whereas radiationless processes are shown using wavy horizontal arrows. Radiationless means that the excited state deactivation is not accompanied by the emission of photons. Before we discuss fluorescence in detail, the different other deactivation processes which can occur subsequent to UV–Vis absorption should be briefly explained. As has been shown in Section 3.9, molecules can absorb light which populates excited electronic states S_1, S_2, and so on according to the orbital and spin selection rules.

Let us assume, as plotted in Figure 3.55, that the S_2 state is the first optically accessible state for UV–Vis absorption from the S_0 ground state, that is, the $S_0 \rightarrow S_2$

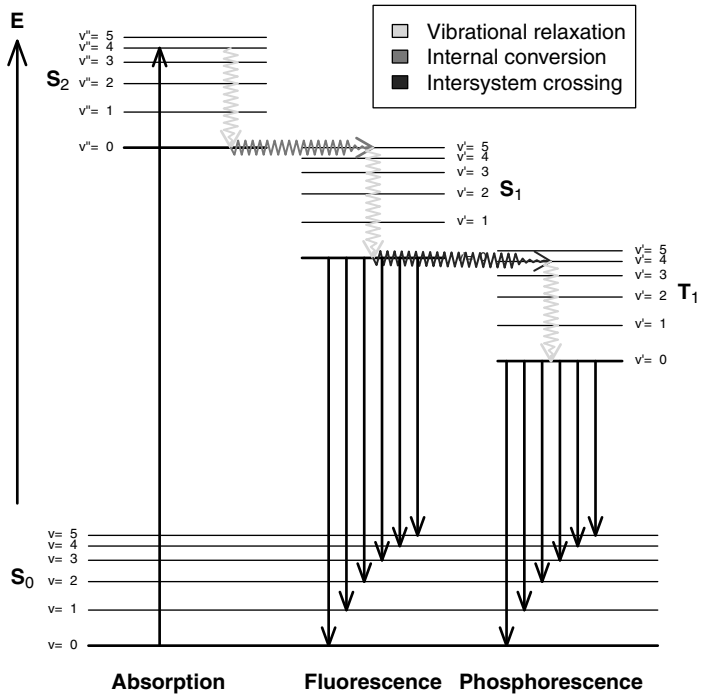

Figure 3.55 Jablonski term scheme for a polyatomic organic molecule (adapted from [20]).

transition is a fully allowed one. The absorption process proceeds according to the Franck–Condon principle and populates excited vibrational states ($v'' > 0$) of Franck–Condon-active modes within the S_2 state.[16] The excess vibrational energy of the S_2 state is dissipated as heat when the vibrationally excited S_2 molecules collide with solvent molecules. This relaxation process which populates the vibrational ground state ($v'' = 0$) of the S_2 state is called vibrational relaxation (vibrational cooling) and takes place on a typical time scale of 10^{-12} s.[17] The $v'' = 0$ level of the S_2 state is usually very close in energy to an excited vibrational level of the S_1 state, facilitating a rapid energy transfer between these two electronic states. Such a radiationless transition between isoenergetic vibronic levels of two different electronic states of the same multiplicity is called internal conversion. Internal conversion has its origin in the breakdown of the Born–Oppenheimer approximation. The Born–Oppenheimer approximation (or adiabatic approximation) is well justified for the ground state S_0 and the first excited state S_1 where the energy gap between these two electronic states is much larger than that between vibrational states. This allows the separate

16) Note that the electronic excitation populates excited vibrational states of Franck–Condon-active normal modes. This excess energy can also be redistributed among other modes that do not accompany the electronic transition, that is, populating vibrational excited states of dark modes.

17) Note that vibrational ground state means that the molecule exhibits in the excited electronic state in terms of all vibrational degrees of freedom q the vibrational quantum number $v_q = 0$.

treatment of electronic and nuclear motions. However, the energy gaps between higher excited electronic states (S_4, S_3, S_2) are relatively small, which means that electronic and nuclear motions cannot be treated independently of each other any longer since they take place on the same time scale and, as a consequence, nuclear motions can induce a radiationless transition between two isoenergetic vibronic levels of two higher excited electronic states. Typical time scales of internal conversion processes between higher excited electronic states are of the order of 10^{-13} s.

After the S_2/S_1 internal conversion process, vibrational relaxation again occurs, populating the vibrational ground state ($v' = 0$) of the lowest excited singlet state S_1. As has been stated above, the much larger energy difference between the S_1 and S_0 states than that between the higher excited electronic states means that internal conversion between S_1 and S_0 proceeds more slowly than that between the upper excited states. Therefore, no matter which upper excited singlet state is populated by the absorption of a UV–Vis photon, vibrational relaxation and internal conversion processes occurring in a matter of picoseconds lead to the population of the $v' = 0$ level of the S_1 state. From there, several relaxation channels can be accessed: (1) radiative transition by emission of a fluorescence photon, (2) S_1/S_0 internal conversion, or (3) intersystem crossing to the first triplet state T_1. This is the statement of Kasha's rule, which says that due to the very rapid depopulation of higher excited electronic states to the lowest vibrational level of the S_1 state, fluorescence emission of electronically excited molecules almost always happens from the lowest vibrational level of the lowest excited singlet state (S_1). In other words, fluorescence from higher excited electronic states is usually unable to compete with internal conversion from these states. Since the S_1/S_0 energy gap is much larger, $S_1 \rightarrow S_0$ fluorescence is able to compete with $S_1(v' = 0) \rightarrow S_0(v = n)$ internal conversion.

Intersystem crossing describes spin-forbidden radiationless transitions between isoenergetic vibrational levels of electronic states of different multiplicity. This spin-forbidden process is driven by spin–orbit coupling (see Section 3.9), which is why its rate can be enhanced by the presence of heavy atoms. Hence the intersystem crossing time scale is variable and depends strongly on the molecular systems. The two radiative excited state deactivation channels fluorescence and phosphorescence are called photoluminescence. Fluorescence involves a radiative decay between two electronic states of the same multiplicity. For most molecular systems, fluorescence starts from the vibrational ground state of the first excited state S_1 and ends in vibrational excited levels of the ground state S_0: $S_1(v' = 0) \rightarrow S_0(v = n) + h\nu$. The intensity of these vibronic fluorescence transitions is determined by the Franck–Condon principle (see also Section 3.9). The time scales of photon emission by fluorescence are in the order of nanoseconds (10^{-9} s). Phosphorescence is a spin-forbidden process which involves the emission of a photon due to a transition between two electronic states of different multiplicity, typically from the vibrational ground state of the first triplet sate T_1 to vibrationally excited levels of the electronic ground state: $T_1(v' = 0) \rightarrow S_0(v = n) + h\nu$. Just as for intersystem crossing, spin–orbit coupling is responsible for this forbidden spin flip process. Hence the time scale for phosphorescence depends on the molecular system (i.e., presence of heavy atoms) but can be really slow, in the order of 10^{-3}–10^{2} s.

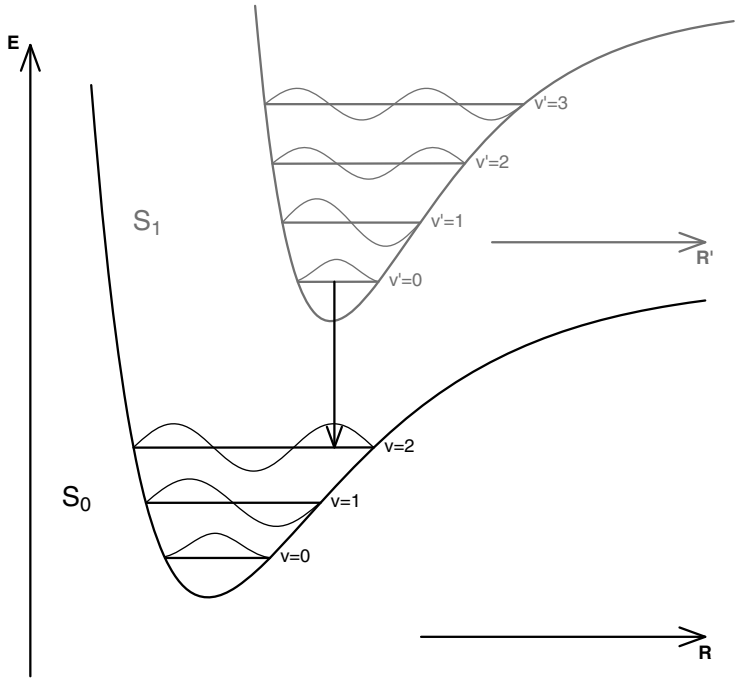

Figure 3.56 Illustration of the Franck–Condon principle for the most probable vibronic fluorescence transition (adapted from [17]).

In the following we characterize the fluorescence emission in more detail. It has been shown above that fluorescence usually originates from the vibrational ground state of the first excited singlet state S_1. Fluorescence transitions, just as absorption processes, are vertical transitions proceeding according to the Franck–Condon principle. Hence the intensities of the different vibronic $S_1(\mathrm{v}' = 0) \rightarrow S_0(\mathrm{v} = n)$ transitions are determined by the respective Franck–Condon integrals $\langle \chi_{\mathrm{v}} | \chi_{\mathrm{v}'} \rangle$ (see Figure 3.9). Figure 3.56 depicts this Franck–Condon principle for the most probable, that is, most intense, vibronic fluorescence transition exhibiting the largest Franck–Condon factor.

Figure 3.57 depicts the Jablonski diagram illustrating the vibronic transitions leading to the $S_0(\mathrm{v} = 0) \rightarrow S_1(\mathrm{v}' = n)$ absorption spectrum and to the $S_1(\mathrm{v}' = 0) \rightarrow S_0(\mathrm{v} = n)$ fluorescence spectrum for a typical organic molecule. The intensities of the vibronic absorption and fluorescence transitions within the absorption and fluorescence spectra (see upper part of Figure 3.57) are determined by the Franck–Condon factors. As has been stated in Section 3.9, the vibronic patterns are often washed out by interaction with the solvent environment and broad and structureless absorption and emission bands result.

The absorption and emission spectra plotted in Figure 3.57 look like mirror images. This is only the case if the vibrational spacings in the ground state S_0 and first excited state S_1 are similar, which occurs if the geometries of S_0 and S_1 states are

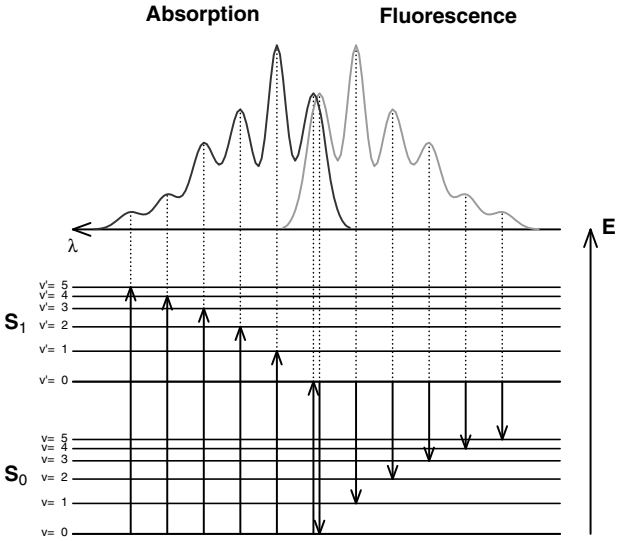

Figure 3.57 Illustration of the vibronic absorption and fluorescence transitions (adapted from [20]).

similar. Such a behavior can be observed for rigid aromatic molecules where there is almost no change in geometry upon electronic absorption. In general, the vibronic pattern of the absorption spectrum resembles the vibrational characteristics of the first excited state while the vibronic structure of the fluorescence spectrum is due to the vibrational level structure of the ground state S_0. According the Stokes rule, the fluorescence emission wavelengths are always red shifted compared with the absorption wavelengths. This phenomenon has its foundation in the rapid vibrational relaxation of vibrationally excited S_1 molecules generated by the absorption process. This means that the excess vibrational energy of the S_1 state is rapidly dissipated as heat to the surroundings prior to fluorescence emission originating from the vibrational ground state ($v = 0$) of the S_1 state. The gap between the intensity maximum of absorption spectrum and that of the fluorescence spectrum is called the Stokes shift.

3.11.2
Basic Concepts of Fluorescence Spectroscopy

In addition to this qualitative picture of fluorescence emission, we aim to establish in the following a quantitative description of fluorescence emission. We start with deriving an expression for the $S_1(v' = 0)$ excited state lifetime. Figure 3.58 recalls all the possible competing intramolecular S_1 deactivation processes with their rate constants:

- k_r^S: rate constant for radiative $S_1 \rightarrow S_0$ decay via fluorescence
- k_{ic}^S: rate constant for internal conversion ($S_1 \rightarrow S_0$)
- k_{isc}: rate constant for intersystem crossing ($S_1 \rightarrow T_1$)

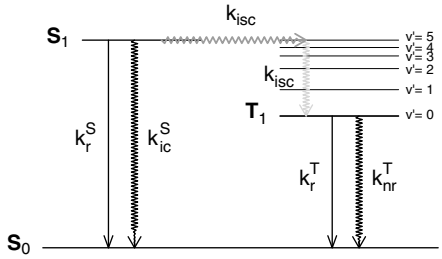

Figure 3.58 Photophysical processes occurring from the $S_1(v' = 0)$ state (adapted from [17]).

- k_r^T: rate constant for radiative decay via phosphorescence ($T_1 \rightarrow S_0$)
- k_{nr}^T: rate constant for nonradiative decay via intersystem crossing ($T_1 \rightarrow S_0$).

The radiationless transitions can be combined to result in an overall nonradiative rate constant $k_{nr}^S = k_{ic}^S + k_{isc}$. The application of standard first-order kinetics yields a rate of disappearance of S_1 excited state molecules $^1A^*$:

$$-\frac{d\left[{}^1A^*\right]}{dt} = \left(k_r^S + k_{nr}^S\right)\left[{}^1A^*\right] \tag{3.136}$$

where $\left[{}^1A^*\right]$ is the concentration of S_1 excited state molecules. Solution of this differential equation yields an expression for the transiently excited S_1 molecule concentration:

$$\left[{}^1A^*\right] = \left[{}^1A^*\right]_0 e^{-\frac{t}{\tau_S}} \tag{3.137}$$

where $\left[{}^1A^*\right]_0$ is the concentration of molecules A promoted to the excited state S_1 by a very short pulse (i.e., short with respect to the inverse of the rate constants listed in Figure 3.58) at time $t = 0$. The S_1 excited state lifetime τ_S is given by

$$\tau_S = \frac{1}{k_r^S + k_{nr}^S}. \tag{3.138}$$

In the following we derive an expression for how the observed fluorescence intensity decays subsequent to an ultrashort pulse excitation. The fluorescence intensity $I_F(t)$ at any time t after excitation is proportional to the concentration of S_1 excited state molecules, that is, $\left[{}^1A^*\right]$, in which the proportionality constant is the rate constant for the radiative decay via fluorescence k_r^S:

$$I_F(t) = k_r^S \cdot \left[{}^1A^*\right] = k_r^S \cdot \left[{}^1A^*\right]_0 \cdot e^{-\frac{t}{\tau_S}}. \tag{3.139}$$

Hence the fluorescence intensity decays monoexponentially with the fluorescence decay time τ_S, which is an important parameter to characterize fluorescent molecules.[18] As mentioned above, the fluorescence lifetime is in the order of nanoseconds.

18) In case that the S_1 state is exclusively deactivated by fluorescence emission, the lifetime is $\tau_r = 1/k_r^S$, which is called the radiative lifetime.

Another important characteristic of a fluorescent molecule is its fluorescence quantum yield, Φ_F, which is defined as the ratio of the number of photons emitted to the number of photons absorbed and can be expressed by

$$\Phi_F = \frac{k_r^S}{k_r^S + k_{nr}^S} = k_r^S \tau_S. \tag{3.140}$$

Integration of the monoexponential decay of the time-dependent fluorescence intensity yields the fluorescence quantum yield:

$$\frac{1}{[^1A^*]_0} \int_0^\infty I_F(t) dt = k_r^S \tau_S = \Phi_F. \tag{3.141}$$

If fluorescence is the only excited state relaxation pathway, then $\Phi_F = 1$, whereas $\Phi_F = 0$ if no fluorescence is observed. Thus the fluorescence quantum yield exhibits values between 0 and 1.

The above relations were deduced for time domain fluorescence experiments where the fluorescence intensity is recorded as a function of time after excitation with a very short light pulse. However, most commonly the fluorescence intensity is recorded under conditions of steady-state illumination where the excitation light source emits a constant amount of photons per unit time (e.g., a lamp). In the following, we derive a quantitative expression for the steady-state fluorescence intensity. The steady-state excitation process can be described as

$$^1A + h\nu \xrightarrow{k_a} {}^1A^* \tag{3.142}$$

where $k_a \approx 10^{15}\ s^{-1}$ is the absorption rate. The concentration of excited state molecules remains constant for such a steady excitation process:

$$\frac{d[^1A^*]}{dt} = 0 = k_a \alpha N_0 - (k_r^S + k_{nr}^S)[^1A^*] \tag{3.143}$$

where N_0 is the constant amount of incident photons under steady-state illumination and $k_a \alpha N_0$ characterizes the number of absorbed photons per unit volume and time (α denotes the fraction absorbed) and can be expressed by the intensity I_0 of the irradiated light, that is, $k_a \alpha N_0 = \alpha I_0$. The steady-state fluorescence intensity I_F is directly proportional to the constant concentration of S_1 excited molecules $[^1A^*]$:

$$[^1A^*] = \frac{\alpha I_0}{k_r^S + k_{nr}^S} \tag{3.144}$$

where the proportionality constant is the rate constant of fluorescence emission k_r^S:

$$I_F = k_r^S [^1A^*] = \alpha I_0 \frac{k_r^S}{k_r^S + k_{nr}^S} = \alpha I_0 \Phi_F. \tag{3.145}$$

Equation 3.145 shows that the ratio of steady-state emitted photons to absorbed photons yields the fluorescence quantum yield:

$$\frac{I_F}{\alpha I_0} = \Phi_F \tag{3.146}$$

All these relations have been derived for an integrated fluorescence intensity, that is, neglecting the different possible energies of the emitted fluorescence photons. Plotting the steady-state fluorescence intensity I_F as a function of the emission wavelength λ_F leads to the fluorescence emission spectra shown in Figure 3.57. This is done by expressing the steady-state fluorescence intensity per absorbed photon as a function of the fluorescence wavelength represented by $F_\lambda(\lambda_F)$. The fluorescence emission spectrum $F_\lambda(\lambda_F)$ mirrors the different vibronic $S_1(v' = 0) \rightarrow S_0(v = n)$ fluorescence transitions and is therefore determined by the corresponding Franck–Condon integrals. Hence the steady-state fluorescence intensity $I_F(\lambda_F)$ is proportional to $F_\lambda(\lambda_F)$ and also to the number of absorbed photons at the excitation wavelength λ_E, which can be expressed by the absorbed light intensity $I_A(\lambda_E)$:

$$I_F(\lambda_E, \lambda_F) = k \cdot F_\lambda(\lambda_F) I_A(\lambda_E) \tag{3.147}$$

where k is a proportionality constant depending on the experimental setup. The absorbed light intensity $I_A(\lambda_E)$ is the difference between the incident $I_0(\lambda_E)$ and the transmitted $I_T(\lambda_E)$ light intensity:

$$I_A(\lambda_E) = I_0(\lambda_E) - I_T(\lambda_E) \tag{3.148}$$

where the transmitted light intensity $I_T(\lambda_E)$ can be expressed by the Lambert–Beer law (Equation 3.122):

$$I_T(\lambda_E) = I_0(\lambda_E) e^{-2.3 \cdot \epsilon(\lambda_E) c \cdot z}. \tag{3.149}$$

By using Equations 3.148 and 3.149 Equation 3.147 can be rewritten:

$$I_F(\lambda_E, \lambda_F) = k \cdot F_\lambda(\lambda_F) I_0(\lambda_E) \left[1 - e^{-2.3 \cdot \epsilon(\lambda_E) c \cdot z}\right]. \tag{3.150}$$

Recording the steady-state fluorescence intensity I_F as a function of the emission wavelength λ_F for a fixed excitation wavelength λ_E yields the fluorescence emission spectrum, that is, it reflects the probability distribution of the different vibronic fluorescence transitions $F_\lambda(\lambda_F)$. Equation 3.150 shows a rather complicated dependence of the steady-state fluorescence intensity on the concentration c. However, for low concentrations the term in square brackets in Equation 3.150 can be approximated as

$$1 - e^{2.3 \cdot \epsilon(\lambda_E) c \cdot z} = 2.3 \cdot \epsilon(\lambda_E) c \cdot z - \frac{1}{2} [2.3 \cdot \epsilon(\lambda_E) c \cdot z]^2 + \cdots \tag{3.151}$$

For dilute solutions, the higher term can be neglected and a direct proportionality between the concentration c and the fluorescence intensity is obtained:

$$\begin{aligned} I_F(\lambda_E, \lambda_F) &= k \cdot F_\lambda(\lambda_F) I_0(\lambda_E) [2.3 \cdot \epsilon(\lambda_E) c \cdot z] \\ &= 2.3 \cdot k \cdot F_\lambda(\lambda_F) I_0(\lambda_E) \cdot A(\lambda_E) \end{aligned} \tag{3.152}$$

where $A(\lambda_E)$ is the absorbance at λ_E (see Equation 3.123). However, for a quantitative analysis of fluorescence emission spectra, one always has to keep in mind that this

linear relationship between the fluorescence intensity and concentration is only valid for dilute solutions, that is, $A \approx 0.01$.

Steady-state fluorescence experiments can be also performed in another way by recording the fluorescence intensity as a function of the excitation wavelength λ_E for a fixed detection wavelength λ_F. This yields a fluorescence excitation spectrum. Equation 3.152 shows that the fluorescence intensity recorded as a function of the excitation wavelength is characterized by the product $I_0(\lambda_E) \cdot A(\lambda_E)$. This means that if it is possible to account for the wavelength dependence of the incoming light intensity, the fluorescence excitation spectrum depends only on the absorption $A(\lambda_E)$, that is, it reflects the absorption spectrum. To be more precise, provided that only one ground-state species exists, the corrected fluorescence excitation spectrum [i.e., compensation of the wavelength dependence of the incoming light $I_0(\lambda_E)$] is identical with the absorption spectrum. Hence a comparison between fluorescence excitation and absorption spectra yields valuable information about the sample species present. Figure 3.59 shows a comparison between the absorption, fluorescence emission, and fluorescence excitation spectra of a dilute aqueous cinoxacin solution.

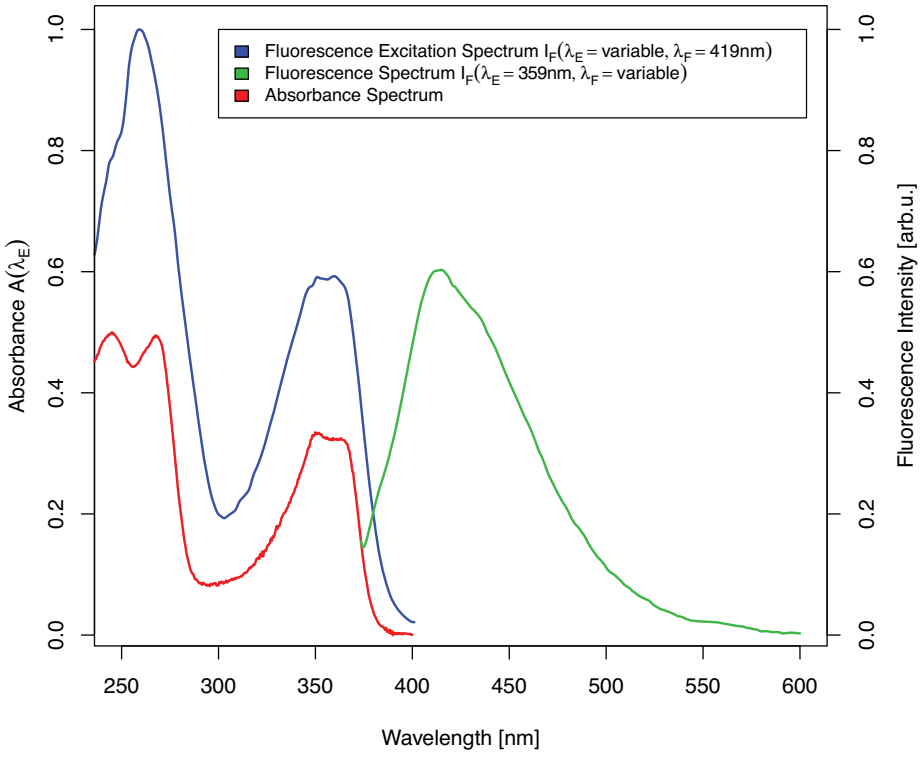

Figure 3.59 Absorption, fluorescence excitation, and fluorescence emission spectra of cinoxacin.

3.11.3
Nonradiative Energy Transfer

So far, we have only considered intramolecular S_1 deactivation channels (see Figure 3.58) when deriving the above-mentioned quantitative fluorescence intensity expressions. However, the interaction of electronically excited molecules with other molecules may compete with fluorescence emission if these intermolecular interactions take place on similar time scales as the excited state lifetime. The intermolecular deactivation of an excited molecule by another molecular system is called fluorescence quenching. Several intermolecular fluorescence quench processes exist. Most of these processes involve a fast transfer process from a donor to an acceptor such as electron, proton, or energy transfer. In the following we focus on radiationless excitation energy transfer from an electronically excited donor to an acceptor, since this is the basis of one of the most important fluorescence techniques in biophotonics to quantify such important processes, for example, protein–protein and protein–DNA interactions or conformational changes of proteins, and so on.

Nonradiative energy transfer requires a significant spectral overlap of the emission spectrum of the donor D with the absorption spectrum of the acceptor A. This means that for a nonradiative energy transfer, the existence of isoenergetic vibronic transitions of the donor and acceptor is required. In other words, these transitions are in resonance, that is, they are coupled (see Figure 3.60).

Various interaction/coupling mechanisms between donor D and acceptor A responsible for the energy transfer exist. In Section 3.9 (see footnote 14 on page 172), we have seen that the coupling between two states $|\psi_i\rangle$ and $|\psi_f\rangle$ is usually expressed by a coupling matrix element $\langle\psi_f|\hat{V}|\psi_i\rangle$ with the perturbation $\hat{V}$. Let us assume that the energy transfer process can be described by one electron of the donor D and one electron of the acceptor A. For this assumption, the initial and final wavefunctions can be expressed by

$$\begin{aligned}\psi_i &= \frac{1}{\sqrt{2}}[\psi_{D^*}(1)\psi_A(2) - \psi_{D^*}(2)\psi_A(1)] \\ \psi_f &= \frac{1}{\sqrt{2}}[\psi_D(1)\psi_{A^*}(2) - \psi_D(2)\psi_{A^*}(1)]\end{aligned} \tag{3.153}$$

where the wavefunction ψ_i represents the situation where the electron on the donor D is excited (D^*) and that on A is not and the final wavefunction ψ_f characterizes the situation after the energy transfer, that is, the electron on A is excited (A^*) and that on D is not. The numbers 1 and 2 symbolize the two electrons involved in the energy transfer process. The form of the wavefunctions (antisymmetrized product wavefunctions) takes into account that electrons are not distinguishable. Hence the coupling matrix element U between donor D and acceptor A due to a perturbation $\hat{V}$ reads as follows:

$$U = \langle\psi_{D^*}(1)\psi_A(2)|\hat{V}|\psi_D(1)\psi_{A^*}(2)\rangle - \langle\psi_{D^*}(1)\psi_A(2)|\hat{V}|\psi_D(2)\psi_{A^*}(1)\rangle. \tag{3.154}$$

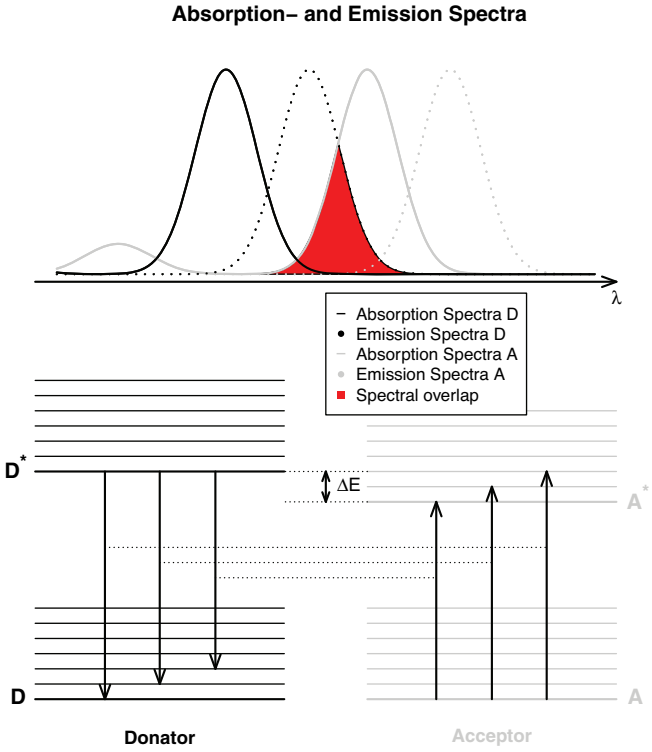

Figure 3.60 Energy level diagram representing the resonance (coupling) of donor and acceptor vibronic transitions (adapted from [19]).

The first term is called the Coulomb term and represents the situation where the initially excited electron on D returns to the ground state whereas simultaneously the electron on A is becoming excited. It is referred to as Coulomb energy transfer because it is a consequence of the electrostatic repulsions between the electron at the donor and that at the acceptor. The second term describes the exchange of two electrons between A and D and is therefore called the exchange term. These two terms are characterized by different operating distances r between the donor and acceptor. The exchange term is a short-range process because it describes an energy transfer process by an exchange of an electron due to intermolecular orbital overlap. However, the Coulomb term can be approximated by a long-range dipole–dipole interaction between the transition dipole moments of the donor $\mu_{fi}^{D} = \langle D^* | \hat{\mu} | D \rangle$ and acceptor $\mu_{fi}^{A} = \langle A^* | \hat{\mu} | A \rangle$ transitions $D \rightarrow D^*$ and $A \rightarrow A^*$, respectively (Figure 3.61). In other words, the electron relaxing from D^* to D generates a transition dipole moment μ_{fi}^{D} which can interact with the transition dipole moment μ_{fi}^{A} simultaneously created by the excitation from A to A^*.

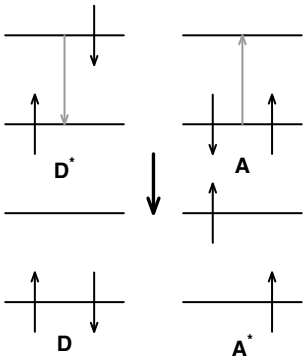

Figure 3.61 Illustration of long-range dipole–dipole Coulomb interaction.

It should be noted that in contrast to the exchange interaction, the Coulombic dipole–dipole interaction does not require contact between donor and acceptor as it is a long-range interaction. The Coulombic mechanism is equivalent to the energy being transferred across the space between the donor and acceptor. The Coulombic term of Equation 3.154 can be expressed under the approximation of a dipole–dipole interaction between the transition dipole moments μ_{fi}^{D} and μ_{fi}^{A} as follows:

$$U^{dd} \sim \frac{|\mu_{fi}^{D}| \cdot |\mu_{fi}^{A}|}{r^3}(\cos\vartheta_T - 3\cos\vartheta_D\cos\vartheta_A) \tag{3.155}$$

where r is the distance between the donor D and the acceptor A. The angles ϑ_T and ϑ_A describe the orientation between the two transition dipole moments and are defined in Figure 3.62.

Equation 3.155 shows that the long-range dipole–dipole interaction is large if the two transitions $D \rightarrow D^*$ and $A \rightarrow A^*$ are fully allowed, that is, their transition dipole moments are large. Furthermore, the dipole–dipole interaction strength depends on the mutual orientation of the transition dipole moments (see Figure 3.62).

3.11.3.1 Förster Resonance Energy Transfer (FRET)

The Coulombic dipole–dipole energy transfer is called Förster resonance energy transfer after Theodor Förster, who developed a detailed theory for such a long-range Coulombic dipole–dipole energy transfer. FRET is considered to be a very weak coupling process. This means that the absorption spectrum of the coupled donor–-acceptor system is almost identical with the sum of the absorption spectra of the individual components. This is the case if the vibrational relaxation in the excited donor D^* is much faster than the energy transfer to the acceptor. The transfer rate for a FRET process can be derived with the help of Fermi's golden rule (see footnote 14 on page 172), employing Equation 3.155 as the coupling matrix element. The density of states ρ is expressed by the spectral overlap between the donor emission spectrum and the acceptor absorption spectrum. Hence the following expression for the FRET transfer rate can be derived:

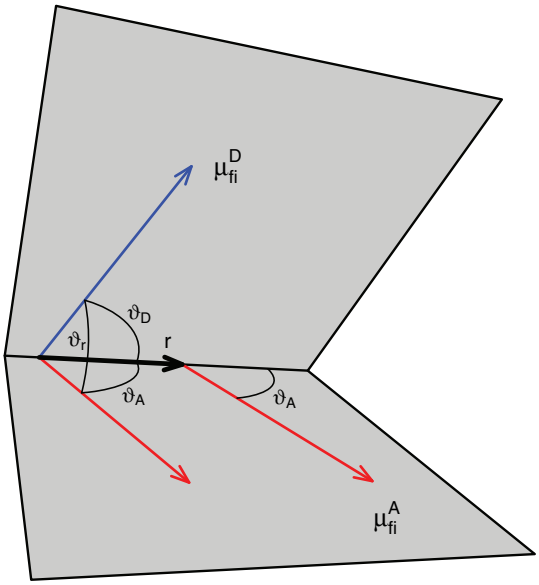

Figure 3.62 Illustration of angles ϑ_T and ϑ_A describing the orientation of the two transition dipole moments μ_{fi}^{D} and μ_{fi}^{A} (adapted from [17]).

$$k_{D\to A}^{dd} = k_D\left(\frac{R_0}{r}\right)^6 = \frac{1}{\tau_D^0}\left(\frac{R_0}{r}\right)^6 \tag{3.156}$$

where k_D is the radiative decay rate of the donor, τ_D^0 is the excited state lifetime of the donor in the absence of energy transfer, and R_0 is the Förster radius, namely the distance at which the intensity decreases caused by energy transfer and spontaneous internal decay are equal, that is, $k_{D\to A}^{dd} = k_D$. The r^6 dependence of the transfer rate on the donor–acceptor distance is a result of the square modulus of the dipole–dipole interaction $\left|U^{dd}\right|^2$ in Fermi's golden rule. The Förster radius can be determined from the spectral overlap of the fluorescence emission spectrum of the donor and the absorption spectrum of the acceptor:

$$R_0^6 = \frac{9000\cdot \ln 10\cdot \kappa^2 \Phi_D^0}{128\cdot \pi^5 N_L n^4}\int_0^\infty I_D(\lambda)\epsilon_A(\lambda)\lambda^4 d\lambda \tag{3.157}$$

where $\kappa^2 = (\cos\vartheta_T - 3\cos\vartheta_D\cos\vartheta_A)^2$ is the orientational factor (see Figure 3.62 and Equation 3.155), Φ_D^0 is the donor fluorescence quantum yield in the absence of the acceptor, n is the average refractive index of the medium for the wavelengths of the spectral overlap, $I_D(\lambda)$ is the normalized fluorescence spectrum of the donor [i.e., $\int_0^\infty I_D(\lambda)d\lambda = 1$], and $\epsilon_A(\lambda)$ is the extinction coefficient of the acceptor. Typical values for the Förster radii, that is, for distances over which energy transfer is important, lie in the range of 15–60 Å. The transfer efficiency can be expressed by

$$\Phi_{D\to A}^{dd} = \frac{k_{D\to A}^{dd}}{k_D + k_{D\to A}^{dd}} = \frac{k_{D\to A}^{dd}}{\frac{1}{\tau_D^0} + k_{D\to A}^{dd}}. \tag{3.158}$$

In combination with the distance dependence of Equation 3.156, it follows for the transfer efficiency:

$$\Phi_{D\to A}^{dd} = \frac{1}{1+\left(\frac{r}{R_0}\right)^6} = 1-\frac{\tau_D}{\tau_D^0} \tag{3.159}$$

where τ_D and τ_D^0 are the excited state lifetimes of the donor D^* (i.e., decay of the donor fluorescence subsequent to pulse excitation) in the absence and presence of the acceptor, respectively. The transfer efficiency also relates to the fluorescence quantum yield of the donor as follows:

$$\Phi_{D\to A}^{dd} = 1-\frac{\Phi_D}{\Phi_D^0} \tag{3.160}$$

where Φ_D and Φ_D^0 are the donor fluorescence quantum yields in the presence and absence of the acceptor, respectively.

As has been stated above, in addition to the distance r between the donor and acceptor, the relative orientation of the transition dipole moments of the donor μ_{fi}^D and acceptor μ_{fi}^A also plays a crucial role in the energy transfer efficiency (see Figure 3.62). The relative orientation is expressed by the orientational factor $\kappa^2 = (\cos\vartheta_T - 3\cos\vartheta_D\cos\vartheta_A)^2$ (see Equation 3.157). For systems where the orientation remains constant during the energy transfer (e.g., use of highly viscose solvents or rigid coupling of donor and acceptor to large and stiff molecules), κ^2 can reach values between 0 (transition dipole moments are orthogonal) and 4 (collinear arrangement). For parallel transition dipole moments, $\kappa^2 = 1$. If both donor and acceptor can rotate, the orientational factor must be replaced by an average: if both chromophores D and A undergo fast isotropic rotation, that is, rotation is considerably faster than the energy transfer rate, the average orientational factor is given by $\kappa^2 = 2/3$. If the donor and acceptor are freely movable but the rotation is significantly slower than the energy transfer, the orientational factor results in $\kappa^2 = 0.476$.

The importance of FRET for biophotonics results in its potential to act as an "optical nano ruler" in the range 10−100Å. The donor–acceptor distance can be determined by either time-resolved or steady state fluorescence measurements via the energy transfer rate (see Equations 3.159 and 3.160):

$$r = \left(\frac{1}{\Phi_{D\to A}^{dd}} - 1\right)^{\frac{1}{6}} R_0. \tag{3.161}$$

The distance between the donor and acceptor should be in the range $0.5R_0 < r < 1.5R_0$ because the Förster radius R_0 is a benchmark for donor–acceptor distances, which can be determined via FRET.

Advances in fluorescence labeling techniques (see The Appendix of this chapter) to introduce fluorophores selectively in biomolecules or in living biological cells (in particular the availability of genetically encoded fluorescent proteins) have allowed the visualization of cellular and single protein processes by means of FRET. This means that FRET measurements are predominantly utilized in biophotonics as a molecular ruler to determine distances between biomolecules labeled with appropriate donor and acceptor chromophores, that is, which are attached to special sites of biomolecules such as proteins. Then it is possible to monitor dynamic molecular processes such as conformational changes manifesting themselves by alterations in the donor–acceptor distances; for example, the donor–acceptor distance in the normal protein is too large for FRET to take place but, as a result of a conformational change of the protein, the donor–acceptor distance is reduced and FRET can occur. Other processes that can be monitored via FRET include (1) conformational changes (e.g., protein folding), (2) ligand receptor interactions or protein–protein aggregation, and (3) protein hydrolysis (see Figure 3.63). For all these processes, the donor–acceptor distance changes from distances where FRET cannot take place to distances where FRET can occur, or vice versa.

Hence the FRET technique adapted to modern fluorescence microscopy is unique in generating fluorescence images (FRET efficiency images) sensitive to molecular dynamics such as conformational changes (e.g., protein folding), ligand-receptor interactions (e.g., protein–protein and protein–DNA interactions), and so on. As mentioned above, FRET manifests itself either through a decrease in the fluorescence lifetime of the donor, or in a quenching of the donor fluorescence intensity and a simultaneous increase in the acceptor fluorescence. Therefore, different methods exist to record FRET efficiency images. Usually it is advantageous to plot the acceptor emission at donor excitation $I_A(\lambda_{abs}^D, \lambda_F^A)$ divided by the donor emission at donor excitation $I_D(\lambda_{abs}^D, \lambda_F^D)$. Such FRET ratio images yield better signal-to-noise ratios than

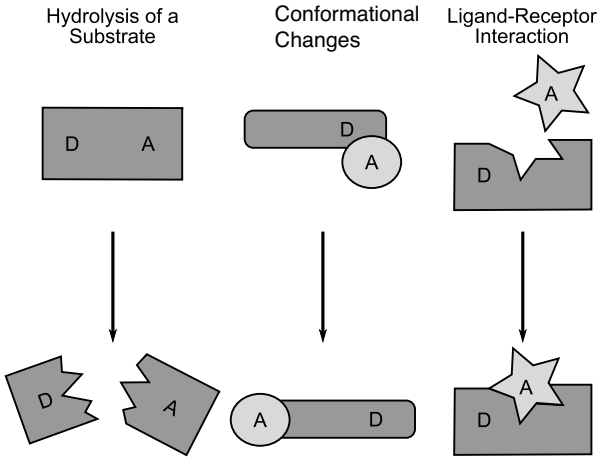

Figure 3.63 Illustration of FRET applications (adapted from [17]).

when solely recording the acceptor fluorescence at donor excitation since both donor decrease and acceptor increase contribute to the signal. Very often it is also necessary to correct for cross-talk, that is, direct excitation of the acceptor when exciting the donor if the donor and acceptor absorption spectra overlap. This can be done by control measurements with samples that are only labeled with the acceptor. Further, it is often required to correct for bleedthrough of donor fluorescence into the acceptor fluorescence detection window in the absence of FRET. This correction is accomplished by control measurements for samples that contain only the donor. An easier way of recoding FRET images which are independent of the above-mentioned spectral contaminations cross-talk and bleedthrough consists in recording the fluorescence lifetime of the donor fluorescence which is reduced if FRET occurs. The generation of fluorescence images based on differences in the exponential decay times of fluorescence is called fluorescence lifetime imaging microscopy (FLIM). In other words, FLIM yields images with the intensity of each pixel determined by the fluorescence lifetime τ and therefore allows viewing of the contrast between fluorophores with different decay times or changes in the decay time of one particular fluorophore due to intermolecular interactions such as in FRET imaging.

3.11.4 Photobleaching

One problem in fluorescence spectroscopy/microscopy with fluorescently labeled biomolecules is photobleaching, which is the permanent loss of the fluorescence emission of a fluorophore due to its exposure to the excitation light. Photobleaching is a dynamic process where the fluorophore molecules are photochemically destroyed on exposure to the excitation light. The average number of absorption fluorescence emission cycles that a fluorophore can carry out before being destroyed by photobleaching depends on the excitation light intensity, the molecular structure of the fluorophore and its chemical environment. Some fluorophores are already bleached after the emission of a few photons whereas others can run through thousands or millions of excitation and emission cycles until photobleaching occurs. The molecular mechanism of photobleaching is only poorly understood. Photobleaching is a matter of different photochemical reactions leading to light-induced damage or modification of the fluorophore. Electronically excited molecules might react with other molecules, leading to irreversible covalent changes of the fluorophore. Furthermore, a fluorophore which ends up in a long-lived triplet state has much more time to react with other molecules in its environment.

Hence the observation of fluorophores in fluorescence microscopy might be hampered because the fluorophores will be destroyed at a certain point by photobleaching due to exposure to the excitation light. However, photobleaching can also be exploited in fluorescence microscopy to characterize the motion or diffusion of molecules. This technology is called fluorescence recovery after photobleaching (FRAP), where a fluorophore is intentionally photobleached by strong laser irradiation. After photobleaching, the fluorescence intensity recovers because fluorophores might diffuse from the environment into the bleaching (i.e., measuring)

area. The recovery of the fluorescence intensity depends on the mobility of the fluorophore. Hence FRAP allows the determination of diffusion coefficients and further parameters determining the mobility of molecules. Additionally, the overall fluorescence intensity decreases due to photobleaching of a certain region can also be monitored. This decrease in fluorescence intensity is caused by the diffusion or transport of molecules into the bleaching region. This fluorescence microscopy approach is called fluorescence loss in photobleaching (FLIP).

3.11.5
Multi-Photon Excited Fluorescence

The recent progress in the development of high-intensity ultrashort laser sources revolutionized fluorescence microscopy by utilizing nonlinear optical phenomena to create a higher microscopic contrast. These ultrashort laser pulses, if focused down, generate extremely high light intensities. As we have seen in Section 3.6, such high intensities allow one to induce multi-photon absorption processes. Multi-photon absorption leads to a simultaneous absorption of $m \geq 2$ photons by a fluorophore. Such a nonlinear dependence can be utilized for applications in which a reaction should be initialized out of only a small spatial area. Thus multi-photon absorption is especially suited to microscopic applications. By the application of a femtosecond titanium:sapphire laser (see Section 3.7) providing excitation wavelengths in the range 800−960 nm, fluorophores absorbing at 400−480 nm (absorption of two photons) or 270−320 nm (absorption of three laser photons) can be excited and their red-shifted fluorescence can subsequently be detected (see Figure 3.64).

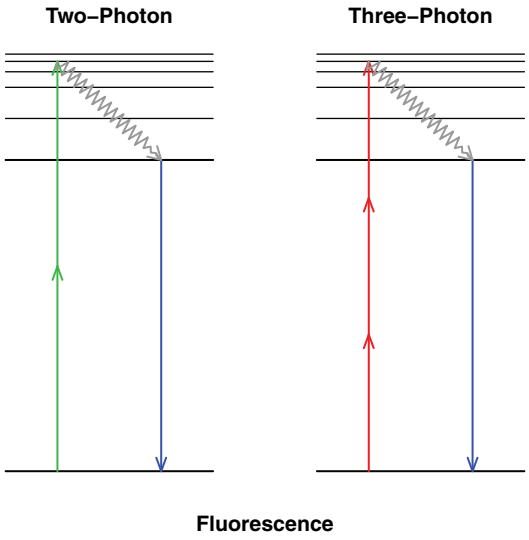

Figure 3.64 Illustration of multi-photon fluorescence emission.

The simultaneous absorption of two or three photons results in a very good localization of the fluorescence light, since such a nonlinear absorption process can only take place in an extremely small volume. Hence multi-photon absorption yields an inherent three-dimensional effect making the application of a confocal pinhole unnecessary, see page 439 (6.1.5.4). There are other advantages of multi-photon absorption fluorescence microscopy. (1) Since the fluorophores are not excited by one high-energy photon but rather through the simultaneous absorption of many low-energy photons, sensitive living biological samples can be investigated in a sparing way. Both the emission of fluorescence and possible bleaching effects, that is, photochemical or thermal degradation of the sample, are limited to a small volume. (2) The excitation wavelength and the fluorescence wavelength are spectrally far apart, resulting in low background noise since the detection of fluorescence light is not disturbed by the broadband excitation laser. Two- or multi-photon absorption fluorescence spectroscopy has emerged since its discovery in 1990 as an indispensable biophysical method providing valuable information about subcellular biochemical processes within living cells. Furthermore, multi-photon imaging by means of NIR femtosecond lasers is characterized by high penetration depths and therefore allows the description of biological tissue with high spatial resolution and good contrast.

3.11.6
Fluorescence Nanoscopy

At the end of this section, recent advances in significantly reducing the spatial area from which fluorescence light can emerge should be briefly summarized. This concept, which is called reversible saturable (or switchable) optical linear fluorescence transitions (RESOLFT) is based on having fluorescent molecules which can exist in two distinct states A and B.[19] Whereas A is a bright state (i.e., shows fluorescence emission), the molecular state B is a dark state (i.e., does not fluoresce). The transition from state A to B can be induced by light and the back reaction from B to A can be either spontaneous or effected by light, heat, and so on:

$$\mathrm{A} \underset{k_{\mathrm{BA}}}{\overset{k_{\mathrm{AB}}}{\rightleftharpoons}} \mathrm{B} \tag{3.162}$$

where k_{AB} and k_{BA} are the rate constants for the transitions $\mathrm{A} \rightarrow \mathrm{B}$ and $\mathrm{B} \rightarrow \mathrm{A}$, respectively. Hence the changes in the normalized populations N_{A} and N_{B} of the states A and B are

$$\frac{\mathrm{d}N_A}{\mathrm{d}t} = -k_{AB}N_A + k_{BA}N_B = -\frac{\mathrm{d}N_B}{\mathrm{d}t}. \tag{3.163}$$

19) It will be shown later that A and B can be two different electronic states of the same molecule or of two different molecules that can be converted into one another by, for example, reversible photoisomerization.

Solving this first-order differential equation yields an expression for the variation of the population of A with time. As $t \to \infty$, the population of state A reaches its equilibrium value, which is given by

$$N_A^{\infty} = \frac{k_{BA}}{k_{AB} + k_{BA}}. \tag{3.164}$$

The rate constant k_{AB} for the light induced depletion of state A is given by

$$k_{AB} = \sigma \cdot I \tag{3.165}$$

where σ is the molecular absorption cross-section and I the light intensity inducing the transition $A \to B$. The molecular absorption cross-section is given by the molar absorption coefficient ϵ : $\sigma = \frac{\epsilon}{N_L}$, where N_L is Avogadro's number.

Equation 3.164 together with Equation 3.165 yields

$$N_A^{\infty} = 1 - N_B^{\infty} = \frac{k_{BA}}{\sigma I + k_{BA}} = \frac{1}{1 + \left(\frac{\sigma}{k_{BA}}\right) I} = \frac{1}{1 + \frac{I}{I_{sat}}}. \tag{3.166}$$

The saturation intensity $I_{sat} = k_{BA}/\sigma$ is the intensity where 50% of the molecules are in state A and 50% in state B. Figure 3.65 shows the dependence of the normalized populations N_A and N_B as a function of the applied light intensity.

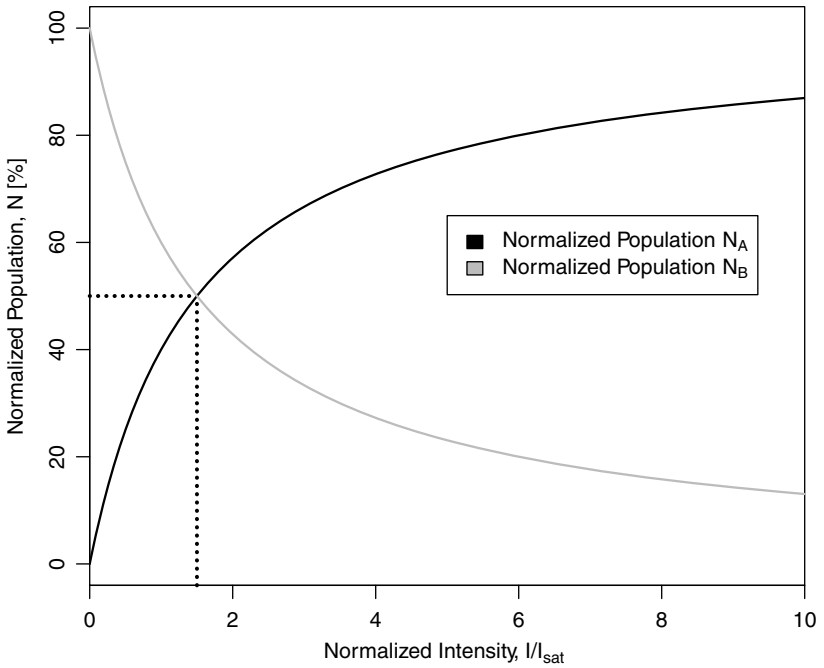

Figure 3.65 Plot of the normalized populations N_A and N_B as a function of I/I_{sat} (adapted from [25]).

It can be seen that for $I \gg I_{sat}$ all molecules end up in the nonfluorescent state B, that is, $N_A^{\infty} \to 0$. Hence it is possible to switch off the fluorescence by shifting all molecules from the bright state A into the dark state B. The principle of reducing the spatial area of fluorescence emission is now based on confining the spatial area of molecules in state A by an intensity naught and simultaneously parking the fluorophores outside the naught in the dark state B. This can be achieved by applying a spatial intensity distribution I for which the intensity at one point x_i equals $I(x_i) = 0$. For one dimension, such an intensity naught can be best realized by a standing wave:

$$I(x) = I_0 \sin^2\left(2\pi n \frac{x}{\lambda}\right) \tag{3.167}$$

where n is the refractive index and λ the wavelength of the light. If this intensity distribution is applied to a spatial distribution of molecules $C(x)$ which are initially in the bright state A for $I_0 \gg I_{sat}$, practically all molecules will be transferred to the dark state B except those which are located around the small area around x_i (see Figure 3.66).

The larger the ratio $I_0/I_{sat} \gg 1$, the smaller the spatial region in which state A is populated becomes. It can be shown that the minima of the standing wave intensity distribution create regions of molecules in the bright state A with a full width at half-maximum (FWHM) of

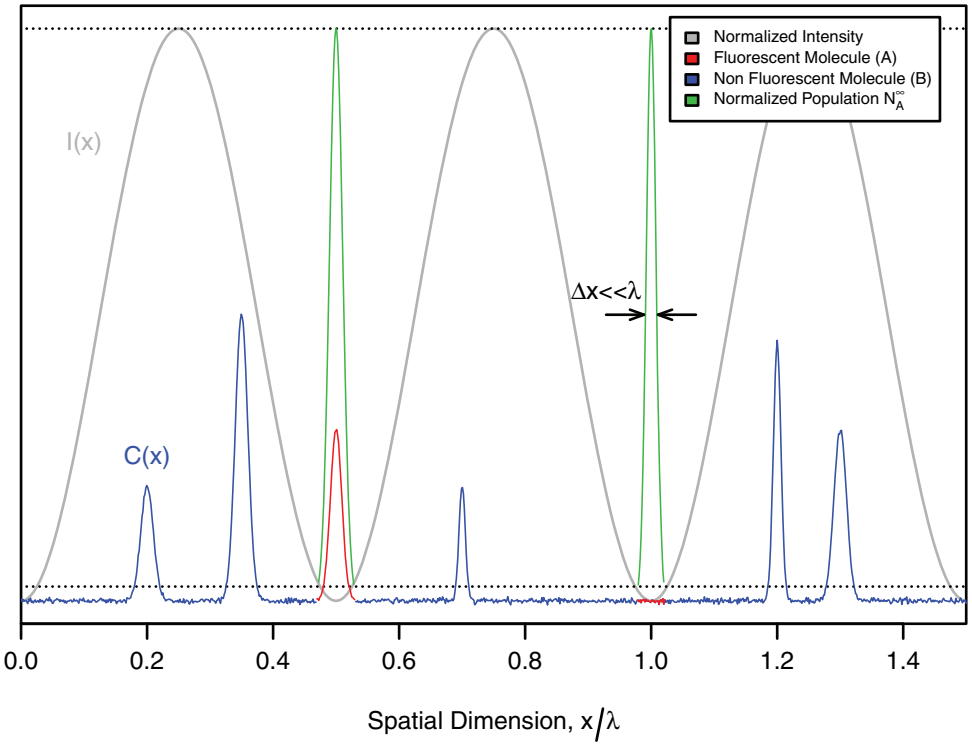

Figure 3.66 Illustration of the RESOLFT principle to create arbitrarily sharp regions of fluorescent molecules (adapted from [24]).

$$\Delta x \approx \frac{\lambda}{\pi n \sqrt{\frac{I_0}{I_{\text{sat}}}}}. \tag{3.168}$$

Thus, if already a small fraction of the overall intensity I_0 is sufficient to promote the molecules into the dark state B, the areas of finding molecules in the bright fluorescent state A are confined to the minima (nodal points) of the standing waves (see Figure 3.66). The fluorescence image is generated by scanning the intensity nodes across the sample $C(x)$. By doing so, all the molecules initially in state A will be temporally transferred to state B except those molecules situated at the nodes. The object $C(x)$ is displayed by the fluorescence observed from the molecules in the bright state A squeezed to an area much smaller than $\lambda/2$. A sequential readout of these transient ultrasharp bright areas yields a high-resolution fluorescence image. The spatial resolution of this image is then determined by the ratio I_0/I_{sat}, which determines the spatial area of the bright state A (see Equation 3.168).

The important relationship $\Delta x \approx (I_{sat}/I_0)^{\frac{1}{2}}$, which was derived for one dimension, is commonly valid for every applied spatial intensity distribution around a naught x_i. If the naught is generated by a lens with an aperture angle α and the fluorescence light is collected by the same lens, the spatial resolution can be approximated by the following relationship:

$$\Delta x \approx \frac{\lambda}{2n \cdot \sin\alpha \sqrt{1 + \frac{I_0}{I_{sat}}}} \tag{3.169}$$

which can be seen as an extension of Abbe's equation (see Section 6.2.2.5).

3.11.6.1 **Stimulated Emission Depletion Microscopy (STED)**

The first experimental realization of the RESOLFT principle is called stimulated emission depletion microscopy (STED). Here, the S_1 state of the fluorophores is the bright state A and the S_0 state is the dark state B. The light-induced transition between the bright S_1 state and the dark S_0 state is accomplished by stimulated emission (see Section 3.7). This means that the S_1 fluorescence is suppressed by stimulated emission from the S_1 (A) into the S_0 (B) state. In doing so, stimulated emission is used to quench the spontaneous emission of fluorescence light in such a manner that only fluorescence at the edge of the fluorescence spot is quenched. Figure 3.67 displays the excitation scheme applied for this stimulated fluorescence quenching called "stimulated emission depletion."

The molecules are excited into an electronically excited state by an excitation laser from where the molecules would normally relax back into the electronic ground state spontaneously by emission of fluorescent light on a nanosecond time scale. However, the application of a high-intensity STED laser pulse that is red shifted and slightly shifted in time compared with the excitation laser leads to stimulated emission of the electronically excited molecules into excited vibrational states of the electronic ground state before they have the chance to fluoresce spontaneously, since stimulated emission is much faster than spontaneous emission. These vibrationally excited

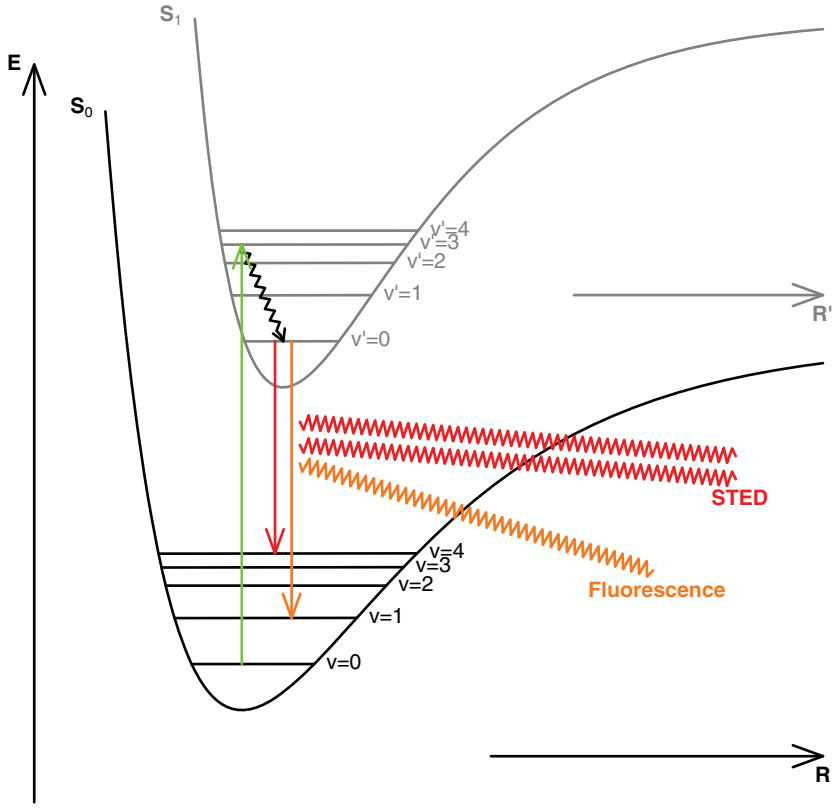

Figure 3.67 Illustration of the STED excitation scheme.

ground-state molecules cannot be excited by the excitation laser any longer. If one chooses a donut beam profile for the STED laser pulse with a central naught which is overlapped with the excitation laser, that is, the STED laser profile is almost dark within the focal point of the excitation laser but very intensively circularly symmetric to the excitation laser, an extreme reduction in the size of the focal spot occurs since only molecules inside both laser foci are not affected by the de-excitation process. Thus the fluorescence light originates from an extremely sharp spot of only a few nanometers in size. Excitation and subsequent de-excitation by the doughnut-shaped STED beam is achieved by synchronized femto- or picosecond pulses allowing the temporal separation of excitation and de-excitation by stimulated emission. The energy of the formerly excited molecule is carried as a further photon in the STED beam. STED microscopy reduces the investigation volume to 0.67 al (attoliters), which is 18 times smaller than that which can be obtained by conventional confocal fluorescence microscopy. The spatial resolution is determined by the intensity of the STED pulse: the more intense the donut beam, the more strongly the effective S_1 population is squeezed to the middle of the donut. The spatial area for which fluorescence is allowed becomes smaller with an increasing STED beam intensity

because then a large fraction of the donut intensity is lying above the saturation intensity I_{sat} and prevents population of the bright state S_1. However, regardless of how high the STED beam intensity is, fluorophores situated at the donut naught will always emit fluorescence light because at the naught no stimulated emission takes place. Hence by scanning the naught across the sample, structures much beyond the diffraction limit are obtained.

The saturation intensity given by $I_{sat} = k_{BA}/\sigma$ depends on the fluorophores or, more precisely, on the two states A and B. The saturation intensity I_{sat} can be approximated by

$$I_{sat} = \frac{1}{\sigma \cdot \tau} \tag{3.170}$$

where τ is the spontaneous emission lifetime of state A. Hence for STED, fairly large saturation intensities are required to reach high spatial resolutions due to the rather short fluorescence lifetime of the S_1 state in the nanosecond range. However, high intensities might lead to sample degradation or photobleaching. Therefore, the application of lower saturation intensities is preferable.

In general, the longer living both states A and B are, the smaller I_{sat} becomes and therefore according to Equation 3.169 the smaller the intensity I_0 becomes that is necessary to go beyond the diffraction limit and coming close to achieving molecular resolution. Therefore, other bright–dark pairs A and B besides S_1 and S_0 in fluorophores with long lifetimes are required to achieve low saturation intensities. The ultimate form of "optical saturation" (see Figure 3.65) is optical switching, that is, the employment of optically bistable molecules where only the bright state A yields fluorescence by excitation to a transient fluorescent state A * (A $\leftrightarrow$ A*) (e.g., photo-transformable *cis–trans* isomers where only one isomer yields fluorescence). These molecular photoswitches allow very low saturation intensities, if it is possible to switch between the long lived fluorescent (A $\leftrightarrow$ A*) and dark (B) states.

3.11.6.2 Photoactivated Localization Microscopy (PALM) and Stochastic Optical Reconstruction Microscopy (STORM)

At the end of this chapter, two other fluorescence microscopy methods achieving nanometer resolution, namely photoactivated localization microscopy (PALM) and stochastic optical reconstruction microscopy (STORM) should be briefly explained. Both PALM and STORM are based on the readout of single molecules from random coordinates. This is achieved by switching on molecules into a bright state A so that only fluorophores that are far apart from each other can be identified as single fluorescent molecules. This means that at the beginning all molecules are switched off, that is, are in state B. Then the molecules are switched on into the fluorescing state A with such a low intensity that the switched-on molecules are further away than half the wavelength. This means that statistically molecules in the direct neighborhood remain in the dark state B. The molecules which were switched on are fluorescence excited several times (A $\rightarrow$ A*) and N photons are detected. In other words, PALM and STORM utilize a molecular process leading to an emission of N photons from the same spot. Subsequently the molecules return spontaneously

(by photobleaching) to the dark state B′ (PALM) or they are sent systematically into the dark state B (STORM). If the movement of the molecules is negligible, each molecule leaves single, separable diffraction broadened spots on the camera whose centroid is determined by a fitting procedure. Each diffraction spot belongs to a single molecule. Fitting an image consisting of N photons can also be seen as N measurements of the fluorophore position in which every measurement has an uncertainty determined by the point spread function (PSF), which describes the response of an imaging system to a point source or point object. The precision with which a single switched-on fluorophore can be localized is given by

$$\Delta_{\mathrm{loc}} = \frac{\Delta_{\mathrm{PSF}}}{\sqrt{N}} \tag{3.171}$$

where Δ is the width of the PSF. A high-resolution image is constructed sequentially by stochastic registration of single switched-on molecules and plotting their position Δ_{loc} as a point. Figure 3.68 illustrates a typical PALM imaging cycle.

First, all fluorescent molecules (red dots) in the field of view are switched off (green dots) by a strong red laser. In a second step, only a small percentage of fluorescent molecules (green light) are switched on such that their images do not overlap. Third, the fluorescence emission of the switched-on molecules is recorded. This fluorescence emission is used to localize the fluorophore position (gray dot) with nanometer accuracy.

The molecule within these single-molecule techniques STORM and PALM has to pass through the bright–dark cycle $[\mathrm{B} \rightarrow \mathrm{A}(\leftrightarrow \mathrm{A}^*) \rightarrow \mathrm{B}(\mathrm{B}')]$ only once since the emission of the N photons takes place via multiple excitation steps in the fluorescent state A^*. In other words, the high-resolution image is assembled molecule by molecule via a single switching cycle $\mathrm{B} \rightarrow \mathrm{A} \rightarrow \mathrm{B}(\mathrm{B}')$ per single molecule. The difference between PALM and STORM is that for PALM photobleaching due to the exposure to the fluorescence excitation light is utilized to switch off A. This means that for PALM the switching cycle is $\mathrm{B} \rightarrow \mathrm{A} \rightarrow \mathrm{B}'$, that is, B′ is different to B. For STORM, B equals B′ since the molecules are actively switched from A to B.

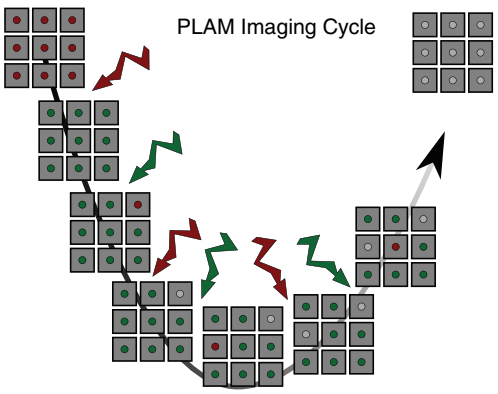

Figure 3.68 Illustration of PALM imaging cycle (adapted from [23]).

This is in contrast to RESOLFT, where constant cycling is required since ensuring state A for a chosen nodal point requires nearby molecules to be switched to the dark state B.

3.12 Elastic Light Scattering

Inhomogeneities inside a medium can also lead to scattering, which is a second effect in addition to absorption (see Section 3.4) that leads to a decrease in the intensity of transmitted light. This section deals with elastically scattered light, which refers to the fact that the wavelength of the light remains unchanged as no energy loss or gain has occurred, very much like a rubber ball which hits a wall, thereby changing only direction but not speed. Scattering is a process which depends strongly on the wavelength of light. Generally, it increases rapidly with decrease in wavelength.

This section aims a short introduction to elastic light scattering. For further reading, [3, 18] are recommended.

There are two mechanisms which are responsible for a decrease in the intensity of a light wave while propagating through a medium. As already detailed (see Section 3.4), one of these mechanisms is the absorption of radiation, during which the energy of the wave is dissipated and which leads to a decrease in the amplitude of the wave. A second mechanism, which also decreases transmission through a medium, is scattering, where light is either elastically or, with a much lower probability, inelastically scattered (see Section 3.13). The former effect is exploited, for example, in nephelometry, where laser light is passed on into a dilute suspension of small particles and the light scattered elastically under an angle of $70-75^\circ$ is collected and investigated to determine the levels of certain proteins.

In analogy with the Lambert–Beer law (Equation 3.38), the dependence of the intensity $I(z)$ with increasing travel distance along the z-direction is given by

$$I(z) = I_0 \exp(-S'z) \tag{3.172}$$

where S' is the scattering coefficient. For dilute solutions, it is possible to determine the so-called scattering cross-section σ_s with a conventional spectrometer directly from the opacity of the sample:

$$S' = N \cdot \sigma_s \tag{3.173}$$

where N represents the number of particles per unit volume. The scattering cross-section is the effective cross-section of the scattering particles within which an incident photon can be deflected.

In the following, we deal only with elastic light scattering, also known as Rayleigh scattering. Inelastic light scattering (Raman sattering) will be treated in detail in Section 3.13.

In the case of elastic light scattering, the incoming electric field induces a time-dependent dipole moment $\mu_{ind}(t)$ and forces the dipole to vibrate. The dipole in turn emits radiation as a consequence with an intensity I_s. Due to the incoming electric field $E = E_0\cos(\omega_0 t)$ at the scattering center ($z = 0$), an oscillating dipole results, which is given by

$$\mu = \alpha \cdot E = \alpha \cdot E_0 \cos(\omega_0 t). \tag{3.174}$$

If the scattering centers are much smaller than the wavelength λ, the Rayleigh equation holds, which is given by

$$\frac{I_s}{I_0} = \frac{16\pi^4\alpha^2}{r^2\lambda^4}\sin^2\varphi. \tag{3.175}$$

It describes the distribution of the Rayleigh scattering, which in the case of monochromatic, perpendicularly polarized light is independent of the azimuth angle ϑ but depends strongly on the zenith angle φ. As can be seen from Equation 3.175, the intensity is indirectly proportional to the fourth power of the wavelength λ or directly proportional to ω^4. The emitted intensity possesses a maximum perpendicular to the dipole axis, as can be seen from Figure 3.69, and is zero along the dipole axis. It is proportional to the square of the dipole moment and indirectly proportional to the square of the distance r from the emitting dipole.

Fairly often, however, the incoming light is unpolarized. In this general case, a superposition of light waves with all possible polarizations results in

$$\frac{I_s}{I_0} = \frac{8\pi^4\alpha^2}{r^2\lambda^4}\left(1 + \cos^2\vartheta\right). \tag{3.176}$$

If there is more than one scatterer in a comparably small volume (multiple scattering, for example molecules in a solution), the scattered waves are nearly always in-phase and interfere constructively. If the scatterers are not small compared with the wavelength, for example in the case of macromolecules, then the scatterer itself consists of a number of scattering centers. Light that is scattered from different scattering centers is generally excited out-of-phase (the wave hits the center at different times and therefore with different phase) and therefore the emitted waves also have different phase and the interference can be both constructive and destructive.

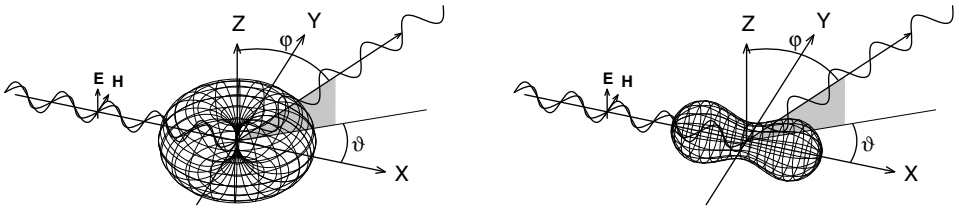

(a) Polarized light (b) Unpolarized light

Figure 3.69 Illustration of the orientation dependence of Rayleigh scattering (adapted from [18]).

Macromolecules in a liquid are usually not perfectly dissolved by a liquid but lead to a colloid or even a suspension. Colloids or suspensions show certain degrees of opacity or turbidity, the investigation of which is carried out by nephelometry (see above).

The theoretical treatment of elastic light scattering can become rather complicated. Originally this problem was solved by Gustav Mie in 1908 for a homogeneous dielectric sphere. Mie's original problem was to understand the various colors in absorption and scattering exhibited by small colloidal particles of gold suspended in water. To obtain the solution, the incident plane wave and also the scattering field can be expanded into radiating spherical vector wavefunctions, while the internal field is expressed as regular spherical vector wavefunctions. By applying the boundary condition on the spherical surface, the expansion coefficients of the scattered field can be computed. A comparably modern way of solving such problems is the *T*-matrix approach. Within this approach, the scattering from anisotropic and anisometric particles can also be treated. Since an exhaustive treatment of this theory is well beyond the scope of this book, we just discuss some of the most important results. One of these results is that the variation of extinction (i.e., absorption + scattering) with frequency depends strongly on the size of the particles. In frequency regions with weak absorptions, the variation of extinction with frequency shows three characteristics: (1) the interference structure which dominates and tends to look like a damped harmonic oscillation; (2) the ripple structure, which is an irregular fine structure; and (3) a monotonically increasing extinction with increasing frequency for the range in which the particle diameter is smaller than the wavelength of light. The last chracteristic implies that the onset of the extinction due to scattering is strongly dependent on the particle size as a result of Mie theory, which explains the various colors of the colloidal gold particles in water (or in glass) as being due to diameter variations of the particles. Figure 3.70 displays the scattering

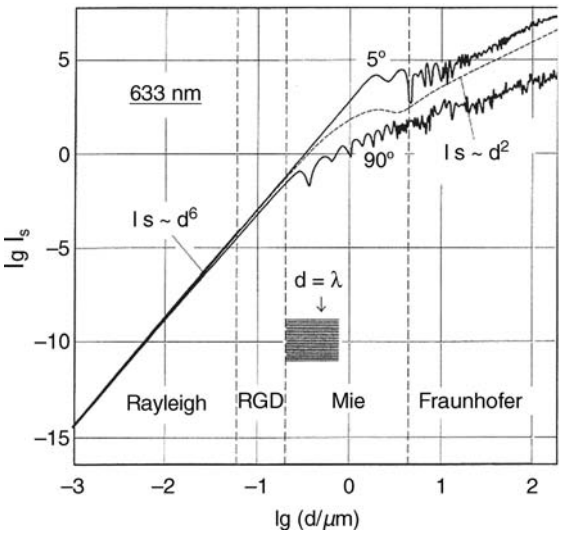

Figure 3.70 Scattering intensity I_S as a function of the particle diameter d (taken from [18]).

intensity I_s as a function of the particle diameter d. It can be seen that the scattering intensity increases by 20 orders of magnitude whereas the particle diameter increases only by five orders of magnitude. For smaller particles, the scattering intensity increases with the sixth power of the particle diameter. For larger diameters d in the range of the wavelength of light, the scattering dependence becomes more complicated and the scattering intensity varies rapidly with the particle diameter. Furthermore, it can be seen that the curve bends down in the area of the wavelength of visible light and the scattering intensity increases only about quadratically with the particle diameter.

3.13
Inelastic Light Scattering (Raman Scattering)

In Section 3.8, it was shown that the direct absorption of IR radiation can promote molecules from their vibrational ground state into the first excited molecular vibrational state. Such vibrational transitions depend directly on the atoms present in the molecule and in particular how these atoms are chemically bonded to each other. Therefore, the vibrational IR absorption pattern of a particular molecule can be seen as its molecular fingerprint and tells a lot about the molecule itself and about the surroundings in which it is embedded. Vibrational transitions can also take place via an inelastic scattering process that was first discovered 1928 by C.V. Raman. This so-called Raman effect marks an indirect approach to excite molecular vibrations. The Raman effect can be interpreted quantum mechanically as an inelastic collision between photons and molecules. Raman and IR spectroscopy are therefore complementary methods exhibiting different selection rules determining which vibration of a molecule can be excited by what method. Although Raman scattering is a fairly weak effect compared with direct IR absorption, Raman spectroscopy has proven in the last few decades its feasibility as a very flexible method in biophotonics. The application of IR absorption spectroscopy for *in vivo* studies is strongly limited by the broad and intense IR absorbance of water. However, unlike IR, water does not interfere with Raman spectroscopy since water has a very weak Raman signal. Hence Raman spectra can be easily collected from aqueous solutions, which is why Raman spectroscopy is perfectly suited for *in vivo* studies. Raman-based methods have emerged in recent years as an extremely powerful method for bioanalytical and biomedical applications, that is, to study biological samples such as cells and tissues. The principle is that Raman spectra contain information on molecular vibrations that provide a highly specific fingerprint of the molecular structure and biochemical composition of cells, tissues, and so on. Diseases and other pathological anomalies are accompanied by changes in these properties. The method provides this information without external markers such as stains or radioactive labels. Raman spectroscopy is a nondestructive technique and, in general, requires only minimal or no sample preparation. However, although the specificity of Raman spectroscopy is very high, its sensitivity, that is, the cross-section of the

Raman effect is rather poor. Since only a small proportion of the incident photons are inelastically scattered, the detection of molecules that are present in very low concentrations is limited. To overcome the disadvantage of low signal intensities from most biomolecules, special Raman signal-enhancing techniques can be applied. The two most prominent approaches are the resonance Raman effect and surface-enhanced Raman scattering (SERS). In addition to these two linear Raman signal-enhancing techniques, the nonlinear variant of Raman spectroscopy CARS also belongs to the most promising Raman techniques because it combines signal enhancement due to the coherent nature of the process with further advantages such as directional emission, narrow spectral bandwidth, and no disturbing interference with autofluorescence. In the following, an introduction to the basic theoretical concepts of linear and nonlinear Raman scattering is given.

The following section provides a rapid introduction to inelastic light scattering. Interested readers are referred to [5]. Nonlinear Raman-techniques are described in [10].

3.13.1
Theoretical Description of Inelastic Light Scattering

Earlier (see Sections 3.1,3.2 and 3.12), it was shown that light can polarize molecules. For visible wavelengths, mainly the electrons contribute to the induced polarization by becoming distorted against the atomic nuclei through the interacting electromagnetic field. Thus the interaction of light with matter induces an electric dipole moment within the molecules (see Equation 3.174). The polarizability α is a measure of how easily electrons can be distorted within a molecule.[20)] The induced dipole moment oscillating with the frequency of the electromagnetic field emits an electromagnetic wave in all directions. If the polarizability α does not change with time, the frequency of the emitted secondary wave corresponds to the frequency of the oscillating induced dipole, that is, the frequency of the external electromagnetic wave inducing the dipole. This type of elastic scattering is called Rayleigh scattering (see Section 3.12).

However, since molecules are always vibrating, the polarizability α is not constant over time, but changes according to the different vibrational frequencies of the molecular normal modes q (see Section 3.8). In other words, the nuclear motions modify the polarizability as the electron density rapidly (adiabatically) adjusts to the momentarily nuclear geometry to minimize overall the energy of the system. The dependence of the polarizability on the nuclear coordinate q can be expressed by expanding the polarizability into a Taylor series around the equilibrium nuclear geometry $q = 0$:

20) It should be noted that α represents a third-rank tensor. If not explicitly mentioned, the tensor characteristics can be neglected for most of the expressions derived in this section.

$$\alpha = \alpha(q) = \alpha(0) + \left(\frac{\partial\alpha}{\partial q}\right)\Big|_{q=0} \cdot q + \cdots . \tag{3.177}$$

The nuclear oscillation with a characteristic frequency ω_R along each normal coordinate q can be approximated by a harmonic oscillation (see Section 3.8):

$$q = q_0 \cdot \cos(\omega_R \cdot t). \tag{3.178}$$

Inserting Equations 3.177 and 3.178 into Equation 3.174 yields for the induced dipole moment:

$$\mu = \left[\alpha_0 + \left(\frac{\partial\alpha}{\partial q}\right)\Big|_{q=0} \cdot q_0 \cos\omega_R t\right] E_0 \cdot \cos\omega_0 t. \tag{3.179}$$

With the help of common trigonometric relations, Equation 3.179 can be rewritten as

$$\begin{aligned}\mu = \alpha_0 E_0 \cos\omega_0 t \quad &+ \frac{1}{2}\left(\frac{\partial\alpha}{\partial q}\right)\Big|_{q=0} \cdot q_0 E_0 \cos(\omega_R - \omega_0)t \\ &+ \frac{1}{2}\left(\frac{\partial\alpha}{\partial q}\right)\Big|_{q=0} \cdot q_0 E_0 \cos(\omega_R + \omega_0)t.\end{aligned} \tag{3.180}$$

Equation 3.180 shows that the time-dependent induced dipole moment, which acts as a source of the scattered radiation, oscillates on three distinct frequencies: the first term oscillating on the frequency ω_0 of the incoming electromagnetic wave represents the elastic light scattering [i.e., Rayleigh scattering (see Section 3.12)] whereas the second and third terms which oscillate with the difference or sum frequency between the incoming light ω_0 and normal mode frequency ω_R express the inelastic or Raman scattering activity. The second term oscillating on the difference frequency is the source for the so-called Stokes scattering, which is red shifted with respect to the excitation frequency ω_0. The Stokes scattered light contains information about the molecular scattering system due to its dependence on ω_R. The third term represents the source of inelastically scattered light which is blue shifted with respect to the incoming frequency ω_0 and is called anti-Stokes Raman scattering. Since the frequency of the anti-Stokes radiation also depends on the normal mode frequency, it also yields molecular information.

Consequently, the secondary radiation emitted by the molecule is a superposition of the exciting frequency and the various vibrational frequencies of the molecule. Dispersing this secondary radiation into its frequency components yields, in addition to the strong Rayleigh scattering, also weak sidebands. The distance between the Rayleigh wavelength and the wavelength of the sidebands corresponds to the vibrational frequencies of the molecule. The appearance of these sidebands due to an inelastic light scattering process was first discovered by C.V. Raman in 1928.

It is also possible to derive an expression for the intensity of the inelastically scattered light based on the classical description of light scattering, that is, the classical picture of interaction between an oscillating electromagnetic field and

a molecular system. The starting point for these considerations is the total power $\mathcal{P}$ emitted by an oscillating Hertzian dipole μ, which is given by

$$\mathcal{P} = \frac{1}{6\pi\varepsilon_0 c^3}\left|\frac{d^2\mu}{dt^2}\right|^2 \tag{3.181}$$

where $d^2\mu/dt^2$ is the second derivative of the dipole moment μ with respect to time t. Since each oscillating induced dipole serves as a Hertzian dipole, that is, as an antenna emitting secondary scattered radiation, μ in Equation 3.181 can be replaced by the induced dipole given in Equation 3.180. In the following we concentrate on the term of the induced dipole moment which leads to the Stokes radiation:

$$\mu_{\text{Stokes}}(t) \sim \frac{1}{2}\left(\frac{\partial\alpha}{\partial q}\right)\Big|_{q=0} \cdot q_0 E_0 \cos(\omega_R - \omega_0)t. \tag{3.182}$$

Inserting the second derivative of the induced Stokes dipole moment $\mu_{\text{Stokes}}(t)$ with respect to the time t yields for the average power

$$\bar{\mathcal{P}} = \frac{q_0^2}{12\pi\varepsilon_0 c^3}\left[\left(\frac{\partial\alpha}{\partial q}\right)\Big|_{q=0}\right]^2 \cdot (\omega_0 - \omega_R)^4 |E_0|^2. \tag{3.183}$$

Here an averaging over time has been performed (i.e., temporal average over the oscillating part). The intensity observed at 90° is given by

$$I = \frac{3 \cdot \bar{\mathcal{P}}}{8\pi}. \tag{3.184}$$

Inserting Equation 3.183 into Equation 3.184 and using the relationship $I_0 \sim |E_0|^2$ yields an expression for the scattered Stokes intensity:

$$I_{\text{Stokes}} = \text{constant} \cdot I_0 \cdot (\omega_0 - \omega_R)^4 \cdot \left[\left(\frac{\partial\alpha}{\partial q}\right)\Big|_{q=0}\right]^2. \tag{3.185}$$

From this classical description of the Raman scattering intensity, it can be seen that the inelastically scattered light intensity depends on the derivative of the electronic polarizability at the equilibrium geometry along the normal coordinate q: $(\partial\alpha/\partial q)|_{q=0}$. Hence for a normal mode q to be visible in a Raman spectrum the polarizability must change along the normal coordinate with a nonzero gradient at the equilibrium geometry $q = 0$. Therefore, $(\partial\alpha/\partial q)|_{q=0}$ and ω_R in Equation 3.185 depend on the molecular system under study whereas ω_0 and I_0 are experimental parameters determining the experimentally observed Raman intensity. This means that the Raman scattering intensity can be increased by increasing the Raman excitation intensity or by using higher excitation frequencies, that is, shorter Raman excitation wavelengths.

The classical description of Raman scattering provides a qualitative or intuitive understanding of inelastic light scattering. However, for a quantitative description of inelastic light scattering, a quantum mechanical approach is required. An obvious

example where the classical description falls short is its failure to account for the different intensities of Stokes versus anti-Stokes radiation. The Raman effect can be interpreted quantum mechanically as an inelastic collision between photons and vibrating molecules. Photons can be scattered from molecules. This scattering process corresponds to a transition into an extremely short-lived transition state, the so-called virtual level (see Figure 3.71). This virtual level is a state of a photon and a molecule during an infinitesimally short time period, that is, a collective quantum energy state of the entity molecule and photon. The molecule can subsequently relax back from this virtual level into the original (starting) molecular state or into an energetically excited molecular state. If the scattering process starts from the vibrational ground state and ends up in a vibrational excited state via a transition into the virtual state, it is called Stokes Raman scattering (see Figure 3.71). If the molecules are initially already in a vibrationally excited state and are transferred by the

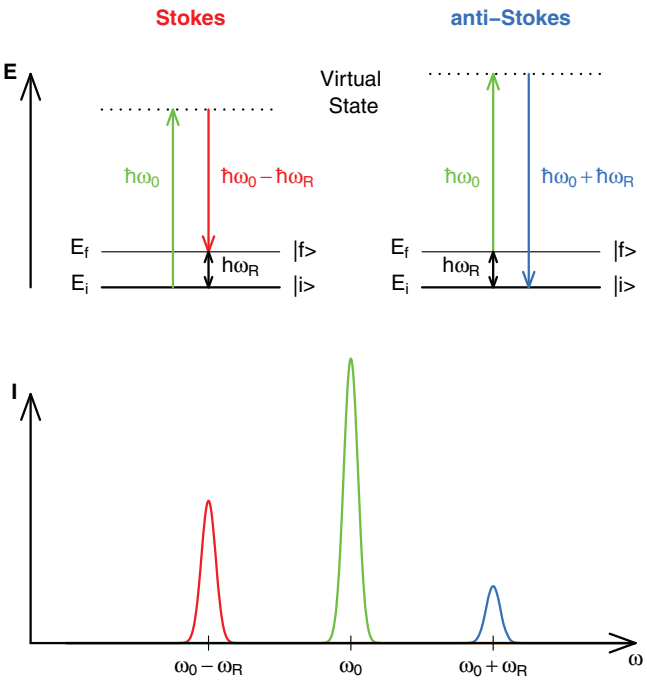

Figure 3.71 Illustration of inelastic light scattering (Raman effect) on a quantized molecular system. Note that the intensity ratio between Stokes Rayleigh and anti-Stokes scattering displayed in the lower part was chosen for the sake of clarity of presentation and is not in accordance with what is experimentally observed. Approximately only one in 10^6 photons is inelastically scattered. The Stokes to anti-Stokes intensity ratio, which would be identical according to the classical dipole model (see Equation 3.180), is determined by the population density ratio between the initial ($|i\rangle$) and final ($|f\rangle$) states determined by the Boltzmann distribution. This means that the Stokes to anti-Stokes intensity ratio depends on the energy difference between the initial ($|i\rangle$) and final ($|f\rangle$) states, that is, on the population of the excited state ($|f\rangle$).

scattering process into the vibrational ground state, it is referred to as anti-Stokes Raman scattering (see Figure 3.71). Since at room temperature the vibrational ground state is usually, according to the Boltzmann distribution (see Equation 3.114), significantly more populated than the vibrationally excited states, the Stokes Raman spectrum of a sample is more intense than the anti-Stokes Raman spectrum. For Rayleigh scattering, the states before and after the scattering process are the same (see Figure 3.71). These scattering processes are classified as two-photon processes since two photons are involved. It should be mentioned that inelastic light scattering (Raman scattering) can occur with a change in vibrational, rotational, or electronic energy of a molecule. In other words, Raman scattering is the inelastic light scattering on a quantized system, that is, energy is exchanged between the incident photons and the molecules where the exchanged energy can be equal to the rotational, vibrational, or electronic energy levels of the molecular scattering system. However, the majority of Raman studies are primarily concerned with the vibrational Raman effect.

The two vibrational spectroscopic methods Raman and IR absorption spectroscopy (see Section 3.8) are complementary methods based on two different light–matter interaction phenomena, thus exhibiting different selection rules. Selection rules determine which vibration of a molecule can be excited by what method. In the case of IR absorption, one photon directly promotes the molecule via an absorption process into a higher vibrational state whereas in the Raman scattering process two photons are involved. In order for a molecular vibration to absorb an IR photon, the dipole moment of the molecule has to change during the course of the vibration, that is, only those vibrations are IR active which give rise to an oscillating dipole. However, as shown above (see Equation 3.185), the polarizability has to change during the vibration so that a molecular vibration can be promoted via an inelastic scattering process into a higher vibrational state.

Raman spectra are usually plotted as the intensity of scattering versus the shift in the wavenumber values of the scattered light from the incident light (see Figure 3.72). Therefore, it is not the absolute wavenumber value that is plotted as in IR absorption spectra (see Figure 3.43), but rather the Raman shift (i.e., relative wavenumber values = wavenumber differences), that is, the shift of the detected wavenumber value with respect to that of the excitation laser. As has been mentioned above, Stokes lines which have a longer wavelength than the incident wavelength (Rayleigh line) due to an energy exchange to the molecules usually display a much higher intensity than anti-Stokes lines which originate from an energy gain from the scattering sample. Therefore, usually the more intense Stokes Raman spectrum (i.e., inelastically scattered light on the long-wavelength side of the excitation line) is observed/recorded.

The combination of Raman spectroscopy with a conventional microscope (micro-Raman spectroscopy) allows for the spatial investigation of samples in the sub-micrometer range. In other words, Raman microscopy allows one to record "molecular" maps of heterogeneous samples such as biological cells or tissue. Therefore, Raman imaging combines the spectral fingerprint information with the lateral information on a cellular and even subcellular level. Raman spectroscopy belongs to the molecular spectroscopic methods with one of the highest information

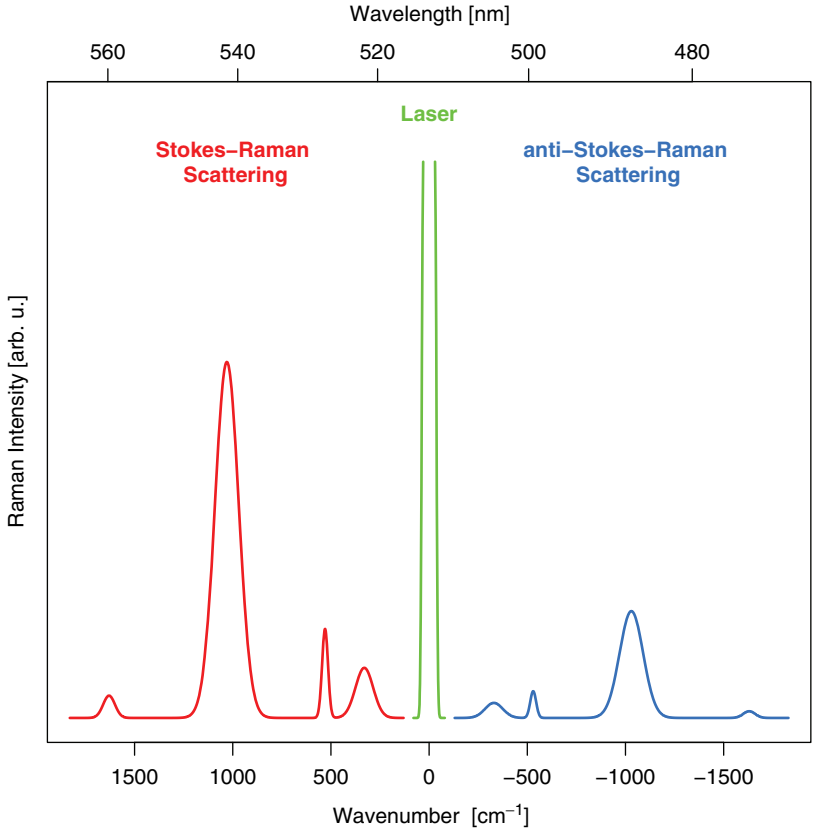

Figure 3.72 Illustration of Stokes versus anti-Stokes Raman scattering.

contents. However, although Raman spectroscopy is characterized by an unprecedented high molecular specificity, its sensitivity, that is, the conversion efficiency of the Raman effect, is rather poor. Since only a small proportion of the incident photons are inelastically scattered, the detection of molecules that are present in very low concentrations is extremely limited. Furthermore it takes a relatively long time to record a complete Raman image of a larger sample area.

Cells and tissues are mainly composed of proteins, nucleic acids, lipids, and carbohydrates. These biological macromolecules consist of defined monomeric subunits such as amino acids and nucleosides. Due to the small Raman cross-sections of these molecules, the Raman spectra of cells and tissues have low intensities. As a consequence of the small number of different subunits, the spectra of cells and tissues often share some similarities that require data with high signal-to-noise ratios to identify the specific spectral signature. To overcome the disadvantage of low signal intensities from most biomolecules, Raman signal enhancement effects were utilized, such as resonance Raman scattering (RRS) and SERS. Whereas the former technique probes vibrations of electronic chromophores, the latter depends

on short-range interactions with metal surfaces in the nanometer range. In the following, these two Raman signal-enhancing effects are discussed in more detail.

3.13.2
Resonance Raman Scattering (RRS)

We start the discussion by reviewing the concepts of RRS, where we particularly focus on theoretical aspects that are of importance for the application of resonance Raman spectroscopy in biophotonics. The classical description of Raman scattering as shown in Equation 3.185 provides a starting point for the discussion of ways in which to enhance the weak Raman scattering cross-sections. Equation 3.185 reveals that the Stokes scattering intensity depends on the polarizability α, or more precisely on $(\partial\alpha/\partial q)|_{q=0}$ and on the incident light intensity I_0. Consequently, the two commonly applied Raman signal-enhancing mechanisms RRS and SERS utilize these two quantities. However, for a quantitative description of resonance Raman spectroscopy, we have to move on to a more detailed explanation of Raman scattering based on the semi-classical picture of Raman scattering, which treats the molecule quantum mechanically (i.e., the polarizability is expressed fully quantum mechanically by means of perturbation theory) but considers the electromagnetic field classically (scattering from a Hertzian dipole). In other words, $\left|(\partial\alpha/\partial q)|_{q=0}\right|^2$ in Equation 3.185 is replaced by the square modulus $|\alpha|^2$ of the quantum mechanical expression of α (because α is a complex quantity):

$$I_{\text{Stokes}} = \text{constant} \cdot I_0(\omega_0 - \omega_R)^4 \cdot |\alpha|^2 \tag{3.186}$$

In resonance Raman spectroscopy, the dispersion relation of the polarizability α (i.e., its frequency dependence) is utilized to enhance the Raman scattering intensity. For the derivation of the polarizability tensor components, second-order perturbation theory must be applied since Raman scattering is a two-photon process. By doing so, Kramers, Heisenberg, and Dirac derived an expression for the transition polarizability tensor:

$$(\alpha_{\sigma\rho})_{\text{fi}} = \sum_{\psi_r} \left(\frac{\langle\psi_f|\hat{\mu}_\rho|\psi_r\rangle\langle\psi_r|\hat{\mu}_\sigma|\psi_i\rangle}{\hbar\omega_{ri} - \hbar\omega_0 - i\Gamma_r} + \frac{\langle\psi_f|\hat{\mu}_\sigma|\psi_r\rangle\langle\psi_r|\hat{\mu}_\rho|\psi_i\rangle}{\hbar\omega_{rf} + \hbar\omega_0 - i\Gamma_r} \right) \tag{3.187}$$

where

$\alpha_{\rho\sigma}$	component of the polarizability tensor $\alpha(\rho, \sigma)$ of the Raman transition $i \rightarrow f$ (i.e., ρ, σ refer to the molecule fixed Cartesian vectors x, y, z)
σ	polarization of the incident light
ρ	polarization of the scattered light (Raman)
$\|\psi_i\rangle$, $\|\psi_f\rangle$, $\|\psi_r\rangle$	initial, final, and intermediate states of the Raman scattering process
ω_0	angular frequency of the incident radiation
ω_{ri}	angular frequency of the transition $i \rightarrow r$

r	sum over all unperturbed intermediate states
Γ_r	damping, which correlates with the lifetime of the intermediate states ψ_r.

The transition dipole moments (see Equation 3.121) in the nominator of Equation 3.187 are illustrated in Figure 3.73.

Equation 3.187 can be interpreted such that Raman scattering is a two-photon process which involves a virtual dipole transition from the initial state $|\psi_i\rangle$ to the complete manifold of intermediate eigenstates $|\psi_r\rangle$ of the unperturbed molecule followed by another virtual dipole transition to the final state $|\psi_f\rangle$. For nonresonant Raman scattering ($\omega_{ri} >> \omega_0$ see Figure 3.73a), the weighted summation over all possible states results in no information on the eigenstates $|\psi_r\rangle$. The initial $|\psi_i\rangle$ and final $|\psi_f\rangle$ states play the determining role.

That changes when the angular frequency of the excitation light ω_0 approaches the transition angular frequency ω_{ri} of an electronic absorption band of the molecule (see Figure 3.73b). Equation 3.187 reveals that for such a case, that is, when $\omega_0 \approx \omega_{ri}$, the polarizability α will be increased dramatically because the denominator of the first

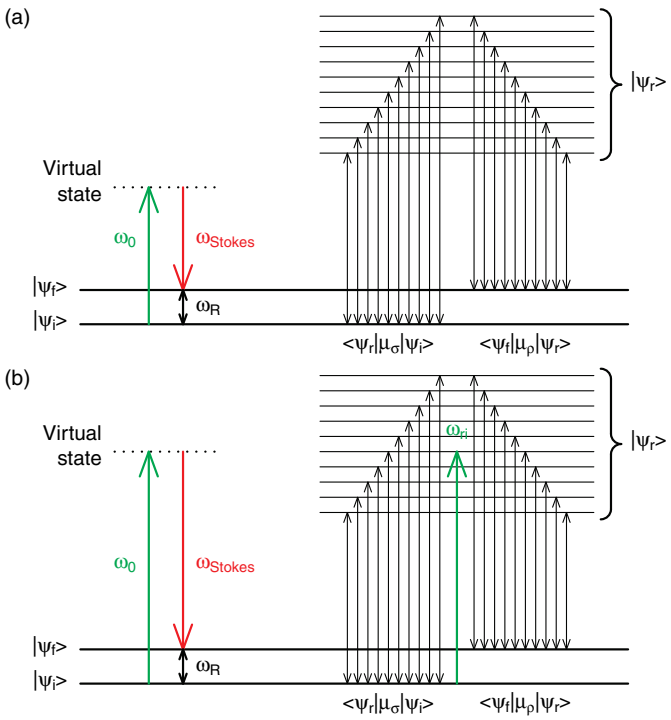

Figure 3.73 Energy level diagram illustrating the sum-over-states description of the Raman transition polarizability tensor (see Equation 3.187). (a) Nonresonant Raman scattering; (b) resonance Raman scattering where the Raman excitation frequency matches the electronic transition of the molecule, that is, $\omega_0 \approx \omega_{ri}$.

term in the sum in Equation 3.187 becomes small, causing the first term to become very large. This explains the Raman signal enhancement of up to six orders of magnitude that is observed for resonance Raman as compared with normal Raman scattering. Therefore, in resonance Raman spectroscopy, the Raman excitation wavelength is chosen to be in or near resonance with an electronic absorption of the molecular scattering system (see Figure 3.73b). For such resonance Raman conditions ($\omega_0 \approx \omega_{ri}$) the first term in Equation 3.187 dominates over the second term and the Raman polarizability in Equation 3.187 reduces to

$$(\alpha_{\sigma\rho})_{fi} = \sum_{\psi_r} \left(\frac{\langle \psi_f | \hat{\mu}_\rho | \psi_r \rangle \langle \psi_r | \hat{\mu}_\sigma | \psi_i \rangle}{\hbar\omega_{ri} - \hbar\omega_0 - i\Gamma_r} \right). \tag{3.188}$$

This expression for the transition polarizability tensor in electronic resonance can be further simplified by utilizing the same assumptions as outlined in Section 3.9, Equations 3.128 and 3.129. This means that rewriting the transition dipole moments in the nominator of Equation 3.188 by applying the Born–Oppenheimer approximation and the Condon approximation results in

$$(\alpha_{\sigma\rho})_{fi} = \sum_{\psi_{el'}} \bar{\mu}^{(0)}_{\rho,\psi_{el}\psi_{el'}} \bar{\mu}^{(0)}_{\sigma,\psi_{el'}\psi_{el}} \sum_{\chi_{v'}} \left(\frac{\langle \chi_{v_f} | \chi_{v'} \rangle \langle \chi_{v'} | \chi_{v_i} \rangle}{\hbar\omega_{ri} - \hbar\omega_0 - i\Gamma_{\psi_{el'}\chi_{v'}}} \right). \tag{3.189}$$

As discussed in Section 3.9, $\bar{\mu}^{(0)}_{\rho,\psi_{el}\psi_{el'}}$ and $\bar{\mu}^{(0)}_{\sigma,\psi_{el'}\psi_{el}}$ are the electronic transition dipole moments at the equilibrium nuclear geometry for the electronic resonant transitions $\psi_{el} \rightarrow \psi_{el'}$ and $\psi_{el'} \rightarrow \psi_{el}$, respectively. In the context of resonance Raman spectroscopy, we are mainly concerned with the vibronic part of the polarizability tensor:

$$(\alpha_{\sigma\rho})_{fi} = \sum_{\chi_{v'}} \left(\frac{\langle \chi_{v_f} | \chi_{v'} \rangle \langle \chi_{v'} | \chi_{v_i} \rangle}{\hbar\omega_{ri} - \hbar\omega_0 - i\Gamma_{\psi_{el'}\chi_{v'}}} \right) \tag{3.190}$$

which is determined by the vibrational overlap integrals (i.e., Franck–Condon factors) for the upward and downward transitions (see Figure 3.73b), that is, between the final vibrational wavefunction of the electronic ground state $|\chi_{v_f}\rangle$ and the vibrational wavefunction $|\chi_{v'}\rangle$ of the resonant electronic excited state, $\langle \chi_{v_f} | \chi_{v'} \rangle$ and between $|\chi_{v'}\rangle$ and the intial vibrational wavefunction of the ground state $|\chi_{v_i}\rangle$, $\langle \chi_{v'} | \chi_{v_i} \rangle$. From Equation 3.190, it can be seen that in resonance Raman spectroscopy only those normal modes which possess large Franck–Condon factors are resonantly enhanced. These are exactly those modes which also account for the vibrational structure in the electronic absorption spectra, that is, the Franck–Condon active modes. In Section 3.9, it was shown that Franck–Condon active modes are vibrations whose equilibrium positions are most greatly changed by the electronic transition. However, while the vibronic pattern in absorption spectra is often washed out due to solvent–solute interactions, resonance Raman spectroscopy is the method of choice to identify these Franck–Condon active modes. Moreover, a quantitative resonance Raman intensity analysis allows one to derive the displacement Δ of the equilibrium

position of the resonant excited electronic state with respect to the ground electronic state. It can be shown that for small displacements of the resonantly excited electronic state potential surface along the resonance Raman-active normal modes, the resonance Raman intensity is approximately proportional to Δ^2. Therefore, resonance Raman spectroscopy and in particular the analysis of resonance Raman excitation profiles (i.e., recording the intensity of resonantly enhanced modes versus excitation wavelength) allows one to deduce valuable information about the structure of electronically excited states by determining the atomic displacement Δ between the ground and excited electronic states and thus the change in bond lengths and bond angles while going from the ground to the excited state. However, resonance Raman spectroscopy in biophotonics is mainly applied not because of its potential to interrogate the Franck–Condon point/region[21)] of an excited electronic state, but rather because of its high, dramatically increased sensitivity as compared with nonresonant Raman scattering.

The selection of a Raman excitation wavelength in resonance with an electronic absorption band increases the Raman cross-section of those modes which are coupled to the resonant electronic transition (i.e., the Franck–Condon active modes) of a factor of up to 10^6 as compared with nonresonant Raman scattering. This enhancement of the Raman scattering intensity significantly improves the signal-to-noise ratio and allows the detection of low-concentration substances in solution. Since resonance Raman spectra are dominated by modes characteristic of the geometric changes of the molecules during the electronic transition, resonance Raman spectra are less complex than their nonresonant counterparts since fewer vibrations contribute to the spectrum. Therefore, special emphasis can be placed selectively on these enhanced vibrations. Furthermore, the selective excitation of vibrational modes of certain electronic chromophores (e.g., of chromophores pivotal for the biological activity of the molecule) becomes possible by choosing the appropriate excitation wavelength in resonance with the electronic chromophore. Therefore, such a site specificity due to the choice of different resonance Raman excitation wavelengths is a great advantage when investigating biological samples with more than a single electronic chromophore, since it allows the selective investigation of smaller subunits in large assemblies, for example, probing the active center in proteins, which is pivotal for the function of the respective molecules, or the selective excitation of macromolecules such as proteins or DNA in the presence of other molecules, for example, in whole cells. The high sensitivity and selectivity have led to various important applications of resonance Raman spectroscopy in biological, biochemical, and medical research in recent years.

However, despite all these advantages, there are also some drawbacks when using resonance Raman spectroscopy. First, the absorption of the resonance Raman excitation light often causes photo degradation of the sample, which is why it is

21) The Franck–Condon point is geometrically identical with the minimum in the ground state, but located in the excited electronic state. However, Franck–Condon region would be more precise since a vertical transition starting from the nuclear equilibrium geometry of the ground state just represents the most probable transition. Hence the region of the excited state potential which is accessed by the vertical transitions (see Figure 3.50) is called the Franck–Condon region.

necessary to rotate the sample quickly to avoid heating (i.e., excitation light always hits a fresh sample spot). Hence the combination of the resonance Raman technique with microscopy to study biological samples is very difficult. Furthermore, reabsorption of the scattered light makes quantitative evaluation of the Raman intensity difficult and internal standards have to be used.

In Section 3.11, it was shown that an electronic absorption into the first excited singlet state S_1 is often followed by the emission of fluorescence light. Hence the greatest drawback in resonance Raman spectroscopy might be the simultaneous excitation of intense fluorescence with which resonance Raman spectroscopy has to compete if resonance Raman spectroscopy occurs also via the S_1 excited electronic state from which the fluorescence emission originates. Since the cross-section for fluorescence can be much larger than the resonance Raman cross-section, the observation of Stokes-scattered resonance Raman light is often obscured by the presence of fluorescence. This is especially the case when the Stokes shift, that is, the energy difference between the absorption maximum and the fluorescence maximum, is small. Therefore, the simultaneous observation of fluorescence and RRS becomes possible for large fluorescence Stokes shifts so that the fluorescence emission and the Stokes scattered resonance Raman light are spectrally separated (see Figure 3.74).

The masking of resonance Raman signals by fluorescence can be also avoided by the application of excitation wavelengths in the deep UV region (< 250 nm), which excite higher electronic excited states (S_n with $n > 1$). While RRS occurs directly from the Franck–Condon point of the highly excited electronic state and within about 5−10 fs after electronic absorption, fluorescence originates in most cases according to Kasha's rule (see Section 3.11) from the vibrational ground state of the first excited electronic state S_1, resonance Raman and fluorescence are energetically far away from each other, that is, spectrally well separated.

Another approach to separate RRS from fluorescence consists in utilizing the different time scales on which the two processes take place. RRS occurs immediately after electronic excitation that is within a time window of about 5−10 fs after photon absorption, the fluorescence emission decays on a nanosecod time scale. Thus, the application of ultrafast Kerr shutters allows the observation of the resonance Raman signal without emission contributions by temporally separating RRS from fluorescence emission.

3.13.3
Surface-enhanced Raman Spectroscopy (SERS)

Another way to overcome the drawback of low scattering intensity of normal Raman spectroscopy is to use SERS. The SERS effect corresponds to the enhancement (by a factor of up to 10^{11-14}) of the Raman scattering of a molecule situated in the vicinity of nanosized metallic structures (e.g., Ag or Au). The exact mechanism of the enhancement effect of SERS is still a matter of debate in the literature. There are two primary enhancement mechanisms, namely electromagnetic and chemical enhancement.

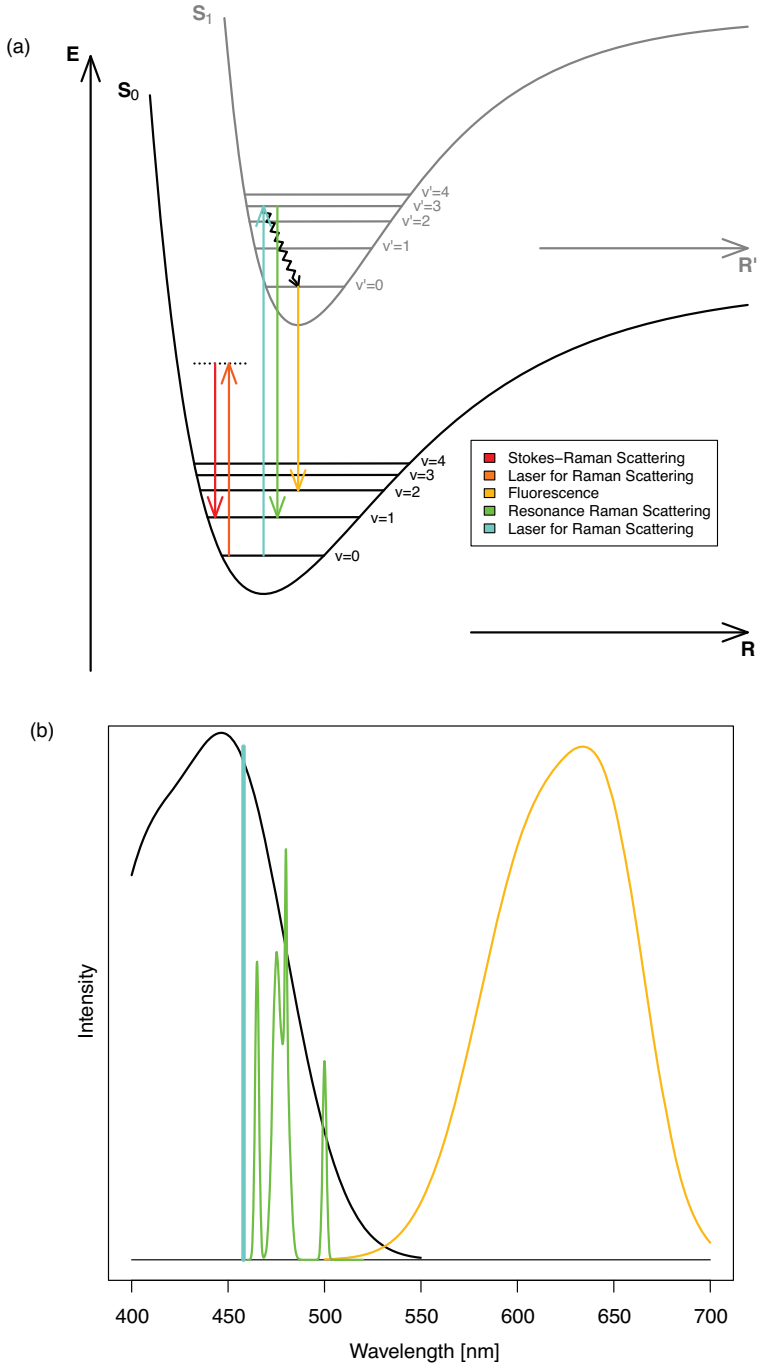

Figure 3.74 Comparison of resonance Raman spectroscopy and fluorescence emission (a). For large Stokes shifts, resonance Raman and fluorescence do not interfere (b).

The classical description of Raman scattering discussed above revealed that the Raman intensity corresponds to the total power emitted by a Hertzian dipole and is proportional to the square of the second time derivative of the induced dipole moment μ (see Equation 3.181). According to $\mu = \alpha \cdot E$, there are two ways to increase the Raman scattering intensity: first by increasing the electromagnetic field E and second by enhancing the transition polarizability tensor α. The first is named the electromagnetic field enhancement mechanism and the second the charge transfer or chemical enhancement mechanism. Although these mechanisms are substantially different from each other, distinguishing them experimentally has not been straightforward. Discussions about the relative contributions of the two mechanisms to the total enhancement are still ongoing.

The electromagnetic enhancement mechanism is based on a local increase in the electromagnetic field at metal surfaces due to the excitation of surface plasmon resonances. Plasmons can be described in the classical picture as collective oscillations of the free electron gas (conduction electrons against the fixed positive ion cores of the metal). One differentiates between bulk plasmons, which denote electron oscillations inside the bulk, and surface plasmons, which are collective charge density fluctuations at the metal/vacuum or metal/dielectric interface. In other words, surface plasmons are surface electromagnetic waves (evanescent waves) that propagate in a direction parallel to the metal/dielectric (or metal/vacuum) interface. If the metal surface is roughened the plasmons are no longer confined and the electric field can radiate in both parallel and perpendicular directions to the surface. The excitation of the plasmons in metal nanoparticles results in a polarization and an electric field exceeding that of the exciting light. Locally these fields might be much higher than the incident field, often referred to as field enhancement. For metals such as Ag, Au, and Cu, the plasmon resonances are in the visible region of the electromagnetic spectrum. Particle size and shape (morphology) were found to have a strong influence on the resonance frequency. The metallic nanoparticles should be smaller than or roughly equal in size to the wavelength of the excitation light, that is, typically sizes of up to 100 nm are used. The field enhancement should be most intense at edges where the curvature of the particle is high, and therefore the density of the electric flux is highest (lightning rod effect). If a sample is brought into close contact with a rough metal surface and the surface plasmons of the metal are excited with a laser, the enhanced evanescent electromagnetic field causes an enhanced Raman signal with a scattering cross-section 3–15 orders of magnitude larger than those for normal Raman scattering.

The simplest model to describe the electromagnetic enhancement consists in a quasi-static treatment of a single isolated metal sphere. This single metal sphere has a dielectric constant ε_i in a medium which is small compared with the wavelength, or in vacuum with the electric permittivity of free space ε_0. As shown in Section 3.1, the dielectric constant ε_i is a complex value. Furthermore, it is assumed that ε_i of the metal sphere is independent of its size. Figure 3.75 illustrates the electromagnetic enhancement mechanism. A metal sphere embedded in a medium is in the close vicinity of a molecule.

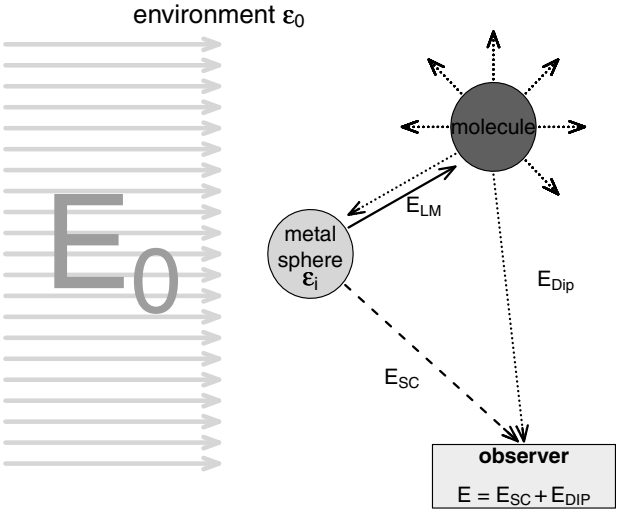

Figure 3.75 Illustration of electromagnetic enhancement.

The incident electromagnetic wave E_0 excites surface plasmons within the metal nanoparticle which induces the electromagnetic field E_{LM} which is largest directly at the surface of the particle and decreases on going into the space. The SERS signal intensity I_{SERS} is proportional to the square of the induced electromagnetic field E_{LM}:

$$E_{\mathrm{LM}}^2 = E_0^2 \cdot |g|^2 \left(1 + 3\cos^2 \vartheta\right) \tag{3.191}$$

where ϑ denotes the angle relative to the applied field direction and g is given by

$$g = \frac{\varepsilon_{\mathrm{i}} - \varepsilon_0}{\varepsilon_{\mathrm{i}} + 2\varepsilon_0}. \tag{3.192}$$

Equation 3.191 reveals that the largest field strengths are reached for $\vartheta = 0^\circ$ and 180°. The field intensity can be also increased by maximizing g, that is, the strongest field enhancements for a certain geometry are achieved for $\mathrm{Re}(\varepsilon_{\mathrm{i}}) \approx -2\varepsilon_0$ and $\mathrm{Im}(\varepsilon_{\mathrm{i}}) \ll 1$, which means that the plasmon resonance relation is met. Hence the plasmon resonance is characterized by ε_{i}. As shown in Figure 3.75, the exciting field acting on the molecule is the sum of E_{LM} and E_0, which induces a dipole in the molecule which is the source of emission of a dipole field E_{Dip} according to the radiation characteristic of a Hertzian dipole (dotted line). This emitted light can again be enhanced through the vicinity to the metal surface. This enhanced field is called E_{SC} (dashed line). The signal detected by the observer is then the sum of E_{Dip} and E_{SC}.

In summary, the metal particles act as dipoles, similarly to the molecules in the Raman scattering process as discussed above, and are the source of localized strong fields. The excited metal surface plasmons enhance both the local laser field experienced by a molecule, E_0, and the Stokes-shifted light scattered by the molecule. Hence the metal nanoparticle acts as an antenna, efficiently amplifying the Raman signal. The electromagnetic enhancement depends on, in addition to the other

parameters mentioned earlier (e.g., size and form of metal nanoparticle, plasmon resonance) the distance between the analyte and metal sphere. The range of the electromagnetic field of the excited surface plasmons quickly decreases with distance d from the surface of a spherical metal particle with radius r. A single molecule close to the metal surface experiences the following distance dependence of the electromagnetic enhancement EM_{enhance}:

$$EM_{\text{enhance}} \sim \left(\frac{r}{r+d}\right)^{12}. \tag{3.193}$$

This equation shows that larger metal particles produce an electromagnetic enhancement with further spatial range. Overall SERS uses the optical (plasmonic) properties of nanostructures to enhance the intrinsically weak Raman signal.

The second SERS enhancement mechanism, called charge transfer enhancement, can be interpreted as a surface-induced resonance Raman effect resulting from the direct chemisorption of the adsorbate on the metal surface, forming a surface complex. This interaction with the conduction and/or valence bands of the metal surface (ligand-to-metal and/or metal-to-ligand charge-transfer interactions) causes changes in the electronic structure of the analyte. If the exciting laser light is in resonance with the charge-transfer absorption of the surface–analyte complex, RRS occurs (see Section 3.13.2). As the mechanism depends on a metal–adsorbate bond, it effectively operates only on the first layer of adsorbates (absolute first-layer enhancement). Compared with normal Raman spectra, surface enhanced Raman spectra might exhibit shifted vibrational bands and a changed intensity pattern due to the selective enhancement of the vibrational modes coupling to the excited electronic transitions of the analyte–metal complex.

It should be mentioned that separation of the two SERS enhancement mechanisms is very difficult and it is almost impossible to differentiate between them in a SERS spectrum.

SERS is a very sensitive technique capable of obtaining rich chemical information on the substances in close contact with the metal. Due to the surface enhancement, the sensitivity is increased compared with normal Raman spectroscopy by 3–15 orders of magnitude. This lowers the detection limit and analytes at very low concentrations down to 10^{-11} M can be detected. It was even possible to record surface-enhanced Raman spectra from single molecules. For the interpretation of the spectra, surface selection rules have to be applied and also Raman-inactive bands may become observable. In their simplest form, those Raman bands that originate from vibrations with an induced polarization of the adsorbate electron cloud perpendicular to the metal surface are predicted to show the highest intensity.

The application of SERS in biophotonics puts some important constraints on the type of appropriate SERS substrates: (1) they must be non-toxic for the biological system under investigation, (2) they should be stable, and (3) most importantly, they should allow reproducible and quantitative SERS measurements.

Commonly metal colloids are applied as SERS substrates since they are simple to produce and easy to use. However, they exhibit a poor reproducibility since the

enhancement depends strongly on the state of aggregation because of enhanced electromagnetic field intensities between nanoparticles in the direct neighborhood. Hence the main drawback from which SERS suffers is its poor quantitative reproducibility, since the SERS signal is extremely sensitive to the nature and shape of the metal surface roughness, and to a number of factors involving the adsorption. Great research effort is therefore being put into the development of reproducible SERS substrates with well-defined shapes and hence exactly controlled plasmonic properties. The very high sensitivity of SERS allows single-molecule detection. However, it can also be possible that an impurity within a sample or a species formed by surface photochemistry is preferentially enhanced. The exclusion of such unwanted signals can sometimes be difficult, since the specific selection rules of SERS might make it complicated to relate the SERS spectra to the Raman scattering from the parent species before adsorption. Furthermore, since the analyte requires being in close proximity to a suitable roughened surface, one has to be aware of contamination of the sample with the SERS substrate metal colloid.

3.13.4
Hyper-Raman Effect

In Section 3.6, it was shown that the employment of intense light sources leads to the induction of a nonlinear polarization, that is, the induced dipole moment of a molecule is no longer proportional to the applied electric field. This nonlinearity between the induced dipole moment and the electric field strength is expressed by a power series:

$$\begin{aligned} \mu &= \alpha \cdot E + \frac{1}{2}\beta E \cdot E + \frac{1}{6}\gamma E \cdot E \cdot E + \cdots \\ \mu &= \mu^{(1)} + \mu^{(2)} + \mu^{(3)} + \cdots \end{aligned} \tag{3.194}$$

where β is the first hyperpolarizabilty ($\beta \ll \alpha$) and γ is the second hyperpolarizability ($\gamma \ll \beta$). Thus the induced dipole moment can be expressed by a linear term $\mu^{(1)}$ and nonlinear contributions $\mu^{(2)}$, $\mu^{(3)}$, and so on. Further, it has been shown in Section 3.13.1 that the polarizability α need not be constant and can be modified by the nuclear motions q. The dependence of α on q has been expressed by expanding the polarizability into a Taylor series around the equilibrium nuclear geometry $q = 0$. The first, second, and higher hyperpolarizabilty also depend, of course, on the nuclear motion q and this dependence can be also expressed by an expansion of β or γ around $q = 0$. For the first hyperpolarizability β, this expansion results in

$$\beta = \beta(q) = \beta_0 + \left(\frac{\partial \beta}{\partial q}\right)\Big|_{q=0} \cdot q + \cdots . \tag{3.195}$$

Inserting Equation 3.195 together with $E = E_0 \cos(\omega_0 t)$ and $q = q_0 \cos(\omega_R t)$ into Equation 3.194 yields for the second-order nonlinear induced dipole moment:

$$\mu^{(2)} = \frac{1}{2}\beta E^2 = \frac{1}{2}\left[\beta_0 + \left(\frac{\partial\beta}{\partial q}\right)\Big|_{q=0} \cdot q_0 \cos\omega_R t\right] E_0^2 \cos^2\omega_0 t. \tag{3.196}$$

With the help of common trigonometric relations, Equation 3.196 can be rewritten as

$$\begin{aligned}\mu^{(2)} = {} & \frac{1}{4}\beta_0 E_0^2 + \frac{1}{4}\beta_0 E_0^2 \cos 2\omega_0 t + \frac{1}{4}\left(\frac{\partial\beta}{\partial q}\right)\Big|_{q=0} \cdot q_0 E_0^2 \cos\omega_R t \\ & + \frac{1}{8}\left(\frac{\partial\beta}{\partial q}\right)\Big|_{q=0} \cdot q_0\, E_0^2 \cos(2\omega_0 + \omega_R)t \\ & + \frac{1}{8}\left(\frac{\partial\beta}{\partial q}\right)\Big|_{q=0} \cdot q_0\, E_0^2 \cos(2\omega_0 - \omega_R)t.\end{aligned} \tag{3.197}$$

Equation 3.197 shows that the second-order nonlinear induced dipole moment, which acts also as a source of scattered radiation, can oscillate at four different frequencies. The second term leads to the so called hyper-Rayleigh scattering at the frequency $2\omega_0$. The fourth and fifth terms, which vibrate with the sum and difference frequency between $2\omega_0$ and the vibrational frequency ω_R, are the source of the so-called anti-Stokes hyper-Raman ($2\omega_0 + \omega_R$) and Stokes hyper-Raman ($2\omega_0 - \omega_R$) scattering. Additionally, a term oscillating in the IR region at ω_R and a constant term which results in no radiation exist. All these classically derived frequency components can be seen in the scattered light when using an intense light source such as ultrashort laser pulses. Of particular relevance for biophotonics is hyper-Raman scattering, which is illustrated in Figure 3.76 in the form of an energy level diagram.

The hyper-Raman effect corresponds to a two-photon transition into a virtual state (see above) from where the molecule can relax back into the starting molecular state, which results in hyper-Rayleigh scattering or in an energetically excited state leading to Stokes hyper-Raman radiation. If the two-photon transition into the virtual state originates from a vibrationally excited molecule, the scattering can also end up in the vibrational ground state, resulting in anti-Stokes hyper-Raman scattering, which is usually much less intense than Stokes hyper-Raman radiation since normally for room temperature the vibrational ground state is more populated than the vibrational excited state. Since hyper-Raman scattering is overall a three-photon process, it exhibits different selection rules to linear Raman scattering (which is a two-photon process) and IR absorption (i.e., dipole transition of an IR photon). The derivation of the selection rules would go beyond the scope of this book. However, there are special normal modes which are neither Raman nor IR allowed that can be excited by hyper-Raman scattering.

3.13.5
Coherent Raman Spectroscopy

So far, all of the inelastic scattering processes discussed are considered to be spontaneous. Spontaneous means that the vibrations of the individual molecules

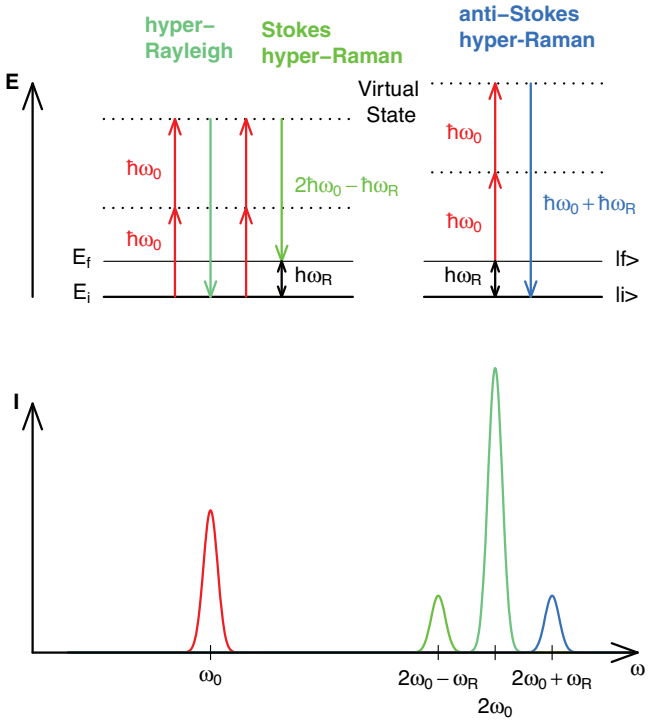

Figure 3.76 Illustration of hyper-Raman scattering on a quantized molecular system.

are all excited independently by a single exciting frequency ω_0, that is, the excited vibrations exhibit a random mode-to-mode phase relationship. The observed spontaneous Raman spectrum is just the result of a simple superposition of the excited vibrations of all molecules. In the following we introduce coherent Raman scattering processes where the irradiation of at least two laser beams of different frequencies ω_L and ω_S (L = laser, S = Stokes) generates coherently driven molecular vibrations (i.e., where the phases of the excited vibrations are locked). The establishment of a fixed phase relationship between the excited normal modes can be achieved by tuning the frequency difference between the laser frequency ω_L and the Stokes frequency ω_S to match the molecular vibrational frequency ω_R, that is, $\omega_R = \omega_L - \omega_S$. By doing so, all molecules within the common focus of the two lasers ω_L and ω_S experience ("see") the beat frequency $\omega_L - \omega_S = \omega_R$, that is, their own vibrational frequency, which results in the excitation of coherent molecular vibrations (see Figure 3.77).

3.13.5.1 Coherent Anti-Stokes Raman Spectroscopy (CARS)

In the following, we aim to give a classical description of the excitation of coherent molecular vibrations. Let us start with the assumption of having a Raman scattering medium with N harmonic oscillators per volume element that experience a displacement q under the influence of the two laser waves with frequencies ω_L and ω_S and the total field strength:

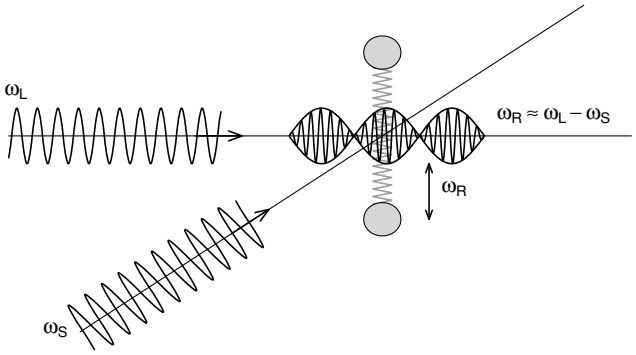

Figure 3.77 Illustration of excitation of coherent molecular vibrations within the common focus of two laser beams whose difference frequency $\omega_L - \omega_S \approx \omega_R$ matches a molecular vibrational frequency.

$$E = E_L + E_S = E_L^0 e^{i(\omega_L t - k_L z)} + E_S^0 e^{i(\omega_S t - k_S z).} \tag{3.198}$$

This displacement q leads to an electrostatic energy (potential energy) W that is stored within the molecules:

$$W = -\mu \cdot E. \tag{3.199}$$

Equation 3.199 together with the following relations derived above,

$$\mu = \alpha(q)E \tag{3.200a}$$

with

$$\alpha(q) = \alpha_0 + \left(\frac{\partial \alpha}{\partial q}\right)\Big|_{q=0} \cdot q + \cdots \tag{3.200b}$$

yields an expression for the driving force F acting on a molecule:

$$F = -\frac{\partial W}{\partial q} = \left(\frac{\partial \alpha}{\partial q}\right)\Big|_{q=0} \cdot E^2. \tag{3.201}$$

The vibration enforced by F can be described by a damped harmonic oscillator (see Equation 3.16) with a reduced mass m, eigenfrequency $\omega_R = \sqrt{k/m}$, and damping constant Γ, which is related to the linewidth of the Raman band. The classical equation of motion for this enforced vibration is obtained by considering all acting forces, that is, applying the force equilibrium condition:

$$m\frac{\partial^2 q}{\partial t^2} + \Gamma\frac{\partial q}{\partial t} + \omega_R^2 \cdot m \cdot q = F = \left(\frac{\partial \alpha}{\partial q}\right)\Big|_{q=0} E^2 \tag{3.202}$$

where the first term on the left-hand side represents the inertia force (Newton's second law), the second term considers the damping force, and the third term corresponds to the restoring force. The right-hand side of Equation 3.202

corresponds to the driving force F expressed in Equation 3.201. Inserting the solution approach $q = q_0 e^{i\omega t}$ into Equation 3.202 and also applying Equation 3.198 results in

$$\left(\omega_R^2 - \omega^2 + i\gamma\omega\right) q_0 e^{i\omega t} = \frac{1}{2m}\left(\frac{\partial\alpha}{\partial q}\right)\Big|_{q=0} \cdot E_L^0 E_S^0 e^{i[(\omega_L-\omega_S)t-(k_L-k_S)z]} \tag{3.203}$$

with $\Gamma = \gamma/m$. Since Equation 3.203 must be valid for all times, a comparison of the exponents on the left- and right-hand sides yields the frequency condition: $\omega = \omega_L - \omega_S$. This means that molecules are excited by the simultaneous interaction with the two light fields E_S and E_L to enforced vibrations on the difference frequency $\omega_L - \omega_S$. Equation 3.203 yields the following equation for the amplitude q of these enforced vibrations which propagates together with the two waves in the medium:

$$q = \frac{1}{2m}\left(\frac{\partial\alpha}{\partial q}\right)\Big|_{q=0} \frac{E_L^0 E_S^0}{\omega_R^2 - (\omega_L-\omega_S)^2 + i\gamma(\omega_L-\omega_S)} e^{i[(\omega_L-\omega_S)t-(k_L-k_S)z]}. \tag{3.204}$$

Equation 3.204 reveals that a non-vanishing amplitude q is only obtained if $(\partial\alpha/\partial q)|_{q=0} \neq 0$. This means that only Raman-active vibrations can be coherently driven. Furthermore, the resonance denominator in Equation 3.204 shows that large amplitudes q are obtained if $\omega_R^2 - (\omega_L-\omega_S)^2$, that is, for $\omega_R = (\omega_L-\omega_S)$. Therefore, if the difference frequency between the two lasers is tuned to be in resonance with the molecular vibrational frequency, the molecules are most efficiently excited to perform coherent molecular vibrations. These coherent molecular vibrations (excited by ω_L and ω_S) are able to modulate a third light wave E and thus induce a total polarization P given by

$$P = \varepsilon_0\chi E = \varepsilon_0 N\alpha(q)E = \varepsilon_0 N\left[\alpha_0 + \left(\frac{\partial\alpha}{\partial q}\right)\Big|_{q=0} \cdot q + \ldots\right] \cdot E. \tag{3.205}$$

The term with α_0 can be neglected since it leads to Rayleigh scattering. For the third wave, one does not necessarily have to apply a wave with a different frequency, it is sufficient if, for example, $E = E_L$. Hence the nonlinear term of the polarization P can be expressed by

$$P_{NL} = \varepsilon_0 N\left(\frac{\partial\alpha}{\partial q}\right)\Big|_{q=0} \cdot q \cdot E_L. \tag{3.206}$$

Equation 3.206 expresses the nonlinear polarization P_{NL} generated by the coherent molecular vibrations q which modulate the third wave E_L. With $E_L = E_L^0 e^{i(\omega_L t - k_L z)}$ and Equation 3.204, it follows that

$$P_{NL} = \varepsilon_0 \frac{N}{2m}\left[\left(\frac{\partial\alpha}{\partial q}\right)\Big|_{q=0}\right]^2 \cdot \frac{1}{\omega_R^2 - (\omega_L-\omega_S)^2 + i\gamma(\omega_L-\omega_S)} \times \left(E_L^0\right)^2 E_S^0 \cdot e^{i[(2\omega_L-\omega_S)t-(2k_L-k_S)z]}. \tag{3.207}$$

Comparing this equation with the expression for the nonlinear polarization introduced in Section 3.6 (see, e.g., Equation 3.79), P_{NL} can be identified as a third-order nonlinear polarization:

$$P_{NL} = \varepsilon_0 \chi^{(3)} E_L^2 \cdot E_S^* \tag{3.208}$$

with

$$\chi^{(3)} = \varepsilon_0 \frac{N}{2m} \left[\left(\frac{\partial \alpha}{\partial q} \right) \Big|_{q=0} \right]^2 \cdot \frac{1}{\omega_R^2 - (\omega_L - \omega_S)^2 + i\gamma(\omega_L - \omega_S)}. \tag{3.209}$$

The polarization P_{NL} is the source term for the irradiation of a new electromagnetic wave:

$$E_{aS} = E_{aS}^0 e^{i(\omega_{aS} t - k_{aS} z)} \tag{3.210}$$

with $E_{aS}^0 = (E_L^0)^2 E_S^0$ and

$$\begin{aligned} \omega_{aS} &= 2\omega_L - \omega_S = \omega_L + \omega_L - \omega_S = \omega_L + \omega_R \\ \omega_L + \omega_L &= \omega_S + \omega_{aS}. \end{aligned} \tag{3.211}$$

Hence the coherent molecular vibrations excited by the two laser fields with frequencies ω_L and ω_S modulate a third wave with frequency ω_L and generate a coherent light beam at the anti-Stokes frequency $\omega_{aS} = 2\omega_L - \omega_S$. This nonlinear version of Raman spectroscopy is called coherent anti-Stokes Raman scattering (CARS) (see Figure 3.78).

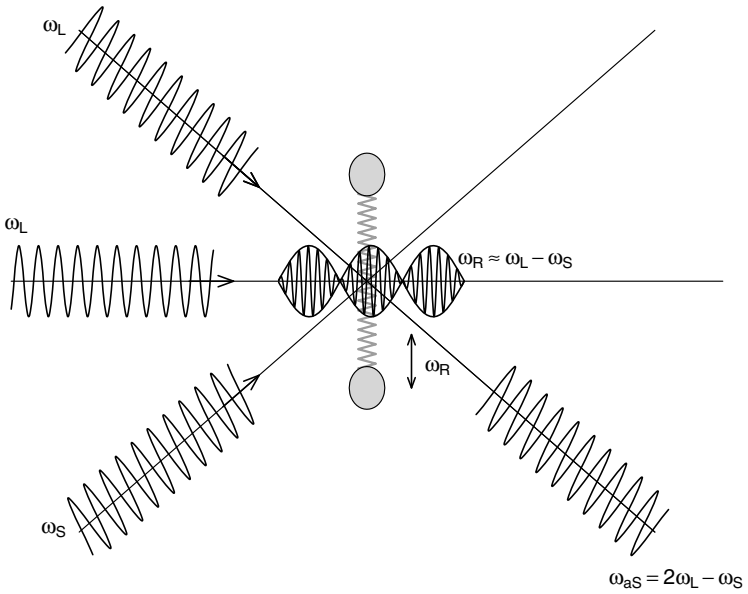

Figure 3.78 Illustration of of coherent anti-Stokes Raman scattering (CARS).

Thus, in a CARS process three laser pulses interact with the sample and generate a coherent spatially directed CARS signal (i.e., fourth pulse). CARS spectroscopy is based on the fact that two laser pulses with frequencies ω_L and ω_S drive the molecules to vibrate coherently, that is, in-phase if the energy difference between the two lasers corresponds to a Raman transition (i.e., $\omega_L - \omega_S = \omega_R$). Another photon of frequency ω_L can be subsequently scattered inelastically off this ensemble of coherently excited vibrational modes by emitting a blue-shifted, compared with the excitation lasers, anti-Stokes signal of frequency ω_{aS}. The frequency of the anti-Stokes signal arises from energy conservation, which can be derived from Equation 3.211 as follows:

$$\hbar\omega_L + \hbar\omega_L = \hbar\omega_S + \hbar\omega_{aS}. \tag{3.212}$$

The energy conservation corresponds to the generation (i.e., Stokes process) and annihilation (anti-Stokes process) of a vibrational quantum:

$$(1) \qquad \hbar\omega_L - \hbar\omega_S = \hbar\omega_R \rightarrow \text{Stokes process (generation)}$$

$$(2) \qquad \hbar\omega_L + \hbar\omega_R = \hbar\omega_{aS} \rightarrow \text{anti-Stokes process (annihilation)}$$

$$(1)+(2) \quad 2\hbar\omega_L + \hbar\omega_S = \hbar\omega_{aS} \rightarrow \text{CARS signal.} \tag{3.213}$$

This photon energy conservation can be also expressed in an energy level diagram (see Figure 3.79), which reveals that in total CARS can be seen as a four-photon process (or often referred to as four-wave mixing process).

The direction of the CARS signal is determined by the photon momentum (wavevector) conservation, which is known as the phase-matching condition (see Section 3.6). That means the sum of the wavevectors of the four participating photons must equal zero for the CARS signal to become maximum (see also further below):

$$\vec{k}_{aS} = 2\vec{k}_L - \vec{k}_S. \tag{3.214}$$

The momentum conservation for a CARS process can be also seen as the generation and annihilation of a photon momentum:

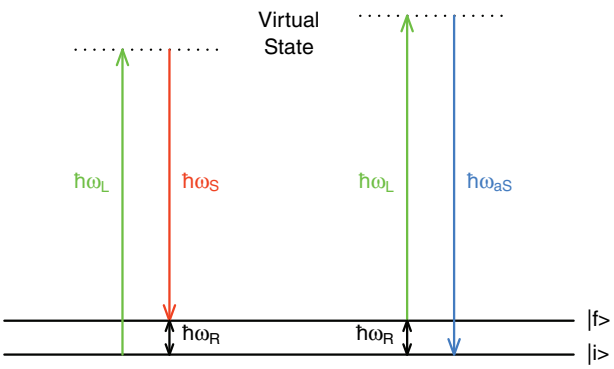

Figure 3.79 Energy level diagram representing the CARS process.

$$(1) \qquad \vec{k}_L - \vec{k}_S = \vec{k}_R \rightarrow \text{generation of photon momentum}$$

$$(2) \qquad \vec{k}_L + \vec{k}_R = \vec{k}_{aS} \rightarrow \text{annihilation of photon momentum}$$

$$(1)+(2) \quad \vec{k}_L + \vec{k}_L = \vec{k}_S + \vec{k}_{aS} \rightarrow \text{momentum conservation.} \qquad (3.215)$$

The CARS phase-matching condition is realized experimentally by special laser beam arrangements. This means that the incident laser beams have to be aligned in a precise manner such that the CARS process is properly phase matched. For gases where the linear refractive index is almost constant (i.e., $n = 1$) for a large frequency range a collinear beam arrangement can be chosen (see Figure 3.80a). However,

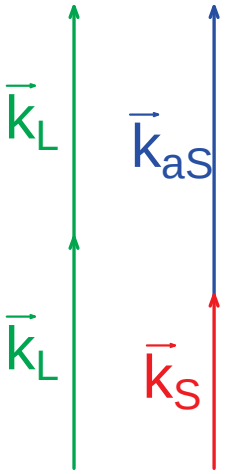

(a) Collinear CARS

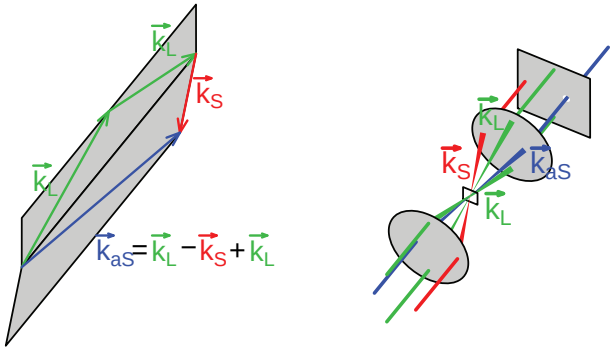

(b) Folded BOXCARS

Figure 3.80 (a) Momentum conservation for a collinear CARS beam arrangement in dispersionless media. (b) Folded BOXCARS beam arrangement to satisfy phase matching in dense media.

in condensed phases the dispersion of the refractive index, that is, $n_i = n(\omega)$ ($i = \mathrm{L,S,aS}$) must be considered. Because $\left|\vec{k}_i\right| = \omega_i n_i / c$, it is obvious that a collinear arrangement between the four waves is not possible. Therefore, special beam geometries (CARS excitation schemes) satisfying the CARS phase-matching condition in dispersive media are required. The so-called folded BOXCARS phase-matching geometry shown in Figure 3.80b is a commonly applied non-collinear beam arrangement which is used to achieve CARS phase matching in dense media.

The starting point for the derivation of an expression for the CARS intensity is the nonlinear CARS polarization (Equation 3.207). Employing this nonlinear CARS polarization (Equation 3.207) as the source term within the Maxwell equations results in a nonlinear wave equation for the anti-Stokes amplitude E_{aS} (see also Section 3.6.1), which can be used to express the CARS signal intensity I_{aS}:

$$I_{\mathrm{aS}} \sim |E_{\mathrm{aS}}|^2 = \frac{\pi}{2n_{\mathrm{aS}} \cdot c} \omega_{\mathrm{aS}}^2 L^2 \left|\chi^{(3)}\right|^2 I_{\mathrm{L}}^2 I_{\mathrm{S}} \cdot \mathrm{sinc}^2 \left(\frac{\left|\Delta\vec{k}\right| L}{2} \right) \tag{3.216}$$

where $\Delta\vec{k} = \vec{k}_{\mathrm{aS}} - (2\vec{k}_{\mathrm{L}} - \vec{k}_{\mathrm{S}})$ and L is the interaction length over which the beams interact within the sample. $\Delta\vec{k}$ is a direct consequence of the phase-matching condition discussed above. Equation 3.216 reveals that for phase-matched conditions (i.e., $\left|\Delta\vec{k}\right| = \Delta k = 0$) the CARS signal intensity increases with L^2. For non-phase-matched conditions, however (i.e., $\left|\Delta\vec{k}\right| = \Delta k \neq 0$), the CARS signal only builds up over the coherence length $l_{\mathrm{Ph}} \approx \pi / \Delta k$ while after this a spatial–time-periodic intensity modulation due to constructive and destructive interference of the four beams that are mixed within a CARS process occurs (see Figure 3.81). This

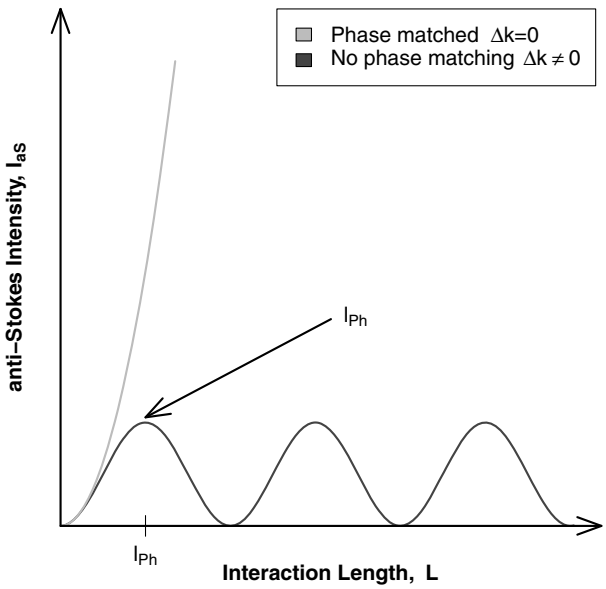

Figure 3.81 CARS signal intensity for phase-matched ($\Delta k = 0$) and non-phase-matched ($\Delta k \neq 0$) conditions.

means that for non-phase-matched beam geometries the CARS signal oscillates as a function of L with a periodicity of $\lambda_{aS}/(2\Delta n)$ and the buildup of a macroscopic CARS signal is prevented. However, $|\Delta\vec{k}|^{-1}$ is the critical interaction length for which phase matching can be neglected. Further below when discussing CARS microscopy, it will be shown that for tight focusing conditions by the use of a microscope objective with large numerical aperture it is possible to go below this critical interaction length.

In the following, linear spontaneous Raman scattering is briefly compared with its nonlinear variant CARS. It has been shown that Raman scattering is a non-directional and incoherent process with small scattering cross-sections. In contrast, CARS leads to a directed and coherent signal, which is why the weak Raman scattering intensity is enhanced significantly. The Stokes Raman signal appears at longer wavelengths compared with the excitation laser, which is why it is often masked by the simultaneous excitation of disturbing fluorescence. The CARS signal, however, emerges at shorter wavelengths than the excitation lasers and therefore experiences no disturbing interference with autofluorescence. Whereas the Raman scattering intensity is direct proportional to the volume density of scattering molecules N, the CARS signal intensity scales with N^2. The latter is a consequence of the dependence of I_{aS} (Equation 3.216) on the square modulus of the CARS susceptibility, $|\chi^{(3)}|$ (Equation 3.209), which scales linearly with N. Linear Raman scattering, that is, Stokes and anti-Stokes radiation, can be interpreted as an energy exchange between the scattered photon and the molecule or vice versa. The nonlinear CARS process can be seen as a sequence of a Stokes and anti-Stokes processes where the molecule finally ends up in the same state as that from which the CARS process started (see Figure 3.82).

As can be seen in Figure 3.82, a CARS spectrum is recorded by keeping the laser wavelength λ_L fixed and tuning the wavelength of the Stokes laser λ_S. Whenever the difference frequency between the two laser pulses hits a Raman transition ω_R (i.e., $\omega_L - \omega_S = \omega_R$), a CARS signal is generated.

However, whereas linear Raman spectroscopy leads to Raman lineshapes that are easy to interpret, CARS spectra are often characterized by complex line profiles. In the following, the CARS line profiles are discussed in more detail. The starting point is Equation 3.209, the CARS susceptibility, which can be rewritten in the close vicinity of a Raman resonance (i.e., for $\omega_L - \omega_S = \omega_R$) to yield

$$\chi^{(3)} = \frac{\chi_R}{2\delta + i\gamma} \tag{3.217}$$

where χ_R defines the Raman cross_section:

$$\chi_R = \frac{N}{2m\omega_R}\left[\left(\frac{\partial\alpha}{\partial q}\right)\Big|_{q=0}\right]^2 \tag{3.218}$$

and $\delta = \omega_R - (\omega_L - \omega_S)$ is called Raman detuning. Equation 3.217 shows that the CARS susceptibility is a complex value:

$$\chi^{(3)}_{CARS} = \chi' + i\chi'' \tag{3.219}$$

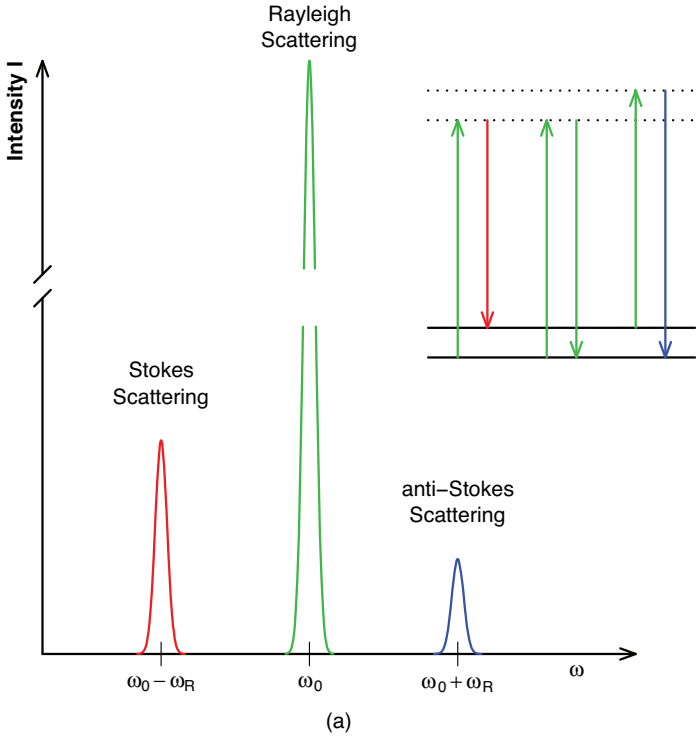

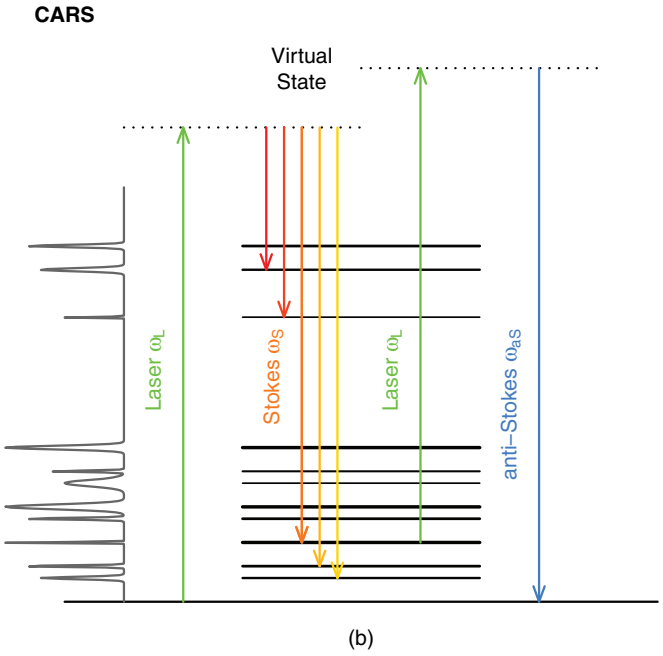

Figure 3.82 Comparison of (a) linear Raman scattering and (b) CARS.

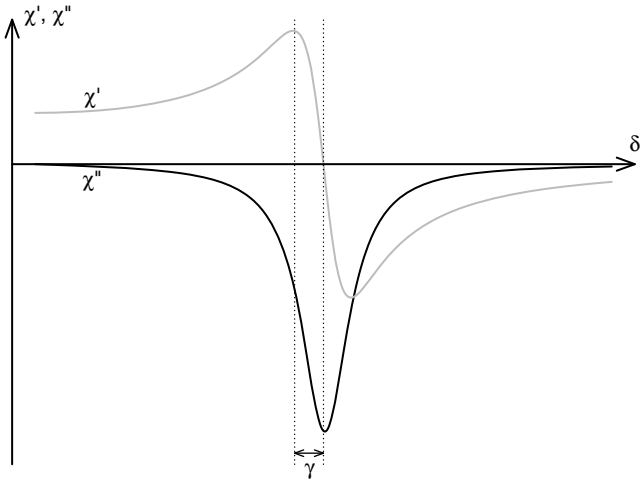

Figure 3.83 Dependence of the real χ' and imaginary part χ'' of the CARS susceptibility.

with a real part

$$\chi' = \frac{2\chi_R \cdot \delta}{4\delta^2 + \gamma^2} \tag{3.220}$$

and an imaginary part

$$\chi'' = \frac{\chi_R \cdot \gamma}{4\delta^2 + \gamma^2}. \tag{3.221}$$

The resulting functions are displayed in Figure 3.83 (see also Figure 3.8). For Raman resonance conditions (i.e., where $\delta = 0$), the real part χ' of the CARS susceptibility becomes zero and the CARS susceptibility is solely determined by its imaginary part χ''. Therefore, the CARS signal intensity in resonance with a single Raman transition is directly proportional to $\chi^{(3)}_{CARS} = \chi''$. Figure 3.83 shows that the imaginary part of the CARS susceptibility χ'' is characterized by a Lorentz profile, which is why the CARS signal for a single isolated Raman transition (see also further below) exhibits a Lorentzian lineshape. However, in addition to these resonant CARS susceptibilities due to molecular vibrations, a nonresonant contribution χ_{NR} mostly originating due to the electronic structure of the medium must also be considered. Figure 3.84 illustrates the Raman resonant CARS susceptibility and the nonresonant susceptibility due to the electronic enhancement of the medium in the form of energy level diagrams[22)].

The nonresonant contribution χ_{NR} is considered to be a real value, which is true if the two-photon transitions shown in Figure 3.84 are away from a two-photon

22) It should be noted that further energy level diagrams exist which also contribute to the nonresonant susceptibility.

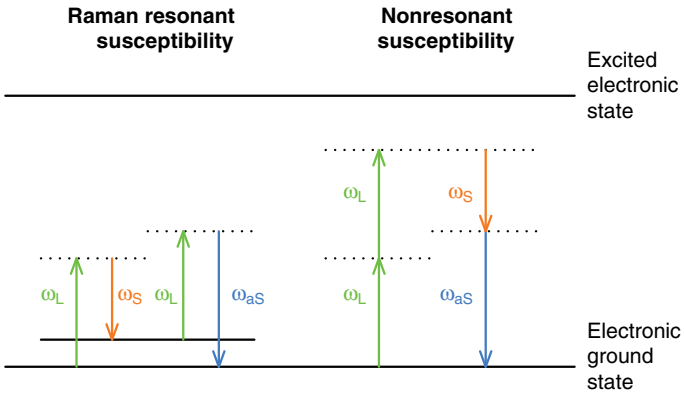

Figure 3.84 Comparison of resonant versus nonresonant CARS susceptibility.

electronic absorption (see Figure 3.83: in the case of resonant conditions the imaginary part of the susceptibility is the dominant contribution whereas for nonresonant conditions the susceptibility is mainly dominated by its real part). Furthermore, χ_{NR} does not display a strong frequency dependence, which means that χ_{NR} can be considered constant in the vicinity of a Raman transition. Hence the square modulus of the CARS susceptibility including nonresonant contributions reads as follows:

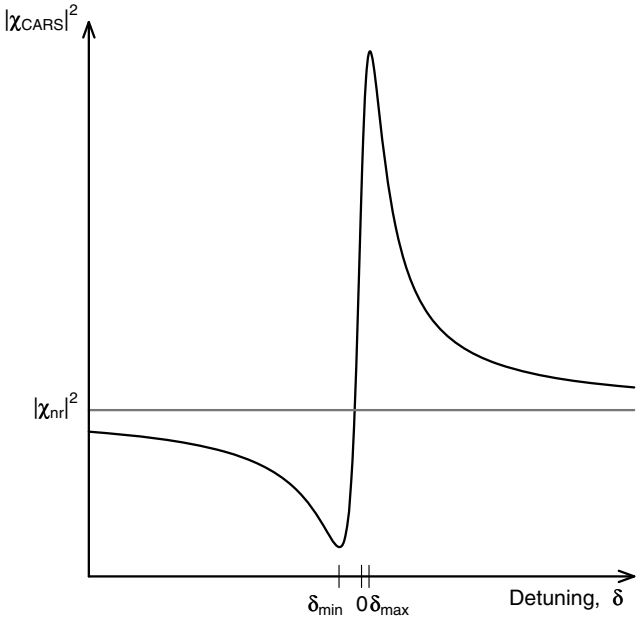

Figure 3.85 Typical dispersive CARS line profile.

$$\left|\chi^{(3)}_{\mathrm{CARS}}\right| = \left|\chi' + i\chi''\right|^2 = \chi'^2 + \chi''^2 = \left(\chi_{\mathrm{NR}} + \frac{2\chi_{\mathrm{R}}\cdot\delta}{4\delta^2+\gamma^2}\right)^2 + \left(-\frac{\chi_{\mathrm{R}}\cdot\gamma}{4\delta^2+\gamma^2}\right)^2. \tag{3.222}$$

The lineshapes observed in CARS spectra are determined by Equation 3.222. Figure 3.85 displays the square modulus of the CARS susceptibility as a function of the detuning $\delta = \omega_{\mathrm{R}} - (\omega_{\mathrm{L}} - \omega_{\mathrm{S}})$. It can be seen that the nonresonant susceptibility χ_{NR} leads to asymmetric CARS lineshapes. Depending on the magnitude of χ_{NR}, the observed CARS lines can become complex and difficult to interpret.

The situation becomes even more complicated if several Raman transitions are lying close together or spectrally overlap. Here, highly asymmetric and complicated lineshapes are observed due to interference effects among the complex resonant CARS susceptibilities of adjacent Raman transitions and/or interference with the nonresonant background, that is, χ_{NR}. Therefore, even background-free CARS spectra (if nonresonant contributions can be neglected, that is, $\chi_{\mathrm{NR}} = 0$) only lead to line profiles comparable to those observed in spontaneous nonlinear Raman scattering (i.e., Lorentzian shape) if the Raman resonant transitions are spectrally well separated from each other. If this is not the case and the Raman transitions are spectrally overlapping, interference effects between the respective Raman resonant CARS susceptibility contributions have to be considered and determine the CARS line profile. Depending on the ratio between real and imaginary parts of the various Raman resonant contributions, the observed CARS line profiles can vary drastically. Hence a quantitative CARS lineshape analysis is a complicated process.

CARS Microscopy The nonlinear variant of Raman spectroscopy CARS belongs to the most promising biophotonic techniques because it combines signal enhancement due to the coherent nature of the CARS process with further advantages such as directional emission, narrow spectral bandwidth, and no disturbing interference with autofluorescence. Particularly the introduction of CARS as a microscopic contrast mechanism allows the recording of vibrational (molecular) images (more precisely, the spatial CARS intensity distribution of one particular molecular vibration) in real time, that is, with video repetition rate. However, the combination of CARS with a conventional light microscope raises the question of how to satisfy the phase-matching condition, since it has been shown above that a collinear beam arrangement cannot be applied to dense media. However, collinear CARS microscopy is possible since for tight focusing conditions with a high numerical aperture microscope objective the phase-matching condition becomes uncritical because (1) the large angle of aperture of the microscope objective provides in the focus for every wavevector component of the laser beam ($\vec{k}_{\mathrm{L}}$) the corresponding component of the Stokes beam ($\vec{k}_{\mathrm{S}}$) required to fulfill the CARS phase-matching condition (see Figure 3.86); and (2) the CARS signal is only generated over an extremely short interaction length L. This means that tight focusing by means of a microscope objective goes below the CARS coherence length l_{Ph} (see Figure 3.81) and the interaction length is too short for a large phase mismatch to occur.

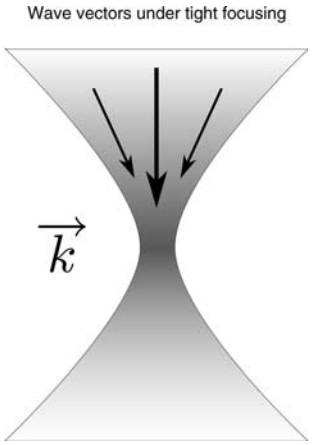

Figure 3.86 Illustration of phase matching under tight focusing conditions.

The CARS signal can be detected in either the forward (F-CARS) or backward (EPI-CARS/E-CARS) direction (see Figure 3.87). Since the wavevector mismatch for F-CARS microscopy is almost zero (i.e., $|\Delta\vec{k}| = \Delta k \approx 0$) because of the large k vector distribution generated by a high numerical aperture microscope (see Figure 3.86), all

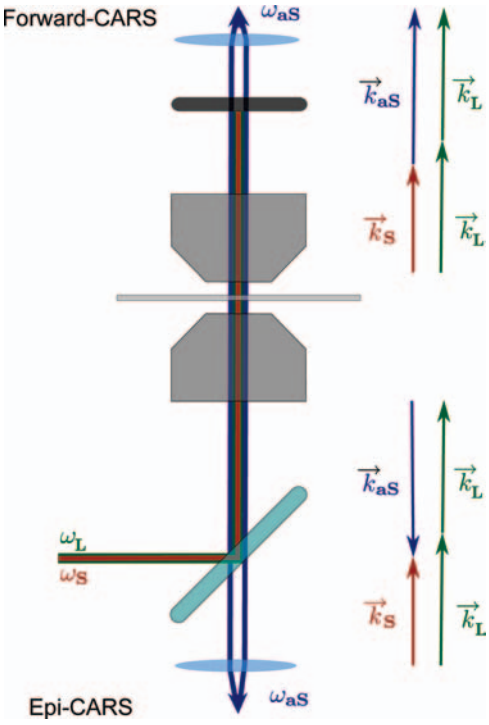

Figure 3.87 Schematic diagram of a F- and EPI-CARS microscopy.

scattering objects lead to large F-CARS signals. This is in contrast to EPI-CARS where the phase mismatch of $|\vec{\Delta}k| = \Delta k \approx -2|\vec{k}_{aS}| = 4\pi n/\lambda_{aS}$ is significant. Hence an EPI-CARS signal is only generated for scattering objects smaller than half of the anti-Stokes wavelength. Here, the magnitude of the phase mismatch acts as a filter for scattering objects of a certain size where the interaction length is below the CARS coherence length (see above).

By selectively scanning the samples, 2D- and 3D-CARS images of special molecular vibrations can be obtained. These CARS images yield detailed chemical structure information about the investigated sample. However, it has been shown above that the CARS process is not background free due to the presence of nonresonant contributions χ_{NR} to the CARS susceptibility. Hence CARS microscopy is also not background free and the Raman resonant CARS contrast is reduced due to nonresonant background signals, for example because of the electronic structure of the medium. Furthermore, water present in almost all biological samples leads, due to its spectrally broad Raman bands, to rather strong resonant background signals. These background signals are often troublesome for F-CARS microscopy since they reduce the molecular contrast due to Raman resonant signals. Here, the Raman resonant CARS signal of a small scattering object is superimposed by the much stronger, due to the larger interaction length, CARS signal of the medium (e.g., water). This large background leads to a reduced contrast for the CARS image of the object. In contrast to F-CARS, E-CARS detection allows imaging with a much better contrast because the E-CARS signal of the medium disappears due to destructive interference. However, this is not true for the E-CARS signal of the scattering object if its size is comparable to the anti-Stokes wavelength where exclusively the object contributes to the image contrast. Background reduction in CARS microscopy is a subject of current research in CARS microscopy and several approaches have been developed to reduce the background. However, a detailed discussion of these approaches would go beyond the scope of this general introduction to CARS microscopy.

Another important issue in CARS microscopy is the appropriate choice of excitation lasers. Due to the nonlinearity of the CARS process, high field strengths are required to generate a CARS signal. However, the spectral pulse widths should be as small as possible in order to excite predominantly Raman resonances and therefore generate only a small amount of the almost frequency-independent and contrast-reducing nonresonant CARS signals. In other words, the applied pulse lengths should be as short as possible for efficient CARS signal generation but on the other hand not too short that the spectral width of the pulses becomes larger than that of the Raman resonances. Therefore, picosecond pulses are usually applied in CARS microscopy.

3.13.5.2 Stimulated Stokes- and Anti-Stokes Raman Scattering

When the two laser beams with frequencies ω_L and ω_S travel through a Raman-active medium, the longer wavelength beam ω_S can experience optical amplification at the expense of the shorter wavelength beam ω_L. This effect, which is represented schematically in Figure 3.88, is called stimulated Raman scattering.

Figure 3.88 shows that the incident beam (L) loses an energy quantum $\hbar\omega_L$ whereas an energy quantum $\hbar\omega_S$ is added to the Stokes beam (S). Hence the

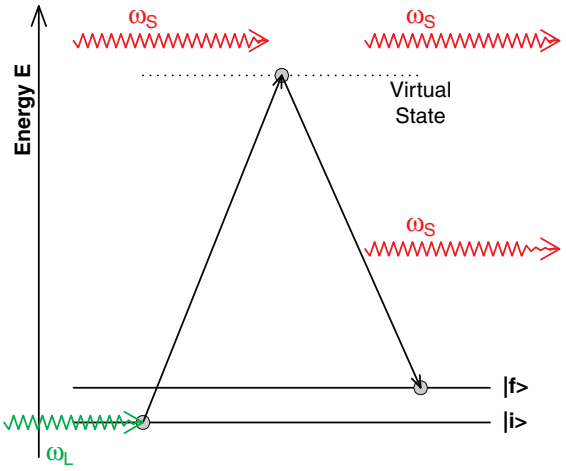

Figure 3.88 Schematic illustration of stimulated Raman scattering.

stimulated Raman effect leads to an amplification of the Stokes beam since from one excitation ω_L and one Stokes photon ω_S two Stokes photons are generated.

Stimulated Raman scattering can also occur by irradiating the Raman-active medium with just one intense input laser field with frequency ω_L because for high laser intensities the number of inelastically scattered Stokes photons can be possibly so high that stimulated Stokes scattering takes place. This means that for high laser intensities the spontaneous Stokes Raman scattering can be so strong that its influence on the molecules cannot be neglected any longer. The molecules interact simultaneously with two light waves, namely the laser wave ω_L and the Stokes wave $\omega_S = \omega_L - \omega_R$, that is, both waves are coupled by the molecules vibrating at the frequency ω_R. This parametric interaction allows an energy exchange between the laser wave as pump wave and the Stokes wave and can lead to the generation of an intensive directed radiation at the Stokes frequency $\omega_S = \omega_L - \omega_R$ (see also Figure 3.89).

In Section 3.13.5.1 an expression for the amplitude q of the enforced vibrations at the difference frequency $\omega_R = \omega_L - \omega_S$ induced by the interaction with both the light fields E_L and E_S was derived (see Equation 3.204). The induced vibrating dipoles lead to a polarization where the contribution P_S oscillating at the Stokes frequency ω_S and responsible for the Stokes Raman scattering is given by (see Equation 3.182)

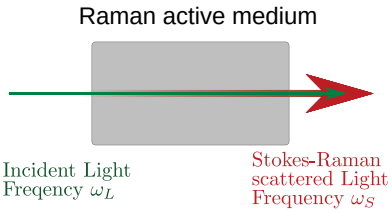

Figure 3.89 Illustration of stimulated Raman scattering, that is, the interaction of an intense laser beam leads to the generation of a forward-directed Stokes beam.

$$P_S = N \cdot \frac{1}{2}\left(\frac{\partial\alpha}{\partial q}\right)\Big|_{q=0} \cdot q \cdot E. \tag{3.223}$$

Together with q given by Equation 3.204 and $E = E_L + E_S = E_L^0 e^{i(\omega_L t - k_L z)} + E_S^0 e^{i(\omega_S t - k_S z)}$, Equation 3.223 can be rewritten to yield a nonlinear polarization:

$$P_S^{NL} = N \cdot \frac{\left[\left(\frac{\partial\alpha}{\partial q}\right)\Big|_{q=0}\right]^2 (E_L^0)^2 E_S^0}{4m[\omega_R^2 - (\omega_L - \omega_S)^2 + i\gamma(\omega_L - \omega_S)]} e^{-i(\omega_S t - k_S z)}. \tag{3.224}$$

Hence a polarization wave is propagating through the medium whose contribution oscillating at the Stokes frequency k_S has the same wavevector k_S as the Stokes wave, which is why it can enhance the Stokes wave. The enhancement factor g can be calculated as follows:

$$g \sim \left(\frac{\partial\alpha}{\partial q}\right)\Big|_{q=0} \frac{\gamma}{(\omega_L - \omega_S - \omega_R)^2 + \gamma^2}. \tag{3.225}$$

Equation 3.225 shows that for $\omega_R = \omega_L - \omega_S$, the enhancement factor becomes largest:

$$g \sim \left(\frac{\partial\alpha}{\partial q}\right)\Big|_{q=0} \cdot \frac{1}{\gamma}. \tag{3.226}$$

This means that a coherent Stokes wave (see Figure 3.89) is generated for such Raman modes which exhibit the best ratio between their Raman cross-section $(\partial\alpha/\partial q)|_{q=0}$ and linewidth γ. Very often the generated coherent Stokes wave is still so intense that a further second coherent overtone wave with the frequency $\omega_L - 2\omega_R$ can be excited, which itself excites a third coherent overtone Stokes wave, and so on (see Figure 3.90).

Whereas for spontaneous Raman scattering the anti-Stokes intensity is rather low because of the small thermal population of excited vibrational levels, the detection of anti-Stokes radiation with stimulated Raman scattering becomes possible. A considerable amount of molecules is pumped into excited vibrational levels by the intense incoming laser or pump wave and thus a strong anti-Stokes radiation at the frequency $\omega_{aS} = \omega_L + \omega_R$ can be observed (see Figure 3.91).

From Figure 3.91, it is obvious that stimulated anti-Stokes Raman scattering can be seen as a four-wave mixing process (see also Figure 3.91). Earlier it was shown that four-wave mixing processes require correct phase matching. This means that a macroscopic stimulated anti-Stokes beam can only build up if the phase-matching condition $2\vec{k}_L = \vec{k}_S + \vec{k}_{aS}$ is fulfilled. Figure 3.92 depicts the phase-matching geometry for induced anti-Stokes radiation as a four-wave interaction. Here, the Stokes (S) and anti-Stokes (aS) waves are confined to conical beams coaxial with the pump or laser beam (L). The cones can be created by rotating the plane of Figure 3.92 around k_L. Hence the radiation of a Raman-active medium with a single intense laser beam (L) generates higher order coherent Stokes beams (see Figures 3.89 and 3.90) and anti-Stokes radiation (see Figure 3.93), which is emitted in a cone whose axis is determined by the direction of the incoming laser beam L (see Figure 3.93). The

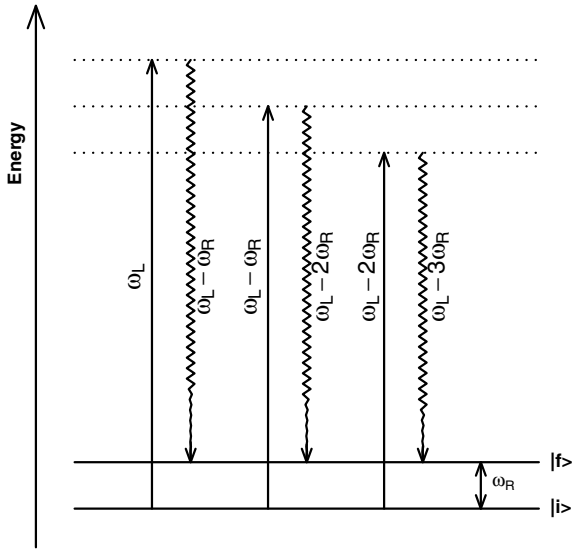

Figure 3.90 Illustration of the generation of coherent Stokes radiation and coherent overtone Stokes waves.

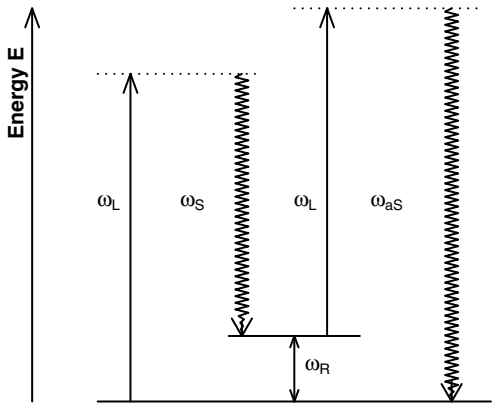

Figure 3.91 Illustration of stimulated anti-Stokes Raman scattering as a four-wave mixing process.

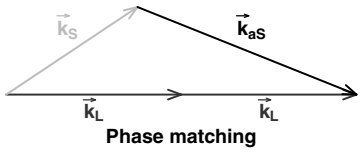

Figure 3.92 Illustration of phase-matching geometry for stimulated anti-Stokes Raman scattering.

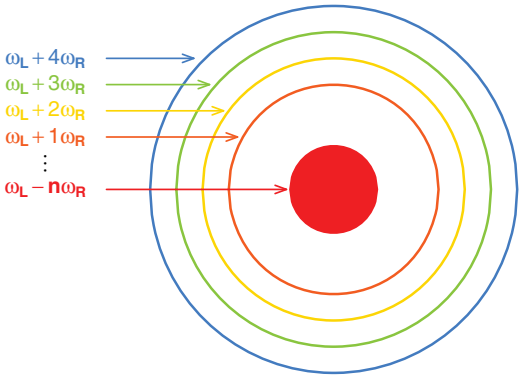

Figure 3.93 Schematic diagram of fundamental and higher order stimulated Stokes and anti-Stokes Raman radiation.

generation of stimulated Stokes and anti-Stokes Raman radiation which is depicted schematically in Figure 3.93 is often used for frequency shifting of pulsed lasers.

Stimulated Raman Scattering Microscopy Very recently stimulated Raman scattering microscopy has demonstrated its potential in biophotonics for quantitative, background-free, real-time vibrational imaging. Earlier it was shown that irradiating a Raman-active medium by two laser beams with frequencies ω_L and ω_S leads to an amplification of the Stokes beam (S) and an attenuation of the laser beam (L) due to stimulated Raman scattering (see Figure 3.88). Measuring the gain in power of the Stokes beam (S) is called stimulated Raman gain spectroscopy (SRGS) and the detection of loss of power in the laser beam (L) is called stimulated Raman loss spectroscopy (SRLS) (see Figure 3.94).

Recording the gain (SRGS) or loss (SRLS) of power of the two laser beams due to stimulated Raman scattering offers some advantages over CARS, as can be seen from the expressions describing the intensities of SRGS and SRLS:

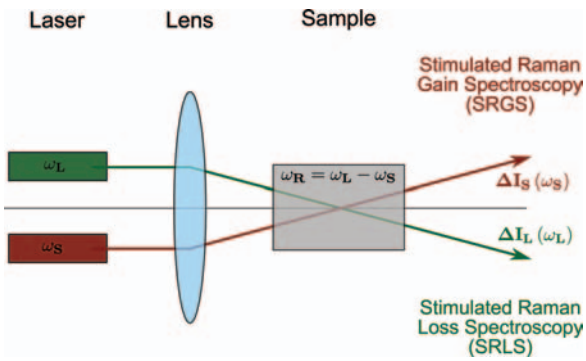

Figure 3.94 Illustration of stimulated Raman gain and Raman loss spectroscopy.

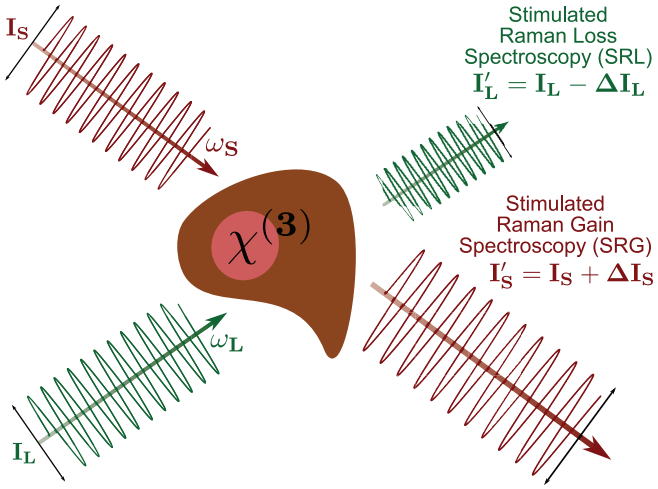

Figure 3.95 Schematic illustration of stimulated Raman microscopy.

$$\Delta I_S \sim N \cdot \left(\frac{\partial \alpha}{\partial q}\right)\Big|_{q=0} \cdot I_S \cdot I_L$$
$$\Delta I_L \sim -N \cdot \left(\frac{\partial \alpha}{\partial q}\right)\Big|_{q=0} \cdot I_S \cdot I_L. \tag{3.227}$$

The intensities scale linearly with the concentration. Furthermore, stimulated Raman scattering is background free since SRGS or SRLS signals are only generated if $\omega_L - \omega_S$ matches a Raman resonance. Hence quantitative measurements are possible. However, the loss or gain in intensity is rather small, that is, small quantities need to be detected on a large background, which is why sophisticated detection methods (heterodyne detection by means of lock-in amplifiers) are required. Figure 3.95 depicts schematically the principle of stimulated Raman scattering microscopy.

References

1 Atkins, P.W. (1996) *Physikalische Chemie*, 2nd edn, Wiley-VCH Verlag GmbH, Weinheim.
2 Hecht, E. (2005) *Optik*, Oldenbourg Wissenschaftsverlag, Munich.
3 Jackson, J.D. (1999) *Classical Electrodynamics*, 3rd edn, John Wiley & Sons, Inc., New York.
4 Zinth, W. and Zinth, U. (2005) *Optik*, Oldenbourg Wissenschaftsverlag, Munich.
5 Schrader, B. and Bougeard, D. (1995) *Infrared and Raman Spectroscopy: Methods and Applications*, Wiley-VCH Verlag GmbH, Weinheim.
6 Tuchin, V. (ed.) (2002) *Handbook of Optical Biomedical Diagnostics*, SPIE Publications, Bellingham, WA.
7 Born, M. and Wolf, E. (1997) *Principles of Optics: Electromagnetic Theory of Propagation, Interference and Diffraction of*

Light, Cambridge University Press, Cambridge.
8 Yeh, P. (2005) *Optical Waves in Layered Media*, John Wiley & Sons, Inc., New York.
9 Mayerhöfer, T.G. (2004) Modelling IR-spectra of single-phase polycrystalline materials with random orientation – a unified approach. *Vib. Spectrosc.*, 350 (1–2), 67–76.
10 Boyd, R.W. (1992) *Nonlinear Optics*, Academic Press, New York.
11 Butcher, P.N. and Cotter, D. (1991) *The Elements of Nonlinear Optics*, Cambridge University Press, Cambridge.
12 Mukamel, S. (1995) *Principles of Nonlinear Optical Spectroscopy*, Oxford University Press, New York.
13 Shen, Y.R. (1984) *The Principles of Nonlinear Optics*, John Wiley & Sons, Inc., New York.
14 Demtröder, W. (1991) *Laserspektroskopie*, Springer, Berlin.
15 Rulliere, C. (2005) *Femtosecond Laser Pulses: Principles and Experiments*, Springer, Berlin.
16 Telle, H.H., Ureña, A.G., and Donovan, R.J. (2007) *Laser Chemistry: Spectroscopy, Dynamics and Applications*, John Wiley & Sons, Inc., New York.
17 Valeur, B. (2002) *Molecular Fluorescence*, Wiley-VCH Verlag GmbH, Weinheim.
18 Schmidt, W. (2000) *Optische Spektroskopie*, Wiley-VCH Verlag GmbH, Weinheim.
19 Turro, N.J. (1991) *Modern Molecular Photochemistry*, University Science Books, Mill Valley, CA.
20 Wardle, B. (2009) *Principles and Applications of Photochemistry*, John Wiley & Sons, Inc., New York.
21 Barron, L.D. (2004) *Molecular Light Scattering and Optical Activity*, Cambridge Univ Press, Cambridge.
22 Lakowicz, J.R. (2004) *Principles of Fluorescence Spectroscopy*, vol. 9, Springer, New York.
23 Fernández-Suárez, M. and Ting, A.Y. (2008) Fluorescent probes for super-resolution imaging in living cells. *Nat. Rev. Mol. Cell Biol.*, 90 (12), 929–943.
24 Hell, S.W. (2003) Toward fluorescence nanoscopy. *Nat. Biotechnol.*, 210 (11), 1347–1355.
25 Hell, S.W. (2009) Microscopy and its focal switch. *Nat. Methods*, 60 (1), 24–32.
26 Hell, S.W. (2007) Far-field optical nanoscopy. *Science*, 3160 (5828), 1153–1158.

Appendix 3.A
Fluorescence Labeling Strategies for Proteins

Ingo Kleppe and Klaus Weisshart

3.A.1
Introduction

There is an increasing demand in modern biology to understand cellular processes with high temporal and spatial resolution. Recording of the underlying kinetic processes necessitates the quantification of molecule numbers, diffusion, and interaction networks within the cellular context [A1]. Specific labeling techniques in combination with sophisticated optical instruments and paired with computational power have boosted our ability to study dynamic processes and structures within a cell [A2]. In particular, fluorescence microscopy has revolutionized research in the life sciences. Combined with functionalized fluorophores, they provide an extremely powerful experimental toolbox [A3]. Modern fluorescence microscopes

offer the possibility of imaging with molecular specificity and the necessary sensitivity to view molecules in their natural environment down to the single molecule level [A4].

Labeling in principle has two major obstacles to overcome: the potential interference of the label with the function of the labeled structure and the difficulty of bringing the label to the desired target. The development of labeling techniques over the last 15 years has made these issues negligible for a very large class of molecules: the proteins [A5]. Since the decoding of entire genomes, proteins have become the biomacromolecules attracting the greatest attention as they not only shape cells through the cytoskeleton, but are also indispensable for the catalysis of biochemical reactions. As macromolecular assemblies they are involved in diverse processes such as immune responses, cell signaling, cell adhesion, and the cell cycle, to name just a few of their functions.

In recent times, new techniques have been developed to mark proteins with small organic fluorophores and semiconductor nanocrystals, but the most rapid advances have been seen in the employment of fluorescent proteins [A6]. The landmark here was the discovery of the green fluorescent protein (GFP) from the jellyfish *Aequorea victoria* in 1962 that led to a complete new labeling strategy, using the cell itself for generating the label and targeting the molecules of interest by means of molecular biology. At the top of these developments there is the enormous variety of transgenic animal strains today expressing various fluorescent proteins in different parts of their body without loss of physiological function.

The choice of a specific labeling technique depends very much on the scientific questions asked (Table 3.A.1). However, there are some general criteria to consider for the best choice of dye and labeling technique. By far the largest differentiation is the nature of the sample, that is, a solution, a fixed specimen, or a living cell [A7]. Other parameters to be taken into account are the photostability of the dye, its phototoxicity, and its photophysical properties [A8]. The size of the dye can also have a major impact, as the molecule of interest to which the tag is attached might be inactivated by steric interference.

3.A.2
General Labeling Strategies for Organelles and Biomacromolecules

Many of the dyes used as fluorescent labels are derived from molecules found in Nature. An example of a natural fluorophore is phycobilin, which is employed by cyanobacteria and red algae to collect light for photosynthesis. Although natural labels have been successfully applied for cytology and immunochemistry applications, their properties cannot be controlled sufficiently to assign broader usage to them. In addition, naturally fluorescent dyes are fairly large in size, and can interfere with molecule function.

Since the aromatic or conjugated nature of bonds in fluorophores is well understood, chemical synthesis has allowed tailoring of the properties of organic dyes with respect to photostability, spectral emission, and size [A9]. Organic dye molecules can consist of

Table 3.A.1 Strategies used for protein labeling and their applications.

	Small organic dye and Qdots	Antibody (Ab) and ligands	Fluorescent proteins (FPs)	Tags with small dyes
Labeling	Chemically linked to a protein of interest	Ab and ligand is directly coupled to organic dye or Qdot; Ab can also be detected by secondary labeling	Genetically linked to a protein of interest	Genetically linked to a protein of interest
Delivery	Administered to solution or cell medium	Administered to solution or cell medium	*In situ* expression	*In situ* expression of peptide, delivery of cell-permeable dye in medium
Application	Solution and chip assays to probe conformational changes and interactions	Detection of proteins in fixed and permeabilized cells to probe localization; detection of receptors on cell membrane	Dynamic and interactions studies in live cells	Dynamic and interaction studies in live cells
Advantages	High brightness; photostability; small size	High specificity; amplification; multicolor	High specificity; low background; live cell; multicolor	Small size; live cells; multicolor
Shortcomings	Exogenous labeling; low specificity	Fixed cells only or restricted to cell surface; huge size; intensive washing needed to reduce background	Environmental sensitivity; ectopic expression; oligomerization; low brightness	Environmental sensitivity; toxic; intensive washing needed to reduce background

just a few atoms, rendering them the ideal tools to intercalate into larger biomacromolecules without causing too much steric hindrance. Their hydrophobicity or affinity to certain chemical groups will decide on their affinity to biological structures.

A group of dyes called cell function probes are able to integrate into or penetrate the membrane and act as sensors [A10]. For example, the high hydrophobicity of DiI and derivatives enables these dyes to intercalate into membranes. Since they are specific for certain lipids, they act as markers of the membrane composition [A11]. Some membrane-permeable dyes stain specific structures or organelles, such as MitoTracker, a mitochondrial selective fluorescent label. Others are indicators of a metabolic state. For example, the fluorescence of Indo-1 and Fluo-3 is sensitive to the calcium concentration within the cell. Yet other dyes are voltage sensitive or are used to probe the pH of the microenvironment [A12]. Hoechst 33342, DAPI, TOTO, and EtBr are examples of nucleic acid staining dyes and they can have selectivity for DNA, RNA, AT pairs or GC pairs, but otherwise they are unspecific, staining the molecule throughout its length [A13]. In contrast to lipids and nucleic acids, intercalating dyes for proteins are sparse as they do not form as readily stacked structures into which a dye can intercalate. Most common are those protein dyes that bind to hydrophobic pockets in the protein or attach to certain side chains. No intercalating dye, however, will stain all proteins to the same extent and, due to their unspecific binding, intercalating protein dyes are most commonly used to stain proteins in gels, such as the SYPRO dyes [A14].

3.A.3
Protein Labeling Strategies

Labeling with a fluorescent probe has become the most commonly used protein modification in scientific research. Labeling with reactive organic dye molecules and quantum dots and the use of labeled antibodies or ligands having affinities to specific peptide sequences have been and are still heavily used for *in vitro* investigations in solution or the fixed cells. On the other hand, expression of autofluorescent proteins and selective chemical modifications by genetic engineering are the techniques of choice when it comes to live cell imaging (Figure 3.A.1) [A15].

3.A.4
Direct Labeling Strategies for Fixed Cells and Solution

To label a protein stably, an organic fluorescent dye must be functionalized with a reactive group that in turn will react with specific functional groups within amino acids, the building blocks of proteins. Functionalized dyes can react with amino groups via active ester, carboxylate, isothiocyanate, or hydrazine, with carboxyl groups via carbodiimide, and with thiol groups via maleimide or acetyl bromide. The result is a covalent linkage between the protein and the fluorophore (Figure 3.A.2). Common dye families include xanthene derivatives (fluorescein, rhodamine, eosin, etc.), cyanine derivatives (cyanines, carbocyanines, etc.), and coumarin derivatives [A11].

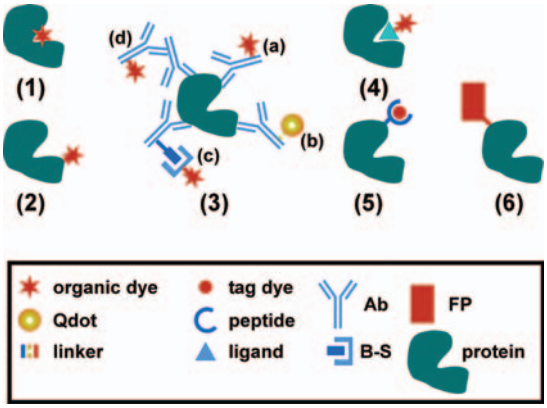

Figure 3.A.1 Labeling strategies for proteins. Fluorescent organic dyes with affinities for hydrophobic pockets or specific amino acid side chains can be used to mark proteins noncovalently and nonspecifically (1). Organic dyes can be functionalized to react with certain chemical groups of amino acids to form a covalent linkage (2). As these chemical groups exist in virtually all proteins, labeling is rather unspecific. Specific labeling is achieved by the employment of antibodies (Ab) raised against the protein (3). The antibodies recognize either sequence stretches or conformational epitopes. The primary antibody can be labeled itself with an organic dye (a) or a quantum dot (b). In sandwich techniques, the primary antibody will not be directly coupled to a fluorescent dye molecule. Instead, it is either tagged with biotin to which streptavidin conjugated to a fluorophore can bind (biotin–streptavidin system, B-S) (c), or is detected by a secondary antibody that bears the label (d). The protein can also be indirectly labeled if it can bind a ligand to which the label has been attached, as is the case, for example, for many cell membrane receptors (4). Since antibodies, quantum dots, and many ligands and organic dyes are non-cell permeable, labeling has to occur in solution and their use is restricted to *in vitro* studies or the surface of living cells. *In vivo* labeling techniques, on the other hand, include the fusion of either a self-labeling peptide sequence, to which a dye specific for such a tag will bind (5), or a fluorescence protein (FP) (6) to the protein of interest. Care must be taken not to disturb the function of the protein by these fluorescent tags.

Companies often supply these under special group names such as BODIPY, Alexa Fluor (both from Invitrogen), Atto (from Sigma Aldrich), DyLight Fluor (from Thermo Scientific), and FluoProbes (from Interchim). As these reagents represent newer generation fluorophores, they in general perform better in terms of photostability, brightness, and environmental insensitivity compared with classical dyes such as fluorescein. There is a variety of synthetic dyes available nowadays that cover the whole visible spectrum (Figure 3.A.3).

Specificity in labeling will only be obtained if the protein is in its pure form when being modified, because contaminant proteins present in the reaction mixture and harboring the functional groups of interest will also be labeled to the same extent. However, one can tailor the site of labeling by the introduction of specific amino acids at certain positions, taking care that the structure and function of the protein is not disturbed. Due to the chemical nature of the label, the reaction can only be controlled

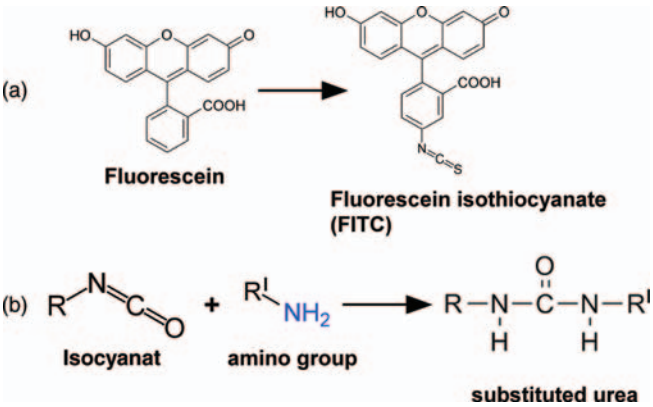

Figure 3.A.2 Functionalization and reaction of organic dye molecules. Dye molecules must be functionalized with a reactive group in order to be able to link them covalently to amino acid side chains of a protein. The example shows FITC, a derivative of fluorescein to which an isothiocyanate group has been added (a). The isothiocyanate group can react with amino groups of amino acids to attach the dye covalently to the protein (b).

to a certain extent. For example, all amino groups in the protein are potential targets for an amine reactive dye. Hence it cannot always be predicted which position will be labeled and if one or more dye molecules will be covalently linked to the protein. Fortunately, there are kits available from a variety of companies, which make the labeling procedure straightforward and allow for even tiny amounts of protein to be labeled efficiently with a defined stoichiometry.

In addition to organic dye molecules, quantum dots have also been a favorite tool for labeling proteins [A16]. Their advantage lies in their broad excitation spectra, so many wavelengths can be used to excite them, and they all show narrow emission bands. Quantum dots come in a size range between 2 and 10 nm and the larger they

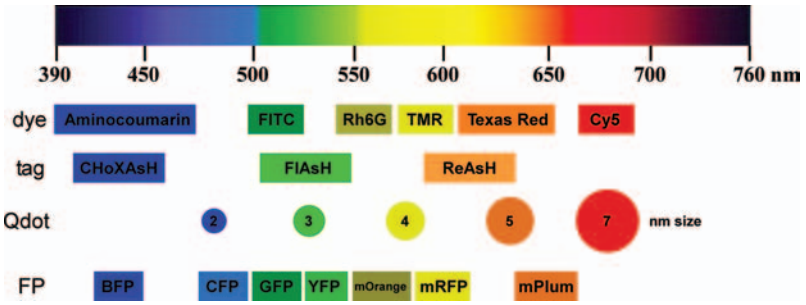

Figure 3.A.3 Spectral range of fluorophores. Common organic dyes (dye), quantum dots (Qdot), dyes binding to self-labeling peptides (tag), and fluorescent proteins (FP) are placed at the position of the spectrum according to their emission wavelength to demonstrate that each class covers a broad range of the visible spectrum. An extended list of fluorophores can be found at http://home.earthlink.net/pubspectra/ [A6].

are the more red shifted their emission wavelength is (Figure 3.A.3). Quantum dots are semiconductors and, since their core and shell are made up of heavy metal ions, they can be toxic to cells. To reduce their deleterious effects, they can be coated with biomaterial on their exterior.

3.A.5
Indirect Labeling Strategies for Fixed Cells and Solution

To provide for high specificity in labeling proteins, the employment of so-called secondary labels is of great advantage. Rather than labeling the protein directly with the organic dye molecule (or quantum dot), the fluorophore is attached to an antibody or, if appropriate, a ligand, which in turn will specifically bind to the protein of interest (Figure 3.A.1) [A7]. Antibodies are the proteins that are elicited as a defense against foreign antigens and they have the property of binding to specific epitopes or peptide stretches within a protein. They therefore represent an ideal tool to detect, for example, one sort of a molecule within a million. They can be produced against virtually every peptide sequence in different animals, allowing multiple staining of various proteins in a cell if each class of antibody is labeled with a specific dye. Polyclonal antibodies isolated from serum after triggering an immune response against an administered protein are specific for multiple parts of the antigen, whereas monoclonal antibodies recognize just one specific epitope of the target molecule, increasing the specificity of the reaction. Other strategies in antibody labeling aim at boosting the signal by sandwich technologies. In this case, it is not the primary antibody specific for the protein that is labeled with the dye, but rather a secondary one, that is specific for the primary antibody. For example, if the primary antibody was produced in mice, the secondary antibody will be an anti-mouse antibody, maybe derived in a sheep.

Another popular method is provided by the biotin–streptavidin system (Figure 3.A.1). Biotin is a vitamin that is bound by streptavidin, a bacterial protein produced in the species *Streptomyces* and consisting of four identical subunits. The biotin–streptavidin interaction is one of the strongest known biological noncovalent linkages. The primary or secondary antibody is biotinylated and then stained with streptavidin that is coupled to an appropriate dye. The advantage of such a system is that with the same primary antibody different stains are possible, depending on the dye attached to the streptavidin. Antibodies are, however, large proteins with a size of around 20 nm, so, like other labeled proteins, quantum dots, or labeled ligands, they are normally not cell permeable and are therefore restricted to cell surfaces with regard to live cell imaging (Figure 3.A.4). The constant F_c part of antibodies can also be bound by specific receptors on some immunologically relevant cells. In such cases, it is mandatory to use only the flexible F_{ab} fragments, which are made up solely by the specific binding sites to avoid unspecific staining. Antibody and ligand staining procedures are most commonly used on fixed and permeabilized cells in immunofluorescence and imunohistochemistry applications (Figure 3.A.5).

The only way to deliver labeled proteins into the cell would be by microinjection or electroporation procedures, which are stressful to some cell types (Figure 3.A.6).

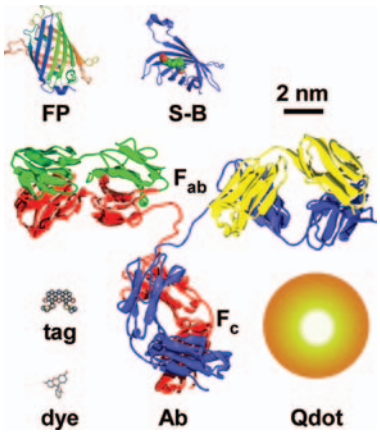

Figure 3.A.4 Sizes of protein labels. Depicted to scale are the dimensions of fluorescein (dye), ReAsH (tag), a medium-sized quantum dot (Qdot), a typical IgG (Ab) with its F_c and F_{ab} fragments indicated, the biotin–streptavidin (monomeric) complex (B-S), and GFP (FP). Typical protein sizes are above the size of GFP, but below the size of IgG.

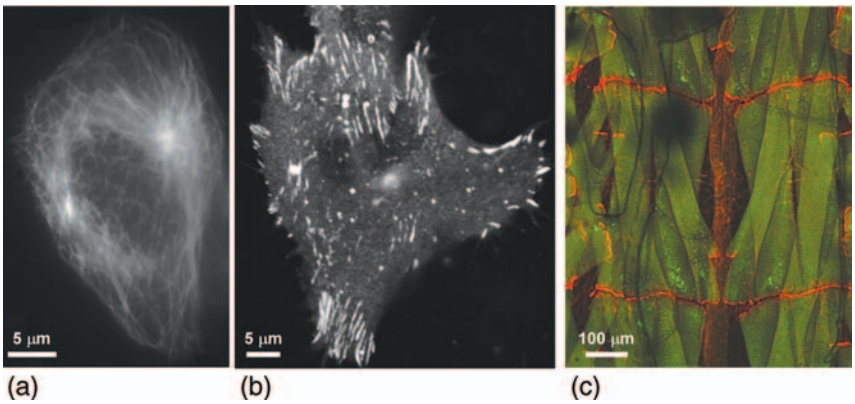

Figure 3.A.5 Use of protein labels. (a) Fixed and permeabilized HepG2 cell stained with a microtubule-specific antibody coupled to Alexa 647. Microtubules provide one component of the cell's cytoskeleton. (b) Live HepG2 cell transiently expressing paxillin fused to tdEOS. Paxillin is involved in the formation of focal adhesions, which are the attachment points of a cell to the substrate. (c) Section of a third instar larva of *Drosophila melanogaster* expressing mCD8 fused to GFP (green channel) and stained with an integrin-specific antibody coupled to Cy3 (red channel). Individual channels are false colored and merged. mCD8 is an ectopically expressed mouse protein, which is membrane linked and highlights the muscle cells. Integrins are receptors that mediate the contact of a cell with the tissue surrounding it, which can be either other cells or the extracellular matrix.

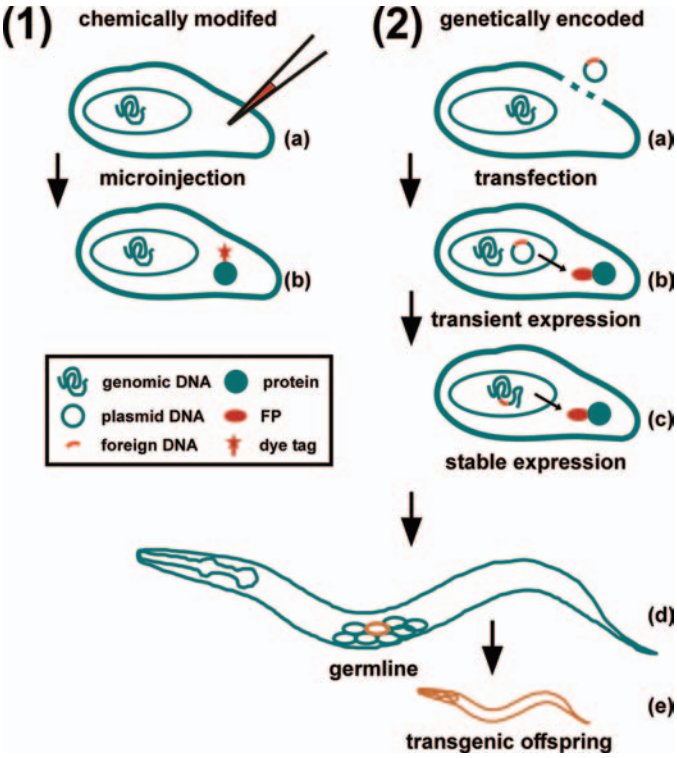

Figure 3.A.6 Methods of delivery of fluorophores into cells. Proteins chemically linked to a fluorophore (or exogenously expressed and purified fluorescence fusion proteins) can be administered into the cell by microinjection (1). The amount delivered can be controlled by adjusting the microinjected volume (a). Experiments are usually carried out immediately after injection, as proteins will be degraded over time and would be diluted out during cell division (b). To express a peptide sequence or a fluorescence protein (FP) fused to a protein of interest in a cell, their coding DNA sequences are cloned into a plasmid (2). The plasmid is delivered into the cell by transfection (a). Depending on the promoter, different levels of the fusion will be expressed. Experiments are normally done within days, since the protein is only transiently expressed as the cell tends to degrade the plasmid with the foreign DNA (b). By introducing a resistance marker along with the plasmid, cells expressing the resistance gene can be selected for. With time the foreign DNA will be integrated into the genome to result in a stably transfected cell line (c). If the cell is from the germline, it can be re-transplanted into the ovary or developing embryo, resulting in a transgenic organism that depending on the promoter used expresses the fusion protein tissue and developmental specific (d). Alternatively, in invertebrate model organisms such as the nematode *Caenorhabditis elegans* (d), the fruit fly *Drosophila melanogaster* and the zebra fish *Danio rerio*, the DNA can be injected directly into the egg with the offspring expressing the protein fusion (e).

Although the protein concentrations administered can be controlled to a certain extent using these techniques, the disadvantages are that it is a laborious technology, requires experimental skills, and proteins will dilute out during cell division. Moreover, degraded proteins cannot be replenished, in contrast to strategies involving endogenous expression. This is where autofluorescent proteins have their great advantage.

3.A.6
Direct Labeling Strategies for *In Vivo* Studies with Autofluorescent Proteins

Since the discovery of the GFP from the jellyfish *Aequorea victoria*, there has been an explosion in the isolation and creation of new fluorescent proteins (FPs) from various organisms covering a wide range of the visible spectrum (Figure 3.A.3) [A6]. Two strategies have been employed to expand the variety of available FPs even further: first, by saturated mutagenesis of known sequences and screening for desired properties of the mutants; and second, by rational design, where crucial amino acids responsible either for building the chromophore or contributing to its direct environment are deliberately altered. The latter approach has yielded, for example, numerous GFP-derived FPs that cover a broad spectral emission range. Since they have been termed according to the matching color of fruits such as banana, cherry, and plum, they are known as the fruit basket of FPs [A8].

The beauty of FPs is that they can be easily cloned from organisms and genetically linked to any protein of interest with modern molecular biological approaches. It can be decisive for the preservation of function as to which end, N- or C-terminal, the FP is attached to its target, and this can often only be established by trial-and-error experiments. Nevertheless, DNA recombinant technologies are nowadays well established, so that creating a fusion between an FP and the protein of interest is straightforward and commonplace in many biological laboratories.

Several options exist to express an FP-tagged protein in a cell. The most commonly used approach is transient expression of the fusion protein (Figure 3.A.6). To this end, an expression vector harboring the construct is transfected into cells with a suitable protocol and the cells are cultivated for the time required to express the fusion. Expression levels can partly be tailored by using differently powerful promoters, which represent the control sequences for expression in a cell. There will always be, however, a distribution of expressed quantities in the expressing cell population. On the other hand, this can be used as an advantage, since cells with desired or physiological expression levels can be screened and selected for. It should be noted that all FP proteins have a maturation time and can change their fluorescence properties until their mature state, so the time point at which the experiment is scheduled could well influence the outcome [A18]. The downside of transient expressions is their variability in efficiencies and only a certain percentage of cells will have the construct expressed.

If a selection marker, such as an antibiotic-resistance gene, is cloned along with the fusion protein, a selective pressure can be used to establish stably transfected cell lines that integrate the foreign piece of DNA over time into the cellular genome. This

procedure can last for months, but once in hand, a stably transfected cell line has the huge advantage that all the cells will express the fusion at approximately the same level. How strongly the protein is expressed depends on both the promoter used and the integration site within the genome. Hence it is possible to select for cell lines having just the right expression levels.

If an embryonic stem cell or a germ cell was the target for expression, it can be re-implanted into the developing embryos and all descendant cells of that particular stem cell will express the FP-tagged protein, if it is under a constitutive promoter (Figure 3.A.6). By choosing specific promoters, expression can be even limited to certain developmental stages or tissues. One should keep in mind that not only the recombinant stem cell will contribute to the cell mass of the developed organism and in this case will often be mosaic. If the gene was introduced directly into the germline, all cells of the offspring can potentially express the construct (Figure 3.A.6).

The greatest uncertainty when working with FP-tagged proteins is the precise concentration of the endogenous protein. Even if the concentration is known, it is unclear what the active fraction of it really is. Hence it is difficult to judge whether the expression levels of the fusion can be regarded as representative of the native pool. In a best case scenario, the tagged protein would completely replace the endogenous one in quantities and function.

There are several possibilities to interfere with or prevent the expression of the endogenous protein. One technique is the so-called knock-out technology, in which both copies of the gene are specifically removed from the diploid genome by DNA recombination. Even lethal knock-outs can be cultivated, when the missing protein is compensated for by its transient ectopic expression. Finally, to create an only fusion construct, a knock-in of the respective sequences can be performed, leading to the replacement of the endogenous by the tagged product. A second approach is RNA interference (RNAi). Messenger RNAs coding for a protein can be targeted for destruction by small complementary RNAs. If they are specific for the endogenous protein, it is only this type that will be destroyed, leaving the fusion untouched.

The properties of the dyes will in the end decide if they will be appropriate for the experiment in mind. The FP fused to a protein of interest should have the ability to be expressed in a cell in sufficient quantities. It also should show a high enough brightness and photostability in order to provide for sensitivity and longevity of the experiment in mind and should not be toxic to the cell. Next, the FP should not oligomerize to prevent ambiguities in interpretation, especially when interactions are the object of study. Also, the fluorescence of the FP should be insensitive to local environmental influences that might confound quantitative data interpretation.

There are many applications of fluorescent proteins (Figure 3.A.7) [A15]. The classical use is to study the localization of a labeled protein (Figure 3.A.5). However, more advanced methods have been developed over time that involve two or more different labeled species and that allow the dynamics and turnover of proteins to be studied. If the emission spectra of two FPs are well separated, they can be used for co-localization studies with a minimum of cross-talk. If the emission spectrum of one FP overlaps the excitation spectrum of the other, the pair of them can be used in interaction studies using FRET, a non-radiative process where the energy of the donor

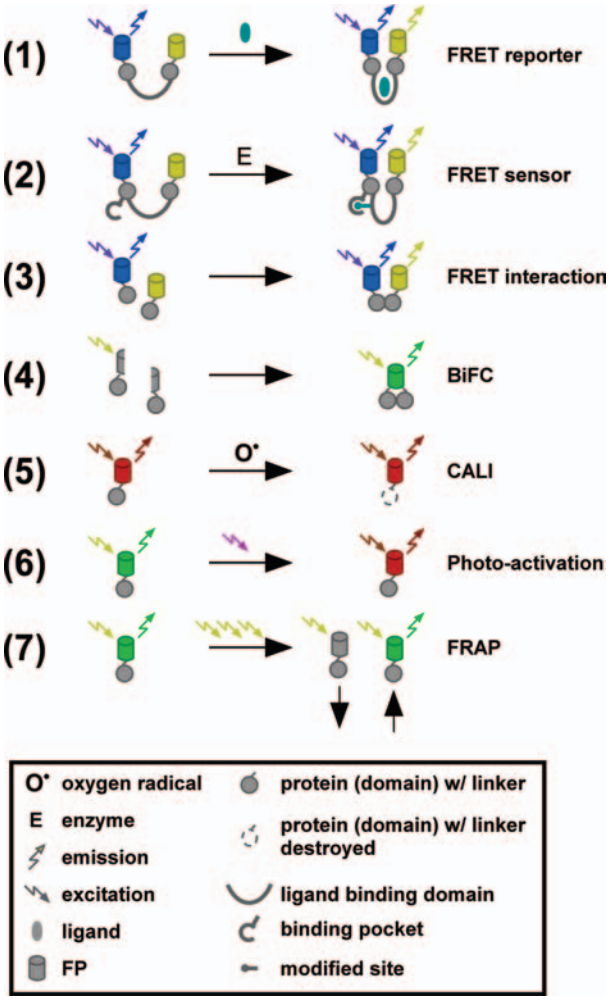

Figure 3.A.7 Advanced applications of fluorescent proteins. Conformational changes induced by binding of a ligand (1) or a modification such as phosphorylation by an enzyme (E) (2) brings the acceptor in close proximity to the donor, both of which are bound at different sites to the same protein. The acceptor fluorescence by FRET acts as a reporter or sensor on the conformation. Likewise, FRET can indicate interaction of two proteins as their conjugated donor and acceptor FP come in close proximity upon binding (3). Interaction can also be measured by bimolecular fluorescence complementation (BiFC), where two split parts of the FP attached to the two interacting partners can fold and form the chromophore when in close proximity (4). High-intensity illumination of certain FPs such as KillerRed leads to the production of oxygen radicals that can destroy the attached protein or a structure to which it binds via a process called chromophore-activated light inactivation (CALI) (5). Some FPs called optical highlighters can change their spectrum when illuminated with wavelength in the violet spectral range (6). This allows tracking of the movement of the activated versus the unchanged proteins. In FRAP, high-intensity illumination is used to bleach fluorophores at a defined site. The speed of redistribution of non-bleached fluorophores from the vicinity into the bleached area is a measure of the diffusion of these molecules.

can be transmitted on to the acceptor if both molecules are in very close proximity. If the donor is excited with its specific wavelength, an emission from the acceptor would be indicative of a very close proximity of the proteins with the two FPs attached [A19]. FRET can also be used for sensing. For example, calmodulin fused to the FRET pair CFP–YFP can be used for Ca^{2+} detection. Upon binding of calcium, calmodulin changes its conformation to allow energy transfer between CFP (donor) to YFP (acceptor) [A20]. Another way to study interactions is to provide the protein binding partners of interest with only parts of the same FP, for example, one obtains the N-terminal and the other the C-terminal end of it. On their own, both fusions are nonfluorescent as they cannot form the conjugated system necessary for fluorescence. If their attached proteins come into close proximity, however, both ends can complement each other and properly fold to restore the chromophore. If the FP can be switched, activated, or converted from one fluorescence state to the other by light induction, for example, from a dark to a bright state or between different spectral states, they can be used for turnover studies as the fate of only the switched FPs can be studied against the background of the non-switched molecules. Another use of these so-called optical highlighter proteins is in super-resolution microscopy. Here molecules are so sparsely activated that only a few at a time are visible and non-overlapping, making it possible to determine their localization precisely [A21]. FPs susceptible to rapid photobleaching can be used in a technique called fluorescence recovery after photobleaching (FRAP). A small area of the cell is bleached and the kinetics of recovery of the FP into the bleached area can be used to estimate its diffusion coefficient [A22]. Even phototoxicity can be of use for some settings. For example, KillerRed readily produces reactive oxygen species upon excitation, which in turn can wreak havoc in the vicinity of where they are produced. This opens up the possibility of locally destroying certain cellular structures or organelles if KillerRed is targeted to them [A23].

3.A.7
Indirect Labeling Strategies for *In Vivo* Studies Using Self-Labeling Protein Tags

Genetic engineering has made it possible to introduce sequences within a protein that can bind to low molecular weight compounds [A24]. Care should be taken that this so-called self-labeling tag is introduced at a site that does not interfere with protein function. Since the compound is labeled externally, it must be cell permeable and excess unbound label has to be removed for high-contrast images. Using self-labeling tags, protein expression and labeling are uncoupled and hence cannot interfere with each other.

Three types of peptide or protein tags for fluorescence labeling have been established for broader usage. The tetracysteine tag (TC-tag or Lumio tag) consists of the hexapeptide sequence Cys–Cys–X–X–Cys–Cys. It is bound specifically by biarsenic fluorophores CHoXAsH, FlAsH (fluorescent arsenical helix binder) and ReAsH (resorufin arsenical helix binder) that emit in different spectral windows (Figure 3.A.3) [A20]. In the reaction, the labeling reagents increase dramatically in their fluorescence. However,

the reagents can bind as well to analogous sequences with two closely spaced Cys residues, making background levels higher compared with the use of FPs. Also, arsenic compounds can be toxic to cells exposed to them for long periods and antidotes have to be delivered simultaneously. In addition, the labeling reagent binds the cysteines only in their reduced state and hence the labeling efficiency is affected by the pH.

Other tags are derived from enzymes and hence are relative large in size [A25]. The HaloTag, for example, a derivative of a dehalogenase enzyme, has a molecular weight of 33 kDa. A variety of HaloTag labeling reagents are available, including two fluorescent labels based on fluorescein and tetramethylrhodamine, and also a biotin-derivative. The SNAP-tag, on the other hand, is a derivative of human protein alkylguanine-DNA-alkyltransferase (AGT) 20 kDa in size, which reacts with a variety of substrates that can deliver a dye.

3.A.8 Prospects

FPs have made a major impact on the analysis of molecular dynamics, localization, and behavior *in situ*. There certainly are needs for brighter, more photostable and redder shifted variants and efforts will be made to close that gap. Tailoring the properties of FPs will doubtless expand their usage in new and evolving technologies such as super-resolution and photosensitizing [A23]. If an adverse effect on the proper function is introduced by the relatively huge FP tags, resorting to small-sized tags such as the TC-tag or even organic dyes might be beneficial [A8]. One exciting avenue is the incorporation of optical switches and triggers into proteins to render them amenable to photomanipulation [A26]. Optogenetics is another emerging field where light is used to modulate specific responses [A27]. As fluorescence techniques ensure high spatial and temporal resolution and demonstrate their compatibility with live cells and organisms by being nondestructive, they will continue to be an important tool in the analysis of protein dynamics and networks in the future.

Acknowledgments

The authors thank Julia Sellin, University of Osnabrück, Germany, for the *Drosophila* sample, Peter Hemmerich, Fritz Lipman Institute for Age Research, Jena, Germany, for the HepG2 cell line and transfections; and Monika Marx, Carl Zeiss MicroImaging GmbH, Jena, Germany, for preparing images.

Appendix References

A1 Lock, J.G. and Stromblad, S. (2010) Systems microscopy: an emerging strategy for the life sciences. *Exp. Cell Res.*, 316 (8), 1438–1444; 1438.

A2 Lippincott-Schwartz, J., Snapp, E., and Kenworthy, A. (2001) Studying protein dynamics in living cells. *Nat. Rev. Mol. Cell Biol.*, 2 (6), 444–456.

A3 Lichtman, J.W. and Conchello, J.A. (2005) Fluorescence microscopy. *Nat. Methods*, 2 (12), 910–919.

A4 Michalet, X., Kapanidis, A.N., Laurence, T., Pinaud, F., Doose, S., Pflughoefft, M., and Weiss, S. (2003) The power and prospects of fluorescence microscopies

and spectroscopies. *Annu. Rev. Biophys. Biomol. Struct.*, 32, 161–182.

A5 Yang, H. (2009) Progress in single-molecule spectroscopy in cells. *Curr. Opin. Chem. Biol.*, 14 (1), 3–9.

A6 Miyawaki, A., Sawano, A., and Kogure, T. (2003) Lighting up cells: labelling proteins with fluorophores. *Nat. Cell Biol.* (Suppl.), S1–S7.

A7 Suzuki, T., Matsuzaki, T., Hagiwara, H., Aoki, T., and Takata, K. (2007) Recent advances in fluorescent labeling techniques for fluorescence microscopy. *Acta Histochem. Cytochem.*, 40 (5), 131–137.

A8 Shaner, N.C., Steinbach, P.A., and Tsien, R.Y. (2005) A guide to choosing fluorescent proteins. *Nat. Methods*, 2 (12), 905–909.

A9 Tsien, R.Y., Ernst, L and Waggoner, A. (2006) Fluorophores for confocal miroscopy. Photophysics and Photochemistry, in *Handbook of Biological Confocal Microscopy*, 3rd edn (ed. J.B. Pawley), Springer, New York., pp. 338–352.

A10 Petit J.M., Denis-Gay, M., and Ratinaud, M.H. (1993) Assessment of fluorochromes for cellular structure and function studies by flow cytometry. *Biol. Cell*, 78 (1–2), 1–13.

A11 Haugland, R.P. (2005) *The Handbook – A Guide to Fluorescent Probes and Labelling Technologies*, 10th edn, Molecular Probes, Eugene, OR.

A12 Johnson, I. (1998) Fluorescent probes for living cells. *Histochem. J.*, 30 (3), 123–140.

A13 Neto, B.A. and Lapis, A.A. (2009) Recent developments in the chemistry of deoxyribonucleic acid (DNA) intercalators: principles, design, synthesis, applications and trends. *Molecules*, 14 (5), 1725–1746.

A14 Sasse, J. and Gallagher, S.R. (2003) Staining proteins in gels, in *Current Protocols in Molecular Biology*, Wiley Interscience, (eds. F.M. Ausubel, R. Brent, R.E. Kingston, D.D. Moore, J.G. Seidman, J.A. Smith and K. Struhl), New York, pp. 10.6.1–10.6.25.

A15 Giepmans, B.N., Adams, S.R., Ellisman, M.H., and Tsien, R.Y. (2006) The fluorescent toolbox for assessing protein location and function. *Science*, 312 (5771), 217–224.

A16 McNamara, G., Gupta, A., Reynaert, J., Coates, T.D., and Boswell, C. (2006) Spectral imaging microscopy web sites and data. *Cytometry A*, 69 (8), 863–871.

A17 Smith, A.M., Duan, H., Mohs, A.M., and Nie, S. (2008) Bioconjugated quantum dots for *in vivo* molecular and cellular imaging. *Adv. Drug Deliv. Rev.*, 60 (11), 1226–1240.

A18 Verkhusha, V.V. and Lukyanov, K.A. (2004) The molecular properties and applications of anthozoa fluorescent proteins and chromoproteins. *Nat. Biotechnol.*, 22 (3), 289–296.

A19 Miyawaki, A. (2003) Visualization of the spatial and temporal dynamics of intracellular signaling. *Dev. Cell*, 4 (3), 295–305.

A20 Zhang, J., Campbell, R.E., Ting, A.Y., and Tsien, R.Y. (2002) Creating new fluorescent probes for cell biology. *Nat. Rev. Mol. Cell Biol.*, 3 (12), 906–918.

A21 Lukyanov, K.A., Chudakov, D.M., Lukyanov, S., and Verkhusha, V.V. (2005) Innovation: photoactivatable fluorescent proteins. *Nat. Rev. Mol. Cell Biol.*, 6 (11), 885–891.

A22 Lippincott-Schwartz, J., Altan-Bonnet, N., and Patterson, G.H. (2003) Photobleaching and photoactivation: following protein dynamics in living cells. *Nat. Cell Biol.* (Suppl.), S7–S14.

A23 Remington, S.J. (2006) Fluorescent proteins: maturation, photochemistry and photophysics. *Curr. Opin. Struct. Biol.*, 16 (6), 714–721.

A24 Chattopadhaya, S., Abu Bakar, F.B., and Yao, S.Q. (2009) Expanding the chemical biologist's tool kit: chemical labelling strategies and its applications. *Curr. Med. Chem.*, 16 (34), 4527–4543.

A25 Eisenstein, M. (2006) Helping cells to tell a colorful tale. *Nat. Methods*, 3 (8), 647–655.

A26 Gorostiza, P. and Isacoff, E. (2007) Optical switches and triggers for the manipulation of ion channels and pores. *Mol. Biosyst.*, 3 (10), 686–704.

A27 Zhang, F., Aravanis, A.M., Adamantidis, A., de Lecea, L., and Deisseroth, K. (2007) Circuit-breakers: optical technologies for probing neural signals and systems. *Nat. Rev. Neurosci.*, 8 (8), 577–581.

4
Light Sources

Rainer Riesenberg and Andreas Wutting

4.1
Introduction

Radiation emitted by light sources can be characterized by its spectral properties, spatial power density, power per unit area, solid angle (radiance), spatial homogeneity, polarization properties, coherence properties, and the reproducibility of all this, to name only a few. These properties depend on the process in which the light is generated and also any subsequent influence by light propagation, light–matter interaction, and so on.

To cope with this situation, the first part of this chapter reviews some of the most important properties of light, and the second part addresses fundamental principles of light generation and the corresponding light sources and devices. We only consider artificial light sources and many source types and aspects can be treated only briefly, otherwise this chapter would require a whole book volume. The main attention is directed to the application relevance in chemistry, biology, and medicine. For more detailed information, we recommend specialized technical literature and for specific construction forms and designs of light sources we recommend consulting manufacturers' catalogues and Internet sites.

4.2
Brief Review of Light Properties

4.2.1
Spectrum

Light as an electromagnetic phenomenon propagates through space as a transversal, polarized wave. In addition to the polarization properties described later in this chapter, light is particularly characterized by its wavelength or, in the case of non-monochromatic light, by the composition of components with different wavelengths.

At not too high irradiance levels, most materials respond linearly to incident light, allowing the light–material interaction to be considered separately for each

Handbook of Biophotonics. Vol.1: Basics and Techniques, First Edition.
Edited by Jürgen Popp, Valery V. Tuchin, Arthur Chiou, and Stefan H. Heinemann.

wavelength. As a consequence, it is possible to define material properties such as refractive index, absorption, birefringence, and so on as a function of the wavelength and it becomes useful to characterize non-monochromatic light by its spectrum, that is, the above-mentioned composition of monochromatic light components with different wavelengths.

Light–matter interactions will then influence the shape of the spectrum, allowing information to be deduced about the material. If this happens through a linear physical process (i.e., one that responds linearly to the field amplitude of the light), the light source must deliver sufficient intensity throughout the spectral range of interest and its spectrum must be known well and should be stable. Examples of measurement approaches using such linear processes are absorption spectrometry and spectrally resolved reflectometry. In nonlinear processes due to the amplitude, such as Raman scattering or fluorescence, energy is transferred between different wavelengths and it is often advantageous or even necessary to irradiate a sample only with monochromatic light of a known single wavelength or a specific combination of several monochromatic contributions.

The range of all wavelengths is coarsely subdivided into several main ranges, as shown in Figure 4.1. The visible (VIS) spectral range of light lies between a minimum wavelength of about 400 nm and a maximum wavelength of about 750–800 nm (depending on the conditions), corresponding to oscillation frequencies between 7.5×10^{14} and 3.7×10^{14} Hz. To longer wavelengths and lower oscillation frequencies, the spectrum extends into the infrared (IR), terahertz, microwave, and radio-frequency ranges, whereas to shorter wavelengths it extends into the ultraviolet (UV), extreme ultraviolet (EUV, XUV), X-ray and gamma-ray ranges. For biological applications usually only the UV, VIS, and near-infrared (NIR) to mid-infrared (MIR) regions will be of interest.

It should be noted that exactly monochromatic waves are a purely theoretical construct, since they would require an infinite duration of the wave train. Every temporal restriction, that is, pulsing, of such an exactly monochromatic wave corresponds to a mixture of several infinite waves with slightly different wavelengths and thus to an effective spectral broadening. For pulse durations in the range of

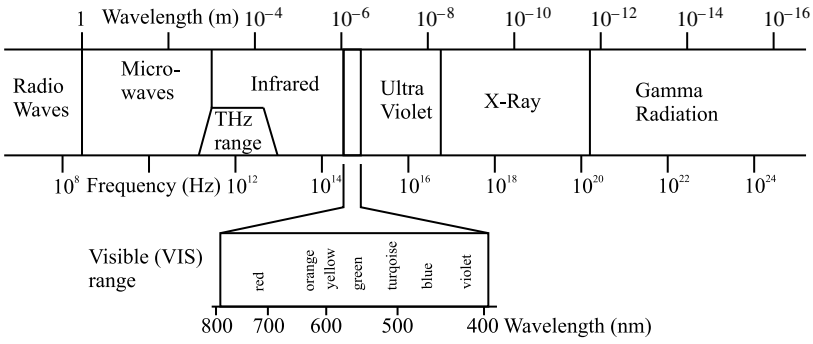

Figure 4.1 The wavelength ranges of electromagnetic radiation.

nanoseconds or longer, this spectral broadening can usually be ignored, but for shorter pulse durations it increases significantly and for pulse durations in the femtosecond range it comes into the order of the wavelength itself.

4.2.2
Radiometric Properties and Beam Parameter Product

The basic radiometric property to which all other properties can be traced back is the so-called optical flux ϕ, which effectively is a power and can be measured in watts. The flux describes, for instance, the optical power emitted by a light source or entering an aperture or optical system. In a next step, the total flux can be related to an area, a wavelength range, a solid angle, or any combination of them, leading to seven more radiometric properties, which are listed in Table 4.1.

In addition to the flux, as the second basic radiometric property, sometimes the optical energy Q is of interest, which simply describes the integral of the flux over a certain time interval and can therefore be used to describe light pulses or results of an integration process in a measurement. According to the flux itself, seven more radiometric properties can be defined by relating Q to an area, wavelength range, or solid angle. Not considered here are the so-called photometric properties, which are very similar to the radiometric properties, but related to the spectral sensitivity of the human eye.

Light originating from different light sources can be focused on a sample with different efficiencies, depending on the light generation process and the actual physical conditions in this process. Depending on the light source, either the radiance or the flux [1] or their respective spectral counterparts are best suited to characterize the "intensity" (in its loose meaning) of the light source.

Table 4.1 Overview of radiometric properties of optical radiation.

Name/symbol	Description	Typical unit
(Radiant) flux ϕ	Total optical power	W
Non-spectral properties		
(Radiant) intensity I	Flux per unit solid angle in a given direction	W sr^{-1}
Irradiance E	Flux per unit area at a given surface element;	W cm^{-2}
(also radiant exitance)	For sources the term "radiant exitance" is used	
Radiance L	Flux per unit solid angle in a given direction and projected unit area	W sr^{-1} cm^{-2}
Spectral properties		
Spectral flux ϕ_λ	Flux per unit wavelength at a given wavelength	W nm^{-1}
Spectral intensity I_λ	Intensity per unit wavelength	W sr^{-1} nm^{-1}
Spectral irradiance E_λ	Irradiance (exitance) per unit wavelength	W nm^{-2} nm^{-1}
(also spectral exitance)		
Spectral radiance L_λ	Radiance per unit wavelength	W nm^{-2} nm^{-1} sr^{-1}

4.2.2.1 Diffuse Sources

When considering the irradiance at a detector or sample to be maximized, the radiance or spectral radiance is the essential parameter of a diffuse source, because there exists no passive, linear optical system that could increase the irradiance above the value observed at the surface of a completely diffuse radiator, often referred to as Lambertian radiator. For such radiators the radiance and irradiance (radiant exitance) directly at the surface become identical up to a factor of π, that is,

$$E_{\text{Source}}(\lambda) = \pi L_{\text{Source}}(\lambda). \tag{4.1}$$

The radiance itself is constant in optical systems without diffusers or absorbers and otherwise can only decrease. A passive optical system violating this observation would also violate the second law of thermodynamics.

The change of the irradiance in an optical system is furthermore closely related to the spatial coherence properties of the light, which are discussed below. At the surface of a completely diffuse radiator, the spatial coherence of the radiation has a minimal value. Increasing the spatial coherence (and thus making the light focusable) always requires a corresponding reduction of the irradiance (by reducing the solid angle at constant radiance), and vice versa, focusing of diffuse radiation increases the solid angle and reduces the spatial coherence. At a constant irradiance, the spatial coherence in an optical system can only be decreased, for instance by a diffuser which diffuses the light in a non-recoverable way, or for constant spatial coherence the radiance and irradiance can only be decreased, for instance by an absorber. Summarizing, if a sample is to be examined using a diffuse light source, the maximally achievable irradiance at a target surface, for example, the sample or the detector, is given by

$$E_{\text{Target}}(\lambda) \leq \frac{\pi L_{\text{Source}}(\lambda)}{1 + \cot^2\alpha} \tag{4.2}$$

where α is the half-angle under which the target is illuminated (Figure 4.2).

In a similar manner, the irradiance at a (perfectly) diffusely scattering sample or optical element limits the maximal irradiance in all subsequent parts of the optical

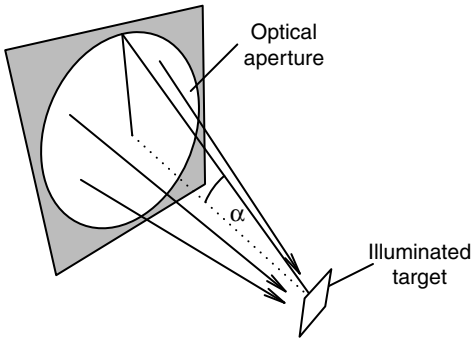

Figure 4.2 The maximal irradiance that can be achieved at an illuminated target surface depends on the radiance and the angle under which the target is illuminated by the optical system.

system, even if the sample is illuminated with a nondiffuse light source. In such cases, the scattering surface has to be considered as a new light source whose irradiance determines the radiance in the subsequent parts of the optical system. Thus, if low irradiance at the final detector is a problem, one should aim for the best possible focusing at the sample.

4.2.2.2 Nondiffuse Sources

If a nondiffusely radiating light source such as a laser is used in a measurement system, often the (spectral) flux is better suited to describe the intensity of the light, since in principle it can be focused down to the diffraction limit. This is exactly possible if the source emits a single, fixed, and known spatial radiation mode and the subsequent optics are matched to that mode. The term "mode" here denotes only a radiation distribution with a fixed amplitude and phase relation between all its points and with a single, fixed wavelength. If there is a small number of additional modes, the properties of the light can be described appropriately by the flux and an additional parameter M^2 describing the mode quality, in terms of the focusability of the light. A value of $M^2 = 1$ is perfect; single-mode lasers typically have values better than 1.3 and multimode lasers can have values in the range of hundreds to thousands. For higher numbers of spatial modes, the source must again be considered as a diffuse radiator with a certain radiance.

With the M^2 parameter, it is possible to define the so-called beam parameter product (BPP), which relates the radius w_0 of a focused spot to the half opening angle φ of the convergent beam:

$$\mathrm{BPP} = \varphi w_0 = M^2(\lambda/\pi). \tag{4.3}$$

M^2 thus describes the broadening of the spot compared with a (Gaussian or Airy) single-mode spot. For a nearly diffraction-limited spot with a small M^2 parameter and the definitions made in Figure 4.2, the effective peak irradiance in the center of the Airy diffraction disk is given by

$$E_{\mathrm{Peak}} = \phi \cdot \frac{\tan^2\alpha}{2\lambda^2 M^4}. \tag{4.4}$$

4.2.3 Coherence

Coherence is the ability of a light field to show interference effects between different spatial points at the same time (spatial coherence), between different time points at the same spatial position (temporal coherence), or a mixture of both (spatio-temporal coherence). Interference effects in turn are effects where the time-averaged flux or radiance of the sum of two or more light fields differs from the sum of their individual fluxes or radiances, that is, there occurs mutual enhancement or suppression of the intensities.

For the most general case of spatio-temporal coherence, the coherence can be described by a four-dimensional function with a large number of degrees of freedom.

So, for instance, the coherence function at the entrance pupil of a camera contains the whole (colored) image information of the scene which is imaged by that camera. This is in spite of the fact that the camera pupil itself is practically homogeneously illuminated by the scene, when only the intensity of the light is considered. The camera optics here undertake the task of a computer, which reconstructs the information contained in the coherence function into an image by bringing different points of the entrance pupil to interference in the detector plane with a certain relative temporal delay.

From this example, it should be clear that also the coherence properties of a single light source cannot always be described analytically and that it will often be necessary to resort to simplifying models. On the other hand, manipulation of the coherence function of a light source can also be used to achieve particular effects. In the following, some basic aspects of temporal and spatial coherence are discussed.

4.2.3.1 Temporal Coherence

The temporal (self-) coherence function of a light source, that is, the autocorrelation of the field strength over time, is equal to the normalized Fourier transform of the spectrum of the light source. The narrower the spectrum of the light source, the larger is its coherence length. This dependence is known as the Wiener–Khinchin theorem. For a nearly Gaussian spectral intensity distribution with an FWHM (full width at half-maximum) of $\Delta\lambda$ around a center wavelength λ, the coherence length is given by

$$L_C = \frac{2\ln(2)}{\pi} \cdot \frac{\lambda^2}{\Delta\lambda}. \tag{4.5}$$

Examples of coherence functions are given in Figure 4.3. Typical coherence lengths [2, 3] range from 600 nm for sunlight or the continuum light of a short arc mercury lamp, over 300 μm to 300 mm for single lines of spectral lamps, a few meters for standard lasers, to more than 30 000 km for specially stabilized He–Ne lasers.

A large temporal coherence can turn out to be disadvantageous if the light passes multiple interfaces or surfaces of optical elements, because the parasitic reflections created at these surfaces can come to interference and create disturbing structures, which moreover are extremely sensitive to temperature changes, mechanical vibrations, or changes of the optical system, and therefore cannot be calibrated out of the measurement result. Figure 4.4 shows the difference between holographic microscopy images obtained with a strongly coherent laser light source and a short arc lamp, where a prominent line was filtered out, giving a temporal coherence length of about 15 μm (and a spatial coherence diameter of about 60 μm) [4]. For the long coherence laser, parasitic reflections at optical interfaces such as lenses or sample holder slides lead to disturbing interferences. These vanish if the coherence length is less than the distances between the optical surfaces. It can, however, still be large enough to enable coherent techniques, such as the computer-based reconstruction of the recorded holograms, to be used.

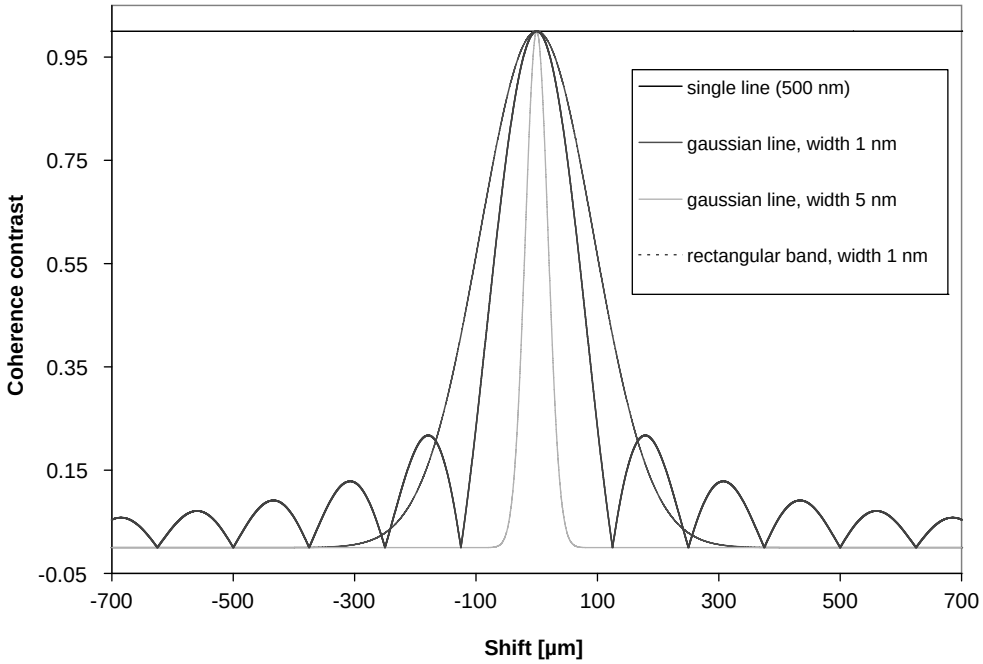

Figure 4.3 Coherence functions for different spectra. A single, monochromatic line has a constant unit coherence function. Gaussian lines (here 1 and 5 nm FWHM around a center wavelength of 500 nm) also have a Gaussian coherence function and a rectangular band spectrum leads to an abs(sinc)-shaped coherence function with a central peak and side lobes.

4.2.3.2 **Spatial Coherence**

Many light sources generate light inside a surface or volume through statistically unrelated elementary processes, for instance, thermal light sources, plasma light sources, or fluorescent dyes. As a consequence, the light emitted from different points of such sources is uncorrelated and thus mutually incoherent. This does not mean, however, that at later stages in an optical system the incoherence is preserved. Instead one of the fundamental theorems of optics, the van Cittert–Zernike theorem states that the spatial coherence of light increases as it moves away from the source. For the degree of coherence between two points of a light field, it is essential how far these points are separated and under which angle (along the direction, which links the two points) the light source appears to each of them. Roughly, the mutual coherence increases with a lower apparent angle of the source and with a shorter distance between the points. Particularly for a circular light source, the distance d_c between two points at which the first minimum of the mutual coherence occurs is given by

$$d_c \approx 1.22 \cdot \frac{\lambda}{\sin \alpha} \tag{4.6}$$

where α is the half-angle under which the source appears to the two points. One may note that the coherence diameter d_c is exactly the diameter of the diffraction Airy disk, and indeed the partial spatial coherence can be considered a result of diffraction-

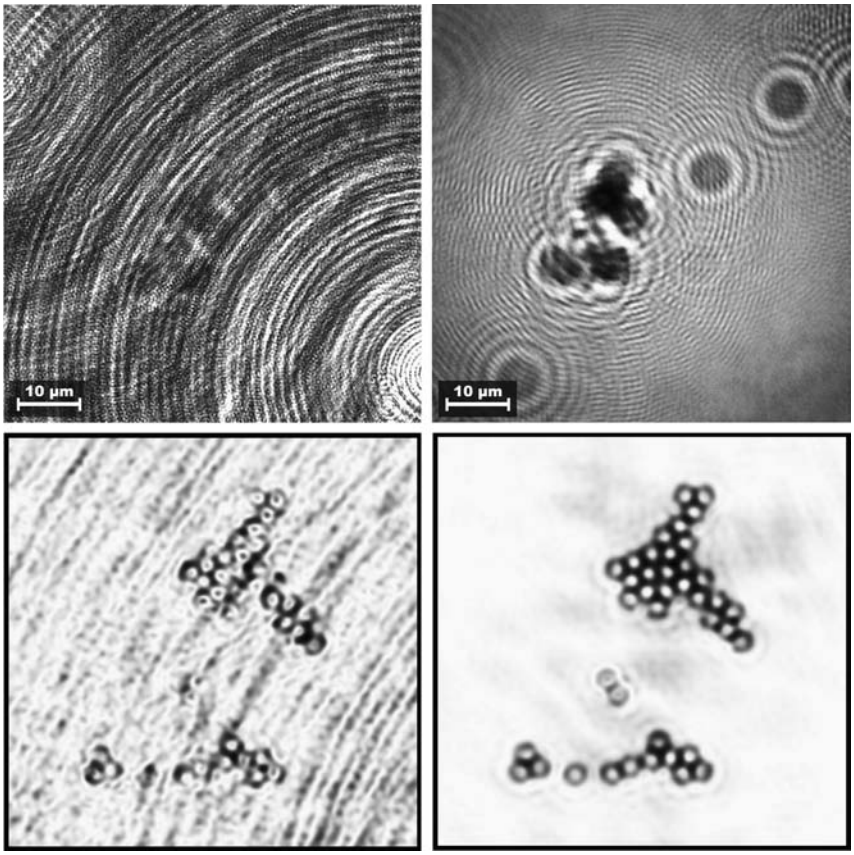

Figure 4.4 Difference between holographic microscopy recordings for high coherence and application-adapted coherence length of the light source. The top images show the holograms and the bottom images the computationally reconstructed object intensity distributions of a cluster of 1 µm polymer beads. In the left column a long coherency laser has been used, leading to parasitic interferences from optical surfaces and an accordingly low quality of the reconstruction. In the right column a light source with a coherence length of approximately 15 µm has been used. Parasitic interferences are efficiently suppressed, but the numerical reconstruction still works well, although the method requires coherent light.

caused broadening of incoherently illuminated points in the plane of the measurement, that is, the light field can be viewed as a superposition of extended, but mutually incoherent diffraction figures, such as the Airy disk in the case of a round source. Accordingly, it is even possible to set up an equation for the propagation of the coherence function that closely resembles the propagation equation for a fully coherent light field. This would, however, go far beyond the scope of this book. The only important thing here is the fact that the minimal spatial coherence diameter in any plane of an incoherently illuminated optical system – even after passing simple optical elements such as lenses – is determined by the angular shape under which the source appears to the considered point. The coherence diameter can be increased further or the coherence function can be modeled into complicated shapes by

interference optical elements or nonregular optical elements such as lens arrays, screens with multiple apertures, diffusers, and so on.

4.2.4 Polarization

Light is a transversal electromagnetic wave, that is, in isotropic media electric and magnetic components of the field are orthogonal to the propagation direction and the direction of energy transport. For plane, monochromatic electromagnetic waves, this allows two base polarization directions for the electrical field component inside the plane of the wave to be introduced (Figure 4.5). Monochromatic here means that the wave contains only a single wavelength or oscillation frequency and that the field strength of any field component varies over time proportional to a phase-shifted sine. The two base polarization directions can then be assigned individual amplitudes and a relative phase shift, to model any possible electrical polarization state of the wave. Depending on phase shift and amplitudes, linear polarization with any direction inside the wave plane, circular polarization, or general elliptical polarization results. Linear polarization in this case means that the electrical field vector oscillates only in a single direction, whereas for elliptical polarization the field vector follows the shape of an ellipse one time per oscillation period.

Matter – for instance in optical devices, examined chemicals, and so on – can respond sensitively to the polarization of the light or change it, if it has anisotropic, chiral, or inhomogeneous properties. This is the case, for instance, for several types of crystals (birefringence), materials under mechanical stress (stress birefringence), certain materials in a magnetic field (Faraday effect), chiral organic molecules, colloidal structures, and many more. Also, light scattering processes or non-perpendicular passing of optical surfaces usually influence polarization properties. In sensitive or quantitative measurements, this can lead to measurement errors, which are often hard to avoid. The strong polarization sensitivity of some scattering

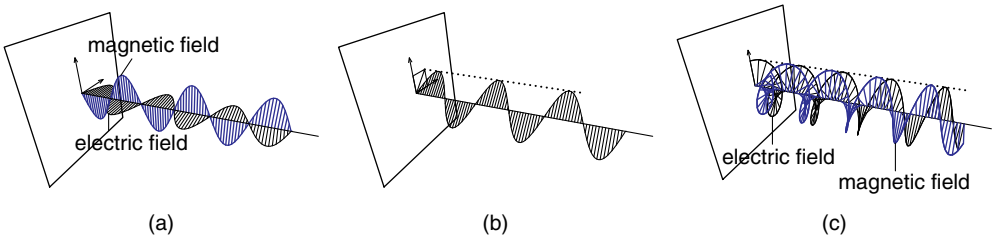

Figure 4.5 Polarization of light. (a) Monochromatic, linearly polarized light shows a sinusoidal electrical field strength which varies along one direction when the time or propagation position coordinate is changed. The magnetic field vector varies proportionally to the electric field vector, but is perpendicular to it. (b) A linear wave with an electric field vector varying along a direction between the coordinate axes can be described as a linear superposition of two waves varying along the coordinate axes and having a zero phase difference between each other. (c) If the phase difference in the latter example becomes non-zero, an elliptical or circular wave will result.

processes furthermore leads to severely nonrotationally symmetric angle distributions of the scattered light, if the illumination is done with linearly polarized light. This can reduce or increase the efficiency of light collection when the detector is oriented at an angle to the illumination, and therefore has to be carefully considered in system designs, which use such setups for the optical examination of samples. An example could be a Raman spectrometry setup where the sample is illuminated from the side by a laser and a centrally placed microscope lens collects the scattered light. The dependence between polarization of incident light and Raman scattered light is given by the so-called Raman scattering tensor, which depends on the incident and scattered wavelengths, the scattering material, and its orientation in case of an anisotropic material. Also, the Rayleigh scattering, that is, elastic scattering of the incident radiation without a wavelength shift, leads to a spatially varying distribution of the scattered light, which can be used, for instance, to suppress this normally unwanted contribution of the signal.

When spectral properties, directional distribution, and polarization properties including relative phase information are put together, a classical light field can be described completely by a three-dimensional vector function (polarization amplitudes + relative phase) of three parameters (wavelength + two angles for the propagation direction or alternatively a three-dimensional wavenumber vector). Between the vacuum wavenumber vector $\vec{k}$ (Figure 4.6), the vacuum wavelength λ, the oscillation frequency ν, and the tilt angles with respect to the x- and y-axes, α and β, the following relations exist:

$$\lambda = 2\pi/\|\vec{k}\| \tag{4.7}$$

$$2\pi\nu = c \cdot \|\vec{k}\| \tag{4.8}$$

$$kx = \|\vec{k}\| \sin\alpha \tag{4.9}$$

$$k_y = \|\vec{k}\| \sin\beta. \tag{4.10}$$

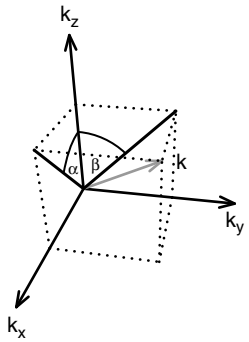

Figure 4.6 The wavenumber vector and the propagation angles.

4.3
Light Generation and Light Sources

4.3.1
Processes of Light Generation

4.3.1.1 General Emission Processes

In most cases light is generated when an electrically charged particle or particle system changes from a state of higher energy to one of lower energy. The energy difference then will be equal to the energy of the emitted radiation plus eventually generated mechanical energy (heat). Exceptions to this fundamental type of light generation are direct particle reactions such as the radiant annihilation of an electron–positron pair or nonlinear processes such as the decay of one photon into a multitude of photons with the same total energy inside a nonlinear optical material.

The usual light sources for practical applications are nearly always based on the transition of an electron system from a state of higher energy to one of lower energy. Inside this class of light sources, one often finds a strict subdivision into thermal and nonthermal light sources. However, the main difference between these two groups is simply the fact that the population of states of higher energy in a thermal light source is driven only by temperature effects near a thermal equilibrium state, whereas nonthermal light sources usually use more direct mechanisms for populating the higher states.

The thermal activation in a thermal light source has the consequence that at any wavelength the spectral radiance of the light source cannot be larger than the value given by Planck's blackbody radiation equation, that is,

$$L_{\text{Source}}(\lambda, T) = u(\lambda, T) \cdot \frac{2\pi hc^2}{\lambda^5 \left[\exp\left(\frac{hc}{\lambda k_B T}\right) - 1\right]} \tag{4.11}$$

where k_B is the Boltzmann constant, h is Planck's constant, c is the speed of light, and $u(\lambda, T)$ is a wavelength-, temperature-, and material-dependent emission coefficient. Typical blackbody radiation curves for the temperatures of the Sun, incandescent lamps, and halogen lamps are given in Figure 4.7 for $u = 1$. In the case of the lamps, u is, however, only about 0.5.

For pure blackbody radiation ($u = 1$), the spectral source radiance has a peak at a wavelength

$$\lambda_{\text{Peak}}(T) = b/T \tag{4.12}$$

where $b = 2.8977685 \times 10^{-3}$ m K is called Wien's displacement constant. The relation is known as Wien's displacement law. The total radiance produced by a blackbody is given by the Stefan–Boltzmann law, which states that the surface radiant exitance is given by

$$E_{\text{Source}}(T) = \sigma T^4 \tag{4.13}$$

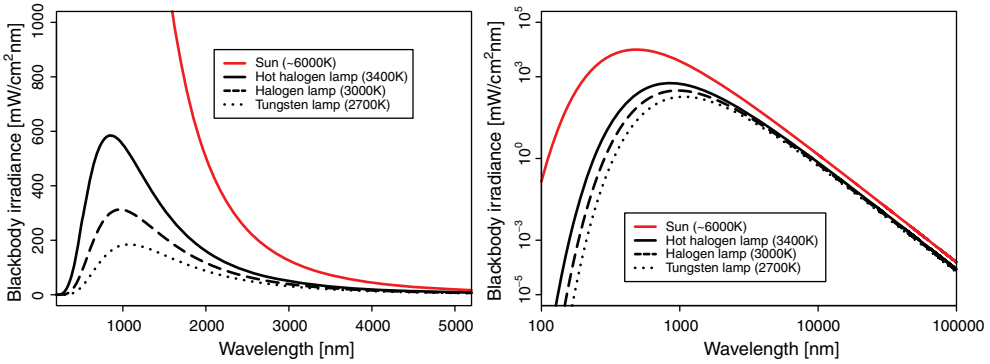

Figure 4.7 Spectral surface irradiance (exitance) distributions for thermally radiating blackbodies at different temperatures; Particularly for the tungsten and halogen lamps, the really observable surface spectral exitances will be about 50% of these values, since they are bad blackbodies with a low emission coefficient. Furthermore, the most energy is emitted in the NIR region, leading to low efficiency for illumination purposes.

with the Stefan–Boltzmann constant $\sigma = 5.670400 \times 10^{-8}\ \mathrm{W\,m^{-2}\,K^{-4}}$. Due to the freedom of the emission coefficient, the spectrum is, however, in no way limited to resembling the shape of the pure blackbody radiation with $u = 1$. This is particularly true for low-pressure, single-atom, light-emitting gases, whose thermal emission spectra practically consist only of very narrow, gas-specific emission lines. In the opposite direction, the radiating subsystem of a nonthermal light source can practically always be assigned a thermodynamic temperature, which then differs strongly, however, from the temperature of the remainder of the light source, leading to a situation where one is far away from thermal equilibrium of the total system.

Aside from thermal activation, there exist a large number of technically used excitation processes. Some of them are listed in Table 4.2.

Table 4.2 Some excitation processes and according light sources.

Excitation process	Example light sources
Thermal	Incandescent light bulb, high-pressure gas emission lamp (secondary excitation process)
Collision (mostly due to a flowing current or in a plasma)	Gas laser, gas discharge lamp
Optical excitation	Fluorescent dyes, solid-state lasers
Charge carrier injection in diodes	Light-emitting diode (LED), diode laser
Chemical reaction	Chemoluminescent substances, chemical laser
Direct acceleration of charge carriers	Synchrotron light source, X-ray tube
Other nonlinear optical processes/ inelastic scattering	Raman laser, optical parametric oscillator

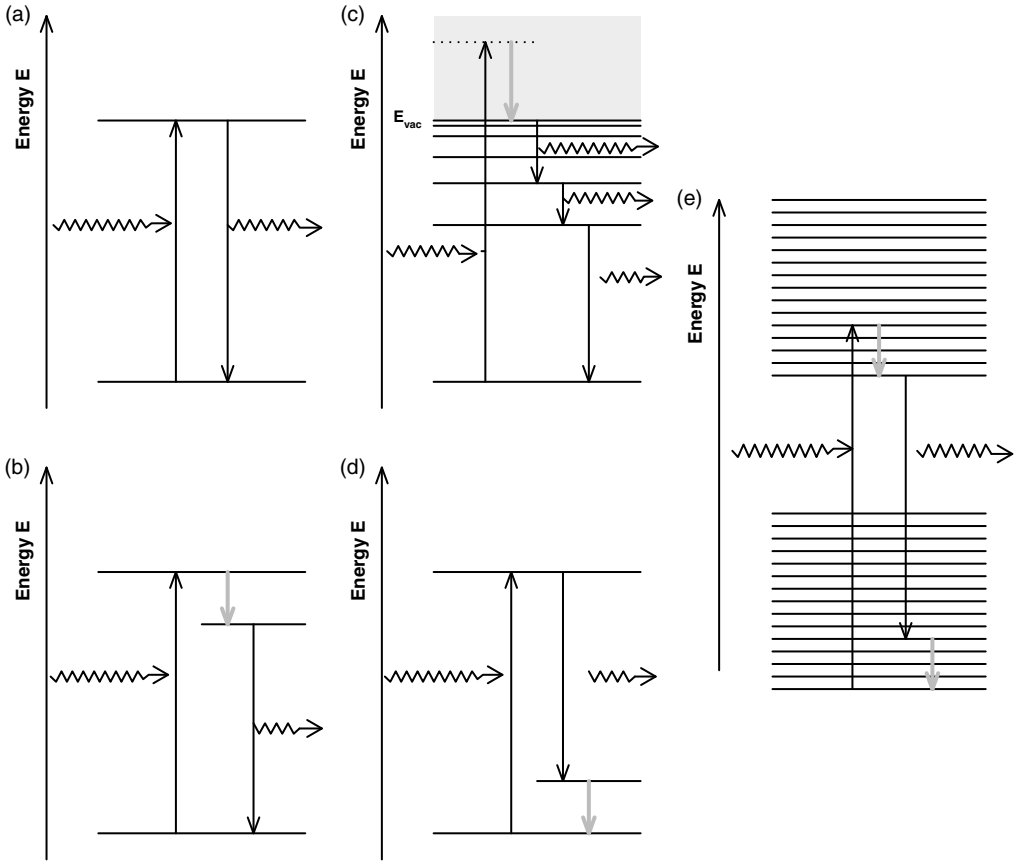

Figure 4.8 Some basic schemes of excitation and light emission. (a) Simple model of a two-level system; (b) plasma excitation and emission of a gas; (c) simple three-level system; (d) Raman Stokes scattering in a three-level system; (e) excitation and emission in a fluorescent dye molecule.

Figure 4.8 shows some examples of excitation and light emission processes that can occur in light sources. In detail, the following processes are shown:

- Simple model of a two-level system: the excitation energy and energy of the emitted photon are identical; if the system is already excited, it will be de-excited by the excitation source with the same probability as a nonexcited state will be excited.
- Plasma excitation and emission of a gas: an outer electron is excited from its bound ground level to a virtual level above vacuum energy E_{Vac}, leading to ionization. Excitation here can occur, for instance, by collision with a fast, free electron (collision ionization) or with another gas molecule. The free energy ground state is then repopulated from a vacuum state. This can occur directly or via intermediate higher energy levels, leading to the emission at different, gas-specific emission levels.

- Simple three-level system: an electron is excited to a higher energy level and then decays rapidly to a somewhat lower third level by a nonradiative decay. Such a level will eventually not be de-excited by the excitation source and can be relatively stable, leading to a low spontaneous emission and allowing laser action through stimulated emission.
- Raman Stokes scattering in a three-level system: an incident photon excites the system from the ground state and then first returns to a state above the ground state, emitting a red-shifted photon. The system later returns to the ground state in another process such as nonradiative relaxation.
- Excitation and emission in a fluorescent dye molecule: the dye molecule will normally be in or near the ground state and can be excited into one of the states of a higher band by a short-wavelength photon. Then it usually relaxes by nonradiative processes to the lower edge of the upper band, from where it can recombine to one of the levels of the lower band, emitting a photon at a longer wavelength than the exciting photon. The cycle closes with a nonradiative decay to the ground state.

4.3.1.2 **Laser Emission**

One of the most important types of light source in analytical applications is the laser, since it can produce extremely coherent, monochromatic, often strong and non-diffuse radiation, which can be focused down to or near the diffraction limit. There is a huge variety of laser types and principles and the underlying theory is considerably more complex than the theory of other light sources, since lasers are strongly nonlinear devices. We will not attempt to go into all these details but rather describe some fundamental properties of lasers. For those interested in a deeper understanding we recommend reading the textbook by Svelto [5]. This section on laser principles is given before the sections on individual types of light sources, since many of these light source types can be modified to operate as lasers. Instead of discussing these sources twice, we will include the laser aspects in their general discussion. For instance, lasers are available based on light-emitting diodes (LEDs), low-pressure gas discharge, hollow-cathode emission, fluorescent dyes, fluorescence in solids, Raman processes, optical down-conversion in nonlinear materials, and chemoluminescence, to name just a few. The important difference between the non-laser and the laser light sources is that in the latter the stimulated emission is made the dominant light generation mechanism by appropriate arrangements. The term "laser" accordingly means "light amplification by stimulated emission of radiation." The characteristic features of a laser are a medium that can emit light through a stimulated emission process (an optical amplifier) and a means for feedback of part of the generated light (Figure 4.9). There are also a few devices that do not need the feedback unit, since their amplification is large enough to permit laser-like action without it. Such devices are called superlasers or superluminescent sources.

Stimulated emission can occur when a photon hits a quantum mechanical system in an excited state, there is a lower, free state which can be reached in a radiating transition, and the energy difference between this state and the current state of the system corresponds to the wavelength of the photon. The quantum mechanical

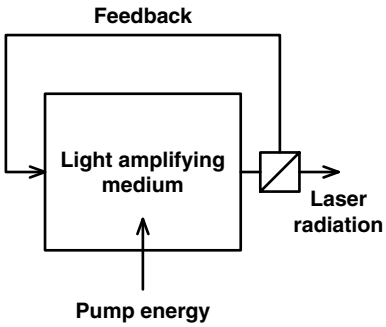

Figure 4.9 Basic principle of a laser. A medium capable of amplifying light by a stimulated emission process is pumped, that is, excited into a higher energy state with inversion. From there, it can return to the ground state by spontaneous or stimulated emission. A feedback unit directs a part of the emitted light back into the medium. The combination of an amplifier and a feedback unit makes the arrangement strongly nonlinear and works as an optical oscillator. If the spontaneous decay rate is low enough and the fraction of the fed back light is large enough, stimulated emission will become dominant, creating a strong, coherent emission.

system can be, for instance, an excited atom or molecule or a more complex system. In the following we will simply speak of an atom, keeping in mind the other possibilities. If the above-mentioned conditions are met, then there is a certain probability P_1 that the incident photon de-excites the atom and generates a second photon, which then will have exactly the same phase, polarization, and wavelength as the incident photon. To achieve a high ratio between stimulated and spontaneous emission, the initial higher energy state should be metastable, that is, have a low spontaneous decay rate, no matter whether the decay corresponds to the laser transition or another transition. Furthermore, if the atom is in the lower state, the incident photon will excite it with the same probability P_1 into the higher state. Hence, to achieve a net amplification, more atoms have to be in the higher state than in the lower state, which is called an inversion.

To achieve this inversion, the higher state of the laser transitions has to be populated to a high fraction of the atoms. Populating a higher state is possible by collision effects or semiconductor charge injection, but also by direct optical pumping from the ground state. However, then the pumping photons would also lead to stimulated emission from the higher state to the ground state, limiting the population of the upper state to below 50% and avoiding inversion. In a more advantageous scheme, the pumping will thus not be done directly from the ground state to the upper laser state, but to a higher, intermediate state, which quickly decays to the upper laser state, so that the pumping radiation will not stimulate a transition to the ground state. This scheme corresponds to the three-level system shown in Figure 4.8c. The drawback of this simple system is that the laser radiation, which can cause stimulated emission from the upper to the lower laser level, can also be absorbed by the laser transition, if many atoms are in the lower state of the laser transition. Since this lower level is the ground state, the population density will be

high, particularly when the stimulating field is strong, leading to reduced amplification efficiency due to re-absorption.

Another, but exotic, possibility to achieve inversion is to have a lower state of the laser transition, which is sparsely populated, and to populate the upper state to a higher degree. Here, the lower state of the laser transition has to be somewhat higher than the ground state and should rapidly decay to it. As a result, the population density of that state will be low. Hence again this results in a three-level system, but this time the excitation and emission form a Raman-like process, as shown in Figure 4.8d. One drawback here is that atoms which have already been pumped to the higher laser state can be de-excited by the pump radiation, which again limits the efficiency of the process. Moreover, the pump transition will normally lead to a rapid decay from the upper state, circumventing the laser transition and mainly yielding Rayleigh scattering in the amplifier material. The most advantageous laser schemes thus have at least four levels, as shown in Figure 4.10.

Such a system combines the two advantageous aspects of the previously discussed three-level systems and avoids their drawbacks. In contrast, as described above, an optically pumped pure two-level system will combine the drawbacks of the two types of three-level system in such a way that it becomes impossible to achieve inversion. If the pumping is done through another mechanism, some types of two-level systems can also achieve inversion.

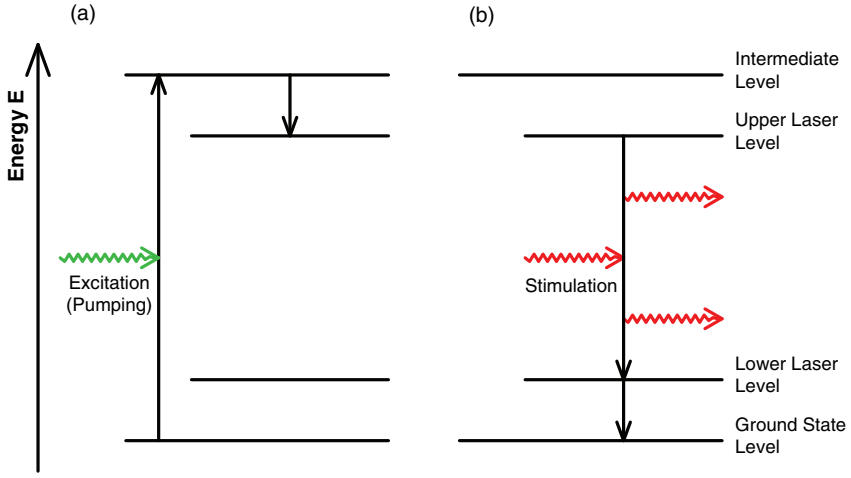

Figure 4.10 Stimulated emission with the example of a four-level system as one of a number of possible stimulated emission schemes for lasers. In a first step, an upper laser level is populated by a pumping process, usually via an intermediate level. An incident photon with an energy corresponding to the laser transition can stimulate the transition, leading to the emission of a second photon. The latter will have the same properties as the stimulating photon, that is, exactly share its wavelength, polarization, and propagation direction. Instead of an upper intermediate level, there is often a broader so-called pump band, which allows optical pumping with a broader spectral bandwidth of the pump radiation.

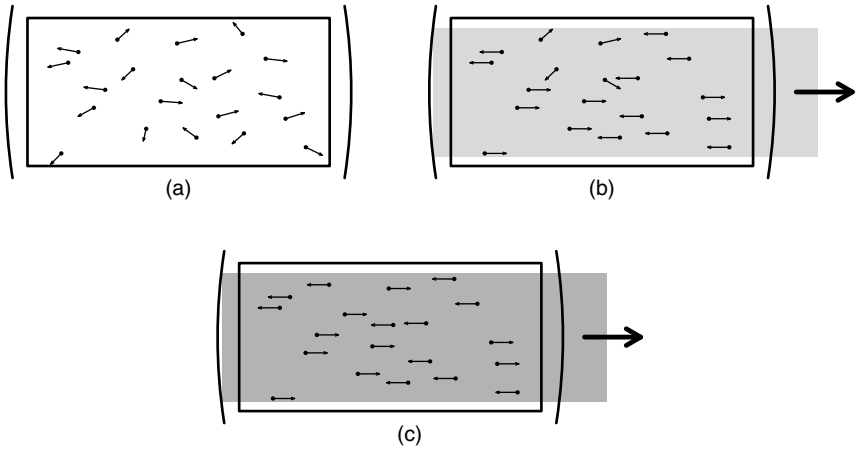

Figure 4.11 Build-up of a laser process; In the example a laser medium between two mirrors, one fully reflecting and one partially transparent, is shown. The mirrors form the feedback unit and act as a Fabry–Pérot resonator. (a) Directly after pumping, the medium starts to emit radiation randomly by spontaneous emission. Only photons reflected by one of the mirrors will re-enter the laser medium. (b) Photons, which re-entered the laser medium after reflection can stimulate further excited atoms or molecules in the laser medium, transferring their own wavelength and phase to the newly emitted photons. Due to the Huygens principle, a field starts to build up with a directional distribution and wavelength spectrum dictated by the mirrors. (c) After several rounds between the mirrors, the field becomes so strong, that practically all still excited atoms or molecules will emit their energy by stimulated emission. Since different wavelength and spatial modes of propagation are partially competing with each other, one or a few modes will win over others.

If inversion is achieved and feedback is established, laser emission can build up. Figure 4.11 shows the build-up of a laser process for a laser medium in a Fabry–Pérot cavity, consisting of two mirrors. Initially starting with spontaneous emission, the cavity will select certain propagation modes and wavelengths which can build a stable field. Since the stimulated emission amplifies a present field, the medium will emit an increasing fraction of its stored energy into this field. The cavity acts as a resonator, which is dedamped by the laser medium, turning the arrangement into an optical oscillator which can have a high Q factor and an accordingly small bandwidth. An oscillation, that is, a laser activity will take place if the losses after one round trip through the laser cavity (including the losses of the light exiting the cavity) are smaller than the inverse amplification factor, which is caused by the active medium during one round trip. As a second condition, the light field has to be stable, that is, reproduce its shape and phase after one round trip, otherwise the fields resulting after different round trips would interfere destructively. Due to the latter condition, the field in the cavity and in any optical oscillator can be decomposed into several discrete modes of different spatial distribution and/or wavelength.

Depending on the amplification properties of the laser medium, these modes may be amplified by the same excited atoms or by different subgroups of them. In the first case, the mode which best fits to the cavity and the amplification properties will

stimulate most of the excited atoms, thereby suppressing the other modes. This is called a mode competition. After a short time, only the dominant mode will survive. The best fitting mode will usually be the mode which has the largest cross-section with the laser medium and has a wavelength next to the peak amplification wavelength of the medium.

In the second case, multiple modes which are in not too strong competition with each other can survive. Such a situation can arise if the modes have a low spatial cross-section (for instance, a centered mode and a ring or "donut" mode) or if they have such different wavelengths that they will be amplified by different sub-species of the atoms. This is typical of, for instance, laser diodes. If several similarly well-fitting modes are in competition with each other, in either of the two cases a jumping between different modes – so-called mode hopping – can occur for different reasons. To achieve stable, single-mode laser emission, additional stabilization precautions will be necessary.

4.3.2
Thermal Sources

One of the best-known groups of thermal radiators for technical illumination purposes is the group of tungsten filament lamps and halogen lamps. In addition to these types of lamps, ceramic radiators and thin-layer radiators also belong to the thermal light sources. Other light sources also emit thermal radiation, such as high-pressure gas discharge lamps; however, the thermal emission there is not the main or only mechanism and these light sources will not be discussed in this section.

4.3.2.1 Tungsten Filament Lamps

Tungsten filament lamps, such as the well-known incandescent light bulb, are based on a tungsten filament as the light-emitting element. The filament is either a spiral or double-spiral wound tungsten coil or a flat ribbon, the latter giving a better defined geometry. The filament is heated by an electric current to a temperature of 2700 K to maximally 3400 K, so that it accordingly emits an approximate continuous blackbody radiation spectrum with an intensity maximum between 1080 and 730 nm. Compared with a pure Planck-type blackbody radiator, the spectral flux is reduced by the spectral emission coefficient of tungsten. For a wavelength of 200 nm and for usual working temperatures, this coefficient is about 0.5 and drops to less than 0.2 for a wavelength of 3 μm. Directly at the filament surface, the peak spectral radiance is in the order of 100–300 mW sr^{-1} cm^{-2} nm^{-1}, but particularly for the coil-type filament the distribution of radiance is inhomogeneous and the average radiance is below the value at the surface. To protect the tungsten filaments from oxygen – which would immediately react with the tungsten at high temperatures – the filament is placed inside a glass tube or bulb. In former times the latter was evacuated, but nowadays it is filled with a protective gas for different reasons. Energy losses due to convection and thermal conduction by the gas can be minimized best by using a protective gas with a high molecular weight and a low number of rotational degrees of freedom. Consequently, the noble gases xenon and krypton are used for high-quality lamps, whereas in cheaper lamps often a nitrogen–argon mixture is used.

For emission in the VIS region between 400 and 800 nm, the highest efficiencies would result for a working temperature of about 7000 K, but even tungsten, which has one of the highest melting points, melts at 3695 K. For a working temperature of 3400 K, the lifetime of the lamp shortens to a few hours, compared with about 1000 h for a temperature of 2700 K.

4.3.2.2 Halogen Lamps

Halogen lamps are a special type of tungsten lamp. Through the operation of a normal tungsten lamp, part of the tungsten filament sublimes and evaporates the wall of the glass bulb, creating a black, absorbing layer. To limit the sublimation rate, the working temperature and therefore the efficiency of the lamp have to be limited, and furthermore the glass bulb must be made sufficiently large to avoid too high absorption by the deposited tungsten layer which develops during the lamp lifetime.

In halogen lamps, the net sublimation rate and the tungsten deposition are limited by using a halogen additive in the filling gas. The sublimed tungsten reacts with the halogen and is stopped from settling down at the glass bulb. Near the filament, the tungsten halide decomposes because of the high temperature, so that the tungsten can settle back on the filament, which in this way can at least partly be regenerated. These mechanisms allow comparatively small glass bulbs to be used and the working temperature to be increased to about 3000 K to achieve a higher lamp efficiency. At the same time, the average lamp lifetime can be increased from 1000 h for a conventional tungsten lamp to about 3000 h. It is possible to operate halogen lamps up to about 3400 K, but only at the price of a drastically reduced lifetime.

4.3.3 Low-Pressure Gas Discharge Lamps

Low-pressure gas discharge lamps include a large number of construction types, filling gases, spectral properties and excitation types. All these sources have in common light generation by a radiative electron recombination or a radiative transition between different molecular excitation states in a plasma, that is, a partly ionized gas. The excitation of the gas can be accomplished by different physical processes, the most usual ones being direct excitation by a flowing current (arc lamps), capacitive excitation by a high-frequency electric alternating field, or inductive excitation by a magnetic alternating field, which generates a closed electrical current inside the plasma. The gas from which the plasma is generated is often a noble gas such as argon, neon or xenon, a metal vapor, or a mixture of both. In such a case there are no molecules in the gas and the emitted spectrum mainly consists of narrow, atomic transitions. If the lamp is filled with a molecular gas, the emitted spectra will be broader or continuous. Depending on the conditions, there are three different types of electrical discharge in a gas, of which two are used for light generation purposes, the glow discharge and the arc discharge. Figure 4.12 shows the basic dependence between the electrical voltage across and the electrical current through a gas in a strongly simplified diagram. The three types of discharge are distinguished by different currents and are separated by unstable ignition breakdown

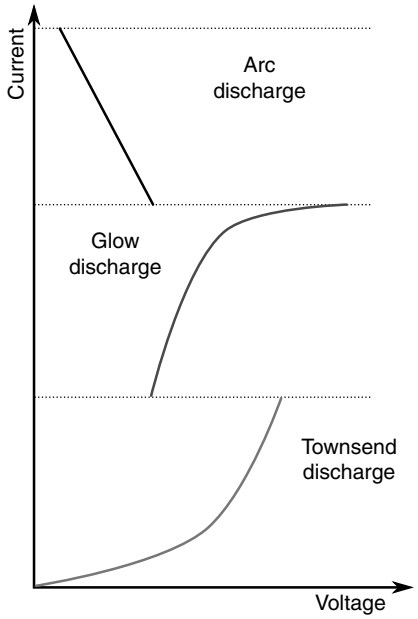

Figure 4.12 Basic discharge types in a gas. Glow discharge and arc discharge produce a plasma and can be used for lighting applications.

processes. The arc discharge furthermore has a negative differential resistance, requiring arc discharge light sources to be operated with a resistor.

4.3.3.1 Cold Cathode Fluorescent Lamps and Spectral Lamps

Cold cathode fluorescent lamps (CCFLs), sometimes also called neon lamps, consist of a glass or silica (quartz) tube with two electrodes and are filled with a (atomic) noble gas and eventually a metal vapor. A voltage applied to the electrodes leads to a glow discharge current, which excites the atoms by collision processes. Depending on the lamp type, the light emission takes place only near the cathode or at higher voltages additionally in the so-called positive column. Whereas lamps emitting only in the negative column are useful only for small indicator lamps, lamps emitting in the positive column usually give more light and can emit it nearly over the full length of the tube. Particularly for atomic gases, the emitted spectra consist of a number of lines which are very narrow and can be used for absolute wavelength calibration and also the determination of the spectral smear of spectrometers. Spectral lamps containing argon and mercury are particularly useful in the UV range, where they have a very strong emission line at 253.6 nm and further, weaker emission lines at some more wavelengths below 400 nm, which mainly originate from the mercury component. More lines occur in the VIS and NIR regions, where the latter are mainly caused by the argon component. Other lamp types and their predominant colors include pure helium (white–pink), neon (red–orange), argon (blue), krypton (white),

or xenon (violet) lamps and are – in addition to versions with mercury addition – frequently used for artistic illumination purposes and luminous advertising.

4.3.3.2 Energy-Saving Lamps

Energy-saving lamps are based on mercury arc-based lamps which are coated with a fluorescent dye or a mixture of multiple fluorescent dyes. In contrast, they usually have a heated cathode to allow electron emission at lower voltages. The dyes are optimized for efficient absorption of the dominant 253.6 nm peak of the mercury spectrum and are tailored to produce a certain color or color temperature, for instance to achieve an enjoyable room illumination or to achieve suitability for photographic purposes. However, the dye mixtures usually do not exhibit a continuous spectrum, but a spectrum with 3–6 more or less isolated emission ranges, rendering them less usable for spectroscopic purposes.

4.3.3.3 Hollow-Cathode Lamps

Similarly to spectral lamps, hollow-cathode lamps deliver spectra with a multitude of well-defined, narrow spectral emission lines. A larger variety than in the case of arc discharge lamps is possible due to a larger possible variety of emitting materials. Practically every metal and even a number of nonmetals and material combinations can be used as a characteristic material. The materials are placed in a hollow cathode inside a glass tube which is filled with an inert gas (Figure 4.13).

By applying a large voltage across the electrodes, a plasma discharge builds up in the buffer gas and the cathode material is gradually evaporated due to a sputtering process. The evaporated material is subsequently excited and ionized by collision with charge carriers and other particles in the plasma and starts to emit its own, characteristic radiation. The main application of hollow-cathode lamps is in atomic absorption spectrometry (AAS), since the light source spectra can be matched to the absorption spectra of the substances to be detected, leading to significant sensitivity increases of up to several orders of magnitude in comparison with nonspecific light sources.

The lifetime of the hollow cathode is limited by the cathode material which is available for sputtering. Since the sputtering speed is approximately proportional to the current, the lifetime is given in milliampere hours. Typical lifetimes of

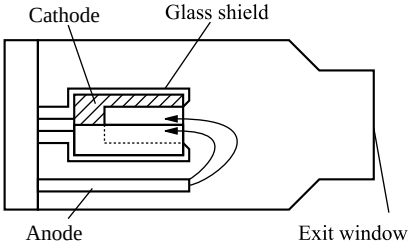

Figure 4.13 Basic layout of a hollow-cathode lamp.

commercial hollow cathode lamps are around 5000 mAh. A comprehensive overview of hollow-cathode lamps and their spectral lines is given in, for instance, [6].

4.3.3.4 Hydrogen and Deuterium Lamps

If broadband emission is required in the UV region, hydrogen and deuterium arc discharge lamps are a good choice. Of the two, the deuterium lamp provides a somewhat higher intensity. Both types can produce stable, well-characterized outputs and are therefore employed as irradiance standard sources. Although these lamps are operated at low to medium pressures, they do not deliver line spectra, but really continuous spectra. The reason for this is that the excitation and emission process is not a plain electronic one, but involves transitions between different molecular states and even dissociation of the gas molecules. The lifetime of these lamps is typically about 2000 h, but can range between 1000 and 5000 h.

4.3.4 High-Pressure Gas Discharge Lamps

High-pressure gas discharge lamps are filled with a plasma-generating gas, which at room temperature is already at or above normal pressure and will have increased pressure during operation. The gas is excited either by an incident radiofrequency radiation or alternating magnetic field (as for sulfur lamps), or by an arc discharge. Due to the high pressure there is a high probability that an excited atom will collide with another atom before it radiatively returns to the ground state. On the one hand, this causes the normally narrow spectral emission peaks of atomic gases to broaden significantly. On the other, it leads to a conversion of a large fraction of the electrically induced energy into heat of the plasma. The plasma therefore can gain higher temperatures than any solid and particularly in lamps with a very high pressure it can emit a corresponding thermal broadband radiation. Due to the high temperature, the pressure increases significantly when the lamp is in use.

4.3.4.1 Short Arc Lamps/High-Intensity Discharge (HID) Lamps

The predominant type of high-pressure gas discharge lamps are arc lamps with a short electrical arc, so-called short arc lamps. These lamps typically have a very high pressure of about 10–40 MPa (when in use) and can produce broadband radiation with extremely high radiances. The arc length typically is only a few millimeters and the most intense radiation is produced near the cathode (Figure 4.14). Depending on the lamp type, a second intense radiance maximum can exist near the anode.

Example emission spectra from one xenon and one xenon–mercury lamp with a 2 mm short arc are shown in Figure 4.15. At a distance of 50 cm from the lamps, the spectral irradiance of the xenon lamp is about one-tenth the value of the solar irradiance at sea level, except for the spectral absorption features of the atmosphere and some more narrow extra emission bands of xenon. The average spectral irradiance between 250 and 2000 nm is about 1 $\mu W\ cm^{-2}\ nm^{-1}$ and more than 50% of this irradiance originates from a region significantly smaller than 1 mm^2. Precise measurements of the spectral radiance distribution inside a xenon short arc

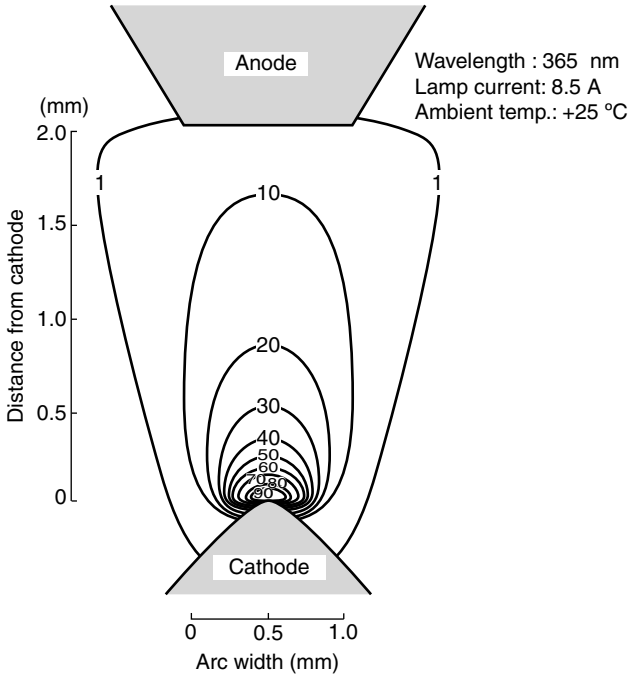

Figure 4.14 Typical cross-sectional view of the intensity distribution in the flare of a high-pressure xenon short arc lamp, here with the example of a Hamamatsu L2273. The radiance increases dramatically towards the cathode (image: Hamamatsu datasheet.)

lamp (Figure 4.16) have been performed by, for instance, Nakar *et al.* [7]. Results for measured spectral radiances in a 2 mm gap, 150 W short arc xenon lamp were presented, which show that in the brightest spot near the cathode the spectral radiance peaks at about 2 W sr^{-1} cm^{-2} nm^{-1}; for shorter wavelengths the measured values decrease because of the measurement method and would otherwise increase slightly further. Compared with peak radiances of about 90 mW sr^{-1} cm^{-2} nm^{-1} at $\lambda = 1073$ nm for a tungsten lamp operating at 2700 K or about 160 mW sr^{-1} cm^{-2} nm^{-1} at $\lambda = 966$ nm for a halogen lamp operating at 3000 K, this is a 12–22 times larger peak spectral radiance, which furthermore occurs at much shorter wavelengths.

Short arc lamps are therefore particularly well suited for creating high-intensity illumination of samples, for non-laser-based beam scanning confocal microscopy, for fluorescence excitation, for projecting brilliant images, or for illuminating objects at larger distances.

4.3.4.2 Other High-Pressure Gas Discharge Lamps

Further prominent gas discharge lamps which are not short arc lamps are the sulfur lamp and the high-pressure sodium (HPS) lamp. Both lamps are used because of their high efficiency for lighting applications and can produce high luminous fluxes

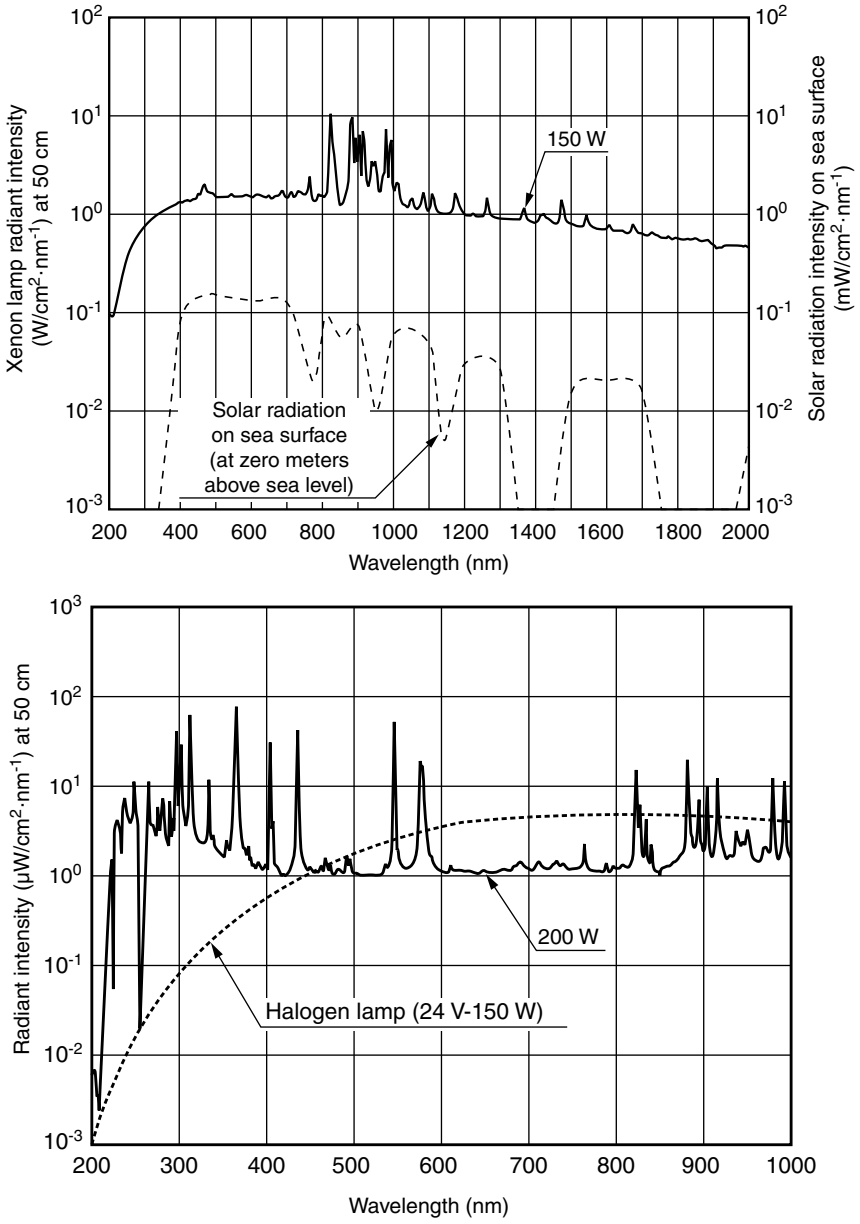

Figure 4.15 Spectral irradiances of a 150 W xenon arc lamp (Hamamatsu L2273) and a closely related 200 W mercury–xenon arc lamp (Hamamatsu L2423) at a distance of 50 cm. The addition of mercury particularly increases the UV emission, but also adds additional spectral peaks and absorption features. Note the different scales of the two charts (charts taken from Hamamatsu datasheet.)

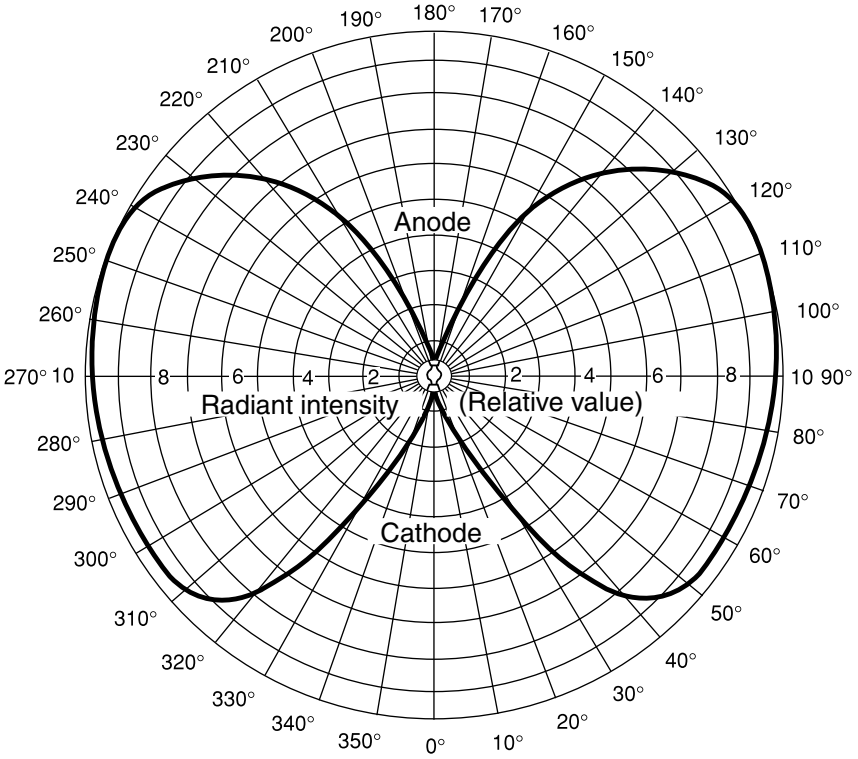

Figure 4.16 Typical angular radiance distribution of a short arc lamp with the example of a Hamamatsu L2273 150 W xenon lamp (chart taken from Hamamatsu datasheet).

but not high radiances, since the light generation occurs in relatively large volumes. The HPS lamp is an arc lamp with a long arc, whereas the sulfur lamp is electrodeless and uses a magnetron to excite the sulfur vapor with 2.45 GHz microwave radiation. Whereas the HPS lamp produces mainly yellow light, the sulfur lamp emits through nearly the whole visible spectral range, but only very little in the IR and UV ranges.

4.3.4.3 Gas Lasers

The principle of the low-pressure gas discharge emission lamp can be extended to build lasers. The first gas laser ever build was a helium–neon (HeNe) laser which was directly pumped by an electrical current. In contrast to normal gas discharge arc lamps, the energy scheme here is more complicated, to achieve good laser conditions. Helium and neon are mixed with relative partial pressures of approximately 10:1 at a total pressure of about 100 Pa. The electrical current first excites the helium atoms into the 2^1s or the 2^3s state, which then transfer their energy to the neon atoms, exciting them into the $3s$ or $2s$ state in a collision process. These states are metastable and can go to the $3p$ and $2p$ states by stimulated emission. The corresponding wavelengths are 632.816, 1152.3, and 3391.2 nm and have a very narrow spectral width. From the $3p$ and $2p$ states the neon atoms can return to the ground state by

spontaneous emission. Because of the very narrow amplification profiles, HeNe lasers can be made very stable with a highly precise emission wavelength and coherence lengths of several thousand kilometers. Even for nonstabilized HeNe lasers the coherence length is already in the range of the resonator length. A second important gas laser is the argon ion laser, which can produce up to 10 different laser wavelengths and high radiant fluxes of up to several watts. The most important of the large number of emission lines of the argon ion laser are at wavelengths 514.5, 496.5, 488.0, 467.5, 457.9, and 351 nm, with the first one giving the highest output power.

Further gas lasers in use are krypton ion lasers, argon–krypton lasers, helium–cadmium lasers, copper vapor lasers, and certain lasers based on hollow cathodes.

4.3.5
Light–Emitting Diodes (LEDs)

Light-emitting diodes (LEDs) are semiconductor devices in which the excitation of electrons is a direct effect of an electrical current flowing across a p–n junction. The current, which flows in the forward direction of the diode, injects conduction electrons from the n region and conduction holes from the p region of the device into the depletion zone, where they recombine with each other. The basic principle is shown in Figure 4.17.

In semiconductor materials with a direct bandgap, the recombination has a large probability of being radiative, that is, of producing photons. A direct bandgap is one

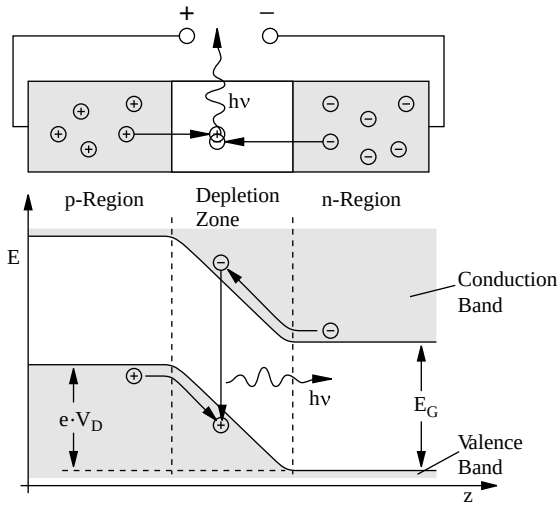

Figure 4.17 Principle of the LED. A semiconductor diode is operated in the forward direction, leading to injection of holes from the p region and of electrons from the n region of the diode into the depletion zone. There they will recombine, eventually emitting a photon with a frequency equal to or slightly larger than the bandgap energy E_G, divided by Planck's constant.

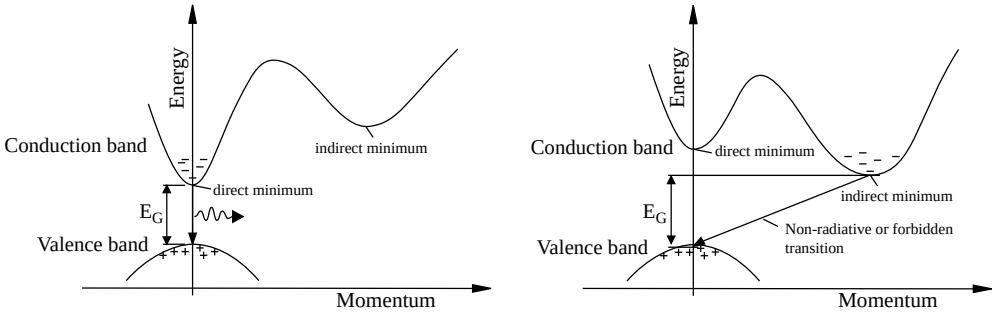

Figure 4.18 Direct and indirect semiconductors in the momentum–energy diagram. In direct semiconductors the transition of an electron from the conduction to the valence band is possible with a small or no change of the momentum, so that photons can be emitted. In indirect semiconductors, the lowest energy states of the conduction band differ significantly from the lowest energy hole states of the valence band in their electron momentum. If only such states are populated, the transition between the conduction and valence band is connected to a large momentum change, which cannot be accomplished by a photon. The material will not show optical activity.

where the mechanical momentum of the electron or hole does not change between conduction band and valence band, so that the energy can be transferred to a photon which has a negligible mechanical momentum. The process of light generation is called electroluminescence. In contrast, for indirect bandgaps, the recombination happens non-radiatively and mostly produces heat if no further modifications are made to the material. The large momentum change during recombination in an indirect semiconductor can only be accomplished by coupling to phonon modes of the semiconductor grid, preventing the emission of photons. Typical materials with a direct bandgap are GaAs, GaN, InP, certain GaAsP alloys, and AlGaAs, whereas SiC, GaP, silicon or germanium belong to the indirect bandgap materials. The difference between direct and indirect bandgap materials is sketched in Figure 4.18.

By introducing localized impurities (or "traps") in indirect bandgap materials, additional energy levels are created. Because of the localization, these traps can interact with a wide range of electron and hole momentum values, thereby connecting the minimum of the conduction band with the maximum of the valence band. Holes from the valence band and electrons from the conduction band can convert to the trap energy levels with emission of a photon. An electron and a hole at a trap create a so-called exciton, which can recombine. These possibilities of incorporating indirect bandgap materials in LEDs are shown in Figure 4.19.

Early LEDs were mainly based on the materials $GaAs_{1-x}P_x$, $Al_xGa_{1-x}As$, and GaP, partly with additional dopings, and emitted at wavelengths between 555 nm (yellowish green) and 940 nm, and beyond this range multiple quantum well systems of InGaAs and InP have been used for the range between 940 and about 1600 nm. LEDs for shorter wavelengths became possible more recently due to new material and technology developments based on GaN, InGaN, InAlGaN, AlGaN, ZnO, ZnSe, AlN, InN, and diamond and also SiC as a substrate material. Currently, LEDs with wavelengths down to 247 nm are commercially available [8], shorter wavelength

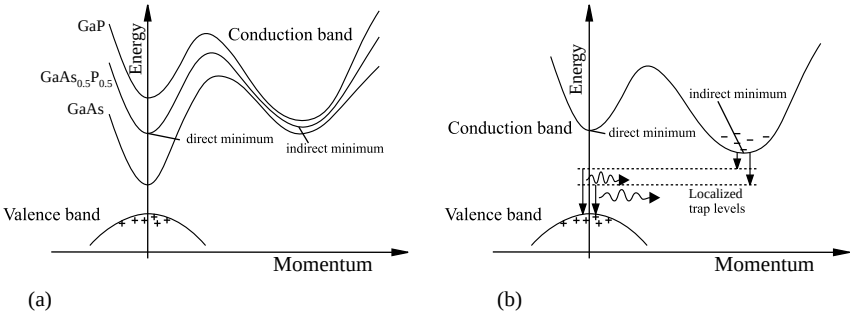

Figure 4.19 Possibilities for emitting photons from an indirect semiconductor material. (a) By creating alloys (here $GaAs_{1-x}P_x$) between an indirect semiconductor (GaP) and a direct semiconductor (GaAs), the relation between indirect and direct minima can be shifted, so that from a certain point a direct semiconductor alloy results. This method also allows one to tune the bandgap and the emitted color in a certain range. (b) By introducing local impurities (trap atoms or molecules), the momentum change between conduction and valence band states can be bridged and photon emission becomes possible. The energy of the photons depends on the trap energy levels and thus on the type of impurity. More specifically, so-called excitons, that is, electron–hole pairs, form at the traps, which have a high probability of recombination.

devices down to 230 nm are under development [9], and devices down to about 200 nm can be imagined based on the mentioned materials. A main direction of the developments is an increase in the radiant flux of LEDs, to make them suitable for lighting applications. These developments have already led to LED devices which, in addition to a high flux, can produce a relatively high radiance and spectral radiance and can therefore be very interesting for measurement applications, where gas discharge lamps are too large, energy consuming, expensive, or otherwise not well suited. Table 4.3 list some recent (mid-2010) high-power LEDs and their properties.

As can be seen from the table, source radiant exitances of up to $90\,W\,cm^{-2}$ and spectral source exitances of up to $4\,W\,cm^{-2}\,nm^{-1}$ can be delivered by the devices, particularly in the blue and violet spectral region, where halogen lamps deliver significantly less than $100\,mW\,cm^{-2}\,nm^{-1}$.

A further advantageous property of LEDs is their direct electrical modulation capability, which in addition to information transfer permits lock-in measurements without a mechanical chopper or stroboscopic measurements. The maximally possible modulation frequency depends on the recombination time of the electron–hole pairs in the depletion zone and can vary widely between different LED types. Typical recombination times are between about 1 μs for older homojunction GaAs LEDs and less than 10 ns for newer LEDs, leading to modulation frequencies from below 1 MHz to more than 100 MHz. For higher frequencies, operation as a laser diode (see the next section) is advantageous.

4.3.5.1 **Laser Diodes**

A wide range of LEDs can be operated as lasers. In contrast to other laser types using optical pumping or excitation through collision processes, an LED can produce an

Table 4.3 Some properties of current commercial high-power LEDs[a].

Type	Wavelength (nm)[b]	Bandwidth (nm)	Chip area or junction area (mm^2)	Output power (mW or lm)	Material	Approx. Radiant exitance ($mW\ cm^{-2}$)	Approx. spectral exitance ($mW\ cm^{-2}\ nm^{-1}$)
Philips Lumileds							
1W Blue Luxeon (GaN)	425	20	1	600 mW	GaN	60 000	3000
Osram high-power IR LEDs							
SFH 4258-AW	850	35	0.09	45 mW		50 000	1429
SFH 4850	850	42	0.09	50 mW		55 556	1323
Cree XBright and EZBright series							
Cree XB900	455–475 (505, 527)	21	0.72	165 mW	InGaN on G-SiC	22 945	1093
Cree XB500	460 (470, 505, 527)	21	0.20	55 mW	InGaN on G-SiC	27 404	1305
Cree EZ700	450 (445–475, 527)	21	0.42	300 mW	InGaN	71 006	3381
Cree EZ1000	445–475 (527)	21	0.90	380 mW	InGaN	42 105	2005
Cree EZ600	445–475	21	0.30	240 mW	InGaN	79 339	3778
Cree EZ400	445–465 (527)	21	0.123	105 mW	InGaN	85 714	4082
Osram Golden Dragon series							
LD W5AP-3V8A-35	455	25	2	1800 mW	Thin GaN	90 000	3600
LB W5AP-JYKY-35	470	25	2	97 lm	Thin GaN	78 033	3121
LT W5AP-LYMZ-36	528	33	2	280 lm	Thin GaN	24 649	747
LY W5AP-KYLZ-36	590	18	2	180 lm	Thin-film InGaAlP	17 407	967
LA W5AP-LXMY-24	617	18	2	240 lm	Thin-film InGaAlP	42 073	2337
LR W5AP-KZMX-1	625	18	2	210 lm	Thin-film InGaAlP	47 596	2644

a) The radiant and spectral exitance values are estimated based on the chip areas and the radiant flux values of the output power (datasheet). For LEDs, where only lumen (lm) values are given, the radiant flux was additionally estimated based on the wavelength. Further chips with a potentially high radiance are those produced by Nichia Corp., but here no reliable data on chip areas were available.

b) Values in parentheses are additionally available.

inversion directly through the injection process [10]. As a result, only two energy levels are necessary for the laser process and the only remaining critical parameters are the relation between the probabilities for stimulated and spontaneous emission and the amplification per unit length. In many LED materials, these parameters are well suited to create a laser even with very short lengths of the active medium. This is particularly true at longer wavelengths.

In the simplest case, a laser diode consists of an edge-emitting LED with a waveguide structure, concentrating the radiation along a line and with facets at the end of this structure, which act as mirrors and create a Fabry–Pérot cavity. Often, no additional reflection layers are necessary for the mirrors, because the high refractive index of the semiconductor leads to a sufficiently large reflection coefficient. Another simple diode laser type is vertically emitting laser diodes, so-called vertical cavity surface-emitting lasers (VCSELs), which consist of a very thin – that is, short – laser cavity between mirror layers. The thickness of the laser cavity can be as small as three wavelengths.

As for all lasers, the radiance limitations of the underlying light source, that is, the LED, are overcome. Also, due to the stimulated emission, which de-excites the higher laser levels faster than a spontaneous emission would do, diode lasers allow even higher modulation frequencies than their LED counterparts. However, to avoid frequency-limiting oscillations connected to the switching between lasing and non-lasing states, the laser diode needs to be held in a lasing state all the time and modulation would be done between two different intensities. Direct modulation frequencies of up to 66 GHz have been reported for special VCSELs [11].

Because of the spectrally very broad amplification profiles and the high amplification, usually several laser modes will oscillate in a diode laser. This leads to a spectral width of the laser that is broader than for other lasers and results in a short coherence length in the range of the cavity length, but with periodic revivals. In applications where a small emission bandwidth is needed, more advanced implementations such as distributed feedback (DFB) lasers or external cavity diode lasers (ECDLs) with additional tuning elements can be used. In the DFB diode laser, the active region itself or a part of it is structured and forms a Bragg grating, which only permits efficient amplification of a single laser mode. Simple designs provide a fixed wavelength, whereas more advanced designs permit wavelength tuning by temperature control or electro-optic effects. The external cavity diode laser uses a dispersive element such as a reflection grating outside the diode as one of the two mirrors. Figure 4.20 shows the basic layout of an ECDL in a Littrow arrangement. Again, only one wavelength is reflected back in such a way that laser amplification can occur and this wavelength can be tuned through the amplification bandwidth of the laser medium by aligning the dispersive element.

Currently, diode lasers with wavelengths down to 375 nm are commercially available and shorter wavelength devices (partially with indirect, optical pumping) are under development. Diode lasers can therefore potentially serve in applications for which currently often large, expensive, and energy-consuming lasers with frequency conversion or excimer lasers with toxic gases are needed.

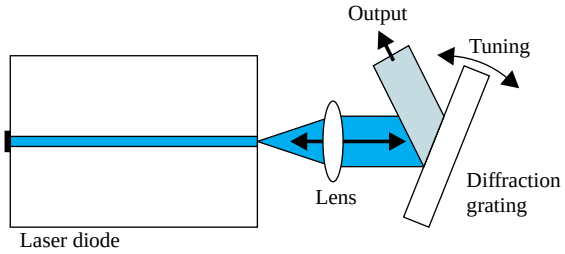

Figure 4.20 External cavity diode laser with a grating in Littrow configuration.

4.3.5.2 Optically Pumped Semiconductor Lasers

In addition to laser diodes which are pumped directly through the injection current, there also exist semiconductor lasers which are pumped optically by an LED. With such lasers, already significantly shorter emission wavelengths than for directly pumped diode lasers have been reported. Particularly lasing at a wavelength as low as 231.8 nm for a cooled AlGaN multiple quantum well laser and 241.5 nm for an uncooled one have already been demonstrated in the laboratory [12].

4.3.5.3 Other Sources

There exists a wide range of other light sources that have not been discussed here. One important type is the diode-pumped solid-state (DPSS) laser. Here, a laser medium such as a neodymium-doped yttrium–aluminum–garnet (Nd:YAG) crystal is pumped optically by one or a number (called a stack) of high-power IR laser diodes. The Nd:YAG laser, as one of the currently most important types of DPSS laser, can emit strong laser radiation at a wavelength of 1064 nm and less strong laser radiation at 946, 1320, and 1444 nm. Output powers can reach at high as 10 kW and it is possible to operate in a continuous wave or pulsed mode. Due to the high power of the primary laser radiation, it is possible to create shorter wave laser sources by frequency conversion, for instance the green 532 nm line, which is achieved by frequency doubling. The latter is often done inside the laser cavity. It is also possible to create the third and fourth harmonic waves, leading to emission wavelengths of 355 and 266 nm.

Fiber lasers are a special version of DPSS lasers. Here, a fiber with a doped core is pumped from one end. The pumping radiation is coupled into a wider core, which surrounds the doped core. Due to the large length of the fiber, the pumping radiation can be efficiently absorbed by the doped core and be converted into laser radiation with a low (i.e., good) M^2 parameter. In this way, even the very faint Raman process can be used to produce a laser. Before laser diodes were available for pumping, gas discharge lamps were used to pump solid-state lasers, such as the first laser ever, the ruby laser.

Supercontinuum light sources – sometimes called white light lasers – are light sources which use optically nonlinear effects to broaden spectrally the initially monochromatic or low bandwidth radiation of a laser. For short and very intense pulses from femtosecond lasers, crossing of a medium such as a fluid or even air is

often sufficient to achieve this effect; for longer pulse durations or continuous laser radiation, the transmission through a long optical fiber with nonlinear effects is necessary. The great advantage of a supercontinuum source is the production of nondiffuse, that is, diffraction-limited, very intense broadband radiation or white light, which cannot be produced by other light sources. Such radiation is useful, for instance, for white light confocal microscopy, spectroscopy, or optical coherence tomography (OCT), sometimes also referred to as white light interferometry.

Dye lasers are optically pumped lasers, similar to solid-state lasers. Instead of a spectrally relatively narrow laser transition in a solid body, these lasers use dyes (often in a liquid), which can have a very broad amplification bandwidth. It is therefore possible to tune the wavelength of the laser emission of a dye laser in a very wide range of typically 30–60 nm bandwidth by changing the laser resonator. Dye lasers are available from the near-UV to the MIR region.

Tunable monochromatic laser-like radiation can also be produced by a so-called optical parametric oscillator (OPO). This device mainly consists of an optically nonlinear crystal in an optical resonator. It converts an incident monochromatic laser beam into two beams whose oscillation frequencies add up to the oscillation frequency of the incident radiation, that is, the energy of each incident photon is distributed to two new photons. The underlying physical process is called parametric three-wave mixing. Tuning is achieved by appropriately aligning the optical resonator and the crystal; however, the alignment of an OPO is complicated and small instabilities or misalignments – for instance due to temperature changes – can lead to an interruption of the conversion process. OPOs are therefore primarily used in scientific laboratories and less often in industrial applications.

References

1 Pedrotti, F., Pedrotti, L., Bausch, W., and Schmitt, H. (2005) *Optik für Ingenieure: Grundlagen*, Springer, Berlin.

2 Bergmann, L. and Schäfer, C. (2004) *Lehrbuch der Experimentalphysik III*, vol. 9, Walter de Gruyter, Berlin.

3 Hecht, E. (2005) *Optik*, Oldenbourg Wissenschaftsverlag, Munich.

4 Petruck, P., Riesenberg, R., Kanka, M., and Huebner, U. (2009) Partially coherent illumination and application to holographic microscopy. In 4th EOS Topical Meeting on Advanced Imaging Techniques Conference, pp. 71–72.

5 Svelto, O. (2010) *Principles of Lasers*, Springer, New York.

6 Bass, M. and Casimer, D. (1995) *Handbook of Optics*, vol. **I**, McGraw-Hill, New York.

7 Nakar, D., Malul, A., Feuermann, D., and Gordon, J.M. (2008) Radiometric characterization of ultrahigh radiance xenon short-arc discharge lamps. *Appl. Opt.*, **47** (2), 224–229.

8 Gaska, R. and Zhang, J. (2006) Deep-UV LEDs: physics, performance and applications. *Proc. SPIE*, **6037**, 603706–603711.

9 Hirayama, H., Yatabe, T., Noguchi, N., Ohashi, T., and Kamata, N. (2007) 231–261nm AlGaN deep-ultraviolet light-emitting diodes fabricated on AlN multilayer buffers grown by ammonia pulse-flow method on sapphire. *Appl. Phys. Lett.*, **91**, 071901.

10 Paschotta, R. (2008) *Encyclopedia of Laser Physics and Technology*, Wiley-VCH, Weinheim

11 Zhao, X., Parekh, D., Lau, E.K., Sung, H.K., Wu, M.C., Hofmann, W., Amann, M.C., and Chang-Hasnain, C.J. (2007) Novel cascaded injection-locked 1.55-μm VCSELs with 66 GHz modulation bandwidth. *Opt. Express*, **15**, 14810–14816.

12 Takano, T., Narita, Y., Horiuchi, A., and Kawanishi, H. (2004) Room-temperature deep-ultraviolet lasing at 241.5nm of AlGaN multiple-quantum-well laser. *Appl. Phys. Lett.*, **84**, 3567.

5
Optical Detectors

Rainer Riesenberg and Andreas Wuttig

5.1
Introduction

The main focus of this chapter will be CMOS (complementary metal–oxide–semiconductor) and CCD (charge-coupled device) technologies and the photodiode/photoconductor technology on which they are based, since they are most relevant for biophotonics applications. Other light detection technologies are only briefly mentioned to give a coarse overview.

5.2
Devices for Light Detection

5.2.1
Sensitivity and Detectivity of Light Detectors

5.2.1.1 Responsivity

The term responsivity denotes the strength of a light detector's output current in relation to the power of the incident light [1], measured in amperes per watt ($\mathrm{A\,W^{-1}}$). Such a figure is typically only valid for a single wavelength, since in semiconducting detectors, for instance, the generated photocurrent is more related to the incidence rate of photons. Furthermore, the efficiency of light-to-current conversion is itself dependent on the wavelength via the quantum efficiency $\eta(\lambda)$. For example, for a photodiode without internal gain it can be calculated as

$$R = \eta(\lambda)\frac{e\lambda}{hc} \tag{5.1}$$

where $\eta(\lambda)$ is the quantum efficiency of the electron–hole generation process, h is Planck's constant, e is the charge of the electron and c is the speed of light. In addition to material-related properties, the quantum efficiency may also subsume the transmissivity of the detector surface, that is, the efficiency at which light enters the detector. In this case, it is also referred to as external quantum efficiency, otherwise as

Handbook of Biophotonics. Vol.1: Basics and Techniques, First Edition.
Edited by Jürgen Popp, Valery V. Tuchin, Arthur Chiou, and Stefan H. Heinemann.

internal quantum efficiency. For other semiconducting detectors, the responsivity–wavelength behavior may differ from the above equation by a gain factor, describing the internal multiplication of an initially generated photoelectron or electron–hole pair. For thermal detectors, which are based on the measurement of incident energy rather than incident photon flux, the responsivity looks completely different and may even be constant over certain wavelength ranges. For other detectors, responsivity may not be a useful figure at all, since their output may not be described properly by a current.

5.2.1.2 Noise, Sensitivity, and Detectivity

In contrast to responsivity, the figure of sensitivity loosely speaking describes the lowest detectable amount of light of a given wavelength, and as such is always a useful performance figure for a detector. The sensitivity of a detector is closely related to its dark noise, that is, the nonsystematic uncertainty involved in a measurement, and more precisely describes the amount of light for which a specific minimal signal-to-noise ratio SNR_{req} of the output of the detector is achieved. For low light levels, the noise of a detector can often be considered independent of the signal. For this case, the sensitivity can be characterized by the noise equivalent power (*NEP*), which is connected to the noise level σ and the responsivity R of the detector by

$$NEP = \frac{\sigma}{R}. \tag{5.2}$$

The noise elongation r of a single measurement of the detector output will be centered to zero, that is, the expectation value $\langle r \rangle$ is zero, since a nonzero expectation value can be subsumed under the systematic measurement errors. The square of the noise level, called the noise variance, is then given by the expectation value of r^2, that is, $\sigma^2 = \langle r^2 \rangle$. The value σ itself is often referred to as the root mean square (rms) of the noise. If the noise generation processes yield a white or pink noise, that is, noise with constant spectral power density at least up to a certain frequency limit, the relevant noise variance itself depends on the bandwidth of the system consisting of detector and measurement electronics and will be proportional to it. Furthermore, the ultimate limit of noise generation of a detector is very often given by statistical noise processes, which take place independently at different points inside the sensitive area or volume of a detector. If the thickness of the sensitive area is chosen to be an optimal value, the surface remains the only important parameter for these processes and the noise variance becomes proportional to the detector area. Taking these influences together, a new property of a detector, its so-called detectivity or specific detectivity, D^*, can be defined:

$$D^* = \frac{\sqrt{A \cdot \Delta f}}{NEP} \tag{5.3}$$

where A is the sensor area, Δf is the bandwidth, and *NEP* is the noise equivalent power, that is, the radiant flux, which generates a signal with $SNR = 1$. D^* describes the quality of a detector or the performance of a detector technology.

5.2.2
Light Detection Through Thermal Effects/Thermal Detectors

If light is absorbed by a material, its energy will cause a transition from a lower to a higher energy state. These transitions can be electronic transitions, changes of molecular energy levels, or lattice vibrations of a solid-state body. If from this higher level a radiative transition to a lower level is improbable or impossible, the energy can gradually be converted into vibrational energy, that is, heat. This heat can then be detected in a temperature measurement, giving an indirect measure of the incident light intensity. Thermal detectors make use of exactly this measurement scheme, combining a good absorber with a low specific heat capacity and a sensitive temperature sensor. Since absorbers can be made efficient over wide wavelength ranges, thermal sensors are cost-efficient detectors for wavelength ranges, where otherwise only very expensive or even no detectors would be available. The most frequently used thermal detectors are uncooled bolometers, thermopiles, and pyropiles, which have typical detectivities in the range 10^8 to $10^9\,\mathrm{cm{\cdot}Hz^{0.5}{\cdot}W^{-1}}$. This is relatively low compared with most other detector technologies. In contrast, the most sensitive thermal detectors are superconducting edge transition bolometers, which achieve detectivities higher than $10^{10}\,\mathrm{cm{\cdot}Hz^{0.5}{\cdot}W^{-1}}$.

5.2.3
Light Detection Using the Photoelectric Effect

The photoelectric effect is the emission of electrons (so-called photoelectrons) from a material when it is illuminated with photons. The latter are absorbed by the material in such a way that the energy is transferred to an electron. If the energy of the photon is higher than the binding energy of the electron, it can leave the material. The effect thus works particularly well for short wavelengths and is used in a number of photodetectors.

5.2.3.1 **Phototube**
The simplest photodetector based on the photoelectric effect is the phototube. It consists of a gas-filled or vacuum tube with a photocathode and an anode. Photons absorbed by the cathode lead to emission of electrons from the cathode, which then move to the anode and generate a current pulse. Simple phototubes without amplification capabilities are outdated, since detector technologies now exist that are cheaper and better.

5.2.3.2 **Photomultiplier**
The photomultiplier or photomultiplier tube (PMT) is a phototube that is capable of multiplying single photoelectrons several million times, each time generating a large current pulse. In the more recent types of PMTs, the amplification is achieved by a number of so-called dynodes, which are electrodes at voltage levels between those of the anode and cathode. The voltages between all the electrodes in the PMT are tailored in such a way that the photoelectron emitted from the cathode is first accelerated

towards the first dynode. Upon its impact on the dynode, it already has such a high kinetic energy that several secondary electrons will be emitted from the dynode as a result of the impact. The electron packet created is then accelerated towards the next dynode, where every electron again creates several secondary electrons. This process is repeated until the anode is hit by a large packet of electrons coming from the last dynode.

PMTs are still in use because they permit relatively sensitive detection of light. However, their sensitivity compared with other detector types is often overestimated. Taking the poor IR sensitivity and the high effort for the electronics on the one hand and the semiconductor-based alternatives on the other (see below) into account, however, this is not one of the best reasons for using them as photodetectors. The more important properties of a photodetector are their very high temporal resolution, the large sensitive area, which can be achieved at low noise levels, and the fact that the gain factor can be varied by several orders of magnitude by simply changing the voltages of the dynodes.

5.2.4
Light Detection Using Internal Photoelectric Effects

The term "internal photoelectric effects" here will subsume all effects where absorbed light generates free charge carriers inside a medium, leading to changed electrical properties of a device containing such a medium. Normally, the medium will be a semiconductor and the free charge carriers will be generated as electron–hole pairs, when the absorbed photons elevate electrons from the valence band to the conduction band of the semiconductor. This can lead to the effect of photoconductivity and to the photovoltaic effect, depending on the device.

5.2.4.1 **Photoconductor**

The photoconductor is the simplest semiconducting optical detector. It has a resistance that is indirectly proportional to the incident intensity. Photoconductors are usually made of an amorphous film of the semiconducting material, coated on an insulating substrate and connected by metal contacts. The latter often have a so-called interdigital shape to increase the overall conductivity and the gain of the device (Figure 5.1). Typical semiconductor materials for optical detectors and their most important physical properties are given in Table 5.1.

Once a photon has been absorbed by the photoconductor material, an electron–hole pair is created, that is, an electron is elevated into the conduction band and a hole is created in the valence band. Such an absorption can occur when the energy of the incident photon is higher than the bandgap energy of the semiconductor, that is,

$$E_{\mathrm{Phot}} = \frac{hc}{\lambda} \geq E_{\mathrm{G}}. \tag{5.4}$$

According to this, there exists a cutoff wavelength above which the material will not be sensitive to incoming radiation. After generation, photoelectron and hole diffuse through the photoconductor until they recombine with other holes and electrons.

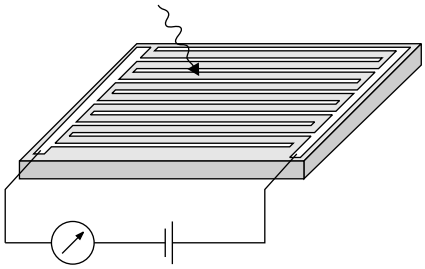

Figure 5.1 Photoconductor interdigital electrodes. Incident photons create free charge carriers, which cause a current, if an external voltage is applied.

The mean time until recombination is given by the inverse of the so-called recombination rate. If a voltage is applied at the metal contacts, an electrical field is generated inside the photoconductor. As a result, the diffusion motion of the charge carriers will change into a directed drift motion and a global current, the photocurrent, can be observed. For usual detector geometries and applied voltages, the time it takes an electron to travel through the detector is much shorter than the recombination time. If an electron reaches the positive metal electrode and is extracted from the semiconductor, another conduction band electron will be injected for it at the negative electrode to retain electrical neutrality. A photoelectron thus effectively can travel several times through the detector and the observed global current will be increased by an according factor, the gain factor G. The highest values

Table 5.1 Bandgaps and corresponding cut-off wavelengths for different semiconductors at temperatures of 300 and 4 K, compiled from Wagemann and Schmidt [2], Jones [3], Nahory *et al.* [4], and Hansen and Schmit [5].

Material	300 K		4 K	
	E_G (eV)	λ_{cut} (μm)	E_G (eV)	λ_{cut} (μm)
Si	1.11	1.12	1.20	1.03
Ge	0.67	1.85	0.74	1.68
PbS	0.41	3.02	0.29	4.28
PbSe	0.29	4.28	0.15	8.27
GaP	2.26	0.55	2.34	0.53
CdTe	1.50	0.83	1.60	0.77
CdS	2.24	0.515	—	—
CdSe	1.73	0.715	—	—
InAs	0.36	3.45	—	—
InSb	0.18	6.89	—	—
$In_{1-x}Ga_xAs$[a)]	0.36–1.43	0.87–3.44	—	—
$Hg_{1-x}Cd_xTe$[a)] (MCT)	−0,14–1.49	>0.83	−0.26–1.65	>0.75

a) Bandgaps depending on material composition; InGaAs given in [4], MCT given in [5].

that have been achieved for G are in the region of 10^5. Since the recombination rate of electrons increases with increase in the number of available holes and the recombination rate of holes increases with increase in the number of available electrons, the responsivity will become nonlinear. The average recombination time of the detector itself determines the time constant of the detector, that is, the speed at which it responds to changes in the incident intensity. For a given detector geometry and operation voltage, larger gain factors can therefore only be achieved at the expense of slower detection.

5.2.4.2 **Photodiode**

Photodiodes of the basic type (Figure 5.2) are formed by a p–n junction in a semiconductor, that is, by a contact between a p-doped region, in which charge transport only takes place in the form of hole conduction, and an n-doped region, where electrons are responsible for charge transport. Between these two regions an insulating zone without free charge carriers builds up due to diffusion processes of electrons and holes, because free electrons will recombine and be captured in the p zone (loading it negatively) and free holes will do the same in the n zone. Inside the insulating zone, called the depletion zone, an electrical field is generated due to the capture of the two types of charge carriers on the two different sides of the p–n junction. Finally, the system of n zone, p zone, and depletion zone effectively forms a charged capacitor. Similarly to the case of the photoconductor, incident light with a photon energy higher than the bandgap energy E_G generates electron–hole pairs, which without an electrical field would diffuse through the device but with an electrical field will generate a photocurrent.

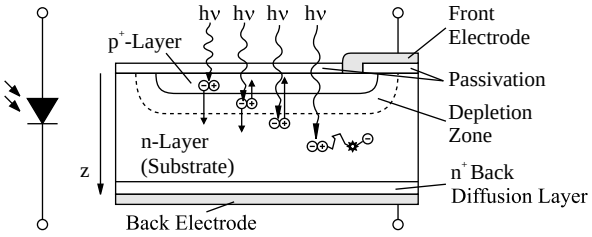

Figure 5.2 Basic layout of a photodiode. Below a transparent and probably anti-reflective passivation layer (in silicon photodiodes typically SiO_2 or Si_3N_4) a thin, n- or p-type layer is processed on to a substrate of opposite weak doping by thermal diffusion. The back side of the substrate is heavily doped with the same type of doping as the substrate itself as a transition to the back-side metal electrode. The top layer (here the p region) is connected to a further front-side metal electrode. At the interface between p- and n-type layers a depletion zone with an internal electrical field builds up, expanding mainly into the weakly doped substrate. If photons are absorbed inside or near the depletion zone, electron–hole pairs generated by the absorption will be separated due to the field of the depletion zone, leading to a measurable voltage or current at the electrodes. Photons absorbed at a larger distance from the depletion zone will in contrast be very unlikely to lead to a signal, since the generated charge carriers will only diffuse randomly through the material until they recombine with other charge carriers or are eventually captured by the depletion zone with a very low probability.

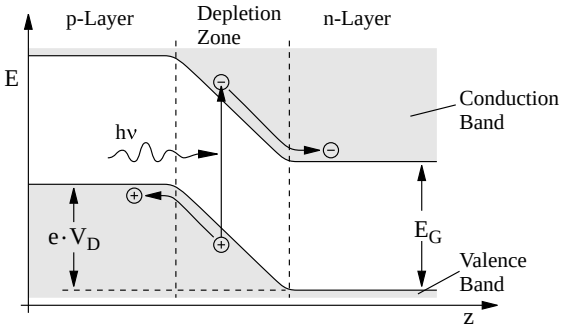

Figure 5.3 Energy diagram for the photodiode shown in Figure 5.2. An electron–hole pair is generated when the energy of an incident photon is absorbed by elevating an electron from the valence band to the conduction band. For this, the photon energy $h\nu$ needs to be larger than the bandgap energy E_G. If the absorption process takes place in or near to the depletion zone, the two charge carriers will be separated due to the spatial variation of the band energies.

As a first fundamental difference from the photoconductor, the electrical field will only be observed in the depletion zone between the n- and the p-conducting parts. Additional fields applied from the outside will only lead to a change in the width of the depletion zone and the voltage drop V_D (see Figure 5.3) about it. If the photon is absorbed inside the depletion zone, the electrical field will drag the electron into the n region and the hole into the p region, thereby creating a photocurrent which can either be extracted from the photodiode through contacts at the n and p regions or which otherwise leads to a charge and voltage change of the diode capacitance. According to this, photodiodes can be operated in the photoconduction mode or in the photovoltaic mode, depending on their bias voltage (Figure 5.4):

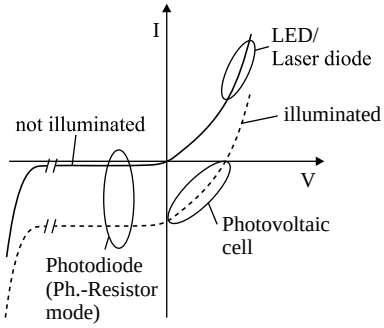

Figure 5.4 Depending on its operational conditions, a photodiode acts as a photoconductor, a photovoltaic cell, or a light-emitting device, each located in a certain quadrant of the voltage–current (V–I) diagram. Different diode designs and materials are, however, differently well suited for each of the modes. Particularly for light emission, a number of additional conditions, such as having a direct semiconductor or exciton levels, have to be met, otherwise the diode will only heat up instead of emitting light.

- **Operation as a photovoltaic cell**: A photodiode illuminated by light in its sensitive region will generate a photovoltage and drive a photocurrent, if it is properly connected in an electric circuit. This mode is employed in, for example, solar cells, which are just photodiodes with a large collecting area. If the photodiode runs free or is operated at a large load impedance, the photoinduced voltage will approach the open-circuit voltage, which has a disadvantageous dependence on the illuminated power. Such an operation regime would therefore not be useful for light intensity measurements, as long as the voltage is not being reset between readouts. At low impedance values of the external load or in short-circuit operation, the current will become proportional to the incident intensity. For most sensitive measurements without an amplifier, the external impedance should be set to the effective impedance of the photodiode. In this mode of operation, the photodiode will, however, be relatively slow and the dependence between illumination power and output power of the photodiode is nonlinear, so a good calibration is required. Faster operation with a higher measurement precision due to a linear response is possible if the photodiode is operated in the short-circuit mode and the resulting current is measured using a current-to-voltage converter.
- **Operation with reverse bias voltage**: If a voltage in the reverse direction is applied to the photodiode, incident light will still lead to a photocurrent. Since this current is also directed in the reverse direction, the photodiode effectively acts like a photoconductor, but without the gain mechanism observed in real photoconductors, since no replacement electrons can be injected into the hole-conducting p region of the photodiode. Because of the applied voltage, the depletion zone will broaden, leading to a lower capacity and a faster response, so detection of faster signals will become possible. The bias voltage will, however, also lead to a temperature-dependent dark current, which in turn leads to an associated shot noise and a degraded linearity between incident power and total output current. If the bias voltage is raised above a certain device-dependent level, the photodiode will act as an avalanche photodiode. Due to an avalanche effect, every absorbed photon will lead to an avalanche breakdown, resulting in an internal gain of the photoinduced charges. This increases the effective responsivity of the device, which makes it easier to read out the signals of single photons. This is described in more detail in a separate section.

At low photon energies, that is, energies inducing only one electron–hole pair per absorbed photon, the theoretical responsivity limit for a monochromatic wavelength is given by Equation 5.1. This limit can only be achieved if the wavelength corresponds to the energy of the bandgap. Shorter wavelengths will yield at best the same current per number of photons, which means a lower current per incident power. Figure 5.5 shows a comparison between the sensitivities achieved by real detectors and the maximal responsivity for the case of a quantum efficiency of 100%. Typical features of detectors are illustrated in Figures 5.6–5.10 and Table 5.2.

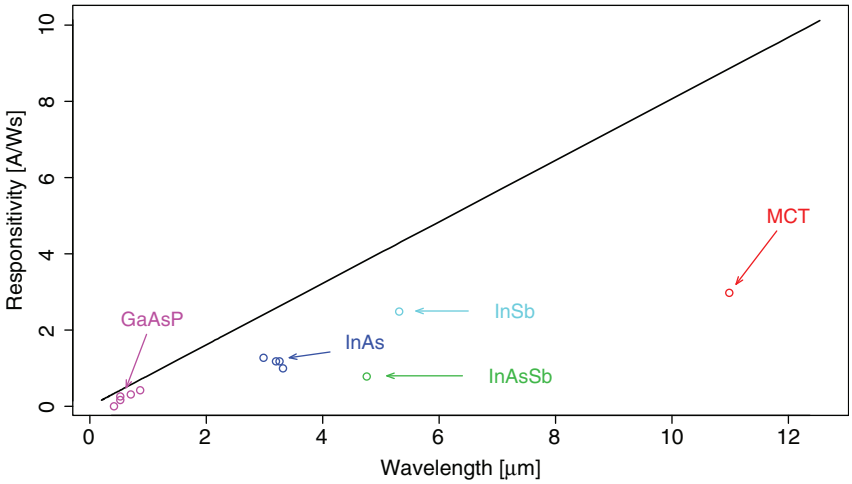

Figure 5.5 Maximal theoretically possible responsivity of photodiodes and responsivities achieved by real photodiodes and a photoconductor (MCT) [6].

5.2.4.3 PIN Photodiode

The PIN (positive–intrinsic–negative) photodiode is a special type of a photodiode, which has an intrinsic (i.e., weakly doped or undoped) region between the positively and negatively doped regions (Figure 5.11). The insertion of an intrinsic region has two advantageous effects:

- Most photons are absorbed in the intrinsic region. Due to the electric field present, the photoinduced charge carriers will be directed quickly to the p- and n-doped regions instead of eventually getting there by a drift process. At the same time, due to the greater thickness of the depletion zone, the capacity of the device is comparatively low. Together, this leads to a very quick response of the PIN photodiode to changing light intensities. The operating frequencies of the fastest PIN photodiodes are in the range of tens of gigahertz, making them ideal for optical communication applications.

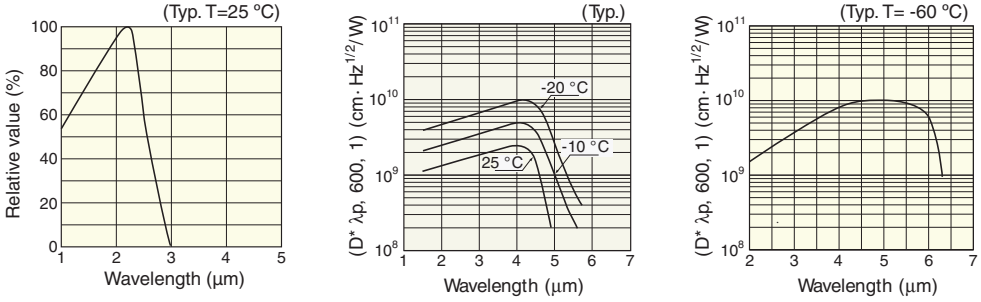

Figure 5.6 Typical spectral detectivities of PbS, PbSe, and InSb detectors manufactured by Hamamatsu.

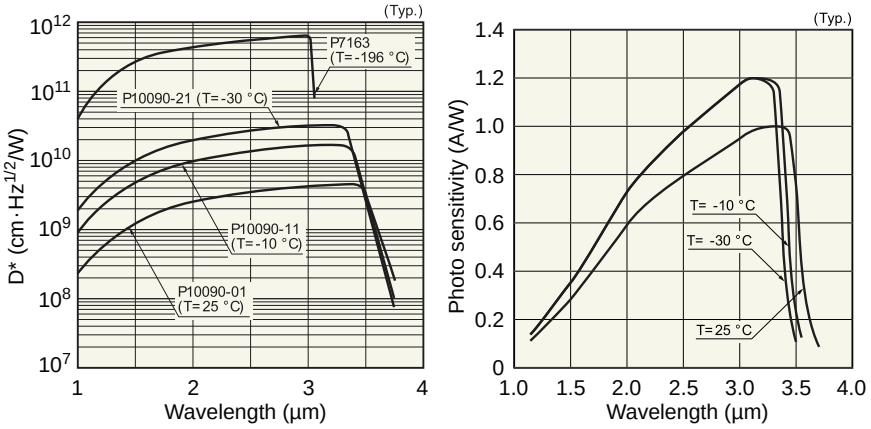

Figure 5.7 Typical detectivities and responsivities (referred to as "photosensitivities") of InAs detectors manufactured by Hamamatsu (diagrams taken from Hamamatsu datasheet).

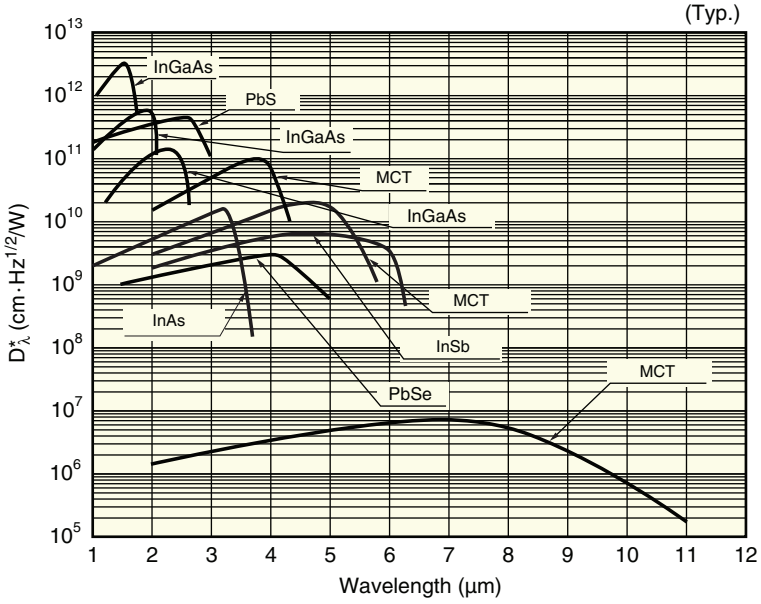

Figure 5.8 Spectral detectivity chart of different cooled photodetector devices manufactured by Hamamatsu (diagram taken from Hamamatsu datasheet). The sensitivities depend not only on the material, but also on the material modification, the operating conditions, and the device layout. A larger long-wavelength cutoff normally implies a lower sensitivity. Beyond 10 µm this relation is partly reversed, but lower detector temperatures have to be used.

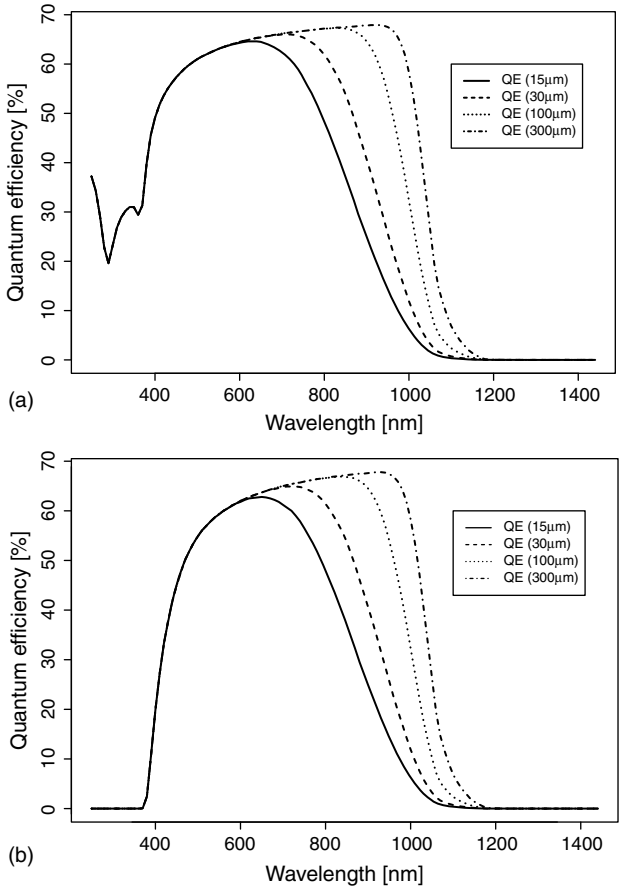

Figure 5.9 Theoretical maximum quantum efficiencies of silicon photodiodes with thicknesses of the depletion zone between 15 μm (solid lines) and 300 μm (dashed-dotted lines), thicknesses of the non-sensitive part of the top layer of 5 nm (a) and 100 nm (b) , and no antireflective coating. The quantum efficiencies are calculated only from the wavelength-dependent refractive indices and absorption coefficients.

- The larger sensitive volume compared with a normal (p–n) photodiode leads to a more efficient collection of light, particularly at the long-wavelength end of the sensitivity region, where photons start to pass through the diode material without being absorbed.

5.2.4.4 **Pinned Photodiode**

The "pinned" photodiode is mentioned here because it must not be confused with the PIN photodiode. Pinning is a method to reduce the dark current of a photodiode working in the accumulation regime by three or more orders of magnitude. Pinning

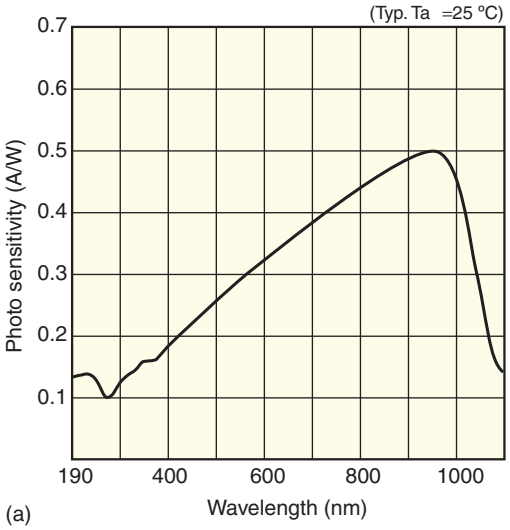

(a)

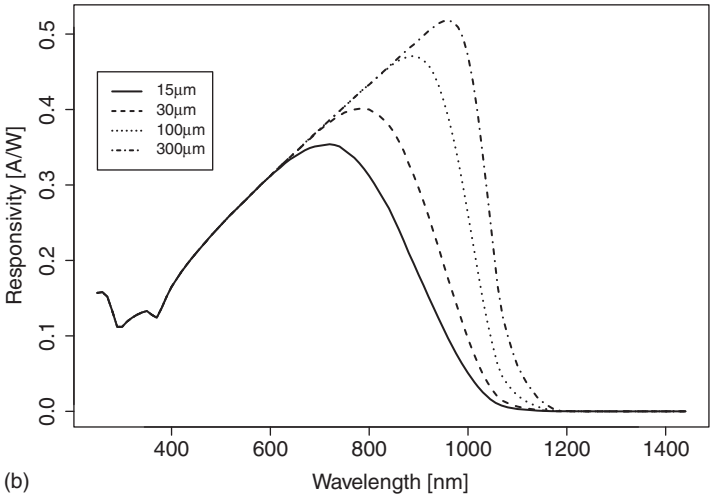

(b)

Figure 5.10 (a) Responsivity ("photosensitivity") of a silicon photodiode manufactured by Hamamatsu (diagram taken from Hamamatsu datasheet) and (b) theoretical responsivity for silicon photodiodes with thicknesses of the depletion zone varying between 15 and 300 μm, with a non-sensitive top layer of 1 nm thickness, and without anti reflective coating. The shape of the responsivity curve of the real detector indicates a thickness of the sensitive region of at least 300 μm.

is practically only employed in image sensors of the CCD or CMOS type, particularly for cooled, high-performance devices, where it raises the usual silicon photodiode peak detectivities from values in the range $10^{12}-5\times10^{14}$ to $>10^{17}$ cm·Hz$^{0.5}$·W^{-1}. Pinning will be discussed in more detail in Section 5.3.2.7.

Table 5.2 Photosensitive semiconductor materials and properties of some corresponding detectors available from Hamamatsu. Particular properties depend on the material modification, for instance the quantitative composition of HgCdTe.

Material	Peak wavelength (μm)	Responsivity at peak wavelength (A W^{-1})	Max. wavelength (μm)
PbSe	4.0–4.3	—	4.8–5.2
PbS	2.2	—	2.9
InSb	4.5–5.3	Typically 2.5	5.5–6.7
InAs	3.0–3.35	1.0–1.3	
HgCdTe (MCT)	3.6–17	Typically 3	4.3–22
Si	0.7–0.96	0.25–0.72	1.1
GaP/GaAsP	0.37–0.71	0.06–0.4	0.4–0.76

5.2.4.5 **Avalanche Photodiode**

If the voltage across a depletion zone of a photodiode is made sufficiently large, charge carriers generated by photon absorption will be accelerated so much that they gain enough energy to generate secondary electron–hole pairs which again are accelerated, and so on. By this so-called avalanche effect, every absorbed photon will induce a large number of charge carriers and an accordingly large current pulse. This internal gain mechanism is used in avalanche photodiodes (APDs), which can be operated in two main modes, the linear mode and the Geiger mode. In the linear mode, the APD is operated below the breakdown voltage. As described above, an initially generated electron–hole pair will be multiplied by a certain factor, leading to an increased total responsivity. Typical gain factors are 10–50 for germanium and InGaAs APDs and 100–1000 for silicon APDs. After the single initial electron–hole pair has been multiplied and contributed a certain current pulse to the total

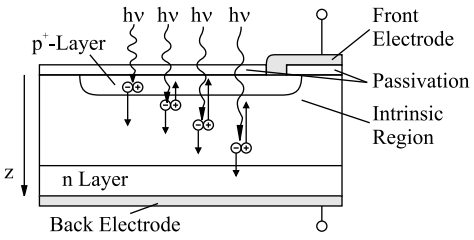

Figure 5.11 The PIN photodiode is similar to the standard photodiode, but it has a large intrinsic (undoped) region between the p and n layers. Since the intrinsic region has no free charge carriers, there is an electrical field, which can separate photocharge pairs, making the intrinsic region photosensitive. Particularly long-wavelength radiation, which is not well absorbed by silicon, can be detected better because of the greater thickness of the sensitive volume.

photocurrent, it will not lead to further generation of secondary charge carriers. The multiplication process itself is subject to two main noise contributions. The first contribution is a result of the statistical nature of the charge amplification and increases as the square of the shot noise level by a factor of 2. The second contribution is excess noise, which is related to the statistics of ionization by different charge carrier types. The square of this factor typically ranges between 3 and 10, depending of the APD type. The main advantage of an APD operated in the linear mode is that very low light levels can be detected at a high speed using relatively simple preamplifiers. Due to the shot noise amplification they are, however, not adequate for high-precision measurements of extremely low light levels.

The problem of shot noise amplification is partly overcome in the second operation mode, the Geiger mode. This mode is also frequently referred to as the "photon counting mode," since here single photon absorption events are detected and counted. In the Geiger mode, the APD is operated at a reverse voltage beyond the breakdown voltage, leading to a very high gain of 10^5–10^8. Normally, an APD operated above the breakdown voltage would be permanently conducting a large current even without incidence of light or generation of dark charge carriers. An additional external current limiter will, however, induce a statistical fluctuation of the current, which also includes a fluctuation to a zero current with a high probability. Once the current becomes zero, it requires a photoinduced or dark charge carrier to trigger a revival of the current. The average time until the current drops to zero is called the recovery time of the APD and if the photon rates and dark charge generation rates are significantly below the inverse of this time, the APD can be used to count photons directly, avoiding excess noise due to the amplification process. The new limiting factors are the dark charge generation rate (which, however, already contributed in the linear mode), the recovery time, an excess noise related to the probability of the incidence of two or more photons within the recovery time, and the phenomenon of afterpulsing, that is, the generation of further current pulses after the pulse due to an absorbed photon. Afterpulsing is mainly caused by temporary trapping and later release of individual charge carriers. For typical detectors, the recovery time varies between about 100 ns and 1 ms, essentially limiting the operating frequency to values between 1 kHz and about 10 MHz [7] and the acceptable photon rates to a fraction of these values, depending on the application. Faster recovery times down to less than 2 ns have been reported, however, for InGaAs APDs [8].

Summarizing, APDs can be used for measurements at high precision, high temporal resolution, or high speed, but they will not be as sensitive as a photodiode with a good preamplifier. Particularly when measurement speed or temporal resolution is not critical, cooled integrating photodiodes such as pinned photodiodes will yield a higher precision and at the same time allow for a relatively large photon flux.

5.2.4.6 **Metal–Semiconductor–Metal (MSM) Photodetectors**

Consisting of a semiconductor between two metal electrodes, the metal–semiconductor–metal (MSM) type of detector looks much like a photoconductor; however, there is a fundamental difference, namely a Schottky contact instead of an

ohmic contact between the metal electrodes and the semiconductor. The Schottky contacts of the MSM act like diodes and avoid injection of charge carriers from the metal into the semiconductor. The response time of the MSM is thus determined by the short average time that a charge carrier needs to reach an electrode and not by the much longer charge carrier recombination time, making the MSM detector very fast. The MSM detector is even faster than a PIN photodiode and reaches operating frequencies of hundreds of gigahertz [9, 10], but dark current values of current MSM detectors are 10–100 times larger than those of very sensitive PIN photodiodes [11, 12] and the quantum efficiency is limited due to the necessity for dense interdigital metal electrodes on the front side of the detector. MSM detectors are therefore mainly of interest for high-speed optical communication. As a further consequence of the diode nature of the metal–semiconductor contacts, there is no internal gain in an MSM detector.

5.2.4.7 **Phototransistor**

A phototransistor effectively is a normal transistor which is housed in a transparent material. The base–collector junction here acts as a photodiode but, due to the amplification of the transistor, the overall device has an internal gain. Phototransistors are a convenient means of achieving a high responsivity with a minimum of external electronics, which is advantageous for low-cost optical data transmission or devices such as light barriers. For measurement applications, however, the poor linearity of phototransistors is a disadvantageous feature.

5.2.4.8 **Remarks on the Sensitivity of Semiconducting Light Detectors With and Without Internal Gain Mechanisms**

Photoconductors, avalanche photodiodes, and phototransistors have significantly larger responsivities than photodiodes without internal gain mechanisms, that is, the current observed at their output is larger for the same incident intensity. This does not mean, however, that they are more sensitive to light. Whether or not a sensitivity gain or loss is achieved depends mainly on the quality of the readout electronics under comparison, the readout mode, and the working temperature of the photosensitive device. In general, the noise of an intensity measurement cannot be lower than the noise of the light. For classical light, this is at best the shot noise of the photons, which for practically all relevant light sources is given by a Poisson distribution with a variance equal to the number of detected photons. The best-case noise level of a measurement will therefore become equal to the square root of the number of detected photons:

$$\sigma_{\text{phot}} = \sqrt{N_{\text{phot}}}. \tag{5.5}$$

This fundamental noise level is raised further due to internal noise of the detector, readout noise, or noise induced by the gain mechanism. In more complex devices such as CCDs (discussed below), other noise contributions such as clock-induced noise or reset noise may arise.

5.2.5 Noise of Semiconducting Photodetectors

5.2.5.1 Dark Current Noise

Dark current noise, also referred to as dark current shot noise, is an intrinsic, signal-independent noise caused by the detector. Due to thermal activation, doping, material defects, or material interfaces, free charge carriers are present in a semiconducting light detector even if no light is irradiated on it. Since the generation of different electron–hole pairs is statistically independent, the probability of the generation of a certain number of dark charge pairs within a fixed period of time is given by a Poisson distribution with an average of μ and a variance, which is also μ. Whereas the average charge per unit time, the so-called "dark current," can be determined by careful calibration of the detector and then subtracted from the measured signals, the variance implies a noise, which cannot be removed from the measured signals. It is therefore important to minimize the dark current for sensitive measurements. Several optimizations contribute to this:

- **Cooling of the detector**: The dark current grows exponentially with the temperature. For silicon photodiodes, the dark current will increase by a factor of approximately 10 for every 20 K temperature increase (see Figure 5.12).
- **Minimizing the detector area to an optimal value**: The dark current of a detector with a given technology is directly proportional to its sensitive area. Small light spots should therefore preferably be measured by small detectors and large light spots by large detectors. Whether in the optimal case the detector should cover the whole spot or cut it at some point depends on the shape of the spot and the relative strength of other noise sources.

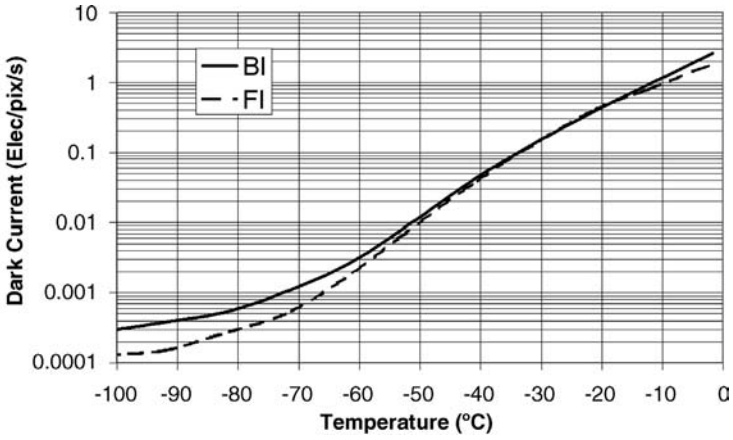

Figure 5.12 Temperature dependence of the dark current of a scientific CCD (Camera: Andor Newton DU940N using an e2v CCD42-10 detector chip with multi pinned phase operation; figure taken from datasheet; pixel size in each direction is 13.5 μm).

- **Using a detector technology with a low dark current**: Using photodiodes instead of photoconductors or thermal detectors, using devices with pinned photodiodes instead of standard photodiodes, and so on.

5.2.5.2 Nyquist–Johnson Noise

If the photodetector has certain electrical properties of a resistor – no matter whether it is a photoconductor, photodiode, or something else – it will show a fundamental thermal noise, the Nyquist–Johnson noise. If the parallel connection to the detector and the input impedance of the amplifier have a resistance R, it will produce a voltage noise with an expectation value of its variance of

$$\langle V^2 \rangle = 4k_B T \cdot R \cdot \Delta f. \tag{5.6}$$

In photodiodes, the resistance R corresponds to the sum of the series resistance and the so-called shunt resistance, the meaning of which is depicted in Figure 5.13.

Depending on the input impedance of the amplifier, this will translate into an according current noise of

$$\langle I^2 \rangle = \frac{4k_B T \cdot \Delta f}{R} \tag{5.7}$$

which adds to the measured signal. To minimize the Nyquist–Johnson current noise, the shunt resistance and amplifier input impedance should be high and the photodiode should be cooled.

5.2.5.3 Flicker Noise and 1/f Noise

$1/f$ noise, as its name implies, is a noise whose intensity is indirectly proportional to the frequency. $1/f$ noise does not originate from a particular single source, but is created in all places where physical processes reduce their intensity at higher "speeds" or show a certain kind of recurrence. In fact, however, it is not yet fully understood.

Flicker noise looks much like $1/f$ noise, but it can have a steeper frequency slope and may even have a peak at a low nonzero frequency. Flicker noise is connected to a current flow and originates, for instance, from generation and recombination of charge carriers, impurities in a conductor, or electrical contacts.

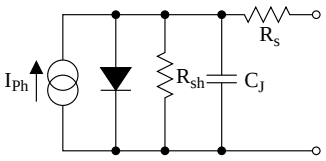

Figure 5.13 Equivalent circuit diagram of a real photodiode, consisting of an ideal current source, which produces a load-independent photocurrent I_{Ph}, an ideal diode, a shunt resistance R_{sh}, a junction capacitance C_J, and a series resistance R_S.

5.2.5.4 Excess Noise

The term "excess noise" covers several noise mechanisms in the detector, which increase the noise to be expected due to photon and dark current statistics. Flicker noise is one type of excess noise. Other excess noise is generated in most internal signal amplification mechanisms, which thus sometimes decrease the sensitivity.

5.2.5.5 Read Noise

The term "read noise" subsumes all noise contributions which are contributed by the readout process of the detector, particularly in amplification, charge-to-voltage conversion, or digitization. There are signal-independent and signal-dependent contributions and individual contributions may be specific for a particular readout technology. Therefore, only the most prominent read noise contributions will be briefly listed here.

- **Quantization noise**: If the signal is digitized, there will be an uncertainty of $\pm^1/_2$ least significant bit (LSB) of the A/D converter. Additionally, the quantization levels of the A/D converter are never exactly equally spaced, for lower quality A/D converters there may even be missing codes (i.e., some quantization levels will never be seen), or the dependence between input signal and code output may be non-monotonic. Quantization noise can be eliminated when the system is operated in a photoelectron counting mode, where every photocharge leads to a change of the A/D output by more than one LSB. This is only useful, however, in low light situations.
- **Amplifier shot noise**: Similarly to amplification mechanisms inside the detector, amplification of a signal in an amplifier is a statistical process and will create an excess noise which depends on the particular design of the amplifier electronics. Optimally, a photocharge signal will thus not be amplified itself, but instead amplification will be applied to a current or voltage signal, which is derived from the charge that is held statically in a capacitance. The relative amplifier shot noise will thus decrease with the inverse square root of the readout time and in this way can in principle be reduced to values below a single photocharge, if the readout time is made large enough.
- **Amplifier thermal noise**: As the readout amplifier is an electronic device, it will contribute some noise due to leak currents, which are equivalent to the dark current in the photodetectors. Furthermore, a Nyquist–Johnson noise will be created by the input impedance of the amplifier, particularly if this impedance is neither very high nor very low. Cooling the first amplifier stage or increasing the readout time helps to reduce these contributions.
- **Output capacitor reset noise**: Some advantageous detector designs require a charge-to-voltage conversion, which uses a small capacitance (i.e., one with a high conversion factor) as the converter. At the beginning of the readout process, the voltage of the output capacitor has to be reset to a reference level, which never succeeds exactly, so there is a so-called reset noise. This noise can be reduced by several approaches, which are discussed later in the sections on image detectors.

5.3
Image Detectors

5.3.1
Pixel-Based Image Detectors

Pixel-based image detectors consist of a plurality of light-sensitive detector elements such as those described above. Part of the existing image detectors, among them the most common types of image detectors, CCD and CMOS or active pixel sensor (APS) detectors, additionally contain some electronics to address the individual pixels and direct their signal to one or more electrical outputs. In this way, the signals can be serialized for further processing by a computer or other electronics. Other imaging devices with a low total number of pixels may not contain pixel selection electronics; instead, the signals of the pixels are directed individually to separate outputs and an external multiplexer will be needed to serialize them if needed. Besides their differences, all those devices can be characterized by some common properties, which will be discussed in the following.

5.3.1.1 Pixel Number, Pixel Pitch and Nyquist Frequency

The pixel number gives the number of individually addressable light-sensitive detector elements of an image detector. The most common pixel arrangement is the rectangular arrangement. In the most common case, detector elements are arranged in a Cartesian grid with a certain number N_y of identical and equidistantly spaced pixel rows, each containing N_x equidistantly spaced, identical detector elements or pixels. Thus a rectangular array with $N_x \times N_y$ pixels will be formed. For the special case of $N_y = 1$, the image detector is called a linear array, otherwise a two-dimensional array. Array sizes vary from 2×1 to thousands by thousands. For example, the high-resolution photographic-purpose CCD chip CCD595 from Fairchild Imaging has a pixel number of 9216×9216, giving a total of about 85 megapixels.

The pixel pitches along the x- and y-directions are often equal and normally driven by considerations of sensitivity, application constraints, technology constraints, or cost optimization. For UV–VIS image detectors, current pixel pitches range from 1.5 μm for low-cost CMOS image detectors to about 26 μm for very sensitive scientific CCDs. IR image detectors can have even larger pixel pitches of up to several hundred micrometers, depending on their application area, but typically they are also in the range up to 25 μm for semiconducting 2D IR detectors.

In addition to the rectangular arrangement, there are a number of special arrangements, for instance with different types of detector elements, pixel rows which are tilted by 45° with respect to the image rectangle (Fuji Super CCD), or pixels which are arranged in a hexagonal grid instead of a Cartesian grid. Special care has to be taken when the performance of such devices is compared with those of the usual rectangular pixel arrangements.

An array with a pixel pitch Δx along a certain direction can resolve a sine-shaped periodic spatial intensity variation which has maximally one local maximum and one

local minimum over a distance of $2\Delta x$, that is, a period which is less than $2\Delta x$ or a spatial frequency which is lower than $1/(2\Delta x)$. Any signal with a shorter period will lead to aliasing and look like a periodic signal of another, lower frequency inside the allowable range. Non-sinusoidal signals can be decomposed into a series of sinusoidal signals (Fourier transform). To reproduce such signals correctly, the maximal non-vanishing spatial frequency must be lower than the so-called Nyquist frequency $1/(2\Delta x)$. This is known as the Nyquist–Shannon sampling theorem or, in brief, sampling theorem. A signal which complies with the given condition is called Nyquist sampled or Nyquist–Shannon sampled by a detector with pitch Δx.

5.3.1.2 Pixel Geometry and Spatial Pixel Response

In every regular pixel arrangement, a pixel can be assigned a unit cell, which in the rectangular arrangement can be chosen as a rectangle with side lengths equal to the pixel pitches in the x- and y-directions. Ideally for most applications, the pixel would be 100% sensitive to light which is absorbed inside the unit cell and would not respond to light absorbed outside. This ideal situation cannot be accomplished in reality, however. On the one hand, large parts of the unit cell may not be light sensitive due to shading from conduction structures or since they contain some per-pixel electronics; on the other hand, light absorbed in the unit cell of one pixel may also contribute to the signal of the neighboring pixels, making it impossible to predict safely which pixel will collect a photoelectron generated at a certain position of the image detector. The latter is typically a result of the finite absorption depth and of photocharge drift effects in the detector material.

Both effects can be jointly described either in the form of a spatial pixel response or of a so-called modulation transfer function (MTF). For a more precise treatment, the angular distribution of the incident light and the wavelength would also have to be considered.

The MTF is the Fourier transform of the spatial pixel response. It directly describes how the modulation depth of a fully modulated sine-shaped intensity distribution with a certain period is reduced due to the spatial pixel response. An MTF value of $+1$ means that after the detection the modulation depth still is maximal, and a value of zero means that only the average intensity of the incident sine wave is seen by the detector and that the details on the modulation are completely lost. At negative values of the MTF, the sine wave is registered inversely, that is, dark parts are seen as bright parts and vice versa. Figure 5.14 shows real pixel responses of an IR detector and Figure 5.15 gives some typical idealized spatial pixel responses and their corresponding MTFs.

As discussed above, the Nyquist frequency of the image detector lies at a spatial frequency of a half inverse pixel pitch. MTF values below this frequency should be large to achieve a high sensitivity and resolution. Whether MTF values for higher frequencies should be large or small depends strongly on the systems in which the image detector is used, since larger spatial frequencies of the incident light will be folded into the Nyquist range due to the Moiré effect. This Moiré effect is used in subpixel detection systems such as double-array spectrometer [14] or scanning multichannel spectroscopy arrangements [15]. In normal imaging systems, where each

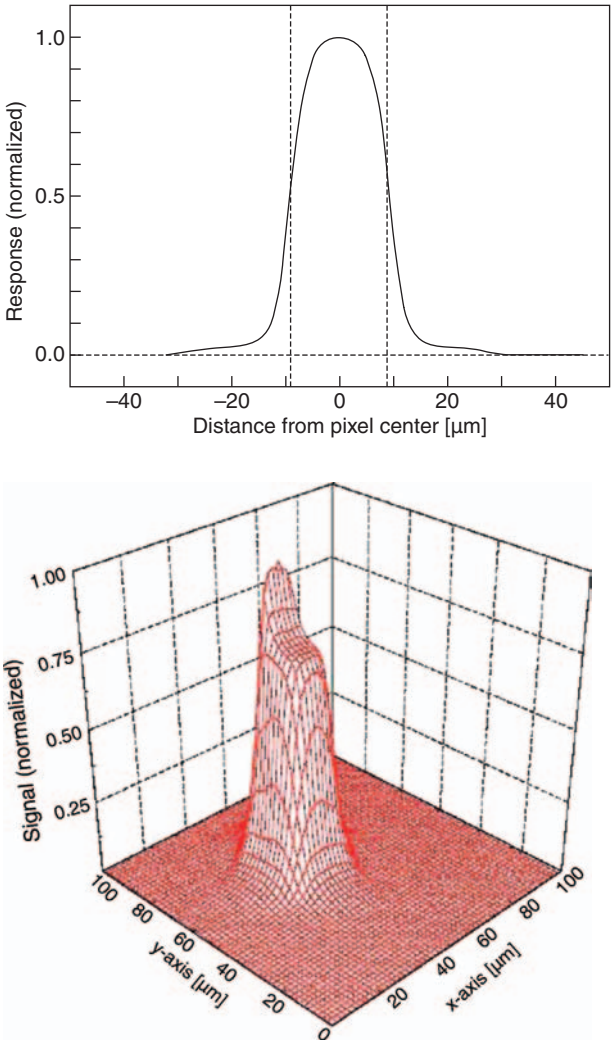

Figure 5.14 One- and two-dimensional pixel response of an MCT image sensor (Teledyne H2RG #40) at a wavelength of 1300 nm as determined experimentally by Barron *et al.* [13].

image is treated individually, Moiré effects will be very annoying. Good imaging systems therefore either contain a spatial low-pass filter in front of the detector or they are dimensioned such that the Abbé cutoff frequency of the optics lies near or below the Nyquist frequency of the detector.

5.3.1.3 Image Acquisition Timing

The acquisition of an image by an image detector consists of two main parts, image exposure and image readout. Image exposure is the exposure of the image detector to

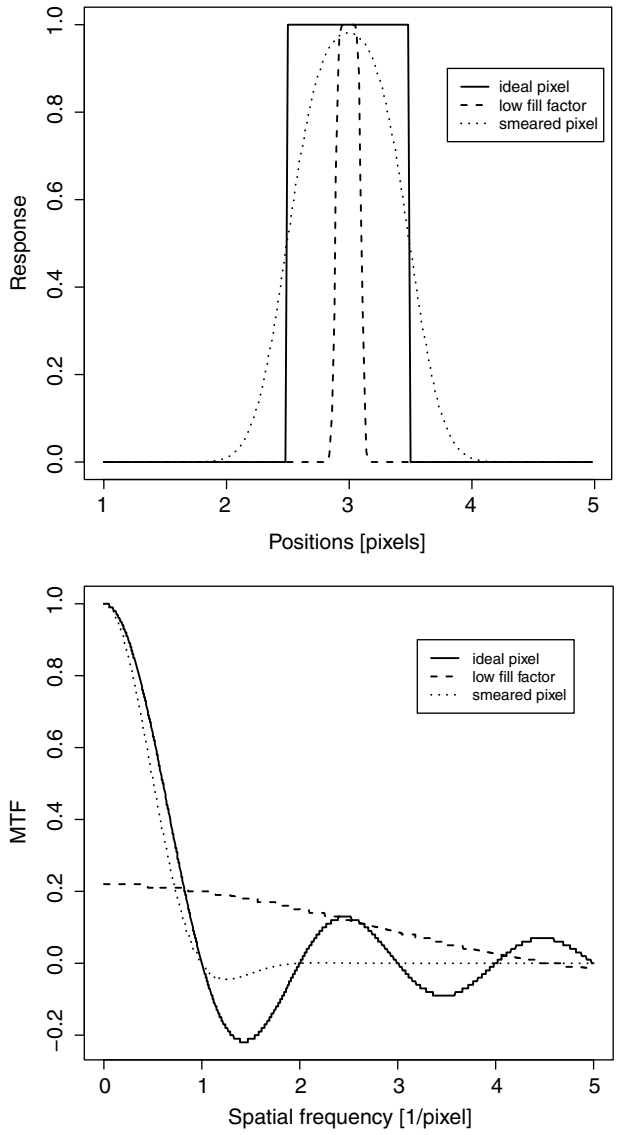

Figure 5.15 Different spatial pixel responses and their corresponding modulation transfer functions; Shown are an ideal pixel with rectangular response and a fill factor of one, a slightly smeared pixel with a low fill factor, such as could be found in a CMOS APS detector, and a smeared pixel with 100% fill factor, as can be observed at back-illuminated CCDs. The Nyquist frequency of the MTF lies at 0.5 per pixel. All given spatial pixel responses lead to MTFs which are non-zero beyond this point, meaning that aliasing could occur.

light, allowing the detector elements to change their state depending on the incident radiation. Two fundamental types of behavior of the detector elements can be distinguished.

The first is characterized by the change in a physical parameter towards an equilibrium value which depends on the incident radiation. The most important example of such a system is an array of thermal detectors, which change their temperature as a reaction to the incident radiation. If the radiation intensity changes from one value to another, the temperature follows with a certain time constant. Consider an image acquisition consisting of an exposure followed by a single temperature readout for each pixel. Exposing the detector to the radiation much longer than the time constant of the detector elements will not yield any significant signal-to-noise gain compared with an exposure which is about 2–3 times the time constant. Not taking into account any errors made in the readout process, the precision of the intensity measurement will depend on the time constant rather than the exposure time. For exposures much shorter than the detector time constant, this will change to the opposite. This type of behavior is not limited to thermal detectors, however, but would also apply to semiconductor detectors, which average incident radiation only by means of a low pass and are read out at a discrete point in time for each measurement. This type of detector will here be referred to as an averaging detector.

The second type of behavior, the accumulating behavior, can be observed in semiconductor detectors with a per-pixel integration capacitance. Here every photon which is absorbed and converted into a photocharge pair will immediately lead to a change of the stored photocharge of the capacitor by one electron. Unless no saturation of the capacitor occurs, the capacitor voltage thus changes practically instantaneously and proportionally to the absorbed energy. In contrast, for the above-described detector behavior, it would have changed proportionally to the incident intensity, showing a delay due to the time constant. For a detector of the accumulating type, the observed signal will on average be directly proportional to the integration time.

Therefore, provided that no saturation occurs, a higher precision of the measured intensity value can be achieved by increasing the exposure time. Figure 5.16 shows an example series of photon incidences and corresponding changes of the temperature signal of an averaging thermal detector and of the accumulated charge of an accumulating detector. Both detectors are modeled as ideal detectors; nonetheless, the thermal detector shows a much worse output signal than the accumulating detector. To circumvent the problems of an averaging detector, its time constant can be made small and a signal accumulation circuit can be connected to its output, so that the overall system behaves approximately like an accumulating detector.

Before the exposure in an accumulating detector starts, the accumulation capacitor of the detector element or a separate accumulation circuit have to be reset. Depending on the technology, the pixels can have some reset gate, which generates a short cut of the capacitors, loads it to a reference voltage, or extracts the charges. Particularly for CCD pixels, the photocharges have to be shifted out of the pixels. In case of a reset, the remaining photocharge in the capacitors will not be exactly zero or at a reference value, but some additional, random charge will remain, which is known as reset

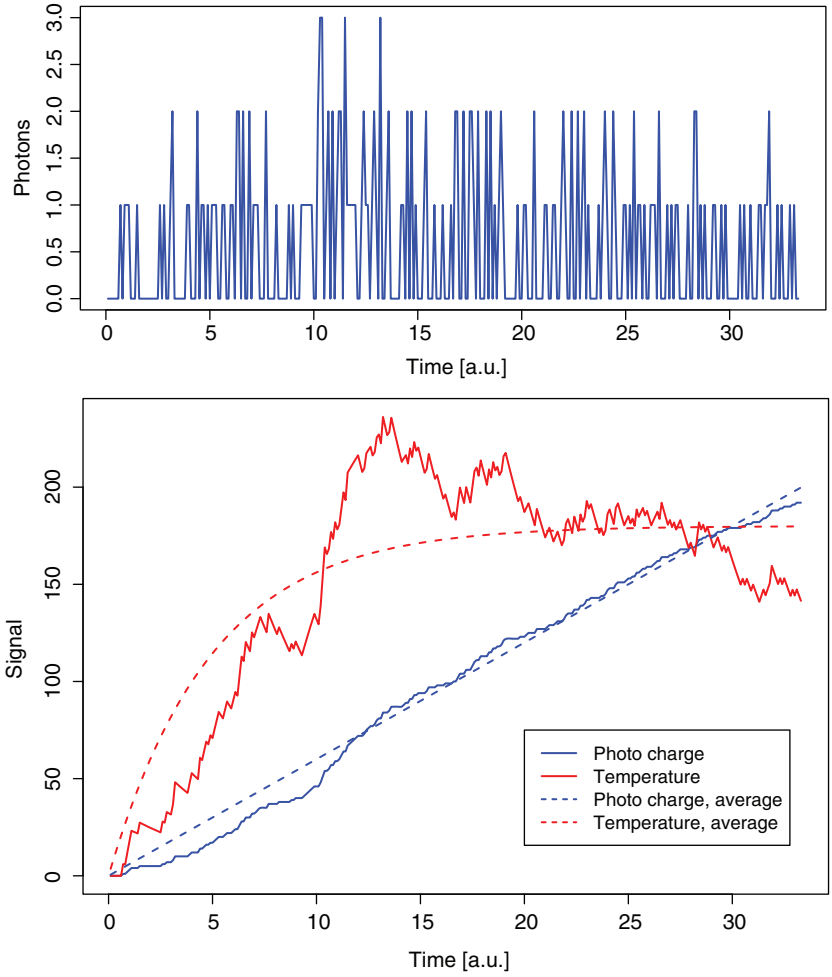

Figure 5.16 Example of statistical incidence of photons and corresponding observed temperature and photocharge of a thermal and a semiconducting (accumulation-type) detector. It can easily be seen that the statistical nature of the light leads to large uncertainties of the measured temperature value and the derived average intensity value, while the accumulated photocharge increases relatively linearly with time and gives a good measure of the average intensity.

noise. For detectors with a possibility of a nondestructive pixel charge readout, such as many CMOS active pixel sensor detectors, the residual charge could be measured right after the reset and before starting the exposure, so it could be subtracted after finishing the measurement. This timing regime is known as double sampling or correlated double sampling and is the simplest timing where the charge readout is not only done after finishing the exposure. More advanced timing regimes for high-sensitivity applications are Fowler sampling, where multiple charge measurements

are performed in the first and in the last third of the exposure time, and sampling-up-the-ramp, where charge measurements are performed continuously during the exposure. After such a measurement, the incident intensity can be determined by fitting a linear function to the series of obtained charge values. Figure 5.17 gives an overview of these readout schemes.

In contrast to image detectors with a nondestructive readout capability, CCD detectors will only be read out after exposure. Since in a CCD detector photocharges are shifted laterally through the chip for readout, there are still several timing parameters that influence the sensitivity and noise of the image acquisition. Also, the summation of pixel charges, the so-called binning, is accomplished by special timing schemes. These timing schemes will be discussed in more detail in the section on CCD operation modes.

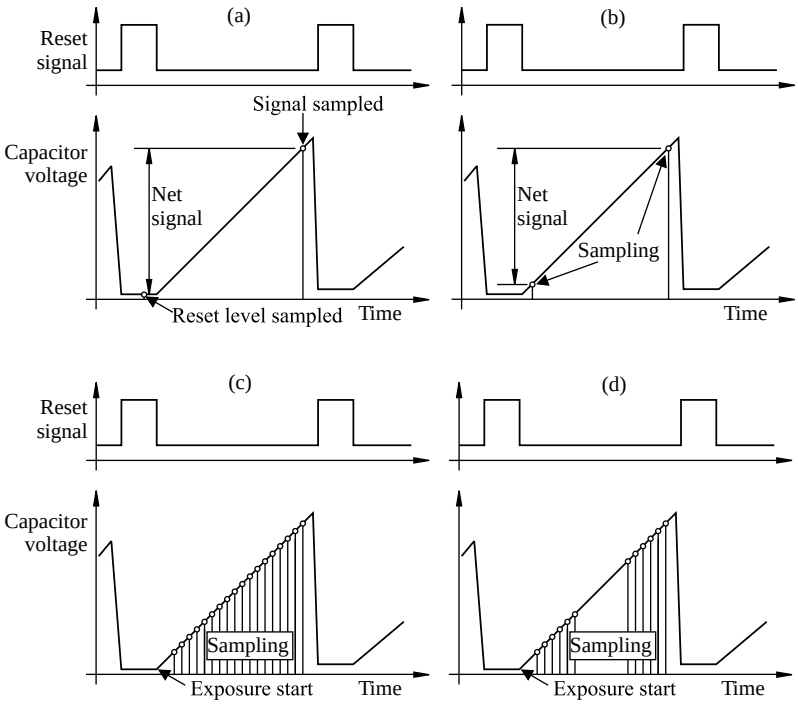

Figure 5.17 Fundamental sampling regimes during exposure of a CMOS detector pixel with non-destructive readout capability. (a) Double sampling or correlated double sampling, recording the reset voltage level and the signal level after integration; in a device with correlated double sampling, the differencing between the two levels is done in the analog hardware path. (b) A double sampling scheme could also be sampling two extreme points during integration, which are separated by a specified time. However, this is not commonly done. (c) Sampling-up-the-ramp, determining the slope of the capacitor voltage by continuous sampling during the integration period. (d) Fowler sampling, determining the voltage slope by sampling during the first and the last third of the integration time.

After all, the user of an image detector will usually be confronted with two main timing parameters, the exposure time and the readout time. The latter can be measured in seconds per pixel and is the time that the output amplifier and A/D converter are given to acquire the signal of a single pixel.

5.3.2 Charge-Coupled Devices (CCDs)

The invention of the CCD image detector was a by-product of the development of an analog shift register for data storage applications. This shift register was initially intended to replace the magnetic memory which was used at that time.

CCDs are almost always silicon-based image detectors. In the UV–VIS spectral region they belong to the most sensitive available detectors and can even be applied for single photon detection. However, the potential of a high sensitivity is not tapped in all CCD types and implementations. Instead, available CCD chips differ significantly in their properties not only between cheap consumer CCDs and high-performance scientific CCDs, but also within these groups. There is no such thing as the best CCD, which is superior in all applications. To select the appropriate CCD for a given application thus requires a basic knowledge about different CCD types and their characteristics and limits. It is the aim of this section to give a coarse overview of the most relevant topics without going too much into the details.

5.3.2.1 General Principle of CCD Operation

CCD image sensors are arrays of photodiodes with an internal capacitance for accumulating photocharges and a capability to shift these charges through the array. Figure 5.18 shows the schematic layout of a simple CCD pixel of a so-called three-phase CCD along with its potential diagram. On a heavily doped substrate an epitaxial layer with a relatively low doping, that is, a high resistivity is grown. The top of this layer is oxidized to create an insulator. Gate electrodes on top of the oxide layer can create a potential well in the epitaxial layer (the substrate is drawn to ground), where charges can accumulate. In the figure, such a potential well is formed below the electrode set to positive voltage, whereas below the electrodes under negative voltage no potential well is created. Accumulated charge carriers will therefore collect below the positive electrode and cannot escape laterally. By repeating the arrangement of positively and negatively loaded electrodes, a lateral pixel structure can be created. The system consisting of top electrode, oxide, and silicon here forms a so-called metal–oxide–semiconductor (MOS) capacitor and the system of differently doped silicon layers acts like a photodiode, including a depletion zone. The electrodes are made of an optically transparent material, so light can enter the silicon and create electron–hole pairs. If this happens inside the depletion region, the charge pairs are separated, so that one species of charge carriers is always drained into the substrate and the other accumulates below the oxide. This simple type of CCD is called a surface channel CCD.

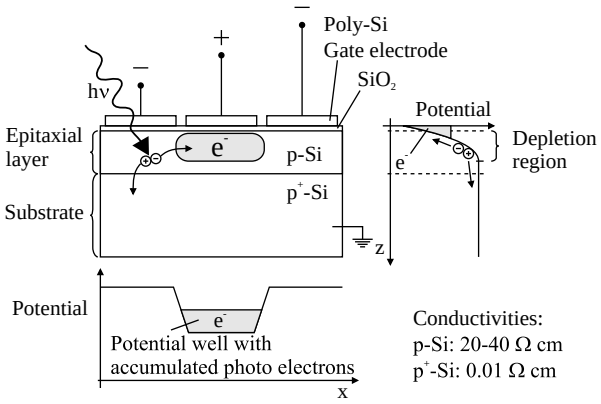

Figure 5.18 General layout of a single pixel of a three-phase CCD (surface channel, i.e., no buried channel) and situation during exposure. Photons absorbed in the approximately 5–10 μm thick depletion region of the CCD will be captured with nearly 100% efficiency in the potential well generated due to the applied voltage, while photoelectrons generated in the bulk of the substrate will undergo a random walk and either recombine with holes or eventually move into the depletion region where they will be captured.

So far, we have only considered a linear structure. Figure 5.19 shows the corresponding two-dimensional arrangement. Whereas in one direction (here tagged the "transfer direction") the described electrode structure leads to a pixelation, in the orthogonal direction different rows of pixels have to be separated by a so-called channel stop. This is a lateral interruption of the lightly doped regions of the epitaxial layer by heavily doped stripes. These stripes have a doping similar to the substrate and are therefore at the same voltage potential, which leads to a fixed lateral confinement of the potential wells along the direction perpendicular to the transfer direction. To

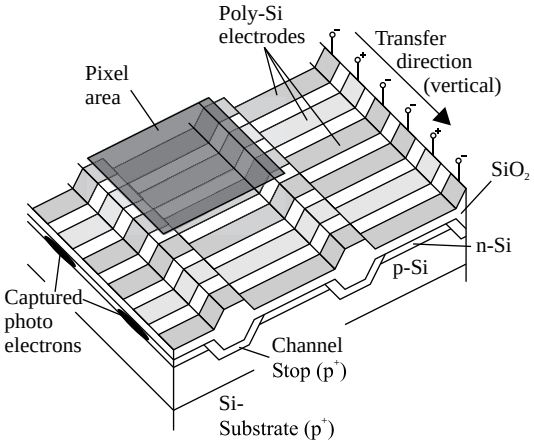

Figure 5.19 Simplified layout of a three-phase front-illuminated p-type buried-channel CCD.

avoid a high electrical capacity between the electrodes and the substrate, the thickness of the gate oxide is increased in the channel stop regions. A pixel of the CCD area now extends over the range between two channel stops and one group of electrodes, that is, three electrodes in the case of a three-phase CCD.

5.3.2.2 Full Well Capacity and Blooming

As described before, the photocharges are collected by a potential well. The depth of the potential well, however, is itself dependent on the number of collected charges. At some point, the well will vanish and additional photocharges can no longer be captured by the well and will spill out laterally. The limit of the number of charges is called the full well capacity and the lateral spill is called blooming. For a given layer structure of a CCD, the full well capacity of a pixel is proportional to its area, that is, larger pixels will commonly provide a larger full well capacity. Typical values are between 15 000 electrons for small pixel consumer CCDs and around 500 000 electrons for scientific CCDs with 26 μm pixel pitch.

The full well capacity limits the dynamic range of a CCD, which effectively is given by the ratio between the full well capacity and the noise level. Cooled scientific CCDs with a pixel size of 26 μm and readout noise of three electrons achieve typical dynamic ranges of larger than 150 000:1 or ∼100 db, while consumer CCDs have typical dynamic ranges of 3000:1 to 5000:1.

Excess charges leaking from a filled potential well will migrate to neighboring pixels, where they will be captured, until these pixels also achieve their full well charge. One intensively illuminated pixel or even a so-called hot pixel, that is, a pixel with a significantly increased dark current, can thus flood a whole number of pixels in its vicinity, mostly along the transfer direction. There exist certain improved types of CCDs which remove excess charges through a so-called anti-blooming (AB) gate. The principle of the AB gate is shown in Figure 5.20. An additional gate electrode, which is placed next to the pixels and parallel to the channel stop, lowers the potential below it so much that excess charges will not flow to other pixels, but through the gate. Behind the gate the charges are extracted through a drain electrode. One drawback of the

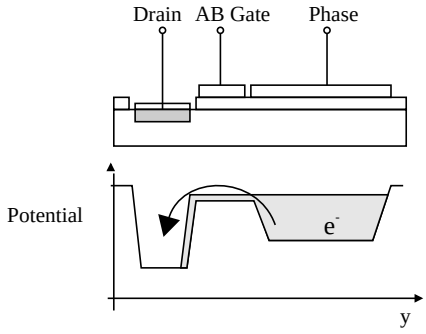

Figure 5.20 Principle of the AB gate. A gate electrode which is located next to a pixel slightly reduces the potential height, so that excess charges will flow through it. After passing the AB gate, the electrons arrive at a drain electrode, through which they can be removed from the chip.

anti-blooming gate is a reduction of the fill factor of the CCD, so for low-light applications it is often better to omit it, whereas for applications with high intensities it may be essential to achieve acceptable results. Additionally, the use of an AB gate considerably reduces the full well capacity of the pixels. Since a lower full well capacity means a lower dynamic range of the CCD, and a high dynamic range is particularly important for high-intensity applications, the latter will suffer from anti-blooming when the pixel size becomes too small.

5.3.2.3 Charge Transfer and Electronic Shutter Capabilities

In a CCD, the photocharges accumulated through the exposure time are not read out directly in the place where the exposure occurred. Instead, they are shifted out of the detector area to one or more sites where they are measured. The basic readout process for the example of a three-phase CCD is shown in Figure 5.21. By setting the gate electrodes of the CCD to different voltage levels, the lateral position and width of the potential well can be altered. The photocharges will always follow the well and can thus be shifted through the detector towards a detector edge.

In addition to the three-phase operation, there are also other operation schemes, using from one to four phases and partly involving a laterally varying doping to create the potential well and define a shifting direction for the photocharges. The laterally varying doping is at least necessary for all CCD types with less than three phases; however, these schemes will not be discussed here. To read out a two-dimensional image, in the simplest case the whole image is first shifted along the transfer direction of the light-sensitive area – which is often referred to as the vertical direction – by one pixel, so that the lowest pixel row is shifted out of the light-sensitive area and transferred into a one-dimensional CCD structure, whose transfer direction is

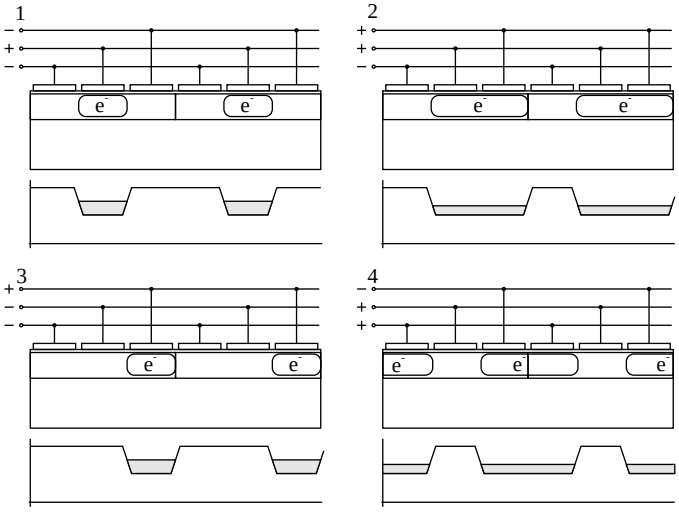

Figure 5.21 Principle of charge transfer at readout time for a three-phase CCD. Shown are the first four of the six steps necessary to shift the charges by the distance of one pixel pitch.

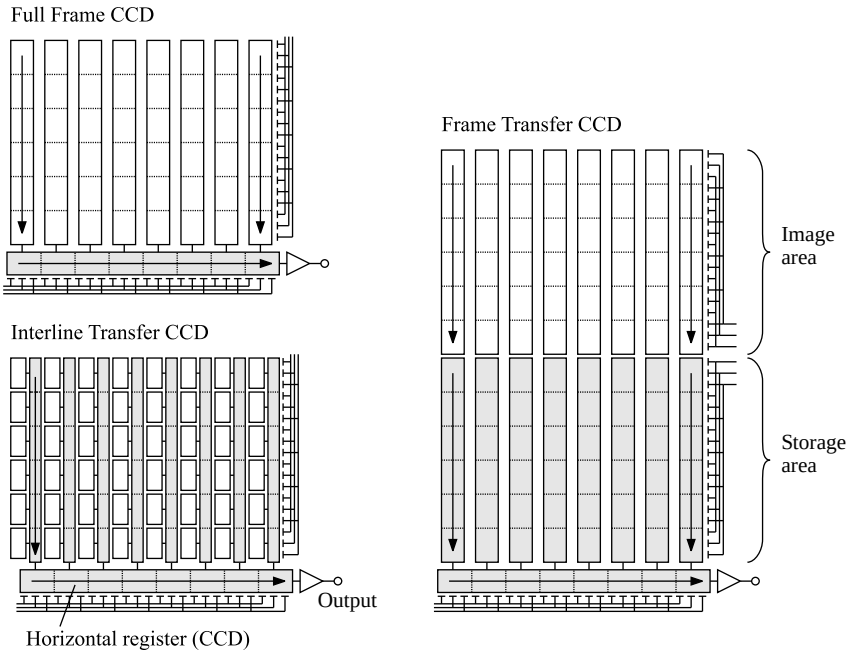

Figure 5.22 Basic CCD image transfer modes.

perpendicular to that of the light-sensitive area and which is shielded from light. This CCD structure is called the readout register or the horizontal shift register. Once an image row has been transferred into this register, the charges can be shifted towards an output node at the end of the shift register, where they can be measured and subsequently discarded. When the shift register is emptied, the next image row can be transferred into it by a vertical shift of the image. The CCD type implementing this fundamental readout scheme is called the "full frame CCD" (see Figure 5.22).

One problem with the full frame CCD is that the light-sensitive area of the image remains light sensitive also during readout. If light continues to fall on to the CCD, accumulation will continue, but since the image is progressively shifted through the CCD, the light will contribute to pixels at the wrong vertical coordinate, leading to a vertical smear effect. One possibility to avoid this is the use of a mechanical shutter or a pulsed light source, but often both possibilities are problematic for reasons that will not be discussed here. Hence certain CCD schemes have been developed to achieve an electronic shuttering capability. For high-quality applications the so-called frame transfer CCD is frequently used. In a frame transfer CCD, the light sensitive "image area" is complemented by an equally large shielded "storage area." After an exposure has finished, the whole image can be shifted rapidly from the image area into the storage area. Then the readout is started from the storage area, as was done from the light-sensitive area of a full frame CCD. By separating the vertical shift electrodes of storage and image areas, the next exposure can be started immediately after the image has been shifted into the storage area and continue during readout. The fast transfer

of the image from the image to the storage area still leads to a certain smear, which is very small, however, compared with the image intensity and can usually be ignored, particularly for long integration times. Otherwise it is at least very well correctable by computational methods because of its low amplitude.

A third scheme, which is in widespread use in consumer devices, is interline transfer. Here, the light-sensitive pixels are not directly connected to the vertical transfer electrodes but are linked to a shielded vertical CCD readout structure by a transfer gate (also a MOS capacitor). For every column of pixels, there exists an adjacent vertical readout register, so that the fill factor of the light-sensitive area is significantly below 100%. After an exposure, the transfer gates are opened, so that the photocharges are transferred into the shielded vertical readout registers. From there they can be read out similarly to the full frame CCD or the frame transfer CCD. Also, the next exposure can start immediately after the transfer, which takes only one or a few clock periods. In addition to the lower fill factor, another drawback of the interline transfer CCD is a limited electronic separation between light-sensitive pixels and the vertical registers, so that through exposure photocharges can be captured directly in the vertical registers, leading to a vertical smear effect.

For frame transfer CCDs and interline transfer CCDs, additional variants exist that permit interlaced readout, that is, for first reading all odd and then all even rows of an image. Interlaced readout modes were introduced for older television standards and are not of interest for scientific applications and of only secondary interest for the recently introduced high-definition video formats, so they will not be discussed here.

For high data or frame rate applications, the number of readout nodes of a CCD can be increased, for instance by subdividing the light-sensitive area into an upper and a lower part, which are shifted to the upper and lower edge, respectively, for readout. Additionally, the readout register can be separated into two parts, one leading to an output node at the left and the other leading to an output node at the right side. If all this is not enough, the shift register can be separated into shorter pieces, each with its own output node, and in extreme cases, such as CCDs for adaptive optics control, every pixel column can have its own output node [16].

5.3.2.4 **Charge Readout**

To read out the charge from the CCD, a so-called floating diffusion (FD) site is used. This is a direct electrical contact (i.e., the oxide is removed) which acts like a capacitor and thus generates a charge-proportional voltage, which can be measured by an external high-impedance amplifier. The term floating diffusion was coined, since this voltage "floats" depending on the charge. Figure 5.23 shows the basic arrangement of the overall output node.

The FD capacitance is placed directly at the end of the horizontal shift register. Charges from this register can therefore be shifted directly into the FD. Immediately after the FD, a single MOS transistor, the reset gate (RG), follows. This gate links the FD to a second direct electrical contact, the reset drain (RD), which is held at a low potential and will thus drain any charge which flows in through the RG. The capacitance of the floating diffusion capacitor is made small to achieve a large conversion coefficient, that is, voltage per unit charge. This small capacitance,

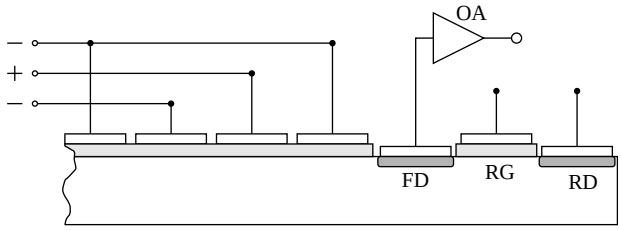

Figure 5.23 Typical output node at the end of a horizontal shift register; Charges are shifted by the shift register into the floating diffusion (FD) output capacitance, which acts as a charge-to-voltage converter, so the charge can be measured by an output amplifier (OA). To remove the charges from the FD, a reset gate (RG) can be opened, transferring the charges to the reset drain (RD), from where they can be extracted from the chip.

however, causes certain noise in the reset process, that is, the draining of the charges through the RG and RD. To remove this noise from the final measurement result, the already mentioned correlated double sampling is used, that is, the charge inside the FD is measured a first time immediately after the reset and a second time after the pixel charge has been shifted into the FD. Subsequently, the difference value is taken, preferably by a hardware-based analog differencing unit. After draining the charge to the RD, the next measurement cycle can be started. As described in the next section, it is also possible to shift the charges of multiple pixels into the FD, holding the reset gate closed.

5.3.2.5 **Binning and Windowing**

By employing the charge shifting capabilities of a CCD in the right way and using some additional structure for erasing charges, so-called dump gates, CCDs can easily be timed in such a way that sub-frames of the full image can be detected and that the charges of adjacent pixels can be combined into a sum charge, which is only read out once and thus is disturbed only once by the readout noise of the readout circuit. Reading out sub-frames is called windowing. Along the vertical direction, a subset of the image rows can be selected for readout by discarding unwanted rows, once they have arrived in the horizontal readout register instead of shifting them to the output node and measuring the charges. The skipping is achieved by opening a reset gate (a MOS transistor) below the shift register, which connects to a dump gate, that is, a direct electrical connection (the oxide layer here is removed), from where charges can be drained out of the chip. Immediately after the content of the register has been discarded, the next image row can be shifted into it. In the horizontal direction the selection of certain image columns is achieved by skipping over unwanted pixels. Similarly to the vertical skipping, they are simply quickly transferred to a reset drain or dump gate by means of a reset gate. The vertical reset gate can be omitted, however, then unwanted image lines would have to be discarded by shifting them to the horizontal reset drain, which would take significantly more time.

Binning, that is, the co-addition of charges inside the CCD, uses the same mechanisms of skipping over certain lines and pixels during readout, but does not

use the vertical reset gate and applies a different timing on the horizontal reset gate. Consider that again an image line which arrived in the readout register is not transferred to the output node, but instead the next image line is shifted into the horizontal register. In contrast to the previously discussed dumping of the charges from the previous line by means of the vertical reset gate, this time the charges of the previous line will still be present in the horizontal register. Then the charges of the second line are added to those charges already present, effectively leading to an addition of the two adjacent image rows. This process can be carried on until the full well capacity of the horizontal register is achieved. Similarly, pixels lying in the horizontal shift register can be co-added along the horizontal direction by skipping over individual pixels without dumping their charge to the reset drain through the reset gate. The charges will be accumulated in the floating diffusion gate and can be measured together after the accumulation. With a CCD it is therefore possible to bin (i.e., co-add) an arbitrary number of adjacent horizontal image lines in a free, arbitrary pattern and discard other lines. This is supported by most scientific CCD controllers. Within each image line or group of binned lines, adjacent pixels could be binned along the horizontal direction and others could be discarded in an arbitrary pattern, which could differ between different line groups. Although easily implementable, such operations are only supported by a few scientific controllers. The whole set of controllers only allows a fixed, regular binning and windowing of only one sub-window along the horizontal direction but several identical windows along the vertical direction.

5.3.2.6 **Charge-Transfer Efficiency (CTE) and Buried Channel CCD**

When an image is read out from the CCD, it has to be shifted through a large number of MOS capacitors; for a pixel located diametrical to the output node, a total of $N_x \pm N_y$ individual shift steps has to be performed. It is very undesirable to lose a significant fraction of photocharges through the whole shifting procedure or to smear the charges over multiple pixels. This makes it essential to have a very high charge-transfer efficiency (CTE) between subsequent MOS capacitors. Consider, for instance, a 1000×1000 pixel CCD. If the CTE in one shift step is as high as 99.99%, that is, one electron per 10 000 would be lost, the overall transfer efficiency for a charge packet undergoing 2000 transfers would still only be a poor value of 81.9%. To achieve an overall efficiency of, say 99%, the CTE here would have to be at least 99.9995%. For larger CCDs the situation is even more demanding; thus for the largest current CCD with 9216×9216 pixels, the same figure of 99% total efficiency would require a CTE of 99.99995%. Unfortunately, at the semiconductor–oxide interface, there is a large number of charge traps, which extract or temporarily capture charges during readout. It is therefore not possible to achieve a sufficiently high CTE for moderately sized to large CCDs with certain quality requirements using a surface-channel CCD.

The issue of surface traps is overcome by adding an additional layer to the CCD, generating a buried channel. This layer is doped inversely to the doping of the substrate and deforms the potential well in such a way that the charge collection will occur at some distance from the surface, as shown in Figure 5.24.

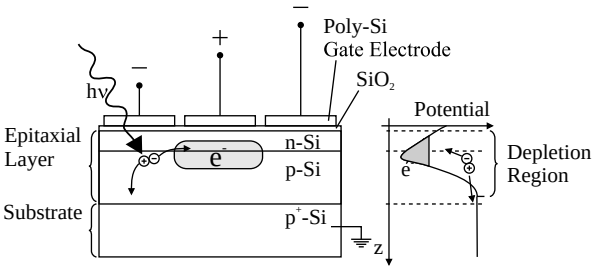

Figure 5.24 To reduce the influence of surface charge traps, increase the charge transfer efficiency, and suppress surface dark current, an additional n-doped layer (p-doped layer for n-type substrates) is employed. This layer deforms the charge collection potential and separates the photocharges from the surface, provided that the gate voltages are in a proper range. This type of CCD is called a "buried channel CCD."

5.3.2.7 **Multi-Pinned Phase (MPP)**

Multi-pinned phase (MPP) operation of a buried channel CCD is an essential step in suppressing the surface dark current, which is usually the largest noise source inside the detector array. In the MPP mode, all gate electrodes are held or clocked in the so-called "inverted state" during integration, that is, the applied gate voltage is driven so much into the negative range (for a CCD based on a p-type substrate) that holes from the channel stop region migrate to the Si–SiO_2 interface and thus populate the n channel. In the inverted state the accumulated holes shield the potential from the gate voltage; thus lowering the gate voltages below the level, where inversion occurs, will no longer alter the potential. This behavior is called pinning and the potential is said to be in a pinned state. In the pinned state the dark current is reduced by approximately three orders of magnitude (Figure 5.26).

If a normal CCD would be set into the fully inverted state, there would be no lateral potential wells and confining potential barriers along the translation direction of the CCD, which could define a pixel. To allow charge accumulation in the fully inverted state, an additional doping below part of the electrodes is introduced into the manufacturing process. This doping leads to a different potential than in neighboring undoped regions, as shown in Figure 5.25. Here a p-type doping is added below

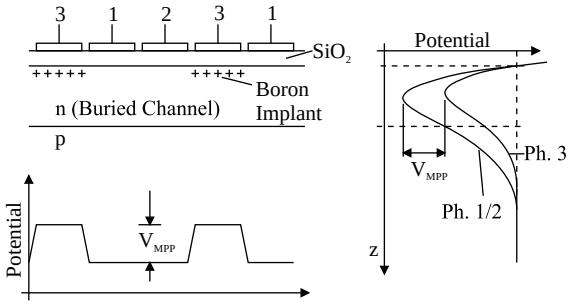

Figure 5.25 Layout and potential diagrams of a three-phase MPP CCD.

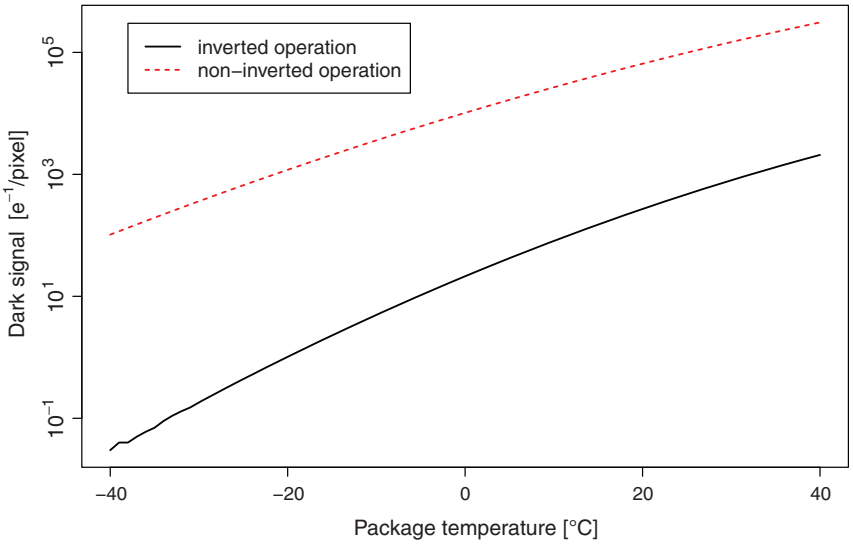

Figure 5.26 Comparison of temperature-dependent dark current for two versions of the same CCD detector. The lower, solid line shows the dark current for the front-illuminated e2v sensor chip CCD30-11 with "advanced inversion mode," a type of MPP; the higher, dashed line shows a front-illuminated CCD30-11 with deep depletion and noninverted operation. The dark current of the latter is roughly 1000 times larger, which is mainly attributed to the noninverted operation.

the electrodes of phase 3, leading to a relative potential barrier of height V_{MPP} below these electrodes in the fully inverted state. Photocharges will therefore accumulate below the electrodes of phases 1 and 2.

The fully inverted state is only left for vertically shifting the image, that is, for the short periods of time between the readout of two adjacent horizontal image lines through the horizontal CCD register. The horizontal register itself is not operated in MPP mode and has no corresponding doping structures, since this would not make any sense and instead lead to spurious charge generation, which is an unwanted noise contribution.

5.3.2.8 Back Side Thinning and Back Illumination

Although the gate electrodes of the CCD are made of a transparent material such as polysilicon, they reduce the quantum efficiency of the CCD by blocking part of the light. Below a wavelength of about 400 nm they even block all the incident radiation. A fundamental solution to this problem is provided by a back-thinned, back-illuminated CCD. In such a CCD, the material, at least in the image area, is etched down from the back side to thicknesses of 10–15 μm, approximately to the interface between the epitaxial layer and p^+-doped substrate. The interface here is used as an etch-stop for a selective etching agent. In early back-thinned CCDs, etching was carried out in such a way that a free-standing silicon membrane inside a thick silicon frame resulted. The mechanical properties and the homogeneity of such a system are

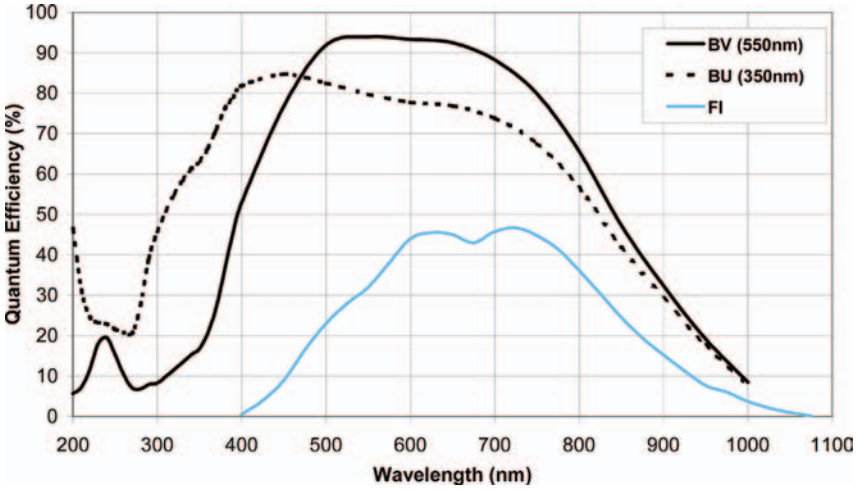

Figure 5.27 Comparison of quantum efficiencies of front- (FI) and back-illuminated (BU/BV) CCDs with the example of an e2v CCD42-10 for two different VIS anti-reflective coatings of the back-illuminated types and at a temperature of −90 °C (diagram from Andor DU-440 datasheet).

not very desirable, however. In newer back-thinned CCDs, the front side of the chip is bonded to a second silicon substrate before thinning and effectively, after the thinning, a thick and stable CCD chip with buried electrode structures results. The entry of light into the sensitive region is now only impaired by the Fresnel reflections at the surface and a usually extremely thin layer with reduced efficiency. The latter results from charge traps at the back side and a finite probability that photoelectrons will thermally diffuse to these traps against the global electrical field direction. The Fresnel reflections can be reduced further by an anti-reflective coating. Figure 5.27 shows a comparison of two typical quantum efficiency curves achieved by a front-illuminated and a back-illuminated high-performance scientific CCD. The back-side operation not only permits detection in the UV range, but also increases the quantum efficiency in the VIS and NIR range. For high-sensitivity applications, back-illuminated CCDs have therefore become a standard.

In addition to many critical issues involved in the manufacturing of good back-illuminated CCDs, however, there are some properties of these devices that limit their applicability in some cases. One of these properties is a reduced short-wavelength MTF performance. Short-wavelength photons are absorbed near to the back side. The generated photocharges have to move almost through the whole thickness of the thinned chip, until they can be captured by the potential well at the front-side buried channel, which also constrains their lateral position. Before this capture occurs, the photocharges have to cross a region with lower electrical field strength. In improperly designed, processed, or operated CCDs there may even remain a region which is not depleted and thus shows no electrical field. Since the charge carriers show a temperature-induced diffusion motion additionally to their directed motion in the electrical field, they will not move to their capture sites along a

straight line, but also show a stochastic lateral movement. In the regions with a weak field, the relation between lateral motion and motion towards the front side will become particularly large and this allows some charge carriers to drift to neighboring pixels before they are captured. This causes an electronic blur, that is, the MTF of the CCD is degraded particularly in the UV spectral range. In scientific back-illuminated CCDs with standard operation conditions a blur in the region of 15 μm [full width at half-maximum (FWHM)] can be observed. With the usual pixel sizes of scientific CCDs this will not be a problem, provided that no sub-pixel information is involved in a measurement approach. At wavelengths longer than 600 nm, the MTF performance will be approximately the same as for front-illuminated CCDs, but here another problem, so-called etaloning, arises due to multiple reflections between the front and back sides of the chip.

Alternative methods for achieving UV sensitivity without back-side thinning are the use of a fluorescent coating on top of the electrode structure or of so-called open electrodes, which do not cover the entire pixel area and thus allow part of the UV radiation to enter the photosensitive layer directly. These techniques will not achieve the same high quantum efficiencies as back-thinned CCDs, but are less expensive and furthermore may have better MTF characteristics, particularly at shorter wavelengths and for the open electrode type.

5.3.2.9 **Etaloning at Long Wavelengths and Deep Depletion CCDs**

In the NIR range beyond about 600 nm, silicon becomes increasingly transmissive and an ever larger fraction of the incident radiation can pass through the whole CCD thickness without being absorbed. This not only limits the NIR sensitivity of the CCD, but also leads to an additional annoying effect, so-called etaloning. Since the CCD chip is transmissive but has a large surface reflection coefficient because of its high refractive index of about 3.5–4 in the NIR region, it starts to act as a Fabry–Pérot etalon, where light is reflected forwards and backwards several times, causing interference fringes. Etaloning leads to a preference of certain wavelengths over others with a very strong dependence on the thickness. Since thickness – particularly in back-thinned CCDs – varies spatially, a monochromatic image will be disturbed by a fringe structure, and precise quantitative measurements will become very difficult. The effects are most severe for back-thinned CCDs and can lead to intensity modulations of more than 50% of the total intensity.

One way to reduce etaloning and achieve a higher quantum efficiency in the NIR region is to use a CCD with deep depletion. The thickness of the sensitive (depleted) layer here is increased to about 40 μm using a high-resistivity silicon. Back-illumination and back-thinning can still be used, and the latter accounts for the increased thickness of the depleted layer, that is, the thickness of a back-thinned deep depletion CCD will be much larger than that of a standard back-thinned CCD. The drawback of deep depletion CCDs is that they cannot be operated in fully inverted (i.e., MPP) mode, so the dark current at a given temperature is about 1000 times larger than that of a CCD using MPP operation at the same temperature and deeper cooling is necessary to achieve the same dark current values. For applications with

short integration times, however, an increased dark current may be acceptable as a price for the increased IR quantum efficiency.

For radiation with a coherence length (see Chapter 4) below the doubled optical thickness of the CCD, the etaloning will vanish. For example, at a wavelength of 1000 nm (the refractive index here is 3.57) and a thickness of 40 μm, this coherence length is about 285 μm. Care still has to be taken if the investigated radiation is known to have highly monochromatic peaks, for instance from a laser line which is mixed into another spectral distribution, or if the CCD is used in a spectrometer with such a high resolution that the coherence length of a single channel becomes larger than the critical value. Particularly the limit of the spectral with (FWHM) is given by

$$\Delta\lambda \geq \frac{\ln 2}{\pi} \frac{\lambda^2}{d_{\mathrm{CCD}} \cdot n_{\mathrm{Si}}(\lambda)} \tag{5.8}$$

where d_{CCD} is the thickness of the CCD and n_{Si} is the refractive index. For the above example, a spectral resolution of better than 1.5 nm (corresponding to a wavenumber resolution of 15 cm^{-1}) could lead to etaloning despite the deep depletion CCD. For methods such as Raman spectroscopy this is not a particularly high resolution, so etaloning is likely to occur if no further precautions are taken. In addition to anti-reflective coatings, which can substantially suppress etaloning, these precautions can include roughening of the back side (with respect to the incident radiation). In fact, a certain "roughening" already occurs due to the electrode structure and the channel stops. Roughening will suppress etaloning if the spatial coherence diameter of the incident radiation is significantly smaller than the spatial spread which is caused by the roughening. Otherwise, it will lead to speckle noise. In well-designed spectroscopic devices, however, the spatial coherence diameter should be smaller than a pixel pitch, at least along the direction of the dispersion, so the etaloning/speckle noise will be reduced significantly. In a spectroscopic system with an anti-reflective coated, back-side roughened, deep depleted CCD, the spectra will look visually smooth and free of etaloning. However, if precise quantitative measurements have to be performed, one should be aware that none of the anti-etaloning precautions can really eliminate etaloning completely.

5.3.3
Photodiode Arrays (PDAs), Active Pixel Sensors (APSs/CMOS), and IR Focal Plane Arrays (FPAs)

As in the previous section on CCDs, it is the aim of this section to give some fundamental properties of photodiode array (PDA), active pixel sensor (APS), and focal plane array (FPA) detectors and here particularly on CMOS APS sensors, since these are most relevant for many applications. This knowledge should enable one to choose among different available sensors for a certain application. Since APS technology is much more variable and heterogeneous than CCD technology, currently developments in this sector are extremely fast, and future developments can only be foreseen to a small extent, it is particularly important to understand some basic principles and their implications for device performance. In contrast, it would

be useless simply to list different APS types and their performance parameters. For a complete understanding of this section and for complementary information, it is recommended also to read Section 5.3.2 on CCDs.

5.3.3.1 Plain Photodiode Arrays and Focal Plane Arrays

In addition to CCDs, monolithically integrated arrangements of photodiodes without a charge shifting capability can be used to record one- or two-dimensional intensity distributions. In the simplest case, these PDAs do not contain any readout electronics or pixel addressing capability and partly also have no relevant photocharge integration capability. Such pure PDAs are usually only used if either the technology of the PDA does not easily allow the integration of readout electronics, if different pixels have to be read out truly parallel at a high speed, or if a very small total number of pixels makes the integration of readout electronics useless or inefficient. Examples of technologies that do not easily allow for the integration of readout electronics are in principle all non-silicon-based types of photodiodes, which are particularly interesting in the IR region, and technologies with processes that are incompatible with standard electronic processes. Further, they also include types of photodiodes with incompatible voltage levels of signals or bias voltages, such as avalanche photodiodes.

For PDAs without readout electronics, which are linear, or have a small number of pixels, connections for each pixel are usually drawn out to the lateral boundaries of the array, where they can be connected individually to some follow-up electronics. If the latter can be used to address the photodiodes individually to reset their accumulated charges or connect them to one or a few outputs, it is called a multiplexer and is often based on CMOS technology. Sometimes a CCD-like device may also be used, but this is less common.

For PDAs with larger pixel numbers it will not be possible to connect every pixel individually from the lateral border. This situation is typical of IR image detectors, often referred to as FPAs. Here a hybrid solution is used, where a PDA chip of some IR-sensitive semiconductor material is placed on top of a silicon-based so-called readout integrated circuit (ROIC) chip, that is, a two-dimensional multiplexer. The two chips are connected by indium solder bumps (Figure 5.28).

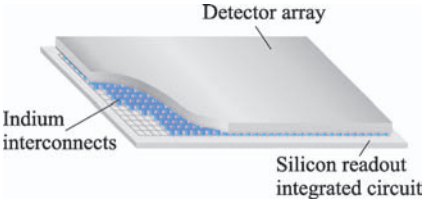

Figure 5.28 Basic scheme of a hybrid IR FPA. The FPA consists of an array of IR-sensitive photodiodes, photoconductors, or sometimes other detector types without any readout electronics. The readout is accomplished by a separate silicon ROIC, which is bonded to the detector array using indium bumps. The ROIC is a complete CMOS imager, but without integrated photodiodes. These are replaced by the contacts below the indium bumps.

The term FPA is also used for image detectors which use light-sensitive elements other than photodiodes, such as thermal detectors and photoconductors. Except for the photodiodes or other light-sensitive elements, which are replaced by contact structures, ROICs are very similar to the CMOS active pixel sensors discussed in the next section, and work as multiplexers with or without integrating capacitors. For some imagers the ROIC may also be based on a CCD instead of a CMOS design. Furthermore, sometimes even silicon-based PDAs are connected to a separate ROIC in a hybrid arrangement. One reason, as before, can be incompatible production processes for readout and PDA; a second reason is, however, the wish to achieve a high fill factor. Particularly, if there is a lot of functionality in each pixel, the achievable fill factors of a monolithic sensor are very limited.

The hybrid technology of FPAs is very complex for several reasons, such as the connections between light-sensitive chip and ROIC, thermal expansion mismatch between the different materials, or the processing steps which are necessary to make the light-sensitive elements electrically connectable from the back side. In addition to the already high costs of good IR photodiode or photoconductor arrays, this complexity is the second main cost factor of FPAs, which are still relatively expensive.

Once a photodetector array has been connected to a multiplexer or ROIC, it practically becomes an APS with all of its possibilities and limitations. The details of the operation of such a device will therefore be discussed only in the section on APS image detectors, without explicitly mentioning the applicability to PDAs and FPAs.

5.3.3.2 CMOS Image Detectors/Active Pixel Sensors

The APS [17] is characterized by the fact that every pixel contains its own readout amplifier, addressing and reset electronics, and probably further elements. In addition to different possible technologies for the intra-pixel electronics, APSs also cover a wide range of light detector technologies and can be monolithically integrated as well as hybrid devices. Usually they will be based on a photodiode or pinned photodiode as the detector element, but may also use a thermal or photoconducting detector or borrow from CCD technology in the form of the photogate.

The APS is often simply referred to as a CMOS image sensor. However, on the one hand it is not limited to a CMOS technology and on the other it would also be possible to manufacture a passive pixel sensor on a CMOS technology base. Except for pixel electronics designs which share transistors between pixels, the simplest pixel design has three transistors and is therefore called a 3T pixel. Here one transistor is needed to reset the accumulated pixel charge, one is needed to address the pixel, and one realizes the amplifier functionality. The principle of an APS with 3T pixels is shown in Figure 5.29, the realization with three MOS transistors is shown in Figure 5.30, and a typical signal diagram of the capacitor voltage is show in Figure 5.31.

The number of transistors per pixel is not limited to any maximum value, and every pixel can in principle have very complex signal-processing capabilities. Typically, the number of transistors varies from three to seven, allowing for more or less complex timing, exposure, and shutter modes and for different handling of over-exposure situations. For more special demands, there are, however, pixels with

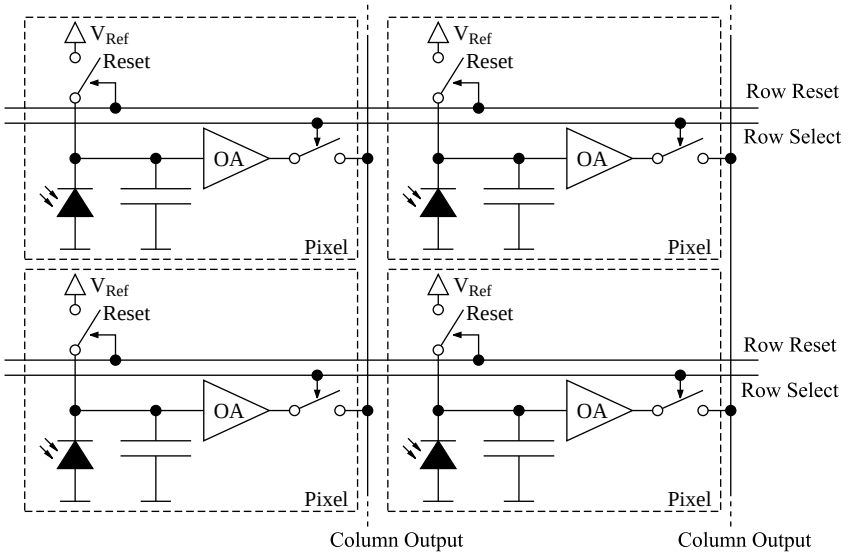

Figure 5.29 Coarse principle of a simple 3T pixel architecture: Before an integration starts, an integration capacitor in each pixel is reset to a reference voltage V_{DD}. When illuminated, the photodiode in each pixel discharges the capacitor, whose voltage is amplified by a per-pixel output amplifier (OA). By setting one row select signal active, all pixels of this row are enabled to forward their OA signal to their according column output line. At the end of each line for instance an individual analog-to-digital converter exists, or a further switch per column allows one of the columns to be forwarded to a common chip output or ADC.

a much larger number of transistors, such as a 37 transistor pixel design with per-pixel analog-to-digital conversion for a high-speed image sensor reported by Kleinfelder *et al.* [18].

The main problem with too many transistors per pixel is a low resulting fill factor, but this can be overcome, at least partly, by using a hybrid approach or

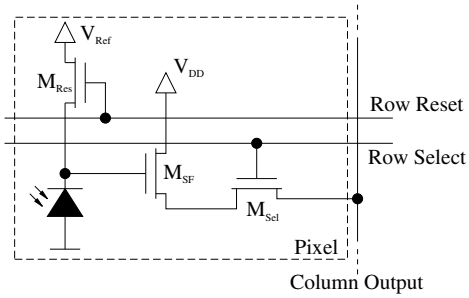

Figure 5.30 Realization of a 3T pixel with three MOSFET transistors. Transistor M_{Sf} is a so-called source follower and acts as the output amplifier. By activating the row select line, its output is transferred to the column output line via the transistor M_{Sel}. Transistor M_{Res} is used for charge reset, the charge is stored inside the photodiode capacitance.

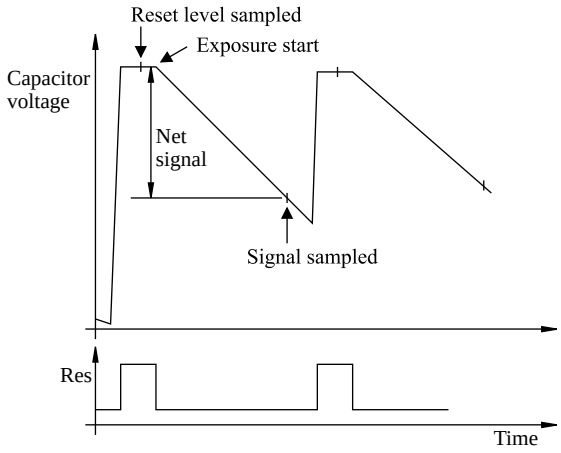

Figure 5.31 Typical exposure timing of a 3T APS pixel. The integration capacitance is first reset to a reference voltage level, which is then immediately sampled before the start of the integration to suppress reset noise. After an exposure time, the now reduced capacitor voltage is sampled a second time to determine the signal (i.e., the accumulated intensity).

back-illumination. Also, lens arrays on top of the APS are used to increase the fill factor. However, they also cause some problems for scientific applications, which will not be discussed here.

5.3.3.3 Double Sampling and Correlated Double Sampling (CDS) in APS Imagers

One common feature of most APS imagers is that at some stage a per-pixel capacitance will be used either to integrate a photocurrent or to convert a stored charge into a voltage using a capacitance. Before the integration or the charge transfer, the capacitance needs to be reset to a reference voltage. Similarly to the reset noise at the floating diffusion site of a CCD output node, this does not work perfectly. Instead, a reset noise occurs when the capacitance is reset to the reference voltage. Moreover, the average reset level varies from pixel to pixel, which is called fixed pattern noise (FPN).

These noise contributions can be eliminated by double sampling (DS) (not to be confused with the statistical method) or correlated double sampling (CDS). In APS detectors, the CDS scheme is based on a hardware feature which generates the difference signal between the two sampled values of one pixel integration in the analog domain. For this purpose, at the end of each column output line, there exists one dedicated CDS circuit, which can store the two values in two separate sample-and-hold units and derives the difference voltage. The principle of such a unit is shown in Figure 5.32. Since the CDS unit needs the two sampled voltages of one pixel directly after each other, it is clear that the pixel itself needs to have a possibility to store the reset voltage throughout the integration period and transfer it to the column output line on demand. This is not possible with a 3T pixel design and requires at least a 4T pixel. For pixel architectures where the reset noise is generated in

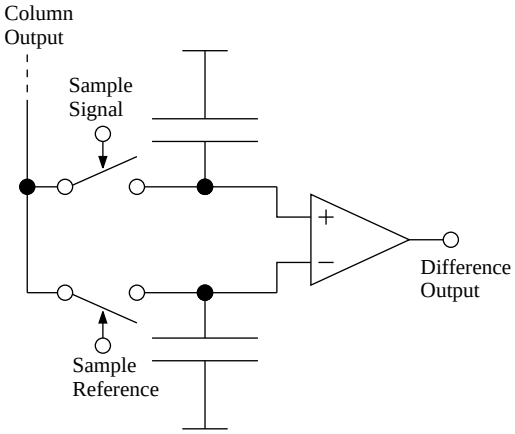

Figure 5.32 Schematic principle of a correlated double sampling circuit at the end of each column output line of a CDS capable APS imager; Two parallel sample-and-hold circuits, each mainly consisting of a switch and a storage capacitor, are used to sample the reference and the signal level of a pixel sequentially. A differential amplifier produces a new signal, which is corrected for the reference level.

a charge readout after the exposure, an extra charge storage capability is not necessary.

The two DS schemes can be used to solve the problems of reset noise and FPN; however, they produce their own, weaker noise and errors. In the case of DS, an additional noise contribution is added due to the second necessary voltage measurement, and in the case of CDS, the CDS circuitry causes a column fixed pattern noise, which has to be removed by further means. The DS approaches furthermore only work well if the output amplifiers respond linearly to the photocharge. It should be mentioned that in contrast to the term "correlated double sampling," the term "double sampling" is not in widespread use in the context of measuring electrical properties.

5.3.3.4 **Exposure Integration Schemes**

One criterion to categorize APS pixels is the way in which the integration of the incident light is done. This issue is closely related to the type of light-sensitive element.

Many APS detectors are based on photocurrent-producing light-sensitive elements such as standard photodiodes or photoconductors. The operation of a pixel here starts with preloading the accumulation capacitance with a certain charge (i.e., to a certain voltage), which is then drained by the photocurrent of the light-sensitive element. One drawback of this approach is a reduced sensitivity for low intensities, since it is much harder to detect a small number of missing charges on a large charge background than to detect the charges themselves as an absolute signal. This is complicated by reset noise and FPN, which have to be corrected particularly well in order to achieve a good low light sensitivity.

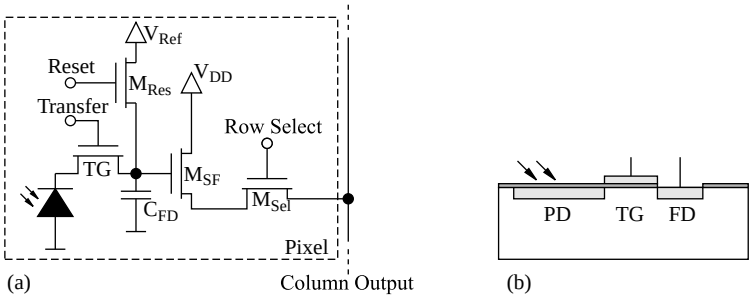

Figure 5.33 Design of a simple 4T pixel with pinned photodiode (PD), transfer gate (TG) and floating diffusion (FD) as a storage/measurement capacitance. (a) General pixel design; (b) the three elements in a cross-sectional view; The arrangement resembles the combination of transfer gate and floating diffusion as known from the readout node of a CCD. Instead of a pixel of the CCD readout register, the pinned diode is directly connected to the transfer gate.

More sensitive pixel designs are based on a photogate or pinned photodiode, which in a similar manner to CCDs accumulate photocharges in a local potential well (Figure 5.33). These elements are not available in all technologies, however. In the pinned photodiode, the potential well is created by the structure of the doping, usually a buried n channel, and in the photogate it results from a voltage which is applied to a transparent electrode above the sensitive area. Although the photogate effectively is a MOS transistor, we will not count it here in the number of transistors of the pixel. Before the exposure, the potential wells are flushed to a zero charge. Photocharges are then collected during integration. After the integration, the charge is transferred to a small capacitance, where it is converted into a voltage that can be read out in the usual way. The charge transfer is accomplished by a transfer gate, that is, an additional MOS transistor between the light sensitive element and the measurement capacitance. The latter is usually laid out as a floating diffusion capacitor. This arrangement closely resembles the readout node of a CCD (see Section 5.3.2.4) and the charge transfer between light-sensitive element and floating diffusion capacitance is accomplished by a deeper potential well of the floating diffusion capacitor than of the light-sensitive element.

Reset noise and FPN here mainly apply to the capacitance and not to the light-sensitive element. The DS or CDS operation here therefore compares the voltage of the measurement capacitance before and after the charge is transferred to it. Both values can be determined after the integration, so CDS can be implemented already in the simple types of photogate- or pinned photodiode-based pixels. In contrast to pixels based on plain photodiodes or photoconductors, the charge of the photogate or pinned photodiode cannot be read out nondestructively during the exposure. For the pinned photodiode, however, it would be possible to transfer photocharges repeatedly to the floating diffusion capacitor during the exposure time without resetting the latter during this time. This would permit an indirect kind of Fowler or up-the-ramp sampling (Figure 5.17) by a simple change of the timing.

5.3.3.5 Electronic Shutter Modes

As opposed to the CCD, pixels of an APS sensor can be read out and reset more or less randomly and their charge will not be shifted through the light-sensitive area. Hence in principle no shutter capability is needed to avoid spatial blur in the readout process. However, as a minimum requirement for the acquisition of usable images without an external shutter or a pulsed illumination, it should additionally be possible to achieve equal exposure times for all pixels. The starting point of an exposure is always determined by the resetting (photodiode/photoconductor) or flushing (pinned photodiode/photogate) of the integration capacitance and can be done individually for every pixel row or globally for all pixels, even for the simplest pixel types. The true problem, particularly for simple pixel types, is to set the end point of the exposure integration. In the 3T pixel the exposure is effectively stopped when the pixel charge is read out and cannot be stopped in another way. Since only one row can be read at a time and different rows must be read sequentially, the only possibility for maintaining a constant exposure time for all pixels of the array is also to start the exposure of different pixel rows sequentially. This cheapest of all shutter approaches is called a "rolling shutter." The array exposure starts with resetting the first row, waiting for one row readout time, resetting the second row, and so on. One exposure time after resetting the first row, the accumulated charges of the first row are read out, then the second row follows, and so on. The readout of the lower row may already start when the resetting of the higher rows is still in progress. In an extreme case, the exposure time can even be shorter than the row readout time; however, this has to be supported by the on-chip control logic.

The rolling shutter approach works well for capturing fixed or slowly changing intensity distributions, but for fast processes or dynamic scenes it produces artifacts. Here a snapshot operation – also called global shutter operation – of the image sensor is desirable. To achieve a real snapshot capability, that is, start and stop the exposure interval for all pixels simultaneously, a second charge storage capability in addition to the integrating capacitance is required, such as is present in the 4T pixel of APS with a pinned photodiode or photogate. A usual 3T pixel can be extended in a similar manner to a 4T pixel with a standard photodiode or photoconductor by adding one transistor and one storage capacitor. In both types of 4T pixels, however, the snapshot operation is in conflict with the CDS capability. The reason is simple: the exposure is in both cases stopped by transferring the accumulated charge to the floating diffusion node or the newly introduced storage capacitor. To achieve snapshot operation, this would have to be done simultaneously for all pixels. However, as pointed out above, for CDS operation the charge transfer has to be done row by row with a sampling by the CDS circuits before and after each transfer. The same 4T pixel can thus be used for snapshot operation and for CDS operation, but not for both at the same time. Again, the choice is determined by the readout timing of the on-chip control logic. To achieve CDS and snapshot operation simultaneously, at least a 5T pixel design is necessary. Further transistors may be added to achieve anti-blooming (i.e., prevent spill-out of excess charges in an over-exposure situation), improve performance parameters of the pixel, or add preprocessing capabilities to the pixels (intelligent sensors).

5.3.3.6 Back-Side Thinning of CMOS Image Detectors

Starting from the first decade of the twenty first century – and even earlier in astronomy research – back-illumination has also been introduced in CMOS APS technology. This development was driven by sensitivity problems with consumer cameras with large numbers of small pixels, but also by the fact that it has major advantages for scientific applications. With the introduction of back-illumination, APS devices start to offer the same potential for scientific applications as CCDs, particularly high sensitivity and detection down to the deep-UV region. At the same time, they retain their specific advantages over CCDs, particularly a much simpler external electronic circuitry, significantly lower power consumption, and the potential for much smaller pixels. Consequently, the development of scientific back-illuminated APS devices is particularly interesting for the space sector [19].

References

1 Paschotta, P. (2008) *Encyclopedia of Laser Physics and Technology*, Wiley-VCH, Berlin.

2 Wagemann, H.G. and Schmidt, A. (1998) *Grundlagen der Optoelektronischen Halbleiterbauelemente*, Teubner, Stuttgart.

3 Jones, K.A. (1990) *Introduction to Optical Electronics*, Harper & Row, New York.

4 Nahory, R.E., Pollack, M.A., Johnston, W.D. Jr., and Barns, R.L. (1978) Band gap versus composition and demonstration of Vegard's law for InGaAsP lattice matched to InP. *Appl. Phys. Lett.*, **33**, 659.

5 Hansen, G.L. and Schmit, J.L. (1983) Calculation of intrinsic carrier concentration in HgCdTe. *J. Appl. Phys.*, **54**, 1639.

6 Hamamatsu Global, http://www.hamamatsu.com/. (July 2010).

7 Brivitch, I. and Renker, D. (2006) Measurements of the recovery time of Geiger-mode avalanche photodiodes. *Nucl. Instrum. Methods Phys. Res.*, **567** (1), 260–263.

8 Dixon, A.R., Dynes, J.F., Yuan, Z.L., Sharpe, A.W., Bennett, A.J., and Shields, A.J. (2009) Ultrashort dead time of photon-counting InGaAs avalanche photodiodes. *Appl. Phys. Lett.*, **94**, 231113.

9 Chou, S.Y., Liu, Y., Khalil, W., Hsiang, T.Y., and Alexandrou, S. (1992) Ultrafast nanoscale metal–semiconductor–metal photodetectors on bulk and low-temperature grown GaAs. *Appl. Phys. Lett.*, **61** (7), 819.

10 Koscielniak, W.C., Pelouard, J.L., and Littlejohn, M.A. (1989) Dynamic behavior of photocarriers in a GaAs metal–semiconductor–metal photodetector with sub-half-micron electrode pattern. *Appl. Phys. Lett.*, **54**, 567.

11 Honkanen, K., Hakkarainen, N., Määttä, K., Kilpelä, A., and Kuivalainen, P. (1999) High-speed metal–semiconductor–metal photodetectors fabricated on SOI-substrates. *Phys. Scr.*, **1999**, 127.

12 Dobrzanski, L., Jagoda, A., Gora, K., and Przyborowska, K. (2002) Properties of metal–semiconductor–metal and Schottky barrier GaN detectors. *Opto-Electron. Rev.*, **10**, 291–293.

13 Barron, N., Borysow, M., Beyerlein, K., Brown, M., Weaverdyck, C., Lorenzon, W., Schubnell, M., Tarle, G., and Tomasch, A. (2006) Sub-pixel response measurement of near-infrared sensors. Arxiv preprint astro-ph/0611339.

14 Wuttig, A., Riesenberg, R., and Nitzsche, G. (2002) Subpixel analysis of a double array grating spectrometer. *Proc. SPIE*, **4480**, 334.

15 Deckert, V., Liebler, W., Eck, R., and Kiefer, W. (1997) New device for Raman difference spectroscopy with multichannel and scanning multichannel detection. *Appl. Spectrosc.*, **51** (7), 939–943.

16 Janesick, J.R. (2001) *Scientific Charge-Coupled Devices*, Society of Photo-Optical Instrumentation Engineers (SPIE), Bellingham, WA.

17 Yang, G., Cunningham, T., Ortiz, M., Heynssens, J., Sun, C., Hancock, B., Seshadri, S., Wrigley, C., McCarty, K., and Pain, B. (2002) Integrated imaging sensor systems with CMOS active pixel sensor technology. Presented at the 201st Meeting of the Electrochemical Society, Philadelphia.

18 Kleinfelder, S., Lim, S.H., Liu, X., and El Gamal, A. (2001) A 10000 frames/s CMOS digital pixel sensor. *IEEE J. Solid-State Circ.*, **36** (12), 2049–2059.

19 Waltham, N.R., Prydderch, M., Mapson-Menard, H., Pool, P., and Harris, A. (2007) Development of a thinned back-illuminated CMOS active pixel sensor for extreme ultraviolet spectroscopy and imaging in space science. *Nucl. Instrum. Methods Phys. Res. A*, **573** (1–2), 250–252.

6
Instruments in Biotechnology and Medicine

Andreas Voss, Karl-Heinz Feller, and Dieter Beckmann

Biophotonics is a fusion of photonics and biology and represents interactions between light and biological material; it combines optical technologies, microelectronics, and imaging for applications in medicine and biotechnology. The increasingly aging world population increases tremendously the financial pressure on our health care systems. Efforts are under way to develop technologies that increase the efficiency of the patient care process. One such technology is biophotonics.

The application of biophotonics in diagnostics and therapy has already and will continue to have an increasing major impact on health care and the health care industry. This chapter is intended as an introduction to applications of biophotonics in medicine and biotechnology, not as an in-depth, exhaustive, and complete treatise on this field. The objective is to provide a basic knowledge of a range of topics to stimulate the reader to learn and think further about the challenges of biophotonics and to initiate and intensify studies in this field.

6.1
Photonic Instruments in Medicine

6.1.1
Introduction

6.1.1.1 Optical Window of Cells and Tissues

Concerning the irradiation of human tissue with light, different aspects of light–matter interactions have to be discussed. In general, the effects of light on human tissue depend on the wavelength of the irradiated light and, of course, on the intensity of the light. Furthermore, the duration of application (skin effect) is of great importance. In this respect light–(human) matter interactions are of very complex nature. Concerning the wavelength dependence of light penetration into cells and tissues, as shown in Figure 6.1 [1, 2], absorption and multiple scattering affect the penetration of the light. At short wavelengths [in the deep ultraviolet (UV) region], the penetration is short due to high absorption coefficients (ε in $mM^{-1}\,cm^{-1}$) and strong Rayleigh scattering. In the visible region, the absorption decreases (no water

Handbook of Biophotonics. Vol.1: Basics and Techniques, First Edition.
Edited by Jürgen Popp, Valery V. Tuchin, Arthur Chiou, and Stefan H. Heinemann.

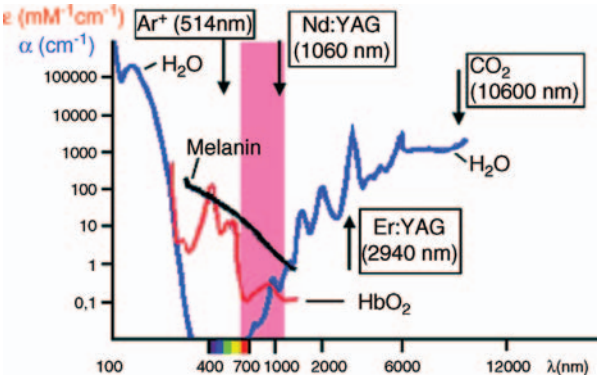

Figure 6.1 Optical window of cells and tissue with water, melanin, and oxyhemoglobin absorption coefficients [3].

absorption) and the Rayleigh scattering vanishes with λ^4. In the near-infrared region, the water absorption increases again and multiple scattering in heterogeneous media becomes more and more dominant. In connection with this behavior, different actions can be taken in different wavelength regions.

In Figure 6.1, the different penetration depths of light as a function of the wavelength are shown and the absorption spectra of the important components water, melanin, and oxyhemoglobin are depicted. It becomes clear that between 400 and 700 nm a so-called "optical window" of the tissue appears where neither water absorption nor scattering diminishes the penetration depth significantly. In this manner, the "optical window" is defined as the range of wavelengths where the light has its maximum depth of penetration into the tissue. Further in Figure 6.1 some examples of lasers are indicated (with their wavelengths) preferentially used in laser therapy for different indications.

6.1.1.2 Laser Light–Matter Interaction as a Function of Intensity

Light–matter interaction in biophotonics is based on the intensity of light (power flow density) treating the matter and the application time (which is often directly correlated with the peak intensity due to the effect of producing higher peak intensities by pulse shortening).

The dependence on the energy density or better reflected by the power flow density as shown in Figure 6.2. Different processes in cells and tissues occur in the human body [1, 2, 4], which will be discussed in more detail in the following chapter. As already mentioned, the other parameter is the application time: at long application times reflecting the accumulation of energy (or simply photons) in the body, at short times more reflecting the dependence of the peak intensities obtained with powerful lasers from the extremely shortened pulse length.

6.1.1.3 Photochemical Treatment of Tissues

At the lowest photon densities, processes occur which are well known in photophysics and photochemistry, such as the photoinduced isomerization process. An

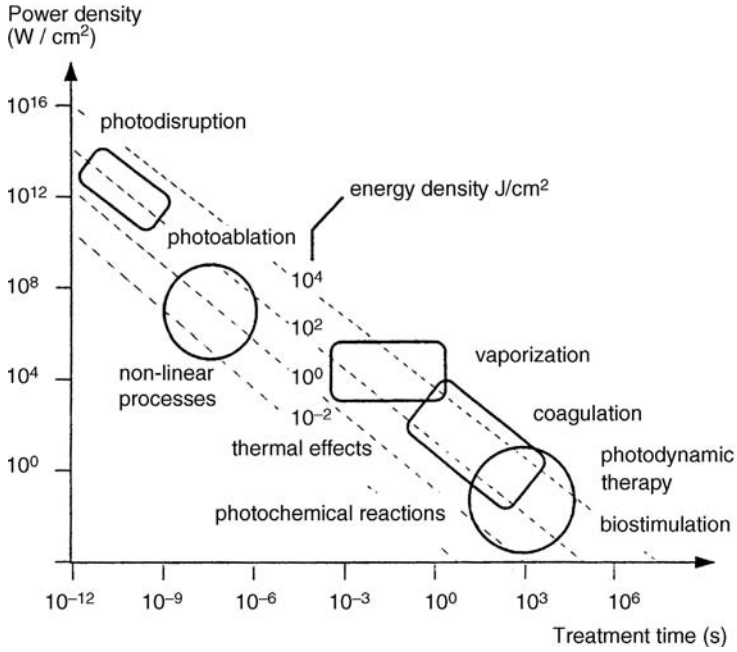

Figure 6.2 Laser light–matter interaction effects as a function of power density ($W\,cm^{-2}$) and treatment time (s). Dotted straight lines indicate the energy density region ($J\,cm^{-2}$). (with permission from Ringelhan [5]).

important example of such processes is the *cis–trans* isomerization of rhodopsin as the basis of the vision process in the human eye. A medical application is the treatment of hyperbilirubinemia, the cause of icterus (jaundice) in newborn babies, the basis of which is increased levels of bilirubin. Another example is photodynamic therapy where the patient is treated with HPD (hematoporphyrin derivative) (see Figure 6.3 for structure), which is selectively bound to cancer cells. After irradiation of the tissue, the excited HPD transfers the energy to the oxygen (in the surrounding) via a dynamic quenching process to create singlet oxygen. This further creates hydroxyl radicals, which destroy the cancer cells [6].

Other examples of processes that occur in this intensity region are photoinduced synthesis in plants and UV-induced melanin production in skin. The basis of life on Earth is the photoinduced charge separation in the reaction center as the primary process of photosynthesis.

It should be added that biostimulation also belongs to this intensity region. Biostimulation is defined as a process of laser treatment at extreme low intensities (below the threshold of reversible tissue damage, Section 6.1.3). So far, no results have been published which prove that biostimulation of human cells and tissues makes any impact.

All these processes have in common that compared with usual photon densities in laser applications, they proceed at very low intensities. In principal they need no laser irradiation and could be performed with classical light sources. The advantage of

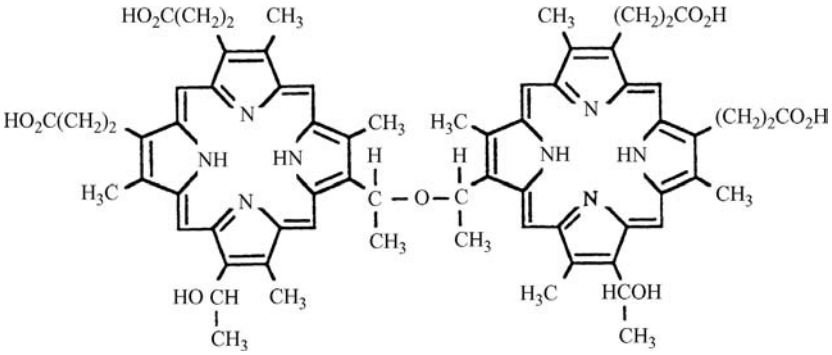

Figure 6.3 HPD – hematoporphyrin derivative.

lasers in this intensity region is often connected with proper guidance of the light to the tissue.

6.1.1.4 Thermal Processes in Light–Matter Interaction

At higher intensities, thermal effects play a crucial role in the understanding of light–matter interactions. Thermal effects depend strongly on the wavelength. On the one hand, the absorption in water is the main cause of thermal changes in cells and tissues, and on the other, the shorter the wavelength the higher is the amount of energy deposited in the tissue or cell. In general, thermal treatment of tissue is connected with different damage regions. When the tissue is vaporized under peak power irradiation, this sharp cut is surrounded by an irreversibly damaged zone covered by a carbonized interface (or called the necrosis zone). As can be seen in the Figure 6.4, at lower excitation intensities, lower heating of the tissue leads to reversible effects (for more details, see [1, 2, 4, 7]).

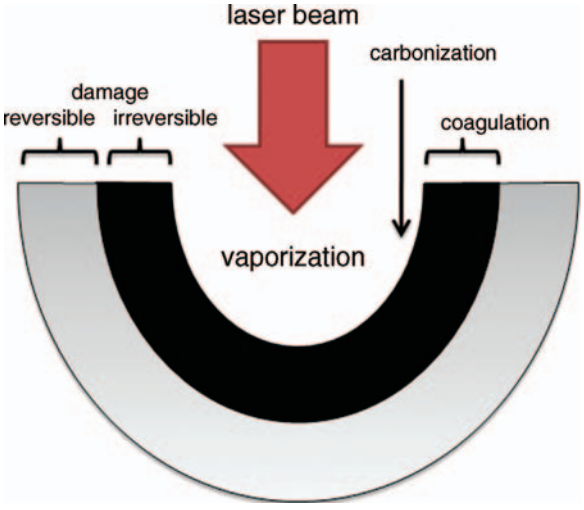

Figure 6.4 Zones of thermal treatment of skin at high laser intensities.

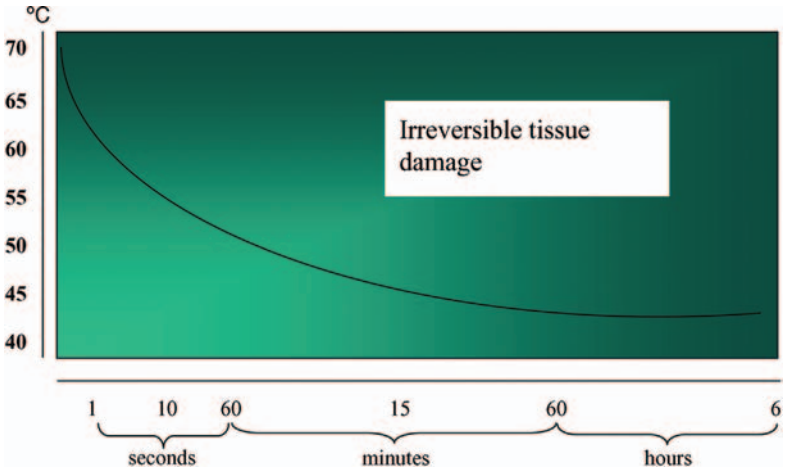

Figure 6.5 Reversible and irreversible damage of tissues as a function of the application time.

Depending on the applied wavelength and the intensity, these zones have different sizes. The longer the wavelength, the larger is the zone of irreversible damage. Further, the thermal damage depends on the application time, as shown in Figure 6.5.

As is clearly seen, increasing application times are connected with irreversible damage at lower temperatures, or the reverse: Short application times are connected with less damage of the tissue (skin effect). This effect is even more pronounced if the nanosecond time scale is reached because thermal diffusion times in tissues are in the nanosecond time scale (rate constants in the region of $10^{10}\,s^{-1}$). Shorter pulse lengths of the irradiation pulse lead to local effects in the tissue without thermal diffusion into the neighborhood. In this respect, ultrafast processes in light–matter interaction have minimal side effects (thermal damage effects) if the interaction process (and the resulting energy dissipation) proceeds faster than the diffusion time constants [4, 7]. In Figure 6.6, the laser beam penetrations as a function of the intensity and the respective treatment zones (thermal. optical, ablative) are depicted for comparison.

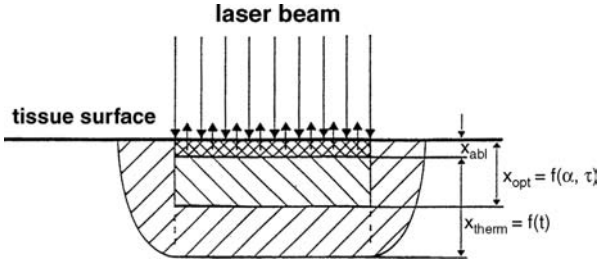

Figure 6.6 Influence of laser treatment on depth of tissue ablation, optical and thermal behavior. (with permission from Ringelhan 1992 [5]).

6.1.1.5 Nonlinear Processes in Light–Matter Interaction (Not to Be Confused with Nonlinear Optics)

In the late 1970s, Srinivasan and co-workers [8] were the first to show that under strong laser excitation in polymers a process occurs that is not longer explained by the action of one photon to create a single change in the material. It was shown that the cooperative action of multiple photons creates an avalanche process in the material which is energy dependent and has a well-defined threshold. This process was called "ablation" and has distinct different properties in comparison with the thermal treatment discussed before applying much lower intensities. Srinivasan and co-workers proposed the "photochemical model of ablation," which is based on the assumption that ablation proceeds above the bond energy by the cleavage of the chemical bond in the material (a process which is completed within picoseconds) and the fragments of the molecules are in the vapor phase, released from the irradiated area at high speed and without thermal dissipation into the surroundings. This model was proven by the ablation process in poly(methyl methacrylate) (PMMA) (see Figure 6.7). It was possible to show that the ablation process starts (threshold) if the loss effects are overcompensated by the production of molecule fragments in the irradiated volume. In this respect, the ablation process is a multi-photon process with single-photon excitation. This proceeds hold for the photoablation of tissue at high intensities with a UV laser, for example, an excimer laser. This process is used, for example, in ophthalmology (for more details, see [8]).

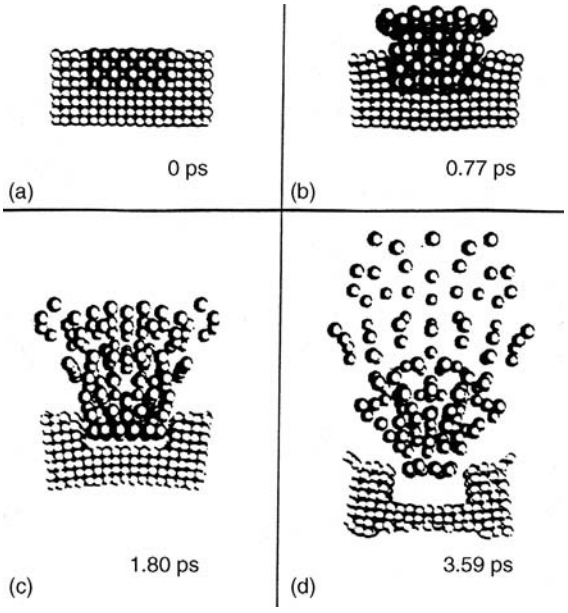

Figure 6.7 Photoablation scheme in PMMA [8]. (a) Starting point of ablation by irradiation of the ablated area; (b) release of the molecules from the layer, crystalline structure still unaffected; (c) build-up of the ablation bloom; (d) total release of the ablated material, finish of ablation process.

In addition to ablation by means of bond cleavage, it was shown that ablation can be achieved with the same minimized side effects (no thermal diffusion into the surrounding tissue) at wavelengths below the bond energy. In this case, the so-called *thermal model of ablation* provides an explanation of the effects that occur. The thermal ablation procedure is connected with multi-photon absorption at the surface. Under these multi-photon conditions, the heating of the irradiated region is connected with restricted thermal diffusion. This process holds for near-infrared (NIR) ablation with Nd:YAG and Er:YAG lasers. It was shown that this process is a cascade process of multi-photon absorption rather than a simultaneous absorption of more than one photon.

6.1.2
Minimally Invasive Diagnostics – Endoscopy

Endoscopy means looking inside the body for any medical reason using an optical-based medical device called an endoscope. The word endoscopy is derived from the two Greek words *endo* meaning "inside" and *skopein* meaning "to see."

Endoscopes can be inserted into the body through a natural opening, such as the throat, anus, or urethra. Alternatively, they can be inserted through a small surgical incision made in the skin.

Further, endoscopy permits minimally invasive surgery, making many operations simpler for the surgeon and safer, more effective, and often less painful for the patient, while significantly shortening the necessary stay in hospital.

For therapeutic reasons, the endoscope often has one or more channels for suction, which also serves as an instrument channel for the passage of biopsy forceps, retrieval forceps, cytology/culture brushes, and other accessories. Most endoscopes also have a separate channel for insufflations of air and water, thus enabling the endoscopist to distend the gastrointestinal tract during viewing and wash debris off the lens.

Endoscopic technology has advanced rapidly over the past 40 years, becoming an integral part especially in various fields of clinical and internal medicine. The utilization of endoscopy for both diagnostic evaluation and screening has markedly increased over the last two decades. Many innovations have extended indications for endoscopy. However, the largest factor to increase clinical endoscopic volumes in recent years has been the adoption of colorectal cancer screening through colonoscopy. The global endoscopy market is forecast to grow at a compound annual growth rate of 30% between 2008 and 2015 [9].

However, one major design problem with endoscopes remains – the necessary small external diameter. Within this small space, a lens system or a charge-coupled device (CCD) chip, a lighting fiber bundle, and useful instrument and flow channels have to be installed.

6.1.2.1 History

The first person in modern times to invent an instrument intended to illuminate the inner cavities of the human body was Philipp Bozzini. He published his first extensive medical report on his "light conductor" (*Lichtleiter*) in 1806. In 1960, Harold

H. Hopkins patented the rod lens system, which improved the previous Nitze system of a train of glass lenses by interspersing neutral gas between them instead of air. The optical features were improved ninefold by lowering the refractive index and increasing the functional diameter of the lenses. Fernando Alves Martins, from Portugal, invented the first fiber optics endoscope in 1963. Karl Storz in 1965 produced the first endoscope combining rod lenses for image transmission with fiber optics (fiber bundles) for illuminating (cold light) the biological object. The first solid-state camera was introduced in 1982. This was the basis for video endoscopy, starting with systems where the camera was mounted on the eyepiece of a traditional endoscope. The introduction of digital imaging with CCD image sensors in 1985 was a breakthrough. The chips could be miniaturized, and starting in the 1990s whole imaging procedure was placed at the tip of the endoscope. Interestingly, the CCD was first invented by researchers William S. Boyle and George E. Smith (awarded the Nobel Prize for Physics in 2009) at Bell Laboratories as a new type of computer memory. Soon it became apparent that it could be used as a light-sensitive element, which could capture images similarly to a film in a camera. The fiber bundles and optics used in fiber endoscopes to guide the light from the tip to the display could be replaced by simple wires.

Spectral endoscopy has evolved using different (no white light) illumination techniques and allows the detection or easy diagnosis of additional diseases. Fluorescence endoscopy is one example of the discriminative power of spectral endoscopy indicating tumorous growth on the bladder wall. In 2001, Given Imaging [10] introduced the first wireless pill-sized endoscopic capsule with a camera that is given to the patient for swallowing. With this technique, the small intestine can be examined, which was not possible before.

Finally, modern endoscopes are combined with other technologies such as endoscopic ultrasound or confocal endomicroscopy to enhance and optimize complex clinical investigations or treatments.

6.1.2.2 Types and Components of Endoscopes

Typical components of endoscopes are the following:

- tube (either rigid or flexible)
- light source (normally outside the body)
- light delivery system (fiber optics) for illuminating the organ or object under inspection
- in traditional endoscopes an optical lens or fiber optics system and/or in video endoscopes an information delivery system [images from CCD or CMOS (*complementary metal–oxide–semiconductor*) chip camera]
- a guiding system for additional manipulation (e.g., surgery, flushing) or diagnosing systems (e.g., biopsy probe sampling)
- image processing and documentation.

Light Sources Light sources for the illumination of the visual field of endoscopes (cold light) are typically connected to the endoscope via a flexible fiber-optic cable.

The most prominent light sources are the following:

- A halogen lamp cold light source is sufficient for most rigid endoscopy using the eyepiece.
- A metal halide lamp is an often used light source for fiber-optic scopes.
- Xenon is more powerful light source and is essential when dealing with video endoscopy and reduced light transmission of flexible endoscopes.
- Miniaturized light-emitting diode (LED) (in modern systems directly mounted at the tip of the endoscope).
- Laser light (for special applications such as fluorescence microendoscopes).

Imaging Depending on the visualization principle different imaging techniques are applied, such as

- white light imaging
- narrow band imaging
- fluorescence imaging.

The quality and sensitivity of imaging methods are strongly influence by features such as

- illumination of the region of interest (brightness)
- color fastness, depth of field
- resolution
- contrast
- vignetting
- depth of sharpness
- photosensitivity (electronic image transmission)
- signal-to-noise ratio of the implemented optical and electronic components.

Image Processing Systems in Video Endoscopes Image processing in endoscopy provides manipulation and enhancement of the video images. Image processing is a crucial part of the efforts to increase the quality and significance of medical images. Numerous filtering and image quality enhancement techniques (e.g., contrast enhancement, error reduction, distortion correction) have been introduced for various modalities and situations.

Visualization and Documentation Direct visualization of endoscopic images by eye is being more and more replaced by the introduction of video camera systems that present the images on a screen. This offers the opportunity for several observers to observe the endoscopic examination at the same time.

Modern video camera systems consist of an objective, a CCD or CMOS chip and a control unit mounted within a box. This kind of visualization provides analog or digital storage of endoscopic images and videos in modern documentation and clinical information systems. Image documentation is of high relevance for clinical follow-up and quality management of medical services. Further, the stored digital data offer new possibilities for digital signal processing, leading to increased quality

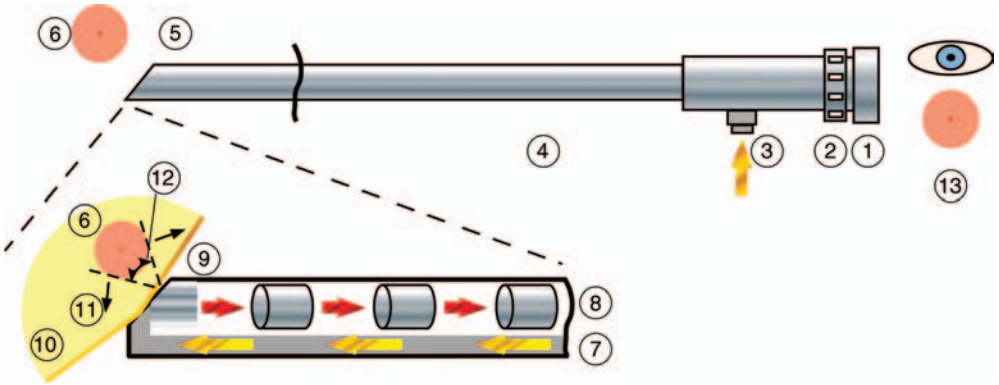

Figure 6.8 Rigid endoscope: 1, ocular; 2, focusing; 3, connector for fiber light guide cable; 4, telescope including fiber bundle for light transmission; optical lens system for image transmission and depending on application further channels for any manipulation; 5, endoscope tip; 6, object to be investigated; 7, fiber bundle for light transmission; 8, optical lens system (e.g., rod or achromatic) for image transmission; 9, objective lens; 10, illuminated area; 11, changeable direction of view (e.g., detectable tip); 12, lateral viewing angle (changeable, e.g., by type of included objective lens); 13, image of the object to be investigated within the field and angle of view.

of the images and extraction of new features from these images, increasing the precision of diagnosis that would not be possible with simple visualization.

Types of Endoscopes

Rigid Endoscope Rigid endoscopes (Figure 6.8) are small tubular telescopes to look inside the body and, in addition to diagnostic purposes, to carry out surgical procedures using special endoscopic instruments.

The optical element for rigid endoscopic systems is the telescope. It is an integral part of the system that provides both the image and the light transmission. The telescope is both the most expensive and most fragile part of the endoscope system. In rigid endoscopes, the optical lens train transfers the image to the eye of the user or to a video monitor. The lens train is comprised of precisely aligned lenses, spacers, and mirrors. Visualization occurs when light is transferred from a light source through the glass fibers distributed around the lens train. Rigid rod lens optics provides high-quality endoscopic images [11] (Figure 6.9).

The disadvantage of low light transmission in endoscopes with smaller diameter is compensated by the use of rod lens systems (Figure 6.9a). Endoscopes with an outer

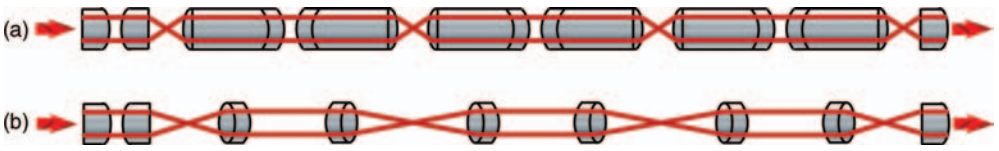

Figure 6.9 Lens systems in rigid endoscopes: (a) rod lens system; (b) achromatic lens system.

diameter of 6 mm and larger often include achromatic lens systems (Figure 6.9b), leading to higher stressability by holding nearly the same optical features.

The newest designed rod lens systems in combination with optimized glass fiber arrangements for lighting provide high-resolution images with sharpness up to the edges. Recent optical systems provide detailed recognition of the smallest visible anatomical structures.

A deflectable endoscope tip provides the maneuverability and access required for endoscopic single-site surgery.

Flexible Endoscope Flexible endoscopes are useful for viewing the inside of, for example, the stomach and intestines, where the endoscope may have to pass a long distance into the body, and around twists and curves. Flexible endoscopes are long, flexible tubes (Figure 6.10). In addition to visual and enhanced diagnostic purposes, flexible endoscopes enable (as rigid ones) surgical procedures to be carried out using special endoscopic instruments.

Fiber-optic lines are strands of optical glass (or special optical plastics) as thin as a human hair that carry digital information over long distances.

The single optical fibers (Figure 6.11) consist of three parts:

- **Core**: – Thin glass center of the fiber – transmits the light or optical information.
- **Cladding**: – Outer optical material surrounding the core – reflects the light back into the core.
- **Buffer coating**: – Plastic coating – protects the fiber from damage and moisture.

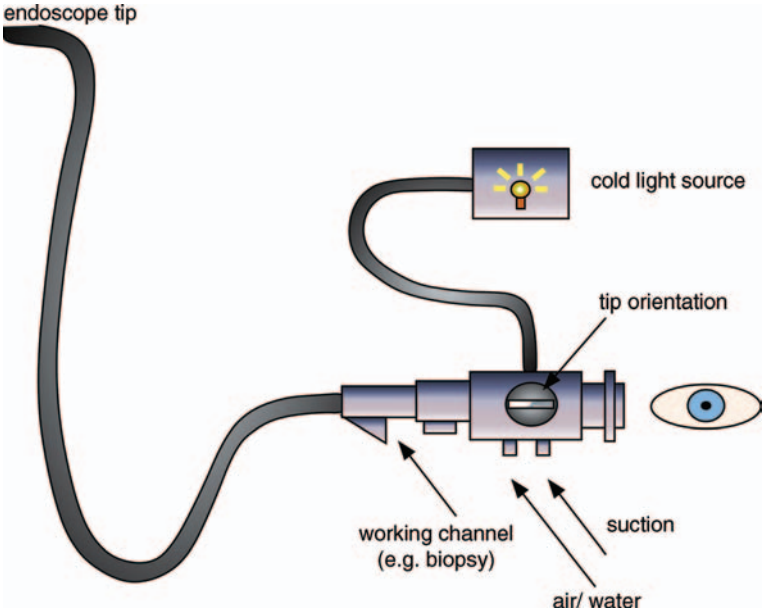

Figure 6.10 Flexible endoscope.

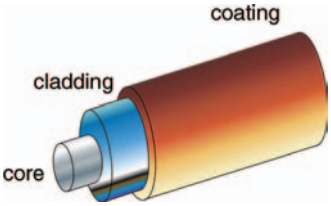

Figure 6.11 Single optical fiber.

The light in a fiber-optic cable travels through the core by constantly bouncing from the cladding based on the principle of total internal reflection (Figure 6.12).

The critical angle φ_C can be calculated from Snell's law, putting in an angle of 90° for the angle of the refracted ray φ_1. This gives φ_2, where n_1 and n_2 are the refractive indices of core and cladding material, respectively.

$$\varphi_1 = \arcsin\left(\frac{n_2}{n_1} \cdot \sin\varphi_2\right) \tag{6.1}$$

with $\varphi_2 = 90°$ and $\sin\varphi_2 = 1$ is $\varphi_C = \varphi_1 = \arcsin(n_2/n_1)$.

Thousands of these optical fibers are arranged in a bundle (Figure 6.13). This bundle is protected by an outer covering. Optical fibers come in two types depending on the type of light to be transmitted: single-mode and multi-mode fibers. A mode describes the distribution of light energy across the fiber (the patterns depend on the wavelength of light transmitted and on the variation in refractive index that shapes the core).

In fiber-optics endoscopes there are two separate fiber bundles, one for viewing and the other for transmitting light. The fibers in the viewing bundle are spatially

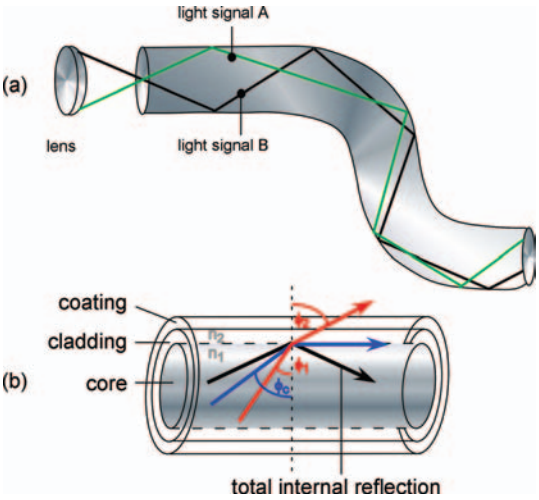

Figure 6.12 Schematic of (a) transmission in glass and (b) total reflection.

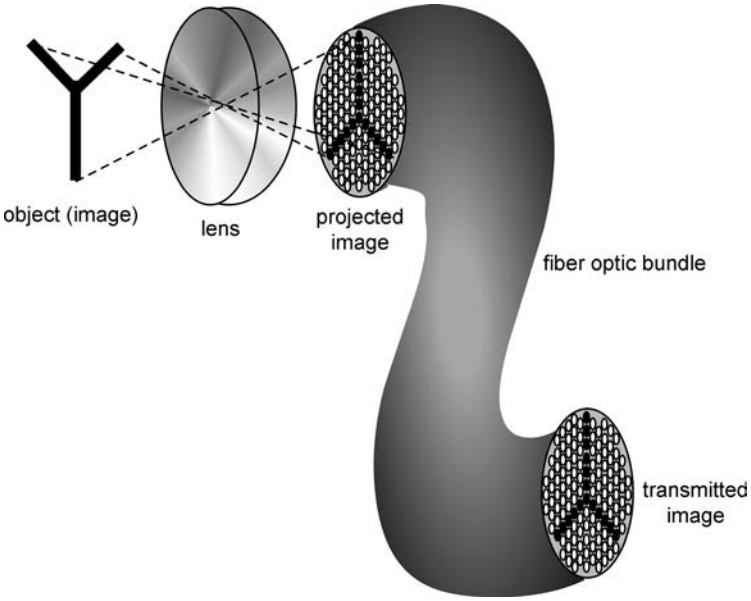

Figure 6.13 Fiber optic bundle (thousands of optical fibers are arranged in a bundle).

oriented so that the top of the object at one end corresponds to the top of the object at the other end (Figure 6.13). A lens focuses the image at the distal end and a magnifying lens enlarges the image at the eyepiece. Light is transmitted from a remote light source so that there is no heat at the end of the scope. The resolution of a fiber-optics endoscope is limited to about 100.000 pixels depending on the number and kind of bundled fibers (leading to an optical resolution of 1 pixel per fiber).

Video Endoscope The electronic video endoscope is based on a rigid or flexible endoscope and uses a computer chip camera as an imaging device. The most important part of the camera is a CCD or a CMOS sensor. These sensors convert the optical image into an electronic signal that is transmitted via wires to an external microprocessor, whose circuitry converts the signal to a video image, which is then processed and displayed on a high-resolution monitor.

CCD or CMOS sensors are composed of millions of photodiodes or photogates (Figure 6.14b), which convert photons into electric current that is later transformed into voltage, amplified, and converted to a digital form.

The signal path for a single pixel is as follows:

$$\text{photons}(\text{ph}\ \ \text{s}^{-1}) \Rightarrow \text{photocurrent}(\text{A}) \Rightarrow \text{charge}(\text{column}) \Rightarrow \text{voltage}(\text{V}).$$

CCD chips have a photoactive (photodiodes/photogates, Figure 6.14b) and a transmission region (yellow arrows in Figure 6.15). An image is projected through a lens on to the photoactive region, and each capacitor accumulates an electric charge proportional to the light intensity at that location. A control circuit then causes each photoactive region to transfer its contents to its neighbor. This circuit operates as

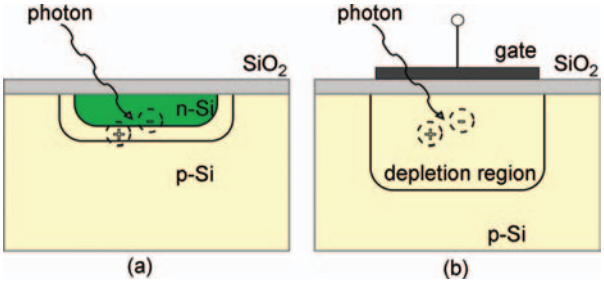

Figure 6.14 Schematic of (a) a photodiode and (b) a photogate of one silicon pixel from a CCD/CMOS image sensor (+ represents a hole and − an electron) (adapted from [11]).

a shift register (the original task of a CCD), transferring the electric charge sequentially, row by row, column by column, to a common output structure that converts the charge to a voltage. The color accuracy of the CCD camera allows enhanced visualization of reproduced images. Other advantages of the CCD camera are the improved resolution and quality of the images achieved when three chips are present (one each for red, blue, and green light). Most small endoscopes use a single chip in which these color distinctions are created by filters (e.g., Bayer filter).

CMOS chips, likewise, are capable of electronic registration of images projected on to their surface through the lens of a camera, and also provide image capture to a grid of pixels formed by photoelectric elements. The resultant electric charges are "read" by a sensor (Figure 6.15) and a process of analog-to-digital signal conversion is required to produce images that can be stored. In a CMOS sensor – in contrast to the CCD – each pixel acts as its own independent amplifier of the image signal, which limits noise as the charge-to-voltage conversion takes place within each pixel. However, these sensors are (still) less sensitive and noisier than CCDs. On both types of chips, the information is transferred to a controller box for image presentation or storage.

In comparison with CCD sensors, CMOS technology offers improved integration (more functions on the chip), lower energy consumption, faster processing, less heat

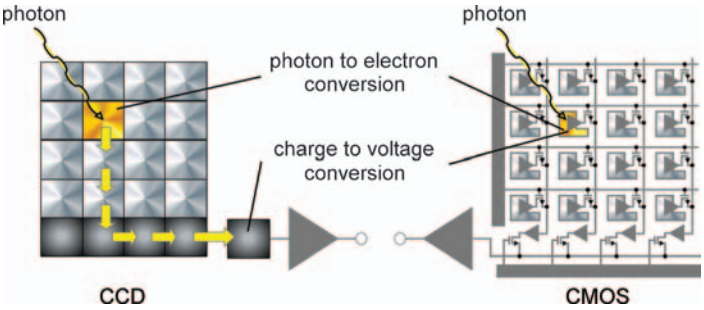

Figure 6.15 Schematic of CCD and CMOS image sensor arrays. CCDs (left) move photogenerated charge from pixel to pixel and convert it to voltage at an output node; CMOS (right) imagers convert charge to voltage inside each pixel (adapted from [11]).

production, and no smear effects. Additionally, CMOS technology requires fewer electronic components, which allows such chips to be smaller and more compact. However, to date, the advantages of CMOS chips often come at the expense of image quality and device cost. CMOS cameras still generally require companion chips to optimize image quality (e.g., to compensate for the lower light sensitivity and rolling shutter effects), which increases costs and power consumption.

Technological developments have allowed the production of CMOS sensors with high energy efficiency, high spatial resolution, high speed, low power consumption, and low cost. In the future, CMOS camera endoscopes might reduce device costs and facilitate the spread of distal sensor endoscopy. Sophisticated new microlenses with tiny gaps between them appreciably increase the efficiency of CMOS sensor light gathering [12–14].

Video endoscope with proximal camera: Conventional rigid and fiber-optic endoscopes can be converted to a video endoscope with a proximally mounted video camera on the eyepiece (Figure 6.16). Input to this sensor is the light transmitted either through a lens system or through fiber bundles (here the quality of the image is dependent on the quantity and quality of the fiber bundles).

Video endoscope with distal camera: Here the chip camera is mounted directly behind a lens system on the tip (distal) of the endoscope (Figure 6.17) and replaces either the lens system or the viewing fiber optic bundle in fiber-optic endoscopes. The quality of the image is dependent only on the quality of the CCD or CMOS chip (resolution). These image sensors are smaller than 2 mm in diameter. An optical magnification (zoom) can be added. With this technology, resolutions of $\gg$400 000 pixels are typical. The newest processors enhance the image to HD TV 1080i. The

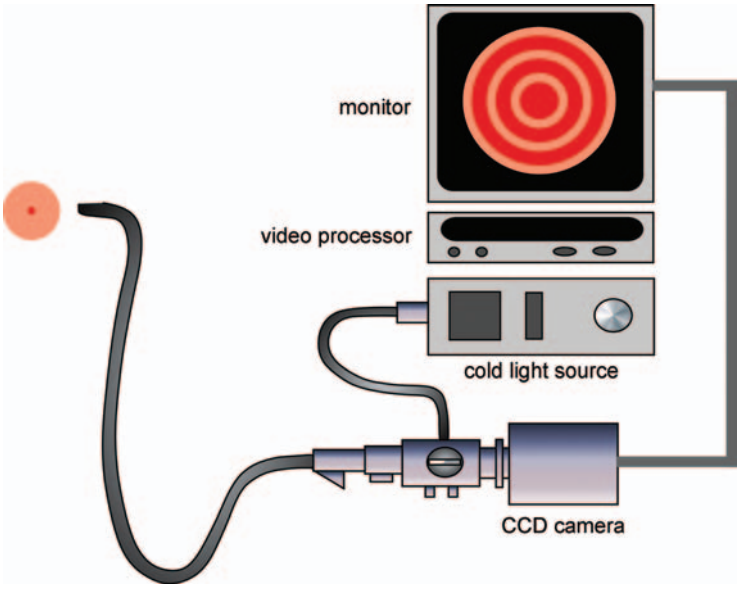

Figure 6.16 Schematic of a video endoscope with proximally mounted video camera.

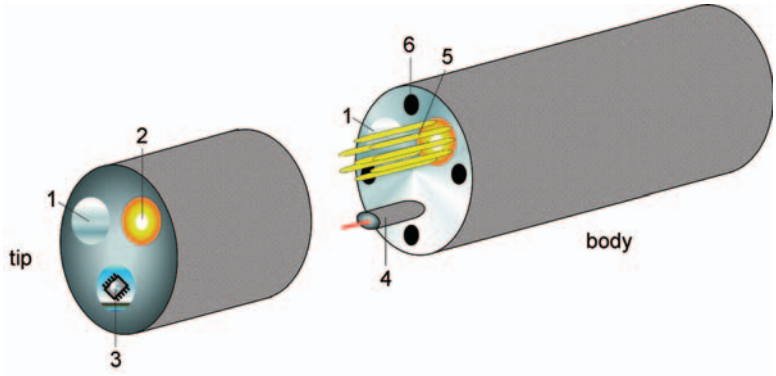

Figure 6.17 Schematic of flexible endoscope with distal mounted camera: 1, working channel/micro tools; 2, light; 3, tip-mounted camera with CCD/CMOS chip and lenses; 4, video cable; 5, light fiber bundle; 6, articulation control wires.

resolution of the newest Pentax CCD chip is 1280×1024 pixels (approximately 1.25 million pixels) and displays at native resolution [15].

High-resolution endoscopes are partly equipped with an optical zooming facility comprising a movable motor-driven lens in the tip of the scope that, controlling the focal distance, can move very close to the surface providing the magnified image. These scopes – magnification endoscopes – are referred to as magnifying endoscopes and increase the level of magnification, discriminating detail so that suspicious small lesions in the unmagnified overview image can be detected, reducing the surface area that is visualized [16].

The images can be further enhanced by the topical application of stains or pigments such as methylene blue, indigo carmine, and acetic acid, a technique known as enhanced magnifying endoscopy [17].

Capsule Endoscopy Esophageal capsule endoscopy is a new and exciting technique that uses a dual-camera wireless capsule endoscope [10], which offers an alternative approach to visualize the esophagus without the need for sedation, and without the discomfort and risks of conventional endoscopy. This technique may be helpful in finding the source of bleeding, pain, or other symptoms that may be coming from the small intestine, but it is also useful for looking at the colon and other parts of the body [18].

Capsule endoscopes are approximately 2.6 cm in length, the size of a large pill. The approved capsule [19] had a camera at one end that took two images per second as the capsule traveled through the digestive tract. The capsules were propelled from the mouth to the anus by the peristalsis of the digestive tract, and the images were transmitted to a recorder worn by the patient. Approximately 50 000 images were collected during the 8 h that the capsule was traveling through the body, and these were then downloaded to a computer. The associated computer program was configured to erase duplicate images, so that if the capsule was in

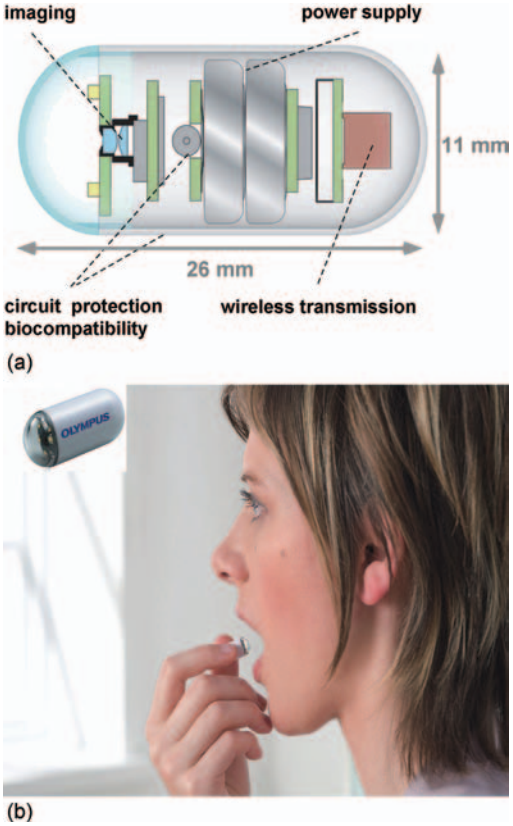

Figure 6.18 Capsule endoscope (Olympus EC Type 1). (a) Schematic diagram of the capsule endoscope; (b) the capsule endoscope and its ingestion.

one location for 15 min, not all of the images from that location would be downloaded. Figure 6.18 shows the scheme and the newest Olympus capsule endoscope.

Behind real-time monitoring of the capsule's transition, a system-integrated workstation contains software with overview and express viewing functions to shorten the time spent analyzing results (Figure 6.19). These functions are based on analysis of the motion grade between consecutive images to help decrease the number of redundant images for more efficient analysis (Olympus WS-1).

However, many of the already performed outcome studies have potential biases and confounding and do not provide sufficient evidence to determine the effect of capsule endoscopy on patient health outcomes. The use of capsule endoscopy of the colon allows visualization of the colonic mucosa in most patients, but its sensitivity for detecting colonic lesions is (so far) lower than with the use of optical colonoscopy [20].

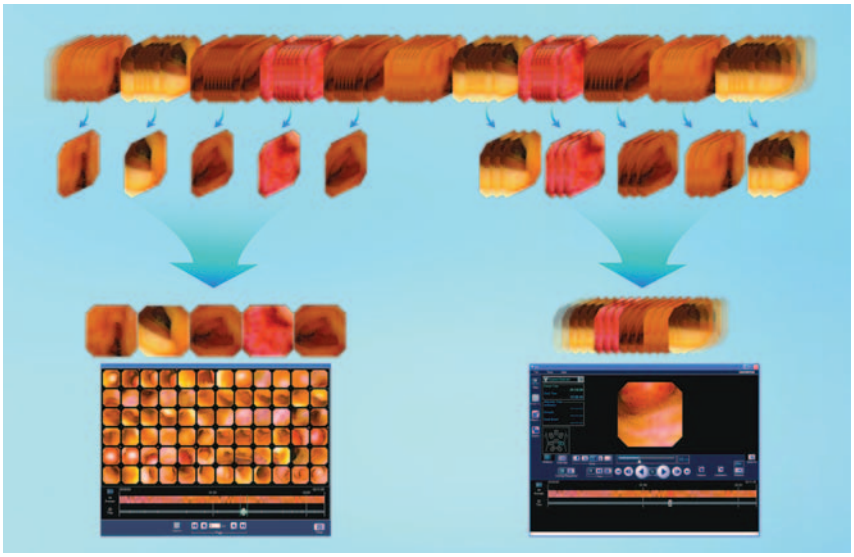

Figure 6.19 Workstation (Olympus WS-1) with overview and express-viewing facilities to optimize analyzing efforts.

6.1.2.3 **Advantages and Disadvantages of Endoscopy**

Advantages are:

- Enhances diagnostics (direct viewing interior of an organ often improves determination of the cause of disease or complication and is very helpful in establishing a diagnosis).
- Minimum stress and mortality.
- Faster recovery after intervention.
- Offers parallel interventions (e.g., biopsy probe sampling, endoscopic ultrasound).

Disadvantages are [21]:

- Requires rather expensive equipment and specialized setup.
- Biopsies are usually adequate but not as good as full thickness.
- Cannot examine every part of the organ (depending on diameters and bending radius) and lesions and other problems may be beyond the reach of the endoscope.
- Cannot determine if an ulcer is going to rupture or bleed.
- There is a small chance of herniation of abdominal contents after laparoscopy.
- There is always the possibility of the introduction of an unsterilized instrument into the body.
- Inexpert handling of the endoscope may lead to a punctured organ with variable effects.

- Reactions to the sedation can occur, although they are rare. For this reason, breathing, blood pressure, heart rate, and oxygen level have to be monitored during endoscopy.

6.1.2.4 **Application Fields**

The following conditions and illnesses are most commonly investigated or diagnosed with an endoscope:

- breathing disorders
- chronic diarrhea
- incontinence
- internal bleeding
- irritable bowel syndrome
- stomach ulcers and helicobacter
- urinary tract infections.

The choice of endoscope depends on which part of the digestive tract is to be examined. Some types of endoscopes and the areas of the body that they are used to view are listed in Table 6.1.

6.1.2.5 **Combination of Standard White Light Endoscopic with Other Diagnostic Methods**

Light interacts with tissue in a variety of ways, including absorption, fluorescence, elastic scattering, and Raman scattering. These interactions enable a number of promising technologies to be considered for endoscopic diagnosis. Other diagnostic procedures include cell and tissue sample collection by brush or biopsy forceps.

Some of the most promising newer methods combining with traditional endoscopy are briefly described below.

Fluorescence Endoscopy In contrast to the anatomical information provided by white light endoscopy (based mainly on the analysis of reflected light), fluorescence imaging provides biochemical and metabolic information [23] (Figure 6.20).

The principle of fluorescence diagnosis is based on the interaction between light at a specific wavelength and fluorophores in tissue. Light sources that can be used include incoherent light sources (e.g., xenon) and monochromatic laser light. When light penetrates tissue, it causes not only reflection and absorption, but also fluorescence. Depending on the fluorophore used, only light at a specific wavelength is maximally absorbed, and in turn variably emitted. As a result of the stimulation process, blue stimulation light, for example, loses some of its energy and is therefore given off as longer wavelength green or red fluorescence [24] (Figure 6.21). "Color differences" between, for instance, normal and neoplastic tissue arise here as a result of endogenous and exogenous fluorophores [25].

Fluorescence endoscopy is a wide-area imaging technique, with the ability to examine rapidly a large surface area of various organs such as gastrointestinal mucosa, bladder, or lung to detect small areas of dysplasia or cancer. It has potential in diseases such as Barrett's esophagus, ulcerative colitis, and gastric cancer, in which

Table 6.1 Types of endoscopes and their applications [18, 22].

Type of endoscope	Insertion	Body area(s) examined	Name(s) of procedures
Arthroscope	Incision near joint	Joints	Arthroscopy
Bronchoscope	Mouth or nose	Trachea (windpipe) and bronchi (tubes inside the lungs)	Bronchoscopy, flexible bronchoscopy
Capsule endoscope	Mouth	Upper and lower gastrointestinal tract	Capsule endoscopy
Colonoscope	Anus	Colon (large intestine)	Colonoscopy, lower endoscopy
Colposcope	Vagina	Vagina, cervix, and vulva	Colposcopy
Cystoscope	Urethra	Bladder, urethra, urinary tract, uteral orifices, and prostate (men)	Cystoscopy, cystourethroscopy
Esophagogastroduodenoscope	Mouth	Esophagus (swallowing tube), stomach, and duodenum (first part of small intestine)	Esophagogastroduodenoscopy (EGD), panendoscopy, upper endoscopy, gastroscopy
Hysteroscope	Vagina	Inside uterus	Hysteroscopy
Laparoscope	Incision(s) in abdomen	Space inside abdomen and pelvis	Laparoscopy, peritoneal endoscopy
Laryngoscope	Mouth or nose	Larynx (voice box)	Laryngoscopy
Mediastinoscope	Incision above sternum (breastbone)	Mediastinum (space between the lungs)	Mediastinoscopy
Nasopharyngoscope	Nose	Nasal cavity, maxillary sinus, nasopharynx, vocal cords	Nasopharyngoscopy
Neuroendoscope	Small incision, opening in the skull, supraorbital	Skull, brain, and spine	Neuroendoscopy
Otoscope, auriscope	Ear	Outer and middle ears	Otoscopy
Sigmoidoscope (flexible sigmoidoscope)	Anus	Rectum and sigmoid colon (lower part of large intestine)	Sigmoidoscopy, flexible sigmoidoscopy, proctosigmoidoscopy
Thoracoscope	Incision(s) in chest	Pleura, pleural spaces, mediastinum, pericardium	Thoracoscopy, pleuroscopy

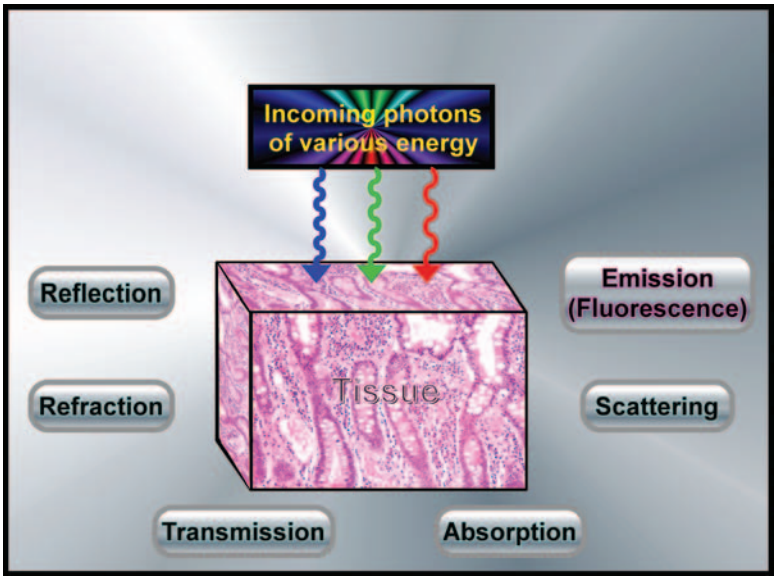

Figure 6.20 Interaction of light with tissue.

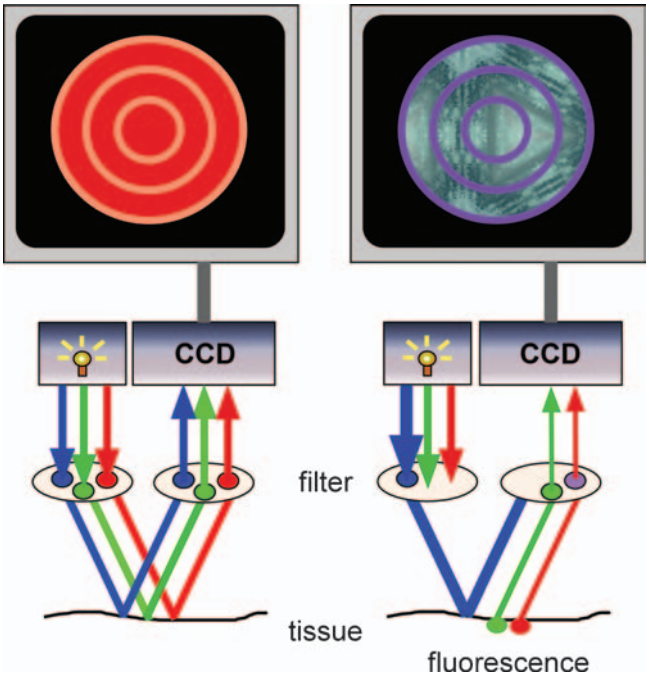

Figure 6.21 Schematic of fluorescence endoscope (adapted from [23]).

large areas of mucosa may harbor areas of dysplasia or superficial cancer not visible on conventional or high-definition white light endoscopy [26].

Fluorescence spectroscopic techniques are classified into two main types: autofluorescence diagnosis (using endogenous fluorophores), which utilizes inherent tissue autofluorescence, and photodynamic diagnosis (PDD) (exogenous fluorescence) using fluorescent drugs called photosensitizers, which react to various wavelengths of light [24].

When tissue is illuminated with UV or short-wavelength visible light from a laser source or a filtered lamp, fluorescence light of a longer wavelength is emitted by endogenous molecules (fluorophores) within the tissue. This "autofluorescence" arises from several components of connective tissues (collagen, elastin), cellular metabolism-related coenzymes, aromatic amino acids, by-products of heme biosynthesis, and lipopigments. Different excitation wavelengths activate different groups of fluorophores, each of which emits in a different range of wavelengths.

As their excitation and emission bands are fairly broad and often show spectral overlapping, it is still difficult to distinguish between these fluorophores. It is only when a suitable stimulation wavelength is selected that the individual fluorophores causing autofluorescence can be distinguished. A number of different pathological processes (neoplasias, inflammation, and ischemia) affect the metabolic, oxidative condition of the cells and thus their autofluorescence [24].

In contrast with autofluorescence, various exogenous photosensitizers (e.g., porphyrins) are used when fluorescence is induced by a drug in the PDD technique. However, the use of exogenous substances that produce a stronger and clearer fluorescence signal because of comparatively specific accumulation also has some disadvantages. In addition to the necessity to administer a chemical substance to the patient, it is often associated with brief but non-negligible photosensitization of the skin, so that the patient needs to be protected from sunlight for about a day [27].

The detection of abnormal lesions with autofluorescence depends on changes in the concentration or depth distribution of the endogenous fluorophores, changes in the tissue microarchitecture, or both, including altered mucosal thickness or blood concentration, that can affect the fluorescence intensity or spectrum because of wavelength-dependent light absorption. With exogenous fluorophores, lesion detection is based on selective drug uptake or retention by a target tissue relative to the uptake by normal tissue.

Endomicroscopy The Pentax confocal laser endoscope [28] and the Leica FCM1000 endoscopic confocal microscope (especially for animal experiments) [29] represent a fusion of endoscopy and confocal microscopy.

The components of a confocal laser endoscope are based on the integration of a confocal laser microscope in the distal tip of a conventional video endoscope, which permits confocal microscopy in addition to standard video endoscopy. The diameter of both the distal tip and the insertion tube is less than 13 mm. The distal tip contains an air and water jet nozzle, two light guides, an auxiliary water jet channel (used for topical application of the contrast agent) and a 2.8 mm working channel. Actuation of

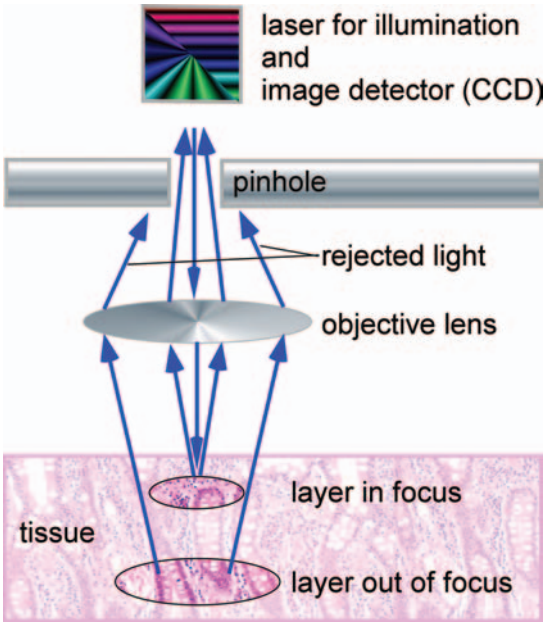

Figure 6.22 Schematic of confocal laser optical unit.

the imaging plane depth relative to the surface of the tissue is controlled using two additional buttons on the endoscope control body.

To create confocal images, blue laser light is focused on the desired tissue via the distal end. Applied fluorescent materials are excited by the laser light, and the special confocal optical unit (Figures 6.22 and 6.23) detects exclusively the fluorescing light in an exactly defined horizontal level. This produces high-resolution microscopic images, making it possible to assess structures down to the size of the cell nucleus (Figure 6.24).

In vivo confocal laser endomicroscopy is a newly developed diagnostic tool allowing virtual *in vivo* histology of the mucosal layer during ongoing endoscopy.

Summarizing the features of endomicroscopy, one can state the following characteristics and possibilities:

- *In vivo* microscopy during routine endoscopy.
- Real-time tissue diagnosis.
- Very high precision and correlation with histology.
- Simple pattern classification for diagnosis.
- Detection of neoplasias and *Helicobacter pylori* possible.
- Penetration into deeper layers (0–250 μm).
- Cell nucleus can be imaged in conjunction with topical staining.
- Vascular morphology can be assessed.
- Tissue can be examined over a greater area.
- No substantial material consumption (stains).

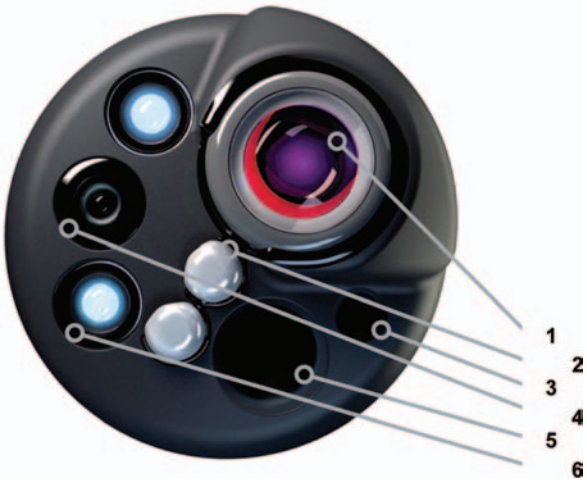

Figure 6.23 Distal part of a confocal laser endoscope [28]: 1, confocal microscope; 2, air/water nozzles; 3, water jet; 4, objective lens; 5, instrument channel; 6, light guide.

- Future (currently the only) technology platform for gastrointestinal molecular fluorescence markers.

The potential benefits can be summarized as follows:

- Early, improved tumor detection in a curable stage as a promising strategy for reduction of tumor mortality.
- Fewer conventional biopsies thanks to specific "smart biopsy."
- Optimized work processes in endoscopy (e.g., immediate therapeutic decision).
- Incorporation of progress from the fields of immunology and genomics in endoscopy (molecular markers).
- Efficient use of new, specific therapeutic measures (e.g., microscopic/molecular monitoring of efficacy).

Endoscopic Ultrasound Diagnostic procedures include the use of ultrasound-equipped endoscopes to evaluate blood flow or provide imaging of lesions. Endoscopic ultrasound can provide information (e.g., the depth and extent of lesions) that is not available via conventional endoscopy. Endoscopic ultrasound is increasingly used to assess gastrointestinal and lung diseases [30].

Further Approaches Chromoendoscopy still holds a place for detecting especially flat lesions in high-risk patients such as those with ulcerative colitis. Digital chromoendoscopy techniques such as narrow-band imaging (NBI), i-scan, and Fuji intelligent chromoendoscopy offer new possibilities of easily and reversibly obtaining enhanced tissue contrast. Autofluorescence imaging uses tissue function to yield a pseudocolored image, and has the potential to serve, for example, as a red flag technique for the detection of neoplastic lesions [31].

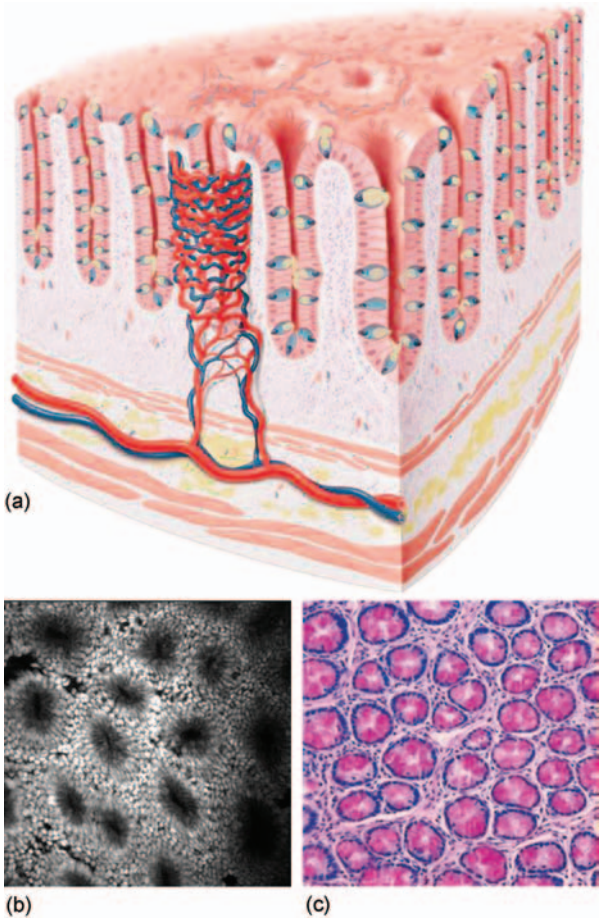

Figure 6.24 Colorectal cancer: screening with PENTAX 3618 endomicroscope. (a) Scheme of a horizontal slice; (b) conventional histology, horizontal slice; (c) endomicroscopy, horizontal slice (images courtesy of Uniklinik Mainz/Kiesslich).

Reflectance spectroscopy is an emerging technology which provides rapid and safe evaluation of tissue for dysplasia and ischemia. The probe-based devices can be passed through most endoscopes. Current applications include detection of dysplasia in Barrett's esophagus, colitis, and colon polyps [32].

6.1.2.6 **Some Trends in Endoscopy**

Colorectal cancer (CRC) is the second leading cause of cancer death, after bronchial carcinoma, in the West. Current estimates suggest that the disease affects in excess of 22 000 and 148 000 people annually in the UK and the US, respectively, where 50% die as a consequence of their disease [33]. New data suggest that early-stage disease (if diagnosed correctly in time) can be treated with "curative intent" using novel endoluminal resection techniques such as endoscopic mucosal resection (EMR)

and endoscopic submucosal dissection (ESD). Furthermore, novel adjunctive endoscopic imaging technology in the form of high-magnification endoscopy, colonic chromoscopy, confocal laser scanning endomicroscopy, NBI, "mini probe" endoscopic ultrasound, and autofluorescence now offer the endoscopist an unparalleled choice of diagnostic tools that improve early recognition of, for example, neoplastic disease and in general allow accurate *in vivo* morphological and now histopathological interpretation, in addition to "on-table" staging to enhance patient selection for further endoscopic surgical treatment. These technologies will be partly combined in the near future and enhanced by applying sophisticated imaging and image processing techniques.

NBI dramatically improves the detection of premalignant and early neoplastic lesions, particularly in combination with magnifying endoscopy. This allows the endoscopist to accomplish accurate diagnosis and better targeting of biopsy and improved and more appropriate treatment, and thereby contribute to optimal quality of life and patient survival [34].

Huang *et al.* [35] introduced integrated Raman spectroscopy and trimodal (white light reflectance, autofluorescence, and narrow-band) imaging techniques for real-time *in vivo* tissue Raman measurements with endoscopy. A special 1.8 mm endoscopic Raman probe with filtering modules was developed, permitting effective elimination of interference of the fluorescence background and silica Raman in fibers while maximizing tissue Raman collections. They demonstrated that high-quality *in vivo* Raman spectra of the upper gastrointestinal tract can be acquired within 1 s or less under the guidance of wide-field endoscopic imaging modalities, greatly facilitating the adoption of Raman spectroscopy into clinical research and practice during routine endoscopic inspections.

Advances in optical coherence tomography (OCT) may lead to a new class of endoscopic, image-guided therapies that target disease with microscopic precision. Fibered OCT in conjunction with natural orifice transluminal endoscopic surgery (NOTES) could provide a facility for rapid, *in situ* pathological diagnosis of intraperitoneal tissues in a truly minimally invasive fashion [36].

Further enhancements in software technology and image processing will lead to 3D surface reconstruction from endoscopic images [37] in combination with 360° forward life view (augmented reality) [38] and additionally displayed patient data for optimum (and automatic) navigation.

Lasher *et al.* [39] applied spatial modeling and analysis of living cardiac tissue based on 3D image data obtained by scanning confocal microscopy. For that purpose, they developed a novel method for the local delivery of fluorescent dye and labeling of cardiac tissue, which they characterized with standard inverted and catheter-based confocal microscopy systems. They introduced a methodology to process stacks of microscopic images and applied it to obtain detailed spatial models (Figure 6.25) and quantitative data on cardiac microstructure. These models and data promise to constitute an important input for tissue characterization and computational modeling of cardiac function.

Further, molecular imaging is a rapidly growing new discipline, for instance in gastrointestinal endoscopy. It uses the molecular signature of cells for minimally

Figure 6.25 Three-dimensional model of ventricular tissue shown from endocardial surface. The model includes 11 complete myocytes and 11 partial myocytes (scale: 50 mm) (courtesy of University of Utah, Salt Lake City/Sachse and © 2009 IEEE [35]).

invasive, targeted imaging of gastrointestinal pathologies. Molecular imaging comprises wide-field techniques for the detection of lesions and microscopic techniques for in vivo characterization. Exogenous fluorescent agents serve as molecular beacons and include labeled peptides and antibodies, and probes with tumor-specific activation. Most applications have aimed at improving the detection of gastrointestinal neoplasia with either prototype fluorescence endoscopy or confocal endomicroscopy, and the first studies have translated encouraging results from rodent and tissue models to endoscopy in humans. Even with the limitations of the currently used approaches, molecular imaging has the potential to impact greatly on future endoscopy in gastroenterology [40].

Virtual endoscopy is an imaging test. It uses a special computed tomography (CT) (or other modality) scan to look at the inside surfaces of organs such as the lungs (virtual bronchoscopy) or colon (virtual colonoscopy, also called CT colonography). Patients have the procedure just as they would any other CT scan – that is, they lie still on a table while a large ring (the CT scanner) passes over the part of the body being imaged. Unlike normal CT scans, which result in images in two dimensions, virtual endoscopy uses a computer to combine many images to create a 3D picture. Doctors can even use the images to create a black-and-white "fly-through" view on the screen, which looks much like it would if they were performing an actual endoscopy.

In recent years, endoscopic image quality has improved as the devices have advanced technologically. Although techniques such as chromoendoscopy, high-resolution and magnification endoscopy, narrow-band imaging, and autofluorescence imaging improve the visualization and detection of mucosal and other lesions, biopsy of the targeted lesion must still be performed for a formal histological diagnosis of cellular and architectural atypia. It would be ideal if a definite diagnosis could be made during endoscopy without a biopsy.

Virtual endoscopy has some advantages over standard endoscopy in that it is noninvasive and does not require any type of anesthesia. It also allows the doctor to change the angle or magnify the image, which can help with diagnosis. However, there are also some disadvantages. Although virtual endoscopy does show good detail, it is not quite as good at showing fine detail as standard endoscopy (for example, it cannot show color differences). It also exposes the patient to some radiation – about the same amount as a standard CT. Finally, because it is not invasive, it does not allow the doctor to take biopsy samples while it is being done. This means that if something abnormal is found, the patient may still need a standard endoscopy so that a biopsy sample can be taken.

6.1.3
Noninvasive Diagnostics – Photoplethysmography

6.1.3.1 Introduction

Photoplethysmography (PPG) is an optical measurement technique that can be applied to determine changes in blood volume in the microvascular bed of body tissue. It utilizes the optical characteristic of blood to absorb light strongly. It is applied on the surface of the skin, usually a finger tip or an earlobe, and working with light in the visible or NIR spectrum [41]. Therefore, it is an absolutely noninvasive and nonhazardous method.

There is a wide range of clinical applications, most commonly pulse oximetry to monitor blood oxygen saturation, but also various diagnostic methods to assess the cardiac and the vascular system. The technical effort and its handling are relatively small and simple compared with other assessment techniques such as vascular catheter or CT. Basically, the technical equipment consists of only two optical elements: a light source to illuminate the region of interest and a photodetector to measure the intensity variations of light beyond the volume. This correlates with the changes in blood volume in the examined body part, representing the peripheral pulse wave and therefore providing information about the cardiovascular system.

6.1.3.2 Characterization of the PPG Signal

The PPG signal consists of a pulsatile component, the AC component that results from the small variations in the blood volume during a heart period and a DC component that is related to the tissues surrounding the vessel and the basic average blood volume.

Hertzman, who was one of the pioneers in the field of PPG, and Spealman first described the characteristics of the pulse wave form in 1937 [42]. They defined two phases, first the rising edge of the pulse associated with the systole, and second the falling edge of the pulse associated with the diastole and the peripheral wave reflections (Figure 6.26). Also a dicrotic notch in the second phase is typical for subjects with normal compliance of arteries. The DC component can also vary, mainly due to respiration and vasomotor activities.

In several studies on the ability of PPG to assess the vascular system, many features of the pulse wave form have been investigated, such as the rise time, the pulse-transit

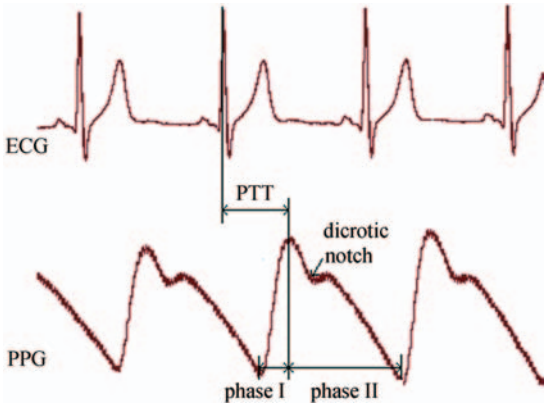

Figure 6.26 Typical PPG signal and extracted parameters in relation to ECG.

time (PTT) [time from the R wave in simultaneous electrocardiogram (ECG) recording to the maximum amplitude of pulse wave], the amplitude and shape, and also the variability of these parameters [43].

6.1.3.3 Signal Acquisition

Several studies [44–46] have found that the main factors affecting the amount of light received by the optical detector are the following:

- blood volume
- movement of blood vessel walls
- orientation of the red blood cells.

Another important aspect is the choice of wavelength that is used. There are three limiting considerations:

1) The optical characteristics of water, which is the main constituent of body tissue, need to be considered. It absorbs light strongly at the UV and long infrared (IR) wavelengths and therefore inhibits the light from passing on to the blood vessels. At the visible and NIR wavelengths the absorption of water is weaker, hence these wavelengths are usually used for PPG [47].
2) The isosbestic wavelengths play an important role, especially for the measurement of blood oxygen saturation. At these wavelengths compared with others there is no significant difference in the absorption between oxyhemoglobin and reduced hemoglobin. Hence the PPG signal is independent of the amount of oxygen in the blood volume [48].
3) The tissue penetration depth is also dependent on the operating wavelength [49]. It has been proven that light with longer wavelength can penetrate deeper into the tissue than light with shorter wavelength; for example, for a wavelength of 600 nm the penetration depth is 0.55 mm, whereas for a wavelength of 1000 nm it is 1.5 mm [50].

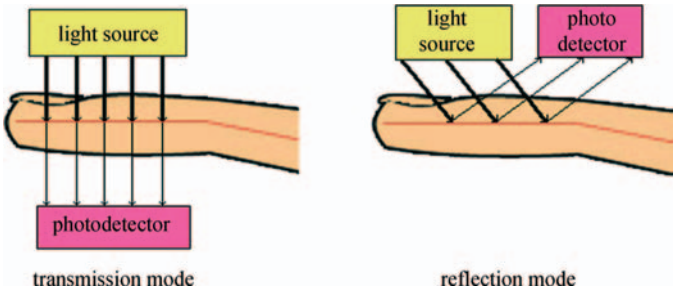

Figure 6.27 The principle of transmission mode and reflection mode.

Modern PPG sensors are usually built with semiconductor technology with LED and photodetector devices working at the red and NIR wavelengths (600–1000 nm). LEDs have several advantages compared with conventional illuminants:

- a narrow bandwidth
- compactness and robustness
- long operation time
- relative independence of temperature [51].

There are two different measuring realizations available (Figure 6.27). In the transmission mode, the tissue sample is placed between the light source and the photodetector. Therefore, its application is limited to only very few body parts that are thin enough to pass light. In the reflection mode, the light source and the photodetector are placed on the same side of the sample.

Several requirements have to be met to minimize measurement errors:

- Good contact with the skin.
- Movements between the sample and the sensor should be avoided.
- Probe attachment with a dark cuff and damping light in the measurement area, hence the signal is not influenced by ambient light interactions with the sensor.
- Filtering and artifact reduction by suitable electronic components and signal processing techniques.

6.1.3.4 Clinical Applications

Patient Monitoring – Blood Oxygen Saturation, Heart Rate The development of pulse oximetry is one of the most important improvements in the field of clinical monitoring in the last few decades. It involves the determination of the amount of oxygen in the blood and also the observation of the heart rate. Simple handling and rapid results acquisition allow application in many fields, such as in hospitals and in emergency medical care, and also in sports medicine and veterinary medicine.

For the calculation of the blood oxygen saturation, two different wavelengths are required, one in the red light and the other in the NIR light band. At these wavelengths, the absorption characteristics of oxyhemoglobin (HbO_2) and reduced

hemoglobin (Hb) are different. From the amplitudes at both wavelengths the oxygen saturation (SpO_2) can be calculated:

$$SpO_2 = \frac{HbO_2}{HbO_2 + Hb}. \tag{6.2}$$

To determine the impact of ambient light, a measurement without a signal of the light source as a reference is performed, and the resulting absorption amplitudes are subtracted from the original result of measurement. Usually an empirically derived calibration curve is needed [51, 52].

Since the AC component is synchronous with the heart beat, the PPG signal can be used to provide the heart rate, which is also an important parameter in monitoring of patients. A typical example of a pulse oximeter is shown in Figure 6.28.

Continuous Blood Pressure Measurement The determination of the arterial blood pressure is very important in the monitoring of patients, especially in intensive care units. Usually an invasive catheter is needed to provide this information. However, this method carries some disadvantages for the patient, such as the risk of infection or the dependence on hospitalization. Several studies have shown that a beat-to-beat evaluation of the changes in blood pressure [blood pressure variability (BPV)] is a potential tool for diagnosing cardiovascular diseases and for risk stratification.

The Finapres™ (now Portapres™) device (Figure 6.29) was one of the first medical instruments that provided noninvasive and continuous tracking of the blood

Figure 6.28 Pulse oximeter (Covidien-Nellcor™); transmission mode, display with blood oxygen saturation (left) and heart rate (right).

Figure 6.29 Portapres™ (Finapres Medical Systems BV) blood pressure monitor; inflatable finger cuff and control unit.

pressure wave form. It was developed in the 1980s and is based on the volume-clamp method that was first introduced by Penaz in 1967 [53]. With this method, the finger arterial pressure is measured using a finger cuff and an inflatable bladder in combination with an IR PPG sensor. The IR light is absorbed by the blood and the pulsation of arterial diameter during a heart beat causes a pulsation in the light detector signal. The first step in this method is determination of the proper unloaded diameter of the finger arteries, the point at which finger cuff pressure and intra-arterial pressure are equal. Then the arteries are kept at this unloaded diameter by varying the pressure of the finger cuff. Hence the cuff pressure provides an indirect measure of intra-arterial pressure [53, 54].

In several studies, parameters from the BPV provided by the Finapres were analyzed in order to examine the autonomic regulation system. For example, it was shown that measures from BPV analysis revealed highly significant differences discriminating patients with dilated cardiomyopathy from a reference group [55]. In another interesting study, it was found that the analysis of the baroreflex sensitivity is a potential tool in the prediction of pre-eclampsia, which is the most dangerous complication in pregnancy [56]. For the calculation of the baroreflex sensitivity, the determination of beat-to-beat changes in blood pressure is required. Furthermore, subjects with acute schizophrenia showed a reduction in baroreflex sensitivity (calculated from blood pressure and heart rate) accompanied by tachycardia and greatly increased left ventricular work index [57].

Assessment of the Peripheral Vascular System Arteriosclerosis and the resulting peripheral arterial occlusive disease (PAOD) play a significant role in arterial diseases, especially in elderly patients. It is also correlated with an increased risk of coronary artery disease and stroke. The PPG provides a potential diagnostic method as the peripheral pulse is usually damped, delayed, and diminished according to the stage of disease [58, 59]. In general, this is diagnosed through a site-to-site comparison, mostly performed at the lower limbs. A study by Simonson *et al.* [60] found significant changes in the rise time in impaired arteries. The potential of differences in PTT between the left and the right sides was further stated in recent

studied [61, 62]. It was also shown that frequency analysis of the PPG signal can reveal differences between healthy arteries and those with arteriosclerosis [63]. The shape of the pulse wave also contains diagnostic information. This was proven by Allen and Murray applying a neural network for classification [64]. They also introduced the shape index as a measure of the abnormal distortion of the pulse contour that provided a very high accuracy of >90% [65, 66].

A further new development is the application of photoplethysmography for the determination of the ankle brachial index (ABI). This is usually performed by using two pressure cuffs placed on the upper arm and lower limb (Figure 6.30) and a pocket Doppler ultrasound device. The ABI test is a potential method for the noninvasive assessment of PAOD [67]. Studies have shown a sensitivity of 90% with a corresponding 98% specificity for detecting hemodynamically significant stenosis (diameter of occlusion >50%) in major leg arteries [68]. The Doppler device registers the peripheral pulse while the pressure cuffs are inflated over the artery until the pulse

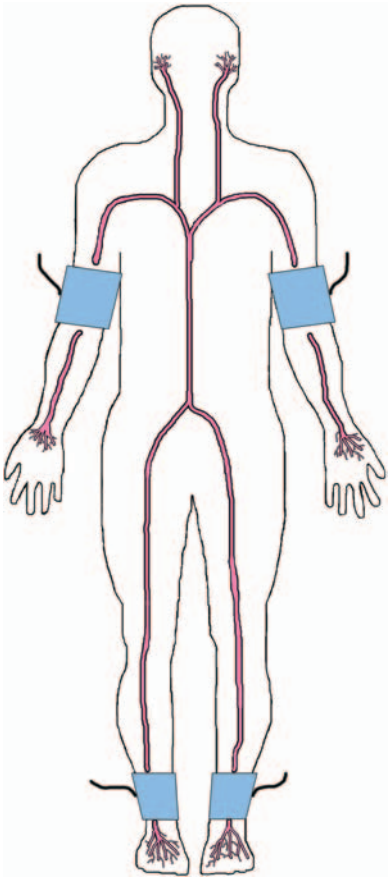

Figure 6.30 The principle of arrangement for measuring ABI.

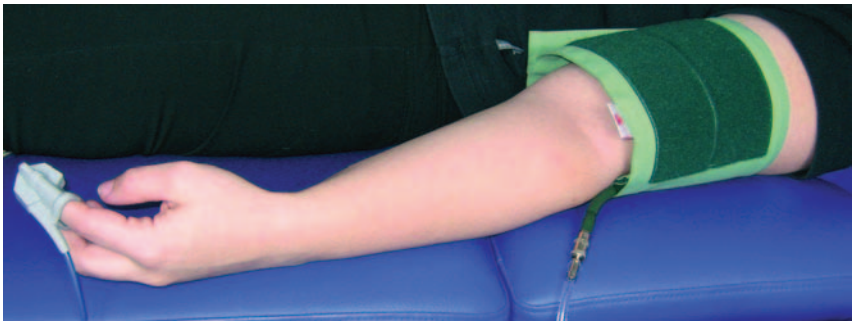

Figure 6.31 Placement of the pressure cuff and the PPG sensor on the left arm for determining the ABI (Vascular Explorer, enverdis GmbH, Jena).

ceases. The cuff is then slowly deflated. The corresponding pressure at the moment the pulse signal returns provides the systolic blood pressure reading for the given artery. A recently developed device (Figures 6.31 and 6.32) uses a PPG sensor instead of the Doppler device to detect automatically the diminishing and return of the pulse wave.

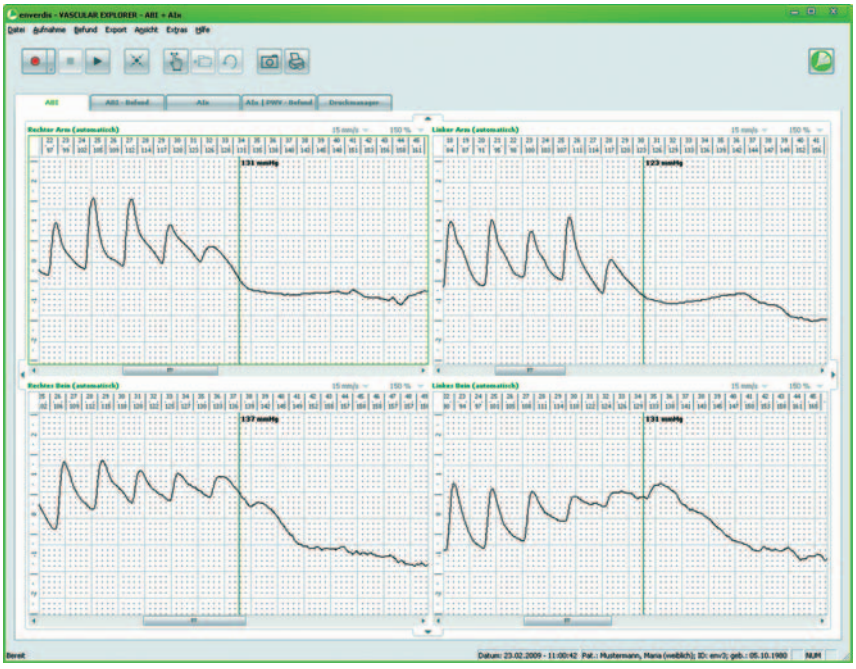

Figure 6.32 Display of the peripheral pulse wave in the measured limb: top left, right arm; top right, left arm; bottom left, right leg; bottom right, left leg. Marker represents the artery occlusion pressure which is the moment when the pulse wave disappears.

Further, chronic venous insufficiency can be detected with PPG by analyzing the DC component. The amount of blood increases in the venous system in a standing position due to the damaged valves in the vessels. This volume increase can be tracked with PPG. This method is also known as light reflection rheography [69, 70].

Assessment of the Microvascular Blood Flow In peripheral tissues, oxygen is distributed by the capillaries to the cells (Figure 6.33). Due to their small diameters, conventional techniques such as angiography and ultrasound are not capable of analyzing these vascular segments. "Tissue photospectrometry" is a technique to provide information on the condition of the microvascular system.

Measurement of the tissue perfusion is important for the assessment of, for example, viability and wound healing. A new technology which is realized in the O2C (Oxygen to See; LEA Medizintechnik, Giessen, Germany) (Figure 6.34) is a multiple-channel system which makes it possible to determine perfusion quantities and oxygen values within different tissue depths. This technology is a combination of laser Doppler spectroscopy for determination of blood flow and white light spectroscopy for determination of blood oxygen saturation and the amount of hemoglobin (Figure 6.35). Laser light determines perfusion quantities in tissue. A Doppler shift is caused by the movement of the red blood cells. This Doppler shift of the detected laser light is analyzed and displayed as the blood flow velocity (laser device class 3 B, protective class I, wavelength 830 nm, power <30 mW). The detected laser signal correlates with the number of moving red blood cells within the tissue. This quantity and the blood flow velocity are used to calculate the blood flow. Different applications

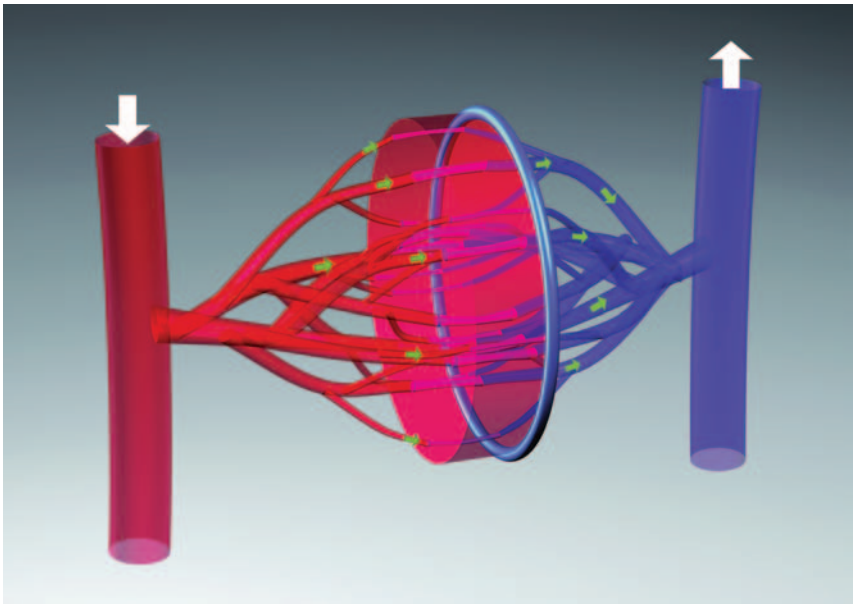

Figure 6.33 The capillary system.

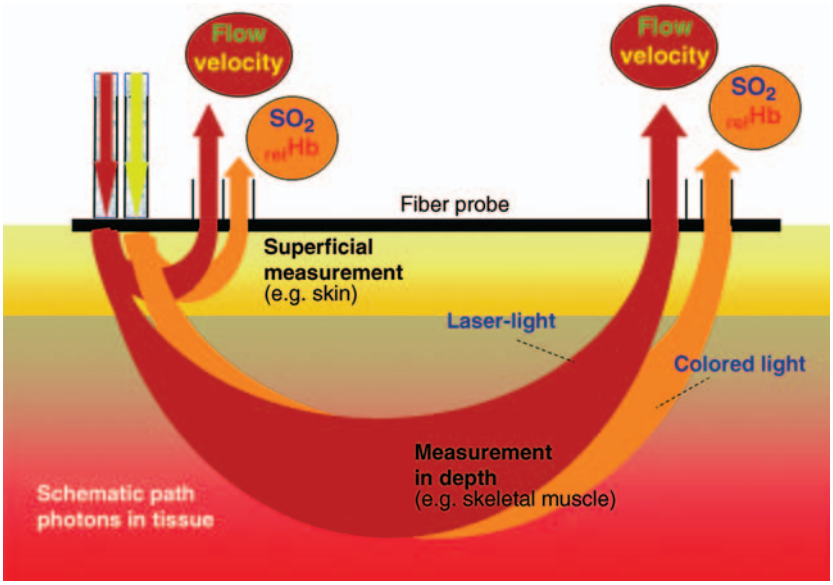

Figure 6.34 Principles of measurement of the microvascular blood flow and oxygen saturation (LEA Medizintechnik, Giessen). The O2C works simultaneously with white and laser light. The light in tissue is scattered at the mitochondria and reflected to the surface. There it is detected and analyzed. The white light allows the determination of the oxygen saturation. The shift in frequency of the laser light carries the information about the blood flow.

at the skin and in internal organs and the intestinal tract are possible using flexible glass fiber probes. Applying this technology allows the assessment of the healing of wounds, for example in patients with diabetic foot ulcers [71]. Another approach showed that the combined use of laser light spectroscopy and PPG allows continuous and noninvasive monitoring of organ reperfusion and oxygen metabolism during simultaneous pancreas–kidney transplantation [72].

Figure 6.35 (a) Display of the O2C: continuous data on oxygen saturation and blood flow over time (top); instantaneous values of oxygen saturation and blood flow in different tissue depth (right); spectrum and observation of signal quality (bottom left). (b) Sensor with white light and laser light source and detection unit.

6.1.3.5 Summary

Photoplethysmography is a technology that has a wide range of applications in the assessment of the cardiac and vascular system. It is a noninvasive, simple, and inexpensive method. The improvements in semiconductor optical components and computer-based signal processing have further increased its abilities. Conclusively PPG has great potential in the field of cardiovascular screening and monitoring of patients.

6.1.4 Noninvasive Diagnostics – Ophthalmology

6.1.4.1 Introduction

Ophthalmology is concerned with diseases and dysfunctions of the human eye, including structures surrounding the eye such as the retina, pupil, iris, vitreous body, and gland of the eye. The human eye is a complex photosensitive organ that enables analysis of the form, light intensity, and reflected light to be performed. Therefore, the eye contains different functional components: a lens system which focuses the image, a nervous system, and a layer with photosensitive cells that collect, process, and assign information to the brain [73]. The structure of the eye is shown in Figure 6.36. The eye consists of three layers, the outer, the middle, and the inner layer. The outer layer includes the cornea and the sclera and the middle layer consists of the iris, ciliary body, and choroid. The inner layer consists of the retina (nervous tissue), which is part of the optical nerve system and converts the light in electrical impulses.

The inner layer of the eye can be divided into different compartments: the anterior chamber, posterior chamber, and vitreous chamber [73, 75, 76]. The principle of image formation in the eye is demonstrated in Figure 6.37. A light beam is travels through the cornea, where the light is refracted and passes through the lens.

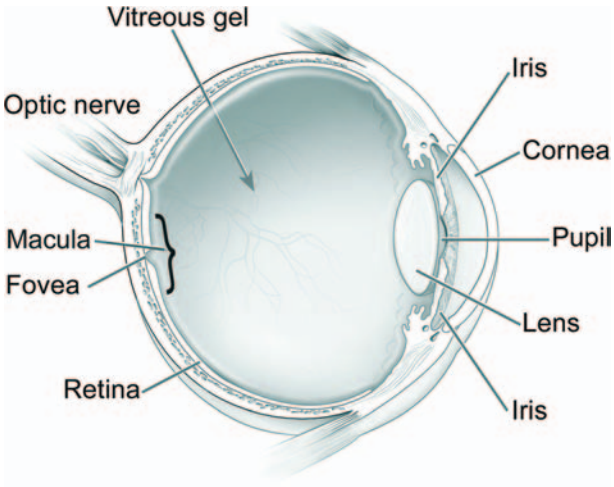

Figure 6.36 Structure of the eye [74].

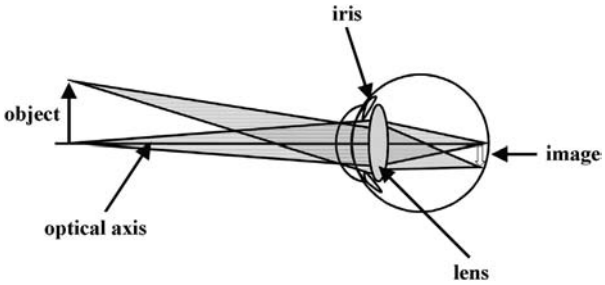

Figure 6.37 Process of a light beam in the eye (adapted from [76]).

The iris is located between the cornea and the lens and controls the size of the incoming light beam by the pupil. The lens focuses the light at the retina. The retina is a light-sensitive tissue where an inverted image of the visual field is formed [73].

Alterations in the eye are related to diseases such as hypertension and blinding conditions generated by glaucoma and macular degeneration [77]. In the following, some of the most important eye diseases are briefly described.

A scotoma is an area of partial or complete blindness within the visual field. The defect ranges from barely detectable loss of visual acuity to absolute blindness. It is due to retinal choroid or optic nerve disorder. There are three types of scotoma: absolute, relative, and scintillating scotoma [78].

A *cataract* is a gradual thickening of the lens that causes the lens to become so clouded that light is either distorted or cannot reach the back of the eye (the retina) for transmission to the brain [79]. It is opacity to different degrees of the lens of the eye [80]. Cataracts are the leading cause of treatable blindness in all areas of the world, especially in adults with an age of 55 years or more [81].

Glaucoma is a progressive disease of the optical nerve. Among other reasons it can be based on increased intraocular pressure (IOP). There are two main types of glaucoma: angle-closure glaucoma and open-angle glaucoma. For open-angle glaucoma, the risk increases with, for example, age over 45 years, family history of glaucoma, diabetes. or low blood pressure, and for closed angle glaucoma it increases with, for example, age over 55 years (especially in females), family history of glaucoma, or the use of certain drugs with cholinergic inhibition [82].

The macula is the part of the eye that is needed for seeing fine detail and central vision. Degenerative changes in the macula results in state known as macular degeneration. The disease is due to no apparent cause and usually occurs after the age of 50 years. The first symptom of macular degeneration is the painless loss of central visual acuity [83].

Keratoconus is characterized by a conical, usually bilateral, central deformation of the cornea with parenchymal opacification and thinning of the cornea. The risk of keratoconus increases with family history of the disease, and women are more likely to be affected than men [84].

There are different methods to diagnose the discussed diseases, outlined below.

One of the simplest methods for examining the anterior eye segmented is the slit lamp. The slit lamp (e.g., Slit Lamp SL 130, Carl Zeiss Meditec, Jena, Germany [85]) is

an instrument that consists of a high-intensity light source that can be focused to shine in a thin beam that is usually combined with a microscope. A variable narrow light beam (e.g., 1–2 mm) is focused on the curved surface of the cornea. This allows an optical section through the clear segments of the eye tissue. The split lamp is used for the examination of ocular tissue and surface, especially corneal injury. If the observer is using various handheld or split lamps equipped with lenses, it is possible to visualize the optic nerve, posterior vitreous, and retina [86].

The following sections discuss some of the common diagnostic methods (e.g., corneal topography, perimetry, scanning laser polarimetry, and wave front analysis) and their applications and give an overview of typical components, advantages, and disadvantages.

6.1.4.2 **Corneal Topography**

Corneal topography or videokeratography (see Figure 6.38) is a method for mapping the surface curvature of the cornea.

The patient is looking into a light bowl that consists of a pattern with concentric rings (placido disc). The light ring of the placido disc (Figure 6.39) shines on to the corneal surface. In the center of the placido disc an aperture measures the reflected rings from the cornea using a CCD camera.

The results are displayed in a color-coded topographic map of the cornea and computer software calculates different parameters characterizing the corneal surface [88–90]. An example of a pupil videokeratoscopic image is shown in Figure 6.40 and a color-coded topographic map is depicted in Figure 6.41 [87, 90].

Figure 6.38 Atlas Model 9000 (Carl Zeiss Meditec, Jena).

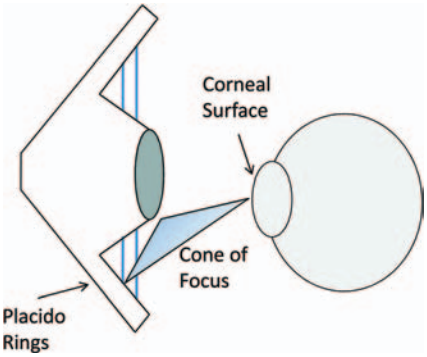

Figure 6.39 Structure of the placido disc with a cone of focus and the corneal surface where the placido rings are projected (adapted from [87]).

Applications Corneal topography is used for fitting contact lenses and identifying distortions such as keratoconus or scarring of the cornea. It is also needed for the evaluation of patients before and after surgical procedures. Another application of corneal topography is the analysis of the degree of corneal steepness [88, 91].

Typical Components of a Corneal Topographer A corneal topographer consists of a placido disc. The placido disc is a flat, lit disc and is composed of a pattern of concentric dark and light rings such as black and white rings. A placido disc can have

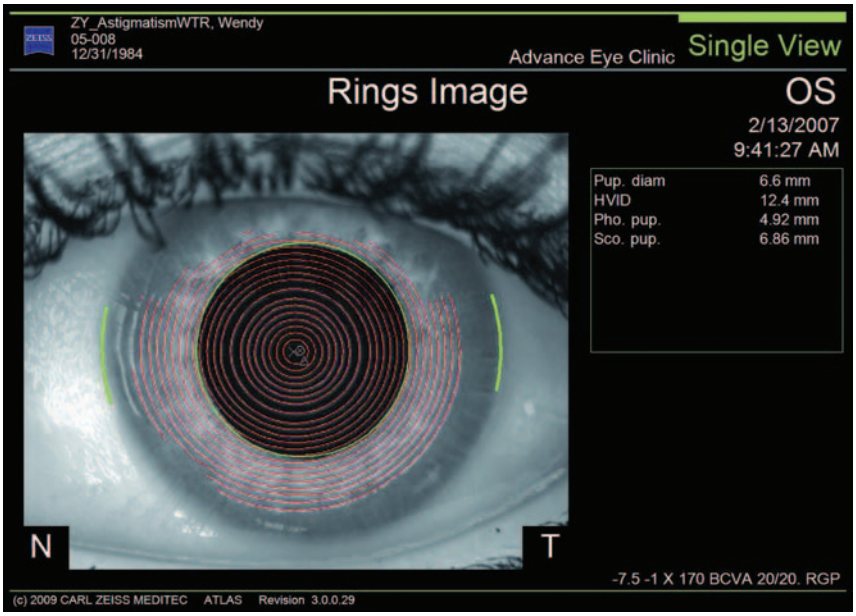

Figure 6.40 Videokeratoscopic image showing the projected rings from the placido disc on the corneal surface.

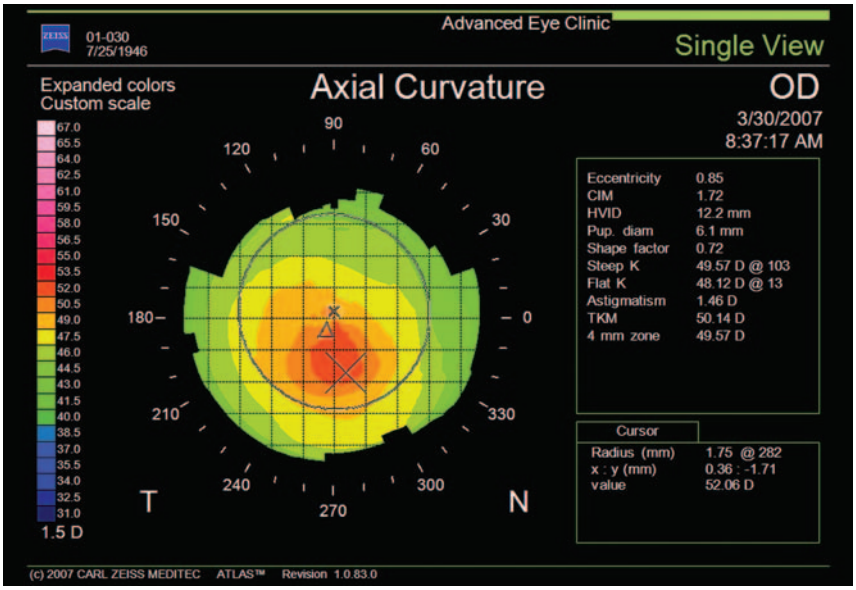

Figure 6.41 A color-coded topographical map displaying the curvature, elevation, and corneal wavefront. Blue represents the flattest area and red the mean steepness.

different sizes (a small or a large placido disc target) depending on the number of rings and the producer. In front of the placido disc the patient is held still by a chin rest. Another component of a corneal topographer is an imaging system with objective lens and a camera recording the reflected pattern of the cornea. The data analysis is performed by a computer system.

There are two approaches concerning the placido disc: on the one hand (I) the use of a large placido disc target and a long working distance to project images of mires on to the corneal surface and on the other (II) a small placido disc target with a short working distance [91, 92].

Corneal topography is a noninvasive, painless, and rapid method. The measurement has the ability to measure directly in the corneal height, detect irregular corneal surfaces, and perform analysis accurately across the whole cornea [91]. Approach I has the advantage of less critical focus whereas approach II has greater potential coverage of the corneal surface [92].

Corneal topography consisting of a large placido disc target and a long working distance (approach I) has the disadvantage of corneal shadows created by the brow and the nose. The disadvantage of the small placido disc target with a short working distance (approach II) is higher sensitivity to errors in focusing [92].

6.1.4.3 **Perimetry**

Perimetry uses different light sensitivities to verify the visual field. Here the patient is seated in front of the bowl and is held still with a chin and head rest. Figure 6.42 shows the principle of perimetry.

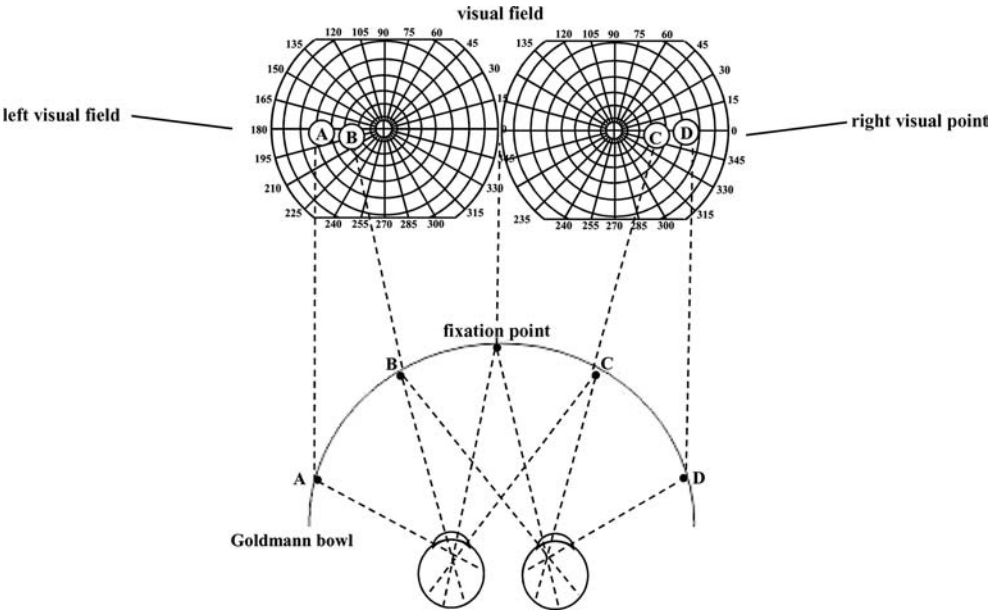

Figure 6.42 Scheme of perimetry with a Goldmann perimeter. The Goldmann chart represents the peripheral boundary of the visual field (adapted from [93]).

A light target is projected on a defined background (Goldmann perimeter). If the patient recognizes the light target he/she presses a button. This procedure is used for many light targets from different peripheral points. These recognized points are then plotted in the graph of the visual field [94].

Perimetry includes kinetic perimetry and static perimetry; both methods can be performed manually or automatically. In recent years, fundamental findings of automatic perimetry were reported [95, 96]. The Humphrey matrix perimeter was developed by Carl Zeiss Meditec AG (Figure 6.43) and is an example of an automated perimeter.

Applications Perimetry is used to explore the boundaries of the visual field, identifying visual abnormalities. Perimetry detects vision loss in the peripheral visual field caused by glaucoma and detects scotomas [97].

Typical Components of a Perimeter The major component of a standard perimeter is a hemispherical bowl with a white surface and a radius of 30 cm (Goldmann bowl). The patient is held still in front of the bowl by a fixation mechanism and in the back of the bowl is a telescope allowing the observer to adjust the patient's position. A light target is projected on to the inside of the white surface and its intensity and size are varied.

The basic equipment of an automated perimeter is a hemispherical bowl or a spherical Goldmann bowl, a patient fixation system such as a chin rest and head rest, a signal button, a monitor (flat-screen monitor) for real-time display, and

Figure 6.43 Humphrey Matrix™ Perimeter (Carl Zeiss Meditec, Jena).

a computer system. The automated perimeter can be used with different software solutions to analyze different states of glaucoma and scotomas, e.g., standard automated perimetry (SAP), frequency doubling perimetry (FDP), and short-wavelength automated perimetry (SWAP). SAP (or the so-called white-to-white perimetry) is the gold standard for testing functional changes in glaucoma. This technique measures light sensitivity thresholds at each retinal location. However, the method is not selective for the detection of particular glaucoma-related retinal ganglion cell (RGC) damage [98]. FDT perimetry is based on a frequency-doubled sinusoidal grating stimulus and was developed to detect damage to magnocellular ganglion cells, which are preferentially affected in glaucoma patients [98–100]. SWAP is used for the early detection of glaucoma. SWAP utilizes a bright yellow background and a large short-wavelength ("blue") stimulus to isolate and measure the sensitivity of short-wavelength chromatic mechanisms. From this basis the sensitivity of the middle ("green") and long ("red") wavelength mechanism is actuated [101].

Kinetic Perimetry A mobile light target (stimulus) is moved by a Goldmann perimeter from a non-seeing area to a seeing area of the visual field. When the spot light is noticed, the patient presses a button. Kinetic perimetry presents the visual field in a topographic map as depicted in Figure 6.44 [95, 102].

Kinetic perimetry is a noninvasive method to characterize an entire peripheral visual field [95].

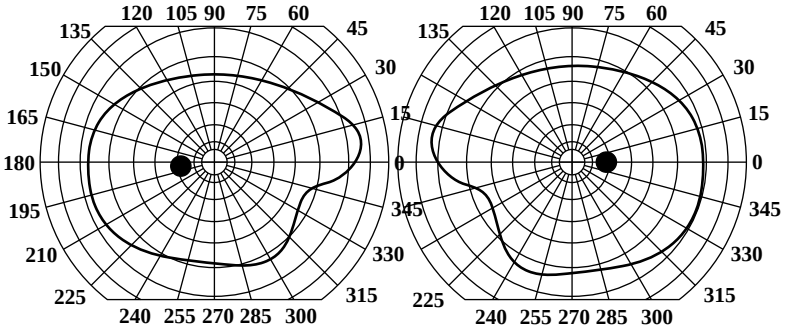

Figure 6.44 Perimetric results of a normal visual field. The optic disc makes a black point on the topographic map which is called the blind spot (adapted from [103]).

The results are dependent on the perimetrist because the exposure time is variable, there are different speeds of movement, and the point location of the stimulus is moved by hand. The measurement of the full field is time consuming, tedious, and requires good patient cooperation [95, 104]. Intensive training is necessary for the application of kinetic perimetry [105].

Static Perimetry Static perimetry is generally an automated method. The intensity and size of a light target will be increased or decreased until the patient notices. That means that the spot light does not move, in contrast to kinetic perimetry [102]. Figure 6.45 presents results for a defective visual field [106].

Static perimetry is a noninvasive method to characterize the central visual field. This computerized method uses a software package for fast data analysis, storage, and comparison with normative data [95]. The tests in static perimetry are performed by a computer, hence the measurements are reproducible, automatically calibrated, and performed under standardized conditions [107].

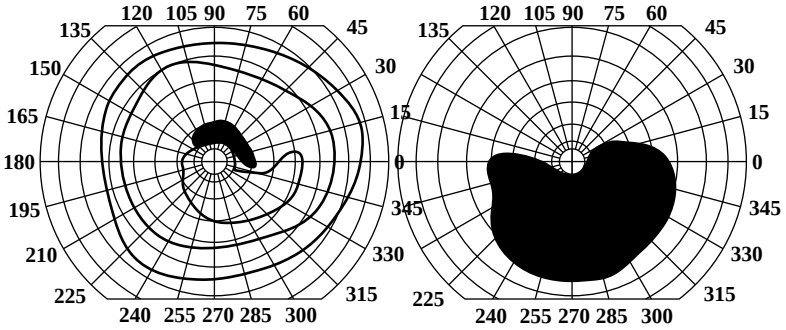

Figure 6.45 Perimetric results of defected visual fields. On the left side is an immediate visual loss and on the right is an advanced visual loss, e.g., due to glaucoma (adapted from [106]).

Static perimetry has increased cognitive demands and lack of flexibility for patients. Automated perimetry has high maintenance and acquisition costs [95, 97].

6.1.4.4 Optical Biometry

Optical biometry is a noninvasive optical biometric imaging technology which is based on the method of partial coherent interferometry (PCI). It measures directly biometric data such as the axial length along the eye's visual axis from the lens to the macula, as shown in Figure 6.46.

The measurement principle of optical biometry using a Michelson interferometer is demonstrated in Figure 6.47. A laser diode generates IR light (wavelength 780 nm) with a short coherence length. The laser beam passes through a beamsplitter, which produces two coaxial beams with mutual time delay by means of the interferometer mirrors (a fixed reference mirror and a moving measurement mirror).

These coaxial beams pass directly into the eye and are reflected on the surface of the cornea and the retina. A PCI signal is detected by a photodetector. The displacement of the moving mirror allows an accurate measurement of the axial length [108, 109]. The IOL-Master measures the anterior chamber depth (ACD), axial length, corneal radius, and white-to-white distance [110] (Figure 6.48).

Applications Optical biometry set a new standard for highly accurate, precise measurements of all ocular characteristics. Three measurements are executed for the calculation of intraocular implant lenses: the axial length of the eye, central cornea curvature, and ACD.

Figure 6.46 Optical biometry system: the IOL-Master (Carl Zeiss Meditec, Jena).

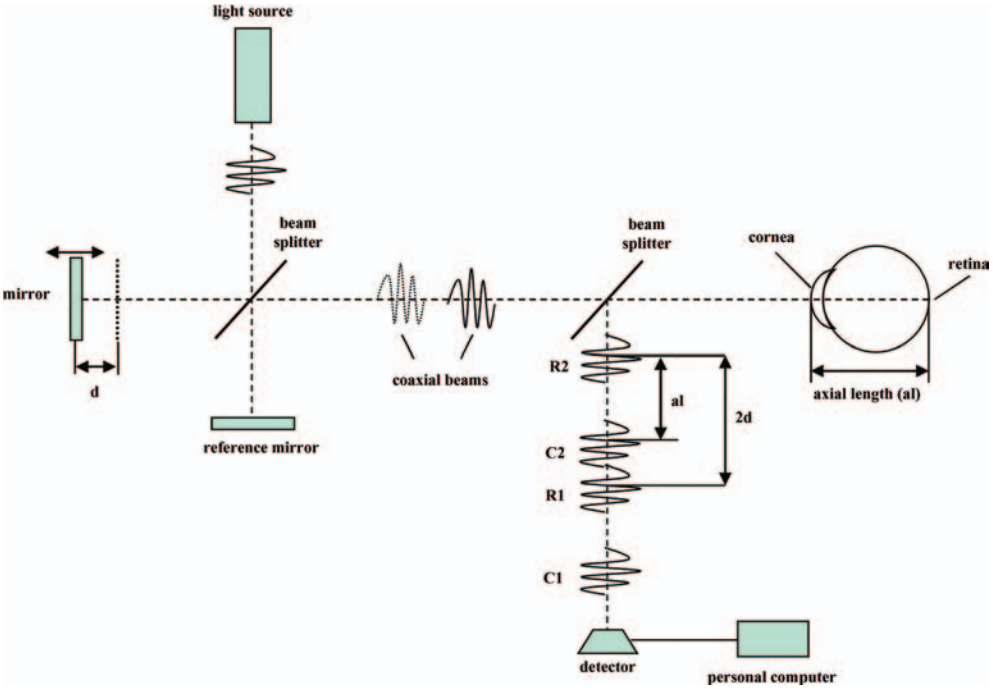

Figure 6.47 Operating principle of the IOL-Master device with a dual-beam partial coherence interferometer. The interferometer generates two coaxial beams with a mutual time delay (interferometer arm length differences *d*). Both coaxial beams pass through the eye and are reflected at the anterior surface of the cornea (C_1, C_2) and at the retinal (R_1, R_2) interface. An interference signal is detected at the photodetector with the help of the displacement of the moving mirror which is related to the coherence of the light source and the reflected signal (adapted from [108]).

Typical Components of the IOL-Master Optical Biometry System An optical biometry system such as the IOL-Master consists of a measurement aperture including an IR laser diode (wavelength 780 nm), beamsplitter, photodetector and video camera. A joystick is used for raising and lowering the IOL-Master scanning device. A patient module (chin rest and head rest) for the patient's positioning and a computer system

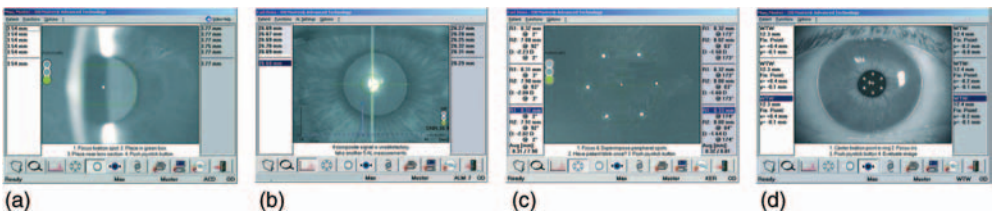

Figure 6.48 Measurements with the IOL-Master: (a) anterior chamber depth; (b) axial length; (c) corneal radius; (d) white-to-white distance.

with an integrated software package for data analysis, storage, and documentation of the results are also included [111].

Optical biometry is a noninvasive procedure that is easy to use for the operator and with less discomfort for the patient. The measurement is made without any anesthesia [112].

Optical biometry is not applicable in various cases, such as severe tear film problems, corneal scarring, mature cataract, respiratory distress, tremor, membrane formation, keratopathy, lid abnormalities, vitreous hemorrhage, and retinal detachment [112]. A new generation of optical biometry device is the Lenstar LS900®all-in-one optical biometer (Haag-Streit AG, Koeniz, Switzerland). The Lenstar LS900 measures nine different eye parameters: corneal thickness, ACD, lens thickness, axial length, keratometry, white-to-white distance, pupillometry, eccentricity of the visual axis, and retinal thickness at the point of fixation (macula). The measurement is based on the principle of optical low-coherence reflectometry (Michelson interferometry) [113].

6.1.4.5 **Retinal Imaging and Glaucoma Diagnostics**

Optical imaging is a standard method for detecting changes in the optic nerve head and retinal nerve fiber layer (RNFL). Some optic diagnostic imaging methods specialized for glaucoma management are scanning laser ophthalmoscopy (SLO), scanning laser polarimetry (SLP), optical coherence tomography (OCT), and the retinal thickness analyzer (RTA) [105], and are discussed in the following.

Scanning Laser Ophthalmoscopy (SLO) SLO is based on the technique of confocal scanning laser microscopy. The principle of SLO is shown in Figure 6.49. A laser beam passes through a pinhole aperture and is situated in a conjugate plane with a small focus point that scans the retina surface horizontally and vertically.

The scanning depth is adjusted by shifting the confocal aperture. The detector measures the reflected light and records this on a fundus camera [115, 116].

The Heidelberg retina tomograph (HRT) (Figure 6.50) generates two-dimensional images Figure 6.51 by an array of pixels and is also designed for acquisition and analysis of three-dimensional images of the posterior segment. It allows the quantitative assessment of the topography of ocular structures and the precise follow-up of topographic changes [114].

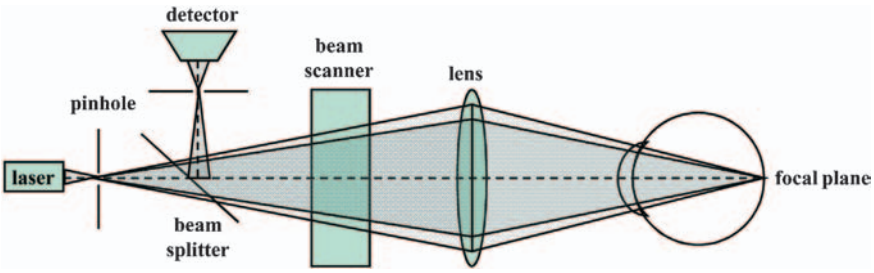

Figure 6.49 Scheme of a scanning laser ophthalmoscope (adapted from [114]).

Figure 6.50 HRT 3 scanning laser ophthalmoscope (Heidelberg Engineering GmbH, Heidelberg).

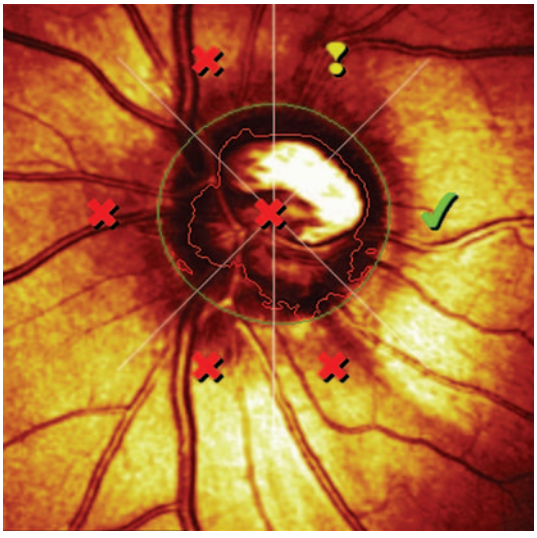

Figure 6.51 HRT image: reflectance map image of an optic nerve head [117].

Application SLO imaging is used for diagnostics of the retina or cornea and glaucoma, macular degeneration, and other retinal disorders. Some topographic parameters are estimated such as disc area, RNFL thickness, cup depth, and shape [105, 116].

Typical Components of SLO The light source of the HRT is a diode laser (wavelength 670 nm). The patient is held still with a patient module such as head rest and chin rest. A standard personal computer is used with a software package including data analysis and storage of the results [117].

HRT is a noninvasive method and the topography image is acquired without pupil dilation. HRT images are of high contrast and are available in real time [105].

Some HRT measurements require a reference plane for the exact calculation of some diagnostic parameters. Further, it needs some expertise to draw a initial contour line to define the optic disc margin. Another limitation of HRT is the influence of the intraocular pressure [105].

Scanning Laser Polarimetry (SLP) SLP uses polarized light to determine the thickness of the RNFL. The method is based on the property of birefringence of nerve fiber layers. The scanning laser polarimeter [118] (Figure 6.52) is based on confocal scanning laser ophthalmoscope [119].

Figure 6.53 shows the basic principle of SLO. A polarized laser beam is projected into the eye and is reflected by the retina. The amount of light reflected is detected and analyzed. The RNFL produces birefringence, changing the state of polarization. This

Figure 6.52 Scanning laser polarimeter: the GDx™ (Carl Zeiss Meditec, Jena) measures the birefringence of the RNFL and includes analysis for glaucoma. Some instruments have a variable corneal compensation (VCC), reducing the anterior segment birefringence of the eye and eliminating RNFL inaccuracies in the image.

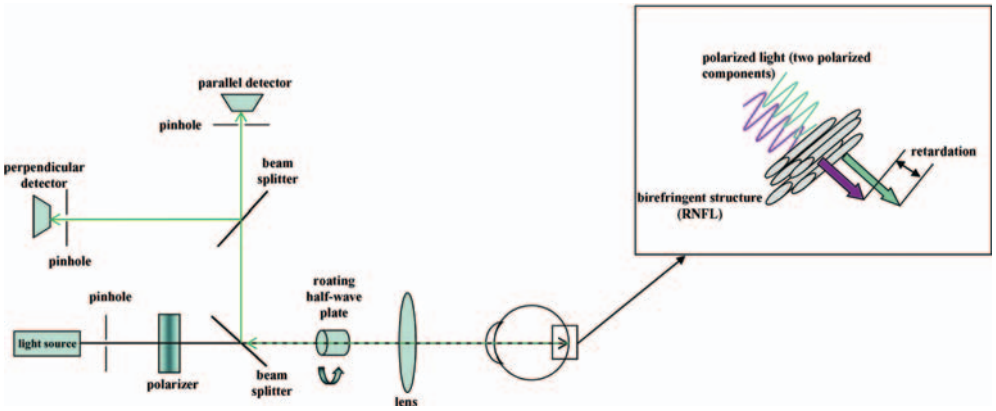

Figure 6.53 Principle of scanning laser polarimetry (adapted from [120, 121]).

procedure, called retardation, is detected by an analyzer. The value of retardation directly correlates with the thickness of the nerve fiber layer and is displayed in the retardation map [120]. Some scanning laser polarimeters have variable corneal compensation (VCC) for adjusting the corneal birefringence.

Figure 6.54 presents the standard GDx printout with the fundus image, the thickness map or retardation map, the deviation map and TSNIT (temporal–superior–nasal–inferior–temporal) graph and RNFL parameter. The fundus image displays

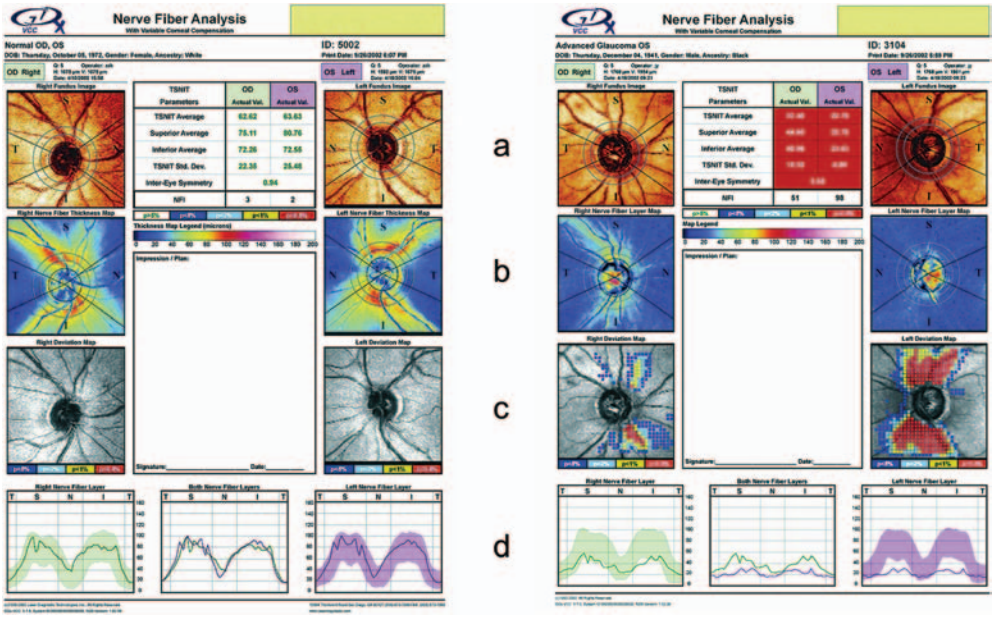

Figure 6.54 Standard GDx printout of a healthy eye (left) and a glaucoma eye (right): (a) fundus image; (b) thickness map or retardation map; (c) deviation map; (d) TSNIT graph.

a color intensity map of the reflectance. The retardation map shows a color-coded RNFL thickness, which means that thicker areas are displayed in warm colors (yellow, orange, and red) and thinner areas in colder colors (blue and green).

The deviation map compares each RNFL scan with a normative database. A color scale characterizes the locations and magnitudes of the RNFL defects. The TSNIT graph represents the RNFL thickness values along the calculation circle; normal values are in the shaded area and abnormal values are below the shaded area [105].

Application SLP detects structural changes and defects of the RNFL and enhances the diagnostics of early glaucoma.

Typical Components of an SLP The light source of an SLP is a helium–neon diode (wavelength 632.8 nm) or argon laser (514 nm). A polarization modulator changes the polarization states of the laser beam. The laser beams are moved horizontally and vertically on the retina by a scanning unit. The polarization detector detects the reflected polarized light from the cornea. A computer analyzes and stores the results. Some instruments have a joystick for pupil alignment [119].

A measurement can be performed without pupil dilation and is independent of a reference plane and magnification effects. SLP is a noninvasive method and easy to handle [105, 122].

Erroneous images and measurements could be obtained in the case of eyes with peripapillary embossment. It is not possible to generate images from eyes with nystagmus. Other problems in SLP imaging are atypical birefringence patterns and abnormal polarization at the anterior segment [105, 122].

Optical Coherence Tomography (OCT) OCT generates high-resolution images of the ocular structure. The principle of this optical technology is similar to that of ultrasound, but low-coherence light is used instead of sound. OCT is based on the Michelson interferometer technique (Figure 6.55).

In Figure 6.56, a schematic OCT setup is shown. Low-coherent light (consisting of a finite bandwidth of frequency) is focused through a Michelson interferometer. A beamsplitter in the interferometer breaks the light into a reference beam and sample beam. The sample beam passes directly through the retina and the light is reflected from structures at different depths. The reference beam is reflected on the reference mirror. The two reflected beams are recombined at the same beamsplitter and transmitted to a photosensitive detector.

OCT generates a final image which is a color-coded map with the help of a special image processing software package. A printout of an OCT scan is shown in Figure 6.57, including the RNFL thickness [105, 123].

There are different basic principles of OCT: time domain optical coherence tomography (TDOCT), frequency domain optical coherence tomography (FDOCT), which is also called Fourier domain OCT or spectral domain OCT, and polarization-sensitive optical coherence tomography (PS-OCT).

In contrast to FDOCT, where the mirror is kept stationary, in TDOCT the mirror moves to match the delay in various layers of the sample. The resulting interference

Figure 6.55 Optical coherent tomography with Stratus OCT (Carl Zeiss Meditec, Jena).

signal is processed to produce the axial scan waveform. The reference mirror must move one cycle for each axial scan, which limits the speed of the image acquisition. In FDOCT, the mirror is stationary and the spectral pattern of the interference between the sample and the reference reflections is measured and the interferogram is Fourier transformed to provide an axial scan. FDOCT offers higher resolution than TDOCT (5 μm versus 10 μm axial resolution) [125–127].

PS-OCT uses depth-dependent changes in the polarization states of backscattered light. Its application is to measure the birefringence of the RNFL. The reference arm consists of a quarter-wave plate (polarization modulator) and a moving mirror. In the

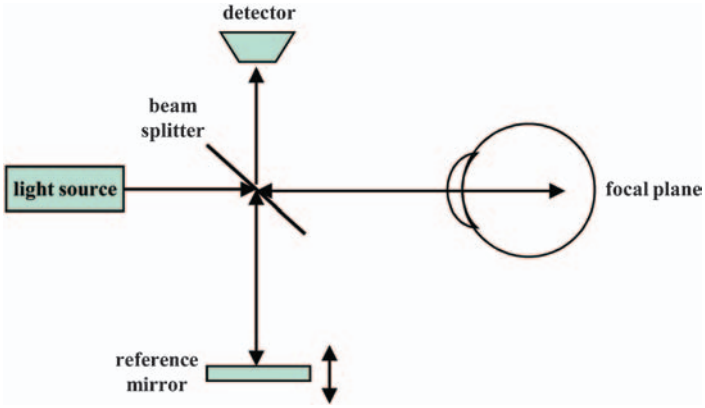

Figure 6.56 Operating principle of an OCT using an interferometer (adapted from [123]).

sample arm is also located a quarter-wave plate and a lens. The backscattered light of the reference arm is combined with the light of the sample arm and the resulting interfered beam is split by a polarization beamsplitter. The resulting beams are detected by two separate detectors [125, 128].

Application OCT is used to diagnose posterior segment and anterior segment disorders of the eye. The application of OCT in the posterior segment has contributed to the understanding of macular holes and vitreomacular traction. It is also a quantitative method of detecting changes in retinal thickness due to diabetes, cystoid macular edema, and epiretinal membrane.

The use of OCT in the posterior segment is helpful in imaging and measuring complex details of corneal pathologies and structural changes of the chamber angle and iris. OCT supports research on and treatment of glaucoma [123].

Typical Components of OCT The light source in OCT is a super-luminescent diode (wavelength 830 nm for the posterior segment and 1310 nm for the anterior segment) [122]. A photodetector records images. The patient is held still with a patient module such as head rest and chin rest and a joystick is needed for pupil alignment. A computer includes software packages for storage, analysis, viewing and importing of the OCT data [124].

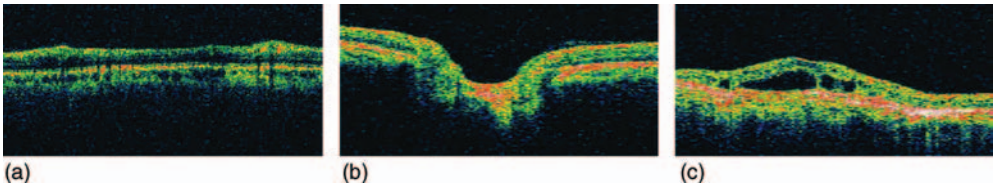

Figure 6.57 OCT scan with (a) thickness of RNFL; (b) optic nerve head; (c) macula [124].

OCT is a noninvasive diagnostic method which produces high-resolution images. It does not need a reference plane for measuring the RNFL thickness. It is possible to measure without pupillary dilation [105].

The measurements with OCT are dependent on the position of the individual scans and their overlap [129]. Many patients need pupillary dilation for good-quality images [105].

A problem with the OCT tomogram is to establish an accurate segmentation and layer thickness measurement of the retinal layer. Mishra *et al.* [130] developed an image processing method for the segmentation of all intra-retinal layers. The algorithm was performed on retinal images from healthy and diseased rodent models. The study presented a new method allowing much more accurate segmentation even in sub-optimal conditions of low image contrast and the presence of irregularly shaped structural features in the OCT images. The recently developed spectral domain OCT allows the image speed to be increased 100-fold compared with the first-generation TDOCT and allows three-dimensional imaging and real-time imaging of fast-moving structures. OCT has the potential to improve the precision of surgical interventions and may provide new interventions [131].

Retinal Thickness Analyzer (RTA) The RTA (Figure 6.58) is a device for mapping and quantitative measurement of the thickness of a selected retinal area in various regions of the fundus disc topography. The method is based on the principal of slit lamp biomicroscopy. A green helium–neon laser (543 nm) projects narrow light slits

Figure 6.58 RTA 3 retinal thickness analyzer (Talia Technology Ltd., Israel).

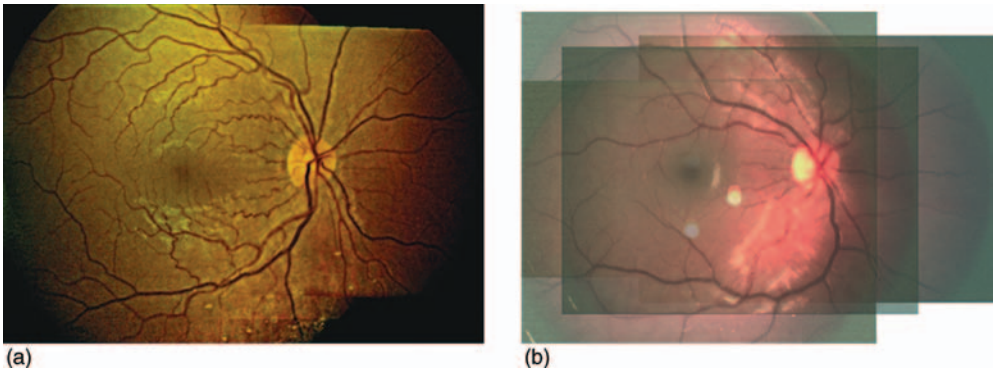

Figure 6.59 Standard RTA fundus image: (a) stand-alone fundus image; (b) overlapping of high-resolution fundus images.

on the retina and scans, in steps, across the retina. A CCD camera records the reflected light from the retinal pigment epithelium (RPE) and RNFL [105, 132, 133].

The recorded fundus images (Figure 6.59a) were analyzed by using an image registration algorithm. Thereby subsequent scans are overlaid (Figure 6.59b) while a color-coded retinal thickness mapping is performed. This allows an accurate follow-up of the vasculature of the fundus.

Furthermore, the RTA data provide information about topography maps, deviation probability maps from a normative database, quantitative numerical values, optical cross-sections, and unique interactive 3D cut sections [133].

Application The RTA is used for detection and follow-up investigations of glaucoma, diabetic retinopathy, age-related macular degeneration, and other retinal pathologies [133].

Typical Components of an RTA The RTA consists of a laser source such as a solid-state laser (wavelength 532 nm), a CCD camera which records the backscattered light, and a computer system including a software package for automatic registration, analysis and storage of high-resolution fundus images from the camera.

RTA is a noninvasive method and scans a wide area of the retinal tissue in a short acquisition time [105, 134].

Pupillary dilation is needed to obtain acceptable RTA images such as a macular scan. It is also possible to obtain optic disc images without pupillary dilation. For a continuous retinal thickness map an interpolation is necessary, but focal defects in retinal thickness or disc topography could be overlooked [105]. Furthermore, the image is adversely affected by media opacities [135].

6.1.4.6 Fluorescein Angiography

Fluorescein angiography (Figure 6.60) uses the dye tracing technique for examining the blood circulation within the retinal vessels.

Figure 6.60 Fluorescein angiography system combined with spectral-domain OCT: Spectralis HRA + OCT (Heidelberg Engineering GmbH, Heidelberg).

A fluorescent dye is injected into a vein in the patient's arm. After the dye injection, a series of photographs are taken and an angiogram is obtained for documentation. An exemplary fluorescein angiogram is presented in Figure 6.61. The fluorescein angiogram can be divided into six phases (choroida, arterial, capillary, venous, recirculation, late phase) with normal transit times [136, 137].

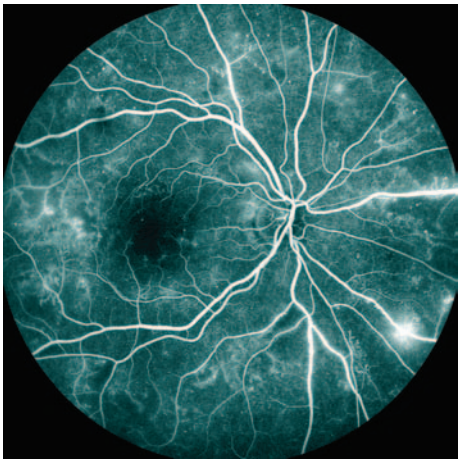

Figure 6.61 Fluorescein angiogram of retinal blood vessels.

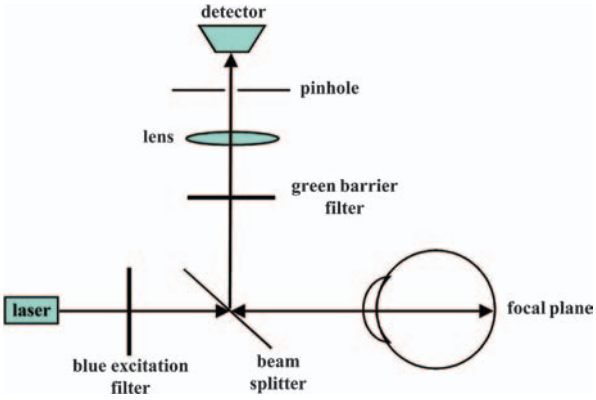

Figure 6.62 Principle of fluorescein angiography (adapted from [140]).

Sodium fluorescein has the property to fluoresce, which is the absorption of light with a specific wavelength inducing emission of light with a higher wavelength. A wavelength between 485 and 500 nm (blue) is the suitable for stimulating sodium fluorescein that consequently emits light with a wavelength between 520 and 525 nm (yellow–green). In the following, the basic principle of a fluorescein angiography system is described.

A monochromatic laser beam passes through an excitation filter that is only transparent to blue light. Accordingly, this blue light enters the eye and excites the fluorescein present in blood vessels. This procedure is called the excitation phase. Subsequently yellow–green and blue light emerge from the eye and pass through another barrier filter. This filter is only transparent to yellow–green light, which is detected by the camera (emission phase) [138, 139]. In Figure 6.62 the basic form of fluorescein angiography is shown.

Another type of fluorescein angiography is indocyanine green (ICG) angiography. ICG dye is a fluorescent substance which produces a weaker fluorescence. In this context, the wavelength of the excitation light ranges from 780 to 805 nm while light with a slightly higher wavelength (820–850 nm) is emitted. ICG is a useful method for investigating the choroidal circulation [140, 141].

Application Fluorescein angiography is used for the diagnosis of various posterior segment diseases such as macular diseases, retinal vascular diseases, optic nerve disorders, inflammatory retinal/choroidal diseases, and tumors [139].

Typical Components of a Fluorescein Angiography System The Spectralis HRA fluorescein angiography system consists of an optical system with a laser source (diode laser, wavelength 790 or 820 nm) and filter system. The angiography images can be recorded with a camera. A patient module (e.g., chin rest and head rest) is used to keep the patient still. It also has a computer system with an integrated software platform for image acquisition, processing, and archiving [142]. The fluorescent agent supports the ability to visualize dynamic processes in the retina [129].

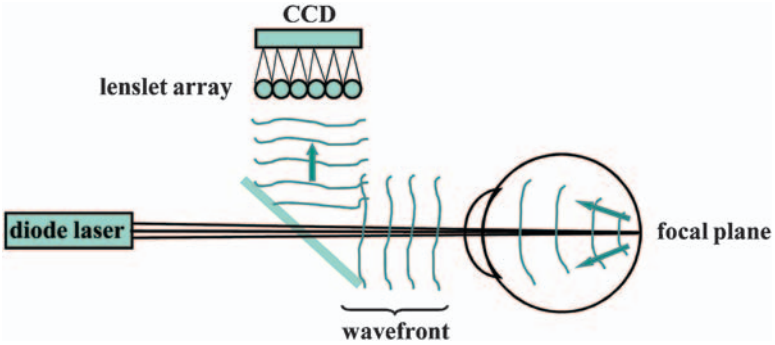

Figure 6.63 Schematic diagram of the Shack–Hartmann aberrometer (adapted from [144, 145]).

Fluorescein angiography is a less invasive imaging method with pupillary dilation [129]. Side effects of fluorescent dye injection are nausea, emesis, pruritus, and vasovagal symptoms. Further, the fluorescent dye stains the skin (yellow) and the urine [136].

6.1.4.7 **Wavefront Analysis**

The wavefront measures and treats small vision errors (higher order aberrations) that scatter light in a pattern that is unique to every person. Aberrations of the eye are results of optical contradictions within media and local irregularities of the optical surfaces. A wavefront analyzer (aberrometer) is based on a Shack–Hartmann sensor or a Tscherning sensor [143]. The working principle of both aberrometers is to measure the reflected wavefront of light that is coming out of the eye [144].

A Shack–Hartmann aberrometer consists of an aperture where the beams of a diode laser are focused to a point on the retina. The reflected wavefront that returns out of the eye passes through a lenslet array and subdivides the wavefront into multiple beams. All the reflected light generates multiple images of the retinal spot and is detected by a CCD camera. Figure 6.63 shows the principle of a Shack–Hartmann aberrometer [144–146].

The Tscherning aberrometer is a device where the laser beam (wavelength 670 nm) passes through a dot mask which forms a bundle of thin parallel beams [147] (Figure 6.64). This light beams are projected into the eye and a retinal spot pattern is generated of the eye's aberrations. The retinal spot pattern image is recorded with a CCD camera. The differences between the original image and the reflected image are analyzed mathematically. The basic principle of a Tscherning aberrometer is shown in Figure 6.65 [144, 148].

Application The wavefront analysis diagnoses lower and higher order vision errors represented by the way the eye refracts or focuses light. Lower order aberrations are more typical vision errors such as nearsightedness, farsightedness, and astigmatism whereas higher order aberrations are more complex vision errors.

Figure 6.64 Tscherning aberrometer:ALLEGRO Analyzer (WaveLight AG, Erlangen).

Typical Components of an Aberrometer An aberrometer typically consists of a light source, beamsplitter, lens system, and camera recording the returning wavefront from the eye. A patient module is used to keep the patient still and a computer analyzes and displays the measurement data.

Shack–Hartmann aberrometry [144,149]: The principle of Shack–Hartmann aberrometry is the generation of images with high resolution, accuracy, and reproducibility. The method needs a short measuring time and fast performance

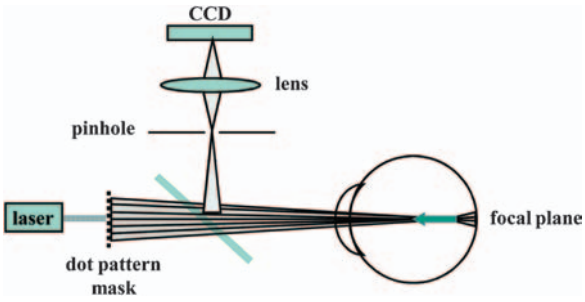

Figure 6.65 Schematic diagram of the Tscherning aberrometer (adapted from [144]).

of data analysis is possible. Furthermore, it is less sensitive to scattering and provides information about the central cornea. Shack–Hartmann aberrometry uses the outgoing path and an expensive sensor technique. Another disadvantage is the deeper penetration in the macula.

Tscherning aberrometry [142,147]: Tscherning aberrometry has a low penetration into the fovea and is a fast measuring technique. It is limited in the imaging resolution and also in the patient setup, and the analysis is more time consuming. Furthermore, it is sensitive to scattering due to the diffraction of the laser beam caused by the pinholes which affects the results. There is also a disturbing visible ash for patients during the measurement.

6.1.5
In Vitro Diagnostics – Microscopy

Microscopes are devices that are used to magnify small objects that are too small to be viewed by the unaided human eye. Objects with a size from millimeters down to nanometers can be visualized. The limits of resolution are shown in Figure 6.66.

In the following we consider only microscopes with a biophotonic background (other existing technologies, such as electron microscopes, are not considered).

There are different types of microscopes classified by shape, size, functional principle, illumination source, and image processing. Some major application fields of microscopy are hematology, pathology, cytology, gynecology, cancer research, brain research, analysis of samples, and *in vitro* fertilization.

Microscopy is an essential tool for functional studies on specimens of biological structures, molecules, and pathways in living organisms. Major innovations in microimaging technology during recent decades (e.g., confocal microscopy, fluorescent proteins) improved the resolution and sensitivity of microscopes. This enabled scientists to understand cellular functions and to determine the molecular

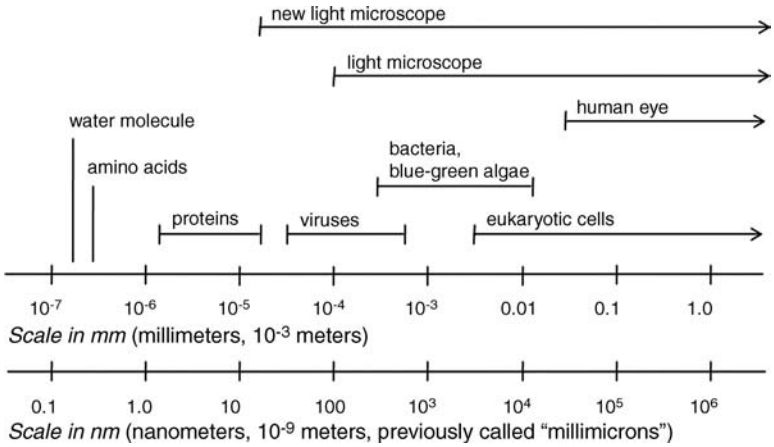

Figure 6.66 Limits of resolution in microscopy. In cell biology, the micrometer and nanometer scales are of most interest (adapted from [152]).

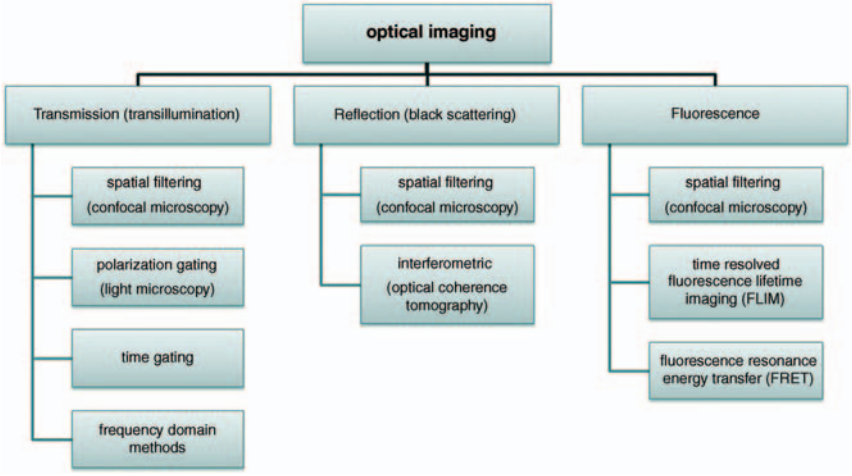

Figure 6.67 Optical methods of imaging (adapted from [153]).

mechanisms of diseases such as cancer and Alzheimer's disease [150]. We can differentiate different basic principles of optical imaging (Figure 6.67) suitable for microscopy:

- Transmitted light microscopy (with is based on the transmission by light of thin specimens, for example, cell cultures or biopsy samples).
- Reflected light microscopy (which is based on examination of the light reflected by thicker specimens).
- Fluorescence microscope (which is based on the phenomenon that certain materials emit energy detectable as visible light when irradiated with light of a specific wavelength) [151].

Further, we can differentiate between the following:

- "**Wide-field" microscopy**: The entire specimen is bathed in light and the image can be viewed directly by the eye or with a detector (e.g., CCD camera).
- **Laser scanning microscopy**: Only a disc-shaped area of the fluorescently labeled or autofluorescent sample is illuminated by a focused laser beam via a pinhole and the sample is scanned point-to-point. A detector pinhole focused on the same plane eliminates light scattered outside the focus plane. The image is reconstructed electronically by computer [151].

Due to this wide variety of existing microscopy techniques, detailed descriptions of each application would go beyond the scope of this chapter. Therefore, only a few techniques (light microscopy, fluorescence microscopy, confocal microscopy, Raman microscopy) have been selected for a more detailed description. In Section 6.2.2.5 on advanced microscopic techniques, some further important microscopic techniques for biotechnology are described.

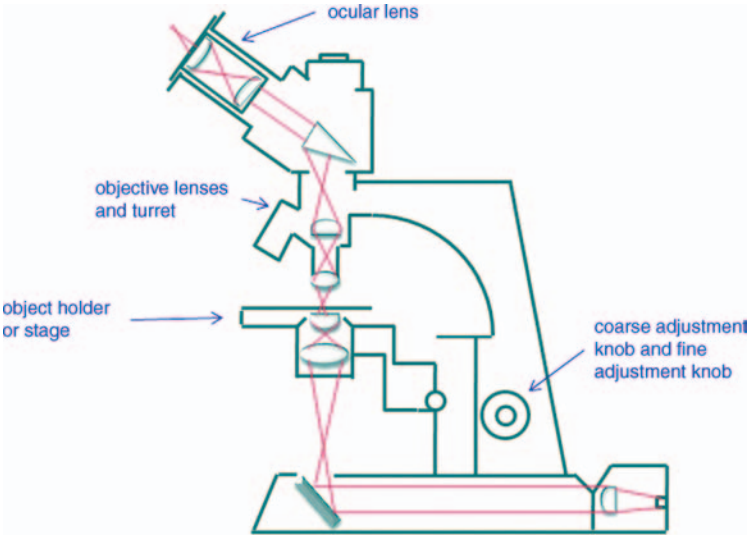

Figure 6.68 Basic components of a light microscope (adapted from [155]).

6.1.5.1 Light Microscope

The light microscope is a type of optical microscope which uses visible light and a system of lenses to magnify images of small samples. The basic components and the light path are illustrated in Figure 6.68 [154].

The main disadvantage of a standard light microscope is the limited spatial resolution of 200 nm. Other types of light microscopes include the inverted microscope (a microscope with its light source and condenser on the top, above the stage pointing down, while the objectives and turret are below the stage pointing up; it is useful for observing living cells or organisms at the bottom of a large container) and the stereomicroscope (which uses two separate optical paths with two objectives and two eyepieces to provide slightly different viewing angles to the left and right eyes).

6.1.5.2 Fluorescence Microscope

A fluorescence microscope is a light microscope used to study the properties of organic or inorganic substances using the phenomena of fluorescence and phosphorescence instead of, or in addition to, reflection and absorption [156]. Fluorescence microscopy the most frequently used microscopy procedure in biology and medicine [151].

In addition to the basic components (Figure 6.69) of a light microscope, typical components of a fluorescence microscope are the following [158]:

- a light source (xenon arc lamp, mercury vapor lamp, or laser)
- an excitation filter
- a dichroic mirror (or dichromatic beamsplitter).

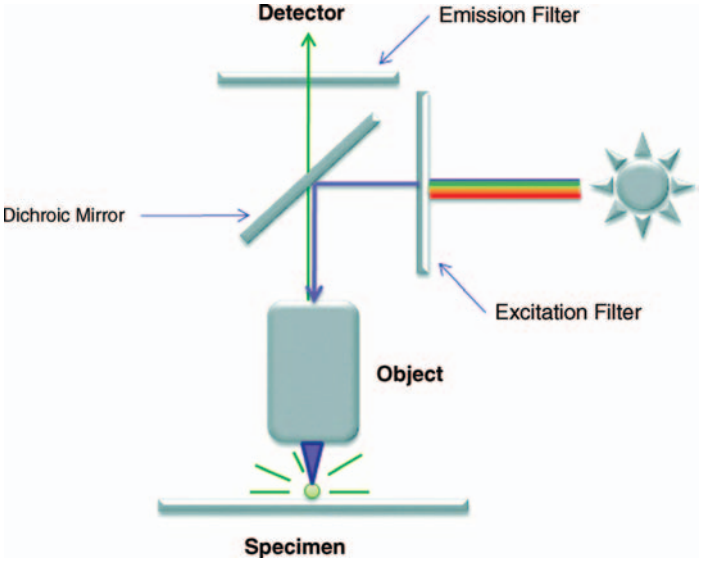

Figure 6.69 Light path in a fluorescence microscope. The specimen is illuminated with light of a specific wavelength (selected with excitation filters) which is absorbed by the fluorophores. The fluorescent light can be separated from surrounding light with special (emission) filters. The observer views only the part of tissue that is fluorescing (adapted from [157]). Copyright Spectrum Akademisches Verlag/Springer – Verlag Gmbtt

With total internal reflection fluorescence (TIRF) microscopy (see also Sections 6.1.2.2 and 6.1.2.5), extraordinarily sharp and detailed images of the cell surface are possible by eliminating fluorescence from within the cell. This allows researchers to study cellular signaling processes, exo- and endocytosis, the principles of cell adhesion, and cell-to-cell interactions.

The analysis of images acquired with conventional wide-field fluorescence excitation near the cell membrane is difficult due to the background fluorescence from other planes which are not in focus. Only under TIRF conditions can a resolution of $<$200 nm on the z-axis be achieved by selective illumination. This resolution is not achieved by either epifluorescence or confocal microscopy. The problem is solved by a technique in which fluorochromes are excited within a thin layer only. TIRF microscopy is particularly suited to the task, as the principle allows only those molecules to be excited which are in a layer of typically 100–200 nm above the cover-slip [159, 160].

For the transition from the glass cover-slip (refractive index $n_1 = 1.518$) into water ($n_2 = 1.33$), a critical angle of 61° results (Figure 6.70). With total reflection, a stationary evanescent (= decaying) wave is formed at the interface between the two media. The intensity of this wave decays exponentially with increasing distance from the interface:

$$I_z = I_0 \cdot \exp\left(-\frac{z}{d}\right) \tag{6.3}$$

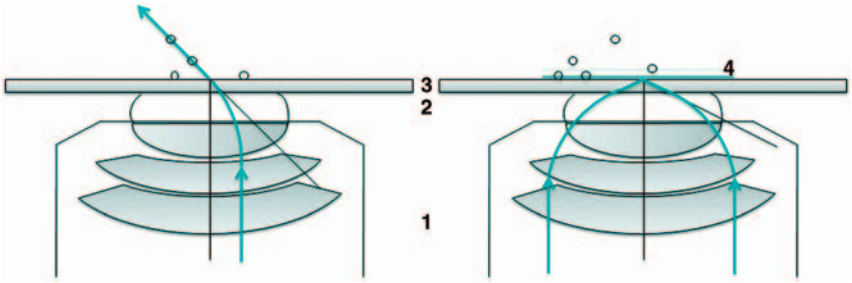

Figure 6.70 Beam path of incidence at less than the critical angle (left pathway) and beam path of total reflection (right pathway): 1, objective; 2, immersion oil, $n = 1.518$; 3, cover-slip, $n = 1.518$; 4, evanescent field (adapted from [160]).

where I_z is the intensity at a distance z from the interface and I_0 the intensity at the interface.

The penetration depth of the evanescent field is defined as the distance d from the interface at which the energy of the light has dropped to 37% of the original level. This distance depends on the angle of incidence and the wavelength of the light used. The distance d is calculated by

$$d = \frac{\lambda_0}{4\pi n_2 \sqrt{\left(\frac{\sin\alpha_1}{\sin\alpha_g}\right)^2 - 1}}. \tag{6.4}$$

6.1.5.3 New Fluorescence Microscope Techniques

The resolution limitation of light microscopy is overcome by several new microscopy technologies which allow structures smaller than 200 nm to be studied. Various approaches of microscopy techniques and different characteristics are listed in Table 6.2.

Table 6.2 Summary of the various described approaches and comparison of the different characteristics [161].

Method	Acquisition method	Lateral resolution (nm)	Axial resolution (nm)	Time required per image acquisition	Time required per image processing
Confocal laser scanning	Scanning	200	500	<1 s	
Structured illumination	Wide-field	50–120	150–350	<1 min	1–10 min
PALM	Wide-field	20–40		5–10 min	<1 h
TIRF	Wide-field	200	<100	0.2–0.4 s	

Photoactivated localization microscopy (PALM) offers biomedical researchers effective lateral resolution down to 20 nm. The technology employs photoswitchable dyes to enhance the resolution significantly.

With the method of structured illumination microscopy (SIM), researchers can image any fluorophore in living cells with twice as much lateral and axial resolution as with current light microscopes [150].

PALM and SIM enable scientists to analyze functionally even smaller cellular structures without the applicative limitations of electron microscopy (disadvantage: no colored picture) and other high-resolution techniques. For example, neuronal synaptic vesicles are about 50 nm in size and were previously not visible under the light microscope. The same is true for visualizing interactions between single pairs of proteins in living cells [150].

In addition to laser scanning microscopy, a wide range of other optical sectioning technologies is available addressing the needs of specific biological applications [161].

3D Structured Illumination Microscopy (3D-SIM) SIM can image any fluorophore, fixed or live, with up to twice the resolution possible using deconvolution or confocal microscopy. This is made possible by combining precise spatial modulation of the excitation light with an algorithm that computes super-resolution information from interference patterns in the raw data.

Super-resolution structured illumination microscopy (SR-SIM) provides up to double the resolution in all dimensions, without compromising on dyes and without special sample treatment. It relies on state-of-the-art algorithms to reconstruct a super-resolution image in 3D (see Figure 6.71).

Considering the two overlapping grids in Figure 6.72, tilted at 5° against each other, one can observe a real and visible pattern of approximately perpendicular dark and light bands superimposed on the parallel lines. This is a phenomenon called Moiré fringes, originating from the interaction of the optical patterns of lines. The fringes contain super-resolution information that otherwise escapes detection.

This is exactly the principle that is used in SR-SIM. A known pattern is projected into the image plane and interferes with sample structures, creating Moiré fringes. Super-resolution information can now be captured by the microscope from these structures. All that remains to be done is to restore this information into a super-resolution image by high-end algorithms.

Photoactivated Localization Microscopy (PALM) PALM (Figure 6.73) allows scientists to produce light microscopic images with effective lateral resolutions down to 20 nm. This is achieved by successively localizing single molecules with high precision. A wide range of fluorophores can be visualized in this way, from special GFP (green fluorescent protein) mutants to organic dyes such as Cy5. For uncompromised results, it is of paramount importance to achieve the highest system sensitivity and precise optical sectioning [150].

PALM permits scientists to visualize cells with far more detail than with conventional light microscopes, which are inherently limited by the wavelength of light. To achieve this resolution, PALM uses different fluorescent labels that can be turned on

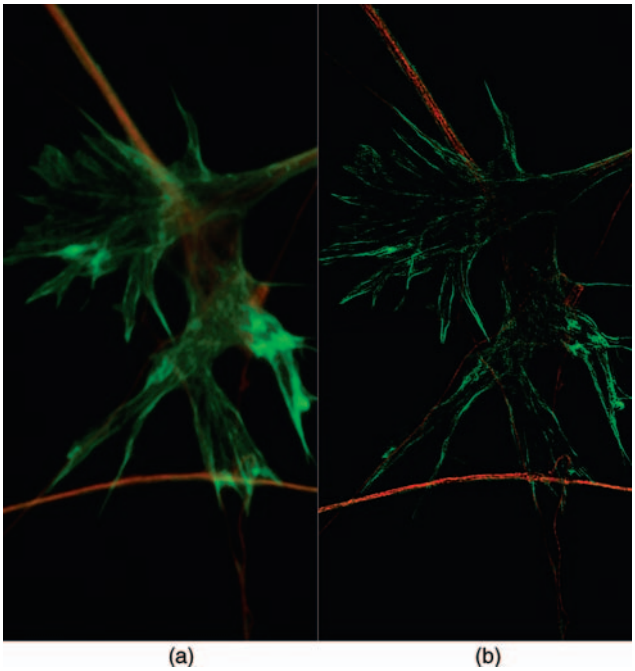

Figure 6.71 (a) Widefield image and (b) SIM image of neuronal growth cones. Staining for tubulin (red) and F-actin (green) (specimen: M. Fritz and M. Bastmeyer, University of Karlsruhe, Germany [150]).

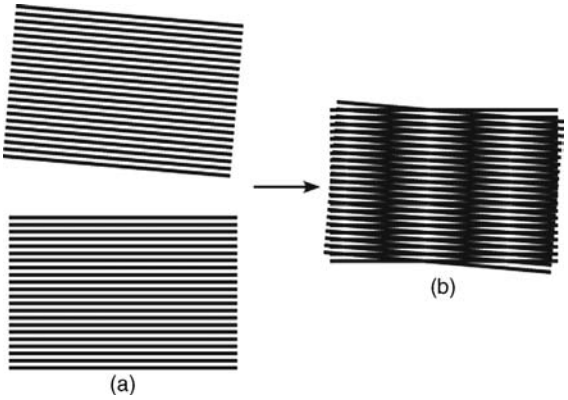

Figure 6.72 Moiré patterns formed by superimposed grids. (a) An image and the same image turned 5°; (b) the overlapped grids generated Moiré fringes, which contain super-resolution information [162].

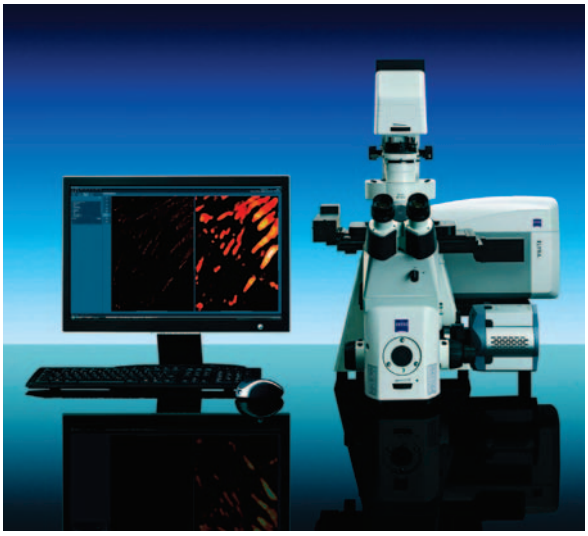

Figure 6.73 ELYRA P.1 photoactivated localization microscope (Carl Zeiss MicroImaging GmbH, Jena) offers fluorescence imaging with single-molecule discrimination, down to effective resolutions of 20 nm [164].

and off with a pulse of light. Cells whose proteins are tagged with these labels are imaged repeatedly with PALM, with only a tiny subset of the fluorescent molecules turned on in each image. PALM records many thousands of these images to illustrate each fluorescently tagged protein. Hence PALM creates a complete picture of the structure under study. As a result, the observer obtains a much clearer picture than the overlapping haze that results when all of the tagged proteins are lit up at the same time, as in traditional fluorescence microscopy [163, 164] (see Figure 6.74).

6.1.5.4 **Confocal Microscopy**

The principle of confocal microscopy (see Figure 6.75) was originally patented by Marvin Minsky in 1957. The development of lasers for confocal laser scanning microscopy (CLSM) became a standard technique towards the end of the 1980s. Thomas Cremer and Christoph Cremer designed in 1978 a laser scanning process which scans point-by-point the three-dimensional surface of an object by means of a focused laser beam and creates the overall image via a photomultiplier (similar to those used in scanning electron microscopes). The key feature of confocal microscopy is its ability to acquire in-focus images from selected depths (a process known as optical sectioning); images are acquired point-by-point and reconstructed with a computer. As only one point in the sample is illuminated at a time, 2D or 3D imaging requires scanning over a regular raster (i.e., a rectangular pattern of parallel scanning lines). The thickness of the focal plane is defined mostly by the inverse of the square of the numerical aperture of the objective lens, and also by the optical properties of the specimen and the ambient refractive index. The thin optical sectioning possible

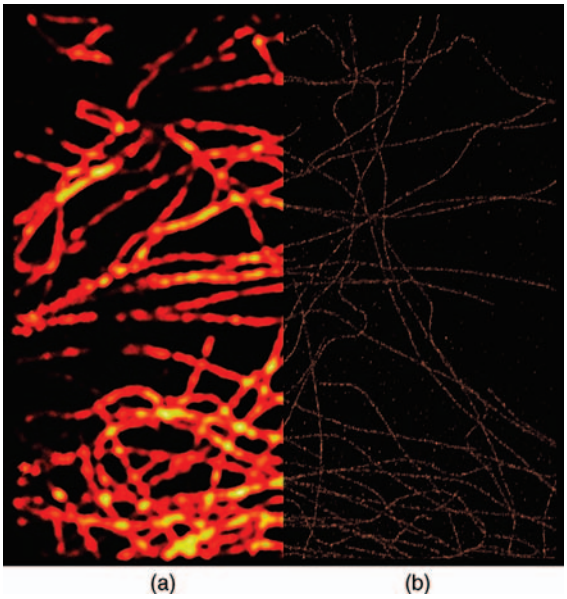

Figure 6.74 (a) Total internal reflection microscope image and (b) PALM image of antibody staining for tubulin in a cultured cell (specimen: S. Niwa, University of Tokyo, Japan [150]).

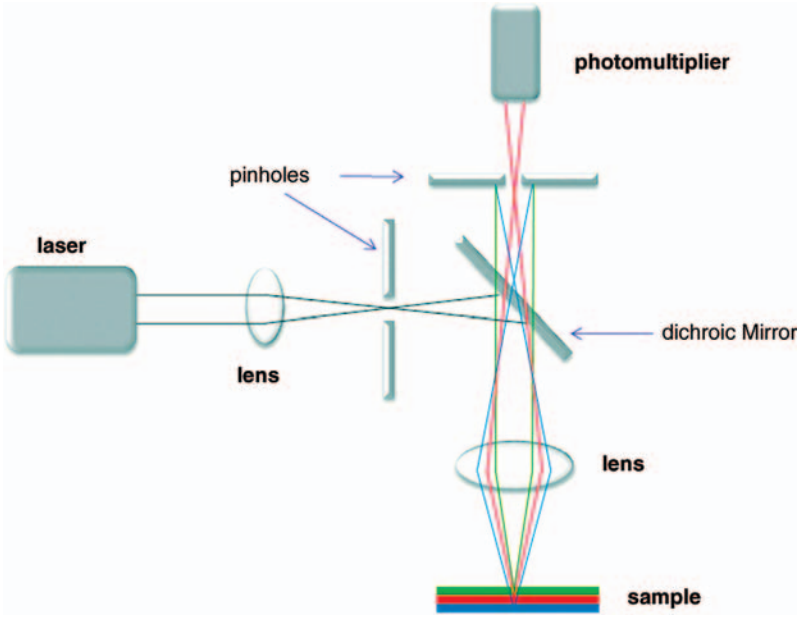

Figure 6.75 Light path and components in a simple confocal laser microscope. Interfering intensity from outside this plane is canceled out by a pinhole. Therefore, it is possible to obtain spatial resolution and additionally very detailed intensity information not only in the *xy*-direction but also in the *z*-direction (adapted from [167]).

makes these types of microscopes particularly suitable for 3D imaging of samples [165, 166].

In comparison with the conventional "wide-field" microscope, the following advantages result [151]:

- improved lateral resolution
- increased contrast
- electronic zoom
- increased sensitivity
- information in the *z*-direction (for 3D imaging).

Traditional fluorescence microscopes can focus on a certain region of the specimen, but the fluorescence background from the out-of-focus part distorts the in-focus signal. Historically, the only way to obtain a clearer and sharper image of a thicker sample was physically to cut thin sections of the sample, a technique which was time consuming, likely to introduce artifacts, and not suitable for imaging living samples.

During the last few decades, a large number of techniques have been developed that allow the contributions from these out-of-focus regions to be removed. This led to a much clearer image of the specimen in the focal plane without any sample manipulation.

The best known optical sectioning method is confocal or laser scanning microscopy (LSM) (see also Section 6.1.2.5); for an example, see Figure 6.76. Confocal microscopy systems enable researchers to study living, 3D samples with significantly improved sensitivity and higher resolution images compared with conventional fluorescence microscopy [150, 166].

Confocal microscopy allows the tracking of specifically labeled (e.g., GFP or fluorescent antibodies) proteins in living cells and organisms. The simultaneous

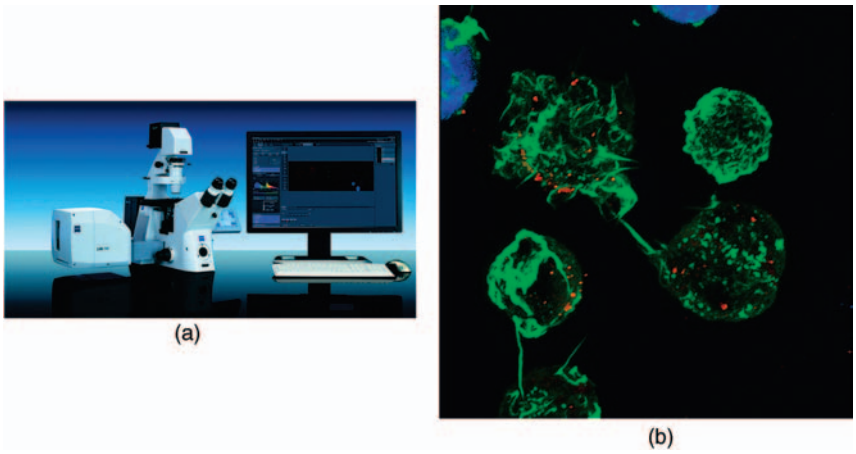

Figure 6.76 (a) LSM 700 confocal laser microscope (Carl Zeiss MicoImaging GmbH, Jena): (b) human lymphocytes transmitting the HIV virus from cell to cell [168].

spectral imaging capabilities and low signal-to-noise ratios of modern LSM systems allow the interactions of several different proteins to be observed at the same time. With such analyses, fundamental cellular pathways can be discovered and morphology can be linked to function. By combining several confocal images with 3D images, unprecedented insights into the molecular morphology and function of cells, tissues, and organisms have become possible [150].

6.1.5.5 **Raman Microscopy**

In addition to the fluorescence microscope, Raman-based techniques have became increasing evident in recent years. Raman spectroscopy allows one to derive detailed and specific information on a molecular level that other laser spectroscopic methods can provide to only a limited extent, and is a technique used to study vibrational, rotational, and other low-frequency modes in a sample [169, 170]. Confocal Raman microscopy combines the 3D optical resolution of confocal microscopy and the sensitivity to molecular vibrations which characterizes Raman spectroscopy (Figure 6.77).

Raman spectroscopy is based on the inelastic scattering of monochromatic light when the frequency of photons changes upon interaction with a sample. The photons of the laser light are absorbed by the sample and subsequently re-emitted. The frequency of the re-emitted photons is shifted up or down in comparison with the original monochromatic frequency, which is known as the Raman effect and provides molecular fingerprints.

The advantages of Raman spectroscopy are that it can be applied to any optically accessible sample, pretreatment of the sample is not or almost not necessary and in contrast to fluorescence spectroscopy it works completely without external markers.

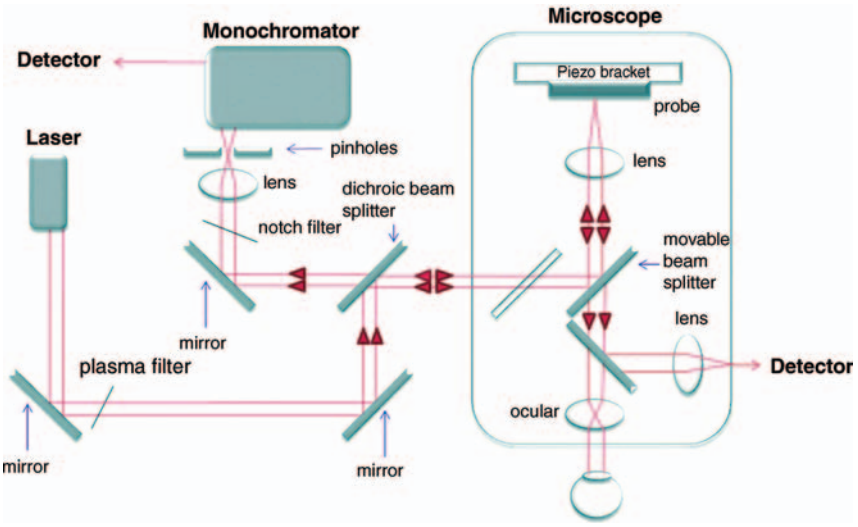

Figure 6.77 Raman microscopy: light path and components (adapted from [171]).

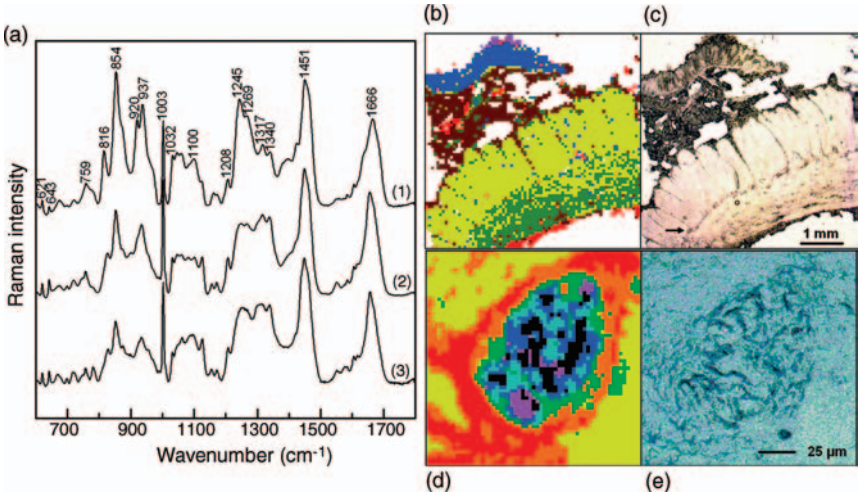

Figure 6.78 Raman spectroscopy of a dried intestinal sample. (a) Representative Raman spectra of connective (1), muscle (2), and epithelium tissues (3). (b) 79 × 79 Raman map with a step size of 62 µm. (c) The arrow in the light-microscope image shows the position of a ganglion. (d) 59 × 59 Raman map with a step size of 2.5 µm; the colors within the Raman maps correlate with group classifications performed by cluster analysis. (e) Zoomed ganglion from (c) [170]. Copyright Spektrum Akademischer Verlag/Springer Verlag GmbH.

An example of Raman spectroscopy of a dried intestinal sample is shown in Figure 6.78.

However, although the specificity of Raman spectroscopy is very high, its sensitivity, that is, the conversion efficiency of the Raman effect, is rather poor. Since only a small number of the incident photons are inelastically scattered, the detection of molecules present in very low concentrations is limited. To circumvent such problems, special Raman signal-enhancing techniques can be applied [169], such as resonance Raman spectroscopy, surface-enhanced Raman scattering (SERS), coherent anti-Stokes Raman scattering (CARS), and tip-enhanced Raman spectroscopy (TERS).

The use of SERS continues to be increasingly important for analytical applications of Raman spectroscopy. Patel *et al.* [172] used a combination of SERS with principal component analysis (PCA) to provide a barcoding methodology for pathogen identification in bacterial cells and to show how this approach potentially provides a rapid diagnostic tool for bacterial pathogens.

A key biological molecule is DNA. Benevides *et al.* [173] used NIR laser excitation to probe drug–DNA interactions. They compared the Raman spectra of complexes of ethidium bromide, 9-aminoacridine, and proflavin with DNA and showed that the Raman signatures reveal the specific structural changes induced at the drug–DNA intercalation sites. The results were discussed in relation to frameshift mutagenic activities of the intercalating drugs. Another theme in this context is the use of Raman spectroscopy to address medically related problems. Pawlak *et al.* [174] reviewed results from a program designed to investigate the potential of Raman microscopy as

a probe technique to address important problems in ophthalmology, looking at the disease age-related macular degeneration (AMD), the leading cause of irreversible blindness in the West.

Downes *et al.* demonstrated the integration of Raman spectroscopy and CARS into one instrument, to combine the benefits of both techniques for stem cell differentiation [175]. In the future, multiplex CARS promises to be the technique of choice for all platforms, due to its combined attributes of speed, full spectral analysis, and applicability to individual live cells.

6.1.6
In Vitro Diagnostics – Digital Slides and Virtual Microscopy

In the last few years, telepathology has benefited from the progress in the technology of image digitization and transmission through the World Wide Web. The applications of telepathology and virtual imaging are more current in research and morphology teaching. In the daily practice of surgical pathology, this technology still has limits and is more often used for case consultation. Many of the limitations of virtual imaging for the surgical pathologist reside in the capacity for storage of images, which so far has hindered the more widespread use of this technology. Overcoming this major drawback may revolutionize the surgical pathologist's activity and slide storage [176].

At present, telepathology serves as a promoter for a complete new landscape in diagnostic pathology, the so-called virtual pathology institution. Industrial and scientific efforts will probably allow the implementation of this technique within the next 2 years, with exciting diagnostic and scientific perspectives [177].

A digital slide in pathology is a digital scanned image of a specimen. The advantages of digital slides are their global management (access, storage, image processing, distribution) with the help of a picture archiving and communication

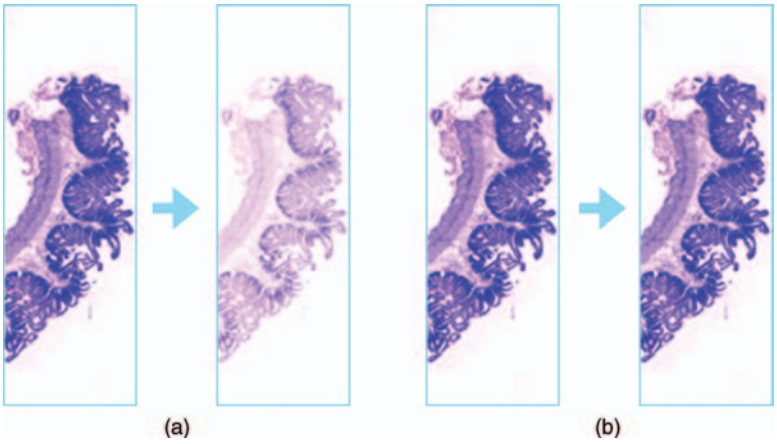

Figure 6.79 Digital slides: a stained specimen on a glass slide will fade over time (a) , whereas a digital slide does not change at all (b) [179].

system (PACS), no fading over time (Figure 6.79), and very fast access for teleconsultation services [178].

The main applications of digital slides are the following:

- **Teleconsultation**: Pathologists are able to view and discuss histology with other colleagues via the Internet.
- **Computer-aided diagnosis**: Interactive quantification allows pathologists to quantify immunohistochemical (IHC)-stained histology sections.
- **Education**: Gives medical students the opportunity to navigate even through rare cases like viewing them under a "real" microscope.

6.1.7
In Vitro Diagnostics – Optical Methods in Clinical Analysis System

6.1.7.1 Optical Spectroscopy of Blood and Urine Components

In addition to electrode measurements in clinical analysis, optical methods have been applied for many years. Usually a chemical reaction is used to convert the component of interest in the analytical solution (blood, urine, or other body liquids) into a colored species. For example, in the case of creatinine the well-known Jaffe's method is used, where the creatinine is converted into a complex which shows good discrimination against other blood components. In such commercially available creatinine detection kits, the absorption of the reaction product at an appropriate wavelength (here 530 nm) is a direct measure of the analyte concentration [180].

More sophisticated methods use more selective reactions to discriminate between the analyte of interest and other components in the highly complex investigation solution (see Table 6.3). First there are enzymatic reactions that can be used. Very often these enzymatic reactions do not lead to a colored species for optical detection. In this case, a side product is usually used to account for the analyte concentration. Commonly used side products for optical detection are oxygen (production or consumption), carbon dioxide, and pH changes. In some cases, when the main products have no significant absorption or absorb only in the deep-UV region (e.g., if NADPH or $NADP^+$ analogs are side products), a secondary reaction is used to detect the analyte concentration via an absorption or fluorescence measurement of the secondary products (see Figure 6.80).

6.1.7.2 Optical Spectroscopy of Tissues and Vessels

Optical spectroscopy of tissues and vessels is a long- and well-established method to detect and analyze components inside and outside cells. Problems arise if the absorption of these native chromophores is in the UV or deep-UV range, because in theses cases direct imaging using one-photon excitation is severely limited by photodamage to living specimens, in addition to indiscriminate background absorption or fluorescence. In these cases, multi-photon excitation can be used to overcome these problems. In fluorescence microscopy (see Section 6.1.5.2), either the fluorescence (autofluorescence) of the native components is visualized or the tissue is labeled selectively with fluorescence markers (such as labeled antibodies

Table 6.3 Clinical chemical blood parameters (selection) and the possibility of their optical detection.

Blood parameters	Detection method	Optical detection methods
Total and direct bilirubin	Complex building reaction with diazotized sulfanilic acid	Red colored azobilirubin detection wavelengths 578 nm (total), 546 nm (direct)
Total protein	Antigen reaction	Colored with 4-chloro-1-naphthyl
Alkaline phosphatase (AP)	Hydrolysis of a phosphate ester substrate [e.g., 2′-(2-benzothiazolyl)-6′-hydroxybenzothiazole phosphate (BBTP)] to a benzothiazole [e.g., 2′-(2-benzothiazoyl)-6′-hydroxy-benzothiazole (BBT)]	Detection of the BBT fluorescence
Lactate dehydrogenase (LDH)	Surface plasmon resonance (SPR) sensing	Measurement of intensity changes of light in an optical fiber
Glutamate dehydrogenase (GLDH)	Interaction with rhodamine–dextran substrate (e.g., SNARF 1-dextran)	Fluorescence detection
Creatine kinase (CK)	Fluoroimmunoassay	Fluorescence detection
Metabolites		
Lactate	SPR sensing	Measurement of intensity changes of light in an optical fiber
Glucose	Interferometric detection	Measurement of refractive index changes
Urea	Enzymatic reaction with urease in a polypyrrole matrix	Absorption measurement
Creatinine	Jaffé method	Absorption measurement
Minerals		
Calcium (Ca) Magnesium (Mg) Phosphorus (P) Sodium (Na) Potassium (K)	Insertion in calixarene receptors with fluorescence markers	Fluorescence measurements
Serum iron (Fe)	Serum transferrin receptor (TfR) measurements	Absorption measurement
Triglycerides	Enzymatic detection	Measurement of secondary products

or by transfection with fluorescent proteins) to discriminate between different components and to localize them. One of the advantages of direct imaging via fluorescence labeling is the visualization of intrinsic chromophores such as nicotinamide adenine dinucleotide (NADH), tryptophan, and serotonin. Especially investigations with endogenous fluorophores of the skin such as tryptophan,

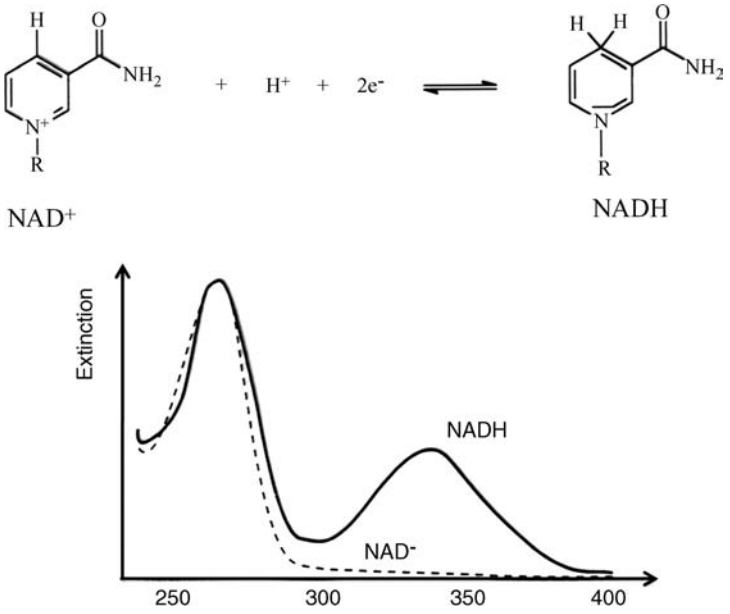

Figure 6.80 NADH transformation and the corresponding spectra.

collagen, elastin, keratin, flavins, melanin, and porphyrins have been discussed in the literature [181].

Two-photon-excited cellular autofluorescence from intrinsic chromophores such as NAD(P)H has been used to study the cellular metabolic state. As an

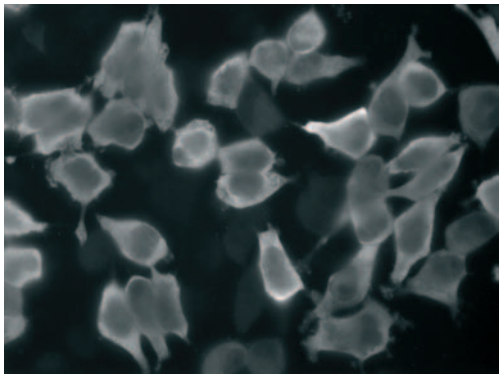

Figure 6.81 NADH autofluorescence. Intrinsic NADH autofluorescence is visualized by using 700 nm pulsed excitation. In this image, the NADH localization in HeLa cells is shown.

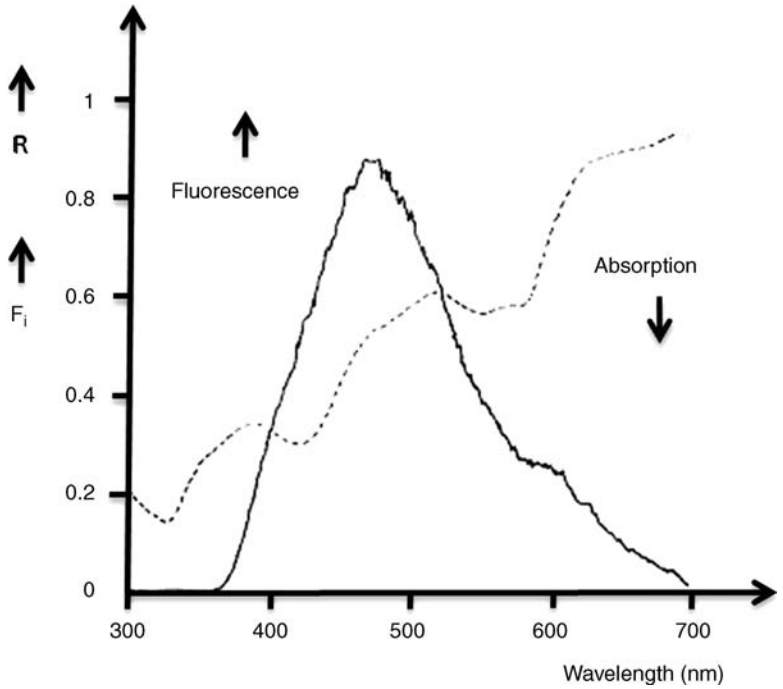

Figure 6.82 Fluorescence and absorption spectra (diffuse reflectance spectrum) of a human hand palm in arbitrary units [184].

example, Figure 6.81 shows two-photon-excited NADH autofluorescence in living cells [182].

In the case of labeling, maintenance of the native biochemical character of the tissue has to be taken into account. Therefore, fluorescent dyes are usually introduced into the biological system at neutral pH, in mild isotonic salt buffers. It must be ensured that the probe is soluble in the labeling buffer and that it can penetrate the hydrophobic membrane of the cells [183].

A noninvasive approach is shown in Figure 6.82, which represents an example of the investigation of autofluorescent tissue. The spectrum was recorded *in vivo* by the reflectance mode of irradiation of the palm of a human hand [184]. Fluorescence originates mainly from NADH, but often its spectrum is overlaid by additional long-wavelength absorbers, as can be seen in the diffuse reflectance absorption spectrum of the palm presented in Figure 6.82.

It is very useful to apply NIR fluorimetry (up to 1600 nm) in tissues, because this technique enables a greater penetration depth of the (NIR) radiation in organic matter to be used to obtain a well-defined region of excitation, for example, in single cells or mammalian tissue.

Other advantages afforded by NIR over UV–visible fluorescence techniques include the following:

- reduced Rayleigh scattered excitation (this being proportional to the inverse fourth power of wavelength)
- low absorption coefficient in many organic media, for example, tissue (results in less background)
- increased photochemical stability.

Additionally, longer absorption and emission wavelengths allow the use of inexpensive light sources such as LEDs and diode lasers, which are available mainly in the red and NIR region. Due to the reduced absorption of human tissue at wavelengths longer than 600 nm, this spectral region is very relevant to clinical applications [185].

Thus a laser beam of around 400 nm might be expected to penetrate only a few micrometers into the skin of a subject due to strong scattering and absorbance by hemoglobin (see below), whereas a light beam of about 830 nm would penetrate some centimeters due to the 16-fold lower scattering and also much reduced absorbance. We can imagine interrogating implanted fluorophores through the skin for a variety of diagnostic purposes, such as blood glucose monitoring [186]. In mammalian tissue at visible wavelengths, the principal absorbing species is, of course, hemoglobin, due to its strong absorbance and high concentration. All derivatives of hemoglobin exhibit significant absorbance at wavelengths longer than 700 nm; absorbance spectra are depicted in Figure 6.83. The measurement principle is used in the well-known noninvasive pulse oximetry. Every species (hemoglobin derivative) has its own optimal detection region. The calculation of the concentrations of the components can be made with respect to isosbestic points (e.g., at 805 nm) [187].

Other NIR applications of tissue and vessel imaging include optical time-domain reflectometry and photon migration in tissue [188, 189]. Furthermore, laser-induced autofluorescence studies of human tissue are widely used in modeling of human cutaneous tissue using spectroscopic measurements. This is possible simply because human tissue contains many components that fluoresce. This creates a readily

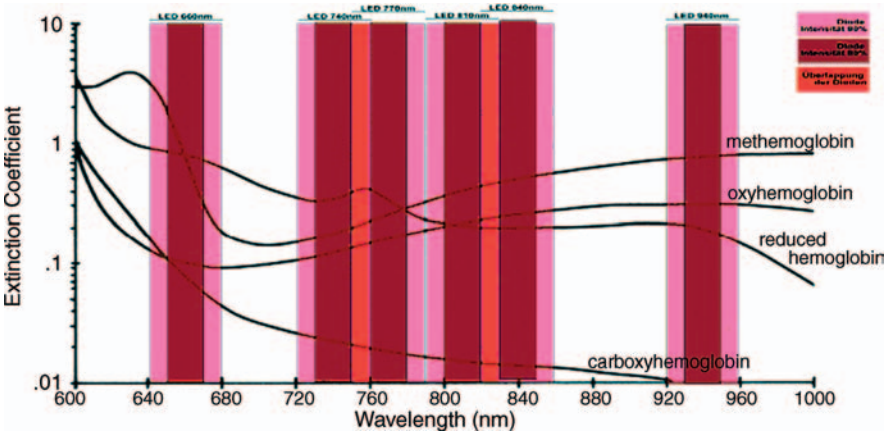

Figure 6.83 Absorbance of hemoglobin derivatives in the red and near-IR region.

detectable fluorescence background, but on the other hand is an important feature that limits the sensitivity of labeled fluorescence applications in tissue characterization. In this respect, laser-induced autofluorescence spectroscopy provides excellent possibilities for medical diagnostics of different tissue pathologies, including cancer, because cancer cells have a different metabolism than healthy cells and exhibit a much stronger fluorescence background than healthy reference tissue [23].

Another very important method for the investigation of cells and other tissue components is flow cytometry. Flow cytometry is a method of fluorescence-activated cell sorting (FACS) and is widely used in the diagnosis of cell diseases such as leukemia [190, 191]. In flow cytometry, the sample is irradiated with a continuous-wave laser light beam and the fluorescence light is detected as an indicator of cell type-specific antigens, cell–cell interactions, cell diseases, and mutagenic changes (see Figure 6.84). Most applications of flow cytometry are based on the presence or absence of cell-surface antigens, or the presence of one or two copies of the DNA, as determined by measurement of the fluorescence intensity of cells labeled with fluorescent antibodies or nucleic acid stains such as 4′,6-diamidino-2-phenylindole (DAPI). Multidimensional slit-scan flow cytometers have also been developed and used successfully for the automated detection of different types of cancer cells [190, 191].

In general, the time resolution of the fluorescence light is a very powerful tool for investigating environmental effects upon the cells and other components in tissues and vessels. This is due to the high sensitivity of the fluorescence lifetime to the

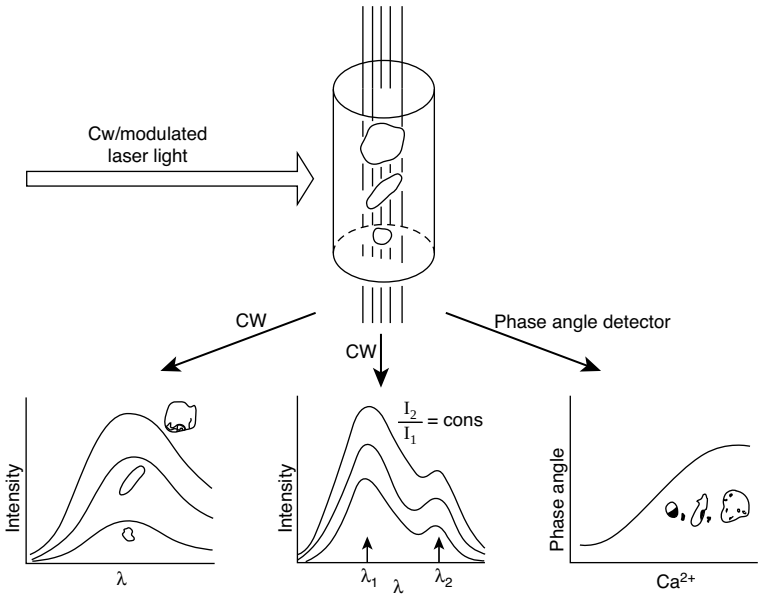

Figure 6.84 Principle of cell-by-cell measurements in flow cytometry (cw = continuous wave) (adapted from [192, 193]).

solvent or the viscosity and polarity of the surroundings of the cell. Therefore, lifetime imaging and fluorescence lifetime measurements play an important role in the optical characterization of human tissues.

Fluorescence lifetime imaging (FLIM) allows image contrast creation based on the lifetime of the probe at each point in the image. There is significant interest in creating 2D or even 3D fluorescence lifetime images, and for this purpose several techniques have recently been described. If the probe lifetime is sensitive to a naturally occurring analyte, one now has the ability to create (chemical and biochemical) images of cells and tissues (for more details, see [192, 193] and the references therein).

6.1.7.3 Optical Spectroscopy of Agglutination and Precipitation – Nephelometry, Turbidimetry

In addition to absorption of electromagnetic radiation, we observe scattered radiation if photons impact on matter (e.g., Raman scattering).

In the case of elastic light scattering, the relative molecular mass M_r of the scattering particle can be calculated from the analysis of the scattered radiation. Furthermore, information can be obtained about the molecular dimensions and the interaction between macromolecules, and parameters such as the diffusion coefficient of the scattering particle can be estimated.

In general, various scattering processes have to be taken into consideration:

- **Elastic light scattering**: Incident and scattered light have the same frequency.
  - –If the dimensions of the scattered particles are small in comparison with the wavelength, $d \ll \lambda/2$, Rayleigh scattering is observed.
  - –If the dimensions of the scattered particles are large in comparison with the wavelength, $d \gg \lambda$, Mie scattering occurs.
- **Quasi-elastic scattering**: Change in the frequency of the scattered light due to translational movement of the scattered particle (Doppler effect, frequency chirp).
- **Inelastic scattering**: Excitation of molecular vibration due to interaction with the incident light (Raman scattering).

Nephelometry is an optical analysis method to determine the concentration of colloidal dispersed small particles, in most cases in solution.

In the following, the scattering behavior of particles in solution is considered. This is necessary to understand the kind of representation of the results usual in nephelometry and the parameters deduced from the plots. The scattering of monochromatic polarized light at an isolated, isotropic molecule with the field strength leads to the induction of an electrical dipole moment (see Figure 6.85):

$$E = E_0 \cos\left[2\pi\nu\left(t - \frac{x}{c}\right)\right]. \tag{6.5}$$

The resulting oscillating dipole emits radiation, the field strength of which is proportional to

$$\frac{d^2\mu}{dt^2} = f(\varphi). \tag{6.6}$$

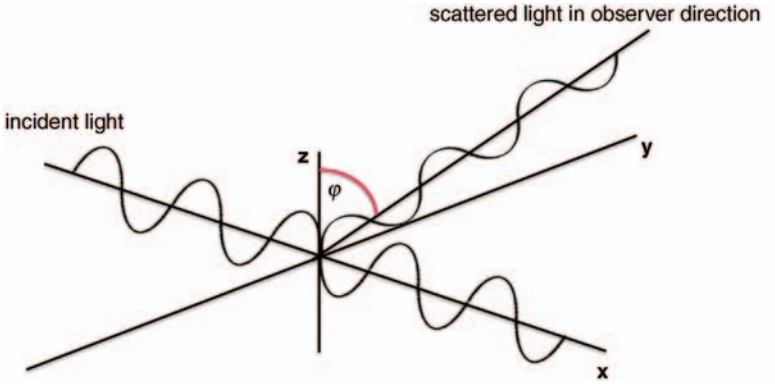

Figure 6.85 Scheme of scattering of incident irradiation at an object at (0, 0, 0) indicating the scattering angle φ under which the scattered light occurs.

For isolated molecules in solution, the resulting equation for the relative scattered light intensity is

$$\frac{I_s}{I_0} = \frac{2\pi^2(1+\cos^2\varphi)n_0^2}{r^2 \cdot L \cdot \lambda^4} \cdot \left(\frac{dn}{dc}\right)^2 \cdot cM_r \tag{6.7}$$

where I_s is the scattered light intensity, I_0 is the incident light intensity, φ is the angle of detection, n_0 is the refraction index of the solvent, n the refraction index of the solution, r is the radius of the particle, L is the Loschmidt number, c is the concentration of the molecules and M_r is the relative molecular mass.

With the help of some abbreviations like the Rayleigh rate R_0 and a constant K

$$R_0 = \frac{I_s}{I_0} \cdot \frac{r^2}{1+\cos^2\varphi} \tag{6.8}$$

and

$$K = \frac{2\pi^2 n_0^2}{L\lambda^4} \cdot \left(\frac{dn}{dc}\right)^2 \tag{6.9}$$

Equation 6.7 can be transformed. For ideal solutions, Equation 6.7 results in [194, 195]

$$\frac{K \cdot c}{R_0} = \frac{1}{M_r} \tag{6.10}$$

Taking into consideration a real solution with the experimentally determined concentration dependence of the scattered light intensity, the following equation results:

$$\frac{K \cdot c}{R_0} = \frac{1}{M_r} + 2Bc + \ldots \tag{6.11}$$

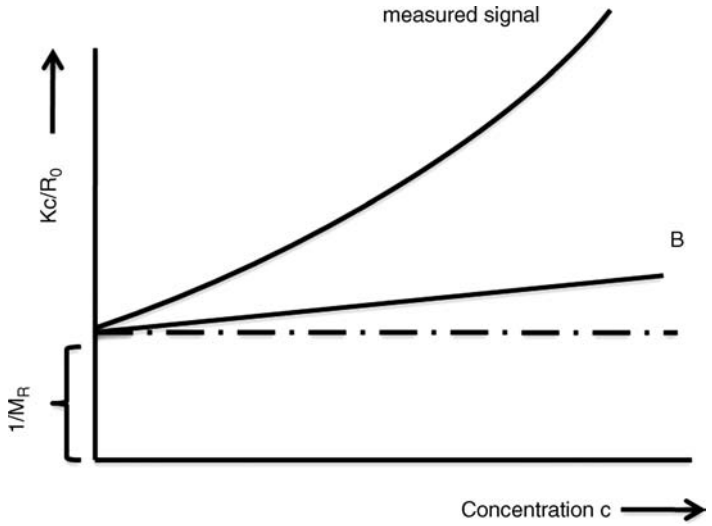

Figure 6.86 Typical measuring curve for $K \cdot c/R_0$ as a function of the concentration c of scattering particles. The ordinate section gives the molecule mass; the ascent of the curve at low concentrations gives the second virial coefficient B (with permission of H.-J. Galla [194]).

From this dependence, the molecular mass and the second virial coefficient B (the interaction strength between the particles) can be deduced (see Figure 6.86).

In the case of Mie scattering, the particle can no longer be handled as a point; the phase of the interacting light has different values at different places in the particle. In general, the contributions to the overall scattered light intensity must be summarized. This procedure is very time consuming and involves the calculation of so-called Mie integrals. Even more sophisticated is the application of a correction function which involves all aberrations of the Mie scattered light intensity behavior depending on the measuring angle compared with the Rayleigh scattered light intensity [194, 195]:

$$P(\varphi) = 1 - \frac{16\pi^2 R_G^2}{3\lambda^2} \sin^2\left(\frac{\varphi}{2}\right). \tag{6.12}$$

This correction term goes to zero if the wavelength becomes large, the radius of gyration R_G becomes small, and the detection angle becomes zero. On the other hand, this correction term fully describes the shape of the scattered light intensity in the case of Mie scattering from the detection angle. Equations 6.11 and 6.12 give

$$\frac{K \cdot c}{R_0} = \frac{1}{P(\varphi)} \left(\frac{1}{M_r} + 2Bc\right). \tag{6.13}$$

The abbreviated equation for the scattered light intensity in this case becomes [194, 195]

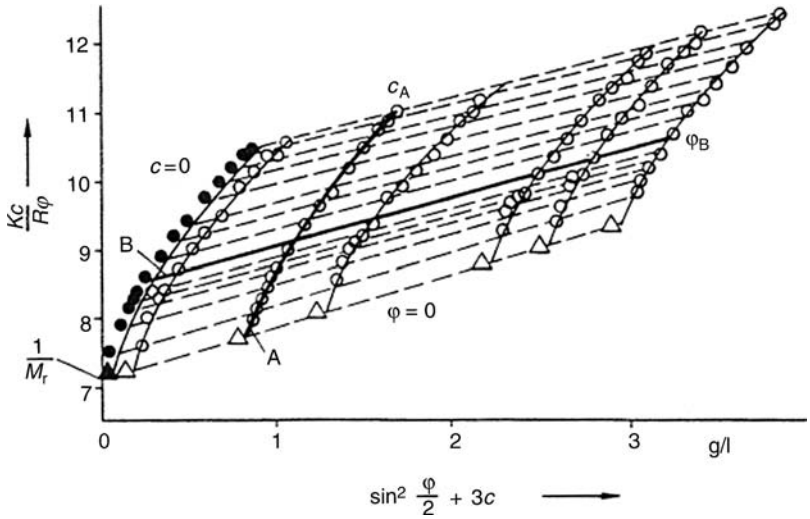

Figure 6.87 Zimm diagram (adapted from [194, 195]).

$$\frac{K \cdot c}{R_0} = \frac{1}{\left[1 - \frac{16\pi^2 R_G^2}{3\lambda^2} \sin^2\left(\frac{\varphi}{2}\right)\right]} \left(\frac{1}{M_r} + 2Bc\right). \tag{6.14}$$

In the case of Mie scattering, it is no longer sufficient to measure the scattered light intensity at one angle only. At least the detection of the scattered light intensity of a half circle is necessary (see Figure 6.87).

Measurement of the scattered light intensity as a function of the concentration and the detection angle leads to the well-known Zimm diagram (see Figure 6.88).

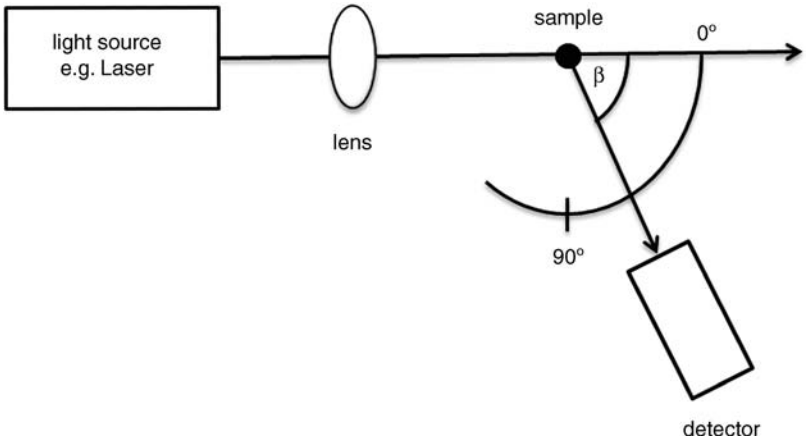

Figure 6.88 Scheme of half-circle detection for detecting scattered light intensity (with permission of H.-J. Galla [194]).

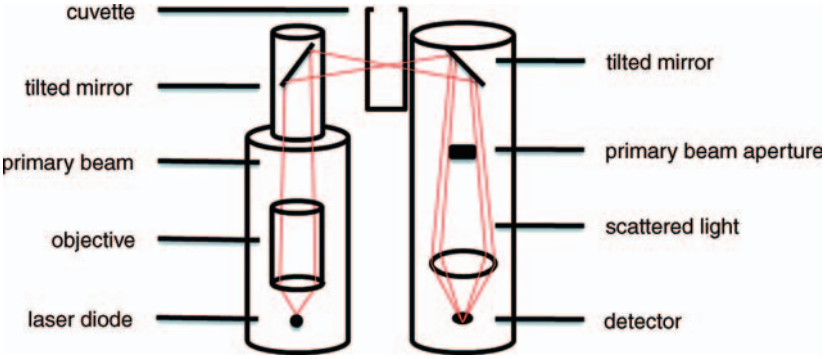

Figure 6.89 Principle of turbidimetry. Only scattered light intensity as an overall signal is detected.

Mie scattering delivers, in addition to the molecular mass and the virial coefficient via the radius of gyration, information about the dimension and the shape of the scattering particle.

In the case of turbidimetry, only the scattered light intensity as an overall signal is detected, as can be seen in the measuring scheme in Figure 6.89. The primary beam is blended out after the samples, and with a lens the whole of the scattered light is directed on to the detector. The scattered light intensity is in this case directly proportional to the concentration of the sample.

Typical precipitation reactions in clinical analysis can be checked by means of scattered light analysis. In the simplest case, the "apparent absorption" is measured and plotted against time to obtain a kinetic description of the precipitation reaction. Plotting the apparent absorption against the concentration leads to the well-known nonlinear form of the calibration curve of immunological reactions (see Figure 6.90).

6.1.8
In Vitro Diagnostics – Blood Gas Pressure Measurements

6.1.8.1 Optical Detection of pO_2 in Blood

In addition to the amperometric detection of gas pressure (oxygen gas pressure in blood), gas components in human blood can also be detected by means of optical methods. In this case the optical fiber connected with the light source (usually a diode laser in the green or blue region) is covered on the tip with an immobilized dye embedded in a polymer which is gas permeable and cleanable with respect to contamination of the analyte solution (blood, urine). The dye is irradiated with the excitation light and fluorescence emission is obtained in the red-shifted wavelength region [196] (see Figure 6.91).

As oxygen is an effective quencher, the permeated oxygen in the analyte solution quenches the fluorescent light. Plotting of the fluorescence intensities in a Stern–Volmer plot leads to a straight-line dependence between the fluorescence intensities (I_0/I) and the oxygen concentration:

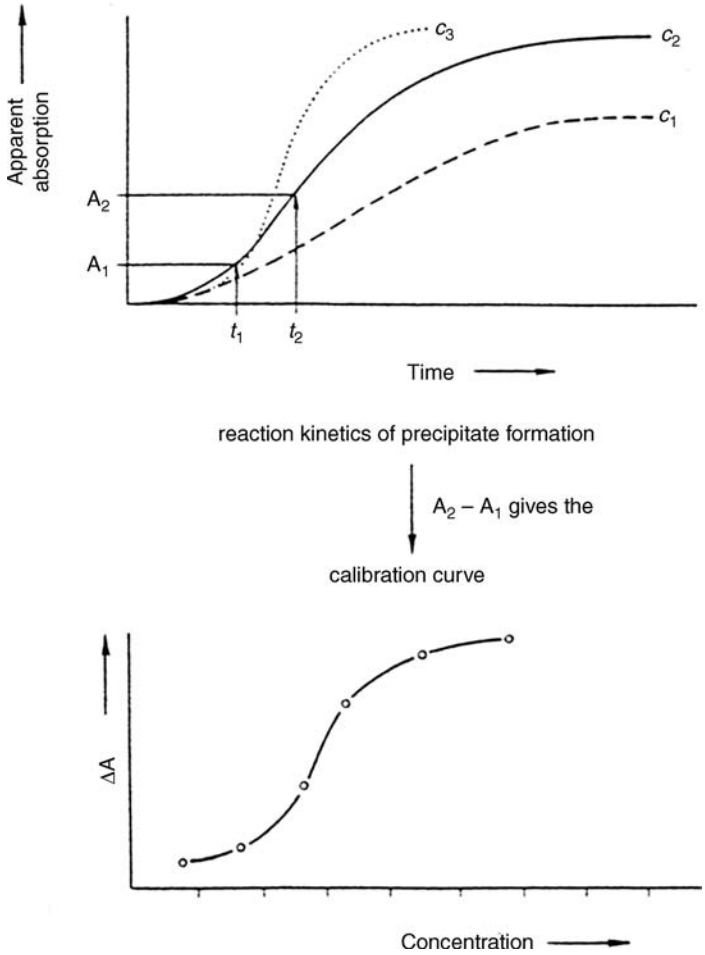

Figure 6.90 Scheme of kinetic–turbidimetric measurements of immunological reactions and transformations in a calibration curve.

$$\frac{I_0}{I} = 1 + k_q \tau_F [Q] \tag{6.15}$$

where k_q is the quenching rate constant, τ_F is the fluorescence lifetime, and [Q] is the quencher (oxygen) concentration. The term $k_q\tau_F$ is the "half quenching concentration," which is the quencher concentration at which the quenching effect is 50%.

With the help of the linear dependence between fluorescence intensity and quencher concentration, the oxygen concentration in blood can be determined.

The great advantage of the optical system is the possibility of minimally invasive permanent monitoring of the oxygen (and carbon dioxide) partial gas pressure in intensive medical monitoring.

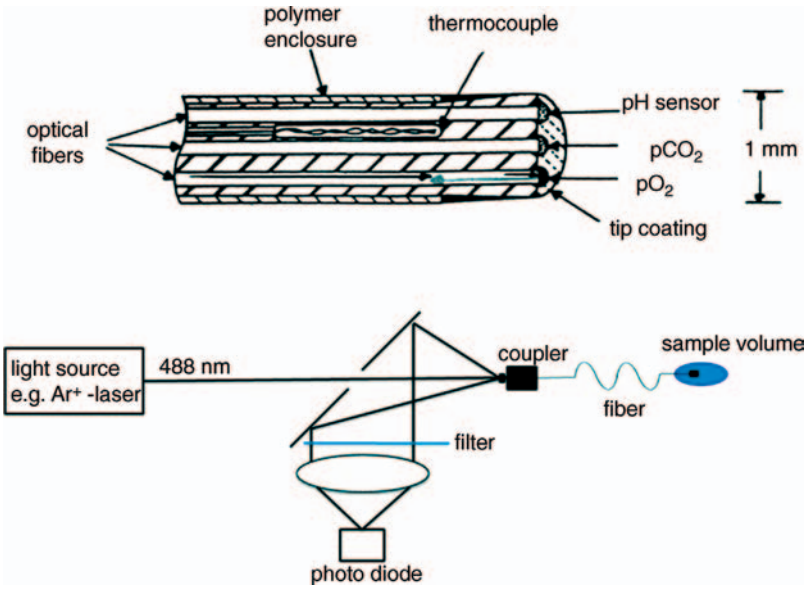

Figure 6.91 Experimental set-up of the fiber-optic partial gas pressure measuring system.

6.1.8.2 Optical Detection of pCO_2 in Blood

The basic principle of the pCO_2 measurement method adapts the Lambert–Beer law and the embodied system using the nondispersive infrared (NDIR) method. Since CO_2 gas reacts to a 4.3 μm wavelength, this wavelength is selected using an optical filter, and the energy decrease due to molecule oscillations is used. The CO_2 concentration is then measured by a mass flow controller (MFC) using basic steps, instead of collecting pCO_2 gas by applying heat to the outer skin. The measuring system consists of an IR lamp, optical filter, optical reaction chamber, pyroelectric sensor, and signal processor. To make the sensor system portable, the length of the optical reaction chamber is minimized to 1 mm using an Si wafer based on MEMS (microelectromechanical systems) technology. When CO_2 gas is injected into the optical reaction chamber, a result of 4.3 mV was confirmed when using a photoreaction path of 1 mm with a CO_2 gas reaction. The response time of the system was within 2 s, which is fairly fast [197].

6.1.8.3 Optical Detection of Further Monitoring Parameters in Intensive Care (Temperature, pH)

Novel methods of temperature measurement use optical fibers and luminescent materials to convert absorption into a temperature-dependent luminescent signal. For example, the delay time of an excited state in an inorganic material has been shown to vary with temperature, and this is readily measured via the phase-shift technique [198]. Other approaches use the creation of an acoustic wave due the conversion of excitation energy into heat and sensitive detection by a microphone for

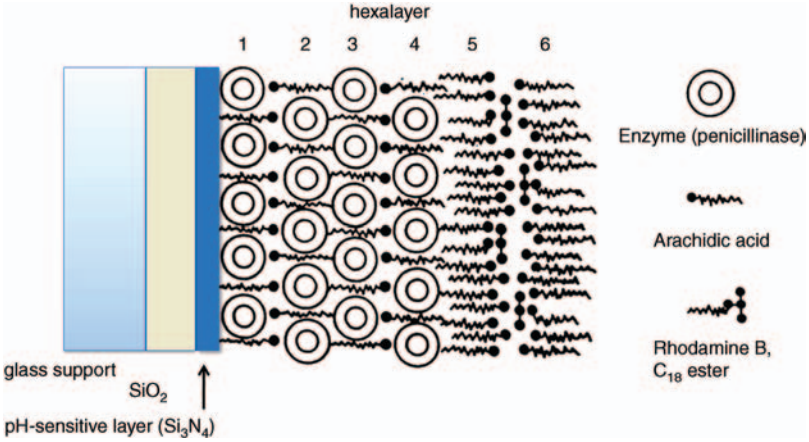

Figure 6.92 Scheme of an optical pH meter composed of Si_3N_4 semiconductor material and a potential-sensitive dye in the layer.

temperature measurement. This method is rather similar to photoacoustic spectroscopy (for more details, see Section 6.1.9).

Optical pH measurements combine the use of semiconductor materials such as Si_3N_4 to create potential changes in the medium with the incorporation of a potential-sensitive fluorescent dye in the layer (see, e.g., [199] and Figure 6.92).

6.1.9
In Vitro Diagnostics – Photoacoustic Spectroscopy

Photoacoustic spectroscopy goes back to Alexander Graham Bell in 1880, who observed that modulated sunlight directed into a gas chamber or on to a thin membrane emits sound. He further discovered that the sound became louder if the sample in the gas chamber was darker (higher light absorption) or the surface became larger. One year later, Tyndall and Röntgen discovered that the sound is also emitted without a solid component in the gas chamber if modulated heat radiation (IR radiation) is directed into the chamber. H_2, O_2, and air gave no sound whereas illuminating gas (CH_4, CO) and ammonia were connected with a loud tone [200–203].

The reason for this effect is that periodic light absorption leads to thermal oscillations in the gas chamber. These thermal oscillations are connected with density oscillations which in its part create sound (sonic) waves that can be detected by a microphone.

In principle, the photoacoustic spectrometer (Figure 6.93) measures the heat production in the sample or, in other words, the contribution of nonradiative deactivation channels in the molecules to the overall relaxation process after absorption. The advantages of the photoacoustic spectroscopy are manifold. First, photoacoustics needs no transmittive sample. The heat and therefore the signal are produced from the front side of the sample. Furthermore, with photoacoustics very

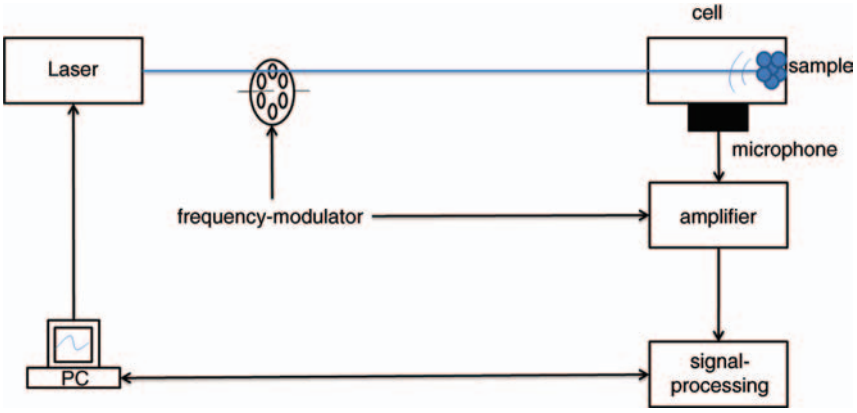

Figure 6.93 Scheme of photoacoustic spectrometer.

high and also very low absorption can easily be detected. The signal is directly proportional to the absorbed power (in solids: absorbed power within the thermal diffusion length). Hence there are decisive advantages in comparison with conventional absorption spectroscopy:

- direct measurement (no difference)
- no transmitted light beam necessary.

The application of photoacoustic spectroscopy in medicine is directed to the investigation of non-transparent samples, for example

- biological samples such as leaves, apple parings, and flowers
- medical samples such as blood, skin, and vessels.

Information given by the photoacoustic spectrum, in addition to the concentration and the spectral characteristics of the samples, includes

- demolition-free depth profiles, material defects
- fluorescence quantum yield, heat capacity, thermal conductivity.

6.1.10 Therapy

6.1.10.1 Introduction

Today, a multitude of therapeutic applications based on the biophotonics concept are available in the medical and cosmetic surgical fields, for example:

- Photodynamic therapy (PDT) [202–207] is used in dermatology for the treatment of viral warts, acne, psoriasis, actinic keratoses, Bowen's disease, basal cell carcinoma, and so on; in oncology for the treatment of cancer of the skin, bladder, breast, stomach, oral cavity, and so on; in ophthalmology for the treatment of wet macular degeneration, subfoveal choroidal neovascularization, pathological

myopia, and presumed ocular histoplasmosis syndrome; in cosmetic surgery as therapy for photoaging, cosmetic skin improvement, oily skin, enlarged sebaceous glands, wrinkles, rejuvenation, and so on; see Section 6.1.1.3.

- Refractive surgery [208–212] alters the curvature of the cornea to improve the focusing characteristics of the eye and can be divided into flap surgery [laser-assisted *in situ* keratomileusis (LASIK), intralase-LASIK, femto-LASIK, intra-LASIK, laser-LASIK, all-laser-LASIK] and surface surgery [photorefractive keratectomy (PRK), laser epithelial keratomileusis (LASEK)] and epithelial *in situ* keratomileusis (epi-LASIK).
- Laser-induced photothermolysis [213–215] is used for removing abnormal cutaneous vessels (telangiactasias, port wine stains, capillary hemangiomas, etc.), for laser skin resurfacing (e.g., treatment of fine wrinkles, photodamaged skin, acne and surgical scars, melasma, uneven skin coloring, stretch marks, keloids, xanthelasma), for laser removal of tattoos and permanent makeup, and for laser removal of undesired hair.
- Photobiomodulation (low-level laser therapy, cold or soft laser therapy, laser biostimulation) [216–218] is applied for the therapy of, for example, wound management, soft tissue injuries, inflammation, arthritis, chronic pain, dermatological conditions, myofascial trigger point therapy, acupuncture, allergy, and tinnitus.
- Photoactivated disinfection (PAD) [219] is an antibacterial dental treatment of, for example, endodontics, periodontics, caries, peri-implantitis, and so on.
- Laser conization [220, 221] is used for cervical intraepithelial neoplasia.
- Laser tonsillotomy [222, 223] is applied for tonsillar hyperplasia.
- Laser interstitial thermal therapy (LITT) [224, 225] is used for the treatment of, for example, brain and spinal cord tumors and breast cancer.
- Percutaneous laser disc decompression (PLDD) [226, 227] can be used to treat back and neck pain caused by a herniated disc.
- Photoselective vaporization of the prostate (PVP) [228, 229] (also known as GreenLight HPS, GreenLight PV, laser prostatectomy, laser TURP) is used to treat benign enlargement of the prostate gland.
- Laser lithotripsy [230, 231] is a surgical procedure to remove a kidney stone, urethral stone, or bladder stone.

Due to this wide variety of existing biophotonics applications in therapy, detailed descriptions of each application would go beyond the scope of this chapter. Therefore, as just one example, refractive surgery, as a widely used laser light therapeutic application in ophthalmology, is described in a more detailed manner in the following section.

6.1.10.2 **Laser Therapy in Ophthalmology – LASIK (Refraction Correction by Cornea Treatment)**

Laser therapy for refraction corrections goes back to Trokel *et al.* [232],who reported the first laser application in ophthalmology in 1983. In 1987 the first commercial cornea surgery laser (>250 000 patients) was introduced.

Direct cornea ablation (photorefractive keratectomy) is preferentially carried out with an excimer laser at a wavelength above the photodecomposition energy of 3.5 eV

(XeCl, ArF, etc.) and the mechanism is ablation by photodecomposition with a precision of $<0.5\,\mu m$ and a typical ablation depth of $100\,\mu m$.

Radial Keratectomy (RK) The idea of surgical vision correction is not new. In the early 1970s, Svyatoslav Fyodorov, a Russian ophthalmologist, developed a procedure called radial keratotomy (RK). He noticed that after removing splinters of glass from a patient's eye, the patient's distance vision improved. In 1978, the procedure was introduced in the US. Surgeons perfected the procedure by creating incisions in the cornea to flatten the front of the eye and to refocus light on to the retina. Unfortunately, it was not a good procedure for patients with higher prescriptions, so surgeons started to search for a new procedure to reshape the cornea.

RK involves the placement of microscopic incisions outside the central optical zone. This weakens the outer perimeter of the cornea and causes it to flatten, thereby moving the point of focus from in front of the retina to the periphery of the retina [233].

Photorefractive Keratectomy (PRK) The next procedure to be developed, photorefractive keratectomy (PRK), approved by the US Food and Drug Administration (FDA) in 1996, uses an excimer laser to resurface the cornea. Because of pain receptors in the surface of the cornea, PRK turned out to be a painful procedure and surgeons looked towards a new approach. Furthermore, the surface of the cornea changed by creating cicatrices in the long term, which reduced the effect of cornea resurfacing dramatically (see Figure 6.94).

Laser-Assisted *In Situ* Keratomileusis (LASIK) Finally, LASIK surgery was developed. LASIK combines the creation of a corneal flap with laser resurfacing. Because there are no pain receptors in the under-layers of the cornea, the creation of the flap proved to eliminate pain involved in the procedure and led to a quicker recovery (see [209] and references therein, and Figure 6.95).

LASIK is a procedure that permanently changes the shape of the cornea, the clear covering of the front of the eye, using an excimer laser. A knife, called a microkeratome, which is better with femtosecond laser pulses (Carl Zeiss Meditec, Jena, Germany), is used to cut a flap in the cornea. A hinge is left at one end of this flap. The flap is folded back, revealing the stroma, the middle section of the cornea. Pulses from a computer-controlled laser vaporize a portion of the stroma and the flap is replaced.

6.2
Photonic Instruments in Biotechnology

6.2.1
Introduction

Much attention has been devoted recently to defining biotechnology. The European Federation of Biotechnology defined biotechnology as the integration of natural sciences and engineering sciences in order to achieve the application

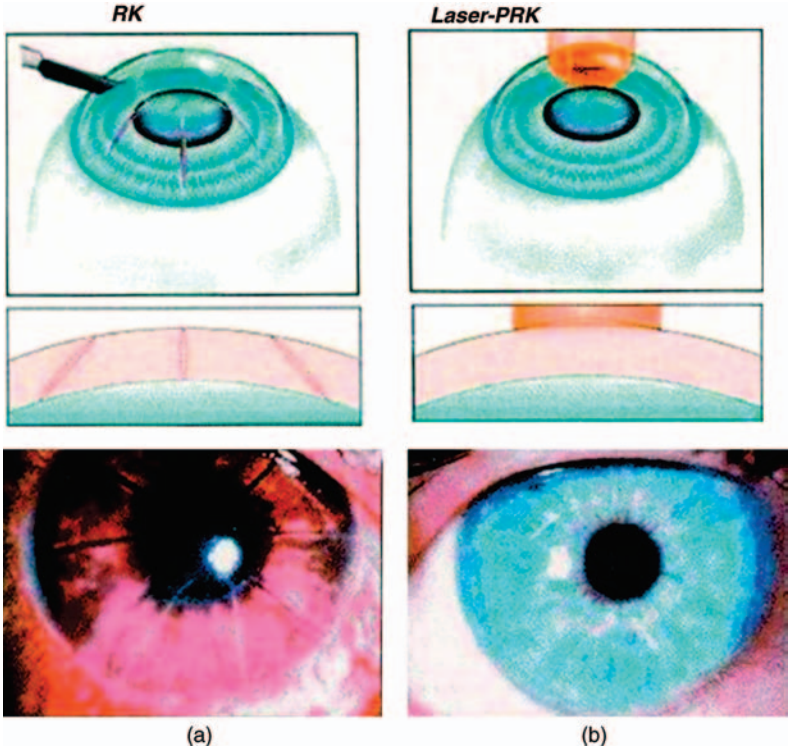

Figure 6.94 Eye after RK (a) and eye 1 day after laser PRK (b).

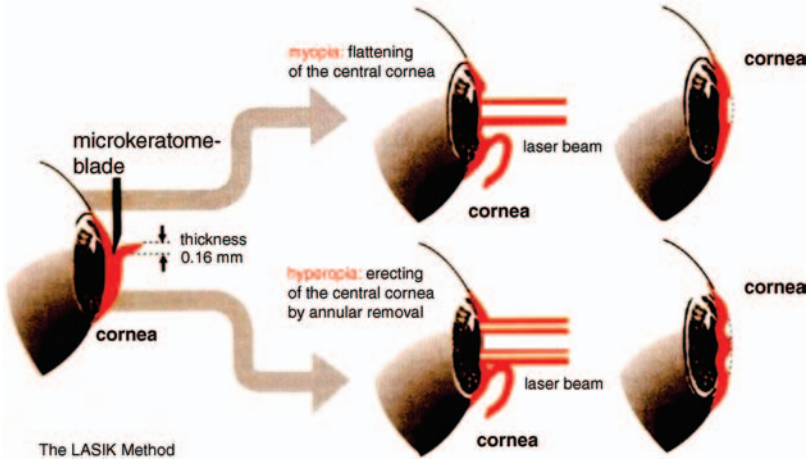

Figure 6.95 LASIK ablative surgery in cases of myotropia and hypermetropia.

of organisms, cells, parts thereof, and molecular analogs for products and services [234].

The interrelation between chemistry, chemical engineering, and the burgeoning areas of molecular biology is especially important as chemical industrial processes incorporate recombinant DNA techniques. In a wider community of chemists, an understanding of the so-called "new" biology enhanced research opportunities and communication in related fields. Frequently, the language of a given discipline creates a barrier to interactions with other disciplines. Rapid developments, such as micro- and nanotechnology have been witnessed in the last few years in the multidisciplinary field of biotechnology, exacerbate this problem [235].

Despite this discussion, biotechnology is one of the oldest technologies of mankind. Depending on the point of view and with consideration of different incisive scientific and technological developments, several steps can be defined [236].

The production of early foodstuffs such as bread, cheese, and sour milk products and also alcoholic beverages such as beer and wine was for thousands of years often characterized by the unwitting use of the metabolism of microorganisms.

The second developmental stage is characterized by biotechnological treatments without prevention of foreign microorganisms. Louis Pasteur (1822–1895) and other microbiologists investigated the metabolic reactions in microorganisms and Robert Koch (1843–1910) developed the technology for the production of microorganisms in monoculture, but often in corresponding processes infections by microorganisms different from those being cultivated could not be excluded. This period was marked by the production of primary metabolic substances such as lactic and citric acid, ethanol, and butanol and the development of the first waste water treatment plants at the end of the nineteenth century.

The next step is to consider the biotechnological manufacture of products with exclusion of foreign microorganisms. The discovery of the antimicrobial action of penicillin by Alexander Fleming (1881–1955) stimulated large-scale production. Sophisticated process technology made the growth of microorganisms under optimal conditions possible. Sterilizability of plant components which are in contact with the fermentation medium was a necessary condition. Following the discovery of further antibiotics, a wide range of secondary metabolic products such as vitamins and pharmaceutical substances came into biotechnological production. This period is still continuing.

One important turning point was, of course, the discovery of the genetic code by James Watson (born 1928) and Francis Crick (1916–2004) in 1953. This fourth period is denoted, in general, by the transfer of knowledge from basic research to biotechnology. Many results in microbiology, biochemistry, enzyme research, molecular biotechnology, genetic engineering, and process engineering are combined into modern biotechnology. All of these disciplines use photonic instruments for the investigation of biological objects and organic and inorganic substances.

On the other hand, material research is also increasingly influencing biotechnology and biotechnological production processes. The selected material itself as well as the interactions between technical/inorganic phase and biologic system/organic material are of considerable importance for optimized biotechnological processes

and technical systems, respectively. Much research work is done with respect to the functionalization of material surfaces and interfaces. The control of structure and surface-relevant interactions at this interface is an essential requirement for innovative developments and products in biotechnology. Examples are the cultivation of adherent cells with ceramic or polymer materials and also modern biosensors and biochips.

Biotechnology today provides products in various application fields with growing markets, employment, and turnover [237]. Meanwhile, a classification by colors has been introduced (e.g., red, medicine/pharmaceuticals; green, agriculture, plant biotechnology; gray, waste management; white, biotech products, industrial processes [238]).

Biotechnological production processes are highly sophisticated and specially adapted and optimized to the relevant biological system (microorganisms, cells, biomolecules) and the desired product [236, 239]. In general, and in brief, the first step is the screening, investigation, and optimization (among others by genetic engineering, and the independent field of Research Technology & Development) of the biological component including the exploration of the optimal process conditions. This is a wide field of application of photonic instruments.

The basic production step, fermentation, involved the transformation of raw material (substrate) into the desired product by microorganisms, cells, or biomolecules or the cultivation of the biomass as the product itself. The technical device used, the fermenter, is a highly sophisticated system. To realize the optimal biochemical change, optimized cultivation conditions (e.g., temperature, pH, dissolved oxygen, stirrer speed for mixing, ion concentration, concentration of substrate and product components, and many more) are controlled by the fermenter. Therefore, fermentation is also an important field of application for analytical and photonic instruments.

Fermenters are available with a broad range of special equipment adaptable for every organism, strain, and metabolic product and therefore for different kinds of processes (see Section 6.2.4). Its volume can vary from a few milliliters to thousands of cubic meters. In parallel with the first step mentioned above, the selection and composition of the nutrient broth, the substrate, is realized. The substrate contains all the necessary components for the maintenance of the microbial or cellular metabolism or for an optimal biochemical reaction.

After sterilization and filling of substrate (or vice versa), the fermenter is inoculated with the organism that will be cultivated.

As result of the fermentation process, the fermentation broth contains the desired final product in a mostly very complex substrate. For this reason, treatment steps are normally necessary to isolate the end product (e.g., by filtration in different forms, centrifugation, digestion, evaporation extraction, crystallization). The monitoring of the product quality and purity is a further field of application for photonic instruments.

However, sensors and analytical systems for the huge range of all biotechnological process steps and every signal level are necessary in general and are widely available for in-line, on-line and off-line measurements. In addition to others, especially

electrochemical devices, numerous optical photonic systems are used. Process coupling is increasingly at the center of attention but the problems of sampling are often neglected.

6.2.2 Selected Analytical Methods

6.2.2.1 Introduction

In biotechnology, a broad range of different measuring systems is used. They can be discriminated by different criteria. One important classification describes the series of steps of the analytical process with respect to the prespecified problem of the measurement [240] (Figure 6.96). An important aspect of this consideration is related to the sampling problem, which is often disregarded.

The analytical principle as the first step of the measurement is quantitatively describable by the underlying natural law. For example, light is absorbed by molecules of a solution; the Lambert–Beer law describes the extinction as a function of concentration.

The analytical method furthermore comprises parts of the sample preparation and the evaluation of the measured value. It realizes a strategic concept for extracting the optimal information content from the object. With respect to the absorption of light, the method includes, for example, rules about how to dilute the sample and how to fill and handle the cuvette, and also instructions about the calculation of the result.

The analytical procedure contains complex protocols including, on the one hand, instructions about the sampling from the measured object or the process and, on the other, sample preparation, the arrangement of measuring equipment, the calibration functions, the possible errors, and so on. In the case of a fermentation process, it could be important, for instance, to prescribe the sample port and the sterile interface to obtain a sample for flow through the cell of a photometer and also the use of calibration curves for the determination of the biomass content from the extinction of the photometer.

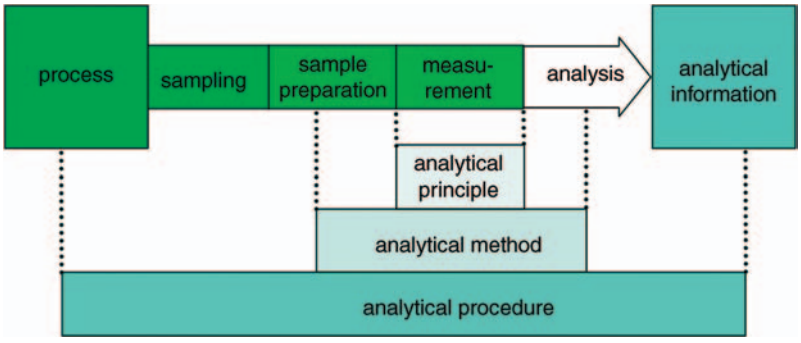

Figure 6.96 Analytical principle, analytical method, analytical procedure.

It is important to state that sensors cannot be classified in this system. In contrast, sensors are in direct contact with the object or the process. In combination with data recording and acquisition by electronics, they are independent systems which are able to record physical or chemical properties of the environment qualitatively and/or quantitatively.

On the other hand, the underlying principles are used both in analytical systems and in sensors. In the context of this chapter, we distinguish here between the methods and the sensors. However, it is important to state that in real practice the relationship is smooth.

6.2.2.2 **Reflectometric Interference Spectroscopy (RIfS)**

Reflectometric interference spectroscopy (RIfS) is based on the multiple reflection of white light at interfaces between thin transparent layers with different refractive indices. The basic principle is Fabry–Pérot interferometry. It is suited to the determination of the thickness of thin transparent layers [241].

At each interface, the light beam is partly transmitted and partly reflected (Figure 6.97 [242]). The reflected beams cover different optical paths. Any change

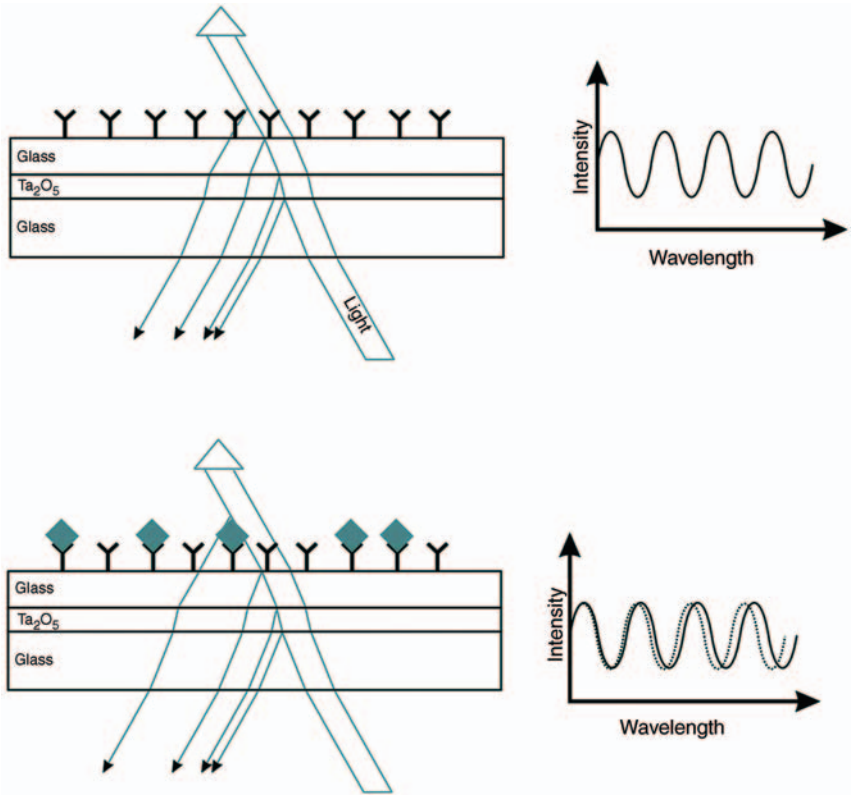

Figure 6.97 RIfS: light is partly reflected and partly transmitted at the glass–antibody layer and also at the antibody–antigen layer.

in optical thickness (represented by *nd*, where *n* is the refractive index and *d* the thickness) will lead to changes in the interference spectrum of the recombined fractions of the reflected light due to constructive and destructive interference of the individual single beams.

Reflection also takes place at biologically activated surfaces (receptors) and at receptor–analyte complexes (e.g., antibody–antigen system). The temporal shift of the position of a selected extremum provides information about interactions between surface-immobilized biomolecules and molecules of the analyte. In combination with a fluidic system, RIfS permits time-resolved, label-free measurement of the real-time kinetics of analyte binding to a surface-immobilized sensor molecule.

As a laboratory method RIfS has also been evaluated for use in different experiments, for example, for bacterial infections [243], testing of biocompatibility [244], and coupling with other highly sophisticated methods {e.g., matrix-assisted laser desorption/ionization time-of-flight (MALDI-TOF) mass spectrometry for the determination of binding interaction of antibiotics [245]}, in addition to being used as a bridging technology for different high-content screening approaches in the development chain of leading structures for the pharmaceutical industry or during the identification and validation processes of new biomarkers [246].

The RIfS method is widely used in biosensors (see below), but analytical systems are also commercially available. Analytik Jena (Jena, Germany) offers the BIAffinity® system [247] for the measurement of concentrations (10^{-3}–10^{-10} M), kinetics (association rate k_a 10^3–$10^6\,M^{-1}\,s^{-1}$, dissociation rate k_d 10^{-5}–$10^{-1}\,s^{-1}$), and affinities (10^4–$10^9\,M^{-1}$). Label-free real-time detection of interactions is possible with simultaneous presentation of the interference spectrum.

Depending on the application, different materials are usable as transducers. Glass slides are coated with niobium pentoxide, titanium dioxide, indium tin oxide and TOPAS® (a cyclic olefin copolymer). The use of a wide range of "classical" bioreceptors has been described (e.g., antibodies, antigens [248], cells [249], oligonucleotides). Modern analytics also applies bioanalogs (e.g., aptamers) and synthetic molecules [e.g. prepared by molecular imprinting (MIP)] [250, 251].

6.2.2.3 **Surface Plasmon Resonance (SPR)**

Label-free interaction analysis is of increasing importance for scientists in the academic, pharmaceutical, biotechnology, and diagnostic markets. SPR, in addition to RIfS, is such a label-free interaction analytical technique. SPR was first demonstrated in 1983 [252, 253].

Plasmons are quantized density oscillations of charge carriers in metals and semiconductors. On irradiating the interface between a glass substrate coated with a thin gold layer and a liquid medium, total reflection can be observed (Figure 6.98) [254]. Normally the gold layer has no influence if it is thin enough. However, at a definite angle and under special conditions of polarization (use of totally internally reflected parallel polarized light) of the incident monochromatic wave, the evanescent field goes into resonance with the electrons of the gold layer and light energy of the reflected light is absorbed. The diffusion and immobilization of a layer of analyte molecules or analyte receptor complexes at the gold surface

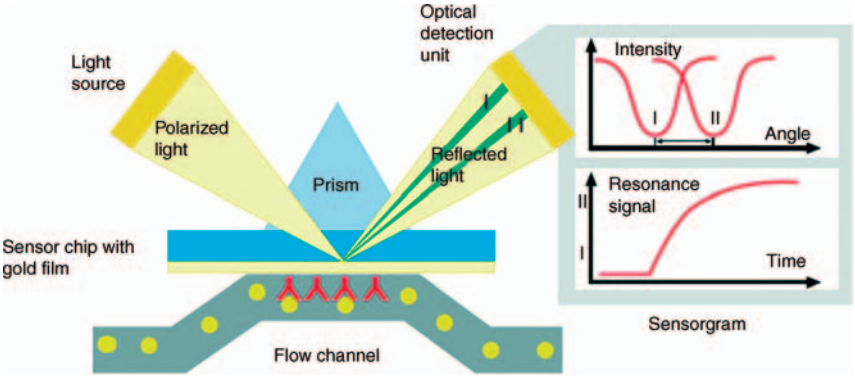

Figure 6.98 The Biacore detector with sensor chip and integrated microfluidics cartridges. © 2010 General Electric Company. Reproduced by permission of the owner.

influence the resonance condition and the maximum signal is detectable at a different angle. The deviation is a measure of the concentration of the substances. Together with a selected receptor, this principle allows specific and quantitative detection. A good overview of SPR is given in [255].

In the same way as RIfS, SPR was developed only as biosensor technology. However, in current biotechnology it is mostly used as sophisticated analytical system using a flow system for sample transport (Figure 6.98) [256]. Biacore (Uppsala, Sweden) commercialized its SPR systems in 1990 [257]. The systems permit label-free interaction analysis in real time and are applicable for concentration measurement in the nanomolar range, compound-target-binding assays in the range 50–2000 ng ml^{-1}IL-6 (interleukine-6), and anti-drug-antibody (ADA) detection. The data give insights into protein functionality, elucidate disease mechanisms, and play a key role in the critical decisions needed for efficient development and production of therapeutics. Numerous research articles deal with special applications [258].

SPR is particularly interesting if more than one receptor is immobilized at the surface. Using a variety of different molecules, for example, by application of biochips with numerous receptor dots, a CCD matrix scans the signals and the interaction analysis of potential binding partners is possible. Some further interesting developments are the extension to complex analytical systems, for example, combination with MALDI-TOF mass spectrometry [259, 260] (see Section 6.2.2.2), miniaturization, the detection of whole cells, the option of remote sensing (by coupling with light fibers), the use of gold nanoparticles in solution instead of a gold layer (which allows, for instance, tumor diagnostics), and multichannel analysis. For future trends, see also [255]; selected applications are described in [261].

6.2.2.4 Fluorescence Methods

Application of Green (GFP) and Other Fluorescent Proteins Since its incidental discovery in 1962 [262], green fluorescent protein (GFP) has become one of the most important tools [263] of molecular biology (Nobel Prize in Chemistry, 2008).

The oxoluciferase aequorin from the jellyfish *Aequorea victoria* fluoresces after excitation by blue or ultraviolet light with the same emission spectrum as the tissue of the jellyfish itself and is associated with a green fluorescent protein. This shows that the GFP is excited by the aequorine. Additionally, no cofactors are necessary for fluorescence. It has two absorption maxima (395 and 475 nm) but only one emission maximum (509 nm). GFP is very stable over a broad pH range and denatures only at temperatures higher than 65 °C. In jellyfish, the excitation energy is provided by radiationless energy transfer from the aequorin protein.

It was found that GFP can be gene-specifically fused with different proteins without loss of fluorescence. Since 1994, GFP has been used as marker for these proteins [264, 265] and this technology has become a standard method in cell biology and genetic engineering, because genetic expressions can be viewed.

GFP can be expressed by numerous organisms and many variants (seven different groups, additionally enhanced variants; see Chapter 7) with different emission spectra have been synthesized by mutagenesis. Today, further proteins obtained (e.g., from corals or *Escherichia coli* [266]) with very different emission spectra (e.g., blue 440 nm, red 610 nm) are available. With these proteins it is possible to monitor the spatial and temporal distribution of different proteins of living cells to which the fluorescent proteins are bound.

Förster/Fluorescence/Bioluminescence Resonance Energy Transfer (FRET, BRET) Fluorescence resonance energy transfer (FRET) and bioluminescence resonance energy transfer (BRET) are useful tools for investigating molecular interactions, biochemical reaction kinetics and their location in living organisms.

FRET (described in 1948 by Thomas Förster and often referred to as Förster resonance energy transfer [267]) is a distance-dependent interaction between excited electronic states of two dye molecules with energy transfer and without transfer of photons. In a typical FRET experiment, the regions of interest are labeled with different fluorophores [e.g., blue fluorescent protein (BFP), cyan fluorescent protein (CFP), and yellow fluorescent protein (YFP)] [268], the donor and the acceptor. It is performed with a fluorescence spectrometer by observing the fluorescence intensity of the donor, and if possible also that of the acceptor, or by specially adapted microscopes, offered by different companies, for example [269]. More complicated but more convincing is the measurement of the fluorescence decay time.

The absorption of the donor takes place at a shorter wavelength than that of the acceptor and the FRET efficiency E_{FRET} can be detected by the appearance of sensitized fluorescence of the acceptor by quenching of donor fluorescence. The efficiency of this process depends on the inverse of the sixth power of the intermolecular distance [270]:

$$E_{FRET} = \frac{1}{1 + \left(\frac{R}{R_0}\right)^6} \tag{6.16}$$

where R is the distance between fluorophores and R_0 is the Förster radius, which is the distance at which 50% of the donor fluorescence is quenched.

The spatial resolution of a conventional fluorescence microscope is limited by the Rayleigh criterion to about 200 nm. FRET permits the determination of the closeness of the molecules within a few nanometers (Förster radius), depending on the fluorescence quantum yield of the donor (e.g., 4 nm for BFP–GFP, 5 nm for CFP–YFP). The process can take place when the donor fluorophore in the electronically excited state transfers its excitation energy to the nearby acceptor. If the fluorescence emission spectrum overlaps the absorption spectrum of the acceptor molecule, the donor transfers the energy by long-range dipole–dipole intermolecular coupling.

A limitation of FRET is the requirement for external illumination to initiate the fluorescence transfer, which can lead to background noise in the results from direct excitation of the acceptor or to photobleaching. To avoid this drawback, BRET was developed. This technique uses a bioluminescent luciferase rather than CFP to produce an initial photon emission compatible with YFP.

FRET has become a standard tool in molecular biology {e.g., real-time quantitative polymerase chain reaction (PCR) [271–273]}, biochemistry (e.g., hetero- and oligodimerization, reconnaissance of signal transduction pathways [274]) and cell biology [275, 276] for the detection of protein–protein, protein–nucleic acid, and nucleic acid–nucleic acid interactions [277]. It is also used for spectroscopy and in combination with confocal microscopy. FRET and BRET in research are also used for the study of molecular motors, that is, the molecular machines for the movement of living organisms. Furthermore, by labeling different ends of a molecule, the kinetics of fragmentation can be observed in real time.

Flow Cytometry/FACS The key technology of cytometry was developed in 1968 by Wolfgang Göhde and Wolfgang Dittrich [278, 279] and has been commercialized by several companies. Flow cytometry combines fluorescence and stray light measurement into a powerful technique which can be used for the analysis of multiple parameters, especially for counting and examining microscopic particles. In biotechnology it is used for a wide range of applications from individual cells within populations, chromosomes, and ploidy analysis to GFP expression analysis [280, 281]. For descriptive introductions see [282–284].

Cells are suspended in a fluidic stream (Figure 6.99 [282]) until thousands per second are passing a laser beam and the fluorescent and forward- and side-scattered light emerging from each cell is captured and statistically evaluated in real-time. Relevant parameters are, for example, size, components, complexity, and phenotype.

The sample is transported to the interrogation point by a flow system. Lasers are used as light source. The optics gathers and directs the emerging light to the detectors. The operation and data evaluation are substantially computer controlled.

Laser light and the sample intersect at the interrogation point. The sample stream containing the cells is injected into the fluid stream by hydrodynamic focusing. Due to the higher pressure of the outer sheath stream, the inner sample stream is formed into a thin thread. In consequence, the cells pass through the laser beam one at a time. In practice, cytometers can detect cells with diameters between 1 and 15 μm. Specialized systems can detect particles outside this range.

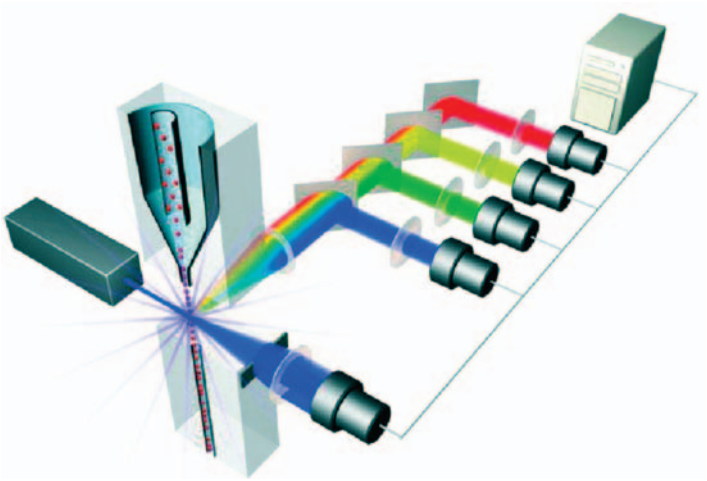

Figure 6.99 Basic design and optical path of the flow cytometer (Invitrogen).

Stray light from the interrogation point can be measured at different angles. Routine devices besides fluorescence are designed to measure low-angle scattered light and/or light scattered at a right-angle. The forward-scattered light is nearly proportional to the cell size. Hence the scattered light received by the detector is proportional to the cell size and results in a histogram of the diameter distribution. The side-scattered light characterizes the granularity and structural complexity inside the cell. Separate detectors sample this light as a function of the wavelength also as histograms. The combination of both measurements is a 2D histogram with patterns characterizing the different particles of the sample.

A third signal, the fluorescence of different marker molecules (dyes) applied to label cells is measured as a function of wavelength by the same detectors again as a one- or two-color histogram. Using two dyes, a two-color histogram can be evaluated as a two-color dot plot. Dichroitic filters separate the different emission wavelengths of the different markers. The spectral overlap of the filters depends on their characteristics and on the fluorescence spectra.

Because it is possible to sort cells according to the measured characteristics, cytometers are often also termed fluorescence-activated cell sorters (FACS), despite the fact that this is a registered trade mark of the Becton-Dickinson [285] company. Separation is possible by tagging of cells of interest with an antibody linked to a fluorescent dye. This antibody must be bound to a protein expressed in the cells of interest. Ultimately cells are sorted by electrical charge, which is computer controlled, applied to the drops before being formed at the end of the flow stream. These charged drops are then deflected to sample tubes.

In addition to biotechnology, there are also numerous applications in medicine, for example, blood analysis [286, 287], bone marrow diagnostics [288, 289], immune phenotyping [290, 291], and AIDS research [292].

Fluorescence *In Situ* Hybridization (FISH) Fluorescence *in situ* hybridization (FISH) is a special form of *in situ* hybridization, a molecular method to detect nucleic acids (DNA or RNA) in tissues, cells, or metaphase chromosomes by fluorescence. It rests on the pairing of complementary bases of single nucleic acid strands. One of these is previously labeled (e.g., with haptens, in the case of FISH directly with fluorescing molecules) and the other is the strand to be detected.

6.2.2.5 Advanced Microscopic Techniques (Selection)

Some of the available advanced microscopic techniques are also based on fluorescence. According to classical physics (Abbe's theory of image formation, Rayleigh criterion of resolution; see below), until not very long ago it was accepted that two objects limited by diffraction can be resolved only if they are not closer than about half of the wavelength of light, that is, about 240 nm.

The lateral two-point resolution is calculated by

$$\Delta r = \frac{0.61\lambda}{n \sin \alpha} \tag{6.17}$$

where n is the refractive index and α half the aperture angle. The product $n\alpha$ (n sinα) is called the numerical aperture.

The axial two-point resolution is given by

$$\Delta z = 2\frac{n\lambda}{(n \sin \alpha)^2}. \tag{6.18}$$

Many biological objects of interest are smaller. By the end of the last century, new concepts and technical developments overcame the diffraction criterion and allowed the transition from microscopy to nanoscopy. Some ideas that emerged from scanning and fluorescence microscopy (e.g., labeling) recently resulted in a large number of microscopic methods. To present them all would go beyond the scope of this chapter (see [293, 294]) and here are only a few principles are mentioned.

Confocal Laser Scanning Microscopy (CLSM) Confocal laser scanning microscopy (CLSM) is distinguished by enhanced lateral resolution (about 200 nm) and depth selectivity. In contrast to classical fluorescence microscopy, only a disc-shaped area of the fluorescently labeled or autofluorescent sample is illuminated by a focused laser beam via a pinhole and the sample is scanned point-to-point (Figure 6.100 [295]). A detector pinhole focused to the same plane eliminates light scattered outside the focus plane. The image is electronically reconstructed by computer. By the reduction of the out-of-focus blur, the image definition of opaque samples is enhanced, allowing better surface profiling and to a certain extent (non-opaque samples, light absorption) virtual 3D images with a depth penetration from some tens to a few hundred micrometers are possible. Comprehensive image processing software supports this option [296, 297]. Although already patented in 1957, it needed further technical developments in other fields to make this system suitable for research and routine uses, especially lasers and computer technology.

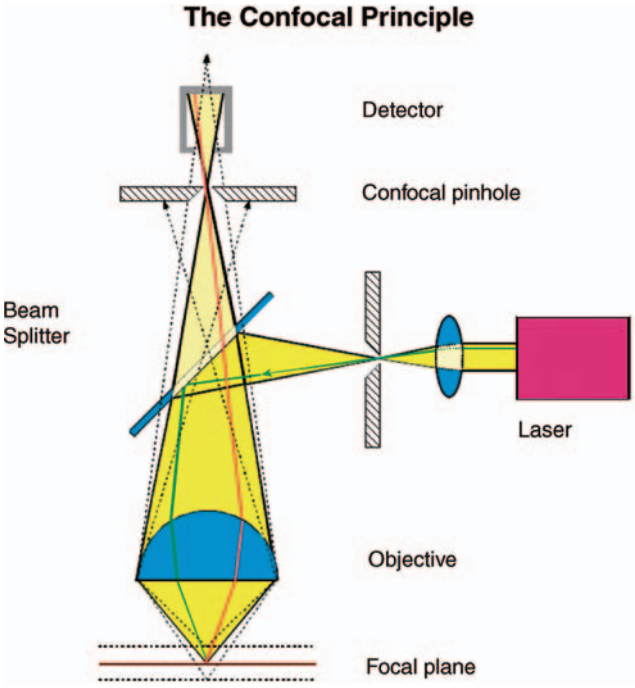

Figure 6.100 Principle of CLSM. Copyright (2010) Leica Microsystems CMS GmbH.

CLSM is used for innumerable applications. Especially in biotechnology and medicine [293], new options are opened up for the investigation of cells and tissues [298–301].

Two-/Multi-photon Laser Scanning Microscopy (TPLSM, MPLSM) In multi-photon laser scanning microscopy (MPLSM), the fluorescence of the (labeled) sample is excited by a pulsed solid-state laser. In CLSM, the energy of the excitation light corresponds to the difference in the energetic levels of the ground and excited states of the fluorescing molecules (one-photon excitation). whereas in MPLSM, the energy of the exciting electron due to quantum effects can be smaller than the energetic distance of the two levels provided that the excitation of the two or more photons takes place nearly simultaneously (the excitation probability is proportional to the reciprocal pulse duration) and with high intensity. Both requirements are fulfilled by femtosecond lasers (pulses of 10^{-15} s, e.g., titanium sapphire laser).

A major advantage of these nonlinear processes is the limitation of the excitation to the focus volume. As a consequence, the fluorescence is also generated mainly in this focus region. A second result is the excitation of the fluorescence with (in the case of two photons) half of the energy, which is especially advantageous for the investigation of sensitive samples such as biological objects. By both effects the unobserved

regions of the sample are less charged with energy and the bleaching of the fluorescent dyes is reduced. Further, the longer wavelength used in two-photon laser scanning microscopy (TPLSM) penetrates the sample up to five times deeper. Because the signal is generated only in the focus, no pinhole is necessary. Therefore, photons from the focus scattered by other sample compartments can contribute to the image.

As in CLSM, in TPLSM the sample is scanned and the signal of every scattered focus point contributes to the computer-generated 3D image. Different scanning modes are available [302] (Figure 6.101). Derived from theoretical considerations, the lateral resolution of the TPLSM is about 1.5–2 times better than that of the CLSM and typically reaches about 300 nm; the axial resolution is of the order of micrometers. It should be mentioned that in addition to the use of labels [303] and of autofluorescence, the application of the above-mentioned fluorescent proteins is common.

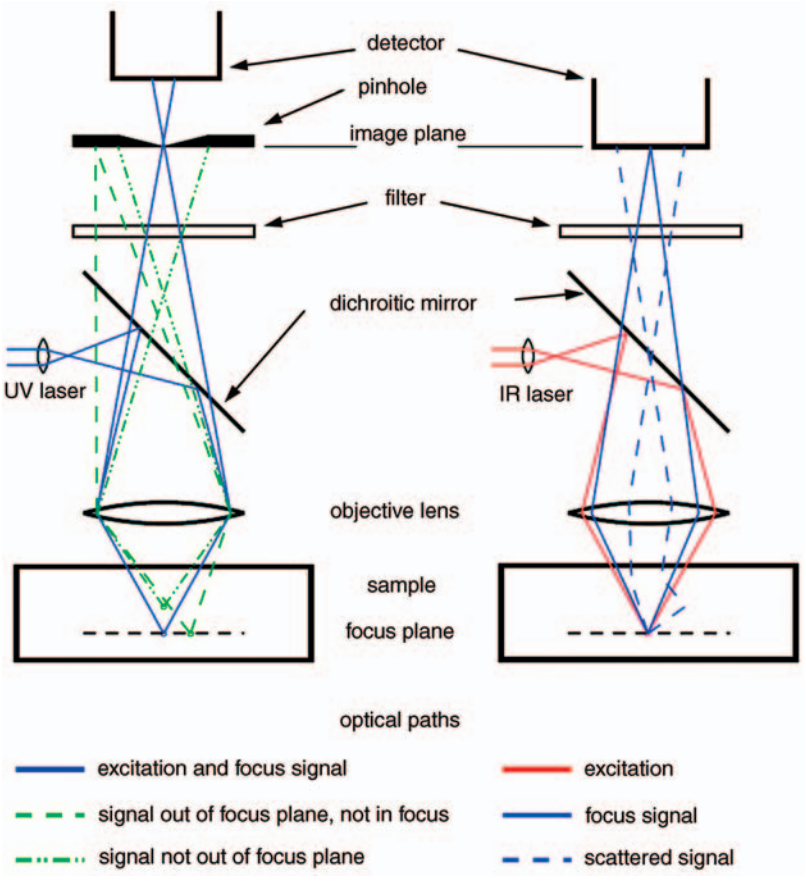

Figure 6.101 Comparison of CLSM and TPLSM: in both cases a laser beam (UV or IR) is focused via a dichroitic mirror and the objective on the sample. Fluorescence is projected on detector. The filter blocks the excitation light.

Applications in biology and medicine are numerous, for example, the investigation of cell interactions [304], imaging of neurons [305], tissue remodeling [306], and tumor research [307].

Resulting from the advantage that the exciting energy is generated only in the focus, TPLSM is used for other working methods. The option to adjust the energy in the focus point, on the one hand, enables one to destroy structures specifically. This can be used, for instance, for the investigation of structure–function relations of macromolecules or cells. On the other hand, it becomes possible to dose energy, for example, for the triggering of polymerization reactions on the nanoscale, for instance to generate predetermined structures.

4Pi Microscopy (4Pi) 4Pi microscopy (4Pi) is a far-field fluorescence 3D microscopic method and a version of confocal microscopy. In consequence of the previously mentioned Abbe criterion and because many biological objects (cell organelles, viruses, genes) are smaller than the minimal resolution in fluorescence microscopy, objects are with increasing regularity observed indirectly by fluorescence labeling (e.g., GFP). The lens projection of a point light source to a focus point caused by the wave character of light does not result in a point image but in an intensity distribution around this point, which has a greater extension in the z-direction than in the x,y-directions. If the projection of the complete solid angle 4π were possible, the resolution could be increased. It could be shown that it is possible to minimize the spread of the focus to the minimal distance given by Abbe by the so-called point spread function engineering [308].

Using a beamsplitter cube [309] (Figure 6.102), the excitation light of the laser source is split into two beams with the same intensity and projected by two opposing lenses of high numerical aperture. The counterpropagating spherical wavefronts are

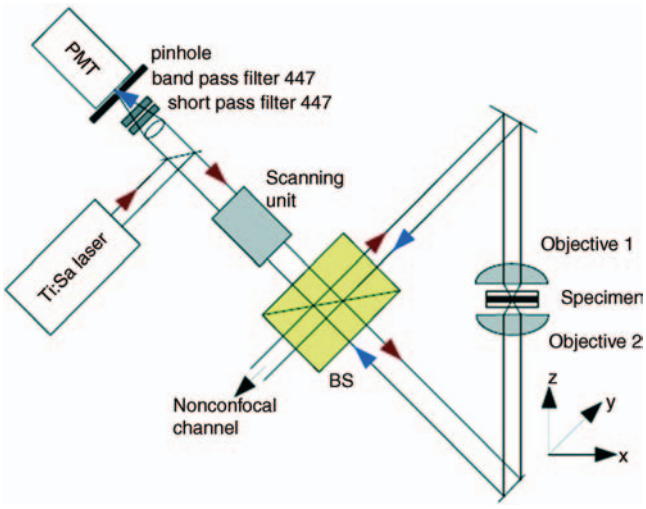

Figure 6.102 Principle of beam path of 4Pi microscope. BS, beamsplitter.

coherently summed at the focal point. The sample is scanned in the axial direction. The fluorescent light is recorded by both objectives, recombined by the beamsplitter and back-reflected to the confocal scanner, where it is spectrally detected.

As a result, the axial resolution is improved 3–7-fold down to 100 nm. 4Pi is mostly applied in cell imaging for biology and medicine [310–312].

Stimulated Emission Depletion (STED) Microscopy Stimulated emission depletion (STED) microscopy is another variant of non-diffraction-limited far-field fluorescence microscopy [294, 313] that has recently found application in biology and medicine [314, 315]. Fluorescence markers are applied for labeling of small components of the sample. When irradiated by a focused laser beam, molecules emit [316] (Figure 6.103) light within a few nanoseconds. In STED microscopy the effective excitation is limited to a small spatial extent. This is facilitated by a second laser beam which is focused like a donut with central zero intensity. Its wavelength and energy are in the red region and therefore too low to excite the molecules, but it is adapted to de-excite molecules by stimulated emission.

The donut shape of the laser beam de-excitation of the molecules in the outer zone of the excitation beam is achieved to confine molecules in the ground state whereas the molecules in the middle of the donut remain excited and fluorescent. In this way, resolutions of better than 20 nm ($\sim \lambda/50$, 15 times better than confocal microscopy) are possible. Excitation and de-excitation are realizable by synchronized laser pulses of shorter than 100 ps and longer than 300 ps, respectively.

It should be mentioned that several different methods and variants of STED microscopy have been reported, for instance, reversible saturable/switchable optically linear fluorescence transition (RESOLFT) and ground-state depletion (GSD) microscopy [294].

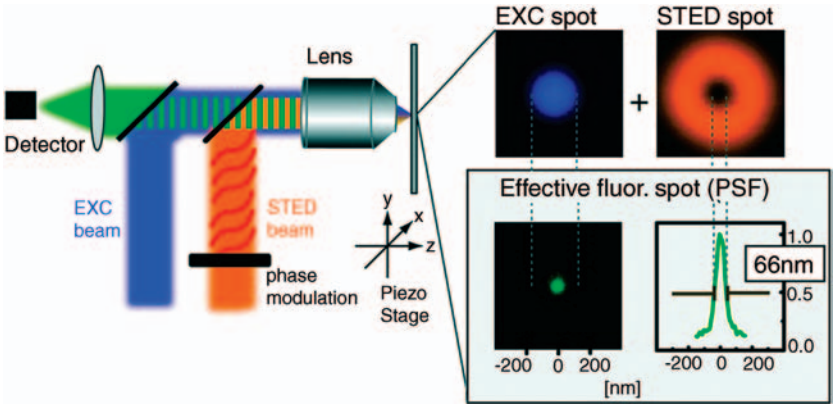

Figure 6.103 STED: exciting and de-exciting light pulses are coupled in simultaneously. The exciting laser generates a diffraction spot of >250 nm whereas the wave front of the STED beam is modified by a phase shift and generates a "donut." in this way, at the edge of the donut fluorescence is prevented. In the middle of the spot fluorescence can be observed.

Scanning Near-Field Optical Microscopy (SNOM, NSOM) Compared with the microscopes mentioned above, scanning near-field optical microscopy (SNOM or NSOM) is a near-field technique. SNOM yields high-resolution topographic and optical images and is an important technique for visualizing biological systems.

The theory was originally proposed in 1928. The Abbe diffraction limit is circumvented by SNOM because the light is generated, scattered, and detected in the near-field. Illumination of the sample is realized through an aperture with a diameter significantly smaller than wavelength of the light. Resolutions of 50 nm can be realized.

A point light source is placed within nanometers of the surface of interest, different modes are known (transmitting, reflecting, collecting, and illumination/collection mode imaging, depending on the illumination and the detected light [317]; see Figure 6.104). A few different light sources are available (tapered optical fibers, cantilevers used in atomic force microscopy with a centered hole for laser illumination, pipets filled with light-emitting or luminescent compounds). The tip is positioned within a few nanometers above the surface and controlled by special feedback mechanisms. The sample is scanned.

Changes in refractive index, reflectivity, transparency, and polarization, and also fluorescent and excited molecules (e.g., Raman) are usable for image generation [317].

Combinations with atomic force microscopy, laser tweezers, and immunolabeling, among others, extend the opportunities for application in life sciences from single fluorescently labeled molecules such as DNA or proteins up to whole cells and chromosomes (for examples, see [317–322]). SNOM is particularly suited to labeling cell surface membrane proteins, since the illumination depth is limited to tens of nanometers. This allows good discrimination between proteins at the cell membrane and those in the cytoplasm [323]. Fluorescent labeling of chromosomes is also

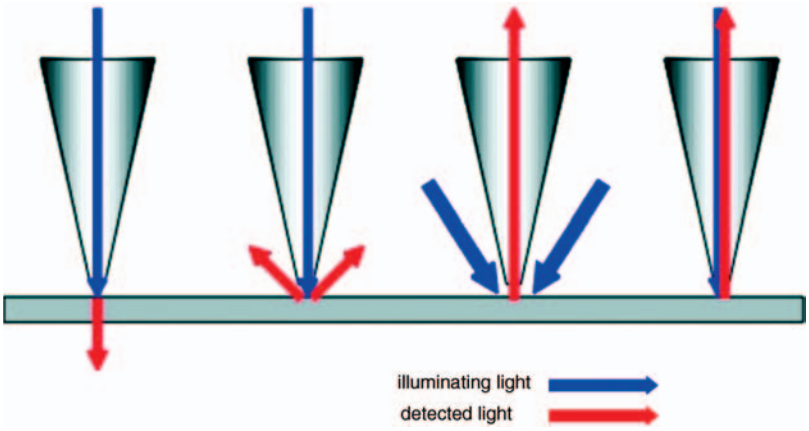

Figure 6.104 SNOM: modes of illumination of the sample and detection of light (for explanation, see text).

common, using FISH or other techniques to label particular areas, which can then be identified in the topography images.

6.2.2.6 Enzyme-Linked Immunosorbent Assay (ELISA)

Enzyme-linked immunosorbent assay (ELISA) is a common serological test for the presence of particular antibodies or antigens. It was developed simultaneously with but independently of enzyme immunoassay (EIA) [324]. It is based on the principle of immunoassay, that is, the interaction of antibodies and antigens of the immune system, and can measure their concentrations sensitively. The principle is similar to radioimmunoassay (RIA), which needs a radioactively labeled detection reagent for quantitative measurement.

In principle, the examined substance (e.g., the antigen) is bound to a solid surface of a microtiter plate, which is immobilized with a specific antibody. Subsequently a second enzyme-labeled antibody is added. The enzyme is used for colorimetric or fluorimetric detection.

Today ELISA represents a standard method in biotechnological and medical laboratories and is applied in numerous detection applications, for example, for low molecular weight compounds (hormones, toxins, pesticides) and also for proteins and viruses [325–328].

Several different technologies have been developed over time. The basic technology is the sandwich ELISA in which, complementary to the basic principle, a secondary antibody bounds at a different site of the antigen [329] (see (4) in Figure 6.105). The method is more universal because this secondary antibody is usable for several different detections.

Competitive ELISA as a further method uses a labeled structural analog, a synthetic antigen, instead of the antibody that competes with the analyte for the binding site.

The indirect ELISA test determines whether a specific antibody is present in the sample. This technique first immobilizes the appropriate antigen to the walls of the microtiter plate [330].

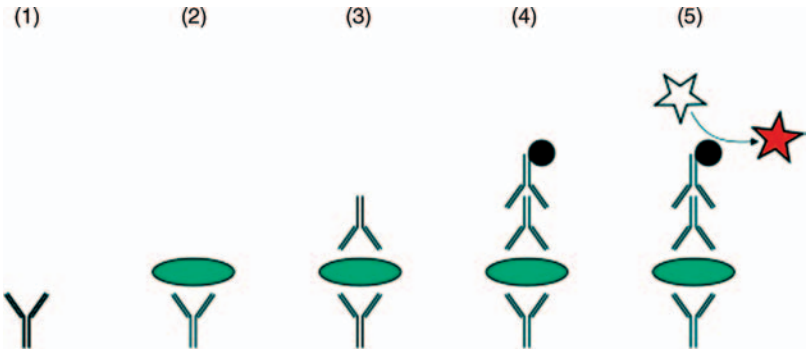

Figure 6.105 Sandwich-ELISA.

6.2.2.7 Optical Biosensors, Biochips, Miniaturized Analytical Systems

Optical Biosensors Chemoreceptors of cells have binding sites for specific substances. Following a binding reaction of this substance with the receptor, the protein structure is changed and an ion channel is opened for transporting ions.

Biosensors are technical analogs of the chemoreceptors of cells. They are defined [331] as self-contained integrated devices which are capable of providing specific quantitative or semiquantitative information using a biological recognition element (biochemical receptor) that is in direct spatial contact with a technical transduction element. The biological recognition element has to identify a substance specifically (key–keyhole principle) and to generate a signal resulting from the contact with this analyte (see Figure 6.106). The technical component has to transduce this signal into a technically processable signal.

This definition is partially outdated because of two developments. Today, the recognition elements are not only biological receptors but increasingly also biotechnological, biomimetic, and synthetic substances. The second reason is that the receptor and transducer are no longer just in direct spatial contact, they are highly integrated, for example, in the form of biochips.

In general, biosensors are classified into two main groups: bioaffinity and metabolism biosensors [332, 333]. This reflects what happens between the receptor and the analyte. Not discussed further here, sometimes one encounters additionally the group of coupled and hybrid sensors and also biomimetic biosensors.

At the surface of a *bioaffinity sensor*, the analyte A is bound with a receptor R as a stable complex characterized by the alteration of the electron density:

$$A + R \Leftrightarrow AR \tag{6.19}$$

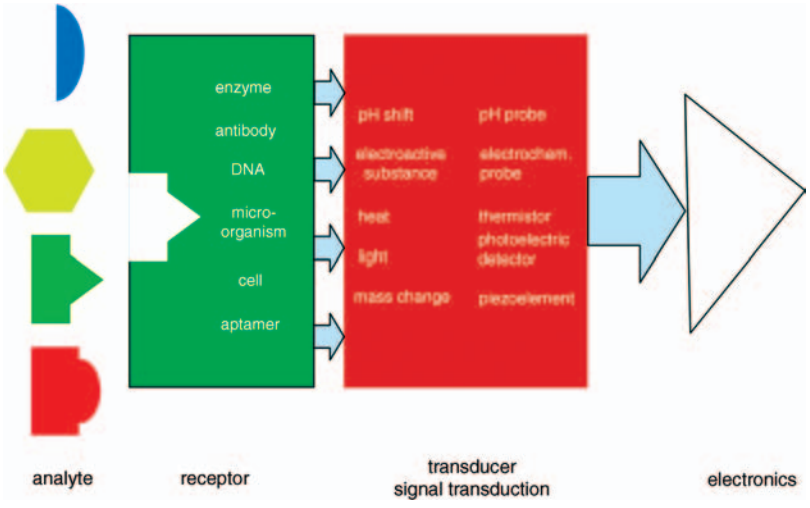

Figure 6.106 Schematic principle of a biosensor.

A typical example is an immunosensor. The related physico-chemical alteration, for instance, layer thickness, refractive index, light absorption, or electrical charge, can be measured by different optoelectronic sensors, based on a quartz microbalance, by surface acoustic waves, and others. The initial state has to be recovered by splitting of the complex.

In the case of *metabolism biosensors* the molecular recognition of analytes by the receptor is coupled with the chemical conversion of the analyte into a product:

$$A + R \Leftrightarrow AR \Leftrightarrow P + R. \tag{6.20}$$

Here an enzyme biosensor typically represents the principle. Mostly electrochemical transducers are used, sometimes also thermometric biosensors, and less frequently optical sensors. It is important to state that the analyte is consumed and the receptor is available in the initial state again.

Other classifications [332] (Table 6.4) distinguish between the different kinds of receptors (e.g., enzymatic, immuno, cell-based, synthetic biosensors, molecular imprinted) or transducers (e.g., electrochemical, optical, piezoelectric, thermal biosensors) [334, 335].

Table 6.4 Recognition elements and transducers of various configurations generate data which are differently analyzed (selection).

Recognition element	Transducer	Measured data/ evaluation	Configuration
Biologic Enzymes Antibodies Nucleic acids Cells *Biotechnological* Designed enzymes Transgenic cells Variants of antibodies *Biomimetic* Highly affine aptamers Peptide nucleic acids *Synthetic* Synzymes Molecular imprints	*Electrochemical* Amperometric Potentiometric Conductometric Capacitive Impedance Microelectrodes ISFET's *Optical* Photometric Interferometric Fluorimetric Optical light guides *Mechanical/ Thermodynamical* Thermistors Piezoelements (Quartz micro balance) Surface acoustic wave	Threshold values Digital single Concentrations Biological effects Pattern recognition	Sensor/probe Microanalytical system Microfluidic systems Micro-total analysis Systems (μ-TAS) Micro-electro-mechanical systems (MEMS) Highly parallel systems (biochips)

In biosensors, three processes proceed successively:

- specific recognition of the analyte
- transformation of the physico-chemical alteration caused by the interchange with the receptor into an electrical signal
- signal processing.

Applications of biosensors are very diverse [334, 336], extending from biotechnology to food technology and from environmental monitoring to forensic and human medicine.

Probably the first and most important stimuli for the development of biosensors arose from medicine. In 1962, Clark and Lyons [337, 338] developed the first biosensor for the determination of glucose in blood. Based on the electrochemical oxygen probe, invented by Clark, the enzyme glucose oxidase was immobilized between two membranes on top. The glucose concentration could be measured from the change in the oxygen concentration due to the oxidation of glucose by the catalytic action of the enzyme. As a result of investigations in different scientific disciplines (e.g., biochemistry) and technological developments (e.g., biotechnology, sensor technology), a vast number of biosensors have now been developed. This progress has culminated in the presentation of modern biochips and microanalytical systems (see the subsections Biochips and Miniaturized Analytical Systems below) with incorporated (bio)sensors.

In medicine, point-of-care testing (POCT) [339] means the use of small, robust, and simple to handle instruments with less consumption of substance and without sample preparation. Instruments in this class allow fast analysis, need no sample transport, and are not integrated in the time flow of the laboratory. Short turnaround times (TATs) permit optimization of therapy [340] (Table 6.5).

One of the goals with the glucose sensor mentioned above was the improvement of the monitoring of diabetes patients. Especially the monitoring of critical states and self-control of patients were targeted. During the last decades, numerous of new and especially miniaturized sensors were developed. These miniaturized sensors based on electrochemical transducers are often combined with other sensors and integrated in analytical hand-held systems, and some of these developments are suitable for patient self-control [341].

Table 6.5 Typical turnaround times (TATs).

POCT parameter	TAT (min)
Metabolic (glucose, bilirubin, lactate)	30
Coagulation	30
Fertility	
Hematology	30
Cardiology [troponine, CK-MB (creatine kinase muscle–brain)]	Immediately
Kidney function	<60
Blood gas	Immediately
Electrolytes	30
Infection serology	<60

With respect to the subject matter of this book, in the following only biosensors based on optical effects (e.g., diffraction, interference, total refraction) or transducers will be discussed. Sometimes more than one effect is used in this kind of biosensor (e.g., diffraction and SPR).

- **Evanescent field biosensors, total internal reflection fluorescence (TIRF)**: Inside an optical waveguide, light is totally or partially reflected at the interface between the core (with lower refractive index) and the surrounding cladding (with higher refractive index). However, the amplitude outside the core does not decrease discontinuously to zero, it decays exponentially. This evanescent part of the wave can be used for the detection of binding events between analytes (e.g., pure or labeled antigens) and a receptor (e.g., antibody), which is immobilized at the surface of the core without the cladding. One option is to compare the light absorbed by the receptor with and without bound analyte. The other opportunity is the excitation of fluorescence of the (labeled) analyte and the measurement of the fluorescent light irradiated back into the waveguide.
- **Interferometric biosensor, reflectometric interference spectroscopy (RIfS)**: Another group of biosensors is based on the principle of interference. In a basic type, light from a waveguide is split into two arms, a sensing arm with the appropriate immobilized receptor and the reference arm (Mach–Zehnder interferometer). In the sensing arm, interaction between light and receptor–analyte complex takes place by evanescent waves. After passing the arms, recombination of the waves allows the observation of constructive and destructive interferences depending on the concentration of the analyte. The principle of RIfS is more often used. The label-free multiple reflection of light at interfaces between thin transparent layers with different refractive indices is the underlying principle of this biosensor type. The principle is described above. RIfS systems provide measurement of real-time kinetics of a bioanalyte binding to a surface-immobilized sensor molecule (see Section 6.2.2.2) and also the investigation of conformational changes in the receptor, leading to the activation or inhibition of the receptor-dependent pathways [342] and much more (see the references in Section 6.2.2.2). Application to fermentation control has also been described [343].
- **Grating couplers**: Often the variation of the refractive index is used to monitor the reaction between analyte and receptor. The grating coupler (in addition to the prism coupler, which is not discussed here) offers a method to determine the refractive index via the evanescent field of the waveguided light. A surface grating is used to couple or decouple light into the waveguide. The effective refractive index influences the grating constant and therefore also the interference characteristics of the electromagnetic wave. Depending on the wavelength, constructive interference only takes place at well-defined angles, that is, only at these angles can light be coupled in or decoupled out of the waveguide. The evanescent wave is influenced by the addition of the analyte and the subsequent shift of the coupling angle is detectable. Different types of grating couplers are used (input, output, reflected mode, wavelength-interrogated couplers).

- **Surface plasmon resonance (SPR)**: This type of biosensor is mostly used as a complete analytical system. The principle is described in Section 6.2.2.3. SPR biosensors are used in drug discovery [344] for some hundreds of assays per day.

Biochips Biochips are small sample carriers constructed from different materials (glass, plastics, silicon). At their surface in parallel hundreds or thousands of sensitive spots with immobilized biological material are arranged as sensitive elements (targets), comparable to the receptor of a biosensor. Each spot realizes a biochemical detection reaction. For this reason, advantageous parallelized and miniaturized analysis is possible.

For the interpretation of the results, it is necessary to know which analyte from the sample is bound at which spot or was detected with which receptor. Therefore, the target spots are structured as an array, with respect to their dimensions often also denoted as microarray. Optical and electrical biochips can be distinguished depending on the method of signal acquisition and processing. For detection of a certain molecule, the characteristic molecular interaction with its target is used, for example, the sequence-specific hybridization of nucleic acids or the affinity of antigens and antibodies.

Huge quantities of target molecules can be generated by synthetic procedures, for instance by amplification of clones sampled in DNA libraries in a PCR.

There are many methods for coating the spots with the target molecules. Sometimes they are similar to microfabrication processes developed by the electronics industry (photolithography), but it is also possible by, for example, piezoelectric (like an air jet) or micro contact printing. In a few square centimeters one can generate some tens of thousands of these spots.

In the past, by combining biochips with flow cells an increase in the probe number was possible because of the relatively high sample concentration in the small chamber volume and hence by the acceleration of the hybridization reaction. Another advantage of flow systems is that the applicability of different fluorescent dyes with similar quantum efficiency opens up the possibility of competitive hybridization for labeling of different targets (e.g., oligonucleotides of different tissue types), which allows the direct comparison of their relative amounts.

For optical detection, the analyte molecules are labeled with a dye, for instance with a fluorescent label. Because the binding of the analyte to the target is specific (e.g., between DNA strands), the binding position at the biochip can be recorded by a sensitive microarray scanner (CCD) or photomultiplier) with high spatial resolution. Another method is the use of glass fiber bundles which read out the spots of the biochip. Furthermore, the waveguides used are similar to those mentioned earlier. The detected signals are analyzed by specific software with pattern recognition.

Since the beginning of this century, many biochips have become commercially available. Their development boomed particularly after the first encodings of the genome of microorganisms starting in the mid-1990s. The first yeast DNA chip possessed a sequence motive of more than 6000 genes in an area of 18×18 mm. The basic principle of biochips was applied to different target molecules such as biomolecular probes (oligonucleotides, cDNA, DNA, RNA), peptides, proteins, and cells.

Biochips are widely used in biological, molecular biological, and biomedical research and also in pharmaceutical drug screening. By miniaturization, automation, and parallelization the throughput efficiency, sensitivity, and reliability are improved, which is not possible with conventional serial methods of biotechnology. Biochip-based analytical systems are being progressively used in clinical and diagnostic fields, for example, for genotyping, mutation analysis, and infection diagnosis.

Miniaturized Analytical Systems These previously mentioned examples present a cross-section of the versatile opportunities for biosensor and biochip applications. However, biosensors suffer from one important bottleneck: because of their biochemical nature, receptors are very sensitive to extreme ambient conditions such as temperature, pH, high salt concentrations, high viscosity, and so on. For this reason, they are often used in the protected surroundings of fluidic systems [e.g., flow injection analysis (FIA); see Section 6.2.3], which are complete analytical systems allowing preconditioning of the sample.

Generally (and independently of the need for biosensors), as a result of the progress in science and technology, miniaturized analytical systems were developed for several advantageous reasons, among others faster response time and analysis, saving of reagents, lower sample and waste volumes, and the compactness of the analytical system.

Micro electromechanical systems (MEMS) are a consequence of the progress in modern microelectronics in the middle of the twentieth century that made sub-micrometer-sized mechanical structures in silicon wafers possible. Subsequently, a further logical step was the consequent integration of fluidic channels and fluid handling modules (dosing devices, valves, pumps) into miniaturized CMOS-compatible systems, denoted lab-on-a-chip (LOC) [345, 346] (Figure 6.107).

Other materials used are glass, ceramics, and polymers. For example, one of the first systems was a gas chromatograph for environmental application [347, 348]. The dimensions of LOCs are in the square millimeter to square centimeter range, liquid volumes down to picoliters are handled, and single or a few functions are integrated. Although the terminology is not consistent, micro total analysis system (μTAS) is used mostly synonymously, whereas the microfluidic systems [349] further also integrate pretreatment steps of the laboratory to a complete laboratory analysis. In microfluidic systems (Figure 6.108), the samples and fluidic elements are mostly handled serially, except that the different components are supplied to points of reaction. Sophisticated systems are able to process some tens of thousands of samples per day.

Related to the numerous applications, a differentiation and systematic classification into the above-mentioned groups is not always possible – the boundaries are fluid. Such miniaturized analytical devices are applied in a wide range of scientific and technological fields, for example, biotechnology [350], medical research [351–353], centralized laboratory analysis, POCT, and pharmaceutical high-throughput screening (HTS) (see Section 6.2.2.8). Optical systems are integrated advantageously, for example, as sensors [354] or for the manipulation [355] of cells and particles.

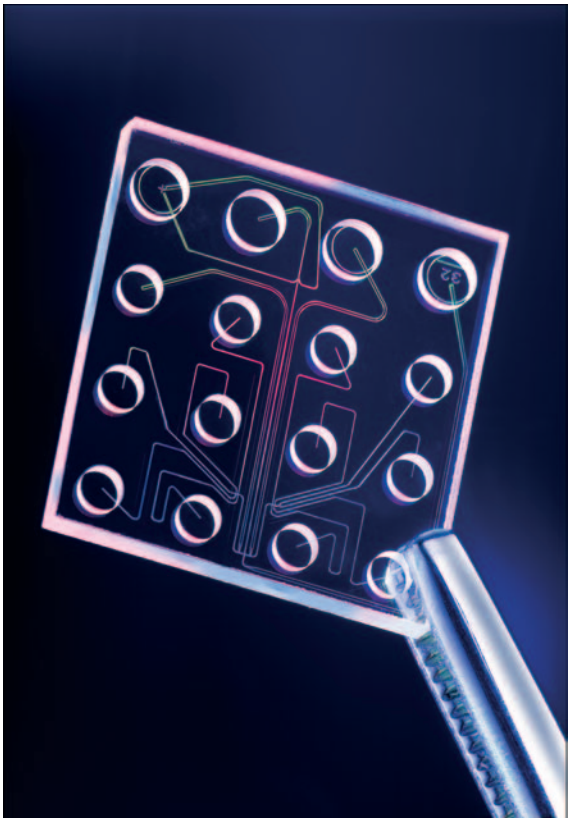

Figure 6.107 Lab-on-a-chip module of Agilent Technologies, Inc. (Waldbronn, Germany) for sample handling, mixing, dilution, electrophoresis, and chromatographic separation. Copyright (2010) Agilent Technologies, Inc. Reproduced with permission.

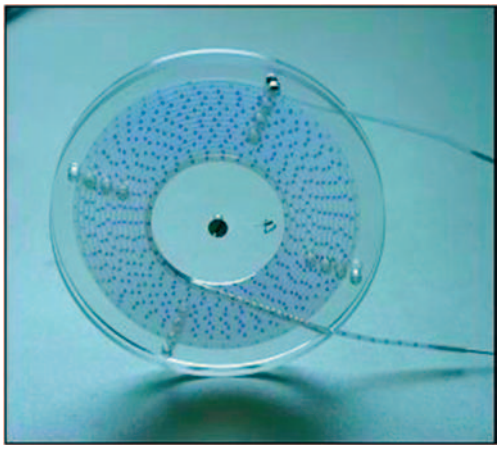

Figure 6.108 Storage coil of a microfluidic system (pipe-based bioreactor, pbb®, Institut für Bioprozess- und Analysenmesstechnik, Heiligenstadt, Germany). Picoliter droplets (stained blue for better visualization) can be used for cell cultivation under sterile conditions.

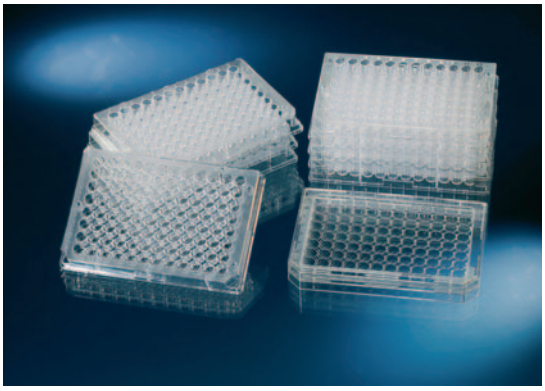

Figure 6.109 Thermo Scientific Nunc 96 Micro Well™ plates. Copyright (2010) Thermo Fisher Scientific. (www.thermofisher.com, 14. 01. 2011)

6.2.2.8 High-Throughput Screening (HTS)

In contrast to microfluidic systems, HTS is a highly parallelized automatic method for liquid handling. Up to millions of samples per day can be processed [for more than 10^5 per day the process is termed ultra-high-throughput screening (UHTS)]. Developed for pharmacological, genetic, and biochemical applications, HTS is mostly used in pharmaceutical research to identify new lead compounds for drugs. The center piece is the microwell or microtiter plate (Figure 6.109) with 96–1536 or more wells in which the assays take place. Especially the interaction of test substances with pathogenic target structures (proteins, cells, microorganisms) is investigated as a (competitive) binding assay with labeled ligands resulting (predominantly) in an optical signal.

HTSs are partly or fully automated systems for liquid handling with statistical data evaluation. Microplates can be supplied by stackers to the system. Corresponding to the highly parallel sample handling and data acquisition, the measurement of the optical signals must also be highly parallelized.

Highly sophisticated microplate readers are filter- and/or monochromator-based detection systems [356] (Figure 6.110) which can address the necessary microplate-based applications to detect the reaction events in the wells. Depending on their special application, they are equipped with suitable optical modules for sample excitation and measurement of sample emission (color intensity, absorbance, polarization, time-resolved fluorescence and luminescence) in the UV–VIS–NIR spectral range. The measuring time necessary is in the range from a few to tens of seconds, depending on the measurement method and the number of wells. However, many variations of detection methods are available, from label-free measurement to the use of imaging of the wells or the whole well plate.

6.2.3
Sample Preparation: Flow Injection Analysis

Parallel to the progress of modern analytical measurement techniques due to technical developments in the twentieth century arose the demand for automation of test routines. However, in general it is important to state that sampling is an often

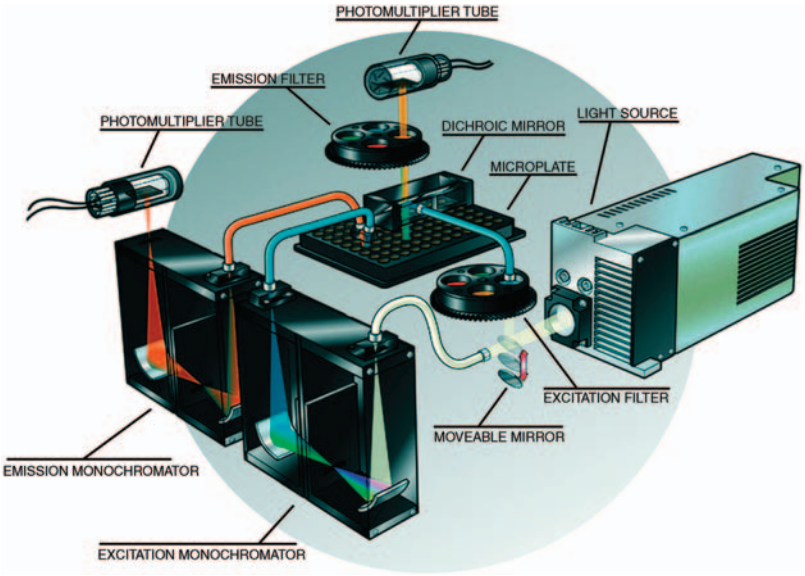

Figure 6.110 Combined filter-based system with monochromator-based optics of the BioTek Synergy 4 Hybrid Multi-Mode Microplate Reader (BioTek, Winooski, VT, USA).

underconsidered field of analytics, above all in process monitoring. In addition to cost efficiency, automation, and some other aspects, a general problem is to separate different samples taken at different times, at different sites, or from different patients for an unambiguous correlation at every later time. Additionally in other applications, it can be important to protect the sample or the process or to condition the sample (e.g., chemical reaction, dilution, preconcentration, and debubbling).

Parallel to autoanalyzers used in clinical laboratories and resulting from their particular disadvantages (use of bubbles for sample segmentation and carryover between the different samples), FIA was developed, defined by three criteria:

1) sample injection into the flow stream by a special injection valve
2) reproducible timing of all processes by computer control
3) controllable dispersion.

A basic FIA system consists of two pumped fluidic lines, the carrier (C) and the reagent (R) line (Figure 6.111) [357]). The sample (S) is injected into the carrier as a plug, undergoing dispersion on the way to the detector and leaving the FIA system as waste (W). A myriad of setups differing from this basic mode are used, depending on the special application of the system.

Dispersion takes place because the center of the flow zone is moving faster than the edges against the wall, as wall drag slows the molecules.

The dispersion coefficient D is defined [358] as the amount by which the chemical signal is reduced by dispersion in an FIA system according to

$$D = \frac{C_0}{C_{\max}} \tag{6.21}$$

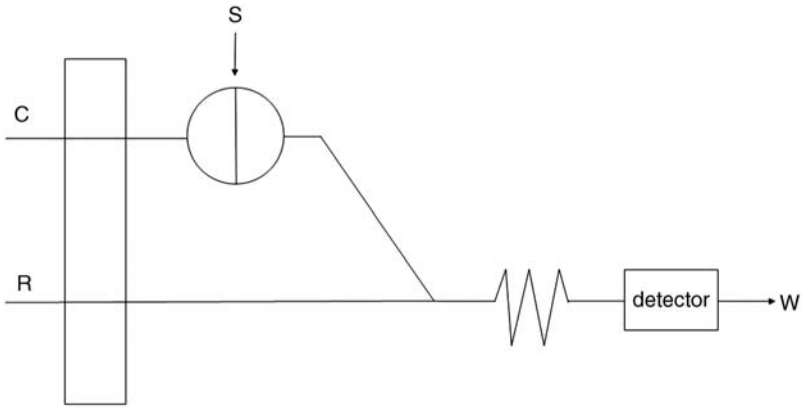

Figure 6.111 Schematic diagram of the basic FIA system.

where C_0 is the maximum signal without dispersion, determined experimentally by filling the FIA system with a pure dye, and C_{max} is the concentration of the same dye injected in a nonreactant carrier flow.

Because of the physical FIA characteristics, it was shown that the flow stream has a reproducible spectrum of corresponding concentrations in the ascending and the descending parts of the curve, depending on the time after injection, that is also at the detection point (if the design of the FIA is not changed). In practice, this so-called gradient method has some advantages, for example, for measuring concentration as a function of the injection time or for providing concentrations beyond the measurement range of the detector.

However, in addition to reproducible sampling, another important advantage of FIA is the usability of numerous highly sophisticated analytical systems as detectors (e.g., high-performance liquid chromatography HPLC). Of course, optical systems can also be coupled to FIA systems, for example, luminometers [359], spectrometers [360, 361], and fluorimeters [362].

6.2.4
Fermentation as a Central Process of Biotechnology

6.2.4.1 General Aspects

Fermenters are bioreactors available with a broad range of special equipment adaptable for every organism, strain, and metabolic product and therefore for different kinds of processes. Fundamentally, depending on their construction, fermenters with mechanical stirrers, pneumatic agitation, and membrane separation between the sensitive biomass and the agitated fermentation broth are used (e.g., aerobic, anaerobic, stirred, air-lift, tower-loop, bubble columns, submerged or adherent cultivation). Fermenters are operated in continuous, batch, and fed-batch mode depending on whether the substrates are supplied and the products are downstreamed.

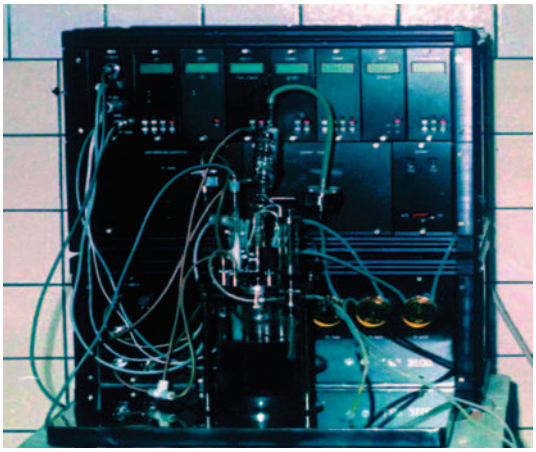

Figure 6.112 Bench-top laboratory-scale stirred-tank fermenter of 1 l volume.

The volume ranges from a few milliliters (mostly laboratory scale and research; see Figure 6.112) to thousands of cubic meters (production scale), depending on the particular process (organism, product, application). By means of today's microsystem technology, it is already possible to use microfluidic-generated droplets in the nanoliter range (Figure 6.113) to cultivate and handle single cells inside for special purposes, for example, testing of individual cells against chemical stress or encapsulation to protect the cells against surrounding media [363, 364]. They are often termed microbioreactors.

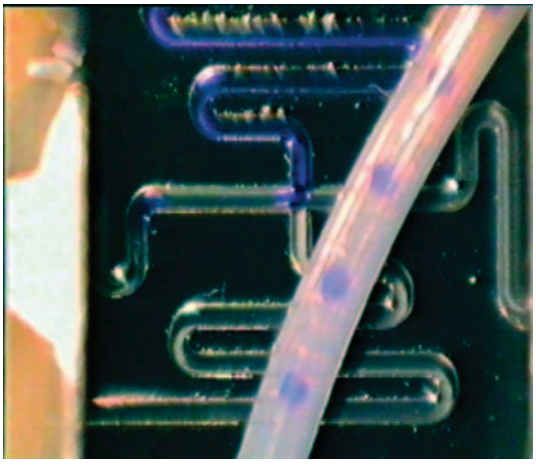

Figure 6.113 Microfluidic system for sterile handling of single or a few cells inside droplets (blue points) of some tens of nanoliters.

Apart from a few exceptions (unsterile processes such as biogas production and waste water treatment), the necessity for sterilization of fermenters to exclude germs in competition with the production organism is an aggravating constraint. The most common method to avoid foreign organisms is heat sterilization by steam at 125 °C. This requires all components to be resistant to steam contact. Often it excludes the in-line application of otherwise reliable analytical systems and sensors and demands sample taking and off-line measurement. The problem can mostly be solved only by help of a sterile interface in a coupling system (sample port, flow systems such as FIA [357, 365]) providing protection against the harsh conditions (on-line mode). Among others (financial pressure, accepted materials), this condition also resulted in the use of disposable bioreactors (characterized by a cultivation chamber or bag made of plastic materials), especially in cell cultivation for the development of biopharmaceutical products [366].

After sterilization and filling with substrate (or vice versa), the fermenter is inoculated with the organism to be cultivated. The system is operated by highly sophisticated digital systems for measurement and control. Different operating modes are usual (batch, fed-batch, repeated fed-batch, semicontinuous, continuous fermentation) depending on the kind of system used (e.g., closed, open, partly cyclic).

As a result of the fermentation process, the fermentation broth contains the desired final product in a mostly very complex substrate. For this reason, treatment steps are normally necessary to isolate the product (e.g., filtration in different forms, centrifugation, digestion, evaporation extraction, crystallization). The monitoring of the product quality and purity is a further field for application of photonic instruments.

In both process development and biotechnological production it is necessary to obtain information about the state of the process by the measurement of characteristic variables. In contrast to more or less calculable chemical processes, in fermentation the biomass and its growth often influence the process unpredictably. For this reason, in addition to temperature, pH, substrate and product concentrations, masses, mass flow rates, and impeller speed, especially biomass concentration, dissolved oxygen, and intermediates are examples of typical process characteristic variables to be taken into consideration.

With respect to measurement, general consideration of the hierarchical signal level in a biotechnological process is necessary. The example of the fermentation process shows how it is obvious to differentiate.

First one can gain information at the level of the substrate mixture. It contains all the necessary feed components (carbon and nitrogen sources, carbon hydrates, organic acids, oxygen, etc.), the inoculated organisms, and its products. The substrate shows physicochemical parameters typical for the process state. Measurement parameters are temperature, pH, ions, dissolved oxygen, glucose, biomass concentration, secondary metabolites, antibiotics, and so on.

The metabolic level is the second item of information. The measurand is the metabolic activity of the microorganism or cell, characterizable by different parameters such as adenosine triphosphate (ATP), NAD(P)H, intermediate metabolites, enzymes, and coenzymes.

Third, subcellular epigenetic level nucleic acids and their components (nucleosides, nucleotides, nucleic acid bases) are observed. Modern biochips have improved the possibilities to measure this group of substances.

The delays between external influences and the measurable reaction (minutes to days) are often too long for effective process control because exertion of the influence is no longer possible. This illustrates the necessity to control biotechnological processes as early as possible after process-changing incidents. The problem of nonsterilizability of most sensors and measuring systems and the resulting necessity to use sampling ports and/or flow systems or to measure off-line magnify the problem.

6.2.4.2 **Fermentation Control**

Measurement systems, probes, and sensors are available for all three hierarchical signal levels. With respect to the content of this book, only examples of sterilizable and in-line or on-line coupled systems [367] are mentioned here.

Biomass is an important parameter because it allows insight to be gained into the process by the activity of cell growth and the optimization of the process. Different systems are commercially available, from electrical impedance spectrometers to especially optical probes. Probably the most widespread are sterilizable turbidimetric probes for real-time monitoring of cell growth, measuring the absorption in the NIR spectrum and calibrated with the cell number or optical density of laboratory analyses. By varying the optical pathlength, a wider concentration range can be measured. The biomass concentration is directly monitored in grams per liter, percent dry matter, or optical density (OD) [368]. This approach is used for active control of the fermentation. Another example if the use of optical detection at this level is nephelometric biomass detection by scattered light measurement [369].

Recently, new emphasis has been placed on the use of optical oxygen sensors, but they are temperature sensitive and not sterilizable. In the biotechnological and medical fields, the measurement of the oxygen partial pressure by these sensors is a standard diagnostic tool (e.g., for blood and tissue). One reason for the increasing interest in optical sensors is the ready availability of fiber-optic technologies and of oxygen-sensitive dyes. These sensors use oxygen-sensitive molecules immobilized in oxygen-permeable and nonpolar polymers. Oxygen quenches the luminescence or lifetime of numerous dyes. In this way, the intensity of the emitted light and the relaxation to the ground state depend on the oxygen concentration [370, 371]. The probes of dissolved oxygen measurement in the parts per million (milligrams per liter) range show percentage-level accuracy, for example [372].

On-line monitoring of intracellular proteins and enzymes is an important factor with regard to fermentation process development and optimization. Disintegration of cells under sterile conditions is required. The necessary sample preparation and disintegration of cells (e.g., by ultrasonics) under sterile conditions can be performed by FIA. Using special reaction protocols, for example, the quantification of intracellular lactate dehydrogenase (LDH) during fermentation is possible [373]. LDH oxidizes lactate to pyruvate enzymatically with simultaneous reduction of NAD^+ to NADH. Nicotinamide adenine dinucleotide (NADH, oxidized as NAD^+, reduced as

NADH) is a coenzyme of living cells and is involved in redox reactions as an electron carrier. However, NADH itself also presents an example of measurement of fluorescent substances at the metabolic level. The oxidized and reduced states differ in their fluorescence (NADH is fluorescent at 460 nm, NAD^+ is nonfluorescent) and the fluorescence changes with binding to protein [374]. Despite the option of coupling a fluorimeter with FIA, in the past several attempts have been made to develop *in situ* fluorosensors [375].

Another example is the measurement of ATP concentration. All living cells contain intracellular ATP needed for the regulation of stored metabolic energy, for the maintenance of enzyme systems and for biosynthesis of cellular constituents during all phases of growth. In dead cells, ATP is broken down by autolysis within a few minutes. ATP can therefore be used as a measure of microbial biomass. Linear relationships have been found between intracellular ATP levels and the total number of colony-forming units (CFUs) with bacteria and with yeast. In addition to the more conventional measurement of the intracellular ATP level mediated by the luciferin–luciferase reaction and detection with an (FIA-coupled) luminometer [376], in other reports [377, 378] microorganisms were genetically modified, for example, by inserting cDNA for firefly luciferase resulting in specific activity of luciferase during different growth phases due to ATP utilization in the presence of added D-luciferin. Using fiber optics, the luminescent light emitted inside the fermenter is guided to a photometer.

6.2.4.3 **Photobioreactors**

About 400 000 different algae populate very diverse biotopes on earth. Worldwide about 16 million tonnes of algae were produced in 2007 [379] and processed into foodstuffs, feeds, cosmetics and fertilizers. By use of light, chlorophyll of phototropic microorganisms such as algae and cyanobacteria in photosynthesis produce energy-rich substances and biomass from CO_2.

Bioenergy from biomass can contribute to solving the global energy problem. Biomass can be converted into biofuel (fuel of the third generation), for example, by alcoholic fermentation. Their light conversion effectiveness differs but in general especially microalgae offer a 10-fold higher biomass yield than terrestrial plants.

At present, open land and offshore systems for algae production dominate. However, various different types of closed photobioreactors have been developed by numerous companies and research institutions [380]. They provide an artificial environment for the chemical conversion on the scale of liters to cubic meters. Attempts have also been made to use micro system technology for this process [381]. In addition to the availability of carbon dioxide in huge quantities (1.8 tons for 1 ton of biomass), one of the technical problems is the optimization of photobioreactor design with respect to the light regime necessary for optimal growth of algae [382]. The general objective is to avoid artificial lighting. Because absorption takes place according to the Lambert–Beers law, the light intensity decreases exponentially with depth and with the algae concentration. Hence flat planar or tubular systems of different types (e.g., flat plate, airlift, column; see Figure 6.114 [383]) and materials (e.g., glass, PVC foil) are mostly used.

Figure 6.114 Column photobioreactor (Hielscher Ultrasonics GmbH, Teltow, Germany).

6.2.5
Optical Trap/Optical Tweezers

Already in the 1970s lasers were used to trap various atoms and particles. The first optical traps used visible light. Starting in the mid-1980s, optical traps were used to trap biological particles. Arthur Ashkin [384, 385] is thought to be the pioneer of optical tweezers. His group at AT&T Bell Laboratories trapped individual viruses and *E. coli* bacteria as early as 1985. In a study performed in 1987, the viruses were able to resist the power created by a 1064 nm laser, whereas the *E. coli* bacteria always exploded at around 100 mW. In order to reduce biological damage, using IR lasers in the 780–950 nm range proved to be useful, especially for bacteria which under these conditions can survive the trap for hours without damage [386].

Microscopic objects are moved in the laser light in the direction of the optical axes. The change in direction of the light is connected with a change in the momentum transferred to the biological cell. In Figure 6.115, in partial beam "a" the light has the momentum F_a (inwards) out of the whole beam, and in partial beam "b" the momentum F_b (outwards) is effective. In a homogeneous laser profile this would result in a movement in the beam direction. Because the field is inhomogeneous (see the laser profile), the resulting force is directed in the direction of the beam center.

In principle, light acts as force on an object (impact of photon and object, like a pressure model in a gas cell). For an illustration of the scale of the effect, two examples can be given:

- A car in sunlight is ~1 mg (better millipond) heavier than in the shadow.
- The tail of a comet is "pushed away" on approaching to the Sun.

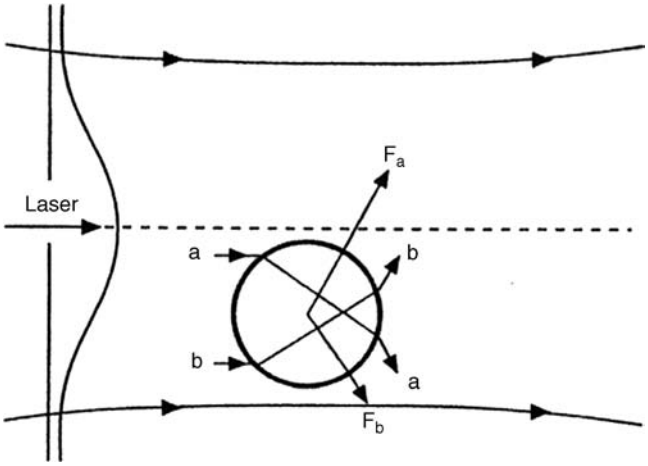

Figure 6.115 Scheme of laser irradiation of a spherical particle and the resulting momentum (F_i) as a function of the beam intensity (a larger than b).

The force of a laser F with power P in watts is given by

$$F = \gamma P/c \tag{6.22}$$

where γ is the gravity constant and c is the velocity of light.

If laser light of 1 W is focused on to a cell of 10 μm diameter, a pressure of ~5 bar acts on the cell. Due to its small mass, the cell will be accelerated to extremely high speeds (700 000 times the acceleration due to gravity). The acceleration is connected with the pressure in the following way:

$$p = \frac{F}{A} = \frac{m \cdot a}{A}. \tag{6.23}$$

Hence the velocity is

$$v = a \cdot t = \frac{p \cdot A \cdot t}{m}. \tag{6.24}$$

The speed of the acceleration cell results in Equation 6.24. Taking a 100 kW laser instead of a 1 W laser will result in catapulting of microscopic objects. In such cases, the speed can be as high as 1one-tenth of the speed of light [387].

6.2.5.1 Basic Scheme of Laser Tweezers and Micromanipulation

The realization of laser tweezers is achieved by a combination of a UV laser (diffraction limited) with a powerful NIR laser. In normal cases, this pair consists of an Nd:YAG laser (as the NIR laser) and an N_2 laser (or even better is an excimer laser) as the UV laser; in some cases green lasers are also used. The NIR laser acts as an optical tweezer and due to the wavelength has a small (or vanishing) absorption with a large penetration depth. Whereas the UV laser acts as an optical treatment

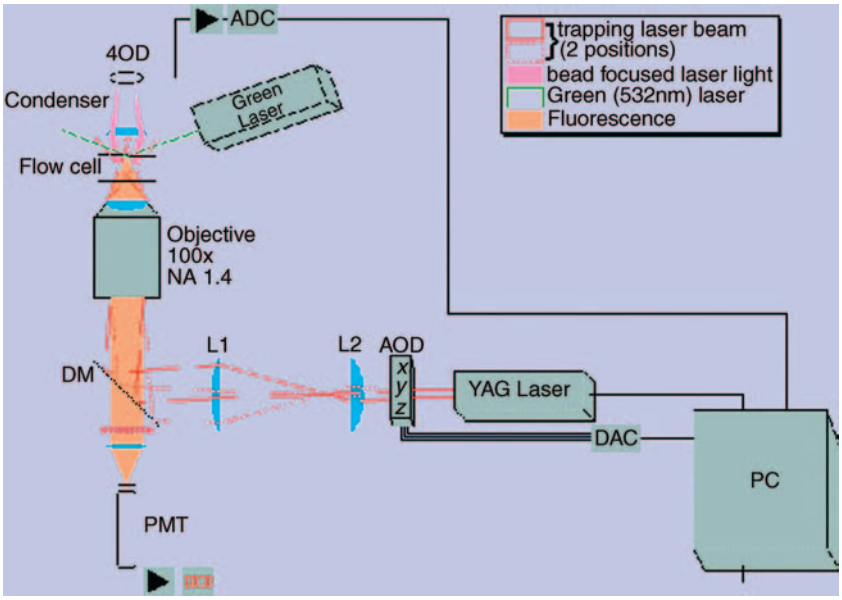

Figure 6.116 Scheme of optical tweezers [3].

(cutting) tool, UV light is absorbed by the cell. Short, powerful pulses lead to extremely high local temperatures. Of decisive importance is that the surrounding tissue is not or only marginally damaged by the laser energy. The requirements for achieving this effect are the possibility of high focusability and an excellent beam profile with low thermal diffusion effects [388].

The basic equipment is an optical microscope (e.g., Zeiss Axiovert) with UV lenses as shown in Figure 6.116. Via the in-coupling of the illumination light, the two laser beams are also coupled in. With the microscope the image is zoomed into the object cell and the laser tweezers and the UV laser are aligned with respect to the object. The object is captured, the UV laser vaporizes cell parts, drills microholes, and destabilizes the cell walls, as shown in Figure 6.117.

6.2.5.2 Applications of Optical Tweezers

Optical tweezers have been used since 1987 for medical purposes. For example, the manipulation of red blood cells (see Figure 6.118) can be performed by rotating them. They can also be stretched, moved, and even dissected using an optical tweezer/scalpel.

Helical modes of light can be focused into toroidal optical traps known as optical vortices, which are capable of localizing and applying torques to small volumes of matter. Measurements of optical vortices created with dynamic holographic optical tweezers (see Figure 6.119) reveal an unsuspected dependence of their structure and angular momentum flux on their helicity. There is novel optical ratchet potential in practical optical vortices [389].

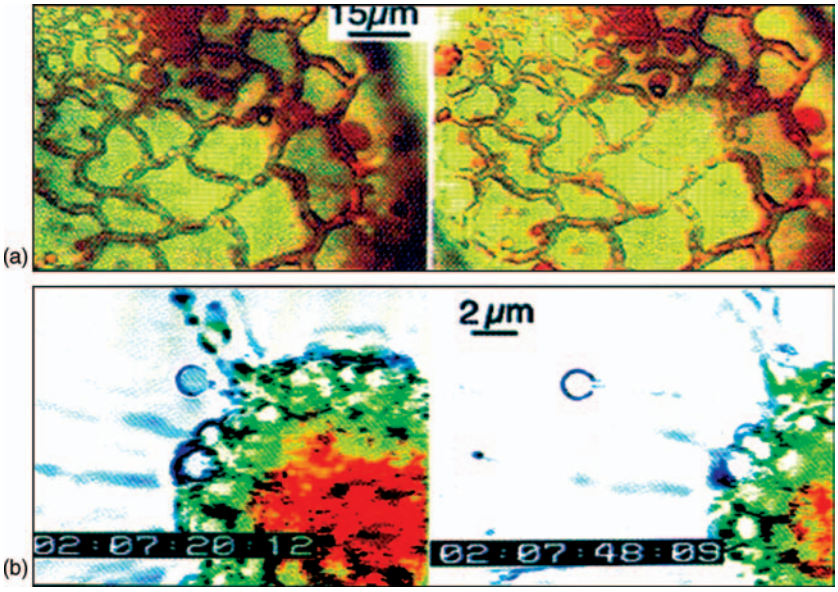

Figure 6.117 (a) Modification of the surface structure of a lily pollen. The resolution of the laser beam is $>1\,\mu m$, so it is possible to modify the structure of the pollen surface without influencing the cell wall. (b) Movement of subcellular structures through optical tweezers in unopened cells of the alga *Pyrocystis noctiluc*. The cell is irradiated from below through the cell wall (no absorption) and subcellular structures at the opposite wall are accelerated so strongly that they are catapulted out of the cell and can be caught in microreaction vessels and prepared as single subcellular structures (courtesy of K. O. Greulich, Leibniz-Institut für Altersforschung, Jena).

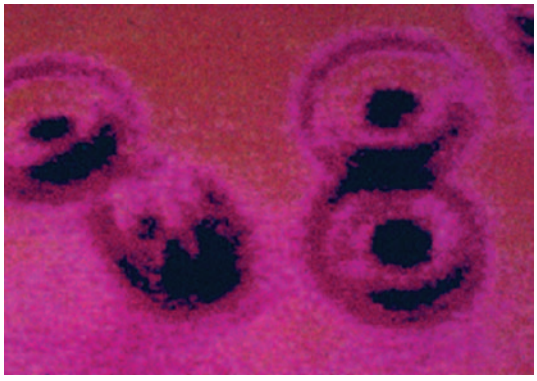

Figure 6.118 Red blood cells manipulated with optical tweezers [389].

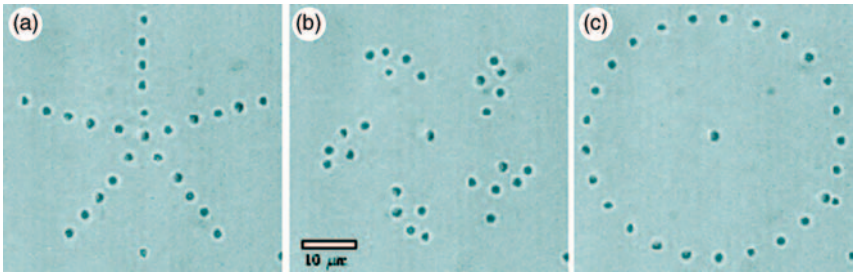

Figure 6.119 A pentagonal pattern of 26 colloidal silica spheres 0.99 μm in diameter is transformed into a circle using dynamic holographic optical tweezers. (a) The original configuration; (b) after 16 steps; (c) the final configuration after 38 steps of illumination [390].

Beams of light with helical wave fronts focus to rings, rather than points, and also carry orbital angular momentum that they can transfer to illuminated objects. When focused strongly enough, such helical modes form toroidal optical traps, whose properties present novel opportunities for scientific research and technological applications. For example, optical vortices should be ideal actuators for MEMS, and arrays of optical vortices have shown a promising ability to assemble colloidal particles into mesoscopic pumps for microfluidic systems.

Further applications of optical tweezers are shown in Figure 6.120, where the fusion of two lymphoblast cells after perforation of the cells by a strong UV laser and transportation of one of the cells via laser tweezer to another is shown in (a). In (b), laser-supported fertilization is shown where the optical tweezer guides the sperm cell to the perforated egg cell. In (c), laser microcutting of a chromosome is depicted where the two chromosomes indicated an arrows are cut along their long axes to separate the two chromatides [391].

The list of possible applications of optical tweezers could in principle be almost infinite. Optical tweezers can be calibrated for position measurements because of the 3D force is quantitative. Therefore, it is possible to measure movements and forces generated by single motor proteins.

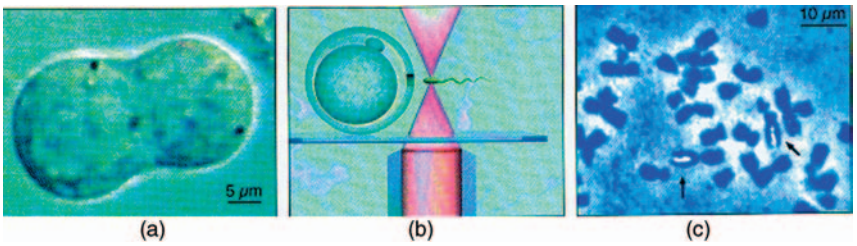

Figure 6.120 (a) Fusion of a long-living lymphoblast cell with a B-cell lymphoblast of a mouse for antibody production. (b) Principle of laser-supported fertilization: the egg cell is already perforated and the optical tweezer/trap is used to guide the sperm cell to the entrance of the perforation channel. (c) *In vitro* laser microcutting of a chromosome: two chromosomes are cut along their long axes to separate the two chromatides (courtesy of K. O. Greulich, Leibnitz-Institut für Altersforschung, Jena).

References

1 Eichler, J. and Seiler, T. (1991) *Lasertechnik in der Medizin*, Tuebner Studienbücher Physik, Berlin.
2 Eichler, J. and Eichler, H.-J. (1998) *Laser: Grundlagen, Systeme, Anwendungen*, Springer, Berlin.
3 König, K. (2000) Multiphoton microscopy in life sciences, *J. microsc.*, **200** (Pt2), 83–104.
4 Niemz, M.H. (1996) *Laser–Tissue Interactions*, Springer, Berlin.
5 Kar, H. and Ringelhan, H. (1992) grundlagen und Technik der Photoablation, *Advances in Laser Medicine Series*, No. **6**, ecomed.
6 Wilson, B.C. and Patterson, M.S. (2008) The physics, biophysics and technology of photodynamic therapy. *Phys. Med. Biol.*, **53** (9), R61–R109.
7 Waynant, R.W. (2001) *Lasers in Medicine*, CRC Press, Boca Raton, FL.
8 Srinivasan, R., Braren, B., and Casey, K.G. (1990) Ultraviolet laser ablation and decomposition of organic materials. *Pure Appl. Chem.*, **62**, 1581–1584.
9 Free-Press-Release Inc. The Endoscopy Market Research Review, http://www.free-press-release.com/news/200904/1239873767.html. 2009, (11 January 2011).
10 Given Imaging Ltd. Esophageal Capsule Endoscopy, http://www.givenimaging.com. 2009, (11 January 2011).
11 DALSA Corporation. Image Sensor Architectures for Digital Cinematography, www.dalsa.com. 2009, (11 January 2011).
12 Natalin, R.A. and Landman, J. (2009) Where next for the endoscope? *Nat. Rev. Urol.*, **6**, 622–628.
13 Theuwissen, A.J.P. (1995) *Solid-State Imaging with Charge-Coupled Devices*, Kluwer, Dordrecht.
14 Yang, D.X.D., El Gamal, A., Fowler, B., and Tian, H. (1999) A 640×512 CMOS image sensor with ultra wide dynamic range floating-point pixel-level ADC. *IEEE J. Solid State Circuits*, **34**, 1821–1834.
15 Nelson, L.J. Micro-Imaging Solutions, http://www.advancedimagingpro.com/print/Advanced-Imaging-Magazine/Advances-in-Endoscopy/1$5670, Cygnus Business Media. 2009, (11 January 2011).
16 Galli, J., Cammarota, G., Rigante, M., De Corso, E., Parrilla, C., Passali, G.C., Almadori, G., and Paludetti, G. (2007) High resolution magnifying endoscopy: a new diagnostic tool also for laryngeal examination? *Acta Otorhinolaryngol. Ital.*, **27** (5), 233–236.
17 Mine, T. (2006) The role of magnifying endoscopy in the diagnosis of early gastric carcinoma. *J. Gastroenterol.*, **41** (4), 397–398.
18 American Cancer Society. Capsule Endoscopy, http://www.cancer.org/docroot/PED/content/PED_2_3X_Endoscopy.asp. 2009, (11 January 2011).
19 Baillie, J. (2005) Advances in endoscopy. *Gastroenterol. Hepatol.*, **1** (2), 105–106.
20 Van Gossum, A., Munoz-Navas, M., Fernandez-Urien, I., Carretero, C., Gay, G., Delvaux, M., Lapalus, M.G., Ponchon, T., Neuhaus, H., Philipper, M., Costamagna, G., Riccioni, M.E., Spada, C., Petruzziello, L., Fraser, C., Postgate, A., Fitzpatrick, A., Hagenmuller, F., Keuchel, M., Schoofs, N., and Deviere, J. (2009) Capsule endoscopy versus colonoscopy for the detection of polyps and cancer. *N. Engl. J. Med.*, **361** (3), 264–270.
21 Bhoi, D.B. Endoscopy, http://www.authorstream.com/Presentation/drdhirenvet-241392-endoscopy-dr-dhiren-bhoi-vardhari-ta-lunawada-dist-panchmahals-gujarat-india-education-ppt-powerpoint/, authorSTREAM. 2009, (11 January 2011).
22 Kramme, R. (2007) *Medizintechnik Verfahren-System-Informationsverarbeitung*, Springer, Berlin.
23 DaCosta, R.S., Wilson, B.C., and Marcon, N.E. (2005) Optical techniques for the endoscopic detection of dysplastic colonic lesions. *Curr. Opin. Gastroenterol.*, **21** (1), 70–79.
24 Ell, C. (2003) Improving endoscopic resolution and sampling: fluorescence techniques. *Gut*, **52** (Suppl 4), iv30–iv33
25 Stepp, H., Sroka, R., and Baumgartner, R. (1998) Fluorescence endoscopy of

gastrointestinal diseases: basic principles, techniques, and clinical experience. *Endoscopy*, **30** (4), 379–386.
26 Falk, G.W. (2009) Autofluorescence endoscopy. *Gastrointest. Endosc. Clin. N. Am.*, **19** (2), 209–220.
27 Endlicher, E., Knuechel, R., Hauser, T., Szeimies, R.M., Scholmerich, J., and Messmann, H. (2001) Endoscopic fluorescence detection of low and high grade dysplasia in Barrett's oesophagus using systemic or local 5-aminolaevulinic acid sensitisation. *Gut*, **48** (3), 314–319.
28 PENTAX Corp. Konfokale Endomikroskopie – Das Verborgene Sichtbar Machen, http://www.pentax.de/de/media/8ed15928970c8c93cef9c4e0018cdd19/3618_Endomicro_DE_WEB.pdf. 2009 (11 January 2011).
29 Scouten, C.W. Deep Brain Visualisation and Surgery in Animal Research, http://www.leica-microsystems.com/press-media/newsletters/research-resolution/march-2009-test/deep-brain-visualisation-and-surgery-in-animal-research/, Leica Microsystems. 2009, (11 January 2011).
30 Singh, S. and Thakur, M. (2009) Diagnosis of recurrent lung cancer in the mediastinum using endosonographically guided fine-needle aspiration biopsy. *J. Clin. Ultrasound*, **37** (4), 230–232.
31 Goetz, M. and Kiesslich, R. (2009) Advanced imaging of the gastrointestinal tract: research vs. clinical tools? *Curr. Opin. Gastroenterol.*, **25** (5), 412–421.
32 Wallace, M.B., Wax, A., Roberts, D.N., and Graf, R.N. (2009) Reflectance spectroscopy. *Gastrointest. Endosc. Clin. N. Am.*, **19** (2), 233–242.
33 Hurlstone, D.P. Early Colorectal Cancer Detection with Confocal Endomicroscopy and Other Novel Endoscopic Techniques, http://www.touchgastroenterology.com/files/article_pdfs/gastro_7846, Business Briefings, Ltd. 2007 (11 January 2011).
34 Muto, M., Horimatsu, T., Ezoe, Y., Morita, S., and Miyamoto, S. (2009) Improving visualization techniques by narrow band imaging and magnification endoscopy. *J. Gastroenterol. Hepatol.*, **24** (8), 1333–1346.
35 Huang, Z., Teh, S.K., Zheng, W., Mo, J., Lin, K., Shao, X., Ho, K.Y., Teh, M., and Yeoh, K.G. (2009) Integrated Raman spectroscopy and trimodal wide-field imaging techniques for real-time *in vivo* tissue Raman measurements at endoscopy. *Opt. Lett.*, **34** (6), 758–760.
36 Cahill, R.A., Asakuma, M., Trunzo, J., Schomisch, S., Wiese, D., Saha, S., Dallemagne, B., Marks, J., and Marescaux, J. (2009) Intraperitoneal virtual biopsy by fibered optical coherence tomography (OCT) at natural orifice transluminal endoscopic surgery (NOTES). *J. Gastrointest. Surg.*, **14** (4), 732–738.
37 Zhou, J., Das, A., Li, F., and Li, B. (2008) Circular Generalized Cylinder Fitting for 3D Reconstruction in Endoscopic Imaging Based on MRF, 9th IEEE Computer Society Workshop on Mathematical Methods in Bio-medical Image Analaysis MMBiA 08, 1–8. (IEEE DOI Link 0806).
38 Caversaccio, M., Garcia Giraldez, J., Thoranaghatte, R., Zheng, G., Eggli, P., Nolte, L.P., and Gonzalez Ballester, M.A. (2008) Augmented reality endoscopic system (ARES): preliminary results. *Rhinology*, **46** (2), 156–158.
39 Lasher, R.A., Hitchcock, R.W., and Sachse, F.B. (2009) Towards modeling of cardiac micro-structure with catheter-based confocal microscopy: a novel approach for dye delivery and tissue characterization. *IEEE Trans. Med. Imaging*, **28** (8), 1156–1164.
40 Goetz, M. and Wang, T.D. (2010) Molecular imaging in gastrointestinal endoscopy. *Gastroenterology*, **138** (3), 828–833.
41 Allen, J. (2007) Photoplethysmography and its application in clinical physiological measurement. *Physiol. Meas.*, **28** (3), R1–R39.
42 Hertzman, A.B. and Spealman, C.R. (1937) Observations on the finger volume pulse recorded photoelectrically. *Am. J. Physiol.*, **119**, 334–335.
43 Murray, W.B. and Foster, P.A. (1996) The peripheral pulse wave: information overlooked. *J. Clin. Monit.*, **12** (5), 365–377.

44 Hertzman, A.B. and Randall, W.C. (1948) Regional differences in the basal and maximal rates of blood flow in the skin. *J. Appl. Physiol.*, **1** (3), 234–241.

45 Kamal, A.A., Harness, J.B., Irving, G., and Mearns, A.J. (1989) Skin photoplethysmography – a review. *Comput. Methods Programs Biomed.*, **28** (4), 257–269.

46 Naslund, J., Pettersson, J., Lundeberg, T., Linnarsson, D., and Lindberg, L.G. (2006) Non-invasive continuous estimation of blood flow changes in human patellar bone. *Med. Biol. Eng. Comput.*, **44** (6), 501–509.

47 Jones, D.P. (1987) Medical electro-optics: measurements in the human microcirculation. *Phys. Technol.*, **18**, 79–85.

48 Gordy, E. and Drabkin, D.L. (1957) Spectrophotometric studies. XVI. Determination of the oxygen saturation of blood by a simplified technique, applicable to standard equipment. *J. Biol. Chem.*, **227** (1), 285–299.

49 Murray, A. and Marjanovic, D. (1997) Optical assessment of recovery of tissue blood supply after removal of externally applied pressure. *Med. Biol. Eng. Comput.*, **35** (4), 425–427.

50 Anderson, R.R. and Parrish, J.A. (1981) The optics of human skin. *J. Invest. Dermatol.*, **77** (1), 13–19.

51 Webster, J.G. (1997) *Design of Pulse Oximeters*, Institute of Physics Publishing, Bristol.

52 Kyriacou, P.A. (2006) Pulse oximetry in the oesophagus. *Physiol. Meas.*, **27** (1), R1–R35.

53 Penaz, J. (1973) Photoelectric measurements of blood pressure, volume and flow in the finger. In 10th Int. Conf. Med. Biol. Eng, Dresden, Germany, p. 104.

54 Imholz, B.P., Wieling, W., van Montfrans, G.A., and Wesseling, K.H. (1998) Fifteen years experience with finger arterial pressure monitoring: assessment of the technology. *Cardiovasc. Res.*, **38** (3), 605–616.

55 Voss, A., Schroeder, R., Truebner, S., Goernig, M., Figulla, H.R., and Schirdewan, A. (2007) Comparison of nonlinear methods symbolic dynamics, detrended fluctuation, and Poincaré plot analysis in risk stratification in patients with dilated cardiomyopathy. *Chaos*, **17** (1), 015120.

56 Malberg, H., Bauernschmitt, R., Voss, A., Walther, T., Faber, R., Stepan, H., and Wessel, N. (2007) Analysis of cardiovascular oscillations: a new approach to the early prediction of pre-eclampsia. *Chaos*, **17** (1), 015113.

57 Bar, K.J., Boettger, M.K., Berger, S., Baier, V., Sauer, H., Yeragani, V.K., and Voss, A. (2007) Decreased baroreflex sensitivity in acute schizophrenia. *J. Appl. Physiol.*, **102** (3), 1051–1056.

58 Heck, A.F. and Hall, V.R. (1975) An on-line system for measurement of opacity pulse propagation times in atraumatic screening of patients for occlusive vascular disease. *Med. Instrum.*, **9** (2), 88–92.

59 Osmundson, P.J., O'Fallon, W.M., Clements, I.P., Kazmier, F.J., Zimmerman, B.R., and Palumbo, P.J. (1985) Reproducibility of noninvasive tests of peripheral occlusive arterial disease. *J. Vasc. Surg.*, **2** (5), 678–683.

60 Simonson, E., Koff, S., Keys, A., and Minckler, J. (1955) Contour of the toe pulse, reactive hyperemia, and pulse transmission velocity: group and repeat variability, effect of age, exercise, and disease. *Am. Heart J.*, **50** (2), 260–279.

61 Erts, R., Spigulis, J., Kukulis, I., and Ozols, M. (2005) Bilateral photoplethysmography studies of the leg arterial stenosis. *Physiol. Meas.*, **26** (5), 865–874.

62 Spigulis, J. (2005) Optical noninvasive monitoring of skin blood pulsations. *Appl. Opt.*, **44** (10), 1850–1857.

63 Oliva, I., Ipser, J., Roztocil, K., and Guttenbergerova, K. (1976) Fourier analysis of the pulse wave in obliterating arteriosclerosis. *Vasa*, **5** (2), 95–100.

64 Allen, J. and Murray, A. (1993) Development of a neural network screening aid for diagnosing lower limb peripheral vascular disease from photoelectric plethysmography pulse waveforms. *Physiol. Meas.*, **14** (1), 13–22.

65 Allen, J., Oates, C.P., Lees, T.A., and Murray, A. (2005) Photoplethysmography detection of lower limb peripheral arterial occlusive disease: a comparison of pulse timing, amplitude and shape characteristics. *Physiol. Meas.*, **26** (5), 811–821.

66 Allen, J., Overbeck, K., Stansby, G., and Murray, A. (2006) Photoplethysmography assessments in cardiovascular disease. *Meas. Control.*, **39**, 80–83.

67 Diehm, C., Schuster, A., Allenberg, J.R., Darius, H., Haberl, R., Lange, S., Pittrow, D., von Stritzky, B., Tepohl, G., and Trampisch, H.J. (2004) High prevalence of peripheral arterial disease and co-morbidity in 6880 primary care patients: cross-sectional study. *Atherosclerosis*, **172** (1), 95–105.

68 McDermott, M.M., Criqui, M.H., Liu, K., Guralnik, J.M., Greenland, P., Martin, G.J., and Pearce, W. (2000) Lower ankle/brachial index, as calculated by averaging the dorsalis pedis and posterior tibial arterial pressures, and association with leg functioning in peripheral arterial disease. *J. Vasc. Surg.*, **32** (6), 1164–1171.

69 Belcaro, G., Veller, M., Nicolaides, A.N., Cesarone, M.R., Christopoulos, D., DeSanctis, M.T., Dhanjil, S., Geroulakos, G., Griffin, M., Fisher, C., Helmis, E., Gizzi, G., Tegos, T., Lennox, A., Incandela, L., Labropoulos, N., Laurora, G., Leon, M., Malouf, M., Myers, K., Ramaswami, G., Szendro, G., Vasdekis, S., Venniker, R., and Fernandes e Fernandes, J. (1998.) Noninvasive investigations in vascular disease. St Mary's Fellows. ISVI (Italian Society for Vascular Investigations). *Angiology*, **49** (9), 673–706.

70 Incze, A., Lazar, I., Abraham, E., Copotoiu, M., and Cotoi, S. (2003) The use of light reflection rheography in diagnosing venous disease and arterial microcirculation. *Rom. J. Intern. Med.*, **41** (1), 35–40.

71 Beckert, S., Witte, M.B., Konigsrainer, A., and Coerper, S. (2004) The impact of the Micro-Lightguide O2C for the quantification of tissue ischemia in diabetic foot ulcers. *Diabetes Care*, **27** (12), 2863–2867.

72 Fertmann, J.M., Arbogast, H., Sajzewa, E., Tarabichi, A., Liner, W.D., Land, W., and Hoffmann, J.N. (2003) Measurement of regional perfusion and oxygen saturation during human simultaneous pancreas–kidney transplantation – correlation with intravital microscopy (Poster, 11th ESOT Congress 2003 & 13th ETCO Congress 2003).

73 Junqueira, L.C. and Carneiro, J. (2005) *Basic Histology: Text and Atlas*, 11th edn, McGraw-Hill, New York.

74 Retina Vitreous Center PA. Vitrectomy, http://www.retinavitreouscenter.com/procedures_vitrectomy.html. 2010 (11 January 2011).

75 Grierson, I. (2000) *The Eye Book: Eyes and Eye Problems Explained*, Liverpool University Press, Liverpool.

76 Atchison, D.A. and Smith, G. (2000) *Optics of the Human Eye*, Butterworth-Heinemann, Edinburgh, pp. 3ff.

77 Galloway, N.R., Amoaku, W.M.K., Galloway, P.H., and Browning, A.C. (2006) *Common Eye Diseases and Their Management*, 3rd edn, Springer, London.

78 McCann, J.A.S. (2008) *Nursing*, Interpreting signs and symptoms. Lippincott Williams & Wilkins, 546–548.

79 Alcon Laboratories, Inc. Learn About Cataracts: Facts, Stats, and FAQs, http://www.cataractsurgery.com/docs/CS-PDF_FactsStatsFAQ.pdf. 2010 (11 January 2011).

80 Steinert, R.F. (2004) *Cataract Surgery: Techniques, Complications and Management*, 2nd edn, Elsevier, Philiadelphia, PA.

81 Alcon Laboratories, Inc. Learn About Cataracts. What are Cataracts?, http://www.cataractsurgery.com/learn-about-cataracts/what-are-cataracts.asp. 2010 (11 January 2011).

82 Griffith, H.W., Moore, S., and Yoder, K. (2006) *Complete Guide to Symptoms, Illness and Surgery*, 5th edn, Penguin Group, New York.

83 Falvo, D.R. (2005) *Medical and Psychosocial Aspects of Chronic Illness and Disability*, 3rd edn, Jones and Bartlett Publishers, Sudbury, MA.

84 Lang, G.K. and Gareis, O. (2007) *Ophthalmology: a Pocket Textbook*

Atlas, 2nd edn, Georg Thieme, Stuttgart.
85 Carl Zeiss Meditec AG. SL 130 Slit Lamp: Maximum Quality for Optimum Performance, http://www.meditec.zeiss.com/88256DE3007B916B/0/002D7D01B318A333882571B1005DED1A/$file/sl130_en-final.pdf. 2010 (11 January 2011).
86 Henretig, F.M. and King, C. (1997) *Textbook of Pediatric Emergency Procedures*, Williams & Wilkins, Baltimore, MD.
87 Carl Zeiss Meditec AG. ATLAS Corneal Topography System: Simply Accurate For Maximum Productivity, http://www.meditec.zeiss.com/88256DE3007B916B/0/D9D6543C9F4DACE88825763F006610EA/$file/atlas_brochure_atl_1587revb.pdf. 2010 (11 January 2011).
88 Fung, M.W., Raja, D., Fedor, P., and Kaufman, S.C. Corneal Topography and Imaging, http://www.meditec.zeiss.com/88256DE3007B916B/0/D9D6543C9F4DACE88825763F006610EA/$file/atlas_brochure_atl_1587revb.pdf, Medscape. 2009 (11 January 2011).
89 Berwick Eye Centre Pty Ltd. Cataract Surgery, http://www.berwickeye.com.au. 2010 (11 January 2011).
90 Carl Zeiss Meditec AG. ATLAS Review Software: Greater Productivity Through Connectivity, http://www.meditec.zeiss.com/88256DE3007B916B/0/818357754D88D1BE882576620078AB5E/$file/atlas_reviewsoftwareds_atl_2492.pdf. 2009 (11 January 2011).
91 Agarwal, A. (2006) *Step by Step Corneal Topography*, 2nd edn, Japee Brothers Medical Publisher, New Delhi.
92 Wang, M. (2006) *Corneal Topography in the Wavefront Era: a Guide for Clinical Application*, SLACK, Thorofare, NJ.
93 Purves, D., Augustine, G.J., Fitzpatrick, D., Katz, L.C., LaMantia, A.-S., McNamara, J.O., and Williams, S.M. (2001) *The Retinotopic Representation of the Visual Field. Neuroscience*, vol. **2**, Sinauer Associates, Sunderland, MA.
94 Mayer, L. Visual Field Tests, http://www.e-advisor.us/vf/tests.html, ADVISOR Project Coordinating Center, Children's Hospital Boston. 2010, (11 January 2011).
95 Morrison, J.C. and Pollack, I.P. (2003) *Glaucoma: Science and Practice*, Thieme Medical Publishers, Stuttgart.
96 Imaging and Perimetry Society. What is Perimetry?, http://www.perimetry.org/Perimetr.htm. 2008, (11 January 2011).
97 Miller, N.R., Newman, N.J., Biousse, V., and Kerrison, J.B. (2005) *Walsh and Hoyt's Clinical Neuro-Ophthalmology: the Essentials*, 6th edn, Lippincott Williams & Wilkins, Philadelphia, PA.
98 Park, S.B., Nam, Y.P., Sung, K.R., and Kook, M.S. (2009) Structural and functional relationships in glaucoma using standard automated perimetry and the Humphrey Matrix. *Korean J. Ophthalmol.*, **23** (3), 176–182.
99 Stamper, R.L., Lieberman, M.F., and Drake, M.V. (2009) *Becker–Shaffer's Diagnosis and Therapy of the Glaucomas*, MOSBY Elsevier, Philadelphia, PA.
100 Zeppier, M. and Johnson, C.A. Frequency Doubling Technology (FDT) Perimetry, http://webeye.ophth.uiowa.edu/ips/PerimetryHistory/FDP/index.htm, Imaging and Perimetry Society. 2008, (11 January 2011).
101 Miller, N.R., Walsh, F.B., and Hoyt, W.F. (2005) *Walsh and Hoyt's Clinical Neuro-Ophthalmology*, 6th edn, vol. **3**, Lippincott Williams & Wilkins, Philadelphia, PA.
102 Morin, J.D. (1979) Changes in the visual field in glaucoma: static ans kinetic perimetry in 2,000 patients. *Trans. Am. Ophthalmol. Soc.*, **77**, 622–642.
103 Augenklinik Tausendfensterhaus. Krankheitsbilder und ihre Behandlung. Der Grüne Star/Glaukom, http://www.augenklinik-tausendfensterhaus.de/krankheitsbilder-und-ihre-behandlung/der-gruene-starglaukom.html. 2010 (11 January 2011).
104 Nova Southeastern University. Goldmann Perimetry, http://www.nova.edu/hpd/otm/otm-d/fields/goldmann.html. 2010 (11 January 2011).
105 Grehn, F. and Stamper, R. (2004) *Glaucoma*, Springer, Berlin.
106 Herrmann, R.G. http://www.beepworld.de/members/

dr-herrmann/gesichtsfeld.htm, Augenarztpraxis Dr. Herrmann und Kollegen. 2010 (11 January 2011).
107 Tasman, W. and Jaeger, E.A. (2001) *The Wills Eye Hospital Atlas of Clinical Ophthalmology*, 2nd edn, Lippincott Williams & Wilkins, Philadelphia, PA., 114–120.
108 Haigis, W., Lege, B., Miller, N., and Schneider, B. (2000) Comparison of immersion ultrasound biometry and partial coherence interferometry for intraocular lens calculation according to Haigis. *Graefes Arch. Clin. Exp. Ophthalmol.*, **238** (9), 765–773.
109 Santodomingo-Rubido, J., Mallen, E.A.H., Gilmartin, B., and Wolffsohn, J.S. (2002) A new non-contact optical device for ocular biometry. *Br. J. Ophthalmol.*, **86** (4), 458–462.
110 Carl Zeiss Meditec AG. IOLMaster: the Gold Standard in Biometry, http://www.meditec.zeiss.com/88256DE3007B916B/0/BB738EE51A2BEE91882571B1005DED29/$file/iolmaster_en-final.pdf. 2010 (12 January 2011).
111 Carl Zeiss Meditec AG. IOLMaster – End User Training Version 5, http://www.meditec.zeiss.com/C125679E00525939/EmbedTitelIntern/TrainingIOLMforallversions/$File/IOLMaster_Training_Slides.pdf. 2010, (12 January 2011).
112 Kohnen, T. (ed.) (2002) *Modern Cataract Surgery. Developments in Ophthalmology*, vol. **34**, Karger, Basel.
113 Rohrer, K., Frueh, B.E., Walti, R., Clemetson, I.A., Tappeiner, C., and Goldblum, D. (2009) Comparison and evaluation of ocular biometry using a new noncontact optical low-coherence reflectometer. *Ophthalmology*, **116** (11), 2087–2092.
114 Allingham, R.R. and Shields, M.B. (2005) *Shields' Textbook of glaucoma*, 5th edn, Lippincott Williams & Wilkins, Philadelphia, PA.
115 Sharp, P.F. and Manivannan, A. (1997) The scanning laser ophthalmoscope. *Phys. Med. Biol.*, **42**, 951–966.
116 Fellers, T.J. and Davidson, M.W. Introduction to Confocal Microscopy, http://www.olympusconfocal.com/theory/confocalintro.html, Olympus Corporation. 2009 (12 January 2011).
117 Heidelberg Engineering. HRT Retina Module, http://www.heidelbergengineering.com/international/products/hrt-retina. 2010 (12 January 2011).
118 Choplin, N.T. (2006) GDx Scanning Laser Polarimeter, http://www.meditec.zeiss.com/C125679E00525939/EmbedTitelIntern/GDx/$File/GDx.pdf. 2006 (12. 01. 2011).
119 Knighton, R.W., Huang, X.-R., and Greenfield, D.S. (2002) Analytical model of scanning laser polarimetry for retinal nerve fiber layer assessment. *Invest. Ophthalmol. Vis. Sci.*, **43** (2), 383–392.
120 Carl Zeiss Meditec AG. Primer Excerpts – Clinical Guidance for Using the GDx, http://www.zeiss.de/C125679E0051C774/Contents-Frame/477FEB6A209C2C4E882570 FF0066A42B. 2010 (22. 06. 2010).
121 Grehn, F. and Stamper, R. (2008) *Essentials in Ophthalmology. Glaucoma: Progress III*, Springer, Berlin.
122 Kampik, A. and Grehn, F. (2003) *Augenärztliche Diagnostik*, Georg Thieme, Stuttgart.
123 Bouma, B.E. and Tearney, G.J. (2002) *Handbook of Optical Coherence Tomography*, Marcel Dekker, New York.
124 Carl Zeiss Meditec AG. Direct Cross-Sectional Retinal Imaging, http://www.meditec.zeiss.com/88256DE3007B916B/0/540AF97E5601FAA6C125755C0051F1A7/$file/poster_stratus_700x1000_e-final.pdf. 2009 (12 January 2011)
125 Drexler, W. and Fujimoto, J.G. (2008) *Optical Coherence Tomography: Technology and Applications*, Springer, Berlin.
126 Steinert, R.F. and Huang, D. (2008) *Anterior Segment Optical Coherence Tomography*, SLACK, Thorofare, NJ.
127 Schulze, A., Lamparter, J., and Hoffmann, E.M. (2009) New options of high resolution optical coherence tomography in glaucoma diagnostic. *Ophthalmologe*, **106** (8), 702–704, 706–708.
128 Xie, T., Guo, S., Zhang, J., Chen, Z., and Peavy, G.M. (2006) Use of polarization-

sensitive optical coherence tomography to determine the directional polarization sensitivity of articular cartilage and meniscus. *J. Biomed. Opt.*, **11** (6), 064001.

129 Heimann, H., Kellner, U., and Foerster, M.H. (2006) *Atlas of Fundus of Angiography*, Georg Thieme, Stuttgart.

130 Mishra, A., Wong, A., Bizheva, K., and Clausi, D.A. (2009) Intra-retinal layer segmentation in optical coherence tomography images. *Opt. Express*, **17** (26), 23719–23728.

131 Hüttmann, G., Lankenau, E., Schulz-Wackerbarth, C., Müller, M., Steven, P., and Birngruber, R. (2009) Optical Coherence Tomography: from Retina Imaging to Intraoperative Use – a Review. Technical Report, Institut für Biomedizinische Optik, Klinik für Augenheilkunde, Lübeck.

132 Weinberger, D., Axer-Siegel, R., Landau, D., and Yassur, Y. (1998) Retinal thickness variation in the diabetic patient measured by the retinal thickness analyser. *Br. J. Ophthalmol.*, **82** (9), 1003–1006.

133 Talia Technology Ltd. Retinal Thickness Analyzer, http://www.talia.com/. 2010, (12 January 2011).

134 Pires, I., Bernardes, R.C., Lobo, C.L., Soares, M.A., and Cunha-Vaz, J.G. (2002) Retinal thickness in eyes with mild nonproliferative retinopathy in patients with type 2 diabetes mellitus. *Arch. Ophthalmol.*, **120** (10), 1301–1306.

135 Kremser, B., Troger, J., Baltaci, M., Kralinger, M., and Kieselbach, G.F. (1999) Retinal thickness analysis in subjects with different refractive conditions. *Ophthalmologica*, **213** (6), 376–379.

136 Arevalo, J.F. (2009) *Retinal Angiography and Optical Coherence Tomography*, Springer Verlag + Business Media, LLC, New York.

137 St. Luke's Cataract and Laser Institute. Fluorescein Angiogram (FA), http://www.stlukeseye.com/eyeq/FluoresceinAngiogram.html. 2010 (12 January 2011).

138 Chua, C.N. Principles of Fluorescein Angiography, http://www.mrcophth.com/ffainterpretation/ffamainpage.html, UNIMAS, Kota Samarahan. 2010 (12 January 2011).

139 Wong, T.Y. (2001) *The Ophthalmology Examinations Review*, World Scientific, Singapore.

140 Agarwal, A. (2008) *Fundus Fluorescein and Indocyanine Green Angiography: a Textbook and Atlas*, SLACK, Thorofare, NJ.

141 Hayashi, K., Hasegawa, Y., and Tokoro, T. (1986) Indocyanine green angiography of central serous chorioretinopathy. *Int. Ophthalmol.*, **9** (1), 37–41.

142 Heidelberg Engineering, Inc. Spectralis HRA, http://www.heidelbergengineering.com/products/spectralis-hra/. 2010 (12 January 2011).

143 Topcon Europe BV. Topcon KR-9000PW, http://www.tag-ps.com/index.asp?pageid=2e5fe758c13d4618a83fede988e4a15e. 2010 (12 January 2011).

144 Glasmacher, M. (2006) Wavefront Aberrometers, unpublished.

145 Thibos, L.N. (2000) Principles of Hartmann–Shack aberrometry. *J. Refract. Surg.*, **16**, 563–565.

146 Probst, L.E. and Doane, J.F. (2001) *Refractive Surgery: a Color Synopsis*, Georg Thieme, New York.

147 WaveLight GmbH. See the Difference, http://www.wavelight.com/?cjt=3JoOhD6SHUYAAGNpeXQAAAAC. 2010 (12 January 2011).

148 Pretoria Eye Institute. The Allegretto Wave Excimer Laser, http://www.eyeinstitute.co.za/serv_news_009.asp. 2010 (12 January 2011).

149 LEC LASIK Eye Centres, Inc. Wavefront, http://www.lasikeyecentres.com/Wavefront.aspx. 2010 (12 January 2011).

150 Opitz, F. (2009) *Super-resolution Optical Sectioning*, Carl Zeiss, Jena.

151 Ekbert, H. and Rolf, M. (eds) (2006) *Photonik – Grundlagen, Technologien und Anwendung*, vol. **1**, Springer, Berlin.

152 Department of Integrative Biology, University of California-Berkeley. The Compound Microscope, http://ib.berkeley.edu/courses/bio1b/labschedfall09/labexercises/MicroscopeTutorial2_3.pdf. 2008 (11 January 2011).

153 Prasad, P.N. (2003) *Introduction to Biophotonics*, John Wiley & Sons, Inc., Hoboken, NJ.

154 Abramowitz, M., Keller, H.E., Spring, K.R., Flynn, B.O., Long, J.C., Parry-Hill, M.J., Tchourioukanov, K.I., and Davidson, M.W. Optical Microscopy Primer: Anatomy of the Microscope, http://micro.magnet.fsu.edu/primer/anatomy/anatomy.html, Molecular Expressions. 2008 (11 January 2011).

155 Lichtscheidl, I.K. Durchlichtmikroskop, http://www.univie.ac.at/mikroskopie/1_grundlagen/mikroskop/bauarten/2_durchlicht.htm. 2010 (11 January 2011).

156 Spring, K.R. and Davidson, M.W. Microscopy: the Source for Microscopy Education, http://www.microscopyu.com/articles/fluorescence/fluorescenceintro.html, Molecular Expressions, Florida State University (FSU), and Nikon, Inc. 2010 (11 January 2011).

157 Wikipedia. Fluorescence Filters, http://en.wikipedia.org/w/index.php?title=Fluorescence_microscope&oldid=364754293. 2010 (12 January 2011).

158 Axelrod, D., Herman, B., Frohlich, V.E.C., Lakowicz, J.R., Murphy, D.B., Piston, D.W., Hardee, C., Kinoshita, R., Wakefield, T., Johnson, R., Erdogan, T., Abramowitz, M., Fester, W.K., Kawano, Y., Enders, R.G., Spring, K.R., Parry-Hill, M.J., Fellers, T.J., Claxton, N.S., and Davidson, M.W. Optical Microscopy Primer: Anatomy of the Microscope, http://micro.magnet.fsu.edu/primer/techniques/fluorescence/fluorhome.html, Molecular Expressions. 2009 (12 January 2011).

159 Axelrod, D., Long, J.C., and Davidson, M.W. Optical Microscopy Primer: Anatomy of the Microscope, http://micro.magnet.fsu.edu/primer/java/tirf/reflect/index.html, Molecular Expressions. 2007 (12 January 2011).

160 Carl Zeiss MicroImaging GmbH. Applications for Light Microscopy – BioMed, http://www.zeiss.de/C12567BE0045ACF1/ContentsWWWIntern/A470B15C96F23953C1256E4B0051249D. 2010 (11 January 2011).

161 Ankerhold, R., Kempe, M., and Wolleschensky, R. (2008) High-resolution light microscopy – methodical approaches and their application possibilities. *BioPhotonics*, **2**, 28–31.

162 Carl Zeiss MicroImaging GmbH. Structured Illumination Microscopy, http://www.zeiss.de/c12567be0045acf1/Contents-Frame/1736b900a71d4300c125758d0021d760. 2010 (11 January 2011).

163 Török, P. and Kao, F.-J. (2003) *Optical Imaging and Microscopy: Techniques and Advanced Systems*, Springer, Berlin.

164 Carl Zeiss MicroImaging GmbH. LSM 71 ELYRA P.1, http://www.zeiss.de/c12567be0045acf1/Contents-Frame/ba65c4744bda515cc125764a0061fa9c. 2010 (11 January 2011).

165 Murray, J.M., Spring, K.R., Johnson, I., Metcalfe, W.K., Lerant, A., Riddle, K.A., Bass, H.W., Fajer, P., Cusma, A.M., Parry-Hill, M.J., and Davidson, M.W. Laser Scanning Confocal Microscopy, http://micro.magnet.fsu.edu/primer/virtual/confocal/index.html. Molecular Expressions. 2006 (12 January 2011).

166 Pawley, J.B. (1995) *Handbook of Biological Confocal Microscopy*, Springer, Berlin.

167 Jurkiewicz, A., Albrektsen, A., Madsen, E., Broghammer, A., and Grossmann, C.Detection of fluorescence, 2009. Centre for Carbohydrate Recognition and Signalling.

168 Carl Zeiss MicroImaging GmbH. Laser Scanning Microscopes, http://www.zeiss.de/c12567be0045acf1/Contents-Frame/a22821a1bdcaae49c12574e80030638e. 2006 (12 January 2011).

169 Schmitt, M. and Popp, J. (2006) Raman spectroscopy at the beginning of the twenty-first century. *J. Raman Spectrosc.*, **37**, 20–28.

170 Schmitt, M., Kraft, C., and Popp, J. (2008) Raman imaging: molekulares imaging: Raman, CARS und TERS. *Biospektrum*, **14**, 605–607.

171 Kador, L. and Bezold, T. Confocal Raman and Luminescence Microscopy at Room Temperature, http://www.agkador.phy.uni-bayreuth.de/en/projects_web/Konfokale_Ramanspektroskopie/index.html, Physikalisches Institut, University of Bayreuth. 2010 (11 January 2011).

172 Patel, I.S., Premasiri, W.R., Moir, D.T., and Ziegler, L.D. (2008) Barcoding bacterial cells: a SERS-based methodology for pathogen identification. *J. Raman Spectrosc.*, **39** (11), 1660–1672.

173 Benevides, J.M., Kawakami, J., and Thomas, G.J. Jr. (2008) Mechanisms of drug–DNA recognition distinguished by Raman spectroscopy. *J. Raman Spectrosc.*, **39** (11), 1627–1634.

174 Pawlak, A.M., Beattie, J.R., Glenn, J.V., Stitt, A.W., and McGarvey, J.J. (2008) Raman spectroscopy of advanced glycation end products (AGEs), possible markers for progressive retinal dysfunction. *J. Raman Spectrosc.*, **39** (11), 1635–1642.

175 Downes, A., Mouras, R., and Elfick, A. (2010) Optical spectroscopy for noninvasive monitoring of stem cell differentiation. *J. Biomed. Biotechnol.*, **2010**, 101864.

176 Rocha, R., Vassallo, J., Soares, F., Miller, K., and Gobbi, H. (2009) Digital slides: present status of a tool for consultation, teaching, and quality control in pathology. *Pathol. Res. Pract.*, **205** (11), 735–741.

177 Kayser, K., Kayser, G., Radziszowski, D., and Oehmann, A. (1999) From telepathology to virtual pathology institution: the new world of digital pathology. *Rom. J. Morphol. Embryol.*, **45**, 3–9.

178 Molnar, B., Berczi, L., Diczhazy, C., Tagscherer, A., Varga, S.V., Szende, B., and Tulassay, Z. (2003) Digital slide and virtual microscopy based routine and telepathology evaluation of routine gastrointestinal biopsy specimens. *J. Clin. Pathol.*, **56** (6), 433–438.

179 Carl Zeiss MicroImaging GmbH. Digital Slide, http://www.zeiss.de/c12567be0045acf1/Contents-Frame/65d0a7975c51782dc1257129003df6d4. 2010 (11 January 2011).

180 Grabowska, I., Chudy, M., Dybko, A., and Brzozka, Z. (2005) Determination of creatinine in clinical samples based on a flow-through system. *Anal. Chim. Acta*, **540**, 181–185.

181 Banerjee, B., Miedema, B., and Chandrasekhar, H.R. (1998) Emission spectra of colonic tissue and endogenous fluorophores. *Am. J. Med. Sci.*, **316** (3), 220–226.

182 Lakowicz, J.R. (2002) *Nonlinear and Two-Photon Induced Fluorescence. Topics in Fluorescence Spectroscopy*, vol. **5**, Kluwer, New York.

183 Wansink, D.G., Schul, W., van der Kraan, I., van Steensel, B., van Driel, R., and de Jong, L. (1993) Fluorescent labeling of nascent RNA reveals transcription by RNA polymerase II in domains scattered throughout the nucleus. *J. Cell Biol.*, **122** (2), 283–293.

184 Benson, D.M. and Knopp, J.A. (1984) Effect of tissue absorption and microscope optical parameters on the depth of penetration for fluorescence and reflectance measurements of tissue samples. *Photochem. Photobiol.*, **39** (4), 495–502.

185 Thompson, R.B. (2002) *Red and Near-Infrared Fluorometry. Topics in Fluorescence Spectroscopy*, vol. **4**, Plenum Press, New York.

186 Lakowicz, J.R., Johnson, M.L., Lederer, W.J., Szmacinski, H., Nowaczyk, K., Malak, H., and Berndt, K. (1992) Fluorescence lifetime sensing generates cellular images. *Laser Focus World*, **28** (5), 60–80.

187 Zijlstra, W.G., Buursma, A., and van Assendelft, O.W. (2000) *Visible and Near-IR Spectra of Human and Animal Haemoglobin*, VSP, Utrecht.

188 Ripamonti, G. and Cova, S. (1986) Optical time-domain reflectometry with centimeter resolution at fW sensitivity. *Electron. Lett.*, **22**, 818–819.

189 Ripamonti, G. and Cova, S. (1991) Time-resolved spectroscopy and imaging of tissues. *Proc. SPIE*, **1431**, 1–335.

190 Lakowicz, J.R., Szmacinski, H., Nowaczyk, K., Lederer, W.J., Kirby, M.S., and Johnson, M.L. (1994) Fluorescence lifetime imaging of intracellular calcium in COS cells using Quin-2. *Cell Calcium*, **15** (1), 7–27.

191 Morgan, C.G., Mitchel, A.C., and Murray, J.G. (1992) In *situ* fluorescence analysis using nanosecond decay time imaging. *Trends Anal. Chem.*, **11**, 32–41.

192 Robinson, R.D., Reeder, J.E., and Wheeless, L.L. Jr. (1989) Technique for cellular fluorescence distribution analysis. *Cytometry*, **10** (4), 402–409.

193 Robinson, R.D., Wheeless, D.M., Hespelt, S.J., and Wheeless, L.L. (1990) System for acquisition and real-time processing of multidimensional slit-scan flow cytometric data. *Cytometry*, **11** (3), 379–385.

194 Galla, H.-J. (1988) *Spektroskopische Methoden in der Biochemie*, Georg Thieme, Stuttgart.

195 Kronman, M.J., Timasheff, S.N., Colter, J.S., and Brown, R.A. (1960) Light-scattering studies on ascites tumor cell RNA. *Biochim. Biophys. Acta*, **40**, 410–417.

196 Gehrich, J.L., Lubbers, D.W., Opitz, N., Hansmann, D.R., Miller, W.W., Tusa, J.K., and Yafuso, M. (1986) Optical fluorescence and its application to an intravascular blood gas monitoring system. *IEEE Trans. Biomed. Eng.*, **33** (2), 117–132.

197 Janata, J., Josowicz, M., and DeVaney, D.M. (1996) Chemical sensors. *Anal. Chem.*, **33** (12), 207R–228R.

198 Klimant, I., Kühl, M., Glud, R.N., and Holst, G. (1997) Optical measurement of oxygen and temperature in microscale: strategies and biological applications. *Sens. Actuators B*, **38**, 29–37.

199 Urbano, E., Offenbacher, H., and Wolfbeis, O.S. (1984) Optical sensors for continuous determination of halides. *Anal. Chem.*, **56**, 427–429.

200 Bell, A.G. (1880) On the production and reproduction of sound by light: the photophone. *Am. J. Sci.*, **20**, 305.

201 Bell, A.G. (1881) Upon the production of sound by radiant energy. *Philos. Mag.*, **11**, 510–528.

202 Tyndall, J. (1881) Action of an intermittent beam of radiant light upon gaseous matter. *Proc. R. Soc. London*, **31**, 307–317.

203 Röntgen, W.C. (1881) On tones produced by the intermittent irradiation of a gas. *Philos. Mag.*, **11**, 308.

204 Rao, J. Photodynamic Therapy for the Dermatologist, http://emedicine.medscape.com/article/1121517-overview, Medscape. 2010 (11 January 2011).

205 National Cancer Institute, Photodynamic Therapy for Cancer, http://www.cancer.gov/cancertopics/factsheet/Therapy/photodynamic

206 Brancaleon, L. and Moseley, H. (2002) Laser and non-laser light sources for photodynamic therapy. *Lasers Med. Sci.*, **17** (3), 173–186.

207 Jampol, L.M. and Scott, L. (2002) Treatment of juxtafoveal and extrafoveal choroidal neovascularization in the era of photodynamic therapy with verteporfin. *Am. J. Ophthalmol.*, **134** (1), 99–101.

208 Carl Zeiss Meditec AG. MEL 80 Excimer Laser, http://www.meditec.zeiss.com/88256DE3007B916B/0/7F59B179A0C9A92B882571 B1005DED25/$file/080331_1526-092_mel80_e_final.pdf. 2010 (11 January 2011).

209 Sakimoto, T., Rosenblatt, M.I., and Azar, D.T. (2006) Laser eye surgery for refractive errors. *Lancet*, **367** (9520), 1432–1447.

210 LASIK Zentren GmbH. Epi-LASIK, http://www.lasik-center.com/lasik/epi-lasik.html. 2010 (11 January 2011).

211 Ceatus Media Group LLC. Refractive Surgery News, http://www.lasiksurgerynews.com/. 2010 (11 January 2011).

212 Bansal, A.K. and Veenashree, M.P. (2001) Laser refractive surgery: technological advance and tissue response. *Biosci. Rep.*, **21** (4), 491–512.

213 Asclepion Laser Technologies GmbH. MeDioStar Effect, http://www.asclepion.com/root_corporate/mediostar_effect_687_ENG_Corporate.aspx. 2010 (11 January 2011).

214 Quantum Radiophysics Department, Lebedev Physics Institute. Yachroma-Med the Copper Vapor Laser System for Dermatological Surgery, http://www.yachroma.com/slcEng.htm. 2010 (22 June 2011),

215 Rokhsar, C.K. and Fitzpatrick, R.E. (2005) The treatment of melasma with fractional photothermolysis: a pilot study. *Dermatol. Surg.*, **31** (12), 1645–1650.

216 MKW Therapie-Systeme GmbH. The New Generation of Laser Showers, http://www.mkw-laser.de/de/Produkte/

laserdusche_powertwin21.html. 2010 (11 January 2011).
217 Karu, T. (1999) Primary and secondary mechanisms of action of visible to near-IR radiation on cells. *J. Photochem. Photobiol. B*, **49** (1), 1–17.
218 Spectra-Medics. What is Low Level Laser Therapy?, http://www.spectra-medics.com/index.php?id=24. 2010 (11 January 2011).
219 Reimers & Janssen GmbH. Photo-Activated Disinfection, http://www.rj-laser.com/english/photo_dynamic_therapy.htm. 2010 (11 January 2011).
220 van Doorn, G.A. and Oosterhuis, G.J.E. (1999) Laser and cold-knife conisation for cervical intraepithelial neoplasia: a long-term follow-up. *Lasers Med. Sci.*, **14** (2), 109–111.
221 Bacon, J.L. (2007) Carbon Dioxide Laser Surgery for Cervical Dysplasia, http://emedicine.medscape.com/article/272382-overview, Medscape. 2007 (12 January 2011),
222 Hüttenbrink, K.B. (2005) *Lasers in Otorhinolaryngology*, Georg Thieme, Stuttgart.
223 Helling, K. and Scherer, H. (2002) Laser-tonsillotomy in infantile tonsillar hyperplasia. *Med. Laser Appl.*, **17** (3), 263–271.
224 Visualase, Inc. Laser Interstitial Thermal Therapy, http://visualaseinc.com/. 2010 (12 January 2011).
225 Haraldsdottir, K.H., Ivarsson, K., Gotberg, S., Ingvar, C., Stenram, U., and Tranberg, K.G. (2008) Interstitial laser thermotherapy (ILT) of breast cancer. *Eur. J. Surg. Oncol.*, **34** (7), 739–745.
226 Schenk, B., Brouwer, P.A., Peul, W.C., and van Buchem, M.A. (2006) Percutaneous laser disk decompression: a review of the literature. *AJNR Am. J. Neuroradiol.*, **27** (1), 232–235.
227 Choy, D.S.J., Tassi, G.P., Hellinger, J., Hellinger, S., and Lee, S.H. (2009) Twenty-three years of percutaneous laser disc decompression (PLDD) – state of the art and future prospects. *Med. Laser Appl.*, **24** (3), 147–157.
228 Gomez Sancha, F., Bachmann, A., Choi, B.B., Tabatabaei, S., and Muir, G.H. (2007) Photoselective vaporization of the prostate (GreenLight PV): lessons learnt after 3500 procedures. *Prostate Cancer Prostatic Dis.*, **10** (4), 316–322.
229 Shergill, I.S. Greenlight Photoselective Vaporization of the Prostate, http://www.futuremedicine.com/doi/pdf/10.2217/14750708.1.2.177?&. 2004 (11 January 2011).
230 Steiner, R. (1988) *Laser Lithotripsy: Clinical Use and Technical Aspects*, Springer, Berlin.
231 Dornier MedTech. Laser Lithotripsy – Treatment, http://www.dornier.com/americas/english_gb/patient/kidney_stones/laser/treatment.htm. 2010 (11 January 2011).
232 Trokel, S.L., Srinivasan, R., and Braren, B. (1983) Excimer laser surgery of the cornea. *Am. J. Ophthalmol.*, **96** (6), 710–715.
233 Bates, A.K., Morgan, S.J., and Steele, A.D. (1992) Radial keratotomy: a review of 300 cases. *Br. J. Ophthalmol.*, **76** (10), 586–589.
234 Nagel, B., Dellweg, H., and Gierasch, L.M. (1992) Glossary for chemists of terms used in biotechnology (IUPAC Recommendations 1992). *Pure Appl. Chem.*, **84** (1), 143–168.
235 IUPAC. Compendium of Chemical Terminology, 2nd edn, (1997) http://old.iupac.org/publications/compendium/B.html, International Union of Pure and Applied Chemistry. 1997 (12 January 2011).
236 Präve, P. (1994) *Handbuch der Biotechnologie*, Oldenbourg Verlag, Munich.
237 van Beuzekom, B. and Arundel, A. (2009) *OECD Biotechnology Statistics*, http://www.oecd.org/dataoecd/4/23/42833898.pdf, OECD. 2009 (11 January 2011).
238 Wikipedia. Biotechnology, http://en.wikipedia.org/w/index.php?title=Biotechnology&oldid=369361253. 2010 (12 January 2011).
239 Präve, P., Faust, U., Sittig, W., and Sukatsch, D.A. (1987) *Fundamentals of Biotechnology*, VCH Verlag GmbH, Weinheim.
240 Schwedt, G. (1997) *The Essential Guide to Analytical Chemistry*, Wiley-VCH Verlag GmbH, Weinheim.

241 Gauglitz, G., Brecht, A., Kraus, G., and Nahm, W. (1993) Chemical and biochemical sensors based on interferometry at thin (multi-)layers. *Sens. Actuators B*, **11**, 21–27.

242 Wikipedia. Reflectometric Interference Spectroscopy (RIfS). http://upload.wikimedia.org/wikipedia/commons/7/74/RIfS_Prinzip_eng_PF.png. 2009 (12 January 2011).

243 Nagel, T., Ehrentreich-Förster, E., Singh, M., Schmitt, K., Brandenburg, A., Berka, A., and Bier, F.F. (2008) Direct detection of tuberculosis infection in blood serum using three optical label-free approaches. *Sens. Actuators B*, **129** (2), 934–940.

244 Lue, X.-Y., Huang, H., Huang, Y., Qian, W.-P., Yuan, C.-W., and Lu, Z. (2001) Using biomedical sensor–reflectometry interference spectroscopy for evaluation of biocompatibility of biomaterials. Annual International Conference of the IEEE vol. 3, pp. 3012–3015. Engineering in Medicine and Biology Society.

245 Mehlmann, M., Garvin, A.M., Steinwand, M., and Gauglitz, G. (2005) Reflectometric interference spectroscopy combined with MALDI-TOF mass spectrometry to determine quantitative and qualitative binding of mixtures of vancomycin derivatives. *Anal. Bioanal. Chem.*, **382** (8), 1942–1948.

246 Proll, G., Steinle, L., Proll, F., Kumpf, M., Moehrle, B., Mehlmann, M., and Gauglitz, G. (2007) Potential of label-free detection in high-content-screening applications. *J. Chromatogr. A*, **1161** (1–2), 2–8.

247 Analytik Jena AG. Biomolekulare Interaktionsanalytik, http://www.analytik-jena.de/de/Life-Science/Pressezentrum__4033/. 2010 (11 January 2011).

248 Yu, F., Yao, D., and Qian, W. (2000) Reflectometry interference spectroscopy in detection of hepatitis B surface antigen. *Clin. Chem.*, **46** (9), 1489–1490.

249 Mohrle, B.P., Kohler, K., Jaehrling, J., Brock, R., and Gauglitz, G. (2006) Label-free characterization of cell adhesion using reflectometric interference spectroscopy (RIfS). *Anal. Bioanal. Chem.*, **384** (2), 407–413.

250 Schütz, A. (2000) Einsatz der reflektometrischen Interferenzspektroskopie (RIfS) zur markierungsfreien Affinitätsdetektion für das Hochdurchsatzscreening. PhD thesis, Universität Tübingen.

251 Belmont, A.S., Jaeger, S., Knopp, D., Niessner, R., Gauglitz, G., and Haupt, K. (2007) Molecularly imprinted polymer films for reflectometric interference spectroscopic sensors. *Biosens. Bioelectron.*, **22** (12), 3267–3272.

252 Liedberg, B., Nylander, C., and Lundstrom, I. (1983) Surface plasmon resonance for gas detection and biosensing. *Sens. Actuators*, **4**, 299–304.

253 SPRpages. Surface Plasmon Resonance, http://www.sprpages.nl/Index.php. 2011 (11 January 2011).

254 Biacore AB. Surface Plasmon Resonance, www.protein.iastate.edu/seminars/BIACore/TechnologyNotes/TechnologyNote1.pdf. 2001 (11 January 2011).

255 Schasfoort, R.B.M. and Tudos, A.J. (2008) *Handbook of Surface Plasmon Resonance*, Royal Society of Chemistry, Cambridge.

256 Biacore AB. An Introduction to Biacore's SPR Technology, http://www.protein.iastate.edu/seminars/BIACore/TechnologyNotes/TechnologyBrochure.pdf. 2001 (11 January 2011).

257 General Electric Company. Label-Free Interaction Analysis in Real Time, http://www.biacore.com/lifesciences/introduction/index.html. 2011 (11 January 2011).

258 General Electric Company. Reference Database, http://www.biacore.com/lifesciences/technology/publications/refdb/index.html. 2011 (11 January 2011).

259 Nedelkov, D. and Nelson, R.W. (2000) Exploring the limit of detection in biomolecular interaction analysis mass spectrometry (BIA/MS): detection of attomole amounts of native proteins present in complex biological mixtures. *Anal. Chim. Acta*, **423** (1), 1–7.

260 Marchesini, G.R., Buijs, J., Haasnoot, W., Hooijerink, D., Jansson, O., and Nielen, M.W. (2008) Nanoscale affinity chip

interface for coupling inhibition SPR immunosensor screening with nano-LC TOF MS. *Anal. Chem.*, **80** (4), 1159–1168.

261 Biacore AB. BIACore Information, http://www.protein.iastate.edu/seminars/BIACore/, Protein Facility of the Iowa State University Office of Biotechnology, Iowa State University. 2002 (11 January 2011).

262 Shimomura, O., Johnson, F.H., and Saiga, Y. (1962) Extraction, purification and properties of aequorin, a bioluminescent protein from the luminous hydromedusan, *Aequorea*. *J. Cell Comp. Physiol.*, **59**, 223–239.

263 Hicks, B.W. (2002) *Green Fluorescent Protein, Applications and Protocols, Methods in Molecular Biology*, vol. **183**, Humana Press, Totowa, NJ.

264 Chalfie, M., Tu, Y., Euskirchen, G., Ward, W.W., and Prasher, D.C. (1994) Green fluorescent protein as a marker for gene expression. *Science*, **263** (5148), 802–805.

265 Lux, K., Goerlitz, N., Schlemminger, S., Perabo, L., Goldnau, D., Endell, J., Leike, K., Kofler, D.M., Finke, S., Hallek, M., and Buning, H. (2005) Green fluorescent protein-tagged adeno-associated virus particles allow the study of cytosolic and nuclear trafficking. *J. Virol.*, **79** (18), 11776–11787.

266 Wildt, S. and Deuschle, U. (1999) cobA, a red fluorescent transcriptional reporter for *Escherichia coli*, yeast, and mammalian cells. *Nat. Biotechnol.*, **17** (12), 1175–1178.

267 Förster, T. (1948) Zwischenmolekulare Energiewanderung und Fluoreszenz. *Ann. Phys.*, **437** (1–2), 55–75.

268 Nguyen, A.W. and Daugherty, P.S. (2005) Evolutionary optimization of fluorescent proteins for intracellular FRET. *Nat. Biotechnol.*, **23** (3), 355–360.

269 Olympus America Inc. Fluorescence Resonance Energy Transfer (FRET) Microscopy, http://www.olympusmicro.com/primer/techniques/fluorescence/fret/fretintro.html. 2010 (11 January 2011).

270 Stryer, L. and Haugland, R.P. (1967) Energy transfer: a spectroscopic ruler. *Proc. Natl. Acad. Sci. USA*, **58** (2), 719–726.

271 Safeukui, I., Millet, P., Boucher, S., Melinard, L., Fregeville, F., Receveur, M.C., Pistone, T., Fialon, P., Vincendeau, P., Fleury, H., and Malvy, D. (2008.) Evaluation of FRET real-time PCR assay for rapid detection and differentiation of *Plasmodium* species in returning travellers and migrants. *Malar. J.*, **7**, 70.

272 Ahmad, A.I. and Ghasemi, J.B. (2007) New FRET primers for quantitative real-time PCR. *Anal. Bioanal. Chem.*, **387** (8), 2737–2743.

273 Sabella, S., Vecchio, G., Cingolani, R., Rinaldi, R., and Pompa, P.P. (2008) Real-time PCR in a plastic chip based on solid state FRET. *Langmuir*, **24** (23), 13266–13269.

274 Wouters, F.S., Verveer, P.J., and Bastiaens, P.I. (2001) Imaging biochemistry inside cells. *Trends Cell Biol.*, **11** (5), 203–211.

275 Chen, H., Puhl, H.L. III, Koushik, S.V., Vogel, S.S., and Ikeda, S.R. (2006) Measurement of FRET efficiency and ratio of donor to acceptor concentration in living cells. *Biophys. J.*, **91** (5), L39–L41.

276 Piljic, A. and Schultz, C. (2008) Simultaneous recording of multiple cellular events by FRET. *ACS Chem. Biol.*, **3** (3), 156–160.

277 Piston, D.W. and Kremers, G.J. (2007) Fluorescent protein FRET: the good, the bad and the ugly. *Trends Biochem. Sci.*, **32** (9), 407–414.

278 Göhde, W. (1968) Automatisches Meß- und Zählgerät für die Teilchen einer Dispersion, patents DE 1815352 (1968), GB 1300585, US3, 738, 759.

279 Dittrich, W. and Gohde, W. (1969) Impulse fluorometry of single cells in suspension. *Z. Naturforsch., Teil B*, **24** (3), 360–361.

280 Ormerod, M.G. (2003) *Flow Cytometry: a Practical Approach*, vol. **3**, Oxford University Press, Oxford.

281 John Wiley & Sons, Inc. Current Protocols. Cytometry, http://www.currentprotocols.com/cytometry. 2001 (11 January 2011).

282 Life Technologies. Introduction to Flow Cytometry, http://probes.invitrogen.com/resources/education/tutorials/

4Intro_Flow/player.html. 2010 (12 January 2011).
283 Rahman, M. Introduction to Flow Cytometry, http://www.abdserotec.com/uploads/Flow-Cytometry.pdf, Serotec Ltd. 2006 (11 January 2011).
284 Ormerod, M.G. The Flow Cytometer, http://flowbook.denovosoftware.com/Flow_Book/Chapter_2meter, De Novo Software. 2010 (12 January 2011).
285 Becton, Dickinson and Company. BD Bioscences, http://www.bdbiosciences.com/home.jsp. 2011 (11 January 2011).
286 Rodriguez-Caballero, A., Garcia-Montero, A.C., Bueno, C., Almeida, J., Varro, R., Chen, R., Pandiella, A., and Orfao, A. (2004) A new simple whole blood flow cytometry-based method for simultaneous identification of activated cells and quantitative evaluation of cytokines released during activation. *Lab. Invest.*, **84** (10), 1387–1398.
287 O'Gorman, M.R. and Corrochano, V. (1995) Rapid whole-blood flow cytometry assay for diagnosis of chronic granulomatous disease. *Clin. Diagn. Lab. Immunol.*, **2** (2), 227–232.
288 Sah, S.P., Matutes, E., Wotherspoon, A.C., Morilla, R., and Catovsky, D. (2003) A comparison of flow cytometry, bone marrow biopsy, and bone marrow aspirates in the detection of lymphoid infiltration in B cell disorders. *J. Clin. Pathol.*, **56** (2), 129–132.
289 Forichon, A., Condevaux, F., Perron-Lepage, M.-F., and Descotes, J. (2006) Bone marrow differentials – comparison of flow cytometry and manual counting in rats treated with compounds inducing hematological changes. *Toxicol. Lett.*, **164** (1), 105.
290 Petkova, S.B., Yuan, R., Tsaih, S.W., Schott, W., Roopenian, D.C., and Paigen, B. (2008) Genetic influence on immune phenotype revealed strain-specific variations in peripheral blood lineages. *Physiol. Genomics*, **34** (3), 304–314.
291 McCarthy, D.A. and Macey, M.G. (2001) *Cytometric Analysis of Cell Phenotype and Function*, Cambridge University Press, Cambridge.
292 Darden, J.M., Polonis, V.R., deSouza, M.S., Chantakulkij, S., Brown, A.E., Birx, D.L., and Pattanapanyasat, K. (2000) A flow cytometric method for measuring neutralization of HIV-1 subtype B and E primary isolates. *Cytometry*, **40** (2), 141–150.
293 Pawley, J. (2006) *Handbook of Biological Confocal Microscopy*, vol. **3**, Springer, Berlin.
294 Hell, S.W. (2009) Microscopy and its focal switch. *Nat. Methods*, **6** (1), 24–32.
295 University of Kassel. Das Konfokale Lasermikroskop, http://www.uni-kassel.de/fb19/cellbio/wwwSeiten/Clsm01.htm. 2010 (13 January 2011).
296 University of Zurich. Introduction to Confocal Laser Scanning Microscopy, http://www.zmb.uzh.ch/resources/download/CLSM.pdf. 2010 (11 January 2011).
297 Engelmann, R. Maximum Sensitivity and Flexibility in a Single System, http://www.zeiss.de/C1256D18002CC306/0/BA710158046BB095C125749B004861E4/$file/60-1-0006.pdf. Carl Zeiss MicroImaging GmbH. 2008 (11 January 2011).
298 Baschong, W., Suetterlin, R., and Laeng, R.H. (2001) Control of autofluorescence of archival formaldehyde-fixed, paraffin-embedded tissue in confocal laser scanning microscopy (CLSM). *J. Histochem. Cytochem.*, **49** (12), 1565–1572.
299 Shirota, T., Yasui, H., Shimokawa, H., and Matsuda, T. (2003) Fabrication of endothelial progenitor cell (EPC)-seeded intravascular stent devices and *in vitro* endothelialization on hybrid vascular tissue. *Biomaterials*, **24** (13), 2295–2302.
300 Feng, Y., Bantseev, V., and Simpson, T.L. (2008) Corneal, limbal, and conjunctival epithelium of bovine eyes imaged *in vitro* by using a confocal laser scanning microscope. *Cornea*, **27** (3), 344–348.
301 Ralphs, J.R. (2008) Confocal laser scanning microscopy in connective tissue research. *Eur. Cells Mater.*, **16** (2), 35.
302 Fricke, M. (2007) Schnelle und hochsensitive multifokale Zwei-Photonen-Laser-Raster-Mikroskopie. PhD thesis, Universität Bielefeld.
303 Bestvater, F., Spiess, E., Stobrawa, G., Hacker, M., Feurer, T., Porwol, T.,

Berchner-Pfannschmidt, U., Wotzlaw, C., and Acker, H. (2002) Two-photon fluorescence absorption and emission spectra of dyes relevant for cell imaging. *J. Microsc.*, **208** (Pt 2), 108–115.

304 Bousso, P., Bhakta, N.R., Lewis, R.S., and Robey, E. (2002) Dynamics of thymocyte–stromal cell interactions visualized by two-photon microscopy. *Science*, **296** (5574), 1876–1880.

305 Denk, W., Delaney, K.R., Gelperin, A., Kleinfeld, D., Strowbridge, B.W., Tank, D.W., and Yuste, R. (1994) Anatomical and functional imaging of neurons using 2-photon laser scanning microscopy. *J. Neurosci. Methods*, **54** (2), 151–162.

306 Agarwal, A., Coleno, M.L., Wallace, V.P., Wu, W.Y., Sun, C.H., Tromberg, B.J., and George, S.C. (2001) Two-photon laser scanning microscopy of epithelial cell-modulated collagen density in engineered human lung tissue. *Tissue Eng.*, **7** (2), 191–202.

307 Boissonnas, A., Fetler, L., Zeelenberg, I.S., Hugues, S., and Amigorena, S. (2007) In *vivo* imaging of cytotoxic T cell infiltration and elimination of a solid tumor. *J. Exp. Med.*, **204** (2), 345–356.

308 Baddeley, D., Carl, C., and Cremer, C. (2006) 4Pi microscopy deconvolution with a variable point-spread function. *Appl. Opt.*, **45** (27), 7056–7064.

309 Sauter, D. (2009) 4Pi live cell imaging. PhD thesis, Ruperto-Carola University of Heidelberg.

310 Arkhipov, A., Huve, J., Kahms, M., Peters, R., and Schulten, K. (2007) Continuous fluorescence microphotolysis and correlation spectroscopy using 4Pi microscopy. *Biophys. J.*, **93** (11), 4006–4017.

311 Egner, A., Verrier, S., Goroshkov, A., Soling, H.D., and Hell, S.W. (2004) 4Pi-microscopy of the Golgi apparatus in live mammalian cells. *J. Struct. Biol.*, **147** (1), 70–76.

312 Huve, J., Wesselmann, R., Kahms, M., and Peters, R. (2008) 4Pi microscopy of the nuclear pore complex. *Biophys. J.*, **95** (2), 877–885.

313 Donnert, G. (2007) Dual-colour STED-microscopy on the nanoscale. PhD thesis, Ruperto-Carola University of Heidelberg.

314 Willig, K.I., Rizzoli, S.O., Westphal, V., Jahn, R., and Hell, S.W. (2006) STED microscopy reveals that synaptotagmin remains clustered after synaptic vesicle exocytosis. *Nature*, **440** (7086), 935–939.

315 Hein, B. (2009) Live cell STED microscopy using genetically encoded markers. PhD thesis, Georg-August-Universität zu Göttingen.

316 Wirsing, B. (2006) Ultrascharfes Lichtmikroskop entschlüsselt grundlegende Mechanismen der Nervenkommunikation. Technical Report, Max-Planck-Gesellschaft, Munich.

317 Nanonics Imaging Ltd. http://www.nanonics.co.il/a-brief-history-and-simple-description-of-nsom-snom-tec.html. Nanonics Ltd. 2007 (11 January 2011).

318 Kim, J.M., Ohtani, T., Sugiyama, S., Hirose, T., and Muramatsu, H. (2001) Simultaneous topographic and fluorescence imaging of single DNA molecules for DNA analysis with a scanning near-field optical/atomic force microscope. *Anal. Chem.*, **73** (24), 5984–5991.

319 Subramaniam, V., Kirsch, A.K., and Jovin, T.M. (1998) Cell biological applications of scanning near-field optical microscopy (SNOM). *Cell. Mol. Biol. (Noisy-le-Grand)*, **44** (5), 689–700.

320 Zweyer, M., Troian, B., Spreafico, V., and Prato, S. (2008) SNOM on cell thin sections: observation of Jurkat and MDAMB453 cells. *J. Microsc.*, **229** (Pt 3), 440–446.

321 Generosi, J., Margaritondo, G., Sanghera, J.S., Aggarwal, I.D., Tolk, N.H., Piston, D.W., Castellano, A.C., and Cricenti, A. (2008) Infrared scanning near-field optical microscopy investigates order and clusters in model membranes. *J. Microsc.*, **229** (Pt 2), 259–263.

322 Hausmann, M., Liebe, B., Perner, B., Jerratsch, M., Greulich, K.O., and Scherthan, H. (2003) Imaging of human meiotic chromosomes by scanning near-field optical microscopy (SNOM). *Micron*, **34** (8), 441–447.

323 JPK Instruments AG. Tutorials – Scanning Near-Field Optical Microscopy (SNOM), http://www.jpk.com/scanning-near-field-opt-microscopy.440.html. 2010 (11 January 2011).

324 Lequin, R.M. (2005) Enzyme immunoassay (EIA)/enzyme-linked immunosorbent assay (ELISA). *Clin. Chem.*, **51** (12), 2415–2418.

325 Guan, M., Chen, H.Y., Foo, S.Y., Tan, Y.J., Goh, P.Y., and Wee, S.H. (2004) Recombinant protein-based enzyme-linked immunosorbent assay and immunochromatographic tests for detection of immunoglobulin G antibodies to severe acute respiratory syndrome (SARS) coronavirus in SARS patients. *Clin. Diagn. Lab. Immunol.*, 11 (2), 287–291.

326 Kifude, C.M., Rajasekariah, H.G., Sullivan, D.J. Jr., Stewart, V.A., Angov, E., Martin, S.K., Diggs, C.L., and Waitumbi, J.N. (2008) Enzyme-linked immunosorbent assay for detection of *Plasmodium falciparum* histidine-rich protein 2 in blood, plasma, and serum. *Clin. Vaccine Immunol.*, **15** (6), 1012–1018.

327 Mishra, A., Goswami, T.K., and Shukla, D.C. (2007) An enzyme-linked immunosorbent assay (ELISA) to measure growth hormone level in serum and milk of buffaloes (*Bubalus bubalis*). *Indian J. Exp. Biol.*, **45** (7), 594–598.

328 Sjogren, A.C., Kaper, J.B., Caprioli, A., and Karpman, D. (2004) Enzyme-linked immunosorbent assay for detection of Shiga toxin-producing *Escherichia coli* infection by antibodies to *Escherichia coli* secreted protein B in children with hemolytic uremic syndrome. *Eur. J. Clin. Microbiol. Infect. Dis.*, **23** (3), 208–211.

329 Vinocur., J.M., ELISA-Sandwich, http://en.wikipedia.org/wiki/File:ELISA-sandwich.svg. 2006 (12 January 2011).

330 Sinauer Associates and Sumanas, Inc. Enzyme-Linked Immunosorbent Assay (ELISA), http://www.sumanasinc.com/webcontent/animations/content/ELISA.html. 2002 (11 January 2011).

331 Thevenot, D.R., Toth, K., Durst, R.A., and Wilson, G.S. (1996) International Union of Pure and Applied Chemistry Physical Chemistry Division, Steering Committee on Biophysical Chemistry Analytical Chemistry Division, Commission V.5 (Electroanalytical Chemistry) Electrochemical Biosensors: Proposed Definitions and Classification Synopsis of the Report. *Sens. Actuators B*, **30** (1), 81.

332 Scheller, F.W. (1998) Neue Aspekte der Biosensorik. 9. Heiligenstädter Kolloquium "Technische Systeme für Biotechnologie und Umwelt", Heiligenstadt, p. 14.

333 Aizawa, M., Nishiguchi, K., Imamura, M., Kobatake, E., Haruyama, T., and Ikariyama, Y. (1995) Integrated molecular systems for biosensors. *Sens. Actuators B*, **24** (1–3), 1–5.

334 Marks, R.S., Lowe, C.R., Cullen, D.C., Weetall, H.H., and Karube, I. (2007) *Handbook of Biosensors and Biochips*, John Wiley & Sons, Inc., Hoboken, NJ.

335 Spichiger-Keller, U. (1998) *Chemical Sensors and Biosensors for Medical and Biological Applications*, Wiley-VCH Verlag GmbH, Weinheim.

336 Yang, V.C. and Ngo, T.T. (2000) *Biosensors and Their Applications*, Kluwer Academic/Plenum Publishers, New York.

337 The Hebrew University. Development of Biosensors, http://chem.ch.huji.ac.il/. 2010 (22 June 2010).

338 Clark, L.C. Jr. and Lyons, C. (1962) Electrode systems for continuous monitoring in cardiovascular surgery. *Ann. N. Y. Acad. Sci.*, **102**, 29–45.

339 Zahn, D., Szeponik, J., and Ganghi, A. (2009) Novel device for quick measurement of glucose in POCT areas without pre-analytical steps based on a multi-way glucose biosensor. *Eng. Life Sci.*, **9** (5), 398–403.

340 Zahn, D., Szeponik, J., and Ganghi, A. (2008) Biosensoren für die Point-of-care-Diagnostik. Technical report. Lecture given at the 14th Heiligenstädter Kolloquium "Technische Systeme für die Lebenswissenschaften"

341 Mendosa, D. The GlucoWatch Biographer, http://www.mendosa.com/glucowatch.htm. 2009 (11 January 2011).

342 Fechner, P., Proll, F., Carlquist, M., and Proll, G. (2009) An advanced biosensor for the prediction of estrogenic effects of

endocrine-disrupting chemicals on the estrogen receptor alpha. *Anal. Bioanal. Chem.*, **393** (6–7), 1579–1585.

343 Tunnemann, R., Mehlmann, M., Sussmuth, R.D., Buhler, B., Pelzer, S., Wohlleben, W., Fiedler, H.P., Wiesmuller, K.H., Gauglitz, G., and Jung, G. (2001) Optical biosensors. Monitoring studies of glycopeptide antibiotic fermentation using white light interference. *Anal. Chem.*, **73** (17), 4313–4318.

344 Myszka, D.G. and Rich, R.L. (2000) Implementing surface plasmon resonance biosensors in drug discovery. *Pharm. Sci. Technol. Today*, **3** (9), 310–317.

345 Herold, K.E. and Rasooly, A. (2009) *Lab-on-a-Chip Technology*, vols. **1** and **2**, Caister Academic Press, Norwich.

346 Agilent. Lab-on-a-Chip, www.chem.agilent.com. 2011 (11 January 2011).

347 Terry, S.C. (1975) A gas chromatographic air analyser fabricated on silicon wafer using integrated circuit technology. PhD thesis, Stanford University.

348 Jerman, J.H. and Terry, S.C. (1981) A miniature gas chromatograph for atmospheric monitoring. *Environ. Int.*, **5**, 77–83.

349 Tian, W.-C. and Finehout, E. (2008) *Microfluidics for Biological Applications*, Springer, Berlin.

350 Hsu, H., Ohta, A.T., Chiou, P.Y., Jamshidi, A., Neale, S.L., and Wu, M.C. (2010) Phototransistor-based optoelectronic tweezers for dynamic cell manipulation in cell culture media. *Lab Chip*, **10** (2), 165–172.

351 Wang, J., Heo, J., and Hua, S.Z. (2010) Spatially resolved shear distribution in microfluidic chip for studying force transduction mechanisms in cells. *Lab Chip*, **10** (2), 235–239.

352 Streng, D.E., Lim, S.F., Pan, J., Karpusenka, A., and Riehn, R. (2009) Stretching chromatin through confinement. *Lab Chip*, **9** (19), 2772–2774.

353 Mahalanabis, M., Al-Muayad, H., Kulinski, M.D., Altman, D., and Klapperich, C.M. (2009) Cell lysis and DNA extraction of Gram-positive and Gram-negative bacteria from whole blood in a disposable microfluidic chip. *Lab Chip*, **9** (19), 2811–2817.

354 Sauer-Budge, A.F., Mirer, P., Chatterjee, A., Klapperich, C.M., Chargin, D., and Sharon, A. (2009) Low cost and manufacturable complete microTAS for detecting bacteria. *Lab Chip*, **9** (19), 2803–2810.

355 Kuhn, S., Phillips, B.S., Lunt, E.J., Hawkins, A.R., and Schmidt, H. (2010) Ultralow power trapping and fluorescence detection of single particles on an optofluidic chip. *Lab Chip*, **10** (2), 189–194.

356 BioTek Instruments, Inc. Biotec Synergy 4 Hybrid Multi-Mode Microplate Reader, http://mktg.biotek.com/Products/Synergy4/Syn4_Combi_Illustration_lrg.jpg. 2010 (12 January 2011).

357 Karlberg, B. and Pacey, G.E. (1989) *Flow Injection Analysis: a Practical Guide*, Elsevier, Amsterdam.

358 Ruzicka, J. and Hansen, E.H. (1975) Flow injection analysis. Part I. A new concept of fast continuous flow analysis. *Anal. Chim. Acta*, **78**, 145–157.

359 Ikebukuro, K., Wakamura, H., Karube, I., Kubo, I., Inagawa, M., Sugawara, T., Arikawa, Y., Suzuki, M., and Takeuchi, T. (1996) Phosphate sensing system using pyruvate oxidase and chemiluminescence detection. *Biosens. Bioelectron.*, **11**, 959–965.

360 Baptista, M.S., Tran, C.D., and Gao, G.H. (1996) Near-infrared detection of flow injection analysis by acoustooptic tunable filter-based spectrophotometry. *Anal. Chem.*, **68** (6), 971–976.

361 Trojanowicz, M. (2000) *Flow Injection Analysis: Instrumentation and Applications*, World Scientific, Singapore.

362 Ocean Optics, Inc. Fluorimeters, http://www.oceanoptics.com/products/fiasialov.asp. 2010 (11 January 2011).

363 Grodrian, A., Metze, J., Henkel, T., Martin, K., Roth, M., and Kohler, J.M. (2004) Segmented flow generation by chip reactors for highly parallelized cell cultivation. *Biosens. Bioelectron.*, **19** (11), 1421–1428.

364 Schumacher, J.T., Grodrian, A., Lemke, K., Römer, R., and Metze, J. (2008) System development for generating homogeneous cell suspensions and

transporting them in microfluidic components. *Eng. Life Sci.*, **8** (1), 49–55.
365 Tzanavaras, P. Flow Injection Analysis, http://www.scitopics.com/Flow_Injection_Analysis.html, Elsevier. 2008 (11 January 2011).
366 Eibl, R. and Eibl, D. (2009) *Disposable Bioreactors*, Springer, Berlin.
367 Ulber, R., Frerichs, J.G., and Beutel, S. (2003) Optical sensor systems for bioprocess monitoring. *Anal. Bioanal. Chem.*, **376** (3), 342–348.
368 optek-Danulat, Inc. Fermenter Control Photometric Converter, http://www.optek.com/Product_Detail.asp?ProductID=24. 2010 (11 January 2011).
369 Madrid, R.E. and Felice, C.J. (2005) Microbial biomass estimation. *Crit. Rev. Biotechnol.*, **25** (3), 97–112.
370 Dremel, B.A.A. and Schmid, R.D. (2004) Optische Sensoren für die Bioprozeß-Kontrolle. *Chem.-Ing.-Tech. – CIT*, **64** (6), 510–517.
371 Schrenkhammer, P. (2008) Optical Biosensors for Uric Acid and Glucose. PhD thesis, University of Regensburg.
372 Cole-Parmer. Fluoroprobe Handheld Optical Dissolved Oxygen Meter, http://www.coleparmer.com/catalog/product_view.asp?sku=0594720. 2010 (11 January 2011).
373 Nandakumar, M.P., Nandakumar, R., and Mattiasson, B. (2000) Fluorimetric quantification of intracellular lactate dehydrogenase during fermentation using flow injection analysis. *Biotechnol. Lett.*, **22** (18), 1453–1457.
374 Luong, J.H.T. and Mulchandani, A. (1990) Application of NADH-dependent fluorescence sensors for monitoring and controlling bioprocesses, in *Sensors in Bioprocess Control* (eds J.V. Twork and A.M. Yacynych), Marcel Dekker, Inc., pp. 75–94.
375 Guenneugues, P., Chibois, S., and Trystram, G. (1990) Application of NADH fluorosensor for on-line biomass measurements in yeast fermentation on whey substrates. *Food Control*, **1** (4), 236–241.
376 Sato, K., Yoshida, Y., Hirahara, T., and Ohba, T. (2000) On-line measurement of intracellular ATP of *Saccharomyces cerevisiae* and pyruvate during sake mashing. *J. Biosci. Bioeng.*, **90** (3), 294–301.
377 Lasko, D.R. and Wang, D.I. (1996) On-line monitoring of intracellular ATP concentration in *Escherichia coli* fermentations. *Biotechnol. Bioeng.*, **52** (3), 364–372.
378 Funabashi, H., Imajo, T., Kojima, J., Kobatake, E., and Aizawa, M. (1999) Bioluminescent monitoring of intracellular ATP during fermentation. *Luminescence*, **14** (6), 291–296.
379 Hennenberg, K.J. Aquatic Biomass: Sustainable Bioenergy from Algae?, www.bioenergywiki.net/images/8/8a/Input-paper.pdf, Öko-Institut eV, Darmstadt. 2009 (11 January 2011).
380 FAO. Algae-Based Biofuels: a Review of Challenges and Opportunities for Developing Countries, ftp://ftp.fao.org/docrep/fao/011/ak333e/ak333e00.pdf, Food and Agriculture Organization of the United Nations (FAO), Environment, Climate Change and Bioenergy Division, Rome. 2009 (12 January 2011).
381 Ackermann, U. (2007) Mikrotechniken für eine effiziente Energierzeugung. Technical Report, Bundesministerium für Bildung und Forschung, Bonn.
382 Barbosa, M.J.G.d.V. (2003) Microalgal photobioreactors: scale-up optimization. PhD thesis, Wageningen University.
383 Hielscher Ultrasonics GmbH. Die Reinigung von Photo-Bioreaktoren mit Ultraschall, http://www.hielscher.com/ultraschall/algae_reactor_cleaning_01.htm. 2009 (11 January 2011).
384 Ashkin, A. (1980) Applications of laser radiation pressure. *Science*, **210** (4474), 1081–1088.
385 Ashkin, A. (1997) Optical trapping and manipulation of neutral particles using lasers. *Proc. Natl. Acad. Sci. USA*, **94** (10), 4853–4860.
386 Perkins, T.T., Quake, S.R., Smith, D.E., and Chu, S. (1994) Relaxation of a single DNA molecule observed by optical microscopy. *Science*, **264** (5160), 822–826.
387 Greulich, K.O. (1999) *Micromanipulation by Light in Biology and Medicine: the Laser Microbeam and Optical Tweezers. Methods in Bioengineering*, Birkhäuser, Boston.

388 Cumpston, B.H., Ananthavel, S.P., Barlow, S., Dyer, D.L., Ehrlich, J.E., Erskine, L.L., Heikal, A.A., Kuebbler, S.M., Lee, I.-Y.S., McCord-Maughton, D., Qin, J., Röckel, H., Rumi, M., Wu, X., Marder, S.R., and Perry, J. (1999.) Two-photon polymerization initiators for three-dimensional optical data storage and microfabrication. *Nature*, **398**, 51–54.

389 Galajda, P. and Ormos, P. (2001) Complex micromachines produced and driven by light. *Appl. Phys. Lett.*, **78**, 249.

390 Curtis, J.E., Koss, B.A., and Grier D.G. (2002) Dynamic holographic optical tweezers, *Opt. Commun.*, **207**, 169–175.

391 Berns, M.W. and Greulich, K.O. (2007) *Laser Manipulation of Cells and Tissue, Methods in Cell Biology*, vol. **82**, Academic Press, New York.

7
Biology

Stefan H. Heinemann, Roland Schönherr, and Toshinori Hoshi

Biophotonics comprises several scientific and technological disciplines that have in common an interaction of light, photons, with biologically relevant material. A prerequisite of research and development in the field of biophotonics is a firm understanding of the structure, function, and organization of organisms and their components, both as a whole and in isolation – a wide area collectively summarized by the term biology. Since a large branch of biophotonics applications involves the diagnosis and treatment of human diseases, knowledge of some fundamentals of medicine is also helpful.

Living material is always organized in cells and a biophotonics experiment most often must extract information from light–cell interactions. Although cells can be extremely diverse in their appearance and function (see Section 7.2), a prototypical cell model as depicted in Figure 7.1a may serve to indicate some common cellular features. Cells are always separated from the environment by a very thin lipid bilayer (about 4 nm), the plasma membrane. Cells also contain a large nucleus (often 5 μm in diameter), which contains the chromosomes holding the genetic information. The power plants of cells are mitochondria; these organelles have a size comparable to that of bacteria (about 1 μm in length). Whereas cell bodies typically range in diameter between 10 and 50 μm, some nerve cells can have very long fiber-like axons, for example, reaching from the spinal cord to the little toe.

Biologically relevant processes span a very wide range of length and time scales and, hence, pose a challenge to the experimenter. As illustrated in Figure 7.1b, biophotonics employs a relatively narrow spectrum of electromagnetic radiation including visible light to gain information about length scales ranging from individual chemical bonds, proteins, and organelles to long cellular structures. The range of time scales of interest in biology is even more impressive, as illustrated in Figure 7.1c. Whereas biologically relevant chemical bonds may be broken and formed in less than 1 ns, molecules holding the genetic information may last for the entire lifespan of an organism.

This chapter on biology provides quick access to the most relevant aspects of the life sciences, with particular reference to potential biophotonics applications. It is primarily intended for students and researchers from outside the field of life

Handbook of Biophotonics. Vol.1: Basics and Techniques, First Edition.
Edited by Jürgen Popp, Valery V. Tuchin, Arthur Chiou, and Stefan H. Heinemann.

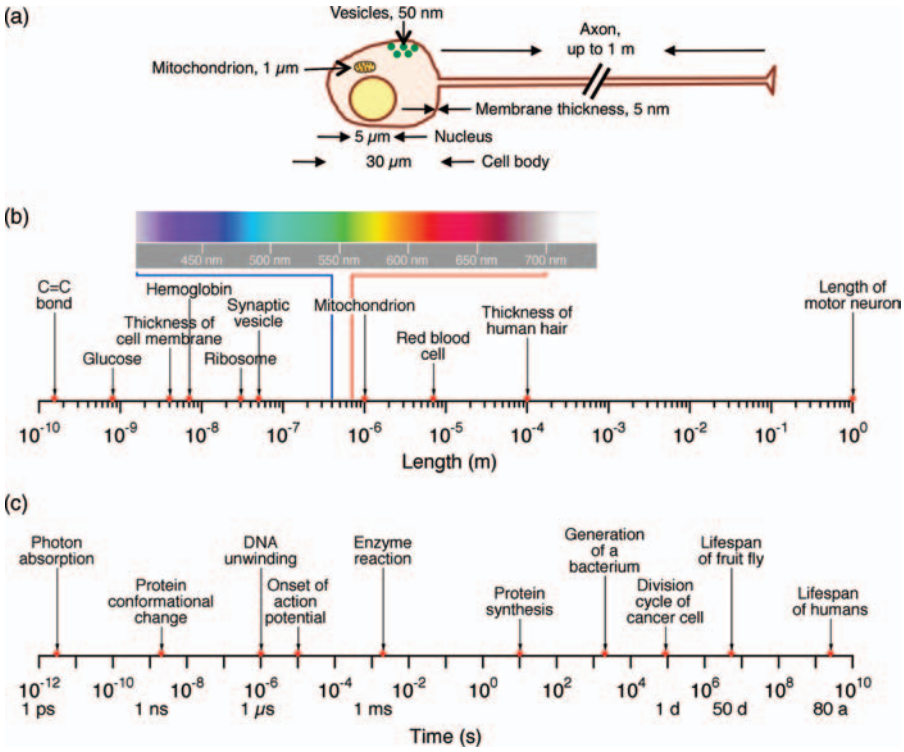

Figure 7.1 Overview of length and time scales. (a) A prototypic neuronal cell with a cell body and a long axon with some typical length scales indicated. (b, c) Selected length and time scales of biological material and processes [parts (b) and (c) adapted from Stryer [1]].

sciences, such as physicists, chemists, and engineers. It is not meant to be a comprehensive source of biology, which can be found in numerous excellent textbooks. Instead, we have attempted to cover selected topics to provide illustrative access to general biological problems and the language of biology, thereby facilitating communication between biophotonicists and biomedical scientists. We are aware that several exciting aspects of biology cannot be discussed in depth here. Nevertheless, summarizing in a somewhat naive way how life works from an engineer's perspective may be a suitable starting point for examining some fascinating aspects of biology and medicine.

We start with a description of the most relevant biomolecules and their properties. Section 7.1, providing a quick reference to biochemistry, will be essential because the biomolecules are the ultimate targets for light–matter interactions. We continue with a presentation of various cell types and the organization of cells in Section 7.2, topics that are usually found in textbooks on cell biology. In Section 7.3, we discuss several ways in which cells communicate with each other and how communication takes place inside cells. Such communication processes are usually termed cell signaling and the corresponding textbooks are on molecular cell biology. The reader may notice the complete absence of references to physiology, organs, and whole organisms –

essentially the most important aspects of biology. Such topics are far beyond the scope of this chapter. Therefore, to illustrate how molecular and cellular dysfunctions alter the whole organism, we discuss in Section 7.4 a few human diseases, their pathomechanisms, diagnosis, and possible therapies. Given the obvious link of biophotonics to biotechnological applications, we present a few standard methods for the handling of biological material in information Boxes. Insight into such methods will help the biophotonicist to evaluate the feasibility of experimental plans.

7.1
Biomolecules: Building Blocks of Living Matter

Even a relatively simple organism, such as the intestinal bacterium *Escherichia coli*, consists of several thousands of different types of molecules. In a typical human cell, there are certainly more than 100 000 types of molecules and many more remain to be identified. Therefore, obtaining information from a spectroscopic experiment in which the light–matter interaction is studied in living cells must appear a tremendously complicated task. However, the situation is not hopeless because the molecules of living material are organized in a hierarchical manner, ranging from free protons, metal ions, and water to macromolecules with a size greater than 1000 Da (the dalton is a unit commonly used in biology. 1 Da is one-twelfth the mass of a ^{12}C atom, that is, 1.66×10^{-27} kg. Proteins mostly have a mass of several thousand daltons, usually abbreviated as kDa). By means of self-aggregation, even greater complexes, so-called molecular aggregates such as membranes and fibers, are formed.

As shown in Table 7.1, about 70% of the mass of a bacterial cell consists of water, and macromolecules account for about 25%. The latter are polymers; chain-like molecules formed from a limited set of smaller units, the monomers. Hence there are many thousands of different types of macromolecules inside a cell, but the unitary elements are always the same, somewhat simplifying the situation. As depicted in Figure 7.2, the most important polymers are nucleic acids built of only eight different

Table 7.1 The approximate chemical composition of a bacterial cell (after Alberts *et al.* [2]).

Component	% of total weight	Number of types of each molecule
Water	70	1
Inorganic ions	1	20
Sugars and precursors	1	250
Amino acids and precursors	0.4	100
Nucleotides and precursors	0.4	100
Fatty acids and precursors	1	50
Other small molecules	0.2	~300
Macromolecules (proteins, nucleic acids, polysaccharides)	26	~3000

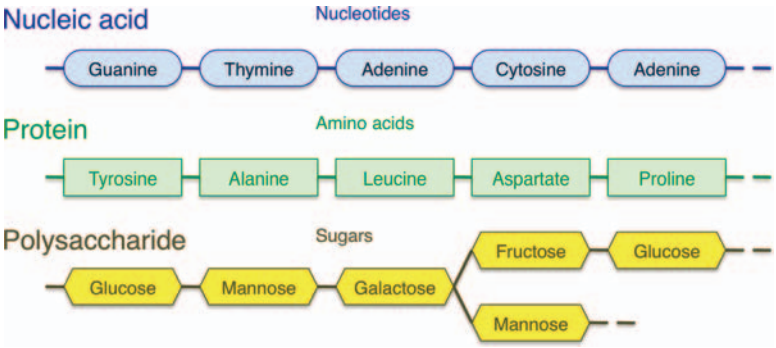

Figure 7.2 Polymeric biomolecules. Whereas nucleic acids and proteins are linear chains of monomers, polysaccharides can form branched chains.

nucleotides (see Section 7.1.1), proteins typically built of 20 different amino acids (see Section 7.1.2), and polysaccharides consisting of different types of sugar molecules (Section 7.1.3). Membranes are formed by various types of lipids (Section 7.1.4); they are more heterogeneous in structure but also harbor modular fatty acid components. The relatively stereotypical structure of polymers can be diversified by specific chemical modification of their components, as discussed below for proteins. Proteins made solely of amino acids cannot achieve some tasks, such as the light harvesting of the protein rhodopsin in the eye. Such special-purpose proteins therefore contain specific prosthetic groups or cofactors, many of which are of particular interest to biophotonics research (Section 7.1.5). Finally, in Section 7.1.6 we address some important nonpolymeric molecules.

7.1.1
Nucleic Acids: Storage of Genetic Information

Virtually all mammalian cells are composed of many proteins, lipids, and sugars, and some nucleic acids (Table 7.2). Since the latter are the storage medium for genetic information and, hence, they contain the information necessary to produce all the other biomolecules and to replicate itself, we start with a description of these very long polymeric molecules.

The key type of macromolecule is deoxyribonucleic acid (DNA); it forms two intertwined chains, each built of individual nucleotides (see Figure 7.4). The nucleotides themselves consist of a sugar moiety, the deoxyribose, a phosphate moiety, and one of four bases: adenine (A), thymine (T), guanine (G), or cytosine (C) (Figure 7.3). Genetic information is encoded by the sequence of these four nucleotides. Since there are four nucleotides, the number of possible combinations of a chain of n nucleotides is 4^n. In molecular biology, the length of DNA typically is expressed in units of bases, that is, one kilobase (kb) or one megabase (Mb) is a nucleic acid molecule 1000 or 1 000 000 nucleotides in length, respectively. Since DNA in the nucleus is a double-stranded molecule, one often refers to base pairs (bp) instead of just bases. In order to distinguish between computer storage (measured in

Table 7.2 Approximate chemical compositions of a bacterium and a typical mammalian cell[a].

	E. coli	Mammalian cell
Water	70	70
Inorganic ions	1	1
Miscellaneous small metabolites	3	3
Proteins	15	18
RNA	6	1.1
DNA	1	0.25
Phospholipids	2	3
Other lipids	—	2
Polysaccharides	2	2

[a]Numbers represent percentage of total cell weight (after Alberts *et al.* [2]).

kilobytes and megabytes) and genetic information, kbp and Mbp are also used. The entire human genome comprises about 3 billion base pairs (3000 Mbp or 3 Gbp). Since nearly every human cell carries its genome in duplicate, having one copy of each chromosome from the father and mother, the total cellular DNA content is 6 Gbp in the so-called diploid cell. In eukaryotic cells, most DNA is organized in 8–60 chromosomes in the cell nucleus, while a very small fraction of DNA exists in the

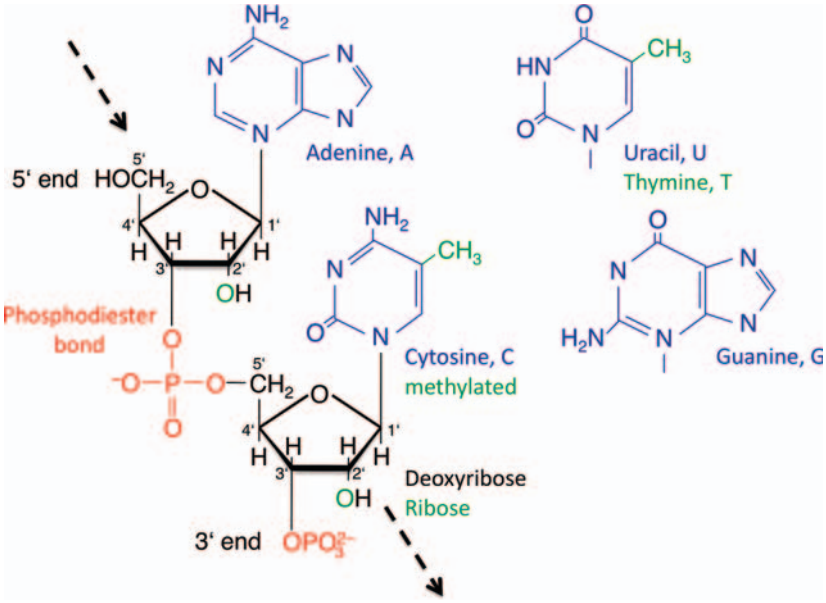

Figure 7.3 DNA and RNA are made by linking individual nucleotides via phosphodiester bonds (red). The coupling occurs between the 3′ and the 5′ carbons of a sugar moiety, a ribose for RNA and a deoxyribose for DNA (black). The nucleotides differ in the structure of their bases (blue). In RNA, uracil is used instead of thymine (5-methyluracil). Also shown is the methylated form of cytosine (5-methylcytosine).

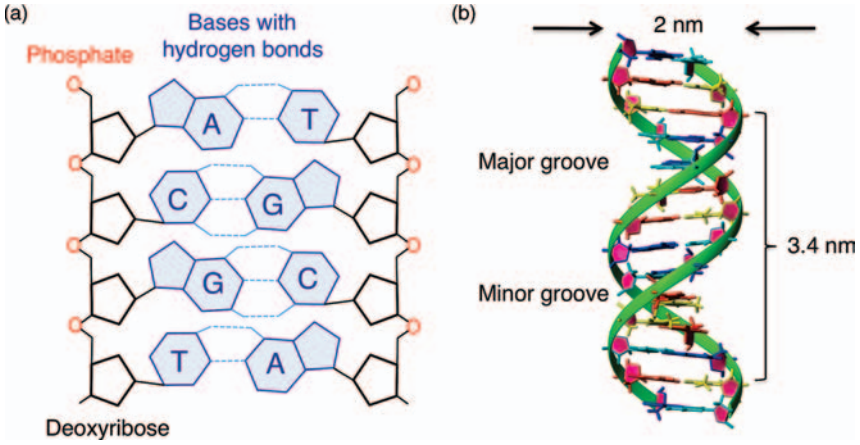

Figure 7.4 Double-stranded DNA. (a) Base pairing by formation of hydrogen bonds between the bases A/T and G/C. (b) Model structure of B-DNA (courtesy of Dr. Matthias Görlach, Jena).

mitochondria, intracellular membrane-bound compartments within a cell (in humans, mitochondrial DNA comprises only 16 569 nucleotides).

The sequence of nucleotides in one DNA chain determines the sequence of the other, complementary, chain. This is because both chains bind to each other via hydrogen bonds between the bases. Two hydrogen bonds can be formed between adenine and thymine, and three between guanine and cytosine (Figure 7.4). Therefore, only the pairs A–T and G–C are allowed when two nucleic acid chains hybridize to form double-stranded DNA. The unambiguous coupling of the nucleotides ensures that one chain is an exact complementary copy of the other. When cells divide, all constituents and also the DNA must be replicated. In this phase, the double-stranded DNA opens, and both chains are the templates for the synthesis of new complementary offspring chains. Therefore, in a daughter cell the DNA consists of one newly synthesized nucleic acid chain and one "inherited" from the parent cell.

The interpretation of the information stored in the DNA sequence implies the definition of so-called genes – regions of the DNA that actually contain the blueprint for the formation of proteins or for functional ribonucleic acid (RNA) molecules, including flanking regions with regulatory function. Surprisingly, there are only a fairly limited number of genes in the human genome (about 20 000–25 000). Moreover, the number of genes is not a good indicator of the complexity of an organism, as exemplified by the worm *Caenorhabditis elegans* (18 300 genes), the fruit fly *Drosophila melanogaster* (13 300 genes), and the plant *Arabidopsis thaliana* (25 700 genes). The largest parts of all DNA sequences have either regulatory function or can be allocated to so-called introns, noncoding regions that are interspersed between the coding regions called exons. In most cases, genes are composed of several exons, linked at later stages by a process termed gene splicing. Only about 2% of the total human genome sequence contains such blueprint information. The remaining part of the DNA sequence does not appear to code for known functional products.

Roughly half of the human genome is covered by so-called *repetitive sequences*, short repeating stretches of nucleotides. Such repetitive regions have a structural role both at the ends and in the central region of each chromosome, the centromere.

According to the so-called *central dogma of molecular biology*, the amino acid sequences of all proteins are unambiguously determined by the gene sequences. For the expression of genetic information, the translation of a gene into a protein sequence, a copy of the DNA is made for a specific gene only. During this process of transcription, a complementary copy of one DNA chain is formed to generate a chain of RNA. This nucleic acid typically is a single-stranded molecule. It has strong similarity to DNA, but the sugar moiety of the monomers is a ribose instead of a deoxyribose; at the 2′ (read as "two prime") position of the sugar ring there is an OH group instead of a proton (Figure 7.3). In addition, in place of the base thymine, a uracil (U) is used. As a consequence, an adenine (A) in the DNA is transcribed to uracil (U) in the RNA. The information stored on the RNA is then translated into a sequence of amino acids to form a protein. In this process, *three* succeeding nucleotides inside a coding reading frame (triplets or codons) always code for *one* amino acid (see Figure 7.7).

Because translation of genetic information from RNA into a protein sequence takes place outside the nucleus, one task of the RNA molecules is to send the message from the DNA to the site of translation, and therefore this type of nucleic acid is called messenger RNA (mRNA). Another form of RNA is transfer RNA (tRNA). On the one hand, they expose a triplet of ribose nucleotides coding for a specific amino acid. On the other, they bind that amino acid as cargo. By means of the triplet-encoded codon, the tRNA *transfers* the amino acid to the correct position of the template mRNA during the process of protein synthesis. In addition, there are regulatory forms of RNA that play a role in how genes are translated into proteins (siRNA and miRNA) (see the following information Box). In general, DNA is largely a stable storage molecule for genetic information, whereas RNA serves more diverse functions and, in some cases, even exhibits enzymatic activity. Regulatory RNAs can be very small and their functional role is only beginning to be elucidated.

Downregulation of Genes by RNA Interference (RNAi)

One mechanism of post-transcriptional gene regulation is based on double-stranded RNA molecules derived from genomically encoded micro-RNAs (miRNAs). After processing in the nucleus and in the cytosol, double-stranded RNA fragments of ~20–25 bp are generated. These small interfering RNAs (siRNAs) inhibit complementary mRNA and, hence, prevent the production of the encoded protein. Using synthetic siRNA molecules, molecular biologists can thus disable the expression of specific genes, referred to as gene silencing or gene knock-down. In an alternative approach, genetically modified viruses can be used to express siRNA precursors that are processed to functional siRNA by the endogenous RNA interference (RNAi) machinery. RNAi technology provides important tools for cell biology and the potential for therapeutic applications in molecular medicine is being evaluated.

7.1.1.1 Structure

The nucleotides used for storage of genetic information harbor bases with either a pyrimidine ring (C, U, T) or a purine heterocycle (A, G).

The bases in DNA can be chemically modified slightly without any fundamental change in the nucleotide sequence to regulate gene expression, a process collectively referred to as epigenetics. One well-known example of an epigenetic phenomenon is methylation of cytosine and adenine.

Individual nucleotides are linked by means of phosphodiester bonds connecting the ribose ring at the 3′-position with the CH_2 group at the 5′-position (Figure 7.3). According to commonly accepted convention, genetic sequences are read from left to right, that is, from the 5′ to the 3′ end, and this is also the direction of synthesis. A sequence coding for a protein read in this direction is referred to as *sense* sequence, and that of the complementary strand as *antisense* sequence.

At a physiological pH of about 7.2, the phosphodiester groups are negatively charged such that DNA and RNA migrate in electric fields, an important feature used for electrophoretic analysis of these molecules (see the following information Box).

Gel Electrophoresis

Most biological macromolecules are charged and, hence, in an electric field they will move according to their overall charge. The average distance moved depends on the electric field and also on the charge, the size, and the surface structure of the molecules. Hence a given mixture of biomolecules exposed for a certain time to an electric field will be separated according to their molecular properties. The resolution power of standard electrophoresis systems is strongly increased by meshed or porous matrices, such as agarose or polyacrylamide gel, through which the biomolecules are forced to move. The electrophoresis of biomolecules through various types of gels is a powerful and inexpensive method commonly used in molecular biology to analyze and separate RNA, DNA, and proteins. Depending on the type of molecule to be analyzed, various staining methods to visualize the biomolecules under study are applied, such as fluorescent ethidium bromide for DNA/RNA and Coomassie Brilliant Blue stain for proteins. As all nucleic acids have identical densities of negative charge, their electrophoretic mobility directly reflects the molecule size if they are assumed to be in the same conformation, such as the linear double-stranded form. By contrast, proteins are much more heterogeneous in size and charge and typically analyzed using sodium dodecyl sulfate polyacrylamide gel electrophoresis (SDS-PAGE). The anionic detergent SDS unfolds the proteins and provides a uniform charge density on the surface such that the electrophoretic mobility of a protein is roughly linear to the logarithm of its molecular weight.

The long DNA molecules adopt specific three-dimensional structures. The most important form, predicted by James Watson and Francis Crick in their pioneering work awarded the Nobel Prize in Physiology or Medicine in 1962, is a double-helical

right-handed spiral, also called B-DNA (Figure 7.4b). This configuration is stabilized by the hydrogen bonds formed between the matching bases A–T and G–C. These so-called Watson–Crick base pairs result in a very stable DNA configuration with the bases, that is, the moieties carrying the information on the DNA, pointing to the center of the strand, and the negatively charged phosphate backbone facing the outside so as to minimize electrostatic repulsion between the individual chains. The helical double strand has a thickness of about 2 nm, and 10 bp are required for one helical turn. The stacked bases are rotated by 36° with respect to the immediate neighbor. The distance from one ribose to the next is about 0.34 nm. Thus, a single copy of the entire human genome would correspond to a linear DNA molecule of about 1 m in length. The binding of complementary single DNA strands to form a double-stranded DNA is referred to as hybridization. The stability of the double-stranded DNA depends strongly on the temperature. Heating beyond a certain critical "melting" temperature results in the separation of the strands.

As the DNA strands wind around each other, they leave gaps between each set of phosphate backbones, revealing the sides of the bases inside. There are two of these grooves twisting around the surface of the double helix: the major groove is 2.2 nm wide and the other, the minor groove, is 1.2 nm wide. The greater accessibility in the major groove means that DNA-interacting proteins such as transcription factors that can bind to specific sequences in double-stranded DNA usually make contacts with the sides of the bases exposed in the major groove.

The double-stranded DNA is stable, but for the synthesis of mRNA, the DNA template must be present as single strands to expose the bases. Specific enzymes are required to open the double strand and to initiate the transcription. The propensity that this actually happens itself is encoded in the DNA sequence using multiple mechanisms. One strategy is based on the difference in binding energy between the base pairs. Because the C–G pair is more stable than the A–T pair, DNA sequences with a high AT content are less stable and easier to "open." Such TATA boxes then often provide access for transcription factors – proteins that regulate (activate or inactivate) the transcription of specific genes.

There are additional, less common forms of DNA whose physiological roles are not yet clear. The A form is a wider right-handed spiral, with a shallow, wide minor groove and a narrower, deeper major groove. The A form occurs under nonphysiological conditions in dehydrated samples of DNA, whereas in the cell it may be produced in hybrid pairings of DNA and RNA strands, and also in enzyme–DNA complexes. Segments of DNA where the bases are methylated may undergo a larger change in conformation and adopt the Z form. Here, the strands turn about the helical axis in a left-handed spiral.

Densely packed DNA strands form chromosomes, which are large structures visible with conventional microscopy. Mammals are typically diploid; every mononucleated somatic cell contains two copies of the set of chromosomes. In humans there are 22 autosomal chromosomes plus the X and Y chromosomes, which determine the gender (female, XX; male, XY). Some individuals with chromosomal disorders carry an extra chromosome, the most common case being trisomy 21, also referred to as Down syndrome. In an extended fashion the helical DNA strand of a

typical human chromosome would have a length of about 50 mm; it would by far not fit into a cell. Moreover, in this configuration the DNA would be inherently unstable. Therefore, in the nucleus the DNA is further condensed with the aid of specialized proteins, the histones. The double-stranded DNA makes two turns while wrapping around a complex of eight histones, thus forming a unit called a nucleosome. These units are cross-linked with H1 histones to form a fiber about 30 nm in diameter. The complex of histones and condensed DNA is referred to as chromatin. The chromatin fiber of a typical chromosome would still have a length of 1 mm. The chromatin is therefore further folded to form the structure of a chromosome. In a configuration in the metaphase of cell division a chromosome can have a length of about 5 μm.

7.1.1.2 Enzymes for DNA and RNA processing

DNA in a chromosome is densely packed with proteins and specific enzymes play key roles in regulating gene transcription. Therefore, under *in vivo* conditions DNA is rarely found in isolation but typically associated with complex clusters of proteins, some of which may have enzymatic activity, facilitating specific chemical reactions. Such enzymatically mediated reactions are necessary to maintain the organization of the supercoiled structure of the very long DNA molecules. DNA pieces need to be cut out and pasted together again to avoid the formation of knots. Replication and transcription are finely regulated and they require the synthesis of new strands of nucleic acids. In particular, because many of these enzymes are valuable tools in molecular biological research, we will briefly address some of them.

Cut and Paste of DNA Nucleases are enzymes that cut DNA or RNA strands by catalyzing the hydrolysis of the phosphodiester bonds (DNAses and RNAses, respectively). Endonucleases cut within a strand whereas exonucleases only remove single nucleotides from the ends. The physiological purpose of DNAses and RNAses is the degradation of the nucleic acids. Experimentally, these enzymes are powerful tools in molecular biology for the targeted isolation of RNA or DNA, respectively. Because of the inherent instability of RNA, trace amounts of RNAses in the laboratory pose a serious problem in handling large RNA molecules. Two DNA strands are rejoined or concatenated (ligated) with the aid of ligases.

Topoisomerases combine the activities of both nucleases and ligases. Thus, they cut a DNA double strand, rotate it, and paste it together again. Topoisomerases therefore reduce the degree of supercoiling when double-stranded DNA is unwound and solve the complex topology problem arising from the helical DNA structure.

Some endonucleases are very specific for the sequence motif at which they cleave the DNA. Such *restriction* endonucleases are indispensable tools in molecular biology as they allow site-specific fragmentation of DNA, for example, for the generation of restriction maps. In addition, restriction enzymes are used to extract specific stretches of DNA from larger DNA structures (e.g., plasmid DNA) for further processing. Most restriction endonucleases originate from bacteria and the enzyme names indicate the origins. For example, the enzyme *Eco*RV comes from *E. coli* and it recognizes the 6-base sequence 5′-GAT|ATC-3′ and cuts at the vertical line, thus leaving "blunt" DNA ends. Other restriction enzymes cut in an asymmetric manner.

The restriction enzyme *Hin*dIII from *Haemophilis influenzae* cuts at the sequence 5′-G|AATTC-3′, leaving single-strand overhangs of four nucleotides, so-called "sticky ends."

Synthesis of New DNA or RNA DNA replication and gene transcription, that is, the synthesis of mRNA, require access to the base sequence of the DNA. The inner-facing hydrogen-bonded bases are not accessible from the outer perimeter in double-helical DNA and the double strand must be "opened." This task is achieved with the aid of energy-consuming enzymes, the helicases; they break the hydrogen bonds between bases and unwind the double-helical DNA into single strands.

The exposed bases are used to synthesize a new complementary strand of DNA or RNA by DNA or RNA polymerases, respectively. These polymerases bind to the single-strand DNA template and join individual nucleoside triphosphates, always working from the 5′ to the 3′ end. DNA replication catalyzed by DNA polymerase is a critical step in biology because a perfect complementary copy of the genome must be synthesized in every cell division. Therefore, many polymerases have a so-called proofreading activity to check and correct for mistakes in DNA synthesis. Transcription or RNA synthesis requires DNA-dependent RNA polymerases; they take single-stranded DNA as a template but synthesize the complementary RNA sequence. Transcription is initiated by binding of the RNA polymerases to specific promoter sequences preceding the actual coding region of a gene and by unwinding the DNA. Transcription terminates at termination sequences encoded in the DNA.

Polymerase Chain Reaction (PCR)

The polymerase chain reaction (PCR) is a fast and simple method to amplify specific parts of a DNA strand. This is important because standard molecular biology techniques such as DNA sequencing, gel electrophoresis, or the recombination of DNA fragments are not applied to single molecules, but typically require at least picomolar DNA concentrations. The power of PCR is based on the fact that both strands of any double-stranded DNA can be used as templates to generate new double strands; n repetitive steps of strand separation (*denaturation* step), hybridization of specific starting oligonucleotides (primers, *annealing* step), and synthesis of new complementary strands (*elongation* step) lead to an exponential amplification of the starting material according to $f(n) = 2^n$. Denaturation typically is performed at around 95 °C for 20 s; annealing occurs, depending on the length of the primers, at 50–65 °C, and thermostable DNA polymerases synthesize the new strands at about 70 °C. PCR is used to produce identical copies of DNA sections for later use (*preparative* PCR) or for the analysis of trace amounts of DNA in modern diagnostics or forensics (*analytical* PCR). Quantification of analytical PCR is achieved by instruments measuring the time course of DNA synthesis (*real-time* PCR). RNA molecules can be subjected to PCR methods subsequent to a reverse transcription into DNA (*RT*-PCR).

The synthesis and analysis of DNA *in vitro* are an indispensable step in most molecular biological experiments. By means of the PCR, DNA sequences are amplified for preparative and analytical/diagnostic purposes (see the information Boxes on PCR and DNA sequencing).

DNA Sequencing

Many experimental steps in molecular biology require the knowledge of the exact sequence of bases in DNA molecules. Various methods to determine DNA sequences exist, but the one most commonly used relies on a combination of DNA synthesis and gel electrophoresis according to Sanger. A template DNA to be sequenced is incubated with a short sequence-specific oligonucleotide and a DNA synthesis reaction mix composed of a polymerase and the four nucleotides (A, T, G, C). The polymerase starts to synthesize new DNA strands by adding complementary nucleotides to the priming oligonucleotide that binds to the template. Instead of performing one reaction with standard A, T, C, and G nucleotides only, the reaction is split into four, each one being supplemented with small amounts of one of the four modified nucleotides (A^*, T^*, C^*, G^*) that cannot be linked to additional nucleotides and, hence, will terminate the chain reaction. At the end, each reaction tube will contain a mixture of oligonucleotides of various lengths, always terminating at either A^*, T^*, C^*, or G^*. Electrophoresis of these four reaction mixes in parallel then reveals a correlation of "size" and "terminating nucleotide," providing the complementary sequence of the template.

A special form of DNA polymerase frequently used in molecular biology is reverse transcriptase. This enzyme takes RNA as a template and synthesizes a complementary DNA (cDNA). It is a valuable tool for the cloning of intron-free coding sequences from processed mRNA molecules isolated from cells.

DNA Propagation in *E. coli*

One of the practical challenges in molecular biology is to identify and isolate specific DNA macromolecules in a mixture with numerous other known and unknown molecules. For example, if a DNA fragment is amplified by a PCR reaction, how is this fragment isolated and produced in large amounts? Typically, such fragments are inserted into a circular DNA (plasmid) by a ligation reaction. The plasmids are subsequently incorporated into bacteria, typically *E. coli* – the bacteria are transformed. Plasmids replicate within the bacteria and amplify with the bacterial culture. However, since bacterial transformation is a very inefficient process, untransformed bacteria without plasmids must be eliminated. This is achieved by a gene on the plasmid coding for a protein that makes the bacteria resistant to an antibiotic. Hence, in the presence of the selection antibiotic, only the transformed bacteria will survive. When bacteria are seeded at very low

concentration on a solid substrate (agar dish), individual colonies of bacteria – all originating from the same "mother bacterium" – will appear. As a result, identical copies of one original DNA molecule – a clone – can be isolated from the descendants of a single bacterial colony.

7.1.1.3 **Mutations, Damage and Repair of DNA**

The DNA sequence remains essentially constant throughout our lives. However, surprisingly, the DNA molecule itself is one of the least stable molecules in the cell. *In vivo*, DNA is always accompanied by water molecules, making the nucleic acid prone to hydrolytic cleavage. In fact, cleavage of the backbone phosphodiester bonds (single-strand break) is a very common reaction under physiological conditions. About 50 000 events of this type are estimated to occur per genome in 24 h. However, also the glycosidic bonds of the purine bases (A, G) are very susceptible to hydrolytic attack and so-called depurinations have an estimated daily frequency of 10 000. The pyrimidines (C, T) are more stable, with cleavage events about 20-fold lower than purine removal. These are just examples of the most common challenges to DNA integrity, but other modifications are also known, including those caused by oxidation.

Oxygen is required for cell survival, especially for energy production, but the oxygen usage itself creates highly reactive oxygen-derived species capable of damaging cell constituents, including DNA. One oxidative damage to human DNA is estimated to occur every 9 s. The DNA stability is further compromised by alkylating agents and electromagnetic radiation such as X-rays and ultraviolet (UV) light. In addition, several chemicals have a tendency to bind to DNA and affect replication and transcription, ultimately leading to changes in nucleotide sequence. Such chemical mutagens are usually planar aromatic substances that fit into the space between two adjacent bases. This process of intercalation may alter transcription and DNA replication and manifest itself as a mutation.

The long list of DNA modifications, either spontaneous or induced by mutagens, raises the question of how DNA can serve as a blueprint of life. In fact, the system would not work without the existence of an elaborate DNA repair machinery. Several independent repair mechanisms are known, including base excision repair and nucleotide excision repair. The *base* excision repair system comprises glycosylases, endonucleases, and polymerase activity, which allow the replacement of a single incorrect *base*. By contrast, enzymes involved in *nucleotide* excision repair remove short nucleotide stretches containing multiple bases in a single DNA strand, followed by a fill-up reaction guided by the sequence of the complementary strand.

The balance between DNA damage and repair, which together define the net mutation frequency, is the basis of all evolutionary processes. Under some conditions, the repair mechanisms are not sufficient and may leave a mutation unrepaired. A DNA mutation occurring in a germ cell can be propagated to the offspring where it has potential to cause a functional or developmental change. In an extreme case, the mutation may be so detrimental that the offspring may not be able to develop properly. In other cases, the consequences of a DNA mutation may not hamper

immediate survival and the mutation may persist and spread among the offspring. One example is single-nucleotide polymorphisms (SNPs); some individuals harbor DNA sequences that vary only at specific single bases. Such SNPs may cause a predisposition for the development of an inherited disease. When located in a noncoding region, it may not have an immediate impact on health, but it can contribute to a diversification of DNA and, hence, might be used for forensic identification.

In contrast to the mutations in germ cells, in cells whose genetic information is not inherited to the next generation, the so-called somatic cells, mutations often affect the process of controlled cell division (see also Section 7.4.1). Thus, chemical mutagens are potentially carcinogenic and must be handled with great care. An example is ethidium bromide, routinely used in molecular biology to visualize DNA in an electrophoresis (see the information Box on electrophoresis). Others are benzopyrenes and aflatoxin. Some intercalating substances, such as the chemotherapeutic drug daunomycin, are used specifically to combat cancer cells, which rely heavily on the replication machinery due to their rapid growth.

Of particular importance for biophotonics applications in living systems is the inherent risk of photons directly damaging DNA. UV light, for example, can induce a cross-linking reaction between adjacent pyrimidine bases, thus producing thymine dimers. Maybe even more importantly, reactive species generated by light, such as free radicals and hydrogen peroxide, also damage DNA by chemically modifying bases or by breaking the DNA double strand. Whereas damage occurring in only one strand can be repaired efficiently by the DNA repair systems, double-strand lesions are difficult to repair and often lead to adverse consequences. Therefore, when using photons for clinical applications, it is imperative to evaluate the photodamage risk carefully.

Detection of Molecules in Cells/Tissue

Despite the immense number of different molecules inside a cell, various methods are available to "visualize" molecules in a very specific manner. DNA and RNA molecules typically are detected by binding cDNA molecules (probes) to them, a process termed hybridization. Such probes are detected either via a fluorescent moiety that they carry or by means of an enzymatic activity with which they are equipped. The cytogenetic technique to localize specific DNA sequences on chromosomes is termed fluorescence *in situ* hybridization (FISH). For the detection of proteins or other molecules the use of antibodies is instrumental (see the information Box on antibodies below). Visualization of specific antigens in biological tissues using antibodies is referred to as *immunohistochemistry* (IHC).

7.1.1.4 UV Absorption and Fluorescent Nucleic Acids

DNA strongly absorbs UV light of wavelength 260 nm. This absorption characteristic is utilized to measure the DNA concentration and purity. In addition, a change in light absorption when DNA molecules are denatured provides information on the melting temperature of DNA and on its content of guanine and cytosine (GC content).

As mentioned in the previous section, some substances show a strong propensity to intercalate into DNA. Such compounds are potentially carcinogenic; however, they have proven to be useful tools in detecting and quantifying DNAs in a variety of manners. For example, the DNA-binding dye ethidium bromide is routinely used to visualize DNA in gel electrophoresis experiments aimed at measuring the size of DNA fragments. For the analysis of the exact DNA sequence various methods exist. Mostly they rely on the synthesis of cDNA from the DNA template to be sequenced. Such reactions are performed four times, each one with a small fraction of a specific variant of the nucleotides (A, T, C, G) such that the reaction is terminated once one of those nucleotides is incorporated. Hence a mix of DNA of various lengths is generated. For the measurement of these lengths, and consequently the association of the terminating nucleotides, the DNAs are separated by electrophoresis and identified by means of fluorescently labeled nucleotides.

The use of fluorescently labeled nucleotides is also the basis of the detection of specific DNA sequences (or specific gene) in cells. Small complementary stretches of single-stranded DNA (oligonucleotides) are labeled with specific dyes. Upon binding of these oligonucleotides to DNA in a cell, the process called hybridization (see above), DNA harboring the matching sequence is detected by fluorescence microscopy. With the FISH technology mentioned earlier, many different genes (or chromosomes) can therefore be detected in cells simultaneously when using oligonucleotides with different fluorescent properties (colors). In a somewhat similar fashion, modern chip technology uses fluorescently labeled RNA probes to evaluate the expression of entire genomes (e.g., measurements of the relative concentration of DNA coding for about 20 000–40 000 genes are performed for pan-genomic human arrays).

7.1.2
Proteins: Scaffolds and Molecular Machines

Proteins are probably the most diverse group of biomolecules in cells. Likewise, their functional roles range from structural scaffolds to ensure cell shape and integrity, to cell communication, catalysis of numerous biochemical reactions, and energy-harvesting and energy-consuming molecular machines. In short, proteins participate in almost all functions required for life.

7.1.2.1 Amino Acids

Amino acids, the building blocks of proteins, are diverse in structure, but have in common a carboxylic acid group and an amino group linked by a central carbon atom (α-carbon) (Figure 7.5). The third bond of this α-carbon is made to a hydrogen atom. The fourth bond is to a variable group (side chain), specifying the type of amino acid (an exception is proline; see below). The tetrahedral arrangement of bonds to the α-carbon confers optical activity on amino acids; the amino acid is chiral and will change the polarization of light on interacting with photons. The mirror-image L-isomer and D-isomer forms exist, but nearly all amino acids in naturally occurring proteins are L-isomers.

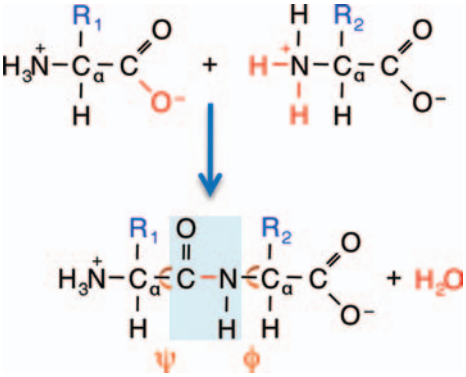

Figure 7.5 Peptide bond formation. Two amino acids with side chains R_1 and R_2 form a dipeptide with the concomitant release of water. The peptide bond is indicated in red and the plane formed by the peptide bond and the carbonyl oxygen in blue. Also indicated are the dihedral angles of rotation, ψ and φ.

The side chain (R_1 and R_2 in Figure 7.5) can be small such as the proton in glycine or large such as the indole group in tryptophan. The chemical nature of this side chain largely determines the properties of the amino acid and, hence, the properties of the proteins made of them. Although there are many different types of amino acids, in nature only 20 L-amino acids are commonly used to build proteins (there are modifications of such amino acids, some of which will be discussed in Section 7.1.6), no matter whether in bacteria, plants, or humans. The strong diversity of the chemical properties of these 20 standard amino acids provides an immense variability of protein structures and therefore functions. At the same time, it is remarkable that the standard amino acids, and therefore most native proteins – without considering modifications occurring after protein synthesis in Section 7.1.2.5 or cofactors (Sections 7.1.2.6 and 7.1.6) – consist of only five chemical elements: carbon (C), hydrogen (H), oxygen (O), nitrogen (N), and sulfur (S) [a few proteins contain selenocysteine instead of cysteine and, therefore, selenium (Se) is another naturally occurring element in native proteins].

Three nomenclature systems, the full names (e.g., arginine), the three-letter code (Arg), and the single-letter code (R) (see Figure 7.6), are in place to describe different amino acid residues. The single-letter code is often used for the description of protein sequences because they can contain more than 1000 amino acid residues.

Amino acids can be classified according to various parameters, as illustrated in Figure 7.6. Among them are the mass, the volume, the electric charge, the pH value at which the residues are half-protonated (pK_R), and a measure of how the side chain interacts with water, hydropathy. According to the last aspect three groups can be defined:

1) non-polar side chains (Gly, Ala, Val, Ile, Met, Pro, Phe, Trp)
2) uncharged but polar side chains (Ser, Thr, Gln, Tyr, Cys)
3) charged polar side chains (Lys, Arg, His, Asp, Glu).

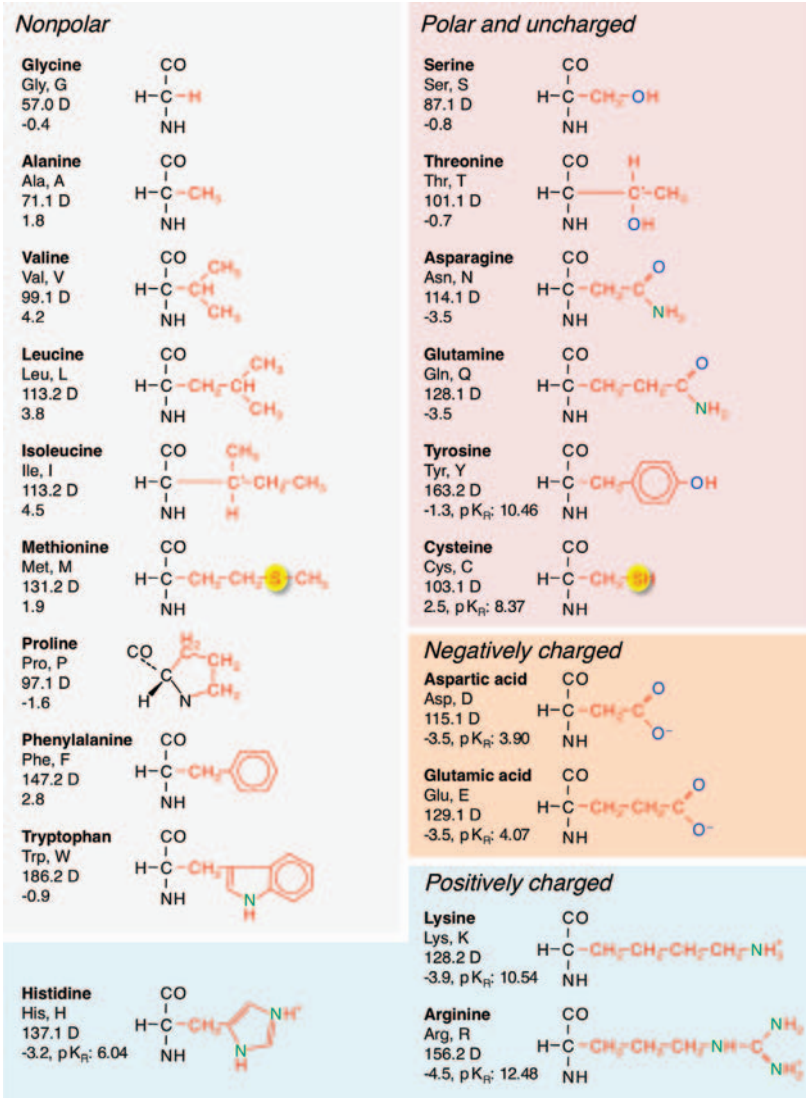

Figure 7.6 The 20 natural amino acid residues as they occur in a polypeptide. Full name, three-letter code, single-letter code, molecular mass of the residue, hydropathy index, and pK_R values for charged residues are indicated. In the chemical structures, the backbone atoms are drawn in black, the side chain atoms are colored. Side-chain atoms sulfur, oxygen, and nitrogen are highlighted (numeric values from Voet *et al.* [3]; hydropathy values from Kyte and Doolittle [4]).

Typical pK_R values of the protonatable side chains are indicated in Figure 7.6. The histidine side chain is partially protonated at physiological pH between 7.2 and 7.4. It is important to note that exact pK_R values vary markedly depending on temperature, ionic strength, and the immediate environment of the ionizable group. For example,

inside a protein the effective pK_R value of a histidine can deviate considerably from 6.04 if there are charged residues nearby.

The amino acid proline is a special case because the hydrogen atom at the backbone is replaced by a bond to the side chain (Figure 7.6). Therefore, proline residues introduce a "kink" in the polypeptide backbone structure (see Section 7.1.2.3). Glycine's side chain is only a proton and, hence, the amino acid glycine is not chiral. Subsequently, glycine exhibits greater structural flexibility than other amino acids (Section 7.1.2.3).

7.1.2.2 Protein Translation – the Standard Genetic Code

Proteins are linear chains of amino acids covalently bonded together and the amino acid sequences contained therein are specified by the genes consisting of DNA base sequences. To synthesize a protein from the corresponding DNA sequence, the first step is to transcribe the DNA into mRNA, which is then transported outside the nucleus to the cytosol, the site of protein synthesis. Here, mRNA binds to ribosomes, large subcellular structures designed to comprise a complex machinery that "reads" the mRNA sequence and then "synthesizes" a protein by linking the correct matching amino acids loaded on to tRNAs ("charged tRNAs"). Since there are only four bases in the DNA or RNA sequence but 20 amino acids, three base positions are utilized to describe an amino acid, defining the so-called standard genetic code. A triplet of bases, a so-called codon, "codes" for an amino acid in mammals according to the scheme illustrated in Figure 7.7. Some features of the genetic code are readily apparent:

- Some amino acids are coded for by four different codons (Leu, Val, Ser, Pro, Thr, Ala, Arg, Gly), some by three, two, or only one codon (Met, Trp).
- Some codons do not code for any amino acid; they are called missense or stop codons.

One consequence is that those amino acid residues coded by four codons are less prone to amino acid-altering mutations because the base at the third position is redundant. A mutation of the base sequence that does not lead to a change in the translated protein sequence is referred to as a "synonymous" mutation or a type of "silent" mutation. Because only a single codon exists for Met or Trp, any change in base sequence coding for Met or Trp will necessarily lead to a coding (non-silent) mutation.

The RNA codon AUG (or ATG in DNA sequence) is of particular importance. It not only codes for the amino acid methionine (Met) but is also the so-called eukaryotic start codon; translation can only start at a base triplet AUG. In this way, the interpretation of the following base triplets – the reading frame – is defined. The structure of the ribosome ensures that, once initiated at an AUG element, the reading frame is maintained; the mRNA always advances by exactly three bases before the next amino acid is attached to the protein sequence. Another consequence is that directly after synthesis all proteins start with a methionine residue.

Pos 1		Pos 2							Pos 3
		U		C		A		G	
U	Phe	UUU	Ser	UCU	Tyr	UAU	Cys	UGU	U
		UUC		UCC		UAC		UGC	C
	Leu	UUA		UCA	stop	UAA	stop	UGA	A
		UUG		UCG	stop	UAG	Trp	UGG	G
C	Leu	CUU	Pro	CCU	His	CAU	Arg	CGU	U
		CUC		CCC		CAC		CGC	C
		CUA		CCA	Gln	CAA		CGA	A
		CUG		CCG		CAG		CGG	G
A	Ile	AUU	Thr	ACU	Asn	AAU	Ser	AGU	U
		AUC		ACC		AAC		AGC	C
		AUA		ACA	Lys	AAA	Arg	AGA	A
	Met	AUG		ACG		AAG		AGG	G
G	Val	GUU	Ala	GCU	Asp	GAU	Gly	GGU	U
		GUC		GCC		GAC		GGC	C
		GUA		GCA	Glu	GAA		GGA	A
		GUG		GCG		GAG		GGG	G

Figure 7.7 Standard genetic code describing how RNA codons are translated into amino acid residues. Coding sequences always start with AUG, also coding for methionine residues. Translation is terminated whenever one of the stopcodons is encountered. Coloring denotes nonpolar (gray), polar and uncharged (pink), negatively charged (orange), and positively charged (blue) residues.

In many cases, however, such leading sequences are removed in subsequent protein processing steps.

Translation is terminated once a stop codon is encountered. In the standard genetic code there are three stop codons: UGA determines the end of about 50% of all human protein sequences and UAA or UAG are found in the rest of the mRNAs.

The fact that organisms as different as a human, an oak tree, and a tiny bacterium virtually "speak" the same genetic language may seem surprising, but it reflects that all organisms are derived from a common ancestor. During the enormous number of generations that separate the mentioned species, very many small variations have occurred and accumulated, and have since been conserved in individual genetic codes. Such deviations from the standard code are particularly evident in mitochondria, small endosymbionts in animal and plant cells (Section 7.2.1.5) that carry some of their own genetic material. In the human mitochondrion, unlike the universal code, UGA codes for tryptophan instead of terminating the translation. AUA codes for methionine instead of isoleucine, and AGA and AGG are stop codons. In addition to such alterations in the meaning of individual codons, the selection of redundant codons for the same amino acid is not identical in different organisms. Depending on the species, the translation machinery prefers some codons over others. Thus, in a given organism the presence of individual tRNA molecules reflects the frequency at which the respective codon is used in the genome of this species. This so-called codon

usage is of practical importance if a gene from one species is to be expressed in a host system of another species; this can result in a very small protein yield if the codon usage is incompatible. For example, the codons AGG and AGA, both encoding arginine, occur with very low frequencies of about 1.5 per 1000 in the genome of the bacterium *E. coli*. In the human genome, each of these codons occurs at a higher frequency of about 12 per 1000 codons. This corresponds to a probability of 42% that one of the two codons appears in the mRNA sequence, whenever an arginine occurs in the protein sequence. As a consequence, efficient production of a human protein in *E. coli* may require adapting the codon usage such that rare tRNAs of *E. coli* will not limit the yield of the translation process.

Genome Projects and Protein Sequences The amino acid sequences of all proteins are specified by the mRNA sequences, which reflect the corresponding complementary DNA sequences. Thus, the information obtained from mRNA has been used to deduce the amino acid sequences of proteins and also to gain additional information about the genome. Typically, mRNA sequences are reverse transcribed or copied into cDNA and used for standard DNA sequencing approaches. Although this approach provided a wealth of information, the sequence coverage for humans and other species was far from being complete. With the development of new shotgun sequencing methods, very large stretches of genomic DNA could be sequenced. With the successful sequencing of the complete human genome, the public availability of gene sequences reached a new quality. In addition, the genomes of many important model organisms and also pathogenic organisms have been sequenced completely. *In principle*, this allows the prediction of all proteins that can be made by cells of these organisms.

Naming genes and gene products (proteins) often has a historical background and it is no rare event that identical genes have various different names. Recently the Human Genome Nomenclature Committee has introduced the standardized HUGO nomenclature of human genes, facilitating searches for genes of specific properties (http://www.genenames.org/). There are several Internet-based resources where information on genes and proteins can be found, for example, http://www.ncbi.nlm.nih.gov/ and http://www.ebi.ac.uk/embl/.

7.1.2.3 Peptide Bonds, Polymerization, and Secondary Structure

Two amino acids are joined to form a dipeptide by a peptide bond between the carboxy group of the first and the amino group of the second amino acid (Figure 7.5). The carbonyl oxygen, its carbon, the nitrogen, and the proton of the amide group are in a plane, mostly in a *trans* configuration, so that the oxygen and the proton point in opposite directions. The bond between the carbonyl carbon and the nitrogen is rigid. The bonds of the α-carbon to the carbonyl carbon and the nitrogen, however, are single bonds and therefore can rotate along the axis. The respective angles of rotation, the dihedral angles ψ and φ, thus provide a considerable degree of rotational freedom.

As a consequence, the side chains of two succeeding amino acids typically point in different directions. Addition of another amino acid yields a tripeptide, and so forth.

Short sequences of amino acid chains are called peptides (or oligopeptides). Starting from a somewhat arbitrary size of about 40 residues, one refers to such polypeptides as proteins. The linear sequence of a protein, the list of amino acid residues starting from the amino-terminal end, is called the *primary sequence* or *primary structure* of the protein.

Upon peptide bond formation, a linear chain of amino acids consists of the backbone, formed by two carbons and one nitrogen atom per residue, one proton of the amide group, one of the α-carbons, a carbonyl oxygen, and the side chain.

Based on the nature of the peptide bond and the available side chains, there is only a limited set of structural configurations that a polypeptide can adopt. A presentation of the dihedral angle ψ plotted versus the dihedral angle φ – the so-called Ramachandran plot – provides a prediction for the formation of secondary structural elements and shows that only relatively small domains of ψ−φ combinations give rise to secondary structural elements. Such structural modules have a low potential energy and therefore form larger building blocks inside protein structures.

The α-Helix The first secondary structure identified was the α-helix (Figure 7.8a). This common structure forms spontaneously and is stabilized by hydrogen bonding between amide nitrogens and carbonyl oxygens of peptide bonds spaced four residues apart. Thus, in an α-helix all CO and NH groups of the backbone are hydrogen bonded. The orientation of the hydrogen bonding produces a helical coiling of the peptide backbone such that the side-chain groups lie on the exterior of the helix and perpendicular to its axis. Typical figures for an α-helix are a diameter of the backbone of about 0.5 nm, a height per turn of about 0.54 nm, and approximately 3.6 residues per turn. Along the helix axis the residues are thus separated by 0.15 nm and are rotated by 100° with respect to the next neighbor. The helical twist in proteins is right-handed. In three-dimensional space, residues separated by three or four positions on the primary sequence are in close proximity.

Not all amino acids favor the formation of the α-helix due to steric constraints of the side-chain groups. Amino acids such as Glu, Met, Ala, Leu, Lys, and Phe favor the formation of α-helices, whereas Gly and Pro favor disruption of the helix. This is particularly true for Pro since it is a pyrrolidine-based imino acid whose structure significantly restricts movement about the peptide bond, interfering with extension of the helix. The disruption of the helix is important as it introduces additional folding of the polypeptide backbone to allow the formation of globular proteins.

Another helical secondary structure much less frequently found is the 3_{10} helix. This is a right-handed helix with three residues per turn and a translation of 0.2 nm along the helical axis. Some protein segments may exhibit transitions between the 3_{10} and α-helical secondary structures.

β-Strands and β-Sheets Whereas an α-helix is composed of a single linear array of helically arranged amino acids, β-sheets are composed of two or more different β-strands, that is, regions of stretches of at least 5–10 amino acids. The folding and alignment of stretches of the polypeptide backbone beside one another to form β-sheets are stabilized by hydrogen bonding between amide nitrogens and carbonyl

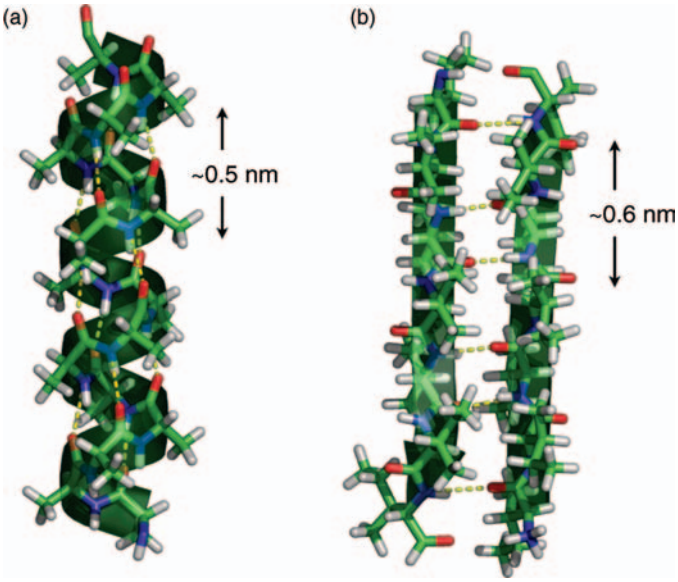

Figure 7.8 Secondary structural elements. (a) α-helix; (b) β-sheet. The hydrogen bonds stabilizing these structures are indicated in yellow.

carbons, thereby using the full hydrogen-bonding capacity of the polypeptide backbone (Figure 7.8b). However, the hydrogen-bonding residues are present in adjacently opposed stretches of the polypeptide backbone in contrast to a linearly contiguous region of the backbone in the α-helix. β-Sheets have a rippled appearance and they are said to be pleated. This is due to positioning of the α-carbons of the peptide bond, which alternates above and below the plane of the sheet; as a consequence, the β-sheet is slightly shorter than an extended polypeptide. Neighboring side chains point in opposite directions and a typical distance between one and the next residue is about 0.7 nm.

β-Sheets are either parallel or antiparallel. In parallel sheets, adjacent peptide chains proceed in the same direction (i.e., the direction of N-terminal to C-terminal ends is the same), whereas in antiparallel sheets adjacent chains are aligned in opposite directions. In proteins, β-sheets can contain between two and 22 strands, with each strand up to 15 residues in length. The average length is six residues. The amino acids Val, Ile, Tyr, Trp, and Leu are most frequently found in β-sheets; Pro and Gly are rarely found in β-sheets.

Coiled Coils α-Helices are perfectly suited to form fibrous proteins: long fiber-like structures that play a supportive and connective role in living organisms. A prominent example is α-keratin, a protein that occurs in hair, nails, and other relatively hard biological structures. Two α-helices wind around one another to form a left-handed coiled-coil structure. Depending on the type of keratin, this structure is stabilized by disulfide bridges. Chemical cleavage of these bonds can result in weakening of the structure; re-formation of disulfide bonds in a curled configuration

can stabilize such a curled structure, as practiced to generate a "permanent wave" of hair. Another example is collagen, forming a coiled-coil structure of three helices twisted around one another. Collagens are stabilizing proteins found in connective tissue such as bone, cartilage, tendons, and skin. They consist of about one-third of glycine and 15–30% of proline and 4-hydroxproline (Hyp). The latter is the result of a post-translational modification of proline with the aid of prolyl hydroxylases, an enzyme that requires vitamin C (ascorbic acid) for its activity. Deficiency of vitamin C can thus result in an impairment of collagen formation as found in scurvy.

Turns, Loops and Random Coils In proteins that do not form long fibrous structures, so-called globular proteins, individual secondary structural elements (α-helices and strands of β-sheets) must be interconnected. The common feature of such structures is that they cause abrupt changes in direction, such as in reverse turns or β-turns connecting strands of β-sheets. Some protein segments, mostly found at the surfaces, form loops. They play important roles in how proteins are recognized by other proteins. In addition, there are countless structural configurations that appear totally disordered or random and cannot be associated with a well-defined structural class, thus referred to as random coil or intrinsically disordered structures. Although such structures appear "random," this characteristic may be well suited for the functions of the proteins.

7.1.2.4 Tertiary and Quaternary Protein Structure

The globular structure of a single polypeptide chain (protein) is referred to as tertiary structure. In many cases, specific function can only be acquired when several identical or different polypeptides or protein *subunits* form homomeric or heteromeric protein complexes, respectively. The overall structure of such complexes is called *quaternary structure*. An example of a protein structure and an illustration of various ways of its visualization are given in Figure 7.9.

Owing to the tremendous number of degrees of freedom, a protein with a given primary sequence can theoretically adopt countless structural configurations and yet in nature, its structural appearance is limited and reproducible; a polypeptide with a given sequence always folds into the same or at least a small number of tertiary structures. Which factors thus determine the final three-dimensional structure of a protein? We have already seen that, mostly by formation of a dense network of hydrogen bonds, secondary structural elements adopt low-energy states and, hence, are fairly stable. Another important driving force is the so-called hydrophobic force, largely expressing how nonpolar residues are stabilized by avoiding contact with water. This tendency is expressed by the hydropathy index (see Figure 7.6) of side chains. Hydrophobic areas will be largely buried inside the protein, whereas hydrophilic parts may face the surface and, hence, may interact with water molecules. In addition, formation of salt bridges, that is, electrostatic interactions of electric charges, contributes substantially to the overall energy of a protein structure. Quantitative descriptions of these physical forces form the basis of molecular dynamics simulations of proteins. Nevertheless, just by these physical forces alone – electrostatics,

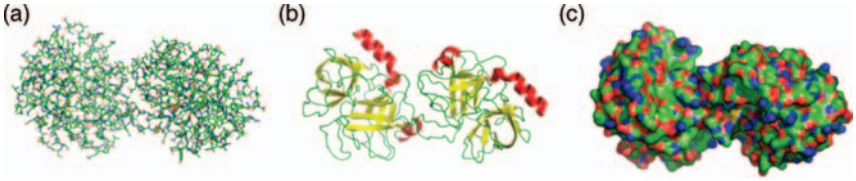

Figure 7.9 Tertiary structure of trypsin represented in three ways: (a) ball and stick, (b) cartoons, and (c) surface. PDB ID: 1TRN.

hydrogen bonds, and hydrophobic forces – most linear polypeptides will not spontaneously assume a tertiary structure with a desired function.

Disulfide Bonds The formation of reversible covalent bonds between the nucleophilic thiol groups (−SH) of two cysteine residues (Figure 7.10) helps to stabilize globular structures. In particular, large extracellular protein loops often require such stabilization in order to adopt the correct structure. The intracellular milieu, with the exception of the ER, is a more reducing environment and therefore the overall likelihood of disulfide formation is lower. However, some intracellular disulfide bonds may be formed and broken, depending on the local redox environment. Disulfide bonds can be formed within the same polypeptide chain, but they are also used to link different chains within a protein complex. During folding of a protein, the formation of disulfide bridges is often catalyzed by protein disulfide isomerases (PDIs).

For *in vitro* analysis, it is often necessary to disrupt the protein structure without destroying the peptide chain. This process is called denaturation and is achieved in part by the addition of strong reducing agents such as mercaptoethanol to break disulfide bonds.

Chaperones Chaperones are proteins that assist the noncovalent folding/unfolding and the assembly/disassembly of other protein structures by transiently interacting with the target protein during synthesis. Some chaperones provide steric information for the new protein to fold. More frequently, however, chaperones prevent both newly synthesized polypeptide chains and assembled subunits from aggregating into nonfunctional structures. These chaperones are typically so-called heat shock proteins. They are synthesized when the temperature is elevated and, hence, when there

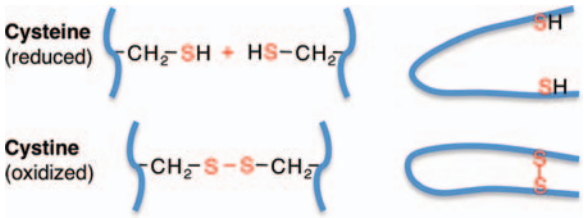

Figure 7.10 Protein stabilization by the formation of disulfide bridges between two cysteine residues. The typical S–S distance is about 0.2 nm.

is an increased tendency for proteins to be denatured by stress. The exact molecular function of chaperones is only beginning to be understood.

Structural Classification of Proteins – Folds The tertiary structures of proteins are much less variable than expected from the vast number of naturally occurring primary sequences. This is because proteins often adopt structures that have an overall similar topology, albeit varying in sequence and function. Since the two well-defined secondary structural units of helices and sheets are abundant in proteins, families of protein structures have been classified by a system based upon the α-helix and β-sheet and their general topological properties. Each different topology may be considered as a fold. Current thinking suggests that there are a limited number of folds, about 1000, in naturally occurring proteins.

Thus, the tertiary structure of a protein can be thought of as a composition of structural modules. Starting from the secondary structural elements discussed above, one defines so-called *supersecondary structures*. These are small structural motifs composed of combinations of α-helices and β-sheets. Prominent examples are antiparallel βαβ-motifs, antiparallel β-hairpin motifs, and antiparallel αα-motifs. A long β-hairpin folded over in the middle results in a Greek key motif.

A single protein can harbor several folds or areas of specific structure and function. Such protein *domains* play a pivotal role in their classification and they are often used when a protein is to be characterized by simpler means than the three-dimensional structure. In particular in the cell biological literature, proteins are often presented in a simplified fashion by denoting such domains without referencing to the real three-dimensional structure. An example is shown in Figure 7.11.

β-Barrels Very common folds are so-called β-barrels – proteins in which β-strand elements are arranged to form a cylindrical structure. These can be arrays of β-strands with alternating directions or more complicated constructs in which the neighboring sheets are not necessarily neighbors in sequence (e.g., jelly roll or Swiss roll barrel). A TIM (triosephosphate isomerase) barrel or α/β-barrel is a complex fold of eight β-strands forming an inner barrel surrounded by eight α-helices forming an outer barrel. The green fluorescent protein (GFP) adopts a fold called β-can – a cylinder of 11 β-strands with a central α-helix holding the chromophore (see Figure 7.20a).

There are various theoretical approaches for the classification of protein structures. The most common ones are SCOP (Structural Classification of Proteins), which defines a hierarchy of "class–fold–superfamily–family–protein–species" and CATH (class, architecture, topology, homology), which uses the four attributes listed as

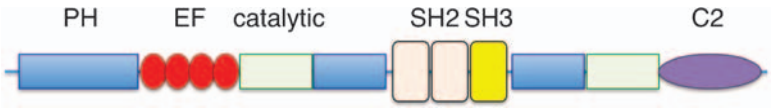

Figure 7.11 Functional domains of phospholipase γ1 (PLCγ1). PH, pleckstrin homology domain; EF, Ca^{2+}-binding EF-hand domains; SH, Src homology domains; C2, Ca^{2+}-dependent phospholipid binding domain (after Cockcroft [5]).

order criteria [6]. For a detailed description and classification of protein folds, see also [7] and [8].

More general classifications of protein structures are guided by their overall appearance of localization: globular, structural, and membrane proteins. Globular proteins are mostly found in the cytosol; typically they are soluble and adopt a compact structure. Structural proteins often tend to aggregate or to polymerize to form large filamentous structures. Membrane proteins are characterized by a hydrophobic core with which they are stabilized in the lipid bilayer membrane.

7.1.2.5 Post-translational Modifications: Dynamics of Protein Structure and Function

A protein, with a three-dimensional structure defined by its primary amino acid sequence coded by DNA, performs specific functions in a cell. If the cellular environment changes, such as a change in oxygen level, the cell may respond by changing gene expression, leading to the synthesis of new proteins with different properties. This strategy, transcriptional regulation, requires an expenditure of cellular energy to synthesize new molecules and it is often slow. In contrast, existing proteins may be modified to regulate their functions rapidly, a process termed post-translational modification. Numerous such modifications have been documented and a few selected examples are presented below. A more detailed treatment of the topic can be found in textbooks on biochemistry.

Cleavage by Peptidases Peptide bonds linking amino acid residues in proteins can be cleaved by specific enzymes, referred to as proteases or peptidases, with varying degrees of specificity to the amino acid sequence. Peptidases are present in the cytosol, in intracellular organelles, or are even secreted to the extracellular space. The secreted peptidases, such as matrix metallo-proteinases (MPPs), are essential in structuring the tissue by modification of those proteins forming the extracellular matrix, playing critical roles in development, remodeling, and cell migration.

The first residue to be synthesized in most proteins is methionine. Following this N-terminal methionine, some proteins may contain special-purpose sequences that are required to target the proteins to specific sites inside a cell, for example, into the mitochondria. Such *signal sequences* are address labels that may not be needed any longer once the desired location has been reached. Therefore, specialized peptidases cleave off such sequences. Other proteins, such as the peptide hormones insulin and enkephalin and the amyloid precursor protein, remain inactive until they are processed via peptidases.

Protein Phosphorylation By far the most important structural and functional regulator of proteins is the covalent attachment of negatively charged phosphate groups (PO_4^{3-}) to specific amino acid residues. This phosphorylation process is catalyzed by protein kinases, which transfer phosphate moieties most commonly from ATP (adenosine triphosphate) to the target proteins, often causing noticeable changes in their functions. The reverse process, removal of phosphate, is catalyzed by phosphatases. Both the phosphorylation and dephosphorylation processes are

subject to fine tuning, and kinases and phosphatases themselves may be phosphorylated.

Protein phosphorylation usually occurs at serine, threonine, and tyrosine residues in eukaryotic proteins. In addition, the basic amino acid residues histidine, arginine, and lysine in prokaryotic proteins may undergo phosphorylation. Histidine and aspartate phosphorylation in eukaryotic cells is less frequent but is receiving increasing attention. Structurally, the addition of a phosphate molecule to a polar group of an amino acid side chain can turn a hydrophobic portion of a protein into a polar and extremely hydrophilic moiety, causing a conformational change in the structure of the protein via interaction with other hydrophobic and hydrophilic residues. In Figure 7.12, phosphorylated serine, threonine, and tyrosine are illustrated.

Antibodies

Antibodies are large molecules generated by the immune system that specifically bind to (mostly) small sections of proteins, also called *epitopes*. While in the immune system antibody binding is a signal for the destruction of the respective target, scientists make use of antibodies to label proteins specifically on or inside cells. Antibodies to a protein of interest are generated in animals (e.g., rabbit, mouse, sheep, horse, chicken) in response to injection of the whole or a small fragment of the protein. The resulting antibodies are diverse in nature, recognizing different aspects of the protein, and are referred to as polyclonal antibodies. By fusion of cancer cells with antibody-producing B-cells in cell culture, permanent hybridoma cell clones can be generated that produce antibody molecules of only one type (monoclonal antibodies). For optical detection, antibodies are often labeled with fluorescent dyes. Since the labeling process is expensive, one often first binds a specific primary antibody (e.g., from mouse) to the target protein and subsequently a secondary, fluorescently labeled antibody that recognizes mouse antibodies is bound to the first one. Fluorescently labeled antibodies can be used

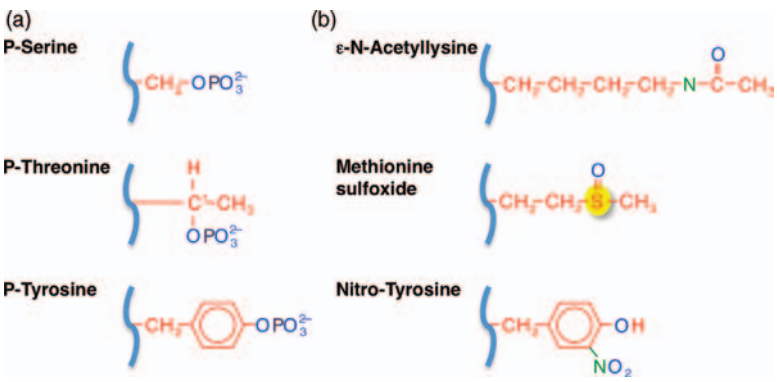

Figure 7.12 (a) Protein phosphorylation: *O*-phosphoserine, *O*-phosphothreonine, and *O*-phosphotyrosine. (b) Acetylated lysine, one epimeric form of methionine sulfoxide, and 3-nitrotyrosine. The side chains only are illustrated.

to detect surface proteins on living cells and to separate such cells in a fluorescence-activated cell sorter (FACS). If antibodies are used to label proteins that have been separated upon gel electrophoresis, this is referred to as Western blot.

A high degree of sequence specificity for protein kinases exists. For example, a given kinase does not phosphorylate every serine residue in a protein. The selectivity arises because most kinases require the target side chains, such as those of serine and threonine, to bind the enzymes transiently as specified by the three-dimensional structure imposed by the neighboring residues. Such phosphorylation *consensus sites*, typically described using the primary sequence, are known for several kinases, but they are much less stringent than, for example, recognition sites for DNA endonucleases. For instance, many kinases specific for serine and threonine residues require positive charges (Arg, Lys) being located N-terminal to the target residue. The mitogen-activated protein kinase (MAPK) prefers the consensus site P–X–S/T–P, where X is any residue. It should be noted, however, that such recognition motifs are an oversimplification as they cannot take into account the three-dimensional structure of the motifs. Experimental evidence is necessary to prove that a specific residue is indeed phosphorylated. For the detection of phosphorylated protein moieties, antibodies specific for a protein structural element encompassing the phosphorylated site (epitope) are instrumental. In particular, antibodies raised against phosphotyrosine are very important because consensus sites for tyrosine kinases are not well defined.

Protein Acetylation Most proteins undergo acetylation as a co-translational modification and/or as a post-translation modification. Most importantly, the N-terminal amide is often acetylated by the aid of *N*-α-acetyltransferases. Of the protein side chains, lysine is a typical target of histone acetyltransferase (HAT), an enzyme that modifies histones and thereby regulates gene transcription. Acetylated lysine (Figure 7.12) is modified back to lysine by histone deacetylase (HDAC). Both HAT and HDAC also exhibit activity with respect to proteins other than histones.

Protein Oxidation Almost all protein side chains can be oxidized, but the sulfur-containing residues cysteine and methionine are most susceptible and enzymes for their reduction exist. Oxidative modification of cysteine with a thiol group (−SH) was discussed in Section 7.1.2.4. Methionine is also oxidized by the addition of an oxygen atom to the sulfur atom, resulting in two epimeric forms of methionine sulfoxide: Met-(*S*)-sulfoxide (Figure 7.12), and Met-(*R*)-sulfoxide. Specific enzymes (methionine sulfoxide reductases A and B, respectively) reduce such moieties back to methionine and thereby play an important role in the antioxidant mechanism.

Protein Nitration Under oxidative conditions, nitric oxide (NO) can lead to formation of peroxynitrite ($ONOO^-$), which then reacts with tyrosine to form nitrotyrosine (Figure 7.12). Tyrosine nitration is speculated to play a role in degenerative phenomena under nitrosative stress conditions.

7.1.2.6 Noncovalent Structural Regulation

In addition to the covalent protein changes discussed in Section 7.1.2.5, more subtle modifications of the protein or its environment can have a consequence for its structure and function. One such regulatory mechanism is reversible binding of a ligand to the protein. Among the diverse ligands, ions, often metal ions, are very commonly utilized.

The smallest ion ligand is the proton, H^+. As illustrated in Figure 7.6, several amino acid side chains harbor structural groups whose degree of protonation depends on the local pH value. For example, the imidazole side chain of histidine has an apparent pK_R value of ~6, and its electric charge varies according to the pH. The functional consequence of the protonation may be dramatic. Some proteins acquire a certain function under the matching proton concentration whereas other proteins are kept in an inactive state while being stored in acidic intracellular organelles; once released to neutral pH media (e.g., the cell cytosol or the extracellular space), they obtain their full function.

Another biologically important ligand is Ca^{2+}. The importance of Ca^{2+} as a regulator is indicated by the existence of specialized, often small, Ca^{2+}-binding proteins. Such proteins undergo substantial conformational changes upon binding of one or more Ca^{2+} ions and they transmit the binding signals to other specific interacting proteins by physical association. The most prominent example of such a Ca^{2+}-binding protein is calmodulin. This small protein, with <150 amino acid residues, is ubiquitously present in eukaryotic cells and harbors four so-called EF-hand domains that bind Ca^{2+}. Two of the domains are half-saturated with Ca^{2+} at about 100 nM and the other two domains at about 1 μM. By physically interacting with other proteins, Ca^{2+}-binding proteins, such as calmodulin, confer robust Ca^{2+} sensitivity to the resulting protein complexes.

In other proteins, binding of metal ions such as Zn^{2+} plays an important role for the establishment of the correct 3D structure. Moreover, metal ions integrated into the protein structure are often essential for the establishment of the catalytic activity of some enzymes.

7.1.2.7 UV Absorption and Fluorescence of Proteins

Polypeptides strongly absorb light in the UV region of the spectrum. The peptide groups of the protein backbone absorb in the far-UV range (180–230 nm). The major contribution of the side chains comes from the aromatic residues Trp, Tyr, and Phe (in that order). Their molar extinction coefficients are as follows Trp, 5050 $M^{-1}\,cm^{-1}$ (at 280 nm); Tyr, 1440 $M^{-1}\,cm^{-1}$ (at 274 nm); and Phe, 220 $M^{-1}\,cm^{-1}$ (at 257 nm). Therefore, from the absorbance at 280 nm the content of aromatic residues can be estimated in protein samples; the maximum absorbance of nucleic acids is at about 260 nm, hence the ratio of the absorbance at 260 nm to that at 280 nm provides an estimate for the purity of a DNA or RNA sample.

Tryptophan is fluorescent with a peak of emission at about 355–360 nm at pH 7.4 and can therefore be utilized for experiments relying on autofluorescence of proteins. Above ~400 nm, proteins do not generally absorb appreciably unless they harbor chromophores (see Section 7.1.5.1).

Owing largely to the absorbance of the aromatic residues, proteins are sensitive to UV light. Molecular damage of residues or cross-linking reactions induced by photons may cause loss of protein function. In addition, secondary reactive species generated by absorption of UV photons in living cells may oxidatively modify proteins, in particular by reacting with the sulfur-containing Cys and Met residues. Therefore, great care must be taken when assaying proteins in a photonic experiment using short-wavelength excitation.

Pigments Biophotonics experiments can be compromised when the object under study contains autofluorescent materials or pigments that markedly absorb light. The most prominent pigment in humans is melanin, a class of compounds derived from the amino acid tyrosine. Among the several melanin-related compounds present in biological samples, eumelanin is a brown–black polymer of dihydroxyindole, dihydroxyindolecarboxylic acid, and their reduced forms. Another common form of melanin is pheomelanin, a red–brown polymer of benzothiazine units largely responsible for red hair and freckles. In human skin (see Section 7.2.2.3), the production of melanin is stimulated by UVB radiation, leading to the development of a tan. Since melanin absorbs UV light and converts its energy to heat, it is a very effective photoprotectant, diminishing DNA damage. The central nervous system also contains melanin-related pigments in selected areas, such as the substantia nigra, giving the areas a dark-brown appearance. Neuromelanin in the substantia nigra may play an important role in the pathogenesis of Parkinson's disease (see Section 7.4.5), by interacting with the neurotransmitter dopamine in a redox-sensitive manner.

In many macroscopic biological preparations, however, the strongest light absorption is due to the content of red blood cells (see Section 7.2.2.6) via the hemoglobin (see Figure 7.19b). Depending on the saturation level with oxygen, hemoglobin strongly absorbs light up to about 620 nm. Therefore, any blood contamination of samples may pose a serious problem. If it is inevitable to perform experiments in the presence of blood/hemoglobin, if possible wavelengths above 620 nm should be used to limit the interference. The absorbance of water sets the limit towards longer wavelengths, thus defining an "optical window" of about 620–1100 nm.

7.1.3
Carbohydrates: Energy Storage and Structural Elements

Carbohydrates or saccharides are polymeric macromolecules formed from individual carbohydrate units, the monosaccharides. Unlike DNA, these sugar-related molecules cannot replicate themselves and they do not have enzymatic functions as found with some proteins. Nevertheless, saccharides are of vital importance not only as an energy source for the cellular metabolism but also as structural materials. In addition, they can be specifically attached to proteins and lipids – a process called glycosylation – and thereby they tremendously increase the versatility of those molecules. Exposed to the extracellular face, they play a pivotal role in the immune response and cell–cell recognition.

7.1.3.1 Sugars, Monosaccharides, and Polysaccharides

Carbohydrates and saccharides are made of only carbon, oxygen, and hydrogen, fewer atom types than those required for nucleic acids and proteins. Yet the complexity of carbohydrate-containing molecules can be enormous.

Monosaccharides The individual building blocks of carbohydrates are sugars or monosaccharides, consisting of a chain of at least three carbon atoms with the center carbons being hydroxy alcohols (HCOH). The number of carbon atoms in the chain determines the primary names such as triose, tetrose, pentose, hexose, and heptose. The nature of the carbonyl determines a secondary name: a sugar with an aldehyde is an aldose (e.g., glucose), a sugar with a ketone is a ketose (e.g., fructose) (Figure 7.13).

There are always two mirror images of sugars, referred to as the D- and L-forms. The D-configurations are more relevant in nature, hence the prefix D- is often omitted. In addition, in the n carbon atoms in linear aldoses, $n-2$ are chiral. Thus, for glucose, there are $2^4 = 16$ possible stereoisomers – all of them having different names. Stereoisomers that vary only in the configuration of one hydroxy alcohol are called epimers. In Figure 7.13 it is illustrated that glucose and mannose are C_2 epimers of an aldohexose, whereas psicose and fructose are C_3 epimers of ketohexose.

The linear form of sugars is not very stable and therefore the carbonyl easily reacts with one of the hydroxyl moieties to form a ring structure. Six-membered rings (pyranoses) and five-membered rings (furanoses) are the most common. The

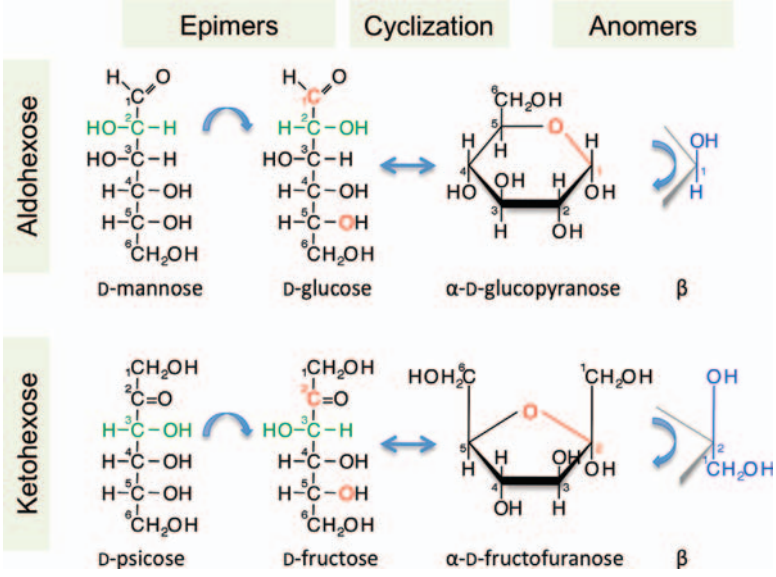

Figure 7.13 Monosaccharides. Typical examples of aldohexoses and ketohexoses. D-Mannose and D-glucose and also D-psicose and D-fructose are stereoisomers with respect to the highlighted carbon atom (green), that is, they are epimers. Cyclization of D-glucose and D-fructose leads to α-D-glucopyranose and α-D-fructofuranose, respectively. Exchanging the direction of the functional groups at the anomeric carbon leads to the β-anomers.

formation of α-D-glucopyranose from D-glucose and α-D-fructofuranose from D-fructose is illustrated in Figure 7.13. The ring closure has the consequence that the carbonyl carbon, here called the anomeric carbon, becomes a chiral center leading to α- and β-variants. The carbon atoms of the rings are not in a plane but adopt so-called chair structures that can interconvert fairly freely. In contrast, anomeric and epimeric forms are fairly stable.

The individual groups of sugar molecules are reactive and therefore many sugar derivatives exist. It is far beyond the scope of this chapter to address such modifications systematically. A couple of common examples are noteworthy. If the aldehyde group is replaced with a carboxy group (COOH), an aldonic acid results. Upon attachment of an OH group, the sugars carry the suffix "itol," such as in the important lipid component inositol. If a proton replaces one of the OH groups at the sugar backbone, the monosaccharides are called deoxy sugars. A prominent example is deoxyribose as it occurs in DNA (Figure 7.3). In amino sugars, one or more of the OH groups are replaced with an amino group (NH_2). An important variant is *N*-acetylneuraminic acid: it is a mannose moiety with an acetylated amine and a pyruvic acid group. *N*-Acetylneuraminic acid and its derivatives, referred to as sialic acids, are important components of glycoproteins and glycolipids (see Figure 7.15).

Polysaccharides Individual monosaccharides can be linked by glycosidic bonds between their hydroxyl groups, giving rise to a very wide range of possible polymeric molecules, also referred to as glycans. Since glycosylic bonds can be formed between any hydroxyl groups, such polysaccharides are not only linear chains of identical or different monosaccharides, they also can be branched to form tree-like structures (see Figure 7.15).

Linkage of two monosaccharides results in disaccharides. An important example is lactose, the component of milk formed by the coupling of galactose and glucose. Another is sucrose, also known as table sugar, in which glucose is linked to fructose as illustrated in Figure 7.14. Tri- and oligosaccharides are less common.

Higher order polysaccharides serve as structural and energy storage molecules. Linkage of several thousand glucose units yields cellulose (Figure 7.14), the primary component of plant cell walls. Cellulose strands form hydrogen-bonded fibers, which are virtually insoluble in water. They give plant cell walls and wood their mechanical strength and require specific enzymes for their degradation. Chitin, which forms the exoskeleton of insects, spiders, and crustaceans, is a polysaccharide made of *N*-acetylglucosamine units. Cellulose and chitin together are very abundant in nature – they are the major carbon storage units in the biosphere.

Glycosaminoglycans are linear polysaccharides of alternating uronic acid and hexosamine units. Together with collagen and other proteins, they form the extracellular matrix in connective tissues such as skin, tendon, and cartilage and provide viscosity and elasticity. An important example is hyaluronic acid, a glycosaminoglycan whose viscoelastic properties make it a perfect natural lubricant and shock absorber. The sulfated glycosaminoglycan heparin occurs in intracellular granules of mast cells in arterial walls. It prevents blood clotting and is therefore an indispensable clinical tool.

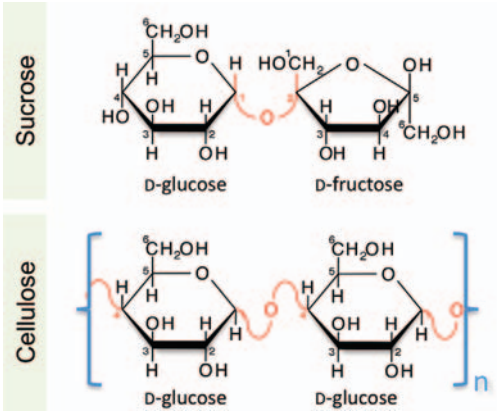

Figure 7.14 Polymerization of monosaccharides. The disaccharide sucrose is formed by linkage of the anomeric carbons of glucose and fructose via a glycosidic bond (red). Cellulose is a long chain of glucose units linked between their C-1 and C-4 carbons.

By means of covalent linkages, glycosaminoglycan can be attached to proteins. The meshwork of covalently and noncovalently aggregated glycosaminoglycans and proteins forming the extracellular matrix is called proteoglycan. Such molecules can reach gigantic sizes of several million daltons. The cell walls of bacteria are composed of a covalently linked mixture of glycosaminoglycans and peptide, the peptidoglycan. This structure is of major medical importance because it largely

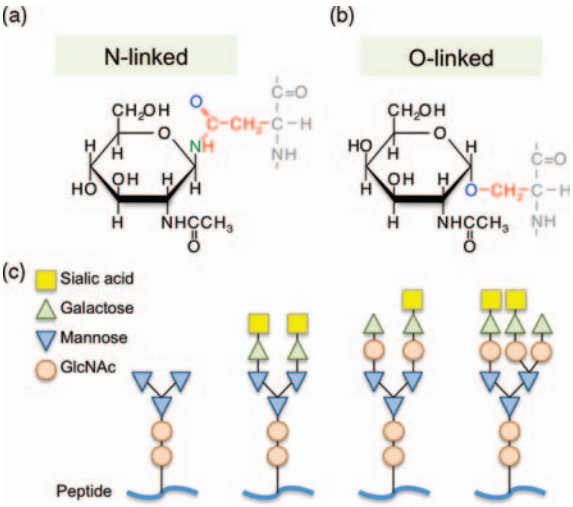

Figure 7.15 Glycosylation of proteins. (a) Formation of an *N*-glycosylic bond between *N*-acetylglucosamine (GlcNAc, black) and asparagine. (b) Formation of an *O*-glycosylic bond between *N*-acetylgalactosamine (GalNAc, black) and serine. The peptide backbones are shown in gray. (c) *N*-Linked oligosaccharides attached to a peptide. The first pentasaccharide consisting of two GlcNAc and three mannose units is an invariable component of *N*-linked protein glycosylation (adapted from Voet *et al.* [3]).

determines the virulence of bacteria and, in some cases, the cell wall alone can evoke symptoms of an infection (see Section 7.4.4).

Living organisms store energy in the form of large polysaccharide molecules. In plants, the principal form is starch, a mixture of α-amylose and amylopectin, both having long chains of glucose units. Starch is the major energy source for humans; it is degraded by digestive enzymes to a variety of disaccharides, trisaccharides, and oligosaccharides (dextrins). Animals use the polysaccharide glycogen as one of the ways to store energy, mainly in skeletal muscle cells and the liver. Glycogen is a heavily branched polymer of glucose residues. Enzymatic cleavage of such branches ensures rapid energy mobilization.

7.1.3.2 Glycosylation of Proteins and Lipids

Glycosylation is the enzymatic process that connects saccharides to produce glycans, either free or attached to proteins and lipids.

Protein Glycosylation This enzymatic process provides a co-translational and post-translational modification mechanism that modulates the structure and function of membrane and secreted proteins. The degree of glycosylation can be high such that some glycoproteins can obtain about twice the mass of the corresponding non-glycosylated proteins. Whereas the protein synthesis strictly follows the genetic blueprint provided by the DNA sequence (see Section 7.1.2.2), the polysaccharide chains are subject to greater environmental fluctuations and the carbohydrates of glycoproteins exhibit a certain degree of variability.

Glycan can be attached to proteins by either *N*- or *O*-glycosidic bonds. *N*-Linked glycosylation starts co-translationally at the rough ER by attaching a tree of 14 sugar residues to the nitrogen of the residue asparagine (Asn), when it occurs second next to serine (Ser) or threonine (Thr), Asn–xxx–Ser or Asn–xxx–Thr, where xxx denotes an arbitrary residue except proline (Pro) or aspartate (Asp). Further processing inside the ER and the Golgi apparatus results in a diversity of sugar chains with a core pentasaccharide of two *N*-acetylglycosamines and three branched mannose groups (Figure 7.15). In addition, fructose can be attached to the first *N*-acetylglycosamine.

O-Linked glycosylation is a post-translational modification, mostly taking place in the Golgi apparatus. Sugar chains starting with *N*-acetylgalactosamine (GalNAc) are attached to the OH group of the residues serine (Figure 7.15) or threonine, independently of their neighboring amino acid sequence.

The key enzymes required for the processing of polysaccharides are glycosidases that cleave off monosaccharides and glycosyl transferases that attach individual sugar groups.

Lipid Glycosylation Lipids are glycosylated by the attachment of glycans to ceramide, as discussed in Section 7.1.4.1.

Because of the immense complexity of polysaccharides attached to proteins and lipids, their specific functions are not known in detail, but they are certainly diverse. The carbohydrate shell of a glycoprotein can protect the polypeptide from proteolytic attacks, can assist in correct protein folding, and may serve as a quality check in

protein processing, that is, proteins without the appropriate glycosylation may be recognized as immature. In addition, sugar residues at proteins function as an address label such that proteins are transported to the correct location inside a cell (protein targeting). Polysaccharides exposed on the cell surface are important for cell–cell recognition; such inter-cell contacts are mediated by proteins (lectins and selectins) that bind to specific polysaccharides. Moreover, the composition of carbohydrates exposed on cell surfaces is a valuable immunological marker, forming the basis for the ABO blood group system.

7.1.4 Lipids and Membranes

Lipids are the fourth large group of biomolecules. Unlike nucleic acids, proteins, and carbohydrates, they do not polymerize. Nevertheless, owing to their hydrophobicity they aggregate to form the structural matrix of biological membranes. In this function, they not only separate the cell interior from the extracellular space, they also form intracellular organelles and are scaffolds for important biochemical reactions. In addition, lipids function as energy storage molecules and they also serve as signaling molecules, playing roles both in normal physiology and in disease states (Section 7.3.2).

7.1.4.1 Lipids: Fatty Acids and Head Groups

The structures of lipids are much more diverse than those of amino acids and nucleic acids because, strictly speaking, most biological molecules soluble in organic solvents can be considered as lipids. Here we only address a few classes that are particularly important for the formation of lipid membranes – fatty acids, triacylglycerols, glycerophospholipids, sphingolipids, and cholesterol. Membrane lipids often consist of one or more nonpolar fatty acid chains and one hydrophilic headgroup.

Fatty Acids The hydrophobic moiety of lipids is formed by fatty acids, which are carboxylic acids with hydrocarbon side chains (a series of CH_2 groups), typically with 14–20 carbons. More than half of the naturally occurring fatty acids are unsaturated; their hydrocarbon tail chain contains one or more double bonds so that the tail carbon atoms could accept additional hydrogen atoms. In addition to several commonly used names, a systematic nomenclature system exists to cope with the vast structural diversity of lipids. For example, stearic acid [octadecanoic acid, $CH_3(CH_2)_{16}COOH$)] is a fatty acid with 18 carbons and no double bond, and hence is denoted 18:0. Oleic acid [9-octadecenoci acid, $CH_3(CH_2)_7CH{=}CH(CH_2)_7COOH$] also has 18 carbons, but there is a double bond between carbons 9 and 10, hence the short form is 18:1*n*-9. In polyunsaturated fatty acids, the double bonds typically occur at every third carbon atom. Double bonds in hydrocarbon chains produce a kink in the structure (Figure 7.16a) and therefore they decrease the melting point of fatty acids. As a consequence, the fluidity of lipid membranes increases with the degree of unsaturation of the fatty acids or the number of double bonds present in the membrane lipids.

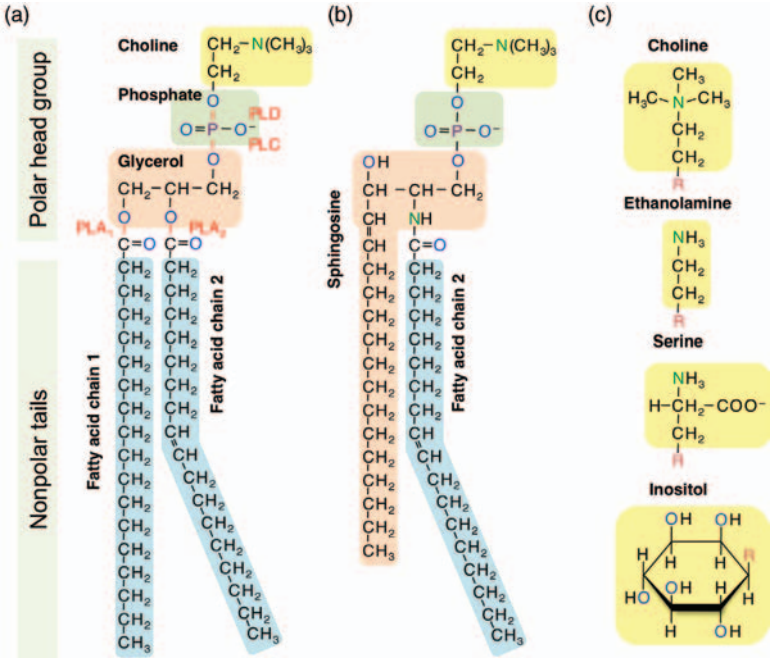

Figure 7.16 Structural elements of a lipid molecule, exemplified for phosphatidylcholine (a) and sphingomyelin (b). Cleavage sites for some phospholipases are indicated in red. (c) Chemical structures of some typical lipid headgroups. R refers to the phospholipid scaffold.

Triacylglycerols (Triglycerides) A common way to store energy is based on triacylglycerols, glycerol molecules in which fatty acid chains are attached to each of their three OH groups. In humans, about one-quarter of the body mass is fat (21% for men, 26% for women), forming an energy reserve that lasts much longer than the stored content of carbohydrates.

Glycerophospholipids The major types of membrane lipids are glycerophospholipids. These lipids are based on glycerol units with fatty acid side chains attached to the first two carbons. The third carbon holds a phosphoryl group, which is then typically linked to a hydrophilic headgroup. In phosphatidic acid this headgroup is just a proton. The structure of phosphatidylcholine is illustrated in Figure 7.16a. It has a saturated fatty acid chain at the C-1 position and an unsaturated chain at the C-2 position. The phosphoryl group together with the choline residue are hydrophilic such that the entire molecule has an amphiphilic character with a nonpolar tail and a polar headgroup. The amphiphilicity of lipids is a major requirement for their self-aggregation into larger structures such as membranes.

Common phospholipids such as occur in biological membranes are phosphatidylethanolamine, phosphatidylserine, and phosphatidylcholine (Figure 7.16).

Sphingolipids Another group of lipids important for biological membranes is based on the amino alcohol sphingosine, comprising 18 carbon atoms. Addition of a fatty acid chain to the amide group at the C-2 position in sphingosine creates a biologically important sphingolipid, ceramide, which plays a role as a messenger within in a cell (Section 7.1.4.3). A related molecule, sphingomyelin (Figure 7.16b), a sphingolipid that contains a phosphocholine as the headgroup, is a vital component of the myelin sheath surrounding and insulating nerve cell axons. In cerebrosides, the headgroup of a ceramide is a sugar residue. Gangliosides are complex lipids consisting of a ceramide with an attached oligosaccharide including at least one sialic acid. Such glycosylated lipids play an important role in cell–cell recognition.

Cholesterol Cholesterol is a slightly amphiphilic structure of three six-membered rings and one five-membered ring. Although infamous for its association with cardiovascular disease, cholesterol is essential for life. In plasma membranes, cholesterol makes up about 30–40 mol% of all lipid molecules and influences membrane fluidity. Cholesterol is also a precursor to very important steroid hormones such as cortisol, aldosterone, estrogens, testosterone, and vitamin D.

7.1.4.2 Formation of Membranes and Vesicles

Lipids do not polymerize but they can form large structures by spontaneous aggregation. The structural prerequisite for this feature is their amphiphilic nature; they are composed of a hydrophobic tail and a hydrophilic headgroup. In an aqueous phase lipid molecules are barely soluble. At fairly low concentrations they tend to form micelles (Figure 7.17b), spherical structures in which the headgroups face the water and fatty acid tails fill the interior.

Although the dimensions of the lipids limit the sizes of micelles, self-aggregation to bimolecular layers gives rise to very large molecular assemblies. The hydrophobic tails form a core region and the headgroups face the water. Depending on the ratio of headgroup surface area and the space-filling volume of the hydrocarbon chains, lipid bilayers may form concave, convex, or planar structures. Small lipid vesicles (Figure 7.17c) are used for storage of transmitter molecules, for example. Lipid membranes (Figure 7.17d) with various degrees of curvature are the basis of membranes delimiting cells (plasma membranes) and organelles.

The formation of membranes does not involve covalent bonds; they are entirely held together by various non-covalent forces, largely so as to minimize the interaction of hydrocarbon tails and to maximize the interaction of the headgroups with water. By virtue of these hydrophobic forces driving the process of self-aggregation, membranes are self-sealing; small holes are spontaneously closed, parts of the membranes can be separated off to form independent vesicles (budding), and vesicular membranes can be incorporated in a larger membrane (exocytosis, endocytosis). Thus, lipid membranes are highly dynamic.

The thickness of a lipid bilayer membrane differs somewhat depending on the lipid composition and the incorporation of membrane proteins. A thin membrane has a thickness of about 4 nm and thick membranes can be about 7 nm.

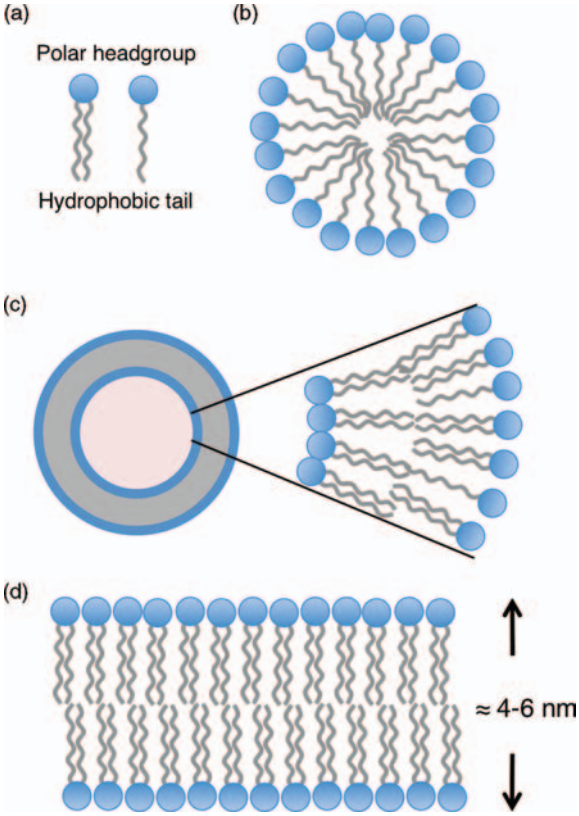

Figure 7.17 Self-aggregation of lipids. (a) Schematic presentation of lipid molecules with one or two fatty acid chains comprising a polar headgroup and a hydrophobic tail. (b) In micelles the hydrophobic tails cluster together to form a sphere with the headgroups pointing towards the aqueous phase. (c) Vesicles are spheres formed of lipid double layers; the composition of the inner and outer layers can be substantially different. (d) A planar lipid bilayer membrane.

As the layer separating the cell interior from the extracellular space, the plasma membrane is the most apparent membrane structure in cells, but it typically makes up less than 10% of the total cellular membrane. The remaining membrane is used to form organelles and small vesicular structures.

Lipid membranes are very effective barriers for polar molecules because of the hydrophobic core region. Therefore, pure lipid membranes are nearly perfect electrical insulators, providing the basis for the establishment of electrical membrane potentials. Hydrophobic substances, such as urea and glycerol, permeate readily through membranes. Water molecules also permeate across membranes. Larger molecules or charged molecules require specific transport proteins that aid them in crossing the membrane (see Section 7.3.2).

7.1.4.3 Lipids as Signaling Molecules

Lipids and lipid-derived molecules not only serve a role as the matrix for biological membranes or as an energy reserve, they also function as signaling molecules. Some phospholipids are phosphorylated and dephosphorylated and hence change their electric charge and functional properties mediated by the action of lipid kinases and phosphatases. The most prominent example is the membrane component phosphatidylinositol-4,5-bisphosphate (PIP_2). Dephosphorylation results in PIP and PI3-kinases phosphorylate PIP_2 to PIP_3.

Membrane phospholipids such as PIP_2 are hydrolyzed into smaller but important lipid-derived signaling molecules by the action of phospholipases, which cleave specific bonds in phospholipids. Phospholipase A_1 hydrolytically excises the fatty acid chain at the C-1 position whereas phospholipase A_2 does so at the C-2 position (Figure 7.16). The latter leaves a lipid with only one fatty acid chain – a so-called lysophospholipid. As the name suggests, this form of lipid destabilizes membranes. Arachidonic acid, a precursor for many local messengers, is also released with the aid of phospholipase A_2 from membrane-bound phosphatidylinositol and other phospholipids. Phospholipase D cleaves off the headgroup after the phosphorus atom, while phospholipase C (PLC) cleaves it off before the phosphorus atom. PLC thus produces the important messengers diacylglycerol (DAG) and inositol-1,4,5-trisphosphate (IP_3) from PIP_2 (see also Section 7.3.2).

7.1.4.4 Interaction of Lipids with Light

Many pigments in biological materials that absorb light strongly or that display fluorescence are lipids. Aromatic structures with delocalized electrons typically are soluble in organic solvent and therefore tend to partition in the hydrophobic center of proteins or inside membranes. Vitamin D and vitamin A (retinol), the latter derived from the red pigment β-carotene, are good examples. Retinal, the oxidized form of retinol, is the pigment in the photoreceptors in the eye.

Like other biological material, lipids can be oxidatively modified and, hence, excessive irradiation with light of low wavelength will directly or indirectly cause lipid peroxidation. Since this process likely results in deleterious effects on biological membranes, Nature has devised some protective measures. One is α-tocopherol, a variant of vitamin E, which is incorporated into membranes and acts as a strong antioxidant, protecting lipids and membrane proteins from oxidative damage.

7.1.5 Special-Purpose Proteins: Cofactors and Prosthetic Groups

Protein complexes made of one or more polypeptide chains containing up to 20 amino acid types (Figure 7.6) with possible co-translational and post-translational modifications (Figure 7.12) can perform a diverse array of functions. However, in some cases, additional inorganic and organic molecules, collectively referred to as cofactors or prosthetic groups, are incorporated into proteins to confer novel functionalities, typically catalytic in nature. Some cofactors are simple metal ions, such as copper, iron, manganese, nickel, and zinc, and others are larger organic

compounds, such as flavin adenine dinucleotide (FAD), nicotinamide adenine dinucleotide (NAD^+), nicotinamide adenine dinucleotide phosphate ($NADP^+$), and heme. The degree of association between the cofactors and the parent proteins can be variable. Some cofactors are bound so tightly that the proteins are almost always found with the cofactors included, referred to as holoproteins, whereas in others the association is not as stable and fractions of the proteins may be found without the cofactors (apoproteins). The proteins with cofactors/prosthetic groups are of special interest in biophotonics because many of them exhibit light-sensitive characteristics. Selected examples are briefly discussed below.

7.1.5.1 Opsins Exemplified by Rhodopsin

Opsins are the best-known family of light-harvesting proteins and serve multiple physiological functions. For example, the sensitivity and acuity of our visual experience is enabled by opsin proteins in rod and cone photoreceptor cells in the retina.

Cylindrical rod photoreceptor cells are present throughout the retina with a couple of notable exceptions including the very center, and the rods are particularly important in dim-light monochromatic vision or scotopic/mesopic vision. The sensitivity to light is so high that a single photon can be readily detected by a rod photoreceptor cell. The first event in the high-sensitivity light transduction process is absorption of a photon by the visual pigment rhodopsin, a G protein-coupled receptor protein with seven transmembrane helical segments that contains retinal, a vitamin A aldehyde, as the chromophore cofactor (Figure 7.18). In the dark, the retinal in the kinked 11-*cis* form is covalently linked to the nitrogen atom of a lysine side chain in a transmembrane helical segment via a protonated Schiff base linkage. An incident photon with a wavelength centering 500 nm (blue–green) isomerizes the retinal around the C-11=C-12 double bond with a quantum yield of ~0.67 within 0.2 ps, forming linear all-*trans*-retinal. The opsin protein undergoes multiple conformational changes and eventually assumes a conformation known as Meta II. Metarhodopsin II activates the adjacent G protein (*transducin*), which initiates a series of biochemical reactions involving cGMP (cyclic guanosine monophosphate) to amplify the original signal, ultimately resulting in a visual experience sometime later ($\geq$100 ms). Following activation of the intracellular signaling cascade, the all-*trans*-retinal dissociates from the protein (bleaching). Eventually, through a multi-step reaction taking place in the retinal pigment epithelium, all-*trans*-retinal is recycled to an 11-*cis*-retinal precursor, which is then incorporated back into rhodopsin in rod photoreceptor cells. At different stages in the light transduction process, the chromophore has distinct spectral characteristics and this feature has allowed time-resolved biophotonics approaches, such as time-resolved variants of fluorescence microscopy, infrared microscopy, and Raman spectroscopy, to provide detailed mechanistic information.

Cone photoreceptor cells, with a more tapered appearance, are located almost exclusively near the center of the retina and mediate our high-acuity color vision under well-lit conditions or photopic vision. The biochemical reactions taking place in cone photoreceptor cells are similar to those occurring in rod photoreceptors; photons induce isomerization of the chromophore 11-*cis* retinal contained in cone opsin proteins, leading to activation of nearby G proteins. A distinct opsin with a

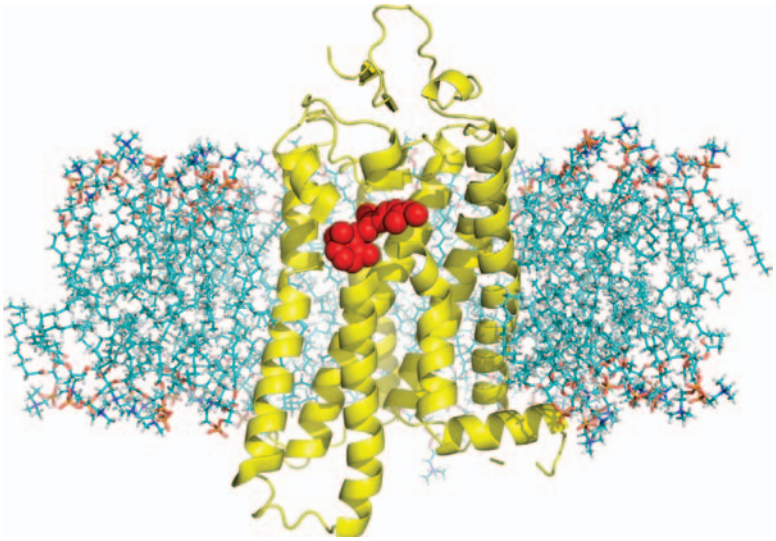

Figure 7.18 Structure of bovine rhodopsin (PDB ID: 1GZM) in its bilayer environment highlighting the retinal (red).

characteristic light absorption spectrum is present in each of three classes of cone photoreceptor cells in the human retina. Accordingly, the three human cone photoreceptor cells are often referred to as blue or S cones with a maximum absorption at ~420 nm, green or M cones with a maximum absorption at ~530 nm, and red or L cones with a maximum absorption at ~560 nm. The differential but overlapping spectral characteristics of the cone opsins are conferred by amino acid differences near the chromophore in the transmembrane segments and also those near the C terminus in the cytoplasmic compartment. The overall light sensitivity of cone photoreceptor cells is not as exquisite as that of rod photoreceptor cells, in part because the biochemical amplification gain in the cone cells is smaller. However, differential excitation of the three classes of cone photoreceptor cells by a light stimulus forms the basis of our color vision.

Opsins are also found in many prokaryotic organisms such as bacteria and algae, in which retinal-containing opsin proteins typically perform light-activated transport of ions across cell membranes. Recently, channelrhodopsins from green algae have been expressed in the brains of rodents and nonhuman primates so that their brain electrical activity and behavior can be experimentally manipulated by flashes of light.

7.1.5.2 **Porphyrin Proteins**

Heme (iron protoporphryin IX, Figure 7.19a) is a planar tetrapyrrole macrocycle synthesized through a series of reactions taking place in both the cytoplasm and mitochondria, and incorporated into numerous proteins as their prosthetic factor. Detailed mechanisms of heme binding to proteins vary but an interaction between the heme iron center and the imidazole side chain of histidine (His) is common. Functionally, the presence of the redox-sensitive iron center (Fe^{2+}/Fe^{3+}) in the heme

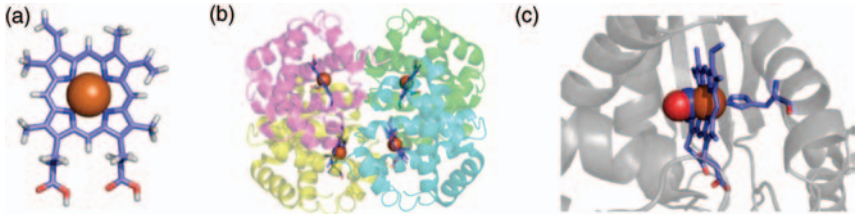

Figure 7.19 Heme, hemoglobin, and soluble guanylyl cyclase. (a) Heme. (b) Four-chain hemoglobin complex with four heme cofactors (PDB ID: 3HHB). (c) Soluble guanylyl cyclase (PDB ID: 2O0C), illustrating coordination of heme with a histidine side chain (right) and an interaction of NO with the iron center.

moiety is utilized for gas transport, gas detection, and catalysis through electron transfers. For example, the O_2 and carbon monoxide (CO) sensitivity of hemoglobin responsible for oxygen delivery is well known (Figure 7.19b) and the enzyme-soluble guanylyl cyclase (Figure 7.19c) involved in numerous processes including blood vessel dilation is an NO- and CO-sensitive heme protein.

7.1.5.3 Living Colors: Fluorescent and Phosphorescent Proteins

GFP from the bioluminescent jellyfish *Aequorea victoria* is intrinsically fluorescent without any special prosthetic group. In GFP, consisting of 238 amino acid residues, a ring is formed spontaneously among the succeeding residues Ser–Tyr–Gly. The resulting conjugated double bonds are fluorescent with an ideal excitation at 400 nm and an emission at 508 nm (green). A three-dimensional structure of an engineered form of GFP, enhanced green fluorescent protein (EGFP), is shown in Figure 7.20a, highlighting the optically active site. Numerous variants of EGFP with altered spectral properties exist; mutations in the GFP protein shift the emission to lower [cyan fluorescent protein (CFP)] or higher wavelength [yellow fluorescent protein (YFP)], for example (e.g., [9]).

Because EGFP and its variants are intrinsically fluorescent without any cofactor, these relatively small proteins have emerged as very powerful tools in cell biology. Fused to other proteins, GFP moieties are used to visualize the expression and location of engineered proteins, as illustrated in Figure 7.20b. Equipped with specific signal sequences, expressed GFP can mark organelles such as mitochondria or the nucleus. Meanwhile, an array of available GFP variants gives the experimenter the opportunity to label proteins specifically with different colors such that many more than one type of protein can be monitored at a time in single cells or whole organisms.

Since the photonic properties of GFP molecules depend on the immediate environment of the chromophore, several methods were devised to use GFP as reporter for intracellular events. For example, GFP moieties fused to a Ca^{2+}-sensing protein and genetically expressed in every cell or select cells in a living organism including mice can be utilized for *in vivo* measurements of the intracellular concentration of Ca^{2+}. GFP variants with extra cysteine residues, so-called roGFPs, change their fluorescence properties when two of such cysteines form a disulfide bridge and thereby report on the intracellular redox milieu.

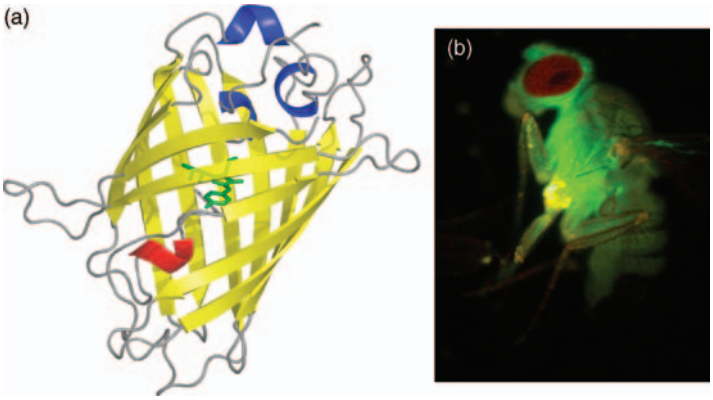

Figure 7.20 (a) Structure of GFP (PDB ID: 1EMA). On the outside, 11 antiparallel β-strands (yellow) form a very compact cylinder. Inside this β-structure there is an α-helix (red), in the middle of which is the chromophore (green). There are also short helical segments (blue) on the end of the can. The cylinder has a diameter of about 2.5 nm and a length of about 3 nm. (b) Fluorescence image of a transgenic fruit fly expressing an EGFP-tagged protein in nervous tissue.

Genetically Modified Animals: Knock-out and Transgenic Animals

Various methods exist to manipulate the genome of laboratory animals. The easiest is the destruction of a gene such that no corresponding functional protein can be generated. Such animals are then referred to as knock-out animals; a mouse having gene *ABC* deleted on both chromosomes (homozygous) would be termed $ABC^{-/-}$. To generate a knock-out mouse, embryonic stem (ES) cells are manipulated in cell culture, such that the normal gene is inactivated and a selectable marker, such as an antibiotic resistance gene, is inserted instead. Such modified ES cells are reintroduced into early-stage mouse embryos and implanted into the uterus of a female mouse. After several rounds of cross-breeding this will finally generate mice with a deficiency in just one specific gene. Using more involved strategies, gene knock-out can be designed such that it is controlled by exogenous factors (*inducible knock-out*). Gene knock-out can be combined with tissue specificity so as to affect gene expression in specific organs only. *Transgenic animals* are those that carry a new gene or a mutated gene. The time and financial resources required to produce such genetically modified animals vary greatly with the species. Whereas transgenic plants and fruit flies can be generated within a few weeks, gene knock-out in mammals often takes many months.

Variants of EGFP are also useful for fluorescence resonance energy transfer (FRET) experiments reporting on the distance between two chromophores and thereby providing insight into the dynamics of cellular proteins. The physical

proximity, typically less than 10 nm, can be inferred if excitation of one chromophore (donor) influences the status of the other chromophore (acceptor). In a related measurement method called bimolecular fluorescence complementation (BiFC), two fragments of a GFP are expressed in two proteins and, if the two proteins physically interact, functional GFPs are formed and the fluorescence is observed. The contribution of GFP-based technology was recognized with the Nobel Prize in Chemistry in 2008 awarded to Osamu Shimomura, Martin Chalfie and Roger Y. Tsien.

7.1.6
Low Molecular Weight Molecules

In addition to lipids and the polymeric macromolecules discussed thus far, the cytosol of cells contains very many different types of molecules of lower molecular weight. It would be far beyond the scope of this brief introduction to discuss those in detail and, therefore, we will consider just a few molecules important for biophotonics research.

7.1.6.1 Adenosine Phosphates

The most important molecule for short-term energy storage and exchange is adenosine-5′-triphosphate (ATP). It is a nucleotide with a molecular mass of about $507\,\mathrm{g\,mol^{-1}}$ and provides energy to cellular reactions by hydrolysis to adenosine diphosphate (ADP), yielding $-30.5\,\mathrm{kJ\,mol^{-1}}$, or adenosine monophosphate (AMP), yielding $-45.6\,\mathrm{kJ\,mol^{-1}}$. Since ATP is unstable, it is immediately used and must be recycled constantly. Therefore, humans at rest produce about 70 kg of ATP per day. The intracellular concentration of ATP is between 1 and 10 $\mathrm{mmol\,l^{-1}}$. The ATP:ADP concentration ratio provides an estimate of the energy status of a cell.

ATP is not only used as "energy currency" inside the cell, it also serves roles as extracellular and intracellular signaling molecule (see Section 7.3) and takes part in DNA replication and transcription.

7.1.6.2 Nicotinamide Adenine Dinucleotide

NAD^+ and the protonated form NADH are coenzymes functioning as a redox pair, that is, NAD^+ is the oxidizing agent accepting electrons from other molecules while the reducing agent NADH is an electron donor. NAD^+, with a molecular mass of about $663\,\mathrm{g\,mol^{-1}}$, exists in all cells and is of vital importance for various redox reactions. Therefore, the NAD^+:NADH concentration ratio is a measure of the redox state of a cell, thereby providing information on the metabolic state and the cell's health. Typical ratios are around 700. The concentration of NAD^+ and NADH in the cytosol depends on the cell type but it is on the order of 1 $\mathrm{mmol\,l^{-1}}$.

These molecules are important for photonic research because both absorb UV light strongly. NAD^+ has an absorption peak at 259 nm with an extinction coefficient of $16\,900\,\mathrm{M^{-1}\,cm^{-1}}$; NADH has an additional absorption peak at 339 nm with an extinction coefficient of $6220\,\mathrm{M^{-1}\,cm^{-1}}$. Therefore, from the absorbance at 340 nm one can easily infer the NAD^+:NADH concentration ratio and, hence, the redox

state. In addition, NADH undergoes fluorescence with an emission peak at about 460 nm, whereas NAD^+ does not fluoresce. This provides another means of monitoring the redox state via fluorescence microscopy. Around 260 nm excitation the fluorescence of NADH dominates the autofluorescence of virtually all cells.

7.1.6.3 Glutathione

The tripeptide Glu–Cys–Gly [glutathione (GSH), reduced form] forms a dimeric disulfide-linked structure, glutathione disulfide (GSSG, oxidized form) and thereby reduces other targets. GSH therefore is an antioxidant that helps to protect cells from reactive oxygen species. GSSG needs to be regenerated to GSH by means of glutathione reductase. The equilibrium between GSH and GSSG is another indicator of the cellular redox state. In a healthy cell, typically 90% of glutathione exists as GSH and only 10% as GSSG. Elevated oxidative stress manifests as an increased GSSG:GSH ratio. The cellular concentration of GSH is typically a few millimoles per liter.

Owing to the potential hazard imposed by light-generated reactive species in cells, in particular long-term photonic experiments on living material require the maintenance of a healthy cell state. Control of cytosolic ATP, NADH, and GSH can be used as a quality check and supplementation of the cytosol with these factors can help to diminish oxidative damage during a photonic experiment.

7.2 Cells

The principal unit of life is the cell. This simple statement is just as fundamental for biological science as the atomic theory is for chemistry. In the 1830s, Matthias Schleiden and Theodor Schwann proposed the cell theory, stating that all organisms are composed of one or more cells. In 1855, this was extended by Rudolf Virchow, who found that cells never arise from non-cellular material but only by division from pre-existing cells. A closer look at this basic unit is not only important for microbiologists who study unicellular bacteria, but also for others studying multicellular organisms with intricate interactions among the cells.

7.2.1 Compartments of a Human Cell

About 10^{14} individual cells form the body of an adult human, and despite an enormous degree of cellular differentiation, all of these cells have the same principal building plan. Human cells share this concept with the cells of our closer relatives, for example, all mammals including important biomedical model organisms like mice and rats. Later we will compare cellular principles in mammalian cells and those of other life forms, such as plants or the unicellular protozoa and bacteria.

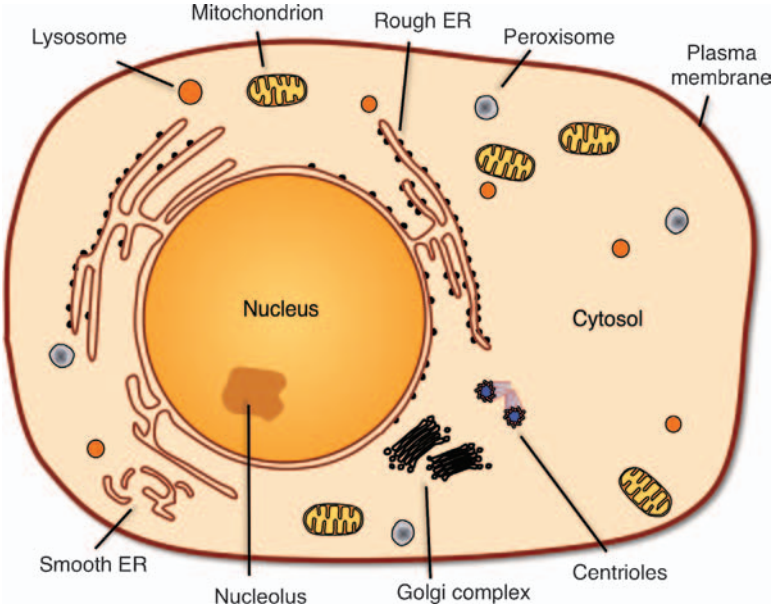

Figure 7.21 Structural organization of a prototypical human cell. The dimensions are not to scale to enhance clarity. For example, the thickness of cellular membranes is exaggerated.

Shape and size of human cells can vary substantially. Red blood cells have diameters below 10 μm, whereas a secondary oocyte, waiting to be fertilized, is about 100 μm across and visible to the naked eye. The longest cells in our body are the sensory neurons connecting the toes with the spinal cord over a distance up to 1.5 m. Despite these huge differences, the structural organization within most of the cells follows the same blueprint. Figure 7.21 is a schematic diagram of a prototypic human cell with a size of approximately 20 μm across.

The cell is separated from its external environment by the plasma membrane. This allows a complex organization of the cell interior and the accumulation of energy-rich metabolites. Inside the cell, additional membranes enclose compartments called organelles, the biggest of which is the nucleus. Typically this is a near spherical structure with a diameter of about 5–10 μm and it harbors most of the genetic information in form of the chromosomes. Within the nucleus a region of higher density, called nucleolus, is often visible by light microscopy. In contrast to other organelles, the nucleolus is poorly demarcated and not surrounded by a membrane. The volume between the nuclear membrane and the plasma membrane, the cytoplasm, comprises an aqueous phase – the cytosol –, and additional organelles.

Directly contiguous with the nucleus is the membrane of the ER, a widespread tubular system involved in synthesis, transport, and secretion of various important biomolecules. Closer examination using electron microscopy often reveals a dense decoration of the cytosolic ER surface with uniformly sized particles, the *ribosomes*. These areas are called rough ER, in contrast to the smooth ER, lacking ribosomes. The presence of ribosomes is a marker for ongoing synthesis of proteins designated

for export or for other compartments being restocked via the ER. By contrast, smooth ER is involved in the biosynthesis and modification of other biomolecules, such as lipids and carbohydrates. Most of the macromolecules from the ER are further modified and sorted in the *Golgi complex*, stacks of membrane-surrounded, flattened compartments that were first described in 1898 by Camillo Golgi. *Mitochondria*, the organelles that generate most of the cell's energy currency ATP, are surrounded by a double-membrane system. More than 1000 mitochondria are typically found in each cell. Their shapes range from filamentous tubules to almost spherical bodies resembling bacteria. In fact, according to the now undisputed "endosymbiotic theory," mitochondria were originally derived from bacteria that have been engulfed by larger cells and since then remained there to the benefit of both parties. This explains the double-membrane system and the presence of a genetic code specific for mitochondria (Sections 7.1.1 and 7.1.2.2). *Endosomes*, *lysosomes*, and *peroxisomes* are additional membrane-delimited vesicular structures of a human cell. Furthermore, several large intracellular structures exist without a membranous envelope. As the definition of the term "organelle" has never been precise, some of these structures, including the centromeres are traditionally also called organelles.

7.2.1.1 **The Plasma Membrane and Its Transport Proteins**

The plasma membrane is the interface between every cell and its environment and, just like the walls surrounding ancient cities, the membrane protects the cell from the loss of valuables and allows tight control of cargo transport into and out of the cell. The design principle of the membrane as a barrier is simple but very efficient. It builds on the fact that the hydrophobic parts of lipids and hydrophilic environments are incompatible. The cell interior, and also the extracellular space, are dominated by the omnipresence of water and the cellular content is adapted to this aqueous environment. Thus, a contiguous envelope, consisting of lipid molecules, is a perfect way to separate the hydrophilic biomolecules on the two sides.

The amphiphilic nature of phospholipids drives these molecules to form bilayers in aqueous environments with no energetic costs to the cell (see Section 7.1.4.1). Hence a lipid layer, only ~4–5 nm thick, is wrapped around every cell of our body, prohibiting efflux and influx of ions and of hydrophilic biomolecules such as sugars, proteins, and nucleotides. Biomembranes are called bilayers, because they are formed by two closely packed layers of molecules, the inner and outer leaflets. Functionally, we could also name them trilayers, as a lipid core layer is shielded from water by the headgroup layers on either side. With extensive electron microscopy studies since the late 1950s, it became clear that not only the plasma membrane but also all intracellular membranes of the organelles have the same ultrastructure.

Membrane Fluidity In contrast to the metaphor of a city wall, the plasma membrane is anything but rigid. The founders of the modern membrane concept, Jonathan Singer and Garth Nicolson, in 1972 used the term "fluid mosaic" to account for the exquisite freedom of motion for all phospholipids at body temperature. Rotational diffusion lets phospholipid molecules turn around their own lateral axis 10^8 times per second. In addition, lateral diffusion makes neighboring phospholipids change their

places in less than 1 μs. In addition, the membrane as a whole can undergo wavelike, undulating motions on a microsecond time scale, preventing any loss of membrane integrity, even under pressure. It is obvious that the actual shape of a cell cannot be constrained by a fluid membrane layer. The typical discoid shape of a red blood cell (erythrocyte) and the branching structures of neuronal dendrites require a more rigid support. Proteins of the cytoskeleton provide the structuring components that determine a cell's actual shape. Typically, a dense protein network located underneath the plasma membrane is further connected to structural proteins extending throughout the cytosol.

Membrane Proteins Having a tight, lipid-based envelope is advantageous for the cell, but gates are needed for nutrient import and for export of a variety of molecules. In fact, every cellular membrane incorporates proteins that fulfill the task of controlled transport or the propagation of signals across the membrane. As a rule of thumb, about 50% of the plasma membrane mass is formed by membrane proteins. The set of 20 natural amino acids allows the construction of proteins to accommodate both the aqueous environment and the lipid part of the membrane. Amino acids such as alanine, leucine, and isoleucine are characterized by nonpolar side chains. Polypeptide stretches made from such hydrophobic amino acids therefore tend to position away from water and to insert into membranes. On the other hand, polar amino acid residues in a membrane protein can form cavities or pores to fit hydrophilic cargo such as proteins, sugars, and ions. Despite the huge diversity in potential protein folding patterns, the architecture of proteins in the plasma membrane follows a stereotypic concept. One or multiple α-helical stretches of approximately 20 amino acid residues are the basic building block of any mammalian transmembrane protein. These helices can be formed solely from hydrophobic residues or, if several helices are contacting each other, amphipathic helices can be organized in a way that places only the lipophilic faces towards the surrounding lipid, while hydrophilic sides are facing each other. As we will discuss later, proteins of mitochondrial membranes are an exception to this construction principle. Whereas the transmembrane parts of plasma membrane proteins are fairly uniform, extracellular and intracellular loops linking the transmembrane helices can adopt very diverse folding patterns and domain structures.

Membrane Anchors Peripheral membrane proteins do not span the membrane but they are tightly associated with it, mostly by means of membrane anchors. These are lipid moieties covalently linked to residues of the respective proteins. Three major classes of such lipid modifications can be distinguished: acylation, prenylation, and linkage of so-called glycosylphosphatidylinositol (GPI) anchors. The fatty acids myristate (C_{14}) and palmitate (C_{16}) are common acyl anchors, typically attached to an N-terminal glycine residue. Farnesyl (C_{15}) or geranylgeranyl (C_{20}) moieties are anchored to one or more cysteine residues near the C terminus. Both anchor types attach proteins to the cytoplasmic surface of the plasma membrane. The typical anchor for the external surface is GPI, being attached to the cleaved C-terminal end of a protein. The protein to be modified contains a stretch of hydrophobic amino acids at

its C-terminal end, anchoring the protein initially in the membrane of the ER during biogenesis. This membrane anchor is then cleaved off and replaced by the membrane-bound GPI. In this structure, the inositol ring of a phosphatidylinositol (PI) molecule is followed by glucosamine, three mannoses, and phosphoethanolamine, which is coupled via its amino group to the new carboxyl end of the protein.

Membrane Asymmetry Membrane proteins are not only involved in transport processes across the membrane, they also help lipid molecules to move *within* the membrane. As described above, membranes in a human cell are energetically stable bilayers, assembled from various phospholipids, sphingolipids, and cholesterol (Figure 7.22). However, all living cells invest energy to establish a strong asymmetry of lipid distribution between the outer and inner leaflets. The outer leaflet of a typical plasma membrane is mainly formed of phosphatidylcholine (PC) and sphingomyelin (SM), the two membrane lipids with choline as the headgroup (Figure 7.16). By contrast, the aminophospholipids phosphatidylethanolamine (PE) and phosphatidylserine (PS) and also PI form the inner leaflet. Cholesterol, with its very small headgroup, is found in both layers as it can interchange between them. The membrane-resident proteins responsible for the strong asymmetry are commonly called flippases and floppases. These lipid translocases belong to the class of active

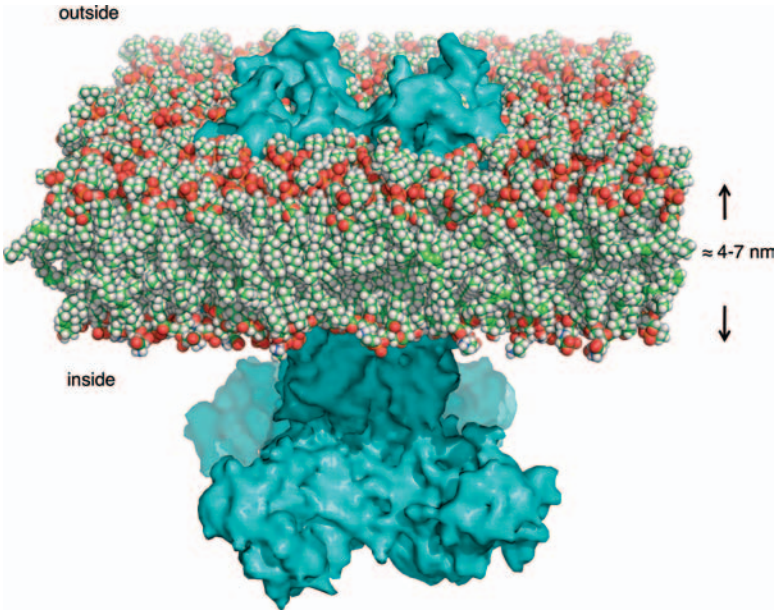

Figure 7.22 A single voltage-gated potassium channel embedded in a lipid bilayer containing phosphatidylcholine, phosphatidylserine, phosphatidylethnolamine, and cholesterol. The channel (PDB ID: 2R9R) is depicted using its molecular surface representation (cyan) and the membrane components are shown using spheres. Green, carbon; white, hydrogen; blue, nitrogen; red, oxygen; orange, phosphate. The image was rendered using MacPyMol. Ions and water molecules are not shown for simplicity.

transporters or pumps, working against a chemical gradient at the expense of ATP. Whereas flippases continually work on the inward movement of PE, PS, and PI, floppases transport PS and SM to the outer leaflet.

Membrane asymmetry has fundamental biological consequences, as we may illustrate with the specific role of PS as a signaling molecule. The flippases, responsible for keeping PS in the inner leaflet, are strongly inhibited by Ca^{2+} ions in the cytosol. Under resting conditions the cytosolic Ca^{2+} concentration is very low. Damage of a cell mostly manifests as an increase in the cytosolic Ca^{2+} concentration and hence inhibits flippase activity. At the same time, a third type of lipid translocase, scramblases, is activated by Ca^{2+}. Scramblases are passive transporters, accomplishing a rapid but unspecific phospholipid exchange between the layers, driven by the existing gradients. In consequence, PS headgroups will appear on the outer cell surface, where they indicate that the cell is in an unhealthy situation. This is a signal to the immune system to activate *phagocytes*, immune cells that are specialized to engulf other cells or cellular debris (see Section 7.2.1.7).

Lateral Mobility of Membrane Proteins According to the fluid mosaic model, not only membrane lipids but also the embedded transmembrane proteins are free to move laterally within the membrane (Figure 7.22). Now we know that lateral movements are much more restricted in biological membranes. Such limitations in fluidity occur when membrane proteins have cytosolic contacts to the cytoskeleton. Anchoring to intracellular proteins is in fact very common and holds membrane proteins in place. For example, in intestinal epithelial cells, a protein can be confined to the apical membrane area facing the gut lumen. Typical contact motifs often reside in the distal C terminus of the membrane protein. The presence of a hydrophobic residue in the very last position and a Ser or Thr in the −3 position of the C terminus provides a docking site for so-called PDZ domains. This domain was named after three proteins for which it was originally described: post-synaptic density, discs large, and zona occludens-1. PDZ domains, comprising about 90 amino acid residues, are typically found in adapter proteins, linking integral membrane proteins to actin fibers of the cytoskeleton.

Lipid Rafts Restricted lateral mobility can also be a result of heterogeneity in the membrane lipid composition. One such phenomenon of the plasma membrane is the formation of so-called *lipid rafts*. The outer leaflet can form small, dynamic zones enriched in sphingomyelin and cholesterol. The surface area of these rafts is typically below the resolution limit of light microscopy. Because of the small size, the exact dimensions and the lifetime of rafts are still a matter of intense debate. However, the protein makeup in rafts appears different from that in the rest of the membrane. For instance, GPI-anchored proteins are enriched in raft compartments. The inner leaflet area under the raft is rich in cholesterol and phospholipids carrying predominantly saturated acyl chains. Notably, typical proteins in these areas are dual-acylated kinases and small guanosine triphosphatases (GTPases). Most likely this arrangement of surface receptors and intracellular signaling proteins promotes a rapid transfer of extracellular signals into the cytoplasm.

Glycoproteins and Glycolipids In addition to lipids and proteins, the plasma membrane also contains carbohydrate, up to 10% by weight. Sugars can be covalently linked to both proteins and lipids, but glycoproteins account for ~90% of the sugar in the plasma membrane. Virtually all of the sugar moieties, regardless of the linked structures, face the extracellular space. The exact functions of glycosylation are far from being understood, but sugars are certainly involved in sorting processes, intercellular recognition, and interaction with the cell environment. Of high practical relevance in medicine are carbohydrates linked to lipids in the plasma membrane of human red blood cells, forming the basis of the ABO blood grouping system. The last moiety in a short chain of sugars determines the blood group. All members of blood group A carry *N*-acetylgalactosamine in this position whereas blood group B is determined by a galactose moiety instead. As these sugars are well exposed on the surface of the blood cells, they are recognized readily by cells of the immune system. If a blood transfusion delivers cells with the incompatible sugar, it would trigger defense reactions of the immune cells. Interestingly, the two enzymes, responsible for the linkage of either *N*-acetylglucosamine or galactose, are encoded by two variants of the same gene. As every individual has two copies of this gene, one from each parent, many individuals have a mixed genotype and both alternative enzymes are formed. They form blood group AB, characterized by the presence of both sugar types in their blood cells. As a fourth alternative, the members of blood group O did not receive a functional gene copy and neither *N*-acetylglucosamine nor galactose is coupled to their glycolipids. As a consequence, type O individuals could donate blood to any other individual; however, they cannot receive blood from other ABO groups because both sugars are "foreign" to the immune system of type O individuals.

7.2.1.2 The Nucleus

The nucleus houses the vast majority of the genetic material of the cell and separates the space where protein building plans (mRNA) are synthesized, the nucleoplasm, from the area where they are translated into protein, the cytoplasm. The nuclear envelope is formed by two adjacent lipid bilayer membranes, the inner and outer nuclear membranes. They are separated by about 10–50 nm and the volume between them is contiguous with the ER lumen. The outer nuclear membrane is in direct contact with the rough ER and shares a similar set of proteins, whereas the inner nuclear membrane has its own distinct set of proteins. Mechanical support of the envelope is provided by a protein network attached to the nucleoplasmic surface of the inner nuclear membrane, the nuclear lamina. This network is built of intermediate protein filaments, one of three categories of cytoskeletal proteins (see Section 7.2.1.8).

DNA Packing in the Nucleus In addition to stabilization of the nuclear envelope, the nuclear lamina also serves as an attachment site for chromatin fibers. Chromatin is a generic term for the complexes formed by DNA, histones, and nonhistone proteins. The well-known structures of highly condensed chromosomes exist for only a short period of time in the life of a cell. Maximum condensation of the DNA allows the

equal distribution of the chromosomes between daughter cells during cell division. When a division is completed, the DNA no longer forms visible chromosomes, but appears as rather diffuse matter, filling the nucleoplasm. Despite their disorganized appearance in light microscopy, fluorescence staining of individual chromosomes shows that these decondensed chromosomes are not randomly intermingled, but rather restricted to specific regions. Inspection of the nucleoplasm by electron microscopy does not identify individual chromosomes, but typically distinguishes compacted, denser areas in the nucleoplasm, the so-called heterochromatin, from a more dispersed euchromatin. Heterochromatin is a macroscopic reflection of gene silencing. This inactive state is constitutive for the distal ends of all chromosomes, the telomeres, and the central parts of the chromosomes, the centromeres. In contrast, any active use of DNA for transcription or replication requires the decondensation of the genetic material. For the major parts of all chromosomes, the degree of condensation is dynamic and depends on the differentiation of an individual cell. In females, a complete chromosome, one of the two X chromosomes in each cell, is typically inactivated as facultative heterochromatin, the *Barr body*. Inactivation of one of the X chromosomes ensures that male and female cells produce about the same amounts of X-encoded proteins. X chromosome inactivation in females is a random process in early embryogenesis and the condensed state of the X-chromosomes is subsequently transmitted to all descendant cells. As hair/fur pigmentation in mammals is partly determined by a gene product of the X chromosome, this can result in random patches of different coat color, as seen in the so-called calico cats. Accordingly, male cats, that do not inactivate X chromosomes, do not show calico color patches.

The Nucleolus The largest substructure in the nucleus visible in light microscopy is the nucleolus, an irregular region of higher density. Unlike other organelles, the nucleolus is not surrounded by a membrane. The higher density is due to the accumulation of rRNAs, RNA-processing enzymes, and partly assembled ribosomes as the nucleolus is the site of ribosome production. The large and small ribosomal subunits, huge complexes formed of several rRNAs and proteins, are exported from the nucleus after assembly to act as protein synthesis factories in the cytoplasm. Three of four different rRNAs are encoded by a single gene, which is located in multiple copies on five different chromosomes of the human cell. Thus, in a diploid cell, 10 chromosomes carry rRNA genes at their distal ends. During rRNA synthesis, these ends stick together closely and form the center of the ribosome production factory. The size of the nucleolus is variable and depends on the need for ribosomes in the cytosol. In active cells producing very large amounts of protein, the size of the nucleolus can reach up to 25% of the nuclear volume.

Nuclear Pores The nuclear envelope keeps the genetic material away from the sites of active metabolism, but exchange and communication between nucleoplasm and cytoplasm are vitally important. Since the sequence information for protein synthesis at cytoplasmic ribosomes is carried by mRNA, continual export of mRNA from the nucleus to the cytoplasm is required. As mentioned before, the ribosomal subunits

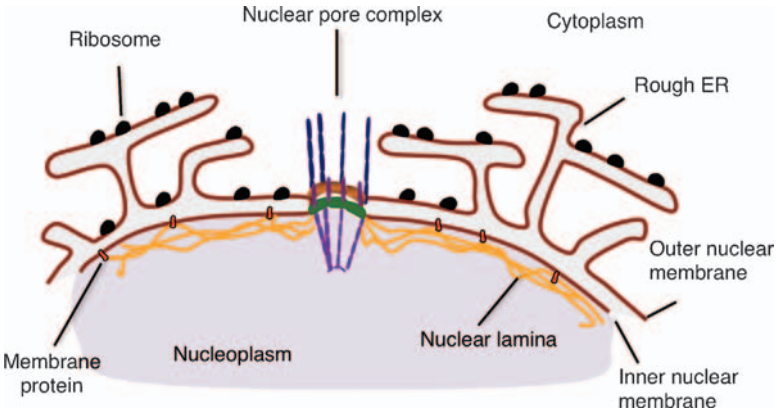

Figure 7.23 Structure of the nuclear envelope in contact with the ER.

are also formed in the nucleolus and need to be exported. For actively growing human cells in culture, it is estimated that over 10 000 ribosomal subunits leave the nucleus per minute. Ribosomal proteins themselves are synthesized by ribosomes in the cytoplasm and need to be imported into the nucleus. Other proteins with high import rates are the histones, needed to build the nucleosome structures with the DNA. Other candidates for nuclear import are RNA polymerases and regulatory proteins responsible for gene transcription. To meet all these transport demands, the nuclear envelope is perforated with several thousand pores (Figure 7.23).

Each of these pores is formed as an immense protein assembly, termed the *nuclear pore complex* (NPC). With a total mass of about 80 000 kDa, the NPC is one of the largest structures of the cell. Multiple copies of about 30 different proteins, the nucleoporins, are organized such that electron microscopy images from the cytosolic side reveal a ring-like structure with octameric symmetry. On its cytoplasmic side, eight filaments of about 800 nm length extend into the cytoplasm. Views from the nucleoplasmic side show analogous filaments, but joined at their ends to form a basket-like structure (Figure 7.23). The whole membrane-embedded ring structure connects both nuclear membranes and it is in direct contact to the nuclear lamina.

Nuclear Import and Export The inner diameter of the nuclear pores is not fixed but dynamic; the nucleoporins form a flexible aperture-like ring. This structure accommodates small proteins of 50 kDa or less, in addition to huge complexes such as small and large ribosomal subunits with 1400 and 2800 kDa mass, respectively. Ions, metabolites, and proteins below 50 kDa diffuse passively through the NPC, whereas all larger proteins need helper proteins, the so-called importins and exportins, to pass in and out through the NPC. This guided transport relies on short amino acid motifs in the cargo proteins. A classical nuclear-localization signal (NLS) is formed by seven amino acids with mostly positively charged side chains near the C-terminus of an imported protein. Transport through the NPC is not only specific but also requires energy, such that NLS-tagged proteins can be accumulated in the nucleus. Direction

of the translocation process and energy input are brought about by the small GTPase Ran. In its guanosine triphosphate (GTP)-bound state, Ran can drive the outward movement of the protein importins or exportins through the NPC. After an importin has conveyed a cargo protein into the nucleoplasm, release of the cargo is triggered by binding of Ran-GTP to the importin. The complex of importin and Ran-GTP then leaves the nucleus through an NPC. In the cytoplasm, Ran is activated to cleave its GTP and to unbind from the importin. This hydrolysis of GTP to guanosine diphosphate (GDP) and P_i provides the energy that drives the cyclic process. Now, the importin is free to bind another cargo protein and to re-enter the nucleus, while Ran-GDP independently travels back to the cytosol. To complete the cycle, in the nucleus the Ran-bound GDP is replaced by GTP. Other proteins are exported through the NPC in a similar manner, but unlike the extrusion of importin, a Ran-GTP-bound exportin will carry a third partner, a protein with a nuclear export signal.

The export of mRNA also depends on guidance by bound proteins, but does not involve the Ran protein. Importantly, the export-competent complex of binding proteins and mRNA is only formed after excision of introns from the precursor mRNA, such that mostly mature messengers come in contact with the ribosomes in the cytoplasm. Some exceptions exist; in those cases mRNA is spliced inside the cytosol.

Nucleus and Cell Division Prior to cell division, the genome has to be replicated and the nucleus must be divided into two daughter nuclei. In human cells, this is accomplished by a complete breakdown of the nucleus followed by the re-formation of two new nuclear envelopes. During mitosis, the process leading to chromosome segregation, the filament proteins of the nuclear lamina are phosphorylated and the resulting negative charges trigger disintegration of the network, followed by a retraction of the nuclear envelope into the ER. Similarly, phosphorylation of the proteins of the NPC leads to reversible dissociation of the pore complexes. At the end of mitosis, the nuclear envelope is reformed from tubular ER, a complex process that is induced by contacts between ER and the chromosomes.

7.2.1.3 Endoplasmic Reticulum (ER)

The largest membrane system in the eukaryotic cell is formed by the ER, a network of flattened tubes and sacs called cisternae. It comprises roughly 50% of the cellular membrane surface and about 10% of the total cell volume. Major ER functions include protein synthesis and modification, synthesis of lipids and steroid hormones, detoxification, and Ca^{2+} sequestration. Rough and smooth areas of the ER can be distinguished by electron microscopy. Both parts of the vesicular systems are contiguous, but the resident proteins in rough and smooth areas are specialized, reflecting different enzymatic activities. The rough endoplasmic reticulum (RER) is directly connected to the nucleus and ongoing protein synthesis in this area is morphologically visible by the presence of ribosomes on the cytoplasmic membrane surface. Proteins synthesized at these ribosomes are either transferred into the lumen of the ER or they reside in the ER membrane. However, only a small fraction of the proteins synthesized at the RER remain there as resident proteins. Most of the

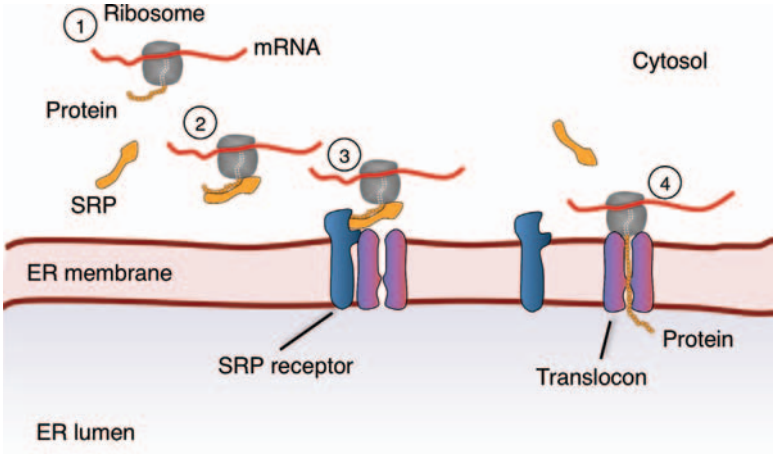

Figure 7.24 Synthesis of secreted proteins at the ER membrane. Ribosomal synthesis of all proteins starts in the cytosol (1). Binding of the signal recognition particle (SRP) to the N-terminal signal sequence of a membrane protein halts the synthesis (2). The complex of mRNA, ribosome, nascent protein, and SRP is translocated to the SRP receptor in the ER membrane (3), where it comes in close contact with the translocon complex. Following release of the SRP and tight docking of the ribosome to the translocon, protein synthesis is resumed and the growing polypeptide is threaded through the translocon pore (4).

proteins are destined for other compartments and the ER is only the first transit station on their journey.

Signal Sequences Direct Proteins to the ER The first events of protein synthesis take place in the cytoplasm, as small and large ribosomal subunits assemble around a molecule of mRNA. Initiation and elongation of the translation process need additional helper proteins, but the major translation machine is the ribosome itself. The growing polypeptide chain leaves the ribosome and globular cytoplasmic proteins will immediately start to fold into their native structure. These proteins are released into the cytoplasm when the last amino acid is attached. By contrast, a large group of proteins has a unique property: the N-terminal end of the growing polypeptide chain carries the information to stop the synthesis process until the whole complex of ribosome, mRNA, and the growing protein make contact with the ER membrane (Figure 7.24). In fact, the N-terminal residues of these proteins are used as a "sorting code" by the ER. The critical event is the binding of a *signal-recognition particle* (SRP), a large RNA–protein complex, to a stretch of about 15 residues at the N-terminus of the nascent protein. The amino acid sequences of these signals are not very conserved, but all contain at least eight hydrophobic residues in the center, often preceded by one or more basic amino acids. The mammalian SRP itself is a complex formed of one small RNA molecule and six distinct proteins. One of these proteins forms a signal-binding pocket lined by hydrophobic residues. Binding of the N-terminal signal sequence of the nascent protein in this pocket immediately stops the ongoing protein synthesis at the respective ribosome. The

complex of SRP and mRNA is then translocated to the ER, where it is recognized and bound by an ER-resident protein called SRP receptor. This membrane protein brings the SRP and the ribosome in close proximity to a gated pore complex in the ER membrane, the translocon. Upon binding of the ribosome, this pore lines up with the large ribosomal subunit such that the growing polypeptide slides directly into the aqueous translocon pore. The contact between the ribosome and the translocon complex is perfectly tight such that no ions pass through the channel during protein transfer. Ribosomes sitting in such complexes on the ER surface cause the rough texture of the RER.

Protein Folding in the ER Depending on the hydrophobicity profile of the growing protein, it will either be completely transferred into the ER lumen or, if hydrophobic helices are formed, these transmembrane-spanning helices anchor the new polypeptide in the ER membrane. The signal sequences of soluble proteins are usually cleaved after translocation by the membrane-bound signal peptidase. In transmembrane proteins, the signal can be cleaved, but it can also be preserved in the mature protein. The RER is not only an important starting point for protein sorting, but is also crucial for protein folding and glycosylation. For many soluble proteins and also membrane proteins, the formation of disulfide bridges is required to stabilize their native structure, a process called oxidative folding. This task cannot be accomplished under the reducing conditions of the cytoplasm; a set of proteins present in the lumen of the ER fulfills this task. The initial event, the *de novo* formation of a disulfide link, is accomplished by the enzyme Ero1p. It uses the oxidizing power of molecular oxygen to link two of its own cysteines. This disulfide can be transferred to protein disulfide isomerases, which then pass it on to substrate proteins.

Protein Glycosylation Another important function of the RER is protein glycosylation. Regardless of their final destination, both soluble proteins and membrane proteins are usually modified by addition of sugar moieties. In the ER the targets of modification are asparagine (Asn) residues in the newly synthesized proteins. While the exact amino acid sequence of any protein can be determined by the encoding gene, the sequence of added sugars depends on the action of gylcosyltransferases and their spatial localization. Hence genome sequencing or determination of mRNA sequences cannot fully predict the final structure of a glycosylated protein. The basal sugar structure added to proteins in the ER is a preformed assembly of 14 sugars (see Section 7.1.3.2). This invariant structure is assembled on a lipid carrier in the ER membrane and subsequently transferred to proteins by the ER enzyme oligosaccharyltransferase. Mutations blocking this basal modification system are lethal. Other enzymes subsequently modify the original 14-unit sugar structure by adding or trimming off some of the sugar moieties.

In addition to functions in the mature protein, glycosylation has an important role in quality control for virtually all proteins in the ER. The basic sugar structure contains three terminal glucose moieties that are fully removed during further processing steps in the ER. However, if a protein is not yet properly folded, a glycosidase will add a new, single glucose moiety to the structure. This glucose

tag induces the retention of the protein in the ER lumen, where it is bound by the ER-resident membrane protein calnexin. The folding process in the ER lumen is usually assisted by helper proteins, so-called chaperones. Thus longer retention periods in the ER increase the chance of complete folding. Nevertheless, disulfide formation, folding, and oligomerization of subunits are not very efficient processes. For some proteins the estimated "success rates" of folding are far below 50%. Hence the ER needs a way to clear this ballast of inefficient protein production. This is accomplished by export of misfolded proteins through the same translocon structures that are used for protein import.

Retention and Retrieval of ER Proteins For most proteins that are produced, folded, and glycosylated in the RER, these steps are just the starting point of a journey to their final destinations, such as other organelles or the plasma membrane. This transport is based on the formation of small vesicles, formed from the ER membrane, leaving with destination to the next station of protein traffic, the *cis*-side of the Golgi complex (see below). However, ER-resident proteins must be retained from this constant flow of material in order to keep the ER compartment functional. This is accomplished by retention and retrieval mechanisms. Soluble resident ER proteins are marked with a short retrieval sequence, formed by the amino acids Lys–Asp–Glu–Leu (KDEL) at the C-terminus. This short motif is recognized and bound by the *KDEL receptor*, a membrane protein that loads the protein into budding vesicles that will be sent back from the Golgi compartment to the ER (retrograde transport; see Figure 7.25). For

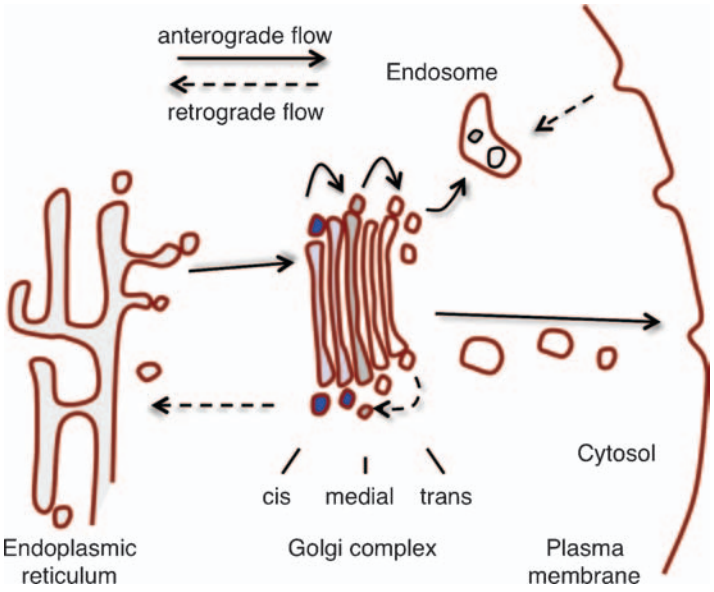

Figure 7.25 The Golgi complex as central sorting station of the cell. Solid arrows indicate the vesicle-mediated transport of proteins from the ER via the Golgi complex to endosomes or the plasma membrane. Retrograde transport between the same compartments is indicated by dashed arrows.

resident membrane proteins, analogous signals determine retrieval and retrograde transport in a similar fashion. These retrieval mechanisms capture proteins that escaped the ER, but packing of resident proteins into vesicles is *per se* less frequent than for secreted proteins. The mechanisms underlying this active retention are not well established, but it is assumed that resident proteins of ER or other compartments have the general tendency to aggregate into larger complexes that are just too big to enter vesicles.

The Smooth ER In contrast to the flattened structures of the RER, areas of smooth endoplasmic reticulum (SER) typically appear as a network of branched tubules, although this morphological distinction is not true for all cell types. The SER has metabolic functions including lipid and steroid hormone synthesis. The latter is a characteristic of endocrine cells in the gonads, usually reflected by more extended regions of SER. The synthesis of membrane lipids is of general importance in all cells and the majority of all lipids in plasma membrane and intracellular membranes originate from the SER. Interestingly, this does not mean that all membranes within a single cell have approximately the same phospholipid composition. For example, the content of phosphatidylcholine is usually much higher in the ER than in the plasma membrane, whereas phosphatidylserine has a higher concentration in the plasma membrane. Another important feature of the SER is its role in the sequestration of Ca^{2+} ions. The cytosolic concentration of free Ca^{2+} ions in the cytoplasm is typically very low (see Section 7.3.2.1), in part because it is actively pumped into the SER, which function as Ca^{2+} reservoirs. Upon specific triggers, Ca^{2+} is released back into the cytoplasm, initiating cellular responses. In skeletal muscle cells a specialized form of SER, the sarcoplasmic reticulum (SR), rapidly releases Ca^{2+} ions in response to electrical stimulation and hence initiates muscle contraction.

7.2.1.4 The Golgi Complex

Whereas the ER is a major site of protein synthesis and modification, the Golgi complex, or Golgi apparatus, can be envisioned as *central sorting station* of the cell. Proteins and also lipids coming from the ER are handled in the Golgi complex, further modified, and targeted to their final destinations. The classical morphology of the Golgi compartment resembles a stack of pancakes with frayed rims, formed of flat membrane-enclosed cisternae (Figure 7.25). Each stack comprises about 4–7 disk-like elements with a diameter up to 1 μm. Human cells typically contain many of these Golgi stacks, linked by tubular connections and thereby forming a complex located near the nucleus. This spatial organization is achieved by connecting microtubules of the cytoskeleton. The individual stacks can be morphologically and functionally divided into three distinct compartments. The *cis* face comprises the cisternal elements in proximity to the ER, followed by *medial-* and *trans-Golgi cisternae*. Thin networks of tubules and vesicles on either side of the stack are called *cis-Golgi network* and *trans-Golgi network*. The spatial organization is accompanied by a clear functional compartmentalization, such that specific enzymes of the glycosylation machinery are located in distinct cisternae of the *cis*, medial, or *trans* part of a stack.

Golgi Stacks Are Dynamic Interestingly, resident membrane proteins of the Golgi are distinguished from membrane proteins of other compartments by shorter transmembrane helices, comprising around 15 amino acids instead of the typical 20–25 amino acid helices in most other proteins. This difference provides the basis for a Golgi retention mechanism. Vesicles leaving the *trans*-Golgi are thicker than the membrane of the Golgi membranes themselves, thereby excluding transmembrane proteins with too short transmembrane segments. The precise organization of the Golgi stacks rises the question of how these structures are generated and maintained. Two alternative models are under discussion, the "vesicular transport model" and the "cisternal maturation model." The former model assumes a static position of the Golgi cisternae with a fixed set of enzymes in each part of the structure. Transit molecules would primarily move in forward-directed vesicles and retrograde vesicles would return enzymes that escaped from their major site of activity. By contrast, in the maturation model, complete cisternae would move through the Golgi stack and thereby take along proteins and lipids from the *cis* to the *trans* side. During this movement, the enzyme equipment of individual cisternae would mature. Enzymes belonging to the early *cis* face would permanently move backwards from medial disks to newly formed disks on the *cis* side and medial enzymes would travel back from disks that just reached the *trans* side. More recent studies, using spatially focused photobleaching of fluorescent proteins in distinct cisternae, favor a rather static model. However, in contrast to the classical vesicular model, transit between disks is not only mediated by vesicle transport, but may also be carried out in large part by a direct equilibration between individual disks through connecting tubules.

Protein Handling in the Golgi Stacks Newly synthesized and folded proteins from the ER typically leave the RER in vesicles and enter the *cis* face of a Golgi stack. They are then passed along through medial and *trans* discs. Transport in ER and Golgi is not necessarily unidirectional, but vesicles connecting the individual compartments can also move in a retrograde manner. This is especially important to bring ER-resident proteins back from the Golgi complex to their ER destination and to ensure a specific enzyme composition in each of the three Golgi compartments. One of the major processing steps in the Golgi complex is to continue and complete the protein modifications that have been initiated in the ER. Processing of the N-linked oligosaccharides includes further removal of mannose, addition of *N*-acetylglucosamine, galactose, and the negatively charged sialic acid. Furthermore, *O*-linked glycosylation on Ser and Thr amino acid residues only takes place in the Golgi complex. Despite a good knowledge of sugar modifications on proteins and the compartments for individual processing steps, for the majority of the glycosylated proteins the functional impact is still largely elusive. Another post-translational modification that is specifically accomplished in *trans*-Golgi cisternae is the addition of sulfate to tyrosine residues. Tyrosine sulfation of exported proteins or on extracellular epitopes of plasma membrane proteins was found to strengthen protein–protein interactions.

7.2.1.5 Mitochondria are the "Power Plants" of the Cell

Among the most complex organelles in the human cell are the mitochondria, membrane-enclosed structures in the cytoplasm that can be visualized by light microscopy. Most human cells carry several hundred to thousands of individual mitochondria. The volume typically occupied by the mitochondria makes up between 10 and 25% of the total cell volume. Depending on the cell type, the size and shape of the mitochondria can be diverse. The overall structure of a mitochondrion can resemble a cylinder with a diameter of about 1 μm and a length of 4 μm, whereas in other cells mitochondria appear as long tubules or even as branched, interconnected networks. These structures are usually dynamic because mitochondria can fuse with one another. New mitochondria are generated from existing mitochondria by a process called fission. This multiplication of mitochondria is important in dividing cells, as the organelles cannot be formed *de novo* and must be inherited to the daughter cells. About 100 years ago, Konstantin Sergejewitsch Mereschkowski proposed that mitochondria are not innate parts of the cell, but rather descended from bacteria that have been engulfed by another cell. This "endosymbiotic theory" was initially greeted with skepticism but, with the finding of DNA present in mitochondria and the analysis of mitochondrial genes in the 1980s, the idea gained strong support and is now fully accepted.

Compartments of the Mitochondria Mitochondria are more than a simple enveloped vesicle. A closer look shows the existence of two juxtaposed membranes, the *outer mitochondrial membrane* and the *inner mitochondrial membrane*. The inner membrane forms characteristic infoldings, the cristae, reaching into the inner lumen called *mitochondrial matrix*. Practically, five compartments of the mitochondrion can be distinguished: the outer membrane, the intermembrane space, the lumen of the cristae, the inner membrane, and the matrix (Figure 7.26). The outer membrane encloses the whole organelle and separates it from the cytoplasm. This membrane, with a total protein content of about 50%, is similar to other cellular membranes, but in remarkable contrast, the transmembrane segments of the resident proteins of this membrane are typically folded as β-sheets, instead of the common α-helical segments. This folding pattern resembles the structure of the porin proteins in the outer membrane of *E. coli* and other so-called Gram-negative bacteria. Because of these membrane proteins, the outer mitochondrial membrane partly allows the exchange of ions and small molecules between the cytosol and the intermembrane space.

The Inner Mitochondrial Membrane In contrast to the outer mitochondrial membrane, the inner membrane provides a tight permeation barrier that separates the matrix from the intermembrane space. This membrane is devoid of cholesterol, but contains a high concentration of cardiolipin, a "double lipid" with four fatty acids, which is otherwise found only in bacteria. The invaginated inner membrane surrounds the cristae and its surface area can make up to one-third of the total membrane area of the cell. The density of cristae in a mitochondrion is especially high in those cells with a high energy consumption such as heart muscle cells. The inner mitochondrial membrane is exceptionally rich in proteins, with at least 3:1 ratio

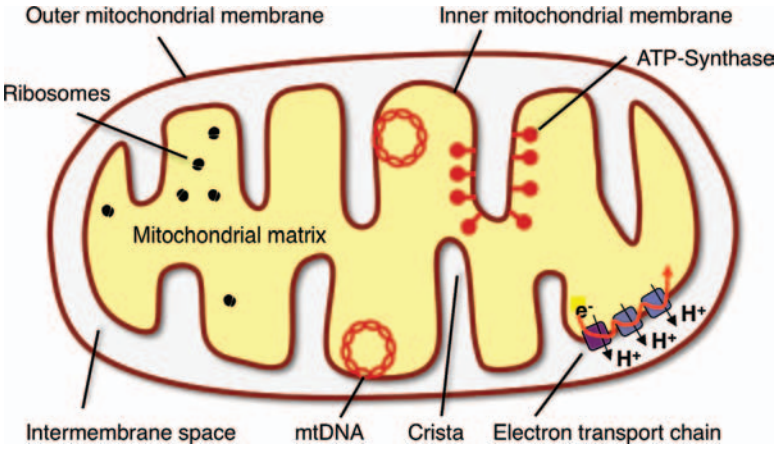

Figure 7.26 Cartoon of a mitochondrion with its compartments. Five functional compartments can be distinguished: the outer membrane, the intermembrane space, the inner membrane with the electron transport chain, the cristae, and the inner matrix. Cristae are invaginations of the inner membrane; they are in contact with the intermembrane space, but local solute concentrations can differ.

of protein to lipid. The enzymes incorporated here are essential for oxidative phosphorylation, the process that generates most of the cellular energy in the form of ATP. The electron transport chain transfers electrons from NADH to molecular oxygen and utilizes the energy difference to drive protons (H^+) from the matrix into the intermembrane space or the lumen of the cristae. The ATP–synthase complexes in the same membrane act like turbines, coupling the energy stored in the electrochemical gradient of protons to the production of ATP from ADP.

The Mitochondrial Matrix Along with the ER lumen, the mitochondrial matrix is considered an important site for the storage of Ca^{2+} ions and the triggered release of these ions acts as an intracellular signal. The matrix also contains the enzymes required for the final metabolism of pyruvate and fatty acids to gain the end product CO_2 and NADH, the energy-rich substrate for the ATP-producing electron-transport chain of the inner membrane. Additional important components of the mitochondrial matrix are DNA molecules, tRNA, ribosomes, and proteins of the transcription–translation machinery. Mitochondria were originally derived from free bacteria and, during a long process of evolution as symbiont in the nucleated cell, most of the mitochondrial genes have been translocated to the central genome in the nucleus. Nevertheless, mitochondria retained some genes and ribosomes of their own to produce proteins in the mitochondrial matrix (see below). In contrast to the chromosomes in the nucleus, mitochondrial DNA has a ring-shaped structure and is devoid of histone proteins.

Mitochondrial Protein Import The interaction of mitochondria with the rest of the cell is characterized on the one hand by busy export of the valuable energy source ATP.

On the other hand, 99% of the mitochondrial proteins must be imported from the cytosol in order to maintain ATP synthesis. This high import demand exists because most mitochondrial genes have been translocated to the nuclear genome and only 13 proteins are still encoded by the organelle's own DNA. Proteins destined for a mitochondrial compartment do not follow the main secretory pathway along the ER and Golgi and ribosomal synthesis is typically completed in the cytosol. To facilitate transport of mitochondrial proteins, chaperones bind to the nascent polypeptide chains and prevent their final folding. Supported by a transport receptor protein, the new protein is then threaded into a β-barrel protein complex of the outer mitochondrial membrane, the TOM complex. Matrix proteins typically have N-terminal signal sequences, analogous to the ER-targeting signals. The mitochondrial import signals typically form amphipathic α-helices of 20 or more amino acids with positive charges (Arg, Lys) on one side of the helix and hydrophobic residues on the opposing side. Such proteins will continue their way through TIM23, a translocator in the inner mitochondrial membrane. TIM and TOM proteins come in close proximity during transport and both membranes (Figure 7.27) appear in direct contact in electron microscopy images of active translocator sites. Once a protein has reached the matrix, a mitochondrial protease cleaves the mitochondrial signal sequence and the protein folds into its final tertiary structure and reaches the mitochondrial matrix. Proteins destined for the inner mitochondrial membrane will be processed by TIM22. This complex allows the lateral release of hydrophobic helices of the transported protein into the inner membrane. By contrast, proteins targeted to the outer mitochondrial membrane enter the intermembrane space before being retrieved back into the outer membrane. The pore formed by the β-barrel-shaped TOM complex is tightly closed all around and does not allow a lateral release of cargo proteins directly into the outer

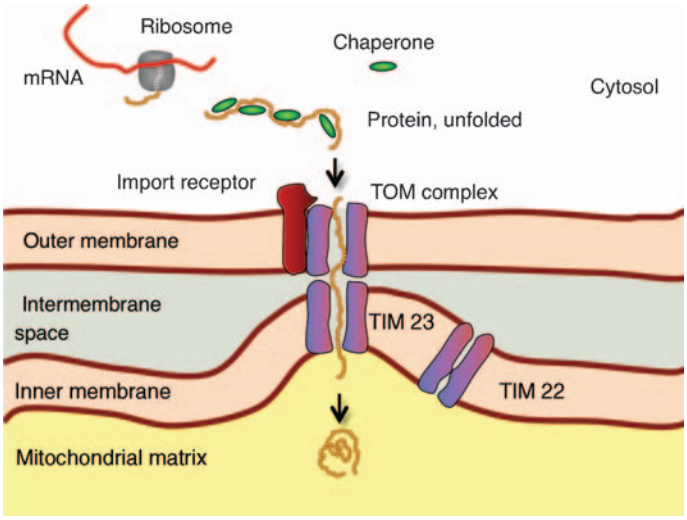

Figure 7.27 The mitochondrial import system for proteins from the cytosol.

membrane. In contrast to the co-translational transport of growing proteins into the ER, the post-translational protein import into mitochondria needs additional input of energy provided by the hydrolysis of ATP.

7.2.1.6 **Peroxisomes**

Peroxisomes are morphologically rather unobtrusive, round organelles, surrounded by a bilayer, and with diameters of about 0.1–1 μm. It was not until the middle of the twentieth century that peroxisomes, and also lysosomes, were identified and described by Christian de Duve. This relatively recent discovery may be explained by the small size and the unremarkable appearance of peroxisomes. In some mammalian cells they contain electron-dense crystals, but human peroxisomes are usually without noticeable inner structures. Several hundred peroxisomes are typically found distributed throughout the cytosol of every cell. Like mitochondria, they proliferate by fission of existing peroxisomes. This fact led to a long-lasting discussion about a potential endosymbiotic origin of the peroxisomes. However, unlike mitochondria, they contain neither DNA nor ribosomes of their own. The name of the organelle refers to the presence of enzymes involved in the handling of peroxides. Hydrogen peroxide (H_2O_2), a toxic and reactive oxidant, can arise from several sources but peroxisomes themselves also generate H_2O_2 as a common product of resident enzymes. D-Amino acid oxidase, glycolate oxidase, and other peroxisomal enzymes utilize molecular oxygen (O_2) to oxidize their substrates and generate H_2O_2 as the secondary product. The peroxisomal enzyme catalase is required for the immediate breakdown of H_2O_2, yielding water (H_2O) and O_2 as final products. Many of the oxidative reactions performed by peroxisomal enzymes resemble enzymatic activities in the mitochondria, with the notable difference that peroxisomes do not directly produce energy. A prominent example is the stepwise breakdown of fatty acid molecules, β-oxidation. In this sequential reaction, fragments comprising two carbon atoms are released and exported as acyl-CoA to the cytosol. This energy-rich compound can be reused in biosynthetic reactions or further processed to gain energy. Another important function of peroxisomes, especially in liver and kidney cells, is the detoxification of toxic compounds such as ethanol, phenol, or formaldehyde. About 25% of the ethanol consumed is oxidized to acetaldehyde in peroxisomes. Importantly, peroxisomes are also involved in functions other than degradation and detoxification processes. An essential biosynthetic function of peroxisomes is the formation of phospholipids with ether-linked fatty alcohols, instead of the standard, ester-linked fatty acid chains. These *plasmalogens* are important phospholipid components of the myelin sheets, insulating membrane layers surrounding nerve axons.

Protein Import to Peroxisomes Like mitochondria, peroxisomes are not part of the major vesicle traffic pathways emerging from ER and Golgi. Consequently, all enzymes of the peroxisomal lumen and the surrounding membrane need to be imported from the cytosol. The import machinery is not well characterized, but more than 20 proteins, the so-called peroxins, are involved in the ATP-driven uptake of proteins. In contrast to the mitochondrial import machinery, peroxisomes can take

up proteins that have already adopted their final structures. However, the enzymes catalase and peroxidase receive their prosthetic heme group only after import into the organelle is completed. The sorting codes, determining a peroxisomal protein's destination, can sometimes be found at the N termini of peroxisomal proteins, but in most cases a short amino-acid motif at the distal C terminus is responsible for uptake. Artificial transfer of the short amino-acid sequence Ser–Lys–Leu to the C terminus of a cytosolic protein is sufficient to direct the recombinant protein into peroxisomes. The importance of a functional peroxisome import system is underscored by the finding that various peroxin gene mutations, known to deactivate the uptake system, lead to relatively rare human diseases collectively termed the Zellweger syndrome. In the patient's cells, peroxisomes are still visible, but they lack their resident proteins at least in part. The Zellweger syndrome is typically characterized by severe failures of the liver, kidneys, and brain, leading to death within the first few months after birth.

7.2.1.7 **Lysosomes**

The second organelle discovered by de Duve, the lysosome, is not uniform in either shape or size, ranging from small vesicles of around 20 nm up to more irregular structures up to 1 μm in diameter. The lysosomes are equipped with a variety of hydrolytic enzymes, enabling them to act as the cell's central "recycling station." A lysosome can hold at least 50 different enzymes: proteases, glycosidases, RNases, DNases, lipases, and many others. Equipped with these enzymes, lysosomes are prepared for the destruction of practically all cellular biomolecules and even foreign molecules, as the enzyme lysozyme can degrade peptidoglycan, a major component of bacterial cell walls. All these hydrolases share a requirement for low pH between 4.5 and 5.0. This low pH is the major characteristic of the lysosomal lumen and serves as an important safeguarding system. The assembly of destructive enzymes in the lysosome is potentially dangerous for all other constituents of the cell. However, in case of their liberation into the cytosol, the acid hydrolases will be inactive in the practically neutral milieu around pH 7.2. The exceptionally low pH of the lysosome is sustained by proton ATPases in the lysosomal membrane. These transporters pump H^+ from the cytosol into the organelle lumen – a process that is driven by the hydrolysis of ATP. The resident lysosomal proteins in the acidic environment seem to be protected from destruction by an unusually high degree of glycosylation.

Transport to Lysosomes Lysosomes are equipped for the degradation of virtually all possible macromolecules, but efficient transport routes must exist to bring the material destined for degradation into the lysosomal compartment. This is established via different vesicular transport pathways. As depicted in Figure 7.28, a major degradation route starts with small vesicles, pinching off the plasma membrane, a process called endocytosis. This import pathway takes up material from the extracellular space, encapsulated in endocytic vesicles. Lipids and proteins of the plasma membrane themselves also take part in this passage to destruction. Transport to lysosomes is the classical way to remove membrane proteins and also membrane lipids. Just as in all other compartments, the lipids and proteins of the plasma membrane are subject to a continual replacement. Primary vesicles from the

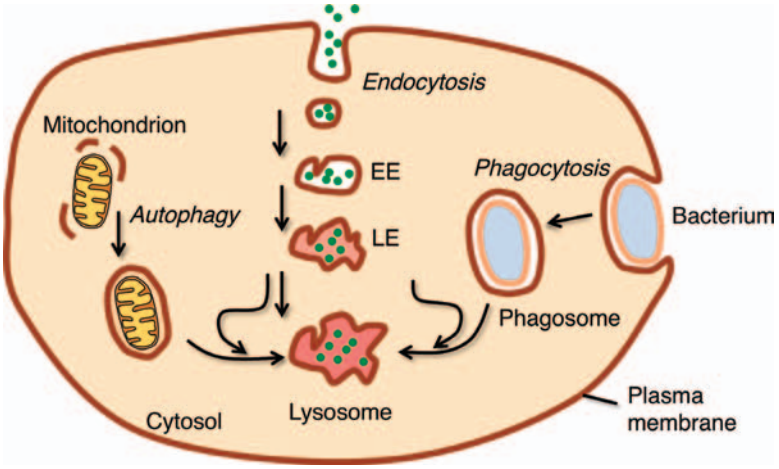

Figure 7.28 Lysosome traffic. Alternative pathways leading to degradation in lysosomes. Maturation of early endosomes (EEs) to late endosomes (LEs) and lysosomes is associated with a gradual reduction of the internal pH value.

plasma membrane will fuse with others and increase in size. In addition, vesicles coming from the Golgi complex will fuse to such *early endosomes* and bring lysosomal hydrolases. Endosomes are subject to a maturation process, during which the internal pH is decreased until the *late endosome* will finally have all characteristics of a lysosome. Another important pathway to degradation is the engulfment of bacteria or viruses at the plasma membrane. This process (*phagocytosis*) produces an internalized particle completely surrounded by a cellular membrane, the phagosome. These organelles can be fused to mature lysosomes and the content of the phagosome will be degraded. An analogous pathway starts at the ER membrane that eventually envelopes inner organelles, such as complete mitochondria or peroxisomes. This process (*autophagy*) allows for the complete renewal of cellular organelles over time. It is also a mechanism to gain new material for the cellular synthesis machinery in times of nutrition deprivation.

Transport of Hydrolases to Lysosomes The central role of lysosomes as the recycling site for all classes of molecules requires a continual replenishment of acid hydrolases to the lysosomal compartment. In contrast to peroxisomes and mitochondria, lysosomes do not possess a proprietary protein import machinery. Instead, lysosomes make use of the main protein traffic route, starting in the ER and proceeding through the Golgi complex (Figure 7.25). In the Golgi compartment, the fate of lysosomal proteins must differ from exported proteins or from resident proteins of the plasma membrane. In fact, so-called signal patches, short amino acid motifs on the protein surface, are recognized by the glycosylation machinery of the Golgi complex. As a result, *N*-linked oligosaccharides will be modified such that a mannose 6-phosphate (M6P) group is formed on the oligosaccharide tree. In the late stacks of the *trans*-Golgi network, membrane-resident receptor proteins bind this modified sugar with high affinity and thereby anchor the labeled hydrolases to the membrane.

In the *trans*-Golgi network, distinct types of vesicles are continually formed, one class of which is explicitly enriched in M6P receptor proteins. Hence the vesicles are loaded with various hydrolases marked with the M6P tag. After fusion to endosomes, the inner side of the vesicles becomes part of the endosomal lumen. Just like lysosomes, the endosomes are more acidic than the surrounding cytosol. Acidification is caused by the activity of proton ATPases in the endosomal membrane. As a result, the maturation process of vesicles to early and late endosomes is accompanied by a decrease in the internal pH. Interestingly, the affinity of M6P receptors to M6P is strictly regulated by pH. With lowered pH, this binding affinity decreases and the captured hydrolases are released to the lumen of late endosomes or lysosomes. Vesicles rich in M6P receptors are formed at the endosomal membrane. They bud off from the endosome to be relocated to the *trans*-Golgi stacks, ready to bind new target proteins at neutral pH.

7.2.1.8 **The Cytoskeleton**

The membrane bilayers surrounding the cell and its internal compartments are highly flexible and the actual shape of the cell and its compartments is not determined by the membrane but stabilized by a network of proteins. Underneath the plasma membrane, a dense protein meshwork defines the overall structure of the cell. Similarly, structural support of the nuclear membrane is provided by the underlying lamin network inside the nucleus. Cytoskeletal structures not only align with membranes, but also traverse the cytoplasm in all directions, thereby providing a scaffold to mount intracellular organelles such as mitochondria and peroxisomes. The contacts between organelles and the cytoskeleton are not static attachments, but motor proteins can drive a busy traffic along the cytoskeletal routes inside cells. Three major types of cytoskeletal protein structures can be recognized: *actin filaments*, *intermediate filaments*, and *microtubules*, in part distinguished by their characteristic diameters of 7, 10, and 25 nm, respectively. All three cytoskeletal components are aggregates of smaller subunits collectively forming extended, filamentous structures. In the case of actin filaments and microtubules, the basic structures have a globular shape, whereas intermediate filaments are formed as assemblies of extended, helical proteins. The cytoskeletal protein assemblies are stabilized without covalent bonds between the subunits, allowing the rapid association and dissociation of cytoskeletal structures. Three major functions can be attributed to the cytoskeleton:

1) structural stabilization of the cell
2) movements within the cell such as vesicle transport or the segregation of chromosomes during cell division
3) cell movements such as muscle contraction and cell migration.

Such diverse activities are possible because the cytoskeletal proteins provide binding platforms for a variety of more specific, associated proteins, including the molecular motor proteins.

Actin Filaments The actin filament is a two-stranded helical polymer with a diameter alternating between 5 and 9 nm (Figure 7.29). The basic subunit is the globular actin

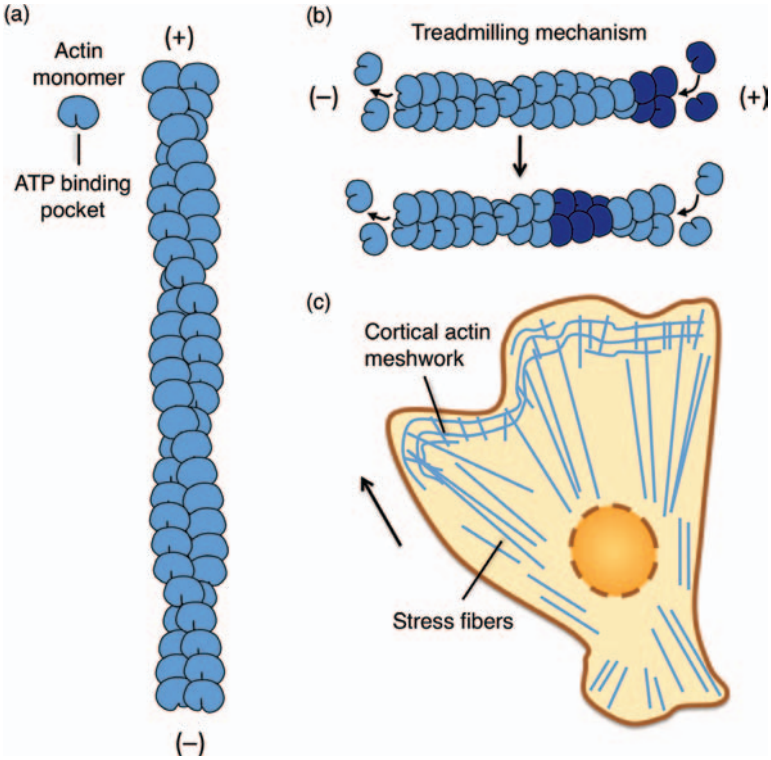

Figure 7.29 The actin cytoskeleton. (a) The two-stranded helical structure of actin microfilaments. (b) The actin filament turnover follows a treadmilling mechanism. (c) Typical subcellular localization of actin filaments in a migrating cell. The arrow indicates the direction of cell movement.

monomer (G-actin) that binds the energy-rich nucleotide ATP in a cleft on one side of the protein. Upon assembly of actin monomers into filaments (F-actin), all subunits align such that the ATP-binding cleft is directed to one side, the minus end of the filament. This gives polarity to the overall structure of the filament. After entry into the polymer, the bound ATP is hydrolyzed to ADP that stays bound in its binding pocket. As a consequence, a small conformational change in the actin molecule lowers its affinity for other actin subunits. Typically, ATP-carrying actins are added to the filament whereas ADP-bound actins have a tendency to leave the polymer structure. Assembly and disassembly can occur at both ends of the filament but the ratio of assembly to disassembly is higher at the plus end of the filaments such that actin filaments with two free ends will grow at their plus ends and shrink at the minus end. When both processes are in a steady state, the filament undergoes *treadmilling*, a mechanism that keeps the overall length of the polymer constant, while new subunits are constantly added at the plus end, move through the entire filament, and finally leave it at the minus end. Thus, existing actin filaments in the cell are not static but undergo constant reconstruction. When ADP-bound actin has left the

polymer, its nucleotide can be exchanged for ATP, and the subunit is ready for a new round through a filament.

The overall organization of actin filaments can vary with their localization in the cell and is determined by accessory cross-linking proteins. One group of such cross-linking proteins, including filamin, joins the actin filaments such that loose three-dimensional networks of gel-like consistency are formed. This is the typical appearance of the actin cytoskeleton in the cell cortex, the cytosolic region beneath the plasma membrane. Another group of actin-bundling proteins couples actin filaments in parallel arrangements. The so-called *stress fibers* are contractile actin bundles with antiparallel organization of the filaments. Stress fibers typically extend from the center of a cell towards the periphery and α-actinin is one of the major cross-linkers in these fibers. As determined by the dimensions of α-actinin, the lateral distances between the bundled actin filaments are about 30 nm. The ability of the stress fibers to contract is provided by myosin molecules, the typical motor proteins of actin filaments, which can bind between the loosely arranged α-actinin molecules. By contrast, parallel actin bundles formed by the cross-linking protein fimbrin are more densely packed with distances around 15 nm and they are not contractile. Such parallel bundles are typically found in a thin projection at the leading edge of a migrating cell, the so-called *filopodia*. Very regular parallel assemblies of 20–30 actin fibers can be formed by villin, another small bundling protein. These villin-linked bundles form the core of the microvilli, finger-like extensions of the plasma membrane with a length of about 1 μm and diameters around 80 nm. These very regular cell structures can largely expand the surface area of a cell. Microvilli are found on the apical side of many epithelial cells, for example, in the intestine, where the uptake of nutrients through the plasma membrane takes place.

Microtubules In contrast to actin, the building blocks forming microtubules are not homomeric, but heteromeric dimers of α-tubulin and β-tubulin (Figure 7.30). The polymeric structure formed from the tubulin dimers is a stiff, hollow cylinder formed from 13 protofilaments that are aligned in parallel. This cylinder with an outer diameter of 25 nm is stabilized by noncovalent contacts between heads and tails of the tubulin dimers in the longitudinal axis and by lateral contacts between tubulins in neighboring filament strings. These lateral bonds connecting the protofilaments are homotypic contacts between two α-tubulins or between two β-tubulins. Like actin filaments, the microtubule has a polarity defined by the orientation of its subunits. β-tubulins are exposed to the plus end of the tube, whereas α-tubulins mark the minus end. In principle, both ends of the microtubule can grow or shrink, but in the living cell all microtubules are fixed with their minus ends to the *microtubule-organizing center* (MTOC), an amorphous protein-rich structure in the vicinity of the nucleus. In animal cells the MTOC also harbors the centrioles, two barrel-shaped structures formed by nine triplets of microtubules. During cell division, the centrioles are involved in the formation of a microtubule spindle apparatus that separates the chromosomes between the two daughter cells. At the plus end of a microtubule, the type of nucleotide bound to β-tubulin determines growth or disassembly. Just like actin, both tubulins have a nucleotide binding site, but they bind GTP instead of ATP.

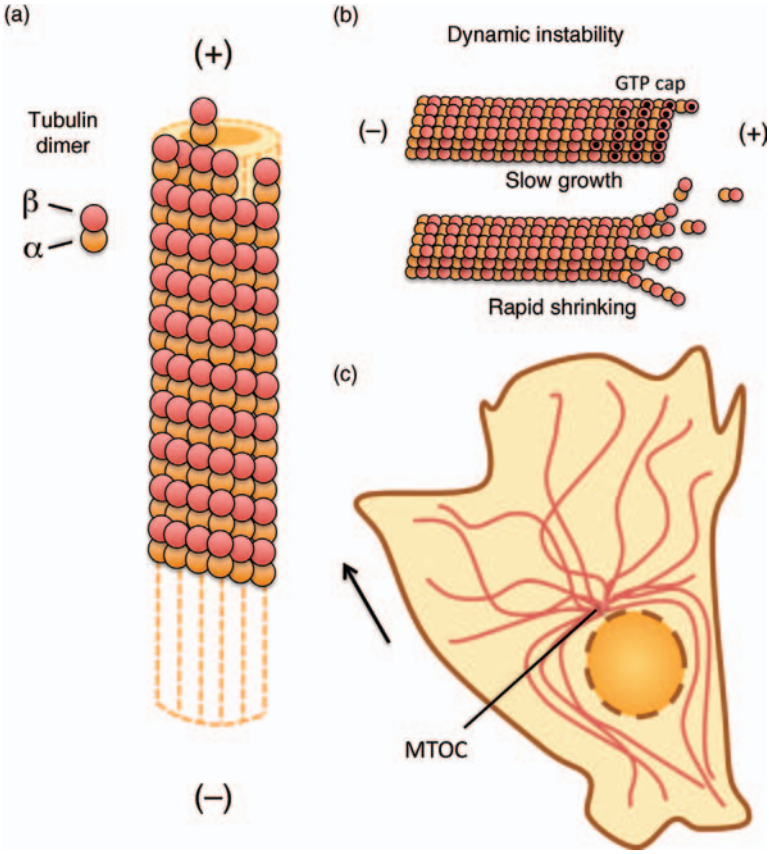

Figure 7.30 Microtubules. (a) Microtubules are long, hollow cylinders composed of 13 parallel protofilaments. The protofilaments are strings of tubulin dimers, each consisting of α-tubulin and β-tubulin. (b) Microtubule turnover is governed by dynamic instability of the plus end. GTP–tubulin dimers (with black dot on β-tubulin) stabilize the plus end of the microtubule. (c) Subcellular localization of microtubules in a migrating cell. All microtubules arise from the microtubule-organizing center (MTOC) near the front of the nucleus. The arrow indicates the direction of cell movement.

In the dimeric subunits, both tubulins are tightly connected such that the GTP bound to α-tubulin is trapped by the coupled β-tubulin and the nucleotide is neither released nor hydrolyzed. In contrast, GTP in the β-tubulin can be hydrolyzed to GDP. Similarly to actin filaments, this conversion of bound GTP to GDP is associated with a lowered binding affinity of the respective tubulin dimer. The turnover of microtubules is characterized by periods of slow growth typically alternating with shorter periods of very rapid disassembly, a mechanism called *dynamic instability*. During the growth periods, the addition of tubulin dimers with GTP-loaded β-tubulin exceeds the rate of GTP hydrolysis in the incorporated tubulin dimers. This results in the formation of a so-called GTP cap at the plus end, stabilizing the

overall structure. However, when the rate of dimer incorporation falls below the rate of GTP hydrolysis, the GTP cap is lost and rapid disassembly occurs. This abrupt shrinking process is enforced by the inherent tendency of GDP-containing filaments to assume a curved shape. Only upon more rapid association of new GTP-containing subunits is the microtubule rescued and the protofilaments are forced into a linear conformation.

Intermediate Filaments The third kind of cytoskeletal polymers are the intermediate filaments, a more heterogeneous group of polymer-forming proteins. Several families of filament proteins are known, but all share a similar central domain with a long α-helical secondary structure. These domains contain a series of 40 or more heptad repeat amino-acid motifs that stabilize the lateral assembly of coiled-coil dimers. These parallel-oriented coiled-coiled protein aggregates are the underlying building blocks of all intermediate filaments, which are formed as rope-like lateral assemblies of the long dimers. In a typical intermediate filament, the cross-section has a diameter of 10 nm and consists of 16 dimers, eight of them oriented in each direction. As already described, *lamins* are the typical components of the nuclear lamina that stabilizes the nuclear envelope beneath the inner nuclear membrane. The keratins are a large intermediate filament family of proteins found in epithelial cells and also in hair and nails. *Vimentin* and vimentin-like proteins are the typical intermediate filament proteins in all types of muscle cells. Three different *neurofilaments* are the main cytoskeletal intermediate filament component in neuronal axons. The neuronal intermediate filaments grow with the outgrowing axon and the thickness of the filament bundles determines the diameter of the axon.

7.2.1.9 Transport Vesicles, Exocytosis and Endocytosis

Transport Vesicles The membrane-enclosed organelles of a living cell are in constant communication with each other and soluble molecules and also lipids must be exchanged among the different compartments. Much of this transport is accomplished by vesicles, budding off one membrane and fusing with another membrane. Such vesicles can be diverse in diameter and shape; some are small and spherical whereas other vesicles have more irregular or tubular shapes. Despite this variability, transport vesicles can be grouped according to the coat proteins that form a cage-like structure when the vesicle buds off from the donor membrane. Coat proteins are required to shape the donor membrane such that a basket-like deformation of the membrane appears, which is finally pinched off as a closed vesicle (Figure 7.31). In addition to this mechanical function, the coat proteins help to assemble those membrane proteins in the deforming membrane patch that are to be incorporated into the vesicle. In turn, these membrane proteins can bind soluble proteins to pack them into the transport vesicle.

The assembly of coat proteins is not constitutive, but requires the binding of a GTPase with bound GTP. As already described for the Ran GTPase, the small GTPases exist in two conformations, the GTP-bound and the GDP-bound state. Thereby, the state of GTPases required for coat assembly provides a control

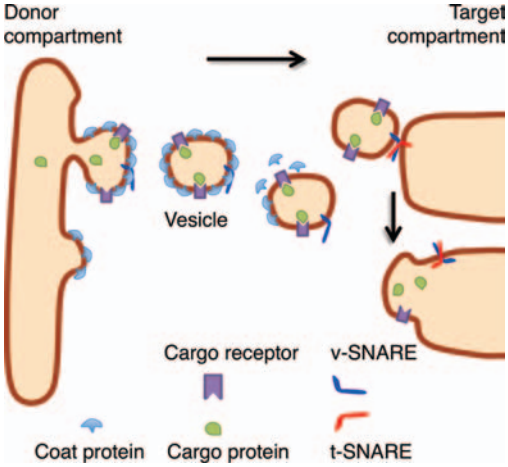

Figure 7.31 Intracellular vesicle transport. Vesicles budding from a donor have characteristic coat complexes. Cargo receptor proteins assemble proteins to be loaded into a budding vesicle. Specific binding and vesicle fusion to a target membrane depend on the matching interaction of vSNAREs and tSNARES on vesicle and target membrane, respectively.

mechanism to keep the membrane traffic balanced. Three major types of vesicles can be distinguished based on their coat protein complexes: the COP I-coated, COP II-coated, and clathrin-coated vesicles. COP II is the typical coat complex of vesicles in the anterograde transport from ER to the *cis*-Golgi network, whereas retrograde transport, for example, in the retrieval pathway from Golgi to ER, uses vesicles with COP I coats. The best-defined and most regular structure is found in clathrin-coated vesicles. Clathrin subunits are formed by three large and three small subunits assembled in a three-legged structure. These stable structures assemble with each other to form coated pits, and finally geometrically spherical structures consisting of hexagons and pentagons. This assembly shapes the donor membrane to form uniform vesicles. The final release of such vesicles requires the GTPase dynamin. Dynamin assembles around the neck of the budding vesicle and triggers its final release. Regardless of the type of vesicles, all have in common that the coats are removed after detachment from the donor membrane. Coat disassembly is triggered by the hydrolysis of GTP bound to the GTPase that previously had induced the assembly process. Loss of the vesicle coat is prerequisite for the later fusion of the vesicle with a target membrane.

Traffic Along Microtubules The movement of a vesicle between donor and target membrane is not random diffusion through the cytosol. This would be too slow for long-distance traffic, for example, along the axon of a peripheral nerve cell. The solution to this problem is a close connection of all vesicles to microtubules of the cytoskeleton, which are oriented with plus ends in the cell periphery and minus ends being attached to the MTOC in the vicinity of the nucleus. Docking of a vesicle to a microtubule not only provides direction but also, more importantly, allows active and

rapid transport. Two types of motor proteins link vesicles to a microtubule: kinesins, moving to the plus end of a microtubule, and dyneins, moving to the minus end. Thus, vesicles from the *trans*-Golgi network that are bound for the cell periphery will be linked to kinesin motor proteins. Each single step of such molecular motors is driven by the hydrolysis of one ATP molecule. The speed of this transport depends on the ATP concentration and on the presence of additional microtubule-associated proteins or other vesicles on the same microtubule. Under ideal conditions in a test tube, dyneins move at rates around 10 $\mu m\, s^{-1}$, whereas kinesins are somewhat slower with rates about 3 $\mu m\, s^{-1}$. In a cell with a diameter of 20–50 μm, this means that budding, transport, and fusion of a vesicle can be accomplished in just a few seconds. By contrast, transport along a neuronal axon can take a few days from a cell soma in the spinal cord to the periphery of the same neuron in a leg or arm.

Vesicle Fusion, SNARE Proteins, and Exocytosis Just like the formation of vesicles, the fusion of vesicles to their target membranes must also be controlled with respect to specificity and timing. Specificity is brought about by anchor proteins in the vesicle and in the target membrane, the SNAREs (soluble *N*-ethylmaleimide-sensitive-factor attachment receptors). This is a protein family with more than 20 members, sharing extended helical domains that can form intertwining complexes with the helix of another SNARE. The tSNAREs are anchored in a target membrane and vSNAREs are linked to the vesicle membrane. A vesicle carrying a certain type of vSNARE will only dock to a membrane equipped with a compatible type of tSNARE. If liposomes with matching SNAREs are mixed they will start to fuse. As SNAREs spontaneously form close complexes, the separation of two SNAREs requires energy input. In fact, the specialized ATPase NSF (*N*-ethylmaleimide-sensitive factor) can bind to SNARE complexes and unravel the intertwined helical domains at the expense of ATP hydrolysis. This mechanism allows SNAREs to be recycled and used for another fusion event. At the same time the activity of NSF defines the susceptibility of the target membrane for further vesicles. In a living cell, docking and fusion are distinct processes and in many cases a signal is required to initiate the final fusion of vesicles that are already docked by SNARE complexes. The classical signal to initiate the final tight contact between SNAREs is a sudden increase in the intracellular Ca^{2+} concentration in the close vicinity of the vesicles.

In the case of vesicle fusion to the plasma membrane, the consequence of the fusion event is that the vesicle content is secreted or released to the extracellular space. The specific term *exocytosis* is used to describe this type of fusion. One of the best-studied examples of exocytosis is the secretion of synaptic vesicles. Synapses are the contact sites between two nerve cells or between a nerve cell and a muscle cell. Importantly, the secretion of transmitters must follow the high frequency of electrical signals reaching the synapse (see Section 7.3.1.4). This could not be accomplished if vesicle transport along the microtubules were a rate-limiting step. To achieve extremely fast secretion, a pool of transmitter-loaded vesicles is usually docked to the presynaptic membrane, waiting for Ca^{2+} ions as a trigger for final membrane fusion and rapid transmitter release.

Endocytosis The term endocytosis describes the uptake of material from the extracellular space into the cell by vesicle formation at the plasma membrane. Three uptake mechanisms can be distinguished: *phagocytosis* describes the inclusion of particles into endocytic vesicles, *pinocytosis* is the uptake of fluids, and *receptor-mediated endocytosis* describes the uptake of specific molecules that are bound by receptor proteins in the plasma membrane. All three processes typically start with a small invagination of the plasma membrane extending to a deeper infolding that is finally released as vesicle into the cytosol. Depending on the size of the engulfed particle, phagocytosis vesicles can be large. Typically, the endocytosed vesicles, or *endosomes*, will be gradually converted to lysosomes through fusion with acidic vesicles, filled with lysosomal hydrolases (Figure 7.28). Similarly to phagocytosis, vesicles formed during pinocytosis can be variable in size. By contrast, receptor-mediated endocytosis is typically accomplished with vesicles of defined diameter. In the best-studied case, clathrin-dependent endocytosis, this vesicle diameter is about 100 nm. Clathrin is the typical coat protein of vesicles arising from the plasma membrane. Vesicles arising from clathrin-coated pits are enriched in transmembrane proteins with highly selective extracellular receptor domains. Ligand binding to the receptor proteins promotes their closer assembly and a deeper infolding of the pit. The exact shape of the vesicle formed is determined by the geometry of the surrounding clathrin structure. An important clathrin-*independent* endocytosis pathway is associated with lipid rafts, specialized cholesterol-rich areas, in the plasma membrane. In this case, vesicle formation requires incorporation of the protein caveolin into the vesicle membrane.

7.2.2 The Differentiated Cell

7.2.2.1 Cell Lineage and Tissue Types

In multicellular organisms, all individual cells have specific functions and, despite their largely identical genetic resources, mature cells differ in morphology and functionality according to their specific roles in the organism. A general principle of cell differentiation is that only a subset of the available genes is used in any given cell. In extreme cases such as red blood cells, the nucleus with the chromosomes is lost completely; the cell lives for a limited time without any further flow of information from the genome. However, specialization alone is not sufficient to form a viable organism. Importantly, the differentiated cells must act in a coordinated fashion and structural and/or functional contacts between cells are required to build up higher order structures, the tissues. Tissues are functional units of cells that interact closely and they typically contain more than one cell type. In higher organisms, different tissues can be organized together to form the individual organs. Despite a huge variability of tissues, three major classes can be distinguished according to the cell types and cell–cell contacts: *epithelial tissue*, *muscle tissue*, and *nervous tissue*. A fourth class of tissue is the "*connective tissue*," a commonly used term for all remaining types of cell clusters including bone cells, cartilage, and the various blood cells.

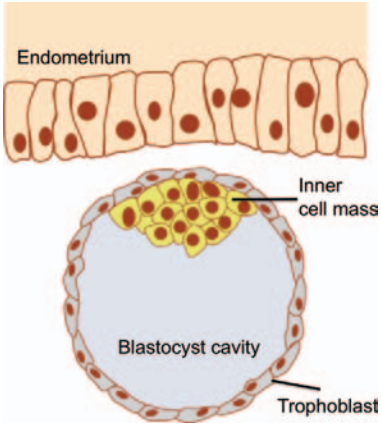

Figure 7.32 The blastocyst has two cell types. Schematic drawing of a mammalian blastocyst at an early stage of embryogenesis before nidation. The cells of the inner cell mass will later develop the embryo, whereas trophoblast cells are responsible for nutrition and contact with the endometrium.

Cell Lineage As multicellular organisms grow from a single cell – the fertilized egg or zygote – that cell must have the capacity to develop into all other cell types of the adult organism. This initial *totipotency* is lost when cells differentiate. For example, a normal keratinocyte of the skin does not retain the potential to form a muscle cell although the genetic information for the required proteins is still present in its chromosomes. The program of differentiation starts shortly after fertilization. During the first cell divisions, all cells have the same appearance and function but already at day five of the human embryogenesis two different cell types exist. In the blastocyst, a single layer of *trophoblast* cells surrounds a fluid-filled cavity and the inner cell mass (Figure 7.32).

This inner cell mass, or embryoblast, develops into the embryo, while the trophoblast provides nutrients to the embryo and will later form the placenta. The decision whether a cell becomes part of the inner cell mass or the trophoblast is the first differentiation step, and many more are to follow throughout the organism's life. At this stage, before implantation in the endometrium of the uterus, the blastocyst consists of about 150 cells. Figure 7.33 depicts the principle of serial decisions on the way from a totipotent cell to numerous terminally differentiated cells.

The full pattern of cell divisions that lead to a certain cell type is called *cell lineage*. To study the mechanisms underlying the decisions that drive a cell in one or another direction, scientists can isolate cells from the inner cell mass and apply different signals, such as hormones or growth factors, to these *embryonic stem cells*. The term stem cell indicates that a cell has on the one hand the potency for numerous divisions in an undifferentiated state (self-renewal), and on the other it is able to generate more differentiated cells. This differentiation is typically an asymmetric process: a stem cell divides into one new stem cell and one further differentiated cell. As a general principle, with every decision on the pathway of cell lineage the degree of potency is reduced. At an intermediate stage, *committed progenitor cells* still have the potential to

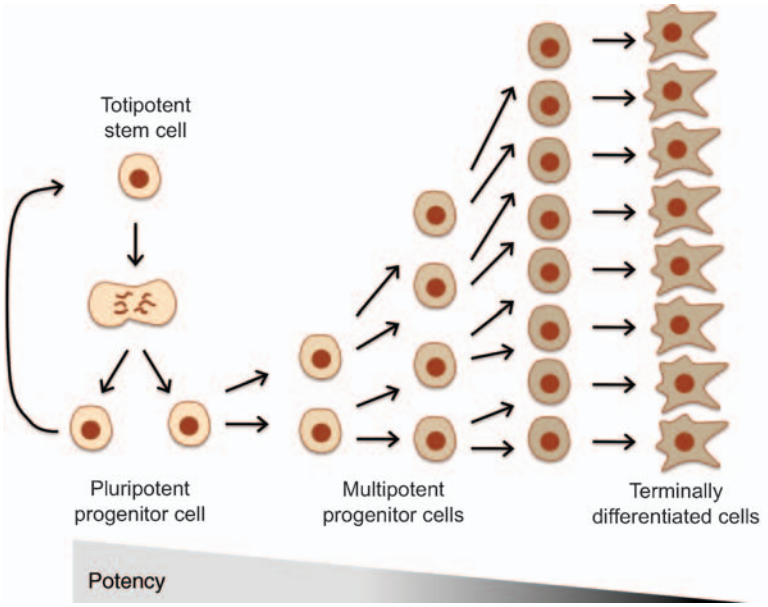

Figure 7.33 Cell differentiation. Progressive cell differentiation and loss of potency on cell lineage pathways from totipotent stem cells to terminally differentiated cells.

develop into more than one cell type, but they cannot generate cells of a completely different lineage that separated off at an earlier stage in the pathway of divisions.

Given this concept, adult organisms would have no potential to regenerate defect tissues, to heal wounds, or to create new cells, such as blood cells. It is now clear that *adult stem cells* with some residual potency of differentiation reside throughout life in specific niches of the adult organism. These cells are less potent than embryonic stem cells, but they can be progenitors for more than one type of terminally differentiated cell types. Adult stem cells are only a minor fraction of cells in a given tissue and they usually undergo very slow rounds of self-renewal during the lifetime of the organism. One of the challenges in regenerative medicine today is to develop a safe method to coerce terminally differentiated adult somatic cells into pluripotent stem cells, induced pluripotent stem (iPS) cells.

7.2.2.2 **Blood Cells**

The concept of stem cells and cell lineage was largely developed based on studies of blood cells and their continuous renewal. All cells in the blood have a limited lifetime, hence stem cells must exist to ensure the supply of new blood cells. Despite the clear differences in shape and function, all blood cells are derived from the same progenitors, the *hematopoietic stem cells*. Together with other types of stem cells, they are found in the bone marrow of large hollow bones. A simplified scheme of hematopoiesis is given in Figure 7.34. The multipotent hematopoietic stem cells divide at very low rates. The daughter cells can either be new self-renewing stem cells or committed hematopoietic progenitors. The latter cell type is still multipotent, but it

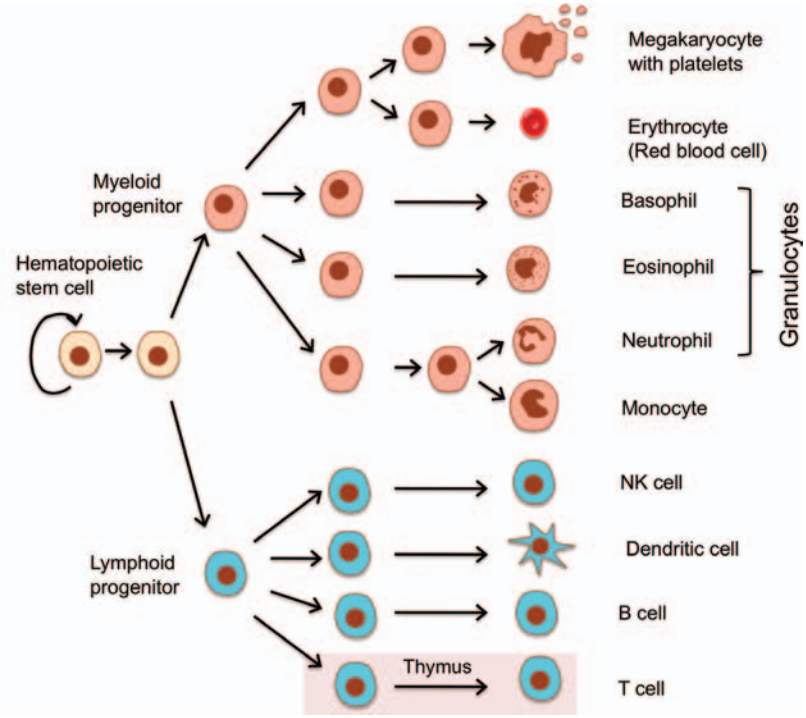

Figure 7.34 Hematopoiesis – development of blood cells. Simplified scheme of the lineage pathways leading from hematopoietic stem cells in the bone marrow to differentiated blood cells. Not all cell types circulating in the blood are represented.

has lost the self-renewing potency. At this point, descendants are committed to undergo either lymphoid or myeloid differentiation. The lymphoid line leads to four types of immune cells: natural killer (NK) cells, dendritic cells, B cells, and T cells. The myeloid line gives rise to erythrocytes (red blood cells), which are the most common blood cells, and among others, granulocytes, monocytes, and platelets. All blood cells other than erythrocytes and platelets are commonly termed white blood cells or leukocytes.

Erythrocytes With about $2–3 \times 10^{13}$ cells in the human adult, the erythrocytes comprise about one-quarter of the total body cell number and they are by far the most common cells in the blood. Corresponding to their role as oxygen transporters for all body organs, erythrocytes are packed with hemoglobin, making up more than 90% of the total protein content. This high concentration and the huge number of erythrocytes in all parts of the body make hemoglobin one of the major obstacles for biophotonic *in vivo* experiments or optical analysis of tissue samples. The mature erythrocyte is practically devoid of all of the normal cellular organelles such as a nucleus, ER, and mitochondria. A human erythrocyte is much smaller than most other cells, with a diameter of about 7 μm and a thickness of 2 μm. With the typical discoid shape, red blood cells can be squeezed through small capillaries of less than

half of their own diameter. The red blood cell is highly flexible and easily deformed but, due to a dense network of proteins lining the inner face of the plasma membrane, they immediately recover their discoid shape when the compression is relieved.

The average lifetime of human erythrocytes is 120 days, after which they are removed by macrophages in the spleen, liver, or bone marrow. The production of new erythrocytes in the bone marrow (erythropoiesis) is stimulated by erythropoietin (EPO), a glycoprotein hormone. EPO is produced by endothelial cells in the kidney and liver, a process that is regulated by the relative oxygen concentration. In the circulating blood, part of the EPO is always bound to erythrocytes, such that a reduced number of cells lead to more free EPO. This mechanism ensures tight coupling of erythropoiesis and removal of red blood cells. The process of erythropoiesis in the bone marrow takes about 8 days and follows the myeloid pathway of differentiation (Figure 7.34). During the first 5 days, the progenitor cells start to differentiate, but they also divide several times to increase the number of cells. After day five, the cells differentiate without further cell divisions. The last group of cells before reaching the mature erythrocyte is the reticulocyte, a cell without a nucleus derived from an erythroblast. Reticulocytes leave the bone marrow and circulate for one more day before maturation to an erythrocyte is complete. In the blood, these immature cells make up about 1% of the total red blood cells.

Leukocytes The white blood cells, or leukocytes, are part of the immune system. Leukocytes can be derived from both myeloid and lymphoid progenitor cells. *B cells* are the producers of antibodies, the primary weapon of the humoral immune response, whereas *T cells* have a central role in cell-mediated immunity. Notably, T cells do not mature in the bone marrow, but progenitor cells travel through the bloodstream to reach the thymus gland, where they expand to large populations of immature cells, the thymocytes. The mature T cells express distinct, individual T-cell receptors on their surface. T cells and B cells are part of the specific, *adaptive immune response*. By contrast, the NK cell, another descendant of the lymphoid lineage, is an important player of the *innate immune response* that provides the first line of defense against pathogens, before the slower adaptive system can react. Immune cells from the myeloid lineage comprise *monocytes* and *granulocytes*, the latter showing characteristic granules in their cytoplasm. Like NK cells, the neutrophil granulocytes are part of the innate immune system. Due to their segmented nuclei, they are also called polymorphnuclear cells. Neutrophils are distinguished from *eosinophil* and *basophil granulocytes* by a different staining behavior in cytological preparations. Monocytes are moving in the bloodstream, but they are still progenitor cells, responsible for the continuous supply of the antigen-presenting dendritic cells and macrophages, specialized phagocytic cells that engulf cellular debris and pathogens. At sites of infection, monocytes can also leave the bloodstream into the infected tissue, where they differentiate to resident macrophages or dendritic cells.

In contrast to the blood cells of the immune system, *platelets* (thrombocytes) have their unique function in the control of bleeding. When blood vessels are injured, collagen of the basement membrane becomes exposed to the blood and serves as a signal to activate platelets, which in turn secrete proinflammatory cytokines and the

platelet-derived growth factor (PDGF) that triggers new blood vessel formation. The platelets are also directly involved in wound closure, as they can form insoluble clots upon activation. With diameters around 3 μm, the platelets, without a nucleus, are the smallest cell type in blood. In fact, they are only small anucleated cell fragments of a much larger progenitor cell, the *megakaryocyte*. A constitutive release of platelets is important, as the average lifetime of the mature platelet in blood is only about 10 days. Megakaryocytes, from which platelets are derived, are huge cells with a diameter of up to 100 μm. During growth, they replicate their DNA several times without division of the cell.

7.2.2.3 Cell Contacts and Extracellular Matrix

Cellular contacts are crucial for the three-dimensional organization and integrity of tissues. The contacts involved in tissue formation follow common principles of architecture that are found throughout the human body. According to morphology and function, three major classes of such cell contacts can be distinguished: *communicating contacts*, *barrier contacts*, and *anchoring contacts*.

Gap Junctions Communicating contacts of mammalian cells are formed as symmetric assemblies of *connexin* proteins. The members of this multigene family share a uniform structure comprising four transmembrane segments. Six connexin proteins form the *connexon*, a hemichannel in the plasma membrane. Two hemichannels in membranes of neighboring cells can assemble to form a functional gap junction, bridging the cytoplasm of both cells. In this configuration, the two adjacent plasma membranes are separated by a distance of about 3 nm. This characteristic "gap" between the two cells is reflected in the name of this junction type (Figure 7.35).

Typically, gap junctions are clustered in regions up to 300 nm in diameter, the plaques. The hydrophilic pore in the center of each gap junction allows free diffusion of molecules with molecular weight up to 1000 Da. Hence both ions and small regulatory substances such as cyclic nucleotides can equilibrate between the

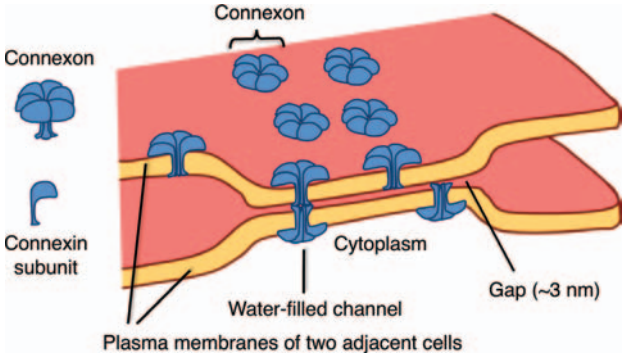

Figure 7.35 Gap junctions. Two adjacent plasma membranes connected by gap junctions. Connexons are hemichannels composed of six connexin proteins. Functional intercellular channels are formed by the connection of two adjacent hemichannels.

connected cells. Proteins and other large molecules are generally precluded from passage through gap junctions. However, gap junction channels are not simply size-exclusion filters. Individual differences in the selectivities of specific gap junctions are determined by the composition of the connexin proteins. A hemichannel can exist as a homomer formed of identical subunits, but heteromeric connexons are also widespread. Gap junctions can switch between open and closed configurations, but the exact gating mechanisms are not well understood. Apart from disassembly of both hemichannels, closure can also be triggered in the joined configuration, for example, by phosphorylation of critical amino acids in connexin subunits. Channel closure is also induced by high concentrations of intracellular Ca^{2+}, a signal that can eventually induce cell death and therefore must be prevented from spreading across the cell cluster. The exchange of small messenger molecules between cells has important physiological consequences. Groups of cells in a tissue can act as a synchronized functional unit. If only a few cells in a connected cluster are stimulated by a hormone, the whole cell cluster can respond in a coordinated fashion. In the same way, the flux of ions allows the electrical synchronization of cell clusters. In the heart, such electrical contacts between neighboring cells are of vital importance. Electrical impulses from the pacemaker region can spread rapidly from cell to cell as ions flow through the gap junctions, a prerequisite for the synchronous contraction of heart muscle cells (also see Section 7.3.1.4). Abnormal coupling of heart muscles can lead to a potentially deadly irregular heartbeat.

Tight Junctions In many epithelial tissues, a tightly sealed cell layer functions as a barrier precluding solutes from uncontrolled access to the underlying tissue. Classical examples are epithelial cells of the gut and the lung. In both cases, a space being in contact with the body's outer environment, for example, the intestinal lumen, is separated from inner tissues. Epithelial cells are organized like a well-laid mosaic with only small interstices between the individual cells. Nevertheless, the tiny space between neighboring plasma membranes would be sufficient to allow free access of small water-soluble molecules. The body would lose these molecules and, on the other hand, potentially harmful molecules, for example from the gut lumen, could enter the intercellular space of a tissue. Such an uncontrolled exchange is prevented by tight junctions that function as seals running all around the epithelial cells. In contrast to gap junctions, there is no space between the opposing membranes of two adjacent cells (Figure 7.36a).

The occluding tight-junction contacts typically contain two types of transmembrane proteins, claudins and occludins, both forming homomeric complexes with each other. These protein interactions bring the plasma membranes of two cells in close contact and seal the space between them. Whereas in some tissues the tight junction permeability is extremely low, in other tissue types the sealing property of the contact is less pronounced. These differences depend on the type of claudin proteins involved in the structure. Claudins form a family of closely related proteins with more than 20 members. Tight junctions not only serve as a diffusion barrier, but also define an important border between the upper (apical) and lower (basolateral) parts of epithelial cells.

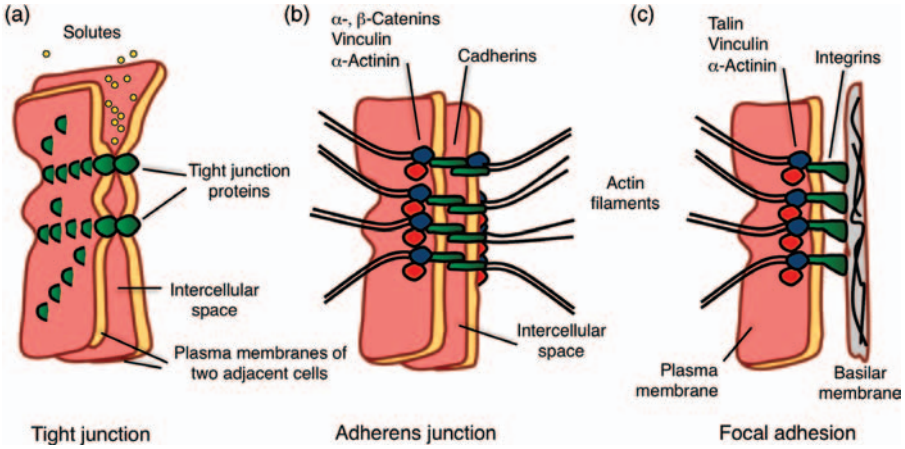

Figure 7.36 Tight junctions, adherens junctions, and focal adhesions. (a) Tight junctions seal the cell–cell contacts in epithelia. (b) Adherens junctions are based on homophilic interactions between cadherins in neighboring cells. In the cytosol, cadherins are linked via adapter proteins to the actin cytoskeleton. (c) Focal adhesions are integrin-mediated contacts of the cell membrane to proteins of the extracellular matrix, for example, the basilar membrane.

Anchoring Junctions Anchoring junctions can make contacts between two cells, and also contacts between a cell and proteins outside the cell, the *extracellular matrix*. In both cases the principle is the same, as contacts are made by a transmembrane protein that is itself connected to either actin filaments or intermediate filaments of the cytoskeleton. Figure 7.36 shows two junctions that are both connected to intracellular actin filaments, the *adherens junction* with cadherins as the binding component (b), and *focal adherens junction* with integrins as the binding transmembrane protein (c). Classical cadherins are single-pass transmembrane proteins, forming lateral dimers in the plasma membrane. The extracellular ends of such dimers make strong homophilic contacts with an identical cadherin dimer of a neighboring cell. These contacts depend on the presence of Ca^{2+}, keeping the extracellular cadherin domains in a rigid and extended conformation. Most classical cadherins are associated with catenins as cytosolic adapter proteins that link the complex to actin filaments. In epithelial cells, adherens junctions often form a belt-like ring around the cells, localized below the tight-junction ring. By contrast, the focal adhesions in epithelial cells are concentrated on the basal part of the membrane, where the extracellular domains of integrins bind to the underlying basilar membrane. In this way, the whole cell layer has a firm hold on the extracellular matrix. Similarly, muscle cells use focal adhesions to attach to their tendons. The muscle-specific integrin α7 is important for the attachment of muscle cells to laminins in the extracellular matrix. Genetic loss of this integrin is the molecular basis for a severe form of congenital muscle dystrophy. Integrins and cadherins can also couple to intermediate filaments instead of the actin cytoskeleton. The corresponding junc-

tions are called *desmosomes* for cadherin-mediated contacts between neighboring cells and *hemidesmosomes* for integrin contacts to extracellular matrix proteins.

Nonjunctional Adhesion Contacts Cell adhesions can manifest in microscopically distinct structures, but they can also occur without visible structures around the connected sites. Such "nonjunctional" adhesions are often involved in weaker, transient contacts between cells or between cells and matrix. Just like in junctional contacts, cadherins and integrins act as major binding proteins. Other transmembrane proteins forming nonjunctional adhesions are *selectins* and Ig-CAMs (*immunoglobulin-like cell adhesion molecules*). Selectins are single-pass transmembrane proteins with a "lectin" domain at the distal, extracellular end. Lectins are sugar-binding entities that can make specific contacts with oligosaccharides on other cells. Heterophilic contacts of this type are especially important for making initial contacts between blood cells and endothelial cells. L-selectins, found on leukocytes, mediate contacts with glycoproteins on endothelial cells and thereby facilitate the entry of blood cells into secondary lymphoid organs. On the other hand, endothelial cells can also express E-selectins in response to an inflammation and slow the movement of passing leukocytes. Supported by subsequent stronger contacts, the leukocytes finally come to a stop and squeeze between the endothelial cells to migrate into the infected tissue. The Ig-CAMs mediate Ca^{2+}-independent cell–cell contacts. A common feature of this protein class is the presence of one or more immunoglobulin domains in the extracellular part. Such domains, stabilized by disulfide bridges, are also characteristic of antibody molecules. In neurons, the expression of so-called N-CAMs is important for initial contacts with other neurons, especially during embryonic neural development. Interestingly, N-CAMs can also have opposing effects, preventing the contact with other cells. This is accomplished by modification of the N-CAM protein with long polysialic acid chains that hinder attachments between other adhesion molecules. Whereas N-CAMs typically form homophilic contacts, the *intercellular adhesion molecules* (ICAMs) use a heterophilic mechanism, for example, by binding to integrins on adjacent cells.

The Extracellular Matrix In higher multicellular organisms, the space between the cells is not just filled with liquid. In order to provide a tear-resistant structure, cells actively secrete a matrix that allows the cells to adhere and that provides orientation for the cellular assembly. The major constituents of the extracellular matrix (ECM) can be divided in two classes of molecules: (a) polysaccharides that can be covalently linked to proteins and (b) fibrous proteins, including collagen, fibronectin, and laminin. The ECM contributes significantly to the autofluorescence of human tissues because collagen and elastin are natural fluorophores with a high quantum yield.

Glycans of the ECM The typical glycans are highly hydrated and form a gel-like structure that resists compression but allows free diffusion of nutrients or hormones. The polysaccharide macromolecules are mostly formed as unbranched chains of 50 or more disaccharide repeats. As one of the sugars in the disaccharide units is always an amino sugar (e.g., *N*-acetylgalactosamine), these macromolecules are termed

glycosaminoglycans (GAGs) (see Section 7.1.3.1). The amino sugar moieties are in most cases sulfated, resulting in a highly negative charge of the long chains. *Hyaluronan* is a simple type of GAG that lacks sulfation. With a length of up to 25 000 disaccharides per chain, it is one of the largest molecules in the body. Hyaluronan is found in most body fluids and serves as a lubricant in the joints. Most other GAGs are proteoglycans, with covalently linked core proteins. These GAGs are assembled in the Golgi apparatus, where a tetrasaccharide is first linked to a serine residue of the protein. The sugar chain is then extended with the typical disaccharides by serial activities of glycosyltransferases in the Golgi compartment and later secreted through exocytosis. In contrast to secreted glycoproteins, the carbohydrate content of the end product can exceed the molecular weight of the core protein by up to 20-fold. Once a proteoglycan is secreted, it can associate with other GAGs to form huge polymeric complexes with dimensions of several micrometers.

Proteins of the ECM The most abundant proteins in the human body are the collagens, members of a family of fibrous molecules. They can assemble to form stiff, rope-like structures that further polymerize to extended fibrils, for example, in skin, cartilage, or blood vessels. Collagen fibrils are typically grouped in bundles of 2 μm or more in diameter. In the tissue, such bundles are arranged as banded patterns with high periodicity. This has an important consequence for the analysis of skin and other collagen-rich tissues with optical methods because the periodic fluctuation of the refractive index in collagen aggregates causes intense Rayleigh scattering in mammalian tissue. Collagen is also a major source of autofluorescence, with an emission maximum of about 380 nm. Collagen proteins are secreted via the secretory pathway involving ER and Golgi complexes (Figure 7.37). In the Golgi lumen, proline and lysine residues in the protein chains are hydroxylated to form hydroxyproline and hydroxylysine. These modified polypeptides assemble to form triple-stranded helical molecules that are stabilized by interchain hydrogen bonds between the hydroxylated amino acids. Following secretion of the procollagen, the triple helices are further modified. Residues at the N- and C-terminal ends of each polypeptide chain are cleaved off by exoproteases and procollagen modules assemble to larger fibrils. The stability of the fibrils is greatly increased by covalent cross-links between lysine residues. Unlike the collagens, fibronectin, another major protein of the ECM, does not self-assemble into fibrils. On the surface of a cell, however, fibril formation can be induced by contacts to integrins in the plasma membrane. The salient structure of fibronectin is a dimer built of two glycoprotein chains that are linked by disulfide bonds at one end of the dimer.

Elastin, another ECM protein, is the main component of elastic fibers in connective tissues. In contrast with collagens and fibronectin, elastin is not glycosylated. The polypeptide chain comprises hydrophobic segments that are interspersed with alanine- and lysine-rich α-helical segments. The hydrophobic elements are important for the elastic properties, whereas the α-helical segments are required to cross-link elastin monomers into larger networks. Elastin is also an important endogenous fluorophore in tissue with an emission peak around 410 nm.

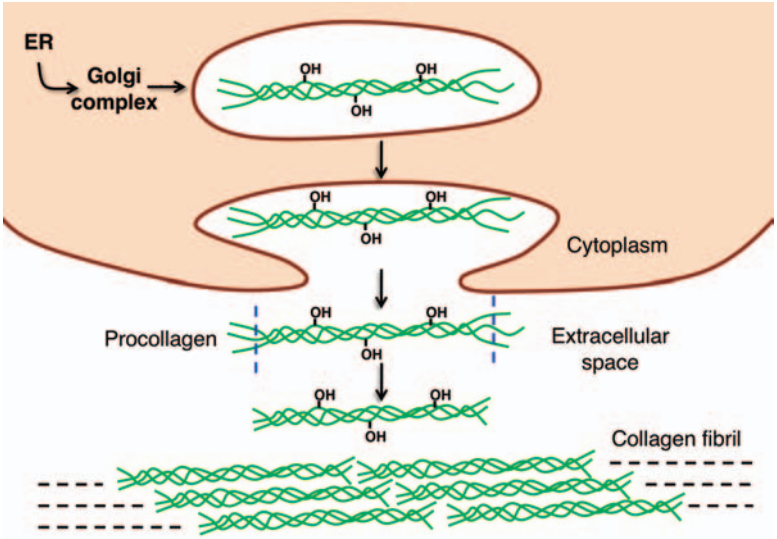

Figure 7.37 Synthesis of collagen fibrils of the extracellular matrix. Triple helices of collagen are formed in the Golgi complex and secreted through vesicles. Proline and lysine residues are hydroxylated and form hydrogen bonds that help to stabilize the triple-stranded helix. Following export, the propeptides are proteolytically shortened on both ends and triple helices assemble into large fibrils. Hydroxylation of polypeptide chains in the final fibril is not shown for simplicity.

7.2.2.4 **Epithelial Cells**

The cells lining the inner or outer surfaces of the body form *epithelial tissues*. The common characteristics of this tissue type are the presence of a lumen-exposed surface on one side and of a basement membrane on the other side. The functions of epithelia can differ markedly, but they always act as barriers, separating underlying tissues from the environment or from an internal lumen. Hence epithelial cells are functionally contiguous with one another and the intercellular space between them is very limited.

All glandular organs such as the salivary gland, sweat glands, and liver contain epithelial cells and all ducts and tubes of the body are lined by epithelia. The epithelium forming the inner surface of the blood vessels is usually called the *endothelium*. With a total number of about 10^{13}, endothelial cells are one of the most abundant cell types in the human body. Tight junctions are important connections between epithelia cells, but additional contacts, such as adherens junctions or gap junctions, are also established. Depending on the density of the tight junctions and the exact protein composition therein, some epithelia are completely impermeable whereas others may not act as a tight barrier.

Some epithelia are responsible for the uptake of material from the environment, such as the intestinal epithelium. Other epithelia, especially those in glands, function to secrete their own products such as hormones, sweat, or breast milk.

The overall structure of an epithelium differs depending on the number of layers that it contains. In the *simple epithelium*, all cells are arranged in a single layer. If two or

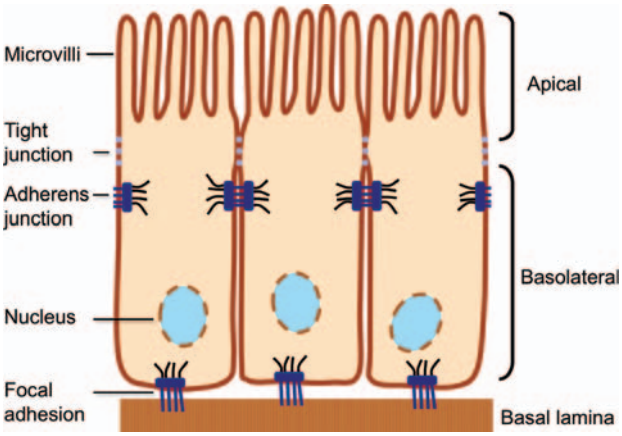

Figure 7.38 A simple columnar epithelium. The cells have a clear polarity, with an apical side and a basolateral side, being separated by tight junctions. An epithelium of this type covers the surface of the small intestine, where the apical surface area of the cells is increased by microvilli, reaching into the intestinal lumen. On the basal side, the cells are anchored to the upper layer of the basement membrane, the basal lamina.

more cellular layers are formed, the epithelium is called *stratified*. A *squamous* simple epithelium consists of a single layer of flat-shaped cells. Typical examples are the lung alveolar epithelium or the blood vessel endothelium. An epithelium is *cuboidal* if the cells are nearly equal in width and height, as found in many kidney tubules. Figure 7.38 shows a *simple columnar epithelium*, characterized by single-layered epithelial cells with a cell height clearly exceeding the width. The densely packed microvilli on the apical surface are typical of the epithelia of the small and large intestine. The enlarged cell surface allows the mass transport of nutrients across the barrier. The structure of these cell extensions is determined by parallel bundles of about 25 actin filaments. The densely packed microvilli have very regular diameters of around 100 nm, hence they are not optically resolved by conventional light microscopy. Owing to a fuzzy appearance in the light microscope, the zone of the microvilli has been termed the brush border.

Stratified epithelia are formed by more than one cellular layer. In many glands, such as mammary glands or salivary glands, the basal layer is formed by actin-rich contractile cells, the myoepithelial cells. Other cells that produce the specific secretory product are arranged in layers on top of these cells. Contraction of the myoepithelial cells then allows the active secretion of the glandular products. The terminology for epithelia comprising more than one cell type in different layers follows the pattern of the outermost layer. Accordingly, the epidermis of the skin is called a stratified squamous epithelium because the outermost cells have squamous shape, whereas cells in the basal layer are cuboidal.

The epidermis is a good example of the continuous renewal processes in many tissues, involving cell differentiation, morphology changes, and terminal cell death. A simplified cartoon of the epidermal cell layers is shown in Figure 7.39. The

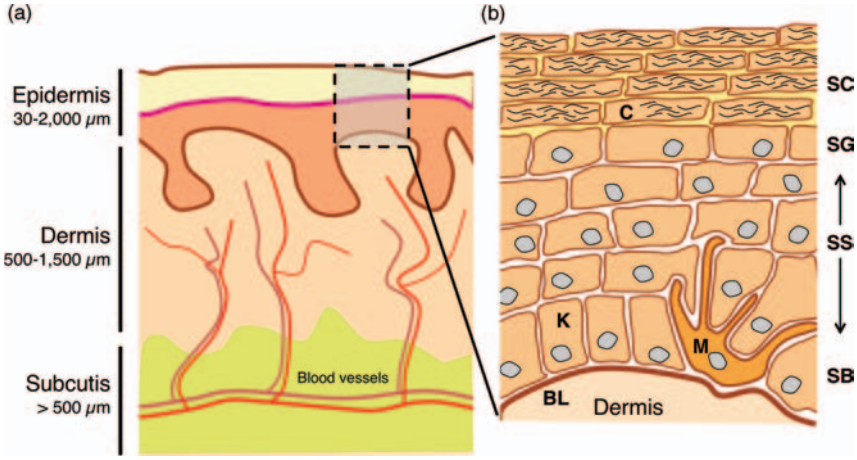

Figure 7.39 Schematic drawing of the epidermis (b) and its location in the skin (a). The epidermis forms the outermost layer of the human body. It is separated from the underlying dermis and by a basal lamina (BL). Keratinocytes (K) are organized in the layers *stratum basale* (SB), *stratum spinosum* (SS), and *stratum granulosum* (SG). The *stratum corneum* (SG) is made of terminally differentiated keratinocytes. These corneocytes (C) are dead cells without a nucleus. They are filled with keratin and embedded in a lipid-rich matrix. Melanocytes (M) are interspersed in the *stratum basale*, where they produce the pigment melanin that is transferred to keratinocytes.

dominant cell type of this epithelium is the keratinocyte. The cuboidal keratinocytes in the lowest layer are in contact with the basal lamina and they continually divide to renew the cell layers above. One of the two daughter cells will remain in the basal layer, whereas the other descendant moves upwards into the stratum spinosum. On their migration through this layer, the cells begin to flatten and to produce keratin, an insoluble intermediate filament protein. In the thin granular layer, or stratum granulosum, the keratinocytes contain visible granules filled with the intermediate filament protein keratohyalin. In the outermost layer, the keratinocytes become corneocytes, anucleated flattened cells surrounded by a dense layer of lipids. This is the final differentiation stage that a keratinocyte reaches about 5 weeks after its "birth" in the basal layer. The highly enriched keratin in the interior of these cells gives the epidermis mechanical stability. The secreted "cement" around the cells is made of lipids such as ceramides, cholesterol, and fatty acids. With these substances the stratum corneum makes an effective barrier against water and all soluble substances. In the outermost cell layers of the horny part of the epidermis, the stratum corneum, the cells start to weaken their cell–cell contacts, so that they are continually lost during washing and rubbing.

There are additional cell types residing in the skin. A dense layer of bacteria lives between the loosely connected outermost cells and feeds on the cell debris and the lipids. About 1000 bacteria per square millimeter find their natural habitat here. In the deeper layers of the epidermis, immune cells (*Langerhans cells*) patrol between the keratinocytes. Merkel cells are mechanoreceptor cells in the basal layer that are

connected to sensory nerve endings. Together with the nerve cell, they function as touch sensors of the skin, responsible for the sensation of gentle touch and the discrimination of shapes and textures. Another prominent cell of the basal layer is the pigment-producing *melanocyte*. The skin pigment melanin is stored and transported in the melanosomes, specialized vesicular organelles similar to the ubiquitous lysosomes. The melanosomes are transported along dendritic processes of the melanocyte from which they are finally released to be taken up by connected keratinocytes. The melanocytes comprise less than 10% of the cells in the basal layer of the epidermis. The skin color is not determined by the number of melanocytes in the skin, but rather by the amount of melanin they produce and transfer to the neighboring keratinocytes.

The Basal Lamina All epithelia are separated from underlying stroma by a dense network structure with a thickness between 30 and 120 nm, the *basal lamina*. A similar extracellular matrix structure is wrapped around muscle cells, separating them from connective tissue. The major protein components of the basal laminae are type IV collagen and laminins. Laminins are glycoproteins with the inherent ability to self-assemble as trimeric complexes with a cross-like structure. The long arm of the cross can be used to anchor cells, whereas the three shorter arms are connected to other components of the basal lamina. Ultrastructurally, the basal lamina can be divided into a lighter upper zone (*lamina lucida*) and an electron-dense lower layer, called the *lamina densa*. The latter is tethered to an underlying thick layer of collagen fibrils. This whole arrangement is usually called the *basement membrane*. Basal laminae are more than a structural foundation that anchors epithelia or muscle tissue. They also influence the connected cells, induce polarity, and promote cell survival and proliferation.

7.2.2.5 Nerve Cells and Glial Cells

The nervous tissue is built of two very different cell types: *neurons* and *glial cells*. Neurons, or nerve cells, are the electrically excitable cells of the nervous tissue, responsible for the propagation of electrical signals through the body. The major functions of glial cells are to accompany neurons, provide physical support, buffer ions, and supply nutrients and oxygen. In the human brain, both cell types are found in an approximate 1:1 ratio.

The human body contains nervous tissue in three functional entities: the brain, the spinal chord, and the *peripheral nervous system* (PNS). The first two are also called the *central nervous system* (CNS). They have in common that nerve cells are concentrated at high densities and that a bone structure provides mechanical protection, whereas the *blood–brain barrier* shields the nerve cells from chemical threats. This barrier is constituted by the endothelial cells in the CNS vessels tightly controlling the exchange of soluble molecules between the cerebrospinal fluid surrounding the nerve cells and blood. Endothelial cells in the CNS are connected by tight junctions that almost completely restrict the passage of solutes, whereas hydrophobic hormones and also O_2 and CO_2 can pass. Entry of soluble molecules, including glucose as the major source of energy, depends closely on transmembrane

transporters in the plasma membrane of endothelial cells. The blood–brain barrier represents an important factor in the design of therapeutic agents; those designed to treat the brain must pass the blood–brain barrier easily whereas those destined for other tissues should not pass the barrier.

The PNS resides mainly outside this protected area because it connects the CNS with all inner organs, the limbs, and the skin. Two types of directional nerves accomplish this connection. Neurons of the *afferent* nerves relay information from the periphery to the CNS, and *efferent* neurons deliver signals from the CNS to effector organs, glands, and muscles. The PNS can be further divided into the *autonomic nervous system* and *somatic nervous system*. The former controls all functions of the body that are not under deliberate, conscious control, such as heart rate, respiration rate, digestion, and many others. The tissues controlled by the autonomic nervous system are smooth muscles, cardiac muscle, and glandular tissues. By contrast, skeletal muscles are controlled by the somatic nervous system. The efferent fibers of this system transmit signals from the CNS to the skeletal muscles and allow the voluntary control of muscle activity. Afferent fibers of the somatic nervous system deliver signals from peripheral sensory neurons to the CNS.

Nerve Cells Neurons come in very different sizes and shapes, but a unifying morphological feature, applicable to most of them, is a composition of three functional units, namely cell body (soma), axon, and the dendrites. This basic structure is depicted in Figure 7.40. The soma contains the nucleus and most of

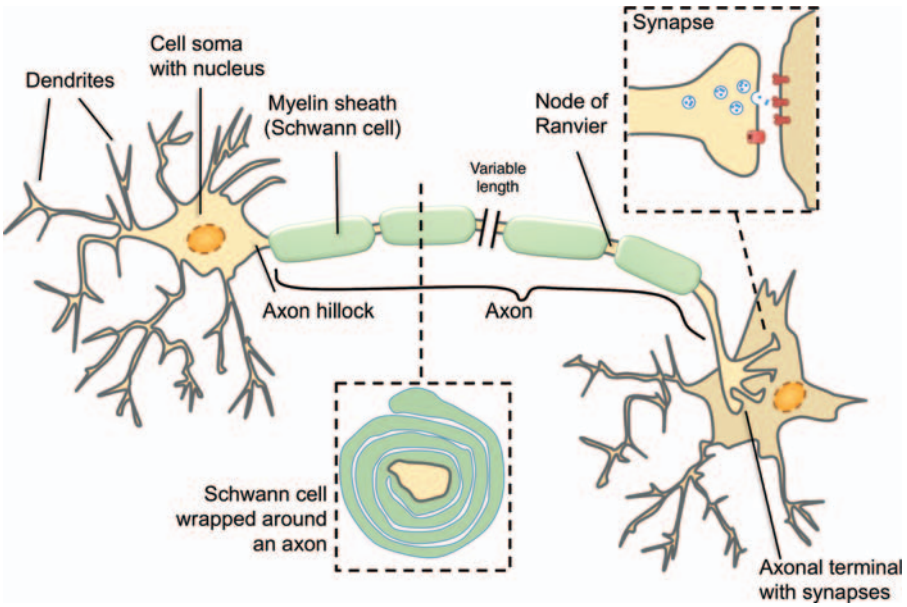

Figure 7.40 Basic structure of a neuron with a myelinated axon. The magnified sections show cross-sections through the axon with the myelin sheath and a synaptic contact.

the cellular synthesis takes place here. Hence proteins or neurotransmitters produced in the soma need to be transported into dendrites and into the axon. This long-distance traffic is accomplished as active transport of vesicles along microtubules.

The dendrites are cellular extensions that often resemble the branching pattern of a tree. For most neurons, the dendrites are the major entrance sites for incoming electrical signals. They are docking platforms for the synapses from other neurons and deliver the signal further down to the soma. In addition, incoming synapses can also be connected to the plasma membrane of the soma itself.

The axon is a long extension of the nerve cell that transmits the electrical signals, often over long distances. The axon hillock, an area at the beginning of an axon, is densely packed with voltage-gated sodium channels enabling the cell to generate action potentials or nerve impulses, the electric information unit of a neuron (see Section 7.3.1). Two main types of axons can be distinguished, the fast-conducting myelinated axons and slow-conducting non-myelinated axons. The myelin sheath is wrapped around the axon, except at the nodes of Ranvier. The myelin layer is formed by closely attached glial cells; in the PNS these are Schwann cells and in the CNS oligodendrocytes. At contact sites to the axon, the membrane of the glial cell grows continuously until several layers of plasma membrane are concentrically wrapped around the axon. In the final state, these membrane layers are tightly packed with no cytoplasmic content lying in between. In contrast to most plasma membranes, the bilayers in myelin sheaths are enriched in lipids, with a lipid-to-protein ratio of about four. The main function of the myelin layer is to provide electrical insulation for the axon, analogous to the plastic insulation of a power cable. It increases the electrical resistance across the axon membrane more than 1000-fold and strongly reduces the electrical capacitance. As a consequence, myelinated axons can conduct electrical impulses about 50 times faster than non-myelinated axons of the same diameter. Slowly conducting nerve fibers without myelin sheath are typically found in the autonomic nervous system. For the continuous control of functions such as heart rate and digestion, the speed of electrical signal transmission is not critical and myelination is dispensable. By contrast, skeletal muscles are innervated by myelinated axons of the somatic nervous system to allow fast responses.

Glial Cells Schwann cells and oligodendrocytes forming the myelin sheath in the PNS and CNS, respectively, belong to the *macroglial cells*. The largest fraction of macroglia in the CNS are the star-shaped *astrocytes*. Cells of this type have a direct role in the formation of the blood–brain barrier as they form tight complexes with endothelial cells of the capillaries. Importantly, the functions of astrocytes are not restricted to the passive support of neurons. More recently, it became evident that astrocytes may participate directly in neurotransmission by releasing neurotransmitters such as glutamate. Linked by gap junctions, astrocytes can form large syncytial complexes and Ca^{2+} flux along these connected cells can trigger the release of neurotransmitters. Additionally, astrocytes are also involved in the reuptake and clearance of neurotransmitters. In the PNS, satellite cells play a similar role. Like astrocytes, they can form complexes that are interconnected by gap junctions and Ca^{2+} waves can travel along such cell complexes. Various functions are adopted by

microglia cells, in both the PNS and CNS. This cell type comprises mobile cells that are capable of phagocytosis and they provide the main immune defense of the CNS. Microglia cells do not descend from neural progenitor cells like neurons and other glial cells, but they are derived from precursor cells in the bone marrow and travel into the CNS.

7.2.2.6 **Muscle Cells**

Muscles convert chemical energy from ATP into mechanical energy, causing the movement of organs within the organism or motion of the whole organism. The fundamental unit of a muscle is the muscle cell with a contractile machinery formed by actin and myosin filaments. This section is focused on morphology and specific properties of these cells. Regardless of the type of muscle cell, repeated conformational changes of myosin proteins cause the myosin filaments to slide along actin filaments, such that the overall protein assembly and the muscle cell itself are shortened. In contrast, the relaxation and stretching of muscle cells are passive processes. Three types of muscle cells can be distinguished based on tissue organization and function: *smooth muscle* cells, *skeletal muscle* cells, and *cardiac muscle* cells (Figure 7.41). Like neurons, many muscle cells have excitable plasma membranes to generate and propagate action potentials. The plasma membrane of the muscle cells is commonly termed *sarcolemma*.

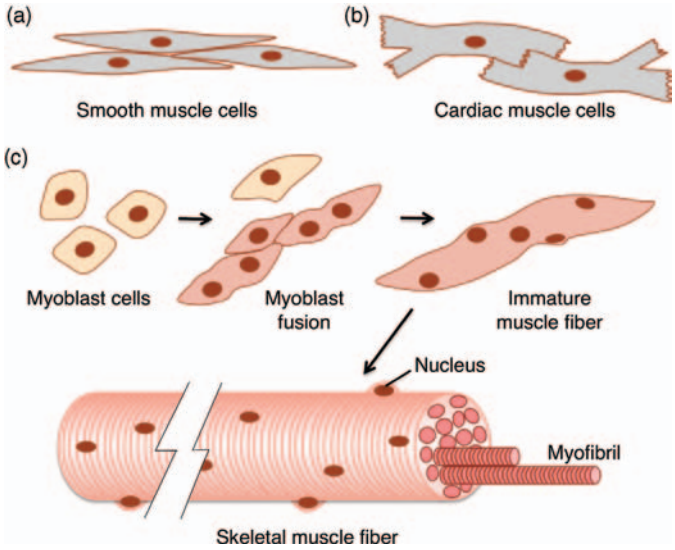

Figure 7.41 Three types of muscle cells. (a) Smooth muscle and (b) cardiac muscle tissues consist of single contractile cells. Cardiac cells can be branched; they are tightly connected to neighboring cells at the undulated blunt ends. (c) Skeletal muscles consist of large polynucleated cells (muscle fibers) generated by fusion of progenitor cells (myoblasts). The assembly of myosin and actin filaments in myofibrils causes a striped (striated) appearance of skeletal muscle fibers.

Smooth Muscle Cells Smooth muscles consist of spindle-shaped cells (Figure 7.41a) with a length ranging from 10 μm in artery walls to 600 μm in the uterus during pregnancy. Consistent with their involvement in involuntary contraction, smooth muscles are innervated through the autonomous nervous system. In multi-unit muscles, innervation is directed to individual, functionally independent muscle cells. In single-unit smooth muscle, for example in the intestinal walls, the cells are connected by gap junctions. This allows electrical contact and concerted contractions of a larger cluster. Such muscle cell clusters contract spontaneously if stretched. In the cytoplasm of smooth muscle cells, bundles of actin filament are arranged such that one end of the bundle is fixed to *dense bodies* in the cytoplasm, while the other end is connected to a second actin bundle via intercalating myosin filaments. Repeated sets of this structure are coupled in long chains (*myofibrils*) through the whole cytoplasm of the cells. On the surface of the plasma membrane, these myofibrils are fixed to *attachment plaques*. As the repeating structures in the myofibrils are not aligned between neighboring cells, the overall appearance of the tissue is smooth and not striped as in skeletal muscle cells. The contraction of smooth muscle cells is slower than in skeletal muscle, but the contracted state can be much more sustained.

Skeletal Muscle Cells Skeletal muscles consist of cylindrical-shaped muscle fibers with an average length of 1–3 cm and diameters ranging from 10 to 100 μm. The longest fibers of about 30 cm are found in the sartorius muscle that runs down the thigh. Each muscle fiber is a huge cell with many nuclei, originating from the fusion of committed progenitor cells, the myoblasts (Figure 7.41c). In the mature muscle fiber, the individual nuclei are located underneath the sarcolemma. The outer surface of the sarcolemma is covered with a thin and flexible layer of collagens and polyglycans. Importantly, the cytoplasmic protein dystrophin is a central part of a protein complex that connects the cytoskeleton through the membrane to the surrounding extracellular matrix. Mutation or loss of dystrophin causes Duchenne muscular dystrophy, a severe and eventually lethal disease. The fusion of myoblasts occurs both during development and throughout adulthood when muscles grow or need regeneration. In the adult muscle, small *satellite* cells are closely attached to the muscle fibers. They represent persistent myoblasts that are needed to regenerate the multinucleated muscle fibers after damage. The innervation of skeletal muscle cells comes from the somatic nervous system and allows voluntary control of muscle contractions.

As in smooth muscle, the basic unit of skeletal muscle contraction is the myofibril. In the cytoplasm of skeletal muscle cells, these long bundles of actin and myosin filaments are organized in parallel, such that the muscle fiber has a striped or *striated* appearance. Each stripe is formed from two sets of actin filaments and an intercalated set of myosin filaments. The outer ends of the actin proteins are fixed at the Z-discs. Contraction is brought about by a sliding filament mechanism in which the myosin filaments move deeper between the actin filaments. In the relaxed muscle, each sarcomere has a length of approximately 3 μm, whereas contracted sarcomeres are on average 1.5 μm long. As an important specialization of the skeletal muscle cell, the ER, here called SR, is organized as an envelope around each of the myofibrils. The SR

structure does not form a tight seal around the filaments, but rather looks like a curtain with many holes. The purpose of the SR is to store and quickly release Ca^{2+} ions in response to excitation and Ca^{2+} ions are the trigger for the sliding movement of myosin filaments.

Cardiac Muscle Cells Cardiac muscle cells (*cardiomyocytes*) are not fused (Figure 7.41b), but with close end-to-end connections each cell acts like a block in a tightly assembled pavement. The mature tissue has no prominent progenitor cell population like the satellite cells of skeletal muscle and cardiac muscle tissue hardly regenerates after injuries and cell death. However, more recent evidence suggests that some cardiac progenitor cells exist even in adult tissue. Given the high mortality rates caused by myocardial infarction, there is a strong research interest in cardiac stem cells, but the therapeutic potential awaits further clarification. The contractile machinery of cardiomyocytes follows a similar building plan as in skeletal muscle, although the cells are not fused. The myofibrils are also striated with repeated modules of actin and myosin filaments between Z-discs. At the cell membrane the filaments end in *intercalated discs* instead of a Z-disc. At these blunt ends, each cardiomyocyte is closely connected to the next cardiomyocyte, forming a system of functionally coordinated cells. The inner cell architecture and the SR also resemble the skeletal muscle, but only one set of T-tubules is found per sarcomere. The cardiac muscle is not under voluntary control as it is innervated by the autonomous nervous system.

7.2.3 The Biological Diversity of Cells

7.2.3.1 Biological Diversity and Taxonomy

All living cells share principal structures such as DNA, proteins, or lipid bilayers; the life of all cells involves common principles such as the universal genetic code or the use of energy-rich ATP to drive enzyme reactions. However, based on this common ground, over some billions of years evolution has generated an enormous diversity of cells and organisms and it is obvious that bacteria, single-celled algae, and mammalian cells differ significantly in many of their cellular structures and biochemical properties. In consequence, experiments with biological samples from different organisms require at least some knowledge of the specific properties of the object under study and of the phylogenetic relations between different species.

It is a common practice to employ model organisms for the investigation of biological principles that can be extrapolated to other organisms of interest. This can have practical or ethical reasons, for example, the genome of a mouse can be specifically altered to study gene function with relevance for other mammals including humans. However, every model has its limitations and transfer of knowledge from one organism to another requires great caution. For example, the bacterium *E. coli* is routinely used to propagate and manipulate human DNA, but it is important to remember that bacterial cells have no nucleus and, hence, human gene regulation cannot be studied easily in this model organism.

This section cannot provide a comprehensive introduction to biological diversity, rather it is aimed at giving a first insight into the major classes of organisms and at highlighting phylogenetic relationships between them.

Taxonomy Taxonomy is the science of classification of living beings. The modern system of scientific classification aims for an unbiased representation of the phylogenetic relatedness between species, regardless of superficial analogies in the outer appearance. Based on its position in the classification system, every species then derives its unambiguous scientific name. The so-called *binomial nomenclature* system for organisms dates back to Carl Linnaeus who published a systematic overview of life forms in the eighteenth century. According to his system, all species are named such that the two lowest scientific ranks, genus and species, form the name of an organism. For instance, in the name *Homo sapiens*, "*Homo*" is the more generic term, which includes many extinct relatives such as *Homo neanderthalensis* and *Homo erectus*. The specific name "sapiens" refers to the species. By definition, this is a group of organisms capable of interbreeding and separated from other groups with which no interbreeding occurs. According to scientific standards, *italic* letters are used to highlight scientific species names in the literature. If there are no ambiguities possible, the genus name is often abbreviated, for example, *E. coli*. A scheme depicting the current hierarchical rank system is shown in Figure 7.42.

Three Domains of Life Linnaeus divided all organisms into two kingdoms: animals and plants. The modern taxonomy system now distinguishes six kingdoms: bacteria, archaea, animals, plants, fungi, and protists. On top of this, a new category, the *domain*, was installed when the microbiologist Carl Woese had analyzed and

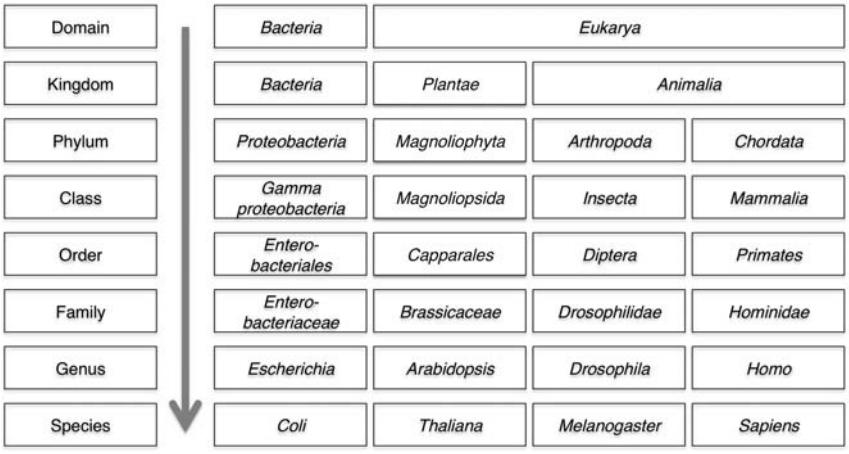

Figure 7.42 Hierarchy of biological classification ranks. The two lowest levels, genus and species, are used to build the unambiguous scientific names for all organisms. In addition to ourselves (*Homo sapiens*), typical model organisms are shown: the bacterium *Escherichia coli*, the mouse-ear cress *Arabidopsis thaliana*, and the fruit fly *Drosophila melanogaster*.

compared ribosomal RNA sequences between species. Ribosomes are common to all known organisms and the vital function of this protein-producing machine caused a stable conservation of rRNA sequences over extremely long periods of evolution. Molecular phylogeny assumes that the degree of divergence between the gene sequences in two given species correlates with the evolutionary distance between them. The most conserved sequences, such as rRNA, can be used to judge the evolutionary distance between non-related species, whereas more specialized genes, undergoing more rapid changes, allow closer relatives to be differentiated. Based on Woese's comparisons, it became evident that the evolutionary distance between certain bacterial species is just as large as the distances of both kinds of bacteria to animals or plants. There is now general agreement to divide all life forms into three major categories or "domains": archaea, eukarya, and bacteria (Figure 7.43).

Despite the superficial morphological resemblance of archaea (or archaebacteria) and "normal" bacteria (eubacteria), sequence similarities imply that archaea and eukarya separated later during evolution. The three-domain system replaced the formerly used differentiation between *eukaryotes* and *prokaryotes*. Nevertheless, both categories are still commonly used to distinguish cells with a membrane-surrounded nucleus (eukaryotes) from bacterial cells without nucleus (prokaryotes). For archaea and bacteria, the domain category is equivalent to the "kingdom." The domain eukarya is further divided into four kingdoms: animals, plants, fungi, and protists.

It is obvious today that the kingdom "protists" does not reflect a homogenous, monophyletic category, but rather comprises several more or less unrelated groups. The *slime molds* resemble fungi, as they typically use spores to reproduce. In contrast, plant-like photoautotrophic protists, called protophyta, are able to gain energy from

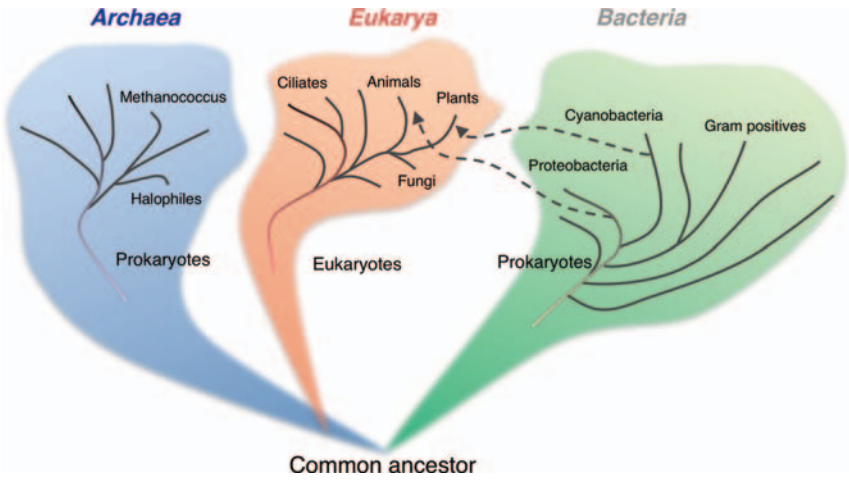

Figure 7.43 Three domains of life. The represented phylogenetic relationship tree is based on the comparison of ribosomal RNA sequences. It assumes that all organisms descended from a common type of progenitor cell. Irrespective of the phylogenetic distance, archaea and bacteria are often grouped together as "prokaryotes" to distinguish them from organisms with nucleated cells, the "eukaryotes."

sunlight. Other protists, called protozoa, have animal-like characteristics, such as a dependence on the uptake of other organisms or at least of energy-rich parts of other organisms. This group includes, for example, the genus *Paramecium* and also the malaria parasites of the genus *Plasmodium*.

The kingdom *animals* appears most familiar, as the colloquial term animal is often associated with the closer relatives of humans, the vertebrates. It is important to know that these animals with a vertebral column and spinal chord, including fish, amphibians, reptiles, birds, and mammals, form only one of many groups in the animal kingdom. The larger diversity within this kingdom may be illustrated by a single example of a more distant relative, the jellyfish. This organism is now prominent in biophotonics, as the green fluorescent protein (GFP) was isolated from the species *Aequoria victoria*, living in the Pacific Ocean. Jellyfish are unrelated to vertebrate fish and the commonly known umbrella-shaped type of jellyfish represents only one step in a two-stage life cycle. In the first stage of the cycle, jellyfish form sessile stalks with feeding tentacles. These polyps can asexually produce the free-floating, umbrella-shaped medusae, which are either male or female. Upon sexual reproduction between them, the life cycle starts again with a polyp. The bioluminescent medusa can generate flashes of blue–green light. The emission is triggered by calcium ions that induce conformational changes in the photoprotein aequorin, a 22 kDa molecule carrying coelenterazine as a prosthetic group. Upon oxidation, this cyclic organic molecule is converted into an excited state from which it relaxes with the emission of blue light. Part of the energy is transmitted by FRET (Förster resonance energy transfer) to the GFP, finally resulting in green fluorescence emission. Surprisingly, it is still unknown what the benefit of this sophisticated bioluminescence system is for the animal.

7.2.3.2 **Plant Cells**

Plants are one of the kingdoms already introduced by Linnaeus, but since then several refinements in the definition have occurred. Fungi and some groups of algae were separated to form their own branches of eukarya. Plants can be divided into four major groups: *seed plants*, *green algae*, *ferns* and their relatives, and the *bryophytes*, a group including the mosses. Among all plant species that have been identified thus far, the seed plants are by far the largest group with over 250 000 species. *Gymnosperms* are seed plants with unenclosed "naked" seeds, a group that includes the conifers and the Gingko tree. The colloquial term "plant" is most often used for the largest group of seed plants, the *angiosperms* or *flowering plants*. A typical cell of a flowering plant is shown as a cartoon in Figure 7.44.

As an important difference from animal cells (Figure 7.21), the flowering plant cell is surrounded by a stable *cell wall* composed of cellulose and hemicellulose fibrils embedded in a matrix of pectin. This wall around the plasma membrane provides physical rigidity and prevents the plant cell from swelling by water influx. Cellulose is built of glucose, the same compound as in starch but with a reverse orientation of the bonds between the glucose molecules. The pectins are more complex heterosaccharides containing galacturonic acid residues. With increasing age, the cell walls gain higher mechanical stability and hydrophobicity through incorporation of lignin, a

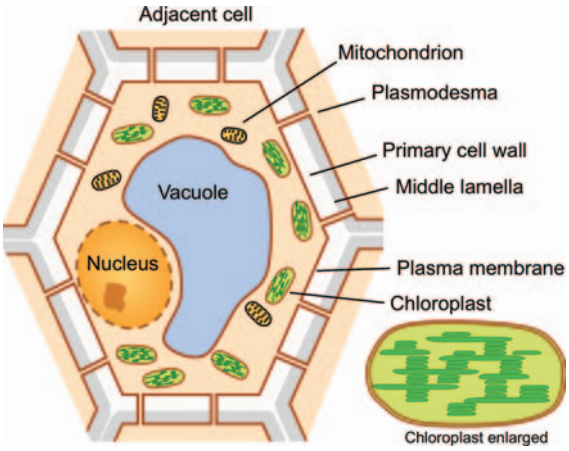

Figure 7.44 A typical cell of a flowering plant. The plant cell is surrounded by a stable primary cell wall. When the cell stops growing, a secondary wall can be formed between plasma membrane and primary wall. Plasmodesmata are cytosol bridges that connect neighboring cells. The vacuole, surrounded by the tonoplast membrane, is functionally related to lysosomes in animal cells. Chloroplasts are the sites of photosynthesis in plant cells. They are endosymbiotic organelles derived from cyanobacteria.

huge phenol-containing macromolecule that cross-links to the polysaccharides of the cell wall. The wooden parts of a plant are usually rich in lignin. Enclosed in the corset of their cell walls, plant cells still have direct contacts to their neighboring cells via the plasmodesmata. These small tunnels with diameters around 50 nm are surrounded by the plasma membrane. Between 1000 and 10 000 plasmodesmata connect the cytoplasm of a single cell with its neighboring cells. Small water-soluble molecules and even small proteins can pass through the plasmodesmata, such that all cells of the plant form an interconnected system, the so-called symplast.

A striking peculiarity within the cytoplasm of most plant cells is the vacuole, a water-filled organelle surrounded by a membrane, the tonoplast. Vacuoles have an acidic pH and in many respects they fulfill the role of the lysosomes in animal cells, as they contain hydrolytic enzymes and they are involved in autophagy, the breakdown of other organelles. In addition, the vacuole with its large content of small, osmotically-active molecules is important for the hydrostatic pressure of the plant cell. In plants without rigid cell walls this pressure, or turgor, is responsible for keeping the whole plant erect. Another difference from animal cells is the lack of centrioles in the centrosomes of the plant cell. Nevertheless, plant centrosomes have similar functions to their animal counterparts, serving as anchor sites for the minus ends of microtubules. Apart from microtubules, the cytoskeleton of a plant cell also contains actin filaments, but intermediate filaments are usually rare or even absent in plant cells.

Chloroplasts Maybe the most important achievement of the plant cell is *chloroplasts*. It can be assumed that cyanobacteria, as progenitors of the modern chloroplast, were taken up by eukaryotic cells as a second endosymbiotic organelle besides mitochondria. Chloroplasts still have their own genome and bacterial-type ribosomes, but like

mitochondria, many of the genes required to build the functional chloroplast were translocated into the nucleus of the host cell during evolution. Thus, chloroplasts cannot live outside the host cell and plant cells depleted of their chloroplasts are unable to regenerate the organelles *de novo*. Due to the endosymbiotic origin of the chloroplasts, the stroma of the chloroplast is surrounded by two membranes, the inner one originally belonging to the cyanobacterium and an outer membrane derived from the eukaryotic host cell plasma membrane.

Sequence analysis of the chloroplast genomes from many different plants implies that the uptake of cyanobacteria by a eukaryotic cell was no unique event, but may have occurred several times during evolution. Interestingly, not only were cyanobacteria integrated into nucleated cells, but also eukaryotic algae with chloroplasts can be engulfed by another eukaryotic cell. An example is the marine alga *Guillardia theta* that contains four different genomes: in its own nucleus, in the mitochondria, in the vestige of the co-opted nucleus (the nucleomorph), and in the chloroplasts of the engulfed cell.

The great benefit of cyanobacteria uptake by the host is that the organism can switch from a heterotrophic lifestyle with the dependence on energy-rich nutrition to an autotrophic way of life. A cell with chloroplasts is able to use the energy from sunlight to build up organic material from CO_2 and water. During evolution, multicellular plants gradually developed from simple unicellular algae, but chloroplasts remain vital for the whole organism. In a seed plant, not all cells are exposed to sunlight and consequently not all cells have green chloroplasts. In the developing plant, chloroplasts are derived from undifferentiated precursors, the proplastids. In light-exposed cells, the proplastids differentiate to mature chloroplasts, but in other tissues, such as the roots, they can also give rise to other plastids, for example, the starch-storing amyloplasts. When a proplastid develops into a mature chloroplast, a prominent structural change is the formation of disk-like membrane-surrounded suborganelles, the thylakoids. The thylakoid membranes harbor the light-harvesting pigments: the porphyrin chlorophyll and different carotinoids, which are isoprenoid molecules with 40 carbon atoms. Several thylakoids are typically assembled as stacks, the so-called grana. In the mature stage, the chloroplast lumen, or stroma, is densely filled with these grana. The pigments in the thylakoid membranes form light-harvesting complexes in which the energy of absorbed photons is funneled to central chlorophyll molecules by resonance energy transfer. From these central chlorophylls, excited electrons are transferred to neighboring acceptors and at the end of a chain reaction NADPH is formed in the chloroplast stroma. The reducing power of this molecule can be used in light-independent reactions to generate sugar molecules from CO_2. The ATP required for this synthesis is also generated at the thylakoid membrane. In the thylakoid lumen, protons are set free through the light-dependent lysis of water molecules. The accumulation of protons in the thylakoids generates a steep concentration gradient towards the chloroplast lumen and the flux of protons through a membrane-spanning ATPase drives the formation of ATP on the stroma side. Oxygen, produced as a byproduct of water photolysis, leaves the plant as a gas. This is of vital importance for the life of humans and many other organisms on Earth that need oxygen to gain energy from their food.

Plant Cell Differentiation and Tissues Just like animal cells, most cells in a plant are differentiated to take on a specific task in a tissue. In a flowering plant, different cell types are found in roots, stem, and leaves. Importantly, the stem forms two types of vascular systems to mediate transport from root to leaves and vice versa. The *xylem* system is responsible for the transport of water and inorganic solutes, whereas transport of organic molecules is performed in the *phloem* system. The source for the growth and regeneration of all plant tissues is undifferentiated meristematic cells. Just like animal stem cells, these cells undergo asymmetric cell divisions, producing a new stem cell and a more differentiated cell. Primary *meristem* zones are found at the tip of the roots and at apical shoot tips in specific growth zones. To allow secondary growth of a plant, lateral, secondary meristems surrounding the stem promote the formation of secondary xylem and phloem such that the plant can grow in diameter. In a tree, xylem forms the central wooden part, whereas only the inner part of the bark is phloem.

7.2.3.3 Bacterial Cells

Bacteria were neglected for a long time because they are too small to be identified with the naked eye. Bacterial cells are about 10 times smaller than most animal cells with dimensions between 0.5 and 5 μm. It was in 1676 when the Dutch tradesman Antoni van Leeuwenhoek reported that he had seen little "animalcules" in pond water and in saliva through his home-made one-lens microscope. At that time the relevance of his observation was not realized and it was only in the second half of the nineteenth century when Louis Pasteur and Robert Koch found that bacteria can be causative agents of diseases.

Today it is clear that bacteria colonize almost every place on the planet and that pathogenic germs are only a small minority among the prokaryotes. In contrast to eukaryote cells, the outer shape of bacterial cells is not characterized by wide variability. Most prokaryotic cells fall in the categories of either round cells (cocci), elongated rod-like cells (bacilli), or spiral cells (spirochetes). More complex shapes such as comma forms and cells with long appendages exist, but the degree of morphological diversity by no means compares with the differences between, for example, neurons, retinal sensory cells, and blood cells. The variability of bacteria becomes more obvious when the metabolic properties of these cells are inspected. Bacteria can be classified according to their relation to oxygen. *Aerobic* bacteria require the presence of oxygen, whereas *anaerobes* can only live in the total absence of gaseous oxygen, such as in deep-sea sediments. A third group of bacteria, the facultative anaerobes, prefer to live with oxygen, but can also grow without. Alternatively, bacteria can be classified according to their preferred source of energy. *Photoautotrophic* bacteria make use of the energy from light to fix carbon from carbon dioxide, whereas chemoautotrophs gain their energy by the oxidation of sulfur, nitrogen, or other elements. By contrast, the *heterotrophs* must take up energy-rich molecules from their surroundings. The breakdown of these nutrients can occur either in the presence of oxygen (respiration) or in the absence of oxygen (fermentation). Traditionally, these and other metabolic properties were used to classify bacteria, but DNA sequence comparisons indicate that the criteria do not reflect the underlying phylogenetic relationships.

As outlined above, the most extensive reorganization of bacterial classification was introduced to distinguish between archaebacteria and eubacteria. Regardless of the relatively large phylogenetic distance between the two groups, a common characteristic of both is the lack of a membrane-surrounded nucleus. Prokaryotic chromosomal DNA is usually a single ring structure that is localized in a confined area of the cytosol, the nucleoid. In contrast to eukaryotic chromosomes, the DNA is optimized as a compact, space-saving array of genes that usually lack introns. However, introns in principle could have existed in bacteria and archaebacteria in the past and whether the lack of intron sequences in prokaryotic genes now is just due to a secondary loss during evolution is unclear. Another similarity between the prokaryotes of both domains concerns the translation machinery. Whereas archaea and eubacteria have ribosomes of 70S (according to their Svedberg sedimentation coefficient), eukaryotes harbor 80S ribosomes.

Eubacteria The relations between the major eubacterial groups or *phyla* are too complex to be discussed in brief and a large number of bacterial organisms have not even been grouped yet. Importantly, a major distinction in the eubacterial domain can still be made on the basis a simple staining technique that Hans Christian Gram empirically invented and published in 1884. Using his method, typical *Gram-positive* cells are stained purple, whereas *Gram-negative* bacteria remain unstained or pink. The reason for this difference is a 20–80 nm thick mesh-like cell wall of Gram-positives that retains the applied dye (Figure 7.45). This cell wall is formed of peptidoglycan (murein) – a polymer of sugars and amino acids. Gram-negatives also have a peptidoglycan layer, but at about 7 nm it is just as thick as lipid bilayer. It should be noted that Gram-positive staining behavior is not exclusive to eubacteria, as some archaebacteria with complex-polymer cell walls are also positive for the Gram staining procedure.

The eubacterial Gram-positives form a rather homogeneous phylogenetic group with well-known genera such as the round-shaped *Streptococcus* and *Staphylococcus*, or rod-like members of the genera *Bacillus* or *Clostridium*. Some Gram-positives have a flagellum, a whip-like filament built of the protein flagellin. Flagella are anchored with ring-like structures in the peptidoglycan layer and in the plasma membrane. A proton gradient across the plasma membrane can be used by the bacterium to rotate the flagellum and thereby to drive a forward movement of the entire cell. In some species of Gram-positives the thick peptidoglycan is not the outermost boundary of the cell, but an extensive layer of polysaccharides, the capsule, can be found on top of the cell wall. In pathogenic bacteria such as *Streptococcus pneumoniae* and *Staphylococcus aureus*, the capsule can be an important virulence factor that protects the bacteria from the host immune cells. The water-rich polysaccharide layer also forms a barrier for hydrophobic molecules. In combination with the hydrophobic plasma membrane, this results in protection of the bacterium against potentially harmful small molecules, including antibiotics.

Gram-negatives The Gram-negative eubacteria form several distinct phylogenetic groups. Apart from the thinner peptidoglycan, another important characteristic is

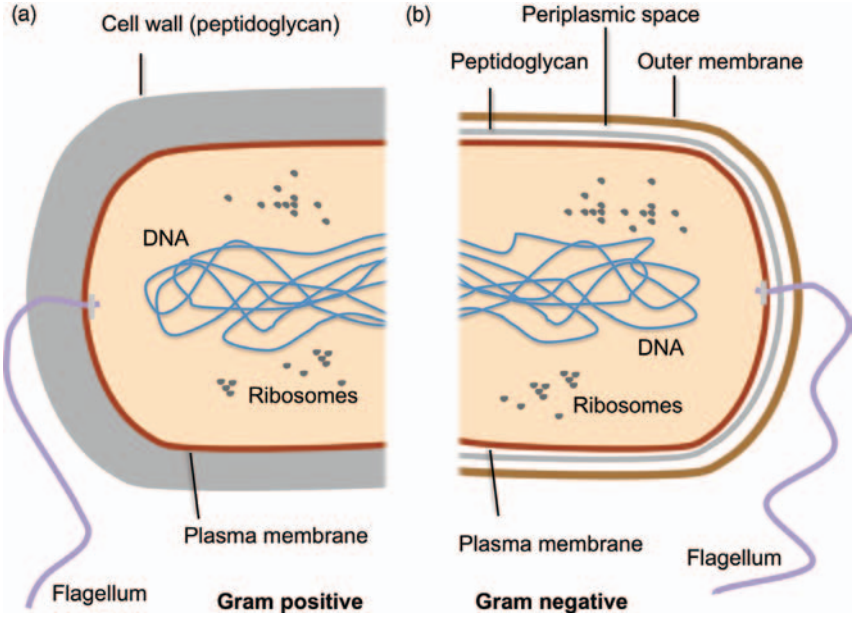

Figure 7.45 Comparison of Gram-positive and Gram-negative bacterial cells. Gram staining is determined by the thickness of the peptidoglycan cell wall. (a) Gram-positive cells have a thick, multilayered peptidoglycan but no outer membrane. (b) In Gram-negative cells, a thin peptidoglycan layer is found between the plasma membrane and outer membrane. The compartment between the two membranes is the periplasmic space. Both bacterial cell types can have rotating flagella for cell motility.

the *outer membrane*. As depicted in Figures 7.45 and 7.46, a second bilayer surrounds the peptidoglycan layer and, due to a constant distance between them, an additional cellular compartment is formed, the *periplasmic space*. Importantly, there is no ATP in the periplasm and no proton gradient is established across the outer membrane. The outer membrane is firmly anchored to the peptidoglycan by lipoproteins. A lysine residue at the C-terminal end of this protein is covalently bound to residues of the peptidoglycan layer, whereas at the opposite side of the lipoprotein cysteine-linked lipids are embedded in the inner leaflet of the outer membrane.

The outer membrane bilayer has a very specific and asymmetric composition. Whereas the inner leaflet resembles a normal, phospholipid-dominated membrane layer, the outer leaflet mainly contains lipopolysaccharides (LPS) or endotoxin. These molecules comprise three parts, the *lipid A* structure in the membrane, a conserved core domain of a polysaccharide chain, and a variable outer part of the polysaccharide. The polysaccharides exposed as the outermost layer serve a similar function to hydrophilic capsules, forming a hydrophilic barrier for hydrophobic molecules. An additional layer of free capsule polysaccharides can also be assembled on top of the LPS. For pathogens, such as *Salmonella typhi* and disease-causing strains of *E. coli*, the variable outer parts of the polysaccharides constitute an important strategy for

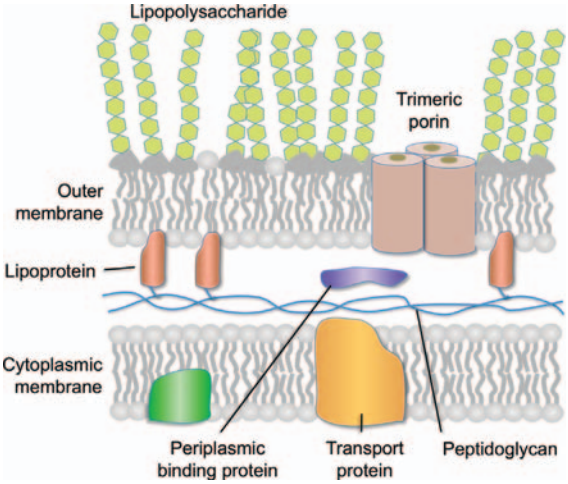

Figure 7.46 Membrane structure of Gram-negative bacteria. In addition to a normal cytoplasmic membrane, Gram-negative eubacteria are enveloped by an outer membrane. This bilayer is highly asymmetric, with lipopolysaccharides (LPS) dominating the outer leaflet. In pathogenic Gram-negatives, variability of the outer sugar chain ends of LPS serve as an immune-escape mechanism. The outer membrane is covalently attached to a thin layer of peptidoglycan via lipoproteins. The periplasmic space between the two membranes is in direct contact with the extracellular medium; small solutes pass freely through porins in the outer membrane.

escaping the host's immune system. Immune cells that could remove the bacteria identify the enemy by its outer layer. Owing to the variability in the sugar patterns of bacterial LPS, the resistance of a host organism can never be perfect. During the long co-evolution of humans and pathogenic germs, the immune system developed a sophisticated early warning system: whenever the hydrophobic membrane anchor of an LPS molecule, the *lipid A* moiety, is recognized in the bloodstream, this is a first indicator of a bacteremia and triggers a generalized activation of the immune system and fever. LPS is first bound by a soluble lipid-binding protein (LBP) and this complex in turn activates membrane-standing receptor proteins of the immune cells. Via internal signaling cascades, this will finally trigger the release of proinflammatory cytokines to stimulate other immune cells. This is beneficial for the infected individual, but an overshooting reaction is dangerous as it can cause septic shock, a major cause of death in intensive care units.

The outer membrane provides a protective layer for the bacterium, but it also necessitates additional transport functions to ensure the uptake of nutrients. The outer membrane is typically rich in *porins*, β-barrel-type transmembrane proteins with a water-filled pore that allow the free diffusional exchange of small hydrophilic molecules between the exterior and the periplasmic space. In addition, more specific porins act as gated pores for the uptake of amino acids, sugars, and iron complexes. For pathogenic bacteria, the extremely low availability of free iron in the body fluids is a growth-limiting factor and several independent iron-uptake receptors can exist in

the outer membrane of a Gram-negative bacterium. The subsequent translocation of cargo from the outer membrane into the cytosol involves soluble periplasmic binding proteins and transporter proteins in the cytoplasmic membrane.

Archaebacteria The domain archaea is divided into four phyla, but further groups might exist. The classification is difficult, as the majority of archaebacterial species cannot be studied in the laboratory. The name archaea was inspired by many archaebacterial species living in ecological niches resembling the geological conditions of the early Earth. This includes hot springs, salt lakes, and even hydrothermal vents in the deep sea. Being adapted to such habitats, many species can live at temperatures around 100 °C. However, not all archaebacteria are extremophiles, for example, methanogenic archaebacteria live as commensals in the guts of humans and cattle. In contrast to eubacteria, no pathogenic archaea are known although humans have always had contact with archaeal species.

The adaptation of many archaea to extreme temperatures makes them an important source of thermostable enzymes for biotechnology. Life at high temperatures not only requires proteins with higher thermal stability, but also the cell membranes must be adapted. Normal phospholipid membranes become more fluid with increasing temperature and at 100 °C the integrity of human or eubacterial membranes would be completely lost. In archaebacterial membranes, the phospholipids carry isoprenoid side chains instead of fatty acids. Methyl side groups in these structures reduce the rotational mobility and make the membranes more compact. In extreme cases, archaebacterial membranes are composed of phospholipids with isoprenoid chains that are fused in the middle, such that a very stable monolayer is built from molecules with hydrophilic headgroups on both sides.

7.3 Cell Signaling

Cells of multicellular organisms are not self-sufficient and isolated – they need to communicate with one another to exchange material and information and to ensure proper coordination of vital functions. Complex molecular languages have evolved to accomplish these tasks. To tackle the problem, collectively termed "cell signaling," we will define a *signal* in terms of cellular communication and discuss according to the medium (carrier, *mediator*) of the signal, how signals travel (*signal transmission*), and how they are converted to signals of other kinds (*signal transduction*).

A cellular signal can be any molecular or cellular state characterized by well-defined parameters. It becomes a meaningful signal when a state or a set of states has some functional interpretation. Signals (or states) therefore can be extremely diverse and can only be interpreted in a context-dependent manner. In Figure 7.47, typical signaling mechanisms are illustrated. In (a) the mediator of the signal may be a molecule that first needs to travel through the plasma membrane; it then enters the nucleus, and finally alters the gene transcription program in a specific manner, here indicated by a change in nucleus color from blue to yellow. This is a typical example of

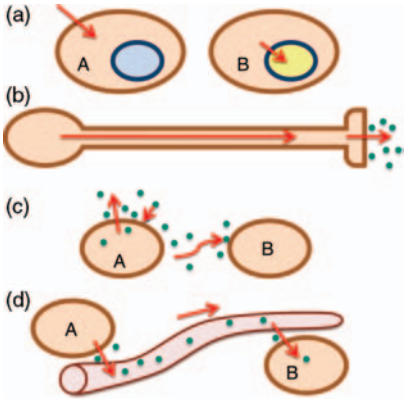

Figure 7.47 Types of cell signaling. (a) Signal transduction mediated by an extracellular signaling molecule that crosses the plasma membrane and subsequently enters the nucleus to affect gene transcription and, hence, renders the cell in an altered state. (b) Transmission of signals along neurons and the subsequent release of synaptic signaling molecules. (c) Release of signaling molecules from a cell can affect itself (A to A: autocrine) or a cell within the diffusion distance (A to B: paracrine). (d) Endocrine signaling: hormones released from cell A are circulated with the blood and affect cell B at some distance away.

hormone signaling in which the active gene transcription pattern is considered a state. In (b) is illustrated a case in which an electrical signal is sent along a neuronal axon. At the nerve ending, the synapse, the electrical signal triggers the release of a chemical messenger – a case of signal transduction. Part (c) illustrates two cases of chemical signal transmission. A chemical mediator released from cell A feeds back to the same cell, a process called autocrine signaling. When the mediator travels to a cell nearby (cell B), that represents a case of paracrine signaling. Classical hormone signaling is shown in (d), where a chemical mediator is released from cell A, distributed via the bloodstream in the body to exert its effect at a far distance at the target cell (B), a process termed endocrine signaling.

In the following section we first address electrical and rapid chemical signaling as it occurs in neurons, muscle, and endocrine cells. Then chemical signaling, in particular involving secondary intracellular mediators, is discussed, followed by some examples of hormone signaling with long-term consequences for the gene transcription profile. "Signaling pathways" provide a brief insight into contemporary thinking of how intracellular signals are processed in a parallel manner.

7.3.1 Electrical and Rapid Chemical Signaling

7.3.1.1 Ions and Membrane Potential

One parameter characterizing the state of a cell is the electrical membrane potential or the voltage between the cytosol and the extracellular space. By convention, the bulk extracellular space is set to zero potential. The membrane potentials of cells in a resting state, the resting membrane potentials, typically are between −40

and −90 mV. Excitable cells such as neurons and skeletal muscle cells can generate action potentials, that is, paradigmatic changes in the membrane potential. These action potentials are sometimes called nerve/muscle impulses or spikes. Also in nonexcitable cells the membrane potential is of vital importance because it largely determines the gradient for the import and export of molecules.

Alteration of the membrane voltage, for example action potentials of a neuron, on the one hand can be considered a signal. On the other hand, changes in membrane potential will change the equilibrium concentrations of ions and other molecules. The signaling aspect is always coupled to a transport of material and vice versa.

The physical reason for that coupling is expressed by the definition of electrochemical gradients. If an ion species is distributed in an unequal manner between the inside and the outside of the cell, and when the membrane is only permeable to that ion species, then the diffusion of ions along their concentration gradient can be exactly compensated by an electrical potential difference, called the Nernst potential or the equilibrium potential:

$$E_{\text{ion}} = \frac{RT}{zF} \ln\left(\frac{[\text{M}]_{\text{out}}}{[\text{M}]_{\text{in}}}\right) \tag{7.1}$$

where R is the gas constant, T the absolute temperature, z the valence of the ion under consideration, F the Faraday constant, and [M] the ion concentrations on either side of the plasma membrane. In Figure 7.48a, typical distribution of the most relevant ions is illustrated for a human skeletal muscle cell with the arrows indicating the direction of the concentration gradients. The extracellular solutions are usually rich in Na^+ and Cl^-, whereas in the cytosol K^+ ions are most abundant.

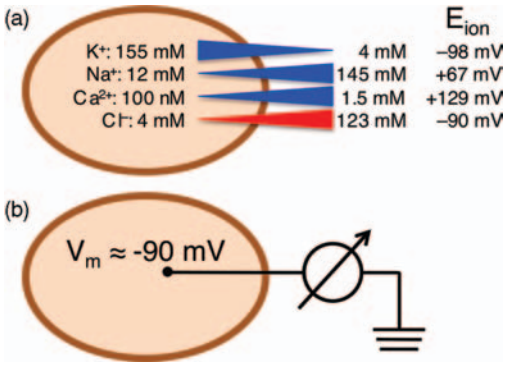

Figure 7.48 Ion distributions and membrane potential. (a) Distributions of the major small ions in a typical human skeletal muscle cell. The arrows indicate the chemical gradients to the extracellular space. Also indicated are the Nernst potentials (E_{ion}) predicted for the given gradients at 37 °C. Note that in some other cell types the intracellular Cl^- concentration can be substantially higher. Bulk electroneutrality is established by a high concentration of intracellular organic anions (note depicted). (b) The membrane potential is defined as the electrical voltage of the cell interior with respect to a ground electrode in the extracellular space. A typical resting membrane potential of a skeletal muscle cell is −90 mV.

In real cells, the ion flux through membranes is never governed by one ion species only. Therefore, to estimate the net ion flux for a given membrane voltage, other contributing ion species, weighted by their permeabilities, must be considered – typically using a formalism referred to as the Goldman–Hodgkin–Katz equation. The membrane voltage at which the net electric current vanishes is called the reversal potential, E_{rev}.

The reversal potential of typical Na^+ conductance is positive ($> +40$ mV), whereas the reversal potentials of K^+ and Cl^- conductances are typically negative (-70 to -90 mV). Hence in excitable cells, resting membrane potentials are largely determined by the gradient of K^+ and Cl^-; the asymmetric distributions of these ions work to hyperpolarize the membrane. Any Na^+ conductance will counteract this process and, hence, it will *depolarize* the membrane.

Free Ca^{2+} ions are a special case because their bulk cytosolic concentration typically is very low, about 100 nM. The Ca^{2+} concentration in the extracellular space is between 1 and 2 mM. Therefore, the equilibrium potential for Ca^{2+} is very high (>100 mV) and Ca^{2+} influx also depolarizes the membrane.

The fluxes of the mentioned ions manifest themselves as a transport of electric charge through ion-selective channel proteins (see below), measurable as electric current. For the example shown in Figure 7.48 and a membrane potential of 0 mV, the flux of Ca^{2+} and Na^+ ions will result in an inward flux of cations, that is, a negative electric current. K^+ ions would leave the cell and Cl^- ions would enter the cell; because of their opposite electrical charges, both would give rise to a positive electric current. Net negative currents promote depolarization whereas net positive currents promote hyperpolarization of the membrane.

7.3.1.2 Action Potentials – Coding of Information

Excitable Cells Excitable cells have the ability to develop temporal changes in the membrane potential in a relatively stereotypical manner, referred to as action potentials. Depending on the cell type, these waveforms of membrane potential can be rather brief (less than 1 ms in neurons), intermediate (a few hundred milliseconds in cardiac muscle cells), or very slow (several seconds in some smooth muscle cells). The maximum amplitude of an action potential largely depends on the type of ion responsible for the depolarization of the membrane. Most commonly in mammals that is Na^+; according to Figure 7.48a, the Nernst potential for Na^+ is about $+50$ mV and, hence, the peak amplitude of an action potential driven by Na^+ influx cannot be greater than that value. Other types of action potentials are driven by Ca^{2+} influx; they are typically slower than those driven by Na^+. The action potential of cardiac cells is triggered by Na^+ current but then sustained by Ca^{2+} influx.

Although the shapes and durations of action potentials can vary substantially, all have in common that they work essentially according to an all-or-none principle, that is, typically an action potential only develops when the membrane potential crosses a certain threshold value. Within the limit of this simplification, the action potential itself does not contain much more information than a single bit, that is, "on" or "off."

The information transmitted by neurons is then provided not by the quality of action potentials but largely by their frequency of occurrence.

This situation is illustrated in Figure 7.49, showing a schematic sensory neuron. Let us suppose that the ending of this neuron resides in a fingertip and extends via its long axon to the spinal cord where it makes contact with another neuron, ultimately sending signals to the brain. The cell body, the soma, of this neuron is not directly in line with the axon. The task of this sensory neuron is to transmit electrical signals reporting on an external stimulus. In this example, this stimulus is a mechanical agitation of the nerve ending, and thus it is a mechano-sensitive neuron. If the nerve ending is stimulated by a brief and weak pressure, the membrane of the nerve ending is depolarized in a graded manner causing a *receptor potential*. This receptor potential then spreads passively along the axon while decreasing in size. It reaches a trigger zone close to the first myelinated section, that is, the electrically insulated area of the axon formed by wrapped-around Schwann cells. If the receptor potential at the trigger

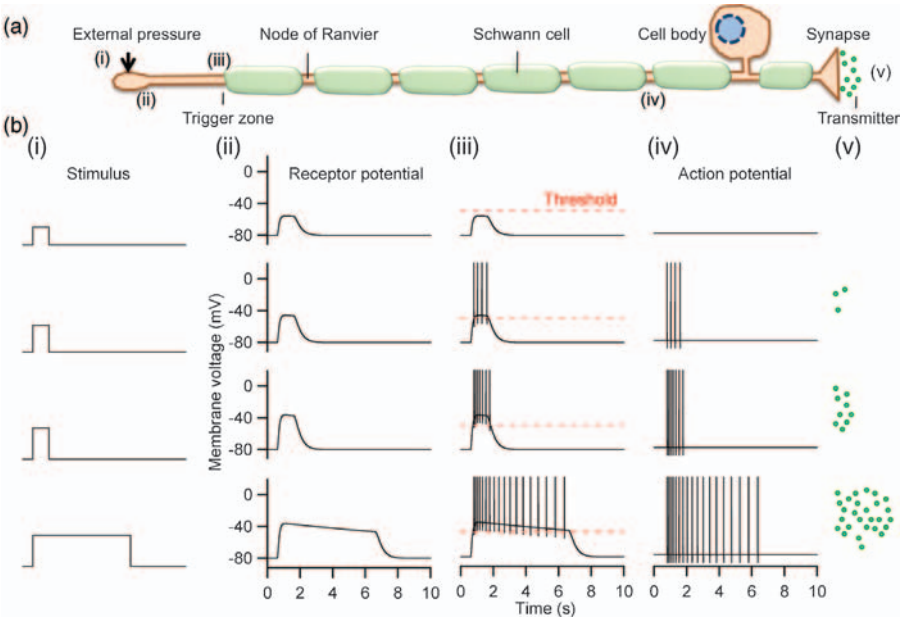

Figure 7.49 Schematic presentation of electrical signal coding by a sensory neuron. (a) Cartoon of a sensory neuron with the nerve ending acting as transduction site, the myelinated axon, the cell body, and a synapse. (b) Four scenarios of how a mechanical agitation of the transduction site generates a receptor potential, how this triggers action potentials, and finally how the transmitted action potentials result in transmitter release at the synapse: (i) mechanical stimulus, (ii) receptor potential at transduction site, (iii) membrane potential at trigger zone, (iv) membrane potential at the synapse, (v) released transmitter molecules. The sensory neuron acts as complex DA/AD converter with integrating and differentiating capacity. Small Roman numerals in (a) indicate where signals shown in (b) were measured (adapted from Kandel *et al.* [10]).

zone exceeds a certain threshold, an action potential is generated – on top of the receptor potential. Generation of an action potential is said to be an active process.

Stronger and more extended receptor potentials generate more and more frequent action potentials. This electrical activity is then transmitted passively through the axonal cable to the next node of Ranvier where it is actively amplified. In this way, the signal travels section by section, that is, from one node of Ranvier to the next. This process of saltatory conduction results in very rapid signaling of up to $100\,\mathrm{m\,s^{-1}}$ in humans, ensuring that the brain receives the sensory information within $\sim$10 ms.

Owing to the combination of passive signal transport under the myelin sheath and active action potential generation at the nodes, the DC component of the initial signal, that is, the receptor potential, is filtered such that only a sequence of action potentials arrives at the synapse (DC filtering). Since at this point the entire information of the mechanical stimulus is encoded as a sequence of action potentials, the signal underwent an analog-to-digital conversion. At the synapse the opposite process takes place. The more action potentials arrive at the synapse, the more Ca^{2+} can enter the cytoplasm from the extracellular space during the brief depolarization episodes. Since Ca^{2+} is constantly cleared from the synapse by active mechanisms (see below), the intracellular Ca^{2+} concentration in the synapse is a measure of a transient integral (or running average) of the incoming action potentials. The local Ca^{2+} concentration in turn determines how much neurotransmitter (Section 7.3.1.4) is released from the synapse to stimulate the receiving cell.

This simple example shows that already a single nerve cell – consider that there are about 100 000 000 000 (10^{11}) neurons in a human brain – can perform complex tasks, e.g., it can transduce an external signal (here mechanical) into an analog electrical signal (receptor potential), reject sub-threshold input, encode the analog signal by a series of action potentials, remove DC values by differentiation, integrate digital electrical input to produce an analog chemical signal (Ca^{2+} concentration) in the synapse, and finally send a chemical message (neurotransmitter) to the next neuron.

Nonexcitable Cells Even in nonexcitable cells, those which do not generate action potentials, the electrical membrane potential serves an important functional role. Here, excursions in membrane potential do not occur with a stereotypical time course but vary with the cellular state and quality and also with the degree of external stimulation. Often one end result of depolarization is, as in excitable cells, an increase in the intracellular Ca^{2+} concentration and, hence, a trigger for the release of chemicals such as liberating hormones in gland cells. In addition, the membrane voltage regulates the transport of ions across the plasma membrane – an important task in all epithelial cells. Therefore, in a simplified manner, we can state that excursions of the electrical membrane voltage are either a "signal" to be transmitted or a "driving force" for the transport of material. While both aspects are always coupled, the signal aspect is more relevant in excitable cells and the transport is the important feature in nonexcitable cells.

Measurement of Electrical Cell Signals Electrical membrane potentials are typically recorded with electrophysiological methods. They require an electrical contact with

the cell interior for measuring the voltage difference between "inside" and "outside" of the cell. Various methods exist to insert fine-tipped electrodes, either electrolyte-filled glass capillaries or metal electrodes, into individual cells and sensitive amplification electronics permits the registration of electrical signals of individual cells. Depending on the mode of operation, one even can record the membrane potential while maintaining a desired current flow (*current clamp*) or record the current through the plasma membrane at a given voltage (*voltage clamp*). Although such methods are extremely powerful and indispensable for physiological research, they are very tedious, expensive, and time consuming. In addition, they are typically only suited for recording signals from individual cells – or just a few cells. Moreover, impalement of cells with electrodes requires direct access and often is not feasible in a noninvasive manner.

Voltage-Sensitive Dyes Therefore, great effort has gone into the development of optical methods for monitoring the electrical cell potential. Several amphiphilic dyes are available that partition into the plasma membrane and undergo conformational changes depending on the membrane voltage. Such changes then result in an alteration the dye's spectral properties. Some voltage-sensitive dye systems rely on fluorescent resonance energy transfer between two dyes (e.g., dibutylbarbituric acid–trimethine oxonol and coumarin). Further, a great variety of such dyes are available according to their speed (i.e., how quickly they respond to changes in the membrane potential), their spectral properties, or the signal intensity. Commonly used fast voltage-sensitive dyes are substituted aminonaphthylethenylpyridinium (ANEP) dyes, such as di-4-ANEPPS and di-8-ANEPPS. ANNINE-6plus is a voltage-sensitive dye with a very fast response time in the nanosecond range and high voltage sensitivity. Recent years have seen development and deployment of genetically encoded voltage-sensitive fluorescent proteins. Although the field may still be in its early stages, the approach holds great promise.

7.3.1.3 Ion Channels, Transporters and Pumps

Electrical signals, as discussed above, are changes in the transmembrane voltage necessarily accompanied by the transport of charges, typically ions, across the membrane. Thus, for generating an electrical signal, cells need to be equipped with very specific mechanisms regulating the transport of ions through the membrane. As discussed in Section 7.2.1.1, an artificial lipid bilayer is a nearly perfect electrical insulator. Only lipophilic or small uncharged molecules can easily traverse the bilayer in a passive manner (Figure 7.50a). Charged molecules, such as the physiologically most relevant ions H^+, Na^+, K^+, Ca^{2+}, and Cl^-, require specialized membrane proteins – *ion channels* (Figure 7.50b) or *carriers* – to cross the membrane according to their respective electrochemical gradients.

However, ions and other molecules are also transported against their electrochemical gradients at the expense of energy from other sources. One distinguishes between *primary active* and *secondary active* transporters. Primary active transporters are so-called *ion pumps*. These proteins transport one or more types of ions against their electrochemical gradients often at the expense of ATP, which is hydrolyzed to

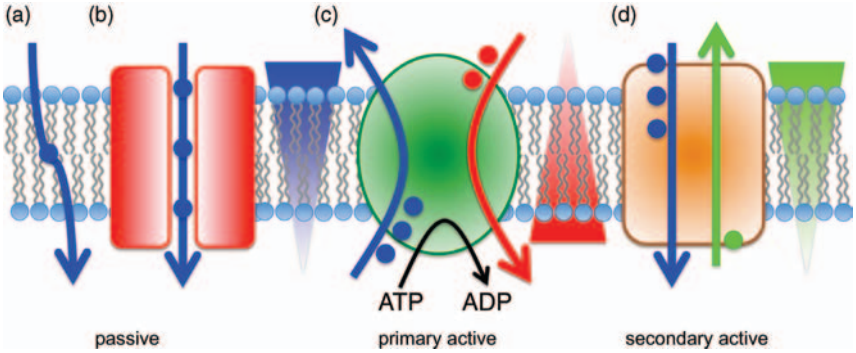

Figure 7.50 Membrane transport – illustration of pathways by which molecules can cross biological membranes. (a) Passive diffusion. (b) Ion channels. (c) Active transporter or pump. At the expense of ATP these proteins pump molecules against their electrochemical gradient into or out of the cell. (d) Secondary active transporters. The example shows an antiport, that is, a transport protein that exchanges two molecule species. Typically the gradient for the one species is used to transport the other species against its gradient. The examples indicate an Na^+/K^+ pump (c) and an Na^+/Ca^{2+} exchanger (d). Large arrow heads indicate electrochemical driving forces.

ADP for each transport cycle (Figure 7.50c). The electrochemical gradients thus established are in turn the energy sources for secondary active transport systems. One of these cases is illustrated in Figure 7.50d, showing a so-called *antiport* or *exchanger*, that is, a transport protein that transports one type of molecule in one direction while transporting another one in the opposite direction. If one molecule follows its electrochemical gradient, say the one indicated by the blue arrow, the other can be transported against its gradient provided that the overall energy balance permits that process. In *symports*, two types of molecules are simultaneously transported in the same direction using the gradient of one type. One example in mammals is the secondary transport of glucose, driven by the primary gradient of Na^+ ions.

Ion Pumps Some ion pumps, in particular those transporting protons (H^+), obtain their energy from absorbed photons or redox processes. In mammals, however, the most common forms are powered by hydrolysis of ATP, and therefore they are often referred to as ATPases. Na^+/K^+-ATPase is a fundamentally important transporter in animals. For every molecule of ATP hydrolyzed, this protein complex physiologically transports three Na^+ ions out of the cell while importing two K^+ ions. Because the net transport of charge is $+1$, this pump is electrogenic. By means of Na^+/K^+-ATPase, the intracellular concentration of Na^+ is kept low (about 5–15 mmol l^{-1}) and the concentration of K^+ high (120–150 mmol l^{-1}). The net export of ions is important for an osmotic balance; a failure of Na^+/K^+-ATPase, such as when an individual suffers an ischemic stroke, ultimately would lead to cell swelling. Whereas the gradient of K^+ is used in most cells to establish or to maintain the resting membrane voltage (see below), the Na^+ gradient serves as an energy source for the secondary transport of other types of molecules.

An example of a secondary transport, coupled to the Na^+ gradient, is the extrusion of Ca^{2+} ions from the cytosol of cardiac muscle cells via the Na^+/Ca^{2+} exchanger (antiport, Figure 7.50d). Along with the action of a plasma membrane Ca^{2+} pump, the Na^+/Ca^{2+} exchanger keeps the intracellular Ca^{2+} concentration at a low level such that the cardiac muscle cells contract at a submaximal force level. Once the Na^+/K^+-ATPase has been blocked by specific inhibitors such as digoxin (or digitalis), a cardiac glycoside extracted from the foxglove plant, the Na^+ gradient is diminished. As a consequence, Ca^{2+} cannot be cleared efficiently from the cytosol via the Na^+/Ca^{2+} exchanger, resulting in stronger cardiac muscle contractions. High doses of digoxin, however, can be fatal.

Ion Channels Ion channel proteins mediate the passive flow of ions across cell and organelle membranes down their respective electrochemical gradients. Typically, ion channels are complexes formed from several protein units. In humans, a very large number of genes, close to 1000, code for ion channel proteins or proteins that take part in directly forming ion channel complexes; hence here we can only concentrate on some of the fundamental features and functional principles.

The most remarkable feature that distinguishes ion channels from other ion transport mechanisms, such as transporters and pumps, is their typically large transport rate, on the order of up to 10^7 ions s^{-1}. For a monovalent ion, say Na^+, this transport is equivalent to an electric current of $10^7\ s^{-1}$ times the elementary charge e_0, that is, $\sim 1.6 \times 10^{-12}$ A (1.6 pA). Although this is an incredibly small current, it can be measured when a very small area of cell membrane containing one channel (sometimes more) is sealed on to the tip of a fine glass capillary tube connected to amplification electronics. The development of this so-called *patch-clamp method* permits the direct real-time observation of how individual proteins, down to a single protein, operate; the discovery earned Erwin Neher and Bert Sakmann the Nobel Prize in Physiology or Medicine in 1991. Although nowadays proteins are typically classified according to the respective genes based on homology and phylogenetic relationships, classification of ion channel proteins according to (a) the ion selectivity, that is, the types of ions that can pass a channel, and (b) the mode of operation, that is, by which means an ion channel is triggered to open or close, is very practical.

Some channel types are very specific for a certain type of ion, some do not distinguish much among the monovalent cations and only exclude anions and multivalent cations, others only discriminate between anions and cations, and yet others are also completely nonselective channels passing both ions and larger molecules.

Because the physiologically most relevant ions are H^+, Na^+, K^+, Ca^{2+}, and Cl^-, it does not come as a surprise that there are ion channels specialized to conduct exactly these ions only – or at least preferentially. For example, K^+ channels are typically very selective, that is, K^+ permeates through them >100 times better than Na^+. Na^+ channels and Ca^{2+} channels are slightly less selective. Cl^- channels do not need to be very selective because Cl^- is virtually the only small anion available. Therefore, under physiological conditions, an open Cl^- channel only conducts Cl^- ions. The effectively high selectivity of K^+ and Cl^- channels is an important

prerequisite for them acting as channels to determine the resting membrane voltage, which is then largely defined by the gradient of K^+ or Cl^- ions. For the generation of an action potential, the membrane needs to be depolarized – a task that is typically accomplished by Na^+ and/or Ca^{2+} channels. Termination of an action potential and its exact shape and repetition frequency depend on many factors such as the spontaneous closure of Na^+ and Ca^{2+} channels once the action potential starts, and the activity of K^+ channels that open only under depolarized conditions – to counteract the influx of Na^+ and/or Ca^{2+}.

What becomes clear in this scenario is that at least those ion channels being involved in the rapid electrical signaling need to be controlled by the membrane voltage itself. Such voltage-gated ion channels form a large superfamily of proteins, most of them being selective for K^+, Na^+, or Ca^{2+}. These channels are typically closed at resting membrane voltage. Moderate depolarizations, induced by receptor potentials (Figure 7.50) or by the activity of so-called pacemaker channels, may increase the probability that voltage-gated Na^+ or Ca^{2+} channels open. In particular Na^+ channels can then open their gates very quickly ($\sim$100 µs) in a very steeply voltage-dependent manner to depolarize the membrane further in an all-or-none fashion. The activity of Na^+ channels is self-limiting because the Na^+ influx diminishes when the potential comes close to the Nernst potential for Na^+. In addition, the channels undergo very rapid inactivation; they spontaneously close within about 1 ms after opening. Moreover, the delayed opening of voltage-gated K^+ channels helps to terminate the action potential by bringing the membrane potential back to the resting voltage. Among others, depending on the Na^+ channels' recovery from inactivation and the closure of K^+ channels, the next action potential can be fired, resulting in a train of electrical activity. This fundamental basic principle of nerve and muscle electrical excitability (illustrated in Figure 7.51) was reported in 1952 by Alan L. Hodgkin and Andrew F. Huxley, who received the Nobel Prize in Physiology or Medicine in 1963 together with John C. Eccles.

As we will see below, alteration in the membrane voltage is not the only stimulus by which ion channels are gated. In the example shown in Figure 7.49, the development of a receptor potential by mechanical agitation of a nerve ending is brought about by the activation of mechano-sensitive ion channels. Likewise, there are ion channel types being activated by chemicals (extracellular or intracellular), heat/cold, the absorption of photons, or intracellular chemical reactions; some channel types do not appear to be "gated" at all – they are open throughout their lifetime and are only regulated by means of protein synthesis and degradation.

7.3.1.4 **Synapses and Chemical Signaling**

For the transmission of electrical signals from one cell to another, they need to make physical contacts. In a simple case, two cells are in close proximity and the adjacent membranes are physically coupled by so-called cell–cell channels or gap junctions (Figure 7.35). Such channel complexes consisting of two six-subunit proteins, one from each cell, form large channels with little ion selectivity and they establish electrical contacts between the cells; a change in membrane potential in one cell is also experienced by the neighboring cell, attenuated by the electrical impedance

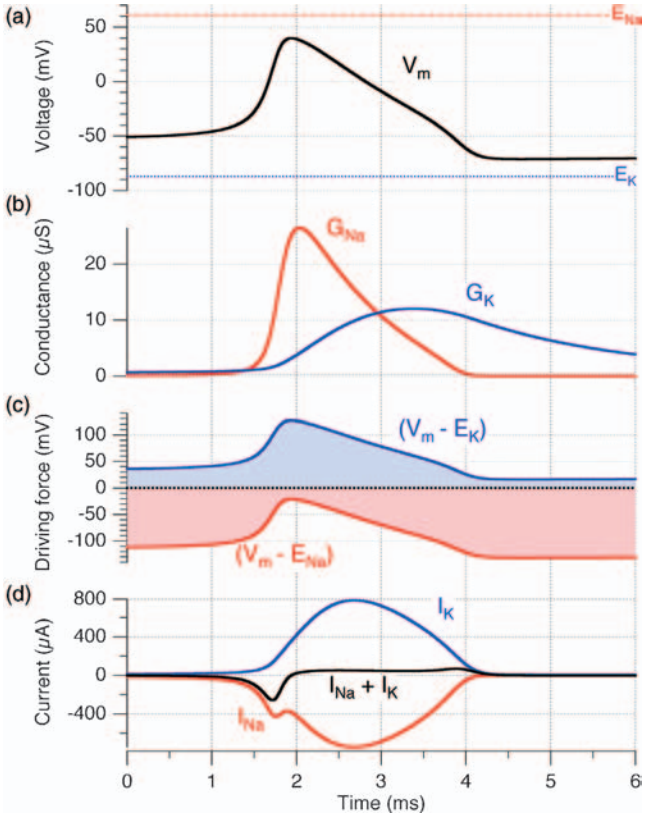

Figure 7.51 Components underlying a neuronal action potential. (a) Time course of an action potential with an indication of the equilibrium potentials for Na^+ and K^+. (b) Membrane conductance during the action potential, separated in those of Na^+ and K^+. (c) Driving forces. (d) Net ion current flowing across the membrane (black) and the underlying Na^+ and K^+ currents flowing in opposite directions. The results depicted schematically represent a large invertebrate nerve action potential.

formed by the resistance of the gap junctions and the membrane capacitance. These *electrical synapses* play an important role when cells in an organ are to be synchronized, as is required, for example, for the concerted contraction of muscle cells in the heart. If cells in a tissue are electrically coupled in such a manner, they are said to form a *syncytium*.

The great advantage of an electrical synapse is its coupling speed; however, it is largely bidirectional and does not provide much specificity. More complex rapid cell–cell communication therefore happens via *chemical synapses*, which means a "sending" presynaptic cell liberates a chemical, termed a transmitter, which then diffuses to the "receiving" postsynaptic cell to elicit a response. The speed of this signaling largely depends on the diffusion of the transmitter from the sending to the receiving cell and, therefore, the synaptic cleft usually is very narrow (20–100 nm).

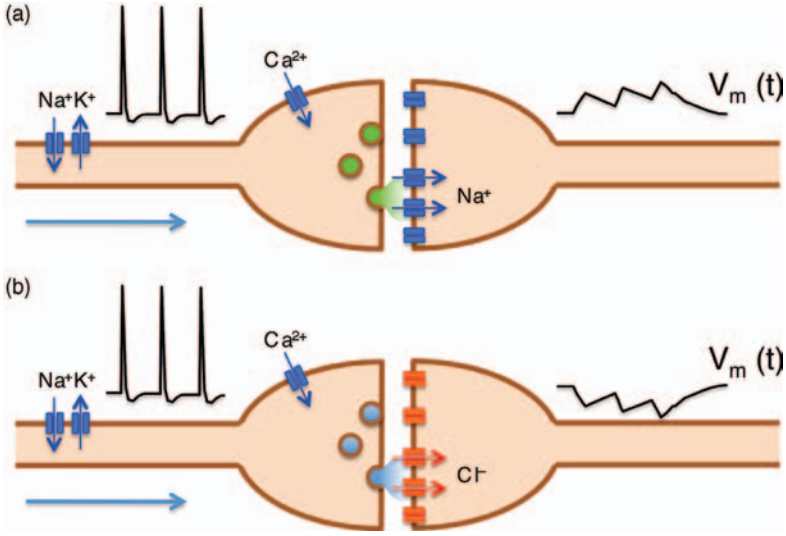

Figure 7.52 Chemical signaling via synapses. Synaptic cell contacts formed by a presynaptic (left) and a postsynaptic (right) terminal separated by the synaptic cleft. Incoming action potentials generated by Na^+ and K^+ channels depolarize the synapse to open Ca^{2+} channels. The Ca^{2+} influx triggers the release of neurotransmitter, stored in vesicles. Upon diffusion to the postsynaptic membrane, the neurotransmitter opens ligand-gated ion channels and changes the postsynaptic potential, $V_m(t)$. (a) Excitatory synaptic contact: an excitatory neurotransmitter, for example, acetylcholine or glutamate, is released. This opens cation-selective ligand-gated ion channels in the postsynaptic membrane to generate an EPSP (excitatory postsynaptic potential). (b) Inhibitory synaptic contact: an inhibitory neurotransmitter, for example, glycine, activates Cl^--selective ion channels to generate an IPSP (inhibitory postsynaptic potential).

The size and shape of synapses can vary substantially depending on the cell type, but usually they are confined cellular areas forming so-called nerve terminals (Figure 7.52). Since these terminals (both presynaptic and postsynaptic) are small and topologically confined, they are specialized sites with local properties regarding membrane potential and intracellular milieu (e.g., Ca^{2+} concentration). Local membrane potentials of synaptic terminals in presynaptic and postsynaptic cells are referred to as pre- and postsynaptic potentials, respectively.

Action potentials, mostly created by the activity of voltage-gated Na^+ and K^+ channels, arrive at the presynaptic terminal where they activate voltage-gated Ca^{2+} channels. The resulting increase in the local intracellular Ca^{2+} concentration is the trigger for a reservoir of transmitter-filled vesicles to fuse with the synaptic membrane (see Section 7.2.1.9), and to liberate their content into the synaptic cleft. This process is also very rapid because the vesicles are already in place, closely attached to sites of fusion, the active zone.

At the postsynaptic membrane, the transmitter molecules bind to their specific receptors, many of which are also ion channels. They subsequently open and permit an ion flow that contributes to an alteration of the postsynaptic potential.

The specificity of synaptic transmission resides in both the type of transmitter released and the type of receiving receptor, which together determine whether a synaptic contact is *excitatory* or *inhibitory*. As illustrated in Figure 7.52a, the transmitter of an excitatory synapse activates ion channels in the postsynaptic cell that depolarize the membrane, that is, they excite the cell and potentially generate a new action potential. In mammals, typical excitatory transmitters are acetylcholine and glutamate; they open postsynaptic ligand-gated cation channels, in the first place resulting in a postsynaptic influx of Na^+ and (in some cases) Ca^{2+} and causing an excitatory postsynaptic potential (EPSP). A single action potential arriving at the presynaptic terminal may not be sufficient to elicit a postsynaptic action potential. Only when the frequency of action potentials is high enough will many EPSPs integrate in the postsynaptic cell finally to trigger firing and propagation of an action potential.

Figure 7.52b shows the scenario for an inhibitory synapse. Here the typical transmitters are glycine and γ-aminobutyric acid (GABA); they activate Cl^--permeable ligand-gated channels in the postsynaptic membrane, thus typically (but not necessarily) causing a hyperpolarization [inhibitory postsynaptic potential (IPSP)] and damping electrical activity.

Some neurons utilize more than one transmitter type, which often operate on different time scales (e.g., milliseconds versus seconds). Typically, however, neurons are classified according to their principal neurotransmitter type that they release. For example, glutaminergic neurons release glutamate and GABAergic neurons release GABA. The receiving postsynaptic cell receives inputs from a variety of presynaptic neurons and possesses the appropriate receptors to detect the neurotransmitters. As a consequence, the electrical activity of a neuron in the brain is determined by the temporal and local superposition of many excitatory and inhibitory inputs.

Ligand-Gated Ion Channels The examples above showed that there are several types of ion channels activated by extracellular ligands or neurotransmitters. These channels typically are formed from up to five protein subunits and are classified according to their ion selectivity (cation or anion selective) or their specific activating ligand. Typical examples of ligand-gated cation channels are those activated by acetylcholine (nicotinic acetylcholine receptor channel) and glutamate. Whereas acetylcholine is a transmitter often mediating signal transmission in peripheral cells, for example, at the interface between neurons and muscle cells (neuromuscular junction), glutamate is a transmitter primarily found in the CNS. Both acetylcholine receptor channels and glutamate receptor channels exist as various isoforms and some are able to conduct Ca^{2+} in addition to monovalent cations. Typical examples of Cl^--permeable ligand-gated ion channels are those activated by the amino acid glycine and by GABA. Both glycine receptor channels and $GABA_A$ receptor channels play an important role in inhibitory signal transduction in the CNS, including the brain stem and spinal cord.

Learning and Memory A human brain consists of about 10^{11} neurons in addition to about the same number of glial cells that are increasingly recognized to participate in

information processing. Each of the neurons has on average 7000 synaptic connections to other neurons. Although this impressive number of about 10^{15} synapses per brain decays in the adult by about one order of magnitude, the remaining 10^{14} synapses form the basis of the gigantic cognitive power of a human brain. Given that a synapse can either be excitatory or inhibitory, a tremendously complex meshwork of electrical wiring can be achieved. However, a chemical synapse is by no means a static element like a connection in an electronic circuit. Synapses exhibit a high degree of plasticity, that is, their transmission efficiency is subject to activity-dependent regulation. The *use* of a synapse, that is, the frequency of action potentials arriving, will change the synaptic strength on various time scales. Some of the long-term changes in synaptic strength studied by neurobiologists include long-term potentiation (LTP) and long-term depression (LTD). The strengthening or weakening of synaptic contacts is a cellular basis for such complex phenomena as learning and memory. For more insight, the interested reader may refer to textbooks on neurobiology.

7.3.2
Ligands, Receptors and Second Messengers

In the previous sections we have already made use of the terms *ligand* and *receptor*. Here we will consider how to distinguish various types of ligands and receptors and how signals, encoded by ligands, are processed.

In Figure 7.53, several terms used in this context are illustrated. A ligand is a diffusible molecule (chemical signaling) that binds to a specific receiving molecular complex – a receptor. Ligands can have various names depending on their specification; we have already discussed hormones and transmitters (e.g., neurotransmitters). Since ligands usually mediate a specific response, they are often referred to as mediators. If mediators are not responsible for a major cellular response but only alter this response in a graded manner, they may be called modulators. When "activating" a receptor they are referred to as *agonists*, but if they inhibit a receptor often the name *antagonist* is used.

The chemical structures of ligands range from large peptide structures (e.g., the hormone insulin and the immune system signal interferon), amino acids (e.g., glycine) and low molecular weight compounds such as acetylcholine, ATP and steroids, to ions such as H^+, Ca^{2+} and Zn^{2+}. The size and physicochemical properties of a ligand largely determine how quickly and where it reaches its target. Large or permanently charged ligands will not be able to enter a cell and therefore can only bind to receptors situated on the plasma membrane. Others, such as steroid hormones, are readily membrane permeable and can bind to receptors in the cytosol or even directly in organelles such as the nucleus.

Receptors typically are proteins with binding sites for their specific ligands. Depending on the receptor type, they transmit the received signal in various ways. The processes involved in the reception of a signal by a receptor and the generation of subsequent signals are collectively referred to as *signal transduction*, to be detailed in the following sections. As illustrated in Figure 7.53, receptors delimited to the

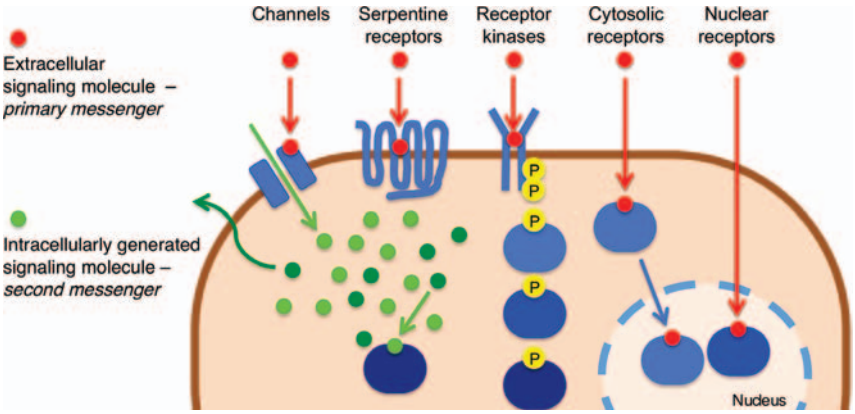

Figure 7.53 Signal transduction. Schematic illustration of how diffusible extracellular signaling molecules (red), so-called primary messengers, are received by various membrane-delimited and intracellular receptors (blue). Recognition of the initial signal either directly initiates a cellular response or it is only the first step in a signaling cascade. Small intracellular signaling molecules, second messengers, play an important role; most of them bind to intracellular constituents and thus relay the "message," others can even leave the cell to initiate retrograde signaling. Many receptors can activate further signaling proteins by direct association or by post-translational modification such as protein phosphorylation.

plasma membrane can largely be grouped into those acting as ion channels, receptors that in effect produce or release another ligand, a so-called second messenger, receptors that "activate" other cellular proteins, and receptors that acquire enzymatic activity when stimulated. This list is by no means complete or exclusive; some receptors have multiple functions and depend strongly on the cellular state itself. Only some ligands directly produce a cellular response by binding to membrane receptors. In many cases the initial binding to a receptor – either in the plasma membrane or somewhere intracellularly – is only the first step in a so-called *signaling cascade* (see Section 7.3.4), often involving intracellular second messengers, formation and breakage of protein complexes, and post-translational protein modifications.

7.3.2.1 **Second Messengers**

A second messenger is a chemical substance whose concentration is altered in response to a primary signal mediated by a primary messenger (ligand). It can be synthesized by enzymes or released by ion channels. Removal of second messengers from the cytosol involves chemical breakdown by specific reactions or active export. The principal purpose of second messengers is to relay extracellular signals, which cannot cross the cell membrane, to intracellular sites. Here they trigger signal cascades and finally result in a cellular response to the primary stimulus.

In addition to accomplishing the mere signal transduction, second messenger systems fulfill more complex tasks (Figure 7.54). In most cases they strongly amplify the chemical signal. For example, a single neurotransmitter molecule bound to a plasma membrane ion channel may open that channel to permit the influx of many

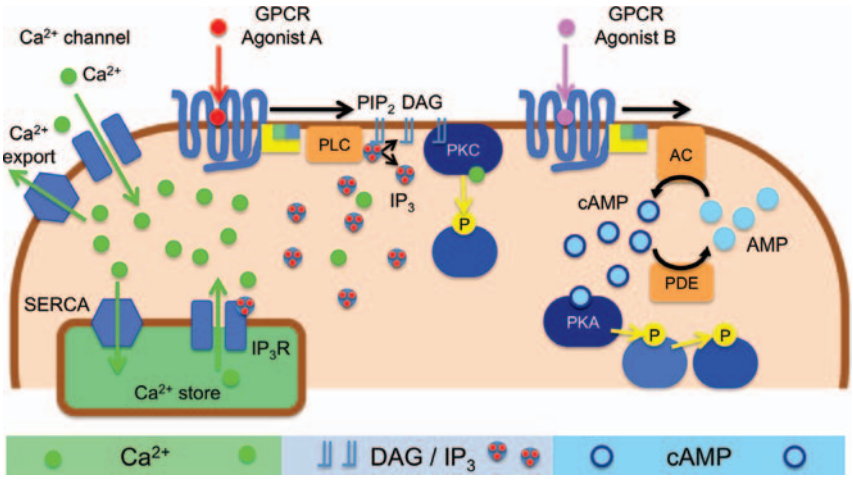

Figure 7.54 Second messenger systems. Schematic presentation of three selected second messenger systems coexisting in a cell. *Left*, Ca^{2+} system. Ca^{2+} ions enter the cytosol via Ca^{2+} channels in the plasma membrane or in intracellular Ca^{2+} stores; this influx is antagonized by Ca^{2+} export systems such as SERCA. *Center*, inositol–lipid system. Activation of a G protein-coupled receptor (GPCR) by an extracellular agonist liberates the heterotrimeric G protein that subsequently activates phospholipase C (PLC). PLC cleaves the membrane lipid PIP_2 into the second messengers DAG (diacylglycerol) and IP_3 (inositol triphosphate). DAG is an activator of the Ca^{2+}-dependent kinase PKC, whereas IP_3 liberates Ca^{2+} from internal stores by binding to IP_3-receptor channels. *Right*, cAMP system. Agonist binding to a GPCR activates adenylate cyclase (AC) mediated by a G protein. AC produces cAMP from AMP and is antagonized by phosphodiesterases (PDE). cAMP is an activator of protein kinase A (PKA), which then phosphorylates target proteins at specific serine and/or threonine residues.

millions of Ca^{2+} ions, which act as second messenger molecules. Various different types of extracellular stimuli may affect the same second messenger and, hence, may induce signal integration. Another important feature is that the production and breakdown of second messengers can be local such that a cell is capable of simultaneously performing multiple spatially separated signaling tasks.

There are three basic types of secondary messenger molecules. Hydrophilic messengers are water soluble, relatively free to diffuse in the cytosol or stored in organelles (Ca^{2+}, cAMP, cGMP, IP_3). Hydrophobic messengers typically are derived from membrane lipids; they are poorly soluble in water and therefore remain preferentially in the lipid phase where they can reach and regulate effector proteins in or at the membrane [diacylglycerol (DAG), phosphatidylinositols, arachidonic acid]. Finally, there are gaseous second messenger molecules that readily diffuse through the cytosol and across membranes so as to reach neighboring cells [nitric oxide (NO), carbon monoxide (CO), hydrogen sulfide (H_2S)].

In the following we will briefly discuss the most important second messengers, their generation and some of their secondary effectors.

Calcium Free Ca^{2+} ions are a special case of second messengers because they are not synthesized and degraded by enzymatic activity but enter the cytosol via Ca^{2+}-permeable channels in the plasma membrane and they are released from Ca^{2+}-loaded intracellular stores such as the ER (or SR in muscle cells) and the mitochondria. Ca^{2+} is by far the most important and versatile intracellular messenger as numerous molecular processes taking place in the cytosol depend on the intracellular free Ca^{2+} concentration, $[Ca^{2+}]_i$. In resting cells $[Ca^{2+}]_i$ is very low (about 100 nM), whereas the Ca^{2+} concentration is typically high (>1 mM) in the extracellular space and in the Ca^{2+} stores.

Ca^{2+} influx into the cytosol mainly is mediated by specific Ca^{2+}-permeable ion channels. In the plasma membrane these are typically voltage-gated Ca^{2+} channels (CaV), which open when the membrane is depolarized such as when an action potential reaches the respective site. In addition, there are several other types of ion channels that are selective to cations and, hence, upon activation contribute to an increase in $[Ca^{2+}]_i$. To name a few, there are transient receptor potential (TRP) channels and specific forms of ligand-gated channels responding to the transmitters glutamate [NMDA (*N*-methyl D-aspartate) receptors] or acetylcholine (nicotinic acetylcholine receptors). Intracellular Ca^{2+} stores release their Ca^{2+} into the cytosol by means of ligand-gated Ca^{2+} channels such as ryanodine receptors (RyRs) and IP_3 receptors. Some RyRs are specialized to permit very rapid Ca^{2+} release from the SR in skeletal muscle cells by directly coupling to select CaVs in the plasma membrane. In contrast, release of Ca^{2+} via IP_3 receptors is typically a slower process. In addition, there are so-called store-operated Ca^{2+} channels in the plasma membrane that permit Ca^{2+} influx from the extracellular space once the intracellular stores send an "empty" signal.

An increase in $[Ca^{2+}]_i$ typically is a transient event as Ca^{2+} is constantly removed from the cytosol. In the plasma membrane there are two important Ca^{2+} export systems: the plasma membrane Ca^{2+}-ATPase and Na^+/Ca^{2+} exchangers (see Section 7.3.1.3). The major system for refilling the intracellular Ca^{2+} stores is the ion pump SERCA (sarcoplasmic/endoplasmic reticulum Ca^{2+}-ATPase). SERCA itself is under the control of phospholamban, a protein whose activity is regulated by phosphorylation by protein kinase A (PKA).

Because very many cellular constituents bind Ca^{2+}, there is a great difference between the free and total (bound plus free) concentrations of intracellular Ca^{2+}. For example, inside the SR the protein calsequestrin strongly binds Ca^{2+} and thereby reduces the concentration of free Ca^{2+}. The gradient of free Ca^{2+} against which SERCA must pump is thus diminished, although the total Ca^{2+} concentration inside the SR can be 10 000 times higher than in the cytosol. Another consequence of the presence of cytoplasmic mobile and stationary Ca^{2+}-binding molecules (Ca^{2+} buffers) is that the distribution of free Ca^{2+} inside the cytosol is not determined solely by the diffusion of Ca^{2+} in solution and that $[Ca^{2+}]_i$ is by no means homogenous inside a cell. At the sites of Ca^{2+} influx, local $[Ca^{2+}]_i$ can be much higher (>>1 μM) than $[Ca^{2+}]_i$ averaged over the entire cytosol, allowing for local and temporally limited Ca^{2+} signaling inside a cell. Typical phenomena observed in this

context are Ca^{2+} sparks (local transients in $[Ca^{2+}]_i$) and Ca^{2+} waves (spatial and temporal oscillations in $[Ca^{2+}]_i$).

We have briefly mentioned prominent examples of Ca^{2+}-triggered processes such as muscle contraction and the release of transmitters (exocytosis). However, many other cellular functions, in one way or the other, depend on Ca^{2+} ions and therefore the effector proteins of the second messenger Ca^{2+} are extremely diverse. Some proteins possess specific Ca^{2+}-binding moieties such that Ca^{2+} binding exerts a conformational change, leading to a change in function of the respective protein. For example, Ca^{2+} entering the cell during an action potential may bind directly to the cytosolic domain of a Ca^{2+}- and voltage-activated K^+ channel. This channel then opens and the resulting efflux of K^+ hyperpolarizes the cell. In many cases, however, the effector protein itself does not have an intrinsic capacity to bind Ca^{2+} directly. Instead, specific Ca^{2+}-binding proteins are utilized to "sense" the intracellular Ca^{2+} concentration and relay that information to the effector protein. Among the very many Ca^{2+}-binding proteins, the most ubiquitous is calmodulin (CaM); it harbors four so-called EF-hand structures and undergoes a substantial conformational change when Ca^{2+} is bound to them. When associated with an effector protein, CaM thus transmits the "Ca^{2+} signal" to the target protein. Owing to the different Ca^{2+} sensitivities of the EF-hand motifs, such signaling can occur at low and high $[Ca^{2+}]_i$ levels. Other Ca^{2+} signaling steps involve chemical reactions such as protein phosphorylation. Specific Ca^{2+}-dependent kinases (e.g., CDPK) or Ca^{2+}/calmodulin-dependent kinases (CaMKs) phosphorylate the effector protein in response to an increase in $[Ca^{2+}]_i$. Ultimately, Ca^{2+}-dependent molecular processes may affect gene transcription, thus exerting long-term changes to the cell.

Cyclic Nucleotides *Cyclic adenosine monophosphate* (cAMP) is a second messenger controlled by enzymatic reactions for its generation and removal. The precursor of cAMP is ATP (see Section 7.1.6), which is dephosphorylated and cyclized to cAMP by the enzyme adenylate cyclase [synonymous with adenylyl cyclase (AC)]. In turn, AC itself is activated by receptor stimulation and stimulatory G proteins (see below). The lifespan of cAMP is limited by phosphodiesterases (PDEs), a large class of enzymes that hydrolyze cAMP to yield AMP.

The primary effector proteins of the second messenger cAMP are cAMP-dependent protein kinases (PKA)s. Once activated, the enzymes phosphorylate a multitude of target proteins such as phospholamban, as mentioned above. Another prominent example of a PKA-mediated process is the liberation of glucose in muscle cells upon stimulation by the stress hormone adrenaline (synonymous with epinephrine). As for Ca^{2+}-dependent kinases, the activation of PKAs can lead to long-lasting alterations of cellular states by modulating gene transcription.

Cyclic guanosine monophosphate (cGMP) is chemically very similar to cAMP. It is produced from GTP by the action of guanylate cyclase [synonymous with guanylyl cyclase (GC)]. GCs are either membrane receptors, activated by ligands, or soluble in the cytosol (sGC), activated by nitric oxide. As for cAMP, breakdown of cGMP is mediated by PDEs.

In addition to the effects mediated by kinases, both cAMP and cGMP also have direct impacts on proteins such as cyclic nucleotide-gated ion channels (cNGCs). These channels play an important role in the sensing of odorants (cAMP) and light (cGMP) (see Section 7.3.2.2).

The balance between the concentrations of free AMP versus cAMP and that between GMP versus cGMP, respectively, are tightly controlled by the activity of PDE. The action of caffeine, for example, is partly mediated by an inhibition of PDE, thus slowing the decay of cAMP. On the other hand, the hormone insulin activates PDE, thus lowering the concentration of cAMP and limiting the liberation of glucose. One of the major effects of cGMP is relaxation of smooth muscle cells. Since penile erection relies on the relaxation of vascular smooth muscles in the *corpus cavernosum*, inhibition of the cGMP-specific PDE-5 by sildenafil is a way to treat erectile dysfunction by maintaining an elevated cGMP concentration.

Lipid-Derived Second Messengers Two second messengers belonging to the phosphoinositol system are released upon enzymatic cleavage of a membrane lipid molecule. When stimulated by a receptor (see below), the membrane-delimited enzyme PLC cleaves PIP_2 (see Section 7.1.4.3), to yield DAG and IP_3.

DAG largely remains in the membrane compartment and is a potent activator of the Ca^{2+}-dependent protein kinase C (PKC), thus initiating a cascade of phosphorylation events. IP_3 is a water-soluble molecule that diffuses inside the cytosol to activate IP_3 receptor channels to liberate Ca^{2+} from intracellular stores. This is an example where Ca^{2+} could be considered a third messenger, because it is "activated" by the second messenger IP_3. As we shall see below, the concept of third- and higher order messengers has limited usefulness because all second messenger systems are highly coupled and interdependent.

By the action of the enzyme phospholipase A_2 (PLA_2), the polyunsaturated fatty acid arachidonic acid is cleaved from membrane phospholipids. Alternatively, it is derived from DAG. It acts as a lipid second messenger and stimulates secretion. In addition, it is a precursor of a large family of tissue hormones – the prostaglandins. Because arachidonic acid is lipid soluble, it can pass the plasma membrane and can affect neighboring cells.

Gaseous Messengers – NO and CO Gaseous messengers such as nitric oxide (NO) and carbon monoxide (CO) can diffuse freely beyond cell borders and therefore are both *second* messengers within the parent cell and *primary* messengers for the neighboring cells. NO is generated from the amino acid arginine by specific enzymes, the nitric oxide synthases (NOSs). As mentioned above, a prime target of NO is the soluble guanylate cyclase containing heme as the prosthetic group. By means of cGMP production, NO therefore plays an important role as a vasodilator by relaxing vascular smooth muscle cells. In specialized glutamatergic synapses, NO acts as so-called retrograde messenger; produced by activation of the postsynaptic cell (via increased Ca^{2+} levels), NO diffuses back to the presynaptic cell to close ion channels. This feedback system is an important element in the priming of synaptic contacts and it is probably one key component in learning and memory.

CO is increasingly recognized as a second messenger. It is largely generated during the breakdown of the blood pigment heme by heme oxygenase (HMOX) and contributes to the relaxation of smooth muscle cells.

Photonic Detection and Manipulation of Second Messengers Owing to the central role of second messengers in controlling cellular functions, there is tremendous interest in measuring their concentrations in living cells at high temporal and spatial resolution and to manipulate their concentrations in the cytosol. Biophotonic experimental approaches are well suited for these tasks. A variety of Ca^{2+}-selective dyes are available to measure $[Ca^{2+}]_i$. The selection depends on the range of Ca^{2+} concentrations to be observed, the speed of response, and the instrumentational availability of excitation and emission wavelengths. One dye frequently used is FURA-2; excited with about 340 and 380 nm light, it can provide relatively accurate measurements of $[Ca^{2+}]_i$ in a ratiometric manner. Likewise, there are systems for the visualization of cAMP and cGMP, based on either engineered proteins or low molecular weight compounds. Quantitative measurement of other second messengers – remember that we have addressed a few prominent examples only – is still an active field of research.

So-called caged compounds are used to liberate second messengers inside a cell upon stimulation by light. Typically these are light-sensitive substances that bind a messenger and release it once the compound is photochemically cleaved or has undergone a photoinduced conformational change. For the liberation of Ca^{2+} with near-UV light, substances such as DM-nitrophen [1-(2-nitro-4,5-dimethoxyphenyl)-1,2-diaminoethane-*N*,*N*,*N*′,*N*′-tetraacetic acid] and NP-EGTA (nitrophenyl ethylene glycol tetraacetic acid) are often used.

7.3.2.2 G Protein-Coupled Receptors

The physiological generation of most second messengers typically requires the activation of a membrane receptor by an extracellular stimulus. The information about receptor activation must be relayed to other downstream components in the cytosol through a second messenger. The coupling interface between the numerous types of transmitters or agonists that carry a chemical signal to the cell on the one hand and the second messenger systems and effector proteins on the other is a double-layered system of (very many) receptor proteins and (much fewer) heterotrimeric GTP-binding proteins, so-called G proteins (Figure 7.55a).

The receptor proteins that belong to that system are referred to as G protein-coupled receptors (GPCRs). They all have in common a topology with seven transmembrane helical elements (therefore they are also called serpentine receptors or 7-helix receptors) with a central binding site for a specific agonist. The agonists vary in size and structure; they include light-sensitive compounds, odor molecules, pheromones, hormones, and neutrotransmitters. GPCRs are by far the largest family of membrane receptor proteins (>1000 in humans). Typically they are classified according to their functional properties and agonists. In the neurobiological literature, GPCRs are often called *metabotropic* receptors in order to distinguish them from *ionotropic* receptors, that is, ligand-gated ion channels. For

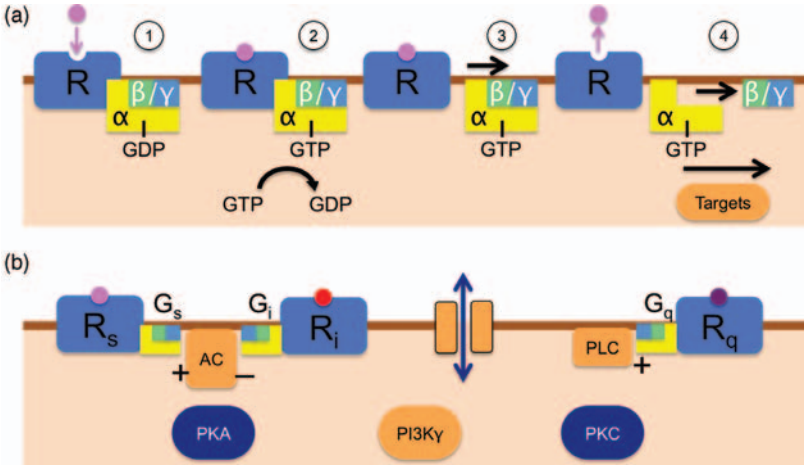

Figure 7.55 G protein-coupled receptors. (a) Sequence of G protein activation. (1) The receptor (R) is associated with the GDP-bound G protein complex consisting of α and β/γ subunits. (2) Upon agonist binding to the receptor, GTP is exchanged for GDP at the α subunit. (3) The G protein complex dissociates from the receptor. (4) The GTP-bound α subunit dissociates from β/γ. Both are now free to interact with downstream targets. (b) GPCRs selectively couple to different types of G proteins: stimulatory G_s and inhibitory G_i proteins regulating the activity of adenylate cyclase (AC), and also G_q proteins leading to phospholipase C (PLC) activation. While the generated second messengers subsequently regulate kinases (e.g., PKA, PKC) and ion channels, G proteins also directly interact with targets such as the protein and lipid kinase (PI3K γ) and ion channels.

example, whereas the nicotinic acetylcholine receptor (nAChR) is an ion channel, the metabotropic acetylcholine receptor (mAChR) is a GPCR. Likewise, there are metabotropic glutamate and serotonin receptors.

Activation of a GPCR is terminated by dissociation of the agonist. In addition, the sustained presence of an agonist in many cases results in receptor desensitization; the receptor progressively loses its sensitivity towards the respective agonist. This feedback process is an important mechanism by which the sensitivity of a receptor is adjusted, effectively increasing the dynamic range of detection.

GPCRs play key roles in modern medicine; about 30% of all prescribed drugs act on GPCRs and some are prescribed fairly frequently, such as β-blockers, neuroleptics, antihistamines, opiates, and sympathomimetics. For example, β-blockers are used for multiple forms of cardiovascular disease, including high blood pressure.

Heterotrimeric G Proteins The activity of GPCRs is signaled to the cell interior by means of heterotrimeric G proteins. These are membrane-associated proteins consisting of three distinct subunits, α, β, and γ. In an inactive form, GDP is bound to the α subunit in the complex. The GPCR, in close contact with the G protein, undergoes a conformation change upon ligand binding and thereby acquires a function as a guanine nucleotide exchange factor (GEF). This activity facilitates the exchange of GDP for a GTP molecule at the G protein and the GTP-bound G protein

is released from the GPCR. The GTP-bound α subunit then separates from the β/γ complex (Figure 7.55a). Depending on the exact situation, an activated G protein, the liberated α subunit, or the β/γ subunits can then interact with target proteins. With time, the α subunit hydrolyzes the bound GTP to GDP and reassociates with the β/γ complex, terminating the signal.

Typically, G proteins are classified according to the functional impact of their activated α subunit. Stimulatory G_s proteins activate whereas inhibitory G_i proteins inactivate the cAMP pathway. G proteins of the G_q subfamily activate the phosphoinositol messenger system (Figure 7.55b). In addition, both G-α and G-β/γ can directly affect other proteins such as ion channels. For example, activation of a G protein cascade may hyperpolarize a cell by opening of K^+ channels by the G-α subunit. On the other hand, the β/γ complex can increase the open probability of Ca^{2+} channels, hence leading to cell depolarization. Some ion channels are controlled by GPCRs in a twofold manner: rapid activation by direct G protein binding is followed by a delayed modulation via a second messenger.

For studying G protein-mediated cell signaling, two molecules are of particular interest. The GTP analog GTP-γ-S is not easily hydrolyzed by the G-α subunit under physiological conditions. When applied to a cell it binds to G proteins in an irreversible manner, causing sustained G protein activation. GDP-β-S is a GDP analog; when bound to a G protein it cannot be exchanged for GTP and, hence, causes G protein inhibition. Both analogs exist in labeled forms (radioactive or fluorescent) and provide experimental insight into the complex processes underlying G protein signaling.

Photoreception As discussed in Section 7.1.5.1, rhodopsins (see Figure 7.18), the photoreceptor proteins in the rods of the eye retina, are a special group of GPCRs. Here the "agonist" is the prebound retinal that becomes active upon photon absorption. The activated rhodopsin then activates the associated G protein, here called transducin, which in turn directly activates a class of cGMP phosphodiesterase. The latter catalyzes the breakdown of the second messenger cGMP to 5′-GMP. In the plasma membrane of rod cells, there are cation-selective cGMP-activated ion channels creating an influx of Na^+ and some Ca^{2+} when the cGMP concentration is high – the dark current. A decrease in the cGMP concentration as a result of photon absorption closes the ion channels and hyperpolarizes the rod cell, providing a signal that is relayed to the synapse of the photoreceptor cell. This process is very efficient: by means of G protein coupling, the absorption of one photon by the retinal in rhodopsin can lead to the hydrolysis of about 100 000 cGMP molecules. This is a good illustration of how the second messenger system is used to amplify the primary signal, one photon in this example.

7.3.3
Receptor Kinases, Hormones, and Transcription Regulation

Whereas ion channels have an immediate impact on cell function by permitting ions to cross the cell membrane, GPCRs also affect cell functions via G proteins and

second messengers. The latter then often activate kinases that phosphorylate (and thereby activate or inactivate) a wide range of target proteins. In many cases, however, the initial activation of a kinase is only the beginning of a phosphorylation cascade, that is, a sequence of phosphorylation events in which the initial "signal" is relayed from one kinase to the next and so forth. Moreover, the primary receptor can be a kinase itself – a so-called receptor kinase.

By means of a sequence of molecular events, the initial chemical signal eventually leads to an alteration of gene transcription, thus modifying the "state" of a cell. The latter often is classified according to rather coarse cellular phenotypes such as "proliferation" (cells divide), "migration" (cells move), "differentiation" (cells change morphology and adopt a more specialized function), or "apoptosis" (cells undergo a programmed cell death). In the following we discuss a few steps in this "signaling cascade."

7.3.3.1 **Receptor Tyrosine Kinases**

Tyrosine kinases are enzymes that phosphorylate proteins at tyrosine side chains. In humans there are 90 genes coding for tyrosine kinases, and 58 encode those that are also capable of receiving chemical signals – the receptor tyrosine kinases (RTKs). RTKs are localized at the cell surface and they typically respond to the binding of peptide signaling molecules such as growth factors, cytokines, and hormones. We discuss RTKs in more detail because of their pivotal role in regular cell functions and also their implication in the development and progression of various types of cancer (see Section 7.4.1).

Although diverse in structure, RTKs have in common a single transmembrane segment anchoring them in the plasma membrane, a variable extracellular structure with specific binding motifs for their ligands, and a more conserved intracellular catalytic domain harboring kinase activity (Figure 7.56). Ligand binding to the receptor triggers a sequence of molecular events, here exemplified for the epidermal growth factor receptor (EGFR); activation of the EGFR can lead to cell proliferation and migration, hence this receptor plays an important role in some forms of cancer. Once the agonist, epidermal growth factor (EGF), is bound to the extracellular binding site, two receptor monomers form an active dimer, stabilized by a disulfide bridge. The conformational change is transmitted to the catalytic domains, which then phosphorylate themselves. The catalytic domain, phosphorylated at tyrosine residues, then forms the target of a class of proteins that bind via their SH2 (Src Homology 2) domain. One such adapter protein is Grb-2 (growth factor receptor-bound protein 2). Grb-2 attracts the guanosine nucleotide exchange factor protein SOS (Son of Sevenless), which transiently interacts with and activates a small G protein (see Section 7.3.2.2), finally triggering an avalanche of further signaling event (see below).

RTKs are diverse in both structure and function, and can deviate markedly from the example above. RTKs are grouped into about 20 different classes; a few prominent examples are the following:

- the ErbB family, of which EGFR is a member
- insulin receptors

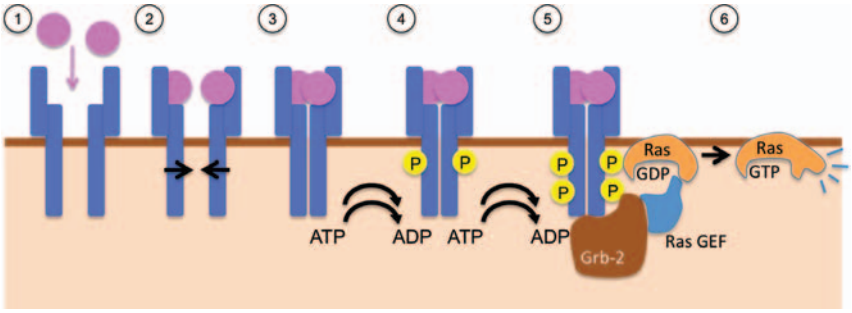

Figure 7.56 Receptor tyrosine kinase (RTK). Sequence of events during the activation of an RTK, for example the epidermal growth factor receptor (EGFR). (1) An agonist, here the small signal protein epidermal growth factor (EGF), binds to the receptor, which is anchored in the plasma membrane with only one transmembrane α-helix. (2) Upon binding, two activated receptors associate to form a dimer (3). (4) Their intrinsic tyrosine kinase activity results in autophosphorylation of their intracellular catalytic domains. (5) Once phosphorylated, the receptor becomes a binding target for adapter proteins, such as Grb-2 (growth factor receptor-bound protein 2). (6) Further association of guanosine nucleotide exchange factor proteins (GEF), such as SOS, activate the small G protein Ras by exchange of GTP for GDP. Activated Ras then starts a signaling cascade involving a series of phosphorylation events (see Figure 7.57).

- receptors for various growth factors such as PDGF (platelet-derived growth factor receptor), FGR (fibroblast growth factor receptor), and VEGF (vascular endothelial growth factor).

They all have in common that the binding of the specific agonist activates the receptor, which then stimulates subsequent intracellular events, in many cases manifesting itself as an alteration of the gene transcription pattern.

RTK signaling is terminated by dephosphorylation of the receptor. This is achieved by protein tyrosine phosphatases (PTPs). Since PTPs are the natural counterparts of RTKs, they are important elements regulating the "level of activation." Therefore, like RTKs, PTPs are involved in cellular processes such as cell growth, differentiation, mitosis, and oncogenic transformation, that is, a dysfunction of PTPs may cause cancer and can have fatal consequences.

7.3.3.2 Small G Proteins – Intracellular Bimodal Switches

Extracellular signals relayed into the cell by membrane receptors are frequently "translated" into second messengers or the activation of membrane-bound heterotrimeric G proteins (large G proteins). Receptor tyrosine kinases also follow the general paradigm with the exception that, rather than activating a heterotrimeric G protein, they are coupled to a class of so-called small G proteins (20–25 kDa). The latter are similar to the α subunits of heterotrimeric G proteins and they belong to the Ras superfamily of small GTPases.

Small G proteins to a certain extent can be considered as second messengers, because they carry a message depending on their association with guanosine

nucleotide. When bound to GDP, small G proteins are in an inactive form; they are activated when GDP is exchanged for GTP. This reaction is facilitated by GEF proteins, such as SOS (Figure 7.56). GEF actually helps GDP to dissociate from the G protein and, because of the cytosolic excess of GTP, separation of GEF will most likely result in a reassociation of GTP, thus completing the exchange cycle. The G protein is inactivated by hydrolysis of GTP, and this reaction is catalyzed by *GTPase-activating proteins* (GAPs). *Guanosine nucleotide dissociation inhibitors* (GDI) keep the G protein in its GDP-bound inactive form. The balance between GEF, GAP, and GDI activity determines the guanine nucleotide status of Ras proteins. The small G proteins therefore are bimodal "on/off switches". Because they are small and often soluble in the cytosol, small G proteins can carry the information stored in their activation state to various sites inside a cell.

There are more than 100 members in the superfamily of Ras proteins, including Rho, Ran, Rab, Arf, and many more. The Ras family is generally responsible for cell proliferation, Rho for cell morphology, Ran for nuclear transport, and Rab and Arf for vesicle transport. Owing to their involvement in elementary cell functions such as proliferation and migration, Ras proteins are so-called proto-oncogens, that is, excess Ras activity can lead to uncontrolled cell growth and tumor formation.

Ras proteins have various effector proteins such as lipid kinases (PI3K). A very well studied signal cascade triggered by Ras is the mitogen-activated protein kinase pathway, which starts with the Ras-mediated activation of Raf (rapidly growing fibrosarcoma) proteins.

7.3.3.3 **Mitogen-Activated Protein Kinase**

Ras initiates a phosphorylation cascade, culminating in the activation of MAPK, which enters the nucleus and phosphorylates various nuclear transcription factors (such as Elk1). This general complex of signal transduction is presented in a simplified manner in Figure 7.57a. An extracellular ligand binds to a receptor. Upon binding, the receptor becomes a target for adapter proteins – intracellular proteins that bind to the receptor at cytosolic moieties. This complex formation is an important aspect in cell signaling and it strongly determines cellular states. It not only happens at membrane-spanning receptor proteins but is practically relevant for all signaling proteins found throughout the cell. The adapter proteins may then "recruit" further proteins into the complex. In our example in Figure 7.57 these are GEFs that activate nearby small G proteins. This is the starting point of a so-called phosphorylation cascade. This means that a protein becomes phosphorylated with the aid of the activated G protein. The target protein, however, is a kinase itself, such that it can now – in its activated form – phosphorylate additional proteins, which can be kinases again. In the example discussed here, the final kinase is the mitogen-activated protein kinase MAPK. Therefore, kinases phosphorylating MAPK are referred to as mitogen-activated protein kinase kinases (MAPKKs), and so forth. From a signaling point of view, the "information" now resides in the phosphorylation status of a sequence of proteins. Depending on the final target, that is, the regulation of a transcription factor in the nucleus, signal transduction results in a long-lasting cellular response such as "proliferation." It is

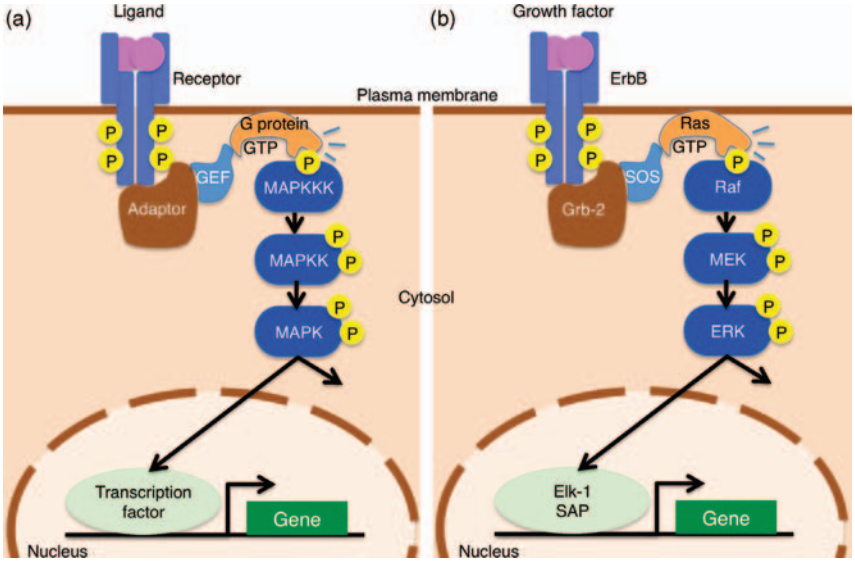

Figure 7.57 Mitogen-activated protein kinase pathway. (a) Signal transduction via the MAPK pathway, starting with the activation of a membrane receptor and subsequently of a G protein. The latter activates a kinase that phosphorylates further kinases, finally the MAP kinase. MAPK then affects transcription factors in the nucleus, that is, proteins that regulate how a gene is transcribed into mRNA. (b) The same pathway as in (a) showing a specific example (for details, see text).

very obvious that complex processes such as "proliferation" cannot be elicited by only turning one knob inside a cell. Therefore, to understand the final cellular outcome of an extracellular chemical signal one must consider all possible reactions (for clarity we show only one here) and, instead of setting individual switches by activated MAPK, rather a complex program of altered gene transcription is typically launched.

In Figure 7.57b, a specific example of MAKP signaling is illustrated. The membrane receptor is here the RTK ErbB. Autophosphorylated RTK recruits the adapter protein Grb-2 and the guanine nucleotide exchange factor SOS. Membrane-delimited Ras is activated, starting a phosphorylation sequence involving the serine/threonine kinases Raf, MEK (mitogen-activated kinase kinase), and ERK (extracellular signal-regulated kinase). ERK is the actual MAP kinase and can, among other reactions, affect the transcription factors Elk-1 and SAP in the nucleus.

7.3.3.4 **Nuclear Receptors**

The extracellular chemical signals discussed thus far are received by the cell via receptor proteins residing in the plasma membrane. Such signals can then be relayed into the nucleus to alter transcription using second messengers, MAPK, or related pathways. However, some ligands, such as steroids, thyroid hormones, vitamin A, and vitamin D, are hydrophobic enough to pass through the plasma membrane.

Hence these ligands can directly reach their receptors within the interior of the cell or even inside the nucleus. In the first place, such *nuclear receptors* regulate gene expression and thereby control complex cellular functions such as development and metabolism. In contrast to the signaling proteins discussed thus far, nuclear receptors have the ability to bind to DNA and function as transcription factors. Owing to the profound importance of nuclear receptors for development, these proteins are promising therapeutic drug targets. However, lipophilic xenobiotics binding to nuclear receptors can cause severe intoxication and developmental disorders.

Two major groups of nuclear receptors are recognized according to their localization and the mechanism of activation. Nuclear receptors of type I reside in the cytosol as a component of multimeric protein complexes; when bound to a ligand, type I receptors are liberated from the protein complexes and are transported into the nucleus (nuclear translocation). In the nucleus they bind to genomic DNA at specific sequences, the hormone response elements (HREs). Binding of the receptor to DNA then triggers the association of additional proteins that finally regulate the transcription of a gene downstream of the HRE. Examples of hormones binding to type I nuclear receptors are androgens, estrogen, progesterone, and glucocorticoids.

Nuclear receptors of type II are always inside the nucleus, associated with DNA. Ligand binding initiates a conformational change of the receptor, enabling it to change its interaction with other proteins (e.g., corepressor and coactivator proteins) that actually regulate gene transcription. Type II receptors include the retinoic acid receptor and the thyroid hormone receptor.

7.3.3.5 Gene Regulation

The term *gene regulation* comprises all molecular steps necessary to transcribe specific genes into mRNA and, finally, to generate the corresponding proteins. These include the regulation of the chromosomal structure, that is, the arrangements of chromatin domains, the transcription, post-transcriptional modification (e.g., mRNA splicing and editing, regulatory RNAs), transport of mRNA, the translation, and finally the termination of translation regulated by mRNA degradation.

All these steps are tightly regulated by numerous proteins. External signaling input to cells often cumulates in an effect on gene regulation, thus enabling the cell to change its state within a few minutes. Such altered "states" can be transient but they can also be stabilized to last for very long time – as for example during the differentiation of stem cells to specialized neurons (see Section 7.2.2.1). Although discussed here as the final result of a signaling cascade, gene regulation can also be considered the birth of a new signal (or multiple signals), thus being part of a gigantic meshwork of mutual dependences continuously changing with time.

Site-Specific Labeling of Proteins

When a protein is to be monitored in living cells, its intrinsic photonic properties may not be sufficient for efficient detection. One may employ fluorescently labeled antibodies that bind to specific epitopes at the protein. However, antibodies have several disadvantages, such as limited accessibility and localization of the epitope

(see the Box "Antibodies" in Section 7.1.2.5) and time and costs required for antibody production. An alternative is to perform a direct covalent coupling of a fluorescent dye to a specific site on the protein. Although such couplings are in principle possible at any amino acid, the easiest and most relevant side chain used cysteine. By means of a disulfide formation bond, dyes with a free thiol group can be coupled to proteins efficiently. Although native cysteines are sometimes used for labeling, a more frequently used approach is to introduce cysteines at specific sites of the protein by mutating the coding DNA and by heterologously expressing the protein in a host cell system. Such methods are often applied to extracellularly accessible domains of membrane proteins. Typical examples of cysteine-specific labeling compounds are methanethiosulfonate (MTS) reagents.

One of the major challenges in biophotonics research is to shed light on this puzzling complexity, for example, to provide tools allowing for the spatially and temporally resolved visualization of gene activity. A combinatorial approach utilizing multiple fluorescent markers, such as enhanced blue/cyan/green/yellow fluorescent proteins, may allow such visualization in the future.

7.3.4
Signaling Pathways

The examples discussed above give us a simplified view of how cellular signals are processed inside a cell. Signals thereby are manifested as "states," that is, a specific structural property of the cells such as the local concentration of second messengers, the status of proteins being activated by phosphorylation or by binding of nucleotides, or by the formation or dissociation of protein complexes, to name just a few. Such "states" then often propagate inside a cell, giving rise to terms such as "signaling cascade" or "signaling pathway." Hence we may talk about a cAMP pathway or a MAPK pathway, for example. When characterizing such pathways, the direction is indicated, referring to *upstream* and *downstream* events, where the start of a pathway usually is the initial binding of an extracellular ligand to a receptor in the plasma membrane or inside a cell.

Among the obvious reasons for having such signaling pathways in cellular systems is their potential for signal amplification: a single transmitter molecule can trigger an avalanche of cellular reactions. In addition, multi-step signaling enables a cell to generate responses with different time courses: while the intracellular Ca^{2+} concentration rises locally within a few 100 μs upon an activation of a Ca^{2+} channel in the plasma membrane, subsequent Ca^{2+}-mediated alterations of the gene transcription program may take minutes or hours. The cell hence has capabilities of effectively processing initial signals such as to perform temporal and spatial differentiation and/or integration.

Cellular signaling pathways are enormously complex; there are numerous pathways and there are alternative routes in the downstream and upstream directions. As a consequence, the physiological outcome of activated signaling pathways can only be understood when all other pathways are properly controlled. Activation of pathway A,

for example, may cause the inhibition or activation of pathway B, leading to concepts such as *signal*, *crosstalk*, and *transactivation*.

The only way to deal with this bewildering complexity is a systematic approach of pathway analysis. On the one hand complete experimental data sets are needed to describe the activity of genes, the existence of proteins (maybe even including their state of modification), and the existence and concentration of all other metabolites inside cells. Such data sets are now compiled using modern microarray technologies to detect mRNA (genomics) and proteins (proteomics) of the entire genome under consideration (pangenomic arrays). In addition, high-end mass spectrometric methods provide detailed and quantitative insight into the cellular content of proteins and metabolites (metabolomics). This very rich source of experimental results needs to be processed so as to gain manageable information reflecting a biologically relevant meaning. This urgent need has triggered the development of *systems biology* as a new branch of science that tries to describe biological systems (e.g., microorganisms, cells, or even higher organisms) as one unit composed of very many interacting elements.

Information from highly parallel "omics" experiments is then analyzed with systems biological methods to isolate individual pathways and to detect their coupling to other pathways. An example illustrating several pathways in one cell is shown in Figure 7.58. Meanwhile there are many databases available providing

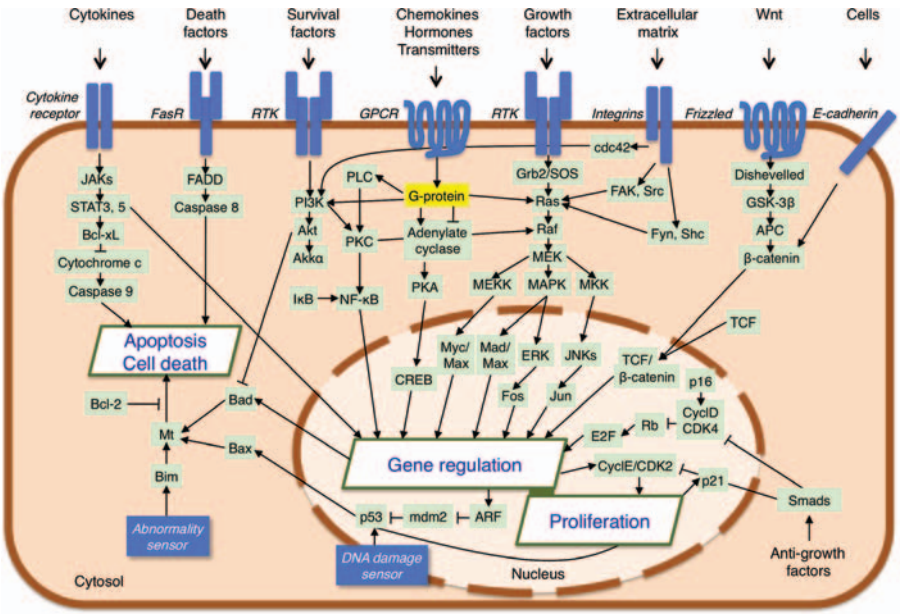

Figure 7.58 Pathway analysis and crosstalk. Schematic description of a few pathways important in cellular signaling. This illustration, although showing only a very small subset of cellular signaling components, already indicates that there are very many more types of receptors, adaptors, mediators, and effectors than discussed in this brief overview of cell signaling. Not illustrated are diffusible second messengers, such as Ca^{2+} and cAMP, which also strongly modulate the individual intracellular reactions.

information on pathways in cellular signaling. Owing to the complexity, these are often specialized to certain scientific subtopics such as a disease or a specific drug or protein. The reader may try to localize such information on the Internet by searching for "cancer signaling pathway" or may look at the Kyoto Encyclopedia of Genes and Genomes (KEGG) database.

Although of impressive complexity and completeness, the currently available data that form the basis of contemporary pathway analysis often lack sufficient temporal and spatial resolution. In addition, in many cases only rough estimates regarding the concentrations of interaction partners and activated elements are available. Therefore, future research will aim at the analysis of cell signaling in living cells in real time with subcellular resolution. The development and use of methods from biophotonics are a logical approach because of the advantage of the minimal invasiveness of light–matter applications.

7.4 Some Examples of Diseases

A disease is any condition in which the normal body function is impaired. The cause of the condition (*etiology*) and the disease progression (*pathogenesis*) vary widely. Many diseases remain *idiopathic*; their causes are unknown. Selected examples are presented below to illustrate the disease diversity.

7.4.1 Cancer – Loss of Proliferation Control

Cancer is a group of frequently fatal diseases characterized by uncontrolled cell growth. *Cancer* is a general term referring to a disease state with dysregulated cell growth, whereas a *tumor* is a solid accumulation of cancer cells. Primary cancer manifested as a tumor in one organ may spread via lymph or blood, and invade other organs, forming metastatic cancer elsewhere. The risk of cancer development is markedly influenced by both genetic factors and environmental factors, including exposures to toxins and viruses. Mechanistically, cancer is a dysfunction of cell growth; as such, a primer of cell division and cell cycle is presented below before our discussion of select cancer cases and potential therapy options.

7.4.1.1 Cell Division

All cells of an adult human are the result of serial cell divisions starting with the fertilized oocyte, as the founder cell of the whole organism. The process by which a cell is split in two, *cytokinesis*, involves the equatorial assembly of a contractile ring made from actin and myosin filaments. This ring of motor proteins constricts the cell membrane to form a deepening cleavage furrow that eventually splits the cell into two daughter cells. Tightly linked to cytokinesis is a process called *mitosis*, during which

all chromosomes are symmetrically arranged and evenly distributed between the two cell halves. This separation of chromosomes follows a strictly organized program that involves the transient halt of RNA synthesis, maximum condensation of all chromosomes, disassembly of the nuclear envelope, and the fixation of the chromosomal centromeres to microtubules arising from microtubule-organizing centers (see Section 7.2.1.8) in both hemispheres of the cell. These microtubules are responsible for the mechanical work that drives two sets of chromosomes into each half of the dividing cell. At the end of mitosis, nuclear envelopes are re-formed in both daughter cells, chromosomal packaging is loosened, and normal transcriptional activity resumes. Mitosis and cytokinesis are precisely coordinated and the whole process takes about an hour in most animal cells. Importantly, cell division and the mechanical separation of chromosomes are only the final steps of a more complex series of events, the *cell cycle*.

Cell Cycle Phases and Checkpoint Control Animal cell growth is not a simple continuous process of macromolecule accumulation and increase in cell volume, but can be divided into four discrete functional phases (G_1, S, G_2, and M) (Figure 7.59). Cell cycle progression is also by no means automatic, but requires the cell to make decisions at several checkpoints. Immediately after a new cell results from division, it starts to produce mRNA and proteins and the overall production of macromolecules proceeds until the next mitosis starts. However, DNA replication, the duplication of chromosomes, is delayed for at least several hours. This first cell cycle period with no replication activity is called G_1 (first gap) phase, as it separates mitosis and the DNA synthesis (S) phase. The duration of G_1 is not only dependent on the availability of nutrients and thereby the speed of cell growth, but is also

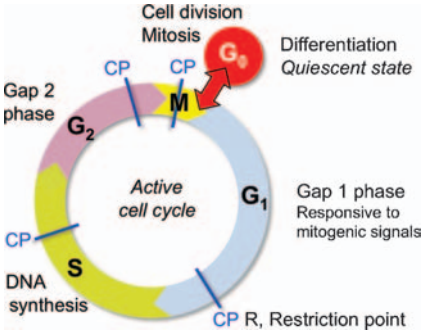

Figure 7.59 The cell cycle of a mammalian cell. Dividing cells pass through four distinct phases with checkpoints (CP) to ensure that progression is linked to specific conditions. Major prerequisites for S, G_2, and M phase progression are genome integrity, completed replication, and proper chromatid assembly, respectively. In G_1, the cell is primarily controlled by extracellular signals that decide if progression to DNA synthesis occurs or if the cell enters the quiescent state G_0. The molecular basis of the control system is provided by cyclins, which are present at oscillating concentrations, and cyclin-dependent protein kinases (CDKs).

characterized as a period of pronounced responsiveness to extracellular signals. As outlined in Section 7.3, mitogenic signals that can stimulate cell proliferation via membrane receptors and downstream signaling pathways are normally required to drive cell proliferation. The G_1 phase is the time period during which a cell is responsive towards this kind of extracellular signals and, even if nutrients are available in abundance, it will not proceed to the S phase without such a signal.

However, extracellular signals not only trigger cell *proliferation* but also control cell *differentiation*. If a cell in G_1 experiences an excess of differentiation signals over proliferative signals, it will not proceed to DNA replication, but rather remain in a stable, differentiated state called the G_0 phase. By contrast, if sufficient proliferative signals were received, the cell will proceed past the so-called restriction point ("R point") (Figure 7.59) and from there on behave largely independently of extracellular signals. Shortly after passing the R point, during the S phase the cell duplicates all chromosomes, a mandatory requirement for the next cell division. The S phase also includes a checkpoint and replication will be halted if any DNA damage is detected at this stage. Only if repair enzymes successfully restore genome integrity can a halted cell proceed past this point. The S phase is complete when all chromosomes have been replicated. The cell will not directly enter mitosis, but remain in a second gap phase (G_2) for at least some hours. Another checkpoint at the entrance of the M phase blocks the cycle again if the genome duplication is not fully completed. Once the cell has passed this point, the mitosis proceeds according to a predetermined program, unless at the "spindle attachment checkpoint" chromatids are not properly assembled on the mitotic microtubule spindle. Overall, the mammalian cell cycle is a process with four clearly distinct phases and multiple checkpoints at which a clear decision is required before the cell is allowed to proceed.

Cyclins and Cyclin-Dependent Kinases When the cell cycle works much like a precision clock, what controls speed, direction, and potential halts at the checkpoints? A first insight came from studies on mitosis in frog embryos, which revealed very precise and synchronous oscillations of concentration of a protein termed *cyclin B*. A gradual increase in cyclin B concentration is followed by a rapid degradation of the protein that is triggered by polyubiquitin chains added by a specific ubiquitin ligase. Later it was found that other cyclins show very similar fluctuations but with peaks at other points of the cell cycle. The complete absence of cyclin B after mitosis prevents any cell from direct re-entry into mitosis, as this would be fatal before DNA replication. Whereas cyclins B, E, and A are regulated by rapid protein degradation, cyclin D1 and other D cyclins that peak during G_1 are not degraded, but exported from the nucleus into the cytosol and thereby rendered inactive. This mobile characteristic of the D cyclins is important for the role of conveying extracellular signals to the cell cycle. Incoming mitogenic signals can cause D cyclins to migrate back into the nucleus and thereby promote cell cycle progression. The two described mechanisms underlying cyclin fluctuations explain the timing of the different phases and unidirectional progression, but the actual effectors of checkpoint decisions are protein kinases that must form heterodimers with individual cyclins to become active, the *cyclin-dependent kinases* (CDKs). One activity of the cyclin B–CDK1 complex

is to phosphorylate nuclear lamins, thereby triggering nuclear lamina breakdown during mitosis. Another prominent example of CDK activity is phosphorylation of the retinoblastoma protein (pRb) by cyclin D–CDK4/6 complexes and by cyclin E–CDK2 during G_1. The tumor suppressor protein pRb with no or only a few phosphorylated sites can bind and inactivate transcription factors required for the progression beyond the restriction point. In contrast, hyperphosphorylation of pRb by the cumulative activities of both cyclin–CDK complexes prevents this inhibiting function of pRb and, hence, drives cell progression beyond the G_1 phase into the S phase.

7.4.1.2 **Cell Death**

Cell death is not necessarily a misadventure in multicellular organisms, but rather a normal process occurring throughout the organism's life, during both development and adulthood. For instance, normal sculpting of the fingers requires that cells in the areas of the hand that are supposed to become the intervening spaces die during development. This controlled interdigital cell death follows a stereotypical signaling program called *apoptosis*, a form of programmed cell death (PCD). Apoptotic cells not only stop their metabolism and destroy their own DNA, but they also signal phagocytic cells to engulf the dead cells or their resulting fragments in membrane vesicles called apoptotic bodies. This apoptosis program is needed during development but it also provides an important safety mechanism throughout adult life. Whenever cells experience unusual challenges, such as DNA damage, viral infection, or severe dysregulation of signaling pathways, induction of apoptosis is a common way to avert damage to the surrounding tissue and the whole organism. However, apoptotic cell death is not the only way to end the life of a cell. In many surface epithelia such as the intestine or the epidermis of the skin, old and inactive cells are continuously shed to the exterior (Section 7.2.2.4). Epidermal keratinocytes in their terminal differentiation state in the outermost cell layers of the skin are dead and without a nucleus; the cells are not actively removed by other cells but simply lost upon washing or rubbing. Loss of selected cells such as exfoliation of the skin cells does not pose a problem for the organism. However, if metabolically active cells are damaged and cannot be cleared, the leakage of cell contents might severely damage neighboring cells of the tissue. This uncontrolled cell death or *necrosis* is a common consequence of burns and frostbite. In contrast to apoptosis, the cell remnants are not trapped in membrane-sorrounded vesicles, but cytosol and even the content of lysosomes packed digestive enzymes can be released. Necrotic wounds are therefore dangerous for the organism and they often impair wound healing.

Apoptosis Signaling The program of apoptotic cell death is inherent to all cells of the body and the signaling system effecting this event must be tightly controlled to avoid unwanted loss of cells. The last steps and the terminal result of apoptosis are always similar, but with respect to the initiating steps, *intrinsic* and *extrinsic* pathways need to be distinguished (see Figure 7.60). Intracellular (intrinsic) apoptosis signals can be triggered by DNA damage through UV radiation, by cytotoxic drugs, or by oxidative stress. The intracellular signals typically lead to the same critical event, namely the

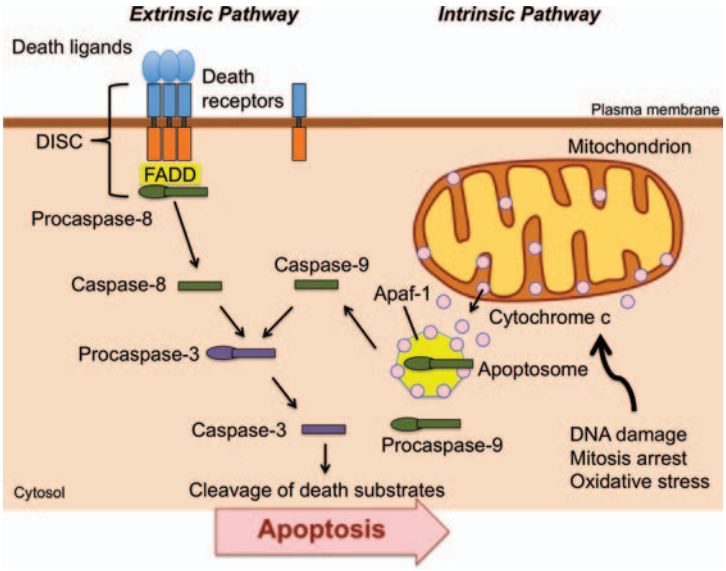

Figure 7.60 Apoptosis – programmed cell death. Controlled cell death enables the organism to remove individual cells during development or in response to cell stress and damage. Cell death commands are conveyed by caspases, proteinases that are primed by proteolytic cleavage of procaspases. Initiation of a caspase cascade can be triggered either by the activation of death receptors or by cytochrome *c* release from mitochondria. Caspase 3 and other effector caspases at the end of the signaling cascade cleave various protein targets in the cell and thereby cause apoptotic cell death.

release of the small heme protein cytochrome *c* from the mitochondrial intermembrane space into the cytosol. Here, cytochrome *c* binds to the protein Apaf-1 and together they form a wheel-like structure with sevenfold symmetry, the apoptosome. This complex then binds and activates the protein procaspase-9. *Caspases* are a family of cysteine-dependent aspartate-directed proteases. They are produced as inactive precursor proteins that can be activated by cleavage of the inhibiting prodomain. Two functional classes of caspases are known: *initiator caspases* that cleave and activate other caspases, and *effector caspases* that cleave other substrates. Caspase-9 acts as an initiator and activates procaspase-3. The active caspase-3 in turn cleaves a broad variety of substrates including actin, tubulin, and pRb, with the inevitable consequence of apoptotic cell death.

Whereas many internal signals finally affect the mitochondrial membrane and its permeability to cytochrome *c*, extrinsic signals use a separate pathway to activate the caspase cascade. The membrane receptors responsible for conveying extracellular apoptosis signals are called *death receptors*. Activating ligands can be soluble proteins but also membrane-bound proteins on the surface of immune cells. Thus, monocytes or other immune cells can instruct a suspicious cell to undergo apoptosis as a suicide program. This is particularly important for the control and removal of tumor cells or virus-infected cells. Death ligand binding causes death receptor trimerization and in turn triggers the binding of cytosolic proteins to the receptor. The Fas-associated

death domain (FADD) protein is such a cytosolic adapter protein and together with the death receptor and procaspase-8, it forms the death-inducing signaling complex (DISC). Active caspase-8 formed by this complex can directly cleave the effector caspases such as caspase-3. Thus, extrinsic and intrinsic pathways converge and result in very similar final stages of apoptosis. One typical hallmark of apoptosis is the fragmentation of chromosomal DNA such that pieces 130–180 bp in length are generated. Another important step is the activation of scramblases in the plasma membrane due to increased cytosolic Ca^{2+} levels. As a consequence, the phospholipid phosphatidylserine, which is normally localized to the inner leaf of the plasma membrane, will appear on the outer surface of the cell membrane as a signal for macrophages to remove the apoptotic cell.

7.4.1.3 Cancer – Diagnosis and Therapy

Cancer is a general term for a diverse and large group of diseases that can affect all parts of the body. A common feature in cancer is the uncontrolled growth of abnormal cells that grow beyond their normal tissue boundaries, often forming a tumor or a neoplasm, and eventually invade other parts of the body. This process, termed metastasis, is the major cause of cancer mortality. With nearly 8 million deaths, cancer accounted for ~13% of all deaths worldwide in 2007. Cancer has long been recognized as a severe health issue throughout the history of medicine, but it was not until the twentieth century that the molecular mechanisms underlying this group of diseases began to emerge. A major breakthrough came in the 1970s, when Varmus and Bishop provided evidence for genetic mechanisms underlying the uncontrolled growth of cancer cells. We now know that tumors can arise from normal cells if mutations in otherwise normal genes occur or if the expression level of a group of genes is strongly altered.

Cancer Types and Cancer Risk Cancers are typically grouped according to the tissue from which they arise and approximately 110 different cancerous diseases have been categorized in this way. Although almost any tissue type can become cancerous, the incident is not uniform across different tissue types. In those tissues with highly differentiated cells that do not appreciably undergo cell divisions, such as nerve tissue, tumor formation is relatively uncommon. By contrast, the epithelium of the colon, with a high rate of cell division, is a very common site of cancer emergence. The leading causes of worldwide cancer deaths are tumors arising in the lung, followed by the stomach, colon, liver, and breast. The first morphological evidence for a cancer is enhanced cell growth or the occurrence of less mature cells in a tissue. Such *dysplasias* are classified as *benign* as long as they do not invade nearby tissues. As soon as such cells grow beyond the normal tissue borders, the tumor is called *malignant*. Malignant cell growth in epithelia, termed *carcinoma*, is responsible for over 80% of cancer deaths, including carcinomas of the mammary gland, stomach, intestine, lung, and liver. Nonepithelial cancers arising from connective tissues or from myocytes are commonly termed *sarcomas*. Another major group of cancers are the *leukemias* and *lymphomas*, both arising from cells of the hematopoietic lineage. The *neuroectodermal* tumors are a group of cancers arising from the outer cell layer

of the early embryo. They include different kinds of glioma, neuroblastoma, and malignant melanoma. The distribution of cancer entities in the body can vary markedly in different populations. For example, the risk of malignant melanoma of the skin is about 150-fold higher in Australia than in Japan, and the incidence rate for cancer of the nasopharynx is 100-fold higher in Hong Kong than in the United Kingdom. Such extreme differences are in part due to genetic differences between the populations, but individual lifestyle and environmental factors are even more important risk determinants. In the United States and Northern Europe, the majority of lung cancers can be attributed to active smoking and the lung cancer incidence rates strictly follows the habit of cigarette smoking. Other risk factors with proven association with cancer incidences comprise diets with high fat, high nitrate, or low fiber and exposure to specific carcinogenic agents such as radium, arsenic, benzene, and asbestos.

Oncogenes and Tumor Suppressor Genes Many human diseases are caused by pathogens such as bacteria and viruses. In 1910, Peyton Rous showed that cancer can be an infectious disease spread by viruses. He found that a sarcoma in the muscle of a chicken is transferred to other chickens by the Rous sarcoma virus (RSV). Similarly, human cancers can be caused by viral infection. Examples are cervical cancer caused by the human papilloma virus (HPV) and adult T cell lymphoma caused by the human T cell leukemia/lymphotropic virus type 1 (HTLV-I). However, for the majority of all cancers no infectious agents could be identified, and it became clear that alterations in the human genome can have similar effects as viral infections, leading to a *transformed* phenotype of individual cells. Detailed analysis of the viral life cycle within host cells eventually identified molecular mechanisms of tumor formation that apply to both virally spread and nonviral forms of cancer. In the genome of RSV, a single gene termed *src* for sarcoma is responsible for the transforming activity but is not required for normal viral replication. Bishop and Varmus showed that *src* is not restricted to viral genomes, but that a gene closely related to *src* is found in the chicken genome itself and also in humans. With this observation, the first cellular *oncogene* was discovered, establishing the concept that normal genes can have the potential to drive cancerous cell growth. More precisely, the intact gene is called a *proto-oncogene*, and mutations can render it hyperactive and induce its oncogenic activity. In the case of *src*, it became evident that ~12% of advanced human colon carcinomas carry mutations in this gene. Thus, *src* can induce cell transformation independent of any viral activity. Today, a large number of proto-oncogenes are known in the human genome and they have in common that the encoded proteins are in one way or another involved in cell cycle control, such that hyperactivity causes increased cell proliferation. The mutations that activate proto-oncogenes are not always simple single-point mutations. In more than 90% of all patients with chronic myeloid leukemia (CML), a translocation of genetic material between chromosomes 9 and 22 is present in bone marrow stem cells. At the breakpoint of this rearrangement on chromosome 22, the "Philadelphia chromosome," part of the *bcr* gene is fused to the tyrosine kinase gene *abl*, with the consequence that the fusion protein BCR/ABL has increased tyrosine kinase activity.

The Src protein is also a tyrosine kinase and one of its target proteins is the growth factor ErbB (Figure 7.57), which initiates signaling along the MAPK pathway. Thus, a signaling pathway that normally drives cell proliferation in response to extracellular mitogenic signals can be dysregulated such that growth factor-independent cell proliferation occurs. Following this rationale, it is no surprise that the receptor ErbB itself was also found to have significant oncogenic activity. In over 30% of all human breast cancers, multiple copies of the *erbB-2* gene (also called HER-2/*neu*) are found. This gene amplification leads to higher densities of the receptor on the cell surface and thereby enhanced mitogenic signaling at normal growth factor concentrations. Even more direct activation of cell proliferation programs can be triggered if the machinery driving gene transcription is hyperactive, irrespective of the signaling cascades. This is the case in juvenile neuroblastoma, where the transcription factor gene N-*myc* is often found in 10 or more copies in the genome. This amplification leads to increased levels of the transcription factor protein and correlates with a poor prognosis. Irrespective of the cellular role of an oncogene, increased activity often leads to faster proliferation. Alternatively, oncogenic proteins can increase the cell's potential to migrate and to invade into foreign tissues, and even the formation of new blood vessels, angiogenesis, can ultimately be triggered by oncogenic factors (Figure 7.61).

In the normal cell, proliferation is not simply controlled by activating signals, but rather determined by the balance between activating and inhibitory signals. Hence any failure of an inhibitory protein can have similar consequences as the increased activity of a proto-oncogene. The class of genes encoding such inhibitory proteins is called *tumor suppressor genes*. Like oncogenes, they can affect all levels of cell signaling, from membrane receptors down to transcription factors (Figure 7.61). A prominent example is the *p53* gene, encoding a master regulator protein of cellular apoptosis. Cell-cycle abnormalities and DNA damage, as they often occur in fast-growing tumors, would normally lead to cell cycle arrest and induction of controlled cell death. However, in a large fraction of tumors, the transcription factor protein p53 is not present in normal amounts, leading to survival of the tumor cells. The lack of a tumor suppressor protein, such as p53, can be caused by mutations that affect the protein function. Alternatively, reduced expression of the otherwise normal gene can be caused by hypermethylation of the promoter or other genetic events.

Tumorigenesis The risk of developing cancer increases appreciably with age. This characteristic is consistent with the notion that tumor formation is not induced by a single oncogenic event but it is the consequence of multiple genetic alterations. Accordingly, identical twins with an inherited oncogenic alteration will not necessarily both develop cancer. As soon as a second, rate-limiting genetic event occurs, a tumor may become clinically apparent. This multiplicity of genetic alterations is required because cellular signaling is governed by multidimensional networks (Figure 7.58), in which dysregulation of a single switch is normally not sufficient to reprogram the whole system. Furthermore, tumor formation is a multi-step and multi-dimensional process that depends on more than just enhanced and uncontrolled cell growth. Most cancers develop in discrete steps, such as dysplastic tissue

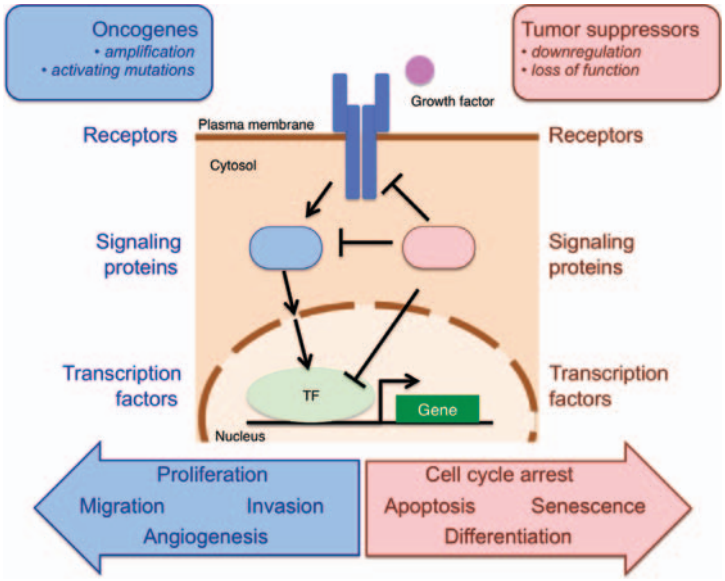

Figure 7.61 Oncogenic signaling. Signaling in tumor cells is characterized by an unbalance between proliferative signals by oncogenic factors (left) and inhibitory signals from tumor suppressors (right). Oncogenes and tumor suppressors can be found on all levels of cell signaling, from membrane receptors down to nuclear transcription factors. Cellular events that either increase the activity of oncogenes or decrease tumor suppressor functions can promote uncontrolled cell division, metastasis, and the formation of tumor blood vessels (angiogenesis).

growth, neoplastic growth into neighboring tissues, spreading along the lymphatic system, or the dissemination through blood vessels that eventually leads to distant metastases. During these phases, the requirements for the tumor cells may vary and a selective advantage at one stage may be irrelevant or even a disadvantage in a different stage.

A long-standing concept in cancer biology hypothesized that accumulation of mutations allows the tumor cell population to acquire new properties, finally leading to a highly malignant and aggressive cell type. This sequential model was challenged by the later finding that not all cells in a tumor are functionally equivalent. Just like stem cells in normal tissues, small subpopulations of slowly dividing cells with self-renewing capacity have been identified in otherwise rapidly dividing leukemias and also in breast cancer and other solid tumors. Such *cancer stem cells* are thought to initiate new tumors and to give rise to the more aggressive, fast-dividing cell type. Whether or not cancer stem cells have common functions and importance in all types of cancer must be clarified in the future. In any case, tumors are heterogeneous assemblies of different cell populations.

Cancer Treatment The standard treatment for most solid tumors is surgical resection in combination with follow-up radiotherapy and/or chemotherapy. The surgical

removal of cancer cells is of limited success if dissemination has occurred. By contrast, chemotherapy reaches wider areas of the body, including any distant metastases. The major obstacle in this approach is the lack of selectivity and consequently often severe side effects. Most commonly administered drugs are designed to interfere with DNA replication and thus cell division – cytostatic agents. As a consequence, cancer cells with high proliferation rates are more susceptible than slowly dividing cells. As many tissues including intestinal epithelia or bone marrow also need rapid cell division of normal progenitor cells, chemotherapy with cytostatics has serious limitations. The finding that slowly dividing cancer stem cells can reside within the tumor cell mass provides a mechanistic explanation for the frequent observation that a life-threatening cancer relapse can follow an initial reduction of the cancer cell mass. These cells with stem cell-like properties are often more resistant to standard therapeutic treatments than the majority of the tumor cells. If they survive the therapeutic intervention, this cell population is the seed for new tumors.

Rational Tumor Therapy The identification of cellular oncogenes and a growing knowledge of intracellular signaling networks in cancer cells have created new opportunities. Given the importance of individual oncogene products, it appeared reasonable to search for drugs that specifically target those signaling proteins instead of using classical cytostatic drugs made to interfere with the process of DNA replication. To be "druggable," an oncoprotein should have a substrate binding pocket that allows the high-affinity binding of small molecules. One of the first prominent successes of rational drug design targeting an oncoprotein was imatinib, a small multi-ring compound now marketed as Gleevec® or Glivec®. This small molecule binds to the active site of the hyperactive tyrosine kinase BCR-ABL responsible for over 90% of all cases of CML. The drug was approved for the treatment of CML and found to be more effective than previous standard treatments, leading to complete remissions in a majority of the treated patients. Imatinib is well tolerated, but long-term side effects remain to be evaluated fully. The success story of imatinib is not without a down side, as it has become evident that long-term treatment with the drug can induce a selective pressure for BCR-ABL point mutations that interfere with drug binding. Modified imatinib variants were introduced as second-generation drugs to overcome this problem. Interestingly, imatinib is not selective for BCR-ABL but c-kit and the platelet-derived growth factor (PDGF) receptor are also inhibited by the drug. This finding makes imatinib an important new drug to treat gastrointestinal stromal tumors (GIST). In up to 90% of the GIST patients, a mutation of the *c-kit* gene, important for tumor progression, is present and those GIST patients with normal copies of *c-kit* often possess mutations in the PDGF receptor gene. Consequently, imatinib is now frequently and successfully used to treat patients after surgical removal of the tumor. Imatinib is only one of many examples of *targeted therapy* approaches, and many other drugs are currently in clinical trials or even approved for cancer treatment. Such drugs are not in all cases small molecules but larger monoclonal antibodies can be valuable tools for the specific intervention with oncoproteins. For example, cetuximab, marketed under

the brand name Erbitux®, is a monoclonal antibody against the external domain of the EGF receptor. This antibody is approved for the treatment of squamous cell carcinoma of head and neck and for colorectal cancer. Trastuzumab (Herceptin®), a monoclonal antibody against the receptor HER-2, is approved for the treatment of HER-2-positive breast cancer.

Given the large number of oncogenes and the heterogeneous pattern of mutations in most tumor types, it is unlikely that we will find drugs that cure all patients suffering from a given tumor or create a "magic bullet" drug for all cancer types. However, if the diagnosis of an individual patient allows identification of the specific oncogenes involved in the pathogenesis of each patient's tumor, it may be possible to replace the non-selective chemotherapy with an individually tailored targeted therapy approach. This way to combine refined diagnosis techniques with very specific drugs is called *personalized therapy/personalized medicine* (see Section 7.4.7).

7.4.2 Cardiovascular Disease

The cardiovascular system, consisting of the heart and blood vessels, supplies blood carrying oxygen and nutrients to organs and tissues throughout the body, including the heart and vessels themselves. The cardiovascular system is a large multi-component system and prone to dysfunction. In fact, cardiovascular disease (CVD), a collection of numerous different pathologies often interacting with the immune system, is the leading mortality cause worldwide, accounting for more than 25% of all deaths in recent years, and the figure is likely to increase. Heart attack, stroke, heart failure, and high blood pressure are some of the CVD forms well known to the public. Mechanistically, CVD involves a variety of underlying mechanisms including arteriosclerosis or hardening of the arteries, ischemia or diminished blood flow, infection by bacteria or viruses that often affect the heart valves, and/or abnormal prenatal development. Various genetic factors contribute to the pathogenesis, making some individuals more predisposed to develop certain forms of CVD and modulating the severity of the disease. Certain lifestyle factors, such as cigarette smoking and a diet rich in saturated fats, are also well-recognized risk factors. A few examples of CVD are briefly summarized below.

Atherosclerosis One of the most important and extensively studied contributing factors in many different forms of CVD is atherosclerosis, a chronic inflammatory vascular condition under which atheromas or cholesterol-containing plaques form immediately beneath the inner blood-facing surface (the endothelium) of medium- and large-sized arteries. The vascular endothelium ("intima") is a one-cell layer lining blood vessels located on top of the smooth muscle cell layer ("media") and produces a large number of vasoactive signaling molecules including endothelin, bradykinin, and nitric oxide. What triggers development of atherosclerotic plaques in the first place is not entirely clear, but it is believed that an injury to the endothelium caused by a mechanical or a shear stress typically initiates a vicious cycle of atheroma formation. Injured endothelial cells exhibit enhanced vascular permeability, allowing various

molecules to traverse the vascular wall. The dysfunctional endothelial cells also alter their gene expression pattern. As a result, the endothelial cells start to express cell-adhesion molecules that facilitate attachment of circulating white blood immune cells to the injured area, creating a local inflammation and oxidative stress. The presence of low-density lipoprotein (LDL), which is often referred to as "bad cholesterol," is also an important contributing factor. The immune cells infiltrate and migrate beneath the endothelium and facilitate the formation of an atheroma just outside the normal smooth muscle layer boundary ("internal elastic lamina"). During plaque formation, infiltrated immune cells generate reactive species capable of oxidizing cell components, including LDL. Oxidized LDL is taken up by infiltrated macrophages, which then transform themselves into foam cells that store oxidized LDL in their cytoplasm. Furthermore, the infiltrated immune cells release a variety of autocrine and paracrine signals (see Section 7.4.3.1) and accelerate the development of atheroma. A collagen fibrous cap eventually surrounds the plaque, which, at the end, contains cholesterol deposits, ectopic migrated smooth muscle cells, and newly formed small blood vessels (Figure 7.62). The formation of a mature atheroma protruding the endothelium to the artery lumen interferes with the laminar flow of blood, potentially seeding additional plaques nearby.

Heart Attack and Stroke Large atherosclerotic plaques decrease the inner diameter of the afflicted arteries and compromise supplies of oxygen and nutrients to the organs and tissues. If this occurs in coronary arteries, ischemic heart disease results, which in turn may cause other secondary changes in the heart. Stenosis or narrowing of coronary arteries by atherosclerotic plaques itself is a serious medical issue, often manifesting as a form of angina or chest pain called stable angina. The situation becomes much more urgent if the plaques rupture, exposing the plaque core to the bloodstream. Plaque rupture can lead to the formation of thrombi or blood clots

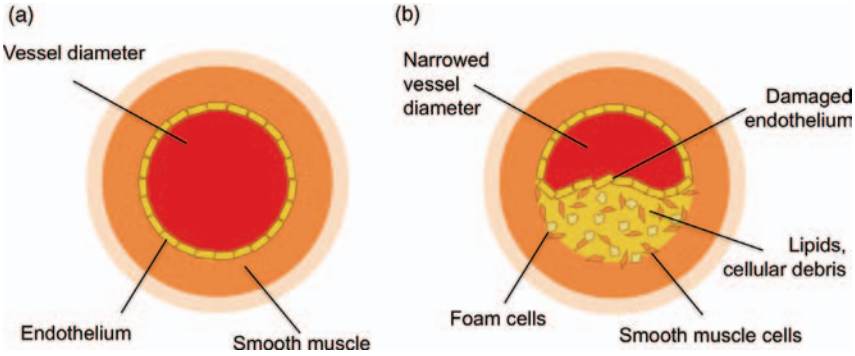

Figure 7.62 Atherosclerosis in artery. (a) Section through a blood vessel. A medium to large artery is illustrated here. The layer containing the endothelium is known as the tunica intima or simply the intima. The layer containing smooth muscle cells is called the tunica media or the media. The outermost layer is called the tunica adventitia. (b) Mature atherosclerotic plaque causing arterial stenosis (narrowing cross-section).

capable of obstructing blood flow, potentially leading to acute coronary syndrome (ACS) and to myocardial infarction (heart attack). Without adequate blood supply, the cells in the affected area die and are eventually replaced with collagen if the patient survives. The diagnosis of myocardial infarction is aided by measurements of serum biomarkers, such as troponin released from the cytoplasm of dying cardiac muscle cells. An ischemic stroke results when a similar plaque rupture occurs in an artery supplying blood to the brain. In some cases, a thrombus may break loose from the vascular wall and becomes an embolus, which may clog blood flow elsewhere – a case of embolism.

Hypertension Hypertension is a definitive risk factor for many forms of CVD and also for other diseases, such as renal disease. Today, normal blood pressure is a systolic pressure of less than 120 mmHg and a diastolic pressure of less than 80 mmHg (120/80). Those individuals with pressure levels of 120/80 to 139/89 mmHg are said to be prehypertensive and those with levels $\geq$140/90 mmHg are considered to be hypertensive. The majority of hypertension cases ($\sim$95%) are essential or primary; no specific cause can be attributed. Undoubtedly, both genetic and lifestyle factors are at play. Some of the known risk factors include family history, age, cigarette smoking, diet as such excessive sodium intake, low physical activity level, and high body weight. Physiologically, blood pressure is a function of two major variables: the cardiac function and the vascular resistance. Each of the two variables in turn depends on numerous factors, making the overall process of blood pressure regulation extraordinarily complex and the majority of the hypertension cases essential. Many prehypertensive and hypertensive patients are typically treated with medications designed to affect the contractility of blood vessels and/or the fluid handling in the kidney.

Heart Failure When the heart is beating but is not performing well enough to supply sufficient blood to organs and tissues, the condition is called heart failure. Heart failure can be caused by insufficient filling of the heart with blood, known as diastolic heart failure, and/or by ineffective ejection of blood by the heart, termed systolic heart failure. Normally, as the heart is filled with a greater volume of blood (diastolic volume), the heart output (stroke volume) increases, as described by the Frank–Starling law. In systolic heart failure, the slope of the curve relating the cardiac output and the diastolic volume is noticeably less than that in healthy hearts so that, for a given diastolic volume, the stroke volume is less. Heart failure often leads to serious secondary pathologies in end organs, such as the lungs, liver, and kidneys. The underlying etiology of heart failure is diverse, but therapeutic strategies typically involve lowering blood pressure by manipulating the fluid handling by the kidney and modulation of vascular and cardiac muscle contractility.

Cardiac Arrhythmia The rhythmic activity of the heart originates as a spontaneous action potential in the primary pacemaker cells in a small area in the right atrium called the sinoatrial (SA) node, which then spreads to the atria. The atrial electrical excitation is transmitted, through the atrioventricular (AV) node, to the ventricles. Within the ventricles, the action potential spreads through the bundle of His and

Purkinje fibers, which are essentially modified neuronal cells, and initiate coordinated ventricular muscle contraction. Cardiac arrhythmia or irregular heartbeat may result when any of the above processes is impaired and this is clinically confirmed using electrocardiography (ECG/EKG). Arrhythmias are frequently observed following myocardial infarction because the normal electrical pathway described above is disturbed by the nonfunctional cardiac cells. One example of arrhythmia is ventricular fibrillation, observed frequently in patients with ischemic heart disease; the electrical activity in the ventricle becomes unsynchronized and interferes with effective blood ejection, potentially leading to sudden cardiac death. Genetic mutations, often in those genes coding for the cardiac ion channel proteins responsible for generating and shaping the cardiac action potential, predispose the afflicted individuals to arrhythmia.

Biophotonics in CVD Technological advances, including those utilizing biophotonic approaches, have made significant contributions to our understanding of the normal heart function and also to CVD. Using optical methods, it is now feasible to visualize the spread of electrical activity and changes in intracellular Ca^{2+} (see Section 7.3.2.1) in a beating heart. The beating heart of a patient can be now visualized noninvasively using an echocardiogram. Biophotonics methods, such as Raman microscopy and fluorescent microscopy, have been utilized to analyze atheromas. Some commercial instruments use optical methods, such as measurements of optical density, to detect blood clots. It is anticipated that biophotonics will continue to play an important role in the cardiovascular physiology and pathophysiology.

7.4.3
Malfunction of the Immune System

Failures of the immune system can fall in one of three main categories: immunodeficiency, autoimmune disease, and hypersensitivity (allergy). Before discussing selected examples for each category, the following sections give an introduction to general aspects of the human immune system.

As multicellular eukaryotic organisms evolved, not only did they compete with single-celled bacteria for nutrition resources but the organisms themselves happened to be ideal, energy-rich habitats where bacteria could thrive. Successful evolution therefore required effective defense strategies to keep bacteria out or at least to restrict their growth and to prevent their attack of the host's cells. The human immune system is much more than a class of defensive blood cells; it involves a collection of multiple defense systems, employing both passive and active safeguard strategies. In general, two types of immune responses are recognized, the *innate* and the *adaptive*. The innate immune response is already active at birth and it is nonspecific; it acts rapidly against a wide variety of pathogens in a relatively generalized and stereotypical manner. In contrast, the adaptive immune system responds to specific pathogens and improves through multiple exposures to pathogens. The memory of adaptive immune cells allows faster and stronger reactions against previously encountered pathogens.

7.4.3.1 Immune Cells and Their Functions

The innate immune system can be divided into two parts: the *first-line defense* is provided by multiple barriers of different types to prevent pathogens from entering body tissues and the *second-line defense* involves all other mechanisms that kill those pathogens that crossed the first-line barriers. The skin provides a physical barrier surrounding the whole body. Tightly packed dead cells of the outer epidermal layers are embedded in secreted ceramides and other lipids; this barrier is nearly waterproof and difficult to penetrate. Importantly, the epidermis is not traversed by blood vessels such that invading bacteria cannot spread but remain localized. At body orifices, additional barrier mechanisms come into play, such as the lacrimal apparatus of the eyes and the saliva in the mouth. The constant secretion of tears from the lacrimal glands flushes potential pathogens and particulate matter out of the eye. This fluid also contains the antibacterial enzyme lysozyme and IgA immunoglobulins. Both protective molecules are also found in saliva. Other parts of the body with a continual inrush of pathogens are covered with mucous membranes. Such major portals of entry are the respiratory and the genitourinary tracts. Mucus layers on the outer epithelia help to trap microorganisms that can be removed by the rhythmic movements of cilia, the hair-like outer appendages of many epithelial cells. An important chemical barrier is provided by the extreme acidic environment of the gastric juice. In the genitourinary tract, lactic acid in the urine and frequent flushing reduce bacterial growth.

Second-line Defense of Innate Immunity Despite the barrier mechanisms in place described above, numerous bacterial cells and viruses manage to enter the human body every day. The second line of the protective mechanisms against these invaders includes cellular responses and chemical activities. A prominent component of the chemical response is the *complement system*, a set of about 30 circulating serum proteins that becomes activated in a cascading manner, leading to multiple consequences including inflammation, recruitment of phagocytes that engulf the foreign bodies, and lysis of invading cells such as bacteria. As the terminal reaction of the complement cascade, a membrane attack complex forms on bacterial surfaces that punches holes into the membrane. The complement cascade can be triggered in multiple ways, one of which involves the presence of antibody–antigen complexes. Hole formation in the bacterial plasma membrane causes a breakdown of the vital proton gradient across this membrane and kills the microbe. The same complement complex can also form holes in viral coats. This does not remove the virus, but with a perforated envelope it can no longer infect host cells. Other key reactions of the second-line response are inflammation and fever, the first being a mainly localized reaction, whereas fever is a systemic increase of the body temperature. Inflammation includes the release of histamine, leukotrienes, and prostaglandins. Together, these mediators cause vasodilation and the migration of phagocytes. Vasodilation increases the diameter of blood vessels in the affected areas and thereby delivers more immune cells. These cells, attracted by local chemical signals, leave the bloodstream and migrate into the tissue, a process termed extravasation. The general increase in body temperature during fever is triggered by breakdown products of bacteria such as

lipopolysaccharide (LPS) from the outer membranes of Gram-negative bacteria. Up to a point, fever is beneficial for the organism as the elevated temperature inhibits bacterial growth and bacterial toxins become less active.

Blood Cells Involved in Innate Immunity Several types of white blood cells (see Figure 7.34) contribute to the nonspecific immune response. Normal *monocytes* in the blood stream are nonphagocytic, but when they reach sites of infection, chemical signals released from other local cells trigger their maturation to become macrophages. This immune cell type has very high phagocytic activity and is responsible for removing bacteria, fungi, or even virus-infected cells. Macrophages not only appear on acute infections, but also persist in many different tissues as resident macrophages. In some tissues, they were given specific names, such as microglia in the brain and Kupffer cells in the liver. Other cells contributing to innate immunity are neutrophil, basophil, and eosinophil granulocytes. Neutrophils are also phagocytes and they are important in guarding mucous membranes and the skin. An important task for all immune cells is to distinguish between *self* and *nonself*, otherwise also cells of the own body could become targets of their attack. For immune cells of the innate response, the identification of nonself largely depends on *toll-like receptors* (TLRs). This family of membrane receptors is specialized to bind molecules that are common to many potential pathogens. The list of such molecules includes LPS from Gram-negative bacteria, lipoteichoic acid from Gram-positive bacteria, and double-stranded or single-stranded RNA found in many viruses. Activation of TLRs triggers intracellular signaling pathways that lead to activation of the immune cell.

7.4.3.2 Adaptive Immune Response

In contrast to innate immunity, the acquired immunity changes with every exposure to pathogens and the set of cells involved in the immune response changes and adapts to specific challenges. Central elements of acquired immunity are immunoglobulins with very specific antigen-binding sites. Antigens can be virtually any foreign molecules that enter the body. A given immunoglobulin does not recognize the whole antigen structure, but instead binds to very delimited surface areas, so-called *epitopes*. Figure 7.63 illustrates the overall structure of the IgG immunoglobulin. These proteins can either be secreted as antibodies or they can reside on the surface of B lymphocytes. IgG antibodies are composed of two heavy and two light chains linked by disulfide bonds. A constant region is common to all antibodies, but the variable region of the antibody forms a highly specific antigen-binding site. The stupendous antibody repertoire is made possible because the antibody proteins are coded by multiple genes that are assembled in a highly complex mix-and-match manner, often referred to as V(D)J recombination (see below). The term *adaptive* does not mean that antibodies adapt to fit to their targets but that selection of the best-fitting antibodies from a huge repertoire adapts the system to recognize all antigens that have been encountered over time. Five different isotypes of immunoglobulins exist: IgG, IgA, IgD, IgE, and IgM, with IgG being the predominant antibody in blood and IgA being secreted into the mucous layers of the intestine and the respiratory tract. IgM molecules are structurally different as they form large pentameric structures.

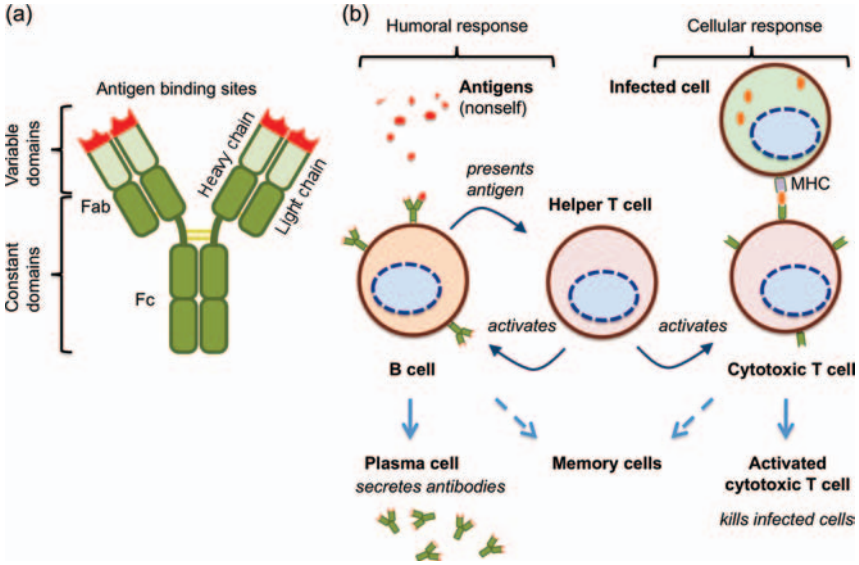

Figure 7.63 Antibodies and immune cells. (a) An IgG antibody comprising two light chains and two heavy chains. The chains are connected via disulfide bonds (yellow). The variable domains harbor the antigen binding sites. (b) Interplay of humoral (antibody) and cellular immune response. Antigen binding and activation by helper T cells induce B cells to become antibody-secreting plasma cells. A smaller fraction of the activated B cells remains as memory cells to allow a faster and stronger response upon subsequent encounters of the same antigen. Cytotoxic T cells become activated when virus-infected cells or tumor cells present an antigen on the major histocompatibility complex (MHC). Also activation of cytotoxic T cells needs support from helper T cells. Most activated T cells will attack and kill infected cells, but a smaller population remains as memory cells.

The binding of antibodies to a virus particle or to a bacterium has three important effects: (i) a pathogen is coated with a layer of antibodies so that it cannot adhere to body cells any longer; (ii) antibodies cause opsonization of the pathogen, that is, they mark it for phagocytosis; (iii) antigen–antibody complexes activate the complement cascade of the innate immune system.

B and T Lymphocytes The cellular carriers of adaptive immunity are B cells and T cells. B cells are responsible for antibody production, the *humoral* response, whereas T cells carry the *cellular* response. A common feature of the two cell types is their ability to produce antigen-binding proteins. In contrast to the Y-shaped antibodies, the membrane-bound T-cell receptors comprise only one antigen-binding site. The names of the lymphocytes refer to their site of maturation: the bone marrow for B cells and the thymus for T cells. Before maturation is completed, the immunoglobulin genes of the precursor cells are irreversibly rearranged, such that millions of different B and T cells arise, each being able to produce just one specific type of immunoglobulin. In a process called *clonal selection*, all cells that bind self antigens are later deleted to prevent their reaction with the own body cells. The remaining B and T lymphocytes are so-called naive cells. They become

activated upon binding of an antigen to their surface immunoglobulin. Activation is a complex process that can involve the mutual interaction of two lymphocytes.

If surface immunoglobulins on a B cell bind an antigen, both receptor and antigen are taken up by endocytosis. The antigen is degraded into small fragments and the epitope is returned to the surface, where it is presented to T cells. Binding of a T cell in turn activates the B cell, which will start to proliferate and differentiate into plasma cells. A plasma cell secretes large amounts of its specific antibody into the blood. Plasma cells can have lifetimes between days and months, but typically their blood concentration drops when the pathogen is cleared. Importantly, a small fraction of activated B cells becomes *memory cells*. These memory B cells persist and, if they ever encounter their antigen again, they allow much faster proliferation of the appropriate B cell population.

The T lymphocytes involved in B cell activation belong to the *T helper cell* population. Another group of T helper cells exists to activate macrophages specifically. Both helper T cells can be identified by a common cell surface protein, termed CD4. Another cell surface protein, CD8, is prominently found in a second group of T cells called *cytotoxic T cells*. These killer T cells biochemically induce death in virus-infected cells, cells that carry intracellular pathogenic bacteria, and tumor cells. The T cell can successfully identify its targets even in tissues with mainly healthy cells because it recognizes pathogen-specific antigens present on the surface of a target cell. Unlike phagocytes, a T cell does not engulf its target cell, but releases a mixture of cytotoxic proteins that damage the other cell and induce cell death by apoptosis. As with B cells, a small population of activated T cells differentiates into memory T cells, which allow a more rapid immune response upon any secondary contact with the same antigen on target cells.

Vaccination The ability of lymphocytes to generate memory cells is an efficient protection against subsequent infections, provided that the patient survived the first encounter. However, the same protective benefit can be induced not only with the whole pathogen itself but also with a characteristic antigen thereof. Such an antigen may exist on related but less virulent pathogen species, on attenuated or dead pathogens, or even as isolated proteins or protein fragments. The first reported successful vaccination was performed in 1796 by Edward Jenner. Jenner realized that milkmaids who were often exposed to cowpox were insensitive to the otherwise highly fatal smallpox infection. Jenner used material from cowpox blisters to immunize healthy individuals effectively against smallpox. Today, vaccination is a powerful way to prevent many serious diseases and it is particularly important for viral diseases, for which treatment options are limited (see Section 7.4.4.2). Modern vaccines are in most cases attenuated virus strains or purified virus proteins administered via many routes, including oral and injection.

7.4.3.3 Failure of the Immune System

Primary Immunodeficiency Diseases Proper function of the human immune system requires the activity of a large set of genetically encoded components, including antibodies, receptors, cytokines, and enzymes. As a consequence, any defect in one of

the underlying genes could severely compromise the immune system function. In general, immunodeficient patients are more susceptible to infectious diseases but the actual symptoms differ significantly. Some inherited immunodeficiencies are so mild that they may remain unnoticed for many years whereas others are severe and afflicted newborns may require immediate treatment.

The defects in inherited immunodeficiencies primarily affect B cells and T cells; however, a loss of phagocyte functions or a loss of individual complement components may have similar phenotypic effects. *Severe combined immunodeficiency* (SCID) is characterized by a lack of functional T cells. As helper T cells are required to activate B cells properly to produce specific antibodies in large quantities, both arms of the adaptive immune response, cellular and humoral, are severely debilitated. Most cases of SCID are due to a defect in the gene encoding an interleukin-2 receptor subunit, known as X chromosome-linked SCID. With the lack of functional interleukin receptors, T cell progenitors cannot respond to interleukin signals and proper T cell maturation is impaired. A second common cause of SCID is a mutation in the gene encoding adenosine deaminase, leading to accumulated ATP breakdown products, which are toxic to B and T lymphocytes. Other defects concern factors of the complement cascade or the function of phagocytic cells. In chronic *granulomatous disease*, the phagocytic cells are unable to produce hydrogen peroxide, required to kill ingested bacteria. Consequently, patients suffer from infections by opportunistic pathogens, which are unable to infect healthy individuals. Prominent examples are bacteria of the genera *Serratia*, *Klebsiella*, and *Salmonella* and fungi of the genera *Aspergillus* and *Candida*.

Acquired Immunodeficiency Disease (AIDS) Suppression of immune functions is not necessarily the result of genetic defects. The most important and best-studied case of a life-threatening immunosuppression caused by a pathogen is acquired immunodeficiency disease (AIDS), a disease caused by the human immunodeficiency virus (HIV). The World Health Organization (WHO) estimates that about 33 million HIV-infected people lived worldwide in 2008 and that about 2 million died of the disease in the same year. The target cells for HIV are helper T cells expressing the membrane protein CD4, as the viral infection relies on binding to this receptor protein. Cytotoxic T cells also can clear such infected helper T cells; however, a small population of infected helper T cells typically remains during an asymptomatic phase that can last for several years. Following a slow increase in the number of infected cells, patients eventually enter an acute phase of the disease, during which also the number of cytotoxic T cells drops. Without treatment, the death of the infected individual is usually caused by opportunistic infections, such as pulmonary bacterial diseases or infections with oncogenic viruses. Treatment for HIV infections consists of the combined application of three drugs, known as *highly active antiretroviral therapy* (HAART). This medication targets the viral enzymes reverse transcriptase and protease. The drug regimen is effective but does not cure the disease because the virus cannot be completely cleared from the body. Hence lifelong treatment is required, a demand that cannot be achieved for most patients worldwide because of the high drug cost.

Autoimmune Diseases The immune system is powerful enough to protect the organism against most invading pathogens. However, the immune cells occasionally become overactive and turn against any normal substance or tissue in the own body, causing serious problems – autoimmune diseases. While the prevalence of autoimmune diseases seems to be increasing, most prominently in more economically developed countries, the underlying disease causes are not understood and therapies are often limited to symptom management and palliative care. In *multiple sclerosis* (MS), the immune system attacks the myelin sheaths around nerve axons in the brain and in the spinal chord, and demyelination impairs the conduction of voltage signals in the affected nerves. MS is not considered a hereditary disease, but some genetic alterations may increase the susceptibility to develop the disease. Multiple subtypes of MS are recognized. In progressive MS cases, the immune system steadily attacks and damages the nerves and the patients experience increasing disability. The relapsing-remitting subtype of MS is characterized by relatively discrete periods of increased disability followed by periods with no noticeable change in the disease severity. Myelinated axons coordinate a large number of functions in the body, and MS patients can therefore experience a broad range of neurological symptoms, including cognitive impairment and depression, pain, muscle weakness, and urinary incontinence. The fundamental cause of MS is yet to be elucidated but several immunomodulators and immunosuppressants have been approved to reduce the frequency and severity of MS attacks.

Other autoimmune diseases include myasthenia gravis (MG), rheumatoid arthritis (RA), and diabetes mellitus type I (discussed in Section 7.4.6), to name just a few. MG is an autoimmune channelopathy with antibodies directed against *nicotinic acetylcholine* (ACh) receptors located on the skeletal muscle fiber, a transmitter-gated ion channel. MG is characterized by progressive skeletal muscle weakness during periods of activity that improves with periods of rest. First signs are often weaknesses of the eye muscles or of muscles involved in facial expression or chewing. Typical treatment mainly involves cholinesterase inhibitors to increase the concentration of ACh to improve muscle excitation or immunosuppressant drugs to reduce the autoimmune reaction against the channel protein. RA is a systemic inflammatory disorder that mainly attacks synovial joints of the hands and feet but sometimes also larger joints such as the knees. Symptoms include painful swelling of the joints, stiffness, and destructive erosion of the joint surfaces. Although it is widely accepted that autoimmunity plays an important role in RA, the molecular pathogenesis is only poorly understood. Apparently, abnormal interactions between B cells and T cells result in the excessive production and release of inflammatory cytokines; treatment with anti-inflammatory drugs can be used to suppress the symptoms.

Hypersensitivity *Allergy* is the most common type of immune dysfunction, characterized by an exaggerated inflammatory response to otherwise normal environmental substances, known as allergens. Allergic reactions may be elicited by a huge palette of stimuli, including airborne particles such as pollen and fungal spores, food, antibiotics, and latex. In the acute phase of the disorder, a subset of helper T cells stimulates B cells to produce and release IgE-type antibodies against the allergen.

Circulating IgE antibodies then bind to the surface of mast cells and basophil granulocytes. With the bound antibodies, both immune cells are sensitized to the allergen and upon exposure they will release potent inflammatory chemical mediators, such as histamine, leukotrienes, and prostaglandins. The symptoms such as tissue swelling and itchiness can either be localized to the sites of allergen exposure or systemic, affecting the whole body. Treatment can include drugs that interfere with the inflammatory mediators, such as antihistamines or anti-leukotrienes. If specific allergens could be determined by allergy tests, avoidance of the allergen often solves the problem. If that is not practical, desensitization is a gradual vaccination procedure against specific allergens. This can be achieved by subcutaneous injections or sublingual administration of progressive allergen doses with the aim of inducing the production of IgG antibodies against it. These antibodies are supposed to neutralize and clear the allergen, thereby preventing it from interactions with IgE antibodies.

7.4.4 Infectious Diseases

All infections, whether caused by bacteria, viruses, or parasites, follow similar general principles: (i) the pathogen must find a way to get into the host; (ii) the pathogen must be able to deal with the immune responses to remain inside the host; (iii) the pathogen must find ways to exit the host and to be transmitted to another host. These three requirements are sufficient for a successful life cycle of the pathogen. To make the whole process a disease, the pathogen must cause damage to the host in some form. If the relationship has no obvious disadvantage for the host, the intruder would rather be called a commensal. This is the case for many of the bacteria in the human mouth flora or in the intestine.

As outlined before, major entry sites into the human body are the mucous membranes of the respiratory tract, the gastrointestinal tract, and the genitourinary tract. Together, these surfaces make about 400 m^2 of mucous membrane in a human adult and, despite the defense mechanisms of innate immunity, numerous bacteria and viruses have evolved to use the aforementioned entry sites. By contrast, the intact skin is a near-perfect protective barrier, but the so-called parenteral route of infection usually depends on breaks in this barrier. Apart from injuries, parenteral infection can also occur very efficiently if an invader uses biting insects as transmission vector. This is a common entryway for many parasites, including *Plasmodium*, the malaria agent.

Following the entry, the second task of the invading pathogen is to establish a pathogen colony. Bacteria physically attach themselves to the host cells using their filamentous fimbriae or sticky glycolipids (adhesins). Viruses attempt to gain entry into the cell cytosol to avoid being flushed out or cleared by macrophages (Figure 7.64). Some pathogens, such as *Vibrio cholerae*, responsible for cholera, and *Neisseria meningitidis*, responsible for bacterial meningitis, grow rapidly within the host whereas others, such as herpes simplex viruses and Epstein–Barr virus, can remain in a latent state that allows them to stay life long with one host organism.

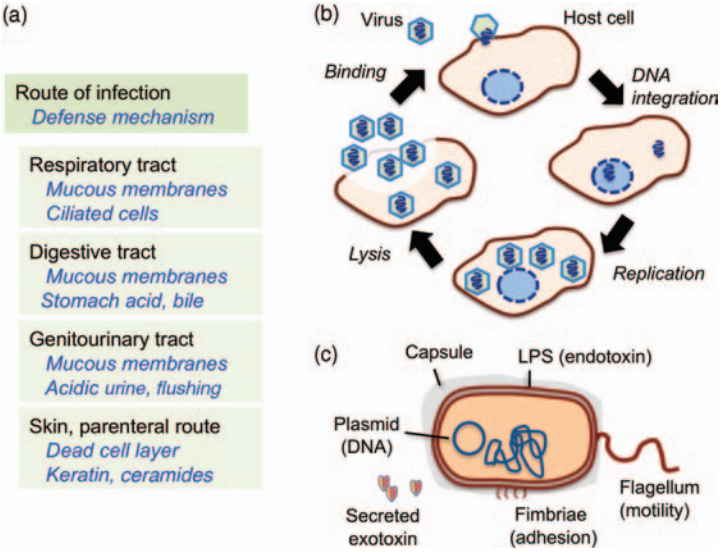

Figure 7.64 Principles of infection. (a) Typical routes of entry of bacterial and viral pathogens and defense strategies of the host (blue). (b) Scheme of a viral lytic cycle. (c) Gram-negative bacterium and virulence factors.

Finally, to ensure survival of the pathogen as a species, mechanisms of transmission to a new host must exist. The major transmission routes are contact transmission, vehicle transmission, and vector transmission. A typical example of contact transmission is the transfer of common cold-causing viruses via direct contact of the hands. Vehicle transport means that the pathogen takes a "piggyback ride" on something else, for example, contaminated food, dust particles, or water. If the carrier itself is an organism, the transfer is called vector transmission. Such vectors can be insects that sting or bite humans, but the carryover of pathogens on human food is also a vector transmission. A common example is the spread of bacteria on houseflies that are often found to shuttle between feces and food products.

In the following sections, bacterial and viral infections are briefly discussed. Although both agents account for the majority of infectious diseases in humans, one should keep in mind that fungi and parasitic protozoans can be extremely potent human pathogens. Parasite-mediated diseases such as malaria, the African sleeping sickness, and the American Chagas disease (trypanosomiasis) cause enormous medical and economic problems.

7.4.4.1 **Bacterial Infection**

Pathogenic strains are found among both Gram-positive and Gram-negative eubacteria but not among archaebacteria (Figure 7.43). Closely related strains from one species can behave either as harmless commensals or as causative agents of severe diseases. The distinguishing factor between such strains is their ability to produce *virulence factors* (Figure 7.64). Passive virulence factors protecting the bacterium

include slimy capsules composed of polysaccharides, the variable O-antigens of the outer membrane LPS in Gram-negatives, and a waxy coating on the outer surface, as produced by *Mycobacterium tuberculosis*. Active factors can be pore-forming cytolytic toxins (hemolysin) or toxins that disturb signaling pathways in the host cells. Importantly, the genes encoding bacterial virulence factors are often found on large plasmids, circular DNA molecules that are inherited in parallel to the bacterial chromosome. Such collections of virulence genes can be easily transferred between bacterial strains, such that nonpathogens can become virulent in very short time.

The Gram-negative pathogen *E. coli* belongs to the Enterobacteriaceae. Other important pathogens of this group are found in the species *Salmonella* and *Shigella*. Common to all three species is their typical fecal-to-oral transmission. Most species that are transferred on this route cause, among other symptoms, severe forms of diarrhea, a factor that supports their rapid and sometimes epidemic spread. Another prominent example is the Gram-negative bacterium *V. cholerae*. The cholera toxin can induce such severe water loss that untreated patients can die within hours. Even more potent toxins are made by some Gram-positive bacteria. The *anthrax toxin* produced by *Bacillus anthracis* is like a tripartite weapon consisting of the proteins edema factor, lethal factor, and protective antigen. Once in the acidic conditions of an endosome, edema factor and lethal toxin are converted to their active conformations. Together with the protective antigen, these toxic proteins inactivate macrophages and neutrophils of the immune system, cause tissue swelling (edema), and finally kill the host.

B. anthracis is a good example of another dangerous property of many pathogens: the ability to persist for long time as a dormant spore. When such spores are inhaled or ingested, they are reactivated and begin to proliferate inside the host. This toxic potency of the dry spores makes anthrax a deadly biological weapon. Another deadly spore-forming toxin is *Clostridum botulinum*, a Gram-positive bacterium that is sometime found in improperly prepared food items and produces neurotoxic botulinum toxins.

The toxins contain a complex of several proteins that become dissociated and activated in the host cells. Deadly paralysis is caused as the toxins bind and cleave t-SNAREs and v-SNAREs in neurons that innervate muscle cells. As described in Section 7.2, SNAREs are indispensable facilitators of synaptic exocytosis and the release of neurotransmitters. The toxin causes death as soon as muscles required for respiration are inhibited. Although this toxin can be deadly, one component in the toxin mixture has found therapeutic applications for excessive sweating and skin wrinkles. When the facial muscles that contract to form wrinkles are paralyzed by the toxin, wrinkle formation is prevented.

Antibiotics The most important finding for the treatment of bacterial diseases was that microbes produce substances to protect themselves against other microbes. In 1928, Alexander Fleming incidentally found that the fungus *Penicillium* produces a substance that kills the bacterium *S. aureus*. Later, it became evident that other bacterial species, most prominently of the genus *Streptomyces*, also produce antibacterial toxins. These newly identified and purified substances became powerful weapons for medicine to defeat bacterial infection.

Later, the active compounds could also be produced as synthetic or semi-synthetic molecules. Importantly, antibiotics directed at bacteria-specific targets were identified, allowing for a thorough antibacterial treatment without severe side effects for the human host. For example, the target of penicillin and many other antibiotics is peptidoglycan of the bacterial cell wall, a molecule that is not found in mammalian cells. Other antibiotics such as erythromycin or tetracyclin inhibit translation in bacteria; the drugs interfere with bacterial ribosomes but have no activity against eukaryotic ribosomes. Other antibiotics inhibit common prokaryotic enzymes involved in transcription and DNA replication.

Unfortunately, with the rising use of antibiotics, it has become evident that bacteria can acquire antibiotic resistance. For instance, the bacterial enzyme β-lactamase cleaves the important β-lactam ring of penicillin. Other resistance mechanisms include small mutations in the antibiotic target molecules, such that the antibiotic no longer binds to the original target and the activity of the target is preserved. The intensive use of antibiotics in hospitals puts strong selective pressure on bacteria and resistant strains have become more and more common in this sensitive environment. Pathogenic *S. aureus* strains with penicillin resistance were found shortly after the introduction of the antibiotic. Some decades later, new strains emerged that were also insensitive to the approved treatment with the β-lactamase-stable antibiotic methicillin/meticillin. These dangerous strains were named methicillin-resistant (or multidrug-resistant) *Staphylococcus aureus* (MRSA). Vancomycin has become the last line of defense against strains, but more recently even vancomycin-resistant strains (VRSAs) have been discovered, necessitating the use of even newer antibiotics.

7.4.4.2 **Viral Infection**

The most important difference between viruses and bacteria is that a virus is not an independent organism but a parasite of a host cell; a virus needs energy and the enzyme machinery of the host to multiply. Reflecting this infectious arrangement, it has been challenging to design specific and effective anti-viral drugs. The salient structure of a virus is a protein coat or shell (capsid) that covers genetic material, either DNA or RNA. Both types of nucleic acids can be packed as either double strands or single strands. In complex viruses, a phospholipid membrane with glycoproteins serves as an additional outer envelope surrounding the capsid.

Two basic capsid structures can be distinguished: icosahedral shapes and helical shapes. Icosahedral viruses have a capsid with 20 triangular surfaces whereas helical capsids can be filamentous or rod shaped. Although viruses do not have an independent life of their own, their *infection cycle* in many respects resembles the life of a real organism. During this cycle, the genetic material is duplicated and a new generation of virus particles is released. Mutations during the replication process allow the evolution of new traits and new strains evolve from existent strains.

Virus infection of a host cell does not necessarily mean that new virus particles are made in large numbers immediately. In a *lysogenic cycle*, viral DNA becomes integrated into the chromosomal DNA of the host. This ensures that the viral genetic

material is replicated by the host and transferred to the daughter cells upon mitosis. Only if such a "sleeper" virus is activated by unusual stress to the host cell or other triggers does it resume the lytic cycle and capsid protein is made to pack viral nucleic acid. With the release of virus particles, a new lytic cycle begins. As long as they are inside the host somewhere, virus particles can attack previously uninfected cells. The first step is attachment to the membrane or to specific receptor proteins followed by endocytosis. The endocytosis pathways used by viruses include clathrin-mediated uptake, caveolar endocytosis, and other mechanisms. To make use of its genetic material, the viral genetic material must be released from its capsid and envelope. This can occur at the cell membrane in some cases, but in many cases it happens in the endosome or even later in the process. For RNA viruses, replication of the genome includes a transient conversion into DNA by means of a viral reverse transcriptase. Following genome multiplication, new viral proteins are made to form new capsids and package nucleic acids. Specific packaging signals on viral nucleic acids identify them to the capsids to ensure that no host nuclei acid is packed. The final release of the new virus particles relies either on death and lysis of the host cell or budding from the plasma membrane. The former is typical for viruses with nonenveloped capsids, whereas the latter is more frequently used with enveloped viruses.

Viral dissemination and transmission occur via multiple pathways, just like bacterial infections. The most common entry site is the respiratory tract, as virus-containing aerosols are easily inhaled. The digestive tract is another common entry site; however, viruses using this route must be resistant to acid, bile, and proteolytic enzymes. The urogenital tract is the entry pathway for sexually transmitted viruses, including HIV, the causative agent of AIDS. As many of the steps in a viral life cycle involve enzymatic activities of the host, the development of selective antiviral agents is appreciably more challenging than that of antibiotics. Nevertheless, viruses often have Achilles' heels and some drugs are in fact available to make use of them. Acyclovir is a nontoxic nucleoside analog of guanine, a building block of DNA. In the cells infected with herpes simplex virus, this analog is activated by the viral enzyme thymidine kinase. Acyclovir is then incorporated into DNA, leading to death of the infected cell. Zanamavir is an inhibitor of the neuraminidase enzyme of the influenza virus and specific protease inhibitors such as indinavir are used to treat HIV infections. These antiviral agents offer some hope, but prevention of viral infection by vaccination remains the most powerful way to combat viral diseases.

7.4.5
Degenerative Diseases Exemplified by Neurodegenerative Diseases

In degenerative diseases, select body functions become progressively impaired over time. Numerous degenerative human diseases are known, afflicting different organs and tissues. Some believe that aging in itself is a degenerative disease that could be treated. Although the exact nature of aging is a matter of debate, aging is associated with many degenerative conditions. Among them are neurodegenerative diseases of the CNS, exemplified by Huntington's disease, transmissible spongiform encephalopathies, Parkinson's disease, and Alzheimer's disease, which illustrate the

diversity in etiology and pathogenesis while causing progressive loss of neurons in different areas of the brain. Because the regenerative capability of the brain is very limited, the impairment is not currently reversible and there is no cure for any of the aforementioned conditions today. It is hoped that the ongoing intensive multidisciplinary investigations, including those utilizing biophotonics, will soon lead to improvements in treatment and care, and eventually to cure and prevention.

Huntington's Disease Huntington's disease is an inherited neurodegenerative disease characterized by progressive impairments in movement and emotional and cognitive abilities. The initial symptoms, such as abnormal jerky and involuntary movements, are frequently recognized at age $\sim$40 years followed by death typically 10–20 years later from a variety of causes. The disease is autosomal dominant and caused by mutation in the huntingtin gene on chromosome 4. The gene codes for a large protein called huntingtin expressed in many tissues, especially in the brain. The huntingtin protein in Huntington's disease patients contains an abnormally greater and variable number of glutamine residues in a row, referred to as polyglutamine (polyQ) repeats, coded by CAG repeats (trinucleotide repeats) in the huntingtin gene. The number of CAG repeats in the gene can be used to predict whether an individual develops Huntington's disease, and genetic testing for the disease is available. The functions of normal huntingtin are not yet clear but recent evidence suggests that the protein has a critical role in the neuronal metabolism of cholesterol, which regulates the cell membrane fluidity. Mutant huntingtin proteins with polyglutamine repeats are suspected to accumulate in nerve cells and interfere with proper cholesterol metabolism, eventually causing cell death. Huntington's disease is only one of so-called trinucleotide/polyQ diseases and other notable examples include spinocerebellar ataxias and dentatorubral-pallidoluysian atrophy.

Creutzfeldt–Jakob Disease In inherited diseases such as Huntington's disease, the transmission agent is nuclear DNA. In contrast, other neurodegenerative diseases may involve genetic and nongenetic factors. Such a multicausal characteristic is well evident in Creutzfeldt–Jakob disease, a relatively rare but fatal neurodegenerative disease that causes dementia. Creutzfeldt–Jakob disease has three forms, depending on the etiology: sporadic, familial (inherited), and acquired. The sporadic and familial forms account for the vast majority, $>$99%, but the acquired form has been well publicized in part because of its similarity to bovine spongiform encephalopathy (BSE) or mad cow disease. The initial symptoms of Creutzfeldt–Jakob disease may include emotional and cognitive changes. Following the symptom onset, patients deteriorate very rapidly and usually die within 12 months. Postmortem examination of the brain typically reveals numerous characteristic "holes," thus giving rise to the name spongiform encephalopathy.

Creutzfeldt–Jakob disease involves conversion of normal prion proteins into abnormal pathogenic conformations. The misshaped prion proteins accumulate, leading to neuronal death. The normal prion protein is a glycosylated membrane-anchored protein with a large α-helical content. The normal functions of prion proteins are yet to be established thoroughly but its participation in proper formation

of insulation around nerve axons (myelination) is likely. One notable characteristic of prion diseases, including Creutzfeldt–Jakob disease, is that abnormal prion proteins drive other surrounding normal prion proteins to assume abnormal pathogenic conformations, which in turn coerce additional prion proteins to be pathogenic. This vicious cycle may contribute to the rapid progression of the disease. In the familial form of the disease, a genetic mutation facilitates the conformational conversion of prion. In the acquired form, it is the abnormal prion proteins themselves that transmit the disease. "Prion infection," although rare, does occur by exposure to tissues containing pathogenic prion proteins isolated from Creutzfeldt–Jakob disease patients. Decontamination of prion poses a serious challenge because abnormal pathogenic prion proteins are notoriously difficult to destroy.

Parkinson's Disease Parkinson's disease is a relatively common degenerative disease, disproportionately afflicting older individuals. Parkinson's disease patients slowly lose their motor coordination, typically exhibiting bradykinesia, impaired posture control, and muscle rigidity. Additional nonmotor symptoms may be observed and, during end stages, different degrees of dementia may be present. Multiple causal and contributing factors for Parkinson's disease are known. A small fraction of Parkinson's disease cases are inherited and genetic mutations in several genes are linked with Parkinson's disease, including those in α-synuclein, parkin, UCH-L1, DJ-1, PINK-1, ATP13A2, OMI/HTRA2, and LRRK2. Functions of the proteins coded by these genes are not yet clearly known, but they may have diverse cellular functions, including a role in synaptic transmission, protein degradation, and protein phosphorylation. Environmental factors may also contribute to the development of the disease. Although inconclusive, chemicals contained in drugs of abuse, insecticides/pesticides/herbicides, exposure to metals that cause oxidative stress, viruses, and head trauma have been implicated. The aforementioned diverse factors eventually destroy the melanin/dopamine-containing neurons in the substantia nigra in the basal ganglia of the midbrain. The surviving neurons in the brain of a typical Parkinson's disease patient contain intracellular inclusions called Lewy bodies filled with α-synuclein fibrils. Whether the α-synuclein-containing inclusions represent a causal factor for the disease or a cellular defense mechanism against the disease is uncertain. The presence of Lewy bodies is not a unique characteristic of Parkinson's disease; similar intracellular inclusions are also found in other dementia-causing neurodegenerative diseases, including Lewy body disease (LBD).

Because Parkinson's disease involves destruction of the substantia nigra neurons that release dopamine as the neurotransmitter, one of the common treatments is to administer exogenous dopamine precursors, such as levodopa, which are then converted into dopamine in the surviving neurons. The levodopa treatment is not entirely satisfactory and new therapeutic options are being actively explored. One such method is deep brain stimulation, which involves surgical implantation of an electrical stimulator into the brain. The exact mechanism of the action of deep brain stimulation is only beginning to be elucidated and a new experimental approach using genetically engineered light-sensitive ion channels coupled with optical fibers is providing promising information.

Alzheimer's Disease The most common cause of dementia in the older population today is Alzheimer's disease, which afflicts >50% of the individuals over the age of 85 years. Because this age group is projected to increase steadily in number in many countries, Alzheimer's disease is a significant health and social concern. Alzheimer's disease patients show progressive impairment of cognitive skills, especially short-term memory, and subsequent autopsies typically show marked brain atrophy and secondary expansion of fluid-filled ventricles. Such postmortem examination of the brain of a typical Alzheimer's disease patient using silver stain reveals two microscopic characteristics of the disease, amyloid plaques and neurofibrillary tangles. The plaques are extracellular deposits outside neuronal cell bodies and dendrites made of multiple proteins. The plaques are found in all individuals as they age but they are much more prominent in Alzheimer's disease patients. The primary component of the plaques in the Alzheimer's disease brain is amyloid β42 (Aβ42), with the number indicating the number of amino acid residues present. Aβ42 is one of the several peptides formed from the larger single-transmembrane protein amyloid precursor protein (APP). Proteolytic cleavage of the extracellular domain of APP by the sequential actions of the proteases α- and γ-secretase produce nonamyloid peptide fragments, but the processing by β- and γ-secretases forms amyloid peptides of two different lengths, 40 and 42 residues. Of the two forms, Aβ42 is more intimately implicated for Alzheimer's disease; aggregation or oligomerization of Aβ42 is suspected to impair normal neuronal communication, eventually leading to cell death and brain atrophy. In addition to the extracellular plaques, intracellular insoluble aggregates consisting of hyperphosphorylated tau proteins, referred to as neurofibrillary tangles, are readily observed in the Alzheimer's disease brain.

Both genetic and nongenetic factors are clearly involved in Alzheimer's disease. Rare early onset forms of the disease are familial or inherited; mutations in multiple genes, including those coding for amyloid precursor protein and presenilin, a component in γ-secretase, are known to be associated with Alzheimer's disease. However, most Alzheimer's disease cases are sporadic. Although the etiology remains to be elucidated, it is believed that certain genetic and environmental factors may modulate the disease onset and pathogenesis. As is the case for Parkinson's disease, exposure to certain metals, pesticides, and brain trauma are suspected to increase the disease risk. In contrast, changes in diet and lifestyle may offer some protection. However, once Alzheimer's disease has been diagnosed, the only therapeutic options widely available are to preserve the remaining brain function by reinforcing the endogenous cholinergic synaptic pathway with inhibitors of cholinesterase that hydrolyzes the neurotransmitter acetylcholine and to minimize neuronal death caused by overexcitation by blocking glutaminergic synaptic pathways.

7.4.6
Diabetes: Malfunction of Blood Sugar Regulation

Diabetes mellitus is a group of diseases affecting glucose metabolism. Glucose, a primary cellular energy source, is transported from the extracellular medium to the

cell interior across the cell membrane by the action of specific glucose transport proteins. The glucose uptake facilitated by selected glucose transporters in the liver, muscle, and fat cells is enhanced by the peptide hormone insulin released from the β cells in the islets of Langerhans in the pancreas. The insulin release into the blood occurs in a fluctuating and pulsatory manner from the β cells in response to many stimuli, including the blood glucose level. The mechanism of glucose utilization is disrupted in type 1 and type 2 diabetes mellitus in different ways, both resulting in hyperglycemia, an increase in blood glucose level. Among the initial symptoms useful for diagnosis of diabetes are the presence of glucose in the urine (glycosuria), frequent urination (osmotic diuresis), and subsequent dehydration.

Type 1 diabetes, sometimes referred to as juvenile diabetes as its symptoms typically but not exclusively develop relatively early in life, is accompanied by hypoinsulinemia caused by the destruction of insulin-secreting β cells. Without insulin to stimulate glucose transport into cells, the blood glucose level remains elevated and cells are forced to utilize an alternative energy source. In particular, the liver cells breakdown stored fat into fatty acids and ketone bodies, the latter of which in turn cause acidification of the blood known as diabetic ketoacidosis. The underlying cause or etiology of destruction of the insulin-secreting β cell observed in type 1 diabetes is not well understood, but it is clearly autoimmune in nature with the pathogenesis process taking place over days to weeks, possibly precipitated by viral infection. The hyperglycemia in type 1 diabetes can be managed by exogenous insulin by injections of insulin or through an insulin pump; however, a cure itself is not currently available but cell replacement therapy using stem cells holds promise.

In type 2 diabetes patients, β cells typically remain intact and insulin is released at least initially but cells in the body fail to respond to insulin: insulin resistance. Without the uptake of glucose normally observed, hyperglycemia results even in the presence of normal or sometimes greater than normal levels of insulin. Many type 2 diabetic patients are obese and may also suffer from metabolic syndrome. Epidemiologically, the incidence of type 2 diabetes, by far the most common form of diabetes (>90%), has increased noticeably in recent years. It is speculated that some lifestyle habits increase whereas others lower the disease risk. The molecular etiology of type 2 diabetes remains elusive; however, several classes of therapeutic agents targeting different aspects of the glucose regulatory pathway have been developed. For example, sulfonylureas facilitate insulin secretion from the β cells by inhibiting their plasma membrane ATP-dependent K^+ channels that otherwise keep the cells electrically inactive. Thiazolidinediones, in contrast, enter the insulin-target cell nucleus and alter gene expression to increase the insulin sensitivity.

Long-term consequences of hyperglycemia in untreated diabetes are numerous and serious, often leading to kidney failure, atherosclerosis, neuropathy, limb amputation, and blindness. Many of the complications are consequences of the vascular abnormalities caused by excess nonenzymatic glycosylation of serum proteins. Accordingly, measurement of glycosylated hemoglobin (HgA1c) is frequently used to monitor the disease progression in diabetic patients. Our understanding of the physiology and pathophysiology of blood glucose regulation has been

aided by several biophotonic approaches. Time- and spatially resolved fluorescence microscopy has been used successfully to monitor the exocytotic release of insulin from β cells. Clinically, portable devices based on near-infrared diffuse reflectance spectroscopy may allow noninvasive monitoring of blood glucose levels.

7.4.7
Personalized Medicine and Outlook

Each and every one of us is different: no two individuals are exactly alike in their genomic makeup, epigenetic makeup, and environmental experience. The effectiveness of a given medical intervention, whether preventive or curative, could vary from one individual to the next and an ideal therapeutic plan should be tailored to each person – *personalized medicine*. The premise of personalized medicine based on the molecular genetic mechanistic knowledge and its promise are obvious. Some genetic variations may increase the risk of developing a disease; establishment of proper genetic markers may permit earlier screening and detection. Other genetic variations may influence how well patients respond to different drugs – *pharmacogenomics*. Ineffective drugs with adverse off-target effects could be avoided and only the most effective drugs could be administered. Although the potential of personalized medicine is vast, its implementation, with notable exceptions in the field of oncology noted earlier, will require additional effort. The reasons for this challenge are manifold. One of the cornerstones in the implementation of personalized medicine is to develop reliable disease and therapeutic biomarkers, and this is not an easy task. Many genes may contribute to the overall risk of developing a disease and each of the single nucleotide variations may make only a minor contribution to the risk. The development of epigenetic biomarkers, such as DNA methylation and histone acetylation, is still in its infancy. Undoubtedly, personalized medicine based on the molecular genetic information will be complemented with other promising therapeutic approaches, including stem cell-based regenerative medicine. In many of these new therapeutic paradigms, biophotonics is expected to play a leading role – mostly with respect to diagnosis but likely also in some therapeutic strategies.

References

1 Stryer, L. (1988) *Biochemistry*, 3rd edn, Freeman, New York.
2 Alberts, B., Bray, D., Lewis, J., Raff, M., Roberts, K., and Watson, J.D. (2002) *Molecular Biology of the Cell*, Garland Publishing, New York.
3 Voet, D., Voet, J.G., and Pratt, C.W. (2006) *Fundamentals of Biochemistry – Live at the Molecular Level*, 2nd edn, John Wiley & Sons, Inc., Hoboken, NJ.
4 Kyte, J., and Doolittle, R.F. (1982) A simple method for displaying the hydropathic character of a protein. *J. Mol. Biol.*, **157**, 105–132.
5 Cockcroft, S. (2006) The latest phospholipase c, plc, is implicated in neuronal function. *Trends Biochem. Sci.*, **31**, 4–7.
6 Russel, R.B. (2002) Classification of protein folds. *Mol. Biotechnol.*, **20**, 17–28.

7 Thornton, J.M., Orengo, C.A., Todd, A.E., and Pearl, F.M.G. (1999) Protein folds, functions and evolution. *J. Mol. Biol.*, **293**, 333–342.

8 Cuff, A.L., Sillitoe, I., Lewis, T., Redfern, O.C., Garratt, R., Thornton, J., and Orengo, C.A. (2009) The cath classification revisited – architectures reviewed and new ways to characterize structural divergence in superfamilies. *Nucleic Acids Res.*, **37**, D310.

9 Shaner, N.C., Steinbach, P.A., and Tsien, R.Y. (2005) A guide to choosing fluorescent proteins. *Nat. Methods*, **2**, 905–909.

10 Kandel, E.R., Schwartz, J.H., and Jessell, T.M., (1991) *Principles of Neural Science*, Elsevier, New York.

1
Microscopic and Spectroscopic Methods

Brent D. Cameron

Microscopy is a term used to refer to methods that allow for the visual examination of the physical properties of a sample on a micron-level scale. Although there are a wide variety of microscopic methods ranging from optical to electron microscopy, the focus of this chapter will concentrate on light-based methods. Although microscopy by itself sheds insight into the physical structure of a sample, optical spectroscopic methods, which concentrate on how photons of light interact with a sample (e.g., absorbed or scattered), can be used to examine a sample's chemical structure. Spectroscopic methods can be performed using single-point measurements or integrated with microscopic methods to allow for chemical imaging; also known as microspectroscopy.

1.1
Bright Field Microscopy

One of the most basic microscopy techniques is known as bright field microscopy. In this approach, sample illumination occurs in transmission mode through the bottom of the sample under investigation. Visual observation of the sample occurs from the top through standard microscope optics to allow for image magnification up to 1000×. Although this is one of the most common microscopy methods, bright field microscopy suffers from contrast limitations and often has difficulty with thick samples [1], as a considerable amount of the sample under investigation will be out of focus, which hinders the image resolution. Bright field microscopy often requires samples to be stained or have sufficient natural pigmentation to allow for proper viewing [1, 2]. This approach is also well suited for visualization of living preparations, such as single-cell organisms.

1.2
Dark Field Microscopy

To deal with some of the contrast issues associated with bright field imaging, especially when dealing with unstained samples, dark field microscopy is commonly

Handbook of Biophotonics. Vol.2: Photonics for Health Care, First Edition. Edited by Jürgen Popp, Valery V. Tuchin, Arthur Chiou, and Stefan Heinemann.

employed. For this approach, the configuration uses an opaque disc placed in front of the light source and behind the condenser lens [1, 2]. At this point, the light interacts with the sample and only the scattered light is collected due to a direct light block. This method can significantly improve image contrast and does not require sample staining [1]. This technique, however, is limited in terms of the intensity of the image and therefore often requires very intense illumination, which may degrade or damage the sample. Dark field configurations are commonly used as low-cost alternatives to phase contrast approaches.

1.3 Phase Contrast Microscopy

When working with biological specimens, a significant amount of the detail is undetectable when using bright field microscopy due to contrast limitations, especially for microstructures with similar pigmentation or transparencies. In 1934, a Dutch physicist, Frits Zernike, described a technique known as phase contrast microscopy. This approach can greatly enhance the contrast of transparent samples, such as microstructures contained in living cells, microorganisms, and thin tissues [3]. The phase contrast method translates minute variations in a specimen's refractive indices, which alters the phase relationships within the electric field of light into corresponding changes in amplitude [1–4]. These changes can then be visualized as differences in image contrast, and therefore details that would normally be transparent or invisible in bright field imaging can now be easily observed. Furthermore, living cells can be examined in their natural state without being fixed and/or stained. Such ability allows the dynamics of various biological processes to be observed and recorded in significant detail.

In terms of implementation, light is focused on to a specialized annulus positioned in the condenser prior to the sample (i.e., front focal plane) [1]. The light then illuminates the sample, at which point it will either pass straight through (i.e., unaltered) or will be diffracted and/or retarded in phase by structures in the specimen. Both the undeviated and diffracted light collected by the objective is then segregated at the back focal plane by a phase plate and focused on to an intermediate image plane to form the final phase contrast image. It should be noted that without the phase plate, there would be no destructive interference and therefore no significant improvement in contrast. The phase plate allows for the slight phase variations to be converted into visible amplitude changes, which provide for the contrast enhancement.

1.4 Differential Interference Contrast Microscopy

Differential interference contrast (DIC) microscopy is another technique used to improve the contrast of highly transparent or unstained samples. DIC microscopy is

somewhat similar to phase contrast microscopy in that it converts changes in the phase shift of the electric field of light, due to variations in refractive index, into detectable intensity or amplitude changes. The resulting image is similar; however, it is not plagued by the sometimes distracting bright diffraction halo [3, 5]. DIC microscopy also depicts differences in optical density as something like a three-dimensional relief image, although this sometimes may not entirely correctly represent actuality, as the occurrence is due to an optical effect instead of physical geometry.

With regard to implementation, the illumination source is initially linearly polarized at an angle of 45° and enters an optical component known as a Nomarski-modified Wollaston prism [5]. This component separates the light into its two orthogonal polarization components. One ray will be used as the sampling ray and the other as a reference. The microscope condenser focuses the rays through the sample; however, they will be slightly spatially offset to each other. Therefore, the rays may experience slightly different refractive indices and/or sample thicknesses, resulting in different optical pathlengths. The resulting rays are then focused by an objective lens and travel through a second Nomarski–Wollaston prism, which recombines the beams. At this point, the rays will interfere with each other, either constructively or destructively, leading to either bright or dark enhancements, respectively, depending on the corresponding optical path difference.

1.5
Confocal Microscopy

One of the most significant advances in the field of optical microscopy was the development of confocal microscopy. The popularity of this approach lies in its ability to examine the three-dimensional structure of thick biological samples. Confocal microscopy produces an optical image using an alternative approach to the traditional wide-field microscope. This method relies on the use of a scanning point approach instead of full sample illumination, which provides slightly higher resolution and considerable enhancement in the optical sectioning of the sample by eliminating the influence of out-of-focus light that would otherwise distort the image [6, 7]. In applications where it is desired to investigate the three-dimensional structure of a sample, confocal microscopy is commonly employed. Lastly, in terms of implementation, confocal microscopy may be combined with fluorescence spectroscopy, which allows for further exploration of biological samples.

1.6
Fluorescence Spectroscopy

Fluorescence spectroscopy is a popular research method used in biomedical research and clinical pathology. Applications include organic compound analysis,

DNA sequencing, the study of protein conformational changes, medical diagnostics, and so on. Although fluorescence measurements can be performed using single-point detectors, image-based analysis is very commonplace today. Fluorescence imaging/microscopy can provide for localization of intracellular compounds and in certain implementations detection at the level of single molecules.

Fluorescence is related to the luminescence family of processes in which certain molecules have the ability to emit light when they are in an excited state. The two categories of luminescence include fluorescence and phosphorescence, which specifically depend on the electronic configuration of the excited state and the emission pathway [8, 9]. Specifically, fluorescence is a property of certain molecules (e.g., aromatic molecules) that absorb light at a given wavelength which excites the species from its ground state to one of the various vibrational levels in an excited electronic state [8]. When the molecule falls back to a specific vibrational level of the ground state, a photon of light will be emitted in the process. Depending on the energy level in the drop, this will determine the frequency or wavelength of light emitted. Therefore, by measuring the emitted wavelengths (i.e., emission spectra) along with their respective intensities, significant information about the molecule under investigation can be determined.

In fluorescence microscopy, the fluorescence emission can be characterized not only by intensity and spatial position, but also by lifetime [10], polarization, and wavelength. Therefore, fluorescence microscopy is commonly performed using a variety of configurations. Some of these configurations include epifluorescence or incident light fluorescence [8], laser scanning fluorescence [6], confocal fluorescence [6], fluorescence lifetime imaging [10], and two-photon excitation fluorescence microscopy [11].

1.7 Infrared Spectroscopy

Infrared (IR) spectroscopy is a well-established technique for the identification of organic molecules. Specifically, it is a subcategory of spectroscopy which employs the IR region of the electromagnetic spectrum, which is normally broken up into the near-infrared (NIR) (0.78–2.5 μm), mid-infrared (MIR) (2.5–50 μm), and far-infrared (FIR) (50–1000 μm) spectral regions [12]. The method is based on vibrations of atoms within a molecule. For analysis, an IR spectrum is normally obtained by passing IR radiation through a sample and then determining which wavelengths are absorbed and to what extent. From this analysis, considerable information on the molecular and bonding structure of the sample can be determined. For biological analysis, IR spectroscopy allows for detailed examination of complex biomolecules, including proteins, lipids, carbohydrates, and nucleic acids [13].

In terms of implementation, the two main methods include a dispersive approach and the more common Fourier transform infrared (FTIR) spectrometer configuration, which is based on optical interference [12]. Detection can be made as

single-point, line, or image-based measurements. MIR spectroscopy can distinguish very subtle changes in chemical structure and therefore often this range is used in the identification of unknown substances. However, since this region of the electromagnetic spectrum is highly subject to water absorption, analysis of aqueous samples can prove extremely difficult and often requires alternative sample preparation (e.g., desiccation) or alternative sampling methods such as attenuated total reflectance (ATR). NIR spectroscopy is better suited to handle aqueous samples and is more commonly employed for applications in medical diagnostics, pharmaceutical analysis, and biological investigations [13–15]. NIR spectra consist of molecular overtones and combination bands of the fundamental molecular absorptions found in the MIR region. Therefore, NIR spectra generally consist of overlapping vibrational bands that may appear nonspecific and/or difficult to resolve. However, through the use of chemometric multivariate processing techniques, both qualitative and quantitative analyses have proven fairly successful [16, 17].

1.8 Raman Spectroscopy

Raman spectroscopy has become an important analytical tool in a multitude of research disciplines. It can be used for applications ranging through pharmaceuticals, forensics, DNA analysis, and medical diagnostics [18, 19]. The technique can provide significant information that may be used for chemical identification, bonding effect analysis, and characterization of molecular structures. Raman spectroscopy is a powerful light-scattering technique, which in simple terms can be thought of as a process in which a photon of light at a specific wavelength interacts with a sample and scattered light at different wavelengths result. This scattered light can then be analyzed to characterize the internal structure of molecules.

More specifically, Raman emissions are generated based on the concept of inelastic scattering of monochromatic light. The source excitation is usually provided by a laser source in the visible to NIR region of the electromagnetic spectrum [20]. In the case of inelastic scattering, depending on the molecular and bonding structure of the sample, a small amount of the light will experience a change in energy. In the case of reduced energy, longer wavelengths will be emitted that are unique to the sample. These are referred to as the Stokes bands and are more commonly used for analysis. In the case of higher energy (due to the molecule already being in an excited vibrational state), shorter wavelengths will be emitted, also unique to the sample. These are commonly referred to as the anti-Stokes bands. Inelastic scatter is very uncommon and accounts for only about 0.001% of the scattered light coming from the sample; most of the light is elastically scattered at the same wavelength of the excitation source.

As with IR spectroscopy, in terms of implementation, the two main methods include a dispersive approach and a Fourier transform (FT) spectrometer configu-

ration [20]. The information contained in Raman spectra is commonly complementary to MIR absorption spectroscopy and both organic and inorganic materials possess Raman spectra. These normally include sharp bands that are representative of the chemical structure of the sample under investigation. It should be noted, however, that since Raman measurements are commonly collected in the visible range of the electromagnetic spectrum, sample autofluorescence can sometimes mask the weak Raman signature, especially for biological samples [21]. Moving the excitation source out to the NIR region can normally help minimize this effect. A main benefit of Raman measurements compared with MIR spectroscopy is that the sample requires little to no preparation and water absorption is not a problem (i.e., sample desiccation is not required), hence the approach is well suited to biological samples.

It should be noted that several variations of Raman spectroscopy are used in practice. These variants are usually implemented to improve sensitivity or spatial resolution, or to acquire specific types of information. Some of these techniques include surface-enhanced Raman spectroscopy (SERS), Raman optical activity (ROA), coherent anti-Stokes Raman spectroscopy (CARS), and resonance Raman spectroscopy [21].

References

1 Leng, Y. (2008) *Materials Characterization: Introduction to Microscopic and Spectroscopic Methods*, John Wiley & Sons (Asia) Pte. Ltd., Singapore.

2 Bradbury, S. and Bracegirdle, B. (1998) *Introduction to Light Microscopy*, BIOS Scientific Publishers, Oxford.

3 Ruzin, S.E. (1999) *Plant Microtechnique and Microscopy*, Oxford University Press, New York.

4 Bennett, A., Osterberg, H., Jupnik, H., and Richards, O. (1951) *Phase Microscopy: Principles and Applications*, John Wiley and Sons, Inc., New York.

5 Murphy, D. (2001) *Fundamentals of Light Microscopy and Digital Imaging*, Wiley-Liss, New York.

6 Pawley, J.B. (ed.) (1995) *Handbook of Biological Confocal Microscopy*, Plenum Press, New York.

7 Wilson, T. (ed.) (1990) *Confocal Microscopy*, Academic Press, London.

8 Lakowicz, J.R. (2006) *Principles of Fluorescence Spectroscopy*, Springer, New York.

9 Rost, F. (1991) *Quantitative Fluorescence Microscopy*, Cambridge University Press, Cambridge.

10 Suhling, K., French, P.M., and Phillips, D. (2005) Time-resolved fluorescence microscopy. *Phtochem. Photobiol. Sci.*, **4** (1), 13–22.

11 So, P.T., Dong, C.Y., Masters, B.R., and Berland, K.M. (2000) Two-photon excitation fluorescence microscopy. *Annu. Rev. Biomed. Eng.*, **2**, 399.

12 Hsu, C.P.S. (1997) Infrared spectroscopy, in *Handbook of Instrumental Techniques for Analytical Chemistry* (ed. F. Settle), Prentice Hall, Englewood Cliffs, NJ, pp. 247–283.

13 Manitsch, H.H. and Casal, H.L. (1986) Biological applications of infrared spectrometry. *Fresenius' Z. Anal. Chem.*, **324**, 655–661.

14 Burns, D. and Ciurczak, E. (2001) *Handbook of Near-Infrared Analysis*, Marcel Dekker, New York.

15 Ciurczak, E. and Drennen, J. (2002) *Near-Infrared Spectroscopy in Pharmaceutical and Medical Applications*, Marcel Dekker, New York.

16 Martens, H. and Naes, T. (1992) *Multivariate Calibration*, John Wiley and Sons, Ltd., Chichester.

17 Mark, H. and Workman, J. (2003) *Statistics in Spectroscopy*, Elsevier, Amsterdam.

18 Choo-Smith, L.P., Edwards, H.G., Endtz, H.P., Kros, J.M., Heule, F., Barr, H., Robinson, J.S. Jr., Bruining, H.A., and Puppels, G.J. (2002) Medical applications of Raman spectroscopy: from proof of principle to clinical implementation. *Biopolymers*, **67** (1), 1–9.

19 Shih, W., Bechtel, K.L., and Feld, M.S. (2008) Quantitative biological Raman spectroscopy, in *Handbook of Optical Sensing of Glucose in Biological Fluids and Tissues* (ed. V.V. Tuchin), Taylor & Francis, Abingdon, pp. 354–381.

20 Colthup, N.B., Daly, L.H., and Wiberley, S.E. (1990) *Introduction to Infrared and Raman Spectroscopy*, Academic Press, New York.

21 Laserna, J.J. (ed.) (1996) *Modern Techniques in Raman Spectroscopy*, John Wiley and Sons, Ltd., Chichester.

2
Glucose Sensing and Glucose Determination Using Fluorescent Probes

Mark-Steven Steiner, Axel Duerkop, and Otto S. Wolfbeis

2.1
Why Glucose Sensing?

The measurement of glucose is among the most important analytical tasks. It has been estimated that about 40% of all blood tests are related to it. In addition, there are numerous other situations where glucose is to be determined, for example, in biotechnology, the production and processing of all kinds of food, in biochemistry in general, and in numerous other areas. The continuing interest in sensing glucose, mainly in blood, is one result of the increasing age and (alarming) size of the world's population, and the fact that about 4% of its (Caucasian) population suffers from diabetes. Normal blood glucose levels range from 3 to 10 mM (54–180 mg dl^{-1}).

The market for glucose sensors is probably the biggest single one in the diagnostic field, its size being about US$40 billion per year at present. Given this size, it does not come as a surprise that any true improvement in sensing glucose represents a major step forward. The greatest need at present is, however, for continuous sensors.

Both optical and electrochemical sensors can be manufactured at costs that are so low that they can also be of the disposable type. Clinical multiparametric instrumentation (e.g., for sensing glucose and blood parameters such as pO_2, pH, Na^+, K^+, Cl^-, lactate, and urea) relies on reusable sensors. In this case, a blood sample is inserted into the instrument, a reading is made, the surface of the sensor is washed, and the sensor is recalibrated before the next sample is introduced. Electrochemical methods are mainly used in stand-alone instruments in clinical laboratories and in near-patient testing. Millions of disposable electrochemical (mediator-based) blood glucose meters are used in homecare devices that enable glucose to be determined within less than 1 min in blood samples as small as 0.3 µl [1]. Electrical wiring of enzymes [2] has led to smaller quantities of blood being taken, thus leading to almost painless sampling in a new generation of glucose sensors that have had tremendous commercial success.

Optical methods are based on the measurement of photons rather than of electrons. The absence of electrodes can be advantageous in the case of patients with heart pacemakers. Although optical schemes for sensing glucose have not had

Handbook of Biophotonics. Vol.2: Photonics for Health Care, First Edition. Edited by Jürgen Popp, Valery V. Tuchin, Arthur Chiou, and Stefan Heinemann.

the success of electrochemical schemes, they still are a topic of highly active research. In addition to color test strips, a couple of reversible optical sensors rely on the measurement of the consumption of oxygen. Among the optical methods, photometry (and reflectometry), fluorescence, and surface plasmon resonance (SPR) have had the greatest success. Almost all optical sensors for continuous monitoring rely on either fluorescence or SPR. Not a single reflectometric method is known for use in continuous sensing. This chapter is restricted to luminescence-based methods.

2.2 Classification of Sensors According to the Recognition Scheme

This review is subdivided into sections according to the method for recognition of glucose. Once selective recognition of glucose has occurred, it has to be transduced into (optical) information. The first fundamental type of glucose sensor is based on the recognition of glucose by certain enzymes (or coenzymes) that subsequently undergo changes in their intrinsic absorption and/or fluorescence, or carry a label placed near the site of interaction and capable of reporting the interaction with glucose. The second class of sensors measure (kinetically) the formation/consumption of metabolites of enzyme activity, mainly of glucose oxidase (GOx). One scheme is based on the measurement of the quantity of oxygen consumed according to Eq. (2.1). Alternatively, the hydrogen peroxide (HP) formed according to Eq. (2.1) may be determined by electrochemical or optical means. A third option consists in the determination of the quantity of protons formed (i.e., the decrease in pH) [Eq. (2.2)].

$$\beta\text{-D-glucose} + O_2 \rightarrow \text{D-glucono-1, 5-lactone} + H_2O_2 \tag{2.1}$$

$$\text{D-glucono-1, 5-lactone} + H_2O \rightarrow \text{gluconate} + H^+ \tag{2.2}$$

The enzyme glucose dehydrogenase has also been used. It catalyzes the conversion of glucose to form NADH according to

$$\beta\text{-D-glucose} + NAD^+ \rightarrow \text{D-glucono-1, 5-lactone} + NADH \tag{2.3}$$

The amount of NADH formed according to Eq. (2.3) may be measured, for example, by photometry at 345 nm or by measuring its fluorescence peaking at 455 nm, but this reaction is not reversible and comes to an end once all the NAD^+ has been consumed. Hence it is less suited (and less elegant) in terms of continuous sensing.

The third large group of sensors relies on organic boronic acids that act as molecular receptors for 1,2-diols and saccharides. The high affinity of boronic acids towards saccharides facilitates recognition of glucose levels in blood samples (3–50 mM). When coupled to a conjugated π-system (a dye), these show a change in the optical properties as a result of binding glucose [3, 4]. The fourth large group of receptors exploits the capability of glucose-binding proteins (GBPs) to bind glucose with high specificity. This includes concanavalin A (ConA) based sensor schemes and apo-GOx, a glucose oxidase whose coenzyme has been removed. On binding glucose,

some proteins undergo changes in their intrinsic optical properties in the ultraviolet (UV) region. In order to shift analytical wavelengths into the (longwave) visible region, they have been labeled with fluorophores. Methods based on labeled proteins are preferred because the choice of a proper label enables the optical properties of the system to be fine-tuned.

2.3 Glucose Sensing via the Optical Properties of Oxidative or Reductive Enzymes

2.3.1 Nonlabeled Enzymes

The first group of recognition schemes comprises enzymes and coenzymes that undergo optical changes in their spectral properties (e.g., GOx [5, 6], glucose dehydrogenase, glucokinase [7], and apo-GOx). The optical changes usually occur in the UV region (based on the intrinsic tryptophan fluorescence of GOx) and in the visible region [the coenzyme flavin adenine dinucleotide (FAD) [8] of GOx]. These respective enzymes have also been labeled with fluorophores in order to shift the analytical wavelength into the visible region. Longwave sensing is highly desirable in view of the reduced absorbance and fluorescence of blood and serum at >600 nm. Labeling usually does not strongly affect the binding constants of the enzymes.

$$\beta\text{-D-glucose} + \text{FAD} \rightarrow \text{D-glucono-1, 5-lactone} + \text{FADH}_2 \tag{2.4}$$

$$\text{FADH}_2 + \text{O}_2 \rightarrow \text{FAD} + \text{H}_2\text{O}_2 \tag{2.5}$$

$$\text{D-glucono-1, 5-lactone} + \text{H}_2\text{O} \rightarrow \text{gluconate} + \text{H}^+ \tag{2.6}$$

Changes of the intrinsic fluorescence may involve (a) the UV fluorescence of tryptophan groups [excitation/emission maxima ($\lambda_{ex}/\lambda_{em}$) at 295/330 nm] in the protein [5], (b) the fluorescence of FAD (Figure 2.1) ($\lambda_{ex}/\lambda_{em}$ 450/520 nm) [8], or (c) NAD^+ ($\lambda_{ex}/\lambda_{em}$ 340/460 nm) [9]. An interesting competitive FRET (Förster resonance energy transfer) assay was presented by D'Auria *et al.* [10]. They used the intrinsic tryptophan fluorescence of glucose kinase as donor whereas glucose derivatized with *o*-nitrophenyl-β-D-glucose-co-pyranoside is the acceptor. Addition of glucose increases donor emission and decreases FRET. The analytical range of these sensors is typically from 0.5 to 20 mM, and rarely up to 200 mM [7].

2.3.2 Labeled Enzymes

In addition to the intrinsic optical properties of glucose-specific enzymes, the optical properties of labels of the enzyme may be exploited. Fluorescein [11, 12] and coumarin [13] are among the most commonly used labels. Excitation at above 400 nm

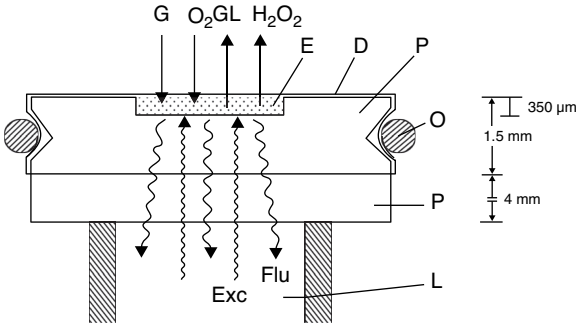

Figure 2.1 Cross-section through the sensing platelet of a fiber-optic glucose sensor. P, Plexiglas; D, dialyzing membrane; E, enzyme solution; O, O-ring; L, light guide. The arrows indicate the diffusion processes involved (G, glucose; GL, gluconolactone). The directions of the exciting light (Exc) and fluorescence (Flu) are also shown. The platelet has o.d. 20 mm; diameter of cavity, 4 mm [8]. Reprinted from W. Trettnak and O.S. Wolfbeis, Fully reversible fiber-optic glucose biosensor based on the intrinsic fluorescence of glucose oxidase, *Anal. Chim. Acta*, 1989, **221**, 195–203, with permission from Elsevier.

is more adequate for determination of glucose in real samples because of the ubiquitous UV absorption of proteins and other compounds in these samples.

2.4
Fluorescent Sensing of Glucose via Measurement of the Consumption of Oxygen Caused by the Action of GOx

The measurement of the consumption of oxygen [Eq. (2.1)] via quenchable probes (luminescent complexes of ruthenium, platinum, or palladium) immobilized in a sensor layer together with the enzyme is a fairly successful approach. The sensors described in the literature differ from each other mainly in the kind of fluorescent probe and the type of polymer matrix [hydrogels, sol–gels, polystyrene (PS)]. Among the technical layouts, optodes (optical fibers with the sensor layer fixed at the tip) and planar sensors in microwells or in a microfluidic flow cell have been reported. Continuous sensing using such enzymes and reversible oxygen sensors became available in the 1980s.

2.4.1
Planar and Fiber-Optic Sensors

The luminescence of probes such as decacyclene [14], complexes of Pt(II) [15, 16] or Pd(II) with porphyrins, Ru(phen) [17], Ru(bpy) [18] and Ru(dpp) [19], and Al-Ferron [20] have been reported to be quenched by molecular oxygen. The metal complexes can be excited in the visible spectrum, show large Stokes shifts, and have comparatively long decay times and good photostability. The signal increases strongly

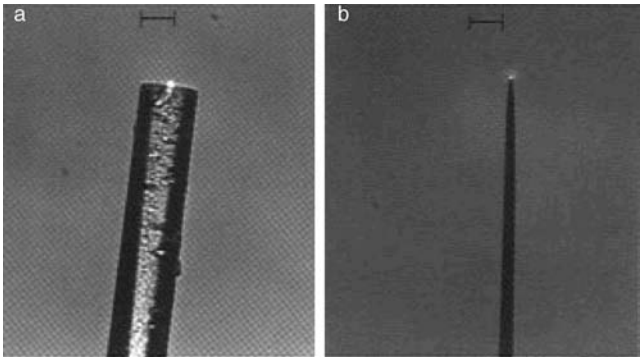

Figure 2.2 Photographs of fiber-optic glucose biosensors. (a) Sensor prepared from an unpulled, single-mode, 3–5 μm core optical fiber. The scale bar represents 50 μm. (b) Sensor prepared from a pulled, micrometer-sized optical fiber tip. The scale bar represents 10 μm [17]. Reprinted with permission from Z. Rosenzweig and R. Kopelman, Analytical properties and sensor size effects of a micrometer-sized optical fiber glucose biosensor, *Anal. Chem.*, 1996, **68**, 1408–1413. Copyright 1996 American Chemical Society.

on addition of glucose (because of the consumption of oxygen). Both fluorescence intensity and lifetime increase. Most common GOx–O_2 sensors consist of the enzyme immobilized on, or in a polymer film (2–5 μm), mostly a hydrogel or polyacrylamide (PAA) [17]. The oxygen-sensitive indicator dye is immobilized in a second polymer, preferably absorbed on silica gel beads, and incorporated in a silicone film [21]. This type of sensor with Ru(dpp) as the probe for oxygen is the only optical sensor produced commercially in very large numbers. Sensors are also known where the enzyme and dye are embedded in the same layer. The sensing layers are then attached to a support such as PS, controlled-pore glass (CPG) [15], or an optical fiber (Figure 2.2), and are often shielded by a diffusion barrier layer [22].

A fiber-optic dual sensor for the continuous and simultaneous determination of glucose and oxygen with $Ru(bpy)_3$ as O_2 transducer was described in 1995 [18]. The sensor comprises two sensing sites in defined positions on the distal end of an imaging fiber (Figure 2.3). Each sensing site contains an individual polymer cone covalently attached to the activated fiber surface using localized photopolymerization. The fluorescence images of both sensing sites are captured with a charge-coupled device (CCD) camera and oxygen quenching data for both sensing sites are fitted by a two-site Stern–Volmer quenching model. Within response times from 9 to 28 s, glucose can be detected in the range 0–20 mM with this self-referenced scheme.

Further glucose biosensors have used unusual supports (eggshell membranes or swim bladder membranes) on which GOx was immobilized [23, 24]. The glucose biosensor has a long shelf-life and was successfully applied to the determination of glucose in a beverage sample in a flow cell.

A limitation of oxygen-based detection schemes in general and oxygen-depleting detection schemes in particular is based on the varying background of oxygen in samples. This may be overcome by using a large excess of air-saturated buffer

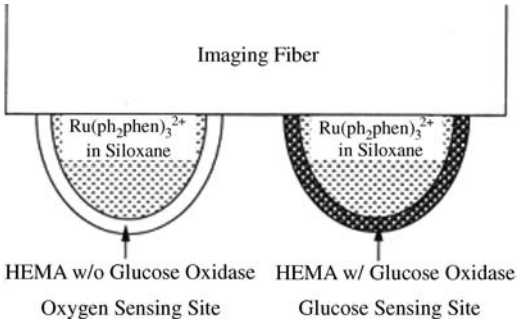

Figure 2.3 Schematic showing a cross-sectional view of the glucose and oxygen sensing sites of a fiber-optic dual sensor for the continuous and simultaneous determination of glucose [18]. Reprinted with permission from L. Li and D.R. Walt, Dual-analyte fiber-optic sensor for the simultaneous and continuous measurement of glucose and oxygen, *Anal. Chem.*, 1995, **67**, 3746–3752. Copyright 1995 American Chemical Society.

solution, or by compensating the variable oxygen background by determining it independently, for example, with a second sensor. This kind of dual sensor was reported first by Li and Walt [18], subsequently by Wolfbeis *et al.* [22], and more recently by Klimant's group [25, 26]. They used a dual sensor, consisting of two commercially available oxygen optodes in close proximity, where one had been modified with GOx and the other served as a reference (Figure 2.4). This sensor is unaffected by fluctuations of the oxygen concentration in the sample and also allows for the compensation of slight temperature fluctuations. Comparable sensor schemes have been patented [27–29].

2.4.2
Sensors Based on the Use of Microparticles (μPs) and Nanoparticles (NPs)

Particle-based sensors have attracted substantial interest for intracellular glucose testing in recent years. They may be applied in the future in the bloodstream as molecular analytical machines reporting blood glucose levels, provided that the optical signal they are giving can be interrogated. Xu *et al.* incorporated GOx, sulfo-Ru $(dpp)_3$ and Oregon Green 488–dextran (as a reference-dye) in 45 nm diameter PAA nanoparticles to obtain so-called PEBBLE sensors for self-referenced ratiometric measurements [30]. The PEBBLEs were implanted into living cells with minimal physical and chemical perturbations to their biological functions. Another implantable microsensor was reported by Brown and co-workers (Figure 2.5) [31, 32].

GOx and horseradish peroxidase (HRP) conjugated CdSe/ZnS core–shell quantum dots (QDs) were used for FRET-based glucose sensing. Upon irradiation, the QDs shuttle electrons to GOx and HRP, upon which they rapidly oxidize glucose to gluconic acid and reduce H_2O_2 (or O_2). This nonradiative energy transfer results in quenching of the QD emission proportional to the concentration of glucose up to 28 mM with a 30 min response time [33].

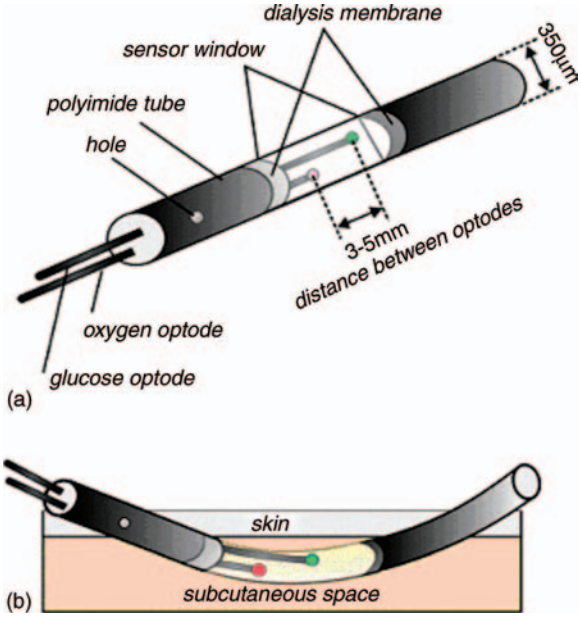

Figure 2.4 Schematic representation of (a) hybrid sensor and (b) implanted hybrid sensor [26]. Reprinted from A. Pasic, H. Koehler, I. Klimant, and L. Schaupp, Miniaturized fiber-optic hybrid sensor for continuous glucose monitoring in subcutaneous tissue, *Sens. Actuators B*, 2007, **122**, 60–68, with permission from Elsevier.

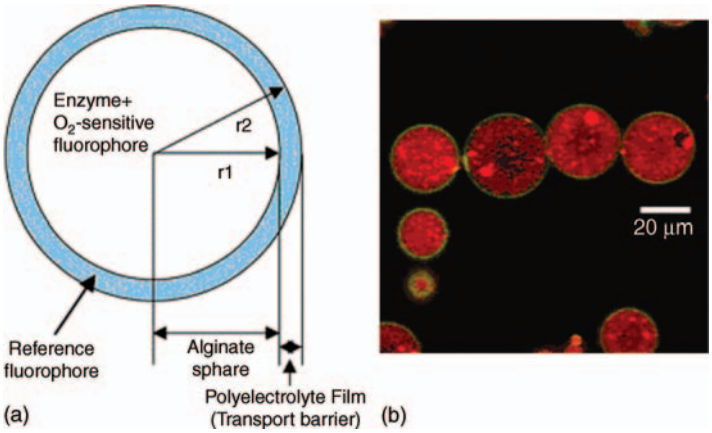

Figure 2.5 (a) Functional schematic of nanoengineered optical glucose sensors; (b) CLSM image of spheres used for glucose sensitivity experiments [31]. Reprinted from J.Q. Brown, R. Srivastava, and M.J. McShane, Encapsulation of glucose oxidase and an oxygen-quenched fluorophore in polyelectrolyte-coated calcium alginate microspheres as optical glucose sensor systems, *Biosens. Bioelectron.*, 2005, **21**, 212–216, with permission from Elsevier.

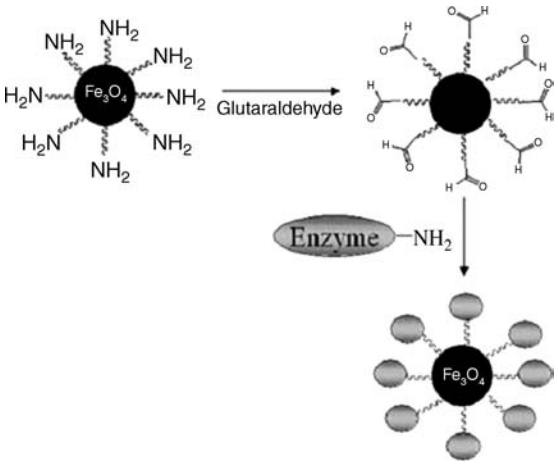

Figure 2.6 Covalent conjugation of glucose oxidase to amino-functionalized magnetic nanoparticles [34]. Reprinted from L.M. Rossi, A.D. Quach, and Z. Rosenzweig, Glucose oxidase–magnetite nanoparticle bioconjugate for glucose sensing, *Anal. Bioanal. Chem.*, 2004, **380**, 606, with permission from Springer Science + Business Media.

GOx-coated magnetite (Fe_3O_4) nanoparticles with $Ru(phen)_3$ can be used as nanometric glucose sensors in glucose solutions (Figure 2.6) [34]. This allows the magnetic separation of the nanoparticles from the analyte sample, permitting reuse in multiple samples.

The O_2 transducer is often influenced by temperature. This drawback can be compensated for by dual sensors that sense both oxygen and temperature [35]. Here, the oxygen probe Pt(porph) in a layer of PS and the europium complex $Eu(tta)_3(dpbt)$ in a layer of poly(vinyl methyl ketone) as the temperature probe allow dual lifetime determination to monitor the consumption of oxygen at varying temperatures. The layers lie upon one another on a polyester support.

2.5
Fluorescent Sensing of Glucose via Measurement of the Formation of Hydrogen Peroxide Caused by the Action of GOx

HP produced in the enzymatic reaction can be linked to the concentration of glucose, as shown in Eq. (2.1). Monitoring of HP has the advantage of a measurement against an almost zero background. Only few sensors for continuous mode operation have been reported.

A probe for HP was reported consisting of a conjugated cationic polymer incorporated with boronate-protected peroxyfluorescein. HP deprotects the fluorescein to create anionic fluorescein, which interacts electrostatically with the cationic fluorene. The FRET between fluorene (donor) and fluorescein (acceptor) can be used to monitor glucose in the nanomolar [36] to micromolar range [37].

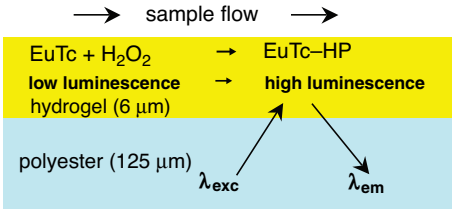

Figure 2.7 Cross-section of the membrane of a glucose biosensor using luminsecent EuTc–HP.

An enzymatic assay for glucose based on luminescent europium(III) tetracycline (EuTc) was described [38]. Weakly luminescent EuTc and enzymatically generated HP form a strongly luminescent complex (EuTc–HP). The probe can be excited at 400 nm and emits at 616 nm. It responds to HP by a 15-fold increase in luminescence and a strong increase in lifetime. This permits lifetime-based measurements of glucose with a substantially reduced luminescence background (Figure 2.7).

The reaction of EuTc with HP is fully reversible but takes about 10 min in both directions and is strongly pH dependent. The complex was used for time-resolved imaging of glucose [39]. Furthermore, GOx was covalently labeled to Mn-doped ZnS QDs. HP produced in the presence of glucose quenches the emission of the dots. The nanosensors were successfully applied to serum samples (Figure 2.8) [40].

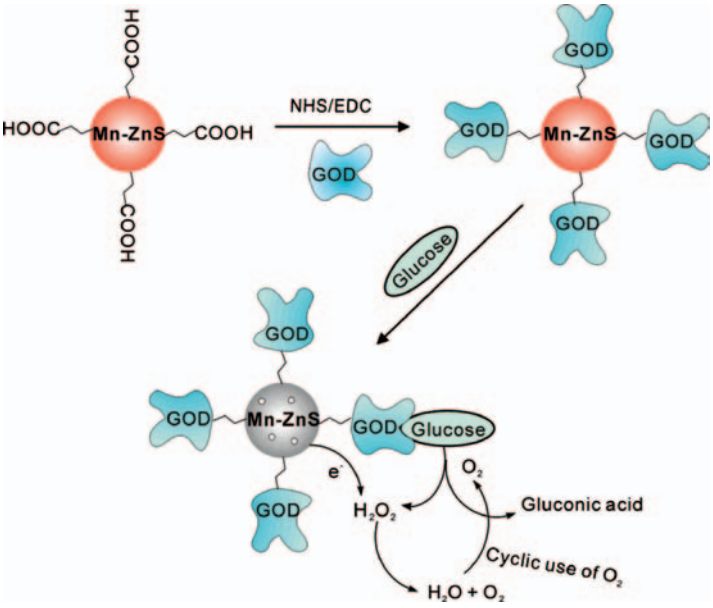

Figure 2.8 Schematic diagram for the preparation and application of GOx–Mn-doped ZnS QD bioconjugate for glucose sensing [40]. Reprinted with permission from P. Wu, Y. He, H.-F. Wang, and X.-P. Yan, Conjugation of glucose oxidase onto Mn-doped ZnS quantum dots for phosphorescent sensing of glucose in biological fluids, *Anal. Chem.*, 2010, **82**, 1427–1433. Copyright 2010 American Chemical Society.

2.6
Enzymatic Sensing of Glucose via Changes of pH

Changes of pH may also serve as analytical information to sense glucose according to Eq. (2.2). However, this approach is limited because often the initial pH of the sample and its buffer capacity are unknown. Therefore, only a few optical biosensors make use of pH transducers.

McCurley reported on a cadaverine unit linked to rhodamine that was incorporated into a hydrogel (along with GOx and catalase) placed at the end of an optical fiber [41]. The cadaverine moiety is protonated on the enzymatic reaction of glucose, which causes swelling of the hydrogel. This, in turn, decreases the fluorescence intensity of the rhodamine in the 0–1.6 mM glucose range.

Tohda and Gratzl [42] covalently immobilized GOx on cellulose acetate beads and embedded a pH-sensitive phenoxazine derivative in polymer microbeads. These beads, along with white reference beads, were arranged in a microarray to read the reversible color change caused by pH with a CCD camera. Another scheme comprises internally cationically charged biocompatible capsules containing the pH probe 8-hydroxypyrene-1,3,6-trisulfonic acid (HPTS) and electrostatically adsorbed GOx. pH changes induce ratiometric changes of emission spectra and are monitored as a function of glucose concentration in the physiological range [43]. Two different sensors with a pH-sensitive azlactone and GOx embedded in a sol–gel were reported [44]. A setup with immobilization of GOx and fluorescein isothiocyanate (FITC) as pH reporter in a polymer at the end of an optical fiber was patented by Applied Research Systems [45].

2.7
Fluorescent Sensing of Glucose via Synthetic Boronic Acids

Boronic acids can reversibly react with 1,2- or 1,3-diols in aqueous solution to form five- or six-membered cyclic esters. The state of the art in optical boronate probes for saccharides has been reviewed recently [3]. The rigid *cis*-diols found in many saccharides generally form stronger complexes than acyclic diols such as ethylene glycol and *trans*-diols. On binding a saccharide, the neutral trigonal boronic acid transforms into the anionic tetrahedral form and releases a proton (Figure 2.9). This change in geometry is accompanied by a reduction in the pK_a from ~9 to ~6 because the electrophilicity of the boronic acid group is enhanced on interaction with a diol. Hence the trigonal form is present at pH values below the pK_a but in the presence of a saccharide it is converted into its tetrahedral anionic form. The pK_a of the boronic acid is tunable to lower values with electron-withdrawing groups, whereas electron-donating groups increase the pK_a. When attached to an appropriate fluorophore, the changes in the symmetry of the boronic acid also induce changes in fluorescence emission (intensity, lifetime, and polarization). One fundamental disadvantage of most boronic acid-based probes for glucose sensing is either a higher selectivity for fructose than for glucose or/and a stronger response to fructose than to glucose.

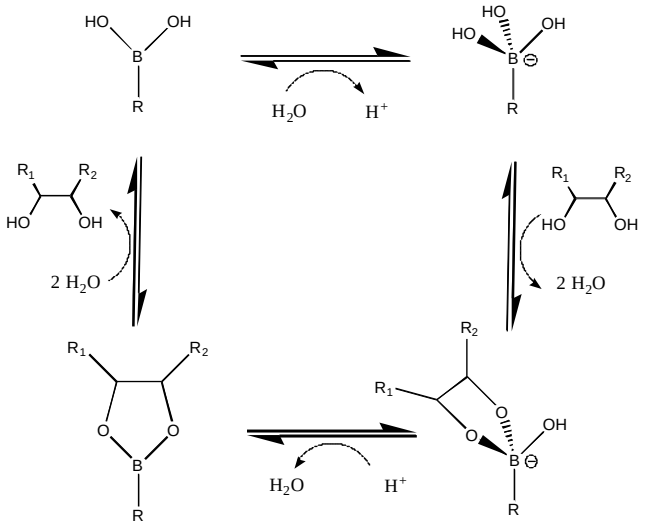

Figure 2.9 Geometries of reaction products of boronic acids with water or 1,2-diols (e.g., glucose).

Three quinoline-based probes for the determination of glucose in tear fluid were presented [46, 47]. The probes were structurally modified to allow compatibility with disposable plastic contact lenses. The sugar-bound pK_a is reduced, favorable with the mildly acidic lens environment. One probe shows a similar affinity for both glucose and fructose from the emission decrease at 450 nm. Glucose and fructose were determined at sub-millimolar levels with a response time of 10 min (Figure 2.10). The probe showed negligible leaching and was quenched only modestly by chloride.

Competitive assay schemes use the reversible interaction between Ru(2,2′-bipyridine)$_2$-(5,6-dihydroxy-1,10-phenanthroline) and arylboronic acid derivatives at pH 8 [48, 49]. Complexation is accompanied by a strong increase in fluorescence intensity at 620 nm. Addition of glucose reduces emission intensity because of intercepting the binding between boronic acid and the metal complex. The ruthenium complex may also be incorporated into a glucose-permeable and implantable polymer [50, 51].

Singaram and co-workers [52] reported on a two-component system comprising an anionic fluorescent dye and a cationic viologen quencher containing a bisboronic acid functionality to form a nonfluorescent ion pair. Their electrostatic interaction is reduced when a saccharide binds to the viologen to yield a negatively charged boronate ester and the fluorescence intensity is increased (Figure 2.11). A modular ensemble composed of three different viologen quenchers was also shown. The increase in luminescence of 11 anionic fluorescent dyes (e.g., HPTS) on addition of 12 saccharides in the presence of these three quenchers was determined and evaluated via two-dimensional linear discriminant analysis. Differentiation between glucose, fructose, mannose, and galactose at a concentration of 2 mM was accomplished [53].

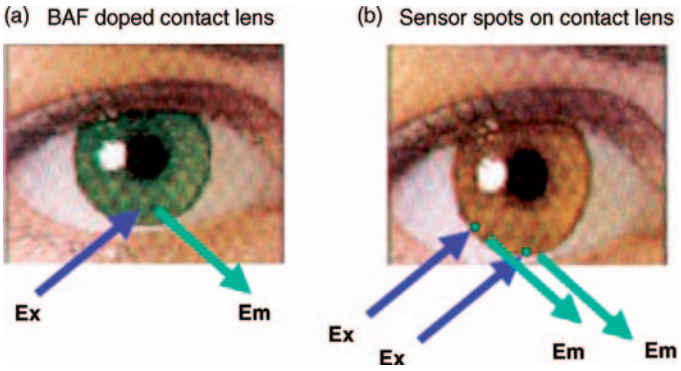

Figure 2.10 Potential methods for noninvasive continuous tear glucose monitoring. (a) Contact lens doped with optical probe for glucose. (b) Sensor spots on the surface of the lens to monitor additionally other analytes in addition to glucose, such as chloride or oxygen. Sensor spot regions may also allow for ratiometric, lifetime, or polarization based fluorescence glucose sensing [47]. Reprinted from R. Badugu, J.R. Lakowicz, and C.D. Geddes, A glucose sensing contact lens: a non-invasive technique for continuous physiological glucose monitoring, *J. Fluoresc.*, 2003, **13**, 371, with permission from Springer Science + Business Media.

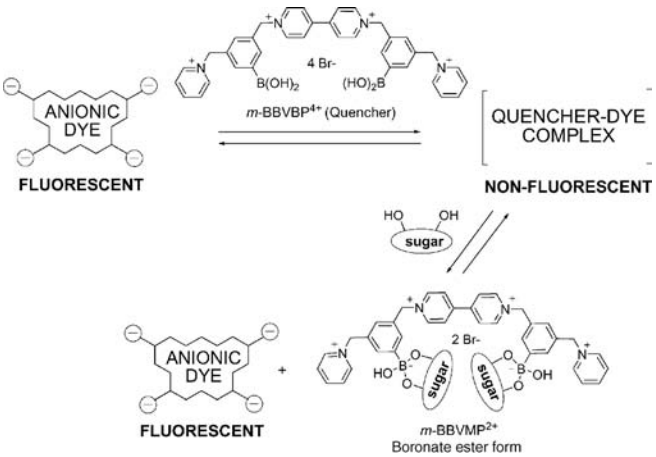

Figure 2.11 General sensing mechanism with the boronic acid-functionalized viologen quencher *m*-BBVBP^{4+} used as the saccharide receptor unit. Viologens quench the luminescence of dyes through an ionic attraction to form a nonfluorescent complex. Upon saccharide binding to the boronic acid of the viologen quencher, the negatively charged boronate ester causes a diminished electrostatic attraction resulting in a fluorescence increase [52]. Reproduced from D. B. Cordes, A. Miller, S. Gamsey, S. Zach, P. Thoniyot, R. Wessling, and B. Singaram, Optical glucose detection across the visible spectrum using anionic fluorescent dyes and a viologen quencher in a two-component saccharide sensing system, *Org. Biomol. Chem.*, 2005, **3**, 1708–1713, with permission from The Royal Society of Chemistry.

CdSe QDs were utilized as fluorescent reporters in combination with a viologen quencher with a boronic acid functionality as the glucose receptor. The fluorescence of the reporter is quenched by the viologen before addition of glucose. When glucose is added to the solution, the emission at 604 nm recovers. Both carboxy- and amino-substituted QDs are quenched by a viologen in aqueous solution at pH 7.4 [54].

2.8
Fluorescent Sensing of Glucose via Concanavalin A

ConA is a plant lectin protein originally extracted from jack beans. The ConA tetramer consists of two dimers and has four binding sites for glucose. Its specific function involves the agglutination of biologically relevant complexes such as glycoproteins, starches, and erythrocytes. ConA is used traditionally in a competitive assay where glucose and another carbohydrate such as dextran mannoside or glycated proteins compete for the lectin-binding sites. The protein and the competitor are generally labeled with appropriate fluorescent dyes. An inherent but often disregarded problem with ConA-based sensors regarding sensor stability is that unbound lectin tends to aggregate irreversibly over a period of some hours.

Schultz *et al.* [55] described a glucose sensor in which ConA is immobilized inside a hollow dialysis fiber connected to a fluorescence detection system by a single optical fiber. FITC-labeled dextran was the competing ligand to pass in and out of the fiber. Glucose displaces the competitor from ConA and increases the concentration of free dextran and, consequently, the fluorescence. Optimization steps comprised immobilization of ConA on Sepharose [56] and optical readout to reduce response times to 5 to 7 min [57].

Transdermal glucose monitoring was achieved [58] by confining Alexa488-labeled ConA and colored macroporous beads inside a sealed, small segment of a hollow-fiber dialysis membrane. Immobilized pendant glucose moieties inside the colored beads compete with glucose for binding of ConA. In the absence of glucose, the excitation and emission of Alexa488 is blocked. Glucose diffuses through the membrane into the sensor chamber and competitively displaces Alexa 488–ConA from the glucose residues of the beads. Consecutively, Alexa488–ConA is fully exposed to the excitation light, and the increase in fluorescence at 520 nm is measured (Figure 2.12). The sensor exhibits the strongest signal change between 0.2 and 30 mM, with a response time of around 4 min. *In vivo* tests were conducted with a ratiometric FRET system consisting of Cy7-labeled agarose-immobilized ConA as acceptor/quencher and unbound Alexa647–dextran as donor. In the absence of glucose, dextran is bound to ConA, therefore both are in close proximity, enabling a FRET. Glucose displaces dextran from ConA, which results in decreased FRET and an increase in Alexa647 fluorescence at 670 nm. *In vivo* tests with a small hollow fiber implanted in dermal skin tissue revealed a delay of 5–15 min in actual blood glucose concentrations [59]. PreciSense has patented a similar but lifetime-based sensor setup [60].

A hollow-fiber setup [61] uses FRET between rhodamine-labeled ConA and fluorescein-labeled dextran. The emission of dextran is restored on addition of

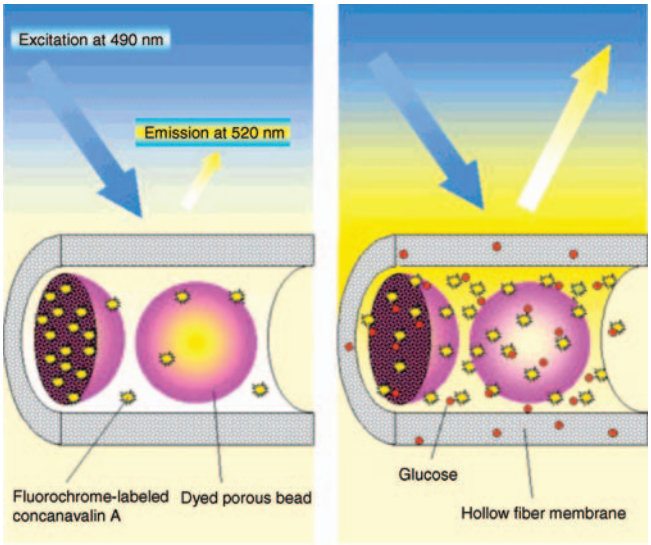

Figure 2.12 In the absence of glucose, fluorochrome-labeled ConA is bound to fixed glucose residues inside the porous beads (a) in a hollow fiber. The beads are colored with dyes to prevent the excitation light from penetrating into them and inducing ConA to fluoresce, thus keeping the fluorescence emission at 520 nm. After diffusion of glucose through the hollow-fiber membrane, ConA is displaced from the beads and diffuses out of them, and hereby fluorochrome-labeled ConA becomes exposed to excitation light, resulting in a strong increase in fluorescence (b) [58]. Reprinted with permission from R. Ballerstadt and J.S. Schultz, A fluorescence affinity hollow fiber sensor for continuous transdermal glucose monitoring, *Anal. Chem.*, 2000, **72**, 4185–4192. Copyright 2000 American Chemical Society.

glucose due to competitive displacement. Novartis has patented a related sensor that can be incorporated into a contact lens and an apparatus to irradiate the sensor dyes and detect FRET [62]. Cheung *et al.* [63] reported on a similar system in microplates (MTP). Donor and acceptor were incorporated into hydrogel pads that were then attached to hydrophobic surfaces of the wells of a microtiter plate (Figure 2.13). A layer-by-layer (LbL) self-assembly process was used to coat the surface of the hydrogel pads with polyelectrolyte multilayers with the aim of creating a permeability-controlled membrane with nanometer thickness. LbL hydrogel pads allow regeneration within 17 min with a signal reproducibility of more than 90% to yield a reusable and reagentless optical bioassay platform.

Birch and co-workers developed a non-radiative FRET sensing setup [64]. Con A was labeled with the NIR fluorescent protein allophycocyanin (APC) as donor and dextran labeled with Malachite Green (MG) as acceptor, which shields APC emission as long as dextran is bound to the lectin. Glucose competitively displaces dextran–MG and leads to restoration of the APC fluorescence at 663 nm, quantified by time-domain fluorescence lifetime measurements. Another setup exploits the luminescence decay time of Cy5-labeled ConA [65] as a FRET donor. The acceptor consisted of

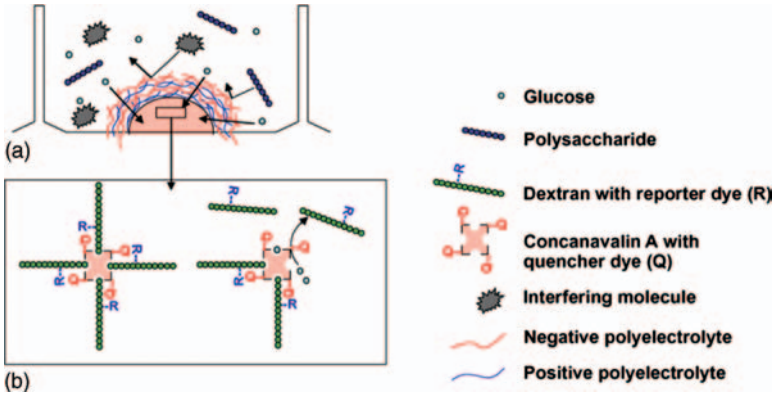

Figure 2.13 Schematic diagram of a LbL hydrogel pad (a) and the entrapped Q–ConA/R–dextran glucose sensing system (b) [63]. Reprinted from K.Y. Cheung, W.C. Mak, and D. Trau, Reusable optical bioassay platform with permeability-controlled hydrogel pads for selective saccharide detection, *Anal. Chim. Acta*, 2008, **607**, 204–210, with permission from Elsevier.

insulin covalently linked to MG and to maltose (MIMG) to provide binding affinity for ConA. MIMG was displaced competitively from ConA in the presence of glucose, and the Cy5 emission and lifetime increased. This sensor has the advantage of a reduced rate of aggregation and better reversibility in comparison with other setups by using a protein as glucose competitor instead of dextran. A further benefit is its NIR emission, allowing measurement of decay times through skin. This suggests the possibility of application as an implantable glucose sensor. Further experiments were carried out with the sensing setup, where the Cy5 label of ConA was replaced with Ru $(bpy)_3$ [66]. The advantages here are the large Stokes shift and long decay times, which simplifies instrumentation for phase-modulation lifetime measurements.

Another sensor based on FRET was described by Liao *et al.* [67]. They used QDs labeled with ConA as donor. Rhodamine-labeled β-cyclodextrin served as acceptor, showing a lower affinity to ConA to improve the signal detection sensitivity 60-fold while preserving glucose sensitivity in the physiological range. ConA and the dextrin were photopolymerized in a hydrogel at the end of an optical silica fiber with a diameter of only 250 μm (Figure 2.14). This permitted interstitial and minimal invasive *in vivo* glucose determination. The ratio of the emission at 525 and 570 nm correlated linearly with the glucose concentration up to 28 mM.

A related sensing scheme by Tang *et al.* [68] comprised ConA-labeled CdTe QDs and β-cyclodextrin-modified gold nanoparticles (AuNPs). In absence of glucose, FRET is observed between QDs as donors and AuNPs as acceptors. In the presence of glucose, the AuNP–CDs are displaced competitively by glucose, resulting in recovery of the QD fluorescence. The setup was also applied to direct glucose determination in human serum with satisfactory results.

The first solution-phase nanotube affinity sensor is based on dextran-modified single-walled carbon nanotubes (SWNTs) [69]. These were aggregated by ConA,

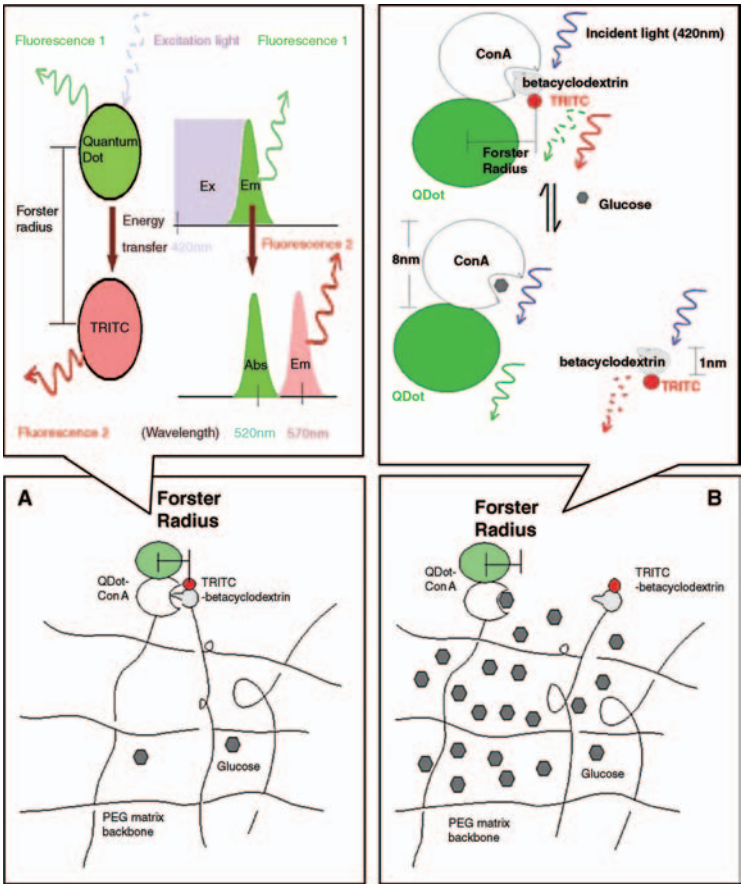

Figure 2.14 Changes in FRET between fluorophores covalently immobilized on the flexible PEG matrix depend on changes in the distance between them, which in turn depends on the competitive natural affinity between Con A and various saccharides such as betacyclodextrin and glucose.

resulting in quenched SWNT photoluminescence ($\lambda_{ex}/\lambda_{em}$ 633/>900 nm). Addition of glucose restored the initial luminescence.

2.9
Fluorescent Sensing of Glucose using Glucose-Specific Apoenzymes

In this (non-kinetic) scheme, the enzyme acts as both a molecular receptor and transducer. It represents an attractive alternative to sensing schemes utilizing the specific binding of glucose to ConA or to a bacterial or engineered glucose-binding protein. Typical enzymes used in this format include GOx and glucose

dehydrogenase (GDH). In order to prevent the oxidation or reduction of glucose but to retain enzyme specificity, the cofactors FAD or NAD, respectively, have to be removed from the holoenzyme, resulting in apo-GOx or apo-GDH. Two major sensing schemes have been reported for apo-enzyme affinity assays:

1) labeling of apo-enzyme with a polarity-sensitive dye and utilization of conformational changes on binding glucose
2) competitive assay similar to ConA using a labeled dextran as a competitor.

Lakowicz and co-workers [70] found that on binding glucose to the apo-GOx, a decrease of up to 18% of its intrinsic tryptophan fluorescence occurs. As UV wavelengths are not useful for routine diagnostic purposes, apo-GOx was non-covalently labeled with the environment sensitive dye 8-anilino-1-naphthalenesulfonate (ANS). In the presence of glucose, both the fluorescence intensity and the mean lifetime of the bound ANS decreased due to conformational changes of apo-GOx. These results suggest that apo-glucose oxidase can be used as a reversible sensor for glucose which – unlike in the case of functional enzymes – is not consumed [71]. A further approach was described using apo-GDH with similar sensitivity [72].

Chinnayelka and McShane [73] described an example of a competitive FRET assay scheme comprising tetramethylrhodamine isothiocyanate (TRITC)-labeled apo-GOx and FITC-labeled dextran. On competitive binding of glucose, a reduction in the efficiency of FRET occurs when the apo-GOx–dextran complex dissociates. A glucose concentration range from 0 to 90 mM can be monitored. The system was applied in an implantable minimally invasive sensor using the LbL self-assembly technology of the former ConA sensor [74]. TRITC–apo-GOx and FITC–dextran were encapsulated in LbL-assembled semipermeable microcapsules (Figure 2.15). These capsules showed five times better specificity for glucose over other saccharides [75]. The sensor design was later extended to longer wavelength emission [76].

2.10
Fluorescent Sensing of Glucose via Glucose-Binding Proteins

The periplasm of Gram-negative bacteria such as *Escherichia coli* comprises a family of proteins [referred to as glucose-binding proteins (GBPs)] with highly specific binding of sugars and other ligands. These proteins are primary receptors for transport and have a very similar structure in common. The monomeric arrangement consists of two globular domains linked by a hinge. The GBPs also show a minute affinity for galactose. The binding constant of native GBP for glucose is in the micromolar range and therefore not very appropriate for sensing in the physiological range. Hence engineered GBPs were developed with mutations of the binding pocket for reduced affinity to glucose. GBP-based sensing schemes are superior to enzyme-based glucose sensors in that they are not limited by enzyme substrates such as

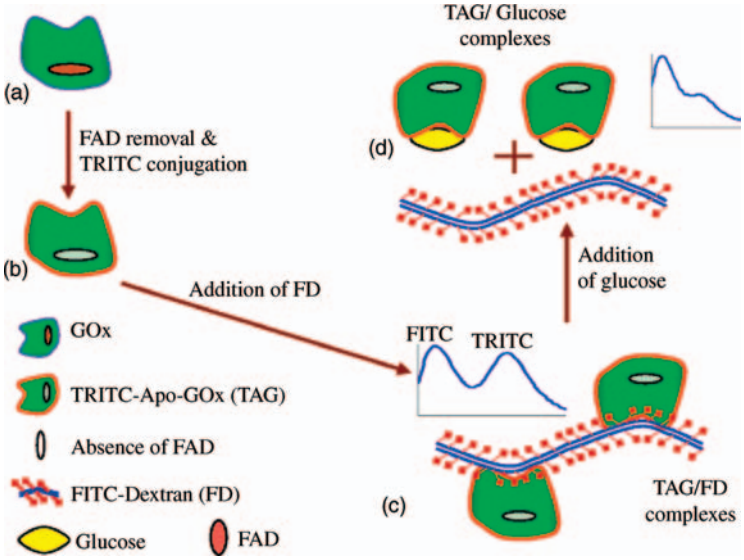

Figure 2.15 Schematic of the RET glucose assay based on competitive binding between dextran and glucose for binding sites on apo-GOx.5 [75]. Reprinted with permission from S. Chinnayelka and M.J. McShane, Microcapsule biosensors using competitive binding resonance energy transfer assays based on apoenzymes, *Anal. Chem.*, 2005, 77, 5501–5511. Copyright 2005 American Chemical Society.

oxygen or potentially toxic reaction products such as HP. Therefore, they are often referred to as reagentless sensors. All sensing schemes utilizing native or engineered GBPs are based on the large change in conformation that occurs on binding of glucose. Hence the binding event can be transduced by site-specifically attached and polarity-sensitive luminophores. Two basic approaches are reported, that is, either one fluorophore labeled on GBP or two fluorophores for ratiometric measurements. The latter have the advantage of being unaffected by variations in excitation light intensity, light path, sample positioning, reagent concentration, and so on.

In the first report on a genetically engineered GBP for use in a glucose sensor [77], two fluorophores were covalently attached to cysteines next to the ligand-binding site. The fluorescence of the first was quenched, whereas the fluorescence of the other was enhanced on addition of glucose due to changes in the polarity of the microenvironment. A series of patents cover this sensing scheme [78–80]. GBP is most often labeled with dyes such as Cy3, Cy5 [81], IANBD, Nile Red derivatives [82], and dyes with a coumarin or benzodioxazole nucleus. The conjugate is then embedded in a polymer and often attached to the end of an optical fiber.

Ye and Schultz [83] were among the first to report on a continuous dialysis hollow-fiber microsensor based on an engineered GBP showing a FRET. The so-called glucose indicator protein (GIP) contains a UV-excitable green fluorescent protein (GFPuv) and a yellow fluorescent protein (YFP) fused to the GBP. The reporter

permits efficient FRET in the absence of glucose, whereas on addition of glucose the distance between the two fluorescent proteins increases accompanied by a decreased FRET (Figure 2.16). A similar setup was used to monitor intracellular glucose levels. GBP was labeled with cyano fluorescent protein and YFP to create a FRET system. Again, addition of glucose decreased the emission of YFP at 535 nm. The developed GBP mutant showed a K_d of ~600 μM, which allowed specific monitoring of the glucose distribution and levels in cells [84]. An implantable glucose-sensing device based on the GIP–FRET sensing scheme was patented [85].

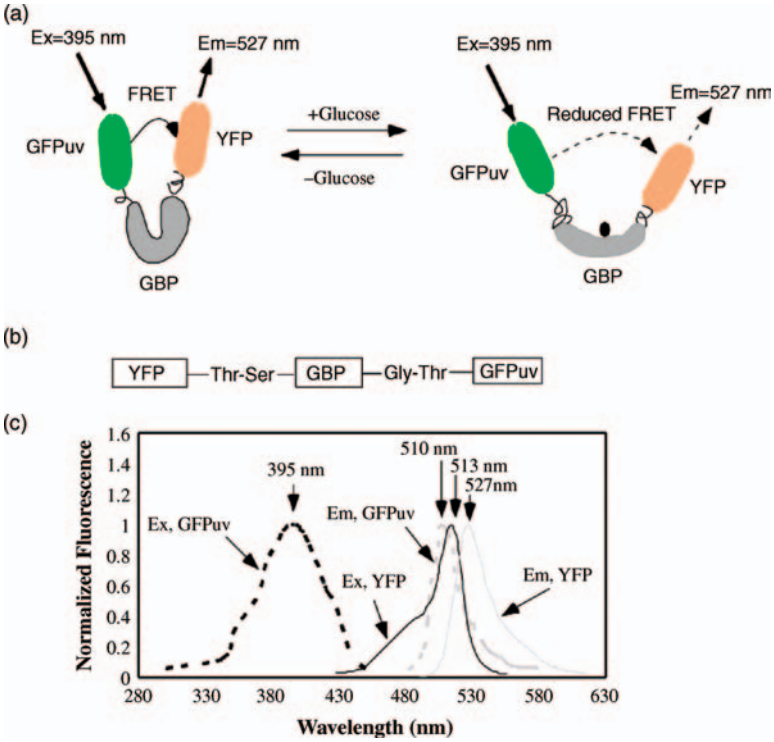

Figure 2.16 Design of a GIP (glucose indicator protein) for sensing glucose based on FRET. (a) Diagram of the GIP structure showing how FRET between two GFPs can measure glucose concentration. The GBP adopts an "open" form in the presence of the glucose, which triggers a conformation change, causing two GFPs apart from the center of GBP leading to the change in FRET. The large dot at the GBP on the right panel represents one molecule of glucose bound to the binding cleft of the GBP. (b) Domain structure of the GIP. GFPuv, green fluorescent protein with several mutations to enhance the excitation by UV light; YFP, yellow fluorescent protein; GBP, glucose-binding protein. (c) Spectral overlap of GFPuv and YFP. The absorbance spectra are denoted by black lines and the emission spectra by gray lines [83]. Reprinted with permission from K. Ye and J.S. Schultz, Genetic engineering of an allosterically based glucose indicator protein for continuous glucose monitoring by fluorescence resonance energy transfer, *Anal. Chem.*, 2003, **75**, 3451–3459. Copyright 2003 American Chemical Society.

2.11 Conclusion and Outlook

Fluorescent technologies, many involving FRET, provide attractive methods for sensing glucose. They have specific features that make them applicable to challenges not covered by electrodes, for example, intracellular sensing and imaging. Clinical sensing of glucose is the largest market and is dominated by electrochemical sensors. All the optical sensors used for routine clinical assays are based on the use of the (very robust) enzyme GOx and fluorimetric measurement of the oxygen consumed. The other schemes presented here still await commercialization. Notwithstanding this, they represent valuable tools for research and, predictably, will find their use in clinical situations where existing sensors cannot be applied.

References

1 Kondepati, V.R. and Heise, H.M. (2007) Recent progress in analytical instrumentation for glycemic control in diabetic and critically ill patients. *Anal. Bioanal. Chem.*, **388**, 545–563.

2 Heller, A. (1999) Implanted electrochemical glucose sensors for the management of diabetes. *Annu. Rev. Biomed. Eng.*, **1**, 153–175.

3 Mader, H.S. and Wolfbeis, O.S. (2008) Boronic acid based probes for microdetermination of saccharides and glycosylated biomolecules. *Microchim. Acta*, **162**, 1–34.

4 James, T.D., Phillips, M.D., and Shinkai, S. (2006) Boronic acids in saccharide recognition, in *Monographs in Supramolecular Chemistry* (ed. J.F. Stoddard), Royal Society of Chemistry, Cambridge.

5 De Luca, P., Lepore, M., Portaccio, M., Esposito, R., Rossi, S., Bencivenga, U., and Mita, D.G. (2007) Glucose determination by means of steady-state and time-course UV fluorescence in free or immobilized glucose oxidase. *Sensors*, **7**, 2612–2625.

6 Sierra, J.F., Galbán, J., and Castillo, J.R. (1997) Determination of glucose in blood based on the intrinsic fluorescence of glucose oxidase. *Anal. Chem.*, **69**, 1471–1476.

7 Hussain, F., Birch, D.J.S., and Pickup, J.C. (2005) Glucose sensing based on the intrinsic fluorescence of sol–gel immobilized yeast hexokinase. *Anal. Biochem.*, **339**, 137–143.

8 Trettnak, W. and Wolfbeis, O.S. (1989) Fully reversible fibre-optic glucose biosensor based on the intrinsic fluorescence of glucose oxidase. *Anal. Chim. Acta*, **221**, 195–203.

9 Narayanaswamy, R. and Sevilla, F. III (1988) An optical fibre probe for the determination of glucosebased on immobilized glucose dehydrogenase. *Anal. Lett.*, **21**, 1165–1175.

10 D'Auria, S., Di Cesare, N., Siaano, M., Gryczynski, Z., Rossi, M., and Lakowicz, J.R. (2002) A novel fluorescence competitive assay for glucose determinations by using a thermostable glucosecokinase from the thermophilic microorganism *Bacillus stearothermophilus*. *Anal. Biochem.*, **303**, 138–144.

11 De Marcos, S., Galindo, J., Sierra, J.F., Galban, J., and Castillo, J.R. (1999) An optical glucose biosensor based on derived glucose oxidase immobilised onto a sol–gel matrix. *Sens. Actuators B*, **57**, 227–232.

12 Sanz, V., Galban, J., de Marcos, S., and Castillo, J.R. (2003) Fluorometric sensors based on chemically modified enzymes: glucose determination in drinks. *Talanta*, **60**, 415–423.

13 Sierra, J.F., Galban, J., de Marcos, S., and Castillo, J.R. (1998) Fluorimetric–enzymatic determination of glucose based on labelled glucose oxidase. *Anal. Chim. Acta*, **368**, 97–104.

14 Trettnak, W., Leiner, M.J., and Wolfbeis, O.S. (1988) Fibre optic glucose biosensor with an oxygen optrode as the transducer. *Analyst*, **113**, 1519–1523.

15 Papkovsky, D.B., Ovchinnikov, A.N., Ogurtsov, V.I., Ponomarev, G.V., and Korpela, T. (1998) Biosensors on the basis of luminescent oxygen sensor: the use of microporous light-scattering support materials. *Sens. Actuators B*, **51**, 137–145.

16 Collins, T.C., Munkholm, C., and Slovacek, R.E., assigned to Bayer Corporation (2000) Optical oxidative enzyme-based sensors. PCT Int. Appl. WO 2000011205.

17 Rosenzweig, Z. and Kopelman, R. (1996) Analytical properties and sensor size effects of a micrometer-sized optical fiber glucose biosensor. *Anal. Chem.*, **68**, 1408–1413.

18 Li, L. and Walt, D.R. (1995) Dual-analyte fiber-optic sensor for the simultaneous and continuous measurement of glucose and oxygen. *Anal. Chem.*, **67**, 3746–3752.

19 Neubauer, A., Pum, D., Sleytr, U.B., Klimant, I., and Wolfbeis, O.S. (1996) Fibre-optic glucose biosensor using enzyme membranes with 2-D crystalline structure. *Biosens. Bioelectron.*, **11**, 317–325.

20 Valencia-Gonzalez, M.J., Liu, Y.M., Diaz-Garcia, M.E., and Sanz-Medel, A. (1993) Optosensing of D-glucose with an immobilized glucose oxidase minireactor and an oxygen room-temperature phosphorescence transducer. *Anal. Chim. Acta*, **283**, 439–446.

21 Moreno-Bondi, M.C., Wolfbeis, O.S., Leiner, M.J., and Schaffar, B.P. (1990) Oxygen optrode for use in a fiber-optic glucose biosensor. *Anal. Chem.*, **62**, 2377–2380.

22 Wolfbeis, O.S., Oehme, I., Papkovskaya, N., and Klimant, I. (2000) Sol–gel based glucose biosensors employing optical oxygen transducers, and a method for compensating for variable oxygen background. *Biosens. Bioelectron.*, **15**, 69–76.

23 Choi, M.M.F., Pang, W.S.H., Wu, X., and Xiao, D. (2001) An optical glucose biosensor with eggshell membrane as an enzyme immobilisation platform. *Analyst*, **126**, 1558–1563.

24 Zhou, Z., Qiao, L., Zhang, P., Xiao, D., and Choi, M.M.F. (2005) An optical glucose biosensor based on glucose oxidase immobilized on a swim bladder membrane. *Anal. Bioanal. Chem.*, **383**, 673–679.

25 Pasic, A., Koehler, H., Schaupp, L., Pieber, T.R., and Klimant, I. (2006) Fiber-optic flow-through sensor for online monitoring of glucose. *Anal. Bioanal. Chem.*, **386**, 1293–1320.

26 Pasic, A., Koehler, H., Klimant, I., and Schaupp, L. (2007) Miniaturized fiber-optic hybrid sensor for continuous glucose monitoring in subcutaneous tissue. *Sens. Actuators B*, **122**, 60–68.

27 Slate, J.B., and Lord, P.C., assigned to Minimed Inc. (1996) Optical glucose sensor. Can. Pat. Appl. CA 2152862.

28 Curry, K.M., assigned to Baxter International, Inc. (1989) Fiber optic biosensor containing oxygen-quenching fluorescent dyes and gas-permeable polymers. Eur. Pat. Appl. EP 309214.

29 Wagner, D.B., assigned to Becton, Dickinson and Co. (1988) Method and apparatus for monitoring glucose. Eur. Pat. Appl. EP 251475.

30 Xu, H., Aylott, J.W., and Kopelman, R. (2002) Fluorescent nano-PEBBLE sensors designed for intracellular glucose imaging. *Analyst*, **127**, 1471–1477.

31 Brown, J.Q., Srivastava, R., and McShane, M.J. (2005) Encapsulation of glucose oxidase and an oxygen-quenched fluorophore in polyelectrolyte-coated calcium alginate microspheres as optical glucose sensor systems. *Biosens. Bioelectron.*, **21**, 212–216.

32 Brown, J.Q., Srivastava, R., Zhu, H-g., and McShane, M.J. (2006) Enzymatic fluorescent microsphere glucose sensors: evaluation of response under dynamic conditions. *Diabetes Technol. Ther.*, **8**, 288–295.

33 Duong, H.D. and Rhee, J.I. (2007) Use of CdSe/ZnS core–shell quantum dots as energy transfer donors in sensing glucose. *Talanta*, **73**, 899–905.

34 Rossi, L.M., Quach, A.D., and Rosenzweig, Z. (2004) Glucose oxidase–magnetite nanoparticle bioconjugate for glucose sensing. *Anal. Bioanal. Chem.*, **380**, 606–613.

35 Nagl, S., Stich, M.I.J., Schäferling, M., and Wolfbeis, O.S. (2009) Method for simultaneous luminescence sensing of two species using optical probes of different decay time, and its application to an enzymatic reaction at varying temperature. *Anal. Bioanal. Chem.*, **393**, 1199–1207.

36 He, F., Tang, Y., Yu, M., Wang, S., Li, Y., and Zhu, D. (2006) Fluorescence-amplifying detection of hydrogen peroxide with cationic conjugated polymers, and its application to glucose sensing. *Adv. Funct. Mater.*, **16**, 91–94.

37 He, F., Feng, F., Wang, S., Li, Y., and Zhu, D. (2007) Fluorescence ratiometric assays of hydrogen peroxide and glucose in serum using conjugated polyelectrolytes. *J. Mater. Chem.*, **35**, 3702–3707.

38 Wolfbeis, O.S., Schaeferling, M., and Duerkop, A. (2003) Reversible optical sensor membrane for hydrogen peroxide using an immobilized fluorescent probe, and its application to a glucose biosensor. *Microchim. Acta*, **143**, 221–227.

39 Schäferling, M., Wu, M., and Wolfbeis, O.S. (2004) Time-resolved fluorescent imaging of glucose. *J. Fluoresc.*, **5**, 561–568.

40 Wu, P., He, Y., Wang, H.-F., and Yan, X.-P. (2010) Conjugation of glucose oxidase onto Mn-doped ZnS quantum dots for phosphorescent sensing of glucose in biological fluids. *Anal. Chem.*, **82**, 1427–1433.

41 McCurley, M.F. (1994) An optical biosensor using a fluorescent, swelling sensing element. *Biosens. Bioelectron.*, **9**, 527–533.

42 Tohda, K. and Gratzl, M. (2006) Micro-miniature autonomous optical sensor array for monitoring ions and metabolites 2: color responses to pH, K^+ and glucose. *Anal. Sci.*, **22**, 937–941.

43 Nayak, S.R. and McShane, M.J. (2006) Fluorescence glucose monitoring based on transduction of enzymatically-driven pH changes within microcapsules. *Sensor Lett.*, **4**, 433–439.

44 Ertekin, K., Cinar, S., Aydemir, T., and Alp, S. (2005) Glucose sensing employing fluorescent pH indicator: 4-[(*p-N,N*-dimethylamino)benzylidene]-2-phenyloxazole-5-one. *Dyes Pigm.*, **67**, 133–138.

45 Attridge, J.W. and Robinson, G.A., assigned to ARS Holding 89 (1993) Enzyme biosensor with optical waveguide for optical assay. PCT Int. Appl. WO 9325892.

46 Badugu, R., Lakowicz, J.R., and Geddes, C.D. (2005) Boronic acid fluorescent sensors for monosaccharide signalling based on the 6-methoxyquinolinium heterocyclic nucleus: progress toward non-invasive and continuous glucose monitoring. *Bioorg. Med. Chem.*, **13**, 113–119.

47 Badugu, R., Lakowicz, J.R., and Geddes, C.D. (2003) A glucose sensing contact lens: a non-invasive technique for continuous physiological glucose monitoring. *J. Fluoresc.*, **13**, 371–374.

48 Murtaza, Z., Tolosa, L., Harms, P., and Lakowicz, J.R. (2002) On the possibility of glucose sensing using boronic acid and a luminescent ruthenium metal–ligand complex. *J. Fluoresc.*, **12**, 187–192.

49 Lakowicz, J.R. and Murtaza, Z., assigned to the Regents of the University of Maryland (2000) Glucose biosensor using fluorescent metal–ligand complexes. PCT Int. Appl. WO 2000043536.

50 Satcher, J.H. Jr, Lane, S.M., Darrow, C.B., Cary, D.R., and Tran, J.A., assigned to the Regents of the University of California and Minimed Inc. (2001) Glucose sensing molecules having selected fluorescent properties. PCT Int. Appl. WO 2001020334.

51 Satcher, J.H., Lane, S.M., Darrow, C.B., Cary, D.R., and Tran, J.A., assigned to University of California and Minimed Inc. (2004) Saccharide sensing molecules having enhanced fluorescent properties. U.S. Pat. 6673625.

52 Cordes, D.B., Miller, A., Gamsey, S., Zach, S., Thoniyot, P., Wessling, R., and

Singaram, B. (2005) Optical glucose detection across the visible spectrum using anionic fluorescent dyes and a viologen quencher in a two-component saccharide sensing system. *Org. Biomol. Chem.*, **3**, 1708–1713.

53 Schiller, A., Wessling, R.A., and Singaram, B. (2007) A fluorescent sensor array for saccharides based on boronic acid appended bipyridinium salts. *Angew. Chem. Int. Ed.*, **46**, 6457–6459.

54 Cordes, D.B., Gamsey, S., and Singaram, B. (2006) Fluorescent quantum dots with boronic acid substituted viologens to sense glucose in aqueous solution. *Angew. Chem. Int. Ed.*, **45**, 3829–3832.

55 Schultz, J.S., Mansouri, S., and Goldstein, I.J. (1982) Affinity sensor: a new technique for developing implantable sensors for glucose and other metabolites. *Diabetes Care*, **5**, 245–253.

56 Schultz, J.S., assigned to United States Department of Health, Education, and Welfare (1980) Optical sensor for blood plasma constituents. U. S. Pat. 4344438.

57 Mansouri, S. and Schultz, J.S. (1984) A miniature optical glucose sensor based on affinity binding. *Bio/Technology*, **2**, 885–890.

58 Ballerstadt, R. and Schultz, J.S. (2000) A fluorescence affinity hollow fiber sensor for continuous transdermal glucose monitoring. *Anal. Chem.*, **72**, 4185–4192.

59 Ballerstadt, R., Evans, C., Gowda, A., and McNichols, R. (2006) *In vivo* performance evaluation of a transdermal near-infrared fluorescence resonance energy transfer affinity sensor for continuous glucose monitoring. *Diabetes Technol. Ther.*, **8** (3), 296–311.

60 Kristensen, J.S., Gregorius, K., Struve, C., Frederiksen, J.M., and Yu, Y., assigned to Precisense A/S (2006) Sensor for detection of carbohydrate. PCT Int. Appl. WO 2006061207.

61 Meadows, D. and Schultz, J.S. (1993) Design, manufacture and characterization of an optical fiber glucose affinity sensor based on an homogeneous fluorescence energy transfer assay system. *Anal. Chim. Acta*, **280**, 21–30.

62 March, W.F., assigned to Novartis AG and Novartis-Erfindungen Verwaltungsgesellschaft mbH (2002) Apparatus for measuring blood glucose concentrations. PCT Int. Appl. WO 2002087429.

63 Cheung, K.Y., Mak, W.C., and Trau, D. (2008) Reusable optical bioassay platform with permeability-controlled hydrogel pads for selective saccharide detection. *Anal. Chim. Acta*, **607**, 204–210.

64 McCartney, L.J., Pickup, J.C., Rolinski, O.J., and Birch, D.J.S. (2001) Near-infrared fluorescence lifetime assay for serum glucose based on allophycocyanin labelled concanavalin A. *Anal. Biochem.*, **292**, 216–221.

65 Tolosa, L., Malak, H., Rao, G., and Lakowicz, J.R. (1997) Optical assay for glucose based on the luminescnence decay time of the long wavelength dye Cy5. *Sens. Actuators B*, **45**, 93–99.

66 Tolosa, L., Szmacinski, H., Rao, G., and Lakowicz, J.R. (1997) Lifetime-based sensing of glucose using energy transfer with a long lifetime donor. *Anal. Biochem.*, **250**, 102–108.

67 Liao, K.-C., Hogen-Esch, T., Richmond, F.J., Marcu, L., Clifton, W., and Loeb, G.E. (2008) Percutaneous fiber-optic sensor for chronic glucose monitoring *in vivo*. *Biosens. Bioelectron.*, **23**, 1458–1465.

68 Tang, B., Cao, L., Xu, K., Zhuo, L., Ge, J., Li, Q., and Yu, L. (2008) A new nanobiosensor for glucose with high sensitivity and selectivity in serum based on fluorescence resonance energy transfer (FRET) between CdTe quantum dots and Au nanoparticles. *Chem. Eur. J.*, **14**, 3637–3644.

69 Barone, P.W. and Strano, M.S. (2006) Reversible control of carbon nanotube aggregation for a glucose affinity sensor. *Angew. Chem. Int. Ed.*, **45**, 8138–8141.

70 D'Auria, S., Herman, P., Rossi, M., and Lakowicz, J.R. (1999) The fluorescence emission of the apo-glucose oxidase from *Aspergillus niger* as probe to estimate glucose concentrations. *Biochem. Biophys. Res. Commun.*, **263**, 550–553.

71 Lakowicz, J.R. and D'Auria, S., assigned to the Regents of the University of Maryland

(2001) Inactive enzymes as non-consuming sensors. PCT Int. Appl. WO 2001018237.

72 D'Auria, S., Di Cesare, N., Gryczynski, Z., Gryczynski, I., Rossi, M., and Lakowicz, J.R. (2000) A thermophilic apoglucose dehydrogenase as nonconsuming glucose sensor. *Biochem. Biophys. Res. Commun.*, **274**, 727–731.

73 Chinnayelka, S. and McShane, M.J. (2004) Resonance energy transfer nanobiosensors based on affinity binding between apo-GOx and its substrate. *Biomacromolecules*, **5**, 1657–1661.

74 Chinnayelka, S. and McShane, M.J. (2004) Glucose-sensitive nanoassemblies comprising affinity-binding complexes trapped in fuzzy microshells. *J. Fluoresc.*, **5**, 585–595.

75 Chinnayelka, S. and McShane, M.J. (2005) Microcapsule biosensors using competitive binding resonance energy transfer assays based on apoenzymes. *Anal. Chem.*, **77**, 5501–5511.

76 Chinnayelka, S. and McShane, M.J. (2006) Glucose sensors based on microcapsules containing an orange/red competitive binding resonance energy transfer assay. *Diabetes Technol. Ther.*, **8**, 269–278.

77 Marvin, J.S. and Hellinga, H.W. (1998) Engineering biosensors by introducing fluorescent allosteric signal transducers: construction of a novel glucose sensor. *J. Am. Chem. Soc.*, **120**, 7–11.

78 Hellinga, H.W., assigned to the Regents of Duke University (1998) Biosensor. US Pat. 6277627.

79 Jacobson, R.W., Weidemaier, K., Alarcon, J., Herdman, C., and Keith, S., assigned to Becton Dickinson (2005) Fiber optic device for sensing analytes and method of making same. US Pat. Appl., US 20050113658 A1.

80 Pitner, B.J., Sherman, D.B., Ambroise, A., and Thomas, K.J., assigned to Becton Dickinson (2006) Long wavelength thiol-reactive fluorophores. US Pat. Appl., US 20060280652 A1.

81 Tian, Y., Cuneo, M.J., Changela, A., Höcker, B., Beese, L.S., and Hellinga, H.W. (2007) Structure-based design of robust glucose biosensors using a *Thermotoga maritima* periplasmic glucose-binding protein. *Protein Sci.*, **16**, 2240–2250.

82 Thomas, J.K., Sherman, D.B., Amiss, T.J., Andaluz, S.A., and Pitner, J.B. (2006) A long-wavelength fluorescent glucose biosensor based on bioconjugates of galactose/glucose binding protein and nile red derivatives. *Diabetes Technol. Ther.*, **8**, 261–268.

83 Ye, K. and Schultz, J.S. (2003) Genetic engineering of an allosterically based glucose indicator protein for continuous glucose monitoring by fluorescence resonance energy transfer. *Anal. Chem.*, **75**, 3451–3459.

84 Fehr, M., Lalonde, S., Lager, I., Wolff, M.W., and Frommer, W.B. (2003) *In vivo* imaging of the dynamics of glucose uptake in the cytosol of COS-7 cells by fluorescence nanosensors. *J. Biol. Chem.*, **278**, 19127–19133.

85 Gross, Y. and Hyman, T., assigned to Glusense Ltd. (2007) Implantable biosensor comprising live cells producing fluorescent proteins and an analyte-binding protein, for monitoring a body fluid analyte, such as glucose. PCT Int. Appl. WO 2007110867.

3
Biochips as Novel Bioassays

Bettina Rudolph, Karina Weber, and Robert Möller

3.1
Introduction

Through new methods in molecular biology, biochemistry, and the humane genome project, the amount of genetic information and the information on biomolecules and their interactions has risen exponentially in recent years. This new information allows the in-depth investigation of biological systems but also demand simple, fast, cheap, and miniaturized analytical tools, which can be produced in large numbers. Classical bioassays, which investigate the effect of a substance on a biomolecule, cell, or even organisms, were normally performed in batch experiments, meaning that the interactions between the investigated substance and a particular biomolecule of interest were performed as one experiment. To investigate the interactions of the same substance with another biomolecule, a new experiment had to be conducted. This experimental setup was time consuming and also needed large amounts of reagents. To save time and reagents, bioassays were miniaturized, for example, using microtiter plates, and molecules were immobilized to surfaces to allow the parallel testing of multiple molecules in one experiment. These approaches for the development of paralleled and miniaturized bioassays led to the development of biochips or microarrays.

Biochips normally consist of a planar solid substrate, on which known biomolecules are immobilized in an ordered fashion. The immobilized biomolecules, which are also referred to as capture molecules, are bound to the surface in spots and each spot contains molecules of the same kind. The biochip is then incubated with a solution containing target molecules that can bind specifically to the surface-immobilized capture molecules.

Because of sophisticated production processes, a high spot density can be achieved. Typical feature sizes for DNA chips produced by photolithography are $100\,\mu m^2$ per spot, which allows the immobilization of an enormous amount of different DNA sequences even on $1\,cm^2$. Hence a biochip permits miniaturized, highly parallel investigations of biomolecular interactions.

Handbook of Biophotonics. Vol.2: Photonics for Health Care, First Edition. Edited by Jürgen Popp, Valery V. Tuchin, Arthur Chiou, and Stefan Heinemann.

In this chapter, we introduce the basics of biochip technology and their use in pathogen detection and clinical diagnostics, and also innovative trends in this field aimed at increasing the applicability and efficiency of biochip-based detection of biomolecules.

3.2 Types of Microarrays

In molecular biology and medicine, miniaturized multiplexed systems are increasingly of importance for highly complex and simultaneous (parallel) testing of tens of thousands of probes. Microarrays, also called biochips, have evolved to a mainstream tool of life science research. Depending on the immobilized biological recognition systems, microarrays can be classified in different types. A classification by the type of transducer/detection method is another possibility, but in this chapter we describe types of microarrays depending on their immobilized receptor. The most common types of microarrays are DNA microarrays. Oligonucleotide arrays provide a powerful tool to study molecular basics and interactions on a scale that is impossible using conventional methods [1]. Further applications of microarrays based on immobilization of, for example, proteins, cells, or tissues are described in the following. Nowadays, many commercial standardized microarrays with different immobilized biological recognition systems, especially oligonucleotides or antibodies, are supplied by a variety of companies, for example, Affymetrix, Agilent, Illumina, GE Healthcare, Applied Biosystems, and Agendia. Most of these companies provide custom-made microarrays for individual research. Another common option is to manufacture specific microarrays directly in the laboratory by using different commercially available technologies for their individual production.

3.2.1 DNA Microarrays

Historically, microarray technology evolved from blotting methods. DNA microarrays are based on the Southern blot [2], which is used in medical diagnostics to control DNA sequences in a DNA sample. Instead of DNA fragments, RNA can be analyzed in a Northern blot. These conventional methods are often time consuming and not effective for investigating large numbers of genes. Hence DNA microarrays became a mainstream method in research for investigations of thousands of genes simultaneously.

Basically, there are three strategies for the development of a DNA chip for gene expression studies, which were described by Lemieux *et al*. [3]. First a strategically selection of known genes that play an important role in biological pathways is necessary. A second way uses clones from a library [4] restricted to cDNA microarrays. Third, the complete expressed sequence content of an organism is used for the production of a microarray [5]. For that purpose, a DNA microarray

can consist of hundreds of thousands of spots of DNA oligonucleotides, called captures or probes. Each spot includes a specific DNA sequence, which binds complementarily to a target molecule in the investigated sample. Depending on the application, there exist different special arrays for genomic DNA, cDNA, RNA, plasmids, polymerase chain reaction (PCR) products, or long oligonucleotides. Usually complementary binding of capture and target molecules is detected and quantified by optical methods to determine the relative abundance of a nucleic acid target sequence in the sample.

Since the early 1990s, the field of DNA microarray technology has seen a constant technological evolution and intensive studies have been carried out. In 1991, Fodor and the company Affymetrix pioneered oligonucleotide arrays [6]. Numerous reviews and articles have reported and discussed the different possibilities and applications of DNA microarrays [7–25]. In 1999, *Nature Genetics* published a series of reviews about DNA microarrays and their fabrication and detection [26], gene expression profiling [27, 28], resequencing and mutational analysis [29], and also applications in drug discovery [30]. Furthermore, Southern *et al.* reported molecular interactions on microarrays [1]. In recent years, really intensive studies were carried out in the field of genomic research, pathogen detection, and clinical diagnostics, as described in Section 3.4.

In 1994, the HIV GeneChip of Affymetrix was the first commercially available DNA microarray, and is now the most widely known and applied microarray platform [31]. A good overview of the current status of used DNA microarrays was given by Shi *et al.* [15]. MammaPrint, a prognostic test for breast cancer from Agendia, became the first *in vitro* diagnostic multivariate index assay (IVDMIA) to acquire clearance from the US Food and Drug Administration (FDA) in 2007. Finally, the importance of DNA microarray technology is evidenced by its extensive literature and still increasing market share. Since the beginning of DNA microarray technology, these novel aspects of bioassays have become ubiquitous in a variety of applications in biological and medical research and drug discovery.

3.2.2 Protein Microarrays

DNA microarrays were the first described biochips applied in the investigation of the expression level of various genes of an organism. However, the evaluated results allow only a limited insight into the process of actual protein expression. Additionally, DNA microarrays provide no information about protein–protein interactions. Most of the protein monitoring on biochips is based on the analysis of the mRNA expression level. However, the data do not always correlate with the corresponding protein abundance. The main reasons for this effect are the post-translational protein modifications, which make the human proteome much more complex in composition than the coding portion of the genome. Therefore, protein microarrays notably increased the applications of biochips in many different fields, due to availability of much new and additional information.

Standard methods to analyze proteins and protein profiles are usually 2D gel electrophoresis and mass spectrometry. An alternative to standard methods is protein microarrays, which are utilized in research to analyze changes in the abundance and existence of proteins in a very high dynamic range in biological samples. Bilitewski reviewed protein-sensing assay formats and devices in general in 2006, based on affinity reactions between an immobilized capture agent and the target protein [32]. Nowadays, optimal ways to immobilize proteins to 2D surfaces to assure the retention of their biological activity and shape is a major challenge to create point-of-care devices for multianalyte diagnosis [33]. Due to their high specificity and affinity, antigen–antibody reactions are the most important tool for protein microarrays in diagnostics and biological studies. The development of protein microarrays and diagnostic applications has been reported in depth by various groups [34–42]. Critical points in antibody microarrays are the selection, production, and purification of suitable antibodies with high affinity and a reduced cross-reactivity to target molecules. Protein microarrays could be a powerful tool for the identification of biomarkers, for example, in tumor–antigen discovery and cancer diagnostics. For instance, Miller *et al.* [43] and Bouwman *et al.* [44] used antibody microarrays for the detection of prostate cancer. Other antibody applications examine the analysis of cytokine secretion by human dendritic cells with lipopolysaccharide or tumor necrosis factor-α [45] and the detection and quantification of cardiovascular risk markers [46]. Protein microarrays can also be used to identify specific targets of pharmaceutical intervention [47, 48].

A second important application of protein microarrays is to examine a multitude of protein–protein, receptor–ligand, protein–peptide [39, 49], protein–carbohydrate, and enzyme–substrate interactions and also protein interactions with small molecules. The knowledge of these interactions is important in applications of protein network profiling, drug discovery, and drug target confirmation [42, 50, 51]. Uttamchandani and Yao also gave an overview of peptide microarrays used in profiling, detection, or diagnostic applications to sense protein activity or act as ligands for potential therapeutic leads [52].

3.2.3 Tissue Microarrays

The understanding of the association between molecular changes and clinical pathology and the validation of new biomarkers are important in clinical research. Current tissue- and cell-based microarrays combine the analysis of tissue morphology with the identification, localization, and characterization of biomolecules in biological systems.

Tissue microarrays (TMAs) allow traditional tissue analysis of conventional histological paraffin blocks to become miniaturized and high throughput to study molecular alterations at the DNA, RNA, and protein level in multiple individual tissue types. Novel targets can be analyzed in hundreds to thousands of tissue samples with molecular pathology techniques in parallel on one slide.

For the construction of a tissue microarray, cylindrical core tissue biopsies from different donor paraffin-embedded tissue blocks were punched and precisely re-embedded in a blank paraffin block [53, 54]. From this new master block, several hundred to thousands of consecutive sections can be cut and molecular alterations can be detected in parallel in up to 500 or more different tissues. TMAs can be used in many fields such as cancer research and inflammatory, cardiovascular, and neurological diseases.

Today, in cancer research, different types of TMAs exist and allow the analysis of molecular alterations in multiple tumor types (multitumor TMA) or in different stages of one particular tumor (progression TMA). Also, (novel) prognostic parameters can be identified in TMAs containing tumor samples from patients with known clinical follow-up data and clinical endpoint or value testing for molecular alterations to predict chemotherapeutic agents.

The combination of tissue and cDNA microarrays will be a powerful approach for the rapid identification and evaluation of genes with clinical relevance in diagnostics and prognostics, or as therapeutic markers [55, 56].

Alterations in molecular targets such as DNA, RNA, and proteins can be visualized by classical histochemical and molecular detection techniques, for example, immunohistochemistry (IHC), *in situ* hybridization (ISH), fluorescent *in situ* hybridization (FISH), *in situ* PCR, RNA or DNA expression analysis, or TUNEL (terminal dUTP nick-end labeling) assay to detect apoptotic cells and for morphological and clinical characterization of patient tissues. Hence TMAs combine all the advantages of microarrays – low cost, high parallelism, and data collection with many other techniques of biomolecular diagnostics.

3.2.4
Cell-Based Microarrays (Transfection Microarrays)

Cell-based microarrays or so-called reverse transfection microarrays allow functional analysis in mammalian cells in parallel in a format without wells. In this array, nanoliter quantities of cDNA- or siRNA-expressing vectors and also small molecules (e.g., drug-like molecules) are printed in defined areas on a slide surface. Adherent cells are cultured on the top of the array and take up the printed molecules and create spots of localized transfections within a lawn of non-transfected cells. Each feature of 100–250 μm in diameter contains a cluster of 30–80 cells, for example, over- or underexpressing a special gene product, or are under the influence of a drug-like molecule [57]. Cell-based microarrays can be examined when the cells are still alive to visualize cellular processes in real time or after fixation. Also, a variety of detection assays can be applied such as *in situ* hybridization, immunofluorescence, autoradiography and also Western blot by transferring the cells on to nitrocellulose [51, 57]. A special form of cell-based microarrays is lentivirus-infected and *Drosophila* cell microarrays, which provide a platform for effective high-throughput loss-of-function screens through expression of short hairpin RNA/RNAi [58–61]. Lentiviruses infect a wide variety of mammalian cells but can also infect non-dividing cells, which is important for the study of primary cell types [14, 62].

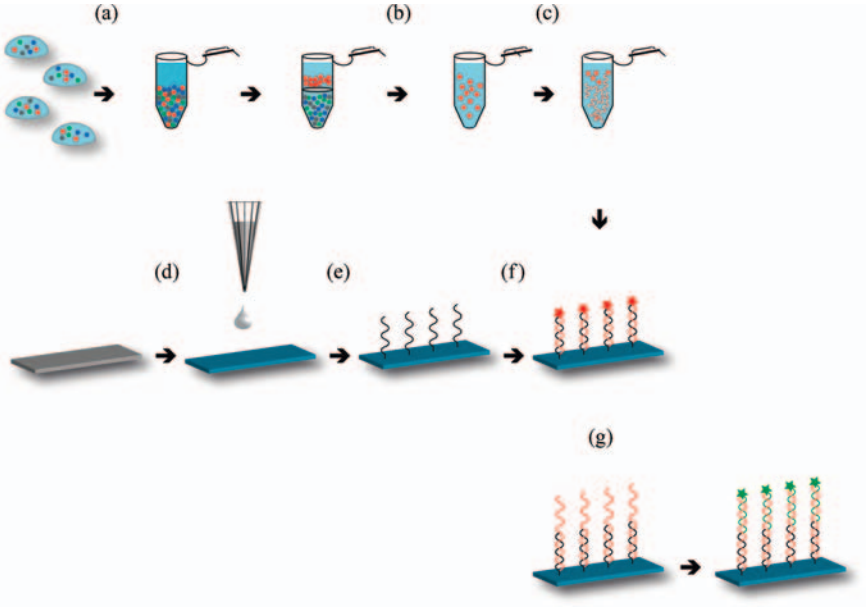

Figure 3.1 Principle process of a microarray experiment. The basic steps include sample preparation (a), purification (b), and target amplification and labeling (c). The functionalization of the solid substrate with capture molecules (e) needs a prior chemical modification of the biochip surface (d). The following hybridization of amplified and labeled target molecules (f) allows the final readout of the specific biomolecular interaction on the chip surface. Alternatively to the direct labeling of the target molecules during the amplification process, the necessary label can be introduced by a sandwich process (g).

3.3 Principle Steps of an Experimental Microarray Process

This section is focused on the microarray experimental setup process especially for DNA/RNA and protein probes. A typical microarray experiment is depicted schematically in Figure 3.1. It involves the basic steps of sample preparation (a), purification (b), target amplification, and labeling (c). The functionalization of the solid substrate with capture molecules (e) needs a prior chemical modification of the biochip surface (d). The subsequent hybridization of amplified and labeled target molecules (f) allows the final readout of the specific biomolecular interaction on the chip surface. Alternatively to the direct labeling of the target molecules during the amplification process, the necessary label can be introduced by a sandwich process (g). Finally, the huge amount of data must be analyzed by means of computational and statistical tools to generate a profile of, for example, expressed genes in a cell [63–67]. A variety of books and overviews have covered microarray analysis and different technical aspects [19, 28, 68–73].

3.3.1 Basics

The underlying principle of a microarray is based on a capture probe immobilized on a solid surface that can bind to a complementary target probe contained in a complex sample. Depending on the amount and density of spots, an array can be subdivided into low-, medium-, and high-density arrays, but overall have the same fundamental principle. Traditionally, an array consists of DNA fragments, but it also can contain other biological recognition units such as antigens or proteins. Often DNA microarrays, for example, in gene expression profiling, belong to high-density arrays due to the presence of hundreds of thousands of probes. It is possible to detect a small amount of target probes in the nanomolar to picomolar range.

3.3.1.1 Surface Biofunctionalization

Surface chemistry and modification are of great importance in microarray technology for binding capture molecules [74–76]. Especially protein immobilization is much more difficult than the immobilization of oligonucleotides or cDNA. Proteins have to be immobilized in their active form in order to bind specifically to their complementary target [33, 77, 78].

The requirements for optimal microarray performance are (a) the stable and covalent immobilization of biomolecules on the chip surface and (b) suitable mechanical and chemical properties of the substrate used [79]. Three different kinds of surfaces are used for the fabrication of microarrays: first, 2D solid structures, such as glass, silicon, silicon nitride, or gold layers, all of which have chemical modifications located on the surface, for instance thiol [80–82], amine [83], epoxy [84], or aldehyde [85] groups; second, 3D coated structures based on the gelation or polymerization of monomers, such as agarose gels [86, 87] or thin layers of polyacrylamide [88, 89], which are commonly immobilized on solid structures for support (e.g., glass); and thirdly, 3D solid structures based on mechanically stable polymeric materials such as poly(methyl methacrylate) [75] and polydimethylsiloxane [90], which do not require a mechanical support.

The advantages of the 2D solid structures are the ease and low cost of fabrication. In addition, some 2D solid structures are transparent towards different light wavelengths, hence making them the substrates of choice for optical detection. Furthermore, their mechanical rigidity allows the deposition of electrodes on their surface, making them compatible with electrochemical detection. Nevertheless, the surface of 2D solid structures is chemically inert. Therefore, these biochip substrates need chemical modification for the stable binding of biomolecules, hence the need to apply chemical reagents or coatings with gels or non-rigid polymers, increasing their fabrication costs.

Therefore, despite the advantages provided by the 2D solid structures and 3D coated structures, it is evident that the development of new materials is required. The 3D solid structures based on polymeric materials can be functionalized during their fabrication procedure. These polymeric materials can be functionalized for

biomolecule immobilization by already embedded functional groups in their monomers, gaining the advantages of 3D coated substrates, but retaining the desired mechanical properties (e.g., transparency and rigidity) of 2D solid structures without reducing the ease or increasing the costs of their fabrication.

Depending on surface modifications, the array can be prepared with capture probes, for example, oligonucleotides with defined length [normally between 20 and 60 base pairs (bps)] or proteins. Oligonucleotides bind on surfaces using combinatorial chemistry and photolithographic techniques. Affymetrix pioneered the fabrication of microarray platforms with high-density arrays. The Affymetrix GeneChip arrays use photolithography techniques for the *in situ* synthesis of oligonucleotides. Semiconductor fabrication, solid-phase chemical synthesis, combinatorial chemistry, and molecular biology are integrated in a robotic manufacturing process [6, 15, 31, 91]. Agilent used Hewlett-Packard's inkjet printing technology for array preparation [92]. Analogous to printing a document, nucleotides are printed on glass slides coated with a hydrophobic surface [15, 93].

Instead of synthesizing capture molecules directly on the surface, another method is the spotting of presynthesized oligonucleotide probes (e.g., GE Healthcare's CodeLink system, Applied Biosystems' Genome Survey Microarrays, custom microarrays printed with Operon's oligonucleotide sets) on modified surfaces. An approach to immobilization of modified oligonucleotides even on unmodified glass surfaces can be made by UV cross-linking [94]. This well known method is widely used in different applications for the attachment of DNA or proteins on membranes, solid surfaces, and polymers [95, 96]. However, the exposure to UV light can damage the DNA [97].

An innovative tool for DNA or RNA studies in genetic analysis is the Illumina bead-based microarray (BeadChip microarray), where presynthesized oligonucleotide probes are deposited on beads. The highest density array platform which is currently available is the Sentrix BeadChip from Illumina, containing 6.5 million features that are just 3 μm wide [98]. The bead-based technology represents an alternative technique that is an accurate, scalable, and flexible approach to a microarray [99].

A detailed comparison of different platforms as tools for functional genomics based on microarray technology was made by Wick and Hardiman [100] and Shi *et al.* also gave a good overview of the current status of DNA microarrays [15].

3.3.2
Preparation of Biomolecules (Sample Preparation)

3.3.2.1 DNA

The ability to extract pure DNA from a variety of sources is an important step in many molecular biological assays. Many different protocols exist for the preparation of genomic DNA. All methods include three steps: cell lysis, deproteination, and concentration/precipitation of DNA. Commonly used protocols are alkaline lysis of cells and phenol–chloroform extraction followed by ethanol precipitation of the nucleic acid. In recent years, traditional purification methods have been replaced by a variety of commercial kits available from many companies (e.g., Qiagen, Invitrogen,

Roche Applied Science, Promega). These kits include necessary solutions for preparation and solubilization of the DNA and columns for anion-exchange chromatography or glass beads. The DNA binds on the silica membranes or glass beads of the spin columns during the separation from contaminating RNA, proteins, and metabolites and can subsequently be easily eluted with high-salt buffer and should be desalted and concentrated before use. A further approach is adsorption of DNA on carboxylated magnetic beads after cell lysis. Subsequently the DNA–magnet particle complex is separated from any residual contaminants by applying a magnetic field. After separation, the purified DNA is released by heating the complex. In this way, a high yield of pure DNA can be produced quickly and conveniently [101, 102].

3.3.2.2 **RNA**

The preparation of high-quality, intact RNA is the first and often the most critical step in performing many molecular biology experiments. This procedure is complicated by the ubiquitous presence of ribonuclease enzymes in cells and tissues, which can rapidly degrade RNA.

The cell probes are first lysed in the presence of a highly denaturing guanidinium isothiocyanate buffer, which immediately inactivates ribonucleases. Then RNA is fractionated from other cellular components via phenol extraction and under conditions that suppress any RNase activity and subsequently concentrated by alcohol precipitation [103].

Several kits for RNA isolation are commercially available, including guanidinium thiocyanate/phenol–chloroform mixtures or silica membrane/glass bead spin columns for RNA extraction without organic solvents. The use of oligo[dT]-cellulose columns or oligo[dT]-magnetic beads selects mRNA from total RNA. Magnetic bead separation allows mRNA to be purified in a single tube by application of a magnetic field, thus eliminating potential sample loss during liquid handling [101, 103].

RNA extraction kits for different starting materials and applications are offered by various companies such as Qiagen, Invitrogen, and Promega.

3.3.2.3 **Proteins**

The first step in protein analysis for any cell line of interest is the lysis of cells and the extraction of total proteins. Typically, a detergent-based method is applied. The lysis method should be mild enough to deliver active and native conformation proteins. Additives such as protease inhibitors protect the proteins from enzymatic degradation whereas nucleases digest DNA. Cell debris and total protein fraction are separated by centrifugation [104].

3.3.3
Target Amplification and Labeling

Because of minimal amounts of starting material, for example from needle biopsies, cell sorting, and laser capture microdissection, an amplification step before use in analytical assays is required in most applications.

3.3.3.1 PCR – Polymerase Chain Reaction

The PCR is a rapid procedure for *in vitro* amplification of a specific DNA region. The process based on the sequence-specific annealing and extension of two oligonucleotide primers which bracket the target DNA region. Three steps, denaturation of the double-stranded target DNA by heating, specific annealing of the primer during temperature reduction, and polymerase-catalyzed extension of the primer sequences in 5′–3′ orientation, define one PCR cycle. The target DNA is enriched exponentially during each PCR cycle and the amplicons produced are also used as templates for subsequent cycles [105, 106].

For the detection of RNA, the PCR procedure is adapted to RNA templates. In this reaction, a defined primer complementary to the polyadenylated tail on the 3′ end of most eukaryotic mRNAs was used and also the reverse transcriptase substitutes/replaces the polymerase. The so-called reverse transcriptase polymerase chain reaction (RT-PCR) produces a cDNA copy of the RNA which can be used in the same context as DNA [107, 108].

During the amplification processes, the amplicon can be modified via the incorporation of altered primers or dNTPs. Hence the introduction of labels such as fluorescent dyes, radioactivity, digoxigenin (DIG), or biotin and also mutations or restriction sites are possible.

3.3.3.2 *In Vitro* Transcription – cDNA/IVT

The so-called Eberwine method and its modifications is a strategy for mRNA amplification by template-directed *in vitro* transcription. In the first step, the poly(A) + RNA pool is reverse transcribed using an oligo-dT primer bearing a specific promoter site for phage RNA polymerases. After the second strand synthesis, cRNA can be amplified by RNA polymerase using the double-stranded cDNA as template. The common RNA polymerases used in *in vitro* transcription reactions are SP6, T7, and T3 polymerases [109].

3.3.3.3 Bio-Barcode Amplification of Nucleic Acids and Proteins

The bio-barcode technology does not include enzymatic target or signal amplification, but is based on nanoparticle technology. In this two-sided sandwich system, the target is immobilized on a solid surface capture probe and is detected through binding a detection probe.

Magnetic-based microparticles of one to several diameters interact with the target molecule through biological recognition (DNA–DNA interaction or antigen–antibody interaction) and allow the separation of the sandwich from unreacted material and medium. Amplifier nanoparticles recognize and bind the target–magnetic particle complex through immobilized detection probes (Figure 3.2). Additionally bound bio-barcode oligonucleotides specific for each target can be released for representing and amplifying the target in a subsequent detection assay [110–113]. Hundreds to thousands of barcodes of one nanoparticle provide a 2–3 log amplification of a target that has been successfully captured and sandwiched. Typical materials for amplifier nanoparticles are gold and polystyrene [114].

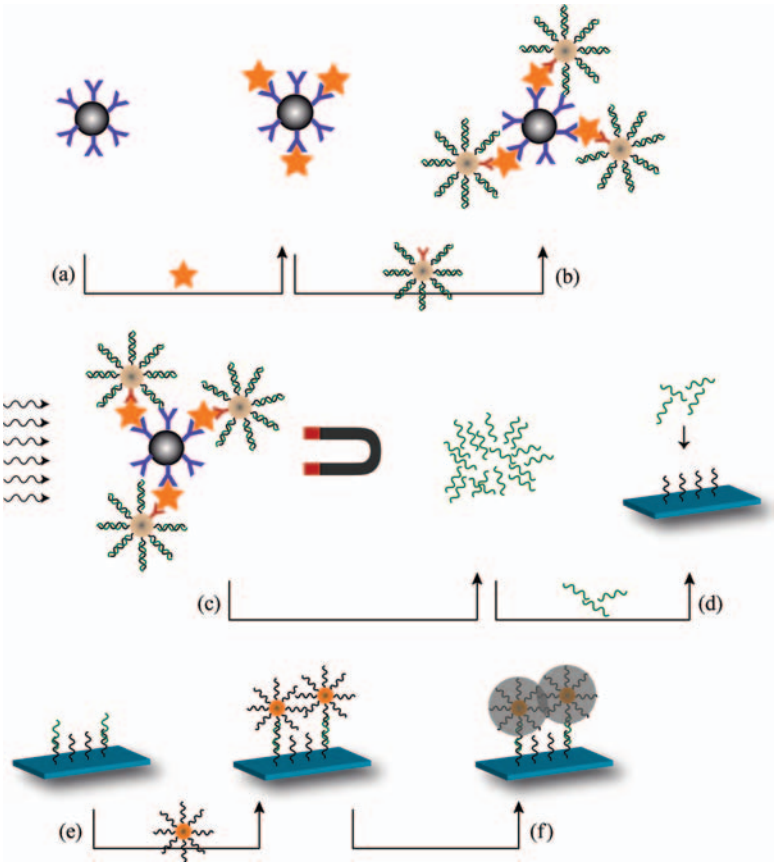

Figure 3.2 Principle of bio-barcode nanoparticle-based PCR-less DNA amplification. An antibody-labeled nanoparticle binds to the analyte (a). A second DNA-labeled magnetic nanoparticle can also bind via antibody–antigen interaction to the analyte (b). In a magnetic separation process (c) followed by barcode DNA denaturation (d), the free amplified bio-barcode DNA can hybridize to a biochip (e). After nanoparticle labeling and silver enhancement, the signal can be optically detected (f).

3.3.3.4 **Radioactive and Fluorophore Labeling**

The visualization of biomolecules can be mediated by labeling with radioactive, fluorescent, luminescent, or other chemical modifications. In nucleic acids, the incorporation of radioactive and nonradioactive labels is common. The label can be attached to one of the dNTPs or the 5′ end of one or both primers, which will be enzymatically incorporated in the amplicon [115, 116].

The efficiency of enzymatic incorporation of labeled nucleotides may be impaired due to steric effects of the bulky label. Also, the use of labeled nucleotides is more costly per reaction than 5′-labeled oligonucleotides. An indirect labeling, for example, with aminoallyl-dNTPs or DIG, allows subsequent conjugation of a fluorescent dye to

the purified amplicon, but it is more time consuming because incubation and washing steps are required.

Proteins commonly will be covalently linked to a nucleoside or nucleotide which carries radioactivity. The radioactivity can be anywhere on the nucleoside (C, N, H, S, I, Hg). Labeling of proteins is performed by reactions of the label with the N- and C-terminus or functional groups of side chains on the surface such as an amino group of lysine, sulfhydryl group of cysteine, or carbohydrate group of the protein [117].

Radioactive labeling provides a highly sensitive method for detection. However, radioisotopes are expensive, have a short half-life, and require a long exposure time before detection. Radioactive materials are also potentially hazardous and their use requires adherence to strict safety precautions. The majority of radioisotopes used in biological experiments emit ionizing radiation and impart energy in living cells. In large enough doses, this energy can damage cellular structures, such as chromosomes and membranes. Such damage can kill the cell or impair its normal functionality.

Nonradioactive labels such as fluorophores become more important due to their sensitivity and easy handling compared with radioactive labels. A wide variety of fluorophores in many different colors are available and compatible with the usual excitation/emission systems. Current fluorescent dyes achieve levels of sensitivity comparable to radioactivity and can be detected immediately, in contrast to isotope labels. Disadvantages of fluorophores are photobleaching and quenching of the fluorescence signal. Additionally, fluorescence detection requires extensive equipment such as an excitation energy source (laser beam) and can be performed only with specialized scanners and image acquisition systems.

3.3.3.5 **Enzymes**

Enzyme assays represent a special group in the field of bioassays [118]. In this labeling method, the substrate of the enzyme is often used as the analyte to be detected. However, also cofactors or even the enzyme itself, for example in clinical diagnostics, can be analyzed by enzyme assays. The advantage of this method is the high specificity. Hence there is no need for a sophisticated sample preparation to eliminate negative matrix effects. Even the investigation of complex probe material can be managed rapidly and easily by enzyme assays, without the use of expensive chromatographic processes. In most cases these assays are based on redox-active enzymes that catalyze the creation of a soluble dye in the presence of specific cofactors (e.g., nicotinamide adenine dinucleotide (NAD) or by co-products of the enzymatic reaction (e.g., H_2O_2). From the analytical point of view, the oxidoreductases and also the hydrolases are of main interest. For example, glucose oxidase and horseradish peroxidase (both belong to the group of oxidoreductases) or alkaline phosphatase and acetylcholinesterase (both belong to the group of hydrolases) are typical representatives and widely used in enzyme-based bioanalytical investigations. A further benefit of enzymes is the wide knowledge about their reactions, kinetics, structure, substrate specificity, and inhibition of catalytic processes. Nowadays, traditional systems such as enzyme-linked immunosorbent assay (ELISA) [119] and

the Western blot [120, 121] are still used as standard analytical methods in biomolecular and immunological laboratories.

3.3.3.6 **Nanoparticles**

Metallic nanoparticles have attracted increasing interest as alternative labels in analytical biochip-based assays. Due to their unique properties, metal nanoparticles allow the development of various novel approaches for the detection of biomolecules. Their attributes depend strongly on the size, shape, and composition of the single particles [122]. A large variety of fabrication methods have already been described in the literature. Different metals can be used to produce nanoparticles, such as Au, Ag, Cu, Pd, and Pt. Since the properties of metallic nanoparticles depend on their shape, a variety of shapes, such as prisms, rods, and cubes, have been synthesized in addition to the common spherical structure. A further important factor for their use in biochip and bioassay applications is the stable and reliable biofunctionalization of the metallic nanoparticles [123, 124]. The coupling of suitable ligands allows the subsequent specific interaction with complementary biomolecules. Functionalization has been studied with high intensity especially on gold surfaces, because this material provides the simplest and most stable conjugation [125].

Because of their high extinction coefficients and also the large scattering coefficients, metal nanoparticles can be used in optical setups based on absorption or scattering processes [126, 127].

In addition to their special optical properties, metal nanoparticles can be used further in electrical, electrochemical, and electromechanical setups [128–130]. By measuring the electrical conductivity of metallic nanoparticles between an electrode gap, a robust and simple approach for the detection of biomolecules can be realized [131].

Furthermore, these metallic nanoscopic structures can be used as reaction seeds for a specific, reductive metal deposition process [132]. The additional metal deposition leads to so-called "core–shell" structures. During the "core–shell" process, the metal nanoparticles increase in size, which leads in many different systems to an improvement of the sensitivity.

3.3.4 **Readout/Detection**

A key step in the microarray experimental process is the detection method or readout after the hybridization event. Therefore, optical detection methods remain the preferred technique in genomic and proteomic chip-based applications. For the evaluation of detection techniques, some criteria must be considered [23, 133].

Figure 3.3 illustrates the most frequent detection methods for optical biochips. In addition to fluorescence (a), metal nanoparticles can be used in absorbance (light microscopy in transmission mode) (b) and light-scattering setups (c). The approach to detect the scattered light of metal nanoparticles enables a multilabeling system comparable to modern fluorescence setups to be developed.

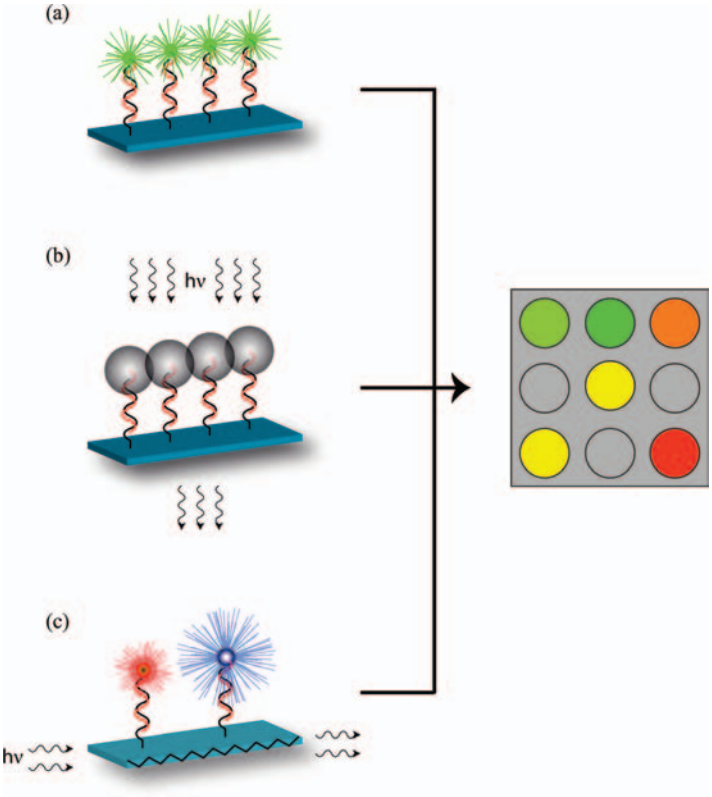

Figure 3.3 The optical detection on biochips is mainly dominated by fluorescence (a). This readout technology allows highly sensitive multilabeling of biomolecules. An alternative approach is the utilization of metal nanoparticles. In both absorbance (b) and scattering setups (c), metal nanoparticles showed the potential to replace traditional markers in biochip technology.

3.3.4.1 **Radioactivity**

Radioactive signals can be captured using autoradiography films, storage phosphor screens, and image acquisition systems, depending on the labeling method and the required levels of sensitivity and resolution. Autoradiography films are commonly used; they are inexpensive, reliable, and provide a good level of sensitivity and resolution. Results obtained with this method can be scanned and analyzed using image analysis software. Scanner-based image acquisition systems are able to detect radioactive signals using a storage phosphor screen, which is about 10 times faster than regular autoradiography films [134].

For the detection of radioactive spots on a microarray, the array is coated with a photographic emulsion. After drying, the sealed slides are stored for a few days in a radiation box. Subsequently the signals are developed with a photographic emulsion.

The reduced silver ions then can be detected and imaged with a scanning light microscope [GE Healthcare (Amersham Biosciences)].

3.3.4.2 **Fluorescence/Absorbance**

Fluorescence is the most commonly applied detection technology in biological and clinical research and drug discovery. Therefore, most of the current commercial microarrays use fluorescence signals for their readout. Reviews have already surveyed fluorescence-based nucleic acid detection methods and microarrays [19, 135–137]. Bally *et al*. described different optical sensing techniques based on microarrays and their applications [133]. Fluorescence immunoassays have largely replaced radioimmunoassay, and fluorescence dominates other detection techniques because of its high sensitivity, dynamic range, and high spatial resolution.

Briefly, the fluorescence process involves the emission of visible light by electronic excitation of molecules, called a fluorophore or fluorescent dye. These molecules have a specialized conjugated π-electron system so that they are capable of absorbing light of different, shorter wavelength than the emission wavelength. Detailed descriptions of the principle of fluorescence have been given in a variety of books and reviews and will not be repeated in this chapter [135, 138]. Microarray technology often uses organic fluorophores as labels due to their characteristics of functionalization, high stability, solubility, and biocompatibility in aqueous solutions [137, 139, 140]. Primary factors limiting fluorescence detectability are photobleaching and quenching processes. Photobleaching is a dynamic process, in which excited fluorophores undergo irreversible destruction under high-intensity illumination conditions and thus lose their ability to emit light [141]. Also, the fluorescence signal depends strongly on the environmental conditions.

In addition to the relatively small size of the microarray, a large periphery is necessary for detection and data interpretation, for instance, light sources, optical instruments, photomultipliers, or a charged-coupled device (CCD) camera. Conventional instruments include scanners and imagers – the two main designs of detection instruments. Scanners are distinguished from imagers in moving their position from the substrate or optics as a function of spatial coordinates in two dimensions. Scanner techniques include laser scanning methods and often photomultipliers for detection. Imagers often use white light sources and CCD technology to achieve images in a single step. A powerful analytical method is required for rapid and automatic data acquisition. Subsequently, the huge amount of data must be analyzed and interpreted by means of bioinformatics [142, 143].

Based on fluorescence, there are different parameters that characterize fluorescent molecules, such as fluorescence quantum yield, wavelength, and lifetime. For instance, information about the lifetime and decay of fluorescence signals is used in DNA microarray [144, 145] and protein array technology [146]. Cubeddu *et al*. presented an overview of time-resolved fluorescence in biology and medicine [147].

Förster resonance energy transfer (FRET), a special form of fluorescence quenching, is often used in biophysics and biochemistry to quantify molecular interactions

such as protein–protein or DNA–protein interactions and also protein conformational changes. FRET also plays an important role in microarray analysis. However, FRET depends strongly on the distance between two molecules, a donor and an acceptor molecule. It depends on the spectral overlap between the emission spectrum of the donor and the absorption spectrum of the acceptor. The fluorescence signals are generated or quenched due to the spatial separation of these two fluorophores. A pair of interactive fluorophores are attached to the ends of two different oligonucleotides or to the two ends of the same oligonucleotide probe. There are two possibilities for detecting the hybridization between capture and target molecules that are used in microarray technology. One possibility is a nonradiative energy transfer from donor fluorophore to acceptor fluorophore if they are in close proximity to each other. If the acceptors are quenchers, the fluorescence emission intensity of the donor fluorophore is decreased. However, if the acceptors are also fluorescent molecules, which are activated by the emission of the donor, the binding event leads to an increase in the emission intensity of the acceptor fluorophore. The other method is to separate the two fluorophores from each other to prevent the energy transfer and generate the donor characteristic emission spectrum uninfluenced by the acceptor fluorophore [11, 136, 148–152]. For instance, a microarray analysis of protein–protein interactions based on FRET using the fluorescence lifetime as an analytical parameter was investigated in the model system of bovine serum albumin and streptavidin [152].

Bio- and chemiluminescence are also useful techniques in biomedical research, diagnostics, and drug discovery and development. Chemiluminescence microscope imaging is a valuable tool for localizing and quantitating enzymes, metabolites, antigens, and nucleic acids in many kinds of specimens [153–157]. In comparison with fluorescence light emission, chemiluminescence is generated by a chemical reaction under exclusion of light. This is advantageous for this technique owing to a lower nonspecific signal and absence of light scattering. However, a disadvantage is that the light-emitting chemical reaction could be uncontrollably inhibited, enhanced, or triggered by sample matrix constituents [158]. A new chemiluminescence-based Ziplex gene expression array technology was evaluated based on Affymetrix GeneChip profiles and applied in ovarian cancer research [159].

Similarly to other methods such as localized surface plasmon resonance (LSPR) and surface-enhanced Raman spectroscopy (SERS), a surface-enhanced fluorescence effect can occur when fluorophores are in close proximity to metal nanoparticles [160]. Lakowicz *et al.* reported on plasmon-controlled fluorescence and the properties of fluorophore–metal interaction bioassays [161].

Absorption measurements have also been used in microarray analysis. Although this method is less sensitive than fluorescence, its simplicity makes it interesting and gives advantages in certain applications. In principle, absorption techniques are based on attenuation of incident light as a function of wavelength. Microarray experimental processes often detect changes in the optical density or the color of probes [162]. Metal nanoparticles have been used in absorption measurements of DNA microarrays as a novel technique [163]. Thus, binding events of target DNA to capture DNA tagged with nanoparticles can be visualized using reflection or

transmission of light depending on some characteristics of particles such size, shape, composition, and environment. Furthermore, nanoparticles are used in DNA microarray scattering detection based on by the extremely large scattering coefficient [125, 163].

3.3.4.3 Surface Plasmon Resonance

Apart from readout-based techniques such as radioactivity and fluorescence, only the development of surface plasmon resonance (SPR)-based biosensors has achieved commercial success (e.g., the Biacore system) [164]. SPR is an optical method that can be used for the real-time and label-free detection of biomolecular recognition reaction [165, 166]. This approach makes use of the interaction of plane polarized light with the free electrons at a metal surface [167]. Under certain conditions, the energy carried by the photons can be transferred to collective oscillations of the electrons, which are called plasmons [168]. The energy transfer occurs only at a specific resonance wavelength of light when the momentum of the photons and that of the plasmons are matched. To excite surface plasmons, in SPR systems, a laser beam is focused on the back of a prism covered with a thin film of metal, mostly gold or silver with a thickness of 40–50 nm. At a defined angle of incidence, the intensity of the reflected light decreases significantly. This effect appears to be due to energy absorption followed by the creation of surface plasmons at the metal surface. The surface plasmons can propagate along the metal surface, but they are not strictly located at the surface. The intensity of their electromagnetic field can be drastically decayed on going from the metal surface into the adjacent medium. Concerning the bioanalytical interest of SPR, the position of the critical angle and thereby the adsorption depend on the evanescent wave and therefore it is sensitive to the environment up to a distance close to the wavelength from the actual metal surface. When using SPR systems in bioanalytics, a major advantage is the label-free detection of biomolecules [169]. These detection units are ideally suited for the direct monitoring of binding events without the need for additional labeled substances. However, the additional use of metal nanoparticles increases the sensitivity up to the picomolar region [170, 171]. Nevertheless, the major problem in every analytical SPR-based system is the unspecific adsorption of the biological target components to the sensor surface. More recently, novel biochip assays have been combined with SPR technology to create a fast and sensitive detection system for different biomolecules [133, 172].

3.4 Examples of Biochip Applications in Biology and Medicine

3.4.1 Genomic Research

The aim of genomic research is the identification of new genes and the understanding of their function and expression levels under different conditions. Two main

applications can be identified: (1) identification of gene mutation (sequence analysis) and (2) determination and monitoring of expression level (gene expression profile) for rapid mapping and identification of disease-related genes [3, 173]. The goal of this research is not only to catalog all genes and their characteristics but also to understand how the components work together to comprise functioning cells and organisms [13]. Pastinen *et al*. developed a powerful approach to scan all possible sequence variations provided by minisequencing assays based on high-density DNA–chip arrays [174]. Several reviews of microarray technologies and applications used in genomic research have been published [14, 175–182]. Grant and Hakonarson provided an overview of recent advances and further expectations within this field [182]. Comparative genome hybridization (CGH) has been mainly used to identify relatively large insertions and deletions in cancer cell lines, for example by cDNA expression arrays [183].

cDNA microarrays are a powerful technique to identify novel biomarkers for potential use as diagnostic, prognostic, and therapeutic tools in clinical diagnosis. They facilitate the analysis of the expression of thousands of genes simultaneously to provide static and dynamic information about expressed genes [91, 184]. It is based on the same principle as Northern blot and RT-PCR analysis. An overview of cDNA microarray technology was given by de Mello-Coelho and Hess [9]. Basically, cDNA microarrays are used for identifying the role of several genes involved in cellular processes. cDNA microarray techniques play an important role in research on human cancers and are used for studying distinct types of cancers, for example, lung cancer [185–187], prostate cancer [188, 189], breast cancer [183, 190–193], and ovarian cancer [194, 195], and also the pathogenesis of infectious diseases [196, 197]. Furthermore, differentiation in gene expression patterns of nondiseased and diseased tissues has contributed to a better understanding of the regulation of molecular mechanisms and potential for therapeutic use towards personalized medicine [198]. Parissenti *et al*. demonstrated gene expression profiles as biomarkers for the prediction of chemotherapy drug response in human tumor cells [179]. Different applications of cDNA microarrays include life science areas of endocrinology, microbiology, immunology, oncology, toxicogenomics, development, genetics, endocrinology, and gerontology [9, 199].

3.4.1.1 **SNP Detection**

A large number of variations in DNA sequence, mainly single nucleotide polymorphism (SNP), are revealed with the complete sequencing of the humane genome. Millions of SNPs are deposited in public databases [200, 201]. These variations in DNA sequence play a major role in the diagnosis of a variety of genetic diseases and cancer and in drug development. SNPs serve as genomic markers for assessing disease predisposition and prediction medication [202, 203]. The analysis of SNPs can help in understanding genetic differences between individuals and disease states and will be also useful in helping researchers to determine and understand why individuals differ in their response to absorb or clear certain drugs for the improvement of medical treatments [180, 204].

The application of oligonucleotide arrays for the detection of particular mutations or polymorphism was first reported in 1989 by Saiki *et al.* [205]. They described the genetic analysis of amplified DNA (HLA-DQA genotyping and 3-thalassemia mutations) with immobilized sequence-specific oligonucleotide probes on a nylon membrane.

Commercial SNP arrays are provided by numerous companies for numerous applications. For example, Illumina has developed a bead-based flexible, accurate, highly multiplexed SNP genotyping assay. Up to 1536 SNPs can be detected in a single DNA sample with this system [204]. Each bead contains hundreds of thousands of covalently attached oligonucleotide probes. For instance, in a cDNA-mediated annealing, selection, extension, and ligation assay, 1152 cSNPs derived from 380 cancer-related genes can be investigated. In this assay, information about both genomic DNA and RNA and also allele-specific expression is obtained, which is important for studying variations and origins of diseases. Owing to the variability and scalability of the Illumina platform, the user can perform small pilot studies or large-scale SNP genotyping studies for human genetic diseases, pharmacogenomic applications, or rapid development of molecular diagnostics [99, 204]. An automated magnetic bead-based platform for pretreatment of human leukocytes, gDNA extraction, and fast analysis of genetic genes was demonstrated by Lien *et al.* [206]. Furthermore, a comparison of genotyping kits and arrays from Applied Biosystems and Affymetrix was made by Selmer *et al.* [207].

A novel genotyping technique that employs a peptide nucleic acid (PNA) zip-code microarray [208] method was described by Mun *et al.* [209]. The zip-code array technique involves unique and distinct short oligonucleotides designed for the purpose of addressing complementary target sequences. It has become an interesting method for conducting routine genetic assays, for instance, investigating mutations in susceptibility gene BRCA1, which is considered to be involved in the development of breast and ovarian cancer. Based on a zip-code microarray mutation, detection of BRCA1 was described [195, 210, 211]. Further applications based on zip-code microarrays include investigations of diabetes caused by HNF-1α mutations [212].

Other applications have been reported for sensing of low-abundance DNA point mutation in K-*ras* oncogenes, which have a high diagnostic value for colorectal cancers [95, 148]. Generally, reviews and articles have focused on the wide range of applications of SNP microarray analysis in cancer research and potential applications in cancer risk assessment, diagnosis, prognosis, and treatment selection [12, 16, 198, 213–216]. Loss of heterozygosity (LOH), genomic copy number changes, and DNA methylation alterations [217, 218] of cancer cells can be determined by SNP array genotyping [216, 219]. LOH of chromosomal regions bearing mutated tumor suppressor genes involve genomic alterations [185, 186, 189, 220]. Also in molecular karyotyping, SNP arrays are used for genome-wide genotyping [221]. Bruno *et al.* studied the feasibility of replacing targeted testing of patients with mental retardation and/or congenital abnormalities using SNP arrays [222].

3.4.1.2 Gene Expression Profile Analysis

Point mutations in the DNA sequence are mainly identified by using SNP analysis. In gene expression profiling, the analysis of point mutations is not preferentially considered. Gene expression profile analysis is used for the monitoring and determination of expressed genes. Depending on their environmental conditions, different expression patterns of genes can be obtained. SNPs are genetic variations and almost unaffected by their environment.

High-throughput molecular technologies are reshaping our understanding of diseases, and microarray-based gene expression has attracted the most attention for performing massive parallel profiling of gene expression from a single sample. General reviews of DNA microarrays include gene expression profiling by Hughes and Shoemaker [223] and also by Deyholos and Galbraith [224]. A technology review about navigating gene expression using microarrays was presented given by Schulze and Downward [225]. Gene expression profile analysis has been successfully used to derive a molecular taxonomy to gain biological insights into basic biochemical pathways and molecular mechanisms of diseases and their regulatory circuits to generate a multitude of prognostic/predictive signatures. Cancer research is one of the most important clinical fields based on microarray technology [175]. The application of biochip technologies in cancer research as a basis for individualized treatment of cancer patients was reported by Kallioniemi [198]. Polyak and Riggins included in a review the serial analysis of gene expression techniques and the implications for cancer research [226]. Other reviews have described the contribution of gene expression profiling to our understanding of breast cancer [227] and its clinical management and what still remains be done for these classifiers to be incorporated in clinical practice [192, 228].

The first customized microarray-based gene expression diagnostic breast cancer array, accepted by US FDA in 2007, called MammaPrint, was developed based on the Agilent two-color platform and method [229]. Breast cancer is the most common research field for gene expression profile analysis and the application of microarrays. Another review covered genome-wide profiling of genetic alterations in acute lymphoblastic leukemia [230]. Also, results of genomic analysis revealed few genetic alterations in pediatric acute myeloid leukemia [231]. Nannini *et al.* analyzed the state of the art of gene expression profiling in colorectal cancer using microarray technology [232]. In addition to gene expression profiling in cancer research, other exciting examples covering fields such as cardiovascular diseases [233, 234] and psychiatric disorders [222, 235] are being researched. Furthermore, gene expression analysis plays an important role in human embryonic stem cell research and the differentiated progeny [236]. It is useful for the treatment of a variety of inherited and acquired diseases. Gene expression profiles can also serve as transcriptional "fingerprints," for example to determine the target of a drug [237, 238]. Another field of expression profiling analysis is the investigation of proteins. However, achieving the equivalent genome-wide profiling of proteins is technically more difficult than investigations of DNA or RNA, due to the already described problems with the complexity of capture molecules and their immobilization [239, 240].

In addition to cancer analysis by microarray techniques, several other diseases have also been investigated, including muscular dystrophy [241], Alzheimer's disease [242–244], schizophrenia [245, 246], and HIV infection [247, 248].

3.4.1.3 **Pharmacogenomics and Toxicogenomics**

Pharmacogenomics means the application of genomic technologies to drug discovery and development. Usually, drug discovery started with a biochemical pathway implicated in a pathophysiological process, and an appropriate enzyme commonly from the rate-limiting step in the pathway or a receptor was characterized, purified, and screened against a variation of structurally diverse small molecules. Today, the monitoring of genetic polymorphisms and differential expression patterns are the most biologically informative application of microarray technology and will be an important improvement in drug discovery [249].

Genetic polymorphisms (SNPs, cSNPs) represent inherited differences in drug-metabolizing capacity. Most drugs interact with specific target proteins to exert their pharmacological effects, such as receptors, enzymes, or proteins involved in signal transduction, cell cycle control, and many other cellular events. In many cases, genetic polymorphisms are associated with altered activity of encoded proteins which influence pharmacokinetics and pharmacologic effects, and as a consequence the sensitivity of specific medications. In drug discovery, genetic polymorphism analyses will be the initiating step followed by biochemical and clinical studies to evaluate the phenotypic consequences of these polymorphisms [250].

Another approach for the discovery of potential drug targets is the investigation of differential expression patterns. The gene expression in a variety of tissues can be compared: normal, diseased, and also drug-affected tissues, in addition to model organisms, examining the effects of selected overexpressed genes or drug treatment. Yeast and mouse models are commonly used. Drug-induced gene products can be used as surrogate markers to follow readily the effect and dose of a drug in the clinical setting. Also, a highly selective tissue expression of a drug target is attractive, as the potential for unwanted side effects may be more restricted [30].

The study of pathogen gene expression during the time of acute infection or during latency and also the identification of genes and gene products turned on by the response of the host against the pathogen is a further approach to establishing new therapeutic targets.

Microarrays are a powerful tool for *in vitro* target identification. They determine drug efficacy and toxicity and improve the understanding of the mechanism of drug action. Various companies are involved in the application of pharmacogenomic technology [238] for drug target validation and identification of secondary drug target effects facilitated by DNA microarrays [251].

The field of toxicogenomics contains global mRNA, protein, and metabolite analysis to study molecular and cellular effects in relation to exposure to toxic elements. The prediction of possible side effects of pharmaceuticals is an important part of the preclinical drug development process. The comparison of gene expression patterns from toxicant-treated organisms versus a control sample, healthy versus

diseased tissue, and susceptible versus resistant tissue helps us to understand the influence of hazards and environmental stressors in biological systems.

There are increasing online resources for biological data and information for toxicogenomic studies (e.g., TOXNET, NIEHS, NCT, TRC, CEBS, and other) [252]. Toxicology microarray data sets comprising genes of different subject areas such as apoptosis, DNA repair, DNA damage, inflammation, and cell proliferation and also cell response to oxidative stress and xenobiotic metabolism have been reported. For the selection of genes from the knowledge-based microarrays, the ratio of the intensities is calculated and the induction and repression of genes inferred. Optimal microarray measurements can detect differences as small as a 1.2-fold increase/decrease in gene expression. Gene expression changes are more sensitive and comprehensive markers of toxicity than typical toxicological endpoints such as morphological changes, reproductive toxicity, and carcinogenicity [253].

Toxicology arrays, for example, the ToxBlot [254] and ToxChip [255] from the National Institute of Environmental Health Sciences Microarray Group, include gene classes related to cancer, immunology, endocrinology, neurobiology, investigative toxicology, predevelopment toxicology, and safety assessment. ToxChips will also be developed to monitor drinking water quality and identify microorganisms [256]. Toxicology biochips determine the relative security of natural and synthesized compounds and chemical mixtures to which humans are exposed.

3.4.2 Pathogen Detection and Clinical Diagnosis

3.4.2.1 Pathogen Detection

The detection and identification of pathogens are essential for ensuring the safety of humans [257]. The difficulty in implementing pathogen detection in biochip and bioassay technology lies in the complexity of most of the samples, making it hard to ensure the sensitivity and specificity of the method. Nowadays, many microbiological laboratories working on pathogen detection have to use microbiological culturing techniques to identify the pathogens reliably. After the culturing process, biochemical and immunological methods are used to detect specific antigens of the pathogen [258]. However, this procedure is very time consuming, and additionally the traditional tests do not provide information about the potential pathogenicity of the organisms.

New biochip approaches facilitate pathogen analysis. The main factors influencing this development are the assay speed, information content, and costs. Further promising opportunities such as miniaturization and integration allow the construction of "lab-on-a-chip" devices for on-site testing [259]. These point-of-care systems permit the analysis of pathogens even for slow-growing organisms. Pathogen detection at the bedside will lead to faster diagnosis and initiation of an appropriate therapy.

In recent years, many groups made remarkable progress in biochip-based pathogen detection [260]. In 2002, Wang *et al.* demonstrated the detection of viral pathogens [261]. They successfully developed a biochip platform to detect PCR products, labeled with a fluorescent dye, of 140 different viruses. Garaizar *et al.* listed a number of bacterial pathogens investigated by biochip studies [262]. A further point of interest is the analysis of host–pathogen interactions. Such an interaction causes substantial changes of the host and also the pathogen. The biochip-based detection of host–pathogen interactions was demonstrated by Diehn and Relman [263]. Especially new spectroscopic methods have the potential for the sensitive and specific detection of pathogens. Identification at the subspecies/strain level on the basis of the SERS fingerprint was reported in 2003 by Grow *et al.* [264]. The highly specific SERS fingerprint could also reflect the physiological state of the bacterial pathogens. A proof-of-principle for the point-of-care-analysis of *Escherichia coli*- and *Bacillus subtilis*-infected samples was developed by Yeung *et al.* in 2006, including sample preparation, amplification, and specific detection [265].

3.4.2.2 **Clinical Diagnosis**

In clinical diagnosis, novel biochip systems have been used in gene analysis for prognosis and treatment. The innovative biochip technology showed the ability to change the current molecular diagnosis to point-of-care analytics that allow the integration of diagnostics with therapeutics and the development of personalized medicine [213, 266]. Personalized medicine will improve the precision and outcome of treatment. Tailor-made therapy for individual patients is based on transcriptional profiling. Additionally, biochips can investigate specific factors of a disease, such as the presence of specific cell types (e.g., white blood cells), proteins, and different kinds of enzymes, in a rapid and efficient manner. For this purpose, the body fluids (e.g., blood), exhaled air, and tissue samples from the patient serve as probe materials for the final biochip analysis. Especially in cancer diagnosis, research in recent years has led to considerable progress in prognosis and tumor classification, where so-called methylation chips served for the diagnosis and prognosis of different cancer types [267].

Aberrant DNA methylation has frequently been found in cancer cells, which silenced different tumor suppressor genes and genes important for cell cycle function and DNA repair. Therefore, various groups tried to detect tumor tissue based on the investigation of DNA methylation. Yan *et al.* presented a tumor classification of breast cancer patients on the basis of their hormone receptor status and clinical aggressiveness [304]. Shi *et al.* detected and identified unique genes preferentially methylated in particular tumors [268]. DNA microarrays were used to analyze DNA methylation. Therefore, the authors analyzed methylated and unmethylated DNA targets on a chip surface after amplification (bisulfite-PCR) and hybridization of the amplified targets to the immobilized capture molecules. In 2006, Schumacher *et al.* developed a technology for unbiased, high-throughput DNA methylation profiling of large genomic regions [269]. Uunmethylated and methylated DNA fractions were enriched using a series of treatments with methylation-sensitive

restriction enzymes, and interrogated on microarrays. Estécio *et al.* introduced the methylated CpG island amplification (MCAM) technique in 2007 [270]. This technique was stated to be a suitable method to discover methylated genes and to profile methylation changes in clinical samples in a high-throughput fashion. Further array-based detection of DNA methylation in cancer diagnosis was described by Melnikov *et al.* [271] and Kimura *et al.* [272]. Other studies targeted the detection of special proteins for cancer diagnosis. Thus, in 2001 Askari *et al.* introduced the anti-p53 tumor suppressor gene antibody in human serum on a biochip [273]. A review by Pollard *et al.* addressed the development and application of protein microarrays for cancer diagnosis and clinical proteomics [34].

Of course, cancer diagnosis and prognosis represent one of the largest fields in clinical diagnosis, although smaller research topics include the investigation and detection of Alzheimer's disease [244] and autism spectrum disorders (ASDs) [180]. However, the application of microarrays in clinical diagnosis is constantly growing.

3.5 Trends in Biochip Research

A wide variety of novel exciting technologies are becoming available with potential use in analytical applications. These innovative, novel sensing techniques have great promise in the analysis of a wide range of targets and various properties in biological, chemical, and immunological problems. In this connection, most notably nanoparticles, quantum dots, and novel enzymatic technologies show the potential to improve or to replace current analytical methods. Especially with respect to the development of point-of-care systems, the new labeling methods offer robust and easy-to-use detection units that can be applied outside specialized laboratories. Another important point is the stability of the signals, which is of interest for comparisons of the received data and storage.

These methods form the basis for a new generation of biochip platforms that allow fast and sensitive on-site detection of biomolecules.

3.5.1 Metal Nanoparticles

The main reasons for the development of innovative bioanalytical approaches based on metal nanoparticles include the stability of the signals, the high signal intensities, and harmless reagents. Additionally, the utilization of metal nanoparticles allows the construction of robust, cost-effective, and portable read-out devices to realize easy-to-use point-of-care systems.

Using the scattered light of metal nanoparticles permits sensitive imaging and quantification of biomolecules. The spectrum of the scatted light is dependent on the attributes of the nanoparticles [126, 127]. As the spectrum depends on particle size, shape, and composition, a multi labeling system based on metal

nanoparticles has been demonstrated [163]. A common glass slide, functionalized with oligonucleotides, was used as a planar wave guide. After specific hybridization with target oligonucleotides, labeled with different sizes of metal nanoparticles, the size-selective scattered light could be used for sequence specific differentiation between the immobilized oligonucleotides.

Furthermore, Quinten demonstrated the influence on plasmon resonance of the interparticle spacing [274]. With this effect, a simple colorimetric DNA detection using gold nanoparticles could be realized [275, 276]. Mirkin's group modified different batches of gold nanoparticles with different sized oligonucleotides [275]. Due to mixing of the batches and by adding a single-stranded target DNA, which was complementary to the two oligonucleotides bound to the different sized particles, the particles formed DNA-linked aggregates. Thereby, the color of the colloidal nanoparticle solution shifted from red to blue. Since this color change was caused by DNA–DNA interactions, heating of the solution above the melting temperature of the double-stranded DNA removed the single-stranded target DNA. Consequently, the nanoparticle aggregate was resolved, resulting in a color shift back to red. By transferring the hybridized particle aggregate to a chromatography plate, the test could be permanently recorded [275].

In addition to the detection of light scattered directly from metal nanoparticles, metal surfaces can enhance electromagnetic fields, which has been exploited in SERS [277, 278], which is an emerging technology in the field of analytics [279]. In comparison with other spectroscopic detection techniques such as fluorescence, Raman spectroscopy is hampered by the inherently small scattering cross-section, which prevents the detection of low analyte concentrations [280, 281]. The huge SERS enhancement of more than 10^6 times the weak Raman signal was considered to be caused by interactions between the analyte molecule and a metallic surface having nanostructured morphology. Since the discovery of the SERS technique, it has become a versatile tool for chemical analysis, environmental monitoring, and biomedical applications, applying the unique properties of Raman spectroscopy, for example, the highly specific molecular fingerprint spectrum [282, 283]. Wabuyele and Vo-Dinh demonstrated the use of plasmonics-based nanoprobes that act as molecular sentinels for DNA diagnostics [284]. The plasmonics nanoprobe consists of a metal nanoparticle and a stem–loop DNA molecule tagged with a Raman label. As long as the hairpin loop is active, the Raman label is in close proximity to the metal nanoparticle, so an intense SERS signal can be detected. In the presence of a complementary target DNA, the hairpin loop will be disrupted. Thereby, the SERS signal will be decreased by removing the Raman label form the metal nanoparticle (Figure 3.4).

3.5.2 Quantum Dots

Quantum dots are most useful in biomedical research and for *in vitro* and *in vivo* clinical diagnostics. These monodisperse semiconductive nanocrystals have dimensions

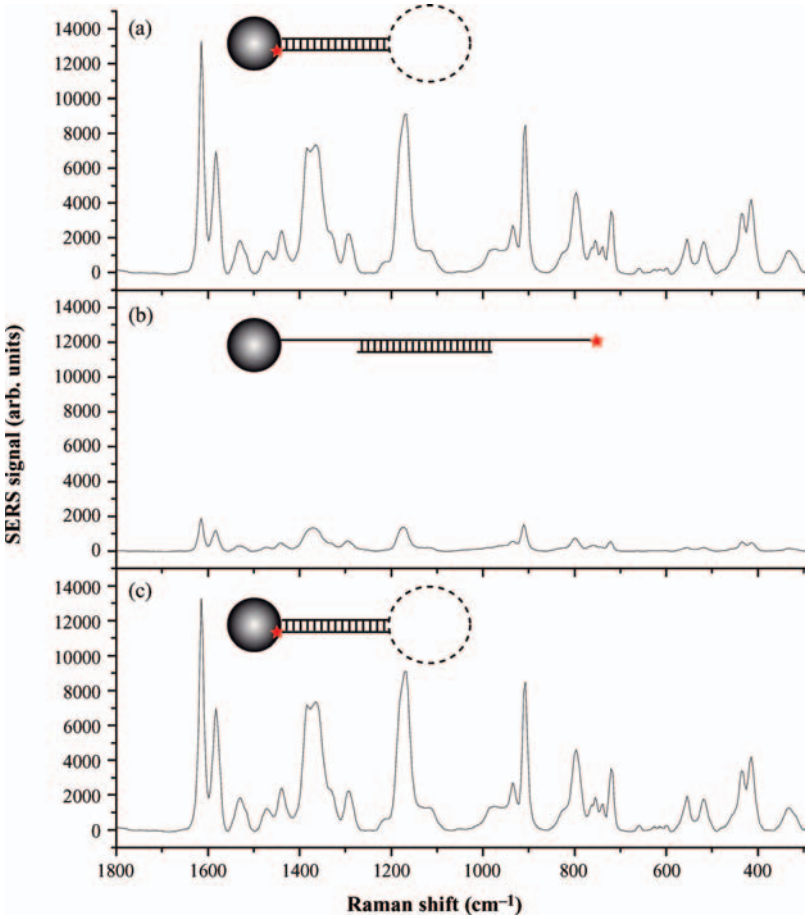

Figure 3.4 SERS intensity dependent on the presence of a plasmonic-based nanoprobe, consisting of a metal nanoparticle and a stem–loop DNA molecule tagged with a Raman label. With a closed hairpin loop the SERS signal can be detected (a). Due to the hybridization of a complementary target DNA, the hairpin loop will be disrupted (b). The SERS signal will be automatically decreased. Heating above the melting temperature of the DNA construct will rearrange the hairpin loop and consequently the SERS signal (c).

between 1 and 10 nm. Because of the small dimensions, the physicochemical properties of quantum dots depend strongly on their size. Colloidal semiconductor quantum dots are single crystals whose size can be controlled by the synthesis conditions. They have very high extension coefficients, much higher than those of organic fluorophores, and these particles adsorb light over a wide range of wavelengths. Quantum dots represent an alternative to organic or natural fluorophores with a variety of advantages, for instance, their large quantum yields, ability to excite a wide range of sizes, with emission ranging from the visible to the near-infrared region with

one laser frequency, and longer fluorescence lifetimes. Furthermore, these nanocrystals offer high photostability, in contrast to organic fluorophores there is no bleaching effect, and their optical attributes allow their use in multiplexed applications for biological microarrays [285].

Especially for *in vivo* applications, significant concerns about the use quantum dots limit their utilization in various applications. The toxicology of quantum dots is determined by their chemical make-up. An inorganic coating of quantum dots insulates the core, amplifies the optical properties, and provides chemical stability. Then an organic coating is necessary for coupling biomolecules [11]. Quantum dots can also be incorporated into latex particles (quantum beads), making them more useful to those attempting antibody conjugation. Basically, chemical coatings (silica and other materials) should provide solubility and the possibility of functionalizing the particles with biomolecules, including DNA, proteins, and antibodies. The toxicology of quantum dots is a combination of the metal, the chemical coating, and the functionalization.

Smith and Nie in 2004 reported details of surface chemistry and bioconjugation, current applications in bioanalytical chemistry and cell biology, and future research directions of quantum dots [286]. Quantum dots are utilized in fluorescence *in situ* hybridization, DNA and protein analysis, and targeting a variety of cell components. In 2005, the Ting's group demonstrated the quantum dot-based detection of proteins via biotin–streptavidin interactions [287]. Additionally, Roullier *et al.* showed the potential of the direct visualization of protein–protein interactions at the single molecule level [288]. Recent reviews have underlined the applicability of quantum dots and the challenges to be overcome to make them commercially available [137, 289–291]. Nowadays, several quantum dot antibody and secondary detection reagents, labels, and labeling kits are commercially available from different companies, for example, Invitrogen and Evident Technologies.

Figure 3.5 illustrates selected applications of quantum dots in biomolecule diagnostics: fluorescence *in situ* hybridization, donors in fluorescence resonance energy transfer, labels for microarray hybridization, and for spectral bar coding [292].

3.5.3 Enzymes

In recent years, much effort has been directed at using enzymes as catalysts to generate metal nanoparticles. The combination aimed at the fusion of the fast and highly specific enzymatic reaction with the unique properties of metal nanoparticles. This technology extended the field of application of enzymes in bioanalytics because of the generation of insoluble stable products. An enzyme-induced growth of metal nanoparticles leads to stable signals that do not fade or bleach.

The use of enzymatic reactions to generate metal nanoparticles was described for the first time in the field of immunohistology and *in situ* hybridization [293, 294].

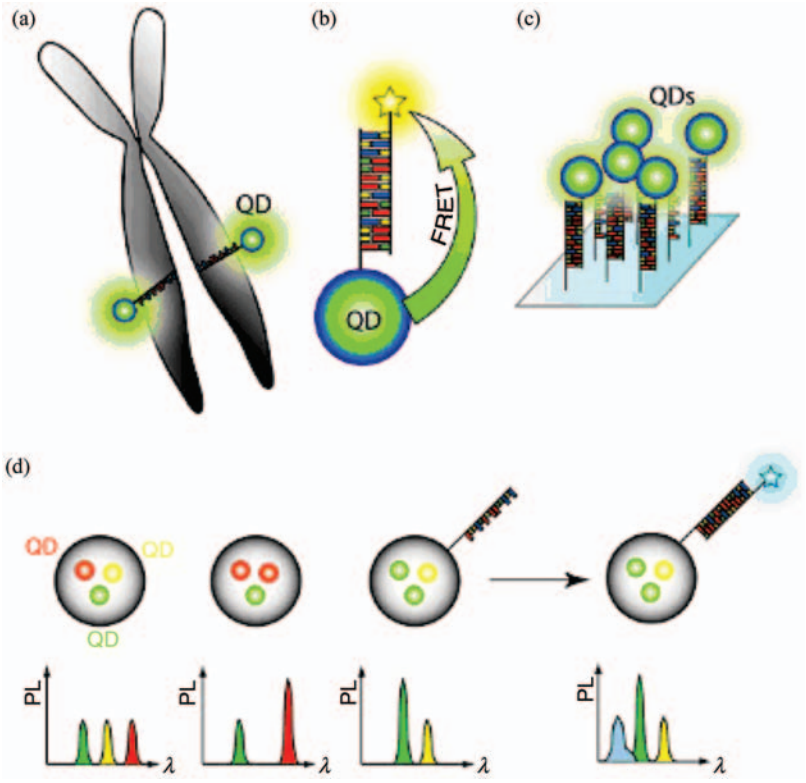

Figure 3.5 Selected applications of quantum dots in nucleic acid diagnostics: (a) quantum dots as labels for fluorescence *in situ* hybridization (FISH); (b) quantum dots as donors in hybridization-mediated fluorescence resonance energy transfer (FRET); (c) quantum dots as labels for biochips/solid-phase hybridization; (d) encapsulated combinations of quantum dots for spectral barcoding. From Algar *et al.* [292].

Both methods used enzymes as labels for the production of specific dyes. However, the enzymatically converted molecules started to diffuse after a short time into neighboring tissue, which led to a decrease in sensitivity and a reduction in resolution. Based on the demonstrated advantages such as the efficient reaction, stability, and reproducibility, different enzymes were investigated in terms of their ability to generate metal nanoparticles. The electrochemical detection of silver nanoparticles deposited by alkaline phosphatase is one of the first described reactions for a chip-based investigation of biomolecules [295–297]. In 2005, Fritzsche's group introduced the horseradish peroxidase-induced growth of silver nanoparticles [298]. The particle growth and the kinetics of the reaction were further investigated at the single-particle level to illustrate the reaction mechanism [299]. Further enzymes, widely used in molecular biological tests, such as glucose oxidase and acetylcholinesterase,

were found to be possible initiators for the enzyme-induced growth of nanoparticles [300, 301]. Silver nanoparticles produced by alkaline phosphatase were used to produce nanoscopic metallic conductor paths by Dip-Pen nanolithography [302]. In addition to nanoparticles, enzymes can generate insoluble colored products that also can be exploited to detect different microorganisms [303]. This detection method is used in biochip applications by CLONDIAG Chip Technologies (Jena, Germany).

The successful combination of enzymes and metal nanoparticles represents a powerful technique that can be used to improve analytical methods in terms of sensitivity and specificity.

3.6 Conclusion

In the last decade, biochips have revolutionized analytical diagnostics. Because of their high throughput ability, biochips save time and costs in experiments. Advantages such as miniaturization and automation led to the further development of this technology. For this purpose, different scientific and engineering fields worked closely together. Due to the collaboration of workers involved in microfabrication, microelectronics, the computer industry, molecular biology, and so on, biochip technology is rapidly growing, with a large number of applications in pathogen detection, clinical diagnosis, genomic research, gene expression profiling, toxicogenomics, and pharmacogenomics.

The method of choice for chip-based biomolecule detection is fluorescence. This technique is well established and widely used in scientific laboratories. Despite all their advantages and the wide applicability of biochips, the technology is still limited to research applications. This is generally caused by a lack of reproducibility and reliability. The rapid development of the technology led to a large number of different biochip systems using various chip platforms, materials, labeling techniques, immobilization strategies, and detection units. Unfortunately, the comparability between these different systems, in terms of sensitivity and specificity, is uncertain. Nevertheless, the development of a new biochip generation, the so-called point-of-care systems, is promising for on-site testing and will continue to advance the technology. Due to the use of alternative labels such as metallic nanoparticles, quantum dots, and enzymes, biochips can be turned into robust and mobile analytical systems. Compared with fluorescence, the nanoparticle-based automation of biochips (e.g., integration in microfluidic systems) will significantly improve the reproducibility and reliability of these on-site diagnostic devices. The required high robustness and short analysis times of point-of-care systems allow their use outside specialized laboratories.

Finally, the biochip technology has already prepared the ground for a new class of bioanalytical tools in order to realize fast, sensitive, easy-to-use, mobile, and reliable diagnostics.

References

1 Southern, E., Mir, K., and Shchepinov, M. (1999) Molecular interactions on microarrays. *Nat. Genet.*, **21**, 5–9.
2 Southern, E.M. (1975) Detection of specific sequences among DNA fragments separated by gel electrophoresis. *J. Mol. Biol.*, **98** (3), 503–517.
3 Lemieux, B., Aharoni, A., and Schena, M. (1998) Overview of DNA chip technology. *Mol. Breed.*, **4** (4), 277–289.
4 Schena, M. (1996) Genome analysis with gene expression microarrays. *Bioessays*, **18** (5), 427–431.
5 DeRisi, J.L., Iyer, V.R., and Brown, P.O. (1997) Exploring the metabolic and genetic control of gene expression on a genomic scale. *Science*, **278** (5338), 680–686.
6 Fodor, S.P., Read, J.L., Pirrung, M.C. *et al.* (1991) Light-directed, spatially addressable parallel chemical synthesis. *Science*, **251** (4995), 767–773.
7 Green, N.S. and Pass, K.A. (2005) Neonatal screening by DNA microarray: spots and chips. *Nat. Rev. Genet.*, **6** (2), 147–151.
8 Greenberg, S.A. (2001) DNA microarray gene expression analysis technology and its application to neurological disorders. *Neurology*, **57** (5), 755–761.
9 de Mello-Coelho, V. and Hess, K.L. (2005) A conceptual and practical overview of cDNA microarray technology: implications for basic and clinical sciences. *Braz. J. Med. Biol. Res.*, **38** (10), 1543–1552.
10 Stoughton, R.B. (2005) Applications of DNA microarrays in biology. *Annu. Rev. Biochem.*, **74**, 53–82.
11 Ng, J.H. and Ilag, L.L. (2003) Biochips beyond DNA: technologies and applications. *Biotechnol. Annu. Rev.*, **9**, 1–149.
12 Heller, M.J. (2002) DNA microarray technology: devices, systems, and applications. *Annu. Rev. Biomed. Eng.*, **4** (1), 129.
13 Lockhart, D.J. and Winzeler, E.A. (2000) Genomics, gene expression and DNA arrays. *Nature*, **405** (6788), 827–836.
14 Aburatani, H. (2004) Functional genomics analysis on DNA microarray. *Tanpakushitsu Kakusan Koso*, **49** (11 Suppl), 1853–1858.
15 Shi, L., Perkins, R.G., and Tong, W. (2009) The current status of DNA microarrays, in *Microarrays Integrated Analytical Systems* (eds K. Dill, R. Liu, and P. Grodzinsky), Springer, New York, pp. 3–24.
16 Guo, Q.M. (2003) DNA microarray and cancer. *Curr. Opin. Oncol.*, **15** (1), 36–43.
17 Hardiman, G. (2008) Applications of microarrays and biochips in pharmacogenomics. *Methods Mol. Biol.*, **448**, 21–30.
18 Jordan, B.R. (2001) *DNA Microarrays: Gene Expression Applications*, Springer, Heidelberg.
19 Schena, M. (2003) *Microarray Analysis*, John Wiley & Sons, Inc., Hoboken, NJ.
20 Watson, S.J. *et al.* (2000) The "chip" as a specific genetic tool. *Biol. Psychiatry*, **48** (12), 1147–1156.
21 Ehrenreich, A. (2006) DNA microarray technology for the microbiologist: an overview. *Appl. Microbiol. Biotechnol.*, **73** (2), 255–273.
22 Wang, J. (2000) From DNA biosensors to gene chips. *Nucleic Acids Res.*, **28** (16), 3011–3016.
23 Schena, M. (ed.) (1999) *DNA Microarrays: a Practical Approach*, Oxford University Press, Oxford.
24 Ramsay, G. (1998) DNA chips: state-of-the-art. *Nat. Biotechnol.*, **16** (1), 40–44.
25 Southern, E.M. (1996) DNA chips: analysing sequence by hybridization to oligonucleotides on a large scale. *Trends Genet.*, **12** (3), 110–115.
26 Cheung, V.G. *et al.* (1999) Making and reading microarrays. *Nat. Genet.*, **21**, 15–19.
27 Brown, P.O. and Botstein, D. (1999) Exploring the new world of the genome with DNA microarrays. *Nat. Genet.*, **21**, 33–37.
28 Duggan, D.J. *et al.* (1999) Expression profiling using cDNA microarrays. *Nat. Genet.*, **21**, 10–14.
29 Hacia, J.G. (1999) Resequencing and mutational analysis using

oligonucleotide microarrays. *Nat. Genet.*, **21**, 42–47.
30 Debouck, C. and Goodfellow, P.N. (1999) DNA microarrays in drug discovery and development. *Nat. Genet.*, **21**, 48–50.
31 Dalma-Weiszhausz, D.D. *et al.* (2006) The Affymetrix GeneChip(R) platform: an overview. *Methods Enzymol.*, **410**, 3–27.
32 Bilitewski, U. (2006) Protein-sensing assay formats and devices. *Anal. Chim. Acta*, **568** (1–2), 232–247.
33 Rusmini, F., Zhong, Z.Y., and Feijen, J. (2007) Protein immobilization strategies for protein biochips. *Biomacromolecules*, **8** (6), 1775–1789.
34 Pollard, H.B. *et al.* (2007) Protein microarray platforms for clinical proteomics. *Proteomics Clin. Appl.*, **1** (9), 934–952.
35 Schena, M. (ed.) (2005) *Protein Microarrays*, Jones & Bartlett, Sudbury, MA.
36 Zhu, H. and Snyder, M. (2003) Protein chip technology. *Curr. Opin. Chem. Biol.*, **7** (1), 55–63.
37 Templin, M.F. *et al.* (2002) Protein microarray technology. *Trends Biotechnol.*, **20** (4), 160–166.
38 Emili, A.Q. and Cagney, G. (2000) Large-scale functional analysis using peptide or protein arrays. *Nat. Biotechnol.*, **18** (4), 393–397.
39 Panicker, R.C., Huang, X., and Yao, S.Q. (2004) Recent advances in peptide-based microarray technologies. *Comb. Chem. High Throughput Screen.*, **7** (6), 547–556.
40 Liotta, L.A. *et al.* (2003) Protein microarrays: meeting analytical challenges for clinical applications. *Cancer Cell*, **3** (4), 317–325.
41 MacBeath, G. and Schreiber, S.L. (2000) Printing proteins as microarrays for high-throughput function determination. *Science*, **289** (5485), 1760–1763.
42 Tomizaki, K.Y., Usui, K., and Mihara, H. (2005) Protein-detecting microarrays: current accomplishments and requirements. *ChemBioChem*, **6** (5), 783–799.
43 Miller, J.C. *et al.* (2003) Antibody microarray profiling of human prostate cancer sera: antibody screening and identification of potential biomarkers. *Proteomics*, **3** (1), 56–63.
44 Bouwman, K. *et al.* (2003) Microarrays of tumor cell derived proteins uncover a distinct pattern of prostate cancer serum immunoreactivity. *Proteomics*, **3** (11), 2200–2207.
45 Schweitzer, B. *et al.* (2002) Multiplexed protein profiling on microarrays by rolling-circle amplification. *Nat. Biotechnol.*, **20** (4), 359–365.
46 Gul, O. *et al.* (2007) Sandwich-type, antibody microarrays for the detection and quantification of cardiovascular risk markers. *Sens. Actuators B Chem.*, **125** (2), 581–588.
47 Wilson, D.S. and Nock, S. (2003) Recent developments in protein microarray technology. *Angew. Chem. Int. Ed.*, **42** (5), 494–500.
48 Kumble, K.D. (2007) An update on using protein microarrays in drug discovery. *Expert Opin. Drug Discov.*, **2** (11), 1467–1476.
49 Falsey, J.R. *et al.* (2001) Peptide and small molecule microarray for high throughput cell adhesion and functional assays. *Bioconjug. Chem.*, **12** (3), 346–353.
50 Uttamchandani, M. *et al.* (2005) Small molecule microarrays: recent advances and applications. *Curr. Opin. Chem. Biol.*, **9** (1), 4–13.
51 Bailey, S.N., Wu, R.Z., and Sabatini, D.M. (2002) Applications of transfected cell microarrays in high-throughput drug discovery. *Drug Discov. Today*, **7** (18), S113–S118.
52 Uttamchandani, M. and Yao, S.Q. (2008) Peptide microarrays: next generation biochips for detection, diagnostics and high-throughput screening. *Curr. Pharm. Des.*, **14** (24), 2428–2438.
53 Kononen, J. *et al.* (1998) Tissue microarrays for high-throughput molecular profiling of tumor specimens. *Nat. Med.*, **4** (7), 844–847.
54 Battifora, H. (1986) The multitumor (sausage) tissue block: novel method for immunohistochemical antibody testing. *Lab. Invest.*, **55** (2), 244–248.
55 Bubendorf, L. *et al.* (1999) Survey of gene amplifications during prostate cancer

progression by high throughput fluorescence *in situ* hybridization on tissue microarrays. *Cancer Res.*, **59** (4), 803–806.

56 Moch, H. *et al.* (1999) High-throughput tissue microarray analysis to evaluate genes uncovered by cDNA microarray screening in renal cell carcinoma. *Am. J. Pathol.*, **154** (4), 981–986.

57 Ziauddin, J. and Sabatini, D.M. (2001) Microarrays of cells expressing defined cDNAs. *Nature*, **411** (6833), 107–110.

58 Bailey, S.N. *et al.* (2006) Microarrays of lentiviruses for gene function screens in immortalized and primary cells. *Nat. Methods*, **3** (2), 117–122.

59 Wheeler, D.B. *et al.* (2004) RNAi living-cell microarrays for loss-of-function screens in *Drosophila melanogaster* cells. *Nat. Methods*, **1** (2), 127–132.

60 Wheeler, D.B., Carpenter, A.E., and Sabatini, D.M. (2005) Cell microarrays and RNA interference chip away at gene function. *Nat. Genet.*, **37**, 25–30.

61 Kulkarni, M.M. *et al.* (2006) Evidence of off-target effects associated with long dsRNAs in *Drosophila melanogaster* cell-based assays. *Nat. Methods*, **3** (10), 833–838.

62 Federico, M. (ed.) (2003) *Lentivirus Gene Engineering Protocols, Methods in Molecular Biology*, vol. **229**, Humana Press, Totawa, NJ

63 Bono, H. and Nakao, M.C. (2003) Introduction to the practical analysis of DNA microarray data. *Tanpakushitsu Kakusan Koso*, **48** (2), 167–172.

64 Do, J.H. and Choi, D.K. (2008) Clustering approaches to identifying gene expression patterns from DNA microarray data. *Mol. Cells*, **25** (2), 279–288.

65 Fan, J. and Ren, Y. (2006) Statistical analysis of DNA microarray data in cancer research. *Clin. Cancer Res.*, **12** (15), 4469–4473.

66 Hanai, T., Hamada, H., and Okamoto, M. (2006) Application of bioinformatics for DNA microarray data to bioscience, bioengineering and medical fields. *J. Biosci. Bioeng.*, **101** (5), 377–384.

67 Hackl, H. *et al.* (2004) Analysis of DNA microarray data. *Curr. Top. Med. Chem.*, **4** (13), 1357–1370.

68 Barbulovic-Nad, I. *et al.* (2006) Bio-microarray fabrication techniques – a review. *Crit. Rev. Biotechnol.*, **26** (4), 237–259.

69 Thompson, M. and Furtado, L.M. (1999) High density oligonucleotide and DNA probe arrays for the analysis of target DNA. *Analyst*, **124** (8), 1133–1136.

70 Pirrung, M.C. (2002) How to make a DNA chip. *Angew. Chem. Int. Ed.*, **41** (8), 1277.

71 Dill, K., Liu, R.H., and Grodzinski, P. (eds.) (2009) *Microarrays: Preparation, Microfluidics, Detection Methods, and Biological Applications (Integrated Analytical Systems)*, Springer Science + Business Media, New York.

72 Nguyen, D.V. *et al.* (2002) DNA microarray experiments: biological and technological aspects. *Biometrics*, **58** (4), 701–717.

73 Pasquarelli, A. (2008) Biochips: technologies and applications. *Mater. Sci. Eng. C Biomimet. Supramol. Syst.*, **28** (4), 495–508.

74 Oh, S.J. *et al.* (2006) Surface modification for DNA and protein microarrays. *OMICS*, **10** (3), 327–343.

75 Henry, A.C. *et al.* (2000) Surface modification of poly(methyl methacrylate) used in the fabrication of microanalytical devices. *Anal. Chem.*, **72** (21), 5331–5337.

76 Pirrung, M.C., Davis, J.D., and Odenbaugh, A.L. (2000) Novel reagents and procedures for immobilization of DNA on glass microchips for primer extension. *Langmuir*, **16** (5), 2185–2191.

77 Kohn, M. (2009) Immobilization strategies for small molecule, peptide and protein microarrays. *J. Pept. Sci.*, **15** (6), 393–397.

78 Uttamchandani, M., Wang, J., and Yao, S.Q. (2006) Protein and small molecule microarrays: powerful tools for high-throughput proteomics. *Mol. Biosyst.*, **2** (1), 58–68.

79 Schena, M. *et al.* (1998) Microarrays: biotechnology's discovery platform for functional genomics. *Trends Biotechnol.*, **16** (7), 301–306.

80 Lamture, J.B. *et al.* (1994) Direct detection of nucleic acid hybridization on the

surface of a charge-coupled device. *Nucleic Acids Res.*, **22** (11), 2121–2125.
81 Rogers, Y.-H. *et al.* (1999) Immobilization of oligonucleotides onto a glass support via disulfide bonds: a method for preparation of DNA microarrays. *Anal. Biochem.*, **266** (1), 23–30.
82 Chrisey, L.A., Lee, G.U., and Oferrall, C.E. (1996) Covalent attachment of synthetic DNA to self-assembled monolayer films. *Nucleic Acids Res.*, **24** (15), 3031–3039.
83 Diehl, F., Beckmann, B., Kellner, N. *et al.* (2002) Manufacturing DNA microarrays from unpurified PCR products, *Nucleic Acids Res.*, **30** (16), e79.
84 Lamture, J.B. *et al.* (1994) Direct detection of nucleic acid hybridization on the surface of a charge coupled device. *Nucleic Acids Res.*, **22** (11), 2121–2125.
85 Schena, M. *et al.* (1996) Parallel human genome analysis: microarray-based expression monitoring of 1000 genes. *Proc. Natl. Acad. Sci. U. S. A.*, **93** (20), 10614–10619.
86 Dufva, M. *et al.* (2004) Characterization of an inexpensive, nontoxic, and highly sensitive microarray substrate. *Biotechniques*, **37** (2), 286–296.
87 Belleville, E. *et al.* (2003) Quantitative assessment of factors affecting the sensitivity of a competitive immunomicroarray for pesticide detection. *Biotechniques*, **35** (5), 1044–1051.
88 Pemov, A. *et al.* (2005) DNA analysis with multiplex microarray-enhanced PCR. *Nucleic Acids Res.*, **33** (2), e11.
89 Miller, J.C. *et al.* (2003) Antibody microarray profiling of human prostate cancer sera: antibody screening and identification of potential biomarkers. *Proteomics*, **3** (1), 56–63.
90 Liu, D. *et al.* (2004) Immobilization of DNA onto poly(dimethylsiloxane) surfaces and application to a microelectrochemical enzyme-amplified DNA hybridization assay. *Langmuir*, **20** (14), 5905–5910.
91 Lockhart, D.J. *et al.* (1996) Expression monitoring by hybridization to high-density oligonucleotide arrays. *Nat. Biotechnol.*, **14** (13), 1675–1680.
92 Hughes, T.R. *et al.* (2001) Expression profiling using microarrays fabricated by an ink-jet oligonucleotide synthesizer. *Nat. Biotechnol.*, **19** (4), 342–347.
93 Wolber, P.K. *et al.* (2006) The Agilent *in situ*-synthesized microarray platform. *Methods Enzymol.*, **410**, 28–57.
94 Duroux, M. *et al.* (2007) Using light to bioactivate surfaces: a new way of creating oriented, active immunobiosensors. *Appl. Surf. Sci.*, **254** (4), 1126–1130.
95 Soper, S.A. *et al.* (2005) Fabrication of DNA microarrays onto polymer substrates using UV modification protocols with integration into microfluidic platforms for the sensing of low-abundant DNA point mutations. *Methods*, **37** (1), 103–113.
96 Nahar, P., Naqvi, A., and Basir, S.F. (2004) Sunlight-mediated activation of an inert polymer surface for covalent immobilization of a protein. *Anal. Biochem.*, **327** (2), 162–164.
97 Sinha, R.P. and Hader, D.P. (2002) UV-induced DNA damage and repair: a review. *Photochem. Photobiol. Sci.*, **1** (4), 225–236.
98 http://www.illumina.com/Documents/products/techbulletins/techbulletin_rna.pdf; Gene expression profiling with Sentrix Focused Arrays; 2005 Illumina, Inc. 2011/07/20.
99 Fan, J.B. *et al.* (2006) Illumina universal bead arrays. *Methods Enzymol.*, **410**, 57–73.
100 Wick, I. and Hardiman, G. (2005) Biochip platforms as functional genomics tools for drug discovery. *Curr. Opin. Drug Discov. Dev.*, **8** (3), 347–354.
101 Ausubel, F.M., Brent, R., Moore, D.D., Seidman, J.G., Smith, J.A., and Stuhl, K. (eds) (2010) Current Protocols in Molecular Biology, Chapter 4: Preparation and Analysis of RNA, John Wiley & Sons Inc.
102 Sambrook, J. and Russell, D. (2001) *Molecular Cloning: a Laboratory Manual*, 3rd edn, Cold Spring Harbor Laboratory Press, Cold Spring Harbor, NY.
103 Stull, D. and Pisano, J.M. (2001) Purely RNA: new innovations enhance the quality, speed, and efficiency of RNA isolation techniques. *Scientist*, **15** (22), 29–31.

104 Qiagen (2006). *Qproteome Mammalian Protein Preparation Handbook*, Qiagen, Hilden.

105 Saiki, R.K. *et al.* (1985) Enzymatic amplification of beta-globin genomic sequences and restriction site analysis for diagnosis of sickle cell anemia. *Science*, **230** (4732), 1350–1354.

106 Saiki, R.K. *et al.* (1988) Primer-directed enzymatic amplification of DNA with a thermostable DNA polymerase. *Science*, **239** (4839), 487–491.

107 Frohman, M.A., Dush, M.K., and Martin, G.R. (1988) Rapid production of full-length cDNAs from rare transcripts: amplification using a single gene-specific oligonucleotide primer. *Proc. Natl. Acad. Sci. U. S. A.*, **85** (23), 8998–9002.

108 Berchtold, W. (1989) A simple method for direct cloning and sequencing cDNA by the use of a single specific oligonucleotide and oligo(dT) in a polymerase chain reaction (PCR). *Nucleic Acids Res.*, **17** (1), 453.

109 van Gelder, R. *et al.* (1990) Amplified RNA synthesized from limited quantities of heterogeneous cDNA. *Proc. Natl. Acad. Sci. U. S. A.*, **87** (5), 1663–1667.

110 Nam, J.-M., Stoeva, S.I., and Mirkin, C.A. (2004) Bio-bar-code-based DNA detection with PCR-like sensitivity. *J. Am. Chem. Soc.*, **126** (19), 5932–5933.

111 Nam, J.-M., Thaxton, C.S., and Mirkin, C.A. (2003) Nanoparticle-based bio-bar codes for the ultrasensitivedetection of proteins. *Science*, **301** (5641), 1884–1886.

112 Stoeva, S.I. *et al.* (2006) Multiplexed DNA detection with biobarcoded nanoparticle probes. *Angew. Chem. Int. Ed.*, **45** (20), 3303–3306.

113 Oh, B.-K. (2006) A fluorophore-based bio-barcode amplification assay for proteins. *Small*, **2** (1), 103–108.

114 Muller, U.R. (2006) Protein detection using biobarcodes. *Mol. Biosyst.*, **2** (10), 470–476.

115 Brown, T.A. (2002) DNA labeling, in *Genomes*, 2nd edn, Wiley-Liss, Oxford, p. 163.

116 Zhu, Z. *et al.* (1994) Directly labeled DNA probes using fluorescent nucleotides with different length linkers. *Nucleic Acids Res.*, **22** (16), 3418–3422.

117 Chen, J., Strand, S.-E., and Sjögren, H.-O. (1996) Optimization of radioiodination and biotinylation of monoclonal antibody chimeric BR96: an indirect labeling using *N*-succinimidyl-3-(tri-*n*-butylstannyl) benzoate conjugate. *Cancer Biother. Radiopharm.*, **11** (3), 217–226.

118 Goddard, J.-P. and Reymond, J.-L. (2004) Enzyme assays for high-throughput screening. *Curr. Opin. Biotechnol.*, **15** (4), 314–322.

119 Engvall, E. and Perlmann, P. (1971) Enzyme-linked immunosorbent assay (ELISA). Quantitative assay of immunoglobulin G. *Immunochemistry*, **8** (9), 871–874.

120 Renart, J., Reiser, J., and Stark, G.R. (1979) Transfer of proteins from gels to diazobenzyloxymethyl-paper and detection with antisera: a method for studying antibody specificity and antigen structure. *Proc. Natl. Acad. Sci. U. S. A.*, **76** (7), 3116–3120.

121 Towbin, H., Staehelin, T., and Gordon, J. (1979) Electrophoretic transfer of proteins from polyacrylamide gels to nitrocellulose sheets: procedure and some applications. *Proc. Natl. Acad. Sci. U. S. A.*, **76** (9), 4350–4354.

122 Liz-Marzan, L.M. (2006) Tailoring surface plasmons through the morphology and assembly of metal nanoparticles. *Langmuir*, **22** (1), 32–41.

123 Nuzzo, R.G. and Allara, D.L. (1983) Adsoption of bifunctional organic disulfides on gold surfaces. *J. Am. Chem. Soc.*, **105**, 4481–4483.

124 Xiao, S. *et al.* (2002) Selfassembly of metallic nanoparticle arrays by DNA scaffolding. *J. Nanopart. Res.*, **4**, 313–317.

125 Fritzsche, W. and Taton, T.A. (2003) Metal nanoparticles as labels for heterogeneous, chip-based DNA detection. *Nanotechnology*, **14** (12), R63–R73.

126 Yguerabide, J. and Yguerabide, E.E. (1998) Light-scattering submicroscopic particles as highly fluorescent analogs and their use as tracer labels in clinical and biological applications. I. Theory. *Anal. Biochem.*, **262** (2), 137–156.

127 Yguerabide, J. and Yguerabide, E.E. (1998) Light-scattering submicroscopic particles as highly fluorescent analogs and their use as tracer labels in clinical and biological applications. II. Experimental

characterization. *Anal. Biochem.*, **262** (2), 157–176.

128 Wang, J., Liu, G., and Merkoci, A. (2003) Electrochemical coding technology for simultaneous detection of multiple DNA targets. *J. Am. Chem. Soc.*, **125** (11), 3214–3215.

129 Dequaire, M., Degrand, C., and Limoges, B. (2000) An electrochemical metalloimmunoassay based on a colloidal gold label. *Anal. Chem.*, **72** (22), 5521–5528.

130 Okahata, Y. *et al.* (2000) Quantitative detection of binding of PCNA protein to DNA strands on a 27MHz quartz-crystal microbalance. *Nucleic Acids Symp. Ser.* (44), 243–244.

131 Möller, R. *et al.* (2001) Electrical classification of the concentration of bioconjugated metal colloids after surface adsorption and silver enhancement. *Langmuir*, **17**, 5426–5430.

132 Steinbrück, A. *et al.* (2006) Preparation and optical characterization of core–shell bimetal nanoparticles. *Plasmonics*, **1** (1), 79–85.

133 Bally, M. *et al.* (2006) Optical microarray biosensing techniques. *Surf. Interface Anal.*, **38** (11), 1442–1458.

134 Johnston, R.F., Pickett, S.C., and Barker, D.L. (1990) Autoradiography using storage phosphor technology. *Electrophoresis*, **11** (5), 355–360.

135 Lakowicz, J.R. (2006) *Principles of Fluorescence Spectroscopy*, 3rd edn, Springer, Berlin.

136 Epstein, J.R., Biran, I., and Walt, D.R. (2002) Fluorescence-based nucleic acid detection and microarrays. *Anal. Chim. Acta*, **469** (1), 3–36.

137 Nagl, S., Schaeferling, M., and Wolfbeis, O.S. (2005) Fluorescence analysis in microarray technology. *Microchim. Acta*, **151** (1), 1–21.

138 Valeur, B. (2001) *Molecular Fluorescence Principles and Applications*, Wiley-VCH Verlag GmbH, Weinheim, p. 388.

139 Sebat, J. *et al.* (2004) Large-scale copy number polymorphism in the human genome. *Science*, **305** (5683), 525–528.

140 Ekins, R.P. and Chu, F.W. (1991) Multianalyte microspot immunoassay – microanalytical compact-disk of the future. *Clin. Chem.*, **37** (11), 1955–1967.

141 Song, L.L. *et al.* (1995) Photobleaching kinetics of fluorescein in quantitative fluorescence microscopy. *Biophys. J.*, **68** (6), 2588–2600.

142 Timlin, J.A. (2006) Scanning microarrays: current methods and future directions. *Methods Enzymol.*, **411**, 79–98.

143 Huang, G.L. *et al.* (2008) Digital imaging scanning system and biomedical applications for biochips. *J. Biomed. Opt.*, **13** (3), 034006.

144 Valentini, G. *et al.* (2000) Time-resolved DNA-microarray reading by an intensified CCD for ultimate sensitivity. *Opt. Lett.*, **25** (22), 1648–1650.

145 Waddell, E. *et al.* (2000) High-resolution near-infrared imaging of DNA microarrays with time-resolved acquisition of fluorescence lifetimes. *Anal. Chem.*, **72** (24), 5907–5917.

146 Striebel, H.M. *et al.* (2004) Readout of protein microarrays using intrinsic time resolved UV fluorescence for label-free detection. *Proteomics*, **4** (6), 1703–1711.

147 Cubeddu, R. *et al.* (2002) Time-resolved fluorescence imaging in biology and medicine. *J. Phys. D Appl. Phys.*, **35** (9), R61–R66.

148 Wabuyele, M.B. *et al.* (2003) Approaching real-time molecular diagnostics: single-pair fluorescence resonance energy transfer (spFRET) detection for the analysis of low abundant point mutations in K-ras oncogenes. *J. Am. Chem. Soc.*, **125** (23), 6937–6945.

149 Cardullo, R.A. *et al.* (1988) Detection of nucleic-acid hybridization by nonradiative fluorescence resonance energy-transfer. *Proc. Natl. Acad. Sci. U. S. A.*, **85** (23), 8790–8794.

150 Mere, L. *et al.* (1999) Miniaturized FRET assays and microfluidics: key components for ultra-high-throughput screening. *Drug Discov. Today*, **4** (8), 363–369.

151 Marras, S.A., Kramer, F.R., and Tyagi, S. (2002) Efficiencies of fluorescence resonance energy transfer and contact-mediated quenching in oligonucleotide probes. *Nucleic Acids Res.*, **30** (21), e122.

152 Nagl, S. *et al.* (2008) Microarray analysis of protein–protein interactions based on FRET using subnanosecond-resolved

fluorescence lifetime imaging. *Biosens. Bioelectron.*, **24** (3), 397–402.
153 Fan, A.P., Lau, C.W., and Lu, J.Z. (2005) Magnetic bead-based chemiluminescent metal immunoassay with a colloidal gold label. *Anal. Chem.*, **77** (10), 3238–3242.
154 Li, H.G. and He, Z.K. (2009) Magnetic bead-based DNA hybridization assay with chemiluminescence and chemiluminescent imaging detection. *Analyst*, **134** (4), 800–804.
155 Marquette, C.A. and Blum, L.J. (2006) Applications of the luminol chemiluminescent reaction in analytical chemistry. *Anal. Bioanal. Chem.*, **385** (3), 546–554.
156 Roda, A. *et al.* (2003) Analytical bioluminescence and chemiluminescence. *Anal. Chem.*, **75** (21), 463A–470A.
157 Seidel, M. and Niessner, R. (2008) Automated analytical microarrays: a critical review. *Anal. Bioanal. Chem.*, **391** (5), 1521–1544.
158 Roda, A. *et al.* (2005) Bio- and chemiluminescence imaging in analytical chemistry. *Anal. Chim. Acta*, **541** (1–2), 25–35.
159 Quinn, M.C.J. *et al.* (2009) The chemiluminescence based Ziplex(R) automated workstation focus array reproduces ovarian cancer Affymetrix GeneChip(R) expression profiles. *J. Translat. Med.*, **7**, 53.
160 Zhang, J. *et al.* (2008) Plasmon-coupled fluorescence probes: effect of emission wavelength on fluorophore-labeled silver particles. *J. Phys. Chem. C*, **112** (25), 9172–9180.
161 Lakowicz, J.R. *et al.* (2001) Intrinsic fluorescence from DNA can be enhanced by metallic particles. *Biochem. Biophys. Res. Commun.*, **286** (5), 875–879.
162 Myers, F.B. and Lee, L.P. (2008) Innovations in optical microfluidic technologies for point-of-care diagnostics. *Lab Chip*, **8** (12), 2015–2031.
163 Taton, T.A., Lu, G., and Mirkin, C.A. (2001) Two-color labeling of oligonucleotide arrays via size-selective scattering of nanoparticle probes. *J. Am. Chem. Soc.*, **123** (21), 5164–5165.
164 Karlsson, R. (2004) SPR for molecular interaction analysis: a review of emerging application areas. *J. Mol. Recognit.*, **17** (3), 151–161.
165 Wegner, G.J. *et al.* (2004) Real-time surface plasmon resonance imaging measurements for the multiplexed determination of protein adsorption/desorption kinetics and surface enzymatic reactions on peptide microarrays. *Anal. Chem.*, **76** (19), 5677–5684.
166 Liedberg, B., Nylander, C., and Lundstrom, I. (1995) Biosensing with surface plasmon resonance – how it all started. *Biosens. Bioelectron.*, **10** (8), i–ix.
167 Peterlinz, K.A. and Georgiadis, R.M. (1996) *In situ* kinetics of self-assembly by surface plasmon resonance spectroscopy. *Langmuir*, **12**, 4731–4740.
168 Georgiadis, R.M., Peterlinz, K.A., and Peterson, A.W. (2000) Quantitative measurements and modeling of kinetics in nucleic acid monolayer films using SPR spectroscopy. *J. Am. Chem. Soc.*, **122** (13), 3166–3173.
169 Perkins, E.A. and Squirrell, D.J. (2000) Development of instrumentation to allow the detection of microorganisms using light scattering in combination with surface plasmon resonance. *Biosens. Bioelectron.*, **14** (10–11), 853–859.
170 Stuart, D.A. *et al.* (2005) Biological applications of localised surface plasmonic phenomenae. *IEE Proc. Nanobiotechnol.*, **152** (1), 13–32.
171 Lyon, L.A., Musick, M.D., and Natan, M.J. (1998) Colloidal Au-enhanced surface plasmon resonance immunosensing. *Anal. Chem.*, **70** (24), 5177–5183.
172 Hoa, X.D., Kirk, A.G., and Tabrizian, M. (2007) Towards integrated and sensitive surface plasmon resonance biosensors: a review of recent progress. *Biosens. Bioelectron.*, **23** (2), 151–160.
173 Vo-Dinh, T. (2003) Biochips and microarrays: tools for the new medicine, in *Biomedical Photonics Handbook* (ed. T. Vo-Dinh), CRC Press, Boca Raton, FL, p. 51-1.
174 Pastinen, T. *et al.* (1997) Minisequencing: a specific tool for DNA analysis and

diagnostics on oligonucleotide arrays. *Genome Res.*, **7** (6), 606–614.
175 Macgregor, P.F. (2003) Gene expression in cancer: the application of microarrays. *Expert Rev. Mol. Diagn.*, **3** (2), 185–200.
176 Meldrum, D. (2000) Automation for genomics, part two: sequencers, microarrays, and future trends. *Genome Res.*, **10** (9), 1288–1303.
177 Mockler, T.C. and Ecker, J.R. (2005) Applications of DNA tiling arrays for whole-genome analysis. *Genomics*, **85** (1), 1–15.
178 Morozova, O. and Marra, M.A. (2008) Applications of next-generation sequencing technologies in functional genomics. *Genomics*, **92** (5), 255–264.
179 Parissenti, A.M. *et al.* (2007) Gene expression profiles as biomarkers for the prediction of chemotherapy drug response in human tumour cells. *Anticancer Drugs*, **18** (5), 499–523.
180 Shen, Y. and Wu, B.L. (2009) Microarray-based genomic DNA profiling technologies in clinical molecular diagnostics. *Clin. Chem.*, **55** (4), 659–669.
181 Waddell, N. (2008) Microarray-based DNA profiling to study genomic aberrations. *IUBMB Life*, **60** (7), 437–440.
182 Grant, S.F.A. and Hakonarson, H. (2008) Microarray technology and applications in the arena of genome-wide association. *Clin. Chem.*, **54** (7), 1116–1124.
183 Pollack, J.R. *et al.* (1999) Genome-wide analysis of DNA copy-number changes using cDNA microarrays. *Nat. Genet.*, **23** (1), 41–46.
184 Schena, M. *et al.* (1995) Quantitative monitoring of gene expression patterns with a complementary DNA microarray. *Science*, **270** (5235), 467–470.
185 Janne, P.A. *et al.* (2004) High-resolution single-nucleotide polymorphism array and clustering analysis of loss of heterozygosity in human lung cancer cell lines. *Oncogene*, **23** (15), 2716–2726.
186 Lindblad-Toh, K. *et al.* (2000) Loss-of-heterozygosity analysis of small-cell lung carcinomas using single-nucleotide polymorphism arrays. *Nat. Biotechnol.*, **18** (9), 1001–1005.
187 Santos, E.S., Perez, C.A., and Raez, L.E. (2009) How is gene-expression profiling going to challenge the future management of lung cancer? *Future Oncol.*, **5** (6), 827–835.
188 Bubendorf, L. *et al.* (1999) Hormone therapy failure in human prostate cancer: analysis by complementary DNA and tissue microarrays. *J. Natl. Cancer Inst.*, **91** (20), 1758–1764.
189 Lieberfarb, M.E. *et al.* (2003) Genome-wide loss of heterozygosity analysis from laser capture microdissected prostate cancer using single nucleotide polymorphic allele (SNP) arrays and a novel bioinformatics platform dChipSNP. *Cancer Res.*, **63** (16), 4781–4785.
190 Brennan, D.J. *et al.* (2005) Application of DNA microarray technology in determining breast cancer prognosis and therapeutic response. *Expert Opin. Biol. Ther.*, **5** (8), 1069–1083.
191 Cheang, M.C.U., van de Rijn, M., and Nielsen, T.O. (2008) Gene expression profiling of breast cancer. *Annu. Rev. Pathol. Mech. Dis.*, **3**, 67–97.
192 Geyer, F.C. and Reis, J.S. (2009) Microarray-based gene expression profiling as a clinical tool for breast cancer management: are we there yet? *Int. J. Surg. Pathol.*, **17** (4), 285–302.
193 Lacroix, M. *et al.* (2002) A low-density DNA microarray for analysis of markers in breast cancer. *Int. J. Biol. Markers*, **17** (1), 5–23.
194 Fehrmann, R.S.N. *et al.* (2007) Profiling studies in ovarian cancer: a review. *Oncologist*, **12** (8), 960–966.
195 Lux, M.P., Fasching, P.A., and Beckmann, M.W. (2006) Hereditary breast and ovarian cancer: review and future perspectives. *J. Mol. Med.*, **84** (1), 16–28.
196 Bednar, M. (2000) DNA microarray technology and application. *Med. Sci. Monit.*, **6** (4), 796–800.
197 Yoo, S.M. and Lee, S.Y. (2008) Diagnosis of pathogens using DNA microarray. *Recent Pat. Biotechnol.*, **2** (2), 124–129.
198 Kallioniemi, O.P. (2001) Biochip technologies in cancer research. *Ann. Med.*, **33** (2), 142–147.

199 Anisimov, S.V. (2007) Application of DNA microarray technology to gerontological studies. *Methods Mol. Biol.*, **371**, 249–265.

200 Sachidanandam, R. *et al.* (2001) A map of human genome sequence variation containing 1.42 million single nucleotide polymorphisms. *Nature*, **409** (6822), 928–933.

201 NCBI. Single Nucleotide Polymorphism, http://www.ncbi.nlm.nih.gov/SNP/., National Center for Biotechnology Information, Bethesda, MD (last accessed 26 March 2011).

202 Hirschhorn, J.N. and Daly, M.J. (2005) Genome-wide association studies for common diseases and complex traits. *Nat. Rev. Genet.*, **6** (2), 95–108.

203 Collins, F.S. *et al.* (2003) A vision for the future of genomics research. *Nature*, **422** (6934), 835–847.

204 Shen, R. *et al.* (2005) High-throughput SNP genotyping on universal bead arrays. *Mutat. Res.*, **573** (1–2), 70–82.

205 Saiki, R.K. *et al.* (1989) Genetic-analysis of amplified DNA with immobilized sequence-specific oligonucleotide probes. *Proc. Natl. Acad. Sci. U. S. A.*, **86** (16), 6230–6234.

206 Lien, K.Y. *et al.* (2009) Extraction of genomic DNA and detection of single nucleotide polymorphism genotyping utilizing an integrated magnetic bead-based microfluidic platform. *Microfluidics Nanofluidics*, **6** (4), 539–555.

207 Selmer, K.K. *et al.* (2009) Genome-wide linkage analysis with clustered SNP markers. *J. Biomol. Screen.*, **14** (1), 92–96.

208 Zabarovsky, E.R. *et al.* (2003) Restriction site tagged (RST) microarrays: a novel technique to study the species composition of complex microbial systems. *Nucleic Acids Res.*, **31** (16), e95.

209 Mun, H.Y. *et al.* (2009) SNPs detection by a single-strand specific nuclease on a PNA zip-code microarray. *Biosens. Bioelectron.*, **24** (6), 1706–1711.

210 Girigoswami, A. *et al.* (2008) PCR-free mutation detection of BRCA1 on a zip-code microarray using ligase chain reaction. *J. Biochem. Biophys. Methods*, **70** (6), 897–902.

211 Jung, C. *et al.* (2008) Microarray-based detection of Korean-specific BRCA1 mutations. *Anal. Bioanal. Chem.*, **391** (1), 405–413.

212 Song, J.Y. (2005) *et al.* Diagnosis of HNF-1 alpha mutations on a PNA zip-code microarray by single base extension. *Nucleic Acids Res.*, **33** (2), e19.

213 Anderson, J.E. *et al.* (2006) Methods and biomarkers for the diagnosis and prognosis of cancer and other diseases: towards personalized medicine. *Drug Resist. Updat.*, **9** (4–5), 198–210.

214 Zhao, X.J. *et al.* (2004) An integrated view of copy number and allelic alterations in the cancer genome using single nucleotide polymorphism arrays. *Cancer Res.*, **64** (9), 3060–3071.

215 Ohira, M. *et al.* (2005) A review of DNA microarray analysis of human neuroblastomas. *Cancer Lett.*, **228** (1–2), 5–11.

216 Dutt, A. and Beroukhim, R. (2007) Single nucleotide polymorphism array analysis of cancer. *Curr. Opin. Oncol.*, **19**, 43–49.

217 Gebhard, C. *et al.* (2006) Genome-wide profiling of CpG methylation identifies novel targets of aberrant hypermethylation in myeloid leukemia. *Cancer Res.*, **66** (12), 6118–6128.

218 Adrien, L.R. *et al.* (2006) Classification of DNA methylation patterns in tumor cell genomes using a CpG island microarray. *Cytogenet. Genome Res.*, **114** (1), 16–23.

219 Mao, X.Y., Young, B.D., and Lu, Y.J. (2007) The application of single nucleotide polymorphism microarrays in cancer research. *Curr. Genomics*, **8** (4), 219–228.

220 Wang, Z.G.C. *et al.* (2004) Loss of heterozygosity and its correlation with expression profiles in subclasses of invasive breast cancers. *Cancer Res.*, **64** (1), 64–71.

221 Rauch, A. *et al.* (2004) Molecular karyotyping using an SNP array for genomewide genotyping. *J. Med. Genet.*, **41** (12), 916–922.

222 Bruno, D.L. *et al.* (2009) Detection of cryptic pathogenic copy number variations and constitutional loss of heterozygosity using high resolution SNP microarray analysis in 117 patients referred for cytogenetic analysis and impact on clinical practice. *J. Med. Genet.*, **46** (2), 123–131.

223 Hughes, T.R. and Shoemaker, D.D. (2001) DNA microarrays for expression profiling. *Curr. Opin. Chem. Biol.*, **5** (1), 21–25.

224 Deyholos, M.K. and Galbraith, D.W. (2001) High-density microarrays for gene expression analysis. *Cytometry*, **43** (4), 229–238.

225 Schulze, A. and Downward, J. (2001) Navigating gene expression using microarrays – a technology review. *Nat. Cell Biol.*, **3** (8), E190–E195.

226 Polyak, K. and Riggins, G.J. (2001) Gene discovery using the serial analysis of gene expression technique: implications for cancer research. *J. Clin. Oncol.*, **19** (11), 2948–2958.

227 Stadler, Z.K. and Come, S.E. (2009) Review of gene-expression profiling and its clinical use in breast cancer. *Crit. Rev. Oncol. Hematol.*, **69** (1), 1–11.

228 Geyer, F.C., Decker, T., and Reis-Filho, J.S. (2009) Genome-wide expression profiling as a clinical tool. *Pathologe*, **30** (2), 141–146.

229 Glas, A.M. *et al.* (2006) Converting a breast cancer microarray signature into a high-throughput diagnostic test. *BMC Genomics*, **7**, 278.

230 Mullighan, C.G. and Downing, J.R. (2009) Genome-wide profiling of genetic alterations in acute lymphoblastic leukemia: recent insights and future directions. *Leukemia*, **23** (7), 1209–1218.

231 Radtke, I. *et al.* (2009) Genomic analysis reveals few genetic alterations in pediatric acute myeloid leukemia. *Proc. Natl. Acad. Sci. U. S. A.*, **106** (31), 12944–12949.

232 Nannini, M. *et al.* (2009) Gene expression profiling in colorectal cancer using microarray technologies: results and perspectives. *Cancer Treat. Rev.*, **35** (3), 201–209.

233 Boerma, M. *et al.* (2005) Microarray analysis of gene expression profiles of cardiac myocytes and fibroblasts after mechanical stress, ionising or ultraviolet radiation. *BMC Genomics*, **6** (1), p. 6.

234 Yanagawa, B. *et al.* (2005) Affymetrix oligonucleotide analysis of gene expression in the injured heart. *Methods Mol. Med.*, **112**, 305–320.

235 Ducray, F., Honnorat, J., and Lachuer, J. (2007) DNA microarray technology: principles and applications to the study of neurological disorders. *Rev. Neurol.*, **163** (4), 409–420.

236 Bhattacharya, B., Puri, S., and Puri, R.K. (2009) A review of gene expression profiling of human embryonic stem cell lines and their differentiated progeny. *Curr. Stem Cell Res. Ther.*, **4** (2), 98–106.

237 Marton, M.J. *et al.* (1998) Drug target validation and identification of secondary drug target effects using DNA microarrays. *Nat. Med.*, **4** (11), 1293–1301.

238 Jain, K.K. (2000) Applications of biochip and microarray systems in pharmacogenomics. *Pharmacogenomics*, **1** (3), 289–307.

239 Zhu, H., Bilgin, M., and Snyder, M. (2003) Proteomics. *Annu. Rev. Biochem.*, **72**, 783–812.

240 Boguski, M.S. and McIntosh, M.W. (2003) Biomedical informatics for proteomics. *Nature*, **422** (6928), 233–237.

241 Chen, Y.W. *et al.* (2000) Expression profiling in the muscular dystrophies: identification of novel aspects of molecular pathophysiology. *J. Cell Biol.*, **151** (6), 1321–1336.

242 Galvin, J.E. and Ginsberg, S.D. (2004) Expression profiling and pharmacotherapeutic development in the central nervous system. *Alzheimer Dis. Assoc. Disord.*, **18** (4), 264–269.

243 Ginsberg, S.D. *et al.* (2006) Single cell gene expression profiling in Alzheimer's disease. *NeuroRx*, **3** (3), 302–318.

244 Georganopoulou, D.G. *et al.* (2005) Nanoparticle-based detection in cerebral spinal fluid of a soluble pathogenic biomarker for Alzheimer's disease. *Proc. Natl. Acad. Sci. U. S. A.*, **102** (7), 2273–2276.

245 Mirnics, K., Levitt, P., and Lewis, D.A. (2004) DNA microarray analysis of postmortem brain tissue. *Int. Rev. Neurobiol.*, **60**, 153–181.

246 Mirnics, K. *et al.* (2001) Analysis of complex brain disorders with gene expression microarrays: schizophrenia as a disease of the synapse. *Trends Neurosci.*, **24** (8), 479–486.

247 Geiss, G.K. *et al.* (2000) Large-scale monitoring of host cell gene expression during HIV-1 infection using cDNA microarrays. *Virology*, **266** (1), 8–16.

248 van't Wout, A.B. *et al.* (2003) Cellular gene expression upon human immunodeficiency virus type 1 infection of CD4(+)-T-cell lines. *J. Virol.*, **77** (2), 1392–1402.

249 Braxton, S. and Bedilion, T. (1998) The integration of microarray information in the drug development process. *Curr. Opin. Biotechnol.*, **9**, 643–649.

250 Evans, W.E. and Relling, M.V. (1999) Pharmacogenomics: translating functional genomics into rational therapeutics. *Science*, **286** (5439), 487.

251 Marton, M., Derisi, J., and Bennett, H. (1998) Drug target validation and identification of secondary drug target effects using DNA microarrays. *Nat. Med.*, **4**, 1293–1301.

252 Lee, K.M., Kim, J.H., and Kang, D. (2005) Design issues in toxicogenomics using DNA microarray experiment. *Toxicol. Appl. Pharmacol.*, **207** (2 Suppl), 200–208.

253 Hamadeh, H.K. *et al.* (2002) An overview of toxicogenomics. *Curr. Issues Mol. Biol.*, **4**, 45–56.

254 Pennie, W.D. (2000) *et al.* The principles and practice of toxicogenomics: applications and opportunities. *Toxicol. Sci.*, **54** (2), 277–283.

255 Nuwaysir, E.F. *et al.* (1999) Microarrays and toxicology: the advent of toxicogenomics. *Mol. Carcinog.*, **24** (3), 153–159.

256 Lemarchand, K., Masson, L., and Brousseau, R. (2004) Molecular biology and DNA microarray technology for microbial quality monitoring of water. *Crit. Rev. Microbiol.*, **30** (3), 145–172.

257 Uttamchandani, M. *et al.* (2009) Applications of microarrays in pathogen detection and biodefence. *Trends Biotechnol.*, **27** (1), 53–61.

258 Kostrzynska, M. and Bachand, A. (2006) Application of DNA microarray technology for detection, identification, and characterization of food-borne pathogens. *Can. J. Microbiol.*, **52** (1), 1–8.

259 Schulze, H. *et al.* (2009) Multiplexed optical pathogen detection with lab-on-a-chip devices. *J. Biophotonics*, **2** (4), 199–211.

260 Garaizar, J. *et al.* (2006) Use of DNA microarray technology and gene expression profiles to investigate the pathogenesis, cell biology, antifungal susceptibility and diagnosis of *Candida albicans*. *FEMS Yeast Res.*, **6** (7), 987–998.

261 Wang, D. *et al.* (2002) Microarray-based detection and genotyping of viral pathogens. *Proc. Natl. Acad. Sci. U. S. A.*, **99** (24), 15687–15692.

262 Garaizar, J., Rementeria, A., and Porwollik, S. (2006) DNA microarray technology: a new tool for the epidemiological typing of bacterial pathogens? *FEMS Immunol. Med. Microbiol.*, **47** (2), 178–189.

263 Diehn, M. and Relman, D.A. (2001) Comparing functional genomic datasets: lessons from DNA microarray analyses of host–pathogen interactions. *Curr. Opin. Microbiol.*, **4** (1), 95–101.

264 Grow, A.E. *et al.* (2003) New biochip technology for label-free detection of pathogens and their toxins. *J. Microbiol. Methods*, **53** (2), 221–233.

265 Yeung, S.W. *et al.* (2006) A DNA biochip for on-the-spot multiplexed pathogen identification. *Nucleic Acids Res.*, **34** (18), e118.

266 de Leon, J. *et al.* (2009) DNA microarray technology in the clinical environment: the AmpliChip CYP450 test for CYP2D6 and CYP2C19 genotyping. *CNS Spectr.*, **14** (1), 19–34.

267 Hatada, I. *et al.* (2002) A microarray-based method for detecting methylated loci. *J. Hum. Genet.*, **47** (8), 448.

268 Shi, H. *et al.* (2003) Oligonucleotide-based microarray for DNA methylation analysis: principles and applications. *J. Cell Biochem.*, **88** (1), 138–143.

269 Schumacher, A. *et al.* (2006) Microarray-based DNA methylation profiling: technology and applications. *Nucleic Acids Res.*, **34** (2), 528–542.

270 Estécio, M.R.H. *et al.* (2007) High-throughput methylation profiling by MCA coupled to CpG island microarray. *Genome Res.*, **17** (10), 1529–1536.

271 Melnikov, A.A. *et al.* (2008) Array-based multiplex analysis of DNA methylation in

breast cancer tissues. *J. Mol. Diagn.*, **10** (1), 93–101.

272 Kimura, N. *et al.* (2005) Methylation profiles of genes utilizing newly developed CpG island methylation microarray on colorectal cancer patients. *Nucleic Acids Res.*, **33** (5), e46.

273 Askari, M. *et al.* (2001) Application of an antibody biochip for p53 detection and cancer diagnosis. *Biotechnol. Prog.*, **17** (3), 543–552.

274 Quinten, M. (2001) Local fields close to the surface of nanoparticles and aggregates of nanoparticles. *Appl. Phys. B*, **73** (3), 245–255.

275 Elghanian, R. *et al.* (1997) Selective colorimetric detection of polynucleotides based on the distance-dependent optical properties of gold nanoparticles. *Science*, **277** (5329), 1078–1081.

276 Storhoff, J.J. *et al.* (1998) One pot colorimetric differentiation of polynucleotides with single base imperfections using gold nanoparticle probes. *J. Am. Chem. Soc.*, **120** (9), 1959–1964.

277 Fleischmann, M., Hendra, P.J., and McQuillan, A.J. (1974) Raman spectra of pyridine adsorbed at a silver electrode. *Chem. Phys. Lett.*, **26** (2), 163–166.

278 Freeman, R.G. *et al.* (1995) Self-assembled metal colloid monolayers: an approach to SERS substrates. *Science*, **267** (5204), 1629–1632.

279 Petry, R., Schmitt, M., and Popp, J. (2003) Raman spectroscopy – a prospective tool in the life sciences. *ChemPhysChem*, **4** (1), 14–30.

280 Schmitt, M. and Popp, J. (2006) Raman spectroscopy at the beginning of the twenty-first century. *J. Raman Spectrosc.*, **37** (1–3), 20–28.

281 Haynes, C.L., McFarland, A.D., and Van Duyne, R.P. (2005) Surface-enhanced Raman spectroscopy. *Anal. Chem.*, **77** (17), 338A–346A.

282 Hering, K. *et al.* (2008) SERS: a versatile tool in chemical and biochemical diagnostics. *Anal. Bioanal. Chem.*, **390** (1), 113–124.

283 Cao, Y.C., Jin, R., and Mirkin, C.A. (2002) Nanoparticles with Raman spectroscopic fingerprints for DNA and RNA detection. *Science*, **297** (5586), 1536–1540.

284 Wabuyele, M.B. and Vo-Dinh, T. (2005) Detection of human immunodeficiency virus type 1 DNA sequence using plasmonics nanoprobes. *Anal. Chem.*, **77** (23), 7810–7815.

285 Han, M. *et al.* (2001) Quantum-dot-tagged microbeads for multiplexed optical coding of biomolecules. *Nat. Biotechnol.*, **19**, 631–635.

286 Smith, A.M. and Nie, S.M. (2004) Chemical analysis and cellular imaging with quantum dots. *Analyst*, **129** (8), 672–677.

287 Howarth, M. *et al.* (2005) Targeting quantum dots to surface proteins in living cells with biotin ligase. *Proc. Natl. Acad. Sci. U. S. A.*, **102** (21), 7583–7588.

288 Roullier, V. *et al.* (2009) High-affinity labeling and tracking of individual histidine-tagged proteins in live cells using Ni^{2+} tris-nitrilotriacetic acid quantum dot conjugates. *Nano Lett.*, **9** (3), 1228–1234.

289 Jain, K.K. (2007) Applications of nanobiotechnology in clinical diagnostics. *Clin. Chem.*, **53**, 2002–2009.

290 Michalet, X. *et al.* (2005) Quantum dots for live cells, *in vivo* imaging, and diagnostics. *Science*, **307** (5709), 538–544.

291 Lucas, L.J., Chesler, J.N., and Yoon, J.-Y. (2007) Lab-on-a-chip immunoassay for multiple antibodies using microsphere light scattering and quantum dot emission. *Biosens. Bioelectron.*, **23** (5), 675–681.

292 Algar, W.R., Massey, M., and Krull, U.J. (2009) The application of quantum dots, gold nanoparticles and molecular switches to optical nucleic-acid diagnostics. *TrAC Trends Anal. Chem.*, **28** (3), 292–306.

293 Hainfeld, J.F. *et al.* (2002) Enzymatic metallography: a simple new staining method, in *Proceedings of Microscopy and Microanalysis 2002* (eds. E. Voekl *et al.*), Cambridge University Press, New York, p. 916CD.

294 Mayer, G. *et al.* (2000) Introduction of a novel HRP substrate–Nanogold probe for signal amplification in

immunocytochemistry. *J. Histochem. Cytochem.*, **48** (4), 461–469.

295 Hwang, S., Kim, E., and Kwak, J. (2005) Electrochemical detection of DNA hybridization using biometallization. *Anal. Chem.*, **77**, 579–584.

296 Fanjul-Bolado, P. *et al.* (2007) Alkaline phosphatase-catalyzed silver deposition for electrochemical detection. *Anal. Chem.*, **79** (14), 5272–5277.

297 Zhang, P. *et al.* (2008) Electrochemical detection of point mutation based on surface ligation reaction and biometallization. *Biosens. Bioelectron.*, **23** (10), 1435–1441.

298 Möller, R. *et al.* (2005) Enzymatic control of metal deposition as key step for a low-background electrical detection for DNA chips. *Nano Lett.*, **5** (7), 1475–1482.

299 Schüler, T. *et al.* (2008) Enzyme-induced growth of silver nanoparticles studied on single particle level. *J. Nanopart. Res.*, **11**, 939–946.

300 Willner, I., Basnar, B., and Willner, B. (2007) Nanoparticle–enzyme hybrid systems for nanobiotechnology. *FEBS J.*, **274**, 302–309.

301 Willner, I., Baron, R., and Willner, B. (2006) Growing metal nanoparticles by enzymes. *Adv. Mater.*, **18** (9), 1109–1120.

302 Basnar, B., Willner, I., and Willner, B. (2006) Synthesis of nanowires using Dip-Pen nanolithography and biocatalytic inks. *Adv. Mater.*, **18** (6), 713–718.

303 Felder, K.M. *et al.* (2009) A DNA microarray facilitates the diagnosis of *Bacillus anthracis* in environmental samples. *Lett. Appl. Microbiol.*, **49** (3), 324–331.

304 Yan, P.S., Chen, C.H., Shi, H.D. (2001) Dissecting complex epigenetic alternations in breast cancer using CpG island microarrays. *Cancer Research*, **61** (23), 8375–8380.

4
Microstructure Fibers in Biophotonics

Aleksei M. Zheltikov

4.1
Introduction: From Early Concepts of Fiber-Based Bioimaging to Biophotonics with Specialty Fibers

The development of fiber-based methods of biomedical imaging spans more than eight decades [1]. The capability of optical fibers to transfer images was first realized in the late 1920s. In 1927, Clarence Hansell, an electronic engineer at the Radio Corporation of America, filed a patent on fiber-based imaging [2], which covered the use of optical cables consisting of many fibers. In 1929, Heinrich Lamm, a medical student at the University of Munich, reported the first successful experiments on image transfer through a bundle of optical fibers [3], motivated by the development of a flexible gastroscope (see [4] for a detailed account of the early days of the history of fiber optics). These early inventions and pioneering concepts had to wait for several decades, however, before fiber fabrication technologies and low-loss fiber materials became mature enough to support the creation of practical fiber imaging systems, leading to revolutionary breakthroughs in biophotonics.

Modern fiber-optic technologies [5] provide an advanced platform for the creation of novel fiber-based imaging systems [6, 7], optical endoscopes [8, 9], biophotonics-oriented fiber laser sources [10], and optical neural interfaces [11, 12]. Although standard single-mode fibers (SMFs) can help implement many of the biophotonic protocols in the endoscopic mode, guiding continuous-wave radiation to the area of interest in living organisms, such fibers are much less efficient in delivering ultrashort laser pulses, needed for multiphoton bioimaging, and in collecting the incoherent optical response from biotissues. The group-velocity dispersion of such fibers tends to stretch ultrashort light pulses, while the numerical aperture of SMFs is typically too low to permit efficient collection of incoherent radiation.

Novel micro- and nanostructured optical fibers, also referred to as photonic-crystal fibers (PCFs) [13, 14], have been shown to offer attractive solutions to these problems [15]. Both group-velocity dispersion and numerical aperture can be tailored in PCFs through fiber structure engineering [16]. Fibers of this class have been used to improve substantially the signal collection efficiency in nonlinear microscopy [17] and have allowed the creation of nonlinear optical fiber endoscopes [18, 19].

Handbook of Biophotonics. Vol.2: Photonics for Health Care, First Edition. Edited by Jürgen Popp, Valery V. Tuchin, Arthur Chiou, and Stefan Heinemann.

Advanced PCF lasers [10, 20], and also PCF frequency converters [16] and supercontinuum sources [21, 22], are gaining growing applications in bioimaging based on coherent anti-Stokes Raman scattering (CARS) [23]. Hollow-core PCFs [24, 25] allow the delivery of high-energy, ultrashort laser pulses for biomedical applications [26]. These fibers also offer much promise for the creation of tunable wavelength shifters for multiphoton microscopy and CARS microspectroscopy [27, 28]. The low nonlinearity of the gas filling the core of the fiber and the choice of the central wavelength of laser pulses to the zero group velocity dispersion (GVD) wavelength of the fiber help to reduce temporal envelope distortions of the transmitted light signal. In this chapter, we give a brief overview of recent developments in biophotonics based on the use of microstructure fibers

4.2
Microstructure Fiber Sensors

Microstructure fibers suggest a variety of attractive strategies for optical sensing. The most common approach involves using the evanescent field of waveguide modes, confined to a high refractive index material in a waveguide, to produce a fluorescent signal, which is employed to detect species of a certain type in the gas, liquid, or solid phase. When implemented with PCFs [29–38], this sensing strategy allows the creation of compact fiber format sensors of gas-phase media [36–38] and biomolecules in aqueous solution [31]. Another widespread approach to sensing with advanced waveguide components is based on interferometric techniques [39], most often the Mach–Zehnder interferometer configuration, intended to detect small changes in the phase of an optical signal transmitted through a waveguide sensor. Devices based on this principle can sense small changes in the refractive index of an analyte or detect the formation of thin molecular layers on a waveguide cladding.

Owing to the remarkable flexibility of their core–cladding structure (Figure 4.1), PCFs offer attractive and often unique options for biosensing. For example, double-clad PCFs, as shown elegantly by Myaing *et al.* [40], can substantially improve the efficiency of two-photon fluorescence detection of biomolecules with the fluorescence signal delivered to the detector in the backward direction through the same fiber. The possibility of extending the concept of fiber grating-based sensing to PCFs has been demonstrated by Eggleton *et al.* [41]. Rindorf *et al.* [33] developed PCF-based sensors with long-period gratings for the detection of molecular monolayers containing immobilized DNA. Advanced fiber micro- and nanostructuring technologies have been shown to permit the creation of high-performance DNA sensors for gene-expression analysis [42], and also specific genomics- and proteomics-oriented sensor systems designed to detect specific genes and proteins (see [43] for a review).

Air-guided modes of hollow-core PCFs (Figure 4.1e) have been shown to be ideally suited for gas-phase sensing using linear [44] and nonlinear [45] optical methods. The biosensing ability of ring-cladding hollow-core PCFs has been demonstrated [46]. The ring cladding in such waveguides, conveniently implemented in a PCF design, serves as a built-in Fabry–Pérot interferometer, allowing the detection of thin

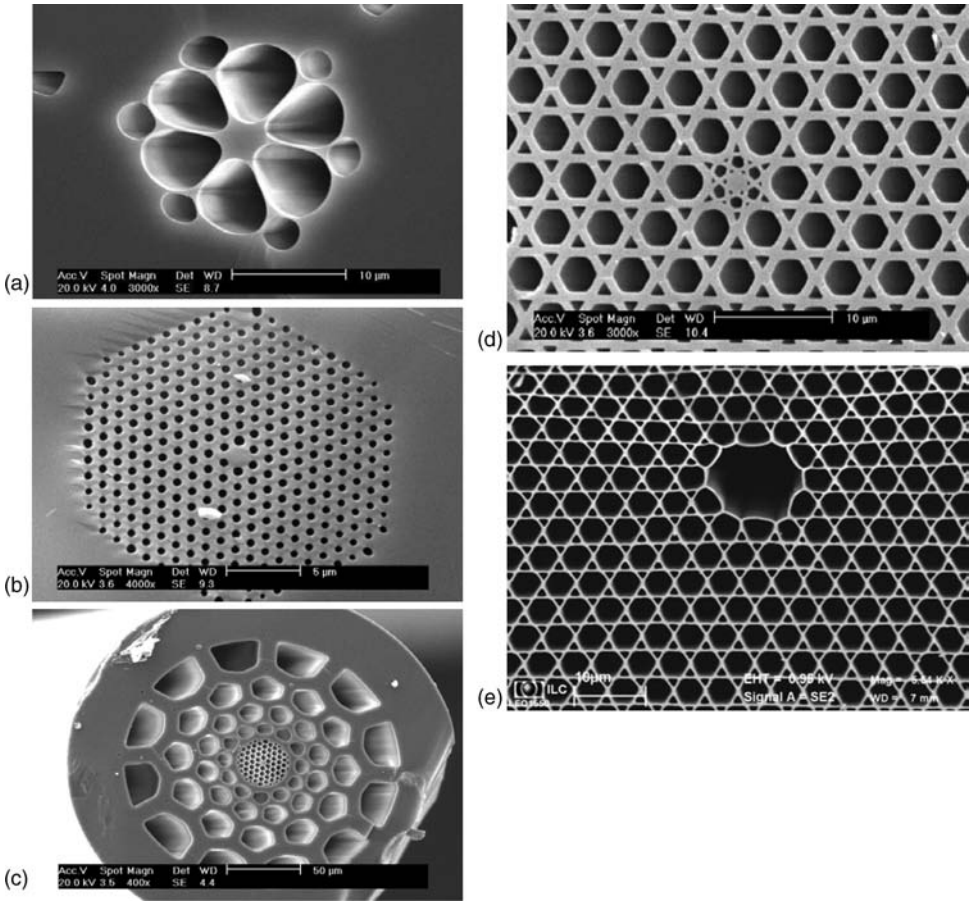

Figure 4.1 SEM images of PCFs: (a) solid-core high refractive index-step silica PCFs with a few-airhole-ring cladding; (b) periodic cladding PCF; (c) solid-core silica PCF with a dual microstructure cladding; (d) multicomponent glass PCF with a nanohole array-modified core; (e) hollow-core PCF.

molecular layers and ensuring a high sensitivity of transmission spectra of waveguide modes to small changes in the refractive index of an analyte filling the hollow core of the waveguide and air holes in the fiber cladding. We show that waveguides of this type offer a platform for the creation of compact and efficient biochemical sensors and sensor arrays. Components of this type can sense biolayers a few nanometers thick and provide a high sensitivity with respect to refractive index changes of an analyte filling the air holes of the waveguide structure.

A diversified architecture of photonic-crystal fibers (Figure 4.1) suggests various approaches to optical sensing. Experiments reported by Konorov *et al.* [32] provide a quantitative comparison of two protocols of optical sensing with PCFs. In the first protocol, diode-laser radiation is delivered to a sample through the central core of a dual-cladding PCF with a diameter of a few micrometers, while the large-diameter

fiber cladding serves to collect the fluorescent response from the sample and to guide it to a detector in the backward direction. In the second scheme, liquid sample is collected by a microcapillary array in the PCF cladding and is interrogated by laser radiation guided in PCF modes. For sample fluids with refractive indices exceeding the refractive index of PCF material, fluid channels in PCFs can guide laser light by total internal reflection, providing an 80% overlap of interrogating radiation with sample fluid. Specially designed PCFs have been shown to integrate an optical sensor with a micropipette, a sample collector, and a microfluidic polycapillary array in a single fiber-optic component, which is ideally suited for "lab-on-a-chip" applications, offering an attractive platform for fiber-based sensors and probes for genomics and proteomics.

4.3 Designing Specialty Fibers for High-Resolution Imaging

The development of subdiffraction microscopy techniques is one of the key tendencies in modern optical physics. Rapidly progressing methods of near-field microscopy [47] provide an unprecedentedly high spatial resolution on specific samples, giving an access to a unique information on the structure of matter and physical processes in subsurface layers. Methods of near-field microscopy, however, face serious difficulties when applied to a broad class of problems related to processes and details of structure in the bulk of a material and in living systems. Problems of this class can be attacked by using novel physical principles of far-field microscopy, such as multiphoton microscopy [48, 49], microscopy based on CARS [50], and stimulated Raman scattering [51], and also microscopy using stimulated emission depletion (STED) [52]. New methods of far-field microscopy have been shown to provide spatial resolution as high as a few tens of nanometers (in certain cases better than 20 nm [53]). These techniques find growing applications in studies of intracellular processes in living organisms, single-molecule detection, and analysis of a broad class of nanostructures and nano-objects.

Modern fiber-optic technologies allow the creation of optical micro- and nanowaveguide systems, including submicrometer-core optical fibers [16]. Such components open up wide opportunities for the implementation of novel methods of microscopy in the fiber format. Rapidly growing research in this field includes the development of fiber-optic sources and systems for the delivery of ultrashort light pulses for nonlinear optical endoscopy and mapping of neuronal activity in the living brain [54, 55]. Unique opportunities offered by fiber-format ultrahigh-resolution microscopy call for a detailed understanding of fundamental physical factors controlling the confinement of electromagnetic field in waveguide systems and analysis of methods of transmission of ultracompact light beams in fiber-optic networks.

The spatial resolution of fiber-based optical imaging is controlled by the confinement of the light field in the fiber core, which can be quantified in terms of the effective mode radius:

$$w = (S/\pi)^{\frac{1}{2}} \tag{4.1}$$

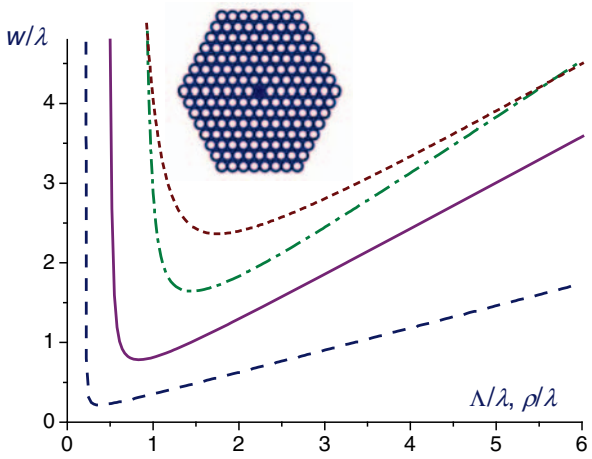

Figure 4.2 Effective radius of the PCF mode as a function of the pitch Λ of the hexagonal fiber cladding for $\lambda = 1\,\mu m$, $d/\Lambda = 0.3$ (dashed-dotted line), 0.5 (solid line), and 0.9 (dashed line). The dotted line shows the effective radius of the fundamental mode of a standard fiber with $n_1 - n_2 = 0.01$ as a function of the core size ϱ. A PCF with a hexagonal-lattice cladding is shown in the inset.

where

$$S = 2\pi\left[\int_0^\infty |F(r)|^2 r\mathrm{d}r\right]^2\left[\int_0^\infty |F(r)|^4 r\mathrm{d}r\right]^{-1} \tag{4.2}$$

is the effective mode area, $F(r)$ being the transverse field profile in the fiber mode. The mode radius w is sensitive to the refractive index contrast, $\Delta = n_1 - n_2$, where n_1 and n_2 are the refractive indices of the fiber core and fiber cladding, respectively, and generally differs from the physical size of the fiber core ϱ. This difference may become especially significant in the case of fibers with very small, subwavelength cores, where diffraction arrests a tight localization of the light field in the fiber core, making a significant fraction of the mode power propagate as the evanescent field outside the fiber core [56, 57].

Figure 4.2 compares the typical behavior of the effective mode radius w as a function of the physical radius of the fiber core ϱ in the case of a conventional step-index fiber (dotted line) and a generic-type PCF with a hexagonal structure of the cladding with a lattice constant Λ (shown in the inset). Calculations presented in Figure 4.2 suggest [58] that the light confinement in the PCF core and, hence, the spatial resolution provided by a PCF probe can be controlled through fiber structure engineering. Larger d/Λ ratios, as can be seen from Figure 4.2, provide a tighter localization of the light field in the fiber core, translating into a higher spatial resolution of a fiber probe. With $d/\Lambda = 0.9$, the minimum mode radius, achieved when $\Lambda \approx 0.4\lambda$, is $w_{\min} \approx 0.2\lambda$ (the dashed line in Figure 4.2), allowing fiber-based

optical probing of areas adjacent to the fiber end with subwavelength resolution. Interestingly, and quite importantly, for smaller core sizes, the field confinement in the fiber core becomes weaker, because of strong diffraction, leading to larger effective mode sizes (see Figure 4.2), with a significant fraction of mode power guided outside the fiber core. All these predictions are fully confirmed by fiber-probe experiments on test objects [59].

4.4 Fiber-Based Imaging of Diffusively Scattering Tissues

To illustrate the significance of the fiber structure for the regime of collection of a fluorescence signal from a diffusively scattering tissue, we consider a generic fiber (Figure 4.3a) consisting of a core with a diameter d_c, which is used to deliver the laser light to a tissue, and a cladding that includes a ring (similar to a ring seen in the PCF structure in Figure 4.1c) with an inner diameter d_r, which serves to pick up the fluorescent response from the tissue within its larger aperture. The case of $d_c = d_r$ corresponds to a standard optical fiber. In a PCF, a cross-section structure can be designed in such a way as to isolate a signal-collecting cladding ring from the central core of the fiber. When a fiber probe with such a design is used to detect the fluorescence response from a uniformly scattering biotissue, the probability of the ring in the fiber cladding to pick up a fluorescent photon generated at a depth z (measured from the fiber tip, Figure 4.3a) peaks, due to the general properties of diffusive scattering of optical signals in random media [60, 61], at $z = L_0$. The full width at half-maximum, δz, of the axial profile $I_{fl}(z)$ of fluorescence collected by the cladding ring is controlled by scattering and absorption of the tissue, and also the diameter of the ring d_r, its thickness t_r, and the refractive index step $\delta n = n_r - n_{eff}$, where n_r is the refractive index of the material of the ring ($n_r \approx 1.45$ for a silica ring in our experiments) and n_{eff} is the effective refractive index of the microstructure surrounding this ring. A ring with a larger diameter d_r will probe tissue layers lying at larger distances L_0 from the fiber tip at the cost of lower axial resolution (larger δz). The thickness of the tissue layer providing the main contribution to the signal detected by the outer ring of the PCF can be reduced by lowering the refractive index contrast δn and decreasing the thickness of the ring t_r. For the PCF shown in Figure 4.1c with $d_r \approx 300\,\mu m$ and $t_r \approx 25\,\mu m$, numerical simulations for typical brain-tissue parameters (reduced scattering coefficient $\mu'_s \approx 1\,mm^{-1}$ and the absorption coefficient $\mu_a \approx 0.1\,cm^{-1}$ [62]) give $L_0 \approx 250\,\mu m$ with $\delta z \approx 160\,\mu m$. The lateral dimensions of the interrogated volume are determined by the outer diameter of the signal-collecting aperture of the fiber probe. In our experiments, this diameter was about 325 μm.

Special measurements were performed to test how well the fluorescence-collecting ring in the PCF cladding is isolated from the central fiber core for PCFs with different cladding-ring diameters. To this end, the intensity I_s of the signal collected by PCFs of different types was measured as a function of the displacement ϱ of the fiber core with respect to a 2 μm spot of a tightly focused laser beam, intended to mimic a point light source. Results of these measurements are presented in Figure 4.3b. For a PCF

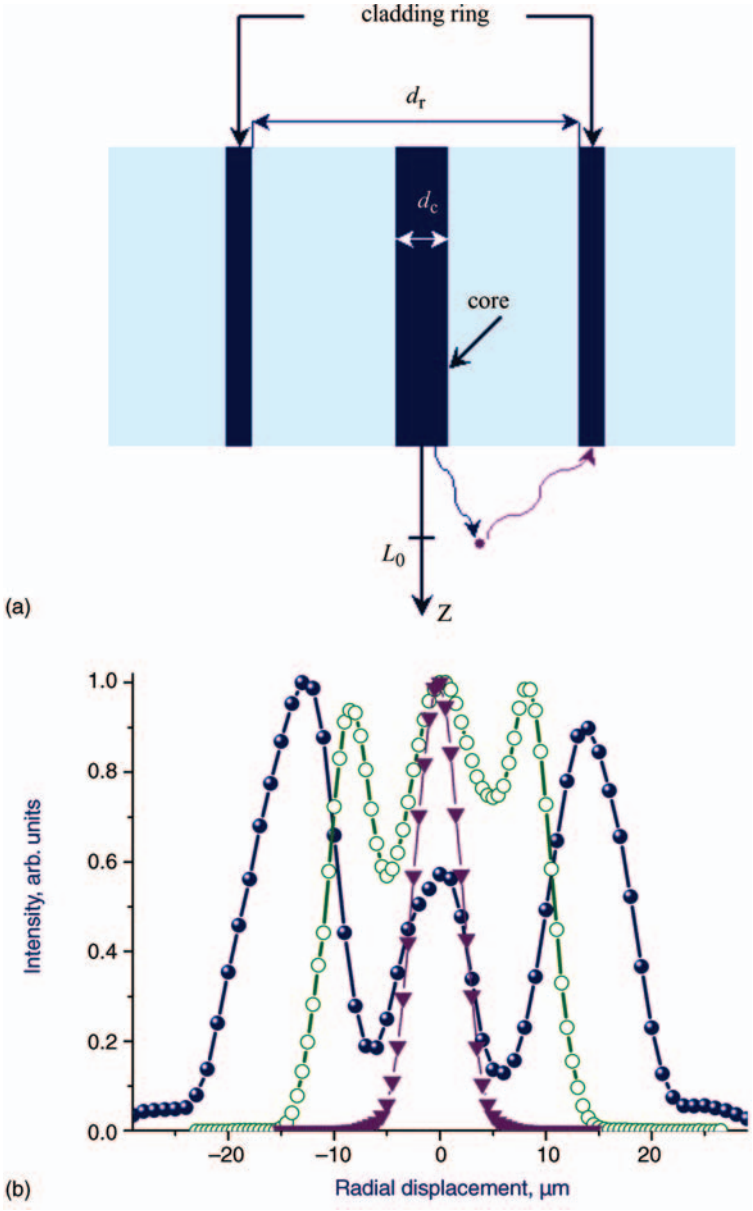

Figure 4.3 (a) Fiber probe with a fluorescence-collecting ring in the cladding. (b) Intensity of the signal collected by a PCF with a cross-section structure shown in Figure 4.1a (filled and open circles) and Figure 4.1d (triangles) measured as a function of the displacement of the fiber core with respect to a 2 μm radiation source. The diameter of the outer light collecting ring in the core of PCF shown in Figure 4.1a is 18 μm (open circles) and 28 μm (filled circles).

without a signal-collecting cladding ring (Figure 4.1a), the measured radial profile $I_s(\varrho)$ features only one maximum (triangles in Figure 4.3b), corresponding to the center of the fiber core. For fibers with signal-collecting cladding rings (Figure 4.1c), the $I_s(\varrho)$ profile displays three peaks (solid and open circles in Figure 4.3b), corresponding to the signal delivered through the central core and the cladding ring. Whereas for fibers with $d_r \leq 20\,\mu m$, the signal transmitted through the cladding ring suffers from interference due to radiation transmitted through the core and the inner part of the microstructure cladding (open circles in Figure 4.3b), PCFs with $d_r \geq 25\,\mu m$ show well-resolved peaks in the $I_s(\varrho)$ profile (solid circles in Figure 4.3b), indicating almost no interference between the signals transmitted through the central core and the signal-collecting cladding ring. The experimental results thus support numerical simulations, confirming that properly designed fiber probes can effectively resolve the fluorescence response from a brain tissue along the axial coordinate even in the regime of single-photon excitation, where high laser intensities, typically required for multiphoton methods, are not needed.

4.5 Enhancement of Guided-Wave Two-Photon-Excited Luminescence Response with a Photonic-Crystal Fiber

Two-photon absorption (TPA) is the backbone of a broad variety of bioimaging techniques and biomedical strategies, including high-resolution microscopy [48, 49, 63], photodynamic therapy [64, 65], and drug-delivery monitoring and drug activation [66]. Luminescence of TPA-excited molecules provides a measurable optical response that allows imaging of TPA-excited regions in two-photon microscopy and helps to visualize tiny objects and identify fine details of structure and morphology inside biological tissues [48, 49]. A combination of TPA approaches with capabilities of fiber-optic probes [54] offers numerous advantages [67], suggesting a convenient format for beam delivery, facilitating manipulation of excitation radiation, and allowing this excitation to be applied locally and selectively. Although many attractive fiber solutions have been developed to meet the needs of TPA-based technologies, collection of the two-photon-excited luminescence (TPL) response still leaves much room for optimization, with the main source of problems being related to the small aperture of fiber probes, making it difficult to collect efficiently the TPL signal, which is uniformly emitted in a 4π solid angle.

PCFs can substantially improve the collection efficiency of the TPL response from TPA-excited molecules in waveguide modes [68], thus allowing the sensitivity of TPA-based techniques to be radically improved. In the earlier relevant work, PCFs of various types were shown to offer numerous advantages as efficient optical sensors [30–32] and compact wavelength-tunable sources for nonlinear microspectroscopy [16, 23]. Dual-cladding PCFs have been employed to enhance the efficiency of two-photon biosensing [40]. As shown by Fedotov *et al.* [68], with only a few nanoliters of TPA-excited molecules filling air holes in a specifically designed PCF, the guided-wave TPL signal can be enhanced by two orders of magnitude relative to

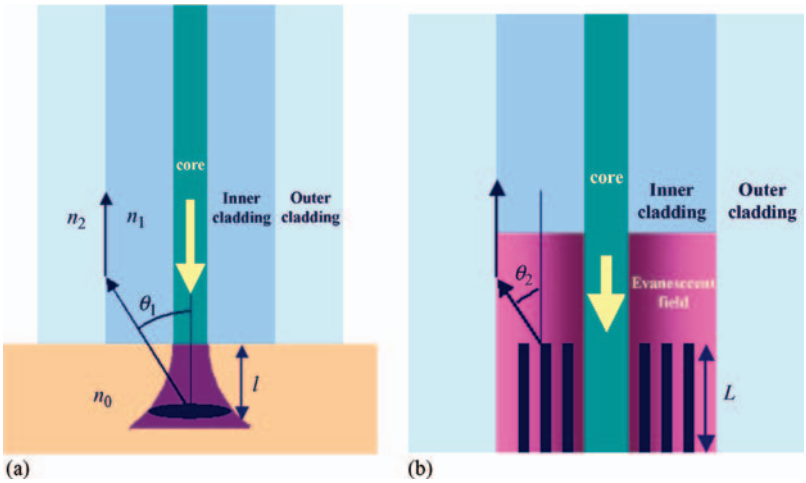

Figure 4.4 TPA excitation and TPL response collection with a dual-cladding fiber probe: (a) excitation light is delivered through the fiber core to an object adjacent to the fiber end, while the TPL signal is collected by a high numerical aperture inner part of the fiber cladding; (b) an evanescent field of the mode guided along the fiber core generates the TPL signal through a TPA excitation of dye molecules in a solution filling the air holes in the PCF cladding, with the inner part of the fiber cladding capturing the TPL response into a waveguide mode and delivering this signal to a detection system.

the maximum TPL signal attainable from a cell with the same dye excited and collected by the same PCF.

We compare two arrangements for the collection of the TPL response with a dual-cladding fiber. In the first scheme (Figure 4.4a), excitation light is delivered along the fiber core to an object adjacent to the fiber end. The TPL signal is then collected by the inner part of the fiber cladding. As shown by Myaing *et al.* [40], this method of TPA excitation using dual-cladding PCF probes offers important advantages for TPA bioimaging. In the second approach (Figure 4.4b), we let a tiny amount of the liquid- or gas-phase substance fill the air holes of the PCF. The TPL signal is then excited by the evanescent field of the mode guided along the fiber core and is captured into a waveguide mode inside the inner part of the fiber cladding.

The total TPL signal collected by the fiber probe in the first experimental arrangement (Figure 4.4a) is

$$P_1 = 2\pi \int_0^a \sigma_1 I_1(r) r \mathrm{d}r \tag{4.3}$$

where

$$I_1(r) = \mu\beta l I_0{}^2 [f_1(r)]^2 \tag{4.4}$$

is the intensity of the TPL signal, σ_1 is the TPL signal collection efficiency, μ is the quantum yield of TPA-induced luminescence, β is the TPA coefficient, l is the length

of the interaction region, I_0 is the on-axis intensity of the waveguide mode, a is the radius of the fiber core, and $f_1(r)$ is the radial profile of field intensity distribution.

The TPL signal collection efficiency σ_1 is given by

$$\sigma_1 = 2\pi \int_0^{\theta_1} \sin\xi \, d\xi \tag{4.5}$$

where θ_1 is the maximum acceptance angle of the high numerical aperture inner part of the fiber cladding:

$$\sin\theta_1 = \frac{n_1}{n_0}\left[1-\left(\frac{n_2}{n_1}\right)^2\right]^{\frac{1}{2}} \tag{4.6}$$

where n_0 is the refractive index of the medium adjacent to the fiber probe end and n_1 and n_2 are the refractive indices of the inner and outer sections of the fiber cladding, respectively.

With $({n_1}^2-{n_2}^2)/{n_0}^2 \ll 1$, integration of Eq. (4.5) yields

$$\sigma_1 \approx \pi{\theta_1}^2 \approx \pi\left(\frac{NA_1}{n_0}\right)^2 \tag{4.7}$$

where $NA_1 = ({n_1}^2 - {n_2}^2)^{1/2}$ is the numerical aperture of the inner cladding of the fiber probe.

In the case of a Gaussian field intensity profile, $f_1(r) = \exp(-r^2/{r_1}^2)$, where r_1 is the effective field intensity radius, Eqs. (4.3), (4.4), and (4.7) give

$$P_1 \approx \pi\mu\beta l {I_0}^2 \frac{S_1}{2}{\theta_1}^2\left[1-\exp\left(-2\frac{a^2}{{r_1}^2}\right)\right] \tag{4.8}$$

where $S_1 = \pi{r_1}^2$ is the effective mode area.

For a large-core fiber with $(a/r_1)^2 \gg 1$, Eq. (4.8) reduces to

$$P_1 \approx \pi\mu\beta l {I_0}^2 S_1 {\theta_1}^2 \tag{4.9}$$

For the second experimental scheme (Figure 4.2b), the total TPL signal collected by the fiber probe is

$$P_2 = 2\pi \int_a^R I_2\left[f_2(r)\right]^2 r dr \tag{4.10}$$

where $f_2(r)$ is the radial profile of field intensity distribution in a liquid-filled fiber, R is the radius of the inner part of the cladding, and the TPL intensity I_2 can be found from the equation

$$I_2 = \mu\beta\sigma_2 \int_0^L \frac{{I_0}^2 dx}{(1+\beta I_0 x)^2} \tag{4.11}$$

where L is the length of the interaction region, σ_2 is the TPL signal collection efficiency defined by

$$\sigma_2 \approx \pi\theta_2{}^2 \approx \pi\left(\frac{NA_2}{n_{co}}\right)^2 \tag{4.12}$$

θ_2 is the maximum acceptance angle, $NA_2 = (n_{co}{}^2 - n_{cl}{}^2)^{1/2}$, n_{co} is the effective refractive index of the inner part of the liquid-filled fiber bounded by the outer cladding, and n_{cl} is the refractive index of the outer part of the cladding.

Integration of Eq. (4.11) yields

$$I_2 = \mu\beta\sigma_2 \frac{I_0{}^2 L}{1 + \beta I_0 L} \tag{4.13}$$

with $\beta I_0 L \ll 1$ and a Gaussian field intensity profile, $f_2(r) = \exp(-r^2/r_2{}^2)$, r_2 being the effective field intensity radius in a liquid-filled fiber, Eqs. (4.10), (4.12), and (4.13) lead to

$$P_2 \approx \pi\mu\beta\theta_2{}^2 I_0{}^2 L \frac{S_2}{2} \exp\left(-2\frac{a^2}{r_2{}^2}\right) \tag{4.14}$$

where $S_2 = \pi r_2{}^2$ and we assume that $r_2 \ll R$.

The length of the interaction region in the first experimental scheme (Figure 4.4a) is dictated by diffraction and can be estimated as $l \approx 2\pi a^2/\lambda$, λ being the radiation wavelength, we find that the second experimental arrangement provides the following TPL signal collection enhancement with respect to the first scheme implemented with a large-core fiber with $(a/r_1)^2 \gg 1$:

$$\eta = \frac{P_2}{P_1} \approx \frac{\theta_2{}^2}{\theta_1{}^2} \frac{S_2}{S_1} \frac{L\lambda}{2\pi a^2} \exp\left(-2\frac{a^2}{r_2{}^2}\right) \tag{4.15}$$

from which it can be seen that the enhancement of the TPL response provided by a fiber with air holes partially filled with a liquid under study scales linearly with the length L of the interaction region and rapidly decreases [$\propto a^{-2} \exp(2a^2/r_2{}^2)$] with an increase in the fiber core radius a because of the evanescent character of the field inducing the TPL response in the second experimental arrangement. For typical parameters of experiments described below, with $\lambda \approx 0.8\,\mu$m, $a \approx 2.3\,\mu$m, $r_2 \approx 2.5\,\mu$m, and $L \approx 1.5$ cm, we find $L/l \approx 360$, and Eq. (4.15) gives $\eta \approx 200$. Waveguide collection of the luminescence signal using an appropriately designed fiber probe can thus provide orders of magnitude enhancement of the TPL response relative to the maximum TPL signal attainable from a cell with the same TPA medium.

Fiber probes used in experiments [68] were based on suitably designed fused-silica PCFs, produced by means of standard PCF fabrication technology. A Ti:sapphire laser, delivering 40 fs, 0.5 W pulses of 805 nm radiation at a pulse repetition rate of 90 MHz, was employed as a source of light inducing two-photon luminescence in solutions of various dyes. Light pulses with an average power of ~50 mW were coupled into the fiber probe with a micro-objective. Because of the nonlinear nature

of the TPA process, efficient TPL generation requires excitation of molecules by light pulses with a sufficiently high peak power. It is therefore critical for highly efficient TPL excitation to minimize temporal spreading of femtosecond light pulses transmitted through the fiber. To this end, the PCF was designed in such a way as to provide a low GVD at the central laser wavelength. In experiments, a laser pulse with an input pulse width of 40 fs transmitted through a 50 cm long piece of PCF with a GVD parameter $\beta_2 \approx 5 \times 10^{-3}\,\mathrm{ps}^2\,\mathrm{m}^{-1}$ was stretched up to 75 fs. This pulse width was still short enough to provide a sufficient laser peak power for efficient TPA excitation of Rhodamine 6G molecules.

In the first scheme of TPL detection, laser pulses were delivered to a 10^{-3} M solution of Rhodamine 6G in a cell through the central core of the fiber with a

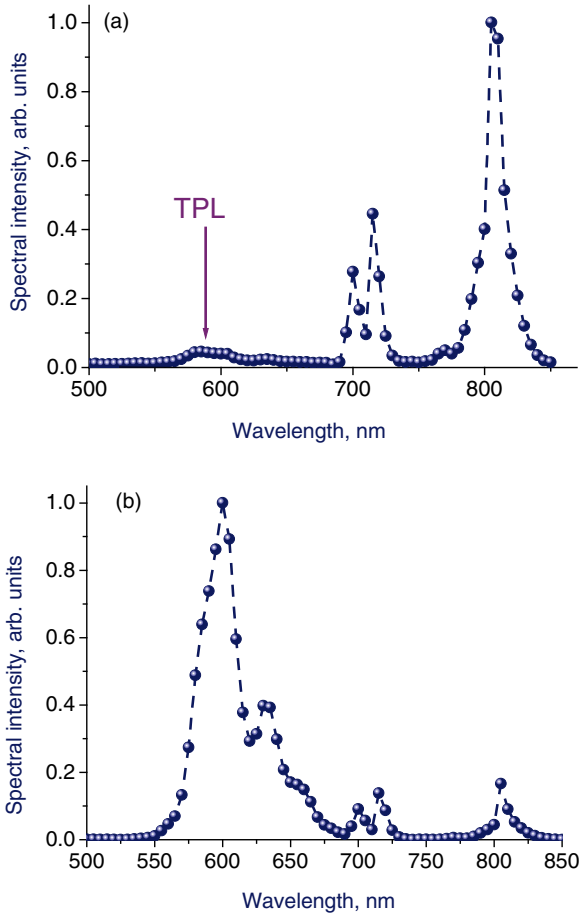

Figure 4.5 Spectra of the optical response of Rhodamine 6G solution excited by femtosecond Ti:sapphire laser pulses with a central wavelength of 805 nm detected (a) from dye solution in a cell (as sketched in Figure 4.4a) and (b) from dye solution filling the air holes in the PCF cladding (as shown in Figure 4.4b).

diameter of 2.3 μm in accordance with the generic approach illustrated in Figure 4.4a. The inner fiber cladding serves to collect the TPL response from the sample and to guide it in the backward direction, towards the input end of the fiber. Outside the fiber, the TPL signal is separated from the 800 nm light and is sent to a detection system by a dichroic mirror. In this regime, the TPL signal is reliably detectable, but is much weaker than the background signal in the spectral range 690–810 nm (Figure 4.5a), which includes back-reflected laser light centered at 805 nm and the nonlinear signal in the spectral region of 700–715 nm generated in the PCF through dispersive-wave emission by optical solitons. This type of emission originates from the instability of solitons induced by higher order dispersion [69]. Its central frequency is controlled by phase matching between the soliton and dispersive waves [70]. The dispersion profile of the PCF used in our experiments dictates emission of dispersive waves that are blue shifted relative to the central wavelength of a soliton. The ratio of the amplitude of the TPL peak in the spectrum of optical response in Figure 4.5a to the amplitude of the peak corresponding to the back-reflected laser light at 805 nm is $\xi_1 \approx 0.04$.

In the second scheme of TPL detection, sketched in Figure 4.4b, a PCF is brought in contact with a liquid-phase sample (a 10^{-3} M solution of Rhodamine 6G in our experiments) so that a small amount of liquid fills the air holes in the fiber cladding due to sample flows induced by surface tension. Dye molecules in the liquid filling the air holes in the fiber cladding are interrogated with the evanescent field of PCF waveguide modes. The TPL signal generated by dye molecules is detected in the backward direction using a dichroic mirror, a monochromator, and a photomultiplier. The fiber infiltration length was estimated from an abrupt change in the level of scattered continuous-wave laser light detected with a standard fiber probe scanned along the infiltrated fiber. With such an experimental arrangement, the ratio of the amplitude of the TPL peak in the spectrum of an optical response from Rhodamine 6G dye penetrating into the air holes inside the PCF over $L \approx 1.5$ cm is $\xi_2 \approx 6.3$ times higher than the intensity of the back-reflected laser signal at 805 nm (Figure 4.5b). The overall volume of interrogated dye solution in this experiment is about 4 nl. Using the back-reflected signal at 805 nm as a reference, we then find that the enhancement of the TPL response provided by the second regime of TPL fiber probing is $\eta = (\xi_2/\xi_1)(P_{02}/P_{01})$, where P_{02} and P_{01} are the powers of the back-reflected signal at 805 nm in the first and second schemes, respectively. With $\xi_1 \approx 0.04$, $\xi_2 \approx 6.3$, and $P_{02}/P_{01} \approx 0.85$, we find $\eta \approx 130$. This estimate agrees well with the analysis presented in the previous section. As a demonstration of a biophotonic application of the developed approach, the dual-cladding PCF shown in Figure 4.1c was used to perform TPL measurements on the Alexa Fluor® family of dyes, which are commonly used as labels in cell biology and fluorescence microscopy, and on green fluorescent protein (GFP), which has gained wide acceptance as a reporter of gene expression [71, 72].

A PCF is thus shown to increase substantially the guided-wave luminescent response from molecules excited through TPA by femtosecond near-infrared laser pulses. With only a few nanoliters of TPA-excited molecules filling air holes in a specifically designed PCF, the guided-wave two-photon-excited luminescence signal

is enhanced by more than two orders of magnitude relative to the maximum TPL signal attainable from a cell with the same dye excited and collected by the same PCF. Biophotonic implications of this waveguide TPL response enhancement include fiber-format solutions for online monitoring of drug delivery and drug activation, interrogation of neural activity, biosensing, endoscopy, highly parallelized gene and protein detection in genomics and proteomics, and locally controlled singlet oxygen generation in photodynamic therapy.

4.6
Microstructure Fibers for Nonlinear Optical Microspectroscopy

CARS [73] has long been established as a powerful tool for time-resolved studies of ultrafast molecular dynamics and diagnostics of excited gases, combustion, flames, and plasmas [74–77]. Because of the nonlinear nature of this type of scattering, the CARS field-interaction region is strongly confined to the beam-waist area, suggesting an attractive approach for microscopy and high-spatial-resolution imaging [50, 78]. Recent advances in femtosecond laser technologies have given a powerful momentum to the development of CARS imaging techniques, making CARS a practical and convenient instrument for biomedical imaging and visualization of processes inside living cells [78, 79].

In the early days of CARS, stimulated Raman scattering (SRS) was successfully used to generate the Stokes field for time-resolved measurements [74] of vibrational lifetimes of molecules in liquids and phonons in solids. Dye lasers and optical parametric sources later proved to be convenient sources of wavelength-tunable Stokes radiation [80, 81], giving a powerful momentum to CARS as a practical spectroscopic tool. The rapid progress of femtosecond lasers and the advent of novel highly nonlinear fibers put a new twist on the strategy of Stokes field generation in CARS, allowing the creation of compact and convenient SRS-based wavelength-tunable fiber-format ultrashort-pulse Stokes sources for a new generation of CARS spectrometers and microscopes [82, 83]. Below in this section, we discuss a compact CARS apparatus that relies on the use of an unamplified femtosecond laser output and two types of PCFs optimized for the generation of wavelength-tunable Stokes field and spectral compression of the probe pulse.

CARS involves coherent excitation of Raman-active modes with a frequency Ω_p by pump and Stokes fields, whose central frequencies, ω_1 and ω_2, are chosen in such a way as to meet the condition of a two-photon, Raman-type resonance, $\omega_1 - \omega_2 \approx \Omega_p$. The third (probe) field with a central frequency ω_3 is then scattered off the coherence induced by the pump and Stokes field to give rise to the anti-Stokes signal at the central frequency $\omega_a = \omega_1 - \omega_2 + \omega_3$, thus reading out the information on the physical properties of the medium projected on the Raman mode. Experiments described below in this section employed a two-color version of CARS with the pump and probe fields delivered by the same light source, implying that $\omega_1 = \omega_3$ and $\omega_a = 2\omega_1 - \omega_2$.

The CARS system that we developed recently [84, 85] (Figure 4.6) is based on a specifically designed long-cavity Cr:forsterite laser oscillator [86]. With a 10 W pump

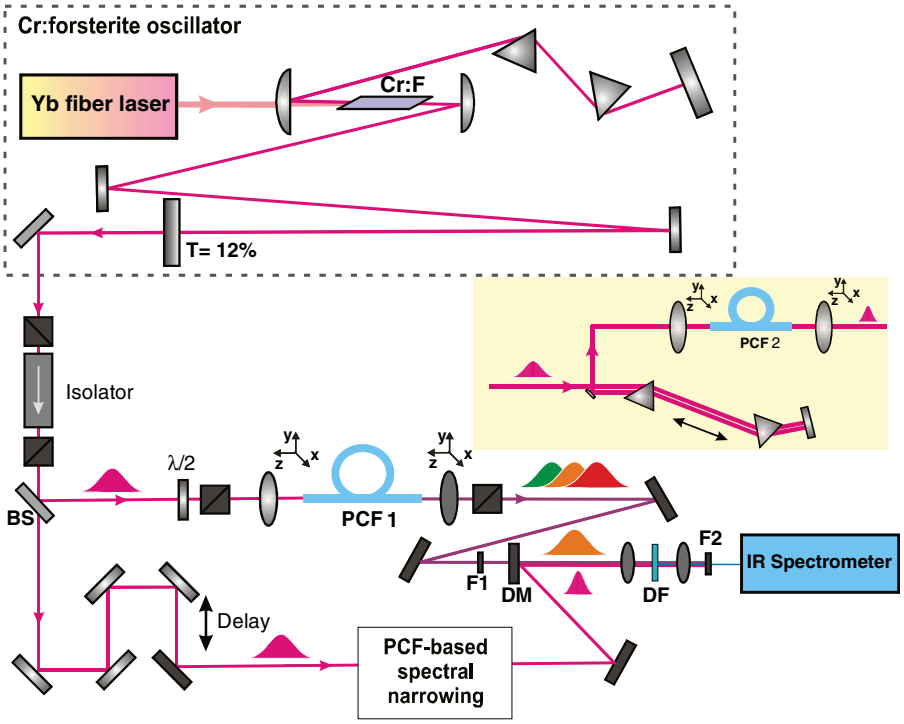

Figure 4.6 Diagram of the experimental setup: Cr:F, Cr:forsterite crystal; BS, beam splitter; PCF1, PCF2, PCFs; F1, F2, filters; DM, dichroic mirror; DF, diamond film. The PCF-based scheme of spectral narrowing is shown in the inset.

provided by an ytterbium fiber laser, the Cr:forsterite oscillator delivered 70 fs, 340 mW light pulses with a central wavelength of 1.25 m at a repetition rate of 18 MHz. A beam splitter (BS in Figure 4.6) was used to divide the Cr:forsterite laser output into two beams. The first beam was launched into a first PCF (PCF1) for the generation of a frequency-tunable Stokes field through soliton self-frequency shift. CARS with a PCF-based soliton frequency shifter as a Stokes source was demonstrated earlier by Andresen *et al.* [82] and Sidorov-Biryukov *et al.* [83]. By varying the power of laser pulses launched into the PCF, we were able to tune the soliton PCF output within the range of wavelengths from 1.35 to 1.75 μm (Figure 4.7a). The smoothly tunable wavelength-shifted soliton output of the PCF was characterized by means of cross-correlation frequency-resolved optical gating (XFROG), implemented in our experiments by mixing the PCF output with reference pulses from the Cr: forsterite laser. Typical XFROG traces of a frequency-shifted PCF1 output measured in experiments with different input peak powers are presented on one map in Figure 4.7a, with the pulse width of the PCF output varying within the range 55–65 fs for different output wavelengths. As can be seen from these XFROG traces, the PCF1 output is nearly transform limited, owing to the soliton regime of wavelength shift,

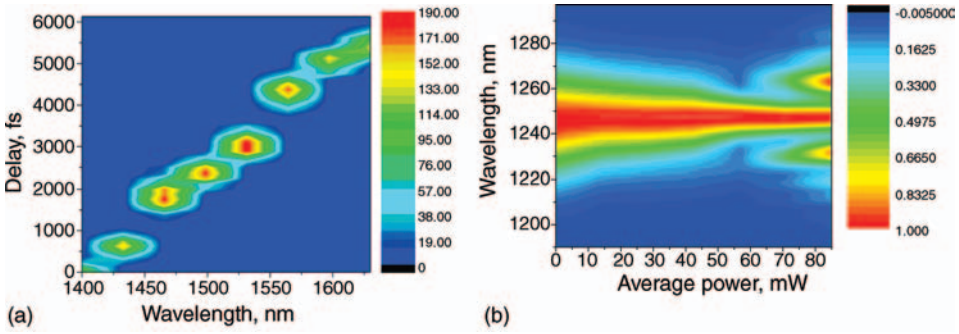

Figure 4.7 (a) A map showing XFROG traces of the frequency-tunable PCF1 output. Traces with different central wavelengths and different delay times were measured in experiments with different input peak powers. (b) Spectra of the output of the photonic crystal fiber (PCF2) used for the spectral narrowing of Cr:forsterite laser pulses measured as a function of the average power of input light pulses.

which helps to avoid unwanted oscillations in CARS spectra due to the interference of resonant and nonresonant parts of the nonlinear signal.

The second beam was intended to provide the pump and probe fields for the CARS process. To improve the spectral resolution and to enhance nonresonant background

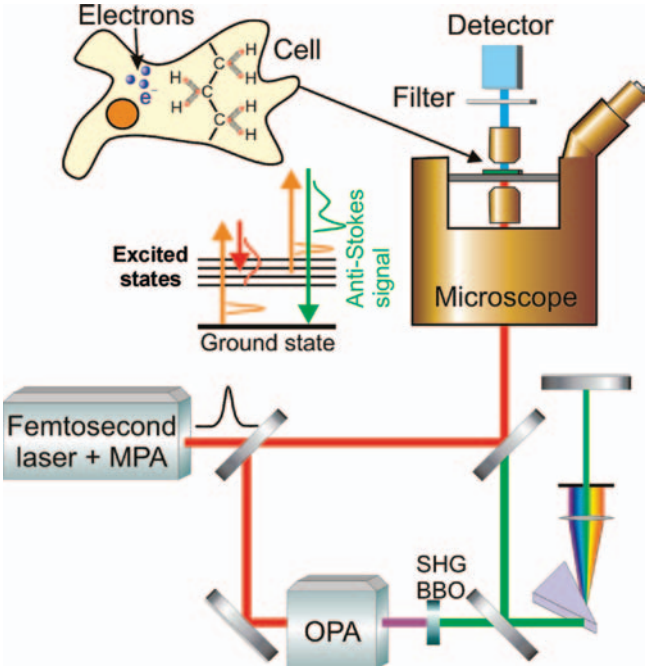

Figure 4.8 Diagram of CARS apparatus: MPA, multipass amplifier; OPA, optical parametric amplifier; SHG BBO, second-harmonic generation in a BBO crystal. A diagram of photons and quantum states involved in CARS is also shown.

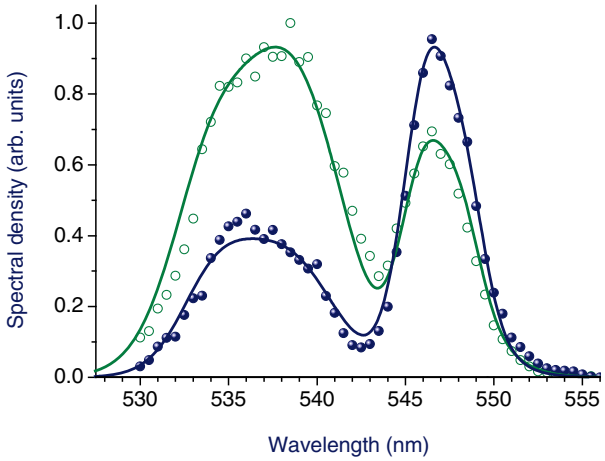

Figure 4.9 Typical CARS spectra from two different regions of mouse brain with a high (open circles) and low (filled circles) content of water versus the results of simulations (solid lines) using the model of the Raman response as described in [90].

suppression in CARS spectra, we used a second PCF (PCF2), which was adjusted to narrow the spectrum of laser pulses through a self-phase modulation process [87–89]. For efficient spectral compression, the light pulses were negatively prechirped with a prism pair, which stretched the pulses to ~700 fs, before they were launched into the PCF. Self-phase modulation in a medium with a positive nonlinear refractive index tends to red shift the leading edge of the pulse and blue shift its trailing edge. For a pulse with an initial negative chirp, such a temporally nonuniform spectral shifting transfers the energy from the wings of the field spectrum toward its central part, thus narrowing the spectrum. Figure 4.7b displays the spectra of the PCF output measured as a function of the input average power of light pulses. Spectral compression ratios of 3.5–4.0 provided an adequate level of spectral resolution in our CARS measurements with the output of the PCF spectral compressor used as a source of pump and probe fields in CARS. Although the spectral compression improves the spectral resolution and helps to suppress the nonresonant background in CARS spectra, a strong chirp of pump and probe pulses should be avoided, as it induces unwanted oscillations due to the interference of resonant and nonresonant parts of the nonlinear signal.

Typical CARS spectra from a coronal section of mouse brain measured [90] with a broadband Stokes field, as shown in Figure 4.8, are presented in Figure 4.9. These spectra are dominated by the lipid symmetric CH stretch vibrational modes (the peak centered at 547 nm in Figure 4.9), and also by the symmetric and asymmetric H_2O stretch vibrational modes of liquid water (merging into the peak centered at 537 nm in Figure 4.9). The ratio of the amplitudes of the 547 and 537 nm peaks is controlled (Figure 4.9) by the content and orientation of lipids and water in the brain tissue region probed by the focused laser beams. Myelin sheaths are especially rich in CH bonds, allowing white matter to be readily distinguished by their high CARS contrast

from gray matter in CARS images of brain tissues [91]. CARS spectra from dehydrated brain samples did not display any feature at 537 nm, confirming the assignment of this peak to vibrational modes of liquid water.

4.7 Microstructure Fibers for Neurophotonics

Advanced fiber-optic components open up a variety of new opportunities in neuroscience, including *in vivo* brain imaging, functional studies of neurons in the brain [92, 93], and the creation of unique optical neural interfaces [11, 12], allowing control over the activity of neurons with light and leading to revolutionary breakthroughs in cognitive sciences. The recently developed advanced fiber tools for high-speed fluorescence microscopy of freely moving animals [54] help to confront the long-standing challenges in experimental studies of neuronal bases of cognition and memory. Specifically designed PCFs have been shown to enhance the two-photon-excited luminescence response from fluorescent protein biomarkers and neuron activity reporters [55].

In vivo work typically imposes demanding requirements on fiber components with regard to their flexibility, compactness, and the ability to integrate multiple functions, such as an optimal geometry local optical excitation of biomolecules, pickup of optical response, and low-loss pump and signal delivery. Several attractive and elegant fiber-format solutions have been developed [5], based on advanced fiber technologies, to meet the needs of biophotonics. A combination of the capabilities of fiber-optic probes with approaches based on multiphoton absorption (MPA) techniques [48, 49, 63] offers numerous advantages, suggesting a convenient format for beam delivery, facilitating manipulation of excitation radiation, and allowing this excitation to be applied locally and selectively. However, three serious problems need to be adequately addressed to make fiber solutions fully compatible with MPA-based technologies. The first difficulty is related to fiber dispersion, which stretches ultrashort laser pulses, reducing the MPA efficiency. The second problem originates from a small aperture typical of a fiber probe, which makes it difficult to collect efficiently the MPA-excited luminescence response, which is uniformly emitted in a 4π solid angle. Finally, the third issue is the laser damage of biotissues, which imposes strict limitations on laser intensity in *in vivo* work and calls for solutions enabling the enhancement of the MPA-excited luminescence response of biomarker molecules. In this section, we show that a new generation of optical fibers offers a promising platform for the creation of wavelength-tunable sources for MPA-based imaging of stained cells and biotissues, including neural activity visualization and brain imaging applications.

In a fused-silica PCF used in experiments [55] (Figure 4.1c), a 2.7 μm diameter core serves to deliver ultrashort laser pulses to the region of TPL interrogation. The inner part of the microstructure cladding with a diameter of 20 μm is designed to provide a high optical nonlinearity and the desired dispersion profile of the fundamental waveguide mode. Along with its outer ring boundary with a diameter of 24 μm, this section of the fiber serves as a high numerical aperture ($NA \approx 0.55$) multimode

waveguide for the collection and guiding of the TPL response signal from dye molecules excited via TPA. Advantages of dual-core PCFs with a high-*NA* inner cladding for luminescent response collection have been demonstrated earlier in experiments on two-photon biosensing [40] and remote analyte detection [32].

The design of the central fiber core and the inner part of the microstructure cladding of the PCF is targeted towards achieving high nonlinearity and a dispersion profile providing (i) anomalous dispersion at the central wavelength of laser radiation used in experiments (800 nm), (ii) soliton self-frequency shift (SSFS) to a desired wavelength needed for efficient TPL excitation, and (iii) two zero points of GVD for SSFS stabilization. As a short-pulse Ti:sapphire-laser output with a central wavelength of 800 nm enters this dual-cladding two zero GVD point PCF (with zero GVD points at 690 and 1050 nm), it tends to evolve toward a soliton. In Figure 4.10, we present the results of numerical analysis of this soliton dynamics for femtosecond 800 nm input laser pulses mimicking the output of the mode-locked Ti:sapphire laser used in our experiments. Simulations were performed by numerically solving the generalized nonlinear Schrödinger equation (GNSE) [22, 94]. High-order fiber dispersion induces soliton instabilities with respect to the emission of dispersive

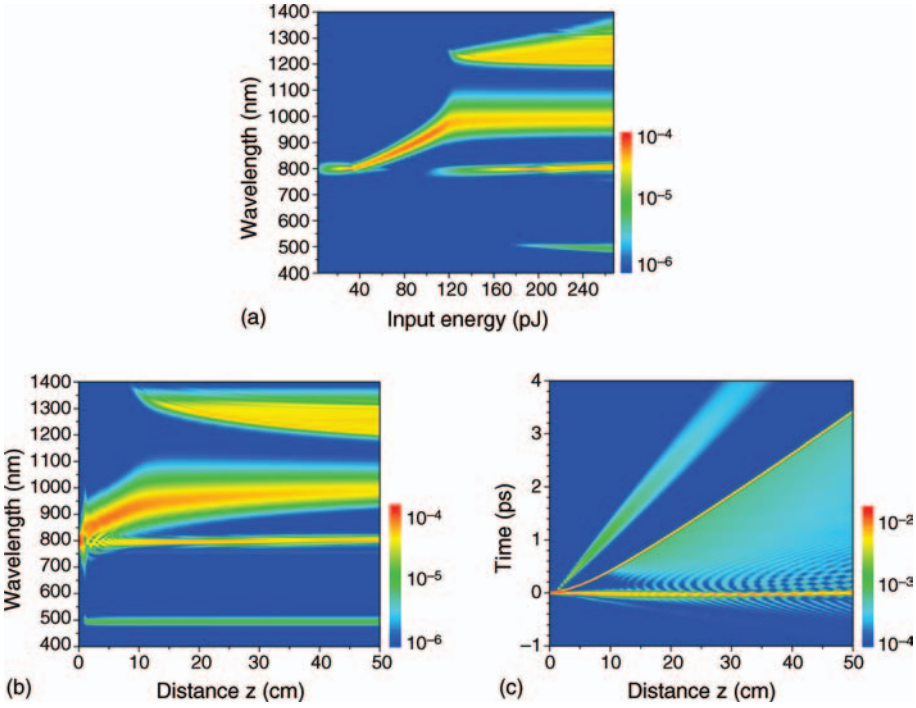

Figure 4.10 Spectrally (a, b) and temporally (c) resolved output of the dual-cladding, two zero GVD point PCF calculated with the use of the GNSE as a function of (a) the input energy and (b, c) the propagation distance *z* along the fiber: (a) the fiber length is 50 cm; (b, c) the input pulse energy is 265 pJ.

waves – a phenomenon that is often referred to as Cherenkov radiation by optical solitons [69]. At the initial stage of pulse evolution in the PCF (propagation distance z ranging from 1 to 10 cm in Figure 4.10a), phase matching between the soliton and a dispersive wave dictates a predominant emission of blue-shifted dispersive waves, observed in GNSE simulations (Figure 4.10a and b) as an intense spectral component centered at the wavelength $\lambda_b \approx 490$ nm. In the time domain, this blue-shifted dispersive-wave radiation is seen as a clearly resolved feature that branches off the soliton part of the field around $z \approx 1$ cm and becomes dispersed by normal fiber dispersion in the process of field evolution (Figure 4.10c).

The Raman effect induces a continuous red shift of a soliton. This effect is clearly seen in Figure 4.10a and b as a well-resolved feature that sweeps over the range of wavelengths from 800 to 990 nm as the pump pulse energy changes from 30 to 120 pJ and the propagation distance increases from 1 to 12 cm. Due to fiber dispersion, the red-shifted soliton accumulates a time delay of about 3.4 ps at the output of a 50 cm piece of PCF (Figure 4.10c). As the central wavelength of a soliton is shifted to the region of a negative slope of the fiber dispersion profile ($z > 10$ cm in Figure 4.10b and c), phase matching between a soliton and a dispersive wave [95] allows efficient generation of red-shifted dispersive waves, observed as a spectral component centered at $\lambda_r \approx 1300$ nm in Figure 4.10a and b. In the time domain, the red-shifted dispersive-wave radiation becomes clearly visible for $z > 10$ cm as a dispersed part of the field adjacent to the red-shifted soliton branch (Figure 4.10c). For input pulse energies exceeding 120 pJ, the central wavelength of the red-shifted soliton becomes insensitive to variations in the input peak energy (Figure 4.10a and b) and stays constant within a broad range of input pulse energies at least up to 800 pJ. This stabilization of the SSFS relative to variations in the pump power, verified by experimental results presented in the inset in Figure 4.11a, and also by earlier experiments [96], is due to the spectral recoil of a soliton by the red-shifted dispersive wave, which exactly compensates [95] for the SSFS induced by the Raman effect.

With its dispersion and nonlinearity designed to generate a stabilized frequency-shifted soliton centered at a desired wavelength, the PCF offers an ideal source for the excitation and detection of the TPL response from a variety of dyes, including fluorescent proteins used as markers of neuron activity, and also brain tissue-labeling dyes. With appropriate modifications of the PCF structure, frequency-shifted ultrashort pulses optimized for the detection of the TPL response of such dyes have been generated. In particular, the fiber design presented in Figure 4.1c, providing a stabilized soliton output with a central wavelength of 980–990 nm (inset in Figure 4.11b), is ideally suited for efficient TPA excitation of Alexa Fluor 488 dye, which is commonly used as a label in cell biology and fluorescence microscopy. Filled circles in the inset in Figure 4.11b display the spectrum of the TPL response of Alexa Fluor 488 dye, measured for a dye solution in a quartz cell with the TPL response collected by the inner, 24 μm diameter part of the microstructure cladding. Our measurements suggest that the use of a frequency-shifted PCF output enhances the TPL response power collected by the fiber by more than an order of magnitude relative to the level of TPL response attainable with a frequency-unshifted, 800 nm, 40 fs output of the Ti:sapphire laser with the same field intensity. This not only opens

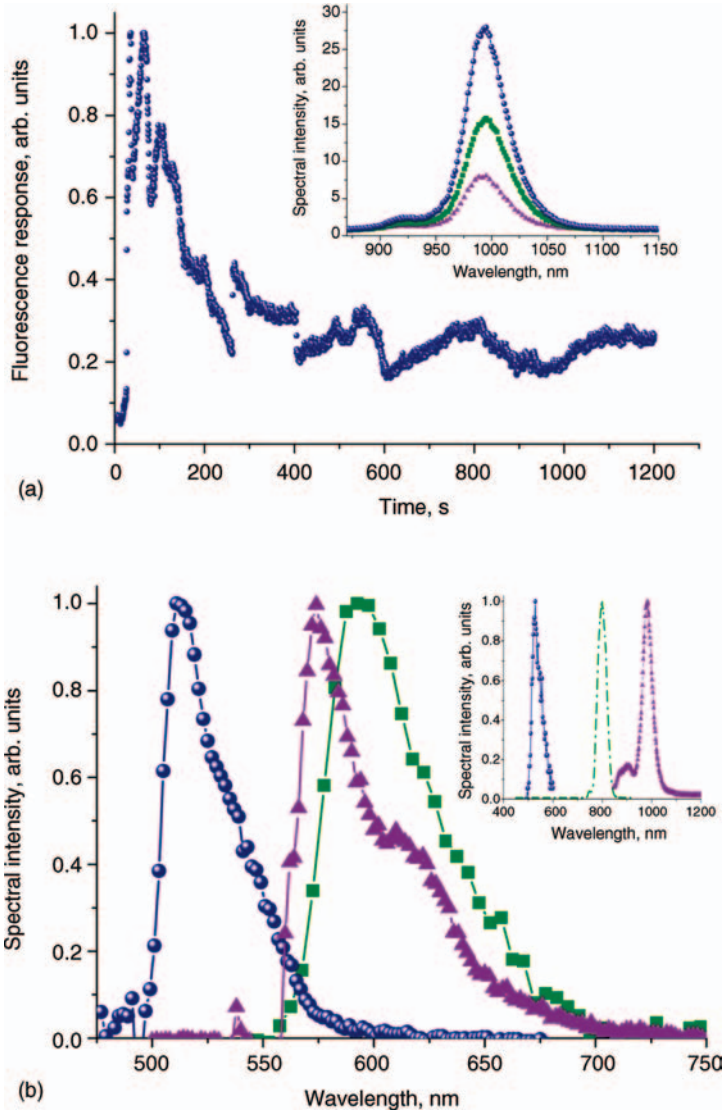

Figure 4.11 (a) Decay kinetics of the fluorescent response of EGFP from the brain of a transgenic mouse in open-skull experiments. The inset shows the spectrum of the PCF output measured for three different input energies of Ti:sapphire laser pulses: triangles, 150 pJ; rectangles, 250 pJ; and filled circles, 400 pJ. (b) Spectrally resolved fluorescent response of EGFP in the brain of a transgenic mouse (filled circles), DsRed2 fluorescent protein in the tail of a *Xenopus laevis* tadpole (rectangles), and Alexa Fluor 555 dye in stained mouse brain (triangles). The inset shows the fluorescent response of Alexa Fluor 488 dye (filled circles) TPA-excited by the frequency-shifted soliton output of a highly nonlinear PCF (triangles). The spectrum of the laser pulse is shown by the dashed-dotted line in the inset.

the ways for a higher speed and improved quality of neuron activity mapping, but also helps to maintain moderate levels of laser intensity in *in vivo* work, making it possible to reduce the laser-induced heat load and avoid radiation damage to biotissues.

The rectangles in Figure 4.11b present the results of spectrally resolved *in vivo* measurements performed on the optical response of DsRed2 fluorescent protein in the muscle tissue of a *Xenopus laevis* tadpole. In these experiments, the DsRed2 reporter gene is controlled by an actin promoter gene. Actin protein produced as a result of promoter gene expression helps build a scaffold, necessary for muscle contraction due to the force generated by myosin proteins. *In vivo* work on neuron activity mapping in brain was performed on transgenic mice, in which the expression of enhanced green fluorescent protein (EGFP) is controlled by an immediate early gene promoter, encoding the *zif*268 mammalian transcription factor. Optical detection of EGFP can thus visualize an accumulation of *zif*268, which is coordinated by a Ca^{2+} influx into a cell and indicates activation of neurons [71, 97]. For the maximum efficiency of TPL detection of EGFP, the absorption of which peaks at $\lambda_{EGFP} \approx 480$ nm, a PCF was designed to deliver a wavelength-shifted soliton centered at $2\lambda_{EGFP} \approx 960$ nm. The pulse width of this wavelength-shifted soliton PCF output was estimated as 25 fs. The spectrum of the TPL response of EGFP expressed in the brain of a transgenic mouse is shown by filled circles in Figure 4.11b. The overall fall-off kinetics of this response (Figure 4.11a), measured in experiments with an open-skull transgenic mouse, reveal the decaying activity of neurons in a fading brain. The maximum intensity of light pulses used for TPL excitation in our *in vivo* experiments (on the order of 10 GW cm^{-2}) was well below the level of light intensities where photodamage of biotissues and photobleaching of dye or fluorescent protein biomarkers became noticeable. With slight modifications of the fiber structure, a wavelength tunability range as broad as 600 nm (from 800 to 1400 nm) could be achieved for the soliton output of the type of PCF considered, suggesting a strategy for multiplex multicolor bioimaging with an appropriate combination of dye and fluorescent-protein biomarkers.

Dye–cell measurements and *in vivo* experiments [55] demonstrated that a dual-cladding PCF with two zero GVD points and properly engineered dispersion profile can substantially enhance the TPL response of fluorescent protein biomarkers and neuron activity reporters. The SSFS, stabilized against laser power fluctuations in a two zero GVD point PCF, has been shown to allow the wavelength of the soliton PCF output to be accurately matched with the TPA spectrum of dye or fluorescent protein biomarker molecules, enhancing their TPL response and allowing laser damage of biotissues to be avoided.

4.8
Toward Fiber-Based Multicolor Imaging

The use of fluorescent proteins for the simultaneous detection of multitudes of neurons in a living brain is one of the most exciting recent achievements of optical technologies in neuroscience [98]. Implementation of this technique in the

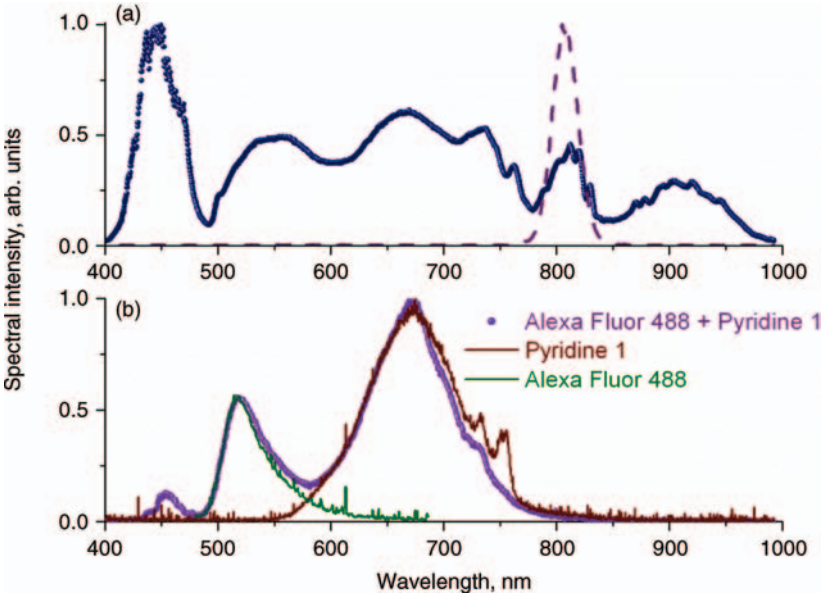

Figure 4.12 Spectrum of the mode-locked Ti:sapphire laser output (a, dashed line) and the spectrum of supercontinuum (a, filled circles) from the highly nonlinear PCF used for the simultaneous measurement of the fluorescent response of Alexa Fluor 488 and Pyridine 1 dyes in a mixture. Also shown are (b) the individual fluorescent responses of the dyes.

endoscopic mode is a challenging task and a highly promising direction for biophotonics. We show below that PCFs offer an attractive platform for the integration of fiber-optic light delivery and fluorescent response pickup with a compact fiber-format multicolor light source for a multiplex optical interrogation of a variety of fluorescent-protein reporters.

The key technology behind the integration of a multicolor light source into a fiber endoscope for neuroscience applications is supercontinuum generation [21, 22] – dramatic spectral broadening of optical waveforms induced by an involved combination of nonlinear optical effects, including self- and cross-phase modulation, pulse self-steepening, wave-mixing phenomena, and solitonic transformations of optical fields assisted by the Raman effect. In experiments [59], efficient supercontinuum generation for multicolor imaging was provided by a highly nonlinear PCF with a core diameter less than 2 μm pumped by a Ti:sapphire laser output with a typical energy of a few nanojoules, a central frequency of 810 nm, and a pulse width of 50 fs at a pulse repetition rate of 90 MHz. The spectrum of the Ti:sapphire laser output is shown by the dashed line in Figure 4.12a. The highly nonlinear PCF is optimized to transform Ti:sapphire laser pulses into a broadband supercontinuum radiation with a spectrum spanning over more than an octave from 420 to 960 nm (filled circles in Figure 4.12a), with a radiation power contained in the 400–700 nm spectral region estimated as approximately 3 mW. The supercontinuum PCF output was focused

with an objective into a beam spot with an area of about $10\,\mu m^2$. With a supercontinuum pulse width on the order of 100 fs and a pulse repetition rate of 90 MHz, such a focusing corresponds to a maximum field intensity of about $3\,GW\,cm^2$. A Keldysh-type formalism of ionization in biotissues [99] estimates the electron density induced by a 100 fs pulse with an intensity in a water-type dielectric such as $n_e \approx 10^3\,cm^{-3}$, indicating that ionization effects are negligible in this regime. The situation becomes radically different, however, in the range of intensities needed for multiphoton brain-tissue excitation and probing. In the case of two-photon excitation of EGFP with 960 nm femtosecond pulses, more than one free electron is generated per laser pulse per each photon emitted through two photon absorption-induced fluorescence (with the cross-section of TPA estimated as $\sigma_{TPA} \approx 6.5\,GM = 6.5 \times 10^{-50}\,cm^4\,s^{-1}$ per photon for wild-type GFP) for sub-TW cm^{-2} field intensities [100]. In this regime, special care should be taken in choosing the repetition rate of excitation pulses in order to prevent the accumulation of free electrons in the laser–tissue interaction region.

The supercontinuum PCF output is used to induce fluorescence in an aqueous solution of Alexa Fluor® 488 and Pyridine 1 dyes, intended to mimic a two-component mixture of fluorescent biomarkers. When this mixture of dyes was irradiated with the entire supercontinuum spectrum, a fluorescent response from both dyes was observed in the spectrum of the fluorescence signal collected with an additional standard optical fiber and studied with a spectrum analyzer. To provide individual excitation of the dyes in the solution, appropriate filters were inserted into the beam of supercontinuum in front of the cell. The spectra of the individual fluorescence responses of Alexa Fluor 488 and Pyridine 1 are shown by the solid lines in Figure 4.12b. The spectrum of the fluorescence response from the mixture of these dyes collected with a standard optical fiber is represented by the bold line in Figure 4.12b. The spectral brightness and the overall intensity of the supercontinuum output of the PCF used in our experiments were found to be ideally suited for experiments on living brain, providing a high efficiency of fluorescence response excitation and producing no photodamage of brain tissues.

References

1 Hecht, J. (1999) *City of Light: the Story of Fiber Optics*, Oxford University Press, Oxford.
2 Hansell, C.W. (1927) Picture transmission, US Patent 1,751,584, filed 13 August 1927, issued 25 March 1930.
3 Lamm, H. (1930) *Z. Instrumentenkd.*, **50**, 579.
4 Hecht, J. (1999) *Opt. Photon. News*, **10** (11), 26.
5 Flusberg, B.A., Cocker, E.D., Piyawattanametha, W., Jung, J.C., Cheung, E.L.M., and Schnitzer, M.J. (2005) *Nat. Methods*, **2**, 941.
6 Lin, C.H. and Webb, R.H. (2000) *Opt. Lett.*, **25**, 954.
7 Bird, D. and Gu, M. (2002) *Opt. Lett.*, **27**, 1031.
8 Jung, J.C. and Schnitzer, M.J. (2003) *Opt. Lett.*, **28**, 902.
9 Liang, C., Sung, K.B., Richards-Kortum, R., and Descour, M.R. (2002) *Appl. Opt.*, **41**, 4603.
10 Limpert, J., Röser, F., Schreiber, T., and Tünnermann, A. (2006) *IEEE*

J. Sel. Top. Quantum Electron., **12**, 233.
11 Boyden, E.S., Zhang, F., Bamberg, E., Nagel, G., and Deisseroth, K. (2005) *Nat. Neurosci.*, **8**, 1263.
12 Aravanis, A.M., Wang, L.P., Zhang, F., Meltzer, L.A., Mogri, M.Z., Schneider, M.B., and Deisseroth, K. (2007) *J. Neural Eng.*, **4**, S143.
13 Russell, P.St.J. (2003) *Science*, **299**, 358.
14 Knight, J.C. (2003) *Nature*, **424**, 847.
15 Zheltikov, A.M. (2000) *Phys. Usp.*, **43**, 1125.
16 Zheltikov, A.M. (2007) *Phys. Usp.*, **50**, 705.
17 Myaing, M.T., Ye, J.Y., Norris, T.B., Thomas, T., Baker, J.R. Jr., Wadsworth, W.J., Bouwmans, G., Knight, J.C., and Russell, P.St.J. (2003) *Opt. Lett.*, **28**, 1224.
18 Flusberg, B., Jung, J., Cocker, E., Anderson, E., and Schnitzer, M. (2005) *Opt. Lett.*, **30**, 2272.
19 Fu, L., Jain, A., Xie, H., Cranfield, C., and Gu, M. (2006) *Opt. Express*, **14**, 1027–1032.
20 Fang, X.-H., Hu, M.-L., Liu, B.-W., Chai, L., Wang, C.-Y., and Zheltikov, A.M. (2010) *Opt. Lett.*, **35**, 2326.
21 Dudley, J.M., Genty, G., and Coen, S. (2006) *Rev. Mod. Phys.*, **78**, 1135.
22 Zheltikov, A.M. (2006) *Phys. Usp.*, **49**, 605.
23 Zheltikov, A.M. (2007) *J. Raman Spectrosc.*, **38**, 1052.
24 Cregan, R.F., Mangan, B.J., Knight, J.C., Birks, T.A., Russell, P.St.J., Allen, D., and Roberts, P.J. (1999) *Science*, **285**, 1537.
25 Smith, C.M., Venkataraman, N., Gallagher, M.T., Muller, D., West, J.A., Borrelli, N.F., Allan, D.C., and Koch, K. (2003) *Nature*, **424**, 657.
26 Konorov, S.O., Fedotov, A.B., Mitrokhin, V.P., Beloglazov, V.I., Skibina, N.B., Shcherbakov, A.V., Wintner, E., Scalora, M., and Zheltikov, A.M. (2004) *Appl. Opt.*, **43**, 2251.
27 Ivanov, A.A., Podshivalov, A.A., and Zheltikov, A.M. (2006) *Opt. Lett.*, **31**, 3318.
28 Zheltikov, A.M. (2005) *Nat. Mater.*, **4**, 267.
29 Monro, T.M., Richardson, D.J., and Bennett, P.J. (1999) *Electron. Lett.*, **35**, 1188.
30 Monro, T.M., Belardi, W., Furusawa, K., Baggett, J.C., Broderick, N.G.R., and Richardson, D.J. (2001) *Meas. Sci. Technol.*, **12**, 854.
31 Jensen, J.B., Pedersen, L.H., Hoiby, P.E., Nielsen, L.B., Hansen, T.P., Folkenberg, J.R., Riishede, J., Noordegraaf, D., Nielsen, K., Carlsen, A., and Bjarklev, A. (2004) *Opt. Lett.*, **29**, 1974.
32 Konorov, S., Zheltikov, A., and Scalora, M. (2005) *Opt. Express*, **13**, 3454.
33 Rindorf, L., Jensen, J.B., Dufva, M., Pedersen, L.H., Høiby, P.E., and Bang, O. (2006) *Opt. Express*, **14**, 8224.
34 Cordeiro, C.M.B., Franco, M.A.R., Chesini, G., Barretto, E.C.S., Lwin, R., Brito Cruz, C.H., and Large, M.C.J. (2006) *Opt. Express*, **14**, 13056.
35 Jensen, J., Hoiby, P., Emiliyanov, G., Bang, O., Pedersen, L., and Bjarklev, A. (2005) *Opt. Express*, **13**, 5883.
36 Hoo, Y.L., Jin, W., Ho, H.L., Wang, D.N., and Windeler, R.S. (2002) *Opt. Eng.*, **41**, 8.
37 Hoo, Y.L., Jin, W., Shi, C., Ho, H.L., Wang, D.N., and Ruan, S.C. (2003) *Appl. Opt.*, **42**, 3509.
38 Pickrell, G., Peng, W., and Wang, A. (2004) *Opt. Lett.*, **29**, 1476.
39 Alfernes, R.C. (1988) in *Guided Wave Optoelectronics* (ed. T. Tamir), Springer, Berlin, p. 145.
40 Myaing F M.T., Ye, J.Y., Norris, T.B., Thomas, T., Baker, J.R. Jr., Wadsworth, W.J., Bouwmans, G., Knight, J.C., and Russell, P.S.J. (2003) *Opt. Lett.*, **28**, 1224.
41 Eggleton, B., Kerbage, C., Westbrook, P., Windeler, R., and Hale, A. (2001) *Opt. Express*, **9**, 698.
42 Ferguson, J.A., Christian Boles, T., Adams, C.P., and Walt, D.R. (1996) *Nat. Biotechnol.*, **14**, 1681.
43 Deiss, F., Sojic, N., White, D.J., and Stoddart, P.R. (2010) *Anal. Bioanal. Chem.*, **396**, 53.
44 Ritari, T., Tuominen, J., Ludvigsen, H., Petersen, J., Sørensen, T., Hansen, T., and Simonsen, H. (2004) *Opt. Express*, **12**, 4080.
45 Fedotov, A.B., Konorov, S.O., Mitrokhin, V.P., Serebryannikov, E.E., and Zheltikov, A.M. (2004) *Phys. Rev. A*, **70**, 045802.

46 Zheltikov, A.M. (2008) *Appl. Opt.*, **47**, 474.
47 Kawata, S., Ohtsu, M., and Irie, M. (2002) *Nano-Optics*, Springer, Berlin.
48 Zipfel, W.R., Williams, R.M., and Webb, W.W. (2003) *Nat. Biotechnol.*, **21**, 1369.
49 Helmchen, F. and Denk, W. (2005) *Nat. Methods*, **2**, 932.
50 Evans, C.L. and Sunney Xie, X. (2008) *Annu. Rev. Anal. Chem.*, **1**, 883.
51 Freudiger, C., Min, W., Saar, B., Lu, S., Holtom, G., He, C., Tsai, J., Kang, J., and Sunney Xie, X. (2008) *Science*, **322**, 1857.
52 Hell, S.W. (2009) *Nat. Methods*, **6**, 24.
53 Bates, M., Huang, B., Dempsey, G.P., and Zhuang, X. (2007) *Science*, **317**, 1749.
54 Flusberg, B.A., Nimmerjahn, A., Cocker, E.D., Mukamel, E.A., Barretto, R.P.J., Ko, T.H., Burns, L.D., Jung, J.C., and Schnitzer, M.J. (2008) *Nat. Methods*, **5**, 935.
55 Doronina, L.V., Fedotov, I.V., Voronin, A.A., Ivashkina, O.I., Zots, M.A., Anokhin, K.V., Rostova, E., Fedotov, A.B., and Zheltikov, A.M. (2009) *Opt. Lett.*, **34**, 3373.
56 Snyder, A.W. and Love, J.D. (1983) *Optical Waveguide Theory*, Chapman and Hall, London.
57 Zheltikov, A.M. (2005) *J. Opt. Soc. Am. B*, **22**, 1100.
58 Zheltikov, A.M. (2010) *JETP Lett.*, **91**, 378.
59 Doronina-Amitonova, L.V., Fedotov, I.V., Ivashkina, O.I., Zots, M.A., Fedotov, A.B., Anokhin, K.V., and Zheltikov, A.M. (2010) *J. Biophoton.*, **3**, 660.
60 Farrell, T.J., Patterson, M.S., and Wilson, B.C. (1992) *Med. Phys.*, **19**, 879.
61 Hull, E.L., Nichols, M.G., and Foster, T.H. (1998) *Appl. Opt.*, **37**, 2755.
62 Bevilacqua, F., Piquet, D., Marquet, P., Gross, J.D., Tromberg, B.J., and Depeursinge, C. (1999) *Appl. Opt.*, **38**, 4939.
63 Denk, W., Strickler, J.H., and Webb, W.W. (1990) *Science*, **248**, 73.
64 Bhawalkar, J.D., Kumar, N.D., Zhao, C.-F., and Prasad, P.N. (1997) *J. Clin. Lasers Med. Surg.*, **15**, 201.
65 Wilson, B.C., Olivo, M., and Singh, G. (1997) *Photochem. Photobiol.*, **65**, 166.
66 Fisher, W.G., Partridge, W.P. Jr., Dees, C., and Wachter, E.A. (1997) *Photochem. Photobiol.*, **66**, 141.
67 Ye, J.Y., Myaing, M.T., Norris, T.B., Thomas, T., and Baker, J. Jr. (2002) *Opt. Lett.*, **27**, 1412.
68 Fedotov, I.V., Fedotov, A.B., Doronina, L.V., and Zheltikov, A.M. (2009) *Appl. Opt.*, **48**, 5274.
69 Akhmediev, N. and Karlsson, M. (1995) *Phys. Rev. A*, **51**, 2602.
70 Herrmann, J., Griebner, U., Zhavoronkov, N., Husakou, A., Nickel, D., Knight, J.C., Wadsworth, W.J., Russell, P.St.J., and Korn, G. (2002) *Phys. Rev. Lett.*, **88**, 173901.
71 Chalfie, M., Tu, Y., Euskirchen, G., Ward, W.W., and Prasher, D.C. (1994) *Science*, **263**, 802.
72 Tsien, R.Y. (2005) Breeding molecules to spy on cells, in *The Harvey Lectures, Series 99*, John Wiley & Sons, Inc., Hoboken, NJ, pp. 77–93.
73 Eesley, G.L. (1981) *Coherent Raman Spectroscopy*, Pergamon Press, Oxford.
74 von der Linde, D., Laubereau, A., and Kaiser, W. (1971) *Phys. Rev. Lett.*, **26**, 9541971.
75 Eckbreth, A.C. (1988) *Laser Diagnostics for Combustion Temperature and Species*, Abacus, Cambridge, MA.
76 Zheltikov, A.M. and Koroteev, N.I. (1999) *Phys. Usp.*, **42**, 321.
77 Zheltikov, A.M. (2000) *J. Raman Spectrosc.*, **31**, 653.
78 Zumbusch, A., Holtom, G.R., and Xie, X.S. (1999) *Phys. Rev. Lett.*, **82**, 4142.
79 Evans, C.L., Potma, E.O., Poureshagh, M., Coté, D., Lin, C.L., and Xie, X.S. (2005) *Proc. Natl. Acad. Sci. U. S. A.*, **102**, 16807.
80 Akhmanov, S.A., Dmitriev, V.G., Kovrigin, A.I., Koroteev, N.I., Tunkin, V.G., and Kholodnykh, A.I. (1972) *JETP Lett.*, **15**, 425.
81 Levenson, M.D., Flytzanis, C., and Bloembergen, N. (1972) *Phys. Rev. B*, **6**, 3962.
82 Andresen, E.R., Birkedal, V., Thøgersen, J., and Keiding, S.R. (2006) *Opt. Lett.*, **31**, 1328.

83 Sidorov-Biryukov, D.A., Serebryannikov, E.E., and Zheltikov, A.M. (2006) *Opt. Lett.*, **31**, 2323.

84 Mitrokhin, V.P., Fedotov, A.B., Ivanov, A.A., Alfimov, M.V., and Zheltikov, A.M. (2007) *Opt. Lett.*, **32**, 3471.

85 Savvin, A.D., Lanin, A.A., Voronin, A.A., Fedotov, A.B., and Zheltikov, A.M. (2010) *Opt. Lett.*, **35**, 919.

86 Fedotov, A.B., Voronin, A.A., Fedotov, I.V., Ivanov, A.A., and Zheltikov, A.M. (2009) *Opt. Lett.*, **34**, 851.

87 Oberthaler, M. and Hopfel, R.A. (1993) *Appl. Phys. Lett.*, **63**, 1017.

88 Planas, S.A., Pires Mansur, N.L., Brito Cruz, C.H., and Fragnito, H.L. (1993) *Opt. Lett.*, **18**, 699.

89 Sidorov-Biryukov, D.A., Fernandez, A., Zhu, L., Pugžlys, A., Serebryannikov, E.E., Baltuška, A., and Zheltikov, A.M. (2008) *Opt. Express*, **16**, 2502.

90 Voronin, A.A., Fedotov, I.V., Doronina-Amitonova, L.V., Ivashkina, O.I., Zots, M.A., Fedotov, A.B., Anokhin, K.V., and Zheltikov, A.M. (2010) Presented at the European Conference on Nonlinear-Optical Spectroscopy, Bremen, June 2010.

91 Evans, C.L., Xu, X., Kesari, S., Sunney Xie, X., Wong, S.T.C., and Young, G.S. (2007) *Opt. Express*, **15**, 12076.

92 Mehta, A.D., Jung, J.C., Flusberg, B.A., and Schnitzer, M.J. (2004) *Curr. Opin. Neurobiol.*, **14**, 617.

93 Jung, J.C., Mehta, A.D., Aksay, E., Stepnoski, R., and Schnitzer, M.J. (2004) *J. Neurophysiol.*, **92**, 3121.

94 Agrawal, G.P. (2001) *Nonlinear Fiber Optics*, Academic Press, San Diego, CA.

95 Skryabin, D.V., Luan, F., Knight, J.C., and Russell, P.St.J. (2003) *Science*, **301**, 1705.

96 Liu, B.-W., Hu, M.-L., Fang, X.-H., Li, Y.-F., Chai, L., Wang, C.-Y., Tong, W., Luo, J., Voronin, A.A., and Zheltikov, A.M. (2008) *Opt. Express*, **16**, 14987.

97 Dynes, J.L. and Ngai, J. (1998) *Neuron*, **20**, 1081.

98 Livet, J., Weissman, T.A., Kang, H., Draft, R.W., Lu, J., Bennis, R.A., Sanes, J.R., and Lichtman, J.W. (2007) *Nature*, **450**, 56.

99 Vogel, A., Noack, J., Huttman, G., and Paltauf, G. (2005) *Appl. Phys. B*, **81**, 1015.

100 Voronin, A.A. and Zheltikov, A.M. (2010) *Phys. Rev. E*, **81**, 051918.

5
Identification and Characterization of Microorganisms by Vibrational Spectroscopy

Stephan Stöckel, Angela Walter, Anja Boßecker, Susann Meisel, Valerian Ciobotă, Wilm Schumacher, Petra Rösch, and Jürgen Popp

5.1
Introduction

Vibrational spectroscopy has been successfully applied to the characterization, identification, and classification of microorganisms [1–5]. In this chapter, the applicability of vibrational spectroscopy to clinically relevant microorganisms is demonstrated.

Infrared (IR) absorption spectroscopy and Raman spectroscopy – the two main vibrational spectroscopic techniques – are based on energetic characteristics of molecular vibrations of major biopolymeric constituents within microorganisms, such as nucleic acids, proteins, lipids, and carbohydrates. Hence specific spectral information within the low-wavenumber region of the IR absorption spectra and the Raman scattering spectra can be achieved, since microorganisms exhibit complex substance compositions of varying concentrations, which depend on phylogenetic characteristics and growth conditions, for example, age, temperature, and nutrition availability [6–8]. Therefore, the fingerprint region of IR absorption and Raman spectra contains specific information, which functions as a molecular fingerprint for classification and identification. In addition to high specificity, IR absorption and Raman spectroscopy exhibit further advantages which are complementary to both techniques [9].

The investigation of microorganisms by means of IR absorption spectroscopy has been increasingly performed since the 1950s [10]. Fourier transform infrared (FTIR) spectrometers have improved the acquisition of IR absorption spectra and by introducing micro-FTIR spectroscopy – the combination of FTIR absorption spectroscopy with a microscope – spatially resolved detection of certain microcolonies was achieved [11]. FTIR absorption analyses can be performed in either transmission or reflectance mode with the transmission mode resulting in high-quality spectra provided that homogeneity and a small sample thickness are maintained. The signal intensity within the IR spectrum correlates with the polarity of particular bonds. This is extremely high for water, which consequently exhibits intense signals and masks

Handbook of Biophotonics. Vol.2: Photonics for Health Care, First Edition. Edited by Jürgen Popp, Valery V. Tuchin, Arthur Chiou, and Stefan Heinemann.

other relevant peaks within the IR absorption spectrum. This characteristic of IR absorption spectroscopy limits the application to biological samples since water is omnipresent in microorganisms, cells, and tissues.

In contrast to the IR absorption process, the scattering mechanism of Raman spectroscopy correlates with the polarizability of molecular bonds. Thus, water causes no intense signals within the fingerprint region of Raman spectra. This facilitates the analysis of microorganisms under *in vivo* conditions. Additionally, the drying step can also be omitted, which simplifies the sample preparation tremendously [12]. Micro-Raman spectroscopy, which results in better spatial resolution than micro-IR absorption spectroscopy, is capable of focusing on single bacterial cells. A preceding sample cultivation step to generate sufficient biomass for the measurements is therefore dispensable. Raman spectroscopy has been proven to be suitable for the fast and reliable investigation of microorganisms with high throughput providing real-time monitoring [13, 14].

Raman spectroscopy is limited by the weak intrinsic scattering, which has been overcome by two enhancement techniques: UV–resonance Raman (UVRR) spectroscopy and surface-enhanced Raman spectroscopy (SERS) [15, 16]. For resonance Raman spectroscopy, the excitation wavelength is shifted to an electronic absorption of the target chromophores to enhance selectively the related chromophore vibrations. An intensity increase of up to 10^6 compared with the non-resonant Raman scattering can be achieved. Hence certain biomolecules can be detected selectively and sensitively in complex biological environments even if present only in low concentrations. Within UVRR spectra excited, for example, at 244 or 257 nm, DNA and proteins are selectively enhanced, where the former functions potentially as a taxonomic marker in genotypic studies.

SERS is another approach to increase the weak Raman signal in which either silver or gold substrates are applied to accomplish an electronic enhancement in the order of 10^5–10^{14} [17].

The combination of SERS with atomic force microscopy (AFM) results in tip-enhanced Raman spectroscopy (TERS). TERS combines the high specificity of Raman spectroscopy with the high spatial resolution of AFM [16].

To illustrate the application of vibrational spectroscopy in medicine and medical-related fields, several examples especially concerning the investigation of biofilms, influence of antibiotics on microorganisms, food-borne pathogens, and epidemiological studies are introduced later in the chapter. Additionally, commonly applied sample preparation procedures are presented in the next section. Since vibrational spectroscopy of microorganisms always deals with huge databases, the necessary preprocessing and data evaluation are also discussed.

5.2
Sample Preparation Techniques

Each vibrational spectroscopic method requires its own characteristic sample preparation technique and specific sample substrates. Since both IR absorption and

Raman spectra are sensitive towards changes in environmental parameters such as different nutrition media, temperature, light, or cultivation age, these parameters should be considered for each study and implemented within databases. For bulk measurements, which require pre-cultivation, this can be achieved by rigid standardization of the cultivation conditions. For single cell measurements, all relevant parameters have to be included in the database [4].

Since the identification of bacteria was first established by means of IR absorption spectroscopy, all further preparation methods are variations of the original protocol established by Naumann [18]. Here, bacterial strains are grown on agar plates applying the so-alled four-quadrant streak pattern. For the IR measurements, a small amount of a colony is removed from the third quadrant. The bacteria are suspended in 80 µl of distilled water and an aliquot of 30 µl is then transferred to a ZnSe optical plate. Subsequently,, the bacterial suspension is dried under moderate vacuum conditions (2.5–7.5 kPa) to form a transparent film [19]. In addition to ZnSe, Si plates are also utilized as substrate for IR absorption spectroscopy [2].

The sample preparation for UVRR spectroscopy [20–22] and Raman spectroscopy with excitation wavelengths in the visible [7] and near-infrared (NIR) regions [23] is similar to that described for IR absorption spectroscopy. For Raman spectroscopic studies, either fused-silica slides or CaF_2 are utilized as substrates. Alternatively, for Raman excitation in the visible and NIR regions, bacterial smears can also be used for investigation [24, 25].

For the application of SERS, the sample preparation varies slightly. The collected bacteria are directly suspended in the corresponding colloid and not in water as described above. For the measurements, both bacteria and colloids are dried on the substrates, either CaF_2 or fused-silica slides [26, 27].

Whenever a microscope is included in the experimental setup, IR and Raman spectroscopy are additionally capable of investigating small micro-colonies [24]. For IR microscopy, a special stamping device is applied which transfers the micro-colonies from the agar plates on to the ZnSe substrate [9]. Using micro-Raman spectroscopy, it is even possible to measure the micro-colonies from the agar plates directly and the sample preparation step can therefore be omitted. Whenever micro-colonies are too small, the medium makes a contribution to the Raman spectrum, which has to be removed [24, 28].

In addition to bulk measurements, investigations of single bacterial or yeast cells can also be performed by means of micro-Raman spectroscopy. For the investigation of single bacterial cells, bacterial smears with well-separated cells are prepared [4, 25, 29]. For the localization of single bacteria inside heterogeneous sample matrices, even conventional fluorescence staining methods can be applied [30].

5.3
Statistical Analysis of Vibrational Spectroscopic Data

Spectroscopic investigations of microorganisms result in datasets which cannot be handled without statistical evaluation. First, the datasets are usually too

extensive, so an intuitive registration is impossible. Second, the chemical variations between different species or strains are so minor that the impact on the spectra cannot be seen with the naked eye. These are the two main reasons why investigations of microorganisms cannot be discussed separately from statistical analysis. Statistical analysis is able to handle huge datasets and is very sensitive to small spectral changes. Therefore, statistical methods offer immense possibilities for the evaluation of biological data but also bear the risk of interpretations induced by artifacts. Artifacts can derive from several sources, for example, sample preparation, measurement procedures, and the measurement setup. Therefore, sample preparations and measurement procedures have to be standardized and the spectrometer must be carefully calibrated. Since variances due to varying laser power intensity and varying sample thickness cannot be completely avoided, careful preprocessing has to be implemented within the data analysis. The preprocessing usually involves, for example, cosmic spike removal, baseline correction, normalization, and dimension reduction. The preprocessed dataset can then be subjected to the statistical methods, which can be divided into supervised and unsupervised methods. For supervised methods, such as artificial neural networks (ANNs), a training procedure is carried out aiming for the optimal output of the algorithm regarding the given labels. Hence, *a priori* knowledge is induced which enables the classification to be validated. Unsupervised methods, such as hierarchical cluster analysis (HCA) and principal component analysis (PCA), instead cluster the data regarding their position within the feature space and not because of their group membership. For unsupervised methods, the actual dataset is used without further information.

A crucial part of the data mining is the preprocessing step. Therefore, before the actual statistical methods are presented, the steps for preprocessing will be discussed.

One very important part is the removal of cosmic spikes. Cosmic spikes are the result of photons which are not caused by the scattering of the laser light of the sample, but derive from outer space. These signals distort the measured spectrum and change the results of the chemometric analysis, so their removal is essential. Because of their origin, the cosmic spikes are detected randomly, and as they are not correlated in either time or space they can therefore be localized by repeating the measurement were measured time or space. If, for example, two Raman spectra in at the same measuring position, a cosmic spike would increase the counts in one channel. The intensity difference between the two spectra would increase abruptly in this channel compared with all other channels of the spectra.

This property enables the algorithm to find spikes by spectra subtraction. In Figure 5.1, the result for this cosmic spike removal procedure is visualized for two Raman spectra, which are depicted in black and red. The black spectrum contains a cosmic spike and the green line is the absolute value of the difference between the black and the red spectra. The distinct green peak determines the localization of a cosmic spike within the black spectrum. With several statistical techniques, it is possible to detect the outlier (very high count) in the green spectrum and so it is possible to detect the cosmic spikes. This method is generalizable for more spectra or spectra of the same sample for different points in space.

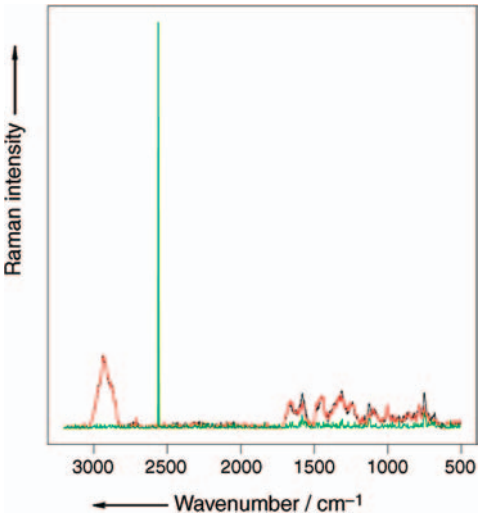

Figure 5.1 Visualization of the cosmic spike removal procedure: two Raman spectra of *P. aeruginosa* were measured at exactly the same position. The first spectrum is represented by the black line and the second by the red line. The green line is the absolute value of the difference of both spectra and clearly helps to identify the channels containing a spike.

The next important preprocessing step is background removal. Not all measured counts result from Raman scattering; other effects such as fluorescence also contribute to the spectra. Fluorescence is a much more likely process than Raman scattering and overlaps or even obscures the Raman signal. Because fluorescence changes over time and may not be constant over the whole sample, it would distort the learning procedure of the supervised method. This has an undesired impact on the outcome of the chemometric analysis and has to be minimized. Characteristically, fluorescence signals vary more slowly than the desired Raman signal over the wavenumber region. This characteristic offers the possibility to detect and remove the spectral background. There are several algorithms to accomplish this task. The most common ones are the SNIP algorithm and Lieber's algorithm [31, 32]. The SNIP algorithm is a composite of a low statistic filter and a peak clipping algorithm. The low statistic filter smoothes domains low statistics (low information) containing with a wide smoothing window. The peak clipping algorithm localizes peaks in order to remove them from the spectra. Both algorithms combined are able to estimate the background. A "background-free" spectrum is achieved by subtracting the estimated background from the measured spectrum. Exemplarily, the result of the SNIP algorithm performed on a spectrum is plotted in Figure 5.2, where the original spectrum is depicted in black, the estimated background is represented by the red line, and the green line is referred to as the preprocessed spectrum.

Lieber's algorithm is based on the assumption that the background changes much more slowly than the actual spectrum. The measured spectrum is a superposition of a

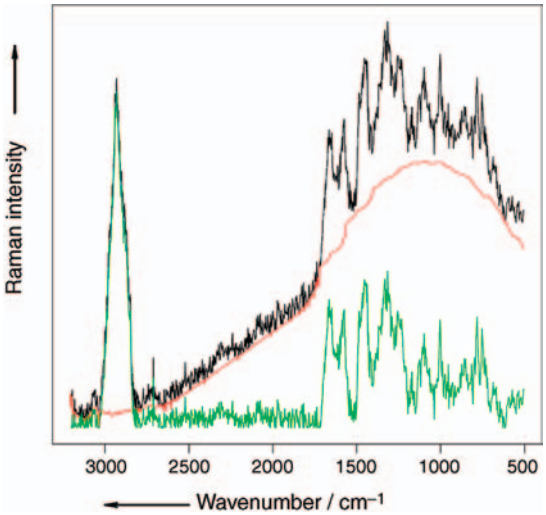

Figure 5.2 Background removal procedure: the black line is the original micro-Raman spectrum of *P. aeruginosa* and the red line shows the estimated background by the SNIP algorithm. The green line presents the difference of the original spectrum (black) and the background (red), which is then referred to as the background corrected spectrum.

rapidly changing positive spectrum and a slowly varying irrelevant background. The spectrum is fitted with a polynomial function of appropriately choser order. Every channel that is bigger than the fit is decreased to the level of the polynomial function and the algorithm starts again. This procedure is repeated until no channel is manipulated any longer.

A further preprocessing step is the normalization of the spectra. The absolute intensity values of the spectra depend on the measurement time, laser intensity, and the scattering properties of the sample. Consequently, it is important to achieve intensity-comparable spectra. There are several normalization techniques available. The first is normalization referring to one band. If all spectra share a common band, it is possible to divide the spectra by the maximum value or the area of this band. This method suffers from the presupposition that one common band is required in all spectra. Another, more general method, the so-called vector normalization, involves normalization by the area of the complete spectrum. For this method, the spectrum is divided by the area of the spectrum, which is calculated as the Euclidean distance of the spectrum to the zero spectrum (2-norm). This procedure has no further prerequisites but is not as selective as the previously mentioned procedure.

Most often the number of spectra is much smaller than or comparable to the number of spectral channels. Therefore, the dimension of the space of the spectra has to be reduced. There are several methods to reduce the dimension of the problem without losing relevant spectral information. The two most common techniques are the independent component analysis (ICA) and the PCA [33, 34]. The latter

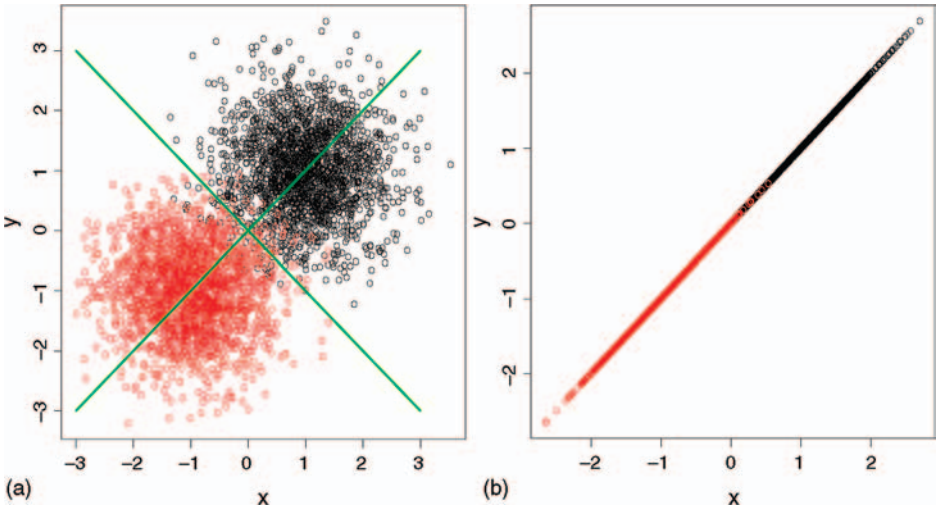

Figure 5.3 Classification of a dataset via PCA: (a) an artificial two-dimensional dataset, where the black and red points represent different classes. The green lines are the axes of the rotated feature space (PCA loadings). (b) the points in (a) projected on the first axis of the new space to achieve a group discrimination based on reduced dimensions of the dataset.

searches for a new orthogonal vector system reconstructing the spectra space. The new coordinates are sorted with falling diversity over the coordinates for the data cloud. High dimensions containing white noise can only be removed without loss of significant spectral information.

An artificial example of a PCA is shown in Figure 5.3, where Figure 5.3a contains the original positions of the elements belonging to the red and the black classes, which are depicted in a two-dimensional space. The green lines represent the new coordinate system in which the two classes are transformed to by the PCA. In Figure 5.3b, the projection of the data points to the first axis of the new space is shown and the dataset is separated into the red and the black groups. A PCA allows classification based on dimensionally reduced data. The ICA works similarly with the difference that no assumption of orthogonality between the new coordinates is required.

The reduction of the dimension has several advantages. First, it decreases the computational power needed, second, it reduces the white noise, and finally, it avoids overfitting. Overfitting is one of the major problems in chemometrics. The learning algorithms of the classifier are very powerful and are capable of learning ever white noise, which increases the accuracy of the classifiers on the training set but decreases the accuracy on unknown data. This problem is called overfitting.

The evaluation of extended datasets containing spectra with high similarities, which cannot be differentiated by the naked eye, is usually accomplished by statistical analysis. One of the most commonly applied statistics is unsupervised HCA [35]. The dataset is analyzed without any *a priori* information. The grouping is based on the

similarities of the spectra – the spectral distances. The spectral distance determines how the similarities of two elements (spectra) are calculated and depends on the applied distance measurements. Two examples are the Euclidian and Pearson correlation coefficient distance measurements. The Euclidian distance measurement refers to the geometric distance, which can corresponds to the area of the difference spectrum. Two different spectra result in a difference spectrum with intense signals and a large area below the curve. Two similar spectra create a difference spectrum with minimal spectral features and a small area below the curve. The Pearson correlation coefficient is the multiplication of two preprocessed spectra. The internal preprocessing includes the subtraction of a spectral mean and the normalization within the spectrum. This preprocessing results in spectra that contain minimized element values. By multiplying those spectral intensities, only values between 1 and −1 can be obtained. Whenever two spectra are very similar, the size of the Pearson coefficient, which is also described as degree of dissimilarities, is close to 1.

After determining the spectral distances, a clustering algorithm follows to depict the results in a tree-like structure called a dendrogram. The *x*-axis of a dendrogram represents the heterogeneity between the spectra and visualizes the spectral distances of all elements from each other by the characteristic of the dendrogram paths. The length of a dendrogram path along the *x*-axis symbolizes the heterogeneity of the connected spectra. The *y*-axis of the dendrogram does not contain any further relevant information apart from the sectioning of the cluster. The most similar spectra within a dataset are connected by short paths along the *x*-axis, which represent low heterogeneity and therefore short spectral distances. Spectra of low heterogeneity are connected via a node and are collected in subclusters. The subclusters are combined in higher level clusters via longer paths along the *x*-axis which represent higher spectral heterogeneity. The intra-cluster heterogeneity is therefore lower than the inter-cluster heterogeneity. The clusters and subclusters contain spectra of certain spectral distances which are determined by a pure mathematical procedure and based on spectral features. That does not necessarily result in classes, which can be compared with the results of microbiological methods such as phenotypic and genotypic identification. Usually the spectral distance does not exhibit "pure" genotypic or phenotypic features; more often a combination of both is expected because the complete microbes with all cell components and metabolites are measured.

The HCA is an attractive analysis method in biological and biomedical applications, since dendrograms, representing phylogenetic trees, are commonly used in "biological-related" sciences. Phylogenetic trees represent the degree of relationship between bacterial strains, species, genera, and other compared classes. The presentation of HCA in the form of a dendrogram offers easily accessible and intuitive comprehension of the results for fast visualization and interpretation. However, besides the advantages of the HCA, an objective application is challenging. The existing risks are outlined in the following after the theoretical background of supervised chemometric methods is presented.

There are numerous supervised classifiers and some of them exhibit very interesting and unique properties. Here only one will be discussed exemplarily. We

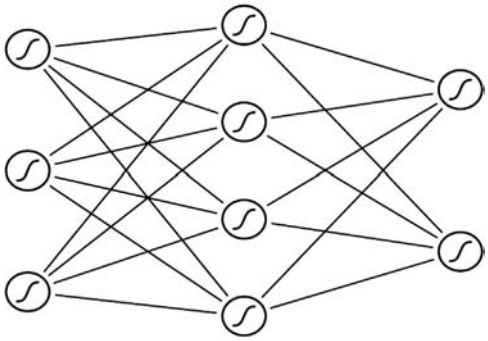

Figure 5.4 Schematic diagram of a feed-forward ANN: the input becomes first mapped to the excitation by the activation function, depicted by the line in the neurons. Subsequently, the excitation becomes mapped weighted by the weights of every connection and the procedure starts again. In this case, it is done twice. The output of the last layer is the output of the whole net.

chose the ANN, because it is one of the strongest classifiers and there are some examples of its application present in the literature [36].

ANNs comprise supervised and unsupervised statistical methods, depending on the used topology of the applied neural network. Most commonly feed-forward neural networks, a supervised technique, are applied. An example is given in Figure 5.4. The ANN is in some aspects modeled after the human brain. ANNs are basically a net of neurons with weighted connections between them. Every neuron contains a function, the so called activation function, which determines. At one step every, neuron collects the excitations of all neurons which are connected to it and sums over the neurons output for a given input weighted with the weights of every connection. The neuron reacts to this weighted sum with excitation or input disexcitation, depending on the activation function. Which activation function is used for in particular depends on the applied net.

For feed-forward nets, several layers exist and every neuron of one layer is connected to every neuron of the next layer. The excitation is propagated forwards layer by layer, giving rise to the net's name. It is obvious that the critical point of the ANNs is the right choice of the connections. Finding the best connections is called training, where several methods exist. The most prominent method for feed-forward nets is the so-called back-propagation algorithm. A systematic introduction to this field of research was given by Rojas and Feldman [36].

To emphasize the different advantages of unsupervised HCA and supervised ANNs, two examples are discussed in the following, focusing on the statistical approach.

Maquelin *et al*. presented results for the identification of pathogenic microorganisms by employing statistical analysis [24]. Figure 5.5a shows Raman spectra of clinically relevant bacterial strains: (a) *Staphylococcus aureus* ATCC 29213, (b) *Staphylococcus aureus* UHR 28624, (c) *Staphylococcus epidermidis* UHR 29489, (d) *Escherichia*

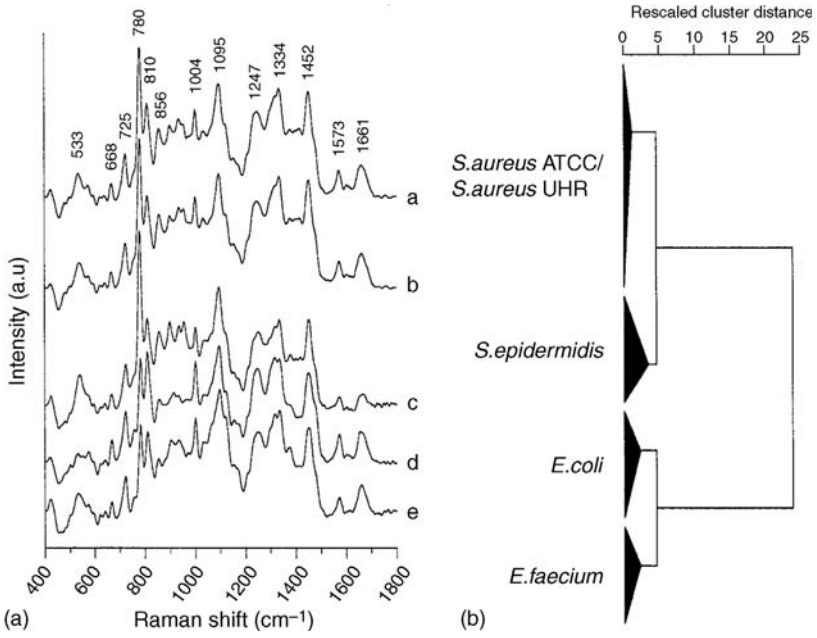

Figure 5.5 (a) Representative micro-Raman spectra of (trace a) *S. aureus* ATCC 29213, (trace b) *S. aureus* UHR 28624, (trace c) *S. epidermidis* UHR 29489, (trace d) *E. coli* ATCC 25922, and (trace e) *E. faecium* BM 4147. (b) Dendrogram as a result of the HCA performed on the principal component scores of the vector-corrected Raman spectra [24].

coli ATCC 25922, and (e) *Enterococcus faecium* BM 4147. The bacterial spectra were measured by micro-Raman spectroscopy directly from the agar plate after a cultivation time of 6 h. The spectra were recorded with an excitation wavelength of 830 nm. The Raman spectra of *Staphylococcus* spp. (Figure 5.5a–c) exhibit an intense band at 780 cm^{-1} assigned to uracil, whereas the representative spectrum of *E. coli* and *E. faecium* (Figure 5.5d and e) feature a more intense Raman signal at 1004 cm^{-1} originating from the phenylalanine vibration. With the application of an HCA, the classification of the spectra was successfully carried out and is depicted as a dendrogram in Figure 5.5b. The dendrogram is divided into two main branches: one cluster contains all *Staphylococcus* species and the other cluster combines the *E. coli* strain and the *E. faecium* strain, which are clearly divided into two clusters on a lower level. Within the *Staphylococcus* cluster, a distinct division between the *Staphylococcus* species *S. aureus* and *S. epidermidis* is obtained, but the two *S. aureus* strains cannot be differentiated and are unified in one subcluster. In the case discussed here, the HCA is capable of differentiating bacterial genera and *Staphylococcus* spp. by means of their Raman spectra, but fails to distinguish between the two *S. aureus* strains.

The phylogenetic interpretation of a dendrogram resulting from statistical analysis is limited. It seems to be certain that the *Staphylococcus* spp., which are combined in

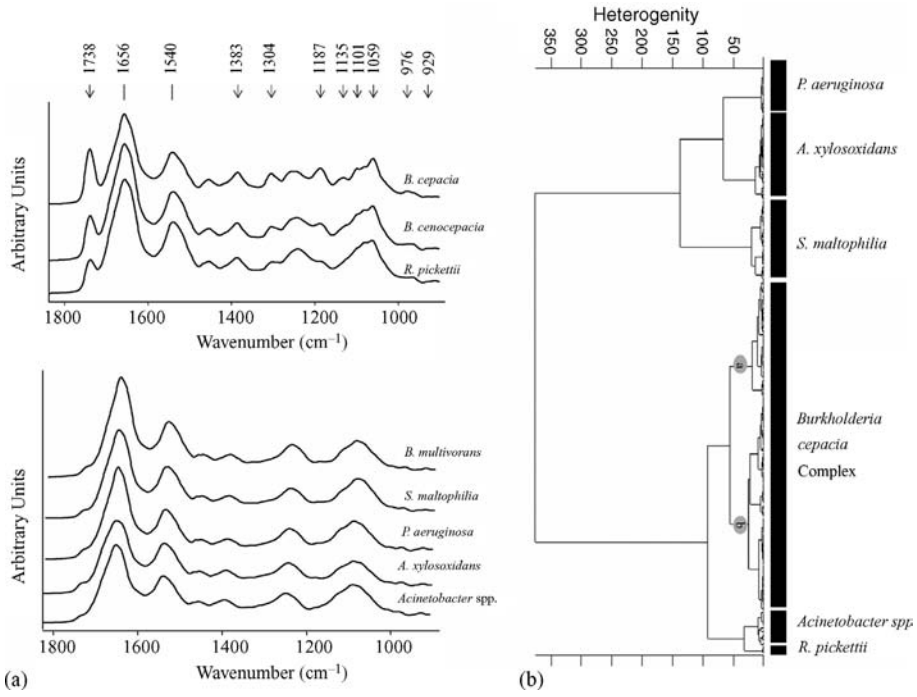

Figure 5.6 (a) IR spectra of the bacterial groups which were isolated from CF patients. (b) Dendrogram of the HCA clustering of the first derivative of the spectra within three spectral windows [38].

one main cluster, are most closely related to each other. It is also reasonable to interpret the dendrogram structure by concluding that the heterogeneity between the two main clusters is higher compared to each intra-cluster heterogeneity. However, it cannot be argued that *S. epidermidis* is genetically more similar to the closer neighbor *E. coli* than to *E. faecium* from the dendrogram, since the clusters can be reflected at their nodes, resulting in opposite relations.

Providing the phenotypic variance or heterogeneity of the culture condition is one of the challenges for the application of statistics such as HCA. Willemse-Erix *et al.* applied hierarchical cluster analysis to a Raman dataset of 785 nm excitation to differentiate between five isolates of *S. aureus* [37]. To ensure that the classification of the five isolates is based on strain specificities and not on differing growth behavior, the influence of growth was included by sampling at 18, 20, 22, and 24 h after incubation. Again, the application of the HCA is suitable to a certain extent, since two isolates could not be separated from each other.

The second example is a study by Bosch *et al.* to differentiate bacterial groups isolated from cystic fibrosis (CF) patients: *Pseudomonas aeruginosa*, *Ralstonia pickettii*, *Achromobacter xylosoxidans*, *Actinobacter* spp., *Stenotrophomonas maltophilia*, and

Burkholderia cepacia complex (BCC) by means of IR spectroscopy in combination with statistical analysis [38]. At first the sample preparation was carefully standardized and the HCA and ANN methods were applied. Figure 5.6 shows (a) the IR spectra and (b) the dendrogram resulting from the HCA. The dendrogram shows clearly six defined groups representing the six bacterial genera. However, a clear distinction of the different BCC strains could not be achieved, but a separation into two groups appeared. One subcluster contained the reference strains, whereas the second subcluster combined the clinical isolates. Although several approaches were implemented to investigate the BCC bacteria, all resulted in division of the clinical and reference isolates. The HCA model discriminated successfully between the six groups (*P. aeruginosa*, *R. pickettii*, *A. xylosoxidans*, *Actinobacter* spp., *S. maltophilia*, and BCC bacteria) but failed to differentiate between the BCC species. The presented misidentifications are considered to be caused by the insufficient phenotypic variance presented by the measured strains within the bacterial species.

The spectral data were also subjected to a two-level ANN model. Both ANN levels were independent and had different tasks that demanded individual preprocessing steps and net characteristics. The first level was applied to identify whether the spectrum originated from one of the six Gram-negative groups. The second level was switched on whenever the bacterium was identified as belonging to the BCC group to continue the identification on the species level. The complete dataset contained around 2000 spectra comprising clinical isolates and reference strains. The results of the ANN model were verified twice, by internal and external validation. For this, the complete dataset was divided into a training dataset and a test dataset. The model was exclusively trained by the training dataset and the internal validation was performed by removing spectra randomly and testing for correct identification, which resulted in 100% correct identification. The external validation was carried out by a completely independent training dataset containing spectra of clinical isolates. The combined ANN model was able to classify correctly 98.1% at the genus level and 93.8% at the BCC species level. Hence the ANN was able to differentiate on BCC species level, which could not be accomplished by the unsupervised HCA method described earlier.

5.4 Monitoring of Biofilms

The self-organization of various microorganisms in biofilms leads, especially in the field of healthcare, to serious problems. The potential of such well-organized organisms to cause infections in patients with indwelling medical devices increases in proportion to their resistance to antimicrobial agents. The process of biofilm formation takes place on either living surfaces such as tooth enamel, heart valves, the lung, and middle ear, or on inanimate surfaces such as catheters, any kind of artificial prosthesis, and intrauterine devices. Biofilm-associated microorganisms commonly isolated from selected indwelling medical devices are, for example, *Candida albicans*, *S. aureus*, *P. aeruginosa* and *E. coli* [39]. This section introduces the examination of

biofilm models by different vibrational spectroscopic techniques, which offer a beneficial approach in medical microbiology.

The multifarious aggregations of different groups of attached microbes with their excretory products have different phenotypes and antibiotic susceptibility compared with their planktonic (suspended) organisms [40]. The nondestructive (i.e., leaving the sample intact during the analysis) and direct analysis of such a multilateral matrix is essential to understand the role of biofilms in infections. Fingerprint spectra display the chemical composition of cells and allow the rapid characterization of microbial strains. The application of vibrational spectroscopic techniques is suitable for fundamental biofilm research and also for the monitoring of biofilm formation [41]. Of these techniques, IR and Raman spectroscopy are complementary concerning spectral information [9].

Investigation of biofilms that develop directly on IR-transparent materials is possible in the transmission mode. Nevertheless, this sample preparation is difficult to standardize and to integrate into a routine protocol. It also limits the possibility of analyzing intact larger samples and the utilization of thick or opaque surfaces. Recent advances in detector sensitivity allow the use of reflectance micro-FTIR spectroscopy for the analysis of raw materials without the need for previous treatment. The penetration depth of the IR beam ranges from 2 to 5 μm. Ojeda *et al.* showed that the reflectance mode is a suitable technique for studying the functional groups in biofilms in opaque or thick samples, such as stainless steel, without sample preparation [42]. The characterization of the biofilm formation of *Aquabacterium commune* was carried out by applying reflectance micro-FTIR spectroscopy. Sterile stainless-steel slides were left on the culture medium with *A. commune* to be colonized at pH 7 for 100 h. Figure 5.7 shows an optical image of stainless steel and an *A. commune* biofilm. The false color images (b–f) of the scanned sample depict the location of different molecules. Thus, the reflectance micro-FTIR analysis showed reliable results for the location of different functional groups in *A. commune* biofilms on stainless steel. According to "free" (not attached) bacteria from planktonic suspension, the carboxylate and phosphoryl groups in the biofilm could play an important role in the adhesion to stainless steel [42].

Attenuated total reflection (ATR) offers a further possibility for FTIR techniques for the observation of biofilms formed directly on the surface of an ATR crystal. Investigations can be carried out without sample preparation and spectra can be obtained nondestructively, *in situ*, and in real time. The ATR crystal is the so-called internal reflection element (IRE). It has a higher refractive index than the sample or the surrounding medium. The beam penetrates through the interface into the sample, which is adjacent to the crystal surface. If the sample absorbs part of the radiation, the reflection will be attenuated. The penetration depth of the light depends on the wavelength of the light, the incident angle, and the refractive indices of the sample and crystal [43]. Immersion of the IRE in a liquid allows the observation of the subsequent colonization of the surface by bacteria and other microorganisms. With this setup, biofilm studies can be carried out in a flow-through cell, where a biofilm grows directly on the crystal surface. Observation of biofilm formation over many days can thus be performed with such an experiment by recording absorption

spectra, which depend on the chemical nature of the cells attached to the crystal surface, which was explored by Delille *et al.* [43]. Here *Pseudomonas fluorescens* bacteria were pumped as a suspension in Luria–Bertani (LB) medium through the cell and the appropriate biofilm was formed on a germanium crystal. Figure 5.8 illustrates the accumulation of biomass on the IRE surface depicted by the acquired spectra over this period and the microscope image shows an increase in the IRE surface coverage by bacteria. After the initial bacterial attachment and biofilm detachment, the authors observed regrowth kinetics depending on the dissolved organic carbon level determined from changes in the areas of bands associated with proteins and polysaccharides [43].

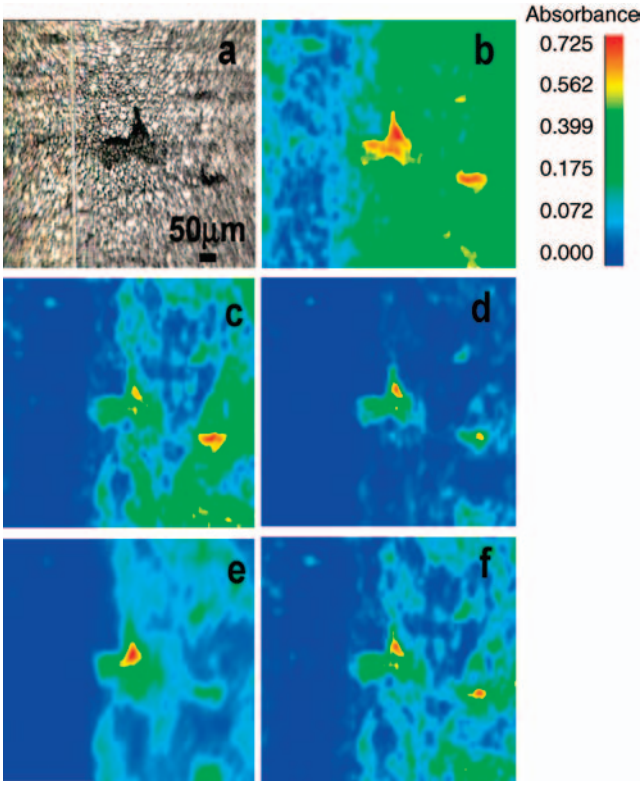

Figure 5.7 (a) Optical image of stainless steel and *Aquabacterium commune* biofilm. (b) Full-range false color image (4000–700 cm^{-1}). (c) Location of molecules with intrinsic absorption bands of amides (N—H stretching at 3550–3200, amide I at 1690, and amide II at 1540 cm^{-1}). (d) Location of molecules with absorption bands intrinsic of C—H, C=O, and C—O. (e) Location of molecules with absorption bands intrinsic of phosphorylated proteins, polyphosphates, and phosphodiester groups (1270–1220, 1100–1070, 1000–950 cm^{-1}). (f) Location of molecules with absorption bands intrinsic of hydroxyl groups (3600–3200 cm^{-1}) [42].

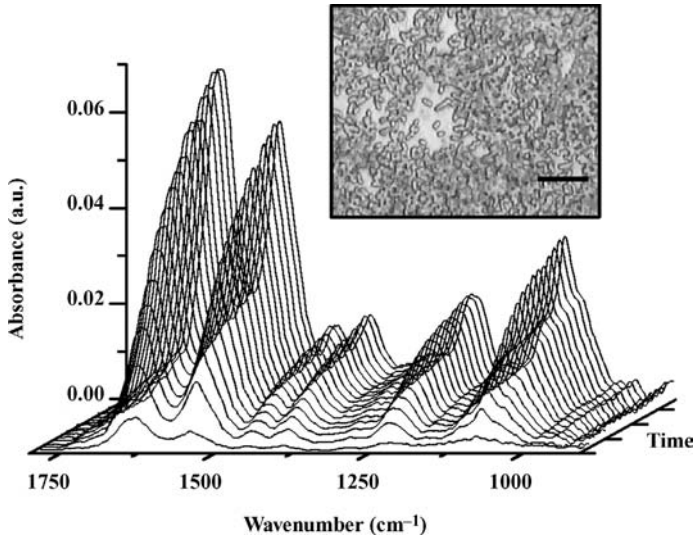

Figure 5.8 Temporal evolution of ATR–FTIR spectra during initial attachment of *P. fluorescens* to the germanium IR [43].

In fact, various groups were able to investigate the development of biofilms by means of IR absorption spectroscopy correlated with the corresponding changes in carbohydrate and protein expression or changes in persistence [42, 43]. This analytic approach could also be used to address the role of individual virulence factors, resistance against antimicrobial agents, and shear stress in the development and adhesion of pathogens grown on surfaces.

Complementary to IR absorption, a Raman "fingerprint" of the sample can be measured. This facilitates an additional analysis of hydrated and living bacterial biofilms under *in vitro* conditions. Therefore, Raman spectroscopy proved to be a suitable technique to investigate the effects of various additives and environmental factors on biofilm growth. The excitation with visible light (e.g., 532 nm) allows the use of common standard optics. Under these conditions, the sample can be visualized by a bright field image and spectra can be processed at different locations within the biofilm. Additionally, it is possible to record vertical and horizontal maps to show the spatial distribution of molecular or cellular species. The nondestructive character of Raman spectroscopy permits the observation of biofilm development and its spatial heterogeneities over a period of time. Raman spectra are furthermore considered to be more specific than IR spectra as they generate sharper bands. The spatial distribution of the biofilm biomass, for example, was analyzed by means of micro-Raman spectroscopy. The chemical mapping was successfully employed to probe directly the water and the biomass distribution within biofilms after only minimal sample treatment. The authors suggested that with this method, the penetration of solutes in biofilms can be determined [44, 45].

The composition of different microorganisms and other substances (minerals) inside an intact multispecies biofilm was characterized by Pätzold *et al.* [46]. The analyses were based on the identification of specific bands in correlation with reference materials. Ivleva *et al.* demonstrated that Raman spectroscopy can correlate various structural appearances within the biofilm to variations of its chemical composition and provide detailed chemical information about the different constituents in this complex matrix [47].

Biofilm analysis by means of SERS is characterized by a higher number of distinguishable peaks in the spectra, suggesting a promising potential of SERS to probe components of the biofilm matrix even at low concentrations. Ivleva *et al.* reported on reproducible *in situ* SERS analysis of biofilm. A heterotrophic biofilm was cultivated on a glass slide and immersed in a silver colloid suspension. SERS spectra from different constituents of multispecies biofilm were recorded [48].

The application of TERS to alginates for analyzing nanostructures in biofilm was reported by Schmid *et al.* [49]. A problem with the interpretation of TERS spectra are contaminated tips since they have a significant influence on the spectrum in contrast to weak analyte signals. An appropriate background subtraction and a careful selection of reference materials are indispensable.

5.5
Role of Vibrational Spectroscopy in Epidemiological Studies

In this section, an overview is given of recent developments in optical typing methods, namely IR and Raman spectroscopy. Here, vibrational spectroscopic methods are successfully applied as identification modalities in clinical environments. This outline mainly comprises investigations on clinical isolates of medically relevant microorganisms to validate the discriminatory power of the spectroscopic approaches and further to perform epidemiological analysis.

While micro-Raman spectroscopic identification at the single cell level allows direct presumptive analysis of isolates, in most of the publications cited here the investigated strains were precultured prior to the actual measurement. Thus, not only enough biomass is generated to perform measurements on bulk material and micro-colonies, but also possible background interferences due to the matrices, from which the microorganisms were isolated, are minimized. Although the mandatory culturing steps contradict the time efficiency of the spectroscopic methods to a certain extent, the achievable gain in time is still significant compared to the most preferred genotyping techniques up to now. In fact, in the case of epidemiological surveillance of microorganisms, pulsed field gel electrophoresis (PFGE) and multi-locus sequence typing (MLST) are mostly applied in retrospective analysis of outbreak situations due to their long turnaround times (48–72 h when starting from a pure culture) and low sample throughput.

Vibrational spectroscopy meets the requirements for a high-throughput, fast, and reliable typing method to provide real-time monitoring of the spread of bacterial

isolates, as demonstrated in several publications. The common strategy in those studies was to classify and consequently identify medically relevant microorganisms originating from clinical isolates by means of vibrational spectroscopic measurements combined with chemometric analyses. The identification results were accomplished by comparing them with typing results obtained via common established daily routine techniques, including DNA sequencing or PFGE [50].

For example, Willemse-Erix *et al.* [37] employed a custom-built Raman setup with 785 nm laser excitation to validate spectroscopic typing using the methicillin-sensitive *Staphylococcus aureus* (MSSA) and methicillin-resistant *Staphylococcus aureus* (MRSA) isolates of four different collections (118 isolates). MRSA is known to be a leading cause of hospital-acquired infections and therefore a candidate for rapid epidemiological surveillance in clinics. The reproducibility of Raman spectroscopy was tested and also its discriminatory power in comparison with established typing techniques, such as PFGE and *spa* typing. Furthermore, the concordance of the Raman spectroscopic results with epidemiological data was checked. Thus, 20 well-characterized HRSA isolates were classified by performing an HCA on their Raman spectra. Isolates with different PFGE patterns were distinguished by using Raman spectroscopy, whereas PFGE-identical isolates were not. In another retrospective study, a collection of 78 MRSA isolates, retrieved from patients and hospital staff members collected in a Dutch hospital during five outbreaks in 2002, were evaluated by two PFGE analyses and Raman spectroscopy. Raman spectroscopy differentiated 72 out of 78 isolates with an accuracy of 92–95% identical with the two PFGE results and identified the majority of unique PFGE isolates as unique Raman types. In total, only three discrepancies were documented between the three typing methods – the HCA clustering of the Raman spectra thus attained good agreement with the epidemiological data [37]. In the same study, Willemse-Erix *et al.* collected four MRSA isolates (one from an index patient and three from a colonized staff member) during a contact screening at a Dutch hospital [37]. Based on the Raman spectroscopic data, it was possible to confirm within 1 day that no transmission between the index patient and the staff member occurred. Four days later, PFGE results reaffirmed these results. This significant gain of time is based upon the protocol employed: starting from positive microbial cultures, only 45 min are needed to prepare 24 isolates for Raman measurement, which usually takes 10 s–1 min per sample or 1 s per spectrum. This rapidity of signal collection is a crucial requirement for preliminary real-time identification of clinical isolates and is achieved due to constant improvement of the Raman equipment, which entails both simplification and improved sensitivity and robustness of the spectrometer combined with a powerful laser (220 mW with 785 nm excitation).

One drawback of non-resonant Raman spectroscopy is the low probability of Raman scattering, with typically only 1 in 10^6 photons Raman scattered, which leads to rather long Raman spectra collection times. An alternative to the classical non-resonant Raman scattering is UVRR scattering, which was described earlier.

An application of this resonant Raman technique in the field of identifying pathogenic organisms is in the discrimination of urinary tract infection (UTI) bacteria [21]. The typical causal agents of UTI are Enterobacteriaceae, especially

E. coli and *Klebsiella* spp. in addition to Gram-positive enterococci [51]. Twenty well-characterized and identified clinical bacterial isolates from patients with UTI from a hospital were obtained belonging to *E. coli*, *Klebsiella oxytoca*, *Klebsiella pneumoniae*, *Enterococcus* spp., and *Proteus mirabilis*. All isolates were cultured for 12 h and were analyzed by means of UVRR spectroscopy with 0.1 mW laser power on the sample and a 120 s integration time for a single spectrum of the bacterial bulk material. This rather long accumulation time despite the aforementioned enhancement mechanism is due to the photochemical destruction or "burning effects" in the sampled microorganisms because of the high energetic nature of UV photons. The applicable laser power on the samples and thus the minimal integration time are therefore limited for the sake of the spectral quality.

The measured and preprocessed resonance Raman spectra of the UTI bacteria were analyzed chemometrically with respect to similarities among them with numerous clustering algorithms. Each of the four classes/genera analyzed was correctly resolved into four separate groups, which leads to the assumption that discrimination between these main causal agents of UCI was achieved. However, because only four *a priori* groups were fed into the cluster algorithms, the resolution at strain level was still low.

Research has also been carried out recently on the spectroscopic identification of nonfermenting Gram-negative rods isolated from sputum samples of cystic fibrosis (CF) patients. Although the major causes of the morbidity and mortality in patients with CF are chronic lung infections caused by *P. aeruginosa*, *S. aureus*, and *Haemophilus influenzae*, an increased fraction of CF patients has been colonized by other bacilli, such as members of the Burkholderia cepacia complex (BCC) [52]. Because of their high transmissibility and multiple antibiotic resistances, BCC infections are difficult to treat once a patient has become infected. Currently, the BCC comprises a group of genetically distinct but phenotypically similar bacteria and contains 17 recognized species. Despite the importance of the rapid and accurate identification of this group, only a few studies using vibrational spectroscopy have been published.

In 2008, Bosch *et al.* employed FTIR spectroscopy to identify bacteria isolated from sputum samples of CF patients [38], including *P. aeruginosa*, *R. pickettii*, *A. xylosoxidans*, *Actinobacter* spp., *S. maltophilia* and BCC bacteria in combination with HCA and ANNs. From 150 CF patients attending three different hospitals in Argentina, 169 clinical isolates of nonfermenting Gram-negative bacteria were studied in combination with 15 reference strains. The clinical isolates were characterized according to guidelines for clinical microbiology practices for respiratory tract specimens from CF patients. In particular, BCC bacteria were further identified by *recA*-based PCR followed by restricted fragment length polymorphism (RFLP), and 165 rRNA gene sequencing was performed on some bacterial species belonging to genera different from BCC. FTIR spectra have been acquired of all strains to establish a database containing 2000 IR spectra, which were fed into the statistical algorithms. Bosch *et al.* [38] managed to discriminate successfully between the six groups with the help of an HCA model. However, differentiation within the BCC was not accomplished [38]. The two-level ANN model proved to be superior to the HCA in this

respect, since a differentiation at the BCC species level was eventually achieved with a classification rate of 93.8%.

However, not only chemical modifications of the bacteria due to cultivation, sampling, and measurement parameters can be a limiting factor for some of the spectroscopic typing methods, which probe the complete biochemical makeup of the microorganisms: chemical modifications resulting from adaptation strategies to the CF lung stress environment, for example, aggressive and prolonged antibiotic therapy, can also affect the discriminatory power. The influence of the phenotypic variability of BCC isolates, for example caused by CF therapeutic procedures, on IR spectroscopy-based models for species and ribopattern discrimination was studied by Coutinho *et al.* [53]. A collection of 185 BCC isolates, representing four different BCC species, from respiratory secretions of 35 patients with CF from a Portuguese hospital, gathered from January 1995 to March 2006, was analyzed. All were previously classified by established molecular methods at species and ribopattern levels. On the basis of discriminant partial least-squares (DPLS) calculations performed on the FTIR absorption spectra, misclassification error rates at the ribopattern level of 2–8% and at the species level of 10% for the hospital isolates and 32% for the reference strains were achieved. This result indicates that the model calibrated with the hospital strains cannot be used to predict the reference strains. Whereas the latter originated from different sources, the isolates obtained in the hospital were sequential isolates from a limited number of different patients, several of them exhibiting the same ribopattern. This demonstrates the restricted generalization ability of a model calibrated with only a limited number of samples. Also, an important degree of variability for isolates belonging to the same species, same ribopattern, and collected from the same patient during prolonged colonization was registered. This may, on the other hand, indicate the possibility of revealing changes in the biochemical composition of the microorganisms due to adaptation strategies to the CF lung stressing environment by means of FTIR spectroscopy.

Another widespread cause of hospital-acquired sepsis is *Candida* spp. This serious noscomial pathogen strikes preferentially in surgical services, and especially in non-neutropenic critically ill patients in intensive care units (ICUs). *Candida*-associated infections exhibit high mortality rates of up to 46–75% and they represent the fourth most commonly recovered organisms from blood cultures [54]. Hence early and systematic antifungal therapy has a tremendously positive effect on the outcome of patients with invasive candidiasis in respect of morbidity and (attributable) mortality. Fluconazole followed by amphotericin B is often the first choice for prophylactic or empirical antifungal therapy. Unfortunately, there exist a number of fluconazole-resistant non-*albicans Candida* spp. and also the fluconazole-resistant *Candida albicans*. A prompt identification of significant isolates to the species, or even strain level, is therefore imperative to be able to decide which initial regimen for prompt antifungal therapy is appropriate, since susceptibility data for isolates may not be available immediately. However, at present the conventional yeast identification is based on an extensive series of biochemical assays, following an obligatory culture period sufficient to obtain a biomass of 10^6–10^8 cells and thus leading to up to 4 days

before a definitive report reaches the clinician. Vibrational spectroscopy might render assistance in this context: a clinical study was reported by Ibelings *et al.*, where Raman spectra of microcolonies 10–100 μm in diameter were obtained after only a 6 h incubation period [55]. Upon arrival in the microbiology laboratory, each specimen was divided into two groups, with one part used for conventional microbiological identification (via a commercially available yeast identification panel with a turnaround time of 48–96 h), and the other for identification by Raman microspectroscopy (within 1 day). A collection of 93 reference *Candida* strains, comprising 10 different *Candida* spp., backed up the Raman spectroscopy-based identification of 88 pertioneal specimens obtained from peritonitis patients from a surgical ICU and a general surgical ward. Spectra obtained from patient specimens were analyzed with a sequential identification model based on six linear discriminant models (LDAs). In three of the 29 *Candida*-positive cases, a difference between the microbiological and Raman identifications occurred, giving a prediction accuracy of 90% by Raman spectroscopy, if the conventional microbiological method is interpreted as the reference method. In a similar study by Maquelin *et al.*, an accuracy of even 97–100% for the Raman identification of *Candida* spp. was obtained with the same method but including 42 reference strains [56].

Similar approaches concerning epidemiological investigations of *Candida* have also been performed with FTIR spectroscopy. Essendoubi *et al*. studied 29 *Candida glabrata* isolates from patients within a two-step procedure [57], as described in the following. First, an internal validation phase with 16 strains was carried out to determine the statistical parameters which result in the highest discriminatory power. A genotypic technique based on randomly amplified polymorphic DNA analysis (RAPD) confirmed the outcomes of this validation step. Second, the 13 remaining clinical strains of *C. glabrata*, isolated from multiple sites in four ICU patients, were tested by FTIR and HCA in order to eliminate the possibility of inter-human infection by comparing the spectral signatures of all patient strains. In the end, six spectral groups (four from the patients and two from reference strains) led to the conclusion that no cross-infection had occurred. Again, the saving of time compared with conventional approaches is striking, since the FTIR spectra were recorded after only 24 h of cultivation of the isolates. Also, a decrease in growth time to 10–18 h seems within reach to gain enough microcolonies for FTIR microspectroscopy.

Recent studies regarding spectroscopic species identification in a clinical diagnostic setting were also focused on cultured mycobacteria. The genus *Mycobacterium* comprises more than 80 species, some of which are potentially pathogenic to humans and animals. Whereas the classically defined lung tuberculosis is predominantly caused by *M. tuberculosis* complex (TB), an increasing number of incidents of pulmonary disease are caused by nontuberculous *Mycobacteria* (NTM) [58, 59]. The clinical features of the NTM-derived disease are in some cases indistinguishable from those of tuberculosis. To stipulate an appropriate therapy and to offer comprehensive infection control, a timely and correct discrimination between TB and NTM and also an identification of causative NTM at the species and strain levels is

mandatory. A large number of commercial techniques are available for a limited number of frequently encountered species, which are rapid but expensive. For rarely emerging *Mycobacterium* isolates, DNA sequencing of the 16S rRNA gene is usually performed in reference laboratories. However, the implementation of these techniques in peripheral laboratories has various drawbacks, such as high cost, complexity, and the absence of clear, unambiguous interpretations and peer-reviewed databases. The spectroscopic data for TB and NTM isolates suggest so far that vibrational spectroscopy may provide a practical solution to identify unknown isolates rapidly in routine clinical–microbiological laboratories.

Buijtels *et al*. presented the first study on the use of Raman spectroscopy for the identification of *M*. *tuberculosis* and the most frequently encountered NTM species with the objective of assessing the reproducibility of the Raman spectra of inactivated *Mycobacteria* versus viable *Mycobacteria* and to compare the performance of this method with that of 16S rRNA sequencing [60]. The pilot inactivation study in Buijtels *et al.*'s publication on 12 level two NTM species revealed that heat inactivation is superior to formalin inactivation. Raman spectra of heat-inactivated samples showed the highest resemblance to those of viable cells. Heat inactivation did not decrease either the classification rate or the intra-species reproducibility substantially. In a subsequent identification study, a collection of 63 *Mycobacterium* strains, comprising eight different *Mycobacterium* species, was identified species-wise first with 16S rRNA sequencing before the Raman measurements were performed. The main differences in the Raman spectra of the eight *Mycobacterium* species were found in the intensity of peaks due to carotenoid vibrations. The similarity between the Raman spectra of the samples was calculated using a squared Pearson correlation coefficient (R^2). Species identification was performed via a leave-one-out approach, by which the R^2 value of one sample relative to all the other measured samples was calculated. The predicted species of a sample was assumed to be identical with the species of the sample with which the highest correlation occurred. This leave-one-out approach simulated the situation in a diagnostic setting where a new measurement is compared with an existing database.

In this study, the classification results of Raman spectroscopy versus 16S rRNA sequencing predicted 60 of 63 strains correctly at the species level, which represents an overall classification rate of 95.2%. These outcomes were achieved within 3 h after a positive signal from the automated culture system. For all strains, the differentiation between *M*. *tuberculosis* and NTM was correct. Since the model in this work was based on only a limited number of species, future research is suggested in order to extend the spectral database with more spectra of other TB and NMT strains with a larger number of isolates per species.

A promising approach to achieve cultivation-independent measurements is the analysis of single bacterial cells directly after their isolation from a patient's sample. Simple and fast enrichment and purification steps remain obligatory, but a prolonged preanalytical cultivation to gain sufficient biomass becomes obsolete, when techniques such as micro-Raman spectroscopy need hundreds of intact bacterial cells only,

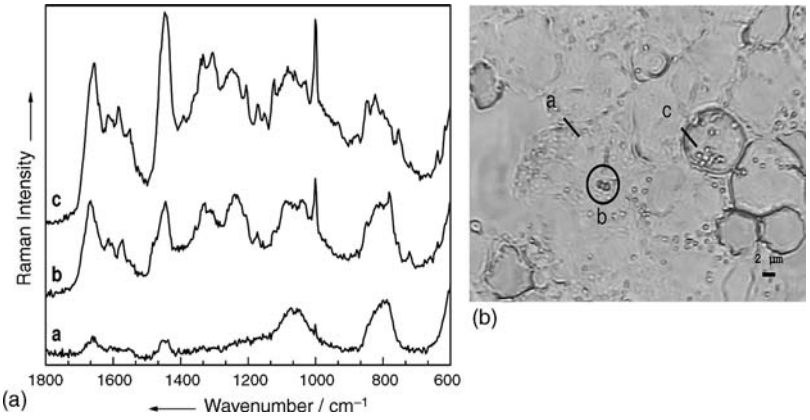

Figure 5.9 (a) Raman spectra of meningococcal patient's sample sedimented via cytocentrifugation: (trace a) background, (trace b) bacteria, and (trace c) leukocyte. (b) Microscopic image of a meningococcal patients sample: (a) background, (b) bacteria, and (c) leukocyte [61].

instead of billions in the case of measurements on bulk samples and microcolonies, as is the case in, for example, FTIR microspectroscopy.

Harz *et al.* proved in a pilot study the capability of micro-Raman spectroscopy to classify bacterial contaminants directly in the cerebrospinal fluid (CSF) of a meningococcal patient [61]. The sample was obtained from a patient with bacterial meningitis caused by *Neisseria meningitides*, who was already being treated with antibiotics. The preparation consisted simply of sedimentation of the cellular components onto fused silica slides by cytocentrifugation followed by a hot-air fixation (10 min at 110 °C) to inactivate the pathogens.

Direct targeting of individual cells, which were localized in the microscope's brightfield image as shown in Figure 5.9, was ensured due to the micro-Raman setup, which provided a focused laser beam approximately 0.8 μm in diameter. Thus, only an individual bacterial cell was probed and delivered a Raman spectrum after 30–60 s, as shown exemplarily in spectrum b in Figure 5.9. The Raman spectra a and c originated from the CSF matrix and a neighboring leukocyte, respectively. It is obvious that, except for contributions of the fused-silica substrate, the CSF did not give any strong Raman signals, which could have a serious impact on the bacterial Raman spectra. The intense Raman spectrum of the leukocyte (c) posed no problem since by targeting only the single bacterial cell any spectral disturbance of the blood cell could be avoided.

The measured spectra from the patient's sample were compared via hierarchical cluster analysis with spectra obtained from bacteria that had been cultivated *in vitro*. Among them are typical causative agents of bacterial meningitis such as *Neisseria meningitis*, *Streptococcus pneumoniae*, and *Listeria monocytogenes*. All of the patient's sample bacteria spectra were correctly placed in the *N. meningitis* cluster; the overall

classification rate at the species level was 95.7% (121/127 spectra). It could be shown that the CSF matrix did not mask the signals of bacterial cells. Furthermore, other cellular components such as leukocytes also did not seriously hamper the detection of individual meningococci cells. In cases with lower cell numbers, where the localization time might increase to impractical dimensions, direct fluorescence staining of the bacteria can be advantageous, requiring an appropriate dye [62]. With a fluorescence detection modality it is then possible to find stained bacteria selectively.

Overall, it can justifiably be concluded that vibrational spectroscopy is suitable for real-time application in medical microbiology. In short, clinicians can benefit from spectroscopy based typing methods because of several advantages: Recording vibrational spectra does not require qualified specialists, the number of essential or expensive chemicals is limited, and, above all, microbial fingerprints are generated at tremendously high speed while still allowing a good discriminatory power. An appropriately equipped medical diagnostic laboratory therefore has the means to identify microbial cultures rapidly, preferably on the same day that an initial culture is obtained from patient material. Additionally, as the spectroscopic methods rely on the identification of variable biological and biochemical features of bacterial strains and thus are phenotypic methods, they supplement perfectly molecular methods, such as sequence-based identification schemes, for example, pulsed-field gel electrophoresis (PFGE) and multilocus sequence typing (MLST), which are mostly applied in retrospective analyses of outbreak situations due to their long turnaround times (48–72 h when starting from a pure culture) and low sample throughput [24, 63].

5.6
Effect of Antibiotics on Microorganisms

During the last two decades, the number of newly discovered antimicrobial agents has decreased drastically with a concomitant increase in multidrug-resistant pathogens. This alarming development is partially due to the prescription frequency of antibiotics and the use of a broad spectrum of antibacterial agents. The only solution for the increasing bacterial resistance is to continuously develop new drugs. However, the development of new antibiotics is affected by the lack of detailed information about the modes of action of various antibacterial agents [64].

To establish a detailed understanding of bacterial metabolism and the effectiveness of various antibacterial agents, noninvasive, highly sensitive techniques are required. In recent years, different vibrational spectroscopic methods have been applied to characterize the interaction between various bacteria and drugs. The vibrational spectroscopic approaches were applied to unravel the mode of action of the antibiotics.

For example, the investigation of the effects of β-lactam antibiotics on microorganisms can be performed successfully by means of the SERS technique [65]. β-Lactam substances inhibit the biosynthesis of the cell wall. The SERS enhancement

originates from the strong optical intensity localized within 10 nm from the surface of metallic nanostructures. Hence SERS is particularly suitable for investigating the interactions of the antibiotics with the microbial cell wall. For example, oxacillin, a β-lactam agent, was found to affect the cell wall of the Gram-positive (*S. aureus*) and Gram-negative (*E. coli*) bacteria differently due to the diverse cell wall composition. The concentration of oxacillin used in the experiment was five times the minimal inhibitory concentration (20 mg l^{-1}). After the initial SERS perturbation of oxacillin, the Gram-positive *S. aureus* bacteria exhibited a transitory SERS recovery. The compensation of synthesis inhibition by the thick peptidoglycan layer is discussed as a possible explanation. Gram-negative bacteria do not possess any reserve of peptidoglycan and their response to oxacillin was found to be irreversible. The time required by β-lactam agents to affect the cell wall integrity was found to be ∼1 h. The changes in the SERS spectra of the investigated microorganisms were related to the destruction of the cell wall. SERS spectra of the Gram-positive *S. aureus* treated with antibiotics that inhibit protein synthesis, for example, gentamicin and tetracycline, exhibited changes after relatively long treatment times of about 9–12 h. This is due to the maintenance of the cell wall integrity during the inhibition of the protein synthesis [65].

Huleihel *et al.* investigated the effect of the commonly applied β-lactam antibiotic ampicillin (100 μg l^{-1}) on Gram-negative bacteria (*E. coli*, *Serratia marcescens*, *P. aeruginosa*, *H. influenza*, and *Salmonella enteridis*) and also on Gram-positive bacteria (*S. aureus*, *Staphylococcus olysgalacticae*, *Staphylococcus mitis*, *Bacillus subtilis*, *Bacillus cereus*, *Bacillus megaterium*, and *Bacillus thuringiensis*) by means of FTIR spectroscopy [66]. In contrast to SERS, which provides chemical information only about the bacterial cell wall, FTIR spectroscopy gives information about all the bacteria cell components. In contrast to the previously presented study, no spectral changes were detected 2 h after the antibiotic (β-lactam) treatment of a bacterial culture. This outcome was attributed by the authors to the relatively low sensitivity to cell wall composition of the FTIR technique compared with SERS. Moreover, no differences in the spectral response between Gram-positive and Gram-negative bacteria treated with antibiotics were observed on applying FTIR spectroscopy.

Huleihel *et al.* also compared the impact of ampicillin on the effect of caffeic acid phenylethyl ester (CAPE) on bacteria [66]. CAPE is a protein synthesis inhibitor and therefore changes of the relative proteins to nucleic acids ratios within the cells were expected. Significant spectral changes were observed 2 h after treatment. Interestingly, Gram-positive and Gram-negative bacteria presented distinctive changes in the biochemical composition. Considerable increases in band areas assigned to proteins and sugars were detected for Gram-positive bacteria, concomitant with major reductions in band areas arising from nucleic acid vibrations. These alterations were considered to be due to the reduced activity of the treated microorganisms, thereby causing an accumulation of carbohydrates in the cells. The increase in the protein level was reasoned to result from an overexpression of other bacterial genes. The IR spectra of Gram-negative bacteria showed an increase in the relative sugar to

protein content. The reported results suggest that FTIR spectroscopy can be used as an effective tool to evaluate rapidly the efficiency of the antibacterial effect of various protein synthesis inhibitors.

In contrast, investigations focused on fluoroquinolones targeting the bacterial enzyme gyrase were mainly performed by means of UVRR spectroscopy [67–70]. This technique was preferred due to the abundant information supplied regarding the DNA/RNA and aromatic amino acids within the investigated microorganisms. Gyrase catalyzes the introduction of negative coils into the DNA structure. Thus, the DNA transcription and replication is blocked by binding the fluoroquinolones to the gyrase–DNA complex. UVRR spectroscopy is applied to study minor modifications of the nucleic acid and protein contents within bacteria. The effect of ciprofloxacin (0.9 and 5 $\mu g\,ml^{-1}$) as a representative of the fluorquinolones on *Bacillus pumilus* was investigated by Neugebauer *et al.* by means of UVRR spectroscopy in combination with statistical methods (PCA and HCA) [67, 69]. By increasing the concentration of ciprofloxacin, notable changes in the band intensity of nucleic acids and proteins were detected. The main changes in the spectra were assigned to nucleic acids, especially guanine and adenine, to proteins represented by tyrosine and tryptophan, and to a CC-stretching vibration assigned to the drug ciprofloxacin itself. For more precise assignment of the detected changes, the Raman spectrum of a relaxed plasmid was compared with that of a superhelical plasmid and also with a spectrum recorded from a mixture of a relaxed plasmid with a subunit of gyrase. The outcome suggests that the Raman spectra of the bacterial cells contain valuable information about the DNA topology and the impact of antibiotics on the DNA structure can be detected by means of UVRR spectroscopy.

The effect of various concentrations of moxifloxacin, another fluoroquinolone drug, on *Streptococcus epidermidis* bacteria was investigated using complementary spectroscopic techniques including FTIR absorption, nonresonant Raman and UVRR spectroscopy [71]. Although the IR spectra of *S. epidermidis*, recorded 80 min after the drug addition appeared to be very similar, quantitative differences according to the drug concentration could be found. HCA was used successfully to differentiate between untreated bacteria and bacteria exposed to small amounts of moxifloxacin (0.08 and 0.16 $\mu g\,ml^{-1}$). The Raman spectra of the bacteria exposed to higher doses of the drug (0.27 and 0.63 $\mu g\,ml^{-1}$) were combined in one cluster and were therefore not differentiated. The results suggest that the antibiotic applied at low concentrations (around the minimal inhibition concentration) did not reach the saturation level and the effect of the drug on the bacteria was still increasing. At high concentrations, saturation was achieved and no further changes in the chemical composition of the cells were detected with increasing amount of drug.

The underlying variances in the IR spectra were elucidated by means of the PCA. Moxifloxacin targets mainly the DNA and protein structures. The drug causes structural changes in the DNA backbone, which suggested to involve reorientation of the phosphate groups, and an additional decrease in the phosphate bindings was observable. Also, an increase of intermolecular β-sheet aggregates (characteristic of

denatured proteins) concomitant with a decrease in ordered α-helical and β-sheet proteins was deduced from the IR absorption spectra. Neugebauer *et al*. interpreted this as a consequence of protein (gyrase)–drug interaction. The nonresonant Raman measurements were performed using an excitation laser in the green region at 532 nm. HCA applied to IR absorption spectra resulted in clear separation of untreated and treated bacteria. The bacterial spectra formed individual clusters dependent on moxifloxacin concentration, exhibiting the inner-class variation. To identify the main changes in the bacterial spectra, PCA was additionally applied. Drug treatment induces an intensity increase in Raman bands assigned to guanine and adenine, to adenosine and thymidine, to glycosidic linkages, and to the phosphate stretching vibration of the DNA backbone. Additionally, an increase in random coil structure upon drug addition was obtained within the Raman spectra. A simultaneous interaction of moxifloxacin with DNA and the protein gyrase was concluded to be the reason.

The results obtained by means of UVRR spectroscopy are in good agreement with the FTIR results, since similar bacteria clusters were obtained using HCA. The PCA outcomes supported the proposed mechanism of interaction between drug and bacteria by focusing on DNA and protein moieties.

The mode of action of amikacin, an aminoglycoside drug, on *P. aeruginosa* bacteria was monitored using UVRR spectroscopy [64]. In contrast to the above-mentioned studies, the antibiotic was provided in various sub-inhibitory concentrations. The spectral changes were ascribed to tryptophan and tyrosine. To study the dynamic nature of the spectral changes over the full antibiotic range below the inhibitory concentrations, the authors applied two-dimensional (2D) correlation analysis.

Generalized 2D correlation spectroscopy is a cross-correlation method that provides information regarding the dynamic spectral changes due to an external perturbation of the system such as increasing antibiotic concentration. The synchronous 2D correlation spectra are characterized by autopeaks along the diagonal and cross-peaks off the diagonal for bands that exhibit similarities in the dynamic behavior. In turn, the asynchronous 2D correlation spectrum contains only cross-peaks that reveal out-of-phase (dissimilar) behavior of two bands. Peaks that do not change their intensities throughout the series will not appear in the 2D spectra. Thus, 2D correlation asynchronous analysis provided information about the order of the changes registered in the Raman spectra [72].

The 2D correlation synchronous spectra obtained by Lopez-Diez *et al.* [64] indicated a decrease in protein signals with increasing amikacin concentration, whereas DNA bands increased. Also, a shift of the protein band was observed from the 2D correlation analysis. The shift of the protein band is consistent with the fact that, as the amount of newly synthesized proteins decreases and amino acids are misincorporated into proteins, the molecular environment of the proteins changes. The 2D correlation asynchronous spectra indicated that the nucleic bands are affected at lower concentration than the protein-related peaks. From the reported Raman results, the mode of action of the amikacin could clearly be described. The drug

targeted the ribosomal RNA and thereby inhibited new protein synthesis and induced misincorporation of amino acids in proteins [64].

5.7 Detection and Identification of Food-Borne Pathogens

In 1999, Mead *et al*. calculated that ~76 million illnesses were caused by spoiled food in the United States each year [73]. Some of the main causes are pathogens (bacteria, viruses, and parasites), toxins, and metals. In the same context, Mead *et al*. defined also that *Salmonella*, *Listeria*, and *Toxoplasma* bacteria are responsible for about 1500 deaths each year. Additionally, other illnesses-causing bacteria including *E. coli*, *Shigella* spp., *Brucella* spp., *Campylobacter* spp., and *B. cereus* exist.

In most cases, medical diagnostics is highly correlated with the knowledge of the anamnesis for distinct identification. This includes the origin, the outbreak, and the spread of a disease, especially when pathogenic microorganisms are involved in this process. The demand on the scientists is to link a pathogenic isolate from a patient to the source of infection to decrease the risk of similar outbreaks. Since microorganisms are ubiquitous, contact cannot be avoided and risk of infections is relatively high. In this context, sources of infection include contaminated food products such as meat, fruits, milk, and juices.

Identification is always a time-sensitive matter. Protecting the public against disease-causing bacteria depends on the efficiency and reliability of the methods designed to detect these pathogens, requiring rapid, sensitive, and accurate procedures. Almost all conventional techniques used today to identify specific pathogens in foods need from not less than 48 h up to 1 week [74]. In addition to immunological and molecular genetic approaches, modern detection systems based on the analysis of a specific spectroscopic signature allow potentially faster identification with enhanced sensitivity and detection limits down to the single-cell level [75]. For that reason, investigations on food-borne pathogens by means of vibrational spectroscopy are considered below.

One method that is used for the classification of various pathogens is FTIR spectroscopy. In this context, Al-Holy *et al*. published a classification of *B. cereus*, *Salmonella enterica*, *E. coli*, and *Listeria* spp. at genus and strain levels based on pattern recognition. The separation of bacterial strains was considered to be due to differences in the structure and quantity of cell wall polysaccharides, lipids, and proteins, which are reflected in the IR spectra between 1700 and 700 cm^{-1} [76]. Furthermore, clear distinctions between different genera, species, and strains of bacteria were observed by PCA. The same method was used by Lin *et al*. to show discrimination between intact and sonication-injured *L. monocytogenes* and to distinguish this strain from other selected uninjured *Listeria* strains [77].

A more complex study based on FTIR spectroscopy was presented by Yu *et al*. [78]. The analysis was applied to the differentiation and quantification of microorganisms in apple juice in comparison with plate counting methods. Eight different pathogenic

strains of bacteria (e.g., *Salmonella* spp., *Enterobacter* spp., and *Pseudomonas vulgaris*), which are known to cause gastroenteric diseases, were investigated. A concentration series was generated by diluting a bacterial starting concentration of 10^9 CFU ml^{-1} (CFU, colony-forming units) with autoclaved juice to six different concentrations from 10^8 to 10^3 CFU ml^{-1}. Exactly 2 min after sample preparation, measurements were made to assure that the number of cells settled on the ATR crystal was proportional to the concentration of the microbial suspension. By using a PCA in combination with canonical variate analysis (CVA), it could be shown that differentiation of microorganisms in apple juice is feasible down to a low concentration level of 10^3 CFU ml^{-1} [78]. CVA, performed on the spectral dataset within the concentration range mentioned above, resulted in consistent and satisfactory separation. Only the three lowest concentrations (10^3–10^5 CFU ml^{-1} apple juice) of *P. vulgaris* were difficult to separate in the chemometric studies (PCA and CVA). To validate the discriminant model, spectra of unknown samples were obtained and their concentrations were predicted, resulting in good agreement with the plate counting method.

Al-Holy *et al*. also published results concerning the identification of pathogens from juice by means of FTIR spectroscopy, especially focusing on the separation of *E. coli* O175:H7 leerzeichen from others. In contrast to the aforementioned method, the inoculated juices were treated with several purification steps, including centrifugation and two washing steps with 0.9% saline solution, to remove juice components and concentrate bacteria. Thereby a pure bacterial pellet was prepared before the spectroscopic analysis was commenced [79] and separation of *E. coli* at the strain level was achieved.

Whittaker *et al*. studied the identification of bacterial pathogens by ATR–FTIR spectroscopy basing on cellular fatty acid methyl esters (FAMEs) [80]. Lipid cellular components, which are responsible for bacterial speciation, are commonly analyzed only by using capillary gas chromatography with flame ionization or mass spectrometric detection. Whittaker *et al*. showed that the identification of FAME mixtures from pathogenic bacteria such as *B. cereus*, *Shigella sonnei*, and *E. coli* is feasible by applying FTIR spectroscopy in combination with data analysis such as PCA and SIMCA.

The described studies emphasize the potential of FTIR spectroscopy to identify pathogenic microorganisms in liquid foods such as juices, and similar food systems, after extraction. Nevertheless, direct measurements on the food matrices are desirable. In this context, food-borne microorganisms have been analyzed directly on food surfaces by means of Fourier transform Raman spectroscopy.

Yang and Irudayaraj demonstrated the characterization and classification of six different bacteria including the pathogenic *E. coli* O157:H7 on whole apples by means of FT-Raman spectroscopy [74]. The apples were carefully covered with the bacterial suspension and then analyzed. The spectrum of the apple skin and the spectra of the apples skin smeared with the different microorganisms were very similar, as shown in Figure 5.10.

Minor spectral differences were localized within the fingerprint region between 1800 and 600 m^{-1} which are due to varying protein and lipid contents within the

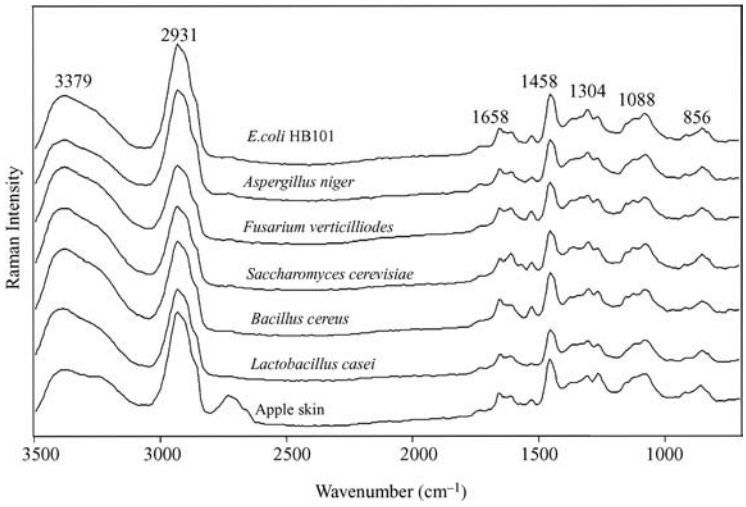

Figure 5.10 FT-Raman spectra of uncontaminated apple and apple contaminated with different types of microorganisms [74].

microbial cells. In this context, spectral analyses were performed with focus on differentiation between various *E. coli* strains. By using multivariate statistics (PCA and CVA), *E. coli* strains were successfully classified and separated into pathogens and nonpathogens according to Figure 5.11. Whereas the pathogenic strain *E. coli* O157:H7 was classified separately from the five different nonpathogenic *E. coli* strains by means of the first two CV scores according to Figure 5.11,

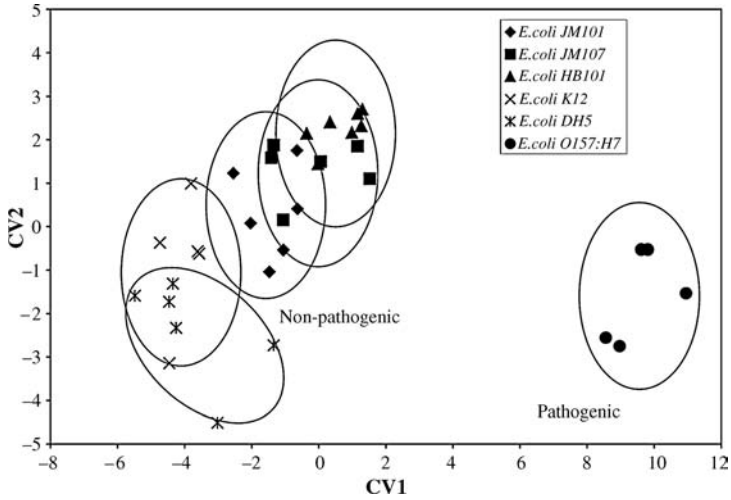

Figure 5.11 Canonical variate analysis based on the first two canonical variates from the spectra of whole apple surface contaminated with nonpathogenic and pathogenic strains of *E. coli* [74].

the nonpathogenic strains overlapped in their clusters. By considering only the nonpathogenic *E. coli* strains in a separate classification by using the first two scores again, different clusters for the strains JM101, JM107 and HB101 without overlapping were also achieved. The clusters of the two other strains, K12 and DB5alpha, still overlap.

The results indicate that Raman spectroscopy is a promising technique, because the sample or the food product can be placed directly under the laser focus and any further sample preparation can be omitted [74].

In 2008, Luo and Lin reported an analysis for discrimination of food-borne pathogens with a dispersive Raman system by using SERS on the basis of silver colloidal nanoparticles for enhanced signals. Spectra of three food-borne pathogens were processed, resulting in clear identification on the basis of their unique spectral bands [81].

All the investigations discussed above have not been introduced in the analytical industry so far, because some obstacles concerning sample preparation and handling practices still have to be overcome. Batt *et al.* pointed out that locating pathogens in complex matrices is not possible by simple physical means, for example, centrifugation [75]. The extraction procedure for bacteria in water differs from that for the same bacteria from juices or milk, depending on the complexity of the matrix composition. Advances in techniques regarding those complex issues will play an important role in food safety and, along with this, in the detection and reduction of illnesses caused by food-borne pathogens.

Ravindranath *et al.*, developed a pathogen sensor for food matrices addressing the above problems regarding the complexity of food matrices. Biofunctionalized magnetic nanoparticles in combination with mid-IR analysis were employed. The nanoparticles were functionalized with antibodies of two well-known food-borne pathogens: *E. coli* 0175:H7 and *Salmonella typhimurium* [82]. The separate isolation of both species from a mixture of other bacteria was achieved and these microorganisms were detected in food matrices by means of FTIR spectroscopy. This advanced technology can also be integrated in a portable device, which enables this approach to be used as a point-of-care technology. Ravindranath *et al.* reported that highly selective detection was achieved in less than 30 min with both investigated strains in complex matrices, such as milk and spinach extract, with a detection limit of 10^4–10^5 CFU ml^{-1}. On-site food-borne pathogen monitoring, with an in-built extraction step using magnetic nanoparticles combined with the specificity of IR spectra, offers the possibility of complementing the conventional and still established microbiological methods with molecular innovative methods [82].

Recent outbreaks of food-borne illnesses were associated with bacterial contamination. Therefore, not only the identification of bacterial cells but also processes of food spoilage by microorganisms concerning, for example, meat or dairy products are investigated. Especially pathogenic microorganisms, such as *Listeria* spp., *Salmonella* spp., *Campylobacter jejuni*, and *Yersinia enterolytica*, trigger food-borne illnesses. It is generally accepted that organoleptic changes result from microbial

spoilages and that the compounds responsible for these changes are various metabolites produced by the enzymatic activity and growth of microorganisms [83]. For example, milk is certainly an ideal medium for microbial growth because of the high water content, the large variety of available nutrients, and the almost neutral pH. Nicolaou and Goodacre investigated spoilage in milk using FTIR spectroscopy and chemometrics [83]. They tested ATR and HT (high-throughput) FTIR techniques in combination with principal component–discriminant function analysis (PCA–DFA) and partial least-squares regression (PLSR) in comparison with the total viable cell counts by plating with three different kinds of milk (whole, skimmed, and semi-skimmed). The FTIR data for the different milk samples showed reasonable results for bacterial loads above 10^5 CFU ml^{-1}. However, HT FTIR spectroscopy provided higher accuracy for lower viable bacterial counts down to 10^3 CFU ml^{-1} for whole milk and 4×10^2 CFU ml^{-1} for semi-skimmed and skimmed milk [83]. Summarizing, they pointed out that by using these techniques in combination with PLSR, rapid acquisition of a metabolic fingerprint and accurate quantification of the microbial load of milk samples with reduced sample preparation are feasible.

FTIR spectroscopy was also applied by Ellis *et al.* to detect microbial spoilage of meat [84]. Organoleptic changes, including discoloration, slime formation, changes in taste or other attributes, lower muscle food quality to an unacceptable limit. These changes result from the decomposition and the formation of metabolites caused by bacterial growth. In this context, it is known that spoilage organisms belong primarily to the genus *Pseudomonas* and other major members of spoilage flora, such as *Moraxella* spp., *Psychrobacter* spp., and *Acinetobacter* spp. Ellis *et al.* exploited the information about microbial spoilage of chicken breast by spectroscopic analysis [84]. The spectra were recorded directly from the meat surface and integrated for 60 s. The authors demonstrated that the application of HATR (horizontal attenuated total reflectance) FTIR and PLS analysis are able to acquire a metabolic snapshot and quantify noninvasively the microbial load of food samples accurately and rapidly in 60 s, directly from the sample surface.

5.8 Conclusion

The application of different vibrational spectroscopic techniques such as IR absorption and Raman spectroscopy allows the rapid and reliable identification of microorganisms. Depending on the application different specialized setups can be applied in order to meet the specific requirements. For FTIR absorption spectroscopy either a fast identification routine of bulk samples can be established or by means of an ATR setup or an IR microscope the heterogeneity of a sample e.g. a biofilm can be analysed. Using Raman spectroscopy with excitation wavelength from the ultraviolet over the visible up to the infrared region allows for a screening and identification of microbial bulk samples or single cells which are related to epidemiological studies or

food safety. Even the impact of antibiotics on bacteria and their internal mode of action can be addressed.

The variety of applications allows an identification of microorganisms within hours and will therefore play a central role in future bacterial identification routines when a fast diagnosis is required.

References

1 Helm, D., Labischinski, H., Schallehn, G., and Naumann, D. (1991) Classification and identification of bacteria by Fourier-transform infrared spectroscopy. *J. Gen. Microbiol.*, **137**, 69–79.

2 Naumann, D. (2001) FT-infrared and FT-Raman spectroscopy in biomedical research, in *Infrared and Raman Spectroscopy of Biological Materials* (eds. H.-U. Gremlich and B. Yan), Marcel Dekker, New York, pp. 323–378.

3 Kirschner, C., Maquelin, K., Pina, P., Thi, N.A.N., Choo-Smith, L.P., Sockalingum, G.D., Sandt, C., Ami, D., Orsini, F., Doglia, S.M., Allouch, P., Mainfait, M., Puppels, G.J., and Naumann, D. (2001) Classification and identification of Enterococci: a comparative phenotypic, genotypic, and vibrational spectroscopic study. *J. Clin. Microbiol.*, **39**, 1763–1770.

4 Harz, M., Rösch, P., and Popp, J. (2009) Vibrational spectroscopy – a powerful tool for the rapid identification of microbial cells at the single-cell level. *Cytometry A*, **75**, 104–113.

5 Rösch, P., Harz, M., Schmitt, M., and Popp, J. (2005) Raman spectroscopic identification of single yeast cells. *J. Raman Spectrosc.*, **36**, 377–379.

6 Escoriza, M.F., Vanbriesen, J.M., Stewart, S., and Maier, J. (2006) Studying bacterial metabolic states using Raman spectroscopy. *Appl. Spectrosc.*, **60**, 971–976.

7 Harz, M., Rösch, P., Peschke, K.-D., Ronneberger, O., Burkhardt, H., and Popp, J. (2005) Micro-Raman spectroscopical identification of bacterial cells of the genus *Staphylococcus* in dependence on their cultivation conditions. *Analyst*, **130**, 1543–1550.

8 Schuster, K.C., Urlaub, E., and Gapes, J.R. (2000) Single-cell analysis of bacteria by Raman microscopy: spectral information on the chemical composition of cells and on the heterogeneity in a culture. *J. Microbiol. Methods*, **42**, 29–38.

9 Choo-Smith, L.P., Maquelin, K., Van Vreeswijk, T., Bruining, H.A., Puppels, G.J., Thi, N.A.N., Kirschner, C., Naumann, D., Ami, D., Villa, A.M., Orsini, F., Doglia, S.M., Lamfarraj, H., Sockalingum, G.D., Manfait, M., Allouch, P., and Endtz, H.P. (2001) Investigating microbial (micro)colony heterogeneity by vibrational spectroscopy. *Appl. Environ. Microbiol.*, **67**, 1461–1469.

10 Heber, J.R.S. and Orvil, E.A.B. (1952) Infrared spectrophotometry as a means for identification of bacteria. *Science*, **116**, 111–113.

11 Naumann, D. (1998) Infrared and NIR Raman spectroscopy in medical microbiology, infrared spectroscopy: new tool in medicine. *Proc. SPIE*, **3257**, 245–257.

12 Petry, R., Schmitt, M., and Popp, J. (2003) Raman spectroscopy – a prospective tool in the life sciences. *ChemPhysChem*, **4**, 14–30.

13 Rösch, P., Harz, M., Peschke, K.-D., Ronneberger, O., Burkhardt, H., Schuele, A., Schmauz, G., Lankers, M., Hofer, S., Thiele, H., Motzkus, H.-W., and Popp, J. (2006) On-line monitoring and identification of bioaerosols. *Anal. Chem.*, **78**, 2163–2170.

14 Kalasinsky, K.S., Hadfield, T., Shea, A.A., Kalasinsky, V.F., Nelson, M.P., Neiss, J., Drauch, A.J., Vanni, G.S., and Treado, P.J. (2007) Raman chemical imaging

spectroscopy reagentless detection and identification of pathogens: signature development and evaluation. *Anal. Chem.*, **79**, 2658–2673.

15 McHale, J.L. (2002) Resonance Raman spectroscopy, in *Handbook of Vibrational Spectroscopy* (eds. J. Chalmers and P. Griffiths), John Wiley & Sons, Ltd., Chichester, pp. 534–556.

16 Hering, K., Cialla, D., Ackermann, K., Dörfer, T., Möller, R., Schneideweind, H., Mattheis, R., Fritzsche, W., Rösch, P., and Popp, J. (2008) SERS: a versatile tool in chemical and biochemical diagnostics. *Anal. Bioanal. Chem.*, **390**, 113–124.

17 Nie, S. and Emory, S.R. (1997) Probing single molecules and single nanoparticles by surface-enhanced Raman scattering. *Adv. Drug Deliv. Rev.*, **275**, 1102–1106.

18 Naumann, D. (2000) Infrared spectroscopy in microbiology, in *Encyclopedia of Analytical Chemistry* (ed. R.A. Meyers), John Wiley & Sons, Ltd., Chichester, pp. 102–131.

19 Naumann, D., Keller, S., Helm, D., Schultz, C., and Schrader, B. (1995) FT-IR spectroscopy and FT-Raman spectroscopy are powerful analytical tools for the noninvasive characterization of intact microbial-cells. *J. Mol. Struct.*, **347**, 399–405.

20 Gaus, K., Rösch, P., Petry, R., Peschke, K.-D., Ronneberger, O., Burkhardt, H., Baumann, K., and Popp, J. (2006) Classification of lactic acid bacteria with UV–resonance Raman spectroscopy. *Biopolymers*, **82**, 286–290.

21 Jarvis, R.M. and Goodacre, R. (2004) Ultra-violet resonance Raman spectroscopy for the rapid discrimination of urinary tract infection bacteria. *FEMS Microbiol. Lett.*, **232**, 127–132.

22 Lopez-Diez, E.C. and Goodacre, R. (2004) Characterization of microorganisms using UV resonance Raman spectroscopy and chemometrics. *Anal. Chem.*, **76**, 585–591.

23 Maquelin, K., Choo-Smith, L.-P.i., Endtz, H.P., Bruining, H.A., and Puppels, G.J. (2000) Raman spectroscopic studies on bacteria. *Proc. SPIE*, **4161**, 144–150.

24 Maquelin, K., Choo-Smith, L.-P.i., Van Vreeswijk, T., Endtz, H.P., Smith, B., Bennett, R., Bruining, H.A., and Puppels, G.J. (2000) Raman spectroscopic method for identification of clinically relevant microorganisms growing on solid culture medium. *Anal. Chem.*, **72**, 12–19.

25 Rösch, P., Harz, M., Schmitt, M., Peschke, K.-D., Ronneberger, O., Burkhardt, H., Motzkus, H.-W., Lankers, M., Hofer, S., Thiele, H., and Popp, J. (2005) Chemotaxonomic identification of single bacteria by micro-Raman spectroscopy: application to clean-room-relevant biological contaminations. *Appl. Environ. Microbiol.*, **71**, 1626–1637.

26 Jarvis, R.M., Brooker, A., and Goodacre, R. (2006) Surface-enhanced Raman scattering for the rapid discrimination of bacteria. *Faraday Discuss.*, **132**, 281–292.

27 Jarvis, R.M., Brooker, A., and Goodacre, R. (2004) Surface-enhanced Raman spectroscopy for bacterial discrimination utilizing a scanning electron microscope with a Raman spectroscopy interface. *Anal. Chem.*, **76**, 5198–5202.

28 Maquelin, K., Kirschner, C., Choo-Smith, L.P., Ngo-Thi, N.A., van Vreeswijk, T., Stammler, M., Endtz, H.P., Bruining, H.A., Naumann, D., and Puppels, G.J. (2003) Prospective study of the performance of vibrational spectroscopies for rapid identification of bacterial and fungal pathogens recovered from blood cultures. *J. Clin. Microbiol.*, **41**, 324–329.

29 Rösch, P., Harz, M., Peschke, K.-D., Ronneberger, O., Burkhardt, H., and Popp, J. (2006) Identification of single eukaryotic cells with micro-Raman spectroscopy. *Biopolymers*, **82**, 312–316.

30 Krause, M., Rösch, P., Radt, B., and Popp, J. (2008) Localizing and identifying living bacteria in an abiotic environment by a combination of Raman and fluorescence microscopy. *Anal. Chem.*, **80**, 8568–8575.

31 Lieber, C.A. and Mahadevan-Jansen, A. (2003) Automated method for subtraction of fluorescence from biological Raman spectra. *Appl. Spectrosc.*, **57**, 1363–1367.

32 Ryan, C.G., Clayton, E., Griffin, W.L., Sie, S.H., and Cousens, D.R. (1988) SNIP,

a statistics-sensitive background treatment for the quantitative analysis of PIXE spectra in geoscience applications. *Nucl. Instrum. Methods B*, **34**, 396–402.

33 Comon, P. (1994) Independent component analysis, a new concept? *Signal Process.*, **36**, 287–314.

34 Pearson, K. (1901) Principal components analysis. *Philos. Mag.*, **2**, 559–572.

35 Fraley, C. and Raftery, A.E. (1998) How many clusters? Which clustering method? Answers via model-based cluster analysis. *Comput. J.*, **41**, 578–588.

36 Rojas, R. and Feldman, J. (1996) *Neural Networks: a Systematic Introduction*, Springer, Berlin.

37 Willemse-Erix, D.F.M., Scholtes-Timmerman, M.J., Jachtenberg, J.-W., van Leeuwen, W.B., Horst-Kreft, D., Bakker Schut, T.C., Deurenberg, R.H., Puppels, G.J., van Belkum, A., Vos, M.C., and Maquelin, K. (2009) Optical fingerprinting in bacterial epidemiology: Raman spectroscopy as a real-time typing method. *J. Clin. Microbiol.*, **47**, 652–659.

38 Bosch, A., Minan, A., Vescina, C., Degrossi, J., Gatti, B., Montanaro, P., Messina, M., Franco, M., Vay, C., Schmitt, J., Naumann, D., and Yantorno, O. (2008) Fourier transform infrared spectroscopy for rapid identification of nonfermenting Gram-negative bacteria isolated from sputum samples from cystic fibrosis patients. *J. Clin. Microbiol.*, **46**, 2535–2546.

39 Donlan, R.M. (2001) Biofilm formation: a clinically relevant microbiological process. *Clin. Infect. Dis.*, **33**, 1387–1392.

40 Donlan, R.M. (2001) Biofilms and device-associated infections. *Emerg. Infect. Dis.*, **7**, 277–281.

41 Heitz, E., Flemming, H.-C., and Sand, W. (eds.) (1996) *Microbially Influenced Corrosion of Materials: Scientific and Engineering Aspects*, Springer, Berlin.

42 Ojeda, J.J., Romero-Gonzalez, M.E., and Banwart, S.A. (2009) Analysis of bacteria on steel surfaces using reflectance micro-Fourier transform infrared spectroscopy. *Anal. Chem.*, **81**, 6467–6473.

43 Delille, A., Quiles, F., and Humbert, F. (2007) *In situ* monitoring of the nascent *Pseudomonas fluorescens* biofilm response to variations in the dissolved organic carbon level in low-nutrient water by attenuated total reflectance–Fourier transform infrared spectroscopy. *Appl. Environ. Microbiol.*, **73**, 5782–5788.

44 Marcotte, L., Barbeau, J., and Lafleur, M. (2004) Characterization of the diffusion of polyethylene glycol in *Streptococcus mutans* biofilms by Raman microspectroscopy. *Appl. Spectrosc.*, **58**, 1295–1301.

45 Huang, W.E., Ude, S., and Spiers, A.J. (2007) *Pseudomonas fluorescens* SBW25 biofilm and planktonic cells have differentiable Raman spectral profiles. *Microb. Ecol.*, **53**, 471–474.

46 Pätzold, R., Keuntje, M., and Anders-von Ahlften, A. (2006) A new approach to non-destructive analysis of biofilms by confocal Raman microscopy. *Anal. Bioanal. Chem.*, **386**, 286–292.

47 Ivleva, N., Wagner, M., Horn, H., Niessner, R., and Haisch, C. (2009) Towards a nondestructive chemical characterization of biofilm matrix by Raman microscopy. *Anal. Bioanal. Chem.*, **393**, 197–206.

48 Ivleva, N.P., Wagner, M., Horn, H., Niessner, R., and Haisch, C. (2008) *In situ* surface-enhanced Raman scattering analysis of biofilm. *Anal. Chem.*, **80**, 8538–8544.

49 Schmid, T., Messmer, A., Yeo, B.-S., Zhang, W., and Zenobi, R. (2008) Towards chemical analysis of nanostructures in biofilms II: tip-enhanced Raman spectroscopy of alginates. *Anal. Bioanal. Chem.*, **391**, 1907–1916.

50 Maquelin, K., Cookson, B., Tassios, P., and van Belkum, A. (2007) Current trends in the epidemiological typing of clinically relevant microbes in Europe. *J. Microbiol. Methods*, **69**, 222–226.

51 Bitsori, M., Maraki, S., Raissaki, M., Bakantaki, A., and Galanakis, E. (2005) Community-acquired enterococcal urinary tract infections. *Pediatr. Nephrol.*, **20**, 1583–1586.

52 Hutchison, M.L. and Govan, J.R.W. (1999) Pathogenicity of microbes associated with cystic fibrosis. *Microb. Infect.*, **1**, 1005–1014.

53 Coutinho, C.P., Sá-Correia, I., and Almeida Lopes, J. (2009) Use of Fourier

transform infrared spectroscopy and chemometrics to discriminate clinical isolates of bacteria of the *Burkholderia cepacia* complex from different species and ribopatterns. *Anal. Bioanal. Chem.*, **394**, 2161–2171.

54 Pfaller, M.A. and Diekema, D.J. (2007) Epidemiology of invasive candidiasis: a persistent public health problem. *Clin. Microbiol. Rev.*, **20**, 133–163.

55 Ibelings, M.S., Maquelin, K., Endtz, H.P., Bruining, H.A., and Puppels, G.J. (2005) Rapid identification of *Candida* spp. in peritonitis patients by Raman spectroscopy. *Clin. Microbiol. Infect.*, **11**, 353–358.

56 Maquelin, K., Choo-Smith, L.P., Endtz, H.P., Bruining, H.A., and Puppels, G.J. (2002) Rapid identification of *Candida* species by confocal Raman microspectroscopy. *J. Clin. Microbiol.*, **40**, 594–600.

57 Essendoubi, M., Toubas, D., Lepouse, C., Leon, A., Bourgeade, F., Pinon, J.-M., Manfait, M., and Sockalingum, G.D. (2007) Epidemiological investigation and typing of *Candida glabrata* clinical isolates by FTIR spectroscopy. *J. Microbiol. Methods*, **71**, 325–331.

58 Martin-Casabona, N., Bahrmand, A.R., Bennedsen, J., Ostergaard Thomsen, V., Curcio, M., Fauville-Dufaux, M., Feldman, K., Havelkova, M., Katila, M.L., Koeksalan, K., Pereira, M.F., Rodrigues, F., Pfyffer, G.E., Portaels, F., Rossell-Urgell, J., Ruesch-Gerdes, S., Tortoli, E., Vincent, V., and Watt, B. (2004) Non-tuberculous mycobacteria: patterns of isolation; a multi-country retrospective survey. *Int. J. Tuberc. Lung Dis.*, **8**, 1186–1193.

59 Griffith, D.E., Aksamit, T., Brown-Elliott, B.A., Catanzaro, A., Daley, C., Gordin, F., Holland, S.M., Horsburgh, R., Huitt, G., Iademarco, M.F., Iseman, M., Olivier, K., Ruoss, S., von Reyn, C.F., Wallace, R.J. Jr., Winthrop, K., ATS Mycobacterial Diseases Subcommittee, American Thoracic Society , and Infectious Disease Society of America (2007) An official ATS/IDSA statement: diagnosis, treatment, and prevention of nontuberculous mycobacterial diseases. *Am J. Respir. Crit. Care Med.*, **175**, 367–416.

60 Buijtels, P.C.A.M., Willemse-Erix, H.F.M., Petit, P.L.C., Endtz, H.P., Puppels, G.J., Verbrugh, H.A., van Belkum, A., van Soolingen, D., and Maquelin, K. (2008) Rapid identification of mycobacteria by Raman spectroscopy. *J. Clin. Microbiol.*, **46**, 961–965.

61 Harz, M., Kiehntopf, M., Stöckel, S., Rösch, P., Straube, E., Deufel, T., and Popp, J. (2009) Direct analysis of clinical relevant single bacterial cells from cerebrospinal fluid during bacterial meningitis by means of micro-Raman spectroscopy. *J. Biophotonics*, **2**, 70–80.

62 Krause, M., Radt, B., Rösch, P., and Popp, J. (2007) The investigation of single bacteria by means of fluorescence staining and Raman spectroscopy. *J. Raman Spectros.*, **38**, 369–372.

63 Maquelin, K., Kirschner, C., Choo-Smith, L.P., van den Braak, N., Endtz, H.P., Naumann, D., and Puppels, G.J. (2002) Identification of medically relevant microorganisms by vibrational spectroscopy. *J. Microbiol. Methods*, **51**, 255–271.

64 Lopez-Diez, E.C., Winder, C.L., Ashton, L., Currie, F., and Goodacre, R. (2005) Monitoring the mode of action of antibiotics using Raman spectroscopy: investigating subinhibitory effects of amikacin on *Pseudomonas aeruginosa*. *Anal. Chem.*, **77**, 2901–2906.

65 Liu, T.-T., Lin, Y.-H., Hung, C.-S., Liu, T.-J., Chen, Y., Huang, Y.-C., Tsai, T.-H., Wang, H.-H., Wang, D.-W., Wang, J.-K., Wang, Y.-L., and Lin, C.-H. (2009) A high speed detection platform based on surface-enhanced Raman scattering for monitoring antibiotic-induced chemical changes in bacteria cell wall. *PLoS ONE*, **4**, e5470.

66 Huleihel, M., Pavlov, V., and Erukhimovitch, V. (2009) The use of FTIR microscopy for the evaluation of anti-bacterial agents activity. *J. Photochem. Photobiol. B*, **96**, 17–23.

67 Neugebauer, U., Schmid, U., Baumann, K., Holzgrabe, U., Ziebuhr, W., Kozitskaya, S., Kiefer, W., Schmitt, M., and Popp, J. (2006) Characterization of bacterial growth and the influence of antibiotics by means of UV resonance Raman spectroscopy. *Biopolymers*, **82**, 306–311.

68 Neugebauer, U., Schmid, U., Baumann, K., Simon, H., Schmitt, M., and Popp, J. (2007) DNA tertiary structure and changes in DNA supercoiling upon interaction with ethidium bromide and gyrase monitored by UV resonance Raman spectroscopy. *J. Raman Spectrosc.*, **38**, 1246–1258.

69 Neugebauer, U., Schmid, U., Baumann, K., Ziebuhr, W., Kozitskaya, S., Holzgrabe, U., Schmitt, M., and Popp, J. (2007) The influence of fluoroquinolone drugs on the bacterial growth of *S. epidermidis* utilizing the unique potential of vibrational spectroscopy. *J. Phys. Chem. A*, **111**, 2898–2906.

70 Neugebauer, U., Szeghalmi, A., Schmitt, M., Kiefer, W., Popp, J., and Holzgrabe, U. (2005) Vibrational spectroscopic characterization of fluoroquinolones. *Spectrochim Acta A Mol. Spectrosc.*, **61**, 1505–1517.

71 Neugebauer, U., Schmid, U., Baumann, K., Ziebuhr, W., Kozitskaya, S., Deckert, V., Schmitt, M., and Popp, J. (2007) Towards a detailed understanding of bacterial metabolism: spectroscopic characterization of *Staphylococcus epidermidis*. *ChemPhysChem*, **8**, 124–137.

72 Noda, I. (1993) Generalized two-dimensional correlation method applicable to infrared, Raman, and other types of spectroscopy. *Appl. Spectrosc.*, **47**, 1329–1336.

73 Mead, P.S., Slutsker, L., Dietz, V., McCaig, L.F., Bresee, J.S., Shapiro, C., Griffin, P.M., and Tauxe, R.V. (1999) Food-related illness and death in the United States. *Emerg. Infect. Dis.*, **5**, 607–625.

74 Yang, H. and Irudayaraj, J. (2003) Rapid detection of foodborne microorganisms on food surfaces using Fourier transform Raman spectroscopy. *J. Mol. Struct.*, **646**, 35–43.

75 Batt, C.A. (2007) Materials science: food pathogen detection. *Science*, **316**, 1579–1580.

76 Al-Holy, M.A., Lin, M., Cavinato, A.G., and Rasco, B.A. (2006) The use of Fourier transform infrared spectroscopy to differentiate *Escherichia coli* O157:H7 from other bacteria inoculated into apple juice. *Food Microbiol.*, **23**, 162–168.

77 Lin, M., Al-Holy, M., Al-Qadiri, H., Kang, D.-H., Cavinato, A.G., Huang, Y., and Rasco, B.A. (2004) Discrimination of intact and injured *Listeria monocytogenes* by Fourier transform infrared spectroscopy and principal component analysis. *J. Agric. Food Chem.*, **52**, 5769–5772.

78 Yu, C., Irudayaraj, J., Debroy, C., Schmilovtich, Z., and Mizrach, A. (2004) Spectroscopic differentiation and quantification of microorganisms in apple juice. *J. Food Sci.*, **69**, 268–272.

79 Al-Holy, M.A., Lin, M., Al-Qadiri, H., Cavinato, A.G., and Rasco, B.A. (2006) Classification of foodborne pathogens by Fourier transform infrared spectroscopy and pattern recognition techniques. *J. Rapid Methods Autom. Microbiol.*, **14**, 189–200.

80 Whittaker, P., Mossoba, M.M., Al-Khaldi, S., Fry, F.S., Dunkel, V.C., Tall, B.D., and Yurawecz, M.P. (2003) Identification of foodborne bacteria by infrared spectroscopy using cellular fatty acid methyl esters. *J. Microbiol. Methods*, **55**, 709–716.

81 Luo, B.S. and Lin, M. (2008) A portable Raman system for the identification of foodborne pathogenic bacteria. *J. Rapid Methods Autom. Microbiol.*, **16**, 238–255.

82 Ravindranath, S.P., Mauer, L.J., Deb-Roy, C., and Irudayaraj, J. (2009) Biofunctionalized magnetic nanoparticle integrated mid-infrared pathogen sensor for food matrixes. *Anal. Chem.*, **81**, 2840–2846.

83 Nicolaou, N., and Goodacre, R. (2008) Rapid and quantitative detection of the microbial spoilage in milk using Fourier transform infrared spectroscopy

and chemometrics. *Analyst*, **133**, 1424–1431.

84 David I. Ellis, David Broadhurst, Douglas B. Kell, Jem J. Rowland, and Royston Goodacre (2002) Rapid and quantitative detection of the microbial spoilage of meat by fourier transform infrared spectroscopy and machine learning. *Appl. Environ. Microbiol.*, **68**, 2822–2828.

6
Cell Sorting

Jochen Guck

6.1
Conventional Techniques in Cell Sorting

The standard technique for the sequential characterization and sorting of cells is fluorescence-activated cell sorting (FACS) [1]. A cell suspension, in which cells of interest are labeled with one or several fluorescent antibodies against specific surface markers, is flowed through a nozzle such that the resulting droplets are charged and each contains a single cell. This stream of droplets then passes a detector that analyzes each drop for the presence of fluorescence. Triggered by a fluorescence signal, the drop is deflected by electric fields and collected. Current high-speed sorters are capable of reliably sorting on the order of 10^4 cells s^{-1} [2].

A variant of fluorescent antibodies is the use of antibodies conjugated with paramagnetic beads. Cells labeled with such beads can then be sorted from a mixed population by magnetic gradients. This magnetic-activated cell sorting (MACS) can process on the order of 10^6 cells s^{-1} [3]. In contrast to FACS, which analyzes many single cells sequentially, MACS is a bulk technique, where cell classification and sorting are achieved in a single step. Bulk sorters generally have a higher throughput rate but are limited in the number of different parameters that can be used simultaneously.

6.2
Photonic Techniques in Single-Cell Sorting

The basis for all photonic techniques used to sort cells is the fact that light carries momentum and can exert forces. In contrast to electric and magnetic forces, optical forces are much weaker because the momentum of photons, and hence their ability to exert forces, are comparatively small. Therefore, lasers are required to achieve photon fluxes sufficient for the manipulation of micron-sized objects, such as cells, with light. A pioneer of such optical manipulation was Arthur Ashkin, who showed in

Handbook of Biophotonics. Vol.2: Photonics for Health Care, First Edition. Edited by Jürgen Popp, Valery V. Tuchin, Arthur Chiou, and Stefan Heinemann.

the early 1970s that small glass beads can be moved by laser beams and that two counterpropagating laser beams can trap small objects in their middle [4]. The optical force has two components: the scattering force pushes the object away from the light source, while the gradient force acts along the gradient of light intensity – in a nonfocused laser beam with Gaussian intensity distribution towards the axis of the beam (see Figure 6.1a).

The most common trap built with optical forces is optical tweezers, which are ideal for single-molecule manipulations and have been used extensively in biophysical studies [5, 6]. In the context of cell characterization and sorting, these optical forces can be used to hold single cells in place during investigation or to move them about for sorting [7]. Here, nonfocused laser beams, such as in dual-beam laser traps, are often better suited than optical tweezers because they allow manipulation of cells of arbitrary size and with reduced light intensities, which could otherwise endanger the integrity of the cell [4, 8–10]. Such optical traps are usefully combined with microfluidics into "lab-on-a-chip" systems for the efficient transport, analysis, and sorting of cells [10–13]. In such lab-on-a-chip systems, cells in suspension are serially delivered into the trapping region where the optical trap (e.g., two counterpropagating laser beams perpendicular to the flow direction) attracts the cell, centers it automatically, and holds it in place for any characterization desired (see Figure 6.1b). While trapped, the cell can be tested for an overall fluorescence signal in analogy to normal FACS machines. In contrast to FACS, however, the cell can be held stationary for an arbitrary number of other assays until a final verdict about the nature of the cell is reached. For example, the cell can be analyzed with microscopy for size, morphology, and structure [9] or with spectroscopy for biochemical information [14]. Optical forces can also be used to rotate the cell [15], so that tomographic information can be obtained, or even to deform the cell in a controlled way to obtain mechanical information [16]. Since the mechanical properties of cells are intricately linked to cell function, this mechanical phenotyping of cells with optical forces represents a powerful new option for cancer diagnosis [17, 18] and stem cell identification [19], and suggests the development of elasticity-activated

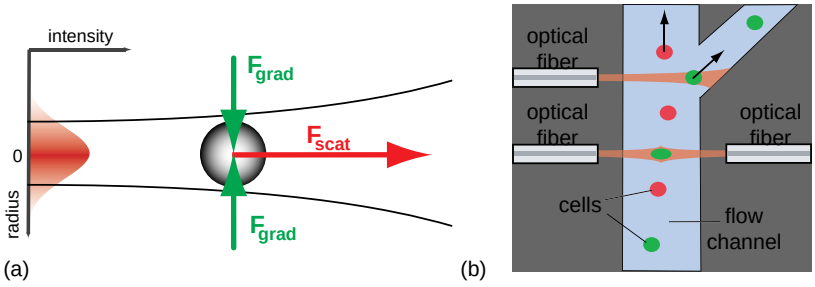

Figure 6.1 Cell sorting with optical forces. (a) Illustration of the direction of scattering and gradient forces acting on a cell in a Gaussian laser beam. (b) Combination of optical forces with a microfluidic system for analysis and sorting. A pair of counterpropagating laser beams, emerging from optical fibers, center and trap single cells sequentially for analysis. A third laser beam then deflects cells of interest into a sorting channel.

cell sorting (EACS) [10]. Once the cell has been identified, it can be released from the optical trap and flowed to the sorting region. Here, another laser beam perpendicular to the flow direction can be used to deflect cells into a sorting channel [20] (see Figure 6.1b). Once sorted, the cells can then be subjected to further analysis such as single-cell polymerase chain reaction (PCR) on the same chip [11] or collected for culture and analysis off-line.

There is also another approach for isolating cells with photonic techniques, called laser microdissection and pressure catapulting (LMPC) [21]. Rather than dissolving tissue to yield a cell suspension, tissue slices can be used directly as a source of cells. Once a cell in the tissue has been identified, for example, using standard histological staining, it is cut out of the tissue slice using a tightly focused UV or IR laser as an optical scalpel. The cut-out cell is then catapulted into a collection reservoir by a laser pulse. LMPC can be used to obtain cells, or even the DNA from within cells, with no contamination because the sample is never in contact with any physical surface – only with light.

6.3 Photonic Techniques in Bulk Sorting

Optical forces can also be used for bulk sorting, where cells are not analyzed serially but analysis is intimately coupled to the sorting process and many cells are sorted simultaneously. MACS is one such bulk technique. One purely optical approach to bulk sorting analyzes the size or optical properties of cells. A cell in an optical lattice, for example, generated by interfering two laser beams, feels a higher deflection force when its refractive index is higher or when its size is comparable to that of the interference pattern spacing. Larger cells, or cells with a lower refractive index, are less affected. When a cell suspension is flowed through such an extended lattice, cells are sorted based on these parameters [22]. The intensity pattern can also be generated by the use of a spatial light modulator [23] or nondiffracting Bessel beams [24]. The throughput of this optical fractionation technique can exceed that of FACS sorters, with a sorting efficiency approaching 100% [22], but obviously at the cost of the amount of specific information used for the distinction. One application of bulk optical fractionation is the sorting of white blood cells from whole blood as they have different size and refractive index to red blood cells. Although sorting by size can also be achieved with micropillar arrays [25], which let smaller cells pass while larger cells are retained, there is an obvious advantage to the optical technique in that it can never clog up. Once the light has been turned off, the sorting mechanism is gone.

In summary, optical forces have their place in both single-cell and bulk sorting applications. In sequential single-cell sorting, the main advantage over conventional sorting approaches such as FACS is that an individual cell can be held stationary by optical forces for high-content analysis, leading to very high purity of the sorted cells at the cost of high throughput. In bulk sorting, optical techniques can operate at sorting rates even in excess of other standard techniques and offer, in addition to size, new sorting parameters such as refractive index that have not yet been explored.

In both cases, optical forces are generally very mild as there is no physical contact involved that could cause unwanted cell activation or alteration. Some 50 years after the invention of the laser, optical cell sorting is another field where its application is set to increase.

References

1 Orfao, A. and Ruiz-Arguelles, A. (1996) General concepts about cell sorting techniques. *Clin. Biochem.*, **29**, 5–9.

2 Ibrahim, S.F. and van den Engh, G. (2003) High-speed cell sorting: fundamentals and recent advances. *Curr. Opin. Biotechnol.*, **14**, 5–12.

3 Miltenyi, S., Müller, W., Weichel, W., and Radbruch, A. (1990) High gradient magnetic cell separation with MACS. *Cytometry*, **11**, 231–238.

4 Ashkin, A. (1970) Acceleration and trapping of particles by radiation pressure. *Phys. Rev. Lett.*, **24**, 156–159.

5 Ashkin, A. (1986) Observation of a single-beam gradient force optical trap for dielectric particles. *Opt. Lett.*, **11**, 288–290.

6 Kuo, S.C. (2001) Using optics to measure biological forces and mechanics. *Traffic*, **2**, 757–763.

7 Jonas, A. and Zemanek, P. (2008) Light at work: the use of optical forces for particle manipulation, sorting, and analysis. *Electrophoresis*, **29**, 4813–4851.

8 Constable, A., Kim, J., Mervis, J., Zarinetchi, F., and Prentiss, M. (1993) Demonstration of a fiberoptic light-force trap. *Opt. Lett.*, **18**, 1867–1869.

9 Grover, S.C., Skirtach, A.G., Gauthier, R.C., and Grover, C.P. (2001) Automated single-cell sorting system based on optical trapping. *J. Biomed. Opt.*, **6**, 14–22.

10 Lincoln, B., Schinkinger, S., Travis, K., Wottawah, F., Ebert, S., Sauer, F., and Guck, J. (2007) Reconfigurable microfluidic integration of a dual-beam laser trap with biomedical applications. *Biomed. Microdevices*, **9**, 703–710.

11 Sims, C.E. and Allbritton, N.L. (2007) Analysis of single mammalian cells on-chip. *Lab Chip*, **7**, 423–440.

12 Eriksson, E., Scrimgeour, J., Graneli, A., Ramser, K., Wellander, R., Enger, J., Hanstrop, D., and Goksor, M. (2007) Optical manipulation and microfluidics for studies of single cell dynamics. *J. Opt. A Pure Appl. Opt.*, **9**, S113–S121.

13 Bellini, N., Vishnubhatla, K.C., Bragheri, F., Ferrara, L., Minzioni, P., Ramponi, R., Cristiani, I., and Osellame, R. (2010) Femtosecond laser fabricated monolithic chip for optical trapping and stretching of single cells. *Opt. Express*, **18**, 4679–4688.

14 Jess, P.R.T., Garcés-Chávez, V., Smith, D., Mazilu, M., Paterson, L., Riches, A., Herrington, C.S., Sibbett, W., and Dholakia, K. (2006) Dual beam fibre trap for Raman micro-spectroscopy of single cells. *Opt. Express*, **14**, 5779–5791.

15 Kreysing, M.K., Kiessling, T., Fritsch, A., Dietrich, C., Guck, J.R., and Käs, J.A. (2008) The optical cell rotator. *Opt. Express*, **16**, 16984–16992.

16 Guck, J., Ananthakrishnan, R., Mahmood, H., Moon, T.J., Cunningham, C.C., and Käs, J. (2001) The optical stretcher: a novel laser tool to micromanipulate cells. *Biophys. J.*, **81**, 767–784.

17 Guck, J., Schinkinger, S., Lincoln, B., Wottawah, F., Ebert, S., Romeyke, M., Lenz, D., Erickson, H.M., Ananthakrishnan, R., Mitchell, D., Käs, J., Ulvick, S., and Bilby, C. (2005) Optical deformability as an inherent cell marker for testing malignant transformation and metastatic competence. *Biophys. J.*, **88**, 3689–3698.

18 Remmerbach, T.W., Wottawah, F., Dietrich, J., Lincoln, B., Wittekind, C., and Guck, J. (2009) Oral cancer diagnosis by mechanical phenotyping. *Cancer Res.*, **69**, 1728–1732.

19 Lautenschläger, F., Paschke, S., Schinkinger, S., Bruel, A., Beil, M., and Guck, J. (2009) The regulatory role of cell mechanics for migration of

differentiating myeloid cells. *Proc. Natl. Acad. Sci. U. S. A.*, **106**, 15696–15701.

20 Wang, M.M., Tu, E., Raymond, D.E., Yang, J.M., Zhang, H., Hagen, N., Dees, B., Mercer, E.M., Forster, A.H., Kariv, I., Marchand, P.J., and Butler, W.F. (2005) Microfluidic sorting of mammalian cells by optical force switching. *Nat. Biotechnol.*, **23**, 83–87.

21 Schütze, K., Niyaz, Y., Stich, M., and Buchstaller, A. (2007) Noncontact laser microdissection and catapulting for pure sample capture. *Methods Cell Biol.*, **82**, 649–673.

22 MacDonald, M.P., Spalding, G.C., and Dholakia, K. (2003) Microfluidic sorting in an optical lattice. *Nature*, **426**, 421–424.

23 Ladavac, K., Kasza, K., and Grier, D.G. (2004) Sorting mesoscopic objects with periodic potential landscapes: optical fractionation. *Phys. Rev. E*, **70**, 010901.

24 Paterson, L., Papagiakoumou, E., Milne, G., Garces-Chavez, V., Briscoe, T., Sibbett, W., Dholakia, K., and Riches, A.C. (2007) Passive optical separation within a 'nondiffracting' light beam. *J. Biomed. Opt.*, **12**, 054017–054013.

25 Panaro, N.J., Lou, X.J., Fortina, P., Kricka, L.J., and Wilding, P. (2005) Micropillar array chip for integrated white blood cell isolation and PCR. *Biomol. Eng.*, **21**, 157–162.

7
Laser Microtomy

Holger Lubatschowski, Fabian Will, Sabine Przemeck, and Heiko Richter

7.1
Cutting by Optical Breakdown

The key technology of a laser microtome is an ultrashort (femtosecond) pulsed laser, emitting light in the near-infrared (NIR) range. Due to the rapid development of commercially available turn-key laser systems in recent years, the use of ultrafast laser technology has become much easier and has opened up new applications in the life sciences field.

Laser light in the NIR range around 1000 nm is well suited for the processing of biological material, since most biological tissues have a very low absorption coefficient at this wavelength. Hence manipulation of tissue is not just limited to the surface, but can even be performed inside the material.

While cutting, the laser beam of a laser microtome is tightly focused into the specimen by a high numerical aperture objective. Due to the extreme intensities of up to $1\,\mathrm{TW\,cm^{-2}}$ inside the focus, multi-photon absorption causes ionization of the tissue. This process is called optical breakdown and leads to the formation of plasma [1, 2]. The rapid expansion of the plasma causes disruption of the tissue and is responsible for the cutting process (Figure 7.1).

If the pulse duration is sufficiently short (100–500 fs) and the diameter of the focal spot is nearly diffraction limited (1 μm), only a very low pulse energy of ~10–100 nJ is needed to induce the optical breakdown. This limits the interaction range to diameters below 1 μm. The material separation only takes place within the focal region. Outside this region, no thermal or mechanical damage can be detected.

7.2
The Laser Microtome at a Glance

The main component of a typical laser microtome (Figure 7.2) is a high-power femtosecond oscillator emitting ultrashort laser pulsing with a wavelength of 1030 nm, a pulse duration of about 300 fs, and a pulse repetition rate variable

Handbook of Biophotonics. Vol.2: Photonics for Health Care, First Edition. Edited by Jürgen Popp, Valery V. Tuchin, Arthur Chiou, and Stefan Heinemann.

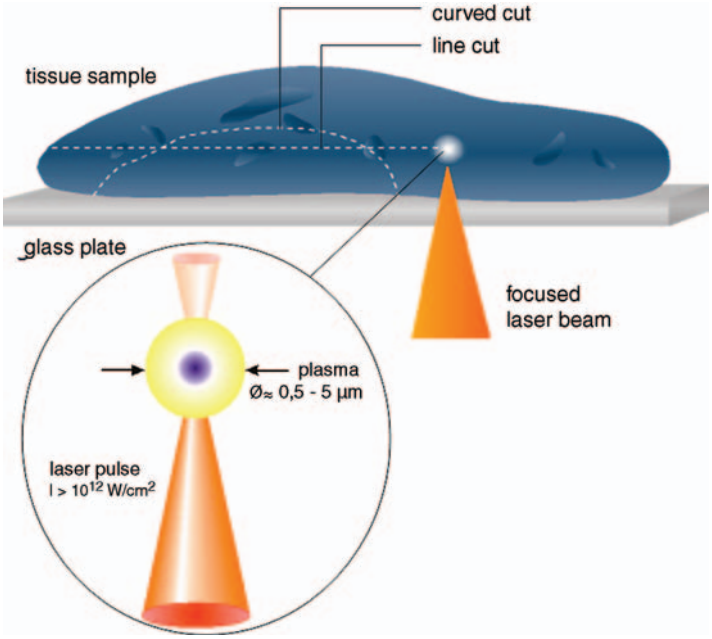

Figure 7.1 Working principle of the laser microtome. A laser-induced plasma is used to cut the tissue without any mechanical forces being applied. The NIR radiation of the laser penetrates the tissue up to 1 mm.

ranging from some kHz to 10 MHz. The maximum average power is ~2.5 W, where laser pulse energies of up to 100 nJ were focused into the sample with a high numerical aperture (>0.5).

The laser beam is deflected by a fast scanner device for lateral deflection whereas the *z*-direction is controlled by a piezo-driven positioning stage. Parameters such as pulse overlap, slice thickness, and the size of the cutting area can be set by the user. Typically, an area of up to 14 × 14 mm can be processed. Larger areas are possible. The cutting speed depends on the properties of the sample, 1 $mm^2 s^{-1}$ being typical. At present slices of 5–100 µm thickness are generated. Thinner slices are also possible, but handling of such tissue slices following removal of the sample bulk is more difficult. For light microscopic examinations, a thickness of 5–10 µm is in most cases sufficient. However, thicker slices are of interest for, for example, primary culture, neurobiological experiments, and pretreatment of samples for ultra microtomy.

7.3 Preparing and Sectioning the Tissue Samples

Because no mechanical forces are applied to the sample, tissue can be processed in its native state and does not need prior fixation, embedding, or freezing. The tissue

Figure 7.2 The laser microtome as a stand-alone system.

sample is placed on a conventional glass microscope slide. In order to achieve good results, the tissue surface has to be plane with good optical contact with the glass slide. If needed, a small drop of liquid is helpful to assist refractive index matching. Saline solutions are as good as most of the media used for cell culture (Figure 7.3).

The software allows three cutting modes: cutting of the whole field (maximum size and maximum time), of a defined rectangular field (e.g., 5×6 mm), or of a customized field by setting position markers. According to the precision of the z-axis, the thickness of the slices can be controlled with an accuracy of better than 3 μm.

During the cutting process, a live video of the sample, that is, the cutting plane, is shown on the control screen. This allows the user to observe whether the cutting procedure is successful or not. A rapidly growing field of microbubbles is a typical indication of the occurrence of photodisruption and therefore a sign of correct cutting. After the cutting process, the tissue section is separated from the

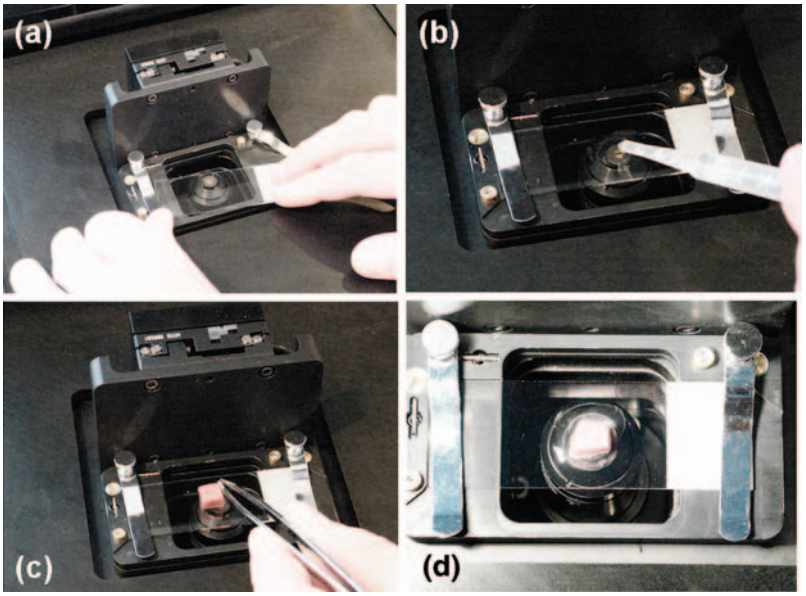

Figure 7.3 Preparation of the sample. (a) A conventional microscopic glass slide acts a tissue holder. (b) A small drop of liquid is helpful to assist refractive index matching. (c) The fresh tissue is placed on the glass slide and (d) a built-in camera of the laser microtome helps to find the area of interest.

bulk with tweezers and placed on a glass slide. Now it can be stained and covered if necessary.

7.4 OCT Controlled 3D Processing

Cutting of flat sections by femtosecond laser technology is only the first step in a new direction in laser microtomy. As a next step, Optical coherence tomography (OCT) imaging was implemented in the system. OCT [3, 4] is a method for imaging different layers of transparent or scattering tissue by scanning the area of interest with a low coherent light source. The measuring principle is similar to that of ultrasound imaging. As a typical light source, superluminescent diodes or even the femtosecond laser pulses themselves with a broad emission band and a corresponding low coherence length can be used. The penetration depth of the NIR radiation is up to 2 mm into the tissue. Due to differences in their optical pathlengths, photons reflected from different layers inside the tissue can be distinguished by interference measurements with an external reference plane. Figure 7.4 shows an OCT image of corneal tissue where the cut was navigated right below the epithelium.

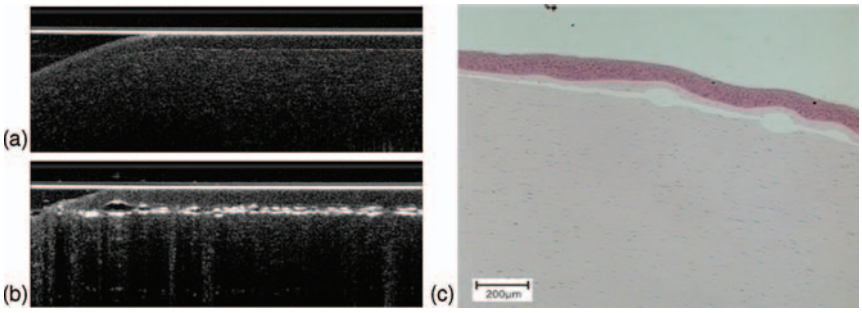

Figure 7.4 Example of an OCT-guided cut below the epithelium of a porcine cornea. (a) OCT image before the cut. The picture is upside down. The bright horizontal line represents the surface of the glass plate. (b) The laser-induced gas bubbles can be monitored as the cutting line right below the epithelium. The bubbles disappear within minutes. (c) Histological section of the cornea after the cut.

Having such a tomographic imaging system implemented, real 3D cutting near the surface of tissue samples is possible, targeting specific areas or volumes of interest.

7.5
Tissue Samples

In principle, every soft tissue with the exception of melanin-containing tissue can be processed, since the 1040 nm radiation is barely absorbed by tissue chromophores. Hard tissues such as bones or of dental origin are also suitable for cutting without decalcifying them. For hard tissues, embedding may be necessary, especially if the tissue is very brittle. The time-consuming preparation of ground sections of embedded hard tissues is therefore shortened. In Figure 7.5, sections of different hard and soft tissue are shown as an example of laser-processed sectioning. The samples show no thermal or mechanical alterations and are well suited for further light microscopic examination. Typical thickness of these slices was 20 µm. Even plastic material can be cut, provided that it has a bright color (Figure 7.6).

7.6
Not for Routine but for Special Cases

Of course, the laser microtome is not a device for routine pathology, as the procedure of tissue separation is too slow. However, it has its clear advantages over standard procedures when preparing tissue in its native state. For investigations based on immunostaining, it can be desirable to keep tissue alive. Furthermore, there are

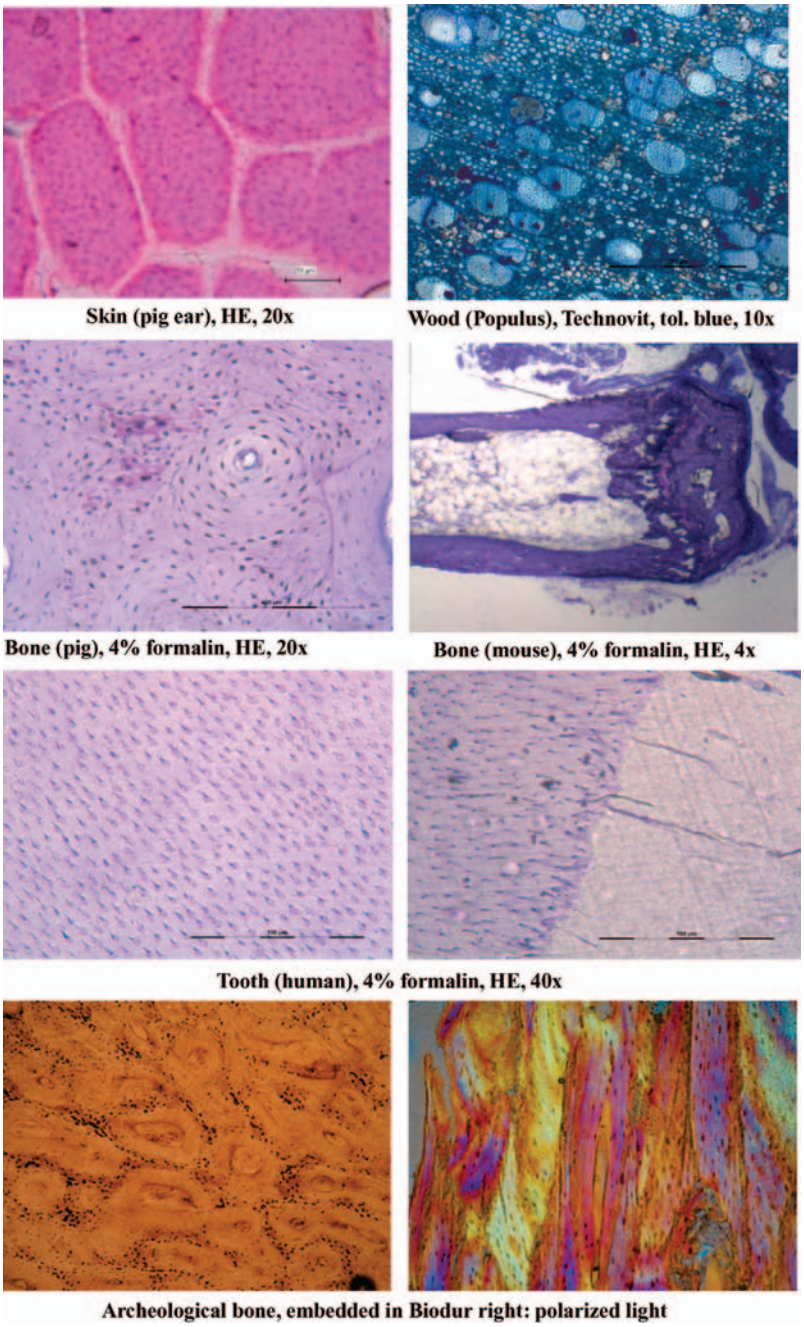

Figure 7.5 Sections of different hard and soft tissues are shown as an example of laser-processed sectioning. The samples show no thermal or mechanical alterations and are well suited for further light microscopic examination. Typical thickness of these slices was 20 μm.

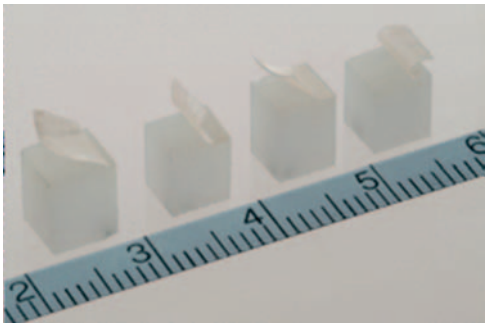

Figure 7.6 Example of Teflon blocks, which were cut into 20 μm slices.

several applications which are, at present, difficult or impossible to realize with conventional sectioning methods, including the cutting of hard tissue, plants, wood, and other materials. The laser microtome might be a good option for these applications. It has the potential to solve different problems in various research fields from plant biology to regenerative medicine.

References

1 Vogel, A. and Venugopalan, V. (2003) Mechanisms of pulsed laser ablation of biological tissues. *Chem. Rev.*, **103**, 577–644.

2 Vogel, A., Noack, J., Hüttman, G., and Paltauf, G. (2005) Mechanisms of femtosecond laser nanosurgery of cells and tissues. *Appl. Phys. B*, **81**, 1015–1047.

3 Huang, D., Swanson, E.A., Lin, C.P., Schuman, J.S., Stinson, W.G., Chang, W., Hee, M.R., Flotte, T., Gregory, K., Puliafito, C.A., and Fujimoto, J.G. (1991) Optical coherence tomography. *Science*, **254** (5035), 1178–1181.

4 Drexler, W. and Fujimoto, J.G. (2008) *Ultrahigh Resolution Optical Coherence Tomography*, Springer, Berlin.

8
Classical Microscopy

Kerstin Roeser, Dietlind Zuehlke, Martin Gluch, Gernoth Grunst, Markus Sticker, Klaus Bendrat, and Axel Niendorf

8.1
Appearance

Classical microscopy relates to light microscopy, that is, incident or transmitted light with a magnification range from 10× to 1000×. This technique has a wide range of applications in the life and material sciences. Here we focus on the role played by classical microscopy in medicine, especially in surgical pathology. However, it is recognized that there is considerable overlap between pathology, anatomy, and the broad field of cell biology.

8.2
Application

Pathology is one of the fundamental diagnostic disciplines. Tissues and cells can be viewed under a microscope and thereby be classified in an order that discriminates between normal, disorders of metabolism, malformation, inflammation, and tumor. In the case of tumor diagnosis, a subclassification into benign and malignant groups is of crucial importance for therapeutic procedures.

8.3
Pathology

Today, more than 90% of a pathologist's work load concerns living patients. One of the most important tasks is to diagnose and classify tumors, which apart from few exceptions is still done by microscopy. The basic requirement is a representative small tissue specimen followed by a optimal processing with the option of subsequent use. After applying selected visualization techniques to give the tissue some contrast or to mark specific molecules, specimens are all examined by means of light microscopic methods. The diagnosis will then be the basis for the risk assessment and also any therapeutic decisions. However, taking into account the fact that a biopsy always

Handbook of Biophotonics. Vol.2: Photonics for Health Care, First Edition. Edited by Jürgen Popp, Valery V. Tuchin, Arthur Chiou, and Stefan Heinemann.

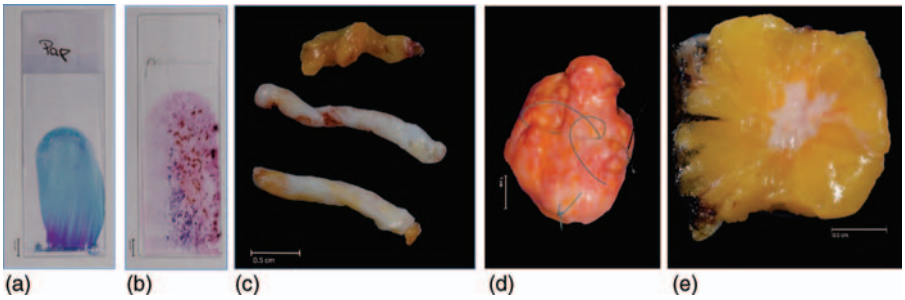

Figure 8.1 Biopsy techniques: (a) cytologic smear; (b) fine needle aspirate (FNA); (c) core biopsies; (d) biopsy; (e) wide excision section.

represents a sample and the microscopic image shows only a section, the need for contextual information leading to a general finding is obvious [1].

This chapter addresses primarily the nonmedical reader and is intended to inform about techniques and procedures in the field of classical microscopy. This is demonstrated exemplarily for breast cancer diagnostics.

8.4 Materials

For diagnostic purposes, tissue samples are used for microscopic investigations. These samples are taken by *biopsy*, which is the removal of cells, tissue, or fluid for diagnosis of diseased tissue.

There are two main techniques to be distinguished: the closed techniques, including *fine needle aspiration* (FNA) and *core needle biopsy*, and the open technique. FNA is a type of biopsy that removes cells trough suction using a syringe. A core needle biopsy is done with a larger needle. Biopsies in the classical sense are the removal of tissue. When a malignancy is suspected, then the tissue specimen is marked to define the margins. However, all techniques correspond to common principles, namely obtaining sufficient tissue for diagnosis and using the least traumatic method (see Figure 8.1).

8.5 Methods (Tissue Processing)

Tissue processing in diagnostic pathology comprises fixation, dehydration, embedding, sectioning, staining, and cover slipping.

Chemical fixatives are used to preserve tissue from degradation and to maintain the structure of cells and their subcellular components. There are five groups of fixatives based on different mechanisms (Table 8.1). The choice of fixative is based on the type of tissue and the histological details to be demonstrated.

Table 8.1 Fixatives used in histology.

Substance	Application	Concentration/content	Advantages/disadvantages	Mechanism of action
Aldehydes	Surgical pathology; autopsy tissue; routine light microscopy	4% formaldehyde in phosphate-buffered saline	Penetrate tissue well, act relatively slowly	Cross-linking proteins
Glutaraldehydes	Electron microscopy	2.5% glutaraldehyde in phosphate-buffered saline	Penetrate poorly; act very quickly; give best overall cytoplasmic and nuclear detail	Deformation of the α-helix structure in proteins
Mercurials	Reticuloendothelial tissue (lymph nodes, spleen, thymus, bone marrow)	Mercuric chloride in Zenker's or B-5 fixative	Penetrate relatively poorly, act fast, give excellent nuclear detail	Unknown
Alcohols	Cytologic smears	95% ethanol	Penetrate cells well, act quickly, give good nuclear detail	Protein denaturation
Oxidizing agents	Electron microscopy; only for special applications	Permanganate, dichromate, osmium tetraoxide	Penetrate relatively poorly	Cross-linking proteins
Picrates	Testis, gastrointestinal tract, endocrine tissue, hematopoietic tissue	Picric acid in Bouin's solution	Penetrate relatively poorly, give good nuclear detail	Unknown

In addition to the nature of the fixatives, there are some critical steps that influence the quality of fixation. First, there must be buffering capacity in the fixative to prevent excessive acidity. Then, the thickness of the tissue sample should be adjusted to the penetration properties of the particular fixative. The fixative will be exhausted during the process, so a 10:1 volume ratio of fixative to tissue is required. Alternatively, interval-type changes of the fixative can solve the problem. By increasing the temperature, the tissue will be fixed faster, but excessive heat will cause artifacts. The concentration of the fixative should be adjusted to the lowest possible level because too high concentrations may adversely affect the tissue and produce artifacts. Also important is the time interval from removal of tissue to fixation. A prolonged dwell time causes artifacts by drying and also the loss of cellular organelles, more nuclear shrinking, and artifactual clumping.

In order to produce microscopic specimen slides, the fixed tissue has to be embedded. Paraffin wax is most frequently used. It is similar in density to tissue, allowing sufficiently thin sections to be cut. Since water and paraffin are immiscible, all traces of water must be removed from tissue. This *dehydration* process is done by passing the tissue through a series of increasing alcohol concentrations. This is followed by a hydrophobic clearing agent (xylene) to remove the alcohol, and finally the infiltration agent (molten paraffin wax), which replaces the xylene. The tissue samples are now ready for external embedding.

During the *embedding* process, the tissue samples are placed in molds along with liquid embedding material, which is then hardened by cooling. The hardened blocks containing the tissue samples are then ready to be sectioned.

Formalin-fixed, paraffin-embedded (FFPE) tissues may be stored at room temperature, and nucleic acids (both DNA and RNA) may be recovered from them decades after fixation, making FFPE tissues an important resource for retrospective studies in medicine. Paraffin-embedded tissues are routinely stored in pathology archives.

Cutting the embedded tissue into sections is done with a microtome. Microtomes have a mechanism for either advancing the block across the knife (rotary microtome) or the knife across the block (sled microtome). *Sectioning* takes much skill and practice and it is important to have properly fixed and embedded tissue to avoid artifacts (tearing, ripping, holes, folding). Sections are floated on warm water to remove wrinkles and mounted on glass microscope slides.

Direct sectioning of a frozen tissue is performed with a cryomicrotome. This method does not need tissue fixation and embedding and therefore has the advantages of speed, maintenance of most enzymes and immunological functions, and relative ease of handling. It has the disadvantage that ice crystals formed during the freezing process will distort the image of the cells. Frozen sections are necessary to obtain rapid diagnosis of a pathological process during surgical procedures (see Figure 8.2).

Figure 8.2 Tissue processing.

8.6 Histological Staining

Staining is employed in both to give contrast to the tissue and to highlight particular features of interest.

To allow water-soluble dyes to penetrate the sections, the paraffin wax has to be removed from the tissue. This is done by running the sections through xylene to alcohol to water. Various dyes are available with different abilities to stain cellular and tissue components. The choice of stain is based on the diagnostic need.

Routine staining is carried out with hematoxylin and eosin (H&E), which is the most commonly used stain in light microscopic histology and histopathology. Hematoxylin, a basic dye, stains nuclei blue, and eosin, an acidic dye, stains the cytoplasm pink.

For special staining, various techniques have been used to stain cells and cellular components selectively; for more details, see Sternberg *et al.* [2]. Stains that are commonly used in breast cancer diagnosis are listed in Table 8.2.

For *immunohistochemistry*, antibodies have been used to visualize specifically proteins, carbohydrate, and lipids. This technique allows the identification of categories of cells under a microscope; more details can be found elsewhere [3–6]. A list of antibodies is given in Table 8.3.

In situ hybridization is used to identify specific DNA or RNA molecules either with fluorescence probes or otherwise labeled nucleic acid probes. To detect fluorescent signals, fluorescence microscopy (see the next section) and confocal microscopy are used, giving good intracellular details [7, 8]; for more details, see Table 8.4.

Table 8.2 Histological stainings used in breast cancer diagnostics.

H&E	General overview staining for histological specimens Nucleus, blue. Cytoplasm, pink. Red blood cell, orange/red. Collagen fiber, pink
Giemsa	General overview staining for cytological specimens and used to differentiate cells present in hematopoietic tissue (lymph nodes) Nucleus, purple–red. Cytoplasm, light blue
EvG (Elastica van Gieson)	Staining to differentiate different types of connective tissue in histological sections Elastic fibers, blue. Nucleus, red. Collagen, light pink. Muscle fibers, light red
PAS (periodic acid–Schiff reaction)	Common staining technique in histology for localizing glycogens and carbohydrates Membranes and mucus, magenta. Nucleus, blue. Cytoplasm, light pink
Iron	Staining to demonstrate ferric iron in tissue sections Iron, blue. Nucleus, red. Background, pink

Table 8.3 Antibodies used for immunohistological staining in breast cancer diagnostics.

Cytokeratins	Monoclonal anti-cytokeratins are specific markers of epithelial cell differentiation and have been widely used as tools in tumor identification and classification. They facilitate typing of normal, metaplastic, and neoplastic cells. They are also useful in detecting micrometastases in lymph nodes, bone marrow, and other tissues and for determining the origin of poorly differentiated tumors
BCL2	BCL2 is an integral outer mitochondrial membrane protein that suppresses apoptosis in a variety of cell systems, including factor-dependent lymphohematopoietic and neural cells. It regulates cell death by controlling the mitochondrial membrane permeability. Heterodimerization with BAX requires intact BH1 and BH2 domains, and is necessary for anti-apoptotic activity
HER2	ErbB 2 is a receptor tyrosine kinase of the ErbB 2 family. It is closely related in structure to the epidermal growth factor receptor. ErbB 2 oncoprotein is detectable in a proportion of breast and other adenocarcinomas, and also transitional cell carcinomas. In the case of breast cancer, expression determined by immunohistochemistry has been shown to be associated with poor prognosis
ER (estrogen receptor)	The estrogen receptor (ER) is a 66 kDa protein that mediates the actions of estrogens in estrogen-responsive tissues. It is a member of a large superfamily of nuclear hormone receptors that function as ligand-activated transcription factors. The ER is an important regulator of growth and differentiation in the mammary gland. The presence of ER in breast tumors indicates an increased likelihood of response to anti-estrogen (e.g., tamoxifen) therapy
PR (progesterone receptor)	The human progesterone receptor (PR) is a member of the steroid family of nuclear receptors. It has been proposed that expression of PR determination indicates a responsive ER pathway, and therefore may predict likely response to endocrine therapy in human breast cancer. A number of studies have shown that PR determination provides supplementary information to ER, both in predicting response to endocrine therapy and estimating survival. PR has proved superior to ER as a prognostic indicator in some studies

Table 8.4 Selection of probes used for *in situ* hybridization in cancer diagnostics.

ERBB2	Epidermal growth factor (EGF) receptor that enhances kinase-mediated activation of downstream signaling pathways. Amplification and/or overexpression of this gene has been reported in numerous cancers, including breast and ovarian tumors
TOP2A	DNA topoisomerase, involved in processes such as chromosome condensation, chromatid separation, and the relief of torsional stress that occurs during DNA transcription and replication. The TOP2A gene functions as the target for several anticancer agents and a variety of mutations in this gene have been associated with the development of drug resistance
cMYC	cMYC functions as a transcription factor that regulates transcription of specific target genes. Mutations, overexpression, rearrangement, and translocation of this gene have been associated with a variety of hematopoietic tumors, leukemias, and lymphomas, including Burkitt lymphoma
CCND1	Cyclins function as regulators of CDK kinases. Cyclin D1 has been shown to interact with tumor suppressor protein Rb. Mutations, amplification, and overexpression of this gene, which alters cell cycle progression, are observed frequently in a variety of tumors and may contribute to tumorigenesis
EGFR	EGFR is a cell surface protein that binds to epidermal growth factor. Binding of the protein to a ligand induces receptor dimerization and tyrosine autophosphorylation and leads to cell proliferation. Mutations in this gene are associated with lung cancer
ESR1	The estrogen receptor, a ligand-activated transcription factor, essential for sexual development and reproductive function, but also plays a role in other tissues such as bone. Estrogen receptors are also involved in pathological processes including breast cancer, endometrial cancer, and osteoporosis
MDM2	MDM2 is a target gene of the transcription factor tumor protein p53. Overexpression of this gene can result in excessive inactivation of tumor protein p53, diminishing its tumor suppressor function. This protein also affects the cell cycle, apoptosis, and tumorigenesis through interactions with other proteins

8.7 Microscopy

The microscope is the enabling tool for the pathologist when it comes to morphological analysis, as it allows viewing of the patient sample from overview up to subcellular resolution. The basic equipment has remained the same for more than 100 years: the compound microscope comprises sample illumination with transmitted light, an objective revolver allows the primary magnification range to be selected between 1× and 100× and the ocular lens delivers the magnified image to the observer. Together with the ocular lens, the total magnification range extends from 10× to 1000×, which corresponds to a field of view between 2.3 mm and 23 μm. In addition to the magnification, the resolution is also important for seeing small object details. The resolution is dependent on the numerical aperture of the objective and illumination, and object structures down to 0.25 μm can be resolved.

In order to make the microscope workplace for the pathologist an efficient tool, many technological improvements have been made over time:

- automatic alignment of the microscope to maintain the highest image fidelity over time
- ocular lenses with a large field of view which allow one to look at large sample areas at high magnification
- ergonomic improvements to minimize stress on neck and hands during day to day operation
- LED illumination with long lifetime and high stability (Figure 8.3).

In addition to these ergonomic additions there are two major additions:

1) With the growing importance of molecular markers, fluorescence has entered routine pathology. It allows visualization of multiple biomarkers on the same sample region, which increases the information density. However, the downside compared with colorimetric staining techniques is that the tissue morphology

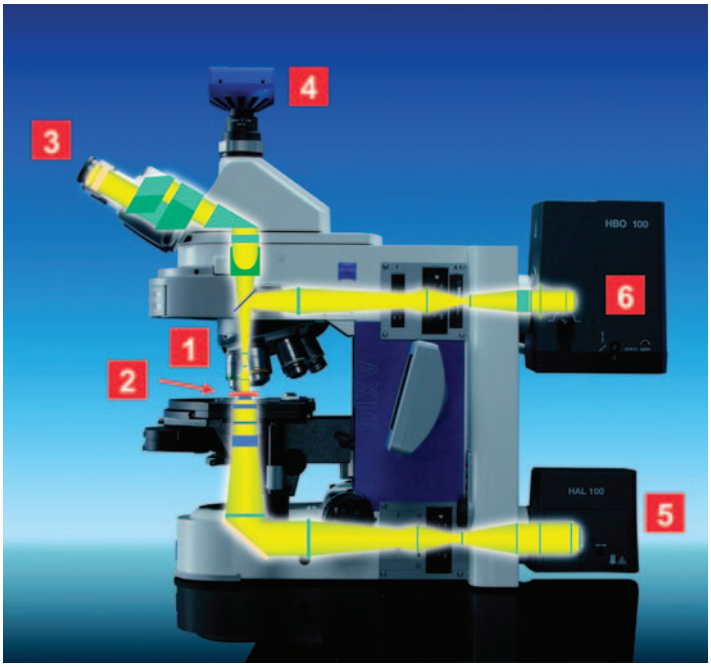

Figure 8.3 Course of beam in light microscopy. In the bright field beam path the objective (1) magnifies the object (2), which can be viewed through the ocular lens (3) or imaged on to a camera (4). The object is illuminated from a white light source (5). In the fluorescence beam path, the sample is illuminated through the objective with a certain wavelength (6), which is absorbed by the fluorophore. The fluorophore emits a longer wavelength which is collected from the objective. After the objective, a dichroic mirror reflects the excitation light and transmits the emission. Only the molecular marker becomes visible for the pathologist.

is not available. So far, fluorescence has been deployed mostly in areas where this is not of crucial importance (e.g., chromosome analysis).

2) Documentation with a digital camera is now an instant easy-to-use option to capture a region of interest. Most of the laboratory information systems today support image attachments, which makes it easy to share images between pathologists for a second opinion.

In the case of unstained samples the pathologist has some contrast techniques that permit the examination of the morphology without staining the sample:

- Dark field contrast shows sample structures where light is scattered or diffracted.
- Polarization contrast shows sample structures due to differences in the birefringent and depolarizing properties of the sample.
- Differential interference contrast and phase contrast make visible small structures that have different refractive indices.

8.8 Diagnostics

8.8.1 Context-Dependent Aspects in Morphological Diagnostics

Diagnostic procedures in surgical pathology are based on the total clinical information and morphological examination at the gross and microscopic levels. The microscopic examination starts with a low magnification to obtain an overview of the whole specimen followed by a selection of areas of interest to be examined in more detail at a higher magnification. Histopathology is a "precision tool" because pathologists are confined to certain (morphological) criteria to define entities. These entities are listed in monographs or, for instance in the case of tumor diagnostics, in series such as the WHO and the Armed Forces Institute of Pathology series, which again are based on the scientific literature. In a practical sense, the pathologist addresses a case with knowledge about the possible single criteria and also the context in which these criteria are likely to occur. In modern pathology, in addition to morphological criteria, biochemical, immunological, and molecular findings become an essential part of the diagnosis. Furthermore, there has been growing interest in tools able to reduce human subjectivity and improve workload. Whole slide scanning technology combined with automated image analysis can offer the capacity to generate fast and reliable results (Figures 8.4–8.7).

8.8.2 Cognitive Aspects of Digital Microscopy

Digital microscopy (DM) can enhance the potential to derive light-based information about reality. Combinable IT modules enable support of human information processing.

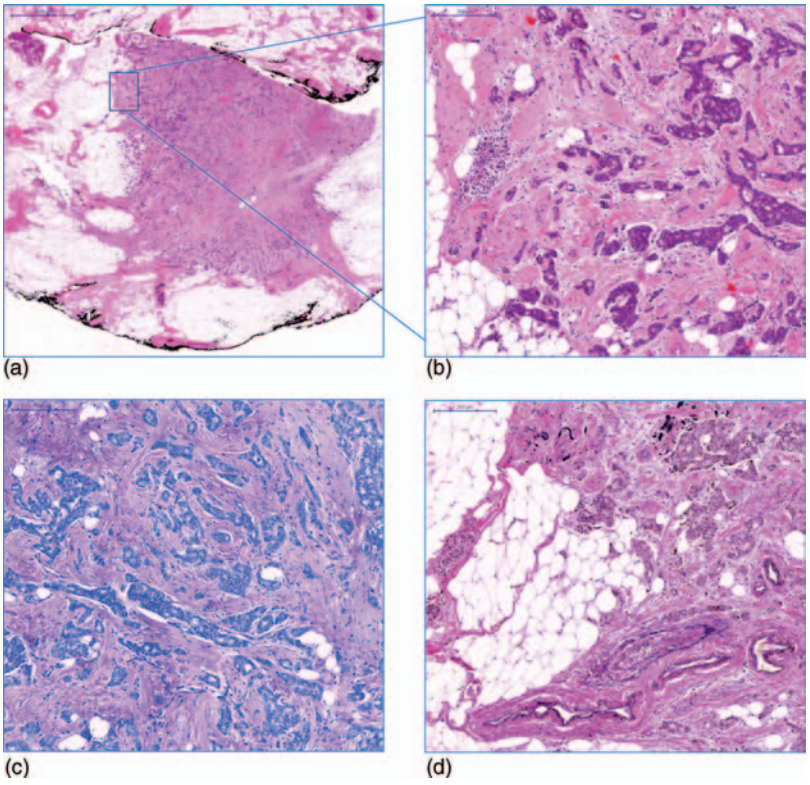

Figure 8.4 Histological analysis. (a) H&E staining is used to identify tumor. Here is shown a classical invasive ductal carcinoma of the breast (G1pT1cpN0V0R0) (×1); (b) H&E staining of the same section (x10); (c) Giemsa staining for improved demonstration of cytological characteristics (×10); (d) EvG staining for more detailed differentiation of connective tissue (×10).

Human experts such as pathologists are forced to focus on the visual data overflow in order to derive relevant information. In contrast, computer-based data handling can take into account extensive and vastly more heterogeneous data. For instance, it is technically possible to merge various images of tissue slices with different staining and to use the integrated information in a common coordinate system.

The amount of data that is produced in this way is huge. Taking into account four different stainings with about 1.5 billion pixels per image (which is the average size of a digital slide with an optical resolution of 40), and relate for image analysis purposes each pixel to a surrounding neighborhood of about 1 cm^2, the resulting data volume is approximately 22 million terabytes! On the other hand, without integration of the analyses into human comprehension processing, the impact of this kind of technical support is without effect in life science research and pathological routine (Figure 8.8).

Digital images in this respect provide a very promising starting point. They can be condensed into semantic units through the application of machine learning-based

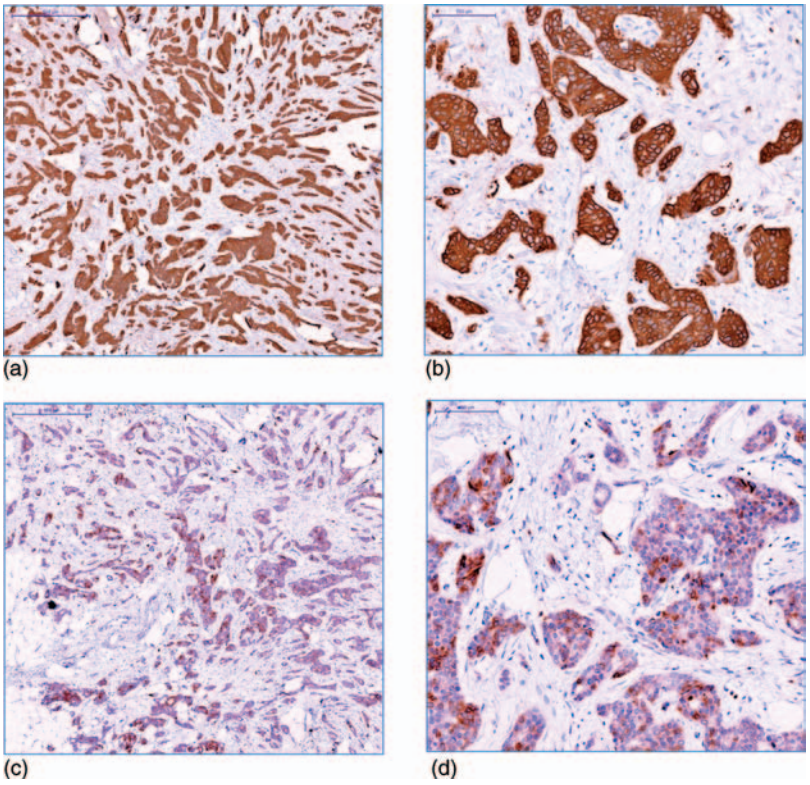

Figure 8.5 Immunohistochemical analysis of tumor marker in breast cancer. (a) Epithelial tumor component demonstrated by expression of cytokeratins (mAB, mouse anti-human pan cytokeratin) (5%). (b) Medium-sized tumor cell islands surrounded by a cell-rich connective tissue (×20); (c) tumor cells of this particular case expresses express bcl-2 in the cytoplasm (mAB, mouse anti-human bcl-2) (×5); (d) stained cells show a distinctive expression level that become obvious at higher magnification by different staining intensities (×20).

image analyses (for an overview, see [9]). The integration process requires mutual "understanding" of humans and machine concerning their respective contributions. Even image experts such as pathologists lack an understanding of what type of additional information can be expected from machine-made image analyses. Therefore, when starting a research program they are unable to give the system cues about important and technically processable image details. Procedures that start with expert labeling of images are called supervised learning methods. From experience concerning DM in life science projects, this is not the most efficient starting point for the integration of human and technical cognition (Figure 8.9).

An alternative is unsupervised learning methods that exploit cluster analyses in order to identify technically manageable image features that can, for example, discriminate various tissue types in pathological slices. The results can be mapped on to the images in the form of color codings for different regions. Visual exploration

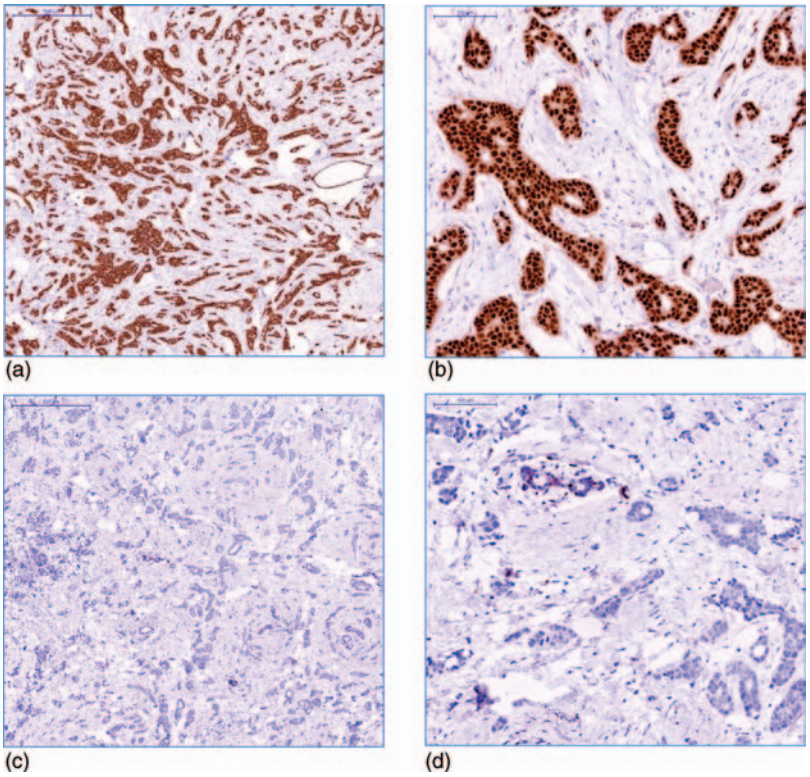

Figure 8.6 Immunohistochemical analysis of steroid receptors in breast cancer. (a) Epithelial tumor component is highly positive (100%) for the estrogen receptor (ER) (mAB, mouse anti-human estrogen receptor) (×5); (b) ER is expressed in the nucleus, in this particular case with a slight cytoplasmic staining (×20); (c) the tumor sample demonstrated here is negative for the progesterone receptor (PR) (mAB, mouse anti-human progesterone receptor) in the epithelial tumor component (×5); (d) only a few cells lining nontimorous ducts show a positive nuclear staining (×20).

and control systems can support the human expert in the necessary validation and adjustment of these findings. If the results are validated by the expert, there is a considerable advantage of technical image analyses. They are comprehensive and therefore applicable to quantitative evaluations of tissue slices that are notoriously problematic for human experts (Figure 8.10).

Results that are obtained in this way can be seen as expedient findings in a diagnostic pattern if they can trigger further experimental steps such as microscopy records applying additional structural and functional staining. Even if senseless "data cemeteries" can be avoided through such interlocking of human–computer interaction, there will arise a multilayered complexity of image-related information that will soon become confusing. In order to support navigation in the growing information space and even the introduction of technical data mining, it is necessary to introduce an image database with pertinent metadata. This combination of machine

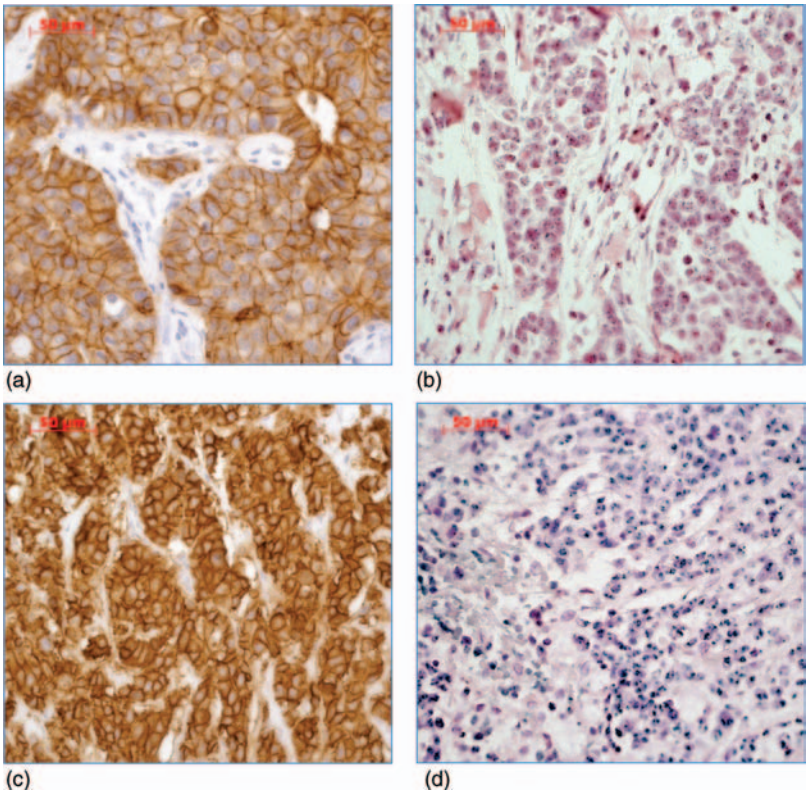

Figure 8.7 Immunohistochemical analysis and *in situ* hybridization for Her-2/neu gene amplification in breast cancer for evaluating Her-2/neu status. (a) Her-2 staining pattern in immunohistochemistry refer to a score of 2 + according to the guideline recommendations for HER2 testing in breast cancer [10] (mAB, mouse anti-human erbB2) (×40); (b) CISH, using dual-color probes against Her-2 (blue) located on chromosome 17 and a probe against the centromeric region of chromosome 17 (red) (ZytoDot 2C Spec HER2/CEN 17) reveals no amplification for Her-2 (×40); (c) another case shows a Her-2 staining pattern that refers to a score of 3 + in immunohistochemistry [10] (×40); (d) CISH reveals an amplification for Her-2 as demonstrated by large dots for the Her-2 signal (blue) and two separate signals for Cen 17 (×40).

learning-based analyses and an image database can considerably enhance the value of DM, especially for the life sciences. Such an enabling environment supports the gradual extension and validation of complex and multilayered knowledge that is impossible without the mutual completion and control of human and machine-made analytical findings.

Digital microscopy renders images of heterogeneous resolution scales and staining. Pathological tissue images can show overviews, cells, and even functional molecules within cells. The spatially correlated evaluation of this heterogeneous information yields a potential for biological and pathological insights that could

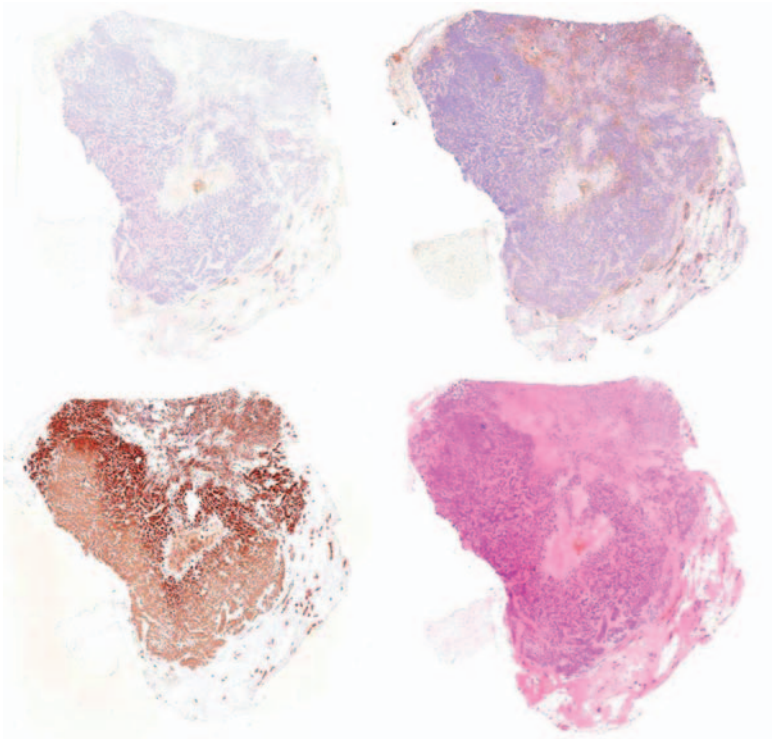

Figure 8.8 Four different histological stainings (CD45, VIM, AE13, HE) for registration into one synthetic image stack.

not be exploited without the described integration of DM and IT modules. For example, it is possible to register different images with structural and functional staining of tissue slices on various magnification levels into one virtual image space that can be analyzed via machine learning algorithms. The combination of identified

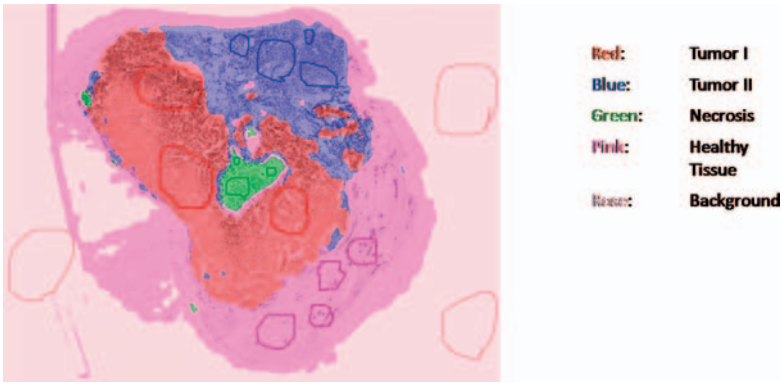

Figure 8.9 Resulting tissue characterization for supervised learning given expert annotations.

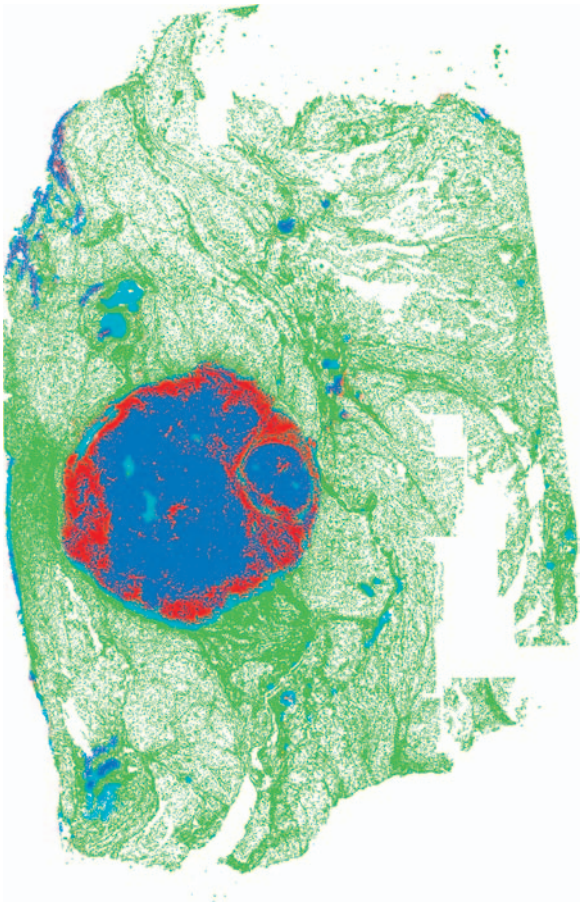

Figure 8.10 Resulting tissue characterization for unsupervised learning with highlighted CD45 (red).

features cannot be "seen" by humans, whereas the resulting classification can be mapped on to color codings of tissue areas and thus show and measure the extension of tumors.

A technical success model for such IT-based integration and graspable presentation of spatially encoded information in a common coordinate system include geographical information environments such as Google Maps.

In conclusion, pathologists and light microscopic analysis of tissue specimens have an integral role in modern cancer units. The information that they provide about tumor type, grade, stage, completeness of excision, and prognosis are derived mainly from traditional methods of histopathology. The information value can be improved as these methods are linked together with advanced techniques such as molecular analyses and automated image analyses. Having said that, we are in accordance with the tenet "pathology is far from dead" [1].

References

1 Lakhani, S.R. and Ashworth, A. (2001) Microarray and histopathological analysis of tumours: the future and the past? *Nat. Rev. Cancer*, **1**, 151–157.

2 Sternberg, S.S. (ed.) (1997) *Histology for Pathologists,* Lippincott Williams and Wilkins, Philadelphia.

3 Hayat, M.A. (2004) *Handbook of Immunohistochemistry and In Situ* Hybridization of Human Carcinomas: *Molecular Genetics – Lung and Breast Carcinomas*, **1**, Academic Press, New York.

4 Pearse, A.G.E. (1980) *Histochemistry: Theoretical and Applied*, **1**, Churchill Livingstone, Oxford.

5 Pearse, A.G.E. (1985) *Histochemistry: Theoretical and Applied*, **2**, Churchill Livingstone, Oxford.

6 Polak, J.M. and Van Noorden, S. (2002) *Introduction to Immunocytochemistry*, Bios Scientific Publishers, Oxford.

7 Gray, J.W., Pinkel, D., and Brown, J.M. (1994) Fluorescence *in situ* hybridization in cancer and radiation biology. *Radiat. Res.*, **137**, 275–289.

8 Jin, L. and Lloyd, R.V. (1997) *In situ* hybridization: methods and applications. *J. Clin. Lab. Anal.*, **11**, 2–9.

9 Caelli, T. and Bischof, W.F. (2008) *Machine Learning and Image Interpretation*, Springer, Berlin.

10 Wolff, A.C., Hammond, M.E., Schwartz, J.N., Hagerty, K.L., Allred, D.C., Cote, R.J., Dowsett, M., Fitzgibbons, P.L., Hanna, W.M., Langer, A., McShane, L.M., Paik, S., Pegram, M.D., Perez, E.A., Press, M.F., Rhodes, A., Sturgeon, C., Taube, S.E., Tubbs, R., Vance, G.H., van de Vijver, M., Wheeler, T.M., Hayes, D.F., American Society of Clinical Oncology , and College of American Pathologists (2007) American Society of Clinical Oncology/College of American Pathologists guideline recommendations for human epidermal growth factor receptor 2 testing in breast cancer. *J. Clin. Oncol.*, **25**, 118–145.

9
Virtual Microscopy

Thorsten Heupel

9.1
Introduction

The basic concept of virtual microscopy is to distribute microscopic images via computer networks. Based on this definition, there are three evolutionary steps along which this technology has developed:

(a) **Static remote microscopy**: From a technology standpoint, this is the easiest way to transmit microscopic images, because only a microscope, a digital camera, and capture software are needed. The operator makes single snapshots from regions of interest and subsequently they can be transferred for example via e-mail to another person for review. The limitations are obvious, such as the possibility of a misaligned microscope, an operator and the physical specimen is always needed, and, the most prominent, only a small part of the specimen can be transferred.

(b) **Dynamic remote microscopy**: Here a motorized microscope is remotely controlled by an operator and a live image from the camera is broadcasted (e.g., via satellite, Internet). This allows one to pan the specimen in the x and y directions, to focus, and to change objectives. Thus the remote person can investigate a complete specimen; some advanced systems even allow switching between slides with a robotic system. This technology was mainly driven by pathologists in order to make remote diagnosis possible, where presence on-site was not possible. Systems were deployed by the US Army to provide expert diagnosis even close to the battlefield. Another application area was instant section diagnosis, allowing remote hospitals with no resident pathologist to obtain the required support during surgery. The term telepathology is a combination of telemedicine and pathology. Telemedicine has been used for several decades (e.g., on-line monitoring of health status by NASA). Telepathology was introduced in 1968 in Boston [1]. In the past, the deployment of telepathology was limited to regions with a mature telecommunication infrastructure. In underdeveloped countries there is a need for telepathology, but so far the infrastructure has mostly been lacking. However, now the increasing coverage of GSM

Handbook of Biophotonics. Vol.2: Photonics for Health Care, First Edition. Edited by Jürgen Popp, Valery V. Tuchin, Arthur Chiou, and Stefan Heinemann.

networks in Africa has triggered the development of telepathology solutions using smartphones [2].

(c) **Static–dynamic hybrid remote microscopy (virtual microscopy):** Virtual microscopy (VM) is a combination of the two technologies described above. The entire sample is automatically scanned at high resolution without user intervention. The user can access the image via the Internet or locally. The remote navigation within the large dataset can be realized with the same technology as for Google Earth. The digitization of the complete sample leads to the so-called virtual slide (VS). VM is becoming the most popular technology, as it paves the way to applications beyond remote viewing of samples. In recent years, the driving forces for VM were the increasing performance of scanners [3] and the exponential growth of information technology (IT), namely cheaper storage, faster processors, and faster Internet connections. In addition to telepathology, new applications are emerging from the biomedical research field. Therefore, it is fair to say that VM has the characteristics of a disruptive technology that will radically change the way in which we use microscopes in the future.

9.2 Principles

A VS is a digital representation of a microscopic specimen. All object regions on a slide are imaged at high magnification and captured with a digital sensor. Scanners use microscope objectives with a high numerical aperture (e.g., 0.8) and a magnification of mainly 20×. The digital sensors used can be divided into two main categories: line sensors (with stripe-wise scanning) and area sensors (with tile-based scanning). After scanning, the stripes or tiles have to be merged together to form a large montage image of the entire specimen. Consequently, most scanners are nowadays closed-box systems with limited functionality, in contrast to research microscopes, which allow for example the selection of multiple magnifications and contrast modes.

Quality of focusing is a critical issue with scanners, because the VS depicts a single focus plane of the specimen and for the viewer the focus dimension is lost. To overcome this drawback, many systems offer the possibility of digitizing the sample at different z levels. Depending on the need, the different z levels are stored or merged into a single plane.

The image size of VS depends on the specimen area on the slide and the scan resolution. The typical scan resolution for VS is between 0.5 and 0.2 μm per pixel, which gives sufficient detail to perform most diagnoses.

Based on the above parameters, the size of the resulting VS is in the range of megabytes to gigabytes. It is obvious that the falling costs of hard disk storage were key for the success of VS. Within 10 years time, the cost of storage space has dropped by a factor of 1000.

The majority of scanners use brightfield illumination as the imaging modality. The reason for this comes from the needs of pathology with standard stains such as H&E (Hematoxylin&Eosin) and PAS (Periodicacid-Schiff stain), where this contrast mode is demanded. With the evolution of new molecular techniques for

pathology (such as fluorescence *in situ* hybridization for HER2/neu) and research applications, the scanning of fluorescently labeled specimens became of increasing importance. This represents a new challenge for scanners also, because scanning of fluorescent samples is much more critical in terms of focus and speed.

9.3 Applications

As already mentioned, telepathology is only one of several application areas for VM technology. The following sections summarize the important areas to date. As the technology is still under development, there will certainly be more applications to follow.

9.3.1 Telepathology

So far, remote access to VS is still a dominant application. In the clinical area, the need for remote consultation is due to the lack of pathologists in certain regions. With VS, their workflow can be optimized, because travel time reduces the effective time of a pathologist. It is as simple as accessing the complete specimen with high resolution from another location. In the case of intraoperative sectioning, it is important to scan with the appropriate resolution very rapidly to obtain a quick feedback from the pathologist (less than 10 min). Outside the clinical environment, peer review is also a well-accepted application field for pharmaceutical companies, because the global distribution of such companies makes it necessary to connect research and validation from different continents (e.g., for toxicology studies) for peer reviews. Another advantage of VS is that once the specimen has been digitized it is preserved (in contrast to physical immunostains, which fade over time). This allows compliance with regulatory procedures which demand that results need to be archived for re-examination if required.

9.3.2 Routine Pathology

In addition to telepathology, the use of VS in routine clinical practice was always considered a major application. However, as of today, the VS has not yet become an integral part of the routine clinical workflow. There are several reasons why this adoption is only slowly taking place. In many cases, pathologists can make their diagnoses faster using glass slides instead of loading and navigating a VS on a PC. The graphical user interface has to be improved, regarding speed and usability, and the software needs an interface to the clinical IT [e.g., PACS (Picture Archiving and Communication System)]. Routine pathology needs faster scanners to handle several hundred slides per day, which means slide processing times of the order of 1 min. Additionally in some countries there are regulatory questions how to use/validate this

technology in routine diagnosis which are not fully answered so far. Combined with image analysis this technology will gain strength in the computer-assisted diagnosis.

9.3.3 Education

In a typical education scenario, there is a lecture room with a set of microscopes for students. One or more students use one microscope to investigate a set of specimens. To make sure that every student can benefit from the tutorial, it is important that all microscopes are perfectly adjusted and every student can investigate the same specimen. This is not trivial as sectioned samples are never identical, and there are rare specimens for which it is impossible to produce the number of samples required for the course. During the course, slides get broken, and microscopes have to maintained and serviced; in summary, the amount of work to keep a microscope training course at a high quality level is fairly high.

Using computer workstations and VS overcomes these problems. Once a specimen has been scanned and the VS put on a server, every student can explore exactly the same specimen. In addition, the lecturer can provide additional information via annotations, or links to notes. Instead of the physical microscope seminar, where the number of participants is limited by the available microscopes and the seminar schedule, VS seminars can be undertaken by students from home. Owing to these clear benefits, implementation of VM in education is already fairly widespread.

9.3.4 Tissue Microarrays

Tissue microarrays (TMAs) are collections of small tissue samples (each tissue is a spot with a diameter of around 1 mm) which are arranged on a slide to form an array. This setup enables the user to place up to several hundred different tissue samples on a slide to perform comparative studies. The first reference to this technique appeared in 1987 [4].

TMA is an enabling tool for clinical research (in particular cancer research). Many clinics have large collections of tissue/tumors built up over the years. These samples originated from patients whose disease record is well known. This allows searching for molecular tissue markers that are specific to known disease patterns. It is possible to investigate these samples for common features, and then correlate these features with characteristics of the disease [5].

The tissue spots are taken from standard tissue blocks, by means of a fine hollow needle. As the spot(s) represent only a small part of the whole block, it is necessary that the researcher/pathologist first investigates the specimen and marks the regions to be used for a TMA. Selecting these regions on a VS allows direct control of the needle for core extraction. This procedure optimizes the whole workflow.

The cores from the several donor blocks are finally transferred to an acceptor (TMA) block. From this acceptor block, several cuts are made for processing

with different stains (e.g., a counterstain and immunohistochemical tumor markers).

In many cases, it is required to quantify the relative stain intensity and covered area over an ensemble of spots (scoring). This can be done by means of image analysis software or manually. Based on the patients' information, the spots can now be filtered and grouped in a gallery, which helps in making side-by-side comparisons.

9.3.5 Research

The number of publications on VM is increasing year by year whereas the number of publications on telepathology is decreasing [6]. With the increased quality and speed of scanning fluorescent probes, this technology is becoming even more interesting for research use. The rapid fading of fluorescent signals makes VS a perfect tool to archive a specimen digitally and to perform off-line image analysis to extract object and pattern information without harming the sample. With this technology also less experienced users can quickly obtain high-quality images. As the VS represents the complete specimen, it is now easy to perform image analysis on larger areas of the specimen. Especially for neurobiology, VM is a technology to acquire a more detailed insight. Research on Alzheimer disease is already utilizing this technology to analyze for example the influence of certain substances or parameters on the formation of plaques [7].

With VM, not only is the complete specimen available, but also together with serial sections it is possible to obtain a three-dimensional representation of the specimen to analyze the structures.

The VS technique is a also a perfect tool to generate high resolution representations of the whole specimen as source for further investigations and combination with other imaging modalities.

9.4 Outlook

It is obvious that future improvements in scanner technology (especially regarding scanning speed with brightfield illumination) and IT will pave the way towards the routine deployment of VS in pathology. In terms of clinical standardization, there is working group 26 within the DICOM organization to define the interface for VS within a standard. This is finalized and will support the implementation into the clinical workflow.

In addition to this prospect, we will also see penetration of this technology in research (universities), especially if the next generations of instruments exhibit increased speed and quality for fluorescence applications.

In the research environment, we will see a fusion between VS and other technologies. The pathologist/researcher will merge other modalities with their classical view of the stained specimen. An example is the combination with MALDI (matrix-assisted laser desorption/ionization) imaging mass spectrometry. This technology is a very

important tool for protein profiling of tissue sections. However, interpretation of the results can only be done in the context of the histological sample. The future will bring more combinations of different technologies besides other imaging modalities with VS, such as proteohistography, tissue microdissection, and mass spectrometry providing data of higher quality and quantity.

VM will support users in the future with more reproducible and quantitative results and this will make it an ideal tool for quality control in the field of material applications but also for food inspection.

Acknowledgment

The author would like to thank Dr. Martin Gluch for the critical review of this chapter and his valuable contribution.

References

1 Kayser, K. (1999) History of Telemedicine and Telepathology, in *Telepathology: Telecommunication, Electronic Education in Pathology* (eds K. Kayser, J. Szymas, and R. Weinstein), Springer, Berlin, pp. 24ff.

2 Zimic, M., Coronel, J., Gilman, R.H., Luna, C.G., Curioso, W.H. *et al.* (2009) Can the power of mobile phones be used to improve tuberculosis diagnosis in developing countries? *Trans. R. Soc. Trop. Med. Hyg.*, **103**, 638–640.

3 Rojo, M.G., García, G.B., Mateos, C.P., García, J.G., and Vicente, M.C. (2006) Critical Comparison of 31 Commercially Available Digital Slide Systems in Pathology. *Int. J. Surg. Pathol.*, **14** (4), 1–21.

4 Wan, W.H., Fortuna, M.B., and Furmanski, P. (1987) A rapid and efficient method for testing immunohistochemical reactivity of monoclonal antibodies against multiple tissue samples simultaneously. *J. Immunol. Methods*, **103**, 121–129.

5 Simon, R., Mirlacher, M., and Sauter, G. (2003) Tissue microarrays in cancer diagnosis. *Expert Rev. Mol. Diagn.*, **3** (4), 421–430.

6 Kayser, K., Molnar, B., and Weinstein, R.S. (2006) *Virtual Microscopy*, VSV Interdisciplinary Medical Publishing, Berlin.

7 Scheffler, K., Stenzel, J., Krohn, M., Lange, C., Hofrichter, J., Schumacher, T., Brüning, T., Plath, A.S., Walker, L., and Pahnke, J. (2011) Determination of spatial and temporal distribution of microglia by 230nm-high-resolution, high-throughput automated analysis reveals different amyloid plaque populations in an APP/PS1 mouse model of Alzheimer's disease. *Curr. Alzheimer Res.*, [Epub ahead of print].

10
In Vitro Instrumentation

Sergio Coda, Rakesh Patalay, Christopher Dunsby, and Paul M.W. French

10.1
Introduction

This chapter describes the application of multidimensional fluorescence imaging techniques to biological tissue, with particular emphasis on fluorescence lifetime imaging. It reviews the main fluorescence measurement and imaging modalities and describes their application to label-free imaging of tissue autofluorescence (AF), concentrating on *ex vivo* measurements, although some of the technology presented has also been applied to *in vivo* imaging.

10.2
Autofluorescence of Biological Tissue

Fluorescence provides a powerful means of achieving optical molecular contrast [1] in single-point (cuvette-based or fiber-optic probe-based) fluorimeters, in cytometers and cell sorters, and in microscopes, endoscopes and multiwell plate readers. Typically for cell biology, fluorescent molecules (fluorophores) are used as "labels" to tag specific molecules of interest. For clinical applications, it is possible to exploit the AF of target molecules themselves to provide *label-free molecular contrast*, which is the main focus of this chapter, although there is an increasing trend to investigate the clinical use of exogenous labels to detect diseased tissue, for example, using photodynamic diagnosis (PDD) [2].

When studying AF of biological tissue, the molecular composition is often unknown and so tissue AF can present a complex signal resulting from an unknown number of endogenous fluorophores present with unknown relative concentrations. Interpretation of AF data is therefore highly challenging, typically requiring *a priori* knowledge of tissue structure and/or physiological function to yield quantitative information. Nevertheless, the potential for label-free molecular contrast as a diagnostic tool is compelling and empirical AF contrast is finding its way into

Handbook of Biophotonics. Vol.2: Photonics for Health Care, First Edition. Edited by Jürgen Popp, Valery V. Tuchin, Arthur Chiou, and Stefan Heinemann.

clinical practice while an increasing number of *ex vivo* and *in vivo* studies are directed at understanding the molecular origins of tissue AF and the contrast available.

In biological tissue, AF can provide a source of label-free optical molecular contrast, offering the potential to discriminate between healthy and diseased tissue. The prospect of detecting molecular changes associated with the early manifestations of diseases such as cancer is particularly exciting. For example, accurate and early detection of cancer allows earlier treatment and significantly improves prognosis [3]. Although the exophytic tumors can often be visualized, the cellular and tissue perturbations of the peripheral components of neoplasia may not be apparent by direct inspection under visible light and are often beyond the discrimination of conventional noninvasive diagnostic imaging techniques. In general, label-free imaging modalities are preferable for clinical imaging, particularly for diagnosis, as they avoid the need for administration of an exogenous agent with associated considerations of toxicity and pharmacokinetics. A number of label-free modalities based on the interaction of light with tissue have been proposed to improve the detection of malignant change. These include fluorescence, elastic scattering, Raman, infrared absorption, and diffuse reflectance spectroscopy [4–7]. To date, most of these techniques have been limited to point measurements, where only a very small area of tissue is interrogated at a time, for example, via a fiber-optic contact probe. This enables the acquisition of biochemical information, but provides no spatial or morphological information about the tissue. AF can provide label-free "molecular" contrast that can be readily utilized as an imaging technique, allowing the rapid and relatively noninvasive collection of spatially resolved information from areas of tissue up to tens of centimeters in diameter. In order to exploit AF for clinical applications, it is first necessary to investigate the AF "signatures" of normal and diseased tissue states, and this has led to a number of *in vitro* studies. The instrumentation applied to such investigations is often similar to that envisaged for *in vivo* clinical applications, although the nature of *in vitro* experiments clearly relax many of the constraints associated with *in vivo* studies and permit the use of more sophisticated (and time consuming) measurements.

The principal endogenous tissue fluorophores include collagen and elastin cross-links, reduced nicotinamide adenine dinucleotide (NADH), oxidized flavins (FAD and FMN), lipofuscin, keratin, and porphyrins. As shown in Figure 10.1 [7], these fluorophores have excitation maxima in the UV-A or blue (325–450 nm) spectral regions and emit Stokes-shifted fluorescence in the near-UV to visible (390–520 nm) region of the spectrum. The actual AF signal excited in biological tissue will depend on the concentration and the distribution of the fluorophores present, on the presence of chromophores (principally hemoglobin) that absorb excitation and fluorescence light, and on the degree of light scattering that occurs within the tissue [6]. AF therefore reflects the biochemical and structural composition of the tissue, and consequently is altered when the tissue composition is changed by disease states such as atherosclerosis, cancer, and osteoarthritis.

Although AF can be observed using conventional "steady-state" imaging techniques, it is challenging to make sufficiently quantitative measurements for diagnostic applications since the AF intensity signal may be affected by fluorophore

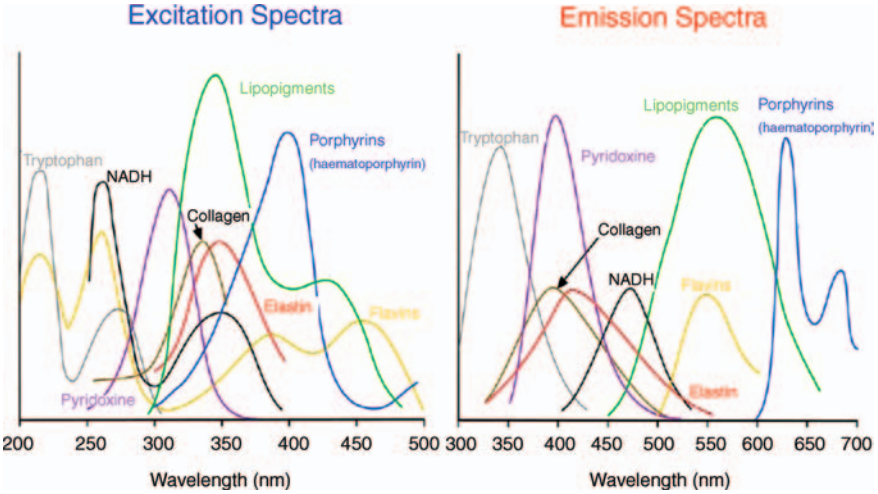

Figure 10.1 Excitation and emission spectra of main endogenous tissue fluorophores. Reproduced with permission from [7].

concentration, variations in temporal and spatial properties of the excitation flux, the angle of the excitation light, the detection efficiency, attenuation by light absorption and scattering within the tissue, and spatial variations in the tissue microenvironment altering local quenching of fluorescence. The remainder of this chapter introduces some of the increasingly sophisticated detection and analysis techniques that aim to overcome these problems.

10.2.1 Fluorescence Contrast

More robust measurements can be made using *ratiometric* techniques, since spectrally and time-resolved measurements can also be sensitive to variations in the local fluorophore environment. In the spectral domain, one can assume that unknown quantities such as excitation and detection efficiency, fluorophore concentration, and signal attenuation will be approximately the same in two or more spectral windows and may be effectively "canceled out" in a ratiometric measurement. This approach is used, for example, with excitation [8] and emission [9] ratiometric calcium sensing dyes and the approach has been demonstrated to provide useful contrast between, for example, malignant and normal tissue [10]. Fluorescence lifetime measurement is also a ratiometric technique as it is assumed that the various unknown quantities do not change significantly during the fluorescence decay time (typically nanoseconds) and the lifetime determination effectively compares the fluorescence signal at different delays after excitation. The fluorescence lifetime is the average time that a fluorophore takes to decay radiatively after having been excited from its ground energy level, and, like the quantum efficiency, it is also a function of the radiative and

nonradiative decay rates and so can provide quantitative fluorescence-based molecular contrast.

10.2.2 Spectroscopic Techniques for Fluorescence Imaging and Metrology

10.2.2.1 Spectral Techniques

The most common and experimentally straightforward approach to tissue spectroscopy has been the acquisition of information about the AF emission spectrum for a fixed excitation wavelength. In its simplest form, this can be implemented using dichroic beamsplitters and multiple detectors, as is often applied to fluorescence microscopy for ratiometric imaging or colocalization studies. This *multispectral* approach is useful when the spectral profiles of fluorophores are known *a priori* and can be used with spectral unmixing techniques to separate contributions from different fluorophore labels or to classify different types and states of tissue using known spectral components.

Without *a priori* knowledge, it is useful to learn as much about the tissue AF as possible and so *hyperspectral* measurements that acquire the full (emission) spectral profile of a fluorescent sample are desirable [6]. For single-channel measurements, for example, made using a spectrofluorimeter, it is straightforward to use a spectrograph that can be read out using a CCD (*charge-coupled device*). Alternative approaches include scanning Fabry–Pérot interferometers, which can be implemented using mechanical scanning or by taking advantage of the electro-optic effect to sweep the refractive index of an étalon. Acousto-optic tunable filters (AOTFs) also provide a means to rapidly scan spectral profiles. Both scanning étalons and AOTFs effectively sample the fluorescence signal, rejecting the "out-of-band" light and so are lossy compared with spectrographs. A more photon-efficient approach is that of a scanning Michelson interferometer, from which the spectrum is obtained by Fourier transformation of the acquired interferogram. Hyperspectral imaging can be readily implemented in laser scanning microscopes by utilizing single-pixel detection techniques, although the rapid raster scanning rates can be a challenge for the read-out rates of the spectral detectors. With no *a priori* knowledge of tissue properties, such rich hyperspectral sets can be analyzed using techniques such as principal component analysis (PCA) that can extract common spectral components from "training sets" of tissue fluorescence data and subsequently be applied for diagnostic purposes, for example. Fluorescence emission data can also be complemented by excitation data.

10.2.2.2 Fluorescence Lifetime Techniques

Increasingly, there is interest in exploiting fluorescence lifetime contrast to analyze tissue AF signals, since fluorescence decay profiles depend on relative (rather than absolute) intensity values and fluorescence lifetime imaging (FLIM) is therefore largely unaffected by many factors that limit steady-state measurements [11]. The principal tissue fluorophores exhibit characteristic lifetimes (ranging from hundreds to thousands of picoseconds) [6, 12] that can enable spectrally overlapping

fluorophores to be distinguished. Furthermore, the sensitivity of fluorescence lifetime to changes in the local tissue microenvironment (e.g., pH, $[O_2]$, $[Ca^{2+}]$) [1] can provide a readout of biochemical changes indicating the onset or progression of disease. FLIM is now being actively investigated as a means of obtaining or enhancing intrinsic AF contrast in tissues [13, 14].

In general, fluorescence lifetime measurement and fluorescence lifetime imaging techniques are categorized as time-domain or frequency-domain techniques, according to whether the instrumentation measures the fluorescence signal as a function of time delay following pulsed excitation or whether the lifetime information is derived from measurements of phase difference between a sinusoidally modulated excitation signal and the resulting sinusoidally modulated fluorescence signal. In principle, frequency and time domain approaches can provide equivalent information, but specific implementations present different trade-offs with respect to cost, complexity, performance, and acquisition time. In general, the most appropriate method should be selected according to the target application. A further categorization of fluorescence lifetime measurement techniques can be made according to whether they are sampling techniques, which use gated detection to determine the relative timing of the fluorescence compared with the excitation signal, or photon counting techniques, which assign detected photons to different time bins. In general, wide-field FLIM is usually implemented with gated or modulated imaging detectors that sample the fluorescence signal whereas photon counting techniques have been widely applied to single-point lifetime measurements. For laser scanning FLIM, single-point fluorescence lifetime measurement techniques can be readily implemented in laser scanning microscopes as modern electronics makes it straightforward to assign detected photons to their respective images pixels. There are extensive reviews of the various techniques [1, 15–17].

10.2.3
Single-Point Spectroscopic Techniques

Single-point spectroscopic measurements are typically made in spectrofluorimeters that are usually designed for cuvette-based solution measurements, although some can be adapted for solid samples. For studying tissue samples, it is common to use a fiber-optic-based probe to deliver the excitation light and collect the resulting fluorescence from a sample. Fiber-optic probes provide experimental convenience, particularly for clinical applications. Such probes are frequently combined with spectrographs that may be used to capture fluorescence emission spectra and also reflected light spectra. With broadband illumination, reflected light spectra can provide information concerning the elastic scattering properties of tissue samples, and this has been used to identify diseased tissue [5]. AF spectra are frequently analyzed using methods such as PCA in order to distinguish different tissue components. Spectral measurements have also been combined with fluorescence lifetime measurements in spectrofluorimeters and fiber-optic probe instruments. Multispectral fluorescence lifetime measurements are often realized

using one or more dichroic filters with multiple time-resolved detection channels or using a scanning spectrometer with a single time-resolved detector [18], and spectrographs have been used with array detectors, including gated intensified CCDs [19], streak cameras [20], and time-correlated single-photon counting (TCSPC) [21, 22].

10.2.4 Fluorescence Microscopy

10.2.4.1 Laser Scanning Confocal/Multiphoton Microscopy

Confocal or multiphoton laser scanning microscopes are used widely for biological imaging because they provide optical sectioning and improved contrast compared with wide-field microscopes. In general, multiphoton excitation permits imaging at greater depths than confocal microscopy due to the reduced scattering and absorption experienced at the longer excitation wavelengths [23], although the longer wavelength leads to a slightly degraded image resolution and multiphoton excitation cross-sections are typically significantly lower than their single-photon counterparts, resulting in increased image acquisition times. Multiphoton excitation confers the benefit of reduced out of focal plane photobleaching compared with confocal microscopy, which is important when acquiring dense *z*-stacks for 3D imaging. The photobleaching process associated with multiphoton excitation is nonlinear, however, and is more severe in the focal volume.

Multichannel spectral detection is routinely implemented in laser scanning microscopes using dichroic beamsplitters and filters, and hyperspectral imaging is realized by directing the collected fluorescence to a scanning spectrometer or to a spectrograph readout using a CCD or multianode photomultiplier array. FLIM is conveniently achieved on laser scanning microscopes using TCSPC [24], photon binning [25] or frequency domain techniques [26].

For all laser scanning microscopes, the sequential pixel acquisition means that increasing the imaging speed requires a concomitant increase in excitation intensity, which can be undesirable due to photobleaching and phototoxicity considerations. In general, parallel pixel excitation and detection are applicable to all laser scanning microscopes and have been extended to optically sectioned line-scanning microscopy, for example, by using line illumination or by using a rapidly scanned multiple beam array to produce a line of fluorescence excitation. The resulting emission can be relayed to the input slit of a spectrograph to facilitate "push-broom" hyperspectral imaging, as discussed below, or to the input slit of a streak camera to implement FLIM [27]. It is also possible to scan multiple excitation beams rapidly in parallel to produce a 2D optically sectioned fluorescence image that can be recorded using wide-field detectors. This has been implemented with single-photon excitation in spinning Nipkow disc microscopes that have been combined with wide-field time-gated detection for FLIM [28–30], and with multibeam multiphoton microscopes that have also been adapted for FLIM [31–33].

10.2.4.2 Wide-Field Fluorescence Imaging

The parallel nature of wide-field imaging techniques can support FLIM imaging rates of tens to hundreds of hertz [34, 35], although the maximum acquisition speed is inevitably limited by the number of photons/pixels available from the (biological) sample. Wide-field FLIM is most commonly implemented using modulated image intensifiers with frequency or time domain approaches proving successful. The frequency domain approach initially utilized sinusoidally modulated laser excitation and the resulting fluorescence was analyzed using a microchannel plate (MCP) image intensifier with a sinusoidally-modulated gain function by acquiring a series of gated "intensified" images at different relative phases between the MCP modulation and the excitation signal [36–38]. In the time domain, FLIM is also realized using modulated MCP image intensifiers to sample the fluorescence decays, but for this approach the MCP image intensifier gain is gated for short periods (pico- to nanoseconds) after excitation [39–41]. The use of gated image intensifiers with a wire mesh proximity-coupled to the MCP photocathode has led to devices with sub-100 ps resolution [42], although it is usually preferable to use longer time gates to increase the detected signal [43].

Although wide-field FLIM can achieve frame rates of around tens of hertz in both the frequency [44] and time [34] domains under the assumption of monoexponential fluorescence decay profiles and has been demonstrated in endoscope systems [34, 45], sampling and fitting of complex decay profiles inevitably increase the FLIM acquisition time since they require significantly more detected photons for accurate lifetime determination. Nevertheless, wide-field FLIM can still be faster than TCSPC implemented in a laser scanning microscope. If high-speed optically sectioned FLIM is required, the fasted systems reported to date have been based on multibeam confocal (Nipkow disc) microscopes with wide-field gated image intensifier detection [28].

10.2.4.3 Multidimensional Fluorescence Microscopy

It can be useful to obtain similar multidimensional fluorescence information from fluorescence imaging experiments, so that functional spectroscopic information can be correlated with morphology. This can be useful for imaging Förster resonance energy transfer (FRET) experiments, where spectral and lifetime measurements can give complementary information [46], for spatially resolved assays of chemical reactions [47], and for studying tissue AF, particularly when investigating samples with no *a priori* knowledge. For example, FLIM can be combined with multispectral imaging, for which time-resolved images are acquired in a few discrete spectral windows [48], or it can be combined with hyperspectral imaging, for which the full time-resolved excitation or emission spectral profile is acquired for each image pixel.

There are several established approaches for implementing hyperspectral imaging. In single-beam scanning fluorescence microscopes, the fluorescence radiation can be dispersed in a spectrometer and the spectral profiles acquired sequentially, pixel by pixel. This is readily combined with FLIM in laser scanning microscopes, for example, using TCSPC systems that incorporate a spectrometer and multi-anode photomultiplier [22, 49]. To increase the imaging rate, it is necessary to move to parallel pixel acquisition, for example, by combining wide-field FLIM with hyperspectral imaging

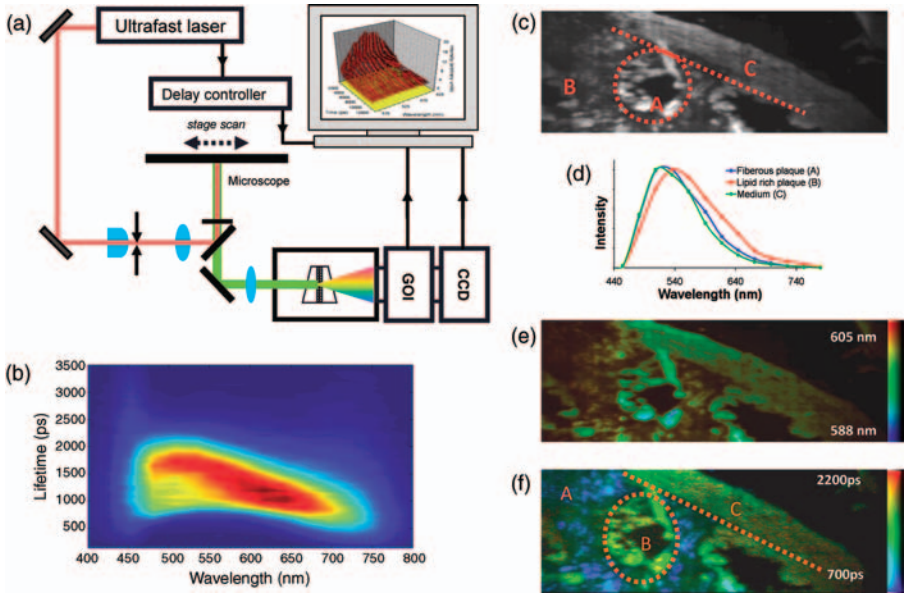

Figure 10.2 (a) Experimental set-up for line-scanning hyperspectral FLIM; (b) integrated intensity image of sample of frozen human artery exhibiting atherosclerosis; (c) time-integrated spectra of sample regions corresponding to medium and fibrous and lipid-rich plaques; (d) AF lifetime-emission matrix; (e) map of time-integrated central wavelength; (f) spectrally integrated lifetime map of sample AF. Adapted from [54].

implemented using filter wheels or acousto-optic [50] or liquid crystal [51] tunable filters to acquire images sequentially in different spectral channels. This approach is not photon efficient because the "out-of-band" light is rejected and the acquisition time will increase with the number of spectral channels. Alternative approaches that can be more efficient include Fourier transform spectroscopic imaging [22] and encoding Hadamard transforms using spatial light modulator technology [52]. In general, however, any approach that requires the final image to be computationally extracted from acquired data can suffer from a reduction in signal-to noise ratio compared with direct image detection. A compromise between photon economy and parallel pixel acquisition that directly detects the spectrally resolved image information is the so-called "push-broom" approach to hyperspectral imaging [53] implemented in a line-scanning microscope. For hyperspectral FLIM, the fluorescence resulting from a line excitation is imaged to the entrance slit of a spectrograph to produce an (x–λ) "sub-image" that can be recorded on a wide-field FLIM detector. Stage scanning along the y-axis then sequentially provides the full (x–y–λ–τ) data set. This approach is photon efficient and the line-scanning microscope configuration provides "semi-confocal" optical sectioning [54]. This instrument was developed to study AF contrast in diseased tissue and Figure 10.2 shows the experimental

configuration and presents multidimensional fluorescence data from a hyperspectral FLIM acquisition of an unstained frozen section of human artery exhibiting atherosclerosis of human cartilage.

This multidimensional fluorescence imaging (MDFI) approach can be further extended if we employ a tunable excitation laser also to resolve the excitation wavelength. Using spectral selection of a fiber laser-pumped supercontinuum source to provide tunable excitation from 390 to 510 nm with this line-scanning hyperspectral FLIM microscope, we demonstrated the ability to acquire the fluorescence excitation–emission–lifetime (EEL) matrix for each image pixel of a sample. Such a multidimensional data set enables us subsequently to reconstruct conventional "excitation–emission matrices" excitation–emission matrix (EEM) for any image pixel and to obtain the fluorescence decay profile for any point in this EEM space. Although this can provide exquisite sensitivity to perturbations in fluorescence emission and can enhance the ability to unmix signals from different fluorophores, we note that the size and complexity of such high content hyperspectral FLIM data sets is almost beyond the scope of *ad hoc* analysis by human investigators. Sophisticated bioinformatics software tools are required to analyze automatically and present such data to identify trends and fluorescence "signatures." The combination of MDFI with image segmentation for high content analysis should provide powerful tools, for example, for histopathology and for screening applications.

10.3
Ex Vivo Tissue Spectroscopy and Imaging: Application to Cancer

In the era of minimally invasive technology, laser-induced fluorescence microscopy and spectroscopy provide label-free highly discriminative intrinsic contrast between benign and neoplastic tissue. This potential has been demonstrated extensively in a multitude of *ex vivo* studies, and nowadays *in vivo* applications of different techniques are opening up a new concept of clinical imaging that can provide both histological and physiological information label-free and in real time. It is not possible to provide a comprehensive review of *ex vivo* studies of tissue AF within this chapter, so this section aims to review some representative examples of the application of fluorescence microscopy, spectroscopy, and endoscopy to a variety of *ex vivo* human tissues. The discussion will be limited to cancer, which is the disease that has attracted the most attention using optical techniques, although we note that multidimensional fluorescence imaging techniques have also been applied to atherosclerosis [55, 56] and other diseases. A review of MDFI applications by tissue type will be given, with a focus on studies using freshly resected biopsy specimens rather than fresh frozen or paraffin-embedded specimens. Important reviews of this field can be found in the literature [4, 5, 57, 58] and the reader is referred to Chapter 11 for a review of *in vivo* studies using fluorescence spectroscopy and imaging.

10.3.1
Oral Cavity

Evaluation of the oral cavity, pharynx, and larynx using AF imaging systems has now become an essential tool for the screening of head and neck squamous cell cancers as a result of pioneering *in vitro* studies [59, 60]. Furthermore, fluorescence spectroscopy and imaging of oral mucosa have been evaluated by several groups with the aim of detecting malignant or premalignant conditions using excitation wavelengths in the UV region [60, 61] and for a wide range of UV and visible wavelengths (250–500 nm) [59].

Uppal and Gupta [62] carried out enzymic measurements of NADH concentrations in samples from nine patients with oral squamous cell carcinoma. All measurements were carried out on malignant tissue and normal-appearing mucosa adjacent to the lesion from the same patient. They showed that the concentrations of NADH in malignant sites of oral cavity tissue were significantly lower than those in the healthy mucosa.

10.3.2
Gastrointestinal Tract

Chwirot and co-workers [63, 64] reported fluorescence imaging of 21 resected specimens of stomach cancers and normal tissues *in vitro* at six visible emission wavelengths and with 325 nm excitation. They observed a significant difference in the fluorescence intensities measured at 440 and 395 nm, both normalized to intensity measured at 590 nm, and used that difference as a diagnostic parameter to classify malignant tissues with high sensitivity and low predictive value.

Abe *et al*. [65] applied an AF endoscopic imaging system [light-induced fluorescence endoscopy (LIFE)-GI system] immediately after surgery to 61 gastric cancers resected from 50 patients. A comparison with conventional histopathology showed that the detection rates increased significantly as the depth of invasion and the mucosal thickening increased (differentiated cancers). Detection rates for undifferentiated cancers were disappointing due to the characteristic dispersion in the modes of invasion, most of which did not alter the mucosal thickness.

Silveira *et al*. [66] used fluorescence spectroscopy with excitation at 488 nm to detect benign and malignant lesions of *ex vivo* human gastric mucosa. Biopsies with endoscopic diagnosis of gastritis and gastric cancer of the antrum were collected from 35 patients during the endoscopic examination. On each biopsy fragment, the AF spectrum was collected at two random points via a fiber-optic catheter coupled to the excitation laser. Analysis of fluorescence spectra was able to identify the normal tissue from neoplastic lesions with 100% sensitivity and specificity.

Xiao and co-workers [67, 68] defined the color characteristics of gastric cancer in AF images using a double-channel laser scanning confocal microscope with an argon ion laser (excitation wavelength 488 nm) and a helium–neon laser (excitation wavelength 543 nm) to detect AF from 16 gastric cancer tissue specimens and

corresponding normal gastric tissue. AF from normal gastric tissue produced a green image whereas a reddish brown image was found to be characteristic of AF in gastric cancer.

Kapadia *et al.* [69] obtained fluorescence emission spectra from 35 normal specimens and 35 adenomatous polyps of the colon with 325 nm excitation. They used multivariate linear regression analysis of the spectra and a binary classification scheme to develop and optimize an algorithm that differentiates adenomatous polyps from normal mucosa and hyperplastic polyps, retrospectively. The algorithm prospectively discriminated 16 adenomatous polyps from 16 hyperplastic polyps and 34 normal tissues, with a sensitivity of 100% and a specificity of 98%.

Richards-Kortum *et al.* [70] measured fluorescence emission spectra from normal colon tissues and adenomatous colonic polyps *in vitro* at a range of excitation wavelengths, spanning the ultraviolet and visible spectrum. They found that the spectral differences between normal and adenomatous colon tissues were greatest with 330, 370 and 430 nm excitation. Furthermore, at an excitation wavelength of 370 nm, fluorescence intensities at 404, 480 and 680 nm were found to be most useful for differentiating adenomas from normal colon tissues.

Yang *et al.* [71] evaluated the ratio of the fluorescence emission intensities at 360 and 380 nm with excitation at 325 nm, and the ratio of the fluorescence emission intensities measured at 450 nm with excitation at 290 and 340 nm. An algorithm based on the ratio of these fluorescence intensities separated adenocarcinomas from normal tissues with 94% sensitivity and 92% specificity.

Chwirot *et al.* [72] investigated whether digital imaging of AF could be applied in the detection of colonic malignancies in a study of 50 resected specimens. AF was excited with 325 nm radiation from an He–Cd laser and images were recorded *in vitro* in six spectral bands. The main result was the observation that for a majority of malignant and premalignant lesions the intensity of AF was lower than for the corresponding normal mucosa in all of the spectral bands selected for imaging. The spectral bands centered around 440 and 475 nm seemed to be most promising in terms of possible future clinical applications.

10.3.3 Bladder

In the bladder, Demos *et al.* [73] imaged a series of fresh surgical specimens obtained following cystectomy or transurethral resection using near-infrared AF under long-wavelength laser excitation in combination with cross-polarized elastic light scattering. The intensity of the near-infrared emission, and also that of the cross-polarized backscattered light, was significantly different in cancerous tissue than the contiguous normal tissue.

Cicchi *et al.* [74] used a combination of four different systems – two-photon excitation intrinsic fluorescence (TPE), second harmonic generation (SHG) microscopy, FLIM, and multispectral two-photon emission (MTPE) detection – to investigate different states of *ex vivo* fresh biopsies of bladder. In particular, they focused on normal mucosa and carcinoma *in situ* (CIS), reporting significant morphological and

spectroscopic differences, in both spectral emission and fluorescence lifetime distribution.

10.3.4 Breast

AF has been evaluated for breast cancer diagnosis using cell cultures, animal models, and human *ex vivo* and *in vivo* tissue. Although results using different models can suggest contradictory conclusions [75, 76], the majority of research using human tissue has confirmed a role for AF in the diagnosis of breast cancer.

Yang *et al.* excited fresh benign and malignant lesions using a range of excitation (275–450 nm) and emission (340–630 nm) wavelengths [77]. The ratios of 289/300 to 289/268 nm in excitation peak intensities for emission at 340 nm were found to be most specific and sensitive for distinguishing benign from malignant pathology.

Breslin *et al.* excited AF in 56 samples of *ex vivo* breast tissue at several wavelengths from 300 to 460 nm [78]. Diffuse reflectance and AF emission spectra were collected between 300 and 600 nm and reduced in dimension using PCA. A sensitivity of 70.0% and a specificity of 91.7% were achieved for distinguishing benign from malignant tissue.

Demos *et al.* imaged *ex vivo* high-grade ductal carcinomas using 532 and 632.8 nm laser excitation and with near-infrared polarized light between 700 and 1000 nm [79]. AF and reflectance images were collected in the 700–1000 nm spectral range. They concluded that there was a significant difference in the tissue AF in this spectral range between cancerous and contiguous non-neoplastic human tissue.

Keller *et al.* used fluorescence spectroscopy and reflectance microscopy on *ex vivo* samples during surgery. An 85% sensitivity and 96% specificity were reported for assessing positive tumor margins [80].

A number of groups have assessed AF imaging in breast ductoscopy [81, 82]. Douplik *et al.* illuminated fresh *ex vivo* breast tissue with blue light (390–450 nm) and collected AF images and point measurements in the green spectral range (490–580 nm). The processed AF images and spectra detected a decrease in green AF from malignant tissue compared with normal breast tissue [82].

Contrast between normal and dysplastic tissue has also been observed using AF lifetime contrast in *ex vivo* specimens with point measurements [83] and lifetime imaging instrumentation [84].

10.3.5 Brain

AF lifetime studies of *ex vivo* brain samples have shown contrast between healthy and normal tissue using both single-point measurements [85, 86] and multiphoton fluorescence imaging has been used in combination with intraperitoneal administration of 5-aminolevulinic acid to identify cancerous tissue [87].

10.3.6 Skin

AF of the skin has been used for diagnosis since the introduction of the Woods lamp (a UV light source) in the earlier part of the twentieth century. Due to its accessibility and the emergence of a clinically licensed and commercially available two-photon microscope [88], there is a rapidly increasing literature concerning the application of MDFI to skin. Although most research has focused on skin malignancies, there is also interest in investigating non-cancer applications such as skin aging [89], inflammatory dermatoses such as eczema [90], and hypertrophic scars [91]. The application of fluorescent precursors to the skin, such as protophorphyrin IX, to aid diagnosis is also being increasingly investigated.

Using a single-point spectral probe, Brancaleon *et al.* measured the emission spectra *in vivo* and from fresh frozen samples of basal cell carcinomas (BCCs)/squamous cell carcinomas (SCCs) [92]. The samples were excited at 350, 360, 390 and 420 nm and fluorescence was collected at 390, 400 and 450 nm. They recorded a loss of AF from a region surrounding the malignant tissue that extended up to three times the size of the tumor. This corresponded to a histologically visible loss of collagen and elastin in 78% of tumors that were studied.

Using two-photon microscopy (TPM) at 810 nm excitation, Eichhorn *et al.* [93] measured the spectra from fresh skin ($n = 150$) and formalin-fixed, unstained sections ($n = 27$) of melanocytic lesions. They observed a single spectral peak at 490 nm in benign nevi and at 600 nm in nodular melanomas, with both peaks appearing in dysplastic nevi. These observations were also reported to be found *in vivo*.

TPM has also been used to study the morphological features of skin malignancies and been reported to show good correlation with histology. Studies of BCC/SCC *ex vivo* samples excited at 780 nm [94] showed irregularly distributed keratinocytes in SCC *in situ* with widened intercellular spaces. In pleomorphic cells and dyskeratotic cells, the cytoplasmic fluorescence intensity was found to be higher than in the surrounding cells. In BCC, nests of BCC cells were found in only one-third of BCCs, although the imaging depth was reported to be insufficient for complete assessment of these tumors. Melanomas have been studied both *ex vivo* and *in vivo* with excitation at 760 nm [95] and were observed to exhibit architectural disarray of the epidermis, poorly defined keratinocyte cell borders, and the presence of pleomorphic or dendritic cells.

In recent years, as FLIM instrumentation has improved, fluorescence lifetime contrast of skin lesions has also been reported. Galletly *et al.* [96] excited freshly excised BCCs at 355 nm and collected fluorescence above 375 nm using a wide-field FLIM system. The observed a significant lifetime difference between BCCs and normal perilesional skin (1.40 ns versus 1.55 ns, respectively) when fitting to a single exponential decay model. In contradiction, however, lifetime data from three out of four BCCs imaged using TPM with excitation at 740 nm by De Giorgi *et al.* [97] demonstrated a shift of 91 ps towards longer lifetimes.

Fluorescence lifetimes obtained *in vivo* and freshly excised *ex vivo* benign nevi and melanomas were recently reported by Dimitrow *et al*. using TPM with 760 nm excitation [98]. Although a difference was seen in the lifetimes (fitted to a double exponential decay model) between keratinocytes and melanocytes, no difference could be detected between benign and malignant tissue.

10.4 Conclusion

A wide range of different types of instrument has been developed for multidimensional fluorescence imaging and many of these have been applied to the study of tissue AF, including *ex vivo* studies of endogenous and exogenous fluorophores. A key outcome of the fluorescence microscopy and spectroscopy of *ex vivo* tissues has been the identification of the main endogenous fluorophores: the cellular components, tryptophan, tyrosine, NADH and FAD, the structural proteins, collagen and elastin, and the porphyrins. These results have provided a sound basis for the application of fluorescence techniques to distinguish between normal and neoplastic tissue *in vivo*.

Acknowledgments

The authors acknowledge funding in part from the UK Engineering and Physical Sciences Research Council (EPSRC), the UK Biotechnology and Biological Sciences Research Council (BBSRC), the Department of Trade and Industry (DTI)/Technology Strategy Board (TSB), the Wellcome Trust, and the European Commission (HEALTH-F5-2008-201577). Paul French acknowledges a Royal Society Wolfson Research Merit Award.

References

1 Lakowicz, J.R. (1999) *Principles of Fluorescence Spectroscopy*, 2nd edn, Kluwer Academic/Plenum Publishers, New York.
2 Borisova, E.G., Vladimirov, B., Terziev, I., Ivanova, R., and Avramov, L. (2009) 5-ALA/PpIX fluorescence detection of gastrointestinal neoplasia, *Proc. SPIE*, **7368**, 241–246.
3 American Cancer Society (2006) *Cancer Facts and Figures 2006*, American Cancer Society, Atlanta, GA.
4 Sokolov, K., Follen, M., and Richards-Kortum, R. (2002) Optical spectroscopy for detection of neoplasia. *Curr. Opin. Chem. Biol.*, **6**, 651–658.
5 Bigio, I.J. and Mourant, J.R. (1997) Ultraviolet and visible spectroscopies for tissue diagnostics: fluorescence spectroscopy and elastic-scattering spectroscopy. *Phys. Med. Biol.*, **42**, 803–814.
6 Richards-Kortum, R. and Sevick-Muraca, E. (1996) Quantitative optical spectroscopy for tissue diagnosis. *Annu. Rev. Phys. Chem.*, **47**, 555–606.
7 Wagnieres, G.A., Star, W.M., and Wilson, B.C. (1998) *In vivo* fluorescence

spectroscopy and imaging for oncological applications. *Photochem. Photobiol.*, **68**, 603–632.

8 Smith, M.W., Phelps, P.C., and Trump, B.F. (1991) Cytosolic Ca^{2+} deregulation and blebbing after $HgCl_2$ injury to cultured rabbit proximal tubule cells as determined by digital imaging microscopy. *Proc. Natl. Acad. Sci. U. S. A.*, **88** (11), 4926–4930.

9 Millot, J.M., Pingret, L., Angiboust, J.F., Bonhomme, A., Pinon, J.M., and Manfait, M. (1995) Quantitative determination of free calcium in subcellular compartments, as probed by Indo-1 and confocal microspectrofluorometry. *Cell Calcium*, **17** (5), 354–366.

10 Andersson-Engels, S., Johansson, J., Stenram, U., Svanberg, K., and Svanberg, S. (1990) Malignant tumour and atherosclerotic plaque diagnosis using laser induced fluorescence. *IEEE J. Quantum Electron.*, **26** (12), 2207–2217.

11 Chen, H.M., Chiang, C.P., You, C., Hsiao, T.C., and Wang, C.Y. (2005) Time-resolved autofluorescence spectroscopy for classifying normal and premalignant oral tissues. *Lasers Surg. Med.*, **37**, 37–45.

12 Elson, D., Requejo-Isidro, J., Munro, I., Reavell, F., Siegel, J., Suhling, K., Tadrous, P., Benninger, R., Lanigan, P., McGinty, J., Talbot, C., Treanor, B., Webb, S., Sandison, A., Wallace, A., Davis, D., Lever, J., Neil, M., Phillips, D., Stamp, G., and French, P. (2004) Time-domain fluorescence lifetime imaging applied to biological tissue. *Photochem. Photobiol. Sci.*, **3**, 795–801.

13 Das, B.B., Liu, F., and Alfano, R.R. (1997) Time-resolved fluorescence and photon migration studies in biomedical and model random media. *Rep. Prog. Phys.*, **60**, 227–291.

14 Dowling, K., Dayel, M.J., Lever, M.J., French, P.M.W., Hares, J.D., and Dymoke-Bradshaw, A.K.L. (1998) Fluorescence lifetime imaging with picosecond resolution for biomedical applications. *Opt. Lett.*, **23** (10), 810–812.

15 Cubeddu, R., Comelli, D., D'Andrea, C., Taroni, P., and Valentini, G. (2002) Time-resolved fluorescence imaging in biology and medicine. *J. Phys. D Appl. Phys.*, **35**, R61–R66.

16 Gadella, T.W. Jr. (ed.) (2008) *FRET and FLIM Imaging Techniques, Laboratory Techniques in Biochemistry and Molecular Biology*, vol. 33, Elsevier, Amsterdam.

17 Esposito, A., Gerritsen, H.C., and Wouters, F.S. (2007) Optimizing frequency-domain fluorescence lifetime sensing for high-throughput applications: photon economy and acquisition speed. *J. Opt. Soc. Am. A*, **24** (10), 3261–3273.

18 Fang, Q., Papaioannou, T., Jo, J.A., Vaitha, R., Shastry, K., and Marcu, L. (2004) Time-domain laser-induced fluorescence spectroscopy apparatus for clinical diagnostics. *Rev. Sci. Instrum.*, **75** (1), 151–162.

19 Pitts, J.D. and Mycek, M.A. (2001) Design and development of a rapid acquisition laser-based fluorometer with simultaneous spectral and temporal resolution. *Rev. Sci. Instrum.*, **72** (7), 3061–3072.

20 Glanzmann, T., Ballini, J.P., van den Bergh, H., and Wagnieres, G. (1999) Time-resolved spectrofluorometer for clinical tissue characterization during endoscopy. *Rev. Sci. Instrum.*, **70**, 4067–4077.

21 O'Connor, D.V. and Phillips, D. (1984) *Time-Correlated Single-Photon Counting*, Academic Press, London.

22 Becker, W. (2005) *Advanced Time-Correlated Single Photon Counting Techniques*, Springer, Berlin.

23 Denk, W., Strickler, J.H., and Webb, W.W. (1990) Two-photon laser scanning fluorescence microscopy. *Science*, **248**, 73–76.

24 Bugiel, I., Konig, K., and Wabnitz, H. (1989) Investigation of cells by fluorescence laser scanning microscopy with subnanosecond time resolution. *Lasers Life Sci.*, **3** (1), 47–53.

25 Gerritsen, H.C., Asselbergs, M.A.H., Agronskaia, A.V., and Van Sark, W.G.J.H.M. (2002) Fluorescence lifetime imaging in scanning microscopes: acquisition speed, photon economy and lifetime resolution. *J. Microsc.*, **206** (3), 218–224.

26 Carlsson, K. and Liljeborg, A. (1998) Simultaneous confocal lifetime imaging of multiple fluorophores using the intensity-modulated multiple-wavelength scanning (IMS) technique. *J. Microsc.*, **191** (2), 119–127.

27 Krishnan, R.V., Saitoh, H., Terada, H., Centonze, V.E., and Herman, B. (2003) Development of a multiphoton fluorescence lifetime imaging microscopy system using a streak camera. *Rev. Sci. Instrum.*, **74** (5), 2714–2721.

28 Grant, D.M., Elson, D.S., Schimpf, D., Dunsby, C., Requejo-Isidro, J., Auksorius, E., Munro, I., Neil, M.A.A., French, P.M.W., Nye, E., Stamp, G.W., and Courtney, P. (2005) Optically sectioned fluorescence lifetime imaging using a Nipkow disc microscope and a tunable ultrafast continuum excitation source. *Opt. Lett.*, **30**, 3353–3355.

29 van Munster, E.B., Goedhart, J., Kremers, G.J., Manders, E.M., and Gadella, T.W. (2007) Combination of a spinning disc confocal unit with frequency-domain fluorescence lifetime imaging microscopy. *Cytometry A*, **71**, 207–214.

30 Grant, D.M., McGinty, J., McGhee, E.J., Bunney, T.D., Owen, D.M., Talbot, C.B., Zhang, W., Kumar, S., Munro, I., Lanigan, P.M.P., Kennedy, G.T., Dunsby, C., Magee, A.I., Courtney, P., Katan, M., Neil, M.A.A., and French, P.M.W. (2007) High speed optically sectioned fluorescence lifetime imaging permits study of live cell signaling events. *Opt. Express*, **15**, 15656–15673.

31 Straub, M. and Hell, S.W. (1998) Fluorescence lifetime three-dimensional microscopy with picosecond precision using a multifocal multiphoton microscope. *Appl. Phys. Lett.*, **73**, 1769–1771.

32 Benninger, R.K.P., Hofmann, O., McGinty, J., Requejo-Isidro, J., Munro, I., Neil, M.A.A., deMello, A.J., and French, P.M.W. (2005) Time-resolved fluorescence imaging of solvent interactions in microfluidic devices. *Opt. Express*, **13** (16), 6275–6285.

33 Leveque-Fort, S., Fontaine-Aupart, M.P., Roger, G., and Georges, P. (2004) Fluorescence-lifetime imaging with a multifocal two-photon microscope. *Opt. Lett.*, **29**, 2884–2886.

34 Requejo-Isidro, J., McGinty, J., Munro, I., Elson, D.S., Galletly, N., Lever, M.J., Neil, M.A.A., Stamp, G.W.H., French, P.M.W., Kellet, P.A., Hares, J.D., and Dymoke-Bradshaw, A.K.L. (2004) High-speed wide-field time-gated endoscopic fluorescence lifetime imaging. *Opt. Lett.*, **29** (19), 2249–2251.

35 Agronskaia, A.V., Tertoolen, L., and Gerritsen, H.C. (2003) High frame rate fluorescence lifetime imaging. *J. Phys. D Appl. Phys.*, **36**, 1655–1662.

36 Morgan, C.G., Mitchell, A.C., and Murray, J.G. (1990) Nanosecond time-resolved fluorescence microscopy: principles and practice. *Trans. R. Microsc. Soc.*, **1**, 463–466.

37 Gratton, E., Feddersen, B., and van de Ven, M. (1990) Parallel acquisition of fluorescence decay using array detectors, *Proc. SPIE*, **1204**, 21–25.

38 Gadella, T.W.J., Jovin, T.M., and Clegg, R.M. (1993) Fluorescence lifetime imaging microscopy (FLIM) – spatial resolution of structures on the nanosecond timescale. *Biophys. Chem.*, **48**, 221–239.

39 Oida, T., Sako, Y., and Kusumi, A. (1993) Fluorescence lifetime imaging microscopy (flimscopy). Methodology development and application to studies of endosome fusion in single cells. *Biophys. J.*, **64**, 676–685.

40 Scully, A.D., MacRobert, A.J., Botchway, S., O'Neill, P., Parker, A.W., Ostler, R.B., and Phillips, D. (1996) Development of a laser-based fluorescence microscope with subnanosecond time resolution. *J. Fluoresc.*, **6** (2), 119–125.

41 Dowling, K., Dayel, M.J., Lever, M.J., French, P.M.W., Hares, J.D., and Dymoke-Bradshaw, A.K.L. (1998) Fluorescence lifetime imaging with picosecond resolution for biomedical applications. *Opt. Lett.*, **23** (10), 810–812.

42 Hares, J.D. (1987) Advances in sub-nanosecond shutter tube technology and applications in plasma physics, *Proc. SPIE*, **831**, 165–170.

43 Munro F I., McGinty, J., Galletly, N., Requejo-Isidro, J., Lanigan, P.M.P., Elson, D.S., Dunsby, C., Neil, M.A.A., Lever, M.J., Stamp, G.W.H., and French, P.M.W. (2005) Toward the clinical application of time-domain fluorescence lifetime imaging. *J. Biomed. Opt.*, **10**, 051403.

44 Holub, O., Seufferheld, M.J., Gohlke, G., and Clegg, R.M. (2000) Fluorescence lifetime imaging (FLI) in real-time – a new technique in photosynthesis research. *Photosynthetica*, **38** (4), 581–599.

45 Mizeret, J., Stepinac, T., Hansroul, M., Studzinski, A., van den Bergh, H., and Wagnieres, G. (1999) Instrumentation for real-time fluorescence lifetime imaging in endoscopy. *Rev. Sci. Instrum.*, **70** (12), 4689–4701.

46 Becker, W., Bergmann, A., Haustein, E., Petrasek, Z., Schwille, P., Biskup, C., Kelbauskas, L., Benndorf, K., Klocker, N., Anhut, T., Riemann, I., and Konig, K. (2006) Fluorescence lifetime images and correlation spectra obtained by multidimensional time-correlated single photon counting. *Microsc. Res. Tech.*, **69**, 186–195.

47 Robinson, T., Valluri, P., Manning, H.B., Owen, D.M., Munro, I., Talbot, C.B., Dunsby, C., Eccleston, J.F., Baldwin, G.S., Neil, M.A.A., de Mello, A.J., and French, P.M.W. (2008) Three-dimensional molecular mapping in a microfluidic mixing device using fluorescence lifetime imaging. *Opt. Lett.*, **33** (16), 1887–1889.

48 Siegel, J., Elson, D.S., Webb, S.E.D., Parsons-Karavassilis, D., Lévêque-Fort, S., Cole, M.J., Lever, M.J., French, P.M.W., Neil, M.A.A., Juskaitis, R., Sucharov, L.O., and Wilson, T. (2001) Whole-field five-dimensional fluorescence microscopy combining lifetime and spectral resolution with optical sectioning. *Opt. Lett.*, **26**, 1338–1340.

49 Bird, D.K., Eliceiri, K.W., Fan, C.H., and White, J.G. (2004) Simultaneous two-photon spectral and lifetime fluorescence microscopy. *Appl. Opt.*, **43**, 5173–5182.

50 Wachman, E.S., Niu, W.H., and Farkas, D.L. (1996) Imaging acousto-optic tunable filter with 0.35-micrometer spatial resolution. *Appl. Opt.*, **35**, 5220–5226.

51 Farkas, D.L., Du, C.W., Fisher, G.W., Lau, C., Niu, W.H., Wachman, E.S., and Levenson, R.M. (1998) Non-invasive image acquisition and advanced processing in optical bioimaging. *Comput. Med. Imaging Graph.*, **22**, 89–102.

52 Hanley, Q.S., Verveer, P.J., and Jovin, T.M. (1999) Spectral imaging in a programmable array microscope by Hadamard transform fluorescence spectroscopy. *Appl. Spectrosc.*, **53**, 1–10.

53 Schultz, R.A., Nielsen, T., Zavaleta, J.R., Ruch, R., Wyatt, R., and Garner, H.R. (2001) Hyperspectral imaging: a novel approach for microscopic analysis. *Cytometry*, **43**, 239–247.

54 De Beule, P., Owen, D.M., Manning, H.B., Talbot, C.B., Requejo-Isidro, J., Dunsby, C., McGinty, J., Benninger, R.K.P., Elson, D.S., Munro, I., Lever, M.J., Anand, P., Neil, M.A.A., and French, P.M.W. (2007) Rapid hyperspectral fluorescence lifetime imaging. *Microsc. Res. Tech.*, **70**, 481–484.

55 Marcu, L., Jo, J.A., Fang, Q.Y., Papaioannou, T., Reil, T., Qiao, J.H., Baker, J.D., Freischlag, J.A., and Fishbein, M.C. (2009) Detection of rupture-prone atherosclerotic plaques by time-resolved laser-induced fluorescence spectroscopy. *Atherosclerosis*, **204** (1), 156–164.

56 Talbot, C.B., McGinty, J., McGhee, E., Owen, D., Grant, D., Kumar, S., De Beule, P., Auksorius, E., Manning, H., Galletly, N.P., Treanor, B., Kennedy, G.T., Lanigan, P.M.P., Munro, I., Elson, D.S., McGee, A., Davis, D., Neil, M.A.A., Stamp, G.W.H., Dunsby, C., and French, P.M.W. (2010) Fluorescence lifetime imaging and metrology for biomedicine, in *Handbook of Photonics for Biomedical Science* (ed. V. Tuchin), Taylor and Francis/CRC Press, Boca Raton, FL, pp. 159–196

57 Andersson-Engels, S., Johansson, J., Svanberg, K., and Svanberg, S. (1991) Fluorescence imaging and point measurements of tissue: applications to the demarcation of malignant tumors and atherosclerotic lesions from normal tissue. *Photochem. Photobiol.*, **53** (6), 807–814.

58 Ramanujam, N. (2000) Fluorescence spectroscopy of neoplastic and non-neoplastic tissues. *Neoplasia*, **2**, 89–117.

59 Ingrams, D.R., Dhingra, J.K., Roy, K., Perrault, D.F. Jr., Bottrill, I.D., Kabani, S., Rebeiz, E.E., Pankratov, M.M., Shapshay, S.M., Manoharan, R., Itzkan, I., and Feld, M.S. (1997) Autofluorescence characteristics of oral mucosa. *Head Neck*, **19**, 27–32.

60 Majumder, S.K., Gupta, P.K., and Uppal, A. (1999) Autofluorescence spectroscopy of tissues from human oral cavity for discriminating malignant from normal. *Lasers Life Sci.*, **8**, 211–227.

61 Wang, C.Y., Chiang, H.K., Chen, C.T., Chiang, C.P., Kuo, Y.S., and Chow, S.N. (1999) Diagnosis of oral cancer by light-induced autofluorescence spectroscopy using double excitation wavelengths. *Oral Oncol.*, **35**, 144–150.

62 Uppal, A. and Gupta, P.K. (2003) Measurement of NADH concentration in normal and malignant human tissues from breast and oral cavity. *Biotechnol. Appl. Biochem.*, **37**, 45–50.

63 Chwirot, B., Jedrzejczyk, W., Chwirot, S., Michniewicz, Z., and Redzinski, J. (1996) Tissue spectroscopy. New generation of optical methods for cancer detection. *Pol. Merkur. Lekarski.*, **1**, 355–358 (in Polish).

64 Chwirot, B.W., Chwirot, S., Jedrzejczyk, W., Jackowski, M., Raczynska, A.M., Winczakiewicz, J., and Dobber, J. (1997) Ultraviolet laser-induced fluorescence of human stomach tissues: detection of cancer tissues by imaging techniques. *Lasers Surg. Med.*, **21**, 149–158.

65 Abe, S., Izuishi, K., Tajiri, H., Kinoshita, T., and Matsuoka, T. (2000) Correlation of *in vitro* autofluorescence endoscopy images with histopathologic findings in stomach cancer. *Endoscopy*, **32**, 281–286.

66 Silveira, L. Jr., Betiol Filho, J.A., Silveira, F.L., Zangaro, R.A., and Pacheco, M.T. (2008) Laser-induced fluorescence at 488 nm excitation for detecting benign and malignant lesions in stomach mucosa. *J. Fluoresc.*, **18**, 35–40.

67 Xiao, S.D., Ge, Z.Z., Zhong, L., and Luo, H.Y. (2002) Diagnosis of gastric cancer by using autofluorescence spectroscopy. *Chin. Dig. Dis.*, **3**, 99–102.

68 Xiao, S.D., Zhong, L., Luo, H.Y., Chen, X.Y., and Shi, Y. (2002) Autofluorescence imaging analysis of gastric cancer. *Chin. Dig. Dis.*, **3**, 95–98.

69 Kapadia, C.R., Cutruzzola, F.W., O'Brien, K.M., Stetz, M.L., Enriquez, R., and Deckelbaum, L.I. (1990) Laser-induced fluorescence spectroscopy of human colonic mucosa. Detection of adenomatous transformation. *Gastroenterology*, **99**, 150–157.

70 Richards-Kortum, R., Rava, R.P., Petras, R.E., Fitzmaurice, M., Sivak, M., and Feld, M.S. (1991) Spectroscopic diagnosis of colonic dysplasia. *Photochem. Photobiol.*, **53**, 777–786.

71 Yang, Y., Tang, G.C., Bessler, M., and Alfano, R.R. (1995) Fluorescence spectroscopy as a photonic pathology method for detecting colon cancer. *Lasers Life Sci.*, **6**, 259–276.

72 Chwirot, B.W., Michniewicz, Z., Kowalska, M., and Nussbeutel, J. (1999) Detection of colonic malignant lesions by digital imaging of UV laser-induced autofluorescence. *Photochem. Photobiol.*, **69**, 336–340.

73 Demos, S.G., Gandour-Edwards, R., Ramsamooj, R., and deVere White, R. (2004) Spectroscopic detection of bladder cancer using near-infrared imaging techniques. *J. Biomed. Opt.*, **9**, 767–771.

74 Cicchi, R., Crisci, A., Nesi, G., Cosci, A., Giancane, S., Carini, M., and Pavone, F.S. (2009) Time- and spectral-resolved multiphoton imaging of fresh bladder biopsies, *Proc. SPIE*, **7367**, 73670M–73679M.

75 Palmer, G.M., Keely, P.J., Breslin, T.M., and Ramanujam, N. (2003) Autofluorescence spectroscopy of normal and malignant human breast cell lines. *Photochem. Photobiol.*, **78**, 462–469.

76 Conklin, M.W., Provenzano, P.P., Eliceiri, K.W., Sullivan, R., and Keely, P.J. (2009) Fluorescence lifetime imaging of endogenous fluorophores in histopathology sections reveals differences between normal and tumor epithelium in carcinoma *in situ* of the breast. *Cell Biochem. Biophys.*, **53**, 145–157.

77 Yang, Y., Katz, A., Celmer, E.J., Zurawska-Szczepaniak, M., and Alfano, R.R. (1997) Fundamental differences of excitation spectrum between malignant and benign breast tissues. *Photochem. Photobiol.*, **66**, 518–522.

78 Breslin, T.M., Xu, F., Palmer, G.M., Zhu, C., Gilchrist, K.W., and Ramanujam, N. (2004) Autofluorescence and diffuse reflectance properties of malignant and benign breast tissues. *Ann. Surg. Oncol.*, **11**, 65–70.

79 Demos, S.G., Gandour-Edwards, R., Ramsamooj, R., and White, R. (2004) Near-infrared autofluorescence imaging for detection of cancer. *J. Biomed. Opt.*, **9**, 587–592.

80 Keller, M.D., Majumder, S.K., Kelley, M.C., Meszoely, I.M., Boulos, F.I., Olivares, G.M., and Mahadevan-Jansen, A. (2010) Autofluorescence and diffuse reflectance spectroscopy and spectral imaging for breast surgical margin analysis. *Lasers Surg. Med.*, **42**, 15–23.

81 Jacobs, V.R., Paepke, S., Schaaf, H., Weber, B.C., and Kiechle-Bahat, M. (2007) Autofluorescence ductoscopy: a new imaging technique for intraductal breast endoscopy. *Clin. Breast Cancer*, **7**, 619–623.

82 Douplik, A., Leong, W.L., Easson, A.M., Done, S., Netchev, G., and Wilson, B.C. (2009) Feasibility study of autofluorescence mammary ductoscopy. *J. Biomed. Opt.*, **14**, 044036.

83 Pradhan, A., Das, B.B., Yoo, K.M., Cleary, J., Prudente, R., Celmer, E., and Alfano, R.R. (1992) Time-resolved UV photoexcited fluorescence kinetics from malignant and non-malignant human breast tissues. *Lasers Life Sci.*, **4**, 225–234.

84 Provenzano, P.P., Eliceiri, K.W., Yan, L., Ada-Nguema, A., Conklin, M.W., Inman, D.R., and Keely, P.J. (2008) Nonlinear optical imaging of cellular processes in breast cancer. *Microsc. Microanal.*, **14**, 532–548.

85 Marcu, L., Jo, J.A., Butte, P.V., Yong, W.H., Pikul, B.K., Black, K.L., and Thompson, R.C. (2004) Fluorescence lifetime spectroscopy of glioblastoma multiforme. *Photochem. Photobiol.*, **80**, 98–103.

86 Butte, P.V., Pikul, B.K., Hever, A., Yong, W.H., Black, K.L., and Marcu, L. (2005) Diagnosis of meningioma by time-resolved fluorescence spectroscopy. *J. Biomed. Opt.*, **10** (6), 064026–064029.

87 Kantelhardt, S.R., Diddens, H., Leppert, J., Rohde, V., Huttmann, G., and Giese, A. (2008) Multiphoton excitation fluorescence microscopy of 5-aminolevulinic acid induced fluorescence in experimental gliomas. *Lasers Surg. Med.*, **40**, 273–281.

88 König, K. (2008) Clinical multiphoton tomography. *J. Biophotonics*, **1** (1), 13–23.

89 Koehler, M.J., Konig, K., Elsner, P., Buckle, R., and Kaatz, M. (2006) *In vivo* assessment of human skin aging by multiphoton laser scanning tomography. *Opt. Lett.*, **31**, 2879–2881.

90 Lee, J.H., Chen, S.Y., Yu, C.H., Chu, S.W., Wang, L.F., Sun, C.K., and Chiang, B.L. (2009) Noninvasive *in vitro* and *in vivo* assessment of epidermal hyperkeratosis and dermal fibrosis in atopic dermatitis. *J. Biomed. Opt.*, **14**, 014008.

91 Chen, G., Chen, J., Zhuo, S., Xiong, S., Zeng, H., Jiang, X., Chen, R., and Xie, S. (2009) Nonlinear spectral imaging of human hypertrophic scar based on two-photon excited fluorescence and second-harmonic generation. *Br. J. Dermatol.*, **161** (1), 48–55.

92 Brancaleon, L., Durkin, A.J., Tu, J.H., Menaker, G., Fallon, J.D., and Kollias, N. (2001) *In vivo* fluorescence spectroscopy of nonmelanoma skin cancer. *Photochem. Photobiol.*, **73**, 178–183.

93 Eichhorn, R., Wessler, G., Scholz, M., Leupold, D., Stankovic, G., Buder, S., Stucker, M., and Hoffmann, K. (2009) Early diagnosis of melanotic melanoma based on laser-induced melanin fluorescence. *J. Biomed. Opt.*, **14**, 034033.

94 Paoli, J., Smedh, M., Wennberg, A.M., and Ericson, M.B. (2008) Multiphoton laser scanning microscopy on non-melanoma skin cancer: morphologic features for future non-invasive diagnostics. *J. Invest. Dermatol.*, **128**, 1248–1255.

95 Dimitrow, E., Ziemer, M., Koehler, M.J., Norgauer, J., Konig, K., Elsner, P., and Kaatz, M. (2009) Sensitivity and specificity of multiphoton laser tomography for

in vivo and *ex vivo* diagnosis of malignant melanoma. *J. Invest. Dermatol.*, **129**, 1752–1758.

96 Galletly, N.P., McGinty, J., Dunsby, C., Teixeira, F., Requejo-Isidro, J., Munro, I., Elson, D.S., Neil, M.A., Chu, A.C., French, P.M., and Stamp, G.W. (2008) Fluorescence lifetime imaging distinguishes basal cell carcinoma from surrounding uninvolved skin. *Br. J. Dermatol.*, **159**, 152–161.

97 De Giorgi, V., Massi, D., Sestini, S., Cicchi, R., Pavone, F.S., and Lotti, T. (2009) Combined non-linear laser imaging (two-photon excitation fluorescence microscopy, fluorescence lifetime imaging microscopy, multispectral multiphoton microscopy) in cutaneous tumours: first experiences. *J. Eur. Acad. Dermatol. Venereol.*, **23**, 314–316.

98 Dimitrow, E., Riemann, I., Ehlers, A., Koehler, M.J., Norgauer, J., Elsner, P., Konig, K., and Kaatz, M. (2009) Spectral fluorescence lifetime detection and selective melanin imaging by multiphoton laser tomography for melanoma diagnosis. *Exp. Dermatol.*, **18**, 509–515.

11
In Vivo Instrumentation

Herbert Schneckenburger, Michael Wagner, Petra Weber, and Thomas Bruns

11.1
Introduction

Optical analysis of human tissue requires homogeneous illumination with thermally tolerable, non-phototoxic light doses, together with high-resolution and sensitive detection. For cell cultures and biopsies, microscopic methods are commonly used, including transillumination, reflection, and fluorescence techniques. For patients, more specific systems have to be applied for various organs, which are based on backscattering or fluorescence measurements. Again, microscopic techniques, but also various endoscopic systems, are appropriate for high-resolution imaging. In addition to these incoherent systems, optical coherence tomography [1] and also interferometric and holographic methods [2] are used increasingly, if high axial resolution is required. These techniques are based on interference of an electromagnetic wave with a reference wave, and only in a well-defined depth of the sample is positive interference attained. In spite of important achievements with these coherent techniques, this chapter focuses on incoherent methods and instrumentation, including microscopy, endoscopy, and imaging equipment.

11.2
Microscopy

Only for thin samples, for example, cell monolayers or thin biopsies, can conventional transillumination microscopy be used. Köhler's illumination and additional equipment for phase contrast or interference contrast microscopy provide optimum image quality. Most *in vivo* samples, however, require epi-illumination either by darkfield equipment (e.g., a darkfield objective lens) for reflection measurements or by a dichromatic mirror in combination with appropriate filters for fluorescence experiments. Fluorescence microscopy currently is the most widespread method, since many cellular compartments or organelles can be stained selectively with various fluorescent dyes or nanoparticles [3], and a large number of fluorescent

Handbook of Biophotonics. Vol.2: Photonics for Health Care, First Edition. Edited by Jürgen Popp, Valery V. Tuchin, Arthur Chiou, and Stefan Heinemann.

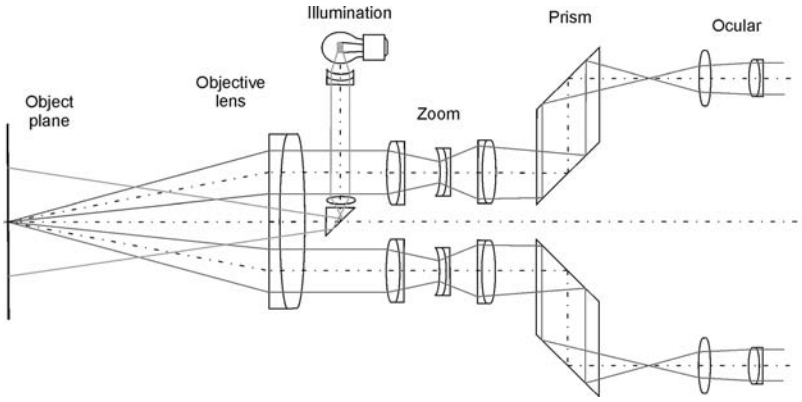

Figure 11.1 Principle of an operation microscope.

proteins can be encoded genetically [4]. Application of fluorescent probes for humans, however, is restricted to very few dyes, for example, fluorescein or indocyanine green used for fluorescence angiography or blood volume determination [5]. Therefore, intrinsic fluorescence, for example, of the free and protein-bound coenzyme nicotinamide adenine dinucleotide (NADH) [6], plays an increasing role in the diagnosis of patients. Whereas conventional fluorescence microscopy generally does not provide axial resolution, laser scanning microscopy [7] and some wide-field techniques using structured [8] or selective plane [9] illumination permit measurements of well-defined layers of a sample and 3D image reconstruction.

In recent years, the operation microscope has become an essential tool in microsurgery with application in many clinical disciplines, for example, ophthalmology, ear, nose, and throat (ENT), gynecology, and neurosurgery. In comparison with *in vitro* microscopy, ultimate resolution is not required, but a large field of vision, high focal depth, long working distance, and stereoscopic observation. Commonly, a binocular tube with an angle ranging from 3 to 10° between individual light paths is used, as depicted in Figure 11.1. An achromatic objective lens with a numerical aperture A_N between 0.01 and 0.05 creates two parallel light beams which are focused to an image plane and further visualized by an ocular. A zoom system may be used to provide variable magnification, which for the whole microscope is between 5× and 20×. With the comparably low A_N, a resolution between 6 and 30 µm and a focal depth up to a few millimeters are attained. Epi-illumination systems including various kinds of light sources, for example, light-emitting diodes (LEDs), halogen or xenon lamps, fiber-optics and specific focusing devices, are commonly used.

11.3 Endoscopy

Endoscopy is the method of choice for measurements inside a body or a specific organ, often in combination with surgery or certain therapies, for example, photo-

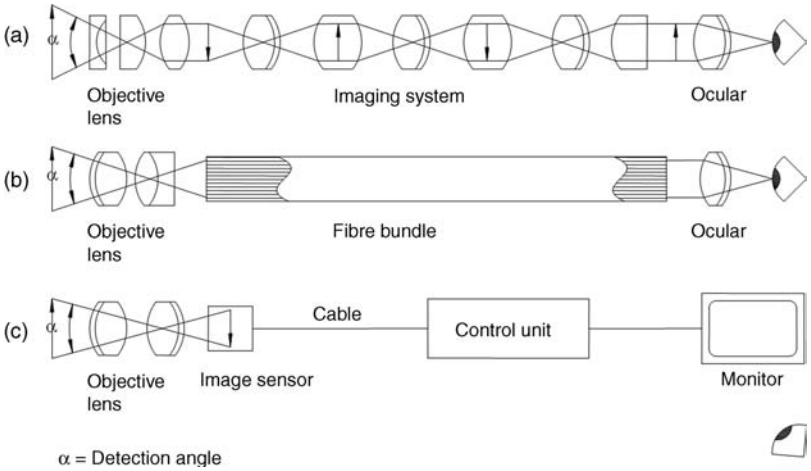

Figure 11.2 Types of endoscopes: (a) rigid endoscope with a system of lenses; (b) flexible endoscope with an oriented fiber bundle; (c) flexible endoscope with electronic image transfer.

dynamic therapy [10]. Different light paths are used for illumination and image detection, in either a reflection or a fluorescence mode. Depending on the specific application, either rigid or flexible endoscopes are preferred, as depicted in Figure 11.2. In rigid endoscopes, the detection path consists of a system of lenses generating an image of the object either in an ocular or on a camera chip. These endoscopes include arthroscopes, laryngoscopes, bronchoscopes, laparoscopes, cystoscopes, and rectoscopes. In contrast, flexible endoscopy is based either on optical image transfer by an oriented fiber bundle or on electronic transfer with an image sensor being located close to the object. Generally, image quality and resolution are better in the latter case. Like rigid endoscopes, flexible endoscopes can be used as bronchoscopes, cystoscopes, or rectoscopes, but there are additional applications in, for example, gastroscopy, choledochoscopy, and coloscopy. For all optical imaging systems, specific techniques can be used, for example, laser scanning endoscopy for high-resolution imaging [11] and integration of grin lenses to keep the diameter of the detection channel small at relatively high numerical aperture [12].

11.4 Imaging Techniques

In modern microscopy and endoscopy visual observation by an ocular is increasingly being replaced by high-performance imaging systems with charge-coupled device (CCD) or electron-multiplying charge-coupled device (EMCCD) cameras whose sensitivities range between about 10^{-13} and 10^{-18} W per pixel. Alternatively, the complementary metal oxide semiconductor (CMOS) detector camera and the image-intensified charge-coupled device (ICCD) camera are becoming more and more popular.

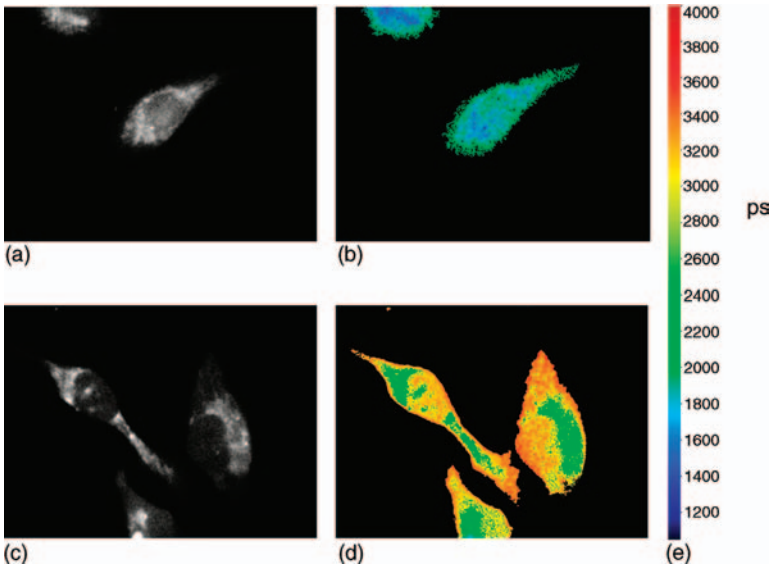

Figure 11.3 Fluorescence intensity (a, c) and lifetime images (b, d) of U251-MG glioblastoma cells (a, b) and U251-MG cells with an activated suppressor gene PTEN (c, d). (e) Scale of fluorescence lifetimes. Excitation wavelength, 375 nm; images measured at $\lambda \geq 420$ nm; image size, $150 \times 200\,\mu$m. Data from BMBF report No. 1792C08 (2010). Cells kindly provided by Professor Jan Mollenhauer, Department of Molecular Oncology, University of South Denmark, Odense, Denmark.

In addition to conventional imaging methods, some special techniques, including spectral imaging, polarization, and fluorescence lifetime imaging (FLIM) are increasingly being used. Together with spatial distribution, spectral or lifetime parameters can give valuable information about molecular or cellular interactions of a metabolite or a dye molecule with its microenvironment. This may include pH values, microviscosities, aggregation, or transfer of optical excitation energy between adjacent molecules. An example of FLIM is given in Figure 11.3 for intrinsic fluorescence of U251-MG human glioblastoma cells (a, b) and U251-MG cells with an activated tumor suppressor gene PTEN. Whereas the fluorescence intensities (a, c) show similar patterns of distribution, the fluorescence lifetimes are generally longer for the less malignant cells (d) than for the tumor cells (b), possibly due to different metabolic pathways. Fluorescence lifetime images can be deduced either from fluorescence decay kinetics recorded for each pixel of a laser scanning microscope [13] or from fluorescence intensities (I_1, I_2) recorded within two sub-nanosecond time gates shifted by a time interval Δt between one another according to the equation $\tau = \Delta t / \ln(I_1/I_2)$, where τ corresponds to the real fluorescence lifetime in the case of a monoexponential decay and to an "effective fluorescence lifetime" in the case of a multi-exponential decay.

References

1 Fujimoto, J.G. (2003) Optical coherence tomography for ultrahigh resolution *in vivo* imaging. *Nat. Biotechnol.*, **21**, 1361–1367.

2 Kemper, B. and von Bally, G. (2008) Digital holographic microscopy for live cell applications and technical inspection. *Appl. Opt.*, **47**, A52–A61.

3 Bruchez, M., Moronne, M., Gin, P., Weis, S., and Alivisatos, A.P. (1998) Semiconductor nanocrystals as fluorescence biological labels. *Science*, **281**, 2013–2016.

4 Rizzuto, R., Brini, M., Pizzo, P., Murgia, M., and Pozzan, T. (1995) Chimeric green fluorescent protein as a tool for visualizing subcellular organelles in living cells. *Curr. Biol.*, **5**, 635–642.

5 Brancato, R. and Trabucchi, G. (1998) Fluorescein and indocyanine green angiography in vascular chorioretinal diseases. *Semin. Ophthalmol.*, **13**, 189–198.

6 Galeotti, T., van Rossum, G.D.V., Mayer, D.H., and Chance, B. (1970) On the fluorescence of NAD(P)H in whole cell preparations of tumours and normal tissues. *Eur. J. Biochem.*, **17**, 485–496.

7 Pawley, J. (1990) *Handbook of Biological Confocal Microscopy*, Plenum Press, New York.

8 Neil, M.A.A., Juskaitis, R., and Wilson, T. (1997) Method of obtaining optical sectioning by structured light in a conventional microscope. *Opt. Lett.*, **22**, 1905–1907.

9 Huisken, J., Swoger, J., del Bene, F., Wittbrodt, J., and Stelzer, E.H.K. (2004) Optical sectioning deep inside live embryos by SPIM. *Science*, **305**, 1007–1009.

10 Dougherty, T.J. and Marcus, S.L. (1992) Photodynamic therapy. *Eur. J. Cancer*, **28**, 1734–1742.

11 de Palma, G.D. (2009) Confocal laser endomicroscopy in the "*in vivo*" histological diagnosis of the gastrointestinal tract. *World J. Gastroenterol.*, **15**, 5770–5775.

12 Fu, L., Gan, X., and Gu, M. (2005) Characterization of gradient-index lens-fiber spacing towards application in two-photon fluorescence endoscopy. *Appl. Opt.*, **44**, 7270–7274.

13 Becker, W. (2005) *Advanced Time-Correlated Single Photon Counting Techniques*, Springer, Berlin.

12
Fluorescent Probes (Fluorescence Standards, Green Protein Technology)

Markus Sauer

Molecules displaying strong fluorescence possess delocalized electrons formally present in conjugated double bonds. Most proteins and all nucleic acids are colorless in the visible region of the spectrum. However, they exhibit absorption and emission in the ultraviolet (UV) region. Natural fluorophores in tissue include nicotinamide adenine dinucleotide (NADH) and flavin adenine dinucleotide (FAD), structural proteins such as collagen, elastin, and their cross-links, and the aromatic amino acids, each of which has a characteristic wavelength for excitation with an associated characteristic emission. A serious limitation of native fluorescence detection of, for example, aromatic amino acids is their low photostability under one- and two-photon excitation conditions, which renders difficult the application of native fluorescence for highly sensitive detection schemes, for example, single-molecule fluorescence spectroscopy [1, 2].

Phycobiliproteins derived from cyanobacteria and eukaryotic algae belong to a class of relatively bright water-soluble natural fluorophores [3]. They absorb light in the visible wavelength range that is poorly utilized by chlorophyll and, through fluorescence energy transfer, convey the energy to the membrane-bound photosynthetic reaction centers where fast electron transfer occurs with high efficiency, converting solar energy to chemical energy. Phycobiliproteins are classified on the basis of their color into phycoerythrins (red) and phycocyanins (blue), with absorption maxima lying between 490 and 570 nm and between 610 and 665 nm, respectively. For example, B-phycoerythrin is comprised of three polypeptide subunits forming an aggregate containing a total of 34 bilin chromophores. It exhibits an absorption cross-section equivalent to that of ~20 rhodamine 6G chromophores and the highest fluorescence quantum yield of all phycobiliproteins of 0.98 with a fluorescence lifetime of 2.5 ns [4–6]. B-phycoerythrin was the first species to be detected at the single-molecule level using laser-induced fluorescence [6–8]. However, single allophycocyanin molecules with a smaller fluorescence quantum yield of 0.68 [9] can also be easily visualized immobilized on a cover-glass surface under aqueous buffer [10].

Organic fluorophores or fluorescent dyes are characterized by a strong absorption and emission band in the visible region of the electromagnetic spectrum

Handbook of Biophotonics. Vol.2: Photonics for Health Care, First Edition. Edited by Jürgen Popp, Valery V. Tuchin, Arthur Chiou, and Stefan Heinemann.

(i.e., between 400 and 700 nm). The long-wavelength absorption band of a fluorophore is attributed to the transition from the electronic ground state S_0 to the first excited singlet state S_1. Since the transition moment for this process is typically very large, the corresponding absorption bands exhibit oscillator strengths on the order of unity. The reverse process $S_1 \rightarrow S_0$ is responsible for spontaneous emission known as fluorescence and for stimulated emission [11]. Since the earlier use of organic fluorescent dyes for qualitative and quantitative determination of analyte molecules (especially for automated DNA sequencing in the 1980s), their importance for bioanalytical applications has increased considerably [12–15]. Owing to the enhanced demand for fluorescent markers, the development of new fluorescent dyes has increased notably in recent years [16–21]. Using fluorescent dyes, extremely high sensitivity down to the single-molecule level can be achieved. Furthermore, time- and position-resolved detection without contacting the analyte is possible. Typically, the fluorescent probes or markers are identified and quantified by their absorption and fluorescence emission wavelengths and intensities. The sensitivity achievable with a fluorescent label is directly proportional to the molar extinction coefficient for absorption and the quantum yield of fluorescence. The extinction coefficient typically has maximum values of about $10^5\,\mathrm{l\,mol^{-1}\,cm^{-1}}$ in organic fluorophores and the quantum yield may approach values close to 100%. Absorption and emission spectra and also the fluorescence quantum yield and lifetime are dependent on environmental factors. Furthermore, for labeling of biological compounds, for example, antibodies and DNA/RNA, the dye must carry a functional group suitable for a mild covalent coupling reaction, preferentially with free amino or thiol groups of the analyte. In addition, the fluorophore should be as hydrophilic as possible to avoid aggregation and nonspecific binding in aqueous solvents. Today, a broad palette of fluorescent dyes (see Figure 12.1) activated as *N*-hydroxysuccinimide (NHS) ester, sulfo-NHS ester, isothiocyanates, or maleimides for mild covalent coupling to amino or thiol groups have been commercialized by several companies (see, e.g., www.invitrogen.com, www.atto-tec.com, www.dyomics.com).

Suitable organic fluorescent dyes are distinguished by a high fluorescence quantum yield. That is, upon excitation into the excited singlet state and subsequent relaxation to the lowest vibronic level of S_1, the radiative decay to the singlet ground state S_0 is the preferred deactivation pathway. However, there are many nonradiative processes that can compete efficiently with light emission and thus reduce fluorescence efficiency to an extent that depends in a complicated fashion on the molecular structure of the dye. Internal conversion, that is, the nonradiative decay of the lowest excited singlet state S_1 directly to the ground state S_0, is mostly responsible for the loss of fluorescence efficiency of organic dyes. In addition to fluorescence quenching via photoinduced electron transfer (PET) or Förster resonance energy transfer (FRET), a molecule excited to S_1 may enter a triplet state and relax to the lowest level T_1. The occupation of triplet states is undesirable with respect to highly sensitive fluorescence applications such as single-molecule fluorescence spectroscopy [23].

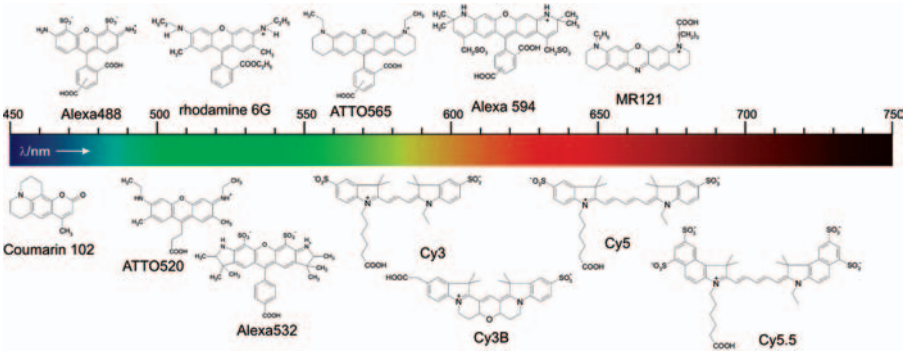

Figure 12.1 Molecular structures of some prominent commercially available organic fluorophores.

Figure 12.1 gives the molecular structures and rough absorption and emission properties of some of the most widely used organic fluorophores. For example, Alexa Fluor 350 and 430 and the two dyes ATTO 390 and ATTO 425 belong to the class of commercially available coumarin derivatives. Their absorption maxima are reflected in their names, that is, the absorptions maxima are at ~350, 430, 390, and 425 nm, respectively. The emission maxima of the three coumarins are located around 445, 545, 480, and 485 nm, respectively. They exhibit extinction coefficients in the range 20 000–50 000 $l\,mol^{-1}\,cm^{-1}$ with fluorescence quantum yields of up to 0.90 and lifetimes between 3 and 4 ns. Today, most (bio)analytical applications requiring high sensitivity use, in addition to carbocyanines, rhodamine dyes that absorb and emit in the wavelength range 500–700 nm. Owing to their structural rigidity, rhodamine dyes show high fluorescence quantum yields. They exhibit a small Stokes shift of about 20–30 nm and are applied as complementary probes together with other fluorophores in double-label staining, as energy donors and acceptors in FRET experiments, and as fluorescent markers in DNA sequencing and immunoassays. To increase the water solubility of the fluorophores for bioanalytical applications, the chromophores are often modified by the attachment of sulfonate groups. There are several functional rhodamine derivatives commercially available for biological labeling: ATTO 488, ATTO 520 and ATTO 532 related to rhodamine 6G, ATTO 550 related to rhodamine B, ATTO 565 related to rhodamine 630, ATTO 590, and ATTO 594. The molecular structures of the Alexa derivatives Alexa 488, Alexa 532, Alexa 546, Alexa 568, Alexa 594, and Alexa 633 are also based on rhodamines (Figure 12.1) [24]. Typically, rhodamine dyes exhibit fluorescence quantum yields close to unity (100%) and a fluorescence lifetime of ~4 ns.

Owing to the small number of compounds that demonstrate intrinsic fluorescence above 600 nm, the use of near-infrared (NIR) fluorescence detection in bioanalytical samples is a desirable alternative to visible fluorescence detection. This has prompted current efforts to use NIR dyes for bioanalytical applications. However, there are few fluorophores that show sufficient fluorescence quantum yields in the NIR region, especially in aqueous surroundings, and that can be coupled covalently to analyte molecules [25]. Otherwise, there are several advantages

of using fluorescent dyes that absorb in the red region over those that absorb at shorter blue and green wavelengths. The most important of these advantages is the reduction in background that ultimately improves the sensitivity achievable. There are three major sources of background: (i) elastic scattering, that is, Rayleigh scattering, (ii) inelastic scattering, that is, Raman scattering, and (iii) fluorescence from impurities. The efficiency of both Rayleigh and Raman scattering are dramatically reduced by shifting to longer wavelength excitation (scales with $1/\lambda^4$). Likewise, the number of fluorescent impurities is significantly reduced with longer excitation and detection wavelengths.

One type of red-absorbing fluorophores is cyanine dyes. Cyanine derivatives belong to the class of polymethine dyes, that is, planar fluorophores with conjugated double bonds where all atoms of the conjugated chain lie in a common plane linked by σ-bonds. Figure 12.1 also gives the molecular structures of some commercially available symmetric cyanine derivatives (Cy3, Cy5, Cy5.5, and the bridged Cy3B). The molar extinction coefficients of cyanine derivatives are comparably high and lie between 1.2×10^5 and $2.5 \times 10^5\,\mathrm{l\,mol^{-1}\,cm^{-1}}$ [26–30]. On the other hand, the fluorescence quantum yield varies only between 0.04 and 0.4 with lifetimes in the range of a few hundred picoseconds (0.2–1.0 ns).

Another class of fluorescent probes, namely fluorescent nanoparticles associated with great promise, is semiconductor nanocrystals (NCs) such as core-shell CdSe/ZnS NCs [31]. Their unique optical properties – tunable narrow emission spectrum, broad excitation spectrum, high photostability, and long fluorescence lifetime (on the order of tens of nanoseconds) – make these bright probes attractive in experiments involving long observation times and multicolor and time-gated detection. Furthermore, the relatively long fluorescence lifetime of CdSe nanocrystals, in the range of several tens of nanoseconds, can be used advantageously to enhance fluorescence biological imaging contrast and sensitivity by time-gated detection [32].

For the investigation of biologically relevant samples, target molecules have to be labeled *in vivo* with a fluorescent tag. Fluorescent labels useful for labeling of biomolecules in living cells have to fulfill special requirements, such as high biocompatibility, high photostability, and retention of biological function. In addition, the observation of the fluorescence signal of a fluorophore is more complicated than *in vitro*, primarily due to strong autofluorescence, especially in the blue/green wavelength region, and concentration control is generally difficult to perform. The first problem, however, is site-specific labeling inside a living cell and some procedures have been described in the literature. A very promising method for *in vivo* labeling with fluorescent probes is protein transduction. Several naturally occurring proteins have been found to enter cells easily, including the TAT protein from HIV [33, 34]. Furthermore, so-called hybrid systems composed of a small molecule that can covalently bind to genetically specified proteins inside or on the surface of living cells have been developed. One of these methods for covalent labeling of proteins in living cells is the tetracysteine–biarsenical system [35], which requires incorporation of a 4-cysteine α-helical motif – a 12-residue peptide sequence that includes four cysteine residues – into the target protein. The tetracysteine motif

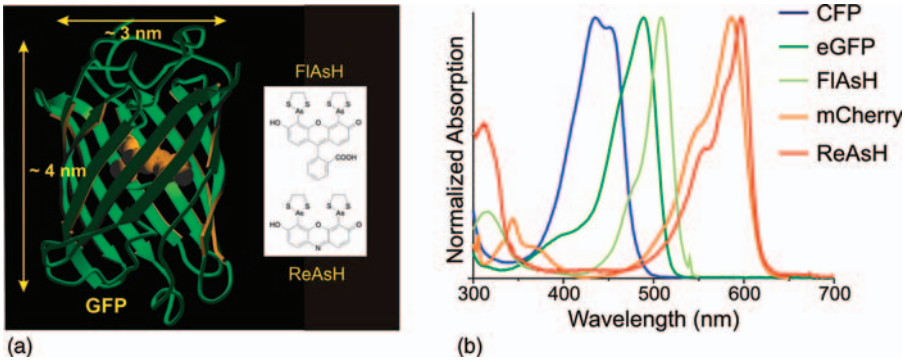

Figure 12.2 (a) Comparison (to scale) of images of the green fluorescent protein (GFP) and the biarsenical fluorophores FlAsH and ReAsH. (b) Normalized absorption spectra of CFP, eGFP, mCherry, and two biarsenical fluorophores in aqueous solvents.

binds membrane-permeable biarsenical molecules, notably the green and red fluorophores FlAsH and ReAsH, with picomolar affinity (Figure 12.2).

On the other hand, the protein of interest can be expressed fused to a protein tag that is capable of binding a small fluorescent ligand [36, 37]. A prominent example uses the enzymatic activity of human O^6-alkylguanine-DNA-alkyltransferase (hAGT) that irreversibly transfers a substrate alkyl group, an O^6-benzylguanine (BG) derivative, to one of its cysteine residues [38]. Kits for genetic labeling of proteins with hAGT are commercially available as SNAP-tags. Alternatively, trimethoprim (TMP) derivatives can be used to selectively tag *Escherichia coli* dihydrofolate reductase (eDHFR) fusion proteins in wild-type mammalian cells with minimal background and fast kinetics [39]. However, one should be aware that the labeling specificity and efficiency of tags in living cells are often reduced due to the attachment of organic fluorophores. Hence all tag technologies require sensitive controls to ensure specific labeling of the desired target protein with minimal perturbation.

The most elegant way to label proteins *in vivo* specifically is direct genetic labeling with fluorescence. The fluorophore used is a genetically encoded protein such as the green fluorescent protein (GFP) or its relatives. GFP from the bioluminescent jellyfish *Aequorea victoria* has revolutionized many areas of cell biology and biotechnology because it provides direct genetic encoding of strong visible fluorescence [40, 41]. GFP can function as a protein tag, as it tolerates N- and C-terminal fusion to a broad variety of proteins, many of which have been shown to retain native function [40–42]. According to this method, the DNA sequence coding for GFP is placed immediately adjacent to the sequence coding for the protein of interest. During biosynthesis, the protein will be prepared as a GFP-fusion protein. GFP is comprised of 238 amino acids and exhibits a barrel-like cylindrical structure in which the fluorophore is highly protected, located on the central helix of the geometric center of the cylinder. These cylinders have a diameter of about 3 nm and a length of about 4 nm, that is, significantly larger than common fluorophores with a size of $\leq$1 nm (Figure 12.2). The fluorophore is a *p*-hydroxybenzylideneimidazolinone formed

from residues 65–67, which are Ser–Tyr–Gly in the native protein. The fluorophore appears to be self-catalytic, requiring proper folding of the entire structure. The protein is relatively stable, with a melting point above 65 °C.

Wild-type GFP has an extinction coefficient of $9500\,l\,mol^{-1}\,cm^{-1}$ at 475 nm and a fluorescence quantum yield Φ_f of 0.79 compared with $53\,000\,l\,mol^{-1}\,cm^{-1}$ at 489 nm in enhanced GFP (EGFP) with $\Phi_f = 0.60$. Further, several spectral GFP variants with blue, cyan, and yellowish green emission have been successfully generated [43, 44]. Proteins that fluoresce at red or far-red wavelengths are of specific interest because cells and tissues display reduced autofluorescence at longer wavelengths. Furthermore, red fluorescent proteins (RFPs) can be used in combination with other fluorescent proteins that fluoresce at shorter wavelengths for both multicolor labeling and fluorescence resonance energy transfer measurements. Here, the discovery of new fluorescent proteins from nonbioluminescent *Anthozoa* species, in particular the red-shifted fluorescent protein DsRed, is of general interest [45]. DsRed (drFP583) has absorption and emission maxima at 558 and 583 nm, respectively. However, several major drawbacks, such as slow maturation and residual green fluorescence, need to be overcome for the efficient use of DsRed as an *in vivo* reporter, especially in Single-molecule fluorescence spectroscopy (SMFS) applications. To improve the maturation properties, and to reduce aggregation, a number of other red fluorescent proteins and variants of DsRed have been developed, for example, DsRed2, DsRed-Express, eqFP611, and HcRed1. The oligomerization problem of DsRed has been solved by mutagenetic means (mRFP1) [46].

In addition to their use for selective fluorescence labeling for dynamic studies, some optical highlighters (photoconvertible or photoactivatable fluorescent proteins such as PA-GFP, Dronpa, and EosFP) and organic fluorophores are also valuable tools in super-resolution fluorescence imaging based on single-molecule detection and precise localization of the position of each fluorophore, for example, PALM, STORM, and *d*STORM [47–50]. These methods rely on the light-induced activation of only a small subset of fluorophores per image spaced further apart than the diffraction limit.

References

1 Lippitz, M., Erker, W., Decker, H., van Holde, K.E., and Basché, T. (2002) *Proc. Natl. Acad. Sci. U. S. A.*, **99**, 2772.

2 Schüttpelz, M., Müller, C., Neuweiler, H., and Sauer, M. (2006) *Anal. Chem.*, **78**, 663.

3 MacColl, R. and Guard-Friar, D. (1987) *Phycobiliproteins*, CRC Press, Boca Raton, FL.

4 Mathies, R.A. and Peck, K. (1990) *Anal. Chem.*, **62**, 1786.

5 Wehrmeyer, W., Wendler, J., and Holzwarth, A.R. (1985) *Eur. J. Cell. Biol.*, **36**, 17.

6 Wu, M., Goodwin, P.M., Ambrose, W.P., and Keller, R.A. (1996) *J. Phys. Chem.*, **100**, 17406.

7 Nguyen, D.C., Keller, R.A., Jett, J.H., and Martin, J.C. (1987) *Anal. Chem.*, **59**, 2158.

8 Peck, K., Stryer, L., Glazer, A.N., and Mathies, R.N. (1989) *Proc. Natl. Acad. Sci. U. S. A.*, **86**, 4087.

9 Oi, V., Glazer, A.N., and Stryer, L. (1982) *J. Cell Biol.*, **93**, 981.

10 Ying, L. and Xie, X.S. (1998) *J. Phys. Chem. B*, **102**, 10399.

11 Schäfer, F.P. (ed.) (1973) *Dye Lasers, Topics in Applied Physics*, vol. **1**, Springer, Berlin.

12 Smith, L.M., Fung, S., Hunkapillar, M.W., and Hood, L.E. (1985) *Nucleic Acids Res.*, **13**, 2399.

13 Prober, J.M., Trainer, G.L., Dam, R.J., Hobbs, F.W., Robertson, C.W., Zagursky, R.J., Cocuzza, A.J., Jensen, M.A., and Baumeister, K. (1987) *Science*, **238**, 336.

14 Smith, L.M. (1991) *Nature*, **349**, 812.

15 Ansorge, W., Sproat, B., Stegemann, J., Schwager, C., and Zenke, M. (1987) *Nucleic Acids Res.*, **15**, 4593.

16 Hemmilä, I.A. (1989) *Appl. Fluoresc. Technol.*, **1**, 1.

17 Whitaker, J.A., Haugland, R.P., Ryan, D., Hewitt, P.C., and Prendergast, F.G. (1992) *Anal. Biochem.*, **207**, 267.

18 Zen, J.M. and Patonay, G. (1991) *Anal. Chem.*, **63**, 2934.

19 Ernst, L.A., Gupta, R.K., Mujumdar, R.B., and Waggoner, A.S. (1989) *Cytometry*, **10**, 3.

20 Sauer, M., Han, K.T., Müller, R., Schulz, A., Tadday, R., Seeger, S., Wolfrum, J., Arden-Jacob, J., Deltau, G., Marx, N.J., and Drexhage, K.H. (1993) *J. Fluoresc.*, **3**, 131.

21 Sauer, M., Han, K.T., Müller, R., Nord, S., Schulz, A., Seeger, S., Wolfrum, J., Arden-Jacob, J., Deltau, G., Marx, N.J., Zander, C., and Drexhage, K.H. (1995) *J. Fluoresc.*, **5**, 247.

22 Coons, H., Creech, H.J., Jones, R.N., and Berliner, E. (1942) *J. Immunol. Methods*, **45**, 159.

23 Tinnefeld, P., Hofkens, J., Herten, D.P., Masuo, S., Vosch, T., Cotlet, M., Habuchi, S., Müllen, K., De Schryver, F.C., and Sauer, M. (2004) *ChemPhysChem*, **5**, 1786.

24 Panchuk-Voloshina, N., Bishop-Stewart, J., Bhalgat, M.K., Millard, P.J., Mao, F., Leung, W.L., and Haugland, R.P. (1999) *J. Histochem. Cytochem.*, **47**, 1179.

25 Soper, S.A. and Mattingly, J. (1994) *J. Am. Chem. Soc.*, **116**, 3744.

26 Boyer, A.E., Lipowska, M., Zen, J.M., Patonay, G., and Tsung, V.C.W. (1992) *Anal. Lett.*, **25**, 415.

27 Southwick, P.L., Ernst, L.A., Tauriello, E.V., Parker, S.R., Mujumdar, R.B., Mujumdar, S.R., Clever, H.A., and Waggoner, A.S. (1990) *Cytometry*, **11**, 418.

28 Mujumdar, R.B., Ernst, L.A., Mujumdar, S.R., and Waggoner, A.S. (1989) *Cytometry*, **10**, 11.

29 Terpetschnig, E., Szmacinski, H., Ozinskas, A., and Lakowicz, J.R. (1994) *Anal. Biochem.*, **217**, 197.

30 Mujumdar, R.B., Ernst, L.A., Mujumdar, S.R., Lewis, C.J., and Waggoner, A.S. (1993) *Bioconjug. Chem.*, **4**, 105.

31 Bruchez, M., Moronne, M., Gin, P., Weiss, S., and Alivisatos, A.P. (1998) *Science*, **281**, 2013.

32 Dahan, M., Laurence, T., Pinaud, F., Chemla, D.S., Alivisatos, A.P., Sauer, M., and Weiss, S. (2001) *Opt. Lett.*, **26**, 825.

33 Torchilin, V.P., Rammohan, R., Weissig, V., and Levchenko, T.S. (2001) *Proc. Natl. Acad. Sci. U. S. A.*, **98**, 8786.

34 Schwarze, S.R., Ho, A., Vocero-Akbani, A., and Dowdy, S.F. (1999) *Science*, **285**, 1569.

35 Griffin, B.A., Adams, S.R., and Tsien, R.Y. (1998) *Science*, **281**, 269.

36 Müller, L.W. and Cornish, V.W. (2005) *Curr. Opin. Chem. Biol.*, **9**, 56.

37 Chen, I. and Ting, A.Y. (2005) *Curr. Opin. Biotechnol.*, **16**, 35.

38 Keppler, A., Gendreizig, S., Gronemeyer, T., Pick, H., Vogel, H., and Johnsson, K. (2003) *Nat. Biotechnol.*, **21**, 86.

39 Miller, L.W., Cai, Y., Sheetz, M.P., and Cornish, V.W. (2005) *Nat. Methods*, **2**, 255.

40 Tsien, R.Y. (1998) *Annu. Rev. Biochem.*, **67**, 509.

41 Baird, D., Zacharias, A., and Tsien, R.Y. (2000) *Proc. Natl. Acad. Sci. U. S. A.*, **97**, 11984.

42 Moores, S.L., Sabry, J.H., and Spudich, J.A. (1996) *Proc. Natl. Acad. Sci. U. S. A.*, **93**, 443.

43 Wiedenmann, J., Oswald, F., and Nienhaus, G.U. (2009) *IUBMB Life*, **61**, 1029.

44 Shaner, N.C., Patterson, G.H., and Davidson, M.W. (2007) *J. Cell Sci.*, **120**, 4247.

45 Matz, M.V., Fradkov, A.F., Labas, Y.A., Savitsky, A.P., Zaraisky, A.G., Markelov, M.L., and Lukyanov, S.A. (1999) *Nat. Biotechnol.*, **17**, 969.

46 Campbell, R.E., Tour, O., Palmer, A.E., Steinbach, P.A., Baird, G.S., Zacharias, D.A., and Tsien, R.Y. (2002) *Proc. Natl. Acad. Sci. U. S. A.*, **99**, 7877.

47 Hell, S.W. (2007) *Science*, **316**, 1153.

48 Betzig, E., Patterson, G.H., Sougrat, R., Lindwasser, O.W., Olenych, S., Bonifacino, J.S., Davidson, M.W., Lippincott-Schwartz, J., and Hess, H.F. (2006) *Science*, **313**, 1642.

49 Rust, M.J., Bates, M., and Zhuang, X. (2006) *Nat. Methods*, **3**, 793.

50 Heilemann, M., van de Linde, S., Mukherjee, A., and Sauer, M. (2009) *Angew. Chem. Int. Ed.*, **48**, 6903.

13
Optical Coherence Imaging for Surgical Pathology Assessment

Wladimir A. Benalcazar and Stephen A. Boppart

Surgical pathology is the field that specializes in assessing surgically removed tissue for disease in order to provide important information to guide surgical intervention and postoperative treatment. In surgical oncology, this includes confirmation of the preoperative diagnosis of the disease, staging the extent or spread of the malignancy, establishing whether the entire affected area was surgically removed, identifying the presence of any unsuspected concurrent diseases, and integrating this information to determine optimal strategies for postoperative treatment.

The entire assessment by a surgical pathologist (so-called intraoperative consultation) requires a combination of macroscopic and microscopic examinations. Whereas a macroscopic examination of tissue specimens can be performed in the operating room by gross examination, a microscopic examination requires that the tissue specimen be frozen or fixed, sectioned into micron-thick slices, placed on microscope slides, and stained for assessment by brightfield microscopy. Frozen sectioning (cryosectioning) can usually be performed within 30 min to provide a fair assessment of the specimen, and has been used most often to confirm if the surgical margins are free of tumor cells. Unfortunately, frozen sectioning has been largely unreliable, and is being used less frequently. More advanced molecular-based immunohistochemical analysis of tissue sections is performed in the pathology laboratory, after the surgical procedure has ended, and often days later. To address some of these limitations, studies have investigated the use of cytology preparations (e.g., touch imprints), polymerase chain reaction (PCR) analysis, and flow cytometry in an effort to provide more information about the disease based on cellular and molecular composition.

Intraoperative consultation is widely used in oncologic surgery. The increase in cancer screening rates in recent years has led to the detection of more tumors at earlier stages of development, which subsequently has resulted in eliminate, more breast-conserving (lumpectomy) surgical procedures. In lumpectomy procedures, the main goal of the surgical pathologist is to inform the surgeon if the surgical

Handbook of Biophotonics. Vol.2: Photonics for Health Care, First Edition. Edited by Jürgen Popp, Valery V. Tuchin, Arthur Chiou, and Stefan Heinemann.

margin is clear of any tumor cells or residual cancer. Therefore, this poses a critical need for fast, high-resolution screening methods that can adequately sample the surgical margin and ensure that it is clear.

The use of frozen section analysis for tumor margin assessment in breast cancer has a sensitivity of 73% and a specificity of 98% compared with the more standard but time-consuming paraffin section analysis [1]. This relatively low quality of frozen section analysis has precluded it from becoming a widely accepted part of the standard of care. In particular, this technique presents problems in sectioning adipose tissue and cannot be done over the entire surface area of the tissue specimen, sampling at best only 10–15% of the surface area, just as with paraffin section analysis [2]. Additionally, this technique adds time (20–30 min) to the surgical procedure and increases costs.

Alternatively, touch preparation cytology can rapidly assess the entire surface area of a surgical specimen while preserving its physical integrity for later histopathologic sectioning and assessment. Although this may be suitable for identifying positive margins, the technique has a reported sensitivity of 75% and a specificity of 82% [2]. The major disadvantage is the requirement for tumor cells to detach from the surface of the examined area, making it unable to provide information about the presence of cancer cells immediately beneath the surface, which is used to determine close and negative margins.

Imaging techniques, such as X-ray mammography, diffuse optical tomography (DOT), ultrasound, and magnetic resonance imaging (MRI), have shown an ability to detect large tumor masses, but lack the resolution and sensitivity to detect the microscopic distribution of tumor cells at the periphery of solid tumors or those tumor cells metastasizing to other sites. Intraoperative radiography provides visualization of the margin in-depth by displaying two-dimensional X-ray projections. However, it does not have the ability to identify diffuse microscopic processes, especially where the tumor boundary is poorly defined. Intraoperative radiography has a sensitivity of only 49% and a specificity of 73% [3]. Alternatively, radiofrequency spectroscopy provides an average measurement over an area with a diameter of 0.7 cm and within a 100 μm depth. It has a sensitivity of 71% and a specificity of 68% [4].

In summary, no intraoperative method currently exists to nondestructively assess the microscopic status of lumpectomy margins in real time. However, high-speed optical imaging and spectroscopy could address this limitation. Optical techniques take advantage of a biological window that exists in the near-infrared region of the optical spectrum, where attenuation of light is governed more by scattering rather than by absorption, so that light at these wavelengths can penetrate into tissue to convey information about its structure or chemical composition. Intraoperative optical imaging with rapid feedback could eliminate the time spent in the surgical pathology laboratory when a fully staffed operating room is waiting for the pathologic assessment of tissue specimens, and could reduce or eliminate the need for reoperations when positive surgical margins are discovered in the pathology laboratory, after the surgical procedure has ended.

13.1
Structural Contrast Imaging

One optical biomedical imaging method that addresses this need for intraoperative, high-resolution imaging is optical coherence tomography (OCT) [5, 6], which interrogates the structure of tissues noninvasively by probing the subsurface refractive index up to 1–2 mm deep into scattering tissue. OCT is attractive because it allows real-time imaging of microstructure *in situ* while avoiding the need for excisions and histologic processing. Initial studies have shown favorable results towards the use of OCT as an intraoperative imaging technique for the assessment of tumor margins [7], lymph nodes [8], and optically guided needle biopsies in the treatment of breast cancer.

OCT is the optical analogue of ultrasound imaging. The contrast mechanism is the change in refractive index and density of tissue structures that cause backscattering of the incident light. Following the illumination of the sample by a focused optical beam, multiple back-reflections are collected and resolved using interferometric detection, which relies on the short coherence length of the incident source to achieve micron-scale axial resolution (i.e., it typically uses sources with a bandwidth of 90 nm centered at 1300 nm for an axial resolution of 6 μm). At a given position of the incident beam, an axial scan is acquired. Two- or three-dimensional images are formed by scanning the beam across the sample. The lateral resolution is limited by the diffraction of the focused incident beam. A system schematic and photograph of a portable OCT system used for intraoperative imaging are shown in Figure 13.1.

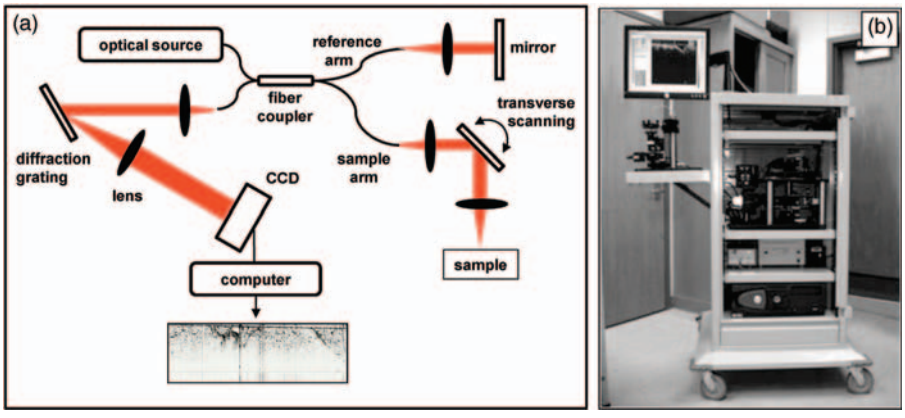

Figure 13.1 (a) Schematic of an OCT setup. A low-coherence optical source (superluminescent diode) is coupled to a fiber-based interferometer, in which a beam splitter (2 × 2 coupler) is used to direct 90% of the power to the sample (sample arm) and the remaining 10% to a mirror (reference arm). The back-reflected optical signals are combined and diffracted into a linear CCD camera to perform spectral interferometric detection. As a result, a depth-resolved profile of the refractive index variations of the sample is obtained. Scanning the beam across the sample allows image formation. (b) Typical implementation of a portable OCT system for intraoperative clinical use.

Since its introduction, advances in OCT technology have enabled significantly increased data acquisition rates to be achieved. Current systems can acquire 200 000 axial scans per second [9] or more, which permits acquisition of 400 frames per second in a range of 10 mm with a lateral resolution of 35 μm. The implementation of compact OCT systems facilitates their use inside the operating room, and the optical imaging beam can be delivered to the patient using hand-held surgical probes [10, 11]. This technique has already found clinical applications in ophthalmology, cardiology, and gastroenterology [12].

OCT imaging of breast tumors has shown that differences in image contrast are correlated with different cell and tissue structures. Adipose tissue, which comprises a large portion of the breast, is less dense and presents a more homogeneous structure than the more structured stromal or epithelial tissue. The same difference in contrast also exists between adipocytes and tumor cells, where the latter are typically densely packed, have an increase in their nuclear to cytoplasm ratio, and are more highly scattering. The large size and low scattering of adipocytes, relative to stromal and tumor cells, provides a method for differentiating these tissue types [13, 14]. In a study that used OCT to classify margins as positive or negative in 20 different lumpectomy specimens after resection but before margin assessment by the pathologist, an overall sensitivity of 100% and a specificity of 82% were achieved [7].

These findings suggest OCT as a potential method for intraoperative margin assessment in breast-conserving surgeries. In particular, following the resection of a tumor mass, OCT can be used to scan the walls of the tumor cavity in the search for tumor cells present at or just beneath the *in situ* surgical margin. Alternatively, resected masses can be imaged on all surfaces to verify a clean surgical margin (Figure 13.2). OCT can typically image to depths of 2 mm in tissue composed primarily of adipocytes and from 0.2 to 1 mm in cell-dense tumor tissue. These depths are comparable to the currently accepted margin widths that classify positive, close, and negative margins [7]. Additionally, although blood is highly scattering, intravascular blood in small vessels and capillaries constitutes a small percentage of the tissue volume and therefore has a minimal effect on the OCT penetration depth. OCT systems using optical sources with center wavelength around 1300 nm are also unaffected by the presence of dyes such as methylene blue and lymphazurin, which are used to map lymph drainage for sentinel and axillary lymph node dissections, because these dyes absorb in the spectral region below 700 nm.

13.2
Molecular Contrast Imaging

Although there is a promising future for OCT in assessing surgical pathology, important challenges and needs for optical microscopy remain, including the detection of tumors and tumor cells at the early stages of development, achieving good differentiation between benign fibrocystic changes and malignant lesions, and

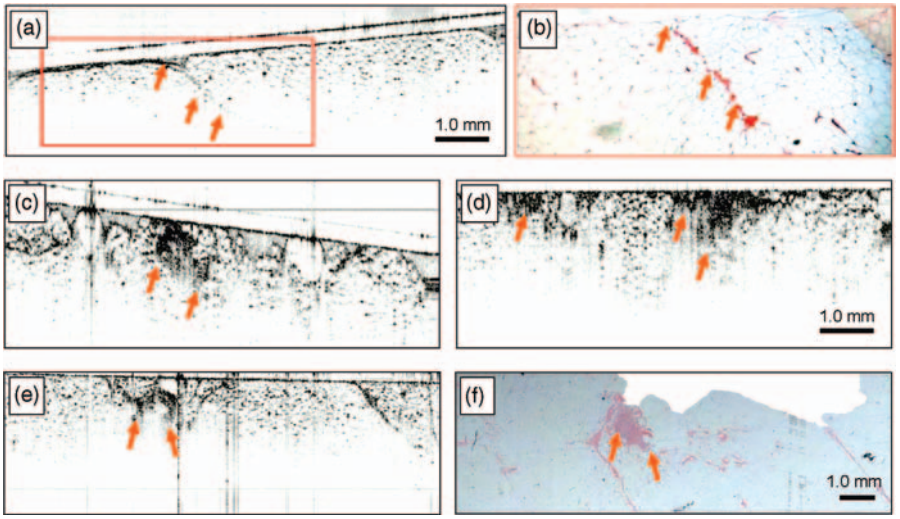

Figure 13.2 Intraoperative surgical margin assessment with OCT, and corresponding histology. (a) OCT image of a negative surgical margin composed primarily of adipose tissue (the small, dark, highly scattering point-like features correspond to individual nuclei of adipocytes, and arrows indicate vasculature) and (b) corresponding histology. (c) OCT image of a positive margin with ductal carcinoma *in situ* (arrows indicate no dense highly scattering features corresponding to tumor cells) and (d) OCT image of a positive margin with invasive ductal carcinoma (tumor cell features indicated by arrows). (e) OCT image and (f) corresponding histology of a small (~1 mm) isolated focus of tumor cells at the surgical margin. Modified figure used with permission from [7].

characterizing tissue at the molecular level. For instance, OCT is limited by the fact that the optical refractive index does not differ significantly between stromal and tumor tissue [15].

In order to overcome these difficulties, OCT with new functional modalities [16, 17] and contrast agents [18, 19] is being investigated. In particular, magnetomotive optical coherence tomography (MM-OCT) has shown selective molecular imaging of tumors by the use of magnetic nanoparticles (MNPs) that target human epidermal growth factor receptor 2 (HER-2/neu) [19] (Figure 13.3).

Working towards more selective and noninvasive microscopy techniques, vibrational spectroscopy has been explored as a label-free method for assessing the molecular composition of tissue. The chemical constituents in breast tissue to which Raman spectroscopy is sensitive have been characterized, and Raman spectroscopy has shown the ability to differentiate normal, malignant (infiltrating ductal carcinoma), and benign (fibrocystic change) human breast tissue [20, 21]. Criteria for classification based on vibrational spectra rely mainly on the higher abundance of proteins in tumors, compared with normal tissue [22]. Other spectral differences suggest a higher presence of myoglobin and a lower degree of oxygenation in infiltrating ductal carcinomas. In specimens with fibrocystic changes, an indicator is a reduction in lipids and carotenoids and an absence of a heme-type signal

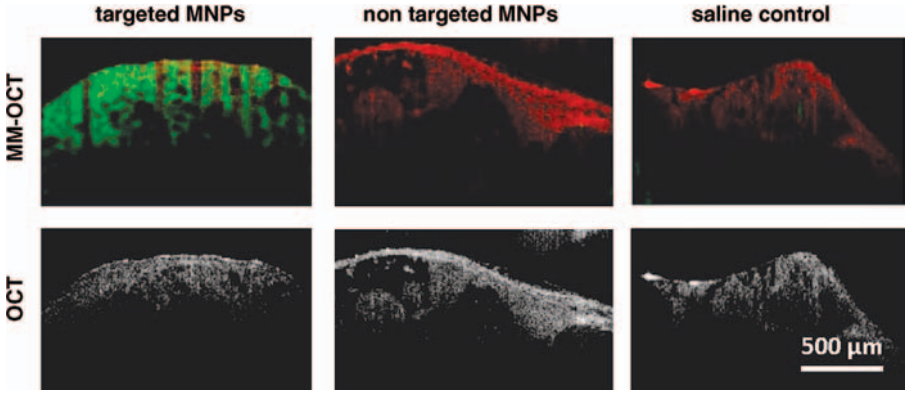

Figure 13.3 Targeted magnetomotive (MM) contrast from *in vivo* MM-OCT using magnetic nanoparticles conjugated to anti-HER-2/neu antibodies for site-specific molecular imaging. MM-OCT (green channel superimposed over red OCT channel, top row) and structural OCT images (bottom row) of tumors from a preclinical carcinogen-induced rat mammary tumor model that recapitulated the progression of human ductal carcinoma *in situ*. Tumors are shown for targeted MNP-injected (left column), nontargeted MNP-injected (center column), and saline-injected rats (right column). The scale bar applies to all six images. Modified figure used with permission from [19].

characteristic of porphyrins [21]. Finally, the degree of saturation in the hydrocarbon chain of lipids is also an important metric, as this varies in normal, benign, and malignant tumor tissues [23].

A study using Raman spectroscopy to identify carcinomas reported a sensitivity of 100%, a specificity of 100%, and an overall accuracy of 93% [24]. Despite these promising findings, Raman spectroscopy is limited by the weak Raman signal, which leads to long integration times (about 1 second per pixel) that make its use impractical for real-time imaging. Coherent anti-Stokes Raman scattering (CARS) microscopy can overcome this issue, but at the cost of generating an unwanted background that coherently interferes with the desired vibrational signal. Furthermore, conventional CARS techniques do not obtain broadband spectra, and the CARS signals are not linearly proportional to the concentration of the molecular species of interest. Despite these limitations, methods based on CARS are emerging, and have shown significant improvements in acquisition rates [25], rejection of background [26, 27], and broadband vibrational acquisition [28].

Techniques such as nonlinear interferometric vibrational imaging (NIVI), which use shaped pulses and interferometric detection, can overcome many of the drawbacks in conventional CARS. In particular, NIVI has been used to acquire background-free, broadband, vibrational spectra from mammary tissue at acquisition rates two orders of magnitude faster than Raman microscopy (Figure 13.4) [29, 30]. Recently, a study of NIVI spectra from various lipids showed its ability to reproduce Raman-like spectra 200 times faster than Raman spectroscopy, and the ability to distinguish (un)saturation levels in fatty acid chains because the NIVI signals are linearly dependent on the concentrations of the molecular bonds [31]. This type of fast

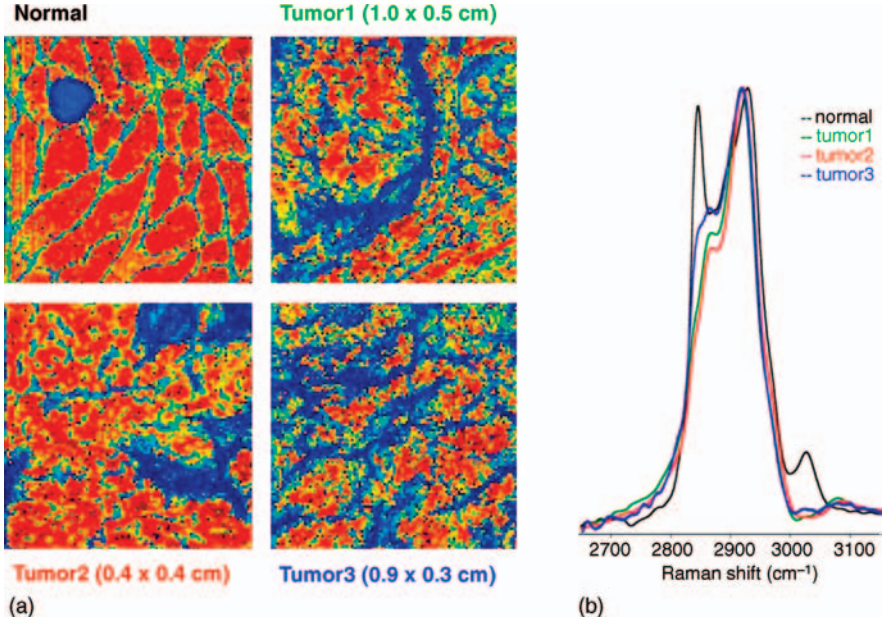

Figure 13.4 Nonlinear interferometric vibrational imaging. Spatial mapping of CH groups (present in different proportions in lipid and protein domains) in mammary tissue. (a) Endogenous-contrast NIVI images ($500 \times 500\,\mu m^2$) (color scale: blue to red, as percentage of CH vibrations) of one normal and three developed mammary tumors of various sizes. (b) Vibrational spectra for images in (a). Images and spectra reveal disruptions of lipid and collagen domains in adipose and tumor tissues, with a predominance of collagen-based structures in tumors.

vibrational spectroscopy could assist surgical procedures by taking spectra or even images from zones deep in the breast using minimally invasive methods involving needle-based probes, or in procedures similar to the commonly used fine-needle aspiration cytology or core-needle biopsies.

Since CARS uses the same contrast mechanism as spontaneous Raman spectroscopy, there is potential for techniques based on CARS to improve the optical diagnosis of breast disease further by adding molecular vibrational contrast to structural and spatial imaging capabilities. The integration of both molecular and morphologic information could contribute significantly to the analysis of disease states, in part because this builds upon traditional cancer histopathology methods that rely on molecularly staining and imaging tissue sections [22]. Currently, however, fast vibrational spectroscopy makes use of nonlinear processes that require two synchronized laser pulses, and the complex setups needed are neither compact nor portable enough for use today in an operating room. Advances are under way, including single-beam approaches to CARS [31], and methods to obtain ultrabroadband spectra free from background, particularly to target the fingerprint region of the vibrational spectrum, where a wealth of valuable molecular information used in spontaneous Raman spectroscopy is present.

13.3 Conclusion

Whether it is by means of providing structural or molecular contrast, coherent optical microscopy and imaging techniques have the potential to assist in advancing our ability to assess surgical pathology. In particular, OCT can be used for real-time identification of tumor margins, and new Raman-based spectroscopic imaging techniques can potentially aid in the fast confirmation of a diagnosis based on molecular signatures. Accompanying these technological advancements, as with all novel imaging techniques, classification and diagnosis will require the study of training and calibration sets by clinicians in order to establish the evaluation methodology and image feature criteria for correct identification. Complementary to this, the information provided by these techniques could eventually lead to automated tissue-type classification algorithms to improve further both the diagnosis at earlier stages and the identification of margins intraoperatively, thereby potentially reducing the need for additional surgical procedures and advancing the diagnostic capabilities in surgical pathology.

References

1 Olson, T.P., Harter, J., Muoz, A., Mahvi, D.M., and Breslin, T. (2007) Frozen section analysis for intraoperative margin assessment during breast-conserving surgery results in low rates of re-excision and local recurrence. *Ann. Surg. Oncol.*, **14** (10), 2953–2960.

2 Valdes, E.K., Boolbol, S.K., Cohen, J.-M., and Feldman, S.M. (2007) Intra-operative touch preparation cytology, does it have a role in re-excision lumpectomy? *Ann. Surg. Oncol.*, **14** (3), 1045–1050.

3 Goldfeder, S., Davis, D., and Cullinan, J. (2006) Breast specimen radiography: can it predict margin status of excised breast carcinoma? *Acad. Radiol.*, **13** (12), 1453–1459.

4 Karni, T., Pappo, I., Sandbank, J., Lavon, O., Kent, V., Spector, R., Morgenstern, S., and Lelcuk, S. (2007) A device for real-time, intraoperative margin assessment in breast-conservation surgery. *Am. J. Surg.*, **194** (4), 467–473.

5 Huang, D., Swanson, E.A., Lin, C.P., Schuman, J.S., Stinson, W.G., Chang, W., Hee, M.R., Flotte, T., Gregory, K., Puliafito, C.A., and Fujimoto, J. G. (1991) Optical coherence tomography. *Science*, **254**, 1178–1181.

6 Drexler W. and Fujimoto J.G. (eds.) (2008) *Optical Coherence Tomography*, Springer, Berlin.

7 Nguyen, F.T., Zysk, A.M., Chaney, E.J., Kotynek, J.G., Oliphant, U.J., Bellafiore, F.J., Rowland, K.M., Johnson, P.A., and Boppart, S.A. (2009) Intraoperative evaluation of breast tumor margins with optical coherence tomography. *Cancer Res.*, **69** (22), 8790–8796.

8 Nguyen, F.T., Zysk, A.M., Chaney, E.J., Adie, S.G., Kotynek, J.G., Oliphant, U.J., Bellafiore, F.J., Rowland, K.M., Johnson, P.A., and Boppart, S.A. (2010) Optical coherence tomography: the intraoperative assessment of lymph nodes in breast cancer. *IEEE Eng. Med. Biol.*, **29**, 63–70.

9 Huber, R., Adler, D.C., and Fujimoto, J.G. (2006) Buffered Fourier domain mode locking: unidirectional swept laser sources for optical coherence tomography imaging at 370,000 lines/s. *Opt. Lett.*, **31** (20), 2975–2977.

10 Boppart, S.A., Bouma, B.E., Pitris, C., Tearney, G.J., Fujimoto, J.G., and Brezinski, M.E. (1997) Forward imaging

instruments for optical coherence tomography. *Opt. Lett.*, **22** (21), 1618–1620.
11 Zysk, A.M., Nguyen, F.T., Chaney, E.J., Kotynek, J.G., Oliphant, U.J., Bellafiore, F.J., Johnson, P.A., Rowland, K.M., and Boppart, S.A. (2009) Clinical feasibility of microscopically-guided breast needle biopsy using a fiber-optic probe with computer-aided detection. *Technol. Cancer Res. Treat.*, **8** (5), 315–400.
12 Zysk, A.M., Nguyen, F.T., Oldenburg, A.L., Marks, D.L., and Boppart, S.A. (2007) Optical coherence tomography: a review of clinical development from bench to bedside. *J. Biomed. Opt.*, **12** (5), 051403.
13 Boppart, S.A., Luo, W., Marks, D.L., and Singletary, K.W. (2004) Optical coherence tomography: feasibility for basic research and image-guided surgery of breast cancer. *Breast Cancer Res. Treat.*, **84**, 85–97.
14 Hsiung, P.L., Phatak, D.R., Chen, Y., Aguirre, A.D., Fujimoto, J.G., and Connolly, J.L. (2007) Benign and malignant lesions in the human breast depicted with ultrahigh resolution and three-dimensional optical coherence tomography. *Radiology*, **244** (3), 865–874.
15 Zysk, A.M., Chaney, E.J., and Boppart, S.A. (2006) Refractive index of carcinogen-induced rat mammary tumours. *Phys. Med. Biol.*, **51** (9), 2165–2177.
16 de Boer, J.F., Milner, T.E., van Gemert, M.J.C., and Nelson, J.S. (1997) Two-dimensional birefringence imaging in biological tissue by polarization-sensitive optical coherence tomography. *Opt. Lett.*, **22** (12), 934–936.
17 Oldenburg, A.L., Crecea, V., Rinne, S.A., and Boppart, S.A. (2008) Phase-resolved magnetomotive OCT for imaging nanomolar concentrations of magnetic nanoparticles in tissues. *Opt. Express*, **16** (15), 11525–11539.
18 Lee, T.M., Oldenburg, A.L., Sitafalwalla, S., Marks, D.L., Luo, W., Toublan, F.J.-J., Suslick, K.S., and Boppart, S.A. (2003) Engineered microsphere contrast agents for optical coherence tomography. *Opt. Lett.*, **28** (17), 1546–1548.
19 John, R., Rezaeipoor, R., Adie, S.G., Chaney, E.J., Oldenburg, A.L., Marjanovic, M., Haldar, J.P., Sutton, B.P., and Boppart, S.A. (2010) *In vivo* magnetomotive optical molecular imaging using targeted magnetic nanoprobes. *Proc. Natl. Acad. Sci. U. S. A.*, **107** (18), 8085–8090.
20 Frank, C.J., Redd, D.C.B., Gansler, T.S., and McCreery, R.L. (1994) Characterization of human breast biopsy specimens with near-IR Raman spectroscopy. *Anal. Chem.*, **66**, 319–326.
21 Redd, D.C., Feng, Z.C., Yue, K.T., and Gansler, T.S. (1993) Raman spectroscopic characterization of human breast tissues: implications for breast cancer diagnosis. *Appl. Spectrosc.*, **47**, 787–791.
22 Kline, N.J. and Treado, P.J. (1997) Raman chemical imaging of breast tissue. *J. Raman Spectrosc.*, **28**, 119–124.
23 Liu, C.-H., Das, B., Glassman, W., Tang, G., Yoo, K., Zhu, H., Akins, D., Lubicz, S., Cleary, J., Prudente, R., Celmer, E., Caron, A., and Alfano, R. (1992) Raman, fluorescence, and time-resolved light scattering as optical diagnostic techniques to separate diseased and normal biomedical media. *J. Photochem. Photobiol. B*, **16**, 187–209.
24 Breslin, T. (2007) *In vivo* margin assessment during partial mastectomy breast surgery using Raman spectroscopy. *Breast Dis. Year Book Q.*, **17** (4), 379–380.
25 Evans, C.L., Potma, E.O., Puoris'haag, M., Côté, D., Lin, C.P., and Xie, X.S. (2005) Chemical imaging of tissue *in vivo* with video-rate coherent anti-Stokes Raman scattering microscopy. *Proc. Natl. Acad. Sci. U. S. A.*, **102**, 16807–16812.
26 Volkmer, A., Book, L.D., and Xie, X.S. (2002) Time-resolved coherent anti-Stokes Raman scattering microscopy: imaging based on Raman free induction decay. *Appl. Phys. Lett.*, **80**, 1505–1507.
27 Cheng, J.X., Book, L.D., and Xie, X.S. (2001) Polarization coherent anti-Stokes Raman scattering microscopy. *Opt. Lett.*, **26**, 1341–1343.
28 Wurpel, G.W.H., Schins, J.M., and Muller, M. (2002) Chemical specificity in

three-dimensional imaging with multiplex coherent anti-Stokes Raman scattering microscopy. *Opt. Lett.*, **27**, 1093–1095.

29 Benalcazar, W.A., Chowdary, P.D., Jiang, Z., Marks, D.L., Chaney, E.J., Gruebele, M., and Boppart, S.A. (2010) High-speed nonlinear interferometric vibrational imaging of biological tissue with comparison to Raman microscopy. *IEEE J. Sel. Top. Quantum Electron.*, **16** (4), 824–832.

30 Chowdary, P. D., Benalcazar, W. A., Jiang, Z., Chaney, E. J., Marks, D. L., Gruebele, M., Boppart, S. A. (2010) Molecular histopathology by nonlinear interferometric vibrational imaging. *Cancer Research*, **70**, 9562–9569.

31 Chowdary, P.D., Benalcazar, W.A., Jiang, Z., Marks, D.M., Boppart, S.A., and Gruebele, M. (2010) High speed nonlinear interferometric vibrational analysis of lipids by spectral decomposition. *Anal. Chem.*, **82** (9), 3812–3818.

32 von Vacano, B., Buckup, T., and Motzkus, M. (2006) Highly sensitive single-beam heterodyne coherent anti-Stokes Raman scattering. *Opt. Lett.*, **31**, 2495–2497.

14
Diffuse Optical Imaging

Jeremy C. Hebden

14.1
Introduction

When a pencil beam of visible or near-infrared light is incident upon biological tissue, profuse scattering ensures that the beam becomes diffuse (i.e., the initial directionality is lost) after penetrating a distance in excess of one transport scattering length, or about 1 mm in most tissues. As a consequence, the formation of images using light which has penetrated more than a few millimeters in tissue is known as diffuse optical imaging (DOI). The simplest and earliest example of DOI is transillumination, which involves viewing or otherwise forming an image when the tissue is illuminated from behind. In 1929, Cutler [1] reported a systematic attempt to detect cancer of the breast by transilluminating with a bright light source in a darkened room. While the study revealed the dominant role played by blood concentration in the degree of opacity of tissue, and showed that solid tumors often appeared to be opaque, it was not possible to differentiate between benign and malignant tumors. In this and subsequent studies, breast transillumination consistently exhibited poor sensitivity and specificity resulting from low inherent spatial resolution.

Interest in DOI has been revived during the past 20 years as a result of developments in two areas of technology. First is the availability of near-infrared sources and sensitive detectors, including low-cost portable devices. Second is the development of sophisticated algorithms for reconstructing images from measurements of diffuse light though tissue, associated with the availability of powerful computers able to perform modeling of photon migration through large thicknesses of biological tissues. Subsequently, two DOI approaches have emerged, known as optical topography and optical tomography (Figure 14.1). Although the distinction between them is somewhat arbitrary, the term optical topography is used to describe techniques which provide maps of changes in hemodynamic parameters (such as blood volume) close to the surface, with little or no depth resolution, whereas optical tomography involves reconstructing an image representing the 3D distribution of optical properties (or a transverse slice

Handbook of Biophotonics. Vol.2: Photonics for Health Care, First Edition. Edited by Jürgen Popp, Valery V. Tuchin, Arthur Chiou, and Stefan Heinemann.

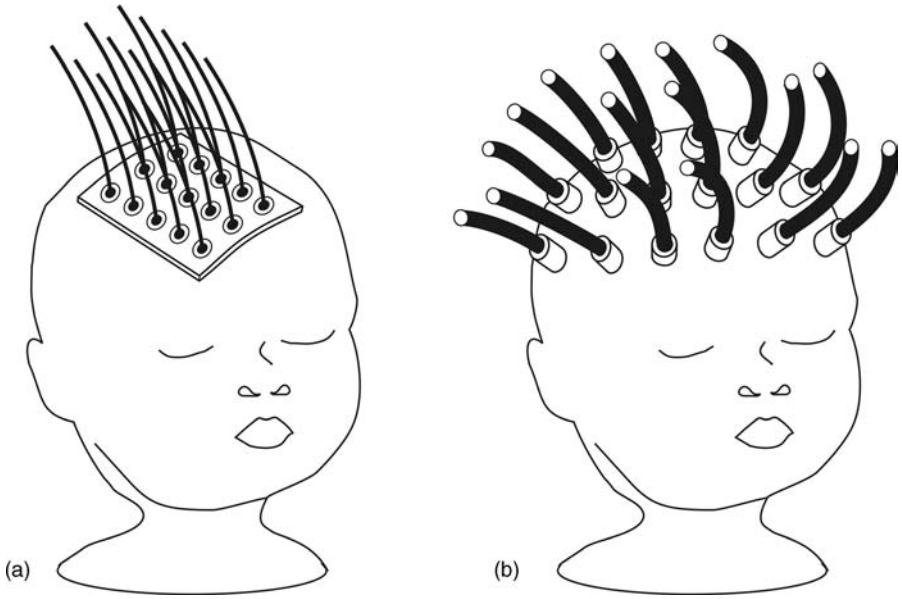

Figure 14.1 Arrangements of sources and detectors for performing a) optical topography, and b) optical tomography of the brain.

across the 3D volume). The distinction has evolved because of the differences in the complexity of the imaging problem and of the associated instrumentation. The two approaches are described in more detail below, with examples of clinical and scientific applications.

14.2 Optical Topography

The imaging technique known as optical topography involves measuring diffusely reflected light between multiple pairs of sources and detectors at discrete locations spread over the area of tissue of interest. The source–detector separations are small enough (a few centimeters or less) to ensure strong enough signals so that measurements can be acquired quickly, enabling images to be displayed in real time at a rate of a few hertz or faster. Fast acquisition is also facilitated by illuminating sources simultaneously, which requires that the detected signal from each source is uniquely identifiable, usually by modulating the intensity of each at a different frequency. The detectors then operate in parallel, employing either lock-in amplifiers or digital processing methods to isolate the signal from each source.

The principle motivation for the development of optical topography has been the display of hemodynamic activity in the cerebral cortex. Measurements of changes in attenuation of signals at two or more wavelengths can be converted

into estimates of changes in concentrations of oxyhemoglobin ([HbO_2]) and deoxyhemoglobin ([Hb]), usually invoking some assumptions about the optical properties of the sampled tissue volume. In addition to monitoring hemodynamic activity, optical techniques have been used to map a so-called "fast" event-related optical signal, where changes observed over a few hundred milliseconds are considered to correspond directly to the neuronal activity associated with information processing.

The probes developed for optical topography systems typically consist of a flexible pad which supports an array of optical fibers, each coupled to either a source (e.g., a laser diode) or a detector (e.g., avalanche photodiode). Securing a probe safely, securely, and comfortably to the head, while minimizing the adverse effects of hair, has always been one of the greatest technical challenges in the implementation of DOI techniques, and a broad variety of solutions have been implemented. Several commercial optical topography systems are now available. For example, the ETG-4000 system developed by Hitachi Medical Corporation (Tokyo, Japan) samples data from up to 52 discrete source–detector pairs at two wavelengths (695 and 830 nm) at a rate of 10 Hz.

14.2.1
Evoked Response to Sensory Stimulation

The regions of the brain associated with processing of sensory information (e.g., touch, sound) are generally cortical areas located within 2–3 cm of the scalp in the adult head. Consequently, measurement of the evoked response of the brain to sensory stimuli has been a major focus of research with optical topography. The additional metabolic demand produced by the stimulus results in an increase in local blood volume and/or a change in blood oxygenation. The technique offers several advantages over BOLD fMRI: optical topography provides greater temporal resolution and signal-to-noise ratio, is portable, less expensive, and is sensitive to changes in both [Hb] and [HbO_2].

Imaging studies have been performed on the response to a variety of visual [2–5], tactile [6], and motor [6–9] stimuli. One of the most dramatic recent illustrations of the potential of optical topography has been presented by Culver and colleagues at Washington University (St. Louis, MO, USA) [5]. A high-density array has been employed to provide phase-encoded mapping of the retinotopic organization within the visual cortex of adult volunteers, allowing the study of subtle inter-subject differences. Figure 14.2a shows the placement of the array over the occipital cortex of an adult, and Figure 14.2b–j show the visual stimuli (a counter-phase flickering checkerboard in one quadrant of the visual field) and the corresponding maps of relative changes in [HbO_2]. All images are posterior coronal projections of a cortical shell, as if looking at the surface of the brain from behind the subject. In order to match the stimulus and response, a 6 s lag between stimulation and maximal response was used. The results show that the hemodynamic response is always maximal in the opposite visual quadrant from the stimulus.

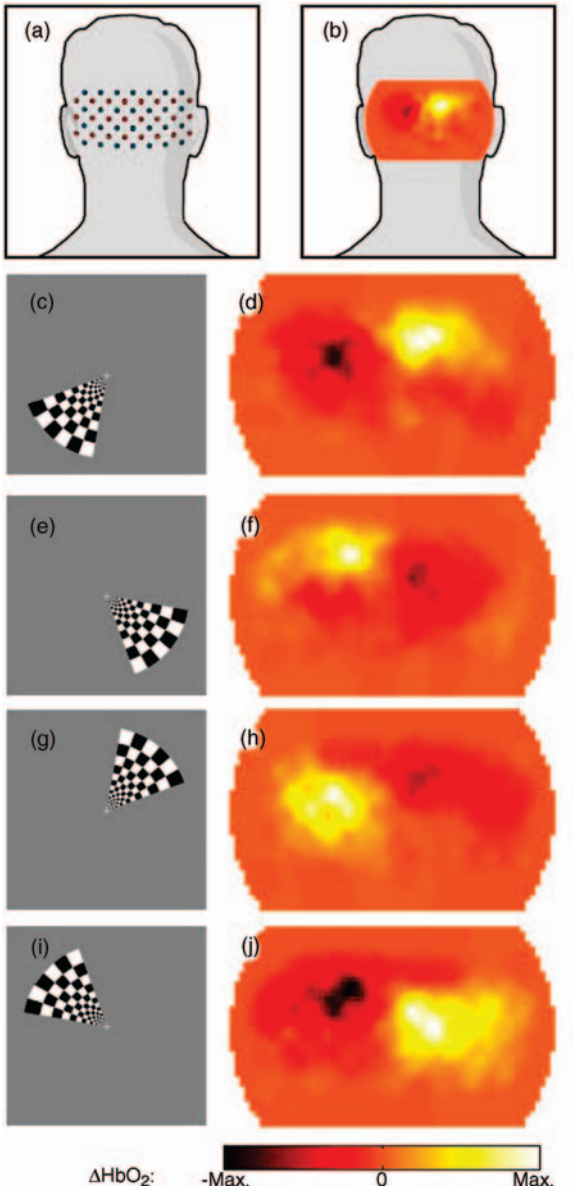

Figure 14.2 Visual activation stimuli and corresponding maps of changes in [HbO_2] the visual cortex. The stimulus is a rotating wedge-shaped flickering checkerboard (a, c, e, g), and the response is always in the opposite visual quadrant. See White and Culver [5] for more details.

14.2.2
Cognitive Activity and Language Processing

Optical topography has evolved into a popular tool for the study of cognitive and psychological processes, and especially for developmental studies on infants and children. The portability and silent function of the hardware make the technique particularly suitable for psychological studies and for use on awake infants. Published results include studies of face perception [10], language processing [11, 12], memory [13], object recognition [14], and post-traumatic stress disorder [15]. The specific application of optical imaging to studies of neurocognitive development in infants has been reviewed by Minagawa-Kawai *et al.* [16].

14.2.3
Epilepsy

Electroencephalography (EEG) is the tool routinely used to diagnose and monitor abnormal electrical activity in the brain, including epileptic seizure. Whereas EEG is sensitive to the electromagnetic dynamics of groups of active neurons, optical imaging provides a means of measuring associated changes in hemodynamic activity as a result of the neurons' increased metabolic demand. Optical topography has been used to display continuous changes in cerebral blood volume during seizure [17, 18]. It has also been combined with simultaneous EEG [19] and magnetoencephalography [20] as a means of studying neurovascular coupling.

14.3
Optical Tomography

Optical tomography involves generating three-dimensional (3D) volume or cross-sectional images using measurements of light transmitted across large thicknesses of tissue. The objective is to acquire maps representing either the spatial variation of optical properties (i.e., the absorption and scattering coefficients) at one or more wavelengths, or the variation in physiological parameters such as concentrations of specific chromophores, blood volume, and blood oxygenation. Typically, measurements are obtained of light transmitted between discrete sources and detectors located over as much of the available surface of the tissue as realistically achievable. Measuring light which is strongly attenuated over large thickness (up to 10 cm) requires powerful sources (consistent with patient safety) and sensitive detectors, and consequently optical tomography has a lower temporal resolution than optical topography. Furthermore, optical tomography requires a method to reconstruct the 3D distribution of optical properties or two-dimensional (2D) cross-section. Although various *ad hoc* back-projection methods have been proposed [21, 22], such approaches are not applicable to imaging arbitrary-shaped volumes. Instead, it is necessary to utilize a model of the propagation of light within the tissue which allows a set of predicted measurements on the surface to be derived for any given

distribution of internal optical properties. Optical tomography is an inverse problem which is nonlinear, severely ill-posed, and generally underdetermined. Consequently, finding reliable and unique solutions for a given set of data involves considerable theoretical and practical difficulties, and various compromises and approximations are unavoidable. A comprehensive examination of the theory of optical tomography image reconstruction was presented by Arridge and Schotland [23]. In order to reduce the ill-posedness of the image reconstruction problem, the development of optical tomography systems has focused on increasing the amount of information available from light transmitted across the tissue. For example, imaging systems have been developed which measure the times-of-flight of photons traveling through the tissue, or measure the modulation and phase delay of light detected from sources modulated at megahertz frequencies. Devices that perform such measurements are known as time-domain and frequency-domain systems, respectively.

14.3.1 Optical Mammography

The principle clinical target of optical tomography has been imaging of the female breast as a means of detecting and characterizing tumors. Several commercial prototypes of so-called optical mammography systems have been produced [24–27], all requiring the patient to lie on a bed with one or both breasts suspended within a cavity surrounded by sources and detectors. Optical tomographic images of the breast typically demonstrate a strong heterogeneity, and significant sensitivity to many types of lesion [28–33]. However, spatial resolution remains low (1–2 cm) and a specificity sufficient for cancer screening remains elusive. The positive and negative aspects of optical mammography are both highlighted in Figure 14.3, which compares optical absorption and magnetic resonance imaging (MRI) images of the same breast cancer patient. The optical image of the right breast reveals the double tumor which is also present in the corresponding contrast agent-enhanced MRI image. However, the optical image of the right breast shows a feature of comparable contrast (lower left), almost certainly due to a surface blood vessel, which has no correlation in the MRI image. Further, optical mammography has demonstrated considerable promise as a mean of monitoring response to primary medical therapy. Since it does not involve ionizing radiation, patients can be scanned at regular intervals to monitor changes over a period of weeks. For example, optical images have exhibited sensitivity to changes in angiogenesis, apoptosis, and hypoxia resulting from neoadjuvant chemotherapy [34, 35].

14.3.2 Optical Tomography of the Brain

Although the attenuation of near-infrared light across the adult head is too great to image the center of the brain, 3D imaging of the entire infant brain is achievable.

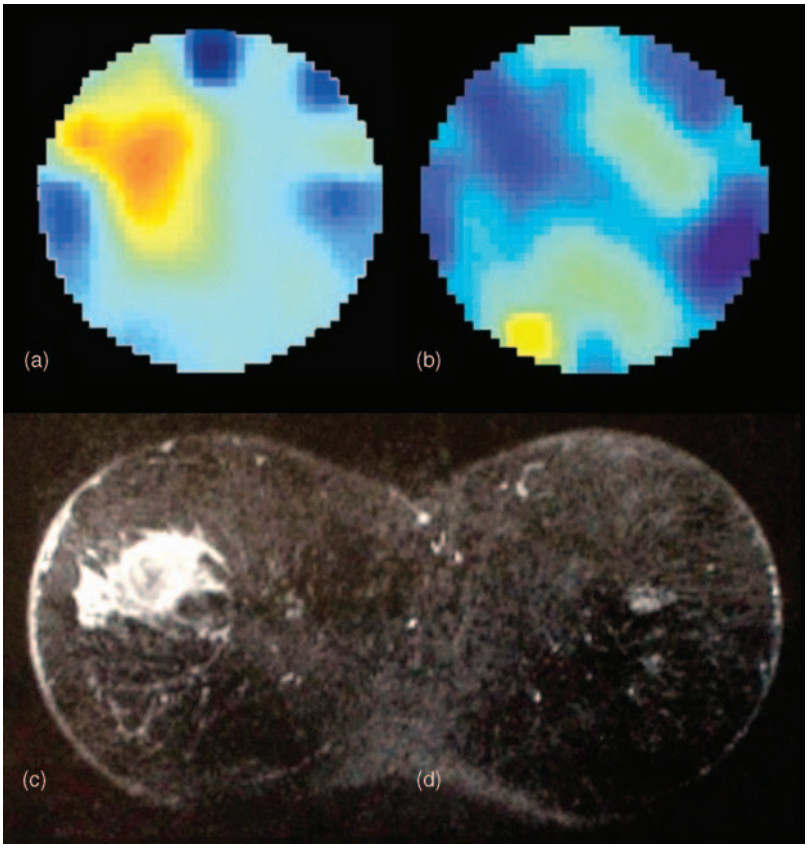

Figure 14.3 Optical absorption (a and b) and magnetic resonance (c and d) images of the left and right breasts of a patient with a malignant lesion in the right breast (a and c).

Optical tomography of the newborn infant brain was first demonstrated by researchers at Stanford University, who acquired images using a time-domain system which revealed intracranial hemorrhage [36], and focal regions of low oxygenation after acute stroke [37]. A more sophisticated time-domain system has been employed at University College London to reconstruct 3D images of the whole infant brain, which have revealed incidence of intraventricular hemorrhage [38] and changes in blood volume and oxygenation induced by small alterations to ventilator settings [39]. The system has also been used to generate 3D images of the entire neonatal head during motor-evoked response [40]. Partial tomographic reconstruction of the adult cortex has also been demonstrated. For example, the Stanford researchers successfully imaged localized contralateral oxygenation increases in the motor cortex of a healthy adult during hand movement [37], and Bluestone *et al.* [41] imaged hemodynamic changes within the frontal regions of the adult brain during the Valsalva maneuver.

14.4 Conclusion

Mapping of cerebral hemodynamic activity using optical topography has evolved into a powerful and widely used research tool, and there are excellent prospects for increased adoption of the technique within a clinical environment, particularly as imaging systems become more portable. The method provides complementary information to established tools such as EEG and functional MRI, with which they can be easily integrated. Optical tomography of the breast and brain has demonstrated the capacity to provide useful research information, and efforts to improve their clinical diagnostic potential are showing promising results.

References

1 Cutler, M. (1929) Transillumination as an aid in the diagnosis of breast lesions. *Surg. Gynecol. Obstet.*, **48**, 721–728.

2 Taga, G., Asakawa, K., Maki, A., Konishi, Y., and Koizumi, H. (2003) Brain imaging in awake infants by near-infrared optical topography. *Proc. Natl. Acad. Sci. U. S. A.*, **100**, 10722–10727.

3 Kusaka, T., Kawada, K., Okubo, K., Nagano, K., Namba, M., Okada, H., Imai, T., Isobe, K., and Itoh, S. (2004) Noninvasive optical imaging in the visual cortex in young infants. *Hum. Brain Mapp.*, **22**, 122–132.

4 Wolf, M., Wolf, U., Choi, J.H., Toronov, V., Paunescu, L.A., Michalos, A., and Gratton, E. (2003) Fast cerebral functional signal in the 100-ms range detected in the visual cortex by frequency-domain near-infrared spectrophotometry. *Psychophysiology*, **40**, 521–528.

5 White, B.R. and Culver, J.P. (2010) Phase-encoded retinotopy as an evaluation of diffuse optical neuroimaging. *Neuroimage*, **49**, 568–577.

6 Franceschini, M.A. and Boas, D.A. (2004) Noninvasive measurement of neuronal activity with near-infrared optical imaging. *Neuroimage*, **21**, 373–386.

7 Yamashita, Y., Maki, A., and Koizumi, H. (2001) Wavelength dependence of the precision of noninvasive optical measurement of oxy-, deoxy-, and total-hemoglobin concentration. *Med. Phys.*, **28**, 1108–1114.

8 Franceschini, M.A., Fantini, S., Thompson, J.H., Culver, J.P., and Boas, D.A. (2003) Hemodynamic evoked response of the sensorimotor cortex measured noninvasively with near-infrared optical imaging. *Psychophysiology*, **40**, 548–560.

9 Hintz, S.R., Benaron, D.A., Siegel, A.M., Zourabian, A., Stevenson, D.K., and Boas, D.A. (2001) Bedside functional imaging of the premature infant brain during passive motor activation. *J. Perinat. Med.*, **29**, 335–343.

10 Blasi, A., Fox, S., Everdell, N., Volein, A., Tucker, L., Csibra, G., Gibson, A.P., Hebden, J.C., Johnson, M.H., and Elwell, C.E. (2007) Investigation of depth dependent changes in cerebral haemodynamics during face perception in infants. *Phys. Med. Biol.*, **52**, 6849–6864.

11 Watanabe, E., Maki, A., Kawaguchi, F., Takashiro, K., Yamashita, Y., Koizumi, H., and Mayanagi, Y. (1998) Non-invasive assessment of language dominance with near-infrared spectroscopic mapping. *Neurosci. Lett.*, **256**, 49–52.

12 Pena, M., Maki, A., Kovacic, D., Dehaene-Lambertz, G., Koizumi, H., Bouquest, F., and Mehler, J. (2003) Sounds and silence: an optical topography study of language recognition at birth. *Proc. Natl. Acad. Sci. U. S. A.*, **100**, 11702–11705.

13 Tsujimoto, S., Yamamoto, T., Kawaguchi, H., Koizumi, H., and Sawaguchi, T. (2004) Prefrontal cortical

activation associated with working memory in adults and preschool children: an event-related optical topography study. *Cereb. Cortex*, **14**, 703–712.

14 Medvedev, A.V., Kainerstorfer, J., Borisov, S.V., Barbour, R.L., and VanMeter, J. (2008) Event-related fast optical signal in a rapid object recognition task: improving detection by the independent component analysis. *Brain Res.*, **1236**, 145–158.

15 Matsuo, K., Kato, T., Taneichi, K., Matsumoto, A., Ohtani, T., Hamamoto, T., Yamasue, H., Sakano, Y., Sasaki, T., Sadamatsu, M., Iwanami, A., Asukai, N., and Kato, N. (2003) Activation of the prefrontal cortex to trauma-related stimuli measured by near-infrared spectroscopy in posttraumatic stress disorder due to terrorism. *Psychophysiology*, **40**, 492–500.

16 Minagawa-Kawai, Y., Mori, K., Hebden, J.C., and Dupoux, E. (2008) Optical imaging of infants' neurocognitive development: recent advances and perspectives. *Dev. Neurobiol.*, **68**, 712–728.

17 Watanabe, E., Maki, A., Kawaguchi, F., Yamashita, Y., Koizumi, H., and Mayanagi, Y. (1998) Noninvasive cerebral blood volume measurement during seizures using multichannel near infrared spectroscopic topography. *J. Epilepsy*, **11** 335–340.

18 Gallagher, A., Lassonde, M., Bastien, D., Vannasing, P., Lesage, F., Grova, C., Bouthillier, A., Carmant, L., Lepore, F., Beland, R., and Nguyen, D.K. (2008) Non-invasive pre-surgical investigation of a 10 year-old epileptic boy using simultaneous EEG–NIRS. *Seizure*, **17**, 576–582.

19 Koch, S.P., Werner, P., Steinbrink, J., Fries, P., and Obrig, H. (2009) Stimulus-induced and state-dependent sustained gamma activity is tightly coupled to the hemodynamic response in humans. *J. Neurosci.*, **29**, 13962–13970.

20 Ou, W., Nissila, I., Radhakrishnan, H., Boas, D.A., Hamalainen, M.S., and Franceschini, M.A. (2009) Study of neurovascular coupling in humans via simultaneous magnetoencephalography and diffuse optical imaging acquisition. *Neuroimage*, **46**, 624–632.

21 Benaron, D.A., Ho, D.C., Spilman, S.D., van Houten, J.C., and Stevenson, D.K. (1994) Tomographic time-of-flight optical imaging device. *Adv. Exp. Med. Biol.*, **361**, 207–214.

22 Walker, S.A., Fantini, S., and Gratton, E. (1997) Image reconstruction by backprojection from frequency-domain optical measurements in highly scattering media. *Appl. Opt.*, **36**, 170–174.

23 Arridge, S.R. and Schotland, J.C. (2009) Optical tomography: forward and inverse problems. *Inverse Probl.*, **25** (12), 123010.

24 Colak, S.B., van der Mark, M.B., Hooft, G.W., Hoogenraad, J.H., van der Linden, E.S., and Kuipers, F.A. (1999) Clinical optical tomography and NIR spectroscopy for breast cancer detection. *IEEE J. Sel. Top. Quantum Electron.*, **5**, 1143–1158.

25 Grable, R.J. and Rohler, D.P. (1997) Optical tomography breast imaging. *Proc. SPIE*, **2979**, 197–210.

26 Intes, X. (2005) Time-domain optical mammography SoftScan: initial results. *Acad. Radiol.*, **12** (8), 934–947.

27 Schmitz, C.H., Klemer, D.P., Hardin, R., Katz, M.S., Pei, Y., Graber, H.L., Levin, M.B., Levina, R.D., Franco, N.A., Solomon, W.B., and Barbour, R.L. (2005) Design and implementation of dynamic near-infrared optical tomographic imaging instrumentation for simultaneous dual-breast measurements. *Appl. Opt.*, **44**, 2140–2153.

28 Grosenick, D., Moesta, K.T., Moller, M., Mucke, J., Wabnitz, H., Gebauer, B., Stroszczynski, C., Wassermann, B., Schlag, P.M., and Rinneberg, H. (2005) Time-domain scanning optical mammography: I. recording and assessment of mmammograms of 154 patients. *Phys. Med. Biol.*, **50**, 2429–2450.

29 Taroni, P., Torricelli, A., Spinelli, L., Pifferi, A., Arpaia, F., Danesini, G., and Cubeddu, R. (2005) Time-resolved optical mammography between 637 and 985 nm: clinical study on the detection and identification of breast lesions. *Phys. Med. Biol.*, **50**, 2469–2488.

30 Yates, T.D., Hebden, J.C., Gibson, A.P., Everdell, N.L., Arridge, S.R., and

Douek, M. (2005) Optical tomography of the breast using a multi-channel time-resolved imager. *Phys. Med. Biol.*, **50**, 2503–2517.

31 Boverman, G., Fang., Q., Carp, S.A., Miller, E.L., Brooks, D.H., Selb, J., Moore, R.H., Kopans, K.B., and Boas, D.A. (2007) Spatio-temporal imaging of the hemoglobin in the compressed breast with diffuse optical tomography. *Phys. Med. Biol.*, **52**, 3619–3641.

32 Tromberg, B.J., Pogue, B.W., Paulsen, K.D., Yodh, A.G., Boas, D.A., and Cerussi, A.E. (2008) Assessing the future of diffuse optical imaging technologies for breast cancer management. *Med. Phys.*, **35** (6), 2443–2451.

33 Wang, X., Pogue, B.W., Jiang, S., Dehgahni, H., Song, X., Srinivasan, S., Brooksby, B.A., Paulsen, K.D., Kogel, C., Poplack, S.P., and Wells, W.A. (2006) Image reconstruction of effective Mie scattering parameters of breast tissue *in vivo* with near-infrared tomography. *J. Biomed. Opt.*, **11** (4), 041106.

34 Choe, R., Corlu, A., Lee, K., Durduran, T., Konecky, S.D., Grosicka-Koptyra, M., Arridge, S.R., Czernieki, B.J., Fraker, D.L., DeMichele, A., Chance, B., Rosen, M.A., and Yodh, AG. (2005) Diffuse optical tomography of breast cancer during neoadjuvant chemotherapy: a case study with comparison to MRI. *Med. Phys.*, **32** (4), 1128–1139.

35 Jiang, S., Pogue, B.W., Carpenter, C.M., Poplack, S.P., Wells, W.A., Kogel, C.A., Forero, J., Muffly, L.S., Schwartz, G.N., Paulsen, K.D., and Kaufman, P.A. (2009) Evaluation of breast tumor response to neoadjuvant chemotherapy with diffuse optical spectroscopic tomography: case studies of tumor region-of-interest changes. *Radiology*, **252** (2), 330–331.

36 Hintz, S.R., Cheong, W.F., van Houten, J.P., Stevenson, D.K., and Benaron, D.A. (1999) Bedside imaging of intracranial hemorrhage in the neonate using light: comparison with ultrasound, computed tomography, and magnetic resonance imaging. *Pediatr. Res.*, **45**, 54–59.

37 Benaron, D.A., Hintz, S.R., Villringer, A., Boas, D., Kleinschmidt, A., Frahm, J., Hirth, C., Obrig, H., van Houten, J.C., Kermit, E.L., Cheong, W.F., and Stevenson, D.K. (2000) Noninvasive functional imaging of human brain using light. *J. Cereb. Blood Flow Metab.*, **20**, 469–477.

38 Hebden, J.C., Gibson, A., Yusof, R., Everdell, N., Hillman, E.M.C., Delpy, D.T., Arridge, S.R., Austin, T., Meek, J.H., and Wyatt, J.S. (2002) Three-dimensional optical tomography of the premature infant brain. *Phys. Med. Biol.*, **47**, 4155–4166.

39 Hebden, J.C., Gibson, A., Austin, T., Yusof, R., Everdell, N., Delpy, D.T., Arridge, S.R., Meek, J.H., and Wyatt, J.S. (2004) Imaging changes in blood volume and oxygenation in the newborn infant brain using three-dimensional optical tomography. *Phys. Med. Biol.*, **49**, 1117–1130.

40 Gibson, A.P., Austin, T., Everdell, N.L., Schweiger, M., Arridge, S.R., Meek, J.H., Wyatt, J.S., Delpy, D.T., and Hebden, J.C. (2006) Three-dimensional whole-head optical tomography of passive motor evoked responses in the neonate. *Neuroimage*, **30**, 521–528.

41 Bluestone, A.Y., Abdouleav, G., Schmitz, C.H., Barbour, R.L., and Hielscher, A.H. (2001) Three-dimensional optical tomography of hemodynamics in the human head. *Opt. Express*, **9**, 272–286.

15
Raman Microscopy

Christoph Krafft and Jürgen Popp

15.1
Introduction

Fluorescence microscopy is the most commonly biophotonic technique applied to assess cells and tissues. Because only a few biomolecules show inherent fluorescence, extrinsic fluorescent probes and molecular stains have been introduced as fluorophores. However, there are sometimes artifacts and drawbacks that have to be taken into account when using fluorophores. Along with the well-known problem of photobleaching, delivering labels can be a problem, particularly for whole organisms. Some labels work only on dead cells; others damage cells or perturb the very processes that they are intended to study. Other measurements destroy cells, creating isolated snapshots of different cells at given points in time. Such data are not particularly useful for heterogeneous cultures containing spontaneously differentiating cells. Label-free and nondestructive microscopy offers a way to investigate living cells while eliminating possible artifacts. Instead of detecting photons emitted from excited fluorophores, alternative techniques detect subtle changes in light as it is absorbed or altered by biological samples relying on linear or nonlinear optical phenomena. Nonlinear phenomena such as second harmonic generation, two-photon fluorescence, coherent anti-Stokes Raman scattering, and stimulated Raman scattering are observed when high-intensity light, in essence pulses of laser light, interacts with matter. They will not be discussed here as the sophisticated and expensive instrumentation is available in only a few specialized laboratories [1]. Raman spectroscopy is a linear optical phenomenon based on inelastic scattering of monochromatic light. It probes molecular vibrations, which are an inherent property of matter. As the spectrum of vibrations provides a specific fingerprint of the chemical composition and structure of samples, Raman spectroscopy has been introduced as a biophotonic tool to characterize cells and tissues. The coupling of a Raman spectrometer with a microscope offers two main advantages. First, lateral resolutions can be achieved down to Abbe's limit of diffraction below 1 μm. Second, maximum sensitivity can be achieved because the photon flux (photon density per unit area) of the focused laser beam on to the sample is at a maximum and the

Handbook of Biophotonics. Vol.2: Photonics for Health Care, First Edition. Edited by Jürgen Popp, Valery V. Tuchin, Arthur Chiou, and Stefan Heinemann.

collection efficiency of scattered photons from the sample is at a maximum. User-friendly, commercial Raman microscopes are available from numerous companies [2]. Of course, Raman microscopy has limitations. Whereas fluorescence labeling can often allow discrimination of single molecules, label-free techniques are less sensitive and specific. To improve the sensitive and specific detection of biomolecules with low scattering intensities or low abundance, signal-enhancement techniques have been developed such as surface-enhanced Raman scattering (SERS) and resonance Raman scattering (RRS). This chapter briefly describes some biomedical examples. Recent reviews give a more comprehensive overview of Raman microscopy of cells and tissues [3] and disease recognition [4].

15.2
Application to Cell Characterization

Single cells are very suitable objects for Raman spectroscopy because of the high concentrations of biomolecules in their condensed volume. Protein concentration as high as 250 $\mu g\,\mu l^{-1}$ and DNA and RNA concentrations in the region of 100 $\mu g\,\mu l^{-1}$ have been reported. These values depend on the cell type, the phase of the cell cycle, and the location within the cell.

Figure 15.1 shows photomicrographs and Raman microscopic images of a dried Hep G2 cell and a fixed macrophage in medium. Hep G2 is a perpetual cell line which was derived from the liver tissue of a 15-year-old male with a well-differentiated hepatocellular carcinoma. The Raman image of 51 × 61 spectra (Figure 15.1b) was collected using a 100 × /NA 0.9 objective with a step size of 500 nm and an exposure time of 6 s per spectrum. The numbers 51 and 61 indicate the spectra in x and y direction, respectively. After low-intensity spectra had been removed and the remaining spectra normalized, the data set was segmented by *k*-means clustering. This algorithm groups the spectra into *k* clusters (here seven) according to their similarity, which is calculated from the Euclidian distance in a given spectral range. The cluster memberships are color coded for display. Averaging all spectra within a cluster offers

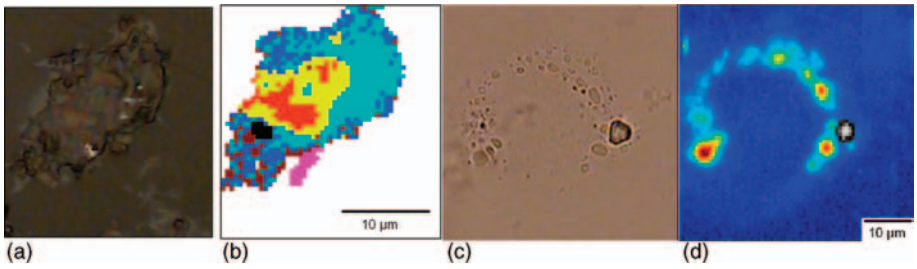

Figure 15.1 (a) Photomicrograph and (b) Raman image of a dried Hep G2 cell. The color code represents the membership of a cluster analysis. (c) Photomicrograph and (d) Raman image of a fixed macrophage in aqueous buffer. The color code indicates the intensity of CH_2 vibrations that corresponds to lipids. The gray scale code shows a foreign particle.

the advantages that pixel-to-pixel variations are reduced and the signal-to-noise ratio is improved compared with a single spectrum.

Macrophages comprise a special class of white blood cells (leukocytes). As phagocytes they engulf and digest cellular debris and pathogens. They are also involved in the uptake of lipids by various mechanisms that create the progressive plaque lesion of atherosclerosis. The Raman image of 78 × 72 spectra (Figure 15.1d) was registered using a 60 × /NA 1.0 water immersion objective with a step size of 700 nm. Typical features of the macrophage are lipid droplets that line the margin of the cell. The most intense Raman bands of lipids are CH_2 stretch vibrations near 2900 cm^{-1} (Figure 15.2). The chemical map in Figure 15.1d plots the intensity distribution of these bands. Under the experimental conditions, larger droplets are resolved; smaller droplets could not be resolved. Higher lateral resolution can be achieved by using a shorter excitation wavelength and a smaller step size.

Figure 15.2a shows five Raman spectra representing the clusters of the Hep G2 cell in Figure 15.1b (traces 1, 2, 3, 5, 6) and a difference spectrum (trace 4 = 2 – 1). Trace 1 represents the cytoplasm (cyan cluster). Spectral contributions of proteins dominate. Bands are assigned to the aromatic amino acid side chains (Phe, 622, 1003, 1032,

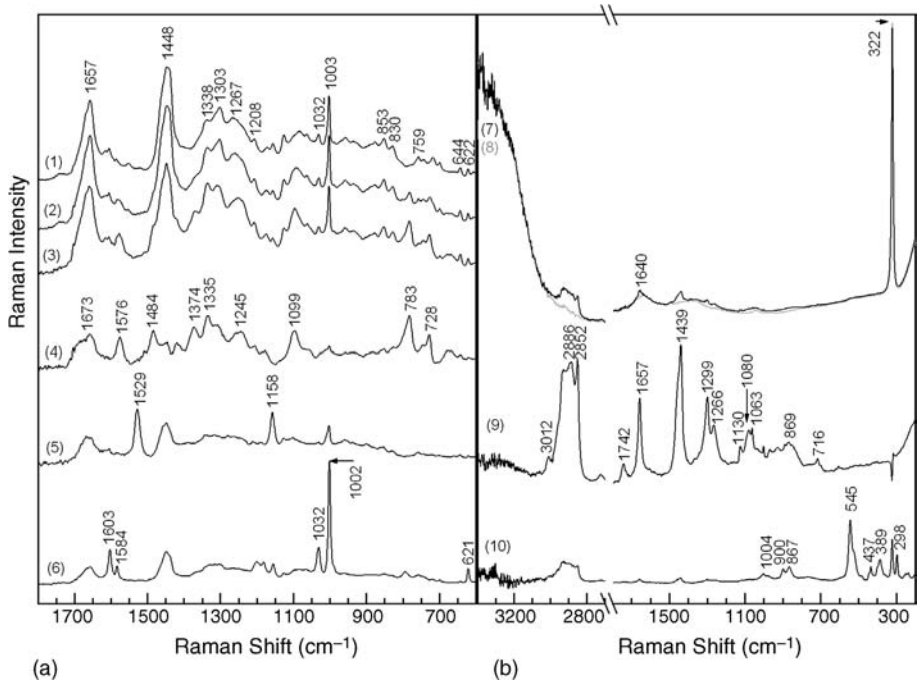

Figure 15.2 Raman spectra representing the clusters of the dried Hep G2 cell in Figure 15.1b (traces 1, 2, 3, 5, 6) and difference spectrum (trace 4 = 2 – 1). Unmanipulated Raman spectra of the macrophage in Figure 15.1d corresponding to the lipid droplets (trace 7) and surrounding medium (trace 8) and difference spectrum (trace 9 = 7 – 8). Raman spectrum of foreign particle (trace 10). The intensity scale was four fold compressed for the range 3400–2700 cm^{-1}.

1208 cm^{-1}; Tyr, 644, 830, 853, 1208 cm^{-1}; Trp, 759 cm^{-1}), aliphatic amino acid side chains (1338, 1448 cm^{-1}), and the peptide backbone (amide III at 1267 cm^{-1}, amide I at 1657 cm^{-1}). Spectral contributions of lipids are resolved at 1303, 1130, 1060, 716, and 700 cm^{-1}. The latter bands are not labeled. The other cytoplasm spectra (blue and brown clusters) deviate only slightly and will not be discussed here. Trace 2 represents the nucleus (yellow cluster). In addition to protein bands that are similar to those in the cytoplasm, spectral contributions of DNA are evident at 783 and 1099 cm^{-1}. As most DNA bands overlap with protein bands, a difference spectrum was calculated (trace 4). Then positive difference bands are assigned to nucleotides (adenine, 728, 1335, 1484, 1576 cm^{-1}; cytosine, 783, 1245 cm^{-1}; thymine, 783, 1374, 1673 cm^{-1}; guanine, 1484, 1576 cm^{-1}) and the phosphate backbone (1099 cm^{-1}). The intensities of DNA bands increase in trace 3, which represents nucleoli (orange cluster). Traces 5 and 6 represent special features (magenta and black clusters, respectively). Bands at 1158 and 1529 cm^{-1} are assigned to carotene. An inherent property of carotene compounds is their high Raman cross-section, which makes them easily detectable in Raman spectra even at low concentrations. Intense bands at 621, 1002, 1032, 1584 and 1603 cm^{-1} are typical of polystyrene. The detection of this polymer bead clearly demonstrates the power of Raman microscopic imaging. The location and distribution of numerous molecules can be assessed by their spectroscopic fingerprint without exogenous labels.

Unmanipulated Raman spectra of the macrophage represent the lipid droplets and the surrounding medium [Figure 15.2b, traces 7 (black) and 8 (gray), respectively]. Spectral contributions are assigned to the substrate calcium fluoride (322 cm^{-1}) and water (1640 and above 3000 cm^{-1}). The overlay of both spectra indicates that the spectral contributions of the lipid droplets are less intense. Subtracting the spectrum of the medium compensates bands of the substrate, water and also constant spectral contributions of optical elements in the light path. The resulting difference spectrum (trace 9) reveals pure lipid bands with a very low background. The bands are assigned to the choline group (716, 869 cm^{-1}), phosphate group (1080 cm^{-1}), ester group (1742 cm^{-1}), and C−C and C−H vibrations of fatty acids (1063, 1130, 1299, 1439, 2852, 2886 cm^{-1}). Bands at 1266, 1657, and 3012 cm^{-1} are indicative of unsaturated fatty acids. The Raman spectrum (trace 9) is consistent with the phospholipid phosphatidylcholine. The Raman spectrum of a foreign particle at the right part of the cell (trace 10) shows bands in the low-wavenumber region at 545, 437, 369, and 298 cm^{-1}. The distribution of the band at 545 cm^{-1} has been included in Figure 15.1d as a gray scale chemical map. This Raman image shows a macrophage at work engulfing a foreign particle.

To improve the sensitive and specific detection of biomolecules with low scattering intensities or low abundance, signal-enhancement techniques have been applied such as SERS and RRS. RRS is observed if the excitation wavelength is matched to an electronic transition of the molecule so that vibrational modes associated with the excited state are enhanced. As the enhancement is restricted to vibrational modes of the chromophore, the complexity of Raman spectra from large biomolecules is reduced. Examples of RRS of cells include the detection of heme and hemozoin in red blood cells (erythrocytes) using 785 nm excitation [5] and cytochrome b_{558} in

neutrophilic granulocytes using 413 nm excitation [6]. SERS utilizes the optical excitation of surface plasmons, i.e., collective vibrations of the free electrons in metals. The result is an amplification of the electromagnetic field in the close vicinity of the metal surface (a few nanometers), which leads to the enhancement of Raman signals from adsorbed molecules. The first SERS experiments used colloidal gold nanoparticles that were taken up by cells. However, due nonspecific binding of biomolecules to these nanoparticles, every spectrum of a Raman image was different and the approach lacked reproducibility [7]. For specific recognition of antigens in cancer cells by SERS microscopy, gold nanoparticles have been functionalized with antibodies [8]. The advantage of the SERS approach compared with the detection of fluorescence labels is the multiplex capacity. The fingerprint of the SERS spectrum allows the simultaneous detection of numerous antigens.

15.3
Application to Tissue Characterization

Histology – the study of the anatomy of tissue – and histopathology – the study of diseased tissue – are performed by examining thin slices (sections) of tissue under a light microscope. The ability to visualize or differentially identify microscopic structures is frequently enhanced through the use of histologic stains because biological tissue has little inherent contrast. Hundreds of techniques exist that have been developed to stain cells and cellular components selectively. As Raman microspectroscopic imaging provides molecular contrast in tissues without stains, it offers prospects to complement established techniques. Instead of staining protocols, sophisticated chemometric tools are applied for the reconstruction and classification of Raman images from tissue sections. In principle, the concepts that have been described in the previous section can be transferred from cell characterization. For example, a SERS marker has been developed to detect the prostate-specific antigen in the context of prostate cancer tissue [9].

Figure 15.3 shows as an example a 70 × 70 Raman image with a 2.5 μm step size of a liver tissue section. A photomicrograph (a), three plots of a vertex component analysis (VCA) (b–d), and a composite image (e) are compared. VCA is a hyperspectral unmixing algorithm that projects the image raw data in a space of smaller dimensionality aiming to retain all information. The scope of VCA is that end-

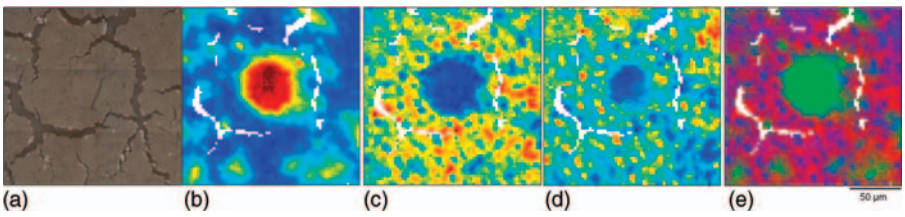

Figure 15.3 (a) Photomicrograph, (b–d) score plots of a vertex component analysis and (e) composite image of the central vein in a liver tissue section.

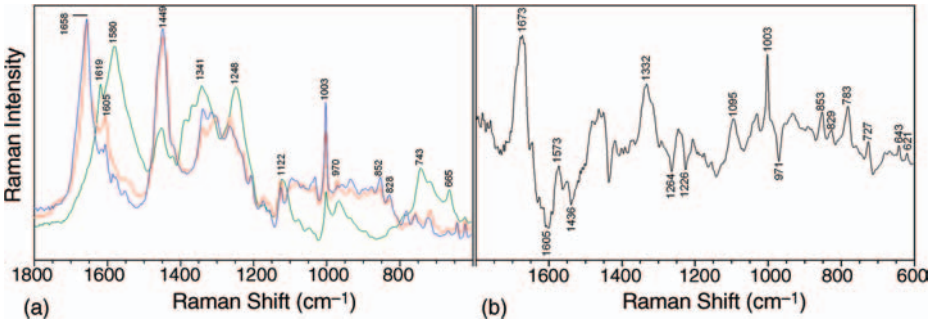

Figure 15.4 (a) Overlay of endmember spectra representing the score plots in Figure 15.3b–d and (b) difference spectrum (black trace = blue – red).

members represent spectra of most dissimilar constituents. It has been found that endmembers have high chemical relevance. Then, scores denote the concentration of the endmember spectra. Details in the context of Raman spectroscopy recently have been published [10]. Considering the bands in the endmember spectra (Figure 15.4) and the location and size of the morphologic features, the score plot in Figure 15.3b is assigned to the central vein and red blood cells, the score plot in Figure 15.3c to liver parenchyma, and the score plot in Figure 15.3d to cell nuclei. If the intensities of the plots in Figure 15.3b–d are converted to green, red, and blue channels, respectively, a composite image can be generated (Figure 15.3e). Such a composite image can be analyzed in a similar way to a histologically stained tissue section.

The endmember spectra are overlaid in Figure 15.4. The color code is analogous to the colors in the composite in Figure 15.3e. This means that the endmember spectrum representing the central vein and red blood cells is plotted green, liver parenchyma red, and cell nuclei blue. The green spectrum is characterized by intense contributions of the heme group at 665, 743, 1122, 1248, 1341, 1580, and 1619 cm^{-1} that are enhanced by a resonance effect. The red and blue spectra are dominated by spectral contributions of proteins near 828, 852, 1003, 1449, and 1658 cm^{-1}. The difference spectrum (black) between the blue and the red was calculated to improve visualization of the variations. Positive difference bands at 727, 783, 1095, and 1573 cm^{-1} are associated with DNA. Further positive difference bands at 621, 643, 829, 853, and 1003 cm^{-1} are assigned to proteins. Positive difference bands at 1332 and 1673 cm^{-1} contain overlapping contributions from proteins and DNA. Negative difference bands at 971, 1226, 1364, 1436, and 1605 cm^{-1} are consistent with bilirubin in bile acid. This result demonstrates the wealth of molecular information that can be obtained simultaneously from the analysis of Raman images of tissue sections.

15.4 Conclusions

Applications of Raman microscopy to cells and tissues are still in their infancy and are expected to grow during the years to come. A prohibitive factor in Raman microscopic

imaging remains the acquisition time. Therefore, technical improvements aim to (i) increase the sensitivity to reduce the exposure time per spectrum and (ii) apply parallel data acquisition strategies to register multiple spectra simultaneously. Innovations include optical filters with higher transmission, spectrographs with reduced light losses, and detectors with optimized quantum efficiency. Modern Raman microscopic instruments are able to collect several hundred spectra per second. Another challenge is the automatic processing of extended Raman microscopic images because the spectral features are often small and distributed over a wide range. In addition to unsupervised segmentation and spectral unmixing algorithms such as cluster analysis, principal component analysis, and vertex component analysis, supervised algorithms such as artificial neural networks, linear discriminant analysis, and support vector machines have to be trained to classify cells and tissues objectively based on their Raman signatures. A full description of all technical and theoretical details is beyond the scope of this chapter. The intention of the chapter was to highlight the potential of Raman microscopy in biophotonics. Further progress requires interdisciplinary efforts of natural scientists, engineers, and physicians.

References

1 Müller, M. and Zumbusch, A. (2007) Coherent anti-Stokes Raman scattering microscopy. *ChemPhysChem*, **8**, 2156–2170.

2 Sage, L. (2009) Raman microscopes. *Anal. Chem.*, **81**, 3222–3226.

3 Krafft, C., Dietzek, B., and Popp, J. (2009) Raman and CARS microspectroscopy of cells and tissues. *Analyst*, **134**, 1046–1057.

4 Krafft, C., Steiner, G., Beleites, C., and Salzer, R. (2008) Disease recognition by infrared and Raman spectroscopy. *J. Biophotonics*, **2**, 13–28.

5 Bonifacio, A., Finaurini, S., Krafft, C., Parapini, S., Taramelli, D., and Sergo, V. (2008) Spatial distribution of heme species in erythrocytes infected with *Plasmodium falciparum* by use of resonance Raman imaging and multivariate analysis. *Anal. Bioanal. Chem.*, **392**, 1277–1282.

6 van Manen, H.J., Uzunbajakava, N., van Bruggen, R., Roos, D., and Otto, C. (2003) Resonance Raman imaging of the NADPH oxidase subunit cytochrome b558 in single neutrophilic granulocytes. *J. Am. Chem. Soc.*, **125**, 12112–12113.

7 Kneipp, K., Haka, A.S., Kneipp, H., Badizadegan, K., Yoshizawa, N., Boone, C., Shafer-Peltier, K.E., Motz, J.T., Dasari, R.R., and Feld, M.S. (2002) Surface-enhanced Raman spectroscopy in single living cells using gold nanoparticles. *Appl. Spectrosc.*, **56**, 150–154.

8 Lee, S., Chon, H., Lee, M., Choo, J., Shin, S.Y., Lee, Y.H., Rhyu, I.J., Son, S.W., and Oh, CH. (2009) Surface-enhanced Raman scattering imaging of HER2 cancer markers overexpressed in single MCF7 cells using antibody conjugated hollow gold nanospheres. *Biosens. Bioelectron.*, **24**, 2260–2263.

9 Schlücker, S., Küstner, B., Punge, A.R.B., Marx, A., and Ströbel, P. (2006) Immuno-Raman microspectroscopy: *in situ* detection of antigens in tissue specimens by surface-enhanced Raman scattering. *J. Raman Spectrosc.*, **37**, 719–721.

10 Miljković, M., Chernenko, T., Romeo, M.J., Bird, B., Matthaus, C., and Diem, M. (2010) Label-free imaging of human cells: algorithms for image reconstruction of Raman hyperspectral datasets. *Analyst*, **135**, 2002–2013.

16
CARS Microscopy

Andreas Zumbusch

16.1
Introduction

Optical microscopy is one of the major tools used in the biological sciences. The interaction between optics and biology has for centuries been enormously fruitful for both areas. In recent decades, especially fluorescence microscopic techniques have found very widespread applications. This is due to their high sensitivity, which can reach the single-molecule detection limit [1], their high specificity achieved by powerful labeling strategies, and the noninvasive character common to most optical microscopy techniques. Despite the great success of fluorescence microscopy, much effort has recently been invested in research on complementary label-free microscopy techniques. The motivation for these efforts is twofold: first, not all samples can be fluorescently labeled, and second, all fluorescent labels suffer from photobleaching, which severely limits the observation times. Ideally, new techniques should – despite working without labels – offer the above-mentioned advantages of fluorescence-based approaches.

In general, if the requirement of offering (molecular) specificity without the use of labels is to be fulfilled, contrast generation should not be based on electronic spectra. This is due to the large linewidths of electronic transitions with respect to the width of the relevant spectral detection window. Concerning this point, vibrational spectra offer much more information, since medium-sized molecules can clearly be identified based on their characteristic vibrational spectra, which typically feature rather narrow linewidths. Vibrational microscopy is mostly performed either by directly monitoring the absorption of infrared (IR) light or by monitoring Raman scattering. Apart from technical problems concerning the relatively low sensitivity and poor spatial resolution, biological applications of IR microscopy suffer especially from the broad and intense absorption bands of water. These two problems are avoided when using spontaneous Raman scattering microscopy. Here, however, low scattering cross-sections and an overwhelmingly strong fluorescence background, which is present in many samples, are new difficulties.

Handbook of Biophotonics. Vol.2: Photonics for Health Care, First Edition. Edited by Jürgen Popp, Valery V. Tuchin, Arthur Chiou, and Stefan Heinemann.

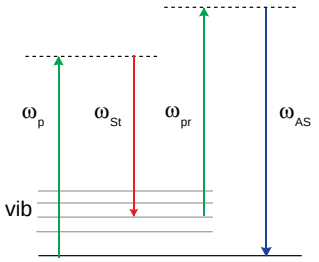

Figure 16.1 Energy level representation of the CARS process.

Despite these problems, Raman-type scattering can be exploited for generating images of unlabeled samples with high spatial resolution if nonlinear optical techniques are used. Since the advent of commercially available laser sources delivering ultrashort pulses, nonlinear optical effects such as two-photon fluorescence excitation [2] and second harmonic generation (SHG) and third harmonic generation (THG) microscopy [3] have been used extensively in optical microscopy. Whereas two-photon excitation as a variant of fluorescent microscopy relies on sample labeling, both SHG and THG microscopy generate contrast in unlabeled specimens. However, both techniques generate structural and not chemically specific contrast. Contrast with chemical selectivity can instead be generated by coherent anti-Stokes Raman scattering (CARS) microscopy [4, 5], a technique which is now commercially available and has found widespread applications.

16.2
Technical Background and Experimental Realizations

CARS is a third-order nonlinear optical process in which three excitation fields interact to produce a fourth field, which is detected. In general, two beams with frequencies ω_p and ω_{St} are tuned such that the frequency difference $\omega_p - \omega_{St}$ coincides with the frequency ω_{vib} of a vibrational transition of the sample molecules. Under this condition, a third beam with frequency ω_{pr} generates a fourth field with frequency $\omega_{AS} = \omega_p + \omega_{vib}$ in a resonance-enhanced manner (Figure 16.1). In most cases, the experiment is performed using a frequency-degenerate scheme with $\omega_p = \omega_{pr}$, such that only two laser beams are necessary for the excitation. The CARS signal intensity depends quadratically on the square modulus of the induced third-order polarization in the sample $I_{AS} \propto \left|\mathbf{P}^{(3)}\right|^2$. $\mathbf{P}^{(3)}$ itself depends on the third-order optical susceptibility $\chi^{(3)}$ as a material-specific parameter that can be decomposed into a resonant and a nonresonant term, and the amplitude of the exciting laser fields $\mathbf{E}$. One obtains

$$\mathbf{P}^{(3)} = \left[\chi_r^{(3)} + \chi_{nr}^{(3)}\right] \mathbf{E}_p \mathbf{E}_{pr} \mathbf{E}_{St}^{*} \tag{16.1}$$

This description already explains many of the features of CARS microscopy. (i) Image contrast is generated with chemical selectivity by tuning the frequency difference between the excitation lasers to ω_{vib}. (ii) Sample autofluorescence does not

interfere with the CARS signal since the latter is blue shifted with respect to the excitation wavelengths. (iii) Three-dimensional images can be obtained without use of a confocal pinhole since CARS is a nonlinear optical process. However, because $\chi^{(3)}$ in all cases is very small, pulsed lasers with high pulse energies have to be used.

A CARS microscopy experiment then consists in tuning the laser wavelengths to the vibrational frequency of interest and then scanning the sample. Microscope setups similar to those used in confocal microscopy are easily adapted to CARS microscopy. This leads to images which represent the spatial distribution of compounds with a specific vibrational resonance. However, the nonresonant part of $\chi^{(3)}$ and the quadratic dependence of I_{AS} on $\chi^{(3)}$ in general make it difficult to extract quantitative information of local molecular concentrations.

16.2.1
Excitation Geometry

The first adaptation of CARS to microscopy was described in the early 1980s [6]. At that time, attempts were made to increase the efficiency of the signal generation process by matching the respective phases of the excitation beams through their geometric separation. However, this severely reduces the effective numerical aperture and therefore no high spatial resolution was achievable. Therefore, CARS microscopy initially did not find any applications. This changed, when it was realized that the reduction in the interaction volume by strong focusing leads to the generation of strong signals [7]. The subsequent development of CARS microscopy was mainly aimed at simplifying the experimental setup and at reducing the nonresonant background due to $\chi_{nr}^{(3)}$.

In most cases, CARS microscopy is carried out in a transmission-type geometry, because most of the signal is generated in the forward direction [8]. However, sample features which are of a size comparable to or smaller than the excitation wavelengths also lead to a strong CARS signal in the backward direction. It has been pointed out, however, that large parts of the strong forward-directed signal can be recovered in an epi-detection scheme due to CARS signal scattering [9]. CARS microscopy can therefore also be performed in a backscattering- or epi-detection scheme. With epi-detection, quantitative image interpretation is impossible, because the signal intensity shows an oscillatory behavior depending on the size of the sample features [10]. The epi-detection scheme is nevertheless of great importance since only one face of the sample has to be accessed for imaging. It is worth mentioning that CARS microscopy has also been performed in a wide-field geometry [11]. This allows very fast image acquisition over large sample areas, but decreases the axial resolution.

16.2.2
Excitation Lasers

Whereas well-established microscope setups can be used for CARS microscopy, much effort has been spent in order to improve the excitation sources used. The most important requirement is that the two (or three) excitation lasers are synchronized to

an extent such that the jitter in the arrival time of the individual laser pulses is less than 300 fs. In addition, the laser system should offer fast tunability in order to address different vibrational resonances and a spectral linewidth of $10\,cm^{-1}$ to ensure high spectral selectivity. At the same time, the pulse duration should be as short as possible for the CARS process to be driven efficiently. The last two requirements are contradictory, since short pulses come with broad spectra. The ideal compromise would consist in using transform-limited pulses with a duration of 1 ps. In practice, most experiments are currently performed by using 5–7 ps pulses available from an optical parametric amplifier system which is pumped by a high repetition rate pump laser at 532 nm [12]. Since in this experiment all excitation beams used are derived from one pump pulse, no timing jitter occurs. The performance of these systems is therefore much better than that of commercially available synchronized Ti:sapphire laser systems [13]. Common to all the laser sources discussed so far is that they are large and rather difficult to operate. Therefore, fiber lasers that are cheaper, more compact, more versatile, and more robust have recently been introduced as an alternative [14].

In contrast to the approach of imaging only one vibrational frequency at a time, so-called multiplexing experiments probe a whole range of frequencies with each excitation cycle. For this purpose, ω_{St} is provided not by a narrowband laser, but instead by a laser covering a broad spectral range [15]. Typically, short laser pulses are used for this purpose. Spectrally resolved detection is then used to gain information about vibrational resonances. Multiplex CARS microscopy is much faster than the single-frequency approach if spectroscopic information of a microscopic volume element is desired. It has therefore been employed successfully in microfluidic measurements [16, 17]. The integration times necessary for recording spectra, however, currently limit its suitability in imaging applications. Also in the field of multiplex CARS microscopy, fiber lasers have recently been used [18]. In this case, they offer the advantage of background-free imaging over the entire vibrational spectral region.

16.3 Applications

CARS microscopy has been developed in order to complement fluorescence microscopic techniques in experiments where fluorescent labeling is not possible. It turns out that especially C−H vibrational resonances lead to very strong CARS signals. Therefore, CARS microscopy has been used extensively to study the lipid distribution in a variety of live cells, live animals, and functional tissues [19]. Early applications of CARS experiments were aimed at following the distribution dynamics of exogenous compounds in live animals. This has the advantage that the vibrational spectra of the compounds of interest are well known. In this respect, mostly permeation studies of the skin were performed [9]. Increasingly, however, CARS microscopy of endogenous structures rich in C−H was performed. Examples are investigations related to atherosclerosis and neuronal damage [20, 21]. None of these experiments could be performed using the labeling strategies necessary for fluorescence imaging. It should be noted that the pulsed excitation employed in CARS microscopy can lead to sample

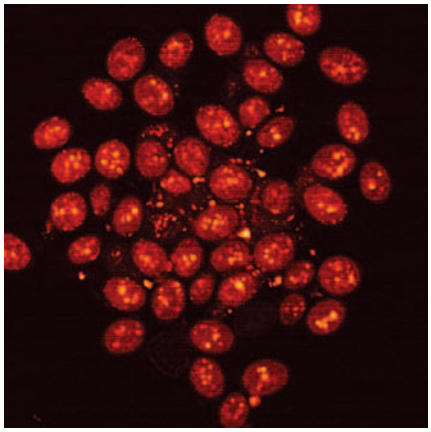

Figure 16.2 CARS images of lipid droplets in live yeast cells recorded at a resonance of 2845 cm^{-1}. Image dimensions are 150 × 150 μm (1024 × 1024 pixels). Integration time, 1 s. M. Winterhalder, unpublished results.

damage. In most cases, however, the excitation intensities necessary are below the threshold for the induction of noticeable damage even to sensitive organisms. As an example, high-resolution CARS microscopy of yeast cells is possible for extended periods without changing their normal behavior, that is, budding and similar processes are not affected (Figure 16.2). Likewise, several CARS microscopic studies on the lipid distribution in live *Caenorhabditis elegans* (Figure 16.3) have been published [22, 23].

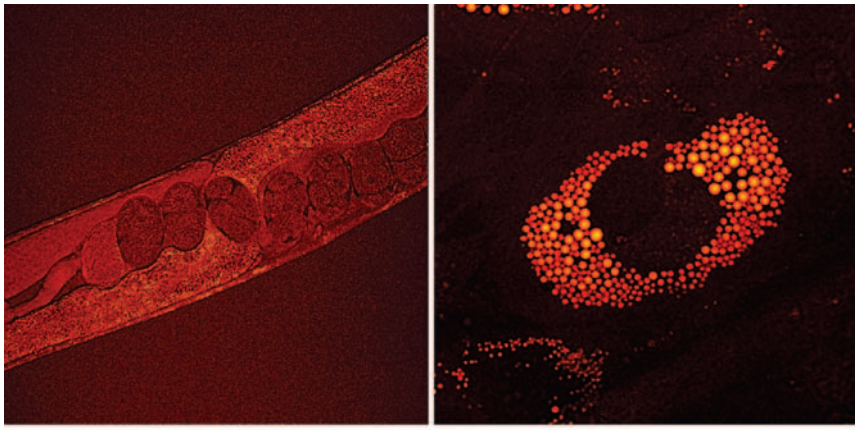

Figure 16.3 (a) CARS image of *C. elegans*. A maximum projection of 54 stacks clearly shows the intestine and fertilized eggs. Lipids mainly located in the intestine generate a strong CARS signal at 2845 cm^{-1}. The image dimensions are 150 × 150 μm (1024 × 1024 pixels). Integration time, 5 s. (b) CARS image of live human adipocytes, recorded at 2850 cm^{-1}. Image size, 84 × 84 μm (1024 × 1024 pixels). Line average, 2; integration time, 2 s. C. Jüngst, unpublished results.

The facts that CARS microscopy can be performed in a truly noninvasive manner, that is, no labeling is necessary, and microscopy with light levels below those causing photodamage to living animals is possible, hold great promise for future medical applications of CARS microscopy. Currently, the main areas of interest in this field are the diagnosis of malignant structures of the skin and intrasurgical application in brain surgery [24]. Although this chapter focuses on biological applications of CARS microscopy, it should nevertheless be mentioned that recently it has also found exciting applications in studies of problems related to material science, such as studies of catalytic processes [25].

16.4 Outlook

CARS microscopy is a new tool for truly noninvasive investigations. Although it does not reach the sensitivity of fluorescence microscopy, it does not require the use of labeling and it can be employed at light levels benign to living organisms, yet it delivers contrast which is molecularly specific. It therefore provides a complementary approach to other microscopy techniques, which is especially interesting for applications in the medical sciences.

References

1 Moerner, W.E. and Orrit, M. (1999) Illuminating single molecules in condensed matter. *Science*, **283** (5408), 1670–1676.

2 Denk, W., Strickler, J., and Webb, W. (1990) Two-photon laser scanning microscopy. *Science*, **248**, 73–76.

3 Olivier, N., Luengo-Oroz, M.A., Duloquin, L., Faure, E., Savy, T., Veilleux, I., Solinas, X., Debarre, D., Bourgine, P., Santos, A., Peyrieras, N., and Beaurepaire, E. (2010) Cell lineage reconstruction of early zebrafish embryos using label-free nonlinear microscopy. *Science*, **329** (5994), 967–971.

4 Müller, M. and Zumbusch, A. (2007) Coherent anti-Stokes Raman scattering microscopy. *ChemPhysChem*, **8** (15), 2156–2170.

5 Evans, C.L. and Xie, X.S. (2008) Coherent anti-Stokes Raman scattering microscopy: chemical imaging for biology and medicine. *Annu. Rev. Anal. Chem. (Palo Alto Calif)*, **1**, 883–909.

6 Duncan, M., Reintjes, J., and Manuccia, T. (1982) Scanning coherent anti-Stokes Raman microscope. *Opt. Lett.*, **7**, 350–352.

7 Zumbusch, A., Holtom, G., and Xie, X. (1999) Three-dimensional vibrational imaging by coherent anti-Stokes Raman scattering. *Phys. Rev. Lett.*, **82**, 4142–4145.

8 Cheng, J.X., Volkmer, A., and Xie, X. (2002) Theoretical and experimental characterization of coherent anti-Stokes Raman scattering microscopy. *J. Opt. Soc. Am. B*, **19**, 1363–1375.

9 Evans, C.L., Potma, E.O., Puoris'haag, M., Côté, D., Lin, C.P., and Xie, X.S. (2005) Chemical imaging of tissue *in vivo* with video-rate coherent anti-Stokes Raman scattering microscopy. *Proc. Natl. Acad. Sci. U. S. A.*, **102** (46), 16807–16812.

10 Cheng, J.X., Volkmer, A., Book, L.D., and Xie, X. (2001) An epi-detected coherent anti-Stokes Raman scattering (E-CARS) microscope with high spectral resolution and high sensitivity. *J. Phys. Chem. B*, **105**, 1277–1280.

11 Heinrich, C., Bernet, S., and Ritsch-Marte, M. (2006) Nanosecond microscopy with spectroscopic resolution. *New J. Phys.*, **8**, 36.

12 Ganikhanov, F., Carrasco, S., Xie, X., Katz, M., Seitz, W., and Kopf, D. (2006) Broadly tunable dual-wavelength light source for coherent anti-Stokes Raman scattering microscopy. *Opt. Lett.*, **31**, 1292–1294.

13 Jones, D., Potma, E., Cheng, J.X., Burfeindt, B., Pang, Y., and Xie, X. (2002) Synchronization of two passively mode-locked, picosecond lasers within 20 fs for coherent anti-Stokes Raman scattering microscopy. *Rev. Sci. Instrum.*, **73**, 2843–2848.

14 Krauss, G., Hanke, T., Sell, A., Träutlein, D., Leitenstorfer, A., Selm, R., Winterhalder, M., and Zumbusch, A. (2009) Compact coherent anti-Stokes Raman scattering microscope based on a picosecond two-color Er:fiber laser system. *Opt. Lett.*, **34** (18), 2847–2849.

15 Müller, M. and Schins, J. (2002) Imaging the thermodynamic state of lipid membranes with multiplex CARS microscopy. *J. Phys. Chem. B*, **106**, 3715–3723.

16 Schafer, D., Squier, J.A., van Maarseveen, J., Bonn, D., Bonn, M., and Müller, M. (2008) *In situ* quantitative measurement of concentration profiles in a microreactor with submicron resolution using multiplex CARS microscopy. *J. Am. Chem. Soc.*, **130**, 11592–11593.

17 Bergner, G., Chatzipapadopoulos, S., Akimov, D., Dietzek, B., Malsch, D., Henkel, T., Schlücker, S., and Popp, J. (2009) Quantitative CARS microscopic detection of analytes and their isotopomers in a two-channel microfluidic chip. *Small*, **5**, 2816–2818.

18 Selm, R., Winterhalder, M., Zumbusch, A., Krauss, G., Hanke, T., Sell, A., and Leitenstorfer, A. (2010) Ultrabroadband background-free coherent anti-Stokes Raman scattering microscopy based on a compact Er:fiber laser system. *Opt. Lett.*, **35** (19), 3282–3284.

19 Le, T.T., Yue, S., and Cheng, J.X. (2010) Shedding new light on lipid biology with coherent anti-Stokes Raman scattering microscopy. *J. Lipid Res.*, **51** (11), 3091–3102.

20 Wang, H.W., Langohr, I.M., Sturek, M., and Cheng, J.X. (2009) Imaging and quantitative analysis of atherosclerotic lesions by CARS-based multimodal nonlinear optical microscopy. *Arterioscler. Thromb. Vasc. Biol.*, **29** (9), 1342–1348.

21 Fu, Y., Sun, W., Shi, Y., Shi, R., and Cheng, J.X. (2009) Glutamate excitotoxicity inflicts paranodal myelin splitting and retraction. *PLoS One*, **4** (8), e6705.

22 Hellerer, T., Axäng, C., Brackmann, C., Hillertz, P., Pilon, M., and Enejder, A. (2007) Monitoring of lipid storage in *Caenorhabditis elegans* using coherent anti-Stokes Raman scattering (CARS) microscopy. *Proc. Natl. Acad. Sci. U. S. A.*, **104** (37), 14658–14663.

23 Yen, K., Le, T.T., Bansal, A., Narasimhan, S.D., Cheng, J.X., and Tissenbaum, H.A. (2010) A comparative study of fat storage quantitation in nematode *Caenorhabditis elegans* using label and label-free methods. *PLoS One*, **5** (9), e12810.

24 Evans, C.L., Xu, X., Kesari, S., Xie, X.S., Wong, S.T.C., and Young, G.S. (2007) Chemically-selective imaging of brain structures with CARS microscopy. *Opt. Express*, **15** (19), 12076–12087.

25 Kox, M.H.F., Domke, K.F., Day, J.P.R., Rago, G., Stavitski, E., Bonn, M., and Weckhuysen, B.M. (2009) Label-free chemical imaging of catalytic solids by coherent anti-Stokes Raman scattering and synchrotron-based infrared microscopy. *Angew. Chem. Int. Ed.*, **48**, 8990–8994.

17
Detection of Viral Infection in Epithelial Cells by Infrared Spectral Cytopathology

Max Diem, Nora Laver, Kristi Bedrossian, Jennifer Schubert, Kostas Papamarkakis, Benjamin Bird, and Miloš Miljković

17.1
Introduction

The Laboratory for Spectral Diagnosis (LSpD) at Northeastern University has been developing methodology for the automatic, infrared spectroscopy-based diagnosis of exfoliated cells [1–3]. These methods will be referred to henceforth as spectral cytopathology (SCP), since they deal with cytology – the "study of cells" using spectral methods. Whereas classical cytology renders a diagnosis based on cell morphology, SCP monitors changes in a cell's biochemical composition. This composition is determined via a global measurement, that is, all cellular biochemical components contribute to the observed infrared spectral pattern based on their abundance. Although infrared spectroscopy of isolated biochemical components can yield a variety of useful information, such as secondary and tertiary structure, degree of hydration and association, and the nature of counter ions, the global measurement of the infrared spectrum of a cell cannot be interpreted in similar detail, since the spectra of all components are superimposed and cannot be decomposed readily into component spectra. Nevertheless, recent advances in the use of multivariate methods of data analysis have produced distinct spectral patterns for a large number of tissue and cell types [4–11], and also for states of health and disease, cellular activity [12], and response to external stimuli [13].

Here, we summarize recent experimental evidence that SCP is able to detect viral infection in exfoliated epithelial cells. The results were unexpected, although some prior *in vivo* Raman results [14] can be interpreted in terms of sensitivity toward viral infections. In this chapter, we report preliminary results from a study of oral and cervical cells for which viral infection status was known *a priori*, or established via standard molecular biology/clinical testing procedures.

Handbook of Biophotonics. Vol.2: Photonics for Health Care, First Edition. Edited by Jürgen Popp, Valery V. Tuchin, Arthur Chiou, and Stefan Heinemann.

17.2 Methods

Clinical samples of cervical and oral exfoliates were obtained from the Department of Pathology at Tufts Medical Center (TMC), Boston, MA. The fixation protocols, handling of samples, and the cell deposition methods have been reported previously. Classical cytopathology, and all testing for high-risk strains of human papillomavirus (HPV, including the most common oncogenic strains 16 and 18) were performed at TMC using the FDA-approved Digene Hybrid Capture II test (see, e.g., [15]).

Spectral data of epithelial cells were collected using a data acquisition procedure referred to as the PapMap approach [16] after deposition by cyto-centrifugation on to infrared reflective slides. In this approach, cellular spectra are reconstructed by averaging between 10 and 100 individual spectra collected from pixels 6.25×6.25 μm in size. Subsequent to spectral data acquisition, cells were stained and imaged. Spectral data collection and viral DNA testing were performed on parallel samples (i.e., a sample aliquot was tested for the virus, while another aliquot was used for spectroscopy). The sample of herpes simplex-infected oral cells was diagnosed by classical cytopathology only.

Raw spectral data were corrected via a universally applicable multivariate procedure known as extended multiplicative signal correction (EMSC) [17, 18] to minimize any residual water vapor spectral contribution, and also light scattered by the cells or subcellular entities such as the nucleus. The correction of raw spectral features for these effects has recently been discussed in a number of papers [19–21]. Spectral datasets were analyzed by principal component analysis (PCA) [22], an unsupervised method which does not require any training or validation datasets. PCA identifies correlated and reproducible spectral differences which may be used to partition data. Spectral types are visualized using scores plots, where correlated variance is indicated by clustering of spectra or items.

17.3 Results and Discussion

Recent results from cervical and oral cell samples diagnosed by classical cytology as "abnormal," but not cancerous [i.e., samples diagnosed as ASCUS (atypical squamous cell of unknown significance) or LGIL (low-grade intraepithelial lesion) in cervical cytology)] showed unexpected SCP results [2, 3]. Most cells from an abnormal sample are nondiagnostic in that they appear morphologically normal. However, these cells exhibit different spectral signatures to those from normal samples. This is shown in Figure 17.1, which shows a scores plot of cellular spectra collected from the tongues of normal subjects and from the tongues of patients with reactive abnormalities, and also cancer of the tongue. Whereas the cancerous cells are morphologically and spectrally very different from normal cells, it is the

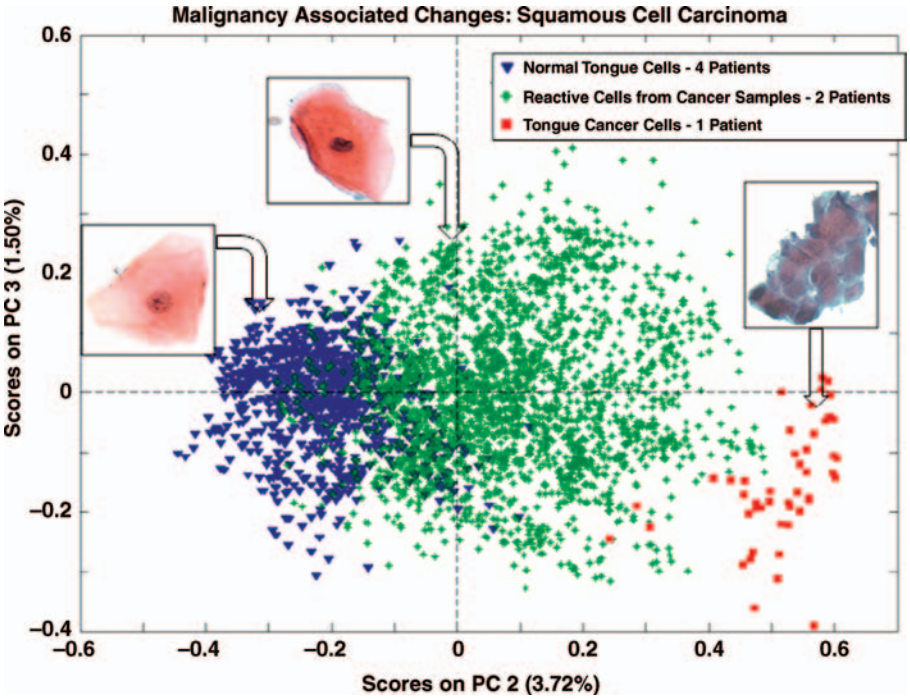

Figure 17.1 Scores plot of spectra from normal, reactive, and cancerous cells from the tongue.

nondiagnostic cells from the samples with reactive abnormalities that are most interesting: despite the fact that these cells exhibit normal morphology, they show spectral differences which range from near normal to near cancerous along the PC2 axis. This is in great contrast to classical cytology, where only 1% or fewer cells show morphologic abnormalities.

Completely analogous results were observed for cancer and premalignant states of other locations in the oral cavity [2]. Furthermore, cells from a patient with an active cold sore, caused by an outbreak of a viral infection (herpes simplex), showed that the infection was persistent in the majority of cells, and caused a gradual change in the spectral patterns between normal cells and cells that were so compromised by the viral infection that they could be diagnosed visually. The majority of cells, however, which exhibited normal morphology, showed spectral patterns that were different from those of normal cells. A comparison of spectral patterns observed for premalignant changes and virally infected cells revealed that there exists a similar change in both (Figure 17.2).

Although these observations do not prove that the precancerous conditions observed in the oral cavity are caused by viruses, recent oncologic studies have implicated both the human papillomavirus (HPV) and the Epstein–Barr (EB) virus as possible causes of head and neck malignancies [23, 24]. Further evidence of SCP

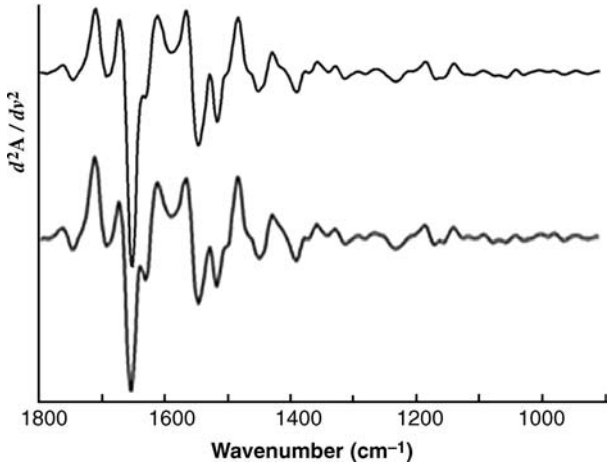

Figure 17.2 Second-derivative spectra of virally infected (top trace) and dysplastic (bottom trace) oral cells.

detecting viral infection (or their consequences) was recently described by preliminary cervical cancer screening efforts in the LSpD. These studies revealed that

- SCP can distinguish between normal [HPV(−)] and HPV-infected [HPV(+)] states.
- Cervical cell samples analyzed by SCP tend to follow the present or most recent HPV status.

Figure 17.3 shows a graphical representation of these two statements, displaying scores plots of cytologically normal cervical cells from HPV(+) samples (pale red) and HPV(−) samples (pale blue) from 10 subjects as a coarse indicator of the separability of these two states. The HPV status was established by DNA-based diagnostics, which detects oncogenic strains of HPV, including strains 16 and 18. Superimposed on this scores plot are samples with a normal cytologic and negative HPV result at the time of sample collection, but with recent histories of abnormal cytology. In Figure 17.3a, the sample had a history of ASCUS with a negative HPV result, and classified with the HPV(−) samples (pale blue). In Figure 17.3b, the sample had a history of HPV(+) ASCUS and LSIL, and classified with the HPV(+) samples (pale red). These results indicate that SCP has the sensitivity to detect the primary response to viral infection and also the effect of recent infection status.

In vivo Raman studies for cervical cancer screening [14, 25] have demonstrated very similar results, which were previously interpreted in terms of malignancy-associated changes (MACs) [26], a loosely defined term with usage similar to "field cancerization" [27], defined as follows: "Patients with a head and neck squamous cell carcinoma (HNSCC) often develop multiple (pre)malignant lesions. This finding led to the field cancerization theory, which hypothesizes that the entire epithelial surface of the upper aero-digestive tract has an increased risk for the development of (pre)malignant lesions because of multiple genetic abnormalities in the whole tissue

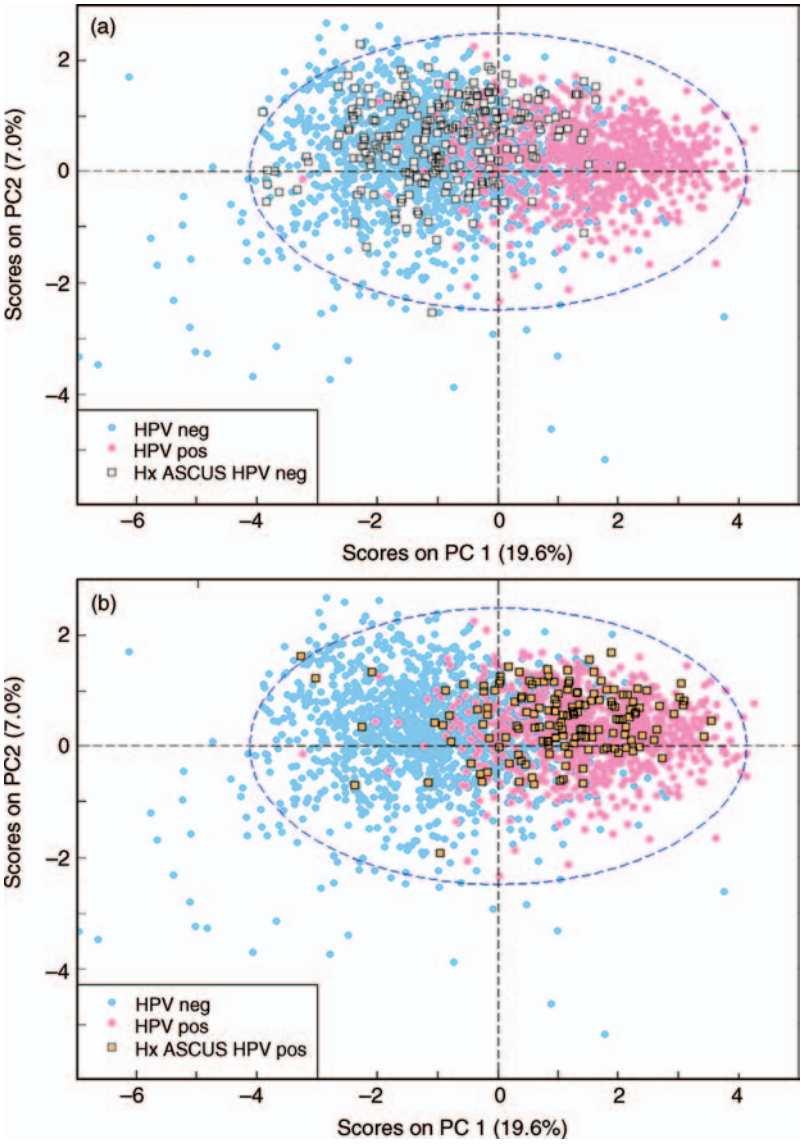

Figure 17.3 Scores plots of cervical cells diagnosed as HPV (−) (pale blue) and HPV (+) (pale red). Superimposed are the scores for an HPV(−) sample with a prior history of ASCUS (a), and a sample with a history of HPV(+), ASCUS, and LSIL (b).

region" [28]. Thus, both "field cancerization" and MACs describe very subtle cellular changes that help explain the occurrence of multiple lesions and the recurrence of HNSCC after treatment of a primary lesion. The results presented here suggest that these subtle morphologic changes could be due to persistent viral infections or their

effects. Normally, viral infections by the HPV or the EB virus are cleared within months by the immune system; however, in cases when the immune system is not able to fight the virus, genital warts or squamous cell cancers may result, as either a direct or indirect result of the viral infection. In addition, recent studies have shown that certain viruses (notably the human herpes virus 6 and 7) can insert their DNA permanently into the human genome; these viruses have been implicated in a number of diseases.

17.4 Conclusions

The results presented here suggest that methods of vibrational (i.e., infrared and Raman) spectroscopy can detect spectral changes that are induced in cells by viral infection. At this point, the nature of the actual spectral change is not understood, and could be due to the presence of the viral genome or the viral proteome, or to the immune response of the body. Recent studies from the LSpD have shown that precancerous and virally infected cells show the largest changes in spectral regions associated with protein vibrations [29], pointing to the detection of either the viral proteome or the immune response. Infrared spectral changes due to the latter case scenario, the immune response, have been observed in serum by Lasch *et al.* [30], manifested by a large variation in the protein composition of the serum.

Acknowledgements

Partial support of this research by grant 090346 from the National Cancer Institute of the National Institutes of Health is gratefully acknowledged.

References

1 Romeo, M., Mohlenhoff, B., Jennings, M., and Diem, M. (2006) Infrared microspectroscopic studies of epithelial cells. *Biochim. Biophys. Acta*, **1758** (7), 915–922.

2 Papamarkakis, K., Bird, B., Schubert, J.M., Miljković, M., Wein, R., Bedrossian, K., Laver, N. and Diem M., (2010) Cytopathology by Optical Methods: Spectral Cytopathology of the Oral Mucosa. *Lab. Invest.*, **90** (4), 589–598.

3 Schubert, J.M., Bird, B., Papamarkakis, K., Miljković, M., Bedrossian, K., Laver, N., and Diem, M. (2010) Spectral cytopathology of cervical samples: detecting cellular abnormalities in cytologically normal cells. *Lab. Invest.*, **90** (7), 1068–1077.

4 Krafft, C. and Salzer, R. (2008) Neuro-oncological Applications of Infrared and Raman Spectroscopy, in *Vibrational Spectroscopy for Medical Diagnosis* (eds Diem, M., Griffith, P. and Chalmer, J.), John Wiley & Sons, Chichester, UK, pp. 231–259.

5 Steller, W., Einenke, J., Horn, L.C., Braumann, U.D., Binder, H., Salzer, R. and Krafft C. (2006) Delimitation of a squamous cell cervical carcinoma using infrared microspectroscopic imaging. *Anal Bioanal Chem.*, **384**, 145–154.

6 Lasch, P., Haensch, W., Naumann, D. and Diem, M., (2004) Imaging of colorectal adenocarcinoma using FT-IR microspectroscopy and cluster analysis. *Biochim Biophys Acta*, **1688** (2), 176–186.

7 Lasch, P., Diem, M., Hänsch, W. and Naumann, D. (2007) Artificial Neural Networks as Supervised Techniques for FT-IR Microspectroscopic Imaging. *JChemometrics.*, **20** (5), 209–220.

8 Gazi, E., Baker, M., Dwyer, J., Lockyer, N.P., Gardner, P., Shanks, J.H., Reeve, R.S., Hart, C.A., Clarke, N.W. and Brown, M.D. (2006) A Correlation of FTIR Spectra Derived from Prostate Cancer Tissue with Gleason Grade, PSA and Tumour Stage. *European Urology*, 750–61.

9 Ly, E., Piot, O., Wolthuis, R., Durlach, A., Bernard, P. and Manfait, M. (2008) Combination of FTIR spectral imaging and chemometrics for tumour detection from paraffin-embedded biopsies. *Analyst*, **133**, 197–205.

10 Wolthuis, R., Travo, A., Nicolet, C., Neuville, A., Gaub, M.-P., Guenot, D., Ly, E., Manfait, M., Jeannesson, P. and Piot, O. (2008) IR Spectral Imaging for Histopathological Characterization of Xenografted Human Colon Carcinomas. *Anal Chem.*, **80**, 8461–8469.

11 Romeo, M., Boydston-White, S., Matthäus, C., Miljkoviać, M., Bird, B., Chernenko, T., Diem M. (2008) Vibrational Microspectroscopy of Cells and Tissues, in *Biomedical Vibrational Spectroscopy* (eds P. Lasch and J. Kneipp), Wiley-Interscience, Hoboken, NJ, pp. 121–152.

12 Boydston-White, S., Romeo, M.J., Chernenko, T., Regina, A., Miljkovic, M., and Diem, M. (2006) Cell-cycle-dependent variations in FTIR micro-spectra of single proliferating HeLa cells: principal component and artificial neural network analysis. *Biochim. Biophys. Acta*, **1758** (7), 908–914.

13 Krishna, C.M., Kegelaer, G., Adt, I., Rubin, S., Kartha, V.B., Manfait, M., and Sockalingum, G.D. (2006) Combined FT-IR and Raman spectroscopic approach for identification of multidrug resistance phenotype in cancer cell lines. *Biopolymers*, **85** (5), 462–470.

14 Utzinger, U., Heintzelmann, D.L., Mahadevan-Jansen, A., Malpica, A., Follen, M., and Richards-Kortum, R. (2001) Near IR Raman Spectroscopy for in vivo detection of cervical precancers. *Appl. Spectroscopy*, **55** (8), 955–959.

15 Ronco, G., Segnan N., Giorgi-Rossi P., Zappa M., Casadei G.P., Carozzi F., Palma, P. D., Del Mistro, A., Folicaldi, S., Gillio-Tos, A., Nardo, G., Naldoni, C., Schincaglia, P., Zorzi, M.l., Confortini, M. and Cuzick, J. (2006) Human Papillomavirus Testing and Liquid-Based Cytology: Results at Recruitment From the New Technologies for Cervical Cancer Randomized Controlled Trial. *J. Natn Cancer Inst.*, **98** (11), 765–774.

16 Schubert, J.M., Mazur, A.I., Bird, B., Miljković, M. and Diem, M. (2010) Single Point vs. Mapping Approach for Spectral Cytopathology (SCP). *Biophotonics*, **3** (8–9), 588–596.

17 Kohler, A., Sule-Sosa, J., Sockalingum, G.D., Tobin, M., BahramiI, F., Yang, Y., Pijanka J., Dumas, P., Cotte, M., van Pittius, D.G., Parkes, G. and Martens, H. (2008) Estimating and Correcting Mie Scattering in Synchrotron-Based Microscopic Fourier Transform Infrared Spectra by Extended Multiplicative Signal Correction. *Appl. Spectroscopy*, **62** (3), 259–266.

18 Kohler, A., Kirschner, C., Oust, A. and Martens, H. (2005) Extended Multiplicative Signal Correction as a Tool for Separation and Characterization of Physical and Chemical Information in Fourier Transform Infrared Microscopy Images of Cryo-sections of Beef Loin. *Appl. Spectroscopy*, **59** (6), 707–716.

19 Bassan, P., Byrne, H.J., Bonnier, F., Lee, J., Dumas, P. and Gardner, P. (2009) Resonant Mie scattering in infrared spectroscopy of biological materials – understanding the 'dispersion artefact'. *Analyst*, **134**, 1586–1593.

20 Bassan, P., Byrne, H.J., Lee, J., Bonnier, F., Clarke, C., Dumas, P., Gazi, E., Brown, M.D, Clarke, N.W. and Gardner, P. (2009) Reflection contributions to the dispersion artefact in FTIR spectra of single biological cells. *Analyst*, **134**, 1171–1175.

21 Bassan, P., Kohler, A., Martens, H., Lee, J., Byrne, H.J., Dumas, P., Gazi, E., Brown, M., Clarke N. and Gardner, P. (2010) Resonant Mie Scattering (RMieS) correction of infrared spectra from highly scattering biological samples. *Analyst*, **135**, 268–277.

22 Adams, M.J. (2004) *Chemometrics in Analytical Spectroscopy*, 2nd edn., RSC Analytical Spectroscopy Monographs (series ed. N.W. Barnett), Royal Society of Chemistry, Cambridge.

23 Sugerman, P.B. and Shillitoe, E.J. (1997) The high risk human papillomaviruses and oral cancer: evidence for and against a causal relationship. *Oral Dis.*, **3**, 130–147.

24 Porter, S. and Waugh, A. (2000) Comment on: oral cancer in young adults. *Br. Dent. J.*, **188** (7), 366.

25 Robichaux-Viehoefer, A., Kanter E., Shappell, H., Billheimer, D., Jones III, H. and Mahadevan-Jansen, A. (2007) Characterization of Raman Spectra Measured in Vivo for the Detection of Cervical Dysplasia. *Appl. Spectroscopy*, **61** (9), 986–993.

26 Ogden, G.R., Cowpe, J.G., and Green, M.W. (1990) The effect of distant malignancy upon quantitative cytologic assessment of normal oral mucosa. *Cancer*, **65**, 477–480.

27 Ha, P.K. and Califano, J.A. (2003) The molecular biology of mucosal field cancerization of the head and neck. *Crit. Rev. Oral Biol. Med.*, **14** (5), 363–369.

28 van Oijen, M.G.C.T. and Slootweg, P.J. (2000) Oral field cancerization: carcinogen-induced independent events or micrometastatic deposits? *Cancer Epidemiol. Biomarkers Prev.*, **9**, 249–256.

29 Diem, M., Papamarkakis, K., Schubert, J.M., Bird, B., Romeo, M.J. and Miljković, M. (2009) The Infrared Spectral Signatures of Disease: Extracting the Distinguishing Spectral Features between Normal and Diseased States. *Appl. Spectroscopy*, **63** (11), 307A–318A.

30 Lasch, P., Beekes, M., Fabian, H. and Naumann D. (2008) Antemortem Identification of Transmissible Spongiform Encephalopathy (TSE) from Serum by Mid-infrared Spectroscopy, in *Vibrational Spectroscopy for Medical Diagnosis* (eds Diem, M., Griffith, P. and Chalmer, J.) John Wiley & Sons, Chichester, UK, pp. 97–122.

18
Clinical and Technical Aspects of Photodynamic Therapy – Superficial and Interstitial Illumination in Skin and Prostate Cancer

Katarina Svanberg, Niels Bendsoe, Sune Svanberg, and Stefan Andersson-Engels

18.1
Background – Cancer and Its Treatment

Worldwide, in almost all countries, the incidence of malignant tumor disease is growing. In developed countries, approximately every third person is diagnosed throughout his/her lifespan with one or more malignancies. With an aging population this figure is growing, as age is the paramount factor for presentation with a malignant tumor. Considering these facts, cancer is defined as one of the world's endemic diseases and the second highest killer in Western countries, out-numbered only by deaths due to heart and vascular diseases. Historically, the evidence for neoplasias of various kinds was described in Indian and Chinese scriptures and Egyptian papyrus rolls as early as 2000 BC. Also, in very old artwork, neoplasias can also be recognized in mummies from both the Old and New World. Already at that time treatment modalities were presented, such as burning sticks, herbal decoctions, and ointments. Surgery was the dominant treatment option until the beginning of the twentieth century, when ionizing radiation was discovered and introduced as another treatment modality. Interestingly, the inventor of ionizing radiation, Konrad Röntgen, became the first Nobel Laureate in 1901, motivated by his paper "Eine neue Art von Strahlen" [1], which was published in 1896. Just a few years later this new treatment modality was introduced in specialized hospitals in Germany, the United Kingdom, and France, and international conferences within this new field were organized and fascinating results presented.

18.2
Phototherapy

Ionizing radiation and also phototherapy (PT) and photochemotherapy (PCT) are treatment modalities within the group of therapies related to physical phenomena arising from the interaction of electromagnetic irradiation with biological tissue. In this chapter, we consider electromagnetic radiation within the visible range, that is, light. PT and PCT differ in the conceptual meaning, namely in PCT a photosensitizing

Handbook of Biophotonics. Vol.2: Photonics for Health Care, First Edition. Edited by Jürgen Popp, Valery V. Tuchin, Arthur Chiou, and Stefan Heinemann.

agent is administered before the light exposure. Both therapies rely on a long tradition and date back to the Greeks, who practiced full-body sun exposure, later termed heliotherapy. A pioneer within the more modern clinical use of PT was Niels Finsen, who was also awarded the Nobel Prize for his discoveries using light in the treatment of cutaneous tuberculosis [2]. Finsen is often referred to as the founder of modern PT, a field which is still very relevant for dermatologic applications, such as for psoriasis and certain other types of dermatitis. Another example of PT is the treatment of juvenile jaundice utilizing UV light. Many mothers have met this type of PT when their newborn babies have been immunized with their own blood, causing a yellowish skin as a sign of jaundice [3]. Historically, these babies were placed in the window niche at the hospital for exposure to sunlight, nowadays more often under a UV lamp. This is the same type of UV lamp that has been used during many years for the diagnosis of cutaneous tinea, and also for the identification of false banknotes and antibacterial effects in laboratories, and in public toilets for camouflaging veins to prevent drug addict injections. A new and interesting field of PT is in psychiatry, where encouraging results have been achieved in the treatment of a particular type of depression called "seasonal affective disorder," as it appears more frequently during the dark season in Nordic countries, where daylight is restricted or absent during the autumn and winter periods [4]. The effect on depression is partly ascribed to a subsequent upgrading of the serotonin levels in the brain receptor transmitting system after light illumination [5].

Already more than 5000 years ago during the Egyptian dynasties and in ancient India, the first known examples of PCT in humans were reported when psoralen plants were used as sensitizing agents in combination with sunlight for the treatment of vitiligo (white/hypopigmented spots in the skin).

The term photodynamic therapy (PDT) refers to a variety of PCT when oxygen must be present in the tissue. There is a resemblance between PDT and photosynthesis of green plants, in which oxygen also is a prerequisite together with a ring-structured light-absorbing molecule, chlorophyll, although photosynthesis leads to build-up of organic material in contrast to tissue destruction in the case of PDT. PDT is a local treatment modality with the potential of being selective due to the tumor-preferred retention of the administered sensitizing agent. The first to demonstrate PDT action was the medical student Oscar Raab in 1898, when he showed the toxic action of acridine on paramecia (a unicellular microorganism) in conjunction with ambient light [6]. He worked in the laboratory of Herman von Tappenier in Munich, who reported in 1904 that the process that Raab had described was dependent on oxygen. Raab was the first scientist to coin the term *photodynamic therapy* to describe the phenomenon of oxygen-dependent photosensitization [7]. Subsequently, von Tappenier performed PDT on humans with skin cancer, cutaneous lupus erythematosis (a rheumatic and inflammatory disease), and genital condylomas (virus-induced warts) using eosin as a photosensitizing agent. Hence he was the first to introduce clinical PDT in modern times. The next step in PDT development occurred in 1908, when the physical properties of the sensitizer hematoporphyrin derivative (HpD) were described. The biological activity of the agent was shown a few years later in 1913 when a German physician, F. Meyer-Betz, injected himself with 200 mg of

HpD. He remained photosensitized for ambient light for 2 months and photographs of him show the typical edema occurring on the sun-exposed areas of his face and on the dorsal part of his hands [8]. The Meyer-Betz sensitization signs are similar to those shown by patients suffering from the inherited disorder porphyria, due to a deficiency of certain enzymes in the heme biosynthetic pathway. These patients accumulate various porphyrins and their precursors in the skin, and thus show the same type of skin sensitization. The anecdote about the mythological creatures called vampires, who were afraid of light as they were sensitized, had long teeth as the light destroyed the soft tissue, and were thirsting for people's blood due to anemia, seems to reflect the classical symptoms of porphyria disease. The term porphyrin comes from the Greek word *purphura*, which means purple pigment and refers to the fact that these patients excrete purple/brown urine. The selective retention of endogenous porphyrins in tumor tissue was first observed in Lyon, France, by Policard in 1924 using a Wood's lamp with UV light exciting fluorescence emission. The selective retention of HpD with fluorescence emission in tumor tissue was demonstrated in 1948 by Figge and Weiland [9, 10]. The modern era of PDT utilizing HpD was initiated in 1960 by Lipson and Baldes in the treatment of breast cancer [11], followed up by Bonnett *et al*. [12], who made a mixture of oligomeric porphyrins. Thomas Dougherty improved the porphyrin mixture mainly by linking it with ester and ether bridges and researched the potential of the PDT technique. Dougherty was instrumental in taking the treatment modality into clinical use [13]. Many review papers on PDT have now published; see, for example, [14–16]. In this chapter, we aim to provide clinical and technical perspectives of PDT and compare challenges in superficial and interstitial light administration.

18.3 Phototoxicity

PDT action relies on three components required in order to cause phototoxicity in targets such as tumors (Figure 18.1). These components are:

- **Photosensitizer (PS)**: A PS or a pro-drug to a PS that is administered (systemically or locally) to the subject. During a certain time interval, the PS is preferentially accumulated to a higher degree in the malignant than the normal surrounding tissue. The role of the PS is to capture/absorb the energy of a light photon and then transfer it to another molecule (the substrate or the tissue oxygen), resulting in tissue toxicity causing necrosis and apoptosis directly or by stimulating the immune system.
- **Light**: Light of an appropriate wavelength matching the peak in the absorption spectrum of the PS is required. Some PS agents have more than one absorption peak (usually in the blue–green and also in the red wavelength region). The depth of light treatment differs with wavelength and is increased in the red part of the spectrum, which is preferably used for deeper PDT action. Only for very thin lesions (less than 1 mm in depth) does blue–green light have therapeutic value.

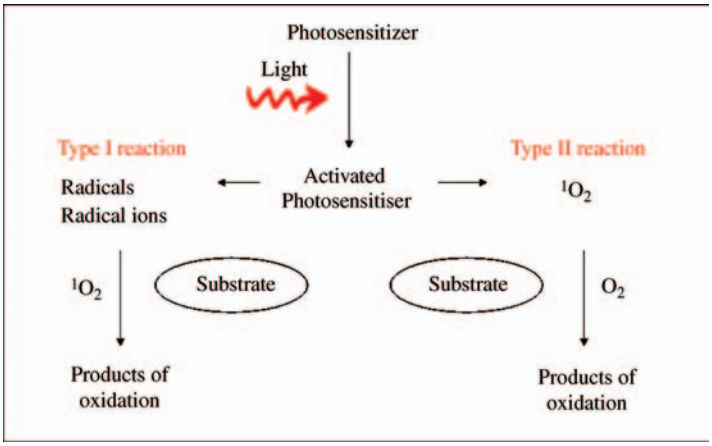

Figure 18.1 The three components of importance for photodynamic therapy: photosensitizer, light and molecular oxygen.

- **Oxygen**: The substrate in the PDT process is the oxygen in the tissue. The oxygen molecule accepts the excess energy gained in the light excitation of the PS. The excited substrate, singlet oxygen, causes chemical destruction of the tumor cells that involves oxidation.

The PDT process is illustrated in Figure 18.2. As light of an appropriate wavelength is sent towards (superficial illumination) or into (interstitially through optical fibers) PS-sensitized tissue, excitation of the PS molecule occurs. Thus, the PS molecule has

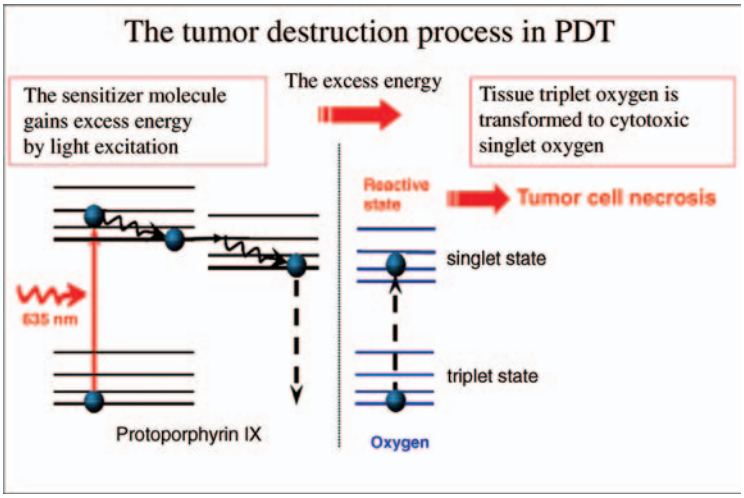

Figure 18.2 The molecular interactions in PDT for the case of protoporphyrin IX as a photosensitizing substance.

gained excess energy. However, as a general phenomenon in nature, nothing remains in an elevated energy level and the excess energy is transferred to the tissue oxygen, which normally resides in a triplet ground state. Cytotoxic singlet oxygen is generated and the PDT action occurs. The phototoxicity in PDT is either a direct momentarily appearing cell kill with breakage of the cell membranes, or a secondary effect after some days or weeks inducing damage to the vascular system or causing necrosis and apoptosis in the cells due to the involvement of the immune system. The action on the cell membrane is explained by the fact that some of the PSs are oligomers and thus lipophilic, and therefore attach to the cell membrane. In a second round, the lipophilic oligomers are split into hydrophilic monomers, which can easily pass through the membrane into the inner part of the cells. There they are mainly attached to the mitochondria or the lysosomes. The intracellular effect is then an action on the respiration of the cell [17–19].

18.4 Photodynamic Procedure

As a principle for cancer treatment, PDT is fairly simple. There are, however, certain important parameters that have to be taken into account for optimizing the therapy results. Examples of these parameters are:

- selection of the PS and mode of administration (local or systemic)
- drug dose for that particular tumor type (percentage of PS or mg/kg body weight)
- time interval between PS administration and light delivery (minutes to days)
- total light dose or light energy delivered (J/cm^{-2})
- light dose rate (W/cm^{-2}) and dose ($s \times W/cm^{-2} = J/cm^{-2}$)
- light fractionation (continuous or intermittent illumination)
- light wavelength (adjusted for the PS absorption property)
- mode of light administration (superficial, interstitial)
- light source (light-emitting diode (LED) or fiber-transmitted laser light).

18.5 Photosensitizers

An optimal photosensitizer for PDT should fulfill certain criteria, namely:

- nontoxic in the absence of light (no “dark” PDT effect)
- high efficiency in absorbing light energy and in transferring it to the substrate (tissue oxygen)
- able to absorb light at “longer” wavelengths, preferably above 600 nm for increased depth of the light penetration
- accumulated preferentially within tumors (high contrast between tumor and normal tissue)
- cleared rapidly from the normal surrounding tissue and organs at risk.

Table 18.1 List of photosensitizers with the major absorption peaks in the red part of the spectrum (names in square brackets are the commercial trade names).

Photosensitizer	Absorption peak wavelength (nm)
Hematoporphyrin derivative (HpD) [Photofrin]	630
δ-Aminolevulinic acid (ALA) [Metvix, Levulan]	635
meso-Tetra(hydroxyphenyl)chlorin (mTHPC) [Foscan]	652
Tin etiopurpurin [Pyrlytin]	660
Benzoporphyrin derivative (BPD) [Verteporfin, Visudyne]	690
Phthalocyanine	720
Lutetium texaphyrin [Lutrin]	732
Bacteriochlorophyll [Tookad]	760

Most probably there is no single sensitizer that fulfills the criteria for being the optimal PS. Different tumors will require specific capabilities of the PSs and substantial efforts have been devoted to developing ideal sensitizers. HpD has been described as belonging to the first generation of PSs and the others in the list above to the second generation.

Sensitizers and the red absorption wavelengths used are listed in Table 18.1. One of the agents in the table differs from the others as it is a precursor to a PS, namely δ-aminolevulinic acid (ALA), which is converted into an active PS following the heme cycle in the cells. All the other PSs are preformed chemical substances. If the wavelengths are translated into corresponding light penetration in the tissue, the depth at which light is attenuated to 37% (1/e) of its initial value, this means approximately a doubling from 630 to 720 nm and in terms of millimeters it corresponds to a change from about 3 to about 6 mm. Thin tumors can be treated efficiently with all these PSs using superficial illumination. Deeper tumors and tumors embedded in the body have to be treated with a different light administration mode – the interstitial mode, with the light transmitted through optical fibers inserted into the tumor mass.

There is a certain preferred time interval between the administration of a PS and the light illumination, and this time span varies from only minutes to days depending on which PS is used. One of the newer PSs, a bacteriochlorophyll (Tookad), exerts its action mainly on the endothelial cells in the vessels and therefore the illumination starts at the same time as the PS is injected. For skin cancer, an important discovery was reported when it was shown that topical application of (ALA) could be used to kill skin cancer and precancer cells [20–22]. In this way, it is possible to avoid one of the undesirable side effects with systemically administered PS, namely that in addition to sensitizing the tumor cells, the PS usually also causes light sensitivity in the skin over a certain time period. Most probably this has delayed the clinical acceptance to introduce PDT, as the patients have to be shielded from strong ambient light for several weeks when administering some of the PSs. However, it should be mentioned that drug-induced photosensitivity also occurs with many other pharmaceutical

agents given to patients in daily practice, including some antibiotics (tetracyclines and sulfonamides), nonsteroidal anti-inflammatory drugs (e.g., naproxen, ketoprofen, and ibuprofen), diuretics (hydrochlorothiazide), and some neuroleptics. The use of some fragrances (e.g., musk perfume) and aspirin can also cause some skin sensitivity. The clinically reversible effects of these drugs and substances are similar to those of systemically administered PSs, with a dry bumpy or blistering rash on the skin.

There are several important physical parameters to take into account concerning the light illumination of PS-sensitized tissue. Most PSs exhibit several light absorption peaks. Usually the peak in the UV or blue part of the spectrum, (e.g., the Soret bands of porphyrins) has a higher amplitude. On the other hand, for therapy of tumors, red absorption is usually chosen owing to the deeper penetration of the activation light compared with UV or blue light.

18.5.1
Laser-Induced Fluorescence for Tumor Detection

The gold standard for diagnosis of a disease is histopathologic investigation of biopsy samples. This procedure is costly and time consuming as the tissue sample has to be fixed, cut, and stained. This conventional technique might be complemented by optical detection with the advantage of giving a diagnosis in real time. The technique is referred to as laser-induced fluorescence (LIF) and two different geometries can be utilized, either point monitoring with the recording of the full spectrum in a single point or an imaging mode over the whole area with a single or a few wavelength bands. The fluorescence excited from the endogenous chromophores is called the autofluorescence. The technique has shown great potential for use in early tumor detection and visualization of shallow lesions.

Blue or UV light is used for the fluorescence excitation. The autofluorescence is broadbanded as it is a composite of various chromophores, such as collagen, elastin, the coenzymes NADH/NAD^+, and others, as shown in Figure 18.3. The composite of the tissue endogenous chromophores differs depending on whether it is normal or malignant tissue and the fluorescence emission varies and can be used for tissue characterization. The endogenous fluorescence emission shows a drastic decrease in intensity in the tumor tissue and is usually also red shifted.

LIF can also be used to localize dysplasia and early cancer before it is possible to identify the affected areas with the naked eye. As an example, the detection of a carcinoma *in situ* in the cervical area in a young woman is shown in Figure 18.4. The five spectra with high-intensity peaking at about 410 nm were all recorded from the squamous and transformation zone of the cervical portio. The fifth spectrum shows a clear decrease in intensity and at the same time a red wavelength shift of approximately 60 nm. In this case, LIF guided the gynecologist to the right location for biopsy sampling and the histopathology showed noninvasive carcinoma of the cervix [23]. On visual inspection no sign of the early cancer was seen. The fluorescence signal corresponds to the early biochemical changes in the tissue. In the transformation process from normal to dysplasia, this status changes earlier than the

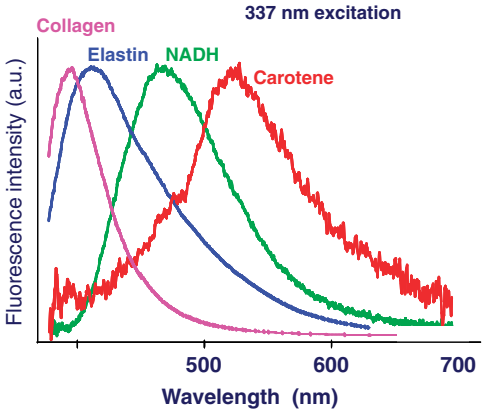

Figure 18.3 Autofluorescence emission spectra from the most important endogenous fluorophores in the tissue excited at 337 nm with a pulsed nitrogen laser. As can be seen, the autofluorescence is broadbanded as it is a composite of different chromophores with the maximum emission at about 470 nm.

cell architecture, which is observed with the naked eye. Therefore, there is a possibility to discover early cancer and precancer by using LIF and thus improve the prognosis for the patient.

As there is a certain preference in uptake of the sensitizers in cancerous and precancer tissue, the fluorescence signal in the red part of the spectrum from these

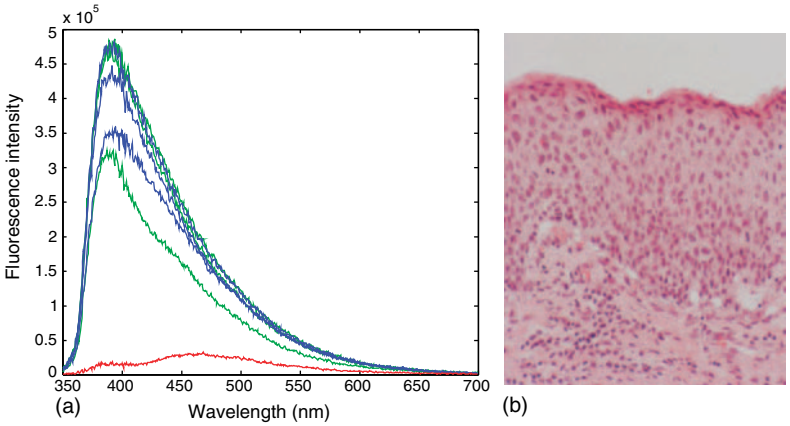

Figure 18.4 (a) Autofluorescence spectra recorded *in vivo* from a patient during an investigation of the cervical area. The fluorescence spectra with overall high intensity represent normal squamous epithelium while the spectrum with the low intensity was recorded from a spot of cancer *in situ* on the portio. In addition to showing a very low signal, the spectrum is shifted towards the red part of the spectrum, both being characteristic of precancer or cancer. (b) The corresponding histopathology from the suspicious area, verifying carcinoma *in situ*.

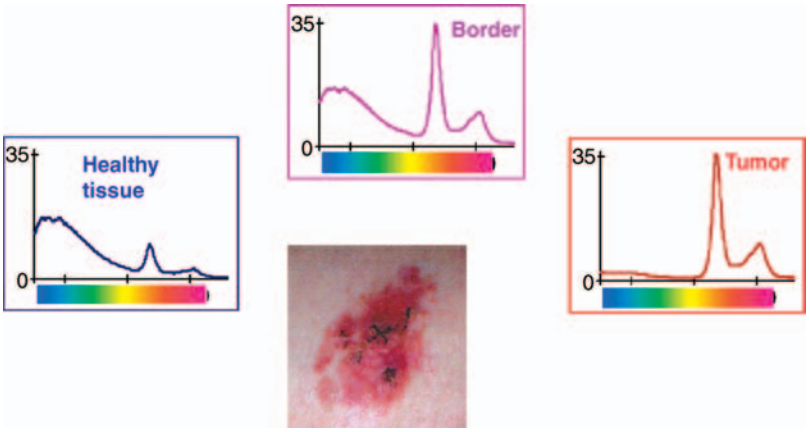

Figure 18.5 Fluorescence spectra from a basal cell carcinoma and the surrounding normal skin. The whole area was topically sensitized with ALA, which induced the protoporphyrin IX, which has an intense emission at about 635 nm. The spectrum from the normal skin shows a weak emission in the red part of the spectrum and a high intensity in the blue–green region. The tumor and the tumor border are characterized by low autofluorescence and high intensity corresponding to the PpIX peak.

agents can be used for enhanced tumor detection and delineation. Three LIF spectra recorded from healthy surrounding skin, tumor border, and tumor center are shown in Figure 18.5. Two main features can be recognized. The autofluorescence shows a decreased signal for the tumor. At the same time, the signal from the ALA-induced protoporphyrin at ~635 nm shows high values for the border and the tumor. If the signal at 635 nm is divided by the signal at 470 nm, a clear demarcation ratio is formed and the tumor including the border is delineated.

The ultimate goal would be to combine LIF and PDT for better tumor target identification. The white light endoscopic image and the processed fluorescence image of the vocal cords are shown in Figure 18.6. The fluorescence image marks out the tumor area on the vocal cord all the way to the commissure between the two folds. The fiber transmits the red PDT light to the tumor area and the PDT treatment is performed guided by the fluorescence image.

18.6 Light Sources

Lasers with monochromatic light emission have been the natural choice for PDT. However, before realistic diode lasers became available, the systems were complicated and required strong support from collaborating physicists. The first lasers in PDT were the Au and Cu vapor lasers and argon ion pumped dye lasers emitting in the red spectral region. Another possibility emerged with the frequency-doubled neodymium:yttrium–aluminum–garnet (Nd:YAG) laser, emitting at 532 nm and

Figure 18.6 A photograph from the operating room at the ENT department at Lund University Hospital, where a patient is being treated with PDT. The white light image and the fluorescence image of the vocal cords were recorded in the pretreatment planning (inset). The tumor is marked out by the fluorescence image and the PDT procedure is guided to the target by the LIF image.

pumping a dye laser. Solid-state diode lasers were introduced in the clinic in the late 1990s. The advantage of lasers in PDT is the possibility of transmitting the light through optical fibers and thus opening up the option of treating tumors in hollow organs, such as the urinary bladder, bronchus, intestine, and esophagus. For superficial illumination, such as for skin, the female gynecologic tract, and the oral cavity, an array of LEDs can fulfill the task. As the PSs do not show very narrow absorption features, the LED with a bandwidth of ~20 nm is advantageous as a treatment light source for superficial PDT. For interstitial PDT, lasers are convenient sources, as the output light can be coupled efficiently to optical fibers for guiding it to the target tissue.

18.7
Photodynamic Therapy as a Clinical Procedure

The most attractive feature of PDT as a local treatment modality is the selective action, causing minor damage to normal adjacent tissue with less scar formation than with alternative treatments. In particular in relation to ionizing radiation, PDT does not cause any DNA damage with the risk of developing secondary malignancies. PDT is characterized by:

- selective action for sensitized cancer/precancer tissue
- possibility of being repeated (in contrast to ionizing radiation)
- no accumulated toxicity
- fast healing with minimal scar formation and good cosmetics
- retained organ function.

18.8
Superficial PDT in Skin Lesions

The most common malignancy in the Western world is skin cancer and the diagnosis and treatment impose huge costs on the healthcare system. Also, the incidence of skin cancer is continuously increasing (10% per year) for several reasons, such as more leisure time with increased sun/UV exposure, an aging population, and for younger persons increased sunbed use. All classical skin cancers, such as basal cell carcinoma (BCC), squamous cell carcinoma (SqCC), and malignant melanoma are related to sun exposure. Also some of the precancerous skin lesions, such as actinic keratosis (AK) and Mb Bowen (SqCC *in situ*) are caused by UV light exposure.

Statistics for Sweden, with a population of approximately 9 million, show that the cost of skin tumor removal amounts to 125 000 000 Euro per year [24]. The corresponding cost for Germany, for example, is 1000 000 000 Euro per year. As there are several treatment options for skin malignancies, such as surgery, cryosurgery, ionizing radiation, and topical cytotoxic drugs, a careful judgment has to be made regarding treatment decisions.

Even though it is a very common disease, the diagnosis of some kinds of skin malignancy is still uncertain and many benign lesions are unnecessarily surgically removed. A clinical estimate shows that approximately nine out of ten removed lesions are benign [25]. Therefore, LIF or other optical detection modalities should be further developed for more convenient and safe diagnosis.

There are several benign, premalignant, and malignant lesions of the skin which are suitable for PDT according to the list below:

Benign lesions

- psoriatic lesions
- acne vulgaris

- verucca vulgaris
- lichen ruber (mucosal).

Potentially malignant lesions

- actinic keratosis
- Mb Bowen (SqCC *in situ*)
- cutaneous lymphoma.

Malignant lesions

- BCC
- SqCC
- Mb Paget
- extramammary Mb Paget (adenocarcinoma *in situ*).

Malignant melanoma is the only primary skin malignancy which is currently not a candidate for PDT. This tumor type has to be surgically removed as soon as possible for extensive histopathologic examination for continued handling and prognostic evaluation. All the other types of skin malignancies can be considered for PDT. A single treatment session is usually sufficient for thin tumors with a thickness of up to 3 mm. Thicker tumors can be retreated after follow-up, or be pretreated with, for example, curettage, which means that some tumor tissue is removed mechanically and PDT is performed to the bottom of the tumor.

PDT has an important role in certain types of skin malignancies, such as:

- in elderly patients
- large tumors (diameter >3 cm)
- multiple tumor locations
- sensitive locations (pretibial, periocular, outer ear)
- recurrent tumors
- earlier radiation treatment
- high need for good cosmetics (face, thoracic wall).

When PDT was introduced clinically, the PS was administered systemically also for skin malignancies [26–29]. As mentioned, an unwanted side effect of systemically applied PS is skin sensitization for a certain period (varying from hours to months) depending of the type of PS given. When topical application of ALA was introduced, PDT for skin malignancies took a large leap forward and a new era within superficial PDT began. ALA is a naturally occurring five-carbon molecule and a straight-chain amino acid. It can easily be dissolved in water and thus mixed in water-based creams for topical use. ALA is the first step in heme synthesis in human cells and given to the organism it enters the endogenous heme cycle in the cells. In this cycle, through many enzymatically driven steps, protoporphyrin IX (Pp IX) is formed, which is a very potent PS. There is a transient build-up in the amount of PpIX in malignant cells due to lower levels of the enzyme ferrochelatase, which transfers PpIX to heme. The process can be followed by LIF, and thus the optimal time window when the contrast normal/tumor ratio is high can be chosen. LIF can also be used for tumor delineation with target definition to increase the treatment radicality.

Figure 18.7 A squamous cell carcinoma *in situ* located on the finger before and after PDT utilizing topical ALA as a sensitizing agent. This tumor location is well suited for PDT as the conventional techniques, such as surgery and ionizing radiation, would not be preferred treatment modalities.

The clinical application of ALA was recognized by Kennedy *et al.*, who showed that ALA–PDT was an efficient treatment for human skin cancer, with the first result being presented in 1990 [21]. In 1991, the Lund group began clinical application of ALA–PDT for skin tumors and via clinical phase III studies introduced the treatment as a clinical routine modality for certain skin malignancies [30, 31]. Two clinical examples of ALA-induced PDT are shown in Figures 18.7 and 18.8. Both tumor locations are interesting for PDT as conventional modalities, such as surgery and ionizing radiation, would not be optimal in any of these cases. The tumors are shown before the ALA–PDT procedures and 3 months post-treatment. The tumor remission results are equal to those with other treatment modalities with a cure rate of ~85% and better cosmetic results compared with other methods [31]. The only modality that shows a lower recurrence rate is Moh's surgery, which is an interactive, time-consuming approach, often with very large areas of tissue being removed.

The light dose used for ALA–PDT of skin malignancies is typically 40–60 J/cm^{-2}. The fluence rate is usually kept below 150 mW/cm^{-2} in order not to heat the tissue. If higher fluence rates are applied, hyperthermic effects may occur, affecting the result of the PDT action with fibrosis induction, organ dysfunction with loss of tissue elasticity, and impaired cosmetic results [32].

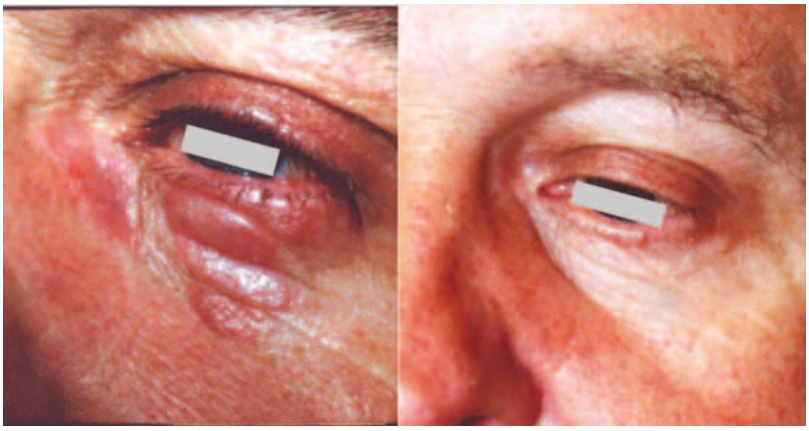

Figure 18.8 A cutaneous T-cell lymphoma tumor located below the margo border of the eye shown before and after ALA–PDT. The patient had gone through six cycles of cytotoxic treatment and had a remaining cutaneous tumor which was resistant to the systemic therapy.

18.9
Interstitial PDT for Prostate Cancer

Prostate cancer is the second most common malignant tumor in men, only outnumbered by skin cancer, and is strongly correlated with age. Prostate cancer is diagnosed based on the occurrence of urologic symptoms and an increased value of the prostate-specific antigen (PSA), which is over-expressed in prostate cancer. An elevated PSA value is a diagnostic indicator of a potential problem but can also be related to benign disorders, such as prostatitis or benign hyperplasia of the gland.

The treatment modality is chosen based on the stage and histopathology of the prostate cancer. For localized tumors, the preferred treatment is surgical prostatectomy. External or internal ionizing radiation is also considered. Hormone therapy is only used in more advanced disease or as a pretreatment to surgery in order to shrink the tumor size. Brachytherapy is administered by the insertion of trocars and sealed needles containing iridium-192 (high dose rate brachytherapy) for a short period (5–15 min), or by permanent implantation of ionizing iodine-125 or palladium-103 seeds (low dose rate brachytherapy). These conventional treatment modalities are all associated with undesired side effects such as urine incontinence, erectile dysfunction, and rectal wall damage with bleeding. These drawbacks open the way for alternative treatment modalities, such as interstitial PDT and the need for individualized dosimetry and treatment control.

Several groups, including our group in Lund, have been developing interstitial PDT to allow treatment of thicker and/or deeply located tumors. When light is delivered into the tissue by optical fibers, the light will be very intense close to the source and the fluence rate will decrease rapidly with distance from the optical fiber. This is one of the reasons why interactive online dosimetry is crucial in interstitial PDT as compared with surface illumination with a wide illumination field. Another

reason is that organs at risk (in prostate cancer the sphincters, the venous/nerve plexus in the capsule, and the rectal wall) are located in the vicinity of the target tumor.

PDT of the prostate was first reported in 1990 by Windahl *et al.*, who successfully treated two patients with localized tumors using Photofrin (porfimer sodium) [33]. It took more than a decade before other groups followed this initial attempt and investigated the safety and feasibility of using ALA-induced PpIX for PDT of prostate cancer [34].

Despite ALA being an interesting candidate as a PS for PDT of malignant tumors, more potent PSs with absorption further towards the infrared region with better light penetration are of interest as the whole prostate gland has to be eradicated in prostate cancer therapy. This is a reason for investigating other PSs, such as *meso*-tetra (hydroxyphenyl)chlorin (mTHPC, FOSCAN, temoporfin) with an activation wavelength at 652 nm as reported by Nathan *et al.* at University College London [35] in patients with local recurrence after radiotherapy. This drug is attractive due to the slightly longer activation wavelength compared with Photofrin and ALA, and also to the higher efficiency of production of toxic reactive oxygen radicals. The same group applied mTHPC–PDT to untreated local prostate cancer in six patients [36]. The outcome was assessed by MRI examinations after the treatment. The treated prostate glands in some patients exhibited distinct features of devascularization, potentially indicating necrosis. The MRI images from some other patients showed patchy areas with reduced contrast uptake, indicating mild tumor response to the treatment. The volume of the prostate increased by ~30% during the first week after treatment. This was interpreted as being caused by induced edema and inflammation. By 2–3 weeks post-treatment, the volume had decreased to ~30% of the baseline volume. Reported complications following PDT were irritation of the urethra, which was cleared in all cases after 4 months. None of these patients needed a urinary catheter, which is common with other treatments.

Another PS investigated for prostate cancer treatment is Lutrin (lutetium texaphyrin), which was administered to patients with localized recurrent prostate cancer after radiotherapy in a trial at University of Pennsylvania [37, 38]. The primary goal of this trial was to assess the maximally tolerated dose of Lutrin–PDT. The drug–light interval between drug administration and the commencement of treatment varied between 3 and 24 h. Several properties, including measurements of the optical properties of the prostate gland [39], fluorescence spectroscopy of the PS [40], and spectroscopic assessment of tissue oxygenation [41], were investigated. Translatable spherical isotropic fiber-optic light diffusers were used for direct measurements of the light fluence rate. The optical measurements performed before, during, and after treatment all indicated substantial heterogeneity of the optical properties of the prostate and accumulation of the PS. The results also indicated that the tissue oxygenation was relatively constant in each patient, but that the total hemoglobin concentration decreased during treatment. The conclusion of the study was that Lutrin–PDT is an attractive alternative to conventional prostate cancer therapy even taking into account the mild, transient complications. Furthermore, the optical heterogeneity of the prostate gland must be considered to ensure correct light delivery. In a subsequent paper by the same group, short- and long-term effects on

PSA levels were described in relation to the PDT light dose [42]. This was defined as the product of the PS concentration and the *in situ* measured light dose. A prolonged delay to the time point when the PSA level began to increase was shown for high-dose as compared with low-dose PDT, 82 and 43 days, respectively. This group has also developed pretreatment dosimetry software intended to optimize various treatment parameters in order to tailor the emitted treatment light according to a predefined dose plan [43].

Trachtenberg and co-workers at the University of Toronto reported on vascular-targeted photodynamic therapy (VTP), using escalating drug doses of the photosensitizer WST09 [44, 45]. Spherical isotropic fiber tips were used as detector probes to study the fluence rate at selected sites during the treatment [46]. Complete response was achieved in 60% of the patients who received high-dose VTP. This assessment was judged using MRI investigation showing avascular areas 1 week after treatment [47]. Also, biopsies from these patients showed no viable cancer after 6 months. The software used in the dosimetry planning of these treatments was presented by Davidson *et al*. [48]. Inter-patient variations in the follow-up were seen. The most probable causes of these treatment response variations were the variability of the PS pharmacokinetics and the PS distribution as a function of time.

Our group started to consider interstitial PDT in localized prostate cancer in 2000 based on our experience of interstitial treatment of thick tumors using optical fibers (see, e.g., [49–53]). We also have long experience in diagnostic measurements, primarily in fluorescence spectroscopy, while dosimetric capability was being developed at that time. The first interstitial treatment system to be developed involved splitting the optical power from a treatment laser into six parts delivered through six individual fibers, which could be inserted into the tumor mass. The first clinical treatments with this system were performed on easily accessible thick skin tumors, intended to gain important clinical experience before moving on to treatment of prostate cancer. A unique feature with this system was that it could intermittently be used in a treatment and dosimetry measurement mode, as illustrated in Figure 18.9. For treatment, all the fibers were used as emitters, to allow the light to be distributed as efficiently and evenly as possible. In the measurement mode, only one fiber at a time was used as an emitter, while the other fibers were used as light sensors. Thus, it was possible to measure the light from one fiber tip to all the others. This dosimetry measurement mode made it possible to monitor the distribution throughout the tumor of fluence rates, PS concentration, and bleaching, and also the oxygenation of the hemoglobin present in the tissue. The system was evaluated in the treatment of experimental tumors in rats [49, 50], and was later used in early treatment of solid human tumors [51–53].

The interstitial PDT studies have contributed to a better understanding of the precise mechanisms of the PDT effects for the development of improved dosimetry models to plan and control the treatment. In order to be able to individualize the treatment as well as possibly, to account for inter-patient variations, it is very useful to be able to monitor all parameters of importance for the treatment outcome. With an improved understanding of the processes involved, would be valuable to know more parameters. It was in this context that the system shown in Figure 18.9 was

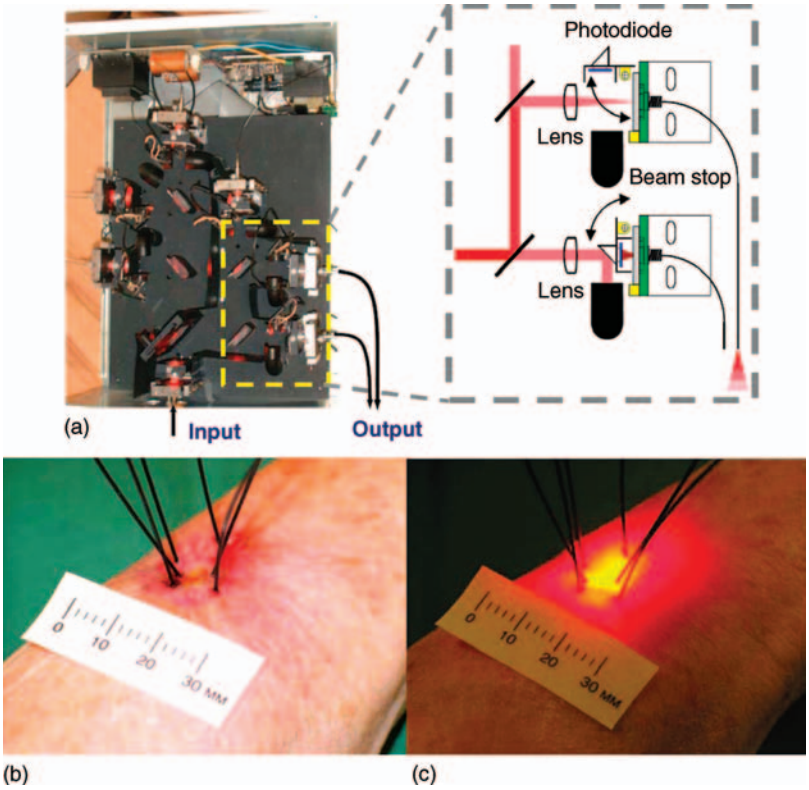

Figure 18.9 (a) Interstitial PDT of skin malignancies using a six-fiber system, where the intensity of light flowing between fibers can be measured by inserting a detector in front of a fiber, while at the same time blocking the treatment light intended for that particular fiber. The situation when one fiber is sending out treatment light and the other five are measuring the received light is shown in (b), and the situation when all six fibers are transmitting treatment light is shown in (c).

developed – a system that had capabilities both for delivering treatment light and also for measuring several parameters of importance for the treatment outcome. The basic elements of this instrument, developed for clinical trials, are presented in Figure 18.10 for the case of six interstitial fibers. Individually adjustable diode lasers were used to supply light to each of the treatment fibers. Photographs from a treatment session for a solid skin malignancy located on the ear are included in Figure 18.10.

Clearly, a system of the kind described above can be fully utilized only in conjunction with advanced dosimetric software, where measured diagnostic signals are fed into a dose distribution calculation program [52–56]. The most common approach is to define a treatment dose from a "threshold dose model" [57, 58]. This means ensuring that a minimum dose, that is, the dose required to induce direct cell

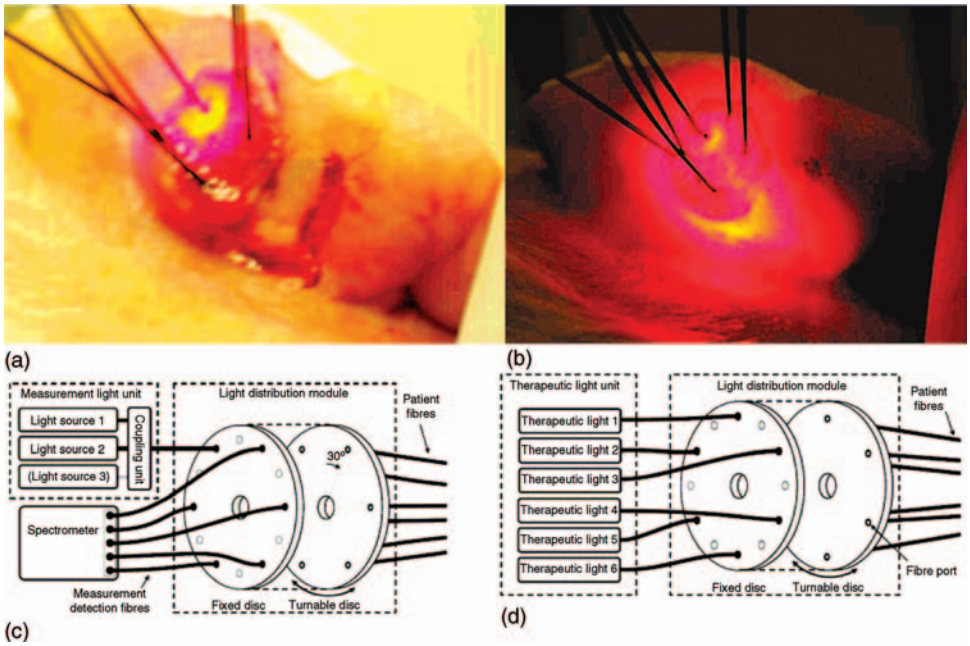

Figure 18.10 Schematic views of a six-fiber system with capability for treatment and also diagnostics of light flux, sensitizer concentration, and tissue oxygenation through the same fibers shown for the treatment situation (c) and for the diagnostic situation (d). Further, in the upper part of the figure a solid tumor is shown, (a) in a diagnostic measurement and (b) in treatment using all fibers Diagrams with fiber arrangement schemes from [54].

death, is delivered to all parts of the target volume, as depicted schematically in Figure 18.11, showing an interstitial PDT treatment session of a prostate with 18 fibers just after initiating the treatment (with small red spheres surrounding each fiber tip, indicating full treatment) and after almost full treatment (with the entire prostate, and some small regions of surrounding tissue being marked as receiving the threshold dose). In practice, the dose can be defined in several ways:

- One option is to multiply the light fluence by the PS concentration to obtain a value related to the amount of excited PS. One then assumes that this value is directly correlated with the amount of oxygen radicals produced and that this amount is related to the tissue damage potential. The idea is that this number should exceed a threshold value for the entire target volume. This means that the PS concentration and light fluence must be quantified in three dimensions.
- If one furthermore assumes that the PS concentration is homogeneously distributed throughout the target volume, it is sufficient to consider only the distribution of the light fluence within the target volume. This will clearly simplify the measurements required to control a treatment.

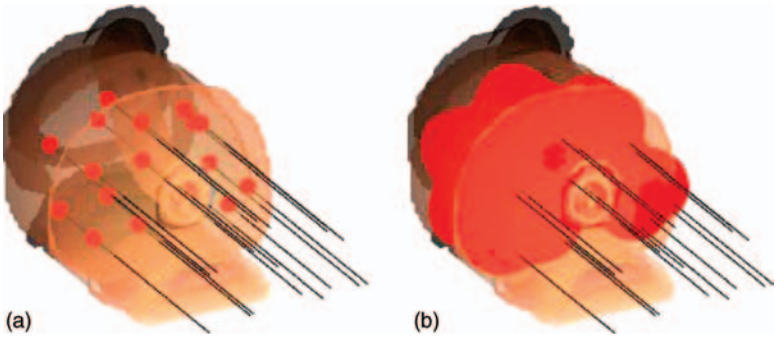

Figure 18.11 Treatment light delivered through multiple optical fibers positioned inside the prostate. Parts (a) and (b) show two different instances of the same treatment session, where the iso-surfaces mark tissue that has received at least the threshold dose.

The fluence rate can be assessed using calibrated optical probes, where integrating the signal over the treatment time yields the fluence dose [59, 60]. Such point measurements are valuable for providing representative values of the light dose delivered at one location. In order to obtain a spatial map of the fluence rate throughout the entire target volume, the photon propagation must be theoretically calculated. The optical properties of the tissue treated are then determined, followed by calculations using a photon propagation model. One example of a theoretical model is the analytical solution to the diffusion equation.

The optical properties in interstitial PDT are typically evaluated through steady-state, spatially resolved measurements [39, 46, 52, 56, 61–63], where absorption and scattering are assumed to be constant throughout the measured tissue. Recently, heterogeneous models of the tissue have been reported utilizing tomographic measurement schemes. The optical properties are then often reconstructed using structural information obtained from prior ultrasound examinations [64, 65] or MRI [66]. This is necessary as the reconstruction is an ill-conditioned and under-determined problem as the number of signals is limited for practical reasons. Many detectors are still essential in order to be able to assess the parameters as a function of position. It therefore quickly becomes a challenge to perform the measurements in the best way and to get the detectors into place. Several studies have been carried out in which the optical fibers delivering and collecting the light were placed transrectally.

Some type of model for the forward light problem calculating the light fluence distribution has to be used both for the evaluation of the optical properties of the tissue (the so-called inverse problem) and in the modeling of treatment light penetration (a true forward problem once the optical properties are known). A wide variety of models have been developed in interstitial PDT dosimetry. For example, accelerated Monte Carlo methods [67], higher order approximations of the radiative transport equation [68, 69], finite element methods [48], and homogeneous models of the diffusion equation [56, 70] have been utilized.

In the pretreatment planning, the issue is to optimize the treatment outcome in terms of destroying the target tissue, while avoiding or minimizing any side effects of

the treatment. This requires modeling of the treatment parameters in every position of the target tissue, and in nearby tissue structures. The intention for the light delivery is to tailor the light distribution so that the entire target volume receives a fluence dose above the threshold. Organs at risk should receive as low a light dose as possible. For this optimization, not only the treatment time but also other parameters have to be considered and optimized. Such parameters are light source positions, shape, and power [43, 48, 55, 56, 70, 71]. The optimization has to take into account clinically realistic light delivery modes, meaning a limited number of optical fibers that can be inserted into the prostate gland.

Most groups utilize optical fiber diffusers to deliver the treatment light, whereas our rationale is to adopt bare-end optical fibers. These fibers allow well-defined positions when using them as sources or detectors, and thus provide a well-defined source–detector distance in any measurements conducted with the fibers. It should therefore be possible to obtain more accurate and robust values of the optical properties of the tissue. It has also been necessary to develop dosimetry software to calculate the optimum positioning of the fibers based on the geometry of the tumor and the nearby organs at risk. Predefined values for absorption and scattering can be assigned to different types of tissue in the pretreatment planning, when no values for the particular patient have yet been obtained. The fiber positions and irradiation times for the individual fibers can then be calculated. The aim of this calculation is to maximize the fluence dose to the prostate gland, while minimizing the dose to the organs at risk. In addition to the pretreatment planning, the instrument developed in our group performs dosimetry calculations during treatment. Thus, the irradiation times can be updated based on treatment-induced changes in the optical properties measured during the treatment. The general procedure is described in detail elsewhere [56, 72].

A clinical trial using an 18-fiber interstitial PDT system, constructed together with the spin-off company SpectraCure (Lund, Sweden) along the principles developed by the Lund University group, has so far involved four prostate cancer patients. The system, procedures, and clinical outcome of these activities have been described recently [73]. Photographs from the clinical procedures are shown in Figure 18.12. In addition to the light flux, the sensitizer concentration and level of oxygenation were also monitored in these treatments. These data, however, were not used to influence the treatment procedure. Incorporation of these data should help to achieve optimized, individually tailored treatments, while the parameters in such a model still have to be defined from real treatments. Several preclinical studies have reported less variation in PDT response when compensating for varying levels of sensitizer in the target medium [74, 75].

Photosensitizer concentration can be assessed through absorption [46] or fluorescence [40] point measurements. Fluorescence was employed in our measurements owing to its higher sensitivity. Such measurements could compensate for both intra- and inter-patient variations. Hence, analogously to the fluence rate calculations, the sensitizer distribution must be assessed in three dimensions. A full tomographic reconstruction of the PS concentration throughout the medium has been conducted, showing an interesting potential also in studying the rate of PS photobleaching as a

Figure 18.12 Photographs from a treatment session of prostate cancer with an 18-fiber system for interstitial PDT with integrated dosimetry feedback functions. Photographs courtesy of SpectraCure AB.

measure to predict treatment outcome. A method of doing this has been reported previously [76].

Interstitial PDT for the treatment of prostate cancer is being continuously developed. Several groups have stressed the need for more sophisticated dose planning approaches. Many aspects must be considered, such as individual variations in blood supply to the gland, type of PS, concentration and localization of PS, the oxygen concentration in and optical properties of the gland, and the size and pathology of the prostate gland. Risk organs in the close vicinity of the prostate must also be considered, for example, the urinary bladder sphincters, to avoid the risk of incontinence. Other potential side effects of the treatment also have to be carefully considered. Thus, the general health status of the patient, the treatment time, and light sensitivity of the patient during and following treatment have to be taken into account in the planning of the treatment. In our opinion, the results obtained so far indicate that this new modality for prostate cancer therapy is very promising. More studies are under way with the aim of getting the treatment modality approved for

treatment of prostate cancer. Interstitial treatments are also under way for other tumors requiring interstitial light delivery, as mentioned above. These attempts to get interstitial PDT approved for these tumor types face very much the same challenges as described for the treatment of prostate cancer – a need for an improved dosimetry and measurements allowing more accurate planning for each individual treatment.

18.10 Discussion

PDT is gaining increased acceptance in the management of malignant disease. Its minimally invasive nature combined with the possibility of retreating without any memory effect are attractive features of this treatment modality. A serious draw-back with the technique is that many sensitizers leave a prolonged light sensitivity to the skin, requiring discipline in not being exposed to strong ambient light for periods which could extend to 1 month. This is not the case with ALA-induced PpIX sensitization, especially useful in the management of non-melanoma skin cancer, which therefore has gained wide application. Interstitial PDT of deep-lying lesions requires a detailed and individualized dosimetry taking spatially resolved light fluence, sensitizer concentration, and tissue oxygenation into account in order to achieve the full advantages of the modality. Several groups, including ours, are addressing this challenge. With more ideal sensitizers, having high tumor specificity, high quantum efficiency, long wavelength activation and fast skin clearance, PDT would gain a strong boost. In this context, extensive efforts along these lines include the development of functionalized nanoparticles.

The development of optimized PDT is a strongly multidisciplinary task where close collaboration between medical doctors of different specialities, physicists, and biochemists is needed. If pursued successfully, PDT might become a treatment of choice for patients with various malignant pathologies. Being minimally invasive and requiring limited infrastructure, this treatment modality could also prove particularly realistic in third-world countries with limited healthcare resources.

Acknowledgments

The authors gratefully acknowledge financial support from VINNOVA, the Swedish Strategic Research Foundation (SSF), the Swedish Research Council through direct grants, and through a Linnaeus Grant to the Lund Laser Center. Further, support from the Lund University Medical Faculty Funds and, the regional hospital organization (Region Skane) was very valuable. We thank a large number of graduate students and clinical collaborators who greatly contributed to our work on experimental and clinical PDT over a 20 year period. They include Göran Ahlgren, Johan Axelsson, Margret Einarsdottir, Ann Johansson, Tomas Johansson, Claes af Klinteberg, K. M. Kälkner, Sten Nilsson, Sara Pålsson, Jenny Svensson, Tomas

Svensson, Marcelo Soto Thompson, and Ingrid Wang. Fruitful collaboration with SpectraCure in developing clinically relevant instrumentation for interstitial PDT is also acknowledged, and thanks go especially to Kerstin Jakobsson, Masoud Khayyami, and Johannes Swartling.

References

1 Röntgen, W. (1895) Über eine neue Art von Strahlen (Vorläufige Mitteilung), in *Aus den Sitzungsberichten der Würzburger Physik.-Mediz. Gesellschaft 1895*, Verlag der Königlicher Hof- und Universitäts- Buch- und Kunsthandlung, Würzburg.

2 Finsen, N.R. (1901) *Phototherapy*, Edward Arnold, London.

3 Urbach, F., Forbes, P.D., Davies, R.E., and Berger, D. (1976) Cutaneous photobiology: past, present and future. *J. Invest. Dermatol.*, **67**, 209–224.

4 Lingjærde, O., Reichborn-Kjennerud, T., Haggag, A., Gärtner, I., Berg, E.M., and Narud, K. (1993) Treatment of winter depression in Norway. I. Short- and long-term effects of 1500-lux white light for 6 days. *Acta Psychiatr. Scand.*, **88**, 292–299.

5 Deguchi, T. (1979) Circadian rhythm of serotonin *N*-acetyltransferase activity in organ culture of chicken pineal gland. *Science*, **203**, 1245–1247.

6 Raab, O. (1899) Untersuchungen über die Wirkung fluorescierender Stoffe. *Z. Biol.*, **39**, 16.

7 von Tappeiner, H. and Jodlbauer, A. (1904) Über Wirkung der photodynamischen (fluorieszierenden) Stoffe auf Protozoan und Enzyme. *Dtsch. Arch. Klin. Med.*, **80**, 427–487.

8 Meyer-Betz, F. (1913) Untersuchungen über die biologische (photodynamische) Wirkung des Hämatoporphyrins und andere Derivate des Blut- und Gallenfarbstoffs. *Dtsch. Arch. Klin. Med.*, **112**, 476–450.

9 Policard, A. (1924) Etudes sur les aspects offerts par des tumeur experimentales examinée à la lumière de Wood's. *C. R. Soc. Biol.*, **91**, 1423–1423.

10 Figge, F.H.J. and Weiland, G.S. (1948) The affinity of neoplastic, embryonic, and traumatized tissue for porphyrins and metalloporphyrins. *Anat. Rec.*, **100**, 659.

11 Lipson, R.L. and Baldes, E.J. (1960) The photodynamic properties of a particular haematoporphyrin derivative. *Arch. Dermatol.*, **82**, 508–516.

12 Bonnett, R., Berenbaum, M.C., and Kaur, H. (1984) Chemical and biological studies on haematoporphyrin derivative: an unexpected photosensitisation in brain, in *Porphyrins in Tumor Phototherapy* (eds. A. Andreoni and R. Cubeddu), Plenum Press, New York, pp. 67–80.

13 Dougherty, T.J. (1979) Photoradiation in the treatment of recurrent breast carcinoma. *J. Natl. Cancer Inst.*, **62**, 231–237.

14 Huang, Z. (2005) A review of progress in clinical photodynamic therapy. *Technol. Cancer Res. Treat.*, **4**, 283–293.

15 Stylli, S.S. and Kaye, A.H. (2006) Photodynamic therapy of cerebral glioma – A review. Part II – Clinical studies. *J. Clin. Neurosci.*, **13**, 709–717.

16 Zeitouni, N.C., Oseroff, A.R., and Shieh, S. (2003) Photodynamic therapy for nonmelanoma skin cancers: current review and update. *Mol. Immunol.*, **39**, 1133–1136.

17 Kessel, D. (1982) Components of hematoporphyrin derivatives and their tumor localization capacity. *Cancer Res.*, **42**, 1703–1706.

18 Kessel, D. and Chou, T.H. (1983) Tumor-localizing components of the porphyrin preparation hematoporphyrin derivative. *Cancer Res.*, **43**, 1994–1999.

19 Bottiroli, G., Doccio, F., Freitas, I., Ramponi, R., and Sacchi, C. (1984) Hematoporphyrin derivative: fluorometric studies in solution and cells, in *Porphyrins in Tumor Phototherapy* (eds. A. Andreoni and R. Cubeddu), Plenum Press, New York, pp. 125–136.

20 Malik, Z. and Lugaci, H. (1987) Destruction of erythroleukaemic cells by photoinactivation of endogenous porphyrins. *Br. J. Cancer*, **56**, 589–595.

21 Kennedy, J.C., Pottier, R.H., and Pross, D.C. (1990) Photodynamic therapy with endogenous protoporphyrin IX: basic principles and present clinical experience. *J. Photochem. Photobiol. B*, **6**, 143–148.

22 Kennedy, J.C. and Pottier, R.H. (1992) Endogenous protoporphyrin IX, a clinically useful photosensitizer for photodynamic therapy. *J. Photochem. Photobiol. B*, **14**, 275–292.

23 Pålsson, S., Stenram, U., Soto Thompson, M., Vaitkuviene, A., Puskiene, V., Ziobakiene, R., Oyama, J., Gustafsson, U., DeWeert, M.J., Bendsoe, N., Andersson-Engels, S., Svanberg, S., and Svanberg, K. (2005) Methods for detailed histopathological investigation and localisation of cervical biopsies to improve the interpretation of autofluorescence data. *J. Environ. Pathol. Toxicol. Oncol.*, **25**, 321–340.

24 Tinghög, G., Carlsson, P., Synnerstad, I., and Rosdahl, I. (2007) *Samhällskostnader för Hudcancer Samt en Jämförelse Med Kostnaderna för Vägtrafikolyckor*, Linköping University Electronic Press, Linköping, http://www.ep.liu.se/ea/cmt/2007/005/.

25 Burton, R.C., Howe, C., Adamson, L., Reid, A.L., Hersey, P., Watson, A., Watt, G., Relic, J., Holt, D., Thursfield, V., Clarke, P., and Armstrong, B.K. (1998) General practitioner screening for melanoma: sensitivity, specificity, and effect of training. *J. Med. Screen.*, **5**, 156–161.

26 Dougherty, T.J., Kaufman, J.E., Goldfarb, A., Weishaupt, K.R., Boyle, D., and Mittleman, A. (1978) Photoradiation therapy for the treatment of malignant tumors. *Cancer Res.*, **38**, 2628–2635.

27 Bandieramonte, G., Marchesini, R., Melloni, E., Andreoli, C., di Pietro, S., Spinelli, P., Fava, G., Zunino, F., and Emanuelli, H. (1984) Laser phototherapy following HpD administration in superficial neoplastic lesions. *Tumori*, **70**, 327–334.

28 Wilson, B.D., Mang, T.S., Cooper, M., and Stoll, H. (1989) Use of photodynamic therapy for the treatment of extensive basal cell carcinomas. *Facial Plast. Surg.*, **6**, 185–189.

29 Tse, D.T., Kersten, R.C., and Anderson, R.L. (1984) Hematoporphyrin derivative photoradiation therapy in managing nevoid basal-cell carcinoma syndrome. *Arch. Ophthalmol.*, **102**, 990–994.

30 Svanberg, K., Andersson, T., Killander, D., Wang, I., Stenram, U., Andersson-Engels, S., Berg, R., Johansson, J., and Svanberg, S. (1994) Photodynamic therapy of non-melanoma malignant tumors of the skin using topical 5-amino levulinic acid sensitization and laser irradiation. *Br. J. Dermatol.*, **130**, 743–751.

31 Wang, I., Bendsoe, N., af Klinteberg, C., Enejder, A.M.K., Andersson-Engels, S., Svanberg, S., and Svanberg, K. (2001) Photodynamic therapy vs. cryosurgery of basal cell carcinomas; results of a phase III clinical trial. *Br. J. Dermatol.*, **144**, 832–840.

32 Cowled, P.A. and Forbes, I.J. (1985) Photocytotoxicity *in vivo* of haematoporphyrin derivative components. *Cancer Lett.*, **28**, 111–118.

33 Windahl, T., Andersson, S.O., and Lofgren, L. (1990) Photodynamic therapy of localised prostatic cancer. *Lancet*, **336**, 1139.

34 Zaak, D., Sroka, R., Höppner, M., Khoder, W., Reich, O., Tritschler, S., Muschter, R., Knüchel, R., and Hofstetter, A. (2003) Photodynamic therapy by means of 5-ALA induced PPIX in human prostate cancer – preliminary results. *Med. Laser Appl.*, **18**, 91–95.

35 Nathan, T.R., Whitelaw, D.E., Chang, S.C., Lees, W.R., Ripley, P.M., Payne, H., Jones, L., Parkinson, M.C., Emberton, M.,

Gillams, A.R., Mundy, A.R., and Bown, S.G. (2002) Photodynamic therapy for prostate cancer recurrence after radiotherapy: a Phase I study. *J. Urol.*, **168**, 1427–1432.

36 Moore, C.M., Nathan, T.R., Lees, W.R., Mosse, C.A., Freeman, A., Emberton, R., and Bown, S.G. (2006) Photodynamic therapy using meso tetra hydroxy phenyl chlorin (mTHPC) in early prostate cancer. *Lasers Surg. Med.*, **38**, 356–363.

37 Du, K.L., Mick, R., Busch, T., Zhu, T.C., Finlay, J.C., Yu, G., Yodh, A.G., Malkowicz, S.B., Smith, D., Whittington, R., Stripp, D., and Hahn, S.M. (2006) Preliminary results of interstitial motexafin lutetium-mediated PDT for prostate cancer. *Lasers Surg. Med.*, **38**, 427–434.

38 Verigos, K., Stripp, D., Mick, R., Zhu, T., Whittington, R., Smith, D., Dimofte, A., Finlay, J., Busch, T., Tochner, Z., Malkowicz, S., Glatstein, E., and Hahn, S. (2006) Updated results of a phase I trial of motexafin lutetium-mediated interstitial photodynamic therapy in patients with locally recurrent prostate cancer. *J. Environ. Pathol. Toxicol. Oncol.*, **25**, 373–387.

39 Zhu, T.C., Dimofte, A., Finlay, J.C., Stripp, D., Busch, T., Miles, J., Whittington, R., Malkowicz, S.B., Tochner, Z., Glatstein, E., and Hahn, S.M. (2005) Optical properties of human prostate at 732 nm measured *in vivo* during motexafin lutetium-mediated photodynamic therapy. *Photochem. Photobiol.*, **81**, 96–105.

40 Finlay, J.C., Zhu, T.C., Dimofte, A., Stripp, D., Malkowicz, S.B., Busch, T.M., and Hahn, S.M. (2006) Interstitial fluorescence spectroscopy in the human prostate during motexafin lutetium-mediated photodynamic therapy. *Photochem. Photobiol.*, **82**, 1270–1278.

41 Yu, G.Q., Durduran, T., Zhou, C., Zhu, T.C., Finlay, J.C., Busch, T.M., Malkowicz, S.B., Hahn, S.M., and Yodh, A.G. (2006) Real-time *in situ* monitoring of human prostate photodynamic therapy with diffuse light. *Photochem. Photobiol.*, **82**, 1279–1284.

42 Patel, H., Mick, R., Finlay, J., Zhu, T.C., Rickter, E., Cengel, K.A., Malkowicz, S.B., Hahn, S.M., and Busch, T.M. (2008) Motexafin lutetium-photodynamic therapy of prostate cancer: short- and long-term effects on prostate-specific antigen. *Clin. Cancer Res.*, **14**, 4869–4876.

43 Altschuler, M.D., Zhu, T.C., Li, J., and Hahn, S.M. (2005) Optimized interstitial PDT prostate treatment planning with the Cimmino feasibility algorithm. *Med. Phys.*, **32**, 3524–3536.

44 Trachtenberg, J., Bogaards, A., Weersink, R.A., Haider, M.A., Evans, A., McCluskey, S.A., Scherz, A., Gertner, M.R., Yue, C., Appu, S., Aprikian, A., Savard, J., Wilson, B.C., and Elhilali, M. (2007) Vascular targeted photodynamic therapy with palladium-bacteriopheophorbide photosensitizer for recurrent prostate cancer following definitive radiation therapy: assessment of safety and treatment response. *J. Urol.*, **178**, 1974–1979.

45 Trachtenberg, J., Weersink, R.A., Davidson, S.R.H., Haider, M.A., Bogaards, A., Gertner, M.R., Evans, A., Scherz, A., Savard, J., Chin, J.L., Wilson, B.C., and Elhilali, M. (2008) Vascular-targeted photodynamic therapy (padoporfin, WST09) for recurrent prostate cancer after failure of external beam radiotherapy: a study of escalating light doses. *BJU Int.*, **102**, 556–562.

46 Weersink, R.A., Bogaards, A., Gertner, M., Davidson, S.R.H., Zhang, K., Netchev, G., Trachtenberg, J., and Wilson, B.C. (2005) Techniques for delivery and monitoring of TOOKAD (WST09)-mediated photodynamic therapy of the prostate: clinical experience and practicalities. *J. Photochem. Photobiol. B*, **79**, 211–222.

47 Haider, M.A., Davidson, S.R.H., Kale, A.V., Weersink, R.A., Evans, A.J., Toi, A., Gertner, M.R., Bogaards, A., Wilson, B.C., Chin, J.L., Elhilali, M., and Trachtenberg, J. (2007) Prostate gland: MR imaging appearance after vascular

targeted photodynamic therapy with palladium-bacteriopheophorbide. *Radiology*, **244**, 196–204.

48 Davidson, S., Weersink, R.A., Haider, M.A., Gertner, M.R., Bogaards, A., Giewercer, D., Scherz, A., Sherar, M.D., Elhilali, M., Chin, J.L., Trachtenberg, J., and Wilson, B.C. (2009) Treatment planning and dose analysis for interstitial photodynamic therapy of prostate cancer. *Phys. Med. Biol.*, **54**, 2293–2313.

49 Stenberg, M., Soto Thompson, M., Johansson, T., Pålsson, S., af Klinteberg, C., Andersson-Engels, S., Stenram, U., Svanberg, S., and Svanberg, K. (2000) Interstitial photodynamic therapy – diagnostic measurements and treatment in malignant experimental rat tumors. *Proc. SPIE*, **4161**, 151–157.

50 Johansson, T., Soto Thompson, M., Stenberg, M., af Klinteberg, C., Andersson-Engels, S., Svanberg, S., and Svanberg, K. (2002) Feasibility study of a novel system for combined light dosimetry and interstitial photodynamic treatment of massive tumors. *Appl. Opt.*, **41**, 1462–1468.

51 Soto Thompson, M., Johansson, A., Johansson, T., Andersson-Engels, S., Bendsoe, N., Svanberg, K., and Svanberg, S. (2005) Clinical system for interstitial photodynamic therapy with combined on-line dosimetry measurements. *Appl. Opt.*, **44**, 4023–4031.

52 Johansson, A., Johansson, T., Thompson, M.S., Bendsoe, N., Svanberg, K., Svanberg, S., and Andersson-Engels, S. (2006) *In vivo* measurement of parameters of dosimetric importance during interstitial photodynamic therapy of thick skin tumors. *J. Biomed. Opt.*, **11**, 34029.

53 Johansson, A., Bendsoe, N., Svanberg, K., Svanberg, S., and Andersson-Engels, S. (2006) Influence of treatment-induced changes in tissue absorption on treatment volume during interstitial photodynamic therapy. *Med. Laser Appl.*, **21**, 261–270.

54 Johansson, A., Johansson, T., Thompson, M.S., Bendsoe, N., Svanberg, K., Svanberg, S., and Andersson-Engels, S. (2006) *In vivo* measurement of parameters of dosimetric importance during interstitial photodynamic therapy of thick skin tumors. *J. Biomed. Opt.*, **11**, 34029.

55 Johansson, A., Soto Thompson, M., Johansson, T., Bendsoe, N., Svanberg, K., Svanberg, S., and Andersson-Engels, S. (2005) System for integrated interstitial photodynamic therapy and dosimetric monitoring, *Proc. SPIE*, **5689**, 130–140.

56 Johansson, A., Hjelm, J., Eriksson, E., and Andersson-Engels, S. (2005) Pre-treatment dosimetry for interstitial photodynamic therapy. Presented at the European Conference on Biomedical Optics (ECBO), Munich, June 2005.

57 Johansson, A., Axelsson, J., Andersson-Engels, S., and Swartling, J. (2007) Realtime light dosimetry software tools for interstitial photodynamic therapy of the human prostate. *Med. Phys.*, **34**, 4309–4321.

58 Berenbaum, M.C., Bonnett, R., and Scourides, P.A. (1982) *In vivo* biological activity of the components of haematoporphyrin derivative. *Br. J. Cancer*, **45**, 571–581.

59 van Gemert, J.C., Berenbaum, M.C., and Gijsbers, G.H. (1985) Wavelength and light-dose dependence in tumor phototherapy with haematoporphyrin derivative. *Br. J. Cancer*, **52**, 43–49.

60 Dimofte, A., Zhu, T.C., Hahn, S.M., and Lustig, R.A. (2002) *In vivo* light dosimetry for motexafin lutetium-mediated PDT of breast cancer. *Lasers Surg. Med.*, **31**, 305–312.

61 Lilge, L., Pomerleau-Dalcourt, N., Douplik, A., Selman, S.H., Keck, R.W., Szkudlarek, M., Pestka, M., and Jankun, J. (2004) Transperineal *in vivo* fluence-rate dosimetry in the canine prostate during SnET2-mediated PDT. *Phys. Med. Biol.*, **49**, 3209–3225.

62 Zhu, T.C., Finlay, J.C., and Hahn, S.M. (2005) Determination of the distribution

of light, optical properties, drug concentration, and tissue oxygenation *in-vivo* in human prostate during motexafin lutetium-mediated photodynamic therapy. *J. Photochem. Photobiol. B*, **79**, 231–241.

63 Wang, K.K.H. and Zhu, T.C. (2009) Reconstruction of *in-vivo* optical properties for human prostate using interstitial diffuse optical tomography. *Opt. Express*, **17**, 11665–11672.

64 Jiang, Z., Piao, D., Xu, G., Ritchey, J.W., Holyoak, G., Bartels, K.E., Bunting, C.F., Slobodov, G., and Krasinski, J.S. (2008) Trans-rectal ultrasound-coupled near-infrared optical tomography of the prostate. Part II: Experimental demonstration. *Opt. Express*, **16**, 17505–17520.

65 Xu, G., Piao, D., Musgrove, C., Bunting, C., and Dehghani, H. (2008) Trans-rectal ultrasound-coupled near-infrared optical tomography of the prostate. Part I: Simulation. *Opt. Express*, **16**, 17484–17504.

66 Li, C., Liengsawangwong, R., Choi, H., and Cheung, R. (2007) Using *a priori* structural information from magnetic resonance imaging to investigate the feasibility of prostate diffuse optical tomography and spectroscopy: a simulation study. *Med. Phys.*, **34**, 266–274.

67 Lo, W.C.Y., Redmond, K., Luu, J., Chow, P., Rose, J., and Lilge, L. (2009) Hardware acceleration of a Monte Carlo simulation for photodynamic therapy treatment planning. *J. Biomed. Opt.*, **14**, 014019.

68 Dickey, D.J., Moore, R.B., Rayner, D.C., and Tulip, J. (2001) Light dosimetry using the P3 approximation. *Phys. Med. Biol.*, **46**, 2359–2370.

69 Dickey, D.J., Partridge, K., Moore, R.B., and Tulip, J. (2004) Light dosimetry for multiple cylindrical diffusing sources for use in photodynamic therapy. *Phys. Med. Biol.*, **49**, 3197–3208.

70 Li, J., Altschuler, M.D., Hahn, S.M., and Zhu, T.C. (2008) Optimization of light source parameters in the photodynamic therapy of heterogeneous prostate. *Phys. Med. Biol.*, **53**, 4107–4121.

71 Rendon, A., Beck, J.C., and Lilge, L. (2008) Treatment planning using tailored and standard cylindrical light diffusers for photodynamic therapy of the prostate. *Phys. Med. Biol.*, **53**, 1131–1149.

72 Johansson, A., Axelsson, J., Swartling, J., Johansson, T., Pålsson, S., Stensson, J., Einarsdottir, M., Svanberg, K., Bendsoe, N., Kälkner, K.M., Nilsson, S., Svanberg, S., and Andersson-Engels, S. (2007) Interstitial photodynamic therapy for primary prostate cancer incorporating real-time treatment dosimetry. *Proc. SPIE*, **6427**, 6427O.

73 Swartling, J., Axelsson, J., Ahlgren, G., Kälkner, K.M., Nilsson, S., Svanberg, S., Svanberg, K., and Andersson-Engels, S. (2010) System for interstitial photodynamic therapy with on-line dosimetry: first clinical experiences of prostate cancer. *J. Biomed. Opt.*, **15**, 058003.

74 Sheng, C., Jack Hoopes, P., Hasan, T., and Pogue, B.W. (2007) Photobleaching-based dosimetry predicts deposited dose in ALA–PpIX PDT of rodent esophagus. *Photochem. Photobiol.*, **83**, 738–748.

75 Zhou, X.D., Pogue, B.W., Chen, B., Demidenko, E., Joshi, R., Hoopes, J., and Hasan, T. (2006) Pretreatment photosensitizer dosimetry reduces variation in tumor response. *Int. J. Radiat. Oncol.*, **64**, 1211–1220.

76 Axelsson, J., Swartling, J., and Andersson-Engels, S. (2009) *In vivo* photosensitizer tomography inside the human prostate. *Opt. Lett.*, **34**, 232–234.

19
Molecular Targeting of Photosensitizers

Hasan Tayyaba, Prakash R. Rai, Sarika Verma, and Xiang Zheng

19.1
Introduction

Photodynamic therapy (PDT) is an emerging, externally activatable treatment modality. It involves the generation of toxic molecular species via excitation of chemicals called photosensitizers (PSs), by light of an appropriate wavelength, generally in the presence of oxygen. PDT is clinically approved for the treatment of neoplastic and non-neoplastic disease and offers several advantages over conventional chemotherapy by providing additional selectivity through the spatial confinement of light required for PS activation. A wide range of PSs have been evaluated and six of these have successfully transitioned from the bench to bedside applications [1]. Despite the regulatory approvals and the clinical success of PDT in oncology, a major limitation of all existing PSs is the lack of high selectivity for target tissue, which precludes its broad application to complex anatomic sites.

A key variable in ensuring favorable PDT outcome and a broader application is selective PS accumulation in the target tissue, thereby confining phototoxic effects to malignant cells. PS selectivity can be enhanced by several methods [2, 3] (Figure 19.1), and can be broadly classified into three categories: (i) molecular modification of the PS by using targeting moieties for improved recognition of target sites, (ii) delivering high PS payloads using passively or actively targeted nanoconstructs, and (iii) biological modulation of target cells to enhance PS concentration.

In this chapter, we discuss some recent advances, spanning the last 5 years, in developing such strategies for efficient PS targeting towards enhancing PDT efficacy against cancers.

Handbook of Biophotonics. Vol.2: Photonics for Health Care, First Edition. Edited by Jürgen Popp, Valery V. Tuchin, Arthur Chiou, and Stefan Heinemann.

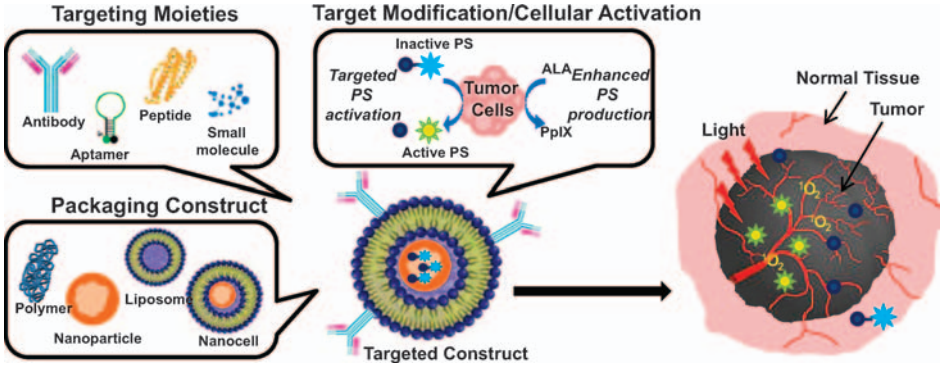

Figure 19.1 Schematic representation of molecular targeting of PS in PDT. Both targeting and packaging strategies can be employed to design efficient PSs, in combination with site-specific activation, to achieve optimum accumulation of PS in tumors.

19.2
Molecular Modifications of Photosensitizers

19.2.1
Small Molecules, Peptides, and Aptamers

Modifications can be made to the inherent structure of a PS by adding a side chain or functional group, or by conjugation of PS to small molecules for delivery such as folate [4], estradiol [5], carbohydrates [6], and fluorescent dyes that localize subcellularly [7]. Peptides have also been extensively used to target the PSs to surface receptors and to intracellular organelles including the nucleus [8]. Cell surface receptors are the most common molecular targets of peptide–PS conjugates and cause improved tumor selectivity over normal cells due to their overexpression on tumor cells. Some recent examples include vascular endothelial growth factor receptor (VEGFR) neuropilin-1, epidermal growth factor (EGF) [21], gastrin-releasing peptide receptor (GRPR), and $\alpha_v\beta_3$-integrin. Other organelles such as Golgi bodies, endoplasmic reticulum, and mitochondria have been explored to understand the effect of intracellular targeting on PDT [9]. As an example, an amphiphilic porphyrin derivative containing a mitochondrial localization sequences (MLS) peptide has been developed [10] and cell-penetrating peptide (CPP) has been used to deliver PSs intracellularly [11, 12]. These studies suggest that stability and affinity are the primary limitations with peptides. Some recent advances that may improve peptide-targeted PDT include the use of peptidomimetics to overcome *in vivo* stability and nanotechnology to enhance affinity to cancer cells. Aptamer–PS conjugates have also been developed for selective *in vitro* PDT targeting of a lymphoma cell line [13]. Thus such peptide– and aptamer–PS conjugates may provide an avenue for the development of highly efficient PDT regimens for clinical applications.

19.2.2
Proteins

Antibody-conjugated PSs were one of the earliest targeting strategies in PDT [14]. Despite all the efforts, antibodies have achieved limited success as targeting agents because of disadvantages such as nonspecific binding of Fc (fragment, crystallizable) receptors in normal cells and poor tumor penetration [15]. Efforts have been made to overcome these limitations using antibody fragments to direct PSs to the tumor [16]. scFv (single-chain fragment, variable) fragments provide efficient tumor penetration and the molecular specificity achieved by these scFvs has been found to vary for different PSs [17]. Some other advances include (i) production of a recombinant immunophotosensitizer [18] using a red fluorescent protein as PS, to overcome the synthetic limitations, such as purification, associated with antibody–PS constructs, and (ii) application of small immune proteins (SIPs) as antibody fragments [19]. SIPs may be preferable for many tumor targeting applications due to their excellent *in vivo* stability, long residence times in tumors, and good selectivity. *In vivo* PDT efficacy was enhanced with a SIP–PS conjugate as compared with an scFv conjugate [19]. Proteins such as transferrin [20] and albumin [22] have also been used for tumor targeting and can improve the specificity and efficiency of PDT [23]. In addition, antibodies have been used as targeting moieties in conjugation with other delivery constructs such as nanoparticles (NPs) [24]. Antibody-targeted PSs have rarely been used clinically, probably owing to the complicated and expensive regulatory process required for such transitions.

19.3
Delivering Photosensitizers via Targeted Nanoconstructs

Many PSs are hydrophobic, reconstitute poorly, have difficult transport in biological systems, and may be rapidly cleared by the reticuloendothelial system (RES) of the body. Preparation of pharmaceutical formulations for parenteral administration of such PSs is greatly hindered because of these limitations and, to overcome this, strategies that employ nanometer-sized delivery vehicles called NPs have been developed in order to permit the stable dispersion of these PSs into aqueous systems. NP encapsulation of PSs has broadened the spectrum of viable PSs for PDT due to the enhanced solubility and stability [24]. The leaky neovasculature of tumors favors accumulation and diminished clearing, often referred to as the enhanced permeability and retention (EPR) effect, helps passively target the tumor. PSs have been encapsulated by different strategies in different NPs, including liposomes, micelles, polymeric NPs, and dendrimers [24]. The use of nanoparticle-encapsulated two-photon dyes or upconversion NPs allows activation with low-energy light which can deeply penetrate tissues [25]. Instead of being mere carriers, these nanoconstructs participate in the actual mechanism of PDT, either by acting as PSs themselves or as transducers of X-rays or near-infrared radiation to emission wavelengths appropriate

for excitation of attached PSs. Further, the NPs can have specific targeting agents such as monoclonal antibodies, aptamers, or peptides for greater selectivity and specificity [24]. Even additional imaging agents may be attached or encapsulated in the NPs to allow for drug/treatment monitoring by fluorescence optical imaging, computed tomographic scan, magnetic resonance imaging, or positron emission tomography [26–28]. It should be emphasized that by appropriate design of the NP, one can circumvent natural barriers to drug delivery, and nanotechnology provides a promising future direction with a platform for the development of multimodal PDT-based combinations for enhanced treatment effects [29, 30]. However, much work still needs to be done and PDT is now at an exciting stage of development. Very few clinical studies have evaluated the effect of the different delivery systems in terms of clinical efficiency. Following extensive characterization, the rapid translation of nanoparticle-encapsulated PSs into the clinic could help validate the potential of PDT towards impacting cancer patients.

19.4
Target Modification/Cellular Activation

Target cell biology has also been modulated to enhance PS accumulation in tumors. ALA (δ-aminolevulinic acid)-mediated treatment provides an excellent example of this technique, where cell differentiation agents are used to increase the conversion of PpIX (protoporphyrin IX) PS from ALA, resulting in increased PDT effectiveness. Differentiating agents that have been used include vitamin D [31], methotrexate [32], and iron chelators (CP94) [33], which are already in clinical use. These agents can induce tumor cell differentiation and upregulate key enzymes involved in PpIX synthesis, thereby rendering tumor cells more susceptible to PDT.

Another upcoming approach is the generation of "Smart PSs." These PSs are initially in a quenched state but can be activated for photokilling by specific components in the tumor region and can provide increased specificity with reduced toxicity. Such "smart PSs" can potentially provide a powerful tool for targeted PDT in cancer. Various activation mechanisms have been explored, including tumor microenvironment (pH, hydrophobicity), enzyme cleavage, and nucleic acid sequence displacement. Lovell *et al*. have reviewed the design and application of such "smart PSs" that provide additional specificity for cancer treatment [34]. Only at the tumor is PS converted from an inactive (quenched) form to an active phototoxic state, thus preventing any collateral damage to the normal tissue. Despite encouraging initial results, further studies are needed before the full potential of such "smart PSs" can be established.

19.5
Conclusion

PS conjugates and supramolecular delivery platforms can improve PDT selectivity by exploiting cellular and physiological markers of targeted tissue. Overexpression of

receptors in cancer and angiogenic endothelial cells allows their targeting by affinity-based moieties for the selective uptake of PS conjugates and encapsulating delivery carriers, while the abnormal tumor neovascularization induces a specific accumulation of PS nanocarriers by the EPR effect. In addition, polymeric prodrug delivery platforms triggered by the acidic nature of the tumor environment or the expression of proteases can be designed. Promising results obtained with recent systemic carrier platforms will, in due course, be translated into the clinic for highly efficient and selective PDT protocols. The overall impact of the development of the more selective PDT agents will result in a broader applicability of this promising platform technology.

References

1 Triesscheijn, M., Baas, P., Schellens, J.H., and Stewart, F.A. (2006) *Oncologist*, **11**, 1034–1044.
2 Solban, N., Rizvi, I., and Hasan, T. (2006) *Lasers Surg. Med.*, **38**, 522–531.
3 Verma, S., Watt, G.M., Mai, Z., and Hasan, T. (2007) *Photochem. Photobiol.*, **83**, 996–1005.
4 Gravier, J., Schneider, R., Frochot, C., Bastogne, T., Schmitt, F., Didelon, J., Guillemin, F., and Barberi-Heyob, M. (2008) *J. Med. Chem.*, **51**, 3867–3877.
5 Swamy, N., Purohit, A., Fernandez-Gacio, A., Jones, G.B., and Ray, R. (2006) *J. Cell Biochem.*, **99**, 966–977.
6 Zheng, X. and Pandey, R.K. (2008) *Anticancer Agents Med. Chem.*, **8**, 241–268.
7 Ngen, E.J., Rajaputra, P., and You, Y. (2009) *Bioorg. Med. Chem.*, **17**, 6631–6640.
8 Schneider, R., Tirand, L., Frochot, C., Vanderesse, R., Thomas, N., Gravier, J., Guillemin, F., and Barberi-Heyob, M. (2006) *Anticancer Agents Med. Chem.*, **6**, 469–488.
9 Kessel, D. (2004) *J. Porph. Phthal.*, **8**, 1009–1014.
10 Sibrian-Vazquez, M., Nesterova, I.V., Jensen, T.J., and Vicente, M.G. (2008) *Bioconjug. Chem.*, **19**, 705–713.
11 Choi, Y., McCarthy, J.R., Weissleder, R., and Tung, C.H. (2006) *ChemMedChem*, **1**, 458–463.
12 Sehgal, I., Sibrian-Vazquez, M., and Vicente, M.G. (2008) *J. Med. Chem.*, **51**, 6014–6020.
13 Mallikaratchy, P., Tang, Z., and Tan, W. (2008) *ChemMedChem*, **3**, 425–428.
14 van Dongen, G., Visser, G.W., and Vrouenraets, M.B. (2004) *Adv. Drug Deliv. Rev.*, **56**, 31–52.
15 Carter, P. (2001) *Nat. Rev. Cancer*, **1**, 118–129.
16 Milgrom, L.R. (2008) *Sci. Prog.*, **91**, 241–263.
17 Bhatti, M., Yahioglu, G., Milgrom, L.R., Garcia-Maya, M., Chester, K.A., and Deonarain, M.P. (2008) *Int. J. Cancer*, **122**, 1155–1163.
18 Serebrovskaya, E.O., Edelweiss, E.F., Stremovskiy, O.A., Lukyanov, K.A., Chudakov, D.M., and Deyev, S.M. (2009) *Proc. Natl. Acad. Sci. U. S. A.*, **106**, 9221–9225.
19 Fabbrini, M., Trachsel, E., Soldani, P., Bindi, S., Alessi, P., Bracci, L., Kosmehl, H., Zardi, L., Neri, D., and Neri, P. (2006) *Int. J. Cancer*, **118**, 1805–1813.
20 Laptev, R., Nisnevitch, M., Siboni, G., Malik, Z., and Firer, M.A. (2006) *Br. J. Cancer*, **95**, 189–196.
21 Gilyazova, D.G., Rosenkranz, A.A., Gulak, P.V., Lunin, V.G., Sergienko, O.V., Khramtsov, Y.V., Timofeyev, K.N., Grin, M.A., Mironov, A.F., Rubin, A.B., Georgiev, G.P., and Sobolev, A.S. (2006) *Cancer Res.*, **66**, 10534–10540.

22 Anatelli, F., Mroz, P., Liu, Q., Yang, C., Castano, A.P., Swietlik, E., and Hamblin, M.R. (2006) *Mol. Pharmacol.*, **3**, 654–664.

23 Sharman, W.M., van Lier, J.E., and Allen, C.M. (2004) *Adv. Drug Deliv. Rev.*, **56**, 53–76.

24 Chatterjee, D.K., Fong, L.S., and Zhang, Y. (2008) *Adv. Drug Deliv. Rev.*, **60**, 1627–1637.

25 Zhang, P., Steelant, W., Kumar, M., and Scholfield, M. (2007) *J. Am. Chem. Soc.*, **129**, 4526–4527.

26 Reddy, G.R., Bhojani, M.S., McConville, P., Moody, J., Moffat, B.A., Hall, D.E., Kim, G., Koo, Y.E., Woolliscroft, M.J., Sugai, J.V., Johnson, T.D., Philbert, M.A., Kopelman, R., Rehemtulla, A., and Ross, B.D. (2006) *Clin. Cancer Res.*, **12** 6677–6686.

27 Koo, Y.E., Reddy, G.R., Bhojani, M., Schneider, R., Philbert, M.A., Rehemtulla, A., Ross, B.D., and Kopelman, R. (2006) *Adv. Drug Deliv. Rev.*, **58**, 1556–1577.

28 Spring, B., Mai, Z., Rai, P., and Hasan, T. (2010) Theranostic nanocells for simultaneous imaging and photodynamic therapy of pancreatic cancer. *Proc. SPIE*, **7551**, 755104.

29 Chen, W. and Zhang, J. (2006) *J. Nanosci. Nanotechnol.*, **6**, 1159–1166.

30 Rai, P., Chang, S., Mai, Z., Neuman, D., and Hasan, T. (2009) Nanotechnology-based combination therapy improves treatment response in cancer models. *Proc. SPIE*, **7380**, 73800W.

31 Ortel, B., Chen, N., Brissette, J., Dotto, G.P., Maytin, E., and Hasan, T. (1998) *Br. J. Cancer*, **77**, 1744–1751.

32 Sinha, A.K., Anand, S., Ortel, B.J., Chang, Y., Mai, Z., Hasan, T., and Maytin, E.V. (2006) *Br. J. Cancer*, **95**, 485–495.

33 Curnow, A. and Pye, A. (2007) *J. Environ. Pathol. Toxicol. Oncol.*, **26**, 89–103.

34 Lovell, J.F., Liu, T.W., Chen, J., and Zheng, G. (2010) Activatable photosensitizers for imaging and therapy. *Chem. Rev.*, **110**, 2839–2857.

20
Photodynamic Molecular Beacons

Pui-Chi Lo, Jonathan F. Lovell, and Gang Zheng

Photodynamic therapy (PDT) is a promising modality for cancer treatment [1, 2]. It involves the combined action of a photosensitizer, light, and molecular oxygen to generate reactive oxygen species (ROS), particularly singlet oxygen, to eradicate tumor cells. Although significant progress has been made over the last two decades in the development of highly efficient photosensitizers [3, 4], a major challenge is to enhance the selectivity of photosensitizers so that damage to surrounding tissues is minimized. To this end, various approaches have been explored to improve the tumor-targeting property of photosensitizers. One of the strategies involves conjugation with monoclonal antibodies or small-molecule ligands that have specific affinity for tumors [5, 6]. An alternative approach is through photosensitizer encapsulation in nanocarriers, such as liposomes, polymeric micelles, lipoproteins, and silica nanoparticles [7–9]. These nanomedicines can achieve long circulation times, allowing significant accumulation in tumors through the enhanced permeability and retention (EPR) effect [10, 11]. Rather than controlling the localization of photosensitizers, an alternative approach is to use activatable photosensitizers, which have recently attracted considerable attention [12–14]. These novel photosensitizers, upon interaction with various tumor-associated stimuli, can be switched "on" for photosensitization, offering a new level of selectivity for therapeutic applications. As shown in Figure 20.1, there are three steps to achieving targeted cell killing using activatable photosensitizers. First, the photosensitizers are delivered to the target cells and surrounding cells. This could be through systemic or topical routes. Next, the photosensitizers are activated only in the target tissue by enzymes or other factors associated with the target (and not the adjacent healthy cells). Finally, the target site is irradiated with light that is usually of a wavelength in the near-infrared range to maximize tissue penetration. Although the light is absorbed by the inactivated photosensitizers in the healthy tissue, the photosensitizers remain quenched and therefore no singlet oxygen is generated. The target cells activate the photosensitizers, and upon irradiation the photosensitizers generate singlet oxygen to kill those cells specifically.

To design an activatable photosensitizer targeting particular cells, several factors must be considered. The active linker, which regulates singlet oxygen

Handbook of Biophotonics. Vol.2: Photonics for Health Care, First Edition. Edited by Jürgen Popp, Valery V. Tuchin, Arthur Chiou, and Stefan Heinemann.

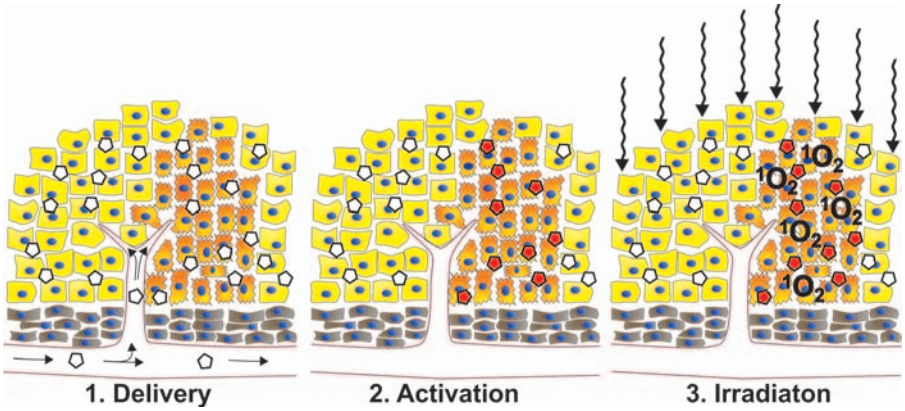

Figure 20.1 General principle of targeted cell killing by activatable photosensitizers.

production, is the centerpiece of the construct. Various activation mechanisms are possible, including the separation of photosensitizer and quencher through linker cleavage by target enzymes or linker elongation by a target nucleic acid. Selection of an appropriate photosensitizer is particularly important. It should absorb light at the appropriate wavelength (near-infrared wavelengths are usually ideal for *in vivo* applications) and have a high singlet oxygen quantum yield. Hydrophobicity should also be considered since very hydrophobic photosensitizers might affect the active linker control mechanism and could make purification more difficult. Finally, the quenching mechanism must be chosen carefully. The simplest quencher can be chosen based on FRET (Förster resonance energy transfer) efficiency with the fluorescence emission of the photosensitizers [15]. Alternatively, self-quenching mechanisms can be used, which often have the advantage of simpler synthesis and more photosensitizers per construct. However, it may be more difficult to predict a design that will ensure efficient self-quenching in the inactive state. Various activation mechanisms are summarized in Figure 20.2 and selected examples of these smart therapeutic agents are highlighted here, focusing on those which can be activated by the environment, enzymes, and nucleic acids.

It has well been documented that the extracellular pH in tumors is relatively low compared with that of normal tissues (about 6.8 versus 7.3) [16, 17]. This characteristic has been employed for the development of various pH-activatable fluorescence probes for cancer imaging [18, 19]. McDonnell *et al.* extended the study to prepare a series of amine-containing BF_2-chelated azadipyrromethenes (Figure 20.3), of which the singlet oxygen generation ability can be switched on and off in *N*,*N*-dimethylformamide (DMF) by changing the pH environment [20]. Under acidic conditions, the amino substituents are protonated, by which the photoinduced electron transfer (PET) process is inhibited. Compound **1**, for example, shows an approximately 10-fold enhancement in singlet oxygen generation efficiency. Compound **2** is a boron dipyrromethene derivative having an additional 15-crown-5 unit.

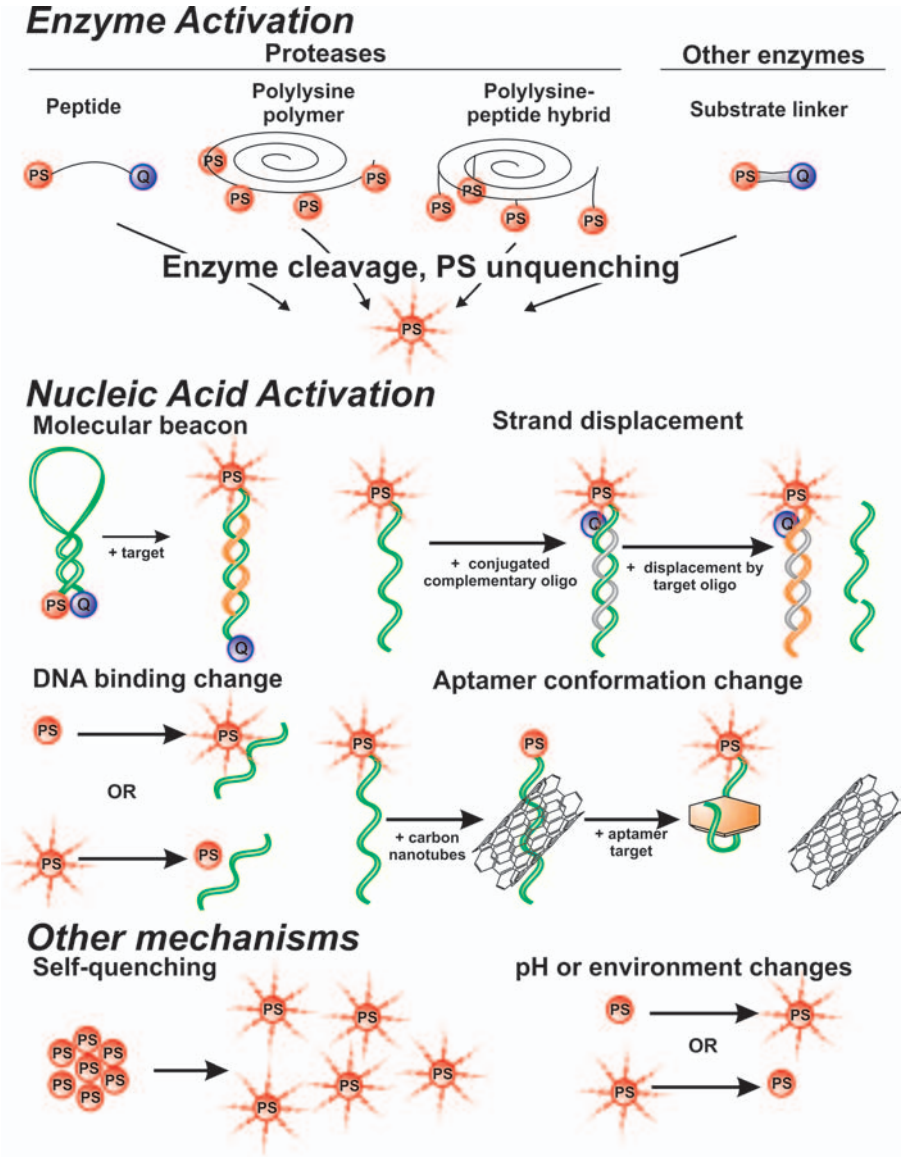

Figure 20.2 Different activation mechanisms of activatable photosensitizers for PDT, with PS representing a photosensitizer and Q representing a quencher.

It is responsive not only to the pH value, but also to the salt concentration, both of which are important physiological parameters [21]. Only at low pH and high salt concentration is this compound activated by hindering the PET process, showing an approximate sixfold increase in singlet oxygen production.

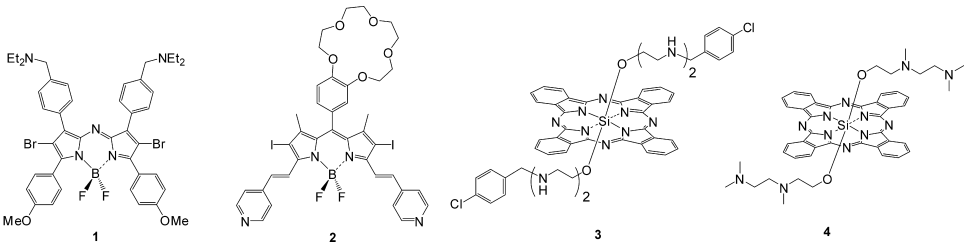

Figure 20.3 Selected examples of pH-activatable photosensitizers.

This approach has also been used by Jiang and co-workers, who synthesized a series of silicon(IV) phthalocyanines with two axial polyamine substituents (Figure 20.3) [22, 23]. The pH-dependent electronic absorption, fluorescence emission, and photosensitizing properties can be modulated by the axial substituents. Compounds **3** and **4** exhibit the most desirable changes in the pH range 5–7, which can roughly differentiate the tumor and normal tissue environments. Their intracellular fluorescence intensity and efficiency in generating singlet oxygen and superoxide radicals are greatly enhanced at lower pH, making them promising pH-controlled and tumor-selective fluorescence probes and photosensitizers for PDT.

Overexpression of specific enzymes is often associated with certain diseases. Proteases, for example, represent an important class of enzymes which are related to cancers, hypertension, AIDS, respiratory diseases, and so on. Therefore, they are the therapeutic targets of many clinically approved drugs for these diseases [24], and should be excellent candidates for activation of photosensitizers. In addition, due to their well-characterized and catalytic action, one enzyme molecule can in principle activate many molecules of the photosensitizer in a specific manner, resulting in high signal amplification. As shown in Figure 20.2, enzyme-activated photosensitizers have focused on enzymatic hydrolysis of covalent bonds that leads to a separation of photosensitizer and quencher. There have been several approaches to developing proteases beacons. Short peptides linking photosensitizer and quencher, polylysine backbones with self-quenched photosensitizers, and also peptide–polylysine hybrids have been described. Other substrates have been used to fuse photosensitizers so that quenching is impacted by enzymatic substrate cleavage. Chen *et al.* employed this concept to report a photodynamic molecular beacon (PMB), **5**, in which a pyropheophorbide *a* (Pyro) photosensitizer is linked to a carotenoid (CAR) quencher via a cleavable caspase-3 substrate, GDEVDGSGK (recognition site underlined; see Figure 20.4) [25]. Owing to the close proximity of Pyro and CAR, the excited state of Pyro is quenched by CAR, inhibiting the generation of singlet oxygen. However, in the presence of caspase-3, the peptide chain is cleaved and the detachment of Pyro and CAR leads to an increase in the singlet oxygen luminescence intensity (by about fourfold) and lifetime (by about 1.3-fold). In this particular PMB, the CAR not only deactivates the excited state of Pyro, but also directly scavenges singlet oxygen, which can minimize photodamage to nontargeted cells [26].

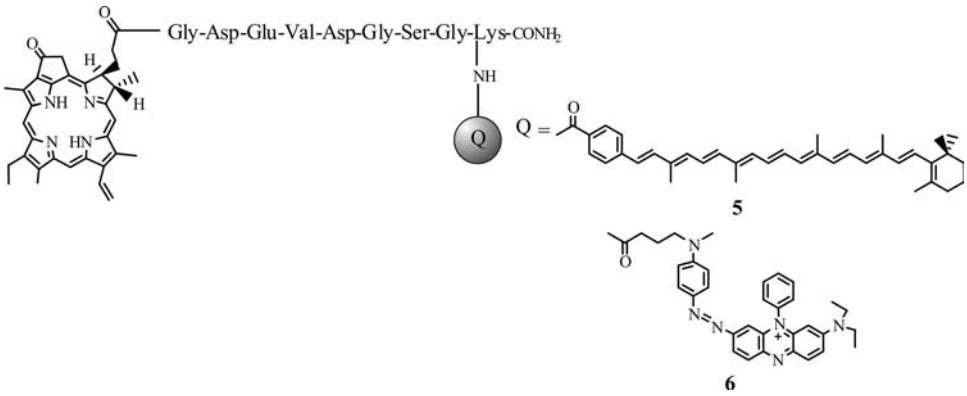

Figure 20.4 Caspase-3-activatable photosensitizers.

On the basis that caspase-3 is one of the executioner caspases involved in apoptosis, this kind of PMB can be used to indicate the occurrence apoptosis. PMB **6** is an analog of **5**, having a black hole quencher 3 (BHQ-3) instead of CAR as the quencher (Figure 20.4) [27]. This agent induces photodamage in irradiated cells by the sensitizing action of Pyro and simultaneously identifies apoptotic cells by the near-infrared fluorescence due to the detached Pyro. Hence this PMB can be considered as having a built-in apoptosis sensor for evaluating its therapeutic outcome *in situ*.

By using a similar strategy, PMBs triggered by matrix metalloproteinase-7 (MMP-7) [28] or fibroblast activation protein (FAP) [29] were also prepared and studied in detail, both *in vitro* and *in vivo*, by the same group. These PMBs are promising for the diagnosis and treatment of epithelial cancers. The studies validate the core principle of the PMB concept, showing that selective PDT-induced cell death can be achieved by controlling the singlet oxygen generation ability of the photosensitizer by responding to specific cancer-associated biomarkers.

One of the factors that affect the efficacy of PMBs is how close the photosensitizer and the quencher can be brought together by the peptide linkage. Different peptide sequences will give different background fluorescence as a result of their distinct natural folding. To overcome this problem, the concept of a "zipper" has been explored, which involves the introduction of two polycationic and polyanionic segments to hold the photosensitizer and the quencher in close proximity by electrostatic interactions. This results in silenced dye activity which is basically independent of the peptide linkage. The hairpin conformation of the substrate sequence can also facilitate the cleavage of the enzyme-specific linker. Chen *et al.* prepared a series of these zipper molecular beacons, in which Pyro connected to a segment of polyarginine and BHQ-3 connected to a segment polyglutamate are linked to two MMP-7-specific peptide sequences, GPLGLARK and RPLALWRSK [30]. It was found that the unsymmetrical beacon (BHQ-3)$(E)_5$GPLGLA$(R)_8$K(Pyro) can optimize the quenching efficiency and readiness of dissociation of the zipper arms after proteolysis. The polyanionic arm of the zipper can prevent the photosensitizer

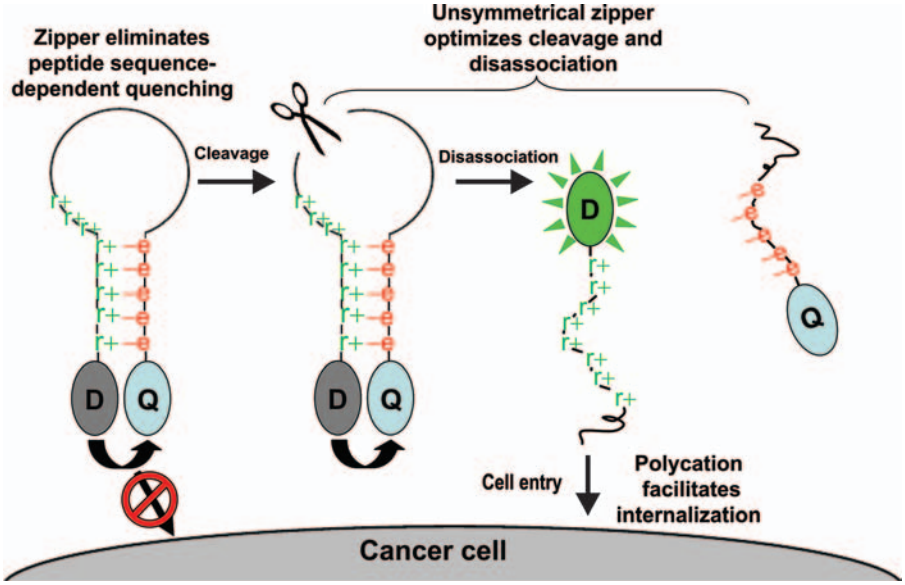

Figure 20.5 Schematic diagram showing the zipper molecular beacon design; D and Q represent the dye and the quencher, respectively. Reproduced with permission from Chen *et al.*, *Bioconjug. Chem.*, 2009, **20**, 1836.

from entering the cells, while the polycationic arm can enhance the cellular uptake of the dye after cleavage (Figure 20.5). This "zipper" concept can become a general approach to improve the functionality of a wide range of diagnostic and therapeutic probes through a simple modification of the substrate sequences.

In addition to these molecular beacons, polymeric protease-mediated photodynamic agents have also been reported [31–33]. Choi *et al.* developed a polylysine–chlorin e6 (Ce6) conjugate in which multiple Ce6 molecules are attached to a biodegradable poly-L-lysine (Lys) backbone grafted with monomethoxy poly(ethylene glycol) (MPEG) side chains (Figure 20.6) [31]. In this polymeric species, the Ce6 molecules are aggregated and the high local concentration of Ce6 causes self-

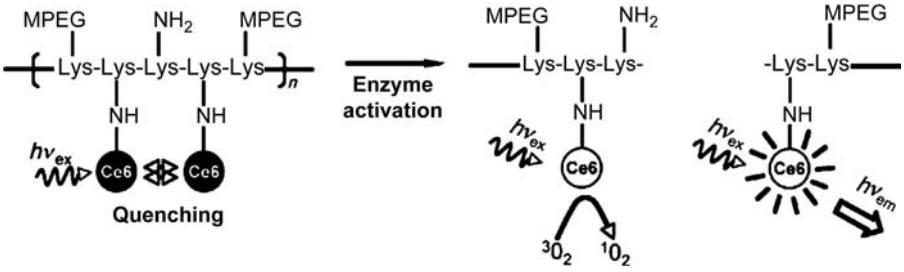

Figure 20.6 Activation of fluorescence emission and singlet oxygen generation of a polylysine–chlorin e6 conjugate by a protease. Reproduced with permission from Choi *et al.*, *Cancer Res.*, 2006, **66**, 7225.

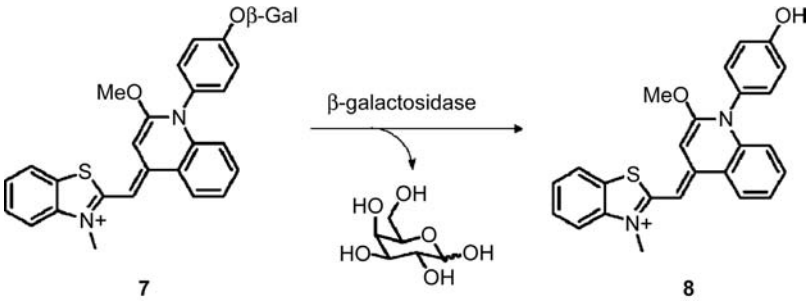

Figure 20.7 Activation of thiazole orange-based photosensitizer **7** by β-galactosidase. Reproduced with permission from Koide *et al.*, *J. Am. Chem. Soc.*, 2009, **131**, 6058.

quenching, resulting in weak fluorescence and low singlet oxygen generation. The aggregation behavior of this polymeric species, however, can enhance the tumor-accumulating property by the EPR effect. In the presence of cathepsin B in buffer, the fluorescence of this polymeric beacon is activated and its singlet oxygen generation efficiency increases sixfold. A similar activation process was also demonstrated *in vivo* using a xenographic tumor model. An intensified fluorescence signal was observed in the animals injected with the agent, which also showed an improved antitumor efficacy compared with controls. Campo *et al.* further improved this system by using a derivatized nicotinic acid polymer with a hydrophilic cationic quaternary amine group, thus eliminating the interference of PEGylation with the photosensitizer interactions that give rise to self-quenching [34].

Nagano and co-workers recently reported another enzymatically activatable photosensitizer based on thiazole orange (**7**, Figure 20.7) [35]. The bulky and hydrophilic β-galactoside moiety of **7** reduces its intracellular fluorescence emission and photosensitizing ability. This may be a result of the blockage of the binding between the dye and biomolecules, especially DNA in the cells. Upon hydrolysis by β-galactosidase, **7** gives the thiazole orange derivative **8** (Figure 20.7), by which both the fluorescence intensity and phototoxicity in cultured cells are greatly increased. The action of **7** on *lac*Z gene-transfected HEK293 *lac*Z(+) cells and untransfected *lac*Z(−) cells has also been examined. β-Galactosidase is encoded by *lac*Z gene from *Escherichia coli*. Interestingly, the HEK293 *lac*Z(+) cells incubated with **7** show a bright fluorescence image and are killed upon irradiation, whereas the *lac*Z(−) cells are only weakly fluorescent and remain essentially unharmed. During the photo-treatment, relocation of the dye to the nucleus was observed only in *lac*Z(+) cells. The results nicely demonstrate that **7** is activated specifically in β-galactosidase-expressing cells.

In addition to applications in cancer imaging and therapy, activatable photosensitizers are also potentially useful for the treatment of localized infections by drug-resistance bacteria. Zheng *et al.* reported a novel β-lactamase activated photosensitizer [36]. The short separation of the two photosensitizer moieties based on 5-(4′-carboxybutylamino)-9-diethylaminobenzo[*a*]phenothiazinium chloride leads to homo- or heterodimerization and eventually quenching of the fluorescence emission.

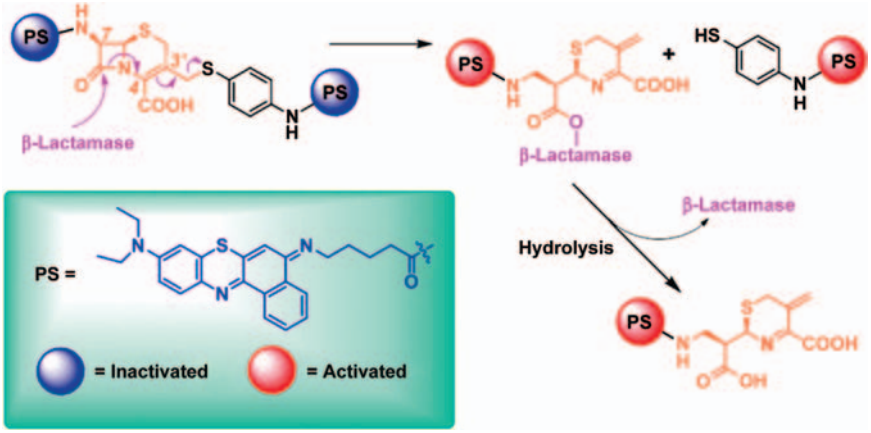

Figure 20.8 Mechanism of the cleavage of a β-lactamase activated photosensitizer. Reproduced with permission from Zheng *et al.*, *Angew. Chem. Int. Ed.*, 2009, **48**, 2148. Copyright Wiley-VCH Verlag GmbH & Co. KGaA.

In the presence of β-lactamase expressed by methicillin-resistant *Staphylococcus aureus* (MRSA), the β-lactam ring is cleaved, releasing activated photosensitizer moieties (Figure 20.8). The results show that photosensitizers can target MRSA selectively and cause less damage to host tissue than PDT with the free photosensitizer.

In addition to enzymes, nucleic acids can also be the targets for PMBs. On the basis that mRNAs have high tumor specificity and their hybridization to the complementary antisense oligonucleotide (AS-ON) sequences through Watson–Crick base pairing is highly selective and efficient, a novel mRNA-triggered PMB has been developed [37]. In this beacon, a Pyro photosensitizer and a CAR quencher are connected to a *c-raf-1* mRNA-targeted AS-ON as the loop sequence. The hairpin effect results in better control of the singlet oxygen production upon target–linker interactions compared with the peptide-based analog [26]. The signal-to-noise ratio is improved more than threefold. This PMB also shows efficient cellular uptake and PDT activation in *c-raf-1* expressing MDA-MB-231 cancer cells. By using a similar approach, Nesterova *et al.* recently prepared two dimer-based molecular beacons in

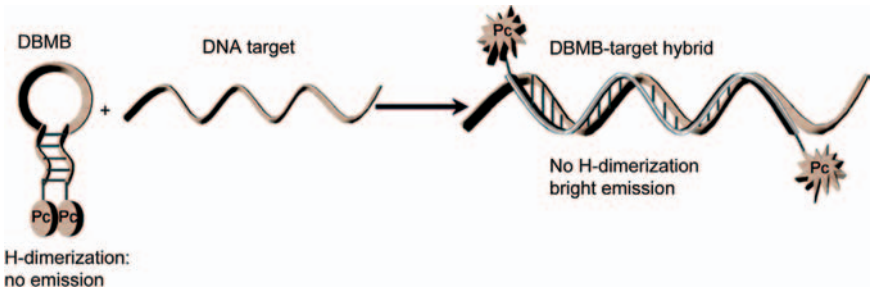

Figure 20.9 Schematic diagram showing the action of phthalocyanine dimer-based molecular beacons. Reproduced with permission from Nesterova *et al.*, *J. Am. Chem. Soc.*, 2009, **131**, 2432.

which two identical zinc(II) phthalocyanine moieties are linked together by an oligonucleotide sequence [38]. Owing to the intrinsic propensity of these phthalocyanines to form nonfluorescent H-type dimers, the beacons are in the "off" state. In the presence of the target DNA, the beacon's loop hybrids to its target, forcing the beacon to open. This disrupts the phthalocyanine dimer, restoring the fluorescence emission (Figure 20.9). Some attractive features of these dimer-based molecular beacons include their strong fluorescence emission in the open form due to the presence of two fluorescent reporter moieties and their relatively straightforward synthesis procedure.

This chapter has highlighted the design and effect of several classes of PMBs which can be activated by different tumor-associated stimuli. They have great potential in killing diseased cells effectively and specifically. Further development of this field of research should be intensified in the years ahead, particularly further improvement of their efficiency and selectivity, discovery of new activation mechanisms, and detailed *in vitro* and *in vivo* studies towards clinical implementation.

References

1 Allison, R.R., Bagnato, V.S., Cuenca, R., Downie, G.H., and Sibata, C.H. (2006) *Future Oncol.*, **2**, 53.
2 Wilson, B.C. and Patterson, M.S. (2008) *Phys. Med. Biol.*, **53**, R61.
3 Detty, M.R., Gibson, S.L., and Wagner, S.J. (2004) *J. Med. Chem.*, **47**, 3897.
4 Nyman, E.S. and Hynninen, P.H. (2004) *J. Photochem. Photobiol. B*, **73**, 1.
5 Sharman, W.M., van Lier, J.E., and Allen, C.M. (2004) *Adv. Drug Deliv. Rev.*, **56**, 53.
6 Verma, S., Watt, G.M., Mai, Z., and Hasan, T. (2007) *Photochem. Photobiol.*, **83**, 996.
7 Nishiyama, N., Jang, W.-D., and Kataoka, K. (2007) *New J. Chem.*, **31**, 1074.
8 Bechet, D., Couleaud, P., Frochot, C., Viriot, M.L., Guillemin, F., and Barberi-Heyob, M. (2008) *Trends Biotechnol.*, **26**, 612.
9 Zheng, G., Chen, J., Li, H., and Glickson, J.D. (2005) *Proc. Natl. Acad. Sci. U. S. A.*, **102**, 17757.
10 Ferrari, M. (2005) *Nat. Rev. Cancer*, **5**, 161.
11 Zhang, L., Gu, F.X., Chan, J.M., Wang, A.Z., Langer, R.S., and Farokhzad, O.C. (2008) *Clin. Pharmacol. Ther.*, **83**, 761.
12 Stefflova, K., Chen, J., and Zheng, G. (2007) *Frontiers Biosci.*, **12**, 4709.
13 Lovell, J.F. and Zheng, G. (2008) *J. Innov. Opt. Health Sci.*, **1**, 45.
14 Lovell, J.F., Liu, T.W., Chen, J., and Zheng, G. (2010) *Chem. Rev.*, **110**, 2839.
15 Lovell, J.F., Chen, J., Jarvi, M.T., Cao, W.-G., Allen, A.D., Liu, Y., Tidwell, T.T., Wilson, B.C., and Zheng, G. (2009) *J. Phys. Chem. B*, **113**, 3203.
16 Stubbs, M., McSheehy, P.M.J., Griffiths, J.R., and Bashford, C.L. (2000) *Mol. Med. Today*, **6**, 15–19.
17 Gerweck, L.E. (2000) *Drug Resist. Updates*, **3**, 49–50.
18 Tang, B., Yu, F., Li, P., Tong, L., Duan, X., Xie, T., and Wang, X. (2009) *J. Am. Chem. Soc.*, **131**, 3016.
19 Urano, Y., Asanuma, D., Hama, Y., Koyama, Y., Barrett, T., Kamiya, M., Nagano, T., Watanabe, T., Hasegawa, A., Choyke, P.L., and Kobayashi, H. (2009) *Nat. Med.*, **15**, 104.
20 McDonnell, S.O., Hall, M.J., Allen, L.T., Byrne, A., Gallagher, W.M., and O'Shea, D.F. (2005) *J. Am. Chem. Soc.*, **127**, 16360.
21 Ozlem, S. and Akkaya, E.U. (2009) *J. Am. Chem. Soc.*, **131**, 48.
22 Jiang, X.-J., Lo, P.-C., Yeung, S.-L., Fong, W.-P., and Ng, D.K.P. (2010) *Chem. Commun.*, 3188.

23 Jiang, X.-J., Lo, P.-C., Tsang, Y.-M., Yeung, S.-L., Fong, W.-P., and Ng, D.K.P. (2010) *Chem. Eur. J.*, **16**, 4777.

24 Turk, B. (2006) *Nat. Rev. Drug Discov.*, **5**, 785.

25 Chen, J., Stefflova, K., Niedre, M.J., Wilson, B.C., Chance, B., Glickson, J.D., and Zheng, G. (2004) *J. Am. Chem. Soc.*, **126**, 11450.

26 Chen, J., Jarvi, M., Lo, P.-C., Stefflova, K., Wilson, B.C., and Zheng, G. (2007) *Photochem. Photobiol. Sci.*, **6**, 1311.

27 Stefflova, K., Chen, J., Marotta, D., and Zheng, G. (2006) *J. Med. Chem.*, **49**, 3850.

28 Zheng, G., Chen, J., Stefflova, K., Jarvi, M., Li, H., and Wilson, B.C. (2007) *Proc. Natl. Acad. Sci. U. S. A.*, **104**, 8989.

29 Lo, P.-C., Chen, J., Stefflova, K., Warren, M.S., Navab, R., Bandarchi, B., Mullins, S., Tsao, M., Cheng, J.D., and Zheng, G. (2009) *J. Med. Chem.*, **52**, 358.

30 Chen, J., Liu, T.W.B., Lo, P.-C., Wilson, B.C., and Zheng, G. (2009) *Bioconjug. Chem.*, **20**, 1836.

31 Choi, Y., Weissleder, R., and Tung, C.-H. (2006) *Cancer Res.*, **66**, 7225.

32 Choi, Y., Weissleder, R., and Tung, C.-H. (2006) *ChemMedChem*, **1**, 698.

33 Gabriel, D., Busso, N., So, A., van den Bergh, H., Gurny, R., and Lange, N. (2009) *J. Control. Release*, **138**, 225.

34 Campo, M.A., Gabriel, D., Kucera, P., Gurny, R., and Lange, N. (2007) *Photochem. Photobiol.*, **83**, 958.

35 Koide, Y., Urano, Y., Yatsushige, A., Hanaoka, K., Terai, T., and Nagano, T. (2009) *J. Am. Chem. Soc.*, **131**, 6058.

36 Zheng, X., Sallum, U.W., Verma, S., Athar, H., Evans, C.L., and Hasan, T. (2009) *Angew. Chem. Int. Ed.*, **48**, 2148.

37 Chen, J., Lovell, J.F., Lo, P.-C., Stefflova, K., Niedre, M., Wilson, B.C., and Zheng, G. (2008) *Photochem. Photobiol. Sci.*, **7**, 775.

38 Nesterova, I.V., Erdem, S.S., Pakhomov, S., Hammer, R.P., and Soper, S.A. (2009) *J. Am. Chem. Soc.*, **131**, 2432.

21
Oxygen Effects in Photodynamic Therapy

Asta Juzeniene

21.1
Introduction

From the early days of photodynamic therapy (PDT), a combination of dyes (photosensitizers) and light has been used to kill cells. However, in 1902, the importance of a third element, molecular oxygen (O_2), was recognized by Ledoux-Lebards [1] and soon afterwards by von Tappeiner and Jesionek [2] and Straub [3]. They demonstrated that photodynamic action is inhibited in the absence of O_2 and concluded that O_2 is required in photosensitization reactions [1–3]. Several hypotheses have been proposed for the role of O_2 in these reactions. In 1931, Kautsky and de Bruijn proposed that O_2 in its singlet excited state could initiate photodynamic reactions [4], and Bäckström in 1934 suggested the involvement of free radicals [5]. Because of the difficulty in identifying and measuring the amounts of the photochemical reaction products *in vitro* and *in vivo*, the processes involved in photosensitization were not understood before the 1960s. In the presence of O_2, the photosensitized oxidation reactions can follow two pathways, called type I and type II reactions [6, 7]. In type I reactions, the triplet state photosensitizer can interact directly with biomolecules, by electron or hydrogen transfer, to form radicals and radical ions which react with O_2 to form oxidized products. In type II reactions (photodynamic action), the triplet state photosensitizer can transfer its energy directly to O_2, generating singlet molecular oxygen ($^1O_2$) [6–8]. Thus, the significance of O_2 in PDT was recognized, and later many important effects related to O_2 levels were observed. These are discussed in this chapter.

21.2
The Role of Oxygen in Photodynamic Therapy: $^1O_2$ Generation

$^1O_2$ is recognized to be the main mediator of photoinactivation of cells sensitized with most clinically used photosensitizers [8, 9]. In 2002, the production of $^1O_2$

Handbook of Biophotonics. Vol.2: Photonics for Health Care, First Edition. Edited by Jürgen Popp, Valery V. Tuchin, Arthur Chiou, and Stefan Heinemann.

during PDT was detected for the first time by direct measurements *in vivo* [10]. This highly reactive form of O_2 reacts with many biological molecules and causes damage that may be lethal for cells. The type II mechanism ($^1O_2$ mechanism) is generally considered to be dominant in PDT. The presence of sufficient O_2 is required for $^1O_2$ production in tissues.

21.3
Dependence of the Photosensitizing Effect on O_2 Concentration

When PDT became a cancer treatment, it was hoped that this treatment would not suffer from any O_2 effect, in comparison with radiation therapy or, at least, would be efficient down to very low O_2 levels. However, in the 1980s it was demonstrated that PDT was not efficient under anoxic conditions, either *in vitro* or *in vivo* [11–16]. The efficiency of photoinactivation of the sensitized cells decreases with decreasing O_2 concentration [12, 15]. The O_2 dependence of the photoinactivation of cells is affected by the type, intracellular concentration, and localization of the photosensitizer, the presence of $^1O_2$ quenchers, pH, and so on. For example, it has been demonstrated that the quantum yield of photoinactivation with hematoporphyrin derivative (HpD) was reduced by 50% when the partial pressure of oxygen (pO_2) was reduced to 7.6 mmHg in NHIK 3025 cells [15]. Similar results were later found *in vivo* by Henderson and Fingar [16].

21.4
The Oxygenation Status in Tumors and Normal Tissues

Oxygen concentrations are significantly lower in some solid tumors than in normal tissue. Up to half of locally advanced solid tumors may exhibit hypoxic and/or anoxic regions [17]. Hypoxic regions may be observed in breast, uterine cervix, vulva, head and neck, prostate, rectum, pancreas, brain tumors, soft tissue sarcomas, and malignant melanomas [17]. Tissue pO_2 is controlled by the O_2 delivery rate and by the O_2 consumption rate of vascular walls and tissues. An imbalance between O_2 supply and consumption in tumors is caused by abnormal structures and functions (tortuosity, leakiness, lack of pericytes, inhomogeneous distribution) of the microvessels, increased diffusion distances between the blood vessels and the tumor cells, and reduced O_2 transport capacity of the blood due to anemia [17]. Hypoxic areas in such tumors are insensitive to PDT [13, 16, 18]. Additionally, hypoxia may indicate an insufficient vascular network, likely to limit photosensitizer delivery.

PDT is now mainly used in dermatology to treat optically available skin cancer. The role of O_2 in cutaneous PDT has previously been described by Fuchs and Thiele [19].

21.5
PDT-Induced Reduction of Tumor Oxygenation

21.5.1
O_2 Consumption (Primary Reduction)

The majority of PDT-induced cytotoxic responses are due to type II reactions ($^1O_2$ generation) which require and consume O_2: one O_2 molecule is consumed for each $^1O_2$ that reacts with and oxidizes another molecule. The O_2 consumption rate depends on the concentration of photosensitizer, the fluence rate, the extinction coefficient of the photosensitizer, the quantum yield of photooxygenation, and so on [20–22]. The photochemical O_2 consumption rates under clinical conditions with Photofrin (porfimer sodium) at fluence rates greater than 100 $mW\,cm^{-2}$ are higher than the metabolic oxygen consumption rates of most tissues and lead to O_2 depletion during exposure to light [23, 24].

21.5.2
Vascular Damage (Secondary Reactions)

Some photosensitizers, especially after shorter incubation times before light exposure, accumulate mostly in blood vessels, and PDT then mainly targets tumor vasculature. Thus, PDT can lead to vasoconstriction and vessel clogging, depending on the conditions such as fluence rate, fluence, drug concentration, and tissue type [25–30]. Vascular damage to the tumor microenvironment is serious, since it inevitably leads to changes in the O_2 supply to the tumor. For example, within minutes of light exposure acute hypoxia in tumors due to vascular damage has been demonstrated during PDT with Photofrin [31, 32]. This almost always limits direct tumor cell photodestruction [31].

21.5.3
Photosensitizer Photobleaching (Secondary Reactions)

In addition to $^1O_2$ reactions with cellular targets, $^1O_2$ may react with the photosensitizer itself. Generally, even under well-oxygenated conditions, the photobleaching reactions also consume O_2. Most photosensitizers used in PDT are photolabile [33, 34]. Photobleaching can decrease the effectiveness of PDT by reducing the photosensitizer and O_2 concentrations. However, it can also be useful for dosimetry [35–37]. Sometimes, when the O_2 concentration is reduced (due to PDT itself or due to hypoxic conditions), the O_2-independent photobleaching mechanism, caused by interactions between excited triplet-state photosensitizer and biological substrates, becomes dominant for tumor and tissue damage. Then, provided that the photosensitizer concentration is lower in the surroundings of the tumor than in the tumor itself, there will be a selective effect on the tumor and

one does not need to worry about normal tissue damage, now matter how much light is delivered.

21.6 Methods to Reduce Tumor Deoxygenation During PDT

It is possible to minimize O_2 depletion during light exposure and to allow tumor reoxygenation.

21.6.1 Low Fluence Rates

Tumor responses to PDT with different photosensitizers depends on O_2 levels and on the fluence rate of the light [24, 38]. A reduction in fluence rate from high (75–200 mW cm^{-2}) to low (10–50 mW cm^{-2}) results in increased PDT efficiency [24, 38–42]. High fluence rate PDT is inefficient, since the consumption of O_2 exceeds the rate at which O_2 can be resupplied from the vasculature, leading to PDT-induced hypoxic tissue regions [24, 43]. O_2 depletion occurs on a time scale of seconds, and depends on the average fluence rate [22]. PDT carried out at a fluence rate of 50 mW cm^{-2} may consume O_2 at a rate of around 6–9 μM s^{-1} [20], whereas the rate is around 32 μM s^{-1} at 100 mW cm^{-2} [22]. There is a lower limit of efficient fluence rates (below 5.5 mW cm^{-2}) [24, 38]. A low fluence rate implies a long exposure time. If this time is too long, vessel damage will occur during exposure and, as a consequence, pO_2 will decrease. Thus, it has been found that low fluence rate PDT causes severe and longer lasting disruption of the microvascular perfusion [42, 44]. This may cause reduced PDT efficiency but may also lead to thrombosis and hemorrhage in tumor blood vessels that subsequently lead to tumor death via deprivation of O_2 and nutrients [42, 44, 45].

Recently, metronomic PDT has been proposed for delivery of ultra-low fluence rates (μW cm^{-2}) and low concentrations of a photosensitizer continuously over several hours, days, or weeks [22, 46].

21.6.2 Fractionated Light Exposure

O_2 consumption is more pronounced at higher fluence rates, and it may take only a few seconds to create anoxia [20]. This aspect is even more crucial when treating solid tumors, as they are often badly oxygenated. Fractionated light exposure regimes have been suggested to overcome this problem, because as long as the microvasculature remains functional, it is possible to stop light exposure for some time and allow reoxygenation. Effective reoxygenation of cells can occur in dark periods of around 30–150 s, depending on the degree of induced hypoxia and on the intactness of the microcirculation [20, 47]. Reperfusion injury can occur during PDT when blood flow is restored after a transient period of ischemia [48]. Furthermore, relocalization of the photosensitizer during the dark period may occur and improve the outcome [49].

21.6.3
Other Methods

Since most normal tissues contain about 5% oxygen, which is supplied by the circulation, they cannot be made more sensitive to PDT by increasing the oxygen tension because the relative quantum yield for $^1O_2$ formation is constant from 5 to 100% O_2, whereas it is halved at 1% oxygen [15, 16]. Hypoxic parts of tumors, however, can be made more sensitive to PDT by overcoming hypoxia. Several methods have been proposed to increase tumor oxygenation: (1) breathing hyperbaric oxygen, (2) using oxygen-carrying fluorocarbons combined with carbogen (95% oxygen) breathing, (3) using nicotinamide injection and carbogen breathing, (4) using oxygen-releasing substances, (5) modulating the oxygen binding capacity of hemoglobin, (6) decreasing the respiration rate, (7) increasing the oxygen solubility, (8) using blood flow modifiers, and (9) destroying hypoxic cells with bioreductive drugs or hypothermia [50]. Several of these methods have been exploited for PDT with promising experimental and clinical results [51–56].

21.7
Changes of Quantum Yields Related to Photosensitizer Relocalization

Under certain conditions, light exposure may result in a transient or permanent intracellular relocalization of photosensitizers (sulfonated *meso*-tetraphenylporphines, sulfonated aluminum phthalocyanines, etc.) [57–59], sometimes even to the nucleus [58–60]. This may lead to the DNA damage and sometimes increase the quantum yield of cell photodestruction [60, 61].

21.8
Changes of Optical Penetration Caused by Changes in O_2 Concentration

The O_2 concentration changes during PDT, as described above. This will lead to a change in the penetration spectrum of light into tissue since hemoglobin and oxyhemoglobin have different absorption spectra. This has to be considered in the choice of optimal wavelength. We have found that as O_2 depletion starts to manifest itself, and the hemoglobin/oxyhemoglobin ratio increases, the optical penetration will increase at 390–422, 455–500, 530–545, and 570–585 nm and decrease at 422–455, 500–530, 545–570, and 585–805 nm [62, 63].

21.9
Conclusion

The efficacy of PDT is crucially dependent on tissue oxygenation, which changes during PDT due to consumption in the photodynamic action itself, to photobleaching, and to vascular damage. The tissue oxygenation influences the penetration depth

of light into tissue during PDT. Reliable, noninvasive methods for monitoring oxygenation during PDT are needed. Optical methods, exploiting differences in the absorption spectra of hemoglobin and oxyhemoglobin, are promising in view of their simplicity and precision.

References

1 Ledoux-Lebards, C. (1902) Action de la lumière sur la toxicité de l'éosine et de quelques autres substances pour les paramècies. *Ann. Inst. Pasteur*, **16**, 587–594.

2 von Tappeiner, H. and Jesionek, A. (1903) Therapeutische Versuche mit fluoreszierenden Stoffen. *Münch. Med. Wochenschr.*, **50**, 2042–2044.

3 Straub, W. (1904) Uber chemische Vorgänge bei der Einwirkung von Licht auf fluoreszierende Substanzen (Eosin und Chinin) und die Bedeutung dieser Vorgänge für die Giftwirkung. *Münch. Med. Wochenschr.*, **51**, 1093–1096.

4 Kautsky, H. and de Bruijn, H. (1931) Die Aufklärung der Photoluminescenztilgung fluorescierender Systeme durch Sauerstoff: die Bildung aktiver, diffusionsfähiger Sauerstoffmoleküle durch Sensibilisierung. *Naturwissenschaften*, **19**, 1043.

5 Bäckström, H.L.J.B. (1934) Der Kettenmechanismus bei der Autoxydation von Aldehyden. *Z. Phys. Chem. B*, **25**, 99–121.

6 Foote, C.S. (1991) Definition of type I and type II photosensitized oxidation. *Photochem. Photobiol.*, **54** (5), 659.

7 Foote, C.S. (1968) Mechanisms of photosensitized oxidation. *Science*, **29**, 963–970.

8 Moan, J., Pettersen, E.O., and Christensen, T. (1979) The mechanism of photodynamic inactivation of human cells *in vitro* in the presence of haematoporphyrin. *Br. J. Cancer*, **39** (4), 398–407.

9 Weishaupt, K.R., Gomer, C.J., and Dougherty, T.J. (1976) Identification of singlet oxygen as the cytotoxic agent in photoinactivation of a murine tumor. *Cancer Res.*, **36** (7 Pt. 1), 2326–2329.

10 Niedre, M., Patterson, M.S., and Wilson, B.C. (2002) Direct near-infrared luminescence detection of singlet oxygen generated by photodynamic therapy in cells *in vitro* and tissues *in vivo*. *Photochem. Photobiol.*, **75** (4), 382–391.

11 Gomer, C.J. and Razum, N.J. (1984) Acute skin response in albino mice following porphyrin photosensitization under oxic and anoxic conditions. *Photochem. Photobiol.*, **40** (4), 435–439.

12 Lee See, K., Forbes, I.J., and Betts, W.H. (1984) Oxygen dependency of photocytotoxicity with haematoporphyrin derivative. *Photochem. Photobiol.*, **39** (5), 631–634.

13 Freitas, I. (1985) Role of hypoxia in photodynamic therapy of tumors. *Tumori*, **71** (3), 251–259.

14 Mitchell, J.B., McPherson, S., DeGraff, W., Gamson, J., Zabell, A., and Russo, A. (1985) Oxygen dependence of hematoporphyrin derivative-induced photoinactivation of Chinese hamster cells. *Cancer Res.*, **45** (5), 2008–2011.

15 Moan, J. and Sommer, S. (1985) Oxygen dependence of the photosensitizing effect of hematoporphyrin derivative in NHIK 3025 cells. *Cancer Res.*, **45** (4), 1608–1610.

16 Henderson, B.W., and Fingar, V.H. (1987) Oxygen limitation of direct tumor cell kill during photodynamic treatment of a murine tumor model. *Cancer Res.*, **47** (12), 3110–3114.

17 Mees, G., Dierckx, R., Vangestel, C., and Van de Wiele, C. (2009) Molecular imaging of hypoxia with radiolabelled agents. *Eur. J. Nucl. Med. Mol. Imaging*, **36** (10), 1674–1686.

18 Henderson, B.W. and Fingar, V.H. (1989) Oxygen limitation of direct tumor cell kill during photodynamic treatment of a murine tumor model. *Photochem. Photobiol.*, **49** (3), 299–304.

19 Fuchs, J. and Thiele, J. (1998) The role of oxygen in cutaneous photodynamic therapy. *Free Radic. Biol. Med.*, **24** (5), 835–847.

20 Foster, T.H., Murant, R.S., Bryant, R.G., Knox, R.S., Gibson, S.L., and Hilf, R. (1991) Oxygen consumption and diffusion effects in photodynamic therapy. *Radiat. Res.*, **126** (3), 296–303.

21 Moan, J. and Juzeniene, A. (2008) The role of oxygen in photodynamic therapy, in *Advances in Photodynamic Therapy. Basic, Translational, and Clinical* (eds. M.R. Hamblin and P. Mroz), Artech House, Boston, pp. 135–149.

22 Wilson, B.C. and Patterson, M.S. (2008) The physics, biophysics and technology of photodynamic therapy. *Phys. Med. Biol.*, **53** (9), R61–R109.

23 Henderson, B.W., Busch, T.M., Vaughan, L.A., Frawley, N.P., Babich, D., Sosa, T.A., Zollo, J.D., Dee, A.S., Cooper, M.T., Bellnier, D.A., Greco, W.R., and Oseroff, A.R. (2000) Photofrin photodynamic therapy can significantly deplete or preserve oxygenation in human basal cell carcinomas during treatment, depending on fluence rate. *Cancer Res.*, **60** (3), 525–529.

24 Henderson, B.W., Busch, T.M., and Snyder, J.W. (2006) Fluence rate as a modulator of PDT mechanisms. *Lasers Surg. Med.*, **38** (5), 489–493.

25 Fingar, V.H., Wieman, T.J., Wiehle, S.A., and Cerrito, P.B. (1992) The role of microvascular damage in photodynamic therapy: the effect of treatment on vessel constriction, permeability, and leukocyte adhesion. *Cancer Res.*, **52** (18), 4914–4921.

26 Fingar, V.H. (1996) Vascular effects of photodynamic therapy. *J. Clin. Laser Med. Surg.*, **14** (5), 323–328.

27 Engbrecht, B.W., Menon, C., Kachur, A.V., Hahn, S.M., and Fraker, D.L. (1999) Photofrin-mediated photodynamic therapy induces vascular occlusion and apoptosis in a human sarcoma xenograft model. *Cancer Res.*, **59** (17), 4334–4342.

28 Fingar, V.H., Taber, S.W., Haydon, P.S., Harrison, L.T., Kempf, S.J., and Wieman, T.J. (2000) Vascular damage after photodynamic therapy of solid tumors: a view and comparison of effect in pre-clinical and clinical models at the University of Louisville. *In Vivo*, **14** (1), 93–100.

29 Krammer, B. (2001) Vascular effects of photodynamic therapy. *Anticancer Res.*, **21** (6B), 4271–4277.

30 Chen, B., Pogue, B.W., Hoopes, P.J., and Hasan, T. (2006) Vascular and cellular targeting for photodynamic therapy. *Crit. Rev. Eukaryot. Gene Expr.*, **16** (4), 279–305.

31 Henderson, B.W. and Dougherty, T.J. (1992) How does photodynamic therapy work? *Photochem. Photobiol.*, **55** (1), 145–157.

32 van Geel, I., Oppelaar, H., Rijken, P.F., Bernsen, H.J., Hagemeier, N.E., van der Kogel, A.J., Hodgkiss, R.J., and Stewart, F.A. (1996) Vascular perfusion and hypoxic areas in RIF-1 tumours after photodynamic therapy. *Br. J. Cancer*, **73** (3), 288–293.

33 Bonnett, R. and Martinez, G. (2001) Photobleaching of sensitisers used in photodynamic therapy. *Tetrahedron*, **57** (47), 9513–9547.

34 Moan, J., Juzenas, P., and Bagdonas, S. (2000) Degradation and transformation of photosensitisers during light exposure, in *Recent Research Developments in Photochemistry and Photobiology* (ed. S.G. Pandalai), Transworld Research Network, Trivandrum, pp. 121–132.

35 Finlay, J.C., Mitra, S., Patterson, M.S., and Foster, T.H. (2004) Photobleaching kinetics of Photofrin *in vivo* and in multicell tumour spheroids indicate two simultaneous bleaching mechanisms. *Phys. Med. Biol.*, **49** (21), 4837–4860.

36 Dysart, J.S. and Patterson, M.S. (2005) Characterization of Photofrin photobleaching for singlet oxygen dose estimation during photodynamic therapy of MLL cells *in vitro*. *Phys. Med. Biol.*, **50** (11), 2597–2616.

37 Weston, M.A. and Patterson, M.S. (2009) Simple photodynamic therapy dose models fail to predict the survival of MLL cells after HPPH-PDT *in vitro*. *Photochem. Photobiol.*, **85** (3), 750–759.

38 Veenhuizen, R.B. and Stewart, F.A. (1995) The importance of fluence rate in photodynamic therapy: is there a parallel with ionizing radiation dose-rate effects? *Radiother. Oncol.*, **37** (2), 131–135.

39 Gibson, S.L., VanDerMeid, K.R., Murant, R.S., Raubertas, R.F., and Hilf, R. (1990) Effects of various photoradiation regimens on the antitumor efficacy of photodynamic therapy for R3230AC mammary carcinomas. *Cancer Res.*, **50** (22), 7236–7241.

40 Feins, R.H., Hilf, R., Ross, H., and Gibson, S.L. (1990) Photodynamic therapy for human malignant mesothelioma in the nude mouse. *J. Surg. Res.*, **49** (4), 311–314.

41 Foster, T.H., Hartley, D.F., Nichols, M.G., and Hilf, R. (1993) Fluence rate effects in photodynamic therapy of multicell tumor spheroids. *Cancer Res.*, **53** (6), 1249–1254.

42 Sitnik, T.M., Hampton, J.A., and Henderson, B.W. (1998) Reduction of tumour oxygenation during and after photodynamic therapy *in vivo*: effects of fluence rate. *Br. J. Cancer*, **77** (9), 1386–1394.

43 Foster, T.H., Murant, R.S., Bryant, R.G., Knox, R.S., Gibson, S.L., and Hilf, R. (1991) Oxygen consumption and diffusion effects in photodynamic therapy. *Radiat. Res.*, **126** (3), 296–303.

44 Henderson, B.W., Sitnik-Busch, T.M., and Vaughan, L.A. (1999) Potentiation of photodynamic therapy antitumor activity in mice by nitric oxide synthase inhibition is fluence rate dependent. *Photochem. Photobiol.*, **70** (1), 64–71.

45 Castano, A.P., Demidova, T.N., and Hamblin, M.R. (2005) Mechanisms in photodynamic therapy: Part three – Photosensitizer pharmacokinetics, biodistribution, tumor localization and modes of tumor destruction. *Photodiagn. Photodyn. Ther.*, **2** (2), 91–106.

46 Bisland, S.K., Lilge, L., Lin, A., Rusnov, R., and Wilson, B.C. (2004) Metronomic photodynamic therapy as a new paradigm for photodynamic therapy: rationale and preclinical evaluation of technical feasibility for treating malignant brain tumors. *Photochem. Photobiol.*, **80**, 22–30.

47 Curnow, A., Haller, J.C., and Bown, S.G. (2000) Oxygen monitoring during 5-aminolaevulinic acid induced photodynamic therapy in normal rat colon. Comparison of continuous and fractionated light regimes. *J. Photochem. Photobiol. B*, **58** (2–3), 149–155.

48 Curnow, A. and Bown, S.G. (2002) The role of reperfusion injury in photodynamic therapy with 5-aminolaevulinic acid – a study on normal rat colon. *Br. J. Cancer*, **86** (6), 989–992.

49 Anholt, H. and Moan, J. (1992) Fractionated treatment of CaD2 tumors in mice sensitized with aluminium phthalocyanine tetrasulfonate. *Cancer Lett.*, **61** (3), 263–267.

50 Vaupel, P., Kelleher, D.K., and Thews, O. (1998) Modulation of tumor oxygenation. *Int. J. Radiat. Oncol. Biol. Phys.*, **42** (4), 843–848.

51 Fingar, V.H., Wieman, T.J., Park, Y.J., and Henderson, B.W. (1992) Implications of a pre-existing tumor hypoxic fraction on photodynamic therapy. *J. Surg. Res.*, **53** (5), 524–528.

52 Ma, L.W., Moan, J., Steen, H.B., and Iani, V. (1995) Anti-tumour activity of photodynamic therapy in combination with mitomycin C in nude mice with human colon adenocarcinoma. *Br. J. Cancer*, **71** (5), 950–956.

53 Tomaselli, F., Maier, A., Sankin, O., Anegg, U., Stranzl, U., Pinter, H., Kapp, K., and Smolle-Juttner, F.M. (2001) Acute effects of combined photodynamic therapy and hyperbaric oxygenation in lung cancer – a clinical pilot study. *Lasers Surg. Med.*, **28** (5), 399–403.

54 Chen, Q., Huang, Z., Chen, H., Shapiro, H., Beckers, J., and Hetzel, F.W. (2002) Improvement of tumor response by manipulation of tumor oxygenation

during photodynamic therapy. *Photochem. Photobiol.*, **76** (2), 197–203.

55 Huang, Z., Chen, Q., Shakil, A., Chen, H., Beckers, J., Shapiro, H., and Hetzel, F.W. (2003) Hyperoxygenation enhances the tumor cell killing of Photofrin-mediated photodynamic therapy. *Photochem. Photobiol.*, **78** (5), 496–502.

56 Skyrme, R.J., French, A.J., Datta, S.N., Allman, R., Mason, M.D., and Matthews, P.N. (2005) A phase-1 study of sequential mitomycin C and 5-aminolaevulinic acid-mediated photodynamic therapy in recurrent superficial bladder carcinoma. *BJU Int.*, **95** (9), 1206–1210.

57 Berg, K., Bommer, J.C., Winkelman, J.W., and Moan, J. (1990) Cellular uptake and relative efficiency in cell inactivation by photoactivated sulfonated *meso*-tetraphenylporphines. *Photochem. Photobiol.*, **52** (4), 775–781.

58 Berg, K. and Moan, J. (1994) Lysosomes as photochemical targets. *Int. J. Cancer*, **59** (6), 814–822.

59 Moan, J., Berg, K., Anholt, H., and Madslien, K. (1994) Sulfonated aluminium phthalocyanines as sensitizers for photochemotherapy. Effects of small light doses on localization, dye fluorescence and photosensitivity in V79 cells. *Int. J. Cancer*, **58** (6), 865–870.

60 Berg, K., Madslien, K., Bommer, J.C., Oftebro, R., Winkelman, J.W., and Moan, J. (1991) Light induced relocalization of sulfonated *meso*-tetraphenylporphines in NHIK 3025 cells and effects of dose fractionation. *Photochem. Photobiol.*, **53** (2), 203–210.

61 Wood, S.R., Holroyd, J.A., and Brown, S.B. (1997) The subcellular localization of Zn (II) phthalocyanines and their redistribution on exposure to light. *Photochem. Photobiol.*, **65** (3), 397–402.

62 Nielsen, K.P., Juzeniene, A., Juzenas, P., Stamnes, K., Stamnes, J.J., and Moan, J. (2005) Choice of optimal wavelength for PDT: the significance of oxygen depletion. *Photochem. Photobiol.*, **81** (5), 1190–1194.

63 Juzeniene, A., Nielsen, K.P., and Moan, J. (2006) Biophysical aspects of photodynamic therapy. *J. Environ. Pathol. Toxicol. Oncol.*, **25** (1–2), 7–28.

22
Organic Light-Emitting Diodes (OLEDs): Next-Generation Photodynamic Therapy of Skin Cancer

Ifor D.W. Samuel, James Ferguson, and Andrew McNeill

22.1
Introduction

The distinctive properties of modern light sources have opened up many uses of light in the diagnosis and treatment of disease. These light sources are particularly relevant in the treatment of skin diseases because the skin is so readily accessible, and as a result light is now used in the treatment of more than 30 skin diseases. A very important and rapidly growing family of skin diseases is skin cancers. Many of these cancers (notably basal cell carcinomas and Bowen's disease) can be treated by photodynamic therapy (PDT), in which a combination of light and a drug is used to cause a photochemical reaction to destroy the tumor.

Over the past 20 years, there has been considerable growth in PDT arising from a combination of advances in light sources and photosensitizers [1–5]. It is the treatment of choice for many skin cancers and is now widely used across Europe and Australia. Although light is used in the treatment of many skin diseases, its use is heavily restricted by constraints imposed by the hospital-based light sources that are typically used [6]. In this chapter, we review the strengths and weaknesses of PDT as currently practiced, introduce organic light-emitting diodes (OLEDs) as novel light sources, and show how wearable light sources inspired by them are transforming PDT.

22.2
PDT of Skin Cancer: Current Approach

Current treatments for skin cancers include surgical excision, cryotherapy, radiotherapy, and various creams. Surgery is very effective but can leave significant scarring and carries a risk of infection. PDT offers a gentler alternative, which can give excellent cosmetic outcomes. This is important as lesions are caused by sunlight

Handbook of Biophotonics. Vol.2: Photonics for Health Care, First Edition. Edited by Jürgen Popp, Valery V. Tuchin, Arthur Chiou, and Stefan Heinemann.

and therefore occur in places that can be seen. The current treatment cycle typically consists of an initial visit to a family doctor, followed by a visit to hospital for the lesion to be identified, two return visits for PDT, and a further return visit for follow-up.

On each of the visits for PDT, the lesion is initially abraided by light curettage (scraping) and a cream of a precursor to the photosensitizer [δ-aminolevulinic acid (ALA) or its methyl analog, Metvix] is applied. This precursor is metabolized to the photosensitizer protoporphyrin IX over the next few hours. Accumulation of protoporphyrin IX occurs preferentially in tumors and so strong selectivity for the tumor is achieved. Four hours after the cream has been applied, the lesion is illuminated under intense red light ($65\,mW\,cm^{-2}$) for 20 min, leading to a dose of $75\,J\,cm^{-2}$. The treatment is often painful and a variety of measures are used to manage the pain, including blowing cool air over the treatment area and in some cases local anesthetic. The procedure is labor intensive as the patient requires supervision to provide appropriate pain relief. The treatment is repeated 1 month later and the two sessions are normally sufficient to kill the tumor.

A variety of light sources are commonly used. These include solid-state diode lasers, filtered lamps, and large arrays of inorganic light-emitting diodes (LEDs). These light sources are expensive and cumbersome, requiring the patient to come to the hospital for treatment, and to lie still under the light source. The number of patients who can be treated is limited by the availability of light sources and supervising staff. From the patient's point of view, the treatment involves a considerable waiting time in hospital. The pain in conventional PDT is also a major concern as median pain scores are 6 on a scale where 10 is extremely severe pain [7]. Even so, the cosmetic results can be impressive.

22.3
Advances in Light Sources: Organic Light-Emitting Diodes

Organic semiconductors are plastic-like materials with semiconducting electronic properties. They combine favorable properties of plastics such as tunability by changing the structure, with scope for simple fabrication and manufacture, so enabling a new generation of semiconductor devices to be made. Many of these devices are related to their inorganic counterparts, and yet with distinctive aspects. For example, these materials can be dissolved and so deposited by simple processes such as ink-jet printing to make devices such as LEDs and transistors. The simplest organic light-emitting diode (OLED) structure consists of one or more ($\sim$100 nm) thin organic layers between contacts. When a voltage is applied, charges are injected and opposite charges can meet up, leading to emission of light.

The materials are amorphous so epitaxy is not required and different colors can be deposited side-by-side. As a result, most work on OLEDs has been directed towards making displays. Many mobile phones now contain OLED displays. Larger and even flexible displays are under development.

22.4
Transforming PDT with Wearable Light Sources

In this section, we show how OLEDs can be used for PDT and could lead to a transformation in the way in which PDT is delivered to patients.

22.4.1
Developing OLEDs for PDT

We recognized an opportunity to use OLEDs to perform PDT in a completely different way. OLEDs could be used to make a small, compact, wearable light source that would enable patients to undergo ambulatory treatment, that is, treatment in which they could move around (Figure 22.1). Displays are orders of magnitude dimmer than PDT light sources, so do not at first sight appear to be obvious candidates for PDT. However, as PDT works by a photochemical reaction, a lower intensity can be used for a longer time to achieve the desired result.

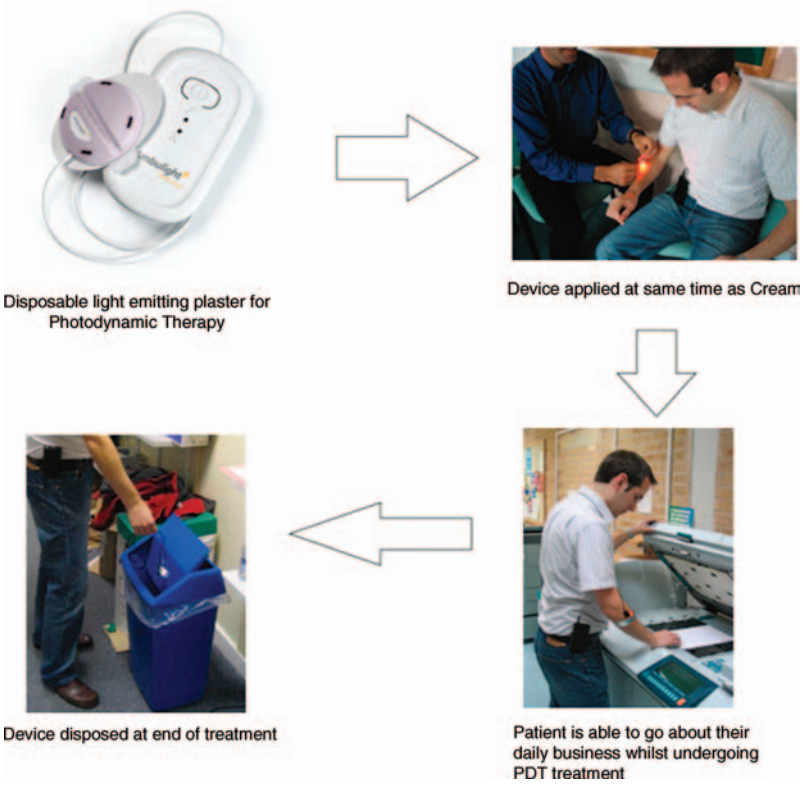

Figure 22.1 Ambulatory PDT. A wearable light source is used to treat skin cancer and is thrown away afterwards.

The demonstration of OLED-PDT required the development of suitable OLEDs. The requirements for OLED-PDT are very different from those for OLED displays. In OLED displays, important issues are achieving pure primary colors, making pixels, and ensuring a sufficiently long lifetime. For OLED-PDT, we envisage a disposable light source, so lifetime is not an issue. However, OLED-PDT requires uniform orange–red illumination over the area to be treated. Many lesions to be treated are small, so a light-emitting area 2 cm in diameter was sufficient for demonstration purposes. The device needs to run at much higher brightness than for a display, and in our initial studies we used OLEDs emitting 5 mW cm^{-2} in the orange–red region of the spectrum. An OLED is a very unusual light source because it emits light from an area, rather than a point. It also has a very distinctive shape – it is very thin. The device consists of two parts – a light-emitting head connected to a power supply containing batteries, that can be worn in a manner analogous to an iPod. Hence the patient can walk around or work during treatment. The light-emitting part of the device is attached to the area to be treated by adhesive tape, much like a sticking plaster.

22.4.2 Testing OLEDs for PDT

After obtaining ethical approval and initial studies on ourselves, we performed a pilot study at Ninewells Hospital, Dundee. The study involved following the same procedure as for conventional PDT, but applying light from an OLED for 3 hours instead of using one of the hospital fixed light sources. Patients could therefore move around during treatment.

Twelve patients with basal cell carcinoma or Bowen's disease were studied and received two treatments of OLED-PDT 1 month apart. At follow-up 6 months after treatment, seven of the 12 patients remained free from their lesions [7]. For the sample size, this is consistent with the normal (70–80%) success rate of PDT. In most cases, the cause of "failure" was a small region at the edge of the lesion in a crescent moon shape. The trial used OLED light sources that were 2 cm in diameter and treated lesions of up to 2 cm in size. It is therefore likely that the failures resulted from a slight misalignment of the light source over the lesion. This has been addressed in subsequent work by making the light source larger so that there is a significant margin of illumination around the lesion, and by introducing an alignment template for the clinician. These two measures now ensure that the entire lesion is treated evenly.

During the trial, patients were asked to rate the pain they felt on a scale from 0 to 10. For OLED-PDT, the median pain score was 1, whereas for conventional PDT the median pain score was 6. This is a remarkable difference and a major advantage of OLED-PDT. It is all the more remarkable as no pain relief was used with OLED-PDT, whereas a Cynosure (cool air) fan was used for all patients receiving conventional PDT. The reason for the reduced pain is that a much lower intensity of light is used for a much longer time.

22.4.3
Ambulatory PDT: a New Paradigm

The results of the pilot trial are extremely encouraging as they demonstrate ambulatory PDT with much reduced pain. There are many implications for treatment. One is that it is much more comfortable and convenient for the patient as they can move around during treatment and experience much less pain. Another is that the number of patients who can be treated is larger as there can be many of the light sources. It is also possible for the patient to return to work or home after the light source has been applied

The real scope for transformation of PDT comes from the possibility of avoiding a hospital visit altogether. Family doctors (general practitioners) could potentially administer the treatment, thereby removing the need for expensive and inconvenient hospital visits.

22.4.4
Commercialization of Ambulatory PDT

We are keen that the advantages of ambulatory PDT should be widely available. The path from concept to approved product is long and expensive and ambulatory PDT is now being commercialized via a spin-off company, Ambicare Health Ltd. The company raised money to enable a product to be designed that meets the requirements for medical CE marking. The medical CE mark has recently been awarded, meaning that the device can now be sold in the European Union. As OLED manufacture is still developing, the first product, Ambulight PDT (Figure 22.2), uses inorganic LEDs in combination with a diffuser as the light source. Future products

Figure 22.2 Ambulight PDT – a wearable light source for skin cancer treatment consisting of a self-adhesive light source and a separate battery-powered control unit.

may use OLEDs because they are area light sources by nature, matching the fact that a lesion is an area to be treated, and they are thin and can be flexible.

22.5 Conclusion

Advances in phototherapy and PDT have been closely linked to advances in light sources. PDT is an attractive treatment for many skin cancers, but its current use is limited by the need for cumbersome, specialized light sources, hospital visits, and many patients finding it painful. We have shown that OLEDs enable compact and convenient *wearable* light sources for PDT to be made, thereby making *ambulatory* treatment possible. This advance has the potential to transform PDT by enabling far more doctors to administer it, far more patients to receive it, and ultimately enabling treatment to take place without the need for hospital visits.

References

1 Babilas, P., Schreml, S., Landthaler, M., and Szeimies, R.M. (2010) *Photodermatol. Photoimmunol. Photomed*, **26**, 118.
2 Braathen, L.R., Szeimies, R.M. *et al.* (2007) *J. Am. Acad. Dermatol.*, **56**, 125.
3 Dougherty, T.J. (2002) *J. Clin. Laser Med. Surg.*, **20**, 3.
4 Ibbotson, S.H. (2010) *Photodiagn. Photodyn. Ther.*, **7**, 16.
5 Morton, C.A., McKenna, K.E., Rhodes, L.E., and The British Association of Dermatologists (2008) *Br. J. Dermatol.*, **159**, 1245.
6 Moseley, H., Allen, J.W. *et al.* (2006) *Br. J. Dermatol.*, **154**, 747.
7 Attili, S.K., Lesar, A. *et al.* (2009) *Br. J. Dermatol.*, **161**, 170.

23
Nanoparticles for Photodynamic Therapy

Wen-Tyng Li

23.1
Introduction

Photodynamic therapy (PDT) can be a curative modality for early or localized cancers and can improve quality of life and lengthen survival for advanced diseases. Owing to its minimal invasiveness and selective therapeutic effect, the applications of PDT have been expanded to treatment of precancerous conditions, infectious diseases, and age-related macular degeneration. Their advantages include cost effectiveness, highly localized treatments, sparing of extracellular matrix that allows regeneration of normal tissue, repetition of therapy without accumulation of toxicity, possibility of combining with chemotherapy, which leads to higher cure rates, and induction of immunity, which may contribute to long-term tumor control and suitability for outpatient therapy [1].

Depending on the part of the body being treated, the photosensitizer is administered by intravenous injection or local application. Light is applied to the area to be treated after the drug has been absorbed by the pathologic tissue. The photosensitizer activated by light forms reactive oxygen species (ROS) that kill the cancer cells directly by way of type I and type II reactions. Type I reaction involves the production of radicals resulting from the activated sensitizer reacting with plasma membrane or other intracellular molecules. Type II reaction involves generation of singlet oxygen ($^1O_2$) upon energy transfer from the activated sensitizer to oxygen. PDT may also work by destroying tumor-associated vasculature, leading to tumor infarction or by alerting the immune system to attack the cancer [2]. Responses to photodynamic treatment are dependent on the type of photosensitizer used, its extracellular and intracellular localization, the total dose administered, the total light exposure dose, light fluence rate, the time between the administration of the drug and light exposure, the oxygenation status of the tissue, and the type of cells involved [3].

Cancer cells respond to photodynamic damage by eliciting a rescue response and/or by undergoing cell death. Rescue responses often involve changes in gene and protein expression of stress proteins, allowing the cells to cope with the damage. PDT

Handbook of Biophotonics. Vol.2: Photonics for Health Care, First Edition. Edited by Jürgen Popp, Valery V. Tuchin, Arthur Chiou, and Stefan Heinemann.

may result in cell death via apoptosis, necrosis, or autophagy, which can be affected by the cell type, the nature of photosensitizers, the incubation protocol, and the light dose [4, 5]. The physical and chemical natures of the photosensitizers, such as hydrophobicity and charge, are of great importance in determining their subcellular localization. The sensitivity of intracellular components to photooxidation via photodynamic action plays an important role in photocytotoxicity. Photosensitizers can localize in mitochondria, lysosomes, endoplasmic reticulum, Golgi apparatus, and plasma membranes, which leads to different signaling pathways involved in cell death.

The essential goal of PDT is to induce efficient damage to tumor tissue while sparing the surrounding tissue. A selective therapeutic effect of PDT is achieved from preferential accumulation of photosensitizers and from irradiation of the target tissue. Some photosensitizers can reach higher concentrations in tumor tissue than in surrounding healthy tissue due to the abnormal physiology of tumors, such as poor lymphatic drainage, leaky vasculature, decreased pH, increased number of receptors for low-density lipoprotein, and abnormal stromal composition [6]. However, most photosensitizers are hydrophobic and tend to aggregate easily in aqueous media, which causes a decrease in its quantum yield and problems for intravenous administration. Although many photosensitizers have been developed, few have made it to clinical trials owing to factors such as poor selectivity in terms of target tissue and healthy tissue, low extinction coefficients, absorption spectra at relatively short wavelengths, and high accumulation rates in skin [7].

Increasing the selective accumulation of the photosensitizers within the tumor tissue allows a lower effective dose of the PDT drug. One can take advantage of the intrinsic features of cancer cells, such as specific surface antigens, low-density lipoprotein (LDL) receptor, and oxidation state [8]. To enhance PDT efficacy, a photosensitizer can be bound to ligands such as monoclonal antibodies or LDL, or can be delivered via carrier systems such as liposomes and micelles [9, 10]. The use of nanoparticles to improve the efficiency of PDT is a promising approach because (1) their large surface area can be modified with functional groups for additional biochemical properties, (2) they have large distribution volumes and are generally taken up efficiently by cells, (3) controlled release of drugs is possible, (4) many synthetic strategies allow transportation of hydrophobic drugs in blood, and (5) preferential accumulation in the solid tumor site is easy due to the enhanced permeability and retention effect [11]. To satisfy the requirements for an ideal PDT drug, some nanoparticles comprising inorganic oxide, metallic, ceramic, and biodegradable polymer nanomaterials have emerged with potential application for PDT. Nanoparticles for PDT were classified into active and passive nanoparticles according to the functional roles in the enhancement of PDT efficacy (Table 23.1) [11]. The former was sub-classified by mechanism of activation into photosensitizer nanoparticles, upconversion nanoparticles, and self-lighting nanoparticles. The latter was sub-classified by material composition into biodegradable and nonbiodegradable nanoparticles. Here, approaches to improving the efficacy of PDT for cancers by using active and passive nanoparticles are described.

Table 23.1 Classification of nanoparticles used for PDT.

Category	Material	Mechanism
Active nanoparticles		
Photosensitizer	CdSe/CdS/ZnS	Indirect excitation of photosensitizer through a FRET mechanism from the nanoparticle to the photosensitizer
	Fullerene	Nanoparticles transfer energy from incident light directly to surrounding oxygen
	SWNTs	CNTs act as quenchers to control and regulate $^1O_2$ generation
Upconverting	$NaYF_4:Yb^{3+},Er^{3+}$	Low-energy light is transduced to higher energy emissions to activate associated photosensitizer
	$NaYF_4:Yb^{3+},Tm^{3+}$	
Self-lighting	$BaFBr:Eu^{2+},Mn^{2+}$	Scintillation on excitation by X-rays activates attached photosensitizer
	$LaF_3:Tb^{3+}$	
Passive nanoparticles		
Biodegradable	Alginate, chitosan, cyclodextrin, albumin	Drug is delivered by micelles, dendrimers, liposomes, or polymeric nanoparticles
	PLA, PLGA, PVAL	Controlled release of encapsulated photosensitizer through biodegradation
Nonbiodegradable	Polyacrylamide	Two-photon dye is encapsulated by microemulsion
	Silica	Photosensitizer is adsorbed/covalently bonded to porous shell
	Gold	Nanoparticles act as pure carrier, no release
	Magnetic iron oxide	Drug is carried directly or co-encapsulated in micelle or polymeric nanoparticle Targeted delivery is achieved by external magnetic field

23.2 Active Nanoparticles for PDT

Regarding active roles in PDT, nanoparticles may act like catalysts to produce free radicals from dissolved oxygen, and serve as ROS modulators or light sources for activating photosensitizers. Nanoparticles such as fullerenes can be generated upon light irradiation, hence they can serve as photosensitizers themselves. Carbon nanotubes (CNTs) are fluorescence quenchers, which can be engineered to modulate $^1O_2$ generation. Nanoparticles such as quantum dots (QDs), upconversion nanoparticles, and scintillation nanoparticles can be used as light sources to activate photosensitizers due to their fluorescence emission properties. To serve as a PDT light source, the nanoparticle selected for activating a photosensitizer must meet the following criteria: (1) its emission spectrum must match the photosensitizer's absorption spectrum, (2) it must have high luminescence efficiency, (3) it must be

easily linked with photosensitizers, and (4) it must be nontoxic, water soluble, and stable in biological environments.

Fullerenes (C_{60}) are composed of 60 carbon atoms arranged in a soccer-ball structure. They absorb visible light, have a high triplet yield, and can generate ROS upon illumination due to their extended π-conjugation [12]. Functionalized fullerene has recently become an attractive tool for photodynamic applications. Depending on the functional groups introduced into the molecule, fullerenes can effectively photoinactivate cancer cells. The ability of fullerenes to generate reactive oxygen species and catalyze the phototoxic reaction after photoexcitation was first demonstrated on thymocytes and Ehrlich ascites cells [13]. One of the major problems in using fullerenes in biological systems is their poor solubility in aqueous solution, which may be overcome by encapsulation in special carriers, suspension with the help of co-solvents, introduction of hydrophilic appendages, or reduction to a water-soluble anion [14]. The photodynamic activity of the functionalized fullerenes as photosensitizers against mouse cancer cell lines was inversely proportional to the degree of substitution of the fullerene nucleus for both the neutral and the cationic groups [15]. Chemical modification of fullerene with poly(ethylene glycol) (PEG) not only made it soluble in water but also exhibited preferential accumulation and prolonged retention in the tumor tissue. PDT with fullerenes has been demonstrated in animal tumor models [16]. The major disadvantage of fullerenes is their optical absorption properties. The absorption spectrum of fullerenes is highest in the UVA and blue regions of the spectrum, where the tissue penetration depth of illumination is shortest due to a combination of light absorption by cellular chromophores and light scattering by cellular structures [12]. It is important to develop fullerenes that absorb red or near-infrared light for clinical application in PDT.

CNTs, which belong to the family of fullerenes, are made up of thin sheets of benzene ring carbons rolled up into the shape of a seamless tubular structure. Based on their structure, CNTs can be classified into single-walled nanotubes (SWNTs) and multi-walled nanotubes (MWNTs). Owing to their ultra-high surface area, molecules such as drugs, peptides, and nucleic acids can be integrated into their walls and tips, which enable them to cross the mammalian cell membrane by endocytosis or to recognize cancer-specific receptors on the cell surface. SWNTs are known to be efficient quenchers of fluorescence probes. A novel molecular complex of a photosensitizer (chlorin e6), an ssDNA aptamer, and SWNTs was engineered to control and regulate $^1O_2$ generation. Target binding with ssDNA aptamers to specific proteins could disturb the interaction between aptamers and SWNTs, resulting in the restoration of $^1O_2$ generation, whereby more selective PDT could be guaranteed [17]. Currently, the knowledge of CNT-based PDT is limited. Further research on the pharmacologic and toxicologic properties of CNTs is required before they could be recommended for routine clinical use [18].

QDs are semiconductor nanocrystals with high quantum yields, high photostability, and fluorescent emission properties which can be tuned from the ultraviolet to the infrared region by changing their size and composition. With a functionalized surface coating, they can be made water soluble and targeted to specific pathologic areas. Cadmium selenide (CdSe) is commonly contained in semiconductor QDs.

The emission of $^1O_2$ at 1270 nm generated by the energy transfer from CdSe QDs alone in toluene under excitation at 488 nm suggested the potential of QDs as possible therapeutic agents for PDT [19]. However, the yield of $^1O_2$ generation (~5%) of QDs was too low for practical applications. Because QDs exhibit broad absorption spectra, the combination of QDs with photosensitizers permits the use of variable excitation wavelengths to activate the photosensitizer. The interaction between CdSe QDs and photosensitizers was first studied using silicon phthalocyanine (Pc). The study revealed that the QDs could be used to sensitize the PDT agent through a Förster resonance energy transfer (FRET) mechanism, or interact directly with molecular oxygen via a triplet energy-transfer (TET) process, which resulted in the generation of ROS that can be used for PDT [20]. A study of the effect of linker chain length on the energy transfer from CdSe QDs to silicon Pc found that the energy-transfer efficiency increased as the chain length increased with maximum efficiency with seven bonds, following a non-Förster-type resonance energy-transfer behavior [21]. Applications of these conjugates may be limited due to the inherent cytotoxicity of core-only Cd-based QDs and the potential instability of charged-assembled complexes in the cellular environment. To enhance its quantum yield, CdSe–core–shell QDs were developed. ZnS shells were also shown to reduce the cytotoxicity of QDs greatly. Covalent conjugation of photosensitizers such as Rose Bengal (RB) and chlorin e6 to CdSe/CdS/ZnS QDs through phytochelatin-related peptides preserved the colloidal and photophysical properties of both the QDs and photosensitizers. Generation of $^1O_2$ was achieved via indirect excitation through FRET from the QDs to the photosensitizer [22]. The application of QDs for PDT has been demonstrated *in vitro*. However, the toxicity of QDs to living cells may limit its application *in vivo* due to release of Cd^{2+} with the protective shell deteriorating after prolonged circulation in the body. Its therapeutic effect for PDT for cancer remains to be determined *in vivo*.

Upconversion nanoparticles are modified nanocomposites which generate higher energy light from lower energy radiation. They are sometimes referred to as upconverting phosphors (UCPs), which are defined as lanthanide-containing, submicrometer-sized ceramic particles that can absorb near-infrared (NIR) or infrared light and emit visible light. $NaYF_4$ is often used as the core material of choice for UCPs. A versatile UCP, $NaYF_4$:Yb^{3+},Er^{3+} nanoparticles coated with a porous, thin layer of silica doped with merocyanine-540 photosensitizer and functionalized with a tumor-targeting antibody, was reported to be a specific PDT agent against MCF-7/AZ breast cancer cells [23]. Another UCP, $NaYF_4$ nanocrystals coated with mesoporous silica-loaded zinc phthalocyanine (ZnPc), was able to convert NIR light to visible light upon excitation by an NIR laser, which further activated the photosensitizer to release $^1O_2$ to kill cancer cells. The photosensitizers loaded into the porous silica shell of the nanoparticles were not released from the silica while they continuously produced $^1O_2$ upon NIR irradiation [24]. To prevent clearance by the reticuloendothelial system, a three-layer UCP composed of an $NaYF_4$:Yb^{3+},Er^{3+} nanoparticle interior, a coating of porphyrin photosensitizer, and a biocompatible PEG outer layer was constructed and millimolar amounts of $^1O_2$ was generated at NIR intensities far less than in two-photon techniques [25]. In addition to the resistance of UCPs to photobleaching,

using UCPs in PDT has other advantages, for example, the excitatory NIR light allows deeper penetration into the soft tissue compared with visible light.

To enhance the effect of PDT without using an external light source, self-lighting PDT was proposed by using scintillation luminescent nanoparticle-attached photosensitizers. Scintillation nanoparticles such as BaFBr:Eu^{2+},Mn^{2+} and LaF_3:Tb^{3+} will emit luminescence to activate the photosensitizers upon exposure to ionizing irradiation; as a result, $^1O_2$ is produced to enhance the killing of cancer cells. In a pilot study, the energy transfer from LaF_3:Tb^{3+} nanoparticles to *meso*-tetra(4-carboxyphenyl)porphyrin (mTCP) was demonstrated by fluorescence quenching techniques in water-soluble LaF_3:Tb^{3+}–mTCP nanoparticle conjugates after exposure to X-irradiation [26]. Persistent-luminescence nanoparticles consisting of luminescent materials with long decay lifetimes will further benefit the PDT method for deep cancer treatment by decreasing the ionization dose and prolonged photosensitizer excitation [27]. However, direct application in biological systems has not yet been reported.

23.3 Nanoparticles as Photosensitizer Carriers for PDT

Many clinically approved photosensitizers often suffer from poor bioavailability and unfavorable biodistribution. The enhanced permeability and retention (EPR) effect caused by the abnormal organization of the tumor neovasculature facilitates both diffusion and retention of photosensitizer carriers in tumors. Nanoparticles can serve as carrier platforms by taking advantage of the EPR effect to improve further the cellular uptake, biodistribution, bioavailability, and pharmacokinetics of the systemic delivery of the photosensitizers [28]. Biodegradable nanoparticles are made of polymers that are often enzymatically hydrolyzed in a biological environment and hence release the photosensitizers. Nonbiodegradable nanoparticles are used to protect the photosensitizers from the fluctuations of the environment, in which the release of the photosensitizers from the nanoparticle carriers is not necessary but oxygen diffusion freely in and out of the nanoparticles is essential [7].

23.3.1 Biodegradable Nanoparticles for PDT

Biodegradable polymer-based nanoparticles have attracted a lot of attention due to their advantages in the possibility of controlling drug release, versatility in material manufacturing processes, and high drug loading. The surface properties, morphologies, and composition of the polymers can be optimized to achieve the desired biocompatibility, controlled degradation rate, and drug release kinetics. The chemical composition and architecture of polymers can be tailored to accommodate photosensitizers with varying degrees of hydrophobicity, molecular weight, charge, and pH. Modifying the surface of nanoparticles with specific moieties also allows for active targeting to specific tissue sites [29].

Photosensitizers may be delivered by using micelles, liposomes, dendrimers, or nanoparticles. Micelles are spherical macromolecular complexes that form spontaneously when amphiphilic copolymers are mixed in an aqueous environment above the critical micelle concentration. The hydrophobic moieties of the polymer aggregate to form the micelle core, while the hydrophilic group forms a hydrated shell around the hydrophobic core. Polymeric micelles have been used to carry hydrophobic photosensitizers, which are physically entrapped in and/or covalently bound to the hydrophobic core. Polymers used for photosensitizer encapsulation include pluronics, PEG–lipid conjugates, pH-sensitive poly(*N*-isopropylacrylamide)-based micelles, and polyion complex micelles [30]. Liposomes are small unilamellar vesicles composed of a phospholipid bilayer membrane enclosing an inner aqueous environment. The phospholipid bilayer of liposomes can dissolve hydrophobic photosensitizers. They can also be used to encapsulate water-soluble molecules. The properties of liposomes can be altered by addition of different molecules to modify their surface to enhance cancer cell targeting specificity and the ability to control the release of photosensitizers [28]. Dendrimers are highly branched macromolecules composed of repetitive units branched on a multivalent core molecule. The photosensitizer can be attached at the periphery of the dendrimer branches or be encapsulated in the core of a dendrimer. The properties of dendrimers are dominated by their functional groups. Nanoparticles are made of natural or synthetic polymers. Photosensitizers can be adsorbed on the porous matrix of polymeric nanoparticles composed of natural or synthetic degradable polymers [28].

Natural degradable polymers including polysaccharides and proteins have been used in drug delivery systems. Commonly used natural biodegradable polymers are alginate, chitosan, dextran, albumin, gelatin, collagen, and agars. Modifications can be made easily to naturally occurring polymers to alter their physico-chemical properties. Alginates, polysaccharides prepared from brown algae, have been used extensively in drug delivery. A novel surfactant–polymer nanoparticle, formulated using the anionic surfactant dioctyl sodium sulfosuccinate [Aerosol-OT, (AOT)] and sodium alginate, was reported to be an efficient encapsulation and sustained delivery system for polar and weak bases such as methylene blue and doxorubicin. Increased ROS production and a higher incidence of necrosis were observed in breast cancer cell lines, MCF-7 and 4T1, following PDT using AOT–alginate nanoparticle-encapsulated methylene blue [31]. Using AOT–alginate nanoparticles for the simultaneous delivery of doxorubicin and methylene blue led to significant inhibition of drug-resistant tumor cell growth and improved survival of JC (mammary adenocarcinoma) tumor-bearing mice [32].

Chitosan is a modified natural carbohydrate polymer prepared by the partial *N*-deacetylation of the crustacean-derived natural biopolymer chitin. Chitosan-based nanoparticles can serve as drug carriers in cancer therapy because of their biocompatibility and biodegradability. Of chitosan derivatives with improved hydrophilicity, glycol chitosan is emerging as a novel carrier of drugs because of its solubility in water and biocompatibility. Hydrophobically modified glycol chitosans (HGCs) prepared by covalent attachment of 5β-cholanic acid to glycol chitosan can self-assemble into nanocarriers under aqueous conditions, that can efficiently take up various

hydrophobic anticancer drugs into their hydrophobic inner cores. The amphiphilic chitosan-based nanoparticles are covered with biocompatible and biodegradable glycol chitosan shells and exhibit enhanced tumor target specificity and a prolonged blood circulation time. The water-insoluble photosensitizer protoporphyrin IX (PpIX) was efficiently encapsulated in chitosan-based nanoparticles (drug-loading efficiency >90%). The PpIX-nanoparticles exhibited phototoxicity against squamous cell carcinoma (SCC-7) cells and enhanced tumor specificity in SCC-7 tumor-bearing mice compared with free PpIX [33].

Cyclodextrins (CDs), produced from starch by means of enzymatic conversion, have wide application in the pharmaceutical industry. They are made of sugar molecules that are connected in a ring and have the ability to form water-soluble complexes encapsulating porphyrins in aqueous solution [34]. Heterotopic colloidal nanoparticles of a cationic amphiphilic cyclodextrin (CD) encapsulating anionic 5,10,15,20-tetrakis(4-sulfonatophenyl)-21*H*,23*H*-porphyrin (TPPS) were found to preserve the photodynamic properties of the entrapped photoactive agent in a range of TPPS:CD molar ratios between 1:10 and 1:50, with photodynamic efficacy proven by *in vitro* studies on tumor HeLa cells [35].

Albumin is a plasma protein responsible for the colloid osmotic pressure of the blood. It is nonantigenic and biodegradable, binds a great number of therapeutic drugs, and has been extensively investigated as a drug carrier. The average half-life of human serum albumin (HSA) is 19 days [36]. The photosensitizer pheophorbide was loaded on HSA nanoparticles with different cross-linked ratios by noncovalent adsorption. The $^1O_2$ quantum yield of pheophorbide-loaded HSA nanoparticles was low due to intramolecular interactions despite the fact that their final phototoxicity was at the same level as induced by free pheophorbide [37]. The results suggest that the photosensitizer loading strategies, biochemical stability, and *in vivo* PDT effect of pheophorbide-loaded HSA nanoparticles still need to be optimized.

Synthetic polymers such as aliphatic polylactide (PLA), polyglycolide (PGA), and their copolymer poly(D,L-lactide-co-glycolide) (PLGA) are often used as drug delivery carriers due to their favorable properties such as good biocompatibility, biodegradability, bioresorbability, and mechanical strength. For example, the photocytotoxicity was found to be more pronounced when EMT-6 mammary tumor cells were treated with PLGA (50:50) nanoparticles incorporated with *meso*-tetra(hydroxyphenyl)porphyrin (mTHPP), which allowed low drug doses and short drug administration–irradiation intervals [38]. To reduce the aggregation of the hydrophobic photosensitizer bacteriochlorophyll-*a* in solution, it was encapsulated into polymeric PLGA nanoparticles. Scanning electron microscopy analysis revealed that these nanoparticles were phagocytosed by P388-D1 cells within a 2 h incubation time [39]. In another study, internalization of PLGA encapsulated *meso*-tetraphenylporpholactol (mTPPL) nanoparticles resulted in 95% cell death of 9L glioblastoma, B16 melanoma, and BT breast carcinoma cells, respectively. *In vivo* experiments showed complete eradication of tumors in nude mice [40]. PLGA nanoparticles were also demonstrated to be a successful delivery system for improving the photodynamic activity of ZnPc in the target tissue in tumor-bearing mice [41]. In a comparative study, both PLGA and PLA were used to encapsulate hypericin. Hypericin-loaded

PLA nanoparticles exhibited a higher entrapment efficiency and photoactivity than PLGA nanoparticles and free drug on the NuTu-19 ovarian cancer cell model. Improved selective accumulation of hypericin in ovarian micrometastases was observed when hypericin-loaded PLA nanoparticles were injected intravenously into Fischer 344 rats bearing ovarian tumors [42, 43].

Disruption of the neovasculature is thought to play an important role in the eradication of tumors by PDT. An *in vitro* model cannot give any information regarding vascular photothrombosis, hence the well-vascularized chorioallantoic membrane (CAM) of the developing chick embryo was used to study the *in vivo* photodynamic activity of photosensitizer-loaded nanoparticles. The photosensitizer mTHPP was found to remain longer in the vascular compartment of CAM when incorporated into PLGA nanoparticles. The use of poly(vinyl alcohol) (PVAL) as stabilizing agent within mTHPP-loaded nanoparticles helped to control the mTHPP release and the photodynamic activity in the CAM model [44]. Analysis of the photodynamic activities of photosensitizers with different hydrophobicities entrapped in poly-D,L-lactic acid nanoparticles showed that the photosensitizer was more effectively entrapped in the polymeric matrix when its degree of lipophilicity increased. *meso*-Tetra-(4-carboxyphenyl)porphyrin (mTCPP) and chlorin e_6 are less hydrophobic than meso-tetraphenylporphyrin (mTPP) and pheophorbide-*a*. The nanoparticles loaded with the most lipophilic molecule (mTPP) induced the highest photothrombic efficiency in the CAM model compared with the other molecules tested [45].

Dendrimers are recognized as the most versatile, compositionally, and structurally controlled nanoscale building blocks. Thus, dendrimers have been investigated in the biomedical field for drug delivery. In 2001, a series of novel 5-aminolevulinate (ALA)-containing dendrimers were synthesized using a convergent growth approach [46]. The ability of the dendrimer conjugated with 18 ALA residues to deliver and release 5-ALA intracellularly for metabolism to the photosensitizer, PpIX, was demonstrated in tumorigenic PAM 212 keratinocytes and human epidermoid carcinoma A431 cells [47]. The dendrimer induced sustained porphyrin production for over 24 h and basal values were not reached until 48 h after systemic intraperitoneal administration, whereas the porphyrin kinetics from ALA exhibited an early peak between 3 and 4 h in most tissues in a murine tumor model [48]. Another group has developed two PEG-attached dendrimers derived from poly(amidoamine) (PAMAM) and poly(propylenimine) (PPI) dendrimers to encapsulate photosensitizers, RB and PpIX. Their results showed that PEG–PPI dendrimer held RB and PpIX in a more stable manner than PEG–PAMAM dendrimer because of their inner hydrophobicity. The complex of PpIX with PEG–PPI exhibited efficient photocytotoxicity in HeLa cells, compared with free PpIX [49]. A novel dendrimer phthalocyanine (DPc)-encapsulated polymeric micelle (DPc/m) was developed recently. The DPc/m might accumulate in the endo-/lysosomes. Both *in vitro* and *in vivo* PDT efficacy were observed in human lung adenocarcinoma A549 cells. Furthermore, DPc/m-treated mice bearing A549 cells did not show skin phototoxicity [50]. The development of dendrimers as nanocarriers with smart functions is expected to be a key to advance further the clinical applications of PDT.

Although synthetic polymers are preferable for use in drug delivery systems due to the ability to tailor their mechanical properties and degradation kinetics to suit various applications, natural polymers remain attractive because they are readily available, relatively inexpensive, and capable of a multitude of chemical modifications. The use of natural biodegradable polymers to deliver drugs will continue to be an area of active research despite the advances in synthetic biodegradable polymers.

23.3.2 Nonbiodegradable Nanoparticles for PDT

Nonbiodegradable nanoparticles play a different role in PDT due to their inability to degrade and release drugs in a controllable fashion. They are not destroyed by the treatment process; therefore, they can be used repeatedly with adequate activation. Nonbiodegradable nanoparticles have several advantages over biodegradable polymeric nanoparticles: (1) their particle size, shape, porosity, and monodispersibility can be easily controlled during the preparation process; (2) some of them are made of inert materials which are stable to environmental fluctuations; (3) they are not subject to microbial attack; and (4) exquisite control of the pore size allows oxygen diffusion in and out of the particles but not for the drug to escape [7, 11]. Similarly to biodegradable nanoparticles, nondegradable nanoparticles can serve as multifunctional platforms for drug delivery.

Polyacrylamide polymers can be used for the synthesis of nondegradable nanoparticles. The photosensitizer can be embedded in the nonporous core of polyacrylamide or sol–gel silica nanoparticles. A novel dynamic nanoplatform composed of polyacrylamide was designed based on a stable photosensitizer-loaded formulation and the concept of delivering $^1O_2$ from the outside of the tumor cells. The encapsulated methylene blue was able to generate sufficient $^1O_2$ upon light irradiation that could diffuse out of the matrix, reach the adjacent cell membranes, and kill rat C6 glioma tumor cells [51]. Furthermore, a polyacrylamide matrix could prevent the embedded methylene blue from being reduced by diaphorase enzymes, thereby retaining the photoactive form of methylene blue for efficient PDT treatment [52].

Most nondegradable nanoparticles are either silica or metallic based. The synthesis of silica nanoparticles has been extensively reported, but their application for drug delivery has not been fully exploited. Silica-based nanoparticles have successfully encapsulated photosensitizers such as mTHPC, Photolon and PpIX [53–55]. The uptake of PpIX-encapsulated colloidal mesoporous silica nanoparticles by tumor cells and the effect of photon-induced toxicity were demonstrated *in vitro* [54]. A highly stable aqueous formulation of organically modified silica-based (ORMOSIL) nanoparticles encapsulating 2-devinyl-2-(1-hexyloxyethyl)pyropheophorbide (HPPH) was developed. The encapsulated HPPH was able to generate $^1O_2$ upon irradiation with light of wavelength 650 nm and thereby caused significant damage to tumorigenic HeLa and UCI-107 cells [56]. The fluorescent dye 9,10-bis[4′-(4″-aminostyryl)styryl]anthracene (BDSA) and

HPPH were co-encapsulated in ORMOSIL nanoparticles with an aim of development for two-photon PDT. BDSA serves as an energy upconverting donor and HPPH serves as an acceptor. HPPH was indirectly activated through efficient two-photon excited intraparticle energy transfer from the BDSA aggregates in the intracellular environment of tumor cells and thereby led to cytotoxic effect on HeLa cells [57]. To prevent drug release from ORMOSIL nanoparticles in systemic circulation, the photosensitizer iodobenzylpyropheophorbide (IP) was covalently incorporated into ORMOSIL nanoparticles while retaining their spectroscopic and functional properties. The phototoxicity of IP–ORMOSIL nanoparticles was further demonstrated in RIF-1 tumor cells [58].

Metallic nanoparticles possess many fascinating properties which have been explored for their biological application in biochemistry as chemical and biological sensors, as systems for nanoelectronics and nanostructured magnetism, and in medicine as agents for drug delivery. Unlike silica-based nanoparticles, photosensitizers can be attached on the surface of the metallic nanoparticles. Because metallic nanoparticles can be confined to an extremely small size, a large dose of photosensitizer can be loaded due to the enormous surface area. Gold nanoparticles are well known for their chemical inertness and minimum acute cytotoxicity [59]. Pc-coated gold nanoparticles were shown to generate $^1O_2$ with enhanced quantum yields and to exhibit double the *in vitro* PDT efficiency on HeLa cells compared with the free drug [60]. To inhibit colloid aggregation in physiologic conditions, PEG was connected to the surface of gold nanoparticles, forming PEGylated gold nanoparticles. PEGylated gold nanoparticles were then conjugated with the photosensitizer Pc4. The dynamics of drug release *in vitro* and in cancer-bearing mice indicated that the process of drug delivery was highly efficient, the drug delivery time required for PDT being greatly reduced from 2 days to less than 2 h [61]. Recently, gold nanoparticles have been used as a vehicle to deliver 5-ALA. It was reported that PpIX accumulated preferentially in fibrosarcoma tumor cells treated with 5-ALA-conjugated nanoparticles while yielding significantly higher reactive oxygen species and 50% greater cytotoxicity than that with 5-ALA [62]. A novel development with gold nanoparticles is the use of intracellular glutathione as a trigger for drug release due to the higher glutathione levels found in cancerous and precancerous cells [63]. Although photosensitizer delivery using gold nanoparticles is still evolving, there is potential for developing multifunctional particles for imaging and drug delivery systems for PDT application. To extend the technique using metallic nanoparticles, magnetic nanoparticles such as iron oxide are used for selectively targeting to tumor tissue. Magnetic nanoparticles also possess other features, such as magnetic resonance imaging (MRI) visibility for MRI imaging and nanoparticle tracking. A nanocarrier consisting of polymeric micelles of diacylphospholipid–PEG co-loaded with the photosensitizer HPPH and magnetic Fe_3O_4 nanoparticles showed excellent stability and efficient uptake by HeLa cells. The magnetic response of the nanocarriers was demonstrated by their directed delivery to tumor cells *in vitro* upon exposure to an external magnetic field. The magnetophoretic control of the cellular uptake provided enhanced imaging and phototoxicity [64]. In another drug delivery system, a chitosan nanoparticle-containing magnetic core and the

encapsulating photosensitizer 2,7,12,18-tetramethyl-3,8-di(1-propoxyethyl)-13,17-bis(3-hydroxypropyl)porphyrin (PHPP) was found to have excellent targeting and imaging ability. Non-toxicity and high photodynamic efficacy on SW480 carcinoma cells both *in vitro* and *in vivo* were achieved with these nanoparticles at the level of 0–100 μM. Photosensitivity and hepatotoxicity could also be attenuated [65]. Despite great enthusiasm in the field of metallic nanoparticle research, reproducible fabrication, aggregation, biocompatibility, nonspecific binding, and toxicity remain challenges to meet [66].

23.4 Conclusion

To improve PDT efficacy for cancers, nanoparticles with active and passive functional roles have been developed. Biodegradable nanoparticles are capable of controlling the drug release; therefore, they often serve as passive carriers for photosensitizers. Nonbiodegradable nanoparticles often resist the fluctuations of the environment and hence play active roles such as catalysts to produce free radicals from dissolved oxygen, ROS modulators, or light sources in PDT. The field of PDT is a quickly evolving technology with new approaches being tested constantly. Molecular strategies are developing to make PDT more efficient and selective. Innovative approaches including specific target moiety conjugates for active targeting, aptamer technology, and combination treatment regimens, which are not discussed here, have been brought into the field in recent years. Each has great advantages over conventional PDT but also comes with significant challenges in developing the process towards clinical application. For nanoparticles used in PDT, the focus is mainly on the enhancement of efficacy and reduction in phototoxicity obtained, whereas the possible toxicity of the residues of nanoparticles is less likely to be considered. Potential hazards with nanoparticles may arise and hence less toxic materials are of great interest for the synthesis of nanoparticles. A conceptual understanding of biological responses to nanoparticles is needed to develop and apply safe nanomaterials in PDT in the future. Long-term follow-up evaluation is necessary owing to the short history of clinical applications of nanoparticles in PDT. In conclusion, much more study remains to be done at the interface between PDT and nanoparticles. Because of its interdisciplinary nature, the application of nanoparticles in PDT is still in its infancy and presents numerous research opportunities to chemists, biologists, engineers, and physicians.

Acknowledgments

During the writing of this chapter, the author was supported by grant NSC 98-2218-E-033-010 from the National Science Council of Taiwan and grant CYCU-98-CR-BE from the project of specific research fields at Chung Yuan Christian University, Taiwan.

References

1 Triesscheijn, M., Baas, P., Schellens, J.H., and Stewart, F.A. (2006) Photodynamic therapy in oncology. *Oncologist*, **11** (9), 1034–1044.

2 Chen, B., Pogue, B.W., Hoopes, P.J., and Hasan, T. (2006) Vascular and cellular targeting for photodynamic therapy. *Crit. Rev. Eukaryot. Gene Expr.*, **16** (4), 279–305.

3 Dolmans, D.E., Fukumura, D., and Jain, R.K. (2003) Photodynamic therapy for cancer. *Nat. Rev. Cancer*, **3** (5), 380–387.

4 Moor, A.C. (2000) Signaling pathways in cell death and survival after photodynamic therapy. *J. Photochem. Photobiol. B*, **57** (1), 1–13.

5 Wyld, L., Reed, M.W., and Brown, N.J. (2001) Differential cell death response to photodynamic therapy is dependent on dose and cell type. *Br. J. Cancer*, **84** (10), 1384–1386.

6 Brown, S.B., Brown, E.A., and Walker, I. (2004) The present and future role of photodynamic therapy in cancer treatment. *Lancet Oncol.*, **5** (8), 497–508.

7 Bechet, D., Couleaud, P., Frochot, C., Viriot, M.L., Guillemin, F., and Barberi-Heyob, M. (2008) Nanoparticles as vehicles for delivery of photodynamic therapy agents. *Trends Biotechnol.*, **26** (11), 612–621.

8 Jori, G. (1996) Tumour photosensitizers: approaches to enhance the selectivity and efficiency of photodynamic therapy. *J. Photochem. Photobiol. B*, **36** (2), 87–93.

9 Solban, N., Rizvi, I., and Hasan, T. (2006) Targeted photodynamic therapy. *Lasers Surg. Med.*, **38** (5), 522–531.

10 Verma, S., Watt, G.M., Mai, Z., and Hasan, T. (2007) Strategies for enhanced photodynamic therapy effects. *Photochem. Photobiol.*, **83** (5), 996–1005.

11 Chatterjee, D.K., Fong, L.S., and Zhang, Y. (2008) Nanoparticles in photodynamic therapy: an emerging paradigm. *Adv. Drug Deliv. Rev.*, **60** (15), 1627–1637.

12 Mroz, P., Tegos, G.P., Gali, H., Wharton, T., Sarna, T., and Hamblin, M.R. (2007) Photodynamic therapy with fullerenes. *Photochem. Photobiol. Sci.*, **6** (11), 1139–1149.

13 Burlaka, A.P., Sidorik, Y.P., Prylutska, S.V., Matyshevska, O.P., Golub, O.A., Prylutskyy, Y.I., and Scharff, P. (2004) Catalytic system of the reactive oxygen species on the C_{60} fullerene basis. *Exp. Oncol.*, **26** (4), 326–327.

14 Doi, Y., Ikeda, A., Akiyama, M., Nagano, M., Shigematsu, T., Ogawa, T., Takeya, T., and Nagasaki, T. (2008) Intracellular uptake and photodynamic activity of water-soluble [60]- and [70] fullerenes incorporated in liposomes. *Chem. Eur. J.*, **14** (29), 8892–8897.

15 Mroz, P., Pawlak, A., Satti, M., Lee, H., Wharton, T., Gali, H., Sarna, T., and Hamblin, M.R. (2007) Functionalized fullerenes mediate photodynamic killing of cancer cells: Type I versus Type II photochemical mechanism. *Free Radic. Biol. Med.*, **43** (5), 711–719.

16 Liu, J., Ohta, S., Sonoda, A., Yamada, M., Yamamoto, M., Nitta, N., Murata, K., and Tabata, Y. (2007) Preparation of PEG-conjugated fullerene containing Gd^{3+} ions for photodynamic therapy. *J. Control. Release*, **117** (1), 104–110.

17 Zhu, Z., Tang, Z., Phillips, J.A., Yang, R., Wang, H., and Tan, W. (2008) Regulation of singlet oxygen generation using single-walled carbon nanotubes. *J. Am. Chem. Soc.*, **130** (33), 10856–10857.

18 Ji, S.R., Liu, C., Zhang, B., Yang, F., Xu, J., Long, J., Jin, C., Fu, D.L., Ni, Q.X., and Yu, X.J. (2010) Carbon nanotubes in cancer diagnosis and therapy. *Biochim. Biophys. Acta*, **1806** (1), 29–35.

19 Samia, A.C., Chen, X., and Burda, C. (2003) Semiconductor quantum dots for photodynamic therapy. *J. Am. Chem. Soc.*, **125** (51), 15736–15737.

20 Samia, A.C., Dayal, S., and Burda, C. (2006) Quantum dot-based energy transfer: perspectives and potential for applications in photodynamic therapy. *Photochem. Photobiol.*, **82** (3), 617–625.

21 Dayal, S., Lou, Y., Samia, A.C., Berlin, J.C., Kenney, M.E., and Burda, C. (2006) Observation of non-Förster-type energy-transfer behavior in quantum dot–phthalocyanine conjugates. *J. Am. Chem. Soc.*, **128** (43), 13974–13975.

22 Tsay, J.M., Trzoss, M., Shi, L., Kong, X., Selke, M., Jung, M.E., and Weiss, S. (2007) Singlet oxygen production by peptide-coated quantum dot–photosensitizer conjugates. *J. Am. Chem. Soc.*, **129** (21), 6865–6871.

23 Zhang, P., Steelant, W., Kumar, M., and Scholfield, M. (2007) Versatile photosensitizers for photodynamic therapy at infrared excitation. *J. Am. Chem. Soc.*, **129** (15), 4526–4527.

24 Qian, H.S., Guo, H.C., Ho, P.C., Mahendran, R., and Zhang, Y. (2009) Mesoporous-silica-coated up-conversion fluorescent nanoparticles for photodynamic therapy. *Small*, **5** (20), 2285–2290.

25 Ungun, B., Prud'homme, R.K., Budijon, S.J., Shan, J., Lim, S.F., Ju, Y., and Austin, R. (2009) Nanofabricated upconversion nanoparticles for photodynamic therapy. *Opt. Express*, **17** (1), 80–86.

26 Liu, Y., Chen, W., Wang, S., and Joly, A.G. (2008) Investigation of water-soluble X-ray luminescence nanoparticles for photodynamic activation. *Appl. Phys. Lett.*, **92** (043901), 1–3.

27 Chen, W. and Zhang, J. (2006) Using nanoparticles to enable simultaneous radiation and photodynamic therapies for cancer treatment. *J. Nanosci. Nanotechnol.*, **6** (4), 1159–1166.

28 Sibani, S.A., McCarron, P.A., Woolfson, A.D., and Donnelly, R.F. (2008) Photosensitiser delivery for photodynamic therapy. Part 2: systemic carrier platforms. *Expert Opin. Drug Deliv.*, **5** (11), 1241–1254.

29 Konan, Y.N., Gurny, R., and Allemann, E. (2002) State of the art in the delivery of photosensitizers for photodynamic therapy. *J. Photochem. Photobiol. B*, **66** (2), 89–106.

30 van Nostrum, C.F. (2004) Polymeric micelles to deliver photosensitizers for photodynamic therapy. *Adv. Drug Deliv. Rev.*, **56** (1), 9–16.

31 Khdair, A., Gerard, B., Handa, H., Mao, G., Shekhar, M.P., and Panyam, J. (2008) Surfactant–polymer nanoparticles enhance the effectiveness of anticancer photodynamic therapy. *Mol. Pharmacol.*, **5** (5), 795–807.

32 Khdair, A., Chen, D., Patil, Y., Ma, L., Dou, Q.P., Shekhar, M.P., and Panyam, J. (2010) Nanoparticle-mediated combination chemotherapy and photodynamic therapy overcomes tumor drug resistance. *J. Control. Release*, **141** (2), 137–144.

33 Lee, S.J., Park, K., Oh, Y.K., Kwon, S.H., Her, S., Kim, I.S., Choi, K., Lee, S.J., Kim, H., Lee, S.G., Kim, K., and Kwon, I.C. (2009) Tumor specificity and therapeutic efficacy of photosensitizer-encapsulated glycol chitosan-based nanoparticles in tumor-bearing mice. *Biomaterials*, **30** (15), 2929–2939.

34 Mazzaglia, A., Angelini, N., Lombardo, D., Micali, N., Patane, S., Villari, V., and Scolaro, L.M. (2005) Amphiphilic cyclodextrin carriers embedding porphyrins: charge and size modulation of colloidal stability in heterotopic aggregates. *J. Phys. Chem. B*, **109** (15), 7258–7265.

35 Sortino, S., Mazzaglia, A., Monsu Scolaro, L., Marino Merlo, F., Valveri, V., and Sciortino, M.T. (2006) Nanoparticles of cationic amphiphilic cyclodextrins entangling anionic porphyrins as carrier–sensitizer system in photodynamic cancer therapy. *Biomaterials*, **27** (23), 4256–4265.

36 Kratz, F. (2008) Albumin as a drug carrier: design of prodrugs, drug conjugates and nanoparticles. *J. Control. Release*, **132** (3), 171–183.

37 Chen, K., Preuss, A., Hackbarth, S., Wacker, M., Langer, K., and Roder, B. (2009) Novel photosensitizer–protein nanoparticles for photodynamic therapy: photophysical characterization and *in vitro* investigations. *J. Photochem. Photobiol. B*, **96** (1), 66–74.

38 Konan, Y.N., Berton, M., Gurny, R., and Allemann, E. (2003) Enhanced photodynamic activity of *meso*-tetra(4-hydroxyphenyl)porphyrin by incorporation into sub-200 nm nanoparticles. *Eur. J. Pharm. Sci.*, **18** (3–4), 241–249.

39 Gomes, A.J., Lunardi, C.N., and Tedesco, A.C. (2007) Characterization of biodegradable poly(D,L-lactide-co-

glycolide) nanoparticles loaded with bacteriochlorophyll-*a* for photodynamic therapy. *Photomed. Laser Surg.*, **25** (5), 428–435.

40 McCarthy, J.R., Perez, J.M., Bruckner, C., and Weissleder, R. (2005) Polymeric nanoparticle preparation that eradicates tumors. *Nano Lett.*, **5** (12), 2552–2556.

41 Fadel, M., Kassab, K., and Fadeel, D.A. (2010) Zinc phthalocyanine-loaded PLGA biodegradable nanoparticles for photodynamic therapy in tumor-bearing mice. *Lasers Med. Sci.*, **25** (2), 283–272.

42 Zeisser-Labouebe, M., Delie, F., Gurny, R., and Lange, N. (2009) Benefits of nanoencapsulation for the hypercin-mediated photodetection of ovarian micrometastases. *Eur. J. Pharm. Biopharm.*, **71** (2), 207–213.

43 Zeisser-Labouebe, M., Lange, N., Gurny, R., and Delie, F. (2006) Hypericin-loaded nanoparticles for the photodynamic treatment of ovarian cancer. *Int. J. Pharm.*, **326** (1–2), 174–181.

44 Vargas, A., Lange, N., Arvinte, T., Cerny, R., Gurny, R., and Delie, F. (2009) Toward the understanding of the photodynamic activity of m-THPP encapsulated in PLGA nanoparticles: correlation between nanoparticle properties and *in vivo* activity. *J. Drug Target.*, **17** (8), 599–609.

45 Pegaz, B., Debefve, E., Borle, F., Ballini, J.P., van den Bergh, H., and Kouakou-Konan, Y.N. (2005) Encapsulation of porphyrins and chlorins in biodegradable nanoparticles: the effect of dye lipophilicity on the extravasation and the photothrombic activity. A comparative study. *J. Photochem. Photobiol. B*, **80** (1), 19–27.

46 Battah, S.H., Chee, C.E., Nakanishi, H., Gerscher, S., MacRobert, A.J., and Edwards, C. (2001) Synthesis and biological studies of 5-aminolevulinic acid-containing dendrimers for photodynamic therapy. *Bioconjug. Chem.*, **12** (6), 980–988.

47 Battah, S., Balaratnam, S., Casas, A., O'Neill, S., Edwards, C., Batlle, A., Dobbin, P., and MacRobert, A.J. (2007) Macromolecular delivery of 5-aminolaevulinic acid for photodynamic therapy using dendrimer conjugates. *Mol. Cancer Ther.*, **6** (3), 876–885.

48 Casas, A., Battah, S., Di Venosa, G., Dobbin, P., Rodriguez, L., Fukuda, H., Batlle, A., and MacRobert, A.J. (2009) Sustained and efficient porphyrin generation *in vivo* using dendrimer conjugates of 5-ALA for photodynamic therapy. *J. Control. Release*, **135** (2), 136–143.

49 Kojima, C., Toi, Y., Harada, A., and Kono, K. (2007) Preparation of poly (ethylene glycol)-attached dendrimers encapsulating photosensitizers for application to photodynamic therapy. *Bioconjug. Chem.*, **18** (3), 663–670.

50 Nishiyama, N., Nakagishi, Y., Morimoto, Y., Lai, P.S., Miyazaki, K., Urano, K., Horie, S., Kumagai, M., Fukushima, S., Cheng, Y., Jang, W.D., Kikuchi, M., and Kataoka, K. (2009) Enhanced photodynamic cancer treatment by supramolecular nanocarriers charged with dendrimer phthalocyanine. *J. Control. Release*, **133** (3), 245–251.

51 Tang, W., Xu, H., Kopelman, R., and Philbert, M.A. (2005) Photodynamic characterization and *in vitro* application of methylene blue-containing nanoparticle platforms. *Photochem. Photobiol.*, **81** (2), 242–249.

52 Tang, W., Xu, H., Park, E.J., Philbert, M.A., and Kopelman, R. (2008) Encapsulation of methylene blue in polyacrylamide nanoparticle platforms protects its photodynamic effectiveness. *Biochem. Biophys. Res. Commun.*, **369** (2), 579–583.

53 Podbielska, H., Ulatowska-Jarza, A., Muller, G., Holowacz, I., Bauer, J., and Bindig, U. (2007) Silica sol–gel matrix doped with Photolon molecules for sensing and medical therapy purposes. *Biomol. Eng.*, **24** (5), 425–433.

54 Qian, J., Gharibi, A., and He, S. (2009) Colloidal mesoporous silica nanoparticles with protoporphyrin IX encapsulated for photodynamic therapy. *J. Biomed. Opt.*, **14** (1), 014012.

55 Yan, F. and Kopelman, R. (2003) The embedding of *meta*-tetra(hydroxyphenyl)-chlorin into silica nanoparticle platforms for photodynamic therapy and their singlet oxygen production and

pH-dependent optical properties. *Photochem. Photobiol.*, **78** (6), 587–591.

56 Roy, I., Ohulchanskyy, T.Y., Pudavar, H.E., Bergey, E.J., Oseroff, A.R., Morgan, J., Dougherty, T.J., and Prasad, P.N. (2003) Ceramic-based nanoparticles entrapping water-insoluble photosensitizing anticancer drugs: a novel drug-carrier system for photodynamic therapy. *J. Am. Chem. Soc.*, **125** (26), 7860–7865.

57 Kim, S., Ohulchanskyy, T.Y., Pudavar, H.E., Pandey, R.K., and Prasad, P.N. (2007) Organically modified silica nanoparticles co-encapsulating photosensitizing drug and aggregation-enhanced two-photon absorbing fluorescent dye aggregates for two-photon photodynamic therapy. *J. Am. Chem. Soc.*, **129** (9), 2669–2675.

58 Ohulchanskyy, T.Y., Roy, I., Goswami, L.N., Chen, Y., Bergey, E.J., Pandey, R.K., Oseroff, A.R., and Prasad, P.N. (2007) Organically modified silica nanoparticles with covalently incorporated photosensitizer for photodynamic therapy of cancer. *Nano Lett.*, **7** (9), 2835–2842.

59 Connor, E.E., Mwamuka, J., Gole, A., Murphy, C.J., and Wyatt, M.D. (2005) Gold nanoparticles are taken up by human cells but do not cause acute cytotoxicity. *Small*, **1** (3), 325–327.

60 Wieder, M.E., Hone, D.C., Cook, M.J., Handsley, M.M., Gavrilovic, J., and Russell, D.A. (2006) Intracellular photodynamic therapy with photosensitizer-nanoparticle conjugates: cancer therapy using a 'Trojan horse'. *Photochem. Photobiol. Sci.*, **5** (8), 727–734.

61 Cheng, Y., Samia, A.C., Meyers, J.D., Panagopoulos, I., Fei, B., and Burda, C. (2008) Highly efficient drug delivery with gold nanoparticle vectors for *in vivo* photodynamic therapy of cancer. *J. Am. Chem. Soc.*, **130** (32), 10643–10647.

62 Oo, M.K., Yang, X., Du, H., and Wang, H. (2008) 5-Aminolevulinic acid-conjugated gold nanoparticles for photodynamic therapy of cancer. *Nanomedicine (Lond.)*, **3** (6), 777–786.

63 Hong, R., Han, G., Fernandez, J.M., Kim, B.J., Forbes, N.S., and Rotello, V.M. (2006) Glutathione-mediated delivery and release using monolayer protected nanoparticle carriers. *J. Am. Chem. Soc.*, **128** (4), 1078–1079.

64 Cinteza, L.O., Ohulchanskyy, T.Y., Sahoo, Y., Bergey, E.J., Pandey, R.K., and Prasad, P.N. (2006) Diacyllipid micelle-based nanocarrier for magnetically guided delivery of drugs in photodynamic therapy. *Mol. Pharmacol.*, **3** (4), 415–423.

65 Sun, Y., Chen, Z.L., Yang, X.X., Huang, P., Zhou, X.P., and Du, X.X. (2009) Magnetic chitosan nanoparticles as a drug delivery system for targeting photodynamic therapy. *Nanotechnology*, **20** (13), 135102.

66 Juzenas, P., Chen, W., Sun, Y.P., Coelho, M.A., Generalov, R., Generalova, N., and Christensen, I.L. (2008) Quantum dots and nanoparticles for photodynamic and radiation therapies of cancer. *Adv. Drug Deliv. Rev.*, **60** (15), 1600–1614.

24
Optical Coherence Tomographic Monitoring of Surgery in Oncology

Elena V. Zagaynova, N.D. Gladkova, N.M. Shakhova, O.S. Streltsova, I.A. Kuznetsova, I.A. Yanvareva, L.B. Snopova, E.E. Yunusova, E.B. Kiseleva, V.M. Gelikonov, G.V. Gelikonov, and A.M. Sergeev

24.1
Introduction

Epithelial cancer is considered to account for the majority of cancer cases and deaths worldwide. The most common urologic cancers, those of the prostate, kidney, and urinary bladder, account for about 300 000 new cases of cancer per year in men with another 32 000 new renal and bladder cancer cases arising in women [1]. In the digestive system, most common are colon and esophageal cancer. Colorectal cancer is one of the leading causes of morbidity and mortality [2]. Colorectal cancer is the third most common cancer in the United States; in 2006, 148 610 new cases of colorectal cancer were registered According to the 2001 records, 13 200 cases of esophageal carcinoma were detected in the United States, of which 12 500 patients died. Adenocarcinoma accounts for about 90% of esophageal carcinoma in the Western hemisphere [3]. Malignant neoplasms of the female reproductive organs, including cervical cancer, are among the principal causes of death. About 510 000 new cervical cancer cases are registered worldwide every year; of these, 288 000 women die, and over US $5–6 billion are spent on patient treatment [4, 5]. A significant increase in the incidence of cervical cancer is observed for women in the early reproductive age group (by 2% yearly on average) [6]. This situation requires new approaches to cervical cancer prevention and diagnosis.

Endoscopic methods are used to diagnose different types of epithelial cancer. However, it is difficult to recognize early neoplasia such as dysplasia and carcinoma *in situ* by endoscopic visualization alone. Random biopsies during white light endoscopy have been used to identify and locate early neoplasia [7], but the sensitivity and specificity are poor. Numerous biopsies can provide histopathologic control only over a very small part of mucosa, for example, in Barrett's esophagus (BE) 3.5% of metaplastic mucosa are analyzed histologically [8].

Handbook of Biophotonics. Vol.2: Photonics for Health Care, First Edition. Edited by Jürgen Popp, Valery V. Tuchin, Arthur Chiou, and Stefan Heinemann.

Initial risk stratification for cervical neoplasia is performed using screening techniques, including Pap smear and HPV (human papilloma virus) testing. The next step in diagnosis is colposcopy guidance biopsy. Histopathologic evaluation of the biopsies serves as a "gold standard" for diagnosis. However, the diagnostic efficacy of colposcopy is limited. Similar colposcopic abnormalities may be observed for a variety of cervical conditions, benign and malignant, which reduces specificity and positive predictive value [9]. Hence the development of new techniques and the elaboration of modern protocols for management of Pap- and HPV-positive women are important for ensuring adequate diagnosis and, at the same time, for avoiding over-referral to colposcopy and over-treatment and to maintain sustainable costs.

In terms of diagnostic tasks, endoscopic methods may be classified into screening (assessment of the entire mucous surface aiming at detecting pathologic zones) and verification (assessment of structural changes with almost cellular resolution without damage to tissue integrity) techniques.

Chromoendoscopy, fluorescence endoscopy, and narrow-band imaging are the screening methods that improve the sensitivity of endoscopic diagnostics. Magnification endoscopy, optical coherence tomography, high-frequency ultrasound, confocal microscopy, and cytoendoscopy are among the verification techniques that enhance diagnostic specificity.

Chromoendoscopy has attracted considerable attention over the past 10 years. Methylene blue, Lugol's solution, and indigo carmine staining of the esophagus have been shown to highlight metaplastic epithelium, and may visualize areas of dysplasia and early adenocarcinoma. Several studies have demonstrated the high diagnostic accuracy of this method [10]. However, this technique is highly operator dependent, with low inter-observer agreement (kappa coefficient 0.36) [11].

Fluorescence imaging is known to have high sensitivity but limited specificity, thereby giving a low positive predictive value, especially for flat lesions. The rate of false-positive readings in fluorescence cystoscopy is high owing to simple hyperplasia of the epithelium, inflammation, and squamous metaplasia [12]. The use of fluorescence, both endogenous (auto) and exogenous, for visualization of high-grade dysplasia (HGD) in BE is particularly efficacious using integral analysis of several fluorescence spectra at several excitation wavelengths (337–620 nm) [13].

Modern verification endoscopic techniques, such as endoscopic confocal microscopy and multiphoton fluorescence microscopy, have cellular spatial resolution, whereas high-frequency ultrasound and optical coherence tomography (OCT), commonly used in clinical practice, have tissue-level resolution. According to some reports, high-frequency ultrasound can indirectly detect intestinal metaplasia by esophageal wall thickening and changed ratio between ultrasonic layers. It was shown that ultrasound is able to diagnose invasive cancer in 23% more patients and to detect lymph node involvement [14]. However, high-frequency ultrasound was shown to be ineffective in the detection of dysplasia or intramucosal carcinoma because its spatial resolution is comparable to the mucosal layer thickness.

24.2 OCT Technique

Since the first report on OCT in 1991 [15], different fundamental and applied studies of the OCT technique have been carried out, resulting in numerous publications. The foundations of OCT are described in a book [16]. A conventional time-domain OCT device uses near-infrared light to allow real-time cross-sectional imaging with high spatial resolution (10–20 μm) at a depth of ~2 mm. When developing a device for clinical application, the fiber-optic modality is evidently to be preferred, allowing for miniaturization [17, 18]. The design of a compact device for effective scanning by Michelson interferometer arms mismatch became a key for such miniaturization. One of the most efficient devices is the controlled piezo-fiber delay line [19] with optical path modulation depth up to several millimeters. A scanning system with such an element can provide high accuracy in keeping a constant Doppler shift of optical frequency mismatch in the interferometer arms, which is necessary for narrow-band signal detection.

The advantages of the fiber-optic OCT modality have also been implemented in the design of endoscopic probes. Endoscopic OCT systems use different models of scanners: catheters with circumferential [20, 21], linear-transverse [22], or longitudinal scanning modality [23, 24], scanners with a built-in endoscope [25], and microelectromechanical systems (MEMS) [26].

Three types of scanning patterns are available for OCT imaging: radial [27], longitudinal [28], and transverse [22, 29]. The radial-scan probe directs the OCT beam radially, giving images that are displayed in a "radar-like" circular plot. Radial scanning can easily image large areas of tissue by moving the probe back and forth over the tissue surface, and has the highest definition when the probe is inserted within a small-diameter lumen, because the OCT images become progressively coarser when a large-diameter lumen is scanned, due to the progressive increase in pixel spacing with increasing distance between the probe and the tissue. The linear-transverse probes scan the longitudinal and transverse positions of the OCT beam at a fixed angle, generating rectangular images of longitudinal and transverse planes at a given angle with respect to the probe. The advantage of linear scanning is that the pixel spacing in the transverse direction is uniform and can better image a definite area of the scanned tissue, especially in the presence of large-diameter and noncircular lumens, where it may be impossible to maintain a constant distance from the probe to the surface over the entire circumferential scan. The transverse scanning modality provides a better depth of field. The depth of field is the range of distances from the probe over which optimal resolution of scanning can be obtained; current OCT scans permit imaging depths up to 1–2 mm in tissues, by using probes with different focuses. In our research, we use flexible endoscopic forward-looking probes 2.7 and 2.4 mm in diameter with linear-transverse scanning that may be introduced through biopsy channels of standard endoscopes to study mucous surfaces. We believe that such an approach to scanning has a number of advantages. The scanning technology implies contact of a probe with the studied object, which minimizes artifacts due to motion and ensures stable focusing of probing radiation.

The possibility of using the effect of tissue compression for obtaining additional information is also significant. The scanner described in this chapter is compatible with the majority of standard endoscopes, thus making OCT a useful technique for many clinical disciplines. Its design meets the requirements for instruments used in clinical practice.

Our previous research showed that conventional OCT technology is informative with regard to structural alterations in tissue, although it did not elucidate the origin of these alterations. Using OCT imaging, it is very difficult to differentiate inflammatory processes, papillomatosis, cancer, and scar changes. This problem may be solved by using polarization optics methods. Some structural components of biotissue can change the polarization state of backscattered radiation. Some visually similar pathologic cases may be differentiated by comparing co- and cross-polarized OCT images [30]. The polarization-sensitive (PS)- and cross-polarization (CP)-OCT techniques have undergone significant development in recent years [31–33]. In PS-OCT, the images obtained allow one to analyze birefringence in biotissues, thus permitting diagnostics, for example, of the state of burned tissues [32] or early glaucoma [34]. CP-OCT permits comparisons of co- and cross-polarization scattering from the sampling volume and, hence, differentiation of biotissue pathology [33]. This method was implemented almost simultaneously in open-space [33] and fiber-optics modalities [30, 35]. In this chapter, we present results of the application of a new tandem-polarization time-domain OCT device that allows one not only to obtain conventional OCT imaging but also to carry out polarization research.

The tandem-polarization time-domain OCT device developed at the Institute of Applied Physics of the Russian Academy of Science (Nizhny Novgorod) operates at 1300 nm with 3 mW power and 35–40 nm bandwidth (light source: SLD 561 HP2). A schematic of the CP-OCT system using two orthogonal polarization modes in an isotropic optical fiber (SMF-28) is shown in Figure 24.1. The full description of the optical scheme can be found elsewhere [36]. The CP-OCT scheme comprises a fiber-based Fizeau interferometer, a common path for signal and reference waves, and an autocorrelator based on a Michelson interferometer with Faraday mirrors [37] that is optimal when an isotropic optical fiber is used.

When operating in the simplest mode, the Fizeau interferometer provides heterodyne detection of weakly scattered light with maximum possible and stable visibility of the interference fringes. Indeed, when the directional pattern of the optical probe is identical for emitted and received light, a wave scattered from nondepolarizing structures and a wave reflected from the fiber tip have identical polarization states. The essential feature of the novel scheme is its ability for simultaneous independent detection of backscattered radiation in both initial and orthogonal polarizations at random polarization states of the probing radiation. The main idea underlying our CP-OCT system consists in creating at the entrance to the optical scheme two strictly orthogonally polarized waves with a predetermined time delay between coherent regions. In a general case, these waves in the probing beam may have arbitrary ellipticity under the condition of their strict mutual orthogonality.

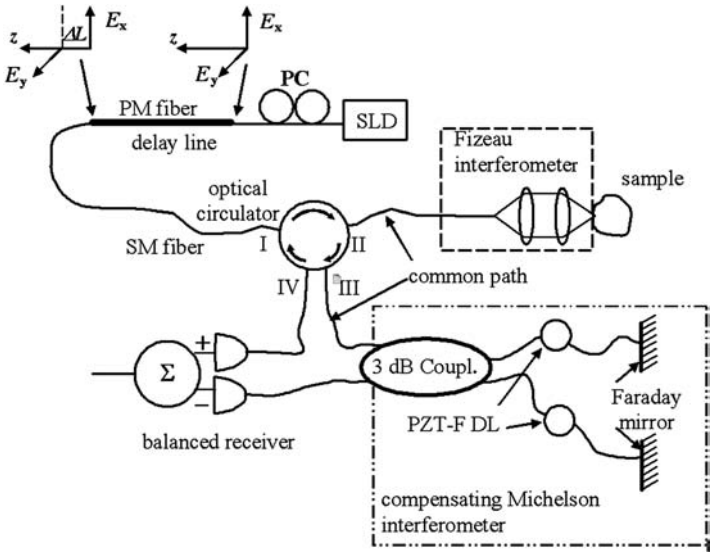

Figure 24.1 Optical scheme of tandem-polarization time-domain OCT device.

A forward-looking OCT probe (2.7 mm o.d.) was used in a routine endoscopic procedure: it was passed through the operating channel of the endoscope and placed in contact with mucosa. The OCT catheter has been developed as a miniaturized electromechanical unit controlling the lateral scanning process [22, 38]. This unit terminates the sampling arm of the fiber interferometer and has a size to fit the diameter and the curvature radius of the biopsy channel of endoscopes. The probe beam moves along the tissue surface within a distance of about 2 mm. The beam deviation system embodies the galvanometric principle, and voltage with a maximum of 5 V is supplied to the distal end of the endoscope. The distance between the output lens and the sample is 5–7 mm and the focal spot diameter is 20 mm. The scanning unit and the extended part of the fiber interferometer are sealed, which allows easy sterilization [22]. Each OCT image, with 200 × 200 pixels, 2 × 2 mm, 19 μm free space in depth resolution (13 μm in tissue), and 25 μm lateral resolution, was acquired in ∼2 s. Images are presented in a pseudo color, "positive" logarithmic palette, that is, the lighter area corresponds to the higher light scattering.

At the current stage of its development, OCT has rich capabilities in oncology. This technique is capable of solving a number of problems: early detection of cancer, targeting biopsy, more precise localization and spread of neoplastic processes, and monitoring results of treatment. There are some publications concerning the application of OCT in examination of the urinary bladder [39–42], digestive tract [43, 44], and cervix [45, 46].

In our recent work, we analyzed material from clinical studies of 895 patients: 175 patients with urinary bladder pathology, 390 with gastrointestinal tract pathology, and 330 with cervical pathology.

In spite of the different morphology of these organs, their study had similar problems that were solved by means of OCT. A multi-center study was carried out. The research was done in the Nizhny Novgorod Regional Hospital (Russia) and in three clinics abroad: Eppendorf Clinic, University of Hamburg (Germany), Cleveland Clinic Foundation (United States), and the George Washington University (GWU) Medical Center (United States). The different clinics used the same protocol, which permitted integration of data when analyzing results. Written informed consent was obtained from all patients.

Earlier studies made it possible to define OCT signs correlating with benign and malignant histopathology and to create a set of images to train observers performing OCT image recognition.

The following retrospectively tested criteria were used for OCT interpretation:

- Sharp, high-contrast horizontal layers through more than 75% of the lateral range. The upper layer (epithelium, glandular mucosa) has a lower signal intensity than the second (submucous) layer– benign images.
- Tissue layers are hardly differentiable, with increased intensity of the upper layer signal and a poorly defined border between the upper and second layers – suspicious images.
- No horizontal layers, or less than 75% (excluding evident motion artifacts) – neoplasia images.
- Very dark pattern of stripes associated with edema is not a diagnostic sign for neoplasia.

Hence the main OCT features characterizing images obtained by means of a transverse scanning probe are the presence or absence of high-contrast horizontal tissue layers and signal level from these layers.

24.3 Urology

The first OCT images of human urologic tissue *ex vivo* were demonstrated in 1997 [47], and the first *in vivo* OCT studies in urology were performed on the bladder urothelium in 1998 [39, 48]. Since then, a number of papers have been published exploring OCT for urologic clinical applications. In brief, the range of potential clinical use includes:

- early detection of bladder neoplasia, including visualization of carcinoma *in situ* (Tis)
- preoperative planning and intraoperative guidance of surgery for adequate resection with maximal bladder preservation
- differentiation of fluorescent bladder lesions
- identification and preservation of neurovascular tissue during prostatectomy
- detection of capsular penetration of prostate cancer during prostatectomy

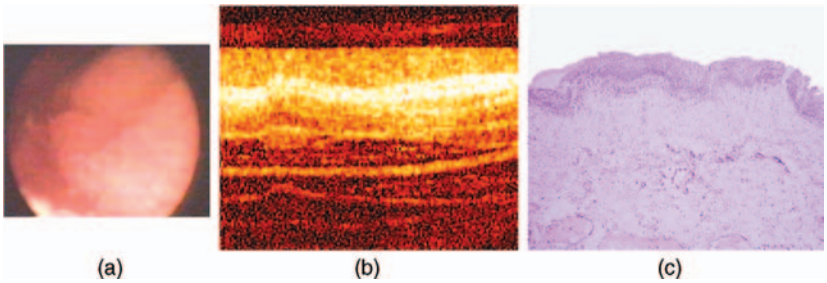

Figure 24.2 Urothelial hyperplasia. (a) Cystoscopic image; (b) OCT image (benign type); (c) corresponding histology (H&E stain).

- preservation of retroperitoneal nerves during lymph node dissection for testicular cancer
- differentiation of renal tumors.

The research done by our group concerns three possible applications of OCT in urologic oncology, outlined below.

24.3.1
Accuracy of OCT in Endoscopic Detection of Early Cancer

It is well known that early cancer in urinary bladder looks like a flat, suspicious lesion. We performed two clinical OCT studies of the urinary bladder: in the Nizhny Novgorod Regional Hospital (Russia) and in the GWU Medical Center (United States). We combined available flat lesion data from both the Russian and the GWU studies to include 80 patients with 114 sites (st) of OCT images with histopathologic and cystoscopic data. Different conditions were histologically diagnosed for each site: benign – urothelial hyperplasia (17 st) (Figure 24.2), von Brunn's nests (15 st), cystitis cystica (6 st), chronic cystitis with exudation (28 st), and chronic cystitis with infiltration (10 st) – and malignant – urothelial dysplasia (5 st), carcinoma *in situ* (10 st), and invasive cancer (2 st).

In both centers, we used a very similar procedure in which the OCT probe was introduced via the working channel of the rigid cystoscope and positioned on the mucosal area of interest under visual control. All images were obtained by placing the en-face OCT probe directly on the desired area normally to the bladder wall. Two or three OCT images were acquired from each site. Biopsies of all scanned areas were performed and submitted for histopathologic analysis. Two respondents made blind recognition of OCT images (Table 24.1).

All histologically confirmed invasive cancer sites had suspicious or abnormal OCT images; 17 of 20 cases of carcinoma *in situ* had suspicious or abnormal OCT images (Figure 24.3). The greatest false-negative error was in recognition of urothelial dysplasia. The cancerous potentiality of dysplasia is still under discussion worldwide.

Table 24.1 Results of blind recognition of OCT images of flat lesions in the urinary bladder.

Parameter	Russia	GWU	Total
Number of zones	61	53	114
Sensitivity (%)	81	88	82
Specificity (%)	78	92	85
Diagnostic accuracy (%)	79	92	85
Positive predictive value (%)	—	—	51
Negative predictive value (%)	—	—	96
Kappa	0.56	0.46	0.6

There are several possible reasons for false-positive OCT readings (benign conditions with suspicious or abnormal OCT image). Inflammatory processes and von Brunn's nest are the most common causes. Severe inflammation can partially or completely obscure the OCT contrast between the urothelium and connective tissue. The mechanism of these changes is still debated; however, it is hypothesized that optical scattering changes are associated with cell infiltration into the lamina propria.

OCT showed good sensitivity (82%) and good specificity (85%) in the identification of flat suspicious zones in the urinary bladder. Diagnostic accuracy at blind recognition of OCT images was higher in the GWU sampling (92%) compared with 79% in Nizhny Novgorod, which is due to different spectra of pathologic states. Based on the fact that OCT properly identified 165 out of 194 benign sites, we can hypothesize that when using white light cystoscopy with OCT, biopsy could have been safely avoided in 85% of cases.

Earlier experimental studies on animals demonstrated that OCT is potentially capable of detecting carcinogenesis in the urinary bladder. The difference between normal urothelium, inflammatory and proliferative changes, and early neoplasia was found [49]. Later, our group made the first clinical studies of the capabilities of OCT for the diagnosis of different clinical states of the urinary bladder [39]. Further, the accumulated clinical material enabled us to carry out preliminary statistical studies [50]. The sensitivity and specificity of OCT in detecting urinary bladder neoplasia were analyzed on the basis of different statistical samplings. However, statistical

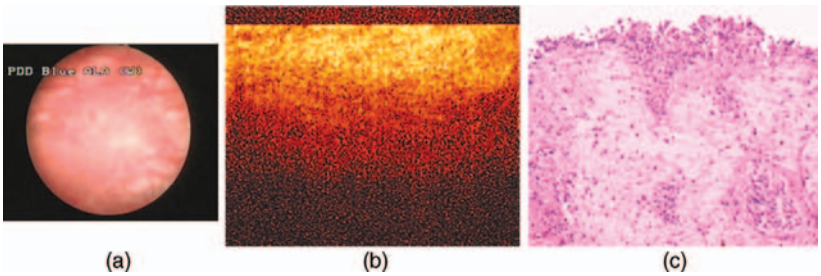

Figure 24.3 High-grade dysplasia (carcinoma *in situ*) in a flat suspicious zone. (a) Cystoscopic image; (b) OCT image (neoplasia type); (c) corresponding histology (H&E stain).

clinical studies in the urinary bladder are very sparse, perhaps owing to the poor adaptation of available probes (rotation probe or rigid OCT cystoscope) to a large, hollow organ. Wang *et al.* reported recent technical improvements of MEMS-based spectral-domain endoscopic OCT and applications for *in vivo* bladder imaging diagnosis. Preliminary clinical studies (20 cases) revealed high sensitivity (91%) and specificity (80%) in the diagnosis of neoplasia [26].

Recent publications confirmed our previous results that OCT was able to differentiate malignant from benign lesions with a positive predictive value of 89% and a negative predictive value of 100%. Benign lesions including cystitis cystica and hyperplasia, and also normal urothelium, had characteristic OCT findings that facilitated distinguishing them from malignant lesions in conjunction with white light cystoscopy [51].

24.3.2
Combined Use of OCT and Fluorescence Imaging for Cancer Detection

The OCT data obtained for bladder cancer suggest that OCT can increase the efficacy of diagnosis and possibly decrease the number of unnecessary biopsies.

Our current study of human fluorescence cystoscopy by means of OCT enrolled 26 patients. In preparation for fluorescence cystoscopy, 50 ml of 3% δ-aminolevulinic acid (ALA) solution was instilled in the bladder 2 h before the procedure. The urinary bladder was first examined in white light, followed by blue light illumination, and the red fluorescent zones were identified. The endoscopic OCT probe was placed through the cystoscope in direct contact with bladder mucosa and biopsy was performed for all fluorescent OCT zones.

A total of 107 fluorescent zones with 18 exophytic tumors and 89 flat suspicious areas were examined and compared with OCT and histology. All 18 cases of exophytic tumors were correctly detected by white light cystoscopy, OCT, and fluorescence cystoscopy. Fluorescence from 18 exophytic tumors verified correct photosensitizer administration. A total of 75 of 89 flat fluorescent zones (84%) had benign histology and, therefore, false-positive fluorescence. Of these 75 lesions, 59 (78.7%) had typical benign stratified OCT images and were considered true negatives (TN). In the remaining 16 histologically benign zones, the OCT images showed a bright or patchy urothelium with poor or no contrast with lamina propria; therefore, these zones had false-positive OCT. Interestingly, most of false-positive OCT cases contained von Brunn's nests and squamous metaplasia. Of the 14 malignant flat zones, OCT correctly revealed 12 areas with neoplastic pathology. OCT worked well in cases of invasive cancer and demonstrated satisfactory results in HGD (Figure 24.4); only two cases of HGD were erroneously recognized as false negative.

Specificity is frequently used to analyze the fluorescence imaging efficacy, but this is not truly accurate because this calculation depends on the arbitrary number of sites without fluorescence chosen for inclusion. Therefore, a positive predictive value (PPV) is a more relevant measure because it represents the ratio between false positives and true positives. In our series, the PPV for flat lesions with fluorescence cystoscopy alone was 16%, while the PPV for the fluorescence

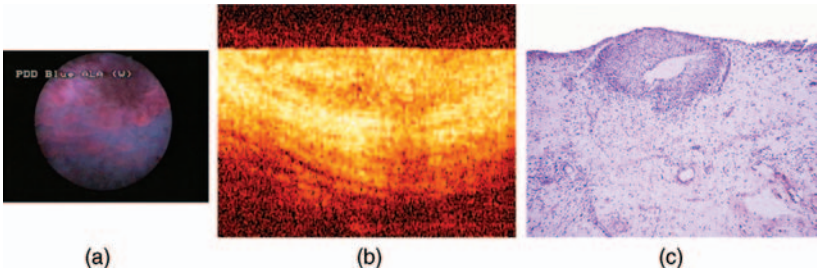

Figure 24.4 High-grade dysplasia. (a) Fluorescent cystoscopic image; (b) OCT image (suspicious type, true positive case); (c) corresponding histology (H&E stain).

cystoscopy combined with OCT increased to 43%, which is a very significant improvement. These data also suggest that 78.7% of the biopsies based on fluorescent positive findings could have been avoided based on OCT results.

Pioneering studies of the combined use of fluorescence and OCT were made on animals. Preliminary results based on rat bladder tumorogenesis studies demonstrate that ALA fluorescence imaging is highly effective and sensitive and covers a large area (diameter 30 mm) of the bladder surface, whereas OCT provides only a cross-sectional scan of 5×2.8 mm. However, because of the superior resolution and the ability to delineate bladder micromorphology, in addition to the detection of a neoplastic lesion, OCT can even detect precancerous lesions that fluorescence may sometimes miss and can differentiate inflammatory lesions that fluorescence may show positive [52]. Here, we present the results of the first clinical study of the combined application of fluorescence cystoscopy and OCT for the diagnosis of early cancer. We demonstrate that fluorescence cystoscopy and OCT do not add diagnostic information in zones of papillary tumors, but OCT greatly increases the specificity and PPV of fluorescence imaging tests in the diagnosis of early cancer in flat suspicious zones to 79% and 43%, respectively.

24.3.3
OCT Guided Surgery in Bladder Cancer (Open Surgery and Transurethral Resections)

The problem of an adequate tradeoff between radical tumor removal and maximum preservation of organs is very important for cancer management and patients' quality of life. We have evaluated OCT for pre- and intraoperative planning of the tumor resection margins on the examples of bladder, esophageal, and rectal carcinoma.

24.3.3.1 Transurethral Resections

OCT was used for intraoperative planning of 44 cases of transurethral resection of bladder tumor (TURBT). The OCT forward-looking probe was introduced through the operating channel of the cystoscope and anchored for TURBT. Under visual control, the probe was pressed directly against the mucosa. Two sites of the tumor and multiple sites along four directional paths around the visual tumor border (up to 2 cm in the 12, 3, 6, and 9 o'clock directions) were imaged.

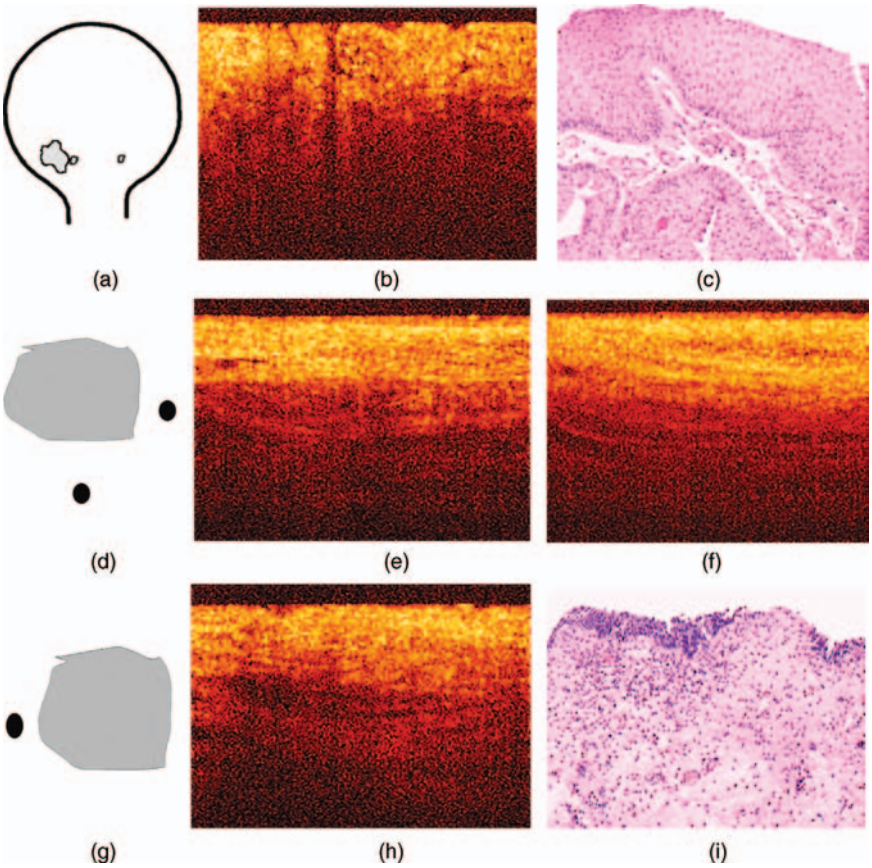

Figure 24.5 Intraoperative OCT planning of resection line during TURBT (T1G2). (a) Scheme of tumor localization; (b) OCT image of tumor focus; (d) scheme of OCT scanning along two directions of conventional clock-dial (6 o'clock); (e, f) OCT images of benign type at 6 o'clock; (g) scheme of localization of OCT image of suspicious type at 9 o'clock; (h) OCT image from the point at 9 o'clock.

To evaluate the postoperative resection margins following TURBT, OCT imaging was performed at the same four directional paths at the line of resection, 0.5 and 1 cm from the postoperative resection line.

All OCT image readings were compared with histologic data from the same site. The OCT and histologic borders coincided in 79% of cases. At the level of the traditional resection line (+ 0.5 cm from the visible tumor border along the perimeter), suspicious OCT images were observed in one-third of the cases (the sensitivity was 93% and specificity 74%). If an abnormal or suspicious OCT image was revealed along the line, then an additional resection was performed accordingly.

Based on OCT data, 14 of 44 TURBT patients with intraoperative resection line examination required additional resection (Figure 24.5). One TURBT patient with postoperative resection line examination required additional resection.

To determine the invasion depth, target investigation of the papillary tumor neck was undertaken in 28 cases. It was found that in the case of superficial tumor (Ta, T1 stages), sharp, high-contrast horizontal layers are visualized throughout the OCT image, whereas in the case of invasive tumor (T2 and higher) *no* horizontal layers were observed in the OCT image. The OCT sensitivity in determining tumor invasion depth by assessing neck image structure was 100% and the specificity was 77%.

24.3.3.2 **Open Surgery**

Using OCT intraoperatively in the open bladder, we can determine the condition of the inferior bladder at the bladder neck for possible preservation, which then may help to preserve normal urinary function for the patient [53]. This OCT study sample included 25 patients who underwent partial cystectomy. Three of 25 PC patients required intraoperative conversion to radical cystectomy as OCT revealed involvement near the bladder neck, while 67% of these patients could have had a more limited resection (Figure 24.6).

OCT can help to define the bladder tumor margins in real time and has the potential to improve the adequacy of bladder resection, optimize bladder sparing, and reduce the recurrence rate.

24.4
Gastroenterology

The history of using OCT in gastroenterology dates back to 1996, when animal organs were studied *ex vivo* and it was shown that OCT is capable of differentiating tissue layers of the wall of hollow organs [54]. The 13 year experience gained by different groups in the application of OCT in gastroenterology is sufficient to discuss its clinical value.

The spectrum of potential clinical use includes:

- OCT for endoscopic BE malignancy monitoring
- OCT for surgical guidance of colon polypscolitis
- OCT in guided surgery of gastrointestinal cancer (esophagectomy and rectoectomy)
- OCT for differential diagnosis of Crohn disease and ulcerative colitis
- OCT of the biliary tract.

Here we present the experience of our group in OCT monitoring surgery in gastroenterology.

24.4.1
OCT for Endoscopic Monitoring of Barrett's Esophagus Malignancy

A total of 78 patients had a complete qualifying set of data for inclusion in the statistical analysis. The protocol for this surveillance for BE was approved by the Cleveland Clinic Institutional Review Board. The protocol and the preliminary

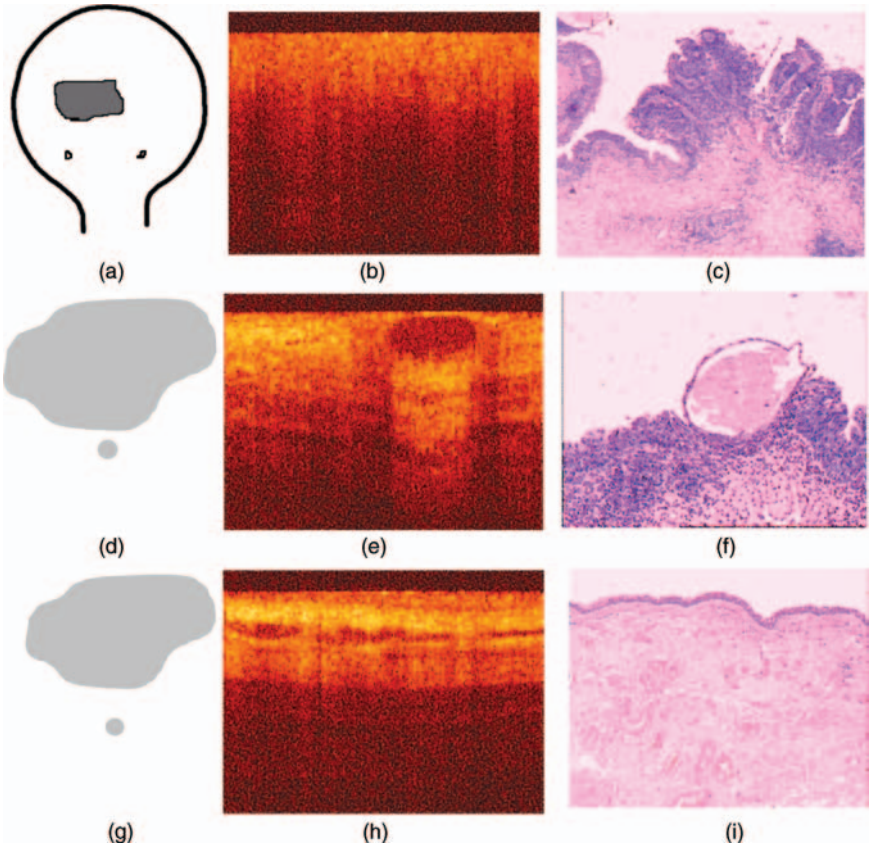

Figure 24.6 Intraoperative OCT planning of resection line during partial cystectomy. (a) Scheme of tumor localization; (b) OCT image of tumor focus; (c) H&E-stained histology section reveals transitional cell-invasive carcinoma (T2GIII); (d) scheme of OCT scanning along direction of conventional clock-dial (6 o'clock tumor border plus 3 mm); (e) OCT image of benign type from point (d); (f) H&E-stained histology section reveals cystitis cystica; (g) scheme of localization of OCT image of 6 o'clock tumor border plus 10 mm; (h) benign OCT image from the point (g); (i) histology section reveals chronic cystitis.

clinical results have been described earlier [55, 56]. Seventeen patients were histologically diagnosed with invasive adenocarcinoma (INVC) originating in the metaplastic epithelium, 17 with intramucosal adenocarcinoma (IMC), 11 with HGD, and 33 with benign BE. According to the Seattle protocol [57], OCT and morphologic analysis were performed on a per level of BE basis (rather than per biopsy site or per patient); 181 levels were analyzed. The analysis included comparison of OCT images and histopathology slides from the same level. For test purposes, histopathologic diagnosis of metaplastic epithelium and low-grade dysplasia (LGD) was considered to be benign (112 levels).

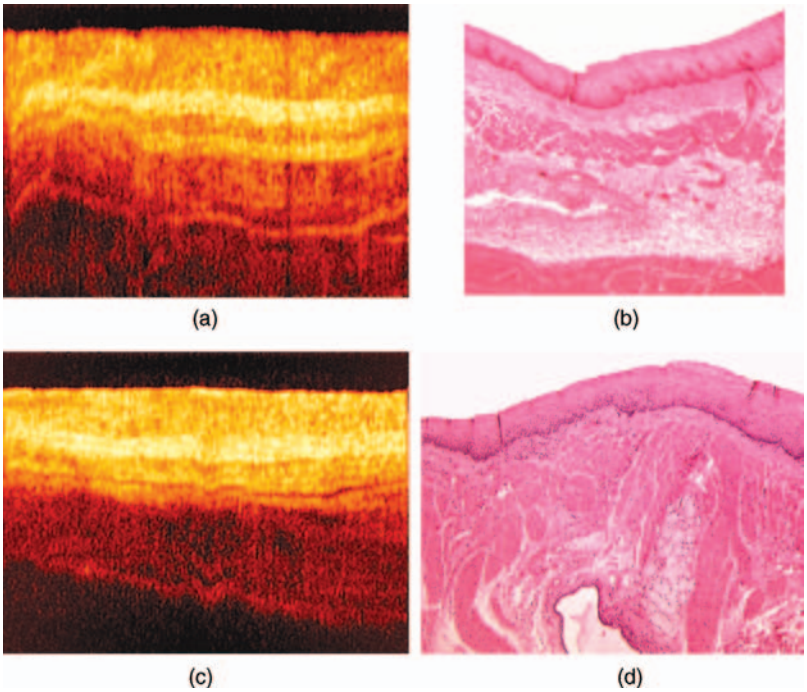

Figure 24.7 Images of normal esophagus: (a) OCT image with distinctive MM layer; (b) corresponding histology (H&E stain); (c) OCT image without distinctive MM layer; (d) corresponding histology (H&E stain). SSE, stratified squamous epithelium; LP, lamina propria; MM, muscularis mucosa; SM, submucosa; MP, muscularis propria (bars = 1 mm).

The following conditions were considered to be malignant: HGD (25 levels), IMC (27 levels), and adenocarcinoma invasive into muscularis propria (INVC) (17 levels). Altogether, 69 levels in malignant state were analyzed.

24.4.1.1 **Differentiation Between Normal Esophagus and Benign BE**

The OCT image of normal squamous esophageal mucosa has a five-layered (Figure 24.7a) or four-layered (Figure 24.7b) structure, depending on how distinctive the muscularis mucosa (MM) layer is.

In both cases, the upper layer with a moderate level of signal and thickness of ~100 μm corresponds to the stratified squamous epithelium (SSE). The second layer with the maximum level of backscattering corresponds to the lamina propria (LP). In the normal esophagus, the SSE layer is well contrasted from LP, and the basal membrane lies at the sharp interface between the two layers. If MM can be differentiated (Figure 24.7b), it will appear darker than the LP and submucosa (SM). In the absence of MM (Figure 24.7d), the contrast between the two connective tissue layers is less pronounced (Figure 24.7c). The fifth layer, muscularis propria (MP), always has low brightness.

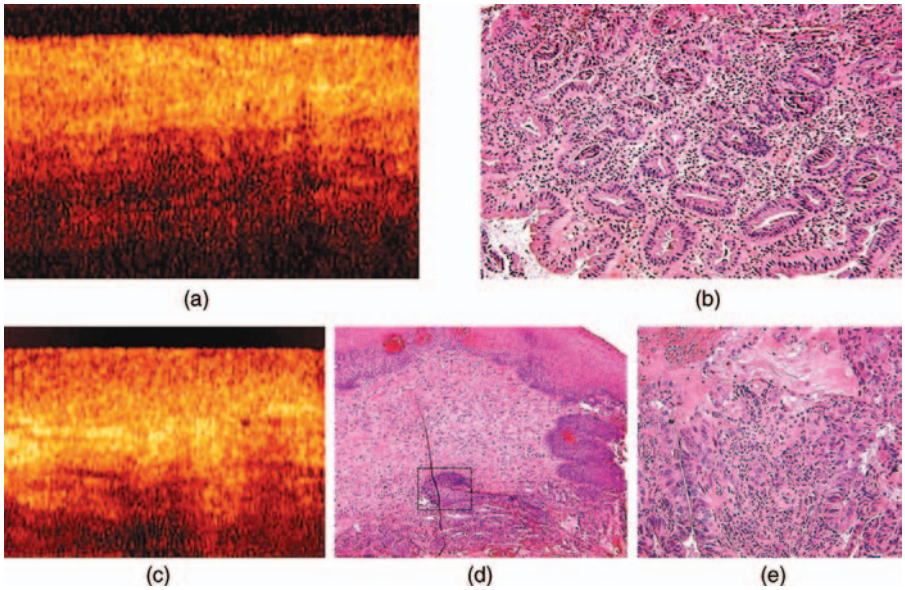

Figure 24.8 HGD of metaplastic epithelium. True-positive case: (a) absence of sharp interface between glandular mucosa and submucosa; (b) corresponding histology (H&E stain). False-negative case: (c) layered OCT image; (d) corresponding histology; (e) area of HGD delineated in a square (H&E stain).

Benign BE also has a layered structure. However, the BE OCT image is different, which is consistent with different histomorphology. Histologically, the upper layer, glandular mucosa (GM), is not a single layer and has a crypt structure with individual crypt size much higher than the resolution of our OCT system. However, the OCT contrast between crypts and mucus is insufficient at this resolution and the GM appears as a single layer.

The SM and MP are contrasted on OCT images of BE, but not so pronounced as in the normal squamous esophagus. As BE has an inflammatory origin, signs of inflammation are often present: dark areas correlating with exudate accumulations. Only three levels out of 112 with benign BE were false negative, the sensitivity of the method to detect BE versus normal esophagus was 97%, and the specificity was 100%.

24.4.1.2 **Differentiation Between HGD and Benign BE**

Loss of OCT contrast between epithelium and connective tissue is the main feature of HGD. This was observed for different types of epithelium, including stratified squamous, transitional, pseudostratified ciliated, and glandular epithelium [58]. OCT images of HGD were characterized by degradation of the sharp interface between GM and SM, and were considered to be positive for malignancy (Figure 24.8a).

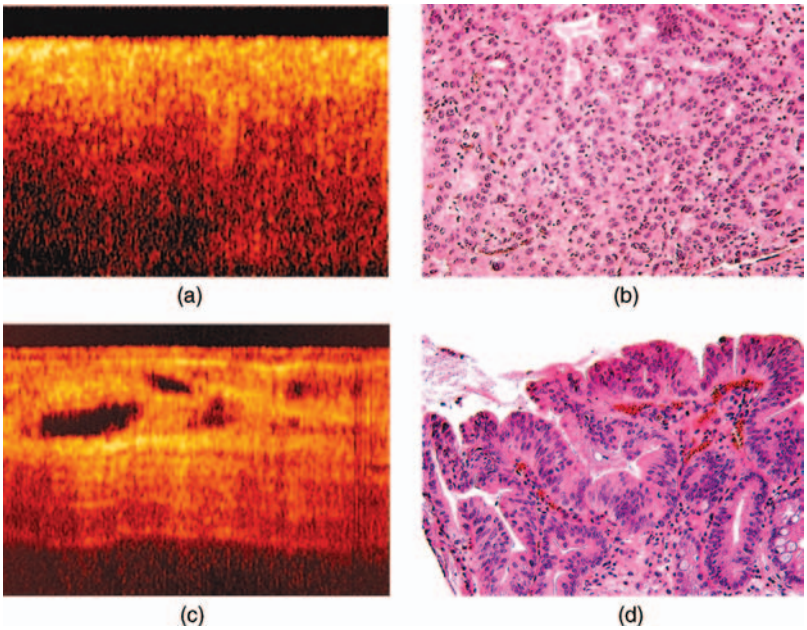

Figure 24.9 Intramucosal ADC. True-positive case: (a) OCT image; (b) corresponding histology (H&E stain). False-negative case: (c) OCT image; (d) corresponding histology (H&E stain).

For patients with BE, the sensitivity and specificity for OCT to detect HGD were 71% and 68%, respectively. Low contrast images of benign BE usually correlated with sites of scarring left from previous biopsies (false positive). Analysis of false negatives revealed that focal areas of SSE were overlapping underlying metaplastic epithelium with HGD (Figure 24.8c–e).

24.4.1.3 **Differentiation Between IMAC and Benign BE**

Adenocarcinoma is characterized by loss of layered structure on OCT images. The GM layer is indistinguishable from the underlying structures (Figure 24.9a).

The sensitivity for the detection of intramucosal adenocarcinoma (IMAC) in patients with BE was 85% and specificity 68%. Four cases out of 27 were false negative (Figure 24.9c), and represented a situation of focal invasion into the SM (when imaging and histology sites are not sufficiently correlated).

Endoscopic data showed that only 14 cases of IMAC were recognized visually by endoscopists. In the remainder of the cases, IMAC was detected in visually unchanged BE.

24.4.1.4 **Differentiation Between Invasive Carcinoma and Benign BE**

The main sign of invasive cancer on OCT images is loss of layered structure (Figure 24.10a). There were no false negatives during identification of invasive adenocarcinoma (INVAC) (sensitivity 100% and specificity 85%).

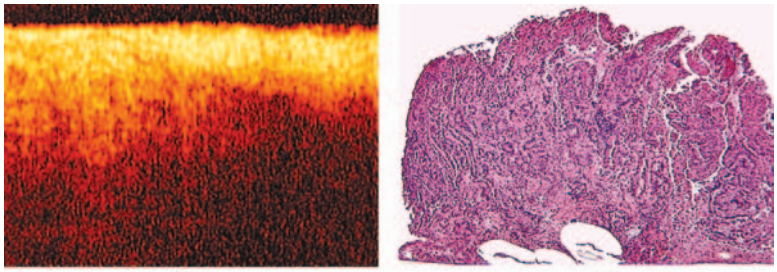

Figure 24.10 Invasive ADC: (a) true-positive OCT image; (b) corresponding histology (H&E stain).

24.4.1.5 **Malignant BE Versus Benign BE**

After combining all malignant states (HGD, IMAC, INVAC), the OCT sensitivity in detection of malignancy was 83% and specificity 68%.

The results of blind recognition of images are summarized in Table 24.2.

BE has been the focus of intense OCT research in the gastrointestinal tract. In Table 24.3, the diagnostic accuracy of OCT in detecting neoplasia in BE is presented. It must be emphasized that these results were obtained using different types of scanning and different criteria of OCT images [29, 55, 56, 59–61].

Evans *et al.* used the longitudinal scanning modality [29]. A catheter of this type exerts no pressure on mucous membrane surfaces, which enables one to observe surface features and differentiate enlarged glands. For diagnosis of IMC/HGD, the authors proposed to use criteria such as surface maturation and gland architecture. They hypothesized that incomplete surface maturation, indicative of dysplasia or regenerative changes, would be seen as a high surface OCT signal compared with the subsurface signal; gland irregularity by OCT might be characterized by irregular size, shape, and distribution of these architectural structures. A total of 177 biopsy correlated images were analyzed. Good correlation between histopathologic diagnosis of IMC/HGD and scores for each image feature [dysplasia index (Spearman correlation coefficient), $r = 0.50$, $p < 0.0001$], surface maturation ($r = 0.48$, $p < 0.0001$), and gland architecture ($r = 0.41$, $p < 0.0001$) was found. When a dysplasia index threshold of >2 was used, the sensitivity and

Table 24.2 Statistical parameters of blind comparison of OCT images and histopathology data.

Parameters	HGD + IMC + INVC	HGD + IMC	HGD	IMC
Sensitivity (%)	83	78	71	85
Specificity (%)	68	68	68	68
Diagnostic accuracy (%)	74	71	69	71
Positive predictive value (%)	62	53	33	39
Negative predictive value (%)	87	87	92	95
Kappa	0.626	0.585	0.562	0.512

Table 24.3 Diagnostic accuracy of OCT in detecting neoplasia in BE in blind recognition (according to data from different studies).

Study	No. of patients (images)	Sensitivity (%)	Specificity (%)	Diagnostic accuracy (%)	Ref.
1. BE/SE, Gastro, Cardia	121	97	92	–	Poneros *et al.*, 2001 [59]
2. BE/LGD, HGD, IMC	23 (152)	69	71	70	Isenberg *et al.*, 2003 [60]
3. BB/LGD, HGD, IMC	33 (314)	68	82	78	Isenberg *et al.*, 2005 [61]
4. BB + LGD/ HGD, IMC, INC	44	75	91	89	Zuccaro *et al.*, 2001 [56]
5. BB/HGD, IMC					Evans *et al.*, 2006 [29]
6. BB + LGD/ HGD, IMC	67 (164)	78	68	70	Gladkova *et al.*, 2007 [55]
7. BB + LGD/ HGD, IMC, INC	78 (181)	83	68	74	Gladkova *et al.*, 2007 [55]

specificity for diagnosing IMC/HGD were 83% and 75%, respectively. The authors concluded that an OCT image-scoring system based on histopathologic characteristics has the potential to identify IMC and HGD in BE. Note that these criteria cease to work for a dysplasia index >2 [29].

The team working at the Division of Gastroenterology in the Case Western Reserve University Hospitals of Cleveland [20, 62] employs endoscopic OCT with radial scanning. In 2005, a double-blinded endoscopic OCT study was performed by four endoscopists in 33 patients with documented BE. A total of 314 pairs of OCT images and jumbo biopsy specimens were analyzed. A cap-fitted, two-channel endoscope and rotation OCT probes were used that ensured target biopsy from the scanned regions. The formulated OCT criteria of BE for a rotation probe have much in common with those of ultrasonic imaging. Dysplasia and adenocarcinoma had the following OCT features: (1) focal areas of decreased light scattering and (2) focal loss of mucosal structure and organization. By using histology as the standard, the endoscopic OCT had sensitivity 68%, specificity 82%, PPV 53%, negative predictive value 89%, and diagnostic accuracy 78%. Based on these results, it was concluded that further modifications, including increased resolution and identification of further potential OCT characteristics of dysplasia, are needed before OCT can be used clinically.

Analysis of analogous groups of patients by our team enables us to argue that OCT is a promising technique for the diagnosis of BE neoplasia, which implies still further clinical experience and also further development of the technology. Making use of the specific OCT features of BE, we found that the sensitivity and specificity of

endoscopic OCT in detecting malignization in BE (HGD, IMAC, INVAC) were 83% and 68%, respectively. However, the OCT sensitivity is rather low when detecting HGD only. Recent research in the field of Doppler OCT [63], ultra-high resolution OCT [64], high scanning speed OCT [65], *in vivo* 3D comprehensive microscopy [66], and computer-aided diagnosis for identification of dysplasia [67] demonstrated additional diagnostic features of the development of early neoplasia in BE, which are expected to increase the diagnostic value of OCT.

24.4.2
OCT for Surgical Guidance of Colon Polyps

The malignancy potential of colorectal polyps is well known in endoscopic practice [68].

Endoscopic OCT was tested as a possible tool for *in vivo* endoscopic differential diagnosis of colon polyps and for assessing the need for their removal during colonoscopy. The studies were undertaken at the Eppendorf Clinic, University of Hamburg (Germany) [69] and the Cleveland Clinic Foundation (United States) [70].

The studies revealed OCT features of adenomas and hyperplastic polyps based on which the diagnostic accuracy of OCT was statistically analyzed; 48 tubular adenomas, 12 tubulovillous adenomas, and 56 hyperplastic polyps were studied. The OCT features of different types of colon polyps were formulated:

1) The hyperplastic polyp is characterized by a three-layer "benign" OCT image, thickening of the upper layer (glandular mucous membrane), and a clear border between the glandular mucous membrane and submucous layer (Figure 24.11a–c).
2) Adenoma, independent of its size, is characterized by an OCT image without layers (Figure 24.11d–f).

Analysis of 116 polyps in the open test showed that OCT differentiates adenomas from hyperplastic polyps with good sensitivity (92%) and specificity (84%).

Our results on the differential diagnosis of colon polyps by the OCT technique agree with preliminary data obtained in clinical studies using an analogous OCT device [69]. Jaeckle *et al.* [69] identified OCT features of adenoma as an image without layers and of hyperplastic polyp as an image in which one can see a glandular mucous membrane, a submucous layer, and a muscular layer. Pfau *et al.* [27] used a rotation probe and also ascertained the capability of OCT to distinguish reliably between hyperplastic and adenomatous polyps. They investigated 44 polyps in 24 patients. Endoscopic optical coherence tomography (EOCT) showed that adenomas were rated significantly more disorganized, with less structure than hyperplastic polyps ($p = 0.0005$). Polyps that were subsequently found to be adenomas in histopathologic evaluation were judged during EOCT to exhibit a significant decrease in light scattering, appearing darker in EOCT images compared with hyperplastic polyps ($p = 0.0007$). It was found that the mean difference in light scattering was significantly greater between adenomas and normal tissue (mean difference = 45.81) than the mean difference in scattering between hyperplastic polyps and normal tissue (mean difference = 14.86) ($p = 0.0001$). The authors

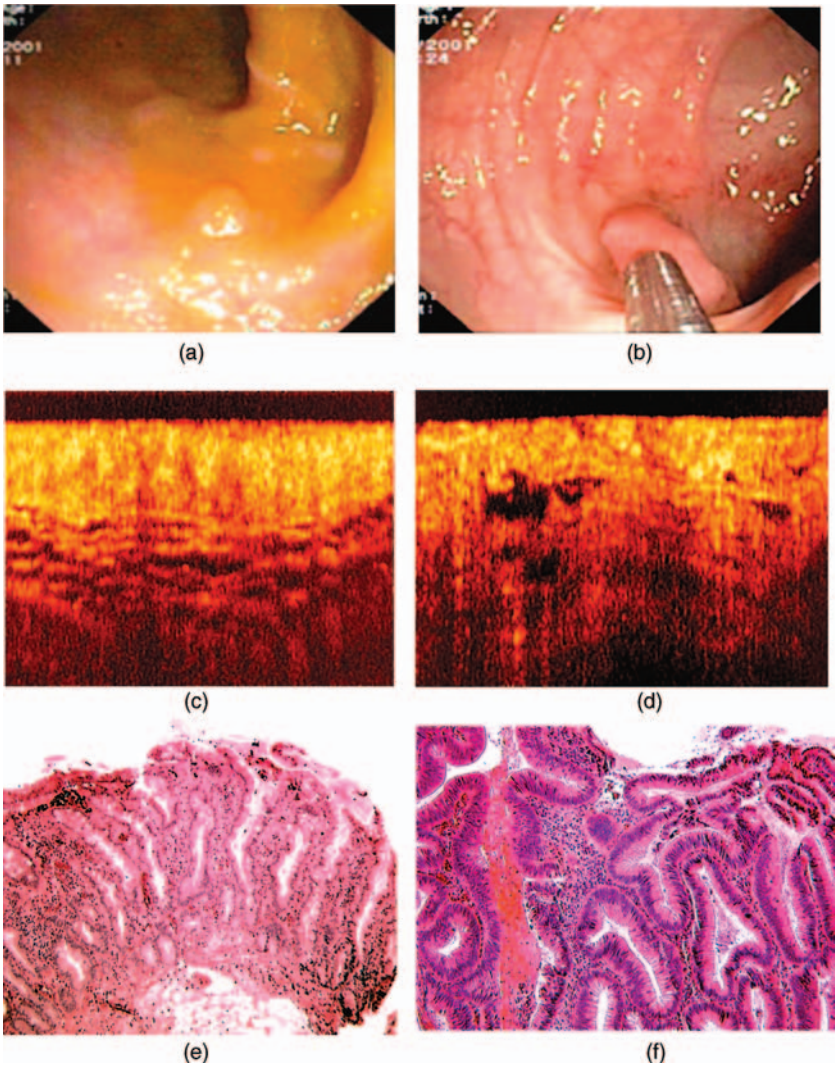

Figure 24.11 Endoscopic OCT and the corresponding histology images of (a–c) hyperplastic polyp and (d–f) adenomatous polyp.

considered that morphologic feature quantification of colonic crypt patterns using a microscope integrated OCT scanner [67] is highly promising for clinical applications.

We defined specific features of OCT images of adenoma and hyperplastic polyps obtained using the forward-looking probe on 116 polyps. It was found that OCT differentiates between adenoma and hyperplastic polyps with good sensitivity (92%) and specificity (84%).

Other groups have also reported on the potential capability of OCT to distinguish flat adenomas from normal mucous membrane of intestines, which is sometimes

difficult in traditional endoscopy. Also reported was a preliminary study of a single case of flat adenoma using Doppler OCT. It was shown that the development of adenoma is accompanied, along with changes in structural features, by changes in the vascular pattern [71].

24.4.3 OCT in Guided Surgery of Gastrointestinal Cancer (Esophagectomy and Rectoectomy)

The problem of adequate tradeoff between radical tumor removal and maximum preservation of organs is very important for cancer management and patient quality of life.

We have evaluated OCT for pre- and intraoperative planning of the tumor resection margins on esophageal and rectal carcinoma. The standard EOCT was used for 19 patients with rectal adenocarcinoma and 24 patients with distal esophageal cancer (14 zsquamous cell, 10 adenocarcinoma, eight cardial type and two Barrett's adenocarcinoma).

This study was performed in the Nizhny Novgorod clinics (Russia). The samples included patients to be operated on for rectal or distal esophageal cancer. Examinations were performed for patients with esophageal cancer located not higher (no more proximal) than 5 cm from the Z-line and rectal adenocarcinoma with tumors in the upper and middle thirds. This inclusion criterion is associated with the possibility of performing organ-preserving surgery.

Taking into account that the endoscopic biopsy involves only the superficial esophageal layers (mucosal and submucosal), the OCT border was determined *ex vivo*, and histopathologic examination of the specimens was performed. We formulated the types of tumor growth along the esophagus and rectum. If the tumor spreads into the mucosa layer, the OCT image has no layers. If the tumor growth occurs along the submucous layer, OCT reveals a contrast border between the mucous and submucous layers, but does not show a contrast border between the submucous and muscle layers.

When the tumor had spread along the muscle layer, we acquired false-negative benign, very well-structured OCT images with two contrast borders. In the cases of mucosal growth, OCT correctly detected tumor borders in all patients with esophageal (4 pt) (Figure 24.12) and rectal cancer (16 pt). In the cases of submucosal tumor growth, OCT worked very well in the detection of tumor borders in all cases of esophageal (16 pt) and rectal cancer (9 pt). However, OCT could not determine tumor borders in patients with muscle cancer that had spread into either the esophagus (4 pt) or the rectum (2 pt).

Based on OCT *ex vivo* data, we developed a technique of endoscopic tumor border detection. Scanning was performed during the presurgery endoscopic examination. The OCT border was detected and marked for further surgery. The EOCT probe investigated the visual border of the tumor (distal for rectal carcinoma and proximal for esophageal carcinoma) along four directions of a conventional dial (12, 3, 6, and 9 o'clock). The above zones were OCT imaged in 0.3–0.5 cm steps until structural

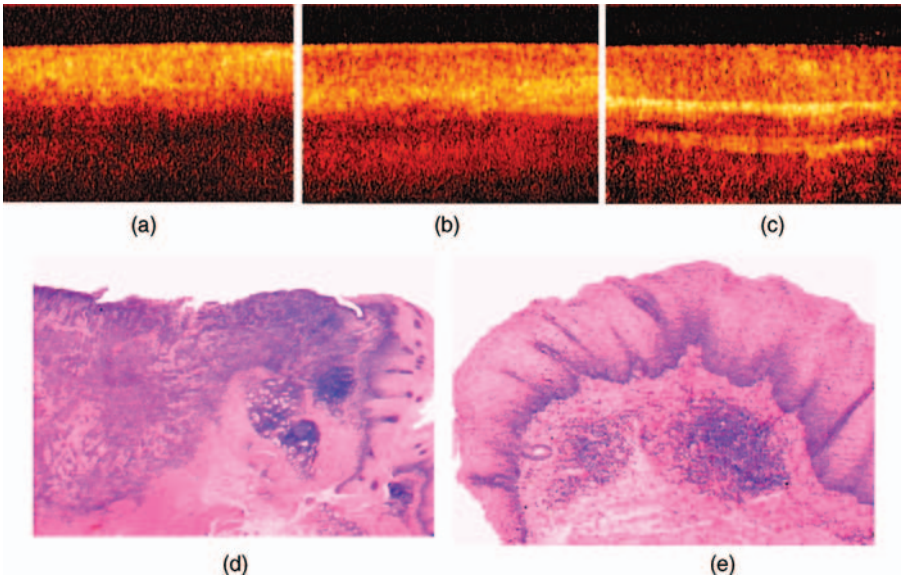

Figure 24.12 Finding the border of mucosal growth of squamous cell carcinoma of esophagus (*ex vivo*). OCT image of tumor focus (a) and the corresponding histology specimen (d); the OCT border (b, arrow) coincides with the histology border of squamous cell nonkeratinizing cancer (d); control OCT and histology study 1 cm from the border did not detect tumor growth (c, e). H&E staining of histology specimens.

images corresponding to normal mucosa were obtained. The OCT border was marked by electrocoagulator or methylene blue tattoo.

24.5 Gynecology

The first *in vivo* OCT images of the uterine cervix were obtained by the Nizhny Novgorod team in 1997 [22]. Later, the clinical feasibility of OCT in gynecology was discussed in a number of papers [72–76], describing the OCT features typical for a normal exocervix, endocervix, and endometrium. It was shown that OCT is capable of detecting neoplastic changes in stratified squamous epithelium. In this section, we demonstrate the potential of the clinical use of a new visualization method in gynecologic practice.

24.5.1 Methodology and Patient Selection

Development of the protocol for uterine cervix target biopsy was done in three stages: initial approbation of OCT for diagnosis of cervical pathology, study of the influence

of acetic acid on OCT images, and development and approbation of the protocol based on OCT colposcopy. In all the stages of the investigation, the female patients had the following indications for colposcopy:

- history of abnormal colposcopic findings
- abnormal results of Pap smear (ASCUS, LSIL; HSIL)
- positive HPV test for oncogenic viral type.

The exclusion criterion was age under 18 years.

The study was approved by the Ethical Committee for scientific studies with human subjects. The patients had to sign an informed consent document stating that they understood the investigational nature of the proposed study.

A typical scenario of the study was similar in all the stages:

- review of patient's history, including cytology and HPV testing results
- colposcopy and identification of regions of interest (ROI)
- OCT of identified ROI
- biopsy of ROI, when clinically appropriate
- histopathology evaluation of biopsy and comparison with OCT and colposcopic findings.

The diagnostic efficiency of OCT in recognizing malignization was studied using blind recognition tests of OCT images.

24.5.2
Guidance Biopsy During Colposcopy

In the first stage, a preliminary investigation of OCT capabilities for detecting neoplasia-induced alterations in the uterine cervix was carried out; 120 patients took part in the study. It was revealed that the most typical OCT feature of malignization was loss of specific image structure, which allowed us to formulate features of "benign" and "malignant" OCT images. Using this approach, we assessed the diagnostic efficiency of OCT for the recognition of cervical malignization. The sensitivity was shown to be 82%, specificity 78%, error 19.2%, and kappa 0.65. It should be noted that the maximum percentage error (Table 24.4) was due to false-negative recognition of metaplasia whose optical images are low structured.

This led us to revise some of the OCT criteria of malignization, for classifying the interpreted images not only as "malignant" or "benign" but also as "suspicious" (Figure 24.13) [92], and for looking for ways to increase the diagnostic efficiency of the technique.

It is worth noting that OCT should not be regarded as an independent diagnostic technique. Research carried out in the first stage demonstrated that to increase the diagnostic quality of cervical pathology, OCT data should be used in combination with information about clinical symptoms, cytology data, and colposcopy results. Therefore, the development of the OCT-based diagnostic protocol demands, in the first place, maximum adaptation of the new method (OCT) to the basic procedure (colposcopy). For validating the OCT–colposcopy technique, in the second stage we

Table 24.4 Distribution of the indices of OCT diagnostic efficiency in recognizing malignization.

Condition	No. of recognitions	True positives	False positives	False negatives	True negatives	Error (%)
Invasive carcinoma	70	62	0	8	0	11.4
Microinvasive carcinoma	28	23	0	5	0	14.2
High-grade dysplasia (HGD)	91	70	0	21	0	23
Inflammation	14	0	0	0	14	0
Metaplasia	56	0	23	0	33	41
Low-grade dysplasia	42	0	2	0	40	4.7

studied the influence of traditional colposcopic tests (application of acetic acid) on the character of OCT images of the uterine cervix.

A total of 120 female patients took part in the study. The structure of the uterine cervix states is presented in Table 24.5.

It was found that local application of a 3% solution of acetic acid in the case of uterine cervical neoplasia reduces the depth of OCT scanning 2–3-fold. We formulated differential criteria for OCT visualization of metaplastic and neoplastic epithelia on local exposure to 3% acetic acid solution, taking into account that interpretation of immature metaplasia is the most difficult for diagnosis in both colposcopy and OCT. In the presence of immature metaplasia, the OCT image persists in being structureless and the depth of scanning does not change, in contrast to the case of severe dysplasia and cervical cancer, when the velocity of signal attenuation becomes very fast, which manifests itself as a pronounced decrease in the size of the image down to half to one-third frames (Figure 24.14).

Being the most difficult for traditional diagnosis and OCT study (the error rate in the previous stage was 41%), cervical metaplasia was chosen for assessing the diagnostic efficiency of the new approach in OCT diagnostics. Results of the "blind" recognition test (Table 24.6) showed that the use of the proposed interpretation criteria enabled the error rate to be reduced to 15%.

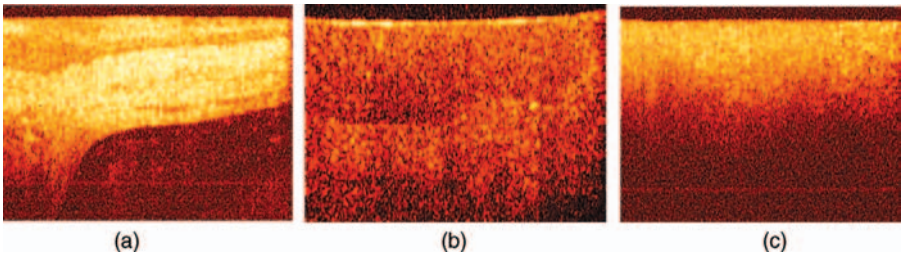

Figure 24.13 Types of OCT images of the cervix: (a) benign, (b) suspicious, and (c) malignant.

Table 24.5 The structure of cervical states.

Norm	21 (17.5%)		
Benign	56 (46.7%)		
Malignant	HGD 26 (21.6%)	Microinvasive carcinoma 5 (4.2%)	Invasive carcinoma 12 (10%)

This research allowed us to formulate the diagnostic protocol for examining the uterine cervix:

- colposcopy using acetic acid
- OCT study taking into account the impact of acetic acid
- target biopsy of the cervical mucous membrane by indications of OCT–colposcopy.

This protocol was tested in clinical conditions with the participation of 90 patients. The study was aimed at evaluating the efficiency of the developed protocol of OCT-colposcopy for taking a decision about uterine cervix biopsy. Examination was carried out following the proposed protocol, but the decision about biopsy was taken by a standard protocol based on colposcopic data. According to our data on abnormal

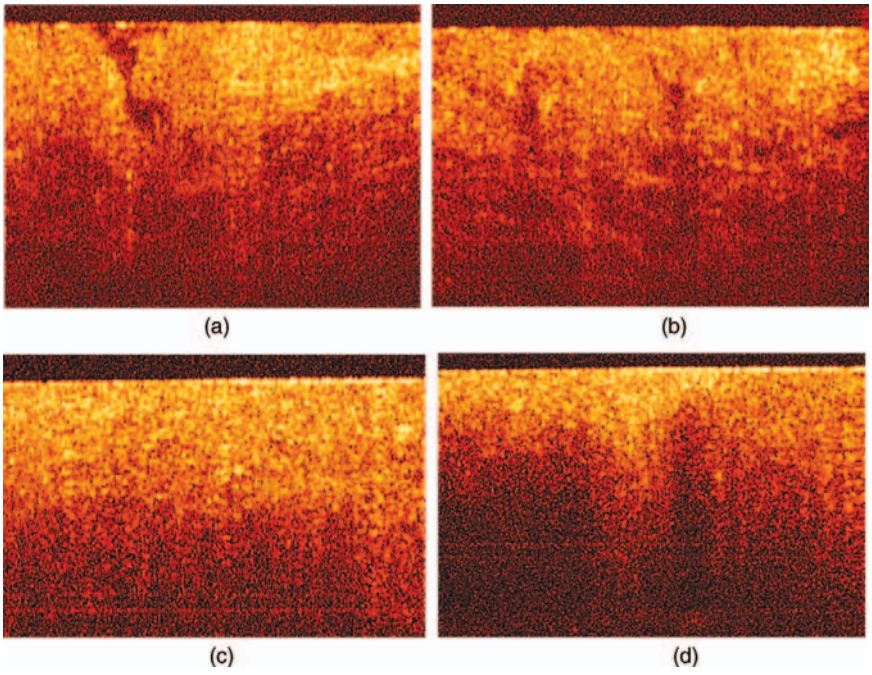

Figure 24.14 OCT images of cervical metaplasia (a, b) and cervical carcinoma (c, d) before (a, c) and after (b, d) application of a 5% solution of acetic acid.

Table 24.6 Diagnostic efficiency of the new approach in OCT diagnostics.

	True positives	False positives	False negatives	True negatives	Sensitivity (%)	Specificity (%)	Error (%)	Kappa
Total recognitions 430	217	20	43	150	83	88	15	0.67

colposcopic findings, 79% of cases had indications for biopsy and only in 36% of cases were malignant and suspicious types of images detected by OCT. Histology studies of biopsy material confirmed the presence of benign states in the benign types of OCT images (Figure 24.15).

We believe that inclusion of OCT in the protocol for uterine cervix examination allows more accurate assessment of the state of the object under study and reduces substantially (by more than 40%) the number of invasive procedures (biopsies) needed, which will have important medical, social, and economic impacts. When no biopsy is taken in the case of benign types of images, OCT may be an objective follow-up technique that will allow timely changes of therapeutic management in case of necessity.

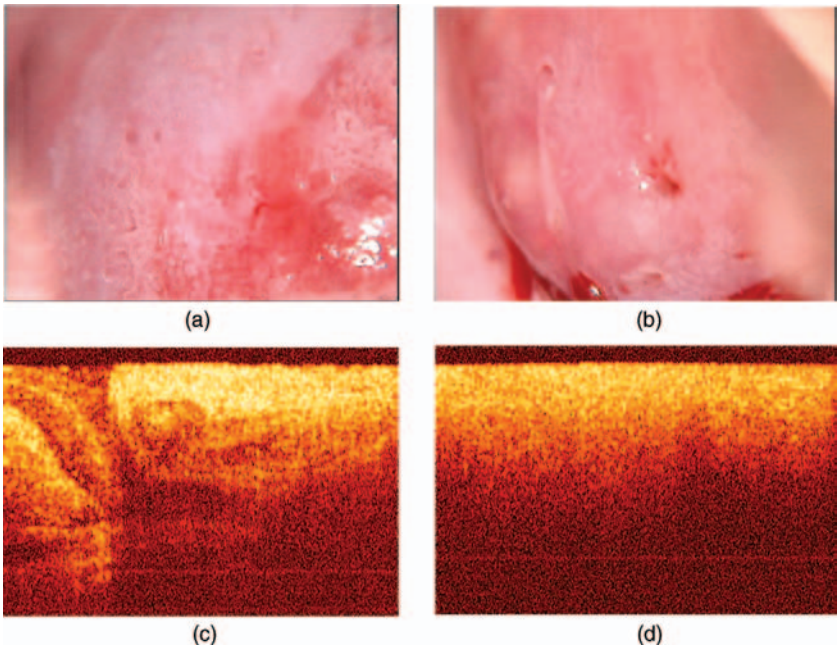

Figure 24.15 Differential diagnosis of colposcopic findings with OCT.

24.6
Cross-Polarization OCT in Oncology

Traditional OCT is most informative for the investigation of layered tissues covered by epithelium. The presence and loss of contrast between the epithelium and the underlying connective tissue are an important diagnostic feature recorded by means of OCT [77]. In some cases, traditional OCT images of benign and malignant tissues are both structureless, which makes them indistinguishable, thus reducing the specificity of the method. Loss of contrast between layers occurs as a result of changes in optical characteristics of the epithelium and also of connective stroma. Standard OCT is not intended for detecting changes in the connective stroma.

Structured components of connective tissue (collagen fibrils and fibers) are formed from collagen. High organization of collagen ensures its capability to change the polarization of light passing through biotissue. In the context of interest to us, collagen is an important birefringent molecule in the human body. Birefringence is the principal polarization characteristic of tissues that may be registered by means of an OCT modality known as polarization-sensitive OCT (PS-OCT) [78].

Another, no less important, polarization characteristic of biotissue is depolarization. Depolarization is the property of material to eliminate polarization in a sum scattered wave. If backscattered radiation contains radiation with polarization orthogonal to that of the probing wave, then it may be recorded by a PS-OCT modality referred to as cross-polarization OCT (CP-OCT) [36].

Neoplasia changes the properties and integrity of healthy tissues, hence it changes the collagen state and polarization features of tissues. That is why detection of birefringence and depolarization properties of tissues by means of PS-OCT may be a useful means for increasing the specificity of traditional OCT.

Elaboration of new polarization techniques is a promising trend in OCT development. Nearly all research groups involved in OCT studies have used polarization methods [79–81].

Histologic methods of assessing collagen and its birefringent properties have been developed, but only *ex vivo*. Of particular interest is the method of light microscopy in polarized light using PicroSirius Red (PSR) staining, which allows the reliable detection of collagen possessing high birefringence. The use of PSR staining in polarized light gives information about the size of the structures, their number, composition, and location, birefringence ability, and, as a consequence, the functional state of tissue [78]. The majority of authors working with PSR staining in polarized light are unanimous in reporting that staining confirms the collagen with enhanced linear birefringence. When stained by PSR, organized collagen shows up as bright regions whose yellow–orange and red colors are typical for thick fibers (type I collagen with fiber diameter 1.6–2.4 μm), and dark green for thin fibers (type III collagen, fiber diameter 0.8 μm) [82–84].

Most researchers have studied birefringence using CP-OCT systems [85, 86], which are a convenient tool for assessing biological tissues with high collagen content. These include tissues that are of low contrast for traditional OCT, such as tendon, articular cartilage [87], and derma [88], as they have a relatively uniform

Table 24.7 Volume of the studied material depending on biological tissue localization.

Object under study	No. of patients	No. of histology specimens	No. of CP-OCT images
Cervical tissue	68	78	148
Urinary bladder tissue	65	72	152
Esophagus tissue	17	23	143
Total	150	173	443

structure. Birefringence is visualized as contrast-alternating bright and dark stripes elongated primarily along the surface, whose spatial period is determined by the magnitude of birefringence. Several such bands may appear in the image at a strongly anisotropic refractive index in biotissue ($\Delta n = 10^{-3}$–10^{-2}).

Two polarization-conjugate images are demonstrated when assessing the depolarization properties of tissue [33, 35]. Comparison of scattering in initial and orthogonal polarizations gives detailed information about microstructures and biochemical alterations depolarizing tissue components, collagen in particular. Our preliminary studies have revealed that the CP-OCT technique may provide clinically important information about mucosa as connective tissue fibers are capable of scattering probing radiation not only to direct but also to orthogonal polarization. Comparison of the patterns of backscattering in direct and orthogonal polarizations proved to be most informative for differentiation between clinically similar cases of esophageal carcinoma and cicatrized esophagus tissue after chemical burning [30], and also for differentiation between cervical leukoplakia and cancer [77].

Thus, the possibility of *in vivo* (noninvasive) observation of collagen changes refines the treatment of suspicious OCT cases and opens up new diagnostic capabilities of OCT.

Cross-polarization investigation of urinary bladder, uterine cervix, and esophageal mucosas was carried out in the course of endoscopic procedures: cystoscopy, colposcopy, and fibrogastroscopy (Table 24.7).

24.6.1
CP-OCT in Oncogynecology

Figures 24.17–24.19 demonstrate two types of OCT images: in direct and in orthogonal polarization. OCT images of the unaltered uterine cervix are shown in Figure 24.16, where a layered horizontally organized mucous structure is visualized. In direct polarization (Figure 24.16a, lower image), the epithelium looks like a moderately uniformly scattering layer that has a sharp border with a more intensely scattering subepithelial tissue. In orthogonal polarization (Figure 24.16a, upper image), the epithelium has, primarily, a cellular structure and is visualized as a very weakly scattering layer. PSR staining of histology specimens in polarized light reveals thick, well-ordered, oriented along the tissue surface, bright-red collagen fibers (type I

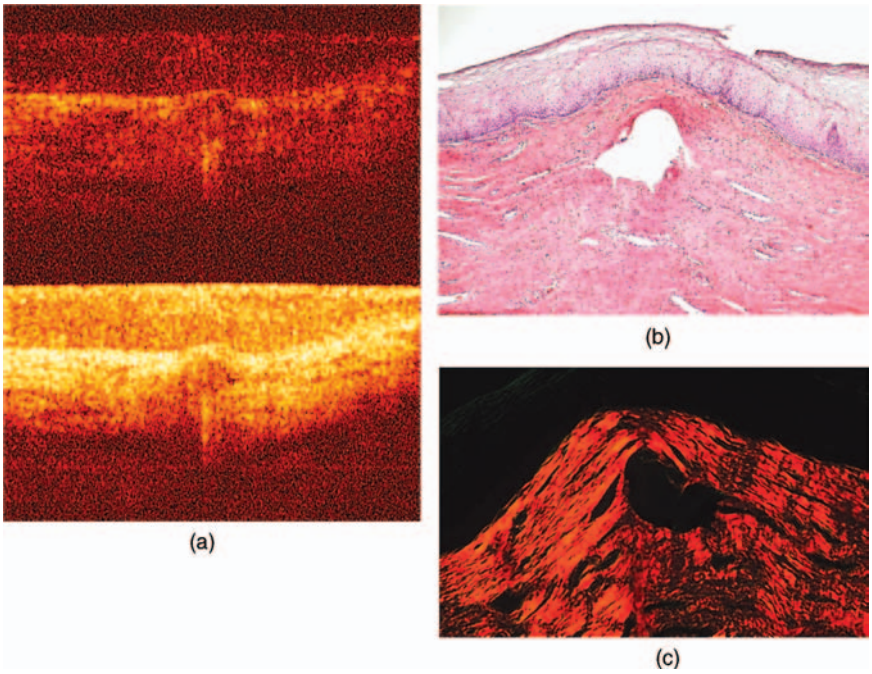

Figure 24.16 Mucous layer of normal uterine cervix. The layers were marked with Safil surgical suture 150 μm in diameter, transparent to OCT probing radiation. The suture was sewn immediately under the epithelium. (a) OCT image in direct (bottom) and orthogonal (top) polarization; (b) histologic specimen, H&E staining, frame size 1.7 × 1 mm; (c) histology specimen, PSR staining in polarized light, frame size 1.7 × 1 mm.

collagen). CP-OCT images of the mucous layer of the normal uterine cervix feature layered tissue structures. Visualization of images in direct and orthogonal polarization allow reliable differentiation of tissue layers with high contrast, and also various inclusions, blood vessels in particular. The signal intensity in orthogonal polarization reflects the presence of type I collagen in stroma.

Two cases where the colposcopic pattern is suspicious for cancer (stippling, mosaic, moderate aceto-white reaction) are illustrated in Figures 24.17 and 24.18. Figure 24.17 demonstrates a mucous layer of the uterine cervix with a growth site of squamous cell nonkeratinous carcinoma with an invasion depth of about 2–3 mm.

Figure 24.18 shows the site of the mucous layer of the uterine cervix (colposcopically suspicious for neoplasia) with histology features of cylindrical epithelium ectopia (immature metaplasia) (without epithelium epidermization and high-grade cellular infiltration of stroma) (benign state).

The presence or absence of a signal in orthogonal polarization may have differential-diagnostic value when traditional OCT images are structureless. Both OCT images are indistinguishable in direct polarization – they have no horizontal layered organization. The typical structureless OCT image depicted in Figure 24.19 may be interpreted as a sign of malignization, which is a false-positive result. In the case of

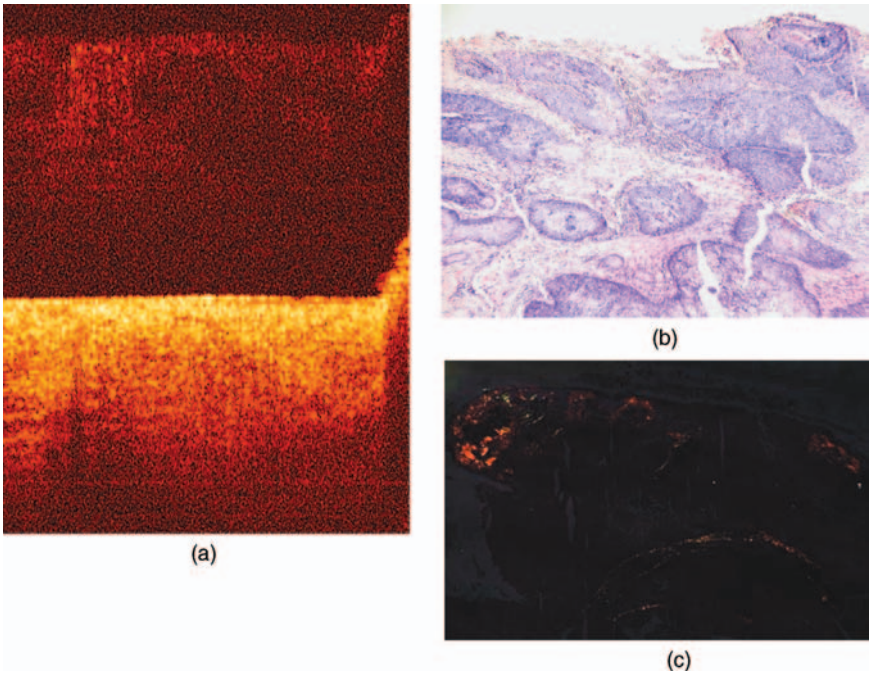

Figure 24.17 Mucous layer of the uterine cervix, growth site of squamous cell nonkeratinous carcinoma with an invasion depth of about 2–3 mm. (a) OCT image in direct (bottom) and orthogonal (top) polarization; (b) histology specimen, H&E staining, frame size 1.7×1 mm; (c) histology specimen, PSR staining in polarized light, frame size 0.75×0.5 mm. PSR staining of the histology specimen in polarized light shows that the area corresponding to cancer complexes is almost non-luminescent. Tumor stroma is represented by sporadic thin yellow–green fibers. OCT image: in direct polarization, the image field is uniform with a high-intensity signal, no layered structure is differentiated. In orthogonal polarization, the image field has no signal; there is signal at a site corresponding to stroma. Invasive squamous cell carcinoma is almost devoid of stroma containing organized collagen. Therefore, in orthogonal polarization, there is almost no signal at the site of cancer, which may be a differential feature of invasive tumor of arbitrary differentiation.

immature metaplasia, a signal is detected in the image in orthogonal polarization because the maturity and orientation of collagen fibers are conserved, in contrast to cancer when disorganized collagen has no polarization characteristics.

Thus, CP-OCT furnishes additional information about the states giving low-contrast images in direct polarization.

24.6.2
CP-OCT in Oncourology

CP-OCT images of normal mucosa of the urinary bladder in direct and orthogonal polarization feature a layered tissue structure. The signal intensity in orthogonal polarization reflects the presence of type I collagen in stroma. Visualization of images

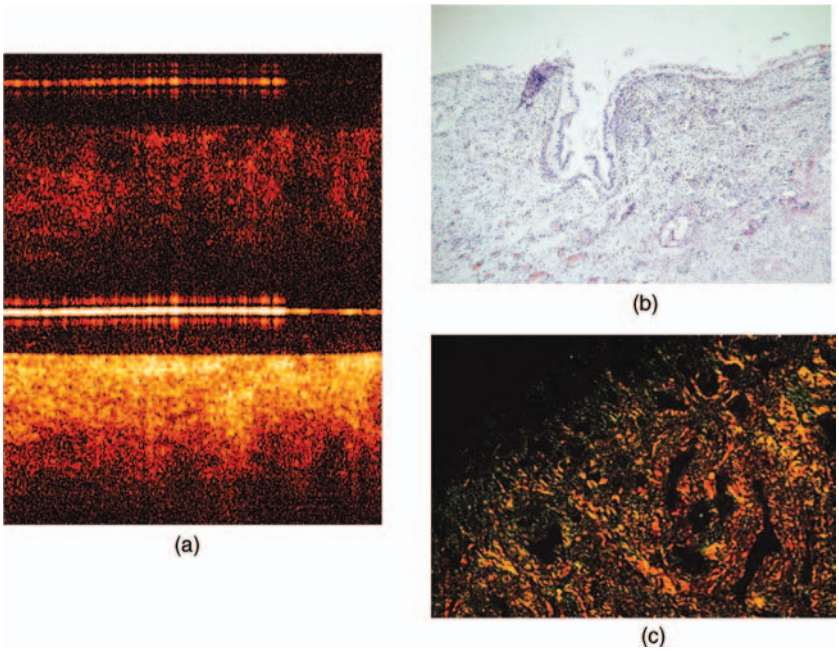

Figure 24.18 Mucous layer of the uterine cervix, cylindrical epithelium ectopia (immature metaplasia). (a) OCT image in direct (bottom) and orthogonal (top) polarization; (b) histology specimen, H&E staining, frame size 1.7×1 mm; (c) histology specimen, PSR staining in polarized light, frame size 0.75×0.8 mm.

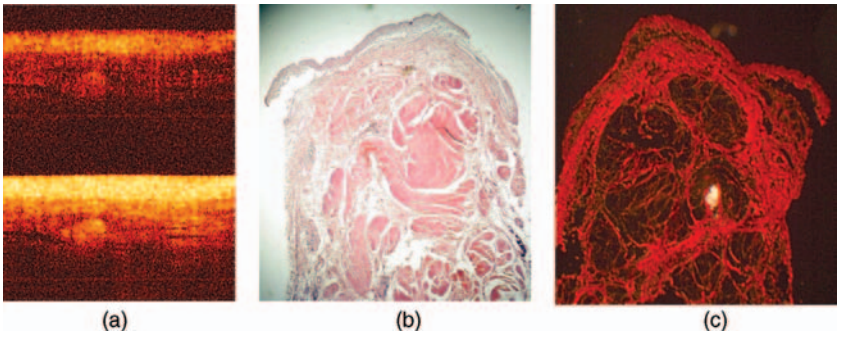

Figure 24.19 Urinal bladder wall specimen sewn with surgical suture transparent to OCT probing radiation. (a) OCT image in direct (bottom) and orthogonal (top) polarization; (b) histology specimen, H&E staining, frame size 1.8×2.3 mm; (c) histology specimen, PSR staining in polarized light, frame size 1.8×2.3 mm. The urinary bladder tissue contracts during OCT examination, hence layer thicknesses do not coincide in OCT and histology images.

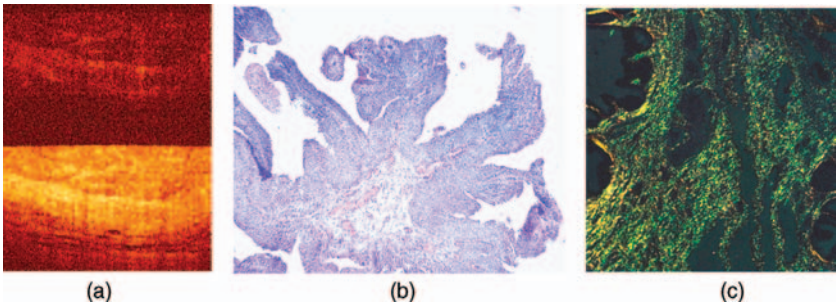

Figure 24.20 Simple urinary bladder papilloma. (a) OCT image in direct (bottom) and orthogonal (top) polarization; (b) histology specimen, H&E staining, frame size 1.8 × 2.3 mm; (c) histology specimen, PSR staining in polarized light, frame size 0.7 × 0.4 mm.

in direct and orthogonal polarizations allows reliable differentiation of all layers of bladder wall tissues with high contrast (Figure 24.19).

Benign states that look like zones of neoplasia at cyctoscopy [for example, papillomatous (exophytic) urinal bladder formation with histology features of simple papilloma without features of cell atypia] (Figure 24.20) give a signal in orthogonal polarization. Connective tissue of benign papilloma gives a signal in orthogonal polarization due to the unchanged mature type I and type III collagen (yellow and green luminescence in PSR-stained histology specimens, Figure 24.20c).

At the same time, exophytic papillomatous growth of urothelial tumors with high-grade differentiation but without signs of invasion into muscular layers (Figure 24.21) gives a structureless image in direct polarization and no signal in orthogonal polarization, because malignant papilloma is almost free of stroma containing organized collagen (Figure 24.21c).

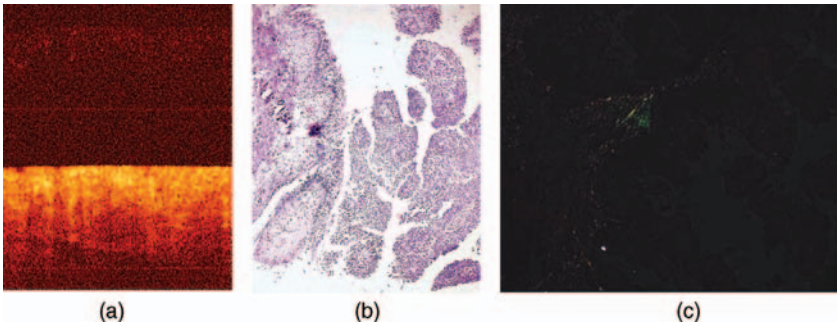

Figure 24.21 Exophytic papillomatous growth of urinary bladder mucosa – high-grade differentiation urothelial tumor without invasion into muscular layer. (a) OCT image in direct (bottom) and orthogonal (top) polarization; (b) histology specimen, H&E staining, frame size 1.7 × 1 mm; (c) histology specimen, PSR staining in polarized light, frame size 0.75 × 0.5 mm.

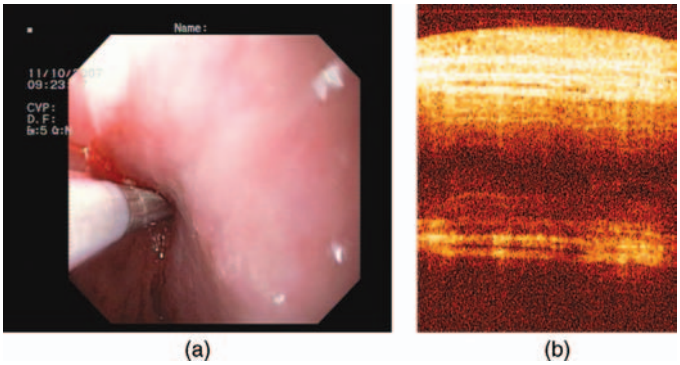

Figure 24.22 Normal squamous cell mucosa of esophagus. (a) Probe in esophagus lumen; (b) OCT image in direct (top) and orthogonal (bottom) polarization.

24.6.3 CP-OCT in Oncogastroenterology

Structured OCT images in standard and orthogonal polarization were also visualized in studying the tissues of the normal gastrointestinal tract (Figure 24.22). Verification of zones suspicious for cancer growth gave low-structured, non-layered cancer-type images (Figure 24.23). Malignant tumor does not depolarize radiation in orthogonal polarization and the OCT signal is minimal.

To conclude, when benign states are scanned, CP-OCT demonstrates structured layered images of benign type. Malignant neoplasms of different localizations are visualized as nonlayered images in standard polarization and are characterized by a weak OCT signal or no signal at all in orthogonal polarization. Some benign states are visualized as structureless images in direct polarization, whereas in orthogonal

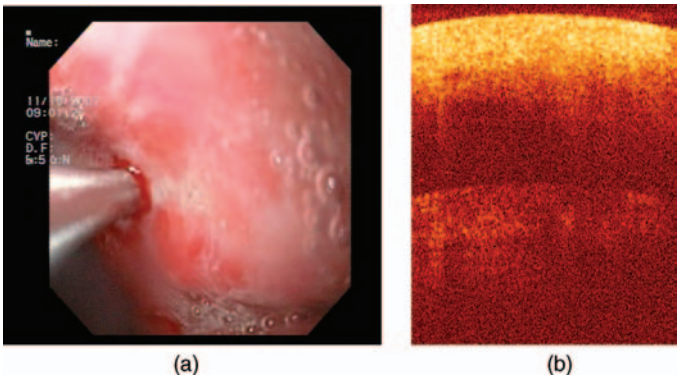

Figure 24.23 Tumor (adenocarcinoma) surface of the middle one-third of stomach body. (a) Probe in stomach lumen; (b) OCT image in direct (top) and orthogonal (bottom) polarization.

polarization a signal is detected, which enhances the specificity of CP-OCT for recognition of neoplasia.

24.7 Conclusion

Earlier pilot studies that used EOCT demonstrated an excellent ability to delineate clearly the layered structure of the esophagus, colon, bladder, vessels, and other biological structures into which the catheter is inserted. This feature of OCT images is universal for the great majority of EOCT devices [42, 75, 89]. Subsequent studies have validated the diagnostic accuracy of OCT for detecting specialized intestinal metaplasia, HGD, and intramucosal carcinoma of the esophagus and bladder [53] and dysplastic colonic polyps [90].

Our studies were aimed at statistical justification of using OCT in endoscopy. The clinical sampling included patients with urinary bladder (164 pt) and gastrointestinal tract (390 pt) pathology. The material was combined into one group as these organs are accessible to OCT. Further, in this fashion we demonstrated that the new diagnostic technique is unique and universal for organs of different morphology. As a result, we analyzed OCT images of pathologic states of the basic types of mucous membranes with transition, multilayer flat, and glandular epithelium.

In our research we used a handy en-face EOCT scanner. Its perpendicular position and moderate pressing on tissue ensure stable images with good tissue contrast; no additional fixing devices are required. The en-face design makes it convenient for investigation of both tubular (gastrointestinal tract) and large, hollow (urinal bladder) organs; further, it is useful for studying skin and mucous membranes of any localization. Its drawback, as in any other linear scanning technique, is the small surface area of a studied sample that is limited by the diameter of the scanner optical window.

Analysis of the results of the application of EOCT enables us to state that this novel visualization technique has found its niche in the diagnostic process. It is capable of solving several diagnostic tasks: early malignancy detection, tumor border marking, tumor removal control, and differential diagnosis of various pathologic forms. In this chapter, we have demonstrated the high diagnostic accuracy of EOCT in specific clinical tasks.

It is difficult to compare results of EOCT diagnostic efficiency obtained by different workers as they investigated different objects (different stages of the neoplastic process) and used different approaches to scanning. Nevertheless, the data presented demonstrate comparability of the independent results obtained. Statistical data for our study show that the diagnostic accuracy of the EOCT technique with criteria for image interpretation proposed by our team is comparable to results reported by other groups, and even better in some cases.

We intend to refine the technique further. The development of high-resolution fast scanning systems is known to be the main direction towards improving OCT. However, it should be taken into account that for promotion into clinical practice,

characteristics such as handy and simple use, portability, and economy are very important. These properties are inherent in our device. We believe that the diagnostic accuracy of such an OCT modality may be enhanced as follows:

- by developing basically new schemes, for example, PS-OCT
- by creating a high-speed scanning system that would enlarge the area of the analyzed surface
- by further minimization of the en-face probe for better matching with standard endoscopic equipment.

Concerning trends in the development the OCT technique as a whole, we hope that a scanning system integrating all the advantages of available approaches will be created and universal criteria of image interpretation will be developed.

Acknowledgments

This work was supported by CRDF, State Contract of the Russian Federation No. 02.522.11.2002, and Presidium of RAS (program "Fundamental Science for Medicine"), Russian Foundation for Basic Research (projects 08.04.97098-r-a, 07-02-01146-a, 08-02-01152, and 08-02-99049-r_ofi), and IMALUX Corporation.

The authors are grateful to Professor M. J. Manyak and his team of the George Washington University Medical Center (United States), Dr. G. Zuccaro and his colleagues at the Cleveland Clinic Foundation (United States), Dr. S. Jäckle and his team at the Eppendorf Clinic, University of Hamburg (Germany), Dr. F. I. Feldchtein, Dr. A. I. Abelevich, Dr. A. N. Denisenko, Dr. V. E. Zagaynov, and A. G. Orlova for their participation in the clinical studies, and N. B. Krivatkina for technical support in this work.

References

1 Jemal, A., Siegel, R., Ward, E., Murray, T., Xu, J. *et al.* (2006) Cancer statistics, 2006. *CA Cancer J. Clin.*, **56**, 106–130.
2 Jemal, A., Siegel, R., Ward, E., Murray, T., Xu, J., and Thun, M. (2007) Cancer statistics, 2007. *CA Cancer J. Clin.*, **57**, 43–66.
3 Koshy, M., Esiashvilli, N., Landry, J., Thomas, C., and Matthews, R.J. (2004) Multiple management modalities in esophageal cancer: epidemiology, presentation and progression, work-up, and surgical approaches. *Oncologist*, **9**, 137–146.
4 Parkin, D.M., Bray, F., Ferlay, J., and Pisani, P. (2005) Global cancer statistics, 2002. *CA Cancer J. Clin.*, **55**, 74–108.
5 Anderson, P. and Runowicz, C. (2001) Beyond the PAP test. New techniques for cervical cancer screening minimizing false-negative results. *Women's Health Prim. Care*, **21**, 753–758.
6 Ronco, G. and Rossi, P. (2008) New paradigms in cervical cancer prevention: opportunities and risks. *BMC Women's Health*, **8**, 23.
7 Oosterlinck, W. (2004) Guidelines on diagnosis and treatment of superficial bladder cancer. *Minerva Urol. Nefrol.*, **56**, 65–72.
8 Tschanz, E.R. (2005) Do 40% of patients resected for Barrett esophagus with high-

grade dysplasia have unsuspected adenocarcinoma? *Arch. Pathol. Lab. Med.*, **129**, 177–180.

9 Burghardt, E., Pickel, H., and Girardi, F. (eds.) (2002) *Primary Care Colposcopy: Textbook and Atlas*, Thieme Medical Publishers, Stuttgart.

10 Sharma, P., Weston, A.P., Topalovski, M., Cherian, R., Bhattacharyya, A., and Sampliner, R.E. (2003) Magnification chromoendoscopy for the detection of intestinal metaplasia and dysplasia in Barrett's oesophagus. *Gut*, **52**, 24–27.

11 Meining, A., Rosch, T., Kiesslich, R., Muders, M., Sax, F., and Heldwein, W. (2004) Inter- and intra-observer variability of magnification chromoendoscopy for detecting specialized intestinal metaplasia at the gastroesophageal junction. *Endoscopy*, **36**, 160–164.

12 Baumgartner, R., Wagner, S., Zaak, D., and Knuchel-Klarke, R. (2000) *Fluorescence Diagnosis of Bladder Tumor by Use of 5-Aminolevulinic Acid: Fundamental and Results*, Endo-Press, Tutlingen.

13 Dacosta, R.S., Wilson, B.C., and Marcon, N.E. (2003) Photodiagnostic techniques for the endoscopic detection of premalignant gastrointestinal lesions. *Dig. Endosc.*, **15**, 153–173.

14 Scotiniotis, I.A., Kochman, M.L., Lewis, J.D., Furth, E.E., Rosato, E.F., and Ginsberg, G.G. (2001) Accuracy of EUS in the evaluation of Barrett's esophagus and high-grade dysplasia or intramucosal carcinoma. *Gastrointest. Endosc.*, **54**, 689–696.

15 Huang, D., Swanson, E.A., Lin, C.P., Schuman, J.S., Stinson, W.G. *et al.* (1991) Optical coherence tomography. *Science*, **254**, 1178–1181.

16 Bouma, B.E. and Tearney, G.J. (eds.) (2002) *Handbook of Optical Coherence Tomography*, Marcel Dekker, New York.

17 Gelikonov, V.M., Gelikonov, G.V., Gladkova, N.D., Kuranov, R.V., Petrova, GA. *et al.* (1995) Coherent optical tomography of microscopic inhomogenities in biological tissues. *Pis'ma Zh. Eksp. Teor. Fiz.*, **61**, 149–153.

18 Gelikonov, V.M., Gelikonov, G.V., Dolin, L.S., Kamensky, V.A., Sergeev, A.M. *et al.* (2003) Optical coherence tomography: physical principles and applications. *Laser Phys.*, **13**, 692–702.

19 Gelikonov, V.M., Gelikonov, G.V., Gladkova, N.D., Leonov, V.I., Feldchtein, F.I. *et al.* (1998) U.S. Pat. US 5835642.

20 Das, A., Sivak, M.V., Chak, A., Wong, R.C.K., Westphal, V. *et al.* (2001) High-resolution endoscopic imaging of the GI tract: a comparative study of optical coherence tomography versus high-frequency catheter probe EUS. *Gastrointest. Endosc.*, **54**, 219–224.

21 Sivak, M.V. Jr., Kobayashim, K., Izatt, J.A., Rollins, A.M., Ung-Runyawee, R. *et al.* (2000) High-resolution endoscopic imaging of the GI tract using optical coherence tomography. *Gastrointest. Endosc.*, **51**, 474–479.

22 Sergeev, A.M., Gelikonov, V.M., Gelikonov, G.V., Feldchtein, F.I., Kuranov, R.V. *et al.* (1997) *In vivo* endoscopic OCT imaging of precancer and cancer states of human mucosa. *Opt. Express*, **1**, 432–440.

23 Bouma, B.E., Tearney, G.J., Compton, C.C., Brand, S., Poneros, J.M. *et al.* (2000) Optical coherence tomography for upper gastrointestinal tract diagnosis. Presented at Biomedical Topical Meetings, Miami Beach, FL.

24 Evans, J.A. and Nishioka, N.S. (2005) The use of optical coherence tomography in screening and surveillance of Barrett's esophagus. *Clin. Gastroenterol. Hepatol.*, **3**, S8–S11.

25 Daniltchenko, D., Konig, F., Lankenau, E., Sachs, M., Kristiansen, G. *et al.* (2005) Utilizing optical coherence tomography (OCT) for visualization of urothelial diseases of the urinary bladder. *Radiologe*, **46**, 584–589.

26 Wang, Z., Lee, C.S., Waltzer, W.C., Liu, J., Xie, H. *et al.* (2007) *In vivo* bladder imaging with microelectromechanical-systems-based endoscopic spectral domain optical coherence tomography. *J. Biomed. Opt.*, **12**, 034009.

27 Pfau, P.R., Sivak, M.V., Chak, A., Kinnard, M., Wong, R.C.K. *et al.* (2003) Criteria for the diagnosis of dysplasia by endoscopic

optical coherence tomography. *Gastrointest. Endosc.*, **58**, 196–202.
28 Bouma, B.E. and Tearney, G.J. (2002) Clinical imaging with optical coherence tomography. *Acad. Radiol.*, **9**, 942–953.
29 Evans, J.A., Poneros, J.M., Bouma, B.E., Bressner, J., Halpern, E.F. *et al.* (2006) Optical coherence tomography to identify intramucosal carcinoma and high-grade dysplasia in Barrett's esophagus. *Clin. Gastroenterol. Hepatol.*, **4**, 38–43.
30 Kuranov, R.V., Sapozhnikova, V.V., Turchin, I.V., Zagainova, E.V., Gelikonov, V.M. *et al.* (2002) Complementary use of cross-polarization and standard OCT for differential diagnosis of pathological tissues. *Opt. Express*, **10**, 707–713.
31 Hee, M.R., Huang, D., Swanson, E.A., and Fujimoto, J.G. (1992) Polarization-sensitive low-coherence reflectometer for birefringence characterization and ranging. *J. Opt. Soc. Am.*, **9**, 903–908.
32 de Boer, J.F., Srinivas, S.M., Malekafzali, A., Chen, Z.P., and Nelson, J.S. (1998) Imaging thermally damaged tissue by polarization sensitive optical coherence tomography. *Opt. Express*, **3**, 212–218.
33 Schmitt, J.M. and Xiang, S.H. (1998) Cross-polarized backscatter in optical coherence tomography of biological tissue. *Opt. Lett.*, **23**, 1060–1062.
34 Cense, B., Chen, H.C., Park, B.H., Pierce, M.C., and de Boer, J.F. (2004) *In vivo* birefringence and thickness measurements of the human retinal nerve fiber layer using polarization-sensitive optical coherence tomography. *J. Biomed. Opt.*, **9**, 121–125.
35 Feldchtein, F.I., Gelikonov, G.V., Gelikonov, V.M., Iksanov, R.R., Kuranov, R.V. *et al.* (1998) *In vivo* OCT imaging of hard and soft tissue of the oral cavity. *Opt. Express*, **3**, 239–250.
36 Gelikonov, V.M. and Gelikonov, G.V. (2006) New approach to cross-polarized optical coherence tomography based on orthogonal arbitrarily polarized modes. *Laser Phys. Lett.*, **3**, 445–451.
37 Gelikonov, V., Gusovsky, D., Leonov, V., and Novikov, M. (1987) Birefringence compensation in single mode optical fibers. *Sov. Tech. Phys. Lett.*, **13**, 775–779.
38 Feldchtein, F.I., Gelikonov, V.M., and Gelikonov, V.M. (2002) Design of OCT scanners, in *Handbook of Optical Coherence Tomography* (eds. B.E. Bouma and G.J. Tearney), Marcel Dekker, New York, pp. 000–000.
39 Zagaynova, E.V., Strelzova, O.S., Gladkova, N.D., Snopova, L.B., Gelikonov, G.V. *et al.* (2002) *In vivo* optical coherence tomography feasibility for bladder disease. *J. Urol.*, **167**, 1492–1497.
40 Koenig, F., Tearney, G.J., and Bouma, B.E. (2002) Optical coherence tomography in urology, in *Handbook of Optical Coherence Tomography* (eds. B.E. Bouma and G.J. Tearney), Marcel Dekker, New York, pp. 000–000.
41 Manyak, M.J., Gladkova, N., Makari, J.H., Schwartz, A., Zagaynova, E. *et al.* (2005) Evaluation of superficial bladder transitional cell carcinoma by optical coherence tomography. *J. Endourol.*, **19**, 570–574.
42 Zagaynova, E.V., Gladkova, N.D., Streltsova, O.S., Gelikonov, G.V., Tresser, N. *et al.* (2008) Optical coherence tomography in urology, in *Optical Coherence Tomography*, Springer, Berlin, pp. 000–000.
43 Jackle, S., Gladkova, N.D., Feldchtein, F.I., Terentieva, A.B., Brand, B. *et al.* (2000) *In vivo* endoscopic optical coherence tomography of the human gastrointestinal tract – toward optical biopsy. *Endoscopy*, **32**, 743–749.
44 Poneros, J.M. and Nishioka, N.S. (2003) Diagnosis of Barrett's esophagus using optical coherence tomography. *Gastrointes.t Endosc. Clin. N. Am.*, **13**, 309–323.
45 Escobar, P.F., Belinson, J.L., White, A., Shakhova, N.M., Feldchtein, F.I. *et al.* (2004) Diagnostic efficacy of optical coherence tomography in the management of preinvasive and invasive cancer of uterine cervix and vulva. *Int. J. Gynecol. Cancer*, **14**, 470–474.
46 Ascencio, M., Collinet, P., Cosson, M., and Mordon, S. (2007) The role and value of optical coherence tomography in gynecology. *J. Gynecol. Obstet. Biol. Reprod.*, **36**, 749–755.

47 Tearney, G.J., Brezinski, M.E., Bouma, B.E., Boppart, S.A., Pitris, C. *et al.* (1997) *In vivo* endoscopic optical biopsy with optical coherence tomography. *Science*, **276**, 2037–2039.

48 Feldchtein, F.I., Gelikonov, G.V., Gelikonov, V.M., Kuranov, R.V., Sergeev, A.M. *et al.* (1998) Endoscopic applications of optical coherence tomography. *Opt. Express*, **3**, 257–269.

49 Pan, Y.T., Lavelle, J.P., Bastacky, S.I., Meyers, S., Pirtskhalaishvili, G. *et al.* (2001) Detection of tumorigenesis in rat bladders with optical coherence tomography. *Med. Phys.*, **28**, 2432–2440.

50 Zagaynova, E.V., Streltzova, O.S., Gladkova, N.D., Shakhova, N.M. and Feldchtein, F.I. *et al.* (2004) Optical coherence tomography in diagnostics of precancer and cancer of human bladder. *Proc. SPIE*, **5312**, 75.

51 Lerner, S.P., Goh, A.C., Tresser, N.J., and Shen, S.S. (2008) Optical coherence tomography as an adjunct to white light cystoscopy for intravesical real-time imaging and staging of bladder cancer. *Urology*, **72**, 133–137.

52 Pan, Y.T., Xie, T.Q., Du, C.W., Bastacky, S., Meyers, S., and Zeidel, M.L. (2003) Enhancing early bladder cancer detection with fluorescence-guided endoscopic optical coherence tomography. *Opt. Lett.*, **28**, 2485–2487.

53 Zagaynova, E., Gladkova, N., Shakhova, N., Gelikonov, G.V., and Gelikonov, V.M. (2008) OCT with forward looking probes: clinical studies in urology and gastroenterology. *J. Biophoton.*, **1**, 114–128.

54 Izatt, J.A., Kulkarni, M.D., Wang, H.-W., Kobayashi, K., and Sivak, M.V. (1996) Optical coherence tomography and microscopy in gastrointestinal tissues. *IEEE J. Sel. Top. Quantum Electron.*, **2**, 1017–1028.

55 Gladkova, N.D., Zagaynova, E.V., Zuccaro, G., Kareta, M.V. and Feldchtein, F.I. *et al.* (2007) Optical coherence tomography in the diagnosis of dysplasia and adenocarcinoma in Barret's esophagus. *Proc. SPIE*, **6432**, 64320A.

56 Zuccaro, G., Gladkova, N.D., Vargo, J., Feldchtein, F.I., Zagaynova, E.V. *et al.* (2001) Optical coherence tomography of the esophagus and proximal stomach in health and disease. *Am. J. Gastroenterol.*, **96**, 2633–2639.

57 Levine, D., Haggitt, R.C., Blount, P., Rabinovitch, P., Rusch, V., and Reid, B.J. (1993) An endoscopic biopsy protocol can differentiate high-grade dysplasia from early adenocarcinoma in Barrett's esophagus. *Gastroenterology*, **105**, 40–50.

58 Feldchtein, F.I., Gladkova, N.D., Snopova, L.B., Zagaynova, E.V., Streltzova, O.S. *et al.* (2003) Blinded recognition of optical coherence tomography images of human mucosa precancer. *Proc. SPIE*, **4956**, 89–94.

59 Poneros, J.M., Brand, S., Bouma, B.E., Tearney, G.J., Compton, C.C., and Nishioka, N.S. (2001) Diagnosis of specialized intestinal metaplasia by optical coherence tomography. *Gastroenterology*, **120**, 7–12.

60 Isenberg, G., Sivak, M.V., Chak, A., Wong, R., Willis, J. *et al.* (2003) Accuracy of endoscopic optical coherence tomography (EOCT) in the detection of dysplasia (D) in Barrett's esophagus (BE). *Gastrointest. Endosc.*, **57**, AB77–AB80.

61 Isenberg, G., Sivak, M.V. Jr., Chak, A., Wong, R.C., Willis, J.E. *et al.* (2005) Accuracy of endoscopic optical coherence tomography in the detection of dysplasia in Barrett's esophagus: a prospective, double-blinded study. *Gastrointest. Endosc.*, **62**, 825–831.

62 Qi, X., Sivak, M.V. Jr., Isenberg, G., Willis, J.E., and Rollins, M.A. (2006) Computer-aided diagnosis of dysplasia in Barrett's esophagus using endoscopic optical coherence tomography. *J. Biomed. Opt.*, **11**, 044010.

63 Standish, B.A., Yang, V.X., Munce, N.R., Wong, K., Song, L.M., Gardiner, G. *et al.* (2007) Doppler optical coherence tomography monitoring of microvascular tissue response during photodynamic therapy in an animal model of Barrett's esophagus. *Gastrointest. Endosc.*, **66**, 326–333.

64 Chen, Y., Aguirre, A.D., Hsiung, P.L., Desai, S., Herz, P.R. *et al.* (2007) Ultrahigh resolution optical coherence tomography of Barrett's esophagus: preliminary

descriptive clinical study correlating images with histology. *Endoscopy*, **39**, 599–605.

65 Chen, Y., Aguirre, A.D., Hsiung, P.L., Huang, S.W., Mashimo, H. *et al.* (2008) Effects of axial resolution improvement on optical coherence tomography (OCT) imaging of gastrointestinal tissues. *Opt. Express*, **16**, 2469–2485.

66 Melissa, J.S., Patrick, S.Y., Benjamin, J.V., Milen, S., Brett, E.B. *et al.* (2008) *In vivo* 3D comprehensive microscopy of the human esophagus for the management of Barrett's patients. *Gastrointest. Endosc.*, **67**, AB99.

67 Qi, X., Pan, Y., Hu, Z., Sivak, M.V., Willis, J. *et al.* (2008) T1853 morphological feature quantification of colonic crypt patterns using microscope-integrated OCT. *Gastroenterology*, **134** (4 Suuppl 1), A577.

68 Park, D.H., Kim, H.S., Kim, W.H., Kim, T.I., Kim, Y.H. *et al.* (2008) Clinicopathologic characteristics and malignant potential of colorectal flat neoplasia compared with that of polypoid neoplasia. *Dis. Colon Rectum*, **51**, 43–49.

69 Jaeckle, S., Gladkova, N.D., Feldchtein, F.I., Terentieva, A.B., Brand, B. *et al.* (2000) *In vivo* endoscopic optical coherence tomography of the human gastrointestinal tract – toward optical biopsy. *Endoscopy*, **32**, 743–749.

70 Zuccaro, G., Gladkova, N., Conwell, D., Feldchtein, F., Vargo, J. *et al.* (2002) Optical coherence tomography (OCT) of the colon in health and disease. *Gastrointest. Endosc.*, **55**, M1951.

71 Yang, V.X.D. (2005) Endoscopic Doppler optical coherence tomography in the human GI tract: initial experience. *Gastrointest. Endosc.*, **61**, 879–890.

72 Pitris, C., Goodman, A., Boppart, S.A., Libus, J.J., Fujimoto, J.G., and Brezinski, M.E. (1999) High-resolution imaging of gynecologic neoplasms using optical coherence tomography. *Obstet. Gynecol.*, **93**, 135–139.

73 Shakhova, N.M., Feldchtein, F.I., and Sergeev, A.M. (2002) Applications of optical coherence tomography in gynecology, in *Handbook of Optical Coherence Tomography* (eds. B.E. Bouma and G.J. Tearney), Marcel Dekker, New York, pp. 000–000.

74 Shakhova, N.M., Sapozhnikova, V.V., Kamensky, V.A., Kuranov, R.V., Loshenov, V.B. *et al.* (2003) Optical methods for diagnosis of neoplastic processes in the uterine cervix and vulva. *J. Appl. Res.*, **3**, 144–155.

75 Kuznetsova, I.A., Gladkova, N.D., Gelikonov, V.M., Belinson, J.L., Shakhova, N.M., and Feldchtein, F.I. (2008) OCT in gynecology, in *Optical Coherence Tomography* (eds. W. Drexler and J.G. Fujimoto), Springer, Berlin, pp. 1211–1240.

76 Zuluaga, A.F., Follen, M., Boiko, I., Malpica, A., and Richards-Kortum, R. (2005) Optical coherence tomography: a pilot study of a new imaging technique for noninvasive examination of cervical tissue. *Am. J. Obstet. Gynecol.*, **193**, 83–88.

77 Gladkova, N., Shakhova, N., and Sergeev, A. (eds.) (2007) *Handbook of Optical Coherence Tomography*, Fizmatlit, Moscow.

78 Brezinski, M.E. (2006) *Optical Coherence Tomography: Principles and Applications*, Academic Press/Elsevier, Burlington, MA

79 Park, B.H., Saxer, C., Srinivas, S.M., Nelson, J.S., and de Boer, J.F. (2001) *In vivo* burn depth determination by high-speed fiber-based polarization sensitive optical coherence tomography. *J. Biomed. Opt.*, **6**, 474–479.

80 Pierce, M.C., Sheridan, R.L., Park, B., Cense, B., and de Boer, J.F. (2004) Collagen denaturation can be quantified in burned human skin using polarization-sensitive optical coherence tomography. *Burns*, **30**, 511–517.

81 Strasswimmer, J., Pierce, M.C., Park, B.H., Neel, V., and de Boer, J.F. (2004) Polarization-sensitive optical coherence tomography of invasive basal cell carcinoma. *J. Biomed. Opt.*, **9**, 292–298.

82 Junqueira, L., Bignolas, G., and Brentani, R. (1979) Picrosirius staining plus polarization microscopy, a specific method for collagen detection. *J. Histochem.*, **11**, 447–455.

83 Borges, L., Gutierrez, P., Marana, H., and Taboga, S. (2007) Picrosirius-polarization

staining method as an efficient histopathological tool for collagenolysis detection in vesical prolapse lesions. *Micron*, **38**, 580–583.

84 Giattina, S.D., Courtney, B.K., Herz, P.R., Harman, M., Shortkroff, S. *et al.* (2006) Assessment of coronary plaque collagen with polarization sensitive optical coherence tomography (PS-OCT). *Int. J. Cardiol.*, **107**, 400–409.

85 de Boer, J.F., Srinivas, S.M., Nelson, J.S., Milner, T.E., and Ducros, M.G. (2002) Polarization-sensitive optical coherence tomography, in *Handbook of Optical Coherence Tomography* (eds. B.E. Bouma and G.J. Tearney), Marcel Dekker, New York, pp. 000–000.

86 de Boer, J.F., Srinivas, S.M., Park, B.H., Pham, T.H., Chen, Z.P. *et al.* (1999) Polarization effects in optical coherence tomography of various biological tissues. *IEEE J. Sel. Top. Quantum Electron.*, **5**, 1200–1204.

87 Herrmann, J.M., Pitris, C., Bouma, B.E., Boppart, S.A., Jesser, C.A. *et al.* (1999) High resolution imaging of normal and osteoarthritic cartilage with optical coherence tomography. *J. Rheumatol.*, **26**, 627–635.

88 Jiao, S., Yu, W., Stoica, G., and Wang, L.V. (2003) Contrast mechanisms in polarization-sensitive Mueller-matrix optical coherence tomography and application in burn imaging. *Appl. Opt.*, **42**, 5191–5197.

89 Terentéva, A.B., Shakhov, A.V., Maslennikova, A.V., Gladkova, N.D., Kamensky, V.A. *et al.* (2008) OCT in laryngology, in *Optical Coherence Tomography* (eds. W. Drexler and J.G. Fujimoto), Springer, Berlin, pp. 1123–1150.

90 Das, A., Sivak, M.V. Jr., Chak, A., Wong, R.C., Westphal, V. *et al.* (2001) High-resolution endoscopic imaging of the GI tract: a comparative study of optical coherence tomography versus high-frequency catheter probe EUS. *Gastrointest. Endosc.*, **54**, 219–224.

25
Intraoperative Optical Coherence Tomographic Monitoring

Alexandre Douplik

25.1
Optical coherence tomography as a Surgery-Assisting Tool

Optical coherence tomography (OCT) is a high-resolution imaging technology analogous to B-mode ultrasound except that it uses infrared light instead of sound. This technique, known as Michelson low-coherence interferometry, which measures the echo delay and intensity of back-reflected or backscattered infrared light from internal tissue microstructure, is used by comparing the reflected light beam with a beam that travels along a reference path. OCT can facilitate imaging close to histologic cross-sections at a high spatial resolution, up to 1–20 μm. Such a resolution is 1–2 orders of magnitude better than a conventional ultrasound. Imaging depths are limited to a few millimeters (2–3 mm) because of optical attenuation due to absorption and scattering; however, these imaging depths are sufficient for many diagnostic applications, including performing intraoperative monitoring [1]. OCT imaging is near real-time (but still lower than a standard PAL or NTSC video rate) and noncontact technique. With recent research advances, OCT imaging of optically scattering, nontransparent tissues has become possible using longer near-infrared (e.g., 1.3 μm) wavelengths where optical scattering is reduced, thus permitting a wide variety of biomedical applications [2]. Contrast in OCT images originates from differences in the reflectivity of different tissues, which are caused by their variations in (complex) refractive index n. Unfortunately, contrast is limited because for most tissues n ranges from 1.3 to 1.4. OCT imaging is sensitive to differences in terms of refraction index of light scattering between different tissues, whereas in histopathology, as in a microscopy, images are generated by differences in either optical reflection or transmission. Hence the inherent appearance of an OCT image is different from that in histopathology and, in general, further studies are required to develop a basis for interpreting OCT images in terms of clinically relevant pathology [3]. Examples of OCT images are provided in Figure 25.1a.

Handbook of Biophotonics. Vol.2: Photonics for Health Care, First Edition. Edited by Jürgen Popp, Valery V. Tuchin, Arthur Chiou, and Stefan Heinemann.

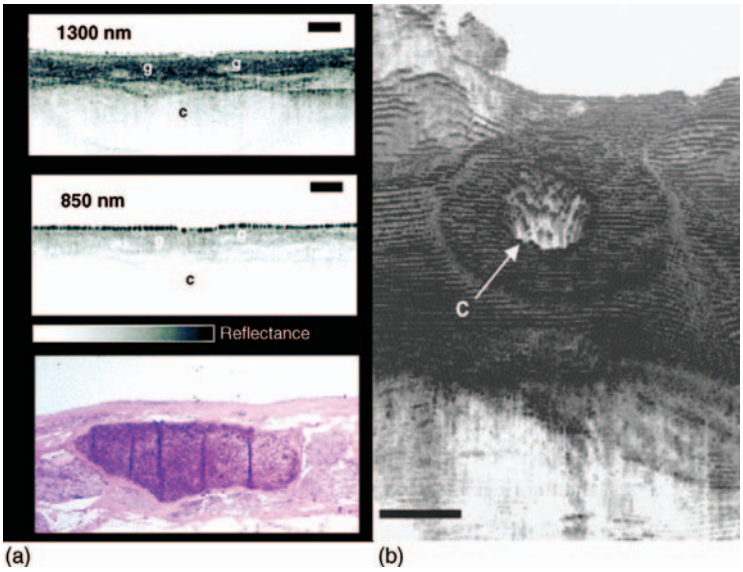

Figure 25.1 (a) Dependence of imaging depth on wavelength of the incident light. A human epiglottis was imaged at both 850 and 1300 nm. The underlying cartilage (c) could be visualized only using longer wavelengths, while a larger reflection at the surface occurred with the 850 nm light. Superficial secretory glands (g) were visualized at both wavelengths. Bars represent 500 μm. In this image, data are displayed as the logarithm of backscattering intensity versus depth (in gray scale) to emphasize deeper structures. Corresponding histology is included (lowest left) [26]. (b) Laser ablation crater. 3D projection illustrates central ablation crater (c) and concentric zones of thermal injury Numbers refer to depth below the surface. Bar represents 1 mm [1]. Courtesy of J. Fujimoto and S. Boppart.

As an intraoperative monitoring tool, OCT is exploited to differentiate normal tissues and recognize the normal and pathology to guide surgery. The intraoperative use of OCT can be invaluable in improving intraoperative evaluation, facilitating surgery, and supporting the surgeon's decision-making process on the fly, thus improving surgical outcomes. The OCT monitoring tools are required not to interfere with the surgery in intensive therapy procedures, either mechanically or using close light wavelengths such as during laser ablation or light interstitial thermotherapy. A 3D OCT image of ablation crater is shown in Figure 25.1b.

25.2
OCT Modalities and Implementations for Intraoperative Assistance

Since the introduction of OCT in 1991, it has been implemented as a time domain technique. The newest extension of OCT exploits frequency domain technology. The latter includes spatially encoded frequency domain OCT [spectral domain (SD) or Fourier domain OCT] and time-encoded frequency domain OCT (also swept-source

OCT) and provides much faster image acquisition relative to time domain technology. High-resolution and 3D OCT require longer data collection times than conventional OCT. Doppler optical coherence tomography (DOCT) is used to obtain information about blood perfusion spatial distribution and vessel reactions. Polarized sensitive (PS) or structural OCT, an extension of classical OCT, is sensitive to birefringence and consequently to anisotropies and stress within a material. The image acquisition in OCT is provided either with hand-held surgical probes, OCT fiber probes compatible with biopsy channels of laparoscopes, catheters, and endoscopes [4, 5] or an OCT system coupled with a surgical microscope (OCT camera) [6].

25.3
Advantages, Limitations, and Reproducibility of Intraoperative OCT Monitoring

Advantages of OCT are a high spatial resolution comparable to conventional histology, fast data collection building up an image nearly in real time, and the capability of acquiring images remotely. Unlike ultrasound, OCT does not require any conducting gel. The principal disadvantage of OCT, as with any optical imaging technique, is that light is highly scattered by most biotissues. In most tissues other than the eyes, optical scattering limits the image penetration depth to between 2 and 3 mm. Another serious limitation of OCT is a relatively small field of view (e.g., hundreds of microns to millimeters), demanding significant time for examination of the region of interest (ROI) and hence limiting the application of OCT for screening surveillance. The larger the area to be scanned, the greater is the probability of "smearing" the OCT image due to motion artifacts. Ho *et al*. reported that OCT imaging in ophthalmology is in general reproducible within 10–20% depending on the particular implementation [7]. High-resolution and 3D OCT require extensive scanning, making OCT imaging subject to motion artifacts when holding the OCT probe still relative to the object is not always possible in organs with high motility such as the gastrointestinal (GI) tract. Pressing the probe against the tissue to stabilize its position may lead to compression of the object, which can affect the measured OCT information [9], though this effect has even been exploited to enhance the OCT contrast [8].

25.4
Specificity and Sensitivity of OCT for Recognizing Normal and Pathologic Tissue

To evaluate the efficiency of the OCT method for the detection of different stages of malignization, three independent blind tests were performed using OCT images of the uterine cervix, urinary bladder, and larynx for diagnosing mucosal neoplasia. The studies showed that the OCT sensitivity was 82, 98, and 77% and specificity 78, 71, and 96%, respectively [9]. The diagnostic accuracy of OCT for recognizing normal and pathologic tissue depends on the particular clinical application and varies from

75 to 86% for sensitivity and 78 to 95% for specificity if H&E histology is used as a gold standard [10, 11]. More detailed analysis of OCT diagnostic accuracy including particular applications is provided in Chapter 2.1.2.4 Optical Coherence Tomography. As a result of providing detailed information on the architectural morphology of the retina at the level of individual retinal layers, OCT has been proposed for the detection of early pathologic changes, even before clinical signs or visual symptoms occur, and it has even been proposed as a new "gold standard" structural test for retinal abnormalities [12]. OCT was found to be a more accurate diagnostic technique than intravascular ultrasound [13].

25.5 Normal Tissue Differentiation with OCT

The high resolution of OCT permits the imaging of features such as tissue morphology and also cellular features. Tissue differentiation is important to avoid accidental destruction of critically important organs and tissues such as blood vessel walls and nerves [14], while accurate identification of pathologic or necrotic tissues assists delineation of the margins of resection. Attempts at localized measurement of the attenuation coefficient μ_t can provide additional information, and may increase the clinical potential of quantitative discrimination between different tissue types by OCT [15]. The ability to see beneath the surface of tissue in real time can guide surgery near sensitive structures such as vessels and nerves and also assist in microsurgical procedures [1, 16, 17]. OCT was integrated with surgical microscopes routinely used to magnify tissue to prevent iatrogenic injury and to guide delicate techniques in ear, nose, and throat (ENT) surgery [18]. Hand-held OCT surgical probes and laparoscopes have also been demonstrated [4]. Miyazawa *et al*. reported that PS-OCT was used for a tissue discrimination algorithm based on the optical properties of tissues. The 3D feature vector from the parameters intensity, extinction coefficient, and birefringence obtained by PS-OCT was calculated. The tissue type of each pixel was determined according to the position of the feature vector in the 3D feature space. The algorithm was applied for discriminating tissues of the human anterior eye segment. The conjunctiva, sclera, trabecular meshwork (TM), cornea, and uvea were well separated in the 3D feature space, and were observed with good contrast [19]. Liang *et al*. used structural OCT to investigate the longitudinal development of engineered tissues and cell dynamics such as migration, proliferation, detachment, and cell–material interactions [20]. Optical techniques that image functional parameters or integrate multiple imaging modalities to provide complementary contrast mechanisms have been developed, such as the integration of optical coherence microscopy with multiphoton microscopy to image structural and functional information from cells in engineered tissue, optical coherence elastography to generate images or maps of strain to reflect the spatially dependent biomechanical properties, and spectroscopic OCT to differentiate different cell types. Hauger *et al*. proposed a surgical system supported by an OCT surface scanner for tissue-differentiated tomography to identify a particular type of tissue [21].

25.6
OCT Biopsy Guidance

A technology capable of performing optical biopsy (defined as imaging tissue microstructure at or near the level of histopathology without the need for tissue excision) has a considerable impact on surgical intervention management such as in situations in which sampling errors severely restrict the effectiveness of excisional biopsy (e.g., the high failure rates associated with blind biopsies used to screen the premalignant conditions of ulcerative colitis or Barrett's esophagus) [22–24] or when conventional excisional biopsy is potentially hazardous in vulnerable regions (e.g., the retina, the central nervous system, the vascular system, the atherosclerotic plaque in the coronary arteries and articular cartilage) [25]. The ability to image at the cellular level could improve the effectiveness of many surgical and microsurgical procedures, including coronary atherectomy, transurethral prostatectomies, and microvascular repair [26]. Fibered OCT in conjunction with natural orifice transluminal endoscopic surgery (NOTES) could provide a facility for rapid, *in situ* pathologic diagnosis of intraperitoneal tissues in a truly minimally invasive fashion [27]. Iftimia *et al.* reported that SD-OCT could help in more precise needle placement during the fine needle aspiration (FNA) breast biopsy and therefore could substantially reduce the number of nondiagnostic aspirates and improve the sensitivity and specificity of the FNA procedures. Over 80% sensitivity and specificity in differentiating all tissue types and 93% accuracy in differentiating fatty tissue from fibrous or tumor tissue were obtained with this technology [28].

25.7
Identifying Malignancy

Intraoperative real-time detection of residual malignant tumor tissue remains an important challenge in surgery. Many malignancy-identifying OCT studies in the 1990s were focused on *in vitro* imaging and correlation with histopathology. *In vitro* studies have been performed to investigate OCT imaging in the GI tract [29], pancreatobiliary tissue [30], urinary system [31], respiratory system [32], and female reproductive tract [33] and in differentiating choroidal nevus from choroidal melanoma in the eye by 3D SD-OCT and OCT characteristics of other choroidal tumors [34]. During the last decade, a number of *in vivo* clinical studies have been performed in dermatology [35], GI tract [36], kidney [37, 38], human brain [39], breast [40], and ENT [41].

25.8
Identifying Atherosclerotic Plaque Composition

The majority of acute coronary events are precipitated by the rupture of a vulnerable atherosclerotic plaque in the coronary system, and subsequent thrombogenesis.

Thus, data on plaque composition and stability, complementing the image, may inform the decision on whether and how to treat a particular section of coronary artery. Van Soest *et al*. concluded from a survey of the complete OCT *in vivo* attenuation coefficient dataset that a high attenuation coefficient in OCT, $\mu_t > 10\,\mathrm{mm}^{-1}$, is associated with two markers of plaque vulnerability: the presence of a necrotic core and macrophage infiltration. More stable forms of atherosclerotic tissue and healthy vessel wall have low attenuation coefficients: $\mu_t \approx 2\text{–}5\,\mathrm{mm}^{-1}$ [42].

25.9
Identifying Necrotic Tissue

Van der Meer *et al*. used OCT to determine the optical properties of human fibroblasts in which necrosis or apoptosis had been induced *in vitro*. The OCT data included both the scattering properties of the medium and the axial point spread function of the OCT system. The optical attenuation coefficient in necrotic cells decreased from 2.2 ± 0.3 to $1.3 \pm 0.6\,\mathrm{mm}^{-1}$, whereas, in the apoptotic cells an increase to $6.4 \pm 1.7\,\mathrm{mm}^{-1}$ was observed. The results from cultured cells, as presented in this study, indicate the ability of OCT to detect and differentiate between viable, apoptotic, and necrotic cells, based on their attenuation coefficient [43]. Standish *et al*. exploited interstitial (IS) DOCT to predict photodynamic therapy (PDT)-induced tumor necrosis deep within solid rat prostate tumors, quantifying the PDT-induced microvascular shutdown rate *in vivo*. A strong relationship ($R^2 = 0.723$) was determined between the percentage tumor necrosis at 24 h post-treatment and the vascular shutdown rate: slower shutdown corresponded to higher treatment efficacy, that is, more necrosis [44].

25.10
Resection Delineation

OCT has already been used *in vitro* for the delineation of fine subtle structures of biotissue to help avoid damage to the normal structure, margins of the spots of the tissue damaged during surgical intervention, and margins of the malignant lesions. Results *in vivo* are expected soon. Thus, an OCT system has been utilized to display the multilayered structure of the airways delineating the subtle architectural differences in three separate anatomic locations, namely trachea, main bronchus, and tertiary bronchus, using fresh pig lung resections [45]. Spectral OCT sensitive to birefringes has been successfully applied for thermally damaged tissue margin delineation [46]. Tsai *et al*. applied swept-source (SS) OCT for the *ex vivo* delineation of an oral cancerous lesion margin sampling with the axial resolution of 8 μm in free space and a system sensitivity of 108 dB via two parameters [47]. One of the parameters was the decay constant in the exponential fitting of the SS-OCT signal intensity to depth. This decay constant decreases as the A-scan point moves laterally

across the margin of a lesion. The other parameter was the standard deviation of the SS-OCT signal intensity fluctuation in an A-scan. This parameter increases significantly when the A-scan point is moved across the transition region between the normal and abnormal portions. Such parameters were used for determining the margins of oral cancer.

25.11
Particular Intraoperative OCT Applications

As follows from the snapshot of the distribution of OCT publications among different clinical applications presented in Figure 25.2, the greatest clinical impact of OCT is in ophthalmologic, cardiovascular, and dermatologic applications. The next impact group includes GI, urologic, osteologic, and neurologic applications. ENT, dental, gynecologic, and pulmonologic applications form the lowest impact group within the OCT research domain.

A similar distribution is expected for intraoperative OCT applications. Below, they are listed and reviewed in order of the priorities mentioned in Figure 25.2.

25.12
Intraoperative OCT Monitoring in Ophthalmology

During laser eye surgery, a surgeon uses a laser device to make permanent changes to the shape of the cornea. The laser used most often is the excimer laser, which produces a beam of ultraviolet light to vaporize tissue. Surgically altering the shape of the cornea can correct mild to moderate refractive errors in most people. However, laser eye surgery also poses certain risks. In general, refractive procedures enjoy very

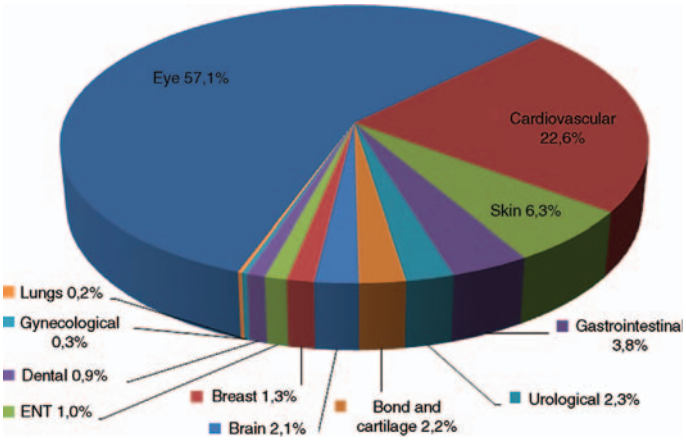

Figure 25.2 Snapshot of distribution of OCT publications among different clinical applications in 1991–2010 (based on ISI Web of Knowledge).

high success rates and are among the most commonly performed elective surgeries in medicine. However, all refractive surgeons must manage unsuccessful cases appropriately. Unsuccessful refractive surgery procedures may relate to each step of the refractive surgery process: preoperative screening, surgical planning, intraoperative events, and postoperative biomechanical or healing anomalies. OCT has demonstrated its ability to reduce these risks. Intraoperative OCT applied in ophthalmology is often coupled with a surgical microscope via adaptation to a slit lamp. Hüttmann *et al.* reported that through the surgical microscope, a volumetric imaging of epithelium, Bowman's and Descemet's membranes, limbus, iris, lens, conjunctiva, and sclera has been demonstrated with a working distance of several tens of centimeters [48]. Instruments and incisions in the cornea were visualized with 20 μm precision. SD-OCT permits wide-field noncontact real-time cross-sectional imaging of retinal structure, allowing for SD-OCT augmented intrasurgical microscopy for intraocular visualization. Real-time imaging and visualization of volumetric OCT data were also demonstrated. Bagayev *et al.* developed OCT for the determination of the removed corneal thickness profile *in situ* with laser ablation to improve the precision of refractive surgery [49]. The precision of measurements of the corneal thickness in preliminary *in vivo* experiments was found to be higher than in *ex vivo* experiments, which is promising for application of the method suggested here in refractive surgery. The ablation of corneal tissue with the excimer laser can be variable and can lead to miscorrections. To avoid that, the intraoperative ablation parameters during laser-assisted *in situ* keratomileusis (LASIK) were evaluated with online optical coherence pachymetry (OCP) [50]. The qualitative and quantitative evaluation of the corneal flap created by a femtosecond laser using anterior segment (AS) OCT before lifting the flap confirmed that the femtosecond laser is a practical intraoperative approach that offers safer surgery [51] as eyes with flat membranes showed strong adhesion to the retinal surface. Potential complications may lead to anterior chamber gas bubbles after LASIK flap formation with a femtosecond laser [52]. OCT has been used as an intraoperative tool for the management of unsuccessful LASIK procedures, focusing on significant advances related to wavefront-guided therapeutic ablations [53]. These studies showed that real-time OCT monitoring of the creation of thin flaps in LASIK using a femtosecond laser is possible, thus ensuring that the flap is created at the desired depth. AS-OCT has been applied to investigate the stromal demarcation line after corneal cross-linking and its influence on the short-term results of cross-linking in patients with progressive keratoconus [54]. A 1310 nm optical coherence tomograph coupled with a beamsplitter on the front lens of an operating microscope has been developed for intraoperative, noncontact visualization of anterior segment procedures by Geerling *et al.* [55]. This modification of OCT technology allowed intraoperative, high-resolution, cross-sectional imaging and pachymetry of the cornea and sclera during anterior segment surgery, which is particularly helpful for lamellae dissection techniques such as deep anterior lamellar keratoplasty and trabeculectomy.

For retinal OCT images, 830 nm wavelength OCT images have been evaluated for surgical indication, intraoperative management, and postoperative outcome of patients with idiopathic epiretinal macular membrane (IEMM) to reveal IEMM

partially separated from the macula, thus guiding the surgeon intraoperatively in the peeling procedures [56]. OCT scans are a valuable adjunct for the pre- and postoperative analysis of staging of idiopathic macular holes [57]. Preoperative assessment of topographic features has the potential to improve surgical strategies in eyes with macular pucker for patients who have undergone full ophthalmologic evaluation including high-definition optical coherence tomography (Cirrus, Carl Zeiss Meditec) prior to a vitrectomy with peeling of the epiretinal membrane (ERM) [58].

Wykoff *et al.* described the use of the intraoperative OCT imaging in macular surgery facilitating by the use of hand-held SD-OCT and providing an efficient method for visualizing macular pathology. This technology may, in certain cases, help confirm or identify diseases that may be difficult to visualize during surgery [59]. Hand-held Fourier domain OCT can be used during Descemet stripping automated endothelial keratoplasty (DSAEK) to assess the donor–host interface in lamellar corneal transplantation surgery [60] or to find interface fluid that is clinically undetectable under the microscope. As such, all patients were able to leave the operating room with a fully attached graft [61].

OCT also has been applied to investigate the long-term mechanical biocompatibility of a polymer microtechnology that can be used to position electrodes in close proximity to the retina [polydimethylsiloxane (PDMS) array implants] in animal studies [62].

OCT has traditionally been used in the outpatient environment as an important diagnostic tool for retinal clinical decision-making. Recent advances in OCT technology have made the intraoperative use of OCT feasible [63].

25.13
Intraoperative OCT Monitoring in Cardiovascular Surgery

Coronary artery bypass grafting (CABG) is the most commonly performed major surgery in the United States. A critical determinant of its outcome has been postulated to be injury to the conduit vessel incurred during the harvesting procedure or pathology pre-existing in the harvested vessel. Brown *et al.* detected by OCT atherosclerotic lesions in the radial arteries radial artery (RA) and discerns plaque morphology as fibrous, fibrocalcific, or fibroatheromatous. OCT is also used to assess intimal trauma and residual thrombi related to endoscopic harvest and the quality of distal anastomosis. The feasibility of OCT imaging as an intraoperative tool to select conduit vessels for CABG has been demonstrated [64]. OCT has been found particularly useful in identifying so-called vulnerable or high-risk plaques which account for many acute coronary events arising from non-flow-limiting coronary lesions. OCT permits excellent resolution of coronary architecture and precise characterization of plaque architecture. Quantification of macrophages within the plaque is also possible. These capabilities allow precise identification of the most common type of vulnerable plaque, thin-cap fibroatheroma [65]. Acute coronary syndromes frequently arise consequent to rupture of an angiographically moderate plaque with occlusive thrombus formation [66]. Plaques prone to rupture have

certain characteristics and are often referred to as vulnerable or high-risk plaques. Such plaques contain a large lipid pool, often covered by a thin fibrous cap, typically less than 65 μm thick [67]. Two-dimensional cross-sectional imaging of the exposed surface of the arterial segments has been performed *in vitro* with OCT by Brezinski *et al*. [26]. A 1300 nm wavelength super-luminescent diode light source was used that allows an axial spatial resolution of 20 μm. The signal-to-noise ratio was 109 dB. Images were displayed in gray scale or false color. Imaging was performed over 1.5 mm into heavily calcified tissue, and a high contrast was noted between lipid- and water-based constituents, making OCT attractive for intracoronary imaging. The 20 μm axial resolution of OCT allowed small structural details such as the width of intimal caps and the presence of fissures to be determined. The extent of lipid collections, which had a low backscattering intensity, was also well documented [26]. OCT, a catheter-based intravascular imaging modality, was used to measure the degree of radial artery spasm induced by means of harvest with electrocautery or a harmonic scalpel in patients undergoing CABG. OCT provides levels of speed and accuracy for quantifying endothelial injury and vasospasm that have not been described for any other modality, suggesting potential as an intraoperative quality assurance tool. Our OCT findings suggest that the harmonic scalpel induces less spasm and intimal injury than electrocautery [68]. Brazio *et al*. used OCT to evaluate the tendency of RAs to spasm when used as a bypass graft [68]. RA conduits otherwise considered acceptable for bypass grafting were often found by OCT imaging to have a substantial amount of lipid, which in turn strongly relates to the risk of postoperative spasm. Screening conduits based on characteristics of intimal quality may improve results following RA grafting [69]. Boppart *et al*. used a 3D-OCT system integrated with a surgical microscope in the assessment of the microsurgical anastomoses of vessels and nerves during microsurgery. 3D-OCT reconstructions depicted the structure within an arterial anastomosis and helped identify sites of luminal obstruction. The longitudinal spatial orientation of individual nerve fascicles was tracked in three dimensions to identify changes in position. *In vitro* human arteries and nerves embedded in highly scattering tissue and not visible on microscopy were located and imaged with OCT at eight frames per second [17]. OCT helped to reveal that intraluminal saphenous vein clot is frequently found after endoscopic vein harvest. In a study by Brown *et al*., systemic heparinization before harvest or an open carbon dioxide endoscopic vein harvest system was recommended as a benign change in practice that can significantly ameliorate this complication [70].

25.14
Intraoperative OCT Monitoring in Dermatology

OCT has been shown to help clinicians to visualize and map the hidden spread of non-melanoma skin cancer (NMSC), such as basal cell carcinomas (BCCs), squamous cell carcinoma (SCC), and the premalignant actinic keratosis (AK) [71] and also for malignant melanomas (MMs) [72]. Mogensen *et al*. described a break-up of the characteristic layering of normal skin is in OCT images of both NMSC and MM

lesions. Several other NMSC features in OCT images have also been described, the most important being focal changes including thickening of epidermis in AK lesions, and dark rounded areas, sometimes surrounded by a white structure in BCC lesions. SCC has mainly been studied on oral mucosal surfaces using OCT but changes similar to those with BCC have been described [73]. OCT has also been applied for monitoring the process of tissue healing of rat skin *in vivo* after laser irradiation [74] and collagen remodeling on opto-thermal response of photoaged skin irradiated with an Er:YAG laser [75].

25.15
Intraoperative OCT Monitoring in Gastroenterology

The intraoperative use of OCT in gastroenterology is mostly part of endoscopic or laparoscopic procedures and facilitated via fiber forward-looking [76] or side-looking fiber probes [77] at wavelength 1300 nm. A few studies assessed OCT guidance by autofluorescence imaging (AFI) in endoscopy [78] and laparoscopy [79]. The advantages of such guidance are a combination of large (AFI) and small (OCT) fields of view and also two different physical imaging modalities that may potentially improve the specificity and sensitivity of cancer diagnostics in the GI tract, particularly revealing cancer in Barrett's esophagus when OCT as a single approach facilitates only 71–85% sensitivity and 68% specificity [78]. OCT has been used as an optical biopsy tool for intraoperative *ex vivo* detection of transmural inflammation in Crohn disease [80].

25.16
Intraoperative OCT Monitoring in Urology

OCT allows imaging of the tissue structure of the bladder wall during cystoscopy with high resolution. OCT systems are currently being studied for potential intraoperative diagnostic use in laparoscopic and robotic nerve-sparing prostate cancer surgery for image-guided cancer removal, prostatectomy, and sperm retrieval.

According to Daniltchenko *et al.*, OCT of normal bladder mucosa clearly shows a differentiation between urothelium, lamina propria, and smooth muscle [81]. Cystitis and metaplasia are characterized by blurring of the laminated structure and thickening of the epithelial layer. In malignant areas, there is complete loss of the regular layered tissue structure. OCT improves the diagnosis of flat lesions of the urothelium and it has the potential for facilitating intraciperative staging of malignant areas in the bladder.

Positive surgical margins represent incomplete resection by the surgeon, and elimination of positive margins represents the only clinical feature during radical prostatectomy that can lead directly to improved cancer outcomes. Skarecky *et al.* reported the union of real-time OCT technology with the da Vinci robotic platform for identification of positive margin sites, and technical advances with wider excisions during surgery suggest promise for further reduction of surgical margins to zero [82].

Two clinical studies by Zagaynova *et al*. have reported 82% sensitivity and 85% specificity, recognizing flat cancer lesions in urinary bladder [78]. They also reported an improvement in OCT diagnostics combined with fluorescence imaging.

Rais-Bahrami *et al*. used OCT for imaging of the cavernous nerve (CN) and periprostatic tissues. The rates of nerve preservation and postoperative potency after radical prostatectomy might improve with better identification of the CN. Seven male Sprague–Dawley rats underwent surgery using a midline celiotomy to expose the bladder, prostate, and seminal vesicles. OCT was also used to image *ex vivo* human prostatectomy specimens differentiating the CN from the bladder, prostate, seminal vesicles, and periprostatic fat. OCT images of the CN and prostate correlated well with the histologic findings. OCT of *ex vivo* human prostatectomy specimens revealed findings similar to those in the rat experiments, with, however, less dramatic architecture being visualized, in part because of the thicker capsule and denser stroma of human prostates [83]. Chitchian *et al*. segmented 2D OCT images of the rat prostate to differentiate the cavernous nerves from the prostate gland. To detect these nerves, three image features were employed: Gabor filter, Daubechies wavelet, and Laws filter using a nearest-neighbor classifier. *N*-ary morphologic post-processing was used to remove small voids. The cavernous nerves were differentiated from the prostate gland with a segmentation error rate of only 0.058 ± 0.019 [84]. Aron *et al*. also found that identification of the neurovascular bundles (NVBs) required an experienced OCT operator to distinguish them from adipose tissue, small vessels, and lymphatics [85]. Parekattil *et al*. showed that OCT with its high-resolution images may improve sperm retrieval rates by better identifying isolated foci of spermatogenesis in men with nonobstructive azoospermia [86].

25.17
Intraoperative OCT Monitoring in Bone and Joint Surgery

Quantitative and nondestructive methods for clinical diagnosis and staging of articular cartilage degeneration are important to the evaluation of potential disease-modifying treatments in osteoarthritis (OA). OCT real-time imaging with 11 μm resolution at four frames per second was performed by Li *et al*. on six patients using a portable OCT system with a hand-held imaging probe during open knee surgery [87]. Structural changes including cartilage thinning, fissures, and fibrillations were observed at a resolution substantially higher than is achieved with any current clinical imaging technology. In addition to changes in architectural morphology, changes in the birefringent or polarization properties of the articular cartilage were observed with PS-OCT, suggesting collagen disorganization, an early indicator of OA supporting the hypothesis that PS-OCT may allow OA to be diagnosed before cartilage thinning.

Using Fourier domain common-path OCT, the characteristic cartilage zones and identity of various microstructured defects in an *ex vivo* chicken knee cartilage were differentiated, thus demonstrating that it could be used to conduct early arthritis diagnosis and intraoperative endomicroscopy [88].

In a study by Chu *et al.*, the hypotheses were tested that OCT can be used clinically to identify early cartilage degeneration and that these OCT findings correlate with arthroscopy results [89]. It was found that both qualitative and quantitative OCT assessments of early articular cartilage degeneration correlated strongly with the arthroscopy results ($p = 0.004$ and $p = 0.0002$, respectively, by the Kruskal–Wallis test).

Meniscal tears are often associated with anterior cruciate ligament (ACL) injury and may lead to pain and discomfort in humans. Maximum preservation of meniscal tissue is highly desirable to mitigate the progression of OA. Images of microstructural changes in meniscus would potentially guide surgeons to manage the meniscal tears better, but the resolution of current diagnostic techniques is limited for this application. Ling *et al.* demonstrated the feasibility of OCT for the diagnosis of meniscal pathology [90]. OCT and scanning electron microscopy (SEM) images of torn menisci were compared and each sample was evaluated for gross and microstructural abnormalities and reduction or loss of birefringence from the OCT images. OCT holds promise in the nondestructive and rapid assessment of microstructural changes and tissue birefringence of meniscal tears. Future development of intraoperative OCT may help surgeons in decision-making in meniscal treatment.

OCT can eventually be developed for use through an arthroscope, having considerable potential for assessing early osteoarthritic cartilage and monitoring therapeutic effects for cartilage repair with resolution close to real time on a scale of micrometers. This technology for nondestructive quantitative assessment of human articular cartilage degeneration may facilitate the development of strategies to delay or prevent the onset of OA.

25.18
Intraoperative OCT Monitoring in Neurology

Intraoperative identification of brain tumors and tumor margins has been limited by either the resolution of the *in vivo* imaging technique or the time required to obtain histologic specimens.

OCT can effectively differentiate normal cortex from intracortical melanoma based on variations in optical backscatter. A portable hand-held OCT surgical imaging probe has been constructed by Boppart *et al.* for imaging within the surgical field. Two-dimensional images showed increased optical backscatter from regions of tumor, which was quantitatively used to determine the tumor margins [91]. The images correlated well with the histologic findings. Three-dimensional reconstructions revealed regions of tumor penetrating the normal cortex and could be resectioned at arbitrary planes. Subsurface cerebral vascular structures could be identified and were therefore avoided.

Detection of residual tumor during resection of glial brain tumors remains a challenge because of the low inherent contrast of adjacent edematous brain, the surrounding infiltration zone, and the solid tumor. Böhringer *et al.* reported the results of a study using a time-domain Sirius 713 tomograph with a central wavelength of 1310 nm and a coherence length of 15 μm equipped with a

mono-mode fiber and a modified OCT adapter containing a lens system for imaging at a working distance of 2.5 cm [92]. A spectral-domain tomograph using 840 and 930 nm superluminescence diodes (SLDs) with a central wavelength of 900 nm was used as a second imaging modality in the same study. Both time-domain and spectral-domain coherence tomography delineated normal brain, the infiltration zone, and solid tumor in murine intracerebral gliomas. Histologic evaluation of H&E-stained sections parallel to the optical plain demonstrated that tumor areas of less than 1 mm could be detected and that not only solid tumor but also brain invaded by low-density single tumor cells which produced an OCT signal different from normal brain. SD-OCT demonstrated a significantly more detailed microstructure of tumor and normal brain up to a tissue depth of 1.5–2.0 mm, whereas the interpretation of time-domain OCT was difficult at tissue depths >1.0 mm.

An OCT integrated endoscope can image the endoventricular anatomy and other endoscopically accessible structures in a human brain specimen. Böhringer *et al,* mounted a Sirius 713 OCT device on a modified rigid endoscope for simultaneous OCT imaging and endoscopic video imaging of the visible spectrum using a graded index rod endoscope [93]. OCT imaging of a human brain specimen in water allowed an in-depth view into structures such as the walls of the ventricular system, the choroid plexus, and the thalamostriatal vein. OCT further allowed imaging of structures beyond tissue barriers or opaque media. In this fixed specimen, OCT allowed discrimination of vascular structures down to a diameter of 50 μm. In vessels larger than 100 μm, the lumen could be discriminated and within larger blood vessels a layered structure of the vascular wall and also endovascular plaques could be visualized. This *in vitro* pilot study demonstrated that OCT integrated into neuroendoscopes may add information that cannot be obtained by video imaging alone. Using an intracranial glioma model according to Böhringer *et al.* [93], it has been shown recently that the working distance of the OCT adapter and the A-scan acquisition rate conceptually allow integration of the OCT applicator into the optical path of the operating microscopes. This would allow a continuous analysis of the resection plane, providing optical tomography, thereby adding a third dimension to the microscopic view and information on the light attenuation characteristics of the tissue. Performing 3D data arrays for multiplanar analysis of the tumor to brain interface, time-domain OCT allows discrimination of normal brain, diffusely invaded brain tissue, and solid tumor [39].

In conjunction with the rapid image acquisition rates of OCT, this technology carries the potential for a novel intraoperative imaging tool for the detection of residual tumor and guidance of neurosurgical resections. OCT technology may provide an extra margin of safety by providing cross-sectional images of tissue barriers within optically opaque conditions.

25.19
Intraoperative OCT Monitoring in Breast Surgery

As breast cancer screening rates increase, smaller and more numerous lesions are being identified earlier, leading to more breast-conserving surgical procedures.

Nguyen *et al*. reported that achieving a clean surgical margin represents a technical challenge with important clinical implications where OCT has been introduced as an intraoperative high-resolution imaging technique that assesses surgical breast tumor margins by providing real-time microscopic images up to 2 mm beneath the tissue surface of the lumpectomy specimens [94]. Based on histologic findings, nine true positives, nine true negatives, two false positives, and no false negatives were found, yielding a sensitivity of 100% and a specificity of 82%.

Another study by the same group reported the use of OCT for the intraoperative *ex vivo* imaging and assessment of axillary lymph nodes from 17 human patients with breast cancer who were imaged intraoperatively with OCT [95]. These preliminary clinical studies identified scattering changes in the cortex, relative to the capsule, which can be used to differentiate normal from reactive and metastatic nodes. These optical scattering changes are correlated with inflammatory and immunologic changes observed in the follicles and germinal centers. The results show the potential of OCT as a real-time method for intraoperative margin assessment in breast-conserving surgeries without having to resect physically and process histologically specimens in order to visualize microscopic features.

25.20
Intraoperative OCT Monitoring in ENT

Shakhov *et al*. applied OCT for intraoperative control in laser surgery of laryngeal carcinoma operated with a surgical YAG:Nd laser at two switchable wavelengths of 1.44 and 1.32 μm by laryngofissure, direct microlaryngoscopy, and fibrolaryngoscopy [96]. Information on structural alterations in laryngeal mucosa to a depth of 2 mm, obtained by OCT, makes it possible to locate tumor borders precisely, thus giving an opportunity to control the surgical treatment of laryngeal carcinoma. Combination of the two wavelengths in a single laser unit and intraoperative OCT monitoring represent a new modality for minimally invasive larynx surgery. The use of biocompatible materials offers new possibilities in ossiculoplasty in middle ear surgery. The exact calculation concerning the length of the implant to be used, however, still poses considerable difficulties and is an additional cause of a remaining air conduction difference or the need for further surgical intervention.

Heermann *et al*. reported the use of an optical coherence interferometer coupled to an operating microscope in five stapedoplasties and five tympanoplasties type III in order to determine the length of the prosthesis to be used [97]. The measurement of middle ear structures has an accuracy of 30 μm. The postoperative audiologic results showed a good auditory performance. Wong *et al*. examined patients undergoing surgical head and neck endoscopy using a fiber-optic hand-held OCT imaging probe placed in near contact with the target site (1.3 μm broadband light source, FWHM = 80 nm, frame rate 1 Hz) in order to study and characterize microstructural anatomy and features of the larynx and benign laryngeal pathology *in vivo*, including information on the thickness of the epithelium, integrity of the basement membrane, and structure of the lamina propria, and also microstructural features such as glands,

ducts, blood vessels, fluid collection/edema, and the transitions between pseudostratified columnar and stratified squamous epithelium [98].

Just *et al.* used a specially equipped operating microscope with an integrated SD-OCT apparatus for standard middle-ear surgical procedures [41]. Intraoperative OCT was evaluated for establishment of the cause of stapes fixation, assessment of the morphology of the stapes footplate in revision stapes surgery, and as an orientation guide in cochlear implantation in congenital anomalies. OCT displays the middle and inner ear structures precisely. Potential areas of application can be defined as a result of these studies: visualization of the oval window niche in revision stapesplasty and reconstructive middle ear surgery, and also during explorative tympanotomy for intraoperative assessment of perilymph fistula, and demonstration of structures of the exposed but not opened inner ear. OCT allowed *in vivo* visualization and documentation of the annular ligament, the different layers of the footplate, and the inner-ear structures, both in non-fixed and fixed stapes footplates. In cases of otosclerosis and tympanosclerosis, an inhomogeneous and irregularly thickened footplate was found, in contrast to the appearance of non-fixed footplates. In both fixed and non-fixed footplates, there was a lack of visualization of the border between the footplate and the otic capsule [99].

Using the Niris OCT imaging system (Imalux, Cleveland, OH, USA), images of benign and premalignant laryngeal disease in 33 patients undergoing surgical head and neck endoscopy were obtained and analyzed by Rubinstein *et al.* [100]. This imaging system has a spatial depth resolution of 10–20 mm and a depth scanning range of 2.2 mm, obtaining images of 200 × 200 pixels at a maximum frame rate of 0.7 Hz. The tip of the probe was inserted through a rigid laryngoscope, and still images of arytenoids, aryepiglottic folds, piriform sinus, epiglottis, and true and false vocal cords were acquired. In patients whose OCT images were taken from normal tissue, the normal microstructures were clearly identified, and also disruption of the latter in malignant pathologies.

OCT imaging potentially offers an efficient, quick, and reliable imaging modality in guiding surgical biopsies, intraoperative decision-making, and therapeutic options of various laryngeal pathologies and premalignant disease. OCT has the unique ability to image laryngeal tissue microstructure and can detail microanatomic changes in benign, premalignant, and malignant laryngeal pathologies.

25.21
Intraoperative OCT Monitoring in Gynecology

Previous studies have correlated cancer recurrence and progression with obtaining clear margins upon resection. The most common need to obtain clear margins with respect to conservative treatment in patients with cervical neoplasia occurs with women who wish to preserve fertility. However, current detection methods are limited and current treatments present additional fertility concerns. In order to provide the best care for patients wishing to retain fertility post-treatment for cervical dysplasia, a superior option for detecting tumor margins accurately at the

microscopic scale must be further explored [101]. A novel prototype intraoperative system combining positron detection and OCT imaging was developed for early ovarian cancer detection by Gamelin *et al*. [102]. The probe employs eight plastic scintillating fiber tips for preferential detection of local positron activity surrounding a central scanning OCT fiber, providing volumetric imaging of tissue structure in regions of high radiotracer uptake. In conjunction with co-registered frequency-domain OCT measurements, the results demonstrated the potential for a miniaturized laparoscopic probe offering simultaneous functional localization and structural imaging for improved early cancer detection.

25.22
Prediction of Future Developments in Intraoperative OCT Monitoring

OCT is a powerful optical biopsy tool although with a small field of view, with nearly real-time imaging. OCT can be guided by a large field of view technique such as spectral or fluorescence imaging [78, 103]. As OCT technology improves, the ability to image cellular level features will increase the range of applicability of OCT imaging. Full use of OCT for guided surgical interventions can be achieved with rapid 3D imaging, thus reducing motion artifacts and improving reproducibility, since otherwise it is difficult to bring the image field in coincidence with the relevant but dynamically changing anatomic structures [48]. Pattern recognition and filter algorithms may improve the discrimination of pathology and consequences of the surgical intervention of the OCT methods [104]. OCT has the potential to improve the efficacy of surgical or therapeutic interventions and may permit new treatment approaches. For instance, further studies are needed to assess possible active control of the laser ablation through real-time OCT clinical feedback, which could improve current ablation efficacy. OCT holds the potential to guide surgical biopsies, direct therapy, and monitor disease, particularly when office-based systems are developed. ENT, dental, gynecologic, and pulmonologic applications have significant potential to be more widely adopted as areas of OCT clinical research.

Acknowledgments

This study was supported by Erlangen Graduate School in Advanced Optical Technologies (SAOT) by the German National Science Foundation (DFG) in the framework of the excellence initiative. The author thanks Ioulia Davydova for helping with the design of the charts.

References

1 Boppart, S.A., Herrmann, J.J., Pitris, C., Stamper, D.L., Brezinski, M.E., and Fujimoto, J.G. (1999) High-resolution optical coherence tomography-guided laser ablation of surgical tissue. *J. Surg. Res.*, **82**, 275–284.

2 Schmitt, J.M., Knuttel, A., Yadlowsky, M., and Eckhaus, M.A. (1994) Optical coherence tomography of a dense tissue – statistics of attenuation and backscattering. *Phys. Med. Biol.*, **38**, 1705–1720.

3 Fujimoto, J.G., Pitris, C., Boppart, S.A., and Brezinski, M.E. (2000) Optical coherence tomography: an emerging technology for biomedical imaging and optical biopsy. *Neoplasia*, **2** (1–2), 9–25.

4 Boppart, S.A., Bouma, B.E., Pitris, C., Tearney, G.J., Fujimoto, J.G., and Brezinski, M.E. (1997) Forward-imaging instruments for optical coherence tomography. *Opt. Lett.*, **22**, 1618–1620.

5 McLaughlin, R.A. and Sampson, D.D. (2010) Clinical applications of fiber-optic probes in optical coherence tomography. *Opt. Fiber Technol.*, **16** (6), 467–475.

6 Probst, J., Hillmann, D., Lankenau, E., Winter, C., Oelckers, S., Koch, P., and Hüttmann, G. (2010) Optical coherence tomography with online visualization of more than seven rendered volumes per second. *J. Biomed. Opt.*, **15** (2), 026014.

7 Ho, J., Sull, A.C., Vuong, L.N., Chen, Y., Liu, J., Fujimoto, J.G., Schuman, J.S., and Duker, J.S. (2009) Assessment of artifacts and reproducibility across spectral- and time-domain optical coherence tomography devices. *Ophthalmology*, **116** (10), 1960–1970.

8 Agrba, P., Kirillin, M., Abelevich, A., Zagaynova, E., and Kamensky, V. (2009) Compression as a method for increasing the informativity of optical coherence tomography of biotissues. *Opt. Spectrosc.*, **107** (6), 853–858.

9 Dolin, S., Feldstein, F., Gelikonov, G., Gelikonov, V., Gladkova, N., Iksanov, R., Kamensky, V., Kuranov, R., Sergeev, A., Shakhova, N., and Turchin, I. (2004) Fundamentals of OCT and clinical applications of endoscopic OCT, in *Handbook of Coherent Domain Optical Methods* (ed. V. Tuchin), Kluwer, Dordrecht, pp. 211–270.

10 Meissner, O.A., Rieber, J., Babaryka, G., Oswald, M., Reim, S., Siebert, U., Redel, T., Reiser, M., and Mueller-Lisse, U. (2006) Intravascular optical coherence tomography: comparison with histopathology in atherosclerotic peripheral artery specimens. *J. Vasc. Interv. Radiol.*, **17** (2 Pt 1), 343–349.

11 Hollo, G., Garas, A., and Kóthy, P. (2010) Comparison of diagnostic accuracy of Fourier-domain optical coherence tomography and scanning laser polarimetery to detect glaucoma. *Acta Ophthalmol.*, **88** (Suppl. s246), on line publication, doi: 10.5301/ejo.5000011.

12 Drexler, W. and Fujimoto, J.G. (2008) State-of-the-art retinal optical coherence tomography. *Prog. Retin. Eye Res.*, **27** (1), 45–88.

13 Suzuki, Y., Ikeno, F., Koizumi, T., Tio, F., Yeung, A.C., Yock, P.G., Fitzgerald, P.J., and Fearon, W.F. (2008) *In vivo* comparison between optical coherence tomography and intravascular ultrasound for detecting small degrees of in-stent neointima after stent implantation. *JACC Cardiovasc. Interv.*, **1** (2), 168–173.

14 Douplik, A., Morofke, D., Chiu, S., Bouchelev, V., Mao, L., Yang, V., and Vitkin, A. (2008) *In vivo* real time monitoring of vasoconstriction and vasodilation by a combined diffuse reflectance spectroscopy and Doppler optical coherence tomography approach. *Laser Surg. Med.*, **40** (5), 323–331.

15 Dirk, J.F., van der Meer, F.J., Aalders, M., and van Leeuwen, C.G. (2004) Quantitative measurement of attenuation coefficients of weakly scattering media using optical coherence tomography. *Opt. Express*, **12** (19), 4353–4365.

16 Brezinski, M.E., Tearney, G.J., Boppart, S.A., Swanson, E.A., Southern, J.F., and Fujimoto, J.G. (1997) Optical biopsy with optical coherence tomography, feasibility for surgical diagnostics. *J. Surg. Res.*, **71**, 32–40.

17 Boppart, S.A., Bouma, B.E., Pitris, C., Southern, J.F., Brezinski, M.E., and Fujimoto, J.G. (1998) Intraoperative assessment of microsurgery with three-dimensional optical coherence tomography. *Radiology*, **208**, 81–86.

18 Justa, T., Lankenaua, E., Hüttmann, G., and Paua, H.W. (2009) Intra-operative application of optical coherence

tomography with an operating microscope. *J. Laryngol. Otol.*, **123** (9), 1027–1030.

19 Miyazawa, A., Yamanari, M., Makita, S., Miura, M., Kawana, K., Iwaya, K., Goto, H., and Yoshiaki, Y. (2009) Tissue discrimination in anterior eye using three optical parameters obtained by polarization sensitive optical coherence tomography. *Opt. Express*, **17** (20), 17426.

20 Liang, X., Graf, B.W., and Boppart, S.A. (2009) Imaging engineered tissues using structural and functional optical coherence tomography. *J. Biophotonics*, **2** (11), 643–655.

21 Hauger, C., Luber, J., Kaschke, M., and Krause-Bonte, M. (2004) Surgical system supported by optical coherence tomography. U.S. Pat. US 6763259.

22 Sampliner, R.E. (2002) Updated guidelines for the diagnosis, surveillance and therapy of Barrett's esophagus. *Am. J. Gastroenterol.*, **97**, 1888–1895.

23 Tearney, G.I., Brezinski, M.E., Bouma, B.E., Boppart, S.A., Pitris, C., Southern, J.F., and Fujimoto, J.G. (1997) *In vivo* endoscopic optical biopsy with optical coherence. *Tomogr. Sci.*, **276** (5), 2037–2039.

24 Tearney, G.J., Brezinski, M.E. *et al.* (1997) Optical biopsy in human gastrointestinal tissue using optical coherence tomography. *Am. J. Gastroenterol.*, **92** (10), 1800–1804.

25 Brezinski, M.E., Tearney, G.J., Boppart, S.A., Swanson, E.A., Southern, J.F., and Fujimoto, J.G. (1997) Optical biopsy with optical coherence tomography: feasibility for surgical diagnostics. *J. Surg. Res.*, **71** (1), 32–40.

26 Brezinski, M.E., Tearney, G.J., Bouma, B.E., Izatt, J.A., Hee, M.R., Swanson, E.A., Southern, J.F., and Fujimoto, J.G. (1996) Optical coherence tomography for optical biopsy. Properties and demonstration of vascular pathology. *Circulation*, **93** (6), 1206–1213.

27 Cahill, R.A., Asakuma, M., Trunzo, J., Schomisch, S., Wiese, D., Saha, S., Dallemagne, B., Marks, J., and Marescaux, J. (2009) Intraperitoneal virtual biopsy by fibered optical coherence tomography (OCT) at natural orifice transluminal endoscopic surgery (NOTES). *J. Gastrointest. Surg.*, **14**, 732–738.

28 Iftimia, N.V., Mujat, M., Ustun, T., Ferguson, R.D., Danthu, V., and Hammer, D.X. (2009) Spectral-domain low coherence interferometry/optical coherence tomography system for fine needle breast biopsy guidance. *Rev. Sci. Instrum.*, **80** (2), 024302.

29 Izatt, J.A., Kulkarni, M.D., Hsing-Wen, W., Kobayashi, K., and Sivak, M.V. Jr. (1996) Optical coherence tomography and microscopy in gastrointestinal tissues. *IEEE J. Sel. Top. Quantum Electron.*, **2**, 1017–1028.

30 Tearney, G.J., Brezinski, M.E., Southern, J.F., Bouma, B.E., Boppart, S.A., and Fujimoto, J.G. (1998) Optical biopsy in human pancreatobiliary tissue using optical coherence tomography. *Dig. Dis. Sci.*, **43**, 1193–1199.

31 Tearney, G.J., Brezinski, M.E., Southern, J.F., Bouma, B.E., Boppart, S.A., and Fujimoto, J.G. (1997) Optical biopsy in human urologic tissue using optical coherence tomography. *J. Urol.*, **157**, 1915–1919.

32 Pitris, C., Brezinski, M.E., Bouma, B.E., Tearney, G.J., Southern, J.F., and Fujimoto, J.G. (1998) High resolution imaging of the upper respiratory tract with optical coherence tomography – A feasibility study. *Am. J. Respir. Crit. Care Med.*, **157**, 1640–1644.

33 Pitris, C., Goodman, A., Boppart, S.A., Libus, J.J., Fujimoto, J.G., and Brezinski, M.E. (1999) High-resolution imaging of gynecologic neoplasms using optical coherence tomography. *Obstet. Gynecol.*, **93**, 135–139.

34 Sayanagi, K., Pelayes, D.E., Kaiser, P.K., and Singh, A.D. (2010) 3D spectral domain optical coherence tomography findings in choroidal tumors. *Eur. J. Ophthalmol.*, **21** (3), 271–275.

35 Strasswimmer, J. (2010) Optical biopsy at the bedside. *Arch. Dermatol.*, **146** (8), 909–910.

36 Bouma, B.E., Tearney, G.J., Compton, C.C., and Nishioka, N.S. (2000) High-resolution imaging of the

human esophagus and stomach *in vivo* using optical coherence tomography. *Gastrointest. Endosc.*, **51**, 467–474.

37 Karl, A., Stepp, H., Willmann, E., Tilki, D., Zaak, D., Knüchel, R., and Stief, C. (2008) Optical coherence tomography (OCT): ready for the diagnosis of a nephrogenic adenoma of the urinary bladder? *J. Endourol.*, **22** (11), 2429–2432.

38 Linehan, J.A., Hariri, L.P., Sokoloff, M.H., Rice, P.S., Bracamonte, E.R., Barton, J.K., and Nguyen, M.M. (2010) Use of optical coherence tomography imaging to differentiate benign and malignant renal masses. *J. Urol.*, **183** (4, Suppl.), e835.

39 Böhringer, H.J., Lankenau, E., Stellmacher, F., Reusche, E., Hüttmann, G., and Giese, A. (2009) Imaging of human brain tumor tissue by near-infrared laser coherence tomography. *Acta Neurochir. (Wien)*, **151** (5), 507–517.

40 Mujat, M., Ferguson, R.D., Hammer, D.X., Gittins C., and Iftimia, N. (2009) Automated algorithm for breast tissue differentiation in optical coherence tomography. *J. Biomed. Opt.*, **14** (3), 034040.

41 Just, T., Lankenau, E., Hüttmann, G., and Pau, H.W. (2009) Optische Kohärenztomographie in der Mittelohrchirurgie. *HNO*, **57** (5), 421–427.

42 Van Soest, G., Goderie, T.P.M., Gonzalo, N., Koljenovic, S., van Leenders, G.L.J.H., Regar, E., Serruys, P.W., and van der Steen, A.F.W. (2009) Imaging atherosclerotic plaque composition with intracoronary optical coherence tomography. *Neth. Heart J.*, **17** (11), 448–450.

43 Van der Meer, F.J., Faber, D.J., Aalders, M.C.G., Poot, A.A., Vermes, I., and van Leeuwen, T.G. (2010) Apoptosis- and necrosis-induced changes in light attenuation measured by optical coherence tomography. *Lasers Med. Sci.*, **25** (2), 259–267.

44 Standish, B.A., Lee, K.K.C., Jin, X., Mariampillai, A., Wood, M.F.G., Wilson, B.C., Vitkin, I.A., Munce, N.R., and Yang, V.X.D. (2008) Interstitial Doppler optical coherence tomography as a local tumor necrosis predictor in photodynamic therapy of prostatic carcinoma: an *in vivo* study. *Cancer Res.*, **68**, 9987.

45 Yang, Y., Whiteman, S., Gey van Pittius, D., He, Y., Wang, R.K., and Spiteri, M.A. (2004) Use of optical coherence tomography in delineating airways microstructure: comparison of OCT images to histopathological sections. *Phys. Med. Biol.*, **49** (7), 1247–1255.

46 De Boer, J.F., Srinivas, S.M., Malekafzali, A., Chen, Z., and Nelson, J.S. (1998) Imaging thermally damaged tissue by polarization sensitive optical coherence tomography. *Opt. Express*, **3**, 212–218.

47 Tsai, M.T., Lee, H.C., Lu, C.W., Wang, Y.M., Lee, C.K., Yang, C.C., and Chiang, C.P. (2008) Delineation of an oral cancer lesion with swept-source optical coherence tomography. *J. Biomed. Opt.*, **13** (4), 044012.

48 Hüttmann, G., Lankenau, E., Schulz-Wackerbarth, C., Müller, M., Steven, P., and Birngruber, R. (2009) Übersicht der apparativen Entwicklungen in der optischen Kohärenztomografie: von der Darstellung der Retina zur Unterstützung therapeutischer Eingriffe. *Klin. Monatsbl. Augenheilkd.*, **226** (12), 958–964.

49 Bagayev, S.N., Gelikonov, V.M., Gelikonov, G.V., Kargapoltsev, E.S., Kuranov, R.V., Razhev, A.M., Turchin, I.V., and Zhupikov, A.A. (2002) Optical coherence tomography for *in situ* monitoring of laser corneal ablation. *J. Biomed. Opt.*, **7** (4), 633–642.

50 Wirbelauer, C., Aurich, H., and Pham, D.T. (2007) Online optical coherence pachymetry to evaluate intraoperative ablation parameters in LASIK. *Graefes Arch. Clin. Exp. Ophthalmol.*, **245** (6), 775–781.

51 Kucumen, R.B., Dinc, U.A., Yenerel, N.M., Gorgun, E., and Alimgil, M.L. (2009) Immediate evaluation of the flaps created by

femtosecond laser using anterior segment optical coherence tomography. *Ophthalmic Surg. Lasers Imaging*, **40** (3), 251–254.

52 Utine, C., Altunsoy, M., and Basar, D. (2008) Visante anterior segment OCT in a patient with gas bubbles in the anterior chamber after femtosecond laser corneal flap formation. *Int. Ophthalmol.*, **30** (1), 81–84.

53 Ambrósio, R., Jardim, D., Netto, M.V., and Wilson, S.E. (2007) Management of unsuccessful LASIK surgery. *Compr. Ophthalmol. Update*, **8** (3), 125–141; discussion 143–144.

54 Doors, M., Tahzib, N.G., Eggink, F.A., Berendschot, T.T.J.M., Webers, C.A.B., and Nuijts, R. (2009) Use of anterior segment optical coherence tomography to study corneal changes after collagen cross-linking. *Am. J. Ophthalmol.*, **148** (6), 844–851.

55 Geerling, G., Müller, M., Winter, C., Hoerauf, H., Oelckers, S., Laqua, H., and Birngruber, R. (2005) Intraoperative 2-dimensional optical coherence tomography as a new tool for anterior segment surgery. *Arch. Ophthalmol.*, **123** (2), 253–257.

56 Azzolini, C., Patelli, F., Codenotti, M., Pierro, L., and Brancato, R. (1999) Optical coherence tomography in idiopathic epiretinal macular membrane surgery. *Eur. J. Ophthalmol.*, **9** (3), 206–211.

57 Gobel, W., Schrader, W.F., Sehrenker, M., and Klink, T. (2000) Findings of optical coherence tomography (OCT) before and after macular hole surgery. *Ophthalmology*, **97** (4), 251–256.

58 Hattenbach, L.O., Höhn, F., Fulle, G., and Mirshahi, A. (2009) Präoperative Diagnostik topografischer Merkmale bei epiretinaler Gliose mittels hochauflösender optischer Kohärenztomografie. *Klin. Monatsbl. Augenheilkd.*, **226** (8), 649–653.

59 Wykoff, C.C., Berrocal, A.M., Schefler, A.C., Uhlhorn, S.R., Ruggeri, M., and Hess, D. (2010) Intraoperative OCT of a full-thickness macular hole before and after internal limiting membrane peeling. *Ophthalmic Surg. Lasers Imaging*, **41** (1), 7–11.

60 Knecht, P.B., Kaufmann, C., Menke, M.N., Watson, S.L., and Bosch, M.M. (2010) Use of intraoperative Fourier-domain anterior segment optical coherence tomography during Descemet stripping endothelial keratoplasty. *Am. J. Ophthalmol.*, **150** (3), 360–365.

61 Ide, T., Wang, J., Tao, A., Leng, T., Kymionis, G.D., O'Brien, T.P., and Yoo, S.H. (2010) Intraoperative use of three-dimensional spectral-domain optical coherence tomography. *Ophthalmic Surg. Lasers Imaging*, **41** (2), 250–254.

62 Güven, D., Weiland, J.D., Maghribi, M., Davidson, J.C., Mahadevappa, M., Roizenblatt, R., Qiu, G., Krulevitz, P., Wang, X., Labree, L., and Humayun, M.S. (2006) Implantation of an inactive epiretinal poly(dimethyl siloxane) electrode array in dogs. *Exp. Eye Res.*, **82** (1), 81–90.

63 Puliafito, C.A. (2010) Optical coherence tomography: a new tool for intraoperative decision making. *Ophthalmic Surg. Lasers Imaging*, **41** (1), 6.

64 Brown, E.N., Burris, N.S., Gu, J., Kon, Z.N., Laird, P., Kallam, S., Tang, C.M., Schmitt, J.M., and Poston, R.S. (2007) Thinking inside the graft: applications of optical coherence tomography in coronary artery bypass grafting. *J. Biomed. Opt.*, **12** (5), 051704.

65 Low, A.F., Tearney, G.J., Bouma, B.E., and Jang, I.-K. (2006) Technology Insight: optical coherence tomography – current status and future development. *Nat. Cardiovasc. Clin. Pract. Med.*, **3** (3), 154–162.

66 Libby, P. (2001) Current concepts of the pathogenesis of the acute coronary syndromes. *Circulation*, **104**, 365–372.

67 Burke, A.P., Farb, A., Malcom, G.T., Liang, Y.-h., Smialek, J., and Virmani, R. (1997) Coronary risk factors and plaque morphology in men with coronary disease who died suddenly. *N. Engl. J. Med.*, **336**, 1276–1282.

68 Brazio, P.S., Laird, P.C., Xu, C.Y., Gu, J.Y., Burris, N.S., Brown, E.N., Kon, Z.N., and Poston, R.S. (2008) Harmonic scalpel versus electrocautery for harvest of radial

artery conduits: reduced risk of spasm and intimal injury on optical coherence tomography. *J. Thorac. Cardiovasc. Surg.*, **136** (5), 1302–1308.

69 Brown, E.N., Burris, N.S., Kon, Z.N., Grant, M.C., Brazio, P.S., Xu, C., Laird, P., Gu, J., Kallam, S., Desai, P., and Poston, R.S. (2009) Intraoperative detection of intimal lipid in the radial artery predicts degree of postoperative spasm. *Arteriosclerosis*, **205** (2), 466–471.

70 Brown, E.N., Kon, Z.N., Tran, R., Burris, N.S., Gu, J., Laird, P., Brazio, P.S., Kallam, S., Schwartz, K., Bechtel, L., Joshi, A., Zhang, S., and Poston, R.S. (2007) Strategies to reduce intraluminal clot formation in endoscopically harvested saphenous veins. *J. Thorac. Cardiovasc. Surg.*, **134** (5), 1259–1265.

71 Steiner, R., Kunzi-Rapp, K., and Scharffetter-Kochanek, K. (2003) Optical coherence tomography: clinical applications in dermatology. *Med. Laser Appl.*, **18** (3), 249–259.

72 Gambichler, T., Regeniter, P., Bechara, F.G., Orlikov, A., Vasa, R., Moussa, G., Stücker, M., Altmeyer, P., and Hoffmann, K. (2007) Characterization of benign and malignant melanocytic skin lesions using optical coherence tomography *in vivo*. *J. Am. Acad. Dermatol.*, **57**, 629–637.

73 Mogensen, M., Lars, T., Jørgensen, T.M., Andersen, P.E., and Jemec, G.B.E. (2009) OCT imaging of skin cancer and other dermatological diseases. *J. Biophoton*, **2** (6–7), 442–451.

74 He, Y., Wu, S., Li, Z., Cai, S., and Li, H. (2010) Monitoring the process of tissue healing of rat skin *in vivo* after laser irradiation based on optical coherence tomography. *Proc. SPIE*, **7845**, 78452E.

75 Zhang, X., Wu, S., and Li, H. (2010) Monitoring collagen remodeling on opto-thermal response of photoaged skin irradiated by Er:YAG laser with optical coherence tomography. *Proc. SPIE*, **7845**, 78450F.

76 Shakhova, N.M., Gelikonov, V.M., Kamensky, V.A., Kuranov, R.V., and Turchin, I.V. (2002) Clinical aspects of the endoscopic optical coherence tomography and the ways for improving its diagnostic value. *Laser Phys.*, **12** (4), 617–626.

77 Yang, V.X.D., Tang, S., Gordon, M.L., Qi, B., Gardiner, G., Cirocco, M., Kortan, P., Haber, G.B., Kandel, G., Vitkin, I.A., Wilson, B.C., and Marcon, N.E. (2005) Endoscopic Doppler optical coherence tomography in the human GI tract: initial experience. *Gastrointest. Endosc.*, **61** (7), 879–890.

78 Zagaynova, E., Gladkova, N., Shakhova, N., Gelikonov, G., and Gelikonov, V. (2008) Endoscopic OCT with forward-looking probe: clinical studies in urology and gastroenterology. *J. Biophotonics*, **1** (2), 114–128.

79 Cahill, R.A. and Mortense, N.J. (2010) Intraoperative augmented reality for laparoscopic colorectal surgery by intraoperative near-infrared fluorescence imaging and optical coherence tomography. *Minerva Chir.*, **65** (4), 451–462.

80 Shen, B., Zuccaro, G., Gramlich, T., Gladkova, N., Delaney, C., Connor, J., Kareta, M., Lashner, B., Bevins, C., Feldchtein, F., Strong, S., Bambrick, M., Trolli, P., and Fazio, V. (2004) Intraoperative *ex vivo* histology-correlated optical coherence tomography in the detection of transmural inflammation in Crohn's disease. *Gastroenterology*, **126** (4), (Suppl. 2) A207–A208.

81 Daniltchenko, D., König, F., Lankenau, E., Sachs, M., Kristiansen, G., Huettmann, G., and Schnorr, D. (2006) Anwendung der optischen Kohärenztomographie (OCT) bei der Darstellung von Urothelerkrankungen der Harnblase. *Radiologie*, **46** (7), 584–589.

82 Skarecky, D.W., Brenner, M., Rajan, S., Rodriguez, E., Narula, N., Melgoza, F., and Ahlering, T.E. (2008) Zero positive surgical margins after radical prostatectomy: is the end in sight? *Expert Rev. Med. Dev.*, **5** (6), 709–717.

83 Rais-Bahrami, S., Levinson, A.W., Fried, N.M., Lagoda, G.A., Hristov, A., Chuang, Y., Burnett, A.L., and Su, L.M. (2008) Optical coherence tomography of cavernous nerves: a step toward real-time

intraoperative imaging during nerve-sparing radical prostatectomy. *Urology*, **72** (1), 198–204.

84 Chitchian, S, Weldon, T.P., and Fried, N.M. (2009) Segmentation of optical coherence tomography images for differentiation of the cavernous nerves from the prostate gland. *J. Biomed. Opt.*, **14** (4), 044033.

85 Aron, M., Kaouk, J.H., Hegarty, N.J., Colombo, J.R. Jr., Haber, G.P., Chung, B.I., Zhou, M., and Gill, I.S. (2007) Second prize: preliminary experience with the Niris optical coherence tomography system during laparoscopic and robotic prostatectomy. *J. Endourol.*, **21**, 814–818.

86 Parekattil, S., Yeung, L.L., and Su, L.-M. (2009) Intraoperative tissue characterization and imaging. *Urol. Clin. North Am.*, **36** (2), 213–221.

87 Li, X.D., Martin, S., Pitris, C., Ghanta, R., Stamper, D.L., Harman, M., Fujimoto, J.G., and Brezinski, M.E. (2005) High-resolution optical coherence tomographic imaging of osteoarthritic cartilage during open knee surgery. *Arthritis Res. Ther.*, **7** (2), R318–R323.

88 Han, J.H., Liu, X., Kang, J.U., and Song, C.G. (2010) High-resolution subsurface articular cartilage imaging based on Fourier-domain common-path optical coherence tomography. *Chin. Opt. Lett.*, **8** (2), 167–169.

89 Chu, C.R., Williams, A., Tolliver, D., Kwoh, K., Bruno, S., and Irrgang, J.J. (2010) Clinical optical coherence tomography of early articular cartilage degeneration in persons with degenerative meniscal tears. *Arthritis Care Res.*, **62** (5), 1412–1420.

90 Ling, C.H.Y., Pozzi, A., Thieman, K.M., Tonks, C.A., Guo, S.G., Xie, H.K., and Horodyski, M. (2010) The potential of optical coherence tomography for diagnosing meniscal pathology. *Meas. Sci. Technol.*, **21** (4), 045801.

91 Boppart, S.A., Brezinski, M.E., Pitris, C., and Fujimoto, J.G. (1998) Optical coherence tomography for neurosurgical imaging of human intracortical melanoma. *Neurosurgery*, **43** (4), 834–841.

92 Böhringer, H.J., Boller, D., Leppert, J., Knopp, U., Lankenau, E., Reusche, E., Hüttmann, G., and Giese, A. (2006) Time-domain and spectral-domain optical coherence tomography in the analysis of brain tumor tissue. *Lasers Surg. Med.*, **38** (6), 588–597.

93 Böhringer, H.J., Lankenau, E., Rohde, V., Hüttmann, G., and Giese, A. (2006) Optical coherence tomography for experimental neuroendoscopy. *Minim. Invasive Neurosurg.*, **49** (5), 269–275.

94 Nguyen, F.T., Zysk, A.M., Chaney, E.J., Kotynek, J.G., Oliphant, U.J., Bellafiore, F.J., Rowland, K.M., Johnson, P.A., and Boppart, S.A. (2009) Intraoperative evaluation of breast tumor margins with optical coherence tomography. *Cancer Res.*, **69** (22), 8790–8796.

95 Nguyen, F.T., Zysk, A.M., Chaney, E.J., Adie, S.G., Kotynek, J.G., Oliphant, U.J., Bellafiore, F.J., Rowland, K.M., Johnson, P.A., and Boppart, S.A. (2010) Optical coherence tomography: the intraoperative assessment of lymph nodes in breast cancer. *IEEE Eng. Med. Biol. Mag.*, **29** (2), 63–70.

96 Shakhov, A.V., Terentjeva, A.B., Kamensky, V.A., Snopova, L.B., Gelikonov, V.M., Feldchtein, F.I., and Sergeev, A.M. (2001) Optical coherence tomography monitoring for laser surgery of laryngeal carcinoma. *J. Surg. Oncol.*, **77** (4), 253–258.

97 Heermann, R., Hauger, C., Issing, P.R., and Lenarz, T. (2002) Erste Anwendungen der optischen Kohärenztomographie (OCT) in der Mittelohrchirurgie. *Laryngorhinootologie*, **81** (6), 400–405.

98 Wong, B.J., Jackson, R.P., Guo, S., Ridgway, J.M., Mahmood, U., Su, J., Shibuya, T.Y., Crumley, R.L., Gu, M., Armstrong, W.B., and Chen, Z. (2005) *In vivo* optical coherence tomography of the human larynx: normative and benign pathology in 82 patients. *Laryngoscope*, **115** (11), 1904–1911.

99 Just, T., Lankenau, E., Hüttmann, G., and Pau, H.W. (2009) Optical coherence tomography of the oval window niche. *J. Laryngol. Otol.*, **123** (6), 603–608.

100 Rubinstein, M., Fine, E.L., Sepehr, A., Armstrong, W.B., Crumley, R.L., Kim, J.H., Chen, Z., and Wong, B.J. (2010) Optical coherence tomography of the larynx using the Niris system. *J. Otolaryngol. Head Neck Surg.*, **39** (2), 150–156.

101 Bickford, L.R., Drezek, R.A., and Yu, T.K. (2007) Intraoperative techniques and tumor margin status-room for improvement for cervical cancer patients of childbearing age. *Gynecol. Oncol.*, **107** (1 Suppl 1), S180–S186.

102 Gamelin, J., Yang, Y., Biswal, N., Chen, Y., Yan, S., Zhang, X., Karemeddini, M., Brewer, M., and Zhu, Q. (2009) A prototype hybrid intraoperative probe for ovarian cancer detection. *Opt. Express*, **17** (9), 7245–7258.

103 Wang, Z.G., Durand, D.B., Schoenberg, M., and Pan, Y.T. (2005) Fluorescence guided optical coherence tomography for the diagnosis of early bladder cancer in a rat model. *J. Urol.*, **174** (6), 2376–2381.

104 Buranachai, C., Thavarungkul, P., Kanatharanaa, P., and Meglinski, I.V. (2009) Application of wavelet analysis in optical coherence tomography for obscured pattern recognition. *Laser Phys. Lett.*, **6** (12), 892–895.

26
Microvascular Blood Flow: Microcirculation Imaging

Martin J. Leahy

26.1
Introduction

Direct (optical) observation of skin and other tissues is of course the oldest method of biomedical imaging. We know that the ancient Greeks already understood that the pallor of the skin was a significant discriminator between health and disease. However, the decomposition of white light, the Doppler effect [1], and the identification of hemoglobin as the substance which changes its color and that of the skin when carrying oxygen provided a scientific basis for reliable measurements of the microcirculation developed over the past 150 years. Over the past 30 years in particular, tremendous progress has been made in single-point biophotonic measurements of microvascular state/activity and more recently imaging of the same.

Blood flow in the skin provides an efficient mechanism for thermoregulation, oxygen transport, mechanical integrity, blood pressure management, and the transport of repair materials. Little is known about the relative importance of these functions in the body's most extensive and accessible organ, which even in resting conditions it is estimated [2] to receive almost 9% of the total cardiac output.

The present understanding of microcirculation (e.g., [3]) assumes that there is little capacity for regulation of blood flow within individual capillaries, and that potential oversupply of oxygen at rest is prevented by alternate shutdown of capillaries. The open capillaries at any instant may be as much as 500 μm apart, contrasting with an actual capillary density of perhaps one per 50 μm. The mechanism for precapillary sphincter closure is under local control at a microregional level, and is triggered by a hyperoxic threshold. Additional regulation is provided by capillary pressure under both local (myogenic) and central (nervous) control mechanisms. These factors must be considered carefully when intending to measure capillary blood flow. If the chosen field of measurement is sufficiently small, the alternating flow/no-flow in individual capillaries may be observed. On the other hand, if the field is so large that a number of capillaries are always open, then the flow pattern will appear smoother, and an average perfusion for this area of tissue is recorded.

Handbook of Biophotonics. Vol.2: Photonics for Health Care, First Edition. Edited by Jürgen Popp, Valery V. Tuchin, Arthur Chiou, and Stefan Heinemann.

Visible and near-infrared light, particularly in the wavelength region 600–1200 nm, offer a window into human and animal tissues due to reduced light scattering and absorption. Nevertheless, the remaining scattering obscures images of the microcirculation everywhere but the eye and nailfold plexus. Although high-frequency ultrasound has been applied to imaging the microcirculation, it has significant limitations in imaging microvessels close to the surface. In this chapter we examine the main biophotonic methods applied to visualization and assessment of the microcirculation and document the progress made over the past 5 years in particular. Applications, particularly in human skin, are of special topical importance due to an improved knowledge of its role and its value as a surrogate for other organs in drug testing at a time when drug development is slowing under the weight of regulation.

Many techniques have been proposed for imaging the microcirculation, from X-rays to thermography, and still more new techniques are emerging, for example, optical coherence tomography (OCT), photoacoustic tomography (PAT), tissue viability (TiVi), and speckle imaging. Magnetic resonance imaging (MRI) and positron emission tomography (PET) are two excellent techniques, but their size and cost render them inaccessible to the majority of patients. Recently developed biophotonic technologies can satisfy the clinical need for simple to use, inexpensive technologies for bedside monitoring and to get to (research) patient groups who cannot attend the small number of locations which house elite equipment. With the exception of the nailfold plexus, light microscopy and direct visual inspection of the skin microcirculation are hampered by scattering, regular reflection from the surface, and absorption by superficial chromophores. Bloodless melanin-free skin provides little absorption but significant scattering across all colors of visible light. Since returning photons are scattered many times within the skin, they are diffuse and therefore the skin appears white.

The vital role of blood supply, and the oxygen it carries, in the health of the individual has ensured that many different techniques for assessing it have been investigated. The principle upon which the methods are based vary widely, as does the suitability, cost of the materials, and technology necessary. A small number of the methods are continuous and even fewer are truly noninvasive. Non-invasive *in vivo* techniques have obvious advantages for the user in providing information without disturbing the normal environment. In the same way, it poses considerable difficulties for developers through the need to make accurate measurements in complex environments subject to enormous (biological) variability.

The imaging technologies discussed here can be separated by physical resolution and sampling depth (Figure 26.1) with confocal microscopy and ultrasound included for completeness. Pixel resolution is improved by two orders of magnitude in commercially available units by going from laser Doppler perfusion imaging (LDPI) to laser speckle perfusion imaging (LSPI) and again from LSPI to TiVi imaging.

Figure 26.1 shows the resolution and sampling depth of the various techniques. The depth of interdisciplinary knowledge required to specify the appropriate technique often means that the wrong technique is used, or that the correct one is used

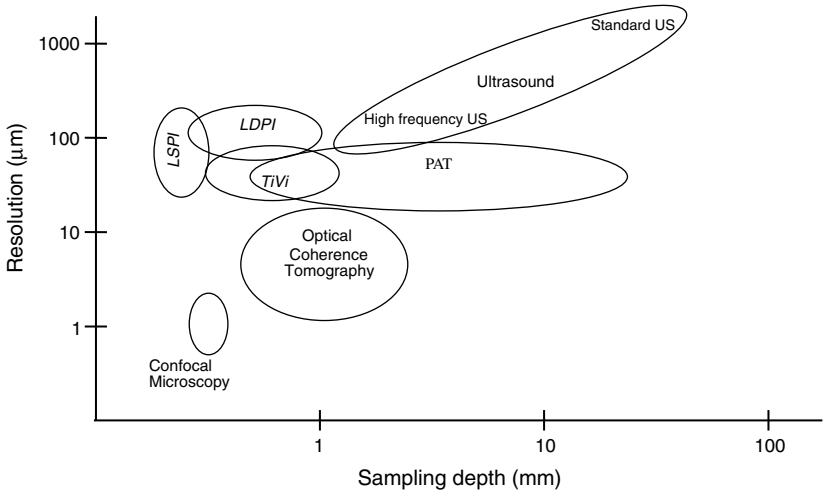

Figure 26.1 Microcirculation imaging domains, including laser speckle perfusion imaging (LSPI), laser Doppler perfusion imaging, tissue viability imaging (TiVi) and photoacoustic tomography (PAT).

inappropriately. This often leads to unfair criticism of techniques used in situations for which they were never designed. The techniques used in the clinical setting tend to have the common advantages of being mobile, inexpensive, or otherwise available as well as the required technical specification. The rush (fashion) for ever more sophisticated technologies, which suggests that expense is somehow an advantage, is not borne out by clinical use. As mentioned above, there is a clinical need for simple to use, inexpensive technologies for bedside monitoring and to get to (research) patient groups who cannot attend the small number of locations which house this elite equipment.

To understand why optical imaging of the skin and microcirculation (Figure 26.2) is not universally applied, it is instructive to consider how light interacts with tissue and which situations allow for direct visualization of the skin. Light microscopy and direct visual inspection are hampered by scattering, regular reflection from the surface, and absorption by superficial chromophores. Bloodless melanin-free skin provides little absorption but significant scattering across all colors of visible light. Since returning photons are scattered many times within the skin, they are diffuse therefore the skin appears white. Regular, mirror-like reflection accounts only for a small percentage of the incident photons. Ultrasound has many advantages due to its low scattering in this tissue matrix and can provide excellent images for larger, deeper vessels. However, it requires higher frequencies for smaller vessels, causing difficulties close to the surface. It is possible to view capillary vessels directly in the nailfold plexus and to view the retinal vessels directly due to the lack of significant absorption/scattering outside these vessels. However, absorption is the main contrast mechanism and backscattering is required to return photons to the detector/eye.

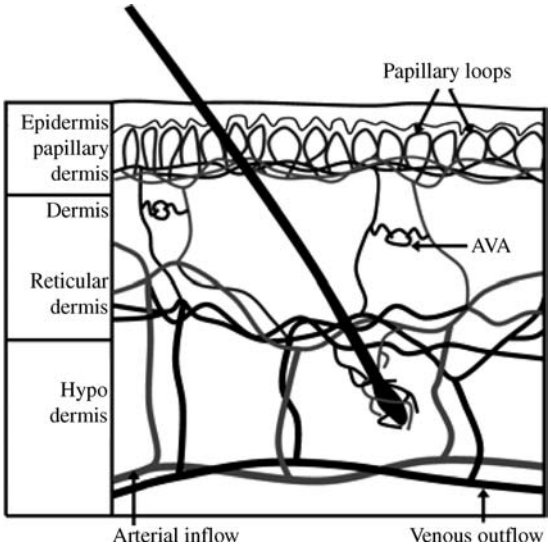

Figure 26.2 Microcirculation in the skin.

26.2
Nailfold Capillaroscopy

One of the most useful methods of assessing blood flow in a small number of blood vessels in the skin is by direct observation using capillary microscopy [4]. Capillaries are the smallest of the blood vessels and their purpose is to link the arterial and venous systems together, allowing the exchange of carbon and oxygen between the tissue and blood cells. Only in certain places in the body do the capillaries come close enough to the surface of the skin to be naturally visible, that is, without the use of specialized optical equipment or optical clearing agents. This is one of the reasons why the study of the skin overlapping the base of the fingernail and toenail is so important. In the nailfold, the capillaries come within 200 μm of the surface of the skin, meaning the methods of examining them are simple. Another reason is that the fingernail is easily fixed in position, free from any movement, due to arterial pulsations or respirations and the capillaries run parallel to the skin surface. Using a microscope with a magnification of between $\times 200$ and $\times 600$, it is possible to see clearly the structure of the blood vessels and, because each vessel is sufficiently transparent, the red blood cell (RBC) motion, in a single capillary, can be measured. If a video camera is attached to the microscope [5, 6], the motion can be examined in a frame-by-frame procedure yielding accurate velocity information for RBC flow in the capillary. The flow may be altered by the fixing procedure and/or the heating effect of the light source. Examining the capillary condition and density can aid the diagnosis of certain diseases. Capillary density and diameter are dependent on age, with younger children having a lower density and capillary thickness than adults [7]. The presence of abnormal vessels, in addition to these factors, has been attributed to

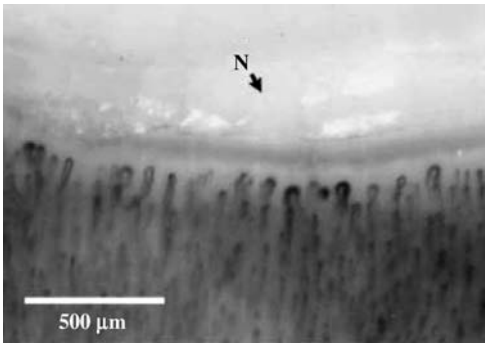

Figure 26.3 Nailfold capillary pattern of a healthy adult [9]. The fingernail is marked as N. A typical capillary density for a healthy adult is approximately 30–40 mm^{-2} [10]. Reproduced with permission from Wiley-Blackwell Publishing Ltd.

various diseases. Some conditions can be detected very early as capillary deformations can be observed before other symptoms occur [8].

Figure 26.3 is an image of a nailfold capillary arrangement of a healthy adult [9]. The capillaries are hairpin-like loops, arranged into regular rows. Each loop consists of two parallel limbs; a thinner arterial limb and a thicker venous limb. The walls of each blood vessel itself are transparent and the RBCs are seen passing through the capillaries [11].

26.2.1 Measurements

A disease-specific "pattern" can be identified by analyzing the geometry and density of the capillaries and the presence of abnormal or very large blood vessels [10]. Other relevant factors include avascular areas (absence of capillaries) [9] and the red blood cell velocity (RBV) through the capillaries [12]. A typical value of RBV would be $\sim 1\ mm\ s^{-1}$ [12]. Examples of avascular areas and giant and dilated capillaries can be seen in Figure 26.4.

The geometry of each capillary is defined by taking measurements at specific points. An example is shown in Figure 26.5.

The most difficult calculation in nailfold capillaroscopy is that of the RBV. There are many different methods of determining this. One such method is laser Doppler flowmetry (LDF). There are two main advantages of nailfold capillaroscopy over this method. The first is that LDF is not limited to a specific area, meaning the measurements are not taken on a specific RBC. As a result, the measurements are made less accurate by cells with various velocities [13]. The second drawback is that the signal produced is in proportion to microvascular perfusion, which is the product of both the velocity and concentration of the RBCs. It not currently possible to measure the absolute units of blood flow [14]. In nailfold capillaroscopy, because individual RBCs can be seen, direct measurement of the RBV is allowed. Several methods of assessing RBC perfusion exist.

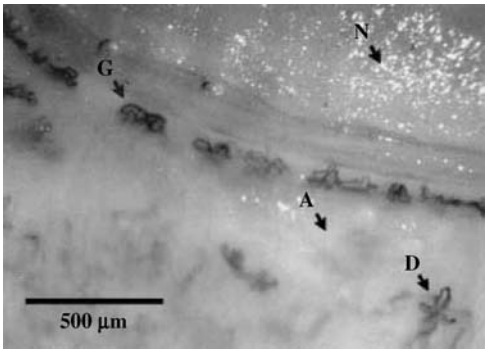

Figure 26.4 Nailfold capillaries in a patient with dermatomyositis. Examples of avascular areas (A), giant capillaries (G), and dilated loops (D) are shown [9]. Reproduced with permission from Wiley-Blackwell Publishing Ltd.

Measurements can be performed in a frame-by-frame analysis of specific patterns of RBC flow (RBCs or plasma gaps) [15]. By tracking the pattern over two consecutive frames, the velocity can be approximated. A drawback of this method is that these patterns are difficult to detect in larger vessels.

Other methods include cross-correlation methods, which can be further subdivided into two methods. The first works by measuring the average intensity at two independent regions of the capillary. Using a temporal cross-correlation and the distance between the regions, the RBV can be calculated [16]. The second method works by creating a series of spatial intensity distributions on a particular section. Using a temporal spatial correlation and the time separation between consecutive frames, the velocity can be calculated [17]. Sourice *et al.* made use of the spatiotemporal autocorrelation function to develop software to perform calculations of the RBV [18].

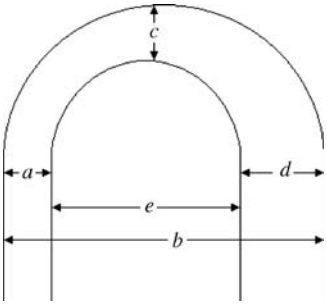

Figure 26.5 Measurements of dimensions of a capillary [10]. *a*, Arterial capillary diameter; *b*, venous capillary diameter; *c*, loop diameter; *d*, width of the capillary; *e*, distance between the limbs.

26.2.2
Experimental Considerations

A typical experimental setup would consist of a microscope, monitor, and video recording system [8, 11, 12, 18]. Fiber-optic illumination is often used [7, 10]. The finger can be immobilized easily by use of a clamp [12]. To increase the transparency of the skin, a clearing agent such as immersion oil is usually applied to the nailfold [7, 8, 11]. A fluorescent solution such as fluorescein can be used to distinguish the capillaries from the surrounding skin [18]. The software used for analyzing the images and the preparation of the subjects is dependent on what is being measured.

Ohtsuka *et al.* [8] showed evidence that for patients with primary Raynaud's phenomenon, the loop diameter, capillary width and capillary length (inner length + outer length/2) were greater in the patients who went on to develop undifferentiated connective tissue disease (UCTD) than those who did not. Bukhari *et al.* [10] studied the dimensions and density of capillaries and showed that there was a significant increase in all dimensions except the distance between the limbs in the patients with Raynaud's phenomenon and systemic sclerosis (SSc) compared to a control group. Also, capillary density is reduced in patients with SSc. Bhushan *et al.* [19] found that there was a decrease in capillary density in the nailfold of patients with psoriasis compared with a control group. Wong *et al.* [20] showed that a characteristic pattern of capillary abnormalities occurred in patients with scleroderma. Aguiar *et al.* [12] studied the RBV, functional capillary density, and capillary morphology differences in patients with primary Sjögren syndrome and a healthy control group. It was found that the affected patients had a higher functional capillary density and lower RBV than the control group.

26.2.3
Limitations and Improved Analysis

The measurements required for analyzing the capillary dimensions and patterns take much longer than the examination itself. Computerized systems have been developed [21–23] for analyzing images of capillary networks and improving their quality by excluding disturbances caused by hair, liquid, reflections, and so on. Combining videocapillaroscopy and various mathematical methods, the statistical properties of the capillaries can be analyzed automatically by extracting capillary count, position, density, size, and so on from the images. Sainthillier *et al.* [21] and Zhong *et al.* [22] used triangulation methods to allow statistical analysis of distances between nearest neighboring capillaries, which is useful for looking at areas that are susceptible to the development of necrosis. Hamar *et al.* [23] are currently developing a Markov chain-based detection algorithm for updating capillaroscopy images to reduce them to a grayscale image containing only the capillaries. These technologies are essential to the development of nailfold microscopy into a more sophisticated method of disease diagnosis.

26.2.4
Conclusion

Although nailfold capillaroscopy is important in the diagnosis of certain connective-tissue diseases, some of the methods described above cannot be applied to other areas of the microcirculation for the simple reason that the capillaries are not clearly visible. This necessitates other methods of measuring the condition and density of the capillaries and RBV.

26.3
Laser Doppler Perfusion Monitoring

Laser Doppler perfusion monitoring (LDPM) refers to the general class of techniques using the Doppler effect to measure changes in blood perfusion in the microcirculation noninvasively. Perfusion has previously been defined as the product of local velocity and concentration of blood cells [24]. The principles behind the technique were first developed by Riva *et al.* [25], who developed a technique to measure RBV in a glass flow tube model; however, the development of LDPM for assessing tissue microcirculation was first demonstrated in 1975 by Stern [26]. Measurement of the velocity of particles in solution by interpreting the Doppler frequency-shifted light backscattered there from had been described by Cummins and Swinney [27], only 4 years after the first working laser was demonstrated by Maiman (1960). However, all commercial devices now rely on the signal processor developed by Bonner and Nossal [28], which, in contrast to laser speckle perfusion monitoring, provides laser Doppler with a sound theoretical base.

The technique operates by using a coherent laser light source to irradiate the tissue surface. A fraction of this light propagates through the tissue in a random fashion and interacts with the different components within the tissue. The tissue consists of both static and moving components. The light scattered from the moving components will undergo a frequency shift which can be explained by the Doppler effect whereas the light scattered from the static components will not undergo any shift. It is almost impossible to resolve the frequency shifts directly. To overcome this, the back-scattered light from the tissue is allowed to fall on the surface of a photodetector where a beat frequency is produced. The typical frequency of this beat detected using a wavelength of 780 nm ranges from 0 to 20 kHz. However, for a 633 nm source the range is smaller, typically 0–12 kHz [24]. The apparent contradiction with the theory that the frequency shift is inversely proportional to wavelength is caused by the deeper vessels probed by the longer wavelengths, which contain faster flowing blood. From this beat frequency, it is possible to determine the speed and concentration of the blood cells. The LDPM technique correlates well with other measurements of skin blood flow, such as venous occlusion plethysmography [33] and xenon washout [34].

LDPM offers substantial advantages over other methods, being very sensitive and able to follow easily changes in local blood perfusion over less than 0.05 s, making it useful for continuous perfusion monitoring. As the probe is not required to touch

the surface of the tissue, the technique can be noninvasive, avoiding any impact on the microcirculation. Where invasive measurements are required, the probes can be as small as a single optical fiber, so that with multichannel devices measurements can be made from several depths or microregions within a tumor, for example. The technique registers tissue perfusion at a single point over time, but microcirculation is known to be heterogeneous, especially in human skin, so a small area of perfusion is not necessarily representative of perfusion in the region of interest [35–37]. Furthermore, the measurements are intrinsically of a relative nature, the measurements are proportional to blood flow. However, the factor of proportionality will be different for different tissues and tissue sites. On the other hand, "correct" values of blood perfusion (ml mg^{-1} s^{-1}) are not generally known, so it is difficult to imagine how absolute values would be used.

LDPM has been revised and improved to remove many of the preliminary issues and has been widely used both in research and more recently as a clinical tool. Guidelines have been published on how to perform measurements using the technique [36]. There are many different types of probes available, each suited for different applications such as fiber probe systems [39] and integrated probe systems [40].

26.3.1
Light Sources

The incident laser light beam has a depth of penetration of ~1 mm depending on the wavelength and configuration of the equipment used. This estimate originates from mathematical modeling of photon diffusion through "imaginary tissues" using Monte Carlo techniques. Therefore, all elements of the dermis may be included, from the superficial nutritional to deeper thermoregulatory vessels.

For a given wavelength of light, the absorption spectrum of components of the tissue determines the interaction that occurs [29]. The penetration depth of light is predetermined by the path the light takes through the skin and is limited by the absorption and scattering effects of the tissue. Another limiting factor is the level of pigmentation of the skin [30].

The absorption of hemoglobin and water is lower towards the red end of the visible spectrum. Because of commercial availability, HeNe lasers (632.8 nm) dominated in earlier LDPM; however, longer wavelengths produced by laser diodes (780, 810 nm) are now preferred owing to increased penetration depth and lower absorption by melanin in the near-infrared region, which shows less dependence on skin color [30]. Also, because the absorption of oxidized and deoxygenated hemoglobin is almost identical at this wavelength, any dependence on oxygen saturation is eliminated. However, systems exist that use dual wavelengths to obtain additional information about the tissue structure [31, 32].

26.3.2
Laser Doppler Perfusion Imaging (LDPI)

The need to study perfusion over larger tissue areas led to the construction LDPI [41, 42]. LDPI is a technique that scans a series of perfusion measurements over a section

of tissue. This is converted into a color-coded image representing the distribution of perfusion over an area of interest.

This technique offers some advantages over the single-probe technique; the blood flow is measured over an area rather than at a single site, which removes some of the difficulties that arise in the LDPM technique such as movement artifacts and site-to-site perfusion variations due to the heterogeneous nature of tissue. The technique requires no contact with the tissue being examined, making it of particular advantage when assessing open, and often infected, wounds.

The technique has limitations; one issue is that several minutes are required to complete a full scan. This can introduce problems in trying to examine a rapid change in blood flow. However, more recent techniques such as line-scanning and full-field laser Doppler offer to improve this considerably. For example, the MK2 moorLDLS (Moor Instruments, Axminster, UK) is an FPGA (Field Programmable Gate Array)-based line-scanning LDPI instrument which acquires 64 pixels simultaneously and the best time for a 256×64 pixel image is 13 s. LDPI provides arbitrary perfusion measurements [35], meaning that the tool is valid for comparative data only and that all measurements must be performed under the same conditions. It is also necessary to consider temporal variations in blood flow over short periods [38] (seconds to minutes) and over extended periods due to seasonal changes [43] while attempting to monitor long-term changes in perfusion to a region.

Another issue with the technique is that due the scanner not being held in contact with the tissue, the distance between the imager and the tissue affects the measured level of perfusion. If this distance changes between subsequent measurements, it will affect the results. There are conflicting opinions on whether the measured perfusion increases [44] or decreases [45] as the distance from the tissue increases. It may be that the algorithms used for signal processing by different machines determine this [46]. In order to make comparable measurements between different systems, a standard calibration and system design is required [24].

Between 1997 and 2002, a standardization project was undertaken by several international research institutes, in which a perfusion simulator for calibration and standardization of LDPM and use of nomenclature was agreed. In 2002, a report on a project named HIRELADO (High Resolution Laser Doppler) from the standardization group of the European society of contact dermatitis published guidelines on the measuring of skin blood flow [47]. This project addressed mainly the technical aspects of how experiments should be performed and what precautions should be taken to ensure valid results. Several different techniques have been developed for producing LDPI data, each with different advantages and disadvantages.

26.3.3 Point Raster Technique

A raster scan laser Doppler image operates by recording a series of point perfusion measurements. This type was the first laser Doppler image system to be developed. The basic schematic is show in Figure 26.6. The imaging is achieved by using a moveable mirror to scan the laser beam over the area to be measured in a raster

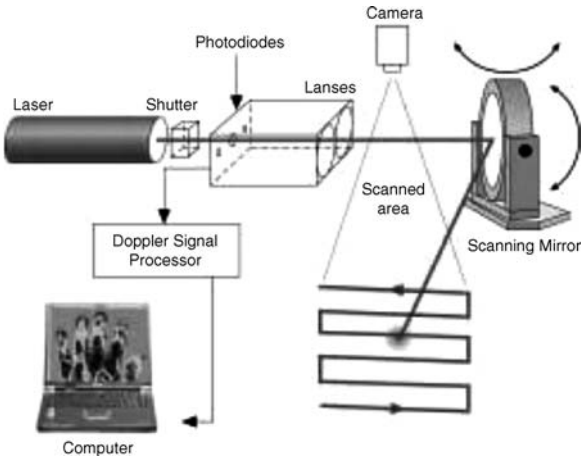

Figure 26.6 Schematic of raster scan laser Doppler imaging system. From moorLDI brochure, Moor Instruments Ltd.

fashion. At each site, an individual perfusion measurement is taken. When the scan is complete, the system generates a 2D map image from the single-point perfusion measurements.

The problem with the technique is the time taken to make measurements. Each individual measurement can be achieved in 4–50 ms; however, shortening the acquisition time results in increased noise in the signal [47]. For time considerations it is important to minimize the number of measured points. This is best achieved if the step length between measurements equals the diameter of the laser beam. For smaller step lengths, the same physiological information is partly collected by neighboring measurements, which increase the overall time without retrieving more information. The moorLDI system reports a capability of capturing a 64×64 pixel perfusion image in 20 s and has a spatial resolution of 0.2 mm at a distance of 20 cm. The system is capable of scanning a region up to 50×50 cm and as small as a single point measurement.

26.3.4
Line Scanning Technique

Laser Doppler line scanning imaging is a new development in LDI technology by Moor Instruments. This technique does not utilize the standard point raster approach but works by scanning a divergent laser line over the skin or other tissue surfaces while photodetection is performed in parallel by a photodiode array. This technique allows a series of perfusion measurements to be performed in parallel. This greatly reduces acquisition time and is bringing laser Doppler imaging one step closer to real-time imaging. A schematic of the system is shown in Figure 26.7. The moorLDLS system utilizes 64 diodes to obtain the perfusion measurements in parallel. The system is capable of measuring each line in times of 100–200 ms.

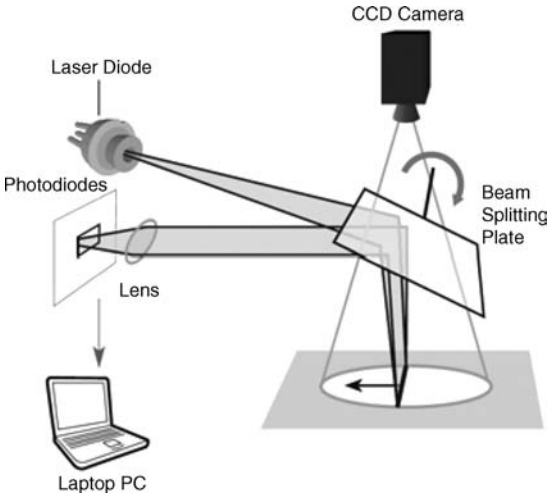

Figure 26.7 Schematic of line scanning laser Doppler system. From moorLDLS brochure, Moor Instruments Ltd.

Regions up to 20 × 15 cm can be imaged and a 64 × 64 pixel perfusion measurement can be produced in 6 s.

26.3.5
Full-Field Scanning Technique

High-speed laser Doppler perfusion imaging using an integrating CMOS (complementary metal–oxide–semiconductor) sensor for full field scanning has been developed by Serov *et al.* [48]. The basic schematic of the system is shown in Figure 26.8. A laser source is diverged to illuminate the area of the sample under investigation and the tissue surface is imaged through the objective lens on to a CMOS camera sensor. This new CMOS image sensor has several specific advantages: first, the imaging time is 3–4 times faster than the current commercial raster scan LDI systems. Second, the refresh rate of the perfusion images is approximately 90 s for a 256 × 256 pixel perfusion image. This time includes acquisition, signal processing, and data transfer to the display. For comparison, the specified scan speed of a commercial laser Doppler imaging system, the moorLDI, is ∼5 min for a 256 × 256 pixel resolution image. However, the scanning imager can only measure areas of up to ∼50 × 50 cm in size whereas the CMOS system at present does not allow imaging of areas larger than ∼50 × 50 mm [49, 50].

26.3.6
Applications

The laser Doppler technique has many medical applications; however, it still has not been fully integrated into clinical settings and is mainly used in research. LDPI

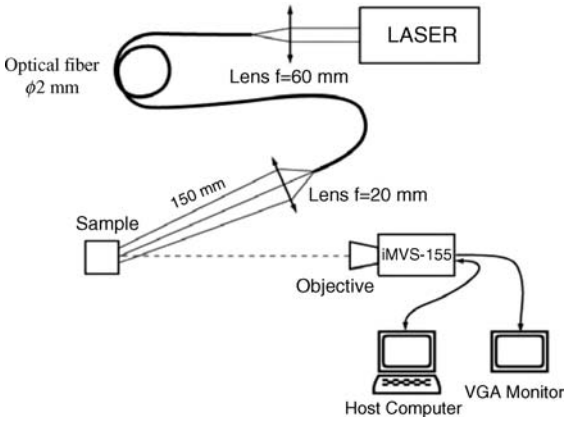

Figure 26.8 Schematic of full-field laser Doppler system [49].

systems have been reported in a wide range of applications from neuroscience [51] to the assessment of burns [52–54]. The use of LDPI is reported to outperform existing methods of assessment of burn wound depth and provides an objective, real-time method of evaluation. Accuracy of assessment of burn depth is reported to be up to 97% using LDPI, compared with 60–80% for established clinical methods [52]. High perfusion corresponds to superficial dermal burns, which heal with dressings and conservative management; burns with low perfusion require surgical management, that is, skin grafts. Correct assessment is of particular importance here as one in 50 grafts fail; if this failure is caught within 24 h, 50% of these cases can be saved [55].

The use of LDPI has also been investigated in different aspects of cancer research and treatment; it has been found that there are higher levels of perfusion in skin tumors which can be detected by the LDPI system [56]. The technique has also been applied to examine how a tumor is responding to different treatments such as photodynamic therapy [57]. Wang *et al.* applied the technique to the assessment of postoperative malignant skin tumors [58]. It has also been applied in many other fields, such as examining allergic reactions and inflammatory responses to different irritants [59–61]. Bjarnason and co-workers applied the technique in the assessment of patch tests [62, 63]. Ferrell *et al.* used the technique to study arthritis and inflammation of joints [64]. It has also been applied in investigating the healing response of ulcers [65] and for examining the blood flow pattern in patients at risk from pressure sores [66].

26.4
Laser Speckle Perfusion Imaging

As the angles in LDP are more or less random and a wide range of velocities are present in the microcirculation, a continuous Doppler frequency spectrum is produced. It is interesting that a similar result can be achieved by considering

the scattering particle to be a moving reflector of light. The reflected light will interfere with the reference beam and the resultant intensity will vary with the difference in optical path between the two beams. The number of interference fringes to pass the detector in time is related to the speed of the moving cells. Each time the mirror (cell) moves through a distance equal to half the wavelength of the light, the detector "sees" an interference fringe pass. That is, a fluctuation in light intensity is recorded. Variations in speckle contrast will then be dependent on the velocity distribution of the scatterers. Therefore, this velocity can be determined using a measurement of the statistical behavior of the speckles over time. The integration time of the detector should be small in comparison with the correlation time of the intensity fluctuations to avoid "averaging out" of the signal [67]. This is similar to the reading given by a laser Doppler measurement, and in fact it has been demonstrated that Doppler and time-varying speckle imaging are two methods of arriving at the same result [68].

When recorded over a finite integration time, the moving scatterers result in a speckle pattern that appears "blurred" or decorrelated. The amount of decorrelation depends on the speed and volume of the RBCs in the tissue [69]. The time-varying component of the speckle can be quantified by comparing the intensity recorded at each pixel in successive scans. The average difference between the two measurements is dependent on flow – large in high-flow regions and small in low-flow areas. A two-dimensional map can be created by scanning the line across a region of interest. Experiments showed a decrease in the blood flow parameter during occlusion of the finger, and an increase was observed across a scar on the back of the hand [70].

26.4.1 Full-Field Measurements

The set-up for full-field laser speckle measurements is shown in Figure 26.9. The tissue is illuminated by an expanded laser beam and the resulting image speckle is recorded by a charge-coupled device (CCD) camera.

The source used is typically a low-power expanded helium–neon (632.8 nm) laser in the 3–30 mW range [71, 72] although the use of 660 [73], 514 [74], 780 [75, 76], and 808 nm [77] wavelengths have also been reported. Typically for studies of capillary perfusion, this is set between 5 and 20 ms [69, 71, 72, 75, 78]. Yuan *et al.* [79] found that the optimal integration time for rodent cerebral blood flow studies was 5 ms.

This technique, originally developed for retinal blood flow imaging [80], uses a short integration time, as mentioned previously, to photograph the illuminated area and produces a high-contrast speckle pattern. The contrast K, is calculated based on small areas of the pattern, typically a sliding 7×7 or 5×5 pixel window [67, 71, 72]. The higher the velocity of the RBCs, the higher is the frequency of the fluctuations. This means that for a given integration time, more averaging will occur and there will be a decrease in contrast. Conversely, an area where blood flow is low will appear as a high-contrast reading. These contrast measurements can therefore be used to build up a two-dimensional map of relative velocities.

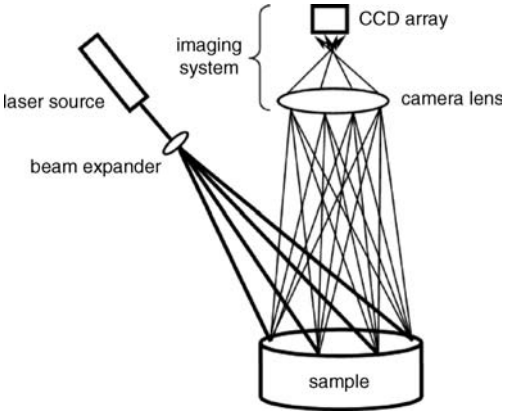

Figure 26.9 Full-field laser speckle contrast imaging. The tissue is illuminated by a laser that has been diverged by a lens. The speckle pattern is then recorded by the CCD camera and the speckle contrast, *K*, is computed.

26.4.2
Limitations and Improved Analysis

The effects of specular reflection can be eliminated with the addition of polarizing filters [69, 73, 81–83]. Multiple scattering can have the effect of blurring the image by influencing the apparent size of the object [83]. Also, the effects of scattering by static tissue must also be considered [73]. As the laser speckle signal is dependent on the fluctuating part of the pattern, static tissue has the effect of reducing the signal-to-noise ratio. Zakharov *et al.* developed a model taking this into account that includes a correction to the equation relating speckle contrast to correlation time [83]. Attempts to limit the effect of static scatterers have also been made in single-point measurements using fiber-optic probes by adjusting the source–detector separation [84]. This limiting effect may be one of the most significant reasons why the speckle technique is suited to more superficial measurements. Indeed, many of the applications reported, as described in Section 26.4.3, involve measurements on surgically exposed tissue.

The main difficulty with using imaging systems based the Laser Speckle Contrast Analysis (LASCA) Algorithm is that the relationship between speckle contrast and red blood cell velocity is nonlinear. Forrester *et al.* developed an improved version of Briers' LASCA system called laser speckle perfusion imaging (LSPI) [69]. A different approach to producing the contrast image is taken by first calculating a reference image by averaging the speckles spatially and temporally. The intensity fluctuations due to blood flow can then be examined by calculating the intensity difference between the corresponding pixels in the reference and newly acquired image. The result is then normalized by the reference in order to negate the effect of nonuniform illumination, or changes in laser output or tissue optical properties. The intensity difference is inversely proportional to the speed of the scatterers: in low-flow regions, a sharp speckle contrast is observed, and a large difference between

the reference and speckle intensities will be recorded. In high-flow regions, a large amount of decorrelation occurs and the difference approaches zero.

An *in vitro* blood flow model was devised to test the response of the LSPI system [81] consisting of a 0.95 mm bore glass tube fixed in a gelatin-set tissue phantom 1 mm below the surface. Red cell concentrations of 0.1–5% were imaged at flow rates in the range 0–800 $\mu l\,min^{-1}$ (corresponding to RBC velocities of 0–18.8 $mm\,s^{-1}$). These parameters cover the typical physiological range [85]. In comparison with a commercially available laser Doppler imager (moorLDI), it was found that at a constant flow rate, LSPI had a similar response to LDPI to changes in RBC concentration (correlation $r^2 = 0.93$). At a constant concentration (1%), LSPI also had a similar response to LDPI to changing red blood cell velocity, with its perfusion index increasing linearly over the range of flow rates ($r^2 = 0.99$).

Speckle imaging systems using the "averaging window" suffer from a loss of resolution (for example, a 7×7 pixel window will produce a speckle image 1/49th the resolution of the original). However, the temporal averaging technique used by the LSPI algorithm means that the full resolution of the CCD can be retained to produce high-detail images of the vascular structure. For higher speed acquisition, however, a spatial averaging mode may be employed [69].

The main advantage over LDPI is the speed at which the images may be acquired. Acquisition speeds at video rates [25 frames per second (fps)] can be attained, making it possible to measure the blood flow response to occlusion and hyperemia (typical LDPI scans are of the order of minutes). Also, the much higher resolution [limited only by the CCD, maximum LDI resolution is 256×256 (moorLDI)] permits more detailed imaging of tissue structures [69].

26.4.3 Microcirculation

The early use of laser speckle imaging of the microvasculature has been reported [67]. However, more recent work incorporating the improvements outlined above, and in particular the advent of video rate acquisition has led to some interesting applications.

Human retinal blood flow has been examined using the technique [77] in a similar method to Briers *et al.* and an *in vitro* calibration model was developed to relate speckle decorrelation to actual readings of velocity. *In vivo* experiments conducted in parallel with electrocardiogram measurements showed that the speckle contrast varied with the heart rate and red blood cell velocity reached a peak corresponding to that of the cardiac cycle. Yaoeda *et al.* [86] adapted the technique developed by Fujii *et al.* [70] to monitor blood flow to the optic nerve head, showing differences between the right and left eyes.

The LSPI system developed by Forrester *et al.* [69] was used to measure changes in flow in the knee joint capsule of a rabbit before and after femoral artery occlusion, recording a 56.3% decrease after the maneuver. The system was also incorporated into a hand-held endoscope for the simultaneous measurement of the same event. The response was validated as before with an *in vitro* model, showing the linear

response over a large flow range (0–800 μl min^{-1}). Equipped with a motion-detection algorithm to limit motion artifact, the endoscopic set-up recorded a similar decrease (58.7%) [73]. Clinical data from human subjects has also been acquired using this endoscopic LSPI system (eLSPI), recording a decrease in blood flow in the medial compartment of the knee after application of a tourniquet. A dose-dependent response to the vasoconstrictor epinephrine was also recorded [87].

Choi *et al.* demonstrated the use of laser speckle imaging in a rodent skin fold model [72] and were able to provide quantitative measurements of relative blood flow in areas of tissue that were otherwise obscured by attached muscle and fat. Selected areas of the tissue were irradiated with a 585 nm laser pulse to stop blood flow locally, and this was seen in the LSI images. Similar animal models were investigated by Cheng *et al.* [71] while testing the effect of varying doses of phentolamine, a vasodilator, on intestinal tissue. In both cases, image processing was conducted offline.

Extensive studies of cerebral blood flow in rodents have been undertaken using various laser speckle imaging techniques to monitor the vascular response to stimuli and chemically induced changes. Cerebral blood flow was monitored in rats to demonstrate its heterogenic response to mild hypotension (induced by withdrawal of blood from the femoral artery). Regional variations in perfusion were recorded [88]. Blood perfusion measurements have also been made on the surgically exposed cerebrum of rodents that show a drop in signal over time after a photochemically induced infarction [76], while Royl *et al.* [89] recorded an increase in flow in the somatosensory cortex during electrical stimulation of the forepaw.

Laser speckle measurements of cerebral blood flow through the intact rat skull (minus the skin) have been presented Li *et al.* [75]. A temporal averaging algorithm was employed that used data from 40 consecutive speckle patterns and computed the difference between the intensity at a pixel of interest and the average intensity calculated for that pixel over the 40 frames. The resulting so-called laser speckle temporal contrast analysis image (LSTCA) was found to be more immune to the effects of static scatterers (such as the skull) than spatial techniques such as LASCA.

The effect of photodynamic therapy (PDT) and pulsed dye laser (PDL) irradiation on the microvasculature in a rodent dorsal skin-fold model was examined using laser speckle contrast analysis (LASCA) [90]. Images taken 18 h after treatment show vascular flow reduction in the exposed area (Figure 26.10).

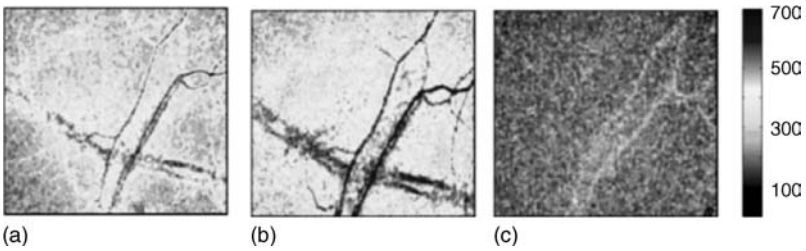

Figure 26.10 Laser speckle contrast maps of blood flow: (a) prior to PDT treatment, (b) immediately after and (c) 18 h after. Reproduced with permission from Wiley-Liss, Inc., a subsidiary of John Wiley & Sons, Inc. [90].

The versatility of the technique has been illustrated by conducting laser speckle analysis in parallel with PDT using a 514 nm argon ion PDT laser as the source for the speckle measurements [74]. The processing algorithm was the speckle reduction technique developed by Forrester *et al*. [69]. Other animal models studied include temperature-induced changes in blood flow in the rodent [78] and wound-healing in porcine subjects [82].

26.4.4 Agreement with Laser Doppler

While accurate absolute measurements of RBV cannot be calculated, all of the above LSI systems can successfully track relative changes in perfusion. Recent developments and *in vitro* experiments have shown that laser speckle images can respond in the same way as laser Doppler to changes in RBC concentration and velocity [81]. *In vivo* experiments have also shown a strong correlation between the techniques [89]. In fact, recent studies on burn scars show a correlation with an r^2 value of 0.86 between the techniques [91]. It should also be noted that the perfusion measurements correlated strongly with the clinical grading of the scar. As each imager used the same wavelength (632.8 nm), Stewart *et al*. stated that the penetration depth was, in theory, the same for each [91]. However, Moor Instruments report that the penetration depth of the "FLPI" system is less than that of the corresponding LDI system. This is due to two factors: first, unlike the laser Doppler signal, the laser speckle signal is not frequency weighted, meaning that photons arriving from the faster moving RBCs in deeper blood vessels cannot be isolated. Second, as the source in laser speckle systems is an expanded beam, the power density is much lower than in the corresponding Doppler system, hence the depth at which noise dominates is more superficial. The first commercial speckle imager, the moorFLPI, could acquire and process images at video rates (25 fps) at high resolution (576×768 pixels) [92].

Laser speckle, which is a confounding phenomenon in some applications such as laser Doppler [93], is proving to be a very useful tool in blood perfusion measurements. Full-field images can be recorded in a single shot containing information on RBC concentration and velocity. Whereas traditional laser Doppler images can take several minutes to acquire and are of limited resolution (256×256 pixels), LSI can show rapid changes in blood flow in real time.

The most popular processing algorithm reported is that based on speckle contrast maps (LASCA) [71, 72, 89] and it is this method that is used in the commercial device [92]. However, a newer algorithm has improved on this, responding linearly to increasing RBV, limiting the effect of static scatterers and specular reflection, and compensating for variations in tissue optical properties. This "reduced speckle" technique is promising as it follows laser Doppler measurements very closely but at a much higher resolution and speed [69, 73, 74, 81, 91]. The low-cost nature of the system, acquisition speed, resolution, and compatibility with existing laser Doppler measurements make LSPI a very attractive technology for studies of blood perfusion in the microvasculature.

26.5
Polarization Spectroscopy

The technique of polarization spectroscopy allows the gating of photons returning from different compartments of skin tissue under examination [94]. Figure 26.11 details the operation of basic polarization imaging, showing that by use of simple polarization filters, light from the superficial layers of the skin can be differentiated from light backscattered from the dermal tissue matrix. When monochromatic or white incoherent light is linearly polarized by a filter and is incident on the surface of the skin, a small fraction of the light (∼5%) is specularly reflected as surface glare (Fresnel reflection) from the skin surface due to refractive index mismatching between the two media. A further 2% of the original light is reflected from the superficial subsurface layers of the stratum corneum. These two fractions of light retain the original polarization state, determined by the orientation of the first filter. The remaining portion of light (∼93%) penetrates through the epidermis to be absorbed or backscattered by the epidermal or dermal matrix. Approximately 46% of this remaining light is absorbed by the tissue and not re-emitted, while 46% is diffusely backscattered in the dermal tissue. This backscattered portion is exponentially depolarized due to scattering centers in the tissue [95], and also by tissue birefringence due to collagen fibers [96].

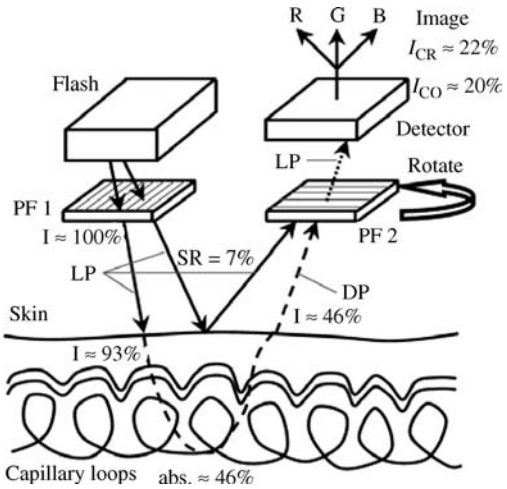

Figure 26.11 Fundamental operation of polarization spectroscopy. This is the foundation of TiVi. Remaining percentages of light intensity are represented by *I*, and 100% intensity is observed after the polarization filter. SR represents specular reflection, a combined effect of Fresnel reflection and light returning after few scattering events from the upper layers of the epidermis. LP and DP represent linear and depolarized light, respectively, and I_{CO} and I_{CR} represent the remaining intensity which contributes to CO or CR data, depending on the two possible states of polarization filter PF2; abs. represents the percentage of light absorbed in the tissue. PF2 can be arranged with pass direction parallel (CO) or perpendicular (CR) to PF1.

The depth of penetration of polarized light is heavily dependent on the optical properties of the medium at each wavelength present [97]. Upon re-emerging from the tissue structure as diffusely reflected light, the remaining fraction of light is almost completely depolarized, and consists of two 22% fractions of parallel and perpendicular polarizations, with respect to the direction of the original filter. This light contains information about the main chromophores in the epidermis (melanin) and dermis (hemoglobin), whereas the surface reflections contain information about the surface topography, such as texture and wrinkles. On detection by a CCD or similar light-collecting device, one can differentiate between detecting the surface reflections or a fraction of the diffusely backscattered light by placing another polarization filter over the detector parallel or perpendicular with respect to the direction of the filter over the light emitter. With both filters oriented parallel or perpendicular with respect to each other, co-polarized (CO) or cross-polarized (CR) data, respectively, are obtained. This allows the gating of photons, and the technique is based on the assumption that weakly scattered light (the surface reflections) retains its polarization state, whereas strongly scattered light will successively depolarize with each scattering event. It has been suggested that more than 10 scattering events are required to depolarize light sufficiently [98, 99].

26.5.1 Current Technology

Polarization gating has been employed in many different technologies, in order to investigate surface details of the skin structure by accepting light scattered from the superficial layers of the tissue. Examples of technologies that have applied polarization filtering include polarization-sensitive optical coherence tomography (PS-OCT), LDPI, Raman spectroscopy, and simple microscopy. The use of polarization filters has been shown to reduce tissue motion artifact in LDPI, while also reducing the overestimation in LDPI readings due to the amplification of specular reflection [100]. Detail of tissue birefringent axes from various layers via phase-sensitive light recording can be extracted by PS-OCT, and the technique can be used to generate 3D images of the polarization state of backscattered light from skin tissue *in vivo* [101, 102]. Raman spectroscopy of layered media will detect chemical signatures from multiple layers, and polarization gating has been successfully employed to generate Raman spectra of only the superficial skin layers [103]. The combination of polarization gating with multiphoton excitation microscopy allows the characterization of fibrous structures in the skin layers, thus verifying the mechanics of transdermal drug delivery and the significance of dermal structural dermal changes [104]. Gating has also been used with laser speckle imaging in the reduction of specular reflection for investigation of the blood vessels in the microcirculation [69].

Polarization cameras and probes employing the gating technique have been developed in order to investigate both the physiology and microcirculation of skin tissue [105, 106]. Orthogonal polarization spectroscopy (OPS) technology is a single-wavelength (548 nm – an isosbestic point of hemoglobin close to peak absorption) video microscopy technique operating at 30 fps, which increases contrast and detail

by accepting only depolarized backscattered light from the tissue into the probe. Single blood vessels are imaged *in vivo* at a typical depth of 0.2 mm and magnification of $\times 10$ between target and image, and information about vessel diameter and RBV are easily obtained. OPS in human studies is limited to only easily accessible surfaces, but can produce similar values for RBV and vessel diameter to those given by conventional capillary microscopy at the human nailfold plexus [107]. It has also been applied to study superficial and deep burns to the skin [108, 109], adult brain microcirculation, and preterm infant microcirculation [110].

Polarization gating images by sequential acquisition of superficial photons (CO) and photons undergoing multiple scattering (i.e., photons interacting with the reticular dermis – CR) have shown cancer, lesion, and burn scar boundaries. A fluorescence method of imaging skin tumors stained with fluorescent dyes rejects excitation light by way of sequential CO and CR image acquisition with a tunable monochromatic source, and details tumor boundaries similar to Mohs surgery, also known as chemosurgery. boundaries [111, 112]. A similar cost-effective method combining polarization imaging with spectroscopy has also been developed to visualize the water content in the superficial layers of the skin, and has shown good comparison with a well-recognized capacitance measurement technique [113]. Another method of polarized light imaging to examine surface skin pathologies in grayscale at 435×548 pixels is capable of distinguishing between freckles, nevii, and carcinomas [114, 115]. An extension of this preliminary technology produced a hand-held cost-effective polarization imaging camera, which operates at 7 fps at 400×400 pixels (15 fps at 250×250 pixels) [116]. Parallel and perpendicular images are acquired simultaneously from two CCDs, and an image processing algorithm is applied which examines only the histologic aspects of the skin surface, with no investigation of the underlying microcirculation. The prototype technology has been successfully examined on melanoma margins.

26.5.2
Image and Data Processing

Image (or data) processing algorithms have generally employed an equation that requires acquisition of both CO and CR images in order to investigate the superficial layers of the tissue [104, 105, 112–114]. The equation represents a normalized difference between the CO and CR images:

$$P = \frac{CO - CR}{CO + CR} \tag{26.1}$$

where P represents a composite image observing surface skin histology. The denominator in Eq. (26.1) represents the normalization of the image, which cancels any nonuniform illumination. P images have been shown to be comparable to histopathology examination, the invasive gold standard of skin examination.

Recent technology [116] analyzes only the RBC concentration in skin microcirculation by way of single-image acquisition or video acquisition by low-cost cameras utilizing orthogonally placed polarization filters. For single-image acquisition, the

flash of a consumer-end RGB digital camera is used as a broadband light source, and the camera CCD acquires an instantaneous image in three 8-bit primary color planes. Color filtering is performed on-camera by three 100 nm bandwidth color filters, blue (~400–500 nm), green (~500–600 nm), and red (~600–700 nm). This represents the first low-cost technique designed to image in real time tissue hematocrit.

Using polarization imaging theory and Kubelka–Munk theory, a spectroscopic algorithm was developed which is not dependent on incident light intensity, taking advantage of the physiological fact that green light is absorbed more by RBCs than red light. For each arriving image, the equation applied is

$$M_{\text{out}} = \frac{M_{\text{red}} - M_{\text{green}}}{M_{\text{red}}} \exp\left[-p\left(\frac{M_{\text{red}} - M_{\text{green}}}{M_{\text{red}}}\right)\right] \tag{26.2}$$

where M_{red} and M_{green} represent the red and green color planes of the image, respectively, and p is an empirical factor to produce the best linear fit between output variable (called TiVi index) and RBC concentration. M_{out} represents a matrix of maximum 3648×2736 TiVi index values for single-image acquisition.

Figure 26.12 shows an example of a TiVi image color coded in a method similar to laser Doppler images where high and low RBC concentrations are represented by blue and red, respectively. The technique has high spatial and temporal aspects, with lateral resolution estimated as 50 μm [116], and has been compared with LDPM and LSPI by O'Doherty *et al.* [117]. The sampling depth in Caucasian skin tissue is estimated approximately from Monte Carlo simulations of light transport in tissue [116]. Topical application of vasoconstricting and vasodilating agents demonstrate the capacity to document increases (erythema) and decreases (blanching) in RBC concentration [118].

Our group is currently developing a real-time system, whereby RBC concentration can be displayed online. Current technology can capture CR frames at 25 fps at a frame size of 400×400 pixels. Video studies will lead to increased temporal

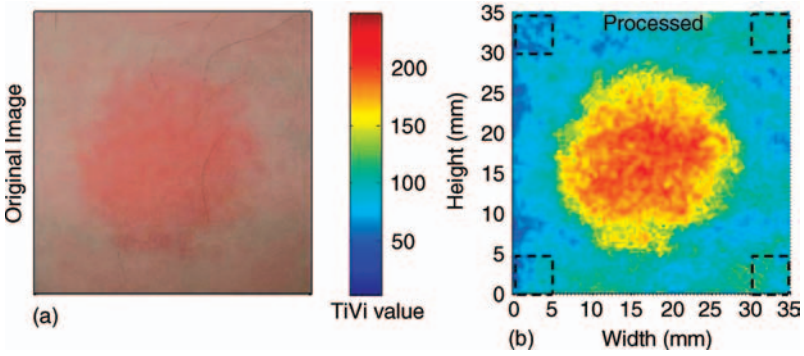

Figure 26.12 Examples of (a) a CR and (b) TiVi image. The CR image was taken of a UVB burn to the volar forearm of a young healthy volunteer. The image was taken 30 h after a 32 s exposure to an 8 mm wide UVB source. The TiVi image shows spatial heterogeneity in the blood distribution over the affected area.

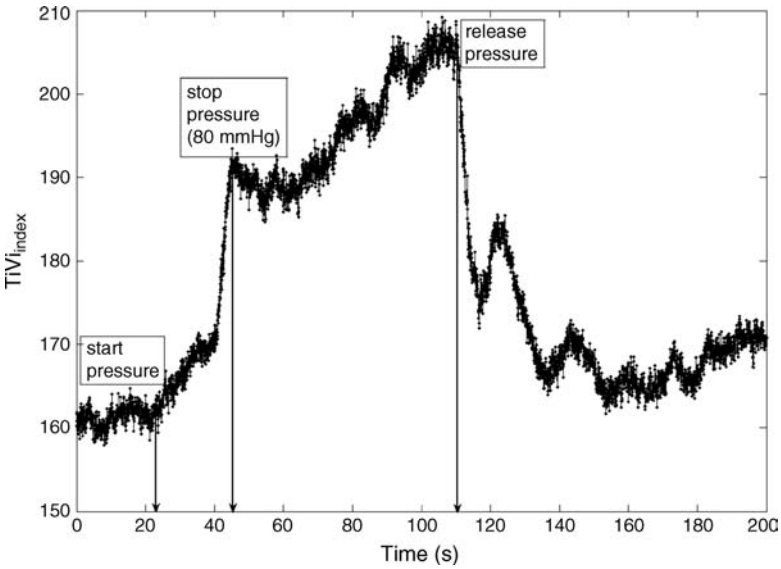

Figure 26.13 Time trace of a 50 × 50 pixel region of the volar forearm of a subject. A pressure cuff on the upper forearm causes an occlusion of the cephalic vein. This demonstration shows clear vasomotion during occlusion and release, and further investigation will focus on pulsatile activity.

resolution, with 0.04 s between each image. Thus, theoretically, the human pulse can be resolved from the time average (duplex) mode of the video imager, and also spatial data over time can be observed. Occlusion of the cephalic vein for the upper arm with 90 mmHg leads to higher RBC concentration due to the RBCs being trapped by the occlusion of the cephalic vein, as the brachial artery pumps RBCs into the area. An example of the duplex mode is shown in Figure 26.13, detailing the average TiVi index of a 50 × 50 pixel region of interest (ROI) on the volar forearm for an acquisition of 25 fps for cephalic vein occlusion. Clear vasomotion of the vessels can be observed at a rate of ∼5 cycles per minute during and post-occlusion and release of the area. Future work will investigate pulsations of the vascular bed, and pulse models have already shown promising results.

Limitations of this new technique include the lack of SI units in measurements, and inaccurate measurements on persons with dark skin due to high absorption of melanin. Light levels are also reduced due to the polarization filters, with only 22.5% of total light intensity reaching the detector. The effect of melanin in the epidermis causes an increase in TiVi index. Image subtraction algorithms have been developed so as to display only the reaction on the skin site, while subtracting out the static components in the CR images. This is also helpful in removing the unwanted effect of deep veins in the volar forearm, a site which is used commonly in routine skin tests. Owing to the availability of measuring tissue hematocrit only, low cost, ease of use, and portability, the TiVi imaging systems are an attractive alternative to expensive and cumbersome equipment such as LDPI and LSPI for the investigation of tissue RBC concentration.

26.6
Photoacoustic Tomography

In recent years, PAT has attracted considerable interest. This is because the technique seeks to combine the best features of biophotonics with those of ultrasound; it offers high optical contrast and high resolution.

The technique operates by irradiating a sample with a laser pulse. When the laser light is absorbed it will produce a pressure wave due to an increase in the temperature and volume. These pressure waves will emanate from the source in all directions. A high-frequency ultrasound receiver can then be used to detect these waves and build a 3D picture of the structure. This is made possible by the much lower speed of sound and lack of scattering or diffusion of ultrasound en route to the receiver. Diffuse, randomized scattering of the light before reaching the microvessels is not a disadvantage and is likely to be useful in providing relatively uniform illumination even to vessels that could not receive ballistic photons due to other vessels in the direct light path.

In PAT, light in the visible to near-infrared region of the spectrum is used. This is because hemoglobin in the blood dominates the optical absorption in most soft tissue. If a tissue sample is irradiated by light in this range, a map of the vessel network within the tissue can be produced. The pulse width is chosen such that it is much shorter than the thermal diffusion time of the system and in this way heat conduction can be neglected [119]. A schematic of the system is shown in Figure 26.14.

The data are processed by a computer and can be output in an image format. Image reconstruction is achieved by various reconstruction algorithms [121, 122].

The technique is capable of diagnosing different physiology conditions. This is because different physiological conditions can change the light absorption properties

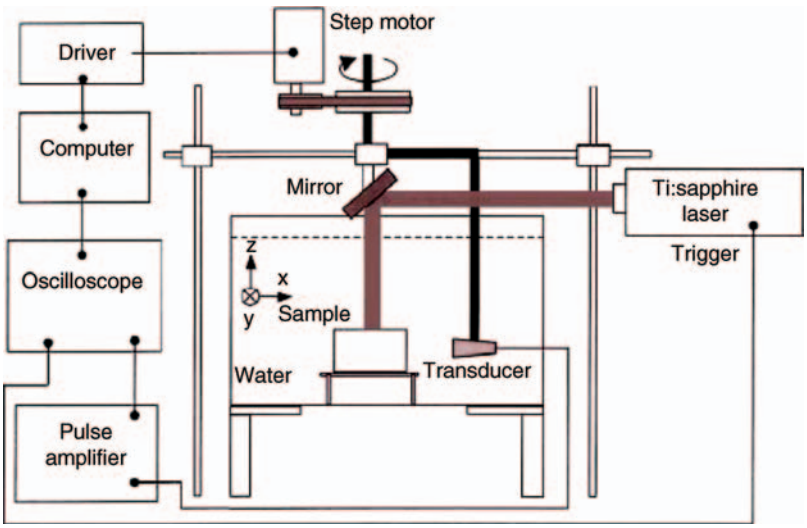

Figure 26.14 Schematic of photoacoustic tomography system [120]. Reproduced with permmission from The American Association of Physicists in Medicine.

of the tissue; for example, absorption contrast between breast tumors and normal breast tissue as high as 500% in the infrared range have been reported [123]. The technique is also capable of detecting hemoglobin levels in tissue with very high contrast. One group has used the technique to acquire 3D data of the hemoglobin level in rat brain [124]. This was achieved using a 532 nm laser source, as the absorption coefficient at this wavelength of whole blood is 100 cm^{-1}, which is much larger than the averaged absorption coefficient of the gray and white matter of the brain, 0.56 cm^{-1}.

The main advantage of combining ultrasound and light is that one can obtain much improved resolution (diffraction-limited) and can image vessels with 60 μm resolution [120]. The Wang laboratory at the University of Washington in St. Louis, MO, has built a system with 5 μm resolution and has already been able to produce exquisite 3D images of microvascular architecture in the rat.

One issue with the technique is the time it takes to produce large 3D scans of a region. Times of up to 16 h have been reported to image a region of radius 2.8 cm in the *XY* plane and a depth 4.1 cm in the *Z* plane [123]. However, the use of an ultrasonic transducer array would greatly improve imaging time.

26.7 Optical Microangiography (OMAG)

Optical microangiography (OMAG) has its origins in Fourier domain OCT and is similar to Doppler OCT. It is a recently developed high-resolution 3D method of imaging blood perfusion and direction at capillary level resolution within microcirculatory beds. A typical setup of an OMAG system is shown in Figure 26.15. The technique itself does not rely on the phase information of the OCT signals to extract the blood flow information. This in turn means that the technique is not sensitive to the environmental phase stability. This allows OMAG to compensate for the inevitable sample movement using the phase data, thus limiting noise through post-processing of the data [124].

An example of an OMAG image is shown in Figure 26.16. The acquisition time to obtain the 3D OMAG data shown in Figures 26.12 and 26.13 was about 50 s. However, the processing time required was much longer.

The OMAG technique appears to offer a much greater signal-to-noise ratio than standard Doppler OCT, allowing the system to visualize more features, as shown in Figure 26.17.

Figure 26.17 compares the two imaging modalities *in vivo* on an adult mouse brain. The images were both obtained on the same mouse with the skull intact. The images were then normalized by the maximum pixel value in each image and log compressed [126]. The improved contrast using this technique is clearly visible. OMAG allows for much smaller features to be visualized deeper into the tissue.

Another advantage of the OMAG technique is that it can determine the direction of the flow by applying a Hilbert transformation for each wavenumber along the positions separately. An example of this is shown in Figure 26.18.

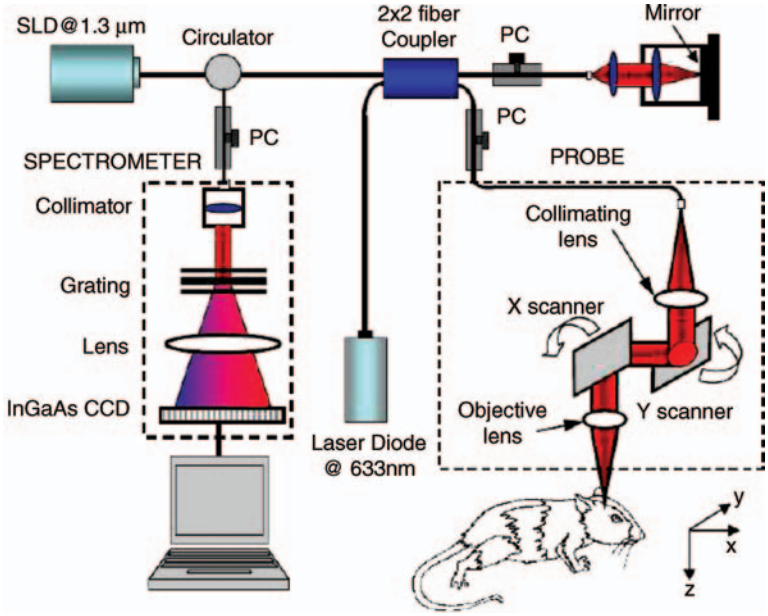

Figure 26.15 Schematic of a typical OMAG system [126]. Reproduced with permmission from The Institute of Physics.

In this experiment, the probe beam was shone from the top on to the sample. The mirror was then modulated using a triangle waveform. The images were generated for (a) the ascending and (b) the descending portion of the wave form. When the mirror moves toward the incident beam, blood perfusion that flows away from the beam direction is determined, and vice versa [127]. The figure shows that the flow direction is clearly determined using this technique. The minimum flow velocity that can be recorded using OMAG is reported to be $\sim 170\,\mu m\,s^{-1}$ and the maximum flow velocity that can be measured is $\sim \pm 2.1\,mm\,s^{-1}$ [124].

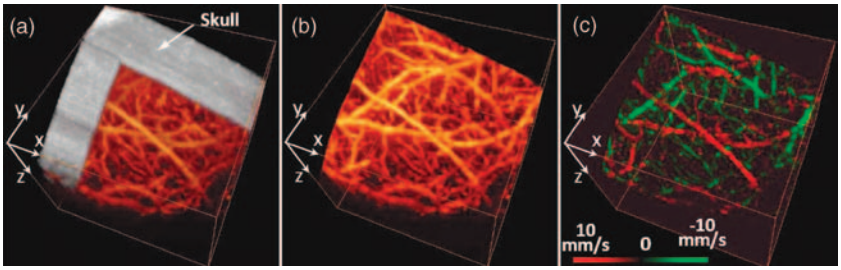

Figure 26.16 *In vivo* 3D OMAG imaging of the cortical brain of a mouse with the skull left intact. The volumetric visualization was rendered by (a) merging the 3D microstructural image with the 3D cerebral blood flow image, (b) the 3D signals of cerebral blood flow only, and (c) the corresponding DOMAG imaging of velocities within the 3D blood flow network in (b). The red color in (c) represents the blood moving towards the incident probe beam, and otherwise the green color. The physical image size was $2.5 \times 2.5 \times 2.0$ (x–y–z) mm^3 [126]. Reproduced with permmission from The Institute of Physics.

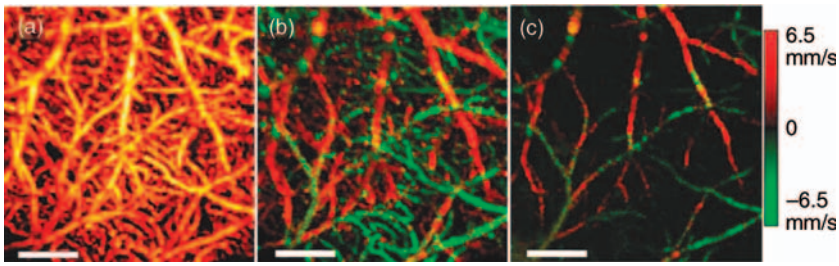

Figure 26.17 Comparison between 3D OMAG and PRDOCT imaging of the cortical brain in mice with the intact skull *in vivo*. Shown are the maximum *x*–*y* projection views of (a) OMAG cerebral blood flow image, (b) DOMAG flow velocity image, and (c) PRDOCT flow velocity image. The physical size of scanned tissue volume was $2.5 \times 2.5 \times 2.0\,mm^3$. White bar = 500 μm.

26.8
Comparison of Planar Microcirculation Imagers TiVi, LSPI, and LDPI

In order to validate the results of any microcirculation techniques, the opinion of a clinical expert is usually required. So far there is no modern technology that has supplanted the fundamental visual observation technique in the clinical environment, even though clinicians' interpretations of images can be bypassed entirely by a computerized analysis, such as neural networks. Limitations of skin assessment

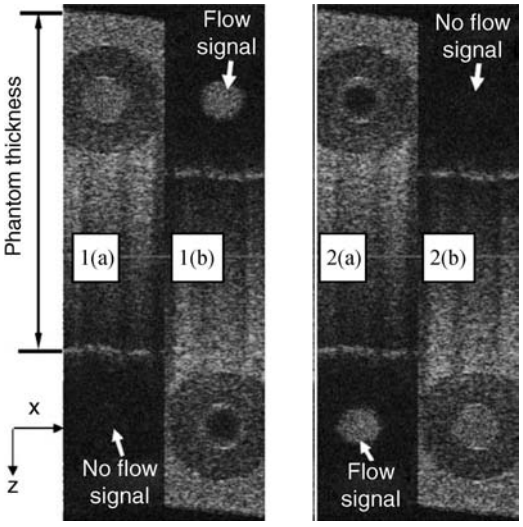

Figure 26.18 Determination of directionality of fluid flow using OMAG. (1) flow is oriented towards scanning beam (2) flow is reversed such that is it oriented away from scanning beam. (a) positive slope of reference mirror; (b) negative slope of reference mirror. The physical dimensions of the image are 1.3×3.1 mm [127]. Reproduced with permmission from osa.

Table 26.1 Comparison table outlining mechanical and operational principles of the different devices evaluated [117]. Reproduced with permmission from SPIE.

Property	LDLS	FLPI	TiVi
Principle	Doppler effect	Reduced speckle contrast	Polarization spectroscopy
Variable recorded	Perfusion (speed × concentration)	Perfusion (speed × concentration)	Relative concentration
Variable units	Perfusion units (PU)	Perfusion units (PU)	$TiVi_{index}$ (AU)
Measurement sites	16 384	431 680	Up to 12 million
Best resolution (μm)	∼500	∼100	∼50
Measurement depth (μm)	∼1000	∼300	∼500
Repetition rate (s)	6 (50 × 64 pixels)	4 (568 × 760 pixels)	5 (4000 × 3000 pixels)
Best capture time (s)	6	4	1/60
Zoom function	No	Yes	Yes
Laser driver	Required	Not required	Not required
Movement artifact sensitivity	Substantial	Dependent on temporal averaging	None
Video mode	No	Yes	Yes
Video rate	—	25 fps	25 fps
Video size (pixels)	—	113 × 152	Up to 720 × 576
Pixel resolution (cm^{-2})	100	40 000	600 000
View angle	Top only	Top only	User selectable
Imager dimensions (cm)	19 × 30 × 18	22 × 23 × 8	15 × 7 × 5
Weight (kg)	Scanner 3.2	2	1
Calibration	Motility standard	Motility standard	None
Ambient light sensitivity	Intermediate	Substantial	Negligible

visual scoring systems such as the skin blanching assay include the requirement for a trained observer to achieve comparable results, the need to make observations in standardized lighting conditions, application of steroids in random order, and assessment by an independent observer.

The following section represents a brief introduction to the instrumentation chosen to perform basic skin tests. A summary of principles and operation of each instrument is presented in Table 26.1. The actual instruments used are briefly described here.

26.8.1
Laser Doppler Imaging – Moor Instruments moorLDLS

The Moor Instruments moorLDLS is a line scanning laser Doppler imager with a 780 nm laser diode.

Owing to the capture of 64 points simultaneously, the temporal resolution is dramatically improved from conventional LDPI. The minimum image acquisition time is dependent on the number of data points per fast Fourier transform (FFT): at maximum resolution (256 × 64 pixels) the best image acquisition time is 13 s for 256 FFTs and 20 s for 1024 FFTs. The best image acquisition time for 64 × 64 pixels is 4 s. The maximum scan area is 20 × 15 cm and the scan distance to the tissue surface (given by the manufacturer) is between 10 and 20 cm. The device is also capable of single-point multichannel acquisition at a sample rate up to 40 Hz for the entire line of detectors simultaneously. The background threshold level was determined automatically by centering of the laser line on the background under laboratory conditions.

26.8.2
Laser Speckle Imaging – Moor Instruments moorFLPI

The Moor Instruments moorLPI system was used for comparison with laser speckle imaging. The laser source (780 nm) is expanded over an area, rather than a line as in LDLS. There is a high-resolution/low-speed temporal mode or a high-speed/low-resolution spatial mode. The integration time is 0.3 s, providing 25 fps at a size of 152 × 113 pixels for the spatial mode. The temporal mode allows an adjustable integration time, constant for temporal averaging (1 s per frame – 25 frames; 4 s per frame – 100 frames; 10 s per frame – 250 frames; 60 s per frame – 1500 frames) at 568 × 760 pixels for each image. The camera gain can be adjusted to increase the image acquisition area, but saturating the CCD must be avoided.

26.8.3
Polarization Spectroscopy – WheelsBridge TiVi Imager

The TiVi imager is a small and portable device for high-resolution imaging of the concentration of RBCs in superficial skin tissue. A white xenon flash lamp provides illumination over the 450–750 nm wavelength region, and a wide area CCD detects the backscattered light from the tissue. The available commercial system utilizes a high-resolution CCD offering instantaneous image acquisition (1/60th of a second) with a refresh rate of one image every 5 s at a resolution of 3648 × 2736 pixels. An enabled macro mode allows focusing at a closest distance of 4 cm from the tissue surface. A research prototype high-speed mode was also tested, allowing 8 fps at 400 × 400 pixels for real-time online viewing and 30 fps at 640 × 480 pixels for offline analysis. This prototype employed a constant broadband light source with the same CCD as used in the high-resolution version of TiVi. The spectra of the light sources are equivalent for both the high-resolution and high-speed TiVi systems.

Occlusion (occlusion of blood vessels using a sphygmomanometer) reactive hyperemia tests were performed on three nonsmoking, healthy subjects (average age 25 years), with no history of skin diseases, who had not used topical or systemic corticosteroid preparations in the previous 2 months. The subjects were acclimatized in a laboratory at 21 °C for 30 min and rested in a seated position with the volar

forearm placed on a flat table at heart level. The instruments were positioned above the forearm for data acquisition.

A reactive hyperemia caused by brachial arterial occlusion using a sphygmomanometer on the upper arm of the test subjects was used to compare the systems in temporal mode (with the high-speed TiVi system used). A baseline level was taken for 1 min, then arterial occlusion was performed by inflating the cuff to 130 mmHg for 2 min. In previous studies with LDPI, upon complete release of the cuff, the resulting increase in blood perfusion is seen, and blood flux oscillations are regularly observed. This phase was observed for a further 3 min. In order to examine further the sensitivity of the TiVi system alone with pressure, a further experiment was conducted in which both the high-speed and high-resolution TiVi systems were arranged to image the volar forearm of a healthy individual at increasing and decreasing pressure steps of 10 mmHg.

Physical size prevented all three technologies being used at the same time on the same test area, meaning that tests with the FLPI had to be carried out separately from TiVi and LDLS studies. The white flash light source on the TiVi did not interfere with the LDLS system, as there are filters present to remove much of the extraneous light. Finally, the TiVi readings were not affected by the scanning beam of the LDLS system as it was outside the sensitive region of the detector.

Imaging comparisons can be carried out by inducing reactions via topical application of different drugs, including vasodilators (e.g., topical analgesic and methyl nicotinate) and vasoconstrictors (e.g., clobetasol-17-propionate). The active ingredient of the analgesic, menthol, induces vasodilation, and caused erythema in all three subjects. Due to percutaneous absorption of methyl salicylate, it was important to note that this analgesic should be used with care on persons sensitive to aspirin or suffering from asthma. None of the subjects were sensitive to aspirin or had asthma, and the analgesic was applied to an unbroken area of skin. The cream was applied to cover an area of $\sim$24 cm^2, in the shape of the letters "UL." A small amount of the cream was applied to the volar forearm and imaged 10 min later. The resulting erythema was imaged with the three devices, and can be seen in Figure 26.20. The images show the same affected area, and clear border discrimination can be seen with the TiVi and FLPI imaging systems. The LDLS however, does not show an increase in perfusion with the shape made by the analgesic cream, and it is proposed that the LDLS imaging system is probing much deeper vessels in the microcirculatory structure.

26.8.4 Results

In order to assess the time acquisition properties, it was decided to observe the commonly studied postocclusive reactive hyperemia at the nailfold of the second finger. Lower and upper pressure values of 90 and 130 mmHg were employed in order to arrest completely the venous and arterial circulation, respectively. Standard baseline was registered for 1 min, a pressure of 130 mmHg was applied using the sphygmomanometer, occluding the blood vessels, and maintained for 2 min.

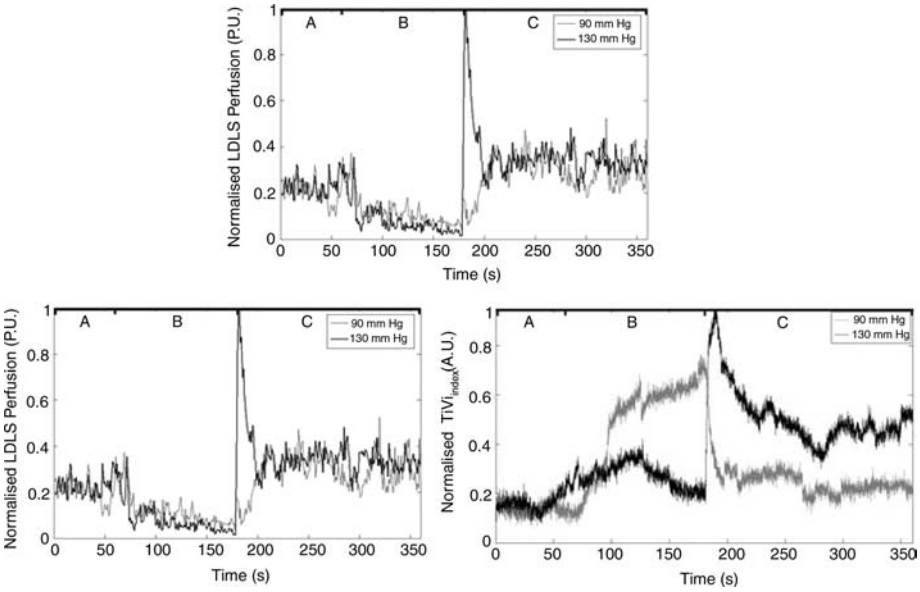

Figure 26.19 Time traces of postocclusive reactive hyperemia. The reaction was sectioned into three; A is the baseline measurement, B is the occlusion for 2 min, and C represents the reactive hyperemia upon removal of the occlusion. Pressure was 130 mmHg except for the TiVi curves, where 90 mmHg pressure was also used to show the TiVi system's (high resolution and high speed) sensitivity to pressure.

The resulting hyperemia upon removal of the occlusion was monitored for 3 min. The areas of the response representing the baseline, occlusion, and hyperemia are labeled A, B and C, respectively, in Figure 26.19. It should be noted that upon application of the sphygmomanometer and subsequent analysis for the TiVi, the curve increased for both 90 and 130 mmHg pressures. This is because the instrument is sensitive to the concentration of RBCs only, and not the speed. This new technology adds a new dimension to the study of postocclusive reactive hyperemia, with a nontraditional time trace sensitive to the concentration of RBCs only. Care has to be taken with the interpretation of these new data, and this is addressed further below.

26.8.5 Discussion

Even with the massive technological advancements of the past 30 years, current "gold standard" methods of examination of skin lesions, erythema and tumors, still involve simple microscope techniques, that is, a closer look at the affected area, carried out by a skilled clinician, be it a pathologist or dermatologist. Similarly, no modern imaging technique has been proven consistently to outperform the opinion of a clinical expert in relation to patch or prick testing [125]. Often, the capital cost of a technology

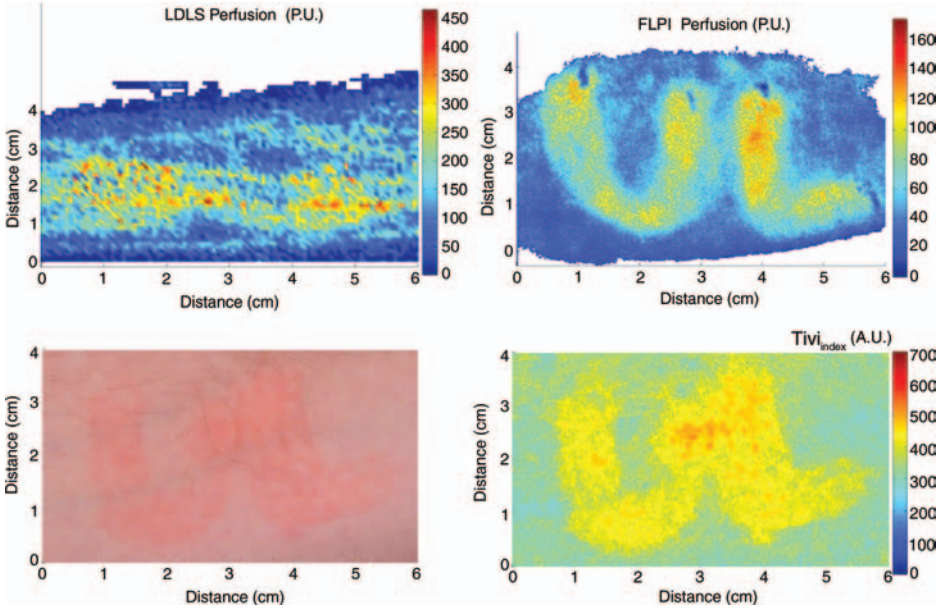

Figure 26.20 Comparison of a topical application of a common analgesic (Deep Heat) as assessed by the LDLS, FLPI, and TiVi imaging technologies. The color visual image is a cross-polarized image from the TiVi imager, which serves as a visual aid, and also the image for subsequent processing. Neither of the other two technologies investigated offers a standard color image [117]. Reproduced with permmission from SPIE.

without an extremely high success rate is not justified, even if the workload of the clinician is drastically reduced.

The ideal blood flow/concentration monitor should have the characteristics of observational measurements, be able to provide reproducible results, have little or no dependence on the tissue optical properties, instantaneous image acquisition (to help against patient motion), and provide a variable in standard SI units. The commercial devices examined in this chapter provide relative changes in flow/RBC concentration due to the random nature of the microvascular architecture. Since LDPI is the oldest technology used in this work (30 years), more research and commercial products exist on LDPI than the other technologies. A full-field laser Doppler imager has been developed and is in commercial production, with Aïmago, providing 256×256 points every 2–10 s [49].

The sensitivity of each device to pressure and the different dynamic reactions can be seen from Figure 26.19, where the concentration of RBCs in the nailfold of the second finger increased upon application of the sphygmomanometer. In the case where 130 mmHg pressure was applied, the arteries and veins were quickly closed, trapping the red blood cells in the tissue at a level not much higher than the baseline. Upon release of the occlusion, the concentration increased rapidly due to the backlog of blood rushing into the area to feed the nutrient-starved tissue. When only

90 mmHg was applied, the arterial inflow remained open while the venous outflow was in stasis. Thus, the concentration of RBCs increased gradually in an almost logarithmic function, and began to reach a plateau, either due to system saturation (the system is linearly calibrated to a physiological RBC concentration of 4% in tissue) or more likely due to a plateau reached by the amount of RBCs that can fit into the vasculature. This section of the curve showed the dynamics of the blood vessels filling up quickly with blood. After the occlusion had been released, the venous outflow was reopened and the RBC concentration decreased rapidly to empty the excess RBCs from the area, and showed signs of returning to a normal state 3 min after release of the occlusion.

The sensitivity of the TiVi imaging system to RBC concentration showed two distinct curves, depending on the pressure of the sphygmomanometer. Since the same CCD was used for both TiVi studies, it was assumed that there were no instrumentation differences. "Biological zero" is a well-known feature of laser Doppler studies and manifests as an offset from instrumental zero seen during occlusion. Total flow arrest would mean that concentration $\times$ velocity would be zero, but Brownian motion and occasionally opening and closing of local shunts, vasodilation, and vasoconstriction of local vessels can all contribute to the nonzero flow registered. A similar situation arises with FLPI as there is still some blurring of the speckle due to RBC movement. However, TiVi is sensitive to concentration alone and would require completely bloodless tissue to register a "zero" reading. The most important feature of the technologies presented is that both the LDLS and FLPI measure perfusion, albeit at different depths in dermal tissue, whereas TiVi technology measures relative concentration in the tissue. It is important to remember that the new TiVi imaging technology does not provide measurements of blood flow. Indeed, it is similar to processing of the unweighted moment of the laser Doppler power spectrum to provide measurement of concentration, except that it is valid only with a low number of scattering events at low concentrations, and is dependent on the total light intensity.

With the larger measurement depth of LDLS compared with the other techniques, it proves to be inefficient for very superficial measurements, such as the erythema produced by the topical analgesic. Acquisition on the temporal scale is also hindered with the LDLS due to rastering of the laser line. As the microcirculation is a highly dynamic environment, its perfusion values can change rapidly. Cardiac pulse ($\sim$1 Hz), breathing ($\sim$0.3 Hz), and vasomotion ($\sim$0.1 Hz) in highly perfused tissues are evidence of the rapid temporal nature of microvascular activity. Thus, in laser Doppler studies and the relatively long acquisition time of a single image, the temporal changes in perfusion may often be misinterpreted as spatial heterogeneity [24]. This occurs because it has to be assumed that the perfusion of the site under investigation is stationary and constant, hence the study of dynamic changes is severely compromised. It remains to be seen if the recent CMOS LDPI technology can bridge the gap in temporal resolution in LDPI.

The laser Doppler and speckle signals are a complex function of many parameters and are also dependent on source wavelength, coherence properties of the laser, tissue optical properties, and distance between the scanner and tissue surface. Additional processing is required to correct for nonlinear behavior at high RBC

concentrations due to the presence of multiple scattering. It should be noted that all three techniques merely provide a ratiometric measurement to aid any clinical observation. The techniques are not to be used for diagnosis independently of clinical observation.

26.8.5.1 Depth of Measurement

Much variation is reported in the literature as to the depth of penetration of a light beam in tissue, which is due to light power and wavelength, and biological factors such as pigmentation level, age, skin transparency, and epidermal thickness. However, the important parameter is measurement depth rather than penetration or even sampling depth. Indeed, the laser Doppler imaging mean measurement depth in the forearm can be from 300 μm to even 600 μm. This measurement depth is highly wavelength dependent, and therefore depends on which device has been employed.

Physiologically, in the vessel compartments the total cross-sectional area (A) increases from the arterioles to the capillaries of the superficial dermal plexus and then decreases in the veins because the blood flow is constant in a closed system and the speed must be proportional to $1/A$. Thus, the speed is lower in the narrower vessels than in the larger (and deeper) vessels. It is for this reason that low and high frequencies are attributed to flux originating in the superficial vascular plexus and the deeper vessels, respectively. Indeed, ~15% of skin blood flow originates from the nutritional flow, while 85% results from the deeper thermoregulatory flow, especially in the presence of arteriovenous shunts, for example, in the palms of the hands.

Use of the laser wavelength for laser Doppler studies is also an issue; the frequency shift for HeNe laser light at 633 nm is 0–12 kHz, but for a 780 nm laser is 0–20 kHz. The difference in frequency shifts occurs due to the longer wavelength penetrating deeper into the microvasculature, thus probing faster flowing blood. However, both the LDLS and FLPI used for studies carried out in this work employed a 780 nm source. Speckle technology probes a shallower depth than laser Doppler for two main reasons. First, the speckle signal is not frequency weighted, and is looking at first-order statistics, whereas laser Doppler looks at second-order statistics. Also for speckle studies, the laser source is expanded over a much larger area than the point for laser Doppler studies, hence there is a reduction in the power density of the beam. This reduction means that the depth at which noise dominates will be more superficial so that the contribution from faster flowing blood in veins (which is enhanced in laser Doppler technology due to frequency weighting) is lost for speckle imaging. The observation that many speckle studies are carried out on surgically exposed tissue and the appearance of microvessels in the processed images can be explained by the choice of tissue and its preparation. In general, the reduced measurement depth of the FLPI system renders it unsuitable for monitoring nonsuperficial vessels. The FLPI imager was also used more frequently for imaging smaller areas more rapidly and at higher resolutions than are commonly used by laser Doppler systems and involve measurements on exposed tissues because the measurement conditions best suit the technique rather than because the technique best suits the measurement. This is an important factor to remember when optimizing

the use of an expensive piece of equipment destined for use in a clinical setting. An interesting comparison should be carried out between the new full-field laser Doppler imager and current commercial laser Doppler technology to examine the depth selection of the signal.

The depth of measurement for TiVi has previously been estimated at 400–500 μm from Monte Carlo simulations of polarized light propagation into simulated dermal tissue [116]. Any future experimentally determined values should verify this model value. It should be noted that the technique is based on polarized light absorption spectroscopy, and does not bear any reference to the moving particles in the tissue. Although the system is not responsive to blood flow, it does return a signal from the deeper veins in the forearm due to the high concentration of blood. Because of the appearance of the blue veins, the TiVi returns an almost zero value in its variable, $TiVi_{\text{index}}$, even though a nearby skin site in the upper microcirculation can have a high $TiVi_{index}$ value. Again, it should be remembered that the TiVi imager is designed to investigate the upper microcirculation and that RBC concentration values from anywhere other than this region may not be accurate. The measurement volume (the volume from which the bulk of the signal is acquired) is well inside the reticular dermis of the microcirculation. For laser Doppler measurements, the measurement volume has been determined as $\sim 1\ \text{mm}^3$ or smaller, and in laser speckle systems the volume is highly dependent on the type of system being used.

26.8.6 Conclusions

We have compared the operation of an established microcirculation imaging technique, laser Doppler (LDPI), with the more recently available laser speckle and TiVi in human skin tissue using the occlusion and reactive hyperemia response. However, TiVi differs from the other techniques in its response to occlusion of the brachial artery. Since this is a global occlusion of the forearm all instruments were sensitive to the effect. LDPI and LSPI showed a large decrease as they are both sensitive to RBC concentration and velocity. However, TiVi, being sensitive to concentration only, showed stasis when a full arterial occlusion (130 mmHg) was applied quickly and an increase in of RBC concentration when the arterial inflow remained open with the venous outflow occluded (90 mmHg). LSPI and TiVi are both welcome tools in the study of the microcirculation, but care must be taken in the interpretation of the images since blood flow and blood concentration in tissue are essentially different parameters. However, LDPI is the only one of these imaging techniques which has been approved by regulatory bodies, including the FDA. Laser Doppler imaging has been shown accurately to assess burn depth and predict wound outcome, with a large weight of evidence [128].

The work described here may motivate further studies of comparisons between noninvasive optical techniques for the investigation of tissue microcirculation.

We have discussed the *modus operandi* and applications of capillaroscopy, LDPI, LSPI, PAT, OCT, and TiVi. Each has had its own peak time and all retain niche applications. Proper application of each is dependent on user knowledge of light

interaction with tissue and the basic workings of the device used. The choice of technology for *in vivo* imaging of the microcirculation is dependent on the sampling depth (nutritional or thermoregulatory vessels), resolution (physical and pixel), field of view, and whether structure or function is to be investigated.

Acknowledgments

The authors are grateful to HEA PRTLI4 (national development plan) funding of the National Biophotonics and Imaging Platform Ireland and IRCSET for supporting this research. They also thank Dr. Rodney Gush of Moor Instruments and Professor Gert Nilsson of WheelsBridge AB, Sweden.

References

1 Doppler, J.C. (1842) Über das farbige Licht der Doppelsterne und einiger anderer Gestirne des Himmels. [On the coloured light from double stars and some other Heavenly Bodies]. *Abhandl. Konigl. Bohmischen Ges. Wiss., 5th Ser.*, **2**, 465 [Treatises of the Royal Bohemian Society of Science].

2 Ostergren, J. and Fagrell, B. (1984) Videophotometric capillaroscopy for evaluating drug effects on skin microcirculation – a double-blind study with nifedipine. *Clin. Physiol.*, **4** (2), 169–176.

3 Schmidt-Nielsen, B. (1994) August Krogh and capillary physiology. *Int. J. Microcirc. Clin. Exp.*, **14** (1–2), 104–110.

4 Ryan, T.J. (1973) Measurement of blood flow and other properties of the vessels of the skin, in *The Physiology and Pathophysiology of the Skin*, vol. 1 (ed. A. Jarrett), Academic Press, London, pp. 653–679.

5 Butti, P., Intaglietta, M., Reimann, H., Holliger, C., Bollinger, A., and Anliker, M. (1975) Capillary red blood cell velocity measurements in human nailfold by video densitometric method. *Microvasc. Res.*, **10**, 220–227.

6 Fagrell, B., Fronek, A., and Intaglietta, M. (1977) A microscope television system for studying flow velocity in human skin capillaries. *Am. J. Physiol.*, **233**, 318–321.

7 Dolezalova, P., Young, S.P., Bacon, P.A., and Southwood, T.R. (2003) Nailfold capillary microscopy in healthy children and in childhood rheumatic diseases: a prospective single blind observational study. *Ann. Rheum. Dis.*, **62**, 444–449.

8 Ohtsuka, T., Tamura, T., Yamakage, A., and Yamazaki, S. (1998) The predictive value of quantitative nailfold capillary microscopy in patients with undifferentiated connective tissue disease. *Br. J. Dermatol.*, **139**, 622–629.

9 Nagy, Z. and Czirják, L. (2004) Nailfold digital capillaroscopy in 447 patients with connective tissue disease and Raynaud's disease. *J. Eur. Acad. Dermatol. Venereol.*, **18**, 62–68.

10 Bukhari, M., Herrick, A.L., Moore, T., Manning, J., and Jayson, M.I.V. (1996) Increased nailfold capillary dimensions in primary Raynaud's phenomenon and systemic sclerosis. *Br. J. Rheumatol.*, **35**, 1127–1131.

11 Allen, P.D., Hillier, V.F., Moore, T., Anderson, M.E., Taylor, C.J., Herrick, A.L., (2003). Computer Based System for Acquisition and Analysis of Nailfold Capillary Images. *Medical Image Understanding and Analysis*, eScholarID:1d32761.

12 Aguiar, T., Furtado, E., Dorigo, D., Bottino, D., and Bouskela, E. (2006) Nailfold videocapillaroscopy in primary Sjögren's syndrome. *Angiology*, **57**, 593–599.

13 Nilsson, G.E., Jakobsson, A., and Wårdell, K. (1992) Tissue perfusion monitoring and imaging by coherent light scattering. *Proc. SPIE*, **1524**, 90–109.

14 Stern, M.D. (1975) *In vivo* evaluation of microcirculation by coherent light scattering. *Nature*, **254**, 56–58.

15 Bollinger, A., Butti, P., Barras, J.P., Trachsler, H., and Siegenthaler, W. (1974) Red blood cell velocity in nailfold capillaries of man measured by a television microscopy technique. *Microvasc. Res.*, **7**, 62–72.

16 Mawson, D.M. and Shore, A.C. (1998) Comparison of capiflow and frame by frame analysis for the assessment of capillary red blood cell velocity. *J. Med. Eng. Technol.*, **22**, 53–63.

17 Rosen, B. and Paffhausen, W. (1993) On-line measurement of microvascular diameter and red blood cell velocity by a line-scan CCD image sensor. *Microvasc. Res.*, **45**, 107–121.

18 Sourice, A., Plantier, G., and Saumet, J.-L. (2005) Red blood cell velocity estimation in microvessels using the spatiotemporal autocorrelation. *Meas. Sci. Technol.*, **16**, 2229–2239.

19 Bhushan, M., Moore, T., Herrick, A.L., and Griffiths, C.E.M. (2000) Nailfold video capillaroscopy in psoriasis. *Br. J. Dermatol.*, **142**, 1171–1176.

20 Wong, M.L., Highton, J., and Palmer, D.G. (1988) Sequential nailfold capillary microscopy in scleroderma and related disorders. *Ann. Rheum. Dis.*, **47**, 53–61.

21 Sainthillier, J.M., Degouy, A., Gharbi, T., Pieralli, C., and Humbert, P. (2003) Geometrical capillary network analysis. *Skin Res. Technol.*, **9**, 312–320.

22 Zhong, J., Asker, C.L., and Salerud, G. (2000) Imaging, image processing and pattern analysis of skin capillary ensembles. *Skin Res. Technol.*, **6**, 45–57.

23 Hamar, G., Horváth, G., Tarján, Z., and Virág, T. (2007) Markov chain based edge detection algorithm for evaluation of capillary microscopic images. Proceedings of the 13th PhD Mini-Symposium, pp. 18–21.

24 Leahy, M.J., de Mul, F.F., Nilsson, G.E., and Maniewski, R. (1999) Principles and practice of the laser-Doppler perfusion technique. *Technol. Health Care*, **7**, 143–162.

25 Riva, C., Ross, B., and Benedek, G.B. (1972) Laser Doppler measurements of blood flow in capillary tubes and retinal arteries. *Invest. Ophthalmol.*, **11**, 936–944.

26 Stern, M.D. (1975) *In vivo* evaluation of microcirculation of coherent light scattering. *Nature*, **254**, 56–58.

27 Cummins, H.Z. and Swinney, H.L. (1970) Light beating spectroscopy. *Prog. Opt.*, **8**, 133–200.

28 Bonner, R. and Nossal, R. (1981) Model for laser Doppler measurements of blood flow in tissue. *Appl. Opt.*, **20**, 2097–2107.

29 Boulnois, J.L. (1985) Photophysical processes in recent medical laser developments: a review. *Lasers Med. Sci.*, **1**, 47–66.

30 Abbot, N., Ferrell, W., Lockhart, J., and Lowe, G. (1996) Laser Doppler perfusion imaging of skin blood flow using red and near-infrared sources. *J. Invest. Dermatol.*, **107**, 882–886.

31 Duteil, L., Bernengo, J.C., and Schalla, W. (1985) A double wavelength laser Doppler system to investigate skin microcirculation. *Trans. Biomed. Eng.*, **32**, 439–447.

32 Gush, R.J. and King, T.A. (1991) Discrimination of capillary and arterio-venular blood flow in skin by laser Doppler flowmetry. *Med. Biol. Eng. Comput.*, **29**, 387–392.

33 Johnson, J.M., Taylor, W.F., and Shepherd, A.P. (1984) Laser Doppler measurements of skin blood flow: comparison with plethysmography. *J. Appl. Physiol. Respir. Environ. Excercise Physiol.*, **56**, 796–803.

34 Holloway, G.A. and Watkins, D.W. (1977) Laser Doppler measurement of cutaneous blood flow. *J. Invest. Dermatol.*, **69**, 306–309.

35 Murray, A.K., Herrick, A.L., and King, T.A. (2004) Laser Doppler imaging: a developing technique for application in the rheumatic diseases. *Rheumatology*, **43**, 1210–1218.

36 Braverman, I.M., Keh, A., and Goldminz, D. (1990) Correlation of

laser Doppler wave patterns with underlying microvascular anatomy. *J. Invest. Dermatol.*, **95**, 283–286.

37 Tenland, T., Salerud, E.G., Nilsson, G.E., and Oberg, P.A. (1983) Spatial and temporal variations in human skin blood flow. *Int. J. Microcirc. Clin. Exp.*, **2**, 81–90.

38 Bircher, A., de boer, E.M., Agner, T., Wahlberg, J.E., and Serup, J. (1994) Guidelines for measurement of cutaneous blood flow by laser Doppler flowmetry. A report from the Standardization Group of the European Society of Contact Dermatitis. *Contact Dermatitis*, **30**, 65–72.

39 Gush, R.J. and King, T.A. (1987) Investigation and improved performance of optical fibers in laser Doppler blood flow measurements. *Med. Biol. Eng. Comput.*, **25**, 391–396.

40 de Mull, F.F.M., van der Plas, D., Greve, J., Aarnoudse, J.G., and van Spijker, J. (1984) Mini laser-Doppler (blood) flow monitor with diode laser source and detection integrated in the probe. *Appl. Opt.*, **23**, 2970–2973.

41 Wårdell, K. (1993) Laser Doppler perfusion imaging by dynamic light scattering. *IEEE Trans. Biomed. Eng.*, **40**, 309–316.

42 Essex, T.J. and Byrne, P. (1991) A laser Doppler scanner for imaging blood flow in skin. *J. Biomed. Eng.*, **13**, 189–194.

43 Gardner-Medwin, J.M., Mac Donald, I.A., Taylor, J.Y., Rikey, P.H., and Powell, R.J. (2001) Seasonal differences in finger skin temperature and microvascular blood flow in healthy men and women are exaggerated in women with primary Reynaud's phenomenon. *Br. J. Clin. Pharmacol.*, **52**, 17–23.

44 Kernick, D.P. and Shore, A.C. (2000) Characteristics of laser Doppler perfusion imaging *in vitro* and *in vivo*. *Physiol. Meas.*, **4**, 222–240.

45 Droog, E.J., Steenbergen, W., and Sjoberg, F. (2001) Measurement of depth of burns by laser Doppler perfusion imaging. *Burns*, **27**, 561–568.

46 Kan, F. and Newton, D. (2003) Laser Doppler imaging in the investigation of lower limb wounds. *Int. J. Lower Extrem. Wounds*, **2**, 74–86.

47 Fullerton, A., Stucker, M., Wilhelm, K.P., Wårdell, K., Anderson, C., Fisher, T., Nilsson, G.E., and Serup, J. (2002) Guidelines for visualization of cutaneous blood flow by laser Doppler perfusion imaging. *Contact Dermatitis*, **46**, 129–140.

48 Serov, A., Steenbergen, W., and de Mul, F. (2002) Laser Doppler perfusion imaging with a complementary metal oxide semiconductor image sensor. *Opt. Lett.*, **27**, 300–302.

49 Serov, A., Steinacher, B., and Lasser, T. (2005) Full-field laser Doppler perfusion imaging and monitoring with an intelligent CMOS camera. *Opt. Express*, **13**, 3681–3689.

50 Serov, A. (2005) High-speed laser Doppler perfusion imaging using an integrating CMOS image sensor. *Opt. Express*, **13**, 6416–6428.

51 Nielsen, A., Fabricius, M., and Lauritzen, M. (2000) Scanning laser-Doppler flowmetry of rat cerebral circulation during cortical spreading depression. *J. Vasc. Res.*, **37**, 513–522.

52 Pape, S., Skouras, C., and Byrne, P. (2001) An audit of the use of laser Doppler imaging (LDI) in the assessment of burns of intermediate depth. *Burns*, **27** (3), 233–239.

53 Brown, R., Rice, P., and Bennett, N. (1998) The use of laser Doppler imaging as an aid in clinical management decision making in the treatment of vesicant burns. *Burns*, **24**, 692–698.

54 Kloppenberg, F., Beerthuizen, G., and ten Duis, H. (2001) Perfusion of burn wounds assessed by laser Doppler imaging is related to burn depth and healing time. *Burns*, **27**, 359–363.

55 Repež, A., Oroszy, D., and Arnež, Z.M. (2007) Continuous postoperative monitoring of cutaneous free flaps using near infrared spectroscopy. *J. Plast. Reconstr. Aesthet. Surg.*, **61** (1), 71–77.

56 Stucker, M., Springer, C., Paech, V., Hermes, N., Hoffmann, M., and Altmeyer, P. (2006) Increased laser Doppler flow in skin tumors corresponds

to elevated vessel density and reactive hyperemia. *Skin Res. Technol*, **12**, 1–6.
57 Hassan, M., Little, R., Vogel, A., Aleman, K., Wyvill, K., Yarchoan, R., and Gandjbakhche, A. (2004) Quantitative assessment of tumor vasculature and response to therapy in Kaposi's sarcoma using functional noninvasive imaging. *Technol. Cancer Res. Treat.*, **3**, 451–457.
58 Wang, I., Andersson-Engels, S., Nilsson, G.E., Wårdell, G., and Svanberg, K. (1997) Superficial blood flow following photodynamic therapy of malignant non-melanoma skin tumours measured by laser Doppler perfusion imaging. *Br. J. Dermatol.*, **136**, 184–189.
59 Fullerton, A. and Serup, J. (1995) Laser Doppler image scanning for assessment of skin irritation , in *Irritant Dermatitis. New Clinical and Experimental Aspects. Current Problems in Dermatology*, Vol. 23 (ed P. Elsner and H.I. Maibach), Karger, Basel, pp. 159–168.
60 Fullerton, A., Rode, B., and Serup, J. (2002) Studies of cutaneous blood flow of normal forearm skin and irritated forearm skin based on high-resolution laser Doppler perfusion imaging (HR-LDPI). *Skin Res. Technol.*, **8**, 32–40.
61 Fullerton, A., Rode, B., and Serup, J. (2002) Skin irritation typing and grading based on laser Doppler perfusion imaging. *Skin Res. Technol.*, **8**, 23–31.
62 Bjarnason, B. and Fischer, T. (1998) Objective assessment of nickel sulfate patch test reactions with laser Doppler perfusion imaging. *Contact Dermatitis*, **39**, 112–1188.
63 Bjarnason, B., Flosadottir, E., and Fischer, T. (1999) Objective non-invasive assessment of patch tests with the laser Doppler perfusion scanning technique. *Contact Dermatitis*, **40**, 251–260.
64 Ferrell, W., Balint, P., and Sturrock, R. (2000) Novel use of laser Doppler imaging for investigating epicondylitis. *Rheumatology*, **39**, 1214–1217.
65 Newton, D., Khan, F., Belch, J., Mitchell, M., and Leese, G. (2002) Blood flow changes in diabetic foot ulcers treated with dermal replacement therapy. *J. Foot Ankle Surg.*, **41**, 233–237.
66 Nixon, J., Smye, S., Scott, J., and Bond, S. (1999) The diagnosis of early pressure sores: report of the pilot study. *J. Tissue Viability*, **9**, 62–66.
67 Briers, J.D. (2001) Laser Doppler, speckle and related techniques for blood perfusion mapping and imaging. *Physiol. Meas.*, **22**, R35–R36.
68 Briers, J.D. (1996) Laser Doppler and time-varying speckle: a reconciliation. *J. Opt. Soc. Am. A*, **13**, 345–350.
69 Forrester, K.R., Stewart, C., Tulip, J., Leonard, C., and Bray, R.C. (2002) Comparison of laser speckle and laser Doppler perfusion imaging: measurement in human skin and rabbit articular tissue. *Med. Biol. Eng. Comput.*, **40**, 687–697.
70 Fujii, H., Nohira, K., Yamamoto, Y., Ikawa, H., and Ohura, T. (1987) Evaluation of blood flow by laser speckle image sensing. *Appl. Opt.*, **26**, 5321–5325.
71 Cheng, H., Luo, Q., Liu, Q., Lu, Q., Gong, H., and Zeng, S. (2004) Laser speckle imaging of blood flow in microcirculation. *Phys. Med. Biol.*, **49**, 1347–1357.
72 Choi, B., Kang, N.M., and Nelson, J.S. (2004) Laser speckle imaging for monitoring blood flow dynamics in the *in vivo* rodent dorsal skin fold model. *Microvasc. Res.*, **68**, 143–146.
73 Forrester, K.R., Stewart, C., Leonard, C., Tulip, J., and Bray, R.C. (2003) Endoscopic laser imaging of tissue perfusion: new instrumentation and technique. *Lasers Surg. Med.*, **33**, 151–157.
74 Kruijt, B., de Bruijn, H.S., van der Ploeg-van den Heuvel, A., Sterenborg, H.J.C.M., and Robinson, D.J. (2006) Laser speckle imaging of dynamic changes in flow during photodynamic therapy. *Lasers Med. Sci.*, **21**, 208–212.
75 Li, P., Ni, S., Zhang, L., Zeng, S., and Luo, Q. (2006) Imaging cerebral blood flow through the intact rat skull with temporal laser speckle imaging. *Opt. Lett.*, **31**, 1824–1826.
76 Paul, J.S. (2006) Imaging the development of an ischemic core

following photochemically induced cortical infarction in rats using laser speckle analysis. *Neuroimage*, **29**, 38–45.

77 Nagahara, M., Tamaki, Y., Araie, M., and Fujii, H. (1999) Real-time blood velocity measurements in human retinal vein using the laser speckle phenomenon. *Jpn. J. Opthalmol.*, **43**, 186–195.

78 Zhu, D., Lu, W., Weng, Y., Cui, H., and Luo, Q. (2007) Monitoring thermal-induced changes in tumor blood flow and microvessels with laser speckle contrast imaging. *Appl. Opt.*, **46**, 1911–1917.

79 Yuan, S., Devor, A., Boas, D.A., and Dunn, A.K. (2005) Determination of optimal exposure time for imaging of blood flow changes with laser speckle contrast imaging. *Appl. Opt.*, **44**, 1823–1830.

80 Briers, J.D. and Fercher, A.F. (1982) Retinal blood-flow visualisation by means of laser speckle photography. *Invest. Ophthalmol. Vis. Sci.*, **22**, 255–259.

81 Forrester, K.R., Tulip, J., Leonard, C., Stewart, C., and Bray, R.C. (2004) A laser speckle imaging technique for measuring tissue perfusion. *IEEE Trans. Biomed. Eng.*, **51**, 2074–2084.

82 Stewart, C.J., Gallant-Behm, C.L., Forrester, K., Tulip, J., Hart, D.A., and Bray, R.C. (2006) Kinetics of blood flow during healing of excisional full-thickness skin wounds in pigs as monitored by laser speckle perfusion imaging. *Skin Res. Technol.*, **12**, 247–253.

83 Zakharov, P., Völker, A., Buck, A., Weber, A., and Scheffold, F. (2006) Quantitative modeling of laser speckle imaging. *Opt. Lett.*, **31**, 3465–3467.

84 Gonik, M.M., Mishin, A.B., and Zimnyakov, D.A. (2002) Visualization of blood microcirculation parameters in human tissues by time-integrated dynamic speckles analysis. *Ann. N. Y. Acad. Sci.*, **972**, 325–330.

85 Sugii, Y., Nishio, S., and Okamoto, K. (2002) *In vivo* PIV measurement of red blood cell velocity field in microvessels considering mesentery motion. *Physiol. Meas.*, **23**, 403–416.

86 Yaoeda, K., Shirakashi, M., Funaki, S., Funaki, H., Nakatsue, T., Fukushima, A., and Abe, H. (2000) Measurement of microcirculation in optic nerve head by laser speckle flowgraphy in normal volunteers. *Am. J. Opthalmol.*, **130** (5), 606–610.

87 Bray, R.C., Forrester, K.R., Reed, J., Leonard, C., and Tulip, J. (2006) Endoscopic laser speckle imaging of tissue blood flow: applications in the human knee. *J. Orthop. Res.*, **24** (8), 1650–1659.

88 Kharlamov, A., Brown, B.R., Easley, K.A., and Jones, S.C. (2004) Heterogeneous response of cerebral blood flow to hypotension demonstrated by laser speckle imaging flowmetry in rats. *Neurosci. Lett.*, **368**, 151–156.

89 Royl, G., Leithner, C., Sellien, H., Müller, J.P., Megow, D., Offenhauser, N., Steinbrink, J., Kohl-Bareis, M., Dirnagl, U., and Lindauer, U. (2006) Functional imaging with laser speckle contrast analysis: vascular compartment analysis and correlation with laser Doppler flowmetry and somatosensory evoked potentials. *Brain Res.*, **1121**, 95–103.

90 Smith, T.K., Choi, B., Ramirez-San-Juan, J.C., Nelson, J.S., Osann, K., and Kelly, K.M. (2006) Microvascular blood flow dynamics associated with photodynamic therapy, pulsed dye laser irradiation and combined regimens. *Laser Surg. Med.*, **38**, 532–539.

91 Stewart, C.J., Frank, R., Forrester, K.R., Tulip, J., Lindsay, R., and Bray, R.C. (2005) A comparison of two laser-based methods for determination of burn scar perfusion: laser Doppler versus laser speckle imaging. *Burns*, **31**, 744–752.

92 Tyrell, J. (2007) Video capability revives interest in laser method. *Opt. Laser Eur.*, **147**, 15–16.

93 Rajan, V., Varghese, B., van Leeuwen, T.G., and Steenbergen, W. (2006) Speckles in laser Doppler perfusion imaging. *Opt. Lett.*, **31**, 468–470.

94 Demos, S.G. and Alfano, R.R. (1997) Optical polarization imaging. *Appl. Opt.*, **36**, 150–155.

95 Ishimaru, A. (1989) Diffusion of light in turbid media. *Appl. Opt.*, **28**, 2210–2215.

96 da Silva, D.d.F.T., Vidal, B.d.C., Zezell, D.M., Zorn, T.M.T., Nunez, S.C., and Ribeiro, M.S. (2006) Collagen birefringence in skin repair to red-polarized laser therapy. *J. Biomed. Opt.*, **11**, 204002.

97 Liu, Y., Kim, Y.Y., Li, X., and Backman, V. (2005) Investigation of depth selectivity of polarization gating for tissue characterization. *Opt. Express*, **13**, 601–611.

98 Schmitt, J.M., Gandjbakhche, A.H., and Bonnar, R.F. (1992) Use of polarized light to discriminate short-pass phonons in a multiply scattering medium. *Appl. Opt.*, **31**, 6535–6539.

99 MacKintosh, F.C., Zhu, J.X., Pine, D.J., and Weitz, D.A. (1989) Polarization memory of multiply scattered light. *Phys. Rev. B*, **40**, 9342–9345.

100 Karlsson, M.G. and Wårdell, K. (2005) Polarized laser Doppler perfusion imaging – reduction of movement-induced artifacts. *J. Biomed. Opt.*, **10**, 064002.

101 Pircher, M., Goetzinger, E., Leitgeb, R., and Hitzenberger, C.K. (2004) Transversal phase resolved polarization sensitive optical coherence tomography. *Phys. Med. Biol.*, **49**, 1257–1263.

102 Goetzinger, E., Pircher, M., Sticker, M., Dejaco-Ruhswurm, I., Kaminski, S., Findl, O., Skorpik, C., Fercher, A.F., and Hitzenberger, C.K. (2003) Three dimensional polarization sensitive optical coherence tomography of normal and pathologic human cornea. *Proc. SPIE*, **5140**, 120–124.

103 Smith, Z.J. and Berger, A.J. (2005) Surface-sensitive polarized Raman spectroscopy of biological tissue. *Opt. Lett.*, **30**, 1363–1365.

104 Sun, Y., Su, J.W., Lo, W., Lin, S.J., Jee, S.H., and Dong, C.Y. (2003) Multiphoton imaging of the stratum corneum and the dermis in *ex-vivo* human skin. *Opt. Express*, **11**, 3377–3382.

105 Jacques, S.L., Ramella-Roman, J.C., and Lee, K. (2002) Imaging skin pathology with polarized light. *J. Biomed. Opt.*, **7**, 329–340.

106 Groner, W., Winkelman, J.W., Harris, A.G., Ince, C., Bouma, G.J., Messmer, K., and Nadeau, R.G. (1999) Orthogonal polarization spectral imaging: a new method for study of the microcirculation. *Nat. Med.*, **5**, 1209–1213.

107 Mathura, K.R., Vollebregt, K.C., Boer, K., DeGraaff, J.C., Ubbink, D.T., and Ince, C. (2001) Comparison of OPS imaging and conventional capillary microscopy to study the human microcirculation. *J. Appl. Physiol.*, **91**, 74–78.

108 Milner, S.M., Bhat, S., Gulati, S., Gherardini, G., Smith, C.E., and Bick, R.J. (2005) Observations on the microcirculation of the human burn wound using orthogonal polarization spectral imaging. *Burns*, **31**, 316–319.

109 Langer, S., Harris, A.G., Biberthaler, P., von Dobschuetz, E., and Messmer, K. (2001) Orthogonal polarization spectral imaging as a tool for the assessment of hepatic microcirculation: a validation study. *Transplantation*, **71**, 1249–1256.

110 Genzel-Boroviczeny, O., Strontgen, J., Harris, A.G., Messmer, K., and Christ, F. (2002) Orthogonal polarization spectral imaging (OPS): a novel method to measure the microcirculation in term and preterm infants transcutaneously. *Pediatr. Res.*, **51**, 386–391.

111 Yaroslavsky, A.N., Salomatina, E.V., Neel, V., Anderson, R., and Flotte, T. (2007) Fluorescence polarization of tetracycline derivatives as a technique for mapping nonmelanoma skin cancers. *J. Biomed. Opt.*, **12**, 014005.

112 Yaroslavsky, A.N., Neel, V., and Anderson, R.R. (2004) Fluorescence polarization imaging for delineating nonmelanoma skin cancers. *Opt. Lett.*, **29**, 2010–2012.

113 Arimoto, H. (2007) Estimation of water content distribution in the skin using dualband polarization imaging. *Skin Res. Technol.*, **13**, 49–54.

114 Jacques, S.L., Roman, J.R., and Lee, K. (2000) Imaging superficial tissues with polarized light. *Lasers Surg. Med.*, **26**, 119–129.

115 Ramella-Roman, J.C., Lee, K., Prahl, S.A., and Jacques, S.L. (2004) Design, testing, and clinical studies of a handheld polarized light camera. *J. Biomed. Opt.*, **9**, 1305–1310.

116 O'Doherty, J., Henricson, J., Anderson, C., Leahy, M.J., Nilsson, G.E., and Sjoberg, F. (2007) Sub-epidermal imaging using polarized light spectroscopy for assessment of skin microcirculation. *Skin Res. Technol.*, **13** (4), 472–484.

117 O'Doherty, J., McNamara, P., Clancy, N.T., Enfield, J.G., and Leahy, M.J. (2009) Comparison of instruments for investigation of microcirculatory blood flow and red blood cell concentration. *J. Biomed. Opt.*, **14** (3), 034025.

118 Leahy, M.J., O'Doherty, J., McNamara, P., Henricson, J., Nilsson, G.E., Anderson, C., and Sjoberg, F. (2006) Diffuse reflection imaging of sub-epidermal tissue haematocrit using a simple RGB camera. *Proc. SPIE*, **6535**, 653503.

119 Diebold, G.J., Sun, T., and Khan, M.I. (1992) In *Photoacoustic and Photothermal Phenomena III* (ed. D. Bicanic), Springer, Berlin, pp. 263–296.

120 Wang, X., Xu, Y., Xu, M., Yokoo, S., Fry, E.S., and Wang, L.V. (2002) Photoacoustic tomography of biological tissues with high cross-section resolution: reconstruction and experiment. *Med. Phys.*, **12**, 2799–2805.

121 Xu, M. and Wang, L.V. (2002) Time domain reconstruction of thermoacoustic tomography in a spherical geometry. *IEEE Trans. Med. Imaging*, **21**, 814–822.

122 Xu, M. and Wang, L.V. (2005) Universal back-projection algorithm for photoacoustic computed tomography. *Phys. Rev.*, **71** (1 Pt. 2), 016706.

123 Yang, D., Xing, D., Tan, Y., Gu, H., and Yang, S. (2006) Integrative prototype B-scan photoacoustic tomography system based on a novel hybridized scanning head. *Appl. Phys. Lett.*, **88** (17), 174101.

124 Wang, X., Pang, Y., Ku, G., Stoica, G., and Wang, L. (2003) Three-dimensional laser-induced photoacoustic tomography of mouse brain with the skin and skull intact. *Opt. Lett.*, **28**, 1739–1741.

125 Lamminen, H. and Voipio, V. (2008) Computer-aided skin prick test. *Exp. Dermatol.*, **17** (11), 975–976.

126 Wang, R.K. (2007) Three-dimensional optical micro-angiography maps directional blood perfusion deep within microcirculation tissue beds *in vivo*. *Phys. Med. Biol.*, **52**, N531–N537.

127 Wang, R.K., Jacques, S.L., Ma, Z., Hurst, S., Hanson, S.R., and Gruber, A. (2007) Three dimensional optical angiography. *Opt. Express*, **15**, 4083–4097.

128 Monstrey, S., Hoeksema, H., Verbelen, J., Pirayesh, A., and Blondeel, P. (2008) Assessment of burn depth and burn wound healing potential. *Burns*, **34** (6), 761–769.

27
Optical Oximetry

Stephen J. Matcher

27.1
Introduction

The most immediate requirement of most eukaryotic life forms is the continued availability of molecular oxygen. The physiology of all animals has evolved to ensure that an adequate supply of oxygen can always be maintained between the atmosphere and the mitochondria within the cells of the body. Oxygen reduces free protons to water in the terminal stage of the oxidative phosphorylation pathway, by which glucose is ultimately converted to CO_2 and water, with the resulting release of energy. Oxidative phosphorylation is the most effective pathway for the synthesis of adenosine triphosphate (ATP), and if this pathway is halted then anaerobic glycolysis alone must meet the body's demand for ATP. Only in a few rare cases (e.g., the cornea of the eye) can glycolysis meet this demand for any appreciable time, so in the absence of oxygen there is an initial decrease in tissue pH (acidosis) and accumulation of lactate, a halt in ATP synthesis followed later by a failure of cell membrane ion pumps, and ultimately hypoxic cell death. In the brain, irreversible damage occurs within just a few minutes. The ability to monitor oxygen delivery to the cells is therefore a major goal of physiological measurement science.

In mammals, oxygen is extracted from the air and transported to cells by a mixture of active and passive (diffusive) transport. The respiratory system extracts O_2 from the air and this is diffusively transported into the blood via close arrangement of alveoli and capillaries in the lungs. Blood is a suspension of erythrocytes in plasma and each erythrocyte (a biconcave anuclear cell about 8 μm in diameter and 2 μm thick) contains the 64 kDa metalloprotein hemoglobin. Each molecule of hemoglobin can physically bind four O_2 molecules. At normal physiological hematocrit, this results in an O_2 concentration nearly 100 times greater than the dissolved O_2 concentration in the plasma. The pulmonary and systemic circulations, powered by the heart, then actively transport this oxygenated blood through the systemic arterial circulation and into the capillary bed. The smallest capillaries are ~10 μm in diameter and all cells of the body that rely on oxidative phosphorylation are located within about 100 μm of a

Handbook of Biophotonics. Vol.2: Photonics for Health Care, First Edition. Edited by Jürgen Popp, Valery V. Tuchin, Arthur Chiou, and Stefan Heinemann.

capillary, so that passive diffusion, driven by the local O_2 partial pressure gradient, then delivers the oxygen through the cell membrane to the mitochondria.

From the previous discussion, we can see the importance of technologies that can monitor all stages of this O_2 transport process, especially in a critical care setting. The need to monitor the correct function of the heart has led to major developments in electrocardiography and lung function is routinely measured by electrical impedance techniques. Likewise, the corresponding systemic blood perfusion pressure can be measured noninvasively by techniques such as oscillometry and also invasively via catheter-based pressure transducers. The resulting volume flow rate of blood can be measured directly using clearance or dilution techniques (although this is not common in critical care medicine) or Doppler ultrasound, and this leaves one final parameter to be determined in order to characterize the supply rate of oxygen to the capillary bed: the overall fraction of blood hemoglobin molecules that are physically bound to oxygen. Denoting the overall concentration of oxygenated hemoglobin in blood as $[O_2Hb]$ and that of deoxygenated hemoglobin as [HHb], then the hemoglobin saturation is defined as $[O_2Hb]/([O_2Hb] + [HHb])$. Given that the majority of the extraction of O_2 occurs in the capillary level, it is clear that this parameter will vary between the main vascular beds, with the arterial saturation exceeding the capillary saturation, which in turn will exceed the venous saturation.

27.2 Co-Oximetry

Oximetry is the name collectively given to techniques that estimate hemoglobin saturation using changes in the optical or near-infrared (NIR) absorption spectrum. It is well known that systemic arterial blood appears vivid crimson whereas systemic venous blood appears a duller brown (and vice versa in the pulmonary circulation). Hemoglobin physically binds oxygen via a conformational change that displaces the iron centers in the molecule, causing a shift in their spectral absorption peaks. Figure 27.1 shows the specific (i.e., molar) extinction coefficient spectra of the two forms of hemoglobin. The large peak in extinction at around 400 nm for both forms accounts for the red hue of blood. In the orange part of the spectrum (450–600 nm), subtle differences occur between the two forms and only at a few specific wavelengths (the "isosbestic points") are the extinction coefficients equal. The extinction coefficients are much lower than in the blue region, which makes it feasible to obtain transillumination spectra across thin samples of undiluted blood. This trend continues into the NIR region (600–1000 nm), where again distinct spectra arise for HHb and O_2Hb and a single isosbestic point occurs at around 800 nm. It is of great significance that the molar extinction coefficient is nearly 100 times lower than in the visible region. This makes it technically feasible to transilluminate intact biological tissue across several centimeters of pathlength and hence obtain spectroscopic information on blood in tissue noninvasively.

A very important application of oximetry is the co-oximeter. This instrument is a bench-top device that accepts blood samples drawn from a patient and automatically

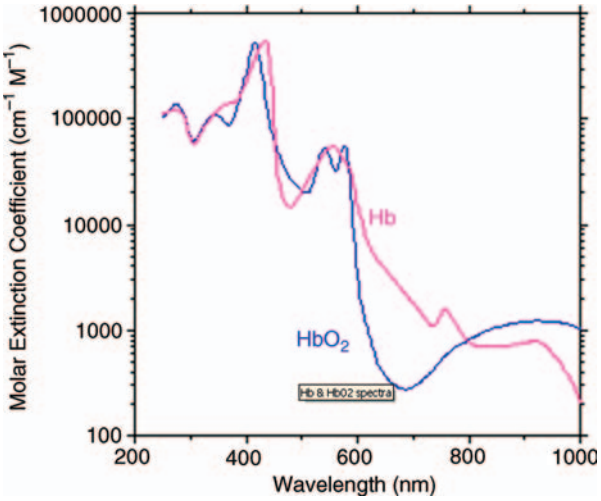

Figure 27.1 Molar extinction coefficient spectra of O_2Hb (HbO_2) and HHb (Hb). Reproduced from http://omlc.ogi.edu/spectra/hemoglobin/index.html (last accessed 3 May 2011).

obtains a visible transillumination spectrum at a number of wavelengths in the visible region. The Beer–Lambert law and multilinear regression are used to convert measurements of light transmission at distinct wavelengths into species concentrations by using the known molar extinction coefficient spectra of the species. Formally, the machine measures the incident and transmitted light intensities I_0 and I when transilluminating a standard pathlength l of blood. Expressing the attenuation in optical density (OD) units, then by the Beer–Lambert law:-

$$\mathrm{OD} = \log_{10}\left(\frac{I_0}{I}\right) = \alpha l = (C_{\mathrm{HHb}}\varepsilon_{\mathrm{HHb}} + C_{\mathrm{O_2Hb}}\varepsilon_{\mathrm{O_2Hb}} + C_{\mathrm{COHb}}\varepsilon_{\mathrm{COHb}} + C_{\mathrm{MetHb}}\varepsilon_{\mathrm{MetHb}})l \tag{27.1}$$

where C_{HHb} is the concentration of HHb and $\varepsilon_{\mathrm{HHb}}$ is the molar extinction coefficient at the measurement wavelength, and similarly for the other species. Repeating the measurements at a series of wavelengths allows the above equation to be written in matrix form:

$$\mathbf{OD} = \varepsilon \cdot \mathbf{C} \tag{27.2}$$

where **OD** and **C** are column vectors of OD measurements and concentrations, respectively, and ε is a matrix of molar extinction coefficients, each row of which relates to a specific species and each column to a specific measurement wavelength. **C** is then obtained from **OD** by a suitable matrix inversion procedure. Evidently measurements are needed to at least two wavelengths if there are two species present in the sample. Although human blood is predominantly composed of either HHb or O_2Hb, in certain situations there can also be significant amounts of other forms, chiefly carboxyhemoglobin (COHb) and methemoglobin (MetHb). Elevated COHb is

associated with carbon monoxide poisoning and leads directly to tissue hypoxia since CO has a binding affinity to hemoglobin that is over 200 times greater than that for O_2. Elevated methemoglobin (an abnormal form of hemoglobin in which the normally ferrous iron Fe^{2+} center in the heme group is replaced by ferric iron Fe^{3+}) indicates methemoglobinemia and again leads to hypoxia as MetHb is unable to bind reversibly to O_2. The co-oximeter therefore uses multiple measurement wavelengths to determine the concentrations of all these distinct hemoglobin species. A potential complication of the measurement is that the measured light attenuation is determined not just by absorption by the hemoglobin species but also by elastic light scattering caused by the red blood cell membranes. This is analogous to the light attenuation caused by fog, which is an aerosol formed by the dispersion of one nonabsorbing substance (water) in another (air). The co-oximeter avoids this problem by lysing the blood cells using detergents or sonication, thereby releasing the hemoglobin into nonscattering solution.

27.3 Pulse Oximetry

In 1942, Glenn Millikan in the United States developed the first practical *in vivo* oximeter. This device transilluminated the pinna of the ear using visible and infrared light and used mechanical pressure from a pneumatic bulb to exsanguinate blood from the tissue and hence collect a blood-free reference measurement. This aimed to estimate the contribution to light attenuation arising purely from tissue scattering. This device was used successfully in a number of physiological studies, especially in military aviation, where transient cerebral hypoxia was a major cause of blackouts experienced by fighter pilots engaged in high-G maneuvers. However, issues surrounding the reproducibility of the oxygenation values and also instrumental stability issues posed challenges to its widespread adoption in critical care medicine. In 1964, Hewlett-Packard commercialized an ear oximeter based on eight separate wavelengths which attempted to measure oxygenation *in vivo* by calibrating some of the scattering-induced background signals using measurements at these extra wavelengths. However, the bulk and expense of this machine meant that it has rarely been used outside specialist physiology laboratories. A major breakthrough occurred in 1975, when Nakajima *et al.* of Minolta Corporation demonstrated that most of the calibration and reproducibility problems generated by tissue scattering could be eliminated by making dynamic measurements of light attenuation between the systolic and diastolic phases of the cardiac cycle. A combination of the elastic compliance of arterial blood vessels and the large pulse pressure amplitudes in the arterial compartment means that the blood volume in this compartment shows measurable pulsatility at the cardiac frequency whereas the capillary and venous compartments do not. By measuring $\Delta OD = OD_{systolic} - OD_{diastolic}$, all contributions due to tissue scattering cancel, as do contributions due to capillary and venous hemoglobin absorption. This results in the determination of the relative proportions of O_2Hb and HHb in the arterial blood, that is, the arterial saturation SaO_2 can be

derived. The great strengths of pulse oximetry are its simplicity, cost, and above all robustness and reliability in a clinical setting. Pulse oximetry is indicated in essentially all critical care and surgical situations and consequently is now ubiquitous in hospital-based medicine. To quote Severinghaus and Astrup: "Pulse oximetry is arguably the most significant technological advance ever made in [critical care] monitoring" [1].

27.4
Near-Infrared Spectroscopy and Imaging

Despite its enormous success, pulse oximetry does have some limitations:

- Only arterial saturation is measured, but venous saturation is also needed in order to estimate O_2 consumption.
- Scattering effects can still influence results indirectly via wavelength-dependent changes in the effective light pathlength and so empirical algorithms are frequently built in to pulse oximeters to obtain acceptable results.
- There is no direct spatial localization available, in contrast to imaging techniques for blood flow such as Doppler ultrasound.
- Only peripheral oxygenation is measured, common sites being the pinna of the ear or the finger-tip.

In 1977, Franz Jöbsis published a landmark paper in which he demonstrated that oxygen-dependent data could be obtained *in vivo* by transilluminating the intact skull of a cat using NIR light [2]. The original paper actually attempted to measure the oxidative phosphorylation pathway directly by detecting redox-dependent changes in the NIR absorption of cytochrome oxidase, a redox-active enzyme which forms part of the electron transport chain in the mitochondrial inner membrane. However, interest soon shifted to oximetry, in part because the inherent concentration of cytochrome oxidase in tissue is so low that hemoglobin absorption generally dominates over cytochrome oxidase absorption. In 1988, Cope and Delpy demonstrated the first clinically useable NIR spectrometer which used laser diodes and photomultipliers to provide deep tissue oxygenation data over 40 mm or more of transilluminated tissue [3]. This machine was soon commercialized by Hamamatsu Photonics as the NIRO-1000, and the field of clinical tissue near-infrared spectroscopy (NIRS) was born.

The NIRO-1000 was a "first-generation" NIRS system that did not provide an absolute value either for the total tissue hemoglobin concentration or the saturation. This was because the scattering offset was not removed by using pulsatile signals, as the aim of this device is to measure signals from all three compartments simultaneously. It is also impractical to obtain a blood-free reference using mechanical exsanguination on such large tissue volumes. Hence first-generation systems function as a trend monitor, that is, a baseline spectrum is recorded at a particular time and then the change in attenuation ΔOD relative to that baseline is recorded. The result of linear regression calculation is then the change in

hemoglobin concentration in the tissue relative to the starting point. Unlike the pulse oximeter, the tissue NIRS system records the change in concentration of both species that is, it records $\Delta HHb(t)$ and $\Delta O_2Hb(t)$. It is therefore incapable of measuring the absolute level of hemoglobin saturation which is required to measure O_2 delivery. Worse still, in the absence of direct information on the photon pathlength l, it cannot quantify the magnitude of the change in absolute units such as mM; instead the units are unquantified mM cm. The physical distance between the light source and detector does not relate directly to the photon pathlength l through the tissue because intense scattering of photons causes them to travel in a quasi-random path from source to detector. The low volume fraction of blood in tissue (typically only a few percent) means that scattering is over 100 times more intense than absorption for NIR photons propagating through tissue. This is different to the situation in cuvette-based spectroscopy of nonscattering solutions. Fortunately, a number of technical solutions have been demonstrated that can provide "quantified trend" measurements by measuring the mean photon path length l. In 1988, Delpy *et al*. reported the first *in vivo* measurements of l (generally known as the differential pathlength) in human volunteers using a direct time-of-flight approach [4]. By illuminating the tissue with a picosecond pulse of light from a mode-locked titanium:sapphire laser and recording the transmitted light intensity as a function of time using a streak camera, the mean transit time of the pulse was determined. For a source–detector separation of 40 mm of tissue it was found that the photons had actually traveled over 200 mm, indicating a fivefold path lengthening. As explained, this arises because the photons do not travel directly from source to detector but follow a random path, with changes of direction occurring several times per millimeter. Shortly afterwards, Benaron *et al*. obtained similar measurements by using an intensity-modulated laser beam rather than a pulsed one [5]. By measuring the phase shift of the transmitted light relative to the incident light the mean transit time can again be derived. The phase method is generally cheaper and simpler to implement than the time-domain method. In 1994 Matcher, Cope and Delpy showed that pathlength could be obtained by measuring the apparent strength of the absorption band of water and comparing this with that of pure water [6]. Since the concentration of water in biological tissues is generally known, this provides information on the photon pathlength. At the time of writing, to the author's knowledge, none of these approaches has been implemented into a commercial NIRS system; however, reference values derived using these techniques in laboratory-based studies are incorporated into the software of most NIRS systems, so that quantified trend methods are routinely available.

Quantified trend monitors fall short of what clinicians ideally want in a critical care monitoring situation, namely a continuous absolute measurement of tissue saturation; however, quantitative hemodynamic measurements can be obtained indirectly. Blood flow can be inferred in several ways. In skeletal muscle, occlusion plethysmography can be performed using the NIRS-derived hemoglobin concentration as the volume measurement [7]. In the head, a modified clearance technique can be implemented in which O_2Hb itself is the tracer [8] and blood volume can be

inferred using a similar idea: a dilution measurement is effectively performed using O_2Hb as the tracer [9]. Venous saturation can be inferred if a moderate venous occlusion is performed, again by using the plethysmographic principle and assuming that the resulting hemodynamic change arises solely through the pooling of venous blood [10]. A completely passive approach has been proposed in which respiratory fluctuations are used: changes in blood volume that occur at the respiratory frequency are assumed to arise solely from oscillations in venous blood volume because of the resulting fluctuations in venous pressure and the very high elasticity of the veins [11].

Despite these advances, the clinical uptake of NIRS has been impeded by the lack of a direct measurement of saturation. Responding to this challenge, both researchers and manufacturers have developed a number of approaches to the problem. Fundamentally, the difficulty arises because in a highly scattering medium the Beer–Lambert law no longer strictly applies, that is, the measurement (OD) is not a linear combination of the hemoglobin concentrations. Instead, two new parameters must be introduced, the tissue absorption and modified scattering coefficients μ_a and μ'_s. μ_a is linearly related to the hemoglobin concentrations; however, the measured OD is related in a complicated nonlinear way to both μ_a and μ'_s. In all cases, then, the approach to "absolute" oximetry involves attempting to determine directly the underlying absolute values of μ_a and μ'_s of the tissue given measurements of ODs. If μ_a is available at several wavelengths, then standard multilinear regression can be used to obtain the hemoglobin concentrations. Several distinct approaches have been introduced. Time-resolved spectroscopy uses the temporal distribution of transmitted light resulting from an incident picosecond light pulse to determine μ_a and μ'_s [12]. This distribution $I(t)$ is generally called the temporal point spread function (TPSF). Its mean value gives the differential path length already described. By comparing the TPSF with one predicted by a forward model of light transport in tissue, μ_a and μ'_s can be derived by least-squares fitting. This model is usually the diffusion equation. A variant of this idea is to use frequency-domain measurements. An intensity-modulated laser is used and the mean transit time and attenuation are measured for a variety of modulation frequencies [13]. One can show that this provides equivalent information to the time-domain approach. A third approach is to make measurements of light attenuation for a series of different source–detector spacings [14]. This approach is often referred to as spatially resolved spectroscopy (SRS) and has the major advantage of simplicity as only continuous-wave laser diodes and DC signal detectors are needed. Consequently, this approach has been commercialized in "second-generation" NIRS systems such as the Hamamatsu NIRO-100. A significant challenge for these machines is that they rely on a mathematical model of light transport through the tissue and this model will depend on the specific geometry of the tissue under study. In skeletal muscle studies, for example, the model must account for the thickness of overlying and weakly vascularized adipose layers whereas in the head the effects of extracranial tissues and the CSF layer are important. This points to a general area of research in tissue NIRS involving the need both to quantify and to localize the signals; the interested reader is directed elsewhere to a more extensive discussion of this field [15].

The need to combine NIRS with signal localization has spawned the related field of near-infrared imaging (NIRI). The use of a mathematical model to extract tissue absorption and scattering coefficients from measurements of light attenuation is taken to a greater level of sophistication by using measurements at a large number (tens to hundreds) of source–detector positions and then attempting to determine spatial maps of μ_a and hence oxygenation. This technology has evolved extensively over the last decade; however, routine clinical application has not yet been established. Spatially resolved trend monitors have proven to be valuable in functional studies of brain activation. This is a partial approach to imaging known as "optical topography," and seems to be capable of producing maps of cortical activation in response to a variety of cognitive and motor tasks similar to those obtainable by much more expensive and complicated techniques such as functional magnetic resonance imaging. The interested reader is directed to recent review articles [16].

27.5 New Approaches

No review of current approaches to noninvasive oximetry would be complete without a mention of emerging technologies such optical coherence tomography, hyperspectral imaging, and photoacoustic imaging. All of these techniques provide much higher spatial resolution than NIRS and NIRI at the expense of tissue penetration depth, and the emphasis is on physiological studies rather than clinical monitoring (although photoacoustic imaging has potential for clinical monitoring).

Optical coherence tomography (OCT) is an optical analog of ultrasound imaging with lower tissue penetration (<2 mm) but higher resolution (2–10 μm). Conventional OCT derives contrast from tissue boundaries, similarly to ultrasound; however, variants have been proposed to provide molecular contrast to hemoglobin and other species. The challenge is that the absorption coefficient of hemoglobin is very low in the NIR region, so the contrast generated over the very short pathlengths that characterize OCT is low. One potential solution to this is "pump–probe" OCT, in which transient changes in μ_a are induced by saturating the molecular ground state of the molecule using short pulses of pump radiation [17]. This pump light can lie in the visible range, whereas the imaging (i.e., "probe") OCT beam can be in the infrared region, thus retaining good depth penetration and resolution. This technology is interesting but has yet to demonstrate a clinical impact; the next few years could well clarify the situation.

Interest in the use of the visible spectrum has seen resurgence in recent years through the introduction of multispectral and hyperspectral cameras which can produce 3D data cubes whereby a 2D image gains a third dimension of wavelength information. 2D real-time images of hemoglobin saturation can thus be created with cellular level resolution. The main applications of this technology currently relate to basic physiological studies in animal models; in particular, the hemoglobin saturation in tumor vasculature can be determined [18]. Hypoxia is a characteristic of the tumor microenvironment because of a mismatch between metabolic demand from

the hyperproliferating cells and blood supply. It is therefore important to monitor the effects of pharmacological treatments such as vasculature-targeting combretastatins on this parameter.

Photoacoustic imaging is a rapidly emerging new modality which effectively gives ultrasound imaging sensitivity to molecular absorption. The technique locates areas of high optical absorption, such as a blood vessels, by causing rapid and transient heating using a nanosecond pulse of light whose wavelength matches a peak in the absorption spectrum of compound. The rapidity of this heating and the resulting mechanical expansion of the surrounding water generate a pulse of ultrasound that can be detected on the tissue surface using a conventional ultrasound hydrophone. The amplitude of the ultrasound relates directly to the magnitude of the absorption coefficient and so, by tuning the pulsed light to various NIR wavelengths, the hemoglobin saturation can be determined [19]. A great advantage of this technique is that the arrival time of the ultrasound directly encodes the depth of the blood vessel and so an image can be formed as in conventional ultrasound. The major limitation of optical imaging of biological tissues is poor resolution and depth penetration, which arise because of intense light scattering. Photoacoustic imaging uses optical radiation only as a source of heating, image information is carried by the acoustic wave, and so resolution and depth penetration are fundamentally superior. This technology holds great promise to deliver clinically useful images of tissue oxygen delivery with a resolution matched to the dimensions of the human vasculature. The next few years will doubtless bring many interesting new developments in this area.

27.6 Conclusion

The routine clinical application of oximetry is now over 70 years old and still there is great scope for continued technological innovation and new clinical applications. The co-oximeter and pulse oximeter are standard equipment in the hematology laboratory and intensive care room, respectively, and the advent of second-generation NIRS systems that can measure absolute saturation on the brain and skeletal muscle is pushing this technology into the clinic. It should be noted, however, that debate still exists about whether NIRS technology is currently delivering clinically relevant information, owing to ongoing issues surrounding reproducibility and stability [20]. The combination of oximetry with spatially resolved mapping of the cerebral cortex can provide a viable alternative to functional magnetic resonance imaging (fMRI) in some cases, especially where the use of fMRI is impractical, such as in the neonate. New variants on old methods, especially hyperspectral imaging, are finding applications in nonclinical studies of tumor models and may also find clinical applications in, for example, studies of nonhealing wounds and burns in the skin.

Imaging technologies such as OCT and photoacoustic imaging can also be adapted to provide oximetry data. Photoacoustic imaging in particular could develop into a tool with a unique combination of spectral and spatial resolution combined with depth penetration.

References

1 Severinghaus, J.W. and Astrup, P.B. (1986) History of blood gas analysis. VI. Oximetry. *J. Clin. Monit.*, **2** (4), 270–288.

2 Jöbsis, F.F. (1977) Non-invasive infrared monitoring of cerebral and myocardial oxygen sufficiency and circulatory parameters. *Science*, **198** (4323), 1264–1267.

3 Cope, M. and Delpy, D.T. (1988) System for long-term measurement of cerebral blood and tissue oxygenation on newborn infants by near-infrared transillumination. *Med. Biol. Eng. Comput.*, **26**, 289–294.

4 Delpy, D.T., Cope, M., van der Zee, P., Arridge, S.R., Wray, S., and Wyatt, J. (1988) Estimation of optical pathlength through tissue from direct time of flight measurement. *Phys. Med. Biol.*, **33** (12), 1433–1442.

5 Benaron, D.A., Gwiazdowski, S., Kurth, C.D., Steven, J., Delivoria-Papadopoulos, M., and Chance, B. (1990) Optical pathlength of 754 nm and 816 nm light emitted into the head of infants. *Proc. IEEE Eng. Med. Biol.*, **12**, 1117–1119.

6 Matcher, S.J., Cope, M., and Delpy, D.T. (1994) Use of the water absorption spectrum to quantify tissue chromophore concentration changes in near-infrared spectroscopy. *Phys. Med. Biol.*, **39** (1), 177–196.

7 De Blasi, R.A., Ferrari, M., Natali, A., Conti, G., Mega, A., and Gasparetto, A. (1994) Noninvasive measurement of forearm blood flow and oxygen consumption by near-infrared spectroscopy. *J. Appl. Physiol.*, **76** (3), 1388–1393.

8 Edwards, A.D., Wyatt, J.S., Richardson, C., Delpy, D.T., Cope, M., and Reynolds, E.O. (1988) Cotside measurement of cerebral blood flow in ill newborn infants by near-infrared spectroscopy. *Lancet*, **ii** (8614), 770–771.

9 Wyatt, J.S., Cope, M., Delpy, D.T., Richardson, C., Edwards, A.D., Wray, S., and Reynolds, E.O. (1990) Quantitation of cerebral blood volume in human infants by near-infrared spectroscopy. *J. Appl. Physiol.*, **68** (3), 1086–1091.

10 Yoxall, C.W., Weindling, A.M., Dawani, N.H., and Peart, I. (1995) Measurement of cerebral venous oxyhemoglobin saturation in children by near-infrared spectroscopy and partial jugular venous occlusion. *Pediatr. Res.*, **38** (3), 319–323.

11 Franceschini, M.A., Zourabian, A., Moore, J.B., Arora, A., Fantini, S., and Boas, D.A. (2001) Local measurement of venous saturation in tissue with non-invasive near-infrared respiratory-oximetry. *Proc. SPIE*, **4250**, 164–170.

12 Patterson, M.S., Chance, B., and Wilson, B.C. (1989) Time resolved reflectance and transmittance for the noninvasive measurement of tissue optical properties. *Appl. Opt.*, **28**, 2331–2336.

13 Fantini, S., Franceschini, M.A., Maier, J.S., Walker, S.A., Barbieri, B., and Gratton, E. (1995) Frequency-domain multichannel optical detector for noninvasive tissue spectroscopy and oximetry. *Opt. Eng.*, **34**, 32–42.

14 Matcher, S., Kirkpatrick, P., Nahid, K., Cope, M., and Delpy, D.T. (1994) Absolute quantification methods in tissue near infrared spectroscopy. *Proc. SPIE*, **2389**, 486–495.

15 Matcher, S.J. (2002) Signal quantification and localization in tissue near-infrared spectroscopy, in *Handbook of Optical Biomedical Diagnostics* (ed. V. Tuchin), SPIE Press, Bellingham, WA, pp. 487–584.

16 Wolf, M., Ferrari, M., and Quaresima, V. (2007) Progress of near-infrared spectroscopy and topography for brain and muscle clinical applications. *J. Biomed. Opt.*, **12** (6), 062104.

17 Applegate, B.E. and Izatt, J.A. (2007) Molecular imaging of hemoglobin using ground state recovery pump–probe optical coherence tomography. *Proc. SPIE*, **6429**, 64291Y.

18 Sorg, B.S., Moeller, B.J., Donovan, O., Cao, Y., and Dewhirst, M.W. (2005) Hyperspectral imaging of hemoglobin saturation in tumor microvasculature and

tumor hypoxia development. *J. Biomed. Opt.*, **10** (4), 044004.

19 Laufer, J., Delpy, D.T., Elwell, C., and Beard, P. (2007) Quantitative spatially resolved measurement of tissue chromophore concentrations using photoacoustic spectroscopy: application to the measurement of blood oxygenation and haemoglobin concentration. *Phys. Med. Biol.*, **52**, 141–168.

20 Greisen, G. (2006) Is near-infrared spectroscopy living up to its promises? *Semin. Fetal Neonatal Med*, **11** (6), 498–502.

28
Photonic Therapies

Igor Peshko

28.1
Atrial Fibrillation

Atrial fibrillation (AF) is a heart-rhythm abnormality, which involves irregular and rapid heartbeats. During AF, irregular electrical impulses cause erratic and incomplete activation of the atria. Multiple stray currents (shown as round arrows in Figure 28.1a) result in chaotic short pulses that activate the heart muscle. The surgical maze procedure was the first treatment that offered a permanent solution for maintaining a normal sinus rhythm in patients with AF [1]. This procedure involves the creation of a maze-like series of incisions in the atrium, resulting in isolation of the pulmonary vein (Figure 28.1b). The scarring resulting from the incisions permanently blocks (isolates) the path of the erratic electrical impulses and prevents the arrhythmia. From an "electrical point of view", it does not matter which technology is used to make an incision. The incisions may be done mechanically (scalpel, ultrasound), by strong cooling (cryosurgery), or by strong heating (radio-frequency or microwave irradiation) (see review in [2]). Visible, near-infrared, or mid-infrared light can also be successfully used to initiate the scars. The optical power is easily delivered to any target, through an optical fiber, and can be focused to an area with a size spanning microns due to the small wavelength of the light. To provide an effective AF treatment, one needs a light source/catheter system that will create deep, homogeneous, electrophysiologically inactive scars with a controllable lesion size and a clear-cut lesion border. The fiber photocatheter (FPC) addresses all these requirements [3].

During the last decade, the most successful medical laser applications have been non- or less-invasive: laser trabeculoplasty, hair removal, photodynamic therapy, skin rejuvenation and cosmetology, laser treatments of psoriasis and acne, and laser acupuncture. Laser-based diagnostic tools, such as optical coherent tomography, nonlinear spectroscopy and microscopy, have become routine techniques. Any treatment that was provided with laser technologies can now be done with FPCs, with the added benefit of being used in parts of the human body that are difficult to access. In general, optical fiber technologies can be used for optical power delivery, to

Handbook of Biophotonics. Vol.2: Photonics for Health Care, First Edition. Edited by Jürgen Popp, Valery V. Tuchin, Arthur Chiou, and Stefan Heinemann.

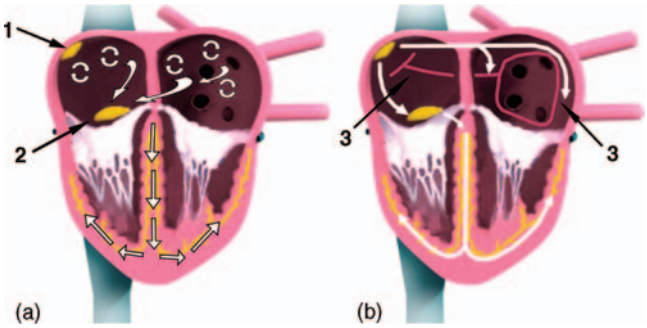

Figure 28.1 Simplified diagrams of the heart with: (a) atrial fibrillation and (b) after the treatment. 1, Sinus node; 2, atrioventricular node; 3, scars, blocking abnormal paths.

act as sensors, and as multifunctional devices controlling the laser's radiation and transferring the optical data.

28.1.1 Fiber Photocatheters

28.1.1.1 What is a Fiber Photocatheter?

A regular catheter is supposed to deliver liquid drugs, dyes, or some microinstrumentation that cannot be directly injected into the tissue. An FPC delivers light power, some optical signals, and/or contains micro-optical devices. Depending on the level of optical power, catheters may be roughly grouped into three main categories: (a) high power delivery (watts to tens of watts): scalpel-free surgery and light therapy; (b) middle (milliwatts to hundreds of milliwatts): precise microsurgery and "soft" light treatment; (c) low (microwatts to hundreds of microwatts): imaging, spectroscopy, microscopy, and so on.

The "photo" in FPC also refers to the fact that optical technologies are used for the fabrication of some parts of the catheter, such as long-period gratings, which can be photoprinted with point-by-point or interference-pattern technologies.

Historically, the first FPCs were applied in therapeutic treatments [4]. The uncoated fiber, which was mechanically scratched and/or chemically thinned, was covered with a special paste containing small particles that effectively scattered the radiation delivered by a fiber [5]. This type of FPC is still in use and is commercially available. However, this FPC is rigid, has a limited length of about 2–5 cm, and is fairly thick – 1–2 mm in diameter. An optically fabricated flexible FPS has been developed for use in photodynamic therapy [4] (Figure 28.2) and surgical treatment of atrial fibrillation with laser radiation [3, 6].

Photocatheters, being fabricated from inert materials such as quartz, Teflon, silicone rubber, and stainless steel, are ideally matched with medical requirements of sterility. Being fabricated from thin fibers (200–50 μm core), catheters are flexible enough to follow curved surfaces of typical tissue or blood-vessel "labyrinths" (inset in Figure 28.2). This makes it possible to act precisely in the intended area without

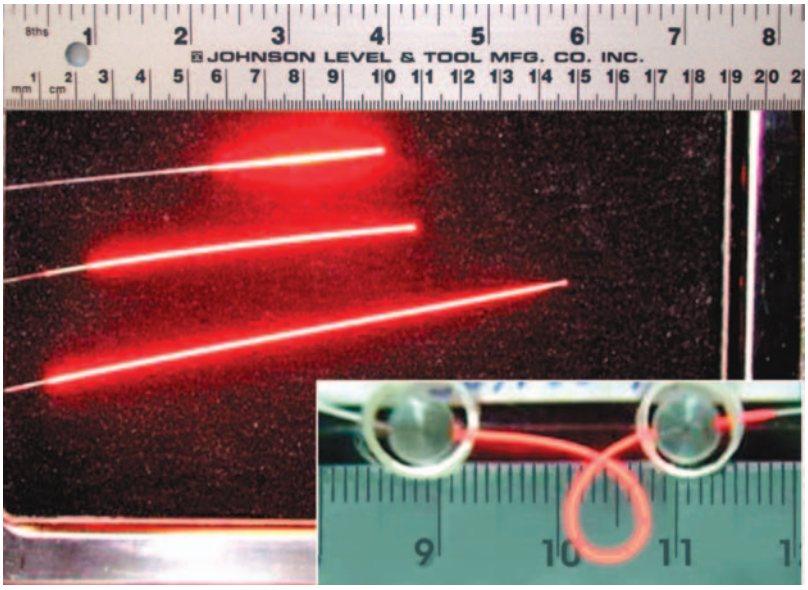

Figure 28.2 Photograph demonstrating FPCs of length 4, 9, and 14 cm. The inset shows a coiled FPC ~1.5 cm in diameter.

affecting surrounding tissue. Moreover, the FPC may be imprinted anywhere along the fiber, not only at the fiber end as a classical diffuser.

28.1.1.2 **Fiber Photocatheter Design**

A photocatheter with a flexible side-emitting optical fiber is based on specific long-period gratings (LPGs) [3, 4, 6] or Bragg gratings (BGs) [7] recorded in the core area of the fiber. These gratings produce a refractive index modulation at the fiber core–cladding interface that disrupts the total internal reflection conditions in the fiber core and enables the light traveling along the fiber to be scattered sideways. These LPGs or BGs operate as diffusers. The significant advantage of the proposed technology is that the output light intensity profile (along the catheter) is preliminarily designable [8]. It may be flat, dashed, decreasing, increasing, or any special shape. By varying the refractive index modulation value, density, and period of the gratings, it is possible to control the energy scattered along the entire length of the diffuser. For constant longitudinal radiant emission, the remaining power inside the fiber core decreases linearly with a corresponding increase in the strength of scattering as a function of the length of the grating. The local transmittance of each diffuser segment falls exponentially, reaching a minimum at the diffuser's end.

Figure 28.3 shows an example of the catheter design and demonstrates the photocatheter prototype [8]. The system includes: an up to 15 cm long, 50–400 μm core fiber diffuser (1); a 20–50 W laser diode; a flexible elliptical or cylindrical reflector (2); an end fiber cooler; a series of openings (3) for rapid self-attachment to the tissue (vacuum holder–gripper); a closed-loop irrigating chamber with circulating coolant

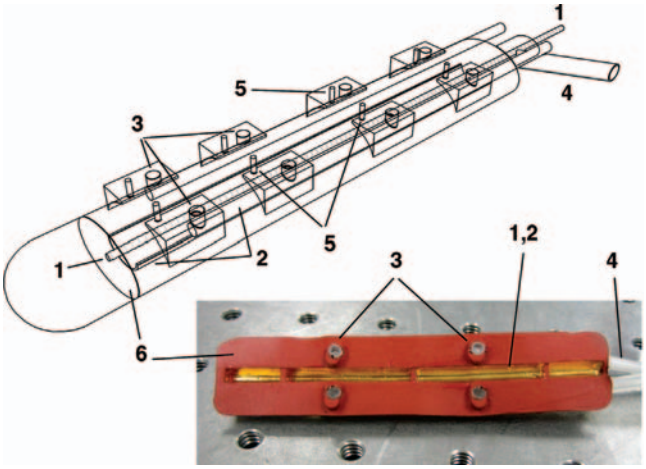

Figure 28.3 Design of the FPC for the atrial fibrillation surgical treatment: 1, Fiber with long period gratings; 2, reflector; 3, suction openings; 4, irrigation channel; 5, thermocouples. The photograph shows the FPC prototype.

(4) to cool the optical diffuser; and thermocouples for temperature control (5). Two or more light sources may be connected to the FPC with scattering of different wavelengths (colors) at different diffuser areas. The reflector is used to condense optical power on the irradiated tissue; alternatively, an LPG, recorded with a slope to reflect power to one side of the catheter, can be used. The fiber catheter body (6) was cast from high-temperature silicone rubber and was then gold coated to form a reflector.

28.2
All-in-One Endoscope Devices

An optical system can be installed at the end of a fiber, effectively transforming the fiber into a remote microscope, an optical tomograph, a spectrometer, or another endoscope instrument. A few examples of optical diagnostic catheters are mentioned below.

1) The feasibility of a time-resolved fluorescence spectroscopy technique (TRST) for intraluminal investigation of arterial vessel composition under intravascular ultrasound has been demonstrated [9]. A catheter combines a side-viewing optical fiber and an intravascular ultrasound catheter. The catheter can locate a fluorophore in the vessel wall, steer the fiber into place, perform blood flushing under flow conditions, and acquire high-quality TRFS data using ultraviolet wavelength excitation. This system has the potential for *in vivo* arterial plaque composition identification using TRFS.
2) A two-axis scanning catheter was developed for 3D endoscopic imaging with spectral domain optical coherence tomography (SD-OCT) [10]. The catheter

incorporates a micromirror scanner implemented with microelectromechanical systems (MEMS) technology. A micromirror is mounted on a two-axis gimbal comprised of folded flexure hinges and is actuated by a magnetic field. The catheter was incorporated with a multifunctional SD-OCT system for 3D endoscopic imaging.

3) An optical coherence tomography catheter–endoscope for micrometer-scale, cross-sectional imaging in internal organ systems has been demonstrated [11]. The catheter–endoscope uses single-mode fiber optics with a transverse scanning design. The distal end of the catheter–endoscope uses a gradient-index lens with a microprism to emit and collect a single spatial-mode optical beam with specific focusing characteristics. The beam is scanned in a circumferential pattern and can image transverse cross-sections through the structure into which it is inserted. An imaging of *in vitro* human venous morphology was demonstrated. A technique for performing an optical biopsy (high-resolution micrometer-scale cross-sectional optical imaging) of tissue architectural morphology, without the need to excise tissue specimens, would have a powerful effect on the diagnosis and clinical management of many diseases.
4) A one-dimensional optical fiber-based imaging catheter, specifically developed for the atherosclerotic plaque detection of emerging novel near-infrared fluorescence imaging agents, has been demonstrated [12]. It was shown that femtomole amounts of fluorochromes can be detected, especially in the presence of a blood-free medium. To detect the fluorescent molecular tags reliably, a dual-wavelength catheter-based system, using different fiber designs tuned to the near-infrared range, has been developed. The ability of the catheter to detect fluorescence signals in human carotid atherosclerotic plaque has also been demonstrated.

A multifunctional device may contain both active (optical surgical instruments) and passive (information channels) components. Devices that provide monitoring, diagnostics, and treatment by the same all-in-one device are currently being developed.

References

1 Cox, J.L., Schuessler, R.B., D'Agostino, H.J. Jr., Stone, C.M., Chang, B.C., Cain, M.E., Corr, P.B., and Boineau, J.P. (1991) The surgical treatment of atrial fibrillation, III. Development of a definitive surgical procedure. *J. Thorac. Cardiovasc. Surg.*, **101**, 569–583.

2 Song, H.K. and Puskas, J.D. Recent advances in surgery for atrial fibrillation, http://www.ctsnet.org/sections/newsandviews/specialreports/article-1.html (last accessed 20 April 2011).

3 Peshko, I., Rubtsov, V., Vesselov, L., Sigal, G., and Laks, H. (2007) Fiber photo-catheters for laser treatment of atrial fibrillation. *Opt. Laser Eng.*, **45**, 495–502.

4 Lilge, L., Vesselov, L.M., and Whittington, W. (2005) Thin cylindrical diffusers created in multimode Ge-doped silica fibers. *Lasers Surg Med.*, **36**, 245–251.

5 Fried, N.M., Lardo, A.C., Berger, R.D., Calkins, H., and Halperin, H.R. (2000) Linear lesions in myocardium created by Nd:YAG laser using diffusing optical fibers: *in vitro* and *in vivo* results. *Laser Surg. Med.*, **27**, 295–304.

6 Rubtsov, V., Laks, H., Levin, M., Akbarian, M., and Peshko, I. (2008) Fiber optic tissue ablation. U.S. Pat. Appl. US 2008/0082091 A1 3 April 2008.

7 Gu, X. and Tam, R. (2002) Optical fiber diffuser. U.S. Pat. US 6398778, filed 18 June 1999, issued 4 June 2002.

8 Peshko, I. and Rubtsov, V. (2007) Fiber photo-catheters with spatially modulated diffusers for laser treatment of atrial fibrillation. *Proc. SPIE*, **6424**, 642421.

9 Stephens, D.N., Park, J., Sun, Y., Papaioannou, T., and Marcu, L., (2009) Intraluminal fluorescence spectroscopy catheter with ultrasound guidance. *J. Biomed. Opt. Lett.*, **14** (3), 030505.

10 Kim, K.H., Park, B.H., Maguluri, G.N., Lee, T.W., Rogomentich, F.J., Bancu, M.G., Bouma, B.E., de Boer, J.F., and Bernstein., J.J. (2007) Two-axis magnetically-driven MEMS scanning catheter for endoscopic high-speed optical coherence tomography. *Opt. Express*, **15** (26), 18130–18140.

11 Tearney, G.J., Boppart, S.A., Bouma, B.E., Brezinski, M.E., Weissman, N.J., Southern, J.F., and Fujimoto., J.G. (1996) Scanning single-mode fiber optic catheter–endoscope for optical coherence tomography. *Opt. Lett.*, **21** (7), 543–545.

12 Zhu, B., Jaffer, F.A., Ntziachristos, V., and Weissleder., R. (2005) Development of a near infrared fluorescence catheter: operating characteristics and feasibility for atherosclerotic plaque detection. *J. Phys. D: Appl. Phys.*, **38**, 2701–2707.

29
Bronchoscopy

Lutz Freitag, Kaid Darwiche, and Dirk Hüttenberger

29.1
Diagnostics

The first report about a direct inspection of the airways of a living human being was published in 1897 [1]. Gustav Killian, an ENT surgeon had removed an aspirated chicken bone from the trachea of a farmer. For this first direct laryngoscopy he had used a rigid tube, inserted into the airways under local anesthesia. The next step was the development of angled rigid telescope lenses in combination with external light sources. This enabled physicians to detect abnormalities in lobar bronchi. Today, rigid bronchoscopy is performed mainly for therapeutic purposes. Interventional procedures, for example, tumor resection and stent insertion, are done faster and more safely with rigid bronchoscopes under general anesthesia and jet ventilation. In 1966, the Japanese thoracic surgeon Shigeto Ikeda built the first flexible fiber-optic bronchoscope. Every pulmonologist in the world knows his slogan, "more hope with the bronchoscope." In the following years, light sources became brighter, photo- and video-cameras were added, and the number of fibers and consequently the resolution were improved. Within the last 10 years, fiber bronchoscopes have been replaced by video-chip bronchoscopes. Figure 29.1 demonstrates the tremendous progress in image quality. The resolution of a routine instrument is so good that even the smallest surface abnormalities and also vessel distortions are visualized. Flexible bronchoscopes are easy to handle, and they have working channels that allow all kinds of optical probes, catheters, brushes, and biopsy forceps to pass. Therapeutic instruments such as laser fibers, electrocautery, and cryo-probes can be guided to targets down to subsegmental bronchi. The latest progress that has extended the use of bronchoscopy is the incorporation of an ultrasound sector scanner. With a modern endobronchial ultrasound (EBUS) bronchoscope, one can not only see the inner surface of the airways but also visualize adjacent anatomic structures. EBUS has revolutionized lung cancer staging. It has become common practice to puncture hilar and mediastinal lymph nodes under ultrasound guidance. Even small forceps biopsies from nodes can be taken (Figure 29.1c). Ideally, the aspirated cells are examined by the pathologist directly in the bronchoscopy suite. By combining flexible

Handbook of Biophotonics. Vol.2: Photonics for Health Care, First Edition. Edited by Jürgen Popp, Valery V. Tuchin, Arthur Chiou, and Stefan Heinemann.

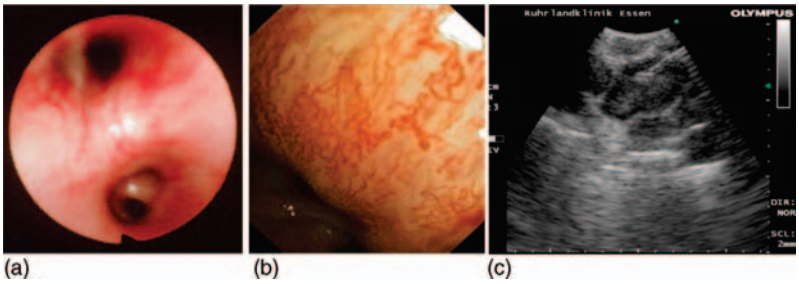

Figure 29.1 Progress of white light bronchoscopy. (a) Fiber-optic bronchoscopy image from 1995; (b) routine video-chip bronchoscope image from 2010; (c) lymph node puncture with endobronchial ultrasound (EBUS) bronchoscope.

bronchoscopy, EBUS, and on-site cytology endoscopic diagnosis, tumor type determination and lymph node staging are accomplished within less than 30 min.

29.1.1 Cancer Detection

Pulmonologists performing bronchoscopy are dealing with one of the most devastating diseases at all, lung cancer. It is estimated that 1.2 million people die every year from this cancer, which is mainly caused by cigarette smoking. Despite all medical progress, the prognosis remains poor because most patients are diagnosed at a stage when curative treatment is no longer possible. Screening and early detection programs are the only hope unless the tobacco industry decides to go out of business voluntarily. A typical squamous cell cancer in a lobar bronchus develops over a time span of more than 15 years. Without causing any symptoms during the first 12 years, it evolves from a tiny dysplastic lesion to a carcinoma *in situ* and then to a mass tumor that can occlude a bronchus and induce metastasis in other organs. Within the next few years the patient becomes incurable. Tumor-associated symptoms such as hemoptysis (coughing up blood) or shortness of breath that would indicate a possible tumor presence occur only in advanced stages. This long period of asymptomatic tumor growth leaves only a small time window for diagnosis. We do not know why many but not all dysplasias progress to squamous cell lung cancers. There are other premalignant changes that can result in deadly tumors. Adenocarcinomas develop from atypical adenomatous hyperplasias. They are usually located more peripherally than squamous cell cancers. Diffuse idiopathic pulmonary neuroendocrine cell hyperplasias (DIPNECH) advance into carcinoids. The technical challenge is to diagnose these tumors preferably in their earliest stages when curative treatment is still possible. Screening programs include computed tomography (CT), sputum cytology, use of molecular markers, and analysis of exhaled breath. If any of these methods indicates the presence of an early cancer, patients are administered bronchoscopy. If the tumor mass is still low, cancer formations are not seen on chest X-rays or CT scans. Bronchoscopy, mostly with a flexible endoscope under mild conscious sedation and local anesthesia, is used to find the tumor spot and take a

biopsy for pathologic examination. Older studies aiming to find radio-occult cancers with white light bronchoscopy had sensitivities lower than 30%, and the detection rates of early invasive cancers were in the region of 60% [2, 3]. However, judging from the results, it is important to realize that these findings were made with fiber-optic scopes with limited resolutions, as shown in Figure 29.1a. It is reasonable to assume that detection rates of early lesions might be higher with current state-of-the-art video-chip endoscopes. Using white light bronchoscopy, early lesions do not differ much in color from normal mucosa and they are especially difficult to find in the presence of mild inflammation that is typical for smokers. There are two main approaches aimed at increasing the contrast between preneoplastic, neoplastic, and normal tissue: filtering parts of the remitted white light or visualization of fluorescence on excitation with non-white light.

29.1.2
Filter-Based Techniques for Tumor Detection

Early stages of tumor development are characterized by changes in cell composition, tissue layer thicknesses, and neo-vascularization. The tumor demands nutrition and it satisfies its need by stimulating angiogenesis. Blood vessels in the mucosa change shape, pattern, and density. This phenomenon can be used for diagnostic purposes with various optical techniques considering that blood has high absorption properties [4]. State-of-the-art light sources are xenon arc lamps. The bright white light is passed through an infrared light filter and transmitted to the bronchoscope via a fiber-optic bundle or a liquid light guide. Under normal conditions, the remitted light is picked up by a color chip camera and the image is displayed on a video screen as unaffected as possible. Vessels appear red on a pale mucosal background. If the remitted light is filtered properly, absorption differences can be emphasized.

To enhance the contrast of the mucosal microvasculature and possible alterations, only parts of the white light spectrum are used for illumination [5–8]. This is accomplished by placing a narrowband filter in front of the white light source. Basically, the absorption properties of blood are used in order to increase the diagnostic yield. One popular device is the EVIS EXERA narrowband imaging (NBI) system from Olympus (Tokyo, Japan). Figure 29.2 shows the enhanced contrast of vascular abnormalities if the system is switched from regular mode to NBI mode. The NBI technique is a well-known method in photography, especially in astrophysics, where the scattered light (for example, from street lights) is suppressed by narrow filters in the red, green, and blue. Emitted light from stars, with a characteristic spectrum, can be selected. For bronchoscopic use, the filter bands are selected to produce the highest contrast between vessels and surrounding tissue. In the aforementioned NBI system, filters are used in the blue and green spectral range. The different depths of penetration of light components lead to different signals. Blue light is absorbed by superficial capillaries and green light is absorbed by blood vessels beneath the mucosa. One main absorption peak of hemoglobin can be found at 415 nm. Structures with high blood content appear

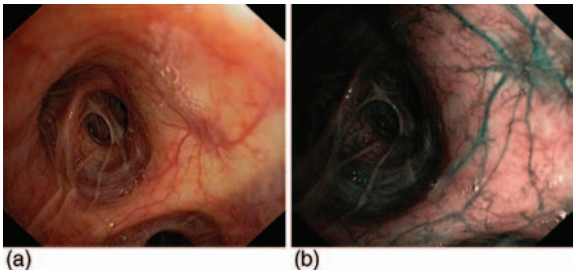

Figure 29.2 (a) White light bronchoscopic image and (b) narrowband image using the same endoscope (Olympus NBI). Mucosal and submucosal vessels and abnormalities become clearly visible.

darker than the surrounding mucosa that reflects the light. Deeper vessels are seen as green light at a secondary absorption maximum at 540 nm. In the digital camera system, the 415 nm signal is linked to the blue and green channels; the superficial vessels are displayed in brown. The red channel of the camera system monitors the reflected light of the green illumination and shows the deeper vessels in cyan. The filters have a bandwidth of about 30 nm. Vessel accumulation, pattern changes such as corkscrew distortions, abrupt stops, or caliber changes are indications of malignant transformations. A clinical study comparing autofluorescence bronchoscopy with narrowband imaging bronchoscopy in 62 patients showed a higher specificity for the filter-based technique [9].

A further step is combination with a magnifying endoscope. Truly microvascular changes are visualized and can be used for diagnostic purposes. In a recent study in 48 high-risk patients, an experimental setup of a high-magnification bronchovideoscope coupled to a narrowband imaging system was used. Angiogenic squamous dysplasia with capillary loops could be clearly differentiated from other premalignant lesions [10].

There have been further developments of band filter techniques. In a three-channel system, the blue channel is linked to 415 nm, the green channel to 445 nm and the red channel to 500 nm. Working with filters is not the only approach. In contrast to NBI, the FICE system (Fuji Intelligent Color Enhancement, Fujinon, Saitama, Japan) uses multi-band imaging (MBI). No optical filters are placed between the light source and the endoscope. A software-driven spectral estimation algorithm calculates and displays single wavelengths of a charge-coupled device (CCD) camera picture [11]. Up to 60 wavelength channels can be selected and varied to enhance the contrast. MBI creates a brighter image than NBI.

For practical purposes, all systems can be easily switched between white light and enhancing mode. In daily practice, the diagnostic yield depends greatly on the experience and concentration of the bronchoscopist. Good pattern recognition ability is required. Blood vessels that are typical for an early tumor are “different.” They have a different pattern but they do not show up in easily recognizable color differences such as we see in competing techniques that use fluorescence abnormalities.

29.1.3
Fluorescence Techniques, Drug Induced Fluorescence

More or less accidentally, substances with fluorescent properties have been found that have higher affinities to neoplastic tissues. The enrichment of these substances in cancer can be due either to higher uptakes or to defects in cellular clearance mechanisms. Several hours after intravenous injection, such a fluorophore remains at a detectable concentration in tumor cells while it has already been cleared from normal tissue. Another possible mechanism is a metabolic difference of cancer cells, for example, an uncontrolled synthesis without competitive inhibition. Typical exogenous fluorophores for tumor detection are porphyrin based. Injected hematoporphyrins are retained in cancer tissue and this can be visualized using their fluorescence. Aminolevulinic acid (ALA) and its derivatives are non-fluorescent precursors of protoporphyrin IX in the heme biosynthetic pathway. After administration, for example as an aerosol, ALA is taken up by tumor cells and converted into a bright fluorescent porphyrin. These drugs have been used for the detection of lung cancer in early stages. Experimental systems in the 1970s required expensive and bulky krypton or helium–cadmium lasers to illuminate the bronchial mucosa with violet light. Bandpass filters with photodiodes and later spectroscopic devices were used to detect the typical fluorescent peak at 630 nm indicating the presence of porphyrins in neoplastic lesions [12–14]. When highly sensitive video cameras became available, images could be obtained and these devices were used for the detection of radio-occult tumors in clinical studies [15]. In order to facilitate interpretation, false-color techniques were used.

Eventually, the lasers could be replaced by mercury or xenon arc lamps and small spectrometers or CCD video cameras were attached to the bronchoscopes. Following Photofrin injection or ALA inhalation, flat tumors unrecognizable to the naked eye can be visualized. Figure 29.3 shows examples of such a system for early lung cancer detection that we used until the late 1990s. A major hurdle for daily practice is the skin sensitivity associated with the injection of the photoactive drugs (see later in this chapter). Attempts were made to lower the amount of the drugs in order to avoid these side effects while still obtaining sufficient tumor signals. The “noise” that limits the

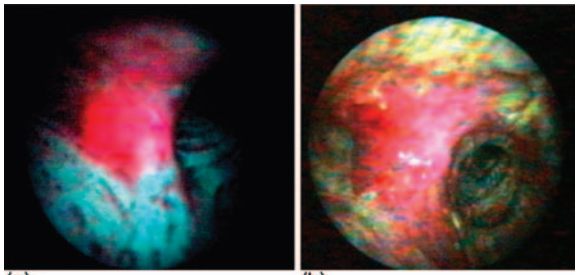

Figure 29.3 Drug induced fluorescence. The tumor lesion shows up bright red 30 min after inhalation of ALA (a) and in another patient 24 h after intravenous injection of Photofrin (b).

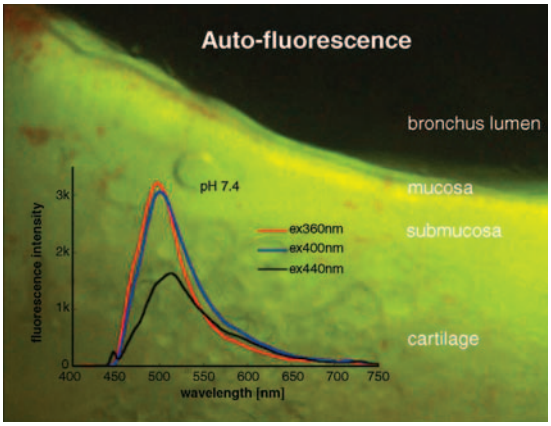

Figure 29.4 Autofluorescence of bronchial tissue. Blue light comes from below, perpendicular to bronchoscopy condition.

dose reduction is autofluorescence. It is well known that biological tissue shows a naturally occurring autofluorescence when excited by UV or visible blue light illumination (about 200–460 nm). Of course, only the visible and harmless range is suitable for medical applications. It was already known that malignant tissue yielded lower fluorescence than normal tissue when excited with UV light [16, 17]. On excitation with blue light (400–450 nm), bronchial tissue appears green when observed through a yellow filter, as shown in Figure 29.4. Like many other groups, we have studied the optical properties of normal and lung cancer cells and tissues with and without photosensitizers (Figure 29.5). Almost by serendipity it was found that there are significant differences in the autofluorescence intensities and compositions of normal bronchial tissue and early cancers on excitation with blue light (404–450 nm) used for porphyrin detection. Figure 29.6 shows the autofluorescence of a normal mucosa and the attenuated signal remitted from a tumor-affected area. The green signal drops considerably more than the red signal. The ratio can be used

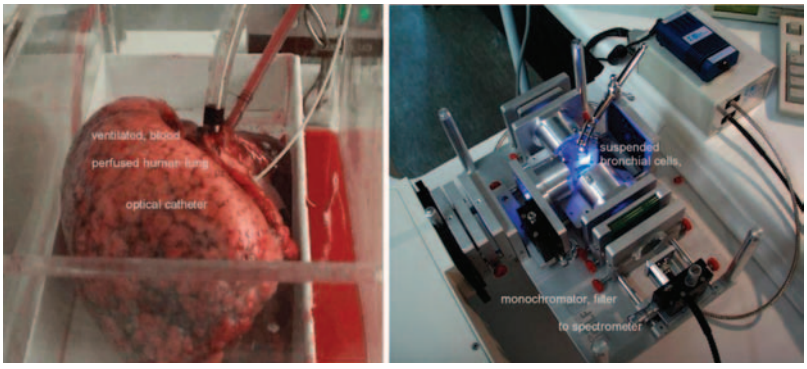

Figure 29.5 Laboratory tests for studying optical properties of bronchial and lung tissue.

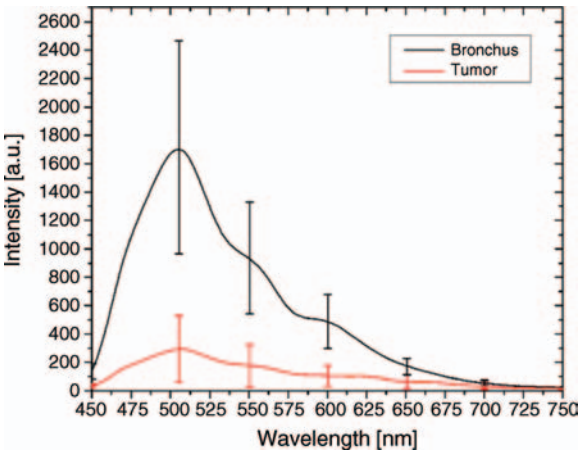

Figure 29.6 Autofluorescence of normal and tumor-affected bronchial mucosa.

for tumor detection. Suddenly there was no longer any need a for exogenous sensitizers with possible side effects. Lung cancer detection systems based on abnormalities of endogenous autofluorescence were developed.

29.1.4
Fluorescence Techniques, Auto-Fluorescence

Most fluorophores that are present in bronchial and lung tissue have been identified [18]. The strongest signal comes from flavins: flavin mononucleotide (FMN) and flavin adenine dinucleotide (FAD), with excitation at 530 nm. Elastin and collagen are architectural proteins with a yellow–green fluorescence giving the background fluorescence in most applications (excitation from 300 to 480 nm). Other optically active substances are the already mentioned porphyrins, which are important in the heme biosynthetic pathway (emission at 610–620 nm). The redox state of the tissue determines how much NADH is present: NADH (excitation at 340 nm/emission at 435 nm), NADPH (excitation at 360 nm/emission at 460 nm). In the deprotonated form (NAD/NADP), the molecules are not fluorescent. Absorption and emission spectra of human tissue are shown in Figures 29.7 and 29.8.

There are many autofluorescence-based systems available for lung cancer detection. The original LIFE system (Xillix Technologies, Richmond, BC, Canada) consisted of a helium–cadmium laser (442 nm) and two image-intensified BW cameras with green (520 nm) and red (>630 nm) filters hanging from the ceiling because they were too heavy to be carried by the physician. The clinical results were very encouraging. The detection rate for moderate and severe dysplasia increased from 38.5 and 40% with white light bronchoscopy to 73.1 and 91.4%, respectively, with the LIFE system [19]. Today, systems from all leading companies use modified xenon lamp white light sources and video-chip bronchoscopes. For the end user, these devices have become very convenient and most pulmonary departments have an

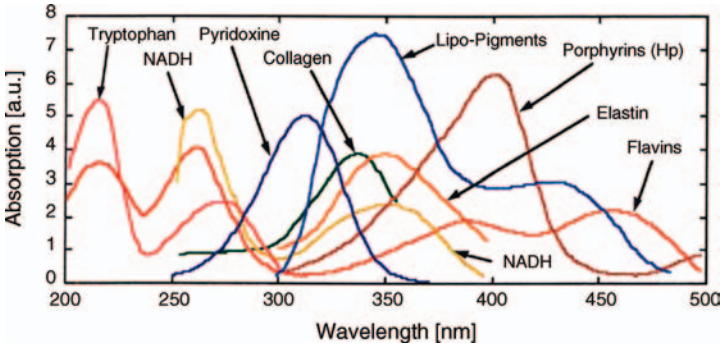

Figure 29.7 Absorption spectra of fluorophores in human tissue.

autofluorescence bronchoscope for clinical routine. However, despite the established application, some questions about the origin of autofluorescence remain unanswered. There are two main explanations for the decreased intensity in tumor tissue in comparison with normal tissue. On the one hand, the tumor has an increased epithelial thickness and therefore has a stronger absorption of excitation and fluorescence light. This architectural effect was first proposed by Qu *et al.* [20] and later confirmed by other groups (e.g., [21]). On the other hand, due to an abnormally high metabolism in tumor cells, there is a high enrichment of different kinds of molecules, as is known from the applications of photodynamic therapy (PDT) [22] or positron emission tomography (PET) techniques [23]. Biochemical effects (pH, metabolic specificities) have influences on the concentration and the spectra of certain fluorophores [24–27]. A third reasonable explanation for the attenuation of visible fluorescence would be increased absorption of the illuminating and/or the fluorescent light. As mentioned earlier, the main absorber in the visible range in human tissue is hemoglobin. Its influence is shown in Figure 29.9a and b. We compared fluorescence signals (405 nm excitation) in lungs that were perfused with blood and with saline solution [28]. The exsanguinated tissue yields a higher fluorescence with a "dromedary curve." The hemoglobin absorption curve [4] is

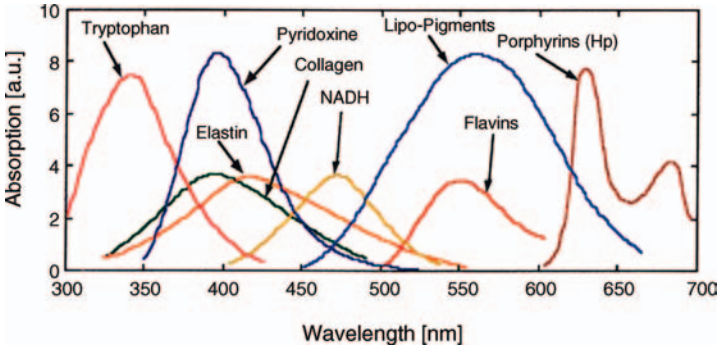

Figure 29.8 Emission spectra of fluorophores in human tissue.

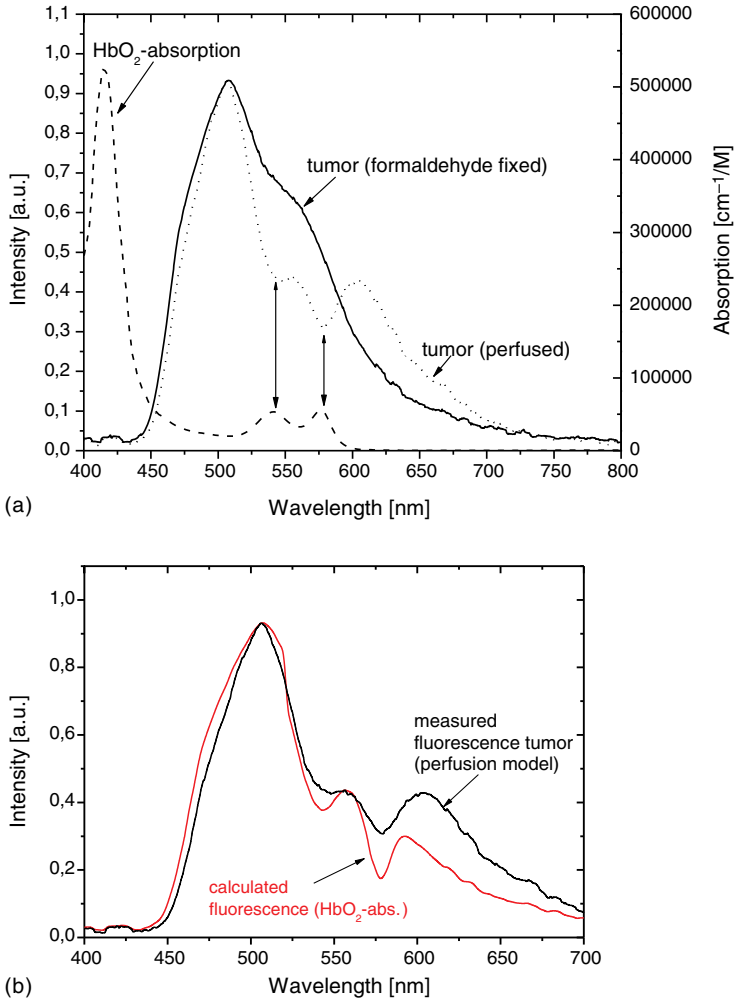

Figure 29.9 (a) Comparison of the fluorescence spectra of perfused tumor and formaldehyde-fixed tumor specimen. (b) Calculated and measured fluorescence signal of tumor tissue.

overlayed in the picture. The characteristic "camel curve" shape with two humps as usually seen in endobronchial fluorescence measurements results from this absorption. Changes in the red to green hump ratio indicate dysplasias or early cancers. We have used these curves in an optical catheter system [29] as shown in Figure 29.10. Excitation light from a mercury lamp or a laser diode (405 nm) is guided through a catheter. The remitted light is analyzed by a PC spectrometer after passing a chopper wheel (Ocean Optics, Duiven, The Netherlands). The continuous white light is replaced by stroboscopic light. Due to the latency of the video chip, the endoscopist sees a normal endoscopic image with a blue spot on the field of interest. During the long (unnoticed) dark phase, spectroscopy is carried out. On the video screen, the

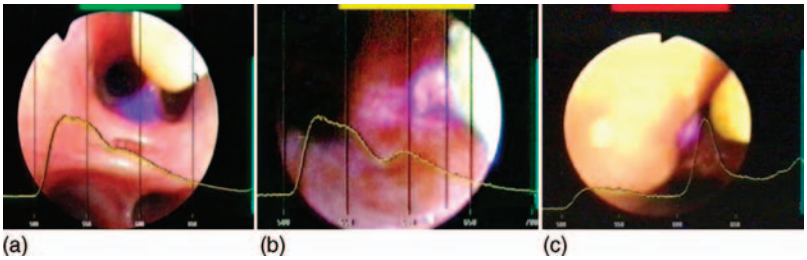

Figure 29.10 Optical catheter *in vivo* showing fluorescence signals of normal mucosa (a), early cancer (b), and drug-induced fluorescence of lung cancer (c).

fluorescence spectrum curve is overlayed on the endoscopic image in real time. The dromedary shape of scar tissue, the deepened dip characteristic of inflammation, and the flattened camel-shaped curves of a carcinoma *in situ* can be clearly differentiated. Most likely, changes in tissue texture, layer thickness, and intracellular metabolism and also changes in blood density contribute to the autofluorescence attenuation phenomenon.

29.1.5 Commercially Available Systems

All major companies offer autofluorescence systems for bronchoscopy; examples of screen images are shown in Figures 29.11–29.15.

The diagnostic autofluorescence endoscopy (DAFE) system of Wolf (Knittlingen, Germany) uses a 300 W xenon lamp as light source and a three-chip CCD camera. A flip-flop filter holder permits a change from white light to blue–violet emission. The bandpass filter allows transmission from 390 to 470 nm, giving the well-known green fluorescence picture behind the yellow blocking filter. Specific to the Wolf system is a variation in the filter behind the light source. A second low transmission (around 665 nm) results in red backscattered light that makes the final image brighter and enhances the contrast by a factor of 2.7 [30]. In the second generation of the DAFE system, the filters in front of the camera have also been modified. Small amounts of

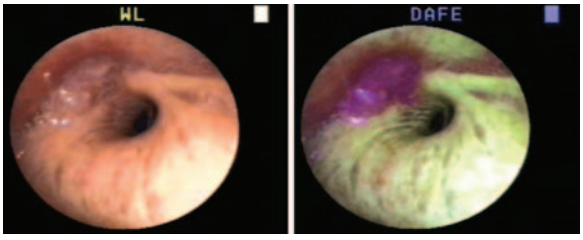

Figure 29.11 White light image and autofluorescence images of a small tumor. First generation of the Wolf DAFE system.

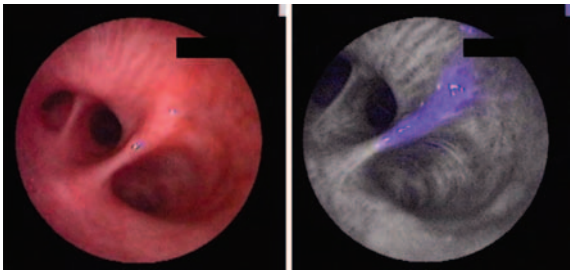

Figure 29.12 White light and auto-fluorescence images of a carcinoma *in situ*. Second generation of the Wolf DAFE system. Image courtesy of Dr. P. Ramon, Lille, France.

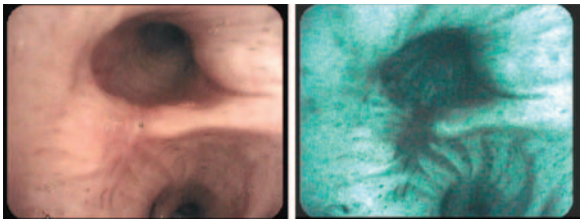

Figure 29.13 Twin mode images of a small carcinoma *in situ* using the Pentax SAFE system. Images courtesy of Dr. M. Wagner, Nürnberg, Germany.

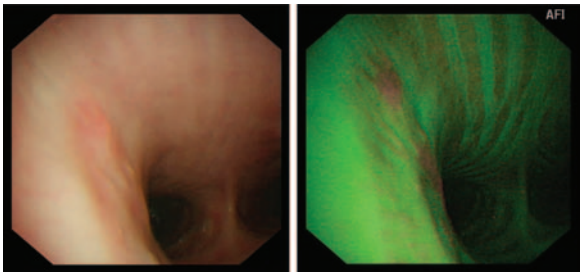

Figure 29.14 Carcinoma *in situ*, visualized by the Olympus LUCERA system.

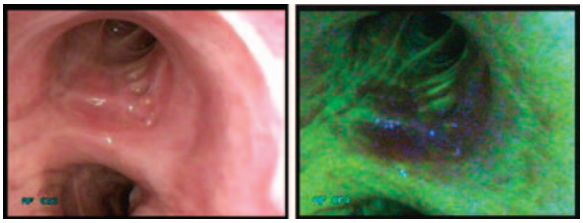

Figure 29.15 Carcinoma *in situ* visualized by the STORZ D-light system (software version currently not released for clinical use).

backscattered blue and white light in the fluorescence mode are detected. This allows better differentiation between premalignant lesions, inflammation, and blood [31].

Pentax (Tokyo, Japan) offers the SAFE system. The first generation (SAFE 1000) used a xenon light source. The imaging system consisted of a relatively bulky camera that could be mounted on any standard fiber bronchoscope. The second generation (SAFE 2000) used a video-chip bronchoscope. Brightness differences in the autofluorescence image could be manipulated electronically. Suspicious areas were rendered in pseudo-color yellow. The actually marketed SAFE 3000 system uses a 300 W xenon white light source and a blue diode laser (408 nm). Unique is the feature of displaying the fluorescence image and the white light image simultaneously on the video screen. This twin mode makes an examination very convenient. Regarding the detection of carcinoma *in situ* and dysplasia, improvements from 65% (white light only) to 90% (fluorescence mode) have been reported [32]. Finally, the brightness information of the autofluorescence image can be used to modify the chroma signal of the white light image. This Multiple Image Xposition (MIX) mode is the latest attempt to improve the specificity and distinguish between precancerous and inflammatory lesions [33].

Olympus Optical (Tokyo, Japan) introduced the EVIS LUCERA system in 2006. It uses a xenon white light source equipped with two switchable wheels containing appropriate filters and a bronchoscope with a triggered BW CCD camera chip at its tip. The RGB filter wheel is used to create high-resolution color images. The other filter wheel is used to excite an autofluorescence image. Similarly to other systems, parts of the reflected light are used to create a false color image with high contrasts. Normal tissue appears green, bronchitis purple, and cancer more reddish.

Xillix Technologies has modified the original LIFE system described above, which can be considered a milestone in fluorescence imaging bronchoscopy [34]. The new generation, called Onco-LIFE, also uses small amounts of red light (675–720 nm) in addition to the blue light (395–445 nm) from a mercury arc lamp for illumination. An area demarcated by a small target in the center of the displayed fluorescence–reflectance image is further processed and a value based on the ratio of reflectance to green fluorescence signal intensities in that area is calculated. The re-emitted diffuse light is used as the reference. In a multicenter, prospective study with 170 individuals, the relative sensitivity on a per lesion basis of white light plus fluorescence bronchoscopy versus white light bronchoscopy alone was determined as 1.5. For a quantified fluorescence reflectance response value of more than 0.4, a sensitivity and specificity of 51 and 80%, respectively, could be achieved for detection of moderate/severe dysplasia, carcinoma *in situ*, and microinvasive cancer [35].

Karl Storz (Tuttlingen, Germany) offers several versions of its D-Light system. A xenon light source with switchable filters is used in all generations. Most studies have been performed with CCD cameras attached to rigid telescope lenses or fiberscopes [21, 36]. Recently, a video-chip bronchoscope has become available for clinical studies. Early malignant lesions appear almost blue whereas inflamed areas look more brownish. The image quality in white light mode is outstanding, and no sacrifices regarding the resolution, dynamics, and brightness have to be made.

The system can be used in combination with exogenous drugs such as ALA, providing high-contrast images with bright red cancerous lesions. Currently, several image processing algorithms are being studied in order to improve the specificity. Results of clinical studies can be expected by the end of 2011.

29.1.6
Remaining Problems

The clinical problem with all systems is the relatively high number of false-positive biopsies. A typical statement from a clinician is that the systems are "too sensitive." The reported specificities for autofluorescence bronchoscopy range from 4 to 94% in various studies [37]. The challenge is to maintain the high sensitivity but improve the specificity. Most recently, attempts have been made to incorporate spectral measurements into imaging systems [38], use color fluorescence ratios in algorithms of fluorescence image analysis [39], or combine autofluorescence and narrowband imaging techniques [40]. The title of the Editorial [41] in the issue in which the last paper [40] appeared summarizes our current knowledge: "Optical diagnosis for preneoplasia, the search continues."

29.2
Therapy

Lung cancer causes symptoms from involvement of the trachea or major bronchi in up to 30% of all cases; 17% of all patients suffer of symptomatic airway obstruction [42]. Post-obstructive pneumonia is a severe consequence but even worse is the impairment of gas exchange. Suffocation is the most feared fate of cancer patients. All efforts are made to establish open airways. The armamentarium includes chemotherapy and radiation therapy and interventional bronchoscopic methods [43]. Compressed bronchi are kept open by placement of airway stents. In emergency cases, endoluminally growing tumors can be cored out mechanically. However, cutting techniques with coagulation options are preferred. The most established techniques for endobronchial tissue removal are electrocautery, cryotherapy, argon plasma coagulation, and laser photo-resection.

29.2.1
Lasers in Bronchology

Lasers are commonly used in pulmonary medicine. Figure 29.16 shows various lasers that are routinely used in the authors' department. Labeled 1 is a VISULAS diode laser emitting at 662 nm for PDT with chlorins. PDT with Foscan is performed with a Biolitec CERALAS (labeled 4) emitting at 652 nm and PDT with Photofrin with a Zeiss diode laser emitting 630 nm (labeled 6). Cutting instruments are the Biolitec Evolve laser (labeled 2), which is available with wavelengths of 980 or 1470 nm, and the Dornier Nd:YAG laser emitting 1064 nm (labeled 5). In addition to arc lamps with

Figure 29.16 Lasers used in interventional bronchology. For detailed descriptions, see the text.

filters, we use small diode laser such as the OXIUS, which delivers monochromatic light at 405 nm for diagnostic and dosimetry excitation of photosensitizers.

29.2.2 Thermal Laser Applications

The classical workhorse in interventional bronchology is the Nd:YAG laser [44]. Its infrared light (1064 nm) is guided with air-cooled fibers through the working channel of the bronchoscope. Low power of 10–20 W is used for coagulation, as

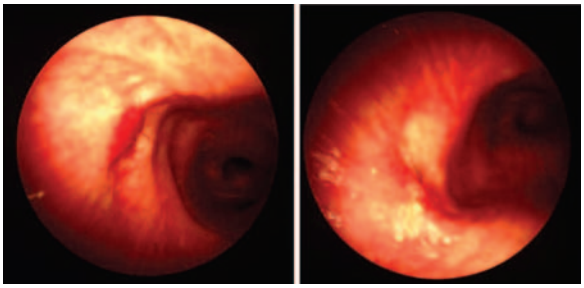

Figure 29.17 Endobronchial hemangioma (Osler disease). Photocoagulation using the Dornier Nd:YAG laser at 1064 nm.

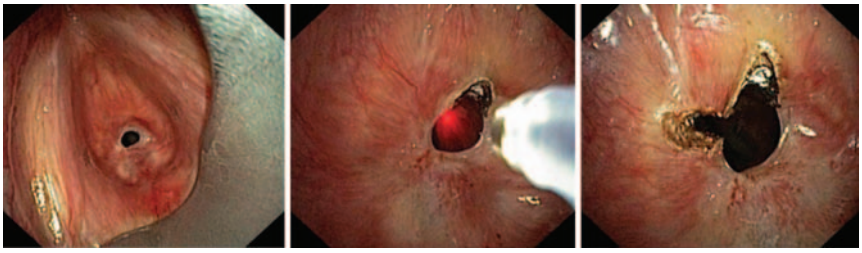

Figure 29.18 Scar tissue causing a subglotic web stenosis. Thermo-photoresection of fibrotic tissue using the Biotitec EVOLVE diode laser at 1470 nm.

demonstrated in Figure 29.17. While argon plasma coagulation has a depth of penetration in the region of 2 mm, YAG lasers are feasible for coagulating blood vessels 5–10 mm below the surface. Even highly vascularized tumors can be coagulated and removed safely. The technique has an excellent safety record, with thousands of applications worldwide [45]. The great advantage over other techniques such as cryotherapy and PDT is the immediate effect [46]. The main reason why other devices endanger the dominance of these thermal lasers is the high cost of the equipment. Recently, other thermal lasers have become available for endobronchial applications. Diode lasers are smaller, less noisy, and less expensive than Nd:YAG lasers. The air-cooled EVOLVE diode laser (Biolitec, Jena, Germany) delivers up to 40 W at 1470 nm. This wavelength matches an absorption maximum of water. The laser is suitable for precise cutting without undesired deep tissue necrosis, as demonstrated in Figure 29.18. Web-type airway stenosis can be treated with such a laser. However, surgery with end-to-end anastomosis remains the treatment of choice for benign tracheal stenosis. Any local treatment, including laser resection, can potentially induce further granulation tissue development. Coagulation in the laryngeal region may affect tissue nutrition, promote peribronchitis, and affect laryngeal nerve function with the risk of speech loss. For tissue removal at the level of the vocal cords where deeper tissue effects are risky, devices such as the CO_2 laser are safer.

29.2.3 Photodynamic Therapy

The method of PDT is based on the enrichment of exogenous chromophores in metaplastic tissue, which has been discussed in the diagnostics section. Most of the fluorophores used for photodynamic diagnostics are also potentially phototoxic. The excitation of those molecules with light leads to intermolecular interactions with molecular oxygen or surrounding molecules. Depending on rate constants, either oxygen radicals, surrounding molecules, or singlet oxygen, which is a highly reactive molecule, will be generated. As the sensitizer molecules are retained in cellular compartments, such as mitochondria or membranes, the reactive species created are able to destroy the cells. Endobronchial PDT is realized with laser systems that emit in the red spectral range because its depth of penetration makes it feasible for the

destruction of mucosal tumors. Highly effective sensitizers need to have absorption spectra with maxima in the far-red region. Ideally, drugs for PDT should also have fluorescent properties as this facilitates tumor detection, therapy planning, and dosimetry. In addition to the penetration depth, which is wavelength dependent, another important parameter for therapy efficacy is the tumor to tissue ratio. A high enrichment in the target area and a low concentration in the surrounding tissues lead to the most specific tumor therapy without collateral tissue damage. A large variety of photosensitizers have been used in preclinical and clinical studies.

ALA and its esters are precursors of protoporphyrin IX as parts of the heme biosynthetic pathway. Administering excess ALA causes visible fluorescence of endobronchial tumors. As discussed above, enrichment in cancer cells is due to a higher metabolism in malignant cells and their lack of several enzymes for the decomposition of protoporphyrin IX. Application of ALA is orally or topically; the esters are synthesized for topical use. Most institutions use ALA for diagnosis only. A single study has been published on ALA PDT in lung cancer [47]. The comparative drug, an intravenously administered hematoporphyrin derivative (Photosan), proved to be superior.

Photofrin is the most commonly used representative of blood-based porphyrin formulations. Early studies had been made with Photofrin I. The currently marketed Photofrin II, which was developed by Dougherty *et al.* [48, 49], has a higher purity. The absorption maximum is in the typical Soret band at 400 nm [50]. Because of the higher light penetration in the red region, a smaller absorption band at 630 nm is used for therapy. A maximum of concentration is reached 48 h after systemic application. Bare fibers, micro-lens fibers, radial diffusers, or balloons are available to illuminate the tumor region. Superficial tumors or carcinoma *in situ* are illuminated with lens fibers; bulky tumors can be treated interstitially. The diffusing fiber can be pushed into such a tumor under direct bronchoscopic vision, as shown in Figure 29.19. The bulky and difficult to manage argon-pumped dye lasers that we had to use until the mid-1990s have been replaced by turn-key diode lasers. They can easily deliver up to 1000 mW, resulting in treatment times of less than 10 min; 100–200 J per centimeter of tumor length are applied in standard protocols. The first reaction to endobronchial PDT is the formation of fibrin plugs, debris, and necrosis

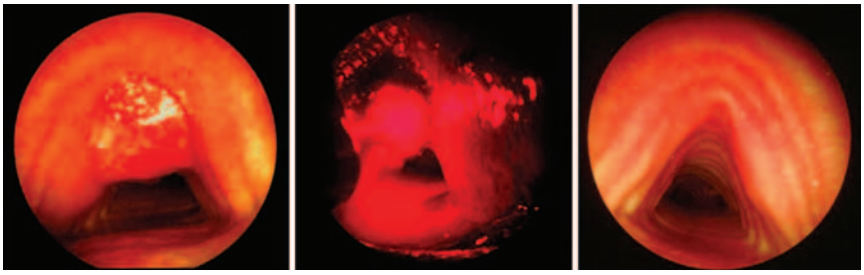

Figure 29.19 PDT of an endotracheal tumor using Photofrin. The 9 mm tumor is treated by interstitial application of red light (630 nm) applied by a cylindrical fiber of 10 mm length. Six months after therapy, no signs of residual tumor.

within 48 h after illumination. This may obstruct airways even further and could result in suffocation unless a clean-up bronchoscopy is performed. If we treat tracheal lesions, we perform these flexible bronchoscopies for removal of debris the next morning. PDT with Photofrin has been used for early [51], recurrent [52], and advanced lung cancers [53, 54].

There are numerous original articles and reviews stating the superior efficacy and cost effectiveness of PDT when compared with thermal YAG laser therapy [55–57]. The depth of penetration of red light at 630 nm is limited to a few millimeters. In small tumors less than 0.5 cm in diameter, cure rates of 95% have been accomplished. If tumors extended to 2 cm in length, the cure rate dropped to 43%, and if they were exophytic, they could be eradicated in only 14% of cases [51]. The response rate is determined by the tumor extension and the depth of infiltration [58]. In a routine clinical setting, early invasive lung cancers can only be cured by Photofrin PDT if they respect the bronchial wall. The method of choice to resolve this problem is endobronchial ultrasonography [58], which has become standard of care to check the depth of tumor infiltration with a balloon ultrasound probe before a decision is made as to whether PDT alone is sufficient to eradicate the tumor. If the tumor depth exceeds 3 mm or if the tumor is longer than 10 mm along any axis, we combine PDT with endobronchial brachytherapy (five times 4 Gy). Using this regime, eradication rates of $>$80% can be accomplished in these cases with Photofrin [59]. Another option for the treatment of these early invasive tumors is the use of other sensitizers.

As only Photofrin has been approved for treatment of lung cancer in Europe, the use of other drugs requires exceptional approvals from ethical committees. *m*-Tetrahydroxyphenylchlorin (mTHPC) (Foscan) is licensed for head and neck cancer PDT. It is a chlorin, not soluble in water. The drug is injected 96 h before the treatment. mTHPC has a higher quantum yield than porphyrins. Treatment times are shorter and the cytocidal effect is greater [61]. The most relevant clinical advantage is the excitation wavelength of 652 nm for maximum therapeutic effects. The depth of penetration is higher and additional brachytherapy can be spared. Used in clinical studies, we have seen very good tumor responses even in larger invasive cancers of the airways (Figure 29.20). Photofrin and Foscan accumulate in bronchogenic

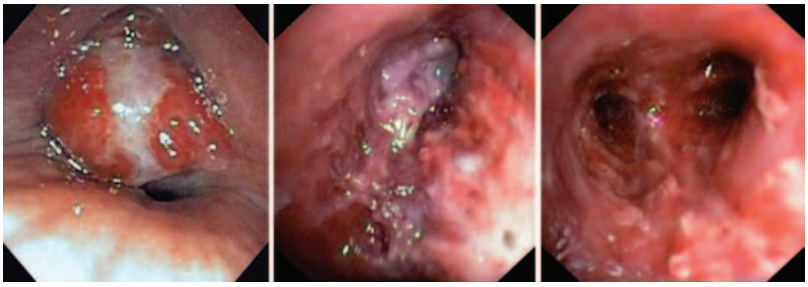

Figure 29.20 PDT of a squamous cell cancer occluding the middle lobe bronchus. PDT with Foscan. Two days after illumination with red light at 650 nm, tumor appears infarcted and necrotic. One week later, still inflammation but the bronchus is open without residual tumor.

Figure 29.21 Severe skin toxicity after use of first-generation PDT drugs. Despite all warnings, patients went out into sunlight for cigarette smoking.

tumors and show visible fluorescence. Through a yellow blocking filter at the ocular of the bronchoscope, the cancer extension can be seen under blue light illumination which facilitates the treatment. The degree of drug retention can be estimated using the above-mentioned optical catheter and spectrometer (Figures 29.3 and 29.10).

A major disadvantage of PDT with the currently available drugs is the long-lasting photoxicity of the skin. The light sensitivity lasts for up to 6 weeks and certainly impairs the quality of life of patients as they are requested to avoid bright artificial light and especially sunlight. Figure 29.21 shows sunburn of patients who did not follow the recommendations. There is a need for new drugs with shorter retention times. Potential candidates are other chlorins, which are reduced, hydrophilic porphyrins with a strong absorption band in the 640–700 nm range. Chelation with metals can alter the absorption properties. A promising drug is chlorin e6. Derived from chlorophyll-*a* ("green porphyrin"), chlorin e6 is monomeric in solution, has a quantum yield of singlet oxygen of 0.7, and, like other sensitizers, has photo-oxidative effects on amino acids, enzymes, and lysosomes. It binds strongly to albumin [63, 64]. The highest accumulation in tumor tissue is reached 2–4 h after drug injection. The drug fluorescence is clearly visible under illumination with blue–violet light. A sharp peak at 670 nm over the tumor proves selectivity (Figure 29.22). The high absorption

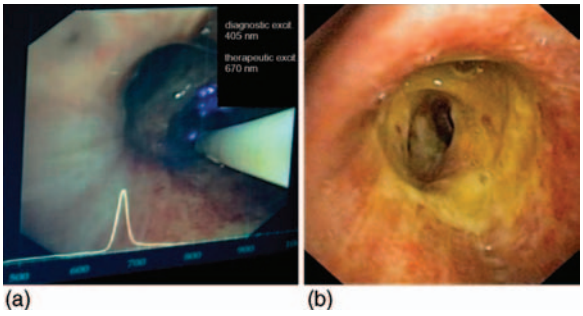

Figure 29.22 Very large area of tumor, extending from mid-trachea to lower lobe bronchus. Experimental treatment with chlorin e6 (Fotolon) and 5 cm long cylindrical fibers. Sharp fluorescence peak at 670 nm during bronchoscopy (a). Unusual yellow fibrin covering of the treated area but histologically no residual tumor (b).

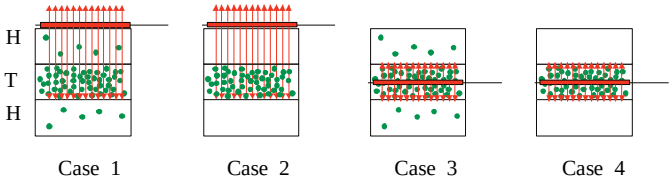

Figure 29.23 Cases of different enrichment and optimization of light delivery in tumor tissue.

at 670 nm allows deep penetration, especially in lung tissue. By 24 h after application the substance is cleared from mucosa and skin. Hence the phototoxic side effect is critical for only about 12 h, which makes PDT with this drug easy and practical. In preliminary studies, we have seen very convincing results with eradication of tumors exceeding several centimeters in length.

There are many other photosensitizers, such as 4-hydroxyphenylpyruvate dioxygenase (HPPD), phthalocyanines, NPe6 (talaporfin), Purlytin, Padoporfinin, lutrin, texaphryrin, and benzoporphynn, under investigation in clinical studies. A review was provided by Allison and Sibata [65]. For practical application, some critical parameters are important. It is mandatory for monitoring and dosimetry that the sensitizer has good visible fluorescence and little photobleaching. Nonfluorescent phototoxic drugs are difficult to use, and side effects can hardly be predicted or avoided [66].

Compared with thermal laser treatment, the advantage of PDT is a relative selectivity resulting from drug accumulation in the target. Submucosal tumors cannot be attacked with electrocautery or conventional laser treatment. At least theoretically, this could be accomplished with PDT. Ideally, there would be no sensitizer molecules in the healthy tissue. The therapeutic light would penetrate healthy tissue without doing any harm (Figure 29.23, case 2). This could be realized by injecting a sensitizer directly into the tumor. In the more realistic case 1 (depending on the threshold for cell destruction), damage to the sound tissue cannot be excluded. For a solid tumor embedded in healthy tissue, an additional reduction of the light can be realized by puncturing the tissue down into the tumor with an illumination fiber. The wavelength that activates the sensitizer will determine the maximum absorbance capacity and, thus, the wavelength of light to be used. The second-generation sensitizers allow the use of light with wavelengths between 600 and 800 nm, allowing an increase in penetration depths compared with first-generation porphyrins [68]. Figure 29.24 shows transmission spectra for therapeutic light of excised lung tissue with and without exsanguinations. The highest transmission is reached at around 670–700 nm. For endoscopic PDT of lung tumors, these wavelengths would be ideal. The knowledge about the transmission characteristics of human tissue gives us the opportunity for sufficiently precise dosimetry. The dose rate can be described by an extended Lambert's law. The dose D_{depth} in the tissue has to be above a threshold $D_S{}^*$ for cell death, that is known [69]. D_{depth} is calculated by the photodynamic dose D^*, which results from the quality of light, its fluence rate,

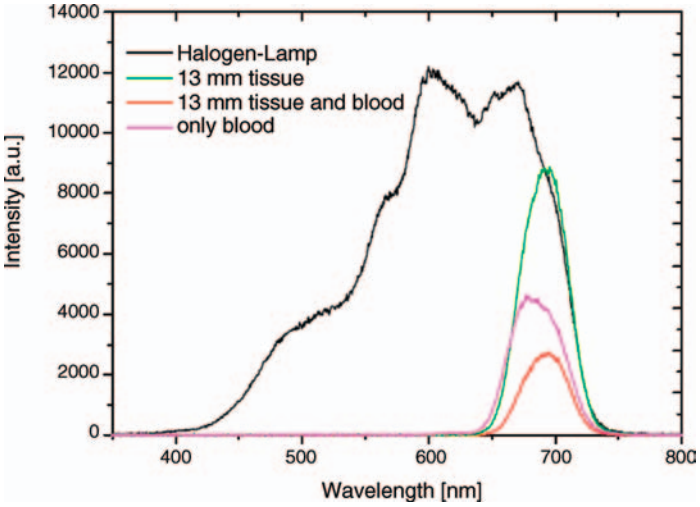

Figure 29.24 Transmission spectra of lung tissue.

the time of illumination, the extinction coefficient, and the density of the tissue. Table 29.1 shows the calculations for a first-generation drug excited at 630 nm and for a second-generation chlorin excited at 670 nm. As a clinical consequence, tumors penetrating the bronchial wall and even outside the airways could be treated effectively through a bronchoscope (Figure 29.25).

It is often argued that PDT has never made it into general pulmonary medical practice despite the fact that is has been available for almost 30 years. There is no reason for nihilism. Progress in pharmacology and technology makes it attractive today and even more in the foreseeable future.

Table 29.1 Calculation of dose rate.

$$D_{\text{depth}} = D^{*} e^{-\frac{z}{\delta}} \quad \text{with} \quad D^{*} = \varepsilon D \Phi t \frac{\lambda}{hc\varrho}$$

Parameter	Symbol	Photofrin	Chlorin e6
Extinction ($cm^{-1} M^{-1}$)	ε	10 000	40 000
Average tissue density (lung) ($g\,cm^{-3}$)	ϱ	0.3–0.48	
Concentration of sensitizer in tumor (M)	D	6×10^{-5}	6×10^{-5}
Illumination time	t		
Necrosis threshold [$p\,g^{-1}$ (photodynamic active units per gram)]	D_S^*	2×10^{19}	
Excitation wavelength (nm)	λ	630	670

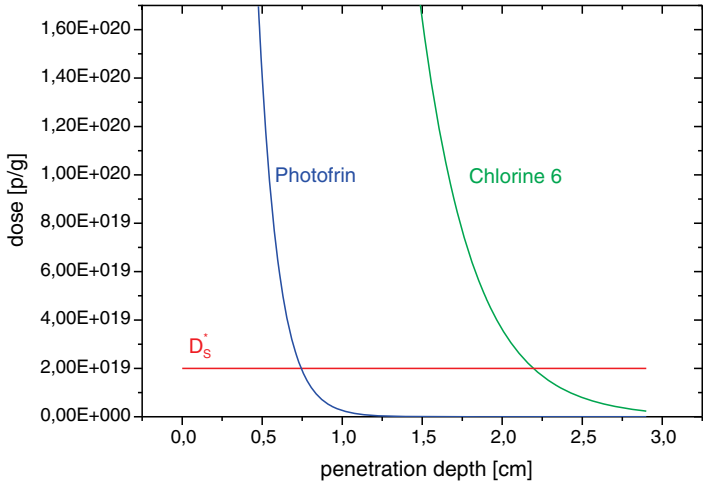

Figure 29.25 Depth of penetration and calculated therapeutic effect of PDT using excitation wavelengths of 630 vs. 670 nm.

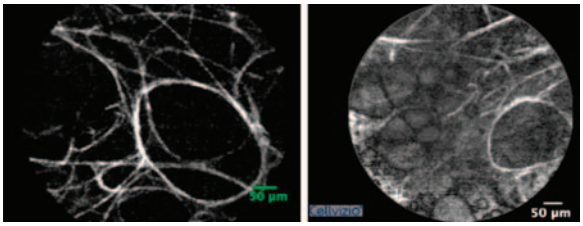

Figure 29.26 Probe-based confocal fluorescence endomicroscopy images using the CellVizio system (Mauna Kea Technologies, Newtown, PA, USA). Images courtesy of Professor Luc Thiberville, Rouen, France.

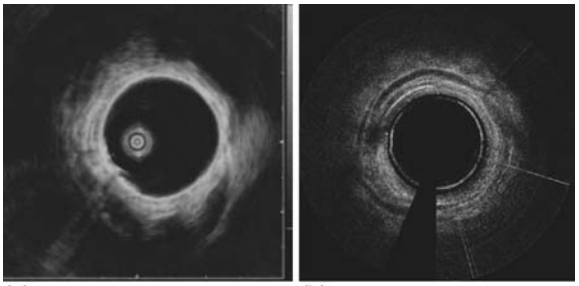

Figure 29.27 Endobronchial ultrasound image (a) and optical coherence tomography (b). OCT images using the OCTIS system (Tomophase, Burlington, MA, USA). Images courtesy of Professor A. Ernst, Boston, MA, USA.

29.3
New Techniques: Fluorescence Microimaging, Optical Coherence Tomography

There are several other promising new techniques that have been applied for bronchoscopic use. Fiber confocal fluorescence microscopy provides microimages from the smallest airways and even from the alveolar sacs (Figure 29.26). We obtain fascinating pictures from formerly inaccessible regions of the lung [70]. The lung parenchyma can be studied through the working channel of a bronchoscope. The combination with fluorescence measurements provides further information [71]. Combined with electromagnetic navigation techniques, optical biopsies from the smallest lung nodules becomes feasible.

An equally fascinating technique is optical coherence tomography (OCT). The already commercially available devices allow the study of airway wall structures with much better resolution than endobronchial ultrasound, as shown in Figure 29.27.

There is no question that optical methods will further boost the use of bronchoscopy. We are privileged to take part in a fascinating journey where the combination of techniques allows insights into bronchi and lungs and where we can help patients suffering from pulmonary diseases. Advances in molecular biology, optical cancer detection methods, and light-based methods provide us with very promising tools in the fight against lung cancer. There is more hope with NBI, PDD, PDT, OCT, and a high-resolution bronchoscope.

References

1 Kollofrath, O. (1897) Entfernung eines Knochenstücks aus dem rechten Bronchus auf natürlichem Wege und unter Anwendung der directen Laryngoscopie. *MMW*, **38**, 1038–1039.

2 Lam, S. and Becker, H.D. (1996) Future diagnostic procedures. *Chest Surg. Clin.*, **6**, 363–380.

3 Thiberville, L. (1999) Precancerous lesions of the bronchi: endoscopic detection. *Eur. Respir. J.*, **14S**, 2475.

4 Prahl, S. and Jacques, S. (1999) Optical absorption of hemoglobin. *Oregon Med. Laser Center Proc.*

5 Gono, K., Obi, T., Yamaguchi, M. *et al.* (2004) Appearance of enhanced tissue features in narrow-band endoscopic imaging. *J. Biomed. Opt.*, **9**, 568–577.

6 Yoshida, T., Inoue, H., Usui, S. *et al.* (2004) Narrow-band imaging system with magnifying endoscopy for superficial esophageal lesions. *Gastrointest. Endosc.*, **59**, 288–295.

7 Muto, M., Katada, C., Sano, Y. *et al.* (2005) Narrow band imaging: a new diagnostic approach to visualize angiogenesis in superficial neoplasia. *Clin. Gastroenterol. Hepatol.*, **3**, 16–20.

8 Kuznetsov, K., Lambert, R., and Rey, J.F. (2006) Narrow-band imaging: potential and limitations. *Endoscopy*, **38**, 76–81.

9 Herth, F.J., Eberhardt, R., Anantham, D. *et al.* (2009) Narrow-band imaging bronchoscopy increases the specificity of bronchoscopic early lung cancer detection. *J. Thorac. Oncol.*, **4** (9), 1060–1065.

10 Shibuya, K., Hoshino, H., Chiyo, M., Iyoda, A., Yoshida, S., Sekine, Y., Iizasa, T., Saitoh, Y., Baba, M., Hiroshima, K., Ohwada, H., and Fujisawa, T. (2003) High magnification bronchovideoscopy combined with narrow band imaging could detect capillary loops of angiogenic squamous dysplasia in heavy smokers at

high risk for lung cancer. *Thorax*, **58**, 989–995.

11 Miyake, Y., Kouzu, T., Takeuchi, S.,*et al.* (2005) Development of new electronic endoscopes using the spectral images of an internal organ. Proceedings of the IS&T/SID's Thirteen Color Imaging Conference, Scottsdale (AZ), pp. 261–269.

12 Profio, A.E., Doiron, D.R., and King, E.G. (1979) Laser fluorescence bronchoscope for localization of occult lung tumors. *Med. Phys.*, **6** (6), 523–525.

13 Doiron, D.R., Profio, E., Vincent, R.G., and Dougherty, T.J. (1979) Fluorescence bronchoscopy for detection of lung cancer. *Chest*, **76**, 27–32.

14 Kato, H. and Cortese, D.A. (1985) Early detection of lung cancer by means of hematoporphyrin derivative fluorescence and laser photoradiation. *Clin. Chest Med.*, **6**, 237–253.

15 Lam, S., Palcic, B., McLean, D., Hung, J., Korbelik, M., and Profio, A.E. (1990) Detection of early lung cancer using low dose Photofrin II. *Chest*, **97**, 333–337.

16 Sutro, C., and Burman, M. (1933) Examination of pathological tissue by filtered ultraviolet radiation. *Arch. Pathol.*, **16**, 346–349.

17 Herly, L. (1944) Studies in selective differentiation of tissues by means of filtered ultraviolet light. *Cancer Res.*, **4**, 227–231.

18 Wagnières, G., Star, W., and Wilson, B. (1998) *In vivo* fluorescence spectroscopy and imaging for oncological applications. *Photochem. Photobiol.*, **68** (5), 603–632.

19 Lam, S., McAulay, C., LeRiche, J.C., Ikeda, N., and Palcic, B. (1994) Early localization of bronchogenic carcinoma. *Diagn. Ther. Endosc.*, **1**, 75–78.

20 Qu, J.Y., MacAulay, C.E., Lam, S., and Palcic, B. (1995) Laser-induced fluorescence spectroscopy at endoscopy: tissue optics, Monte Carlo modeling and *in vivo* measurements. *Opt. Eng.*, **34** (11), 3334–3343.

21 Häussinger, K., Stanzel, F., Hubner, R.M., Pichler, J., and Stepp, H. (1999) Autofluorescence detection of bronchial tumors with the D-Light/AF. *Diagn. Ther. Endosc.*, **5**, 105–112.

22 Kennedy, J.C., Pottier, R.H., and Pross, D.C. (1990) Photodynamic therapy with endogenous Protoporphyrin IX: basic principles and present clinical experience. *J. Photochem. Photobiol. Biol.*, **6**, 143–148.

23 Yamamoto, Y.T., Thompson, C.J., Diksic, M., Meyer, E., and Feindel, W.H. (1984) Positron emission tomography. *Experientia Suppl., Neurosurg. Rev.*, **7** (4), 233–252.

24 Hung, J., Lam, S., LeRiche, J.C., and Palcic, B. (1991) Autofluorescence of normal and malignant bronchial tissue. *Lasers Surg. Med.*, **11**, 99–105.

25 Yang, Y., Ye, Y., Li, F., Li, Y., and Ma, P. (1987) Characteristic autofluorescence for cancer diagnosis and its origin. *Lasers Surg. Med.*, **7**, 528–532.

26 Harris, D.M., and Werkhaven, J. (1987) Endogenous porphyrin fluorescence in tumors. *Lasers Surg. Med.*, **7**, 467–472.

27 Wolfbeis, O. (1985) The fluorescence of organic natural products, in *Molecular Luminescence Spectroscopy: Methods and Applications – Part I* (ed. S.G. Schulman), John Wiley and Sons, Inc., New York, pp. 167–370.

28 Hüttenberger D., Gabrecht, T., Wagnières, G., Weber, B., Linder, A., Foth, H.J., and Freitag, L. (2008) Autofluorescence detection of tumors in the human lung – spectroscopical measurements *in situ*, in an *in vivo* model and *in vitro*. *Photodiagnosis Photodyn. Ther.*, **5** (2), 139–4729.

29 Freitag, L. and Hüttenberger, D. (2007) Autofluorescence bronchoscopy using the Hemer optical catheter and the Wolf DAFE system, in *Autofluorescence Bronchoscopy* (eds. M. Wagner and J.H. Ficker), Unimed Verlag, Bremen, pp. 79–89.

30 Gabrecht, F.T., Glanzmann, T., Freitag, L., Weber, B.C., van den Bergh, H., and Wagnières, G. (2007) Optimized autofluorescence using additional backscattered red light. *J. Biomed. Opt.*, **12** (6), 6401–6406.

31 Gabrecht, T., Radu, A., Grosjean, P., Weber, B., Reichle, G., Freitag, L., Monnier, P., van den Bergh, H., and Wagnières, G. (2008) Improvement of the

specificity of cancer detection by autofluorescence imaging in the tracheobronchial tree using backscattered violet light. *Photodiagnosis Photodyn Ther.*, **5**, 2–9.

32 Ikeda, N., Honda, H., Hayashi, A., Usuda, J., Kato, Y., Tsuboi, M., Ohira, T., Kato, H., Serizawa, H., and Aoki, Y. (2006) Early detection of bronchial lesions using newly developed videoendoscopy-based autofluorescence bronchoscopy. *Lung Cancer*, **52** (1), 21–27.

33 Wagner, M. and Ficker, J.H. (2007) Video-Autofluorescence SAFE-3000, in *Autofluorescence Bronchoscopy* (eds. M. Wagner and J.H. Ficker), Unimed Verlag, Bremen, pp. 19–58.

34 Lam, S., McAulay, C., Hung, J., LeRiche, J., Profio, A.E., and Palcic, B. (1993) Detection of dysplasia and carcinoma *in situ* using a lung imaging fluorescence endoscopy (LIFE) device. *J. Thorac. Cardiovasc. Surg.*, **105**, 1035–1040.

35 Edell, E., Lam, S., Pass, H., Miller, Y.E. *et al.* (2009) Detection and localization of intraepithelial neoplasia and invasive carcinoma using fluorescence–reflectance bronchoscopy: an international, multicenter clinical trial. *J. Thorac. Oncol.*, **4** (1), 49–54.

36 Stanzel, F. (2007) The Storz D-Light system, in *Autofluorescence Bronchoscopy* (eds. M. Wagner and J.H. Ficker), Unimed Verlag, Bremen, pp. 65–77.

37 Kennedy, T.C., McWilliams, A., and Edell, E. (2007) Bronchial intraepithelial neoplasia/early central airways lung cancer. *Chest*, **132**, 221S–233S.

38 Reinders, D., Snead, D., Dhillon, P., and Fawzy, Y. (2009) Endobronchial cancer detection using an integrated bronchoscope system for simultaneous imaging and noncontact spectral measurement. *J. Bronchol. Intervent. Pulmonol.*, **16**, 158–166.

39 Lee, P., van den Bergh, R.M., Lam, S., Gazdar, A.F., Grunberg, K., McWilliams, A., LeRiche, J., Postmus, P., and Sutedja, T. (2009) Color fluorescence ratio for the detection of bronchial dyspalsia and carcinome *in situ*. *Clin. Cancer Res.*, **15** (14), 4700–4705.

40 Nguyen, P.T., Salvado, O., Masters, I.B., Farah, C.S., and Fielding, D. (2010) Combining autofluorescence and narrow band imaging with image analysis in the evaluation of preneoplastic lesions in the bronchus and larynx. *J. Bronchol. Intervent. Pulmonol.*, **17** (2), 109–116.

41 Lee, P. (2010) Optical diagnosis for preneoplasia, the search continues. *J. Bronchol. Intervent. Pulmonol.*, **17** (2), 101–102.

42 Minna, J.D., Higgins, G.A., and Glatstein, E.J. (1985) Cancer of the lung, in *Cancer, Principles and Practice of Oncology*, 2nd edn (eds. V.T. DeVita, S. Hellman, and S.A. Rosenberg), J.P. Lippincott, Philadelphia, pp. 518–526.

43 Freitag, L., Macha, H.N., and Loddenkemper, R. (2001) Interventional bronchoscopic procedures. *Lung Cancer*, **6** (17), 272–304.

44 Dumon, J.F., Shapshay, S., Bourcereau, J., Cavaliere, S., Meric, B., Garbi, N., and Beamis, J. (1984) Principles for safety in application of neodymium–YAG laser in bronchology. *Chest*, **86** (2), 163–168.

45 Cavaliere, S., Foccoli, P., Toninelli, C., and Feijo, S. (1994) Nd:YAG laser therapy in lung cancer: an 11 year experience with 2253 applications in 1585 patients. *J. Bronchol.*, **1**, 105–111.

46 Bolliger, C.T., Sutedja, T.G., Strausz, J., and Freitag, L. (2006) Therapeutic bronchoscopy with immediate effect: laser, electrocautery, argon plasma coagulation and stents. *Eur. Respir. J.*, **27** (6), 1258–1271.

47 Maier, A., Tomaselli, F., Matzi, V., Woltsche, M., Anegg, U., Fell, B., Rehak, P., Pinter, H., and Smolle-Jüttner, F.M. (2002) Comparison of 5-aminolaevulinic acid and porphyrin photosensitization for photodynamic therapy of malignant bronchial stenosis: a clinical pilot study. *Lasers Surg. Med.*, **30** (1), 12–17.

48 Dougherty, T.J., Kaufman, J.E., Goldfarb, A., Weishaupt, K.R., Bouyle, D.G., and Mitleman, A. (1978) Photoradiation for the treatment of malignant tumors. *Cancer Res.*, **38**, 2628–2635.

49 Dougherty, T.J. (1989) Photodynamic therapy – new approaches. *Semin. Surg. Oncol.*, **5**, 151–152.

50 Pass, H.L. (1991) Photodynamic therapy for lung cancer. *Chest Surg. Clin. North Am.*, **1**, 135–151.

51 Furuse, K., Fukuoka, M., Kato, H., Horrai, T., Kubota, K., Kodama, N., Kusunoki, Y., Takifuji, N., Okunaka, T., Konaka, C., Wada, H., and Hayata, Y. (1993) A prospective phase II study on photodynamic therapy with Photofrin II for centrally located early-stage lung cancer. *J. Clin. Oncol.*, **11**, 1852–1857.

52 Freitag, L., Korupp, A., Itzigehl, I., Dankwart, F., Tekolf, E., Reichle, G., Kullmann, H.J., and Macha, H.N. (1996) Experience with fluorescence diagnosis and photodynamic therapy in the multimodality treatment concept of operated, recurrent bronchial carcinoma. *Pneumonologie*, **50** (10), 693–699.

53 Sutedja, T.G. (1999) Photodynamic therapy in advanced tracheobronchial cancers. *Diagn. Ther. Endosc.*, **5**, 245–251.

54 Moghissi, K., Dixon, K., Stringer, M., Freeman, T., Thorpe, A., and Brown, S. (1999) The place of bronchoscopic photodynamic therapy in advanced unresectable lung cancer: experience of 100 cases. *Eur. J. Cardiothorac Surg*, **15** (1), 1–6.

55 Diaz-Jimenez, J.P., Martinez-Ballarin, J.E., Llunell, A., Farrero, E., Rodriguez, A., and Castro, M.J. (1999) Efficacy and safety of photodynamic therapy versus Nd:YAG laser resection in NSCLC with airway obstruction. *Eur. Respir. J.*, **14** (4), 800–805.

56 Furukawa, K., Tetsuya, O., Yamamoto, H., Tsuchida, T., Usuda, J., Kumasaka, H., Ishida, J., Konaka, C., and Kato, H. (1999) Effectiveness of photodynamic therapy and Nd:YAG laser treatment for obstructed tracheobronchial malignancies. *Diagn. Ther. Endosc.*, **5**, 161–166.

57 Moghissi, K. and Dixon, K. (2003) Is bronchoscopic photodynamic therapy a therapeutic option in lung cancer? *Eur. Respir. J.*, **22**, 535–541.

58 Sutedja, T., Lam, S., and LeRiche, I. (1994) Response and pattern of failure after photodynamic therapy for intraluminal stage I lung cancer. *J. Bronchol.*, **1**, 259–289.

59 Miyazu, Y., Miyazu, T., Kurimoto, N., Iwamoto, Y., Kanoh, K., and Kohno, N. (2002) Endobronchial ultrasonography in the assessment of centrally located early-stage lung cancer before photodynamic therapy. *Am. J. Respir. Crit. Care Med.*, **165**, 832–837.

60 Freitag, L., Ernst, A., Thomas, M., Prenzel, R., Wahlers, B., and Macha, H.N. (2004) Sequential photodynamic therapy (PDT) and high dose brachytherapy for endobronchial tumour control in patients with limited bronchogenic carcinoma. *Thorax*, **59** (9), 790–793.

61 Ma, L., Moan, J., and Berg, K. (1994) Evaluation of a new photosensitizer, meso-tetra-hydroxyphenyl-chlorin, for use in photodynamic therapy: a comparison of its photobiological properties with those of two other photosensitizers. *Int. J. Cancer*, **57** (6), 883–888.

62 Spikes, J.D. (1990) Chlorins as photosensitizers in biology and medicine. *J. Photochem. Photobiol. B*, **6**, 259–274.

63 Osbroff, A.R., Ohuoha, D., Hasan, T. *et al.* (1986) Antibody-targeted photolysis: selective photodestruction of human T-cell leukemia cells using monoclonal antibody–chlorin e6 conjugates. *Proc. Natl. Acad. Sci. U. S. A.*, **83**, 8744–8788.

64 Kochubeev, G.A., Frolov, A.A., and Zenkevtch, E.L. (1988) Characteristics of complex formation of chlorin e6 with human and bovine serum albumins. *Mol. Biol.*, **22**, 968–975.

65 Chin, W.W.L., Heng, P.W.S., and Olivo, M. (2007) Chlorin e6 – polyvinylpyrrolidone mediated photosensitization is effective against human non-small cell lung carcinoma compared to small cell lung carcinoma xenografts. *BMC Pharmacol.*, **7**, 15.

66 Allison, R.R. and Sibata, C.H. (2010) Oncological photodynamic therapy photosensitizers: a clinical review. *Photodiagn. Photodyn. Ther.*, **7**, 61–75.

67 Tremblay, A., Leroy, S., Freitag, L., Copin, M.C., Brun, P.H., and Marquette, C.H. (2003) Endobronchial phototoxicity of WST 09 (Tookad), a new fast-acting photosensitizer for

photodynamic therapy: preclinical study in the pig. *Photochem. Photobiol.*, **78** (2), 124–130.

68 Gomer, C.J. (1991) Preclinical examination of first and second generation photosensitizers used in photodynamic therapy. *Photochem. Photobiol.*, **54**, 1093–1107.

69 Jacques, S. (1998) The mathematics of PDT dosimetry for cancer treatment. *Proc. Oregon Med. Laser Center.*

70 Thiberville, L., Moreno-Swirc, S., Vercauteren, T., Peltier, E., Cave, C., and Bourg-Heckly, G. (2007) *In vivo* imaging of the bronchial wall microstructure using fibered confocal fluorescence microscopy. *Am. J. Respir. Crit. Care Med.*, **175**, 22–31.

71 Thiberville, L., Salaun, M., Lachkar, S., Dominique, S., Moreno-Swirc, S., Vever-Bizet, C., and Bourg-Heckly, G. (2009) Human *in vivo* fluorescence microimaging of the alveolar ducts and sacs during bronchoscopy. *Eur. Respir. J.*, **33**, 974–985.

72 Michel, R.G., Kinasewitz, G.T., Fung, K.M., and Keddissi, J.I. (2010) Optical coherence tomography as an adjunct to flexible bronchoscopy in the diagnosis of lung cancer: a pilot study. *Chest*, **138** (4), 984–988.

30
Laser Therapy

Anant Mohan

Laser is an acronym for *Light Amplification by Stimulated Emission of Radiation*. In simpler language, lasers are devices that produce light that becomes transformed into heat upon interacting with living tissue. Three properties differentiate laser light from naturally occurring light [1]:

1) **Monochromaticity**: the laser light contains only one color or a narrow band of wavelengths, unlike natural light that is a blend of various wavelengths.
2) **Spatial coherence**: laser light hardly diverges and maintains its intensity as it travels forwards.
3) **Temporal coherence**: The packets of energy travel in uniform time with equal alignment.

Lasers have become an important diagnostic and therapeutic tool in pulmonary medicine.

Although Albert Einstein recognized the existence of stimulated emissions in 1917, the first description of stimulated optical emissions of monochromatic light occurred in 1960 with the advent of the ruby laser. The utility of lasers stems from their ability to transfer precisely high levels of energy to tissue (a property exploited for photoresection of endobronchial lesions), and also the unique properties of monochromatic (utilized for photodynamic therapy (PDT) and autofluorescence bronchoscopy (AFB).

The use of lasers in pulmonology may be both diagnostic and therapeutic. These are discussed below along with the current status:

30.1
Diagnostic Applications of Lasers

30.1.1
Autofluorescence Bronchoscopy (AFB)

In AFB, bronchial mucosa is illuminated by blue light. Normal mucosa emits autofluorescent light with a peak in the green range. In diseased mucosa (neoplastic or chronic inflammatory), the thickened epithelium reduces the fluorophore

Handbook of Biophotonics. Vol.2: Photonics for Health Care, First Edition. Edited by Jürgen Popp, Valery V. Tuchin, Arthur Chiou, and Stefan Heinemann.

Table 30.1 Indications for the use of autofluorescence bronchoscopy [2].

Evidence-based indications
1. Evaluation of patients with high-grade sputum atypia and normal chest imaging studies
2. Bronchoscopic surveillance of moderate/severe dysplasia and carcinoma *in situ*
3. Guiding of curative endobronchial therapy of microinvasive lesions
4. Evaluation of patients with suspected, known, or previous lung cancer
Preoperative:
• Determination of tumor margins
• Detection of synchronous lesions
Follow-up:
• Detection of recurrence
• Detection of metachronous lesions

concentration and hyperemia, hence the intensity of autofluorescence (AF) emission is significantly reduced and the emission peak shifts from the green to the red range. Therefore, the diseased mucosa shows shadowing and discoloration.

In routine clinical practice, the primary indication for using AFB is for the early detection of intraepithelial malignant disease. The various clinical situations where AFB may be useful are listed in Table 30.1.

Of the several AFB systems available, two models using laser light are the LIFE and SAFE-3000. The LIFE Lung system (Lung Imaging Fluorescence Endoscope, Xillix Technologies, Richmond, BC, Canada) (Figure 30.1) was introduced in 1991 and has been commercially available since 1998. It uses a helium–cadmium laser to illuminate the bronchial mucosa with 442 nm light. The laser beam is conducted to the mucosa via a conventional fiber-optic bronchoscope. The reflected beams of the bronchial mucosa appear at two characteristic spectral bands in the green (480–520 nm) and red (4630 nm) range. Normal mucosa appears light green and neoplastic mucosa reddish brown (Figure 30.2).

The second laser-based system, the SAFE-3000 (Pentax Corporation, Tokyo, Japan) (Figure 30.3) uses a semiconductor laser diode that emits 408 nm light to induce AF and a xenon lamp for white light bronchoscopy (WLB) examination. A single high-sensitivity color charge-coupled device (CCD) sensor detects AF in the green and red range and also reflected blue light (430–700 nm), and generates a combined fluorescence–reflectance image. Both light sources and the video processor are integrated in one device. The white light and AF images can easily be switched using a button on the bronchoscope.

Several trials have compared the relative sensitivity of AFB and WLB for the detection of early cancerous changes in the bronchial mucosa [3–6] (Table 30.2). Although initial studies demonstrated a rather high relative sensitivity of up to 6.2, subsequent larger and better conducted multicenter studies showed a more realistic assessment of the potential of AFB, the relative sensitivity settling down to around 1.5. However, AFB suffers from inferior specificity to WLB due to false-positive results obtained in inflammation and scarring, leading to increases in costs and the number of biopsies.

Figure 30.1 The LIFE Lung system (Lung Imaging Fluorescence Endoscope).

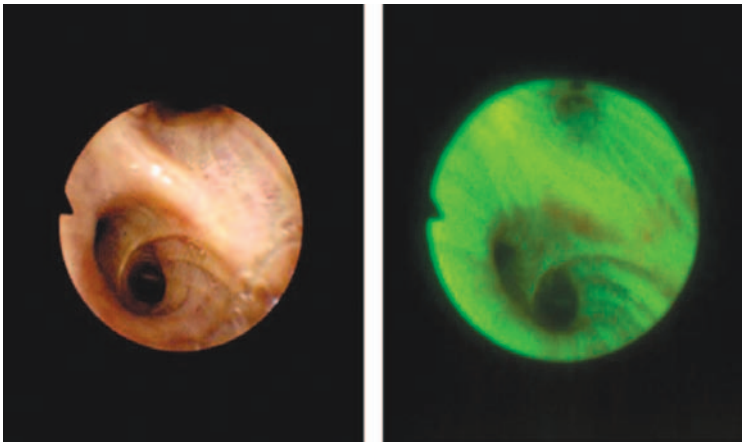

Figure 30.2 Simultaneous display of white light and autofluorescence images.

Figure 30.3 Pentax SAFE-3000 autofluorescence bronchoscopy system with flexible video-chip bronchoscope (Pentax Corporation, Tokyo, Japan).

Table 30.2 Comparative studies of white light and autofluorescence.

Study	No. of patients	Sensitivity (%)		Relative sensitivity	Specificity (%)	
		WLB	WLB + AFB		WLB	WLB + AFB
Lam *et al.* (1998) [3]	173	9	56	6.2	90	66
Khanavkar *et al.* (1998) [4]	165	32	86	2.7	75	31
Ikeda *et al.* (1999) [5]	158	58	92	1.6	62	66
Häussinger (2005) [6]	1173	58	82	1.4	62	58

30.2 Fibered Confocal Fluorescence Microscopy (FCFM)

Confocal fluorescence microscopy is a relatively new optical technology, which uses a laser as light source. It produces real-time dynamic images of living tissue, which due to their high resolution are referred to as "optical biopsies." The technique can be applied endoscopically to the lung via flexible fiber-optic miniprobes. The main

endogenous fluorophore of the lung is elastin. In bronchial mucosa, fibered confocal fluorescence microscopy (FCFM) visualizes the network of elastic fibers in the subepithelial layer. Thiberville *et al.* [7] attempted to establish normal and abnormal patterns of FCFM imaging of the bronchial mucosa in a study of 29 subjects at high risk for lung cancer. They found that the absence of a regular fibered pattern seems to be sensitive for preinvasive lesions. Thus FCFM could be used as an adjunct to AFB, compensating for the low specificity of the latter by *in vivo* differentiation of AF-positive lesions in benign and suspicious samples. Although current data defining FCFM alveolar imaging of the normal lung are limited, the method appears promising because it is minimally invasive and can be repeated serially whenever indicated.

30.3
Therapeutic Uses of Laser

30.3.1
Photodynamic Therapy (PDT)

PDT utilizes the principle of a photosensitizer, which accumulates in tumor tissue, is activated by laser light of a specific wavelength, and in the presence of oxygen in the tissue environment produces reactive oxygen species. These cause cell death by inducing cellular damage, vascular ischemia, and inflammatory and immune responses. The primary clinical indications for using PDT are for curative therapy of early central lung cancer (ECLC) and palliative treatment of advanced lung cancer with bronchial obstruction. In addition, PDT has been tried as experimental therapy in early peripheral lung cancer and for the adjuvant treatment of mesothelioma. PDT is an alternative option in patients not eligible for surgery due to a high operative risk.

A recent review of the literature on PDT of ECLC, comprising 15 studies with 626 patients and 715 early cancers, revealed that almost all patients (99%) experienced at least partial remission while the rate of complete remission varied between 30 and 100% [8]. Overall, 5 year survival was 61%. The complication rate was low and acceptable and included photosensitivity skin reactions in 5–25%, respiratory complications in 13–18%, and nonfatal hemorrhage in 7.8%. Compared with other modalities used for treating central lung cancers, such as electrocautery, cryotherapy, brachytherapy, and photo-resection with the Nd:YAG laser, PDT was considered superior regarding the level of evidence, benefit, and grade of recommendation [9]. Moreover, PDT can be combined easily with other modalities of treatment such as Nd:YAG laser therapy, electrocautery, and brachytherapy. The role of PDT in advanced lung cancer has also been reviewed [10], comprising 12 studies with 636 patients, and it was concluded that PDT is safe and provides symptomatic benefit in patients with advanced lung cancer with a significant endobronchial component but good performance status and without extrathoracic metastasis. However, the cost–benefits of this procedure with respect to other modalities are not yet established. In addition, since it

provides delayed response, PDT is not suitable for use in acute, life-threatening situations.

The recommended light dose for endobronchial PDT is 200 J cm^{-1} tumor length (150–300 J cm^{-1}). The light used for PDT can be generated by an argon laser and various types of dye lasers. More recently, modern diode lasers have served as light sources. The light is delivered through optical fibers, which can be introduced via the working channel of a flexible bronchoscope.

The use of PDT for treating early peripheral lung cancer is still experimental. However, after further development and evaluation of the technique, it could be a promising alternative for those patients who are unfit for surgery or radiotherapy. Similarly, PDT is an experimental tool for treating malignant mesothelioma, mainly due to the high rate of local recurrence.

30.3.2 Laser Therapy

Lasers are extensively used for the palliative treatment of symptomatic central lung cancer. The use of lasers in bronchoscopy started almost three decades ago when Strong and Jako in 1972 used a CO_2 laser to treat various laryngeal disorders [11]. Several types of lasers have been used in medical science over the past three decades (Table 30.3). Of these, the neodymium-doped yttrium aluminum garnet (Nd:YAG) laser is currently the most popular among the various lasers available. Although laser radiation gives the best results in lesions of short length located in the trachea and

Table 30.3 Commonly used medical lasers.

Laser	Wavelength (nm)	Characteristics	Advantages/disadvantages
Nd:YAG	1064	Invisible; absorption proportional to tissue pigmentation	Deep tissue penetration with excellent hemostasis; can be used with flexible scope
KTP	532	Green light; low absorption in water	Delivery via flexible scope possible; more precise cutting than Nd:YAG; useful in endoscopic sinus surgery
CO_2	10 600	Invisible; complicated delivery system required; poor hemostatic effect	Precise cutting but more bleeding; only possible via rigid scope
Argon	488–514	Blue–green; good affinity for hemoglobin	Useful for small cutaneous and retinal vessel coagulation; needs contact with tissue for resection
Xenon-chloride	400	Precise cutting without much scatter	Delivery via flexible scope possible; useful in corneal surgery, angioplasty

mainstem or proximal lower lobe bronchi, which are easily accessible to the rigid bronchoscope, the use of flexible bronchoscopes has expanded the reach to more distal lesions. Laser resection provides significant and rapid improvement in the patient's symptoms, and is at least as effective as other palliative methods such as cryotherapy, PDT, and stent placement, if not more so.

The effect of laser radiation on the tissue depends on several factors, such as the power settings and wavelength employed, distance of the laser tip from the target, duration of impact, and certain physical characteristics of the tissue, mainly its color, surface, and water content. The Nd:YAG laser can penetrate up to 5–10 mm from the focal point and coagulate blood vessels up to 5 mm in diameter, making it an ideal choice for large vascular tumors. However, laser energy has a tendency to scatter and damage the adjoining tissues. Reducing the duration of impact and giving short energy bursts of 0.5 s each instead of a continuous beam can minimize this complication.

It is now clear that relief of central airway obstruction by intraluminal growths, either malignant or benign, constitutes the primary indication for this procedure, but laser therapy also has several other uses (Table 30.4). In the emergency setting, lasers may be used to control acute pulmonary hemorrhage in children. Another common indication for laser usage is in the treatment of tracheal and bronchial stenosis, which may occur as a result of endotracheal intubation or tracheostomy or as a consequence of systemic disorders such as sarcoidosis, tuberculosis, and Wegener granulomatosis. The laser is applied prior to mechanical dilatation using a rigid

Table 30.4 Indications for the Nd:YAG laser.

1	Intrabronchial growth	Benign	Hamartoma
			Chondroma
			Lipoma
			Neurinoma
			Papillomatosis
		Malignant	Carcinoma *in situ* (CIS)
			Early lung cancer
			Typical carcinoid
			Mucoepidermoid carcinoma
			Adenoid–cystic carcinoma
			Metastatic lesion from thyroid, colon, kidney, esophagus, and melanoma
2	Tracheal or bronchial stenosis	After endotracheal intubation or tracheostomy	
		Sarcoidosis	
		Tuberculosis	
		Wegener granulomatosis	
3	Others	To cut metallic stents and foreign bodies prior to removal	
		To close small proximal bronchopleural fistulas occurring after lung resection	
		To control acute pulmonary hemorrhage in children	

Table 30.5 Contraindications for the Nd:YAG laser.

Related to anatomic location of obstruction	Extrinsic lesions without endobronchial growth Lesions bordering or infiltrating adjoining vascular structures, esophagus or mediastinum Total obstruction with inadequate landmarks
Related to patient condition	Coagulation disorders Terminal metastatic disease

bronchoscope or balloon; however, distortion of the airways and scarring are frequent complications. Lasers are also used to cut metallic stents and foreign bodies prior to their removal and to close small proximal bronchopleural fistulas occurring after lung resection. Lasers have also been tried as an adjunct in tuberculosis, but a Cochrane review found insufficient evidence to recommend their use at present [12].

30.4 Contraindications

Table 30.5 lists the various common contraindications for laser procedures.

30.5 Laser Bronchoscopy Procedure

30.5.1 Anesthesia

The type of anesthesia used depends on whether a rigid, flexible, or combined bronchoscopic delivery is planned. Combustible gases, such as halothane, should be strictly avoided. Intravenous propofol supplemented with midazolam and fentanyl is a popular regimen. The inspired oxygen concentration (FiO_2) should be kept below 40% and oxygen saturation by pulse oximetry should be maintained above 90%.

30.5.2 Technique

This procedure requires a combined team effort of the bronchoscopist, anesthetist, laser operator, and nurses. Nd:YAG laser bronchoscopy using a fiber-optic bronchoscope can be performed on awake, spontaneously breathing patients. The instrument is passed transnasally or transorally and then the laser fiber is guided through it until the target lesion is reached. Keeping the tip of the laser fiber at least 1 cm away from the tip of the bronchoscope and 4–10 mm from the lesion to be treated, the laser is fired in pulses of 0.5–1 s at energy settings between 20 and 40 W. The beveled end of

the rigid bronchoscope can sometimes be used to shear off a portion of protruding tissue. The bronchoscopist should be able to vaporize a small lesion completely or cause sufficient sloughing off of the tissue to be easily coughed out or removed using biopsy forceps.

Bronchoscopy should be repeated 2–4 days later to assess the results of treatment. These sessions should be repeated every 2–4 days until maximum benefit is achieved. A complete response is defined as complete clearing of the tumor whereas a partial response is a reduction in tumor size or improvement in the smallest tracheobronchial diameter. Symptomatic improvement of the patient's symptoms, improvement in pulmonary functions, resolution of atelectasis on chest radiograph, and improved performance status as noted by dyspnea indices are other parameters to gage the success of this procedure.

The following safety precautions should be strictly adhered to during laser resection:

- Use the lowest possible oxygen concentration during laser firing.
- Avoid laser firing towards the airway wall.
- Remove all flammable material from the vicinity of the equipment.
- Cover the patient's eyes with saline pads and aluminum foil.
- All personnel in the room should wear goggles.
- Perform frequent bronchial toilet to keep the airway patent.
- Avoid prolonged periods of apnea.
- Use the laser sparingly; rely more on mechanical resection.

30.6 Complications

These procedures are usually well tolerated in experienced hands, as is evident from several large series conducted over the last two decades where the complication rates ranged from 2.3 to 6.5%. The commonly encountered complications are listed in Table 30.6.

30.7 Outcome

The short-term results of endobronchial laser treatment are usually good (Figure 30.4). Immediate success depends more on the location and extent of the lesion in the tracheobronchial tree than on the histology. Personne *et al.* [13] reported the first large series in which they performed 2284 laser sessions on 1310 patients; 25% of their patients survived more than 1 year and more than half of all subjects had significant relief of airway obstruction, with an overall mortality of only 1.6%. In another large case series involving 1838 patients [14], successful de-obstruction after the first laser treatment was achieved with 93% of lesions located in the trachea, main bronchi,and bronchus intermedius, whereas the success rate dropped in lobar

Table 30.6 Complications of laser therapy..

Complication		Management
Common	Hemorrhage	Continuous suctioning, lavage with saline and epinephrine and photocoagulation of the surrounding tissue
	Airway fire	Can be avoided by keeping the laser tip clean to minimize chances of self-ignition, removing all flammable objects from the laser path, avoiding combustible inhaled anesthetics, keeping the FiO_2 below 50%, and delivering laser pulses of 40 W or less
	Airway perforation	The most important preventive strategy against perforation is to use the minimum energy setting for short durations
	Pneumothorax	Avoid laser perforating the bronchial wall or due to a ruptured bleb in a hyperinflated lung
	Hypoxemia	As a result of bronchospasm or laryngospasm; should be treated before proceeding with the laser procedure. Maintaining a good pulmonary toilet and clear airways is the most important precaution against hypoxia.[27]
	Cardiac events	Rarely seen now with better monitoring of cardiac rhythm and oxygen saturation, and can be prevented to a great extent by following the safety measures for bronchoscopic laser therapy
Uncommon	Noncardiogenic pulmonary edema Focal pulmonary hyperinflation Airway scarring/stenosis Systemic/air embolism	

bronchi to between 77% in the lower lobes and 49% in the upper lobes, where more bending of the bronchoscope is required.

Hence the utility of lasers in pulmonary medicine is multifactorial and of both diagnostic and therapeutic importance. Further refinement of the technique and physician expertise is likely to expand its utility and improve patient outcomes following their use.

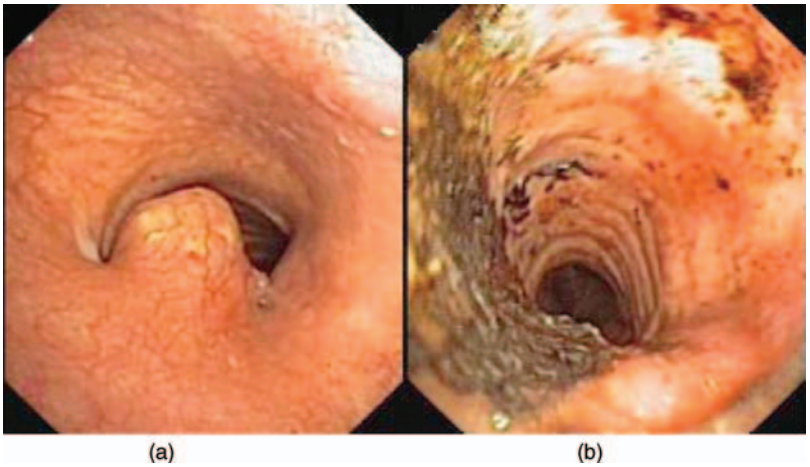

Figure 30.4 Adenoid-cystic carcinoma. (a) Exophytic tumor in the proximal trachea and (b) restored tracheal lumen immediately after laser resection with the Nd:YAG laser.

References

1 Van Der Spek, A.F., Spargo, P.M., and Norton, M.L. (1988) The physics of lasers and implications for their use during airway surgery. *Br. J. Anaesth.*, **60**, 709–729.

2 Kennedy, T.C., McWilliams, A., Edell, E., Sutedja, T., Downie, G., Yung, R., *et al.* (2007) Bronchial intraepithelial neoplasia/early central airways lung cancer: ACCP evidence-based clinical practice guidelines (2nd edition). *Chest*, **132** (3 Suppl.), 221S–233S.

3 Lam, S., Kennedy, T., Unger, M., Miller, Y.E., Gelmont, D., Rusch, V., *et al.* (1998) Localization of bronchial intraepithelial neoplastic lesions by fluorescence bronchoscopy. *Chest*, **113** (3), 696–702.

4 Khanavkar, B., Gnudi, F., Muti, A., Marek, W., Muller, K.M., Atay, Z., *et al.* (1998) Basic principles of LIFE-autofluorescence bronchoscopy. Results of 194 examinations in comparison with standard procedures for early detection of bronchial carcinoma – overview. *Pneumologie*, **52** (2), 71–76.

5 Ikeda, N., Honda, H., Katsumi, T., Okunaka, T., Furukawa, K., Tsuchida, T., *et al.* (1999) Early detection of bronchial lesions using lung imaging fluorescence endoscope. *Diagn. Ther. Endosc.*, **5** (2), 85–90.

6 Häussinger, K., Becker, H., Stanzel, F., Kreuzer, A., Schmidt, B., Strausz, J., *et al.* (2005) Autofluorescence bronchoscopy with white light bronchoscopy compared with white light bronchoscopy alone for the detection of precancerous lesions: a European randomized controlled multicentre trial. *Thorax*, **60** (6), 496–503.

7 Thiberville, L., Moreno-Swirc, S., Vercauteren, T., Peltier, E., Cave, C., and Bourg Heckly, G. (2007) *In vivo* imaging of the bronchial wall microstructure using fibered confocal fluorescence microscopy. *Am. J. Respir. Crit. Care Med.*, **175** (1), 22–31.

8 Moghissi, K. and Dixon, K. (2008) Update on the current indications, practice and results of photodynamic therapy (PDT) in early central lung cancer (ECLC). *Photodiagn. Photodyn. Ther.*, **5** (1), 10–18.

9 Mathur, P.N., Edell, E., Sutedja, T., and Vergnon, J.M. (2003) American College of Chest Physicians. Treatment of early stage non-small cell lung cancer. *Chest*, **123** (1 Suppl.), 176S–180S.

10 Moghissi, K. and Dixon, K. (2003) Is bronchoscopic photodynamic therapy a therapeutic option in lung cancer? *Eur. Respir. J.*, **22** (3), 535–541.

11 Strong, M.S. and Jako, J.G. (1972) Laser surgery in the larynx: early clinical experience with continuous CO_2 laser. *Ann. Otol. Rhinol. Laryngol.*, **81**, 791–798.

12 Vlassov, V.V. and Reze, A.G. (2006) Low level laser therapy for treating tuberculosis. *Cochrane Database Syst. Rev.*2 (Art. No.: CD003490), DOI: 10.1002/14651858.CD003490.pub2.

13 Personne, C., Colchen, A., Leroy, M., *et al.* (1986) Indications and technique for endoscopic laser resections in bronchology. *J. Thorac. Cardiovasc. Surg.*, **91**, 710–715.

14 Cavaliere, S., Venuta, F., Focolli, P. *et al.* (1996) Endoscopic treatment of malignant airway obstruction in 2008 patients. *Chest*, **110**, 1536–1542.

31
Bladder Biopsy with Optical Coherence Tomography

Alexandre Douplik

The American Cancer Society estimates that in 2010 there will be 70 530 new cases and an estimated 14 680 deaths from bladder cancer in the United States [1]. The 5 year survival rate drops from 98% [when cancer is found at early (0) stage or carcinoma *in situ*] to 63% (when cancer is found at stage 3 or invasive tumor), and then to 15% for patients with stage 4 (metastasized) [2]. Hence it is critical to discover bladder cancer at an early stage. Another critical issue in cancer care of the bladder is to identify adequately the resection margins and maximally preserve the adjacent healthy tissue while eradicating cancer lesion(s). Downsizing of the bladder affects patients' quality of life as they may not be able to hold as much urine in the bladder as before surgery and may need to empty it more often [3].

People with bladder cancer sometimes have a similar tumor in the lining of another part of the urinary system. Therefore, when someone is found to have cancer in one part of their urinary system, the entire urinary tract needs to be checked for tumors. Particularly in the case of early cancerous changes, in most cases the lesion cannot be discovered, delineated, or checked for malignancy under conventional endoscopy or intraoperatively and the gold standard remains a biopsy histology examination that usually takes a few hours at least. The technique of optical coherence tomography (OCT) has been proposed to facilitate a biopsy directly during regular cystoscopic surveillance [4] or therapeutic intervention at an image resolution close to standard H&E histology nearly in real time [5]. As the OCT probe can be implemented in a small-diameter fiber probe (1–2 mm), it has been applied in both transurethral [6] and open bladder access [7].

The type of bladder cancer can affect the treatment options because different types respond to different treatments. Transitional cell carcinoma is by far the most common type of bladder cancer. It starts in the urothelial cells lining the bladder. These tumors are divided into grades based on how the cells look under the microscope. If the cells look more like normal cells or are well differentiated, the cancer is called a low-grade cancer. When the cells look very different from normal or are poorly differentiated, the cancer is high grade. Lower grade cancers tend to grow slower and to have a better outcome than higher grade cancers. The much less common other types of malignancy in the urinary system are squamous cell

Handbook of Biophotonics. Vol.2: Photonics for Health Care, First Edition. Edited by Jürgen Popp, Valery V. Tuchin, Arthur Chiou, and Stefan Heinemann.

carcinoma, adenocarcinoma, and small cell cancer [8]. A recent study by Cauberg *et al.* showed *ex vivo* that based on OCT-measured optical attenuation (μ_t), the grade of bladder urothelial carcinoma could potentially be assessed in real time [9].

One of the limitations of OCT imaging is a relatively small field of view (of the order of 1–6 mm^2), making screening of the entire area of interest a considerably time-consuming procedure that is usually unaffordable for endoscopists and surgeons. Hence fluorescence imaging-navigated OCT imaging has been proposed as a small field of view approach to OCT guided by a large field of view technique (fluorescence imaging) [10]. Another advantage of such a combination stems from the different origins of the normal versus pathologic tissue imaging contrast and can improve the combined sensitivity and specificity. Schmidbauer *et al.* reported that using fluorescence cystoscopy in combination with OCT increases the specificity of fluorescence cystoscopy in targeting urothelial carcinoma by 19% at the lesion level and by 25% per patient [11].

OCT images of normal and cancerous bladder tissue demonstrate that well-organized layers can be seen in normal bladder tissue, whereas such clearly defined structures are not present in the invasive tumor [4, 12]. as can be seen in Figure 31.1. Karl *et al.* recently reported an OCT biopsy study of the bladder based on 166 scanned OCT images with 100% sensitivity and 65% specificity [13]. In a study by Zagayanova *et al.*, OCT images of the bladder were evaluated as being either malignant or benign based on the absence of a layering structure with a sensitivity of 98% and a specificity of 72% [14]. The relatively low specificity can be interpreted by the fact that OCT images of squamous metaplasia may be confused with carcinoma *in situ*. Squamous metaplasia is diagnosed when the urothelial transitional cells are replaced by benign squamous cells, with or without evidence of keratinization occurring, for instance, in response to chronic cystitis. The OCT image could have a layered structure; however, the urothelium is thickened and brighter than normal, frequently leading to poor or no contrast with the lamina propria [6].

In order to improve the diagnostics accuracy further, computational methods have been applied for bladder OCT image analysis, including texture analysis [15].

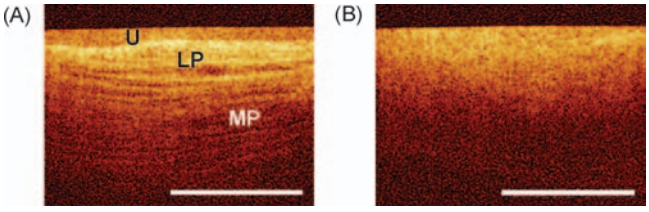

Figure 31.1 Images taken from a patient at the Cleveland Clinic after bladder OCT study using the Imalux Niris Imaging System. (a) The normal bladder (anterior wall) shows a thin urothelium (U) over a bright lamina propria (LP). A well-demarcated border with good contrast is presented between the urothelium and the lamina propria. The muscularis propria (MP) is below the lamina propria, and the border is also demarcated. (b) Image from invasive bladder cancer lesion. Courtesy of Imalux Corporation.

An overview of intraoperative OCT imaging modalities applied in the bladder, including benign tissues and inflammation, can be found in Chapter 25. Intraoperative OCT monitoring (Douplik). The results described in this chapter justify the development of OCT biopsy in the bladder for further clinical studies.

31.1 Acknowledgments

This study was supported by Erlangen Graduate School in Advanced Optical Technologies (SAOT) and by the German National Science Foundation (DFG) in the framework of the excellence initiative. The author is grateful for support from Imalux Corporation (USA) in providing the OCT images.

References

1 American Cancer Society (2010) Cancer facts and figures, www.cancer.org (last accessed: Dec 15, 2010).
2 National Cancer Institute (2010) Annual report to the nation on the status of cancer 1975–2001, with a special feature on survival: questions and answers, http://www.cancer.gov/newscenter/qa/2004/2001-annual-report-survivalqa.
3 National Cancer Institute (2010) Bladder cancer surgery, http://www.cancer.gov/cancertopics/wyntk/bladder/page8#a.
4 Jesser, C.A., Boppart, S.A., Pitris, C., Stamper, D.L., Nielsen, G.P., Brezinski, M.E., and Fujimoto, J.G. (1999) High resolution imaging of transitional cell carcinoma with optical coherence tomography: feasibility for the evaluation of bladder pathology. *Br. J. Urol.*, **72**, 1170–1176.
5 Fujimoto, J.G., Pitris, C., Boppart, S.A., and Brezinski, M.E. (2000) Optical coherence tomography: an emerging technology for biomedical imaging and optical biopsy. *Neoplasia*, **2** (1–2), 9–25.
6 Zagaynova, E.V., Gladkova, N.D., Streltsova, O.S., Gelikonov, G.V., Tresser, N., and Feldchtein, F.I. (2008) Optical coherence tomography in urology, in *Optical Coherence Tomography: Technology and Applications (Biological and Medical Physics: Biomedical Engineering)* (eds W. Drexler and J.G. Fujimoto), Springer, Berlin, pp. 1241–1268.
7 Zagaynova, E., Gladkova, N., Shakhova, N., Gelikonov, G., and Gelikonov, V. (2008) Endoscopic OCT with forward-looking probe: clinical studies in urology and gastroenterology. *J. Biophotonics*, **1** (2), 114–128.
8 University of Virginia Health System. Urinary tract pathology tutorials, http://www.med-ed.virginia.edu/courses/path/urinary/uroth4.cfm (last accessed: Dec 15, 2010).
9 Cauberg, E.C.C., de Bruin, D.M., Faber, D.J., de Reijke, T.M., Visser, M., de la Rosette, J.J.M.C.H., and van Leeuwen, T.G. (2010) Quantitative measurement of attenuation coefficients of bladder biopsies using optical coherence tomography for grading urothelial carcinoma of the bladder. *J. Biomed. Opt.*, **15** (6), 066013.
10 Wang, Z.G., Durand, D.B., Schoenberg, M., and Pan, Y.T. (2005) Fluorescence guided optical coherence tomography for the diagnosis of early bladder cancer in a rat model. *J. Urol.*, **174** (6), 2376–2381.
11 Schmidbauer, J., Remzi, M., Klatte, T., Waldert, M., Mauermann, J., Susani, M., and Marberger, M. (2009) Fluorescence cystoscopy with high-resolution optical coherence tomography imaging as an

adjunct reduces false-positive findings in the diagnosis of urothelial carcinoma of the bladder. *Eur. Urol.*, **56**, 914–919.

12 Manyak, M.J., Gladkova, N.D., Makari, J.H., Shwartz, A., Zagaynova, E.V., Zolgahari, L., Zara, J.M., Iksanov, R., and Feldchtein, F.I. (2005) Evaluation of superficial bladder transitional-cell carcinoma by optical coherence tomography. *J. Endourol.*, **19** (5), 570–574.

13 Karl, A., Stepp, H., Willmann, E., Buchner, A., Hocaoglu, Y., Stief, C., and Tritschler, S. (2010) Optical coherence tomography for bladder cancer – ready as a surrogate for optical biopsy? Results of a prospective mono-centre study. *Eur. J. Med. Res.*, **15** (3), 131–134.

14 Zagayanova, E.V., Streltsova, O.S., Gladkova, N.D., Shakova, N.M., Feldchtein, F.I., Kamensky, V.A., Gelikonov, G.V., Snopova, L.B., and Donchenko, E.V. (2004) Optical coherence tomography in diagnostics of precancer and cancer of human bladder. *Proc. SPIE*, **5312**, 75–81.

15 Lingley-Papadopoulos, C.A., Loew, M.H., Manyak, M.J., and Zara, J.M. (2008) Computer recognition of cancer in the urinary bladder using optical coherence tomography and texture analysis. *J. Biomed. Opt.*, **13** (2), 024003.

32
Advanced Laser Endoscopy in Urology: Laser Prostate Vaporization, Laser Surgery, and Laser Removal of Renal Calculi

Ronald Sroka, Michael Seitz, and Markus Bader

32.1
Introduction

Clinical medical laser application using high-power laser light offers the opportunity to destroy malignant and benign soft and hard tissue. Innovative developments in clinical endoscopic techniques allow for the delivery of high-power laser light in continuous-wave and pulsed modes in the spectral wavelength region 500–2100 nm. Thus covering high-power lasers using second harmonic generation in the visible spectral region, high-power diode laser systems in the near-infrared (NIR) spectral region, and also lasers emitting in the 2 μm region such as solid-state lasers and fiber laser systems, all laser systems are today clinically available. The laser output power ranges from 250 W continuous wave to more than 2 J per pulse at repetition rates of 50 Hz in pulsed mode which can be applied by single fibers. For the treatment of benign prostate hyperplasia (BPH), high-power laser vaporization [1–9] and pulsed techniques for enucleation procedures [1, 2, 10–15] are clinically proven to be reliable, safe, and effective treatment procedures. Recently, a new chapter in BPH laser treatment began with investigations of the laser–tissue interaction of high-power diode laser systems either for vaporization or for enucleation purposes. Although this era is still open and a matter of debate, the basics of preclinical and clinical investigations can be presented. Further, the potential of laser light application in the upper urinary tract is outlined. Urologic stone fragmentation can be conducted with pulsed infrared (IR) laser application. The suitable combination of a laser wavelength and laser power provides the basis for laser–tissue interaction, thus achieving successful treatment.

32.2
High-Power Diode Laser for BPH-Treatment

After the successful clinical introduction of prostate laser vaporization and laser enucleation techniques, diode laser systems have been investigated for the treatment

Handbook of Biophotonics. Vol.2: Photonics for Health Care, First Edition. Edited by Jürgen Popp, Valery V. Tuchin, Arthur Chiou, and Stefan Heinemann.

of benign prostatic enlargement. Using light in the NIR spectral range (800–1100 nm), these devices offer high simultaneous absorption in water and hemoglobin; with lasers emitting in the spectral range 1320–2100 nm, the absorption is dominated by the tissue water. Diode lasers for the treatment of BPH are available at different wavelengths. Whereas low-power diode lasers at wavelengths between 805 and 850 nm have been used for interstitial laser coagulation [16–21], diode lasers emitting light at 940, 980, 1320, and 1470 nm are currently being tested for vaporization of the prostate [22–27].

32.2.1 Preclinical Investigations

To evaluate the coagulation and vaporization properties of these laser wavelengths at high powers, investigations of their effects in different kinds of tissue models have been performed under reproducible conditions. In preclinical studies using an *ex vivo* autologous blood-perfused porcine kidney model, diode lasers at output power $P > 50$ W emitting light at 940, 980, and 1470 nm showed major amounts of tissue ablation in comparison with a 532 nm laser at 80 W, but similar hemostasis. In contrast, the coagulation zones at 50 W differ substantially. Whereas the 532 nm laser gave a coagulation depth of about 1.5 mm, diode lasers emitting light at 940 and 980 nm gave a coagulation depth between 8.4 and 9.6 mm in the kidney model, indicating deeper optical tissue penetration and greater tissue damage [24, 26, 27]. With a coagulation depth of 3.4 mm, the diode laser at 1470 nm seems to be more comparable to the 532 nm laser. Although it is questionable whether the *ex vivo* perfused kidney model mimics the condition in human prostates in every respect, the specific heat capacities in kidney ($3.89\,\mathrm{kJ\,kg^{-1}\,K^{-1}}$) and prostate ($3.80\,\mathrm{kJ\,kg^{-1}\,K^{-1}}$) are almost identical. Therefore, the isolated, blood-perfused, porcine kidney seems to be a valuable model, especially for the investigation of laser procedures, in which the heat sink is of the utmost importance [28, 29].

Another set of preclinical experiments on human cadaver prostates gave similar results to those in the porcine kidney model. In this model, the macroscopic destruction capacity of the diode laser at 980 nm at 100–200 W is 2–3 times larger than the vaporization zone of the 532 nm laser at 80 W and the diode laser at 1470 nm at 50 W. In this human cadaver prostate model also, the diode laser at 980 nm demonstrated more than twofold deeper coagulation than the 532 nm laser at 80 W and the diode laser at 1470 nm at 50 W [24]. In this respect, the diode laser is able to combine very high tissue ablation properties with the benefit of excellent hemostasis due to deep coagulation. However, owing to the laser's deep coagulation zones in the 940 and 980 nm generators, there may be a risk of violating underlying structures such as the neurovascular bundles and the external sphincter, which may cause erectile dysfunction and incontinence [30].

Unfortunately, the value of the human cadaver prostates is limited, since there is no blood perfusion, which is one of the main absorbers in the wavelength range 500–1000 nm. Therefore, *in vivo* studies on canine prostates were carried out to

evaluate the diode laser emitting at 940 nm using a generator output level of 200 W. The mean extension of the coagulation zone was measured as 4.3 mm and the ablation capacity was estimated to be up to 1500 $mm^3\,min^{-1}$ [26]. In comparison, the diode laser at 1470 nm produced a coagulation rim of 2.3 mm and the tissue removal ability reached about 400 $mm^3\,min^{-1}$ [27]. These findings indicate that diode laser vaporization is feasible and might be very effective for acutely relieving bladder outlet obstruction in an *in vivo* setting. Due to the different amounts of coagulation and ablation while showing similar overall destruction capabilities, in the clinical setting it is essential to protect underlying structures such as the neurovascular bundles and the external sphincter from thermal exposure, which may result in erectile dysfunction and incontinence.

32.2.2
Clinical Laser Application for BPH

Currently, only a limited number of studies have investigated the clinical applications of diode laser prostatectomy with a maximum follow-up of 1 year. Although all studies showed high intraoperative safety and excellent hemostatic properties, reports on the long-term durability and safety are inconsistent. In a preliminary clinical study on 10 patients, the diode laser at 1470 nm demonstrated an improvement in the international prostate symptom score (IPSS) after 12 months from 16.3 to 5.0, and the quality of life score (QoL) fell from 3.3 to 0.9. Also, the maximum flow rate (Q_{max}) increased from 8.9 $ml\,s^{-1}$ preoperatively to 22.4 $ml\,s^{-1}$ after the laser intervention. Unfortunately, reoperation rates were 20% due to laser failure in the treatment of a prominent midlobe [23]. In a single-center prospective study comparing a 200 W high-power diode laser emitting at 980 nm with a 120 W laser emitting at 532 nm, 117 patients were treated. Both laser devices provided rapid tissue ablation; the high-power diode laser at 980 nm was more favorable in terms of hemostasis during and after surgery. The higher rates of urinary retention (20%), urgency (24%), urge incontinence (7%), bladder neck strictures (15%), stress incontinence (9%), and tissue necrosis after diode laser ablation of the prostate are indications of deep tissue damage. The authors found high-power diode laser vaporization of the prostate at 980 nm to be in a premature state for treating lower urinary tract symptoms (LUTS) secondary to BPH [30]. Later, others investigated the diode laser at 980 nm at 100 W with a 0.1 s pulse duration and 0.01 s pulse interval in 52 patients and found significant durable improvements in Q_{max}, post-voiding residual urine (PVR), IPSS, and QoL score. In this single-center and single-surgeon series, no severe complications were reported, including any cases of urinary incontinence, significant irritative symptoms, retrograde ejaculation, or worsening of erectile function [30]. A subsequent investigation on diode laser vaporization at 980 nm in 47 patients by a Turkish group revealed a distinct improvement in IPSS and QoL score. There was no deterioration in erectile function. The most common postoperative complications were retrograde ejaculation (31.7%) and irritative symptoms (23.4%) [31].

32.2.3 Summary

In summary, diode laser prostatectomy is feasible. Nevertheless, despite its favorable intraoperative safety, long-term follow-up and large-scale trials will be needed to evaluate the technique finally in the future. From the clinical point of view, diode laser vaporization with generators emitting light between 900 and 1000 nm should be treated with caution owing to the large coagulation depth, which might lead to damage of underlying structures such as the neurovascular bundle, rectum, or external sphincter. On the other hand, diode lasers at 1470 nm have shown not only a good vaporization ability but also a reasonable and safe tissue coagulation capability. This might offer not only a routine operation technique but also a HoLEP (holmium laser enucleation of the prostate)-like procedure with a high safety profile.

32.3 Laser Therapy for the Upper Urinary Tract Tumors

In the treatment of upper urinary tract transitional cell carcinoma (UUTT), laser-guided techniques are mainly used through flexible and semi-rigid ureteroscopes. Nephroureterectomy has been considered as the gold standard for treating UUTT. Ureteroscopically guided laser ablation has been used successfully, resulting in recurrence rates ranging from 31% to 65% and disease-free rates of 35–86%, depending on stage and grade at diagnosis. To obtain the highest treatment success, the initial staging and grading of the tumor are crucial. Owing to the lack of comparable randomized, multicenter trials, the indications for an endoscopic laser treatment option have to be defined based on the patient's individual situation.

The endoscopic treatment of UUTT with a laser requires a light-energy transport via flexible quartz fibers introduced through the working channel of the endoscope. Depending on the laser source and the laser parameters (e.g., output power, fluence, fluence rate), the induced effects on soft tissue vary among coagulation, ablation, vaporization, and incision. Although the application of Nd:YAG and Ho:YAG lasers in urology, including in the treatment of UUTT [32–36], are widespread, innovative thulium laser developments have shown promising initial results with minimal collateral damage under experimental conditions. The roles of the thulium laser emitting in the 2 μm region and other newly evolved diode laser devices have yet to be defined in clinical studies and to produce long-term data.

Ureteral access sheets facilitate easy introduction and re-introduction of flexible ureterorenoscopes for laser treatment throughout the whole collecting system. The new generation of scopes combine excellent intraoperative visualization and maneuverability together with low-pressure, continuous-flow irrigation and working channels of up to 3.6 Fr [36]. The degree of active and passive deflection and the amount of irrigation flow are least affected when utilizing the smallest fibers available. Attention

must always be paid to prevent the laser harming the endoscope. The laser fiber tip should always be visualized a few millimeters beyond the tip of the scope [33, 36].

32.3.1 Laser Interventions

Ho:YAG laser energy is highly absorbed by water and water-containing tissues. As the heat is rapidly dispersed, minimal thermal damage to the surrounding tissue occurs. To achieve tumor ablation, the Ho:YAG laser fiber must be used in full-contact manner. For debulking of papillary urothelial tumors, the Ho:YAG laser parameters should be set in the range 0.6–1.0 J per pulse at repetition rates between 5 and 10 Hz [37, 38]. When tissue adherence to the fiber tip during ablation occurs, interruption of laser intervention and cleaning of the fiber tip are mandatory.

Although the Ho:YAG laser allows tissue ablation under direct vision, it is not possible to coagulate larger tumor vessels [32, 34, 39], and therefore circumferential treatment in the surrounding tissue is indicated [38, 40, 41]. Incomplete resection may be a problem in the case of large tumors (diameter >1.5 cm). Patients with bulky, low-grade, upper-tract tumors frequently require staged ureteroscopic therapy, meaning that the tumor is ablated to the highest amount possible; subsequently, a ureteral stent is placed, and the patient returns after an interval of healing for an additional intervention [36, 37, 39]. Staged therapy is also employed when extensive or multifocal tumor resection is required and when visualization is a constraint [37, 38, 42]. Post-laser operation, most patients require ureteral stents for 1–6 weeks [36, 37, 39]. In the case of vascular and bulky tumors, Nd:YAG laser energy should be used for coagulation because of its greater optical depth of penetration, which provides deeper coagulation and an ablative effect. Nd:YAG laser parameter settings of 20–30 W for 2–3 s using fiber diameters in the range 200–600 μm are suggested. Laser application should be performed in noncontact mode until the tumor coagulation occurs, identified by tissue bleaching and whitening [33, 34, 37–39]. Using the Nd:YAG laser, the risk of subsequent ureteral stricture is significantly higher compared with the Ho:YAG laser due to its deep tissue penetration [34]. Whenever diode laser devices with suitable fibers become clinical available, the first Nd:YAG laser treatment procedures could be replaced.

Ureteroscopic laser treatment has been reported in a relatively small but increasing number of published studies. The rate of disease-specific mortality for low-grade tumors is zero in the majority of the series [37]. Patients with grade 1 and 2 tumors treated ureteroscopically did not progress in grade or stage during close endoscopic follow-up [38]. Tumors larger than 1.5 cm requiring staged treatment showed significantly higher rates of local recurrence [43]. The localization of the tumor is less important [44]. Indications for ureteroscopic therapy initially included a solitary kidney, bilateral disease, renal insufficiency, and the presence of significant medical co-morbidities. The level of acceptance of ureteroscopically guided laser treatment of grade 1 superficial tumors of the renal pelvis is high. A less invasive approach with endoscopic laser ablation and surveillance is favored [45].

32.3.2
Complications

The rate of complication associated with retrograde endoscopic therapy has decreased with innovative developments in instrumentation and technique. Perforation while using the Ho:YAG or Nd:YAG laser can occur if the power settings are too high and the laser light is directed on to the ureteral or pelvic wall rather than the tumor. As the optical penetration depth of the Ho:YAG laser is 0.5 mm and that of the Nd:YAG laser is 5–6 mm, their coagulation effects in issue depth differ significantly. The laser fiber tip should always be visualized a few millimeters beyond the tip of the ureteroscope and directed on to the tumor under direct vision control [33, 37–39]. Owing to the induced thermal effects, there is a risk of scarring and of subsequent stricture formation after laser ablation in the ureter [33, 34, 37]. The reported stricture rate in large series ranged from 5 to 14% [33].

32.4
Laser-Assisted Lithotripsy

The surgical management of nephrolithiasis has undergone tremendous design and development changes over the past 25 years, beginning with the introduction of shockwave lithotripsy (SWL) and percutaneous management of intrarenal calculi [percutaneous nephrolithotomy (PCNL)] in the early 1980s, followed by the further development of semi-rigid ureteroscopes and the advent of actively deflecting endoscopes. Together with the miniaturization of endurologic equipment, the field of ureteroscopy expanded from the distal ureter beyond the proximal ureter to the intrarenal collecting system. With emerging new-generation flexible ureteroscopes with greater angles of maximum active tip deflection and improved durability, the complete collecting system was made accessible for ureteroscopic laser lithotripsy.

32.4.1
Experience from Preclinical Investigations

Clinically available pulsed laser systems emitting in either the infrared (IR) or visible (VIS) spectral region could be compared in reproducible standardized experiments with respect to their impact on phantom stones in underwater laboratory setups. So far, there are three pulsed laser systems emitting light either in the IR ($\lambda = 2100$ nm, Ho:YAG laser) or VIS ($\lambda = 532$ nm/1064 nm, FREDDY laser; 598 nm, FLPD laser) spectral range available. The fragmentation rates could be determined in relation to the fluence (depending on pulse energy and fiber diameter) using artificial stones. The threshold value of the laser pulse energy to induce an ablation of artificial stones induced by the different laser systems showed that even the lowest laser settings induced significant ablation without regard to the repetition rate and fiber diameter. The VIS lasers showed higher fragmentation rates than the IR lasers. However, VIS lasers are useful solely for laser-induced

shockwave lithotripsy of soft stones, whereas IR lasers are also able to fragment the hardest stone composites.

32.4.2 Laser Lithotripsy from the Clinical Point of View

The combination of the newest innovative endoscopic equipment and the Ho:YAG laser, with its precise and powerful thermal decomposition mechanism, has the ability to treat large urinary calculi irrespective of size or chemical consistency [46–50].

The Ho:YAG laser emits light of wavelength 2100 nm with a pulse duration of $250\,\mu s < t_p < 300\,\mu s$ at repetition rates between 3 and 50 Hz. The mechanism of stone fragmentation is based on a plasma-induced shock wave that is generated following the creation of a water channel between the fiber tip and the stone. The laser energy is guided directly on to the stone surface through this channel ("Moses effect"). A primary photothermal mechanism causing photochemical decomposition of the calculus is the dominant mechanism behind Ho:YAG laser lithotripsy. The pressure waves generated at cavitation bubble collapse make little contribution to the fragmentation process. Chemical decomposition as a consequence of a prevalent photothermal mechanism plays the main role in the Ho:YAG fragmentation process, whereas photomechanical forces make little contribution to fragmentation. Close contact between the fiber tip and the stone surface is therefore a precondition for effective Ho:YAG laser lithotripsy that is capable of breaking stones irrespective of their composition.

In addition to the improved accessibility of the collection system due to small-diameter fibers, Ho:YAG laser lithotripsy has another major advantage: the stone debris generated is finer and therefore more likely to pass spontaneously than that from any other lithotripsy device [51, 52]. In addition, soft tissue injury and bleeding are less likely owing to the small depth of optical penetration of the Ho:YAG laser.

Even with a large stone burden (e.g., partial staghorn calculi), Ho:YAG laser lithotripsy has become the procedure of choice for patients who are poor candidates (e.g., bleeding diathesis, severe cardiopulomonary disease, certain anatomic factors, and body mass index >30), for standard percutaneous therapy. In these selected patients, ureteroscopy combined with Ho:YAG laser lithotripsy may allow a decrease in morbidity and hospital stay with a stone-free rate touching that with the PCNL approach.

When treating large upper urinary tract calculi, the prevention of inadvertent laser firing, patience, and clear visibility are essential. Decreased visibility during fragmentation leads to a prolonged operative time and the potential risk of injuring the surrounding tissue or the ureteroscope, making a staged approach ultimately necessary in several cases.

Major complications secondary to ureteroscopy are less common and ureteroscopy has proved to be safe in patients where shock wave lithotripsy is likely to fail or in whom PCNL may be contraindicated (e.g., pregnancy, obese patients, patients with coagulopathy or scoliosis or other body deformities) [53–55]. Due to the decrease in

ureteroscope size, significant complications such as ureteral avulsion and stricture formation are exceedingly rare and have been reported to be as low as 1.5% [56].

The combination of the retrograde ureteroscopic approach and the holmium laser as the lithotrite of choice appears to be an adequate tool to disintegrate all kinds of calculi, independent of stone size or location, throughout the urinary tract. On the downside, generating small fragments or fine debris is a time-consuming procedure resulting in long operative times, making staged therapy necessary especially for large stone burdens in some cases.

32.5 Conclusion

During recent years, the application of thermal lasers in urology has increased. Both benign and malignant operations can be managed effectively. The primary indication for thermal laser treatment is symptomatic prostate enlargement due to BPH which can be treated either by laser enucleation techniques or by laser vaporization. Both procedures are equally effective as standard treatment [57]. Although diode laser applications have shown encouraging results and further lasers systems such as the thulium laser [58–61] are clinically available, the applicability of these laser treatment procedures needs to be confirmed in the future. Latest investigations in clinical laser application in urology report on successfull laparascopic laser assisted partial nephrectomy without need of ischemia [62]. With respect to treating patients suffering from clinical stone diseases, the combination of the retrograde ureteroscopic approach and the Ho:YAG laser as the lithotrite of choice appears to be an adequate tool to disintegrate all kinds of calculi, independent of stone size or location, throughout the urinary tract. Overall, laser assisted endoscopic treatments in urology are widespread and show promising advantages over conventional methods.

References

1 Kuntz, R.M. (2006) Current role of lasers in the treatment of benign prostatic hyperplasia (BPH). *Eur. Urol.*, **49** (6), 961–969.

2 Naspro, R., Bachmann, A., Gilling, P., Kuntz, R., Madersbacher, S., Montorsi, F., *et al*. (2009) A review of the recent evidence (2006–2008) for 532-nm photoselective laser vaporisation and holmium laser enucleation of the prostate. *Eur. Urol.*, **55** (6), 1345–1357.

3 McAllister, W.J. and Gilling, P.J. (2004) Vaporization of the prostate. *Curr. Opin. Urol.*, **14** (1), 31–34.

4 Te, A.E. (2004) The development of laser prostatectomy. *BJU Int.*, **93** (3), 262–265.

5 Hai, M.A. and Malek, R.S. (2003) Photoselective vaporization of the prostate: initial experience with a new 80 W KTP laser for the treatment of benign prostatic hyperplasia. *J. Endourol.*, **17** (2), 93–96.

6 Bachmann, A., Ruszat, R., Wyler, S., Reich, O., Seifert, H.H., Müller, A., *et al*. (2005) Photoselective vaporization of the prostate: the Basel experience after 108 procedures. *Eur. Urol.*, **47** (6), 798–804.

7 Sarica, K., Alkan, E., Lüleci, H., and Taşci, A.I. (2005) Photoselective vaporization of the enlarged prostate with KTP laser: long-term results in 240 patients. *J. Endourol.*, **19** (10), 1199–1202.

8 Ruszat, R., Seitz, M., Wyler, S.F., Abe, C., Rieken, M., Reich, O.,*et al.* (2008) Green light laser vaporization of the prostate: single-center experience and long-term results after 500 procedures. *Eur. Urol.*, **54** (4), 893–901.

9 Hamann, M.F., Naumann, C.M., Seif, C., van der Horst, C., Jünemann, K.P., and Braun, P.M. (2008) Functional outcome following photoselective vaporisation of the prostate (PVP): urodynamic findings within 12 months follow-up. *Eur. Urol.*, **54** (4), 902–907.

10 Kuntz, R.M., Lehrich, K., and Ahyai, S.A. (2008) Holmium laser enucleation of the prostate versus open prostatectomy for prostates greater than 100 grams: 5-year follow-up results of a randomised clinical trial. *Eur. Urol.*, **53** (1), 160–166.

11 Naspro, R., Suardi, N., Salonia, A., Scattoni, V., Guazzoni, G., Colombo, R., *et al.* (2006) Holmium laser enucleation of the prostate versus open prostatectomy for prostates >70 g: 24-month follow-up. *Eur. Urol.*, **50** (3), 563–568.

12 Wilson, L.C., Gilling, P.J., Williams, A., Kennett, K.M., Frampton, C.M., Westenberg, A.M. *et al.* (2006) A randomised trial comparing holmium laser enucleation versus transurethral resection in the treatment of prostates larger than 40 grams: results at 2 years. *Eur. Urol.*, **50** (3), 569–573.

13 Ahyai, S.A., Lehrich, K., and Kuntz, R.M. (2007) Holmium laser enucleation versus transurethral resection of the prostate: 3-year follow-up results of a randomized clinical trial. *Eur. Urol.*, **52** (5), 1456–1463.

14 Gilling, P.J., Aho, T.F., Frampton, C.M., King, C.J., and Fraundorfer, M.R. (2008) Holmium laser enucleation of the prostate: results at 6 years. *Eur. Urol.*, **53** (4), 744–749.

15 Tan, A., Liao, C., Mo, Z., and Cao, Y. (2007) Meta-analysis of holmium laser enucleation versus transurethral resection of the prostate for symptomatic prostatic obstruction. *Br. J. Surg.*, **94** (10), 1201–1208.

16 Pow-Sang, M., Orihuela, E., Motamedi, M., Pow-Sang, J.E., Cowan, D.F., Dyer, R., and Warren, M.M. (1995) Thermocoagulation effect of diode laser radiation in the human prostate: acute and chronic study. *Urology*, **45**, 790–794.

17 Prapavat, V., Roggan, A., Walter, J., Beuthan, J., Klingbeil, U., and Muller, G. (1996) *In vitro* studies and computer simulations to assess the use of a diode laser (850 nm) for laser-induced thermotherapy (LITT). *Lasers Surg. Med.*, **18**, 22–33.

18 Cromeens, D.M., Johnson, D.E., Stephens, L.C., and Gray, K.N. (1996) Visual laser ablation of the canine prostate with a diffusing fiber and an 805-nanometer diode laser. *Lasers Surg. Med.*, **19**, 135–142.

19 Martenson, A.C. and de la Rosette, J.J. (1999) Interstitial laser coagulation in the treatment of benign prostatic hyperplasia using a diode laser system: results of an evolving technology. *Prostate Cancer Prostatic Dis.*, **2**, 148–154.

20 Daehlin, L. and Hedlund, H. (1999) Interstitial laser coagulation in patients with lower urinary tract symptoms from benign prostatic obstruction: treatment under sedoanalgesia with pressure-flow evaluation. *BJU Int.*, **84**, 628–636.

21 de la Rosette, J.J., Muschter, R., Lopez, M.A., and Gillatt, D. (1997) Interstitial laser coagulation in the treatment of benign prostatic hyperplasia using a diode-laser system with temperature feedback. *Br. J. Urol.*, **80**, 433–438.

22 Sroka, R., Ackermann, A., Tilki, D., Reich, O., Steinbrecher, V., Hofstetter, A., Stief, C.G., and Seitz, M. (2007) *In-vitro* comparison of the tissue vaporisation capabilities of different lasers. *Med. Laser Appl.*, **22**, 227–231.

23 Seitz, M., Sroka, R., Gratzke, C., Schlenker, B., Steinbrecher, V., Khoder, W., Tilki, D., Bachmann, A., Stief, C., and Reich, O. (2007) The diode laser: a novel side-firing approach for laser vaporisation of the human prostate – immediate efficacy

and 1-year follow-up. *Eur. Urol.*, **52**, 1717–1722.

24 Seitz, M., Reich, O., Gratzke, C., Schlenker, B., Karl, A., Bader, M., Khoder, W., Fischer, F., Stief, C., and Sroka, R. (2009) High-power diode laser at 980 nm for the treatment of benign prostatic hyperplasia: *ex vivo* investigations on porcine kidneys and human cadaver prostates. *Lasers Med. Sci.*, **24**, 172–178.

25 Seitz, M., Ackermann, A., Gratzke, C., Schlenker, B., Ruszat, R., Bachmann, A., Stief, C., Reich, O., and Sroka, R. (2007) Diode laser: *ex vivo* studies on vaporization and coagulation characteristics. *Urologe A*, **46**, 1242–1247.

26 Seitz, M., Bayer, T., Ruszat, R., Tilki, D., Bachmann, A., Gratzke, C., Schlenker, B., Stief, C., Sroka, R., and Reich, O. (2009) Preliminary evaluation of a novel side-fire diode laser emitting light at 940 nm, for the potential treatment of benign prostatic hyperplasia: *ex-vivo* and *in-vivo* investigations. *BJU Int.*, **103**, 770–775.

27 Seitz, M., Ruszat, R., Bayer, T., Tilki, D., Bachmann, A., Stief, C., Sroka, R., and Reich, O. (2009) *Ex vivo* and *in vivo* investigations of the novel 1470 nm diode laser for potential treatment of benign prostatic enlargement. *Lasers Med. Sci.*, **24**, 419–424.

28 Cooper, T.E. and Trezek, G.J. (1972) A probe technique for determining the thermal conductivity of tissue. *J. Heat Transfer*, **94**, 133.

29 Reich, O., Bachmann, A., Schneede, P., Zaak, D., Sulser, T., and Hofstetter, A. (2004) Experimental comparison of high power (80 W) potassium titanyl phosphate laser vaporization and transurethral resection of the prostate. *J. Urol.*, **171**, 2502–2504.

30 Ruszat, R., Seitz, M., Wyler, S.F., Muller, G., Rieken, M., Bonkat, G., Gasser, T.C., Reich, O., and Bachmann, A. (2009) Prospective single-centre comparison of 120-W diode-pumped solid-state high-intensity system laser vaporization of the prostate and 200-W high-intensive diode-laser ablation of the prostate for treating benign prostatic hyperplasia. *BJU Int.*, **104**, 820–825.

31 Erol, A., Cam, K., Tekin, A., Memik, O., Coban, S., and Ozer, Y. (2009) High power diode laser vaporization of the prostate: preliminary results for benign prostatic hyperplasia. *J. Urol.*, **182**, 1078–1082.

32 Schilling, A., Bowering, R., and Keiditsch, E. (1986) Use of the neodymium–YAG laser in the treatment of ureteral tumors and urethral condylomata acuminata: clinical experience. *Eur. Urol.*, **12** (Suppl 1), 30–33.

33 Chen, G.L. and Bagley, D.H. (2001) Ureteroscopic surgery for upper tract transitional-cell carcinoma: complications and management. *J. Endourol.*, **15**, 399–404.

34 Schmeller, N.T. and Hofstetter, A.G. (1989) Laser treatment of ureteral tumors. *J. Urol.*, **141**, 840–843.

35 Marks, A.J. and Teichmann, J.M.H. (2007) Laser in clinical urology: state of the art and new horizons. *World J. Urol.*, **25**, 227–233.

36 Lam, J.S. and Gupta, M. (2004) Ureteroscopic management of upper tract transitional cell carcinoma. *Urol. Clin. North Am.*, **31**, 115–128.

37 Johnson, G.B. and Grasso, M. (2005) Ureteroscopic management of upper urinary tract transitional cell carcinoma. *Curr. Opin. Urol.*, **15**, 89–93.

38 Grasso, M., Fraiman, M., and Levine, M. (1999) Ureteropyeloscopic diagnosis and treatment of upper urinary tract urothelial malignancies. *Urology*, **54**, 240–249.

39 Grasso, M. (2000) Ureteroscopic management of upper urinary tract urothelial malignancies. *Rev. Urol.*, **2**, 116–121.

40 Elliott, D.S., Blute, M.L., and Patterson, D.E. (1996) Long-term follow-up of endoscopically treated upper urinary tract transitional cell carcinoma. *Urology*, **47**, 819–825.

41 Razvi, H.A., Shun, S.S., and Denstedt, J.D. (1995) Soft-tissue applications of the holmium:YAG laser in urology. *J. Endourol.*, **9**, 387–390.

42 Gerber, G.S. and Lyon, E.S. (1993) Endourological management of

upper tract urothelial tumors. *J. Urol.*, **150**, 2–7.

43 Keeley, F.X., Jr., Bibbo, M., and Bagley, D.H. (1997) Ureteroscopic treatment and surveillance of upper urinary tract transitional cell carcinoma. *J. Urol.*, **157**, 1560–1565.

44 Tawfiek, E.R. and Bagley, D.H. (1999) Upper-tract transitional cell carcinoma. *Urology*, **50**, 321–329.

45 Razdan, S., Johannes, J., Cox, M., and Bagley, D.H. (2005) Current practice patterns in urologic management of upper-tract transitional cell carcinoma. *J. Endourol.*, **19**, 366–371.

46 Grasso, M., Conlin, M., and Bagley, D. (1998) Retrograde ureteropyeloscopic treatment of 2 cm or greater upper urinary tract and minor staghorn calculi. *J. Urol.*, **160**, 346–351.

47 Busby, J.E. and Low, R.K. (2004) Ureteroscopic treatment of renal calculi. *Urol. Clin North Am.*, **31**, 89–98.

48 Mariani, A.J. (2007) Combined electrohydraulic and holmium: YAG laser ureteroscopic nephrolithotripsy of large (greater than 4 cm) renal calculi. *J. Urol.*, **177**, 168–173; discussion 73.

49 Johnson, G.B., Portela, D., and Grasso, M. (2006) Advanced ureteroscopy: wireless and sheathless. *J. Endourol.*, **20**, 552–555.

50 Vassar, G.J., Chan, K.F., Teichman, J.M. *et al.* (1999) Holmium:YAG lithotripsy: photothermal mechanism. *J. Endourol.*, **13**, 181–190.

51 Mariani, A.J. (2007) Combined electrohydraulic and holmium:YAG laser ureteroscopic nephrolithotripsy of large (greater than 4 cm) renal calculi. *J. Urol.*, **177**, 168–173; discussion 73.

52 Teichman, J.M., Vassar, G.J., Bishoff, J.T., and Bellman, G.C. (1998) Holmium:YAG lithotripsy yields smaller fragments than lithoclast, pulsed dye laser or electrohydraulic lithotripsy. *J. Urol.*, **159**, 17–23.

53 Soucy, F., Ko, R., Duvdevani, M. *et al.* (2009) Percutaneous nephrolithotomy for staghorn calculi: a single center's experience over 15 years. *J. Endourol.*, **23** (10), 1669–1673.

54 Busby, J.E. and Low, R.K. (2004) Ureteroscopic treatment of renal calculi. *Urol. Clin North Am.*, **31**, 89–98.

55 Miller, N.L. and Lingeman, J.E. (2007) Management of kidney stones. *BMJ*, **334**, 468–472.

56 Harmon, W.J., Sershon, P.D., Blute, M.L., Patterson, D.E., and Segura, J.W. (1997) Ureteroscopy: current practice and long-term complications. *J. Urol.*, **157**, 28–32.

57 Rieken, M. and Bachmann, A. (2010) Thermal lasers in urology. *Med. Laser Appl.*, **25** (1), 20–26.

58 Bach, T., Wendt-Nordahl, G., Michel, M.S., Herrmann, T.R., and Gross, A.J. (2009) Feasibility and efficacy of thulium:YAG laser enucleation (VapoEnucleation) of the prostate. *World J. Urol.*, **27** (4), 541–545.

59 Bach, T., Herrmann, T.R., Haecker, A., Michel, M.S., and Gross, A. (2009) Thulium:yttrium-aluminium-garnet laser prostatectomy in men with refractory urinary retention. *BJU Int.*, **104** (3), 361–364.

60 Bach, T., Herrmann, T.R., Ganzer, R., Burchardt, M., and Gross, A.J. (2007) RevoLix vaporesection of the prostate: initial results of 54 patients with a 1-year follow-up. *World J. Urol.*, **25** (3), 257–262.

61 Xia, S.J., Zhuo, J., Sun, X.W., Han, B.M., Shao, Y., and Zhang, Y.N. (2008) Thulium laser versus standard transurethral resection of the prostate: a randomized prospective trial. *Eur. Urol.*, **53** (2), 382–389.

62 Khoder, W.Y., Sroka, R., Hennig, G., Seitz, M., Siegert, S., Zillinberg, K., Gratzke, C., Stief, C.G., Becker, A.j. (2011) The 1318-nm diode laser supported partial nephrectomy in larascopic and open surgery: prelimnary results of a prospective feasability study. Lasers Med. Sci. doi 10.1007/s10103-011-0897-y.

33
Barrett's Esophagus and Gastroesophageal Reflux Disease – Diagnosis and Therapy

Jason M. Dunn, Steven G. Bown, and Laurence B. Lovat

33.1
Introduction

The rationale for endoscopic surveillance in patients with Barrett's esophagus (BE) is to detect progression to cancer and to allow early intervention when the disease is curable. Dysplasia arising in BE increases cancer risk, although this risk is variable according to the grade of dysplasia, and is often occult. The four-quadrant biopsy protocol, one biopsy in every quadrant of the Barrett's segment every 1–2 cm, has been shown to detect high-grade dysplasia (HGD) [1] and is recommended for Barrett's surveillance by several professional bodies, including the American Gastroenterology Association (AGA) and the British Society of Gastroenterology (BSG) [2, 3]. Even using these rigorous biopsy protocols, only about 1% of a patient's BE is examined histologically and up to one-third of cases with HGD or early cancer may be missed [4–7]. Furthermore, dysplasia itself is an imperfect marker of cancer risk, with progression rates to cancer varying between 13 and 59% after 5 years with HGD to between 1 and 8% after 5 years with low-grade dysplasia (LGD). The diagnosis of dysplasia is difficult to assess correctly and subject to disagreement between expert gastrointestinal pathologists, 15% of the time for HGD and 80% of the time for LGD [8, 9].

There is a need for more accurate assessment of the Barrett's columnar lined mucosa. Technological advances in gastrointestinal endoscopy since the introduction of conventional white light endoscopes have led to a plethora of potential tools to aid the endoscopist. In scope technologies such as narrow band imaging, magnification endoscopy by optical zoom, and high-definition charge-coupled device (CCD) chips (which produce pixel densities up to 1.25 million) are now widely used. Enhanced identification of intestinal metaplasia has been demonstrated by simple spray techniques, either by altering mucosal topography using acetic acid or chromoendoscopy with methylene blue [10, 11]. Confocal laser endomicroscopy (CLE) and optical coherence tomography (OCT) are promising research tools which inform on tissue characteristics at a cellular level. Despite these technical advances, a significant diagnostic advantage over four-quadrant biopsy has yet to be achieved. The main disadvantage of these examiner-dependent modalities is end-user interpretation,

Handbook of Biophotonics. Vol.2: Photonics for Health Care, First Edition. Edited by Jürgen Popp, Valery V. Tuchin, Arthur Chiou, and Stefan Heinemann.

with inter-observer variability [12] and a learning curve for the procedure [13] contributing significant bias to studies. Spectroscopic techniques also inform on tissue at a nuclear level, and are advantageous as end-user interpretation is removed. The first section of this chapter reviews the evidence for these novel optical techniques for the assessment of BE, with focus on translational research from bench to bedside.

The second section explores recent advances of minimally invasive treatment for dysplasia and early cancer arising in BE. The principle of endoscopic therapy for BE is that the mucosa of columnar lined esophagus may be effectively removed and is replaced, when healing is in an acid-controlled environment, by squamous epithelium (squamous regeneration). The use of biophotonics for this purpose was first demonstrated in 1992 with Nd:YAG laser therapy [14]. Since then, there has been much interest in the use of biophotonic techniques to provide endosopcially delivered therapy for dysplastic BE. These may be broadly categorized into those that utilize thermal energy (argon plasma coagulation and, more recently, radiofrequency ablation) and photodynamic therapy (PDT).

33.2 Diagnosis

33.2.1 Spectroscopy

All spectroscopic modalities analyze light–tissue interactions to yield diagnostic information about the structural (scattering) and molecular (Raman, absorption, fluorescence) composition of tissue. When light of a certain wavelength is used to stimulate tissue, distinct optical signals are produced. These "spectra" can then be correlated with histopathology and analyzed to create algorithms for tissue classification and grading. Spectroscopy offers the potential for real-time endoscopic differentiation of neoplastic and normal mucosa, and has the additional advantage of dispensing with end-user interpretation.

33.2.1.1 Scattering (Reflectance) Spectroscopy

Elastic and Light Scattering Spectroscopy When tissue is interrogated by white light, typically delivered through a fiber, *elastic* scattering events occur that redirect incident photons without a change in wavelength (or energy). Elastic scattering (also known as diffuse reflectance) spectra, which may be detected by either the same fiber or a second collection fiber, are a measure of the behaviour of white light emerging from the tissue surface following these multiple elastic scattering events. These spectra may contain both multiply scattered photons (primarily from the stroma) and photons that have undergone single or few scattering events following their interaction with the epithelium. Incident photons are also sensitive to tissue absorbers, such as hemoglobin, that reduce the intensity of the diffusely reflected light at

particular wavelengths. Elastic scattering spectroscopy (ESS) thus informs on the tissue morphology (predominantly scatter) and tissue biochemistry (predominantly absorption by hemoglobin). The interpretation of these spectra, and how they correlate with the physical properties of preneoplastic and neoplastic tissue, have attracted much interest.

Physical Correlation ESS spectra relate to the wavelength dependence and angular probability of scattering efficiency of tissue micro-components. The size, structure, and refractive indices of the denser subcellular components (e.g., the nucleus, nucleolus, and mitochondria) are known to change upon transformation to premalignant or malignant conditions. Indeed, histopathologists use these nuclear changes to grade dysplasia, that is, the sizes and shapes of nuclei and organelles, the ratio of nuclear to cellular volume (nuclear:cytoplasmic ratio) and clustering patterns (nuclear crowding).

Mourant *et al*. examined the influence of scatterer size in rat tumor cell lines and compared them with normal cells [15]. An optical geometry of 400 nm optical fiber and a 200 nm collection fiber spaced 550 nm away (center-to-center) was used. ESS measurements demonstrated a small but significant difference in optical properties between the two cell lines, with this difference in the scattering rather than the absorption properties of the cells. The authors postulated either that this was due to the average size of a scattering particle being larger in cancer cell lines (e.g., size of nuclei or mitochondria increase), or that there could be a change in the number and distribution of scattering particles (e.g., number of mitochondria increase).

The same group went on to hypothesize that spectral signatures will be altered if the refractive index of the nucleus changes, due to an increase in the amount of deoxyribonucleic acid (DNA) content [16]. By measuring DNA content by flow cytometry, the DNA indices DNA index (DI) were calculated for two different cell lines, and plotted against high-angle scatter (between 110° and 140°). Cell suspensions with higher DI (analogous to abnormal DNA content or aneuploidy) scattered more light than cell suspensions with smaller DI (analogous to normal DNA content or diploid).

Backman *et al*. reported on the correlation of tissue morphology with reflectance spectra using polarized light, which allows the measurement of single scattering events, called light-scattering spectroscopy (LSS) [17]. LSS was evaluated on colonic cell lines and *ex vivo* colonic polyps, where the spectrum of the single backscattering events provided quantitative information about the epithelial cell nuclei such as nuclear size, degree of pleomorphism, degree of hyperchromasia, and amount of chromatin [18].

Clinical Studies of ESS/LSS The largest clinical *in vivo* study of scattering spectroscopy to date evaluated the value of ESS in discriminating dysplastic and nondysplastic tissue in BE [9]. A total of 181 matched biopsy sites from 81 patients, where histopathologic consensus was reached, were analyzed. There was good pathologist agreement in differentiating HGD and cancer from other pathology ($\kappa = 0.72$). Spectral data was analyzed by linear discriminant analysis (LDA) + principle

component analysis (PCA) to form a model which was then tested by leave-one-out cross-validation. Elastic scattering spectroscopy detected HGD or cancer with 92% sensitivity and 60% specificity. If used to target biopsies during endoscopy, the number of low-risk biopsies taken would decrease by 60% with minimal loss of accuracy. ESS had a negative predictive value of 99.5% for HGD or cancer. This group went on to publish, in abstract form, on the accuracy of detection of DNA content abnormalities (aneuploidy/tetraploidy) *in vivo* [19]. A total of 258 biopsies without HGD were collected and analyzed by image cytometric DNA analysis from 60 patients. The sensitivity and specificity for the diagnosis of DNA content abnormalities was 83 and 78% respectively.

There have been two clinical studies of LSS. The first, on 13 BE patients (76 biopsies, four HGDs), found a sensitivity and specificity of 90% [20]. The second study evaluated LSS with ESS and autofluorescence spectroscopy (AFS) as part of a putative "tri-modal spectroscopy" system. Sixteen patients with BE (40 biopsies, seven HGDs) were studied and the sensitivity and specificity for differentiating HGD from non-HGD BE was evaluated. LSS gave a sensitivity and specificity of 100 and 91%, respectively, ESS 86 and 100%, respectively and AFS 100 and 97%, respectively [21]. When all three modalities were combined, the sensitivity and specificity were both reported as 100%, although as only seven sites contained dysplasia, and multiple spectral parameters were evaluated, the possibility of statistical error by overfitting is high.

Angle-resolved low-coherence interferometry (a/LCI) is a recent advance, a probe-based optical biopsy technique that combines OCT with LSS. Data from an *ex vivo* pilot study suggested that a/LCI may inform on nuclear density and the nuclear diameter [22]. Although these data are encouraging, the sample size was small (18 sites) and the device is yet to be tested *in vivo*.

The Field Effect – 4DELF and LEBS Backman's group went on to develop two new approaches that are extensions of LSS, called four-dimensional elastic light-scattering fingerprinting (4D-ELF) and low-coherence enhanced backscattering spectroscopy (LEBS). Both of these techniques may detect field changes in carcinogenesis – the proposition that the genetic/environmental milieu that results in neoplasia in one mucosal region should be detectable at a distant mucosal site [23]. In a landmark clinical study, both LEBS and 4D-ELF were able to detect pancreatic adenocarcinoma from optical measurements taken from the histologically normal duodenal periampullary mucosa [24].

Studies of the azoxymethane-treated rat carcinogenesis model and colonic adenomas in humans have also demonstrated changes in LEBS and 4D-ELF, with the authors suggesting these may be used as novel optical biomarkers for cancer [25, 26]. In addition to changes in tissue organization, 4D-ELF also measures subtle changes in microvascular blood supply [so-called early increase in blood supply (EIBS)] that may inform on field carcinogenesis elsewhere [27]. A recent study using a simplified 4D-ELF probe supports this theory in colon cancer [28]. No studies have been undertaken on patients with BE or early gastric cancer to date. Further large-scale clinical studies of these promising techniques are awaited.

33.2.1.2 Raman Spectroscopy

Raman spectroscopy provides molecular-specific information about tissue based on the detection of *inelastically* scattered light. Following tissue excitation by a laser, a small fraction of the scattered light undergoes "wavelength shifts" relative to the excitation wavelength due to energy transfer between incident photons and tissue molecules. The emitted signal is very weak because only a very small proportion of light interacting with tissue results in the inelastic scattering (compared with elastic scattering and autofluorescence, which are up to 10^6 times and 10^3 times stronger, respectively). Recent developments in instrumentation have permitted its application in tissue to allow the objective identification of molecular markers associated with neoplastic progression [29–31]. Despite promising results *ex vivo*, however, *in vivo* studies in BE are limited because readings take a comparatively long time to collect (around 5 s) and the esophagus is a dynamic organ. In a single-center *in vivo* study of 65 patients, 26 out of 192 biopsy sites showed HGD or early cancer and Raman spectra correctly identified these with a sensitivity of 88% and a specificity of 89% [32].

33.2.1.3 Absorption Spectroscopy

Fourier Transform Infrared Spectroscopy Fourier transform infrared (FTIR) spectroscopy probes the vibrational properties of amino acids and cofactors which are sensitive to minute structural changes [33]. FTIR spectroscopy is advantageous over Raman spectroscopy as it produces large signals that are insensitive to tissue autofluorescence. In the first study of FTIR spectroscopy in BE, Wang *et al*. showed that DNA, protein, glycogen, and glycoprotein comprise the principal sources of infrared absorption [34]. Using LDA with leave-one-out cross-validation on 98 *ex vivo* specimens from 32 patients, squamous mucosa could be distinguished from columnar mucosa (BE and gastric mucosa) with a sensitivity and specificity of 100 and 97% respectively. Moreover, using FTIR to detect dysplastic mucosa resulted in a sensitivity and specificity of 92 and 80%, respectively. Dysplastic Barrett's mucosa was found to have a higher mean DNA content and greater average glycoprotein concentration than nondysplastic BE. This study was limited by its use of partially dehydrated tissue samples. Martin *et al*. commented that "hydrated or *in vivo* samples are a problem for FTIR spectroscopy because the water peak obscures much of the useful information in the biomolecular range" [35].

33.2.1.4 Fluorescence Spectroscopy

Autofluorescence results when a tissue surface is illuminated by short wavelengths, either ultraviolet (400 nm) or short visible light (400–550 nm). The resulting fluorescence is of a longer wavelength and emanates from tissue biomolecules ("fluorophores") that are distributed in varying concentrations in the different layers of the esophagus. The dominant fluorescent layer is the submucosa, which contains highly green-fluorescing connective tissues (collagen and elastin), while a weaker mucosal component arises from epithelium and lamina propria. Different excitation wavelengths activate different groups of fluorophores, each of which

emits at different wavelengths. HGD is characterized by low collagen fluorescence and high nicotinamide adenine dinucleotide phosphate [NAD(P)H] fluorescence, which manifests as an increase in red fluorescence. Although first described in BE using spectroscopic point measurements (AFS), the technology has since been adapted for incorporation into video endoscopes [autofluorescence imaging (AFI)] [36–39].

Autofluorescence Spectroscopy Panjehpour *et al.* were the first to report the *in vivo* use of AFS in the esophagus [40]. Thirty-six patients were studied using a laser-induced fluorescence (LIF) system with an excitation wavelength of 410 nm, which corresponds to the excitation of flavins. Normal esophagus could be distinguished from esophageal cancer with a sensitivity of 100% and a specificity of 98%. The specificity, however, dropped to 28% for the 56 biopsies that demonstrated focal HGD.

Two studies assessed the accuracy of diagnosis of dysplasia when the excitation wavelengths are in the near-ultraviolet range. With 330 nm excitation light, the major endogenous fluorophores contributing to tissue emission are collagen (absorption maximum 335 nm), NADH (absorption maximum 340 nm) and, to a much lesser extent, flavins (absorption maximum 450 nm). Hence, as several fluorophores are involved, more spectral information may be collected.

Bourg-Heckly *et al.* used various excitation ratios of different wavelengths to assess 18 BE, 15 nondysplastic, and three HGD/intramucosal cancer patients [41]. An excitation ratio of 390/550 nm gave the best results, with a sensitivity of 86% and a specificity of 95%.

Another study reported disappointing results using 337 nm excitation, with a sensitivity of 74% and a specificity of 67% for differentiating dysplastic and non-dysplastic Barrett's mucosa [42]. The authors of this study also evaluated time-resolved fluorescence, with the hypothesis that using time- or frequency-domain techniques, changes in tissue constituents or factors such as pH or oxygenation may be evaluated. A previous study had successfully applied this technique in the colon for the detection of adenomatous polyps, with a subsequent increase in diagnostic accuracy [43]. In the study on BE, however, no such improvement was noted.

Drug-Induced Fluorescence Spectroscopy Fluorescence can be enhanced by the addition of exogenous prodrugs that induce endogenous photosensitization. Aminolevulinic acid (ALA) is perhaps the best studied. Administration causes an increase in porphobilinogen deaminase levels and decreased ferrochelatase levels in the tissue, which leads to greater production and retention of protoporphyrin IX (PpIX) in neoplastic cells. Excitation by ultraviolet light from a xenon lamp (375–440 nm) causes emission of fluorescence signals which are stronger than AFS.

Clinical studies of drug-induced fluorescence spectroscopy (DFS) with oral and topical ALA have yet to demonstrate a significant diagnostic advantage over AFS, however [44], and due to the problems of variable drug pharmacokinetics, adverse effects, costs, and regulatory approval, its use is unlikely to gain wider application in Barrett's surveillance.

33.2.1.5 Summary

The understanding of the physical correlation of spectroscopic data and tissue morphology continues to evolve. A correlation with genomic instability both at the site of biopsy and from a field effect has now been shown. In addition, the recent introduction of both CLE and OCT allows real-time *in vivo* assessment at the cellular level. These advances in optical diagnostics may pave the way for a new strategy in Barrett's surveillance, whereby a multimodal approach would allow the endoscopist to quantify accurately an individual's risk of progression to cancer *in vivo*. Furthermore, as endoscopic therapy becomes more commonly employed as a first-line treatment for dysplasia and early cancer in BE, so too will there be a need for accurate assessment of the mucosa, both prior to and after therapy. Indeed, it may be possible for real-time management decisions to be made at endoscopy, based on information from these modalities. Ultimately, the adoption of these advanced optical techniques as standard practice will be based on ease of use, diagnostic accuracy, and cost.

33.3 Therapy

33.3.1 Argon Plasma Coagulation

Argon plasma coagulation (APC) is a noncontact technique in which monopolar energy is delivered to tissue using ionized argon gas, via a probe held a few millimeters from the target surface. There are many studies that report short-term success rates for complete reversal of dysplasia and metaplasia of between 60 and 100%, with efficacy apparently dependent on the power used and total energy delivered to the tissue [45–50]. The long-term efficacy of APC is questionable, however, with recurrence rates as high as 66% in one study [51]. This may be a consequence of the relatively superficial injury inflicted by APC, and also the inherent difficulty in applying the energy uniformly over the area of abnormal mucosa. Serious adverse events reported include esophageal perforations, pneumomediastinum, strictures (4–9%), and significant gastrointestinal bleeding following therapy at higher powers (60–90 W) in 4–9% [48, 52]. These complication rates, and the introduction of newer ablation techniques, have rendered APC largely obsolete for the eradication of BE, although APC could still be used to eliminate small islands of Barrett's metaplasia [53].

33.3.2 Photodynamic Therapy

PDT is a field ablation technique that is potentially an effective lower risk alternative to esophagectomy for the treatment of HGD in BE. It is a two step, nonthermal, photochemical process, which requires the interaction of a photosensitizer, light, and oxygen.

The first step is the administration of the chemical photosensitizer, which becomes concentrated in the abnormal target tissue. The majority of PDT photosensitizers possess a heterocyclic ring structure similar to that of either chlorophyll (chlorine-based photosensitizers) or, more commonly, heme (porphyrin-based photosensitizers). The second step is the application of visible light of appropriate wavelength and energy, which photoactivates the porphyrin molecule. The resulting production of cytotoxic singlet oxygen, or superoxide, contributes to the destruction of the abnormal cells where it is concentrated [54]. The most commonly used PDT light sources are lasers as they produce high-power monochromatic light of a specific wavelength with a narrow bandwidth that can be matched to the absorption peak for specific photosensitizers.

Many parameters may be varied to obtain optimal conditions for PDT, including drug dose, light power, total energy delivered, wavelength of activating light, and the time interval between photosensitizer administration and activation (drug–light interval). Hence, although there are many photosensitizers under development, only the first-generation hematoporphyrin derivative Photofrin (porfimer sodium; Axcan Pharma Inc.), has received Food and Drug Administration (FDA) and National Institute for Health and Clinical Excellence (NICE) approval for the treatment of BE. Both Levulan (5-aminolevulinic acid HCl; DUSA Pharmaceuticals, Inc.) and Foscan (temoporfin, *m*-tetrahydroxyphenylchlorin, mTHPC; Biolitec AG) have been investigated and the results of clinical trials are summarized below.

33.3.2.1 **Photofrin**

Photofrin is a hematoporphyrin derivative (HpD), a mixture of different porphyrins, and dihematoporphyrin ester (DHE). NICE approved Photofrin PDT for treating HGD in BE in 2006. The drug is administered by intravenous injection, 3 days prior to therapy, at a dose of 2 mg kg^{-1} body weight. Photofrin is activated by 630 nm laser light, typically by using a balloon-based cylindrical fiber-optic diffuser (e.g., Wizard X-cell balloon) that is placed endoscopically in the esophageal lumen, and inflated so as to hold position and flatten the esophageal folds [55]. Photosensitivity lasts up to 3 months after drug delivery.

Clinical Studies Early studies of cohort series demonstrated encouraging results for ablation of BE, with reversal of HGD in 88–95% [56–58]. A multicenter, international randomized controlled trial of 200 patients with high-grade dysplasia in BE confirmed the effectiveness of Photofrin PDT [59, 60]. Patients were randomized in a 2:1 ratio to either Photofrin PDT and a proton pump inhibitor (PPI), or PPI alone. Complete reversal of high-grade dysplasia (CR-HGD) at 1 year was achieved with Photofrin PDT in 71% versus 30% in the control group ($p < 0.001$). In the follow-up evaluation at 5 years, CR-HGD was 59% compared with 5% in the control arm [60]. A significant decreased incidence of esophageal adenocarcinoma (13% with Photofrin PDT, 28% with PPI alone) was reported as a secondary end point.

A retrospective study of 199 patients with HGD in BE compared outcomes of Photofrin PDT versus surgery [61]. There was no significant difference in long-term survival, with overall mortality 9% (11/129) for PDT and 8.5% (6/70) in the

esophagectomy group, over a median 5 years of follow-up. None of the patients treated either with surgery or PDT died from esophageal cancer. A more recent study from the same group, comparing outcomes for early intramucosal cancer with PDT plus endoscopic mucosal resection versus surgery, came to a similar conclusion [62].

Several studies have evaluated the cost-effectiveness of PDT, and all have found that Photofrin PDT for HGD is cost-effective in terms of quality-adjusted life-years compared with esophagectomy [63–65].

Adverse Events Two common side effects of PDT using Photofrin are skin photosensitivity reactions and esophageal strictures. Photosensitivity can occur up to 3 months after treatment and is reported in more than 60% of patients. This can lead to severe burns requiring hospital admission and patients are advised to undertake strict light precautions after therapy. In a randomized controlled trial severity was graded as mild in 66%, moderate in 24%, and severe in 1% [59].

As Photofrin is taken up by both the esophageal mucosa and the submucosa, the associated esophageal stricture rate is high: 22% with one treatment and rising to 50% with multiple treatments [56, 66]. Several studies have investigated ways to lower this stricture rate. In a nonblinded dosimetry study, there was a threefold decrease in severe stricture occurrence when light doses below 115 J cm^{-1} (105–85 J cm^{-1}) were used [67]. This occurred, however, at the expense of a reduction in efficacy for ablation of HGD and intramucosal cancer. The same group evaluated the effect of oral steroids after PDT, but this intervention did not reduce the incidence of stricture formation [57].

Other adverse events include pleural effusions, atrial fibrillation [68], nausea and vomiting, and odynophagia. These complications significantly affect the acceptability of Photofrin PDT.

33.3.2.2 Levulan

Levulan is the chemically stable hydrochloride salt of 5-ALA, a naturally occurring five-carbon amino ketone carboxylic acid. It is a recent drug that has come into prominence over the last decade for its potential use in the PDT of superficial, benign, and malignant skin disorders. ALA is not a new chemical entity, however. It is present in virtually all human cells as the first committed intermediate of the biochemical pathway resulting in heme synthesis in humans and chlorophyll in plants. It differs from other types of PDT in that it is not a preformed photosensitizer, but instead a metabolic precursor of the endogenously formed photosensitizer PpIX. The human body is estimated to synthesize 350 mg of ALA per day to support endogenous heme production. The synthesis of ALA is normally tightly controlled by feedback inhibition of ALA synthetase, presumably by intracellular heme levels. ALA, when provided to the cell, bypasses this control point and enters the heme synthesis pathway, which results in the accumulation of PpIX. As in the chemical chain from ALA to heme, the rate-limiting step is the final conversion of PpIX to heme [69]. Free PpIX, unlike heme, does not appear to have intrinsic biological activity. However, PpIX is a potent natural photosensitizer, and irradiation of tissues that have been photosensitized, at sufficient dose rates and doses of light, can lead to significant

photodynamic effects on cells, subcellular elements, and macromolecules via production of singlet oxygen [70].

Clinical Studies The first study of ALA PDT for HGD in BE treated five patients with a median segment length of 5 cm [71]. Oral ALA 60 mg kg^{-1} was administered, followed by 630 nm laser light via a 3 cm cylinder diffuser-tipped fiber optic at a power density of 150 mW cm^{-2} and an energy fluence of 90–150 J cm^{-2}. All healed with squamous regeneration. Two patients were found to have BE buried beneath squamous islands (buried glands), although no remaining HGD was identified.

Gossner *et al*. treated 32 patients with ALA PDT using 60 mg kg^{-1} ALA given orally and 635 nm laser light delivered 4–6 h after drug dosing through a 2 cm cylinder diffuser-tipped fiber optic at a power density of 100 mW cm^{-2} to a light dose of 150 J cm^{-2} [72]. As no balloon size was published, however, it is not possible to establish dosimetry. Ten patients had HGD and the remainder mucosal cancer. Patients were maintained on omeprazole for the duration of the study. Dysplasia was eradicated in all patients with HGD, and there was complete remission of the cancers in 17/22 patients (77%), giving an overall success rate of 27/32 (84%). This remission was maintained during follow-up of 1–30 months (mean 9.9 months). Squamous regeneration was seen in 68%, although the presence of nondysplastic buried glands was noted in some patients. A mean of 1.7 treatment sessions was required for the eradication of mucosal tumors. Of note, no tumor more than 2 mm in depth was included in the study.

In the only double-blind, randomized, placebo-controlled study reported for BE with LGD, 36 patients were randomized to receive oral ALA (30 mg kg^{-1}) or placebo [73]. This was followed 4 hours later by endoscopy and treatment of up to 6 cm of BE using green (514 nm) light. Green light is potentially advantageous as it is more strongly absorbed by the mucosa, although the depth of effect is less. A response was seen in 16/18 (89%) of patients in the ALA group, with a median area decrease of BE of 30% (range 0–60%). In the placebo group, a median area decrease of 0% was seen (range 0–10%). Of those who responded in the ALA PDT group, all maintained regression to normal squamous epithelium over the entire 24 month follow-up period, and no dysplasia was observed in the treated areas of BE which remained. In the placebo group, persistent LGD was found in 12/18 (67%) of patients followed for 24 months ($p < 0.001$). Although this study is encouraging, there are significant problems in performing studies in patients with LGD as there is a low intra- and inter-observer agreement on the diagnosis between pathologists [9, 74]. In this study, although the presence of LGD was confirmed by two independent pathologists, it was only at a single time point prior to PDT.

The optimum parameters for ALA PDT were demonstrated in a series of studies at our center. We recognized that when using a diffuser fiber to deliver light to a length of BE, the total energy delivered was best expressed per centimeter length of BE treated rather than in J cm^{-2}, as the latter measure varied depending on the size of the balloon used, whereas the total number of cells treated did not. When using 60 mg kg^{-1} ALA with red laser light, a light dose of less than 1000 J cm^{-1} was less effective than this highest light dose [75]. In a randomized controlled trial of 27

patients, we went on to demonstrate that red laser light (635 nm) was more effective than green laser light (512 nm) when using ALA 60 mg kg^{-1} [76]. Additionally, patients receiving 30 mg kg^{-1} of ALA relapsed to HGD significantly more frequently than those receiving 60 mg kg^{-1}. Kaplan–Meier analysis of the 21 patients who were subsequently treated with this optimal regimen demonstrated an eradication rate of 89% for HGD and a cancer-free proportion of 96% at 36 months' follow-up.

The first long-term results of ALA PDT in patients with HGD were described by Pech *et al.* [77]. This was a 6 year observational study that evaluated both efficacy and survival rates of 35 patients with a total of 44 ALA PDT procedures. All patients received 60 mg kg^{-1} ALA activated by red laser light. Complete remission was achieved in 34 of 35 (97%) of patients with HGD. Only 6% of patients with HGD had progression to cancer during the median follow-up period of 37 months. Six patients (18%) developed a metachronous lesion, and five of these underwent successful repeat treatment. The calculated 5 year survival was 97%. A further 31 patients with intramucosal cancer were studied with a total of 38 PDT treatments carried out; 29% had recurrence of metachronous lesions during the median follow-up period of 37 months. The calculated 5 year survival in this group was 80%.

Adverse Events Esophageal strictures following ALA occur less commonly than with Photofrin, as the drug is mostly converted to PpIX in the mucosa [78]. Photosensitivity reactions are rare and often mild as patients are sensitive to light for only 36 h. More common adverse reactions from oral ALA are nausea and vomiting and transient increases in serum aspartate aminotransferase (AST) [79]. Other serious adverse reactions reported to date include hypotension and unmasking of angina pectoris, although these appear to be self-limited and manageable in an inpatient setting.

There has been one case of acute neuropathy reported after ALA [80]. The authors surmised that the patient likely had a silent porphyria prior to treatment. On the basis of available evidence, current doses used in PDT are highly unlikely to result in neurologic or other systemic toxicologic findings.

Two early deaths have been reported following ALA PDT in two separate studies [81, 82]. One death was reported as occurring 24 h post-PDT in a patient who was treated in an ambulatory setting. The patient was randomized to receive 13-*cis*-retinoic acid 14 days prior to treatment with ALA PDT and died of acute cardiopulmonary failure; autopsy revealed aspiration pneumonitis [81]. The cause of death in the other study was not identified but also occurred the day after ALA PDT which had been done in an ambulatory setting. In our view, ALA PDT should be limited to inpatients.

33.3.2.3 Foscan

Foscan (*m*-tetrahydroxyphenylchlorin or mTHPC) is a powerful photosensitizer approved in Europe for the palliative treatment of advanced squamous cell carcinoma of the head and neck. Foscan is administered by intravenous injection after a

drug–light interval of 4 days at a wavelength of 652 nm (Summary of Product Characteristics, biolitec Pharma).

Clinical Studies Javaid *et al*. in 2002, successfully treated five out of seven patients with HGD or intramucosal cancer at a median follow-up of 1 year [83]. Another study reported successfully treating 12/12 patients with HGD or intramucosal cancer using green light to activate Foscan for PDT with a median follow-up of 18 months. Just one patient required further PDT and this was successful [84].

Our center has reported a nonrandomized study of 19 patients treated with Foscan PDT which compared red and green light activation via a diffuser balloon and a bare-tipped fiber activated by red light [85]. Seven had HGD and 12 had intramucosal cancer; all were unfit for surgery. The red light diffuser group achieved CR-HGD of 70% (4/6 patients with cancer and 3/4 with HGD); 0/3 patients achieved remission in the green light group. When using the bare-tipped fiber, there was one procedure-related death as described below and only 1/5 patients with cancers were successfully treated. Two others were downgraded to HGD.

Adverse Events There have been two esophageal perforations reported with Foscan PDT, from taking multiple biopsy specimens too soon after therapy [85]. Additional contributory factors were that one patient received a very high light dose to a single area, and the other patient had received Nd:YAG laser irradiation prior to treatment. Skin photosensitivity is comparable to that with Photofrin, up to 1 month after treatment. Stricture formation occurred in 13% (5/38) of patients presented in the three studies above. Foscan is mainly distributed in the submucosa, although more drug is found in the mucosa than with Photofrin [86].

In summary, although isolated studies showed promising initial results of Foscan PDT for HGD in BE, long-term efficacy and safety data are lacking. The data on the use of Foscan for intramucosal cancers are inferior to those with newer techniques for these lesions (Endoscope Mucosel Resection) and serious adverse events are more common. For these reasons, Foscan PDT is rarely used for the treatment of BE.

33.3.3 Radiofrequency Ablation

Radiofrequency ablation (RFA) using the HALO System (Barrx Medical, Sunnyvale, CA, USA) is a new technique for field ablation in the esophagus. The HALO System uses ultra-short pulse radiofrequency energy that delivers a constant power density of 40 W cm^{-2} and energy density 10–15 J cm^{-2}. A uniform ablation depth of 0.5–1 mm is achieved, thereby affecting the mucosa while preserving the submucosa. There are two devices, a balloon-mounted electrode for field ablation ($HALO^{360}$) and a smaller paddle device for focal ablation ($HALO^{90}$). All catheters are single-use disposable devices. Clinical trials in the United States and Europe have suggested that it is safe and effective for treating nondysplastic BE, LGD, and HGD. The HALO Ablation System was most recently reviewed by the FDA in 2006, although the device has been cleared for human use since 2001. These devices also have a Conformité Européene

(CE) mark for use in Europe and have recently been approved in the United Kingdom by NICE for the treatment of HGD arising in BE. The technical setup is simpler than in PDT, with no need for drug administration or hospital admission.

33.3.3.1 Clinical Studies

A randomized controlled trial of 127 patients (63 with HGD and 64 with LGD) treated by RFA or a sham procedure reported complete eradication of BE in 77% (65/84) and 2% (1/43) of patients, respectively, at 12 month follow-up ($p < 0.001$) [87]. The rate of progression from HGD to cancer was significantly lower in those patients treated by RFA than those treated by sham procedure at 12 month follow-up [2% (1/42) and 19% (4/21), respectively] ($p = 0.04$). No LGD patients progressed to cancer in either group. A United States Registry has reported efficacy data on 92 patients with HGD treated by RFA with at least one follow-up endoscopy [88]. Among those patients, CR-HGD was 90% (83/92) at a median 1 year follow-up; 80% (74/92) had no dysplasia and 54% (50/92) had complete reversal of BE with no intestinal metaplasia. Other cases series have reported CR-HGD rates between 79 and 100% at 12 months [89, 90]. Long-term follow-up data, however, are currently lacking.

33.3.3.2 Adverse Events

Perhaps the largest study on safety experience with HALO RFA was of 508 procedures in the United States, with no serious adverse events [91]. Symptom diaries showed mild and transient symptoms after ablation which generally resolved by day 4. Within the randomized controlled trial, adverse events included esophageal stricture formation (6% per patient), gastrointestinal bleeding (1% per patient), and chest pain requiring hospitalization (2% per patient) [87].

33.3.4 Subsquamous specialized intestinal metaplasia SSIM

A concern following all ablative therapies is the partial treatment of Barrett's epithelium with healing and squamous regeneration over the top of the Barrett's mucosa, which is hidden from the endoscopist at follow-up, so-called subsquamous specialized intestinal metaplasia (SSIM). The presence of SSIM is reported following all ablative therapies, with a frequency of 0–40% after PDT and 0–60% after APC. There have been several case reports of adenocarcinoma arising unnoticed underneath normal squamous tissue, at a rate of 0–3.7% [56, 66, 72]. One case series of 52 patients undergoing Photofrin PDT found the rate to be as high as 35.1% [92]. A more recent study, the largest of SSIM to date, evaluated 33 000 esophageal biopsies in patients undergoing PDT within a randomized trial [93]. The rate of SSIM was 5.8–30% of patients treated, but a similar frequency was found in the group treated with PPI alone (2.9–33%). In a recent randomized controlled trial of a new ablative therapy, radiofrequency ablation, the frequency of SSIM was reduced post-therapy (from 25 to 5%) and increased in the PPI alone group (from 25 to 40%) [87]. Other studies have shown that the neoplastic potential of SSIM post-PDT, as measured by Ki67 (a proliferative marker) and DNA ploidy, may be

lower than that of pre-PDT SSIM [94]. The significance of SSIM is yet to be determined.

33.4 Conclusion

The emergence of endoscopic therapy for the treatment of HGD in BE has been paralleled by studies into the use of PDT and APC. These techniques have been shown to be effective in reversing dysplasia and present a viable alternative to esophagectomy. More recent techniques for ablation of Barrett's epithelium are RFA and cryospray ablation with liquid nitrogen, which has shown promising results in single-center studies [95]. These techniques are potentially advantageous over PDT, with no need for drug administration, hospital admission, or general anesthetic, meaning that patients can have the procedure as a day case. Initial efficacy and safety data are promising, although long-term follow-up data are currently unavailable.

Dysplasia is, however, an imperfect marker of cancer risk and convincing evidence of long-term cancer prevention is lacking. Questions also remain regarding the long-term durability of the ablated Barrett's mucosa, and there is much interest in the use of biomarkers as surrogate prognostic biomarkers. Genetic abnormalities, including DNA ploidy, p16, and proliferation markers, have been shown to persist post-PDT and predict recurrent dysplasia [96–98]. Prospective studies on the use of biomarkers to guide further treatment and surveillance intervals are awaited.

In conclusion, endoscopically delivered minimally invasive therapy presents a viable alternative to surgery for patients with HGD in BE. Which therapy is chosen will depend on many factors, including regional availability, institutional expertise, cost, and ultimately patient acceptability.

References

1 Reid, B.J., Weinstein, W.M., Lewin, K.J., Haggitt, R.C., VanDeventer, G., DenBesten, L., and Rubin, C.E. (1988) Endoscopic biopsy can detect high-grade dysplasia or early adenocarcinoma in Barrett's esophagus without grossly recognizable neoplastic lesions. *Gastroenterology*, **94** (1), 81–90.

2 Playford, R.J. (2006) New British Society of Gastroenterology (BSG) guidelines for the diagnosis and management of Barrett's oesophagus. *Gut*, **55** (4), 442.

3 Wang, K.K. and Sampliner, R.E. (2008) Updated Guidelines 2008 for the Diagnosis, Surveillance and Therapy of Barrett's Esophagus. *Am. J. Gastroenterol.*, **103** (3), 788–797.

4 Kara, M.A., Peters, F.P., Rosmolen, W.D., Krishnadath, K.K., ten Kate, F.J., Fockens, P., and Bergman, J.J. (2005) High-resolution endoscopy plus chromoendoscopy or narrow-band imaging in Barrett's esophagus: a prospective randomized crossover study. *Endoscopy*, **37** (10), 929–936.

5 Kara, M.A., Smits, M.E., Rosmolen, W.D., Bultje, A.C., ten Kate, F.J., Fockens, P., Tytgat, G.N., and Bergman, J.J. (2005) A randomized crossover study comparing light-induced fluorescence endoscopy with standard videoendoscopy for the

detection of early neoplasia in Barrett's esophagus. *Gastrointest. Endosc.*, **61** (6), 671–678.

6 Reid, B.J., Blount, P.L., Feng, Z., and Levine, D.S. (2000) Optimizing endoscopic biopsy detection of early cancers in Barrett's high-grade dysplasia. *Am. J. Gastroenterol.*, **95** (11), 3089–3096.

7 Falk, G.W., Rice, T.W., Goldblum, J.R., and Richter, J.E. (1999) Jumbo biopsy forceps protocol still misses unsuspected cancer in Barrett's esophagus with high-grade dysplasia. *Gastrointest. Endosc.*, **49** (2), 170–176.

8 Reid, B.J., Haggitt, R.C., Rubin, C.E., Roth, G., Surawicz, C.M., Van Belle, G., Lewin, K., Weinstein, W.M., Antonioli, D.A., and Goldman, H. (1988) Observer variation in the diagnosis of dysplasia in Barrett's esophagus. *Hum. Pathol.*, **19** (2), 166–178.

9 Lovat, L.B., Johnson, K., Mackenzie, G.D., Clark, B.R., Novelli, M.R., Davies, S., O'Donovan, M., Selvasekar, C., Thorpe, S.M., Pickard, D., Fitzgerald, R.C., Fearn, T., Bigio, I., and Bown, S.G. (2006) Elastic scattering spectroscopy accurately detects high grade dysplasia and cancer in Barrett's oesophagus. *Gut*, **55** (8), 1078–1083.

10 Guelrud, M., Herrera, I., Essenfeld, H., and Castro, J. (2001) Enhanced magnification endoscopy: a new technique to identify specialized intestinal metaplasia in Barrett's esophagus. *Gastrointest. Endosc.*, **53** (6), 559–565.

11 Ngamruengphong, S., Sharma, V.K., and Das, A. (2009) Diagnostic yield of methylene blue chromoendoscopy for detecting specialized intestinal metaplasia and dysplasia in Barrett's esophagus: a meta-analysis. *Gastrointest. Endosc.*, **69** (6), 1021–1028.

12 Meining, A., Rösch, T., Kiesslich, R., Muders, M., Sax, F., and Heldwein, W. (2004) Inter- and intra-observer variability of magnification chromoendoscopy for detecting specialized intestinal metaplasia at the gastroesophageal junction. *Endoscopy*, **36** (02), 160–164.

13 Adler, A., Pohl, H., Papanikolaou, I.S., Abou-Rebyeh, H., Schachschal, G., Veltzke-Schlieker, W., Khalifa, A.C., Setka, E., Koch, M., Wiedenmann, B., and Rösch, T. (2008.) A prospective randomised study on narrow-band imaging versus conventional colonoscopy for adenoma detection: does narrow-band imaging induce a learning effect? *Gut*, **57** (1), 59–64.

14 Brandt, L.J. and Kauvar, D.R. (1992) Laser-induced transient regression of Barrett's epithelium. *Gastrointest. Endosc.*, **38** (5), 619–622.

15 Mourant, J.R., Hielscher, A.H., Eick, A.A., Johnson, T.M., and Freyer, J.P. (1998) Evidence of intrinsic differences in the light scattering properties of tumorigenic and nontumorigenic cells. *Cancer Cytopathol.*, **84** (6), 366–374.

16 Mourant, J.R., Canpolat, M., Brocker, C., Esponda-Ramos, O., Johnson, T.M., Matanock, A., Stetter, K., and Freyer, J.P. (2000) Light scattering from cells: the contribution of the nucleus and the effects of proliferative status. *J. Biomed. Opt.*, **5** (2), 131–137.

17 Backman, V., Wallace, M.B., Perelman, L.T., Arendt, J.T., Gurjar, R., Muller, M.G., Zhang, Q., Zonios, G., Kline, E., McGilligan, J.A., Shapshay, S., Valdez, T., Badizadegan, K., Crawford, J.M., Fitzmaurice, M., Kabani, S., Levin, H.S., Seiler, M., Dasari, R.R., Itzkan, I., Van Dam, J., and Feld, M.S. (2000) Detection of preinvasive cancer cells. *Nature*, **406** (6791), 35–36.

18 Gurjar, R.S., Backman, V., Perelman, L.T., Georgakoudi, I., Badizadegan, K., Itzkan, I., Dasari, R.R., and Feld, M.S. (2001) Imaging human epithelial properties with polarized light-scattering spectroscopy. *Nat. Med.*, **7** (11), 1245–1248.

19 Mackenzie, G.D., Oukrif, D., Green, S., Novelli, M.R., Bown, S.G., and Lovat, L.B. (2007) Elastic scattering spectroscopy for the detection of aneuploidy in Barrett's oesophagus. *Gut*, **56**, A71.

20 Wallace, M.B., Perelman, L.T., Backman, V., Crawford, J.M., Fitzmaurice, M., Seiler, M., Badizadegan, K., Shields, S.J., Itzkan, I., Dasari, R.R., Van Dam, J., and Feld, M.S.

(2000) Endoscopic detection of dysplasia in patients with Barrett's esophagus using light-scattering spectroscopy. *Gastroenterology*, **119** (3), 677–682.

21 Georgakoudi, I., Jacobson, B.C., Van Dam, J., Backman, V., Wallace, M.B., Muller, M.G., Zhang, Q., Badizadegan, K., Sun, D., Thomas, G.A., Perelman, L.T., and Feld, M.S. (2001) Fluorescence, reflectance, and light-scattering spectroscopy for evaluating dysplasia in patients with Barrett's esophagus. *Gastroenterology*, **120** (7), 1620–1629.

22 Pyhtila, J.W., Chalut, K.J., Boyer, J.D., Keener, J., D'Amico, T., Gottfried, M., Gress, F., and Wax, A. (2007) *In situ* detection of nuclear atypia in Barrett's esophagus by using angle-resolved low-coherence interferometry. *Gastrointest. Endosc.*, **65** (3), 487–491.

23 Kopelovich, L., Henson, D.E., Gazdar, A.F., Dunn, B., Srivastava, S., Kelloff, G.J., and Greenwald, P. (1999) Surrogate anatomic/functional sites for evaluating cancer risk: an extension of the field effect. *Clin. Cancer Res.*, **5** (12), 3899–3905.

24 Liu, Y., Brand, R.E., Turzhitsky, V., Kim, Y.L., Roy, H.K., Hasabou, N., Sturgis, C., Shah, D., Hall, C., and Backman, V. (2007) Optical markers in duodenal mucosa predict the presence of pancreatic cancer. *Clin. Cancer Res.*, **13** (15), 4392–4399.

25 Roy, H.K., Kim, Y.L., Liu, Y., Wali, R.K., Goldberg, M.J., Turzhitsky, V., Horwitz, J., and Backman, V. (2006) Risk stratification of colon carcinogenesis through enhanced backscattering spectroscopy analysis of the uninvolved colonic mucosa. *Clin. Cancer Res.*, **12** (3 Pt 1), 961–968.

26 Roy, H.K., Turzhitsky, V., Kim, Y., Goldberg, M.J., Watson, P., Rogers, J.D., Gomes, A.J., Kromine, A., Brand, R.E., Jameel, M., Bogovejic, A., Pradhan, P., and Backman, V. (2009.) Association between rectal optical signatures and colonic neoplasia: potential applications for screening. *Cancer Res.*, **69** (10), 4476–4483.

27 Wali, R.K., Roy, H.K., Kim, Y.L., Liu, Y., Koetsier, J.L., Kunte, D.P., Goldberg, M.J., Turzhitsky, V., and Backman, V. (2005) Increased microvascular blood content is an early event in colon carcinogenesis. *Gut*, **54** (5), 654–660.

28 Gomes, A.J., Roy, H.K., Turzhitsky, V., Kim, Y., Rogers, J.D., Ruderman, S., Stoyneva, V., Goldberg, M.J., Bianchi, L.K., Yen, E., Kromine, A., Jameel, M., and Backman, V. (2009.) Rectal mucosal microvascular blood supply increase is associated with colonic neoplasia. *Clin Cancer Res.*, **15** (9), 3110–3117.

29 Stone, N., Kendall, C., Smith, J., Crow, P., and Barr, H. (2004) Raman spectroscopy for identification of epithelial cancers. *Faraday Discuss.*, **126**, 141–157.

30 Shetty, G., Kendall, C., Shepherd, N., Stone, N., and Barr, H. (2006) Raman spectroscopy: elucidation of biochemical changes in carcinogenesis of oesophagus. *Br. J Cancer*, **94** (10), 1460–1464.

31 Kendall, C., Stone, N., Shepherd, N., Geboes, K., Warren, B., Bennett, R., and Barr, H. (2003) Raman spectroscopy, a potential tool for the objective identification and classification of neoplasia in Barrett's oesophagus. *J. Pathol.*, **200** (5), 602–609.

32 Song, L.M.W.K., Molckovsky, A., Wang, K., Burgart, L., Buttar, N., Papenfuss, S., Lutzke, L., Wilson, B., Dolenko, B., and Somorjai, R. (2005.) Diagnostic performance of near-infrared Raman spectroscopy in Barrett's esophagus. *Gastroenterology*, **128** (4), A51.

33 Berthomieu, C. and Hienerwadel, R. (2009) Fourier transform infrared (FTIR) spectroscopy. *Photosynth. Res.*, **101** (2), 157–170.

34 Wang, T.D., Triadafilopoulos, G., Crawford, J.M., Dixon, L.R., Bhandari, T., Sahbaie, P., Friedland, S., Soetikno, R., and Contag, C.H. (2007) Detection of endogenous biomolecules in Barrett's esophagus by Fourier transform infrared spectroscopy. *Proc. Natl. Acad. Sci. U. S. A.*, **104** (40), 15864–15869.

35 Martin, F.L. and Fullwood, N.J. (2007) Raman vs. Fourier transform spectroscopy in diagnostic medicine. *Proc. Natl. Acad. Sci. U. S. A.*, **104** (51), E1.

36 Haringsma, J., Tytgat, G.N., Yano, H., Iishi, H., Tatsuta, M., Ogihara, T., Watanabe, H., Sato, N., Marcon, N., Wilson, B.C., and Cline, R.W. (2001) Autofluorescence endoscopy: feasibility of detection of GI neoplasms unapparent to white light endoscopy with an evolving technology. *Gastrointest. Endosc.*, **53** (6), 642–650.

37 Ortner, M.A., Ebert, B., Hein, E., Zumbusch, K., Nolte, D., Sukowski, U., Weber-Eibel, J., Fleige, B., Dietel, M., Stolte, M., Oberhuber, G., Porschen, R., Klump, B., Hortnagl, H., Lochs, H., and Rinneberg, H. (2003.) Time gated fluorescence spectroscopy in Barrett's oesophagus. *Gut*, **52** (1), 28–33.

38 Niepsuj, K., Niepsuj, G., Cebula, W., Zieleznik, W., Adamek, M., Sielanczyk, A., Adamczyk, J., Kurek, J., and Sieron, A. (2003) Autofluorescence endoscopy for detection of high-grade dysplasia in short-segment Barrett's esophagus. *Gastrointest. Endosc.*, **58** (5), 715–719.

39 Kara, M.A., Peters, F.P., ten Kate, F.J., Van Deventer, S.J., Fockens, P., and Bergman, J.J. (2005) Endoscopic video autofluorescence imaging may improve the detection of early neoplasia in patients with Barrett's esophagus. *Gastrointest. Endosc.*, **61** (6), 679–685.

40 Panjehpour, M., Overholt, B.F., Vo-Dinh, T., Haggitt, R.C., Edwards, D.H., and BuckleyIII, F.P. (1996) Endoscopic fluorescence detection of high-grade dysplasia in Barrett's esophagus. *Gastroenterology*, **111** (1), 93–101.

41 Bourg-Heckly, G., Blais, J., Padilla, J.J., Bourdon, O., Etienne, J., Guillemin, F., and Lafay, L. (2000) Endoscopic ultraviolet-induced autofluorescence spectroscopy of the esophagus: tissue characterization and potential for early cancer diagnosis. *Endoscopy*, **32** (10), 756–765.

42 Pfefer, T.J., Paithankar, D.Y., Poneros, J.M., Schomacker, K.T., and Nishioka, N.S. (2003) Temporally and spectrally resolved fluorescence spectroscopy for the detection of high grade dysplasia in Barrett's esophagus. *Lasers Surg. Med.*, **32** (1), 10–16.

43 Mycek, M.A., Schomacker, K.T., and Nishioka, N.S. (1998) Colonic polyp differentiation using time-resolved autofluorescence spectroscopy. *Gastrointest. Endosc.*, **48** (4), 390–394.

44 Brand, S., Wang, T.D., Schomacker, K.T., Poneros, J.M., Lauwers, G.Y., Compton, C.C., Pedrosa, M.C., and Nishioka, N.S. (2002) Detection of high-grade dysplasia in Barrett's esophagus by spectroscopy measurement of 5-aminolevulinic acid-induced protoporphyrin IX fluorescence. *Gastrointest. Endosc.*, **56** (4), 479–487.

45 Madisch, A., Miehlke, S., Bayerdorffer, E., Wiedemann, B., Antos, D., Sievert, A., Vieth, M., Stolte, M., and Schulz, H. (2005) Long-term follow-up after complete ablation of Barrett's esophagus with argon plasma coagulation. *World J. Gastroenterol.*, **11** (8), 1182–1186.

46 Attwood, S.E., Lewis, C.J., Caplin, S., Hemming, K., and Armstrong, G. (2003) Argon beam plasma coagulation as therapy for high-grade dysplasia in Barrett's esophagus. *Clin. Gastroenterol. Hepatol.*, **1** (4), 258–263.

47 Basu, K.K., Pick, B., Bale, R., West, K.P., and de Caestecker, J.S. (2002) Efficacy and one year follow up of argon plasma coagulation therapy for ablation of Barrett's oesophagus: factors determining persistence and recurrence of Barrett's epithelium. *Gut*, **51** (6), 776–780.

48 Pereira-Lima, J.C., Busnello, J.V., Saul, C., Toneloto, E.B., Lopes, C.V., Rynkowski, C.B., and Blaya, C. (2000) High power setting argon plasma coagulation for the eradication of Barrett's esophagus. *Am. J. Gastroenterol.*, **95** (7), 1661–1668.

49 Schulz, H., Miehlke, S., Antos, D., Schentke, K.U., Vieth, M., Stolte, M., and Bayerdorffer, E. (2000) Ablation of Barrett's epithelium by endoscopic argon plasma coagulation in combination with high-dose omeprazole. *Gastrointest. Endosc.*, **51** (6), 659–663.

50 Morris, C.D., Byrne, J.P., Armstrong, G.R., and Attwood, S.E. (2001) Prevention

of the neoplastic progression of Barrett's oesophagus by endoscopic argon beam plasma ablation. *Br. J. Surg.*, **88** (10), 1357–1362.

51 Mork, H., Al Taie, O., Berlin, F., Kraus, M.R., and Scheurlen, M. (2007) High recurrence rate of Barrett's epithelium during long-term follow-up after argon plasma coagulation. *Scand. J. Gastroenterol.*, **42** (1), 23–27.

52 Ragunath, K., Krasner, N., Raman, V.S., Haqqani, M.T., Phillips, C.J., and Cheung, I. (2005) Endoscopic ablation of dysplastic Barrett's oesophagus comparing argon plasma coagulation and photodynamic therapy: a randomized prospective trial assessing efficacy and cost-effectiveness. *Scand. J. Gastroenterol.*, **40** (7), 750–758.

53 Spechler, S.J., Fitzgerald, R.C., Prasad, G.A., and Wang, K.K. (2010) History, molecular mechanisms, and endoscopic treatment of Barrett's esophagus. *Gastroenterology*, **138** (3), 854–869

54 Bown, S.G. and Lovat, L.B. (2000) The biology of photodynamic therapy in the gastrointestinal tract. *Gastrointest. Endosc. Clin North Am.*, **10** (3), 533–550.

55 Panjehpour, M., Overholt, B.F., and Haydek, J.M. (2000) Light sources and delivery devices for photodynamic therapy in the gastrointestinal tract. *Gastrointest. Endosc. Clin North Am.*, **10** (3), 513–532.

56 Overholt, B.F., Panjehpour, M., and Haydek, J.M. (1999) Photodynamic therapy for Barrett's esophagus: follow-up in 100 patients. *Gastrointest. Endosc.*, **49** (1), 1–7.

57 Panjehpour, M., Overholt, B.F., Haydek, J.M., and Lee, S.G. (2000) Results of photodynamic therapy for ablation of dysplasia and early cancer in Barrett's esophagus and effect of oral steroids on stricture formation. *Am. J. Gastroenterol.*, **95** (9), 2177–2184.

58 Wang, K.K. (2000) Photodynamic therapy of Barrett's esophagus. *Gastrointest. Endosc. Clin North Am.*, **10** (3), 409–419.

59 Overholt, B.F., Lightdale, C.J., Wang, K.K., Canto, M.I., Burdick, S., Haggitt, R.C., Bronner, M.P., Taylor, S.L., Grace, M.G., and Depot, M. (2005) Photodynamic therapy with porfimer sodium for ablation of high-grade dysplasia in Barrett's esophagus: international, partially blinded, randomized phase III trial. *Gastrointest. Endosc.*, **62** (4), 488–498.

60 Overholt, B.F., Wang, K.K., Burdick, J.S., Lightdale, C.J., Kimmey, M., Nava, H.R., Sivak J Jr., M.V., Nishioka, N., Barr, H., Marcon, N., Pedrosa, M., Bronner, M.P., Grace, M., and Depot, M. (2007.) Five-year efficacy and safety of photodynamic therapy with Photofrin in Barrett's high-grade dysplasia. *Gastrointest. Endosc.*, **66** (3), 460–468.

61 Prasad, GA., Wang, KK., Buttar, NS., Wongkeesong, L., Krishnadath, K.K., Nichols J III, F.C., Lutzke, L.S., and Borkenhagen, L.S. (2007) Long-term survival following endoscopic and surgical treatment of high-grade dysplasia in Barrett's esophagus. *Gastroenterology*, **132** (4), 1226–1233.

62 Prasad, G.A., Wu, T.T., Wigle, D.A., Buttar, N.S., Wongkeesong, L.M., Dunagan, K.T., Lutzke, L.S., Borkenhagen, L.S., and Wang, K.K. (2009) Endoscopic and surgical treatment of mucosal (T1a) esophageal adenocarcinoma in Barrett's esophagus. *Gastroenterology*, **137** (3), 815–823.

63 Shaheen, N.J., Inadomi, J.M., Overholt, B.F., and Sharma, P. (2004) What is the best management strategy for high grade dysplasia in Barrett's oesophagus? A cost effectiveness analysis. *Gut*, **53** (12), 1736–1744.

64 Vij, R., Triadafilopoulos, G., Owens, D.K., Kunz, P., and Sanders, G.D. (2004) Cost-effectiveness of photodynamic therapy for high-grade dysplasia in Barrett's esophagus. *Gastrointest. Endosc.*, **60** (5), 739–756.

65 Comay, D., Blackhouse, G., Goeree, R., Armstrong, D., and Marshall, J.K. (2007) Photodynamic therapy for Barrett's esophagus with high-grade dysplasia: a

cost-effectiveness analysis. *Can. J. Gastroenterol.*, **21** (4), 217–222.

66 Overholt, B.F., Panjehpour, M., and Halberg, D.L. (2003) Photodynamic therapy for Barrett's esophagus with dysplasia and/or early stage carcinoma: long-term results. *Gastrointest. Endosc.*, **58** (2), 183–188.

67 Panjehpour, M., Overholt, B.F., Phan, M.N., and Haydek, J.M. (2005) Optimization of light dosimetry for photodynamic therapy of Barrett's esophagus: efficacy vs. incidence of stricture after treatment. *Gastrointest. Endosc.*, **61** (1), 13–18.

68 Overholt, B.F., Panjehpour, M., and Ayres, M. (1997) Photodynamic therapy for Barrett's esophagus: cardiac effects. *Lasers Surg. Med.*, **21** (4), 317–320.

69 Marcus, S.L., Sobel, R.S., Golub, A.L., Carroll, R.L., Lundahl, S., and Shulman, D.G. (1996) Photodynamic therapy (PDT) and photodiagnosis (PD) using endogenous photosensitization induced by 5-aminolevulinic acid (ALA): current clinical and development status. *J. Clin. Laser Med. Surg.*, **14** (2), 59–66.

70 Poh-Fitzpatrick, M.B. (1986) Molecular and cellular mechanisms of porphyrin photosensitization. *Photodermatology*, **3** (3), 148–157.

71 Barr, H., Shepherd, N.A., Dix, A., Roberts, D.J., Tan, W.C., and Krasner, N. (1996) Eradication of high-grade dysplasia in columnar-lined (Barrett's) oesophagus by photodynamic therapy with endogenously generated protoporphyrin IX. *Lancet*, **348** (9027), 584–585.

72 Gossner, L., Stolte, M., Sroka, R., Rick, K., May, A., Hahn, E.G., and Ell, C. (1998) Photodynamic ablation of high-grade dysplasia and early cancer in Barrett's esophagus by means of 5-aminolevulinic acid. *Gastroenterology*, **114** (3), 448–455.

73 Ackroyd, R., Brown, N.J., Davis, M.F., Stephenson, T.J., Marcus, S.L., Stoddard, C.J., Johnson, A.G., and Reed, M.W. (2000) Photodynamic therapy for dysplastic Barrett's oesophagus: a prospective, double blind, randomised, placebo controlled trial. *Gut*, **47** (5), 612–617.

74 Kerkhof, M., van Dekken, H., Steyerberg, E.W., Meijer, G.A., Mulder, A.H., de Bruine, A., Driessen, A., ten Kate, F.J., Kusters, J.G., Kuipers, E.J., and Siersema, P.D. (2007) Grading of dysplasia in Barrett's oesophagus: substantial interobserver variation between general and gastrointestinal pathologists. *Histopathology*, **50** (7), 920–927.

75 Mackenzie, G.D., Jamieson, N.F., Novelli, M.R., Mosse, C.A., Clark, B.R., Thorpe, S.M., Bown, S.G., and Lovat, L.B. (2007) How light dosimetry influences the efficacy of photodynamic therapy with 5-aminolaevulinic acid for ablation of high-grade dysplasia in Barrett's esophagus. *Lasers Med. Sci.*, **23** (2), 203–210.

76 Mackenzie, G.D., Dunn, J.M., Selvasekar, C.R., Mosse, C.A., Thorpe, S.M., Novelli, M.R., Bown, S.G., and Lovat, L.B. (2009) Optimal conditions for successful ablation of high-grade dysplasia in Barrett's oesophagus using aminolaevulinic acid photodynamic therapy. *Lasers Med. Sci.*, **24** (5), 729–734.

77 Pech, O., Gossner, L., May, A., Rabenstein, T., Vieth, M., Stolte, M., Berres, M., and Ell, C. (2005) Long-term results of photodynamic therapy with 5-aminolevulinic acid for superficial Barrett's cancer and high-grade intraepithelial neoplasia. *Gastrointest. Endosc.*, **62** (1), 24–30.

78 Mackenzie, G.D., Dunn, J.M., Novelli, M.R., Mosse, S., Thorpe, S.M., Bown, S.G., and Lovat, L.B. (2008) Preliminary results of a randomised controlled trial into the safety and efficacy of ALA versus Photofrin photodynamic therapy for high grade dysplasia in Barrett's oesophagus 1. *Gut*, **57**, A14.

79 Regula, J., MacRobert, A.J., Gorchein, A., Buonaccorsi, G.A., Thorpe, S.M., Spencer, G.M., Hatfield, A.R., and Bown, S.G. (1995) Photosensitisation and photodynamic therapy of oesophageal, duodenal, and colorectal tumours using 5-aminolaevulinic acid induced protoporphyrin IX – a pilot study. *Gut*, **36** (1), 67–75.

80 Sylantiev, C., Schoenfeld, N., Mamet, R., Groozman, G.B., and Drory, V.E. (2005) Acute neuropathy mimicking porphyria induced by aminolevulinic acid during photodynamic therapy. *Muscle Nerve*, **31** (3), 390–393.

81 Forcione, D.G., Hasan, T., Ortel, B.J., and Nishioka, N.S. (2004) Optimization of aminolevulinic acid-based photodynamic therapy of Barrett's esophagus with high grade dysplasia. *Gastrointest. Endosc.*, **59** (5), 251.

82 Haringsma, J., Siersema, P.D., and Kuipers, E.J. (2004) Endoscopic ablation of Barrett's neoplasia. Rotterdam results. *Gastrointest. Endosc.*, **59** (5), AB252.

83 Javaid, B., Watt, P., and Krasner, N. (2002) Photodynamic therapy (PDT) for oesophageal dysplasia and early carcinoma with mTHPC (*m*-tetrahydroxyphenyl chlorin): a preliminary study. *Lasers Med. Sci.*, **17** (1), 51–56.

84 Etienne, J., Dorme, N., Bourg-Heckly, G., Raimbert, P., and Flejou, J.F. (2004) Photodynamic therapy with green light and *m*-tetrahydroxyphenyl chlorin for intramucosal adenocarcinoma and high-grade dysplasia in Barrett's esophagus. *Gastrointest. Endosc.*, **59** (7), 880–889.

85 Lovat, L.B., Jamieson, N.F., Novelli, M.R., Mosse, C.A., Selvasekar, C., Mackenzie, G.D., Thorpe, S.M., and Bown, S.G. (2005) Photodynamic therapy with *m*-tetrahydroxyphenyl chlorin for high-grade dysplasia and early cancer in Barrett's columnar lined esophagus. *Gastrointest. Endosc.*, **62** (4), 617–623.

86 Mlkvy, P., Messmann, H., Regula, J., Conio, M., Pauer, M., Millson, C.E., MacRobert, A.J., and Bown, S.G. (1998) Photodynamic therapy for gastrointestinal tumors using three photosensitizers – ALA induced PPIX, Photofrin(R) and MTHPC. A pilot study. *Neoplasma*, **45** (3), 157–161.

87 Shaheen, N.J., Sharma, P., Overholt, B.F., Wolfsen, H.C., Sampliner, R.E., Wang, K.K., Galanko, J.A., Bronner, M.P., Goldblum, J.R., Bennett, A.E., Jobe, B.A., Eisen, G.M., Fennerty, M.B., Hunter, J.G., Fleischer, D.E., Sharma, V.K., Hawes, R.H., Hoffman, B.J., Rothstein, R.I., Gordon, S.R., Mashimo, H., Chang, K.J., Muthusamy, V.R., Edmundowicz, S.A., Spechler, S.J., Siddiqui, A.A., Souza, R.F., Infantolino, A., Falk, G.W., Kimmey, M.B., Madanick, R.D., Chak, A., and Lightdale, C.J. (2009) Radiofrequency ablation in Barrett's esophagus with dysplasia. *N. Engl. J. Med.*, **360** (22), 2277–2288.

88 Ganz, R.A., Overholt, B.F., Sharma, V.K., Fleischer, D.E., Shaheen, N.J., Lightdale, C.J., Freeman, S.R., Pruitt, R.E., Urayama, S.M., Gress, F., Pavey, D.A., Branch, M.S., Savides, T.J., Chang, K.J., Muthusamy, V.R., Bohorfoush, A.G., Pace, S.C., DeMeester, S.R., Eysselein, V.E., Panjehpour, M., and Triadafilopoulos, G. (2008) Circumferential ablation of Barrett's esophagus that contains high-grade dysplasia: a U.S. Multicenter Registry. *Gastrointest. Endosc.*, **68** (1), 35–40.

89 Sharma, V.K., Jae, K.H., Das, A., Wells, C.D., Nguyen, C.C., and Fleischer, D.E. (2009) Circumferential and focal ablation of Barrett's esophagus containing dysplasia. *Am. J. Gastroenterol.*, **104** (2), 310–317.

90 Gondrie, J.J., Pouw, R.E., Sondermeijer, C.M., Peters, F.P., Curvers, W.L., Rosmolen, W.D., Krishnadath, K.K., ten Kate, F., Fockens, P., and Bergman, J.J. (2008) Stepwise circumferential and focal ablation of Barrett's esophagus with high-grade dysplasia: results of the first prospective series of 11 patients. *Endoscopy*, **40** (5), 359–369.

91 Rothstein, R.I., Chang, K., Overholt, B.F., Bergman, J.J., and Shaheen, N.J. (2007) Focal ablation for treatment of dysplastic and non-dysplastic Barrett esophagus: safety profile and initial experience with the Halo90 device in 508 cases. *Gastrointest. Endosc.*, **65** (5), AB147.

92 Mino-Kenudson, M., Ban, S., Ohana, M., Puricelli, W., Deshpande, V., Shimizu, M., Nishioka, N.S., and Lauwers, G.Y. (2007) Buried dysplasia and early adenocarcinoma arising in Barrett esophagus after

porfimer-photodynamic therapy. *Am. J. Surg. Pathol.*, **31** (3), 403–409.

93 Bronner, M.P., Overholt, B.F., Taylor, S.L., Haggitt, R.C., Wang, K.K., Burdick, J.S., Lightdale, C.J., Kimmey, M., Nava, H.R., Sivak, M.V., Nishioka, N., Barr, H., Canto, M.I., Marcon, N., Pedrosa, M., Grace, M., and Depot, M. (2009) Squamous overgrowth is not a safety concern for photodynamic therapy for Barrett's esophagus with high-grade dysplasia. *Gastroenterology*, **136**1), 56–64.

94 Hornick, J.L., Mino-Kenudson, M., Lauwers, G.Y., Liu, W., Goyal, R., and Odze, R.D. (2008) Buried Barrett's epithelium following photodynamic therapy shows reduced crypt proliferation and absence of DNA content abnormalities. *Am. J. Gastroenterol.*, **103** (1), 38–47.

95 Johnston, M.H., Eastone, J.A., and Horwhat, J.D. (2005) Cryoablation of Barrett's esophagus: a pilot study. *Gastrointest. Endosc.*, **62**, 842–848.

96 Dunn, J.M., Mackenzie, G.D., Oukrif, D., Mosse, C.A., Banks, M.R., Thorpe, S., Sasieni, P., Bown, S.G., Novelli, M.R., Rabinovitch, P.S., and Lovat, L.B. (2010) Image cytometry accurately detects DNA ploidy abnormalities and predicts late relapse to high-grade dysplasia and adenocarcinoma in Barrett's oesophagus following photodynamic therapy. *Br. J. Cancer*, **102** (11), 1608–1617.

97 Krishnadath, K.K., Wang, K.K., Taniguchi, K., Sebo, T.J., Buttar, N.S., Anderson, M.A., Lutzke, L.S., and Liu, W. (2000) Persistent genetic abnormalities in Barrett's esophagus after photodynamic therapy. *Gastroenterology*, **119** (3), 624–630.

98 Prasad, G.A., Wang, K.K., Halling, K.C., Buttar, N.S., Wongkeesong, L.M., Zinsmeister, A.R., Brankley, S.M., Westra, W.M., Lutzke, L.S., Borkenhagen, L.S., and Dunagan, K. (2008) Correlation of histology with biomarker status after photodynamic therapy in Barrett esophagus. *Cancer*, **113** (3), 470–476.

34
Noninvasive Fluorescence Imaging in Rheumatoid Arthritis – Animal Studies and Clinical Applications

Andreas Wunder and Bernd Ebert

34.1
Introduction

In rheumatoid arthritis (RA), most of the noninvasive imaging techniques in clinical use visualize anatomic, physiologic, or metabolic heterogeneity rather than identifying specific cellular or molecular events that underlie the disease. Most imaging agents used are unspecific. In consequence, the methods used in the clinic report relatively late in the course of the disease, assessment of disease activity and early monitoring of treatment response are challenging, and little or no information about cellular and molecular mechanisms is provided [1–4]. More specific imaging methods are urgently needed. Such techniques are highly relevant not only clinically, but also as tools for arthritis research in animal disease models [5–7]. It has been shown that new imaging agents that bind specifically to molecules crucially involved in the pathophysiology of the disease permit the visualization, characterization, and quantification of molecular and cellular processes noninvasively within intact living organisms. Such compounds have been developed and are under development for different imaging techniques, including positron emission tomography (PET), single photon emission computed tomography (SPECT), magnetic resonance tomography (MRT), ultrasound (US), and optical imaging techniques [8–10]. In this chapter, we describe the use of fluorescent imaging agents and noninvasive fluorescence imaging techniques for the visualization of arthritis in animal disease models and we discuss possible clinical applications of fluorescence imaging in RA.

34.2
Non-Invasive Fluorescence Imaging Techniques and Fluorescent Imaging Agents

Noninvasive fluorescence imaging techniques are increasingly important tools in biomedical research. Thus, fluorescence imaging systems are most frequently found in research facilities. Several fluorescence imaging systems for small animals with different characteristics are commercially available. These systems are comparatively simple. They consist of one ore more light sources for excitation of fluorochromes

Handbook of Biophotonics. Vol.2: Photonics for Health Care, First Edition. Edited by Jürgen Popp, Valery V. Tuchin, Arthur Chiou, and Stefan Heinemann.

and one or more fluorescence detectors, mostly a highly sensitive charge-coupled device (CCD) camera [11]. The major advantage of fluorescence imaging methods is their high sensitivity. Very small amounts (in the range of nanomoles to femtomoles or less) of an injected fluorochrome located inside the body of laboratory animals can be detected. Furthermore, fluorescence imaging techniques are fast, easy to use, and inexpensive. The major disadvantages of fluorescence imaging techniques are a comparatively low spatial resolution (in the range of millimeters) and depth limit (in the range of centimeters if near-infrared light is used), attributed to absorption and scattering of light in biological tissue. Moreover, absolute quantitation of the imaging signal is challenging [11–13].

Numerous fluorescent imaging agents have been developed, permitting the visualization of a series of biological processes such as increased vessel permeability or tissue perfusion, blood flow, hypoxia, proliferation, cell death, enzyme activity, receptor expression, cell migration, and many more. In most of these studies, the fluorescent imaging agents used absorb and emit light in the near-infrared fluorescence (NIRF) range, because in this spectral range the penetration depth of light is comparatively high and the tissue autofluorescence is comparatively low [14, 15].

Fluorescent imaging agents have been successfully used to study physiology and pathophysiology in different animal disease models, including animal models of cancer [16], vascular diseases [17] such as atherosclerosis [18] and stroke [19], as well as arthritis [20]. Currently, two fluorescent dyes are clinically approved: indocyanine green (ICG), an NIRF dye, and the red fluorescent protoporphyrin IX, which generates from the precursor δ-aminolevulinic acid (ALA). These compounds are relatively small molecules of low molecular weight (775 and 168 Da, respectively). ICG is used clinically in, for instance, angiography [21, 22]. ALA can be applied for the fluorescence diagnosis or for fluorescence-guided resection of both premalignant and nonmalignant diseases [23]. Recently, a pilot study using fluorescence imaging after systemic administration of the fluorescent dye ICG in patients with RA was reported [24]. Further, a fluorescence camera device, Xiralite (mivenion, Berlin, Germany), designed for ICG imaging of patients has been developed. In the following, we first describe the use of noninvasive fluorescence imaging and fluorescent imaging agents in arthritis models. We then describe clinical approaches, followed by a critical overview of fluorescence imaging in arthritis.

34.3
Experimental Studies in Arthritis Models

Imaging agents can be classified into three different groups: nonspecific, targeted, and activatable probes. All three classes of probes have been evaluated in animal models of arthritis. Nonspecific probes do not have a specificity for a certain molecular target. They can be used to assess, for instance, perfusion, blood flow, or the extravasation through blood–tissue barriers. Targeted probes are characterized

by specific binding to a certain molecular target, for example, a receptor. With these probes, the presence of a specific molecular target can be visualized. In contrast to nonspecific and targeted probes, activatable or "smart" sensor probes do not give a signal in the injected state: only after interaction with a certain molecular target is the signal activated. Examples are enzyme-activatable probes, which are activated upon cleavage by the target enzyme. Owing to the low background, this strategy results in excellent signal-to-noise ratios [5].

34.3.1
Nonspecific Fluorescent Imaging Agents in Arthritis Models

In several approaches, nonspecific fluorescent imaging agents were administered to animals with arthritis and thereafter noninvasive fluorescence imaging was performed. The idea behind using nonspecific imaging agents in arthritis is that inflamed joints show a an increased perfusion, a higher rate of extravasation, and a large number of cells with increased metabolism and phagocytosis, which increases the retention of injected compounds in tissues. The interplay of these parameters leads to contrast generation in inflamed joints compared with normal joints [25–27].

Hansch *et al.* injected the NIRF dye Cy5.5 intravenously into mice with antigen-induced arthritis (AIA). Noninvasive NIRF imaging was performed at different time points after administration of the fluorochrome. Fluorescence intensities of arthritic and normal knee joints by region of interest (ROI) analysis were estimated [25]. Figure 34.1a shows that significantly higher fluorescence intensities were found in inflamed knee joints compared with normal knee joints between 2 and 72 h after injection of the nonspecific dye. The ratios between inflamed and normal knee joints that could be achieved in this setting were never higher than 2, decreasing after 24 h. The fluorochrome used in this approach is highly water soluble and has a comparably short half-life in blood (in the range of a few hours). The dye binds *in vivo* to serum proteins, mainly to albumin, and is therefore protected from an even more rapid excretion by the kidneys. By covalent binding of fluorochromes to macromolecular carriers, the contrast between inflamed and normal joints can be increased significantly. Moreover, the contrast decreases less rapidly. In mice with collagen-induced arthritis (CIA), we could demonstrate strong fluorescence in inflamed toes and paws after injection of albumin labeled with aminofluorescein [26]. The high fluorescence intensity in inflamed toes and paws could easily be documented by taking pictures with a conventional camera and a slide film, as shown in Figure 34.1b. The pharmacokinetic data after radiolabeling of the protein showed a 6–7-fold higher uptake in inflamed paws compared with normal paws even 48 h after injection. Fischer *et al.* evaluated two nonspecific NIRF dyes, indocyanine green (ICG) and a hydrophilic carbocyanine derivative, SIDAG [1,1′-bis(4-sulfobutyl)indotricarbocyanine-5,5′-dicarboxylic acid diglucamide monosodium salt], in a mouse model of *Borrelia*-induced Lyme arthritis [27]. ICG is a lipophilic fluorochrome, which is rapidly cleared by the liver [21, 22]. The dye is characterized by high plasma protein binding (98%), whereas the more hydrophilic fluorochrome SIDAG also used in this

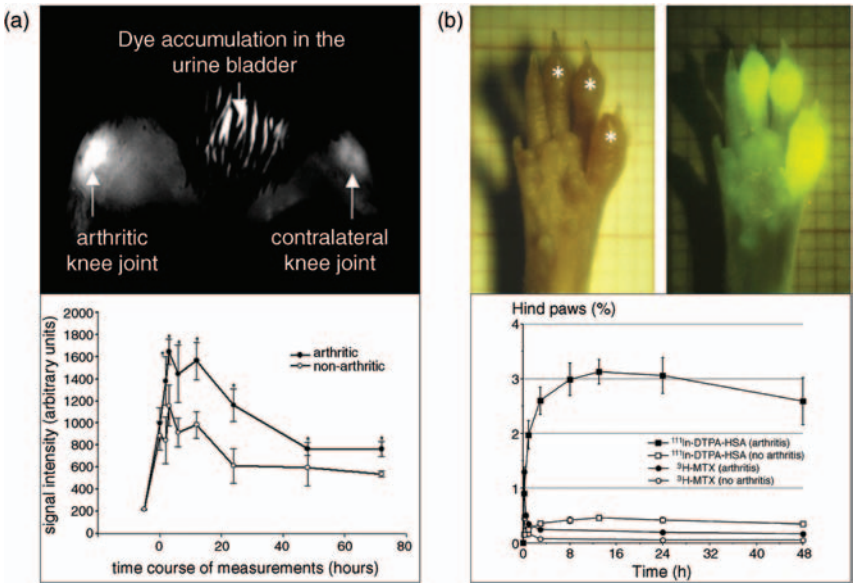

Figure 34.1 Noninvasive visualization of arthritis in animal models using nonspecific fluorescent imaging probes (Cy5.5 and fluorescently labeled albumin). (a) Noninvasive NIRF image of a mouse with AIA affecting the right knee joint taken 2 h after i.v. injection of the nonspecific NIRF dye Cy5.5. The knee joint affected by arthritis shows a higher fluorescence intensity than the normal knee joint. The time-dependent fluorescence signal intensities in arthritic and contralateral joints are depicted in the graph. Significantly higher fluorescence intensities were found in inflamed knee joints compared with normal knee joints between 2 and 72 h after injection. Ratios between inflamed knee joints compared with normal knee joints were about 2 or less, decreasing rapidly. Adapted with permission from [25]. (b) Noninvasive white light (left) and fluorescence image (right) of a paw of a mouse with CIA affecting three toes (indicated by asterisks) 3 h after injection of human serum albumin (HSA) labeled with aminofluorescein, a green fluorescent dye. Only toes affected by arthritis showed strong fluorescence demonstrating the high rate of albumin accumulation in inflamed toes. The uptake kinetics of radiolabeled HSA ([^{111}In]-DTPA-HSA) and radiolabeled methotrex at ([^{3}H]-MTX) in hind paws of mice with and without CIA after i.v. injection is shown in the graph (percentage of the initially administered radioactivity). Significant amounts of albumin accumulated in arthritic hind paws, exceeding the uptake in noninflamed hind paws by 6–7-fold. In contrast, uptake of radiolabeled MTX in arthritic hind paws was found to be significantly less, decreasing rapidly over time. Adapted with permission from [26].

study shows plasma protein binding of only 10% [27]. As shown in Figure 34.2, the pharmacokinetic behavior of the two dyes differs significantly. After injection of ICG, the fluorescence intensity in inflamed and normal joints increased rapidly within the first few seconds after injection and started to decrease about 60 s after injection. The washout of ICG from inflamed joints compared with normal joints was surprisingly even faster. After injection of ICG, significantly lower fluorescence intensities were found in the joints compared with joints of mice injected with SIDAG. After injection of SIDAG, fluorescence intensities in inflamed and normal joints increased within

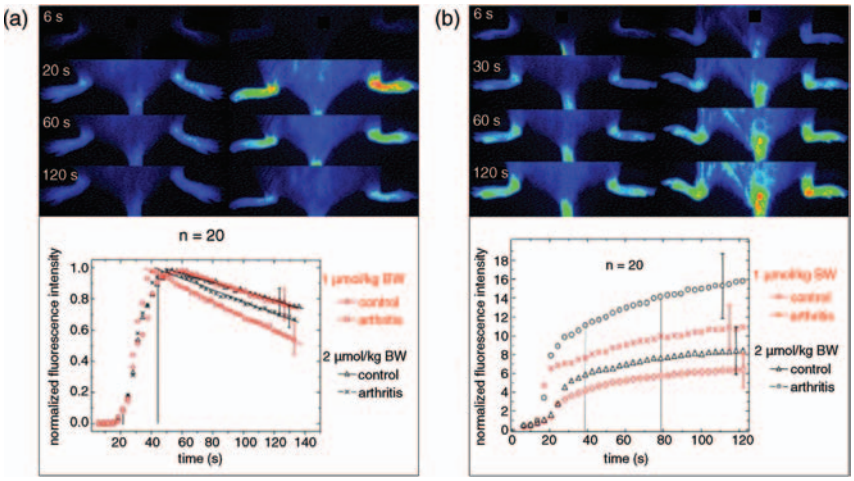

Figure 34.2 Noninvasive visualization of arthritis in animal models using nonspecific fluorescent imaging probes (ICG and a hydrophilic carbocyanine derivative called SIDAG). Color-coded noninvasive NIRF images of mice with *Borrelia*-induced Lyme arthritis after intravenous injection of ICG **(a)** or SIDAG **(b)**. The graphs show the time course of the measured fluorescence intensities over normal and arthritic ankle joints after injection of the two compounds in two different doses. Mice injected with ICG showed a rapid increase in fluorescence intensity over both inflamed and normal joints, decreasing about 60 s after injection. In contrast, in mice injected with SIDAG, significantly higher fluorescence intensities were detected in inflamed joints compared with normal joints. The ratio between inflamed and normal joints increased over time. Adapted with permission from [27].

the observation time of 120 s, with a stronger increase in inflamed joints. The ratios between inflamed and normal joints were about 2. The highest ratios were measure at 24 h after injection. In most animals with Lyme arthritis, no cartilage destruction at the time of imaging was observed, indicating that early stages can be imaged with this technique.

Taking the results of these three studies together, it has been demonstrated that in arthritic mice acceptable ratios between inflamed and normal joints can be achieved by injection of nonspecific imaging agents. This might help in the diagnosis of arthritis. The feasibility of diagnosing early stages of arthritis with such nonspecific imaging agents has to be further supported. The results of these three studies tell one more important story: all approaches with specific compounds need a careful evaluation of the extent to which unspecific distribution contributes to the signal. This is especially true under inflammatory conditions, where this effect can be substantial.

34.3.2
Targeted Fluorescent Imaging Agents in Arthritis Models

Numerous fluorescently labeled ligands that bind specifically to target molecules involved in the pathophysiology of diseases have been developed and evaluated in

different animal disease models, including cancer models, models for vascular diseases, and arthritis models [16–20]. Some examples of the use of targeted fluorescence imaging probes in arthritis models are described in the following:

In patients with RA, it has been shown that the nonepithelial isoform beta of the folate receptor is expressed on activated but not on resting synovial macrophages. Against this background, Chen *et al.* [28] evaluated NIRF-labeled folate receptor targeted imaging probe followed by noninvasive NIRF imaging in two different arthritis models: arthritis induced by intra-articular injection of lipopolysaccharide (LPS) and the KRN serum transfer model. After intravenous injection of the targeted imaging agent and noninvasive NIRF imaging, the authors found about twofold higher fluorescence intensities in the inflamed joints compared with normal joints. As a control, the free, uncoupled NIRF dye was used (see Figure 34.3a). The authors concluded that this folate receptor targeted imaging method might facilitate improved arthritis diagnosis, especially at early stages, by providing an *in vivo* characterization of active macrophage status in inflammatory joint diseases. Moreover, the presented technique might also be helpful in the evaluation of anti-inflammatory treatment [28].

Sensitive imaging strategies for monitoring treatment response would indeed be valuable for facilitating appropriate therapy and dosing, evaluating clinical outcome, and developing more effective drugs in RA. In mice with CIA, we evaluated NIRF-labeled annexin V as a marker for treatment response to methotrexate (MTX), one of the most commonly used drugs in the treatment of RA [29]. Annexin V binds tightly and specifically to phosphatidylserine (PS). In normal cells, PS is almost exclusively restricted to the inner leaflet of the cell membrane. When cells die by apoptosis or necrosis, exposure of PS occurs. Therefore, annexin V is a suitable marker for specific imaging of cell death, which has been shown in several animal disease models and in patients with different diseases using different imaging modalities (for a review, see [30]). Three hours after injection of NIRF-labeled annexin V and noninvasive NIRF imaging, arthritic paws of MTX-treated mice showed a sevenfold higher fluorescence intensity than arthritic paws of untreated mice and a fourfold higher fluorescence intensity than non-arthritic paws of MTX-treated mice. With this approach, we could demonstrate that fluorescent annexin V and NIRF imaging can be used successfully to monitor response to treatment in a mouse model of RA [29].

Vollmer *et al.* investigated a fluorescently labeled single-chain antibody fragment covalently linked to the NIRF dye tetrasulfocyanine (TSC), which binds with high specificity to the extracellular domain B (ED-B) of the extracellular matrix protein fibronectin, as a targeted imaging probe in rats with CIA [31]. ED-B is a highly conserved domain that occurs after alternative splicing, for instance during vascular remodeling processes such as angiogenesis. Since the hallmark of RA is synovitis leading to both angiogenesis in the synovium and the promotion of cartilage and bone disruption, the antibody fragment might be a suitable marker in the clinical diagnostics and in the evaluation of treatment response in RA. The authors labeled the marker with an NIRF fluorochrome, injected the labeled compound intravenously into rats with and without CIA, and performed noninvasive NIRF imaging. As a control, ovalbumin labeled with the same NIRF dye was used. Fluorescence

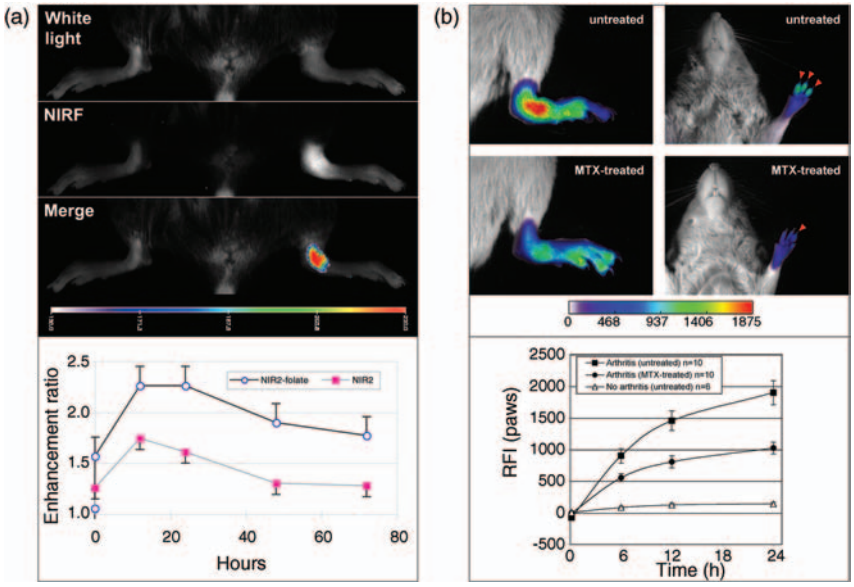

Figure 34.3 Noninvasive visualization of arthritis in animal models using targeted (folate receptor) and activatable (matrix degrading enzymes) fluorescent imaging probes. (a) Noninvasive white light, NIRF image, and color-coded merged image of a mouse that received an intra-articular injection of LPS into the left ankle joint. Images were taken 24 h after i.v. injection of a folate receptor-targeted NIRF imaging probe. In the graph, the time course of the enhancement ratios (fluorescence intensity over the inflamed joint divided by the fluorescence intensity over the opposite joint) after injection of the targeted imaging probe (highest ratio: 2.3:1) and free, uncoupled NIRF dye as a control is depicted. Adapted with permission from [28]. (b) Color-coded noninvasive NIRF images superimposed on white light images of untreated (upper row) and MTX-treated (bottom row) mice with collagen-induced arthritis (CIA) affecting the right hind paw (left) or toes of the left fore paw (right; red arrowheads) 24 h after i.v. injection of a "smart" fluorescence imaging probe that is activated by proteases such as cathepsin B. The time course of the fluorescence intensities in arthritic paws of untreated and MTX-treated mice and nonarthritic paws of untreated mice after probe injection is shown in the graph. Inflamed paws of untreated arthritic mice showed a sevenfold higher fluorescence intensity than paws of untreated healthy mice at 24 h. MTX treatment significantly reduced the fluorescence intensities from arthritic paws compared with untreated mice at 6, 12, and 24 hours. Adapted with permission from [34].

intensity ratios between inflamed joints and the nose of the animals were about 4–6-fold for the antibody fragment and about twofold for ovalbumin.

34.3.3 Activatable Fluorescent Imaging Agents in Arthritis Models

Activatable imaging agents based on different principles have been developed for different imaging modalities, including magnetic resonance imaging (MRI) and

optical imaging, targeting different processes, including enzyme activity [32, 33]. Matrix-degrading enzymes such as matrix metalloproteinases (MMPs) and cathepsins have a substantial role in arthritic joint destruction. Using an enzyme-cleavable NIRF imaging agent that can be activated by cathepsins, we were able to visualize the presence of these enzymes in inflamed joints of mice with CIA noninvasively. Fluorescence intensities were 5–7-fold higher in inflamed compared with normal paws or toes 24 h after injection. With this approach, we could also show that the probe can be used for early monitoring of treatment response to MTX (see Figure 34.3b). The design of this imaging agent nicely illustrates how activatable probes work in principle: multiple Cy5.5 fluorochromes are bound to a graft copolymer backbone of polylysine, to which methoxypolyethylene glycol (MPEG) side chains are attached. Owing to interactions between the fluorochromes, fluorescence quenching occurs. Enzymatic cleavage of the backbone by cathepsins releases Cy5.5 and results in activation of fluorescence [34].

RA is also characterized by high expression levels of reactive oxygen species (ROS) and hyaluronidase, inducing progressive degradation of joint hyaluronic acid (HA) in the extracellular matrix. Lee *et al.* [35] immobilized NIRF-labeled HA on the surface of gold nanoparticles, which resulted in quenching of the fluorochromes. The presence of ROS and hyaluronidase leads to activation of the fluorescence. After intravenous injection of the particles into mice with CIA, about fivefold higher fluorescence intensities were found in inflamed compared with normal limbs, decreasing between 6 and 24 h after injection [35]. Similarly to our approach described above, this activatable imaging agent might also be useful as a marker in early detection of arthritis and for evaluation of treatment efficacy in arthritis.

34.3.4
Monitoring Cell Migration in Arthritis Models

Noninvasive monitoring of the fate of injected cells, also called cell tracking, is highly relevant in biomedical research and in the clinic. Tracking the fate of implanted cells, for example, in stem cell approaches or visualization of leukocyte trafficking, are just two out of numerous examples (for a review, see [36]). Simon *et al.* [37] labeled allogenic leukocytes with a fluorochrome called DID, a lipophilic NIRF dye, and injected 10^7 fluorescent cells intravenously into rats with AIA followed by noninvasive NIRF imaging. At 4 and 24 h post-injection, the fluorescence intensities of arthritic knees were significantly higher than those of normal knees, and of arthritic knees and knees of cortisone treated rats, decreasing between 4 and 24 h. Ratios between arthritic and normal rat knees were around 2:1 or less. This study shows that the infiltration of leukocytes into inflamed joints of rats can be visualized with noninvasive fluorescence imaging. The authors concluded that inflammation imaging with labeled leukocytes might help in the monitoring of new drugs that specific interact with T cells and monocytes in the synovium [37].

Sutton *et al.* [38] labeled human mesenchymal stem cells (hMSCs) with DID, the same dye as mentioned above. Fluorescent hMSCs (from 10^4 up to 10^7 cells) were

administered into the peritoneum of athymic rats with an immune-mediated polyarthritis induced by intraperitoneal injection of peptidoglycan polysaccharide. Evaluating the noninvasive NIRF images, the authors reported that the fluorescence intensity of arthritic ankle joints was significantly higher 24 and 48 h after injection of the cells compared with normal ankle joints, decreasing at 72 h (see Figure 34.4). The data presented led the authors to the conclusion that the described technique might be useful for monitoring the factors that influence the survival of implanted stem cells and therapeutic progress [38].

34.4
Clinical Applications

Optical methods have also been applied to patients with RA. For this purpose, sophisticated imaging systems were designed. Two basically different approaches are described, both using near-infrared light, lasers, and highly sensitive detectors. One strategy is the measurement of intrinsic tissue parameters such as absorption and scattering of light in joints, which are altered under inflammatory conditions. For detailed descriptions of techniques based on intrinsic parameters, the interested reader is referred to [39–43]. The second approach is noninvasive NIRF imaging after injection of a fluorescent compound. Our recent pilot study demonstrates that noninvasive fluorescence imaging of human finger joints after systemic administration of the nonspecific dye ICG is feasible [24]. ICG was used as a fluorochrome because it is the only dye in the NIRF spectral range that is clinically approved. Five patients with clinically active RA and five healthy volunteers were injected with ICG as an intravenous bolus injection at a dose of $0.1\,\mathrm{mg\,kg^{-1}}$, which is lower than that used for other diagnostic investigations. After injection of the compound, fluorescence images of one hand were acquired over a period of 15 min. All participants underwent contrast-enhanced MRI (Gd-DTPA) 1 day before fluorescence imaging. Figure 34.5 shows fluorescence images of RA patients and a healthy volunteer, and also the time course of the detected fluorescence intensities in different regions of interest. The fluorescence imaging data and the MRI data showed a good correlation [24]. The results of an ongoing study with a higher number of subjects are eagerly awaited.

34.5
Critical Overview of Fluorescence Imaging in Arthritis

Noninvasive fluorescence imaging is a powerful tool for studying physiology and pathophysiology in animal models of arthritis. It is easy to use, fast, and inexpensive. If the target tissue is located superficially, highly sensitive imaging can be performed with an acceptable spatial resolution. Rapidly increasing numbers of fluorescent imaging agents are available, targeting different biological processes and offering multiple opportunities in arthritis research. However, absolute quantitation in

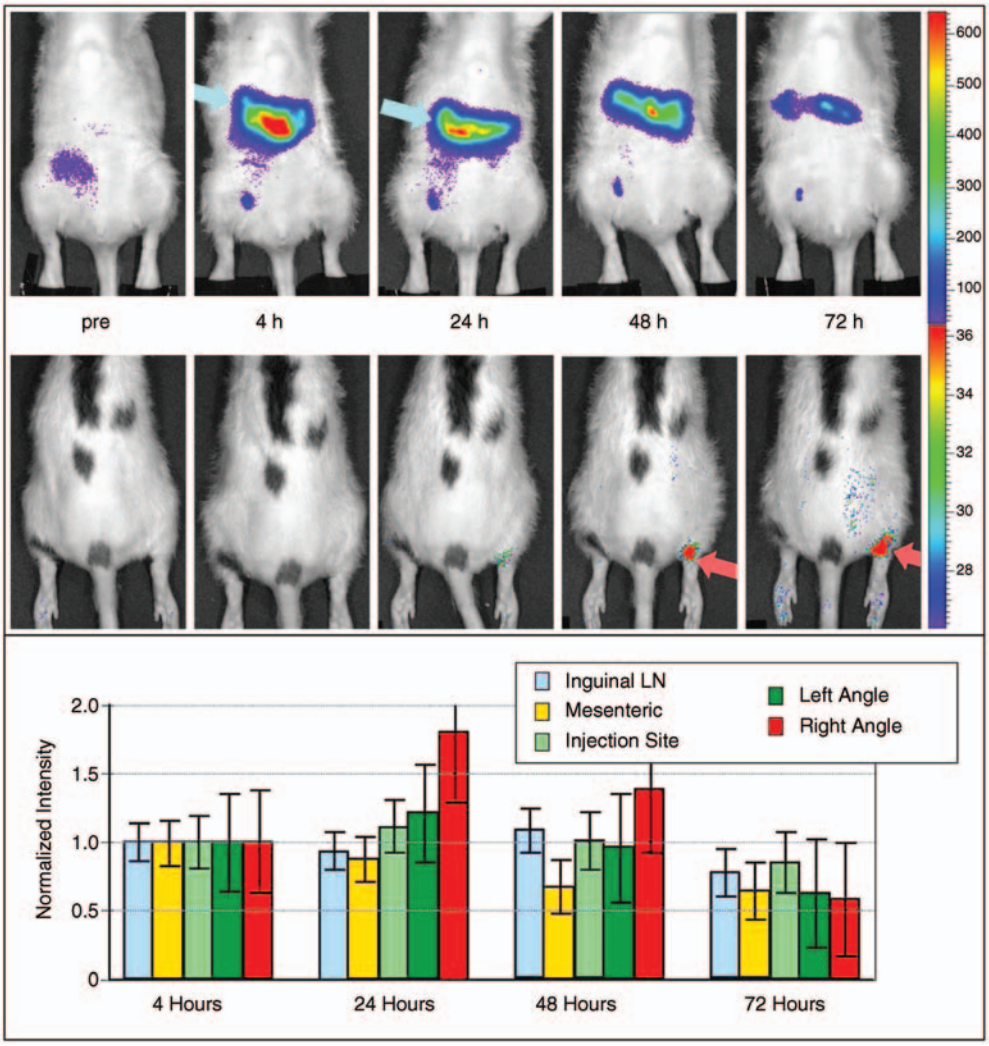

Figure 34.4 Monitoring cell migration in an arthritis model with noninvasive fluorescence imaging. Color-coded noninvasive fluorescence images superimposed on white light images of an athymic rat with an immune-mediated polyarthritis induced by intraperitoneal injection of peptidoglycan polysaccharide before and after i.p. injection of fluorescently labeled hMSCs show fluorescence of the abdomen on early post-injection images (indicated by blue arrow) and a progressively enhanced fluorescence of the right ankle (red arrow). The graphs show the normalized intensity of the fluorescence image at 4 h post-injection within the ROI in the inguinal LN, mesenteric, injection site, and right and left ankle joints after background subtraction (obtained from preinjection image) at different time points post-injection. The fluorescence intensity of arthritic ankle joints was significantly higher 24 and 48 h after injection of the cells compared with normal ankle joints, decreasing at 72 h. Reproduced with permission from [38].

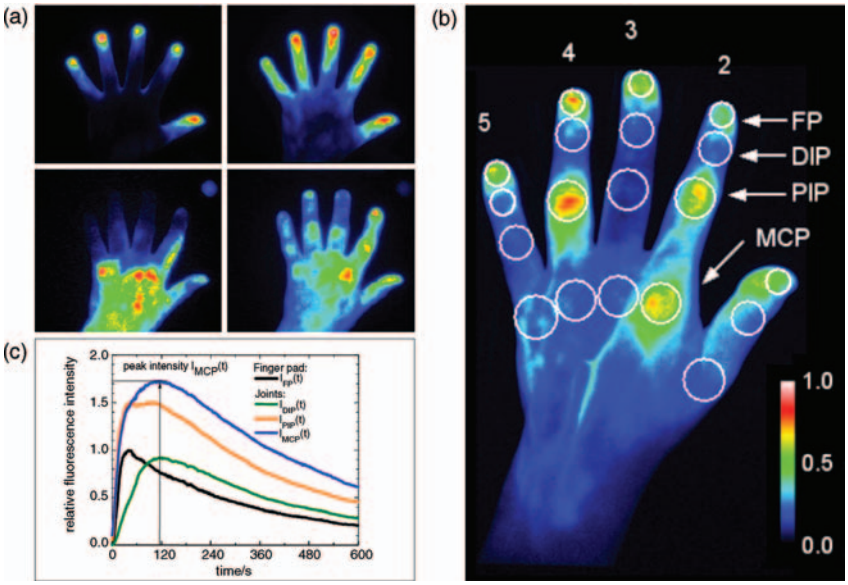

Figure 34.5 Noninvasive visualization of arthritis in patients using a nonspecific fluorescent imaging probe (ICG). (a) Fluorescence images of a hand of a healthy volunteer (upper row) and of a patient with rheumatoid arthritis (lower row) after application of ICG (0.1 mg kg^{-1}). Images were taken 40 s (left) and 65 s (right) after injection of ICG. (b) Location of investigated areas, that is, ROIs indicated as white circles on the dorsal side of the hand. The hand is shown in a normalized false color presentation, corresponding to the color bar at the right side. FP, finger pad; DIP, distal interphalangeal joint; PIP, proximal interphalangeal joint; MCP, metacarpal phalangeal joint. (c) Temporal behavior of 90th percentiles of the fluorescence intensity in selected ROIs of the left forefinger of a patient [see (b)] after injection of ICG. Only the finger pad shows a clear arrival and washout of the ICG bolus. Adapted with permission from [24].

fluorescence imaging is still challenging, which is a clear disadvantage compared with nuclear imaging methods such as PET and SPECT, especially when absolute quantitation of the imaging signal is mandatory. Our first proof-of-concept study with RA patients published in 2010 gives hope that in the near future noninvasive fluorescence imaging after injection of fluorescent reporters can be performed in the clinical routine. Especially the use of specific fluorescent reporter agents for imaging physiology and pathophysiology at the cellular and molecular level will, in our opinion, improve the diagnostic power, and therefore the management, of the disease considerably. Generally, these novel tools will be helpful in evaluating disease processes, facilitating diagnosis, and monitoring therapeutic regimens, to permit a reliable prognosis and to support the development of new therapies. Furthermore, the techniques promise to be safe, simple, cost-effective, and rapid. However, the penetration depth of near-infrared light limits the applicability of fluorescence imaging to finger and foot joints.

References

1 Fouque-Aubert, A. and Chapurlat, R.D. (2010) A comparative review of the different techniques to assess hand bone damage in rheumatoid arthritis. *Joint Bone Spine*, **77** (3), 212–217.

2 Yazici, Y., Sokka, T., and Pincus, T. (2009) Radiographic measures to assess patients with rheumatoid arthritis: advantages and limitations. *Rheum. Dis. Clin. North Am.*, **35** (4), 723–729.

3 Brown, A.K. (2009) Using ultrasonography to facilitate best practice in diagnosis and management of RA. *Nat. Rev. Rheumatol.*, **5** (12), 698–706.

4 Boesen, M., Østergaard, M., Cimmino, M.A., Kubassova, O., Jensen, K.E., and Bliddal, H. (2009) MRI quantification of rheumatoid arthritis: current knowledge and future perspectives. *Eur. J. Radiol.*, **71** (2), 189–196.

5 Wunder, A., Straub, R.H., Gay, S., Funk, J., and Müller-Ladner, U. (2005) Molecular imaging: novel tools in visualizing rheumatoid arthritis. *Rheumatology (Oxford)*, **44** (11), 1341–1349.

6 McBride, H.J. (2010) Nuclear imaging of autoimmunity: focus on IBD and RA. *Autoimmunity*, **43** (7), 539–549.

7 Malviya, G., Conti, F., Chianelli, M., Scopinaro, F., Dierckx, R.A., and Signore, A. (2010) Molecular imaging of rheumatoid arthritis by radiolabelled monoclonal antibodies: new imaging strategies to guide molecular therapies. *Eur. J. Nucl. Med. Mol. Imaging*, **37** (2), 386–398.

8 Jaffer, F.A. and Weissleder, R. (2005) Molecular imaging in the clinical arena. *JAMA*, **293** (7), 855–862.

9 Massoud, T.F. and Gambhir, S.S. (2007) Integrating noninvasive molecular imaging into molecular medicine: an evolving paradigm. *Trends Mol. Med.*, **13** (5), 183–191.

10 Contag, C.H. (2007) *In vivo* pathology: seeing with molecular specificity and cellular resolution in the living body. *Annu. Rev. Pathol.*, **2**, 277–305.

11 Leblond, F., Davis, S.C., Valdés, P.A., and Pogue, B.W. (2010) Pre-clinical whole-body fluorescence imaging: review of instruments, methods and applications. *J. Photochem. Photobiol. B*, **98** (1), 77–94.

12 Ntziachristos, V. (2006) Fluorescence molecular imaging. *Annu. Rev. Biomed. Eng.*, **8**, 1–33.

13 Hilderbrand, SA. and Weissleder, R. (2010) Near-infrared fluorescence: application to *in vivo* molecular imaging. *Curr. Opin. Chem. Biol.*, **14** (1), 71–79.

14 Licha, K., Schirner, M., and Henry, G. (2008) Optical agents. *Handb. Exp. Pharmacol.*, **185** (1), 203–222.

15 Escobedo, J.O., Rusin, O., Lim, S., and Strongin, R.M. (2010) NIR dyes for bioimaging applications. *Curr. Opin. Chem. Biol.*, **14** (1), 64–70.

16 Pierce, M.C., Javier, D.J., and Richards-Kortum, R. (2008) Optical contrast agents and imaging systems for detection and diagnosis of cancer. *Int. J. Cancer*, **123** (9), 1979–1990.

17 Wunder, A. and Klohs, J. (2008) Optical imaging of vascular pathophysiology. *Basic Res. Cardiol.*, **103** (2), 182–190.

18 Jaffer, F.A., Libby, P., and Weissleder, R. (2009) Optical and multimodality molecular imaging: insights into atherosclerosis. *Arterioscler. Thromb. Vasc. Biol.*, **29** (7), 1017–1024.

19 Wunder, A. and Klohs, J. (2010) Noninvasive optical imaging in small animal models of stroke, in *Rodent Models of Stroke,* Neuromethods, vol. **47**, 1st edn (ed. U. Dirnagl), Springer, Berlin, pp. 167–177.

20 Gompels, L.L., Lim, N.H., Vincent, T., and Paleolog, E.M. (2010) *In vivo* optical imaging in arthritis – an enlightening future? *Rheumatology (Oxford)*, **49** (8), 1436–1446.

21 Dzurinko, V.L., Gurwood, A.S., and Price, J.R. (2004) Intravenous and indocyanine green angiography. *Optometry*, **75** (12), 743–755.

22 Rodrigues, E.B., Costa, E.F., Penha, F.M., Melo, G.B., Bottós, J., Dib, E., Furlani, B., Lima, V.C., Maia, M., Meyer, C.H., Höfling-Lima, A.L., and Farah, M.E.

(2009) The use of vital dyes in ocular surgery. *Surv. Ophthalmol.*, **54** (5), 576–617.

23 Krammer, B. and Plaetzer, K. (2008) ALA and its clinical impact, from bench to bedside. *Photochem. Photobiol. Sci.*, **7** (3), 283–289.

24 Fischer, T., Ebert, B., Voigt, J., Macdonald, R., Schneider, U., Thomas, A., Hamm, B., and Hermann, K.G. (2010) Detection of rheumatoid arthritis using non-specific contrast enhanced fluorescence imaging. *Acad. Radiol.* **17** (3), 375–381.

25 Hansch, A., Frey, O., Hilger, I., Sauner, D., Haas, M., Schmidt, D., Kurrat, C., Gajda, M., Malich, A., Bräuer, R., and Kaiser, W.A. (2004) Diagnosis of arthritis using near-infrared fluorochrome Cy5.5. *Invest. Radiol.*, **39** (10), 626–632.

26 Wunder, A., Müller-Ladner, U., Stelzer, E.H., Funk, J., Neumann, E., Stehle, G., Pap, T., Sinn, H., Gay, S., and Fiehn, C. (2003) Albumin-based drug delivery as novel therapeutic approach for rheumatoid arthritis. *J. Immunol.*, **170** (9), 4793–4801.

27 Fischer, T., Gemeinhardt, I., Wagner, S., Stieglitz, D.V., Schnorr, J., Hermann, K.G., Ebert, B., Petzelt, D., Macdonald, R., Licha, K., Schirner, M., Krenn, V., Kamradt, T., and Taupitz, M. (2006) Assessment of unspecific near-infrared dyes in laser-induced fluorescence imaging of experimental arthritis. *Acad. Radiol.*, **13** (1), 4–13.

28 Chen, W.T., Mahmood, U., Weissleder, R., and Tung, C.H. (2005) Arthritis imaging using a near-infrared fluorescence folate-targeted probe. *Arthritis Res. Ther.*, **7** (2), R310–R317.

29 Wunder, A., Schellenberger, E., Mahmood, U., Bogdanov, A. Jr., Müller-Ladner, U., Weissleder, R., and Josephson, L. (2005) Methotrexate-induced accumulation of fluorescent annexin V in collagen-induced arthritis. *Mol. Imaging*, **4** (1), 1–6.

30 Schutters, K. and Reutelingsperger, C. (2010) Phosphatidylserine targeting for diagnosis and treatment of human diseases. *Apoptosis*, **15** (9), 1072–1082.

31 Vollmer, S., Vater, A., Licha, K., Gemeinhardt, I., Gemeinhardt, O., Voigt, J., Ebert, B., Schnorr, J., Taupitz, M., Macdonald, R., and Schirner, M. (2009) Extra domain B fibronectin as a target for near-infrared fluorescence imaging of rheumatoid arthritis affected joints *in vivo*. *Mol. Imaging*, **8** (6), 330–340.

32 Blum, G. (2008) Use of fluorescent imaging to investigate pathological protease activity. *Curr. Opin. Drug Discov. Dev.*, **11** (5), 708–716.

33 Schellenberger, E., Rudloff, F., Warmuth, C., Taupitz, M., Hamm, B., and Schnorr, J. (2008) Protease-specific nanosensors for magnetic resonance imaging. *Bioconjug. Chem.*, **19** (12), 2440–2445.

34 Wunder, A., Tung, C.H., Müller-Ladner, U., Weissleder, R., and Mahmood, U. (2004) *In vivo* imaging of protease activity in arthritis: a novel approach for monitoring treatment response. *Arthritis Rheum.*, **50** (8), 2459–2465.

35 Lee, H., Lee, K., Kim, I.K., and Park, T.G. (2008) Synthesis, characterization, and *in vivo* diagnostic applicationsof hyaluronic acid immobilized gold nanoprobes. *Biomaterials*, **29**, 4709–4718.

36 Arbab, A.S., Janic, B., Haller, J., Pawelczyk, E., Liu, W., and Frank, J.A. (2009) *In vivo* cellular imaging for translational medical research. *Curr. Med. Imaging Rev.*, **5** (1), 19–38.

37 Simon, G.H., Daldrup-Link, H.E., Kau, J., Metz, S., Schlegel, J., Piontek, G., Saborowski, O., Demos, S., Duyster, J., and Pichler, B.J. (2006) Optical imaging of experimental arthritis using allogeneic leukocytes labeled with a near-infrared fluorescent probe. *Eur. J. Nucl. Med. Mol. Imaging*, **33** (9), 998–1006.

38 Sutton, E.J., Boddington, S.E., Nedopil, A.J., Henning, T.D., Demos, S.G., Baehner, R., Sennino, B., Lu, Y., and Daldrup-Link, H.E. (2009) An optical imaging method to monitor stem cell migration in a model of immune-mediated arthritis. *Opt. Express*, **17** (26), 24403–24413.

39 Scheel, A.K., Krause, A., Mesecke-von Rheinbaben, I., Metzger, G., Rost, H., Tresp, V., Mayer, P., Reuss-Borst, M., and Müller, G.A. (2002) Assessment of

proximal finger joint inflammation in patients with rheumatoid arthritis, using a novel laser-based imaging technique. *Arthritis Rheum.*, **46** (5), 1177–1184.

40 Scheel, A.K., Backhaus, M., Klose, A.D., Moa-Anderson, B., Netz, U.J., Hermann, K.-G.A., Beuthan, J., Müller, G.A., Burmester, G.R., and Hielscher, A.H. (2005) First clinical evaluation of sagittal laser optical tomography for detection of synovitis in arthritic finger joints. *Ann. Rheum. Dis.*, **64** (2), 239–245.

41 Hielscher, A.H., Bluestone, A.Y., Abdoulaev, G.S., Klose, A.D., Lasker, J., Stewart, M., Netz, U., and Beuthan, J. (2002) Near-infrared diffuse optical tomography. *Dis. Markers*, **18** (5–6), 313–337.

42 Hielscher, A.H., Klose, A.D., Scheel, A.K., Moa-Anderson, B., Backhaus, M., Netz, U., and Beuthan, J. (2004) Sagittal laser optical tomography for imaging of rheumatoid finger joints. *Phys. Med. Biol.*, **49** (7), 1147–1163.

43 Klose, C.D., Klose, A.D., Netz, U., Beuthan, J., and Hielscher, A.H. (2008) Multiparameter classifications of optical tomography images. *J. Biomed. Opt.*, **13** (5), 050503.

35
Diffuse Optical Tomography of Osteoarthritis

Zhen Yuan and Huabei Jiang

35.1
Motivation

Osteoarthritis (OA) is the most common arthritic condition worldwide and is estimated to affect nearly 60 million Americans. Classically, OA is most often found in the large weight-bearing joints of the lower extremities, particularly the knees and hips. However, there is also a subset of individuals with a predilection for developing OA of the hands and a more generalized form of OA. To diagnose cartilage abnormalities and alterations in the composition of synovial fluid in joints affected by OA, a variety of imaging methods have been developed and tested, such as X-ray methods, ultrasound (US), computed tomography (CT), and magnetic resonance imaging (MRI). While X-ray methods are able to visualize joint space narrowing and osteophyte formation, it is insensitive to changes in cartilage and fluid and therefore incapable of capturing the primary features of the early stage of OA. MRI, another commonly used modality in clinical practice, can reliably detect early-stage OA when high-contrast agents are used. However, it is costly and time consuming. CT has also been employed in the diagnosis of OA. However, it is expensive and provides only qualitative structural information in severe OA. Musculoskeletal US has been the subject of much recent interest in evaluating rheumatoid arthritis and regional musculoskeletal pathology. US is, however, a strongly operator-dependent modality and sensitive only to changes in the boundary layer, limiting its utility in the evaluation of the early stages of OA. Although present therapy is symptomatic, remarkable advances have been made in our understanding of the pathophysiology of OA. Much of the degradation of cartilage is mediated through matrix metalloproteinases, and the development of small-molecule inhibitors has been an area of active research interest. In anticipation of the development of new products with the potential to alter the natural history of OA, it will be crucial to have noninvasive technologies that can detect early-stage OA and monitor the efficacy of therapy [1–7].

Handbook of Biophotonics. Vol.2: Photonics for Health Care, First Edition. Edited by Jürgen Popp, Valery V. Tuchin, Arthur Chiou, and Stefan Heinemann.

35.2
Diffuse Optical Tomography Imaging of Osteoarthritis in the Hands

Owing to its numerous advantages of low cost, portability, and use of non-ionizing radiation, near-infrared (NIR) diffuse optical tomography (DOT) is emerging as a potential tool for imaging bones and joint tissues [1–7]. DOT imaging methods are able to provide a variety of functional and structural information with high sensitivity and specificity compared with other imaging modalities. This is especially true for the joints of the fingers, where the small dimensions and much higher transmitted light intensities should result in better signal-to-noise ratios and greatly improved spatial resolution. In a recent pilot case study, we have shown that the optical contrast between OA and normal joints is high, suggesting that DOT indeed has the potential for detecting OA joints in the hands and for assessing its treatment [1]. Although DOT appears to be especially suited for imaging of the finger joints because of the high signal-to-noise ratio associated with the small volume, the spatial resolution is still relatively low due to light scattering. In addition, X-ray imaging is currently the gold standard imaging method for the detection and quantification of joint destruction in patients with OA with high resolution. To take advantage of the complementary information from the optical and X-ray imaging modalities, an optimized approach that combines X-ray and DOT imaging has been developed for *in vivo* imaging of OA in the finger joints [2, 3]. The basic idea of this multi-modality imaging approach is to incorporate the high-resolution structural X-ray images into the DOT reconstruction so that both the resolution and quantitative accuracy of optical image reconstruction are enhanced.

35.2.1
DOT and Hybrid X-Ray–DOT Systems

The DOT system (Figure 35.1) consists of laser modules, a hybrid light delivery subsystem, a fiber optics–tissue interface, a data acquisition module, and light

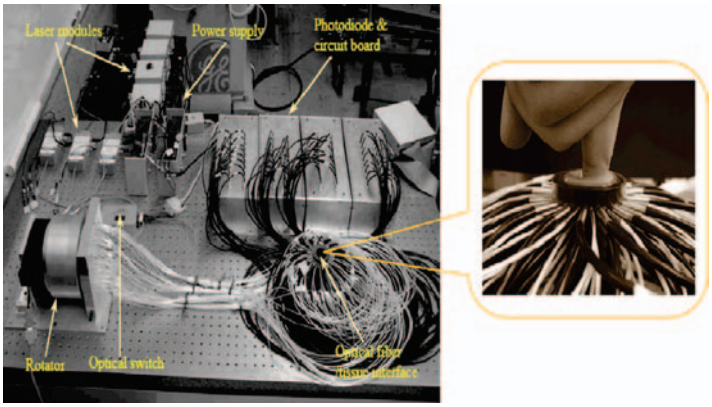

Figure 35.1 Photograph of the DOT imaging system. The inset is a close-up photograph of the finger–coupling medium–fiber optics interface.

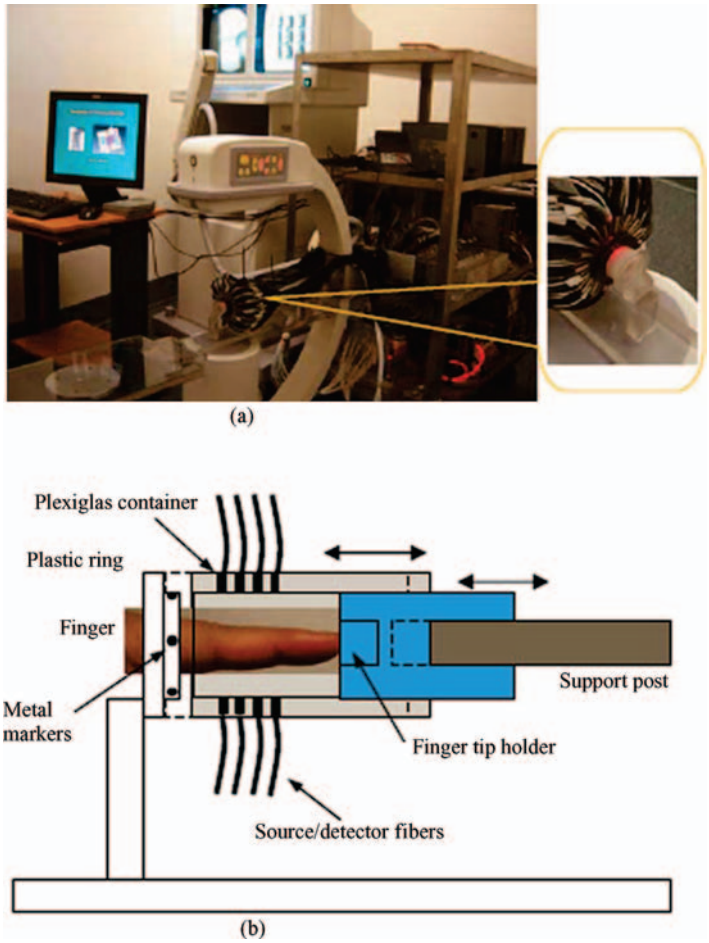

Figure 35.2 (a) Photograph of the integrated hybrid X-ray–DOT system. The inset is a close-up photograph of the finger–fiber optics–X-ray interface. (b) Schematic of the interface.

detection modules [1]. The cylindrical fiber optics–tissue interface is composed of 64 source and 64 detector fiber bundles that are positioned in four layers along the surface of a Plexiglas container and cover a volume of 15×30 mm. In each layer, 16 source and 16 detector fiber bundles are arranged alternately. The space between the finger and the wall of the Plexiglas container is filled with tissue-like phantom materials as coupling media consisting of distilled water, agar powder, Indian ink and Intralipid, giving an absorption coefficient of $0.014\ \text{mm}^{-1}$ and a reduced scattering coefficient of $1.0\ \text{mm}^{-1}$. A total of eight laser modules in the NIR region are available. The hybrid X-ray–DOT imaging system (Figure 35.2) integrates a modified mini C-arm X-ray system (MiniView 6800, GE-OEC, Salt Lake City, UT, USA) with the 64×64-channel photodiode-based DOT system [2]. In the hybrid imaging of joint tissues, the X-ray imaging was performed imme-

diately after the DOT data acquisition. To eliminate the artifacts in the X-ray projections possibly caused by the optical interface [2], we used a co-axial post to support the optical interface so that the interface can be translated along the post (see the inset in Figure 35.2a and the schematic of the interface shown in Figure 35.2b).

35.2.2
DOT Reconstruction Methods

When the data acquisition was finished, the next step was to generate the optical images using a robust 3D reconstruction algorithm. Our existing reconstruction algorithm is based on the following diffusion equation and type III boundary conditions [1]:

$$\nabla \cdot D(r)\nabla\Phi(r) - \mu_a(r)\Phi(r) = -S(r), \quad -D\nabla\Phi \cdot n = \alpha\Phi \tag{35.1}$$

where $\Phi(r)$ is the photon intensity, $D(r)$ the diffusion coefficient, α is a coefficient related to the boundary, $\mu_a(r)$ is the absorption coefficient, and $S(r)$ is the source term. The discretized finite element form of Eq. (35.1) is written as $[A]\{\Phi\} = \{b\}$. The inverse solution is obtained through the following equations:

$$[A]\{\partial\Phi/\partial\chi\} = \{\partial b/\partial\chi\} - [\partial A/\partial\chi]\{\Phi\}, \quad \left(\Im^T\Im + \lambda \boldsymbol{I}\right)\Delta\chi = \Im^T(\Phi^o - \Phi^c) \tag{35.2}$$

where χ expresses D and μ_a, and $\Im$ is the Jacobian matrix formed by $\partial\Phi/\partial\chi$ at the boundary measurement sites. λ is a scalar, $\boldsymbol{I}$ is the identity matrix and $\Delta\chi$ is the updating vector for the optical properties. $\Phi^o = \left(\Phi_1^o, \Phi_2^o, \ldots, \Phi_M^o\right)^T$ and $\Phi^c = \left(\Phi_1^c, \Phi_2^c, \ldots, \Phi_M^c\right)^T$, where Φ_i^o and Φ_i^c are observed and computed photon intensity for $i = 1, 2, \ldots, M$ boundary locations. For X-ray guided DOT reconstruction, the following updating equation is used:

$$\Delta\chi = \left(\Im^T\Im + \Im^T\Im + \lambda I + \boldsymbol{L}^T\boldsymbol{L}\right)^{-1}\left[\Im^T(\Psi^o - \Psi^c)\right] \tag{35.3}$$

where the X-ray structural *a priori* information is incorporated into the iterative process using a spatially variant filter matrix $\boldsymbol{L}$ [2].

35.2.3
Reconstructed Results

From the absorption and scattering images shown in Figures 35.3 and 35.4, we find that the bones are clearly identified. Importantly, compared with the optical parameters of the bones, we observe a significant decrease in the strength of absorption and scattering properties of the healthy joint tissues in the joint space/cavity. However, we see only a small drop for the OA joint tissues. Interestingly, the difference in joint tissues between the OA patients and healthy controls seems apparent from the ratio of the optical properties of joint soft tissues to that of bone [2, 3]. We note that these ratios for the diseased joints are significantly larger than those from the healthy joints [2].

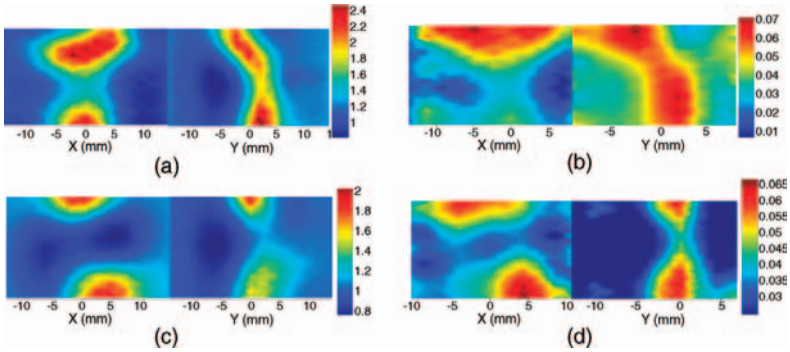

Figure 35.3 Reconstructed low-resolution optical images at 805 nm with selected dorsal/coronal planes: scattering (a) and absorption slices (b) for an OA joint; scattering (c) and absorption slices (d) for a healthy joint. Compared with the optical parameters of the bones, a significant decrease in the values of absorption and scattering properties of the healthy joint tissues surrounding the joint space (c, d) can be observed, whereas the drop for the OA joint is not so significant (a, b).

As shown in Figure 35.4, when a subset of the prior X-ray information on the joint structure was used in the DOT reconstruction, distinct boundaries separating different tissues were clearly recovered, indicating a significant improvement of DOT resolution because of the incorporation of prior X-ray structural information. These optical images show accurate delineation of the joint space and bone geometry, consistent with the X-ray findings. Both the absorption and scattering images reconstructed without X-ray guidance (Figure 35.3) show significantly overestimated thickness of the joint tissues and also increased boundary artifacts. The image quality obtained from the hybrid system is significantly improved over that from DOT alone. We see that the ratios for the diseased joints are significantly larger than those from normal joints. The differences in the ratio between the OA and normal joints

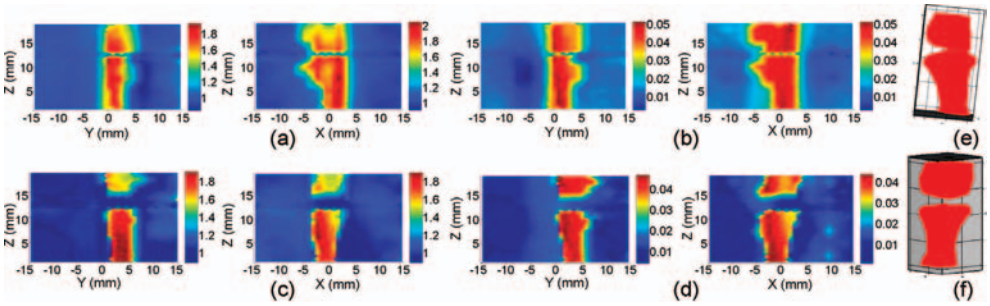

Figure 35.4 Reconstructed scattering (a) and absorption slices (b) for the OA joint with X-ray guidance; scattering (c) and absorption slices (d) for the healthy joint with X-ray guidance; tomographic X-ray image for the OA joint (e) and healthy joint (f). Joint space narrowing is observed for the OA joint (a, b). Importantly, compared with the optical parameters of the bones a significant decrease in the values of optical properties of the healthy joint tissues (c, d) is identified.

estimated from the X-ray-guided DOT reconstruction are notably increased relative to that without X-ray guidance [2].

We have seen that the OA-induced joint changes are quantitatively revealed by DOT. It is noted from the results that the optical properties and also the joint spacing between OA and healthy joints are different, and both can be used as an OA indicator. Our statistical analysis revealed that sensitivity and specificity up to 92 and 100%, respectively, can be achieved when the optical properties of joint tissues are used as classifiers [3].

35.2.4 Diffuse Model Versus Transport Model

Owing to computational complexity, the model used for describing photon migration in biological tissues has usually been limited to the diffusion approximation (DA) to the radiative transport equation (RTE). However, the DA-based method is challenging in imaging small volumes including arthritis in the finger joints. In such cases, the DA is not able to describe the photon migration accurately owing to the small optical distance between sources and detectors. To overcome this limitation, the discrete ordinate approximated RTE has been utilized to recover the optical parameters of small volume tissues. However, this type of reconstruction algorithm is time consuming. We have developed a 3D reconstruction method based on simplified spherical harmonics approximated RTE which is only 1.2 times slower than the DA-based method [4].

As shown in Figure 35.5, the difference in recovered quantitative optical properties between the two models can be as large as 15% [4]. This demonstrates that the RTE

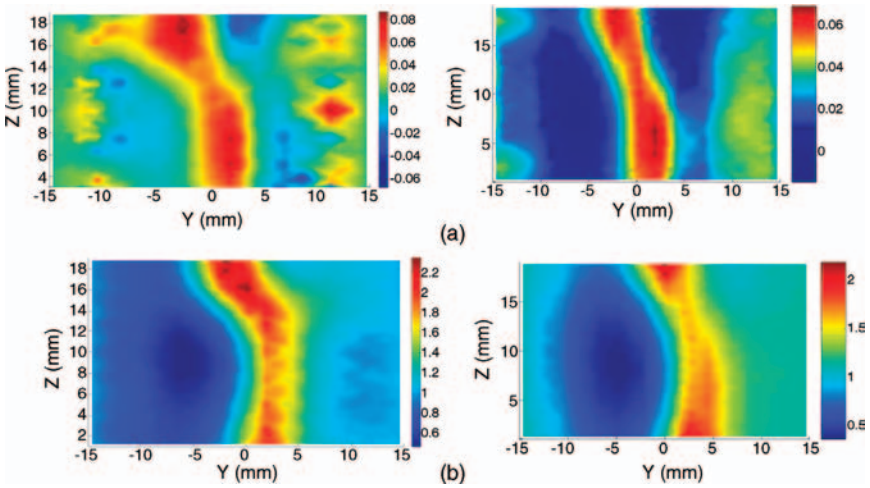

Figure 35.5 Reconstructed absorption (a) and scattering (b) images at selected coronal planes for the OA joint using the DA (left column) and the RTE model (right column). Importantly, boundary effect is significantly reduced for the optical image recovered using the RTE without X-ray guidance (right column).

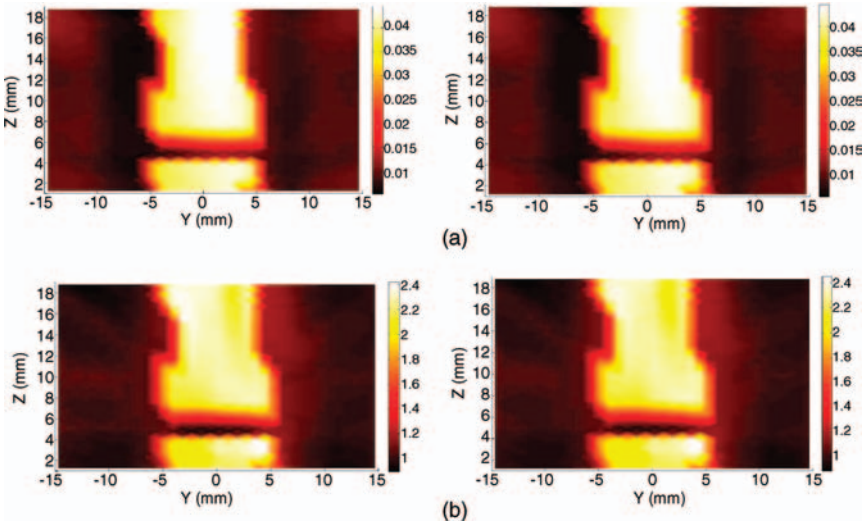

Figure 35.6 Reconstructed absorption (a) and scattering (b) images at selected coronal planes for the healthy joint using DA (left column) and RTE model (right column) with X-ray guidance. The image quality using the RTE is not enhanced when X-ray guidance is available.

model can provide significantly improved reconstruction accuracy for joint imaging. More interestingly, model errors appear to lead to smaller errors in reconstruction when the X-ray *a priori* structural information is incorporated into DOT reconstruction, as shown in Figure 35.6. This is because more accurate modeling of photon migration in tissue can be achieved using the DA when anatomic *a priori* information becomes available. The use of prior structural information eliminates the need to look for spatial/anatomy information in the optical inversion, which ensures that optical property profiles are the only parameter(s) that need to be recovered.

35.3
Image-Guided Optical Spectroscopy in Diagnosis of OA

There is increasing evidence that OA is a disease involving a metabolic dysfunction of bone [3]. It is likely that this metabolic dysfunction of bone, often associated with high metabolism of subchondral bone and connected joint soft tissues, will cause changes in tissue oxygen saturation (S_TO_2), deoxyhemoglobin, oxyhemoglobin, and water content (H_2O). When multiple wavelengths are used, the absorption spectra determine the tissue concentration of S_TO_2, Hb, HbO_2, and H_2O, the dominant NIR molecular absorbers in joint tissues. These quantitative physiological parameters of joint tissues may possibly allow us to detect metabolic changes associated with OA joints. In the spectroscopic experiments conducted, six wavelengths from the laser sources were used to irradiate the finger joint systems (633, 670, 723, 805, 853, and 896 nm) to ensure the reconstruction accuracy and minimize the parameter cross-talk.

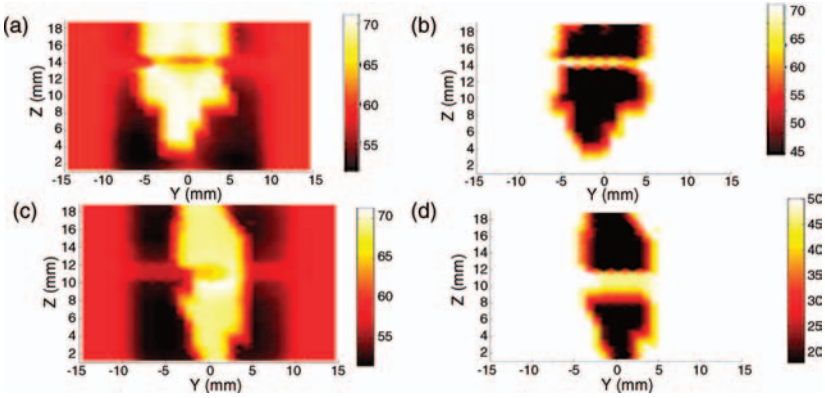

Figure 35.7 Reconstructed images at selected coronal planes: the oxygen saturation (a) and water content slice (b) for an OA finger joint; oxygen saturation (c) and water content slice (d) for a healthy joint. The axes (left and bottom) indicate the spatial scale in millimeters, whereas the color scale gives the oxygen saturation (%) or water content (%). Compared with the S_TO_2 values of bones, a significant decrease in the magnitude of the S_TO_2 value of soft tissues for the OA joints is observed (a) whereas only a small decrease for the healthy one is identified (c); the H_2O content of soft tissues for the OA joints (b) overall is significantly higher than that for the healthy joints (d).

We found that both S_TO_2 and H_2O of joint soft tissues are able to distinguish well between OA and normal joints in the majority of subjects [3], as observed from Figure 35.7. We noted that in most OA cases, the mean S_TO_2 values of joint soft tissues are smaller than those for bones. Further, compared with the S_TO_2 values of bones, we observed a significant decrease in the magnitude of the S_TO_2 value of soft tissues for the OA joints, whereas we saw only a small decrease in this parameter of soft tissues for the healthy joints. In some healthy cases, the S_TO_2 values of soft tissues are comparable to those of the bones. We can also see from Figure 35.7 that the H_2O content of soft tissues for the OA joints is overall significantly higher than that for the healthy joints. The high-resolution metabolic/functional images of joint tissues achievable by X-ray–multispectral DOT may shed light on the very early detection of OA in the finger joints.

35.4 Future Directions

Based on joint morphology and the optical and physiological/metabolic properties recovered, we observed statistically significant differences between healthy and OA finger joints [1–7]. This suggests that these imaging parameters are potential indicators for diagnosing OA and monitoring its progression.

Further large-scale clinical studies are necessary to evaluate prospectively the potential of DOT for finger joint imaging. In addition, there is a need to explore the possibility of DOT imaging in large joints such as the knee. Finally, it is definitely

necessary to study whether this technique can distinguish well between OA and other types of arthritis such as rheumatoid arthritis and psoriatic arthritis.

References

1 Yuan, Z., Zhang, Q., Sobel, E., and Jiang, HB. (2007) *J. Biomed. Opt.*, **12**, 034001.

2 Yuan, Z., Zhang, Q., Sobel, E., and Jiang, HB. (2008) *J. Biomed. Opt.*, **13**, 044006.

3 Yuan, Z., Zhang, Q., Sobel, E., and Jiang, HB. (2009) *Proc. SPIE*, **7174**, 71740K.

4 Yuan, Z., Zhang, Q., Sobel, E., and Jiang, HB. (2009) *J. Biomed. Opt.*, **14**, 054013.

5 Hielscher, A.H., Klose, A.D., and Scheel, A.K. (2004) *Phys. Med. Biol.*, **49**, 1147.

6 Schwaighofer, A., Tresp, V., Mayer, P., Krause, A.,*et al.* (2003) *IEEE Trans. Biol. Eng.*, **50**, 375.

7 Scheel, A.K., Krause, A., Rheinbaben Mesecke-von, I.,*et al.* (2002) *Arthritis Rheum.*, **46**, 1177.

36
Laser Doppler Imaging

Jamie Turner, Bernat Galarraga, and Faisel Khan

In patients with rheumatoid arthritis (RA), the redness and heat associated with articular inflammation are directly related to increased blood flow to the area (hyperemia). It is therefore desirable to measure synovial blood flow *in vivo* since abnormalities in this are indicative of active arthritis and may give information about the extent and development of the disease. One of the more widely used noninvasive techniques for measuring microcirculatory blood flow is laser Doppler flowmetry (LDF). Until relatively recently, its use in rheumatology had been largely confined to research purposes, especially so with the traditional instruments that record perfusion continuously from a small area of tissue. With the advent of scanning laser Doppler imaging, which allows blood flow to be measured over much larger areas, its use has been extended to provide useful clinical information regarding disease severity in various rheumatologic conditions. In addition, laser Doppler imaging can also be used to measure microvascular endothelial function, a key marker of early atherosclerotic disease. This is potentially an extremely useful tool in a condition associated with an increased cardiovascular (CV) morbidity and mortality such as RA.

36.1
Development and Use of Laser Doppler Flowmetry

The development of LDF owes much to the study of the Doppler effect, whereby light waves that have been scattered by, for example, moving red blood cells in tissue undergo a shift in frequency. This phenomenon is utilized in LDF by directing a low-power monochromatic laser beam at the skin surface, which, depending on skin pigmentation, penetrates up to 2 mm into tissue. Light that is reflected off stationary tissue undergoes no shift whereas light that is reflected off moving blood cells with velocity undergoes the aforementioned Doppler shift in proportion to the velocity of the red blood cells. An analyzer/recorder detects this, giving an output of red blood cell flux (number of red blood cells times their velocity), which determines circulation [1].

Handbook of Biophotonics. Vol.2: Photonics for Health Care, First Edition. Edited by Jürgen Popp, Valery V. Tuchin, Arthur Chiou, and Stefan Heinemann.

In vivo measurements of blood flow with this technique were first attempted in animal models using single vessels such as the retinal artery [2] and femoral vein (via a fiber-optic catheter) of the rabbit [3]. Stern [4] first adapted the technique to look at tissue perfusion in humans, specifically in fingertip skin, and showed that the amplitude of the Doppler signal in the 10–12 kHz band varied predictably with challenges in the microcirculation, such as arterial occlusion, and after a vasodilator drug.

Correlation between laser Doppler and other measurements of blood flow, such as venous occlusion plethysmography, has been demonstrated, [5, 6]. However, the laser Doppler instrument cannot be calibrated directly against these other techniques because the anatomic variation of the microcirculation between different sites and different tissues would mean that the calibrations are valid only for that particular tissue and measurement site [7]. An LDF-derived flux value is therefore generally expressed in arbitrary units.

36.2 Laser Doppler Imaging

A major limitation of LDF is that it measures blood flow at only a single point, and with respect to the cutaneous microcirculation there is considerable spatial heterogeneity of blood flow, meaning that tissue perfusion can vary considerably over short distances [8]. This reduces the reproducibility of the measurements, making it difficult to monitor changes in perfusion over time, particularly within an individual where even subtle changes in positioning of the laser probe can lead to significant variations in perfusion.

A recent development to counteract this has been the ability to scan the laser with a motor-driven mirror in a raster fashion over a defined area of tissue to produce a detailed color-coded perfusion map. Scanning LDF or laser Doppler imaging (LDI) therefore allows investigators to compensate for spatial heterogeneity and also allows for the study of large areas of tissue, for example, the ability to obtain noncontact images of perfusion in inflamed joints in RA patients.

Standard laser Doppler imagers employ a helium–neon laser (red, wavelength 632.8 nm), which provides measures of perfusion from the relatively superficial dermis (1–2 mm depth) (Figure 36.1). However, perfusion from deeper levels can be obtained with the use of near-infrared light (wavelength 780 nm) [9]. The latter has been used both in animal models of inflamed joints and in patients with RA, giving an understanding of the development and treatment of joint injury and arthritis and the study of the mechanisms and mediators that may contribute to joint inflammation.

Forrester *et al.* used standard (633 nm) and near-infrared (780 nm) light to measure blood flow changes in the connective tissue of surgically exposed rabbit medial ligaments [10]. LDI has also been used to examine blood perfusion in the medial aspect of an exposed rat knee joint capsule after acute inflammation had been induced via carrageenan injection. This work showed an enhancement of vasodilator

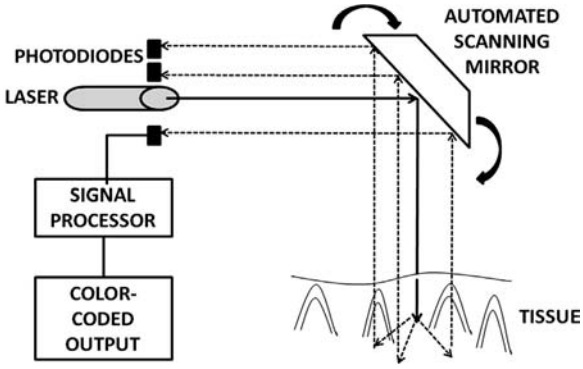

Figure 36.1 Schematic diagram of laser Doppler imager.

responses to substance P and calcitonin gene-related peptide, suggesting that these neuropeptides contained in the articular sensory C-fibers are important in mediating neurogenic joint inflammation [11]. This LDI method for measuring perfusion in inflamed and arthritic rat joints has been utilized in subsequent studies [12, 13].

LDI has also been used to show increased perfusion over the proximal interphalangeal and metacarpophalangeal joint of patients with RA, compared with control subjects [14, 15]. These differences were only seen with the more penetrating near-infrared laser light, confirming that these changes were indeed related to perfusion in the joint rather than the skin microcirculation (Figure 36.2). This was confirmed in a later study in which a red laser source failed to detect any hyperemic areas associated

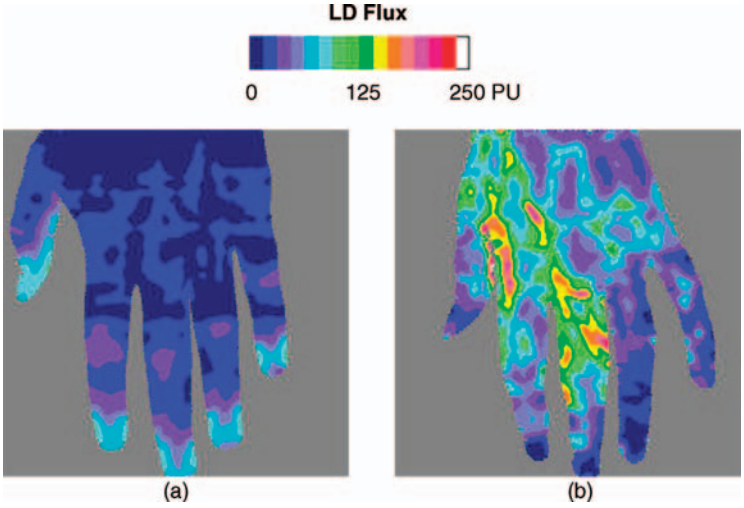

Figure 36.2 Near-infrared laser Doppler images from the hand of: (a) a normal subject, and (b) a patient with rheumatoid arthritis showing increased perfusion over the inflamed joints.

with joint inflammation in patients with osteoarthritis [16]. In future, this near-infrared laser Doppler scanning could provide a potential method for quantification of joint inflammation in patients with RA and permit noninvasive monitoring of the effects of drug therapy targeted at reducing inflammation, especially in longitudinal clinical trials.

36.3 Endothelial Dysfunction

Patients with RA have an increased mortality compared with the general population [17–19], with life expectancy being reduced by 10–15 years [20]. This increase in mortality is largely attributable to CV disease, with CV morbidity also increased in comparison with the general population [21, 22]. Factors that contribute to this excess CV risk include traditional risk factors [e.g., dyslipidemia, diabetes mellitus, hypertension, higher body mass index (BMI), impaired physical fitness], along with manifestations of the disease itself [23]. However, traditional CV risk factors cannot completely explain the increased morbidity and mortality observed in RA.

RA is characterized by inflammation, which also is a key component in the development of atherosclerosis [24, 25]. Inflammation leads to the activation of endothelial cells, which, through an increase in the expression of leukocyte adhesion molecules, promotes a pro-atherosclerotic environment. Pro-inflammatory markers such as C-reactive protein (CRP) levels and tumor necrosis factor alpha (TNFα) have an important role in atherosclerosis and CV mortality in RA [26].

The vascular endothelium is the key site through which inflammation exerts its deleterious effects on atherogenesis and its subsequent progression are intimately related to endothelial dysfunction. The vascular endothelium is the innermost layer of the blood vessels and has an essential role in maintaining the health of blood vessels through the maintenance of vascular tone and through the release of a variety of vasoactive substances and mediators of inflammation and coagulation. One the most important of these substances is nitric oxide (NO); it maintains blood flow by causing vasodilatation, inhibiting platelet aggregation and leukocyte adhesion, and preventing smooth-muscle proliferation.

In endothelial dysfunction, an imbalance between NO and other substances produced in the endothelium creates an environment that promotes vasoconstriction, inflammation, and coagulation, which can lead to both thrombosis and atherosclerotic disease. Endothelial dysfunction is therefore an early preclinical marker of atherosclerosis, and is commonly found in patients with RA.

36.4 LDI and Iontophoresis

Given the importance of endothelial function on the CV health of RA patients, numerous techniques to measure endothelial function in patients have been

developed. A major use of LDI is to measure cutaneous perfusion accompanied by iontophoresis of vascular test drugs as a measure of endothelial function. Iontophoresis involves delivery of ions of soluble salts across the skin (typically in the inner forearm) under the influence of a relatively weak electrical current. Increasing either the current or the time of delivery can increase the total drug administered [27].

Using this technique, drugs such as acetylcholine (ACh) and sodium nitroprusside (SNP) have been tested on the skin and have given some insight into the involvement of endothelial function and NO activity in rheumatologic conditions [28]. ACh is an endothelium-dependent vasodilator that causes normal vasodilatation in the presence of an intact and fully functional endothelium. ACh mediates vasodilatation through the production of NO by NO synthase, with an accessory role for vasodilator prostanoids (e.g., prostacyclin) and endothelium-derived hyperpolarizing factor (EDHF). In contrast, SNP is an NO donor which allows examination of the response of the vasculature to exogenous NO, independently of the endothelium, and is therefore an established test drug for measuring vasculature smooth muscle cell function. Once the iontophoresed ACh/SNP reaches the microvessels of the skin, subsequent vasodilatation is recorded by LDI, which provides a relative measure of skin perfusion.

There is increasing evidence linking microvascular dysfunction to CV outcomes in a range of conditions [29, 30], hence measuring the response of the microcirculation to pharmacologic stimuli could improve our understanding of vascular dysfunction and disease progression. The technique has good reproducibility [31], and appears to be reflective of global endothelial function and CV health. Abnormalities in the microvascular bed have been shown to correlate with CV risk factors [32] and with established coronary artery disease [33]. The association reported between microvascular function and coronary flow reserve in healthy individuals [34] provides further evidence that assessments made in the skin do indeed provide a reliable global measure of microvascular function.

36.5
Studies Using LDI in RA Patients

Given the strong correlation between microvascular function and the presence of CV risk factors, assessment of the microvascular bed could provide a sensitive measure of the early stages of atherosclerosis in RA patients. Studies have shown that endothelial dysfunction in RA is closely associated with inflammation, and therapeutic reduction of inflammation leads to improvements in endothelial function. As such, assessments of microvascular endothelial function could prove to be useful in the identification and monitoring of CV risk in patients with RA. However, to date, not many studies have focused on microvascular function in RA (Figure 36.3). One small-scale study reported microvascular dysfunction in female patients with RA [35], and a pilot study showed improvements in microvascular function in eight patients with RA following anti-inflammatory treatment [36]. The most convincing evidence to date connecting systemic inflammation and microvascular endothelial function in RA was provided by a large, cross-sectional study of 128 patients with RA [37]. In this study, we reported

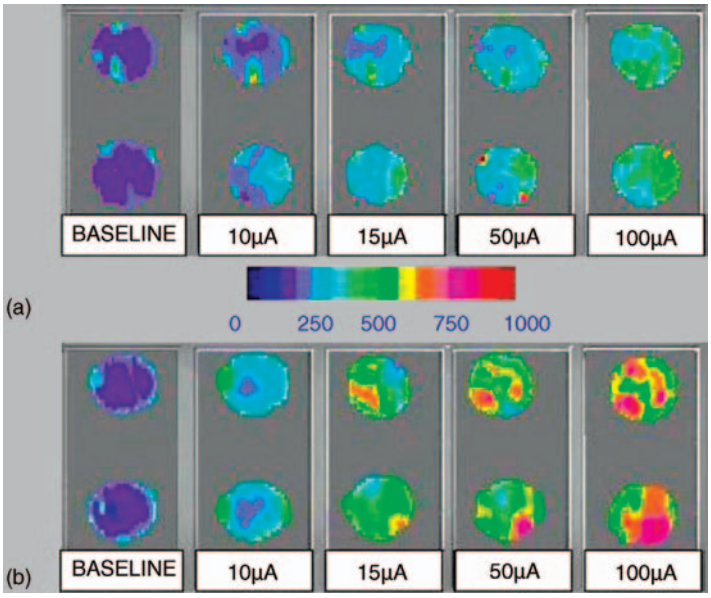

Figure 36.3 Colour-coded LDI output showing skin perfusion response to concurrent iontophoresis of ACh (top) and SNP (bottom) at increasing currents (10-100 uA). There is a clearly reduced response to both drugs in the RA patient (A) compared to the healthy control (B).

that microvascular endothelial dysfunction is directly correlated with CRP level, a key marker of systemic inflammation, independent of other conventional vascular risk factors [37]. We have also reported that vascular function improves in patients who respond to anti-TNF therapy or DMARDs (disease-modifying antirheumatic drugs), suggesting that, in the microcirculation at least, reduction in inflammation, rather than choice of treatment *per se*, can be beneficial [38].

36.6 Conclusion

Laser Doppler flowmetry has great potential in rheumatology in clinical practice, especially with the development of laser Doppler imagers that can measure the progression of the disease in synovial tissue. The noninvasive nature of the instruments and the fact that measurements can be made without contact make them highly acceptable to patients. Many of the inherent difficulties with traditional single-point techniques, such as variability of measurements due to spatial heterogeneity of skin blood flow, can be overcome with the use of imagers.

To date, LDI has been used mostly as a research tool, where it has provided a better understanding of the abnormalities of microvascular endothelial function in RA patients. Increased inflammation and subsequent endothelial dysfunction contrib-

ute to the many factors that lead to increased CV morbidity in RA patients. Hence LDI can become a vital tool for measuring CV risk in future studies of RA patient populations.

References

1 Nilsson, G.E., Tenland, T., and Oberg, P.A. (1980) Evaluation of a laser Doppler flowmeter for measurement of tissue blood flow. *IEEE Trans. Biomed. Eng.*, **27** (10), 597–604.

2 Riva, C., Ross, B., and Benedek, G.B. (1972) Laser Doppler measurements of blood flow in capillary tubes and retinal arteries. *Invest. Ophthalmol.*, **11** (11), 936–944.

3 Tanaka, T. and Benedek, G.B. (1975) Measurement of the velocity of blood flow (*in vivo*) using a fiber optic catheter and optical mixing spectroscopy. *Appl. Opt.*, **14** (1), 189–196.

4 Stern, M.D. (1975) *In vivo* evaluation of microcirculation by coherent light scattering. *Nature*, **254** (5495), 56–58.

5 Saumet, J.L., Dittmar, A., and Leftheriotis, G. (1986) Non-invasive measurement of skin blood flow: comparison between plethysmography, laser-Doppler flowmeter and heat thermal clearance method. *Int. J. Microcirc. Clin. Exp.*, **5** (1), 73–83.

6 Tooke, J.E., Ostergren, J., and Fagrell, B. (1983) Synchronous assessment of human skin microcirculation by laser Doppler flowmetry and dynamic capillaroscopy. *Int. J. Microcirc. Clin. Exp.*, **2** (4), 277–284.

7 Oberg, P.A. (1990) Laser-Doppler flowmetry. *Crit. Rev. Biomed. Eng.*, **18** (2), 125–161.

8 Wardell, K., Braverman, I.M., Silverman, D.G., and Nilsson, G.E. (1994) Spatial heterogeneity in normal skin perfusion recorded with laser Doppler imaging and flowmetry. *Microvasc. Res.*, **48** (1), 26–38.

9 Abbot, N.C., Ferrell, W.R., Lockhart, J.C., and Lowe, J.G. (1996) Laser Doppler perfusion imaging of skin blood flow using red and near-infrared sources. *J. Invest. Dermatol.*, **107** (6), 882–886.

10 Forrester, K., Doschak, M., and Bray, R. (1997) *In vivo* comparison of scanning technique and wavelength in laser Doppler perfusion imaging: measurement in knee ligaments of adult rabbits. *Med. Biol. Eng. Comput.*, **35** (6), 581–586.

11 Lam, F.Y. and Ferrell, W.R. (1993) Acute inflammation in the rat knee joint attenuates sympathetic vasoconstriction but enhances neuropeptide-mediated vasodilatation assessed by laser Doppler perfusion imaging. *Neuroscience*, **52** (2), 443–449.

12 Egan, C.G., Lockhart, J.C., and Ferrell, W.R. (2004) Pathophysiology of vascular dysfunction in a rat model of chronic joint inflammation. *J. Physiol. (Lond.)*, **557** (2), 635–643.

13 McDougall, J.J. (2001) Abrogation of α-adrenergic vasoactivity in chronically inflamed rat knee joints. *Am. J. Physiol. Regul. Integr. Comp. Physiol.*, **281**, R821–R827.

14 Ferrell, W.R., Sturrock, R.D., Mallik, A.K., Abbot, N.C., Lockhart, J.C., and Edmondson, W.D. (1996) Laser Doppler perfusion imaging of proximal interphalangeal joints in patients with rheumatoid arthritis. *Clin. Exp. Rheumatol.*, **14** (6), 649–652.

15 Ferrell, W.R., Balint, P.V., Egan, C.G., Lockhart, J.C., and Sturrock, R.D. (2001) Metacarpophalangeal joints in rheumatoid arthritis: laser Doppler imaging – initial experience. *Radiology*, **220** (1), 257–262.

16 Ng, E.Y.K. and How, T.J. (2003) Laser-Doppler imaging of osteoarthritis in proximal interphalangeal joints. *Microvasc. Res.*, **65** (1), 65–68.

17 Myllykangas-Luosujarvi, R.A., Aho, K., and Isomaki, H.A. (1995) Mortality in rheumatoid arthritis. *Semin. Arthritis Rheum.*, **25** (3), 193–202.

18 Solomon, D.H., Goodson, N.J., Katz, J.N., Weinblatt, M.E., Avorn, J., Setoguchi, S., Canning, C., and Schneeweiss, S. (2006) Patterns of cardiovascular risk in rheumatoid arthritis. *Ann. Rheum. Dis.*, **65** (12), 1608–1612.

19 Van Doornum, S., McColl, G., and Wicks, I.P. (2002) Accelerated atherosclerosis: an extraarticular feature of rheumatoid arthritis? *Arthritis Rheum.*, **46** (4), 862–873.

20 Van Doornum, S., Jennings, G.L.R., and Wicks, I.P. (2006) Reducing the cardiovascular disease burden in rheumatoid arthritis. *Med. J. Aust.*, **184** (6), 287–290.

21 Shoenfeld, Y., Gerli, R., Doria, A., Matsuura, E., Cerinic, M.M., Ronda, N., Jara, L.J., Abu-Shakra, M., Meroni, P.L., and Sherer, Y. (2005) Accelerated atherosclerosis in autoimmune rheumatic diseases. *Circulation*, **112** (21), 3337–3347.

22 Sitia, S., Atzeni, F., Sarzi-Puttini, P., Di Bello, V., Tomasoni, L., Delfino, L., Antonini-Canterin, F., Di Salvo, G., De Gennaro Colonna, V., La Carrubba, S., Carerj, S., and Turiel, M. (2009) Cardiovascular involvement in systemic autoimmune diseases. *Autoimmun. Rev.*, **8** (4), 281–286.

23 Nurmohamed, M.T. (2009) Cardiovascular risk in rheumatoid arthritis. *Autoimmun. Rev.*, **8** (8), 663–667.

24 Ku, I.A., Imboden, J.B., Hsue, P.Y., and Ganz, P. (2009) Rheumatoid arthritis – a model of systemic inflammation driving atherosclerosis. *Circ. J.*, **73** (6), 977–985.

25 Ridker, P.M., Hennekens, C.H., Buring, J.E., and Rifai, N. (2000) C-reactive protein and other markers of inflammation in the prediction of cardiovascular disease in women. *N. Engl. J. Med.*, **342** (12), 836–843.

26 Dixon, W.G. and Symmons, D.P.M. (2007) What effects might anti-TNFα treatment be expected to have on cardiovascular morbidity and mortality in rheumatoid arthritis? A review of the role of TNFα in cardiovascular pathophysiology. *Ann. Rheum. Dis.*, **66** (9), 1132–1136.

27 Khan, F., Davidson, N.C., Littleford, R.C., Litchfield, S.J., Struthers, A.D., and Belch, J.J.F. (1997) Cutaneous vascular responses to acetylcholine are mediated by a prostanoid-dependent mechanism in man. *Vasc. Med.*, **2** (2), 82–86.

28 Cerinic, M.M., Generini, S., and Pignone, A. (1997) New approaches to the treatment of Raynaud's phenomenon. *Curr. Opin. Rheumatol.*, **9** (6), 544–556.

29 Turner, J., Belch, J.J.F., and Khan, F. (2008) Current concepts in assessment of microvascular endothelial function using laser Doppler imaging and iontophoresis. *Trends Cardiovasc. Med.*, **18** (4), 109–116.

30 Huang, A.L., Silver, A.E., Shvenke, E., Schopfer, D.W., Jahangir, E., Titas, M.A., Shpilman, A., Menzoian, J.O., Watkins, M.T., Raffetto, J.D., Gibbons, G., Woodson, J., Shaw, P.M., Dhadly, M., Eberhardt, R.T., Keaney, J.F. Jr., Gokce, N., and Vita, J.A. (2007) Predictive value of reactive hyperemia for cardiovascular events in patients with peripheral arterial disease undergoing vascular surgery. *Arterioscler. Thromb. Vasc. Biol.*, **27** (10), 2113–2119.

31 Newton, D.J., Khan, F., and Belch, J.J.F. (2001) Assessment of microvascular endothelial function in human skin. *Clin. Sci.*, **101** (6), 567–572.

32 Khan, F., Elhadd, T.A., Greene, S.A., and Belch, J.J.F. (2000) Impaired skin microvascular function in children, adolescents, and young adults with type I diabetes. *Diabetes Care*, **23** (2), 215–220.

33 Ijzerman, R.G., De Jongh, R.T., Beijk, M.A.M., Van Weissenbruch, M.M., Delemarre-van De Waal, H.A., Serne, E.H., and Stehouwer, C.D.A. (2003) Individuals at increased coronary heart disease risk are characterized by an impaired microvascular function in skin. *Eur. J. Clin. Invest.*, **33** (7), 536–542.

34 Khan, F., Patterson, D., Belch, J.J.F., Hirata, K., and Lang, C.C. (2008)

Relationship between peripheral and coronary function using laser Doppler imaging and transthoracic echocardiography. *Clin. Sci.*, **115** (9), 295–300.

35 Arosio, E., De Marchi, S., Rigoni, A., Prior, M., Delva, P., and Lechi, A. (2007) Forearm haemodynamics, arterial stiffness and microcirculatory reactivity in rheumatoid arthritis. *J. Hypertens.*, **25** (6), 1273–1278.

36 Datta, D., Ferrell, W.R., Sturrock, R.D., Jadhav, S.T., and Sattar, N. (2007) Inflammatory suppression rapidly attenuates microvascular dysfunction in rheumatoid arthritis. *Atherosclerosis*, **192** (2), 391–395.

37 Galarraga, B., Khan, F., Kumar, P., Pullar, T., and Belch, J.J.F. (2008) C-reactive protein: the underlying cause of microvascular dysfunction in rheumatoid arthritis. *Rheumatology (Oxford)*, **47** (12), 1780–1784.

38 Galarraga, B., Belch, J.J.F., Pullar, T., Ogston, S., and Khan, F. (2010) Clinical improvement in rheumatoid arthritis is associated with healthier microvascular function in patients who respond to antirheumatic therapy. *J. Rheumatol.*, **37** (3), 521–528.

37
Ocular Diagnostics and Imaging

Michael Larsen

37.1
Ocular Diagnosis, Imaging and Therapy

The eye is an optical imaging system with transparent refractive components that permit the projection of an image on its sensory component, the retina, where a neuronal signal is produced an relayed to the brain via the optic nerve (Figure 37.1). The same refractive media can be used to observe the interior of the eye and to apply therapeutic optical radiation to the eye. This chapter presents an overview of the current state of ophthalmic optical technology and the diagnostic use of optics in the study of the eye and its diseases.

37.2
Outline of Anatomy and Physiology

The optical interface between the eye and the surrounding world is the surface of the tear film, a delicate, multilayered film composed of an outer layer of lipid, a fluid layer of electrolytes dissolved in water in the middle, and a bottom of seaweed-like polysaccharide chains that anchor the film to the cells that cover the surface of the cornea [1]. Without a tear film, there is no glimpse (specular reflex) in an eye, there is intense discomfort and blurred vision, and the surface cells of the cornea will soon be lost, as will eventually the transparency of the cornea (Figure 37.2). Two-thirds of the refractive power of the eye is found on the interface between air and tear film.

After the tear film comes the cornea, which is a living tissue supported internally by an ordered network of collagen fibers analogous to the component of skin that is used to make leather. Behind it, the anterior chamber of the healthy eye is filled with clear, watery fluid. The iris forms the pupil, an adjustable aperture located close to the front nodal plane of the eye. The iris covers the anterior surface of the lens to a variable extent. The lens (Figure 37.3) differs from conventional artificial lenses in having the properties of a gradient refractive index (GRIN) lens. It is responsible for one-third of the refractive power of the eye. Behind the lens, a gelatinous structure with a few fibrils, the vitreous body (or simply *the vitreous* in clinical jargon), provides

Handbook of Biophotonics. Vol.2: Photonics for Health Care, First Edition. Edited by Jürgen Popp, Valery V. Tuchin, Arthur Chiou, and Stefan Heinemann.

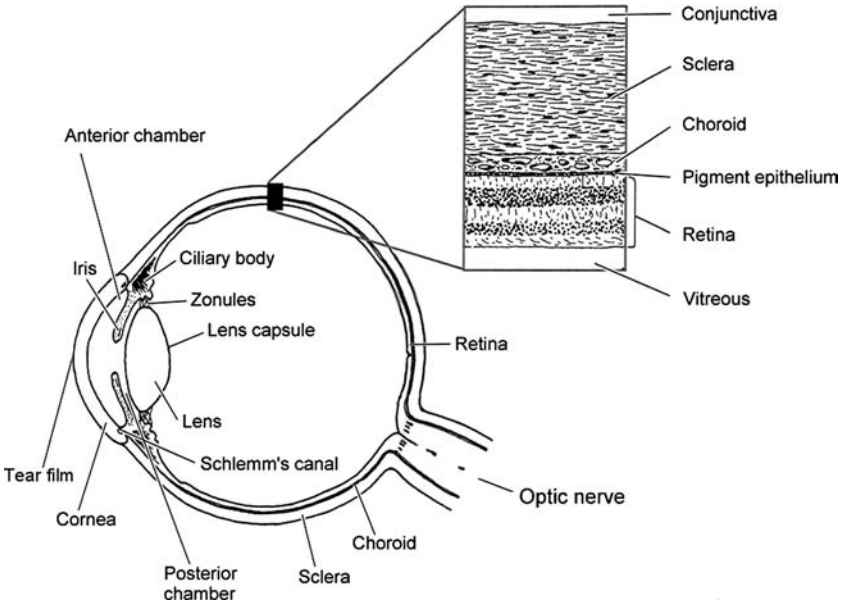

Figure 37.1 Cross-section of the right eye of a human seen from above. The refractive media include the tear film, the cornea, the aqueous humor in the anterior and posterior chambers, the lens, the vitreous body, and the retina. The photoreceptors are located in the outer retina, next the to retinal pigment epithelium.

supplementary mechanical support for the lens. It has no apparent optical role other than being clear and its delicate structure is a rudiment of fetal vessels that is responsible for the phenomenon of seeing "floaters." The posterior inside of the eye is covered by its actual sensory tissue, the retina, the arrayed photoreceptors of which

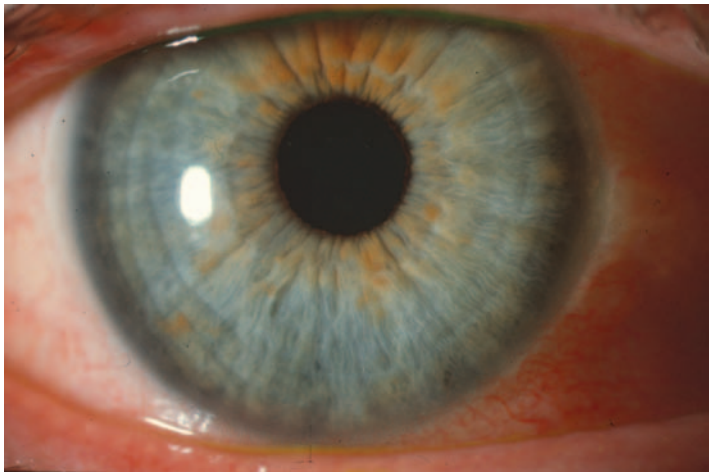

Figure 37.2 The smooth corneal reflex is produced by a contiguous tear film covering the entire surface of the eye, thus forming the primary and most powerfully refracting optical surface of the eye.

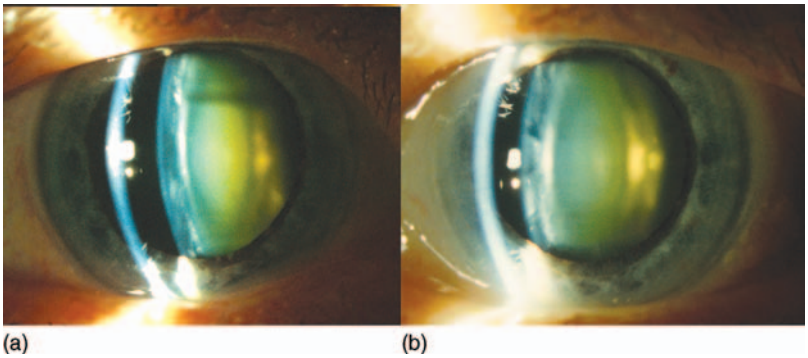

Figure 37.3 The anterior segment of the eye seen in diffuse illumination combined with a narrow vertical beam of intense white light from a slit-lamp illuminating the eye from the left at a 30° angle from the line of sight. The left eye (b) is nearly normal and shows some backscatter of light as the beam passes the cornea (narrow and curved, to the left) and the lens (biconvex and broader, at the center of the pupil). The right eye (a) has a cortical lens opacity that casts a shadow into the upper part of the lens and a highly scattering lens nuclear cataract.

convert incoming photons to neuronal signals that are processed and compressed in the inner layers of the retina before being conveyed to the brain via the optic nerve. Behind the retinal pigment epithelium, which is the outermost layer of the retina, the highly perfused network of blood vessels called the choroid delivers nutrition that diffuses into the retina to supplement the relatively sparse network of retinal vessels. A small depression in the retina near the posterior pole of the eye marks the fovea and its center, the foveola, where the daylight-optimized cone photoreceptors are found at maximum density and where fixation, reading, face recognition, and other high angular resolution tasks are subserved.

Anatomic terminology refers the corneal direction as being anterior and the direction towards the fovea as being posterior, or it may refer to the eye as a globe, the direction toward its center being inside or internal and the direction away from its center being outside or external. In some contexts, the posterior part of the eye may be referred to as though the patient were lying down on an operating table, the choroid being below the retinal pigment epithelium, and so on.

The optical components of the eye are not perfectly aligned on a linear optical axis and the axis of viewing defined by the location of the foveola and the center of the pupil deviates from the geometric axis of the eye by a few degrees. While such theoretical imperfections can be pointed out, there are indications that they help compensate for a number of classical problems in the manufacture of artificial optics. An elegant example is the bowl-shaped sensor, that is, the photoreceptor layer of the retina, the shape of which is a near-perfect match to the curved image plane of the optical apparatus in the anterior segment of the eye. This example shows that what would be considered imperfections on an optical assembly line – a grotesquely curved image plane and a sensor that is not a perfectly flat – combine to form a magnificently compact wide-angle biological camera.

37.3
Basic Optical Instrumentation for Examination of the Eye

The slit-lamp biomicroscope was designed for stereoscopic observation of the anterior segment of the eye at high magnification and with adjustable illumination that can be focused to a narrow slit-shaped beam at the focus of the microscope (Figure 37.4). The light source can be rotated about this focus so that the various tissues can be seen in the optical cross-section provided by light scattered from the semi-transparent tissues (cornea, lens, vitreous, retina) and the aqueous, which is normally free from visible scatter.

Observation of the interior of the eye requires nothing but coaxial illumination. The unaided eye can see all the way to the posterior inside of the eye, if assisted by a suitable source of coaxial illumination. This is the principle of direct ophthalmoscopy (Figure 37.5). Limitations of direct ophthalmoscopy include lack of stereoscopic viewing and a narrow field of view, often less than 5° as seen from outside the eye.

Stereoscopic viewing and a wide field are provided by indirect ophthalmoscopy, where a real image of the fundus is formed between the observer and a lens held close to the eye (Figures 37.4 and 37.6).

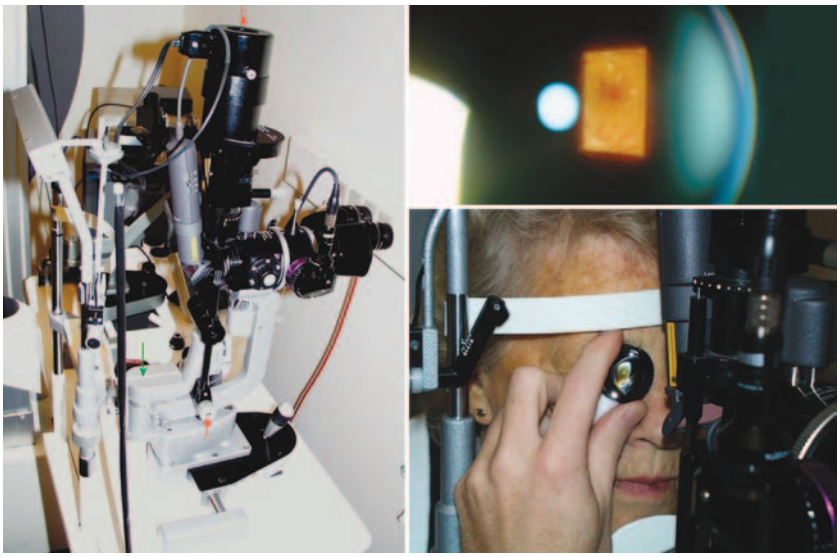

Figure 37.4 Binocular microscope for examination of a seated subject, with his or her head rested on a fixed support, the examiner being seated on the other side of an adjustable table. The light source and the microscope can be moved on the table with the aid of a joystick and can be rotated independently about a common vertical axis (green arrow). The lamp house (upper red arrow) and its optical shutters can be rotated and adjusted by knobs at the lower end of this unit (lower red arrow).

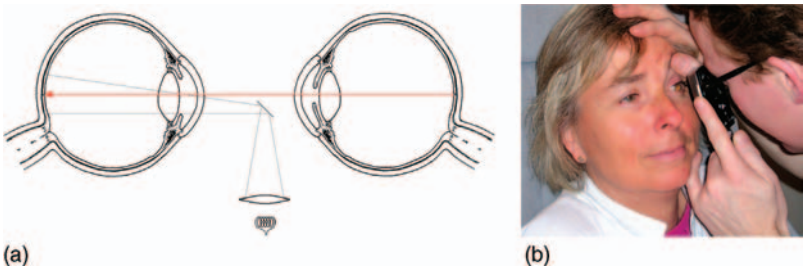

Figure 37.5 Direct ophthalmoscopy. The left eye of the observer views the fovea of the eye of the patient with the aid of a quasi-coaxial light source. The modern hand-held direct ophthalmoscope includes a rotating disk with lenses of various dioptric powers that allow correction for spherical refractive errors in the examiner and the patient. The sketch in (a) shows the eye of the patient to the left, with a pharmaceutically dilated pupil and the observer to the right, both seen from above.

37.4 Fundus Photography

The principle of conventional fundus photography (Figure 37.7) is the same as that of indirect ophthalmoscopy, except that the eye of the observer is replaced by an artificial refractive system and the retina with a film. The source of illumination is built into the camera and the lens in front of the eye is fixed to the camera housing. Alignment of the camera is accomplished by moving the entire camera housing while the patient is seated and fixating a target light with his or her other eye.

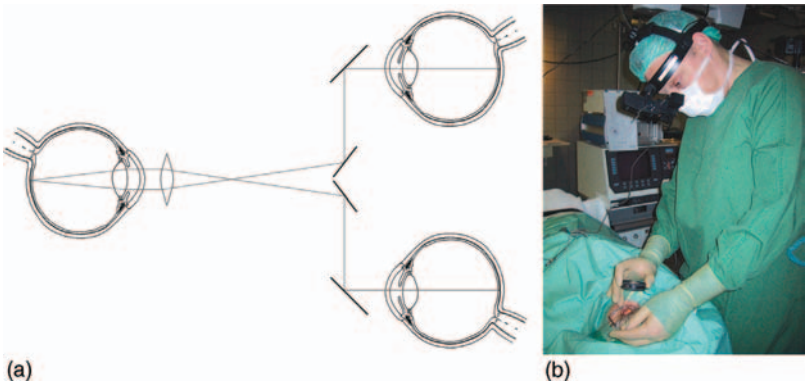

Figure 37.6 Indirect ophthalmoscopy. The fundus of the eye of the patient, shown to the left in (a), is observed with both eyes of the observer at a viewing angle of nearly 7° angular separation inside the eye. This is made possible by using mirrors to narrow the effective distance between the observer's pupils to a few mm. The illumination (not shown on the sketch) is mounted on the axis of symmetry, slightly above the plane of the viewing optics. The two lines of sight are crossing between the physician (b) and the hand-held lens, at a conjugate plane of the fundus where a real image is formed.

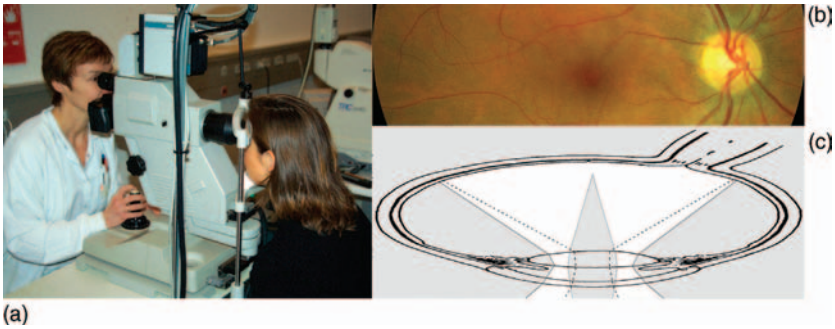

Figure 37.7 (a) Fundus camera with photographer (left) and patient (right). (c) Schematic diagram of the pathways of optical illumination (white) and imaging (stippled outline), which are separated as they pass through the back-scattering media of the cornea and the lens. The layout of these pathways determines how small a pupil the camera can work with. Optical cross-talk between the incoming and outgoing pathways increases with increasing scatter in the lens as it ages or suffers from opacification from other causes.

High-quality fundus photography requires pharmaceutical pupil dilation. Maximum dilation is achieved by combining two mydriatic eyedrops, one of which is an anticholinergic and the other an adrenergic agent, thus paralyzing the circular pupil sphincter muscle while stimulating the radial dilator muscle. Pupil dilation requires about 30 min of preparation (instillation, waiting for the effect to set in, and observing for side effects) and vision will be blurred for 1–3 h after the examination. To provide faster and more convenient examinations, fundus cameras for smaller pupils have been designed. These non-mydriatic cameras provide less lateral resolution, because of the smaller numerical aperture, and less contrast than mydriatic fundus cameras because of the poorer separation between illumination and imaging pathways. Systematic use of non-mydriatic cameras in settings such as diabetic retinopathy screening clinics is problematic because ~25% of patients will be found to need pharmaceutical pupil dilation and the extra work involved tends to offset the time gained in the remainder of the population.

Conventional fundus cameras cover an angle of 30–60 degrees in a single image. Wider coverage can be obtained by pointing the camera in multiple directions. Systematic fundus photography protocols divide the fundus into a number of fields. Systematic screening for diabetic retinopathy is often restricted to a fovea-centered and a disk-centered image (Figure 37.8).

Fundus photographs can be made in stereoscopic pairs by parallel displacement of the camera horizontally away from the centerline of the pupil, as much as can be done without sacrificing the illumination of the fundus (Figure 37.9). Before the development of optical coherence tomography (OCT), stereoscopic biomicroscopy and fundus photography were the only means whereby information about retinal thickening could be obtained.

Digital fundus cameras are made with three-channel image sensors that capture the red, green, and blue components or layers of an object illuminated by white light. The effective illumination varies considerably with the spectral characteristics of the

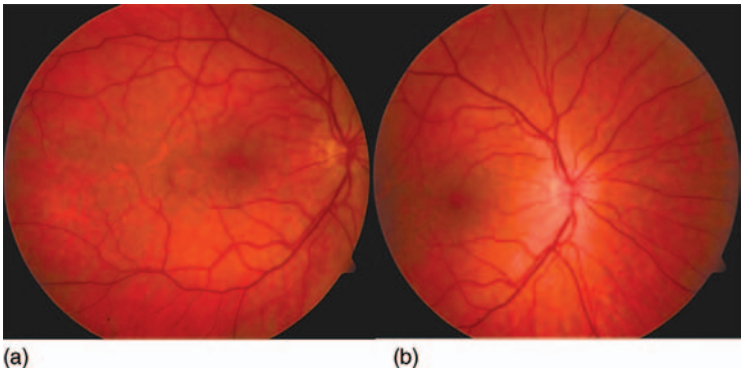

Figure 37.8 Color fundus photographs, each 60° horizontal subtense seen from outside the eye. The image in (a) is centered on the temporal side of the fovea and that in (b) is centered on the optic disk.

crystalline lens. With increasing age comes increasing absorption from the blue end of the spectrum (Figure 37.10). It would be desirable to have fundus cameras that interactively regulate spectral illumination so that it could be tuned to suit the individual eye.

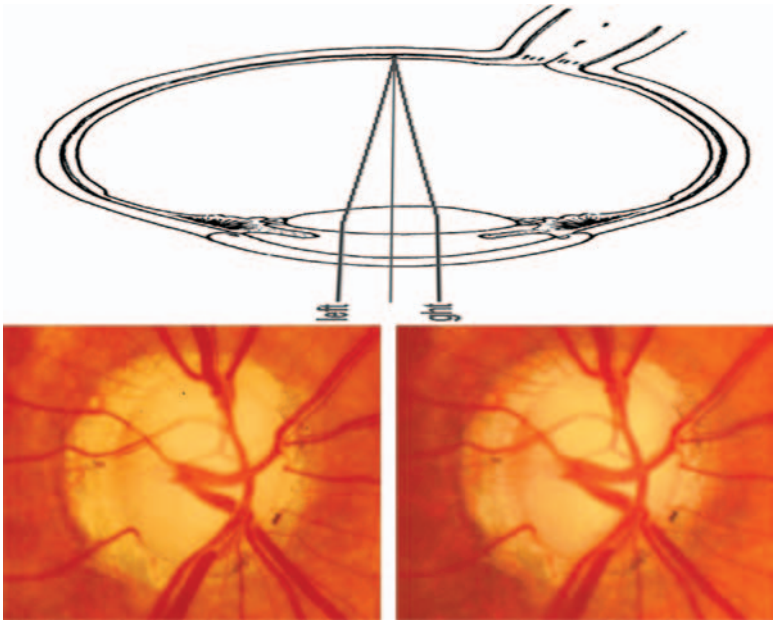

Figure 37.9 Schematic presentation of parallel displacement of fundus camera to record stereoscopic fundus photographs. The pair below have been swapped to allow stereoscopic viewing by crossing one's eyes. Successful viewing is accomplished when one is looking at the middle of three images and perceiving a profound cupping of the optic nerve head.

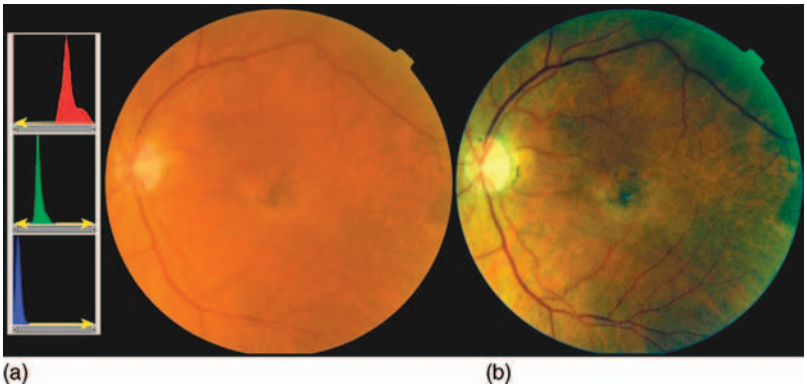

Figure 37.10 Raw color fundus photograph from an elderly person made using a nonmydriatic fundus camera (a) with curves to the left showing the distribution of pixel intensities over the 256-bit dynamic range of the image sensor. The red channel is well exposed, bordering on overexposure, the green channel is moderately underexposed, and the blue channel is severely underexposed. By spreading the signal over the full dynamic range of the display (histogram stretching), as indicated by yellow arrows, a color-selective contrast-enhanced image can be produced (b).

Gray-scale fundus photographs provide superior contrast, the balance between the various features of the normal and diseased fundus varying with the color of the illumination. Briefly, blue light provides optimal viewing of the retinal nerve fiber layer, green light shows blood in high contrast, and red light shows pigmented lesions to advantage. Quantitative spectral analysis of the fundus image has few applications, but retinal oximetry is currently being studied as a means of investigating retinal metabolism. This method of estimating oxygen saturation in the blood is based on a characteristic shift in the absorption spectrum of hemoglobin when it changes between being oxygenated and deoxygenated (Figure 37.11).

Fundus photography can be performed in the infrared region of the spectrum. There is poor contrast, except when densely pigmented structures such as choroidal nevi are present. Infrared fundus video photography is used to monitor aiming and focusing of nonmydriatic fundus cameras because the invisible radiation does not stimulate pupil contraction. Because the infrared image is useless in itself, a flash of white light must be fired to obtain a regular fundus image. Digital nonmydriatic cameras work with low flash settings, thanks to the high sensitivity of digital image sensors, but it is obvious that in many subjects some degree of pupil constriction persists for several minutes after the first image has been shot.

Fundus image analysis has been shown experimentally to be able to separate fundus images with diabetic retinopathy from images without retinopathy with an accuracy that is comparable to that of trained observers [2] (Figure 37.12). The method has been introduced in selected settings as a means of prescreening images to reduce the number of screening images that need to be assessed by graders. Additional uses of digital image analysis include measurement of retinal

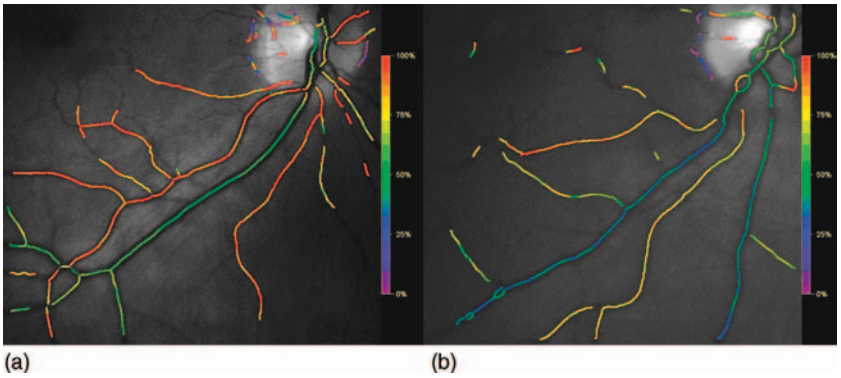

Figure 37.11 Oxygen saturation in retinal vessels of a healthy subject (a) and a patient with severe systemic hypoxia because of a congenital cardiac septum defect (b). A pair of fundus images obtained with 605 nm and 586 nm illumination, respectively, were subjected to computerized analysis of the variation in optical density of the retinal vessels, which varies with oxygen saturation at 605 nm but not at the reference wavelength of 586 nm. The ratio of the optical densities is approximately linearly related to the oxygen saturation of hemoglobin.

vessel diameters, which has shown epidemiological associations with systemic cardiovascular disease but which has yet to find an application in routine clinical practice.

The virtue of fundus photography in blue light as a means of imaging the retinal nerve fiber layer is evident in young subjects (Figure 37.13), whereas in elderly people the aging of the lens makes the method less useful. A range of alternative methods for quantitative characterization of the retinal nerve fiber and ganglion cell layers are available, as will be discussed in the following.

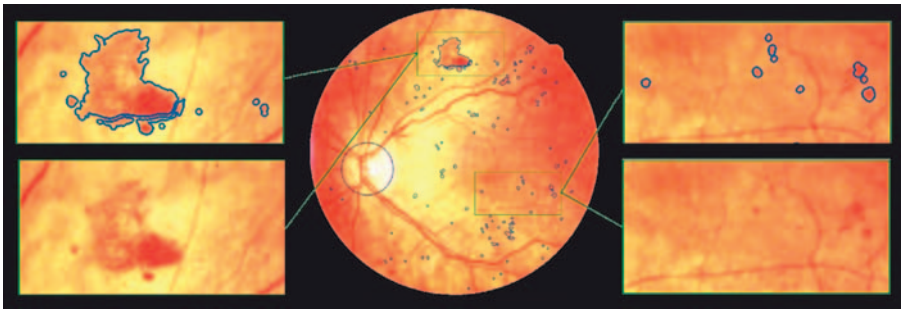

Figure 37.12 Fundus photograph analyzed by a digital algorithm that subtracts the optic disk and the retinal blood vessels, after which it identifies circumscribed dark lesions in the green channel and marks the border of each lesion, so that an observer can be alerted to the presence of abnormalities in the image.

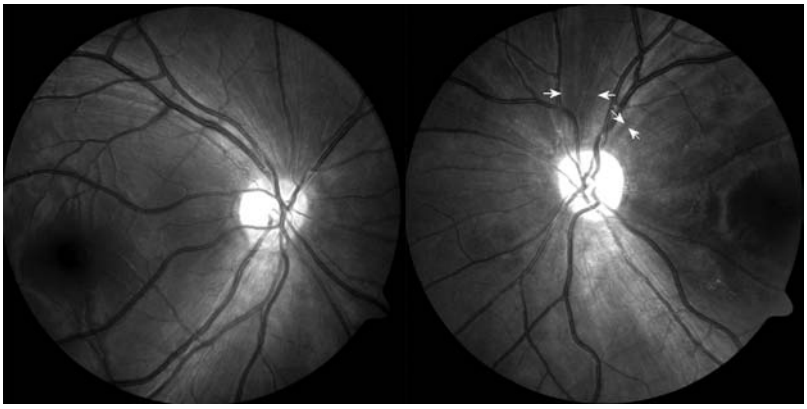

Figure 37.13 Fundus photographs recorded in red-free illumination (white incandescent light source behind red-blocking filter) using a panchromatic digital image sensor. The images are from a 21-year-old man with retinal nerve fiber damage in his left eye. Wedge-shaped defects of the retinal nerve fiber layer (arrows) are seen more readily in the green and blue light. Pure blue illumination is ideal for nerve fiber imaging but in elderly people with glaucoma, where such defects are most common, high absorption and scatter in the aged lens and other age-related changes in the eye make the method less reliable.

37.5 Fluorescence Imaging

Many molecules can be made to fluoresce if struck by photons of sufficient energy to excite an electron to a higher energy level, yet the energy should be small enough not to break covalent bonds, in which case damage to the molecule would occur. Within or near the visible range of electromagnetic radiation, molecules with conjugated double bonds, especially aromatic systems, are likely to have the critical property of being able to absorb a photon, store the absorbed energy in an excited electron with little risk of dissipation of the energy, and then re-emit most of the energy as a single new photon. Because some of the energy stored in the excited state tends to be lost to molecular vibration, the emitted fluorescent photon is generally of a longer wavelength than the absorbed photon. The shift in energy/wavelength is called the Stokes shift. Fluorescence permits imaging of various properties of tissue in an attractive manner. In the case of the fundus of the eye, blue light can be used to excite fluorescence from the retinal pigment epithelium. The intensity of the fundus autofluorescence is so weak that it is overwhelmed by reflected light in most image sensing systems, but colored optical filters can block the exciting light and allow only the fluorescent light to reach an observer or a camera aimed at the fundus. Visual observation was indeed used to make the first observations of the retinal circulation of blood stained with fluorescein (peak excitation at 494 nm, peak fluorescence emission at 521 nm). The intrinsic fluorescence or autofluorescence of the fundus is much weaker and cannot be seen by the observer unless the illumination reaches toxic levels. This happens during photocoagulation treatment (Figure 37.14).

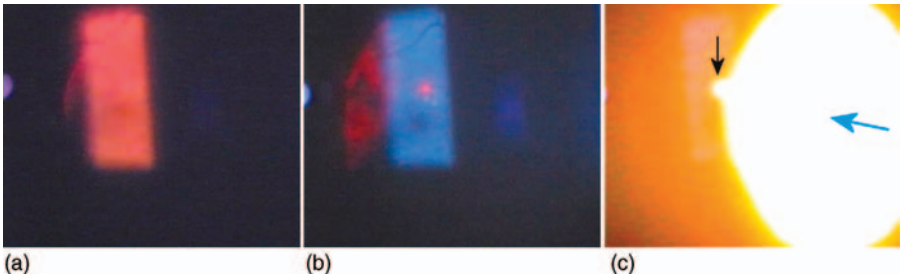

Figure 37.14 View of the fundus of the eye during 532 nm laser photocoagulation treatment. The treating physician is observing the posterior inside of the eye in white light (a) or blue–green light that provides better contrast. (b) The direction of incoming light is from the right. A red aiming spot shows where the laser is aimed. Four bright spots (b) indicate where coagulation has already been applied. The dark area below the aiming beam is the fovea. A barrier filter blocks all 532 nm light from reaching the physician's eye and the monitoring camera. When the physician activates the 532 nm laser by pressing a footswitch, a bright yellow flash of fluorescence is seen from the fundus (black arrow) and from the lens (blue arrow, the direction of which indicates the direction of the incoming light) (c).

At illumination intensities that are tolerable for the eye, the weak fluorescence from the intrinsic fluorophores that are naturally present in the fundus is best imaged by summation of multiple frames recorded by a confocal scanning laser ophthalmoscope (Figure 37.15).

If a conventional fundus camera is used, the powerful fluorescence of the lens, although it is out of focus, will add a veil of background fluorescence that obscures much of the detail in the fundus image (Figure 37.16). This effect is also very noticeable on indocyanine green angiograms.

Fluorescence can be elicited from multiple natural components of the eye, in health and in disease. Aged proteins of the lens are the most prominent source. In the fundus, N-retinylidene-N-retinylethanolamine (A2E) is an important fluorophore. A2E is a byproduct of the biochemical cycle commonly known as the visual cycle that generates photopigment. The photopigment drives vision by capturing photons in the photoreceptors. The most important artificial fluorophores are indocyanine green (peak excitation at 780 nm, peak fluorescence at 830 nm) and fluorescein, both of which can be given intravenously. This is usually done as a rapid bolus injection into a vein in the forearm. A fundus camera with an appropriate set of excitation and barrier filters, or a light source with an appropriate wavelength such as a 488 nm laser for excitation of fluorescein, is used to capture the image of stained blood flowing through the blood vessels of the fundus of the eye (Figures 37.17 and 37.18).

37.6 Photocoagulation Therapy

Photocoagulation treatment of the fundus of the eye is a crude and rather brutal treatment, the direct effect of which is to amputate photoreceptors and

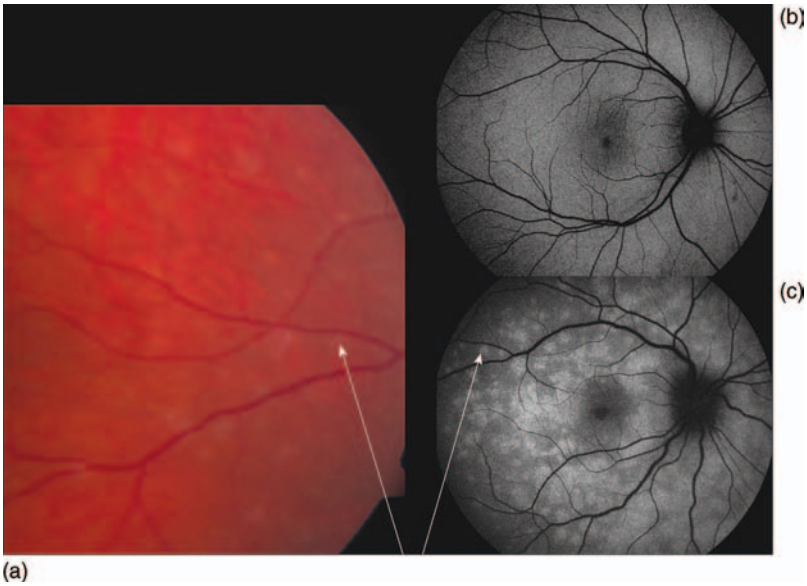

Figure 37.15 Fundus autofluorescence image from a healthy subject (b) and from a patient with the multiple evanescent white dot syndrome (c). The patient's fundus was also photographed in color (a). Arrows indicate white dots that are difficult to discern in color but are very distinct on the fluorescence image.

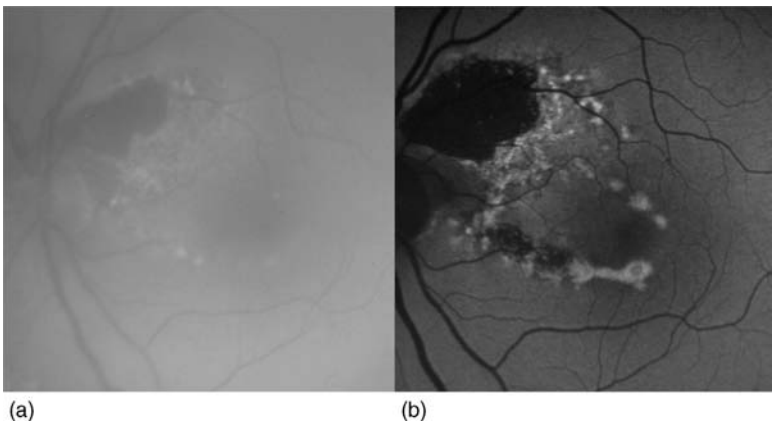

Figure 37.16 Fundus autofluorescence images from a 50-year old phakic man (phakic meaning with an intact lens) with sequels of central serous chorioretinopathy. With a conventional camera (a), the diffuse overlay of lens fluorescence adds a diffuse veil of background fluorescence that severely reduces contrast. An image recorded with a confocal scanning laser ophthalmoscope (b) has better contrast because fluorescence from sources outside the focal plane is effectively rejected.

Figure 37.17 Indocyanine green (a) and fluorescein fundus angiography (b) images from healthy eyes. The infrared light used to excite indocyanine green penetrates the retinal pigment epithelium, thus allowing visualization of the dense network of large choroidal vessels behind the retina. Most of the blue light used to excite fluorescein is absorbed by the pigment epithelium, thus producing a more selective visualization of the vessels of the retina.

pigment epithelial cells [3]. The virtue of the treatment is that it is noninvasive, selective for the outer layers of the retina, and applicable in small, selected locations in the fundus. It is also inexpensive and highly effective in controlling conditions such as proliferative diabetic retinopathy. The lesions are often called laser burns, although no combustion is involved; hence photocoagulation scar is a more precise term. The desired temperature to be reached at the target site during the application of the treatment pulse is 70–90 °C, which leads to coagulation of protein in and around the retinal pigment epithelium, the melanin pigment of which is responsible for the bulk of light absorption in the retina (Figure 37.19). The reason why coagulation can be confined to the outer retina is that the inner retina is transparent, except for its blood vessels. The treating physician therefore aims between, not on, the major blood vessels of the retina.

The photocoagulation lesions are swollen and white like boiled egg-white immediately after the laser application, if sufficient energy to achieve coagulation has been

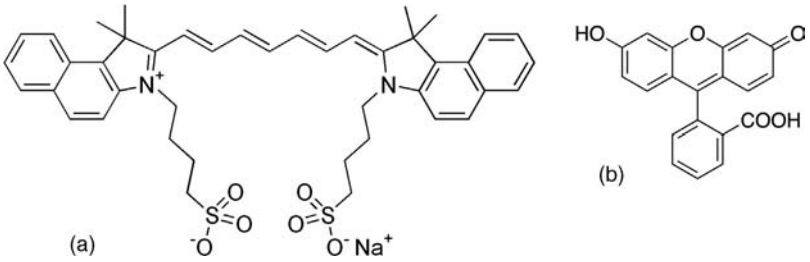

Figure 37.18 Indocyanine green (a) and fluorescein (b), two fluorescent dyes used in clinical practice to visualize the flow of blood through the vessels of the fundus of the eye.

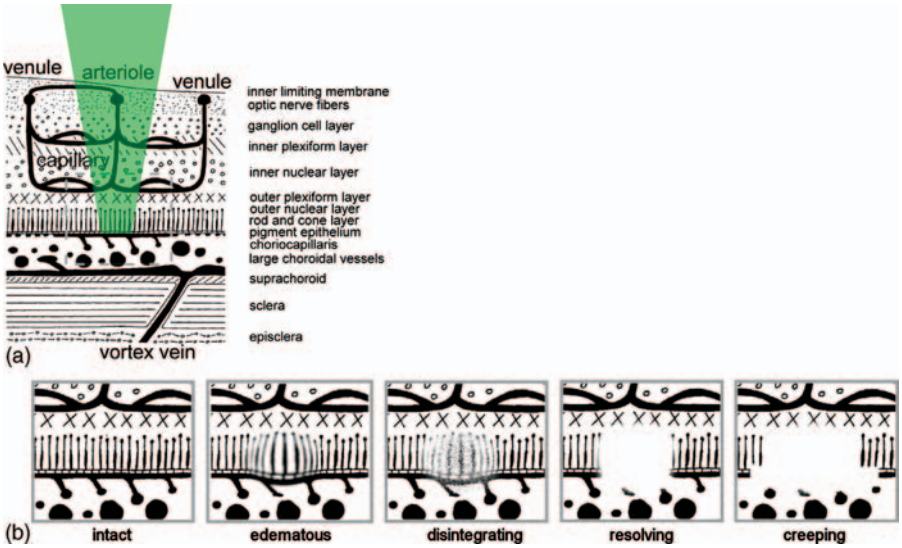

Figure 37.19 (a) Absorption of green light during photocoagulation treatment occurs deep in the retina in the pigment epithelium. Melanin absorbs light throughout the visible and near-ultraviolet range, its absorption wearing off towards the red and infrared regions. The tissue response that follows immediately and over months to years after photocoagulation is outlined in (b).

used (Fig. 37. 19(b), edematous phase). Coagulation leads to immediate cell death, but the dead tissue disintegrates only slowly, over weeks to months, when a scar characterized by loss of tissue and occasionally with hyperpigmentation appears. The resolution of the lesion involves invasion of the retina by macrophages, cells that eat and digest the components of the disintegrating tissue. Subsequently, various degrees of creeping atrophy (secondary withering of cells that were not killed by coagulation) may occur. This process is believed to be the result of a deficit of biochemical stimuli from the cells that were lost to photocoagulation and not a result of sublethal injury during photocoagulation (Figure 37.20).

The complex evolution of the photocoagulation lesions and their considerable variation between individuals demonstrate the dynamic interaction between treatment and tissue response. Photocoagulation is currently made with laser light sources because they are compact, rugged, energy-efficient, and easy to couple to an optical delivery system, but the treatment has not changed fundamentally since the pioneering work was done by using sunlight captured and led to the retina by a system of mirrors.

Photocoagulation of the anterior chamber angle between the cornea and the iris is used to lower intraocular pressure in glaucoma patients. Argon laser trabeculoplasty is applied using a contact lens (Figure 37.21) that allows focused delivery under direct observation of thermal effects to the trabecular meshwork, a filter through which the aqueous leaves the eye to be drained away by veins on the outside of the eye. The trabecular meshwork is involved in controlling the intraocular pressure and can be

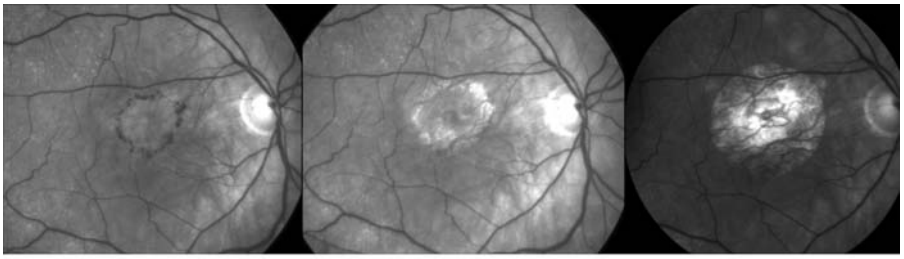

Figure 37.20 Subfoveal choroidal neovascularization (a) in a patient with neovascular (wet) age-related macular degeneration (AMD). The round mat of new vessels is demarcated by a rim of small dark hemorrhages (bleedings) that are visible through the clear neurosensory retina. The hemorrhages and new vessels are found in front of the retinal pigment epithelium and are an example of what is called a classic neovascularization. The new vessels are connected to the choroidal vessels by a vascular stalk that penetrates Bruch's membrane and the retinal pigment epithelium. Because the new vessels were actively growing and loss of residual central vision was imminent, confluent photocoagulation treatment was applied to limit the damage (514.5 nm argon laser, 300 mW, 0.2 s, 200 μm laser spot diameter). Three months later (b), the treated area had lost all traces of pigment epithelium and photoreceptors. Two years later (c), the scar had expanded to a 40% larger diameter because of creeping outer retinal atrophy at the rim of the scar.

manipulated to increase drainage. The laser energy is titrated so that "champagne bubbles" are produced when the 488/514.5 nm light is delivered in pulses of millisecond duration. Selective laser trabeculoplasty is a term that denotes pulsed 532 nm treatment using a laser exposure time (3 ns) that is shorter than the thermal reaction time of melanin. In other words, the exposure is stopped before significant diffusion of heat has occurred beyond the melanin-containing cells that are the intended target of treatment. The treatment is performed using a frequency-doubled 532 nm Q-switched Nd:YAG (neodymium-doped yttrium aluminum garnet) laser with a spot size of 400 mm.

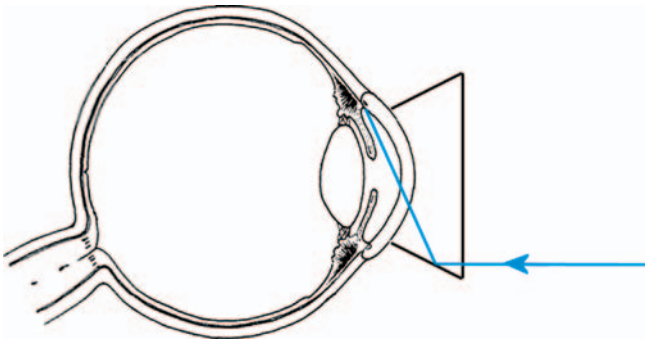

Figure 37.21 Thermal laser treatment of the trabecular meshwork in the anterior chamber angle promotes drainage of the intraocular fluid (aqueous humor or simply aqueous) and lowering of the intraocular pressure, which is useful in selected patients with glaucoma.

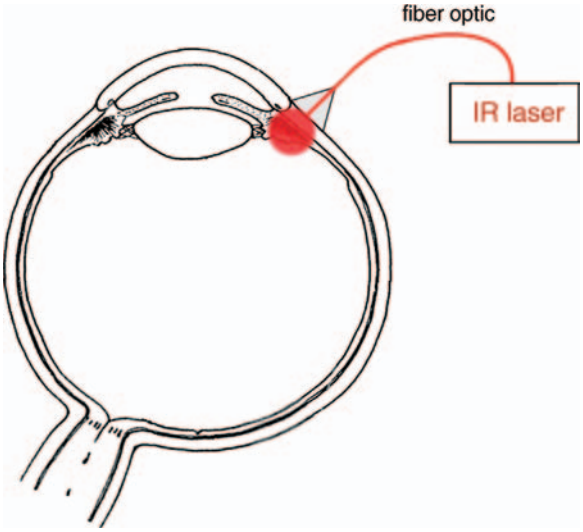

Figure 37.22 Infrared laser cyclodestruction using fiber-optic delivery to the surface of the eye, the infrared light penetrating the unpigmented sclera and exerting its heating effect in the pigmented ciliary body.

A minor application of photocoagulation is in the trans-scleral delivery of infrared light from a fiber-optic system. By placing the tip of the fiber on the outside of the eye over the ciliary body (Figure 37.22), sufficient heat can be generated inside the eye to coagulate the pigmented tissue of the ciliary body inside the eye, thus reducing the production of intraocular fluid. This treatment, cyclodestruction, is often the last resort in the fight against intraocular pressure elevation. It is mainly used in eyes with neovascular glaucoma.

Slow infrared heating of the fundus, called transpupillary thermotherapy (TTT), has been tested as a means of arresting the progression of neovascular age-related macular degeneration. The method failed to demonstrate a significant effect in a well-planned clinical trial. Although the method is believed to be effective, in principle, there is a fundamental problem in that there is no clinically applicable method of monitoring the rise in temperature in the posterior pole of the eye during the treatment. The use of standard parameters across subjects with pronounced variations in fundus pigmentation may not be a viable solution to this problem.

37.7 Photodisruption

Photodisruption is an elegant noninvasive technique based on the unique properties of ultra-short laser pulses that can produce microscopic explosions at precisely targeted locations deep inside the eye. The most common procedure is laser capsulotomy, the splitting of a brittle membranous part of the lens that is left behind

after cataract surgery to hold the artificial implant lens. Lens epithelial cells left behind in the peripheral fold of the lens capsule proliferate and migrate over the posterior aspect of what is left of the lens capsule, leading to opacification of the capsule a year or more after cataract surgery. The alternative to laser capsulotomy is to insert a hooked needle behind the lens and use it to split the capsule [4]. Cataract surgery, as we know it today, would never have reached its current popularity had a convenient, noninvasive technology for capsulotomy not been invented.

The explosive effect of the ultrafast pulsed laser is not based on absorption of light in a chromophore, as happens in photocoagulation or fluorescence. The interaction is more subtle and much faster; it is the interaction that occurs between light and any refractive medium during the propagation of light in matter. It is this interaction that is responsible for the speed of light in matter being slower than in vacuum. The interaction it is extremely weak and over the distances covered in the eye it has no measurable effect at normal light intensities. The typical light source used for photodisruption in the eye, however, generates 1 mJ of photonic energy in the form of infrared photons within 1 ns. This is equivalent to the electricity consumption of a major city during the same time interval. When this radiation is made to converge on a small focus, the flux of photons reaches such a density that the sum of weak interactions becomes large enough to tear electrons from their nuclei and create plasma (photodisruption). The extreme heat causes expansion of the gas-like plasma, which cools very rapidly under the emission of white light (bremsstrahlung) and with the collapse of the plasma bubble. This cavitation event is accompanied by an audible click and often with the release of gas from decomposed molecules and by dissolution of gasses dissolved in the biological fluids. The phenomenon has features in common with a flash of lightning.

The photodisruption laser is housed in a delivery system based on the slit-lamp biomicroscope design. The commonly used light source is an Nd:YAG laser. The operator focuses a red helium—neon aiming beam to the smallest possible spot on the capsule, so that the entire flow of photons is delivered to as small a target area as possible. The beam should be focused precisely on the posterior lens capsule or slightly behind it, to avoid damaging the intraocular implant lens. If no effect is produced with a low initial energy setting, the pulse energy is increased and so on. An abrupt transition will occur, from producing no effect to producing plasma and cavitation (Figure 37.23). This is an example of a nonlinear optical phenomenon where nothing happens below a critical threshold.

If the focus of the Nd:YAG laser is fixed while the pulse energy is increased, it will be observed that with increasing intensity the focus where plasma is formed moves closer to the instrument. This is because the higher photonic flux means that the threshold flux is reached before the light has fully converged at the focus of the instrument.

Nd:YAG lasers are perfectly capable of producing cavitation in air. Because the free particles of the plasma absorb photons of any wavelength, the plasma will form a shield that stops any further advance of the light. This means that unlike photocoagulation systems, pulsed cavitation laser energy cannot be delivered reliably to the posterior segment of the eye using optics that relay the radiation into the eye from a

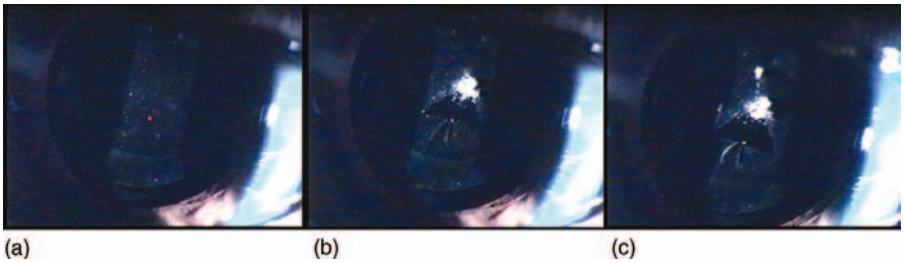

Figure 37.23 Sequences of photographs recorded during photodisruptive Nd:YAG laser treatment of secondary cataract in an eye with a dilated pupil and an artificial implant lens somewhat smaller than the dilated pupil. First, a red aiming beam is focused on the posterior part of the lens capsule that remains after cataract surgery (a). The pulsed infrared laser is fired and 80 ms later (b) the capsule is seen to have been split by the explosive formation of a plasma that also led to the release of a bubble of gas, which is seen 400 ms later (c) to have rise–behind the posterior capsule.

primary focus between the instrument and a lens such as a 90-diopter precorneal lens. If a strand of fibrous tissue has to be transected in front of the retina, or a hemorrhage is to be produced to facilitate development of a chorioretinal anastomosis in an eye with a central retinal vein occlusion, it will have to be done using a corneal contact lens such as the classical planoconvex Goldmann corneal contact lens.

The latest use of photodisruption in ophthalmology is in refractive cornea surgery where infrared femtosecond fiber-optic lasers are being used to produce very rapid sequences of tightly spaced cavitation effects inside the cornea, so that it can be cut in quasi-contiguous planes in preparation for stromal ablation. After the femtosecond procedure, a blunt probe is used to lift the corneal flap while gently breaking residual strands of corneal stroma connecting the two layers that have been prepared. This principle is now replacing the microkeratomes that were originally used in the LASIK procedure. Experimental studies are being conducted where such femtosecond laser instruments are used to cut the cornea in two planes nearly parallel to its surface, thus producing an intrastromal lenticule that can be extracted, leaving the residual corneal tissue with the desired refractive characteristics.

37.8 Photodynamic Therapy

Certain organic molecules, notably those containing a porphyrin ring, a structural motif found also in hemoglobin, can absorb light and expend the energy in the production of free oxygen radicals. New vessels formed under the fovea in neovascular age-related macular degeneration can be treated using verteporfin (Figure 37.24), which accumulates in the endothelial cells of newly formed blood vessels. Here, photochemical activation at 693 nm reaction leads to production of extremely reactive singlet oxygen and other reactive oxygen radicals that are toxic to

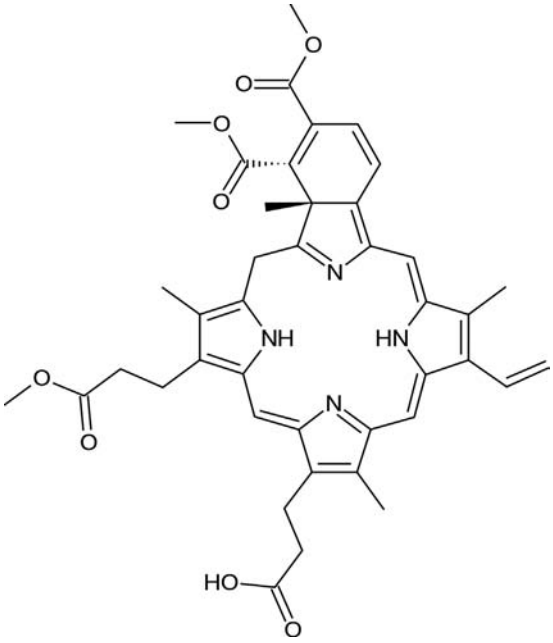

Figure 37.24 Verteporfin, a porphyrin derivative used in photodynamic therapy of diseases of the retina and choroid. Originally developed for the treatment of neovascular age-related macular degeneration, verteporfin is now used mainly in polypoidal choroidal vasculopathy, choroidal hemangioma, and central serous chorioretinopathy.

the endothelial cells and leads to occlusion of the new vessels. Photodynamic therapy includes psoralens for psoriasis and δ-aminolevulinic acid, a porphyrin precursor, for skin cancer. Porphyria cutanea tarda, a hereditary deficiency of the conversion of uroporphyrinogen, a precursor of hemoglobin, leads to accumulation of this intermediate and to phototoxic production of skin blisters.

37.9 Optical Coherence Tomography

Optical coherence tomography (OCT) allows selective registration of reflections from a given optical pathlength inside the eye [5]. The method is based on the principle that light from a light source that is phase-coherent only near the emmitting surface of the light source will be coherent at any conjugate image of the light source, be it inside the eye or on the surface of the reference mirror. By recombining light from the reference mirror with light returned from the eye, constructive interference can be obtained corresponding to the target inside the eye, whereas stray light that can be orders of magnitude more intense than the specular reflection is lost to destructive interference (Figure 37.25).

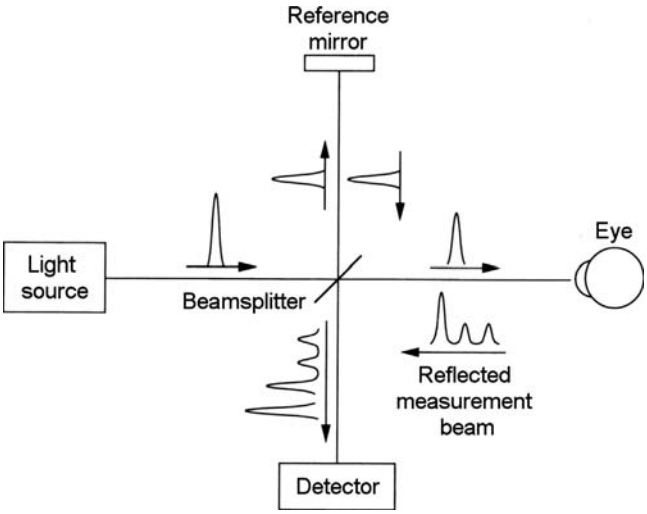

Figure 37.25 Principle of time-domain optical coherence tomography.

The focus of the OCT instrument can be scanned in various patterns over the retina or any other optically accessible part of the eye after which a tomographic reconstruction of the anatomy of the retina can be made (time-domain OCT). State-of-the art systems have progressed to spectral-domain OCT, which is faster and more robust in terms of axial alignment. Furthermore, scans can be aligned with respect to a simultaneously recorded fundus image and summation and averaging of multiple scans can be used to reduce speckle noise (Figure 37.26).

OCT has become an important addition to and to some extent a replacement for biomicroscopy and fluorescein angiography (Figure 37.19). The first applications were mainly in conditions where the retina is thickened or detached, such as diabetic macular edema, neovascular age-related macular degeneration, and central serous chorioretinopathy (Figure 37.27). With increasing resolution OCT has become a valuable tool for the objective characterization of tissue loss in the atrophic conditions that dominate the hereditary retinal degenerations.

The most common atrophic condition in the retina and optic nerve is glaucoma, which is characterized by loss of retinal ganglion cells and nerve fibers (Figure 37.28). OCT is one of the techniques that compete for a place in glaucoma diagnostics and monitoring. The modern definition of glaucoma is that it is a condition where loss of nerve fibers in the inner retina and on the optic disk is accompanied by cupping of the disk of no identifiable cause other than, in some cases, intraocular hypertension. The diagnosis needs to be backed up by the demonstration of subnormal visual field sensitivity, that is, loss of function. Assessment of intraocular pressure is relevant, not only for making the diagnosis of glaucoma, but also to assess the effect of therapy. Temporal arteritis is another cause of nerve fiber loss with cupping of the disk. Nerve fiber loss without cupping is seen in intracranial hypertension, Leber hereditary optic

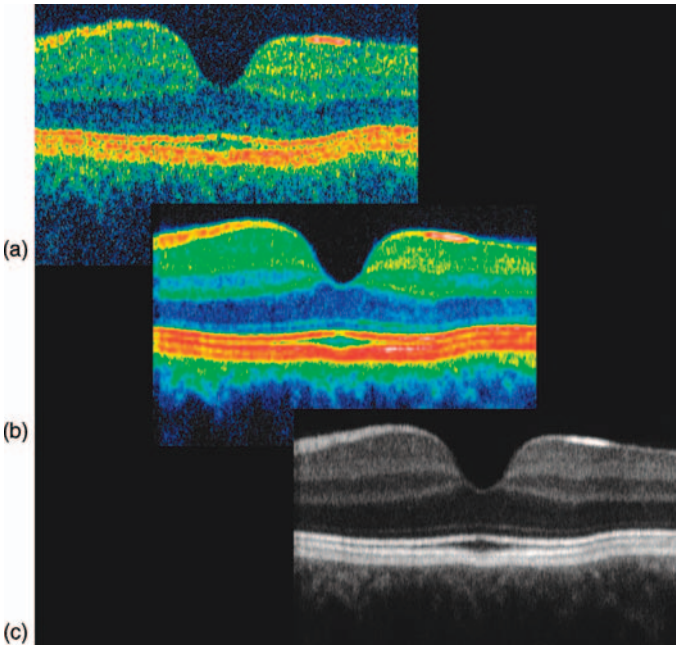

Figure 37.26 Time-domain optical coherence tomography single scan (a) and after summation and averaging of 12 scans, shown in false-color code (b) and in gray-scale reflection intensity (c).

neuropathy, uveitis, optic neuritis, and other diseases with an apparent focus of injury away from the optic disk. The concomitant loss of nerve fibers and the supporting stroma on the disk is one of several indications that the focus of injury is on the disk, another being the occasional observation of hemorrhages among the nerve fibers on the disk. Other conditions are characterized, to variable extents, by stationary nerve fiber deficits, for example, optic nerve hypoplasia. There is no loss or deficit of nerve fibers on the disk, however, without a deficit of retinal ganglion cells in the retina. When ophthalmoscopy and conventional fundus photography were the only means of retinal imaging, however, there was no method of assessing ganglion cell loss in the retina. This has now changed and noninvasive optical methods for nerve fiber and ganglion cell assessment are becoming a diagnostic mainstay in optic nerve disease.

Ophthalmoscopic examination of the optic disk, especially when stereoscopic, provides an impression of the surface contour of the disk, the fullness and vascularization of its nerve fiber rim, and the occasional splinter hemorrhage. Inspection of the peripapillary area gives a view of the delicate, silky gray bundles of nerve fibers as they arch toward the disk. Nerve fiber defects in patients with glaucoma and other optic neuropathies can be immediately obvious to the trained clinician. In these cases, objective methods of nerve fiber mapping are relevant only as a secondary means of measuring disease progression, the primary one being visual

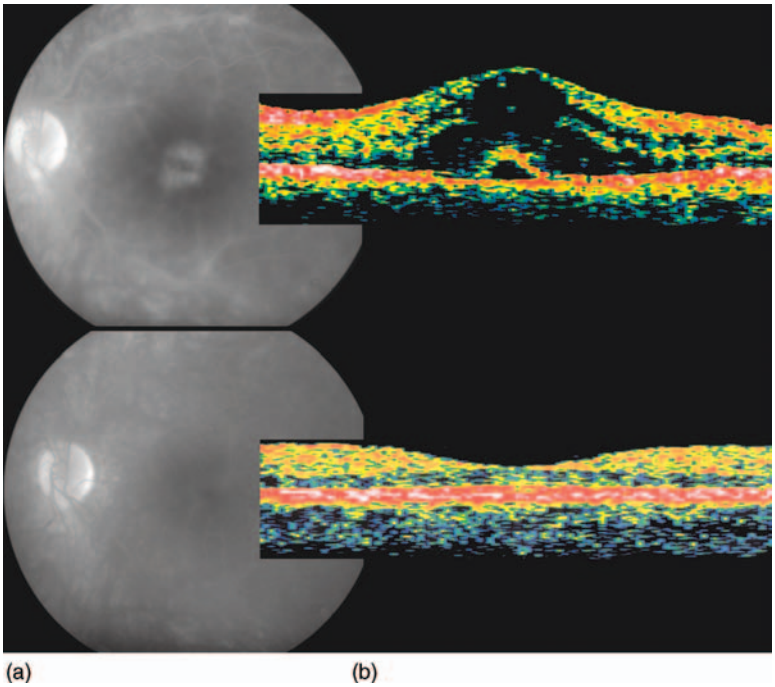

Figure 37.27 Fundus fluorescein angiography (a) and transfoveal optical coherence tomography (b) (first-generation technology) during an attack of retinal vasculitis with exudation and accumulation of fluid in the fovea (above) and after treatment with systemic glucocorticosteroid with subsequent resolution of the edema and normalization of the foveal contour (below). The case illustrates the ability of OCT, a noninvasive method, to replace fluorescein angiography, an invasive method based on intravenous injection of a synthetic dye.

field assessment by computerized perimetry. Objective optical methods have the advantage, in principle, of allowing structural mapping independently of confounding factors such as inability to cooperate with computerized perimetry, a change in optical media quality as a result of cataract surgery, and, to some extent, poor optical quality of the refractive media of the eye.

The rational use of objective biometric measurement in clinical practice requires a base of evidence from normative studies and, preferably, from prospective studies to show that the instrument can help provide a better functional outcome for patients over time. New diagnostic medical equipment is generally authorized for sale with minimal documentation of its diagnostic utility, physicians being expected to know what to do with it based on their biomedical insight. This is good for innovation but leaves many questions about an instrument's practical use unanswered, and years may pass before the necessary research has been completed. Glaucoma diagnostics has been supplemented with a succession of optical instruments that are described in the following.

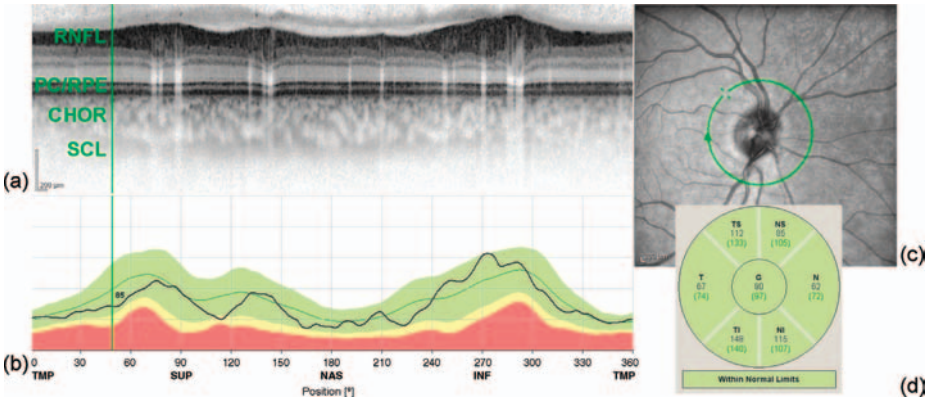

Figure 37.28 Spectral domain optical coherence tomography scan around the optic nerve head (optic disk) (c) in the right eye of a healthy subject (c). The unfolded scan (a) shows the variation in retinal layer thickness, with shadows cast by the major blood vessels. By convention, the scan is shown at a height:width aspect ratio of 2:1. Computerized segmentation of the retinal nerve fiber layer (RNFL) is overlaid on a reference curve collected in a population of healthy subjects. PC/RPE, photoreceptor/retinal pigment epithelium layer; CHOR, choroid; SCL, sclera.

Scanning laser ophthalmoscopy is an imaging technique that mimics essential features of conventional fundus photography but has better spatial selectivity for the plane of interest in the fundus. Because it picks up information only from a small volume in three-dimensional space at any given time and then reconstructs an image from a three-dimensional scanning array of such points, scatter and fluorescence from the anterior segment of the eye is very effectively rejected. Built on the flying-spot scanner principle, it only illuminates a spot with a diameter of a few micrometers at the fundus and then sweeps the spot across the horizontal and vertical directions of an image plane inside the eye it either accepts all reflected light from the fundus at all times or only from a small spot that is confocal with the illumination spot. The confocal method rejects reflected or fluorescent light outside the small sampling volume. By scanning the image plane along the optical axis of the eye, images from various depths can be obtained, provided that there is a transparent optical medium in front of it. Because the neurosensory retina is transparent, sectional images from various depths can be reconstructed, providing information about reflection, back-scatter, and fluorescence.

Additional techniques for objective characterization of optic nerve disease include three-dimensional contour mapping of the disk using confocal scanning laser ophthalmoscopy and assessment of nerve fiber layer thickness by measurement of the optical anisotropy induced by the birefringence of the nerve fibers and their uniform direction. For all technologies, follow-up studies are more informative than single examinations. Normative studies generally lag years to decades behind the marketing of new instruments, meaning that the evidence base for rational application in clinical practice is often weak when the product is launched.

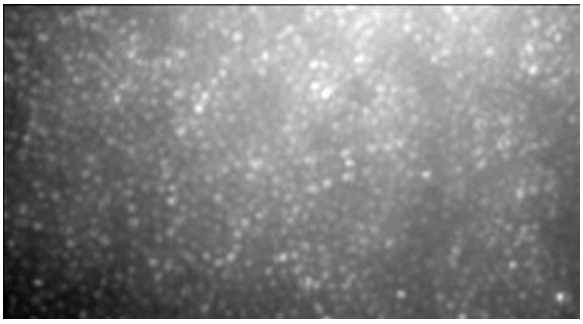

Figure 37.29 Adaptive optics fundus photography of a section of the fundus 2° superior of the fovea showing a normal cone photoreceptor matrix. Faint shadows are cast by the blood vessels anterior of the photoreceptors. The photoreceptors vary in brightness depending on their spectral absorption characteristics and the color of the illumination.

37.10
Adaptive Optics Fundus Photography

Lateral and axial resolution in fundus photography are limited by the optical quality of the anterior segment of the eye. In practice, there are higher orders of aberrations than spherical errors and astigmatism. By focusing on a small area of the fundus and using wavefront analysis to interactively control the properties of a multipoint-deformable mirror, these aberrations can be overcome and sufficient resolution can be achieved to image single photoreceptors [6, 7] (Figure 37.29).

37.11
Refractive Surgery

The prerequisite for correction of refractive errors, be it with spectacles, contact lenses, or refractive surgery, is a precise preoperative characterization of the refractive properties of the eye [8]. The common clinical refractioning procedure consists of a simple titration with spherical and cylindrical trial lenses using tests of foveal angular resolution for high-contrast, single-symbol optotypes (letters, numbers, simple objects). These techniques require no information about how the refractive components of the eye combine to yield the actual refraction of the individual eye, except that contact lenses must fit the surface contour of the eye (Figure 37.30). To achieve this a keratometric measurement of corneal radii of curvature is made, based on the specular reflex of the tear film (Figure 37.31). Subsequently, the actual fit of a selected contact lens can be tested on the eye (Figure 37.32).

Refractive surgery requires additional information because one of the components of the eye is going to be altered and the effect of, say, flattening the corneal

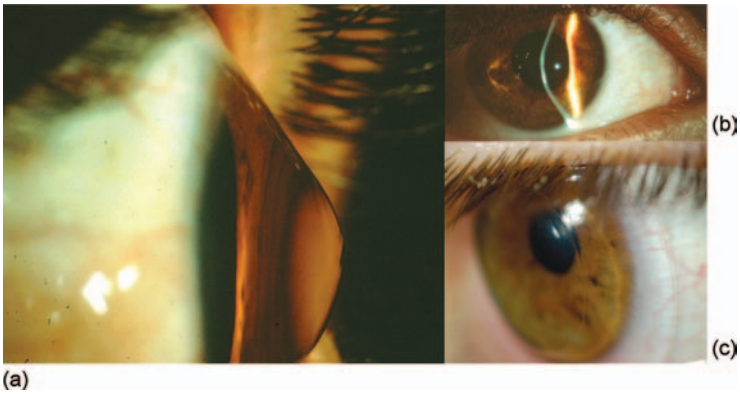

Figure 37.30 Irregular corneal contour in an eye with keratoconus, a condition of progressive attenuation of the corneal stroma where the degree of thinning increases with the distance from the limbus corneae (the transition between the sclera and the cornea) (a). The side view of a slit-beam transecting a section of the cornea (b) can be computer analyzed and used to estimate corneal curvature. A contact lens (c) can be used to bridge the irregularities of the corneal surface and substitute the role of the cornea by forming a regularly shaped interface with the atmosphere.

radius of curvature by 0.5 mm will depend on the axial length of the eye and other parameters of variable importance. The most common refractive surgery procedure is cataract surgery with implantation of an artificial intraocular lens [9]. The two most important parameters used to calculate the power of an implant lens that will produce a desired postoperative refraction is the corneal curvature and the axial length of the eye. The latter is defined as the distance from the apex of the cornea to

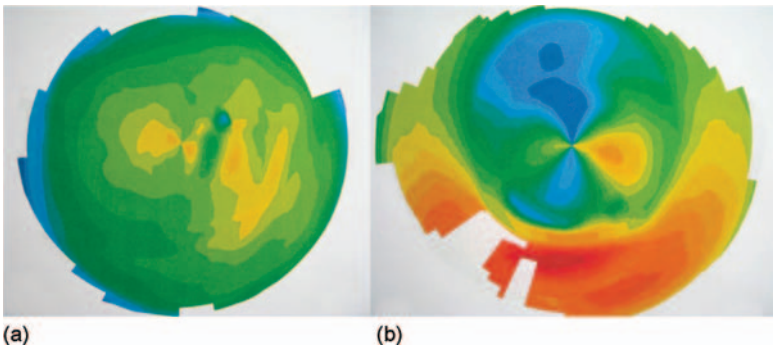

Figure 37.31 Corneal topography maps in color code indicating the local radius of curvature. A healthy eye with normal visual acuity (a) shows little irregularity whereas a cornea that underwent unsuccessful refractive surgery (b) has a highly irregular surface contour.

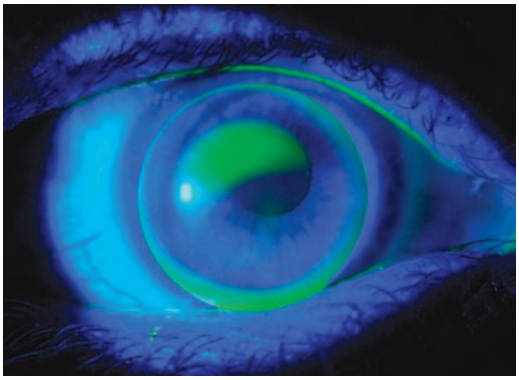

Figure 37.32 The fit between a hard contact lens and the surface of the cornea can be tested after the tear film has been stained using fluorescein. In this patient with keratoconus, the contour is irregular, causing accumulation of fluid in a crescent-shaped pocket under the contact lens right above the apex of the cornea.

the photoreceptor layer of the retina. The techniques for corneal topography can be divided into those that analyze the image formed by the specular reflex of the cornea, for instance the image of a series of concentric rings, and those techniques that observe the corneal contour from the side while a selected section the cornea is intensely illuminated by a slit-beam (Figure 37.30). The Scheimpflug projection (Figure 37.33) is ideal for the latter and is employed in a range of topography instruments.

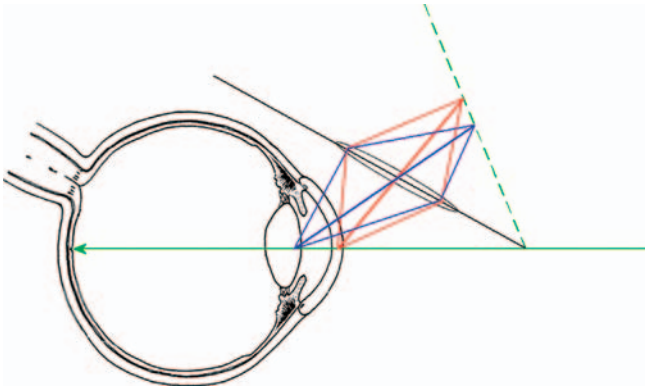

Figure 37.33 Principle of Scheimpflug projection enabling the full depth of an optical section of the anterior segment of the eye (green arrow representing incoming slit-beam of illuminating light) to be in focus on an image sensor placed at the plane indicated by the dashed green line. The lens placed across the black line is projecting the image of the cornea and the lens on the image sensor.

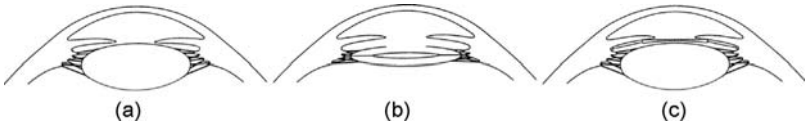

Figure 37.34 Schematic diagram of the normal eye (a), an eye with an implant lens in the bag created out of the lens capsule (b), and a posterior chamber phakic implant lens for high myopia (phakic meaning that the natural lens or phakos remains intact) (c). Lenses made out of polymers with high refractive indices achieve the necessary refractive power with much less substance than the natural lens. in daylight the pupil is rarely dilated beyond the diameter of the optical part of the implant lens. Implant lens dimensions are kept small to avoid having to make large incisions for implantation.

37.12
Intraocular Lens Implantation

Implantation of an intraocular lens in the capsular bag that remains after removal of the contents of the lens through a circular opening of its anterior surface is the standard solution for optical rehabilitation after cataract surgery (Figure 37.34) [10, 11]. The refractive power of the lens to be implanted is calculated based on preoperative measurements of corneal surface radii of curvature and axial length. The latter was previously made using ultrasonography but optical coherence line scanning has better precision and is now the standard of care.

Bifocal (multifocal) implant lenses are available in various designs made to compensate for the presbyopia that follows from the rigidity of implant lenses. All of these lenses sacrifice contrast for depth of focus [12]. Patient satisfaction is highly variable and dependent upon subjective preferences. An alternative solution to presbyopia is to make one eye emmetropic (focused at infinity) while the other eye is optimized for reading (focused at 33 cm). This again is a compromise, now of binocular vision, and again there are patients who are perfectly pleased with this solution whereas others are deeply dissatisfied. This compromise, called monovision, can be tested in a reversible manner using contact lenses.

37.13
Photoablation

Excited dimer or excimer lasers can produce powerful pulses of ultraviolet radiation that disrupt the molecules in a thin surface layer of biological material, thus spending the energy without heating the nonablated substance [13, 14]. Excimer lasers used in ophthalmology include argon fluoride (ArF) lasers operating at 193 nm. Typical pulse durations are 10 ns and repetition rates are from 100 Hz and higher. Because of the short wavelength, mirrors rather than lenses are used to control the beam. Various delivery systems have been designed, beginning with simple circular apertures with a controllable diameter to smaller moving spots. Ablation patterns have developed

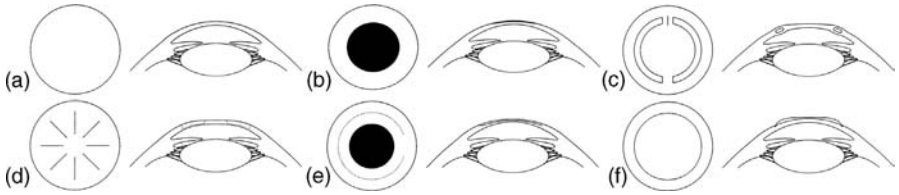

Figure 37.35 Types of refractive cornea surgery: (a) normal anatomy; (b) apical photoablation; (c) intracorneal stromal ring implant; (d) radial keratotomy (2/3 incision to relax pericentral cornea); (e) intrastromal ablation after creation of a corneal flap that is folded away during ablation (LASIK); (f) epikeratophakia (sutured corneal transplant shaped from donor tissue that is eventually covered by the recipient's corneal epithelium).

from one of simple correction for spherical errors to custom ablation in complex patterns calculated on the basis of a preoperative wavefront analysis that includes higher orders of aberration (Figure 37.35) [15].

37.14 Thermal Keratoplasty

Holmium lasers emit at 2.08 μm, a wavelength that is very effectively absorbed in water. Holmium laser radiation has been used experimentally to induce thermal shrinkage of corneal collagen in a limbus-concentric zone at a distance from the limbus. When successful, the treatment produces a steeper curvature of the apical prepupillary cornea. This effect can help correct hypermetropia (far-sightedness). Holmium lasers have also been used to create an artificial passage from the anterior chamber through the sclera at or near the anterior chamber, through the sclera to an opening under the conjunctiva. The aqueous is supposed to seep out at a rate that allows a reduction of the intraocular pressure without inducing hypotony (too low a pressure, for practical purposes below 5 mmHg). The radiation is delivered through a 0.5 mm diameter fiber-optic probe inserted through a surgical opening in the cornea. The probe is advanced toward the angle opposite the point of entry. The pulse energy is 60–150 mJ and the repetition rate 5 Hz. Energy levels of 1.35–6.6 J are sufficient to produce full-thickness tunnels through the sclera. All such types of filtration surgery, which ever way the opening is made, suffer from the consequences of the tissue reaction to the surgical injury. Consequently, long-term success depends not only on the surgical procedure but also very much on postoperative care and pharmaceutical modulation of the healing and scarring processes.

37.15 Blood Flow Measurement

The rates of blood flow through the retina and the choroid are of fundamental interest for the study of the eye. Noninvasive flowmetry in the eye is problematic.

Ultrasonography is very useful in other organs, but in relation to the eye only the vessels on the outside of the sclera in the posterior pole are sufficiently large to permit measurements that are reproducible and reliable. Optical methods include laser speckle flowmetry, which shows movement of particulate matter through the vessels of the fundus but fails to identify direction, volume, or sum in a manner that can be converted to volumetric or linear flow rates. Laser Doppler velocimetry has been studied in great detail and its virtues and limitations are well characterized. A laser pointed at a selected major retinal vessel and a detector that measures the frequency shift of the light reflected by erythrocytes and leukocytes in motion allow determination of peak velocity. According to Poiseuille, volumetric flow can be estimated if the vessel diameter is also known and if the fluid follows the characteristics of isotropic fluids. Laser Doppler flowmetry has found no application outside experimental physiology.

Stroboscopic subtraction imaging of retinal blood flow is a recent invention. By firing apid sequences of flashes and recording a sequence of fundus images without the eye having moved significantly, frame-by-frame subtraction can yield an image in which the faint trace of formed elements of the blood moving through the retinal capillaries stand out against an empty background. The method permits measurement of retinal capillary blood flow is a manner that is comparable to the blue-field entoptic technique a technique, that relies on the patients themselves to observe the rate of flow and compare it with a simulated reference shown to their fellow eye on a video screen.

37.16 Perspectives

Ophthalmic biophotonics is under constant development and several experimental techniques are expected to mature within the next decade, including femtosecond laser treatment of the lens [16], adaptive optics imaging of the fundus, and multimodal imaging and spectral analysis of the various tissues of the eye. The application of sophisticated optical devices outside university hospitals and specialized clinics will be spurred by increasing compactness and affordability.

References

1 Westheimer, G. (2009) Visual acuity: information theory, retinal image structure and resolution thresholds. *Prog. Retin. Eye Res.*, **28** (3), 178–186.

2 Cheung, N., Mitchell, P., and Wong, T.Y. (2010) Diabetic retinopathy. *Lancet*, **376** (9735), 124–136. Epub 2010 Jun 26.

3 Wong, T.Y. and Scott, I.U. (2010) Clinical practice. Retinal-vein occlusion. *N. Engl. J. Med.*, **363** (22), 2135–2144.

4 Buehl, W. and Findl, O. (2008) Effect of intraocular lens design on posterior capsule opacification. *J. Cataract Refract. Surg.*, **34** (11), 1976–1985.

5 Drexler, W. and Fujimoto, J.G. (2008) State-of-the-art retinal optical coherence

tomography. *Prog. Retin. Eye Res.*, **27** (1), 45–88.
6 Godara, P., Dubis, A.M., Roorda, A., Duncan, J.L., and Carroll, J., (2010) Adaptive optics retinal imaging: emerging clinical applications. *Optom. Vis. Sci.*, **87** (12), 930–941.
7 Lombardo, M. and Lombardo, G. (2009) New methods and techniques for sensing the wave aberrations of human eyes. *Clin. Exp. Optom.*, **92** (3), 176–186.
8 Ehlers, N., Hjortdal, J., and Nielsen, K. (2009) Corneal grafting and banking. *Dev. Ophthalmol.*, **43**, 1–14.
9 Gwiazda, J. (2009) Treatment options for myopia. *Optom. Vis. Sci.*, **86** (6), 624–628.
10 Norrby, S., Piers, P., Campbell, C., and van der Mooren, M. (2007) Model eyes for evaluation of intraocular lenses. *Appl. Opt.*, **46** (26), 6595–6605.
11 Olsen, T. (2007) Calculation of intraocular lens power: a review. *Acta Ophthalmol. Scand.*, **85** (5), 472–485.
12 Glasser, A., (2008) Restoration of accommodation: surgical options for correction of presbyopia. *Clin. Exp. Optom.*, **91** (3), 279–295.
13 Krueger, R.R., Rabinowitz, Y.S., and Binder, P.S. (2010) The 25th anniversary of excimer lasers in refractive surgery: historical review. *J. Refract. Surg.*, **26** (10), 749–760.
14 Krueger, R.R., Thornton, I.L., Xu, M., Bor, Z., and van den Berg, T.J. (2008) Rainbow glare as an optical side effect of IntraLASIK. *Ophthalmology*, **115** (7), 1187–1195.
15 Myrowitz, E.H. and Chuck, R.S. (2009) A comparison of wavefront-optimized and wavefront-guided ablations. *Curr. Opin. Ophthalmol.*, **20** (4), 247–250.
16 Binder, P.S. (2010) Femtosecond applications for anterior segment surgery. *Eye Contact Lens*, **36** (5), 282–285.

38
Glaucoma Diagnostics

Marc Töteberg-Harms, Cornelia Hirn, and Jens Funk

38.1
Introduction

Glaucoma is a widespread disease leading to progressive loss of visual function. It is still one of the leading causes of blindness around the world [1, 2] and the number one reason for blindness in industrialized countries [3–5]. Worldwide there are more cases of primary open angle glaucoma than of angle closure glaucoma [3]. Glaucoma is a chronic and progressive neurodegenerative disorder causing loss of retinal ganglion cells and their axons [6]. Characteristically, cupping of the optic disc is seen with a possible loss of visual field. In most cases, the intraocular pressure (IOP) is elevated above the normal [7] range.

IOP is the major risk factor for glaucoma. In addition, some other risk factors are well known, for example, age, family history, and race (e.g., African or Caucasian descent) [8].

Aqueous humor is formed by the ciliary processes [9–14] and drained mainly through the trabecular meshwork into Schlemm's canal [15]. Schlemm's canal communicates with the episcleral veins. This is called the trabecular outflow (83–96% of the aqueous humor outflow) [16–19]. In addition, 5–15% of the aqueous humor is drained via the uveoscleral pathway [17–23]. Usually an increased drain resistance is the reason for elevated IOP [17–25], whereas aqueous humor production is nearly constant [26–28]. The main location of outflow resistance could probably be found in the juxtacanalicular tissue of the trabecular meshwork [29, 30].

In managing glaucoma patients, lowering the IOP is the only treatment, with excellent quality of evidence [31–36]. Medical reduction of IOP is the first-line therapy in most cases [31, 37, 38]. If medical treatment fails, there are several well-established surgical procedures to reduce IOP.

Trabeculectomy (TE) as it is performed today was introduced in 1968 by Cairns [39], and it is still the gold standard in glaucoma surgery. The aqueous flows via a scleral flap from the anterior chamber into the subconjunctival space [40]. TE is very effective in lowering the IOP for long periods [41, 42]. The use of antimetabolites during

Handbook of Biophotonics. Vol.2: Photonics for Health Care, First Edition. Edited by Jürgen Popp, Valery V. Tuchin, Arthur Chiou, and Stefan Heinemann.

Figure 38.1 Typical OCT test setting with patient and examiner.

surgery provides even better long-term IOP control [43–49]. Other surgical procedures include laser surgery of the trabecular meshwork {argon laser trabeculoplasty (ALT) [50–57] and selective laser trabeculoplasty [50, 51, 54, 58–65]} and cyclophotocoagulation (CPC) [66–73] for the ciliary body or shunt implants (e.g., Molteno [74–76], Ahmed [77, 78], and Baerveldt tube [79, 80]).

Managing the glaucoma patient over time by measuring the IOP and testing the visual field is very important. By the time the breakdown of retinal ganglion cells is clinically detected, extended and irreversible damage has already occurred [81, 82]. Since effective therapy can slow the progress of glaucoma, early diagnosis of worsening is one of the main goals in treatment of this disease. It is strongly believed that the thinning of the retinal nerve fiber layer (RNFL) correlates highly with or even precedes visual field loss in glaucoma [83–89]. Well established in detecting early RNFL thinning are optical coherence tomography (OCT) (Figure 38.1), scanning laser ophthalmoscopy with the Heidelberg retina tomograph (HRT) (Heidelberg Engineering, Heidelberg, Germany), and laser scanning polarimetry (GDx) (Carl Zeiss Meditec, Oberkochen, Germany).

38.2 Optical Coherence Tomography

Using OCT, Huang *et al.* were the first to present a noncontact, noninvasive method of using low-coherence interferometry to determine the echo time delay and magnitude of backscattered light reflected off different layers of a structured tissue sample [90]. The unique optic free pathway through the eye made OCT highly applicable to the visualization of retina layers. In 1995, time domain optical coherence tomography (TD-OCT) was introduced as an imaging technique for glaucoma diagnosis [87]. In spectral domain optical coherence tomography (SD-OCT) (or Fourier domain OCT), a moving reference mirror as used in TD-OCT is

no longer needed. SD-OCT provides higher resolution at faster scanning speeds [91, 92].

In TD-OCT, a prism splits an 820 nm infrared light source into two beams. One spreads through the layers of the eye while a reference beam is deflected to a moving reference mirror. For every measurement point detected along an axial depth scan (A-scan), the moving reference mirror has to be readjusted. If the reference mirror is positioned at virtually the same distance from the light source as the backscattering tissue, the reunited light beams will interfere and be detected by an interferometer. Processing multiple A-scans along a scanning line (B-scan) allows for the visualization of retinal layers. TD-OCT provides axial resolutions of up to 10 μm [87, 90, 93, 94].

A major revolution in OCT imaging was the introduction SD-OCT. Instead of time delay as used in TD-OCT, SD-OCT applies Fourier analysis to light wavelengths to determine the spatial location of reflected light [92, 95]. The first ophthalmic SD-OCT *in vivo* scans were introduced by Wojtkowski *et al.* in 2002 [91]. With SD-OCT, all axial data information along one A-scan can be gathered within a single scan. In 2006, the first high-speed, high-resolution OCTs became commercially available. Today, the latest generation of SD-OCT devices provide resolutions that are five times higher and scanning speeds 100 times faster compared to TD-OCT [95, 96]. Owing to the faster scanning speed, more data (A-scans) can be acquired in a given time, allowing SD-OCT devices to generate 3D reconstructions of retina areas [97].

Another development available in recent OCT devices is the implementation of specific algorithms and software to enhance the scanning resolution further and decrease motion artifacts. In 2006, the Spectralis SD-OCT system (Heidelberg Engineering, Heidelberg, Germany) was introduced for retinal imaging. This instrument features two different options to enhance reproducibility. An online eye tracking device (eye tracker) compensates for involuntary eye movements during the scanning process, and a retest function assures that follow-up measurements are taken from the same area of the retina as the baseline examination. The Heidelberg Spectralis is the only commercially available SD-OCT system with an eye tracking function. Both options can be switched off separately. To measure the RNFL circle, scans could be performed around the optic disc with a scanning angle of 12°, which equates to a retinal diameter of 3.5 mm when assuming a standard corneal curvature of 7.7 mm. The SD-OCT Super uses a luminescent diode with a center wavelength of 840 mm. The Spectralis SD-OCT obtains up to 40 000 A-scans per second with a depth resolution of 7 μm in tissue. Transversal resolution depends on the tightness of the A-scans and is up to 5 μm.

With a dual beam, a corresponding scanning laser ophthalmoscope (SLO) fundus image can be captured at the same time as the OCT measurement, enabling the system to link every OCT scan (Figure 38.2a) to its corresponding position on the SLO fundus image (Figure 38.2b). Processing of SLO data and identification of specific patterns in retinal structures such as blood vessels allow scans to be marked as a reference and baseline. In follow-up examinations, the system recognizes the former scanning area on the retina and automatically positions the retest scan on the same location. During the measurement, online eye tracking provides a

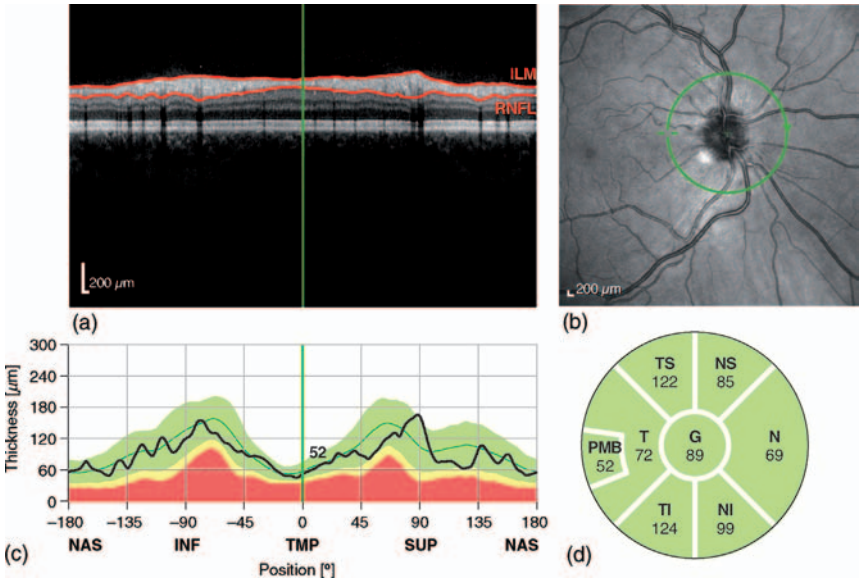

Figure 38.2 Circular peripapillary optical coherence tomogram of a normal right eye (a) with its corresponding fundus image (b) obtained with the dual-beam scanning laser ophthalmoscope. Red lines in the OCT B-scan (a) indicate the inner and outer border of the RNFL found by the algorithm. In (c), measured RNFL thickness is plotted on the thickness values measured in healthy subjects of the same age. The mean RNFL thickness of sectors, the peripapillary bundle, and the global mean RNFL thickness are shown in (d).

real-time adjustment of the OCT scanner on the simultaneously gathered SLO image in order to decrease motion artifacts, and the high scanning speed reduces the time for distracting eye movements to occur. To increase image quality, the Spectralis SD-OCT includes an ART (automatic real time) function. With ART activated, multiple frames (B-scans) are gathered during the scanning process and images are averaged for noise reduction [98, 99]. The number of frames can be adjusted from one to 100.

The SD-OCT devices provide an algorithm to determine the inner and outer borders of the RNFL (Figure 38.2a). OCT data were analyzed by this algorithm to detect the RNFL thickness along the circular scan in micrometers. The median thickness was plotted on a pie chart diagram representing different sectors of the optic disc (Figure 38.2d). The calculated thickness profile (Figure 38.2c) refers to a set of normative RNFL thickness data in healthy subjects [100]. Green areas represent the 95% normal range found in healthy subjects of the same age whereas values outside the 99% confidence interval of the normal distribution ($0.01 < p < 0.05$) are indicated in red. Yellow areas represent values outside the 95% confidence interval but within the 99% confidence interval of the normal distribution. Figure 38.3 shows a typical printout of an OCT RFNL scan of a glaucoma patient.

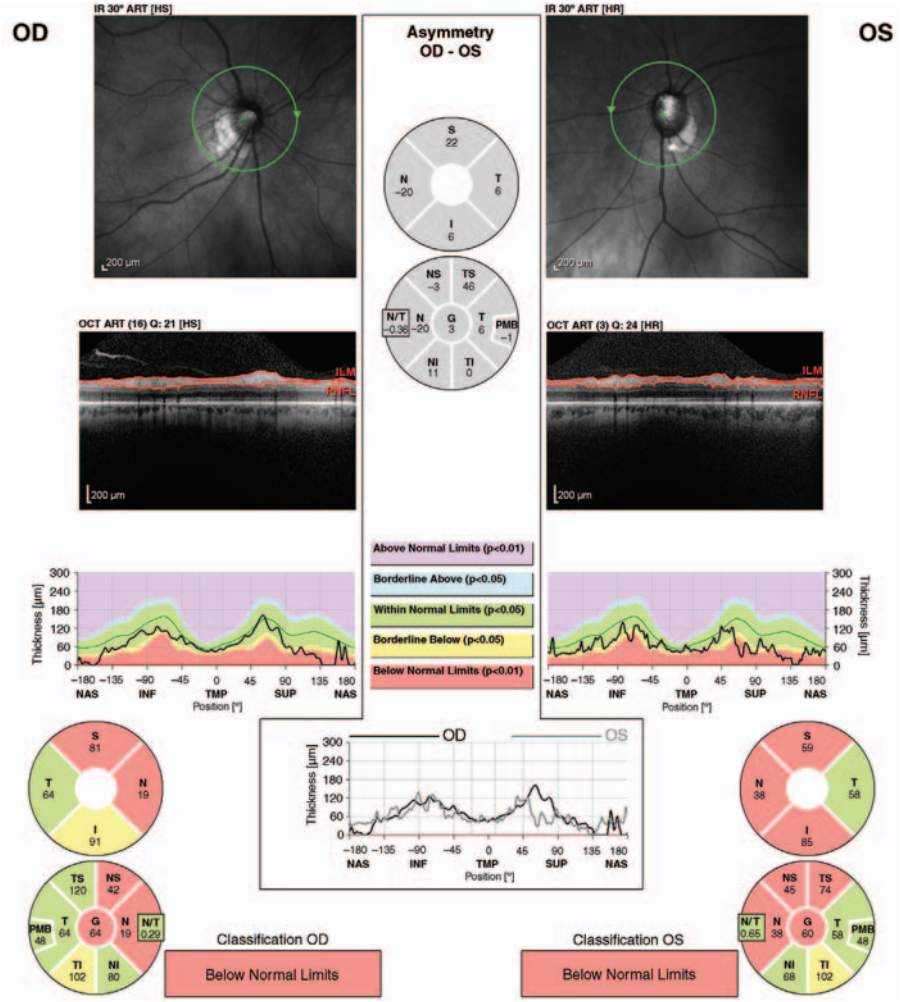

Figure 38.3 Typical printout of OCT RFNL scan of a glaucoma patient.

38.3
Scanning Laser Tomography – Heidelberg Retina Tomography

The aim of optic nerve head (ONH) imaging is to assist in the classification of normal and glaucomatous optic discs on the one hand and to detect glaucoma progression on the other.

The latest version of the HRT system (HRT3) is a confocal scanning laser system for acquisition and analysis of three-dimensional images of the ONH and RNFL.

It allows quantitative assessment of the topography of the ONH and also the follow-up of topographic changes.

Pupil dilation is not required for the examination.

A diode laser with a wavelength of 670 nm is focused and deflected periodically for point-by-point two-dimensional scanning of the posterior pole perpendicular to the optical axis. The intensity of the light reflected from the object is detected separately from the incident laser beam. In confocal scanning laser systems, a diaphragm with a pinhole is placed before the detector. Only light reflected from the focal plane is focused on the pinhole, passes the diaphragm, and is detected; reflections from layers above or below the focal plane are suppressed. This technique is called scanning laser tomography.

The location of the light-reflecting surface allows the determination of the height of the scanned structure. HRT permits image acquisition at different depth locations, providing a series of optical section images forming a layer-by-layer three-dimensional image of the ONH and the peripapillary RNFL. The size of the field of view is set at $15^\circ \times 15^\circ$; the images are digitized in frames of 384×384 pixels. The distance between the focal planes is set at 62.5 μm.

Sets of three images are acquired in one measurement. By translating each specific height location into a specific color, a color-coded mean topography image in addition to a mean reflectance image is computed.

For stereometric measurements and analysis of the ONH, a contour line has to be drawn around the disc margin by the operator; the structure enclosed is analyzed three-dimensionally. Based on the contour line, a reference plane is automatically defined. This reference plane is set parallel to the peripapillary retinal surface and is located 50 μm posterior to the retinal surface of the papillomacular bundle. All structures located below the reference plane are considered to be cup, and all structures located above the reference plane and within the contour line are considered to be rim.

The result of the analysis is a set of stereometric parameters, which are printed in a table and shown in color-coded images and graphs. The most important are disc area, cup and rim area, cup and rim volume, cup to disc ratio, mean and maximum cup depth, and thickness of the RNFL along the contour line. The only parameters independent of the reference plane are the three-dimensional cup shape measure and the height variation of the contour.

Moorfields regression analysis (MRA) is a tool to determine normal or glaucomatous discs by a regression analysis between disc size and rim area [101]. The results of the MRA are superimposed on the reflectance image with a subdivision into six sectors, each marked according to the classification as normal, borderline, or outside normal limits, with red crosses for outside normal, yellow exclamation marks for borderline, and green ticks for within normal limits.

Additional graphs are horizontal and vertical cross-sections of the topography image with a marked line for the reference plane and the optic disc margin, a graph of the height variation of the RNFL following the contour line, representing the RNFL thickness at the disc margin, and the results of the MRA displayed as seven bars – one for each of the six sectors of the ONH and a seventh for the overall optic disc assessment.

When interpreting the results of an HRT examination, classification as normal or glaucomatous based on individual stereometric parameters is rather difficult.

So far, the major drawback in interpretation of the results is that the stereometric parameters are dependent on the reference plane. In addition to an inter-observer variability of the drawing of the contour line [102, 103], a high physiological variation of ONH stereometric parameters adds to changes in the height of the RNFL during the course of the disease and also a physiological reduction in RNFL thickness with age [104]. Therefore, the reference plane is moving posteriorly, leading to underestimation of the cupping and possible progression [105].

Additionally, the IOP has a direct influence on cup volume, cup depth, rim area, and cup to disc area ratio [106, 107].

The coefficients of variation for area and volume parameters are 2–6 and 6–14%, respectively [102, 108].

To improve the diagnostic power, in HRT3 the normative database has been expanded and now offers 215 healthy African-American eyes and 733 healthy eyes of white individuals, and a further database of ~100 Indian (south Asian) eyes is available.

A new tool is the OU report, which compares the subject's stereometric parameters against the normative database and which features an image quality assessment for both eyes, based on the mean pixel height standard deviation, scaled from excellent to very poor quality, with acceptable image quality with standard deviation (SD) less than 35 μm, and good quality images categorized as images with SD less than 25 μm.

A second new tool is the glaucoma probability score (GPS), which aims to discriminate between normal and glaucomatous eyes using a mathematical model of ONH shape [109]. Included in the analysis are horizontal and vertical curvature of the peripapillary retina, cup depth, cup width, and cup wall slope. The advantage of this analysis is that it is independent of the contour line and the reference plane position and therefore not operator dependent.

A graphical representation is used similar to the MRA, with red crosses for outside normal, yellow exclamation marks for borderline, and green ticks for within normal limits.

The GPS shows a sensitivity and specificity of 77.1 and 90.3%, compared with 71.4 and 91.9% for MRA [110].

Data indicate that an abnormal MRA classification is more useful to confirm that a disc is glaucomatous, and MRA better discriminates in more severe glaucoma, whereas a within normal limits GPS classification is more likely to confirm that a disc is normal [111].

Although the MRA is based on the relation between disc size and rim area, the diagnostic precision seems to be reduced in large discs [112, 113].

For progression analysis, there are currently two algorithms: trend analysis examines the change of stereometric parameters over time, and topographic change analysis (TCA) estimates the probability that a change in surface height between baseline and follow up occurred by chance alone [114]. The change probability map combines clusters of 4×4 adjacent height measurements or pixels to give so-called superpixels. The variability of baseline measurements is compared with the

combined variability of the baseline and follow-up measurements. The resulting probability maps are displayed color-coded [107, 114, 115].

In summary, the HRT provides moderate discrimination between normal and glaucomatous ONH, but is promising when it comes to identifying and quantifying progression.

38.4 Scanning Laser Polarimetry – GDx

Thinning of the peripapillary RNFL has been shown to be one of the earlier signs of glaucomatous damage [81, 84, 116], and scanning laser polarimetry (SLP) is a technique developed to evaluate the peripapillary RNFL thickness.

SLP is based on the birefringence of the RNFL, which is due to the parallel alignment of the microtubuli in the nerve fibers. This birefringence induces a change in retardation of polarized light passing through the RNFL.

The GDx uses a diode laser with a wavelength of 780 nm; the scanning area is $15^\circ \times 15^\circ$. The retardation of the reflected laser light is detected with a scanning raster of 256×256 pixels. Pupil dilation is not necessary. Based on experimental conversion factors, the RNFL thickness is estimated [117, 118].

In addition to RNFL, in the anterior segment the cornea and the lens also are birefringent and affect the measurement. To compensate for this effect, a variable corneal compensation (VCC) was developed. In the GDx VCC, initially a macular scan is performed. As there are no retinal nerve fibers in the fovea centralis, all changes in retardation should be due to corneal birefringence. Hence the polarization axis and magnitude of the cornea can be calculated [119]. For subsequent scans of the peripapillary RNFL, those values are applied for correction of the measurement.

For the analysis of the scans, after marking of the ONH margin, a ring (the so-called ellipse) is placed around the optic disc with a diameter of 1.75 mm. Along that ring, the modulation and thickness of the RNFL are calculated. On the printout, there are an ONH image and a color-coded RNFL thickness map and also a deviation map and the TSNIT graph. The TSNIT graph shows the peripapillary height modulation of the RNFL.

Additionally, a number of modulation and thickness parameters are presented, and also a global parameter called the nerve fiber indicator (NFI), which is a support-vector machine-derived parameter for discrimination between healthy and glaucomatous eyes [120, 121]. The coefficient of variation for the GDx VCC is 3–6%.

One drawback with the VCC technique is that corneal compensation is dependent on an intact fovea. In patients with macular diseases, VCC can be severely hindered. In patients with peripapillary atrophy, the ellipse has to be enlarged to spare the areas of atrophy to avoid artifacts.

Typical retardation patterns display larger amounts of retardation superior and inferior to the optic disc, and decreasing amounts of retardation with increasing distance from the optic disc.

Atypical patterns occur in ~10–25% of healthy and 15–51% of glaucomatous eyes [121–124]. They seem to be more frequent in patients with high myopia and lightly pigmented fundi. Therefore, a new method was introduced a few years ago: enhanced corneal compensation (ECC). With this method, the signal-to-noise ratio is improved in cases of atypical retardation patterns.

In contrast to VCC, where the measurement was adjusted to neutralize the corneal birefringence, in ECC an additional amount of birefringence is added to the measurements, thus shifting the measurement into a more sensitive detection range [125, 126]. Hence images showing atypical retardation patterns are reduced compared with the VCC technique at similar levels of reproducibility [127]. The ability to discriminate between healthy and glaucomatous eyes seems to be improved in ECC [124].

Progression analysis is shown in a serial printout with differences between measurements flagged based on arbitrarily chosen cut-off marks.

References

1 Thylefors, B., *et al.* (1995) Global data on blindness. *Bull. World Health Organ.*, **73** (1), 115–121.
2 Resnikoff, S.,*et al.* (2004) Global data on visual impairment in the year 2002. *Bull. World Health Organ.*, **82**, 844–851.
3 Quigley, H.A. and Broman, A.T. (2006) The number of people with glaucoma worldwide in 2010 and 2020. *Br. J. Ophthalmol.*, **90** (3), 262–267.
4 Quigley, H.A. (1996) Number of people with glaucoma worldwide. *Br. J. Ophthalmol.*, **80** (5), 389–393.
5 Thylefors, B. and Negrel, A.D. (1994) The global impact of glaucoma. *Bull. World Health Organ.*, **72** (3), 323–326.
6 Quigley, H.A.,*et al.* (1981) Optic nerve damage in human glaucoma. II. The site of injury and susceptibility to damage. *Arch. Ophthalmol.*, **99** (4), 635–649.
7 Cellini, M.,*et al.* (2008) Matrix metalloproteinases and their tissue inhibitors after selective laser trabeculoplasty in pseudoexfoliative secondary glaucoma. *BMC Ophthalmol.*, **8**, 20.
8 Boland, M.V. and Quigley, H.A. (2007) Risk factors and open-angle glaucoma: classification and application. *J. Glaucoma*, **16** (4), 406–418.
9 Green, K. and Pederson, J.E. (1972) Contribution of secretion and filtration to aqueous humor formation. *Am. J. Physiol.*, **222** (5), 1218–1226.
10 Weinbaum, S.,*et al.* (1972) The role of secretion and pressure-dependent flow in aqueous humor formation. *Exp. Eye Res.*, **13** (3), 266–277.
11 Green, K. and Pederson, J.E. (1973) Aqueous humor formation. *Exp. Eye Res.*, **16** (4), 273–286.
12 Pederson, J.E and Green, K. (1973) Aqueous humor dynamics: experimental studies. *Exp. Eye Res.*, **15** (3), 277–297.
13 Pederson, J.E. and Green, K. (1973) Aqueous humor dynamics: a mathematical approach to measurement of facility, pseudofacility, capillary pressure, active secretion and X c. *Exp. Eye Res.*, **15** (3), 265–276.
14 Bill, A. (1975) Blood circulation and fluid dynamics in the eye. *Physiol. Rev.*, **55** (3), 383–417.
15 Grant, W.M. (1963) Experimental aqueous perfusion in enucleated human eyes. *Arch. Ophthalmol.*, **69**, 783–801.
16 Toris, C.B.,*et al.* (2002) Aqueous humor dynamics in ocular hypertensive patients. *J. Glaucoma*, **11** (3), 253–258.
17 Toris, C.B.,*et al.* (1999) Aqueous humor dynamics in the aging human eye. *Am. J. Ophthalmol.*, **127** (4), 407–412.
18 Jocson, V.L. and Sears, M.L. (1971) Experimental aqueous perfusion in

enucleated human eyes. Results after obstruction of Schlemm's canal. *Arch. Ophthalmol.*, **86** (1), 65–71.
19 Bill, A. and Phillips, C.I. (1971) Uveoscleral drainage of aqueous humour in human eyes. *Exp. Eye Res.*, **12** (3), 275–281.
20 Inomata, H. and Bill, A. (1977) Exit sites of uveoscleral flow of aqueous humor in cynomolgus monkey eyes. *Exp. Eye Res.*, **25** (2), 113–118.
21 Sherman, S.H., Green, K., and Laties, A.M. (1978) The fate of anterior chamber fluorescein in the monkey eye. 1. The anterior chamber outflow pathways. *Exp. Eye Res.*, **27** (2), 159–173.
22 Townsend, D.J. and Brubaker, R.F. (1980) Immediate effect of epinephrine on aqueous formation in the normal human eye as measured by fluorophotometry. *Invest. Ophthalmol. Vis. Sci.*, **19** (3), 256–266.
23 Pederson, J.E., Gaasterland, D.E., and MacLellan, H.M. (1977) Uveoscleral aqueous outflow in the rhesus monkey: importance of uveal reabsorption. *Invest. Ophthalmol. Vis. Sci.*, **16** (11), 1008–1017.
24 Peterson, W.S., Jocson, V.L., and Sears, M.L. (1971) Resistance to aqueous outflow in the rhesus monkey eye. *Am. J. Ophthalmol.*, **72** (2), 445–451.
25 Grant, W.M. (1958) Further studies on facility of flow through the trabecular meshwork. *AMA Arch. Ophthalmol.*, **60** (4 Part 1), 523–533.
26 Becker, B. (1958) The decline in aqueous secretion and outflow facility with age. *Am. J. Ophthalmol.*, **46** (5 Part 1), 731–736.
27 Brubaker, R.F. (1991) Flow of aqueous humor in humans [The Friedenwald Lecture]. *Invest. Ophthalmol. Vis. Sci.*, **32** (13), 3145–3166.
28 Brubaker, R.F.,*et al.* (1981) The effect of age on aqueous humor formation in man. *Ophthalmology*, **88** (3), 283–288.
29 Bill, A. and Svedbergh, B. (1972) Scanning electron microscopic studies of the trabecular meshwork and the canal of Schlemm – an attempt to localize the main resistance to outflow of aqueous humor in man. *Acta Ophthalmol. (Copenh.)*, **50** (3), 295–320.
30 Maepea, O. and Bill, A. (1992) Pressures in the juxtacanalicular tissue and Schlemm's canal in monkeys. *Exp. Eye Res.*, **54** (6), 879–883.
31 Heijl, A.,*et al.* (2002) Reduction of intraocular pressure and glaucoma progression: results from the Early Manifest Glaucoma Trial. *Arch. Ophthalmol.*, **120** (10), 1268–1279.
32 Grant, W.M. and Burke, J.F. Jr. (1982) Why do some people go blind from glaucoma? *Ophthalmology*, **89** (9), 991–998.
33 Collaborative Normal-Tension Glaucoma Study Group (1998) The effectiveness of intraocular pressure reduction in the treatment of normal-tension glaucoma. *Am. J. Ophthalmol.*, **126** (4), 498–505.
34 Collaborative Normal-Tension Glaucoma Study Group (1998) Comparison of glaucomatous progression between untreated patients with normal-tension glaucoma and patients with therapeutically reduced intraocular pressures. *Am. J. Ophthalmol.*, **126** (4), 487–497.
35 The AGIS Investigators (2000) The Advanced Glaucoma Intervention Study (AGIS): 7. The relationship between control of intraocular pressure and visual field deterioration. *Am. J. Ophthalmol.*, **130** (4), 429–440.
36 Palmberg, P. (2001) Risk factors for glaucoma progression: where does intraocular pressure fit in? *Arch. Ophthalmol.*, **119** (6), 897–898.
37 Wilensky, J.T. (1999) The role of medical therapy in the rank order of glaucoma treatment. *Curr. Opin. Ophthalmol.*, **10** (2), 109–111.
38 Feiner, L. and Piltz-Seymour, J.R. (2003) Collaborative Initial Glaucoma Treatment Study: a summary of results to date. *Curr. Opin. Ophthalmol.*, **14** (2), 106–111.
39 Cairns, J.E. (1968) Trabeculectomy. Preliminary report of a new method. *Am. J. Ophthalmol.*, **66** (4), 673–679.
40 Spencer, W.H. (1972) Symposium: microsurgery of the outflow channels.

Histologic evaluation of microsurgical glaucoma techniques. *Trans. Am. Acad. Ophthalmol. Otolaryngol.*, **76** (2), 389–397.
41 Migdal, C., Gregory, W., and Hitchings, R. (1994) Long-term functional outcome after early surgery compared with laser and medicine in open-angle glaucoma. *Ophthalmology*, **101** (10), 1651–1656; discussion 1657.
42 Jay, J.L. and Allan, D. (1989) The benefit of early trabeculectomy versus conventional management in primary open angle glaucoma relative to severity of disease. *Eye (Lond.)*, **3** (Pt 5), 528–535.
43 Yoon, P.S. and Singh, K. (2004) Update on antifibrotic use in glaucoma surgery, including use in trabeculectomy and glaucoma drainage implants and combined cataract and glaucoma surgery. *Curr. Opin. Ophthalmol.*, **15** (2), 141–146.
44 WuDunn, D.,*et al.* (2002) A prospective randomized trial comparing intraoperative 5-fluorouracil vs mitomycin C in primary trabeculectomy. *Am. J. Ophthalmol.*, **134** (4), 521–528.
45 Khaw, P.T.,*et al.* (2001) Modulation of wound healing after glaucoma surgery. *Curr. Opin. Ophthalmol.*, **12** (2), 143–148.
46 Katz, G.J.,*et al.* (1995) Mitomycin C versus 5-fluorouracil in high-risk glaucoma filtering surgery. Extended follow-up. *Ophthalmology*, **102** (9), 1263–1269.
47 Towler, H.M.,*et al.* (2000) Long-term follow-up of trabeculectomy with intraoperative 5-fluorouracil for uveitis-related glaucoma. *Ophthalmology*, **107** (10), 1822–1828.
48 Suzuki, R.,*et al.* (2002) Long-term follow-up of initially successful trabeculectomy with 5-fluorouracil injections. *Ophthalmology*, **109** (10), 1921–1924.
49 Lama, P.J. and Fechtner, R.D. (2003) Antifibrotics and wound healing in glaucoma surgery. *Surv. Ophthalmol.*, **48** (3), 314–346.
50 Damji, K.F.,*et al.* (2006) Selective laser trabeculoplasty versus argon laser trabeculoplasty: results from a 1-year randomised clinical trial. *Br. J. Ophthalmol.*, **90** (12), 1490–1494.
51 Cioffi, G.A., Latina, M.A., and Schwartz, G.F. (2004) Argon versus selective laser trabeculoplasty. *J. Glaucoma*, **13** (2), 174–177.
52 Rouhiainen, H., Terasvirta, M., and Tuovinen, E. (1987) Low power argon laser trabeculoplasty. *Acta Ophthalmol. (Copenh.)*, **65** (1), 67–70.
53 Blondeau, P., Roberge, J.F., and Asselin, Y. (1987) Long-term results of low power, long duration laser trabeculoplasty. *Am. J. Ophthalmol.*, **104** (4), 339–342.
54 Kramer, T.R. and Noecker, R.J. (2001) Comparison of the morphologic changes after selective laser trabeculoplasty and argon laser trabeculoplasty in human eye bank eyes. *Ophthalmology*, **108** (4), 773–779.
55 Grinich, N.P., Van Buskirk, E.M., and Samples, J.R. (1987) Three-year efficacy of argon laser trabeculoplasty. *Ophthalmology*, **94** (7), 858–861.
56 Bergea, B. (1986) Repeated argon laser trabeculoplasty. *Acta Ophthalmol. (Copenh.)*, **64** (3), 246–250.
57 Bergea, B. (1986) Intraocular pressure reduction after argon laser trabeculoplasty in open-angle glaucoma. A two-year follow-up. *Acta Ophthalmol. (Copenh.)*, **64** (4), 401–406.
58 Babighian, S.,*et al.* (2010) Excimer laser trabeculotomy vs 180 degrees selective laser trabeculoplasty in primary open-angle glaucoma. A 2-year randomized, controlled trial. *Eye (Lond.)*, **24** (4), 632–638.
59 Latina, M.A. and Gulati, V. (2004) Selective laser trabeculoplasty: stimulating the meshwork to mend its ways. *Int. Ophthalmol. Clin.*, **44** (1), 93–103.
60 Latina, M.A.,*et al.* (1998) Q-switched 532-nm Nd:YAG laser trabeculoplasty (selective laser trabeculoplasty): a multicenter, pilot, clinical study. *Ophthalmology*, **105** (11), 2082–2088; discussion 2089–2090.
61 Nagar, M.,*et al.* (2005) A randomised, prospective study comparing selective laser trabeculoplasty with latanoprost for the control of intraocular pressure in ocular hypertension and open angle glaucoma. *Br. J. Ophthalmol.*, **89** (11), 1413–1417.

62 Chen, E., Golchin, S., and Blomdahl, S. (2004) A comparison between 90 degrees and 180 degrees selective laser trabeculoplasty. *J. Glaucoma*, **13** (1), 62–65.

63 Song, J.,*et al.* (2005) High failure rate associated with 180 degrees selective laser trabeculoplasty. *J. Glaucoma*, **14** (5), 400–408.

64 Harasymowycz, P.J.,*et al.* (2005) Selective laser trabeculoplasty (SLT) complicated by intraocular pressure elevation in eyes with heavily pigmented trabecular meshworks. *Am. J. Ophthalmol.*, **139** (6), 1110–1113.

65 Latina, M.A. (1995) A technique to evaluate fluid flow in glaucoma shunts. *Ophthalmic Surg. Lasers*, **26** (6), 576–578.

66 Schuman, J.S.,*et al.* (1990) Contact transscleral continuous wave neodymium:YAG laser cyclophotocoagulation. *Ophthalmology*, **97** (5), 571–580.

67 Flamm, C. and Wiegand, W. (2004) Intraocular pressure after cyclophotocoagulation with the diode laser. *Ophthalmologe*, **101** (3), 263–267 (in German).

68 Pucci, V.,*et al.* (2003) Long-term follow-up after transscleral diode laser photocoagulation in refractory glaucoma. *Ophthalmologica*, **217** (4), 279–283.

69 Beckman, H. and Sugar, H.S. (1973) Neodymium laser cyclocoagulation. *Arch. Ophthalmol.*, **90** (1), 27–28.

70 Hennis, H.L. and Stewart, W.C. (1992) Semiconductor diode laser transscleral cyclophotocoagulation in patients with glaucoma. *Am. J. Ophthalmol.*, **113** (1), 81–85.

71 Wilensky, J.T., Welch, D., and Mirolovich, M. (1985) Transscleral cyclocoagulation using a neodymium: YAG laser. *Ophthalmic Surg.*, **16** (2), 95–98.

72 Fankhauser, F.,*et al.* (1986) Transscleral cyclophotocoagulation using a neodymium YAG laser. *Ophthalmic Surg.*, **17** (2), 94–100.

73 Beckman, H.,*et al.* (1972) Transscleral ruby laser irradiation of the ciliary body in the treatment of intractable glaucoma. *Trans. Am. Acad. Ophthalmol. Otolaryngol.*, **76** (2), 423–436.

74 Molteno, A.C. (1969) New implant for drainage in glaucoma. Clinical trial. *Br. J. Ophthalmol.*, **53** (9), 606–615.

75 Molteno, A.C. (1983) The use of draining implants in resistant cases of glaucoma. Late results of 110 operations. *Trans. Ophthalmol. Soc. N. Z.*, **35**, 94–97.

76 Molteno, A.C. and Haddad, P.J. (1985) The visual outcome in cases of neovascular glaucoma. *Aust. N. Z. J. Ophthalmol.*, **13** (4), 329–335.

77 Prata, J.A. Jr.,*et al.* (1995) *In vitro* and *in vivo* flow characteristics of glaucoma drainage implants. *Ophthalmology*, **102** (6), 894–904.

78 Albis-donando, O. (2006) The Ahmed valve, in *Atlas of Glaucoma Surgery* (eds T. Shaarawy and A. Meermoud), Anshan, Tunbridge Wells, pp. 58–76.

79 Lloyd, M.A.,*et al.* (1994) Intermediate-term results of a randomized clinical trial of the 350- versus the 500-mm^2 Baerveldt implant. *Ophthalmology*, **101** (8), 1456–1463; discussion 1463–1464.

80 Britt, M.T.,*et al.* (1999) Randomized clinical trial of the 350-mm^2 versus the 500-mm^2 Baerveldt implant: longer term results: is bigger better? *Ophthalmology*, **106** (12), 2312–2318.

81 Sommer, A.,*et al.* (1991) Clinically detectable nerve fiber atrophy precedes the onset of glaucomatous field loss. *Arch. Ophthalmol.*, **109** (1), 77–83.

82 Mikelberg, F.S., Yidegiligne, H.M., and Schulzer, M. (1995) Optic nerve axon count and axon diameter in patients with ocular hypertension and normal visual fields. *Ophthalmology*, **102** (2), 342–348.

83 Horn, F.K.,*et al.* (2009) Correlation between local glaucomatous visual field defects and loss of nerve fiber layer thickness measured with polarimetry and spectral domain OCT. *Invest. Ophthalmol. Vis. Sci.*, **50** (5), 1971–1977.

84 Tuulonen, A., Lehtola, J., and Airaksinen, P.J. (1993) Nerve fiber layer defects with

normal visual fields. Do normal optic disc and normal visual field indicate absence of glaucomatous abnormality? *Ophthalmology*, **100** (5), 587–597; discussion 597–598.

85 Kerrigan-Baumrind, L.A.,*et al.* (2000) Number of ganglion cells in glaucoma eyes compared with threshold visual field tests in the same persons. *Invest. Ophthalmol. Vis. Sci.*, **41** (3), 741–748.

86 Wollstein, G.,*et al.* (2004) Optical coherence tomography (OCT) macular and peripapillary retinal nerve fiber layer measurements and automated visual fields. *Am. J. Ophthalmol.*, **138** (2), 218–225.

87 Schuman, J.S.,*et al.* (1995) Optical coherence tomography: a new tool for glaucoma diagnosis. *Curr. Opin. Ophthalmol.*, **6** (2), 89–95.

88 Ajtony, C.,*et al.* (2007) Relationship between visual field sensitivity and retinal nerve fiber layer thickness as measured by optical coherence tomography. *Invest. Ophthalmol. Vis. Sci.*, **48** (1), 258–263.

89 Quigley, H.A., Dunkelberger, G.R., and Green, W.R. (1989) Retinal ganglion cell atrophy correlated with automated perimetry in human eyes with glaucoma. *Am. J. Ophthalmol.*, **107** (5), 453–464.

90 Huang, D.,*et al.* (1991) Optical coherence tomography. *Science*, **254** (5035), 1178–1181.

91 Wojtkowski, M.,*et al.* (2002) *In vivo* human retinal imaging by Fourier domain optical coherence tomography. *J. Biomed. Opt.*, **7** (3), 457–463.

92 Drexler, W.,*et al.* (2003) Enhanced visualization of macular pathology with the use of ultrahigh-resolution optical coherence tomography. *Arch. Ophthalmol.*, **121** (5), 695–706.

93 Fercher, A.F.,*et al.* (1993) *In vivo* optical coherence tomography. *Am. J. Ophthalmol.*, **116** (1), 113–114.

94 Hee, M.R.,*et al.* (1995) Optical coherence tomography of the human retina. *Arch. Ophthalmol.*, **113** (3), 325–332.

95 Wollstein, G.,*et al.* (2005) Ultrahigh-resolution optical coherence tomography in glaucoma. *Ophthalmology*, **112** (2), 229–237.

96 Kiernan, D.F., Mieler, W.F., and Hariprasad, S.M. (2010) Spectral-domain optical coherence tomography: a comparison of modern high-resolution retinal imaging systems. *Am. J. Ophthalmol.*, **149** (1), 18–31.

97 Wojtkowski, M.,*et al.* (2005) Three-dimensional retinal imaging with high-speed ultrahigh-resolution optical coherence tomography. *Ophthalmology*, **112** (10), 1734–1746.

98 Sakamoto, A., Hangai, M., and Yoshimura, N. (2008) Spectral-domain optical coherence tomography with multiple B-scan averaging for enhanced imaging of retinal diseases. *Ophthalmology*, **115** (6), 1071–1078 e7.

99 Sander, B.,*et al.* (2005) Enhanced optical coherence tomography imaging by multiple scan averaging. *Br. J. Ophthalmol.*, **89** (2), 207–212.

100 Bendschneider, D.,*et al.* (2010) Retinal nerve fiber layer thickness in normals measured by spectral domain OCT. *J. Glaucoma*, **19** (7), 475–482.

101 Wollstein, G., Garway-Heath, D.F., and Hitchings, R.A. (1998) Identification of early glaucoma cases with the scanning laser ophthalmoscope. *Ophthalmology*, **105** (8), 1557–1563.

102 Miglior, S.,*et al.* (2002) Intraobserver and interobserver reproducibility in the evaluation of optic disc stereometric parameters by Heidelberg retina tomograph. *Ophthalmology*, **109** (6), 1072–1077.

103 Tan, J.C.,*et al.* (2003) Reasons for rim area variability in scanning laser tomography. *Invest. Ophthalmol. Vis. Sci.*, **44** (3), 1126–1131.

104 Garway-Heath, D.F., Wollstein, G., and Hitchings, R.A. (1997) Aging changes of the optic nerve head in relation to open angle glaucoma. *Br. J. Ophthalmol.*, **81** (10), 840–845.

105 Chen, E., Gedda, U., and Landau, I. (2001) Thinning of the papillomacular bundle in the glaucomatous eye and its influence on the reference plane of the Heidelberg

retinal tomography. *J. Glaucoma*, **10** (5), 386–389.

106 Bowd, C.,*et al.* (2000) Optic disk topography after medical treatment to reduce intraocular pressure. *Am. J. Ophthalmol.*, **130** (3), 280–286.

107 Harju, M. and Vesti, E. (2001) Scanning laser ophthalmoscopy of the optic nerve head in exfoliation glaucoma and ocular hypertension with exfoliation syndrome. *Br. J. Ophthalmol.*, **85** (3), 297–303.

108 Sihota, R.,*et al.* (2002) Variables affecting test–retest variability of Heidelberg Retina Tomograph II stereometric parameters. *J. Glaucoma*, **11** (4), 321–328.

109 Swindale, N.V.,*et al.* (2000) Automated analysis of normal and glaucomatous optic nerve head topography images. *Invest. Ophthalmol. Vis. Sci.*, **41** (7), 1730–1742.

110 Harizman, N.,*et al.* (2006) Detection of glaucoma using operator-dependent versus operator-independent classification in the Heidelberg Retina Tomograph-III. *Br. J. Ophthalmol.*, **90** (11), 1390–1392.

111 Zangwill, L.M.,*et al.* (2007) The effect of disc size and severity of disease on the diagnostic accuracy of the Heidelberg retina tomograph glaucoma probability score. *Invest. Ophthalmol. Vis. Sci.*, **48** (6), 2653–2660.

112 De Leon-Ortega, J.E.,*et al.* (2007) Comparison of diagnostic accuracy of Heidelberg Retina Tomograph II and Heidelberg Retina Tomograph 3 to discriminate glaucomatous and nonglaucomatous eyes. *Am. J. Ophthalmol.*, **144** (4), 525–532.

113 Ferreras, A.,*et al.* (2007) Diagnostic ability of Heidelberg Retina Tomograph 3 classifications: glaucoma probability score versus Moorfields regression analysis. *Ophthalmology*, **114** (11), 1981–1987.

114 Chauhan, B.C.,*et al.* (2000) Technique for detecting serial topographic changes in the optic disc and peripapillary retina using scanning laser tomography. *Invest. Ophthalmol. Vis. Sci.*, **41** (3), 775–782.

115 Burk, R.O. and Rendon, R. (2001) Clinical detection of optic nerve damage: measuring changes in cup steepness with use of a new image alignment algorithm. *Surv. Ophthalmol.*, **45** (Suppl 3), S297–S303; discussion S332–334.

116 Quigley, H.A.,*et al.* (1992) An evaluation of optic disc and nerve fiber layer examinations in monitoring progression of early glaucoma damage. *Ophthalmology*, **99** (1), 19–28.

117 Huang, X.R. and Knighton, R.W. (2002) Linear birefringence of the retinal nerve fiber layer measured *in vitro* with a multispectral imaging micropolarimeter. *J. Biomed. Opt.*, **7** (2), 199–204.

118 Weinreb, R.N.,*et al.* (1990) Histopathologic validation of Fourier-ellipsometry measurements of retinal nerve fiber layer thickness. *Arch. Ophthalmol.*, **108** (4), 557–560.

119 Knighton, R.W., Huang, X.R., and Greenfield, D.S. (2002) Analytical model of scanning laser polarimetry for retinal nerve fiber layer assessment. *Invest. Ophthalmol. Vis. Sci.*, **43** (2), 383–392.

120 Reus, N.J. and Lemij, H.G. (2004) Diagnostic accuracy of the GDx VCC for glaucoma. *Ophthalmology*, **111** (10), 1860–1865.

121 Medeiros, F.A.,*et al.* (2004) Comparison of the GDx VCC scanning laser polarimeter, HRT II confocal scanning laser ophthalmoscope, and stratus OCT optical coherence tomograph for the detection of glaucoma. *Arch. Ophthalmol.*, **122** (6), 827–837.

122 Toth, M. and Hollo, G. (2005) Enhanced corneal compensation for scanning laser polarimetry on eyes with atypical polarisation pattern. *Br. J. Ophthalmol.*, **89** (9), 1139–1142.

123 Bagga, H., Greenfield, D.S., and Feuer, W.J. (2005) Quantitative assessment of atypical birefringence images using scanning laser polarimetry with variable corneal compensation. *Am. J. Ophthalmol.*, **139** (3), 437–446.

124 Mai, T.A., Reus, N.J., and Lemij, H.G. (2007) Diagnostic accuracy of scanning laser polarimetry with enhanced versus variable corneal compensation. *Ophthalmology*, **114** (11), 1988–1993.

125 Reus, N.J., Zhou, Q., and Lemij, H.G. (2006) Enhanced imaging algorithm for scanning laser polarimetry with variable

corneal compensation. *Invest. Ophthalmol. Vis. Sci.*, **47** (9), 3870–3877.

126 Zhou, Q. (2006) Retinal scanning laser polarimetry and methods to compensate for corneal birefringence. *Bull. Soc. Belge Ophtalmol.*, (302), 89–106.

127 Sehi, M., Guaqueta, D.C., and Greenfield, D.S., (2006) An enhancement module to improve the atypical birefringence pattern using scanning laser polarimetry with variable corneal compensation. *Br. J. Ophthalmol.*, **90** (6), 749–753.

39
Early Detection of Cataracts

Rafat R. Ansari and Manuel B. Datiles III

Cataracts, the clouding of the eye lens (Figure 39.1), accounts for half of all blindness worldwide [1–3]. Although there is very active research into finding the cause of cataracts, there is no medical (nonsurgical) cure. Cataract surgery is one of the most successful operations in the world today, but requires highly skilled surgeons and complex and expensive equipment and facilities. Up to 7 million cataract operations are performed worldwide each year at considerable cost. In the United States, cataract accounts for 45% of visits to eye doctors and cataract surgery is the most frequently performed surgical procedure among Medicare beneficiaries [4].

In medicine, early detection of disease leads to early treatment while the disease is still reversible. Noncataractous (before the appearance of haze and cloudiness) lens changes occur with normal aging [5, 6] and the clinical difference between early cataract and age-related change is often not clear-cut in transparent lenses. This makes early detection of cataract very difficult, especially with conventional photographic techniques in use today. Patient follow-up examinations help differentiate nonprogressive aging changes from slowly progressive cataractous changes.

This chapter summarizes currently available methods for the evaluation of cataracts and describes briefly promising methods for the early detection of cataracts. Table 39.1 gives a list of these methods. However, light scattering in various forms remains the main mode of operation in these methods. Simply, more light is scattered as a cataract is formed.

39.1
Visual Acuity Testing

Visual acuity testing (for example, the Snellen test originally introduced in 1862) and survey-type questions are very subjective and dependent upon patients' response. These tests (shown as A and B in the table) do not adequately describe the ability to see large but low-contrast patterns such as faces or nearby objects. A cataract may affect the results of the Snellen acuity test minimally, and yet a patient may already

Handbook of Biophotonics. Vol.2: Photonics for Health Care, First Edition. Edited by Jürgen Popp, Valery V. Tuchin, Arthur Chiou, and Stefan Heinemann.

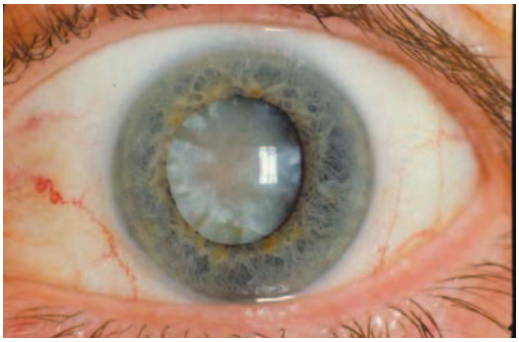

Figure 39.1 Photograph of an eye showing a mature or advanced cataract seen through a dilated pupil.

experience difficulties in daily activities such as driving or walking, especially in bright sunlight or at night, or have difficulty in reading fine print accurately.

39.2 Ophthalmologic Clinical Examinations

39.2.1 Hand-Held Light Examination

A hand-held light in conjunction with a magnifying loupe is the basic tool used for gross examination such as in-field examination of the lens.

39.2.2 Ophthalmoscopy

The direct ophthalmoscope's built-in + 10 lens allows the gross detection of opacities in the lens. The indirect ophthalmoscope may also be useful in making a gross assessment of the clarity of the media as one observes the fundus (back of the eye).

39.2.3 Slit-Lamp Examination

The standard way of examining the lens clinically is using the slit-lamp biomicroscope through a widely dilated pupil. This instrument provides a three-dimensional view of the lens. One can focus on specific areas of the lens from different angles, and at the same time vary the location, direction, and intensity of the illuminating beam independently. The following techniques can be used: (1) direct focal illumination using either a wide or narrow beam; (2) retroillumination; and (3) others, including specular reflection, indirect illumination, diffuse illumination, and use of the light reflected from the iris and posterior capsule.

Table 39.1 Standard methods used in cataract evaluation.

A. Visual acuity/function tests	B. Functional impairment/ quality-of life tests	C. Clinical examination and documentation of physical lens changes
1. Snellen/ETDRS acuity charts or projectors [7]	1. NEI VFQ-25 [13]	1. Clinical examination with hand-held light, slit-lamp biomicroscopy and ophthalmoscopy, and accessory devices [20]
2. Glare and contrast sensitivity tests [8]	2. VF-14 [14, 15]	2. Standardized clinical grading and photographic systems (comparing a patient's cataract with standard photographs)
3. Potential acuity tests	3. Others: Short Form 36 (SF-36) activities of daily vision (ADV), sickness impact profile [16–19]	a. Lens opacities classification system (LOCS), clinical and photographic grading system [21]
a. Pinhole aperture [9]		b. Wisconsin clinical and photographic cataract grading system [22]
b. Entoptic phenomenon [10]		c. Wilmer clinical and photographic cataract grading system [23]
c. Macular function tests: potential acuity meter (PAM), clinical interferometers [11]		d. Oxford clinical cataract grading system [24]
4. Tests for refractive distortions in the lens		e. Age-Related Eye Disease Study (AREDS), clinical and photographic cataract grading system [25, 26]
a. Resolution test target projection ophthalmoscope (acuityscope, Oqual) [12]		f. World Health Organization cataract grading system [27]
b. Wavefront aberrometer, double-pass optical quality analysis system (OQAS II) [18]		3. Modified slit-lamp photography/imaging
		a. Scheimpflug slit-lamp imaging and densitometry systems (Pentacam, Symphony) [28, 29, 32]
		b. Others: laser slit-lamp, sequential color imaging and analysis [33, 34]

New methods currently used in research	Quasi-elastic or dynamic light scattering (QELS or DLS) [45–52]	Optical coherence tomography [33, 34, 54–56]	MRI and NMR spectroscopy [42–44]	Wavefront technology [40]	Raman spectroscopy [35–39]	Autofluorescence [39, 57]

39.2.4
Slit-Lamp Photography of the Lens and Grading of Cataracts

Slit-lamp digital photography documents abnormalities and opacities in the lens. Variables to consider in its use in the lens include the limited depth of field, the variabilities in light intensities with the slit beam, limits of magnification with corresponding limits on the area that can be photographed, limits in the angle of the slit beam used, and limits imposed by pupil size. Recently, cataract classification systems have been developed that use carefully selected slit-lamp photographs of cataracts as standards for comparison with the patient's cataracts. These are enumerated in Table 39.1. These systems provide lens photographs showing various severities or grades of cortical, nuclear, and posterior subcapsular cataracts to be used as standards, which a clinician can then compare with the patient's cataract as seen directly on the slit lamp. For nuclear cataracts, slit photographs of the lens are used (Figure 39.2), and for cortical and posterior subcapsular cataracts, retroillumination photographs are used in which the light is reflected back from the retina (Figure 39.3).

39.2.5
Modified Slit-Lamp Photography

Several instruments have been developed to convert the cataract photographic image into numbers. In nuclear cataracts, densitometric analysis can be performed and clouding of the lens nucleus can be expressed in terms of optical density similarly to turbidity measurements. In cortical and posterior subcapsular cataracts, the area occupied by the cataract inside the pupillary space that is blocking light can be measured. These objective measurements can then be analyzed statistically for research studies.

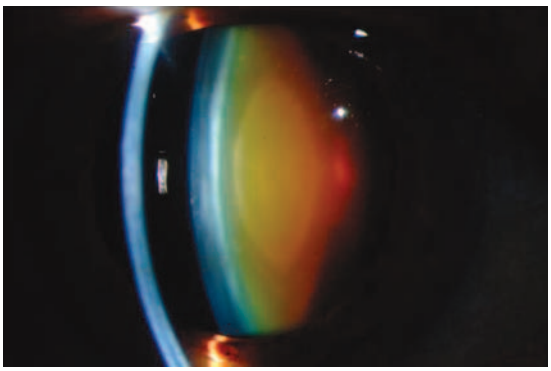

Figure 39.2 Photograph of a saggital section of a nuclear cataract using the slit beam of a slit-lamp camera (note the brownish color or brunesence of nuclear or central core area of the lens).

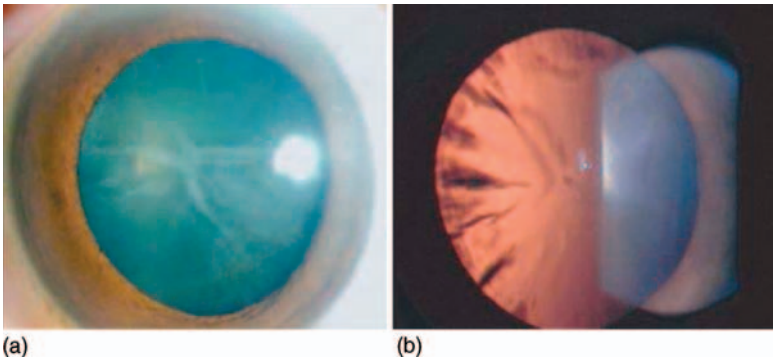

Figure 39.3 Photograph of a cortical cataract seen using direct illumination (a) and using retroillumination (reflection of light from the retina) of a slit-lamp camera (b). Note spoke like opacities.

39.2.6
Scheimpflug Cameras

Slit-lamps modified along the Scheimpflug principle [28, 29] can capture lens images with sufficient depth of focus that the entire anterior chamber from the cornea to the posterior capsule of the lens is in sharp detail. Figure 39.4 shows Scheimpflug images of the front of the eye. Densitometric analysis can be also performed in an area of interest, including the cornea and the lens nucleus. Longitudinal studies to follow the progression of nuclear cataracts can thus be conducted in an objective and masked fashion [29]. A recent review outlined the development of the technique and its introduction into ophthalmology [30].

39.2.7
Retroillumination

Retroillumination cameras [31, 32] can capture images of cortical and posterior subcapsular cataracts using light reflected from the retina as shown in Figure 39.5 and allow the calculation of the size of opacities.

39.3
New Methods Under Development

New technologies are being applied in the early detection of cataracts and show great promise for providing new insights into the cataract problem. In this section, the following devices are discussed: optical coherence tomography (OCT), Raman spectroscopy, autofluorescence, magnetic resonance imaging (MRI), nuclear magnetic resonance (NMR) spectroscopy, wavefront technology, and dynamic light scattering (DLS) [also known as quasi-elastic light scattering (QELS) and photon

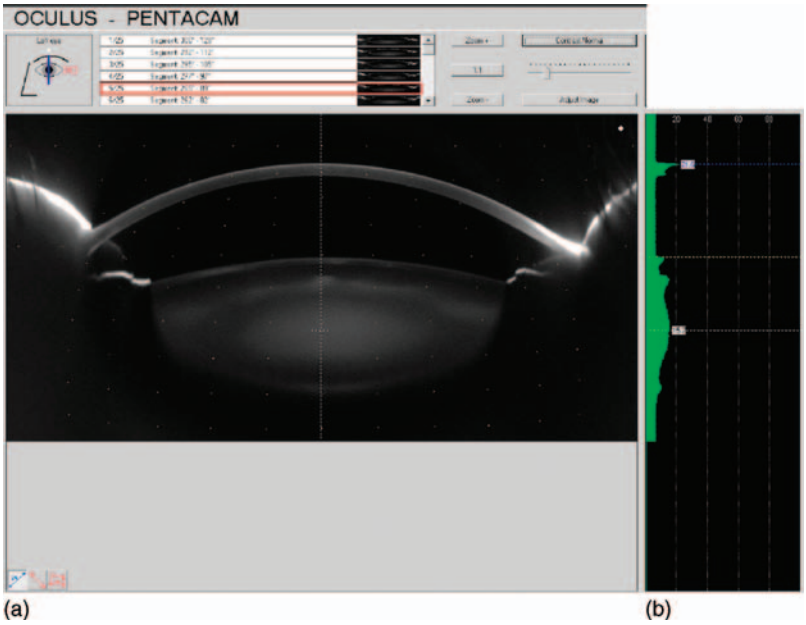

Figure 39.4 (a) Scheimpflug image of the lens with a nuclear cataract showing the automated densitometric measurement through the center [the graph in (b) shows the density across the lens in pixel units]. Currently, the Pentacam Scheimpflug imaging device performs a 360° sweep of the anterior eye segment through the pupillary axis to create a three-dimensional image. It is used routinely to map the cornea for LASIK surgery measurements, but is used here to portray the lens.

correlation spectroscopy (PCS)]. These new noninvasive techniques add to the armamentarium available to cataract researchers.

39.3.1 Optical Coherence Tomography

OCT is a near-infrared optical ranging imaging technique [33]. High-resolution cross-sectional images of the cornea, anterior lens, and retina are obtained by measuring the echo time delay of reflected infrared light using a technique known as low coherence interferometry. The images obtained by OCT are of much higher resolution (~1–15 μm) than images obtained by low-frequency ultrasound pulse-echo imaging (~100 μm). OCT provides more detailed structural information than any other noninvasive ophthalmic imaging technique at present. OCT of the lens and cataracts is limited by the depth of scanning, hence only the anterior half can usually be imaged. It has not yet been used extensively in this area but holds promise in the study of cortical cataracts. Recently, OCT nucleus density measurements correlated well with LOCS III for nuclear opalescence and color [34].

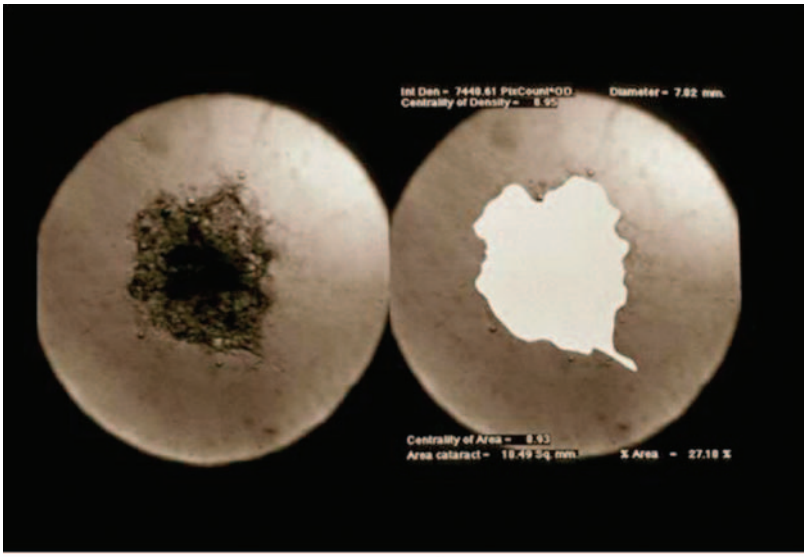

Figure 39.5 Digitized retroillumination image of the lens with a posterior subcapsular cataract (a) and the area of cataract highlighted for measurement (b) using an automated system using thresholding to determine what is an opaque versus nonopaque area.

39.3.2
Raman Spectroscopy for the Detection of Cataract

Raman scattering is the result of inelastic collisions in which the scattered photons exchange energy with the vibrational energy modes of an atom. This frequency shift (or the difference in frequency of an incident photon and the scattered photon) points to specific structural information about a constituent molecule analogous to a certain specific fingerprint that can identify any species present in the system being investigated. However, the Raman signal is very weak. Of 10^6–10^{10} incident photons, only one scattered photon exhibits a Raman shift. Raman spectroscopy has furthered our knowledge of normal aging and pathologic processes in the lens [35], which would not have been possible with other currently available methods. The structural information it provided includes SH, S–S, H_2O, Trp, Try, Phe, and protein secondary structure. Studies can be carried out in the intact living lens. Raman spectroscopy has been used to demonstrate regional swelling of the lens in diabetes. In mildly diabetic rats, the overall increase in lens hydration is hardly detectable. However, regional swelling was demonstrated by Mizuno *et al.* [36]. This method permitted the determination of water content from the periphery of the lens to the center. The advantage of this type of noninvasive technique, similar to that of NMR spectroscopy and QELS, is that it permits the analysis of discrete areas of the lens. Hence these methods may be helpful in determining the changes that occur in certain regions of the lens during cataract formation. The Raman spectra of animal and human lenses have been discussed

by Ozaki in a review article [37]. Raman spectroscopy is very useful for cataract research; it gives unique information about changes in water content and structural alterations in the lens proteins with cataract development. Clinical *in vivo* use of this technology is limited by the need to use high laser power, and comprehensive spectral data libraries must first be generated and established. It can then be used to give searchable fingerprints (indices) for ocular and other diseases.

39.3.3
Autofluoresence for the Detection of Cataract

Ocular tissues exhibit natural or autofluorescence (AF) and it has been found to increase with age in healthy individuals [38]. Accumulation of fluorescent proteins in ocular tissue can result from long-term exposure to the UV or UVA radiation in sunlight. This accumulation of fluorophores may also be responsible for lens opacification and can be considered a risk factor for cataract formation. These fluorophores can be found during cataract formation. In the initial stages these can be characterized by exhibiting fluorescence in the near-ultraviolet and violet regions of the spectrum (340 and 411 nm). However, in advanced stages of cataract development, an increase in the intensity of the long-wave fluorescence of the lipids in the blue–green region (430/480 nm) occurs [39]. AF from transparent (noncataractous) lenses exhibits a strong correlation with age. The increased level of fluorescence from the lens can be attributed to oxidative stress or absorbance of UV light as a function of age. Because the cornea does not absorb UV light, its AF level remains constant. However, both diabetic lens and cornea show significantly increased AF levels.

39.3.4
Wavefront in Cataract Detection

Wavefront aberrometry was introduced in ophthalmologic practice to evaluate visual performance objectively. A wavefront analyzer is used to evaluate the quality of an optical system. The wavefront is the pack of light beams or bundle of rays reflected from the retina and coming out of the eye, which is then detected by a sensor called a Shack–Hartmann wavefront sensor (originally developed for high-energy laser and astronomy applications). The light used in the measurement is in the near-infrared region of the spectrum where the eye is nearly insensitive. The sensor has lenslets which divide the wavefront into parts.

Image degradation in the macula because of cataract may be caused not only by light scattering but also by optical aberrations. As discussed in Section 39.1, several devices such as the Oqual and the resolution test target test have been devised as simple ways to test for the effect of optical degradation in the retina.

A new technology using wavefront analysis to study optical aberrations of the eye and in particular the cornea to enhance the results of refractive surgery in patients has also been used on the lens. Kuroda *et al.* [40], using the Hartmann–Shack aberrometer (Topcon, Tokyo, Japan), found that the ocular total higher order optical aberration in eyes with a cortical or nuclear cataract was significantly higher than in

normal subjects. Corneal total high-order optical aberration in eyes with mild cortical or nuclear cataracts did not differ from that in normal subjects. This suggests that high-order optical aberration increases in eyes with cataract because of the local refractive change in the lens. Another finding was that the polarity of spherical aberration was different between nuclear and cortical cataracts. In nuclear cataracts, the polarity is always negative, suggesting that a delay of the light wavefront occurs when the ray travels inside the hard nucleus with increased refractive index. In contrast, in cortical cataract, the polarity was always positive.

These findings suggest that in mild cortical and nuclear cataracts, not only light scattering but also optical aberrations in the lens contribute to loss of visual function as measured by loss of contrast sensitivity [40]. Hence this new technique may be useful in studying the total effect of early cataracts on visual function, and explain some patients' complaints such as monocular diplopia in the presence of mild lens changes.

39.3.5
Magnetic Resonance Imaging and Nuclear Magnetic Resonance Spectroscopy of the Lens

As any other human tissue, the lens contains carbon and hydrogen atoms in which protons spin around their nuclei in random directions. On application of a magnetic field, these "microscopic magnets" are aligned in a particular (north–south) direction (higher energy state). On turning off the magnetic field, the microscopic magnets return to their original random state (lower energy state). The frequency of rotation is equal to the energy of a photon (normally a known radiofrequency) that would cause the nuclei to flip between these two energy levels. This provides measurements of relaxation rates between different energy states of the nuclei in relation to the applied excitation photon field. Because they are dependent on the hydrogen nuclei densities in the tissue, the relaxation rate information can be translated into images.

MRI provides the ability to probe the chemical and metabolic status of the lens noninvasively. Thus, in response to normal and pathophysiologic conditions, aspects such as lens metabolism, ion concentrations, the state (bound versus free) of lens water, and metabolite and macromolecular motional dynamics may be investigated. Valuable biochemical and biophysical information pertinent to the factors that govern lens transparency, and conversely the medical condition of the cataract, can thus be studied.

MRI has been used to image the eye but problems have been encountered, including poor resolution; limited access to the surface coil, and poor resultant magnetic signal (because of the location of the eye within the bony structure of the orbit); motion artifacts (caused by microsaccadic eye movements, breathing and heartbeat); and the presence of high susceptibility gradients around the eye. Lizak *et al.* [41] used a special technique, magnetization transfer constant enhancement (MTCE), to enhance the lens image successfully and study diabetic and galactosemic animal models of cataract, and applied it to clinical use. MTCE takes advantage of the magnetic interactions between water and macromolecule hydrogen atoms.

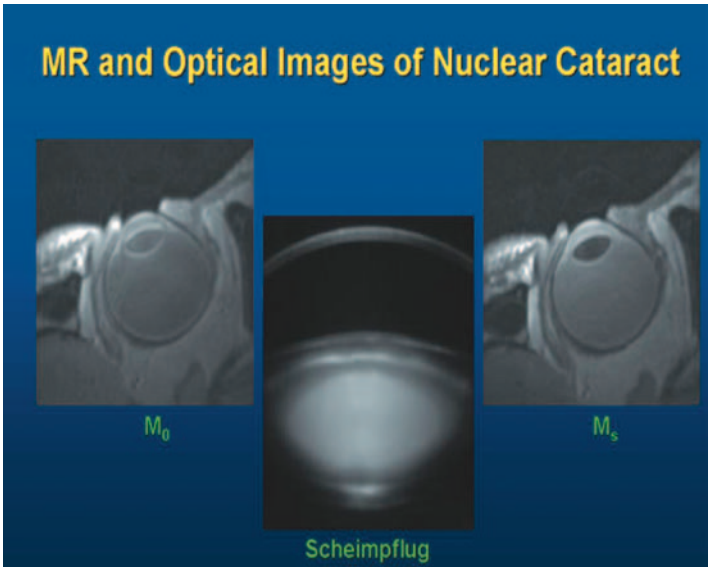

Figure 39.6 An MRI image of the lens compared to a Scheimpflug image of the same lens with nuclear cataract. M_0, magnetic resonance image of a patient's eye with a nuclear cataract; Scheimpflug, image of the same nuclear cataract (LOCS II nuclear opalescence grade 2) taken using a Zeiss Scheimpflug slit-lamp camera (optical/digital); M_s, magnetic resonance image of the same eye with magnetic transfer contrast enhancement [41].

Preliminary clinical studies suggest that cortical lens changes can be better observed with unenhanced magnetic resonance images, whereas nuclear lens changes are better observed by the addition of the MTCE preparation pulse (Figure 39.6). MRI therefore promises to be an imaging method independent of optical imaging that will allow clinicians to monitor metabolic processes in the lens [41]. In a recent study, a new ultra-high resolution MRI instrument with a magnetic field of 7.1 T was used to study the anterior segment of the eye including the crystalline lens of postmortem animal and human eyes and in *in vivo* rabbit experiments [42]. ^{13}C NMR spectroscopy of the intact lens, on the other hand, has provided information about the production, turnover, and inhibition of sorbitol by aldose reductase inhibitors. Proton NMR spectroscopy of ^{13}C-labeled metabolites offers the ability to monitor the reactivation and dynamics of the hexose monophosphate shunt (HMPS), a pathway important for the maintenance of the lens redox state, in real time and noninvasively [43]. ^{31}P NMR spectroscopy allows the monitoring of phosphorus-containing metabolites, thereby permitting the real-time assessment of lens tissue metabolic response to pathophysiologic conditions. Important metabolites, such as adenosine triphosphate, phosphomonoesters, and phosphodiesters, may be monitored. Furthermore, intralenticular pH may be measured. However, no clear correlation between phosphorus metabolite levels and lens clarity has been established to date, despite numerous NMR and classic biochemical studies. This lack of correlation suggests the importance of biophysical investigations

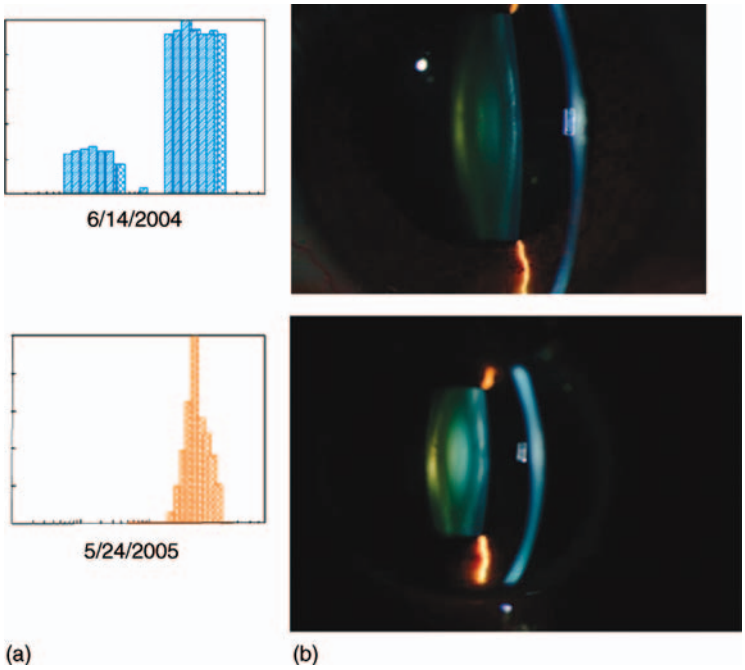

Figure 39.7 A sequential study of an eye which developed a nuclear cataract in a year (b). The dynamic light scattering particle size distribution graphs are shown in (a). The first peak represent the α-crystallin content of the lens, which disappeared by the time the nuclear cataract developed (seen in the photograph). (Reproduced from Datiles *et al.* [50]).

aimed at the interaction behavior and organization of the constituent lens proteins in the cytoplasm, the macromolecular entities responsible for light scattering associated with cataract. NMR spectroscopy may be viewed as an important adjunct to the better established laser light scattering studies of the lens, and has remained mainly a laboratory, rather than a clinical, method of studying the human lens [44].

39.3.6
Dynamic Light Scattering (DLS)

DLS is an established laboratory technique to measure the average size or size distribution of microscopic particles (3 nm to 3 μm) suspended in a fluid medium in which they undergo random Brownian (or thermal) motion. The intensity of light scattered by the particles from a laser beam passing through such dispersion will fluctuate in proportion to the Brownian motion of the particles. Because the size of the particles influences their Brownian motion, analysis of the fluctuations in scattered light intensity yields a distribution of the diffusion coefficient(s) of the suspended particles from which average particle size or particle size distribution can be extracted [45, 46]. Clinically, DLS can be used to study cataracts noninvasively at the molecular level [47, 48]. *In vivo* DLS measurements at the molecular level correlate

well with established laboratory analytical methods such as high-performance liquid chromatography [49, 50]. DLS is safe and fast to use in early cataract evaluation because of the very low laser power (50–100 μW) and short data acquisition time (5 s). In a cold-induced cataract model experiment in which the cataract was simultaneously monitored with both the DLS device and Scheimpflug camera, the DLS picked up subtle changes in the lens faster (2–3 orders of magnitude earlier) than the Scheimpflug camera [51]. The DLS measures the Brownian motion of the crystallins and aggregated proteins inside the lens. The α-crystallins have recently been found to prevent the aggregation of other crystallins and also other proteins such as membranes that have been damaged by oxidative stress. For clinical use, the DLS probe for early cataract detection was successfully integrated into a Keratron device with a three-dimensional aiming system. This aiming arrangement permits consistent remeasurement of changes in the same location in the lens over time. Data obtained from patients in clinical studies have shown good reproducibility [51, 52]. Using this DLS device, it was shown that DLS can measure α-crystallins clinically and noninvasively and that loss of α-crystallins correlated highly with the development of cataract. Hence DLS can measure the reserve of α-crystallins in a given lens and thus assess the risk for cataract development (Figure 39.7) in a patient [53].

39.4 Conclusion

New developments in biophotonics have led to compact and efficient devices showing great potential in aiding researchers to elucidate cataract formation processes *in vivo* and noninvasively. Further improvements and testing on patients will be helpful in moving this field forward and one day help find new ways to prevent or treat cataracts without the need for surgery.

Disclaimer: The views and opinions expressed in this talk are those of the authors and not those of NASA, NIH, and/or the Government of the United States of America.

References

1 Javitt, J. and Wang, F. (1996) Blindness due to cataract: epidemiology and prevention. *Annu. Rev. Public Health*, **17**, 159.

2 Foster, A. (1999) Cataract – a global perspective: output, outcome and outlay. *Eye*, **3**, 449.

3 Kupfer, C. (1985) Bowman Lecture. The conquest of cataract: a global challenge. *Trans. Ophthalmol. Soc. UK*, **104**, 1.

4 National Eye Institute, National Institutes of Health. Vision Research: a National Plan: 1999–2003, Report of the Cataract Panel. US Department of Health and Human Services, NIH Publication No. 98-4120, pp. 59–75.

5 Weekers, R., Delmarcelle, Y., Luyckx-Bacus, J., *et al.* (1973) Morphological changes of the lens with age and cataract, in *The Human Lens – in Relation to*

Cataract (eds. K. Elliott and D. Fitzsimons), Elsevier, Amsterdam, p. 25.
6 Weale F R.A. (1981) Physical changes due to age and cataract, in *Mechanism of Cataract Formation in the Human Lens* (ed. G Duncan), Academic Press, New York, p. 47.
7 Ferris, F.L., Kassoff, A., Bresnick, G.H., *et al.* (1982) New visual acuity charts. *Am. J. Ophthalmol.*, **4**, 91.
8 American Academy of Ophthalmology Committee on Ophthalmic Procedures (1990) Contrast sensitivity and glare testing in the evaluation of anterior segment disease: ophthalmic procedures assessment. *Ophthalmology*, **97**, 1233.
9 Melki, S., Safar, A., Martin, J., *et al.* (1999) Potential acuity pinhole. *Ophthalmology*, **106**, 1262.
10 Sinclair, S.H., Loebl, M., and Riva, C. (1979) Blue field entoptic phenomenon in cataract patient. *Arch. Ophthalmol.*, **97**, 1092.
11 Lasa, M.S.M., Datiles, M.B. III, and Friedlin, V. (1995) Potential vision tests in patients with cataracts. *Ophthalmology*, **102**, 1007.
12 Lobo, R.F. and Weale, R.A. (1993) The objective clinical assessment of the quality of the anterior segment by means of the Oqual. *Doc. Ophthalmol.*, **83**, 71.
13 Mangione, C.M., Lee, P.P., Gutierrez, P.R., *et al.* (2001) Development of the 25-item National Eye Institute Visual Function Questionnaire. *Arch. Ophthalmol.*, **119**, 1050.
14 Steinberg, E.P., Tielsch, J.M., Schein, O.D., *et al.* (1994) The VF-14. An index of functional impairment in patients with cataract. *Arch. Ophthalmol.*, **112**, 630.
15 Cassard, S.D., Patrick, D.L., Damiano, A.M., *et al.* (1995) Reproducibility and responsiveness of the VGF-14. An index of visual impairment in patients with cataracts. *Arch. Ophthalmol.*, **113**, 1508.
16 Lee, P., Spritzer, K., and Hays, R. (1997) The impact of blurred vision on functioning and well being. *Ophthalmology*, **104**, 390.
17 Ware, J.E. and Shelbourne, C.D. (1992) The MOS 36 Item Short Form Health Survey (SF-36): I. Conceptual framework and item selection. *Med. Care*, **30**, 473.
18 Mangione, C.M., Phillips, R.S., Seddon, J., *et al.* (1992) Development of the Activities of Daily Vision Scale. A measure of visual function status. *Med. Care*, **30**, 1111.
19 Berner, M., Bobbitt, R.A., Carter, W.B., *et al.* (1981) The Sickness Impact Profile: development and final revision of a health status measure. *Med. Care*, **19**, 787.
20 Berliner, L. (1949) *Biomicroscopy of the Eye*, vol. II, Paul B. Hoeber, New York, p. 948.
21 Chylack, L., Leske, C., Sperduto, R., *et al.* (1988) Lens Opacities Classification System. *Arch. Ophthalmol.*, **106**, 330.
22 Klein, B.E.K., Klein, R., Linto, K.L.P., *et al.* (1990) Assessment of cataracts from photography in the Beaver Dam Eye Study. *Ophthalmology*, **97**, 1428.
23 Taylor, H.R. and West, S.K. (1989) The clinical grading of lens opacities. *Aust. N. Z. J. Ophthalmol.*, **17**, 81.
24 Sparrow, J., Bron, A., Brown, N., *et al.* (1986) The Oxford clinical cataract classification and grading system. *Int. Ophthalmol.*, **9**, 207.
25 Kassoff, A., Kassoff, J., Mehu, M., *et al.* (2001) The Age Related Eye Disease Study (AREDS) system for classifying cataracts from photographs: AREDS Report No. 4. *Am. J. Ophthalmol.*, **131**, 167–175.
26 Braccio, L., Campirini, M., Graziosi, P., *et al.* (1998) An independent evaluation of the Age Related Eye Disease Study (AREDS) cataract grading system. *Curr. Eye Res.*, **17**, 53.
27 Thyleflors, B., Chylack, L., Konyama, K., *et al.* (2002) A simplified cataract grading system. *Ophthalmic Epidemiol.*, **9**, 83.
28 Dragomirescu, V., Hockwin, H., Koch, H.R., *et al.* (1978) Development of a new equipment of rotating slit image photography according to Scheimpflug's principle. *Interdiscipl. Top. Gerontol.*, **13**, 118.
29 Datiles, M., Magno, B., and Friedlin, V. (1995) Study of nuclear cataract progression using the NEI Scheimpflug system. *Br. J. Ophthalmol.*, **79**, 527.

30 Wegener, A. and Laser-Junga, H. (2009) Photography of the anterior eye segment according to Scheimpflug's principle: options and limitations. *Clin. Exp. Ophthalmol.*, **37**, 144–154.

31 Kawara, T. and Obazawa, H. (1980) A new method of retroillumination photography of cataractous lens opacities. *Am. J. Ophthalmol.*, **90**, 186.

32 Brown, N., Bron, A., Ayliffe, W., *et al.* (1987) The objective assessment of cataract. *Eye*, **1**, 234.

33 Drexler, W., Morgner, V., Ghanta, R., Kastner, F., *et al.* (2001) Ultrahigh resolution OCT. *Nat. Med.*, **7**, 502–507.

34 Wong, A.L., Leung, C.K., Weinreb, R.N., *et al.* (2009) Quantitative assessment of lens opacities with anterior segment optical coherence tomography. *Br. J. Ophthalmol.*, **93** (1), 61–65.

35 McCreery, R.L. (1996) Analytical Raman spectroscopy: an emerging technology for practical applications. *Am. Lab.*, **28**, 34.

36 Mizuno, A., Nozawa, H., Taginuma, T., *et al.* (1987) Diabetic cataracts. *Exp. Eye Res.*, **45**, 185.

37 Ozaki, Y. (1988) Medical application of Raman spectroscopy. *Appl. Spectrosc. Rev.*, **24**, 259.

38 Bursel, S.E. and Yu, N.T. (1990) Fluorescence and Raman spectroscopy of the crystalline lens, in *Noninvasive Techniques in Ophthalmology* (ed. B.R. Masters), Springer, New York. 342–365.

39 Babizhayev, M.A. (1989) Lipid fluorophores of the human crystalline lens with cataract. *Graefes. Arch. Clin. Exp. Ophthalmol.*, **227**, 384.

40 Kuroda, T., Fujikado, T., Maeda, N., *et al.* (2002) Wavefront analysis in eyes with nuclear or cortical cataract. *Am. J. Ophthalmol.*, **134**, 1.

41 Lizak, M., Datiles, M.B., Aletras, A., *et al.* (2000) MRI of the human eye using magnetization contrast enhancement. *Invest. Ophthalmol. Vis. Sci.*, **41**, 3878.

42 Langner, S., Martin, H., Terwee, T., *et al.* (2010) 7.1 T MRI to assess the anterior segment of the eye. *Invest. Ophthalmol. Vis. Sci.*, **51**, 6575.

43 Gonzales, R.G., Willis, J., Aguayo, J., *et al.* (1982) C-13 nuclear magnetic resonance studies of sugar cataractogenesis in the single intact rabbit lens. *Invest. Ophthalmol. Vis. Sci.*, **22**, 808.

44 Williams, W.F., Austin, C.D., Farnsworth, P.N., *et al.* (1988) Phosphorus and proton magnetic resonance spectroscopic studies on the relationship between transparency and glucose metabolism in the rabbit lens. *Exp. Eye Res.*, **47**, 97.

45 Chu, B. (1991) *Laser Light Scattering: Basic Principles*, Academic Press, New York.

46 Bern, B. and Pecora, A. (1976) *Dynamic Light Scattering*, John Wiley and Sons, Inc., New York.

47 Benedek, G.B., Clark, J.I., Serrallad, E.N., *et al.* (1979) Light scattering and reversible cataracts in the calf and human lens. *Philos. Trans. R. Soc. Lond. Ser. A Math. Phys. Sci.*, **293**, 329.

48 Ansari, R.R. (2004) Ocular static and dynamic light scattering: a non-invasive diagnostic tool for eye research and clinical practice. *J. Biomed. Opt.*, **9** (1), 22–37.

49 Simpanya, M.F., Ansari, R.R., Leverenz, V., and Giblin, F.J. (2008) Measurement of lens protein aggregation *in vivo* using dynamic light scattering in a guinea pig/UVA model for nuclear cataract. *J. Photochem. Photobiol.*, **84**, 1589–1595.

50 Datiles, M.B. III, Ansari, R.R., Suh, K.I., Vitale, S., Reed, G.F., Zigler, J.S. Jr., and Ferris, F.L. III (2008) Clinical detection of precataractous lens protein changes using dynamic light scattering. *Arch. Ophthalmol*, **126** (12), 1687–1693.

51 Datiles, M.B., Ansari, R.R., and Reed, G.F. (2002) A clinical study on the human lens with a dynamic light scattering device. *Exp. Eye Res.*, **74**, 93.

52 Thurston, G., Hayden, D.L., Burrows, P., *et al.* (1997) Quasielastic light scattering study of the living human lens as a function of age. *Curr. Eye Res.*, **16**, 197.

53 Steinberg, E.P., Tielsch, J.M., Schein, O.D., *et al.* (1994) The VF-14. An index of functional impairment in

patients with cataract. *Arch. Ophthalmol.*, **112**, 630.

54 Fercher, A.F. (1996) Optical coherence tomography. *J. Biomed. Opt.*, **1**, 15.

55 Izatt, J.A., Hee, M.R., Swanson, E.A., *et al.* (1994) Micrometer-scale resolution imaging of the anterior eye *in vivo* with optical coherence tomography. *Arch. Ophthalmol.*, **112**, 1584.

56 DiCarlo, C.D., Roach, W.P., Gagliano, D.A., *et al.* (1999) Comparison of optical coherence tomography (OCT) imaging of cataracts with histopathlogy. *J. Biomed. Opt.*, **4**, 450.

57 Dochio, F. and Van Best, J.A. (1998) Simple, low-cost, portable corneal fluorometer for detection of the level of diabetic retinopathy. *Appl. Opt*, **37** 4303.

40
Diabetic Retinopathy

Adzura Salam, Sebastian Wolf, and Carsten Framme

40.1
Introduction

Diabetic retinopathy (DR) is the commonest microvascular complication occurring in diabetes mellitus and remains one of the leading causes of vision loss and blindness among adults aged 40 years and older. According to the latest report on "Prevalence of Diabetic Retinopathy in the United States, 2005–2008," the prevalence of diabetic retinopathy and vision-threatening diabetic retinopathy was 28.5 and 4.4%, respectively, among American adults with diabetes [1]. The prevalence of DR among Americans aged 40 years or older with vision-threatening diabetic retinopathy (VTDR) is predicted to triple by 2050, from 5.5 million in 2005 to 16.0 million for DR and from 1.2 million in 2005 to 3.4 million for VTDR [2].

Vision loss occurs in DR due to the development of maculopathy, especially diabetic macular edema (DME), and due to proliferative diabetic retinopathy (PDR). The Wisconsin Epidemiologic Study of Diabetic Retinopathy (WESDR) reported that the prevalence of PDR was 23% in the WESDR younger-onset group, 10% in the WESDR older-onset group who take insulin, and 3% in the group who do not take insulin [3]. The same study reported that hyperglycemia, longer duration of diabetes, and more severe retinopathy at baseline were associated with an increased 4 year risk of developing PDR.

In 2009, another study by the same group, The Wisconsin Epidemiologic Study of Diabetic Retinopathy XXIII, reported that the 25 year cumulative incidence was 29% for DME and 17% for clinically significant macula edema (CSME) [4]. They also concluded that the relatively high 25 year cumulative rate of incidence of DME was related to glycemia and blood pressure.

Both DR and DME share common risk factors, namely the duration of diabetes and severity of hyperglycemia. Others risk factors for progression of DR include coexisting hypertension, hyperlipidemia, renal disease, and pregnancy [5–8]. The WESDR also reported that the incidence of DME was associated with more severe DR, higher glycosylated hemoglobin, proteinuria, higher systolic and diastolic blood pressure, and chronic smoking [4].

Handbook of Biophotonics. Vol.2: Photonics for Health Care, First Edition. Edited by Jürgen Popp, Valery V. Tuchin, Arthur Chiou, and Stefan Heinemann.

40.2 Diagnosis of DR and DME

Traditionally, DR is diagnosed by using slit-lamp biomicroscopy and stereo fundus photography [9, 10]. The gold standard for grading the severity of DR is stereoscopic fundus photography through dilated pupils, using seven standard fields [11–13], and grading guidelines for these photographs were established by the Early Treatment Diabetic Retinopathy Study (ETDRS) group [14]. Clinically, DR can be classified into two stages: nonproliferative diabetic retinopathy (NPDR) and proliferative diabetic retinopathy (PDR) [15] (Table 40.1). The stereo fundus photograph helps in documentation of the clinical findings in DR. NPDR appear as dot-blot hemorrhage, cotton-wool spot, hard exudates, and venous beading depending on the severity (Figure 40.1). The presence of new vessels elsewhere (NVE), new vessels on the disc (NVD), and enhanced epiretinal and intravitreal hemorrhage are the characteristic features of PDR (Figure 40.2).

DME is a common microvascular complication which may appear at any stage of DR. DME is further classified into focal, diffuse, and ischemic maculopathy [16] (Table 40.2). In developed countries, stereo fundus photography is being used in DR screening programs. Such screening programs effectively help to reduce the incidence of blindness secondary to DR [11, 13]. However; in developing countries, the utility of fundus photography as a large-scale screening procedure is limited because of its cost and the requirements for special equipment and trained personnel.

In a further diagnostic step, fluorescein angiography (FA) is frequently used, especially for baseline examination. It is a procedure in which sodium fluorescein is administered intravenously followed by rapid sequence photography of the retina to evaluate its circulation. FA is usually used to evaluate the extent and origin of fluid

Table 40.1 International clinical diabetic retinopathy disease severity scale.

Proposed disease severity level	Findings observable upon dilated ophthalmoscopy
No apparent retinopathy	No abnormalities
Mild nonproliferative diabetic retinopathy	Microaneurysms only
Moderate nonproliferative diabetic retinopathy	More than microaneurysm but less than severe NPDR
Severe nonproliferative diabetic retinopathy	Any of the following: 1. More than 20 intraretinal hemorrhages in each of four quadrants 2. Definite venous beading in two or more quadrants, prominent intraretinal microvascular abnormalities (IRMA) in one or more quadrants, *and* no signs of proliferative retinopathy
Proliferative diabetic retinopathy	One or both of the following: 1. Neovascularization 2. Vitreous/preretinal hemorrhage

Source: Wilkinson *et al*. [16].

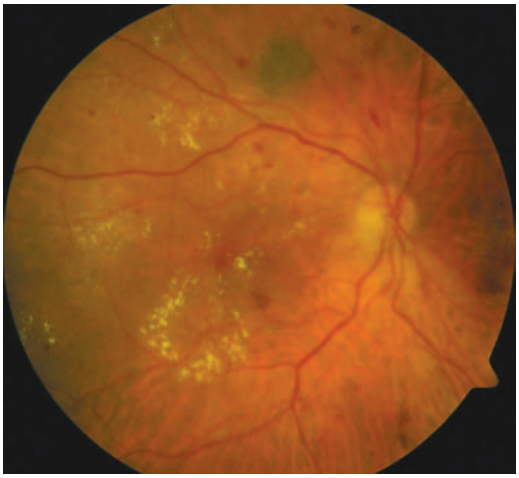

Figure 40.1 Color fundus photograph of the right eye showing severe nonproliferative diabetic retinopathy with diffuse clinically significant macular edema. Note the presence of dot-blot hemorrhage, hard exudates in "succinate ring," cotton-wool spots, and venous beading.

leakage and also the extent of capillary ischemia in DME [17]. The flow and permeability of retinal vessels can be correlated with anatomic changes by using FA (Figure 40.3). FA findings in DME can be categorized into three different types of leakage: (1) focal leakage, (2) diffused leakage, and (3) diffused cystoid leakage. The most important information gained from FA is whether there is presence of macular ischemia, a condition which responds poorly to most conventional DME treatments [17]. However, FA has its limitations: an invasive technique, time constraints, expensive equipment

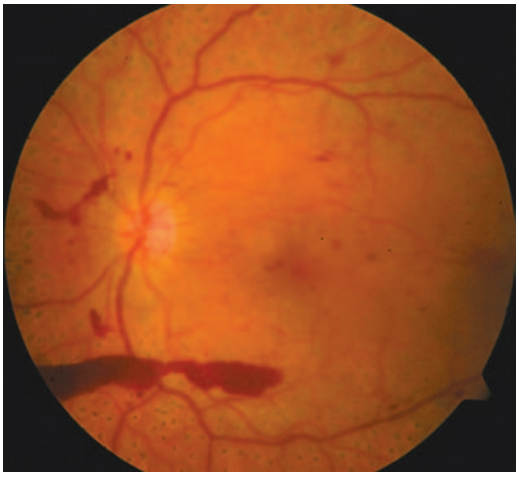

Figure 40.2 Color fundus photograph of the left eye showing proliferative diabetic retinopathy with presence of new vessels at the disc, new vessels elsewhere, and subhyaloid hemorrhage. Note old panretinal laser photocoagulation scars outside the vessel arcades.

Table 40.2 International clinical diabetic macular edema disease severity scale.

Proposed disease severity level	Findings observable upon dilated ophthalmoscopy[a)]
Diabetic macular edema apparently absent	No apparent retinal thickening or hard exudates in posterior pole
Diabetic macular edema apparently present	Some apparent retinal thickening or hard exudates in posterior pole
If diabetic macular edema is present, it can be categorized as follows:	
Diabetic macular edema present	Mild diabetic macular edema: some retinal thickening or hard exudates in posterior pole but distant from the center of the macula Moderate diabetic macular edema: retinal thickening or hard exudates approaching the center of the macula but not involving the center Severe diabetic macular edema: retinal thickening or hard exudates involving the center of the macula

a) Hard exudates are a sign of current or previous macular edema. Diabetic macular edema is defined as retinal thickening; this requires a three-dimensional assessment that is best performed by dilated examination using slit-lamp biomicroscopy and/or stereo fundus photography.

required, and possible allergic-type reactions to sodium fluorescein. Hence FA should be performed only under strong indication or for treatment planning.

The most recent step in diagnostics is provided by optical coherence tomography (OCT), which was first introduced in 1991 by Huang *et al.*, offering a noninvasive, noncontact imaging technology that can image retinal structures *in vivo* [18]. Time-domain OCT uses low-coherence interferometry to provide absolute measurements of retinal thickness and achieves a high axial resolution of ~10 μm (Figure 40.4). OCT is used in clinical routine to assess the posterior pole pathology in various retinal diseases and specifically to analyze DME in DR [19].

40.3 Spectral-domain OCT in DME

The technology of OCT has undergone rapid evolution over the past decade. The most recent advance, spectral-domain optical coherence tomography (SD-OCT), made both high resolution and fast scanning speeds possible, thus improving the quality of images. Various SD-OCT instruments are available: Cirrus HD-OCT (Carl Zeiss Meditec), RTVue-Fourier Domain OCT (Optovue), Copernicus OCT (Reichert/Optopol Technology), Spectral OCT/SLO (Opko/OTI), Spectralis HRA +OCT (Heidelberg Engineering), Topcon 3D OCT-1000 (Topcon), and RS-3000 Retiscan (Nidek). All instruments provide high-quality OCT images and produce three-dimensional images.

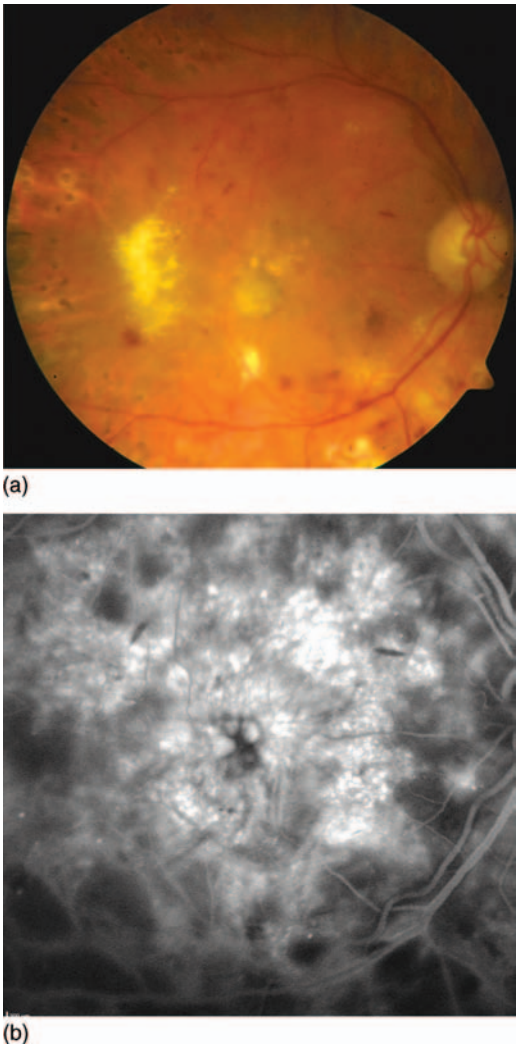

Figure 40.3 Color fundus photograph showing CSMO (a) and hyperfluorescein leakage during fluorescein angiography (b).

SD-OCT reveals various pathologic findings at qualitative and quantitative levels, and also abnormal morphology of retinal layers. The qualitative interpretation includes hyperreflective structures (hard exudates and cotton-wool spots), hyporeflective structures (intraretinal edema, exudative retinal detachment, and cystoid macular edema), and also shadow effects (hemorrhage, exudates, and retinal vessels) [20]. In the past, OCT has been used primarily to analyze macular thickness in DME (Figure 40.5). Various studies have documented changes in retinal thickness, central foveal thickness, and the macular volume among diabetes patient as compared with nondiabetes patients [21, 22]. In addition, some researchers have reported

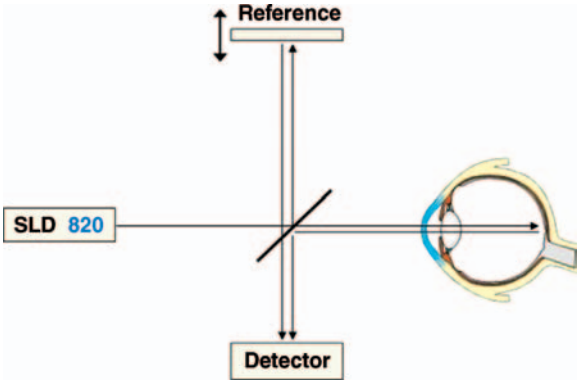

Figure 40.4 Diagram showing the principle of OCT. OCT uses low-coherence interferometry technology to produce a two-dimensional images. A low-coherence near-infrared light beam (820 nm) is directed towards the target tissue. The magnitude and relative location of backscattered light from the internal tissue microstructures are interpreted by the OCT to generate an image.

a modest correlation between macular thickness and best-corrected visual acuity (BCVA) in diabetic eyes [23, 24]. These findings may be useful for early detection of macular thickening and may be indicators for closer follow-up of patients with diabetes. Strøm *et al.* reported close agreement between subjective and objective assessments of retinal thickness; the same study suggested that DME can be accurately and prospectively measured with OCT [25].

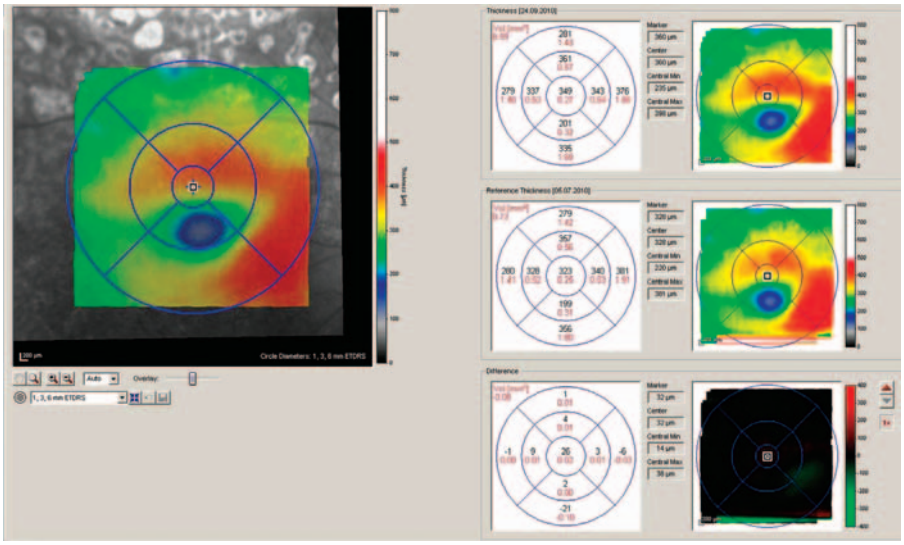

Figure 40.5 Spectralis HRA+OCT retinal thickness scan. Note that the central macular thickness and volume can be compared before and after a treatment.

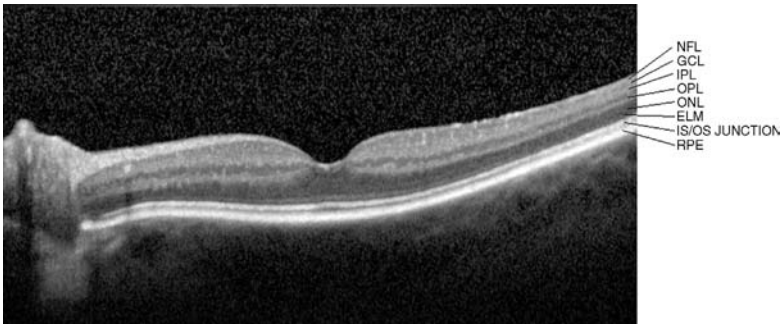

Figure 40.6 Normal retina as imaged by the Spectralis HRA+OCT: ganglion cell layer (GCL), inner plexiform layer (IPL), inner nuclear layer (INL), outer plexiform layer (OPL), outer nuclear layer (ONL), external limiting membrane (ELM), photoreceptor inner segments (IS), outer segments (OS), and retinal pigment epithelium (RPE).

The Spectralis HRA+OCT, used as a standard in our clinic, combines high-resolution SD-OCT with an scanning laser ophthalmoscopy (SLO). The system allows for simultaneous OCT scans with high-resolution scanning laser retinal imaging. The instrument uses broadband 870 nm SLD for the OCT channel. The retina is scanned at 40 000 A-scans per second, creating highly detailed images of the structure of the retina. The OCT optical depth resolution is 7 μm and the digital depth resolution is 3.5 μm. The combination of high-resolution scanning laser retinal images and SD-OCT allows for real-time tracking of eye movements and real-time averaging of scanning laser images and OCT scans, reducing speckle noise of the OCT images [26].

Recent advances in the SD-OCT technique made both high resolution and fast scanning speeds possible. High resolution allows for differentiation of as many as 11 structural characteristics within the retina (Figure 40.6). Other additional information available using SD-OCT includes the structural changes in DME, which can include epiretinal membrane (ERM), retinal swelling, cystoid macular edema (CME), subretinal fluid (SRF) accumulation, and intraretinal fluid (IRF) accumulation (Figure 40.7). SD-OCT imaging allows visualization of the integrity of the outer

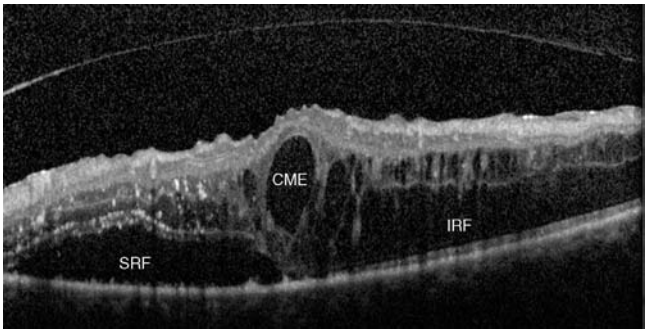

Figure 40.7 The Spectralis HRA+OCT shows cystoid macular edema (CME), intraretinal fluid (IRF), and subretinal fluid (SRF) with subretinal detachment.

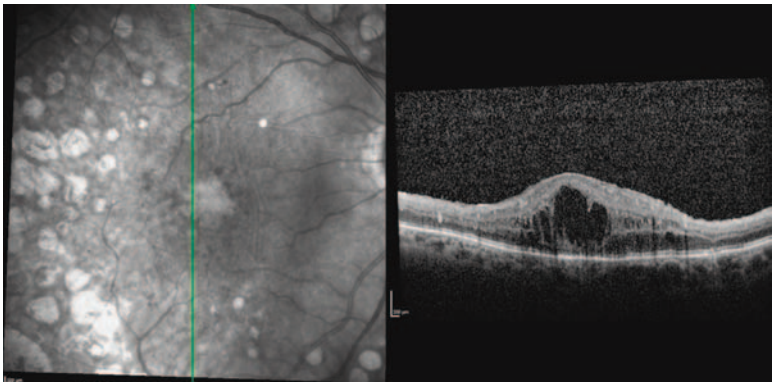

Figure 40.8 The Spectralis HRA+OCT shows disturbed outer and inner segment junction of photoreceptor and external limiting membrane.

retinal layers in DME, which are most important for vision. These include the external limiting membrane (ELM), the photoreceptor inner segment (IS), the outer segment (OS), the retinal pigment epithelium (RPE), and Bruch's membrane (Figure 40.8).

Otani *et al.* were among the earliest researchers to observe three basic structural changes in DME by OCT, namely sponge-like retinal swelling, edema with cystic spaces, and edema with serous retinal detachment [27]. The same study reported a correlation between BCVA and retinal thickness, regardless of the different tomographic features [27]. Panozzo *et al.* introduced vitreo-macular traction (VMT) into the OCT-derived classification of DME and this led to more research into DME [28]. The role of VMT is particularly important in considering possible surgical intervention for DME.

OCT is less invasive than FA for diagnosis of DME in DR patients. Several groups demonstrated that OCT provides an objective documentation of foveal structural changes in eyes with DR [29–31]. Some of the diabetic structural changes such as foveal traction, serous foveal detachment, and CME can be detected by OCT, which may not be evident using ophthalmoscopy and FA. Interestingly, serous macular detachment (SMD) and VMT in the fovea are observable in OCT but not in FA and also not by funduscopy [32].

Koleva-Georgieva *et al.* reported that SD-OCT is useful in diagnosing subclinical SMD in DME and the presence of VMT [33]. VMT appeared as a relative hyperreflective line in the nonreflective space of the vitreous body (Figure 40.9). However, the major drawback of OCT over FA is its incapability to detect macular ischemia, denoted by nonperfusion of the retinal capillaries. Hence FA is still the best diagnostic tool in ischemic DME, as OCT will not be able to give much information regarding this particular condition. Therefore, FA is the most important diagnostic tool in baseline examination in DME to rule out significant macular ischemia, obviating the need for further macular treatments such as laser or intravitreal drug treatment.

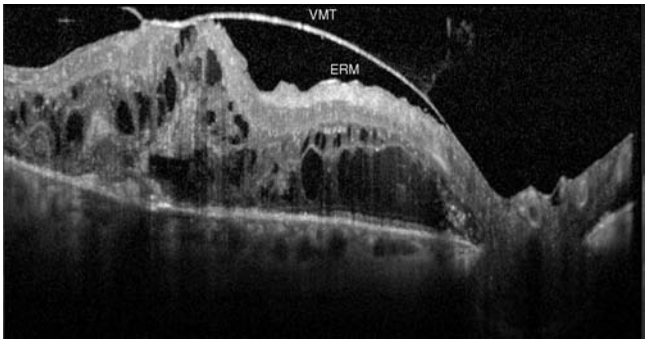

Figure 40.9 The Spectralis HRA+OCT shows vitreo-macular traction (VMT) and epiretinal membrane (ERM) in diabetic macular edema.

40.4
How OCT Changes Our View in Management of DR

OCT technology has changed our perspective in the management of DR, particularly DME. OCT helps the retina physician in accurately diagnosing the different types of DME, especially in the early stages when structural changes may occur that would not be evident with slit-lamp biomicroscopy or FA. In addition, OCT helps in deciding the treatment protocols, either surgical or medical, in DME. Finally, OCT also aids as a noninvasive tool in monitoring the disease progress and the treatment outcome in both DR and DME.

Based on the ETDRS report, the macular photocoagulation laser (MPL) used to be the gold standard in treating DME [34]. Over the last decade, this trend has changed where in cases of refractory DME diagnosed by OCT, which is obviously not be responding to MPL treatment, medical treatment has become the alternative solution. The Intravitreal Triamcinolone for Clinically Significant Macular Edema That Persists After Laser Treatment (TDMO) study reported a reduction in central macular thickness observed by OCT and significant improvement in visual acuity, especially during the initial treatment [35]. In another study, Avitabile *et al*. reported reduced central macular thickness and improved BCVA more in a group of patient treated with intravitreal triamcinolone compared with macular laser grid photocoagulation [36]. It is also important to note that the risk of glaucoma due to steroid response has to be considered in patients who are to be treated with triamcinolone.

In the era of antivascular endothelial growth factors (anti-VEGFs), new drugs such as bevacizumab and ranibizumab have shown promising results in the treatment of DME. The Pan-American Collaborative Retina Study Group (PACORES) reported that primary intravitreal bevacizumab for DME seems to provide stability or improvement in BCVA, OCT, and FA in diffused DME at 12 months [37]. Similarly, results of The RESOLVE Study also showed a promising outcome regarding the safety and efficacy of ranibizumab treatment in patients with DME at 12 months [38].

Framme *et al*. demonstrated postoperative proliferation of the retinal pigment epithelium (RPE), RPE atrophy, and neurosensory retina alteration seen with

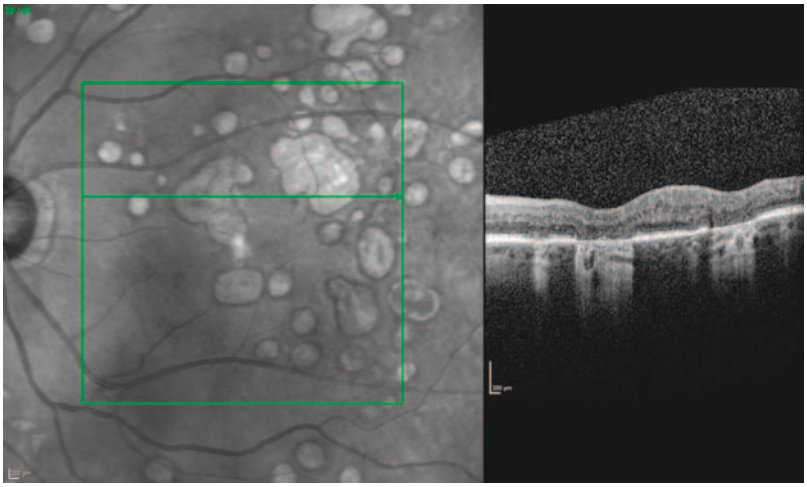

Figure 40.10 The Spectralis HRA+OCT demonstrates postoperative RPE atrophy and neurosensory retina alteration following macular laser photocoagulation.

SD-OCT following MPL [39] (Figure 40.10). Therefore, in the future, treatment of DME will probably be focused more on medical therapy or mild laser treatment, such as selective laser therapy using Nd:YLF laser methods, to prevent such structural damage.

Clinical and anatomic evidence indicates that VMT has been established as one of the known factors in the pathogenesis of CME. A few researchers have reported improvement of BCVA and a significant reduction in macular thickness following vitrectomy for diffused DME combined with VMT [40, 41]. Recchia *et al*. suggested that pars plana vitrectomy with peeling of the inner limitans membrane (ILM) may provide anatomical and visual benefit in DME [42]. In contrast, Shah *et al*. [43] and Dhingra *et al*. [44] reported that vitrectomy and ILM peeling for refractory DME in the absence of VMT failed to improve visual acuity. Hence pars plana vitrectomy with ILM peeling should be reserved for selected cases.

40.5
SD-OCT Scans as a Prognostic Features for DME

The use of SD-OCT is becoming more valuable in the management of DME. SD-OCT imaging enables us to assess the status of the photoreceptor layers. A few researchers have reported a close relationship between this photoreceptor layer status and visual function in various macular diseases such as branch retinal vein occlusion [45], central serous chorioretinopathy [46], age-related macular degeneration [47], retinitis pigmentosa [48], and retinal detachment [49]. Interestingly, an association has been detected between VA and abnormal OCT findings such as those pertaining to the external limiting membrane and the junction between the photoreceptor inner and outer segments (IS/OS) [45–48].

Einbock *et al*. were the first to report an improvement in VA after intravitreal anti-VEGF therapy in DME patients with normal appearance of the external limiting membrane, photoreceptor inner and outer segments, and the RPE [50]. In contrast, patients with disturbed outer retinal layers on SD-OCT showed only a reduction in retinal thickness, without much visual improvement after intravitreal anti-VEGF therapy. Another important finding from the same study was that patients with discontinuity of the inner retinal layer and disturbed outer retinal layers failed to achieve anatomic or visual improvement after intravitreal anti-VEGF in DME (Figures 40.11–40.13).

Forooghian *et al*. observed a stronger correlation of photoreceptor outer segment (PROS) length with VA in DME and suggested that the PROS measures may be more directly related to visual function [51]. In another study, Otani *et al*. reported a

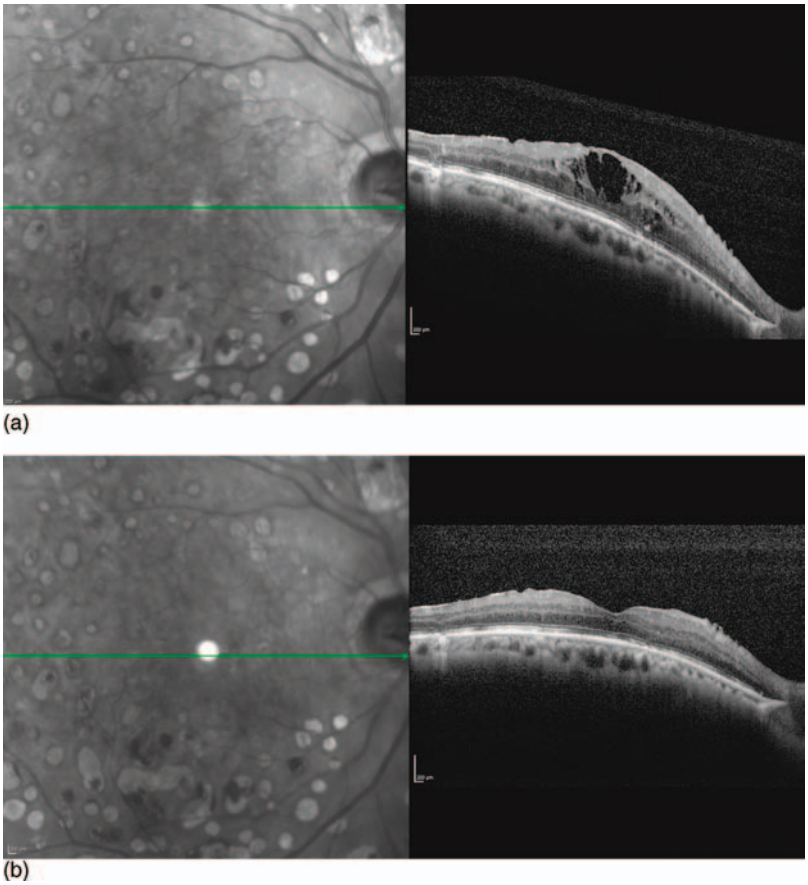

Figure 40.11 Patient with cystoid macular edema before (a) and 3 months after repeated treatment (b) with intravitreal anti-VFGF therapy (ranibizumab). Cystoid edema disappeared and VA improved from 20/60 to 20/30. Note the normal outer retinal layers at baseline. At the inner surface of the retina, an epiretinal membrane was observable.

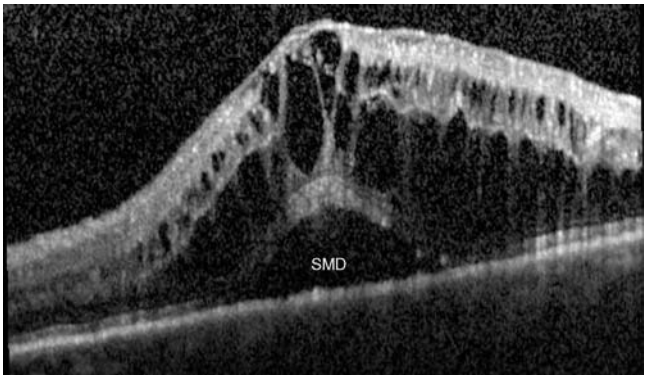

Figure 40.12 Patient with DME and severe cystoid changes. Note that the outer retinal layers such as the external limiting membrane and photoreceptor layers are severely disturbed with serous macular detachment (SMD). VA was unchanged in this patient after anti-VEGF therapy.

significant correlation between the integrity of the external limiting membrane and inner and outer segments of the photoreceptors with best-corrected VA when compared with central subfield thickness in diabetic macular edema [52]. In 2009, Sakamoto *et al*. reported a significant association between foveal photoreceptor status and VA after resolution of diabetic macular edema by pars plana vitrectomy [53]. These findings suggested that integrity of the photoreceptor outer segment plays a significant role in prediction of visual outcome after DME treatment. Such an enormous increase in medical knowledge was only possible due to this OCT technique, which has become one of the most important noninvasive diagnostic tools in ophthalmology.

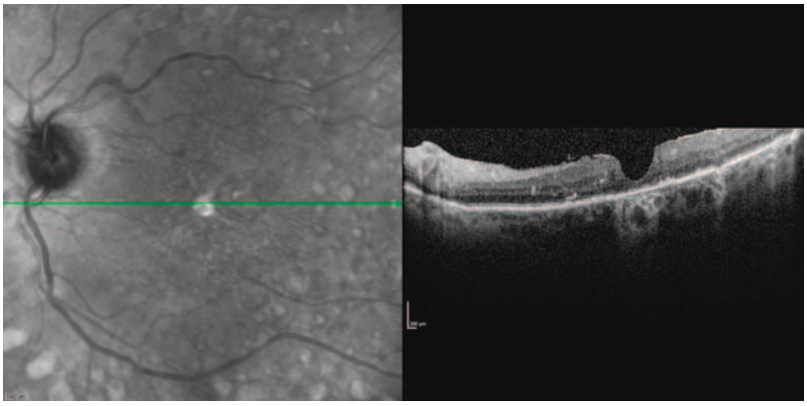

Figure 40.13 Chronic diabetic macular edema patient with discontinuity of the inner retinal layer and disturbed outer retinal layers. This patient failed to achieve anatomic or visual improvement after intravitreal anti-VEGF.

40.6 Summary for the Clinician

- The development of advanced diagnostic instrumental techniques such as SD-OCT has changed our understanding of this disease's pathophysiology, and improved the ability of clinicians to individualize the approach to treatment.
- The integrity of retinal layers can be analyzed with high-resolution OCT scans.
- The presence and integrity of the external limiting membrane, the photoreceptor inner and outer segments, and the retinal pigment epithelium play a significant role in the prediction of visual outcome after DME treatment.

References

1 Zhang, X., Saaddine, J.B., Chou, C.-F., Cotch, M.F., Cheng, Y.J., Geiss, L.J., Gregg, E.W., Albright, A.L., Klein, B.E.K., and Klein, R. (2010) Prevalence of diabetic retinopathy in the United States, 2005–2008. *JAMA*, **304** (6), 649–656.

2 Saaddine, J.B., Honeycutt, A.A., Narayan, K.M.V., Zhang, X., Klein, R., and Boyle, J.P. (2008) Projection of diabetic retinopathy and other major eye diseases among people with diabetes mellitus United States, 2005–2050. *Arch. Ophthalmol.*, **126** (12), 1740–1747.

3 Klein, B.E. and Moss, S.E. (1992) Epidemiology of proliferative diabetic retinopathy. *Diabetes Care*, **15** (12), 1875–1891.

4 Klein, R., Knudtson, M.D., Lee, K.E., Gangnon, R., and Klein, B.E.K. (2009) The Wisconsin Epidemiologic Study of Diabetic Retinopathy XXIII: the twenty-five-year incidence of macular edema in persons with type 1 diabetes. *Ophthalmology*, **116**, 497–503.

5 Klein, R., Klein, B.E.K., Moss, S.E., Davis, M.D., and DeMets, D.L. (1988) Glycosylated hemoglobin predicts the incidence and progression of diabetic retinopathy. *JAMA*, **260**, 2864–2871.

6 Vitale, S., Maguire, M.G., Murphy, R.P., Hiner, C.J., Rourke, L., Sackett, C., and Patz, A. (1995) Clinically significant macular edema in type I diabetes. *Ophthalmology*, **102**, 1170–1176.

7 Chew, E.Y., Klein, M.L., Ferris, F.L., Remaley, N.A., Murphy, R.P., Chantry, K., Hoogwerf, B.J., and Miller, D. (1996) ETDRS Research Group: association of elevated serum lipid levels with retinal hard exudate in diabetic retinopathy: Early Treatment of Diabetic Retinopathy Study (ETDRS) Report No. 22. *Arch. Ophthalmol.*, **114**, 1079–1084.

8 Klein, R., Klein, B.E.K., Moss, S.E., and Cruickshanks, K. (1998) The Wisconsin Epidemiologic Study of Diabetic Retinopathy, XVII: the14-year incidence and progression of diabetic retinopathy and associated risk factors in type I diabetes. *Ophthalmology*, **105**, 1801–1815.

9 Early Treatment Diabetic Retinopathy Study Research Group (1991) Fundus photographic risk factors for progression of diabetic retinopathy. ETDRS Report Number 12. *Ophthalmology Suppl.*, **98**, 823–833.

10 Early Treatment Diabetic Retinopathy Study Research Group (1991) Grading diabetic retinopathy from stereoscopic color fundus photographs – an extension of the modified Airlie House classification. ETDRS Report Number 10. *Ophthalmology Suppl.*, **98**, 786–805.

11 Hutchinson, A., McIntosh, A., Peters, J., O'Keeffe, C., Khunti, K., Baker, R., and Booth, A. (2000) Effectiveness of screening and monitoring tests for diabetic retinopathy: a systematic review. *Diabet. Med.*, **17**, 495–506.

12 American Diabetes Association (2000) Diabetic retinopathy. *Diabetes Care*, **23** (Suppl. 1), S73–S76.

13 Singer, D.E., Nathan, D.M., Fogel, H.A., and Schachat, A.P. (1992) Screening for diabetic retinopathy. *Ann. Intern. Med.*, **116**, 660–671.

14 Early Treatment Diabetic Retinopathy Study Research Group (1991) Grading diabetic retinopathy from stereoscopic color fundus photographs: an extension of the modified Airlie House classification: ETDRS Report No 10. *Ophthalmology*, **98** (Suppl.), 786–806.

15 American Academy of Ophthalmology. The Eye M.D. Association.Year 2011 (last review5.7.2011) http://one.aao.org/CE/PracticeGuidelines/ClinicalStatements_Content.aspx? cid=5e96758f-c10d-41aa-a9b2-fc4d4faac6b9

16 Wilkinson, C.P., Ferris, F.L., Klein, R.E., Lee, P.P., Agardh, C.D., Davis, M., Dills, D., Kampik, A., Pararajasegaram, R., Verdaguer, J.T., and Global Diabetic Retinopathy Project Group (2003) Proposed international clinical diabetic retinopathy and diabetic macular edema disease severity scales. *Ophthalmology*, **110** (9), 1677–1682.

17 Cunha-Vaz, J.G. (2000) Diabetic retinopathy: surrogate outcomes for drug development for diabetic retinopathy. *Ophthalmologica*, **214**, 377–380.

18 Huang, D., Swanson, E.A., Lin, C.P., Schuman, J.S., Stinson, W.G., Chang, W., Hee, M.R., Flotte, T., Gregory, K., and Puliafito, C.A. (1991) Optical coherence tomography. *Science*, **254** (5035), 1178–1181.

19 Wolf, S. and Wolf-Schnurrbusch, U. (2010) Spectral-domain optical coherence tomography use in macular diseases: a review. *Ophthalmologica*, **224** (6), 333–340.

20 Lang, G.E. (2007) Optical coherence tomography findings in diabetic retinopathy. *Dev. Ophthalmol.*, **39**, 31–47.

21 Sánchez-Tocino, H., Alvarez-Vidal, A., Maldonado, M.J., Moreno-Montañés, J., and García-Layana, A. (2002) Retinal thickness study with optical coherence tomography in patients with diabetes. *Invest. Ophthalmol. Vis. Sci.*, **43**, 1588–1594.

22 Massin, P., Erginay, A., Haouchine, B., Mehidi, B., and Gaudric, A. (2002) Retinal thickness in healthy and diabetic subjects measured using optical coherence tomography mapping software. *Eur. J. Ophthalmol.*, **12**, 102–108.

23 Nunes, S., Pereira, I., Santos, A., Bernardes, R., and Cunha-Vaz, J. (2010) Central retinal thickness measured with HD-OCT shows a weak correlation with visual acuity in eyes with CSME. *Br. J. Ophthalmol.*, **94** (9), 1201–1204.

24 Diabetic Retinopathy Clinical Research Network (2007) The relationship between OCT-measured central retinal thickness and visual acuity in diabetic macular edema. *Ophthalmology*, **114** (3), 525–536.

25 Strøm, C., Sander, B., Larsen, N., Larsen, M., and Lund-Andersen, H. (2002) Diabetic macular edema assessed with optical coherence tomography and stereo fundus photography. *Invest. Ophthalmol. Vis. Sci.*, **43**, 241–245.

26 Wolf-Schnurrbusch, U.E., Ceklic, L., Brinkmann, C.K., Iliev, M., Frey, M., Rothenbuehler, S.P., Enzmann, V., and Wolf, S. (2009) Macular thickness measurements in healthy eyes using six different optical coherence tomography instruments. *Invest. Ophthalmol. Vis. Sci.*, **50** (7), 3432–3437.

27 Otani, T., Kishi, S., and Maruyama, Y. (1999) Patterns of diabetic macular edema with optical coherence tomography. *Am. J. Ophthalmol.*, **127**, 688–693.

28 Panozzo, G., Gusson, E., Parolini, B., and Mercanti, A. (2003) Role of optical coherence tomography in the diagnosis and follow up of diabetic macular edema. *Semin. Ophthalmol.*, **18**, 74–81.

29 Özdek, S.C., Erdinç, M.A., Grelik, G., Aydin, B., Bahçeci, U., and Hasanreisoğlu, B. (2005) Optical coherence tomography assessment of diabetic macular edema: comparison with fluorescein angiographic and clinical findings. *Ophthalmologica*, **219**, 86–92.

30 Soliman, W., Sander, B., Hasler, P.W., and Larsen, M. (2008) Correlation between intraretinal changes in diabetic macular oedema seen in fluorescein angiographic and optical coherence tomography. *Acta Ophthalmol.*, **86**, 34–39.

31 Kang, S.W., Park, C.Y., and Ham, D.I. (2004) The correlation between fluorescein angiographic and optical coherence tomography feature in clinically significant diabetic macular edema. *Am. J. Ophthalmol.*, **137**, 313–322.

32 Ozdemir, H., Karacorlu, M., and Karacorlu, S. (2005) Serous macular detachment in

diabetic cystoid macular edema. *Acta Ophthalmol. Scand.*, **83**, 63–66.

33 Koleva-Georgieva, D. and Sivkova, N. (2009) Assessment of serous macular detachment in eyes with diabetic macula edema by use of spectral-domain optical coherence tomography. *Graefes Arch. Clin. Exp. Ophthalmol.*, **247**, 1461–1469.

34 The Diabetes Control and Complications Trial Research Group (1993) The effect of intensive treatment of diabetes on the development and progression of long-term complications in insulin-dependent diabetes mellitus. *N. Engl. J. Med.*, **329**, 977–986.

35 Gillies, M.C., Sutter, F.K., Simpson, J.M., Larsson, J., Ali, H., and Zhu, M. (2006) Intravitreal triamcinolone for refractory diabetic macular edema: two-year results of a double-masked, placebo-controlled, randomized clinical trial. *Ophthalmology*, **113**, 1533–1538.

36 Avitabile, T., Lungo, A., and Reibaldi, A. (2005) Intravitreal triamcinolone compared with macular laser grid photocoagulation for the treatment of cystoid macular edema. *Am. J. Ophthalmol.*, **140**, 695–702.

37 Arevalo, J.F., Sanchez, J.G., Fromow-Guerra, J., Wu, L., Berrocal, M.H., Farah, M.E., Cardillo, J., Rodríguez, F.J., and Pan-American Collaborative Retina Study Group (PACORES) (2009) Comparison of two doses of primary intravitreal bevazumab (Avastin) for diffused diabetic macular oedema: result from the Pan American Collaborative Retina Study Group (PACORES) at 12 months follow up. *Graefes Arch. Clin. Exp. Ophthalmol.*, **247** (6), 735–743.

38 Massin, P., Bandello, F., Garweg, J.G., Hansen, L.L., Harding, S.P., Larsen, M., Mitchell, P., Sharp, D., Wolf-Schnurrbusch, U.E.K., Gekkieva, M., Weichselberger, A., and Wolf, S. (2010) Safety and efficacy of ranibizumab in diabetic macular edema (RESOLVE Study). A 12-month, randomized, controlled, double-masked, multicenter phase II study. *Diabetes Care*, **33**, 2399–2405.

39 Framme, C., Alt, C., Theisen-Kunde, D., and Brinkmann, R. (2009) Structural changes of the retina after conventional laser photocoagulation and selective retinal treatment (SRT) in spectral-domain optical coherence tomography. *Curr. Eye Res.*, **34**, 568–579.

40 Massin, P., Duguid, G., Erginay, A., Haouchine, B., and Gaudric, A. (2003) Optical coherence tomography for evaluating diabetic macular edema before and after vitrectomy. *Am. J. Ophthalmol.*, **135**, 169–177.

41 Shimonagono, Y., Makiuchi, R., Miyazaki, M., Doi, N., Uemura, A., and Sakamoto, T. (2007) Result of visual acuity and foveal thickness in diabetic macular edema after vitrectomy. *Jpn. J. Ophthalmol.*, **51**, 204–209.

42 Recchia, F.M., Ruby, A.J., and Carvalho Recchia, C.A. (2005) Pars plana vitrectomy with removal of internal limiting membrane in the treatment of persistent diabetic macular edema. *Am. J. Ophthalmol.*, **139**, 447–454.

43 Shah, S.P., Patel, M., Thomas, D., Aldington, S., and Laidlaw, D.A.H. (2006) Factors predicting outcome of vitrectomy for diabetic macular oedema: results of a prospective study. *Br. J. Ophthalmol.*, **90**, 33–36.

44 Dhingra, N., Sahni, J., Shipley, J., Harding, S.P., Groenewald, C.I., Pearce, A., Stanga, P.E., and Wong, D. (2005) Vitrectomy and internal limiting membrane (ILM) removal for diabetic macular edema in eyes with absent vitreo–macular traction fails to improve visual acuity: results of a 12 months prospective randomized controlled clinical trial. Presented at the Annual Meeting of the Association for Research in Vision and Ophthalmology, 1–5 May 2005, Fort Lauderdale, FL.

45 Ota, M., Tsujikawa, A., Murakami, T., Kita, M., Miyamoto, K., Sakamoto, A., Yamaike, N., and Yoshimura, N. (2007) Association between integrity of foveal photoreceptor layer and visual acuity in branch retinal vein occlusion. *Br. J. Ophthalmol.*, **91**, 1644–1649.

46 Piccolino, F.C., Longrais, R.R.D.L., Ravera, G., Eandi, C.M., Ventre, L., Abdollahi, A., and Manea, M. (2005) The foveal photoreceptor layer and visual acuity loss in central serous chorioretinopathy. *Am. J. Ophthalmol.*, **139**, 87–99.

47 Hayashi, H., Yamashiro, K., Tsujikawa, A., Ota, M., Otani, A., and Yoshimura, N. (2009) Association between foveal

photoreceptor integrity and visual outcome in neovascular age-related macular degeneration. *Am. J. Ophthalmol.*, **148** (1), 83–89.

48 Oishi, A., Otani, A., Sasahara, M., Kojima, H., Nakamura, H., Kurimoto, M., and Yoshimura, N. (2009) Photoreceptor integrity and visual acuity in cystoids macular oedema associated with retinitis pigmentosa. *Eye*, **23**, 1411–1416.

49 Wakabayashi, T., Oshima, Y., Fujimoto, H., Murakami, Y., Sakaguchi, H., Kusaka, S., and Tano, Y. (2009) Foveal microstructure and visual acuity after retinal detachment repair. Imaging analysis by Fourier-domain optical coherence tomography. *Ophthalmology*, **116**, 519–528.

50 Einbock, W., Berger, L., Wolf-Schnurrbusch, U., Fleischhauer, J., and Wolf, S. (2008) Predictive factors for visual acuity of patients with diabetic macular edema interpreted from the Spectralis HRA+OCT (Heidelberg Engineering). *Invest. Ophthalmol. Vis. Sci.*, **49**, 3432–3473.

51 Forooghian, F., Stetson, P., Scott, M., Chew, E.Y., Wong, W.T., Chukras, C., Meyerle, C.B., and Frederick, L. (2010) Relationship between photoreceptor outer segment length and visual acuity in diabetic macular edema. *Retina*, **30** (1), 63–70.

52 Otani, T., Yamaguchi, Y., and Kishi, S. (2010) Correlation between visual acuity and foveal microstructural changes in diabetic macular edema. *Retina*, **30** (5), 774–780.

53 Sakamoto, A., Nishijima, K., Kita, M., Oh, H., Tsujikawa, A., and Yoshimura, N. (2009) Association between foveal photoreceptor status and visual acuity after resolution of diabetic macular edema by pars plana vitrectomy. *Graefes Arch. Clin. Exp. Ophthalmol.*, **247**, 1325–1330.

41
Glaucoma Laser Therapy

Marc Töteberg-Harms, Peter P. Ciechanowski, and Jens Funk

41.1
Introduction

There are multiple possibilities for lowering intraocular pressure (IOP). Medical therapy is the first-line treatment (http://www.worldglaucoma.org; http://www.eugs.org, http://www.seagig.org). When medical therapy is no longer sufficient, there are many surgical ways to control IOP. Trabeculectomy is still the gold standard. The European Glaucoma Society recommends laser surgery of the trabecular meshwork (TM) before or in addition to medical therapy (see guidelines of the European Glaucoma Society, http://www.eugs.org).

In this chapter, laser trabeculoplasty (LTP), argon laser trabeculoplasty (ALT), and selective laser trabeculoplasty (SLT), and also excimer laser trabeculotomy (ELT) and cyclophotocoagulation (CPC), are described.

For about 35 years, laser therapy has been used to lower IOP [1, 2]. Different laser types could be used, such as the continuous-wave, frequency-doubled neodymium: yttrium aluminum garnet (Nd:YAG) laser (wavelength 1064 and 532 nm), argon laser (488 and 514.5 nm), diode laser (810 nm), excimer laser (308 nm), and krypton laser (647 or 568 nm) [3–6]. The most important parameter of these lasers with regard to lowering the IOP is the energy density delivered to specific tissues.

By decreasing or even replacing the need for topical medications, especially in patients with primary open-angle glaucoma (POAG), laser therapy can reduce systemic [7] and local [8] side effects, or can even avoid the need for surgery.

41.2
Laser Trabeculoplasty (LTP) and Selective Laser Trabeculoplasty (SLT)

In 1973, Krasnov [1] reported the first temporary lowering of IOP via a Q-switched ruby laser. The laser was meant to increase the outflow of aqueous humor within the TM [2, 9].

Handbook of Biophotonics. Vol.2: Photonics for Health Care, First Edition. Edited by Jürgen Popp, Valery V. Tuchin, Arthur Chiou, and Stefan Heinemann.

Different types of lasers are used for LTP: argon laser (488 or 514.5 nm), solid state laser (532 nm) or diode laser (810 nm).

There are several theories about the mechanism of LTP (including ALT and SLT), but it is not yet definitely known. From a biochemical point of view, LTP and SLT could increase the replication of cells which are involved in the outflow of the TM [10–13]. Another theory focuses on the mechanical distortion of the TM.

With ALT, a series of 50 μm laser beam spots (about 20–25 spots within 90° of the TM) with an exposure time of 0.1 s and a power of up to 1000 mW are placed 180–360° around the TM to increase the aqueous humor outflow. If only 180° is used, it is advisable to re-evaluate the patient after 4–6 weeks. This intervention causes thermal coagulative damage and can decrease the IOP by up to 9–10 mmHg [14]. However, filtering surgery should be considered first, if a greater decrease in IOP is needed.

The SLT device in clinical use is a frequency-doubled, Q-switched Nd:YAG laser (532 nm) [15]. Usually 180° or 360° of the TM are treated with 50–100 spots. The spot size is 400 μm, the pulse duration is 3 ns and the power is 0.6–1.0 mJ per pulse on average.

In contrast to ALT, SLT does not cause significant coagulative damage. Despite this, because of a wider beam and a very short exposure time, each SLT pulse delivers less than 0.1% energy in comparison with ALT.

In both laser procedures (ALT and SLT), an IOP spike within the first few hours after treatment can occur. Local medication or systemic carboanhydrase inhibitors can be used to prevent this peak.

For the laser treatment, a gonioscopic lens (e.g., Goldmann three-mirror lens, Latina lens or other gonioscopic lenses) is used under topical anesthesia to focus the laser beam to the TM.

After LTP, most patients require continuing medication; about 30–50% can reduce their level of treatment within the following months.

ALT causes scars in the TM, hence repeated coagulations are not recommended, whereas SLT does not and can be repeated [16].

Both ALT and SLT are favorable ways of lowering the eye pressure in patients who need their IOP to be reduced by around 5–10 mmHg.

41.3 Excimer Laser Trabeculotomy (ELT)

In addition to the methods mentioned above, ELT is mostly used in POAG and also in pseudoexfoliative glaucoma. The excimer laser is short pulsed (80 ns) and uses xenon chloride at a wavelength of 308 nm. ELT delivers photoablative energy and decreases the outflow obstruction at the inner wall of Schlemm's canal and the juxtacanalicular TM [17, 18].

This intervention can be performed with topical anesthesia either in combination with cataract surgery (Phako-ELT) or as monotherapy. A paracentesis is needed to insert a fiber-optic probe and an endoscope or a goniolens is used for observation. Ten pores are usually created in Schlemm's canal.

ELT is an elegant way of reducing the IOP, in particular in combination with cataract surgery. Usually the IOP can be reduced by up to 35%, depending on the level of initial IOP [19–21].

41.4 Cyclophotocoagulation (CPC)

For CPC, different lasers are used: trans-sclerally a 1064 nm wavelength Nd:YAG laser or an 810 nm diode laser [22].

This procedure destroys the ciliary processes and reduces the production of aqueous humor. Because other laser therapies have fewer complications, CPC is often considered just if other attempts at IOP reduction have failed.

For the intervention, short anesthesia or retro-bulbar block is usually required. It is recommended to treat at 270° with 16–18 applications each with an exposure time of 2500 ms and a power of 0.5–2.75 J. The tip is placed at a distance of 0.5–1.5 mm from the limbus and held as perpendicular to the sclera as possible.

In special cases, it is also possible to perform CPC endoscopically (endo-cyclophotocoagulation).

Cyclophotocoagulation can be repeated several times, but because of its possible complications, including inflammation, pain, uveitis, reduction of visual acuity, hypotony, and phthisis bulbi or hemorrhage, the indication has to be carefully considered.

References

1 Krasnov, M.M. (1973) Laseropuncture of anterior chamber angle in glaucoma. *Am. J. Ophthalmol.*, **75** (4), 674–678.

2 Wise, J.B. and Witter, S.L. (1979) Argon laser therapy for open-angle glaucoma. A pilot study. *Arch. Ophthalmol.*, **97** (2), 319–322.

3 Chung, P.Y., *et al.* (1998) Five-year results of a randomized, prospective, clinical trial of diode vs argon laser trabeculoplasty for open-angle glaucoma. *Am. J. Ophthalmol.*, **126** (2), 185–190.

4 Englert, J.A., *et al.* (1997) Argon vs. diode laser trabeculoplasty. *Am. J. Ophthalmol.*, **124** (5), 627–631.

5 Guzey, M., *et al.* (1999) Effects of frequency-doubled Nd:YAG laser trabeculoplasty on diurnal intraocular pressure variations in primary open-angle glaucoma. *Ophthalmologica*, **213** (4), 214–218.

6 Spurny, R.C. and Lederer, C.M. Jr. (1984) Krypton laser trabeculoplasty. A clinical report. *Arch. Ophthalmol.*, **102** (11), 1626–1628.

7 Nelson, W.L., *et al.* (1986) Adverse respiratory and cardiovascular events attributed to timolol ophthalmic solution, 1978–1985. *Am. J. Ophthalmol.*, **102** (5), 606–611.

8 Osborne, S.A., *et al.* (2005) Alphagan allergy may increase the propensity for multiple eye-drop allergy. *Eye (Lond.)*, **19** (2), 129–137.

9 Wickham, M.G. and Worthen, D.M. (1979) Argon laser trabeculotomy: long-term follow-up. *Ophthalmology*, **86** (3), 495–503.

10 Alvarado, J.A., *et al.* (2005) A new insight into the cellular regulation of aqueous outflow: how trabecular meshwork endothelial cells drive a mechanism that

regulates the permeability of Schlemm's canal endothelial cells. *Br. J. Ophthalmol.*, **89** (11), 1500–1505.

11 Ticho, U., *et al.* (1978) Argon laser trabeculotomies in primates: evaluation by histological and perfusion studies. *Invest. Ophthalmol. Vis. Sci.*, **17** (7), 667–674.

12 Van Buskirk, E.M., *et al.* (1984) Argon laser trabeculoplasty. Studies of mechanism of action. *Ophthalmology*, **91** (9), 1005–1010.

13 Wickham, M.G., Worthen, D.M., and Binder, P.S. (1977) Physiological effects of laser trabeculotomy in rhesus monkey eyes. *Invest. Ophthalmol. Vis. Sci.*, **16** (7), 624–628.

14 Starita, R.J., *et al.* (1984) The effect of repeating full-circumference argon laser trabeculoplasty. *Ophthalmic Surg.*, **15** (1), 41–43.

15 Latina, M.A., *et al.* (1998) Q-switched 532-nm Nd:YAG laser trabeculoplasty (selective laser trabeculoplasty): a multicenter, pilot, clinical study. *Ophthalmology*, **105** (11), 2082–2088; discussion 2089–90.

16 Damji, K.F., *et al.* (1999) Selective laser trabeculoplasty v argon laser trabeculoplasty: a prospective randomised clinical trial. *Br. J. Ophthalmol.*, **83** (6), 718–722.

17 Walker, R. and Specht, H. (2002) Theoretical and physical aspects of excimer laser trabeculotomy (ELT) *ab interno* with the AIDA laser with a wavelength of 308 nm. *Biomed. Tech. (Berl.)*, **47** (5), 106–110 (in German).

18 Babighian, S., Rapizzi, E., and Galan, A. (2006) Efficacy and safety of *ab interno* excimer laser trabeculotomy in primary open-angle glaucoma: two years of follow-up. *Ophthalmologica*, **220** (5), 285–290.

19 Pache, M., Wilmsmeyer, S., and Funk, J. (2006) Laser surgery for glaucoma: excimer-laser trabeculotomy. *Klin. Monbl. Augenheilkd.*, **223** (4), 303–307 (in German).

20 Wilmsmeyer, S., Philippin, H., and Funk, J. (2006) Excimer laser trabeculotomy: a new, minimally invasive procedure for patients with glaucoma. *Graefes Arch. Clin. Exp. Ophthalmol.*, **244** (6), 670–676.

21 Töteberg-Harms, M., *et al.* (2011) One-year results after combined cataract surgery and excimer laser trabeculotomy for elevated intraocular pressure. *Ophthalmologe*, 2011 Feb 27. [Epub ahead of print] PMID: 21359550 (in German).

22 Beckman, H. and Sugar, H.S. (1973) Neodymium laser cyclocoagulation. *Arch. Ophthalmol.*, **90** (1), 27–28.

42
Ocular Blood Flow Measurement Methodologies and Clinical Application

Yochai Z. Shoshani, Alon Harris, and Brent A. Siesky

42.1
Background and Significance

Open-angle glaucoma (OAG) is a chronic progressive optic neuropathy representing one of the leading causes of blindness in the United States and worldwide [1]. Elevated intraocular pressure (IOP) is the only current modifiable risk factor [2]; however, many patients with OAG continue to experience progression of the disease despite lowered IOP. This has led to the identification of other risk factors, including low ocular perfusion pressure, vascular dysregulation, and ischemia. Assessment of blood flow and its current clinical implications are discussed in this chapter.

42.2
Blood flow Methodologies

42.2.1
Color Doppler Imaging

Color Doppler imaging (CDI) measures blood flow in the retrobulbar blood vessels supplying ocular tissues. CDI combines two-dimensional structural ultrasound images with velocity measurements derived from the Doppler shift of sound waves reflected from erythrocytes as they travel through blood vessels. The peak systolic velocity (PSV) and end diastolic velocity (EDV) are measured and used to calculate Pourcelot's index of resistivity (RI), a marker of downstream resistance, as RI = (PSV – EDV)/PSV [3].

42.2.2
Laser Doppler Flowmetry and Scanning Laser Flowmetry

Laser Doppler flowmeter measures retinal capillary blood flow noninvasively by utilizing a modified fundus camera combined with a computer system. The

Handbook of Biophotonics. Vol.2: Photonics for Health Care, First Edition. Edited by Jürgen Popp, Valery V. Tuchin, Arthur Chiou, and Stefan Heinemann.

Heidelberg retinal flowmeter (HRF) is one commercially available system that combines laser Doppler flowmetry with scanning laser tomography, providing a two-dimensional map of blood flow to the optic nerve and surrounding retina. This technique is most sensitive to microvascular blood flow changes in the superficial layers of the optic nerve head.

42.2.3 Retinal Vessel Analyzer

The retinal vessel analyzer (RVA), which is composed of a fundus camera, a video camera, a monitor, and a computer with specialized software, permits continuous monitoring of vessels in real time with a maximum frequency of 50 Hz. Each vessel has a specific transmittance profile that is based on the absorbing properties of hemoglobin. The diameter of a vessel is determined using an algorithm converting this profile.

42.2.4 Ocular Pulse Amplitude and Pulsatile Ocular Blood Flow

Dynamic contour tonometry (DCT) is a noninvasive and direct method of continuously measuring IOP over time [4]. The difference between the highest and lowest IOP measurements defines the ocular pulse amplitude (OPA), which is believed to be a result of the changing blood volume of the eye. Similarly to DCT, the sinusoidal pattern of pulsatile ocular blood flow (POBF) can be estimated by quantifying the changes in ocular volume and pressure during the cardiac cycle using a variety of devices.

42.2.5 Laser Speckle Method (Laser Speckle Flowgraphy)

The laser speckle method is a technique based on the interference phenomenon, observed when coherent light sources are scattered by a diffusing surface. The scattered laser light forms a "speckle" pattern, which is imaged and then statistically characterized. The variation in the structure of the pattern changes with the velocity of erythrocytes in the retina.

42.2.6 Digital Scanning Laser Ophthalmoscope Angiography

Retinal blood flow can be directly visualized using sodium fluorescein dye, and choroidal flow using indocyanine green dye, during digital scanning laser ophthalmoscope (SLO) angiography. The fluorescent compound is injected into a vein and observed as it fills the ocular vasculature. A time-based stream of measured intensities is then used to construct a video signal [5]. The amount of time between the first appearance of dye in a retinal artery and the associated vein is called the arteriovenous passage time (AVP), which has been shown to be very sensitive to small

changes in blood flow through the retinal vascular bed, and measurements can be localized to specific quadrants of the retina.

42.2.7
Doppler Optical Coherence Tomography

Doppler optical coherence tomography (DOCT) uses the Doppler frequency shift of backscattered light reflecting off red blood cells in the vasculature to measure blood flow in the retinal arteries in real time. Using Fourier domain OCT, it is possible to combine the high-resolution cross-sectional imaging of OCT with laser Doppler imaging to capture information from the retinal blood vessels in three dimensions in a time period that is only a fraction of the cardiac cycle [6]. DOCT is used to measure both the velocity and volumetric flow rate in the retinal branch vessels (Figure 42.1).

42.2.8
Retinal Oximetry

Retinal oximetry is the noninvasive measurement of hemoglobin oxygen saturation in the retinal vasculature. A linear relationship exists between the oxygen saturation and the ratio of optical densities measured at the two wavelengths. This allows for direct and quantitative mapping of retinal biochemistry [7]. Retinal oximetry is a

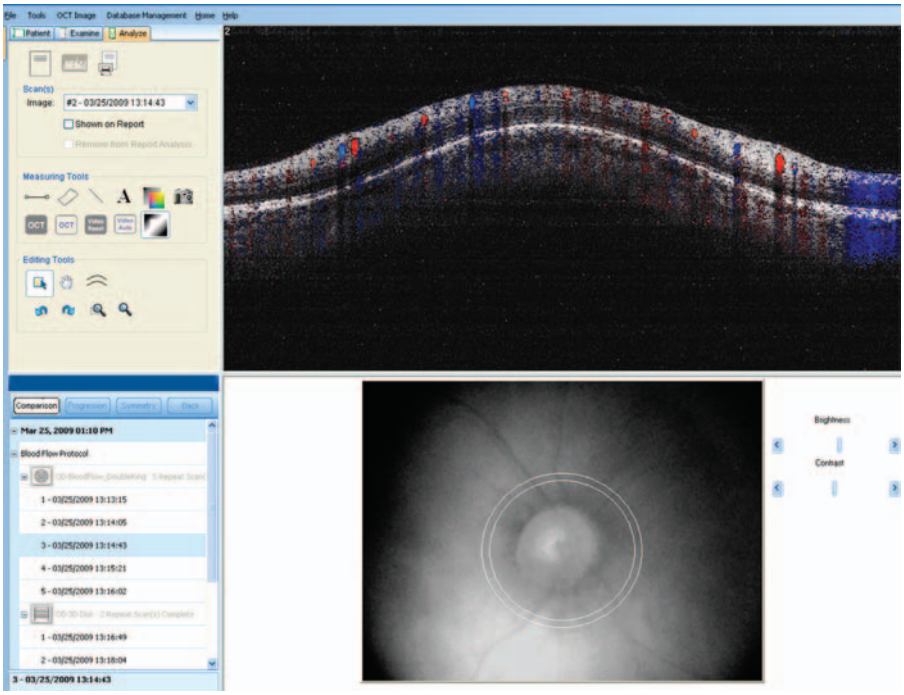

Figure 42.1 Doppler OCT.

novel technique that may help investigators understand the metabolic changes that may contribute to the pathology of glaucoma.

42.2.9
Newly Developed Techniques

In addition to these established techniques, recent developments in high-resolution magnetic resonance imaging (MRI) and its application to image anatomy, physiology, and function in the retina may provide future avenues for assessing the ocular circulation [8]. MRI offers unique advantages over existing retinal imaging techniques, including the ability to image multiple layers without depth limitation and to provide multiple clinically relevant data in a single setting. Functional laser Doppler flowmetry (FLDF), which is the coupling between visually evoked neural activity and vascular activity within the neural tissue of the optic nerve (neurovascular coupling), may also be useful [9]. The application of FLDF in patients with ocular hypertension and early glaucoma demonstrates that the visually evoked hyperemic responses are significantly depressed even when neural retinal activity may still be relatively preserved [9].

42.3
Relationship Between Blood Flow and Visual Function

The retrobulbar circulation of the orbit has been the most studied vascular bed in glaucoma, with dozens of research investigations demonstrating altered blood flow parameters in patients with glaucoma. A correlation between glaucomatous progression and decreased blood flow velocities in the A correlation between glaucomatous progression and decreased blood flow velocities in the short posterior ciliary arteries (SPCAs), the small retrobulbar vessels that supply the optic nerve head, decreased EDV in the central retinal artery (CRA), higher RI in the CRA and SPCA, and a high RI in the ophthalmic artery (OA) have been reported [10, 11]. Both blood flow and velocity in the retinal microcirculation were also demonstrated to be significantly decreased in eyes with worse damage compared with their fellow eyes with less damage [12]. Blood flow at the neuroretinal rim has been shown to correspond to regional VF defects in patients with normal-tension glaucoma (NTG) [13]. Circadian fluctuations of OPP were also found to correlate significantly with VF damage in a group of 132 patients with NTG [14]. Although a causal relationship has yet to be established, ocular blood flow likely plays an integral role in both the pathophysiology and progression of glaucomatous vision loss, and therefore warrants further investigation.

42.4
Relationship Between Blood Flow and Optic Nerve Structure

Several studies have investigated hemodynamic alterations in the SPCA and other retrobulbar blood vessels and also the retina and choroid in relation to ocular

structure. Loss of capillaries was found in the neural tissue of the optic disc in glaucomatous optic atrophy [15]. Characteristic glaucomatous excavation of the optic disc has also been correlated with alterations in the retinal and retrobulbar circulations [16]. Neuroretinal rim damage was found to be associated with a local reduction in blood flow in glaucoma patients [17]. Ocular blood flow was found to be associated with thinning in the retinal nerve fiber layer (RNFL) [18]. A reduction in blood flow with thinning of the RNFL would be expected because capillary loss accompanies loss of neural tissue, which likely has decreased metabolic demands. However, several of the above studies found an increase in local retinal blood flow with thinning of the RNFL. This divergence may be explained by an autoregulatory compensatory response. Initially, blood flow may increase to a region of RNFL thinning; as glaucomatous damage progresses, blood flow may gradually decrease. Unfortunately, no study has examined this relationship in advanced glaucoma patients.

It has been suggested that glaucomatous optic neuropathy may be linked to unstable blood flow and reperfusion injury from either perfusion pressure fluctuations or dysfunctional autoregulation [19]. Larger fluctuations in perfusion and arterial pressure were correlated with reduced RNFL thickness. This suggests that faulty autoregulation during fluctuations in ocular perfusion pressure may cause daily ischemic damage, succeeded by reperfusion injury. Recent evidence from the Thessaloniki Eye Study [20] found that patients on antihypertensive therapy with diastolic blood pressure (DBP) less than 90 mmHg was positively correlated with cup area and cup-to-disc ratio when compared with both patients with high DBP and untreated patients with normal DBP. Low perfusion pressure was also positively associated with cup area and cup-to-disc ratio. The results remained consistent after adjusting for age, IOP, cardiovascular disease, diabetes, and duration of antihypertensive treatment. The findings suggest that blood pressure status is an independent risk factor for glaucomatous damage [20]. Systemic hypertension has also been linked as a risk factor for development of glaucoma. The association of systemic hypertension as a risk factor may be related to its association with elevated IOP. Because the Thessaloniki study adjusted for IOP, its results may more appropriately portray the relationship between blood pressure and cupping [20]. The translamina cribrosa pressure difference, the difference between the IOP and the pressure of the cerebrospinal fluid (CSF) around the optic nerve, may be an important consideration as CSF pressure is likely correlated with blood pressure and was found to be lowered in OAG and NTG patients [21].

The 2009 report of the World Glaucoma Association stressed that only larger, longitudinal multi-center investigations can confirm the relationship between ocular blood flow and visual function and optic nerve structure hinted at in the available pilot research. It is therefore vital that we determine at what levels of (and fluctuations in) IOP and ocular perfusion pressure there is an increase in the probability of glaucoma progression and how altered ocular blood flow may play a role in the development and progression of glaucoma [22].

References

1 Quigley, H.A. (1996) Number of people with glaucoma worldwide. *Br. J. Ophthalmol.*, **80** (5), 389–393.
2 Weinreb, R.N. (2001) A rationale for lowering intraocular pressure in glaucoma. *Surv. Ophthalmol.*, **45** (S4), s335–s336.
3 Pourcelot, L. (1974) Applications of cliniques de l'examinen Doppler transcutane. *INSERM*, **34**, 213–240.
4 Punjabi, O.S., Kniestedt, C., Stamper, R.L., and Lin, S.C. (2006) Dynamic contour tonometry: principle and use. *Clin. Exp. Ophthalmol.*, **34** (9), 837–840.
5 Wolf, S., Arend, O., Toonen, H., *et al.* (1991) Retinal capillary blood flow measurement with a scanning laser ophthalmoscope. Preliminary results. *Ophthalmology*, **98**, 996–1000.
6 Wehbe, H.M., Ruggeri, M., Jiao, S., Gregori, G., Puliafito, C.A., and Zhao, W. (2007) Automatic retinal blood flow calculation using spectral domain optical coherence tomography. *Opt. Express*, **15**, 15193–15206.
7 Alabboud, I., Muyo, G., Gorman, A., *et al.* (2007) New spectral imaging techniques for blood oximetry in the retina. *Proc. SPIE*, **6631**, 6310.
8 Duong, T.Q., Pardue, M.T., Thulé, P.M., *et al.* (2008) Layer-specific anatomical, physiological and functional MRI of the retina. *NMR Biomed.*, **21** (9), 978–996.
9 Riva, C.E. and Falsini, B. (2008) Functional laser Doppler flowmetry of the optic nerve: physiological aspects and clinical applications. *Prog. Brain Res.*, **173**, 149–163.
10 Zeitz, O., Galambos, P., Wagenfeld, L., *et al.* (2006) Glaucoma progression is associated with decreased blood flow velocities in the short posterior ciliary artery. *Br. J. Ophthalmol.*, **90** (10), 1245–1248.
11 Yamazaki, Y. and Drance, S. (1997) The relationship between progression of visual field defects and retrobulbar circulation in patients with glaucoma. *Am. J. Ophthalmol.*, **124**, 287–295.
12 Grunwald, J.E., Piltz, J.E., Hariprasad, S.M., and DuPont, J. (1998) Optic nerve and choroidal circulation in glaucoma. *Invest. Ophthalmol. Vis. Sci.*, **39** (12), 2329–2336.
13 Sato, E.A., Ohtake, Y., Shinoda, K., Mashima, Y., and Kimura, I. (2006) Decreased blood flow at neuroretinal rim of optic nerve head corresponds with visual field deficit in eyes with normal tension glaucoma. *Graefes Arch. Clin. Exp. Ophthalmol.*, **244** (7), 795–801.
14 Choi, J., Kim, K.H., Jeong, J., Cho, H.S., Lee, C.H., and Kook, M.S. (2007) Circadian fluctuation of mean ocular perfusion pressure is a consistent risk factor for normal-tension glaucoma. *Invest. Ophthalmol. Vis. Sci.*, **48** (1), 104–111.
15 Gottanka, J., Kuhlmann, A., Scholz, M., Johnson, D.H., and Lütjen-Drecoll, E. (2005) Pathophysiologic changes in the optic nerves of eyes with primary open angle and pseudoexfoliation glaucoma. *Invest. Ophthal. Vis. Sci.*, **46**, 4170–4181.
16 Hafez, A.S., Bizzarro, R.L.G., and Lesk, M.R. (2003) Evaluation of optic nerve head and peripapillary retinal blood flow in glaucoma patients, ocular hypertensives, and normal subjects. *Am. J. Ophthalmol.*, **136**, 1022–1031.
17 Nicolela, M.T., Drance, S.M., Rankin, S.J.A., Buckley, A.R., and Walman, B.E. (1996) Color Doppler imaging in patients with asymmetric glaucoma and unilateral visual field loss. *Am. J. Ophthalmol.*, **121**, 502–510.
18 Grieshaber, M.C., Mozaffarieh, M., and Flammer, J. (2007) What is the link between vascular dysregulation and glaucoma? *Surv. Ophthalmol.*, **52**, S144–S154.
19 Vulsteke, C., Stalmans, I., Fieuws, S., and Zeyen, T. (2008) Correlation between ocular pulse amplitude measured by dynamic contour tonometer and visual field defects. *Graefes Arch. Clin. Exp. Ophthalmol.*, **246** (4), 559–565.
20 Topouzis, F., Coleman, A.L., Harris, A., *et al.* (2006) Association of blood pressure status with the optic disk structure in non-glaucoma subjects: the Thessaloniki Eye Study. *Am. J. Ophthalmol.*, **142**, 60–67.
21 Berdahl, J.P., Allingham, R.R., and Johnson, D.H. (2008) Cerebrospinal fluid pressure is

decreased in primary open-angle glaucoma. *Ophthalmology*, **115**, 763–768.

22 Weinreb, R.N. and Harris, A. (eds.) (2009) Section V. What do we still need to know?, in *Blood Flow in Glaucoma: the Sixth Consensus Report of the World Glaucoma Association*, Kugler Publications, Amsterdam, pp. 161–163.

43
Photodynamic Modulation of Wound Healing in Glaucoma Filtration Surgery

Salvatore Grisanti

43.1
Introduction

Glaucoma is one of the major causes of blindness in the world. Different factors contribute to the progression of the disease and visual field defects (Figure 43.1a and b). An elevated intraocular pressure plays a pivotal role in most cases. The outflow of aqueous humor through its natural pathway at the trabecular meshwork is somehow reduced (Figure 43.1c). Trabeculectomy is the most frequently applied surgical method to reduce intraocular pressure in these cases (Figure 43.1d and e). The wound healing process and the developing fibrosis at the site of the filtration area (Figure 43.1f), however, lead to failure in about 30% of the cases within 6–8 weeks after surgery [1]. Characteristically, fibroblasts from Tenon's capsule and episclera lead to a fibro-proliferative response involving and closing the created fistula [2–12]. To increase the success rates of filtration surgery, agents such as mitomycin-C and 5-fluorouracil [4, 16–34] have been introduced and are used perioperatively as an antifibrotic therapy. Despite their positive effect on filtration surgery and success rates in cases with poor surgical prognosis, diffusion into adjacent ocular tissues cause toxic effects [35, 36]. New surgical complications, such as hypotony maculopathy, blebitis, endophthalmitis, and an increased incidence of already known postoperative complications, have hampered clinical use and stimulated a search for clinically less harmful alternatives [37, 38].

43.2
Photodynamic Therapy

Photodynamic therapy (PDT) is an alternative method for the treatment of localized pathologies, such as skin cancer [42]. Specific activation of pertinent drugs at the targeted area should avoid side effects. PDT has also been evaluated for some distinct

Handbook of Biophotonics. Vol.2: Photonics for Health Care, First Edition. Edited by Jürgen Popp, Valery V. Tuchin, Arthur Chiou, and Stefan Heinemann.

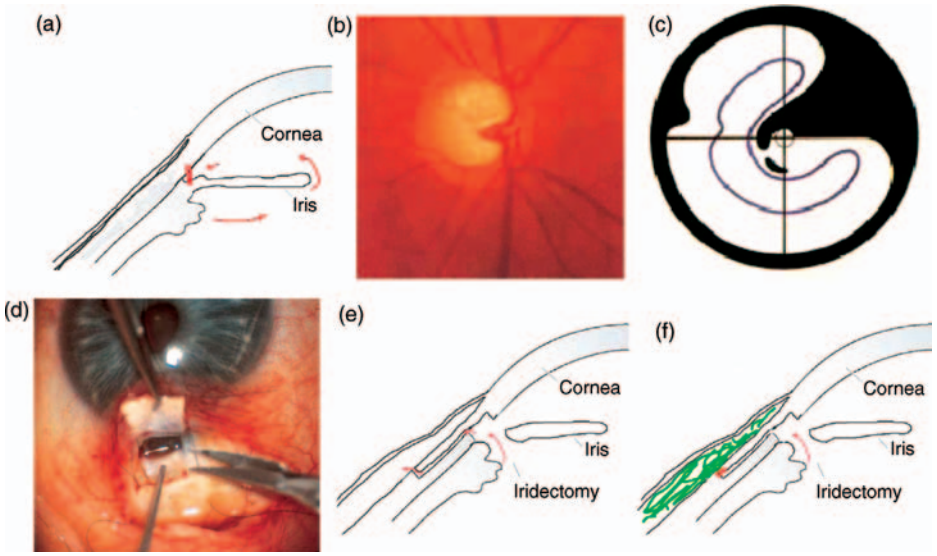

Figure 43.1 Filtration surgery to reduce IOP in glaucoma. (a) A reduction of aqueous humor outflow leads to elevated IOP. Chronic elevation of IOP leads to glaucomatous changes of the optic nerve (b) and visual field defects (c). Filtration surgery (d) allows outflow of aqueous humor into the subconjunctival space (e). (f) Postoperative wound healing and fibrosis (green).

ophthalmic diseases, such as ocular tumors, choroidal and corneal neovascularization, proliferative vitreoretinal disorders, and postoperative fibrosis in glaucoma surgery [41, 43–47]. Hill *et al*. investigated the feasibility of PDT in a rabbit model of filtration surgery. Using ethyletiopurin, a photosensitizer traditionally delivered by intravenous injection, they showed that subconjunctival delivery could have an impact on filtering bleb survival [41].

At about the same time, we had already started to evaluate BCECF-AM [2′,7′-bis (2-carboxyethyl)-5-(and -6)-carboxyfluorescein acetoxymethyl ester] in *in vitro* [39] and *in vivo* [40] studies in order to induce an antiproliferative photodynamic effect.

43.3 Photodynamic Modulation of Wound Healing in Glaucoma Filtration Surgery

43.3.1 Preclinical Studies

BCECF-AM is a cell membrane-permeable compound (Figure 43.2) rendered membrane impermeable and fluorescent upon cleavage by intracellular

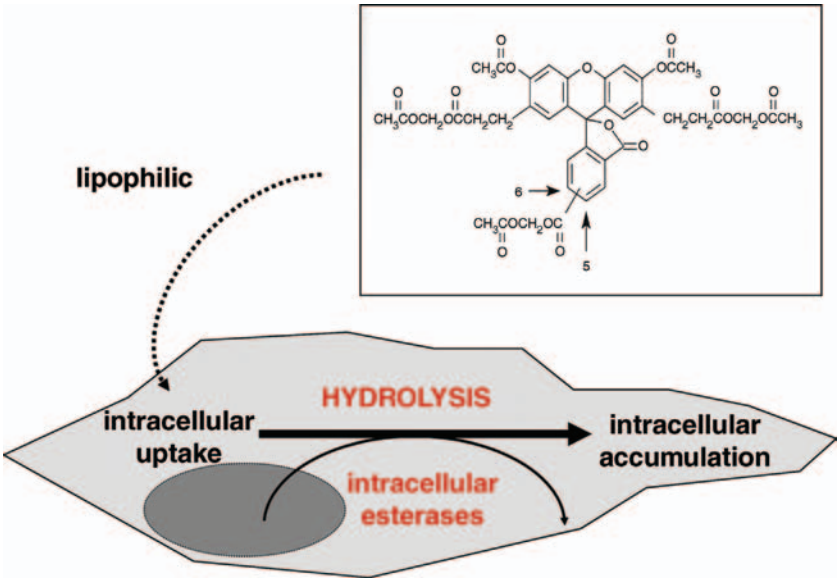

Figure 43.2 The fluorophore BCECF-AM [2′,7′-bis(2-carboxyethyl)-5-(and -6)-carboxyfluorescein acetoxymethyl ester] is lipophilic and therefore cell membrane permeable. After intracellular uptake, esterases and hydrolysis are responsible for the conversion into a lipophobic molecule and intracellular accumulation.

esterases [48–50]. Exposure of cells having incorporated BCECF-AM to light at an appropriate wavelength leads to cellular photoablation (Figure 43.3). PDT is a selective and localized treatment based on the photosensitized oxidation of biological matter [39–42]. A photosensitizer can be used as a mediator of controlled light-induced cell toxicity. The mechanism of action is reported to be due to photooxidative reactions of type I and II. Oxygen is transformed into singlet oxygen, which oxidizes amino acids, nucleic acids, and unsaturated fatty acids. Within hours, the cytotoxic effect is seen at cell membranes (blebs), plasma membranes, mitochondria, lysosomes, and nuclei. Selective activation of the photosensitizer by application of light at an appropriate wavelength limits the drug effect to a selected area [40, 41].

BCECF-AM activated at the appropriate wavelength has been shown to induce cellular damage (Figure 43.4) and inhibit the proliferation of human Tenon's fibroblasts *in vitro* after treatment with 10 μg and irradiation for 10 min [39] (Figure 43.5). In experimental eyes of pigmented rabbits, it was shown to inhibit scarring effectively after filtration surgery and demonstrated a dose–response curve from 40 to 100 μg after irradiation for 10 min [40]. BCECF-AM was injected preoperatively into the subconjunctival space (Figure 43.6a). Thereafter, similarly to surgery in patients, the conjunctiva was opened and the sclera and Tenon's capsule were exposed to illumination to induce the photoreactive effect

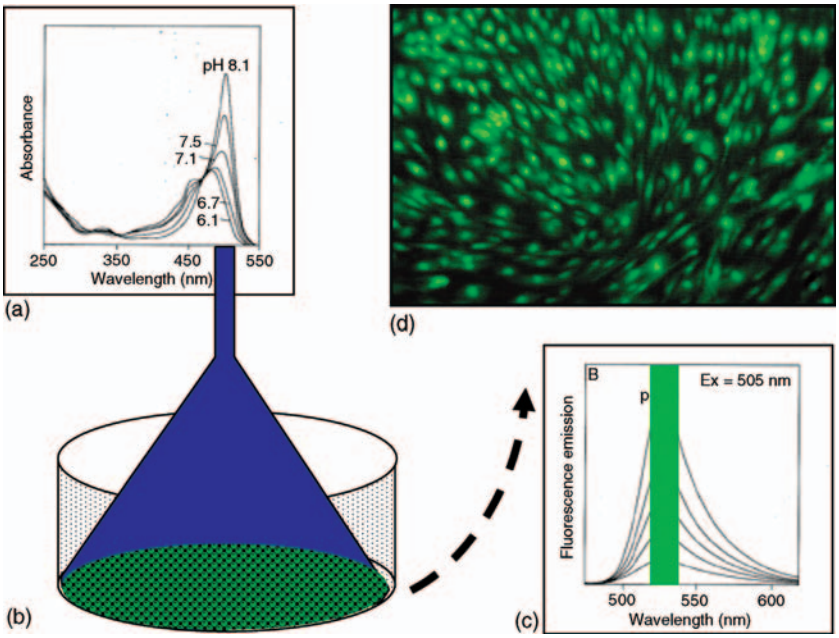

Figure 43.3 Photoactivation of intracellular BCECF-AM with diffuse blue light. (a) BCECF optimal absorbance ranges at a wavelength of 490 nm. (b) Cultured cells previously incubated with BCECF-AM illuminated with diffuse blue light (490 nm) have a peak emission (c) at a wavelength of 505 nm and (d) show a green fluorescence.

(Figure 43.6b). The postoperative phase did not show toxic effects or inappropriate postoperative inflammation (Figure 43.6c and d). The intraocular pressure was significantly reduced for a prolonged time compared with surgery without cellular photoablation. Macroscopic and histological analysis of the surgical site revealed less fibrosis (Figure 43.7).

43.3.2 Clinical Studies

The feasibility, efficacy, and safety shown in the animal experiments led to the first clinical application. An open-label phase II study was initiated to investigate the impact of cellular photoablation mediated by BCECF-AM on the postoperative fibrosis after filtration surgery in human glaucomatous eyes with poor prognosis. All patients had uncontrolled glaucoma due to high intraocular pressure (IOP) despite maximum tolerable medical therapy. Only eyes with advanced glaucomatous damage of the optic nerve head were included after approval by the institutional ethics review board. Each patient gave written informed consent after the purpose of the study and the method of surgery had been explained in detail.

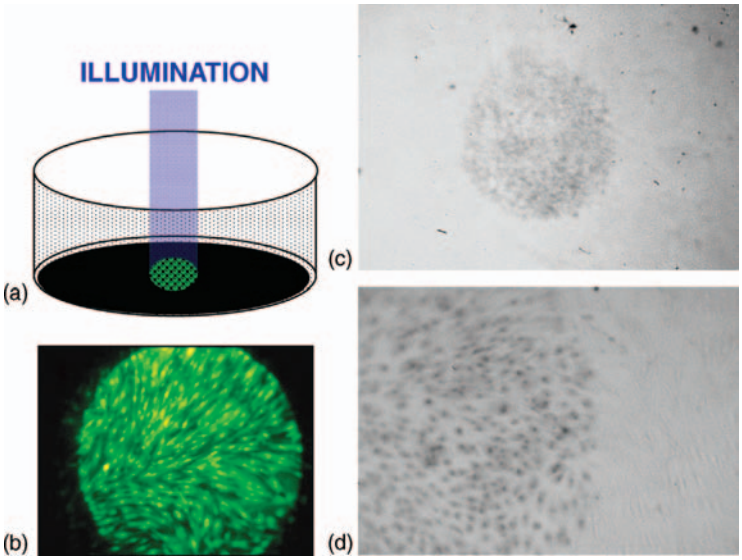

Figure 43.4 Photodynamic effect of intracellular BCECF-AM. (a) Spotlight illumination (diffuse blue light) of a cultured fibroblast monolayer previously incubated (5 min) with BCECF-AM (10 μg). (b) BCECF-AM is activated within the spot of illuminated cells. (c) Trypan blue exclusion test reveals the damaged cells within the round spot that had been previously illuminated. (d) Magnification of the spot edge reveals the demarcation line between damaged (stained) and unaffected (surrounding) cells.

The fluorescent probe BCECF-AM was provided by the pharmacy of the University of Lübeck in tuberculin syringes (Figure 43.8a). A dose of 80 μg was diluted in 300 μl of balanced salt solution and stored at −70 °C. Fifteen minutes prior to surgery, the eye received a single subconjunctival injection of 80 μg of BCECF-AM solution in one superior quadrant where the trabeculectomy was to be performed (Figure 43.8b). Following a limbus-based conjunctival flap, the episcleral Tenon's capsule and the subconjunctival tissue were irradiated. Illumination with diffuse blue light (450–490 nm; $\sim 51.9 \times 10^3$ cd m^{-2}) was performed for 8 min (Figure 43.8c). Photoactivating light was delivered by a portable Zeiss lamp equipped with a blue filter fixed at a distance of about 2 cm from the episclera. Light was focused to an area of about 20 mm in diameter, comprising the subconjunctival and episcleral tissue and sparing the cornea, which in addition was covered with tape. The illuminated area encompassed the consequently produced scleral flap of 3.5×3.5 mm (Figure 43.8d). A standard trabeculectomy and a full thickness iridectomy followed.

The application of BCECF-AM and photoactivation in this group of patients resulted in successful and prolonged reduction of IOP. Slit-lamp microscopy revealed no detectable damage of the conjunctiva or cornea (Figure 43.9). As BCECF-AM is a lipophilic drug, it may diffuse into other tissues adjacent the area of subconjunctival injection. However, subconjunctival injection of BCECF-AM

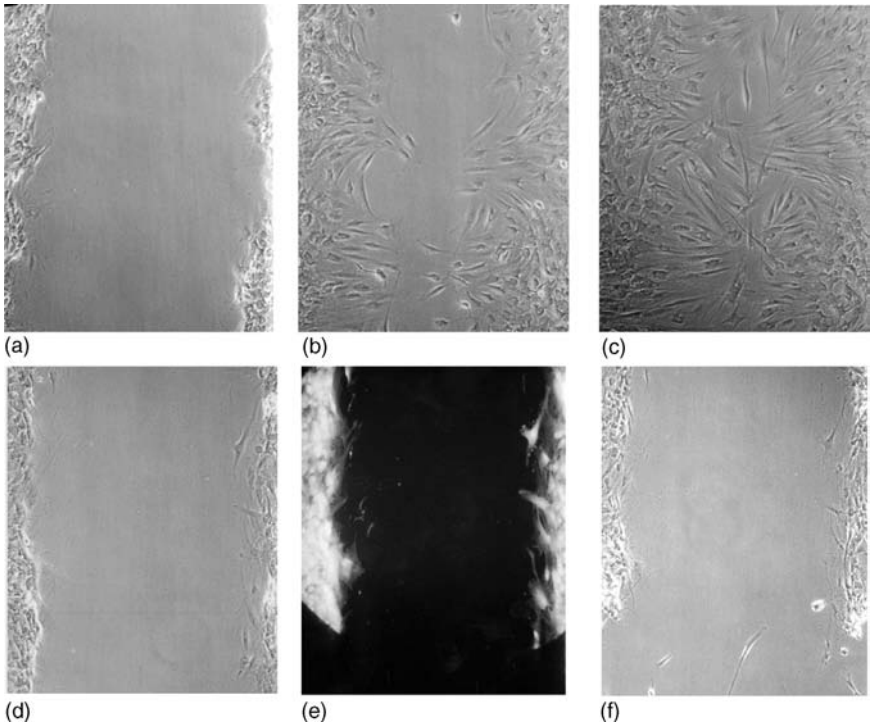

Figure 43.5 Photodynamic effect on an *in vitro* wound model. Photomicrographs showing a monolayer of fibroblasts at time 0 after creating a "wound" by scratching (a, d). The same site as in (a) shown after 12 h (b) and 24 h (c) when remaining untreated. (c) After 24 h the previous "wound" is covered by proliferating cells. (e) Illumination of the same site as in (d) at time 0. (f) Same site as in (d) and (e) after 96 h. The "wound" was not closed by cells.

followed by illumination and surgery did not cause a conjunctival defect. Owing to the promising results after more than 1 year of follow-up, additional patients were included. A subsequent study comprising 42 human glaucomatous eyes confirmed the previous results, showing the effectiveness of the approach. The clinical safety and tolerability were represented by a functioning filtering bleb with prolonged filtration, no signs of local toxicity or intraocular inflammation, and the lack of any discomfort or adverse effects for the patient.

Cellular photoablation seems to be an effective therapeutic approach to control postoperative fibrosis in human glaucomatous eyes with poor surgical prognosis. Various parameters such as light dose, light application, wavelength, irradiation area, total dose of the dye and multiple dosing may be altered in the future to improve the antifibrotic effect of PDT during glaucoma surgery. The safety and efficacy however need to be tested in randomized controlled clinical studies.

The complex issue of modulating the wound healing process after glaucoma filtration surgery has been the target of many experimental and clinical studies. So

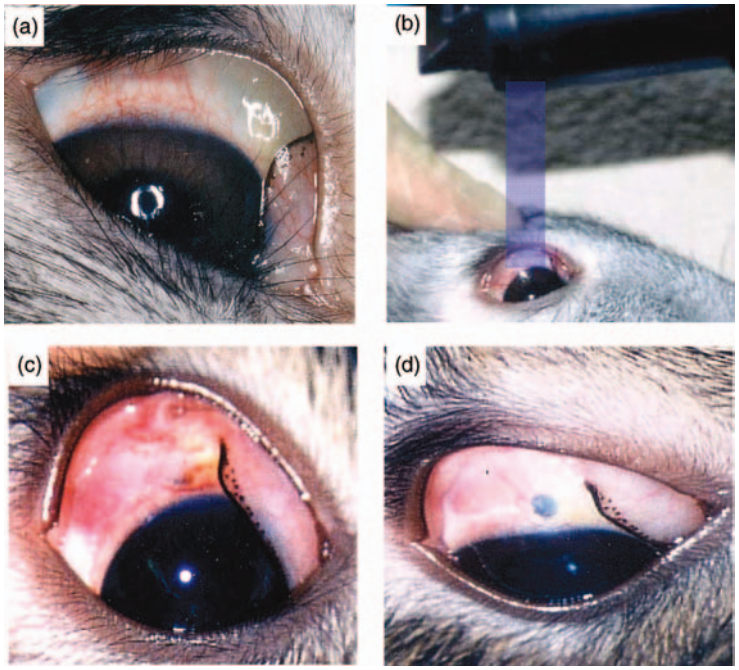

Figure 43.6 PDT in an *in vivo* glaucoma filtration surgery model. (a) The anterior segment of a rabbit eye after subconjunctival injection of BCECF-AM solution displaying a subconjunctival bleb filled with the yellowish solution. (b) Photographs reveal the intraoperative illumination (450–490 nm; $51.9 \times 103\ \mathrm{cd\,m^{-2}}$; 10 min). The same eye is shown (c) 1 day and (d) 2 weeks after surgery and PDT.

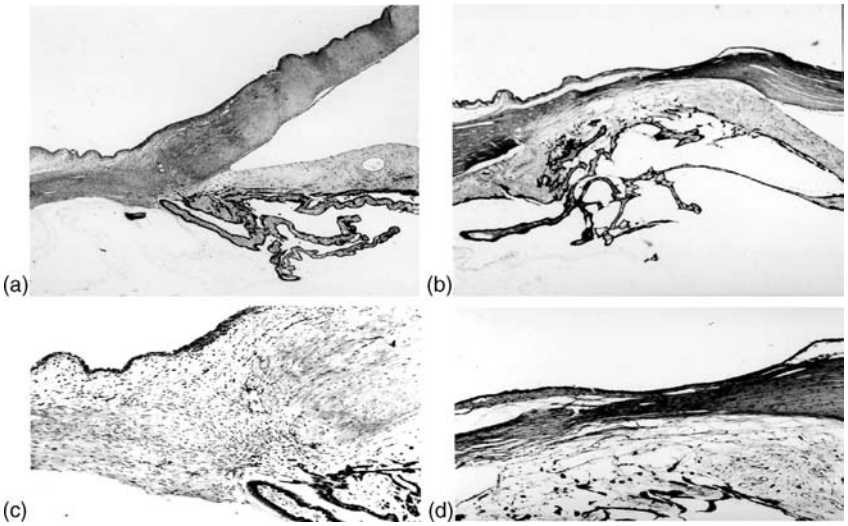

Figure 43.7 PDT in an *in vivo* glaucoma filtration surgery model. Photomicrographs of the surgical site 10 days after filtering intervention without (a, c) adjuvans and combined with photodynamic wound modulation (b, d).

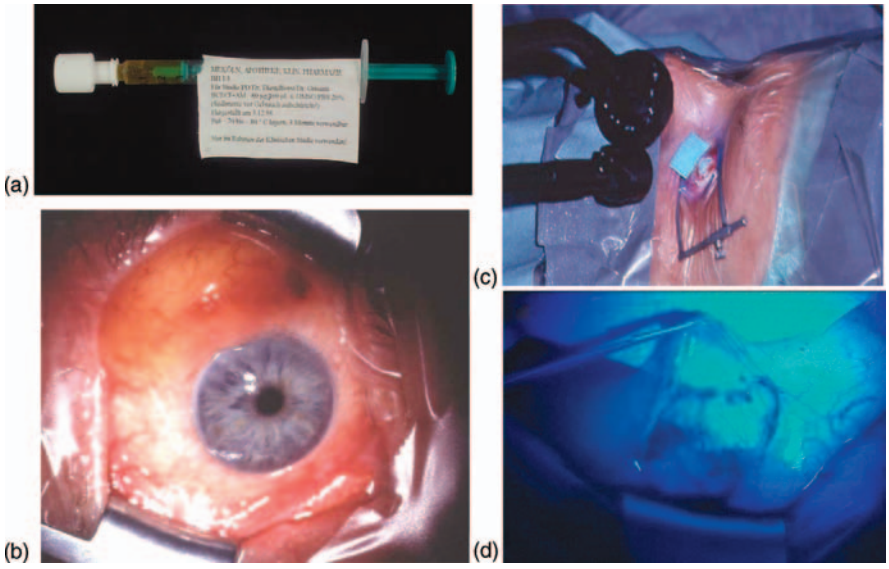

Figure 43.8 PDT in clinical glaucoma filtration surgery. (a) BCECF-AM in a syringe (80 μg diluted in 300 μl of BSS solution) as provided by the pharmacy. (b) Intraoperative site after a single subconjunctival injection of BCECF-AM 15 min. preoperatively. Intraoperative situation depicting the illumination with diffuse blue light (450–490 nm; 51.9 × 103 cd m^{-2}; 8 min).

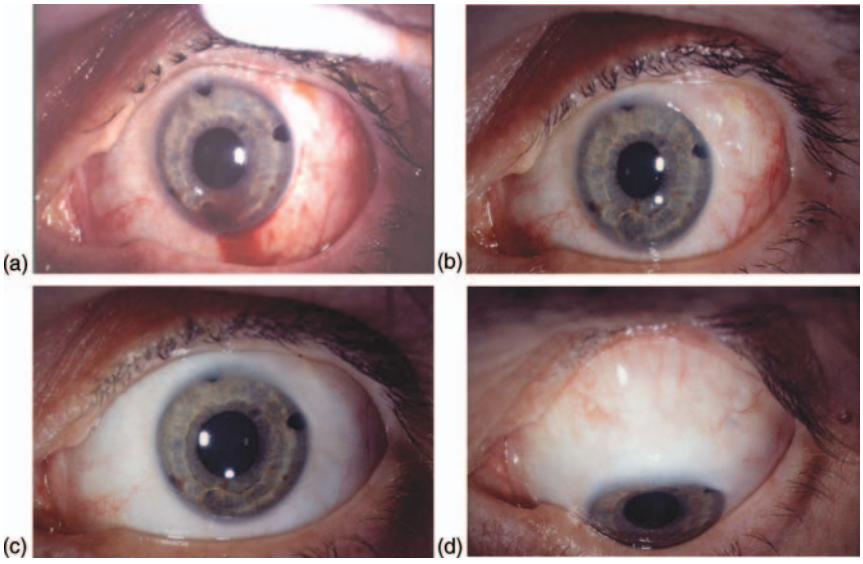

Figure 43.9 PDT in clinical glaucoma filtration surgery. Photographs of the anterior segment 1 (a), 19 (b), and 139 days (c, d) after surgery.

far, no completely suitable method has been established to achieve satisfactory long-term postoperative surgical results with only minimal or no side-effects for the patient, but PDT with BCECF-AM has proved to be a promising approach.

References

1 Diestelhorst, M., Khalili, M.A., and Krieglstein, G.K. (1999) Trabeculectomy: a retrospective follow-up of 700 eyes. *Int. Ophthalmol.*, **22**, 211–220.

2 Maumenee, A.E. (1960) External filtering operations for glaucoma: the mechanisms of function and failure. *Trans. Am. Ophthalmol. Soc.*, **58**, 319–328.

3 Addicks, E.M., Quigley, H.A., Green, W.R., and Robin, A.L. (1983) Histologic characteristics of filtering blebs in glaucomatous eyes. *Arch. Ophthalmol.*, **101**, 795–798.

4 Hitchings, R.A. and Grierson, I. (1983) Clinicopathological correlation in eyes with failed fistulizing surgery. *Trans. Ophthalmol. Soc. U. K.*, **103**, 84–88.

5 Teng, C.C., Chi, H.H., and Katzin, H.M. (1959) Histology and mechanism of filtering operations. *Am. J. Ophthalmol.*, **47**, 16–34.

6 Jampel, H.D., McGuigan, L.J.B., Dunkelberger, G.R., L'Hernault, N.L., and Quigley, H.A. (1988) Cellular proliferation after experimental glaucoma filtration surgery. *Arch. Ophthalmol.*, **106**, 89–94.

7 Costa, V.P., Spaeth, G.L., Eiferman, R.A., and Orengo-Nania, S. (1993) Wound healing modulation in glaucoma filtration surgery. *Ophthalmic Surg.*, **24**, 152–170.

8 Heuer, D.K., Parrish, R.K. II, Gresel, M.G., Hodapp, E., Palmberg, F.F., and Anderson, D.R. (1984) 5-Fluorouracil and glaucoma filtration surgery. II. A pilot study. *Ophthalmology*, **91**, 384–394.

9 Joseph, J.P., Miller, M.H., and Hitchings, R.A. (1988) Wound healing as a barrier to successul filtration surgery. *Eye*, **2**, S113–S123.

10 Skuta, G.L. and Parrish, R.K. II (1987) Wound healing in glaucoma filtering surgery. *Surv. Ophthalmol.*, **32**, 149–170.

11 Tahery, M.M. and Lee, D.A. (1989) Review: pharmacologic control of wound healing in glaucoma filtering surgery. *J. Ocular Pharmacol.*, **5**, 155–179.

12 Weinreb, R.N. (1994) Wound healing in filtration surgery. *Curr. Opin. Ophthalmol.*, **13**, 8–25.

13 Starita, R.J., Fellmann, R.L., Spaeth, G.L., Poryzees, E.M., Greenidge, K.C., and Traverso, C.E. (1985) Short- and long-term effects of postoperative corticosteroids on trabeculectomy. *Ophthalmology*, **92**, 938–946.

14 Sugar, H.S. (1965) Clinical effect of corticosteroids on conjuctival filtering blebs: a case report. *Am. J. Ophthalmol.*, **59**, 854–860.

15 Roth, S.M., Spaeth, G.L., Starita, R.J., Birbillis, E.M., and Steinmann, W.C. (1991) The effect of postoperative corticosteroids on trabeculectomy and the clinical course of glaucoma: five-year follow-up study. *Ophthalmic Surg.*, **22**, 724–729.

16 Skuta, G.L., Beeson, C.C., Higginbotham, E.J., Lichter, P.R., Musch, D.C., Bergstrom, T.J., Klein, T.B., and Falck, F.Y. (1992) Intraoperative mitomycin versus postoperative 5-fluorouracil in high risk glaucoma filtering surgery. *Ophthalmology*, **99**, 438–444.

17 Costa, V.P., Wilson, R.P., Moster, M.R., Schmidt, C.M., and Gandham, S. (1993) Hypotony maculopathy following the use of topical mitomycin C in glaucoma filtration surgery. *Ophthalmic Surg.*, **24**, 389–394.

18 Shields, M.B., Scroggs, M.W., Sloop, C.M., and Simmons, R.B. (1993) Clinical and histopathologic observations concerning hypotony after trabeculectomy with adjunctive mitomycin C. *Am. J. Ophthalmol.*, **116**, 673–683.

19 Xu, Y., Yang, G.H., Gin, W.M., Chen, K.Q., and Song, X.H. (1993) Effect of subconjunctival daunorubicin on glaucoma surgery in rabbits. *Ophthalmic Surg.*, **24**, 382–388.

20 Lee, D.A., Hersh, P., Kersten, D., and Melamed, S. (1987) Complications of subconjuctival 5-fluorouracil following glaucoma filtering surgery. *Ophthalmic Surg.*, **18**, 187–190.

21 Lee, D.A., Lee, T.C., Cortes, A.E., and Kitada, S. (1990) The effect of mithramycin, mitomycin, daunorubicin, and bleomycin on human subconjunctival fibroblast attachment and proliferation. *Ophthalmol. Vis. Sci.*, **31**, 2136–2144.

22 Lee, D.A., Shapourifar-Tehrani, S., and Kitada, S. (1990) The effect of 5-fluorouracil and cytarabine on human fibroblasts from Tenon's capsule. *Invest. Ophthalmol. Vis. Sci.*, **31**, 1848–1855.

23 Bansal, R.K. and Gupta, A. (1992) 5-Fluorouracil in trabeculectomy for patients under the age of 40 years. *Ophthalmic Surg.*, **23**, 278–280.

24 Heuer, D.K., Parrish, R.K. II, Gressel, M.G., Hodapp, E., Desjardins, D.C., Skuta, G.L., Palmberg, P.F., Nevarez, J.A., and Rockwood, E.J. (1986) 5-Fluorouracil and glaucoma filtering surgery. Intermediate follow-up of a pilot-study. *Ophthalmology*, **93**, 1537–1546.

25 Jampel, H.D., Jabs, D.A., and Quigley, H.A. (1990) Trabeculectomy with 5-fluorouracil for adult inflammatory glaucoma. *Am. J. Ophthalmol.*, **109**, 168–173.

26 Patitsas, C.J., Rockwood, E.J., Meisler, D.M., and Lowder, C.Y. (1992) Glaucoma filtering surgery with post-operative 5-fluorouracil in patients with intraocular inflammatory disease. *Ophthalmology*, **99**, 594–599.

27 Rockwood, E.J., Parrish, R.K. II, Heuer, D.K., Skuta, G.L., Hodapp, E., Palmberg, P.F., Gressel, M.G., and Feuer, W. (1987) Glaucoma filtering surgery with 5-fluorouracil. *Ophthalmology*, **94**, 1071–1078.

28 The Fluorouracil Filtering Surgery Study Group (1993) Three-year follow-up of the fluorouracil filtering surgery study. *Am. J. Ophthalmol.*, **115**, 82–92.

29 Bergstrom, T.J., Wilkinson, S., Skuta, G.L., Watnick, R.L., and Elner, V.M. (1991) The effect of subconjuctival mitomycin C on glaucoma filtration surgery in rabbits. *Arch. Ophthalmol.*, **109**, 1725–1730.

30 Khaw, P.T., Doyle, J.W., Sherwood, M.B., Smith, M.F., and McGorray, S. (1993) Effects of intraoperative 5-fluorouracil or mitomycin C on glaucoma filtration surgery in the rabbit. *Ophthalmology*, **100**, 367–372.

31 Liang, L.L. and Epstein, D.L. (1992) Comparison of mitomycin C and 5-fluorouracil on filtration surgery success in rabbit eyes. *J. Glaucoma*, **1**, 87–93.

32 Pasquale, L.R., Thibault, D., Dorman-Pease, M.E., Quigley, H.A., and Jampel, H.D. (1992) Effect of topical mitomycin C on glaucoma filtering surgery in monkeys. *Ophthalmology*, **99**, 14–18.

33 Wilson, M.R., Lee, D.A., Baker, R.S., Goodwin, L.T., and Wooten, F. (1991) The effects of topical mitomycin on glaucoma filtration surgery in rabbits. *J. Ocular Pharmacol.*, **7**, 1–8.

34 Chen, C.W., Huang, H.T., Bair, J.S., and Lee, C.C. (1990) Trabeculectomy with simultaneus topical application of mitomycin C in refractory glaucoma. *J. Ocular Pharmacol.*, **6**, 175–182.

35 Mietz, H., Arnold, G., Kirchhof, B., Diestelhorst, M., and Krieglstein, G.K. (1996) Histopathology of episcleral fibrosis after trabeculectomy with and without mitomycin C. *Graefes Arch. Clin. Exp. Ophthalmol.*, **234**, 364–368.

36 Ustundag, C. and Diestelhorst, M. (1998) Effect of mitomycin C on aqueous humor flow, flare and IOP in eyes with glaucoma 2 years after trabeculectomy. *Graefes Arch. Clin. Exp. Ophthalmol.*, **236**, 734–738.

37 Mietz, H., Addicks, K., Diestelhorst, M., and Krieglstein, G.K. (1995) Intraocular toxicity to ciliary nerves after extraocular application of mitomycin C in rabbits. *Int. Ophthalmol.*, **19**, 89–93.

38 Schraermeyer, U., Diestelhorst, M., Bieker, A., Theison, M., Mietz, H., Ustundag, C., Joseph, G., and Krieglstein, G.K. (1999) Morphologic proof of the toxicity of mitomycin C on the ciliary body in relation to different application methods. *Graefe's Arch. Clin. Exp. Ophthalmol.*, **237**, 593–600.

39 Grisanti, S., Gralla, A., Maurer, P., Diestelhorst, M., Krieglstein, G., and Heimann, K. (2000) Cellular photoablation to control postoperative

fibrosis in filtration surgery: *in vitro* studies. *Exp. Eye Res.*, **70**, 145–152.

40 Grisanti, S., Diestelhorst, M., Heimann, K., and Krieglstein, G. (2000) Cellular photoablation to control postoperative fibrosis in a rabbit model of filtration surgery. *Br. J. Ophthalmol.*, **83**, 1353–1359.

41 Hill, R.A., Crean, D.H., Doiron, D.R., McDonald, T.J., Liaw, L.H., Ghosheh, F., Hamilton, A., and Berns, M.W. (1997) Photodynamic therapy for antifibrosis in a rabbit model of filtration surgery. *Ophthalmic Surg. Lasers*, **28**, 574–581.

42 Bissonnette, R. and Lui, H. (1997) Current status of photodynamic therapy in dermatology. *Dermatol. Clin.*, **15** (3), 507–519.

43 Weissgold, D.J., Hu, L.K., Gragoudas, E.S., and Young, L.H.Y. (1996) Photodynamic therapy (PDT) of pigmented choroidal melanoma via a trans-scleral approach. *Invest. Ophthalmol. Vis. Sci.* **37** (Suppl), S123.

44 Moshfeghi, D.M., Peyman, G.A., Khoobehi, B., Moshfeghi, A., and Crean, D.H. (1995) Photodynamic occlusion of retinal vessels using tin ethyl etiopurin (SnET2): an efficacy study. *Invest. Ophthalmol. Vis. Sci.*, **36** (Suppl), S115.

45 Cox, K.W., Shepperd, J.D., Lattanzio, F.A., and Williams, P.B. (1997) Photodynamic therapy of corneal neovascularization using topical dihematoporphyrin ester. *Invest. Ophthalmol. Vis. Sci.*, **38** (Suppl), S512.

46 Smyth, R.J., Nguyen, K., Ahn, S.S., Panek, W.C., and Lee, D.A. (1993) The effects of photophrin on human Tenon's capsule fibroblasts *in vitro*. *J. Ocular Pharmacol.*, **9**, 171–178.

47 Dacheux, R. and Guidry, C. (1995) Cellular photoablation as a therapy to control proliferative vitreoretinopathy: *in vitro* studies. *Invest. Ophthalmol. Vis. Sci.*, **36** (Suppl), S751.

48 Grimes, P.A., Stone, R.A., Laties, A.M., and Li, M. (1982) Carboxyfluorescein. A probe of the blood–ocular barriers with lower membrane permeability than fluorescein. *Arch. Ophthalmol.*, **100**, 635–639.

49 Hofmann, J. and Sernetz, M. (1983) A kinetic study on the enzymatic hydrolysis of fluorescein diacetate and fluorescein di-beta-D-galactopyranoside. *Anal. Biochem.*, **131**, 180–186.

50 Rotman, B. and Papermaster, B. (1966) Membrane properties of living mamalian cells as studied by enzymatic hydrolysis of fluorogenic esters. *Proc. Natl. Acad. Sci. U. S. A.*, **55**, 134–141.

44
Correction of Wavefront Aberrations of the Eye

Dan Reinstein and Manfred Dick

44.1
Introduction

A plane optical wavefront with no aberrations is in general considered to give the best performance of optical systems. However, especially in the field of refractive corrections of the human eye, only the correction of low-order optical aberrations such as tilt, sphere, and cylinder was possible in the past. With the advent of wavefront aberrometers (e.g., on the basis of Shack–Hartmann sensors) around 2000, monochromatic higher order aberrations such as spherical aberration, trefoil, and coma became measurable and their influence on visual performance could also be studied. The correction of these higher order aberrations, fully or to some extent, was investigated for all vision correction modalities. The aim was to improve visual acuity significantly up to supervision, which is defined as a visual acuity of 20/10 or 20/8 [1].

As the eye, due to its accommodating power, is a dynamic system which is age dependent because of presbyopia, an additional challenge concerning the correction of aberrations arises. Mostly a higher order aberration correction for distance vision and large pupils is performed to achieve the best visual acuity, but it is still limited by retinal resolution and diffraction. Other concepts, especially with LASIK and intraocular lenses, divide the pupil into radial optical zones with different corrections of aberrations, for example, for near and distance vision.

With regard to glasses, the correction of higher order aberrations can be realized for one viewing direction and a fixed position of the pair of glasses, but for all viewing directions and tolerances in position only partial optimization is possible. With the help of the i.Scription wavefront-based refraction glasses, patients had a considerable improvement in night vision [2, 3].

Contact lenses are better suited for correction of higher order aberrations as only one viewing direction is predetermined. The problem with contact lenses is the lateral shift behavior, which could worsen the performance of optical correction. Our own experiments have shown that a decentration of 0.3 mm leads to a 20% reduction in the Strehl intensity ratio.

Handbook of Biophotonics. Vol.2: Photonics for Health Care, First Edition. Edited by Jürgen Popp, Valery V. Tuchin, Arthur Chiou, and Stefan Heinemann.

Intraocular lenses have great potential for the correction of higher order aberrations as biometric diagnosis and also lens calculation algorithms become more and more accurate, in addition to improved surgical techniques [4–7].

As laser refractive surgery of the cornea represents the most stable target for the correction of higher order aberrations, we will concentrate here on excimer laser-based customized refractive surgery [8, 9].

44.2
Excimer Laser-Based Refractive Surgery for Correction of Wavefront Aberrations

All excimer laser platforms now allow the surgeon to include a patient's wavefront data to try to reduce higher order aberrations at the same time as treating the refraction. The micronic accuracy of excimer laser systems means that irregular ablation profiles based on wavefront data can be delivered with confidence. For example, Carl Zeiss Meditec performed laboratory closed-loop experiments to validate the use of the MEL80 for the correction of higher order aberrations. The MEL80 was used to create transparent polymer phase plates with a defined profile that would represent a specific Zernike coefficient of determined amplitude on the polymer surface. The resulting ablated phase plate surface shape was verified independently using a profilometer, and was then used to aberrate a collimated planar wavefront beam and generate a wavefront distortion to be detected by the WASCA. The WASCA and profilometry measurements were used as measures of accuracy in the ability to produce a given wavefront aberration on a phase plate. The WASCA measurement was then imported into a CRS-Master workstation to generate an ablation profile designed to reverse the specific aberration induced. Figure 44.1 depicts a profilometer-based topography measurement and horizontal wavefront section measured after a collimated beam has passed through a phase plate ablated to produce a Z(3,–1) Zernike shape. The agreement between the measured horizontal section and the intended Zernike polynomial can be seen to be very high.

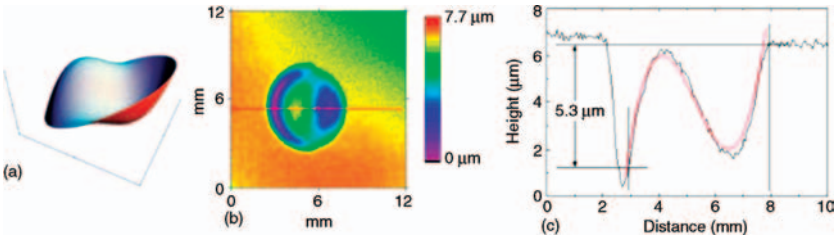

Figure 44.1 Laboratory validation of WASCA and the MEL80 excimer laser as components of a wavefront-guided ablation system: 3D plot of a planned Z(3,–1) Zernike polynomial to be ablated into PMMA (a), 3D profilometry of the surface of the PMMA plate after ablation (b), and a horizontal section (red line) showing the actual profile achieved (c). The attempted shape (red curve) is seen to be very close to the achieved shape (blue curve).

The efficacy of wavefront customized ablation profiles will therefore depend on the accuracy of the higher order aberration measurements (i.e., the aberrometer used), the centration of the ablation profile, and the biomechanical response to the ablation.

Given the fact that all current ablation profiles induce higher order aberrations, particularly spherical aberration, it is interesting to investigate whether simply including the wavefront for primary myopic treatments will be of benefit. It is likely that including the wavefront for primary myopic treatments would be more beneficial for eyes presenting with significant higher order aberrations, whereas, the wavefront ablation profile will only have minor differences from the base ablation profile for a patient presenting with negligible aberrations. Any possible benefit should be weighed against the small increase in ablation depth when including wavefront data.

The known induction of spherical aberration should also be taken into account when planning a wavefront customized ablation for a primary procedure. For example, myopic ablation induces positive spherical aberration (OSA notation), so if the patient's wavefront has negative spherical aberration and is used for treatment, this will increase the amount of induced positive spherical aberration, which would be detrimental to the outcome of the treatment. To account for this, some laser systems, such as the MEL80, allow the surgeon to include specific types of aberration while excluding others so that the ablation profile can be tailored to offer the optimal treatment.

Using the MEL80, we set out to study whether the incorporation of higher order aberrations into the standard aspheric profile would be of further benefit. In this study, carried out between July 2003 and May 2004, 24 consecutive patients recruited for study were given a MEL80 standard aspheric profile in the dominant eye, while receiving a CRS-Master derived wavefront-guided profile in the nondominant eye, which included the nascent higher order aberrations of the patient [10]. Preoperatively, the right and left eyes of each patient were within ± 0.75 D spherical equivalent refraction and cylinder. At a minimum follow-up of 6 months, there were no statistically significant differences between eyes in efficacy (UDVA), accuracy, or safety (changes in CDVA). However, positive improvements were noted in the induction of higher order aberrations for the eyes treated with a wavefront-guided profile. There was 22% less induction in spherical aberration (measured at a 6 mm pupil) in the eyes treated with a wavefront guided profile, which was a statistically significant difference ($p = 0.005$). Contrast sensitivity was equal in right and left eyes preoperatively, but statistically significantly higher in the eyes treated with a wavefront-guided profile at 3 and 6 cpd (cycles per degree) ($p < 0.015$). This study demonstrated that wavefront-guided treatments may indeed offer a small benefit over standard aspheric treatments. However, given the amount of aberrations induced by the base ablation profiles compared with the relatively small amount of higher order aberrations in the majority of untreated eyes, the final solution of actually being able to correct nascent higher order aberrations will have to wait until aberration-free ablation profiles are developed. Many groups are working on this problem.

Wavefront-guided treatments are likely to be most useful for treating highly aberrated eyes, such as are encountered in corneas that have undergone refractive surgery previously with complaints of night vision disturbances. In these cases,

there is often little refraction and so there should not be much induction of higher order aberrations due to any further surgery. Therefore, it is reasonable to treat the higher order aberrations with a wavefront-guided treatment to help alleviate visual difficulties.

We performed a study to investigate the amount of aberrations in post-refractive surgery eyes complaining of night vision disturbances compared with those not complaining after primary myopic LASIK using the standard aspheric MEL80 profile [11]. The repair eye group were found to have 42% more spherical aberration than the post-LASIK control group. This supports the theory that higher order aberrations, especially spherical aberration, are the root cause of night vision disturbances. The repair eye group were also found to have significantly lower contrast sensitivity at all frequency levels; the normalized contrast sensitivity ratio [12] was about 0.80 for the repair eyes (below normal) compared with 1.02 for the post-LASIK control eyes (normal). After wavefront-guided repair, the repair eye group were found to have only 17% more spherical aberration than the post-LASIK control group. Furthermore, the normalized contrast sensitivity ratio was increased to 1.02 (Figure 44.2). The MEL80 wavefront-guided treatment managed to reduce the aberrations to a similar level to that which is commonly found after myopic LASIK with the MEL80. It was found that this reduction was sufficient to restore the contrast sensitivity to the normal range in the majority of cases; 80% of repair eyes had contrast sensitivity in the normal range.

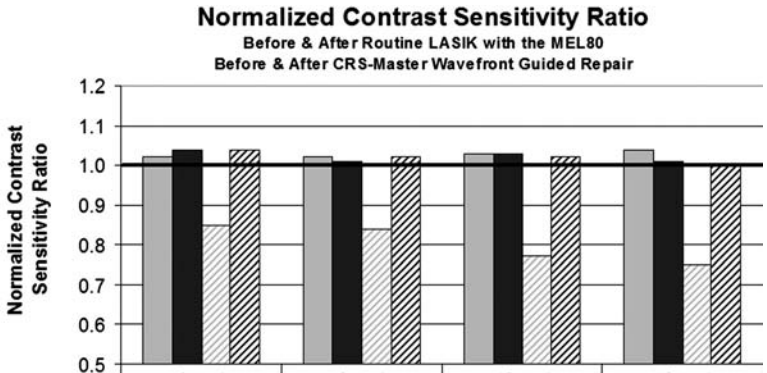

	3 cpd	6 cpd	12 cpd	18 cpd
Control Pre	1.02	1.02	1.03	1.04
Control Post	1.04	1.01	1.03	1.01
Pre CRSM-Repair	0.85	0.84	0.77	0.75
Post CRSM-Repair	1.04	1.02	1.02	1.00

Figure 44.2 Bar chart of the average normalized contrast ratio before and after routine LASIK with the MEL80 and before and after MEL80 wavefront-guided repair. A ratio of 1 is considered normal and is marked on the graph as a dark solid line. The graph shows that the contrast sensitivity remained the same following routine LASIK with the MEL80. It also shows that the contrast sensitivity was restored to the normal range following MEL80 wavefront-guided repair.

This result showed that although the laser ablation was delivering the measured wavefront exactly (as proved by profilometry and described earlier), and the profile included only a small refractive component so there should have been few induced aberrations, the postoperative wavefront was a long way from being flat. The reasons for the undercorrection of the higher order aberrations could be due to a number of factors: (1) the aberrometers may not have high enough accuracy and repeatability, although the resolution and repeatability of instruments such as the WASCA [10, 13] appear to be good enough (Figure 44.3 shows the repeatability of each Zernike coefficient in 70 consecutive measurements of a highly aberrated eye after LASIK in a corneal transplant); (2) there may be diurnal changes in wavefront; (3) the wavefront changes as the pupil diameter changes; and (4) the biomechanical response of the cornea serves partially to reverse some of the intended change (it is possible that a nomogram is required for each Zernike value).

However, the result that the contrast sensitivity was restored to the normal level despite reducing the spherical aberration by only 27% suggests that the goal of wavefront treatments might not have to be to *flatten* the wavefront, but only to reduce the aberrations to a tolerable level. Aberrations are induced in every LASIK patient, but the majority of patients do not complain of night vision disturbances or a decrease in the quality of vision. Therefore, we can conclude that the brain has a tolerance level to aberrations.

Indeed, we can actually take advantage of the ability of the brain to filter a certain amount of aberrations. It has been shown that an increase in spherical aberration is associated with an increase in depth of field [14], and we have employed this increase

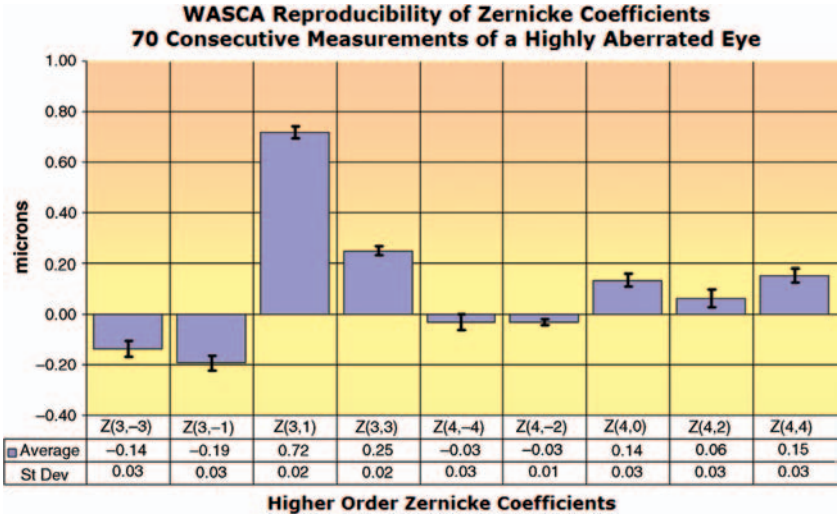

Figure 44.3 Zernike polynomial coefficient mean repeatability (standard deviation) for a consecutive series of 70 measurements for a highly aberrated eye. The *x*-axis shows the Zernike ordinal number. The value of the bar is the mean for each Zernike (Malacara notation) and the repeatability is shown as the error bars.

in depth of field to develop a procedure for the treatment of presbyopic patients using a new nonlinear aspheric ablation profile, a procedure known as laser blended vision [15, 16]. The initial goal was to increase the depth of field sufficiently to provide vision from a distance through intermediate to near; creating an eye that would see 20/20 at a distance, read a computer screen, but also read J1. However, as we learned, visual quality and contrast sensitivity can be compromised by excessive changes in aberrations of the cornea. We discovered that it was possible to safely increase the depth of field of the cornea to 1.50 D for any starting refractive error. However, given a 1.50 D depth of field, it would not be possible to achieve full distance and full near vision monocularly; therefore, we borrowed from the time-tested concept of monovision and set up the nondominant eye to be slightly myopic, so that the depth of field of the predominantly distance (dominant) eye was able to see from a distance down to intermediate, while the predominantly near (nondominant) eye was able to see in the intermediate and near range. In the intermediate region, both eyes have similar acuity, which draws on our knowledge of binocular fusion processing: the horopter, a volume centered on the fixation point that contains all points in space that yield single vision. Monovision, or in this case, micro-monovision, draws on the inherent cortical processes of neuronal gating and blur suppression (the ability for conscious attention to be directed to the part of the visual field with the best image quality).

In all, laser blended vision draws on six mechanisms for its success as a procedure: (1) depth of field increase by a specific controlled increase in corneal aberrations; (2) pupil constriction during accommodation affording a further depth of field increase on the retinal image; (3) retinal and cortical processing for increasing contrast of the retinal image changes produced by spherical aberration; (4) micro-monovision to allow continuous distance to intermediate to near vision between the two eyes; (5) relying on central cortical processing including neuronal gating and blur suppression; and (6) making use of the residual accommodation of the eye.

Customized ablation profiles can also be generated using front surface topography data and some laser systems offer a topography-guided ablation profile. Topography-guided ablation algorithms are designed to calculate an ablation profile that would alter an irregular topography to become a smooth, regular, aspheric surface. An irregular front surface topography will cause significantly higher order aberrations; therefore, the consequence of regularizing the front surface corneal topography will be to reduce higher order aberrations.

Using the MEL80 system, topography-guided ablations are actually more effective in reducing aberrations, particularly spherical aberration, than wavefront-guided ablations. In our study using the MEL80 topography-guided system for post-refractive surgery complications, the spherical aberration was reduced by 41% on average [17]. Topography-guided ablations were found to be particularly successful for the correction of decentrations and for optical zone enlargement. One of the major advantages of topography-guided ablation over wavefront-guided ablation is the centration. By definition, topographic data are centered about the corneal vertex, which approximates the visual axis. On the other hand, wavefront data are currently calculated centered on the entrance pupil center, as decided by the OSA Committee, since wavefront data can only be obtained within the pupil. Therefore, in an eye with a

large angle kappa, the wavefront will not represent the patient's vision since the patient is not looking through the center of the pupil (where the wavefront is centered). This means that using a wavefront custom ablation in eyes with a large angle kappa could result in worsening of the visual symptoms. For this reason, a topography-guided ablation is a much more reliable and effective treatment option for decentration.

However, before a wavefront- or topography-guided ablation is performed, it is important first to have made a confident diagnosis and in particular to have considered the effect of epithelial thickness changes. The epithelium will always remodel itself to compensate for underlying stromal surface irregularities; the epithelium overlying bumps in the stromal surface becomes progressively thinner and the epithelium overlying troughs in the stromal surface becomes progressively thicker [18–25]. The epithelium effectively acts as a low-pass filter over the stoma, regularizing high-frequency noise. The epithelium is regulated by the blinking motion of the eyelid [25, 26] and is therefore designed to improve regularly irregular astigmatism about the visual axis. Unfortunately, this evolutionary power of the epithelium to remodel itself to a smooth surface poses a problem when trying to diagnose subsurface causes of irregularities in corneal front surface shape. We believe that epithelial thickness mapping has the potential to improve greatly our diagnostic capabilities, and also improve treatment planning in the correction of irregular astigmatism. The presence of epithelial thickness profile changes also means that neither wavefront- nor topography-guided ablation will ever be a complete solution because they do not account for epithelial thickness changes.

References

1 Krueger, R.R., Applegate, R.A., and MacRae, S.M. (2004) *Wavefront Customized Visual Corrections: the Quest for Super Vision II*, Slack, Thorofare, NJ.

2 Cabeza, J.M., Mendel, L., and Kratzer, T.C. (2003) The performance of wavefront-based refraction can be proven. *Dtsch Opt Ztg*, (DOZ 4), 68–71.

3 Cabeza, J.M. (2010) Optimized low order prescription by incorporating wavefront data of the eye. *MAFO Ophthalmic Labs Ind.*, **7** (MAFO 4-10), 10–16.

4 Fiala, W. (2009) Remarks on wavefront designed aberraton correcting intraocular lenses. *Optom. Vis. Sci.*, **86** (5), 529–536.

5 Pieh, S., Fiala, W. Malz, A., and Stork, W. (2009) *In vitro* Strehl ratios with spherical, aberration free, average, and customized spherical aberration-correcting intraocular lenses. *Invest. Ophthalmol. Vis. Sci.*, **50** (3), 1264–1269.

6 Nochez, Y., Favard, A. Majzoub, S., and Pisella, P.-J. (2010) Measurement of corneal aberrations for customistion of intraocular lens asphericity: impact on quality of vision after midro-incision cataract surgery. *Br. J. Ophthalmol.*, **94**, 440–444.

7 Preussner, P.-R. and Wahl, J. (2003) Simplified mathematics for customized refractive surgery. *J. Cataract Refract. Surg.*, **29**, 462–470.

8 Mrochen, M. and Seiler, T. (2001) Grundlagen der wellenfront-geführten refraktiven Hornhautchirurgie. *Ophthalmologe*, **98**, 703–714.

9 Mrochen, M. (2001) Aberrationsmessung und wellenfront-geführte refraktive Chirurgie. *Ophthalmochirurg*, **13**, 45–51.

10 Reinstein, D.Z., Neal, D.R., Vogelsang, H., Schroeder, E., Nagy, Z.Z., Bergt, M. *et al.* (2007) Optimized and wavefront guided corneal refractive surgery using the Carl Zeiss Meditec platform:

CRS-Master and MEL80 excimer laser, in *Surgical Techniques in Ophthalmology Series: Refractive Surgery* (ed. F.H. Roy), Saunders Elsevier, Philadelphia, pp. 99–125.

11 Reinstein, D.Z., Archer, T.J., Couch, D., Schroeder, E., and Wottke, M. (2005) A new night vision disturbances parameter and contrast sensitivity as indicators of success in wavefront-guided enhancement. *J. Refract. Surg.*, **21** (5), S535–S540.

12 Wachler, B.S. and Krueger, R.R. (1998) Normalized contrast sensitivity values. *J. Refract. Surg.*, **14** (4), 463–466.

13 Reinstein, D.Z., Archer, T.J., and Couch, D. (2006) Accuracy of the WASCA aberrometer refraction compared to manifest refraction in myopia. *J. Refract. Surg.*, **22** (3), 268–274.

14 Marcos, S., Moreno, E., and Navarro, R. (1999) The depth-of-field of the human eye from objective and subjective measurements. *Vision Res.*, **39** (12), 2039–2049.

15 Reinstein, D.Z., Couch, D.G., and Archer, T.J. (2009) LASIK for hyperopic astigmatism and presbyopia using micro-monovision with the Carl Zeiss Meditec MEL80. *J. Refract. Surg.*, **25** (1), 37–58.

16 Reinstein, D.Z., Archer, T.J., and Gobbe, M. (2011) LASIK for myopic astigmatism and presbyopia using non-linear aspheric micro-monovision with the Carl Zeiss Meditec MEL 80 platform. *J. Refract. Surg.*, **27** (1), 23–37.

17 Reinstein, D.Z., Archer, T.J., and Gobbe, M. (2009) Combined corneal topography and corneal wavefront data in the treatment of corneal irregularity and refractive error in LASIK or PRK using the Carl Zeiss Meditec MEL80 and CRS master. *J. Refract. Surg.*, **25** (6), 503–515.

18 Reinstein, D.Z. and Archer, T. (2006) Combined Artemis very high-frequency digital ultrasound-assisted transepithelial phototherapeutic keratectomy and wavefront-guided treatment following multiple corneal refractive procedures. *J. Cataract Refract. Surg.*, **32** (11), 1870–1876.

19 Holland, S.P., Srivannaboon, S., and Reinstein, D.Z. (2000) Avoiding serious corneal complications of laser assisted *in situ* keratomileusis and photorefractive keratectomy. *Ophthalmology*, **107** (4), 640–652.

20 Reinstein, D.Z., Silverman, R.H., Sutton, H.F., and Coleman, D.J. (1999) Very high-frequency ultrasound corneal analysis identifies anatomic correlates of optical complications of lamellar refractive surgery: anatomic diagnosis in lamellar surgery. *Ophthalmology*, **106** (3), 474–482.

21 Reinstein, D.Z., Rothman, R.C., Couch, D.G., and Archer, T.J. (2006) Artemis very high-frequency digital ultrasound-guided repositioning of a free cap after laser *in situ* keratomileusis. *J. Cataract Refract. Surg.*, **32** (11), 1877–1882.

22 Reinstein, D.Z. and Archer, T.J. (2007) Evaluation of irregular astigmatism with Artemis very high-frequency digital ultrasound scanning, in *Irregular Astigmatism: Diagnosis and Treatment* (ed. M. Wang), Slack, Thorofare, NJ, pp. 29–42.

23 Reinstein, D.Z., Archer, T.J., and Gobbe, M. (2009) Corneal epithelial thickness profile in the diagnosis of keratoconus. *J. Refract. Surg.*, **25** (7), 604–610.

24 Reinstein, D.Z., Archer, T.J., Gobbe, M., Silverman, R.H., and Coleman, D.J. (2010) Epithelial thickness after hyperopic LASIK: three-dimensional display with Artemis very high-frequency digital ultrasound. *J. Refract. Surg*, **26** (8), 555–564.

25 Reinstein, D.Z., Archer, T.J., Gobbe, M., Silverman, R.H., and Coleman, D.J. (2010) Epithelial, stromal and corneal thickness in the keratoconic cornea: three-dimensional display with Artemis very high-frequency digital ultrasound. *J. Refract. Surg.*, **26** (4), 259–271.

26 Reinstein, D.Z., Archer, T.J., Gobbe, M., Silverman, R.H., and Coleman, D.J. (2008) Epithelial thickness in the normal cornea: three-dimensional display with Artemis very high-frequency digital ultrasound. *J. Refract. Surg.*, **24** (6), 571–581.

45
Optical Coherence Tomography of the Human Larynx

Marc Rubinstein, Davin Chark, and Brian Wong

45.1
Anatomy

The larynx is a complex organ composed of cartilage, connective tissue, muscle, and mucosal epithelium that acts in a coordinated fashion to allow sphincteric control of the airway. The larynx has respiratory and digestive functions; it protects the lungs from aspiration of food and water, and it helps in the passage of air, phonation, and in the clearance of secretions. The larynx is divided anatomically into the supraglottic, glottic, and subglottic regions, illustrated in Figure 45.1. The supraglottic region extends from the tip epiglottis superiorly to the false vocal folds inferiorly, the glottic region encompasses the true vocal folds, and the subglottic region extends from the inferior border of the true vocal folds superiorly to the cricoid cartilage inferiorly. The vocal folds (i.e., the vocal "cords") consist of a multilayered structure of nonkeratinized stratified squamous epithelium covering three layers of dense connective tissue; the epithelial layer is separated from the connective tissue by the basement membrane. The basement membrane is a critical tissue layer as cancer cells that spread through this layer gain access to blood vessels and lymphatics. Deep to these layers is the vocal ligament of the thyroarytenoid muscle, illustrated in Figure 45.2 [1–5].

45.2
Clinical Problems

45.2.1
Laryngeal Cancer

Laryngeal cancer is the second most common cancer in the upper aerodigestive tract, with an estimated 12 290 new cases per year in the United States and roughly 3660 annual deaths [6]. Approximately 95% of laryngeal cancers are squamous cell carcinoma (SCC), and the majority occur in patients between the ages of 60 and 70 years [7]. The 5 year overall survival rate for laryngeal SCC is around 64% [8]. The

Handbook of Biophotonics. Vol.2: Photonics for Health Care, First Edition. Edited by Jürgen Popp, Valery V. Tuchin, Arthur Chiou, and Stefan Heinemann.

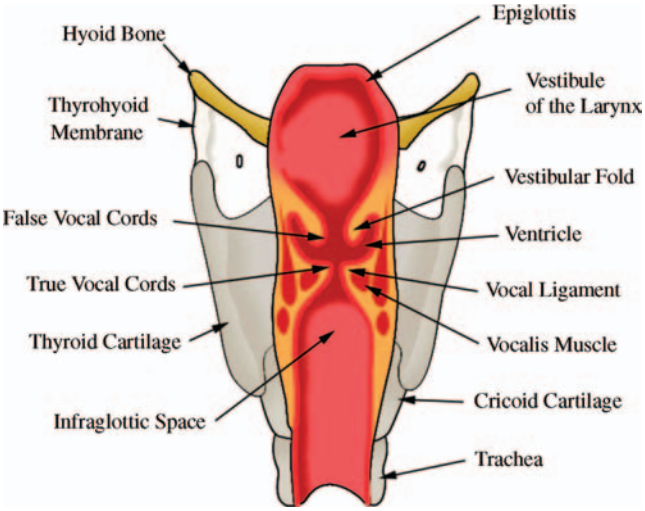

Figure 45.1 Diagram showing the human larynx with its corresponding structures.

risk of developing laryngeal SCC has been closely related to the use of tobacco and alcohol and it is proportional to the amount and duration of use, and when combined they act synergistically [9].

45.2.2 Importance of Laryngeal Optical Coherence Tomography

The cardinal symptom of early laryngeal cancer is hoarseness, but since this is a very innocuous and nonspecific symptom, laryngeal cancer often is not diagnosed until

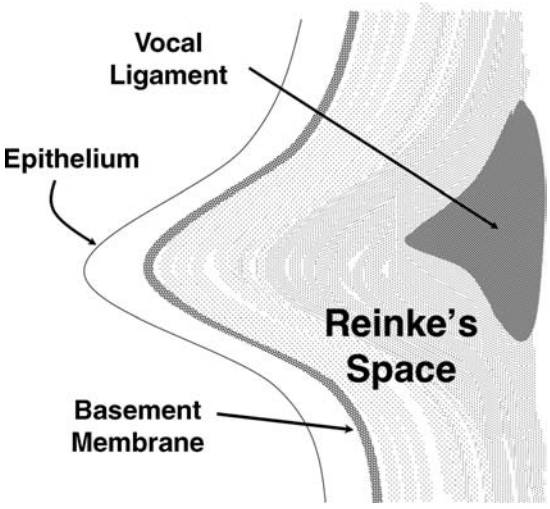

Figure 45.2 Diagram showing the microstructure of the vocal fold.

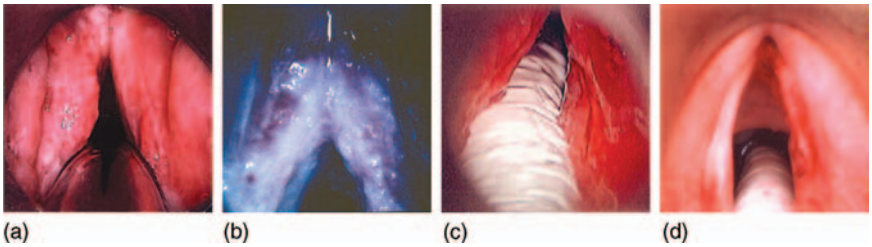

Figure 45.3 Disorders that can mimic laryngeal cancer: (a) chronic inflammation; (b) hyperkeratosis; (c) severe dysplasia; (d) invasive cancer (the white plastic object in the center is the endotracheal tube).

advanced stages. Clinical evaluation relies on using a flexible fiber-optic laryngoscope or a laryngeal mirror, which provides only a two-dimensional view of the laryngeal structures, which in the case of early cancers is generally inadequate to distinguish early malignancy from benign diseases and processes of the larynx. Early diagnosis of laryngeal cancer is key for optimal treatment. The "gold standard" for accurate diagnosis is a biopsy of the suspicious lesion. In general, this has to be performed under general anesthesia. Vocal fold biopsy is not without risk, and injury to the delicate epithelium of the folds may occur. Permanent changes can occur such as scarring, which may alter fold vibration and voice quality.

The spread of cancer cells through the basement membrane into the deeper layers of the vocal fold is the most important feature needed to establish a diagnosis of invasive cancer as opposed to premalignant entities such as dysplasia and carcinoma *in situ* and benign conditions such as chronic laryngitis (Figure 45.3).

Because of the risks associated with biopsy, and the considerable decision an ENT surgeon must make to take a patient to the operating room for a biopsy of the vocal folds under general anesthesia, noninvasive methods of imaging vocal fold microstructure have received significant attention. In particular, optical coherence tomography (OCT) may be used to evaluate the structural integrity of the basement membrane in patients at risk for cancer, and also provide surgeons with a means to guide biopsies towards regions with a greater diagnostic yield. OCT may also potentially be used to monitor the progression of the disease, providing a three-dimensional archive of vocal fold micro-architecture, reducing the reliance upon biopsies for disease surveillance.

45.3
Clinical *In Vivo* Applications

45.3.1
OCT During Microsurgical Endoscopy

In laryngology, the first clinical studies were performed during surgical endoscopy (i.e., under general anesthesia), where the OCT probe was passed through

the working channel of a flexible endoscope to obtain images of the laryngeal mucosa [10–12]. Observing that in OCT images taken from the regions with cancer no structures were identified, as compared with OCT images taken from normal mucosa, it was concluded that OCT has the capability to determine the border of the tumor [12]. Later studies expanded the applications, increased the patient numbers, and broadened the disease classes imaged using OCT in the operating room [13–20]. Most studies used slender rigid or semi-rigid probes. Wong *et al*. [14] imaged normative anatomy and benign lesions in 82 patients. OCT images compared favorably with results obtained using conventional histology. Epithelial thickness measurements were also recorded for specific laryngeal subsites, although these measurements were not directly compared with histology. Armstrong *et al*. [15] imaged 22 patients with laryngeal cancer, where integrity of the basement membrane was identified; disruption of the basement membrane was seen in those patients with histologic diagnosis of cancer, and also the transition zone was identify at the cancer margin. Klein *et al*. [16] used both OCT and polarization-sensitive optical coherence tomography (PS-OCT) to perform preliminary studies in 13 patients in the operating room and in the outpatient clinic, and examined the collagen content in the sub-epithelial tissue. A landmark study by Kraft *et al*. [18] imaged normal, benign, and malignant laryngeal diseases in 193 patients using a commercial OCT system [20]. In all cases, OCT images were compared with histopathology. They concluded that the use of OCT during microsurgical endoscopy yielded a correct diagnosis in 89% of cases compared with a rate of only 80% during microsurgical endoscopy alone. They also observed a higher sensitivity for predicting invasive tumor growth and epithelial dysplasia when using microlaryngoscopy with OCT compared with microlaryngoscopy alone.

Other clinical studies have focused on more specific applications. Shakhov *et al*. [13] used OCT as an aid for intraoperative surgical guidance and targeting of resection margins in laryngeal cancer surgery. Twenty-six patients were imaged during surgery and OCT was used to identify the transition zone between normal tissue and frank invasive cancer, thus increasing the accuracy of the tumor resection. Kaiser *et al*. [19] used OCT to measure the *in vivo* epithelial thickness of six different laryngeal subsites and correlated these measurements with those obtained on fixed anatomic laryngectomy specimens. Ridgway *et al*. [21] used OCT to evaluate the *in vivo* normal anatomy of the upper aerodigestive tract in 15 children. The normal microanatomy of different regions including the pediatric larynx were identified, and also various benign pathologic conditions. In neonates, Ridgway *et al*. [22] used OCT to image the larynx and trachea of 12 newborns who were admitted to the neonatal intensive care unite and required endotracheal intubation. Their study demonstrated that OCT may be capable of functioning as a noninvasive imaging technique to study and monitor changes in the newborn airway during intubation, and possibly reduce the incidence of acquired disorders such as subglottic stenosis. An example of laryngeal OCT is illustrated in Figures 45.4 and 45.5.

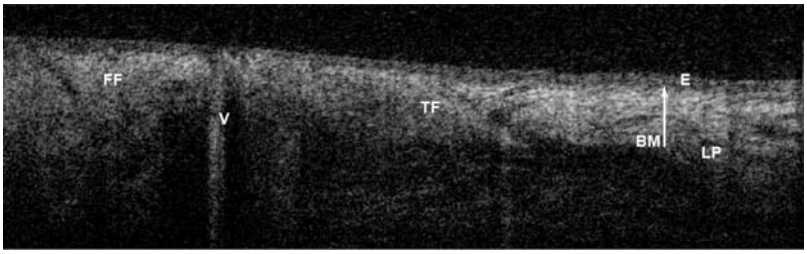

Figure 45.4 OCT image of a newborn's larynx. FF, false vocal folds; V, ventricle; TF, true vocal folds; BM, basement membrane locus; E, epithelium; LP, lamina propria.

45.3.2 Office-Based OCT

With the immense body of data supporting the use of OCT to image the larynx under general anesthesia, the focus has shifted towards developing systems for use in the office with awake, fully conscious patients using only topical anesthetics. An office-based OCT system would allow ENT surgeons to identify suspicious lesions better in the office and thus select patients better to undergo surgical biopsy. An office-based system also provides a means to archive three-dimensional cross-sectional images of suspicious lesions over time, and hence monitor disease progression. Although there are several reports of the use of OCT in the office, a major challenge that clinicians must contend with is motion of the patient's body, the patient's larynx, and the clinicians hand, and the sway of the fiber-optic endoscope or rigid telescope [16, 23]. There are two basic device platforms that are used to image the larynx in the office: flexible fiber-optic laryngoscopes, which are inserted through the nares and passed into the pharynx, and rigid laryngeal endoscopes, which are inserted into the oral cavity to view the larynx from the oropharynx.

Klein *et al.* [16] first reported using OCT in the office, in three patients, although the study did not focus on the feasibility of this technique or the methods used to obtain results. Sepehr *et al.* [23] studied the feasibility of using OCT in the office-based setting in 17 patients using a flexible OCT probe in tandem with a flexible fiber-optic laryngoscope. The instruments were inserted through the nose, and the OCT fiber tip was placed in direct contact with the larynx. They concluded that using this system in the office setting is feasible and could aid in the diagnosis of laryngeal lesions.

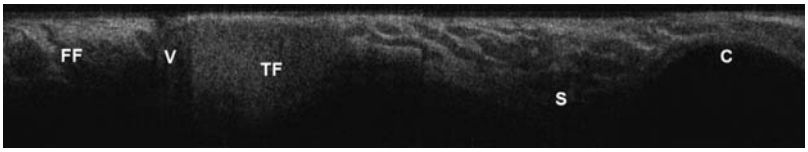

Figure 45.5 OCT image of a pediatric larynx. FF, false vocal folds; V, ventricle; TF, true vocal folds; S, subglottis; C, cricoid cartilage.

An alternative approach is to couple an OCT imaging system with a rigid Hopkins rod endoscope or similar rigid optical device. Using this approach allows the clinician simultaneously to obtain real-time OCT images while examining the patient's larynx [24–27]. This approach has several limitations. First, because the distance from any point in the oropharynx to the vocal folds varies greatly from patient to patient, the working distance also varies and this has to be manually adjusted during imaging, making it a challenge to acquire good images. The image quality is also affected by light dispersion as related to the image working distance. Also, the motion of the clinician's hand or the patients head, neck, or larynx affects the ability to identify the image plane. Finally, some patients may have a strong gag reflex and cannot tolerate imaging with this system configuration. Yu *et al.* [27] recently reported obtaining real-time *in vivo* OCT images at the same time as measuring the vocal fold vibrations. These vocal fold vibrations were recorded in both male and female patients and were successfully correlated with the vocal fundamental frequencies. Different systems have been used to image the human larynx, as summarized in Table 45.1.

45.3.3
OCT Integrated with a Surgical Microscope

The hand-held OCT probes used during laryngeal microsurgery are useful, but are limited in that the surgeon cannot use both hands (and two surgical instruments) during surgery. This also lengthens the surgical time, since the surgeon has to remove the OCT probe in order to introduce a second surgical instrument, which limits real-time imaging surgery *per se*. The probes also occupy space in what is already a narrow working port within a surgical laryngoscope. One approach to overcome these limitations is to integrate an OCT system with a surgical microscope [28, 29]. Vokes *et al.* [28] first reported using this type of integrated system to perform noncontact OCT imaging in 10 patients. The device consisted of an OCT scanner mounted on the objective of a surgical microscope much like conventional laser surgical micromanipulators. Although they reported identifying the vocal fold epithelium and lamina propria, limitations included reduced image resolution and operational challenges such as aligning the OCT beam and adjusting the focal length. Just *et al.* [29], using a different optical design incorporating the native optics of a surgical microscope, reported imaging patients during laryngeal microsurgery. This system effectively addressed some of the limitations previously reported by Vokes *et al.* [28], although with limitations of reduced lateral and axial resolution, which are due to the limited numerical aperture of the system. The potential of these combined systems is promising, although additional improvements need to be made before they can be widely used during laryngeal surgery.

45.4
Other Preclinical Applications of OCT in the Larynx

There are several *ex vivo* imaging studies using OCT in both the human [30, 31] and animal larynx [32–37]. Bibas *et al.* [30] imaged 10 human *ex vivo* laryngeal specimens

Table 45.1 Comparison of different OCT systems used to image the laryngeal tissue in humans.

Authors	Year	Central wavelength (nm)	System[a)]	Speed (kHz)	Axial resolution (μm)	Lateral resolution (μm)	Commercially available	*In vivo*	Type of study
Sergeev *et al.* [10]	1997	830	TD	1	15	17	No	Yes	Direct contact
Feldchtein *et al.* [11]	1998								
Shakhov *et al.* [12, 13]	1999, 2001								
Bibas *et al.* [30]	2004	830	TD	0.7	13	5	No	No	Noncontact
Wong *et al.* [14]	2005	1310	TD	0.5	10	10	No	Yes	Direct contact
Armstrong *et al.* [15]	2006								
Ridgway *et al.* [21, 22]	2007, 2008								
Sepehr *et al.* [23]	2008								
Kaiser *et al.* [19]	2009								
Burns [31]	2005	1310	FD	10	12	25	No	No	Noncontact
Klein *et al.* [16]	2006	1310	FD	10	12	30	No	Yes	Noncontact
Lueerssen *et al.* [26]	2007	1278	TD	0.1	20	30–55	No	Yes	Noncontact
Kraft *et al.* [18]	2008	1300	TD	0.5	15	25	Yes	Yes	Direct contact
Just *et al.* [29]	2009	840	SD	5	12	24	No	Yes	Noncontact
Yu *et al.* [27]	2009	1310	SS	20	8	25	No	Yes	Noncontact
Rubinstein *et al.* [20]	2010	1300	TD	0.75	10–20	25	Yes	Yes	Direct contact

a) TD, time domain; SS, swept source; SD, spectral domain.

using OCT. After the images were reconstructed in 3D, they were compared with histopathology obtained after processing of the same specimens. Burns *et al.* [31] used a combination of OCT and PS-OCT to image three human cadaver larynges; PS-OCT showed an increase in the tissue birefringence in the outer surface of the vocal ligament, which delineates it from the superficial lamina propria, suggesting a potential use for PS-OCT for detecting scar areas within the lamina propria and also to aid OCT in diagnosing subepithelial benign lesions. Several *ex vivo* animal model studies have focused on measuring and characterizing the lesions in the vocal folds [32, 34, 35]. Karamzadeh *et al.* [32] used rabbit models to mimic three different vocal folds lesions: scar formation, edema, and trauma. Other studies have focused on evaluating the injury caused by using a CO_2 laser, demonstrating that OCT can potentially be used in real time to assist surgeons during laryngeal laser surgery [34, 35]. In a more recent study, Burns *et al.* [37] used OCT to track real-time injection of hydrogel into to the vocal folds, and thus provide feedback for phonosurgical operations.

Although OCT may have tremendous potential in helping clinicians to diagnose laryngeal pathology, monitor disease progression and even aid in guiding surgical biopsies, the technology still needs to be improved before its use can spread beyond academic centers. Such limitations are signal penetration, the acquisition speed, and the resolution. Implementing better office-based OCT systems will also increase the usefulness and widespread use of this imaging technique.

References

1 Lorenz, R.R., Netterville, J.L., and Burkey, B.B. (2008) Head and neck, in *Sabiston Textbook of Surgery* (eds C.M. Townsend, R.D. Beauchamp, B.M. Evers, and K.L. Mattox), Saunders Elsevier, Philadelphia, pp. 813–847.

2 Woodson, G.E. (2005) Laryngeal and pharyngeal function, in *Cummings Otolaryngology: Head and Neck Surgery* (eds C.W. Cummings, P.W. Flint, B.H. Haughey, K.T. Robbins *et al.*), Elsevier Mosby, Philadelphia, pp. 1963–1975.

3 Noordzij, J.P. and Ossoff, R.H. (2006) Anatomy and physiology of the larynx. *Otolaryngol. Clin. North Am.*, **39**, 1–10.

4 Merati, A.L. and Rieder, A.A. (2003) Normal endoscopic anatomy of the pharynx and larynx. *Am. J. Med.*, **115** (Suppl 3A), 10S–14S.

5 Armstrong, W.B. and Netterville, J.L. (1995) Anatomy of the larynx, trachea, and bronchi. *Otolaryngol. Clin. North Am.*, **28**, 685–699.

6 Jemal, A., Siegel, R., Ward, E., Hao, Y. *et al.* (2009) Cancer statistics, 2009. *CA. Cancer J. Clin.*, **59**, 225–249.

7 Barnes, L., Tse, L.L.Y., Hunt, J.L., Brandwein-Gensler, M. *et al.* (2005) Tumours of the hypopharynx, larynx and trachea: Introduction, in *World Health Organization Classification of Tumours. Pathology and Genetics of Head and Neck Tumours* (eds L. Barnes, J.W. Eveson, P. Reichart, and D. Sidransky), IARC Press, Lyon, pp. 111–117.

8 Hoffman, H.T., Porter, K., Karnell, L.H., Cooper, J.S. *et al.* (2006) Laryngeal cancer in the United States: changes in demographics, patterns of care, and survival. *Laryngoscope*, **116**, 1–13.

9 Pelucchi, C., Gallus, S., Garavello, W., Bosetti, C., and La Vecchia, C. (2008) Alcohol and tobacco use, and cancer risk for upper aerodigestive tract and liver. *Eur. J. Cancer Prev.*, **17**, 340–344.

10 Sergeev, A., Gelikonov, V., Gelikonov, G., Feldchtein, F. *et al.* (1997) *In vivo* endoscopic OCT imaging of precancerand cancer states of human mucosa. *Opt. Express*, **1**, 432–440.

11 Feldchtein, F.I., Gelikonov, G.V., Gelikonov, V.M., and Kuranov, R.V. *et al.*

(1998) Endoscopic applications of optical coherence tomography. *Opt. Express*, **3**, 257–270.

12 Shakhov, A., Terentjeva, A., Gladkova, N.D., Snopova, L. *et al.* (1999) Capabilities of optical coherence tomography in laryngology. *Proc. SPIE*, **3590**, 250–260.

13 Shakhov, A.V., Terentjeva, A.B., Kamensky, V.A., Snopova, L.B. *et al.* (2001) Optical coherence tomography monitoring for laser surgery of laryngeal carcinoma. *J. Surg. Oncol.*, **77**, 253–258.

14 Wong, B.J., Jackson, R.P., Guo, S., Ridgway, J.M. *et al.* (2005) *In vivo* optical coherence tomography of the human larynx: normative and benign pathology in 82 patients. *Laryngoscope*, **115**, 1904–1911.

15 Armstrong, W.B., Ridgway, J.M., Vokes, D.E., Guo, S. *et al.* (2006) Optical coherence tomography of laryngeal cancer. *Laryngoscope*, **116**, 1107–1113.

16 Klein, A.M., Pierce, M.C., Zeitels, S.M., Anderson, R.R. *et al.* (2006) Imaging the human vocal folds *in vivo* with optical coherence tomography: a preliminary experience. *Ann. Otol. Rhinol. Laryngol.*, **115**, 277–284.

17 Kraft, M., Luerssen, K., Lubatschowski, H., Glanz, H., and Arens, C. (2007) Technique of optical coherence tomography of the larynx during microlaryngoscopy. *Laryngoscope*, **117**, 950–952.

18 Kraft, M., Glanz, H., von Gerlach, S., Wisweh, H. *et al.* (2008) Clinical value of optical coherence tomography in laryngology. *Head Neck*, **30**, 1628–1635.

19 Kaiser, M.L., Rubinstein, M., Vokes, D.E., Ridgway, J.M. *et al.* (2009) Laryngeal epithelial thickness: a comparison between optical coherence tomography and histology. *Clin. Otolaryngol.*, **34**, 460–466.

20 Rubinstein, M., Fine, E.L., Sepehr, A., Armstrong, W.B. *et al.* (2010) Optical coherence tomography of the larynx using the Niris system. *J. Otolaryngol. Head Neck Surg.*, **39**, 150–156.

21 Ridgway, J.M., Ahuja, G., Guo, S., Su, J. *et al.* (2007) Imaging of the pediatric airway using optical coherence tomography. *Laryngoscope*, **117**, 2206–2212.

22 Ridgway, J.M., Su, J., Wright, R., Guo, S. *et al.* (2008) Optical coherence tomography of the newborn airway. *Ann. Otol. Rhinol. Laryngol.*, **117**, 327–334.

23 Sepehr, A., Armstrong, W.B., Guo, S., Su, J. *et al.* (2008) Optical coherence tomography of the larynx in the awake patient. *Otolaryngol. Head Neck Surg.*, **138**, 425–429.

24 Guo, S., Hutchison, R., Jackson, R.P., Kohli, A. *et al.* (2006) Office-based optical coherence tomographic imaging of human vocal cords. *J. Biomed. Opt.*, **11**, 30501.

25 Guo, S., Yu, L., Sepehr, A., Perez, J. *et al.* (2009) Gradient-index lens rod based probe for office-based optical coherence tomography of the human larynx. *J. Biomed. Opt.*, **14**, 014017.

26 Lueerssen, K., Wisweh, H., Ptok, M., and Lubatschowski, H. (2007) Optical characterization of vocal folds by OCT-based laryngoscopy. *Proc. SPIE*, **6424**, 64241O.

27 Yu, L., Liu, G., Rubinstein, M., Saidi, A. *et al.* (2009) Office-based dynamic imaging of vocal cords in awake patients with swept-source optical coherence tomography. *J. Biomed. Opt.*, **14**, 064020.

28 Vokes, D.E., Jackson, R., Guo, S., Perez, J.A. *et al.* (2008) Optical coherence tomography-enhanced microlaryngoscopy: preliminary report of a noncontact optical coherence tomography system integrated with a surgical microscope. *Ann. Otol. Rhinol. Laryngol.*, **117**, 538–547.

29 Just, T., Lankenau, E., Huttmann, G., and Pau, H.W. (2009) Intra-operative application of optical coherence tomography with an operating microscope. *J. Laryngol. Otol.*, **123**, 1027–1030.

30 Bibas, A.G., Podoleanu, A.G., Cucu, R.G., Bonmarin, M. *et al.* (2004) 3-D optical coherence tomography of the laryngeal mucosa. *Clin. Otolaryngol. Allied Sci.*, **29**, 713–720.

31 Burns, J.A., Zeitels, S.M., Anderson, R.R., Kobler, J.B. *et al.* (2005) Imaging the mucosa of the human vocal fold with optical coherence tomography. *Ann. Otol. Rhinol. Laryngol.*, **114**, 671–676.

32 Karamzadeh, A.M., Jackson, R., Guo, S., Ridgway, J.M. *et al.* (2005) Characterization of submucosal lesions using optical coherence tomography in the rabbit

subglottis. *Arch. Otolaryngol. Head Neck Surg.*, **131**, 499–504.

33 Luerssen, K., Lubatschowski, H., Gasse, H., Koch, R., and Ptok, M. (2005) Optical characterization of vocal folds with optical coherence tomography. *Proc. SPIE*, **5686**, 328–332.

34 Nassif, N.A., Armstrong, W.B., de Boer, J.F., and Wong, B.J. (2005) Measurement of morphologic changes induced by trauma with the use of coherence tomography in porcine vocal cords. *Otolaryngol. Head Neck Surg.*, **133**, 845–850.

35 Torkian, B.A., Guo, S., Jahng, A.W., Liaw, L.H. *et al.* (2006) Noninvasive measurement of ablation crater size and thermal injury after CO_2 laser in the vocal cord with optical coherence tomography. *Otolaryngol. Head Neck Surg.*, **134**, 86–91.

36 Wisweh, H., Merkel, U., Huller, A.-K., Luerssen, K., and Lubatschowski, H. (2007) Optical coherence tomography monitoring of vocal fold femtosecond laser microsurgery. *Proc. SPIE*, **6632**, 663207.

37 Burns, J.A., Kim, K.H., Kobler, J.B., deBoer, J.F. *et al.* (2009) Real-time tracking of vocal fold injections with optical coherence tomography. *Laryngoscope*, **119**, 2182–2186.

46
Optical Coherence Tomography of the Human Oral Cavity and Oropharynx

Marc Rubinstein, Davin Chark, and Brian Wong

46.1
Anatomy

The oral cavity (OC) is a complex organ, composed of salivary glands, teeth, muscles, and sensory receptors. It is bounded by the palate above, the floor of the mouth below and the cheek on each side. The OC has several functions, including sense of taste, mastication, deglutition, vocalization, and respiration. The OC can also be divided by subsites, which include the lip, buccal mucosa, floor of mouth, hard palate, oral tongue, alveolar ridges, and retromolar trigone, illustrated in Figure 46.1 [1–3].

The area where the soft palate joins the hard palate is the transition between the OC and the oropharynx (OP). The OP is bounded anteriorly by the soft palate, uvula, and tonsillar pillars, posteriorly it goes from the soft palate to the epiglottis, and laterally by the palatine tonsils. The OP has both respiratory and digestive functions; it is involved in the deglutition, respiration, and phonation process. The OP subsites include the base of the tongue, soft palate, palatine tonsils and posterior pharyngeal wall, illustrated in Figure 46.2 [1–3].

46.2
Progression of Disease

The American Cancer Society estimated that 35 720 new cases of OC and OP cancer was diagnosed in 2009 and accounted for 7600 deaths [4]. In the United States, these malignant neoplasms comprise 3.1% of all cancers in men and 2.5% in women [5]. Approximately 80% of the cancer in the OC and OP is squamous cell carcinoma (SCC) [6]. Premalignant lesions are usually precursors of this type of cancer. Lesions can present as a white lesion (leukoplakia) or red lesion (erythroplakia); although these lesions are not normal, they are not necessarily neoplastic. Currently the only way to differentiate if the lesion is benign, premalignant, or malignant is with a biopsy. Premalignant lesions are called dysplasia, atypical cells

Handbook of Biophotonics. Vol.2: Photonics for Health Care, First Edition. Edited by Jürgen Popp, Valery V. Tuchin, Arthur Chiou, and Stefan Heinemann.

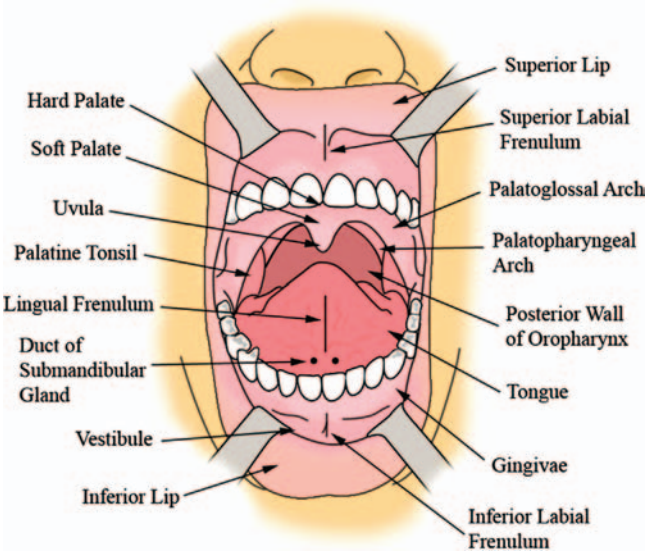

Figure 46.1 Diagram showing the human oral cavity.

that have not invaded the underlying tissue. Although dysplasia can progress to cancer, it can also regress. Erythroplakia is more likely to progress to cancer (51%) than leukoplakia (5%) [7]. The most important factor in long-term survival is early lesion detection and adequate treatment.

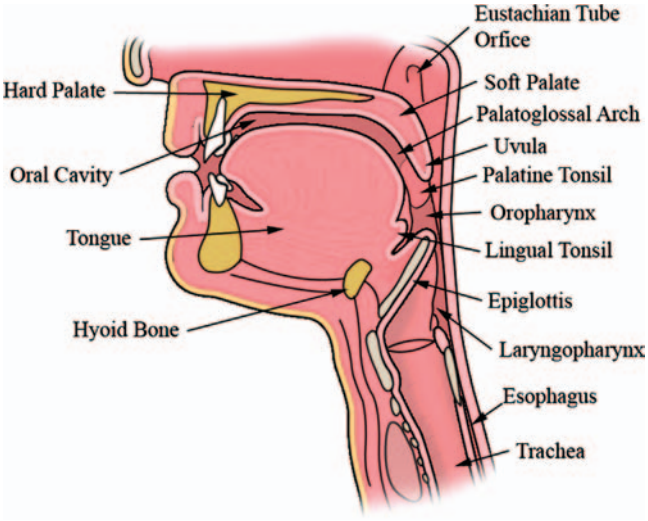

Figure 46.2 Diagram showing the human oropharynx.

46.3 Usefulness of OCT

Although there are many diagnostic tools and techniques for oral cancer management, none at present have shown significantly greater efficacy than conventional clinical examination [8], although this is an evolving situation. Recent human *in vivo* clinical studies have shown the efficacy of diagnosing premalignant and malignant diseases in the OC using optical coherence tomography (OCT) [9–11]. Tsai *et al.* [9] imaged 32 patients using OCT and diagnosed and distinguished epithelial hyperplasia, mild dysplasia, and SCC, differentiating between these three distinct pathologic entities and also from normal mucosa using A-line imaging-derived features. Likewise, Wilder-Smith *et al.* [10] imaged a total of 50 patients with normal mucosa, dysplasia, or malignant lesions. They found that OCT images compared favorably with histology, with high sensitivity and specificity for detecting these different types of lesions. Fomina *et al.* [11] used OCT to detect OC neoplasia *in vivo* in 35 patients, comparing OCT images with histology in benign or dysplastic/malignant lesions. They concluded that OCT has clinical application for diagnosis and treatment guidance and also for cancer screening (sensitivity 83% and specificity 98%).

OCT may also be used to guide surgical biopsies toward regions of higher diagnostic yield. Jerjes *et al.* [12] examined 34 *ex vivo* biopsies of 27 patients, and examined changes in the keratin layer, epithelial layer, and the lamina propria, and for the presence or absence of an intact basement membrane. Based on the architectural changes identified using OCT, biopsies were then performed in the sites of interest. One of the areas where OCT has its greatest clinical use in the OC and OP is in the management of patients with "field cancerization." Field cancerization is the presence of histologically abnormal tissue surrounding primary cancerous lesions of squamous cell carcinomas [13]. Tsai *et al.* [14] reported using an *ex vivo* model to delineate the cancer from normal tissue. Using two parameters, decay constant and standard deviation A-scan, they observed that while the decay constant decreased as the A-scan moved laterally away from the abnormal portion, the standard deviation A-scan increased when it was performed in the abnormal portion of the lesion. Also, having the ability to identify the transition zone between normal epithelium and malignant epithelium makes OCT a useful clinical tool (Figures 46.3 and 46.4).

Another clinical application of OCT is to monitor disease progression and change in a noninvasive manner. Tsai *et al.* [15] evaluated OC lesions in different oncologic stages and were able to differentiate between mild and moderate dysplasia.

OCT has also been used to evaluate and diagnose different pathologic conditions throughout the OC and OP [16–21]. One of the most common side effects of radiotherapy and/or chemotherapy is mucositis. OCT has the capability of detecting, in patients receiving radiotherapy and/or chemotherapy, early microstructural changes in the OC before the clinical manifestations appear, which may provide an effective and noninvasive method to evaluate early mucosal changes, and thus lead to early treatment of mucositis [16–18]. Ridgway *et al.* [21] studied normal and pathologic conditions in the OC and OP in 41 patients, and compared OCT images with histopathology, confirming the feasibility of using OCT to identify differences in

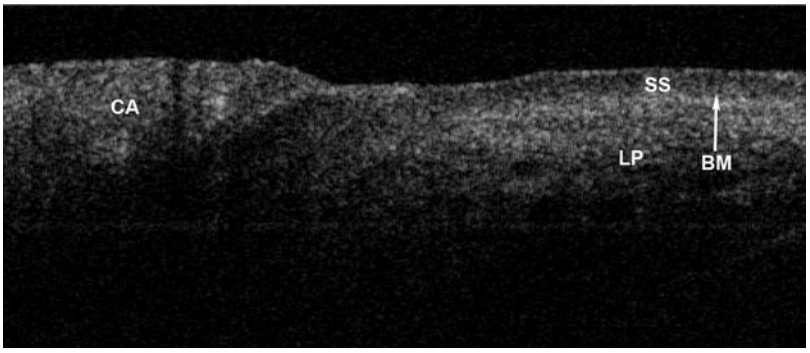

Figure 46.3 OCT image showing the transition zone in the buccal mucosa; note the loss of the basement membrane in the area of the cancer. LP, lamina propria; SS, stratified squamous epithelium; BM, basement membrane locus; CA, cancer.

the mucosal and submucosal tissue of the OC and OP. Other studies imaging the OC have focused on specific disease processes, such as oral submucous fibrosis [19] and vascular anomalies [20].

Several studies focused on imaging only normal healthy mucosa of the OC [22, 23]. Recently, Prestin *et al*. [24] used OCT to measure the epithelial thickness in different areas of the OC; this is an important study as thickness is one factor distinguishing neoplastic from normal tissues. Multiple OCT systems have been used to image the OC and OP; Table 46.1 presents a summary of some of these systems. There have also been several animal studies using OCT to evaluate various benign and malignant processes in the OC [25–31].

Although OCT has potential to aid clinicians in diagnosing OC and OP pathologies, there are limitations with this technology, such as a limited depth of penetration, the acquisition speed and the resolution. Improvements in theses areas are important to obtain better images at a faster rate and thus aid in the diagnosis and treatment of neoplasia.

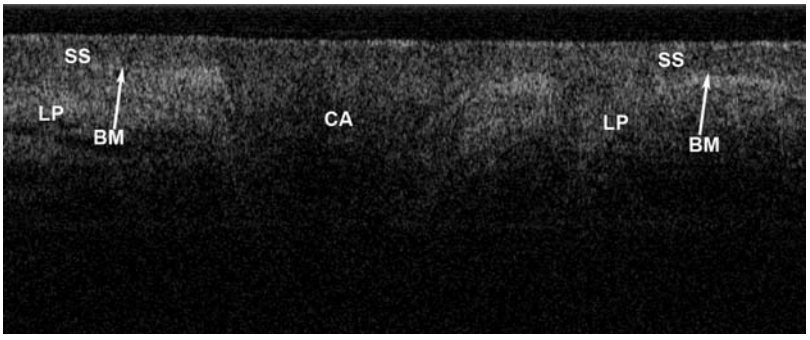

Figure 46.4 OCT image showing transition zones in the buccal mucosa; note the loss of the basement membrane in the area of the cancer. LP, lamina propria; SS, stratified squamous epithelium; BM, basement membrane locus; CA, cancer.

Table 46.1 Comparison of different OCT systems used to image the OC and OP in humans.

Authors	Year	Central wavelength (nm)	System[a)]	Speed (kHz)	Axial resolution (μm)	Lateral resolution (μm)	Commercially available
Feldchtein *et al.* [22]	1998	830 1280	TD	1	13 17	17 22	No
Fomina *et al.* [11]	2004	1270	TD	0.75	15–20		Yes
Gladkova *et al.* [16, 17]	2005, 2006						
Ridgway *et al.* [21]	2006	1310	TD	0.5	10	10	No
Kawakami-Wong *et al.* [18]	2007						
Tsai *et al.* [9, 14, 15, 19]	2008, 2009	1310	SS	20	8	15	Yes
Lee *et al.* [19]	2009						
Ozawa *et al.* [20, 23]	2009	1260–1360	SS	20	11 (air) 8 (tissue)	37	Yes
Jerjes *et al.* [12]	2009	1310	SS	<10	<10	<7.5	Yes
Wilder-Smith *et al.* [10]	2009	1300	TD	0.75	10–20	25	Yes
Prestin *et al.* [24]	2010						

a) TD, time domain; SS, swept-source.

References

1 Travers, J.B. and Travers, S.P. (2005) Oral cavity, pharynx, esophagus, in *Cummings Otolaryngology: Head and Neck Surgery* (eds C.W. Cummings, P.W. Flint, B.H. Haughey, K.T. Robbins, *et al.*), Elsevier Mosby, Philadelphia, pp. 1409–1437.

2 Dhillon, N. (2007) Anatomy, in *Current Diagnosis and Treatment in Otolaryngology—Head and Neck Surgery* (ed. A. Lalwani), McGraw-Hill Medical, New York, pp. 1–30.

3 Lorenz, R.R., Netterville, J.L., and Burkey, B.B. (2008) Head and neck, in *Sabiston Textbook of Surgery* (eds C.M. Townsend, R.D. Beauchamp, B.M. Evers, and K.L. Mattox), Saunders Elsevier, Philadelphia, pp. 813–847.

4 American Cancer Society (2009) *Cancer Facts and Figures*, American Cancer Society, Atlanta, GA.

5 Jemal, A., Siegel, R., Ward, E., Hao, Y. *et al.* (2009) Cancer statistics. *CA. Cancer J. Clin.*, **59**, 225–249.

6 Horner, MJ., Ries, LAG., Krapcho, M., Neyman, N. *et al.* (2009) SEER Cancer Statistics Review, 1975–2006, National Cancer Institute. Bethesda, MD, http://seer.cancer.gov/csr/1975_2006/, based on November 2008 SEER data submission, posted to the SEER web site (last accessed 15 May 2011).

7 Lee, N. and Chan, K. (2007) Benign and malignant lesions of the oral cavity, oropharynx, and nasopharynx, *Current Diagnosis and Treatment in Otolaryngology—Head and Neck Surgery* (ed. A. Lalwani), McGraw-Hill Medical, New York, pp. 356–366.

8 DeCoro, M. and Wilder-Smith, P. (2010) Potential of optical coherence tomography for early diagnosis of oral malignancies. *Expert Rev. Anticancer Ther.*, **10**, 321–329.

9 Tsai, M.T., Lee, H.C., Lee, C.K., Yu, C.H. *et al.* (2008) Effective indicators for diagnosis of oral cancer using optical coherence tomography. *Opt. Express*, **16**, 15847–15862.

10 Wilder-Smith, P., Lee, K., Guo, S., Zhang, J. *et al.* (2009) *In vivo* diagnosis of oral dysplasia and malignancy using optical coherence tomography: preliminary studies in 50 patients. *Lasers Surg. Med.*, **41**, 353–357.

11 Fomina, J.V., Gladkova, N.D., Snopova, L. B., Shakhova, N.M. *et al.* (2004) *In vivo* study of neoplastic alterations of the oral cavity mucosa. Proc. SPIE, 5316, 41–47.

12 Jerjes, W., Upile, T., Conn, B., Hamdoon, Z. *et al.* (2009) *In vitro* examination of suspicious oral lesions using optical coherence tomography. *Br. J. Oral Maxillofac. Surg.*, **48**, 18–25.

13 Slaughter, D.P., Southwick, H.W., and Smejkal, W. (1953) Field cancerization in oral stratified squamous epithelium; clinical implications of multicentric origin. *Cancer*, **6**, 963–968.

14 Tsai, M.T., Lee, H.C., Lu, C.W., Wang, Y.M. *et al.* (2008) Delineation of an oral cancer lesion with swept-source optical coherence tomography. *J. Biomed. Opt.*, **13**, 044012.

15 Tsai, M.T., Lee, C.K., Lee, H.C., Chen, H.M. *et al.* (2009) Differentiating oral lesions in different carcinogenesis stages with optical coherence tomography. *J. Biomed. Opt.*, **14**, 044028.

16 Gladkova, N., Maslennikova, A., Balalaeva, I., Vyseltseva, Y. *et al.* (2006) OCT visualization of mucosal radiation damage in patients with head and neck cancer : pilot study. Proc. SPIE, 6078, 60781J–60788.

17 Gladkova, N., Maslennikova, A., Terentieva, A., Fomina, Y. *et al.* (2005) *Proc. SPIE*, 58610T–58618T.

18 Kawakami-Wong, H., Gu, S., Hammer-Wilson, M.J., Epstein, J.B. *et al.* (2007) *In vivo* optical coherence tomography-based scoring of oral mucositis in human subjects: a pilot study. *J. Biomed. Opt.*, **12**, 051702.

19 Lee, C.K., Tsai, M.T., Lee, H.C., Chen, H.M. *et al.* (2009) Diagnosis of oral submucous fibrosis with optical coherence tomography. *J. Biomed. Opt.*, **14**, 054008.

20 Ozawa, N., Sumi, Y., Chong, C., and Kurabayashi, T. (2009) Evaluation of oral vascular anomalies using optical coherence tomography. *Br. J. Oral Maxillofac. Surg.*, **47**, 622–626.

21 Ridgway, J.M., Armstrong, W.B., Guo, S., Mahmood, U. *et al.* (2006) *In vivo* optical coherence tomography of the human oral cavity and oropharynx. *Arch. Otolaryngol. Head Neck Surg.*, **132**, 1074–1081.

22 Feldchtein, F., Gelikonov, V., Iksanov, R., Gelikonov, G. *et al.* (1998) *In vivo* OCT imaging of hard and soft tissue of the oral cavity. *Opt. Express*, **3**, 239–250.

23 Ozawa, N., Sumi, Y., Shimozato, K., Chong, C., and Kurabayashi, T. (2009) *In vivo* imaging of human labial glands using advanced optical coherence tomography. *Oral Surg. Oral Med. Oral Pathol. Oral Radiol. Endod.*, **108**, 425–429.

24 Prestin, S., Betz, C., and Kraft, M. (2010) Measurement of epithelial thickness within the oral cavity using optical coherence tomography. Proc. SPIE, 7548, 75482F–75489F.

25 Kim, C.S., Wilder-Smith, P., Ahn, Y.C., Liaw, L.H. *et al.* (2009) Enhanced detection of early-stage oral cancer *in vivo* by optical coherence tomography using multimodal delivery of gold nanoparticles. *J. Biomed. Opt.*, **14**, 034008.

26 Hanna, N.M., Waite, W., Taylor, K., Jung, W.G. *et al.* (2006) Feasibility of three-dimensional optical coherence tomography and optical Doppler tomography of malignancy in hamster cheek pouches. *Photomed. Laser Surg.*, **24**, 402–409.

27 Wilder-Smith, P., Hammer-Wilson, M.J., Zhang, J., Wang, Q. *et al.* (2007) *In vivo* imaging of oral mucositis in an animal model using optical coherence tomography and optical Doppler tomography. *Clin. Cancer Res.*, **13**, 2449–2454.

28 Wilder-Smith, P., Krasieva, T., Jung, W.G., Zhang, J. *et al.* (2005) Noninvasive imaging of oral premalignancy and malignancy. *J. Biomed. Opt.*, **10**, 051601.

29 Matheny, E.S., Hanna, N.M., Jung, W.G., Chen, Z. *et al.* (2004) Optical coherence tomography of malignancy in hamster cheek pouches. *J. Biomed. Opt.*, **9**, 978–981.

30 Jung, W.G., Zhang, J., Chung, J.R., Wilder-Smith, P. *et al.* (2005) Advances in oral cancer detection using optical coherence tomography. *IEEE J. Sel. Top. Quantum Electron.*, **11**, 811–817.

31 Wilder-Smith, P., Jung, W.G., Brenner, M., Osann, K. *et al.* (2004) *In vivo* optical coherence tomography for the diagnosis of oral malignancy. *Lasers Surg. Med.*, **35**, 269–275.

47
In Vivo Brain Imaging and Diagnosis

Christoph Krafft and Matthias Kirsch

47.1
Introduction

In general, biophotonic imaging methods give information regarding intrinsic optical properties of brain tissue and the presence or absence of endogenous or exogenous chromophores. The benefits of using light in imaging living tissue include that light can provide high sensitivity to functional changes and can reveal the dynamics of cells in the nervous system, via either absorption of light, emission of light (fluorescence and phosphorescence), and elastic or inelastic scattering. Further advantages are diffraction-limited spatial resolution in the micrometer and even submicrometer range, nondestructive sampling, use of nonionizing radiation, fast data collection, relatively inexpensive instrumentation and reduced infrastructure requirements compared with other clinical imaging methods. A disadvantage of all optical techniques is their limited penetration depth in brain tissue, which is dependent on its absorption and scattering properties. High absorption exists in both the visible wavelength range (350–700 nm), mainly due to hemoglobin, and in the wavelength range above 900 nm, due to lipids, proteins, and water. However, in the range 700–900 nm, the absorption of all biomolecules is weak; hence imaging using light in this interval maximizes tissue penetration while simultaneously minimizing autofluorescence from nontarget tissue. The most widely measured intrinsic chromophores are oxy- and deoxyhemoglobin, alongside cytochromes and metabolites which have distinctive absorption and fluorescence properties. Cytochrome oxidase is a mitochondrial enzyme that plays an important role in oxygen metabolism in the brain. The concentration of cytochrome oxidase in the brain is lower than that of hemoglobin (2–3 μM compared with 40–60 μM). Extrinsic chromophores such as absorbing and fluorescent dyes in addition to transgenic methods can also provide specific optical contrast and are often able actively to report functional parameters. Optical imaging modalities which probe molecular vibrations as an inherent feature of all molecules do not depend on chromophores. Molecular vibrations can be excited by absorption of mid-infrared (MIR) radiation and inelastic scattering of monochromatic light.

Handbook of Biophotonics. Vol.2: Photonics for Health Care, First Edition. Edited by Jürgen Popp, Valery V. Tuchin, Arthur Chiou, and Stefan Heinemann.

Among the first applications of optical brain imaging was a paper by Jöbsis in 1977 [1]. He measured blood and tissue oxygenation changes in the brain of a cat using near-infrared (NIR) light. Since then, the field has grown, encompassing both basic science and diagnostic applications that exploit the interactions between light and tissue to image the brain. Optical *in vivo* imaging of the diseased nervous system [2], optical brain imaging *in vivo* [3], and vibrational spectroscopic imaging in the context of neuro-oncology [4] have recently been summarized. Currently, numerous parts of the nervous system can be visualized by optical *in vivo* imaging, including the cortex, cerebellum, olfactory bulb, retina, spinal cord, peripheral nerves, and autonomic ganglia. Transgenic labels have been developed for tracing many structures in the nervous system, including neurons, axon tracts, most glial populations, oligodendrocytes, brain vasculature, and invading tumor cells. This has allowed a growing number of models to be studied in mice.

Magnetic resonance imaging (MRI), X-ray computed tomography (CT) and positron emission tomography (PET) are valuable and established tools for brain imaging. MRI and X-ray CT require shielded rooms for protection, and PET requires synchrotrons to generate the short-lived radioactive isotopes of carbon, nitrogen, fluorine, or oxygen. X-ray CTs and structural MRI have excellent spatial resolution and allow the detection of morphologic changes in the brain, for example, to delineate tumors. In particular, functional brain imaging has seen significant growth since the availability of functional magnetic resonance imaging (fMRI) in 1990. Applications cover neurosurgical planning, the investigation of the physiologic basis of neurologic diseases such as epilepsy, Alzheimer's disease, and stroke, the development of diagnostic methods, drugs, treatments, and interventions, and the study of cognitive and perceptual responses and developmental changes, to name just a few [5]. Owing to their broad range of contrast mechanisms and their ability to detect and image a wide range of functional parameters, optical imaging technologies can complement the established clinical modalities.

For example, to visualize regions of the brain exhibiting functional changes in response to stimuli, fMRI typically exploits the blood oxygen level-dependent (BOLD) signal, widely thought to correlate inversely with deoxygenated hemoglobin (HbR) concentration. However, a BOLD increase (an HbR decrease) may correspond to an increase in oxygenation, or a decrease in blood volume. Newer fMRI methods such as arterial spin labeling can provide measures of flow, and intravenous contrast agents such as monocrystalline iron oxide nanocompounds can allow cerebral blood volume changes to be observed. These measurements cannot easily be acquired simultaneously and only the combination of the methods provides insight into the true hemodynamic responses and oxygenation dynamics in the brain. PET is performed using contrast agents such as 2-fluoro-2-deoxy-D-glucose containing radioactive isotopes. Subsequently, glucose utilization in the brain can be imaged via the localization of these isotopes. However, resolution is typically poor, data acquisition is slow, and hence dynamics cannot be readily evaluated. Further disadvantages are that contrast agents must be manufactured locally prior to each scan, and radioactive dose limits its use in certain patient populations, especially infants. The major drawback of both fMRI and PET imaging is that they cannot be used during a surgical

procedure or for extensive amounts of time. In addition, especially fMRI is not as reliable as morphologic analysis [6, 7].

A major challenge in optical imaging for noninvasive clinical applications is to overcome the effects of elastic light scattering, which limits the penetration depth and achievable imaging resolution. Therefore, optical imaging encompasses a wide range of measurement techniques with the aim of overcoming the effects of scatter. These range from laser scanning microscopy of surface accessible regions with submicron resolution to diffuse optical tomography of deeper and larger volumes of tissue. According to Abbe's law of diffraction, the lateral resolution of conventional light microscopy is limited to $\delta_{lat} = 0.61\lambda/NA$ and the axial resolution to $\delta_{ax} = 2\lambda n/NA^2$ (where λ = wavelength; n = refractive index; NA = numerical aperture). Although ultraviolet and visible light offer higher resolutions due to smaller wavelengths, clinical optical brain imaging generally uses NIR light to obtain improved penetration through the scalp, skull, and brain due to minimal absorption of intrinsic chromophores.

Optical brain imaging is finding widespread applications as a research tool for both clinical and animal studies of brain functions, diseases, and treatments of pathologies. The structures of the human brain and principles to assess brain tissue composition and brain function using optical brain imaging are displayed in Figure 47.1. However, little is known about the way in which the normal brain functions, in part due to the difficulties of measuring such a complex organ without disturbing or damaging its *in vivo* function. Optical imaging allows the living brain to be closely observed, and many functional interactions and changes to be investigated over various length and time scales. Imaging of animals (commonly mouse, rat, cat, or primate) rather than humans provides more flexibility since preparations can be much more controlled and diseases and treatments can be systematically compared. Furthermore, extrinsic dyes and cross-validation techniques can be utilized and developed without the need for clinical regulatory approval. Since the adverse effects

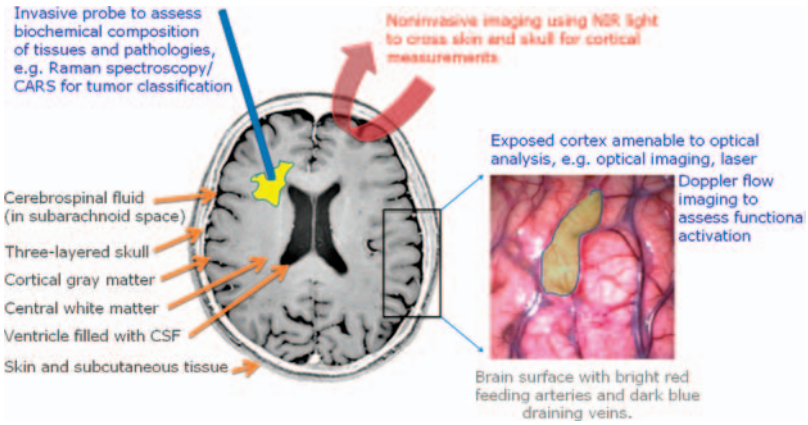

Figure 47.1 Structures of the human brain and principal technologies to assess brain tissue composition and brain function using biophotonic technologies.

of light scattering worsen as the size of the tissue being interrogated increases, imaging of smaller animals therefore also offers significant technical advantages, allowing higher resolution imaging and improved sensitivity and quantitation. For very high-resolution imaging, the cortex can be surgically exposed, allowing direct optical imaging of the brain's surface with only minimal disturbance to normal brain activity. For long-term experiments, the cortex is covered by implanting a permanent cranial window. A small cover-slip is placed over the opening of the skull and is sealed using acrylic cement. This procedure effectively reseals the skull, allows intracranial pressure to re-equalize, prevents contamination or dissolution of ambient gas, and controls brain movement which would otherwise be substantially affected by heart rate and breathing. Exposed cortex optical imaging is highly versatile, and most commonly performed in animals, although it has also been performed on the human brain, for example, during epilepsy surgery. Optical imaging of the exposed cortex is currently the only technique that can provide sufficient resolution to reveal detailed information of functional responses for sensory and cognitive processing research.

In this overview, we describe various optical imaging approaches to brain imaging in neurology and neurosurgery as summarized in Table 47.1. We introduce the techniques concisely in the context of brain imaging. All techniques are described

Table 47.1 Summary of optical imaging techniques.

Technique	Attributes
Optical imaging	Techniques including microscopy and biophotonic methods that use light to visualize the distribution of cells and molecules.
Wide-field microscopy	The entire field of view is illuminated simultaneously to produce an image.
Scanning microscopy	A focused beam of light (usually a laser) is moved (scanned) across the field of view to detect the signal of each spot sequentially (includes confocal microscopy and multiphoton microscopy).
Confocal microscopy	A technique that allows optical sectioning by placing a pinhole in front of the detector to exclude out-of-focus light and generate a sharp image of structures in the focal plane.
Tomography	Imaging approaches in which the object is imaged from multiple angles and mathematical algorithms are used to reconstruct the three-dimensional structure of the signal source.
Intrinsic optical imaging	A technique that detects changes in the optical properties of brain tissue such as absorption or scattering.
Fluorescence microscopy	Detection of fluorescence emission of intrinsic or extrinsic chromophores after absorption of light.
Calcium imaging	Calcium indicator dyes (that is, calcium-dependent fluorophores) in combination with microscopy are used to measure changes in intracellular calcium concentration.
Multiphoton microscopy	Scanning microscopy technique in which a pulsed near-infrared laser is used to achieve optical sectioning by limiting (multiphoton) excitation to the perifocal plane (includes two-photon microscopy and second-harmonic generation).

Table 47.1 (*Continued*)

Technique	Attributes
Second-harmonic generation microscopy	Near-infrared lasers generate frequency-doubled signals from the scattering of light as it interacts with specific macromolecules. Structures such as cytoskeleton and collagen can be visualized.
Two-photon microscopy	Two photons of a pulsed near-infrared laser are absorbed and excite a fluorophore which emits a higher energy photon.
Raman microscopy	Inelastic scattering of monochromatic light probes molecular vibrations (includes nonlinear variant coherent anti-Stokes Raman scattering using high intensity pulsed lasers).
Optical coherence tomography	A technique that uses interferometry of reflected or backscattered light from biological tissues.

more comprehensively in Part I of this Handbook. We then focus on examples of *in vivo* brain imaging: Section 47.3 details the use in neuro-oncology and imaging of functional areas, Section 47.4 covers vascularity and Section 47.5 regeneration.

47.2 Basic Principles

47.2.1 Two-Dimensional Camera-Based Imaging: Absorption

2D camera–based imaging of the exposed cortex is the simplest optical imaging technique and is often referred to as "optical imaging" in the neuroscience literature. The term "optical imaging of intrinsic signals" (OIS) is also known because intrinsic optical properties such as absorption and scattering are detected which can be measured directly at the brain surface. This brain imaging technique can visualize brain compartments with micrometer and millisecond resolution. The most significant absorbers in the brain at visible and NIR wavelengths are oxyhemoglobin (HbO_2) and deoxyhemoglobin (HbR). Their distinctive absorption spectra yield quantitative chemical information about their concentration, blood flow, blood volume, and oxygenation. Blood delivers oxygen to tissue by locally converting HbO_2 to HbR, so changes in the oxygenation state of blood correspond to changes in the relative concentrations of HbO_2 and HbR. Consequently, variations in the amount and oxygenation state of hemoglobin modulate the absorption properties of the brain. By simply shining light into the exposed cortex and taking pictures with a camera, the hemodynamic properties can be readily observed. Furthermore, since HbR and HbO_2 have different absorption spectra, measurements with different wavelengths of light can produce images that are preferentially sensitive to changes in the concentration of either HbO_2 or HbR. At isosbestic points where the HbR and HbO_2 absorptions are approximately the same (e.g., 500, 530, 570, and 797 nm),

changes in total hemoglobin (HbT) concentration ($HbT = HbR + HbO_2$) can be measured independently of changes in blood oxygenation. To calculate the actual changes in the concentrations of HbO_2, HbR, and HbT, the absorption of the brain must be measured at two or more wavelengths. This is expressed by the term hyperspectral imaging. OIS is usually described as an invasive imaging technique because it requires surgery to make the cortex visible. However, as intraoperative OIS is performed in the operating room by attaching a charge-coupled device (CCD) camera and optical filters to the operating microscope, it is noninvasive compared with the current gold standard intraoperative electrophysiologic techniques, which require placing electrodes directly on to the brain. Intraoperative IOS has been demonstrated to be a potentially useful neurosurgical tool for both functional brain mapping and lesion delineation (see overview by Prakash *et al.* [8]).

47.2.2
Two-Dimensional Camera Based Imaging: Fluorescence

The fluorescence of intrinsic and extrinsic chromophores can be imaged by a two-dimensional camera-based setup which consists of an excitation filter of the appropriate wavelength and a long-pass filter in front of the camera to block excitation light and isolate the fluorescence emission. In some cases, a dichroic mirror is used such that the illumination light is reflected on to the brain, and emitted fluorescence passes through the dichroic mirror to the camera.

Extrinsic voltage-sensitive dyes (VSDs) provide a way to detect optically the neuronal activity in the *in vivo* exposed cortex. VSDs are molecules that generally bind across a neuron's membrane. Changes in membrane potential cause measurable changes in the fluorescence of the dye. VSDs can only be used in animals at present, and are usually topically applied directly to the exposed cortex for 1–2 h before imaging commences. Some VSDs have been shown to photobleach quickly or have phototoxic effects, and so illumination times are typically kept to a minimum. Calcium-sensitive dyes (CaSDs) are compounds that increase their fluorescence in response to increases in calcium ion concentration. When cells such as neurons are loaded with CaSDs, it becomes possible to monitor intracellular calcium. Since calcium influx occurs when a neuron fires an action potential, the calcium dye's fluorescence can optically report this, providing a second tool with which to image neuronal activity optically. The challenge with CaSDs is to introduce them into the neurons successfully. Concentration changes in intrinsic flavoproteins (FADs) in the brain can be measured from their intrinsic fluorescence *in vivo*. FADs provide a measure of metabolic changes in cells (neurons and possibly glia), and have a distinct time course compared with shorter neuronal and longer hemodynamic responses.

47.2.3
Two-Dimensional Camera-Based Imaging: Laser Speckle

Laser speckle flow imaging is capable of imaging the blood flow dynamics in the superficial cortex. Flow is a very important parameter if the rate of oxygen delivery

and consumption are to be calculated. Laser Doppler imaging has been widely used to provide point measurements of blood flow in the brain. However, laser speckle flow imaging of the exposed cortex can image the spatial distribution of the flow throughout the vascular network during functional activation. In this case, the light source is replaced with a divergent laser diode. The camera then simply acquires rapid and high-resolution images of the exposed cortex, which appear as low-contrast images of the speckle pattern from the laser illumination. The speckle pattern is caused by the coherent laser light scattering within the brain. If red blood cells are moving within the image, they cause the speckle pattern to vary over time. The rate at which the speckles change relates to how fast the red blood cells are moving.

47.2.4
Two-Dimensional Fiber Bundle-Based Imaging

Although most measurements use anesthetized animals, some studies of native behavior require that the animal be both awake and able to move around freely. Recently, a technique was developed in which the exposed cortex of a mouse could be imaged via a flexible fiber bundle with high temporal and spatial resolution [9]. The principle is that excitation light propagates in one direction through an optical fiber bundle while emitted fluorescence returns via the same path, is reflected by a dichroic mirror, and is imaged by a camera. Microlenses project and enlarge small fluorescent brain structures on to a fiber bundle containing well-ordered arrays of glass cores for flexible image transfer from the mouse to the camera. These fiber bundles typically contain thousands of fiber cores whose centers are spaced by around 10 μm apart. Using a fast CCD camera, the authors achieved image acquisition rates up to 100 Hz over imaging fields of 0.25–0.33 mm.

47.2.5
Three-Dimensional Imaging: Optical Coherence Tomography

Optical coherence tomography (OCT) is analogous to ultrasound imaging except that reflections of NIR radiation, rather than sound, are detected. In ultrasonography, the time delay of reflected sound waves is used to generate an image of tissue structures. Because of the high velocity of light, a time delay of reflected light cannot be measured directly. Therefore, light is split into probe and reference light. The reference light and the probe light are combined by a beamsplitter and registered by a detector. Interference of low-coherence light occurs only when the optical pathlengths of the reference and probe are matched within the coherence length of the light source, which means that the difference between the optical path of the reference and the probe light determines the depth in the sample at which the magnitude of reflection is registered. Interferometers with fiber-optic couplers and beam scanning systems have been implemented to perform OCT measurements through microscopes, fiber-optic catheters, endoscopes, and hand-held probes. The contrast in OCT is generally due to refractive index mismatches. OCT is typically performed using NIR wavelengths >1 μm. OCT synthesizes cross-sectional images from a series of laterally

adjacent depth scans. OCT allows noninvasive real-time *in vivo* imaging of brain tissues up to a 3 mm penetration depth with a spatial resolution of 10–15 μm and in ultrahigh-resolution mode even better (0.9 μm axial, 2 μm lateral) [10, 11].

47.2.6 Confocal Microscopy

Confocal microscopy relies on the rejection of scattered light by isolating signals originating from the focus of the scanning beam. Confocal excitation wavelengths are typically in the visible spectrum, where tissue scatter and absorption are high. Therefore, when using confocal microscopy to image depths beyond 200–300 μm, the laser beam can no longer focus, and images become blurry and lack sensitivity. Confocal microscopy can also be combined with fluorescence emission. While it is assumed that the detected fluorescence light originates from the focus of the scanning beam, some of the detected signal is also generated by excitation and emission light that is scattered or absorbed within the tissue above and below the focus. This light not only contributes to image blurring, but can also result in cumulative photodamage to areas of the tissue that are not actively being imaged.

47.2.7 Two-Photon Microscopy

Since two-photon microscopy was first demonstrated in 1990 [12], it has become an invaluable tool for imaging intact biological specimens at very high resolution, to depths of up to 600 μm. The advantages have been summarized and discussed in depth [13]. Two-photon microscopy has also been applied to *in vivo* imaging of the brain, which has previously been reviewed in the context of brain function monitoring [14]. Although fluorescent contrast is required, two-photon microscopy provides an unprecedented view of *in vivo* brain activity on a cellular and microvascular level. In particular, sophisticated transgenic technology allows the labeling of single cells in the nervous system and permits their function to be monitored. Similarly to confocal microscopy, two-photon microscopy requires a focused beam of laser light to be steered within the tissue, sensing the properties of each location and using them to form a 2D or 3D image. This technique overcomes many of the disadvantages of confocal microscopy. Instead of fluorescence excitation at visible wavelengths, two-photon microscopy utilizes laser light of twice the excitation wavelength. When sufficient photon flux is achieved, it is usually possible for a fluorophore to be excited by two of these lower energy photons arriving in quick succession. Once excited, the fluorophore will emit a photon at or near its usual emission wavelength. This high photon flux is achievable if a pulsed laser is used which delivers high-energy, rapid pulses. Typically, a Ti:sapphire laser is used, which is tunable between 700 and 1000 nm, with 80 MHz pulse repetition, $<$500 fs pulse width, mean power 1 W, and peak power 25 kW. Even with such a high peak power, the nonlinear effect of two-photon excitation will only occur at the tight focus of the laser beam. Consequently, two-photon microscopy can use NIR light to image the

same fluorophores as confocal microscopy. However, since scattering and absorption of NIR light in tissue are much lower than for visible light, the focus of the laser beam can be maintained at depths of >600 μm, depending on the tissue type. The fact that the fluorophore is excited only at the very focus of the beam means that surrounding tissue does not experience significant photodamage. As NIR excitation is generally spectrally well separated from the emission wavelength, excitation light is rejected much more simply than for confocal microscopy. Further, since any light emerging from the tissue is expected at the fluorescent emission wavelength, it can only have originated from the focus of the scanning beam and it is not necessary to reject scattered light as required in confocal microscopy. Sensitive detectors can be placed as close to the tissue as possible to collect all of the emerging emission light. This signal, when reformed according to the beam scanning pattern, produces a high-resolution image of the fluorescent structures within tissue. Whereas traditional microscopy required tissue to be stained and sectioned, two-photon microscopy allows high-resolution 3D imaging of intact, functioning tissue.

47.2.8
Second-Harmonic Generation

Although endogenous multiphoton fluorescence imaging has found a number of applications in brain imaging, the small number of naturally fluorescent compounds limits its general use. Only small modifications are required to equip a laser-scanning two-photon microscope for second-harmonic generation (SHG) imaging microscopy. The nonlinear optical effect SHG is also commonly called frequency doubling. The phenomenon requires intense laser light passing through a highly polarizable material with a noncentrosymmetric molecular organization. Collagen within connective tissue, muscle thick filaments, and microtubule arrays within interphase and mitotic cells belong to the biological material that can produce SHG signals. The second-harmonic light emerging from the material is at precisely half the wavelength of the light entering the material. Hence the SHG process within the material changes two NIR incident photons into one emerging visible photon at exactly twice the energy (and half the wavelength). Like that of two-photon microscopy, the amplitude of SHG is proportional to the square of the incident light intensity. Therefore, SHG microscopy has the same intrinsic optical sectioning characteristics. Hence SHG microscopy offers a contrast mechanism that does not require excitation of fluorescent molecules. The fact that only selected proteins reveal contrast in SHG imaging is a limiting factor. Applications for visualizing biomolecular arrays in cells, tissues, and organisms have been summarized [15].

47.2.9
Inelastic Light Scattering: Raman Spectroscopy

Raman spectroscopy is based on inelastic scattering of monochromatic light. This process can excite molecular vibrations. As numerous vibrations of biomolecules are probed simultaneously, more bands are observed in vibrational spectra of

cells and tissue than in other optical spectra, giving a fingerprint-like signature. These bands provide information about the biochemistry, structure, and composition of the underlying sample. Among the main advantages is that this information is obtained without labels. Potential autofluorescence is reduced and penetration of incident and scattered light is enhanced by excitation with NIR lasers. The relatively weak signals require intense laser excitation and highly sensitive instrumentation. Continuous-wave lasers are operated at powers of a few hundred milliwatts to prevent tissue degradation. Optical components for detection are optimized for high throughput and low light losses. Furthermore, signal amplification methods (resonance Raman scattering, surface-enhanced scattering, coherent anti-Stokes Raman scattering, stimulated Raman scattering) have been developed to increase sensitivity. Raman images which provide molecular contrast are usually registered in the sequential point mapping mode, which means that the laser focus or the sample is moved from one spot to the other.

47.2.10
Noninvasive Optical Brain Imaging: Topography, Tomography

For routine optical brain imaging in humans, it is clearly necessary to develop noninvasive techniques. They must overcome the effects of light scattering, while maintaining the benefits of optical contrast to study functional activation and to investigate pathologies. Since light penetration and scattering are significant obstacles for noninvasive imaging, measurements on children and babies are easier to achieve than on adults. It is often difficult to image these infants and small children using fMRI and PET, so optical imaging provides a unique opportunity to study many aspects of functional brain development. Optical imaging of the adult brain can also provide valuable functional information that complements modalities such as fMRI. As a particular advantage of its ability to image HbO_2, HbR, and HbT simultaneously, optical imaging is widely adopted for studies of the cortical hemodynamic response to a wide range of stimuli.

Direct topography is the most widespread approach to clinical optical brain imaging and is often referred to as near-infrared spectroscopy (NIRS). Optical fibers are generally used to transmit light to and from the head. Instrumentation may be continuous wave (cw), frequency domain (FD), or time domain (TD) using two or more wavelengths. In its simplest form, NIRS uses light source and detector pairs positioned on the head. Light that passes though the skull scatters within the cortex of the brain. Despite significant attenuation, variations in absorption due to changes in local HbT, HbO_2, and HbR concentrations result in detectable modulations in the intensity of the emerging light in the cortical surface of the brain where the majority of functional processing occurs. If an array of sources and detectors is used, the changes measured between a source–detector pair can be approximately mapped or interpolated to the underlying cortex and a low-resolution (>5 mm) 2D topographical map of cortical activation can be produced. Data processing is an important issue to consider systematic errors due to breathing or hearth rate. A further difficulty is reliable placement of sources and detectors on the head. Hair on the head is a major

challenge as it can significantly attenuate light entering and leaving the head, and can cause measurement instability over time if the probes shift. Finally, light propagation in the human head has to be modeled using either Monte Carlo algorithms or the diffusion approximation to the radiative transfer equation.

In addition to absorption, photon emission can be detected, preferentially using NIR fluorescence or red-shifted bioluminescence reporters that take advantage of the low absorption of biological tissues in this spectral window. However, one limitation is the low spatial and temporal resolution of this technique. Although photons from deep within the brain can reach the surface, they are scattered along the way so that their origin is obscured. Another limitation is that biophotonic signals are weakened by absorption, which restricts temporal resolution by long acquisition times. In general, detection of light through >7 cm of tissue will cause around 10^{-7} attenuation. New fluorophores that might improve sensitivity are becoming available, such as quantum dots (that is, semiconductor nanocrystals that have unique fluorescence features).

The most complex approach to optical brain imaging involves performing a full 3D reconstruction of the entire head using an approach similar to X-ray CT. As for tomographic imaging, a series of measurements or projections through the tissue need to be imaged and light has to be transmitted across the whole head; this approach has only been demonstrated on small infants. However, the benefits are that in addition to functional imaging, this approach can potentially permit imaging of pathologies. For reconstructed topography, measurements between sources and detectors with different separations allow some depth-resolved information to be deduced. In tomography, the same basic image reconstruction approach is used, but a larger number of projections through the head at different angles are required to calculate the 3D structure deep within the brain. Fluorescence or bioluminescence imaging requires a 3D reconstruction of the location of the cells that emit the signal. A comprehensive introduction to biophotonic imaging techniques and their current capabilities and limitation has been given elsewhere [16].

47.3 Applications in Neuro-Oncology and Functional Imaging

Surgical removal of brain tumors is the most common initial treatment received by brain tumor patients because it relieves the mass effect of the tumor on neurologic tissue and allows histopathologic diagnosis of the tumor, which directly affects the direction of follow-up therapeutic strategy. Aggressive surgical resection results in prolonged survival of patients with a malignant glioma, may lower the risk of anaplastic progression in a low-grade glial tumor, and may thereby increase the survival length and quality of life in these patients. To achieve this goal with minimal neurologic deficits, an accurate identification of brain tumor margins during surgery is required. However, the intraoperative detection of residual tumor tissue, especially in a low-grade tumor, is difficult because of the low optical contrast between tumor and adjacent brain. Moreover, a glioma lacks a true tumor to brain

interface; instead, single cells migrate along preformed anatomic structures into the adjacent brain beyond the highly cellular margin of the tumor. Currently, neurosurgeons determine brain tumor margins intraoperatively by visual inspection and information provided by surgical navigation systems that are based on X-ray CT/MRI and/or intraoperative ultrasound (IOUS). However, limitations of these techniques include the following:

- The true infiltrating margins may not be visible on X-ray CT/MRI images.
- Registration errors and intraoperative brain shift can degrade the spatial accuracy of the surgical navigation systems.
- Primary brain tumors, unlike most metastatic tumors, do not typically possess clear boundaries, that is, the margins appear blurred in the IOUS images.
- It is often difficult, even for experienced neurosurgeons, to differentiate visually low-grade gliomas and associated tumor margins from normal brain tissue.

Because of their complexity, IOUS and intraoperative MRI cannot provide a continuous online imaging of the resection cavity, and integration of these technologies into microsurgical instruments or operating microscopes is limited. Applications of IOUS and MRI require a pause in the course of the brain tumor resection for intermittent analyses, which is realistic only for a limited number of investigations. Furthermore, the spatial resolution of IOUS in brain tissue is typically no higher than 150–250 μm, and with the advancement of the surgical procedure, artifacts diminish the use of IOUS. In particular, the creation of new surfaces, alteration of the acoustic properties of the tumor–tissue interfaces by surgical interactions, and the introduction of foreign material (e.g., for hemostasis or therapeutic interactions) generate new structures that limit comparability of IOUS images within the same procedure. The spatial resolution of MRI is between 0.5 and 1 mm which is insufficient to resolve tissue microstructure and to discriminate between tissue alterations due to tumor infiltrations and those resulting from surgery. However, the main advantages of both IOUS and MRI are the penetration depth and the routine volumetric sampling. This eases interpretation and co-registration to other imaging modalities.

Biophotonic imaging techniques are attractive candidates for analyzing brain tissue nondestructively in real time and for providing intraoperative *in vivo* diagnosis. It is of clinical interest to obtain data on both the morphology and the composition of the tissues. A combination of biophotonic imaging techniques with conventional imaging should allow for rapid introduction into clinical routine.

47.3.1 Absorption-Based Imaging

Determination of tumor oxygenation at the microvascular level will provide important insight into tumor growth, angiogenesis, necrosis, and therapeutic response. NIRS has the potential to differentiate lesions and hemoglobin dynamics. The vascular status and the pathophysiologic changes that occur during tumor vascularization were studied in an orthotopic brain tumor model [17]. A noninvasive multimodal approach based on NIRS along with MRI was applied for monitoring the

concentrations of HbO_2, HbR, and water within the tumor region. The concentrations of these compounds were determined using 15 discrete wavelengths in a spectral window of 670–780 nm. A direct correlation between tumor size, intratumoral microvessel density, and tumor oxygenation was found.

To clarify the characteristics of the evoked cerebral blood oxygenation changes occurring in stroke and brain tumors, noninvasive NIRS and BOLD fMRI were compared during functional brain activation [18]. NIRS enabled functional brain stimulation and activation to be imaged through measurement of changes in hemoglobin concentrations. The approach was applied to monitor 12 glioma patients during recovery after neurosurgery [19]. The sensitivity and specificity of NIRS for hemoglobin were used to image functional brain stimulation and activation through measurement of changes in hemoglobin concentrations. Functional activation of specific areas of the brain can be elicited by, for example, sensory stimulation of the arm, hand, or leg (somato-sensory evoked potentials). A corresponding region of activation can be correlated with the stimulated area, and the image can be overlaid into an operating microscope and used to guide an intracerebral approach.

47.3.2 Fluorescence-Based Imaging

Autofluorescence with 337 nm excitation can discriminate solid tumors from normal brain tissues based on their reduced fluorescence emission at 460 nm compared with normal tissue. False-positive rates constitute a general problem because not all regions showing reduced fluorescence are tumors [20]. A hand-held optical spectroscopic probe was applied in clinical trials that combined autofluorescence with diffuse reflection spectroscopy [21, 22]. Spectra of brain tumors and infiltrating tumor margins were separated from spectra of normal brain tissues *in vivo* using empirical algorithms with high sensitivity and specificity. Blood contamination was found to be a major obstacle.

Multiphoton-excited autofluorescence using NIR femtosecond laser pulses allows the reconstruction of 3D microanatomic images of native tissues at a subcellular level without the need for contrast-enhancing markers or histologic stains. Multiphoton autofluorescence microscopy could visualize solid tumor, the tumor–brain interface, and single invasive tumor cells in gliomas of mouse brains and of human biopsies [23, 24]. Furthermore, fluorescence lifetime imaging of endogenous fluorophores provides an additional parameter in so-called 4D microscopy, since the different decay times of the fluorescent signal could differentiate tumor and normal brain tissue [16, 25].

47.3.2.1 5-ALA

In order to improve selectivity, fluorescent markers have been applied to malignant brain tissue. These markers include indocyanine green [26], fluorescein [27], and fluorescein–albumin [28]. Fluorescent porphyrins accumulate in malignant brain tissue after administration of the metabolic precursor 5-aminolevulinic acid (ALA) [29]. These fluorophores are taken up by individual glioma cells, but not in

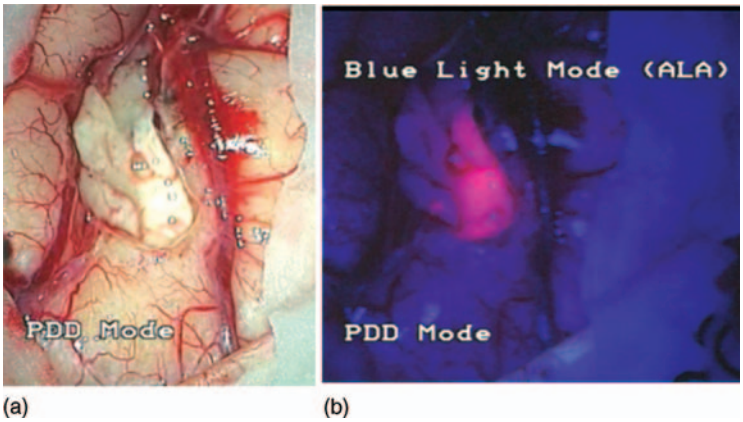

Figure 47.2 Intraoperative macroscopic (~5× magnification) view of subcortical ALA + glioma tissue. (a) Normal white light image of the operative field. The adjacent normal cortical structures and vessels are easily delineated. (b) The ALA-derived fluorescence depicts viable pink fluorescent tumor within the opened cortex. Although being revolutionary to neurosurgery, the images also reveal the limitations: macroscopic resolution, no morphologic information, single pathology classification.

normal brain tissue [29]. Single glioma cells can be detected. However, given the limited magnification usable for a surgical procedure, the ratio of infiltrative cells to normal parenchyma is seen as a shift from bright orange–pink to a soft pinkish tint of the tumor margin (Figure 47.2).

The technique can be integrated in an operating microscope and the fluorescence images permitted intraoperative detection of the brain tumors and a safer tumor resection (Figure 47.2). Results from a human clinical trial showed that ALA-derived fluorescence with peaks at 635 and 704 nm could predict the presence of tumor tissue with a specificity of 100% and a sensitivity of 85% with respect to histopathology [30]. A multicenter clinical phase III trial of 322 patients revealed that this approach led to improved progression-free survival of patients with malignant gliomas [31]. However, identification of low-grade tumors and tumor margins could be problematic. It remains unclear whether the fluorophore requires an opening of the blood–brain barrier which is disturbed within solid glioma tissue, since the current recommendations suggest a combined application of ALA and dexamethasone, a drug that seals the blood–brain barrier and has been shown to improve fluorescence. The technique needs planning and is not available any time or on demand during surgery, since a long metabolic phase has to be taken into account. The substance has to be applied several hours prior to the operation. Second, a certain degree of photobleaching of the fluorophore occurs with fluorescence decay within 25 min for excitation light and ~90 min for white light [29]. Third, ALA-derived fluorescence is only positive in malignant gliomas as a pathognomic sign. Many other brain tumor types are only positive in a small percentage of cases, such as pituitary adenomas, meningiomas, and the frequent cerebral metastases. These problems have diminished the capability of induced fluorescence for brain tumor

demarcation so far. Normal intraoperative magnification of up to 20-fold does not allow for individual cell detection. Moreover, infiltrating glioma cannot be discerned from normal tissue. This exemplifies the need for better imaging tools to delineate fine morphologic structures and their classification with regard to tissue types. ALA-derived imaging is revolutionary to neurosurgery, but is monocentric with regard to its possible applications and does not allow morphologic information to be obtained. It is not available to all patients since contraindications exist with regard to hepatic co-morbidities. Since ALA is given systemically, the patient's skin is also sensitive to bright light exposure. This light sensitivity is mild and temporary as it is attenuated to a normal level within 24 h. However, patients should be exposed for 1 day to ambient light only.

47.3.2.2 **Nanoparticles**

Nanoparticle-based-platforms have attracted considerable attention for their potential effect in oncology and other biomedical fields. A fluorescent nanoprobe was presented that is able to cross the blood–brain barrier and specifically target brain tumors in a genetically engineered mouse model [32]. Animals were investigated *in vivo* using magnetic resonance and biophotonic imaging, and histologic and biodistribution analysis. The nanoprobe consists of an iron oxide nanoparticle coated with biocompatible poly(ethylene glycol)-grafted chitosan copolymer, to which the tumor-targeting agent chlorotoxin and an NIR fluorophore are conjugated. After the nanoparticles have been injected, they accumulate and remained in brain tumors for up to 5 days. The study demonstrated that the nanoparticles can improve contrast in both MRI and optical imaging during surgery. The authors called their technique brain tumor illumination or brain tumor painting.

47.3.2.3 **Quantum Dots**

Quantum dots (QDs) are optical semiconductor nanocrystals that offer prospects as labels due to their stable, bright fluorescence. The intravenous injection of QDs is accompanied by macrophage sequestration. Macrophages infiltrate brain tumors and phagocytize intravenously injected QDs, optically labeling the tumors. Macrophage-mediated delivery of QDs to brain tumors may represent a novel technique to label tumors preoperatively [33, 34]. The surface of QDs can be coupled with antibodies specific to one or several tumor epitopes, leading to selective enhancement of tumor cells rather than indirect labeling by macrophage sequestration [35]. Proven technologies for antibody coupling using streptavidin-conjugated QDs with biotinylated antibodies may soon be employed [36]. This technology is particularly interesting for neurosurgery since many different fluorochromes can be used and different epitopes can be labeled. This extends the potential usability to other pathologies such as Parkinson's disease and other degenerative central nervous system (CNS) disorders. QDs might serve for both detection and delivery of therapeutic substances. QDs within tumors may be detected within 30 min after application [37] employing optical imaging and optical spectroscopy, providing the surgeon with real-time optical feedback during the resection and biopsy of brain tumors.

47.3.3
Bioluminescence Imaging

Bioluminescence imaging (BLI) has emerged as a sensitive imaging technique for small animals. BLI exploits the emission of photons based on energy-dependent reactions catalyzed by luciferases with a maximum depth of 2–3 cm. Luciferases comprise a family of photoproteins that emit photons in the presence of oxygen and adenosine triphosphate (ATP) during metabolism of substrates such as luciferin into oxyluciferin. Luciferins are injected immediately before data acquisition. The light from these enzyme reactions typically has very broad emission spectra that frequently extend beyond 600 nm, with the red components of the emission spectra being the most useful for imaging by virtue of easy transmission through tissues [38]. In the context of neuro-oncology, BLI was used to monitor the formation of grafted tumors *in vivo*, to measure cell numbers during tumor progression and response to therapy [39], and to monitor the proliferative activity of glioma cells and cell cycle in a genetically engineered mouse model of glioma *in vivo* [40]. The ability to image two or more biological processes in a single animal can greatly increase the utility of luciferase imaging by offering the opportunity to distinguish the expression of two reporters biochemically. Dual BLI was used to monitor gene delivery via a therapeutic vector and to follow the effects of the therapeutic protein TRAIL (tumor necrosis factor-related apoptosis-inducing ligand) in gliomas [41]. TRAIL has been shown to induce apoptosis in neoplastic cells and may offer new prospects for tumor treatment.

47.3.4
OCT-Based Imaging

OCT-based noncontact imaging of brain tissue during neurosurgical procedures is challenging because after opening of the dura, the target volume follows the respiratory and arterial cycle, resulting in movements several millimeters in amplitude. Slow scan times will result in distortion of the tissue surface contour or may result in the area of interest moving out of the measurement window. Therefore, short scan acquisition times are crucial. In particular, spectral-domain (SD)-OCT allows rapid scanning times of three images per second, which would be sufficient to suppress motion artifacts of the relatively slow movements of the brain exposed during operations. Both time domain (TD)- and SD-OCT of experimental gliomas in mice and human brain tumor specimens delineated normal brain, infiltration zone, and solid tumor based on the tissue microstructure and signal characteristics [10, 42]. The same authors also presented the first feasibility study of intraoperative OCT [43]. Post-image acquisition processing for noninvasive imaging of the brain and brain tumor was used to compensate for image distortion caused by pulse- and respiration-induced movements of the target volume. Based on different microstructure and characteristic signal attenuation profile, OCT imaging discriminated normal brain, areas of tumor-infiltrated brain, solid tumor, and necrosis. Ultrahigh-resolution OCT discriminated between healthy and pathologic human brain tissue biopsies by

visualizing and identifying microcalcifications, enlarged cell nuclei, small cysts, and blood vessels [44]. The working distance of the OCT adapter recently allowed integration of the OCT applicator into the optical path of operating microscopes. This permits a continuous analysis of the resection plain in neurosurgery, the identification of vocal cord tumors, and *in situ* measurements of the auditory ossicles.

OCT imaging, which is based on reflection of radiation, has its strength in clarifying the architectural tissue morphology. However, for many diseases, including cancer, diagnosis based on such architectural features is not sufficient since the most important diagnostic indicators of neoplastic changes are features such as accelerated rate of growth, mass growth, local invasion, lack of differentiation, anaplasia, and metastasis, which mainly occur on the subcellular and molecular level. An approach to overcome this limitation is the combination of complementary techniques. Optical intrinsic signal imaging (OISI) provides two-dimensional, depth-integrated activation maps of brain activity. OCT provides depth-resolved, cross-sectional images of functional brain activation. Co-registered OCT and OISI imaging was performed simultaneously on the rat somatosensory cortex through a thinned skull during forepaw electrical stimulation, which correlated with OISI relating to the functional activation patterns, indicating retrograde vessel dilation [45].

47.3.5 Raman-Based Techniques

One of the potential advantages of Raman spectroscopy in neuro-oncology is that brain tissue can be characterized label free at the microstructural and/or molecular level with spatial resolution in the single cell range. This permits accurate delineation of tumor margins, and sensitive and specific identification of tumor remnants upon preservation of normal tissue. Raman images of pristine human brain tissue specimens were collected *ex vivo* by a Raman spectrometer coupled to a microscope with a low magnification objective ($10\times$ / *NA* 0.25) [46]. Regions of 2×2 mm of 2 mm tissue sections were covered by a window to prevent drying during data acquisition. Raman images were acquired using a step size of 100 μm. The laser intensity of 60 mW was focused to a spot ~60 μm in diameter. No tissue degradation was observed during signal collection of 20 s per spectrum. Raman spectra of white matter were characterized by maximum spectral contributions of lipids and cholesterol. In the Raman spectra of gray matter, the bands of proteins and water were more prominent whereas bands of lipids were less intense. In Raman spectra of gliomas, spectral contributions of lipids further decreased and spectral contributions of hemoglobin increased, which was consistent with hemorrhage or higher blood perfusion. An interesting feature was the accumulation of phosphatidylcholine, which was indicated by a Raman marker band near 717 cm^{-1} and which was confirmed by NMR spectroscopy and chromatography.

Raman systems can be coupled to fiber-optic probes. This approach has been applied to detect metastasis in mouse brains [47]. Injection of tumor cells in the carotid artery induces tumor development preferentially in one brain hemisphere. The unaffected brain hemisphere can be used as a control for normal murine brain

tissue. Owing to the improved sensitivity of the fiber-optic probe compared with the microscope, Raman images were acquired with a shorter exposure time of 8 s per spectrum. Raman spectra of brain metastases from malignant melanomas showed additional spectral contributions of the pigment melanin. The band intensities were resonance enhanced with 785 nm excitation because the pigment showed electronic absorption of the excitation wavelength. The presence of melanin in brain metastasis of malignant melanomas demonstrated that secondary tumors possess molecular properties of the primary tumors. As Raman spectroscopy probes molecular fingerprint, Raman spectra can be applied to identify the origin the brain metastases. The related vibrational spectroscopy technique of Fourier transform infrared (FTIR) imaging classified the primary tumor of the four most frequent brain metastases [48, 49]. As modern FTIR imaging spectrometers combine the Fourier transform and the multi-channel advantage of IR-sensitive focal plane array detectors, FTIR image acquisition of extended tissue sections took just minutes. However, owing to the high water content of tissue and cells and the strong absorption of MIR radiation by water, the penetration depth is just a few micrometers and application under *in vivo* conditions is limited.

The acquisition time can be further decreased using coherent anti-Stokes Raman scattering (CARS) microscopy, which is a nonlinear variant of Raman spectroscopy using picosecond pulsed lasers. It has been applied to image structure and pathology in fresh unfixed and unstained *ex vivo* brain tissue and tumor [50]. CARS was tuned to specific vibrational bands to provide image contrast with subcellular resolution and near real-time temporal resolution. However, only single bands can be probed in short exposure times. Most frequently, bands near 2845 cm^{-1} are probed that are particularly intense in lipid-rich structures.

47.4 Applications in Neurovascular Pathologies

Diseases that affect the neurovascular unit of the CNS, such as ischemic stroke, are particularly suited to optical *in vivo* studies. Ischemia can be easily induced in animals, and vessels can be outlined by intravenous injection of fluorescent dextran conjugates [51]. The resultant negative contrast of erythrocytes which exclude the dextran can be used to assess blood flow. Earlier, flow measurements were taken in the pia mater and in the upper cortical layers using wide-field or confocal microscopy. Later, measuring changes in cortical blood flow in response to sensory stimulation was one of the first applications of multiphoton microscopy which allowed the visualization of capillary flow down to cortical layer IV in rats (see overview by Misgeld and Kerschensteiner [2]). Transcranial analysis of the vascular architecture was used to monitor tumor vascularization and also to monitor antivascular anti-angiogenic therapeutic effects in tumors [52–55] and to monitor therapeutic pro-angiogenic responses of ischemic lesions.

The intravasal fluorescent dye indocyanine green (ICG), which labels serum proteins in the blood, has been introduced into clinical routine in neurovascular

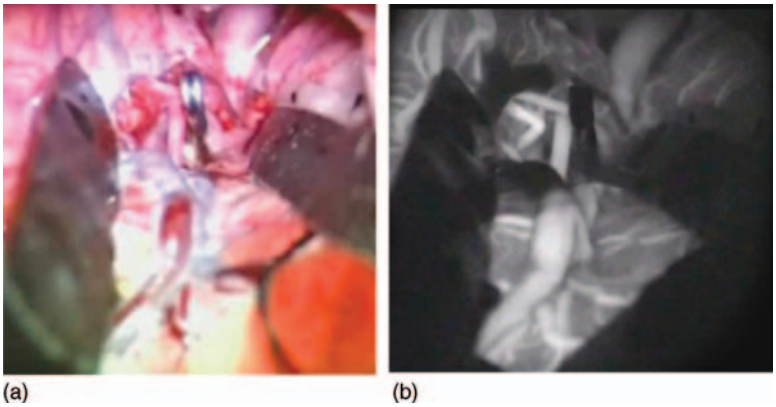

Figure 47.3 Intraoperative vascular fluorescence imaging using ICG. Perfused vessels reveal NIR-fluorescence (b) that can be superimposed on the white light picture (a). The fluorescent bolus of labeled blood can be analyzed using video microscopy and allows one to assess direction of flow, diameter of vessels, and type of vessel since arteries are perfused before and veins after the parenchymal phase.

procedures (Figure 47.3). Operative microscope-integrated ICG video angiography, as an intraoperative method for detecting vascular flow, was found to be rapid, reliable, and cost-effective and possibly a substitute or adjunct for Doppler ultrasonography or intraoperative conventional digital subtraction angiography.

The simplicity of the method, the speed with which the investigation can be performed, and the quality of the images help to improve manipulation of cerebral vessels and to control the surgical manipulations. Using video microscopy, the temporal changes in perfusion of arteries, then tissue perfusion followed by venous drainage, allow quantification of the type of vessel, direction of flow, and the perfusion of the supplied tissue. Perfusion was imaged using ICG in acute stroke patients undergoing decompressive craniotomy to visualize the extent of nonperfused and penumbral tissue [56]. The delineation of the nonperfused tissue can facilitate the placement of parenchymal probes for pO_2/pCO_2 and pH measurements *in situ*.

47.4.1 Absorption-Based Imaging

The growth and expansion of gliomas are highly dependent on vascular neogenesis. An association of microvascular density and tumor energy metabolism is assumed in most human gliomas. Intraoperative NIRS was applied to 13 glioma patients in order to elucidate the relationship between microvascular blood volume, oxygen saturation, histology, and patient survival [57]. High intratumoral blood volume and high oxygen saturation in malignant brain tumors of the glioblastoma multiforme type correlated with a low median survival time. Limitations of oxygen saturation data acquired using NIR technology are that (i) only tumors with appearance on the pial surface are accessible for noninvasive NIR spectroscopy probes and (ii) the total blood volume of

the whole tumor usually cannot be assessed since intraoperative NIR measurements analyze the tumor surface up to a depth of only 4 mm.

47.4.2 Thermography

The local analysis of spontaneous emission of infrared radiation, and therefore of thermal radiation, is termed thermography. Thermography is based on infrared radiation of wavelength 1200–2500 nm. In experimental neurosurgical applications, small differences in temperature have been used to delineate surgically exposed arterial from venous vessels, especially in complex cerebral and spinal vascular lesions [58, 59], and to detect alterations of cortical blood flow [60] as early as 1970. In particular, the control of tissue perfusion during vascular procedures might be feasible in the exposed brain [61, 62]. More complex analysis of thermographic images might help to verify functional areas on the cortical surface during neurosurgical procedures using similar physiologic effects as for intrinsic optical imaging: an increase in blow flow due to local increase in metabolism should result in thermographic differences that correlate with active functional regions [63, 64].

47.5 Applications to Regeneration, Transplantation, and Stem Cell Monitoring

In vivo optical imaging is a powerful tool to study how axons in the peripheral nervous system behave during degeneration and regeneration. Axonal transaction (axotomy) is a common form of neurologic damage. In the peripheral nervous system, axotomy is followed by regeneration and recovery. This is not the case in the CNS, where regeneration fails with the dire consequences that are known from brain and spinal injuries. Axotomy was the first pathologic alteration of the nervous system to be imaged *in vivo* using intrinsic contrast [65, 66]. Further examples are summarized in a review by Misgeld and Kerschensteiner [2].

47.5.1 Identification of Cellular Fractions and Monitoring of Implants in the CNS

The identification of neural stem and progenitor cells (NPCs) using *in vivo* brain imaging could have important implications for diagnostic, prognostic, and therapeutic purposes. In several rodent models using various subtypes of stem cells for targeting lesions of the CNS, the cells were labeled prior to implantation. Labeling with, for example, magnetic iron particles led to improved identification of these cells after systemic or focal injection [67–71]. It was possible to visualize whether the stem cells would migrate to and remain within the lesions. It was not possible to monitor their local differentiation and whether they participated in cellular regeneration. Using a cranial window technique and multiphoton microscopy, cellular movements and vascular growth can be visualized [52, 72–74].

Recently, magnetic resonance spectroscopy defined a fingerprint for neural stem cells in humans using a biomarker in which NPCs are enriched and demonstrated its use as a reference for monitoring neurogenesis [75]. *In vivo* magnetic resonance spectroscopy in rodents and humans helped to identify regions with high expression of the signature indicating higher concentrations of neural stem cells. However, this notion has been challenged since then [76]. Similar purposes can be met using biophotonic techniques, for example, to assess cellular composition for targeting of specific brain regions. An example is the deposition of implants in the degenerated substantia nigra or areas within the basal ganglia. A combination of established electrophysiologic analyses along with newer spectroscopic techniques to verify the biochemical composition of the target area might improve the biological accuracy of the procedure. A second example is based on the current inability of any method to monitor transplants and differentiation of transplanted cells except for biopsies. A biophotonic approach seems feasible to overcome these limitations.

47.6 Conclusions

The potential applications of biophotonic imaging techniques in the field of basic and of clinical neurosciences are numerous. The possibility of probing for morphologic, that is, structural information and also for biochemical information holds great promise for the different modalities. Neurosurgery in particular might benefit from these evolving technologies. They might offer, alone or in combination with existing technologies and routine applications in brain surgery, enhancement of the visual details, and analysis of tissue for both pathologic changes – for example, by Raman spectroscopy or CARS – or to obtain online, label-free information on the functional status of an exposed cortical region (Figure 47.3). From a neurosurgical perspective, intraoperative optical imaging technologies should comply with the following requirements:

- integration into existing intraoperative setups, especially the operating microscope
- wide-field data generation, usually several cm^2
- depth information, generation of volume data sets
- image fusion into volumetric conventional morphologic MRI data sets
- lateral resolution: depiction of morphology
- chemometric resolution: depiction of biochemical composition = classification of tissue types
- temporal resolution: depiction of function
- rapid (online), continuous, or repeatable, reproducible, and robust
- low affection due to frequent intraoperative artifacts, such as contamination by CSF, blood or irrigation
- no time interval for preparation of tissue/patient before/after imaging
- no toxicity from excitation light source.

In spite of numerous successful applications, *in vivo* optical imaging is not without pitfalls. There are two fundamentally different modes of *in vivo* imaging and each has its own problems. On the one hand, real-time observations visualize a process as it happens. On the other hand, intermittent imaging collects multiple observations. Although real-time imaging is more direct, intermittent imaging alleviates many concerns about toxicity. However, finding and orienting cells for each session pose a new set of challenges. Artifacts can be induced by anesthesia, labeling, and surgery. Such invasive procedures can change the normal behavior of cells and the brain might be susceptible to such stress factors. In the future, novel miniature microscopes and fiber optics might permit improved experiments.

Too much light is toxic to cells. Toxic effects of light on cells limit most *in vivo* microscopy experiments. They are caused at least in part by bleaching and associated photochemical generation of free radicals. Phototoxicity itself is unacceptable unless used for therapeutic means, for example, in photodynamic therapy (PDT). Phototoxic damage which is induced in brain structures can be misinterpreted as pathology-related changes. Potential solutions include the following

- using as little excitation light as possible and the most sensitive detector possible
- filtering out irrelevant wavelengths from the excitation light
- considering multiphoton microscopy
- controlling temperature, oxygenation, and pH to reduce cellular stress.

The living brain is in constant motion due to motor activity, respiration, and heartbeat that induce movement and orientation artifacts. Repeatedly identifying and orienting the same cells under the microscope can be challenging during intermittent imaging protocols. Well-engineered equipment (such as stereotactic holders) helps to immobilize the target. Pressure gradients can be reduced by, for example, closing a craniotomy in small animals with agarose and a cover-slip. Image acquisition or illumination can be triggered from the electrocardiogram. Ventilation may be interrupted for short periods of time (<1 min) while collecting images. Fast imaging allows images to be taken that are little affected by pulse-related blurring. Subsequent x–y alignment and averaging can improve the signal-to-noise ratio.

Finally, instruments for *in vivo* imaging, especially multiphoton microscopy, can be expensive. To reduce costs, many parts of the nervous system can be imaged with a relatively affordable wide-field microscope. Furthermore, detailed descriptions have been published about how to build one's own multiphoton microscope. These instruments can be tailored to specific needs, and have often outperformed those available commercially [13].

In summary, an optimistic picture is emerging of what optical *in vivo* imaging could offer to basic and clinical neuroscientists. Further progress will depend on technological innovations and integration with accepted standards in clinical care and clinical technology. Among the most exciting perspectives is a new field, dubbed nanoscopy, which might overcome the ultimate frontier of light microscopy – that is, the diffraction limit of resolution – and which aims to expand light microscopy into the subcellular or even the molecular realm. The fundamental principle is to create excitation volumes that are much smaller than those that can be generated in

conventional microscopy. Current nanoscopic approaches use complicated optical tools. Newly identified proteins that have light-inducible fluorescent properties could permit nanoscopic imaging with simpler optics that is applicable to living multicellular organisms. Therefore, rather than depending on physicists alone, the future development of optical *in vivo* imaging might be a multidisciplinary task with contributions made by chemists and molecular biologists.

References

1 Jöbsis, F.F. (1977) Noninvasive, infrared monitoring of cerebral and myocardial oxygen sufficiency and circulatory parameters. *Science*, **198**, 1264–1267.

2 Misgeld, T. and Kerschensteiner, M. (2006) *In vivo* imaging of the diseased nervous system. *Nat. Rev. Neurosci.*, **7**, 449–463.

3 Hillman, E.M. (2007) Optical brain imaging *in vivo*: techniques and applications from animal to man. *J. Biomed. Opt.*, **12**, 051402.

4 Krafft, C. and Salzer, R. (2008) Neuro-oncological applications of infrared and Raman spectroscopy, in *Vibrational Spectroscopy for Medical Diagnosis* (eds M. Diem, J.M. Chalmers, and P.R. Griffiths), John Wiley&Sons, Ltd, Chichester, pp. 231–259.

5 Matthews, P.M., Honey, G.D., and Bullmore, E.T. (2006) Applications of fMRI in translational medicine and clinical practice. *Nat. Rev. Neurosci.*, **7**, 732–744.

6 Havel, P., Braun, B., Rau, S., Tonn, J.C., Fesl, G., Bruckmann, H., and Ilmberger, J. (2006) Reproducibility of activation in four motor paradigms. An fMRI study. *J. Neurol.*, **253**, 471–476.

7 Rau, S., Fesl, G., Bruhns, P., Havel, P., Braun, B., Tonn, J.C., and Ilmberger, J. (2007) Reproducibility of activations in Broca area with two language tasks: a functional MR imaging study. *AJNR Am. J. Neuroradiol.*, **28**, 1346–1353.

8 Prakash, N., Uhlemann, F., Sheth, S.A., Bookheimer, S., Martin, N., and Toga, A.W. (2009) Current trends in intraoperative optical imaging for functional brain mapping and delineation of lesions of language cortex. *Neuroimage*, **47** (Suppl 2), T116–T126.

9 Flusberg, B.A., Nimmerjahn, A., Cocker, E.D., Mukamel, E.A., Barretto, R.P., Ko, T.H., Burns, L.D., Jung, J.C., and Schnitzer, M.J. (2008) High-speed, miniaturized fluorescence microscopy in freely moving mice. *Nat. Methods*, **5**, 935–938.

10 Böhringer, H.J., Lankenau, E., Rohde, V., Huttmann, G., and Giese, A. (2006) Optical coherence tomography for experimental neuroendoscopy. *Minim. Invasive Neurosurg.*, **49**, 269–275.

11 Giese, A., Kantelhardt, S.R., Oelckers, S., Lankenau, E., Huttmann, G., and Rohde, V. (2008) Certified prototype of an OCT – integrated operating microscope for intraoperative optical tissue analysis. Presented at 59. Jahrestagung der Deutschen Gesellschaft für Neurochirurgie, 3. Joint Meeting mit der Italienischen Gesellschaft für Neurochirurgie, Würzburg, 1–4 June 2008

12 Denk, W., Strickler, J.H., and Webb, W.W. (1990) Two-photon laser scanning fluorescence microscopy. *Science*, **248**, 73–76.

13 Zipfel, W.R., Williams, R.M., and Webb, W.W. (2003) Nonlinear magic: multiphoton microscopy in the biosciences. *Nat. Biotechnol.*, **21**, 1369–1377.

14 Garaschuk, O., Milos, R.I., Grienberger, C., Marandi, N., Adelsberger, H., and Konnerth, A. (2006) Optical monitoring of brain function *in vivo*: from neurons to networks. *Pflugers Arch.*, **453**, 385–396.

15 Campagnola, P.J. and Loew, L.M. (2003) Second-harmonic imaging microscopy for visualizing biomolecular arrays in cells, tissues and organisms. *Nat. Biotechnol.*, **21**, 1356–1360.

16 Ntziachristos, V., Ripoll, J., Wang, L.V., and Weissleder, R. (2005) Looking and listening to light: the evolution of whole-body photonic imaging. *Nat. Biotechnol.*, **23**, 313–320.
17 Saxena, V., Gonzalez-Gomez, I., and Laug, W.E. (2007) A noninvasive multimodal technique to monitor brain tumor vascularization. *Phys. Med. Biol.*, **52**, 5295–5308.
18 Sakatani, K., Murata, Y., Fujiwara, N., Hoshino, T., Nakamura, S., Kano, T., and Katayama, Y. (2007) Comparison of blood-oxygen-level-dependent functional magnetic resonance imaging and near-infrared spectroscopy recording during functional brain activation in patients with stroke and brain tumors. *J. Biomed. Opt.*, **12**, 062110.
19 Fujiwara, N., Sakatani, K., Katayama, Y., Murata, Y., Hoshino, T., Fukaya, C., and Yamamoto, T. (2004) Evoked-cerebral blood oxygenation changes in false-negative activations in BOLD contrast functional MRI of patients with brain tumors. *Neuroimage*, **21**, 1464–1471.
20 Goujon, D., Zellweger, M., Radu, A., Grosjean, P., Weber, B.C., van den Bergh, H., Monnier, P., and Wagnieres, G. (2003) *In vivo* autofluorescence imaging of early cancers in the human tracheobronchial tree with a spectrally optimized system. *J. Biomed. Opt.*, **8**, 17–25.
21 Lin, W.C., Toms, S.A., Johnson, M., Jansen, E.D., and Mahadevan-Jansen, A. (2001) *In vivo* brain tumor demarcation using optical spectroscopy. *Photochem. Photobiol.*, **73**, 396–402.
22 Toms, S.A., Lin, W.C., Weil, R.J., Johnson, M.D., Jansen, E.D., and Mahadevan-Jansen, A. (2005) Intraoperative optical spectroscopy identifies infiltrating glioma margins with high sensitivity. *Neurosurgery*, **57**, 382–391.
23 Kantelhardt, S.R., Leppert, J., Krajewski, J., Petkus, N., Reusche, E., Tronnier, V.M., Huttmann, G., and Giese, A. (2007) Imaging of brain and brain tumor specimens by time-resolved multiphoton excitation microscopy *ex vivo*. *Neuro-Oncology*, **9**, 103–112.
24 Kantelhardt, S.R., Diddens, H., Leppert, J., Rohde, V., Huttmann, G., and Giese, A. (2008) Multiphoton excitation fluorescence microscopy of 5-aminolevulinic acid induced fluorescence in experimental gliomas. *Lasers Surg. Med.*, **40**, 273–281.
25 Leppert, J., Krajewski, J., Kantelhardt, S.R., Schlaffer, S., Petkus, N., Reusche, E., Huttmann, G., and Giese, A. (2006) Multiphoton excitation of autofluorescence for microscopy of glioma tissue. *Neurosurgery*, **58**, 759–767.
26 Haglund, M.M., Berger, M.S., and Hochman, D.W. (1996) Enhanced optical imaging of human gliomas and tumor margins. *Neurosurgery*, **38**, 308–317.
27 Kabuto, M., Kubota, T., Kobayashi, H., Nakagawa, T., Ishii, H., Takeuchi, H., Kitai, R., and Kodera, T. (1997) Experimental and clinical study of detection of glioma at surgery using fluorescent imaging by a surgical microscope after fluorescein administration. *Neurol. Res.*, **19**, 9–16.
28 Kremer, P., Wunder, A., Sinn, H., Haase, T., Rheinwald, M., Zillmann, U., Albert, F.K., and Kunze, S. (2000) Laser-induced fluorescence detection of malignant gliomas using fluorescein-labeled serum albumin: experimental and preliminary clinical results. *Neurol. Res.*, **22**, 481–489.
29 Stummer, W., Stocker, S., Novotny, A., Heimann, A., Sauer, O., Kempski, O., Plesnila, N., Wietzorrek, J., and Reulen, H.J. (1998) *In vitro* and *in vivo* porphyrin accumulation by C6 glioma cells after exposure to 5-aminolevulinic acid. *J. Photochem. Photobiol. B*, **45**, 160–169.
30 Stummer, W., Stocker, S., Wagner, S., Stepp, H., Fritsch, C., Goetz, C., Goetz, A.E., Kiefmann, R., and Reulen, H.J. (1998) Intraoperative detection of malignant gliomas by 5-aminolevulinic acid-induced porphyrin fluorescence. *Neurosurgery*, **42**, 518–525.
31 Stummer, W., Pichlmeier, U., Meinel, T., Wiestler, O.D., Zanella, F., and Reulen, H.J. (2006) Fluorescence-guided surgery with 5-aminolevulinic acid for resection of malignant glioma: a randomised controlled multicentre phase III trial. *Lancet Oncol.*, **7**, 392–401.
32 Veiseh, O., Sun, C., Fang, C., Bhattarai, N., Gunn, J., Kievit, F., Du, K., Pullar, B., Lee, D., Ellenbogen, R.G., Olson, J., and Zhang, M. (2009) Specific targeting of

brain tumors with an optical/magnetic resonance imaging nanoprobe across the blood–brain barrier. *Cancer Res.*, **69**, 6200–6207.

33 Jackson, H., Muhammad, O., Daneshvar, H., Nelms, J., Popescu, A., Vogelbaum, M.A., Bruchez, M., and Toms, S.A. (2007) Quantum dots are phagocytized by macrophages and colocalize with experimental gliomas. *Neurosurgery*, **60**, 524–529.

34 Muhammad, O., Popescu, A., and Toms, S.A. (2007) Macrophage-mediated colocalization of quantum dots in experimental glioma. *Methods Mol. Biol.*, **374**, 161–171.

35 Arndt-Jovin, D.J., Kantelhardt, S.R., Caarls, W., de Vries, A.H., Giese, A., and Jovin Ast, T.M. (2009) Tumor-targeted quantum dots can help surgeons find tumor boundaries. *IEEE Trans. Nanobiosci.*, **8**, 65–71.

36 Sabharwal, N., Holland, E.C., and Vazquez, M. (2009) Live cell labeling of glial progenitor cells using targeted quantum dots. *Ann. Biomed. Eng.*, **37** (10), 1967–1973.

37 Wang, J., Yong, W.H., Sun, Y., Vernier, P.T., Koeffler, H.P., Gundersen, M.A., and Marcu, L. (2007) Receptor-targeted quantum dots: fluorescent probes for brain tumor diagnosis. *J. Biomed. Opt.*, **12**, 044021.

38 Shah, K. and Weissleder, R. (2005) Molecular optical imaging: applications leading to the development of present day therapeutics. *NeuroRx*, **2**, 215–225.

39 Burgos, J.S., Rosol, M., Moats, R.A., Khankaldyyan, V., Kohn, D.B., Nelson M.D. Jr., and Laug, W.E. (2003) Time course of bioluminescent signal in orthotopic and heterotopic brain tumors in nude mice. *Biotechniques*, **34**, 1184–1188.

40 Uhrbom, L., Nerio, E., and Holland, E.C. (2004) Dissecting tumor maintenance requirements using bioluminescence imaging of cell proliferation in a mouse glioma model. *Nat. Med.*, **10**, 1257–1260.

41 Shah, K., Tang, Y., Breakefield, X., and Weissleder, R. (2003) Real-time imaging of TRAIL-induced apoptosis of glioma tumors *in vivo*. *Oncogene*, **22**, 6865–6872.

42 Bohringer, H.J., Boller, D., Leppert, J., Knopp, U., Lankenau, E., Reusche, E., Huttmann, G., and Giese, A. (2006) Time-domain and spectral-domain optical coherence tomography in the analysis of brain tumor tissue. *Lasers Surg. Med.*, **38**, 588–597.

43 Bohringer, H.J., Lankenau, E., Stellmacher, F., Reusche, E., Huttmann, G., and Giese, A. (2009) Imaging of human brain tumor tissue by near-infrared laser coherence tomography. *Acta Neurochir. (Wien)*, **151**, 507–517.

44 Bizheva, K., Unterhuber, A., Hermann, B., Povazay, B., Sattmann, H., Fercher, A.F., Drexler, W., Preusser, M., Budka, H., Stingl, A., and Le, T. (2005) Imaging *ex vivo* healthy and pathological human brain tissue with ultra-high-resolution optical coherence tomography. *J. Biomed. Opt.*, **10**, 11006.

45 Chen, Y., Aguirre, A.D., Ruvinskaya, L., Devor, A., Boas, D.A., and Fujimoto, J.G. (2009) Optical coherence tomography (OCT) reveals depth-resolved dynamics during functional brain activation. *J. Neurosci. Methods*, **178**, 162–173.

46 Krafft, C., Sobottka, S.B., Schackert, G., and Salzer, R. (2005) Near infrared Raman spectroscopic mapping of native brain tissue and intracranial tumors. Analyst, 130, 1070–1077.

47 Krafft, C., Kirsch, M., Beleites, C., Schackert, G., and Salzer, R. (2007) Methodology for fiber-optic Raman mapping and FTIR imaging of metastases in mouse brains. *Anal. Bioanal. Chem.*, **389**, 1133–1142.

48 Krafft, C., Shapoval, L., Sobottka, S.B., Geiger, K.D., Schackert, G., and Salzer, R. (2006) Identification of primary tumors of brain metastases by SIMCA classification of IR spectroscopic images. *Biochim. Biophys. Acta*, **1758**, 883–891.

49 Krafft, C., Shapoval, L., Sobottka, S.B., Schackert, G., and Salzer, R. (2006) Identification of primary tumors of brain metastases by infrared spectroscopic imaging and linear discriminant analysis. *Technol. Cancer Res. Treat.*, **5**, 291–298.

50 Evans, C.L., Xu, X., Kesari, S., Xie, X.S., Wong, S.T., and Young, G.S. (2007) Chemically-selective imaging of brain

structures with CARS microscopy. *Opt. Express*, **15**, 12076–12087.

51 Nishimura, N., Schaffer, C.B., Friedman, B., Tsai, P.S., Lyden, P.D., and Kleinfeld, D. (2006) Targeted insult to subsurface cortical blood vessels using ultrashort laser pulses: three models of stroke. *Nat. Methods*, **3**, 99–108.

52 Read, T.A., Farhadi, M., Bjerkvig, R., Olsen, B.R., Rokstad, A.M., Huszthy, P.C., and Vajkoczy, P. (2001) Intravital microscopy reveals novel antivascular and antitumor effects of endostatin delivered locally by alginate-encapsulated cells. *Cancer Res.*, **61**, 6830–6837.

53 Fukumura, D., Xavier, R., Sugiura, T., Chen, Y., Park, E.C., Lu, N., Selig, M., Nielsen, G., Taksir, T., Jain, R.K., and Seed, B. (1998) Tumor induction of VEGF promoter activity in stromal cells. *Cell*, **94**, 715–725.

54 Brown, E., McKee, T., DiTomaso, E., Pluen, A., Seed, B., Boucher, Y., and Jain, R.K. (2003) Dynamic imaging of collagen and its modulation in tumors *in vivo* using second-harmonic generation. *Nat. Med.*, **9**, 796–801.

55 Jain, R.K., Munn, L.L., and Fukumura, D. (2002) Dissecting tumour pathophysiology using intravital microscopy. *Nat. Rev. Cancer*, **2**, 266–276.

56 Woitzik, J., Pena-Tapia, P.G., Schneider, U.C., Vajkoczy, P., and Thome, C. (2006) Cortical perfusion measurement by indocyanine-green videoangiography in patients undergoing hemicraniectomy for malignant stroke. *Stroke*, **37**, 1549–1551.

57 Asgari, S., Rohrborn, H.J., Engelhorn, T., and Stolke, D. (2003) Intra-operative characterization of gliomas by near-infrared spectroscopy: possible association with prognosis. *Acta Neurochir. (Wien)*, **145**, 453–459.

58 Nakagawa, A., Hirano, T., Uenohara, H., Utsunomiya, H., Suzuki, S., Takayama, K., Shirane, R., and Tominaga, T. (2004) Use of intraoperative dynamic infrared imaging with detection wavelength of 7–14 microm in the surgical obliteration of spinal arteriovenous fistula: case report and technical considerations. *Minim. Invasive Neurosurg.*, **47**, 136–139.

59 Okudera, H., Kobayashi, S., and Toriyama, T. (1994) Intraoperative regional and functional thermography during resection of cerebral arteriovenous malformation. *Neurosurgery*, **34**, 1065–1067.

60 Anderson, R.E., Waltz, A.G., Yamaguchi, T., and Ostrom, R.D. (1970) Assessment of cerebral circulation (cortical blood flow) with an infrared microscope. *Stroke*, **1**, 100–103.

61 Nakagawa, A., Hirano, T., Uenohara, H., Sato, M., Kusaka, Y., Shirane, R., Takayama, K., and Yoshimoto, T. (2003) Intraoperative thermal artery imaging of an EC–IC bypass in beagles with infrared camera with detectable wave-length band of 7–14 microm: possibilities as novel blood flow monitoring system. *Minim. Invasive Neurosurg.*, **46**, 231–234.

62 Okada, Y., Kawamata, T., Kawashima, A., and Hori, T. (2007) Intraoperative application of thermography in extracranial–intracranial bypass surgery. *Neurosurgery*, **60**, 362–365.

63 George, J.S., Lewine, J.D., Goggin, A.S., Dyer, R.B., and Flynn, E.R. (1993) IR thermal imaging of a monkey's head: local temperature changes in response to somatosensory stimulation. *Adv. Exp. Med. Biol.*, **333**, 125–136.

64 Gorbach, A.M., Heiss, J., Kufta, C., Sato, S., Fedio, P., Kammerer, W.A., Solomon, J., and Oldfield, E.H. (2003) Intraoperative infrared functional imaging of human brain. *Ann. Neurol.*, **54**, 297–309.

65 Hollander, H. and Mehraein, P. (1966) On the mechanics of myelin sphere formation in Wallerian degeneration. Intravital microscopic studies of single degenerating motor fibers of the frog. *Z. Zellforsch. Mikrosk. Anat.*, **72**, 276–280.

66 Williams, P.L. and Hall, S.M. (1971) Prolonged *in vivo* observations of normal peripheral nerve fibres and their acute reactions to crush and deliberate trauma. *J. Anat.*, **108**, 397–408.

67 Zhu, W.Z., Li, X., Qi, J.P., Tang, Z.P., Wang, W., Wei, L., and Lei, H. (2008) Experimental study of cell migration and functional differentiation of transplanted neural stem cells co-labeled with superparamagnetic iron oxide and BrdU in an ischemic rat model. *Biomed. Environ. Sci.*, **21**, 420–424.

68 Ruiz-Cabello, J., Walczak, P., Kedziorek, D.A., Chacko, V.P., Schmieder, A.H.,

Wickline, S.A., Lanza, G.M., and Bulte, J.W. (2008) *In vivo* "hot spot" MR imaging of neural stem cells using fluorinated nanoparticles. *Magn. Reson. Med.*, **60**, 1506–1511.

69 Walczak, P., Zhang, J., Gilad, A.A., Kedziorek, D.A., Ruiz-Cabello, J., Young, R.G., Pittenger, M.F., van Zijl, P.C., Huang, J., and Bulte, J.W. (2008) Dual-modality monitoring of targeted intraarterial delivery of mesenchymal stem cells after transient ischemia. *Stroke*, **39**, 1569–1574.

70 Zhu, W., Li, X., Tang, Z., Zhu, S., Qi, J., Wei, L., and Lei, H. (2007) Superparamagnetic iron oxide labeling of neural stem cells and 4.7T MRI tracking *in vivo* and *in vitro*. *J. Huazhong Univ. Sci. Technol. Med. Sci.*, **27**, 107–110.

71 Curtis, M.A., Kam, M., Nannmark, U., Anderson, M.F., Axell, M.Z., Wikkelso, C., Holtas, S., van Roon-Mom, W.M., Bjork-Eriksson, T., Nordborg, C., Frisen, J., Dragunow, M., Faull, R.L., and Eriksson, P.S. (2007) Human neuroblasts migrate to the olfactory bulb via a lateral ventricular extension. *Science*, **315**, 1243–1249.

72 Schaffer, C.B., Friedman, B., Nishimura, N., Schroeder, L.F., Tsai, P.S., Ebner, F.F., Lyden, P.D., and Kleinfeld, D. (2006) Two-photon imaging of cortical surface microvessels reveals a robust redistribution in blood flow after vascular occlusion. *PLoS Biol.*, **4**, e22.

73 Spires, T.L., Meyer-Luehmann, M., Stern, E.A., McLean, P.J., Skoch, J., Nguyen, P.T., Bacskai, B.J., and Hyman, B.T. (2005) Dendritic spine abnormalities in amyloid precursor protein transgenic mice demonstrated by gene transfer and intravital multiphoton microscopy. *J. Neurosci.*, **25**, 7278–7287.

74 Yuan, F., Dellian, M., Fukumura, D., Leunig, M., Berk, D.A., Torchilin, V.P., and Jain, R.K. (1995) Vascular permeability in a human tumor xenograft: molecular size dependence and cutoff size. *Cancer Res.*, **55**, 3752–3756.

75 Manganas, L.N., Zhang, X., Li, Y., Hazel, R.D., Smith, S.D., Wagshul, M.E., Henn, F., Benveniste, H., Djuric, P.M., Enikolopov, G., and Maletic-Savatic, M. (2007) Magnetic resonance spectroscopy identifies neural progenitor cells in the live human brain. *Science*, **318**, 980–985.

76 Loewerbrück, K.F., Fuchs, B., Hermann, A., Brandt, M., Werner, A., Kirsch, M., Schwarz, J., Schiller, J., and Storch, A. (2011) Proton MR spectroscopy of neural stem cells: does te proton MNR peak at 1.28 ppm function as a biomarker for cell type or state? Rejuvenation Res. DOI: 10.1089/rej.2010.1102.

48
Assessment of Infant Brain Development

Nadege Roche-Labarbe, P. Ellen Grant, and Maria Angela Franceschini

48.1
Introduction

Studying the infant's brain has been one of the major applications of *in vivo* optical imaging since the mid-1980s [1–4], for reasons both scientific and technical.

There are very few tools available for noninvasive bedside study of the neonatal brain, and they do not assess local cerebral metabolism and hemodynamics. Electroencephalography (EEG) and amplitude-integrated electroencephalography (aEEG) measure electrical activity, head ultrasound (US) gives structural images, and transcranial Doppler (TCD) ultrasonography estimates blood flow but only in the major arteries. Our current understanding of metabolic and vascular regional brain development in infants is derived from positron emission tomography (PET) [5–8], single photon emission computed tomography (SPECT) [9], and functional magnetic resonance imaging (fMRI) [10–12] studies. However, these techniques are performed rarely, and primarily in clinical populations, because they cannot be used at the bedside and may require sedation. In addition PET and SPECT come with an increased risk from radiation exposure. In contrast, near-infrared spectroscopy (NIRS) and diffuse correlation spectroscopy (DCS) are portable, noninvasive, and safe optical imaging techniques that use nonionizing radiation (near-infrared light) and emit less energy than a head US [13, 14]. For this reason, NIRS and DCS are particularly well suited to neonates and infants.

From a technical point of view, NIRS is particularly optimal for neonatal brain studies because, in addition to being safe and noninvasive, it takes advantage of the thinner scalp and skull layer, smaller head diameter, and smaller amount of hair compared with older children and adults. These characteristics of newborn heads (especially premature newborns) allow for deeper penetration of light into the brain, and a better signal-to-noise ratio [15]. These characteristics also

Handbook of Biophotonics. Vol.2: Photonics for Health Care, First Edition. Edited by Jürgen Popp, Valery V. Tuchin, Arthur Chiou, and Stefan Heinemann.

necessitate shorter source–detector distances, approximately 2 cm as opposed to 4 cm in adults [16].

Optical imaging in neonates and infants uses various NIRS and DCS techniques described below. Applications can be divided into functional and baseline studies of normal and abnormal brain development.

48.2 Techniques

48.2.1 Measurement of Local Oxy- and Deoxyhemoglobin Concentrations

NIRS is the most widely used optical imaging technique in studies of the infant brain. It uses the specific absorption properties of oxyhemoglobin (HbO_2) and deoxyhemoglobin (HbR) in the near-infrared range (around 650–850 nm) to measure the concentration of these molecules in tissues [17].

The first NIRS systems were simple continuous wave (CW) systems introduced in the late 1980s and 1990s, which were used to quantify hemoglobin concentration from tissue absorption. With CW-NIRS systems, light is emitted continuously with a constant or low-frequency (kHz) amplitude, and light attenuation through tissues is measured. Because biological tissues are highly scattering, the Beer–Lambert law, an empirical relationship between light attenuation and chromophore concentration [18], cannot be directly applied. Delpy *et al*. developed a modified Beer–Lambert law [Eq. (48.1)], which takes into account the photon's longer path distribution due to the multiple scattering events [19].

$$OD(\lambda) = \{\varepsilon_{\mathrm{HbR}}(\lambda)[\mathrm{HbR}] + \varepsilon_{\mathrm{HbO_2}}(\lambda)[\mathrm{HbO_2}]\} L\, DPF(\lambda) + G(\lambda) \qquad (48.1)^{1)}$$

where OD is the optical density, λ is the wavelength used, ε is the extinction coefficient of each chromophore, L is the source–detector separation, G is the geometry factor, and DPF is the differential pathlength factor, the term that takes into account the longer photon path in a multiple scattering regime.

The DPF is either assumed or measured with more complex NIRS instruments (see below). The geometry factor is not known but is eliminated if we consider relative changes of hemoglobin instead of quantifying absolute concentrations. By repeating the same measurements at two or more wavelengths, the changes in concentration of HbO_2 and HbR can then be derived. CW-NIRS systems are the simplest, cheapest, and most widely used type of NIRS system. They are optimal for following changes in hemoglobin at a high temporal resolution, and are therefore often used in functional experiments [20–24]. Because the DPF cannot be directly measured with CW

1) In biological tissues, we also need to consider water absorption. Typically for brain applications, water concentration is assumed to be 75–85%. To measure water concentration, wavelengths higher than 900 nm are needed, and such wavelengths are not commonly available in commercial NIRS systems.

systems, CW-NIRS is not optimal for quantifying hemoglobin concentration and total oxygenation index (TOI)[2)], but it is still widely used for this purpose.

Under physiologically induced changes in blood volume [4, 26, 27], CW-NIRS can quantify total hemoglobin concentration ($HbT = HbR + HbO_2$), and from that derive cerebral blood volume (CBV):

$$CBV = \frac{HbT \times MW_{Hb}}{HGB \times D_{bt}} \tag{48.2}$$

where MW_{Hb} = molecular weight of hemoglobin = 64 500 g mol^{-1}, D_{bt} = brain tissue density = 1.05 g ml^{-1}, and HGB = blood hemoglobin measured in g/dl^{-1}.

In the early 1990s a more rigorous theory than the Beer–Lambert law derived from the radiative transport theory [28], the diffusion approximation to the Boltzmann transport equation [29–31], allowed separation of the absorption and scattering contributions and quantification of absolute hemoglobin concentration in highly scattering media. Time-domain (TD) and frequency-domain (FD) NIRS instruments are able to quantify absorption (μ_a) and scattering (μ_s) coefficients if the light temporal profile is acquired in TD systems [32] or if the light attenuation is acquired at multiple frequencies [33] and multiple source–detector distances [34] in FD systems. From the absorption coefficient at two or more wavelengths, HbO_2 and HbR concentrations can be quantified, and HbT, CBV, and total oxygenation ($StO_2 = HbO_2/HbT$) can be derived.

With TD systems, light is emitted as a pulse and its temporal profile is measured. TD is the most sophisticated and sensitive type of NIRS system [1, 35–38]. With FD systems, light is sinusoidally modulated in the radiofrequency range, and light amplitude attenuation and phase delay are measured. FD-NIRS provides a good compromise between performance (absolute quantification) and simplicity, and is especially well suited for clinical and physiological applications when quantification of baseline hemoglobin is needed [34, 39–42].

48.2.2 Local Cerebral Blood Flow Measurement

There have been attempts to measure optically regional cerebral blood flow (CBF) in neonates using NIRS, using either an oxygen bolus obtained by changing the inspired oxygen [43–46], a method applicable only in ventilated infants, or an

2) In the 20+ years of NIRS, hemoglobin concentration and oxygenation have been abbreviated in many different ways by many different groups. Unfortunately, there is still no unified nomenclature. Moreover, especially with CW-NIRS, where several assumptions need to be made, the algorithms used to calculate oxygenation differ between commercial systems [25]. Here, we use TOI for total oxygenation index, as is done with the tissue oxygenation index measured with the NIRO systems (Hamamatsu Photonics, Hamamatsu City, Japan). We prefer to define TOI as total oxygenation index instead of tissue oxygenation index because it better reflects that it measures the sum of arterial and venous hemoglobin oxygenation, and not tissue oxygenation. The regional cerebral oxygen saturation ($rScO_2$) measured with the INVOS (Somanetics Corp., Troy, MI, USA) is calculated with a different algorithm but represents the same quantity.

indocyanine green bolus [47, 48], obtained with the injection of the dye that cannot be performed in healthy infants for ethical reasons. These methods give correct estimates of CBF but are not generally applicable in all infants.

DCS is a more recent technique, providing a measure of tissue perfusion based on the movement of scatterers (i.e., blood cells) inside the tissue [49, 50]. As NIRS, DCS can directly measure tissue perfusion without having to rely on a bolus or oxygen manipulations. DCS was introduced in the early 1990s and has been validated in a number of animal and human studies [50–54] for measuring regional and temporal variations in blood flow. We have recently proven the ability of DCS to quantify an absolute parameter, blood flow index (BF_i), proportional to CBF in the neonatal brain [55].

48.2.3 Estimates of Cerebral Metabolic Rate of Oxygen

To determine the balance between oxygen delivery and oxygen consumption, CW systems can be used to derive an index of the regional oxygen extraction fraction, the relative fractional tissue oxygen extraction (FTOE) [56]:

$$\mathrm{FTOE} = (\mathrm{SaO_2} - \mathrm{TOI})/\mathrm{SaO_2} \tag{48.3}$$

More importantly, following the PET and fMRI literature, NIRS can be used to derive the regional metabolic rate of oxygen ($CMRO_2$) of the infant brain. $CMRO_2$ describes oxygen consumption in relation to oxygen delivery and is a very important parameter in assessing brain metabolism during normal development and disease [5].

Using the Fick principle, estimation of $CMRO_2$ requires a measurement of CBF, HGB, and hemoglobin oxygenation in the arterial (SaO_2) and venous (SvO_2) compartments, that is,

$$\mathrm{CMRO_2} = \frac{\mathrm{HGB} \times \mathrm{CBF} \times (\mathrm{SaO_2} - \mathrm{SvO_2})}{MW_{\mathrm{hb}}} \tag{48.4}$$

SaO_2 is provided by standard pulse oximetry, but SvO_2 is unknown. With NIRS, as defined above, we measure total oxygenation, a weighted sum of arterial and venous oxygenation:

$$\mathrm{StO_2} = a\mathrm{SaO_2} + b\mathrm{SvO_2} \tag{48.5}$$

with $a + b = 1$ [57]. By assuming a and b constant with age and disease, from Eq. (48.4) we can quantify relative $CMRO_2$ without having to measure SvO_2:

$$\mathrm{rCMRO_2} = \frac{\mathrm{CMRO_2}}{\mathrm{CMRO_{2o}}} = \frac{\mathrm{HGB}}{\mathrm{HGB}_o} \times \frac{\mathrm{CBF}}{\mathrm{CBF}_o} \times \frac{\mathrm{SaO_2} - \mathrm{StO_2}}{\mathrm{SaO_{2o}} - \mathrm{StO_{2o}}} \tag{48.6}$$

with the subscript o indicating the reference measure.

Using DCS, CBF can be replaced by BF_i. In CW systems, StO_2 is approximated with TOI, and CBF can be quantified with a bolus perturbation [27, 58, 59]. With NIRS

alone, by assuming a constant power law relation between changes in blood flow and blood volume with age:

$$\frac{\mathrm{CBF}}{\mathrm{CBF}_o} = \left(\frac{\mathrm{CBV}}{\mathrm{CBV}_o}\right)^{\beta} \tag{48.7}$$

with $2 \leq \beta \leq 5$ [60, 61], one can recover rCMRO_2 [40, 62]. While the flow–volume relationship has been validated in healthy adult human subjects with MRI functional studies [63], the relationship may not hold in infants or disease states [55].

48.3 Functional and Cognitive Studies

When a cortical area becomes active, there is a local increase in perfusion to respond to the increased metabolic demand driven by neuronal activity [64]. Increases in oxygen consumption are significantly lower than increases in cerebral blood flow and blood volume caused by the release of vasoactive neurotransmitters [65, 66]. As a result, we see a net increase in the amount of oxygen in the blood and tissue [67–69]. The typical vascular response observed with NIRS following neural activity is an increase in HbT and HbO_2 but a decrease in HbR. Although the decrease in HbR is equivalent to a positive blood oxygen level-dependent (BOLD) signal in fMRI, fMRI is unable to detect changes in HbO_2 or HbT.

For more than a decade, CW-NIRS has been used in functional studies in infants and has been shown to detect vascular changes in response to visual stimulation of the primary visual cortex in newborns [70–72] and infants [21, 23, 72–75], auditory stimulation of the temporal and frontal cortices in newborns [24, 76–79] and infants [73, 80], passive stimulation of the somatosensory cortex in premature [81, 82] and term newborns [83], noxious stimulation of the somatosensory cortex in premature and term newborns [81, 84], and olfactory stimulation of the orbital gyri in newborns [20]. NIRS has also been used to monitor neuronal activation due to spontaneous arousal [85] or spontaneous neuronal activity bursts during slow sleep [86].

In several cases, there have been reports of a "negative" vascular response, that is, an increase in HbR and a decrease in HbO_2 concentration [24, 74, 75] consistent with negative BOLD responses in fMRI studies [10, 87–91]. The cause of these inverted responses to stimulation remains unclear. It might be due to differences in the subjects' vigilance level across studies, or to differences in neurovascular coupling maturation [10, 87–91]. Because of the inconsistency in the signs of HbO_2 and HbR in newborns and infants, and the lack of a plausible explanation for this, the current literature may appear confusing and the results discouraging. Understanding these inverted responses is of paramount importance, and further systematic studies with large samples and multiple modalities are needed.

In the past several years, an increasing number of successful NIRS cognitive studies have been performed. Valuable information was gathered in older infants from the study of facial and social stimuli processing [92–97], object

processing [98–101], language processing [102–105], and habituation/novelty auditory paradigms [106].

For a detailed review of language processing NIRS studies in infants, see [107]; for a comprehensive review of all functional/cognitive NIRS studies in infants, and also infant probes and specific issues, see [108] and [109].

48.4 Baseline Hemodynamic Assessment and Clinical Applications

Baseline hemoglobin concentration and blood flow in the cerebral cortex can be related to neurovascular development and brain health. For more than 20 years, researchers have attempted to establish NIRS as a bedside cerebral monitoring tool in neonatal intensive care units. We can only mention here some of the many CW-NIRS baseline applications in clinical settings.

Autoregulation has been studied in response to peripheral saturation [110], blood pressure [111, 112], pCO_2 [113], and posture changes [114]. The effects of respiratory support on cerebral StO_2 have been studied extensively, including the effect of surfactants [115–117], endotracheal suctioning [118, 119], ventilation methods [46, 120–124], and extracorporeal membrane oxygenation [125, 126]. NIRS has been used as a monitoring tool during surgery [127–130]. There is also a vast literature on the use of NIRS in newborns and infants with congenital heart disease [131–133].

Wardle *et al.* [134] studied the effect of hypotension and anemia on the cerebral fraction of oxygen extraction in premature neonates, Lemmers *et al.* [135] showed that StO_2 is more variable in newborns with respiratory distress syndrome, and several groups have characterized the effect of hypoxia on the newborn brain [2, 136–139]. Initial findings in the study of perinatal asphyxia and subsequent hypoxic–ischemic injury were sometimes inconsistent [4, 140–142], but NIRS measures seemed to correlate with outcome [56, 143]. Despite their prevalence, intraventricular hemorrhage and periventricular leukomalacia studies are still under-represented in the literature. However, CBF [144] and StO_2 [145] at birth have been found to correlate with the occurrence and severity of intraventricular hemorrhage. Roche-Labarbe *et al.* also described different hemodynamic responses to spontaneous bursts of neuronal activity between healthy newborns and patients with intraventricular hemorrhage [86].

For a synthetic review of CW-NIRS baseline hemodynamic studies in newborns and infants before 2003, see [146]. For a comprehensive review of functional and baseline studies of NIRS in neonates, see [109].

Although the efforts to implement NIRS in the NICU generated a large number of publications, there has not been a clear breakthrough leading to the use of NIRS technology as a routine diagnostic tool. Past studies have been very important in opening up the field [25, 56, 147–149]; however there are limitations that CW-NIRS and perturbation approaches cannot overcome [146, 150]. We believe that a new generation of TD, FD, and DCS systems will allow developers to establish NIRS successfully as the technology of choice for bedside monitoring of brain health neonatal intensive care units.

As we stressed in the techniques section, TD, FD, and DCS instruments are able to quantify baseline hemodynamic parameters and metabolism with fewer assumptions. This offers several advantages with respect to the traditional CW systems:

- It allows for absolute measurements, and as a result optical probes do not need to be kept in place for long periods of time, but can be frequently repositioned on the subject's head without losing the reference value. The variability is about 5–10% for FD measurements and 10–15% for DCS measurements [40, 55, 151], and differences in the recovered parameters are due more to tissue heterogeneity than to system calibration issues.
- Blood parameters can be directly quantified without external perturbations, or bolus techniques, that can alter cerebral vascular physiology (thus biasing the results), are not applicable in every infant, require additional expertise, and cannot be performed continuously or frequently.
- As opposed to typical commercial NIRS systems that acquire the minimum number of parameters necessary to resolve oxygenated and deoxygenated hemoglobin, some newer systems acquire additional distances and/or wavelengths and use redundancy in the measurements to assess data quality. This enables preset rejection criteria to be used to discard bad measurements based on statistical results [40, 55].
- The majority of previous work using CW systems focused on determining TOI differences between the healthy and diseased brain. Although TOI and SaO_2 are very sensitive to changes during hypoxic episodes, recent studies suggest that oxygenation saturation is not the best biomarker for detecting brain injury after the insult, because the brain tends to maintain a constant oxygenation saturation level by adjusting perfusion. Across ages [40] and diseases [62], total oxygenation is remarkably constant. On the other hand, CBV and $CMRO_2$ acquired using FD-NIRS seem to discriminate much more effectively between brain-injured and healthy newborns [62]. The same issues are encountered with the oxygen extraction fraction (OEF): PET studies showed that regional OEF is constant across ages [152] and does not predict brain injury as well as CBF or $CMRO_2$ [153].
- Finally, we recently showed that in the neonatal population, the flow–volume relationship [Eq. (48.7)] is not valid, because the term β does not take into account the large decrease in blood viscosity during the first few months of life due to the transition from fetal to adult hemoglobin [154]. Therefore, we cannot replace the CBF ratio with the CBV ratio to calculate $CMRO_2$ using Eq. (48.6). Rather, we need to measure CBF directly, which is made possible by DCS [55].

48.5 Conclusion and Perspectives

NIRS is especially well suited to the study of newborn and infant brain development, and recent technical improvements such as the ability to measure absolute values with TD- and FD-NIRS, and a reliable and safe CBF index with DCS, have made it

suitable for large-scale clinical applications. In the future, multimodal approaches coupling optical imaging with other imaging techniques should allow a more extensive understanding of the developing brain and the incorporation of NIRS into the clinical routine. Although there have been promising attempts at optical tomography, that is, the three-dimensional imaging of newborns' brains with NIRS [35, 37, 38], to date the technique is too complex and time consuming for routine clinical application. The trend is towards more flexible and patient-friendly setups allowing repeated measurements.

With respect to functional and cognitive studies, we are looking forward to more complex experimental designs allowing us to study the details of cognitive development during the first year of life.

References

1 Benaron, D.A. *et al.* (1992) Noninvasive methods for estimating *in vivo* oxygenation. *Clin. Pediatr. (Phila.)*, **31**, 258–273.

2 Brazy, J.E., Lewis, D.V., and Mitnick, M.H. (1985) Noninvasive monitoring of cerebral oxygenation in preterm infants: preliminary observations. *Pediatrics*, **75**, 217–225.

3 Rea, P.A. *et al.* (1985) Non-invasive optical methods for the study of cerebral metabolism in the human newborn: a technique for the future? *J. Med. Eng. Technol.*, **9** (4), 160–166.

4 Wyatt, J.S. *et al.* (1986) Quantification of cerebral oxygenation and haemodynamics in sick newborn infants by near infrared spectrophotometry. *Lancet*, **ii**, 1063–1066.

5 Altman, D.I. *et al.* (1993) Cerebral oxygen metabolism in newborns. *Pediatrics*, **92** (1), 99–104.

6 Chugani, H.T. (1998) A critical period of brain development: studies of cerebral glucose utilization with PET. *Prev. Med.*, **27**, 184–188.

7 Chugani, H.T. and Phelps, M.E. (1986) Maturational changes in cerebral function in infants determined by 18FDG positron emission tomography. *Science*, **231**, 840–843.

8 Shi, Y. *et al.* (2009) Brain positron emission tomography in preterm and term newborn infants. *Early Hum. Dev.*, **85** (7), 429–432.

9 Tokumaru, A.M. *et al.* (1999) The evolution of cerebral blood flow in the developing brain: evaluation with iodine-123 iodoamphetamine SPECT and correlation with MR imaging. *AJNR Am. J. Neuroradiol.*, **20**, 845–852.

10 Arichi, T. *et al.* (2010) Somatosensory cortical activation identified by functional MRI in preterm and term infants. *Neuroimage*, **49** (3), 2063–2071.

11 Fransson, P. *et al.* (2009) Spontaneous brain activity in the newborn brain during natural sleep – an fMRI study in infants born at full term. *Pediatr. Res.*, **66** (3), 301–305.

12 Sander, K., Frome, Y., and Scheich, H. (2007) FMRI activations of amygdala, cingulate cortex, and auditory cortex by infant laughing and crying. *Hum. Brain Mapp.*, **28** (10), 1007–1022.

13 Bozkurt, A. and Onaral, B. (2004) Safety assessment of near infrared light emitting diodes for diffuse optical measurements. *BioMed. Eng. OnLine*, **3** (9), 1–10.

14 Ito, Y. *et al.* (2000) Assessment of heating effects in skin during continuous wave near infrared spectroscopy. *J. Biomed. Opt.*, **5** (4), 383–391.

15 Faris, F. *et al.* (1991) Non-invasive *in vivo* near-infrared optical measurement of the penetration depth in the neonatal head. *Clin. Phys. Physiol. Meas.*, **12** (4), 353–358.

16 Taga, G., Homae, F., and Watanabe, H. (2007) Effects of source-detector distance

of near infrared spectroscopy on the measurement of the cortical hemodynamic response in infants. *Neuroimage*, **38** (3), 452–460.
17 Jöbsis, F.F. (1977) Noninvasive, infrared monitoring of cerebral and myocardial oxygen sufficiency and circulatory parameters. *Science*, **198**, 1264–1267.
18 Beer, A. (1853) Einleitung in die höhere Optik. Published by F. Vieweg und Sohn, Braunschweig, Germany.
19 Delpy, D. *et al.* (1988) Estimation of optical path length through tissue from direct time of flight measurements. *Phys. Med. Biol.*, **33**, 1433–1442.
20 Bartocci, M. *et al.* (2000) Activation of olfactory cortex in newborn infants after odor stimulation: a functional near-infrared spectroscopy study. *Pediatr. Res.*, **48** (1), 18–23.
21 Meek, J.H. *et al.* (1998) Regional hemodynamic responses to visual stimulation in awake infants. *Pediatr. Res.*, **43** (6), 840–843.
22 Taga, G. *et al.* (2000) Spontaneous oscillation of oxy- and deoxy-hemoglobin changes with a phase difference throughout the occipital cortex of newborn infants observed using non-invasive optical topography. *Neurosci. Lett.*, **282**, 101–104.
23 Watanabe, H. *et al.* (2008) Functional activation in diverse regions of the developing brain of human infants. *NeuroImage*, **43** (2), 346–357.
24 Zaramella, P. *et al.* (2001) Brain auditory activation measured by near-infrared spectroscopy (NIRS) in neonates. *Pediatr. Res.*, **49**, 213–219.
25 Toet, M. and Lemmers, P.M. (2009) Brain monitoring in neonates. *Early Hum. Dev.*, **85**, 77–84.
26 Skov, L. *et al.* (1993) Estimation of cerebral venous saturation in newborn infants by near infrared spectroscopy. *Pediatr. Res.*, **33** (1), 52–55.
27 Yoxall, C.W., Weindling, A.M., and Yoxall, C.W. (1998) Measurement of cerebral oxygen consumption in the human neonate using near infrared spectroscopy: cerebral oxygen consumption increases with advancing gestational age. *Pediatr. Res.*, **44** (3), 283–290.
28 Ishimaru, A. (1978) *Wave Propagation and Scattering in Random Media*, Academic Press, New York.
29 Fantini, S. *et al.* (1994) Quantitative determination of the absorption spectra of chromophores in strongly scattering media: a light-emitting-diode based technique. *Appl. Opt.*, **33** (22), 5204–5213.
30 Farrell, T., Patterson, M., and Wilson, B. (1992) A diffusion theory model of spatially resolved, steady-state diffuse reflectance for the noninvasive determination of tissue optical properties *in vivo*. *Med. Phys.*, **19** (4), 879–888.
31 Fishkin, J.B., Gratton, E., and Fishkin, J.B. (1993) Propagation of photon-density waves in strongly scattering media containing an absorbing semi-infinite plane bounded by a straight edge. *J. Opt. Soc. Am. A*, **10** (1), 127–140.
32 Patterson, M.S. *et al.* (1995) Absorption spectroscopy in tissue-simulating materials: a theoretical and experimental study of photon paths. *Appl. Opt.*, **34**, 22–30.
33 Pham, T.H. *et al.* (2000) Broad bandwidth frequency domain instrument for quantitative tissue optical spectroscopy. *Rev. Sci. Instrum.*, **71** (6), 2500–2513.
34 Fantini, S. *et al.* (1995) Frequency-domain multichannel optical detector for non-invasive tissue spectroscopy and oximetry. *Opt. Eng.*, **34**, 34–42.
35 Austin, T. *et al.* (2006) Three dimensional optical imaging of blood volume and oxygenation in the neonatal brain. *Neuroimage*, **31** (4), 1426–1433.
36 Gibson, A.P. *et al.* (2006) Three-dimensional whole-head optical tomography of passive motor evoked responses in the neonate. *NeuroImage*, **30**, 521–528.
37 Hebden, J.C. *et al.* (2004) Imaging changes in blood volume and oxygenation in the newborn infant brain using three-dimensional optical tomography. *Phys. Med. Biol.*, **49** (7), 1117–1130.
38 Hebden, J.C. *et al.* (2002) Three-dimensional optical tomography of

the premature infant brain. *Phys. Med. Biol.*, **47**, 4155–4166.
39 Cerussi, A. *et al.* (2005) Noninvasive monitoring of red blood cell transfusion in very low birthweight infants using diffuse optical spectroscopy. *J. Biomed. Opt.*, **10** (5), 051401.
40 Franceschini, M.A. *et al.* (2007) Assessment of infant brain development with frequency-domain near-infrared spectroscopy. *Pediatr. Res.*, **61** (5), 546–551.
41 Spichtig, S. *et al.* (2009) Multifrequency frequency-domain spectrometer for tissue analysis. *Rev. Sci. Instrum.*, **80** (2), 024301.
42 Zhao, J. *et al.* (2005) *In vivo* determination of the optical properties of infant brain using frequency-domain near-infrared spectroscopy. *J. Biomed. Opt.*, **10** (2), 024028.
43 Edwards, A.D. *et al.* (1988) Cotside measurement of cerebral blood flow in ill infants by near-infrared spectroscopy. *Lancet*, **332** (8614), 770–771.
44 Elwell, C.E. *et al.* (2005) Measurement of $CMRO_2$ in neonates undergoing intensive care using near infrared spectroscopy. *Adv. Exp. Med. Biol.*, **566**, 263–268.
45 Meek, J.H. *et al.* (1998) Cerebral blood flow increases over the first three days of life in extremely preterm neonates. *Arch. Dis. Child. Fetal Neonatal Ed.*, **78**, F33–F37.
46 Noone, M.A. *et al.* (2003) Postnatal adaptation of cerebral blood flow using near infrared spectroscopy in extremely preterm infants undergoing high-frequency oscillatory ventilation. *Acta Paediatr.*, **92** (9), 1079–1084.
47 Patel, J. *et al.* (1998) Measurement of cerebral blood flow in newborn infants using near infrared spectroscopy with indocyanine green. *Pediatr. Res.*, **43** (1), 34–39.
48 Kusaka, T. *et al.* (2001) Estimation of regional cerebral blood flow distribution in infants by near-infrared topography using indocyanine green. *NeuroImage*, **13**, 944–952.
49 Boas, D.A. and Yodh, A.G. (1997) Spatially varying dynamical properties of turbid media probed with diffusing temporal light correlation. *J. Opt. Soc. Am.*, **14** (1), 192–215.
50 Cheung, C. *et al.* (2001) *In vivo* cerebrovascular measurement combining diffuse near-infrared absorption and correlation spectroscopies. *Phys. Med. Biol.*, **46**, 2053–2065.
51 Buckley, E.M. *et al.* (2009) Cerebral hemodynamics in preterm infants during positional intervention measured with diffuse correlation spectroscopy and transcranial Doppler ultrasound. *Opt. Express*, **17** (15), 12571–12581.
52 Culver, J.P. *et al.* (2003) Diffuse optical measurement of hemoglobin and cerebral blood flow in rat brain during hypercapnia, hypoxia and cardiac arrest. *Adv. Exp. Med. Biol.*, **510**, 293–297.
53 Durduran, T. *et al.* (2004) Diffuse optical measurement of blood flow, blood oxygenation, and metabolism in a human brain during sensorimotor cortex activation. *Opt. Lett.*, **29** (5), 1766–1768.
54 Li, J. *et al.* (2005) Noninvasive detection of functional brain activity with near-infrared diffusing-wave spectroscopy. *J. Biomed. Opt.*, **10** (4), 044002.
55 Roche-Labarbe, N. *et al.* (2010) Noninvasive optical measures of CBV, StO_2, CBF index, and $rCMRO_2$ in human premature neonates' brains in the first six weeks of life. *Hum. Brain Mapp.*, **31**, 341–352.
56 Toet, M.C. *et al.* (2006) Cerebral oxygenation and electrical activity after birth asphyxia: their relation to outcome. *Pediatrics*, **117** (2), 333–339.
57 Watzman, H.M. *et al.* (2000) Arterial and venous contributions to near-infrared cerebral oximetry. *Anesthesiology*, **93**, 947–953.
58 Brown, D.W. *et al.* (2003) Near-infrared spectroscopy measurement of oxygen extraction fraction and cerebral metabolic rate of oxygen in newborn piglets. *Pediatr. Res.*, **54** (6), 861–867.
59 Tichauer, K.M. *et al.* (2006) Measurement of cerebral oxidative metabolism with near-infrared spectroscopy: a validation

study. *J. Cereb. Blood Flow Metab.*, **26** (5), 722–730.

60 Boas, D.A. *et al.* (2003) Can the cerebral metabolic rate of oxygen be estimated with near-infrared spectroscopy? *Phys. Med. Biol.*, **48** (15), 2405–2418.

61 Grubb, R.L.J. *et al.* (1974) The effects of changes in $PaCO_2$ on cerebral blood volume, blood flow, and vascular mean transit time. *Stroke*, **5** (5), 630–639.

62 Grant, P.E. *et al.* (2009) Increased cerebral blood volume and oxygen consumption in neonatal brain injury. *J. Cereb. Blood Flow Metab.*, **29** (10), 1704–1713.

63 Chen, J.J., Pike, G.B., and Chen, J.J. (2009) BOLD-specific cerebral blood volume and blood flow changes during neuronal activation in humans. *NMR Biomed.*, **22** (10), 1054–1062.

64 Sherrington, C. (1933) *The Brain and Its Mechanism*, Macmillan, New York.

65 Fox, P.T. and Raichle, M.E. (1986) Focal physiological uncoupling of cerebral blood flow and oxidative metabolism during somatosensory stimulation in human subjects. *Proc. Natl. Acad. Sci. U. S. A.*, **83** (4), 1140–1144.

66 Fox, P.T. *et al.* (1988) Nonoxidative glucose consumption during focal physiologic neural activity. *Science*, **241** (4), 462–464.

67 Malonek, D. and Grinvald, A. (1996) Interactions between electrical activity and cortical microcirculation revealed by imaging spectroscopy: implications for functional brain mapping. *Science*, **272**, 551–554.

68 Meek, J.H. *et al.* (1995) Regional changes in cerebral haemodynamics as a result of a visual stimulus measured by near infrared spectroscopy. *Proc. Biol. Sci.*, **261** (1362), 351–356.

69 Obrig, H. *et al.* (1996) Cerebral oxygenation changes in response to motor stimulation. *J. Appl. Physiol.*, **81** (3), 1174–1183.

70 Hoshi, Y. *et al.* (2000) Hemodynamic responses to photic stimulation in neonates. *Pediatr. Neurol.*, **23** (4), 323–327.

71 Karen, T. *et al.* (2008) Hemodynamic response to visual stimulation in newborn infants using functional near-infrared spectroscopy. *Hum. Brain Mapp.*, **29**, 453–460.

72 Taga, G. *et al.* (2003) Hemodynamic responses to visual stimulation in occipital and frontal cortex of newborn infants: a near-infrared optical topography study. *Early Hum. Dev.*, **75** (Suppl.), S203–S210.

73 Bortfeld, H., Wruck, E., and Boas, D.A. (2007) Assessing infants' cortical response to speech using near-infrared spectroscopy. *NeuroImage*, **34**, 407–415.

74 Csibra, G. *et al.* (2004) Near infrared spectroscopy reveals neural activation during face perception in infants and adults. *J. Pediatr. Neurol.*, **2** (2), 85–89.

75 Kusaka, T. *et al.* (2004) Noninvasive optical imaging in the visual cortex in young infants. *Hum. Brain Mapp.*, **22** (2), 122–132.

76 Kotilahti, K. *et al.* (2005) Bilateral hemodynamic responses to auditory stimulation in newborn infants. *NeuroReport*, **16** (12), 1373–1377.

77 Pena, M. *et al.* (2003) Sounds and silence: an optical topography study of language recognition at birth. *Proc. Natl. Acad. Sci. U.S.A.*, **100** (20), 11702–11705.

78 Saito, Y. *et al.* (2007) The function of the frontal lobe in neonates for response to a prosodic voice. *Early Hum. Dev.*, **83** (4), 225–230.

79 Sakatani, K. *et al.* (1999) Cerebral blood oxygenation changes induced by auditory stimulation in newborn infants measured by near infrared spectroscopy. *Early Hum. Dev.*, **55** (3), 229–236.

80 Taga, G. and Asakawa, K. (2007) Selectivity and localization of cortical response to auditory and visual stimulation in awake infants aged 2 to 4 months. *Neuroimage*, **36** (4), 1246–1252.

81 Bartocci, M. *et al.* (2006) Pain activates cortical areas in the preterm newborn brain. *Pain*, **122** (1–2), 109–117.

82 Hintz, S.R. *et al.* (2001) Bedside functional imaging of the premature infant brain during passive motor activation. *J. Perinat. Med.*, **29** (4), 335–343.

83 Isobe, K. *et al.* (2001) Functional imaging of the brain in sedated newborn infants using near infrared topography during

passive knee movement. *Neurosci. Lett.*, **299** (3), 221–224.
84 Slater, R. *et al.* (2006) Cortical pain responses in human infants. *J. Neurosci.*, **26** (14), 3662–3666.
85 Zotter, H. *et al.* (2007) Cerebral hemodynamics during arousals in preterm infants. *Early Hum. Dev.*, **83** (4), 239–246.
86 Roche-Labarbe, N. *et al.* (2007) Coupled oxygenation oscillation measured by NIRS and intermittent cerebral activation on EEG in premature infants. *Neuroimage*, **36** (3), 718–727.
87 Anderson, A.W. *et al.* (2001) Neonatal auditory activation detected by functional magnetic resonance imaging. *Magn. Reson. Imaging*, **19** (1), 1–5.
88 Heep, A. *et al.* (2009) Functional magnetic resonance imaging of the sensorimotor system in preterm infants. *Pediatrics*, **123** (1), 294–300.
89 Morita, T. *et al.* (2000) Difference in the metabolic response to photic stimulation of the lateral geniculate nucleus and the primary visual cortex of infants: a fMRI study. *Neurosci. Res.*, **38**, 63–70.
90 Yamada, H. *et al.* (1997) A rapid brain metabolic change in infants detected by fMRI. *NeuroReport*, **8**, 3775–3778.
91 Yamada, H. *et al.* (2000) A milestone for normal development of the infantile brain detected by functional MRI. *Neurology*, **55** (2), 218–223.
92 Blasi, A. *et al.* (2007) Investigation of depth dependent changes in cerebral haemodynamics during face perception in infants. *Phys. Med. Biol.*, **52** (23), 6849–6864.
93 Carlsson, J. *et al.* (2008) Activation of the right fronto-temporal cortex during maternal facial recognition in young infants. *Acta Paediatr.*, **97** (9), 1221–1225.
94 Lloyd-Fox, S. *et al.* (2009) Social perception in infancy: a near infrared spectroscopy study. *Child Dev.*, **80** (4), 986–999.
95 Nakato, E. *et al.* (2009) When do infants differentiate profile face from frontal face? A near-infrared spectroscopic study. *Hum. Brain Mapp.*, **30** (2), 462–472.
96 Otsuka, Y. *et al.* (2007) Neural activation to upright and inverted faces in infants measured by near infrared spectroscopy. *Neuroimage*, **34** (1), 399–406.
97 Shimada, S. and Hiraki, K. (2006) Infant's brain responses to live and televised action. *Neuroimage*, **32** (2), 930–939.
98 Baird, A.A. *et al.* (2002) Frontal lobe activation during object permanence: data from near-infrared spectroscopy. *NeuroImage*, **16** (4), 1120–1126.
99 Wilcox, T. *et al.* (2009) Hemodynamic changes in the infant cortex during the processing of featural and spatiotemporal information. *Neuropsychologia*, **47** (3), 657–662.
100 Wilcox, T. *et al.* (2005) Using near-infrared spectroscopy to assess neural activation during object processing in infants. *J. Biomed. Opt.*, **10** (1), 11010.
101 Wilcox, T. *et al.* (2008) Hemodynamic response to featural changes in the occipital and inferior temporal cortex in infants: a preliminary methodological exploration. *Dev. Sci.*, **11** (3), 361–370.
102 Bortfeld, H., Fava, E., and Boas, D.A. (2009) Identifying cortical lateralization of speech processing in infants using near-infrared spectroscopy. *Dev. Neuropsychol.*, **34** (1), 52–65.
103 Homae, F. *et al.* (2006) The right hemisphere of sleeping infant perceives sentential prosody. *Neurosci. Res.*, **54** (4), 276–280.
104 Homae, F. *et al.* (2007) Prosodic processing in the developing brain. *Neurosci. Res.*, **59** (1), 29–39.
105 Minagawa-Kawai, Y. *et al.* (2007) Neural attunement processes in infants during the acquisition of a language-specific phonemic contrast. *J. Neurosci.*, **27** (2), 315–321.
106 Nakano, T. *et al.* (2009) Prefrontal cortical involvement in young infants' analysis of novelty. *Cereb. Cortex*, **19** (2), 455–463.
107 Minagawa-Kawai, Y. *et al.* (2008) Optical imaging of infants' neurocognitive development: recent advances and perspectives. *Dev. Neurobiol.*, **68** (6), 712–728.
108 Lloyd-Fox, S., Blasi, A., and Elwell, C.E. (2010) Illuminating the developing brain: the past, present and future of functional

near infrared spectroscopy. *Neurosci. Biobehav. Rev.*, **34** (3), 269–284.

109 Wolf, M. and Greisen, G. (2009) Advances in near-infrared spectroscopy to study the brain of the preterm and term neonate. *Clin. Perinatol.*, **36** (4), 807–834.

110 Wolf, M. *et al.* (2000) Tissue oxygen saturation measured by near infrared spectrophotometry correlates with arterial oxygen saturation during induced oxygenation changes in neonates. *Physiol. Meas.*, **21** (4), 481–491.

111 De Smet, D. *et al.* (2009) New measurements for assessment of impaired cerebral autoregulation using near-infrared spectroscopy. *Adv. Exp. Med. Biol.*, **645**, 273–278.

112 Wong, F.Y. *et al.* (2008) Impaired autoregulation in preterm infants identified by using spatially resolved spectroscopy. *Pediatrics*, **121** (3), e604–e611.

113 Vanderhaegen, J. *et al.* (2009) The effect of changes in $tPCO_2$ on the fractional tissue oxygen extraction – as measured by near-infrared spectroscopy – in neonates during the first days of life. *Eur. J. Paediatr. Neurol.*, **13** (2), 128–134.

114 Ancora, G. *et al.* (2009) Effect of posture on brain hemodynamics in preterm newborns not mechanically ventilated. *Neonatology*, **97** (3), 212–217.

115 Dorrepaal, C.A. *et al.* (1993) Cerebral hemodynamics and oxygenation in preterm infants after low- vs. high-dose surfactant replacement therapy. *Biol. Neonate*, **64** (4), 193–200.

116 Edwards, A.D. *et al.* (1992) Cerebral hemodynamic effects of treatment with modified natural surfactant investigated by near infrared spectroscopy. *Pediatr. Res.*, **32** (5), 532–536.

117 Roll, C. *et al.* (2000) Effect of surfactant administration on cerebral haemodynamics and oxygenation in premature infants – a near infrared spectroscopy study. *Neuropediatrics*, **31** (1), 16–23.

118 Kohlhauser, C. *et al.* (2000) Effects of endotracheal suctioning in high-frequency oscillatory and conventionally ventilated low birth weight neonates on cerebral hemodynamics observed by near infrared spectroscopy (NIRS). *Pediatr. Pulmonol.*, **29** (4), 270–275.

119 Mosca, F.A. *et al.* (1997) Closed versus open endotracheal suctioning in preterm infants: effects on cerebral oxygenation and blood volume. *Biol. Neonate*, **72** (1), 9–14.

120 Dani, C. *et al.* (2007) Brain haemodynamic effects of nasal continuous airway pressure in preterm infants of less than 30 weeks' gestation. *Acta Paediatr.*, **96** (10), 1421–1425.

121 Milan, A. *et al.* (2009) Influence of ventilation mode on neonatal cerebral blood flow and volume. *Early Hum. Dev.*, **85** (7), 415–419.

122 Palmer, K. *et al.* (1994) Negative extrathoracic pressure ventilation – evaluation of the neck seal. *Early Hum. Dev.*, **37** (1), 67–72.

123 Palmer, K.S. *et al.* (1995) Effects of positive and negative pressure ventilation on cerebral blood volume of newborn infants. *Acta Paediatr.*, **84** (2), 132–139.

124 van de Berg, E. *et al.* (2010) The effect of the "InSurE" procedure on cerebral oxygenation and electrical brain activity of the preterm infant. *Arch. Dis. Child. Fetal Neonatal Ed.*, **95** (1), F53–F58.

125 Ejike, J.C. *et al.* (2006) Cerebral oxygenation in neonatal and pediatric patients during veno-arterial extracorporeal life support. *Pediatr. Crit. Care Med.*, **7** (2), 154–158.

126 Rais-Bahrami, K., Rivera, O., and Short, B.L. (2006) Validation of a noninvasive neonatal optical cerebral oximeter in veno-venous ECMO patients with a cephalad catheter. *J. Perinatol.*, **26** (10), 628–635.

127 Dotta, A. *et al.* (2005) Effects of surgical repair of congenital diaphragmatic hernia on cerebral hemodynamics evaluated by near-infrared spectroscopy. *J. Pediatr. Surg.*, **40** (11), 1748–1752.

128 Toet, M.C. *et al.* (2005) Cerebral oxygen saturation and electrical brain activity before, during, and up to 36 hours after arterial switch procedure in neonates without pre-existing brain damage: its relationship to neurodevelopmental outcome. *Exp. Brain Res.*, **165**, 343–350.

129 Vanderhaegen, J. *et al.* (2008) Surgical closure of the patent ductus arteriosus and its effect on the cerebral tissue oxygenation. *Acta Paediatr.*, **97** (12), 1640–1644.

130 Zaramella, P. *et al.* (2006) Surgical closure of patent ductus arteriosus reduces the cerebral tissue oxygenation index in preterm infants: a near-infrared spectroscopy and Doppler study. *Pediatr. Int.*, **48** (3), 305–312.

131 Maher, K.O., Phelps, H.M., and Kirshbom, P.M. (2009) Near infrared spectroscopy changes with pericardial tamponade. *Pediatr. Crit. Care Med.*, **10** (1), e13–e15.

132 Mascio, C.E. *et al.* (2009) Near-infrared spectroscopy as a guide for an intermittent cerebral perfusion strategy during neonatal circulatory arrest. *ASAIO J.*, **55** (3), 287–290.

133 Tobias, J.D., Russo, P., and Russo, J. (2009) Changes in near infrared spectroscopy during deep hypothermic circulatory arrest. *Ann. Card Anaesth.*, **12** (1), 17–21.

134 Wardle, S.P., Yoxall, C.W., and Weindling, A.M. (2000) Determinants of cerebral fractional oxygen extraction using near infrared spectroscopy in preterm neonates. *J. Cereb. Blood Flow Metab.*, **20** (2), 272–279.

135 Lemmers, P.M. *et al.* (2006) Cerebral oxygenation and cerebral oxygen extraction in the preterm infant: the impact of respiratory distress syndrome. *Exp. Brain Res.*, **173** (3), 458–467.

136 Jenni, O.G. *et al.* (1996) Impact of central, obstructive and mixed apnea on cerebral hemodynamics in preterm infants. *Biol. Neonate*, **70** (2), 91–100.

137 Livera, L.N. *et al.* (1991) Effects of hypoxaemia and bradycardia on neonatal cerebral haemodynamics. *Arch. Dis. Child*, **66** (4 Spec. No.), 376–380.

138 Petrova, A. and Mehta, R. (2006) Near-infrared spectroscopy in the detection of regional tissue oxygenation during hypoxic events in preterm infants undergoing critical care. *Pediatr. Crit. Care Med.*, **7** (5), 449–454.

139 Urlesberger, B. *et al.* (2000) Changes in cerebral blood volume and cerebral oxygenation during periodic breathing in term infants. *Neuropediatrics*, **31** (2), 75–81.

140 Huang, L. *et al.* (2004) Assessment of the hypoxic–ischemic encephalopathy in neonates using non-invasive near-infrared spectroscopy. *Physiol. Meas*, **25** (3), 749–761.

141 Naulaers, G. *et al.* (2004) Continuous measurement of cerebral blood volume and oxygenation during rewarming of neonates. *Acta Paediatr.*, **93** (11), 1540–1542.

142 van Bel, F. *et al.* (1993) Changes in cerebral hemodynamics and oxygenation in the first 24hours after birth asphyxia. *Pediatrics*, **92** (3), 365–372.

143 Meek, J.H. *et al.* (1999) Abnormal cerebral haemodynamics in perinatally asphyxiated neonates related to outcome. *Arch. Dis. Child. Fetal Neonatal Ed.*, **81** (2), F110–F115.

144 Meek, J.H. *et al.* (1999) Low cerebral blood flow is a risk factor for severe intraventricular haemorrhage. *Arch. Dis. Child. Fetal Neonatal. Ed.*, **81** (1), F15–F18.

145 Sorensen, L.C. *et al.* (2008) Neonatal cerebral oxygenation is not linked to foetal vasculitis and predicts intraventricular haemorrhage in preterm infants. *Acta Paediatr.*, **97** (11), 1529–1534.

146 Nicklin, S.E. *et al.* (2003) The light still shines, but not that brightly? The current status of perinatal near infrared spectroscopy. *Arch. Dis. Child. Fetal Neonatal Ed.*, **88** (4), 263–268.

147 Kane, J.M., Steinhorn, D.M., and Kane, J.M. (2009) Lack of irrefutable validation does not negate clinical utility of near-infrared spectroscopy monitoring: learning to trust new technology. *J. Crit. Care*, **24** (3), 472–477.

148 Tina, L.G. *et al.* (2010) S100B protein and near infrared spectroscopy in preterm and term newborns. *Front. Biosci. (Elite Ed.)*, **2**, 159–164.

149 Wolf, M. *et al.* (2007) Progress of near-infrared spectroscopy and topography for brain and muscle clinical applications. *J. Biomed. Opt.*, **12** (6), 062104.

150 Greisen, G. (2006) Is near-infrared spectroscopy living up to its promises?

Semin. Fetal Neonatal Med., **11** (6), 498–502.

151 D'Arceuil, H.E. *et al.* (2005) Near-infrared frequency-domain optical spectroscopy and magnetic resonance imaging: a combined approach to studying cerebral maturation in neonatal rabbits. *J. Biomed. Opt.*, **10**, 011011.

152 Takahashi, T. *et al.* (1999) Developmental changes of cerebral blood flow and oxygen metabolism in children. *Am. J. Neuroradiol.*, **20** (5), 917–922.

153 Gupta, A.K. *et al.* (2002) Measurement of brain tissue oxygenation performed using positron emission tomography scanning to validate a novel monitoring method. *J. Neurosurg.*, **96** (2), 263–268.

154 Oski, F.A. and Naiman, J.L. (1982) *Hematologic Problems in the Newborn*, 3rd edn., Major Problems in Clinical Pediatrics, vol. **4**, Saunders, Philadelphia, pp. 1–360.

49
Revealing the Roles of Prefrontal Cortex in Memory

Hui Gong and Qingming Luo

49.1
Introduction

The major breakthroughs in neuroscience in the past two decades have generated the opportunity to achieve an integrated understanding of the brain's structure and functions [1]. The brain is highly specialized, differentiated, and organized so that different regions of the neocortex simultaneously carry out computations on separate features of the external world. Memory is the process of retaining informations in storage, which can possibly be drawn later on. It is localized in the brain as physical changes produced by experience through years of research [2]. Information is accumulating about how memory is organized and what structures and connections are involved. The prefrontal cortex (PFC) is one of the latest cortices in the human developing process, having attained maximum relative growth in the human brain. The PFC function relies closely on its connections with a vast array of other cerebral structures [3].

There are several non- or minimally invasive neuromonitoring techniques available to examine functional brain activity for psychiatric researcher and clinicians. These methods can be categorized as direct or indirect based on the information acquisition principles. Direct methods include magnetoencephalography (MEG), electroencephalography (EEG), and event-related potentials (ERPs). Among these, EEG and ERPs record the electrical fields generated by neuronal activity, whereas MEG records the magnetic fields induced by such activity. The direct methods have a high speed response to the brain activity but a limited spatial resolution. By monitoring hemodynamic changes consequent to brain electrical activity, positron emission tomography (PET), single positron emission computed tomography (SPECT) and functional magnetic resonance imaging (fMRI) are regarded as indirect methods. PET and SPECT operate by monitoring the decay of blood-borne radioactive isotopes as they pass through the brain. fMRI, in contrast, detects changes in the local concentration of deoxyhemoglobin via its effect on imposed magnetic fields. The indirect methods can only detect neuronal activity after it has been filtered by a complex and poorly understood neurovascular coupling [4]. Human neuropsychology

Handbook of Biophotonics. Vol.2: Photonics for Health Care, First Edition. Edited by Jürgen Popp, Valery V. Tuchin, Arthur Chiou, and Stefan Heinemann.

and neuroimaging studies have begun to provide a broad view of the task conditions in which it is engaged. However, an understanding of the mechanisms by which PFC controls has remained elusive [5].

As a new approach in indirect methods, near-infrared spectroscopy (NIRS) is a noninvasive optical method that utilizes the sensitivity of near-infrared light to hemoglobin oxygenation-state shifts [6]. Since Chance *et al*. [7] proved that hemodynamic signals in the brain could be quantified by NIRS, many studies have demonstrated the validity of this method [8–10]. In comparison with fMRI, NIRS can measure relative changes in blood volume, oxyhemoglobin (Δ[oxy-Hb]), deoxyhemoglobin (Δ[deoxy-Hb]), and cytochrome oxidase redox state [11]. In most cases, Δ[oxy-Hb], Δ[deoxy-Hb], and total hemoglobin (Δ[total-Hb), the sum of Δ[oxy-Hb] and Δ[deoxy-Hb]), act as NIRS parameters that vary with brain cognitive activity [12].

In this chapter, we review the optical approaches to human PFC activation during cognition function for working memory and long-term memory.

49.2
Working Memory Modality

The concept of working memory proposes that a dedicated system maintains and stores information in the short term, and that this system underlies human thought processes [13]. Recently, applications of functional optical methods have begun to shed light on the contributions of specific regions to working memory in humans.

The forward digit span (DF) and backward digit span (DB) tasks are widely used to assess short-term memory in neuropsychologic research and clinical evaluations. Hoshi *et al*. [14] used a 64-channel time-resolved optical tomographic imaging system to demonstrate that the DB task activated the dorsolateral prefrontal cortex (DLPFC) of each hemisphere more than the DF task in healthy adult volunteers. They found that higher performance of the DB task was closely related to the activation of the right DLPFC.

The N-back task combines maintenance and manipulation, which requires the monitoring of a continuous sequence of stimuli. A positive response occurs whenever the current stimulus matches the stimulus *n* positions back in the sequence. The value of *n* is often viewed as proportional to the "working memory load" – the total demand placed on the maintenance and/or manipulation process [15]. We have reported a functional NIRS study on the PFC activation caused by a WM task, a verbal *n*-back task [16]. A portable multichannel continuous-wave (cw) NIRS instrument was developed for monitoring the PFC activity by measuring the local relative hemodynamic changes [17]. The cognition task is a verbal parametric "*n*-back" task in which working memory load increases with *n* from 0 to 3 and a sequence of 45 letters as test presentation. We found that, in 2- and 3-back conditions, the behavior performances are negatively correlated with cerebral activation. Lower accuracy is accompanied by longer response time and stronger PFC activation, which suggests that a subject with difficulty in solving a problem will lead to more significant hemodynamic changes than one without difficulty in solving the same problem. Increasing memory load

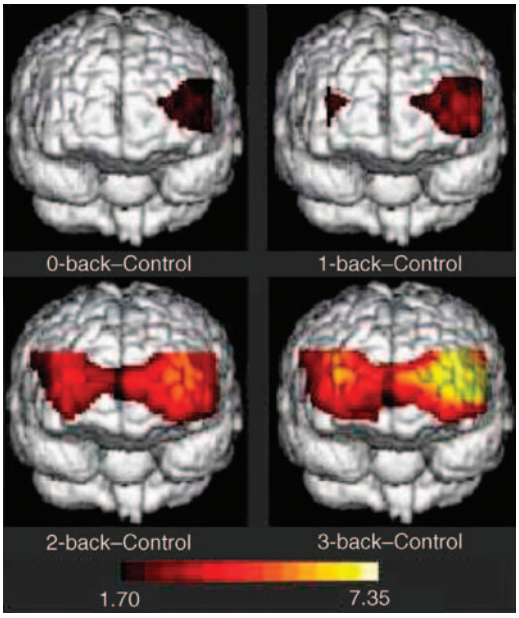

Figure 49.1 Activation distribution in the prefrontal lobe averaged across all the 23 subjects in 0–3-back memory tasks [37].

causes strengthening activation in bilateral polar and DLPFC and the left ventrolateral prefrontal cortex (VLPFC). Figure 49.1 shows the significant activation distribution in the prefrontal lobe averaged across all the 23 subjects in 0–3-back memory tasks. Using the same task, we compared hemodynamic parameters between males and females [18]. Δ[oxy-Hb] and Δ[tot-Hb] exhibited obvious gender differences, but Δ[deoxy-Hb] did not. Males showed bilateral activation with slight left-side dominance, whereas females showed left activation. The activation in males was more widespread and stronger than in females. Furthermore, females required a lower hemodynamic supply than males to obtain comparable performance. Our results suggest that females possess more efficient hemodynamics in the PFC during working memory.

Hoshi used a multichannel cw-NIRS system to monitoring regional cerebral blood flow (rCBF) on the forehead with random digits as a 2-back test presentation [19]. There were no significant changes during the 1-back task, whereas increases in oxy-Hb and tot-Hb with a decrease in deoxy-Hb were observed during the 2-back task. The activated areas correspond to the left DLPFC and no activated areas were seen in the right side. In contrast, in another study, Hoshi *et al.* employed a multichannel cw-NIRS system and a single-channel time-resolved spectroscopy (TRS) instrument to examine changes in rCBF during the performance of an *n*-back task [20]. A sequence of single random digits was used as *n*-back test presentation. It was found that activation from the bilateral VLPFC was prominent with the *n*-back task, but hemispheric dominance was not clearly observed. This study demonstrated that there are overlaps in brain activations across the tasks in each participant.

Schreppel *et al.* used sequences of task-relevant and task-irrelevant faces as the *n*-back test presentation [21]. The analysis of bilateral enhancements of oxygenated hemoglobin showed that the lateral PFC was for remembering relevant faces and the right lateral PFC was for ignoring irrelevant faces. However, oxygenation analysis showed no significant differences between relevant and irrelevant faces, indicating that memory processes and interference resolution were interdependent functions, which were subserved by comparable prefrontal regions. This study supports the notion that the prefrontal activity during working memory tasks reflects not only maintenance processes but also attentional monitoring and selection processes.

Conflict processing, which includes conflict monitoring and solving, is necessary to accomplish a specific task in a complex situation. This solving process typically uses brain function of working memory. The Stroop task is a classical method of studying conflict processing, which was developed in 1935 by John Ridley Stroop, who discovered a cognitive delay when the meaning of a printed word was inconsistent with the color of the word. This phenomenon was dubbed the Stroop effect. Because the Stroop effect reflects conflicts between different pieces of information, it has been widely used in both clinical neuropsychology and experimental psychology. By combining cw-NIRS and event-related potentials (ERPs), we used Chinese character color–word as the Stroop task presentation. Hemodynamic and electrophysiologic signals in the PFC were monitored simultaneously by cw-NIRS and ERPs. We found that P600 signals correlated significantly with the hemodynamic parameters, suggesting that the PFC executes conflict-solving function. Additionally, we observed that the change in deoxy-Hb concentration showed higher sensitivity in response to the Stroop task than other hemodynamic signals [22].

Leon-Carrion *et al.* employ a multichannel cw-NIRS system and used a modified Stroop paradigm to establish the relationship between the hemodynamic response of the PFC and individual differences in cognitive control [23]. Mean concentration levels of oxy-Hb were correlated with behavioral performance in the conflict task. Those with shorter reaction times had higher levels of oxy-Hb concentration in the superior dorsolateral PFC. Negoro *et al.* assessed PFC dysfunction in attention-deficit/hyperactivity disorder (ADHD) children during the Stroop color–word task, using a 24-channel NIRS instrument [24]. During the Stroop color–word task, they found that the oxy-Hb changes in the control group were significantly larger than those in the ADHD group in the inferior prefrontal cortex, especially in the inferior lateral prefrontal cortex bilaterally.

It is well known that the PFC play a central role in working memory, but it remains unknown whether the lateral area of prefrontal cortex (LPFC) of children of preschool age is responsible for working memory. To address this issue, Tsujimoto *et al.* applied optical topography to compare activity in the LPFC between adult subjects and preschool children [25]. The cognitive task is an item recognition test, which requires working memory, under different memory-load conditions. Areas and properties of such activity were similar in adults and preschool children. Data suggest that the LPFC of 5- and 6-year-old children is active during working memory processes; the LPFC has already developed processing of this important cognitive function.

Tsujii *et al*. also used a spatial item recognition working memory task to compare frontal cortical activation in children between 5 and 7 years old using an optical topography system [26]. Behavioral data confirmed that older children performed the working memory task more precisely and more rapidly than younger children. NIRS data showed that older children characterized right hemisphere dominance, but younger children had no significant hemispheric differences. Children with strengthened lateralization showed improved performance from 5 to 7 years old. This study suggests that the right lateralization for spatial working memory may start in children between 5 and 7 years old.

Schroeter *et al*. measured brain activation in the LPFC of children and adults with functional NIRS during an event-related, color–word matching Stroop task. In children, the Stroop task elicited significant brain activation in the left LPFC comparable to adults. The results reveal that brain activation due to Stroop interference increased with age in the DLPFC in correlation with an improvement in behavioral performance and the hemodynamic response occurred later in children than adults [27].

To compare the activity in the left LPFC, Zhang *et al*. employed multichannel cw-NIRS to monitor the concentration changes of rCBF in normal and dyslexic Chinese children, during phonological processing testing. The results show that the degree and the areas of the PFC activity are different between these two groups. During the phonological awareness section, the Δ[deoxy-Hb] in dyslexia-reading children was significantly higher than that in normal-reading children in the left VLPFC. In the phonological decoding section, both normal-reading and dyslexic children had more activity in the left VLPFC, but only normal-reading children had activity in the left mid-dorsal prefrontal cortex [28].

Herrmann *et al*. used multi-channel NIRS to compare the PFC activation between young and older subjects during a verbal fluency task [29]. The results clearly show that the memory test activated the left and right DLPFC with increases in HbO_2 and more localized decreases in deoxygenated hemoglobin (HHb), with an obvious left-hemispheric dominance. The elderly subjects generally exhibited less activation and no left hemispheric lateralization effect.

To study the neural activation regions associated with separable cognitive components of task, Cutini *et al*. used multichannel NIRS to measure brain cortical activity in a task-switching paradigm [30]. The results suggest that factors associated with load and maintenance of distinct stimulus–response mapping rules in working memory are likely contributors to the activation of the LPFC, whereas only activity in the left superior frontal gyrus can be linked unequivocally to switching between distinct cognitive tasks.

49.3
Long-Term Memory Modality

The application of functional neuroimaging techniques to human long-term memory (LTM) has created growing interest in the contribution of frontal lobe

function to these processes [31]. Compared with the working memory of maintaining information temporarily over periods of seconds, the long-term memory has the ability to retain information for much longer periods. Data analysis suggests that PFC activations during LTM tasks reflect control processes that aid and optimize memory encoding and retrieval, rather than more automatic storage processes. Most neuroimaging experiments for LTM study include two phases. One is the study phase, in which multiple stimuli are presented, with or without explicit instruction to remember the stimuli. The other is the test phase, during which these stimuli must be recalled, or recognized from among other stimuli. These studies allow a clear distinction between two types of LTM: semantic memory and episodic memory [15].

To examine the hemodynamic response of the PFC, Matsui *et al*. used a portable NIRS system and verbal learning in a words memory learning task [32]. The results show that [oxy-Hb] increased and [deoxy-Hb] decreased during the memory task. The relative change in [oxy-Hb] during encoding from the first to the second condition was significantly larger than that during retrieval. This study suggests that memory organization is facilitated during encoding of the first condition, and that the retrieval period through two conditions still involves more activation in the prefrontal area than the encoding period. For comparison of verbal and spatial memory effects in PFC, Li *et al*. used a multichannel cw-NIRS system to examine the hemodynamic response during stem recognition [33]. The experimental protocol comprised four test blocks, including verbal control, verbal memory, spatial control, and spatial memory. The results show that the left PFC has more significant hemodynamic changes of verbal memory than that of spatial memory. The oxygenation of spatial memory mainly increased in the middle and right PFC. Kubota *et al*. used a two-channel NIRS system and monitoring of PFC hemodynamics in real time, while subjects studied word lists and subsequently recognized unstudied items (false recognition) [34]. The results show that bilateral increases in the [oxy-Hb] were observed during false recognition compared with true recognition, and a left PFC dominant increase in [oxy-Hb] was observed during encoding phases where subjects later claimed that they recognized unstudied words. Reflected primarily in the left PFC activity, traces of semantic processing could eventually predict whether subjects falsely recognize nonexperienced events.

Yang *et al*. explored the role of the prefrontal cortex in semantic encoding of unrelated word pairs by using a cw-NIRS system [35]. The cognitive tasks of unrelated pairs of Chinese words under both nonsemantic and semantic encoding conditions were presented. Under the nonsemantic conditions, subjects judged whether the two words had similar orthographic structures; under the semantic condition, they generated a sentence involving the presented word pairs. The regions that corresponded to the PFC showed greater activation under semantic than nonsemantic conditions in both the left and right hemispheres, although the extent of the activation was larger in the left than right prefrontal regions. This result was consistent with other neuroimaging studies on unrelated word pairs processing, but did not conform to the strict interpretations of the hemispheric encoding/retrieval asymmetry model. This study suggests that material specificity

is one of the important factors to influence hemispheric asymmetry in memory encoding. Sanefuji *et al.* examined the correlation between old/new effects and task performance during the recognition judgments about old (studied) or new (unstudied) meaningless shapes, by using event-related NIRS [36]. The data show that lateralization of the VLPFC old/new effects may also depend on the type of stimulus and the VLPFC could be associated with retrieval success.

In summary, we have reviewed the NIRS studies for PFC activation of both working memory and long-term memory with different stimulus protocols. As one of the indirect approaches, NIRS has the advantages of simple monitoring of the PFC and easily coupling with other measurements, either direct or indirect methods.

References

1 Pechura, C.M. and Martin, J.B. (eds.) (1991) *Mapping the Brain and Its Functions: Integrating Enabling Technologies into Neuroscience Research*, National Academies Press, Washington, DC.

2 Wilson, R.A. and Keil, F.C. (eds.) (1999) *The MIT Encyclopedia of the Cognitive Sciences*, MIT Press, Cambridge, MA.

3 Fuster, J.M. (2001) The prefrontal cortex – an update: time is of the essence. *Neuron*, **30**, 319–333.

4 Strangman, G., Boas, D.A., and Sutton, J.P. (2002) Non-invasive neuroimaging using near-infrared light. *Biol. Psychiatry*, **52**, 679–693.

5 Miller, E.K. and Cohen, J.D. (2001) An integrative theory of prefrontal cortex function. *Annu. Rev. Neurosci.*, **24**, 167–202.

6 Jöbsis, F.F. (1977) Noninvasive infrared monitoring of cerebral and myocardial oxygen sufficiency and circulatory parameters. *Science*, **198**, 1264–1267.

7 Chance, B., Leigh, J.S., Miyake, H. *et al.* (1988) Comparison of time-resolved and -unresolved measurements of deoxyhemoglobin in brain. *Proc. Natl. Acad. Sci. U. S. A.*, **88**, 4971–4975.

8 Hoshi, Y. (2003) Functional near-infrared optical imaging: utility and limitations in human brain mapping. *Psychophysiology*, **40**, 511–520.

9 Wolf, M., Ferrari, M., and Quaresima, V. (2007) Progress of near-infrared spectroscopy and topography for brain and muscle clinical applications. *J. Biomed. Opt.*, **12** (6), 062104–062114.

10 Izzetoglu, M., Izzetoglu, K., Bunce, S. *et al.* (2005) Functional near-infrared neuroimaging. *IEEE Trans. Neural Syst. Rehabil. Eng.*, **13** (2), 153–159.

11 Chance, B., Luo, Q., Nioka, S. *et al.* (1997) Optical investigations of physiology: a study of intrinsic and extrinsic biomedical contrast. *Philos. Trans. R. Soc. Lond. B Biol. Sci.*, **352**, 707–716.

12 Villringer, A. and Chance, B. (1997) Non-invasive optical spectroscopy and imaging of human brain function. *Trends Neurosci.*, **20** (10), 435–442.

13 Baddeley, A. (2003) Working memory: looking back and looking forward. *Nat. Rev. Neurosci.*, **4**, 829–839.

14 Hoshi, Y., Oda, I., Wada, Y. *et al.* (2000) Visuospatial imagery is a fruitful strategy for the digit span backward task: a study with near-infrared optical tomography. *Brain Res. Cogn. Brain Res.*, **9**, 339–342.

15 Fletcher, P.C. and Henson, R.N.A. (2001) Frontal lobes and human memory: insights from functional neuroimaging. *Brain*, **124**, 849–881.

16 Li, C., Gong, H., Zeng, S. *et al.* (2005) Verbal working memory load affects prefrontal cortices activation: evidence from a functional NIRS study in humans. *Proc. SPIE*, **5696**, 33–40.

17 Lv, X., Zheng, Y., Li, T. *et al.* (2008) A portable functional imaging instrument for psychology research based on near-infrared spectroscopy. *Frontiers Optoelectron. China*, **1** (3–4), 279–284.

18 Li, T., Luo, Q., and Gong, H. (2010) Gender-specific hemodynamics in prefrontal cortex during a verbal working memory task by near-infrared spectroscopy. *Behav. Brain Res.*, **209**, 148–153.

19 Hoshi, Y. (2003) Functional near-infrared optical imaging: utility and limitations in human brain mapping. *Psychophysiology*, **40**, 511–520.

20 Hoshi, Y., Tsou, B.H., Billock, V.A. *et al.* (2003) Spatiotemporal characteristics of hemodynamic changes in the human lateral prefrontal cortex during working memory tasks. *Neuroimage*, **20**, 1493–1504.

21 Schreppel, T., Egetemeir, J., Schecklmann, M. *et al.* (2008) Activation of the prefrontal cortex in working memory and interference resolution processes assessed with near-infrared spectroscopy. *Neuropsychobiology*, **57** (4), 188–193.

22 Zhai, J., Li, T., Zhang, Z., and Gong, H. (2009) Hemodynamic and electrophysiological signals of conflict processing in the Chinese-character Stroop task: a simultaneous near-infrared spectroscopy and event-related potential study. *J. Biomed. Opt.*, **14** (5), 054022.

23 Leon-Carrion, J., Damas-Lopez, J., and Martin-Rodriguez, J.F. (2008) The hemodynamics of cognitive control: the level of concentration of oxygenated hemoglobin in the superior prefrontal cortex varies as a function of performance in a modified Stroop task. *Behav. Brain Res.*, **193** (2), 248–256.

24 Negoro, H., Sawada, M., Iida, J. *et al.* (2010) Prefrontal dysfunction in attention-deficit/hyperactivity disorder as measured by near-infrared spectroscopy. *Child Psychiatry Hum. Dev.*, **41** (2), 193–203.

25 Tsujimoto, S., Yamamoto, T., Kawaguchi, H. *et al.* (2004) Prefrontal cortical activation associated with working memory in adults and preschool children: an event-related optical topography study. *Cereb. Cortex*, **14** (7), 703–712.

26 Tsujii, T., Yamamoto, E., Masuda, S. *et al.* (2009) Longitudinal study of spatial working memory development in young children. *Neuroreport*, **20** (8), 759–763.

27 Schroeter, M.L., Zysset, S., Wahl, M. *et al.* (2004) Prefrontal activation due to Stroop interference increases during development: an event-related fNIRS study. *Neuroimage*, **23** (4), 1317–1325.

28 Zhang, Z., Li, T., Zheng, Y. *et al.* (2006) Study the left prefrontal cortex activity of Chinese children with dyslexia in phonological processing by NIRS. *Proc. SPIE*, **6078**, 607833.

29 Herrmann, M.J., Walter, A., Ehlis, A.C. *et al.* (2006) Cerebral oxygenation changes in the prefrontal cortex: effects of age and gender. *Neurobiol. Aging*, **27**, 888–894.

30 Cutini, S., Scatturin, P., Menon, E. *et al.* (2008) Selective activation of the superior frontal gyrus in task-switching: an event-related fNIRS study. *Neuroimage*, **42** (2), 945–955.

31 Frackowiak, R.S.J., Friston, K.J., Frith, C. *et al.* (eds.) (2004) *Human Brain Function*, Elsevier, Amsterdam.

32 Matsui, M., Tanaka, K., Yonezawa, M. *et al.* (2007) Activation of the prefrontal cortex during memory learning: near-infrared spectroscopy study. *Psychiatry Clin. Neurosci.*, **61**, 31–38.

33 Li, T., Li, L., Luo, Q. *et al.* (2009) Assessing working memory in real-life situations with functional near-infrared spectroscopy. *J. Innov. Opt. Health Sci.*, **2** (4), 423–430.

34 Kubota, Y., Toichi, M., Shimizu, M. *et al.* (2006) Prefrontal hemodynamic activity predicts false memory: a near-infrared spectroscopy study. *Neuroimage*, **31**, 1783–1789.

35 Yang, J., Zeng, S., Luo, Q. *et al.* (2005) Hemispheric asymmetry for encoding unrelated word pairs? A functional near-infrared spectroscopy study. *Space Med. Med. Eng.*, **18** (5), 318–323.

36 Sanefuji, M., Nakashima, T., Kira, R. *et al.* (2007) The relationship between retrieval success and task performance during the recognition of meaningless shapes: an event-related near-infrared spectroscopy study. *Neurosci. Res.*, **59**, 191–198.

37 Gong, H., Li, C., Li, T. *et al.* (2007) Near infrared Optical imaging of prefrontal cortex for working memory. *Sci China Ser G*, **37** (51), 110–117.

50
Cerebral Blood Flow and Oxygenation

Andrew K. Dunn

50.1
Introduction

The hemodynamic state of the brain, including blood flow and oxygenation, is critical for maintaining normal brain function. In diseases such as stroke, blood flow is disrupted, leading to inadequate oxygen supply which results in a cascade of harmful events [1]. Many stroke therapies currently under development target the cerebral vasculature. Therefore, techniques for monitoring blood flow and oxygen levels in the brain with good spatial resolution are essential for evaluating the efficacy of these new treatments. Optical methods are particularly well suited for imaging hemodynamic parameters *in vivo* because exogenous contrast agents are not required for most techniques. Optical methods have been applied to the brain at multiple spatial scales ranging from optical microscopy at the micron scale to noninvasive diffuse optical tomography at the centimeter length scale [2]. In this chapter, we focus specifically on three different optical methods for quantifying hemodynamics on the surface of the cortex in preclinical animal models: laser speckle contrast imaging of blood flow, multispectral reflectance imaging of hemoglobin oxygenation and volume, and phosphorescence quenching for pO_2 mapping using a digital micromirror device.

50.2
Laser Speckle Contrast Imaging of Cerebral Blood Flow

Laser Doppler flowmetry has been used extensively for *in vivo* monitoring of cerebral blood flow (CBF) at a single spatial location in animals under a variety of physiologic conditions. Although laser Doppler flowmetry provides high temporal resolution (millisecond) measurement of relative CBF, the lack of any spatial information is a significant limitation. Scanning laser Doppler can be used to provide some spatial information [3], but is limited in both its spatial and temporal resolutions, since the spatial information is typically obtained at the expense of temporal resolution due to the need for scanning [4–6].

Handbook of Biophotonics. Vol.2: Photonics for Health Care, First Edition. Edited by Jürgen Popp, Valery V. Tuchin, Arthur Chiou, and Stefan Heinemann.

Over the past several years, laser speckle contrast imaging has emerged as a powerful tool for imaging CBF changes with high spatial resolution [7–9]. Speckle imaging is a full-field imaging technique that utilizes a charge-coupled device (CCD) camera, does not require any scanning components or tissue contact, and provides millisecond temporal and tens of microns spatial resolution [9–12]. Therefore, speckle contrast imaging is a relatively simple technique for obtaining the detailed spatiotemporal dynamics of CBF changes.

The basic concept of speckle contrast imaging is straightforward. When the cortex is illuminated with coherent laser light and the reflected light is imaged on to a camera, a dynamic speckle pattern (Figure 50.1) is produced. Because some of the scattering particles are in motion (i.e., blood cells), the speckle pattern fluctuates in time. When the exposure time of the camera (5–10 ms) is longer than the time scale of the speckle intensity fluctuations (typically <1 ms), the camera integrates the intensity variations resulting in blurring of the speckle pattern. In areas of increased motion there is more blurring of the speckles during the camera exposure, resulting in a lower spatial contrast of the speckles in these areas.

Since the motion of the scattering particles (i.e., blood flow) is encoded in the dynamics of the speckle pattern, a measure of blood flow can be obtained by quantifying the spatial blurring of the speckle pattern. This is accomplished by calculating the local speckle contrast (K), defined as the ratio of the standard deviation, σ_s, to the mean intensity of pixel values, $\langle I \rangle$, in a small region of the image [11]:

$$K = \frac{\sigma_s}{\langle I \rangle} \tag{50.1}$$

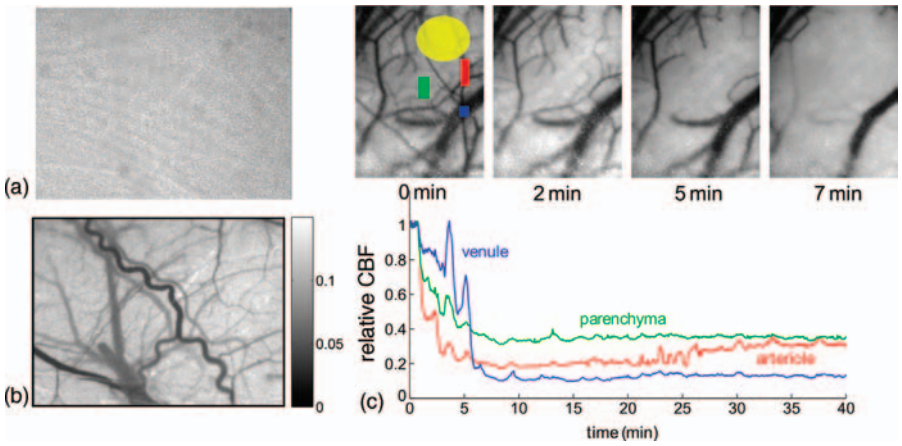

Figure 50.1 Example of raw speckle image (a) and the corresponding speckle contrast image (b) calculated with Eq. (50.1). The gray levels in the speckle contrast image are inversely related to blood flow. The field of view is ~4 mm. (c) Images show changes in speckle contrast following local activation of photothrombosis (green shaded region). The time course of the CBF changes in three regions reveals a significant drop in CBF as vessels are occluded.

A typical example of a raw speckle image of the rat cortex, taken through a thinned skull, and the computed speckle contrast are shown in Figure 50.1a and b. The raw speckle image illustrates the grainy appearance of the speckle pattern. The speckle contrast image, computed directly from the raw speckle image using the Eq. (50.1), represents a two-dimensional map of blood flow. Areas of higher baseline flow, such as large vessels, have lower speckle contrast values and appear darker in the speckle contrast images.

Laser speckle contrast imaging has been widely used to investigate the CBF changes during ischemia in animal models. Figure 50.1c illustrates the speckle contrast and CBF changes in the cortex during photothrombotic stroke in a rat. The series of speckle contrast images illustrates that as the clot is formed, the speckle contrast values decrease and the vessels seem to disappear from the images. This apparent disappearance occurs because the flow in those vessels is greatly reduced and therefore the speckle contrast values increase. The plots show the time course of the actual CBF changes in three particular regions of interest and also highlight the importance of spatially resolved CBF measurements, something that is not possible with traditional laser Doppler flowmetry.

50.3
Multispectral Reflectance Imaging of Hemoglobin Oxygenation

In addition to imaging of CBF changes, optical techniques can be used to determine the changes in hemoglobin oxygenation. Optical imaging of intrinsic signals (OIS) is based on the fact that perfusion related changes lead to changes in the reflectance of the cortical tissue due to hemoglobin absorption. In most OIS measurements, the cortical surface is exposed and illuminated with narrowband ($\sim$10 nm) visible light. OIS has provided numerous insights into the functional organization of the cortex in a number of animal models [13–15].

Despite the success of OIS in revealing detailed changes in the cortex, single-wavelength OIS techniques are unable to quantify the changes in hemoglobin oxygenation and volume. Recently, there has been growing interest in the quantitative determination of the hemodynamic changes within the cortex, such as changes in concentrations of HbO, HbR, and total hemoglobin (HbT). However, full-field imaging of these parameters has been challenging owing to the need to obtain images at a minimum of two wavelengths. Acquisition of this spectroscopic information has been achieved by sacrificing spatial information [16, 17]. These approaches have enabled the temporal dynamics of hemoglobin volume and oxygenation to be studied during functional activation in animal models [18, 19]. However, a major limitation of these techniques is the need to sacrifice spatial information in order to obtain spectroscopic information. To overcome this limitation, we have developed a spectroscopic imaging method that permits full-field imaging of reflectance changes from the cortex at multiple wavelengths by rapid switching of the illumination wavelength using a continuously moving filter wheel [20, 21]. This technique allows quantitative imaging of the concentration

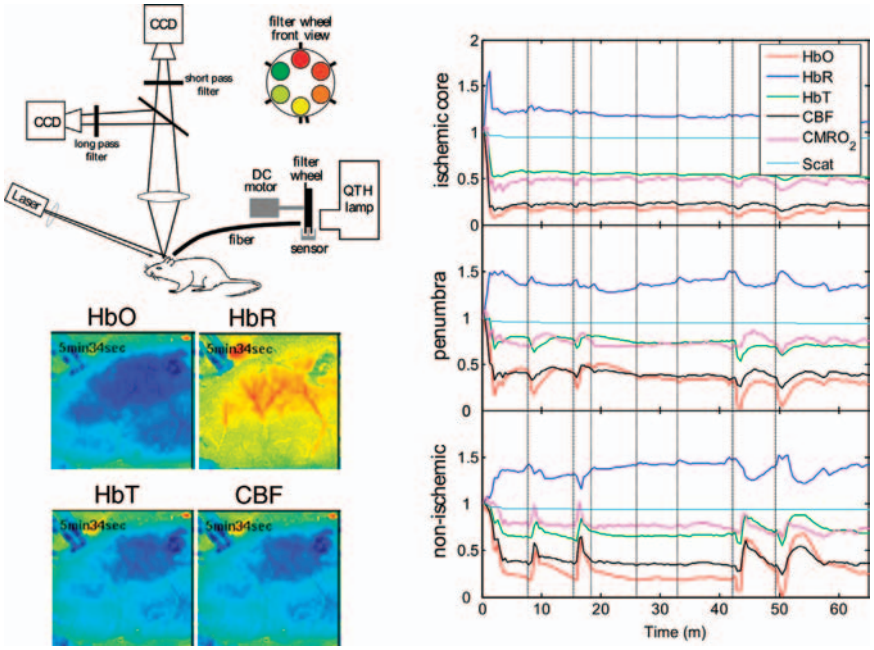

Figure 50.2 Combined laser speckle imaging of CBF and multispectral imaging of hemoglobin oxygenation and saturation. The images demonstrate the spatial changes in each parameter 5 min after stroke induction in a mouse model, and the time courses reveal a complex set of hemodynamic changes that vary depending on the location within the ischemic territory [22].

changes in HbO, HbR, and HbT with the same spatial and temporal resolution as traditional OIS.

Figure 50.2 illustrates how multispectral reflectance imaging (MSRI) can be combined with speckle imaging of CBF to permit simultaneous imaging of CBF, HbO, HbR, and HbT. The multispectral imaging consists of sequential acquisition of reflectance images at illumination wavelengths in the range 560–630 nm. Each set of spectral images is converted to maps of changes in HbO, HbR, and HbT using an appropriate model [20–22]. The images and plots in Figure 50.2 show the spatial and temporal dynamic of the CBF and hemoglobin changes in a mouse model of focal ischemia [22].

50.4 Imaging of pO_2 with Phosphorescence Quenching

In vivo measurement of dissolved oxygen (pO_2) has been accomplished using several different methods, including oxygen-sensitive electrodes, oxygen-dependent phosphorescence quenching, and electron paramagnetic resonance [23]. Oxygen-sensitive

electrodes can provide pO_2 measurements from small tissue volumes (a few μm^3) due to the small size of many electrodes, but suffer from the fact that they are single-point measurements and they are invasive and can lead to tissue damage. Determination of pO_2 using phosphorescence quenching has been shown to be highly effective for *in vivo* measurements due to recent advances in imaging technology and probe design [24–28]. This method is based on the fact that dissolved oxygen quenches the phosphorescence or fluorescence of certain compounds such as porphyrin dyes and ruthenium complexes, resulting in changes in excited-state lifetimes [29]. As a result, the pO_2 can be quantified from the measured lifetime [30] using the Stern–Volmer relationship:

$$\frac{\tau_0}{\tau} = 1 + k_q \tau_0 [pO_2] \tag{50.2}$$

where τ is the measured lifetime, τ_0 is the unquenched lifetime, and k_q is a quenching constant that depends on the properties of the dye and the surrounding environment. Therefore, absolute oxygenation can be quantified from the measured decay time provided that the quenching constant and unquenched lifetime are known. In addition, lifetime-based measurements are not dependent on absolute intensities [29], which eliminates the need to correct for the presence of other tissue chromophores or tissue scattering.

Despite their widespread use, phosphorescence quenching methods are almost always limited to a single spatial location and only a few reports have demonstrated pO_2 imaging or spatial mapping [31–34]. This limitation arises from the need to resolve the phosphorescence lifetime, which makes most cameras extremely difficult to use. Single-point detectors such as avalanche photodiodes and photomultiplier tubes are significantly more sensitive and have sufficient temporal resolution to resolve the phosphorescence decay times.

In order to obtain spatially resolved pO_2 measurements, we have utilized a digital micromirror device (DMD) combined with a sensitive single-element detector such as a photomultiplier or avalanche photodiode [35]. This approach retains the high sensitivity of single-element detectors while still permitting spatially resolved phosphorescence decay measurements (Figure 50.3). A speckle contrast image is first obtained, and several regions of interest are selected from the image of the surface vasculature. Each region is transformed to the DMD coordinates and the appropriate mirrors of the DMD are turned on to restrict the pulsed phosphorescence excitation light to this region. The entire phosphorescence emission from that region is collected by the detector and the decay time is determined and converted to a pO_2 value. The entire system is controlled by custom software and the DMD switches illumination regions at approximately 10 regions per second.

An example of the use of this system in a rodent stroke model is illustrated in Figure 50.3d–f. In this example, eight spatial regions were selected for pO_2 measurement. The CBF (Figure 50.3e) and pO_2 (Figure 50.3f) time courses over the eight regions demonstrate that the changes in these two parameters during the course of ischemia differ, particularly in branches of the arteriole. In particular, the CBF drop is larger than the corresponding decrease in pO_2. This example illustrates the great

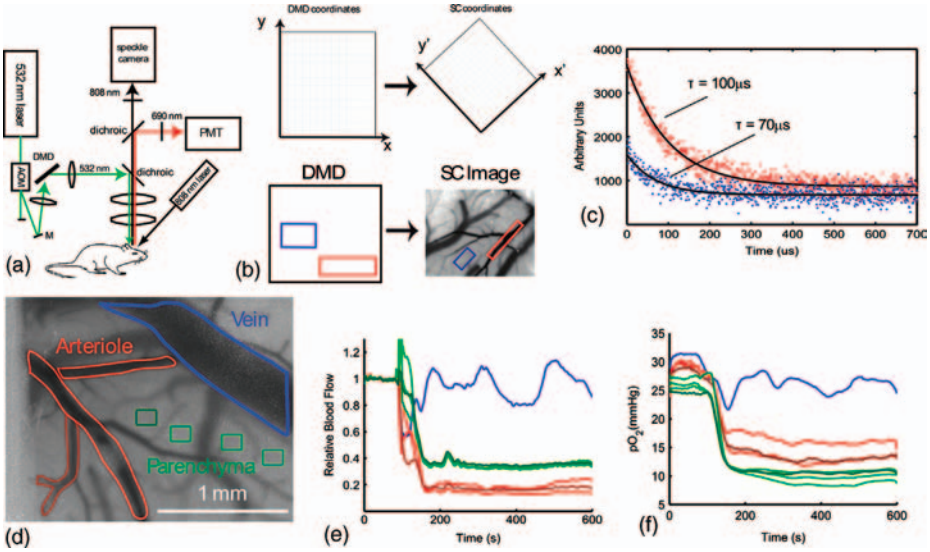

Figure 50.3 (a, b) Combined instrument for simultaneous imaging of CBF and spatial mapping of pO_2. Spatially resolved pO_2 is obtained by spatially restricting phosphorescence excitation light and utilizing a single-element detector to record time-resolved phosphorescence decays (c). (d–f) Measured temporal dynamics of CBF and pO_2 changes in eight different spatial regions following ischemia induction (at $t = 100$ s).

potential of combined optical imaging instruments for revealing the subtleties of hemodynamic changes in the cortex during cerebrovascular pathologies.

References

1 Lo, E.H., Dalkara, T., and Moskowitz, M.A. (2003) Mechanisms, challenges and opportunities in stroke. *Nat. Rev. Neurosci.*, **4** (5), 399–415.

2 Hillman, E.M.C. (2007) Optical brain imaging *in vivo*: techniques and applications from animal to man. *J. Biomed. Opt.*, **12** (5), 051402.

3 Wardell, K., Jakobsson, A., and Nilsson, G.E. (1993) Laser Doppler perfusion imaging by dynamic light scattering. *IEEE Trans. Biomed. Eng.*, **40** (4), 309–316.

4 Ances, B.M., Greenberg, J.H., and Detre, J.A. (1999) Laser Doppler imaging of activation-flow coupling in the rat somatosensory cortex. *Neuroimage*, **10** (6), 716–723.

5 Nielsen, A.N., Fabricius, M., and Lauritzen, M. (2000) Scanning laser-Doppler flowmetry of rat cerebral circulation during cortical spreading depression. *J. Vasc. Res.*, **37** (6), 513–522.

6 Serov, A., Steinacher, B., and Lasser, T. (2005) Full-field laser Doppler perfusion imaging and monitoring with an intelligent CMOS camera. *Opt. Express*, **13**, 3681–3689.

7 Dunn, A.K., Bolay, H., Moskowitz, M.A., and Boas, D.A. (2001) Dynamic imaging of cerebral blood flow using laser speckle. *J. Cereb. Blood Flow Metab.*, **21** (3), 195–201.

8 Boas, D.A. and Dunn, A.K. (2010) Laser speckle contrast imaging in biomedical optics. *J. Biomed. Opt.*, **15** (1), 011109.

9 Briers, J.D. (2001) Laser Doppler, speckle and related techniques for blood perfusion mapping and imaging. *Physiol. Meas.*, **22** (4), R35–R36.

10 Briers, J.D., Richards, G., and He, X. (1999) Capillary blood flow monitoring using laser speckle contrast analysis. *J. Biomed. Opt.*, **4**, 164–175.

11 Briers, J.D. and Webster, S. (1996) Laser Speckle contrast analysis (LASCA): a nonscanning, full-field technique for monitoring capillary blood flow. *J. Biomed. Opt.*, **1**, 174–179.

12 Fercher, A. and Briers, J. (1981) Flow visualization by means of single-exposure speckle photography. *Opt. Commun.*, **37**, 326–329.

13 Grinvald, A., Lieke, E., Frostig, R., Gilbert, C., and Wiesel, T. (1986) Functional architecture of cortex revealed by optical imaging of intrinsic signals. *Nature*, **324**, 361–364.

14 Grinvald, A., Frostig, R., Siegel, R., and Bartfeld, E. (1991) High resolution optical imaging of neuronal activity in the awake mokey. *Proc. Natl. Acad. Sci. U. S. A.*, **88**, 11559–11563.

15 Masino, S. and Frostig, R. (1996) Quantitative long-term imaging of the functional representation of a whisker in rat barrel cortex. *Proc. Natl. Acad. Sci. U. S. A.*, **93**, 4942–4947.

16 Malonek, D. and Grinvald, A. (1996) Interactions between electrical activity and cortical microcirculation revealed by imaging spectroscopy: implications for functional brain mapping. *Science*, **272** (5261), 551–554.

17 Kohl, M., Lindauer, U., Royl, G., Kuhl, M., Gold, L., Villringer, A., and Dirnagl, U. (2000) Physical model for the spectroscopic analysis of cortical intrinsic optical signals. *Phys. Med. Biol.*, **45** (12), 3749–3764.

18 Mayhew, J., Johnston, D., Martindale, J., Jones, M., Berwick, J., and Zheng, Y. (2001) Increased oxygen consumption following activation of brain: theoretical footnotes using spectroscopic data from barrel cortex. *Neuroimage*, **13** (6 Pt 1), 975–987.

19 Jones, M., Berwick, J., Johnston, D., and Mayhew, J. (2001) Concurrent optical imaging spectroscopy and laser-Doppler flowmetry: the relationship between blood flow, oxygenation, and volume in rodent barrel cortex. *Neuroimage*, **13** (6 Pt 1), 1002–1015.

20 Dunn, A.K., Devor, A., Bolay, H., Andermann, M.L., Moskowitz, M.A., Dale, A.M., and Boas, D. (2003) Simultaneous imaging of total cerebral hemoglobin concentration, oxygenation, and blood flow during functional activation. *Opt. Lett.*, **28**, 28–30.

21 Dunn, A.K., Devor, A., Dale, A.M., and Boas, D.A. (2005) Spatial extent of oxygen metabolism and hemodynamic changes during functional activation of the rat somatosensory cortex. *Neuroimage*, **27** (2), 279–290.

22 Jones, P.B., Shin, H.K., Boas, D.A., Hyman, B.T., Moskowitz, M.A., Ayata, C., and Dunn, A.K. (2008) Simultaneous multispectral reflectance imaging and laser speckle flowmetry of cerebral blood flow and oxygen metabolism in focal cerebral ischemia. *J. Biomed. Opt.*, **13** (4), 44007–44011.

23 Tsai, A., Johnson, P.C., and Intaglietta, M. (2003) Oxygen gradients in the microcirculation. *Physiol. Rev.*, **83** (3), 933–963.

24 Wilson, D.F., Rumsey, W.L., Green, T.J., and Vanderkooi, J.M. (1988) The oxygen dependence of mitochondrial oxidative phosphorylation measured by a new optical method for measuring oxygen concentration. *J. Biol. Chem.*, **263** (6), 2712–2718.

25 Shonat, R.D., Wilson, D.F., Riva, C.E., and Pawlowski, M. (1992) Oxygen distribution in the retinal and choroidal vessels of the cat as measured by a new phosphorescence imaging method. *Appl. Opt.*, **31** (19), 3711–3718.

26 Shonat, R.D., Richmond, K.N., and Johnson, P.C. (1995) Phosphorescence quenching and the microcirculation: an automated, multipoint oxygen tension measuring instrument. *Rev. Sci. Instrum.*, **66**, 5075–5084.

27 Vinogradov, S.A., Fernandez-Searra, M., Dugan, B.W., and Wilson, D.F. (2001) Frequency domain instrument for measuring phosphorescence lifetime

distributions in heterogeneous samples. *Rev. Sci. Instrum.*, **7** (8), 3396–3406.

28 Dunphy, I., Vinogradov, S.A., and Wilson, D.F. (2002) Oxyphor R2 and G2: phosphors for measuring oxygen by oxygen-dependent quenching of phosphorescence. *Anal. Biochem.*, **310** (2), 191–198.

29 Lakowicz, J.R. (2006) *Principles of Fluorescence Spectroscopy*, Springer, New York.

30 Vanderkooi, J.M., Maniara, G., Green, T.J., and Wilson, D.F. (1987) An optical method for measurement of dioxygen concentration based upon quenching of phosphorescence. *J. Biol. Chem.*, **262** (12), 5476–5482.

31 Shonat, R.D. and Kight, A.C. (2003) Oxygen tension imaging in the mouse retina. *Ann. Biomed. Eng.*, **31** (9), 1084–1096.

32 Shonat, R.D., Wachman, E.S., Niu, W., Koretsky, A.P., and Farkas, D.L. (1997) Near-simultaneous hemoglobin saturation and oxygen tension maps in mouse brain using an AOTF microscope. *Biophys. J.*, **73** (3), 1223–1231.

33 Helmlinger, G., Yuan, F., Dellian, M., and Jain, R.K. (1997) Interstitial pH and pO_2 gradients in solid tumors *in vivo*: high-resolution measurements reveal a lack of correlation. *Nat. Med.*, **3** (2), 177–182.

34 Sakadzić, S., Yuan, S., Dilekoz, E., Ruvinskaya, S., Vinogradov, S.A., Ayata, C., and Boas, D.A. (2009) Simultaneous imaging of cerebral partial pressure of oxygen and blood flow during functional activation and cortical spreading depression. *Appl. Opt.*, **48** (10), D169–D177.

35 Ponticorvo, A. and Dunn, A.K. (2010) Simultaneous imaging of oxygen tension and blood flow in animals using a digital micromirror device. *Opt. Express*, **18** (8), 8160–8170.

51
Skin Diagnostics

Martin Kaatz, Susaane Lange-Asschenfeldt, Joachim Fluhr, and Johannes Martin Köhler

51.1
Introduction

With an overall size of approximately 2 m^2 human skin is considered the largest organ of the human body and is exposed to the environment. Due to this unique position, the skin and its appendages are susceptible to a great variety of physical, biological, and chemical influences. Owing to its specific features, however, it is able to protect us effectively from many of these influences and to ensure the organism's integrity.

Nevertheless, a considerable number of diseases are manifest on the skin, which may be limited to the skin but may also affect other organ systems. On the other hand, a number of visceral diseases present with cutaneous symptoms, often providing characteristic hints at their true origin. Also, stress factors or emotional challenges may trigger the onset of a skin disease or contribute to its worsening, making the skin a potential reflector of emotional imbalance.

Human skin is easily accessible to clinical evaluation, and also to analysis by invasive and noninvasive examination methods. In recent years, a number of noninvasive *in vivo* diagnostic devices have been developed for the evaluation of skin lesions. This is partly due to the fact that the incidence of many dermatoses, skin cancer in particular, is increasing considerably, thus prompting the need for adjunct diagnostic devices to ensure early diagnosis and treatment. By means of biophotonics, light may be used for diagnosis and therapy of skin diseases. This chapter provides an overview of possible applications of biophotonics in clinical and investigational dermatology.

51.2
Dermoscopy

51.2.1
Technical Principle and Development

Dermoscopy or epiluminescence microscopy is a noninvasive technique for the *in vivo* evaluation and differential diagnosis of skin lesions. It is mainly used as a

Handbook of Biophotonics. Vol.2: Photonics for Health Care, First Edition. Edited by Jürgen Popp, Valery V. Tuchin, Arthur Chiou, and Stefan Heinemann.

hand-held device with light-emitting diodes (LEDs) as internal light source. The objective requires optical coupling with the skin surface by oil, water, or gel in order to achieve translucency of the stratum corneum. Recently developed models use polarized light that permit its use without direct contact with the skin. The combination with digital cameras and computer systems allows not only efficient image analysis and documentation but also software-assisted evaluation of the skin lesions. Furthermore, resolution and magnification can be increased (10–60-fold), thus improving the visualization of dermoscopic criteria.

51.2.2 Applications

51.2.2.1 Pigmented Skin Lesions

Dermoscopy is an important examination method for differentiation between melanocytic (Figure 51.1 and 51.2) and nonmelanocytic skin lesions [1]. Also, the status of many tumors can be evaluated more specifically and more sensitively than by visual inspection alone [2]. The application of digital image acquisition systems allows the storage of additional information of examined lesions for re-evaluation and comparison of follow-up pictures. This facilitates longitudinal monitoring for patients at high risk for skin cancer and allows the early identification of malignant melanomas that do not display sure signs of dysplasia upon initial evaluation.

Chapter 53 provides detailed information on the dermoscopic features.

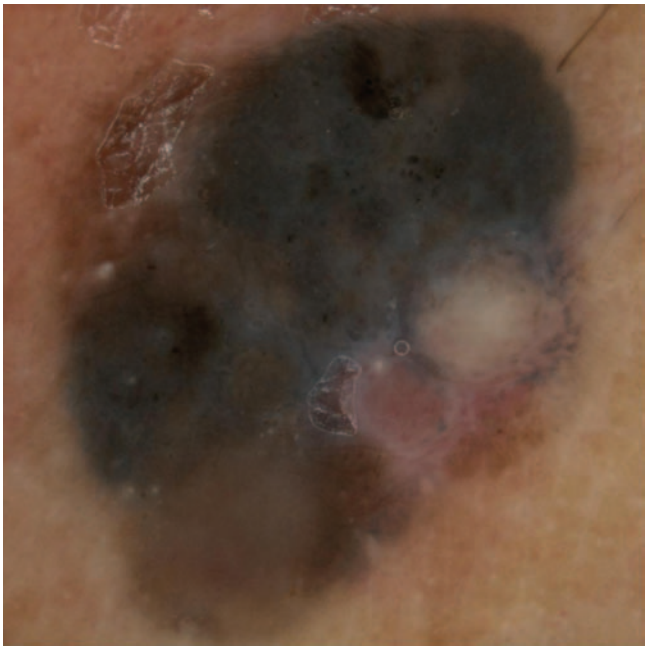

Figure 51.1 Dermatoscopy of a melanoma.

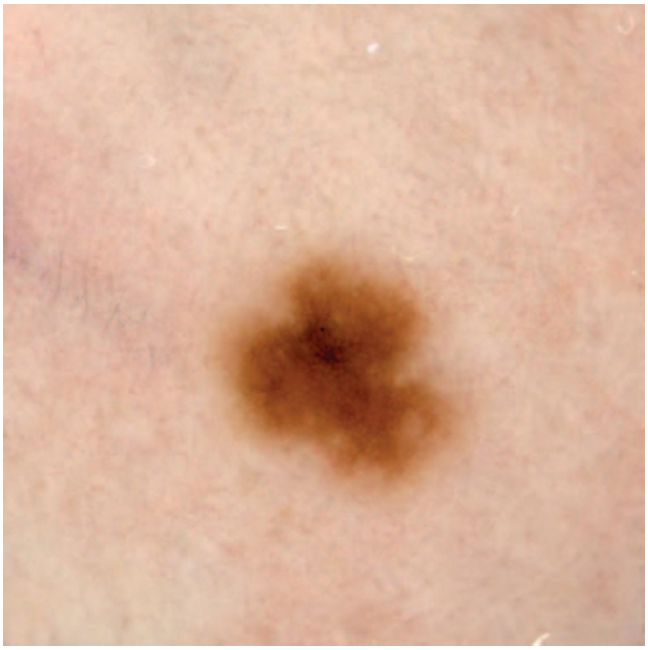

Figure 51.2 Dermatoscopy of a melanocytic nevus.

In addition, dermoscopic criteria that need to be considered in differential diagnosis have been described for other pigmented skin lesions.

Among them, *seborrheic keratoses* are characterized by multiple milia-like cysts, comedo-like openings, light-brown fingerprint-like structures, and/or a cerebriform pattern [1].

Pigmented basal cell carcinomas are diagnosed by characteristic features such as arborizing vessels, leaf-like structures, large blue–gray ovoid nests, multiple blue–gray globules, spoke-wheel areas, and ulceration [3].

The essential dermoscopic features of *pigmented actinic keratoses*, which may be difficult to distinguish from lentigo maligna, are an annular–granular pattern, rhomboidal structures, pseudo-network, black globules, slate-gray globules, black dots, asymmetric pigmented follicular openings, a hyperpigmented rim of follicular openings, and slate-gray areas and streaks.

A clinical discrimination of solar Lentigo from Lentigo maligna is often impossible. The consideration of dermoscopic criteria, however, may help with the differentiation. Important diagnostic features are comedo-like openings, diffuse opaque-brown pigmentation, light-brown fingerprint-like structures, and milia-like cysts [4].

Red–blue lacunae or homogeneous areas are indicators for *benign vascular lesions* such as *cherry angiomas* or *venous malformations*.

51.2.2.2 **Non-Pigmented Skin Lesions**

Dermoscopy is also able to improve diagnostic accuracy in the examination of non-melanoma skin cancer and nontumorous, particularly vascular, lesions.

For nonpigmented skin disease, the vascular structures are of primary importance. A three-step algorithm has recently been proposed [5]. The first step comprises the

assessment of the morphology of vascular patterns, described as linear curved (comma), dotted (globules), linear irregular, linear looped (hairpin), linear coiled (glomerular), or linear serpentine (arborizing), and three specific global patterns: crown, strawberry, and clods. In the second step, the vascular architecture is categorized. The vessel arrangement may be regular, in strings, in clusters, radial, branched, or irregular. The third step consists in the assessment of additional criteria such as duct openings, surface scales, ulcerations, and others. The diagnosis is made based on the combination of the features assessed in the three-step algorithm. For a variety of nonpigmented skin tumors, evidence-based diagnosis and management recommendations have been proposed [5].

Dermoscopic criteria for a broad range of inflammatory and nonpigmented neoplastic skin lesions have been summarized previously [3]. However, in most cases the diagnostic value has not been investigated in larger studies, but only in case reports and smaller case series. However, a number of specific dermoscopic criteria have been defined for some inflammatory diseases, for example, lichen planus, which shows whitish lines in a reticular distribution (corresponding to Wickham striae). Mature lesions also display additional radial capillaries intermingled with the reticular striae. In regressive lesions, the vascular component disappears and gray–blue dots with or without reticular striae become visible.

Dermoscopy may also aid in the diagnosis of contagious skin diseases, including scabies, larva migrans, and tungiasis [3].

A special indication for dermoscopy is the microscopic evaluation of the nailfold capillaries. Here, dermoscopy is used as a capillaroscopic instrument mainly in autoimmune diseases, where characteristic vascular changes may already be detected in early stages [6].

Chapter 52 provides supplementary information on the dermoscopy of nonmelanoma skin cancer.

51.2.3 Conclusion

The advantages of dermoscopy in clinical practice are its time-effective and cost-effective use, an improvement in diagnostic accuracy compared with clinical examination alone, and a moderate training effort. Disadvantages – compared with the (invasive) gold standard histology – are the low magnification and the restriction to mainly superficial skin layers.

51.3 Optical Coherence Tomography (OCT)

51.3.1 Technical Principle and Development

Optical coherence tomography (OCT) as a diagnostic tool was first presented by Huang *et al.* [7]. It is based on the principle of Michelson interferometry using light of

short coherence length. In this process, a light beam is directed into the piece of tissue under examination. The optical pathlength distribution of the sample beam measured by the interference modulation of the axial OCT scan can be interpreted as the depth-resolved reflection signal of the sample. Interference occurs only when the propagation distance of both beams match within the coherence length of the light source. This coherence length also determines the vertical resolution of the system [7].

51.3.2 Applications

In ophthalmology, OCT has been implemented in clinical routine diagnostics for the evaluation of cornea, lens, and corpus vitreum. As early as in the 1990s, however, first studies on cutaneous tissue were performed whereby hyperkeratosis, epidermis, and dermis could be differentiated [8]. In the following years, the value of OCT has been investigated for the diagnosis of a broad range of skin disorders.

51.3.2.1 Skin Tumors

The continuously improving resolution of OCT allowed the examination of both pigmented and nonpigmented skin tumors. At the same time, the penetration depth was measured and compared with histology and high-resolution sonography. Detailed results are given in Chapter 52 (Figures 51.1 and 51.2) Chapter 53 (Figures 53.3 and 53.4).

51.3.2.2 Inflammatory Skin Diseases

In a first study, patients with irritant contact dermatitis ($n = 15$) and psoriasis vulgaris ($n = 16$) were examined by OCT. The findings were compared with the results obtained by biophysical methods. Whereas intact control skin presented with a

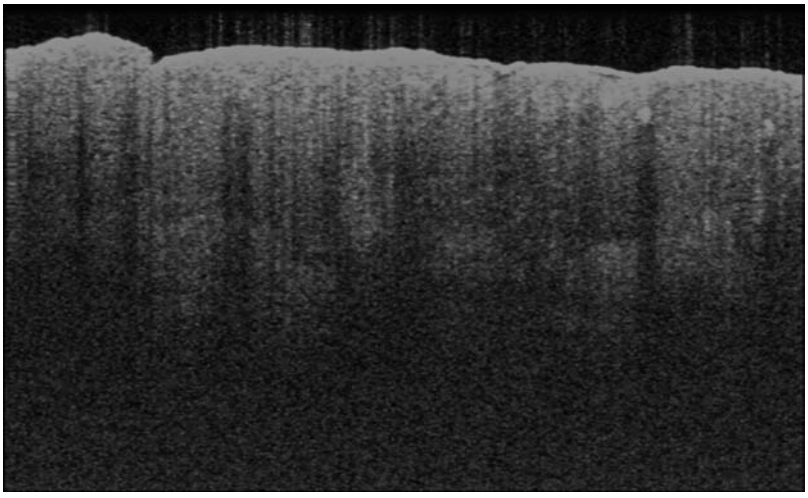

Figure 51.3 OCT of a melanoma at costal arch.

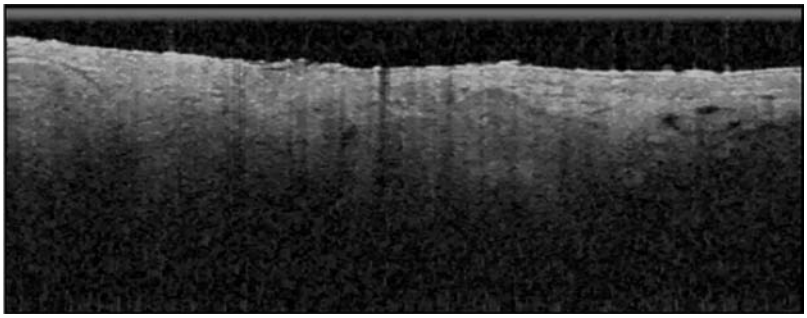

Figure 51.4 OCT of basal cell carcinoma at forehead.

small entrance echo and a clearly defined epidermis, irritated skin caused an increased entrance echo and a thickening of the epidermis [8]. Psoriatic skin presented similarly, with a broadened entrance signal and acanthosis. Intracorneal pustules were depicted as hypo-dense spaces. Longitudinal evaluations following therapy demonstrated a marked regression of these changes [8]. The results were recently confirmed in a separate study including 23 patients. Epidermal thickness of psoriatic and control skin was measured before and after therapy and OCT results correlated well with histologic findings, including a significant decrease in epidermal thickness under therapy [9].

OCT was also applied in the evaluation of contact patch test reactions. Compared with an untreated control area, there was a thickened and/or disrupted entrance signal, pronounced skin folds, and significant acanthosis. Moreover, clearly demarcated signal-free cavities within the epidermis and a considerable reduction in dermal reflectivity are demonstrated by OCT. This result clearly correlated with the clinical characteristics of the patch test result [10].

51.3.2.3 **Wound Healing**

The different phases of wound healing have also been studied by OCT, although to date only in animal models. Individual wound healing phases could be identified after artificial biopsy in mice. The method allowed the description of wound size over time, early re-epithelialization, dermoepidermal junction formation, and differences in wound tissue composition [11]. In another study, performed on rabbits, polarization-sensitive optical coherence tomography (PS-OCT) was employed for monitoring wound healing processes *in vivo* and *in vitro*. Also, several drugs either fostering (sphingosylphosphorylcholines) or hampering (tetraacetylphytosphingosines) wound healing were administered. The evaluation was performed in comparison with an untreated control in correlation with a routine histology. The variations of phase retardation values caused by the collagen morphology changes on wound sites are quantified for all cases. Collagen fiber regeneration could be visualized by means of PS-OCT, and the effects of various drugs on the process of wound healing process were quantified. Different phases of wound healing such as inflammation, re-epithelialization, and collagen remodeling could be identified in the examination of infected and uninfected wounds. Infected wounds were marked

by prominent edema. In the comparison of infected and uninfected wounds, a significantly delayed re-epithelization and collagen remodeling phases were demonstrated [12].

In vivo studies on the longitudinal evaluation of wound healing processes are yet to be performed in order to prove the usefulness of OCT in this area of research.

51.3.2.4 **Bullous Skin Disorders**

OCT allows for morphologic discrimination between different types of bullae. Single patients with bullous pemphigoid, pemphigus vulgaris, Darier disease, subcorneal pustulosis, and burn blisters were examined by OCT [13].

The tense blisters of bullous pemphigoid were seen in OCT images as dark, round, or ovoid, mostly well-differentiated lobules or clefts. Also, in some cases, gray-appearing portions could be detected that corresponded histologically to the intra-bullous eosinophilic infiltrate. Slack blisters (as in pemphigus vulgaris) rather appear gray in OCT images. On the other hand, thermal burns show both intra- and subepidermal blisters. The characteristic skin lesions of subcorneal pustulosis filled by neutrophils are difficult to distinguish from the surrounding area in OCT. They appear as faint gray lobules in the OCT image. The OCT image of a papular lesion such as in Darier disease presents first a disruption of well-defined layering. Also, the epidermis cannot be discriminated from the dermis. With OCT, the depth of bullae development could be clearly defined. Hence OCT can be considered a promising adjunct tool for the classification of bullous dermatoses [13].

51.3.2.5 **Other**

Another possible clinical application is the longitudinal evaluation of topical therapy of benign inflammatory dermatoses. In one study, an unspecific decrease in surface reflexivity was demonstrated by OCT, which was associated with a lowered A scan entrance peak. The application of glycerin resulted in an increase in skin "transparency" by convergence of the refractive indices. At the same time, an increased thickness of the horny layer was observed, likely due to swelling and occlusion effects. Steroid-induced epidermal atrophy was also investigated by OCT [14]. However, further studies to prove the applicability of OCT for morphometric measurement of normal or atrophic epidermis are necessary.

51.3.3 **Conclusion**

Currently, OCT is applicable as an adjunct to high-resolution sonography in the noninvasive imaging of structural alterations of the skin *in vivo* and for the evaluation of epidermal and tumor thickness [10]. The resolution achieved by this method is constantly improving, enabling also microscopic structures to be imaged. OCT allows for the imaging of the skin from the stratum corneum down to the reticular dermis, thus allowing the real-time evaluation of numerous dermatoses, skin tumors and therapeutic effects. In order to judge the diagnostic value of this novel method, further studies have to be performed.

51.4
Laser Doppler Imaging

51.4.1
Technical Principle and Development

In principle, the method is based on the Doppler effect. Frequency changes of monochromatic light reflected by erythrocytes are measured. A distinction is made between laser Doppler imaging (LDI) which allows an extensive perfusion measurement, and the use of laser Doppler flowmetry (LDF) for a selective definition of the blood flow.

In LDI, the area under examination is scanned in a meandering pattern. The result is a two-dimensional image of perfusion differences in the area examined. Owing to technological progress and the continually improving lateral resolution, ($<100\,\mu m$), the method allows for precise perfusion mapping in the area examined.

51.4.2
Applications

51.4.2.1 Skin Tumors
The application of LDI in diagnostics of skin tumors is described in more detail in the respective chapters (Chapter 52 and 53).

51.4.2.2 Inflammatory Skin Diseases
Being an inflammatory dermatosis, psoriasis was supposed to be accompanied by abnormal skin perfusion. Speight *et al.* [15] searched for differences in perfusion within the psoriatic plaques compared with the surrounding skin [15]. A fourfold increase in perfusion was detected within the plaque area compared with surrounding tissue. Even an increased blood flow that, according to clinical evaluation, had not been expected to occur, was detected in the close proximity to the plaques within an diameter of 2–4 mm [15]. Davison *et al.* [16] also were able to prove this fringe of increased perfusion outside the clinical edges of the psoriasis plaques [16]. Krogstad *et al.* [17] defined the histamine release during local anesthesia by microdialysis, and could thus eliminate the impact of histamine as a cause of this increased perfusion [17].

Yosipovitch *et al.* [18] examined the blood flow following a barrier dysfunction by tape stripping in both psoriatic plaques and in normal skin of psoriasis patients and also in healthy test persons [18]. An increased perfusion within the plaques was accompanied by a decreased heat pain threshold, whereas the healthy skin displayed an increased heat pain threshold.

Also in psoriasis, LDI was applied for the evaluation of therapeutic efficacy. Stücker *et al.* employed LDI in order to examine the inflammatory response of psoriasis patients to topical retinoids [19]. The initial irritation of the skin, which is often observed, can be reduced by adaptation of the therapy.

51.4.2.3 Microcirculation of Chronic Wounds
The possible fields of application for the laser Doppler method are broad. Above all they comprise diseases that are accompanied by an impaired microcirculation,

mainly focusing on the chronic venous and arterial wounds. The method has been employed not only for examinations on pathogenesis, but also for reviewing the therapeutic success of other methods of treatment.

In a study performed by Mayrovitz *et al.*, perfusion was measured in the area surrounding the ulcers of patients with venous ulcerations [20]. The perfusion measured was highly dependent on the place measurement and its characteristics. Given good granulation, a high perfusion was measured right inside the ulcer. In cases with absence of granulation, perfusion was shown to decrease significantly, an observation that was also made in the area of normal skin surrounding the ulcer. This study proved not only an increased basal periulcerous flow, but also its causes, being a combination of both increased blood flow velocity and circulating blood volume [20].

Ambrozy *et al.* defined the microcirculation in mixed arterial–venous ulcers and the surrounding skin [21]. In this study, perfusion was found to be highest in the granulation tissue area, whereas the granulation-free parts of the ulcer showed a weak flux only. A high perfusion was also detected in scars. In all areas examined, however, capillary density measured by capillaroscopy was lower than in normal skin [21].

The laser Doppler method is also employed for the evaluation of therapeutic interventions. Jünger *et al.* examined the impact of a low-frequency pulsed current on the microcirculation of venous ulcers [22]. Arora *et al.* [23] showed a significantly improved microcirculation in neuropathic diabetic feet after a successful lower extremity revascularization [23]. Also, its effectiveness was examined with regard to the application of wound dressings to chronic wounds, and to comparison with a vasodilating therapy of peripheral artery occlusire disease [23].

Moreover, the method was also employed for the evaluation of the extent of skin burns. Findings showed a significantly improved predictability of the outcome of a burn wound compared with a merely clinical evaluation [24]. In 1993, a study by Niazi *et al.* showed 100% accord of LDI with histology, whereas the agreement in clinical assessment was only 65% [25]. These findings were confirmed in numerous studies.

51.4.2.4 **Collagenosis and Rheumatic Diseases**

In addition to progressive sclerosis of the skin and viscera, rarefication especially of the terminal vessels is considered one of the most important pathogenetic mechanisms in systemic scleroderma. This rarefication can lead to necroses of the distal phalanges of the finger, being a sure visible sign of the advancement of the disease. At the same time, vascular regulation is faulty, which soon leads to a secondary Raynaud's phenomenon in patients with scleroderma.

In 1994, Seifalian *et al.* [26] examined LDI, LDF, and thermography on both healthy patients and those with systemic scleroderma [26]. Whereas a good correlation was found between LDI and LDF, this did not apply to thermography. Perfusion of the finger in patients with systemic scleroderma was lower than in healthy test persons [26].

Clark *et al.* [27] performed a study of 40 patients with Raynauds's phenomenon (33 of whom suffered from systemic scleroderma), and compared them with 17 healthy volunteers [27]. Hands and fingers of the persons were examined by both LDI and thermography, and the difference between them was measured. The study's focus was on the correlation of these two methods. Only a poor correlation was shown in

this examination. LDI is more sensitive to blood flow changes and therefore more likely to show inhomogeneities than the highly damped temperature response. Therefore, one method cannot substitute for the other [27].

In a study of 44 patients suffering from systemic scleroderma, Correa *et al.* [28] demonstrated a significantly decreased blood flow in the fingers of the patients compared with healthy test persons [28]. The findings could be confirmed at any point in time after cryostimulation. Both in patients and in healthy test persons, blood flow decreased significantly after cryostimulation. In the healthy test persons, however, blood flow recovered after an average of 27 min, whereas this recovery did not occur in the patients with scleroderma. These findings, however, did not correlate with the morphologic microvascular abnormalities detected by nailfold capillaroscopy [28].

Further studies aimed to evaluate the impact of therapies on systemic scleroderma. Sadik *et al.* [29] could not prove an improvement in perfusion by the application of atorvastatin [29]. Rosato *et al.*, however, showed that patients suffering from systemic scleroderma who were administered bosentan because of their pulmonal hypertonia also presented a higher perfusion of the hands [30].

Moreover, LDI has also been applied in inflammatory joint disease. Ferrell *et al.* examined 11 patients with rheumatoid arthritis of the interphalangeal joints [31]. Here, a significantly increased perfusion of the affected joints was detected. The method was also employed in order to prove the impact of locally applied gels or intra-articular steroid injections on the hyperemia [31]. In a later study, Ferrell *et al.* compared LDI with ultrasound and pain score [32]. The results proved particularly the advantages of LDI in the examination of inflammatory joint disease in its early stages [32].

51.4.3
Conclusion

LDI is particularly well suited for the evaluation of blood perfusion, and in that regard for the examination of cutaneous microcirculation. Therefore, LDI has a role in the evaluation of diseases with impaired microcirculation such as chronic wounds, or as an aid in the evaluation of blood flow changes in autoimmune skin disorders including collagenoses. In these diseases, LDI may be useful both for a diagnostic evaluation and for monitoring of therapeutic efficacy. Whether this method will play a role in the routine diagnostic work-up of other diseases remains to be evaluated in future studies and also depends on the continuing development of this methodology.

51.5
Confocal Laser Scanning Microscopy (CLSM)

51.5.1
Technical Principle and Development

The principle of confocal laser scanning microscopy (CLSM) was first described in the 1950s and patented by Minsky in 1961, long before the invention of lasers [33, 34].

The first commercially available system was realized by Rajadhyaksha *et al.* at Harvard Medical School in 1995, based on an 830 nm diode laser that is used as a point light source in a scanning mode providing horizontal tomographic images [35]. The visualization of tissues is based on the different refractive indices of the distinct tissue chromophores and cell structures. This effect is called reflectancy, which is caused by the reflection and scattering of light from the piece of tissue under examination [36]. Owing to the very small aperture, most of the reflected light from outside the focal plane is eliminated. This permits a lateral resolution of 0.5–1 μm and an axial resolution (section thickness) of 3–5 μm. In contrast to routine histology, CLSM imaging is based on optical horizontal sectioning.

For morphologic evaluation, CLSM is generally applied in the reflectance mode without exogenously applied fluorophores. This facilitates its use for imaging of human skin *in vivo*. On the other hand, the application of fluorescent dyes may be useful for the evaluation of cutaneous metabolism, cell to cell contacts, or cell migration, thereby allowing the identification of targets by imaging in the fluorescent mode. Fluorescein sodium is routinely used as a fluorophore (application intradermal or to the skin surface). This fluorophore is safe for human use *in vivo*, whereas many other dyes are permitted only for use *ex vivo* [37].

51.5.2 Applications

51.5.2.1 Topography of Normal Skin

Using CLSM, the selective imaging of single cells and single layers of the epidermis is possible. Due to the horizontal sectioning, the first layer to be evaluated is the stratum corneum, which is characterized by anucleated corneocytes arranged in highly refractive cell clusters. The stratum granulosum consists of 2–4 cell layers, the single cells being between 20 and 25 μm in size. The cell nuclei are displayed in the center as dark, oval, or round structures that are surrounded by a narrow ring of bright, granulous-appearing cytoplasm. The stratum spinosum displays polygonal, rather small cells of size 15–20 μm. These are arranged in a typical honeycomb pattern that, at the papillary tips, shows first signs of pigmented basal cells. The cells of the basal layer are between 10 and 12 μm in size. The basal cell layer itself consists of more or less refractive cells that vary with respective Fitzpatrick skin phototypes, according to their different melanin contents. Here, the content of melanin correlates with the respective reflectancy and, thus, with the image brightness.

At the level of the dermoepidermal junction, the basal cell layer surrounds centrally positioned dark papillae. Often, blood flow can be visualized within the papillae due to the high reflectance of erythrocyte hemoglobin [38].

51.5.2.2 Skin Tumors

The value of CLSM in diagnostics of epithelial and pigmented skin tumors has already been surveyed in numerous clinical studies. Thereby, CLSM may be useful not only for the diagnostic classification of proliferative skin lesions but also for the definition of tumor margins prior to Mohs' surgery or the detection of subclinical

disease. Chapter 52 and 53 provides a detailed outline of the applicability of CLSM for examination of melanoma and non-melanoma skin cancer.

51.5.2.3 **Vascular Skin Lesions**

Reflectance confocal microscopy allows for the examination of small vessels and their anatomic and flow characteristics *in vivo* and in real time. Hence the method is applicable to the evaluation of vascular lesions. Some key features are listed below.

CLSM examination of *spider angioma* produces images of whorled canalicular structures in the mid- and upper dermis. Vessels measure 40–50 μm in diameter and show a high flow [39].

CLSM examination of *cherry angioma* shows a large number of dilated and tortuous dermal capillaries which are up to 50–100 μm wide and of medium flow. The structure is lobular and shows fine fibrous septa [39].

CLSM evaluation of *pyogenic granuloma* shows an increased number of elongated dermal capillaries only 5–10 μm in size. Further characteristics are the detection of lymphocyte rolling and the marked luminescence of canalicular structures. The epidermis additionally shows spongiosis and exocytosis [39].

Kaposi's sarcoma displays inflammatory single cells or aggregates in epidermis and dermis, and also numerous spindle cells. Apart from erythrocyte extravasates and hemosiderin deposits, an increased number of dilated and anastomosed cells can be detected in the stroma [40].

Owing to the small number of cases, the ultimate role of CLSM in the diagnosis of vascular alterations remains to be determined in larger clinical and correlative studies.

51.5.2.4 **Inflammatory Skin Diseases**

Pilot studies have examined a large number of inflammatory skin lesions by CLSM. For most entities, however, randomized multicenter studies are still lacking.

Typical histologic features for acute contact dermatitis could be visualized by CLSM: cell nuclei in the stratum corneum (parakeratosis), intraepidermal vesiculation, inflammatory cells within the epidermis, and an increase in papillary vessels [41].

In search of allergen-specific results of CLSM compared with the clinical evaluation of the patch test (PT), varying images of the reactions to 2% cobalt chloride and 5% nickel sulfate could be proved [41]. The examination of positive patch test reactions showed an increased suprabasal epidermal thickness on days 2 (D2), and 3 (D3) for cobalt chloride. Fairly often, vesicle formation and an overall increased suprabasal epidermal thickness for nickel sulfate appeared in patients with a positive reaction to nickel. In two out of three doubtful positive PTs to cobalt chloride, CLSM images presented characteristics of irritant reactions and one characteristic of a positive allergic reaction [41]. The dynamic evolution of allergic contact dermatitis (ACD) and irritant contact dermatitis (ICD) was also investigated [42]. Here, significant differences in both the time course and the severity of the single features were observed. In this study, structural changes of the stratum corneum were identified as a discriminative feature of ICD. Similarly, the initial presence of superficial disruption is highly indicative of irritant reactions [42]. In ACD, this pattern may only be observed later in the course, or in very extensive reactions.

The degree of epidermal spongiosis, vesicle formation, and exocytosis, however, did not show significant differences between ICD and ACD.

CLSM criteria for the diagnosis of psoriasis correspond well with those established by histology and include hyperparakeratosis, loss of the stratum granulosum, elongation of the rete ridges, and dilatation of the papillary vessels [43]. In a study of 75 patients with psoriasis, a sensitivity of 89% and a specificity of 95% were shown [44]. Further entities examined in this study include mycosis fungoides and lupus erythematodes. In both diseases, the specificity was high (>92%), but the sensitivity was low (63%) [44].

51.5.2.5 **Infections**

Infections of the skin are the cause of many dermatoses. At the same time, they are able to trigger existing dermatoses, especially as a super antigen. Bacterial, mycotic, or viral infections have been studied by CLSM in both reflectance and fluorescence modes.

CLSM was applied to the diagnostics of secondary syphilis. The method allowed for the proof of treponema in the stratum spinosum, but again, these findings are awaiting more extensive evaluations [45].

Staphylococcus and *Candida* strains have also been examined. The yeast and hyphal forms of *C. albicans* could be proved by CLSM within a biofilm using the fluorescence mode (FITC-labeled). These findings allow future studies on the effectiveness of antimicrobial agents in order to eliminate the biofilms, a review of prophylactic application of antimycotics, and examination of biomaterials [46].

51.5.2.6 **Drug Delivery**

CLSM has been applied in numerous surveys in order to study the extent of substance deposition in the skin and their routes of penetration. Owing to improvements of this method by the supplementary implementation of a reflectance mode, examinations can be performed without administration of any additional fluorophores. This permits examinations *in vivo* in humans, and thus a more precise evaluation of locally applied drugs.

In most cases, fluorescent samples were used in order to permit of quantitative measurements. Examination of liposomes and the impact of chemical penetration enhancers were of priority here. Most of the studies, however, were performed on skin models, on skin *ex vivo*, or in animal experiments in order to avoid damage caused by the potential toxicity of the fluorophores applied.

Far-reaching investigations were also performed on matter transportation prior to photodynamic therapy, which plays an important role in the therapy of non-melanoma skin cancer. In these studies, the influence of dimethyl sulfoxide on the penetration of 5-aminolevulinic acid *in vitro* and the resulting protoporphyrin IX accumulation *in vivo* were analyzed by confocal microscopy [47]. Also, the impact of physical methods such as iontophoresis and ultrasound on the penetration were examined [48].

51.5.3 **Conclusion**

Owing to its high resolution and a relatively large imaging area, CLSM allows for the noninvasive evaluation of inflammatory and neoplastic alterations of the skin.

In contrast to routine histology, CLSM permits the imaging of dynamic processes, which allows for evaluation of disease evolution and therapeutic effects. Also, research has shown that CLSM permits the detection of subclinical disease manifestations.

51.6 Multiphoton Laser Imaging

51.6.1 Technical Principle and Development

Maria Goeppert-Mayer described the principle of fluorescence excitation of molecules by multiple photons in 1931, but could not prove the process experimentally [90]. The experimental confirmation of the theoretical prediction was provided by Kaiser and Garrett in 1961 [50], shortly after the development of the first laser systems. On the basis of these findings, the first microscope-based on multiphoton process was developed in 1990 [51]. The effect of the second-harmonic generation (SHG) was already detected at the beginning of the 1960s. In 1974, a microscope was developed based on the SHG effect, which was later refined into a scanning microscope.

The principle of multiphoton imaging is the simultaneous absorption of two or more photons by a fluorophore and emission of one photon at a shorter wavelength, that is, with higher energy. The process requires high photon flux densities that are obtained either by a consistently high laser power or by very short pulses with high peak power [49]. The advantage of using ultra-short pulses is the low average total energy in the tissue, thus avoiding tissue damage.

Owing to the complex structure of the skin, there is a variety of fluorescent biomolecules. Among them, the most important include the nicotinic acid derivatives NADH and NADPH in their reduced state, which contribute significantly to tissue fluorescence [52–54]. Oxidized (NAD and NADP) nicotinic acid derivatives have, however, no fluorescent properties. The highest concentration of NADH and NADPH is found in the mitochondria, but they are also present in the cytoplasm. As an electron transporters and cofactors of numerous redox reactions, they are important indicators of cell metabolism.

With regard to endogenous pigments in cutaneous tissue, melanin and lipofuscin have fluorescent properties. Porphyrins are found as organic dyes in the hemoglobin of red blood cells and show a high absorption in the near-infrared spectral range. Another important and prominent epidermal fluorophore is keratin.

While most of the fluorophores are located intracellularly, elastin and collagen as extracellular matrix proteins also have fluorescent properties. A characteristic phenomenon of fibrillar collagen is its ability for SHG. In sum, the photons emitted from the dermis consist of both autofluorescence and SHG effects [55].

51.6.2 Applications

51.6.2.1 Topography of Normal Skin

The high lateral and axial resolution, each of only a few microns, allows the *in vivo* visualization of microstructures of cutaneous tissue, whereby single cells and even subcellular structures may be described (Figure 51.4). To date, both penetration depth and the field of view are restricted to about 200 μm in *in vivo* multiphoton laser tomography (MLT). Nevertheless, its use in dermatologic science has been proved in several studies. By depth-resolved semiquantitative assessment of autofluorescence (AF) and SHG, it was shown that MLT provides a novel *in vivo* imaging tool for the measurement of epidermal morphometric parameters such as epidermal thickness, which may on the other hand be useful for the observation over time of dynamic changes in skin disorders and therapeutic side effects or in cosmetic research and development [56].

51.6.2.2 Skin Tumors

Multiphoton laser tomography or microscopy has been applied both in the diagnostics of malignant melanomas and in the classification of nonmelanocytic skin tumors. The specific diagnostic criteria and the preciseness that can be achieved by the method are described in Chapter 52 and 53 (Figure 51.5).

51.6.2.3 Skin Aging

Skin aging is essentially characterized by alterations of the elastic and the collagenous fiber network. In the course of the aging process of the skin, so-called solar elastosis

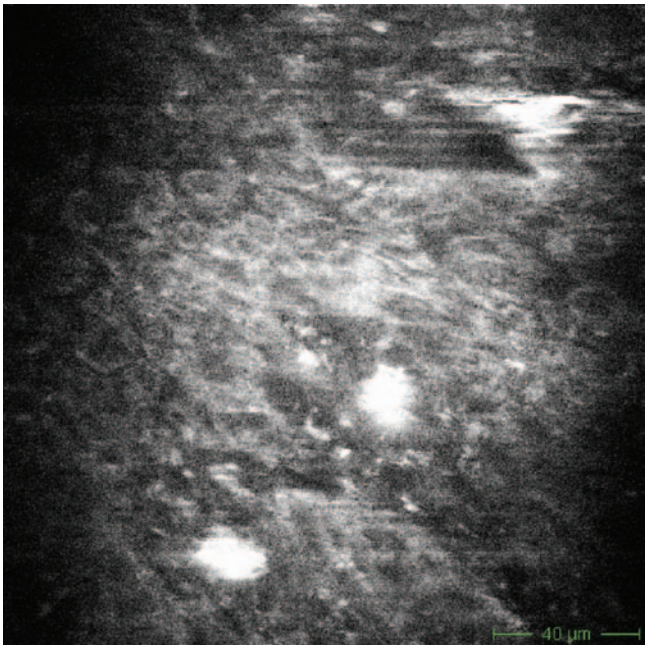

Figure 51.5 Multiphoton laser imaging atypical melanocytes.

appears, which is an accumulation of inferior elastic fibers in the skin. At the same time, the number of mature collagenous fibers decreases. Both fiber qualities can be recorded by MLT. Elastic fibers can be quantified by measuring the autofluorescence caused by multiphoton processes. Collagenous fibers, however, can be recorded via the SHG effect. Since the excitation maximum of both the SHG effect and the AF of elastic fibers lies within the blue spectral range, fibers of both qualities are best excited at 820 nm. In an *ex vivo* study of a few skin samples, Lin *et al.* [57] were able to show for the first time a negative correlation of test persons' age with an index derived from both these values (SAAID). SAAID is defined as: $\mathrm{SAAID} = (\mathrm{SHG} - \mathrm{AF})/(\mathrm{SHG} + \mathrm{AF})$, SHG and AF being a dimension of corresponding numbers of photons measured in a rectangle [57]. These results were reviewed *in vivo*. In this survey, which covered 18 test persons aged between 21 and 84 years, both the AF of the elastic fibers and the SHG effect were measured. SAAID was calculated. The score proved a statistically verified negative correlation with the age of the test persons [58].

In another study, young healthy volunteers using indoor tanning facilities and older people were compared with appropriate controls by semiquantitative evaluation of the dermal matrix composition with a DermaInspect multiphoton laser tomograph. Highly significant differences between the sun-protected volar forearm and the dorsal forearm and also between young and old test persons were found [59].

Another study focused on age-dependent morphologic changes of the dermal fiber network. Using a filter system, the fibers of collagen and elastin were optically separated. Several parameters were defined to describe the fiber network and the parameters were found to be different on comparing young and old volunteers [59] (Figures 51.6–51.9).

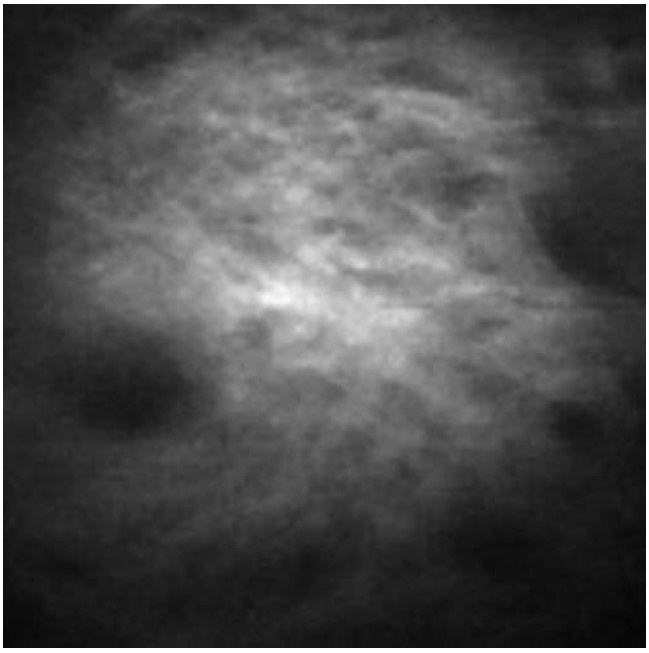

Figure 51.6 Multiphoton laser imaging collagen in young skin.

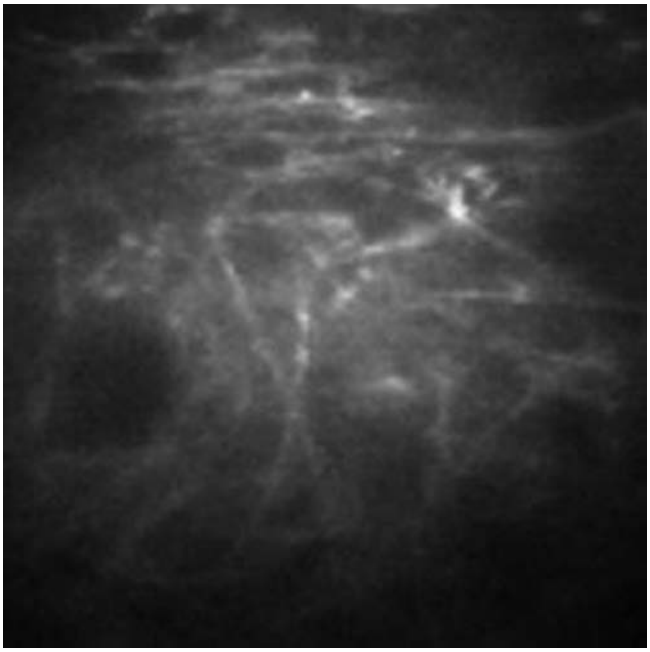

Figure 51.7 Multiphoton laser imaging elastin in young skin.

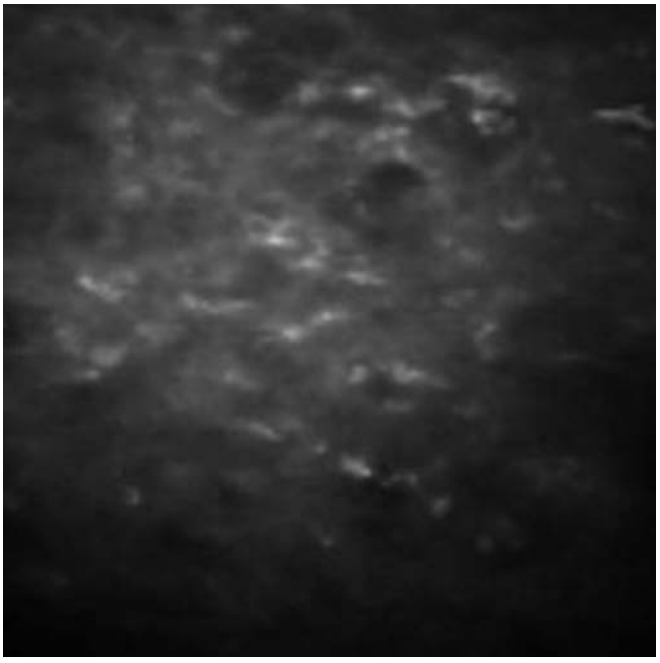

Figure 51.8 Multiphoton laser imaging collagen in old skin.

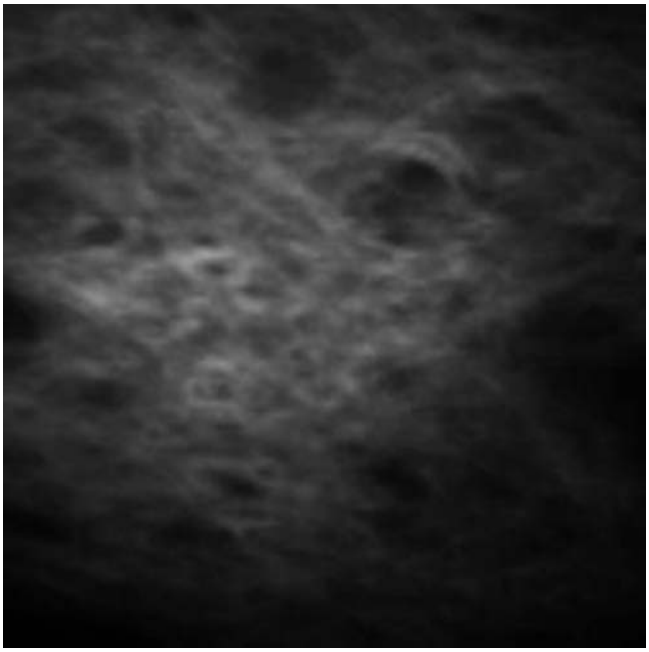

Figure 51.9 Multiphoton laser imaging elastin in old skin.

51.6.2.4 **Drug Delivery**

As a noninvasive imaging tool, MLT is suitable for the measurement of the effectiveness and the kinetics of percutaneous substance transport [60]. After application of different NaCl solutions, swelling and shrinking of corneocytes were observed depending on the salt concentration [61]. Application of penetration enhancers resulted in visible corneocyte disruption, disturbance of the intracellular keratin network, and pore formation [62]. The penetration of fluorescing nanoparticles into hair follicles and wrinkles could be proved by MLT [63]. In a recent study, Gratieri *et al.* examined the penetration characteristics of quantum dot particles (4 nm). Even for those small particles, a penetration into intact skin could not be proved [64]. However, penetration was proved only 10 min after rubbing the particles into damaged skin. Hence, for the time being, nanoparticles are not considered suitable carriers in substance transport [64].

Moreover, MPT results obtained by Lee *et al.* [61] showed the disruption of the intracellular keratin networks and intercellular cohesion of corneocytes by the penetration enhancer of a depilatory cream [61]. Prior treatment of the stratum corneum with a depilatory cream can detach corneocytes and lead to the development of intracellular pores in the remaining corneocytes by disrupting the intracellular keratin. Due to these processes, shunts for drug penetration are created [54].

Furthermore, Yu and co-workers applied various model fluorescent drugs *ex vivo*, the AF characteristics of which differ from those of keratin, thus enabling the dynamics of drug penetration in the stratum corneum to be elucidated [63, 65].

The penetration dynamics of the model substance oleic acid have also been visualized and quantified by MLT [66].

51.6.3 Conclusion

To date, multiphoton imaging is not a diagnostic tool in routine clinical practice, but it has been applied in study settings for the diagnosis of various skin diseases, including skin tumors (malignant melanoma [67], basal cell carcinoma [68], squamous cell carcinoma [69], inflammatory skin disorders (pemphigus vulgaris [70], psoriasis [71], photoaging [72], and intrinsic aging [73]).

The advantages of MLT as a noninvasive method are its high resolution, the specific effect of SHG, and the possibility of fluorescence lifetime detection.

51.7 Raman Spectroscopy

51.7.1 Technical Principle and Development

Raman spectroscopy (RS) helps in gathering information on the molecular architecture, the structure, and the interactions within a sample. In the process, light radiation leads to changes in oscillation and rotational energy levels of the molecules. RS is a method that measures Raman dispersion radiation, that is, nonelastic photon scattering.

Different laser types are employed in Raman spectrometers, including continuously operating gas lasers, Nd:YAG lasers which are mainly employed in the form of Fourier transform spectrometers, and semiconductor junction lasers. The excitation radiation requires monochromatic light in the ultraviolet–visible range and the infrared light of a highly intense radiation beam.

Depending on different wavelengths, RS allows the examination of the stratum corneum, the entire epidermis, and even the chemical architecture down to the dermis. Owing to their maximum penetration depth of 200 μm, shorter wavelengths below 830 nm are only suitable for examinations of the epidermis. Excitation wavelengths of more than 1000 nm, however, also permit examinations of the dermis [74].

When combined with confocal microscopy, RS allows the capture of both the chemical structure and morphologic aspects of the tissue of interest [75]. Thus, the chemical composition of a tissue can be assigned to a specific morphologic structure. At the same time, the sensitivity of substance transport and substance penetration are improved [75].

51.7.2 Applications

51.7.2.1 Molecular Structure of Normal Skin

Gniadecka *et al.* were able to prove significant differences between the Raman spectra of healthy skin, hairs, and nails [76]. The major spectral differences in the confor-

mational behavior of lipids and proteins were of causal nature. Although the examined proteins of all three samples were of the same secondary α-helix structure, there were differences with regard to the positioning of the S-S stretching bands and to the degree of folding. The analysis of the lipid peaks showed a highly ordered, lamellar crystalline structure with an increased lipid fluidity of the entire skin compared with nails and hairs [76].

Detailed analyses performed in subsequent studies focused on the stratum corneum as the primary component of the epidermal barrier function. The thickness of the stratum corneum (axial resolution 2 μm) could be exactly defined by means of confocal RS. Also, the semiquantitative analysis of important components such as stratum corneum lipids or natural moisturizer factor (NMF) components such as lactate, urea, and urocanic acid could be accomplished [77]. The composition and arrangement of lipids in the epidermis, especially in the stratum corneum, are of particular importance for the barrier function. Thus, a subtyping of neutral lipids, (cholesterol, cholesterol esters, cholesterol sulfate, triglycerides, free fatty acids, squalene, and alkanes), polar lipids (phosphatidylcholine, phosphatidylserine, phosphatidylethanolamine, spingomyelin), and sphingolipids (cermamides I–VII, monohexosylceramides) was analyzed based on Raman spectra and supplemented by X-ray diffraction, differential calorimetry, and fluorescence or infrared spectroscopy [78]. Confocal RS also allowed the localization and analysis of substance mixtures of complex structure, such as NMF (main components: 2-pyrrolidone-5-carboxylic acid and urocanic acid). These factors, which are formed by a filaggrin protein breakdown, are useful biomarkers for the filaggrin genotype [79]. RS was also suitable for comparing different methods for distance measurement of the stratum corneum.

In the course of the further development of laser technology, longer excitation wavelengths were applied, allowing the examination of the epidermis, and also the qualitative analysis of the upper dermis. By using a wavelength of 1064 nm, Naito *et al.* were able to examine lipids and proteins of the dermis, but also the cutaneous appendages (sebaceous glands and hair follicles) [74].

Nakagawa *et al.* employed RS in order to analyze the water content of the dermis [80]. By adjusting the exposure time and depth increment, the signal-to-noise ratio of the Raman spectra could be significantly improved. A comparison of different age groups showed a significantly higher water content in the skin of older volunteers. Furthermore, Lademann *et al.* succeeded in defining the contents of β-carotene and lycopene (carotenoids) in the skin [81].

51.7.2.2 **Inflammatory Skin Diseases**

Psoriasis Vulgaris

Psoriasis is a chronic inflammatory disease with a pronounced disorder of the epidermal metabolism and subsequent alterations in the molecular composition of the stratum corneum.

Wohlrab *et al.* examined the stratum corneum of healthy test persons compared with patients suffering from atopic dermatitis and psoriasis vulgaris, applying RS to unaffected skin areas [82]. The *in vitro* Fourier transformed Raman spectra

showed first of all differences with regard to lipids (spectral range 1112–1142 nm). After statistical evaluation, this approach allowed the differentiation of the skin of healthy test persons and both the inflammatory dermatoses even in unaffected skin areas.

The analysis of psoriatic scaling from different areas of the body and of normal skin of healthy test persons showed no differences between the spectra with regard to the anatomic locations. The Raman spectra did not show any significant differences in lipid band positions whereas the crystalline lipid structure was disrupted in psoriatic scales. Nevertheless, there were great spectral differences with regard to the molecular structure of the proteins. Compared with normal skin, the peak position of the amide I band was shifted towards longer wavelengths, suggesting an unfolding of proteins [82].

Atopic Dermatitis

Being a very heterogeneous inflammatory skin disease, atopic dermatitis (AD) is modified and triggered by numerous immunologic, genetic, and environmental factors. The filaggrin gene (FLG), which codes for the protein filaggrin, is of great importance in pathogenesis. The classification of Raman profiles indirectly allows for an evaluation of different filaggrin genotypes which strongly influence the composition of the NMF. O'Regan *et al.* examined 132 well-characterized patients with medium to severe atopic dermatitis [83]. The study was performed using confocal RS, and the results were correlated with the clinical findings and also with the FLG genotype. Based on the examination results, a clear distinction could be made between FLG-related and an unrelated AD. Furthermore, the analysis of the NMF composition allowed the definition of a subset of FLG-related AD, and also differentiation between one or two mutations [83].

Gonzáles *et al.* examined newborns over the course of 1 year, studying the protein filaggrin. Owing to significant differences between the respective Raman spectra, a statistical analysis allowed for prognoses on the development of a filaggrin-related atopic dermatitis [84].

Infections and Wound Healing

In different studies, especially in animal models, RS has been employed for the evaluation of wound healing processes. The definition of specific peaks that correspond to elastin or keratin permits a differentiation between normally healing wounds and those undergoing a retarded healing process. Andrew Chan *et al.* evaluated all phases of acute wound healing (inflammation, proliferation including re-epithelialization and remodeling) after acute traumatization [85]. The protein profiles of the proteins involved in the wound healing process, and also their subclasses, were analyzed. Along with acute wounds, mainly chronic wounds are the target of noninvasive diagnostic methods. This is due to the great impairment of affected patients, and to the limited therapeutic success. Among others, the interaction of oleic acid with wound dressings applied for proteinase inhibition was tested by means of RS. Proteases are of critical importance for wound

chronification. A profile definition may effectively support the choice of suitable local therapy methods.

Not only in wound healing but also in numerous dermatoses, infections are highly relevant. Willemse-Erix *et al*. examined various skin isolates of multiresistant coagulase-negative strains of *Staphylococcus epidermidis* [86]. Here, RS allowed a clear differentiation between the specific isolates. Additionally, the high throughput allows for a similar analysis of multiple colonies in a patient.

Drug Delivery

RS, especially combined with CLSM, is a method suitable for examination of substance transport and substance penetration within and through the skin.

As carotenoids are antioxidant substances, various studies have been performed to analyze their content and distribution in the skin. Owing to their capacity as radical scavenger, carotenoids significantly influence skin aging processes. It has been shown recently that skin with a higher carotenoid content displays less aging signs than skin with a lower carotenoid content [87]. Specific carotenoid profiles could be determined by means of RS. These Raman spectra also permit the semiquantitative definition of carotenoid (e.g., lycopene) and retinol (vitamin A_1) contents. For example, Hesterberg *et al*. showed that a special diet with ecologic eggs led to a significantly increased content of carotenoids in the skin. Also, protective antioxidant effects of carotenoids after exposure of the skin to infrared light has been shown [88].

Further studies were performed on the effectiveness of penetration enhancers, on tolubuterol, and on the quantification of metronidazole in the skin [89].

51.7.3 Conclusion

RS, originally developed for *in vitro* studies, is gaining rapid importance in clinical studies. Especially superficial parts of the skin, that is, stratum corneum and in some cases down to the dermis, can be studied. The composition of the skin and subsequently specific skin diseases have been studied by RS. Recently, alterations at the molecular level have been addressed by RS in atopic dermatitis, psoriasis, infections, and wound healing, and drug delivery studies have also been performed. However many questions are still remain to be answered in this field, for example, standards on the way in which clinic studies can be performed. RS is a powerful tool allowing clinical and basic research to gain rapid *in vivo* insight into molecular processes in the skin.

Acknowledgement

For technical support: Nancy Schmidt, Christine Weidl; for scientific support: Prof. Karsten König, Rainer Bückle, Martin Weinigel, Marcel Kellner-Höfer, Susanne Metz, Enrico Dimitrow.

Figures: OCT (Chapter 51–53): Prof. Julia Welzel, Augsburg; CLSM: Dr. Susanne Lange–Asschenfeldt, Berlin.

References

1 Malvehy, J. *et al.* (2007) Dermoscopy report: proposal for standardization. Results of a consensus meeting of the International Dermoscopy Society. *J. Am. Acad. Dermatol.*, **57**, 84–95.

2 Argenziano, G. *et al.* (2003) Dermoscopy of pigmented skin lesions: results of a consensus meeting via the Internet. *J. Am. Acad. Dermatol.*, **48**, 679–693.

3 Zalaudek, I. *et al.* (2006) Dermoscopy in general dermatology. *Dermatology.*, **212**, 7–18.

4 Tanaka, M. *et al.* (2011) Key points in dermoscopic differentiation between lentigo maligna and solar lentigo. *J. Dermatol.*, **38**, 53–58.

5 Zalaudek, I. *et al.* (2010) How to diagnose nonpigmented skin tumors: a review of vascular structures seen with dermoscopy: Part I. Melanocytic skin tumors. *J. Am. Acad. Dermatol.*, **63**, 361–374, quiz 375–376.

6 Beltrán, E. *et al.* (2007) Assessment of nailfold capillaroscopy by $\times 30$ digital epiluminescence (dermoscopy) in patients with Raynaud phenomenon. *Br. J. Dermatol.*, **156**, 892–898.

7 Huang, D. *et al.* (1991) Optical coherence tomography. *Science*, **254**, 1178–1181.

8 Welzel, J. *et al.* (2003) Optical coherence tomography in contact dermatitis and psoriasis. *Arch. Dermatol. Res.*, **295**, 50–55.

9 Morsy, H. *et al.* (2010) Optical coherence tomography imaging of psoriasis vulgaris: correlation with histology and disease severity. *Arch. Dermatol. Res.*, **302**, 105–111.

10 Gambichler, T. *et al.* (2007) Characterization of benign and malignant melanocytic skin lesions using optical coherence tomography *in vivo*. *J. Am. Acad. Dermatol.*, **57**, 629–637.

11 Cobb, M.J. *et al.* (2006) Noninvasive assessment of cutaneous wound healing using ultrahigh-resolution optical coherence tomography. *J. Biomed. Opt.*, **11**, 064002.

12 Sahu, K. *et al.* (2010) Non-invasive assessment of healing of bacteria infected and uninfected wounds using optical coherence tomography. *Skin Res. Technol.*, **16**, 428–437.

13 Mogensen, M. *et al.* (2008) Optical coherence tomography imaging of bullous diseases. *J. Eur. Acad. Dermatol. Venereol.*, **22**, 1458–1464.

14 Cossmann, M. and Welzel, J. (2006) Evaluation of the atrophogenic potential of different glucocorticoids using optical coherence tomography, 20-MHz ultrasound and profilometry; a double-blind, placebo-controlled trial. *Br. J. Dermatol.*, **155**, 700–706.

15 Speight, E.L. *et al.* (1993) The study of plaques of psoriasis using a scanning laser-Doppler velocimeter. *Br. J. Dermatol.*, **128**, 519–524.

16 Davison, S.C. *et al.* (2001) Early migration of cutaneous lymphocyte-associated antigen (CLA) positive T cells into evolving psoriatic plaques. *Exp. Dermatol.*, **10**, 280–285.

17 Krogstad, A.L. *et al.* (1999) Capsaicin treatment induces histamine release and perfusion changes in psoriatic skin. *Br. J. Dermatol.*, **141**, 87–93.

18 Yosipovitch, G. *et al.* (2003) Thermosensory abnormalities and blood flow dysfunction in psoriatic skin. *Br. J. Dermatol.*, **149**, 492–497.

19 Stücker, M. *et al.* (2002) Instrumental evaluation of retinoid-induced skin irritation. *Skin Res. Technol.*, **8**, 133–140.

20 Mayrovitz, H.N. and Larsen, PB. (1994) Periwound skin microcirculation of venous leg ulcers. *Microvasc. Res.*, **48**, 114–123.

21 Ambrozy, E. *et al.* (2009) Microcirculation in mixed arterial/venous ulcers and the surrounding skin: clinical study using a laser Doppler perfusion imager and capillary microscopy. *Wound Repair Regen.*, **17** (1), 19–24.

22 Jünger, M. *et al.* (1997) Treatment of venous ulcers with low frequency pulsed current (Dermapulse): effects on cutaneous microcirculation. *Hautarzt*, **48**, 897–903.

23 Arora, S. *et al.* (2002) Cutaneous microcirculation in the neuropathic diabetic foot improves significantly but not completely after successful lower extremity revascularization. *J. Vasc. Surg.*, **35** (3), 501–505.

24 La Hei, E.R. *et al.* (2006) Laser Doppler imaging of paediatric burns: burn wound outcome can be predicted independent of clinical examination. *Burns*, **32**, 550–553.

25 Niazi, Z.B. *et al.* (1993) New laser Doppler scanner, a valuable adjunct in burn depth assessment. *Burns*, **19**, 485–489.

26 Seifalian, A.M. *et al.* (1994) Comparison of laser Doppler perfusion imaging, laser Doppler flowmetry, and thermographic imaging for assessment of blood flow in human skin. *Eur. J. Vasc. Surg.*, **8**, 65–69.

27 Clark, S. *et al.* (2003) Comparison of thermography and laser Doppler imaging in the assessment of Raynaud's phenomenon. *Microvasc. Res.*, **66**, 73–76.

28 Correa, M.J. *et al.* (2010) Comparison of laser Doppler imaging, fingertip lacticemy test, and nailfold capillaroscopy for assessment of digital microcirculation in systemic sclerosis. *Arthritis Res. Ther.*, **12**, R157.

29 Sadik, H.Y. *et al.* (2010) Lack of effect of 8 weeks atorvastatin on microvascular endothelial function in patients with systemic sclerosis. *Rheumatology (Oxford).*, **49**, 990–996.

30 Rosato, E. *et al.* (2010) Bosentan improves skin perfusion of hands in patients with systemic sclerosis with pulmonary arterial hypertension. *J. Rheumatol.*, **37**, 2531–2539.

31 Ferrell, W.R. *et al.* (1996) Laser Doppler perfusion imaging of proximal interphalangeal joints in patients with rheumatoid arthritis. *Clin. Exp. Rheumatol.*, **14**, 649–652.

32 Ferrell, W.R. *et al.* (2001) Metacarpophalangeal joints in rheumatoid arthritis: laser Doppler imaging – initial experience. *Radiology*, **220**, 257–262.

33 Minsky, M.Microscopy apparatus. U.S. Pat. US 3013467; http://www.freepatentsonline.com/3013467.html (last accessed 16 May 2011).

34 Minsky, M. Brief Academic Biography of Marvin Minsky, http://web.media.mit.edu/~minsky/minskybiog.html (last accessed 16 May 2011).

35 Rajadhyaksha, M. *et al.* (1995) *In vivo* confocal scanning laser microscopy of human skin: melanin provides strong contrast. *J. Invest. Dermatol.*, **104**, 946–952.

36 Rajadhyaksha, M. *et al.* (1999) Video-rate confocal scanning laser microscope for imaging human tissues *in vivo*. *Appl. Opt.*, **38**, 2105–2115.

37 Suihko, C. *et al.* (2005) Fluorescence fibre-optic confocal microscopy of skin *in vivo*: microscope and fluorophores. *Skin Res. Technol.*, **11**, 254–267.

38 Sauermann, K. *et al.* (2002) Histometric data obtained by *in vivo* confocal laser scanning microscopy in patients with systemic sclerosis. *BMC Dermatol.*, **2**, 8.

39 Astner, S. *et al.* (2010) Preliminary evaluation of benign vascular lesions using *in vivo* reflectance confocal microscopy. *Dermatol. Surg.*, **36**, 1099–1110.

40 Grazziotin, TC. *et al.* (2010) Preliminary evaluation of *in vivo* reflectance confocal microscopy features of Kaposi's sarcoma. *Dermatology*, **220**, 346–354.

41 Astner, S. *et al.* (2005) Pilot study on the sensitivity and specificity of *in vivo* reflectance confocal microscopy in the diagnosis of allergic contact dermatitis. *J. Am. Acad. Dermatol.*, **53**, 986–992.

42 Astner, S. *et al.* (2006) Noninvasive evaluation of allergic and irritant contact dermatitis by *in vivo* reflectance confocal microscopy. *Dermatitis*, **17**, 182–191.

43 Ardigo, M. *et al.* (2009) Concordance between *in vivo* reflectance confocal microscopy and histology in the evaluation of plaque psoriasis. *J. Eur. Acad. Dermatol. Venereol.*, **23**, 660–667.

44 Koller, S. *et al.* (2009) *In vivo* reflectance confocal microscopy of erythematosquamous skin diseases. *Exp. Dermatol.*, **18**, 536–540.

45 Venturini, M. *et al.* (2009) Reflectance confocal microscopy for the *in vivo* detection of Treponema pallidum in skin lesions of secondary syphilis. *J. Am. Acad. Dermatol.*, **60**, 639–642.

46 Peters, BM. *et al.* (2010) Microbial interactions and differential protein expression in *Staphylococcus aureus–Candida albican*s dual-species biofilms. *FEMS Immunol. Med. Microbiol.*, **59**, 493–503.

47 De Rosa, FS. *et al.* (2000) A vehicle for photodynamic therapy of skin cancer: influence of dimethylsulphoxide on 5-aminolevulinic acid *in vitro* cutaneous permeation and *in vivo* protoporphyrin IX accumulation determined by confocal microscopy. *J. Control. Release*, **65**, 359–366.

48 Alvarez-Román, R. *et al.* (2004) Visualization of skin penetration using confocal laser scanning microscopy. *Eur. J. Pharm. Biopharm.*, **58**, 301–316.

49 Kaiser, W. *et al.* (1961) Two-photon excitation in CaF_2:Eu^{2+}. *Phys. Rev. Lett.*, **7**, 229.

50 Denk, W. *et al.* (1990) Two-photon laser scanning fluorescence microscopy. *Science*, **248**, 73–76.

51 König, K. (2000) Robert Feulgen Prize Lecture. Laser tweezers and multiphoton microscopes in life sciences. *Histochem. Cell Biol.*, **114**, 79–92.

52 Masters, B.R. *et al.* (1997) Multiphoton excitation fluorescence microscopy and spectroscopy of *in vivo* human skin. *Biophys. J.*, **72**, 2405–2412.

53 Masters, B.R. *et al.* (1998) Multiphoton excitation microscopy of *in vivo* human skin. Functional and morphological optical biopsy based on three-dimensional imaging, lifetime measurements and fluorescence spectroscopy. *Ann. N. Y. Acad. Sci.*, **838**, 58–67.

54 Zoumi, A. *et al.* (2001) Imaging cells and extracellular matrix *in vivo* by using second-harmonic generation and two-photon excited fluorescence. *Proc. Natl. Acad. Sci. U. S. A.*, **99**, 11014–11019.

55 Koehler, M.J. *et al.* (2010) *In vivo* measurement of the human epidermal thickness in different localizations by multiphoton laser tomography. *Skin Res. Technol.*, **16**, 259–264.

56 Dimitrow, E. *et al.* (2009) Sensitivity and specificity of multiphoton laser tomography for *in vivo* and *ex vivo* diagnosis of malignant melanoma. *J. Invest. Dermatol.*, **129**, 1752–1758.

57 Lin, S.-J. *et al.* (2005) Evaluating cutaneous photoaging by use of multiphoton fluorescence and second-harmonic generation microscopy. *Opt Lett.*, **30**, 2275–2277.

58 Lin, SJ. *et al.* (2006) Prediction of heat induced collagen shrinkage by use of second harmonic generation microscopy. *J. Biomed. Opt.* (2006) **11**, 34020.

59 Koehler, M.J. *et al.* (2008) Morphological skin ageing criteria by multiphoton laser scanning tomography: non-invasive *in vivo* scoring of the dermal fibre network. *Exp. Dermatol.*, **17**, 519–523.

60 Konig, K. *et al.* (2006) *In vivo* drug screening in human skin using femtosecond laser multiphoton tomography. *Skin Pharmacol. Physiol.*, **19**, 78–88.

61 Lee, J. *et al.* (2008) The effects of depilatory agents as penetration enhancers on human stratum corneum structures. *J. Invest. Dermatol.*, **128**, 2240–2247.

62 Luengo, J. *et al.* (2006) Influence of nanoencapsulation on human skin transport of flufenamic acid. *Skin Pharmacol. Physiol.*, **19**, 190–197.

63 Yu, B. *et al.* (2001) *In vitro* visualization and quantification of oleic acid induced changes in transdermal transport using two-photon fluorescence microscopy. *J. Invest. Dermatol.*, **117**, 16–25.

64 Gratieri, T. *et al.* (2010) Penetration of quantum dot particles through human skin. *J. Biomed. Nanotechnol.*, **6** (5), 586–595.

65 Yu, B. *et al.* (2003) Visualization of oleic acid induced transdermal diffusion pathways using two-photon fluorescence microscopy. *J. Invest. Dermatol.*, **120**, 448–455.

66 Lin, S. *et al.* (2006) Discrimination of basal cell carcinoma from normal dermal stroma by quantitative multiphoton imaging. *Opt. Lett.*, **31**, 2756–2758.

67 Dimitrow, E. *et al.* (2009) Spectral fluorescence lifetime detection and selective melanin imaging by multiphoton laser tomography for melanoma diagnosis. *Exp. Dermatol.*, **18**, 509–515.

68 Paoli, J. *et al.* (2008) Multiphoton laser scanning microscopy on non-melanoma skin cancer: morphologic features for future non-invasive diagnostics. *J. Invest. Dermatol.*, **128**, 1248–1255.

69 König, K. *et al.* (2009) Clinical optical coherence tomography combined with multiphoton tomography of patients with skin diseases. *J. Biophotonics*, **2**, 389–397.

70 König, K. *et al.* (2010) Clinical application of multiphoton tomography in combination with high-frequency ultrasound for evaluation of skin diseases. *J. Biophotonics* **3**, 759–773

71 Kaatz, M. *et al.* (2010) Depth-resolved measurement of the dermal matrix composition by multiphoton laser tomography. *Skin Res. Technol.*, **16**, 131–136.

72 Koehler, M.J. *et al.* (2009) Intrinsic, solar and sunbed-induced skin aging measured *in vivo* by multiphoton laser tomography and biophysical methods. *Skin Res. Technol.*, **15**, 357–363.

73 Koehler, M.J. *et al.* (2006) *In vivo* assessment of human skin aging by multiphoton laser scanning tomography. *Opt. Lett.*, **31**, 2879–2881.

74 Naito, S. *et al.* (2008) *In vivo* measurement of human dermis by 1064 nm-excited fiber Raman spectroscopy. *Skin Res. Technol.*, **14**, 18–25.

75 Puppels, GJ. *et al.* (1990) Studying single living cells and chromosomes by confocal Raman microspectroscopy. *Nature*, **347**, 301–303.

76 Gniadecka, M. *et al.* (1998) Structure of water, proteins, and lipids in intact human skin, hair, and nail. *J. Invest. Dermatol.*, **110**, 393–398.

77 Wu, JQ. and Kilpatrick-Liverman, L. (2011) Characterizing the composition of underarm and forearm skin using confocal Raman spectroscopy. *Int. J. Cosmet. Sci.*, **33**, 257–262.

78 Martini, MC. (2003) Biochemical analysis of epidermal lipids. *Pathol. Biol. (Paris)*, **51**, 267–270.

79 Kezic, S. (2008) Methods for measuring *in-vivo* percutaneous absorption in humans. *Hum. Exp. Toxicol.*, **27**, 289–295.

80 Nakagawa, N. *et al.* (2010) *In vivo* measurement of the water content in the dermis by confocal Raman spectroscopy. *Skin Res. Technol.*, **16**, 137–141.

81 Lademann, J. *et al.* (2011) Carotenoids in human skin. *Exp. Dermatol.*, **20**, 377–382.

82 Wohlrab, J. *et al.* (2001) Noninvasive characterization of human stratum corneum of undiseased skin of patients with atopic dermatitis and psoriasis as studied by Fourier transform Raman spectroscopy. *Biopolymers*, **62**, 141–146.

83 O'Regan, G.M. *et al.* (2010) Raman profiles of the stratum corneum define 3 filaggrin genotype-determined atopic dermatitis endophenotypes. *J. Allergy Clin. Immunol.*, **126**, 574–580. e1.

84 González, F.J., Alda, J., Moreno-Cruz, B., *et al.* (2011) Use of Raman spectroscopy for the early detection of filaggrin-related atopic dermatitis. *Skin Res. Technol.*, **17**, 45–50.

85 Andrew Chan *et al.* (2008) A coordinated approach to cutaneous wound healing: vibrational microscopy and molecular biology. *J. Cell Mol. Med.*, **12** (5B), 2145–2154.

86 Willemse-Erix, D.F. (2010) Towards Raman-based epidemiological typing of *Pseudomonas aeruginosa*. *J. Biophotonics*, **3**, 506–511.

87 Lademann, J. *et al.* (2011) Interaction between carotenoids and free radicals in human skin. *Skin Pharmacol. Physiol.*, **24**, 238–244.

88 Hesterberg, K. *et al.* (2009) Raman spectroscopic analysis of the increase of the carotenoid antioxidant concentration in human skin after a 1-week diet with

ecological eggs. *J. Biomed. Opt.*, **14**, 024039.

89 Mélot, M. *et al.* (2009) Studying the effectiveness of penetration enhancers to deliver retinol through the stratum cornum by *in vivo* confocal Raman spectroscopy. *J. Control. Release*, **138**, 32–39.

90 Goeppert-Mayer, M. (1931) Über elementarakte mit zwei quantensprüngen. *Ann Phys*, **9** (3), 273–295.

52
Non-Melanoma Skin Cancer

Martin Kaatz, Susanne Lange-Asschenfeldt, Martin Johannes Koehler, and Uta Christina Hipler

52.1
Introduction

Basal cell carcinoma (BCC) is the most common skin tumor, and overall one of the most frequently occurring tumors. Over the last three decades, incidence rates have increased steadily and about one-third of all Caucasians must be expected to develop a BCC at some point in their lives. Although the tumor is metastasizing only under special circumstances, it may nonetheless pose a considerable therapeutic problem, depending on its size and localization.

Squamous cell carcinoma (SCC) of the skin often develops out of precursors – mainly actinic keratoses – which have histopathologically been classified as *in situ* SCCs. Although early actinic keratoses may undergo a regression process, the probability of developing an invasive SCC increases depending on the thickness of neoplastic alterations, and host factors such as genetic or iatrogenic immunosuppression.

Exposure to UV light poses the most important etiological factor in skin tumorigenesis, hence the preferred development of SCC in sun-exposed parts of the skin, such as the face hands, and forearms. Other possible causes of SCC development include chronic wounds, burn injuries, and exposure to radiation.

Numerous issues arise with regard to the application of noninvasive imaging. These issues cover all areas of tumorigenesis, prevention, diagnostics, and therapy, and also the diagnostic classification of tumors and the assessment of their lateral expansion and penetration depth. This applies particularly to the evaluation of tumor margins, part of which, depending on the tumor type, are clinically not easily determined. Other possibilities are the assessment of preclinical lesions and the monitoring of therapeutic success. Efficacy and tolerance of protective methods also play a role in matters of prevention. Additionally, noninvasive imaging can help clarify scientific issues with regard to tumorigenesis.

Handbook of Biophotonics. Vol.2: Photonics for Health Care, First Edition. Edited by Jürgen Popp, Valery V. Tuchin, Arthur Chiou, and Stefan Heinemann.

52.2 Dermoscopy

52.2.1 Basal Cell Carcinoma

The diagnosis of (pigmented) basal cell carcinomas is based on features such as arborizing vessels, leaf-like structures, large blue–gray ovoid nests, multiple blue–-gray globules, spoke-wheel areas, and ulceration [1–3].

52.3 Optical Coherence Tomography (OCT)

52.3.1 Basal Cell Carcinoma

Epithelial skin tumors and basal cell carcinomas are more easily visualized in optical coherence tomography (OCT) than pigmented lesions due to the usually low melanin content of these tumors. This makes it easier to define clearly the dermoepidermic junction zone [4, 5]. In 2004, Bechara *et al*. employed OCT in order to perform initial studies on the specific features of basal cell carcinomas [6]. The analysis of three superficial BCCs proved subepidermally an echo-rich band that corresponded to the tumor aggregates verified by histology. These aggregates were separated from the surrounding stroma by a narrow, echo-poor band. In a follow-up examination of 43 BCCS, among which there were 23 nodular and 10 multifocal-superficial, OCT allowed the definition of distinctions between different types of BCC. The most important OCT criteria for a BCC were the plug-like signal-intensive structures corresponding to the histology of the dense tumor cell aggregates, honeycomb-like signal-poor structures correlating to the adjacent tumor lobules, and signal-free cavities in the imaging of a supervascularization. The frequency of occurrence of these criteria was found to be different in the single BCC types. The last two of these criteria (70 and 80%, respectively) were found particularly in infiltrative BCC, whereas the plug-like signal-intense structures were detected mainly in the superficial (80%) and, slightly less frequently, in the nodular BCCs (52%). The comparison of penetration depth measurement methods for BCCs <2 mm in size proved an overestimated thickness for both high-resolution ultrasound and OCT. The OCT results, however, were significantly closer to those achieved by histology than the penetration depths measured by high-frequency ultrasound (HFUS). In a blind study, OCT images of 64 BCCs and 39 actinic keratoses were evaluated by dermatologists and pathologists. It was found that dermal tumor cell clusters can be distinguished from the surrounding stroma with sensitivities and specificities of 79–96%. OCT also allowed for the differentiation of solid versus sclerodermatous BCCs. However, a differentiation between BCC and actinic keratosis had an error rate of 50 versus 52% and was thus proved impossible (Figure 52.1).

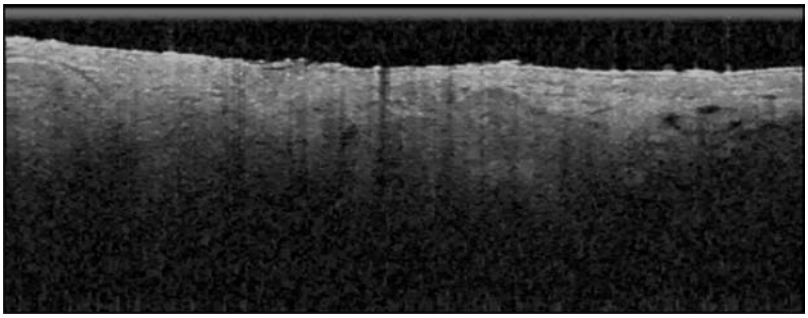

Figure 52.1 OCT of BCC at forehead.

52.3.2
Actinic Keratosis and Squamous Cell Carcinoma

Actinic keratoses predominantly emerge in parts of the body that are exposed to UV light, and that in many cases have already been obviously damaged by sunlight. In several studies, OCT could prove a differentiation between sun-damaged skin and surrounding unaffected areas by detection of a significant thickening of the viable epidermis and/or stratum corneum. Images of sun-damaged skin were characterized by an increased signal in the epidermis and rapid attenuation of light. The imaging of actinic keratoses under examination was characterized by a great variability and heterogeneity, with dark bands in the epidermis possibly corresponding to hyperkeratosis.

The compacted keratin is weakly scattering, and a thickened keratin layer was seen in corresponding histology. In OCT, the epidermis of actinic keratoses often displays distinct horizontal reflections due to flaking within the keratinized region (Figure 52.2). In cases of a significantly widened stratum corneum, a distinct

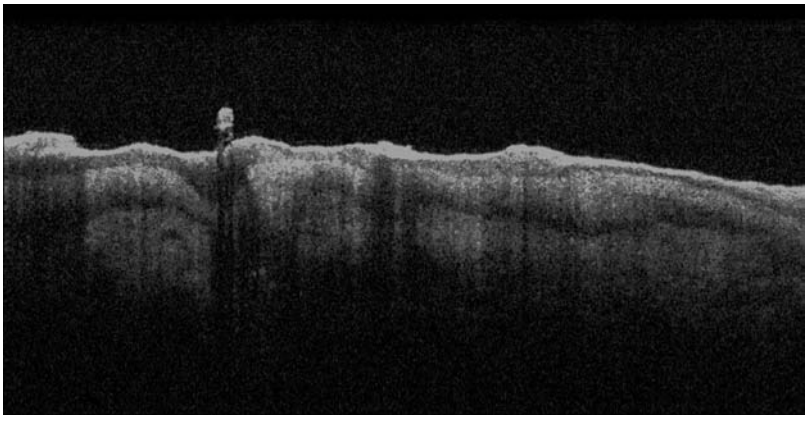

Figure 52.2 OCT of actinic keratosis.

boundary was observed between the keratinized region and underlying epidermis. On comparing intralesional skin with perilesional skin, both OCT and histology could prove an acanthosis. Unlike undiseased skin, the epidermis in actinic keratosis images could appear relatively hyperintense, possibly because of an increased backscatter from the dysplastic cells or parakeratosis. Also, a distinct boundary at a depth consistent with the epidermal–dermal junction was regularly observed. Vertical shadowing from skin flakes was common. Attenuation in the dermis, however, was often strong, similar to severely sun-damaged sites. There were, however, great differences in the comparison of the single lesions. The differentiation of actinic keratoses from the surrounding skin resulted in a sensitivity of 73% and a specificity of 65%. These could even be increased for single OCT criteria (presence of a dark band in the epidermis) to 86% sensitivity and 83% specificity. The clinical–dermatologic assessment achieved a sensitivity of 98% and a specificity of 62%.

The preciseness of thickness measurement in OCT compared with HFUS was also surveyed on actinic keratoses. Results for the lesion thickness were more exact in OCT, even though in actinic keratoses also there was an apparent overestimation [7].

In summary, it can be stated that OCT could prove qualitative and statistically significant quantitative differences in OCT image features of skin with varying degrees of sun damage, and between undiseased skin and actinic keratosis.

Nevertheless, the differentiation between actinic keratoses and BCCs was limited, with a high error rate of ~50% [6, 8].

52.4 Confocal Laser Scanning Microscopy (CLSM)

52.4.1 Basal Cell Carcinoma

In the first study on the noninvasive diagnostics of BCCs by confocal laser scanning microscopy (CLSM), 12 patients with histologically diagnosed BCC were examined. Typical features included an increased number and bore of the vessels, loss of normal architecture, and a strongly reflectant stroma contrasting with the dark tumor parenchyma [9].

Specific criteria were established in 2004 in a multicenter study on 152 lesions, 83 of which were diagnosed as BCC. The criteria comprised elongated, monomorphous cell nuclei, a polarization of these cell nuclei along the same axis (palisading), an inflammatory cell infiltrate, an increase and dilatation of dermal vessels, and a loss of the epidermal honeycomb structure (Figure 52.3). With the presence of four out of five criteria, sensitivity and specificity were 82.9 and 95.7%, respectively. At the same time, CLSM allows for a distinction of BCC subtypes, especially of superficial and solid BCCs. Also, pigmented BCC may be identified by detection of strong contrast due to the high melanin content, whereas the differentiation of the morpheaform

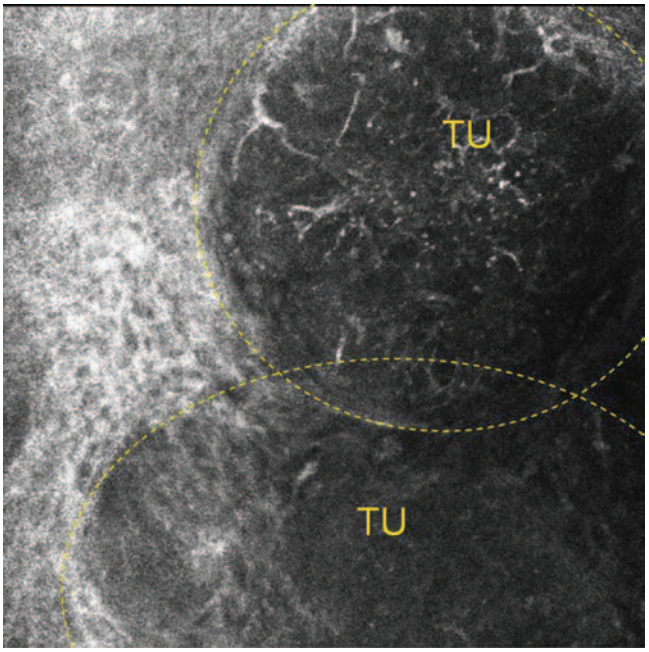

Figure 52.3 CLSM of BCC. Morpheaform variant, tumor lobules (dashed circle, TU), pigmented cells of dendritic shape.

BCC appears to be more difficult due to the few strayed tumor nests extending into the dermis [10].

By means of horizontal mapping, the architecture of larger tumor lobules may be evaluated, allowing the use of CLSM for margin-controlled surgery. One study on 45 excisions reported sensitivity and specificity values of 97 and 89%, respectively, which were confirmed in another study. Since the duration of the CLSM examination was only about 7.5 min, the use of this method promises an acceleration of those surgical procedures [11, 12].

52.4.2 Actinic Keratoses and Squamous Cell Carcinoma

The value of CLSM in diagnostics of epithelial and pigmented skin tumors has already been surveyed in numerous clinical studies. Epithelial *in situ* carcinomas of the actinic keratosis type were examined in 2000 [13]. In that pilot study, hyperkeratosis, pleomorphism, and architectural disarray were described as criteria for actinic keratoses. In subsequent studies, both a high sensitivity (80%) and specificity (96%) of the method compared with routine histology could be proved. In a study on 46 actinic keratoses, sensitivities and specificities of 80–99% were reached [14]. In another study on 30 actinic keratoses, values of 89–94% were obtained. The main features were parakeratosis and/or hyperkeratosis, stratum corneum disruption,

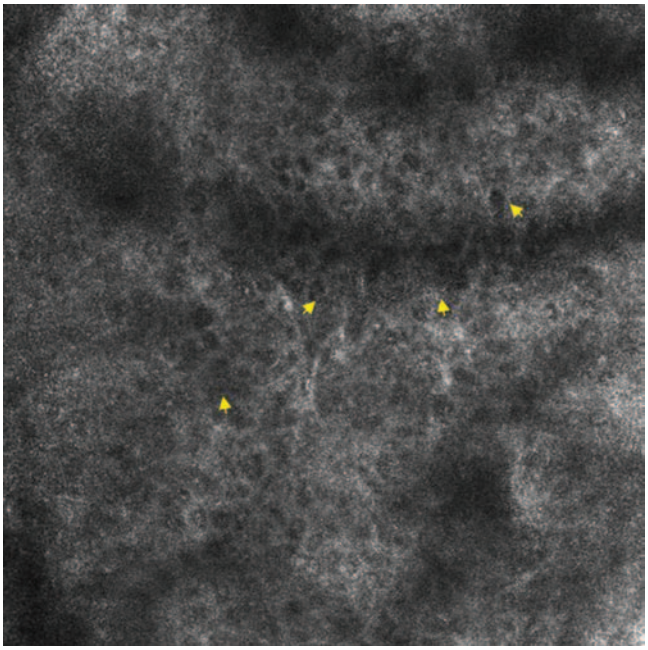

Figure 52.4 CLSM of an actinic keratosis. Clinical II epidermal disarray and keratinocyte pleomorphism (arrowheads) with different shapes and sizes of dark appearing nuclei.

individual corneocytes, pleomorphism, and architectural disruption in stratum granulosum and stratum spinosum [15] (Figure 52.4).

However, in this study, hyperkeratotic actinic keratoses were excluded due to the limited penetration depth allowed by the method. The assessment of the lesion's horizontal extension beyond the clinically visible lesion (subclinical changes) turned out to be excellent. Hence, the method also qualifies for monitoring. Invasive SCC displays similar, if more severe, criteria in CLSM. Vertical extension, however, cannot be recorded owing to the limited penetration depth of the method [13, 16].

52.5 Multiphoton Tomography (MPT)

52.5.1 Basal Cell Carcinoma

Especially superficial BCCs were suitable for examination by multiphoton tomography (MPT), which was mainly due to the limited penetration depth of this method. For nearly all of the lesions examined, a significantly increased epidermal thickness compared with perilesional skin could be proved. Also, a large part of

the BCCs examined showed a pronounced hyperkeratosis that was at least 60 μm thick and highly fluorescent, which hindered the imaging of the underlying epidermis. In these cases, no specific characteristics could be defined in the epidermis. In a large part of the lesions that showed a less pronounced hyperkeratosis, the epidermis was twice as thick as in the surrounding areas of unaffected skin. Therefore, no dermal papillae could be proved even at a depth of 100–130 μm. The tumor cells produced a monomorphous image. Arrangement was, as far as could be evaluated, palisade-like. Also, although rarely, elongated nuclei and cytoplasms could be proved in the lower third of the epidermis, which were oriented in the same direction in the x–y plane, a feature described as nuclei polarization. Speckled perinuclear fluorescence was observed in the subcorneal epidermis of all examined lesions but was also present in the corresponding normal perilesional skin in most cases.

In nodular BCC, in which the important histological alterations of the dermis can be proved, evaluation was limited. Comparing intralesional conditions with those in the surrounding areas, MPT could not detect any differences in the epidermis. Only one-third of the tumors examined presented typical nodular aggregates of tumor cells within the dermis. The tumor nests lacked contiguity with the overlying normal epidermis, and the basal cells within these nests presented large, oval nuclei, little cytoplasm, and peripheral palisading. The autofluorescence of these cells was comparable to that of the cells found in the superficial BCC.

In a further study, additional characteristics of the BCC were defined by multiphoton imaging. In the multiphoton images, BCC was characterized by clumps of autofluorescent cells in the dermis. The tumor cells showed a relatively large nucleus and a higher nucleus-to-cytoplasm ratio. Another prominent feature revealed by multiphoton imaging is the alteration of extracellular matrix in the BCC stroma. In the stroma within and surrounding the cancer clumps, second-harmonic generation (SHG) diminishes whereas autofluorescence signals increase. The decrease in SHG indicates that the collagen molecule packing has been disrupted and can reflect an up-regulated collagenase activity in cancer tissue [17, 18].

52.5.2
Actinic Keratoses and Squamous Cell Carcinomas

In most of the actinic keratoses examined, the stratum corneum proved to be abnormally thick, reaching values up to 30–40 μm. Inside the thickened stratum corneum, fluorescent nuclei compartments within the corneocytes were observed. This morphologic and fluorescent feature has earlier been described to occur in the presence of hyperkeratosis. In two hyperkeratotic lesions, large, rounded bundles of keratin were observed within the stratum corneum, corresponding to so-called keratin pearls. The lower layers of the epidermis displayed an architectural disarray with polymorphous keratinocytes (Figure 52.5). The stratum basale, however, could be submitted to only a limited evaluation, which was due to the limited penetration

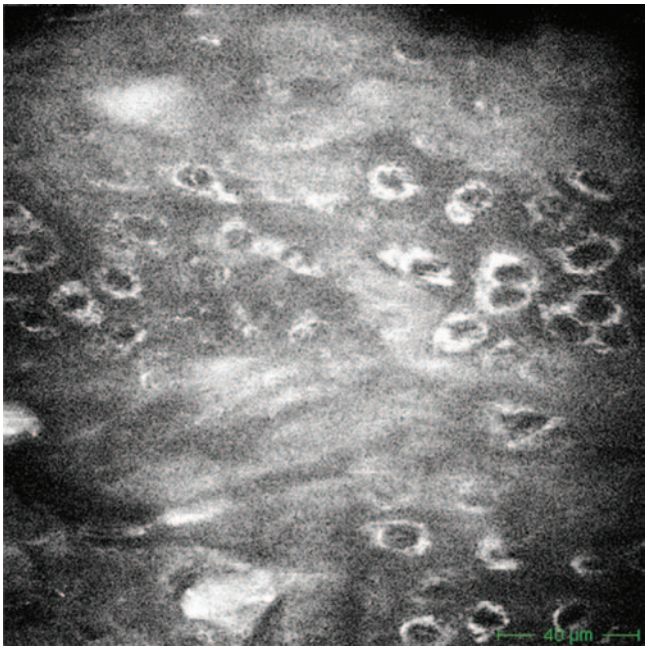

Figure 52.5 MPT of an actinic keratosis. Architectural disarray stratum spinosum.

depth of the method. The reasons for this limitation were the hyperkeratosis and the epidermis widened due to acanthosis [19].

52.6 Laser Doppler Imaging

52.6.1 Basal Cell Carcinoma

Histology shows that expanding tumors, and BCCs in particular, are accompanied by increasing vascularization. Among others, laser Doppler imaging is one way of imaging this vascularization *in vivo*. Stücker *et al.* [20] performed a study on 16 BCCs with this method, providing a two-dimensional image of the blood flow. In the tumor regions, blood flow was always higher than in the surrounding areas, although not as strongly increased as in patients with melanocytic nevi or malignant melanomas. In BCCs, however, a fairly homogeneous increase in perfusion all over the tumor was found. Nevertheless, the peak flow reached lower values than those reached especially in malignant melanomas. Owing to the wide variability of results, a reliable status differentiation by means of laser Doppler imaging is considered impossible [20].

Well-structured studies on the perfusion of actinic keratoses and squamous cell carcinomas are as yet lacking.

52.7
Raman Spectroscopy

52.7.1
Basal Cell Carcinoma

The capabilities of Raman spectroscopy in diagnostics of BCCs have been reviewed in numerous *ex vivo* surveys.

Raman spectral intensities of carotenoids in human skin have been found to be increased in BCC, compared with the surrounding skin. At the same time, differences in lipid and protein structures between BCC and normal skin biopsies were proved. With supplementary employment of the respective Raman intensities, a complete separation between these tissue types could be achieved [21]. Simple analysis of confocal Raman spectra obtained from various skin depths showed a 95% separation between normal skin and BCC [22], Confocal Raman maps of BCC sections have also been shown to identify tumor margins accurately, with 100% sensitivity and 93% specificity. When applying high-wavenumber Raman bands (2800–3125 cm^{-1}), BCC could be discriminated from perilesional tissue.

These results formed the basis for depth-resolved *in vivo* diagnostics using confocal Raman spectroscopy in the form of a hand-held device. The *in vivo* studies achieved a specificity of 100% and a sensitivity of 91%.

Morphometric measurements of the depth of the proximal tumor margin from the skin surface was possible in 66% of cases (six out of the nine BCCs). The measured depths of the tumor margins were 49, 69, 89, 169, 223, 234, 593, 888, and 961 μm from the surface.

Several of these differences reveal that the pathologic spectra can largely be separated by protein- and lipid-related Raman activity.

In addition, compared with conventional Raman spectroscopy, polarized Raman microspectroscopy provides additional relevant information on the molecular ordering of molecular biomolecules. Also, it offers a refined discrimination between the tumor tissue and the normal epidermis.

The depolarization ratios of the bands corresponding to phenylalanine (623, 1339 cm^{-1}), tyrosine (644 cm^{-1}), polysaccharides (1128 cm^{-1}), and *trans* hydrocarbon chains (1128 cm^{-1}) in spectra of the tumor were lower than those recorded in the normal epidermis, representing potential markers to discriminate the tumor tissue and the epidermis. The depolarization ratios of the bands of the peritumoral stroma corresponding mainly to lipids (1065 cm^{-1}), collagens, and various other proteins (920, 940, 1065, and 1128 cm^{-1}) were different from those of the healthy dermis.

The differences in spectra between the peritumoral and the normal dermis were lower than the differences between the tumor tissue and the normal epidermis.

The use of polarized Raman microspectroscopy shows that depolarization ratios of selected vibrations could be potential diagnostic markers to distinguish between the tumor and normal epidermis, and between peritumoral and normal dermis [23].

52.7.2
Actinic Keratoses and Squamous Cell Carcinomas

The spectral intensities of carotenoids were also increased in actinic keratoses, compared with the surrounding skin. At the same time, there were obvious variations in Raman spectra between normal skin and hyperkeratotic lesion samples, which are considered to be related to lipid concentration. In subsequent depth-resolved *in vivo* studies, a correct allocation of abnormal spectra could be achieved in 75% of the actinic keratoses or SCCs. Other than in BCCs, the spectra of SCC tissues generally show a moderate probability for normal tissue [24].

References

1 Zalaudek, I. *et al.* (2006) Dermoscopy in general dermatology. *Dermatology*, **212**, 7–18.
2 Braun, R.P. *et al.* (2005) Dermoscopy of pigmented skin lesions. *J. Am. Acad. Dermatol.*, **52**, 109–121.
3 Campos-do-Carmo, G. and Ramos-e-Silva, M. (2008) Dermoscopy: basic concepts. *Int. J. Dermatol.*, **47**, 712–719.
4 Mogensen, M. *et al.* (2009) Assessment of optical coherence tomography imaging in the diagnosis of non-melanoma skin cancer and benign lesions versus normal skin: observer-blinded evaluation by dermatologists and pathologists. *Dermatol. Surg.*, **35**, 965–972.
5 Jørgensen, T.M. *et al.* (2008) Machine-learning classification of non-melanoma skin cancers from image features obtained by optical coherence tomography. *Skin Res. Technol.*, **14**, 364–369.
6 Bechara, F.G. *et al.* (2004) Histomorphologic correlation with routine histology and optical coherence tomography. *Skin Res. Technol.*, **10**, 169–173.
7 Korde, V.R. *et al.* (2007) Using optical coherence tomography to evaluate skin sun Damage and precancer. *Lasers Surg. Med.*, **39**, 687–695.
8 Mogensen, M. *et al.* (2009) *In vivo* thickness measurement of basal cell carcinoma and actinic keratosis with optical coherence tomography and 20-MHz ultrasound. *Br. J. Dermatol.*, **160**, 1026–1033, Epub 2009 Jan 12.
9 Sauermann, K. *et al.* (2002) Investigation of basal cell carcinoma [correction of carcionoma] by confocal laser scanning microscopy *in vivo*. *Skin Res. Technol.*, **8**, 141–147.
10 Nori, S. *et al.* (2004) Sensitivity and specificity of reflectance-mode confocal microscopy for *in vivo* diagnosis of basal cell carcinoma: a multicenter study. *J. Am. Acad. Dermatol*, **51**, 923–930.
11 Karen, J.K. *et al.* (2009) Detection of basal cell carcinomas in Mohs excisions with fluorescence confocal mosaicing microscopy. *Br. J. Dermatol.*, **160**, 1242–1250.
12 Ziefle, S. *et al.* (2010) Confocal laser scanning microscopy vs 3-dimensional histologic imaging in basal cell carcinoma. *Arch. Dermatol.*, **146**, 843–847.
13 Aghassi, D. *et al.* (2000) Confocal laser microscopic imaging of actinic keratoses *in vivo*: a preliminary report. *J. Am. Acad. Dermatol.*, **43**, 42–48.
14 Ulrich, M. *et al.* (2008) Clinical applicability of *in vivo* reflectance confocal microscopy for the diagnosis of actinic keratoses. *Dermatol. Surg.*, **34**, 610–619.
15 Horn, M. *et al.* (2008) Discrimination of actinic keratoses from normal skin with reflectance mode confocal microscopy. *Dermatol. Surg.*, **34**, 620–625.
16 Ulrich, M. *et al.* (2007) Noninvasive diagnostic tools for nonmelanoma skin cancer. *Br. J. Dermatol.*, **157**, 56–58.

17 Gonzalez, S. and Tannous, Z. (2002) Real-time, *in vivo* confocal reflectance microscopy of basal cell carcinoma. *J. Am. Acad. Dermatol.*, **47**, 869–874.

18 Nori, S. *et al.* (2004) Sensitivity and specificity of reflectance-mode confocal microscopy for *in vivo* diagnosis of basal cell carcinoma: a multicenter study. *J. Am. Acad. Dermatol.*, **51**, 923–930.

19 König, K. and Riemann, I. (2003) High-resolution multiphoton tomography of human skin with subcellular spatial resolution and picosecond time resolution. *J. Biomed. Opt.*, **8**, 432–439.

20 Stücker, M. *et al.* (2002) *In vivo* differentiation of pigmented skin tumors with laser Doppler perfusion imaging. *Hautarzt*, **53**, 244–249.

21 Gniadecka, M. *et al.* (1997) Distinctive molecular abnormalities in benign and malignant skin lesions: studies by Raman spectroscopy. *Photochem. Photobiol.*, **66**, 418–423.

22 Choi, J. *et al.* (2005) Direct observation of spectral differences between normal and basal cell carcinoma (BCC) tissues using confocal Raman microscopy. *Biopolymers*, **77**, 264–272.

23 Lieber, C.A. *et al.* (2008) *In vivo* nonmelanoma skin cancer diagnosis using Raman microspectroscopy. *Lasers Surg. Med.*, **40**, 461–467.

24 Hata, T.R. *et al.* (2000) Non-invasive raman spectroscopic detection of carotenoids in human skin. *J. Invest. Dermatol.*, **115**, 441–448.

53
Pigmented Skin Lesions

Martin Kaatz, Susanne Lange-Asschenfeldt, Peter-Elsner, and Sindy Zimmermann

53.1
Introduction

Cutaneous melanoma is a malignant tumor that arises from melanocytic cells and is potentially the most dangerous form of skin tumor. Simultaneously, cutaneous malignant melanoma is the most rapidly increasing cancer in white populations, increasingly also affecting adolescents and young adults [1, 2]. The frequency of its occurrence is closely associated with the constitutive color of the skin and depends on the geographic zone. The incidence of malignant melanoma in Europe varies from 6–10 per 100 000 per year in Mediterranean countries to 12–20 per 100 000 per year in Nordic countries. Individuals with large numbers of common nevi, congenital nevi and with atypical nevi (dysplastic nevi) are at greater risk [1].

The prognosis for patients with high-risk or advanced metastatic melanoma remains poor, despite advances in this field. Patient outcome and curability depend on timely recognition and excision at early stages of tumor progression. This situation encourages extensive research on new imaging technologies for early melanoma detection and differentiation from benign melanocytic nevi or other non-malignant pigmented lesions.

53.2
Dermoscopy

Dermoscopy **(**epiluminescence microscopy**)** allows for visualization of characteristic features of selected skin lesions that would otherwise be invisible to the naked eye [3–6]. This method has been studied extensively for the evaluation of pigmented skin lesions, where by predictions with respect to the status of the lesion may be made.

Two extensive meta-analyses in which studies from different clinical and experimental settings were assessed showed an increase in the diagnostic accuracy in the detection of melanomas when employing dermoscopy [7–9]. The diagnostic accuracy

Handbook of Biophotonics. Vol.2: Photonics for Health Care, First Edition. Edited by Jürgen Popp, Valery V. Tuchin, Arthur Chiou, and Stefan Heinemann.

expressed as the relative diagnostic odds ratio was 15.6 (95% CI 2.9–83.7) times higher for dermoscopy than for mere visual inspection [10]. It must be kept in mind, however, that the user's experience is crucial to diagnostic accuracy, allowing a decreased excision rate in melanocytic lesions.

According to an expert consensus, after documentation of clinical information on the patient and the lesion, the first dermoscopic step is the distinction between melanocytic and non-melanocytic lesions [6, 11]. In this context, dermoscopic criteria for melanocytic lesions are taken into consideration, including the presence of a pigment network, aggregated globules, streaks, homogeneous blue pigmentation and parallel pattern (Figure 53.1). The second step comprises the description of dermoscopic structures and patterns by standardized terms and optionally the use of a diagnostic algorithm in order to differentiate between benign and malignant tumors. Finally, a specific final diagnosis or differential diagnoses should be provided. With respect to pigmented lesions, the most critical step is the differentiation of benign melanocytic nevi from malignant melanoma. In a study on inter-observer diagnostic agreement, pattern analysis showed the best diagnostic performance among the second-step procedures with an inter-observer agreement of $\kappa = 0.55$ and an intra-observer agreement of $\kappa = 0.85$. Alternative algorithms including the ABCD rule [12], the Menzies score [13], and the seven-point list [14] had inferior diagnostic values. Pattern analysis includes the standardized description of the global pattern, determination of absence or presence and description (typical vs. atypical or regular vs. irregular) of a pigment network, dots/globules, streaks, a

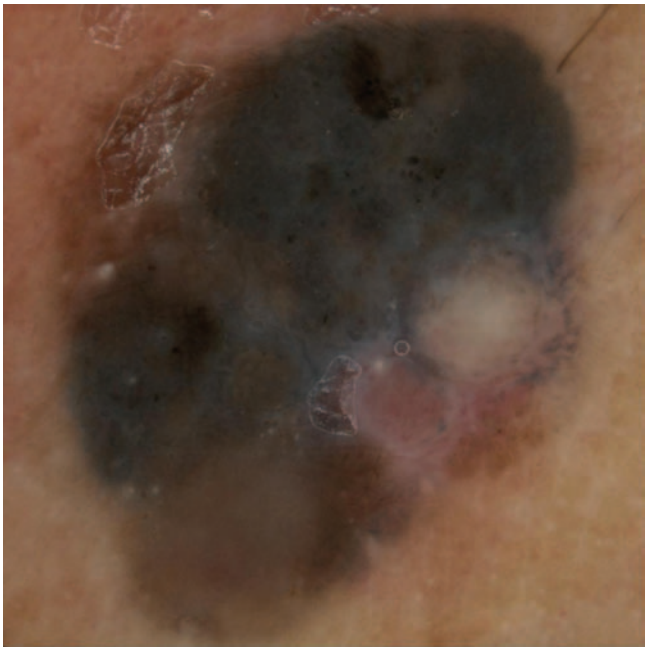

Figure 53.1 Dermoscopy of malignant melanoma.

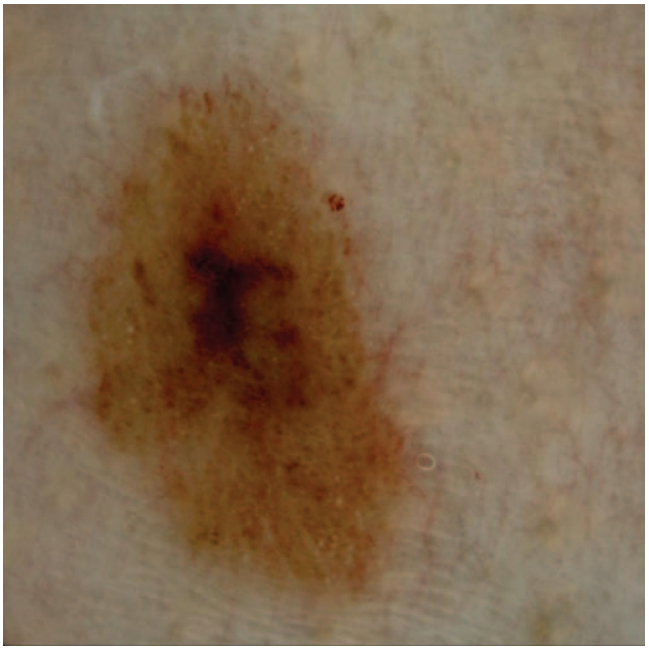

Figure 53.2 Dermoscopy of nevus.

blue–whitish veil, blotchy hypopigmentation, regression structures, and vascular structures [11]. Among these criteria, the most powerful predictors for a melanoma were an atypical pigment network, irregular dots and globules, irregular blotches, and the presence of regression structures, whereas global patterns described as globular, cobblestone, homogeneous, or starburst were most indicative for nevi (Figures 53.1 and 53.2).

Recent advances in computer-assisted dermoscopy may be applied for the follow-up of suspicious melanocytic skin lesions. Sequential digital dermoscopy (SDD) comprises the digital acquisition of dermoscopic images and their storage, allowing for a longitudinal observation of the dynamic changes of a lesion. In several studies, an improvement in the diagnostic power compared with routine dermoscopy was shown [15–17]. These elaborated methods were applied especially for the follow-up of high-risk patients and for the evaluation of the dynamic change of lesions that do not fulfill dermoscopic criteria [8, 18, 19].

53.3
Optical Coherence Tomography (OCT)

Optical coherence tomography (OCT), which is based on the principle of Michelson interferometry using light of short coherence length, has been employed for a variety of dermatologic applications in the past decade. However, few studies evaluated the

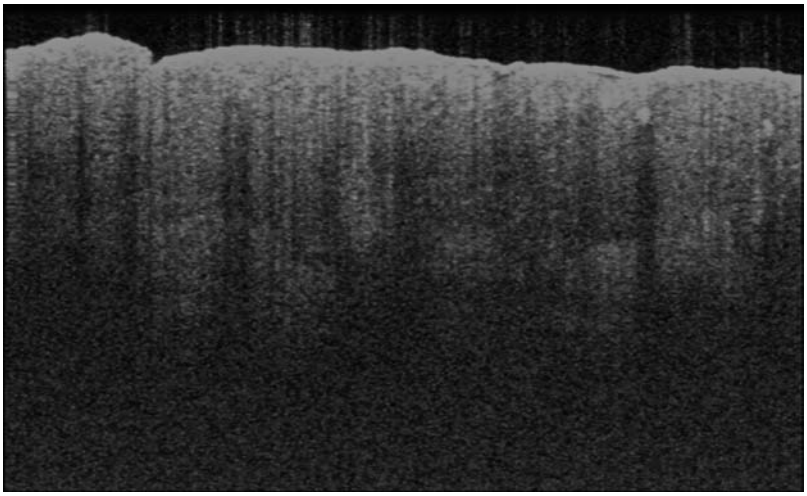

Figure 53.3 OCT of malignant melanoma.

use of this method for the differentiation of melanocytic skin lesions. In a study with 75 patients, criteria for the differentiation of benign and malignant melanocytic lesions by OCT were established by Gambichler *et al.* [20]. Criteria that were more frequently associated with malignant melanoma compared with melanocytic nevi include marked architectural disarray and a blurred dermo-epidermal junction [20] (Figures 53.3 and 53.4). Controlled studies on sensitivity and specificity of the method are lacking, however.

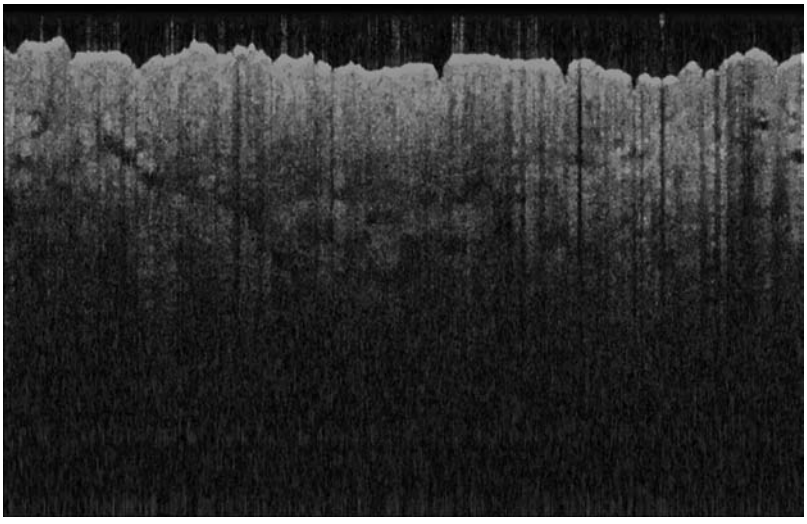

Figure 53.4 OCT of nevus.

53.4
Confocal Laser Scanning Microscopy (CLSM)

Confocal laser scanning microscopy (CLSM) is based on an 830 nm diode laser that is used as a point light source in a scanning mode providing horizontal tomographic images. The visualization of tissues is based on the different refractive indices of the distinct tissue chromophores and cell structures.

There have been numerous studies on CLSM for the evaluation of pigmented skin lesions. Initial investigations have shown that CLSM is particularly suitable for the evaluation of melanocytic lesions, since melanin provides a very strong contrast. In an investigation on 117 melanocytic lesions including 27 malignant melanomas, the sensitivities and specificities of five observers were reported to be 59–96 and 94–100%, respectively [21]. In another study of 125 melanocytic lesions, CLSM was compared with dermoscopy, resulting in similar specificities of 83 and 84%, respectively. In contrast, a much higher sensitivity was obtained by CLSM (97 vs. 89%) [22].

Typical features described for the malignant melanoma include the "non-edged papillae," irregular nests of atypical melanocytes, a pronounced dissolution of the normal epidermal structure, the existence of large, highly refractive cells with a prominent nucleus in the epidermis, and large dendritic cells with long, irregular branches, and also atypical nests of cerebriform morphology [23].

In contrast, benign melanocytic nevi are characterized by small, monomorphic, round to oval cells at the dermo-epidermal junction (junctional nevi), or at the junction and in the superficial dermis (compound nevi). Papillae are particularly well defined (so-called "edged papillae"). Furthermore, both the visualization of regular, homogeneously structured nests of melanocytes and a regular structure of the epidermis are considered to be decisive criteria for the classification of a lesion as benign nevus. Here, the structure of the epidermis may follow either a honeycomb or a cobblestone pattern. Dysplastic nevi display irregularly structured papillae with modified shapes, and also the existence of atypical melanocytes at the junction zone [21, 24] (Figure 53.5).

A number of further skin lesions with pigment disturbance were examined. *Seborrheic keratoses* are characterized by a cerebriform architecture of the epidermis, well-defined, round, black areas filled with whorled refractive material (horn cysts), and enlarged papillary rings lined by brightly refractive cells (pigmented keratinocytes). Plump bright cells (melanophages) may be present in the dermis. Vitiligo presents a complete loss of dermal papillary rings at the dermo-epidermal junction and no bright cells in the epidermis. Dendritic melanocytes may be found at the basal layer in repigmented skin. The features of *lentigo* include hyperrefractive dermal papillary rings with ovoid to annular or polycyclic contours at the dermo-epidermal junction. Plump bright cells (melanophages) may be present in the dermis. *Melasma* is characterized by increased cobblestoning and the presence of dendritic melanocytes at the basal cell layer [25].

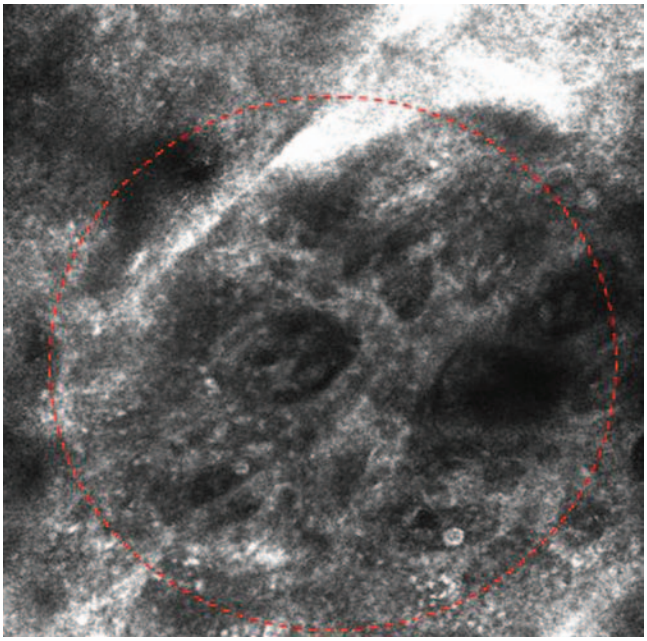

Figure 53.5 Irregular/non-edged papillae with sparse clusters/some large bright cells (circle).

53.5
Multiphoton Laser Tomography (MPT)

The principle of multiphoton imaging is the simultaneous absorption of two or more photons by a fluorophore and emission of one photon at a shorter wavelength, that is, with higher energy. While most of the fluorophores are located intracellularly, elastin and collagen as extracellular matrix proteins also have fluorescent properties. A characteristic phenomenon of fibrillar collagen is its ability for second-harmonic generation (SHG). In sum, the photons emitted from the dermis consist of both autofluorescence and SHG effects. Due to high resolution and the properties of melanin and its components for autofluorescence, a recent study examined the significance of MPT in the diagnostics of malignant melanomas. The investigation included 83 melanocytic skin lesions, including 26 melanomas. In this study, distinct morphologic differences in melanoma compared with melanocytic nevi were identified by multiphoton laser tomography (MLT). Sensitivities and specificities values up to 95 and 97%, respectively, were achieved for diagnostic classification.

The most significant diagnostic criteria include architectural disarray of the epidermis, poorly defined keratinocyte cell borders and the presence of pleomorphic or dendritic cells [26] (Figures 53.6 and 53.7). Remarkable differences

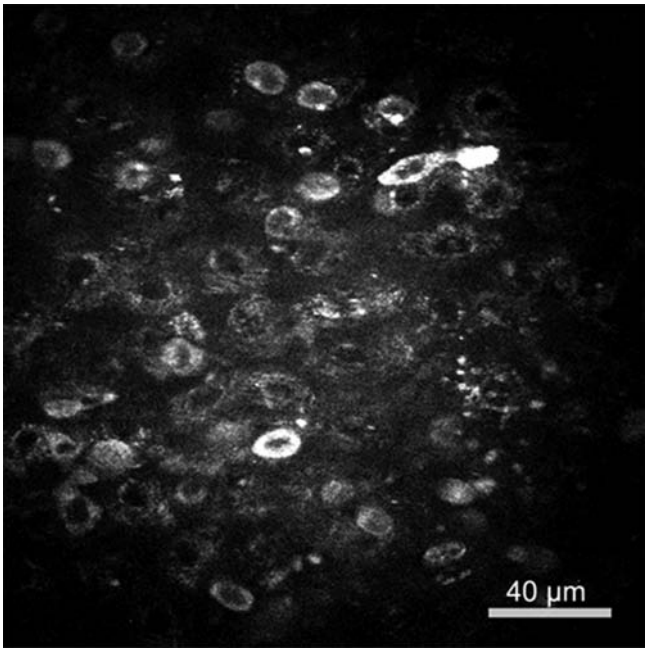

Figure 53.6 MPT of malignant melanoma: stratum granulosum with atypical melanocytes.

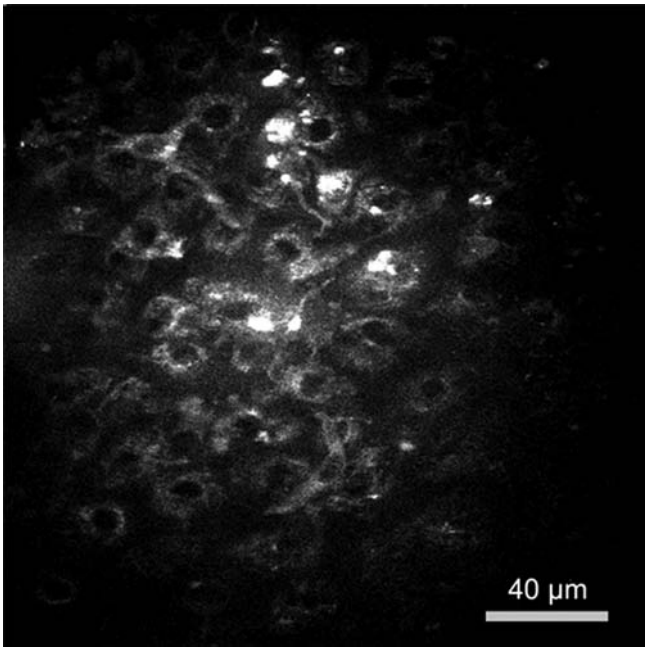

Figure 53.7 MPT of malignant melanoma: stratum spinosum, dendritic cells.

in real-time behavior of keratinocytes in contrast to melanocytes were detected. The fluorescence lifetime distribution was found to correlate with the intracellular amount of melanin [27]. Spectral analysis of melanoma revealed a main fluorescente peak around 470 nm in combination with an additional peak close to 550 nm throughout all epiclermal layers [27].

53.6 Raman Spectroscopy

Raman spectroscopy is an optical technique that probes the vibrational activity of chemical bonds, and each molecule has a spectral signature characteristic of its modes of vibration. These spectral signatures can be used to identify unknown substances in a sample, or to differentiate samples according to their chemical constituency.

Cartaxo *et al*. conducted a survey of 10 excision biopsy samples of malignant melanoma, nine benign melanocytic nevi, and 10 healthy skin samples *ex vivo* [28]. In this pilot study, a high correlation of the Fourier transform Raman spectra was observed between the elements of the same group. A great variation was found in the pigmented nevi and in the malignant melanoma group, whereas no significant variation of the spectra was observed for normal control skin sites. Measured in the vibrational modes for polysaccharides, tyrosine, and amide-I, the discriminatory analysis showed an efficiency of 75.3% in the differentiation of the three groups. In further examinations of small groups of patients, lymph node and brain metastases of malignant melanoma could also be differentiated [29, 30].

53.7 Laser Doppler Imaging

Laser Doppler perfusion imaging (LDPI) is a sophisticated technique for measurement of cutaneous blood flow that possesses broad applications within dermatology. The major advantages of LDPI include measurement of blood flow over an area rather than at a single site and measurement without contacting the skin, which could potentially influence blood flow.

Vascularization is an important element especially of tumor growth. Therefore, for the noninvasive differentiation of skin tumors, the vascular pattern is taken into account, in most examination methods. Stücker *et al*. measured blood flow patterns in basal cell carcinomas, benign nevi, and malignant melanomas with a laser Doppler imager [31]. The results showed the highest perfusion in junctional nevi and malignant melanomas. This technique, however, is preferably employed in combination with other examination methods owing to its low sensitivity and specificity.

References

1 Garbe, C. *et al.* (2010) Diagnosis and treatment of melanoma: European consensus-based interdisciplinary guideline. *Eur. J. Cancer*, **46**, 270–283.

2 Bleyer, A. *et al.* (2006) Cancer in 15- to 29-year-olds by primary site. *Oncologist*, **11**, 590–601.

3 Menzies, S.W. *et al.* (2005) The performance of SolarScan: an automated dermoscopy image analysis instrument for the diagnosis of primary melanoma. *Arch. Dermatol.*, **141**, 1388–1396.

4 Menzies, S.W. and Zalaudek, I. (2006) Why perform dermoscopy? The evidence for its role in the routine management of pigmented skin lesions. *Arch. Dermatol.*, **142**, 1211–1212.

5 Bowling, J. *et al.* (2007) Dermoscopy key points: recommendations from the International Dermoscopy Society. *Dermatology*, **214**, 3–5.

6 Malvehy, J. *et al.* (2007) Dermoscopy report: proposal for standardization. Results of a consensus meeting of the International Dermoscopy Society. *J. Am. Acad. Dermatol.*, **57**, 84–95.

7 Kittler, H. and Binder, M. (2002) Follow-up of melanozytic skin lesions with digital dermoscopy: risks and benefits. *Arch. Dermatol.*, **138**, 1379.

8 Kittler, H. *et al.* (2006) Identification of clinically featureless incipient melanoma using sequential dermoscopy imaging. *Arch. Dermatol.*, **142**, 1113–1119.

9 Bafounta, M.L. *et al.* (2001) Is dermoscopy (epiluminescence microscopy) useful for the diagnosis of melanoma? Results of a meta-analysis using techniques adapted to the evaluation of diagnostic tests. *Arch. Dermatol.*, **137**, 1343–1350.

10 Vestergaard, M.E. *et al.* (2008) Dermoscopy compared with naked eye examination for the diagnosis of primary melanoma: a meta-analysis of studies performed in a clinical setting. *Br. J. Dermatol.*, **159**, 669–676.

11 Argenziano, G. *et al.* (2003) Dermoscopy of pigmented skin lesions: results of a consensus meeting via the Internet. *J. Am. Acad. Dermatol.*, **48**, 679–693.

12 Nachbar, F. *et al.* (1994) The ABCD rule of dermatoscopy. High prospective value in the diagnosis of doubtful melanocytic skin lesions. *J. Am. Acad. Dermatol.*, **30**, 551–559.

13 Menzies, S.W. *et al.* (1996) A sensitivity and specificity analysis of the surface microscopy features of invasive melanoma. *Melanoma Res.*, **6**, 55–62.

14 Argenziano, G. *et al.* (1998) Epiluminescence microscopy for the diagnosis of doubtful melanocytic skin lesions. Comparison of the ABCD rule of dermatoscopy and a new 7-point checklist based on pattern analysis. *Arch. Dermatol.*, **134**, 1563–1570.

15 Haenssle, H.A. *et al.* (2009) Large speckled lentiginous naevus superimposed with Spitz naevi: sequential digital dermoscopy may lead to unnecessary excisions triggered by dynamic changes. *Clin. Exp. Dermatol.*, **34**, 212–215.

16 Rademaker, M. and Oakley, A. (2010) Digital monitoring by whole body photography and sequential digital dermoscopy detects thinner melanomas. *J. Prim. Health Care*, **2**, 268–272.

17 Altamura, D. *et al.* (2008) Assessment of the optimal interval for and sensitivity of short-term sequential digital dermoscopy monitoring for the diagnosis of melanoma. *Arch. Dermatol.*, **144**, 502–506.

18 Menzies, S.W. *et al.* (2009) Impact of dermoscopy and short-term sequential digital dermoscopy imaging for the management of pigmented lesions in primary care: a sequential intervention trial. *Br. J. Dermatol.*, **161**, 1270–1277.

19 Robinson, J.K. and Nickoloff, B.J. (2004) Digital epiluminescence microscopy monitoring of high-risk patients. *Arch. Dermatol.*, **140**, 49–56.

20 Gambichler, T. *et al.* (2007) Characterization of benign and malignant melanocytic skin lesions using optical coherence tomography *in vivo*. *J. Am. Acad. Dermatol.*, **57**, 629–637.

21 Gerger, A. *et al.* (2005) Diagnostic applicability of *in vivo* confocal laser scanning microscopy in melanocytic skin tumors. *J. Invest. Dermatol.*, **124**, 493–498.

22 Langley, R.G.B. *et al.* (2007) The diagnostic accuracy of *in vivo* confocal scanning laser microscopy compared to dermoscopy of benign and malignant melanocytic lesions: a prospective study. *Dermatology (Basel)*, **215**, 365–372.

23 Pellacani, G. *et al.* (2007) The impact of *in vivo* reflectance confocal microscopy for the diagnostic accuracy of melanoma and equivocal melanocytic lesions. *J. Invest. Dermatol.*, **127**, 2759–2765.

24 Gonzalez, S. (2008) *Reflectance Confocal Microscopy of Cutaneous Tumors. An Atlas with Clinical, Dermoscopic and Histological Correlations*, Informa Healthcare, London.

25 Kang, H.Y., *et al.* (2010) Reflectance confocal microscopy for pigmentary disorders. *Exp. Dermatol.*, **19**, 233–239.

26 Dimitrow, E. *et al.* (2009) Sensitivity and specificity of multiphoton laser tomography for *in vivo* and *ex vivo* diagnosis of malignant melanoma. *J. Invest. Dermatol.*, **129**, 1752–1758.

27 Dimitrow, E. *et al.* (2009) Spectral fluorescence lifetime detection and selective melanin imaging by multiphoton laser tomography for melanoma diagnosis. *Exp. Dermatol.*, **18**, 509–515.

28 Cartaxo, S.B. *et al.* (2010) FT-Raman spectroscopy for the differentiation between cutaneous melanoma and pigmented nevus. *Acta Cir. Bras.*, **25**, 351–356.

29 Kirsch, M. *et al.* (2010) Raman spectroscopic imaging for *in vivo* detection of cerebral brain metastases. *Anal. Bioanal. Chem.*, **398**, 1707–1713.

30 de Oliveira, A.F. (2010) Differential diagnosis in primary and metastatic cutaneous melanoma by FT-Raman spectroscopy. *Acta Cir. Bras.*, **25**, 434–439.

31 Stücker, M. *et al.* (1999) Blood flow compared in benign melanozytic naevi, malignant melanoma and basal cell carcinomas. *Clin. Exp. Dermatol.*, **24**, 107–111.

54
Monitoring of Blood Flow and Hemoglobin Oxygenation

Sean J. Kirkpatrick, Donald D. Duncan, and Jessica Ramella-Roman

54.1
Introduction

The primary means of supplying nutrition and oxygen to the skin is the microvasculature. This same network of vessels also plays a key role in wound repair and thermoregulation. Because of this, reliable measures of cutaneous blood flow are necessary for a variety of pharmacological and physiological studies [1], and also for a number of direct clinical applications, including evaluating skin blood flow reserve in diabetic patients [2], assessing cutaneous flow in patients suffering from hypertriglyceridemia [3], determining vascular resistance for the differential diagnosis of vascular disease [4], investigating the effects of locally applied pressure on the development of pressure ulcers [5], studying the changes in blood flow following burns [6], and assessing the changes in the microvascular blood flow dynamics associated with photodynamic therapy [7]. From a historical perspective, there have been numerous approaches for measuring blood flow and inferring perfusion (the product of the scalar flow velocity and the concentration of red blood cells in the probed area). In general, these approaches can be divided into two categories: laser Doppler velocimetry techniques (both point and scanning approaches) and laser speckle techniques. The distinction between the two categories may be somewhat artificial; however, for ease of discussion we will maintain this classification.

The assessment of oxygen saturation of skin has been used in the monitoring of edema and erythema [8], in the demarcation of certain skin lesions and tumors [9, 10], including the evolution of Kaposi's sarcoma (KS) [11], and for monitoring the progress of skin ulcers [12, 13]. Near-infrared imaging spectroscopy [14] was used to obtain maps of oxygen saturation of thermal burns and to separate superficial from deep burns, while other groups showed that SO_2 can be used to quantify skin inflammation due to an irritant [15]. Finally, SO_2 was shown to be a metric of interest when assessing the onset of autonomic dysreflexia [16]. The experimental methodologies mentioned utilize the time averages of skin SO_2, thus implying that the arterial, venous, and capillary SO_2, can be lumped into one unique number (reported SO_2 values vary

Handbook of Biophotonics. Vol.2: Photonics for Health Care, First Edition. Edited by Jürgen Popp, Valery V. Tuchin, Arthur Chiou, and Stefan Heinemann.

between 0.5 and 0.7). When arterial flow is isolated, such as in pulse oximetry, normal values of SO_2 exceed 0.98. Only time-averaged techniques are considered here.

54.2
Laser Doppler Approaches to Quantifying Cutaneous Blood Flow

For cutaneous blood flow, one can generally divide laser Doppler measurements into the categories of point-wise and regional. While both categories rely on the same physical phenomenon, the frequency shift observed when light of a given wavelength is scattered by a moving object, the hardware and software implementations are different. Moreover, the character of the motion estimates is also different. Point-wise measurements rely on a small measurement volume, typically $\sim 0.1\,mm^3$ and less, that is defined by two or more laser beams that cross at an oblique angle. Many commercial systems exist (e.g., TSI, Dantec Dynamics, Measurement Science Enterprise) that are capable of providing (without calibration) absolute velocities in one, two, or three dimensions. Such systems can provide vectorial velocity measurements within vessels of sizes down to the region defined by the beam crossing volume. These systems are typically referred to as heterodyne because one of the laser beams, which is typically frequency shifted, provides an interferometric reference for the other. Because of this frequency shift, the measurement provides both direction and velocity.

Regional measurement is provided by laser Doppler perfusion systems [17]. In this category are the optical fiber-based probe systems [laser Doppler perfusion monitoring (– LDPM] and systems that employ a scanned laser or area illumination and CCD or CMOS detectors [laser Doppler perfusion imaging (–LDPI] (Moor Instruments). All of the LDPx systems rely on a measurement of Doppler shift as well, but have a limiting resolution that is large compared with the cutaneous vasculature structure. The Doppler shift that they perceive is due to motion in a variety of directions, thus resulting in a broadened Doppler spectrum. Multiple scattering within the interrogation volume further broadens this Doppler spectrum [18]. A measure of motion is derived by inspecting the width of this Doppler spectrum. As a result, such measurement concepts provide qualitative measurements of regional flow, that is, perfusion. Such systems are often termed homodyne because the reference is provided by scatter from supposedly stationary tissues outside the vasculature. They have been useful in a variety of research [19] and clinical applications [20] where the objective is to measure perfusion *changes* resulting from some stimulus. Any attempt to provide quantitative assessment of volumetric flow using such systems, however, is fraught with difficulties. An example is the difficulty in establishing a "biological zero" [21], that is, a zero instrument reading when biological motion has supposedly been halted. Such a condition is typically established using a pressure cuff. Motion persists, nonetheless, due simply to Brownian motion. A standardization of sorts for these LDPx measurements can be provided by using an *in vitro* calibration with an aqueous suspension of microspheres. The subsequent *in vivo* measurements, however, still represent a regional, qualitative estimate of motion for the reasons outlined above.

One reoccurring issue with Doppler measurements of whatever kind is that velocity does not equal flow. Although this is true, they are in fact highly correlated. For example, for flow of a Newtonian fluid within a vessel, the velocity profile is parabolic (Poiseuille flow). As a result, the volume flow can be inferred from a measurement of the centerline velocity. Blood, however is non-Newtonian; at low shear rates it displays an elevated viscosity, attributed to the agglomeration of cells, whereas at high shear rates the lowered viscosity is attributed to deformation of cells [22]. Nevertheless, a number of studies [23–25] suggest that for vessels between 155 and 2000 μm the effect can be ignored. As a result, a measurement of centerline velocity together with knowledge of the configuration of the vessel, can be used to infer volume flow rate.

54.3
Laser Speckle Methods for Blood Flow Estimations

The concept of estimating flow based on the contrast of a time-integrated laser speckle pattern was introduced 30 years ago by Fercher and Briers [26]. As originally proposed, the concept was to illuminate a vascularized tissue with a coherent light source and take a photograph with a particular exposure time. The concept relies on the fact that an image formed in coherent illumination has a high-contrast, speckled appearance. Further, if the illuminated object moves, the speckles translate and scintillate. If the exposure time is long compared with the speckle fluctuation time, the imaged speckles are blurred, that is, the contrast is reduced. Contrast, K, is simply defined here as $K \equiv \sigma_I/\mu_I$, where σ_I and μ_I are the standard deviation and the mean of the measured intensity, respectively, typically assessed over a small window of say 5×5 or 7×7 pixels. Therefore, in principle, the idea is to infer a temporal correlation time constant from the observed speckle contrast and subsequently relate this time constant to the flow velocity. Since that time, numerous variations on the same theme have been proposed and implemented [27–30]. Regardless of the specifics, the general concept has remained the same, namely, the idea is to infer a temporal correlation time constant from the observed speckle contrast and subsequently relate this time constant to the flow velocity.

Laser speckle contrast imaging (LASCI), laser speckle contrast analysis (LASCA), and all of the numerous other titles given to this same general approach have strong appeal, namely, the hardware requirements are minimal, requiring only a laser source and a camera, and the technique is full field, thus holding promise for full field velocity estimates. In addition, the approach always yields results (i.e., a moving speckle pattern) and it can be relatively straightforward to demonstrate a correlation between velocity and speckle contrast [27, 31, 32]. The challenge is to provide a *quantitative* relationship between these parameters, and this has yet to be demonstrated in a convincing fashion. A number of the issues that have impeded the progress of LASCI from a correlative technique to a truly quantitative technique were reviewed by Kirkpatrick and co-workers [33, 34]. Recently, Boas and Dunn [35] reviewed the history of and developments in laser speckle contrast imaging, using the

formalisms of quasi-elastic light scattering and diffusing wave spectroscopy as a theoretical starting point. These related techniques have very similar underlying statistical theory; however, their data collection and data analysis requirements differ substantially from those of LSCI, and care must be taken by the user when viewing LSCI from this vantage point.

LSCI has a further advantage, that is, the simplicity at which the spatial resolution can be altered from the size of small arteries and veins up to larger areas. Dunn *et al.* [36] and Zhou *et al.* [37], for example, have exploited the temporal effects in LSCI to investigate changes in regional blood perfusion.

Laser speckle contrast imaging is a promising tool for assessing flow in the cutaneous microvasculature. At present, its greatest potential lies perhaps in assessing relative changes in regional blood perfusion. Challenges such as speckle movement not associated with blood flow (e.g., rigid body motion associated with respiration), multiple scattering, and the presence of a spectrum of decorrelation times in the observed speckle patterns still need to be rigorously investigated and dealt with in order to make LSCI a truly quantitative tool for blood flow velocity measurement.

54.4 Oxygenation

Experimental systems for the assessment of SO_2 in the skin are varied and application dependent. Nevertheless, two main categories can be established – fiber-based systems and imaging systems. When using fiber-based systems, only very localized information can be gathered as fiber probes tend to be only a few millimeters in size. These systems have several advantages, first and foremost being that diffusion-based models of light propagation in the skin may be used (depending on fiber geometry [38]). Moreover, since fibers generally are interfaced with spectrometers, hundreds of wavelengths can be measured in relatively short time. The redundancy in the data can be used to quantify different metrics of interest apart from SO_2, such as melanin, water, or biliriubin content. Imaging systems generate spatial maps of SO_2 and are preferable when monitoring extended lesions. These systems are noncontact and can be useful in clinical scenarios where infection is an issue.

The measurement of skin oxygen saturation starts generally with the assessment of the skin absorption μ_a, scattering coefficient μ_s, or reduced scattering coefficient μ_s. Once these global parameters have been calculated, the specific chromophores and scatterers can be inferred [11, 39]. The assessment of the skin optical properties from skin reflectance spectra or wavelength-dependent images depends largely on the instrumentation used. When fibers are used, diffusion theory may apply provided that the source–detector separation is longer than five mean free paths, $MFP = 1/(\mu_a + \mu_s')$ [10]. Several authors have used this approach [16, 38, 39] using probes arranged in a configuration with one source fiber and several detector fibers at increasing distance from the source. The detectors are connected either to multiple spectrometers [16] or to optical switches and a single spectrometer [9, 40]. This type of

probe can be used to measure oxygen saturation at different depths, where the longest source–detector separation corresponds to the deepest penetration in the tissue. Some uncertainties exist when using diffusion-based models due to boundary conditions and the fact that shallow penetration is desired. A diffusive probe can be used in these cases, [41] where a thin Spectralon slab is inserted between the collector fiber tips and the skin; the slabs act as a diffuser. Yet another approach is the use of look-up table (LUT) inverse models [42], where an LUT is generated from diffuse reflection data obtained with tissue-simulating phantoms. The phantom optical properties at several wavelengths need to be known and are measured with benchtop techniques, such as integrating spheres and inverse adding doubling (IAD) models [40]. An iterative least-squares fit is ultimately used to formulate the inverse model.

Reflectance-based imaging systems are constructed with a black and white imager (CCD or CMOS) combined with either a filter wheel and several narrowband filters or a liquid crystal tunable filter (LCTF). Spectroscopic snapshot systems have also been used based either on division of aperture [13] or the addition of a custom mosaic filter [40]. Often cross-polarizers are used on the source and detector to eliminate specular reflection. Imaging spectroscopy for the assessment of SO_2 relies heavily on empirical parametric models, as even in diffusive media such as skin, diffusion theory cannot be used. Exceptions are structured illumination systems, where the light source is spatially modulated, and contains DC and AC components that can be separated with a phase-shifting technique [43]. From these two components, the bulk absorption and scattering coefficient of skin may be calculated and ultimately oxygen saturation obtained [39].

References

1 Pershing, L.K., Huether, S., Connklin, R.L., and Kreuger, G.G. (1989) Cutaneous blood flow and percutaneous absorption: a quantitative analysis using a laser Doppler velocimeter and a blood flow meter. *J. Invest. Dermatol.*, **92**, 355–359.

2 Rendell, M., Saxena, S., and Shah, D. (2004) Cutaneous blood flow and peripheral resistance in type II diabetes as compared to intermittent claudication patients. *Int. J. Angiol.*, **12** (3), 166–171.

3 Tur, E., Politi, Y., and Rubinstein, A. (1994) Cutaneous blood flow abnormalities in hypertriglyceridemia. *J. Invest. Dermatol.*, **103**, 597–600.

4 Nitzan, M., Goss, D.E., Chagne, D., and Roberts, V.C. (1988) Assessment of regional blood flow and specific microvascular resistance in the foot by means of the transient thermal clearance method. *Clin. Phys. Physiol. Meas.*, **9**, 347–352.

5 Fromy, B., Abraham, P., Bouvet, C., Bouhanick, B., Fressinaud, P., and Saumet, J.L. (2002) Early decrease of skin blood flow in response to locally applied pressure in diabetic subjects. *Diabetes*, **51**, 1214–1217.

6 Jaskille, A.D., Ramella-Roman, J.C., Shupp, J.W., Jordan, M.H., and Jeng, J.C. (2010) Critical review of burn depth assessment techniques: Part II. Review of laser Doppler technology. *J. Burn Care Res.*, **31**, 151–157.

7 Smith, T.K., Choi, B., Ramirez-San-Juan, J.C., Nelson, J.S., Osann, K., and Kelly, K.M. (2006) Microvascular blood flow dynamics associated with photodynamic therapy, pulsed dye laser irradiation and combined regimes. *Lasers Surg. Med.*, **38**, 532–539.

8 Stamatas, G.N., Southall, M., and Kollias, N. (2006) *In vivo* monitoring of cutaneous edema using spectral imaging in the visible and near infrared. *J. Invest. Dermatol.*, **126**, 1753–1760.

9 Yu, C.-C., Lau, C., O'Donoghue, G., Mirkovic, J., McGee, S., Galindo, L., Elackattu, A., Stier, E., Grillone, G., Badizadegan, K., Dasari, R.R., and Feld, M.S. (2008) Quantitative spectroscopic imaging for non-invasive early cancer detection. *Opt. Express*, **16**, 16227–16239.

10 Zonios, G., Perelman, L.T., Backman, V., Manoharan, R., Fitzmaurice, M., Van Dam, J., and Feld, M.S. (1999) Diffuse reflectance spectroscopy of human adenomatous colon polyps *in vivo*. *Appl. Opt.*, **38**, 6628–6637.

11 Vogel, A., Chernomordik, V.V., Riley, J.D., Hassan, M., Amyot, F., Dasgeb, B., Demos, S.G., Pursley, R., Little, R.F., Yarchoan, R., Tao, Y., and Gandjbakhche, A.H. (2004) Using noninvasive multispectral imaging to quantitatively assess tissue vasculature. *J. Biomed. Opt.*, **12**, 051604.1–051604.12.

12 Noordmans, H.J., De Roode, R., Staring, M., and Verdaasdonk, R. (2006) Registration and analysis of *in-vivo* multi-spectral images for correction of motion and comparison in time. *Proc. SPIE*, **7**, 608106.1–608109.

13 Basiri, A., Nabili, M., Mathews, S., Libin, A., Groah, S., Noordmans, H.J., and Ramella-Roman, J.C. (2010) Use of a multi-spectral camera in the characterization of skin wounds. *Opt. Express*, **18**, 3244–3257.

14 Cross, K.M., Leonardi, L., Payette, J.R., Gomez, M., Levasseur, M.A., Schattka, B.J., Sowa, M.G., and Fish, J.S. (2007) Clinical utilization of near-infrared spectroscopy devices for burn depth assessment. *Wound Repair Regen.*, **15**, 332–340.

15 Kollias, N., Gillies, R., Muccini, J.A., Uyeyama, R.K., Phillips, S.B., and Drake, L.A. (1995) A single parameter, oxygenated hemoglobin, can be used to quantify experimental irritant-induced inflammation. *J. Invest. Dermatol.*, **104**, 421–424.

16 Ramella-Roman, J.C. and Hidler, J.M. (2008) The impact of autonomic dysreflexia on blood flow and skin response in individuals with spinal cord injury. Hindawi Publishing Corporation Advances in Optical Technologies Volume 2008, Article ID 797214, 7 pages doi:10.1155/2008/797214.

17 Leahy, M.J., Enfield, J.G., Clancy, N.T., O'Doherty, J., McNamara, P., and Nilsson, G.E. (2007) Biophotonic methods in microcirculation imaging. *Med. Laser Appl.*, **22**, 105–126.

18 Bonner, R. and Nossai, R. (1981) Model for laser Doppler measurements of blood flow in tissue. *Appl. Opt.*, **20** (12), 2097–2107.

19 Jaskille, A.D., Ramella-Roman, J.C., Shupp, J.W., Jordan, M.H., and Jeng, J.C. (2010) Critical review of burn depth assessment techniques: Part II. Review of laser Doppler technology. *J. Burn Care Res.*, **31** (1), 151–157.

20 Ng, E.Y., Fok, S.C., and Goh, C.T. (2003) Case studies of laser Doppler imaging system for clinical diagnosis applications and management. *J. Med. Eng. Technol.*, **27** (5), 200–206.

21 Kernick, D.P., Tooke, J.E., and Shore, A.C. (1999) The biological zero signal in laser doppler fluximetry – origins and practical implications. *Eur. J. Physiol.*, **437**, 624–631.

22 Vennemann, P., Lindken, R., and Westerweel, J. (2007) *In vivo* whole-field blood velocity measurement techniques. *Exp. Fluids*, **42**, 495–511.

23 Charm, S.E. and Kurland, G.S. (1966) On the significance of the Reynolds number in blood flow. *Rheology*, **3** (3), 163–164.

24 Charm, S.E., Kurland, G.S., and Brown, S.L. (1968) The influence of radial distribution and marginal plasma layer on the flow of red cell suspensions. *Biorheology*, **5** (1), 15–43.

25 Charm, S.E. and Kurland, G.S. (1974) *Blood Flow and Microcirculation*, John Wiley & Sons, Inc., New York.

26 Fercher, A.R. and Briers, J.D. (1981) Flow visualization by means of single exposure photography. *Opt. Commun.*, **37**, 326–330.

27 Aizu, Y. and Asakura, T. (1999) Coherent optical techniques for diagnostics of retinal blood flow. *J. Biomed. Opt.*, **4**, 61–75.

28 Ramirez-San-Juan, J.C., Ramos-Garcia, R., Guizar-Iturbide, I., Martinez-Niconoff, G., and Choi, B. (2008) Impact of velocity

distribution assumption on simplified laser speckle imaging equation. *Opt. Express*, **16**, 3197–3203.

29 Li, P., Ni, S., Zhang, L., Zeng, S., and Luo, Q. (2006) Imaging cerebral blood flow through the intact rat skull with temporal laser speckle imaging. *Opt. Lett.*, **31**, 1824–1826.

30 Kirkpatrick, S.J., Duncan, D.D., Wang, R.K., and Hinds, M.K. (2007) Quantitative temporal contrast imaging for tissue mechanics. *J. Opt. Soc. Am. A*, **24**, 3728–3734.

31 Isono, H., Kishi, S., Kimura, Y., Hagiwara, N., Konishi, N., and Fujii, H. (2003) Observation of choroidal circulation using index of erythrocyte activity. *Arch. Ophthalmol.*, **121**, 225–231.

32 Durduran, T., Burnett, M.G., Yu, G., Zhou, C., Furuya, D., Yodh, A.G., Detre, J.A., and Greenburg, J.H. (2004) Spatiotemporal quantification of cerebral blood flow during functional activation in rat somatosensory cortex using laser-speckle flowmetry. *J. Cereb. Blood Flow Metab.*, **24**, 518–525.

33 Duncan, D.D. and Kirkpatrick, S.J. (2008) Can laser speckle flowmetry be made a quantitative tool? *J. Opt. Soc. Am. A*, **25**, 2088–2094.

34 Kirkpatrick, S.J., Duncan, D.D., and Wells-Gray, E.M. (2008) Detrimental effects of speckle-pixel size matching in laser speckle contrast imaging. *Opt. Lett.*, **33**, 2886–2888.

35 Boas, D.A. and Dunn, A.K. (2010) Laser speckle contrast imaging in biomedical optics. *J. Biomed. Opt.*, **15**, 011109.

36 Dunn, A.K., Bolay, H., Moskowitz, M.A., and Boas, D.A. (2001) Dynamic imaging of cerebral blood flow using laser speckle. *J. Cereb. Blood Flow Metab.*, **21**, 195–201.

37 Zhou, C., Yu, G., Furuya, D., Greenburg, J.H., Yodh, A., and Durduran, T. (2006) Diffuse optical correlation tomography of cerebral blood flow during cortical spreading depression in rat brain. *Opt. Express*, **14**, 1125–1144.

38 Farrell, T.J., Patterson, M.S., and Wilson, B. (1992) A diffusion theory model of spatially resolved, steady-state diffuse reflectance for the noninvasive determination of tissue optical properties *in vivo*. *Med. Phys.*, **19**, 879–888.

39 Jacques, S.L. (2005) Spectroscopic determination of tissue optical properties using optical fiber spectrometer, http://omlc.ogi.edu/news/feb06/skinspect/index.htm, Oregon Health and Science University, Portland, OR (last accessed 18 May 2011).

40 Pickering, J.W., Prahl, S.A., van Wieringen, N., Beek, J.F., Sterenborg, H.J.C.M., and van Gemert, M.J.C. (1993) Double-integrating-sphere system for measuring the optical properties of tissue. *Appl. Opt.*, **32**, 399–410.

41 Tseng, S.-H., Bargo, P., Durkin, A., and Kollias, N. (2009) Chromophore concentrations, absorption and scattering properties of human skin in-vivo. *Opt. Express*, **17**, 14599–14617.

42 Rajaram, N., Aramil, T., Lee, K., Reichenberg, J.S., Nguyen, T.H., and Tunnell, J.W. (2010) Design and validation of a clinical instrument for spectral diagnosis of cutaneous malignancy. *Appl. Opt.*, **49**, 142–152.

43 Kong, L., Yi, D., Sprigle, S., Wang, F., Wang, C., Liu, F., Adibi, A., and Tummala, R. (2010) Single sensor that outputs narrowband multispectral images. *J. Biomed. Opt.*, **15** (1), 010502.

55
Sensing Glucose and Other Metabolites in Skin

Elina A. Genina, Kirill V. Larin, Alexey N. Bashkatov, and Valery V. Tuchin

55.1
Introduction

Recent technological advances in the photonics industry have led to a resurgence of interest in optical imaging technologies and real progress towards the development of noninvasive clinical functional imaging systems. Application of optical methods to physiological condition monitoring and cancer diagnostics, and also for treatment, is a growing field owing to the simplicity, low cost, and low risk of these methods. The development of noninvasive measurement techniques for monitoring of endogenous (metabolic) agents in human tissues is very important for the diagnosis and therapy of various human diseases and might play a key role in the proper management of many devastating conditions.

Glucose is a monosaccharide sugar with chemical formula $C_6H_{12}O_6$. It is one of the most important carbohydrate nutrient sources and is fundamental to almost all biological processes as it required for the production of ATP and other essential cellular components. The normal range of glucose in human blood is 70–160 mg dl^{-1} (3.9–8.9 mM; 1 mM = 18.0 mg dl^{-1}) depending on the time of the last meal, the extent of physical tolerance, and other factors [1]. Freely circulating glucose molecules in the bloodstream stimulate the release of insulin from the pancreas. Insulin (a large peptide hormone composed of two proteins bound together) helps glucose molecules to penetrate the cell wall by binding to specific receptors in cell membranes, which are normally impermeable to glucose. Diabetes is a disorder caused by decreased production of insulin, or by decreased ability to utilize insulin in transport of the glucose across cell membrane. As a result, a high and potentially dangerous concentration of glucose can be accumulated in the blood (hyperglycemia) during the disease [2]. Therefore, it is of great importance to maintain blood glucose concentration within the normal range in order to prevent possibly severe complications.

A significant role for physiological glucose monitoring is in the diagnosis and management of several metabolic diseases, such as diabetes mellitus (or simply diabetes). A number of invasive and noninvasive techniques have been investigated

Handbook of Biophotonics. Vol.2: Photonics for Health Care, First Edition. Edited by Jürgen Popp, Valery V. Tuchin, Arthur Chiou, and Stefan Heinemann.

for glucose monitoring [3]; however, the problem of noninvasive glucose monitoring in a clinically acceptable form has not yet been solved.

While the standard analysis of blood currently involves puncturing a finger and subsequent chemical analysis of collected blood samples, in recent decades noninvasive blood glucose monitoring has become an increasingly important topic of investigation in the realm of biomedical engineering. In particular, the introduction of optical approaches has brought exciting advances to this field [4].

Tissue metabolites play an important role in the state of the human organism. For example, bilirubin-IXα, a metabolite of normal heme degradation, occurs in blood as a water-soluble complex with human serum albumin. It can cause life-threatening neurotoxic effects in babies with hyperbilirubinemia if its level becomes too high and it partitions into the brain [5]. Therefore, noninvasive monitoring of the bilirubin level in serum is very important in some clinical cases.

The defense mechanism of the skin is based on the action of antioxidant substances such as carotenoids, vitamins, and enzymes. β-Carotene and lycopene represent more than 70% of the carotenoids in the human organism. The topical or systemic application of β-carotene and lycopene is the general strategy for improving the defense system of the human body. For the evaluation and optimization of this treatment, it is necessary to measure the β-carotene and lycopene concentrations in the tissue, especially in the human skin as the barrier to the environment [6].

Many optical techniques for sensing different tissue metabolites and glucose in living tissue have been developed over the last 50 years. Methods based on fluorescence [7–17], near-infrared (NIR) and mid-infrared (mid-IR) spectroscopic [18–26], Raman spectroscopic [22, 27–29], photoacoustic [30, 31], optical coherence tomography (OCT) [32–36], and other techniques are discussed in this chapter.

55.2 Light–Tissue Interaction

Optical sensing techniques are defined by light–tissue interaction. This interaction depends on the optical properties of tissue components and structures. The absorption depends on the type of predominant absorption centers and water content in tissues. Absorption for most tissues in the visible region is insignificant except for the absorption bands of blood hemoglobin and some other chromophores [37]. The absorption bands of protein molecules are mainly in the near-ultraviolet (UV) region. Absorption in the IR region is essentially defined by the water absorption spectrum and its concentration in tissues. In the NIR spectral range, the main light absorbers are water and lipids, which are present in different tissues in various quantities. In this spectral range, the absorption bands of water in skin with maxima at 930, 970 [38], 1197, 1430, and 1925 nm [39] and lipids with maxima at 1212, 1710, and 1780 nm [40, 41] are observed. The absorption bands of oxyhemoglobin with maxima at about 415, 540, and 575 nm are observed in the visible spectral range [42, 43]. Absorption of water in this spectral range is negligible.

Fluorescence arises upon light absorption and is related to an electronic transition from the excited state to the ground state of a molecule. Fluorescence spectra often give detailed information on fluorescent molecules, their conformation, binding sites, and interaction within cells and tissues or other molecules. On excitation of biological objects by UV light ($\lambda \leq 370$ nm), autofluorescence of proteins and also of nucleic acids can be observed. Autofluorescence of proteins is related to the amino acids tryptophan, tyrosine, and phenylalanine with absorption maxima at 280, 275, and 257 nm, respectively, and emission maxima between 280 nm (phenylalanine) and 350 nm (tryptophan) [44–47]. Fluorescence from collagen or elastin is excited between 400 and 600 nm with maxima around 400, 430, and 460 nm. Fluorescence of collagen and elastin can be used to distinguish various types of tissues, for example, epithelial and connective tissues [46–49].

The reduced form of coenzyme nicotinamide adenine dinucleotide (NADH) is excited selectively in the wavelength range 330–370 nm. NADH is most concentrated within mitochondria, where it is oxidized within the respiratory chain located within the inner mitochondrial membrane, and its fluorescence is an appropriate parameter for detection of ischemic or neoplastic tissues [46, 49]. Flavin mononucleotide (FMN) and flavin adenine dinucleotide (FAD) with excitation maxima around 380 and 450 nm have also been reported to contribute to intrinsic cellular fluorescence [46].

55.3 Fluorescence Measurements

Fluorescent kinetic probes have been used to obtain information on the antioxidant activity of the skin and eye pigment melanin and its biogenetic precursors 5,6-dihydroxyindole and 5,6-dihydroxyindole-2-carboxylic acid [50]. These constitute the major monomeric building blocks of eumelanin, the brown and dark melanin type. These precursors occur in relatively high local abundance in the melanocytes and keratinocytes, and their enhanced blood or urine levels provide biochemical markers for malignant melanoma and a diagnostic tool for its therapy [50].

Porphyrin molecules, for example, protoporphyrin, coproporphyrin, uroporphyrin, and hematoporphyrin, occur within the biosynthetic pathway of hemoglobin, myoglobin, and cytochromes. Abnormalities in heme synthesis, occurring in cases of porphyries and some hemolytic diseases, may enhance considerably the porphyrin level within tissues [44]. Several bacteria, for example, *Propionibacterium acnes*, and bacteria within dental plaque (biofilm), such as *Porphyromonas gingivalis*, *Prevotella intermedia*, and *Prevotella nigrescens*, accumulate considerable amounts of protoporphyrin [51, 52]. Therefore, acne and oral and tooth lesion detection based on measurements of intrinsic fluorescence specific to porphyrin molecules appears to be a promising method of disease diagnostics. For example, time-gated fluorescence spectroscopy was successfully applied to the detection of the tumor within

tissues based on the strong autofluorescence signal coming from accumulated porphyrins [53].

A number of fluorescence-based techniques have been developed and applied in attempts to sense blood glucose concentration [4, 7–10]. The techniques can be subdivided into two general categories: glucose oxidase (GOx)-based and affinity-binding sensors. Sensors in the first category use the electroenzymatic oxidation of glucose by GOx in order to generate an optically detectable glucose-dependent signal [7]. In the late 1990s, research towards a reagentless glucose sensor, using the deactivated apo-GOx enzyme [8], was started, which used the enzyme as a receptor rather than a catalyst. This work showed that apo-GOx retained its high specificity and in many ways paved the way for advances in the development of a new biosensor genre [9, 10]. Several methods for optical detection of the products of this reaction and, hence, the glucose concentration driving the reaction have been presented [11–13]. A simple approach for creating a sensor based on this reaction is to incorporate an oxygen-sensitive dye such as a ruthenium complex [7, 13]. Ruthenium(II) complexes exhibit fluorescence quenching in the presence of oxygen; therefore, a decrease in local oxygen concentration can be detected as an increase in fluorescence of a ruthenium-based dye. Incorporating GOx and a ruthenium dye together results in a sensor whose fluorescence increases with increase in glucose concentration, since increased glucose concentration will lead to an increased consumption of O_2. A disadvantage of this simple approach is that a decrease in local oxygen content may not be distinguished from a rise in glucose concentration.

Fluorescent affinity-binding sensors utilize competitive binding between glucose and a suitable labeled fluorescent compound to a common receptor site. Several methods are based on Förster resonance energy transfer (FRET) and on competition between glucose and dextran for concanavalin-A (ConA) binding sites [7]. The assay components are ConA labeled with an energy acceptor, or an energy donor, and dextran labeled with the complementary molecule for FRET [14, 15]. Glucose displaces the dextran labeled with the fluorophore at the ConA binding sites and consequently FRET-based quenching occurs as its fluorescence it critically dependent on the distance between donor molecule (e.g., ConA) and acceptor molecule (e.g., dextran). The use of ConA as the membrane-bound molecule affords a very sensitive technique because of the strong affinity of ConA to glucose. Using this approach, glucose concentrations can be measured by a decrease in amplitude of the fluorescence peak with increasing glucose concentration. In either approach, the fluorescence techniques appears to be very specific to glucose and sensitive to glucose concentration, without interference from other constituents frequently found in blood and tissues.

Although no fluorescence-based sensing devices are yet commercially available, it appears that a number of the techniques have been sufficiently developed to expect that clinically-viable devices are just over the horizon, and more activity in trials will be observed in the next few years. Advances in nanomaterials such as quantum dots will likely allow improvements in optical stability and choice of excitation/emission wavelengths for various transduction methods [16, 17].

55.4 IR Spectroscopy

Measurements of the absorption and scattering of NIR light traveling through tissue may provide a useful means to quantify functional parameters of tissues, such as total hemoglobin concentration and blood oxygen saturation and glucose [54]. The optical absorption methods for glucose measurements are based on the concentration-dependent absorption of specific wavelengths of light by glucose or other metabolites. In theory, a beam of radiation may be directed through a blood-containing portion of the body and the exiting light analyzed to determine the content of glucose by assessing the absorption spectrum.

For example, the mid-IR spectral bands of glucose and other carbohydrates have been assigned and are dominated by C−C, C−H, O−H, O−C−H, C−O−H and C−C−H stretching and bending vibrations [22]. The 800–1200 cm^{-1} fingerprint region of the IR spectrum of glucose has bands at 836, 911, 1011, 1047, 1076, and 1250 cm^{-1}, which have been assigned to C−H bending vibrations [22]. A 1026 cm^{-1} band corresponds to a C−O−H bending vibration and the 1033 cm^{-1} band can be associated with the ν(C−O−H) vibration [22] or the ν(C−O−C) vibration [55]. Therefore, it might be possible to utilize these spectrum "fingerprints" to quantify the concentration of carbohydrates in the sample with good specificity.

Despite the specificity offered by IR absorption spectroscopy, its application to quantitative blood glucose measurement is limited. A strong background absorption by water and other components of blood and tissues severely limits the pathlength that may be used for transmission spectroscopy to roughly 100 μm or less. Further, the magnitude of the absorption peaks and the dynamic range required to record them make quantification based on these sharp peaks difficult. Nonetheless, attempts have been made to quantify blood glucose using IR absorption spectroscopy *in vitro* and *in vivo* [8, 23–26].

A new concept for *in vivo* glucose detection in the mid-IR spectral range is based on the use of two quantum cascade lasers emitting at wavelengths 9.26 and 9.38 μm to produce photoacoustic signals in the forearm skin [56]. One of the wavelengths correlates with glucose absorption, whereas the other does not. Determination of glucose concentration in the extracellular fluid of the stratum spinosum permits the deduction of the glucose concentration in blood, because the two factors correlate closely with each other. This method allows one to improve glucose specificity and to remove the effect of other blood substances.

In contrast to the mid-IR range, the incident radiation in the NIR spectral range passes relatively easily through water and body tissues, allowing moderate pathlengths to be used for the measurements. Therefore, a large amount of effort has been devoted to the development of NIR spectroscopic techniques for the noninvasive measurement of blood glucose [18]. The NIR region is ideal for the noninvasive measurement of human body compositions because biological tissue is relatively transparent to light in this region, the so-called therapeutic window. The molecular formula of glucose is $C_6H_{12}O_6$ and several hydroxyl and methyl groups are present.

They are mainly hydrogen functional groups whose absorption occurs in the NIR region. For glucose, the second overtone absorption is in the spectral region 1100–1300 nm and the first overtone absorption is in the region 1500–1800 nm [19]. In the range 1400–1500 nm, there is a peak that corresponds to the absorption peak of water. This information provides the theoretical basis for the measurement of blood glucose using NIR spectroscopy [19, 20].

The concept of noninvasive blood glucose sensing using the scattering properties of blood is an alternative to the spectral absorption method. The method of NIR frequency-domain reflectance is based on changes in glucose concentration, which affect the refractive index mismatch between the interstitial fluid and tissue fibers, and hence reduced scattering coefficient μ'_s [57, 58]. The refractive index n of the interstitial fluid modified by glucose is defined by the equation [44]

$$n_{glw} = n_w + 1.515 \times 10^{-6} \times C_{gl} \tag{55.1}$$

where C_{gl} is glucose concentration in $\mathrm{mg\,dl^{-1}}$ and n_w is the refractive index of water [58]. As the subject's blood glucose rise, μ'_s decreases (see Figure 55.1). Key factors for the success of this approach are the precision of the measurements of the reduced scattering coefficient and the separation of the scattering changes from

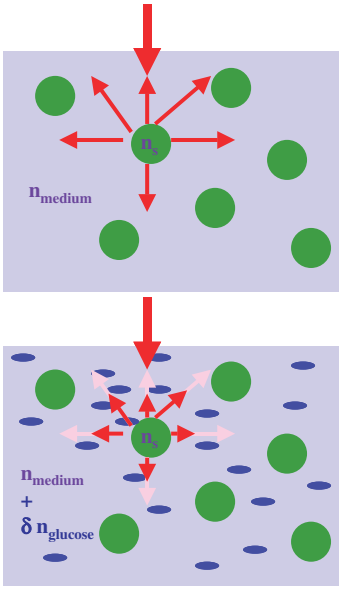

Figure 55.1 Mechanism of glucose-induced changes in the scattering coefficient of a medium: the increase in glucose concentration in the medium (shown as blue ellipses) changes the refractive index of the medium by $+\delta n_{glucose}$, decreases the refractive index mismatch between scattering centers (shown as green circles) and the medium, and, hence, reduces the scattering coefficient (the scattering of light is shown as thin red arrows and incident light is shown as thick red arrows).

absorption changes, as obtained with the NIR frequency-domain spectrometer [57]. Evidently, other physiological effects related to glucose concentration could account for the observed variations of μ'_s and, as it was mentioned earlier, the effect of glucose on the blood flow in the tissue may be one of the sources of the errors in μ'_s measurements.

One critical difficulty associated with *in vivo* blood glucose assay is the extremely low signal-to noise ratio of the glucose peak in the NIR spectrum of human skin tissue. Therefore, the main problem in NIR glucose monitoring is the construction of calibration models [19, 20, 59, 60].

The calibration models typically developed from controlled experiments such as oral glucose tolerance tests might have a better opportunity to provide an acceptable correlation between blood glucose level and the reduced scattering coefficient. At present, the utilization of several experiment data sets for quantitative modeling is most useful to avoid the chance of poor temporal correlation. In one study [59], partial least-squares regression was carried out for the NIR data (total 250 paired data set) and calibration models were built for each subject individually. The selection of informative regions in NIR spectra for analysis can significantly refine the performance of these full-spectrum calibration techniques [60].

A floating-reference method of calibration has been described [20, 21]. The key factor and precondition of the method are the existence of a reference position where diffuse reflectance light is not sensitive to the variations in glucose concentration. Using the signal at the reference position as the internal reference for human body measurement can improve the specification for extraction of glucose information [20].

55.5
Photoacoustic Technique

The photoacoustic technique is based on sensitive time-resolved detection and analysis of laser-induced pressure waves using an ultrasound transducer. Both *in vitro* and *in vivo* studies have been carried out in the spectral range of the transparent "tissue window" around the 1 μm, to assess the feasibility of photoacoustic spectroscopy (PAS) for noninvasive glucose detection [30]. The photoacoustic (PA) signal is obtained by probing the sample with monochromatic radiation, which is modulated or pulsed. Absorption of probe radiation by the sample results in localized short-duration heating. Thermal expansion then gives rise to a pressure wave, which can be detected with a suitable acoustic transducer. An absorption spectrum for the sample can be obtained by recording the amplitude of generated pressure waves as a function of probe beam wavelength [30]. The pulsed PA signal is related to the properties of a turbid medium by the equation [30]

$$PA = k\left(\beta v^n / C_p\right) E_0 \mu_{eff} \tag{55.2}$$

where PA is the signal amplitude, k is a proportionality constant, E_0 is the incident pulse energy, β is the coefficient of volumetric thermal expansion, v is the speed of

sound in the medium, C_p is the specific heat capacity, n is a constant between one and two, depending on the particular experimental conditions, and $\mu_{eff} = \sqrt{3\mu_a(\mu_a + \mu'_s)}$. In the PAS technique, the effect of glucose can be analyzed by detecting changes in the peak-to-peak value of laser-induced pressure waves due to changes in the absorption or scattering as a function of the glucose concentration [31, 61].

Investigations have demonstrated the applicability of PAS to the measurement of glucose concentration [31, 32]. The greatest percentage change in the PA response was observed in region of the C−H second overtone at 1126 nm, with a further peak in the region of the second O−H overtone at 939 nm [30]. In addition, the generated pulsed PA time profile can be analyzed to detect the effect of glucose on tissue scattering, which is reduced by an increase in glucose concentration [62].

Monitoring of the photoisomerization of bilirubin–human serum albumin (BR–HSA) complex is very important in the phototherapy of jaundiced newborns. This complex represents a chromophore–protein interaction. Isomerization reactions of BR–HSA have revealed a detectable structural volume change when studied by photothermal techniques such as laser-induced optoacoustic spectroscopy. The PA signal from solutions of BR–HSA together with the signal amplitude from the calorimetric reference was used to calculate the structural volume change within detection limits [63].

55.6 Raman Spectroscopy

Raman spectroscopy is a powerful technique for the analysis and identification of molecules in a sample. Raman spectroscopy measures inelastically scattered light that results from oscillations and rotations of atoms and atomic groups in molecules (see Figure 55.2). It can provide potentially precise and accurate analysis of metabolite concentrations and biochemical composition. Raman spectra can be utilized to identify molecules because these spectra are characteristic of variations in the molecular polarizability and dipole momentum. Enejder *et al.* [28] accurately measured glucose concentrations in 17 nondiabetic volunteers following an oral glucose tolerance protocol.

β-Carotene and lycopene have different absorption values at 488 and 514.5 nm and, consequently, the Raman lines for β-carotene and lycopene have different scattering efficiencies with 488 and 514.5 nm excitations. These differences were used for the determination of the concentrations of β-carotene and lycopene. The Raman signals are characterized by two prominent Stokes lines at 1160 and 1525 cm^{-1}, which have nearly identical relative intensities [6]. Thus, resonance Raman spectroscopy was used as a fast and noninvasive optical method of measuring the absolute concentrations of β-carotene, lycopene, and other carotenoids in human skin and mucosal tissue [6, 64] and for the determination of the influence of IR radiation on their degradation [65].

In contrast to IR and NIR spectroscopy, Raman spectroscopy has a spectral signature that is less affected by water, which is very important for tissue studies. In addition, Raman spectral bands are considerably narrower (typically

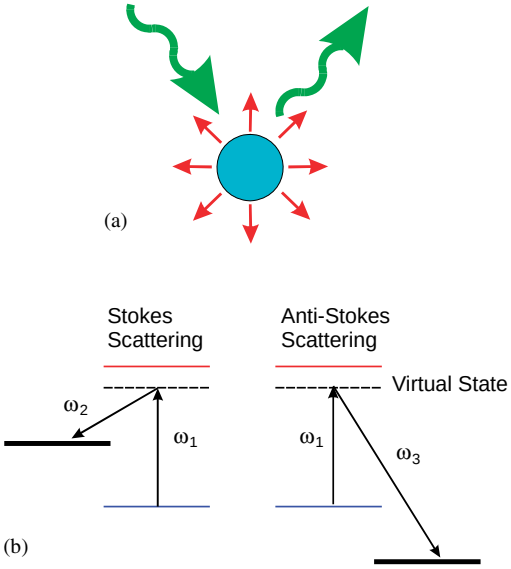

Figure 55.2 Basic principle of Raman spectroscopy: (a) a small portion of photons incident on a target molecule scatters with a shift in photon energy due to molecular vibrations; (b) energy diagram representing the process of Stokes and anti-Stokes scattering (note: there is no transfer of electron population to the "virtual state").

10–20 cm^{-1} [29]) than those produced in NIR spectroscopy. Raman spectroscopy also has the ability for the simultaneous estimation of multiple metabolites, requires minimum sample preparation, and would allow for direct sample analysis [7]. Like IR absorption spectra, Raman spectra exhibit highly specific bands that are dependent on concentration. As a rule, for Raman analysis of tissue, the spectral region between 400 and 2000 cm^{-1}, commonly referred to as the "fingerprint region," is employed.

Different molecular vibrations lead to Raman scattering in this part of the spectrum. In many cases, bands can be assigned to specific molecular vibrations or molecular species, aiding the interpretation of the spectra in terms of biochemical composition of the tissue [7].

Because of the reduction of elastic light scattering on tissue optical clearing, more effective interaction of a probing laser beam with the target molecules is expected. The optical clearing agents increase the signal-to-noise ratio, reduce the systematic error incurred as a result of incompletely resolved surface and subsurface spectra, and significantly improve the Raman signal [66].

55.7 Occlusion Spectroscopy

An approach known as occlusion spectroscopy (OS) was established as a noninvasive method to evoke blood-specific variations of spectral characteristics [67]. The OS

technique is based on the observation that the cessation of blood flow triggers a change in time of the optical characteristics of blood *in vivo*. Because a state of temporary blood flow cessation at the measurement site is created, the average size of aggregates, which are the main scattering centers, begins to grow. Consequently, the mean free path, the light scattering pattern, and the mean absorption coefficients start to evolve with a growth in average size of the scattering particles [68].

The key element of OS is the fact that light scattering changes, originated solely by the blood, drive the optical response of the media. Light scattering fluctuations are associated with both the red blood cells aggregation process and the mismatch of refractive indices of the aggregates and their surrounding media. Glucose present in blood increases the refractive index of plasma and thus decreases the scattering coefficient of blood. Based on a method of parameterization, increased sensitivity to the changes in glucose concentration in blood plasma is achieved [68]. There are still many obstacles in the modeling of aggregation assistance signals in the blood since red blood cells aggregation kinetics vary strongly from subject to subject.

55.8 Reflectance Spectroscopy

The measurement of bilirubin levels in the serum of newborn infants is a very important problem. Hyperbilirubinemia is a common symptom of neonates due to the accumulation of bilirubin in the serum because the liver has not yet developed the enzymes for oxidizing bilirubin for excretion by the kidneys. An optical fiber-based spectrometer has been used for noninvasive monitoring of cutaneous bilirubin (which correlates with serum levels of bilirubin) [69]. It is possible to deduce the bilirubin levels in the skin directly regardless of variations in background scattering, cutaneous melanin, and cutaneous blood content using first principles of optical transport.

The bilirubin absorption adds to the optical density in the region around 480 nm. The bilirubin concentration, C ($\mathrm{mg\,cm^{-3}}$), is related to the absorption coefficient, $\mu_{\mathrm{a.bi1i}}$ ($\mathrm{cm^{-1}}$), by the extinction coefficient, ε [$\mathrm{cm^{-1}\,(mg\,cm^{-3})^{-1}}$]:

$$\mu_{\mathrm{a.bi1i}} = \varepsilon C \tag{55.3}$$

Hence the absorption coefficient $\mu_{\mathrm{a.bi1i}}$ must be deduced in order to specify the amount of bilirubin in the skin. The optical reduced scattering coefficient, μ'_{s}, can be determined by measurement of skin specimens using an integrating sphere spectrophotometer. μ_{a} and μ'_{s} allow the prediction of the reflectance of the skin R and the collection efficiency f [69]. Also, the factor $f_{\mathrm{std}}R_{\mathrm{std}}$ for the Teflon standard has to be determined. The predicted measurement M^* is calculated as $M^* = f^* R$. Then the predicted and measurement values, M^* and M, are compared using a simplex routine and the value of μ_{a} is updated. Iterative cycling of this algorithm converges on a stable deduced value of μ_{a} using the appropriate f^*. This algorithm is applied to each wavelength being considered for analysis. The result is a true absorption spectrum, $\mu_{\mathrm{a}}(\lambda)$, which is then analyzed for the blood and bilirubin content.

This method can be useful to deduce directly the skin bilirubin levels optically without resorting to calibration by a training set of optical versus laboratory serum measurements on some test newborn population [69].

55.9
Polarimetric Technique

The polarimetric technique for blood glucose monitoring utilizes a physical effect such as optical rotation of the polarization plane by glucose molecules. This feature has been used extensively in industry to detect glucose in aqueous solutions. The basic principle of polarimetry is the following: linearly polarized light passing through a medium containing chiral molecules (such as glucose) experiences rotation of a plane of polarization (see Figure 55.3). The degree of this rotation, ϕ, depends on the optical pathlength, L, the concentration of chiral molecules, C, and an intrinsic property of chiral molecules to rotate polarized light, called the specific rotation constant, α:

$$[\phi]^{T}_{\lambda,\mathrm{pH}} = \frac{\alpha}{LC} \tag{55.4}$$

where the subscripts λ and pH and the superscript T indicate dependence of the specific rotation constant on wavelength, pH, and temperature, respectively.

Several groups have tried to utilize this idea to measure glucose concentration in the aqueous humor of the eye [70–73]. A major disadvantage of this method is that glucose-induced changes in the signal are very small and difficult to measure: the angle of rotation for a 1 cm optical pathlength is less than 0.00004° per 1 mg dl^{-1}.

With the exception of transparent ocular tissues, the human body is highly absorbing and scattering in the UV–IR range, and the validity of Eq. (55.4) is questionable. Specifically, (i) light is highly depolarized upon tissue multiple scattering, so even the initial detection of a polarization-preserved signal from which to attempt glucose concentration extraction is a formidable challenge; (ii) the optical pathlength in turbid media is a difficult quantity to define; (iii) other optically active chiral species are present in tissue, thus contributing to the observed optical rotation and hiding/confounding the specific glucose contribution; and (iv) several optical polarization effects occur in tissue simultaneously (e.g., optical rotation, birefringence, absorption, depolarization), contributing to the resultant polarization signals in a complex interrelated way and hindering their unique interpretation [74, 75].

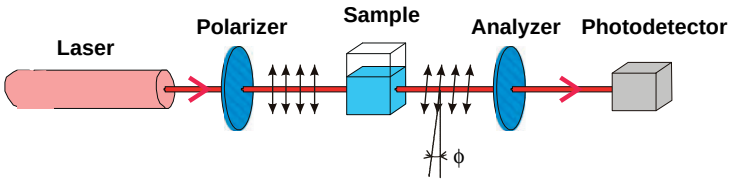

Figure 55.3 Basic principle of the polarimetric approach for glucose monitoring: linearly polarized light passing through a medium containing molecules of glucose experiences rotation of a plane of polarization; ϕ is the degree of this rotation.

Despite these difficulties, it was shown recently that even in the presence of severe depolarization, measurable polarization signals can be obtained reliably from highly scattering media such as biological tissue. Vitkin and co-workers [75] demonstrated surviving linear and circular polarization fractions of light scattered from optically thick turbid media, and measured the resulting optical rotations of the linearly polarized light with the help of a comprehensive turbid polarimetry platform, comprising a highly sensitive experimental system, an accurate forward model that can handle all the complex simultaneous polarization effects manifested by biological tissues, and an inverse signal analysis strategy that can be applied to complex tissue polarimetry data to isolate specific quantities of interest (such as small optical rotation that can be linked to glucose concentration). Additionally, application of this method to relatively transparent tissues (such as the cornea of the human eye) might improve the detection sensitivity of the polarimetric methods [76].

55.10 OCT Technique

An OCT-based method for glucose assessment in tissues has been proposed and its capability for highly sensitive noninvasive monitoring of blood glucose concentration was demonstrated in number of animal and clinical studies [32–35, 77]. The basic principle of this method is to detect and analyze backscattered photons from a tissue layer of interest within the coherence length of a laser source with a two-beam interferometer in the NIR spectral range. OCT technology originates from low-coherence interferometry (a nonscanning/imaging version of OCT) and typically employs a Michelson interferometer, with a broadband laser in the source arm, a beamsplitter, and a photodetector in the detector arm (see Figure 55.4). Light backscattered from the sample is combined with light returned from a mirror in the reference arm of the interferometer, and a photodiode detects the resulting interferometric signal. Interferometric signals can be formed only when the optical pathlength in the sample arm matches the reference arm length within the coherence length of the source. Therefore, by changing the optical pathlength in the reference arm, one-dimensional in-depth profiles of light scattering (A-scans) could be reconstructed in real time with a resolution of about a few microns at depths up to several millimeters.

As mentioned earlier, diffusion of glucose into the interstitial space leads to an increase in the refractive index of the interstitial fluid (ISF), and thus to refractive index matching of collagen fiber (and other tissue components – scatterers) and ISF [64]. Since the scattering coefficient of tissues depends on the refractive index, n, mismatch between ISF and tissue components (fibers, cell components), an increase in tissue glucose concentration will increase the refractive index of the ISF, which will decrease the scattering coefficient of the tissue as a whole. Since the OCT technique measures the in-depth light distribution with high resolution, changes in the in-depth distribution of the tissue scattering coefficient and/or refractive index are reflected in changes in the OCT signal that could be analyzed [32–35, 77].

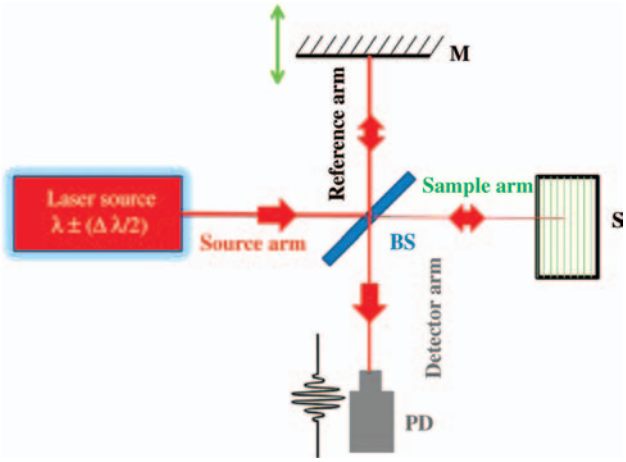

Figure 55.4 General schematic of an OCT system. λ is the central wavelength of the laser source, $\Delta\lambda$ is the bandwidth of the laser source, M is the mirror, S is the sample, BS is the beamsplitter, and PD is the photodetector.

The OCT studies performed in animals (New Zealand white rabbits and Yucatan micropigs) and normal human subjects (during oral glucose tolerance tests) demonstrated (1) capability of the OCT technique to detect changes in scattering coefficient with an accuracy of about 1.5%; (2) a sharp and linear decrease in the OCT signal slope in the dermis with increase in blood glucose concentration; and (3) the accuracy of glucose concentration monitoring may be substantially improved if optimal dimensions of the probed skin area are used [32–35, 77]. The results suggest that the high-resolution OCT technique has a potential for noninvasive, accurate, and continuous glucose monitoring with high sensitivity. However, an OCT method based on analysis of the in-depth amplitude distribution of low-coherent light in skin might have insufficient sensitivity and repeatability and lack of a proper calibration method. Therefore, the development of novel algorithms (e.g., phase-sensitive measurements) and/or combination with other noninvasive sensing modalities are currently being actively investigated by several groups.

55.11 Conclusion

This chapter demonstrates the variety of optical techniques for sensing glucose and other metabolites in skin. Significant efforts have been made by numerous groups and companies in the past two decades to develop a biosensor for noninvasive blood glucose analysis. These approaches include NIR absorption and scattering, polarimetry, Raman spectroscopy, photoacoustics and OCT. The ability of these techniques to assess blood glucose and other metabolites concentration is summarized in Table 55.1.

Table 55.1 Optical techniques for sensing glucose and other metabolites.

Method	Ability	Ref.
Fluorescent glucose-oxidase based sensors	Use the electroenzymatic oxidation of glucose alone or in combination with oxygen-sensitive dye. Fluorescence of the sensor increases with increase in glucose concentration. Sensitivity to decrease in O_2	[7–13]
Fluorescent affinity-binding sensors	Use binding between agent and a labeled fluorescent compound. Fluorescence of the sensor increases with increase in glucose concentration. Specificity to glucose	[14, 15]
NIR absorption spectroscopy	Uses absorption spectral fingerprints of glucose in "therapeutic window." Low sensitivity of agent concentration measurement in physiologic range	[19, 20]
NIR scattering spectroscopy	Use of the change in reduced scattering coefficient with blood glucose concentration due to matching effect. Sensitivity to other physiological effects related to glucose increase	[57, 58]
Mid-IR spectroscopy	Uses spectrum "fingerprints" to quantify the concentration of carbohydrates in tissue with good specificity	[22–26]
Raman spectroscopy	Uses specific spectral bands that are less affected by water. Provides potentially precise and accurate analysis of metabolite concentration. However, it is difficult to isolate glucose from the background spectrum caused by other tissue components	[6, 28, 64, 65]
Occlusion spectroscopy	Uses light scattering fluctuations, originated by the blood. Sensitivity to the changes in glucose concentration in blood plasma	[67, 68]
Reflectance spectroscopy	Uses optical measurements of body composition. Allows noninvasive estimation of cutaneous bilirubin concentration	[69]
Photoacoustic technique	Uses absorption of probe radiation by the sample that results in localized short-duration heating and then gives rise to a pressure wave, which can be detected with a transducer. Sensitivity to the changes in tissue glucose concentration and bilirubin structural volume	[30–32, 63]
Polarimetry technique	Uses optical rotation of the polarization plane by glucose molecules. Measurable polarization signals can be obtained from highly scattering media such as biological tissue. A major disadvantage is that glucose-induced changes in the signal are very small and difficult to measure: the angle of rotation for a 1 cm optical pathlength is less than 0.00004° per 1 mg dl^{-1}	[70–75]
OCT technique	Uses backscattered photons from a tissue of interest within the coherence length of the laser source with a two-beam interferometer in the NIR spectral range. Sensitivity to the changes in blood glucose concentration. Requires proper calibration	[32–35, 77]

Despite significant efforts, the described techniques for noninvasive monitoring of glucose concentration have faced limitations associated with low sensitivity and accuracy and insufficient specificity of glucose concentration measurement in the physiologic range. Therefore, further development of the methods is important for noninvasive diagnosis of various human diseases and blood glucose monitoring and is the subject of current research efforts by several groups.

Acknowledgments

This work was supported in part by the following: 224 014 Photonics4life-FP7-ICT-2007-2; RUB1-2932-SR-08 CRDF; Russian Federation Ministry of Science and Education 2.1.1/4989 and 2.2.1.1/2950, Project 1.4.09 of Federal Agency of Education of the Russian Federation; RFBR-08-02-92224-NNSF_a (Russian Federation–China); RFBR-10-02-90039-Bel_a; and Russian Federation governmental contracts 02.740.11.0770 and 02.740.11.0879.

References

1 Goldstein, D.E., Little, R.R., Lorenz, R.A., Malone, J.I., Nathan, D., Peterson, C.M., and Sacks, D.B. (2004) Tests of glycemia in diabetes. *Diabetes Care*, **27**, 1761–1773.

2 Diabetes Control and Complications Trial Research Group (1997) Hypoglycemia in the diabetes control and complications trial. *Diabetes*, **46**, 271–286.

3 Tuchin, V.V. (ed.) (2009) *Handbook of Optical Sensing of Glucose in Biological Fluids and Tissues*, Taylor & Francis/CRC Press, Boca Raton, FL.

4 Klonoff, D.C. (2005) Continuous glucose monitoring. *Diabetes Care*, **28**, 1231–1239.

5 Williams, R.M., McDonagh, A.F., and Braslavsky, S.E. (1998) Structural volume changes upon photoisomerization of the bilirubin–albumin complex: a laser-induced optoacoustic study. *Photochem. Photobiol.*, **68** (4), 433–437.

6 Darvin, M.E., Gersonde, I., Meinke, M., Sterry, W., and Lademann, J. (2005) Non-invasive *in vivo* determination of the carotenoids beta-carotene and lycopene concentrations in the human skin using the Raman spectroscopic method. *J. Phys. D Appl. Phys.*, **38**, 2696–2700.

7 McNichols, R.J. and Cote, G.L. (2000) Optical glucose sensing in biological fluids: an overview. *J. Biomed. Opt.*, **5**, 5–16.

8 D'Auria, S., Herman, P., Rossi, M., and Lakowicz, J.R. (1999) The fluorescence emission of the apo-glucose oxidase from *Aspergillus niger* as probe to estimate glucose concentrations. *Biochem. Biophys. Res. Commun.*, **263**, 550–553.

9 Mack, A.C., Mao, J., and McShane, M.J. (2005) Transduction of pH and glucose-sensitive hydrogel swelling through fluorescence resonance energy transfer, in *Sensors, 2005 IEEE Conference*, IEEE, (ed. A. Shkel), University of California, Irvine, CA, USA, pp. 912–916.

10 Chinnayelka, S. and McShane, M.J. (2005) Microcapsule biosensors using competitive binding resonance energy transfer assays based on apoenzymes. *Anal. Chem.*, **77**, 5501–5511.

11 Moreno-Bondi, M.C., Wolfbeis, O.S., Leiner, M.J., and Schaffar, B.P.H. (1990) Oxygen optrode for use in a fiber-optic glucose biosensor. *Anal. Chem.*, **62**, 2377–2380.

12 Rosenzweig, Z. and Kopelman, R. (1996) Analytical properties and sensor size effects of a micrometer-sized optical fiber glucose biosensor. *Anal. Chem.*, **68**, 1408–1413.

13 Li, L. and Walt, D.R. (1995) Dual-analyte fiber-optic sensor for the simultaneous and continuous measurement of glucose and oxygen. *Anal. Chem.*, **67**, 3746–3752.

14 McCartney, L.J., Pickup, J.C., Rolinski, O.J., and Birch, D.J.S. (2001) Near-infrared fluorescence lifetime assay for serum glucose based on allophycocyanin-labeled concanavalin A. *Anal. Biochem.*, **292**, 216–221.

15 Rolinski, O.J., Birch, D.J.S., McCartney, L.J., and Pickup, J.C. (2001) Fluorescence nanotomography using resonance energy transfer: demonstration with a protein–sugar complex. *Phys. Med. Biol.*, **46**, N221–N226.

16 Coté, G.L. and McShane, M. (2009) Fluorescence-based glucose biosensors, in *Handbook of Optical Sensing of Glucose in Biological Fluids and Tissues* (ed. V.V. Tuchin), Taylor & Francis/CRC Press, Boca Raton, FL, pp. 331–364.

17 Cordes, D.B., Gamsey, S., and Singaram, B. (2006) Fluorescent quantum dots with boronic acid substituted viologens to sense glucose in aqueous solution. *Angew. Chem. Int. Ed.*, **45**, 3829–3832.

18 Marbach, R., Koschinsky, Th., Gries, F.A., and Heise, H.M. (1993) Noninvasive blood glucose assay by near-infrared diffuse reflectance spectroscopy of the human inner lip. *Appl. Spectrosc.*, **47**, 875–881.

19 Heise, H.M., Lampen, P., and Marbach, R. (2009) Near-infrared reflection spectroscopy for non-invasive monitoring of glucose – established and novel strategies for multivariate calibration, in *Handbook of Optical Sensing of Glucose in Biological Fluids and Tissues* (ed. V.V. Tuchin), Taylor & Francis/CRC Press, Boca Raton, FL, pp. 115–156.

20 Xu, K. and Wang, R.K. (2009) Challenges and countermeasures in NIR non-invasive blood glucose monitoring, in *Handbook of Optical Sensing of Glucose in Biological Fluids and Tissues* (ed. V.V. Tuchin), Taylor & Francis/CRC Press, Boca Raton, FL, pp. 281–316.

21 Luo, Y., An, L., and Xu, K. (2006) Discussion on floating-reference method for noninvasive measurement of blood glucose with near-infrared spectroscopy. *Proc. SPIE*, **6094**, 60940K.

22 Vasko, P.D., Blackwell, J., and Koenig, J.L. (1971) Infrared and Raman spectroscopy of carbohydrates. I: Identification of O−H and C−H vibrational modes for D-glucose, malose, cellobiose, and dextran by deuterium substitution methods. *Carbohydr. Res.*, **19**, 297–310.

23 Hahn, S. and Yoon, G. (2006) Identification of pure component spectra by independent component analysis in glucose prediction based on mid-infrared spectroscopy. *Appl. Opt.*, **45**, 8374–8380.

24 Kim, Y.J., Hahn, S., and Yoon, G. (2003) Determination of glucose in whole blood samples by mid-infrared spectroscopy. *Appl. Opt.*, **42**, 745–749.

25 Martin, W.B., Mirov, W.B., and Venugopalan, R. (2002) Using two discrete frequencies within the middle infrared to quantitatively determine glucose in serum. *J. Biomed. Opt.*, **7**, 613–617.

26 Shen, Y.C., Davies, A.G., Linfield, E.H., Elsey, T.S., Taday, P.F., and Arnone, D.D. (2003) The use of Fourier-transform infrared spectroscopy for the quantitative determination of glucose concentration in whole blood. *Phys. Med. Biol.*, **48**, 2023–2032.

27 Yaroslavskaya, A.N., Yaroslavsky, I.V., Otto, C., Puppels, G.J., Guindam, H., Vrensen, G.F.J.M., Greve, J., and Tuchin, V.V. (1998) Water exchange in human eye lens monitored by confocal Raman microspectroscopy. *Biophysics*, **43**, 109–114.

28 Enejder, A.M.K., Scecina, T.G., Oh, J., Hunter, M., Shih, W.-C., Sasic, S., Horowitz, G.L., and Feld, M.S. (2005) Raman spectroscopy for noninvasive glucose measurements. *J.Biomed. Opt.*, **10**, 031114.

29 Hanlon, E.B., Manoharan, R., Koo, T.W., Shafer, K.E., Motz, J.T., Fitzmaurice, M., Kramer, J.R., Itzkan, I., Dasari, R.R., and Feld, M.S. (2000) Prospects for *in vivo* Raman spectroscopy. *Phys. Med. Biol.*, **45**, R1–R59.

30 MacKenzie, H.A., Ashton, H.S., Spiers, S., Shen, Y., Freeborn, S.S., Hannigan, J., Lindberg, J., and Rae, P. (1999) Advances in photoacoustic noninvasive glucose testing. *Clin. Chem.*, **45**, 1587–1595.

31 Kinnunen, M. and Myllyla, R. (2005) Effect of glucose on photoacoustic signals at the

wavelengths of 1064 and 532 nm in pig blood and intralipid. *J. Phys. D Appl. Phys.*, **38**, 2654–2661.

32 Kinnunen, M., Myllylä, R., Jokela, T., and Vainio, S. (2006) *In vitro* studies toward noninvasive glucose monitoring with optical coherence tomography. *Appl. Opt.*, **45**, 2251–2260.

33 Larin, K.V., Eledrisi, M.S., Motamedi, M., and Esenaliev, R.O. (2002) Noninvasive blood glucose monitoring with optical coherence tomography. *Diabetes Care*, **25**, 2263–2267.

34 Esenaliev, R.O., Larin, K.V., Larina, I.V., and Motamedi, M. (2001) Noninvasive monitoring of glucose concentration with optical coherence tomography. *Opt. Lett.*, **26**, 992–994.

35 Larin, K.V., Akkin, T., Esenaliev, R.O., Motamedi, M., and Milner, T.E. (2004) Phase-sensitive optical low-coherence reflectometry for the detection of analyte concentrations. *Appl. Opt.*, **43**, 3408–3414.

36 Esenaliev, R.O. and Prough, D.S. (2009) Noninvasive monitoring of glucose concentration with optical coherence tomography, in *Handbook of Optical Sensing of Glucose in Biological Fluids and Tissues* (ed. V.V. Tuchin), Taylor & Francis/CRC Press, Boca Raton, FL, pp. 563–586.

37 Young, A.R. (1997) Chromophores in human skin. *Phys. Med. Biol.*, **42**, 789–802.

38 McBride, T.O., Pogue, B.W., Poplack, S., Soho, S., Wells, W.A., Jiang, S., Osterberg, U.L., and Paulsen, K.D. (2002) Multispectral near-infrared tomography: a case study in compensating for water and lipid content in hemoglobin imaging of the breast. *J. Biomed. Opt.*, **7**, 72–79.

39 Palmer, K.F. and Williams, D. (1974) Optical properties of water in the near infrared. *J. Opt. Soc. Am.*, **64**, 1107–1110.

40 Martin, K.A. (1993) Direct measurement of moisture in skin by NIR spectroscopy. *J. Soc. Cosmet. Chem.*, **44**, 249–261.

41 Lauridsen, R.K., Everland, H., Nielsen, L.F., Engelsen, S.B., and Norgaard, L. (2003) Exploratory multivariate spectroscopic study on human skin. *Skin Res. Technol.*, **9**, 137–146.

42 Bashkatov, A.N., Genina, E.A., Kochubey, V.I., and Tuchin, V.V. (2005) Optical properties of human skin, subcutaneous and mucous tissues in the wavelength range from 400 to 2000 nm. *J. Phys. D Appl. Phys.*, **38**, 2543–2555.

43 Prahl, S.A. Optical Absorption of Hemoglobin, http://omlc.ogi.edu/spectra/hemoglobin/index.html, Oregon Medical Laser Center, Portland, OR (last accessed 20 December 2010).

44 Tuchin, V.V. (2007) *Tissue Optics: Light Scattering Methods and Instruments for Medical Diagnosis*, SPIE Press, Bellingham, WA.

45 Lakowicz, J.R. (1999) *Principles of Fluorescence Spectroscopy*, 2nd edn, Kluwer Academic/Plenum, New York.

46 Schneckenburger, H., Steiner, R., Strauss, W., Stock, K., and Sailer, R. (2002) Fluorescence technologies in biomedical diagnostics, in *Optical Biomedical Diagnostics* (ed. V.V. Tuchin), vol. **PM107**, SPIE Press, Bellingham, WA, pp. 827–874.

47 Sinichkin, Yu.P., Kollias, N., Zonios, G., Utz, S.R., and Tuchin, V.V. (2002) Reflectance and fluorescence spectroscopy of human skin *in vivo*, in *Optical Biomedical Diagnostics* (ed. V.V. Tuchin), vol. **PM107**, SPIE Press, Bellingham, WA, pp. 725–785.

48 Zhadin, N.N. and Alfano, R.R. (1998) Correction of the internal absorption effect in fluorescence emission and excitation spectra from absorbing and highly scattering media: theory and experiment. *J. Biomed. Opt.*, **3** (2), 171–186.

49 Drezek, R., Sokolov, K., Utzinger, U., Boiko, I., Malpica, A., Follen, M., and Richards-Kortum, R. (2001) Understanding the contributions of NADH and collagen to cervical tissue fluorescence spectra: modeling, measurements, and implications. *J. Biomed. Opt.*, **6** (4), 385–396.

50 Zhang, X., Erb, C., Flammer, J., and Nau, W.M. (2000) Absolute rate constants for the quenching of reactive excited states by melanin and related 5,6-dihydroxyindole metabolites: implications for their antioxidant activity. *Photochem. Photobiol.*, **71** (5), 524–533.

51 Lucchina, L.C., Kollias, N., Gillies, R., Phillips, S.B., Muccini, J.A., Stiller, M.J., Trancik, R.J., and Drake, L.A. (1996) Fluorescence photography in the

evaluation of acne. *J. Am. Acad. Dermatol.*, **35**, 58–63.

52 Soukos, N.S., Som, S., Abernethy, A.D., Ruggiero, K., Dunham, J., Lee, C., Doukas, A.G., and Goodson, J.M. (2005) Phototargeting oral black-pigmented bacteria. *Antimicrob. Agents Chemother.*, **49**, 1391–1396.

53 Schneckenburger, H., Steiner, R., Strauss, W., Stock, K., and Sailer, R. (2002) Fluorescence technologies in biomedical diagnostics, in *Optical Biomedical Diagnostics* (ed. V.V. Tuchin), SPIE Press, Bellingham, WA, pp. 825–874.

54 Cheng F X., Mao, J.-M., Bush, R., Kopans, D.B., Moore, R.H., and Chorlton, M. (2003) Breast cancer detection by mapping hemoglobin concentration and oxygen saturation. *Appl. Opt.*, **42** (31), 6412–6421.

55 Petibois, C., Rigalleau, V., Melin, A.-M., Perromat, A., Cazorla, G., Gin, H., and Deleris, G. (1999) Determination of glucose in dried serum samples by Fourier-transform infrared spectroscopy. *Clin. Chem.*, **45**, 1530–1535.

56 Von Lilienfeld-Toal, H., Weidenmuller, M., Xhelaj, A., and Mantele, W. (2005) A novel approach to non-invasive glucose measurement by mid-infrared spectroscopy: the combination of quantum cascade lasers (QCL) and photoacoustic detection. *Vibr. Spectrosc.*, **38**, 209–215.

57 Maier, J.S., Walker, S.A., Fantini, S., Franceschini, M.A., and Gratton, E. (1994) Possible correlation between blood glucose concentration and the reduced scattering coefficient of tissues in the near infrared. *Opt. Lett.*, **19**, 2062–2064.

58 Kohl, M., Esseupreis, M., and Cope, M. (1995) The influence of glucose concentration upon the transport of light in tissue-simulating phantoms. *Phys. Med. Biol.*, **40**, 1267–1287.

59 Maruo, K., Tsurugi, M., Tamura, M., and Ozaki, Y. (2003) *In vivo* nondestructive measurement of blood glucose by near-infrared diffuse-reflectance spectroscopy. *Appl. Spectrosc.*, **57**, 1236–1244.

60 Jiang, J.H., Berry, R.J., Siesler, H.W., and Ozaki, Y. (2002) Wavelength interval selection in multicomponent spectral analysis by moving window partial least-squared regression with applications to mid-infrared and near-infrared spectroscopic data. *Anal. Chem.*, **74**, 3555–3565.

61 Larin, K.V. and Oraevsky, A.A. (1999) Optoacoustic signal profiles for monitoring glucose concentration in turbid media. *Proc. SPIE*, **3726**, 576–583.

62 Tuchin, V.V. (2006) *Optical Clearing of Tissues and Blood*, SPIE Press, vol. **PM154**, Bellingham, WA,.

63 Williams, R.M., McDonagh, A.F., and Braslavsky, S.E. (1998) Structural volume changes upon photoisomerization of the bilirubin-albumin complex: a laser-induced optoacoustic study. *Photochem. Photobiol.*, **68** (4), 433–437.

64 Ermakov, I.V., Sharifzadeh, M., Ermakova, M., and Gellermann, W. (2005) Resonance Raman detection of carotenoid antioxidants in living human tissue. *J. Biomed. Opt.*, **10** (6), 064028.

65 Darvin, M.E., Gersonde, I., Albrecht, H., Zastrow, L., Sterry, W., and Lademann, J. (2007) *In vivo* Raman spectroscopic analysis of the influence of IR radiation on the carotenoid antioxidant substances beta-carotene and lycopene in the human skin. Formation of free radicals. *Laser Phys. Lett.*, **4** (4), 318–321.

66 Schulmerich, M.V., Cole, J.H., Dooley, K.A., Morris, M.D., Kreider, J.M., and Goldstein, S.A. (2008) Optical clearing in transcutaneous Raman spectroscopy of murine cortical bone tissue. *J. Biomed. Opt.*, **13** (2), 021108.

67 Fine, I. (2002) Non-invasive method and system of optical measurements for determining the concentration of a substance in blood. U.S. Patent US 6400972.

68 Fine, I. (2009) Glucose correlation with light scattering patterns, in *Handbook of Optical Sensing of Glucose in Biological Fluids and Tissues* (ed. V.V. Tuchin), Taylor & Francis/CRC Press, Boca Raton, FL, pp. 250–292.

69 Jacques, S.L., Saidi, I., Ladner, A., and Oelberg, D. (1997) Developing an optical fiber reflectance spectrometer to monitor bilirubinemia in neonates. *Proc. SPIE*, **2975**, 115–124.

70 Cameron, B.D., Gorde, H.W., Satheesan, B., and Coté, G.L. (1999) The use of polarized laser light through the eye for

noninvasive glucose monitoring. *Diabetes Technol. Ther.*, **1**, 135–143.

71 Cameron, B.D. and Anumula, H. (2006) Development of a real-time corneal birefringence compensated glucose sensing polarimeter. *Diabetes Technol. Ther.*, **8**, 156–164.

72 Pu, C., Zhu, Z., and Lo, Y.H. (2000) A surface-micromachined optical self-homodyne polarimetric sensor for noninvasive glucose monitoring. *IEEE Photon. Technol. Lett.*, **12**, 190–192.

73 Ansari, R.R., Boeckle, S., and Rovati, L. (2004) New optical scheme for a polarimetric-based glucose sensor. *J. Biomed. Opt.*, **9**, 103–115.

74 Wood, M.F.G., Guo, X., and Vitkin, I.A. (2007) Polarized light propagation in multiply scattering media exhibiting both linear birefringence and optical activity: Monte Carlo model and experimental methodology. *J. Biomed. Opt.*, **12**, 014029.

75 Wood, M.F.G., Ghosh, N., Guo, X., and Vitkin, I.A. (2009) Towards noninvasive glucose sensing using polarization analysis of multiply scattered light, in *Handbook of Optical Sensing of Glucose in Biological Fluids and Tissues* (ed. V.V. Tuchin), Taylor & Francis/CRC Press, Boca Raton, FL, pp. 536–574.

76 Malik, B.H. and Coté, G.L. (2010) Real-time, closed-loop dual-wavelength optical polarimetry for glucose monitoring. *J. Biomed. Opt.*, **15** (1), 017002.

77 Larin, K.V., Motamedi, M., Ashitkov, T.V., and Esenaliev, R.O. (2003) Specificity of noninvasive blood glucose sensing using optical coherence tomography technique: a pilot study. *Phys. Med. Biol.*, **48**, 1371–1390.

56
Psoriasis and Acne

Bernhard Ortel and Piergiacomo Calzavara-Pinton

56.1
Psoriasis

Psoriasis is a common skin disease, where areas of affected skin become red, thickened, and scaly, and may be pruritic. Large body areas can be affected. In a susceptible genetic background, the pathogenetic process involves an immune response involving T cells, dendritic cells, polymorphonuclear cells, multiple cytokines, angiogenesis, epidermal hyperplasia, and altered keratinocyte differentiation. Many successful therapies target T lymphocytes that drive the inflammatory process [1].

56.1.1
General Principles of Phototherapies

Photon-based treatments of psoriasis consist of repeated controlled phototoxic exposures of involved skin. Solar phototherapy (heliotherapy) is based on empirical improvement of psoriasis with sun exposure [2]. Artificial radiation sources have made therapeutic applications more available, controllable, and versatile. The availability of ultraviolet (UV)-emitting fluorescent tubes permits the widespread use of phototherapies in modern dermatology. Specific modalities include phototherapy, where UV radiation alone is used, whereas photosensitizers are administered in photochemotherapy and photodynamic therapy. The advantage of the photon-based therapies over other treatment modalities is that photons only reach superficial layers of the skin organ, limiting potential adverse effects.

Treatments are commonly done by whole-body exposure (Figure 56.1), but localized irradiation may be preferable with limited disease. The response of unaffected skin is dose limiting with total body irradiations, as skin affected by psoriasis is more resistant to phototoxic exposures. Initial irradiations are determined by phototesting (quantified erythema response threshold in normal skin) [3] or by estimation of individual sensitivity depending on the skin phototype. Subsequent doses are gradually increased depending on the skin response. Increments are

Handbook of Biophotonics. Vol.2: Photonics for Health Care, First Edition. Edited by Jürgen Popp, Valery V. Tuchin, Arthur Chiou, and Stefan Heinemann.

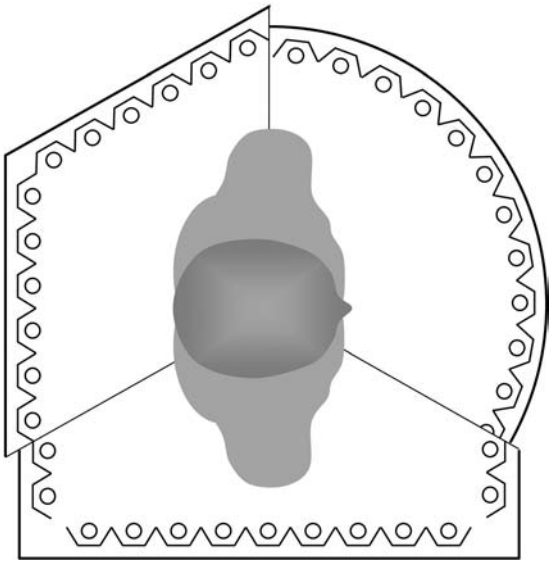

Figure 56.1 Bird's-eye view of a patient in an irradiation device lined by vertical fluorescent tubes with reflectors. The segments of the scheme represent different booth geometries.

either by the same amount or by a percentage of the previous exposure [4]. Linear increases result in slower response and higher cumulative dose. Percentage increases usually yield faster response and lower cumulative exposure, but have a higher frequency of unwanted phototoxicity. Certain protocols do not increase irradiations beyond a fixed target dose. Treatment frequency is two to five times per week for ultraviolet B (UVB) phototherapy and two to four times weekly for photochemotherapy. Some regimens include maintenance therapy, a continued therapy after at least 95% improvement or complete response, with stable radiation dose and progressively reduced frequency [5]. No standard regimens exist for photodynamic therapy. Multiple photosensitizers and different radiation sources make phototherapies very versatile (Figure 56.2).

56.1.2 Ultraviolet B Phototherapy

UVB radiation is delivered by fluorescent tubes, metal halide lamps, or excimer sources. Broadband (280–320 nm), narrowband (311 nm), and monochromatic UVB (308 nm) are available. Most therapeutic radiation sources also emit wavelengths outside the therapeutic spectrum, such as ultraviolet A (UVA), visible, and infrared radiation. Because of the latter, cooling by ventilation may be beneficial to avoid patient discomfort from heat. Moderate doses of unsensitized UVA radiation (320–400 nm) are of limited benefit in psoriasis by itself or if added to UVB. The action spectrum of antipsoriatic efficiency peaks in the wavelength range around

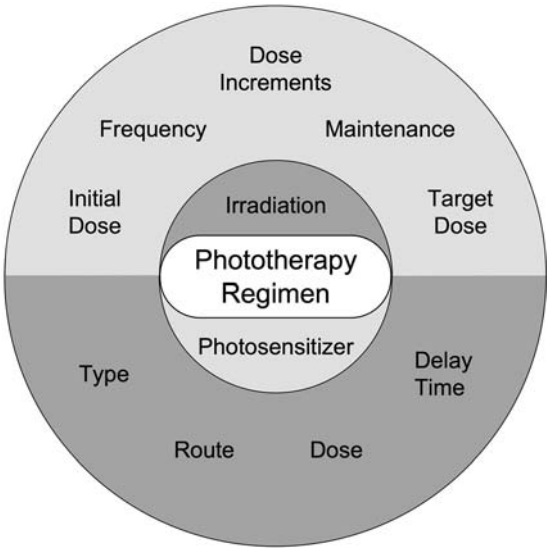

Figure 56.2 Variable parameters are selected for phototherapies of psoriasis, and their multitude illustrates the versatility of photon-based regimens in this common dermatosis.

310–315 nm (Figure 56.3). Several technical developments have applied this finding and removed the shorter, more erythemogenic while therapeutically less effective UVB wavelengths from the treatment spectrum.

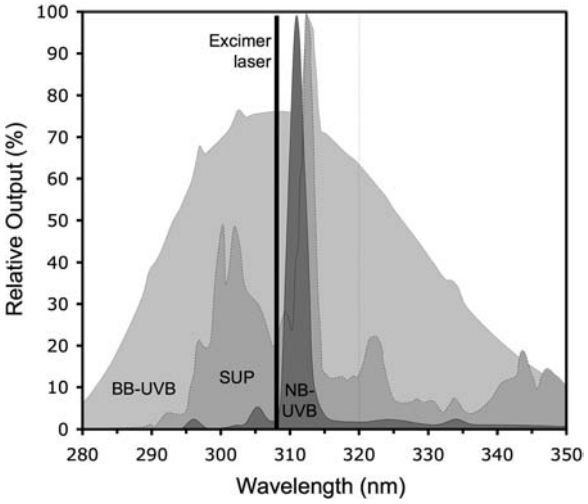

Figure 56.3 Spectra of radiation sources for UVB phototherapy demonstrate the progressive narrowing of the therapeutic spectrum to the wavelength range around 310 nm, where antipsoriatic efficiency is best.

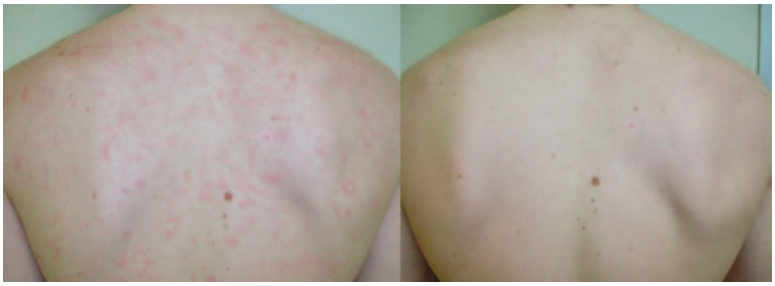

Figure 56.4 A patient with psoriasis before and at the end of a course of phototherapy using NB-UVB fluorescent tubes.

Selective ultraviolet phototherapy (SUP) applied this principle first in a commercial setting and was more efficient than broadband UVB. SUP did not work as well as psoralen with ultraviolet A (PUVA) photochemotherapy [6] and was therefore not very widely used. The more recent availability of narrowband ultraviolet B (NB-UVB, 311 nm) fluorescent tubes coincided with increasing concerns about adverse effects of PUVA. NB-UVB compared favorably with both broadband UVB and PUVA [7, 8]. Therefore NB-UVB is at present the first choice in most phototherapy centers (Figure 56.4). Additional radiation sources include xenon chloride excimer lasers that deliver high-intensity pulse trains of 308 nm radiation, thus requiring only short exposure times, but only of small areas [9]. Excimer lamps are useful for treating larger areas, but their output spectrum may include shorter wavelengths.

56.1.3 Photochemotherapy

PUVA photochemotherapy uses psoralens that are delivered topically or orally to photosensitize skin. The subsequent UVA (320–400 nm) exposure excites the psoralen molecule resulting in photochemical processes that cause a phototoxic reaction. Repeated controlled PUVA exposures lead to remission of psoriasis (Figure 56.5) [10]. Three psoralens are being used for PUVA of psoriasis (8-methoxypsoralen, 5-methoxypsoralen, trimethylpsoralen). Topical delivery may use aqueous solutions of psoralens for soaks of small areas, such as hands or feet, or for whole-body immersion (bath PUVA). Other topical preparations of psoralens are available, such as lotions, gels, and creams. 8-Methoxypsoralen (8-MOP) and 5-methoxypsoralen (5-MOP) are available for oral delivery for treatment of psoriasis. Total body irradiations are done in units as shown in Figure 56.1 that are equipped with UVA fluorescent tubes. Small irradiation units are available for localized exposure, for example, as needed in palmoplantar psoriasis. Metal halide lamps generally have a higher output and therefore require shorter exposure times; however, they require careful filtering of the UVB portion [11]. The spectral sensitivity of psoriasis treated with 8-MOP and UVA appears to be higher in the UVA-2 range (320–340 nm) than in the UVA-1 range

Figure 56.5 A patient before and after a course of oral photochemotherapy using 5-MOP. Note that PUVA induces an intense tan in addition to clearing psoriasis.

(340–400 nm). The fluorescent UVA lamps used most often for PUVA have an emission continuum peaking at 352 nm. Sources peaking around 325 nm appear to be much more efficient but have not been used widely for PUVA [12]. Differences between PUVA and UVB phototherapy include a delayed erythema response after PUVA. Maximum erythema is observed after 72–96 h with oral 8-MOP and at 120 h after bathwater sensitization, while the skin response to UVB peaks within 24 h. Therefore, PUVA exposures are given on two consecutive days only (not more than four per week) to avoid cumulative excessive phototoxicity [13].

56.1.4 Photodynamic Therapy

Photodynamic therapy (PDT) is a modality in which photochemical generation of singlet oxygen plays a central role. Originally devised as cancer treatment, a wide range of applications have been developed over recent decades. The treatment of psoriasis with PDT has been reported with several different sensitizers. Hematoporphyrin derivative [14], tin protoporphyrin [15], and benzoporphyrin derivative [16] have been used for systemic sensitization. Persistent remission in a treated area after a single exposure has been reported, but most regimens require repeated exposures for consistent improvement of psoriatic skin. Topical sensitization has been evaluated with a number of exogenous photosensitizers, but no standard PDT regimen is available at present [17, 18].

Most recently, a specific type of PDT, aminolevulinic acid (ALA)-based PDT (ALA-PDT) has been explored for the treatment of psoriasis. This modality is discussed detail in Chapter 52 for the treatment of skin cancers. In brief, exogenous ALA

[or its methyl ester, methyl aminolevulinate (MAL)] induces the formation of excess protoporphyrin IX in target cells. Psoriatic skin has constitutively elevated levels of endogenous porphyrins, but not enough to be clinically photosensitive [19]. Additional porphyrin accumulation due to ALA exposure sensitizes psoriatic skin sufficiently for PDT [20]. At present, ALA-induced porphyrins are prevalent as photosensitizers. ALA-PDT treatment is complex, requiring topical ALA application to the psoriatic skin, a waiting period for porphyrins to accumulate in the lesions, and subsequent irradiation with visible light [21, 22]. In addition to the need for repeated, time-consuming treatments, ALA-PDT of psoriasis is often intensely painful during irradiation, severely compromising its acceptance by patients [23]. It is safe to say that no convenient or broadly applicable clinical regimen for ALA-PDT of psoriasis is available at present [24].

56.1.5
Laser Therapy

Visible radiation from the pulsed dye laser (PDL, 585–595 nm) is being widely used for the treatment of telangiectasia. Widened capillary loops in the papillary dermis of psoriatic skin have been similarly targeted with good success (Figure 56.6) [25, 26]. The treatment is based on the principle of selective photothermolysis. There is no standard regimen; a range from three to six treatments every 2–6 weeks has been

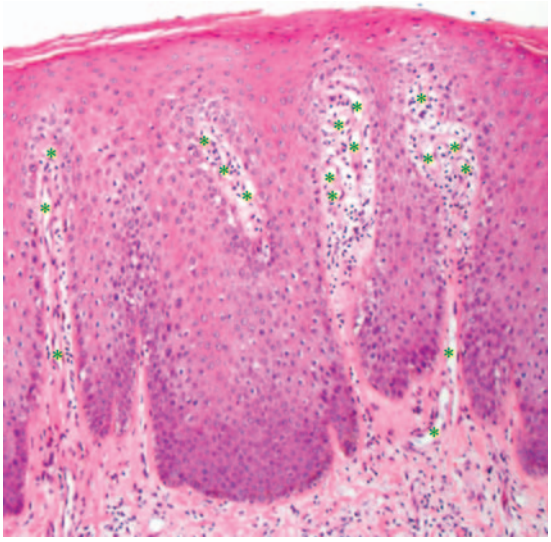

Figure 56.6 Micrograph of psoriatic skin. The capillary loops in the papillary dermis (asterisks) are obliterated by PDL treatments. Other phototherapies primarily target the inflammatory infiltrate cells in the dermis around the vessels.

reported. Although fairly effective, the cost and the small field of laser light delivery make this approach useful only in patients with limited disease.

56.1.6 Mechanisms of Action

Each phototherapeutic modality has its own set of molecular targets and responses. UVB exposure leads to DNA photoproduct formation, predominantly pyrimidine dimers, which result in DNA repair, alterations of transcriptional regulation, cytokine release, and – in those cells that are not reparable – apoptotic cell death. Apoptosis of infiltrating lymphocytes has been associated with therapeutic response to NB-UVB [27]. With UVA exposure, psoralens form cross-links between complementary strands of the DNA helix. Although singlet oxygen production and formation of other psoralen adducts, such as with RNA and proteins, have been demonstrated, the DNA cross-links appear critical for the therapeutic effect. Cross-link formation results in reduced epidermal keratinocyte proliferation. In addition to effects on keratinocytes, the critical effect of both UVB and PUVA in psoriasis appears to be the modulation of cutaneous immunological activities and the induction of apoptosis of lesional lymphocytes [28]. ALA-PDT is mediated predominantly through the action of singlet oxygen and other reactive species. Multiple cellular–molecular effects on cytokine expression and lymphocyte apoptosis are in concordance with the effects of other phototherapeutic modalities [29], but details are yet to be explored. ALA-PDT and other forms of PDT may also target the vasculature in psoriatic skin. In addition, low-dose whole-body exposures to verteporfin have demonstrated immunomodulatory effects that may be beneficial in psoriatic disease [30].

Pulsed laser treatments decimate papillary neovasculature that plays a pathogenetic role in psoriasis. Reduced blood flow and decreased T cell numbers in responsive plaques have been demonstrated [31].

56.1.7 Adverse Effects

The most common short-term side effects of phototherapies are symptoms of excessive phototoxicity, ranging from pruritus over sunburn to painful blistering. Careful dosimetry and patient monitoring help prevent these. If they occur, they are managed by symptomatic treatment and subsequent dose adjustment. Increased pigmentation is an effect that – besides esthetic considerations (that may be favorable) – is not desirable for phototherapy, as it increases the dose requirements; consequently, patients who tan more easily will require longer exposures and higher cumulative irradiations. Tanning is most relevant with PUVA (Figure 56.5) and UVB. Oral 8-MOP can cause nausea and vomiting. 5-MOP is tolerated much better and can be substituted for 8-MOP in patients with such symptoms where available [32]. Uncontrolled environmental UVA exposure has to be carefully avoided after psoralen ingestion to avoid added skin phototoxicity; eye protection

must also be worn after taking psoralens. Other photosensitizers (ALA-derived porphyrins, exogenous tetrapyrroles) also induce various, substance-specific periods of persistent photosensitivity and require protection from accidental light exposure for that time. With ALA-PDT, pain during light exposure is a very common feature and may be ultimately limiting to this application [24]. Oral intake of ALA may cause nausea and hypotension, but this route is not commonly used for psoriasis treatment. The most important unwanted long-term effect of phototherapies is carcinogenesis. UVB is a known complete carcinogen, but the carcinogenic effect of therapeutic exposures to broadband UVB is small compared with PUVA. Extended use and high cumulative exposures to PUVA are associated with increased risks of non-melanoma skin cancer and possibly also melanoma [33]. Interestingly, bath PUVA with trimethylpsoralen (TMP) does not appear to be associated with increased skin cancer rates [34]. NB-UVB therapy does not significantly increase the risk of skin cancers according to recent analysis [35]. PUVA and UVB are immunosuppressive and this effect may contribute to both therapeutic efficacy and carcinogenesis. PDT has not been associated with increased cancer rates, but the observation period and patient numbers are too limited for a reliable assessment. Pulsed visible light is not associated with carcinogenesis.

Additional long-term effects of chronic UVA and UVB exposure include accelerated photoaging with elastosis, wrinkling, dryness, and lentigines.

56.1.8 Summary

Photon-based treatments psoriasis are versatile, cost-effective, and among the most powerful tools in the therapeutic armamentarium for psoriasis. Well-developed designs of the regimens, careful documentation of adverse effects, and a track record of safety and efficacy make phototherapies an important part in everyday management of psoriatic skin disease [4].

56.2 Acne

Acne is a very common dermatosis affecting most teenagers and people at other ages less frequently. It is a disease of the pilosebaceous unit (hair follicle plus sebaceous gland) with a multifactorial pathogenic process involving hormonal sensitivity, bacterial growth, inflammation, and altered epidermal differentiation [36]. Patients affected by acne may present with comedones (open and closed), inflammatory papules, pustules, and deep-seated cysts. Therapy includes daily topical and sometimes oral administration of antibiotics, anti-inflammatory agents, antiseptics, retinoids, and other agents. Many patients desire alternative treatments, and several light-based methods have been promoted.

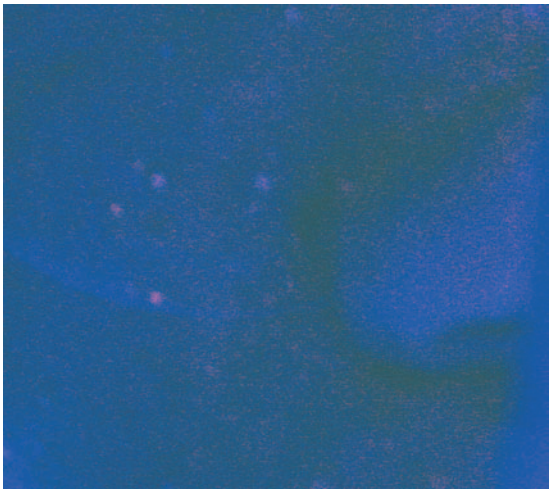

Figure 56.7 Fluorescence image of the cheek of a 13-year-old girl with untreated acne. The comedones show faint red fluorescence of coproporphyrin in the resident *P. acnes*.

56.2.1
General Principles of Phototherapies

Many acne patients experience transitory improvement with sun exposure but it is not certain what part of the solar spectrum contributes most to this effect. Comedones show red fluorescence, which has been correlated with constitutive coproporphyrin accumulation in *Propionibacterium acnes* that populates pilosebaceous units (Figure 56.7). *P. acnes* has been considered an important pathogenic factor. Light therapy aims at destroying *P. acnes* through photosensitization by endogenous porphyrins. In addition, prominent damage to sebaceous glands was reported in mouse skin after PDT with systemic ALA [37]. Also, topical indocyanine green (ICG) appears to penetrate the pilosebaceous unit [38]. These findings indicated the possibility of relatively selective targeting of sebaceous glands in acne patients using photon-based regimens. Conceptually, infrared radiation thermally targets inflammatory infiltrate cells and sebaceous glands.

56.2.2
Ultraviolet Phototherapy and PUVA

UV radiation was considered a useful therapeutic option at a time when few specific agents were available for the management of acne. Critical evaluation showed that PUVA is useless in acne management and unsensitized UV radiation is of very limited therapeutic benefit at best [39]. At present, UV radiation-based treatments are discouraged as acne is often managed using multiple agents, some of which are UV photosensitizers. In addition, UV radiation is considered comedogenic. Long-term adverse effects of UV exposure in young patients are an additional concern.

56.2.3 Visible Light Phototherapy

Light therapy of acne is based on the concept of photosensitizing *P. acnes* by its endogenous porphyrins [40]. Multiple porphyrin absorption peaks allow photoactivation by a number of visible light sources, which differ in relative tissue penetration depth and dose requirements. Fluorescent lamps and light-emitting diodes (LEDs) in the blue and red range, the potassium titanyl phosphate (KTP) laser (532 nm), the PDL (585 nm), and intense pulsed light (IPL) (530–750 nm) have been used with variable success in mild and moderate acne. Regimens vary largely in terms of dosimetry and number and frequency of exposures, ranging from single PDL treatments to twice-daily broadband red light exposures for 8 weeks. One study compared blue and blue plus red light exposures with topical 5% benzoyl peroxide and found the combined blue and red light therapy to be most effective [41]. Infrared-emitting lasers, such as the Nd:YAG laser (1320 nm) and a diode laser (1450 nm), have also been explored. Interestingly, whereas the Nd:YAG laser improved the comedonal components [42], the diode laser persistently reduced inflammatory lesions [43]. Only a few studies included placebo control groups. Because of the large variation of protocols and the multitude of light sources, a champion among acne phototherapies has not evolved. Neither has an action spectrum been established. At present, it appears that phototherapies are definitely not useful for severe and cystic acne. Recent evidence-based review articles evaluated in detail relevant clinical trials of acne phototherapy [44, 45]. A careful comparison showed recently that red light phototherapy was no less effective than PDT using MAL and red light [46].

56.2.4 Photodynamic Therapy

The first study using ALA-PDT in acne showed efficacy of a single and four consecutive weekly exposures [47]. Subsequent studies compared photosensitized acne areas with areas treated with light alone. ALA, MAL, and ICG have been evaluated and several lasers and broadband radiation sources have been used [48]. The difficulty in evaluating PDT regimens lies in the heterogeneity of the protocols. In general, multiple treatments with weekly to monthly intervals work better than single exposures, and the photosensitized areas do better than those treated with light alone. In one study, in which all patients received topical 0.1% adapelene gel, only the control group showed significant improvement, whereas with IPL treatments and PDT using MAL and IPL significance was not attained [49]. Only a few trials have compared photon-based therapies with conventional treatments such as topical 1% clindamycin or 5% benzoyl peroxide, and none compared light-based treatments with standard multi-agent therapies. Finally, side effects may be significant with ALA- and MAL-PDT. Recent reviews are available that compare and critically evaluate various approaches [44, 45]. Although sebaceous gland

targeting was an important concept initially, inflammatory acne lesions generally respond better than comedones.

56.2.5 Mechanisms and Adverse Effects

Very little is known about the mechanisms of phototherapy in acne, although the lethal photosensitization of *P. acnes* was considered an important component [47]. However, several authors refute the relevance of this mechanism [46, 50]. A number of protocols have been shown to reduce sebum excretion, including ALA-PDT and infrared laser treatment. In addition, shedding of infundibular keratinocytes that obstruct the pilosebaceous opening and direct damage to the sebocytes may hypothetically contribute to the therapeutic effect [47], although no data exist to support these claims. It is more likely that sebaceous glands are modified in their function rather than sustaining direct damage [50]. With laser-based therapies, surface cooling reduces unwanted epidermal effects while allowing impact on subepidermal structures. Unsensitized continuous-wave light treatments are not associated with adverse effects. Laser treatments and IPL may cause pain and epidermal damage and topical anesthesia and surface cooling are advisable. Adverse effects during ALA-PDT treatment include pain, burning, and itching. After the treatment, an exacerbation (a folliculitis-like reaction) is common, and epidermal hyperpigmentation may last for months [47]. A conceptual concern about long-term compromise of sebaceous glands is currently not supported by any evidence of their persistent involution after light-based therapies.

56.2.6 Summary

Because of the great efficacy of pharmacotherapies in acne, it is difficult to equal or surpass them with photonic regimens. Phototherapy is an option in patients who cannot use other medications, such as pregnant women. The advantage of light-based approaches lies in the high patient acceptance and the reduced frequency of applications. On the other hand, adverse effects, such as pain, exacerbation, and pigmentation, which accompany the more efficient PDT regimens, compromise their appeal. The use of photon-based therapies in combination regimens deserves further evaluation.

Acknowledgments

We thank Dr. Justin Wasserman, University of Chicago, for providing Figure 56.7 and Saalmann GmbH (Herford, Germany) for the emission spectra of the SUP and NB-UVB lamps.

References

1 Krueger, J.G. (2002) The immunologic basis for the treatment of psoriasis with new biologic agents. *J. Am. Acad. Dermatol.*, **46** (1), 1–23; quiz 23–26.

2 Nilsen, L.T., Soyland, E., and Krogstad, A.L. (2009) Estimated ultraviolet doses to psoriasis patients during climate therapy. *Photodermatol. Photoimmunol. Photomed.*, **25** (4), 202–208.

3 Palmer, R.A., Aquilina, S., Milligan, P.J., Walker, S.L., Hawk, J.L., and Young, A.R. (2006) Photoadaptation during narrowband ultraviolet-B therapy is independent of skin type: a study of 352 patients. *J. Invest. Dermatol.*, **126** (6), 1256–1263.

4 Menter, A., Korman, N.J., Elmets, C.A., Feldman, S.R., Gelfand, J.M., Gordon, K.B., Gottlieb, A., Koo, J.Y., Lebwohl, M., Lim, H.W., Van Voorhees, A.S., Beutner, K.R., and Bhushan, R. (2010) Guidelines of care for the management of psoriasis and psoriatic arthritis: Section 5. Guidelines of care for the treatment of psoriasis with phototherapy and photochemotherapy. *J. Am. Acad. Dermatol.*, **62** (1), 114–135.

5 Stern, R.S., Armstrong, R.B., Anderson, T.F., Bickers, D.R., Lowe, N.J., Harber, L., Voorhees, J., and Parrish, J.A. (1986) Effect of continued ultraviolet B phototherapy on the duration of remission of psoriasis: a randomized study. *J. Am. Acad. Dermatol.*, **15** (3), 546–552.

6 Hönigsmann, H., Fritsch, P., and Jaschke, E. (1977) UV-therapy of psoriasis. Half-side comparison between oral photochemotherapy (PUVA) and selective UV-phototherapy (SUP). *Z. Hautkr.*, **52** (21), 1078–1082.

7 Coven, T.R., Burack, L.H., Gilleaudeau, R., Keogh, M., Ozawa, M., and Krueger, J.G. (1997) Narrowband UV-B produces superior clinical and histopathological resolution of moderate-to-severe psoriasis in patients compared with broadband UV-B. *Arch. Dermatol.*, **133** (12), 1514–1522.

8 Tanew, A., Ortel, B., and Hönigsmann, H. (1999) Half-side comparison of erythemogenic versus suberythemogenic UVA doses in oral photochemotherapy of psoriasis. *J. Am. Acad. Dermatol.*, **41** (3 Pt 1), 408–413.

9 Asawanonda, P., Anderson, R.R., Chang, Y., and Taylor, C.R. (2000) 308-nm excimer laser for the treatment of psoriasis: a dose-response study. *Arch. Dermatol.*, **136** (5), 619–624.

10 Hönigsmann, H. (2001) Phototherapy for psoriasis. *Clin. Exp. Dermatol.*, **26** (4), 343–350.

11 Calzavara-Pinton, P.G. (1997) Efficacy and safety of stand-up irradiation cubicles with UVA metal-halide lamps (and a new filter) or UVA fluorescent lamps for photochemotherapy of psoriasis. *Dermatology*, **195** (3), 243–247.

12 Farr, P.M., Diffey, B.L., Higgins, E.M., and Matthews, J.N. (1991) The action spectrum between 320 and 400 nm for clearance of psoriasis by psoralen photochemotherapy. *Br. J. Dermatol.*, **124** (5), 443–448.

13 Wolff, K.W., Fitzpatrick, T.B., Parrish, J.A., Gschnait, F., Gilchrest, B., Honigsmann, H., Pathak, M.A., and Tannenbaum, L. (1976) Photochemotherapy for psoriasis with orally administered methoxsalen. *Arch. Dermatol.*, **112** (7), 943–950.

14 Diezel, W., Meffert, H., and Sonnichsen, N. (1980) Therapy of psoriasis by means of hematoporphyrin derivative and light. *Dermatol. Monatsschr.*, **166** (12), 793–797.

15 Emtestam, L., Berglund, L., Angelin, B., Drummond, G.S., and Kappas, A. (1989) Tin-protoporphyrin and long wave length ultraviolet light in treatment of psoriasis. *Lancet*, **333** (8649), 1231–1233.

16 Lui, H. (1994) Photodynamic therapy in dermatology with porfimer sodium and benzoporphyrin derivative: an update. *Semin. Oncol.*, **21** (6 Suppl 15), 11–14.

17 McCullough, J.L., Weinstein, G.D., Lemus, L.L., Rampone, W., and Jenkins, J.J. (1983) Development of a topical hematoporphyrin derivative formulation: characterization of photosensitizing effects *in vivo*. *J. Invest. Dermatol.*, **81** (6), 528–532.

18 Takahashi, H., Itoh, Y., Nakajima, S., Sakata, I., and Iizuka, H. (2004) A novel ATX-S10(Na) photodynamic therapy for human skin tumors and benign hyperproliferative skin. *Photodermatol. Photoimmunol. Photomed.*, **20** (5), 257–265.

19 Maari, C., Viau, G., and Bissonnette, R. (2003) Repeated exposure to blue light does not improve psoriasis. *J. Am. Acad. Dermatol.*, **49** (1), 55–58.

20 Boehncke, W.H., Sterry, W., and Kaufmann, R. (1994) Treatment of psoriasis by topical photodynamic therapy with polychromatic light. *Lancet*, **343** (8900), 801.

21 Radakovic-Fijan, S., Blecha-Thalhammer, U., Schleyer, V., Szeimies, R.M., Zwingers, T., Honigsmann, H., and Tanew, A. (2005) Topical aminolaevulinic acid-based photodynamic therapy as a treatment option for psoriasis? Results of a randomized, observer-blinded study. *Br. J. Dermatol.*, **152** (2), 279–283.

22 Collins, P., Robinson, D.J., Stringer, M.R., Stables, G.I., and Sheehan-Dare, R.A. (1997) The variable response of plaque psoriasis after a single treatment with topical 5-aminolaevulinic acid photodynamic therapy. *Br. J. Dermatol.*, **137** (5), 743–749.

23 Warren, C.B., Karai, L.J., Vidimos, A., and Maytin, E.V. (2009) Pain associated with aminolevulinic acid-photodynamic therapy of skin disease. *J. Am. Acad. Dermatol.*, **61** (6), 1033–1043.

24 Schleyer, V., Radakovic-Fijan, S., Karrer, S., Zwingers, T., Tanew, A., Landthaler, M., and Szeimies, R.M. (2006) Disappointing results and low tolerability of photodynamic therapy with topical 5-aminolaevulinic acid in psoriasis. A randomized, double-blind phase I/II study. *J. Eur. Acad. Dermatol Venereol*, **20** (7), 823–828.

25 Katugampola, G.A., Rees, A.M., and Lanigan, S.W. (1995) Laser treatment of psoriasis. *Br. J. Dermatol.*, **133** (6), 909–913.

26 Zelickson, B.D., Mehregan, D.A., Wendelschfer-Crabb, G., Ruppman, D., Cook, A., O'Connell, P., and Kennedy, W.R. (1996) Clinical and histologic evaluation of psoriatic plaques treated with a flashlamp pulsed dye laser. *J. Am. Acad. Dermatol.*, **35** (1), 64–68.

27 Ozawa, M., Ferenczi, K., Kikuchi, T., Cardinale, I., Austin, L.M., Coven, T.R., Burack, L.H., and Krueger, J.G. (1999) 312-nanometer ultraviolet B light (narrow-band UVB) induces apoptosis of T cells within psoriatic lesions. *J. Exp. Med.*, **189** (4), 711–718.

28 Vallat, V.P., Gilleaudeau, P., Battat, L., Wolfe, J., Nabeya, R., Heftler, N., Hodak, E., Gottlieb, A.B., and Krueger, J.G. (1994) PUVA bath therapy strongly suppresses immunological and epidermal activation in psoriasis: a possible cellular basis for remittive therapy. *J. Exp. Med.*, **180** (1), 283–296.

29 Bissonnette, R., Tremblay, J.F., Juzenas, P., Boushira, M., and Lui, H. (2002) Systemic photodynamic therapy with aminolevulinic acid induces apoptosis in lesional T lymphocytes of psoriatic plaques. *J. Invest. Dermatol.*, **119** (1), 77–83.

30 Ratkay, L.G., Waterfield, J.D., and Hunt, D.W. (2000) Photodynamic therapy in immune (non-oncological) disorders: focus on benzoporphyrin derivatives. *BioDrugs*, **14** (2), 127–135.

31 Hern, S., Allen, M.H., Sousa, A.R., Harland, C.C., Barker, J.N., Levick, J.R., and Mortimer, P.S. (2001) Immunohistochemical evaluation of psoriatic plaques following selective photothermolysis of the superficial capillaries. *Br. J. Dermatol.*, **145** (1), 45–53.

32 Calzavara-Pinton, P., Ortel, B., Carlino, A., Honigsmann, H., and De Panfilis, G. (1992) A reappraisal of the use of 5-methoxypsoralen in the therapy of psoriasis. *Exp. Dermatol.*, **1** (1), 46–51.

33 Patel, R.V., Clark, L.N., Lebwohl, M., and Weinberg, J.M. (2009) Treatments for psoriasis and the risk of malignancy. *J. Am. Acad. Dermatol.*, **60** (6), 1001–1017.

34 Hannuksela-Svahn, A., Sigurgeirsson, B., Pukkala, E., Lindelof, B., Berne, B., Hannuksela, M., Poikolainen, K., and Karvonen, J. (1999) Trioxsalen bath PUVA did not increase the risk of squamous cell skin carcinoma and cutaneous malignant melanoma in a joint analysis of 944 Swedish and Finnish patients with

psoriasis. *Br. J. Dermatol.*, **141** (3), 497–501.

35 Hearn, R.M., Kerr, A.C., Rahim, K.F., Ferguson, J., and Dawe, R.S. (2008) Incidence of skin cancers in 3867 patients treated with narrow-band ultraviolet B phototherapy. *Br. J. Dermatol.*, **159** (4), 931–935.

36 Zouboulis, C.C., Eady, A., Philpott, M., Goldsmith, L.A., Orfanos, C., Cunliffe, W.C., and Rosenfield, R. (2005) What is the pathogenesis of acne? *Exp. Dermatol.*, **14** (2), 143–152.

37 Divaris, D.X., Kennedy, J.C., and Pottier, R.H. (1990) Phototoxic damage to sebaceous glands and hair follicles of mice after systemic administration of 5-aminolevulinic acid correlates with localized protoporphyrin IX fluorescence. *Am. J. Pathol.*, **136** (4), 891–897.

38 Lloyd, J.R. and Mirkov, M. (2002) Selective photothermolysis of the sebaceous glands for acne treatment. *Lasers Surg. Med.*, **31** (2), 115–120.

39 Mills, O.H. and Kligman, A.M. (1978) Ultraviolet phototherapy and photochemotherapy of acne vulgaris. *Arch. Dermatol.*, **114** (2), 221–223.

40 Ashkenazi, H., Malik, Z., Harth, Y., and Nitzan, Y. (2003) Eradication of *Propionibacterium acnes* by its endogenic porphyrins after illumination with high intensity blue light. *FEMS Immunol. Med. Microbiol.*, **35** (1), 17–24.

41 Papageorgiou, P., Katsambas, A., and Chu, A. (2000) Phototherapy with blue (415 nm) and red (660 nm) light in the treatment of acne vulgaris. *Br. J. Dermatol.*, **142** (5), 973–978.

42 Orringer, J.S., Kang, S., Maier, L., Johnson, T.M., Sachs, D.L., Karimipour, D.J., Helfrich, Y.R., Hamilton, T., and Voorhees, J.J. (2007) A randomized, controlled, split-face clinical trial of 1320-nm Nd:YAG laser therapy in the treatment of acne vulgaris. *J. Am. Acad. Dermatol.*, **56** (3), 432–438.

43 Jih, M.H., Friedman, P.M., Goldberg, L.H., Robles, M., Glaich, A.S., and Kimyai-Asadi, A. (2006) The 1450-nm diode laser for facial inflammatory acne vulgaris: dose–response and 12-month follow-up study. *J. Am. Acad. Dermatol.*, **55** (1), 80–87.

44 Haedersdal, M., Togsverd-Bo, K., and Wulf, H.C. (2008) Evidence-based review of lasers, light sources and photodynamic therapy in the treatment of acne vulgaris. *J. Eur. Acad. Dermatol. Venereol.*, **22** (3), 267–278.

45 Hamilton, F.L., Car, J., Lyons, C., Car, M., Layton, A., and Majeed, A. (2009) Laser and other light therapies for the treatment of acne vulgaris: systematic review. *Br. J. Dermatol.*, **160** (6), 1273–1285.

46 Hörfelt, C., Stenquist, B., Halldin, C.B., Ericson, M.B., and Wennberg, A.M. (2009) Single low-dose red light is as efficacious as methyl-aminolevulinate – photodynamic therapy for treatment of acne: clinical assessment and fluorescence monitoring. *Acta Derm. Venereol.*, **89** (4), 372–378.

47 Hongcharu, W., Taylor, C.R., Chang, Y., Aghassi, D., Suthamjariya, K., and Anderson, R.R. (2000) Topical ALA-photodynamic therapy for the treatment of acne vulgaris. *J. Invest. Dermatol.*, **115** (2), 183–192.

48 Tuchin, V.V., Genina, E.A., Bashkatov, A.N., Simonenko, G.V., Odoevskaya, O.D., and Altshuler, G.B. (2003) A pilot study of ICG laser therapy of acne vulgaris: photodynamic and photothermolysis treatment. *Lasers Surg. Med.*, **13** (5), 296–310.

49 Yeung, C.K., Shek, S.Y., Bjerring, P., Yu, C.S., Kono, T., and Chan, H.H. (2007) A comparative study of intense pulsed light alone and its combination with photodynamic therapy for the treatment of facial acne in Asian skin. *Lasers Surg. Med.*, **39** (1), 1–6.

50 Pollock, B., Turner, D., Stringer, M.R., Bojar, R.A., Goulden, V., Stables, G.I., and Cunliffe, W.J. (2004) Topical aminolaevulinic acid-photodynamic therapy for the treatment of acne vulgaris: a study of clinical efficacy and mechanism of action. *Br. J. Dermatol.*, **151** (3), 616–622.

57
Wound Healing

Bernard Choi

57.1
Introduction

Wound repair clearly is a critically important function for the human body. Several factors affect the wound-healing process, including age and gender. The manner in which the injury occurs (e.g., electrical burn wound versus scald burn wound) can also modulate the resultant wound repair dynamics. Specific diseases, such as diabetes, can impede the wound-healing process.

To accelerate wound repair, a large variety of methods have been proposed. Wound occlusion with a bandage is one common approach, to maintain a hydrated wound bed and also to restrict access to the wound site by pathogens. A more advanced method of considerable interest is the use of light to modulate cellular function and stimulate the wound-healing process.

The objectives of this chapter are twofold. First, it focuses on the wound-healing response which ensues from selective optical injury to the microvasculature, with application of a method known as selective photothermolysis [1]. Second, a summary is presented of recent applications of optical-based methods for both therapeutic and diagnostic applications in wound healing. The list of applications is not comprehensive; instead, emphasis is placed to give the reader a sense of the diversity of optical-based methods available.

57.2
Wound-Healing Response to Selective Optical Injury to the Microvasculature

Histological and functional analysis of normal and abnormal vasculature irradiated with high-power, pulsed laser irradiation demonstrates that selective photothermal injury can be achieved with minimal perceivable structural alteration of perivascular tissue. This precise outcome is based on the principles of selective photothermolysis

Handbook of Biophotonics. Vol.2: Photonics for Health Care, First Edition. Edited by Jürgen Popp, Valery V. Tuchin, Arthur Chiou, and Stefan Heinemann.

originally proposed by Anderson and Parrish [1]. A clinical application of selective photothermolysis is targeted therapy of subsurface microvasculature, such as port-wine stain (PWS) birthmarks [2]. Despite the immediate stoppage of blood flow which routinely occurs, complete clearance of PWS birthmarks rarely occurs, even after multiple (5–20) treatment sessions.

Hypotheses which describe the reason for the resistance of PWS birthmarks to selective laser therapy are difficult to test, in large part because an animal model with PWS currently does not exist. Nevertheless, one *in vivo* model which has served as an important translational platform for novel treatment discovery is the rodent dorsal window chamber [3]. With this animal model, Babilas *et al.* [4] compared the 24 h microvascular response to selective laser injury with the predictions of photodamage derived from computational modeling data using the finite-element method. They observed that pulsed-dye laser therapy can reliably photocoagulate vessels with diameters $>20\,\mu m$, but this therapy is ineffective at photocoagulating smaller vessels; these experimental findings were in agreement with results of the finite-element modeling. According to the authors, these findings may also offer a hypothesis describing the basis for healing and restoration of the injured vasculature.

Heger *et al.* [5] described, in a comprehensive manner, the biological response to coagulum formation in vessels. Based on published literature describing the impact of specific growth factors and other molecules on thrombus organization, neovascularization, and angiogenesis, they extrapolated these past findings to the biological response of vasculature to photocoagulation. Similarly to Babilas *et al.* [4], they postulated that incomplete photocoagulation, and hence partial thrombus formation, are the primary cause of suboptimal outcomes after laser therapy of PWS birthmarks. They suggested that proposed hypothesis may help to define the role of a combined optical–pharmacologic treatment approach, which could be used to aid phototherapy of PWS birthmarks. This approach would involve photocoagulation accompanied by local release of prothrombotic agents, to enhance the degree of vascular shutdown in damaged vasculature.

Because some PWS birthmarks in patients are known to be resistant to selective laser injury, monitoring the wound-healing response in a longitudinal fashion may offer clues to the underlying reasons. With the rodent dorsal window chamber model of the microvasculature, Choi *et al.* [6] studied the response of the microvascular network to selective optical injury. Results up to 24 h after laser injury support previous work [4, 7] showing acute shutdown of the irradiated blood vessels, presumably due to photocoagulation. The results also suggest that, thereafter, a dramatic remodeling process occurs which involves blood-flow redistribution, vascular repair, and ultimate restoration of blood flow to the injured site (Figure 57.1). The longitudinal investigation of the microvascular hemodynamics in response to selective optical injury may offer a method for future studies to help researchers to understand better the biological factors responsible for the repair process and also to identify novel therapeutic approaches to achieve persistent vascular shutdown. One promising method, identified with the methods described by Choi *et al.*, is the use of combined photodynamic and photothermal therapies [8].

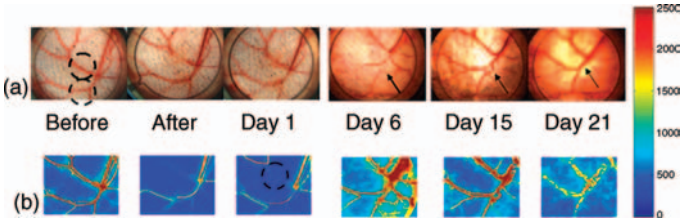

Figure 57.1 Vascular remodeling and blood flow dynamics were evident during the 21 day monitoring period, with the Day 0 "Before" and Day 21 structural images having similar appearances. Methods: a time sequence of wide-field color reflectance images (a) and corresponding speckle flow index images (b) was acquired over a 21 day monitoring period after pulsed laser irradiation of selected sites. Two arteriole–venule pairs (dashed circles in "Before" image) were irradiated with simultaneous 532 and 1064 nm laser pulses (upper circle, five 1 ms laser pulses at 27 Hz repetition rate, 2 J cm^{-2} at 532 nm, 3.6 J cm^{-2} at 1064 nm; lower circle, single 1 ms laser pulse, 4 J cm^{-2} at 532 nm, 7.2 J cm^{-2} at 1064 nm). Note the diffuse appearance of the speckle flow index image at Day 21, due to the presence of a scattering, overlying fascial layer. Color reflectance image dimensions (H × V), 13 × 10 mm; speckle flow index image dimensions, 9 × 7 mm. Adapted with permission from Ref. [4].

Previous research has demonstrated that rapamycin can inhibit angiogenesis. Phung *et al.* [9] and Jia *et al.* [10] reported that topically applied rapamycin can inhibit revascularization of sites irradiated with pulsed laser irradiation. The results suggest that a combined light–drug-based treatment protocol may be appropriate for enhanced therapy of PWS birthmarks and other cutaneous vascular abnormalities.

With microvascular photocoagulation, a purported initial biological response is secretion of angiogenic growth factors by perivascular stromal cells. These growth factors are expected to stimulate angiogenesis and revascularize the injured site. In addition to stromal cells, pluripotent stem cells in the dermis may also modulate the microvascular repair process. Loewe *et al.* [11] used immunohistochemistry to develop a biological model describing the role of stem cells in the overall wound-healing response to selective laser injury. They demonstrated that, following pulsed laser irradiation of *in vivo* human skin bearing PWS vasculature, the expression of Ki-67 (a marker of cell proliferation) and nestin (a stem cell marker) is strongly upregulated. In contrast, markers for circulating endothelial stem cells and mesenchymal stem cells were absent in the histologic sections, suggesting that stem cells are not recruited during the wound-healing process following selective laser injury. From these data, it was postulated that (a) pulsed laser irradiation induces endothelial cell proliferation, hence leading to revascularization of the injured site; and (b) terminally differentiated cells may become activated or "de-differentiated" to modulate the wound-healing process. Loewe *et al.* also reported that the use of topical rapamycin in concert with pulsed laser irradiation reduces the expression of Ki-67 and nestin and enhances the overall therapeutic efficacy. The results are in agreement with previous preclinical findings [9, 10] and collectively support a framework for a combined light–drug-based treatment protocol for PWS birthmarks.

57.3
Recent Applications of Optical-Based Methods in Wound Healing

57.3.1
Low-Level Laser Therapy (LLLT) – Wound Healing

An excellent, concise overview of low-level laser therapy (LLLT) was provided by Pinheiro [12]. Here we focus only on recent findings.

LLLT of biological tissue can affect tissue repair processes *in vitro*. However, several groups have reported that *in vivo* application of LLLT does not improve wound repair. A possible explanation is that LLLT can stimulate bacterial infection of the treated wound site. Nussbaum *et al*. [13] studied bacterial growth at incisional wound sites created on *in vivo* rat dorsal skin and irradiated with either 635 or 808 nm laser light. When compared with bacterial growth at sites 3 days after wound creation, irradiation with 808 nm light resulted in a decrease in normal skin flora and an increase in *Staphylococcus aureus* growth. The research suggests that disruption of normal skin flora enables pathogens such as *S. aureus* to colonize the wound.

Previous research has demonstrated that LLLT can modulate tissue repair processes. However, papers have reported negative findings in terms of the efficacy of LLLT in human subjects. Fulop *et al*. [14] performed a meta-analysis of 23 papers published between 2000 and 2007 to calculate a composite metric of LLLT efficacy in preclinical animal studies and clinical studies. They reported that a significantly positive effect of LLLT was observed in both animal and clinical studies. The calculated efficacy was stronger in animals than in human subjects; it was postulated that this trend is due to the higher degree of experimental control that is present in animal studies. According to the authors, the results demonstrate that LLLT, overall, does improve tissue repair after injury.

Mitomycin C is a chemotherapeutic drug with antineoplastic antibiotic properties, but its effects on wound healing remain to be ascertained. Silva Santos *et al*. [15] studied the effects of LLLT on skin wounds treated with mitomycin C. They postulated that LLLT, which is known to stimulate fibroblast proliferation and collagen production, can modulate the inhibitory effects that mitomycin C on collagen synthesis. They reported that LLLT reduced the inflammatory response and increased both collagen deposition and fibroblast proliferation in scalpel wounds created in the dorsa of a rodent model and subsequently treated with mitomycin C.

57.3.2
LLLT to Aid Cerebral Nervous System Repair Processes

Anders [16] provided an excellent, brief overview of the current state of LLLT to enhance repair of traumatic injury to the central nervous system. Here, we focus on reviewing several key studies published recently.

Tissue plasminogen activator (tPA) is the only treatment option for patients suffering from ischemic stroke. Successful treatment relies on tPA administration within 3 h after stroke onset. As an alternate treatment approach, LLLT purportedly

stimulates mitochondrial function and mitigates the risk of apoptosis in cerebral regions affected by stroke. Zivin *et al.* [17] demonstrated a favorable outcome of ischemic stroke with the use of LLLT. They observed that 36% of patients treated with LLLT achieved a favorable outcome, compared with 31% of patients receiving a sham therapy (i.e., no irradiation with laser light). It is important to note that the difference between patient treatment response was not significant. LLLT can be performed at any time after ischemic stroke, making it an attractive alternative in the clinical management of stroke victims.

Knowledge of the precise mechanisms by which LLLT works could help in the design of robust LLLT-based treatment protocols. One proposed mechanism by which LLLT enhances wound healing is stimulation of mitochondrial activity via absorption of the incident light by cytochrome oxidase *c*. Lapchak and de Taboada [18] employed a luminescence assay to estimate ATP content in excised parietal/occipital cortex from rabbits, after embolization. They performed experiments on three groups of rabbits: (1) negative control (no embolization, no LLLT), (2) embolization without LLLT, and (3) embolization with LLLT. It was found that embolization without LLLT decreases ATP content, and embolization with LLLT increases ATP content by as much as 77% above the content in the negative control group. It was suggested that the potential mechanism by which LLLT improves the outcome of ischemic stroke is enhanced mitochondrial function.

57.3.3
Wound Healing after Laser Cartilage Reshaping

Selective photothermal heating of cartilage can achieve a persistent shape change in the irradiated sample. Recent studies have focused on the effects of laser irradiation on chondrocytes, the cells in cartilage responsible for development of the extracellular matrix in cartilage. Holden *et al.* [19] demonstrated that only collagen type II gene expression, and not that of collagen type I, is observed following laser irradiation of cartilage. They used an Nd:YAG laser to irradiate nasal septum freshly extracted from rabbits and assessed the gene expression of collagen types I and II using reverse transcription polymerase chain reaction (RT-PCR). They determined that collagen type II was absent from the irradiated site but expressed in regions surrounding the site. Collagen type I gene expression was not observed, suggesting that photothermal modulation of cartilage does not induce a traditional wound-healing response. Instead, based on the findings, it was suggested that laser irradiation of cartilage results in the formation of hyaline cartilage, which consists primarily of collagen type II and thus indicates an optimal wound-healing response.

57.3.4
Novel Diagnostic Applications of Biophotonics to Study Wound Healing

Current methods to monitor dermal wound repair are limited. Gross clinical assessment of the wound is highly dependent on the prior experience and training of the clinician. Histologic analysis requires the use of destructive biopsies.

Zhuo *et al*. [20] found that nonlinear optical microscopy (NLOM) is capable of chronic, nondestructive evaluation of scald wound repair in an *in vivo* rodent model. They specifically analyzed second harmonic generation and two-photon excited fluorescence signals. When they transplanted fluorescently labeled bone marrow-derived mesenchymal stem cells (MSCs) to specific wound sites, they were able to monitor the location of the MSCs and the dynamic collagen architecture using NLOM. With the development of clinic-friendly NLOM instruments, clinicians may soon be able to monitor, in a routine manner, the progress of cutaneous wound repair.

57.4 Summary

This chapter has presented a summary of our current knowledge on the biological response of the microvasculature to selective optical injury, followed by an overview of recently published studies describing the application of LLLT to enhance wound healing and optical imaging methods to study noninvasively the wound-healing response. With the current shift towards interdisciplinary preclinical and clinical research, researchers are now well poised to conduct integrated studies at the interface of the cutting edge of both optical technology and biology, to address key fundamental questions on the biological processes which underlie the dynamics of wound healing.

References

1 Anderson, R.R. and Parrish, J.A. (1983) Selective photothermolysis – precise microsurgery by selective absorption of pulsed radiation. *Science*, **220** (4596), 524–527.

2 Kelly, K.M., Choi, B., McFarlane, S., Motosue, A., Jung, B.J., Khan, M.H., Ramirez-San-Juan, J.C., and Nelson, J.S. (2005) Description and analysis of treatments for port-wine stain birthmarks. *Arch. Facial Plast. Surg.*, **7** (5), 287–294.

3 Papenfuss, H.D., Gross, J.F., Intaglietta, M., and Treese, F.A. (1979) Transparent access chamber for the rat dorsal skin fold. *Microvasc. Res.*, **18** (3), 311–318.

4 Babilas, P., Shafirstein, G., Baumler, W., Baier, J., Landthaler, M., Szeimies, R.M., and Abels, C. (2005) Selective photothermolysis of blood vessels following flashlamp-pumped pulsed dye laser irradiation: *in vivo* results and mathematical modelling are in agreement. *J. Invest. Dermatol.*, **125** (2), 343–352.

5 Heger, M., Beek, J.F., Moldovan, N.I., van der Horst, C.M.A.M., and van Gemert, M.J.C. (2005) Towards optimization of selective photothermolysis: prothrombotic pharmaceutical agents as potential adjuvants in laser treatment of port wine stains – a theoretical study. *Thromb. Haemost.*, **93** (2), 242–256.

6 Choi, B., Jia, W.C., Channual, J., Kelly, K.M., and Lotfi, J. (2008) The importance of long-term monitoring to evaluate the microvascular response to light-based therapies. *J. Invest. Dermatol.*, **128** (2), 485–488.

7 Barton, J.K., Hammer, D.X., Pfefer, T.J., Lund, D.J., Stuck, B.E., and Welch, A.J. (1999) Simultaneous irradiation and imaging of blood vessels during pulsed laser delivery. *Lasers Surg. Med.*, **24** (3), 236–243.

8 Channual, J., Choi, B., Pattanachinda, D., Lotfi, J., and Kelly, K.M. (2008) Long-term vascular effects of photodynamic and pulse dye laser therapy protocols. *Lasers Surg. Med.*, **40**, 644–650.

9 Phung, T.L., Oble, D.A., Jia, W., Benjamin, L.E., Mihm, M.C., and Nelson, J.S. (2008) Can the wound healing response of human skin be modulated after laser treatment and the effects of exposure extended? Implications on the combined use of the pulsed dye laser and a topical angiogenesis inhibitor for treatment of port wine stain birthmarks. *Lasers Surg. Med.*, **40** (1), 1–5.

10 Jia, W.C., Sun, V., Tran, N., Choi, B., Liu, S.W., Mihm, M.C.J., Phung, T.L., and Nelson, J.S. (2010) Long-term blood vessel removal with combined laser and topical rapamycin antiangiogenic therapy: implications for effective port wine stain treatment. *Lasers Surg. Med.*, **42** (2), 105–112.

11 Loewe, R., Oble, D.A., Valero, T., Zukerberg, L., Mihm, M.C., and Nelson, J.S. (2010) Stem cell marker upregulation in normal cutaneous vessels following pulsed-dye laser exposure and its abrogation by concurrent rapamycin administration: implications for treatment of port-wine stain birthmarks. *J. Cutan. Pathol.*, **37**, 76–82.

12 Pinheiro, A.L.B. (2009) Advances and perspectives on tissue repair and healing. *Photomed. Laser Surg.*, **27** (6), 833–836.

13 Nussbaum, E.L., Mazzulli, T., Pritzker, K.P.H., Heras, F.L., Jing, F., and Lilge, L. (2009) Effects of low intensity laser irradiation during healing of skin lesions in the rat. *Lasers Surg. Med.*, **41** (5), 372–381.

14 Fulop, A.M., Dhimmer, S., Deluca, J.R., Johanson, D.D., Lenz, R.V., Patel, K.B., Douris, P.C., and Enwemeka, C.S. (2009) A meta-analysis of the efficacy of phototherapy in tissue repair. *Photomed. Laser Surg.*, **27** (5), 695–702.

15 Silva Santos, N.R., dos Santos, J.N., Macedo Sobrinho, J.B., Ramalho, L.M.P., Carvalho, C.M., Soares, L.G.P., and Pinheiro, A.L.B. (2010) Effects of laser photobiomodulation on cutaneous wounds treated with mitomycin C: a histomorphometric and histological study in a rodent model. *Photomed. Laser Surg.*, **28** (1), 81–90.

16 Anders, J.J. (2009) The potential of light therapy for central nervous system injury and disease. *Photomed. Laser Surg.*, **27** (3), 379–380.

17 Zivin, J.A., Albers, G.W., Bornstein, N., Chippendale, T., Dahlof, B., Devlin, T., Fisher, M., Hacke, W., Holt, W., Ilic, S., Kasner, S., Lew, R., Nash, M., Perez, J., Rymer, M., Schellinger, P., Schneider, D., Schwab, S., Veltkamp, R., Walker, M., Streeter, J., and NeuroThera Effectiveness and Safety Trial-2 Investigators (2009) Effectiveness and safety of transcranial laser therapy for acute ischemic stroke. *Stroke*, **40** (4), 1359–1364.

18 Lapchak, P.A. and De Taboada, L. (2010) Transcranial near infrared laser treatment (NILT) increases cortical adenosine-5′-triphosphate (ATP) content following embolic strokes in rabbits. *Brain Res.*, **1306**, 100–105.

19 Holden, P.K., Li, C., Da Costa, V., Sun, C.H., Bryant, S.V., Gardiner, D.M., and Wong, B.J.F. (2009) The effects of laser irradiation of cartilage on chondrocyte gene expression and the collagen matrix. *Lasers Surg. Med.*, **41** (7), 487–491.

20 Zhuo, S.M., Chen, JX., Xie, S.S., Fan, L., Zheng, L.Q., Zhu, X.Q., and Jiang, X.S. (2010) Monitoring dermal wound healing after mesenchymal stem cell transplantation using nonlinear optical microscopy. *Tissue Eng. Part C Methods*, **16** (5), 1107–1110.

58
Diagnosis of Neoplastic Processes in the Uterine Cervix

Natalia Shakhova, Irina Kuznetsova, Ekaterina Yunusova, and Elena Kiseleva

58.1
Introduction

Malignant neoplasms of the female reproductive organs, including cervical cancer, are among the principal causes of death: in 2005, about 500 000 cases of cervical cancer and 260 000 related deaths were reported worldwide [1]. A significant increase in the incidence of cervical cancer is observed for women in the early reproductive age group (by 2% yearly on average) [2]. Detection and treatment of precancerous abnormalities and early-stage cervical cancer can prevent up to 80% of invasive diseases [1]. This situation requires accurate diagnostic techniques providing effective management of women with abnormal screening tests.

The paradigm of colposcopic examination after primary screening (Pap and HPV tests) is still considered the standard for the evaluation of cervical neoplasia. The aim of colposcopy is to identify disease, to obtain representative specimens for histological verification, and to direct patient management. Unfortunately, recent research shows that colposcopic grade and histologic lesion grade are not closely correlated [3]. The sensitivity of colposcopy-guided biopsy for precancerous abnormalities [cervical intraepithelial neoplasia grade 2+ (CIN2 +)] was estimated as only 54%, and for individual physicians this statistical value varies between 28.6 and 81.5% [4, 5]. This is connected with significant errors in colposcopic assessment, subjectivism, and a considerable dependence on the experience of clinicians. However, even when performed by trained and experienced personnel, colposcopic biopsy misses 26–42% of prevalent CIN2+ [6, 7]. The only compensating strategy for timely and accurate diagnosis of early cervical cancer and high-grade premalignant lesion is considered to be morphologic examination of specimens obtained by a large excisional procedure or multiple random biopsies [7, 8]. Such an approach can induce complications due to invasiveness and increase costs and time. In our opinion, complementary application of noninvasive technologies [e.g., fluorescence imaging, high-frequency ultrasound, optical coherence tomography (OCT)] in colposcopy is appropriate for adequate management of Pap and HPV positive women. It allows one to ensure adequate diagnosis and, at the same time, to avoid over-treatment and over-expense.

Handbook of Biophotonics. Vol.2: Photonics for Health Care, First Edition. Edited by Jürgen Popp, Valery V. Tuchin, Arthur Chiou, and Stefan Heinemann.

The goal of this chapter is to demonstrate the efficacy of OCT in the management of cervical neoplasia (early cervical cancer and premalignant abnormalities).

58.2 Materials and Methods

This research was conducted in the Nizhny Novgorod Regional Hospital (Russia). The study was approved by the Ethical Committee for scientific studies with human subjects; written informed consent was obtained from all patients. A total of more than 500 female patients with different cervical conditions have been examined with OCT. The inclusion criterion was indication for colposcopy and the exclusion criterion was age under 18 years.

The standard equipment for colposcopy and methodology with 5% acetic acid local application (traditional colposcopic test) were used. OCT examinations were conducted with a time-domain OCT device (Institute of Applied Physics, Russian Academy of Sciences, Russia). The system has the following technical characteristics: central wavelength, 1300 nm; radiation power, not exceeding 6.0 mW; spatial resolution, 15–20 μm; in-depth scanning range, up to 2 mm; lateral scanning range, 1–2 mm; and acquisition time for two-dimensional 200×200 pixel image, 1.5–2 s. The OCT system for cervical inspection performs using a detachable forward-looking OCT probe with an outer diameter of 2.7 mm. The probe is applied to the cervical area of interest under colposcope control. To reduce artifacts related to unintentional movements of the probe and the studied object, the distal end of the probe has to be in contact with the tissue. The images obtained are interpreted directly during the patient examination.

In the previous stages, the initial approval of OCT for the detection of cervical pathology and adaptation of OCT for the basic colposcopic procedure were carried out. Criteria for OCT detection of cervical neoplasia were elaborated and estimated in a blind recognition test. The sensitivity was shown to be 82%, specificity 78%, and error 19.2%, and the kappa value equals 0.65 [9].

At the present stage of clinical study, 135 female patients of reproductive age (mean age 32 ± 1.3 years) have been examined after primary cervical screening using OCT–colposcopy. Analysis of results was based on morphologic verification (a group of 100 patients) and 3 years of follow-up (a group of 35 patients).

58.3 Results

The suggested approach for increasing the efficacy of cervical cancer and precancer diagnosis is based on the complementary use of colposcopy and OCT, and the method includes the following steps:

- colposcopy with acetic acid test;
- determination of atypical colposcopic findings (ACFs);

- OCT examination of zones with ACFs;
- determination of OCT indications for biopsy;
- biopsy based on OCT indications;
- management of patient depending on histological results.

In previous studies, we distinguished three classes of OCT images: "benign," "suspicious," and "malignant."

We identify three types of images as being in the "benign" class (Figure 58.1). One is two-layer structure with different optical properties of the layers (a moderately scattering upper layer and a strongly scattering lower layer) and a highly contrasted boundary between layers (Figure 58.1a). The second type represents images with a disturbed structure of layers or without layer stratification identified, but with low-scattering areas with high-contrast boundaries (Figure 58.1b). Keeping the imaging depth at about 1.5 mm is an important indicator of "benign"-type images. The third type includes non-structured images but demonstrating a high signal to a depth of 1.5 mm (Figure 58.1c).

The "malignant" class includes two types of images (Figure 58.2). The most typical indicator of "malignant" class is a non-structured image with a large decrease in signal resulting in a low imaging depth (usually 0.5–1 mm) (Figure 58.2a). The other type, which is observed much more rarely than the first type, is a two-layered structure where each layer demonstrates high scattering and a substantial decrease in the signal (Figure 58.2b). The images with a disturbed structure which cannot be clearly identified as "benign" or "malignant" are classified as "suspicious."

Our method of using OCT in cervical diagnostics required revision of the approaches for image interpretation. At present we distinguish two groups of images: "biopsy indication" and "no biopsy indication." In our opinion, the biopsy must be performed for cervical sites characterized by "malignant" or "suspicious" OCT image types.

Approval of this approach was based on 100 clinical cases (randomized group), which showed a high efficiency of OCT–colposcopy. All OCT images obtained in this approval process were verified morphologically by biopsy performed based on colposcopic data according to standard indications. It was shown that the colposcopic data gave an indication for biopsy in 83% of cases whereas cervical neoplasia (CIN2 + and cervical microcarcinoma) was diagnosed in only 37% of cases. OCT images with "biopsy indication" were obtained in only 36% of cases. According to our study, the

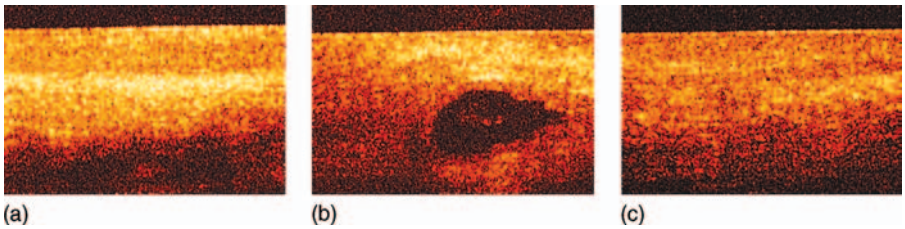

Figure 58.1 Examples of "benign" types of OCT images. All data have been morphologically verified.

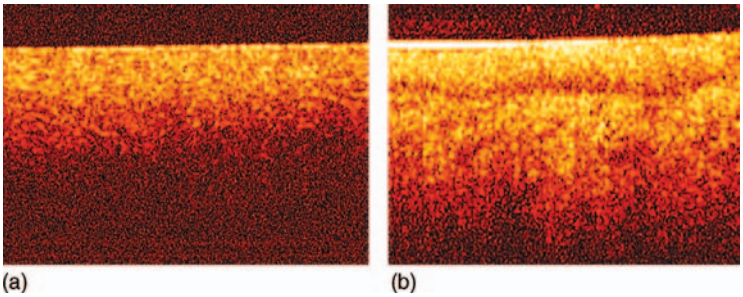

Figure 58.2 Examples of "malignant" types of OCT images. All data have been morphologically verified.

complementary performance of OCT and colposcopy allows the specificity of diagnostics of early-stage cervical cancer to be increased significantly. Concerning the sensitivity of the method, OCT demonstrated "benign" types of images in 1% of cases corresponding morphologically to an in-between state (CIN2) which did not allow us to replace totally the biopsy with OCT inspection in the final protocol. In our opinion, refusal of a biopsy procedure should be accompanied by an OCT follow-up.

The final protocol for early-stage neoplasia (OCT–colposcopy and OCT–follow-up) was performed with the main group of 35 patients of reproductive age. The total follow-up duration was 3 years. The OCT–colposcopy procedures were performed every 6 months. The control group included 20 patients. It was found that in the control group the biopsy was performed for 13 out of 20 patients; in seven cases repeated biopsy was required, and finally cervical neoplasia was diagnosed in two patients. In the main group, indications for biopsy were found for 11 patients out of 35, and indications for repeated biopsy were absent; cervical cancer was diagnosed in six patients. Hence over-biopsy in the control group was performed in 25 cases compared with five cases in the main group. It is worth mentioning that during the 3 year follow-up, no cases of neoplastic changes in the cervix were diagnosed in patients with OCT-based biopsy refusal.

58.4 Discussion and Conclusion

Colposcopy-directed biopsy remains the "gold standard" for cervical cancer diagnosis. However, the shortcomings of colposcopy require the development of new techniques, and OCT is a promising candidate. Improvement of the specificity, but not the sensitivity, by adding OCT to colposcopy was demonstrated in our study. Our results are in agreement with those of other researchers [10].

In spite of some limitations, OCT–colposcopy can be successfully applied in cervical cancer diagnosis. This technique is very helpful in female patients of reproductive age, particularly in cases of questionable interpretation of colposcopic data and limitations of or contraindications to biopsy. For example, 1% of cervical cancers are detected during pregnancy and there are an increasing number of

premalignant lesions in these cases for which diagnosis and evaluation are not easy. Colposcopy in pregnancy does not differ from that in the non-pregnant state, but as the pregnancy advances, interpretation of colposcopy becomes progressively more difficult [10]. OCT could be the method of choice in pregnancy. Another reasonable category for adding OCT to colposcopy is aged patients, as they have a high risk for biopsy complications.

Unfortunately, OCT in some way "suffers" from subjectivism like colposcopy. To minimize this factor, the development of mathematical algorithms for OCT image interpretation is suggested and epithelial brightness has been shown to be a statistically significant distinguishing feature of cervical OCT images [11]. The sensitivity of OCT–colposcopy could be improved by increasing the scanning rate, using a newly designed probe with a larger diameter, and so on [12].

In conclusion:

- OCT is an attractive technique for the detection of cervical neoplasia.
- It should be applied according to relevant indications and in an appropriate scenario.
- Further improvements of the method are required.

Acknowledgments

The Russian Academy of Sciences (Fundamental Sciences for Medicine), the Russian Foundation for Basic Research (RFBR) (07-08-00803, 08-02-99049), and the Science and Innovations Federal Russian Agency (2007-2-2.2-04-01-012) are thanked for financial support.

References

1 World Health Organization (2009) Human papillomavirus vaccines – WHO position paper. *WHO Weekly Epidemiol. Rec.*, **84** (15), 117–132.

2 Ronco, G. and Rossi, P. (2008) New paradigms in cervical cancer prevention: opportunities and risks. *BMC Women's Health*, **8**, 23.

3 Ferris, D.G., Litaker, M.S., and ALTS Group (2006) Prediction of cervical histologic results using an abbreviated reid colposcopic index during ALTS. *Am. J. Obstet. Gynecol.*, **194**, 704–710.

4 The ASCUS-LSIL Triage Study (ALTS) Group (2003) Results of a randomized trial on the management of cytology interpretations of atypical squamous cells of undetermined significance. *Am. J. Obstet. Gynecol.*, **188**, 1383–1392.

5 Pretorius, R.G., Belinson, J.L., and Qiao, Y.L. (2010) Regardless of colposcopic skill, performing more biopsies increases the yield of CIN 3 or cancer. Presented at the Eurogin 2010 Congress. Cervical Cancer Prevention: 20 Years of Progress and a Path to the Future. February 17–20, Monte Carlo, Monaco.

6 Massad, L.S. and Collins, Y.C. (2003) Strength of correlations between colposcopic impression and biopsy histology. *Gynecol. Oncol.*, **89**, 424–428.

7 Stoler, M. (2010) Accuracy and limitations of colposcopic performance. Presented at the Eurogin 2010 Congress. Cervical Cancer Prevention: 20 Years of Progress and a Path to the Future. February 17–20, Monte Carlo, Monaco.

8 Gage, J.C., Hanson, V.W., Abbey, K., Dippery, S. *et al.* (2006) Number of cervical biopsies and sensitivity of colposcopy. *Obstet. Gynecol.*, **108** (2), 264–272.
9 Zagaynova, E.V., Gladkova, N.D., Shakhova, N.M., Streltsova, O.S., *et al.* (2011) Interoperative OCT monitoring, in *Handbook of Biophotonics*, vol. **1** (ed. J. Popp), Wiley-VCH Verlag GmbH, Weinheim.
10 Diakomanolis, S.E. (2010) HPV associated diseases in pregnancy. Presented at the Eurogin 2010 Congress. Cervical Cancer Prevention: 20 Years of Progress and a Path to the Future. February 17–20, Monte Carlo, Monaco.
11 Belinson, S., Belinson, J., Ledford, K., Na, W., *et al.* (2010) Cervical epithelial brightness by optical coherence tomography (OCT) distinguishes grades of dysplasia with statistical significance. Presented at the Eurogin 2010 Congress. Cervical Cancer Prevention: 20 Years of Progress and a Path to the Future. February 17–20, Monte Carlo, Monaco.
12 Liu, Z., Belinson, S.E., Li, J., Yang, B. *et al.* (2010) Diagnostic efficacy of real-time optical coherence tomography in the management of preinvasive and invasive neoplasia of the uterine cervix. *Int. J. Gynecol. Cancer*, **20** (2), 283–287.

59
The Use of Single-Point and Ring-Shaped Laser Traps to Study Sperm Motility and Energetics

Linda Z. Shi, Bing Shao, Jaclyn Nascimento, and Michael W. Berns

59.1
Introduction

Single-point laser trapping is a noninvasive biophysical tool which has been widely applied to study physiologic and biomechanical properties of cells [1, 2]. Over the past three decades, researchers have used laser trapping (tweezers) to quantify sperm motility by measuring swimming forces [3–7]. These studies determined that the minimum amount of laser power needed to hold the sperm in the trap (or the threshold escape power) is directly proportional to the sperm's swimming force according to the equation $F = QP/c$, where F is the swimming force, P is the laser power, c is the speed of light in the medium, and Q is the geometrically determined trapping efficiency parameter [3]. Sperm swimming force measurements have been used to evaluate sperm viability after cryopreservation [5], as a way to evaluate the motility of epididymal versus ejaculated sperm [4], and to examine infertility in human patients [5]. In addition, a relationship between sperm velocity and swimming force (escape power from trap) was found for human and dog sperm [7, 8].

59.2
Single-Point Laser Trap

The more common single-point gradient trap that is used for sperm analysis is shown in Figure 59.1. An Nd:YVO_4 laser operating at 1064 nm is coupled to a Zeiss Axiovert S100 microscope equipped with a phase III, 40×, NA 1.3, oil immersion objective. The laser power in the specimen plane is attenuated by rotating an optical polarizer mounted in a stepper-motor-controlled rotating mount. Two dual video adapters are used to bring the laser into the microscope and simultaneously image the sperm with phase contrast and fluorescence microscopy. The laser beam enters the side port of the first dual video adapter and is transmitted to the microscope. A filter is used to prevent back-reflections of infrared laser light from exiting the top port of the adapter and allow reflected visible light coming from the specimen

Handbook of Biophotonics. Vol.2: Photonics for Health Care, First Edition. Edited by Jürgen Popp, Valery V. Tuchin, Arthur Chiou, and Stefan Heinemann.

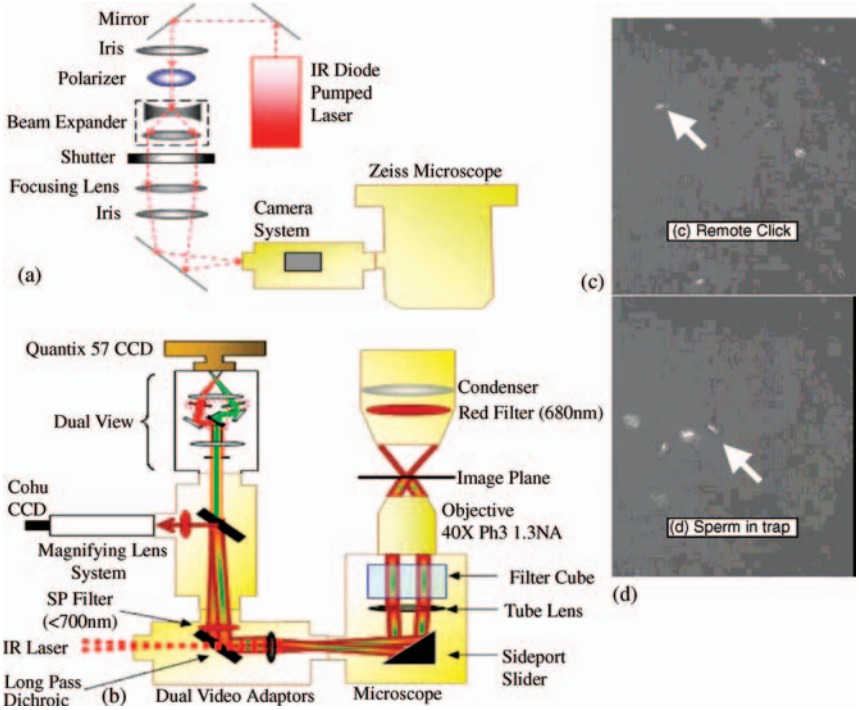

Figure 59.1 (a) Optical schematic showing the components used to generate and control the single-point laser tweezers; (b) imaging setup showing illumination sources, filters, and cameras used to image the sperm in both phase contrast and fluorescence; (c) a collaborator from Australia clicked on a selected swimming dog sperm on the image screen in Australia, which then activated RATTS in the California laboratory, which tracked the sperm for 5 s, and then held it in the trap for 10 s (d).

to pass to the second video adapter. The specimen is viewed in phase contrast using red light from the halogen lamp and viewed in fluorescence mode using the arc lamp as the excitation source. The fluorescence filter cube contains an HQ 500/20 nm excitation filter and a dichroic beam splitter with a 505 nm cut-off wavelength. The second dual video adapter attached to the top port of the first video adapter uses a filter cube to separate the phase information (reflects >670 nm) from the fluorescence (transmits 500–670 nm). The phase contrast images are filtered through a filter and acquired by a charge-coupled device (CCD) camera (operating at 40 frames per second) coupled to a variable zoom lens system (0.33–1.6×) to increase the field of view. For the fluorescent images, a dual-view system splits the red and green specimen fluorescence emitted resulting in an image in each color. Fluorescent emission filters are placed in this emission-splitting system (green fluorescence emitter, HQ 535/40 nm M; red fluorescence emitter, HQ 605/50 nm M). The dual-view system is coupled to a digital camera that captures the images [9].

An integrated system has been developed to analyze individual sperm motility and energetics automatically. A two-level real-time automated tracking and trapping system (RATTS) has been developed to quantify the motility and energetics of sperm using real-time tracking (done by the upper-level system) and fluorescent ratio imaging (done by the lower-level system). The communication between these two systems is achieved by a gigabit network. The RATTS system can be operated remotely through the Internet using the logmein website. Individual sperm can be automatically trapped using laser tweezers to measure sperm swimming forces during real-time tracking. Once the sperm is stably trapped, the custom-built program can gradually reduce the laser power until the sperm is capable of escaping the trap. This escape power can be converted to the actual amount of swimming force needed to escape from the trap. By taking the ratio of the wavelengths of a mitochondrial membrane dye, mitochondrial energetics can be monitored and correlated with both sperm escape power (converted to swimming force in piconewtons by $F = QP/c$) and sperm swimming speed. The latter two parameters are linearly correlated. This two-level system to study individual sperm motility and energetics has not only increased experimental throughput over single-level systems by an order of magnitude, but also allows monitoring of sperm energetics prior to and after exposure to the laser trap [10].

59.3
Ring-Shaped Laser Traps

The experimental setup for a ring-shaped laser trap system is presented in Figure 59.2. The light beam from a continuous-wave ytterbium fiber laser (1070 nm wavelength) is collimated and expanded via the 3× beam expander. For better performance of the trap, a refractive beam shaper is used to convert a Gaussian laser beam into a collimated flat-top beam. A telescope lens pair shrinks the shaped beam so that the thickness of the light cone input to the objective is equal to the diameter

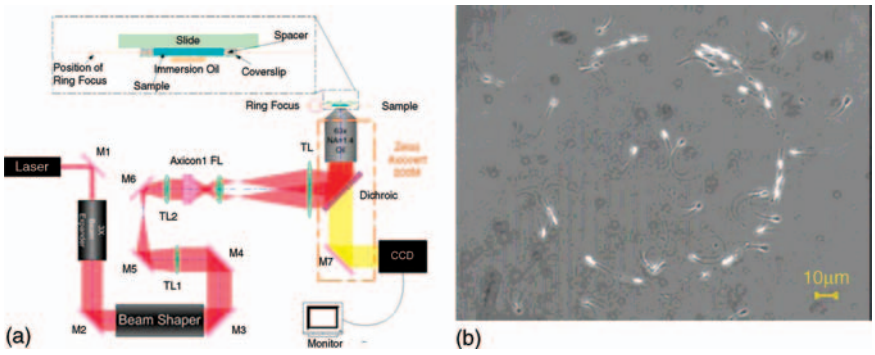

Figure 59.2 (a) Optical setup for ring-shaped laser trap system. (b) Tens of sperm are stopped or moving along the ring focus.

of the back aperture, hence the numerical aperture of the trapping beam is maximized. The laser beam is divided and bent towards the optical axis at an angle upon the Axicon lens, $\beta = \arcsin(n \sin \gamma) - \gamma$, where γ is the base angle and n is the refractive index of the Axicon. At the back focal plane of the focusing lens (FL), a ring image is formed that is conjugate to the ring focus at the specimen plane. After the tube lens (TL), the laser is sent into the microscope and to the objective by the dichroic mirror.

A continuous 3D ring-shaped laser trap can be used for multi-level and high-throughput (tens to hundreds of sperm) sperm sorting and analysis. One potential advantage of the ring trap is that it acts as a force shield for protecting the sperm that are being measured from interference of other sperm. Additionally, the ring-shaped laser trap could potentially be used for parallel sperm sorting based on motility that may be stimulated by chemical agents (chemotaxis). This is a critical feature of sperm in response to the diffusion gradient of chemicals released by the egg and surrounding cells of the cumulus oophorus, which may lead to a better understanding of infertility and provide new approaches for contraception [11]. Differentiating it from the single-spot laser trap, which focuses hundreds of milliwatts on a sperm to achieve trapping, the ring trap utilizes only tens of milliwatts, which allow the sperm to swim along the ring without stopping. As a result, the effect of the optical force on sperm swimming patterns and physiology could be investigated in more detail [2, 12].

59.4 Biological Studies

59.4.1 Sperm Competition

An important and controversial question in evolution is sperm competition. This can be studied in primates using a laser trap in combination with custom-designed computer tracking and trapping algorithms. Semen samples from chimpanzee, rhesus macaque, human, and gorilla were analyzed. The mating systems for both the chimpanzee and the rhesus macaque are multi-male, multi-female (females of these species mate with more than one male within a short period of time). Gorillas are polygynous, defined here as one male, multiple females – that is, the single dominant male mates with the females in the "harem" unit [13] and therefore, from the female point of view, the gorilla is strictly monogamous. Human mating patterns are variable, differing across cultures, but can be considered to be predominantly polygynous (83% of societies), more rarely monogamous (16%), and only very occasionally polyandrous (<1% [13]). Therefore, the sperm analyzed in this study came from primates that represent a variety of mating patterns, ranging from strictly polygynous (gorilla) to multi-male, multi-female (chimpanzee and rhesus macaque).

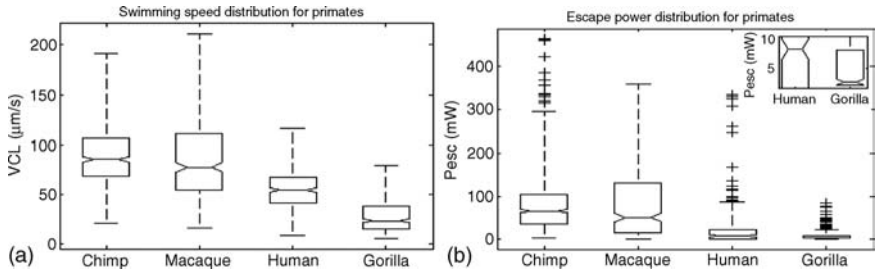

Figure 59.3 Box plots of the distributions of (a) swimming speed (VCL) and (b) escape force (Pesc) for all four primates. Inset in (b) shows an expanded view of human and gorilla distributions to emphasize the difference in median values.

The box plots for distributions of sperm swimming speed (VCL, Figure 59.3a) and escape power (Pesc, indicative of force, Figure 59.3b) for the four primates are shown. Pesc is measured by reducing the laser power after the sperm is trapped until the sperm is capable of escaping the trap. Each species' swimming speed and escape power distributions are statistically different ($p < 0.05$) using the Wilcoxon rank sum test for equal medians. The medians of both measurements, VCL and Pesc, show that rhesus and chimpanzee sperm swim with the fastest speeds and strongest forces, whereas gorilla sperm swim with the slowest speeds and weakest forces. Human sperm swimming speeds and forces lie between these two extremes [14].

59.4.2
Sperm Energetics

The combination of single-point laser tweezers with custom computer tracking software and robotics can be used to analyze motility (speed and force) and energetics [mitochondrial membrane potential (MMP)] of individual sperm. Domestic dog sperm are labeled with a cationic fluorescent probe, $DiOC_2(3)$, that reports the MMP across the inner membranes of the mitochondria located in the sperm's midpiece. Individual sperm are tracked to calculate VCL. The MMP is measured every second over a 5 s interval during the tracking phase (sperm are swimming freely) and continuously during the trapping phase. Figure 59.4 shows the ratio value prior to trapping, during trapping, and after trapping plotted over time for two different sperm. For the sperm in Figure 59.4a, there was an overall decline in ratio value over time as the sperm was held in the trap. Once released from the optical trap, the ratio value increased. However, within 5 s, it did not fully recover to the original value that it had prior to being trapped. Similarly, the sperm swimming speed, VCL, did not recover to its pretrapping value. For the sperm in Figure 59.4b, there was a slight decrease in ratio value while the sperm was in the trap. Again, neither swimming speed nor ratio value fully recovered [15].

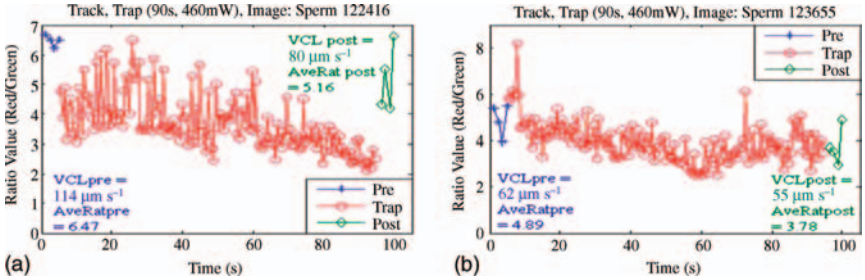

Figure 59.4 Track, trap, and fluorescence of two randomly selected sperm (a) and (b). The ratio value of red/green is plotted against time for the three different phases: prior to, during, and after trapping. Both the average ratio and VCL prior and after trapping are inset in the figures.

59.5 Conclusion

We have described two methods of optical trapping, the more common single-point gradient trap and the ring-shaped laser trap. The single-point gradient trap has found wide application in cell biology, in particular for studies on sperm motility, energetics, evolution (sperm competition), and human infertility. The ring-shaped laser trap is a more recent development, and shows promise for sperm sorting and analytics because of the potential for greater throughput than trapping of single sperm in a point trap.

Acknowledgment

This work was supported by a grant from the Lucille and David Packard Foundation endowment gift to the Beckman Laser Institute Inc. Foundation.

References

1 Berns, M.W. (1998) Laser scissors and tweezers. *Sci. Am. (Int. Ed.)*, **278**, 52–57.
2 Shao, B., Zlatanovic, S., and Esener, S.C. (2004) Microscope-integrated micromanipulation based on multiple VCSEL traps. *Proc. SPIE*, **5514**, 62–72.
3 Konig, K., Svaasand, L., Liu, Y., Sonek, G., Patrizio, P., Tadir, Y., Berns, M.W., and Tromberg, B.J. (1996) Determination of motility forces of human spermatozoa using an 800 nm optical trap. *Cell. Mol. Biol. (Noisy-le-Grand)*, **42**, 501–509.
4 Araujo E. Jr., Tadir, Y., Patrizio, P., Ord, T., Silber, S., Berns, M.W., and Asch, R.H. (1994) Relative force of human epididymal sperm. *Fertil. Steril.*, **62**, 585–590.
5 Dantas, Z.N., Araujo E. Jr., Tadir, Y., Berns, M.W., Schell, M.J., and Stone, S.C. (1995) Evect of freezing on the relative escape force of sperm as measured by a laser optical trap. *Fertil. Steril.*, **63**, 185–188.
6 Patrizio, P., Liu, Y., Sonek, G.J., Berns, M.W., and Tadir, Y. (2000) Evect of pentoxifylline on the intrinsic swimming forces of human sperm assessed by optical tweezers. *J. Androl.*, **21**, 753–756.

7 Tadir, Y., Wright, W.H., Vafa, O., Ord, T., Asch, R.H., and Berns, M.W. (1990) Force generated by human sperm correlated to velocity and determined using a laser generated optical trap. *Fertil. Steril.*, **53**, 944–947.

8 Nascimento, J., Botvinick, E., Shi, L., Durrant, B., and Berns, M.W. (2006) Analysis of sperm motility using optical tweezers. *J. Biomed. Opt.*, **11** (4), 044001.

9 Nascimento, J.M., Shi, L.Z., Tam, J., Chandsawangbhuwana, C., Durrant, B., Botvinick, E.L., and Berns, M.W. (2008) Comparison of glycolysis and oxidative phosphorylation as energy sources for mammalian sperm motility, using the combination of fluorescence imaging, laser tweezers, and real-time automated tracking and trapping. *J. Cell. Physiol.*, **217**, 745–751.

10 Shi, L., Nascimento, J., Chandsawangbhuwana, C., Botvinic, E.L., and Berns, M.W. (2008) An automatic system to study sperm motility and energetics. *Biomed. Microdevices*, **10** (4), 573–583.

11 Eisenbach, M. and Tur-Kaspa, I. (1999) Do human eggs attract spermatozoa? *BioEssays*, **21**, 203–210.

12 Shi, L., Shao, B., Chen, T., and Berns, M.W. (2009) Automatic annular laser trapping: a system for high-throughput sperm analysis and sorting. *J. Biophotonics*, **2** (3), 167–177.

13 Dixson, A.F. (1998) *Primate Sexuality: Comparative Studies of the Prosimians, Monkeys, Apes, and Human Beings*, Oxford University Press, Oxford.

14 Nascimento, J., Shi, L., Meyers, S., Gagneux, P., Loskutoff, N., Botvinick, E.L., and Berns, M.W. (2008) The use of optical tweezers to study sperm competition and motility in primates. *J. R. Soc. Interface*, **5** (20), 297–302.

15 Nascimento, J., Shi, L., Chandsawangbhuwana, C., Tam, J., Botvinic, E.L., and Berns, M.W. (2008) Use of laser tweezers to analyze sperm motility and mitochondrial membrane potential. *J. Biomed. Opt.*, **13** (1), 014002.

60
Laser Thinning of the Zona Pellucida

Hanna Balakier

60.1
The Zona Pellucida

The zona pellucida (ZP) is a specialized extracellular matrix that surrounds mammalian oocytes and early-stage embryos [1]. It is composed of a network of cross-linked filaments usually consisting of three or four highly conserved, zona-specific glycoproteins. The ZP is multifunctional and it plays a crucial role in oogenesis, fertilization, and preimplantation development. The ZP is produced during the early development of the ovarian follicles and it increases in thickness as oocytes increase in diameter [1, 2]. At the blastocyst stage, the ZP is no longer essential and the embryo must hatch out of its coat in order to implant in the uterine endometrium [3, 4]. Any disturbance of this process may cause implantation failure, leading to infertility.

Increased ZP thickness, deficiency in the production of embryonic enzymatic lysins which thin the ZP during embryo development, and the phenomenon of zona hardening are all possible causes of unsuccessful hatching and reduced implantation rates in human IVF (*in vitro* fertilization [3–5]) cycles. It seems that zona hardening may especially influence the implantation potential of the embryo, since although it occurs naturally at fertilization or in aging oocytes, it is increased further by suboptimal *in vitro* culture conditions and oocyte/embryo cryopreservation.

Several experimental techniques have been used to assist embryo hatching in order to improve implantation and clinical pregnancy rates after IVF treatment. Using mechanical and chemical methods, piezo-vibrators, or lasers, ZP manipulations can be performed either by opening the ZP by creating a hole or by zona pellucida thinning (ZPT), reducing zona thickness without breaching it [3, 4]. Regardless of the assisted hatching (AH) technique used, the type of ZP handling (intact or fully-breached) may have important implications for the developmental fate of the embryo [6].

Handbook of Biophotonics. Vol.2: Photonics for Health Care, First Edition. Edited by Jürgen Popp, Valery V. Tuchin, Arthur Chiou, and Stefan Heinemann.

60.2
Laser Assisted Hatching

The introduction of laser techniques in the field of human-assisted reproduction has led to a variety of applications facilitating the efficient manipulation of the ZP and spermatozoa [7, 8]. These include procedures such as laser AH, biopsy of embryonic cells, laser-assisted intracytoplasmic sperm injection (ICSI), sperm viability testing, and the production of hemizone. The use of several types of lasers has been validated in animal and human clinical studies, and currently a noncontact 1.48 μm diode laser system is the simplest, most reproducible, and safest method available for use in IVF laboratories [9].

Laser AH is on course to supersede previous mechanical and chemical methods for opening or thinning the ZP. Of the two methods, laser ZPT appears to be less invasive and associated with higher clinical outcomes than ZP opening [4, 10]. This suggests that breaching of the ZP could be detrimental to the implantation potential of the embryo due to the loss of cells and blastocyst "herniation" through the hole, and it could deprive the embryo of protection by the ZP against infectious or immunologic attacks. Therefore, laser ZPT is more frequently utilized for AH of fresh or frozen embryos before their transfer to the uterus [7, 8].

In theory, the AH by artificial laser ZPT should increase both the hatching potential of the embryo and IVF clinical outcomes. However, the number of studies, especially randomized ones, is limited [6], and the existing data are controversial, showing decreased [11], similar [12], or increased [13–15] implantation/pregnancy rates in the laser ZPT group versus control group without AH. These conflicting results might arise from the study design, patient characteristics, sample size, and variability in the laser technique used, such as the length/depth of ZP thinning and laser pulse duration.

Although clinical indications and the impact of laser ZPT are not yet fully defined, this technique could be particularly beneficial for patients with repeated, unexplained implantation failures [14]. Some embryo implantation problems in these patients may be explained by the inability of the embryos to hatch, but it is unknown whether underlying defects are related to the structure or function of the ZP, the impairment of the production of embryonic/uterine lysins, or other factors.

As recently shown, laser ZPT can also be successfully applied to frozen–thawed human embryos by the slow freezing or vitrification method [13, 15]. It has also become apparent that increasing the area of laser thinning from a small ablation (30–40 μm) to one-quarter or half of the zona may considerably improve IVF outcomes [13–15]. Evaluation of the impact of the size of ZPT area, 25 versus 50%, on vitrified–warmed cleavage-stage embryos, clearly demonstrates that thinning half of the ZP results in much higher implantation/pregnancy rates (32/46.7%) compared with one-quarter of ZPT (16/25.0%) [15]. Interestingly, retrospective analysis of laser AH by the creation of small (40 μm) and large (50% of ZP) holes in the ZP at the blastocyst stage in frozen–thaw cycles suggests that the pregnancy, implantation, and delivery rates are better in the 50% opening group (74, 52, 65%, respectively) compared with the 40 μm opening group (43, 27, 38%) [15].

It is unclear why the ZPT facilitates embryo implantation, and why AH of half rather that one-quarter of the ZP generates better results. Is this simply a matter of the different patterns of embryo hatching, that it is more "natural" and easier to hatch via a wider area versus a smaller "8"-shaped neck in which the embryo can become trapped? Other questions are which ZP structural changes are important, and whether they are related to the immune recognition of the embryo in ways that might enhance implantation? Are such changes induced by the laser ZPT? It is currently hypothesized that the ZP can act as an intrinsic source of signals activating the maternal immune recognition of the developing mammalian embryo [16]. Moreover, blastocyst hatching in different species, including humans, appears to be regulated by trophectodermal projections, which most likely are involved in the delivery of embryo-derived zona lysins to the ZP, causing its lysis [5]. Does AH affect the secretion of embryonic lysins which thin the ZP? A study on mouse embryos has shown that neither ZP thinning nor opening by acid Tyrode's solution changes the secretion of trypsin-like proteases involved in blastocyst hatching [17]. Whether similar mechanisms operate in human embryos awaits further investigations. In summary, the information on the cellular/molecular mechanisms of blastocyst hatching and ZP lysis is scarce and these areas require more systematic and thorough study.

60.3 Laser-Assisted ICSI

Laser ZPT has been proposed as a method to improve the efficiency of routine ICSI procedures, simultaneously providing both a reduction of mechanical stress on the oocytes and AH. This approach may increase oocyte survival rate, embryo hatching, and possibly IVF clinical outcomes, but recent results are preliminary and need to be confirmed by a large randomized study. The size of the thinned area of the ZP prior to ICSI should also be carefully evaluated with regard to safe embryo hatching and avoidance of additional AH at later stages that might create multiple ZP herniations which are known to contribute to monozygotic twinning (MZT; embryo splits into genetically identical embryos). Similar laser ZPT has been adopted recently in animal experiments [7, 8]. This ZP treatment appears to be extremely beneficial, especially in mice, where regular ICSI results in very low survival rates. There is also a potential for future applications of ZPT in domestic and endangered species.

60.4 Safety Aspects of ZPT

The technical and clinical safety aspects of laser ZPT require further investigation. For example, ZPT over a larger area (25 and 50%) of the embryo involves a relatively high amount of energy, which may lead to penetration beyond the ZP, harming the

embryo. To avoid adverse effects, proper laser calibration, short pulse duration, and safe working distance are recommended [18]. Evidently, safety also depends on the properties of the laser. Improvements in noncontact laser technology have achieved better accuracy and safety in ZPT [9]. The earliest laser used pulses as long as 15 ms, later 2–5 ms, and currently it is possible to apply pulses of only 300 μs [15]. It remains to be seen whether a superior laser system can be developed which will be more precise and generate minimal heat.

The recent promising results of laser ZPT need to be confirmed on a larger scale in randomized clinical trials. The other challenge will be to determine the impact of ZPT on several important clinical outcomes, including live birth rate, multiple pregnancies, MZT, congenital malformations, and chromosomal aberrations in children born from this technique [6]. So far, there are only three published follow-up reports on children born after laser ZP opening, and there has been no evidence of increased incidence of chromosomal aberrations or major congenital malformations from the laser treatment [4]. Similar data for laser ZPT are not available. MZT is a particularly important unsolved problem in IVF. The incidence of MZT in assisted conceptions is 2.25 times higher than in natural conceptions, and some techniques such as blastocyst transfer and ICSI seem to carry a higher risk of MZT than the others. The etiology and exact mechanisms leading to this phenomenon are controversial, and the literature provides multiple theories [19]. A combination of factors is likely to be involved, including ovarian stimulation, ICSI, AH, blastocyst culture, and ZP structural changes. Larger scale clinical studies on MZT from single embryo transfers and confirmation of zygosity with DNA analysis are warranted before definitive conclusions can be drawn. Further multidisciplinary studies are also required to define the impact of laser ZPT for optimizing IVF outcomes.

References

1 Wassarman, P.M. and Litscher, E.S. (2008) Mammalian fertilization: the egg's multifunctional zona pellucida. *Int. J. Dev. Biol.*, **52** (5–6), 665–676.

2 Gook, D.A., Edgar, D.H., Borg, J., and Martic, M. (2008) Detection of zona pellucida proteins during human folliculogenesis. *Hum. Reprod.*, **23** (2), 349–402.

3 De Vos, A. and Van Steirteghem, A. (2000) Zona hardening, zona drilling and assisted hatching: new achievements in assisted reproduction. *Cell Tissues Organs*, **166** (2), 220–227.

4 Al-Nuaim, L.A. and Jenkins, J.M. (2002) Assisted hatching in assisted reproduction. *Br J. Obstet. Gynecol.*, **109** (9), 856–862.

5 Seshagiri, P.B., Roy, S.S., Sireesha, G., and Rao, R.P. (2009) Cellular and molecular regulation of mammalian blastocyst hatching. *J. Reprod. Immunol.*, **83** (1–2), 79–84.

6 Das, S., Blake, D., Farquhar, C., and Seif, M.M.W. (2009) *Assisted Hatching on Assisted Conception (IVF and ICSI) Review. The Cochrane Collaboration*, John Wiley & Sons, Ltd., Chichester.

7 Ebner, T., Moser, M., and Tews, G. (2005) Possible application of a non-contact 1.48 μm wavelength diode laser in assisted reproduction technologies. *Hum. Reprod. Update*, **11** (4), 425–435.

8 Montag, M.H.M., Klose, R., Koster, M., Rosing, B., Van der Ven, K., Rink, K., and Van der Ven, H. (2009) Application of non-contact laser technology in assisted

reproduction. *Med. Laser Appl.*, **24** (1), 57–64.

9 Tadir, Y. and Douglas-Hamilton, D.H. (2007) *Laser Effects in the Manipulation of Human Eggs and Embryos for In Vitro Fertilization, Methods in Cell Biology*, vol. 82 (eds M.W. Berns and K.O. Greulich,), Elsevier, Amsterdam, pp. 409–431.

10 Ghobara, T. (2006) Effects of assisted hatching method and age on implantation rates of IVF and ICSI. *RMB Online*, **13** (2), 261–267.

11 Valojerdi, M.R., Eftekhari-Yazdi, P., Karimian, L., Hassani, F., and Movaghar, B. (2010) Effect of laser zona thinning on vitrified–warmed embryo transfer at the cleavage stage: a prospective, randomized study. *RMB Online*, **20** (2), 234–242.

12 Ciray, H.N., Bener, F., Karagene, L., Ulug, U., and Bahceci, M. (2005) Impact of assisted hatching on ART outcome in women with endometriosis. *Hum. Reprod.*, **30** (9), 2546–2549.

13 Ge, H. (2008) Impact of assisted hatching on fresh and frozen–thawed embryo transfer cycles: a prospective, randomized study. *RMB Online*, **16** (4), 689–596.

14 Debrock, S., Spiessens, C., Peeraer, K., and De Loecker, P. (2009) Higher implantation rate using modified quarter laser-assisted zona thinning in repeated implantation failure. *Gynecol. Obstet. Invest.*, **67** (2), 127–133.

15 Hiraoka, K., Hiraoka, K., Horiuchi, T., Kusuda, T., Okano, S., Kinutani, M., and Kinutani, K. (2009) Impact of the size of zona pellucida thinning area on vitrified-warmed cleavage- stage embryo transfers: a prospective, randomized study. *J. Assist. Reprod. Genet.*, **26** (9–10), 515–521.

16 Fujiwara, H., Ariaki, Y., and Toshimori, K. (2009) Is the zona pellucida an intrinsic source of signals activating maternal recognition of the developing mammalian embryo? *J. Reprod. Immunol.*, **81** (1), 1–8.

17 Hwang, S.S., Lee, E.Y., Chung, Y.C., Yoon, B.K., Lee, J.H., and Choi, D.S. (2000) Intactness of zona pellucida does not affect the secretion of a trypsin-like protease from mouse blastocyst. *J. Korean Med. Sci.*, **15** (5), 529–532.

18 Chatzimeletiou, K. (2005) Comparison of effects of zona drilling by non-contact infrared laser or acid Tyrode's on the development of human biopsied embryos as revealed by blastomere viability, cytoskeletal analysis and molecular cytogenetics. *RMB Online*, **11** (6), 697–710.

19 Vitthala, S., Gelbaya, T.A., Brison, D.R., Fitzgerald, C.T., and Nardo, L.G. (2009) The risk of monozygotic twins after assisted reproductive technology: a systematic review and meta-analysis. *Hum. Reprod. Update*, **15** (1), 45–55.

61
Transfection of Cardiac Cells by Means of Laser-Assisted Optoporation

Alena V. Nikolskaya, Vladimir P. Nikolski, and Igor R. Efimov

61.1
Introduction

The first optoporating lasers developed were in the ultraviolet (UV) range because of strong absorption by the membrane constituents in this spectral region [1, 2]. However, the use of UV light could irreversibly damage cells [1, 3, 4]. Alternatively, the use of near-infrared (800 nm) femtosecond and infrared (1064 nm) nanosecond lasers for efficient injection of impermeable dyes and gene transfection has been suggested [5, 6].

The use of visible laser irradiation for optoporation at 488 nm has also been demonstrated. It exploited the fact that the dye Phenol Red, a usual component of cell culture media, has strong absorption at this wavelength. It was hypothesized that laser absorption induced a local rise in temperature, which led to changes in membrane permeability that were considered reversible and relatively harmless to the irradiated cells [4, 7].

However, several cellular components have significant absorption at 488 nm and the possibility of deleterious effects still exists, such as generation of toxic reactive oxygen species (ROS) and irreversible mitochondrial permeability transition pore (mPTP) opening [8–10].

We therefore aimed to improve the laser-assisted optoporation techniques with several impermeable fluorochromes, which could facilitate deposition of energy at the cell membrane and limit damage to intracellular compartments.

61.2
Methods

61.2.1
Primary Cultures of Neonatal Rat Cardiac Cells

Primary neonatal cardiac cells were obtained from ventricles of 3–4-day-old Wistar rat pups (Harlan) using a modification of the method described by Fast and Cheek [11].

Handbook of Biophotonics. Vol.2: Photonics for Health Care, First Edition. Edited by Jürgen Popp, Valery V. Tuchin, Arthur Chiou, and Stefan Heinemann.

The small pieces of ventricle were minced with scissors and dissociated in Hank's balanced salt solution (HBSS, without Ca^{2+} and Mg^{2+}) (Invitrogen) containing trypsin (0.1%) (Boehringer) and pancreatin (60 μg ml^{-1}) (Sigma). The solution of dispersed cells was supplemented with neonatal calf serum (10%) (Boehringer) to stop enzyme activity, centrifuged, and resuspended in UltraCulture medium (BioWhittaker) supplemented with vitamin B_{12} (20 μg ml^{-1}) (Sigma), L-glutamine with penicillin–streptomycin (100 μg ml^{-1}) (Sigma), and bromodeoxyuridine (0.1 mM) (Sigma). The cell suspension was preplated in large culture flasks and incubated for 2 h to isolate the fibroblast-enriched fraction. The myocytes remaining in suspension were collected and plated at a density of 2.5×10^5 cells cm^{-2} on to 300 mm diameter glass-bottomed Petri dishes (EMS) precoated with a collagen, laminin, and fibronectin mixture and grown for 2–7 days before experimentation. The culture medium was exchanged the day after preparation and every second day thereafter. All animal protocols were approved by the Washington University Animal Studies Committee.

61.3 Experimental Design

For all experiments on laser-assisted optoporation, a standard Nikon C1 confocal microscope with a three laser launcher integrated with a fluorescent upright Nikon i80 microscope was used. Transfection and optoporation tests were performed at 21 °C on the microscope stage.

To estimate the size of the effected targeted spot, a glass slide was painted with a marker pen, allowed to dry, and placed in the microscope light path with a 0.45 NA 10× lens. Following focusing, the blue laser pulse was applied, causing the formation of a hole in the paint. The effective size of the hole was estimated to be less than 4 μm, which corresponds to 4× lateral optical resolution ($r = 1.22\lambda/2NA$). The selected areas of cells were located in premarked regions. Cells were selected for transfection using a custom graphic software interface, which allowed us to define the set of targeted positions with individual exposure times on the imaged cell area. This procedure allows desirable patterns to be drawn for beam exposure, making targeted transfection possible. To minimize cell damage while obtaining the initial navigation image and focusing on the area of interest, an He–Ne laser (633 nm, continuous wave, 6.75 mW nominal output power) attenuated 32 times was used in the DIC transmitted light mode.

The blue beam of the argon laser (488 nm, continuous wave, 17 mW nominal output power) was focused at the cell membrane. Laser wounding was done by aiming the beam at a selected position for 2–10 s, depending on the enhancing dye concentration. The total procedure lasted 2–5 min for 20–30 targeted cells. At the site of beam incidence, the cell membrane had modified permeability and allowed impermeable dye or plasmid vector present in the culture media to penetrate inside the cell.

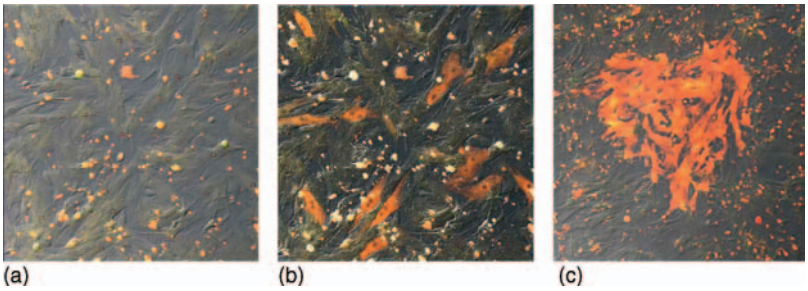

Figure 61.1 Laser-assisted injection of FM 1-43 into cultured cardiomyocytes. (a) Image of the area of interest with cells selected for optoporation in the presence of FM 1-43 in culture media; (b) the same area after optoporation; (c) drawing of specially shaped area.

61.4 Results

We investigated the use of 488 nm laser irradiation for dye-assisted microinjection of membrane-impermeable fluorochromes, such as propidium iodide (PI), and exogenous membrane dyes, such as FM 1-43, and also green fluorescent protein (GFP) encoding plasmid into neonatal cardiac cells. We also investigated the implementation of the same membrane dye, FM 1-43, for further absorption enhancement and perfecting focusing on the membrane surface with additional pharmaceutical treatments for apoptotic and necrotic damage prevention to improve transfection efficiency and ensure cell survival.

The exposure times for reversible membrane permeabilization were established by monitoring accumulation and retention of FM 1-43 (5 $\mu g\,ml^{-1}$) (Invitrogen), PI (20 $\mu g\,ml^{-1}$) (Sigma), and calcein-AM (10 μM) (Invitrogen). The short-term viability of exposed cells was evaluated 15–20 min after irradiation (Figures 61.1 and 61.2). PI membrane-impermeable cationic dye reveals strong red fluorescence after binding to nucleic acids. PI served two purposes: as an indicator of membrane permeabilization when added to the medium before irradiation, and as a vital stain when it was

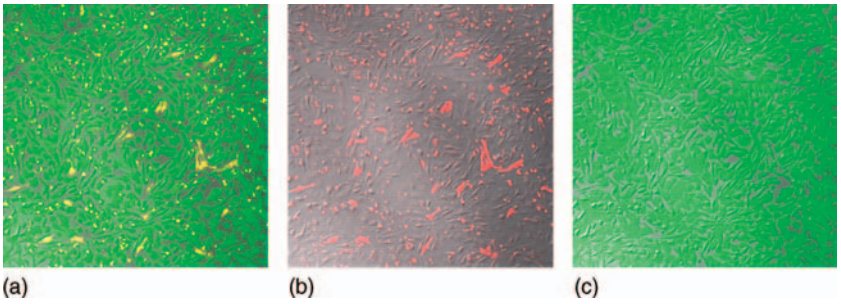

Figure 61.2 Cells optoporated in the presence of FM 1-43 and PI; calcein-AM was added after optoporation. (a) Dual-channel registration (PI, FM 1-43, and calcein) after 5 min of dye accumulation; (b) red channel (PI and FM 1-43) after 5 min; (c) green channel (calcein) after 10 min.

added to the medium 15–20 min after irradiation it distinguished dead from living cells. FM 1-43–styryl dye that has been widely used to demonstrate membrane disruption/resealing [12–14] was used to test membrane injury. This dye is impermeable to intact cell membranes, and specifically fluoresces only when incorporated into the lipid environment such as a cell membrane. The fluorescence of an optoporated cell increases several-fold (with changed emission spectra) owing to the presence of endo-membranes that become stained with the dye. Resealing of the membrane halts this increase in fluorescence. Calcein acetomethyl ester (calcein-AM) is widely used for cell survival assays. The viability of cells subjected to optoporation was assessed by incubating them with calcein-AM for 10 min. Accumulation and retention of this dye in irradiated cells indicate cell viability. For facilitating laser light absorption, in addition to Phenol Red (contained in media), cells were stained with various membrane dyes as further absorption enhancers. We selected FM 1-43 as a nontoxic dye the main absorption band of which corresponds to the laser wavelength. Membrane staining of cultured cells increased the optical density at the wavelength corresponding to the dye absorption spectrum. Moreover, as a membrane fluorescent stain, this dye allowed precise focusing on the membrane itself by means of z-stack positioning with maximum projection fluorescence intensity.

After a series of pilot experiments, exposure times of 10 s for 15 mg l^{-1} and 2 s for 40 mg l^{-1} of Phenol Red were selected for the control transfection procedures. These conditions correspond to the longest irradiation times that allowed transient optoporation of the cells but still did not produce detectable short-term injury to the cells.

The efficiency of optotransfection was assessed by monitoring expression of GFP in cardiac myocytes after laser-assisted optoporation in the presence of 5 μg ml^{-1} of plasmid containing the reporter gene for GFP from *Aequorea victoria* jellyfish.

In order to protect cells against long-term apoptotic damage that may be caused by mPTP irreversible opening or ROS accumulation generated through photodynamic treatment [15], cells were preincubated with cyclosporin A (0.2 μM) (Sigma) for 30 min before laser exposure and supplemented with the ROS scavengers, NO donors SIN-1 (125 μM) (Sigma), and SNAP (100 mM) (Invitrogen).

Before the experiment, regular culture medium was aspirated and substituted with fresh OPTI-MEM (Invitrogen) or M199 (Invitrogen) medium with HEPES buffer. OPTI-MEM was initially phenol free. The nominal concentration of the Phenol Red in M199 medium was 15 mg l^{-1}. In some experiments, culture media was additionally supplemented with Phenol Red solution (Sigma) to obtain the different concentrations (15, 20, 40 mg l^{-1}). In experiments with membrane-stained cells, the cells were incubated with FM 1-43 (5 μg ml^{-1}) (Invitrogen) for 10 min and unbound dye was then removed. GFP plasmids (5 μg ml^{-1}) were added to the culture dishes before irradiation. Assigned areas of individual cells were exposed to the incident laser beam, such that the beam was focused on their membrane.

Following optoporation, cells were incubated for 30 min with the GFP plasmids. After laser exposure, 1000× antioxidant supplement (1 μl ml^{-1}) (Sigma), $CaCl_2$ (2 mM) (Sigma), and surfactant Pluronic-F68 (1 mM) (Sigma) were added to the medium to facilitate membrane resealing. Poloxamer 188 (P188, Pluronic F68) was

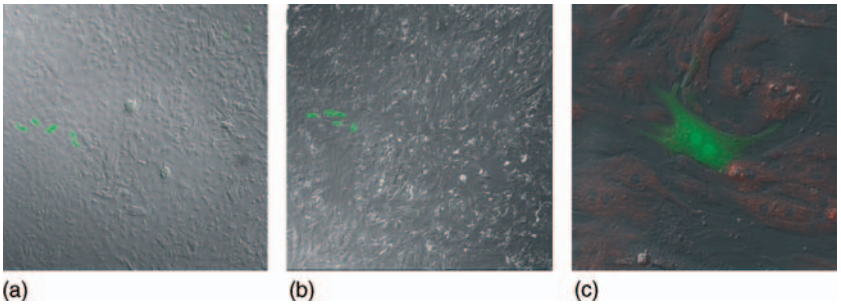

Figure 61.3 Cells optotransfected within selected areas: (a) fibroblast-enriched culture; (b) myocyte-enriched culture; (c) enlarged optotransfected myocyte.

shown to seal cells after electroporation [16–19], heat shock [20, 21], mechanical and barometric traumas [14, 22, 23], and high-dose ionizing radiation [24, 25]. Successful transfection was confirmed after 48–72 h through pronounced green fluorescence, which was at least five times higher than the intrinsic fluorescence of the cells and was distributed over the cytoplasm (Figure 61.3).

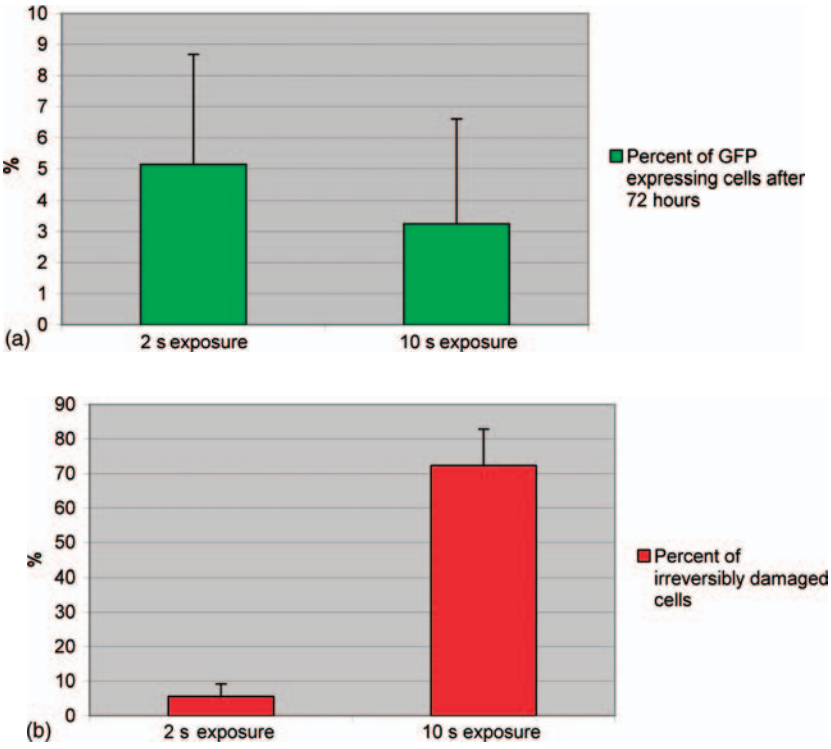

Figure 61.4 Effect of different optoporation parameters on optotransfection outcome: 2 s with 40 mg l^{-1} versus 10 s with 15 mg l^{-1} of Phenol Red. (a) Percentage of optotransfected cells expressing GFP; (b) percentage of irreversibly damaged cells.

The percentage of transfected cells was determined for each area of illuminated cells on the basis of counting individual cells expressing GFP; mean values and standard deviations were calculated from all areas of irradiated cells (Figure 61.4).

The percentages of cells expressing GFP 72 h after optotransfection are shown in Figure 61.4a for the two types of laser exposure: 2 s with 40 mg l^{-1} and 10 s with 15 mg l^{-1} of Phenol Red. From 24 separate experiments, the transfection efficiency for 2 s exposure was estimated as $5.1 \pm 3.5\%$, and from 20 experiments, the transfection efficiency for 10 s exposure was estimated as $3.25 \pm 3.4\%$. The percentage of irreversibly damaged cells for the same exposure conditions was determined through 12 short-term viability assays (PI accumulation and calcein retention) and was $5.6 \pm 3.6\%$ for 2 s exposure and $72.3 \pm 10.5\%$ for 10 s exposure (Figure 61.4b).

When cells were irradiated without light-absorbing dye in OPTI-MEM phenol-free media, the optoporation efficacy was almost negligible, and no short-term membrane damage was observed after several minutes of exposure.

For a comparison of transfection rates, a standard method of lipofection was used. The lipofectamine transfection rate was 10–15%. However, as expected, it was spatially indiscriminate.

61.5 Conclusion

Laser-assisted optoporation appears to be a resourceful tool for cultured, attached cardiac cell transfection. It is possible to perform this method with a standard confocal microscope. It can be applied to different cell types, including those which are not easy to transfect with conventional methods.

Decreasing exposure times sufficient for optoporation resulted in increasing transfection outcome, which could be due to reducing the risk of triggering apoptosis. Results of laser-assisted optoporation were similar to findings reported in the literature for noncardiac cells with the same concentration of Phenol Red. Additional enhancement of light absorbance with the membrane dye FM 1-43 allowed not only an improved focusing technique, but also a further decrease in exposure time sufficient for optoporation, and highlighted the opportunity to use this dye for cell viability and permeability tests.

Acknowledgment

This work was supported by NIH grants HL074283 and HL085369.

References

1 Shirahata, Y., Ohkohchi, N., Itagak, H., and Satomi, S. (2001) New technique for gene transfection using laser irradiation. *J. Investig. Med.*, **49**, 184–190.

2 Tao, W., Wilkinson, J., Stanbridge, E.J., and Berns, M.W. (1987) Direct gene transfer into human cultured cells facilitated by laser micropuncture of

the cell membrane. *Proc. Natl. Acad. Sci. U. S. A.*, **84**, 4180–4184.
3 Lebedeva, L.I., Akhmamet'eva, E.M., Razhev, A.M., Kochubei, S.A., and Rydannykh, O.V. (1990) Cytogenetic effects of UV laser radiation with wavelengths of 248, 223 and 193 nm on mammalian cells. *Radiobiologiia*, **30**, 821–826.
4 Palumbo, G., Caruso, M., Crescenzi, E., Tecce, M.F., Roberti, G., and Colasanti, A. (1996) Targeted gene transfer in eucaryotic cells by dye-assisted laser optoporation. *J. Photochem. Photobiol. B*, **36**, 41–46.
5 Mohanty, S.K., Sharma, M., and Gupta, P.K. (2003) Laser-assisted microinjection into targeted animal cells. *Biotechnol. Lett.*, **25**, 895–899.
6 Tirlapur, U.K. and Konig, K. (2002) Targeted transfection by femtosecond laser. *Nature*, **418**, 290–291.
7 Schneckenburger, H., Hendinger, A., Sailer, R., Strauss, W.S., and Schmitt, M. (2002) Laser-assisted optoporation of single cells. *J. Biomed. Opt.*, **7**, 410–416.
8 Halestrap, A.P., Clarke, S.J., and Javadov, S.A. (2004) Mitochondrial permeability transition pore opening during myocardial reperfusion – a target for cardioprotection. *Cardiovasc. Res.*, **61**, 372–385.
9 Nakajima, M., Fukuda, M., Kuroki, T., and Atsumi, K. (1983) Cytogenetic effects of argon laser irradiation on Chinese hamster cells. *Radiat. Res.*, **93**, 598–608.
10 Peng, T.I. and Jou, M.J. (2004) Mitochondrial swelling and generation of reactive oxygen species induced by photoirradiation are heterogeneously distributed. *Ann. N. Y. Acad. Sci.*, **1011**, 112–122.
11 Fast, V.G. and Cheek, E.R. (2002) Optical mapping of arrhythmias induced by strong electrical shocks in myocyte cultures. *Circ. Res.*, **90**, 664–670.
12 Bi, G.Q., Alderton, J.M., and Steinhardt, R.A. (1995) Calcium-regulated exocytosis is required for cell membrane resealing. *J. Cell Biol.*, **131**, 1747–1758.
13 Togo, T., Alderton, J.M., and Steinhardt, R.A. (2000) The mechanism of cell membrane repair. *Zygote*, **8** (Suppl 1), S31–S32.
14 Yasuda, S., Townsend, D., Michele, D.E., Favre, E.G., Day, S.M., and Metzger, J.M. (2005) Dystrophic heart failure blocked by membrane sealant poloxamer. *Nature*, **436**, 1025–1029.
15 Shanmuganathan, S., Hausenloy, D.J., Duchen, M.R., and Yellon, D.M. (2005) Mitochondrial permeability transition pore as a target for cardioprotection in the human heart. *Am. J. Physiol. Heart Circ. Physiol.*, **289**, H237–H242.
16 Lee, R.C. (2002) Cytoprotection by stabilization of cell membranes. *Ann. N. Y. Acad. Sci.*, **961**, 271–275.
17 Lee, R.C., Hannig, J., Matthews, K.L., Myerov, A., and Chen, C.T. (1999) Pharmaceutical therapies for sealing of permeabilized cell membranes in electrical injuries. *Ann. N. Y. Acad. Sci.*, **888**, 266–273.
18 Lee, R.C., River, L.P., Pan, F.S., Ji, L., and Wollmann, R.L. (1992) Surfactant-induced sealing of electropermeabilized skeletal muscle membranes *in vivo*. *Proc. Natl. Acad. Sci. U. S. A.*, **89**, 4524–4528.
19 Tung, L., Troiano, G.C., Sharma, V., Raphael, R.M., and Stebe, K.J. (1999) Changes in electroporation thresholds of lipid membranes by surfactants and peptides. *Ann. N. Y. Acad. Sci.*, **888**, 249–265.
20 Merchant, F.A., Holmes, W.H., Capelli-Schellpfeffer, M., Lee, R.C., and Toner, M. (1998) Poloxamer 188 enhances functional recovery of lethally heat-shocked fibroblasts. *J. Surg. Res.*, **74**, 131–140.
21 Padanilam, J.T., Bischof, J.C., Lee, R.C., Cravalho, E.G., Tompkins, R.G., Yarmush, M.L., and Toner, M. (1994) Effectiveness of poloxamer 188 in arresting calcein leakage from thermally damaged isolated skeletal muscle cells. *Ann. N. Y. Acad. Sci.*, **720**, 111–123.
22 Fischer, T.A., McNeil, P.L., Khakee, R., Finn, P., Kelly, R.A., Pfeffer, M.A., and Pfeffer, J.M. (1997) Cardiac myocyte membrane wounding in the abruptly pressure-overloaded rat heart under high wall stress. *Hypertension*, **30**, 1041–1046.

23 McNeil, P.L. and Steinhardt, R.A. (1997) Loss, restoration, and maintenance of plasma membrane integrity. *J. Cell Biol.*, **137**, 1–4.

24 Greenebaum, B., Blossfield, K., Hannig, J., Carrillo, C.S., Beckett, M.A., Weichselbaum, R.R., and Lee, R.C. (2004) Poloxamer 188 prevents acute necrosis of adult skeletal muscle cells following high-dose irradiation. *Burns*, **30**, 539–547.

25 Hannig, J., Zhang, D., Canaday, D.J., Beckett, M.A., Astumian, R.D., Weichselbaum, R.R., and Lee, R.C. (2000) Surfactant sealing of membranes permeabilized by ionizing radiation. *Radiat. Res.*, **154**, 171–177.

62
Laser Surgery: an Overview

Roberto Pini, Francesca Rossi, and Fulvio Ratto

62.1
Introduction

Nowadays lasers are in routine clinical use, and the continual development of technological solutions is opening up new frontiers in micro- and nano-surgery, thus enabling the implementation of new surgical applications.

With the use of lasers and delivery systems that may be developed with the current technology on offer, new *minimally invasive* surgical procedures can be conceived. This expression denotes a wide variety of laser procedures, aimed at minimizing the surgical damage to the patient, with the advantages of safer and more effective operations, shorter healing times, and lesser risk of postoperative complications. Examples of these laser surgeries include endoscopic laser surgery, laparoscopic laser surgery, laser-induced suturing, and precise tissue manipulation and cutting.

Endoscopic laser surgery is usually performed with the help of small endoscopic cameras, several thin rigid instruments, and a laser delivery system, which may be either rigid or flexible depending on the particular application. The surgical tools are inserted towards the surgical target through natural body cavities and small artificial incisions (*keyhole surgery*). In comparison with the usual open surgery, there are several advantages for the patient, such as less pain, less strain on the organism, faster recovery, and smaller injuries and scar formation (esthetics). An example of endoscopic laser surgery is *laser lithotripsy*, in which kidney stones are photodisrupted noninvasively by delivering pulsed laser light with optical fibers through the urinary duct. Endoscopic procedures in the human abdomen are typically termed laparoscopy. Originally developed for minimally invasive treatment of the uterus and ovaries, the use of laparoscopic surgery has today expanded to a wide variety of conditions seen by the general surgeon, such as appendectomy and gall bladder removal. Its benefits to the patient over open surgery include faster healing with smaller scars and fewer postoperative infections. These advances, together with the advent of durable delivery fibers, have made laparoscopic laser surgery a cost-effective and convenient solution for patients and physicians alike.

Precise laser microcutting and microsuturing can be included among these minimally invasive laser procedures. An example is intra-tissue cutting by femto-

Handbook of Biophotonics. Vol.2: Photonics for Health Care, First Edition. Edited by Jürgen Popp, Valery V. Tuchin, Arthur Chiou, and Stefan Heinemann.

second lasers, which is currently applied for clinical use in corneal surgery for the resection of accurate corneal flaps during corneal reshaping in order to correct visual defects, and also in transplant of the cornea. In the latter case, femtosecond laser cutting can be associated with another minimally invasive technique, laser welding, which is used to replace conventional suturing, providing lesser inflammation reactions and faster healing times.

In general, laser surgery can be considered minimally invasive provided that most of the side effects are carefully evaluated and controlled, which means that the laser action must be confined to a well-defined volume of tissue, where the surgery is intended to occur. Possible side effects include the following:

1) Uncontrolled heat damage to surrounding healthy tissues, which is mainly due to two factors: (a) incorrect evaluation of the laser penetration depth into the tissue, owing to, for example, underestimation of the light scattering and nonlinear optical absorption processes; (b) diffusion of the heat generated by photothermal conversion well beyond the treatment volume, which may be due to laser pulse durations exceeding the conditions of heat confinement (see Section 62.2.1.3).
2) Mechanical damage to adjacent tissue structures, caused by the development of laser-induced photoacoustic effects, such as thermoelastic stresses within the tissue, recoil pressure pulses generated by material ejection from the tissue surface, cavitation bubble formation in soft tissues, and spallation of superficial tissue layers, up to dramatic photofragmentation processes induced by uncontrolled plasma formation at the laser focus, followed by shock waves expanding at supersonic speed.

In this introduction, we briefly overview the principles of the interactions between laser light and biotissues in order to provide basic and simple arguments which may help to make the application of lasers in surgical procedures safer, more precise, and better controlled.

62.2
Laser–Tissue Interactions

The interaction of light radiation with biological matter depends upon the irradiation parameters (such as wavelength, power/energy, pulse duration, and spot area), and also on the optical properties of the tissue. Despite the structural complexity of and the morphologic differences between organic tissues, in a first approximation the propagation of light radiation (at low intensities) can be described by fundamental optical properties, such as reflection, absorption, scattering, and transmission.

When laser light impinges on the surface of the tissue, a small fraction, typically 4–5%, is diffusively reflected in the backward direction due to the refractive index mismatch between the external environment and biotissue. The fraction of laser radiation remaining after reflection propagates inside the tissue and is subjected to the processes of absorption and multiple scattering.

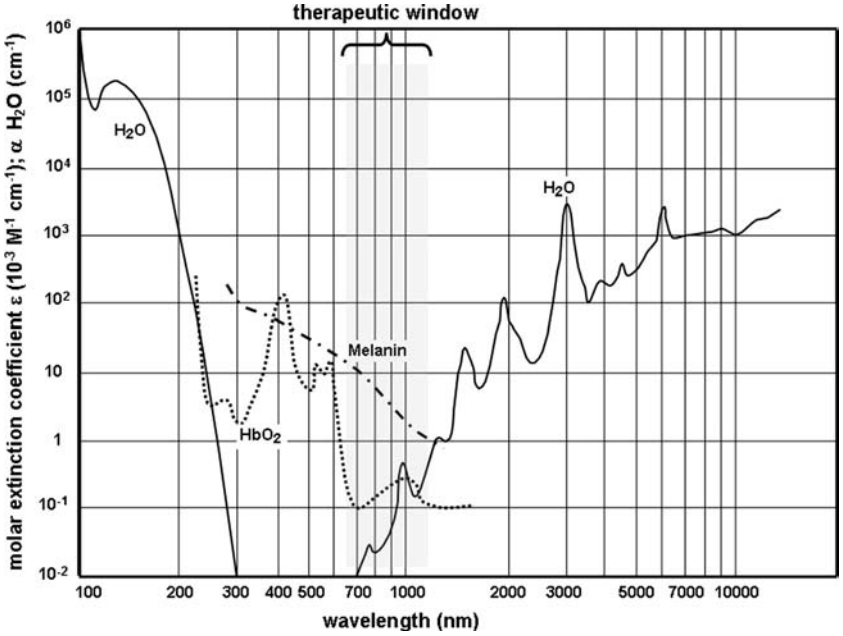

Figure 62.1 Light absorption coefficients of the main absorbers in a biological tissue.

The main absorption features of biotissues are summarized in Figure 62.1, which displays the spectral absorption of water and other biological components. A fundamental role is played by the water content of the tissue, which is the primary absorber in the infrared (IR) spectral region. Moreover, it can be noted that a low absorption of light occurs in the spectral region 700–1300 nm, the so called *therapeutic window* of biological tissues, which is exploited to perform laser treatments or for diagnostic purposes in depth inside the human body.

The process of light absorption in the tissue along the coordinate z, assumed parallel to the optical axis of the light beam and perpendicular to the tissue surface, can be described to a first approximation by the Lambert–Beer law:

$$I(z) = I_0 \exp(-\mu_a z) \tag{62.1}$$

where I_0 is the incident intensity and μ_a is the absorption coefficient, which may be expressed in terms of the *light penetration depth* (also called *extinction length*):

$$L_{ext} = 1/\mu_a \tag{62.2}$$

which represents the distance after which the intensity undergoes a decrease by a factor $1/e$ ($e \approx 2.7$) due to absorption.

In the visible and IR optical bands, large diffusion of light occurs mainly due to the abundance of cellular structures with size comparable to the wavelength of the

propagating light. Schematically, three propagation types can be classified, depending on the light wavelength:

1) *Predominant absorption effects*, occurring at ultraviolet (UV) wavelengths in the range 190–300 nm, for example, those of excimer lasers, and also at IR wavelengths of 2–10 μm, for example, those of Ho:YAG, Er:YAG, and CO_2 lasers. In these cases, the light penetration depth is very short, typically in the range 1–20 μm.
2) *Comparable absorption and scattering effects*, occurring at visible wavelengths in the range 450–590 nm. Here the light penetration depth is about 0.5–2.5 mm. Schematically, the light beam propagating through the tissue may be represented as a collimated component surrounded by a region of multiple scattering phenomena. The backward component of the scattered light constitutes the major fraction of the total reflectance, which can be 15–40% of that of the incident beam.
3) *Predominant scattering effects*, occurring at wavelengths in the range 590 nm–1.5 μm, which exhibit light penetration depths of 2.0–8.0 mm. When the light beam enters the tissue, the collimated component is almost fully converted into diffused light. The backward scattering intensity increases significantly, reaching values as high as 35–70% of that of the incident beam.

According to this simplified picture, most biological tissues can be regarded as turbid media, in which the combination of absorption and scattering produces an effective reduction of the light penetration depth. One may account for this reduction by means of an *effective* absorption coefficient $\mu_{eff} = \mu_a + \mu_s$, which includes both absorption and scattering contributions. The *effective* counterpart of the light penetration depth is

$$L_{eff} = \frac{1}{\mu_{eff}} = \frac{1}{\mu_a + \mu_s} \tag{62.3}$$

This description is strictly true as far as low laser intensities are concerned. Conversely, optical absorption and optical scattering of biotissues may vary significantly under intense laser irradiation, giving rise to nonlinear processes and peculiar spatial and temporal dynamics [1].

The use of lasers as surgical tools requires the emission of high doses of laser power or energy, with emission characteristics which are the key factors to induce particular therapeutic effects in biotissues, which may be otherwise impossible to perform. Lasers are used, for example, to cut, coagulate, weld, ablate, or simply heat the tissue, thus permitting minimally invasive treatments in many surgical fields.

When laser light hits the tissue, several interaction effects are induced, which may be classified schematically into three major types: *photochemical*, *photothermal*, and *photomechanical* effects [2, 3], as sketched in Figure 62.2.

Photochemical effects occur when the absorption of light is able to induce chemical reactions, such as in photodynamic therapies [4]. Photothermal effects are observed when the fraction of laser energy that is absorbed in the tissue

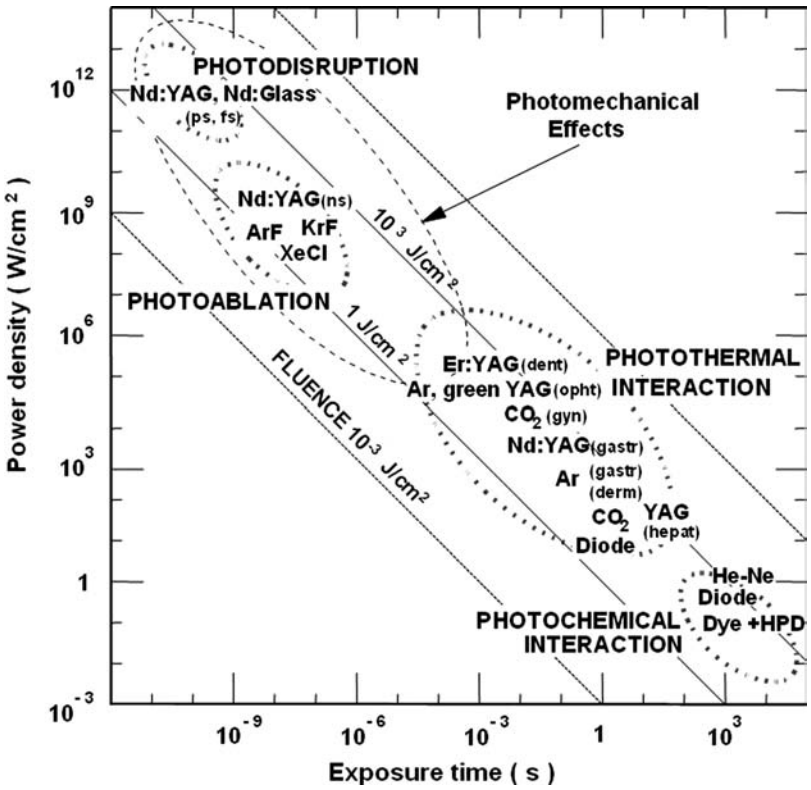

Figure 62.2 Map of laser–tissue interactions: the various types of laser–tissue interactions can be sketched like regions in a logarithmic map, where the abscissa represents the exposure time in seconds, the ordinate expresses the applied power density ($W\,cm^{-2}$), and the diagonals show constant energy fluences ($J\,cm^{-2}$).

becomes converted into heat; this phenomenon is used, for example, for retinal photocoagulation [5] and for the treatment of superficial angiomas [6]. Photomechanical effects instead are generated by the stress associated with the rapid heating and expansion of the illuminated tissue volume, occurring when short laser pulses (pulse durations from microseconds to femtoseconds) are used, thus inducing photoablation or photodisruption of tissues and cells. In most cases, these three phenomena may occur simultaneously during the laser–tissue interaction in different sites of the irradiated tissue volume, which experience different light and heat distributions. However, in the literature, the description of laser–tissue interactions is typically given through the effect which dominates under the irradiation conditions used for the specific treatment. The photochemical effects are beyond the scope of this chapter. In the following, we focus mainly on photothermal and photomechanical effects, which are particularly relevant for the most diffused laser surgical techniques.

62.2.1
Photothermal Effects

Most of the surgical applications of lasers rely on the conversion of radiation energy into thermal energy. At the microscopic level, the photothermal process consists of a two-step reaction: a molecule in the target tissue is brought to an excited state, as a consequence of the absorption of a photon delivered from the laser light. Then the excited molecule decays by collision with the surrounding molecules, which increase their kinetic energy. This nonradiative decay induces rapid heating (in 1–100 ps) around the illuminated volume.

Many observations suggest a schematic classification of the biological effects induced by photothermal processes according to the temperature range realized in the tissue [2, 3]:

- low-temperature effects (43–100 °C), causing different degrees of damage in the tissue as a function of the exposure time (damage accumulation processes) [2, 7];
- medium-temperature effects ($\geq$100 °C), dominated by water vaporization, with confinement and release of heated water vapor from tissues;
- high-temperature ablation or thermoablation ($\sim$300 °C) by tissue vaporization, combustion, molecular dissociation, and/or plasma formation.

These changes may occur simultaneously at different sites within the irradiated volume as a consequence of a nonhomogeneous distribution of the temperature, originated by the differential light penetration through the biological tissue, as depicted in Figure 62.3. The phenomenological description of biological changes as a function of temperature typically applies whenever continuous-wave (cw) laser emission is used. In the case of pulsed irradiation, in addition to the transient temperature rise, the total exposure time still plays a role in the heat-induced effects (see Figure 62.4).

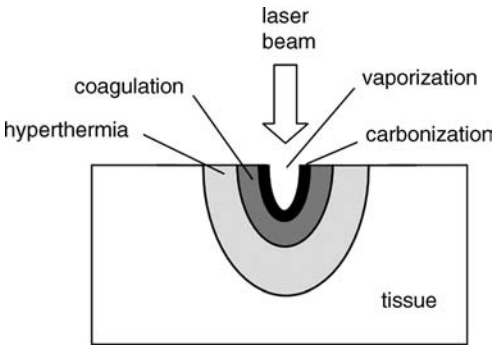

Figure 62.3 Distribution of photothermal effects that may possibly occur in the proximity of the irradiated volume.

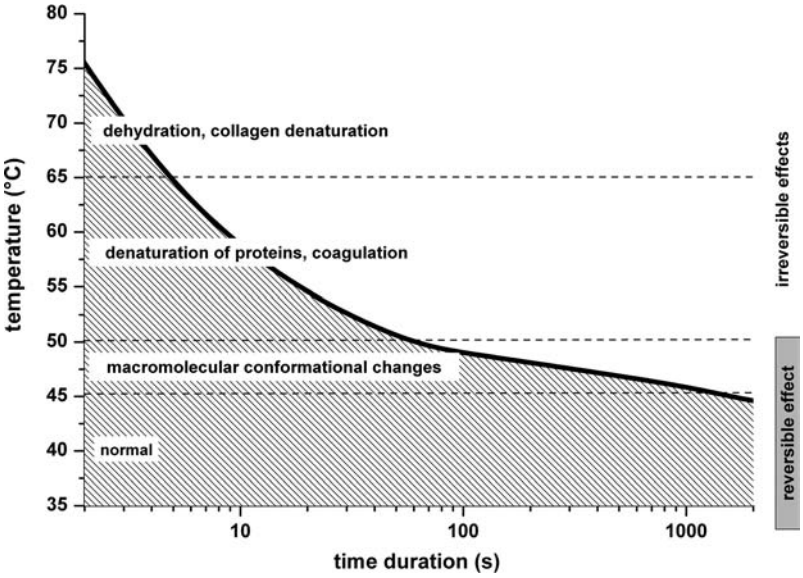

Figure 62.4 Schematic diagram of the low-temperature photothermal effects in biological tissues, depending on the duration of the treatment.

62.2.1.1 Low-Temperature Effects (43–100 °C)

In the case of low-temperature thermal interactions, individual cells and various tissues heated above ~43–45 °C (*hyperthermic range*) can undergo reversible injury which becomes irreversible (cells death) after exposure times ranging from 25 min to hours, depending on the type of tissue and treatment conditions.

The first hyperthermic effects at about 45 °C are modifications of the macromolecular conformations, bond breakage, and membrane alterations, in addition to the onset of the denaturation of biomolecules and their aggregates (collagen, hemoglobin, other proteins, lipids, etc.), such as the rupture of intramolecular hydrogen bonds. In the case of cancerous cells, their viability experiences a significant reduction above these temperatures. This effect is at the basis of the interstitial thermotherapy of tumoral masses performed with cw Nd:YAG or CO_2 lasers.

The denaturation of proteins such as collagen and hemoglobin typically occurs in the range 50–70 °C. In this so-called *coagulative range*, coagulative necrosis of cells and vacuolization in tissues may be observed. The thermal coagulation of tissues is defined as a thermally induced, irreversible alteration of the proteins and other biological molecules, organelles, membranes, cells, and extracellular components observable with the naked eye and microscopic techniques. When inducing temperatures in this range in fibrous collagen (such as type I), rupture of the intermolecular bonds may occur, resulting in a spatial disorganization of its regular structure, macroscopic contraction and swelling of the tissue, and the loss of its opto-physical properties (such as transparency in corneal stroma and birefringence in muscular fibers). The contraction of the intercellular proteins induces a possible collapse of the

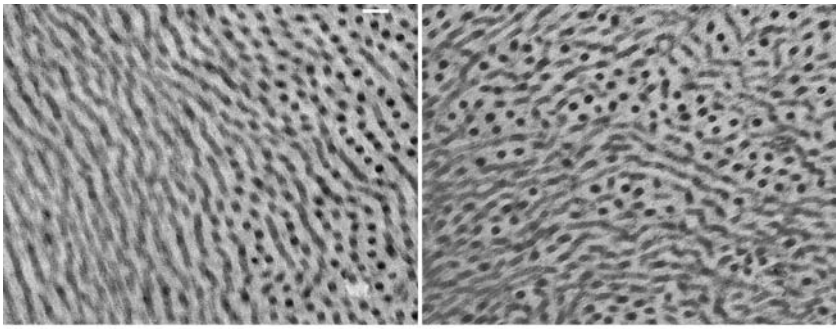

Figure 62.5 Low-temperature effects (at 55–65 °C) in a laser-welded corneal stroma. The transmission electron microscope images (scale bar 90 nm) show the spatial organization of fibrillar collagen in (a) native and (b) laser-welded porcine corneas. In (a), the fibers are organized parallel to each other and grouped in orthogonal lamellar planes; in (b), the individual collagen fibers are preserved, but their spatial distribution appears modified, indicating thermal denaturation of the ground materials which maintain the correct fiber organization (proteoglycan chains).

cytoskeletons, thus producing shrinkage of the coagulated cells. These photocoagulative processes are used, for example, in ophthalmic surgery for reducing retinal detachment and in dermatology for the treatment of vascular or pigmented lesions. The shrinkage of collagen (induced at temperatures higher than 70 °C) is at the basis of some surgical thermal treatments, such as laser capsulorrhaphy [8] and laser thermokeratoplasty [7], while other milder thermal modifications in the spatial distribution of the collagen fibers (see Figure 62.5) are at the basis of the low-power laser welding of corneal tissue, induced at temperatures in the range 55–65 °C) [9].

62.2.1.2 **Medium- and High-Temperature Effects ($\geq$100 °C)**

Thermal effects in this temperature range are mainly dominated by the vaporization of the water component, which may be as high as ~80% in soft tissues. As the tissue temperature approaches the threshold temperature of water vaporization, photothermal effects induced by the laser–tissue interaction are characterized by (1) energy absorption in the liquid–vapor phase transition, (2) tissue drying, and (3) formation of vapor vacuoles inside the tissue. Macroscopically, steam bubbles are formed in the hottest zones below the irradiated tissue surface. When a critical pressure is reached, the thin walls of the tissues including the vacuoles become broken and many vacuoles may aggregate. Under prolonged irradiation, the largest bubbles rupture explosively, causing the so-called *popcorn effect*. Histological analysis of the popcorn effect clearly evidences that the damage induced in the tissue as holes through the surface does not correspond to an actual loss of tissue mass. The hot vapor ejection causes immediate tissue cooling. The water loss diminishes the local heat conductivity and limits heat conduction to surrounding areas.

When the water content of the tissue has completely evaporated, the tissue temperature rises rapidly to >300 °C, which causes high-temperature ablation of

the remaining tissue components by combustion, molecular dissociation, solid material vaporization, and carbonization.

62.2.1.3 **Controlling Heating Effects**

The control of heat effects is a key factor for the effectiveness of the surgical procedure. For this purpose, objective observations of the degree of thermal damage based on the surgeon's experience are not often accurate enough. This control should require in principle the use of noncontact monitoring systems, with high spatial accuracy (in the order of 0.1 mm) and a fast acquisition rate, since the temperature dynamics may develop over the range of milliseconds or shorter times. The available technology does not include any compact, low-cost system which may be effectively used for this purpose during surgery. The thermal analysis is usually performed by the use of an IR thermocamera, which gives a direct measurement of the temperature rise on the external surface of the tissue (see Figure 62.6). In the case of deep penetration of the light into the tissue, in addition to transient heating phenomena with durations shorter than the time acquisition rate of the camera, the temperature dynamics and the temperature distribution inside the tissue under the specific irradiation conditions may become accessible by the development of a mathematical model based on the *bio-heat equation* (see the example in Figure 62.7) [10].

When considering heating and its effects on biological tissues, it is important to control not only the maximum temperature value induced, but also the confinement of the heating to the region where the laser therapy or surgery is required. The results of the laser–tissue interactions may be significantly different whether or not the heated region is restricted to the volume under direct irradiation. Heat confinement

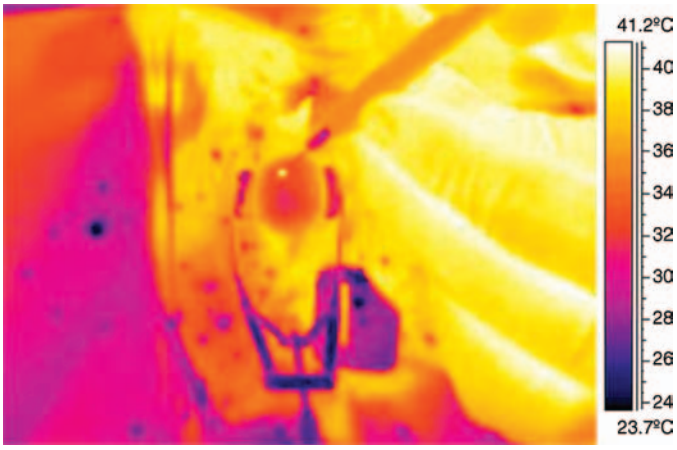

Figure 62.6 IR thermography as a tool to control the surface temperature dynamics during live laser surgery, while performing diode laser welding of the cornea. This image was recorded with a compact IR camera, equipped with software for visualization and analysis. The bright spot corresponds to the temperature rise on the surface of the cornea during irradiation by means of a 300 μm optical fiber operated in noncontact mode.

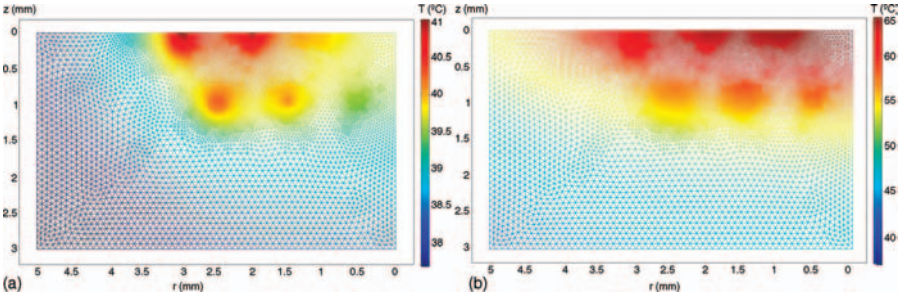

Figure 62.7 Example of a mathematical simulation developed to study spatial and temporal dynamics of laser-induced thermal effects in the upper layers of the skin (including melaninless dermis with blood capillaries of diameters varying in the range 10–200 μm). In this picture, the results of the heating effects induced by cw 300 mW, 405 nm (a) and 470 nm (b), light sources in a 3 mm section of skin are sketched. The model required the solution of the light diffusion and bio-heat equations with the Finite Element Method by the use of commercial software (Comsol Multiphysics).

can be important, for example, to limit the portion of tissue affected by heat damage, especially when precise coagulation has to be realized in the proximity of delicate structures. This result may be achieved by setting the time duration of the laser–tissue interaction process shorter than the time during which heat propagates from the directly irradiated volume to the adjacent tissue.

To provide a quantitative although simplified description of heat confinement during laser irradiation of biotissue, in addition to the laser pulse duration τ_{laser} one has to introduce the *thermal relaxation time* τ_{th}, that is, the time necessary for the propagation of heat over a distance equal to the optical penetration length of the laser light in that particular tissue; τ_{th} thus depends both on the optical absorption coefficient and on the thermal conductivity of the tissue itself. In order to define this parameter, let us introduce the thermal diffusion length L_{th}, which is the distance over which heat diffuses in the time t:

$$L_{th}{}^2 = 4Kt \tag{62.4}$$

where K is the thermal diffusivity of the tissue, which depends on its thermal conductivity, specific heat capacity, and density. For example, in water $K = 1.43 \times 10^{-3}\,\mathrm{cm^2\,s^{-1}}$, hence heat diffuses over a length of 0.8 mm in 1 s. Similarly, considering for simplicity the thermal diffusivity of blood to be the same as that of water, it takes ~170 μs for heat to propagate through a 10 μm diameter blood capillary, and ~17 ms for a 100 μm diameter blood capillary.

If we impose L_{th} to be equal to the optical penetration length L_{ext} defined by Eq. (62.2) (or, in case of absorption and scattering, to the effective penetration length L_{eff}), the thermal relaxation time is given by

$$\tau_{th} = \frac{L_{ext}{}^2}{4K} \tag{62.5}$$

Table 62.1 Typical values of thermal relaxation time for different biological targets of selective photothermolysis.

Target	Thermal relaxation time
Hair follicle, 200–300 μm	40–100 ms
Capillary in port-wine stain, 100 μm	5–100 ms
Epidermis, 20–50 μm	0.2–1 ms
Erythrocytes, 7 μm	20 μs
Melanosome, 1 μm	1 μs
Tattoo cell, 0.1 μm	10 ns

which represents the time necessary for heat to propagate over the optical penetration length. If the laser pulse duration is shorter then the thermal relaxation time, that is, $\tau_{laser} < \tau_{th}$, laser heating is confined in a volume $V = A \cdot L_{ext}$, where A is the area of the irradiated tissue surface. Conversely, when $\tau_{laser} > \tau_{th}$, heat diffuses through the tissue over lengths longer than the optical penetration length, extending the heat-affected zone and eventually the thermal damage to the surrounding tissue volumes.

In a case of practical concern, let us consider the irradiation of soft tissues (assuming for K the value of water) by CO_2 laser emission, which penetrates a length $L_{th} \approx 50\,\mu m$. From Eq. (62.5), one can calculate $\tau_{th} \approx 44\,\mu s$. Therefore, if the CO_2 laser pulse duration is $<40\,\mu s$, then the effect of irradiation will be a highly localized heating to a depth of 50 μm, which may result in vaporization of a very thin layer of tissue, with minimal heat damage to the deeper layers. By adjusting the energy delivered per pulse, the pulse duration, and the repetition rate, the heating effects may thus be controlled, avoiding irreversible thermal damage to sites adjacent to the treatment volume.

The control of heat confinement is at the basis of a specific laser treatment, called *selective photothermolysis*, which employs a green laser, highly absorbed by hemoglobin, which allows, by setting a proper pulse duration, selective coagulation of dilated blood vessels of, for example, port-wine stains, preserving at the same time the small capillaries, and also the overlying skin [11]. Typical values of thermal relaxation time for different biological targets of selective photothermolysis are given in Table 62.1.

62.2.2 Photomechanical Effects

Photomechanical effects become evident when short laser pulses are used to treat biological targets. As the laser pulse duration becomes shorter than a few microseconds, in addition to the purely thermal effects there may also appear significant photomechanical effects, such as pressure pulses propagating both in the air above the irradiated surface and inside the tissue. Depending on the type of interaction, the pressure pulse can be an acoustic pulse, that is, a low-pressure perturbation propagating at the speed of sound, or a shock wave, characterized by a high instantaneous pressure peak, propagating at ultrasound speed.

If tissue irradiation is performed under heat confinement conditions, very high temperatures may develop in a short time within a limited target volume, thus inducing significant photomechanical effects, which may be regarded as a drawback of the laser treatment or otherwise employed for therapeutic purposes, such as to induce fragmentation of hard tissues such as kidney stones, or to permit highly precise cutting of tissues in a controlled way as in the case of femtosecond laser ablation.

When laser irradiation takes place in heat confinement conditions, but at moderate intensities, the induced temperatures and pressure waves may not determine substantial and irreversible structural modifications in the tissue. This is the case in the *thermoelastic* regime, in which only acoustic waves are originated from the irradiated volume.

At higher levels of laser irradiation and for pulse durations in the nanosecond range, photomechanical effects become more evident and can play a fundamental role in the processes of laser ablation of biotissues (*photoablation*), thus increasing the effectiveness of tissue removal during processes of rapid vaporization.

At shorter pulse durations in the pico- to femtosecond regimes (or even in the nanosecond regime, but for very high laser intensities), a process called *photodisruption* can take place, mediated by nonlinear phenomena, such as avalanche ionization of the target materials with the formation of a plasma plume (a cloud of free electrons and ionized atoms) with subsequent microexplosive effects, which may induce the formation of cavitation bubbles inside the tissue. When suitably sized, these bubbles can be used, for example, to perform precise intra-tissue dissections for use in corneal surgery, as described in the following.

In the cases of both *photoablation* and *photodisruption*, one has to bear in mind that tissue removal is accompanied by mechanical stresses inside the tissue, control of which is essential to avoid significant damage to adjacent biological structures. For instance, the retina may by subjected to secondary damage when photorefractive surgery is performed [12–14].

62.2.2.1 **Photoablation with Nanosecond Pulses**

The term *photoablation* means the removal of material (biotissue) by laser irradiation. The photoablation modalities may be very different, depending on the tissue properties (optical, thermal, mechanical, and chemical characteristics of the target tissue), and also on the laser emission parameters and irradiation conditions. In the nanosecond pulse range, in homogeneous or quasi-homogeneous tissues, laser ablation is characterized by a so-called *ablation threshold*, F_{th}, which is the minimum level of laser fluence (i.e., laser energy per unit surface area, typically expressed in $J\,cm^{-2}$) above which material removal starts to occur. The processes taking place around the ablation threshold are displayed schematically in Figure 62.8.

Photoablation behaviors are usually described by the *ablation rate curves* (sketched in Figure 62.9), representing the etching rate (weight of the removed tissue or etching depth per pulse) as a function of the laser fluence. The typical behavior of an ablation rate curve is a quasi-linear dependence of the etching depth on fluence, when a threshold value F_{th} is exceeded. In general, below this threshold fluence, material

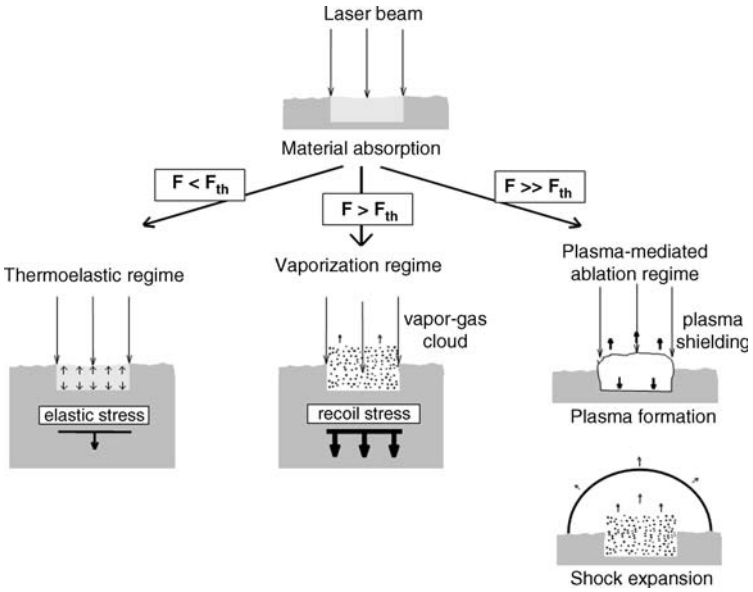

Figure 62.8 Scheme of the physical processes induced by pulsed laser irradiation around the ablation threshold of the target material.

removal does not take place (except for the two cases described in the following), even if photoacoustic effects can still be generated under pulsed irradiation by the thermoelastic effect. On the other hand, above the saturation value F_{sat}, the ablation rate is slowed by nonlinear absorption effects, which may reduce the optical penetration depth or even shield the laser light impinging on the tissue, as in the case of dense plasma formation. The ablation rate curves thus exhibit typical S-shaped behavior, which, for the same type of material, display different threshold values with the laser wavelength (shorter wavelengths exhibit lower threshold values).

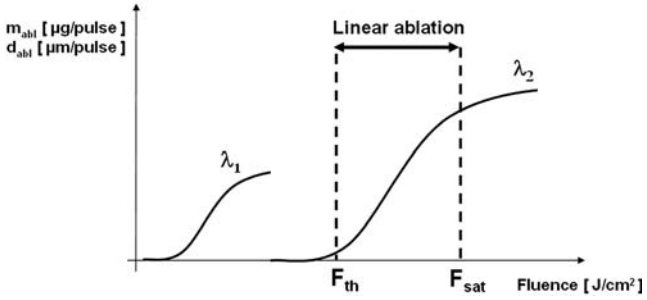

Figure 62.9 Curves of ablation rates for different laser wavelengths.

As the photoablation process is strongly related to the water content of tissues (the energy to vaporize water is about $2500\,J\,cm^{-3}$ under static conditions), it may be useful to characterize two kinds of photoablative regimes, occurring below and above the vaporization threshold.

Photoablation Below the Vaporization Threshold To describe the processes involved better, let us introduce the *stress relaxation time*, τ_{st}, which is the time for a pressure wave to travel a distance equal to the optical penetration length. Below the vaporization threshold of water, material removal under laser irradiation (in the nanosecond regime) may be induced by:

- Pressure peaks due to *inertial confinement*. This is a regime which may occur when the laser pulse duration (typically <10 ns) is so short that the irradiated and heated tissue volume cannot undergo expansion during the pulse, that is, when $\tau_{laser} < \tau_{st}$. Such heat deposition at constant volume results in a rapid increase in the internal pressure, which may give rise to an explosive expansion, eventually causing material ejection.
- *Spallation*. This process consists of the detachment of a superficial layer, rather than a real ejection of vapor or particulate (see Figure 62.10). Spallation is a photoablation condition which is reached when the laser pulse duration is shorter than the thermal relaxation time (heat confinement), but longer than the stress relaxation time: $\tau_{st} < \tau_{laser} < \tau_{th}$. This process originates from thermoelastic expansion inside the tissue, which produces pressure waves propagating in all directions. Let us consider the component of this thermoelastic pulse propagating towards the tissue surface. At the air–tissue interface, due to the mismatch of acoustic impedance, this compressive (positive) pressure peak will be reflected, thus experiencing a phase change π and becoming a rarefaction (negative) pulse peak. The traction exerted by this negative pressure peak may exceed the mechanical resistance of the tissue and cause the detachment of a superficial layer.

Photoablation Above the Vaporization Threshold Tissue removal may be induced by a very rapid vaporization process involving mainly the water content of the tissue, with

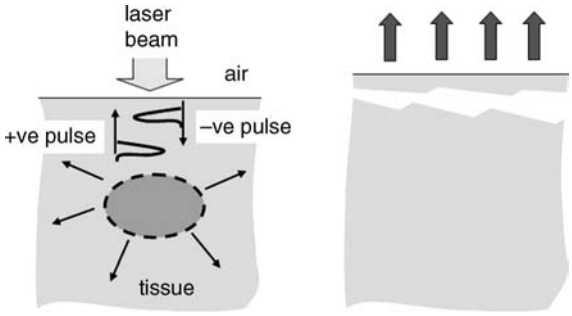

Figure 62.10 Scheme of the laser-induced spallation into biotissue.

explosive characteristics at the microscopic scale. The process is typically induced by laser pulses with durations of 1–100 ns and fluences in the range 0.1–5 J cm^{-2}, depending on the type of tissue. This kind of explosive phase change is one of the most important laser ablation mechanisms in surgical applications whenever controlled removal of soft tissue layers is required with minimal collateral heat effects. Photoablation by fast vaporization is actually the regime in which the description of tissue removal can be given through the ablation rate curves described above. In this respect, control of the laser fluence is important to operate safely in the linear part of the rate curve. Under these conditions, each laser pulse provides fast delivery of energy to the tissue, so as to induce its vaporization in a very short time, thus inducing rapid material ejection in the form of vapor and fine particulate from the surface.

Surgical applications of photoablation processes driven by fast vaporization include: photorefractive keratectomy, in which ablation and reshaping of the cornea are produced by ArF (190 nm) excimer laser pulses for the correction of visual defects, and excimer laser angioplasty, which employs XeCl (308 nm) laser pulses delivered through intraluminal fiber-optic catheters, in order to perform the recanalization of arterial stenoses and obstructions. In the fast vaporization regime, thermal damage to surrounding tissues can be negligible, as most of the delivered energy is used to vaporize the irradiated volume, and because heat confinement conditions are satisfied. In contrast, photomechanical damage may be not negligible, as for example when the rapid material ejection to the air induces a strong recoil and thus a pressure wave propagating in the opposite direction back into the tissue.

62.2.2.2 **Photodisruption**

At very high laser fluences, exceeding the saturation threshold of the typical ablation regime described above, plasma formation can occur, which may become so dense as to absorb the incoming laser light and give rise to a shock wave, which in turn may lead to macroscopically explosive effects, including tissue fragmentation. On the other hand, this disruptive process induced by highly intense nanosecond pulses may find beneficial applications, for example, in the photofragmentation of hard tissues such as kidney stones (laser lithotripsy).

Photodisruption processes in laser–tissue interactions are mediated by the dynamics of a plasma cloud, which is produced by ionization of the atoms of the irradiated material or of the surrounding gas medium [15]. The plasma is a macroscopically neutral gas phase of matter comprising a partially ionized gas, in which a certain proportion of electrons are free. The plasma is ignited when very high laser irradiances exceed the threshold to induce breakdown conditions (*optical breakdown*). The detailed mechanisms behind breakdown with optical pulses depend on the pulse duration. Particularly for femtosecond pulses, multiphoton ionization can efficiently generate free carriers in the initial phase of the pulse, followed by strong absorption by the generated plasma, which leads to further heating and ionization. For long pulses, multiphoton ionization is less important, and the breakdown starts primarily from the few carriers which are already present before the pulse. The random occurrence of such carriers makes optical breakdown less deterministic in the regime

of longer pulses, whereas the breakdown threshold can be very well defined for femtosecond pulses. The conditions for laser breakdown may be reached either at the external surface of a soft or hard target, or in the bulk of a transparent material.

In the case of nontransparent media and pulses in the nanosecond regime or longer, the laser light is absorbed at the air–tissue interface, which induces extraction of free electrons near the surface of the target and then acceleration of these electrons by the electromagnetic field of the laser radiation, which is still present during the evolution of the process. This results in a laser-sustained *avalanche ionization*, which induces a rapid increase in the free electron density, overcoming the losses due to recombination and diffusion. The avalanche ionization thus originates the condition for plasma formation. Very high temperatures ($\sim 10^4\,^{\circ}$C) and high electron densities ($>10^{20}\,\mathrm{cm}^{-3}$) are thus reached. In these conditions, the plasma becomes optically opaque, exhibiting a very high absorption coefficient and very high reflectivity. The consequence is a continuous growth of the plasma electron density and energy, and the formation of a plasma plume towards the external ambient (air), thus shielding further irradiation of the tissue target. The subsequent plasma expansion gives rise to a shock wave that may induce fragmentation and localized ruptures of the tissue.

For optically transparent media, the process is similar to that described above, although in this case the expansion of shock waves developing within the tissue drives the formation of cavitation bubbles with the particular dynamics of fast growth and successive collapse, which thus transmits significant mechanical stresses to the surrounding tissues. The disruptive effects may be enhanced by photochemical effects, with weakening of intra- and intermolecular bonds.

Plasma-mediated processes are at the basis of various laser techniques employed in the surgery of both hard and soft tissues. The former case, typically induced by highly intense nanosecond pulses, has an application in the already mentioned laser-induced fragmentation of kidney stones with Ho:YAG and Er:YAG pulsed lasers. Indeed, in this case it may be preferable to break the stone into small fragments by a few laser shots, instead of slowly ablating layer by layer.

The latter, realized with femtosecond lasers to produce controlled ablation confined to a very thin volume comparable to the focal region of the laser, is described in detail in the following section.

62.2.2.3 **Photoablation with Femtosecond Pulses**

Femtosecond laser (fs-laser)-induced microablation has recently been proposed in cellular and micro-surgery, and in some cases has even reached the phase of clinical applications, for example, for cutting transparent tissues such as the cornea [15–21]. Other intriguing biomedical applications are under study, conventionally indicated as fs-laser *nano-surgery*, which involve intra-cell cutting procedures, with the possibility of manipulating items inside a cell, thus opening up new frontiers in fields such as gene therapy.

The potential of such an fs-laser surgical regime rests on significant properties: when using femtosecond pulses, the confinement of multiphoton absorption in the focal spot and the very low energies required to induce optical breakdown can provide

high precision in cutting biological tissues and, at the same time, a very limited extension of the collateral damage. For example, the optical breakdown threshold can be reduced ~100-fold on passing from 3 ns to 100 fs pulse durations, which results in tissue ablation with less transformation of light energy into destructive mechanical energy. Moreover, in some particular cases, the cutting precision can even exceed the optical diffraction limit by a factor of 2–3, which theoretically determines the minimum size of a focal spot. This can be realized considering that fs-laser photodisruption effects originate from the free-electron distribution. At the focus, the nonlinear absorption process can thus make the electron density distribution narrower than the laser intensity distribution, which results in a better spatial resolution of the fs-laser surgery compared with that obtained in a linear absorption regime (i.e., by cw lasers), where the temperature distribution corresponds to the laser intensity distribution.

There are two main parameter regimes used for micro- and nano-surgery:

1) Long series of pulses emitted from femtosecond oscillators at repetition rates of 80 MHz and pulse energies well below the optical breakdown threshold, which induce accumulative effects; in these conditions, heat-induced damage may occur.
2) Amplified series of femtosecond pulses, (e.g., by means of a regenerative amplifier injected by the femtosecond oscillator) with repetition rates of 1–150 kHz and pulse energies slightly above the threshold for bubble formation; in this case, the effect of each individual pulse can be regarded as independent of each other, and so heat accumulation is negligible.

Let us briefly describe the latter femtosecond regime of those listed above, which is much more within the scope of this chapter. The micrometric photodisruptive effect may be used in notable applications, such as the intra-tissue cutting of ocular structures, and in particular for the cutting and *sculpturing* of the cornea, which is nowadays routinely used in clinics to prepare corneal flaps in the LASIK procedure (laser *in situ* keratomileusis, a type of refractive surgery for correcting myopia, hyperopia, and astigmatism), and also in new procedures of corneal transplant.

Femtosecond laser pulses are used to ablate tissue layers with predefined geometric characteristics, such as thickness, diameter, and lateral profile [16]. Commercially available fs-laser systems may be of various types [22], but in general with emission in the near-infrared (NIR) region, such as Nd:YAG or Nd:glass lasers. This means that laser radiation is well transmitted through transparent tissues such as the cornea. The laser pulses typically have energies in the range 0.5–2.5 μJ, durations of hundreds of femtoseconds and repetition rates in the range 50–150 kHz. Each individual laser pulse is focused to a precise location inside the cornea. This can be achieved, for example, by applanation of the corneal surface by means of a quartz flat connected with the laser beam focusing system. The high laser intensity at the focus creates a microplasma which vaporizes a volume of tissue of a few microns thickness. Then the microplasma drives the creation of a cavitation bubble, which separates the corneal lamellas. The size of this microbubble is governed both by the

size of the focal spot and by the pulse energy. The present fs-laser technology allows for an optimized choice of the emission parameters which permits the controlled production of microbubbles smaller than 10–15 μm. A scanning system moving the focal spot with micrometric precision allows for the delivery of thousands of laser pulses connected together in a raster pattern in order to define a resection plane, which may be horizontal, vertical, or tilted at any arbitrary angle with respect to the optical axis of the laser beam. The distance between the centers of contiguous microbubbles can be adjusted at will: a shorter distance increases the treatment time, but requires lower pulse energies, which increases the precision of the cleavage and minimizes the collateral damage.

The unique capabilities of fs-laser intra-tissue cutting procedures give micrometric precision and repeatability of the same cut pattern in different eyes, thus allowing the sculpturing of identical flaps in both the donor and recipient eyes when performing a lamellar or full thickness transplant of the cornea [20, 23–25].

62.3
Notes on Laser Systems Suitable for Surgical Applications

In this section, we briefly introduce the most common surgical lasers, as summarized in Table 62.2. In the UV region, the most widely used surgical lasers are the excimer lasers, such as the ArF (194 nm) and the XeCl (308 nm) lasers, which permit the so-called *cold ablation* of tissues, which corresponds to the process of fast vaporization described above. This technique is used whenever minimization of heat effects is critical, such as in the reshaping of the cornea (photorefractive keratectomy) and in the recanalization of atherosclerotic arteries. In the visible region, ion lasers such as the argon laser (several emission lines, the main ones at 488 and 514 nm) and krypton laser (several emission lines in the yellow–red region, the main one at 647 nm) were very common in the past, especially for retinal photocoagulation, but are now becoming obsolete owing to their poor efficiency. They are now being replaced by frequency-doubled Nd:YAG lasers emitting in the green (532 nm), which also allow for cw emission, and by diode lasers (630–960 nm). Dye lasers also emit lines in the visible (tunable, e.g., around 550–600 nm), which are mainly used for the treatment of superficial vascular lesions and for laser lithotripsy. In the NIR region, Nd:YAG lasers (1064 nm), operated in the cw, free-running (ms), Q-switching (ns), and mode-locking (ps–fs) regimes, remain the most diffused surgical lasers, used for photocoagulation and photoablation. In the IR region, the emissions of Ho:YAG (2100 nm), Er:YAG (2940 nm), and CO_2 (10 600 nm) lasers are used to excise and vaporize soft tissues, thanks to their high absorption by the high water content of such tissues. This list is, of course, not complete, as many more types of lasers are employed in experimental and preclinical surgery and in very specific medical applications. Moreover, this situation is rapidly changing with new developments in the laser technology, with a trend to replace the old lasers types characterized by high maintenance costs, high electric power consumption, and delicate components, with new compact and cost-effective devices, mainly based on

Table 62.2 Summary of relevant characteristics and surgical applications of the most commonly used lasers (not exhaustive).

Spectral region	Laser	Wavelength (nm)	Operation mode	Energy/power output	Repetition rate (Hz)	Delivery system	Surgical applications
UV	ArF	194	Pulsed: 10 ns	100–500 mJ	10–100	Optical channels with mirrors; no fiber-optic transmission	Photorefractive keratectomy Cardiovascular surgery
	XeCl	308	Pulsed: 10–100 ns	100–500 mJ	10–100	Fiber-optic transmission at moderate energies	Cardiovascular surgery Laser ablation of bones Dermatology: atopical dermatitis, vitiligo, alopecia areata, psoriasis
Visible and NIR	Argon	488–514	cw, pulsed	10 mW–10 W	—	Fiber-optic transmission	Retinal photocoagulation Laser trabeculoplasty Theleangectasia Tattoo removal
	Frequency-doubled Nd:YAG	532	cw and pulsed (ns)	500 mJ	30	Fiber-optic transmission: cw, yes; pulsed, no	Retinal photocoagulation Laser trabeculoplasty Treatment of vascular lesions (e.g. port-wine stains)

(*Continued*)

Table 62.2 (*Continued*)

Spectral region	Laser	Wavelength (nm)	Operation mode	Energy/power output	Repetition rate (Hz)	Delivery system	Surgical applications
	Dye	585–600	Pulsed	1–3 J^2	—	Fiber-optic transmission	Cutaneous vascular lesions
	Diode	630–960	cw Pulsed: pulse width in ms range	1–30 W	—	Optimal fiber-optic transmission	Laser welding Dentistry Facial telangectasias
	Alexandrite	720–800	cw or pulsed	1–10 J	1–100	Fiber-optic transmission	Hair removal Tattoo removal Nevi
	Nd:YAG	1064	Q-switching (short pulse): 10 ns	100–500 mJ	10–100	Fiber-optic transmission at low energies	Laser capsulotomy Deep pigmented lesions Tattoo removal
			Free-running (long pulse): 1 ms	1–2 J	10–100	Optimal fiber-optic transmission	Endoscopic neurosurgery Laparoscopic surgery Laser hair removal Laser lipolysis and treatment of cellulite Treatment of vascular lesions
	Nd:glass	1060	500–800 fs	1–10 μJ	10–150 kHz	Optical channels with mirrors, no fiber-optic transmission	Intra-tissue cutting (e.g., cornea) Tissue flap creation

	Ti:sapphire	700–1000	10–100 fs	1–10 nJ	80 MHz	Optical channels with mirrors, no fiber-optic transmission	Cellular and intracellular surgery
IR	Ho:YAG	2100	0.3 ms	1 J	10	Fiber-optic transmission	Endoscopic surgery Urology Lithotripsy Orthopedics
	Er:YAG	2940	0.2 ms	10–50 J	10	Fiber-optic transmission with special fibers or hollow waveguides	Skin rejuvenation Esthetics Leg veins Acne scars Hair removal Hemangiomas Superficial pigmented lesions
	CO_2	10600	cw, pulsed (100 ms) and super-pulsed (100 µs)	10–100 W	5–100	Transmission through articulated arms or special fibers at low power	Noncontact neurosurgery Ear, nose and throat surgery Gynecology Skin resurfacing Dermatology Tattoo removal Laser welding

solid-state technology. Worth noting also is that high-power lamps and LEDs (light-emitting diodes) are penetrating many surgical application fields that were formerly occupied by lasers.

Table 62.2 also reports the types of delivery systems usable with the various laser sources. The delivery system is a crucial part of the whole laser system, which may either enable or hinder, for example, endoscopic surgical applications, easy access to the treatment site, precise operations under the surgical microscope, or delivery of high laser doses in contact or noncontact modes.

The available delivery systems provided with the most common surgical laser are mainly based on articulated arms, optical fibers, and the direct transmission of laser light through the lens of a surgical microscope. The choice of a particular system clearly depends on the specific surgical application, but is also determined in most practical cases by the capabilities of the delivery medium, which may hinder the transmission of certain wavelengths (e.g., for standard fused-silica optics and optical fibers in the UV and IR regions), and also of high power densities (which may exceed the damage threshold of the light guide).

Articulated arms [26] are based on the reflection of light by multiple mirrors. They are composed of at least two rotating and tilting mirrors, enclosed in linear tubing arrangements and pivot joints, all of which may be arranged in very different setups to satisfy several different surgical needs. A good beam-handling system for surgical applications requires at least five degrees of freedom (three for spatial positioning and two for angular displacement) and terminates in a handpiece operated manually by the surgeon. With the use of these mechanical delivery systems, it is usually not possible to perform minimally invasive surgery inside the human body because of their large size and limited movability, although they may represent the only choice for several UV and IR laser sources and for very high peak power laser pulses. Moreover, they offer good beam quality, preserving the characteristics of the light source, such as its polarization and coherence. A variant of the articulated arms are the motorized optical channels used in clinical fs-laser systems, in which the laser path is based on mirror reflections as above, but controlled by means of a joystick.

Optical fibers [27, 28] are the backbone of minimally invasive surgery. The development of the technology enabling better performance and applicability of this kind of beam handling system is at the basis of modern endoscopy. A fiber-optic is composed of three coaxial cylindrical layers, from the inner part of the fiber, the core, the cladding, and the jacket. The optical properties of the core and the cladding are responsible for the fiber transmission, and the jacket is a protective layer. The principle behind fiber-optic systems may be understood by simple geometric optics arguments, which apply when the size of the fiber core is larger than the wavelength of the light. The core and the cladding are composed of different materials, with refractive index n_{co} and n_{cl}, respectively. If $n_{co} > n_{cl}$, the light ray entering the fiber core with a small enough angle $\alpha < \alpha_{max} = \arccos(n_{cl}/n_{co})$ undergoes total internal reflection at the interface with the cladding. This condition is satisfied at every ray reflection, thus permitting propagation with low losses over long distances (see Figure 62.11).

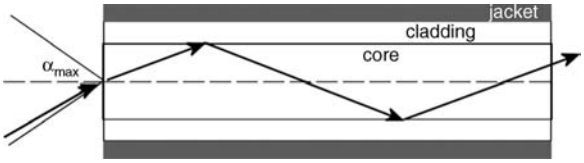

Figure 62.11 Visual representation of light propagation through an optical fiber by means of geometric optics. A light ray enters the fiber core and experiences total internal reflection at the core–cladding interface; α_{max} is the fiber acceptance angle, which defines the maximum angle that the light ray can form with the optical axis to become coupled into the fiber guide.

In surgical applications, because of the requirement to transmit high laser intensities, the core diameters of the fibers employed have to be in the range 100–400 μm. In a description of light propagation by means of electromagnetic fields, these relatively large cores correspond to a large number of electromagnetically guided modes, which mix together during the propagation and provide a homogeneous *top hat* intensity distribution at the fiber output. This intensity profile may be very useful to control the laser–tissue interaction.

Thanks to their flexibility and reduced size, optical fibers are the optimal tools to deliver light radiation inside the human body, thus permitting a wide variety of minimally invasive surgical procedures. The main limitations to their surgical use concern the range of transmitted wavelengths, which depends on the core material (e.g., fused silica gives a good transmission only in the range 300–2000 nm) and on the damage threshold of the fiber itself, which may prevent the transmission of the high laser intensities required to perform specific surgeries, as in the case of laser pulses in the nanosecond range or shorter. In practical medical use, fibers may be either disposable or reusable after sterilization. In some cases, they can be inserted in handpieces to allow easy handling of the fiber tip by the surgeon, especially when used under a microscope.

References

1 Vogel, A. and Venugopalan, V. (2003) Mechanisms of pulsed laser ablation of biological tissues. *Chem. Rev.*, **103**, 577–644.

2 Niemz, M.H. (1996) *Laser–Tissue Interactions*, Springer, Berlin.

3 Thomsen, S. (1991) Pathological analysis of photothermal and photomechanical effects of laser–tissue interactions. *Photochem. Photobiol.*, **53** (6), 825–835.

4 Mitton, D. and Ackroyd, R. (2008) A brief overview of photodynamic therapy in Europe. *Photodiagnosis Photodyn. Ther.*, **5** (2), 103–111.

5 Maguen, E., Chu, T.C., and Boyer, D. (2003) Lasers in ophthalmology, in *Biomedical Photonics Handbook* (ed. T. Vo-Dinh), CRC Press, Boca Raton, FL, pp. 43-9–43-10.

6 Babilas, P., Shafirstein, G., Baumler, W., Baier, J., Landthaler, M., Szeimies, R.M., and Abels, C. (2005) Selective photothermolysis of blood vessels following flashlamp-pumped pulsed dye laser irradiation: *in vivo* results and mathematical modelling are in

agreement. *J. Invest. Dermatol.*, **125** (2), 343–352.

7 Brinkmann, R., Radt, B., Flamm, C., Kampmeier, J., Koop, N., and Birngruber, R. (2000) Influence of temperature and time on thermally induced forces in corneal collagen and the effect on laser thermokeratoplasty. *J. Cataract Refract. Surg.*, **26**, 744–754.

8 Noonan, T.J., Tokish, J.M., Briggs, K.K., and Hawkins, R.J. (2003) Laser-assisted thermal capsulorrhaphy. *Arthroscopy J. Arthrosc. Relat. Surg.*, **19** (8), 815–819.

9 Pini, R., Rossi, F., Matteini, P., and Ratto, F. (2007) Laser tissue welding in minimally invasive surgery and microsurgery, in *Biophotonics* (eds. L. Pavesi and P.M. Fauchet), Springer Verlag Series in Medical Physics, Springer, Heidelberg, pp. 269–296.

10 Rossi, F., Pini, R., and Menabuoni, L. (2007) Experimental and model analysis on the temperature dynamics during diode laser welding of the cornea. *J. Biomed. Opt.*, **12** (1), 014031.

11 Anderson, RR., and Parrish, JA. (1983) Selective photothermolysis: precise microsurgery by selective absorption of pulsed radiation. *Science*, **220** (4596), 524–527.

12 Maatz, G., Heisterkamp, A., Lubatschowski, H., Barcikowski, S., Fallnich, C., Welling, H., and Ertmer, W. (2000) Chemical and physical side effects at application of ultrashort laser pulses for intrastromal refractive surgery. *J. Opt. A Pure Appl. Opt.*, **2** (1), 59–64.

13 Siano, S., Pini, R., Rossi, F., Salimbeni, R., and Gobbi, P.G. (1998) Acoustic focusing associated with excimer laser ablation of the cornea. *Appl. Phys. Lett.*, **72** (6), 647–649.

14 Schumacher, S., Sander, M., Stolte, A., Doepke, C., Baumgaertner, W., and Lubatschowski, H. (2006) Investigation of possible fs-LASIK induced retinal damage. *Proc. SPIE*, **6138**, 61381I-1–61381I-9.

15 Vogel, A., Noack, J., Hüttman, G., and Paltauf, G. (2005) Mechanisms of femtosecond laser nanosurgery of cells and tissues. *Appl. Phys. B*, **81**, 1015–1047.

16 Soong, H.K. and Malta, J.B. (2009) Femtosecond lasers in ophthalmology. *Am. J. Ophthalmol.*, **147**, 189–197.

17 Mian, S.H. and Shtein, R.M. (2007) Femtosecond laser-assisted corneal surgery. *Curr. Opin. Ophthalmol.*, **18**, 295–299.

18 König, K., Krauss, O., and Riemann, I. (2002) Intratissue surgery with 80 MHz nanojoule femtosecond laser pulses in the near infrared. *Opt. Express*, **10** (3), 171–176.

19 Ripken, T., Oberheide, U., Ziltz, C., Ertmer, W., Gerten, G., and Lubatschowski, H. (2005) Fs-laser induced elasticity changes to improve presbyopic lens accommodation. *Proc. SPIE*, **5688**, 278–287.

20 Menabuoni, L., Lenzetti, I., Cortesini, L., Susini, M., Rossi, F., Pini, R., and Parel, J.-M. (2008) Technical improvements in DSAEK performed with the combined use of femtosecond and diode lasers. *Invest. Ophthalmol. Vis. Sci.*, **49**, E-Abstract 2319.

21 Nishimura, N., Schaffer, C.B., and Kleinfeld, D. (2006) *In vivo* manipulation of biological systems with femtosecond laser pulses. *Proc. SPIE*, **6261**, 62611J.

22 Lubatschowski, H. (2008) Overview of commercially available femtosecond lasers in refractive surgery. *J. Refract. Surg.*, **24** (1), S102–S107.

23 Menabuoni, L., Lenzetti, I., Cortesini, L., Pini, R., and Rossi, F. (2009) Technical improvements in PK performed with the combined use of femtosecond and diode lasers. *Invest. Ophthalmol. Vis. Sci.*, **50**, E-Abstract 2220.

24 Menabuoni, L., Lenzetti, I., Rutili, T., Rossi, F., Pini, R., Yoo, S.H., and Parel, J.-M. (2007) Combining femtosecond and diode lasers to improve endothelial keratoplasty outcome. A preliminary study. *Invest. Ophthalmol. Vis. Sci.*, **48**, E-Abstract 4711.

25 Menabuoni, L., Pini, R., Fantozzi, M., Susini, M., Lenzetti, I., and Yoo, S.H. (2006) "All-laser" sutureless lamellar keratoplasty (ALSL–LK): a first case report. *Invest. Ophthalmol. Vis. Sci.*, **47**, E-Abstract 2356.

26 Greve, P. (2003) Beam handling systems, in *Applied Laser Medicine* (eds. H.-P. Berlien and G.J. Müller), Springer, Heidelberg, 137–140.

27 Gannot, I., and Ben-David, M. (2003) Optical fibers and waveguides for medical applications, in *Biomedical Photonics Handbook* (ed. T. Vo-Dinh), CRC Press, Boca Raton, FL, pp. 7-1–7-10.

28 Katzir, A. (1993) *Lasers and Optical Fibers in Medicine*, Academic Press, San Diego, pp. 107–125.

63
Endovenous Laser Therapy – Application Studies, Clinical Update, and Innovative Developments

Ronald Sroka and Claus-Georg Schmedt

63.1
Introduction

The first reports on clinical results of endovenous laser therapy (ELT) were published by Boné [1] and Navarro *et al.* [2] about 10 years ago. By means of ELT, the hemodynamic elimination of incompetent truncal veins should be feasible, which is already possible with other endovenous thermal procedures (radiofrequency ablation) and endovenous chemical procedures (foam sclerotherapy). Using these techniques, the endothermal damage to the vein wall results in consecutive occlusion of the treated vein. The clinical outcome looks very promising. Meta-analysis gives evidence that the innovative endoluminal techniques result in similar clinical outcomes to conventional surgical stripping. From the technical point of view, developments are still continuing. One characteristic of ELT is the broad spectrum of different treatment protocols using a variety of laser systems and forms of endovenous application. In recent years, systematic experimental investigations and the analysis of clinical results have increased our understanding of the connection between particular details of endovenous laser application and clinical results. During laser light application, bare and flat cut fibers are mainly used, causing inhomogeneous circumferential light application to the vessels wall, resulting in non-uniform tissue alteration and perforation. Different kinds of newly developed radial emitting laser fibers are tested in combination with a laser emitting light at 980 and 1470 nm in *ex vivo* model tissue using different treatment parameters. It could be demonstrated that the induced tissue alterations are circumferential uniform without any perforation. Those investigations led to the continuous development and optimization of ELT. This chapter outlines the principles of ELT and experimental developments for optimizing this minimally invasive procedure.

Handbook of Biophotonics. Vol.2: Photonics for Health Care, First Edition. Edited by Jürgen Popp, Valery V. Tuchin, Arthur Chiou, and Stefan Heinemann.

63.2 Clinical Application of ELT

In endovenous application, laser light is introduced into the vein lumen by means of a flexible optical fiber via a sheath system. Depending on the laser wavelength used and on the absorption characteristics of the primary target molecules in the tissue (e.g., water or hemoglobin), laser energy is absorbed and transformed into heat energy. Heating of the tissue leads to cell destruction and collagen shrinkage. Currently, laser systems emitting light of wavelengths in the near-infrared region (810, 940, 980, 1064, 1320, and 1470 nm) are used in clinical practice. In most systems, the light energy is transported via a bare fiber (core diameter of up to 600 μm) which is inserted into the vein via a catheter system.

In principle, for ELT the same indications and contraindications apply as for conventional operative treatment of incompetent truncal veins using crossectomy (high ligation) and stripping. Around 60% of patients suffering from an epifascial vein system were found to be suitable for an endovenous therapy procedure [3]. Contraindications for endovenous thermal application were found to be acute ascending thrombophlebitis, postphlebitic stenosis, segmental obliteration, and aneurysmatic widening of the vein. In the case of marked meandering path of the vein, insertion of the fiber is often impossible. Furthermore, large vein diameters (>20 mm) can also be regarded as a relative contraindication since this makes adequate circular thermal alteration of the vein wall more difficult.

The principle operative procedure of the vena saphena magna is outlined in the following. During the course of preoperative ultrasound diagnosis, the vein diameter should be measured for the precalculation of the appropriate energy density. In principle, ELT can be carried out as an outpatient procedure under local anesthesia (tumescence anesthesia). The great saphenous vein can be treated with ELT in its entire length from the sapheno-femoral junction to the distal lower leg. Particularly in the area of the lower leg, care has to be taken to ensure adequate tumescence and light dosimetry in order to avoid postoperative paresthesia due to the proximity of the saphenous nerve. The use of sonography during operation is an integral part of ELT treatment.

First, the vein is punctured in the area of the distal insufficiency point and a guide wire is introduced. Before introducing the sheath system (Seldinger technique), the bare fiber is inserted into the sheath so that the fiber tip extends ~1–2 cm beyond the end of the sheath. This position should be marked on the fiber. This is important since the fiber tip can be heated to several hundred degrees Celsius during the treatment and if there is insufficient distance from the sheath, this can lead to the melting of the sheath material. Thereafter the sheath system, without fiber, is pushed forward to the sapheno-femoral junction with the aid of the guide wire. After the removal of the guide wire, the bare fiber is inserted with respect to the mark. Together and under sonographic monitoring, the sheath and fiber are then positioned so that the tip of the fiber comes to rest ~1–2 cm distally from the sapheno-femoral junction. The pilot beam can be used to make a rough check of the location of the bare fiber tip as it is visible through the skin. The perivenous tumescence anesthesia is then carried

out under ultrasound supervision. The fluid is to protect the perivenous tissue from thermal damage and reduce the lumen of the truncal vein by compression and spasm.

Two modes of light application are clinically in use. In stepwise pull-back, the fiber with sheath is pulled back by 1–5 mm between each irradiation pulses activated. Using continuous pull-back, continuous irradiation is applied while withdrawing the fiber with sheath at a velocity of 1–3 mm s^{-1}. After pull-back is finished at the distal point of vein incompetence, the vein is ligated after removing the sheath.

Since the damage caused to tissue is proportional to the laser energy applied, the parameter linear endovenous energy density (LEED) is defined, which is proportional to the appropriate level of energy to the length and diameter of the vein segment to be treated in joules per centimeter of vein [4]. Using LEED, the diameter of the vein or the irradiated inner surface of the vein is not taken into consideration. The laser energy applied in relation to the irradiated surface is described as endovenous fluence equivalent (EFE) in J cm^{-2} [4] and uses a cylindrical model of the vein segment, calculating the vein inner surface according to $F = 2r\pi l$ where r is the vein radius and l the length of the treated vein segment. Therefore, the following parameters should be documented for every treatment: vein diameter d (cm), length of the treated vein segment l (cm), laser wavelength λ (nm), laser power P (W), irradiation time t (s) or pull-back speed v (mm s^{-1}) for continuous pull-back. Only in this way LEED and EFE can be calculated for every treatment, thereby making it possible to compare clinical results with different treatment protocols. Clinical analyses suggest that failures in therapy with nonocclusion or recanalization after ELT treatment are observed less when sufficiently high energy density is used – compared with lower LEED or EFE [5–12]. On the other hand, energy densities above a certain level can lead to side effects such as transmural ablation, perforations, and alteration of perivenous tissue [13, 14]. So far it has not been possible to establish generally valid recommendations for appropriate energy density. Table 63.1 gives an overview of recommendations formulated so far by a number of authors. A recent trend of recommendations for higher energy density has been observed.

Table 63.1 Recommended energy density for effective ELT with varying wavelengths[a].

Study	Wavelength (nm)	LEED (J cm^{-1})	EFE (J cm^{-2})
Proebstle *et al.* [5]	940	23.6	13.0
Timperman *et al.* [6]	810/940	>80	n.d.
Proebstle *et al.* [7]	940	n.d.	20.0
Kim *et al.* [8]	980	32.7	9.82
Desmyttère *et al.* [9]	980	50–120	29–41
Kontothanassis *et al.* [10]	980	45–60	n.d.
Vuylsteke *et al.* [11]	980	n.d.	52.0
Elmore and Lackey. [12]	810	109.6	46.6

a) LEED, endovenous energy density; EFE, endovenous fluence equivalent; n.d., not defined.

Clinical and duplex ultrasound examinations should be repeated regularly to ensure the success of the treatment and to exclude possible postoperative thrombosis or thrombus propagation. Also, persistent or recurrent reflux should be ruled out. Directly after the operation, the treated truncal vein can be seen to be somewhat thickened under sonography. The lumen is usually reduced and filled with strongly echoing thrombus material. In the remainder of the vein's path, as a result of repair and scar formation, a stringy, fibrous change may appear or the vein disappears [12].

63.3 Clinical Studies on ELT

After the first clinical reports on ELT in 1999, more recently clinical series with small numbers of cases and relatively short periods of postoperative follow-up have been published. There have occasionally been reports, however, on series and multi-center studies with more than 500 treatments and postoperative observation periods of more than 60 months [9, 12, 15–18]. Today, there are data from more than 60 publications with altogether more than 15 000 ELT treatments available, which have been summarized and evaluated in overviews [19].

With the appropriate selection of patients, ELT treatment can technically be carried out in more than 99% of patients [12] where effective occlusion and hemodynamic elimination can be assumed. The cosmetic results are on the whole very good. However, lack of effectiveness and undesired side effects are also observed [20], for example, 2.3% nonocclusion or early recanalization, 4.5% expected recanalization. The follow-up in the studies analyzed seldom exceeded 6–12 months and the studies showed widely differing results. Recanalization was observed to have occurred with an incidence of up to 24% [3]. Furthermore, the connection between rate of occlusion and endovenously applied laser energy (LEED, EFE) became obvious. Postoperative pain is rated as slight to moderate by most patients (81.5%). However, in a series of 113 patients, 18.5% described the pain as severe to very severe. Postoperative induration of the truncal vein was observed in 78.1% of patients, and perivenous ecchymosis and hematoma in an average of 52% of patients [20]. In a number of studies, however, the incidence of postoperative ecchymosis and hematoma was reported in 60–80% of patients [3, 4]. Phlebitis of the truncal vein was observed in 2.8% of patients, but certain studies reported a significantly higher incidence of up to 17.2% [21]. Further complications such as persistent dysesthesia after nerve lesions (0.8%), burns on the skin (0.5%), thrombus propagation in the deep vein system (0.2%), and pulmonary thrombosis (0.02%) were seldom observed [19].

In Table 63.2, a number of randomized controlled studies comparing ELT with the open surgery techniques of crossectomy and stripping are listed. As the number of these studies is small and the period of postoperative observation is short, a final evaluation is not possible at present. In sum, these studies document, at least initially, effective elimination of the epifascial reflux through ELT accompanied by reduced side effects. Whether refraining from crossectomy in fact leads to an increased incidence of inguinal neo-reflux or even to a reduction in neo-vascularization at the

Table 63.2 Randomized controlled studies comparing ELT with crossectomy and stripping.

Study	Country	No. of procedures	Comparison
de Medeiros and Luccas [40]	Brazil	20	ELT vs. crossectomy/ stripping
Rasmussen *et al.* [41]	Denmark	137	ELT vs. crossectomy/ stripping in local anesthesia
Darwood *et al.* [42]	United Kingdom	103	ELT vs. crossectomy/ stripping
Kalteis *et al.* [43]	Austria	95	ELT vs. crossectomy/ stripping
Disselhoff *et al.* [44, 45]	The Netherlands	120	ELT vs. crossectomy/ cryostripping

sapheno-femoral junction will have to be established in further controlled trials and, in particular, in further postoperative examinations of already randomized patients.

63.4 Analysis of Comparison Studies

Looking at meta-analyses and reviews, it becomes obvious there are some meta-studies available on the one hand evaluating the efficiency and the safety of endoluminal techniques in comparison with conventional surgical stripping and on the other hand comparing the different endoluminal techniques from the clinical point of view.

Although all investigations are of great interest, such studies must be assessed critically because they represent just the short history of about 10 years of the evaluation of innovative laser application techniques which have shown promising successful improvements in finding a more effective treatment protocol and dosimetric concept, including the bare fiber technique that has been improved by the application of radial firing energy. Unfortunately, such developments are so innovative that up to now only reports of single-center clinical studies are available.

In a clinical review, the effects on insufficient veins traditionally treated with high ligation and stripping were compared with minimally invasive techniques including endovenous laser surgery, radiofrequency ablation, and foam sclerotherapy. The authors discussed the mechanism of action of each modality, as well as the techniques for intervention, outcomes, and complications. Minimally invasive treatment of venous insufficiency has replaced open surgical stripping in most cases, with less morbidity than high ligation and stripping, allowing for successful treatment and improved patient satisfaction [22]. A clinical update and clinical hints on how to use ELT clinically was presented [23]. In a histological investigation of ELT using either 940 or 1319 nm light and the bare fiber technique, changes including

acute effects such as loss of intima, vacuolization in the subintima layer and effects at 1 month post-ELT, inflammatory changes, vein wall thickening, intraluminal thrombus, and increased amounts of fibroblasts and collagen could be observed [24].

Meta-analytic studies were performed, comparing the overall outcome of endovenous treatment concepts including ELT with conventional methods. In a meta-analytic survey which included 59 studies of which seven directly compared ELT and surgery (involving ligation and stripping) with respect to safety and efficacy, it was reported that serious side effects are rare in both, whereas minor side effects are more common in ELT. A short-term comparison favored ELT over surgery, showing comparable safety aspects. However, ELT offers short-term benefits and appears to be as clinically effective as surgery up to 1 year after treatment [25]. In another meta-analysis, evidence from the collected data suggests that ELT and radiofrequency techniques are as safe and effective as surgery, particularly in the treatment of saphenous veins. However, most importantly, the type of varicose vein should govern the intervention of choice [26]. A further meta-analysis concluded that endovenous therapies have not yet been compared with surgical ligation and stripping in large randomized clinical trials, especially with long-term follow-up of more than 3 years. In the absence of large, comparative randomized clinical trials, the minimally invasive techniques appear to be at least as effective as surgery in the treatment of lower extremity varicose veins. The results from 64/119 eligible studies with an average follow-up of about 32 months showed that foam therapy and radiofrequency ablation were as effective as surgical stripping. Endovenous laser therapy using bare fiber techniques was significantly more effective than stripping, foam therapy, and radiofrequency ablation. The results of this meta-analysis support the increasing use of minimally invasive interventions in the treatment of lower extremity varicosities. However, large, long-term comparative randomized controlled trials that include patient-reported outcomes, cost-effectiveness analyses, and safety assessment are needed to achieve the highest level of evidence for these novel therapies [27].

ELT using 810 nm light and the bare fiber technique showed thermal damage of the intima and the internal part of the media. Whereas at lower LEEDs of 110–200 J cm^{-1} vascular perforations were observed in less than 10% of cases, at higher LEEDs of 40–880 J cm^{-1} nearly all cases were perforated [28]. As neovascularization is a major cause of recurrent varicosities following surgery, a prospective cohort study was performed comparing recurrence rates and the occurrence of neovascularization after surgery or ELT (810 nm, LEED $<$50 J cm^{-1}, bare fiber) for great saphenous vein reflux. Although the frequencies of recurrent varicosities 2 years after surgery and ELT were similar, neovascularization, a predictor of future recurrence, was less common following ELT. It was supposed that delivering larger LEEDs could reduce recanalization rates and recurrence [29].

The data from a study comparing radiofrequency ablation with 980 nm wavelength ELT (bare fiber technique) at comparable energy densities clearly showed that patients who received radiofrequency ablation recovered more quickly than those who received 980 nm endovenous laser treatment for the first 2 weeks, and then the recovery parameters began to equalize between 2 and 4 weeks after the procedure and were equal at 4 weeks. The authors agreed that the data may differ if different laser

wavelengths are compared with radiofrequency ablation, such as the newer 1319, 1320, and 1470 nm wavelengths [30, 31]. Further comparison studies of radiofrequency ablation versus 980 nm ELT showed that radiofrequency ablation was significantly superior to ELT as measured by post-procedural recovery and quality of life parameters in a randomized prospective comparison between these two thermal ablation modalities for closure of the great saphenous vein within 2 weeks post-treatment [30].

The newer wavelength of 1470 nm was clinically tested in a randomized study using the bare fiber technique. It could be shown that the power of the laser (15W versus 25 W) did not influence the occlusion rate when an appropriate high LEED (110–130 J cm^{-1}) was used. Side effects such as ecchymoses and pain were reduced compared with similar studies using wavelengths of 810 and 980 nm [32]. Furthermore, a prospective follow-up study using the bare fiber technique with a 1470 nm diode laser showed promising clinical results with this minimally invasive, safe, and efficient therapy. It appears that using LEED >100 J cm^{-1}, paresthesia is increased compared with LEED <100 J cm^{-1} at the same occlusion rate of 100% at 1 year follow-up [33].

63.5 Investigations to Improve Light Application

As mentioned earlier, during laser light application, bare and flat cut fibers are mainly used, causing inhomogeneous circumferential light application to the vessels wall, resulting in nonuniform tissue alteration and perforation. The endovenous laser treatment relies on the transformation of luminous energy into heat due to absorption of the photon energy. This process depends on the laser wavelength and on the optical properties of the irradiated tissue. Thus the endoluminal application of laser energy implies a variety of parameters, overall influencing the alterations of the vein wall. Variations in the laser wavelength and power settings result in different temperature levels and thermal alterations. In addition, the light application technique, more precisely the light distribution within the vessel, could also influence the type of response; for example, vessel wall perforation could be observed in the bare fiber technique in combination with special treatment protocols [14, 34, 35]. With respect to this, the blood as the primary medium around the laser fiber tip also influences the mechanism and the process. The purpose of the following study was to investigate in a standardized manner the tissue effects induced by an innovative 360° radial emitting laser fiber which is based upon an interstitial laser light application system for prostate tissue (patent DE 19703208.7).

63.5.1 Experiments

The *ex vivo* model consists of a cow's foot from freshly slaughtered cows (18–24 months of age, weight 550–650 kg, right hind leg) [14, 35]. The subcutaneous veins (V. saphena lateralis and V. digitalis dorsalis communis III, 20.0–25.0 cm in length,

5–8 mm in diameter) are large enough to allow for introduction of the endoluminal application systems and are available for acute *ex vivo* experiments. Leaving these veins *in situ*, appropriate sheath and catheter systems permit perfusion of fluid (e.g., blood, saline) and intraluminal pressure measurement during treatment. After surgical preparation, treatment was performed with endoluminal laser irradiation from the central end (joint) to the peripheral end (hoof).

Laser therapy was performed using a diode laser (Ceralas D15, Biolitec, Bonn, Germany) emitting light of wavelength 1470 nm which is transported via a 600 μm fiber. The 360° radial fiber tip (Biolitec, Bonn, Germany) (Figure 63.1) was polished to emit the light in air radial to the optical axis of the fiber. Retaining this condition, a transparent dome covers the fiber tip and is sealed to prevent blood inflow when used inside the vessel. From the technical point of view, the irradiation profile of the 360° radial fiber was measured using a goniometer setup. With respect to this, the fluence rate delivered through the dome could be calculated and compared with the bare fiber parameters. Experiments on the robustness of the new 360° radial fiber was performed with safety precautions. The fiber robustness under extreme crash conditions was tested by intravenous positioning of the 360° radial fiber without any pull velocity but with blood irrigation and application of an energy of up to 300 J.

For tissue experiments, the 360° radial fiber was introduced into the vein via an introduction sheath. The vein was irrigated using heparinized blood. The pull-back velocity was set to 1 mm s^{-1} for a 3–4 cm vein length. The laser power settings were 3, 6, 10, and 15 W. Thus the applied LEED could be calculated to be 30, 60, 100, and 150 J cm^{-1}, respectively. Each experiment was performed 5–7 times. After treatment, application devices and treated veins were examined macroscopically with standardized *in situ* and *ex situ* preparation and documentation, then the harvested tissues were processed for histology.

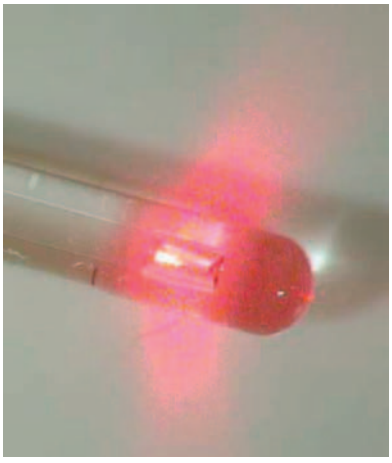

Figure 63.1 360° radial emitting fiber for endoluminal uniform circumferential irradiation of the vein wall.

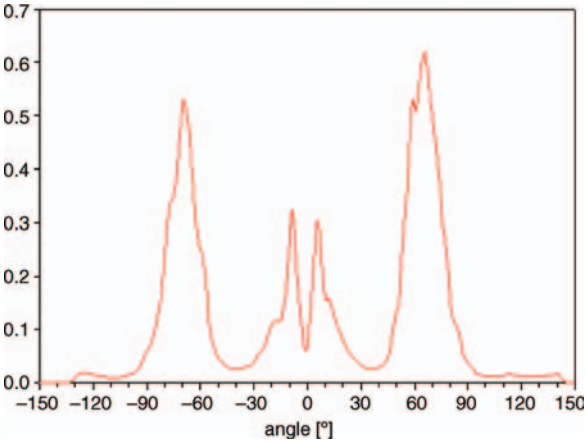

Figure 63.2 Irradiation pattern of the 360° radial emitting fiber tip showing the radial direction of 70° to the optical axis of the fiber and an irradiation divergency of 25–30°.

63.5.2 Experimental Results

Goniometric measurements showed a radial irradiation pattern of the 360° radial fiber with the main deflection axes in the 70° direction with respect to the optical axis of the fiber. As shown in Figure 63.2, the divergence angle of the emitting beam (full width at half-maximum) could be determined as 25–30°. The fiber robustness experiments showed that the fiber remained intact without any damage when a power of 10 W was applied for 30 s. Fiber damage could be observed when using a power of 15 W for more than 20 s. Regarding safety aspects, it should be mentioned that such a situation and such a high dose of light energy should never be reached during endovenous laser treatment. Such a crash situation is far beyond the intended clinical situation.

As shown in Table 63.3, calculations according to the geometric conditions as sketched in Figure 63.3 were performed for a set of vein lumen diameter.

Table 63.3 Calculations of the irradiation area *A* and the applied fluence rate *FR* due to geometric considerations when 10 W laser output power is delivered to 100% of the tissue surface[a)].

Vein diameter, *d* (cm)	Distance from fiber tip or dome to tissue surface, *a* (cm)	A_{radial} (cm^2)	A_{fiber} (cm^2)	FR_{radial} ($W\,cm^{-2}$)	FR_{fiber} ($W\,cm^{-2}$)
0.18	0.00	0.027	0.003	370	3333
0.40	0.10	0.135	0.019	74	526
0.70	0.25	0.413	0.069	24	145
1.00	0.40	0.842	0.149	12	67

a) $A_{radial} = d^2\pi \tan(\alpha_{radial}/2)$; $A_{fiber} = \pi\cdot[(a + x)\tan(\alpha_{fiber}/2)]^2$ with $x = 0.67$ mm with respect to the apex of the divergency.

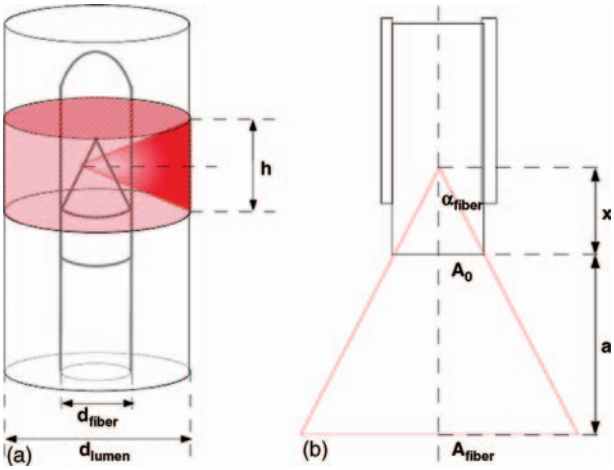

Figure 63.3 Sketch of the geometric conditions for the radial emitting fiber (a) and a bare fiber (b) used for calculations in Table 63.3.

The distance of the fiber, either the tip of the bare fiber (core diameter 0.6 mm) or the dome surface (dome diameter 1.8 mm), to the tissue varied from touching to up to 4 mm, thus affecting the size of the irradiation area (A) due to the beam divergency [α_{fiber}(bare fiber) = 50°; α_{radial}(radial-dome fiber) = 30°]. As a result, the irradiation area in touch of the 360° radial fiber (A_{radial}) differs by a factor of 9 compared with the bare fiber tip (A_{fiber}). Assuming 100% power transmission through the fiber and that no absorption by the blood occurred, it can be calculated that the fluence rate (FR) applied to such an area at a laser output power of 10 W resulted in an FR_{fiber}/FR_{radial} ratio of about 5–9 depending on the vein diameter.

In Table 63.4, the macroscopic observations during the 360° radial application of 1470 nm laser light are summarized, with differentiation between vessel diameters of $d > 7$ mm (large vessel) and $d < 5$ mm (small vessel). The observations were

Table 63.4 Macroscopic evaluation of the tissue alterations due to 360° radial laser light application at $\lambda = 1470$ nm.

Vein diameter (mm)	Power (W)	Rigidity, thickening (class 0–4)	Observations
>7	3	0–1	Boiling noise
<5	3	1–2	Low shrinkage
>7	6	2	Noise, hindered pulling, shrinkage
<5	6	3	Fast shrinkage, hindered pulling
>7	10	2–3	Boiling, shrinkage
<5	10	3	Hard pulling, fast shrinkage
>7	15	3	Shrinkage, sometimes sticking
<5	15	3	Fast shrinkage, sometimes sticking

Table 63.5 Therapeutic options for truncal varicose veins.

Open procedures	Endovenous procedures		
	Endothermal		Chemical
	Radiofrequency ablation	Laser therapy (ELT)	
High ligation	VNUS Closure *Plus*	810–1470 nm	Liquid sclerotherapy
Barrier techniques	VNUS Closure *Fast*	Bare fiber	Foam sclerotherapy
Stripping	Celon RFITT	Cylindrical diffuser	Catheter-based application
Invagination		Radial fiber	
Cryostripping			
Electrical stripping			
Endoscopic stripping			

classified into five groups labeled from 0 to 4, where 0 is defined as normal unaffected tissue, 4 represents burned and carbonized sensations, and classes 1–3 represent different degrees of rigidity concomitant with wall thickening and change of color. The evaluation was performed by three independent investigators. The data in Table 63.4 indicate that sufficient shrinkage with alteration in rigidity and wall thickening could be obtained at applied laser powers of 6 and 10 W, for both vein lumens. Shrinkage was accompanied by increased effort for pulling, especially in small lumen veins. Boiling noise could be experienced in nearly every experiment due to cooking of the fluid inside the vein lumen. Sticking to the tissue occurred especially when moving the fiber through the vein valves.

63.6 Discussion

Endovenous laser therapy has become established in the last few years among the range of therapy options for the treatment of truncal vein insufficiency as listed in Table 63.5. In endovenous radiofrequency ablation (VNUS Closure), reproducible, defined thermal damage to tissue can already be produced through the implementation of feedback mechanisms with automatic generator-steered regulation of energy density and standardized treatment protocols. By contrast, the effects to ELT using the bare fiber technique on tissue, and therefore on the clinical results, are clearly very varied [18, 34]. Because of the use of different wavelengths, different pullback protocols, and different energy densities, ELT can hardly be standardized. Feedback mechanisms through which accurate energy density in ELT can be controlled are lacking. This makes the appropriate dosage of light for the sufficient thermal alteration of tissue more difficult to achieve. In addition to transmural damage, wall perforation is also observed [14], which has the potential for clinically relevant consequences such as ecchymosis and postoperative pain. On the other hand, a locally focused, not completely circular thermal damage of the vein wall leaves

only slightly locally damaged wall areas, which can lead to a higher incidence of nonocclusion or recanalization.

It becomes obvious that a certain level of thermal dose is required to occlude the vein efficiently in a circumferential homogeneous manner. The thermal dose delivered at a specific vein segment is related to both treatment time and temperature. It appears that denaturation of almost all the collagen fibers within the vein wall and consecutive wound healing processes guarantee complete and durable occlusion of the vein [36, 37]. Investigations on mathematical modeling based on optical and thermal parameters of the vessel walls and the perivascular tissue were performed and could serve a useful tools to simulate the mechanisms of action of endovenous laser treatment [38].

Applying a high fluence rate to the tissue ($FR > 1000\,\mathrm{W\,cm^{-2}}$) and exceeding the ablation threshold of the tissue, local perforations could occur [14, 34, 35]. Such tissue effects could be observed during bare fiber light application, especially in cases where the fiber tip is in contact with the tissue. Using the bare fiber tip technique, the mechanism of heat induction and heat transfer to the vessel target has still not been investigated in detail. Hence, with reducing the side effects and clarification of the underlying mechanism in mind, improved and reproducible application of light energy to the vessels wall is required [14, 34, 35].

With respect to this, the innovative 360° radial fiber tip showed promising results in the *ex vivo* experiments. The fluence rate is dramatically reduced below the ablation threshold, so no perforation was observed during experiments. The induced tissue alterations were circumferential and homogeneous. Shrinkage of the vessel due to thickening, loss of flexibility, and change in color as a sign of effective treatment [36] could be observed throughout the complete vessels. Furthermore, shrinkage could be recognized additionally by feeling the improved power needed for pulling the 360° radial fiber through the lumen. As the absorption coefficient of water and blood at a wavelength 1470 nm is superior to that at all other laser wavelengths (810, 940, 980, 1064, 1320 nm) used in this field of laser treatment, an immediate tissue response could be observed already at laser output powers between 6 and 10 W. Hence a continuous pull-back velocity of about $1\,\mathrm{mm\,s^{-1}}$ seems appropriate for reproducible and efficient effects. Based on these experiments, it seems promising that a secure treatment protocol could be developed, depending on the vein lumen diameter, pull-back velocity, and light energy applied. Initial clinical results of ELT treatments with this radial light applicator using a 1470 nm laser generator indicate minimal side effects coupled with a high rate of closure [39]. Long-term studies using the innovative 360° radial fiber should be performed to evaluate the treatment procedure with respect to recanalization, side effects, and other aspects.

63.7 Conclusion

Laser light application in endovenous treatment procedures suffered from inhomogeneous tissue alterations after treatment. Laser treatment parameters showed, in

comparison with radiofrequency ablation, a greater variety of parameters due to wavelength, power, pull-back velocity, compression by tumescence, bare fiber versus cylindrical emitting fibers, and so on. Therefore, a certain treatment protocol was not available. Meta-analysis support the increasing use of minimally invasive interventions such as ELT in the treatment of varicosities which are efficient and with reduced side effects. However, large, long-term comparative randomized controlled trials that include patient-reported outcomes, cost-effectiveness analyses, and safety assessment are needed to achieve the highest level of evidence for these novel therapies.

The latest innovative technologies, such as the 360° radial fiber, seem promising to develop secure, reliable, and reproducible tissue alteration treatments in the acute situation. By means of these optimizations, ELT treatment is coming closer to achieving the goal of standardizing an effective method for the treatment of varicose veins. Further controlled studies are required to compare the results of optimized ELT with those of other endothermal modes of treatment and conventional open surgery.

Acknowledgments

The authors would like to thank the following for supporting these investigations and studies: T. Beck, R. Blagova, C. Burgmeier, V. Hecht, N. Karimi-Poor, R. Meier, M. Sadeghi-Azandaryani, S. Scheibe, I. Sroka, B. Steckmeier, S. Steckmeier, A. von Conta, S. Winter. K. Weick, and B. Steckmeier.

References

1 Boné, C. (1999) *Rev. Patol. Vasc.*, **5**, 35–46.
2 Navarro, L., Min, R.J., and Boné, C. (2001) *Dermatol. Surg.*, **27** (2), 117–122.
3 Sharif, M.A., Soong, C.V., Lau, L.L., Corvan, R., Lee, B., and Hannon, R.J. (2006) *Br. J. Surg.*, **93** (7), 831–835.
4 Proebstle, T.M., Moehler, T., Gül, D., and Herdemann, S. (2005) *Dermatol. Surg.*, **31** (12), 1678–1683; discussion 1683–1684.
5 Proebstle, T.M., Krummenauer, F., Gül, D., and Knop, J. (2004) *Dermatol. Surg.*, **30** (2 Pt 1), 174–178.
6 Timperman, P.E., Sichlau, M., and Ryu, R.K. (2004) *J. Vasc. Interv. Radiol.*, **15** (10), 1061–1063.
7 Proebstle, T.M., Moehler, T., and Herdemann., S. (2006) *J. Vasc. Surg.*, **44** (4), 834–839.
8 Kim, H.S., Nwankwo, I.J., Hong, K., and McElgunn, P.S. (2006) *Cardiovasc. Interv. Radiol.*, **29** (1), 64–69.
9 Desmyttère, J., Grard, C., Wassmer, B., and Mordon, S. (2007) *J. Vasc. Surg.*, **46** (6), 1242–1247.
10 Kontothanassis, D., Di Mitri, R., Ferrari Ruffino, S., Ugliola, M., and Labropoulos, N. (2007) *Int. Angiol.*, **26** (2), 183–188.
11 Vuylsteke, M., Liekens, K., Moons, P., and Mordon, S. (2008) *Vasc. Endovasc. Surg.*, **42** (2), 141–149.
12 Elmore, F.A. and Lackey, D. (2008) *Phlebology*, **23** (1), 21–31.
13 Chang, C.J. and Chua, J.J. (2002) *Lasers Surg. Med.*, **31** (4), 257–262.
14 Schmedt, C.G., Sroka, R., Steckmeier, S., Meissner, O.A., Babaryka, G., Hunger, K., Ruppert, V., Sadeghi-Azandaryani, M.,

and Steckmeier, B.M. (2006) *Eur. J. Vasc. Endovasc. Surg.*, **32** (3), 318–325.
15 Agus, G.B., Mancini, S., and Magi, G. (2006) *Int. Angiol.*, **25** (2), 209–215.
16 Bush, R.G. (2006) *J. Vasc. Surg.*, **43** (3), 642; author reply 642–643.
17 Min, R.J. and Khilnani, N.M. (2005) *J. Cardiovasc Surg. (Torino)*, **46** (4), 395–405.
18 Ravi, R., Rodriguez-Lopez, J.A., Trayler, E.A., Barrett, D.A., Ramaiah, V., and Diethrich, E.B. (2006) *J. Endovasc. Ther.*, **13** (2), 244–248.
19 Schmedt, C.G. and Steckmeier, B.M. (2006) Endoluminale radiofrequenz- und lasertherapie zur therapie der stammveneninsuffizienz, in *Handbuch der Angiologie* (eds. M. Marshall and F.X. Breu), Ecomed, Landsberg, pp. 1–28.
20 Luebke, T. and Brunkwall, J. (2008) *J. Cardiovasc. Surg. (Torino)*, **49** (2), 213–233.
21 Disselhoff, B.C., der Kinderen, D.J., and Moll, F.L. (2005) *Endovasc. Ther.*, **12** (6), 731–738.
22 Brown, K. and Moore, C.J. (2009) Update on the treatment of saphenous reflux: laser, RFA or foam? *Perspect. Vasc. Surg. Endovasc. Ther.*, **21**, 226–231.
23 Schmedt, C.G., Blagova, R., Karimi-Poor, N., Burgmeier, C., Steckmeier, S., Beck, T., Hecht, V., Meier, R., Sadeghi-Azandaryanic, M., Steckmeier, B., and Sroka, R. (2010) Update of endovenous laser therapy and the latest application studies. *Med. Laser Appl.*, **25**, 34–43.
24 Bush, R.G., Shamma, H.N., and Hammond., K. (2008) Histological changes occurring after endoluminal ablation with two diode lasers (940 and 1319 nm) from acute changes to 4 months. *Lasers Surg. Med.*, **40**, 676–679.
25 Hoggan, B.L., Cameron, A.L., and Maddern., G.J. (2009) Systemic review of endovenous laser therapy versus surgery for the treatment of saphenous varicose veins. *Ann. Vasc. Surg.*, **23**, 277–287.
26 Leopardi, D., Hoggan, B.L., Fitridge, R.A., Woodruff, P.W.H., and Maddern., G.J. (2009) Systemic review of treatments for varicose veins. *Ann. Vasc. Surg.*, **23**, 264–276.
27 van den Bos, R., Arends, L., Kockaert, M., Neumann, M., and Nijsten, T. (2009) Endovenous therapies of lower extremity varicosities: a meta-analysis. *J. Vasc. Surg.*, **49**, 230–239.
28 der Kinderen, D.J., Disselhoff, C.V.M., Koten, J.W., de Bruin, P.C., Seldenrijk, C.A., and Moll, F.L. (2009) Histpathologic studies of the below-the-knee great saphenous vein after endovenous laser ablation. *Dermatol. Surg.*, **35**, 1985–1988.
29 Theivacumar, N.S., Darwood, R., and Gough, M.J. (2009) Neovascularisation and recurrence 2 years after varicose vein treatment for sapheno-femoral and great saphenous vein reflux: a comparison of surgery and endovenous laser ablation. *Eur. J. Vasc. Endovasc. Surg.*, **38**, 203–207.
30 Almeida, J.I., Kaufman, J., Göckeritz, O., Chopra, P., Evans, M.T., Hoheim, D.F., Makhoul, R.G., Richards, T., Wenzel, C., and Raines., J.K. (2009) Radiofrequency endovenous ClosureFAST versus laser ablation for the treatment of great saphenous reflux: a multicenter, single-blinded, randomized study (RECOVERY Study). *J. Vasc. Interv. Radiol.*, **20**, 752–759.
31 Lewis, B.D. (2010) Re: radiofrequency endovenous ClosureFAST versus laser ablation for the treatment of great saphenous reflux: a multicenter, single-blinded, randomized study (RECOVERY Study). *J. Vasc. Interv. Radiol.*, **21**, 302; author reply 302–303.
32 Maurins, U., Rabe, E., and Pannier, F. (2009) Does laser power influence the results of endovenous ablation (EVLA) of incompetent saphenous veins with the 1470 nm diode laser? A prospective randomized study comparing 15 and 25 W. *Int. Angiol.*, **28**, 32–37.
33 Pannier, F., Rabe, E., and Maurins., U. (2009) First results with a new 1470-nm diode laser for endovenous ablation of incompetent saphenous veins. *Phlebology*, **24** (1), 26–30.
34 Schmedt, C.G., Meissner, O.A., Hunger, K., Babaryka, G., Ruppert, V., Sadeghi-Azandaryani, M.,

Steckmeier, B.M., and Sroka, R. (2007) *J. Vasc. Surg.*, **45** (5), 1047–1058.
35 Sroka, R., Schmedt, C.G., Steckmeier, S., Meissner, O.A., Beyer, W., Babaryka, G., and Steckmeier, B. (2006) *Med. Laser Appl.*, **21** (1), 15–22.
36 Beck, T.J., Burgmeier, C., Blagova, R., Steckmeier, B., Hecht, V., Schmedt, C.G., and Sroka, R. (2007) *Med. Laser Appl.*, **22** (4), 238–241.
37 Blagova, R., Burgmeier, C., Steckmeier, S., Steckmeier, B., Babaryka, G., Beck, T.J., and Sroka, R. (2007) *Med. Laser Appl.*, **22** (4), 242–247.
38 Mordon, S.R., Wassmer, B., and Zemmouri, J. (2007) *Lasers Surg. Med.*, **39** (3), 256–265.
39 Maurins., U. (2008) Presentation No. 50 at Conference of Deutschen Gesellschaft für Phlebologie, Bochum, 17 October 2008.
40 de Medeiros, C.A. and Luccas, G.C. (2005) *Dermatol. Surg.*, **31** (12), 1685–1694, discussion 1694.
41 Rasmussen, L.H., Bjoern, L., Lawaetz, M., Blemings, A., Lawaetz, B., and Eklof, B. (2007) *J. Vasc. Surg.*, **46** (2), 308–315.
42 Darwood, R.J., Theivacumar, N., Dellagrammaticas, D., Mavor, A.I., and Gough, M.J. (2008) *Br. J. Surg.*, **95** (3), 294–301.
43 Kalteis, M., Berger, I., Messie-Werndl, S., Pistrich, R., Schimetta, W., Pölz, W., and Hieller, F. (2008) *J. Vasc. Surg.*, **47** (4), 822–829; discussion 829.
44 Disselhoff, B.C., der Kinderen, D.J., and Moll, F.L. (2008) *Phlebology*, **23** (1), 10–14.
45 Disselhoff, B.C., der Kinderen, D.J., Kelder, J.C., and Moll, F.L. (2008) *Br. J. Surg.*, **95** (10), 1232–1238.

64
Laser Treatment of Cerebral Ischemia

Ying-Ying Huang, Vida J. Bil De Arce, Luis De Taboada, Thomas McCarthy, and Michael R. Hamblin

64.1
Introduction

Low-level laser (light) therapy (LLLT) has been clinically applied for many indications in medicine that require the following processes: protection from cell and tissue death, stimulation of healing and repair of injuries, and reduction of pain, swelling, and inflammation. The notable lack of any effective drug-based therapies for stroke has rapidly increased researchers' interest in the use of light as a viable approach to mitigating stroke. The fact that near-infrared (NIR) light can penetrate into the brain and spinal cord allows noninvasive treatment to be carried out with a low likelihood of treatment-related adverse events. Although in the past it was generally accepted that the central nervous system could not repair itself, recent discoveries in the field of neuronal stem cells have brought this dogma into question. LLLT may have beneficial effects in the acute treatment of brain damage after stroke or traumatic brain injury (TBI).

64.2
The Problem of Cerebral Ischemia

Stroke is the third leading cause of death in the United States, after heart disease and cancer [1]. Strokes can be classified into two major categories, ischemic and hemorrhagic. Ischemic strokes account for over 80% of all strokes. The most common cause of ischemic stroke is the blockage of an artery in the brain by thrombosis, embolism, or stenosis. Cerebral ischemia is a condition in which there is insufficient blood flow to the brain to meet metabolic demand. This leads to poor oxygen supply or cerebral hypoxia and thus to the death of brain tissue or cerebral infarction/ischemic stroke [2].

Handbook of Biophotonics. Vol.2: Photonics for Health Care, First Edition. Edited by Jürgen Popp, Valery V. Tuchin, Arthur Chiou, and Stefan Heinemann.

64.3
Mechanisms of Brain Injury After Cerebral Ischemia

When a cerebral ischemia occurs, the blood supply to the brain is interrupted, and brain cells are deprived of the glucose and oxygen that they need to function. Normally, the brain requires a large amount of oxygen to generate sufficient adenosine triphosphate (ATP) by oxidative phosphorylation to maintain and restore ionic gradients [3]. The ischemic neuron becomes depolarized as ATP is depleted and membrane ion-transport systems fail. The resulting influx of calcium leads to the release of a number of neurotransmitters, including large quantities of glutamate, which, in turn, activates other excitatory receptors on other neurons. These neurons then become depolarized, causing further calcium influx, further glutamate release, and local amplification of the initial ischemic insult. This massive calcium influx also activates various degradative enzymes, leading to the destruction of the cell membrane and other essential neuronal structures [4]. Reactive oxygen species (ROS), nitric oxide (NO) and arachidonic acid are generated by this process, which lead to further neuronal damage. Within hours to days after a stroke, specific genes are activated, leading to the formation of cytokines and other factors that, in turn, cause further inflammation and microcirculatory compromise [4].

64.4
Current Treatment for Cerebral Ischemia

Thrombolytic therapy is the only intervention of proven and substantial benefit for select patients with acute cerebral ischemia [5]. The main agent that has been employed is recombinant tissue plasminogen activator (t-PA) [6], which works by converting the proenzyme plasminogen to the activated enzyme plasmin, which dissolves fibrin clots into low molecular weight fibrin degradation products. Other thrombolytics that have been used include streptokinase [7, 8]. Time lost is brain lost in acute cerebral ischemia. A pooled analysis of all 2775 patients enrolled in the first six intravenous tPA trials provided clear and convincing evidence of a time-dependent benefit of thrombolytic therapy [9].

64.5
Investigational Neuroprotectants and Pharmacologic Intervention

Neuroprotection is defined as any strategy, or combination of strategies, that antagonizes, interrupts, or slows the sequence of injurious biochemical and molecular events that, if left unchecked, would eventuate in irreversible ischemic injury to the brain. An enormous variety of agents and strategies have received clinical scrutiny, each justified by a pathophysiologic rationale. In all, nearly 165 ongoing or completed clinical trials have been published [10]. There has been an almost universal outcome of failure in all these trials, with exceptions of some small hint of efficacy in only a few cases.

64.6
Mechanism of Low-Level Laser Therapy

The most understood mechanism of action involves the relationship between lasers and cytochrome *c* oxidase. The first law of photobiology states that biological responses of living cells to photon irradiation are initiated by photon absorption in intracellular chromophores or photoacceptors [11]. The absorbed photon's energy excites the photoacceptor molecule into a more energetic (higher) electronic state, resulting in a physical and/or chemical molecular change, ultimately leading to the cell's biological response. It was suggested in 1989 by Karu that the mechanism of LLLT at the cellular level was based on the absorption of monochromatic visible and NIR light by cytochrome *c* oxidase [12] (see Figure 64.1). Cytochrome *c* oxidase is located in the inner mitochondrial membrane and plays a central role in eukaryotic cells. The cytochrome *c* oxidase enzyme complex contains two copper centers, the first of which contains a broad-wavelength absorption peak when oxidized. As a terminal enzyme in the respiratory chain, it delivers protons across the inner mitochondrial membrane and permits the formation of ATP by oxidative phosphorylation [4]. In cerebral ischemia, the neurons become seriously deprived of oxygen and their ATP levels fall precipitously. Laser stimulation of respiration not only increases ATP but also sets in motion several signaling pathways that lead to activation of genes involved in neuroprotection, anti-apoptosis, anti-inflammation, and activation of brain repair processes mediated by neural progenitor cells.

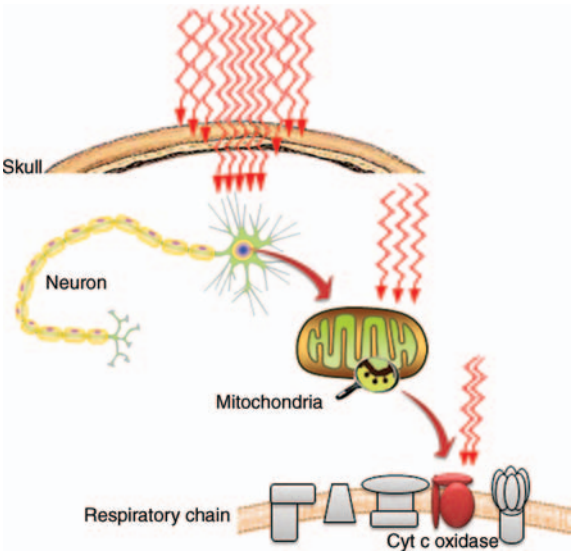

Figure 64.1 Mechanisms of action of transcranial laser therapy for stroke. NIR light penetrates through the scalp and skull and is absorbed by cytochrome *c* oxidase in the mitochondria of the damaged cortical neurons. Signaling pathways are activated that prevent neuronal death and stimulate brain repair.

64.7
LLLT on Neuronal Cells

In cultured human neuronal cells, LLLT resulted in doubling of the ATP content in normal human neural progenitor cells (NHNPs) [13]. LLLT also increased heat shock proteins and preserved mitochondrial function [4]. Ignatov *et al.* [14] showed that He–Ne laser irradiation of a pond snail neuron at a dose of 0.07 mJ increased the amplitude of the potential-dependent slow potassium current. More recently, Ying *et al.* reported that pretreatment with NIR light via a light-emitting diode (LED) significantly suppressed rotenone or 1-methyl-4-phenylpyridinium (MPP)-induced apoptosis in both striatal and visual cortical neurons from newborn rats [15]. These *in vitro* findings suggest that LLLT could have beneficial effects in animal models of neurologic disorders and could be a treatment for stroke.

64.8
LLLT for Stroke in Animal Models

Animals that have been used in cerebral ischemia models for various specific applications include rats, mice, gerbils, cats, rabbits, dogs, pigs, and nonhuman primates. Although there is no one animal model that identically mimics stroke in humans, the use of animal models is essential for the development of therapeutic interventions for stroke. Ischemia is typically induced by occluding the middle cerebral artery (MCA) in the animal. The MCA is most often used to simulate human stroke as most human strokes are due to occlusion of this vessel or one of its branches [16]. Laser treatment for stroke should penetrate the skull bones and scalp. Transmittance of all tissues increases progressively with wavelength from 600 to 814 nm. Tissue thickness, optical absorption, and scattering are major influencing factors [17]. Lychagov *et al.* presented results of measurements of transmittance of high power laser irradiation through skull bones and scalp [18].

Transcranial laser therapy (TLT) at 808–810 nm can penetrate the brain and was shown to lead to enhanced production of ATP in the rat cerebral cortex [4]. Findings of increased neurogenesis in the subventricular zone (SVZ) were reported in an ischemic stroke animal model treated with TLT [19]. Based on these findings, it is thought that TLT may have multiple mechanisms of action and could be beneficial in acute ischemic stroke [20]. Figure 64.2 shows non-invasive delivery of 810 nm laser light into the brain of a rat that had been subjected to stroke induction.

Lapchak and De Taboada [21] were the first to demonstrate that TLT substantially increased cortical ATP production in an embolic stroke model. They hypothesized that this amount should be sufficient to improve or maintain mitochondrial function, improve neuronal survival, and produce behavioral improvement. Given the evidence regarding the anti-apoptotic effect of NIR irradiation and the apparent

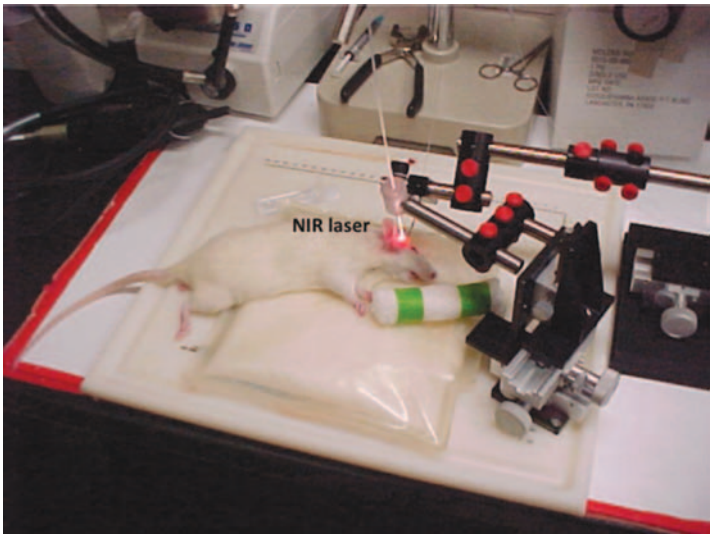

Figure 64.2 Rat model of transcranial laser therapy for stroke. NIR laser fiber allows 810 nm light to penetrate into the stroked rat brain.

extended time window of efficacy, during which apoptotic cell death could still be occurring in the penumbra, it is possible that TLT acts in a neuroprotective fashion. It is also likely that TLT enhances recovery of function because there is evidence that lesion volume is not altered, but neurologic function is restored [19].

For several years, enhanced mitochondrial function with subsequent preservation of the ischemic penumbra and improved outcomes has been the hypothesized mechanism. Only relatively recently has this been demonstrated using an *in vivo* model. In 2004, Lapchak *et al*. [22] used the rabbit small clot embolic stroke model and applied a gallium–arsenic diode NIR laser within 6 h of symptom onset. Significant and sustained improvement was demonstrated in behavioral function measured 24 h after treatment and again at 21 days from stroke onset [23]. Similar studies confirmed this beneficial effect despite using a rodent and a different model of inducing strokes (rat middle cerebral artery occlusion) [2]. There were differences in the treatment times for which TLT was effective, but both models resulted in statistically significant behavioral improvement that warranted human trials.

A recently completed trial using rabbits and an embolic model tested TLT applied after administration of intravenous tPA. The results showed that this combination did not adversely affect hemorrhage rate, volume, or survival compared with tPA alone [24]. Based on this study, and theoretically the different mechanisms of action of TLT and tPA could synergistically treat strokes, a clinical trial testing TLT plus tPA was recommended and is on the horizon.

64.9
TLT in Clinical Trials for Stroke

The NeuroThera effectiveness and safety trial-1 (NEST-1) evaluated the safety and preliminary effectiveness of the NeuroThera Laser System in the ability to improve 90-day outcomes in ischemic stroke patients treated within 24 h from stroke onset [25]. The NEST-1 study indicated that infrared laser therapy had shown initial safety and effectiveness for the treatment of ischemic stroke in humans when initiated within 24 h of stroke onset and a second larger trial was warranted.

Recently, the second clinical trial of the effectiveness and safety trial of NIR laser treatment within 24 h from stroke onset (NEST-2) was completed [26]. This study was a prospective, double-blind, randomized, sham controlled, parallel group, multi-center study that included sites in Sweden, Germany, Peru, and the United States, and enrolled 660 subjects. TLT was applied within 24 h from stroke onset. Comparable results were seen for the other outcome measures. Although no prespecified test achieved significance, a *post hoc* analysis of patients with a baseline National Institutes of Health Stroke Scale (NIHSS) score of <16 showed a favorable outcome at 90 days on the primary end point ($p < 0.044$). Mortality rates and serious adverse events did not differ between groups with 17.5 and 17.4% mortality and 37.8 and 41.8% serious adverse events for TLT and sham control patients, respectively.

64.10
Conclusions and Future Outlook

It is now generally accepted by the LLLT community that NIR (810 nm) laser light applied transcranially can beneficially impact ischemic stroke. It may take somewhat longer to be accepted by the stroke community. Many questions still remain to be answered: for instance, what is the best time after stroke to apply the light; does the use of multiple sessions of treatment (e.g., every day) present any increased benefit over a single treatment session; is pulsed light better that continuous-wave light and if so what are the best pulse parameters; are there any wavelengths that are better than 810 nm? We can envisage the time when all hospital emergency rooms will have the ability to deliver TLT to stroke patients and possibly also TBI patients.

Acknowledgments

This work was supported by Photothera Inc. and grants from the US Air Force MFEL Program (FA9550-04-1-0079), Center for Integration of Medicine and Innovative Technology (DAMD17-02-2-0006), and CDMRP Program in TBI (W81XWH-09-1-0514).

References

1 Wolf, P.A. (1990) An overview of the epidemiology of stroke. *Stroke*, **21**, II4–II6.

2 Ginsberg, M.D. (2009) Current status of neuroprotection for cerebral ischemia: synoptic overview. *Stroke*, **40**, S111–S114.

3 Pasantes-Morales, H. and Tuz, K. (2006) Volume changes in neurons: hyperexcitability and neuronal death. *Contrib. Nephrol.*, **152**, 221–240.

4 Streeter, J., De Taboada, L., and Oron, U. (2004) Mechanisms of action of light therapy for stroke and acute myocardial infarction. *Mitochondrion*, **4**, 569–576.

5 Adams, H., Adams, R., Del Zoppo, G., and Goldstein, L.B. (2005) Guidelines for the early management of patients with ischemic stroke – 2005 guidelines update – a scientific statement from the Stroke Council of the American Heart Association/American Stroke Association. *Stroke*, **36**, 916–923.

6 Barushka, O., Yaakobi, T., and Oron, U. (1995) Effect of low-energy laser (He–Ne) irradiation on the process of bone repair in the rat tibia. *Bone*, **16**, 47–55.

7 Donnan, G.A., Davis, S.M., Chambers, B.R., Gates, P.C., Hankey, G.J., McNeil, J.J., Rosen, D., Stewart-Wynne, E.G., and Tuck, R.R. (1995) Trials of streptokinase in severe acute ischaemic stroke. *Lancet*, **345**, 578–579.

8 Furlan, A., Higashida, R., Wechsler, L., Gent, M., Rowley, H., Kase, C., Pessin, M., Ahuja, A., Callahan, F., Clark, W.M., Silver, F., and Rivera, F. (1999) Intra-arterial prourokinase for acute ischemic stroke. The PROACT II study: a randomized controlled trial. Prolyse in acute cerebral thromboembolism. *JAMA*, **282**, 2003–2011.

9 Hacke, W., Donnan, G., Fieschi, C., Kaste, M., von Kummer, R., Broderick, J.P., Brott, T., Frankel, M., Grotta, J.C., Haley, E.C. Jr., Kwiatkowski, T., Levine, S.R., Lewandowski, C., Lu, M., Lyden, P., Marler, J.R., Patel, S., Tilley, B.C., Albers, G., Bluhmki, E., Wilhelm, M., and Hamilton, S. (2004) Association of outcome with early stroke treatment: pooled analysis of ATLANTIS, ECASS, and NINDS rt-PA stroke trials. *Lancet*, **363** 768–774.

10 Ginsberg, M.D. (2008) Neuroprotection for ischemic stroke: past, present and future. *Neuropharmacology*, **55**, 363–389.

11 Sutherland, J.C. (2002) Biological effects of polychromatic light. *Photochem. Photobiol.*, **76**, 164–170.

12 Karu, T.I. (1989) Laser biostimulation: a photobiological phenomenon. *J. Photochem. Photobiol. B*, **3**, 638–640.

13 Oron, U., Ilic, S., De Taboada, L., and Streeter, J. (2007) Ga–As (808 nm) laser irradiation enhances ATP production in human neuronal cells in culture. *Photomed. Laser Surg.*, **25**, 180–182.

14 Ignatov, Y.D., Vislobokov, A.I., Vlasov, T.D., Kolpakova, M.E., Mel'nikov, K.N., and Petrishchev, I.N. (2005) Effects of helium–neon laser irradiation and local anesthetics on potassium channels in pond snail neurons. *Neurosci. Behav. Physiol.*, **35**, 871–875.

15 Ying, R., Liang, H.L., Whelan, H.T., Eells, J.T., and Wong-Riley, M.T. (2008) Pretreatment with near-infrared light via light-emitting diode provides added benefit against rotenone- and MPP + -induced neurotoxicity. *Brain Res.*, **1243**, 167–173.

16 Philip, M., Benatar, M., Fisher, M., and Savitz., S.I. (2009) Methodological quality of animal studies of neuroprotective agents currently in phase II/III acute ischemic stroke trials. *Stroke*, **40**, 577–581.

17 Salomatina, E., Jiang, B., Novak, J., and Yaroslavsky, A.N. (2006) Optical properties of normal and cancerous human skin in the visible and near-infrared spectral range. *J. Biomed. Opt.*, **11**, 064026.

18 Lychagov, V.V., Tuchin, V.V., Vilensky, M.A., Reznik, B.N., Ichim, T., and De Taboada, L. (2006) Experimental study of NIR transmittance of the human skull. *Proc. SPIE*, **6085**, 60850T

19 Oron, A., Oron, U., Chen, J., Eilam, A., Zhang, C., Sadeh, M., Lampl, Y., Streeter, J., DeTaboada, L., and Chopp, M. (2006) Low-level laser therapy applied transcranially to rats after induction of stroke significantly reduces long-term

neurological deficits. *Stroke*, **37**, 2620–2624.

20 Lampl, Y. (2007) Laser treatment for stroke. *Expert Rev. Neurother.*, **7**, 961–965.

21 Lapchak, P.A. and De Taboada, L. (2010) Transcranial near infrared laser treatment (NILT) increases cortical adenosine-5′-triphosphate (ATP) content following embolic strokes in rabbits. *Brain Res.*, **1306**, 100–105.

22 Lapchak, P.A., Wei, J., and Zivin, J.A. (2004) Transcranial infrared laser therapy improves clinical rating scores after embolic strokes in rabbits. *Stroke*, **35**, 1985–1988.

23 Lapchak, P.A., Salgado, K.F., Chao, C.H., and Zivin., J.A. (2007) Transcranial near-infrared light therapy improves motor function following embolic strokes in rabbits: an extended therapeutic window study using continuous and pulse frequency delivery modes. *Neuroscience*, **148**, 907–914.

24 Lapchak, P.A., Han, M.K., Salgado, K.F., Streeter, J., and Zivin, J.A. (2008) Safety profile of transcranial near-infrared laser therapy administered in combination with thrombolytic therapy to embolized rabbits. *Stroke*, **39**, 3073–3078.

25 Lampl, Y., Zivin, J.A., Fisher, M., Lew, R., Welin, L., Dahlof, B., Borenstein, P., Andersson, B., Perez, J., Caparo, C., Ilic, S., and Oron, U. (2007) Infrared laser therapy for ischemic stroke: a new treatment strategy: results of the NeuroThera Effectiveness and Safety Trial-1 (NEST-1). *Stroke*, **38**, 1843–1849.

26 Zivin, J.A., Albers, G.W., Bornstein, N., Chippendale, T., Dahlof, B., Devlin, T., Fisher, M., Hacke, W., Do, W.H., Ilic, S., Kasner, S., Lew, R., Nash, M., Perez, J., Rymer, M., Schellinger, P., Schneider, D., Schwab, S., Veltkamp, R., Walker, M., Streeter, J., and NeuroThera Effectiveness and Safety Trial-2 Investigators (2009) Effectiveness and safety of transcranial laser therapy for acute ischemic stroke. *Stroke*, **40** (4), 1359–1364.

65
Laser Vision Correction

Diogo L. Caldas and Renato Ambrósio Jr.

65.1
Introduction

Refractive surgery evolved significantly during the last two decades, emerging as a separate ophthalmic sub-specialty when refractive surgical procedures became the most commonly performed elective surgery in medicine [1]. Refractive surgery is classified into three broad categories: refractive keratoplasty (keratoplasty means "molding the cornea"), refractive intraocular lenses (IOLs), and refractive scleral surgery [2]. This classification then divides into various specific surgical techniques, such as refractive keratotomy (RK) or keratomileusis. The advent of the excimer (shortened from excited dimer) laser, a rare gas and halogen argon fluoride (ArF) laser that emits a high-energy ultraviolet (UV) laser beam that is ultimately used to photoablate corneal stroma (i.e., reshaping corneal stroma by microscopically removing portions of the cornea in a precise, accurate, and safe fashion), was a great step forward in refractive surgery and, more specifically, refractive keratoplasty. Laser energy can be delivered either to the Bowman's layer on the corneal stromal surface in surface ablation (SA) procedures or deeper into the corneal stroma by the means of lamellar surgery in which a flap is created and then an excimer laser ablation is performed on the stromal bed in laser-assisted *in situ* keratomileusis (LASIK) [3]. The LASIK flap is created using a mechanical or laser (i.e., using a solid-state femtosecond laser) microkeratome.

Various SA and lamellar techniques are used for correcting myopia, hyperopia, and astigmatism, with high rates of success [95.4% patient satisfaction rate (range: 87.2–100%)] and predictability with few untoward negative consequences [4]. Like any other surgery, refractive surgery has indications and contraindications. In general, myopia up to -10 D, hyperopia up to $+6$ D, and astigmatism up to -6 are the current upper limits for keratorefractive laser vision correction. Each case, however, should be evaluated individually because these limits may change, depending on each individual patient's situation. In fact, currently one in four potential refractive candidates is deemed not a good candidate for refractive surgery. A stable refraction is critical, as also are other criteria (see http://www.fda.gov/

Handbook of Biophotonics. Vol.2: Photonics for Health Care, First Edition. Edited by Jürgen Popp, Valery V. Tuchin, Arthur Chiou, and Stefan Heinemann.

MedicalDevices/ProductsandMedicalProcedures/SurgeryandLifeSupport/LASIK/ucm061325.htm). Additionally, the patient must understand the risks, benefits, limitations including possible complications, and alternatives for these procedures.

65.2
Current Lasers Used in Refractive Surgery

65.2.1
The Excimer Laser

The 193 nm UV wavelength-emitting ArF excimer laser was introduced by Trokel *et al*. [5] in 1983 and was first used on human subjects by McDonald *et al*. in 1987 [6]. Since that time, there has been a tremendous evolution for refining its use in refractive keratoplasty procedures and these improvements in technology (hardware and software) have paralleled the evolution of surgical techniques and our basic scientific understanding of this type of surgery [3].

Early, first-generation excimer laser models used a broad beam with an expanding diaphragm to create simple spherical or spherical–cylindrical ablation profiles [7]. More sophisticated second- and third-generation laser models emerged using large scanning systems or slit beams to create more complicated ablation profiles without the need for masking agents. Further improvements in lasers occurred with the development of smaller beam delivery systems associated with eye trackers, resulting in fourth-generation laser models with more sophisticated algorithms to create smoother, more aspheric, and even custom ablation profiles. For example, the top two most popular lasers currently used by refractive surgeons in world are the VISX Star S4 and Allegretto Eye Q systems. The VISX Star S4 laser (Figure 65.1a) has variable spot scanning with beam diameters from 6.5 to 0.65 mm [3] with a variable repetition rate up to 20 Hz and the Allegretto Eye Q has a fixed flying spot with 0.8 mm and a frequency of 400 Hz (Figure 65.1b).

65.2.2
The Femtosecond Laser

The femtosecond laser produces a short electromagnetic pulse with a time duration on the order of femtoseconds (10^{-15} s) [8]. It therefore belongs in the category of ultrafast lasers and the generation of ultrashort pulses is nearly always achieved with the technique of passive mode locking. These ultrashort pulses are too brief to transfer heat or shock to the material being cut, which means that cutting, drilling, and machining occur with virtually no damage to surrounding material. Furthermore, this revolutionary laser can cut with extreme precision, making hairline cuts in thick materials along a computer-generated path. In the cornea, its automated computer application causes planar dissection possible due to the formation of cavitation microbubbles of CO_2 gas. The laser allows the surgeon to focus the laser energy at a particular depth in the transparent or even the mildly opaque cornea and

(a)

(b)

Figure 65.1 Excimer laser platforms: (a) VISX-AMO; (b) Allegretto Eye Q.

Figure 65.2 Femtosecond laser platform: Intralase iFs, 150 kHz (AMO).

then rapidly cut the tissue at that depth. Automated computer systems controlling the femtosecond laser applications allow the surgeon to pattern and size these cuts into customized shapes, creating a highly precise incision resulting in a perfect match of the donor and host tissue and a stronger junction (Figure 65.2).

While currently being used primarily for cutting LASIK flaps, femtosecond lasers are proving useful in other corneal applications also, including variously shaped and/or sized femtosecond laser-assisted keratoplasty procedures (e.g., geometric-shaped and varying sized penetrating grafts, varying depth and sized lamellar grafts), intracorneal ring segment implantation, astigmatic keratoplasty, and intrastromal inlays [8].

65.3 Refractive Surgery Techniques

The different laser refractive keratoplasty techniques are basically classified into two types: SA and lamellar surgery. Each has certain advantages and disadvantages compared with the other. As the cornea has five layers (epithelium, Bowman's layer, stroma, Descement's membrane, and endothelium) (Figure 65.3), SA techniques involve the removal of the epithelium and ablation of the anterior-most stromal surface (Bowman's layer and then the anterior stroma proper). Lamellar procedures

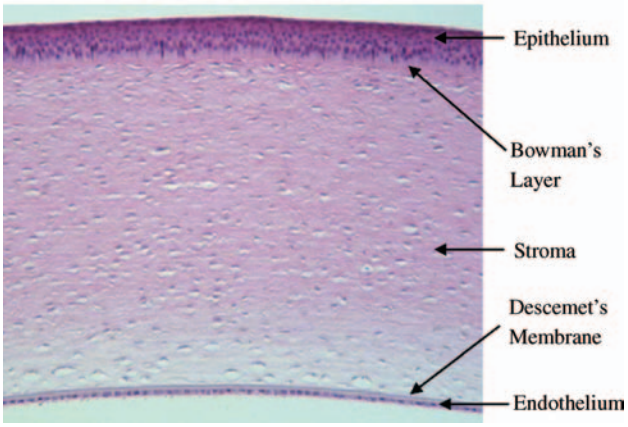

Figure 65.3 Histological section of the human cornea.

involve the creation of a flap containing the epithelium and a thin or thick layer of stroma and subsequent stromal ablation of the bed after the flap is reflected out of the way of the laser beam. At the conclusion of the procedure, the flap is repositioned back into its original place.

65.3.1 Surface Ablation

With SA, various techniques are used to remove the corneal epithelium before the excimer laser is applied to the surface of the corneal stroma. For example, in photorefractive keratectomy (PRK), the epithelium is either scraped or photoablated away. The latter is sometimes referred to as transepithelial PRK. Thus, after PRK or transepithelial PRK, a bare excimer ablated corneal stroma surface is left behind. In comparison, with laser-assisted subepithelial keratectomy (LASEK), instead of removing or excising the epithelium completely as in PRK, the surgeon cuts a round semi-circular area of epithelium with a fine-bladed instrument called a trephine. A dilute alcohol solution is then applied to loosen the cut epithelium inside the semi-circle where it attaches to Bowman's layer, and then the surgeon gently lifts and folds back the hinged loosened epithelial flap, exposing the underlying Bowman's layer and corneal stroma for the excimer laser ablation before repositioning the epithelial flap back into its original location. Finally, with epikeratome laser-assisted *in situ* keratomileusis (EpiLASIK), a unique epikeratome (a microkeratome with a blunt, oscillating blade) is used to separate the epithelium mechanically from the Bowman's layer and stroma, while suction is applied, to make a hinged epithelial flap, similar to a traditional LASIK flap. Unlike LASIK, no sharp blades or intrastromal cuts are made. It is very similar to LASEK, but no alcohol is required. These four techniques have the important advantage of having a high level of safety and security, especially in patients

Table 65.1 Cases where surface ablation may be the best option.

• Patients preference
• Predisposition for contact injury (e.g., martial arts practitioners)
• Anterior basement membrane (Cogan's) dystrophy
• Epithelial sloughing during LASIK in the contralateral eye
• Thin corneas in which the stromal residual bed would be less than 250–300 μm in LASIK
• Deep orbits or tight eyelid fissure causing poor exposure for the microkeratome base
• Flat corneas (<41 D) or steep corneas (>48 D)
• Previous surgery involving the conjunctiva: bleb associated with filtering procedure; scleral buckle for the treatment of retinal detachment
• Moderate dry eye prior to surgery

with thinner corneas or slight changes in its curvature. During wound healing of the corneal surface after the various SA procedures, transient pain or discomfort and blurred vision occur. Usually, the pain or discomfort is relieved by the third or fourth postoperative day and the blurred vision gradually improves during the first week until it stabilizes in at about 1–3 months postoperation. SA procedures typically do not reach the best or uncorrected visual potential of LASIK until the third month postoperatively, but it then tends to surpass LASIK surgery in the longer term in a statistically insignificant manner (Table 65.1). In any of these four techniques, if the subsequent excimer laser ablative step to Bowman's layer and stroma is refractively neutral, this technique is referred to as phototherapeutic keratectomy (PTK).

65.3.1.1 **PRK**

This technique has been used since the early era of excimer lasers, for nearly 20 years. It consists of mechanical removal of corneal epithelium using a scalpel blade, then ablating the anterior stroma with the excimer laser (Figure 65.4).

PRK has been eclipsed by LASIK, mainly because of the faster visual rehabilitation and less discomfort associated the latter during the early postoperative period. Despite this, PRK remains as an excellent option, particularly for mild to moderate corrections [6].

During early phases of corneal wound healing, haze formation associated with myopic treatments over 6 D was the major drawback and limitation of PRK. With the advent of single intraoperative application of topical mitomycin C (MMC), this SA-related wound healing complication has been substantially reduced and has broadened the treatment of SA procedures to higher refractive errors. Cases associated with thin corneas, recurrent erosions, or with a predisposition for eye trauma (martial arts, military, etc.) were among the most important indications for SA procedures since they retain the most biomechanical properties [9].

65.3.1.2 **Transepithelial PRK**

The excimer laser is used to remove the epithelium in transepithelial PRK [9].

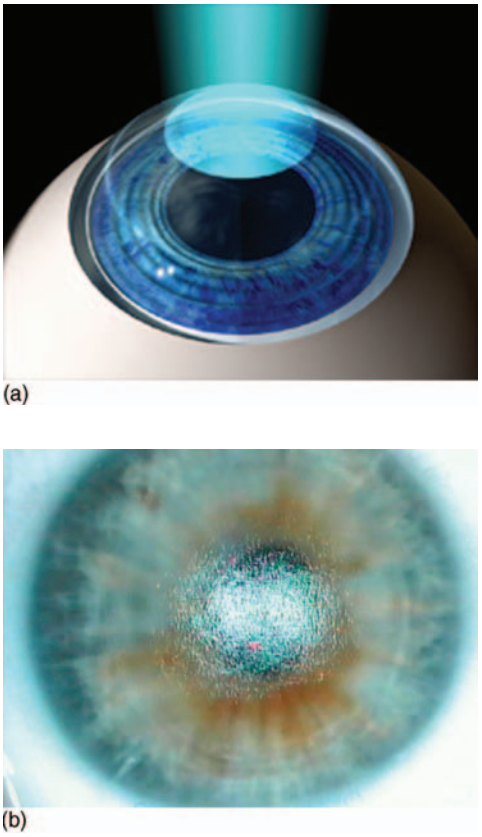

Figure 65.4 Surface ablation: (a) cartoon diagram; (b) perioperative image after laser ablation.

65.3.1.3 **LASEK**

In this technique, an epithelial flap is detached after application of a dilute alcohol solution (typically 18–25%). After laser ablation, the epithelial sheet is repositioned, like the stromal flap is in the LASIK procedure [3]. Most studies suggest that patients with LASEK will experience less pain, faster visual recovery, and less haze compared with PRK or transepithelial PRK [10–18]. The mechanism through which the epithelial flap could provide protection and improve clinical outcomes is not completely understood, but most likely is due to retained epithelial basement membrane, which acts as via bidirectional intrinsic binding and storage properties of wound healing-related cytokines and growth factors.

65.3.1.4 **EpiLASIK**

Here the dissection of the epithelium is carried out with an apparatus similar to the microkeratome, but it is blunt and does not penetrate the Bowman's layer or corneal stroma. It also avoids the use of chemical agents and, at least theoretically, increases the viability of the epithelial cells, which if intact and retain their superficial

squamous layer zonula occludens-type junctional properties, prevent or abrogate exposure to tear film-derived cytokines and growth factors. Some surgeons deviate from conventional EpiLASIK and discard the epithelial flap during the procedure, thus making this latter variant another type of PRK technique since bare ablated stroma remains at the conclusion of the procedure [9].

65.3.2 LASIK

In LASIK, a flap including the epithelium and a portion of the anterior stroma with a total thickness of 120–180 μm is created with the mechanical microkeratome or femtosecond laser and then the stromal bed is accessible for excimer laser ablation [9] (Figure 65.5). The main advantage of LASIK over PRK is related to maintaining an intact, undamaged central corneal epithelium, which increases comfort during the early postoperative period, allows for rapid visual recovery,

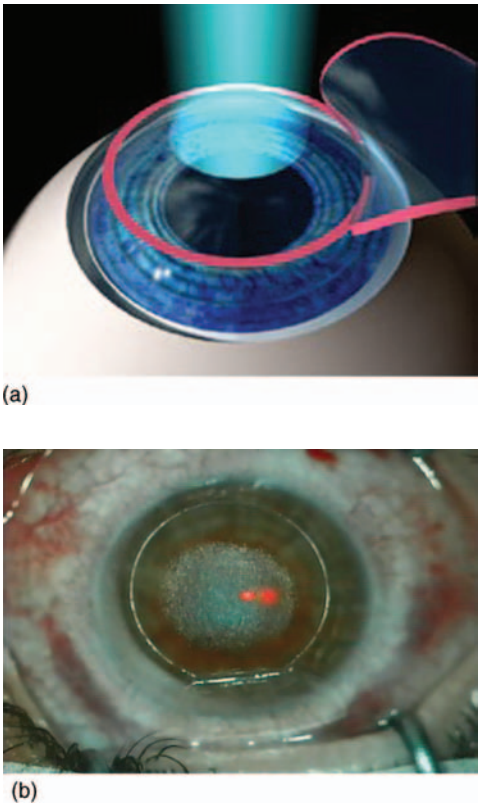

Figure 65.5 LASIK: (a) cartoon diagram; (b) perioperative image after laser ablation.

Table 65.2 Significant advantages of LASIK.

- Faster visual rehabilitation with earlier postoperative stabilization of visual acuity
- Less postoperative patient discomfort
- Attenuated wound healing and less stromal haze formation
- Possibly improved predictability, stability, and corneal clarity in higher correction groups
- Shorter duration of postoperative medications use
- Easier enhancement procedure

and attenuates wound healing response (Table 65.2) [9]. Microkeratome technology has undergone important developments and improvements over the last decade that have improved the overall safety of the LASIK procedure. This further increased the popularity of LASIK, making it the dominant procedure in refractive surgery today [3].

However, it should be mentioned that there are also complications with this procedure (see the FDA website cited in the Introduction), mainly related to long-term biomechanical instability, such as ectasia development or traumatic flap detachments, and infection [19].

65.3.2.1 **Mechanical microkeratome LASIK**

There are several models of mechanical microkeratomes, manual and automated. Automated microkeratomes most commonly have electric motors that drive blade oscillation, translation of the microkeratome head, or both. Hinge location, flap diameter, average flap thickness, suction pressure, and loss of suction cut-off are just a few of the features that vary from model to model. Average flap diameter and flap thickness will be important determinants of the dioptric range and maximum pupil sizes of patients who can be treated with a particular mechanical microkeratome. The chance of complications associated with creating the LASIK flap using the mechanical microkeratome is about one in 500 cases.

65.3.2.2 **Femtosecond laser LASIK**

The laser pulses are focused within the corneal stroma by a computerized system to produce hundreds of spots or cavitation bubbles placed close together in a spiral or rastered pattern to produce a stromal incision below the surface of the cornea. Pulses are stacked along the periphery of the lamellar incision until a cut is made in the corneal surface. One area of the periphery is spared to produce a hinge. Once the flap has been formed with the femtosecond laser, the surgeon peels back the flap and applies the ablation to the stromal bed with the excimer laser.

There are a number of advantages to the femtosecond laser compared with mechanical microkeratomes, including better control over flap thickness, diameter, and hinge position, the manufacture of oval flaps, and the creation of an inverted insertion angle, which increases the biomechanical strength of its adhesion.

65.4
Custom Corneal Ablations

Laser vision correction is intended primarily to fix the spherical and/or cylindrical refractive errors of the eye, which are called lower order aberrations. However, some patients experience unpleasant visual distortions after surgery, such as blurring, ghosting, and halos, especially associated with night vision [20].

New technologies available today allow the study of refractive optics and its application in refractive surgery through the use of computerized corneal topography, tomography, and wavefront analysis. This allows refractive surgeries to be programmed to correct high-order aberrations and sometimes complex corneal irregularities and, thus, improves the quality of vision of patients.

References

1 Ambrósio, R. Jr., Jardim, D., Netto, M.V., and Wilson, S.E. (2007) Management of unsuccessful lasik surgery. *Compr. Ophthalmol. Update*, **8** (3), 125–141; discussion 143–144.

2 Waring, G.O. (2009) Classification and terminology of refractive surgery, in *Corneal Surgery. Theory, Technique and Tissue*, 4th edn (eds F.S. Brightbill, P.J. McDonnell, C.N. McGhee, A.A. Farjo, and O.N. Serdarevic), Mosby Elsevier, St. Louis, MO, pp. 697–709.

3 Ambrósio, R. Jr. and Wilson, S.E. (2003) LASIK vs. LASEK vs. PRK: advantages and indications. *Semin. Ophthalmol.*, **18** (1), 2–10.

4 Solomon, K.D., Fernández de Castro, L.E., Sandoval, H.P., Biber, J.M., Groat, B., Neff, K.D., Ying, M.S., French, J.W., Donnenfeld, E.D., and Lindstrom, R.L. (2009) Joint LASIK Study Task Force. LASIK world literature review: quality of life and patient satisfaction. *Ophthalmology*, **116**, 691–701.

5 Trokel, S.L., Srinivasan, R., and Braren, B. (1983) Excimer laser surgery of the cornea. *Am. J. Ophthalmol.*, **96**, 710–715.

6 McDonald, M.B., Liu, J.C., Byrd, T.J., Abdelmegeed, M., Andrade, H.A., Klyce, S.D., Varnell, R., Munnerlyn, C.R., Clapham, T.N., and Kaufman, H.E. (1991) Central photorefractive keratectomy for myopia. Partially sighted and normally sighted eyes. *Ophthalmology*, **98**, 1327–1337.

7 Dawson, D.G., Manns, F., and Lee, Y. (2009) Excimer laser ablations principles and ablation profiles, in *Corneal Surgery. Theory, Technique and Tissue*, 4th edn (eds F.S. Brightbill, P.J. McDonnell, C.N. McGhee, A.A. Farjo, and O.N. Serdarevic), Mosby Elsevier, St. Louis, MO, pp. 777–787.

8 Farjo, Q.A. and Farjo, A.A. (2009) Femtosecond laser-assisted corneal surgery, in *Corneal Surgery. Theory, Technique and Tissue*, 4th edn (eds F.S. Brightbill, P.J. McDonnell, C.N. McGhee, A.A. Farjo, and O.N. Serdarevic), Mosby Elsevier, St. Louis, MO, pp. 861–870.

9 Ambrósio, R. Jr. and Guerra, F., Refractive laser ablations on the cornea: Understanding new terminology in refractive surgery. *Pearls in Ophthalmology*, http://www.medrounds.org/ophthalmology-pearls/2009/06/refractive-laser-ablations-on-cornea.html (last accessed 28 April 2010).

10 Azar, D.T., Ang, R.T., Lee, J.B., Kato, T., Chen, C.C., Jain, S., Gabison, E., and Abad, J.C. (2001) Laser subepithelial keratomileusis: electron microscopy and visual outcomes of flap photorefractive keratectomy. *Curr. Opin. Ophthalmol.*, **12**, 323–328.

11 Shah, S., Sebai Sarhan, A.R., Doyle, S.J., Pillai, C.T., and Dua, H.S. (2001) The epithelial flap for photorefractive keratectomy. *Br. J. Ophthalmol.*, **85**, 393–396.

12 Lee, J.B., Seong, G.J., Lee, J.H., Seo, K.Y. Lee, Y.G., and Kim F E.K. (2001) Comparison of laser epithelial keratomileusis and photorefractive keratectomy for low to moderate myopia. *J. Cataract Refract. Surg.*, **27**, 565–570.

13 Claringbold, T.V. II (2002) Laser-assisted subepithelial keratectomy for the correction of myopia. *J. Cataract Refract. Surg.*, **28**, 18–22.

14 Kornilovsky, I.M. (2001) Clinical results after subepithelial photorefractive keratectomy (LASEK). *J. Refract. Surg.*, **17**, S222–S223.

15 Scerrati, E. (2001) Laser *in situ* keratomileusis vs. laser epithelial keratomileusis (LASIK vs. LASEK). *J. Refract. Surg.*, **17**, S219–S221.

16 Lee, J.B., Choe, C.M., Seong, G.J., Gong, H.Y., and Kim, E.K. (2002) Laser subepithelial keratomileusis for low to moderate myopia: 6-month follow-up. *Jpn. J. Ophthalmol.*, **46**, 299–304.

17 Vinciguerra, P. and Camesasca, FI. (2002) Butterfly laser epithelial keratomileusis for myopia. *J. Refract. Surg.*, **18**, S371–S373.

18 Rouweyha, R.M., Chuang, A.Z., Mitra, S., Phillips, C.B., and Yee, R.W. (2002) Laser epithelial keratomileusis for myopia with the autonomous laser. *J. Refract. Surg.*, **18**, 217–224.

19 Ambrósio, R. Jr. and Wilson, S.E. (2001) Complications of laser in situ keratomileusis: etiology, prevention, and treatment. *J Refract Surg.*, **17**, 350–379.

20 Netto, M.V., Dupps, W. Jr., and Wilson, S.E. (2006) Wavefront-guided ablation: evidence for efficacy compared to traditional ablation. *Am. J. Ophthalmol.*, **141**, 360–368.

66
Laser Trabeculoplasty

Stephan Eckert

66.1
Laser Systems

Application of lasers to the trabecular meshwork has been used to lower the intraocular pressure (IOP) since the early 1970s [1]. Worthen and Wickham [2] first described an argon laser to perform trabeculoplasty in 1973 and Krasnov used a Q-switched ruby laser to perform goniopuncture or laseropuncture [3]. Wise and Witter described a modified technique which subsequently gained acceptance as an option for the treatment of primary open-angle glaucoma [4]. This procedure was originally, and most often in the past, performed using an argon laser at 488–514 nm. Several other lasers, including diode (810 nm) [5], continuous-wave (1064 nm), and frequency-doubled Nd:YAG (532 nm) [6] lasers, have been described to yield a reduction in IOP similar to that of argon laser trabeculoplasty (ALT) and are often used today (Tables 66.1 and 66.2). Latina and Park conducted a study designed to develop a procedure to target pigmented trabecular meshwork cells selectively while sparing adjacent cells and tissues from collateral thermal damage and to maintain the trabecular meshwork architecture [7]. This study formed the basis of the currently available selective laser trabeculoplasty (SLT) system (532 nm frequency-doubled Q-switched Nd:YAG laser) providing an only 3 ns pulse with a 400 μm beam diameter. Selective absorption of a very short laser pulse generates and spatially confines heat to pigmented targets. The thermal relaxation time of a chromophore is the time required to convert absorbed electromagnetic energy to heat energy. A short pulse duration is critical to prevent collateral tissue damage. If the energy deposition time is short, as in the case of a Q-switched laser, minimal heat transfer takes place. The 1 μs thermal relaxation time of melanin and a 3 ns SLT pulse essentially prevent thermal dissipation to surrounding tissue [8].

66.2
Mechanisms of Action

The exact mechanisms of action of laser trabeculoplasty have not yet been determined. The mechanical theory of IOP reduction proposes that a thermal burn

Handbook of Biophotonics. Vol.2: Photonics for Health Care, First Edition. Edited by Jürgen Popp, Valery V. Tuchin, Arthur Chiou, and Stefan Heinemann.

Table 66.1 Wavelengths of different laser systems for trabeculoplasty.

Laser	Wavelength (nm)
Argon laser (ALT)	514
Nd:YAG	1064, continuous wave 532, frequency-doubled (SLT)
Diode laser	810

Table 66.2 Comparison of different laser systems for trabeculoplasty.

Parameter	ALT	SLT	DLT
No. of spots	50	50	50
Spot size (μm)	50	400	100
Pulse duration	100 ms	3 ns	100–200 ms
Power/energy	600–1200 mW	0.2–2.0 mJ	800–1200 mW

contracts tissue and stretches open adjacent, untreated regions of the trabecular meshwork to increase outflow [9]. However, histologic studies show that coagulative damage and tissue disruption to the trabecular meshwork are associated with ALT [10]. This injury might limit the effectiveness of future retreatment with ALT and theoretically also of other treatment modalities. It is also likely that there are contributing factors at the cellular level such as an increase in the division of trabecular cells and remodeling of the juxtacanalicular extracellular matrix representing a biological theory [11, 12]. Bradley *et al.* showed that laser trabeculoplasty induces the expression and secretion of both interleukin-1β and TNFα within the first 8 h after treatment. These cytokines then mediate increased trabecular stromelysin expression and initiate remodeling of the juxtacanalicular extracellular matrix [13]. After SLT, there was a total absence of coagulative damage with intact beams of the trabecular meshwork [14], supporting the view that the biological theory is the main mechanism for the IOP-lowering effect of SLT.

66.3 Methods of Treatment

Before laser trabeculoplasty, miotics (e.g., 1% pilocarpine) should be applied to ensure optimum access to the trabecular meshwork. With the patient seated in front of the laser slit-lamp system, a Goldmann three-mirror goniolens is coupled to the eye with 1% methylcellulose after application of topical anesthetic. In ALT, the smallest attainable laser spot (typically 50 μm) is placed in the anterior part of the trabecular

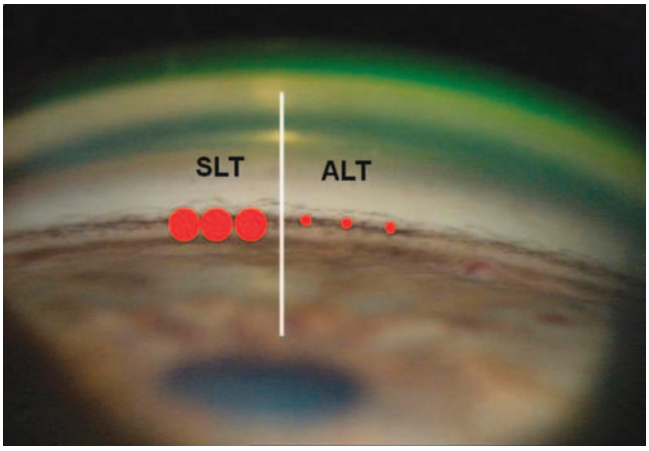

Figure 66.1 Application of laser spots in SLT compared with ALT.

meshwork (Figure 66.1) using 600–1500 mW and a 0.1 s pulse duration. The distance between the laser spots should be 2–3 spot diameters. Standard therapy is to deliver about 50 spots over 180°. Visible endpoints of the treatment are tissue blanching or a large vaporization bubble.

Diode laser trabeculoplasty (DLT) is a variation of ALT. Despite the use of a higher laser power, tissue blanching is less intense than with ALT. Vaporization bubbles are not observed.

In contrast, SLT uses a relatively large laser spot size of 400 μm. This is sufficient to cover the entire width of the trabecular meshwork, making accurate aiming less critical (Figures 66.1 and 66.2). Treatment of Sampaolesi's line should be avoided because it could cause corneal endotheliitis. Standard therapy is to deliver about 50 adjacent but nonoverlapping spots over 180°, or alternatively 100 spots over 360°, of the angle circumference. The energy is initially set at 0.7 mJ per pulse and can be adjusted to the desired treatment endpoint from 0.2 to 2.0 mJ. More heavily pigmented meshwork requires lower power. In contrast to ALT, blanching or large vaporization bubbles within the trabecular meshwork are not seen as an endpoint in SLT; however, tiny "champagne" bubble formation is used as an endpoint for setting the SLT pulse energy. They should be seen at least 50% of the time. Some authors recommend decreasing the energy level by 0.1 mJ when bubble formation is observed [8]. Pretreatment antiglaucoma medications should be resumed after laser trabeculoplasty. Usually the full effect of laser trabeculoplasty is reached after 4–6 weeks. IOP reduction after SLT is often seen even 1 day after treatment, but the period of time can be highly variable. If laser therapy is successful and the IOP reduction is sufficient, antiglaucomatous medication can be reduced.

It is important to check the IOP and exclude increased inflammation on the first postoperative day. Only if increased inflammation is present anti-inflammatory regimens are required (e.g., 1% prednisolone five times per day for 1 week).

Figure 66.2 SLT laser (ARC Laser, Nürnberg, Germany).

66.4 Indications for Laser Trabeculoplasty

Laser trabeculoplasty is a method to reduce IOP in patients with primary open-angle glaucoma and also pseudoexfoliation glaucoma and pigmentary glaucoma. The low risk of adverse effects may make it a good alternative to long-term medical therapy, even in ocular hypertension patients without established glaucomatous optic nerve damage [8].

As an advantage, laser trabeculoplasty can lower IOP without relying on patient compliance with medications, which is a common problem in glaucoma therapy. It can replace or decrease the need for topical medications and therefore reduce systemic and local side effects such as allergy or chronic inflammation.

The IOP before laser trabeculoplasty should not exceed 25 mmHg and the target pressure should not be 25–30% below the preoperative pressure. A larger decrease in IOP cannot be achieved with laser treatment alone. Those patients who have a

baseline IOP >21 mmHg are more likely to have a greater absolute value of IOP reduction and vice versa [15]. This could be the reason why patients with normal tension glaucoma are less successfully treated with laser trabeculoplasty.

Other indications can be old age and patients who refuse operation, have too high risk for operation, or have problems with application of their eyedrops (palsy, tremor).

66.5 Contraindications for Laser Trabeculoplasty

Contraindications for laser trabeculoplasty are neovascular glaucoma, goniosynechiae, post-traumatic glaucoma, and congenital glaucoma.

66.6 Effectiveness of Laser Trabeculoplasty

Clinical studies suggest that laser trabeculoplasty is efficacious in lowering IOP. Average reductions in IOP from 2.7 to more than 6 mmHg or 12–40% depending on the follow up-time have been reported. Response rates within the first postoperative year vary from 59 to 96% according to different definitions (Table 66.3) and usually decline with time. ALT and SLT seem to be equivalent in lowering IOP [8, 16]. Damji *et al.* conducted a prospective randomized trial comparing the effectiveness of a 180° ALT and SLT in lowering IOP in 176 eyes (87 cases of ALT and 89 cases of SLT). Eyes with ALT showed a significant decrease in IOP of 6.04 mmHg and eyes with SLT of 5.86 mmHg after 12 months. Failure rates were 32 and 36% for SLT and ALT, respectively [17]. The Glaucoma Laser Trial showed that in newly diagnosed patients with open-angle glaucoma, ALT was at least as effective as initial medical treatment with 0.5% timolol maleate even after 7 years [14]. In another study, selective laser trabeculoplasty was compared with 0,005% latanoprost. Differences in success rates between latanoprost and 360° SLT did not reach statistical significance [18]. The same study showed that 90° SLT is not effective.

Table 66.3 Studies on laser trabeculoplasty.

Study	Laser	No. of Patients	Follow-up (months)	IOP reduction (mmHg)	IOP reduction (%)
Latina *et al.* (1998) [19]	SLT	30	6	5.8	23.5
Cvenkel (2004) [20]	SLT	44	12	4.4	17.1
Best *et al.* (2005) [21]	SLT	269	24	2.7	12.1
Gracner *et al.* (2006) [22]	SLT	90	72	5.4	22.8
Juzych *et al.* (2004) [23]	ALT	154	60		23.5
Damji *et al.* (2006) [17]	ALT	87	12	6.04	25.8

Because of its nondestructive nature, multiple treatments with SLT are theoretically possible. If IOP reduction is inadequate after 6 weeks, treatment of the untreated 180° may be considered. The fibrosis and scarring that result after ALT do not occur after SLT because of the lack of structural damage to the trabecular meshwork. Hence repeated therapy may result in an additional reduction in IOP [8].

66.7 Complications After Laser Trabeculoplasty

Laser trabeculoplasty, especially SLT, is a very safe procedure, having only minor, transient, self-limiting, or easily controlled side effects [16]. For SLT, a complication rate of 4.5% was observed, much lower than the complication rate in ALT, which may reach up to 34% [8, 14]. Side effects of laser trabeculoplasty are postprocedure IOP spikes (6%), iritis [19], and peripheral anterior synechiae [24].

Early postoperative elevation of IOP in some patients has been observed in all published clinical studies. In all of those cases it resolved quickly with observation or additional antihypertensive treatment [5, 17, 19]. Highly significant IOP elevations have been reported after SLT in some cases of pigmentary glaucoma or glaucoma with heavy angle pigmentation [25]. Therefore, it is recommended to use lower energy or fewer applications, or to treat a smaller proportion of the angle (90°) in such patients. Close IOP monitoring and prophylactic oral carbonic anhydrase inhibitors may be helpful. Postoperative suppression of the inflammatory response may be relatively contraindicated because macrophage response may contribute to IOP lowering. Anterior synechiae appear more often after ALT, but may be prevented when ALT spots are placed in the anterior part of the trabecular meshwork [26].

Other side effects, namely nonspecific conjunctivitis (5%), eye pain (5%), blurred vision (<1%), corneal edema (<1%), and corneal lesion (<1%), have been described as transient and without sequelae [17, 19].

66.8 Conclusion

Laser trabeculoplasty has been shown to be safe, well tolerated, and effective in lowering IOP in patients with open-angle glaucoma. The preservation of the trabecular meshwork makes SLT a safe alternative to ALT that is potentially repeatable.

References

1 van der Zypen, E. and Frankhauser, F. (1982) Laser in the treatment of chronic simple glaucoma. *Trans. Ophthalmol. Soc. UK*, **102**, 147–153.

2 Worthen, D.M. and Wickham, M.G. (1974) Argon laser trabeculotomy. *Trans. Am. Acad. Ophthalmol. Otolaryngol.*, **78**, 371–375.

3 Krasnov, M.M. (1973) Laseropuncture of anterior chamber angle in glaucoma. *Am. J. Ophthalmol.*, **75**, 674–678.

4 Wise, J.B. and Witter, S.L. (1979) Argon laser therapy for open angle glaucoma: a pilot study. *Arch. Ophthalmol.*, **97**, 319–322.

5 Chung, P.Y., Schuman, J.S., and Netland, P.A. (1998) Five-year results of a randomized, prospective, clinical trial of diode vs argon laser trabeculoplasty for open-angle glaucoma. *Am. J. Ophthalmol.*, **126**, 185–190.

6 Guzey, M., Arslan, O., Tamcelik, N., and Satici, A. (1999) Effects of frequency-doubled Nd:YAG laser trabeculoplasty on diurnal intraocular pressure variations in primary open-angle glaucoma. *Ophthalmologica*, **213**, 214–218.

7 Latina, M.A. and Park, C. (1995) Selective targeting of trabecular meshwork cells: *in vitro* studies of pulsed and CW laser interactions. *Exp. Eye Res.*, **60** (4), 359–371.

8 Latina, M.A. and de Leon, J.M. (2005) Selective laser trabeculoplasty. *Ophthalmol. Clin. North Am.*, **18**, 409–419.

9 Van Buskirk, E.M., Pond, V., Rosenquist, R.C. *et al.* (1984) Argon laser trabeculoplasty, studies of mechanisms of action. *Ophthalmology*, **91**, 1005–1010.

10 Kramer, T.R. and Noecker, R.J. (2001) Comparison of the morphologic changes after selective laser trabeculoplasty and argon laser trabeculoplasty in human eye bank eyes. *Ophthalmology*, **108**, 773–779.

11 Parshley, D.E., Bradley, J.M., Fisk, A. *et al.* (1996) Laser trabeculoplasty induces stromelysin expression by trabecular juxtacanalicular cells. *Invest. Ophthalmol. Vis. Sci.*, **37**, 795–804.

12 Bylsma, S.S., Samples, J.R., Acott, T.S., and Van Buskirk, E.M. (1988) Trabecular cell division after argon laser trabeculoplasty. *Arch. Ophthalmol.*, **106**, 544–547.

13 Bradley, J.M.B., Anderssohn, A.M., Colvis, C.M. *et al.* (2000) Mediation of laser trabeculoplasty-induced matrix metalloproteinase expression by IL-1β and TNFα. *Invest. Ophthalmol. Vis. Sci.*, **41**, 422–430.

14 Glaucoma Laser Trial Research Group (1995) The Glaucoma Laser Trial (GLT) and glaucoma laser trial follow-up study, seven-year results. *Am. J. Ophthalmol.*, **120**, 718–731.

15 Johnson, P.B., Katz, L.J., and Rhee, D.J. (2006) Selective laser trabeculoplasty: predictive value of early intraocular pressure measurements for success at 3 months. *Br. J. Ophthalmol.*, **90** (6), 741–743.

16 Barkana, Y. and Belkin, M. (2007) Diagnostic and surgical techniques. *Surv. Ophthalmol.*, **52**, 634–654.

17 Damji, K.F., Bovell, A.M., Hodge, W.G. *et al.* (2006) Selective laser trabeculoplasty versus argon laser trabeculoplasty: results from a 1-year randomized clinical trial. *Br. J. Ophthalmol.*, **90**, 1490–1494.

18 Nagar, M., Ogunyomade, A., O'Brart, D.P.S., Howes, F., and Marshall, J. (2005) A randomized, prospective study comparing selective laser trabeculplasty with latanoprost for the control of intraocular pressure in ocular hypertension and open angle glaucoma. *Br. J. Ophthalmol.*, **89**, 1413–1417.

19 Latina, M.A. *et al.* (1998) Q-switched 532 nm Nd:YAG laser trabeculoplasty (selective laser trabeuloplasty): a multi-center, pilot, clinical study. *Ophthalmology*, **105**, 2082–2088.

20 Cvenkel, B. (2004) One-year follow-up of selective laser trabeculoplasty in open-angle glaucoma. *Ophthalmolojica*, **218**(1), 20–25.

21 Best, U.P., Domack, H., Schmidt, V. (2005) Long-term results after selective laser trabeculoplasty - a clinical study on 269 eyes. *Klin Monbl Augenheilkd*, **222**(4), 326–31.

22 Gracner, T., Falez, M., Gracner, B., Pahor, D. (2006) Long-term follow-up of selective laser trabeculoplasty in primary open-angle glaucoma. *Klin Monbl Augenheilkd*, **223**(9), 743–7.

23 Juzych, M.S., Chopra, V., Banitt, M.R., Hughes, B.A., Kim, C., Goulas, M.T., Shin, D.H. (2004) Comparison of long-term outcomes of selective laser trabeculoplasty versus argon laser

trabeculoplasty in open-angle glaucoma. *Ophthalmology*, **111**(10), 1853–9.

24 Reiss, G.R. *et al*. (1991) Laser trabeculoplasty. *Surv. Ophthalmol.*, **35**, 407–428.

25 Harasymowycz, P.J., Papamatheakis, D.G., Latina, M.A. *et al*. (2005) Selective laser trabeculoplasty complicated by intraocular elevation in eyes with heavily pigmented trabecular meshworks. *Am. J. Ophthalmol.*, **139**, 1110–1113.

26 Traverso, C.E., Greenridge, K.C., and Spaeth, G.L. (1984) Formation of peripheral anterior synechiae following argon laser trabeculoplasty. *Arch. Ophthalmol.*, **102**, 861–863.

67
Laser Photocoagulation

Bettina Fuisting and Gisbert Richard

67.1
Introduction

The penetration depth of laser light and the thermal expansion in ocular tissue depend on the wavelength of the laser light [1, 2]. The amount of laser energy required has to be chosen according to the pigmentation of the fundus and also the transmission of the optic media. Both factors influence the light absorption and temperature rise at the retina. Light absorption is mainly due to melanin. Hence the temperature rise caused by the light energy is higher in highly pigmented fundi. Laser photocoagulation in ophthalmology is used for the treatment of retinal and choroidal diseases. For safety reasons, at the beginning of a laser treatment the laser should be operated with low energy. The laser energy then should be raised carefully to achieve a desired laser effect.

Parameters for laser coagulation are laser spot size = S, duration (time) = T, and laser energy level = E [2, 3].

In ophthalmology, several lasers with different wavelengths are used: argon green (532 nm), dye laser (510–630 nm), double-pulsed Nd:YAG laser (532 nm), and diode laser (532–810 nm) [2, 3].

The laser is fixed either to a slit lamp, (Figure 67.1) to a binocular head ophthalmoscope (indirect ophthalmoscopic laser delivery system), or to an endosonde during vitrectomy [4].

For laser treatment using a slit lamp, special laser contact lenses have to be used (Figure 67.2).

Handbook of Biophotonics. Vol.2: Photonics for Health Care, First Edition. Edited by Jürgen Popp, Valery V. Tuchin, Arthur Chiou, and Stefan Heinemann.

Figure 67.1 Patient and ophthalmologist sitting at a slit lamp during laser treatment.

Figure 67.2 Laser contact lenses: Mainster wide-field lens and Goldmann three-mirror lens.

67.2 Retinal Degeneration

67.2.1 Retinal Tears, Retinoschisis, Retinal Detachment

Purpose: For retinal tears or detachments, a laser is used to create retinochoroidal adherence. Retinal tears are caused by vitreous traction and are often horseshoe-shaped [4] (Figure 67.3).

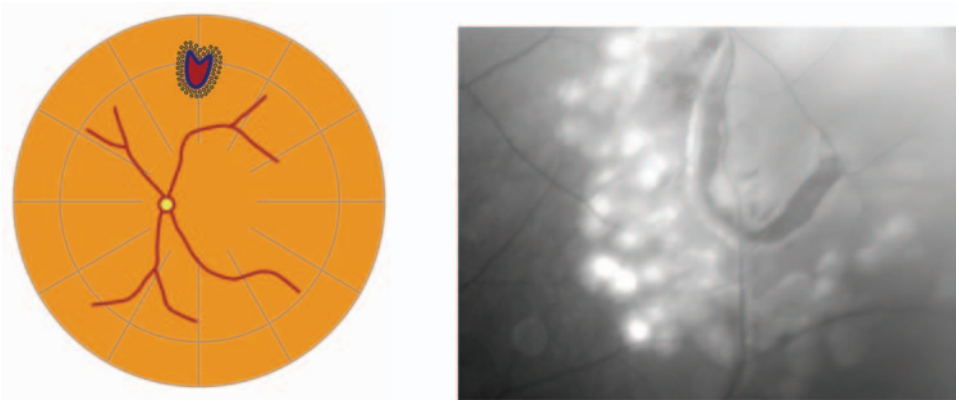

Figure 67.3 Retinal tear with laser treatment.

Laser treatment is applied in several rows (normally 3–4) circular to the retinal tear to avoid retinal detachment. Laser treatment for retinoschisis or small retinal detachments is applied centrally to the retinal pathology. If a vessel rupture due to vitreous traction occurs, so-called "feeder–vessel–treatment" is necessary to obliterate retinal vessels in order to avoid vitreous hemorrhage.

Laser parameters: $S = 200–500\,\mu m$, $T = 0.2–0.5\,s$, $E = 150–500\,mW$.

Visible effect: White to grayish effect.

Complications: Small laser spots with a high energy level can lead to ruptures of Bruchs' membrane. This may cause choroidal neovascularization, retinal holes with retinal hemorrhage, or retinal detachment. An extensive laser treatment may lead to epiretinal membranes, which might need vitrectomy with membrane peeling [5].

67.3 Diabetic Retinopathy (DRP)

67.3.1 Diabetic Macular Edema (DME)

Laser treatment in diabetic retinopathy (DRP) is applied to minimize hypoxic retinal areas and to reduce retinal oxygen demand. Thus the release of vascular endothelial growth factor (VEGF) could be avoided [5, 6].

Indications for focal laser treatment: Diabetic macular edema (DME), non-proliferative DRP without macular edema, combination of DME and DRP. In DRP, microaneurysms should be coagulated directly. Intraretinal hemorrhages and exudates should be surrounded by laser burns.

In DME, *grid laser* coagulation (see Figure 67.4) should be performed to reduce macular edema.

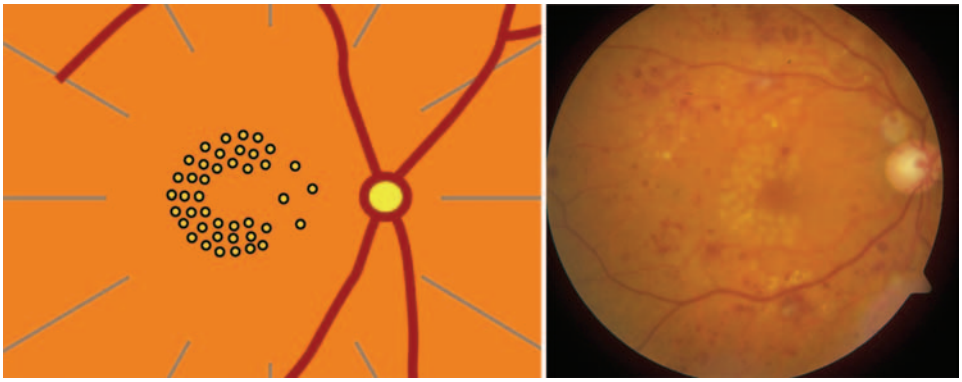

Figure 67.4 Grid laser coagulation.

Laser parameters: $S = 100–150\,\mu m$, $T = 0.1\,s$, $E = 80–150\,mW$.

The distance to the foveola is 300–500 μm. Burns should be barely visible and have a light grayish effect (off-whiteburn). In *ischemic* DRP, laser treatment is *not* indicated. If DRP occurs in combination with DME, DME has to be treated first to avoid an increase in DME.

67.3.2 Proliferative Diabetic Retinopathy

Proliferative retinopathy is the most severe ocular complication of diabetes.

Indications for *pan-retinal* laser treatment are retinal neovascularization or proliferative diabetic vitreoretinopathy (PDVP). Pan-coagulation should be performed between the retinal arcades and equator, placing about 2000 laser spots with a distance of 1–2 laser spot sizes between each other. During one laser session, no more than 500 laser spots should be applied. Laser treatment can be extended up to the outer periphery (see Figure 67.5).

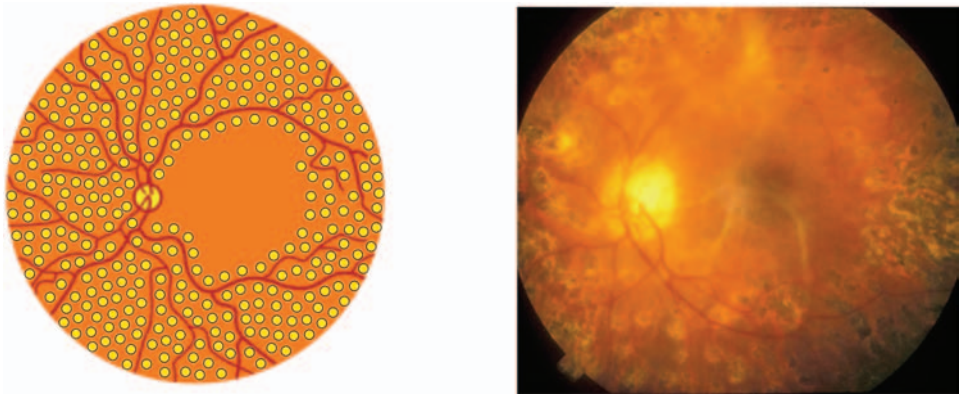

Figure 67.5 Pan-retinal coagulation.

Laser parameters: $S =$ up to 500 µm, $T =$ up to 0.5 s, $E =$ up to 500 mW.

Parameters depend on fundus pigmentation and transparency of optical media.

Visible effect: Grayish effect at the fundus.

Risks: Permanent visual field defects, chorioidal neovascularization, epiretinal membranes, retinal hemorrhage, retinal or choroidal detachment [5].

67.4 Retinal Vein Occlusions

67.4.1 Central Retinal Vein Occlusion (CRVO)

Retinal vein occlusions are common retinal vascular diseases [7, 8]. Central retinal vein occlusion (CRVO) is one of the most common reasons why an eye has to be removed completely by surgery (see Figure 67.6).

Indication: Ischemic central retinal vein occlusion.

Purpose: To avoid retinal neovascularization, macular edema, and rubeosis iridis caused by retinal ischemia (non-perfusion areas).

Laser parameters: $S =$ 200–500 µm, $T =$ 0.2–0.5 s, $E =$ up to 500 mW.

Visible effect: Gray–white burns; pan-retinal laser treatment (scatter treatment).

The distance between the laser spots has to be 0.5–2 laser spot size diameters. Laser spots (up to 2500 burns) should be placed between the hemorrhages.

If macular edema is present, grid laser coagulation (see above) may be indicated [7].

67.4.2 Branch Retinal Vein Occlusion (BRVO)

Branch retinal vein occlusion (BRVO) most often involves the superior or inferior temporal vein. BRVO occurs in older patients showing risk factors such as hyper-

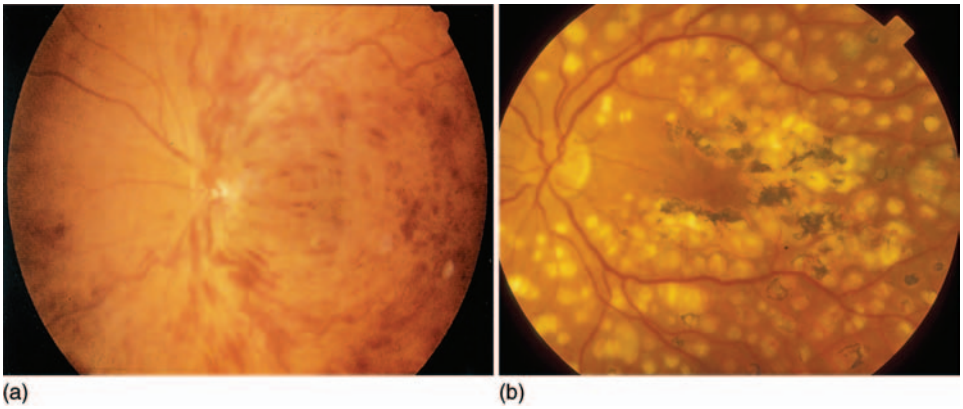

Figure 67.6 CRVO (a) before and (b) after pan-retinal laser treatment.

tension, arteriosclerosis, diabetes, and heart disease. BRVO may occur when retinal arteries and veins share a common adventitia sheath; glaucoma is also a risk factor for BRVO.

Laser parameters: These are similar to the parameters in CRVO: mild scatter treatment in the affected hemisphere.

67.5 Macular Diseases and Choroidal Neovascularization

67.5.1 Age-Related Macular Degeneration (ARMD)

In patients older than 60 years, age-related macular degeneration (ARMD) is the leading cause of legal blindness in industrial countries (see Figure 67.7).

Purpose of laser treatment: Obliteration of abnormal vessels due to parafoveolar choroidal neovascularization (CNV).

Laser parameters: $S = 80–150\,\mu m$, $T = 0.1–0.3\,s$, $E = 100–250\,mW$.

Visible effect: Soft white and confluent.

67.5.2 Transpupillary Thermotherapy (TTT) for the Treatment of CNV

CNV can also be treated by transpupillary thermotherapy (TTT). For TTT, a diode laser with a wavelength of 810 nm is used (see Figure 67.8). After TTT treatment, *no* marked laser effect should be visible at the fundus. The spot size has to overlap the CNV completely [9].

Laser parameters: $S = 2000–3000\,\mu m$, $T = \leq 60\,s$, $E = 400–800\,mW$.

Risks and complications after TTT: Subretinal hemorrhage, iatrogen retinal burns followed by a retinal scar, central scotoma [5, 9].

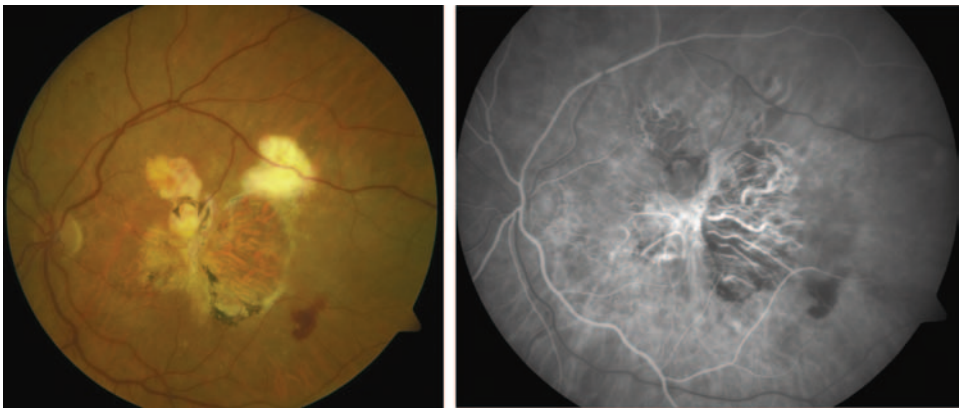

Figure 67.7 Age-related macular degeneration (ARMD).

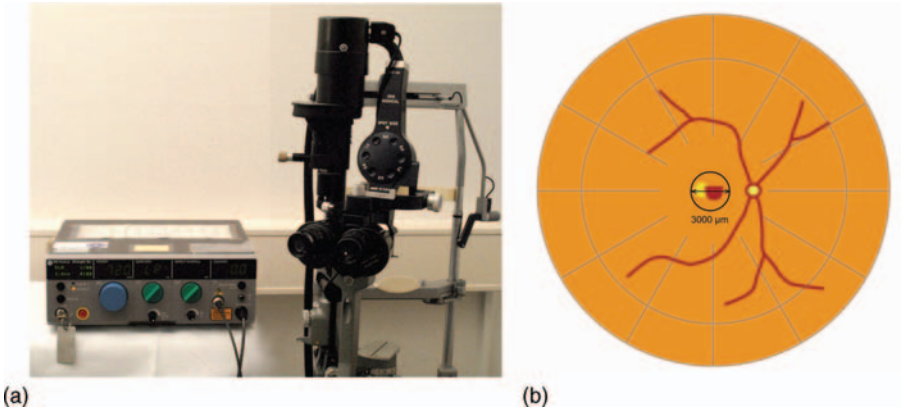

Figure 67.8 (a) TTT laser (diode laser: Ocu Light SLx, 810 nm; Iris Medical, Mountain View, CA, USA) and (b) treatment of ARMD with TTT laser.

67.5.3
Photodynamic Therapy (PDT)

For the sake of completeness, photodynamic therapy (PDT) should be mentioned for the treatment of ARMD, even though PDT is not a coagulative laser treatment. For PDT, a non-thermic laser with a wavelength of 689 nm is used [10].

Purpose: Treatment of subfoveal choroidal neovascularization.

About 15 min before laser treatment, a photosensitive dye (verteporphin, Visudyne®) is injected into a peripheral vein. The dye is activated by a diode laser.

Parameters: $S =$ variable, overlapping the CNV completely, $T = 83$ s, $E = 600\ \mathrm{W\,cm^{-2}}$.

PDT causes a photothrombosis of the CNV. In most patients, PDT has to be performed 2–3 times or even more often, every 3 months. PDT is used for so-called "classical" CNV and CNV due to pathologic high myopia.

67.5.4
Central Serous Chorioretinopathy (CSC)

Clinic: Idiopathic central serous neurosensory retinal detachment.

The subretinal fluid originates from the choroid [4]. Central serous chorioretinopathy (CSC) often affects younger men aged 20–50 years. It may also occur during pregnancy and in patients who have been treated with corticosteroids. Symptoms of CSC are blurred vision, metamorphopsia, and contrast sensitivity loss. In most cases only one eye is affected. Visual acuity ranges from 20/20 to 20/200 and may be improved by hyperopic correction [4]. The most important examination to evaluate CSC is fluorescein angiography (FLA). Fluorescein leaks through a focal defect in the retinal pigment epithelium, causing a "smokestack" configuration [4] (see Figure 67.9). Most patients have spontaneous resolution after 3–6 months. If leakage is still present after this time, laser coagulation has to be considered.

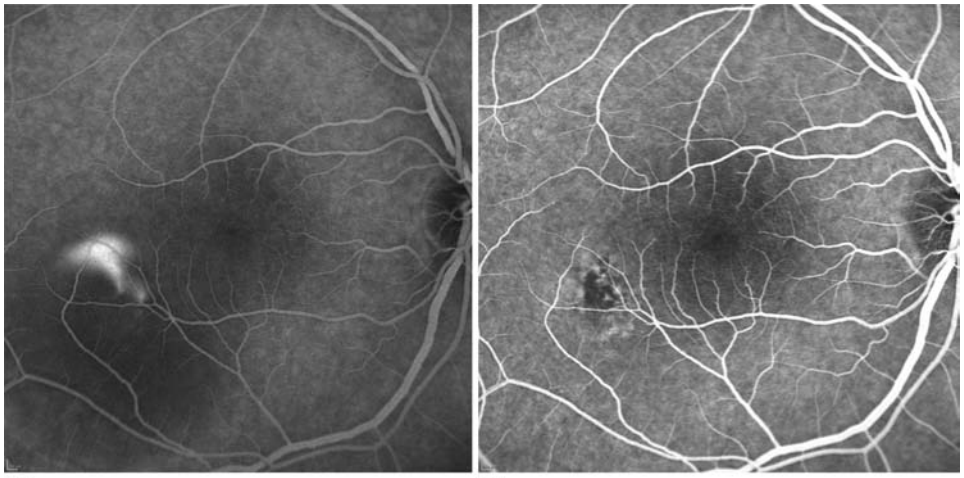

Figure 67.9 CSC (a) before laser treatment (note the typical "smokestack" configuration) and (b) after laser treatment.

Laser parameters: $S = 100–200\,\mu m$, $T = 0.1–0.2\,s$, $E = 80–200\,mW$.
Visible effect: Light gray burns, confluent laser treatment.

In some patients there may be a recurrence of the CSC, in which case additional laser treatment is indicated.

67.6 Choroidal Melanoma

Small choroidal melanoma $\leq 3.0\,mm$ can be treated either by laser or even better by Transpupillary Thermotherapy [11] (see Figure 67.10). The laser energy (E) is ≥ 800

Figure 67.10 TTT laser for small choroidal melanoma.

Table 67.1 Differences between laser techniques.

	Classic laser coagulation	PDT	TTT
Wavelength	Green, yellow, red, and infrared laser (514–810 nm)	Red diode laser (689 nm)	Infrared diode laser (810 nm)
Laser duration	μs	83 s	60 s
Laser–tissue interaction	Photothermal	Photochemical	Photothermal
Retinal irradiation	80 W cm^{-2} (514 nm, 50 mW, with 200 μm spot size)	0.6 mW cm^{-2} (65 mW, with 3.0 mm spot size)	7.5 W cm^{-2} (800 mW, with 3.0 mm spot size)
Assumed maximum rise in temperature on the retina	42 °C (514 nm, 50 mW, 0.1 s, with 200 μm spot size)	2 °C (65 mW, 83 s, with 3.0 mm spot size)	10 °C (800 mW, 60 s, with 3.0 mm spot size)
Invasiveness	Not invasive	Invasive (vein puncture)	Not invasive

Source: modified from Mainster and Reichel [12].

mW for choroidal melanoma. After TTT treatment, a marked laser effect should be visible on the lesion (grayish coagulation effect). The spot size has to overlap the choroidal melanoma by at least 500 μm. Tumors with a larger diameter that cannot be overlapped completely with a single laser spot must be treated with several overlapping laser spots. In TTT for tumor patients, higher energy levels are necessary. This may lead to severe pain, and TTT therefore has to be performed under retrobulbar anesthesia.

Laser coagulation is also used for the treatment of the following rare diseases: retinal teleagiectasia, vascular tumors such as retinal hemangioma and choroidal hemangioma, peripheral retinal neovascularization such as sickle cell retinopathy, retinopathy of prematurity, and fundus alterations due to uveitis, Coats disease, Eales disease, and others [4].

Differences between laser techniques are summarized in Table 67.1. Further information can be found in ophthalmology laser handbooks.

References

1 Rol, P., Fankhauser, F., Giger, H., Dürr, U., and Kwasniewska, S. (2000) Transpupillar laser phototherapy for retinal and choroidal tumors: a rational approach. *Graefe's Arch. Clin. Exp. Ophthalmol.*, **238**, 249–272.

2 Framme, C., Roider, J., Brinkmann, R., Birngruber, R., and Gabel, V.-P. (2008) Grundlagen und klinische Anwendung der Lasertherapie an der Netzhaut. *Klin. Monatsbl. Augenheilkd.*, **225**, 259–268.

3 Augustin, A.J. (2007) *Augenheilkunde*, 3rd edn, chap. **28**, Springer, Berlin, pp. 811–820.

4 Folk, J.C. and Pulido, J.S. (1997) *Laser Photocoagulation of the Retina and Choroid,* American Academy of Ophthalmology Monograph Series, vol. **11**, American Academy of Ophthalmology, San Francisco.

5 Burk, A. and Burk, R. (2005) *Checkliste Augenheilkunde, 3. Auflage*, ThiemeVerlag, pp. 456–460.

6 Early Treatment Diabetic Retinopathy Study Research Group (1987) Treatment techniques and clinical guidelines for photocoagulation of diabetic macular edema. ETDRS Report Number 2. *Ophthalmology*, **94**, 761–774.

7 Central Vein Occlusion Study Group (1995) Evaluation of grid pattern photocoagulation for macular edema in central vein occlusion. *Ophthalmology*, **102**, 1425–1433.

8 Central Vein Occlusion Study Group (1995) Randomized clinical trial of early panretinal photocoagulation for ischemic central vein occlusion. *Ophthalmology* **102**, 1434–1444.

9 Feucht, M., Fuisting, B., and Richard, G. (2006) Stand der TTT bei der Therapie der CNV. *Klin. Monatsbl. Augenheilkd.*, **223**, 802–807.

10 Treatment of Age-Related Macular Degeneration with Photodynamic Therapy (TAP) Study Group (2001) Photodynamic therapy of subfoveal choroidal neovascularization in age-related macular degeneration with verteporfin: two-year results of 2 randomized clinical trials – TAP Report 2. *Arch. Ophthalmol.*, **119**, 198–207.

11 Journee-de Korver, J.G., Oosterhuis, J.A., Kakebeeke-Kemme, H.M., and de Wolff-Rouendaal, D. (1992) Transpupillary thermotherapy (TTT) by infrared irradiation of choroidal melanoma. *Doc. Ophthalmol.*, **82**, 185–191.

12 Mainster, M.A. and Reichel, E. (2000) Transpupillary thermotherapy for age-related macular degeneration: long-pulse photocoagulation, apoptosis and heat shock proteins. *Ophthalmic Surg. Lasers*, **31**, 359–373.

68
Diagnostic Imaging and Spectroscopy

Daniel Fried

68.1
Caries Detection

New diagnostic imaging tools are needed for the detection and characterization of caries lesions (dental decay) in the early stages of development [1]. Conventional methods, visual/tactile and radiographic, have numerous shortcomings and are inadequate for the detection of the early stages of the caries process [2–4]. Radiographic methods do not have sufficient sensitivity for early lesions, particularly occlusal lesions, and by the time the occlusal lesions are radiolucent they have often progressed well into the dentin, at which point surgical intervention is necessary [4–6]. At that stage in the decay process, it is too late for preventive and conservative intervention and a large portion of carious and healthy tissue will need to be removed, often compromising the mechanical integrity of the tooth. If left untreated, the decay will eventually infect the pulp, leading to loss of tooth vitality and possible extraction. The caries process is potentially preventable and curable. If carious lesions are detected in the enamel early enough, it is likely that they can be arrested/reversed by nonsurgical means through fluoride therapy, antibacterial therapy, dietary changes, or low-intensity laser irradiation [1, 7]. Therefore, one cannot overstate the importance of detecting the decay in the early stage of development, at which point noninvasive preventive measures can be taken to halt further decay.

Accurate determination of the degree of lesion activity and severity is of paramount importance for the effective employment of the treatment strategies mentioned above. Since optical diagnostic tools exploit changes in light scattering in the lesion, they have great potential for the diagnosis of the "activity" of the lesion, that is, whether or not the caries lesion is active and expanding or whether the lesion has been arrested and is undergoing remineralization. Such data are invaluable for caries management by risk assessment in the patient and for determining the appropriate form of intervention. A nondestructive, quantitative method of monitoring demineralization *in vivo* with high sensitivity would also be invaluable for use in short-term clinical trials for various anti-caries agents such as new or modified fluoride

Handbook of Biophotonics. Vol.2: Photonics for Health Care, First Edition. Edited by Jürgen Popp, Valery V. Tuchin, Arthur Chiou, and Stefan Heinemann.

dentifrices and antimicrobials. In particular, methods that could be employed in the relevant high-risk areas of the tooth such as the occlusal pits and fissures, would be universally useful. The purpose of this chapter is to describe several recent optically based methods for the detection and imaging of tooth decay.

68.2 Optical Properties of Dental Hard Tissue

68.2.1 Optical Properties of Dental Hard Tissue in the Visible and Near-Infrared Regions

A fundamental understanding of how light propagates through sound and carious dental hard tissues is essential for the development of clinically useful optical diagnostic systems, since image contrast is based on changes in the optical properties of these tissues upon demineralization. Dental hard tissue optics are inherently complex owing to the nonhomogeneous and anisotropic nature of these biological materials. The scattering distributions depend on tissue orientation relative to the irradiating light source [8–11] in addition to the polarization of the incident light [12, 13]. The optical properties of biological tissue can be completely and quantitatively described by defining the optical constants, the absorption (μ_a) and scattering coefficients (μ_s), which represent the probability of the incident photons being absorbed or scattered, and the scattering phase function [$\Phi(\cos\theta)$], which is a mathematical function that describes the directional nature of scattering [14–17]. With knowledge of these parameters, light transport in dental hard tissue can be completely characterized and modeled. Accurate description of light transport in dental hard tissue relies on knowledge of the exact form of the phase function $\Phi(\cos\theta)$ for each tissue scatterer at each wavelength [17].

68.2.2 Optical Properties of Sound Enamel and Dentin

Light absorption by enamel is very weak in the visible and near-infrared (NIR) region ($\mu_a < 1\,\mathrm{cm}^{-1}$, $\lambda = 400$–$1300\,\mathrm{nm}$) and increases in the ultraviolet (UV) region ($\mu_a > 10\,\mathrm{cm}^{-1}$, $\lambda < 240\,\mathrm{nm}$) [18]. The absorption coefficient of dentin is essentially wavelength independent with a value of $\mu_a \approx 4\,\mathrm{cm}^{-1}$ [19] above 400 nm. The optical behavior of enamel and dentin is dominated by scattering in the visible and NIR region [18]. The scattering coefficient of enamel, μ_s, decreases with increasing wavelength from $400\,\mathrm{cm}^{-1}$ in the near-UV region [18] to as low as 2–$3\,\mathrm{cm}^{-1}$ at 1310 and 1550 nm [10, 20] (see Figure 68.1). At longer wavelengths, water absorption increases and dominates the attenuation [21]. The scattering of dentin is variable with position in the tooth and exceeds 100–$200\,\mathrm{cm}^{-1}$ across the visible and NIR region [19]. Measurement of the enamel attenuation coefficients in the NIR region is a particular challenge since the scattering coefficient is almost two orders of magnitude lower than in the visible range, ~ 2–$3\,\mathrm{cm}^{-1}$ at 1310 nm versus $105\,\mathrm{cm}^{-1}$ at 543 nm, and

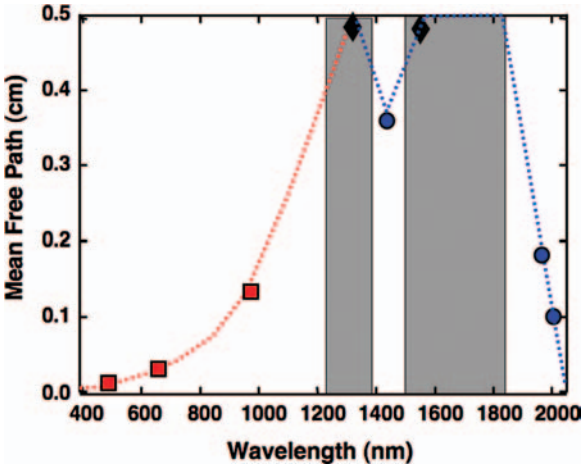

Figure 68.1 Plot of the mean free path of photons in sound dental enamel at visible and NIR wavelengths. The regions of highest transparency are shaded. The red squares are data from ref. [10], the black diamonds are from ref. [20], and the blue circles represent 10% absorption from water taken from ref. [21].

surface scattering can completely mask measurement of the bulk scattering properties [10].

The Monte Carlo (MC) method [22, 23] was used to determine the scattering coefficient and scattering phase function from angular-resolved scattering measurements for dentin and enamel at 543, 632, and 1053 nm. Although the MC method is somewhat labor intensive, it has been shown consistently to yield the most reliable values [14, 17]. The accuracy of the values computed was confirmed by successfully modeling the angular resolved scattering distributions measured for sections of various thickness from 100 μm to 2 mm in the multiple scattering regime. The measured angular resolved scattering distributions could not be represented by a single scattering phase function $\Phi(\cos\theta)$, and required a linear combination of a highly forward-peaked phase function, a Henyey–Greenstein (HG) function, and an isotropic phase function represented by the following equation [10]:

$$\Phi(\cos\theta) = f_d + (1-f_d)\left[\frac{1-g^2}{(1+g^2-2g\cos\theta)^{\frac{3}{2}}}\right] \tag{68.1}$$

The parameter f_d for "fraction diffuse" is defined as the fraction of isotropic scatterers. The average value of the cosine of the scattering angle (θ) is called the scattering anisotropy (g), and $g = 0.96$ and 0.93 for enamel and dentin, respectively, at 1053 nm [10]. The fraction of isotropic scatterers (f_d) was measured to be 36% for enamel and less than 2% for dentin at 1053 nm. Note that Zijp and ten Bosch [8, 11] reported values of $g = 0.4$ for dentin and 0.68 for enamel, calculated by taking the ratio of the forward and backward scattered light. This latter approach is prone to error due

to the contribution of surface scattering [10]. Most scattering biological tissues that can be represented by an HG function have measured g values >0.8 [14]; moreover, the g value should be determined within the context of an appropriate phase function based on the nature of the scatterers in the tissue [24], and subsequently validated through comparison of simulated scattering distributions with measured distributions of various thickness [10].

Light scattering in enamel and dentin is anisotropic, particularly for dentin due to the cylindrical-shaped enamel prisms and dentinal tubules. Altshuler and Grisimov suggested that these structures can act as waveguides to guide visible light [25, 26]. Kienle and co-workers extensively investigated the anisotropy of light scattering in dentin and showed how light is magnified through it [27–31].

68.2.3
Optical Property Changes of Demineralized Enamel

Increased backscattering from the demineralized region of early caries lesions is the basis for the visual appearance of white spot lesions [32, 33]. Attempts at measuring the optical properties of dental caries have been limited to measurements of backscattered light from optically thick, multilayered sections of simulated caries lesions [34–36]. The microstructure of enamel and dentin caries lesions is complex, consisting of various turbid and transparent zones [13, 37]. Highly porous demineralized areas of coronal caries appear whiter and are more opaque. During remineralization, pores and tubules are filled with mineral and those areas are typically more transparent. There have been some attempts to measure and simulate light scattering in artificial and natural lesions [32, 36, 38]. There has not been a major effort to measure and quantify the optical properties of carious lesions in terms of changes in the fundamental optical constants, μ_s and μ_a, and the scattering phase function. This is due in part to the difficulty in acquiring large uniform areas for measurement by conventional means and the highly variable nature of caries lesions. One challenge in quantifying the optical properties of carious lesion areas versus sound tissue areas is the method of index matching. Lesion areas are highly porous, allowing index matching fluids to imbibe into the lesion, effectively eliminating the lesion from an optical standpoint, that is, the lesion becomes more transparent than the sound tissue. One must assume that carious lesions will be filled with fluid in their natural state and that measurement in water replicates the conditions that will be encountered clinically. Darling *et al.* measured the optical properties of lesion areas imbided in water at 1310 nm and compared the increase in the magnitude of the scattering coefficient with mineral loss measured using microradiography [39]. The attenuation in the lesion exceeds $100\,cm^{-1}$, a factor of 50 times higher than that of sound enamel, $2–3\,cm^{-1}$, and is of a similar magnitude to that of the dentin. This difference can be seen in Figure 68.2a, which contains an image of a 200 μm thick tooth section with an interproximal lesion taken with 1310 nm light. The areas of the lesion and dentin are opaque (white) whereas the enamel is highly transparent (dark). A high-resolution digital microradiograph of the demineralized region of the section is shown in Figure 68.2b. The volume-% mineral is represented by the

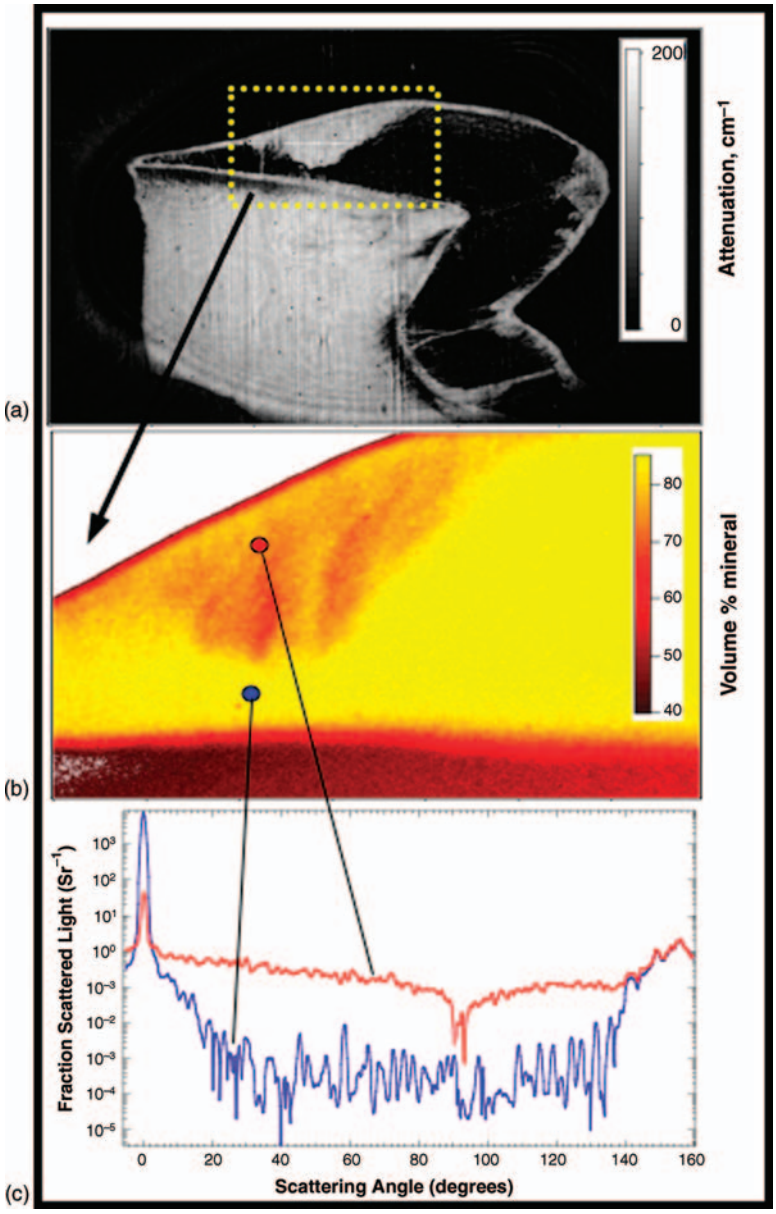

Figure 68.2 (a) NIR transillumination image of 200 μm thick tooth section with demineralization indicated in the yellow box. (b) A high-resolution digital microradiograph of the lesion area shows the volume percent mineral versus position in the lesion area. (c) The fraction of NIR 1310 nm light scattered versus angle in the sound blue and carious black areas of the sample measured with the scattering goniometer. From ref. [39].

yellow–red color table with the areas of lower mineral content, caries lesion and dentin, demarcated in red and the high-mineral areas, namely sound enamel, in yellow. Optical scattering measurements were taken in sound and carious regions of the same section as indicated by the two points, red and blue, in the microradiograph using a 1310 nm diode laser focused to a spot size of 100 μm. Angularly resolved scattering measurements taken at those two points are plotted in Figure 68.2c. The ballistic light is reduced by two orders of magnitude and the intensity of the light scattered at angles $>10^{\circ}$ is 2–3 orders of magnitude higher for the carious tissue over the sound enamel.

NIR optical property measurements during the longitudinal development of early artificial demineralization suggest a rapid exponential increase in optical scattering during initial lesion development followed by a more gradual increase in scattering as the lesion severity increases [39]. Angularly-resolved scattering measurements from artificially demineralized enamel over a period of 5 days show a rapid increase in attenuation after just 1 day followed by an increase in another order of magnitude after the next 4 days. The scattering anisotropy of demineralized enamel also appears to be highly forward directed. This is not entirely unexpected since demineralization proceeds along the core of the enamel rods, hence the scattering centers may be fairly large in the micron range and highly anisotropic.

68.2.4
Optical Properties of Dental Hard Tissue in the IR region

Infrared (IR) wavelengths can be used to monitor changes in the chemical composition and mineral phase crystalline orientation as a result of demineralization and remineralization, and after thermal treatments by lasers to modify the susceptibility to acid dissolution. In the mid-IR region, scattering is negligible and knowledge of the absorption coefficient and the reflectivity are sufficient to describe the optical behavior. The magnitude of the absorption coefficient is high in the mid-IR region due to resonant absorption by molecular groups in water, protein, and mineral. The reflectivity can exceed 50% at wavelengths coincident with mineral absorption bands due to the large increase in the imaginary component of the refractive index. The fraction of incident laser light reflected at the surface of the tooth is described by the Fresnel reflection equation:

$$R = \frac{(n_r - 1)^2 + k^2}{(n_r + 1)^2 + k^2} \tag{68.2}$$

where n_r is the real component of the refractive index and k is the attenuation index. The absorption coefficient (μ_α), k, and the wavelength (λ) are related by the expression $\mu_\alpha = 4\pi k/\lambda$. Hence the reflectance of materials can increase markedly and approach 100% in regions of strong absorption; for example, some metals have absorption coefficients $>10^6\,\mathrm{cm}^{-1}$ and reflectance >99% in the visible and IR region. The reflectance of dentin and enamel was measured at $\lambda = 2.79$, 2.94, 10.6, 10.3,

9.6, and 9.3 μm using a gold-coated integrating sphere [40]. The reflectance of enamel is substantially higher at $\lambda = 9.6$ and 9.3 μm than at $\lambda = 10.6$ μm, near 50%, and must be accounted for when calculating ablation efficiencies, ablation thresholds, and the heat deposition in the tooth when investigating laser interactions with these tissues.

Absorption coefficients corresponding to CO_2 laser lines that could be obtained using conventional transmission measurements were calculated to be $1168 \pm 49\,cm^{-1}$ at 10.3 μm and $819 \pm 62\,cm^{-1}$ at 10.6 μm for enamel and $1198 \pm 104\,cm^{-1}$ at 10.3 μm and $813 \pm 63\,cm^{-1}$ at 10.6 μm for dentin. Enamel absorption coefficients corresponding to Er:YAG (2.94 μm) and Er:YSGG (2.79 μm) were calculated to be 768 ± 27 and $451 \pm 29\,cm^{-1}$, respectively. The absorption coefficient of dentin at 2.79 μm was calculated to be $988 \pm 111\,cm^{-1}$. Those values are shown in Figure 68.3 along with $1/e$ absorption depth, thermal relaxation time, and percentage reflectance. Conventional transmission measurements are not possible for the determination of the optical properties of enamel and dentin at 9.3 and 9.6 μm, therefore an alternative method must be used such as angular-resolved reflection measurements of polarized light and time-resolved radiometric measurements. Previous studies have used angular resolved reflection measurements to estimate IR absorption coefficients in dental enamel. Duplain *et al.* [41] reported absorption coefficients of 6500 and $5200\,cm^{-1}$ at 10.3 and 10.6 μm, respectively. These coefficients were much higher than the dental enamel absorption coefficients determined using direct transmission measurements (1168 and $819\,cm^{-1}$ for 10.3 and 10.6 μm, respectively). Those previously reported values are also not consistent with observed surface modification thresholds based on the known melting range of dental enamel (800–1200 °C). More recent measurements employed time-resolved radiometry measurements coupled with numerical simulations of thermal relaxation in the tissue to measure 8000 and $5250\,cm^{-1}$ at 9.6 and 9.3 μm, respectively [42]. Those values are consistent with time-resolved temperature measurements during laser irradiation and surface melting thresholds [43].

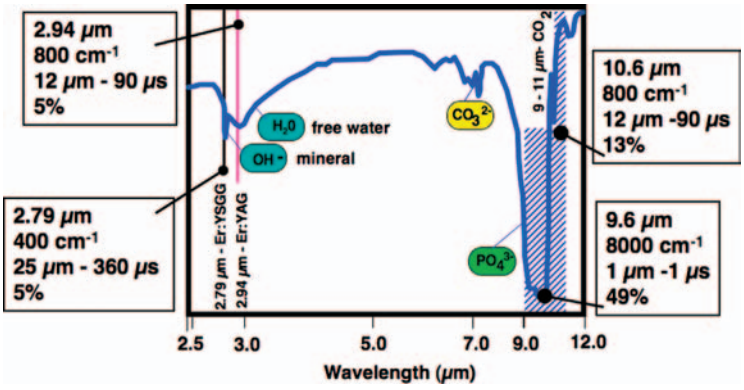

Figure 68.3 Optical properties of human dental enamel and dentin at relevant laser wavelengths. The wavelength, absorption coefficient ($1/e$), absorption depth, thermal relaxation time, and percentage reflectance are listed for each laser wavelength. From refs. [168] and [169].

68.3
Reflectance Spectroscopy

Since the magnitude of light scattering increases markedly in dental hard tissues upon demineralization producing visible white spots on tooth surfaces due to the increased porosity, reflectance spectroscopy is an obvious method for measuring and quantifying lesion severity. In 1984, ten Bosch *et al.* [33] introduced an optical monitor that used optical fibers for reflectance measurements on tooth surfaces. The reflectivity increased from the lesion area with increasing mineral loss [32]. Using the Kubelka–Munk equations, Ko *et al.* [36] showed that the optical scattering power correlated with mineral loss and yielded improved results over reflectance measurements. Benson *et al.* [44] demonstrated that the visibility of scattering structures on highly reflective surfaces such as teeth can be enhanced by the use of crossed polarizers to remove the glare from the surface due to the strong specular reflection from the enamel surface [44, 45]. The contrast between sound and demineralized enamel can be further enhanced by depolarization of the scattered light in the area of demineralized enamel [46, 47]. Blodgett and Webb [48] measured the optical bidirectional reflectance distribution functions (BRDF) and bidirectional scattering distribution functions (BSDF) from the surfaces of human incisors at 632 nm, 1054 nm, and 3.39-μm. Analoui *et al.* [49] showed that multi-spectral La^*b^* color coordinates measured using a diode-array spectrometer in the range 380–780 nm did not correlate well with the depth of artificial lesions.

The contrast between sound and demineralized enamel is greatest in the NIR region due to the minimal scattering of sound enamel (see Figure 68.1) and this can be exploited for reflectance imaging of early demineralization [39]. Wu and Fried [50] reported the high-contrast polarized reflectance images of early demineralization on buccal and occlusal tooth surfaces measured at $\lambda = 1310$ nm and found that the contrast between early demineralization was significantly higher at 1310 nm than in the visible range. Figure 68.4a and b show cross-polarization images of enamel demineralization in the visible and NIR region, showing the marked difference in contrast between the sound and demineralized enamel in these two spectral regions.

68.4
Optical Transillumination

Optical transillumination was used extensively before the discovery of X-rays for the detection of dental caries. Over the past two decades, there has been continued interest in this method, especially with the availability of high-intensity, fiber optic-based illumination systems for the detection of interproximal lesions [51–56]. During fiber-optic transillumination (FOTI), a carious lesion appears dark upon transillumination because of decreased transmission due to increased scattering and absorption by the lesion. A digital fiber-optic transillumination (DIFOTI) system, that utilizes visible light for the detection of caries lesions, has recently been developed by Electro-Optical Sciences (Irvington, NY, USA) [57]. Several studies have been carried

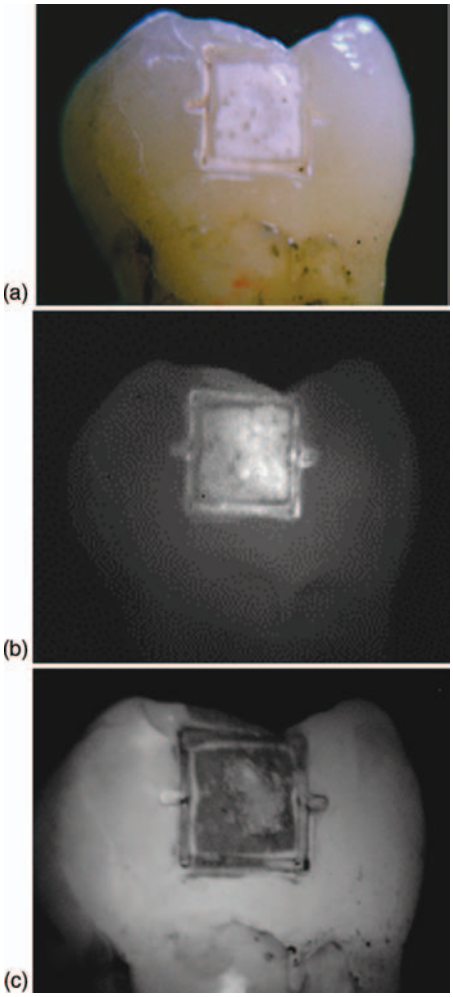

Figure 68.4 Images are shown for the buccal surface of a tooth with a $2 \times 2\,mm^2$ window of demineralization. (a) Visible reflectance with crossed polarizers, (b) NIR reflectance with crossed polarizers, and (c) laser induced fluorescence image ($\lambda = 473\,nm$ excitation, emission $\lambda > 500\,nm$). From ref. [50].

out using visible light transillumination either as an adjunct to bitewing radiography or as a competing method for the detection of interproximal caries lesions [57–62]. However, since FOTI and DIFOTI operate in the visible range, the photon mean free path is limited (see Figure 68.1) and the results are mixed.

Near-IR light can penetrate much further through tooth enamel due to the markedly longer mean free path of the photons [63], that is, enamel is virtually transparent in the NIR region with optical attenuation 1–2 orders of magnitude less than in the visible range (see Figure 68.1). Transmission measurements through demineralized tooth sections at 1310 nm show that the demineralized enamel

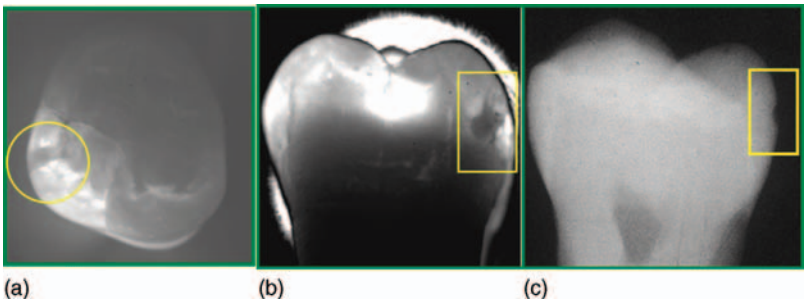

Figure 68.5 Multiple NIR views of a tooth with an interproximal lesion. The radiograph is shown in (c). From ref. [66].

attenuates NIR light by a factor of 20–50 times greater than the sound enamel [64, 65], hence high contrast can be achieved at 1310 nm between demineralized and sound tissues. High-contrast images have been acquired of simulated and natural interproximal lesions on extracted human teeth [66, 67]. Since the tooth manifests such high transparency in the 1310 and 1550 nm NIR regions, multiple imaging configurations can be used to image the decay. Interproximal lesions can be viewed using transillumination with the light source and detector placed on opposite sides of the tooth or NIR light can be delivered near or below the gum-line and both interproximal and occlusal lesions can be imaged from directly above the occlusal surface, as demonstrated in Figure 68.5 for a natural interproximal lesion. Shorter NIR wavelengths have also been investigated in the region that is accessible to conventional silicon-based charge-coupled device (CCD) cameras with the NIR filter removed, namely at 830 nm [68]. Figure 68.6 compares the image contrast of tooth sections of increasing thickness with simulated lesions in the visible region at 830 and 1310 nm [68]. Simulated lesions were produced by drilling small 1 mm diameter cavities on the mesial or distal aspect of tooth sections of varying thickness or whole teeth. The imaging system operating near 830 nm, utilizing a low-cost silicon CCD optimized for the NIR region, is capable of significantly higher performance than a visible system, but the contrast is significantly lower then that attainable at 1310 nm [68]. Owing to the high transparency of the enamel in the NIR region, NIR imaging also has great potential to examine defects in tooth structure and cracks in enamel can be clearly resolved with this method.

68.5
Optical Coherence Tomography

Optical coherence tomography (OCT) is a noninvasive technique for creating cross-sectional images of internal biological structure [69]. The intensity of backscattered light is measured as a function of its axial position in the tissue. Low-coherence interferometry is used to selectively remove or gate out the component of backscattered signal that has undergone multiple scattering events, resulting in

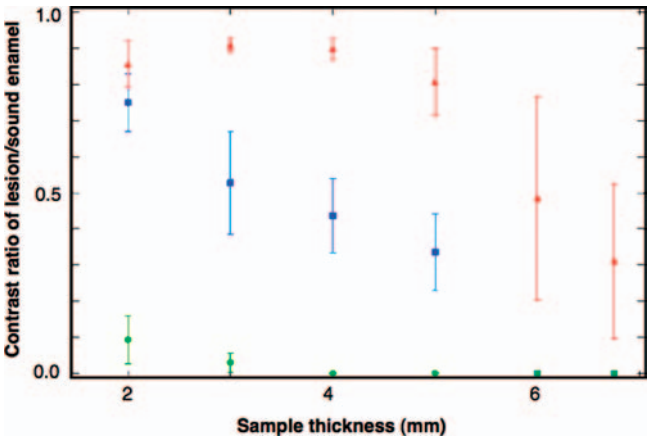

Figure 68.6 Contrast ratio between sound enamel and the simulated lesion for the three imaging systems for varying section thickness: triangles, 1310 nm; squares, 830 nm; circles, visible standard CCD, no filters. From ref. [68].

very high-resolution images (<15 μm). Lateral scanning of the probe beam across the biological tissue is then used to generate a two-dimensional intensity plot, similar to ultrasound images, called a b-scan. The one-dimensional analog of OCT, optical coherence domain reflectometry (OCDR), was first developed as a high-resolution ranging technique for the characterization of optical components [70, 71]. Huang *et al.* [72] combined transverse scanning with a fiber-optic OCDR system to produce the first OCT cross-sectional images of biological microstructure. Excellent books by Bouma and Tearney [69] and Brezinski [73] explain the mechanics of OCT and polarization-sensitive optical coherence tomography (PS-OCT). The first images of the soft and hard tissue structures of the oral cavity were acquired by Colston and co-workers [74–76]. Feldchtein *et al.* [77] presented the first high-resolution dual-wavelength 830 and 1280 nm images of dental hard tissues, enamel, and dentin caries and restorations *in vivo*. OCT has also been used to look at different restorative materials and identify pit and fissure sealants [77, 78]. High-speed Fourier domain (FD)-OCT systems have also been investigated for imaging dental caries [79–82]. OCT images of sound, natural, and artificial demineralized enamel demonstrate that one can image up to 3 mm deep in sound enamel. Although the image depth in enamel is limited to 1–2 mm, highly scattering structures such as the dentin at the dentin–enamel junction (see Figure 68.7) and carious dentin can be detected to a depth of 2–3 mm beneath sound enamel, so that "hidden" dentinal caries can be detected. Figure 68.7 shows an *in vivo* PS-OCT image of the buccal surface of a premolar scanned from the crown to the root showing the excellent optical penetration through the enamel. Identification of caries lesions in OCT images is challenging because the complex signal generation and interpretation of images requires considerable training and experience with the system being used. Since enamel is a weak scatterer, the reflectivity decreases exponentially with depth in sound enamel and subsurface lesions and the reflectivity of a stronger scattering

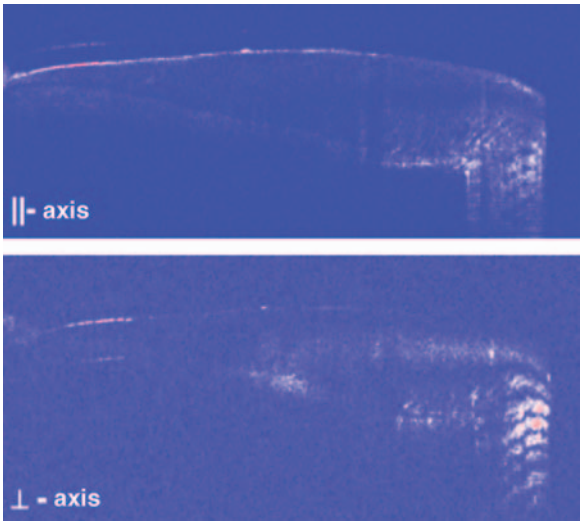

Figure 68.7 *In vivo* PS-OCT images of a sound premolar tooth. The dentinal enamel junction is visible along the entire length from the crown to the root. Banding is caused by tooth birefringence and developmental growth lines.

underlying layer such as dentin or a subsurface lesion can show up even though the signal from sound enamel is no longer visible at that depth. Strong scattering from lesions or developmental defects at the enamel surface can mask the signal from the underlying sound tissues. Moreover, in many cases the reflectivity from the lesion areas can be resolved at greater depths than in sound tissue even though the mean free path of the photons in the sound enamel is two to three orders of magnitude higher than for the caries tissue. Amaechi and co-workers [83, 84] demonstrated that the loss of reflectivity with depth in OCT images correlated with quantitative light fluorescence (QLF) measurements of smooth surface artificial caries. However, as we pointed out above, for some OCT imaging systems the reflectivity actually increases with depth in caries lesions so this approach is not likely to be feasible for natural lesions; however, the rapid loss of reflectivity with depth can be valuable in identifying highly attenuating lesion areas. Enamel and dentin are birefringent and this birefringence can cause bands in OCT images that can be misinterpreted as subsurface caries lesions (see Figure 68.7). Bands are regularly spaced for differentiation from caries lesions. An OCT system with polarization sensitivity can aid in differentiating such structures attributed to birefringence (see below). The incremental growth lines in teeth or striae of Retzius actually scatter light within the tooth and also cause subsurface bands in the images as can be seen in Figure 68.7.

Polarization sensitivity is particularly valuable for imaging caries lesions due to the enhanced contrast of caries lesions caused by depolarization of the incident light by the lesion. Another important advantage is that the confounding influence of the strong surface reflectance of the tooth surface is reduced in the image of the orthogonal polarization state to the incident polarized light. Baumgartner and

co-workers [85–87] presented the first polarization-resolved images of dental caries. PS-OCT images are typically processed in the form of phase and intensity images [45, 88]; such images best show variations in the birefringence of the tissues. Areas of demineralization rapidly depolarize incident polarized light and the image of the orthogonal polarization relative to that of the incident polarization can provide improved contrast of caries lesions [46]. One approach to quantifying the severity of caries lesion is by directly integrating the reflectivity of the orthogonal axis or perpendicular polarization ($\perp$) [46]. There are two mechanisms in which intensity can arise in the perpendicular axis. The native birefringence of the tooth enamel can rotate the phase angle of the incident light beam between the two orthogonal axes (similar to a wave-plate) as the light propagates through the enamel without changing the degree of polarization. The other mechanism is depolarization from scattering in which the degree of polarization is reduced. It is this latter mechanism that can be exploited to measure the severity of demineralization. Complete depolarization of the incident linearly polarized light leads to equal distribution of the intensity in both orthogonal axes. Demineralization of the enamel due to dental decay causes an increase in the scattering coefficient by 1–2 orders of magnitude, thus demineralized enamel induces a very large increase in the reflectivity along with depolarization. This in turn causes a large rise in the perpendicular polarization channel or axis. This can be seen in the PS-OCT images of a premolar with shallow demineralization around the fissure presented in Figure 68.8. The parallel ($\|$)-axis image represents the linearly polarized light reflected in the original polarization incident on the tooth and the $\perp$-axis image represents the light in the orthogonal polarization to the

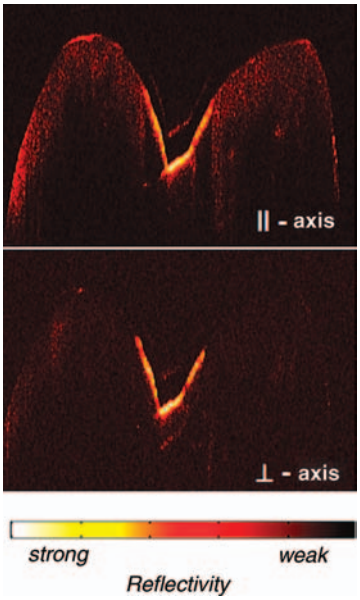

Figure 68.8 PS-OCT images of an area of demineralization in the occlusal pit and fissure of a premolar. From ref. [89].

incident light. The surface of the tooth is less visible in the ⊥-axis image and the lesion appears with higher contrast to the surrounding sound enamel.

This approach also has the added advantage of reducing the intensity of the strong reflection from the tooth surface. The lesion surface zone is very important since this zone can potentially provide information about the lesion activity and remineralization. A conventional OCT system cannot differentiate the strong reflectance from the tooth surface from increased reflectivity from the lesion itself. This facilitates direct integration of the lesion reflectivity to quantify the lesion severity, regardless of the tooth topography and the difficult task of having to deconvolute the strong surface reflection from the lesion surface can be circumvented. The integrated reflectivity of the ⊥-PS-OCT images of natural lesions correlate well with the integrated mineral loss and can thus be used to measure lesion severity directly [46, 89, 90]. Figure 68.9 shows ⊥-axis PS-OCT images, polarized light microscopy (PLM) images, and transverse microradiographs (TMR) of a pigmented interproximal lesion. Five PS-OCT line profiles were taken at different positions in the lesion and each was integrated to yield a total integrated reflectivity for that area of the lesion to a depth of 500 μm. The integrated reflectivity correlated well with the matching mineral density profiles taken from the microradiographs. PS-OCT images also accurately represent the highly convoluted internal structure of caries lesions. Longitudinal studies have demonstrated that PS-OCT can be used for monitoring erosion and demineralization [46, 89, 90]. The progression of artificially produced caries lesions in the pit and fissure systems of extracted molars can be monitored nondestructively [89].

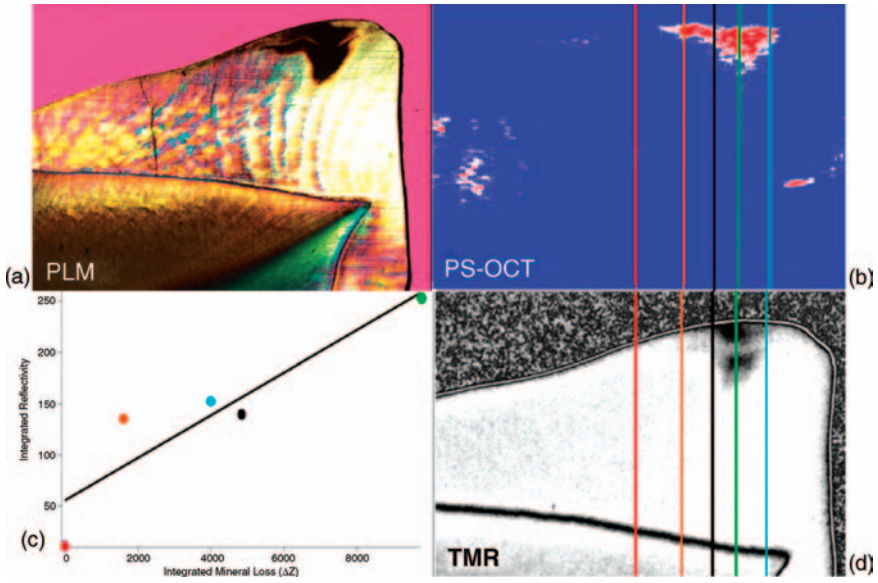

Figure 68.9 Pigmented lesion: (a) reflected light image, (b) ⊥-axis PS-OCT image, and (c) plot of the integrated reflectivity versus the integrated mineral loss to a depth of 500 μm. Each color coded symbol corresponds to the line profiles of (b) and (d). (d) Microradiograph. From ref. [170].

It is not sufficient simply to detect a carious lesion or areas of demineralization – it is also necessary to assess the state of the carious lesion and determine whether it is active and progressing or whether it is arrested and has remineralized. One can take two approaches for determining the state of activity of carious lesions. The first approach is based on monitoring the lesion progression over time to see if it changes. The second approach is to examine the structure of the lesion to determine if there are any definitive features, such as a weakly scattering surface zone, that are indicative of remineralization. Ismail presented a review of visual caries detection criteria [91]. Surfaces of arrested lesions are typically hard and shiny with less light scattering, in contrast to the soft and chalky surface of active lesions. It is likely that if PS-OCT can resolve changes in lesion structure and demineralization, for example the presence of a surface zone of reduced light scattering indicative of remineralization, then this method has potential as a more quantitative diagnostic of the activity of the lesion. Figure 68.10 shows PS-OCT, PLM, and TMR images of human dentin that was exposed to a demineralization solution (left side) and a demineralization solution followed by a remineralization solution (right side). The lower reflectivity surface layer of remineralized dentin is clearly visible in the PS-OCT image.

PS-OCT can also be used to image secondary caries under sealants where the advantage of having the ability to directly integrate the PS-OCT fast axis ($\perp$-axis) images to quantify lesion severity is even more apparent [92]. The imaging depth of PS-OCT through composite is sufficient to resolve early demineralization under the sealant or restoration. Studies also suggest that polarization sensitivity can be used to

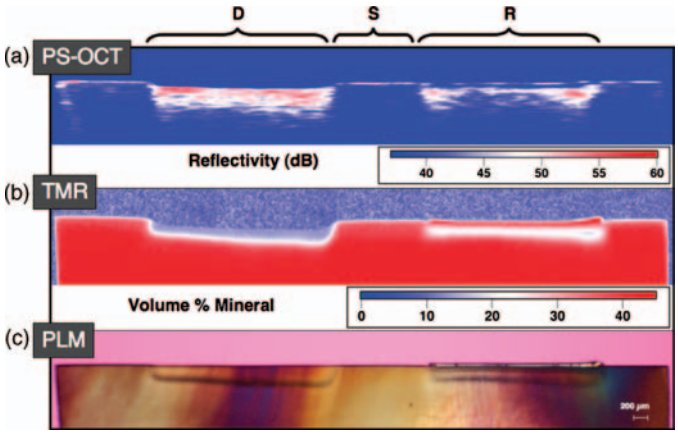

Figure 68.10 (a) ($\perp$-axis) PS-OCT scan taken along long axis of a sample before sectioning. Intensity scale is shown in red–white–blue in units of decibels (dB). Remineralized layer is visible as a blue gap above the remineralized lesion. (b) The corresponding TMR of a 260 μm thick section in a similar orientation to the PS-OCT image. The intensity scale is also shown in red–white–blue with units in volume-% mineral. (c) The PLM image of the same section is shown at 15× magnification. From ref. [171].

differentiate between composites and tooth structure and even differentiate between different composites [92]. The composite reflectivity, depolarization, and penetration depth is not influenced by the composition of the filler; however, the reflectivity was markedly increased in sealants with an added optical opacifier such as titanium dioxide. Therefore, polarization sensitivity can also be advantageous for differentiating demineralized enamel under composite sealants and restorations.

In summary, OCT is an excellent tool for acquiring images of dental caries. However, OCT images are fairly complicated and considerable experience is required to interpret the images. PS-OCT is advantageous for providing a quantitative measure of the lesion severity for monitoring lesion progression and for assessing the success of chemical intervention on arresting and remineralizing lesions.

68.6 Fluorescence Imaging

68.6.1 Quantitative Light Fluorescence (QLF)

Teeth fluoresce naturally upon irradiation with UV and visible light. Alfano *et al.* [93] and Bjelkhagen and Sundstrom [94] demonstrated that laser-induced fluorescence (LIF) of endogenous fluorophores in human teeth could be used as a basis for discrimination between carious and noncarious tissue.

Quantitative light fluorescence (QLF) is the most extensively investigated optical technique for the measurement of surface demineralization. ten Bosch [95] described the mechanism for the QLF phenomenon, that is, the loss of yellow–green fluorescence under illumination with blue light, and it can be solely explained by light scattering effects. Lesion areas appear dark due to increased light scattering in the lesion area that prevents the fluorescence from the underlying collagen in dentin or unknown fluorophores in enamel that are deeper in the tooth from reaching the tooth surface. Excitation wavelengths have varied from 370 nm to 488 nm and blue laser diodes are more typically employed today. Emission spectra are typically independent of excitation wavelengths – Kasha's rule [96]. A study by Amaechi *et al.* [84] compared the loss of reflectivity with lesion depth as measured with OCT with the loss of fluorescence measured with QLF and achieved a very high correlation, suggesting that both experiments measure the same thing, namely increased light attenuation due to an increase in light scattering in the lesion. Fluorescence images provide increased contrast between sound and demineralized tooth structure and avoid the interference caused by specular reflection or high glare from the tooth surface which can interfere with visual detection of white spot lesions. Figure 68.4c shows an LIF image of the buccal surface of a tooth with a demineralized area.

Hafström-Björkman *et al.* [97] established an experimental relationship between the loss of fluorescence intensity and extent of enamel demineralization [97]. The method was subsequently labeled the QLF (quantitative laser fluorescence)

method. An empirical relationship between overall mineral loss (ΔZ) and loss of fluorescence was established that can be used to monitor lesion progression on enamel surfaces [98–100]. The gold standard for quantifying lesion severity and tooth surface and subsurface demineralization is microradiography. The lesion severity is typically reported as the product of the volume-percent mineral loss and the lesion depth, ΔZ (vol.% $\times$ μm). Therefore, it is advantageous to be able to report a similar measure using optical methods. It is important to point out that QLF researchers report changes in fluorescence radiance, ΔF (%), calculated as

$$\Delta F_{\text{Ref}} = \frac{F_{\text{Ref}}(\text{demin})}{F_{\text{Ref}}(\text{sound})} \times 100 \tag{68.3}$$

for comparison with the ΔZ value measured with microradiography. Excellent correlation has been established between ΔF and ΔZ for shallow, uniform, artificial lesions [97, 101]. This approach requires that the user has prior knowledge that the F_{Ref}(sound) measurement is actually in a sound area of the tooth, free of any surface defects. The ΔF value is a ratio of reflectivity of two regions of the tooth; therefore, if there is some complexity to the lesion structure, ΔF may not be meaningful. This is a serious limitation for high-risk areas such as the occlusal pits and fissures. QLF also manifests a strong dependence on the imaging angle and the remaining enamel thickness of the sample. Ando and co-workers [102, 103] established that the ΔF_{Ref} intensity for similar lesions depends on the actual enamel thickness. That result suggests a very serious limitation for clinical implementation since the enamel thickness varies markedly between positions on each tooth and from tooth to tooth. Even though acquiring a reference sound area needed for calculation of ΔF would be challenging in such areas, this method still provides increased contrast for better visualization of the lesion area.

Another complication is that stains and plaque fluoresce strongly, greatly confounding detection. Therefore, QLF has not been successfully validated for quantifying surface demineralization in the pits and fissures of the occlusal surfaces where most lesions are found, and has manifested relatively low specificity in clinical studies on smooth surfaces [101].

QLF has also been used to quantify and measure remineralization both *in vitro* and *in vivo* [104]. Studies have shown optical changes in the fluorescence intensity after exposure of *in vivo* white spot lesions around orthodontic brackets to a remineralization solution or removal of the plaque retention device [105, 106]. However, since QLF cannot produce an image of the structure of the lesion, it cannot be used to determine whether the lesion simply eroded away after removal of the bracket from abrasive action, whether there was a change in the surface roughness of the lesion, or confirm that actual mineral repair has taken place.

In summary, QLF performs well on carefully produced, shallow, uniform lesions on smooth surfaces that are consistent with the proposed fluorescence loss mechanism. However, such performance cannot be expected on highly convoluted occlusal surfaces or for the complex structures of natural lesions. Moreover, stains, plaque, and developmental defects interfere with QLF, which explains the somewhat disappointing clinical performance to date.

68.6.2
DIAGNOdent (Porphyrin Fluorescence)

Bacteria produce significant amounts of porphyrins and dental plaque fluoresces upon excitation with red light [107]. The earliest fluorescence measurements of dental caries showed the distinctive salmon red fluorescence due to porphyrins [93, 94]. A novel caries detection system, the DIAGNOdent (KaVo, Biberach, Germany) has received FDA approval in the United States. This device, shown in Figure 68.11, uses a red diode laser and a fiber-optic probe designed to detect the fluorescence emitted from porphyrins at longer wavelengths. The probe is designed to be inserted in an occlusal pit and fissure and an electronic reading is generated representing the amount of fluorescence from the lesion. Bacteria produce significant amounts of porphyrins and dental plaque fluoresces upon excitation with red light [107]. This device is designed to detect hidden occlusal lesions that have penetrated into the dentin, where the high porosity concentrates porphyrins from bacteria. It is important to note that the primary microorganism responsible for dental decay, *Streptococcus mutans*, does not contain porphyrins and that this method is not an effective means of monitoring cariogenic bacteria. Moreover, this device is designed to detect lesions in the later stage of development after the lesion has penetrated into the dentin and accumulated a considerable amount of bacterial

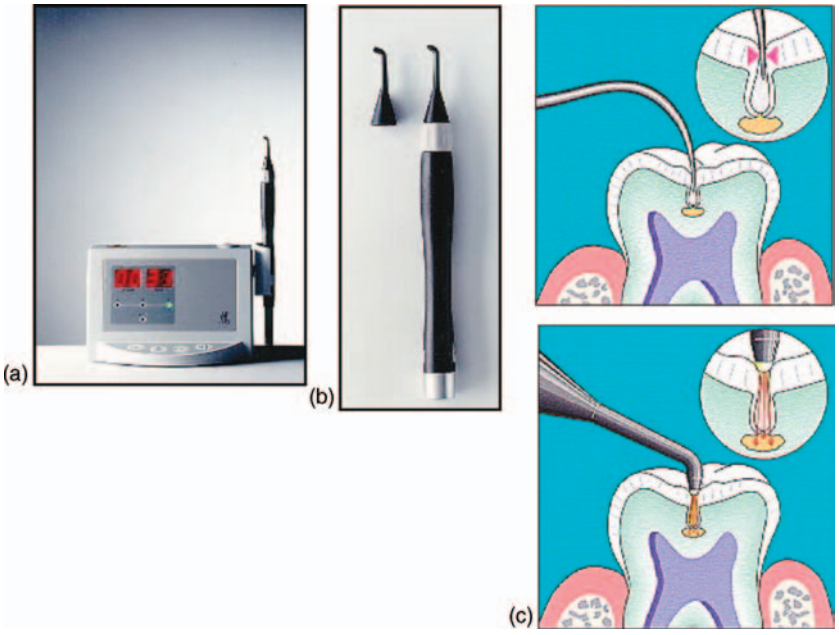

Figure 68.11 Images of (a) the KaVo DIAGNOdent instrument and (b) probes for fluorescence-based detection of caries. The diagrams in (c) compare the use of the DIAGNOdent with the dental explorer for probing the occlusal pits and fissures. Images taken from KaVo web site (http://www.kavo.com/Default.aspx?navid=40&oid=002&lid=En).

byproducts. The DIAGNOdent system has poor sensitivity (~0.4) for lesions confined to enamel [108], since porphyrins have not accumulated in those lesions. Laboratory studies have shown a very good relationship between lesion extent measured histologically after sectioning and the original DIAGNOdent readings [109]. An interproximal caries probe designed to reach proximal surfaces has also been introduced more recently [110]. The DIAGNOdent is well designed for the detection of "hidden" dentinal caries but it does not provide quantitative measurements of demineralization.

68.6.3
Other Fluorescence-Based Imaging Methods

Other fluorescence imaging techniques that have been employed for caries detection include time-resolved fluorescence [111], multiphoton fluorescence [112], dye-enhanced fluorescence [113], confocal fluorescence [100, 114], and modulated fluorescence or luminescence. Confocal fluorescence has considerable promise for studying very early incipient caries lesions.

68.7
Thermal Imaging

Thermal imaging has been used as a tool to measure enamel demineralization. Kaneko *et al*. [115] used a thermal imaging camera to measure the thermal emission from the surface of shallow enamel lesions. The increasing water content of highly porous lesion areas leads to a lower temperature due to evaporative cooling that was clearly discernable in the 3.6–4.6 μm wavelength range.

At highly absorbed wavelengths at which the absorption coefficient greatly exceeds the scattering coefficient, the magnitude of the absorption coefficient can be determined by measurement of the rate of thermal emission from the tooth surface. This is called pulsed photothermal radiometry [116]. Chebotareva *et al*. [117] and Zuerlein *et al*. [42] utilized this approach to determine the magnitude of the absorption coefficient of enamel and dentin at highly absorbed laser wavelengths in the IR region. This approach can also be used to monitor changes in the hard tissues as the absorption coefficient changes with increasing temperature or by modification during laser irradiation [43].

At wavelengths at which there is deep optical penetration such as the visible and NIR region for dental enamel, there can be increased absorption of light by subsurface structures. In theory, the depth of those structures can be calculated by analyzing the temporal profile of the thermal emission from the sample. The incident thermal radiation can be temporally modulated for frequency-domain photothermal radiometry (FD-PTR) and Mandelis and co-workers [118–121] have applied FD-PTR to detect and analyze dental caries, cracks, and other subsurface structures in teeth. Analysis of the phase and amplitude of the PTR signals at different modulation frequencies provides depth-specific information. Mandelis and co-workers indicated

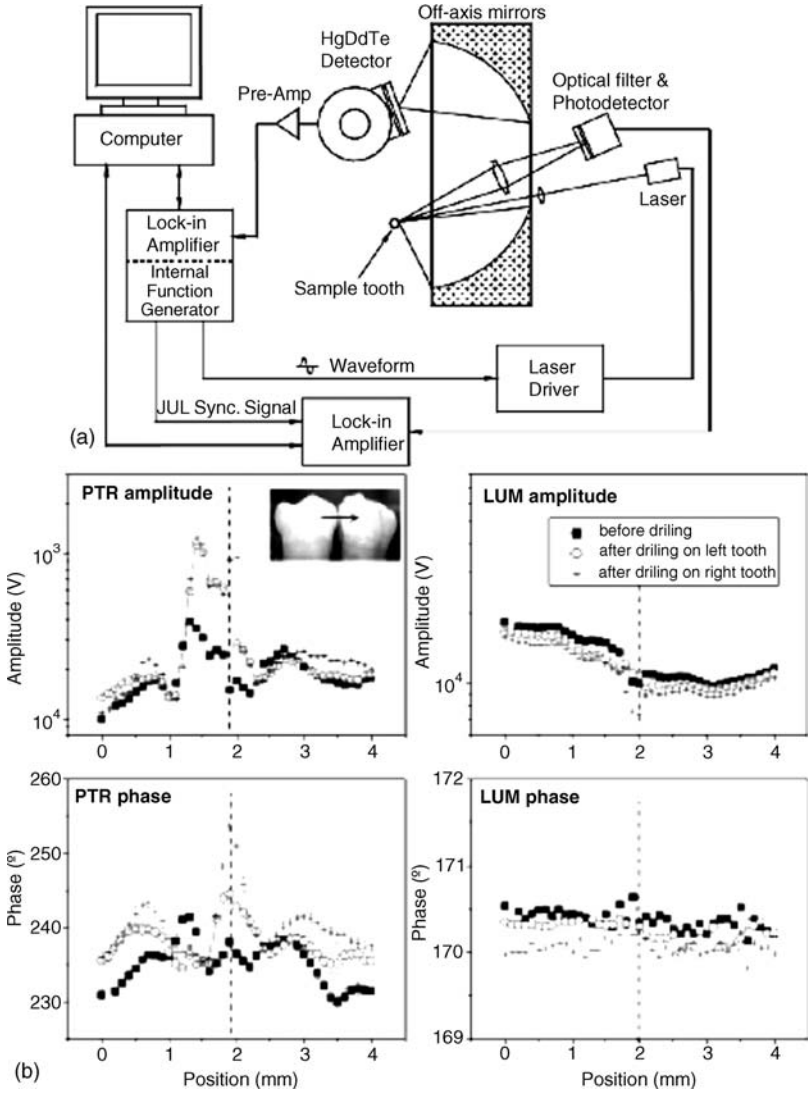

Figure 68.12 (a) Apparatus for frequency-domain IR PTR and modulated luminescence (LUM) imaging. (b) PTR and LUM phase and amplitude measurements at 5 Hz across the proximal contact point before and after drilling holes in each tooth. From reference [118].

that this method can be used potentially to monitor defects up to 3 mm below the surface. The apparatus used to acquire simultaneous FD-PTR signals and modulated fluorescence or luminescence signals is shown in Figure 68.12. Studies have been carried out looking at natural and artificial lesions in enamel and dentin and holes and cracks in teeth. A sample image of holes drilled in teeth positioned at the proximal contact points is also shown in Figure 68.12, indicating that the PTR signals change after drilling holes in the teeth at the appropriate positions. The FD-PTR

signals acquired from artificial lesions show that the PTR signals change with increasing lesion severity, which is consistent to what would be expected with an increase in the scattering coefficient as is observed with other methods.

68.8 Infrared Spectroscopy

Enamel and dentin have distinctive molecular absorption bands in the IR region due to the water, mineral, protein, and lipid components. IR spectra can be used to monitor chemical and crystalline orientational changes in the mineral and organic components of dental hard tissues. The surfaces of mineralized tissues are well suited for probing by light scattering, reflectance, attenuated total reflectance, and photoacoustic IR methods. Transmission measurements are more difficult owing to the high water absorption across the mid-IR region and the extremely high absorption near 3 μm (water) and the mineral phase from 9 to 11 μm. Spectra are useful for determining changes to the organic components, crystalline changes to the mineral phase that are indicative of the formation of either more acid resistance phases, or the disproportionation of hydroxyapatite to form other calcium phosphate phases that are more susceptible to acid dissolution.

IR spectroscopy has been used for half a century to study the structure of bony tissues [122–125]. The most intense absorption bands are due to the phosphate group between 1000 and 1200 cm^{-1}. The spectral properties of the carbonate bands [126, 127] located near 1500 and 800–900 cm^{-1} are of particular importance since it is the carbonate inclusions in the hydroxyapatite mineral phase that make dental enamel highly susceptible to acid dissolution. Fowler and Kuroda [128, 129] used IR transmission spectroscopy to show the chemical changes induced in laser-irradiated dental enamel. Featherstone *et al.* [130] showed that the amount of carbonate in synthetic carbonated hydroxyapatites could be quantified using IR transmission measurements. These early transmission measurements employed the very destructive KBr pellet method, in which the surface of the irradiated enamel is ground away and mixed with KBr to produce a pellet. Fourier transform infrared (FTIR) spectroscopy in specular reflectance mode can provide the same information without destruction of the sample [131]. The principal advantage of this technique is that the tissue reflectance is only influenced by a surface layer with a thickness on the order of the wavelength of the light. FTIR reflectance spectra showing the influence of laser irradiation on the chemical composition of tooth enamel are shown at several irradiation intensities in Figure 68.13. Thermal transformation of the carbonated hydroxyapatite mineral in enamel to a purer phase hydroxyapatite is indicated by the decrease in the area of the carbonate bands between 6 and 8 μm. High-brightness synchrotron radiation sources such as the advanced light source (ALS) provide a means to probe nondestructively specific areas such as laser ablation craters and resolve the laser-induced chemical changes that occur in the mineral phase. During high-intensity laser irradiation, marked chemical and physical changes may be induced in the irradiated dental enamel. Thermal decomposition of the mineral

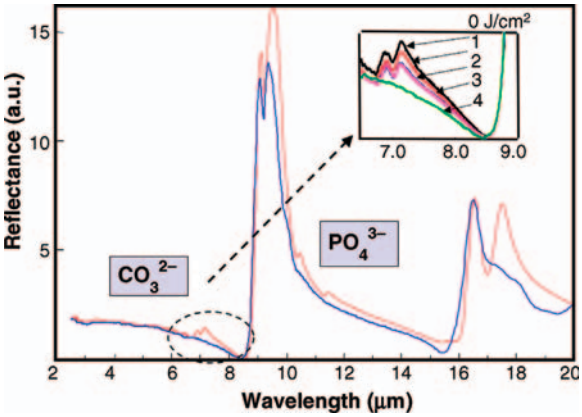

Figure 68.13 IR reflectance spectra of enamel before and after irradiation by a carbon dioxide laser at various irradiation intensities (fluence). The inset shows the area of the carbonate peaks as the carbonate is removed with increasing fluence. From ref. [131].

can lead to changes in the susceptibility of the modified mineral to organic acids in the oral environment. The mineral hydroxyapatite, found in bone and teeth, contains carbonate inclusions that render it highly susceptible to acid dissolution by organic acids generated from bacteria in dental plaque. Upon heating to temperatures in excess of 400 °C, the mineral decomposes to form a new mineral phase that has increased resistance to acid dissolution [132]. Studies have suggested that as a side effect of laser ablation, the walls around the periphery of a cavity preparation will be transformed through laser heating into a more acid-resistant phase with an enhanced resistance to future decay [133–135]. However, poorly crystalline non-apatite phases of calcium phosphate may have an opposite effect on plaque acid resistance [128] and may increase the quantity of poorly attached grains associated with delamination failures.

Polarized IR reflectance measurements can also show orientation changes in the enamel crystals [136]. Such information can be used to show changes to the enamel crystal structure as a result of thermal modification by laser irradiation and chemical changes through acid dissolution and fluoride-enhanced remineralization.

68.9
Raman Spectroscopy and Imaging

Raman spectroscopy has been employed in several studies to measure changes in the mineral phase of demineralized and remineralized enamel and dentin, aid in the discrimination of carious enamel, measure the mineral content of dental calculus, and measure the presence of CaF_2 after fluoride treatments. Raman spectra have been obtained of hydroxyapatite, enamel, dentin, and calculus [137–141]. High-resolution micro-Raman spectroscopy has been used to analyze the chemical composition of the internal interfaces between enamel/dentin and cementum [142].

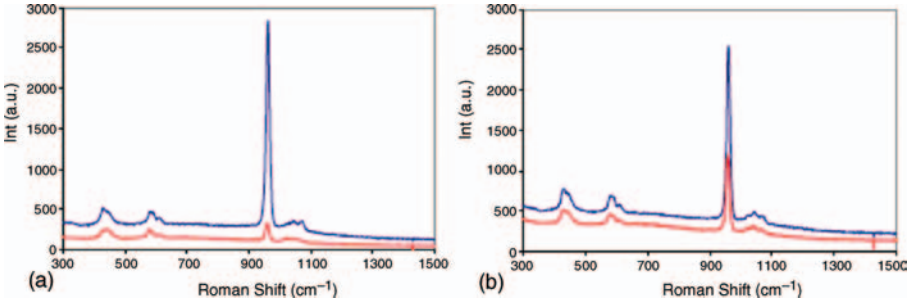

Figure 68.14 Representative parallel- (upper trace) and cross- (lower trace) polarized Raman spectra of (a) sound enamel and (b) caries lesions acquired with the portable Raman spectrometer system. From ref. [144].

Tsuda and Arends [138] used polarization-resolved Raman scattering to gain additional information about changes in the crystal structure of enamel. In a similar manner to IR reflectance spectroscopy [136], polarized Raman analysis can reveal the orientation of single crystals of hydroxyapatite. Such polarized Raman spectra can show the orientation of newly deposited mineral crystals during the repair of the enamel crystals via remineralization and orientational loss during demineralization. It has been well established that caries lesions rapidly depolarize incident light, and Ko and co-workers [143, 144] used polarized Raman spectroscopy to help discriminate caries lesions from sound enamel. Figure 68.14 shows polarized Raman spectra of sound enamel and caries lesions acquired with a portable Raman spectrometer.

Hill and Petrou [145] showed that NIR Raman spectroscopy could be used to differentiate between sound and carious enamel both *in vitro* and *in vivo*. NIR Raman spectroscopy is advantageous for the examination of biological tissues due to the reduced fluorescence background. They used the intensity ratio of the intense 960 cm^{-1} phosphate peak and the background luminescence (fluorescence) at 930 cm^{-1}. Yokoyama *et al.* [146] examined carious lesions with a hollow optical fiber probe that was cemented to a glass ball lens allowing the same fiber to be used for both light delivery and collection. They used the ratio of the 433/446 cm^{-1} peaks, which are peaks due to phosphate that manifest intensity differences in polarized Raman spectra, to indicate caries along with the fluorescence ratio of the 962/930 cm^{-1} peaks. Even though fluorescence is typically considered a major source of unwanted noise in Raman spectroscopy of biological tissues, it can also be exploited in the case of dental caries. Ko *et al.* used polarization ratios of the 959 cm^{-1} band to indicate caries [144]. They also used Raman spectroscopy in conjunction with OCT to help differentiate sound and demineralized enamel [143].

Raman spectroscopy can also be used to monitor changes in the carbonate content of enamel and dentin in a similar fashion to IR spectroscopy [147–150]. Carbonate is preferentially lost during demineralization since those sites on the enamel crystal have a higher solubility than the rest of the mineral phase. Liu and Hsu [151] and Klocke *et al.* [152] showed that changes in the carbonate content could be measured after laser irradiation.

68.10
Ultrasound and Terahertz Imaging

Ultrasound uses high-frequency mechanical pressure waves that are reflected in tissues upon encountering changes in tissue density. Different materials such as enamel dentin and carious tissues manifest different acoustic velocities [153]. Although ultrasound has been highly successful in medicine, bulky probes, the large acoustic impedance mismatch (low coupling efficiency) at the tooth surface due to the high density of the enamel of the tooth, and the relatively low resolution of ultrasound has greatly hindered its use for caries imaging. Ghorayeb *et al.* recently provided a review of ultrasonography for dentistry [154]. Lees and Barber first used ultrasound to measure the internal interfaces in the tooth, namely the enamel–dentin junction and the dentin–pulp junction over 40 years ago [155]. Huysmans and co-workers [156, 157] demonstrated that the a conventional ultrasonic probe could be used with a glycerin coupling agent to measure the remaining enamel thickness for monitoring erosion on extracted human incisors. Culijat *et al.* [158] acquired an entire circumferential scan of a tooth accurately showing the enamel thickness using water as a coupling agent. Blodgett [159] used laser-produced ultrasonic waves to image internal tooth interfaces. A pulsed CO_2 laser was used to produce the ultrasonic waves directly in the tooth, which overcomes the problem of low coupling efficiency.

Several studies have demonstrated that ultrasound can be used to measure tooth demineralization [160, 161]. Ng *et al.* [162] showed that 18 MHz pulse echo ultrasound could be used to differentiate shallow lesions artificially induced on extracted teeth. Teeth were immersed in a water-bath for measurement. Tagtekin *et al.* [160] used an ultrasound probe with glycerin as a coupling agent to measure early white spot lesions on the proximal surfaces of extracted third molar teeth.

Matalon *et al.* [163] demonstrated in both *in vitro* and *in vivo* studies that a hand-held probe that utilizes ultrasonic surface waves (Rayleigh) could be used to detect cavitated interproximal lesions. This device yielded higher sensitivity to cavitated interproximal lesions than bitewing radiographs, but the specificity was lower.

Terahertz radiation is located at wavelengths of ~75 μm–7.5 mm between the far-IR and microwave regions. Biological tissues are semi-transparent and have terahertz fingerprints, permitting them to be imaged, identified, and analyzed. High-intensity synchrotron radiation sources have been used to generate terahertz radiation for imaging. Schade *et al.* [164] acquired multispectral images of teeth in the range 0.06–0.6 THz using a synchrotron. Near-field imaging techniques were employed to increase the resolution. An image of a 2.7 mm thick tooth slab with a lesion through the enamel is shown in Figure 68.15. More portable terahertz imaging systems are now available that utilize pulsed femtosecond lasers and semiconductors [165]. One of the most promising implementations involves terahertz pulse imaging (TPI). This method can be used to measure the remaining enamel thickness to provide a measure of enamel erosion [166]. The large refractive index mismatch at the dentin–enamel junction provides a strong reflective signal in TPI. Crawley *et al.* [165] showed that areas of demineralized and hypomineralized enamel can

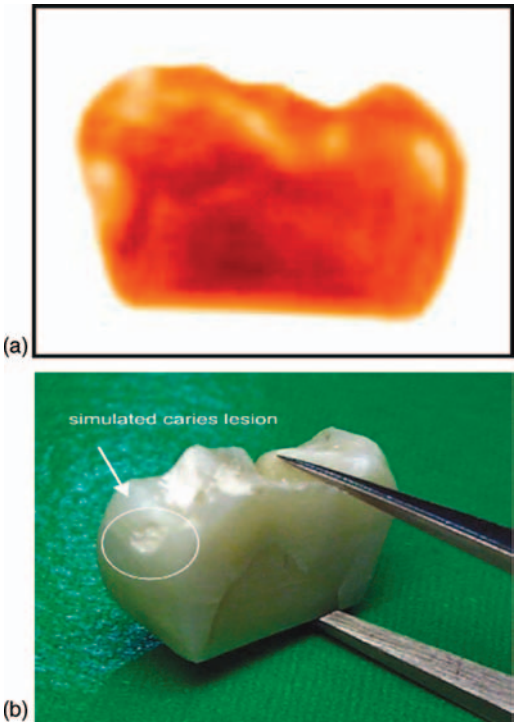

Figure 68.15 A near-field THz image (a) of a 2.7 mm thick human tooth section with an embedded small lesion (b). From ref. [164].

be discriminated from sound tissue in TPI images. The depth of artificial "surface-softened" lesions created in enamel using an acid gel measured by TPI compared well with measurements [167]. These methods appear best suited for measurement of the lesion depth and the remaining enamel thickness for erosion measurements.

References

1 National Institutes of Health (2001) Diagnosis and Management of Dental Caries Throughout Life 1–24, NIH Consensus Statement. National Institutes of Health, Wahington, DC.

2 Lussi, A. (1991) Validity of diagnostic and treatment decisions of fissure caries. *Caries Res.*, **25**, 296–303.

3 Featherstone, J.D.B. and Young, D. (1999) The need for new caries detection methods. *Proc. SPIE*, **3593**, 134–140.

4 Hume, W.R. (1996) Need for change in dental caries diagnosis, in *Early Detection of Dental Caries, Proceedings of the 1st Annual Indiana Conference* (ed. G.K. Stookey), Indiana University School of Dentistry, Indianapolis, IN, pp. 1–10.

5 Featherstone, J.D.B. (1996) Clinical implications: new strategies for caries prevention, in *Early Detection of Dental Caries, Proceedings of the 1st Annual Indiana Conference* (ed. G.K. Stookey), Indiana University School of Dentistry, Indianapolis, IN, pp. 287–295.

6 ten Cate, J.M. and van Amerongen, J.P. (1996) Caries diagnosis: conventional methods, in *Early Detection of Dental Caries, Proceedings of the 1st Annual Indiana Conference* (ed. G.K. Stookey), Indiana University School of Dentistry, Indianapolis, IN, pp. 27–37.

7 Featherstone, J.D.B. (1999) Prevention and reversal of dental caries:role of low level fluoride. *Community Dent. Oral. Epidemiol.*, **27**, 31–40.

8 Zijp, J.R. and ten Bosch, J.J. (1991) Angular dependence of HeNe laser light scattering by bovine and human dentine. *Arch. Oral Biol.*, **36**, 283–289.

9 Zijp, J.R. and ten Bosch, J.J. (1993) Theoretical model for the scattering of light by dentin and comparison with measurements. *Appl. Opt.*, **32**, 411–415.

10 Fried, D., Featherstone, J.D.B., Glena, R.E., and Seka, W. (1995) The nature of light scattering in dental enamel and dentin at visible and near-IR wavelengths. *Appl. Opt.*, **34**, 1278–1285.

11 Zijp, J.R., ten Bosch, J.J., and Groenhuis, R.A. (1995) HeNe laser light scattering by human dental enamel. *J. Dent. Res.*, **74**, 1891–1898.

12 Schmidt, W.J. and Keil, A. (1971) *Polarizing Microscopy of Dental Tissues*, Pergamon Press, Oxfordk.

13 Theuns, H.M., Shellis, R.P., Groeneveld, A., Dijk, J.W.E. and Poole, D.F.G. (1993) Relationships between birefringence and mineral content in artificial caries lesions in enamel. *Caries Res.*, **27**, 9–14.

14 Cheong, W., Prahl, S.A. and Welch, A.J. (1990) A review of the optical properties of biological tissues. *IEEE J. Quantum Electron.*, **26**, 2166–2185.

15 Wilson, B.C., Patterson, M.S., and Flock, S.T. (1987) Indirect versus direct techniques for the measurement of the optical properties of tissues. *Photochem. Photobiol.*, **46**, 601–608.

16 Izatt, J.A., Hee, M.R., Huang, D., Fujimoto, J.G., Swanson, E.A., Lin, C.P., Schuman, J.S., and Puliafito, C.A. (1993) Optical coherence tomography for medical applications, in *Medical Optical Tomography:Functional Imaging and Monitoring* (ed. G. Muller), SPIE, Bellingham, WA, pp. 450–472.

17 Tuchin, V. (2000) *Tissue Optics: Light Scattering Methods and Instruments for Medical Diagnostics*, SPIE, Bellingham, WA.

18 Spitzer, D. and ten Bosch, J.J. (1975) The absorption and scattering of light in bovine and human dental enamel. *Calcif. Tissue Res.*, **17**, 129–137.

19 ten Bosch, J.J. and Zijp, J.R. (1987) Optical properties of dentin, in *Dentine and Dentine Research in the Oral Cavity* (eds. A. Thylstrup, S.A. Leach, and V. Qvist), IRL Press, Oxford, pp. 59–65.

20 Jones R.S. and Fried, D. (2002) Attenuation of 1310 nm and 1550 nm laser light through sound dental enamel. *Proc. SPIE*, **4610**, 187–190.

21 Hale, G.M. and Querry, M.R. (1973) Optical constants of water in the 200 nm to 200-μm wavelength region. *Appl. Opt.*, **12**, 555–563.

22 Wang, L. and Jacques, S.L. (1992) *Monte Carlo Modeling of Light Transport in Multi-Layer Tissues in Standard C*, University of Texas M.D. Anderson Cancer Center, Houston, TX.

23 Wilson, B.C. and Adam, G. (1989) A Monte Carlo model for the absorption and flux distribution of light in tissue. *Med. Phys.*, **10**, 824–830.

24 van der Zee, P. (1993) Methods for measuring the optical properties of tissue in the visible and near-IR wavelength range, in *Medical Optical Tomography: Functional Imaging and Monitoring* (eds. G.H. Mueller *et al.*), vol. **IS11**, SPIE, Bellingham, WA, pp. 450–472.

25 Altshuler, G.B. (1995) Optical model of the tissues of the human tooth. *J. Opt. Technol.*, **62**, 516–521.

26 Altshuler, G.B. and Grisimov, V.N. (1990) New optical model in the human hard tooth tissues. *Proc. SPIE*, **1353**, 97–102.

27 Kienle, A., Forster, F.K., Diebolder, R., and Hibst, R. (2003) Light propagation in dentin: influence of microstructure on anisotropy. *Phys. Med. Biol.*, **48**, N7–N14.

28 Kienle, A., Forster, F.K. and Hibst, R. (2004) Anisotropy of light propagation in

biological tissue. *Opt. Lett.*, **29**, 2617–2619
29 Kienle, A. and Hibst, R. (2006) Light guiding in biological tissue due to scattering. *Phys. Rev. Lett.*, **97**, 018104.
30 Kienle, A., Michels, R. and Hibst, R. (2005) Light propagation in a cubic biological tissue having anisotropic optical properties. *Proc. SPIE*, **5859**, 585917-1–585917-7.
31 Kienle, A., Michels, R., and Hibst, R. (2006) Magnification – a new look at a long-known optical property of dentin. *J. Dent. Res.*, **85**, 955–959.
32 Brinkman, J., ten Bosch, J.J., and Borsboom, P.C.F. (1988) Optical quantification of natural caries in smooth surfaces of extracted teeth. *Caries Res.*, **22**, 257–262.
33 ten Bosch, J.J., van der Mei, H.C. and Borsboom, P.C.F. (1984) Optical monitor of *in vitro* caries. *Caries Res.*, **18**, 540–547.
34 Angmar-Månsson, B. and ten Bosch, J.J. (1987) Optical methods for the detection and quantification of caries. *Adv. Dent. Res.*, **1**, 14–20.
35 ten Bosch, J.J. and Coops, J.C. (1995) Tooth color and reflectance as related to light scattering and enamel hardness. *J. Dent. Res.*, **74**, 374–380.
36 Ko, C.C., Tantbirojn, D., Wang, T., and Douglas, W.H. (2000) Optical scattering power for characterization of mineral loss. *J. Dent. Res.*, **79**, 1584–1589.
37 Wefel, J.S., Clarkson, B.H. and Heilman, J.R. (1985) Natural root caries: a histologic and microradiographic evaluation. *J. Oral Pathol.*, **14**, 615–623.
38 Vaarkamp, J., ten Bosch, J.J., and Verdonschot, E.H. (1995) Light propagation through teeth containing simulated caries lesions. *Phys. Med. Biol.*, **40**, 1375–1387.
39 Darling, C.L., Huynh, G.D., and Fried, D. (2006) Light scattering properties of natural and artificially demineralized dental enamel at 1310 nm. *J. Biomed. Opt.*, **11**, 034023 1–11.
40 Fried, D., Glena, R.E., Featherstone, J.D.B., and Seka, W. (1997) Permanent and transient changes in the reflectance of CO_2 laser irradiated dental hard tissues at $\lambda = 9.3$, 9.6, 10.3, and 10.6 μm and at fluences of 1–20 J/cm^2. *Lasers Surg. Med.*, **20**, 22–31.
41 Duplain, G., Boulay, R. and Belanger, P.A. (1987) Complex index of refraction of dental enamel at CO_2 wavelengths. *Appl. Opt.*, **26**, 4447–4451.
42 Zuerlein, M., Fried, D., Featherstone, J.D.B., and Seka, W. (1999) Absorption coefficients of dental enamel at CO_2 wavelengths. *Spec. Top. J. Quantum Electron.*, **5**, 1083–1089.
43 Zuerlein, M., Fried, D., and Featherstone, J.D.B. (1999) Modeling the modification depth of carbon dioxide laser treated enamel. *Lasers Surg. Med.*, **25**, 335–347.
44 Benson, P.E., Ali Shah, A., and Robert Willmot, D. (2008) Polarized versus nonpolarized digital images for the measurement of demineralization surrounding orthodontic brackets. *Angle Orthod.*, **78**, 288–293.
45 Everett, M.J., Colston, B.W., Sathyam, U.S., Silva, L.B.D., Fried, D., and Featherstone, J.D.B. (1999) Non-invasive diagnosis of early caries with polarization sensitive optical coherence tomography (PS-OCT). *Proc. SPIE*, **3593**, 177–183.
46 Fried, D., Xie, J., Shafi, S., Featherstone, J.D.B., Breunig, T., and Lee, C.Q. (2002) Early detection of dental caries and lesion progression with polarization sensitive optical coherence tomography. *J. Biomed. Opt.*, **7**, 618–627.
47 Fried, D., Featherstone, J.D.B., Darling, C.L., Jones, R.S., Ngaotheppitak, P., and Buehler, C.M. (2005) *Early Caries Imaging and Monitoring with Near-IR Light*, Saunders, Philadelphia, pp. 771–794.
48 Blodgett, D.W. and Webb, S.C. (2001) Optical BRDF and BSDF measurements of human incisors from visible to mid-infrared wavelengths. *Proc. SPIE*, **4257**, 448–454.
49 Analoui, M., Ando, M., and Stookey, G.K. (2000) Comparison of reflectance spectra of sound and carious enamel. *Proc. SPIE*, **3910**, 1017–2661.
50 Wu, J.I. and Fried, D. (2009) High contrast near-infrared polarized reflectance images of demineralization

on tooth buccal and occlusal surfaces at $\lambda = 1310$ nm. *Lasers Surg. Med.*, **41** (3), 208–213.

51 Barenie, J., Leske, G., and Ripa, L.W. (1973) The use of fiber optic transillumination for the detection of proximal caries. *Oral Surg.*, **36**, 891–897.

52 Pine, C.M. (1996) Fiber-optic transillumination (FOTI) in caries diagnosis, in *Early Detection of Dental Caries, Proceedings of the 1st Annual Indiana Conference* (ed. G.K. Stookey), Indiana University School of Dentistry, Indianapolis, IN, pp. 51–66.

53 Peltola, J. and Wolf, J. (1981) Fiber optics transillumination in caries diagnosis. *Proc. Finn. Dent. Soc.*, **77**, 240–244.

54 Holt, R.D. and Azeevedo, M.R. (1989) Fiber optic transillumination abnd radiographs in diagnosis of approximal cariesin primary teeth. *Community Dent. Health*, **6**, 239–247.

55 Mitropoulis, C.M. (1985) The use of fiber optic transillumination in the diagnosis of posterior approximal caries in clinical trials. *Caries Res.*, **19**, 379–384.

56 Hintze, H., Wenzel, A., Danielsen, B., and Nyvad, B. (1998) Reliability of visual examination, fibre-optic transillumination, and bite-wing radiography, and reproducibility of direct visual examination following tooth separation for the identification of cavitated carious lesions in contacting approximal surfaces. *Caries Res.*, **32**, 204–209.

57 Schneiderman, A., Elbaum, M., Schultz, T., Keem, S., Greenebaum, M., and Driller, J. (1997) Assessment of dental caries with digital imaging fiber-optic transillumination (DIFOTI): *in vitro* study. *Caries Res.*, **31**, 103–110.

58 Bin-Shuwaish, M., Yaman, P., Dennison, J., and Neiva, G. (2008) The correlation of DIFOTI to clinical and radiographic images in Class II carious lesions. *J. Am. Dent. Assoc.*, **139**, 1374–1381.

59 Young, D.A. and Featherstone, J.D. (2005) Digital imaging fiber-optic trans-illumination, F-speed radiographic film and depth of approximal lesions. *J. Am. Dent. Assoc.*, **136**, 1682–1687.

60 Young, D.A. (2002) New caries detection technologies and modern caries management: merging the strategies. *Gen. Dent.*, **50**, 320–331.

61 Yang, J. and Dutra, V. (2005) Utility of radiology, laser fluorescence, and transillumination. *Dent. Clin. North Am.*, **49**, 739–752, vi.

62 Keem, S. and Elbaum, M. (1997) Wavelet representations for monitoring changes in teeth imaged with digital imaging fiber-optic transillumination. *IEEE Trans. Med. Imaging*, **16**, 653–663.

63 Jones, R. and Fried, D. (2001) Attenuation of 1310 nm and 1550 nm laser light through dental enamel. *J. Dent. Res.*, **80**, 737.

64 Huynh, G.D., Darling, C.L., and Fried, D. (2004) Changes in the optical properties of dental enamel at 1310 nm after demineralization. *Proc. SPIE*, **5313**, 118–124.

65 Darling, C.L. and Fried, D. (2005) Optical properties of natural caries lesions in dental enamel at 1310 nm. *Proc. SPIE*, **5687**, 34–41.

66 Bühler, C.M., Ngaotheppitak, P., and Fried, D. (2005) Imaging of occlusal dental caries (decay) with near-IR light at 1310 nm. *Opt. Express*, **13**, 573–582.

67 Jones, R.S., Huynh, G.D., Jones, G.C., and Fried, D. (2003) Near-IR transillumination at 1310 nm for the imaging of early dental caries. *Opt. Express*, **11**, 2259–2265.

68 Jones, G., Jones, R.S., and Fried, D. (2004) Transillumination of interproximal caries lesions with 830 nm light. *Proc. SPIE*, **5313**, 17–22.

69 Bouma, B.E. and Tearney, G.J. (eds.) (2002) *Handbook of Optical Coherence Tomography*, Marcel Dekker, New York.

70 Derickson, D. (1998) *Fiber Optic Test and Measurement*, Prentice Hall, Upper Saddle River, NJ.

71 Youngquist, R.C., Carr, S., and Davies, D.E.N. (1987) Optical coherence-domain reflectometry. *Appl. Opt.*, **12**, 158–160.

72 Huang, D., Swanson, E.A., Lin, C.P., Schuman, J.S., Stinson, W.G., Chang, W., Hee, M.R., Flotte, T., Gregory, K., Puliafito, C.A., and Fujimoto, J.G. (1991)

Optical coherence tomography. *Science*, **254**, 1178–1181.

73 Brezinski, M. (2006) *Optical Coherence Tomography: Principles and Applications*, Academic Press, Burlington, MA.

74 Colston, B., Everett, M., Da Silva, L., Otis, L., Stroeve, P., and Nathel, H. (1998) Imaging of hard and soft tissue structure in the oral cavity by optical coherence tomography. *Appl. Opt.*, **37**, 3582–3585.

75 Colston, B.W., Everett, M.J., Da Silva, L.B., and Otis, L.L. (1998) Optical coherence tomography for diagnosis of periodontal diseases. *Proc. SPIE*, **3251**, 52–58.

76 Colston, B.W., Sathyam, U.S., DaSilva, L.B., Everett, M.J., and Stroeve, P. (1998) Dental OCT. *Opt. Express*, **3**, 230–238.

77 Feldchtein, F.I., Gelikonov, G.V., Gelikonov, V.M., Iksanov, R.R., Kuranov, R.V., Sergeev, A.M., Gladkova, N.D., Ourutina, M.N., Warren, J.A., and Reitze, D.H. (1998) *In vivo* OCT imaging of hard and soft tissue of the oral cavity. *Opt. Express*, **3**, 239–251.

78 Otis, L.L., Al-Sadhan, R.I., Meiers, J., and Redford-Badwal, D. (2000) Identification of occlusal sealants using optical coherence tomography. *J. Clin. Dent.*, **14**, 7–10.

79 Madjarova, V.D., Yasuno, Y., Makita, S., Hori, Y., Voeffray, J.B., Itoh, M., Yatagai, T., Tamura, M., and Nanbu, T. (2006) Investigations of soft and hard tissues in oral cavity by spectral domain optical coherence tomography. *Proc. SPIE*, **6079**, 60790N-1–60790N-7.

80 Seon, Y.R., Jihoon, N., Hae, Y.C., Woo, J.C., Byeong, H.L., and Gil-Ho, Y. (2006) Realization of fiber-based OCT system with broadband photonic crystal fiber coupler. *Proc. SPIE*, **6079**, 60791N-1–60791N-7.

81 Yamanari, M., Makita, S., Violeta, D.M., Yatagai, T., and Yasuno, Y. (2006) Fiber-based polarization-sensitive Fourier domain optical coherence tomography using B-scan-oriented polarization modulation method. *Opt. Express*, **14**, 6502–6515.

82 Furukawa, H., Hiro-Oka, H., Amano, T., DongHak, C., Miyazawa, T., Yoshimura, R., Shimizu, K., and Ohbayashi, K. (2006) Reconstruction of three-dimensional structure of an extracted tooth by OFDR-OCT. *Proc. SPIE*, **6079**, 60790T-1–60790T-7.

83 Amaechi, B.T., Higham, S.M., Podoleanu, A.G., Rodgers, J.A., and Jackson, D.A. (2001) Use of optical coherence tomography for assessment of dental caries. *J. Oral. Rehab.*, **28**, 1092–1093.

84 Amaechi, B.T., Podoleanu, A., Higham, S.M., and Jackson, D.A. (2003) Correlation of quantitative light-induced fluorescence and optical coherence tomography applied for detection and quantification of early dental caries. *J. Biomed. Opt.*, **8**, 642–647.

85 Baumgartner, A., Hitzenberger, C.K., Dicht, S., Sattmann, H., Moritz, A., Sperr, W., and Fercher, A.F. (1998) Optical coherence tomography for dental structures. *Proc. SPIE*, **3248**, 130–136.

86 Dicht, S., Baumgartner, A., Hitzenberger, C.K., Sattmann, H., Robi, B., Moritz, A., Sperr, W., and Fercher, A.F. (1999) Polarization-sensitive optical optical coherence tomography of dental structures. *Proc. SPIE*, **3593**, 169–176.

87 Baumgartner, A., Dicht, S., Hitzenberger, C.K., Sattmann, H., Robi, B., Moritz, A., Sperr, W., and Fercher, A.F. (2000) Polarization-sensitive optical optical coherence tomography of dental structures. *Caries Res.*, **34**, 59–69.

88 Wang, X.J., Zhang, J.Y., Milner, T.E., Boer, J.F.D., Zhang, Y., Pashley, D.H., and Nelson, J.S. (1999) Characterization of dentin and enamel by use of optical coherence tomography. *Appl. Opt.*, **38**, 586–590.

89 Jones, R.S., Darling, C.L., Featherstone, J.D.B., and Fried, D. (2004) Imaging artificial caries on occlusal surfaces with polarization sensitive optical coherence tomography. *Caries Res.*, **40**, 81–89.

90 Ngaotheppitak, P., Darling, C.L., and Fried, D. (2006) PS-OCT of natural

pigmented and non-pigmented interproximal caries lesions. *Proc. SPIE*, **5687**, 25–33.

91 Ismail, A.I. (2004) Visual and visuo-tactile detection of dental caries. *J. Dent. Res.*, **83**, C56–C66.

92 Jones, R.S., Staninec, M., and Fried, D. (2004) Imaging artificial caries under composite sealants and restorations. *J. Biomed. Opt.*, **9**, 1297–1304.

93 Alfano, R.R., Lam, W., Zarrabi, H.J., Alfano, M.A., Cordero, J., and Tata, D.B. (1984) Human teeth with and without caries studied by laser scattering, fluorescence and absorption spectroscopy. *IEEE J. Quantum Electron.*, **20**, 1512–1515.

94 Bjelkhagen, H. and Sundstrom, F. (1981) A clinically applicable laser luminescence for the early detection of dental caries. *IEEE J. Quantum Electron.*, **17**, 266–268.

95 ten Bosch, J.J. (1999) Summary of research of quantitative light fluorescence, in *Early Detection of Dental Caries II*, vol. **4**, Indiana University School of Dentistry, Indianapolis, IN, pp. 261–278.

96 Lakowicz, J.R. (1999) *Principles of Fluorecence Spectroscopy*, Kluwer Academic, New York.

97 Hafström-Björkman, U., Sundström, F., de Josselin de Jong, E., Oliveby, A., and Angmar-Månsson, B. (1992) Comparison of laser fluorescence and longitudinal microradiography for quantitative assessment of *in vitro* enamel caries. *Caries Res.*, **26**, 241–247.

98 Ando, M., Gonzalez-Cabezas, C., Isaacs, R.L., Eckert, A.F., and Stookey, G.K. (2004) Evaluation of several techniques for the detection of secondary caries adjacent to amalgam restorations. *Caries Res.*, **38**, 350–356.

99 de Josselin de Jong, E., Sundström, F., Westerling, H., Tranaeus, S., ten Bosch, J.J., and Angmar-Månsson, B. (1995) A new method for *in vivo* quantification of changes in initial enamel caries with laser fluorescence. *Caries Res.*, **29**, 2–7.

100 Fontana, M., Li, Y., Dunipace, A.J., Noblitt, T.W., Fischer, G., Katz, B.P., and Stookey, G.K. (1996) Measurement of enamel demineralization using microradiography and confocal microscopy. *Caries Res.*, **30**, 317–325.

101 Stookey, G.K. (2005) *Quantitative Light Fluorescence: a Technology for Early Monitoring of the Caries Process*, Saunders, Philadelphia, pp. 753–770.

102 Ando, M., Eckert, G.J., Stookey, G.K., and Zero, D.T. (2004) Effect of imaging geometry on evaluating natural white-spot lesions using quantitative light-induced fluorescence. *Caries Res.*, **38**, 39–44.

103 Ando, M., Schemehorn, B.R., Eckert, G.J., Zero, D.T., and Stookey, G.K. (2003) Influence of enamel thickness on quantification of mineral loss in enamel using laser-induced fluorescence. *Caries Res.*, **37**, 24–28.

104 al-Khateeb, S., Oliveby, A., de Josselin de Jong, E., and Angmar-Månsson, B. (1997) Laser fluorescence quantification of remineralisation *in situ* of incipient enamel lesions: influence of fluoride supplements. *Caries Res.*, **31**, 132–140.

105 Tranaeus, S., Al-Khateeb, S., Björkman, S., Twetman, S., and Angmar-Månsson, B. (2001) Application of quantitative light-induced fluorescence to monitor incipient lesions in caries-active children. A comparative study of remineralisation by fluoride varnish and professional cleaning. *Eur. J. Oral Sci.*, **109**, 71–75.

106 al-Khateeb, S., ten Cate, J.M., Angmar-Månsson, B., de Josselin de Jong, E., Sundström, G., Exterkate, R.A., and Oliveby, A. (1997) Quantification of formation and remineralization of artificial enamel lesions with a new portable fluorescence device. *Adv. Dent. Res.*, **11**, 502–506.

107 Koenig, K., Schneckenburger, H., Hemmer, J., Tromberg, B.J., Steiner, R.W., and Rudolf, W. (1994) *In-vivo* fluorescence detection and imaging of porphyrin-producing bacteria in the human skin and in the oral cavity for diagnosis of acne vulgaris, caries, and squamous cell carcinoma. *Proc. SPIE*, **2135**, 129–138.

108 Shi, X.Q., Welander, U., and Angmar-Månsson, B. (2000) Occlusal caries detection with KaVo DIAGNOdent and radiography: an *in vitro* comparison. *Caries Res.*, **34**, 151–158.

109 Lussi, A., Imwinkelreid, S., Pitts, N.B., Longbottom, C., and Reich, E. (1999) Performance and reproducibility of a laser fluorescence system for detection of occlusal caries *in vitro*. *Caries Res.*, **33**, 261–266.

110 Lussi, A., Hack, A., Hug, I., Heckenberger, H., Megert, B., and Stich, H. (2006) Detection of approximal caries with a new laser fluorescence device. *Caries Res.*, **40**, 97–103.

111 Konig, K., Schneckenburger, H., and Hibst, R. (1999) Time-gated *in vivo* autofluorescence imaging of dental caries. *Cell Mol. Biol. (Noisy-le-Grand)*, **45**, 233–239.

112 Hall, A. and Girkin, J.M. (2004) A review of potential new diagnostic modalities for caries lesions. *J. Dent. Res.*, **83** (Spec No. C), C89–C94.

113 Eggertsson, H., Analoui, M., Veen, M.H.V.D., Gonzalez-Cabezas, C., Eckert, G.J., and Stookey, G.K. (1999) Detection of early interproximal caries *in vitro* using laser fluorescence, dye-enhanced laser fluorescence and direct visual examination. *Caries Res.*, **33**, 227–233.

114 Ando, M., Hall, A.F., Eckert, G.J., Schemehorn, B.R., Analoui, M., and Stookey, G.K. (1997) Relative ability of laser fluorescence techniques to quantitate early mineral loss *in vitro*. *Caries Res.*, **31**, 125–131.

115 Kaneko, K., Matsuyama, K., and Nakashima, S. (1999) Quantification of early carious enamel lesions by using an infrared camera, in *Early Detection of Dental Caries II*, vol. **4**, Indiana University School of Dentistry, Indianapolis, IN, pp. 83–99.

116 Tam, A.C. (1985) Pulsed photothermal radiometry for noncontact spectroscopy, material testing and inspection measurements. *Infrared Phys.*, **25**, 305–313.

117 Chebotareva, G.P., Nikitin, A.P., and Zubov, B.V. (1995) Comparative study of CO2 and Er:YAG laser heating of tissue using the pulsed photothermal radiometry technique. *Proc. SPIE*, **2394**, 243–251.

118 Jeon, R.J., Matvienko, A., Mandelis, A., Abrams, S.H., Amaechi, B.T., and Kulkarni, G. (2007) Detection of interproximal demineralized lesions on human teeth *in vitro* using frequency-domain infrared photothermal radiometry and modulated luminescence. *J. Biomed. Opt.*, **12**, 034028.

119 Lena, N., Andreas, M., and Stephen, H.A. (2000) Novel dental dynamic depth profilometric imaging using simultaneous frequency-domain infrared photothermal radiometry and laser luminescence. *J. Biomed. Opt.*, **5**, 31–39.

120 Raymond, J.J., Adam, H., Anna, M., Andreas, M., Stephen, H.A., and Bennett, T.A. (2008) *In vitro* detection and quantification of enamel and root caries using infrared photothermal radiometry and modulated luminescence. *J. Biomed. Opt.*, **13**, 034025.

121 Raymond, J.J., Andreas, M., Victor, S., and Stephen, H.A. (2004) Nonintrusive, noncontacting frequency-domain photothermal radiometry and luminescence depth profilometry of carious and artificial subsurface lesions in human teeth. *J. Biomed. Opt.*, **9**, 804–819.

122 Carden, A. and Morris, M.D. (2000) Application of vibrational spectroscopy to the study of mineralized tissues. *J. Biomed. Opt.*, **5**, 259–268.

123 Brown, P.W. and Constantz, B. (1994) *Hydroxyapatite and Related Materials*, CRC Press, Boca Raton, FL.

124 Elliot, J.C. (1994) *Structure and Chemistry of the Apatites and Other Calcium Orthophosphates*, Elsevier, Amsterdam.

125 Pleshko, N., Boskey, A., and Mendelsohn, R. (1991) Novel infrared spectroscopic method for the determination of crystallinity of hydroxyapatite minerals. *Biophys. J.*, **60**, 786–793.

126 LeGeros, R.Z., LeGeros, J.P., Trautz, O.T., and Klein, E. (1970) *Spectral Properties of Carbonate in Carbonate-Containing*

Apatites, Plenum Press, New York, vol. **7b**, pp. 3–13.

127 LeGeros, R.Z., Trautz, O.R., LeGeros, J.P., and Klein, E. (1968) Carbonate substitution in the apatite structure. *Bull. Soc. Chim. Fr.*, 1712–1718.

128 Fowler, B. and Kuroda, S. (1986) Changes in heated and in laser-irradiated human tooth enamel and their probable effects on solubility. *Calcif. Tissue Int.*, **38**, 197–208.

129 Kuroda, S. and Fowler, B.O. (1984) Compositional, structural and phase changes in *in vitro* laser-irradiated human tooth enamel. *Ca1cif. Tissue Int.*, **36**, 361–369.

130 Featherstone, J.D.B., Pearson, S., and LeGeros, R.Z. (1984) An IR method for quantification of carbonate in carbonated-apatites. *Caries Res.*, **18**, 63–66.

131 Featherstone, J.D.B., Fried, D., and Duhn, C. (1998) Surface dissolution kinetics of dental hard tissue irradiated over a fluence range of 1–8 J/cm^2 at a wavelength of 9.3 μm. *Proc. SPIE*, **3248**, 146–151.

132 Featherstone, J.D.B. and Nelson, D.G.A. (1987) Laser effects on dental hard tissue. *Adv. Dent. Res*, **1**, 21–26.

133 Konishi, N., Fried, D., Featherstone, J.D.B., and Staninec, M. (1999) Inhibition of secondary caries by CO_2 laser treatment. *Am. J. Dent.*, **12**, 213–216.

134 Young, D.A., Fried, D. and Featherstone, J.D.B. (2000) Ablation and caries inhibition of pits and fissures by IR laser irradiation. *Proc. SPIE*, **3910**, 247–253.

135 Fried, D. (2000) IR ablation of dental enamel. *Proc. SPIE*, **3910**, 136–148.

136 Klein, E., LeGeros, J.P., Trautz, O.T., and LeGeros, R.Z. (1970) *Polarized Infrared Reflectance of Single Crystals of Apatites*, Plenum Press, New York, vol. **7b**, pp. 3–13.

137 Nelson, D.G.A. and Williamson, B.E. (1985) Raman spectra of phosphate and monophosphate ions in several dentally-relevant materials. *Caries Res.*, **19**, 113–121.

138 Tsuda, H. and Arends, J. (1994) Orientational micro-Raman spectroscopy on hydroxyapatite single crystals and human enamel crystallites. *J. Dent. Res.*, **73**, 1703–1710.

139 Tsuda, H. and Arends, J. (1997) Raman spectroscopy in dental research: a short review of recent studies. *Adv. Dent. Res.*, **11**, 539–547.

140 O'Shea, D.C., Bartlett, M.L., and Young, R.A. (1974) Compositional analysis of apatites with laser-Raman spectroscopy(OH, F, Cl). *Arch. Oral Biol.*, **19**, 995–1006.

141 Tsuda, H., Ruben, J., and Arends, J. (1996) Raman spectra of human dentin mineral. *Eur. J. Oral Sci.*, **104**, 123–131.

142 Schulze, K.A., Balooch, M., Balooch, G., Marshall, G.W., and Marshall, S.J. (2004) Micro-Raman spectroscopic investigation of dental calcified tissues. *J. Biomed. Mater. Res. A*, **69**, 286–293.

143 Ko, A.C., Choo-Smith, L.P., Hewko, M., Leonardi, L., Sowa, M.G., Dong, C.C., Williams, P., and Cleghorn, B. (2005) *Ex vivo* detection and characterization of early dental caries by optical coherence tomography and Raman spectroscopy. *J. Biomed. Opt.*, **10**, 031118.

144 Ko, A.C., Hewko, M., Sowa, M.G., Dong, C.C., Cleghorn, B., and Choo-Smith, L.P. (2008) Early dental caries detection using a fibre-optic coupled polarization-resolved Raman spectroscopic system. *Opt. Express*, **16**, 6274–6284.

145 Hill, W. and Petrou, V. (2000) Caries detection by diode laser raman spectroscopy. *Appl. Spectrosc.*, **54**, 795–799.

146 Yokoyama, E., Kakino, S., and Matsuura, Y. (2008) Raman imaging of carious lesions using a hollow optical fiber probe. *Appl. Opt.*, **47**, 4227–4230.

147 Nishino, M., Yamashita, S., Aoba, T., Okazaki, M., and Moriwaki, Y. (1981) The laser-Raman spectroscopic studies on human enamel and precipitated carbonate-containing apatites. *J. Dent. Res.*, **60**, 751–755.

148 Penel, G., Leroy, G., Leroy, N., Behin, P., Langlois, J.M., Libersa, J.C., and Dupas, P.H. (2000) Raman spectrometry applied to calcified tissue and calcium-phosphorus biomaterials. *Bull. Group Int. Rech. Sci. Stomatol. Odontol.*, **42**, 55–63.

149 Penel, G., Leroy, G., Rey, C., and Bres, E. (1998) MicroRaman spectral study of the PO_4 and CO_3 vibrational modes in synthetic and biological apatites. *Calcif. Tissue Int.*, **63**, 475–481.

150 de Mul, F.F.M., Hottenhuis, M.H.J., Bouter, P., Greve, J., Arends, J., and ten Bosch, J.J. (1986) Micro-Raman line broadening in synthetic carbonated hydroxyapatite. *J. Dent. Res.*, **65**, 437–440.

151 Liu, Y. and Hsu, C.Y. (2007) Laser-induced compositional changes on enamel: a FT-Raman study. *J. Dent.*, **35**, 226–230.

152 Klocke, A., Mihailova, B., Zhang, S., Gasharova, B., Stosch, R., Guttler, B., Kahl-Nieke, B., Henriot, P., Ritschel, B., and Bismayer, U. (2007) CO_2 laser-induced zonation in dental enamel: a Raman and IR microspectroscopic study. *J. Biomed. Mater. Res. B Appl. Biomater.*, **81**, 499–507.

153 Ng, S.Y., Payne, P.A., Cartledge, N.A. and Ferguson, M.W. (1989) Determination of ultrasonic velocity in human enamel and dentine. *Arch. Oral Biol.*, **34**, 341–345.

154 Ghorayeb, S.R., Bertoncini, C.A., and Hinders, M.K. (2008) Ultrasonography in dentistry. *IEEE Trans. Ultrason. Ferroelectr. Freq. Control*, **55**, 1256–1266.

155 Lees, S. and Barber, F.E. (1968) Looking into teeth with ultrasound. *Science*, **161**, 477–478.

156 Huysmans, M.C. and Thijssen, J.M. (2000) Ultrasonic measurement of enamel thickness: a tool for monitoring dental erosion? *J. Dent.*, **28**, 187–191.

157 Louwerse, C., Kjaeldgaard, M., and Huysmans, M.C. (2004) The reproducibility of ultrasonic enamel thickness measurements: an *in vitro* study. *J. Dent.*, **32**, 83–89.

158 Culjat, M., Singh, R.S., Yoon, D.C. and Brown, E.R. (2003) Imaging of human tooth enamel using ultrasound. *IEEE Trans. Med. Imaging*, **22**, 526–529.

159 Blodgett, D.W. (2003) Applications of laser-based ultrasonics to the characterization of the internal structure of teeth. *J. Acoust. Soc. Am.*, **114**, 542–549.

160 Tagtekin, D.A., Ozyoney, G., Baseren, M., Ando, M., Hayran, O., Alpar, R., Gokalp, S., Yanikoglu, F.C. and Stookey, G.K. (2008) Caries detection with DIAGNOdent and ultrasound. *Oral Surg. Oral Med. Oral Pathol. Oral Radiol. Endodontol.*, **106**, 729–735.

161 Lees, S., Gerhard, F.B. Jr., and Oppenheim, F.G. (1973) Ultrasonic measurement of dental enamel demineralization. *Ultrasonics*, **11**, 269–273.

162 Ng, S.Y., Ferguson, M.W., Payne, P.A., and Slater, P. (1988) Ultrasound studies of unblemished and artificially demineralized enamel in extracted human teeth: a new method for detecting early caries. *J. Dent.*, **16**, 201–209.

163 Matalon, S., Feuerstein, O., Calderon, S., Mittleman, A., and Kaffe, I. (2007) Detection of cavitated carious lesions in approximal tooth surfaces by ultrasonic caries detector. *Oral Surg. Oral Med. Oral Pathol. Oral Radiol. Endodontol.*, **103**, 109–113.

164 Schade, U., Holldack, K., Martin, M., and Fried, D. (2005) THz near-field imaging of biological tissues employing synchrotron radiation. *Proc. SPIE*, **5687**, 46–52.

165 Crawley, D.A., Longbottom, C., Cole, B.E., Ciesla, C.M., Arnone, D., Wallace, V.P. and Pepper, M. (2003) Terahertz pulse imaging: a pilot study of potential applications in dentistry. *Caries Res.*, **37**, 352–359.

166 Crawley, D., Longbottom, C., Wallace, V.P., Cole, B., Arnone, D. and Pepper, M. (2003) Three-dimensional terahertz pulse imaging of dental tissue. *J. Biomed. Opt.*, **8**, 303–307.

167 Pickwell, E., Wallace, V.P., Cole, B.E., Ali, S., Longbottom, C., Lynch, R.J., and Pepper, M. (2007) A comparison of terahertz pulsed imaging with transmission microradiography for depth measurement of enamel demineralisation *in vitro*. *Caries Res.*, **41**, 49–55.

168 Fried, D., Zuerlein, M., Featherstone, J.D.B., Seka, W.D., and McCormack, S.M. (1997) IR laser ablation of dental enamel:mechanistic dependence on the primary absorber. *Appl. Surf. Sci.*, **128**, 852–856.

169 Zuerlein, M., Fried, D., Featherstone, J., and Seka, W. (1999) Optical properties

of dental enamel at 9–11 μm derived from time-resolved radiometry. *Spec. Top. IEEE J. Quantum Electron.*, **5**, 1083–1089.

170 Ngaotheppitak, P., Darling, C.L., and Fried, D. (2005) Polarization optical coherence tomography for measuring the severity of caries lesions. *Lasers Surg. Med.*, **37**, 78–88.

171 Manesh, S.K., Darling, C.L., and Fried, D. (2009) Nondestructive assessment of dentin demineralization using polarization sensitive optical coherence tomography after exposure to fluoride and laser irradiation. *J. Biomed. Mater. Res. B Appl. Biomater.*, **90** (2), 802–812.

69
Optical Coherence Tomography in Dentistry

Natalia D. Gladkova, Yulia.V. Fomina, Elena B. Kiseleva, Maria M. Karabut, Natalia S. Robakidze, Alexander A. Muraev, Stefka G. Radenska-Lopovok, and Anna V. Maslennikova

69.1
Introduction

Studies on the application of optical coherence tomography (OCT) in dentistry were published in 1998 simultaneously by two research teams: one at the Lawrence Livermore Laboratory (Livermore, CA, USA) [1–10] and the other at the Institute of Applied Physics of the Russian Academy of Sciences (Nizhny Novgorod, Russia) [11–14]. Later, a series of studies were launched at the Beckman Laser Institute [15–21]. The majority of dental OCT studies were performed using time domain OCT and later frequency domain OCT systems [22, 23]. There are many publications on time domain polarization-sensitive optical coherence tomography (PS-OCT) [24–31]. The available experience in using OCT for oral cavity examination is sufficiently significant to discuss its clinical value.

In this chapter, we consider the application of OCT in dentistry and present the most significant recent clinical, results obtained by the Russian team with the use of a standard time domain OCT system [32] and a cross-polarization optical coherence tomography (CP-OCT) system described by Gelikonov and Gelikonov [33].

CP-OCT detects light reflected in two polarizations: the polarization of probing light (referred to as co-polarization) and orthogonal polarization (cross-polarization) [34]. The CP-OCT device used by our group acquires two conjugate images (see Figure 69.2b). The image in co-polarization (at the bottom) contains information about the backscattering characteristics of biotissue. The cross-polarized image (at the top) gives an insight not only into the backscattering features but also into the depolarizing properties of collagen, keratin, and other anisotropic structures of biotissue, which can increase the clinical value of OCT substantially [35].

Dental applications of OCT are traditionally focused on three areas: (i) examination of hard tissues (teeth), (ii) periodontal tissues, and (iii) oral cavity mucosa.

Handbook of Biophotonics. Vol.2: Photonics for Health Care, First Edition. Edited by Jürgen Popp, Valery V. Tuchin, Arthur Chiou, and Stefan Heinemann.

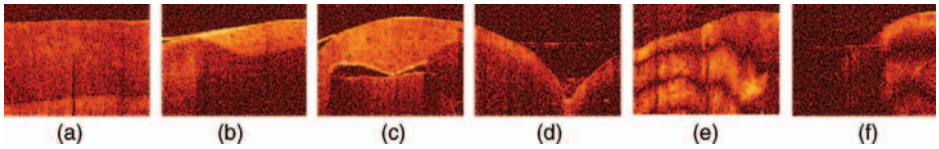

Figure 69.1 OCT images of 11th (a, b, c), 24th (d) and 4th (e, f) teeth. The dentinoenamel junction is seen in a healthy tooth (a); composite material is well distinguished from tooth tissue (b), well seen are small defects of the composite (c); surface caries has no visual manifestations (d). In healthy enamel, the birefringent bands coincide with the orientation of the enamel rods (e); early caries deprives enamel of birefringent properties (f). The cross-section of the OCT images is 1.7 mm.

69.2 Hard Tooth Tissues

The importance of early diagnosis of caries cannot be overestimated as preventive therapy and restoratives may be used at this stage. It is common knowledge that X-ray imaging detects contact caries with moderate sensitivity and high specificity, whereas it is much less efficient in detecting occlusive caries [36, 37]. A diagnostic method of choice for detecting carious cavity is visual examination [38].

Hard tissues are good objects for OCT because of their transparency. Technical characteristics of OCT allow the diagnosis of early carious and noncarious lesions, demineralization, early stages of caries of different localizations (Figure 69.1d and f), and also efficiency of sealant and composite restoration (Figure 69.1b and c) [1–3, 11, 13, 39–41]. Enamel possesses pronounced birefringent properties, which permits additional information to be obtained using PS-OCT. It was found, in particular, that the birefringence and depolarizing properties of healthy enamel and enamel even with early caries are different (Figure 69.1e and f). This phenomenon may be used for preclinical detection of enamel pathology [26, 29].

OCT imaging of subsurface changes in enamel properties and microdefects of composite restorations have no analogs in dental practice and may enhance both diagnosis and quality of dental therapy [2, 11, 19].

69.3 Periodontal Tissues

Periodontal diseases are the main cause of tooth loss. Exact assessment not only of tooth pockets but also of the state of soft tissues is of great significance in periodontology [42]. The OCT technique is a good tool for periodontal diagnosis as it has sufficient penetration depth and high resolution. OCT reliably images borders of soft and hard periodontal tissues [10] and ensures fast, reproducible imaging of surface tissue structure of gingiva, reproducing its specific features in different sections of oral cavity and pocket morphology [22]. OCT gives quantitative information about the thickness and level of gingiva attachment, and also about the position

of alveolar crest. Comparison of OCT images taken at different times enables clinicians to reveal promptly potential sections of disease progression, probably even before clinical manifestations of recession [43]. OCT may be extremely useful for assessing the efficiency of periodontal therapy [19]. Electron recording of clinical data allows the avoidance of subjective and erroneous interpretations inherent in available metrical methods of diagnosis [42].

Dental implants are used to replace missing teeth. An implant is considered to be successful if it does not move, has no periimplantitis, clinical symptoms of infection, discomfort, or pain, and is esthetically pleasant [44–46]. Available diagnostic techniques are based on visual assessment of clinical symptoms of inflammation and are inefficient in detecting periimplantitis at an early stage. Further, it is difficult to control loss of alveolar bone mass around implants. Information provided by OCT may be useful for controlling the volume of attached keratinized gingiva, and also for monitoring gingival inflammatory processes [19, 23].

We studied in a clinical environment healthy volunteers and patients with implants. We analyzed CP-OCT images in co-polarization and cross-polarization of different gingival sections with different degrees of epithelial keratinization and subepithelial collagen organization. For the investigation of specific features of the histomorphology of gum above each tooth, we independently studied tissues postmortem of people without symptoms of gingival pathology. In our histologic analyses we used, in addition to standard hematoxylin–eosin staining, Picrosirius Red (PSR) staining of collagen with subsequent assessment by means of polarization microscopy. This technique allows the detection and differentiation of type I collagen (red and yellow color) from type III collagen (green). The color intensity shows the degree of collagen organization that is directly related to its polarization characteristics [47]. Collagen that has been disorganized in the course of inflammation or neoplasia development produces no color [48].

In a CP-OCT image of healthy gingiva in co-polarization (Figure 69.2b), keratinizing epithelium is not differentiated from connective-tissue stroma because stromal

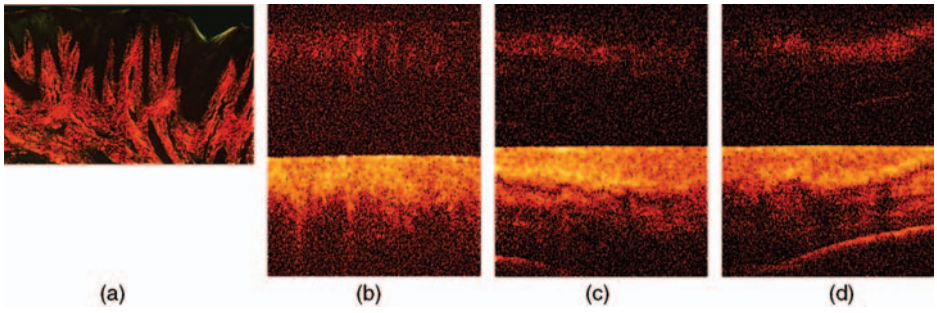

Figure 69.2 Attached gingiva above 11th tooth in norm (a, b): histologic specimen, PSR staining in polarized light, size of histologic frame 1.7 × 1 mm (a); OCT image in co-polarization (bottom) and in cross-polarization (top) (b). Attached gingiva above implant of 11th tooth (c, d): CP-OCT image with signs of gingivitis (c); CP-OCT image illustrating thin gingival biotype. Gingiva thickness 0.7 mm (d). The cross-section of OCT frames is 1.7 mm.

papillae are oriented vertically (Figure 69.2a); hence the image has no layered structure typical of mucosa. In cross-polarization (Figure 69.2b), there is signal from stromal papillae that include vertically oriented fibers, primarily of type I that depolarize light. This is confirmed by histologic data obtained with PSR staining of the specimens and visualized in polarized light (Figure 69.2a).

The CP-OCT image of gingiva above implant clearly demonstrates signs of gingivitis (Figure 69.2c). In co-polarization, inflammation appears as horizontally arranged areas of low signal (signs of edema), but in cross-polarization as regions in which the signal from collagen becomes weaker due to its inflammatory organization. CP-OCT (Figure 69.2d) permits the measurement of the thickness of gingiva above implant thanks to a strong signal from metal gingiva former. Figure 69.2d demonstrates a thin gingival biotype 0.7 mm thick.

69.4
Oral Cavity Mucosa

One of the traditional tasks of OCT is the search for dysplasia and malignization of the epithelium of oral cavity mucosa in patients with leukoplakia and erythroplakia [49–51]. The diagnostic efficiency of OCT and its combinations with various kinds of spectroscopy have been shown in many studies on animal [16] and human [17, 20] models. In all cases, diagnostics is based on the fact that images lose stratification and contrast between epithelium with dysplasia and underlying connective tissue. *In vivo* OCT images demonstrate the excellent capability of OCT for detecting and diagnosing oral premalignancy and malignancy in humans [12, 14, 18].

Our recent unpublished results on the application of CP-OCT for the solution of this important clinical problem demonstrated that, whereas in the case of flat leukoplakia image stratification is still preserved (Figure 69.3c), verrucous leukoplakia without malignization features in co-polarization a low-contrasted image with high-level signal from the keratin layer that obscures the underlying layers (Figure 69.3e). Such an image without contrast also corresponds to carcinoma *in situ* (Figure 69.3g), which reduces the diagnostic value of traditional OCT. In contrast, CP-OCT provides a cross-polarized conjugate image, thus expanding substantially the diagnostic potential of the technique. Fibrillar, highly structured protein keratin, and also organized collagen, depolarizes radiation, leading to the appearance of a signal in the cross-polarized image (Figure 69.3e). Collagen of lamina propria of mucosa immediately under malignant epithelium responds to disturbances of epithelial cell differentiation by collagen destruction, and hence by degradation of its depolarization properties. In this case, there is no signal in the cross-polarized image (Figure 69.3g). The level of signal in cross-polarization agrees well with the intensity of collagen color revealed with PSR staining in polarized light (Figure 69.3b, d, f, and k).

We extended the scope of CP-OCT clinical tasks to the evaluation of microstructural alterations of oral mucosa (in the cheek area, in particular) in patients with inflammatory intestinal diseases, such as Crohn disease and nonspecific ulcerative

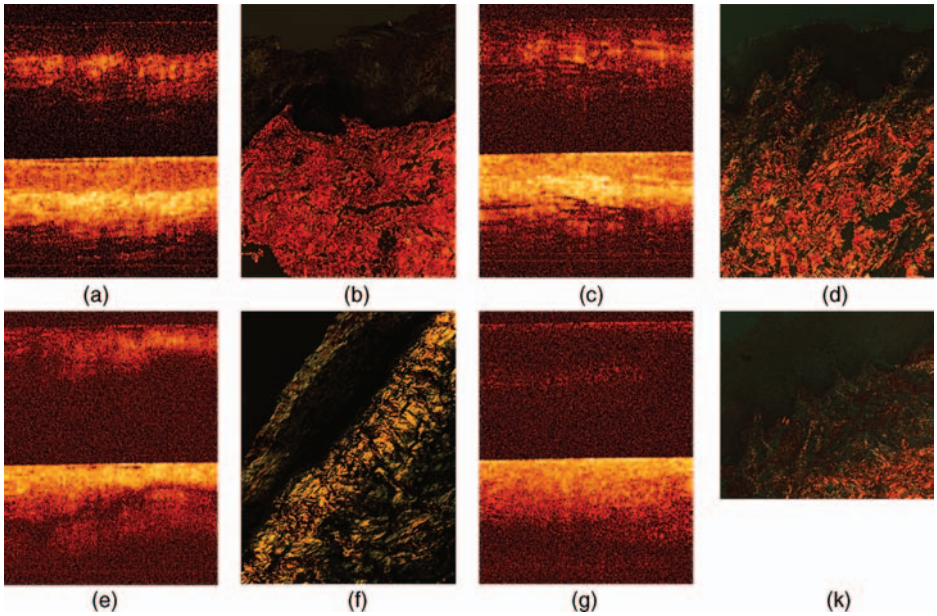

Figure 69.3 Cheek mucosa in norm (a, b), in patients with leukoplakia (c–f) and with cancer (g, k). Healthy cheek mucosa: CP-OCT image (a); the corresponding histologic specimen, PSR staining (b). Flat cheek leukoplakia: co-polarized (bottom) and cross-polarized (top) OCT images (c); histologic specimen, PSR staining in polarized light (d). Verrucous cheek leukoplakia: co-polarized (bottom) and cross-polarized (top) CP-OCT images (e); histological specimen, PSR staining in polarized light (f). Carcinoma *in situ* in cheek area: co-polarized (bottom) and cross-polarized (top) OCT images (g); histological specimen, PSR staining in polarized light (k); histologic frame size, 1.7×1 mm.

colitis. Differential diagnosis of Crohn disease and nonspecific ulcerative colitis is difficult because even "gold standard" histology does not necessarily offer definitive distinguishing features. Diagnosis is usually based on a combination of clinical, endoscopic, and radiologic features [52, 53]. However, a full spectrum of well-known diagnostic techniques is not always sufficient for differential diagnosis of diseases. The role of the oral cavity in a unified model of diagnostic algorithms is currently under active discussion [54]. Some researchers adhere to the opinion that oral mucosa is involved in the inflammatory process in Crohn disease, which is attributed to systemic manifestations of the disease. The susceptibility of the gastrointestinal tract to fibrosis in Crohn disease is regarded as a proven fact [55–57].

We analyzed CP-OCT images of 15 patients and revealed a recurrent phenomenon of a high-intensity signal from fibrous collagen of lamina propria of mucosa in patients with Crohn disease (Figure 69.4a), weak signal intensity in patients with nonspecific ulcerative colitis (Figure 69.4c), and no signal in the aphthae area in patients with stomatitis (Figure 69.4e). The signal level in cross-polarization agrees well with the intensity of collagen color revealed with PSR staining in polarized light (Figure 69.4b, d, and f).

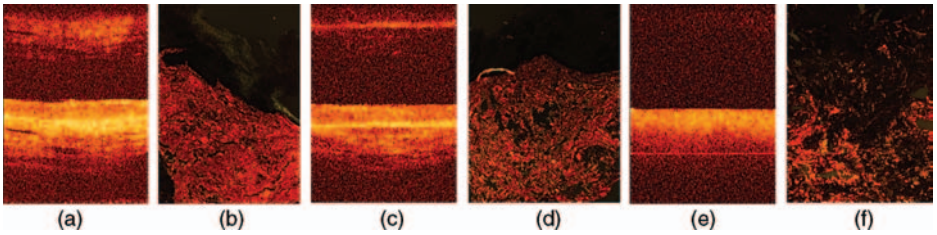

Figure 69.4 Cheek mucosa of a patient with Crohn disease (a, b), with nonspecific ulcerative colitis (c, d), and with aphthous stomatitis (e, f). Co-polarized (bottom) and cross-polarized (top) OCT images (a, c, e); the corresponding histological specimens (b, d, f), PSR staining; histologic frame size, 1.7 × 1 mm.

Such an approach was used by Lee and co-workers for diagnosing oral submucous fibrosis (OSF) [58, 59]. By analyzing OCT scanning results for OSF cases, two indicators, epithelium thickness and standard deviation (SD) of the A-mode scan intensity in the lamina propria layer, were found useful for real-time OSF diagnosis. The statistics showed that the sensitivity and specificity of lamina propria SD can reach 84.1 and 95.5%, respectively. Also, both the sensitivity and specificity of epithelium thickness can reach 100%.

OCT is an attractive tool for noninvasive monitoring of mucositis [15, 21, 60]. OCT proved to be efficient in assessing the dynamics of cheek mucosa microstructure during radio- and radio(chemo)therapy of mucositis in patients with oropharyngeal cancer [61, 62]. Typical OCT manifestations of mucositis were a gradual reduction of contrast of optical layers in OCT images up to their complete disappearance and a decrease in the epithelium layer thickness. The maximum of clinical manifestations of mucositis corresponded to the most pronounced alterations in the OCT images. It was found that the image dynamics depend strongly on mucositis grade, and prognostic criteria of individual radiosensitivity of mucosa were formulated.

For prognosis of mucositis grade in the course of radio- and radio(chemo)therapy of cancer of the oral cavity and pharynx in a specific patient, OCT images of cheek mucosa taken at the same site before treatment and on the day of appearance of the first clinical signs of radioreaction should be compared. Grade 3–4 mucositis is predicted by disappearance in the OCT image of the border between the epithelium and underlying connective tissue (Figure 69.5a and b), and grade 1–2 mucositis is predicted if this border is preserved (Figure 69.5c and d). Numerical analysis of images revealed statistically significant differences in the rates of image contrast reduction as a function of developed mucositis. This information may be extremely important for choosing mucositic prevention and therapy [63].

69.5
OCT Images of Labial Salivary Glands in Norm and Pathology

The main objects of attention for OCT are usually surface layers of superficial tissues: epithelium and subepithelial layers of connective tissue. Recent research [64, 65]

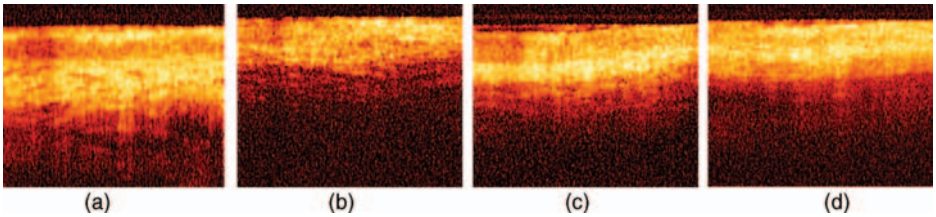

Figure 69.5 OCT images of cheek during radio (chemo)therapy. OCT images showing the alterations caused by mucositis in a 70-year-old male patient with oropharyngeal cancer, stage III (squamous cell keratinizing carcinoma), treated with radio(chemo)therapy resulting in grade 3 mucositis (a, b). Before irradiation, interface between layers is shown by the arrow (a) and after a total dose of 12 Gy with clinically manifested hyperemia and edema (b). The OCT contrast is absent, and no layers can be differentiated. White scale bars measure 1 mm. OCT images showing the alterations caused by mucositis in a 47-year-old male patient with oropharyngeal cancer, stage III (squamous cell non-keratinizing carcinoma), treated with radio (chemo)therapy resulting in a grade 2 mucositis (c, d). Before irradiation (c); after a total dose of 14 Gy with clinically manifested hyperemia and edema (d). The OCT contrast is reduced, but epithelium is still visible. White scale bars measure 1 mm. Interface between the layers is shown by an arrow [63].

demonstrated that labial glands (LGs) located at a depth of 1–1.5 mm in oral mucosa may be visualized by means of OCT. LGs in normal condition have an average size of 1.8 ± 0.8 mm (ranging from 1 to 7 mm, depending on saliva filling and salivation phase). LGs in norm are imaged by OCT in connective tissue stroma as homogeneous regions with low signal and clear contours. When LGs are moderately filled with saliva, lobulous gland structure can be visualized (Figure 69.6a); when LG are well filled with saliva, their size may reach 5–7 mm (Figure 69.6b and c). Ducts of healthy LGs can easily be measured (Figure 69.6d).

Salivary gland diseases in autoimmune processes (primary and secondary Sjögren syndrome), lymphoproliferative lesions, and lymphomas have different clinical courses, in spite of their similarity; therefore, long-term case monitoring is

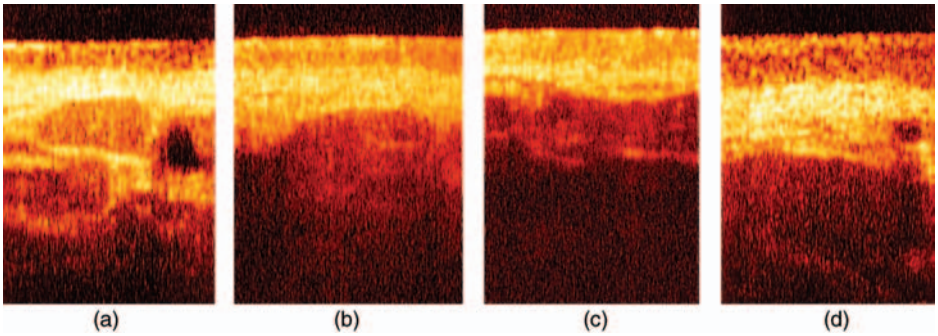

Figure 69.6 Variants of OCT images of LGs and ducts in norm: LG consisting of two lobes and duct, horizontal gland size 0.85 mm (a); LG consisting of two lobes, horizontal gland size 0.85 mm (b). LG with substantial secretion, horizontal gland size 6 mm, only part of the gland is visualized (c). OCT image of LG with excretory duct (d) [33].

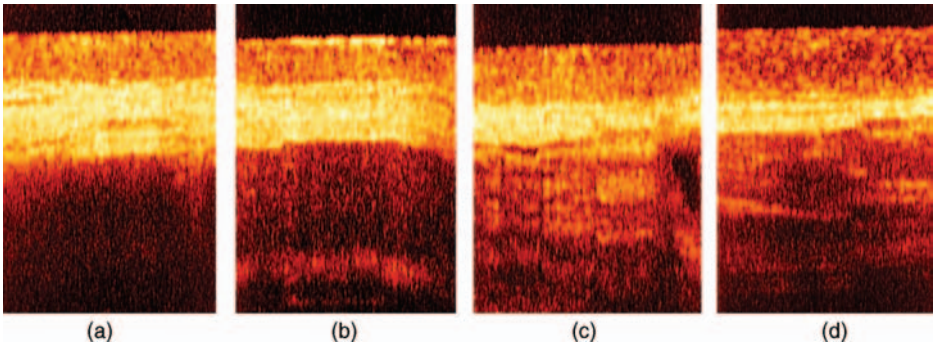

Figure 69.7 OCT images of LGs in a patient with sialadenosis (a, b) obtained with the probe slightly pressed to mucosa (a), and when the probe is strongly pressed to the glandular area so that the bottom of the gland appears (the gland is readily compressed) (b). OCT images of minor salivary glands in a patient with sialadenitis with strongly reduced glandular (c, d) acquired with the probe slightly pressed to mucosa (c); when the probe is strongly pressed, the gland remains almost uncompressed (d) [43].

demanded [66, 67]. The only method of verification is recurrent biopsy. Consequently, objective noninvasive high-resolution techniques that would detect structural changes in salivary glands are highly desirable [68].

We have studied OCT images of LGs in patients with sialadenosis, sialadenitis, and lymphoproliferative alteration lesions. Morphologically, sialadenosis manifests itself as dystrophic alterations of salivary glands without focal or diffuse lymphocytic infiltrations in stroma and with retained functional gland activity. The determining OCT features of sialadenosis are preserved contrast and structure of LGs, and good elasticity ("compressibility") on the OCT probe pressure (Figure 69.7a and b). Being an inflammatory disease, morphologically sialadenitis is characterized by the presence in LG lobes or in periductal space of massive (more than 50 cells in the field of view) focal or diffuse lymphocytic infiltrations (as a manifestation of active immune infiltration inflammation), periductal and interlobular sclerosis (as a consequence of immune inflammation), and disturbance of saliva drainage from small-sized ducts (duct sialadenitis) or disturbance of saliva production (parenchymatous sialedenitis). The OCT features of these structural alterations are a nonuniform signal from the gland with sections of high intensity due to expressed cellular infiltration and stroma sclerosis. The gland remains almost uncompressed in this case (Figure 69.7c and d). Thus, we have shown that OCT adequately identifies the glandular system of oral micosa. The histologic features of sialadenosis, sialadenitis, and benign lymphoproliferative lesion have well-defined OCT equivalents. OCT allows the assessment not only of the structure but also of the function of glands, which is no less important. Noninvasive imaging of LGs by means of OCT may be useful for differential diagnosis of various diseases and also for their monitoring in the course of therapy.

To conclude, OCT, especially its polarization modalities, provides objective information about the properties of biotissues, thus broadening the clinical capabilities of

early diagnosis of dental, periodontium, and soft oral tissue diseases and ensuring their efficient monitoring.

Acknowledgments

This work was supported by the State Contract of the Russian Federation No. 02.740.11.5149 and the Russian Foundation for Basic Research (project 10-02-01175). The authors greatly appreciate the assistance of their colleagues G.V. Gelikonov, V.M. Gelikonov, F.I. Feldchtein, N.B. Krivatkina, V.M. Gubova, V.S. Kozlovsky, L.B. Snopova, E. Yunusova, O.B. Shchukina, A.V. Botina, and S.Yu. Tytyuk.

References

1 Colston, B.W., Everett, M.J., Da Silva, L.B., Otis, L.L. *et al.* (1998) Imaging of hard- and soft-tissue structure in the oral cavity by optical coherence tomography. *Appl. Opt.*, **37** (16), 3582–3584.

2 Colston, B.W., Everett, M.J., Sathyam, U.S., and Da Silva, L.B. (2002) Optical coherence tomography in dentistry, in *Handbook of Optical Coherence Tomography* (eds. B.E. Bouma and G.J. Tearney), Marcel Dekker, New York, pp. 591–612.

3 Colston, B.W., Sathyam, U.S., Da Silva, L.B., Everett, M.J. *et al.* (1998) Dental OCT. *Opt. Express*, **3** (6), 230–238.

4 Otis, L.L., Al-Sadhan, R.I., and Meiers, J. (2003) Identification of occlusal sealants using optical coherence tomography. *J. Clin. Dent.*, **14**, 7–10.

5 Otis, L.L., Al-Sadhan, R.I., Redford-Badwal, D., and Meiers, J. (2000) Identification of occlusal sealants using optical coherence tomography. *J. Dent. Res.*, **79**, 456.

6 Otis, L.L., Colston, B.W., and Everett, M.J. (1998) Dental optical coherence tomography: a novel assessment of oral tissues. *J. Dent. Res.*, **77**, 228.

7 Otis, L.L., Colston, B.W. Jr., Everett, M.J., and Nathel, H. (2000) Dental optical coherence tomography: a comparison of two *in vitro* systems. *Dentomaxillofac. Radiol.*, **29**, 85–89.

8 Otis, L.L., Everett, M.J., and Colston, B.W. (1998) Optical coherence tomography: a novel assessment of coronal restorations. *J. Dent. Res.*, **77**, 824.

9 Otis, L.L., Everett, M.J., Sathyam, U.S., and Colston, B.W. (2000) Optical coherence tomography: a new imaging technology for dentistry. *J. Am. Dent. Assoc.*, **131** (4), 511–514.

10 Otis, L.L. (2005) Optical coherence tomography of periodontal tissues. *Lasers Surg. Med.*, **3**, 19.

11 Feldchtein, F.I., Gelikonov, G.V., Gelikonov, V.M., Iksanov, R.R. *et al.* (1998) *In vivo* OCT imaging of hard and soft tissue of the oral cavity. *Opt. Express*, **3** (6), 239–250.

12 Gladkova, N.D., Fomina, J.V., Shakhov, A.V., Terentieva, A.B. *et al.* (2003) Optical coherence tomography as a visualization method for oral and laryngeal cancer, in *Oral Oncology*, vol. **9** (eds. A.K. Varma and P. Reade), Macmillan Press, New Delhi, pp. 272–281.

13 Ourutina, M.N., Gladkova, N.D., Feldchtein, F.I. and Gelikonov, G.V. *et al.* (eds) (1999) In-vivo optical coherent tomography of teeth and oral mucosa. *Proc. SPIE*, **3567**, 97–107.

14 Fomina, J.V., Gladkova, N.D., Snopova, L.B., Shakhova, N.M. *et al.* (2004) *In vivo* OCT study of neoplastic alterations of the oral cavity mucosa. *Proc. SPIE*, **5316**, 41–47.

15 Wilder-Smith, P., Hammer-Wilson, M.J., Zhang, J., Wang, Q. *et al.* (2007) *In vivo*

imaging of oral mucositis in an animal model using optical coherence tomography and optical Doppler tomography. *Clin. Cancer Res.*, **13** (8), 2449–2454.

16 Wilder-Smith, P., Jung, W.G., Brenner, M., Osann, K. *et al.* (2004) *In vivo* optical coherence tomography for the diagnosis of oral malignancy. *Lasers Surg. Med.*, **35** (4), 269–275.

17 Wilder-Smith, P., Krasieva, T., Jung, W.G., Zhang, J. *et al.* (2005) Noninvasive imaging of oral premalignancy and malignancy. *J. Biomed. Opt.*, **10** (5), 51601.

18 Wilder-Smith, P., Lee, K., Guo, S., Zhang, J. *et al.* (2009) *In vivo* diagnosis of oral dysplasia and malignancy using optical coherence tomography: preliminary studies in 50 patients. *Lasers Surg. Med.*, **41** (5), 353–357.

19 Wilder-Smith, P., Otis, L., Zhang, J., and Chen, Z. (2009) Dental OCT, in *Optical Coherence Tomography: Technology and Applications* (eds. W. Drexler and J. Fujimoto), Springer, Berlin, pp. 1151–1182.

20 Matheny, E.S., Hanna, N.M., Jung, W.G., Chen, Z. *et al.* (2004) Optical coherence tomography of malignancy in hamster cheek pouches. *J. Biomed. Opt.*, **9** (5), 978–981.

21 Kawakami-Wong, H., Gu, S., Hammer-Wilson, M.J., Epstein, J.B. *et al.* (2007) *In vivo* optical coherence tomography-based scoring of oral mucositis in human subjects: a pilot study. *J. Biomed. Opt.*, **12** (5), 051702.

22 Xiang, X., Sowa, M.G., Iacopino, A.M., Maev, R.G. *et al.* (2010) An update on novel non-invasive approaches for periodontal diagnosis. *J. Periodontol.*, **81** (2), 186–198.

23 Ionita, I. and Reisen, P. (2009) Imaging of dental implant osseointegration using optical coherent tomography. *Proc. SPIE*, **7168**, 71682F–71687F.

24 Wang, X.J., Milner, T.E., de Boer, J.F., Zhang, Y. *et al.* (1999) Characterization of dentin and enamel by use of optical coherence tomography. *Appl. Opt.*, **38** (10), 2092–2096.

25 Baumgartner, A., Dichtl, S., Hitzenberger, C.K., Sattmann, H. *et al.* (2000) Polarization-sensitive optical coherence tomography of dental structures. *Caries Res.*, **34** (1), 59–69.

26 Fried, D., Xie, J., Shafi, S., Featherstone, J.D. *et al.* (2002) Imaging caries lesions and lesion progression with polarization sensitive optical coherence tomography. *J. Biomed. Opt.*, **7** (4), 618–627.

27 Chen, Y., Otis, L., Piao, D., and Zhu, Q. (2005) Characterization of dentin, enamel, and carious lesions by a polarization-sensitive optical coherence tomography system. *Appl. Opt.*, **44** (11), 2041–2048.

28 Ngaotheppitak, P., Darling, C.L., and Fried, D. (2005) Measurement of the severity of natural smooth surface (interproximal) caries lesions with polarization sensitive optical coherence tomography. *Lasers Surg. Med.*, **37** (1), 78–88.

29 Kang, H., Jiao, J.J., Lee, C., and Fried, D. (2010) Imaging early demineralization with PS-OCT. *Proc. SPIE*, **7549**, 75490M.

30 Le, M.H., Darling, C.L., and Fried, D. (2010) Automated analysis of lesion depth and integrated reflectivity in PS-OCT scans of tooth demineralization. *Lasers Surg. Med.*, **42**, 62–68.

31 Stahl, J., Kang, H., and Fried, D. (2010) Imaging simulated secondary caries lesions with cross polarization OCT. *Proc. SPIE*, **7549**, 754905.

32 Gelikonov, V.M., Gelikonov, G.V., Dolin, L.S., Kamensky, V.A. *et al.* (2003) Optical coherence tomography: physical principles and applications. *Laser Phys.*, **13** (5), 692–702.

33 Gelikonov, V.M. and Gelikonov, G.V. (2006) New approach to cross-polarized optical coherence tomography based on orthogonal arbitrarily polarized modes. *Laser Phys. Lett.*, **3** (9), 445–451.

34 Schmitt, J.M. and Xiang, S.H. (1998) Cross-polarized backscatter in optical coherence tomography of biological tissue. *Opt. Lett.*, **23** (13), 1060–1062.

35 Zagaynova, E.V., Gladkova, N.D., Shakhova, N.M., Streltsova, O.S. *et al.* (2011) Interoperative OCT monitoring, in *Handbook of Biophotonics*, vol. **2** (ed. J. Popp), Wiley-VCH Verlag GmbH, Weinheim.

36 Lussi, A. (1991) Validity of diagnostic and treatment decisions of fissure caries. *Caries Res.*, **25**, 296–303.

37 Ricketts, D.N.J., Ekstrand, K.R., Martignon, S., Ellwood, R. *et al.* (2007) Accuracy and reproducibility of conventional radiographic assessment and subtraction radiography in detecting demineralization in occlusal surfaces. *Caries Res.*, **41**, 121–128.

38 Versteeg, C.H., Sanderink, G.C.H., and van der Stelt, P.F. (1997) Efficacy of digital intra-oral radiography. *J. Dent.*, **25** (3–4), 215–224.

39 Douglas, S.M., Fried, D., and Darling, C.L. (2010) Imaging natural occlusal caries lesions with optical coherence tomography. *Proc. SPIE*, **7549**, 75490N.

40 Jablow, M. (2009) Caries detection in the 21st century – sharpening our diagnostic abilities. *DentistryIQ,* 11 December 2009.

41 Negrutiu, M.L., Sinescu, C., Rominu, M., Hughes, M. *et al.* (2009) Optical coherence tomography and confocal microscopy investigations of dental structures and restoration materials. *Proc. SPIE*, **7258**, 72584N.

42 Lindhe, J., Karring, T., and Lang, N.P. (2003) *Clinical Periodontology and Implant Dentistry,* 4th edn, Blackwell, Oxford.

43 Baek, J.H., Na, J., Lee, B.H., Choi, E. *et al.* (2009) Optical approach to the periodontal ligament under orthodontic tooth movement: a preliminary study with optical coherence tomography. *Am. J. Orthod. Dentofacial Orthop.*, **135** (2), 252–259.

44 National Institutes of Health (1978) Dental Implants: Benefit and Risk. NIH Consensus Statement Online, National Institutes of Health, Washington, DC, 13–14 June, 1 (3), pp. 13–19.

45 Albrektsson, T., Zarb, G., Worthington, P., and Eriksson, R.A. (1986) The long-term efficacy of currently used dental implants: a review and proposed criteria of success. *Int. J. Oral Maxillofac. Implants*, **1**, 11–25.

46 Iacono, V.J. and Committee on Research, Science and Therapy, the American Academy of Periodontology (2000) Dental Implants in Periodontal Therapy. Academy Report. *J. Periodontol.*, **71** (12), 1934–1942.

47 Junqueira, L., Bignolas, G., and Brentani, R. (1979) Picrosirius staining plus polarization microscopy, a specific method for collagen detection. *Histochem. J.*, **11** (4), 447–455.

48 Borges, L., Gutierrez, P., Marana, H., and Taboga, S. (2007) Picrosirius-polarization staining method as an efficient histopathological tool for collagenolysis detection in vesical prolapse lesions. *Micron*, **38**, 580–583.

49 Clark, A.L., Gillenwater, A., Alizadeh-Naderi, R., El-Naggar, A.K. *et al.* (2004) Detection and diagnosis of oral neoplasia with an optical coherence microscope. *J. Biomed. Opt.*, **9** (6), 1271–1280.

50 Tsai, M.T., Lee, C.K., Lee, H.C., Chen, H.M. *et al.* (2009) Differentiating oral lesions in different carcinogenesis stages with optical coherence tomography. *J. Biomed. Opt.*, **14** (4), 044028.

51 Tsai, M.T., Lee, H.C., Lee, C.K., Yu, C.H. *et al.* (2008) Effective indicators for diagnosis of oral cancer using optical coherence tomography. *Opt. Express*, **16** (20), 15847–15862.

52 Zonderman, J. and Vender, R. (2000) *Understanding Crohn Disease and Ulcerative Colitis*, University Press of Mississippi, Jackson, MS.

53 Sklar, J. (2002) *The First Year: Crohn's Disease and Ulcerative Colitis: An Essential Guide for the Newly Diagnosed*, Marlowe, New York.

54 Bricker, S.L., Landlais, R.P., and Miller, C.S. (eds.) (2001) *Oral Diagnosis, Oral Medicine and Treatment Planning*, BC Decker, Hamilton, ON.

55 Graham, M.F., Diegelmann, R.F., Elson, C.O., Lindblad, W.J. *et al.* (1988) Collagen content and types in the intestinal strictures of Crohn's disease. *Gastroenterology*, **94**, 257–265.

56 Stumpf, M., Krones, C.J., Klinge, U., Rosch, R. *et al.* (2006) Collagen in colon disease. *Hernia*, **10** (6), 498–501.

57 Floer, M., Binion, D.G., Nelson, V.M., Manley, S. *et al.* (2008) Role of MutS homolog 2 (MSH2) in intestinal myofibroblast proliferation during Crohn's disease stricture formation. *Am. J. Physiol. Gastrointest. Liver Physiol.*, **295** (3), G581–G590.

58 Lee, C-.K., Tsai, M-.T., Yang, C.C., and Chiang, C-.P. (2009) Clinical diagnosis of oral submucous fibrosis with optical coherence tomography. *Proc. SPIE*, **7634**, 763405.

59 Lee, C.-K., Tsai, M.-T., Yang, C.C., Lee, H.-C. *et al.* (2009) Diagnosis of oral submucous fibrosis with optical coherence tomography. *J. Biomed. Opt.*, **14**, 054008.

60 Muanza, T.M., Cotrim, A.P., McAuliffe, M., Sowers, A.L. *et al.* (2005) Evaluation of radiation-induced oral mucositis by optical coherence tomography. *Clin. Cancer Res.*, **11** (14), 5121–5127.

61 Gladkova, N., Maslennikova, A., Balalaeva, I., Vyseltseva, Y. *et al.* (2006) OCT visualization of mucosal radiation damage in patients with head and neck cancer: pilot study. *Proc. SPIE*, **6078**, 6071J–6078J.

62 Gladkova, N., Maslennikova, A., Terentieva, A., Fomina, Y. *et al.* (2006) OCT visualization of acute radiation mucositis: pilot study. *Proc. SPIE*, **5861**, 58610T.

63 Gladkova, N., Maslennikova, A., Balalaeva, I., Feldchtein, F. *et al.* (2008) Application of optical coherence tomography in the diagnosis of mucositis in patients with head and neck cancer during a course of radio(chemo)therapy. *Med. Laser Appl.*, **23**, 186–195.

64 Gladkova, N.D., Radenska-Lopovok, S.G., Fomina, Yu.V., Gaydyk, I.V. *et al.* (2006) *In vivo* imaging of labial salivary glands using optical coherence tomography. *Clin. Stomatol.*, **2**, 30–35.

65 Ozawa, N., Sumi, Y., Shimozato, K., Chong, C. *et al.* (2009) *In vivo* imaging of human labial glands using advanced optical coherence tomography. *Oral Surg. Oral Med. Oral Pathol. Oral Radiol. Endodontol.*, **108** (3), 425–429.

66 Fox, R.I., (2005) Sjögren's syndrome. *Lancet*, **366**, 321–331.

67 Vitali, C., Bombardieri, S., Jonsson, R., Moutsopoulos, H.M. *et al.* (2002) Classification criteria for Sjögren's syndrome: a revised version of the European criteria proposed by the American–European Consensus Group. *Ann. Rheum. Dis.*, **61**, 554–558.

68 Xu, K.P., Katagiri, S., Takeuchi, T., and Tsubota, K. (1996) Biopsy of labial salivary glands and lacrimal glands in the diagnosis of Sjogren's syndrome. *J. Rheumatol.*, **23**, 76–82.

70
Fluorescence Spectroscopy

Adrian Lussi

70.1
Introduction

Dental caries is a bacteria-associated progressive process of the hard tissues of the coronal and root surfaces of teeth. Net demineralization may begin soon after tooth eruption in caries-susceptible children without being recognized. This process may progress further, resulting in a caries lesion that is the sign and/or the symptom of the carious process. Caries is, in other words, a continuum which may by assessed falsely when only a certain time point is considered.

Clinical–visual diagnosis may be amenable to longitudinal monitoring even though the assessment is qualitative. It would be easier to have a device that would not only detect caries but also quantify it. Then monitoring progression or arrest would be simple: use the device again and see in what direction the numbers change. This concept is persuading so it is little wonder that researchers have made such efforts to develop, test, and perfect such devices. All of these methods for caries detection are based on the interpretation of one or more physical signals. These are causally related to one or more features of a caries lesion. First, the signals must be received using a receptor device and classified. The classification of a signal is part of the diagnostic decision-making process. However, none of the methods is capable of processing all of these signals to a status that could be called diagnosis. "The art of identifying a disease from its signs and symptoms" [1] is a process that cannot be replaced by a machine or a device. Nevertheless, such devices may be of help especially in the early stage of caries, which may be difficult to diagnose.

The aim of this chapter is to provide insight in today's methods for caries detection based on laser fluorescence.

70.2
Laser/Light-Induced Fluorescence

Fluorescence is a phenomenon by which the wavelength of the emitted light (coming from the light source) is changed into a longer wavelength as it travels back for

Handbook of Biophotonics. Vol.2: Photonics for Health Care, First Edition. Edited by Jürgen Popp, Valery V. Tuchin, Arthur Chiou, and Stefan Heinemann.

detection. The larger wavelength is caused by some loss of energy to the surrounding tissue and therefore will have a different color than the emitting light. By using a filter through which only the fluorescent light may pass, the intensity of the fluorescent light can be measured. The fluorescence of dental hard tissues has been known for a very long time [2]. The chromophores causing the fluorescence of dental hard tissues, however, are not clearly identified. The blue fluorescence was assigned to dityrosine [3]. It seems likely that most of the yellow fluorescence stems from proteinic chromophores, probably cross-links between chains of structural proteins [4]. It has also been discussed whether or not the apatite of dental hard tissues would also contribute [5, 6]. Caries lesions, plaque, and microorganisms also contain fluorescent substances. The difference between the fluorescence of sound tooth tissues and that of a caries lesion can be made visible by the DIAGNOdent method and by quantitative laser- or light-induced fluorescence (QLF).

70.3 DIAGNOdent

The setup and function of the DIAGNOdent (KaVo, Biberach/Riss, Germany) (Figure 70.1) are as follows. Light from a laser diode (655 nm) is coupled into an optical fiber and transmitted to the tooth. The backscattered excitation and short-wavelength ambient light is absorbed by a filter in front of the photodiode detector. To discriminate the fluorescence from the ambient light in the same spectral region, the laser diode is modulated. Owing to its relatively short lifetime, fluorescence follows this modulation. By amplifying only the modulated portion of the signal, the ambient

Figure 70.1 The DIAGNOdent is available with two tips, one for occlusal caries and the other for interproximal caries.

light is suppressed. The remaining signal is proportional to the detected fluorescence intensity and displayed as a number (0–99, in arbitrary units). In order to compensate for potential variations of the system (e.g., laser diode output power), it can be calibrated by a standard of known and stable fluorescence yield. This makes the measurement absolute (although in arbitrary units) and allows comparisons of fluorescing tooth spots over time. A systematic review revealed a high sensitivity of the DIAGNOdent compared with traditional diagnostic methods. However, the method was less specific in that the DIAGNOdent also identified a larger proportion of sound sites as being carious than did the visual method [7]. We recommend this tool as a second opinion in the diagnostic process. Figure 70.2 shows its use on (a) occlusal and (b) interproximal surfaces.

70.3.1 Quantitative Light-Induced Fluorescence (QLF)

Demineralization of a dental hard tissue results in loss of its autofluorescence, the natural fluorescence. As early as the 1920s, this phenomenon was suggested to be useful as a tool for diagnosing dental caries [8]. More recently, laser light was used to induce fluorescence of enamel in a sensitive, nondestructive, diagnostic method for detection of caries [9, 10]. The tooth was illuminated with a broad beam of blue–green light from an argon laser, producing diffuse monochromatic light with a wavelength (λ) of 488 nm. The fluorescence of the enamel occurring in the yellow region was observed through a yellow high-pass filter ($\lambda \geq 520$ nm), which filters out all reflected and backscattered light. Demineralized areas appeared as dark areas because the fluorescence of a caries lesion viewed by QLF is lower than that of sound enamel (Figure 70.3).

Several effects may contribute to the decreased fluorescence of white spot caries lesions, and most probable ones being as follows:

- The light scattering in the lesion, which is much stronger than in sound enamel [11], causes the light path in the lesion to be much shorter than in sound enamel. Therefore, the absorption per unit volume is much smaller in the lesion and the fluorescence is less strong.
- The light scattering in the lesion acts as a barrier for excitation light to reach the underlying fluorescent sound tooth tissues, and as a barrier for fluorescent light from the layers below the lesion to reach the tooth surface. This is one of the reasons for limited depth detection with QLF (up to 400 μm).

The laser fluorescence method was developed further for *in vivo* quantification of mineral loss in natural enamel lesions using a color microvideo charge-coupled device (CCD) camera and computed image analysis [12]. To allow calculation of fluorescence loss in the caries lesion, the fluorescence of the lesion is subtracted from the fluorescence of the surrounding sound tissue. The difference between the actual values and the reconstructed ones gives the resulting fluorescence loss.

QLF is a sensitive, reproducible method for quantification of enamel lesions limited to a depth of only 400 μm. A relationship between mineral loss and fluorescence has been found for artificial and natural caries lesions with correlation

(a)

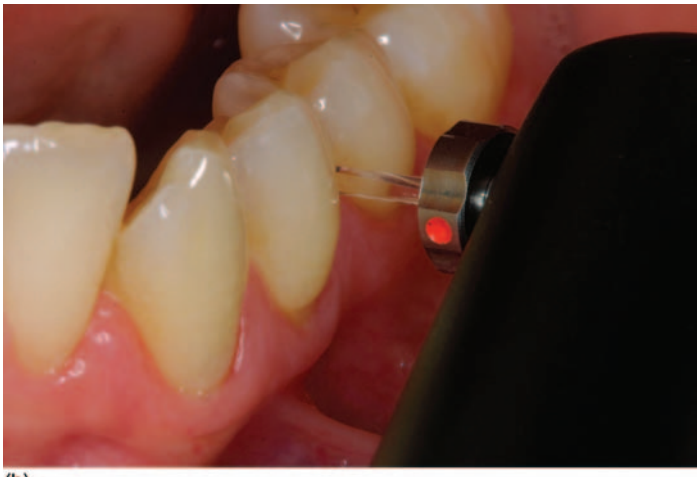

(b)

Figure 70.2 The DIAGNOdent has to be tilted in order to detect the occlusal caries (a) and has to be inserted between two teeth in order to measure fluorescence from interproximal surfaces (b).

Figure 70.3 Appearance of teeth with normal white light (a) and its fluorescence image (b); caries appears as a dark spot (Inspektor Research Systems BV, Amsterdam Netherlands).

coefficients of $r = 0.73–0.86$ [6, 13–15]. Hence a measure of fluorescence may indicate the amount of mineral loss. This device may be used primarily for research purposes where small changes in the outer surface of caries may be of great interest.

References

1 Merriam-Webster (2003) http://www.merriam-webster.com/dictionary/diagnosis.

2 Benedict, HC. (1928) Note on the fluorescence of teeth in ultra-violet rays. *Science*, **67**, 442.

3 Booij, M. and ten Bosch, J.J. (1982) A fluorescent compound in bovine dental enamel matrix compared with synthetic dityrosine. *Arch. Oral Biol.*, **27**, 417–421.

4 Scharf, F. (1971) Über die natürliche Lumineszenz der Zahnhartgewebe 'Schmelz und Dentin'. *Stoma*, **24**, 11–25.

5 Spitzer, D. and ten Bosch, J.J. (1976) The total luminescence of bovine and human dental enamel. *Calcif. Tissue Res.*, **20**, 201–208.

6 Hafström-Björkman, U., Sundström, F., and ten Bosch, J.J. (1991) Fluorescence of dissolved fractions of human enamel. *Acta Odontol. Scand.*, **49**, 133–138.

7 Bader, J.D. and Shugars, D.A. (2004) A systematic review of the performance of a laser fluorescence device for detecting caries. *J. Am. Dent. Assoc.*, **135**, 1413–1426.

8 Benedict, H.C. (1929) The fluorescence of teeth as another method of attack on the problem of dental caries. *J. Dent. Res.*, **9**, 274–275.

9 Bjelkhagen, H. and Sundström, F. (1981) A clinically applicable laser luminescence method for the early detection of dental caries. *IEEE J. Quantum Electron.*, **17**, 266–286.

10 Bjelkhagen, H., Sundström, F., Angmar-Månsson, B., and Rydén, H. (1982) Early detection of enamel caries by the luminescence excited by visible laser light. *Swed. Dent. J.*, **6**, 1–7.

11 ten Bosch, J.J. (1996) Light scattering and related methods, in *Early Detection of Dental Caries: Proceedings of the 1st Annual Indiana Conference* (ed. G.K. Stookey), Indiana University School of Dentistry, Indianapolis, IN, pp. 81–90.

12 de Josselin de Jong, E., Sundström, F., Westerling, H., Tranaeus, S., ten Bosch, J.J., and Angmar-Månsson, B. (1995) A new method for *in vivo* quantification of mineral loss in enamel with laser fluorescence. *Caries Res.*, **29**, 2–7.

13 Hafström-Björkman, U., Sundström, F., de Josselin de Jong, E., Oliveby, A., and Angmar-Månsson, B. (1992) Comparison of laser fluorescence and longitudinal microradiography for quantitative assessment of *in vitro* enamel caries. *Caries Res.*, **26**, 241–247.

14 Emami, Z., Al-Khateeb, S., de Josselin de Jong, E., Sundström, F., Trollsås, K., and Angmar-Månsson, B. (1996) Mineral loss in incipient caries lesions quantified with laser fluorescence and longitudinal microradiography. *Acta Odontol. Scand.*, **54**, 8–13.

15 Al-Khateeb, S., Oliveby, A., de Josselin de Jong, E., and Angmar-Månsson, B. (1997) Laser fluorescence quantification of remineralisation *in situ* of incipient enamel lesions: influence of fluoride supplements. *Caries Res.*, **31**, 132–140.

71
Photothermal Radiometry and Modulated Luminescence: Applications for Dental Caries Detection

Jose A. Garcia, Andreas Mandelis, Stephen H. Abrams, and Anna Matvienko

71.1
Introduction

The traditional methods for dental caries detection, visual examination and radiography, are not effective in detecting early caries lesions [1]. If dental caries is detected early, before a substantial amount of the tooth is destroyed, the area can be remineralized [2], which can prevent invasive procedures, radiation exposure, and create a sound surface devoid of restorations. Recently, a new group of light-based dental diagnostic techniques has been proposed [3]. The group includes techniques such as light-induced fluorescence, digital imaging fiber-optic transillumination (DIFOTI), electrical caries monitoring (ECM), optical coherence tomography (OCT), alternating current impedance spectroscopy, and photothermal radiometry (PTR) with modulated luminescence (LUM).

PTR–LUM combines PTR and LUM for detection and monitoring of carious lesions. In PTR, a beam of energy (typically a laser), intensity modulated at a certain frequency, is focused on the sample surface. The resulting periodic heat flow due to the absorbed optical energy in the material is a diffusive process, producing a periodic temperature rise (spatial distribution) which is called a "thermal wave." This temperature distribution, in turn, causes a modulated thermal infrared (IR) (black-body or Planck radiation) emission which is used to monitor the material under examination. PTR has the ability to penetrate, and yield information about, an opaque medium well beyond the range of optical imaging. Specifically, the frequency dependence of the penetration depth of thermal waves makes it possible to perform depth profiling of materials [4]. In PTR applications to turbid media, such as hard dental tissue, depth information is obtained following optical-to-thermal energy conversion and transport of the incident laser power in two distinct modes: conductively, from a near-surface distance controlled by the thermal diffusivity of enamel (50–500 μm); and radiatively, through blackbody IR emissions from considerably deeper regions commensurate with optical penetration of the diffusely scattered laser-induced optical field (several millimeters) and with the existence of IR spectral "windows" for IR photon transmission.

Handbook of Biophotonics. Vol.2: Photonics for Health Care, First Edition. Edited by Jürgen Popp, Valery V. Tuchin, Arthur Chiou, and Stefan Heinemann.

The term luminescence is used to describe a process in which light is produced when an energy source causes a transition of electrons or other energetic particles from their lowest ("ground") energy state to a higher ("excited") state; subsequent return to the ground state releases the excess energy in the form of light photons of longer wavelength than the optical source (Stokes shift). There are several types of luminescence, each named according to the source of energy, or the trigger for the luminescence, for example, photoluminescence (caused by electromagnetic radiation), or fluorescence (caused by ultraviolet or visible excitation). However, these terms are often used interchangeably in the literature. Many important biological objects containing fluorescing components (fluorophores) exhibit intrinsic fluorescence (or autofluorescence). The reduction in fluorescence when enamel demineralizes has been attributed to the increase in porosity of carious lesions when compared with sound enamel. There is an associated uptake of water and decrease in the refractive index of the lesion resulting in increased scattering and a decrease in light-path length, absorption, and autofluorescence [5]. Additional sources of luminescence decrease are associated with the destruction of the enamel crystalline structure as a result of demineralization. In summary, a combination of PTR and LUM provides valuable complementary information about the conversion pathways of optical energy in a sample.

It has been a decade since the first publications on PTR–LUM for examining hard dental tissue appeared. In this chapter, we review the development of and future outlook for this novel dental diagnostic technology, including the clinical PTR-LUM device (The Canary System).

71.2
Theoretical Modeling

To appreciate better the capabilities of PTR–LUM, it is important to understand how the laser light interacts with turbid media generating two energy fields: optical and thermal. A coupled diffuse photon density and thermal wave model was developed for theoretical analysis of the photothermal field in demineralized teeth [6, 7]. The solution of the radiative transport equation in the limit of diffuse photon density field is considered as a source term in the thermal wave field equation. The chromophore (hydroxyapatite) relaxation lifetimes, optical absorption, scattering, and spectrally averaged IR emission coefficients were determined by fitting the model to the measured PTR–LUM data [6]. The influence of the foregoing optical and thermal parameters (thermal diffusivity and conductivity) of each layer of a demineralized tooth on the diffuse photon density and therma wave depth profiles has recently been analyzed using computer simulations that allow the optimized simultaneous measurement of these major optical and thermal properties of teeth from experimental PTR scans [7].

71.3
Depth Profilometry

One of the main advantages of PTR–LUM, intrinsic to diffusion wave methods, is the ability to perform depth profiling through scanning of the excitation source

modulation frequency. By selecting several modulation frequencies, PTR measurements at different depths in the enamel can be obtained. Studies on the depth profilometric capability of PTR–LUM in dental applications [8] showed that the radiometric amplitude exhibited a superior dynamic range (two orders of magnitude signal resolution) to luminescence (a factor of two only) in distinguishing between intact and cracked subsurface structures in the enamel. Further studies [9] assessed the feasibility of PTR–LUM to detect deep lesions. PTR frequency scans over the surface of a fissure into demineralized enamel and dentin exhibited higher amplitude than those for healthy teeth, and also a pronounced curvature in both amplitude and phase signal channels. These can be excellent markers for the diagnosis of subsurface carious lesions. In addition, PTR exhibited superior sensitivity to the presence of sharp boundaries, and also to changes in natural demineralized regions of the tooth.

71.4
Pits and Fissures Caries Detection

Jeon *et al.* [10] examined pit and fissure caries in 52 extracted human teeth with simultaneous measurements of PTR and LUM. These measurements were compared with conventional diagnostic methods including continuous (DC) luminescence (DIAGNOdent), visual inspection, and radiographs. Sensitivities and specificities were calculated by using histologic observations as the gold standard to compare all examined methods. With the combined criteria of four PTR and LUM signals (two amplitudes and two phases), it was found that the sensitivity of this method was much higher than those of any of the other methods used in this study, whereas the specificity was comparable to that of the DC luminescence. Therefore, the combination of PTR and LUM has the potential to be a reliable tool to diagnose pit and fissure caries and could provide detailed information about deep lesions.

71.5
Interproximal Caries Detection

The interproximal contact area of teeth is a common location for dental caries. Here plaque (containing bacteria in a biofilm) and food particles can become trapped, leading to the creation of carious lesions. Jeon *et al.* used PTR–LUM to examine interproximal caries in extracted human teeth [11]. Three types of lesions were created: with dental burs in a high-speed handpiece, with 37% phosphoric acid, and with demineralization in artificial caries media. Each sample pair was examined before and after bur application, or sequential treatment with acid (etched for 20 s) and gel (time periods spanning from 6 h to 30 days). The results showed distinct differences in the signal for these types of lesions. Dental bitewing radiographs showed no sign of demineralized lesions even for the samples treated for 30 days. Only scanning electron microscopy and micro-computed tomographic imaging, which are destructive, showed visible signs of treatment. PTR further exhibited excellent reproducibility and consistent signal changes in the presence of interproximal

demineralized lesions. The results suggested that PTR can be a reliable probe to detect early interproximal lesions. The LUM channel was also measured simultaneously, but it showed a lower ability than PTR to detect these lesions.

71.6 Early Lesion Detection

There is a great deal of value in detecting carious lesions early. PTR–LUM research in the laboratory setting [12] and observations from an early investigational trial [13] using the clinical version (Canary System), indicated that lesions can remineralize or stabilize if exposed to remineralizing agents such as fluoride and casein phosphopeptide–amorphous calcium phosphate (CCP–ACP). In laboratory studies, PTR–LUM was used to monitor early stages of tooth demineralization and remineralization [12]. Extracted teeth were treated with an artificial demineralization gel to simulate controlled mineral loss on the enamel surface and then exposed to a remineralizing agent. The treated region of the tooth was monitored with PTR–LUM before and after treatment. The results showed that PTR–LUM has very high sensitivity to incipient changes in the enamel structure. The PTR and LUM amplitudes and phases showed gradual and consistent changes with treatment time. There was good correlation of PTR–LUM results with the mineral loss or the lesion depth measured with transverse microradiography (TMR). This indicated that PTR–LUM is capable of monitoring artificially created carious lesions, their evolution during demineralization, and the reversal of the lesions during remineralization.

71.7 Recent Developments

In 2009, The Canary System developed by Quantum Dental Technologies (Toronto, ON, Canada) was used in a Health Canada-approved human investigational trial [13]. In that study, amplitude (A) and phase (P) responses at various modulation frequencies from healthy and carious dental enamel (ICDAS 0–6) were measured. Over 500 regions on healthy tooth surfaces of 50 subjects were used to construct a healthy baseline for each output channel (1-PTR-A, 2-PTR-P, 3-LUM-A, and 4-LUM-P). PTR-A and PTR-P were used to detect near-surface and subsurface lesions, whereas LUM-A and LUM-P were used to detect near-surface lesions. The results indicated that The Canary System did not cause any adverse events or soft or hard tissue trauma. There was no difference in signal from anterior and posterior healthy tooth surfaces, and the presence of surface stain and biofilm did not affect the signal from healthy tooth surfaces. A clear shift from the baseline in both PTR and LUM in carious enamel was observed depending on the type, depth, and nature of the lesion. The results showed that The Canary System is safe and discriminates between healthy and carious enamel. In 2010, a second Health Canada-approved investigational trial has shown the ability of The Canary System to detect carious lesions on smooth surfaces,

occlusal surfaces and around restoration margins [14]. Preliminary results show that the system is safe and provided repeatable measurements that allowed it to monitor lesion growth and response to various remineralization therapies [14].

71.8 Conclusion

This review of the principles of PTR–LUM and its applications to dentistry has highlighted the significant progress in bringing this novel technology to clinical applications. PTR–LUM offers features beyond what is currently available in traditional dental detection methods. These features include the ability to perform depth profilometry and very early caries detection and monitoring on various tooth surfaces. It was also shown that The Canary System, a portable PTR–LUM instrument for clinical applications, is safe and can discriminate healthy and carious tooth tissue.

References

1 Dove, S.B. (2001) Radiographic diagnosis of dental caries. *J. Dent. Educ.*, **65** (10), 985–990.

2 Kidd, E.A. and Fejerskov, O. (2004) What constitutes dental caries? Histopathology of carious enamel and dentin related to the action of cariogenic biofilms. *J. Dent. Res.*, **83** (Spec. No. C), C35–C38.

3 Amaechi, B.T. (2009) Emerging technologies for diagnosis of dental caries: the road so far. *J Appl. Phys.*, **105**, 102047.

4 Munidasa, M. and Mandelis, A. (1992) Photothermal imaging and microscopy, in *Principles and Perspectives of Photothermal and Photoacoustic Phenomena*, vol. **1** (ed. A. Mandelis), Elsevier, New York, pp. 299–367.

5 Bjelkhagen, H., Sundstrom, F., Angmar-Mansson, B., and Ryden, H. (1982) Early detection of enamel caries by the luminescence excited by visible laser light. *Swed. Dent. J.*, **6** (1), 1–7.

6 Nicolaides, L., Feng, C., Mandelis, A., and Abrams, S.H. (2002) Quantitative dental measurements by use of simultaneous frequency-domain laser infrared radiometry and luminescence. *Appl. Opt.*, **41** (4), 768–777.

7 Matvienko, A., Mandelis, A., Jeon, R.J., and Abrams, S.H. (2009) Theoretical analysis of coupled diffuse-photon-density and thermal-wave field depth profiles photothermally generated in layered turbid dental structures. *J. Appl. Phys., Special Issue Appl. Biophys.*, **105**, 102022.

8 Jeon, R.J., Mandelis, A., and Abrams, S.H. (2003) Depth profilometric case studies in caries diagnostics of human teeth using modulated laser radiometry and luminescence. *Rev. Sci. Instrum.*, **74** (1), 380–383.

9 Jeon, R.J., Han, C., Mandelis, A., Sanchez, V., and Abrams, S.H. (2004) Non-intrusive, non-contacting frequency-domain photothermal radiometry and luminescence depth profilometry of carious and artificial sub-surface lesions in human teeth. *J. Biomed. Opt.*, **9** (4), 809–819.

10 Jeon, R.J., Han, C., Mandelis, A., Sanchez, V., and Abrams, S.H. (2004) Diagnosis of pit and fissure caries using frequency-domain infrared photothermal radiometry and modulated laser luminescence. *Caries Res.*, **38**, 497–513.

11 Jeon, R.J., Matvienko, A., Mandelis, A., Abrams, S.H., Amaechi, B.T., and Kulkarni, G. (2007) Detection of interproximal demineralized lesions on human teeth *in vitro* using frequency-

domain infrared photothermal radiometry and modulated luminescence. *J. Biomed. Opt.*, **12** (3), 034028.

12 Jeon, R.J., Hellen, A., Matvienko, A., Mandelis, A., Abrams, S.H., and Amaechi, B.T. (2008) *In vitro* detection and quantification of enamel and root caries using infrared photothermal radiometry and modulated luminescence. *J. Biomed. Opt.*, **13** (3), 048803.

13 Sivagurunathan, K., Abrams, S.H., Garcia, J., Mandelis, A., Amaechi, B.T., Finer, Y., Hellen, W.M.P., and Elman, G. (2010) Using PTR–LUM ("The Canary System") for *in vivo* detection of dental caries: clinical trial results. *Caries Res.*, **44**, 229.

14 Abrams, S., Sivagurunathan, K., Jeon, R.J., Mandelis, A., Silvertown, J.D., Hellen, A., Hellen, W.M.P., Elman, G.I., Ehrlich, B.R., Chouljian, Finer, Y., and Amaechi, B.T. (2011) Multi-center clinical study to evaluate the safety and effectivness of "The canary system" (PTR-LUM Technology), *Caries Res*, **45**, 174–242.

72
Lasers in Restorative Dentistry

Anil Kishen

72.1
Introduction

Current developments in laser technology and laser delivery systems in tandem with an improved understanding of laser–dental tissue interactions have broadened the scope of the application of lasers in dentistry. There has been growing interest among clinicians to apply lasers in different clinical procedures in dentistry. However, the main concern is the lack of sufficient clinical studies that significantly support the advantage of lasers over conventional treatment methods. Dental lasers for clinical procedures operate in the infrared, visible, or ultraviolet range of the electromagnetic spectrum. These lasers are delivered as either a continuous, pulsed (gated), or running pulse waveform. It is imperative for the clinician to determine the specific treatment goals and then select the laser technology best suited to achieve the desired effect(s).

The photons in a laser beam are emitted as a coherent, unidirectional, monochromatic light beam that can be collimated into an intensely focused ray of energy. This focused ray of energy will interact with a target tissue or material by absorption, reflection, transmission, or scattering. The absorbed light energy may result in heating, coagulation, or vaporization of tissues, depending on the laser parameters such as wavelength, power, waveform (continuous or pulsed), pulse duration, energy/pulse, energy density, duration of exposure, angulation of the delivery tip to the target surface, and so on. The optical properties of the target tissue also dictate to a great extent the nature and intensity of interaction with specific laser wavelengths. Pigmentation, water content, mineral content, thermal conductivity, tissue density, and latent heat of transformation are factors that would influence the nature of light–tissue interaction. Furthermore, physiological processes, for instance, tissue vascularity, degree of tissue inflammation, and the presence of progenitor cells to participate in the healing process, will also influence the tissue response to laser radiation.

Handbook of Biophotonics. Vol.2: Photonics for Health Care, First Edition. Edited by Jürgen Popp, Valery V. Tuchin, Arthur Chiou, and Stefan Heinemann.

72.2
Classification of Lasers in Restorative Dentistry

Lasers can be classified as follows:

i. Based on the type of laser medium used:
   - *Gas*
   - *Solid*
   - *Liquid*

ii. Based on the type of delivery system:
   - *Flexible hollow waveguide*
   - *Glass fiber optic cable*

iii. Based on type of interaction with tissue:
   - *Contact lasers*
   - *Noncontact lasers*

iv. Based on the type of application:
   - **Soft tissue lasers (athermic) (~1000 m)**: *The three main types of soft tissue lasers are the helium–neon (He–Ne) diode, gallium arsenide (GaAs), and gallium aluminum arsenide (GaAlAs) lasers.*
   - **Hard tissue lasers (thermic) (~ 3 W or more)**: *The three main types of hard tissue lasers are the argon (Ar), CO_2, and Nd:YAG lasers.*

v. Based on the type by source:
   - **Infrared example**: *CO_2, Ho:YAG, and Nd:YAG lasers*
   - **Visible example**: - *He–Ne and argon lasers*
   - **Ultraviolet example**: - *XeCl, XeF, KrF, and ArF (excimer) lasers*

vi. Based on the type by wavelength:
   - **Long-wavelength**: – *Infrared laser*
   - **Short-wavelength**: – *Ultraviolet laser*

vii. Based on safety (American National Standards Institute Laser Classification)
   - **Class 1**: *Exempt lasers or laser systems that cannot, under normal operation conditions, produce a hazard.*
   - **Class 2**: *Low-power visible lasers or laser systems which, because of normal human aversion responses, do not normally present a hazard, but may present some potential for hazard if viewed directly for extended periods of time.*
   - **Class 3a**: *Lasers or laser systems that normally would not produce a hazard if viewed for only momentary periods with the unaided eye. They may present a hazard if viewed using collecting optics.*
   - **Class 3b**: *Lasers or laser systems that can produce a hazard if viewed directly. This includes intrabeam viewing or specular reflections. Except for the high-power Class 3b lasers, this class of laser will not produce a hazardous diffuse reflection.*
   - **Class 4**: *Lasers or laser systems that can produce a hazard not only from direct or specular reflection, but also from diffuse reflection. In addition, such lasers may produce fire hazards and skin hazards.*

72.3 Lasers and Delivery Systems

The construction of a laser source requires an active medium (gas, liquid, or solid) and a collection of atoms or molecules. The active medium is excited to emit the photons by stimulated emission. The light produced by the laser source is usually coupled to a delivery system and is used for therapeutic purposes. The active medium producing the beam identifies and distinguishes one laser from another. Different types of lasers used in dentistry, such as the carbon dioxide (CO_2), erbium (Er), and neodymium (Nd) lasers, various other substances used in the medium [e.g., yttrium aluminum garnet (YAG) and yttrium scandium gallium, garnet (YSGG), erbium, chromium-doped yttrium scandium gallium garnet (Er,Cr:YSGG)], argon, diode, and excimer types, all produce light of a specific wavelength. The CO_2, Er:YAG, Er,Cr: YSGG, and Nd:YAG lasers emit invisible beams in the infrared range. The argon laser emits a visible light beam at 488 or 514 nm, whereas the excimer lasers, which operate on rare gas monohalides, emit invisible ultraviolet light beams at predetermined wavelengths (ArF, 193 nm; KrF, 248 nm, XeCl, 308 nm).

In clinical applications, it is important to deliver laser energy precisely to the target tissue and ergonomically to the operator. Laser energy is delivered to the target tissue by means of two common delivery systems: (1) a flexible hollow waveguide with mirror finish interior and (2) a glass fiber optic cable. In a flexible hollow waveguide, the laser energy is reflected along this tube and exits through a delivery handpiece with the beam striking the target tissue in noncontact mode. If the delivery probe has to be used in contact mode, then an accessory tip of sapphire or hollow metal may be connected to the end of the waveguide. A glass fiber optic cable can be more flexible and fits snugly into a handpiece with a bare fiber end or attached to a sapphire or quartz tip. A fiber optic delivery system allows greater accessibility to different areas in the oral cavity. Infrared dental lasers are equipped with a separate aiming visible beam that is coaxially superimposed on the infrared beam. This will allow the operator to spot where the infrared laser energy will be focused [1]. Shorter wavelength instruments such as Ar, diode, and Nd:YAG lasers have a small, flexible optical fiber system with bare glass fibers that delivers the laser energy to the target tissue. Er and CO_2 laser devices are constructed with more rigid glass fibers, semiflexible hollow waveguides, or articulated arms to deliver the laser energy to the surgical site [1].

The fiber optic delivery system can be used in either contact or noncontact mode (a few millimeters away from the target). For the optic fiber, the focal point is at or near the delivery tip, and has the greatest energy (focused mode of delivery). The laser beam is divergent and defocused as the handpiece is moved away from the focal point (defocused mode of delivery) (Figure 72.1). At a small divergent distance, the laser light can cover a wider area. At a greater distance, the beam effectiveness decreases because the energy is dissipated. In the defocused mode, there is a wider zone of tissue removal but a shallower depth of penetration. Lasers with shorter emission wavelengths, such as argon, diode, and Nd: YAG lasers, can be designed with small, flexible glass fibers. The Er,Cr:YSGG and Er:YAG devices present challenges to fiber

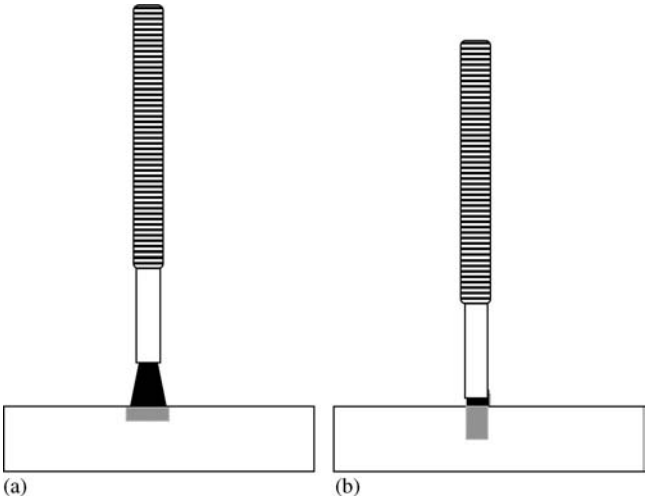

Figure 72.1 Schematic diagram showing the application of laser in (a) defocused and (b) focused modes of delivery. The defocused mode produces a wider zone of tissue removal but shallower depth of penetration compared with the focused mode.

manufacture because their wavelengths are large and do not easily fit into the crystalline molecules of the conducting glass. Further, they are highly absorbed by water, hence a special expensive fiber design with minimal hydroxyl content, peripheral cooling air, and water spray for the handpiece is necessary [1, 2].

72.4 Laser–Dental Tissue Interaction

The nature of laser–tissue interaction is influenced by the properties of the laser (e.g., wavelength, energy density, and pulse duration of the laser radiation) and the characteristics of the tissue (e.g., absorption, reflection, transmission, and scattering). Different types of lasers may produce different effects on the same tissue, and the same laser can have varying effects on different tissues. The nature of absorption and transmission of laser light is primarily wavelength dependent and it is important to note that the intensity of light will not remain constant throughout a definite volume of tissue. Consequently, laser effects will change depending upon their depth of penetration. The clinician controls four parameters while operating a laser system: (a) the level of applied power (power density), (b) the total energy delivered over a given surface area of tissue (energy density), (c) the rate and duration of the exposure to laser energy (pulse repetition), and (d) the mode of energy delivery to the target tissue (i.e., continuous or pulsed energy; direct contact, or no target tissue contact). Four different types of interactions with the target dental tissue have been suggested: (1) photobiological interactions, (2) photochemical interactions, (3) photothermal interactions, and (4) photomechanical and photoelectrical interactions.

1) **Photobiological Interactions:** Transmission of light conducts light energy through the tissue without any interaction and therefore does not have any effect on the tissue. Reflection is another process that does not produce any thermal effect on the tissue. The absorption of laser energy by a tissue is an indication of its ability to produce tissue changes and generation of heat. The nature of the absorption of laser energy by a tissue generally depends upon the laser wavelength and the optical characteristics of the target tissue. In scattering, the light energy is absorbed over a greater surface area, resulting in a less intense and less precise tissue or thermal effect. Scattering is observed to be the most pronounced effect in a tissue, and most tissues behave as a highly scattering turbid medium. The particular properties of each type of laser and the specific target tissue render them suitable for various procedures.

   The CO_2 laser has a high absorption coefficient in water, and is well absorbed by dental hard and soft tissue components. Consequently, it produces effects on most biological soft and hard tissues. However, because of its high thermal absorption, the enamel and dentin surfaces reach very high temperatures on application of a CO_2 laser. The Er:YAG laser is the most efficient for cutting enamel and dentin as its energy is also well absorbed by water and by hydroxyapatite. The argon laser is effective on pigmented or highly vascular tissues, whereas the Nd:YAG laser energy is transmitted through tissues by water and interacts well with dark pigmented tissue. The excimer lasers functions by breaking molecular bonds and reducing the tissue to its atomic constituents before their energy is dissipated as heat.
2) **Photochemical Interactions:** A photochemical effect occurs when there is absorption of laser light by chromophores (natural or artificial) or cellular components to induce biochemical reactions without any thermal effect. Photochemical effects may lead to alterations in the physicochemical properties of the irradiated tissue by photoaddition, photofragmentation, photo-oxidation, photohydration, *cis–trans* isomerization, or photorearrangement. The chemical reaction that leads to the curing of dental composite resin is an example of a photochemical process. Another example of photochemical reactions is photodynamic therapy (PDT). PDT is produced by the absorption of light by the chemicals introduced into a cell or a tissue. The principle of PDT is applied to destroy tumor cells and microbial cells. In PDT, the applied chemical, called a photosensitizer, acts as an exogenous chromophore that performs the function of photosensitization. Photosensitization is the process of sensitizing a photoprocess. The mechanism of most photosensitization reactions involves photoaddition and photo-oxidation.
3) **Photothermal Interactions:** In a photothermal interaction, the laser energy is absorbed by the tissue and the light energy is transformed into heat energy, which is the cause of the final tissue effect. Photothermal interactions can lead to heating with denaturation (45–60 °C), and rapid absorption of laser energy leading to removal of tissue (photoablation) by vaporization or burning away of the tissue by carbonization (photopyrolysis). This interaction forms the basis for many surgical applications of lasers. The photothermal effect on a tissue largely depends on the

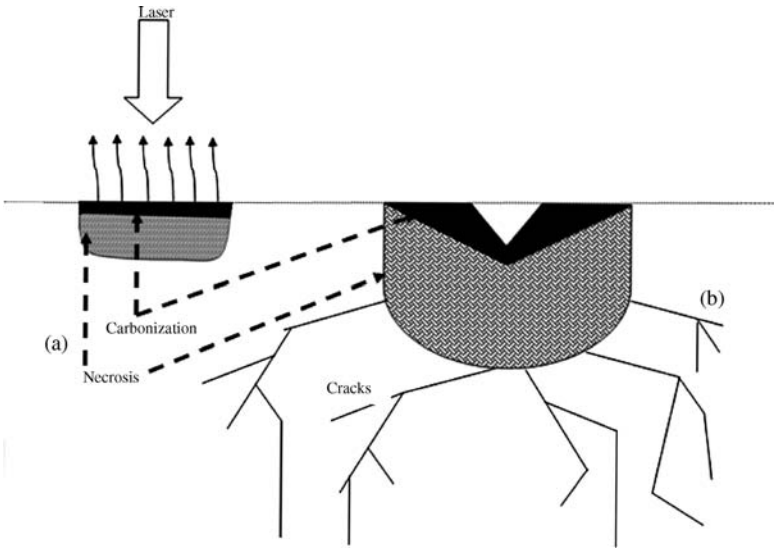

Figure 72.2 Illustration of laser-induced photothermal effects. The laser light energy is absorbed and converted to thermal energy by the lattice vibration of the hard tissue molecules (mainly water). This leads to the heating of surrounding tissues, boiling of water, and drying of tissue. Drying of tissue will cause rapid increase in absorption, carbonization and tissue removal (a). Usually, the surrounding hard tissue damage after treatment is manifested by massive zones of carbonization, necrosis, and cracks in the hard tissue (b) [2].

wavelength of the laser, since the amount of heat generated in the tissue is determined by the extent of absorption of the light. In a photothermal interaction, the laser light is absorbed and converted into thermal energy by stimulating the lattice vibrations of the tissue molecules. The lattice vibrations lead to heating of surrounding tissues and boiling of tissue water. On subsequent to drying, there will be a rapid increase in absorption leading to carbonization and tissue removal. The level of tissue dehydration plays a significant role in the photothermal interaction of lasers with tissue (Figure 72.2).

4) **Photomechanical Interactions:** The photomechanical effect is characteristic of ultra-short pulses of very high energy density. Even a small energy of 1 μJ in 1 ps corresponds to a peak power of 10^6 W and when focused to a 10 m spot would lead to an intensity of about $10^{12}\,\mathrm{W\,cm^{-2}}$. This localized absorption of intense laser irradiation can lead to rapid heating and very large temperature gradients in dental tissues, resulting in enormous pressure waves and photodisruption (or photodisassociation). Photomechanical disruption occurs in three phases: (1) ionization, (2) plasma formation, and (3) shock wave generation.

   The energy levels resulting in shock waves are capable of rupturing intermolecular and atomic bonds due to the conversion of light energy into kinetic energy. In dental hard tissues, a photomechanical shock wave produced by the rapid photovaporization of water leads to a volumetric change of water within the tooth. This change creates high pressures, removing and destroying selective areas of

adjacent tissue. Therefore, it is important to maintain the maximum laser energy density of all pulsed lasers below a certain threshold to avoid microcracks in dental tissues. Er:YAG and Er,Cr:YSGG lasers are known to cause photomechanical effects. This principle is also used to ablate infected dental hard tissue in dental caries (bactericidal effect). Furthermore, the short pulse width associated with high fluence rates in lasers such as the Ho:YAG laser may also induce a photoacoustic interaction, which involves the removal of tissue with shock wave generation. Photoelectrical interactions include photoplasmolysis, which involves the removal of tissue through the formation of electrically charged ions and particles that exist in a semi-gaseous, high-energy state.

5) **Effect of Target Tissue Properties on Laser–Tissue Interaction:** The response of tissues to laser energy is complex and different thermal properties of the target tissue are considered to influence the tissue response. The different thermal properties of interest are the following:
   - **Thermal diffusivity**: This is the ability of the tissue to conduct heat upon exposure to a transient temperature gradient.
   - **Thermal coefficient of expansion**: This property measures the expansion that is experienced by the tissue upon heating.
   - **Heat capacity**: This is the amount of heat energy needed to raise the temperature of 1 cm^3 of tissue by 1 °C.
   - **Phase transformation temperature**: This temperature indicates the melting and vaporization temperatures of the tissue components.
   - **Latent heat of transformation**: This is the characteristic amount of heat absorbed or released by a substance undergoing a change in physical state.

72.5 Laser Effects on Dental Tissues

72.5.1 Laser Effect on Enamel

The laser effect on enamel tissue is primarily due to a temperature effect, which leads to melting and fusion of enamel, vaporization, and crater formation. A pulse mode of application produces less heat than the continuous mode, and therefore melting of the enamel surface can be achieved without vaporization. CO_2 laser radiation is reasonably well absorbed by the enamel, since human enamel has its absorption peak close to the wavelength of the CO_2 laser. Laser energy causes a rapid local temperature rise and prompts melting and cooling of apatite crystals up to a depth of 5 μm. The melting point of human enamel is above 1280 °C. It forms a mixture of β-tricalcium phosphate and tetracalcium phosphate above 1450 °C. These changes were shown either to decrease or increase the solubility of the enamel depending on the calcium: phosphate ratio in the newly formed minerals. Depending on the energy density of the laser irradiation, the chemical and solubility characteristics of enamel tissue can be modified. Low-energy lasing in particular has been shown to increase the acid resistance of enamel, while high-energy density lasing may decrease the acid

resistance. Additionally, lasing of enamel enhances the fluoride uptake, resulting in an increased acid resistance. The laser effect on enamel seems to depend on the structure and orientation of enamel prisms. It was concluded based on this study that the observed resistance of laser-exposed enamel to subsurface demineralization was due to a physical alteration in permeability rather than to a chemical change in solubility [3, 4]. Enamel surfaces exposed to Nd:YAG laser energy show roughness, fused crystallites, charring, and cracking, whereas Er:YAG-lased enamel shows characteristics of cavitated and flaky rough surfaces. An argon laser has a minimal effect on the surface due to reflection of the beam.

72.5.2 Laser Effects on Dentin

The exposure of sound dentin to a CO_2 laser beam causes high absorption of laser radiation by the minerals in the dentin, resulting in an increase in temperature, which after evaporation of water leads to combustion of the organic material and fusion of the hydroxyapatite. Lased dentin recrystallizes while cooling to form a structure that is similar to that of normal enamel [5]. This recrystallized dentin can form a sealed layer [6]. The depth of the sealed layer depends on the energy density used. The recrystallized sealed layer showed a higher mineral content and this layer seemed to be partially acid resistant. However, demineralization of dentin was observed underlying the sealed layer, which was attributed to the acid diffusion that occurs through the unsealed dentin in the laser-treated area and also through the radiation-induced micro-cracking. The level of dentin dehydration plays a significant role in the thermal interaction of lasers with dentin. CO_2 laser energy is easily absorbed by water and therefore results in less carbonization on or heat penetration into the tissue surface that contains water. If the tissue contains no water, carbonization and crack formation occur on the surface of the tissue. It is important to note that the continuous-wave CO_2 laser, when used at energies necessary to ablate the dentin structure, can cause pulpal damage.

Laser irradiation renders the dentin surface harder and more brittle. Different wavelengths of irradiation could provide different surface morphology with less brittle dentin. Laser irradiation of dentin produced a surface morphology characterized by localized melting and recrystallization of dentin which resulted in projections covered with a glaze-like surface that enhanced the mechanical bond of composite restorations. Unfortunately, failures occurred most often within the dentin, indicating that the bond strength of the composite was stronger than the mechanical properties of the dentinal projections [7]. Studies have shown that dentin irradiated with the Nd:YAG laser prior to an adhesive procedure results in a reduction in bond strength with composite resin. This effect is due to the obliteration of the dentinal tubules due to the melting and resolidification of irradiated dentin. In the red and near-infrared electromagnetic spectral region (600 nm–1.5 μm), the tissues have a transmission window so that the absorption of neodymium laser (1064 nm) energy by water and hydroxyapatite is low. Even though the energy is only partially absorbed by dentin, the laser is still able to heat the tissue to the point of carbonization

(600–800 °C). During carbonization, the organic and inorganic materials can melt and vaporize, leading to micro-explosions and ejection of the molten mineral phase, which subsequently resolidifies at the surface. Therefore, the Nd:YAG laser is not indicated for cutting hard tissues or for tissue modification prior to adhesive restoration. Excessive thermal damage has been one of the major problems associated with lasers such as the Nd:YAG and CO_2 lasers when used for cavity preparation due to lower absorption coefficients. Er:YAG laser energy is highly absorbed by water and hydroxyapatite. Er lasers offer the ability to remove enamel, dentin, and carious tissue with minimal tissue disruption of the residual tooth. The absorption of the ArF (193 nm) excimer laser radiation by dentin is considerably higher than that of the XeCl (308 nm) laser. As a result, a much thinner melted layer is formed following Ar:F ablation. It was found that when pulses of extremely short duration are used with this laser, heat accumulation does not occur and thermal damage to the surrounding tissues may be avoided.

72.5.3 Laser Effects on Dental Pulp

The effect of lasers on dental pulp is an important factor that determines the nature of their clinical application. Normally, pulp tissue cannot survive in an environment of elevated temperature for extended periods when the tooth structure is irradiated with lasers [8]. Lasers that produce thermal damage to the pulp are not particularly suitable for cavity preparation. Semiconductor diode laser irradiation has been reported to produce no dental pulp damage, and these lasers having a power of 3–30 W are considered to have potential applications for dental pulp treatment. He–Ne lasers with powers of more than 15 mW are also known not to damage dental pulp. The Nd:YAG laser has a wide energy emission range and its effects should be carefully considered before application. Nd:YAG and CO_2 lasers have the greatest potential for causing damage to the pulp and surrounding tissue. Nd:YAG laser treatment results in total disruption of the normal architecture of the pulp, including destruction of the odontoblastic cell layer and vasculature. There is extravasation of red blood cells and inflammatory cell infiltration consisting of neutrophils, lymphocytes, and plasma cells. The Er:YAG laser has been used to ablate hard and soft tissues under copious water spray without conspicuous damage to dental pulp [9]. Laser preparation of teeth should include short intervals with continuous water application to allow dissipation of heat. This strategy of fractionating the energy and continuous water spray is suggested to minimize the risk of damage to the dental pulp. The Er,Cr:YSGG laser can also be used to ablate hard and soft tissues with a water coolant. The argon laser, which has been used for laser polymerization of dental composite resin, has been reported to cause no significant temperature increase in the pulp tissue [10].

The parameters of the laser that affect the dental pulp tissue are waveform, power, and duration of exposure. Different methods have been utilized to reduce heat transfer from the enamel and dentin surface to the pulp. Pulsing of lasers has been used as an effective method to prevent collateral tissue damage. However, this

method was noted to be effective during soft tissue ablation and less effective when dental hard tissue was involved. The difference is attributed to the difference in the thermal diffusion rate and relaxation time between the hard calcified and soft oral tissues. The use of a combination of air and water spray before, during, and immediately after laser irradiation of enamel and dentin is suggested to be a more effective means of temperature control and reduction of heat transfer to the pulp and surrounding vital structures. Precooling with an air–water spray prior to lasing may be used with laser systems with wavelengths that are more readily absorbed by water (e.g., CO_2, Ho, and Er).

72.6 Lasers in Operative Dentistry

Lasers have been employed for a wide variety of operative procedures on teeth such as bleaching of teeth, adhesive restorations, and soft tissue procedures such as crown lengthening. The treatment goal of applying lasers in operative dentistry is to reduce pain and perform operative procedures as atraumatically as possible.

72.6.1 Laser-Assisted Tooth Bleaching

Laser-assisted tooth bleaching, also called as power bleaching, is carried out for cosmetic purpose and in most cases does not need restoration. Argon, KTP (potassium titanyl phosphate), and diode lasers are most commonly used for this purpose. Laser-assisted tooth bleaching is a method of removing extrinsic and intrinsic stains from teeth. In laser-assisted tooth bleaching, laser activation energy is utilized to trigger faster degradation of the hydrogen peroxide bleaching agent into reactive oxygen free radicals. This in turn increases the rate of tooth bleaching and bleaching efficiency. Certain dental lasers are also used with bleaching products containing a specific chromophore that will absorb the laser wavelength. Studies have recommended minimum laser exposure times to minimize the rise in pulpal temperature. Generally, the rise in laser-induced intra-pulpal temperature is directly proportional to the power of the laser and irradiance and inversely related to tooth thickness [11, 12]. Bleaching gel (absorption agent) is indicated to reduce surface thermal changes and intra-pulpal temperature during laser-assisted bleaching [e.g., titanium dioxide (TiO_2)] [13].

Systems used for laser-assisted tooth bleaching include BritSmile Teeth Whitening System (Discus Dental), LaserSmile Teeth Whitening System (Biolase Technology), LumaArch Teeth Whitening System (Lumalite), and Opus 10 Laser System (Lumenis). In addition to laser systems, light-emitting diode (LED) and halogen light sources are also used for tooth bleaching. The advantages of laser-assisted tooth bleaching are that this approach aids in distributing light energy more uniformly throughout the tooth surface. It has been found that the photochemical activation provides a higher intrinsic

overall radical yield than thermal activation, and that the rate at which reactive radicals are generated is higher than with thermal activation. However, several studies have suggested that laser-assisted tooth bleaching is not more effective than many professional teeth bleaching systems and further research is indicated in this area [14, 15].

72.6.2 Laser-Assisted Cavity Preparation and Caries Removal

In laser-assisted cavity preparation, intense laser energy is used for the ablation of dental hard tissues. The main advantage of laser-assisted cavity preparation is the ability to be specific to the carious lesion and conserve maximum healthy tooth structure. Depending on the wavelength of the light applied, the ablative effect can produce photochemical or photothermal effects on the target tissue. The nature of absorption of light energy is different for different tissues with different textures and water contents [16]. Subsequently, different laser parameters are required for the ablation of enamel, dentin, and carious tissue. Different lasers such as CO_2 and pulsed Nd:YAG lasers have been applied for this caries removal.

The Er-based laser system has been widely used for the preparation of dental hard tissues. During ablation, the main constituent that absorbs the laser energy is the bound water in the tissue. The maximum absorption peak in the infrared range (2.9 μm) matches well with the wavelengths of Er:YAG (2.94 μm) and Er,Cr:YSGG (2.79 μm) lasers. The absorption of water in this range is so high that scattering and absorption of light contributed by other tissue components become insignificant. Since the Er wavelength has an affinity for the water content of hard tissues, (a) it has a small tissue penetration depth and (b) less energy is required to ablate caries (greater water content) than dentin or enamel (lesser water content). When irradiating dentin or enamel with Er-based laser pulses with sufficient pulse energy, the tissue water is heated very rapidly above the boiling point. This causes a micro-explosion, leading to blowing out of the generated small particles (spallation) and mechanical removal of target tissue. Since certain amount of heat conduction cannot be avoided, even though most of the radiation is absorbed by the water, a water-spray has to be used for cooling to prevent damage to pulp tissue. During cavity preparation, a water–air stream is directed on the cutting tip and on to the target tissue. The laser tip should be held perpendicular to the cutting surface to maximize the cutting efficiency. The tip end should be moved constantly to provide effective ablation and better tissue cooling. Once the enamel has been removed, the energy settings must be reduced because dentin and caries have a higher water content than enamel and cut more readily. An alternative approach to changing the operating parameters is to reposition the laser tip to a noncontact mode to decrease the energy density. For deep cutting, the tip is moved up and down as in a pumping action. The operator can also recognize different tooth structures by the sound of ablation (popping sound), which differentiates the tissue types. Both the pitch and resonance of this popping sound are related to the propagation of acoustic shock waves within tooth, and vary according to

the presence or absence of caries. This feature assists the user to confirm if the caries has been removed completely. During interproximal tooth preparation, adjacent teeth should be isolated and protected with the use of a rubber dam or a metal matrix. Laser-based cavity preparation usually results in a cavity with a rough or irregular surface, which is ideal for the placement of a composite resin or glass ionomer restoration.

Lasers have also been applied to prevent enamel and dental caries. The mechanism by which laser irradiation enhances enamel resistance to artificial caries ranges from a physical seal achieved by melting the surface through partial fusion and recrystallization to compositional alteration of enamel [17]. It has been suggested that the thermal treatment converts carbonated hydroxyapatite mineral to a less soluble mineral. Scanning electron microscopic studies have shown that enamel and dentin surfaces subjected to continuous-wave (cw) CO_2 laser radiation (1, 2, 3 W) were sufficiently melted and the smear layer was solidified. This lased region was unchanged even after acid demineralization. This supported the hypothesis that the lased enamel surface is less permeable to diffusion of ions and is resistant to solubility [18]. The formation of a micropore system within the mineral phase in the enamel, dentin, and cementum following laser treatment has also been suggested. The micropore system provides a means for trapping calcium, phosphate, and fluoride ions released during demineralization and these subsequently act as sites for reprecipitation. During the process of demineralization, dissolution of mineral occurs with the mobilization of ions from the affected dental hard tissue. As mineral phases are released from the deeper layers of hard tissue, reprecipitation in the more superficial layer occurs and the surface remains intact [19–21]. It has been shown that irradiation with an argon laser alters the surface layer of enamel by producing microporosities admixed with globular surface coating. This surface is rich in calcium, phosphate, and fluoride. The presence of fine porosities with a confluent globular surface coating suggests that the effect of the argon laser at relatively low fluences (11.5 and 100 J cm^{-2}) may alter or eliminate the organic material overlying and within the surface enamel. Further, it appears as though the mineral phases previously embedded in this organic matrix may form globular precipitates, resembling a calcium fluoride confluent surface [22]. These globular deposits may provide a reservoir for mineral phases during a cariogenic attack.

Nd:YAG, CO_2, and argon lasers have been applied to induce remineralization of subsurface lesions of enamel and dentin, by combining the effect of lasers with fluorides. This treatment approach renders the tooth surface less susceptible to caries. An argon laser has been found to alter the surface characteristics resulting in a significant reduction in its acid solubility. The Nd:YAG laser in combination with acidulated phosphate fluoride application increased the acid resistance of enamel whereas CO_2 laser irradiation created a sealed tissue layer that delayed diffusion of acids into the underlying sound dentin. The lattice strain was decreased after laser irradiation and this resulted in a better arrangement of ions in the crystals of enamel. A slight contraction of the A-axis was observed but the C-axis was not altered by laser

irradiation at an optimal energy density. Reductions of water, carbonate, and organic substances were also revealed in lased enamel. The reduction of carbonate and bound water from the enamel crystals has been suggested to contribute to caries resistance. Even the uptake of fluoride was found to be very high in the lased enamel [23, 24].

72.6.3
Laser-Assisted Adhesion in Tooth Color Restoration

Laser etching is an alternative option to acid etching to bond tooth colored restoration to the tooth structure. Argon, CO_2, Nd:YAG, and excimer lasers are used for this purpose. Laser etching is due to the continuous vaporization of water trapped within the inorganic matrix of enamel and dentin. The laser etching procedure is considered to result in an etched tooth surface, similarly to the acid etching technique. However, conflicting results on bond strength to enamel have been reported after different laser etching. CO_2 laser energy was reported to increase the shear bond strength [7], which exceeded the value obtained for acid etching. These studies supported CO_2 laser etching to improve the bonding of resin composite to enamel [25, 26]. When the bond strengths of porcelain laminate veneers to tooth surfaces after etching with acid and after conditioning with an Er,Cr:YSGG laser was compared, laser-etched bonding produced a similar bond strength to acid-etched bonding of laminate veneers to tooth surfaces [27]. The effect of etching with an Er:YAG laser was also evaluated *in vitro*. There was a significant positive correlation between the etching fluence and the shear bond strength, but pitting of the enamel surface at fluences above 25 J cm^{-2} limited the maximum fluence for etching purposes. It was observed that the shear bond strengths were significantly inferior after Er:YAG laser etching than those obtained using conventional acid etching [28]. In another study, it was shown that laser pretreatment of Ni–Cr alloy increased the bond strength to composite resin compared with sandblasting techniques. Laser pretreatment in combination with sandblasting further increased the bond strengths [29].

72.6.4
Laser-Activated Polymerization of Composite Resin

The argon laser has been found to be useful for polymerizing composite resin. The argon laser emits specific light with wavelengths that correspond to the absorption peak of camphorquinone, the initiator of polymerization for the efficient photopolymerization of resin composite. An *in vitro* experiment has shown that the argon laser is a possible alternative for photopolymerizing composite resin, providing the same quality of polymerization as the halogen lamp. However, none of the photocured units tested in that study completely eliminated microleakage [30]. It is also important to note that laser-induced polymerization can produce an increase in pulpal temperature. However, the magnitude of the heat increase produced would depend upon the polymerization modes and remaining dentin thicknesses. It was

reported that thicker the remaining dentin and the lower the polymerization mode energy, the lower will be the temperature rise [31].

72.6.5
Laser-Assisted Removal of Restorative Materials and Metal Dowels

Lasers are used to remove different restorative materials such as zinc phosphate cement, polycarboxylate cement, glass ionomer cement, polyketone, composites, and silver amalgam. The Er:YAG laser has been shown to be effective in removing these restorative materials with a total energy delivered that was slightly lower than that used on enamel and dentin tissue [32]. The removal of silver amalgam using lasers is not recommended, mainly owing to the high concentration of mercury vapor released during ablation. There are also disadvantages when lasers are applied to remove dowels or endodontic posts: (a) it is difficult to manipulate the fiber optic illumination tip deep within the root canal; (b) some lasers could, directly or indirectly, induce damaging effects on surrounding tissues; and (c) tiny metallic particles are generated during lasing and these particles could be aspirated by the patient or the operator [16]. Further research is required before lasers can be applied for dowel removal. Experiments have also demonstrated that Nd:YAG laser irradiation can be useful for removing obturation materials from the root canal. It has been suggested that these lasing procedures require less time than the conventional method with drills and files. Furthermore, following laser irradiation, the dentin wall was found to be free of debris and the smear layer [33].

72.6.6
Laser-Based Management of Dentin Hypersensitivity

Dentinal hypersensitivity is characterized by pain of short duration arising from the exposed dentin in response to stimuli, typically thermal, evaporative, tactile, osmotic, or chemical. Pain due to dentin hypersensitivity cannot be attributed to any other form of dental defect or pathology. Dental erosion, abrasion, attrition, gingival recession, periodontal treatment, and anatomic defects are risk factors for dentinal hypersensitivity. Hypersensitive tooth surfaces are mostly located at the cervical margin on the buccal surface of the teeth [34]. Brännström *et al*. proposed that the nerve endings in the dentin–pulp interface are activated by the rapid dentinal fluid flow in response to the dentinal stimulation (hydrodynamic theory) [35]. Patent dentinal tubules are the primary factor that leads to sensitivity of exposed dentin and clinical management of dentin hypersensitivity is aimed at blocking the fluid flow through the exposed dentinal tubules. Most in-office treatments for dentin hypersensitivity employ some form of "barrier," either a topical solution or gel or an adhesive-based restorative material to block the dentinal fluid movements. The application of desensitizing agents to reduce neuronal responsiveness to dentinal stimuli has also been investigated. Potassium-containing dentifrices, fluoride-containing medicaments, and agents containing 10% strontium chloride were found to be partially effective in reducing dentinal hypersensitivity. However, to date most

treatment procedures have failed to produce satisfactory long-term treatment outcome in patients with dentin hypersensitivity [36].

The application of lasers in the management of dentinal hypersensitivity is based on two mechanisms. (1) The first is the direct effect of laser irradiation on the neurogenic activity of the nerve fibers. The GaAlAs (diode) laser wavelengths (780, 830, and 900 nm) were considered to produce an analgesic effect by depressing the nerve transmission by blocking the depolarization of C-fiber afferents. (2) The second is sealing of the dentinal tubule by the melting and fusing of dentin tissue/smear layer. The different lasers used for the management of dentin hypersensitivity are He–Ne (632.8 nm), GaAlAs (780 nm), GaAlAs (830 nm), Nd:YAG (1.064 μm), and CO_2 (10.6 μm). The CO_2 laser has been applied to fuse or recrystallize the dentin surface [37]. However, the possibility of carbonization of organic material together with the melting of dentin cannot be avoided. The CO_2 laser at moderate energies produces mainly sealing of dentinal tubules, and also a reduction in permeability [38]. Nd:YAG laser energy (3 W) was also used to manage dentin hypersensitivity [39] by occluding the open dentinal tubules. The sealing depth of Nd:YAG laser irradiation on dentinal tubules measured less than 4 μm [40]. Direct nerve analgesia and a suppressive effect achieved by blocking the depolarization of A-delta and C-fibers were also considered possible mechanisms of action for Nd:YAG laser irradiation in the treatment of dentin hypersensitivity [41]. The Er:YAG laser at a low power has also been used for the treatment of dentin hypersensitivity. However, addition of sodium fluoride was found to enhance markedly the occlusion produced by CO_2 and Er:YAG lasers. Excimer lasers have also been highlighted as a potential treatment option to manage dentin hypersensitivity and prevent bacterial penetration through dentinal tubules. A possible advantage of using excimer lasers could be the lack of thermal damage to the surrounding tissues [42, 43].

72.7
Application of Lasers in Endodontics

The goals of endodontic therapy are to (1) debride and disinfect the infected root canal, (2) shape the root canal, and (3) completely seal the root canal space. Currently, lasers are applied for the diagnosis of pulpal health, pulp capping, pulpotomy, root canal disinfection, root canal obturation, endodontic retreatment, and apical surgery.

72.7.1
Application of Lasers to Diagnose Dental Pulp Health

The selection of a tooth for root canal treatment depends on the pulp health or vitality. Pulp vitality depends on the presence of intact blood supply in dental pulp microvasculature. Nevertheless, the location of dental pulp within a rigid and calcified dental hard tissue has made measuring this parameter very difficult clinically. The current vitality tests do not aid in assessing the pulp vitality. Laser Doppler flowmetry (LDF) was developed to assess the blood flow in pulpal microvasculature, and

subsequently the health of dental pulp. This method is useful for diagnosing the health of pulp in clinical cases of pulp revascularization 3–4 months ahead of electric pulp testing [44].

LDF is a noninvasive method, which assess the blood flow in the microvasculature of dental pulp. This system uses He–Ne and diode lasers at a low power of 1–2 mW. The dentinal tubules in the dentin are said to act as light guides and direct the light incident on the tooth surface into the pulp. Moving red blood cells cause the frequency of the laser beam to be Doppler shifted and some of the light to be backscattered out of the tooth. The scattered light is detected by a photocell that is placed on the surface of the tooth. The measured output is proportional to the number and velocity of the blood cells. The mean blood flux level in teeth with vital pulp tissue is significantly higher than for teeth with non-vital pulp. However, in teeth with vital pulp with impaired blood supply, the flux level can be low and in such cases the presence of pulsation is the only indication of pulp vitality.

Laser light can be directed to the tissue surface via an optical fiber or as a light beam. If an optical fiber-based delivery system is used then the optical fiber can terminate as a probe, which can be placed directly on the tissue surface. One or more light-collecting optical fibers also terminate in the probe head (all-in-one bundle probe). In this case, the collecting optical fibers would transmit a proportion of the scattered light to a photodetector and the signal/image processing systems. Generally, this system will measure blood flow in a tissue volume of typically 1 mm^3 or smaller. The measured blood flow change in a small tissue volume is generally considered to be a representation of the larger volume. Optical probe stability on the tooth surface is very important during laser Doppler measurements. Comparison of a flux trace measured from the contralateral healthy tooth often aids the diagnosis of vitality. Improved signal processing techniques permit diagnosis with a sensitivity and specificity of over 90%.

The advantages of LDF are that (1) it is an objective measurement of the pulpal vitality, (2) in comparison with other vitality tests, it does not rely on the sensation of pain to determine the vitality of a tooth, and (3) this method can be useful in patients, especially young children, who have difficulty in communicating and teeth that have experienced recent trauma. The disadvantages of LDF are that (1) it is difficult to calibrate the measurements in absolute units and their output may not be linearly related to blood flow, (2) the anterior teeth, in which the enamel and dentin are thin, do not present a problem, but molar teeth, with their thicker enamel and dentin and the variability in the position of the pulp within the tooth, may cause deviations in pulpal blood flow and blood flow measurements, (3) differences in the sensor output and inadequate calibration by the manufacturer may indicate the use of multiple probes for accurate measurement, and (4) the system is expensive [44, 45].

72.7.2
Laser-Assisted Pulp Capping and Pulpotomy

Pulp capping is defined as a procedure in which a biomaterial is placed over an exposed or nearly exposed pulp tissue to encourage the formation of an irritational dentin bridge at the location of exposure. Pulpotomy also involves the surgical

removal of a small portion of vital pulp tissue as a means of preserving the remaining coronal and radicular pulp tissues. Pulp capping is indicated when the pulp exposure occurs during the removal of healthy dentin tissue and when the pulp exposure size is very small ($\leq$1.0 mm). Pulp capping is recommended only on uninflamed pulp tissue since the pulp tissue should possess the capacity to form tertiary dentin.

Pulpotomy is indicated when the young pulp is exposed to caries and the root formation is not complete. Restorative materials such as calcium hydroxide [$Ca(OH)_2$], bioactive molecules, or mineral trioxide aggregate (MTA) is used during pulp capping to encourage the formation of reparative dentin. Traditionally, $Ca(OH)_2$ is used widely as a pulp capping agent. When $Ca(OH)_2$ is applied to pulp tissue, a necrotic layer is formed subjacent to which a dentin bridge is expected to form. The disadvantage of this process is that the necrotic zone may allow bacterial growth if the restoration leaks. MTA shows favorable results when applied to exposed pulp. It produces more dentinal bridge in a shorter time with significantly less inflammation than $Ca(OH)_2$. However, a long setting time (3–4 h) is required for the complete setting of MTA [46, 47].

CO_2, Nd:YAG, and Er:YAG lasers have been used to manage exposed pulp tissue. The most important effect of CO_2 laser irradiation is the ability to sterilize and form scar tissue in the irradiated area due to thermal effects, which in turn would aid in protecting the pulp from bacterial invasion. A bloodless field would be easier to achieve owing to the ability of the laser to vaporize tissue, coagulate, and seal small blood vessels. Further, laser treatment may directly stimulate dentin formation [48]. The CO_2 laser was observed to produce new mineralized dentin without cellular modification of pulp tissue when tooth cavities were irradiated in beagles and primates [49, 50]. Jerkit *et al.* [51] studied the histological response of the direct pulp capping after laser irradiation for pulpotomy in the premolars and molars of dogs. An energy level of 1 W with a 0.1 s exposure time and 1 s pulse intervals was applied until the exposed pulp area was completely irradiated. They were then dressed with $Ca(OH)_2$. This study reported more predictable results (90%) with pulp capping performed using laser of different wavelengths than traditional procedures that report a success rate of $\sim$60%. The long intervals (1 s) between the pulses (0.1 s), the relatively low power setting (1 W), and the wavelength (10.6 μm), which is absorbed within 100 μm by water, seem to be sufficient to avoid any thermal damage to the pulp. The final restoration of the cavity is done after 6 months. The high success rate is thought to be due to control of hemorrhage, disinfection, sterilization, carbonization, and stimulation effects on the dental pulp cells. It causes scar tissue formation in the irradiated area due to thermal effects, which may help to preserve the pulp from bacterial invasion. In addition, the laser minimizes the formation of hematoma between the pulp tissue and the $Ca(OH)_2$ dressing, allowing close contact between the dressing and the exposed pulp.

The Nd:YAG laser has been applied in laser-assisted pulp capping procedures. A study showed that the success rate after direct pulp capping with an Nd:YAG laser and Vitrebond are significantly higher than in conventional $Ca(OH)_2$ treatment [52]. However, another study revealed that Nd:YAG and CO_2 laser irradiation of exposed pulp tissue caused carbonization, necrosis, infiltration of inflammatory cells, edema,

and hemorrhage in the pulp tissue [53]. Under the conditions of this experiment, there was little histologic evidence of repair on treated pulp, which was in contrast to the control samples treated with $Ca(OH)_2$-containing cement. Studies have also examined the application of argon, semiconductor diode and Er:YAG lasers for direct pulp capping. Interestingly, more dentin formation and better healing capacity were observed in the Er:YAG laser group than in the conventional control treatment group. Nevertheless, further investigations were suggested to study the effect of the blood extravasation, which appeared near the Er:YAG laser exposure sites [54].

72.7.3 Laser-Assisted Root Canal Disinfection and Shaping

Most current lasers, such as Nd:YAG, diode, and Er:YAG lasers, have bactericidal effects *in vivo* and *in vitro*. Laser radiation produces a bactericidal effect by causing alterations to the bacterial cell wall. Delivery of laser energy through an extremely thin, flexible fiber optic system is important in endodontics. However, the bactericidal effect of laser radiation deep within the dentin differs because of the different absorption of the different wavelengths of lasers. The disadvantage of endodontic irrigants (disinfectants) is that their bactericidal effect is limited to the main root canal lumen. The penetration depth of chemical disinfectants into the dentinal tubules is suggested to be 100 μm [55]. However, laser light is shown to penetrate more than 1000 μm into the dentin. Although different studies have highlighted that the energy from a laser declines as it penetrates into the dentin, the bactericidal effect is found to be effective even to a depth of 1000 μm or more [56]. It was noted that Gram-negative bacteria showed a higher resistance against laser irradiation than Gram-positive bacteria. This higher resistance of Gram-negative bacteria was attributed to their cell wall characteristics.

The laser is an effective tool for killing microorganisms because of the laser energy and wavelength characteristics. Nd:YAG, semiconductor diode, and Er:YAG lasers have commonly been used for endodontic disinfection. However, complete disinfection of the root canal system is very difficult. Additionally, a smear layer is always formed on the instrumented root canal wall. The smear layer, which forms a superficial layer on the surface of the root canal wall, is ~1–2 μm thick. A deeper smear layer packed into the dentinal tubules is also observed to a depth of up to 40 μm (smear plug). The smear layer contains inorganic and organic substances that include microorganisms and necrotic pulp debris. In addition to the possibility that the smear layer itself may be infected, it also can protect the bacteria already present in the dentinal tubules. A smear layer containing bacteria or bacterial products might provide or serve as a reservoir of irritants. During endodontic disinfection, it is vital not only to remove microorganisms from the root canals, but also remove the smear layer formed on the root canal wall and dentinal tubules. In most cases, the effect is directly related to the amount of irradiation and to its energy level. It has also been documented in numerous studies that CO_2 [57], Nd:YAG [58], argon [59], Er,Cr:YSGG [60], and Er:YAG [61] laser irradiation has the ability to remove debris and the smear layer from the root canal walls following instrumentation. KTP laser irradi-

ation was able to remove smear layer and debris from the root canals. At specific fluences, the XeCl laser (wavelength of 308 nm) can melt dentin and seal exposed dentinal tubules [63]. The ArF excimer laser emitting at 193 nm caused significant removal of peritubular dentin at relatively high fluence (10–15 J cm^{-2}) [64]. Inspite of this tremendous interest of using laser in endodontics, studies have stressed the possible limitations of the use of lasers in the root canal system.

The task of cleaning and disinfecting a root canal system that contain microorganisms gathered in a biofilm becomes very difficult. Certain bacterial species become more virulent when harbored in a biofilm demonstrating stronger pathogenic potential and increased resistance to antimicrobial agents as biofilms have the ability to prevent the entry and action of such agents. To increase the effect of disinfection of the infected root canal, black Indian ink or 38% silver ammonium solution was placed in the root canal before irradiating with pulsed Nd:YAG. Rooney *et al.* [65] reported disinfection rates of 80% to 90% with Nd:YAG, whereas others have reported rates of 60%, depending on the condition of the root canals, the type of laser device, the application parameters and the techniques. Bergmans *et al.* [66] tried to define the role of the laser as a disinfecting tool by using Nd:YAG laser irradiation on some endodontic pathogens *ex vivo*. They concluded that Nd:YAG laser irradiation is not an alternative but a possible supplement to existing protocols for canal disinfection, as the properties of laser light may allow a bactericidal effect beyond 1 mm of dentin. Endodontic pathogens that grow as biofilms are difficult to eradicate even upon direct laser exposure.

There are several limitations that may be associated with the intracanal use of lasers that cannot be overlooked. (1) The emission of laser energy from the tip of the optical fiber or the laser guide is directed along the root canal and not necessary laterally to the root canal walls. Thus it is almost impossible to obtain uniform coverage of the canal surface using a laser [67, 68]. (2) The safety of such a procedure is another limitation because potential thermal damage to the periapical tissues is possible. (3) Direct emission of laser irradiation from the tip of the optical fiber in the vicinity of the apical foramen of a tooth may result in transmission of the irradiation beyond the foramen. This transmission of irradiation, in turn, may adversely affect the supporting periradicular tissues of the tooth and can be hazardous in teeth with close proximity to the mental foramen or to the mandibular nerve [68].

The Er:YAG laser is mostly applied for root canal preparation. It has the ability to remove smear layer and open the dentinal tubules. Harashima *et al.* [58, 60] compared 17% EDTA with 6% phosphoric acid and Er:YAG laser energy. The results showed that the Er:YAG laser was the most effective at removal of the smear layer from the root canal walls. When Er:YAG lasers were compared with other lasers, notably argon and Nd:YAG lasers, the results showed that the Er:YAG laser had the most effective wavelength and was more effective than 17% EDTA in removal of the smear layer from the root canal walls. It is suggested that the removal of the smear layer and debris by lasers is possible; however, it is difficult to clean all root canal walls. Therefore, further research is necessary to improve the endodontic tip to permit irradiation of the entire root canal walls. A modified beam delivery system has been

tried for the Er:YAG laser. This system consists of a hollow tube allowing lateral emission of the radiation (side firing), rather than direct emission through a single opening at its terminal end [69].

This new endodontic side-firing spiral tip (RCLase, Opus Dent, Tel Aviv, Israel) was designed to fit the shape and volume of root canals prepared by nickel–titanium rotary instrumentation. It emits the Er:YAG laser irradiation laterally to the walls of the root canal through a spiral slit located all along the tip. The tip is sealed at its far end, preventing the transmission of irradiation to and through the apical foramen of the tooth. The prototype of the RCLase side-firing spiral tip is shown in the root canal of an extracted maxillary canine in which the side wall of the root was removed to allow visualization of the tip. Studies have shown that bacteria and their byproducts, present in infected root canals, may invade the dentinal tubules. The presence of bacteria in the dentinal tubules of infected teeth at approximately half the distance between the root canal walls and the cementodentinal junction was also reported. These findings justify the rationale and need for developing effective means of removing the smear layer from root canal walls following biomechanical instrumentation. This removal would allow disinfectants and laser irradiation to reach and destroy microorganisms in the dentinal tubules.

72.7.4 Laser-Assisted Root Canal Obturation

The thermoplastic properties of gutta-percha are utilized during laser-assisted root canal obturation. The laser energy is used to melt the gutta-percha and the heat-softened gutta-percha is vertically compacted into the root canals. The first laser-assisted root canal filling procedure involved using the argon 488 nm laser. This wavelength, which can be transmitted through dentin, was used to polymerize a resin that was placed in the main root canal. The ability of this obturating material to penetrate into the accessory root canals was tested and it was shown that the resin in the lateral canals was readily polymerized at a low energy level (30 mW). Argon, CO_2, and Nd:YAG lasers have been used to soften gutta-percha [70], and the results indicate that the argon laser can be used for this purpose to produce a good apical seal. The photopolymerization of camphorquinone-activated resins for obturation is possible using an argon laser (477 and 488 nm) [71]. The results indicate that an argon laser coupled to an optical fiber could become a useful modality in endodontic therapy. Er:YAG lasers have shown a remarkable ability to enhance the results of the obturation process. Application of the Er:YAG laser energy to the root canal wall has been shown to increase the adhesion of epoxy-based root canal sealers (AH-26, AH plus, Topseal, Sealer 26, and Sealer Plus) to the canal wall [72].

Studies have shown that laser irradiation using Nd:YAG (100 mJ per pulse, 1 W, 10 Hz) and Er:YAG (170–250 mJ, 2 Hz) lasers improves the apical seal by hindering apical leakage [61, 73]. Since the Nd:YAG laser is very well absorbed by black color, an absorbent paper point soaked with black ink was introduced to the working length and the apical root canal was painted [74]. Maden *et al.* [75] used the dye penetration method to measure apical leakage by comparing lateral condensation, System B

technique, and Nd:YAG-softened gutta-percha. No statistically significant differences were reported. In another study, Anić and Matsumoto [70] demonstrated that the temperature elevation induced on the outer root surface when Nd:YAG and argon lasers were used ranged from 12.9 °C (argon laser) to 14.4 °C (Nd:YAG laser). Such an increase in temperature may be detrimental to the tissues of the attachment apparatus of the teeth. The implication of such methodologies remains questionable. Experiments also evaluated the degree of apical leakage *in vitro* after root canal preparation using Er:YAG laser irradiation. Er:YAG laser irradiation at parameters of 2 Hz and 170–230 mJ per pulse was employed. After obturation, the teeth were immersed in a vacuum flask containing 0.6% rhodamine for 48 h, longitudinally bisected, and observed by stereoscopy and scanning electron microscopy (SEM). It was observed that the degree of apical leakage from the teeth prepared by the laser was not significantly less than that from control teeth. Morphologic findings showed that contact between the root canal walls and obturated materials was hermetic in both groups, but canal walls prepared by laser irradiation were rough and irregular. These results show that root canal preparation by laser irradiation does not affect apical leakage after obturation compared with leakage in canals prepared using the conventional obturation methods [74].

Eriksson and Albrektsson [76] found that the threshold level for bone survival was 47 °C for 1 min. The effects of Nd:YAG laser irradiation on periradicular tissues was examined using a mongrel dog model. The results showed that Nd:YAG laser-treated teeth exhibited ankylosis, cemental lysis, and major bone remodeling 30 days after treatment. The parameters used in this study (3 W and 25 pps for 30 s) were excessive. Since that time, many other studies on periodontal effects of lasers in dogs and rats have been published [77]. According to Kimura *et al.*, the effect on the periodontal ligament when using Er:YAG laser energy is minimal, and no discernible effects on the periodontal ligament were noted [78]. They suggested that the Er:YAG laser can be used for root canal preparation if appropriate parameters are selected.

72.7.5
Laser-Assisted Root Canal Retreatment

The rationale for using laser irradiation in nonsurgical retreatment may be ascribed to the need to remove foreign material from the root canal that may be otherwise difficult to remove using conventional methods. However, studies conducted in this line to evaluate the efficacy of Nd:YAP laser radiation to remove gutta-percha, zinc oxide–eugenol sealer, silver cones, and broken instruments noted that laser radiation alone would not completely remove debris and obturating materials from the root canal. When used at 200 mJ with a pulse duration of 150 ms, an exposure time of 1 s, and a frequency of 10 Hz, the Nd:YAP laser preserved the dentinal walls of the root canal and permitted root canal retreatment without thermal damage to the periodontal tissue. It was concluded that, in combination with hand instruments, the Nd:YAP laser is an effective device for root canal preparation in endodontic retreatment [79]. In another study, an Nd:YAG laser was used at three power outputs (1, 2, and 3 W) to remove gutta-percha and broken files from the root canal. It was

suggested that they were able to remove the obturating materials in more than 70% of the samples, whereas broken files were removed in 55% of the samples [80]. In straight root canals, laser irradiation at appropriate parameters was useful in removing root canal filling materials. The time required to remove any root canal filling material using laser ablation was shorter than that required for conventional methods. However, following laser irradiation, some orifices of the dentinal tubules were noted to be blocked following the melting or ledging of the root canal dentin.

72.7.6 Laser-Assisted Apical Surgery

Endodontic surgery (apicoectomy) is indicated when teeth do not respond to conventional nonsurgical endodontic treatment or when they cannot be treated appropriately by nonsurgical methods. Persistence of irritants in the root canal system zinc oxide eugenol sealer has been observed to be the cause of inflammation of the periapical tissue. The CO_2 laser was first used to irradiate the apex of a tooth during apicoectomy. The advantages of using a laser for this application are (1) improved hemostasis and concurrent visualization of the operating field, (2) reduction in the permeability of the lased dentin, (3) potential disinfection of the contaminated root apex, and (4) ability to achieve recrystallization of the apical root dentin which appeared smooth and ideal for the placement of apical filling material. However, results from an *in vivo* study on dogs showed that the success rate following apicoectomy using the CO_2 laser was not superior and failed to support the use of the CO_2 laser [81]. In another prospective clinical study of two apical preparations with and without a CO_2 laser, in which 320 cases were evaluated, the results did not show that a CO_2 laser improved the healing process [82]. *In vitro* studies with Nd:YAG lasers have shown a reduction in penetration of dye or bacteria through resected roots [83, 84, 85]. It was suggested that the reduced permeability in the lased specimens was probably the result of structural changes in the dentin following laser application [85]. Although SEM examination showed melting, solidification, and recrystallization of hard tissue, the structural changes were not uniform and the melted areas appeared connected by areas that looked like those in the non-lased specimens. It was postulated that this was the reason why the permeability of the dentin was reduced but not completely eliminated.

The Er:YAG laser has been applied for apical cavity preparation of extracted teeth [86]. No significant difference in dye penetration was found between the laser-treated groups and those in which ultrasonic tips were used. This finding was attributed to the inability of the Er:YAG laser to melt or seal dentinal tubules. Further, it has been reported that when using an Er:YAG laser with a low output power in apical surgery, it was possible to resect the apex of extracted teeth. Smooth and clean resected surfaces devoid of charring were observed [87, 88]. It was suggested that although the cutting speed of the Er:YAG laser was slightly slower than that of a conventional high-speed bur, the absence of vibration and discomfort, the smaller chance of contamination of the surgical site, and reduced risk of trauma to adjacent tissues may compensate for the additional time [89]. In a 3 year clinical study [90], a new protocol for lasers in

apical surgery was reported. An Er:YAG laser was used for osteotomy and root resection, whereas Nd:YAG laser irradiation served to seal the dentinal tubules to reduce possible bacterial contamination of the surgical cavity. Improvement in healing was achieved with the use of a LILT GaAlAs diode laser. It has been suggested that after the appropriate wavelength to melt the hard tissues of the tooth has been established, the main contribution of laser technology to surgical endodontics is to convert the apical dentin and cementum structure into a uniformly glazed area that does not allow egress of microorganisms through the dentinal tubules or other openings in the apex of the tooth. Hemostasis and sterilization of the contaminated root apex will have an additional significance. Further, laser treatment in endodontics appears to potentiate spreading of bacterial contamination from the root canal to the patient and the clinicians via the laser plume produced by the laser. This may lead to bacterial dissemination unless precautions are taken to protect against spreading infections while using lasers.

72.8
Lasers in Periodontal Therapy

The applications of lasers in periodontics can be categorized as follows:

1) periodontal soft tissue management
2) removal of periodontal pocket lining
3) disinfection of periodontal pocket
4) removal of calculus, root surface planning
5) periodontal hard tissue management.

The advantages of applying lasers in periodontal treatment are (a) effective and efficient soft and hard tissue ablation with a greater degree of hemostasis, (b) their bactericidal effect, (c) minimal wound contraction, (d) minimal collateral damage with reduced use of local analgesia, and (e) better patient compliance. The disadvantages are that (a) if appropriate power settings are not used, the irradiation of root surfaces can cause detrimental effects, (b) precautions need to be taken during clinical application, (c) laser-based treatment is not very cost-effective, (d) the size of the laser device is cumbersome in the setup involved, (e) application of lasers requires trained personnel, and (f) there is still a need for more sound evidence-based clinical studies.

72.8.1
Laser-Assisted Periodontal Soft Tissue Management

Lasers are mostly used to prepare soft incisions in periodontics. Three methods are commonly used to prepare soft tissue incisions in dentistry: scalpel, electrosurgery, and laser. Each of these methods is effective; however, they differ with respect to hemostasis, healing time, cost of instruments, width of the cut, anesthetic requirement, and disagreeable characteristics such as production of smoke, odor, and

undesirable taste. Many reports have confirmed the safety and efficacy of CO_2 and Nd:YAG lasers, commonly for soft tissue application in periodontics [91]. These lasers can be used for procedures such as frenectomy, gingivectomy, and gingivoplasty, de-epithelization of reflected periodontal flaps, removal of granulation tissue, second-stage exposure of dental implants, lesion ablation, incisional and excisional biopsies of both benign and malignant lesions, coagulation of free gingival graft donor sites, and gingival depigmentation.

The use of surgical lasers in periodontology has been explored in three areas of treatment: (1) removal of diseased pocket lining epithelium, (2) bactericidal effect of lasers on pocket organisms, and (3) removal of calculus deposits and root surface disinfection. Current dental lasers such as diode laser, Nd:YAG, Er,Cr:YSGG, Er:YAG, and CO_2 lasers are advocated for the treatment of sulcular debridement, elimination of bacteria, and removal of calculus. In addition to the current wavelengths, the recently developed frequency-doubled Nd:YAG laser at 532 nm, termed the KTP laser, which has a range of actions similar to the diode laser, has been used for periodontal therapy. It is important to realize that many local and systemic factors influence the treatment outcome in the management of periodontal diseases. The application of most laser delivery systems depend on an axial, end-on emission of light energy, which predisposes the target tissue to a potential build-up of direct and conductive heat effects. Therefore, the applied laser power has to be as low as possible to obtain the desired effect without any unwanted interaction with the tooth or the supporting tissues. In view of the above, blind treatment procedures that lack tactile feedback must be carried out with great caution.

72.8.2
Laser-Assisted Management of Periodontal Pocket

The development of the quartz optic fiber delivery system associated with the diode and Nd:YAG group of lasers, with diameters of 200–320 μm, makes access into the periodontal pocket easy. Longer wavelengths usually rely on fine-bore waveguide probes and sapphire handpiece tips, which are designed for treatment purposes. Following the removal of all hard and soft tissue deposits, the pocket depth is reassessed. The laser fiber is measured to a distance of 1–2 mm short of the pocket depth and inserted at an angle to maintain contact with the soft tissue walls at all times. Using power values sufficient to ablate the epithelial lining (~0.8 W cw diode, 100 mJ/20 pps, 2.0 W Nd:YAG, and Er:YAG/YSGG, 1.0 W cw CO_2), the laser probe is used in a light contact, sweeping mode to cover the entire soft tissue lining. Ablation should commence near the base of the pocket and proceed upwards by slowly removing the probe. Some bleeding of the pocket site may occur due to the disruption of the fragile inflamed pocket epithelium. Each pocket site should be treated for 20–30 s, amounting to possibly 2 min per tooth site with retreatment at approximately weekly intervals during any 4 week period. If the pocket is infra-bony, a number of procedures have been advocated, including laser-ENAP (excisional new attachment procedure), where the Nd:YAG (1064 nm) laser is used in a non-flap procedure to reduce the pocket depth by several millimeters, through a succession of treatment appointments.

72.8.3
Bactericidal Effect of Lasers on Periodontal Pocket

Bacteria have been implicated as one of the major causative factors in periodontal disease. Many studies have demonstrated the ability of laser energy to disinfect periodontal pockets [92–94]. The additional role of lasers in disinfecting infected tissue when used in conjunction with scaling and root planning was also noted [93]. Studies have addressed some of the difficulties of using wavelengths in the range 810–830 nm in the periodontal pocket. The build-up of char and denatured protein material on the delivery fiber of the diode laser results in the development of a carbonized tip, with the temperature rising to $>700\,^{\circ}C$. If it is not removed, it can lead to attenuation of the subsequent laser beam, replaced by the secondary emission of radiant thermal energy from the carbonized deposits (the "hot-tip effect"). The conductive heat would lead to unwanted damage to the delicate tissues [94].

72.8.4
Laser-Assisted Calculus Removal

Er:YAG and Er,Cr:YAG lasers together with innovative near-ultraviolet wavelengths such as frequency-doubled alexandrite (wavelength 377 nm) have been safely applied to remove calculus. Access to the calculus deposits was achieved by utilizing specific laser handpiece tips. The poorly calcified deposits together with a higher water content rendered supra- and sub-gingival calculus susceptible to defragmentation through photomechanical ablation with the erbium group [95]. Potentially this enables deposits to be removed using laser energy levels lower than those required to ablate dental hard tissues. In a study by Aoki *et al.* [96], laser power levels as low as 0.3 W were shown to be sufficient to ablate calculus.

72.8.5
Laser-Assisted Management of Oral Hard Tissues

Since laser–hard tissue interactions are photothermal events which are wavelength dependent, with the possible exception of two wavelengths (Er:YAG and Er,Cr:YSGG), the effect of most dental lasers on bone is generally detrimental. Bone tissue heated to $>47\,^{\circ}C$ is known to undergo cellular damage, leading to osseous resorption, while heating bone tissue to $>60\,^{\circ}C$ would result in tissue necrosis [76]. However, few investigations have examined bone surface temperatures while the overlying soft tissues are being irradiated by a dental laser. A study by Fontana *et al.* [97] examined the temperature increase at the bone surface while using an 810 nm diode laser applied within the periodontal pockets in rats. Following 9 s of irradiation using laser powers of 800 mW, 1.0 W, and 1.2 W delivered through a 300 μm optical fiber, they reported 10 and $11\,^{\circ}C$ increases in bone surface temperature. Only at a 600 mW setting was the bone surface temperature below the threshold of inducing cellular damage. If the exposure time was shortened to 3 s, all power selections resulted in temperature increases that remained below the

critical threshold. In another *in vitro* study [98] CO_2 and Nd:YAG lasers using comparable energy densities were compared for their effects on bone surface temperature while ablating overlying soft tissues. The results showed that the bone surface temperature increase ranged from 1.4 to 2.1 °C for the CO_2 laser and from 8.0 to 11.1 °C for the Nd:YAG laser. These results indicated that when ablating relatively thin, soft tissues supported by subjacent bone, the Nd:YAG laser should be used at lower energy densities for short intervals; otherwise there is a risk of irreversible bone damage. Severe secondary tissue damage has been identified as a major factor in delayed healing of laser-induced bone incisions. Studies have been carried out to compare the osteotomies created by the Er:YAG laser with those created by rotary burs and the CO_2 laser [99, 100]. Overall, the two studies indicated that the Er:YAG laser when used at a peak pulse energy of 100 mJ per pulse and 10 Hz produced well-defined intra-bony incisions without any evidence of melting and carbonization, whereas CO_2 laser-induced osteotomies exhibited extensive charring, melting of the mineral phase, and delayed healing.

72.8.6
Laser-Assisted Management of Dental Hard Tissue

Surface modifications of cementum and dentin have been studied using a variety of laser wavelengths, primarily CO_2, Nd:YAG, Er:YAG, and to a lesser extent diode lasers [101]. A major consideration is the selection of a wavelength that will effectively remove calculus while suppressing both thermal damage to the pulp tissue and undesired removal of sound root structure. The mineral phase of both dentin and cementum is a carbonated hydroxyapatite that has intense absorption bands in the mid-infrared region. Consequently, an Er:YAG laser would appear to be the optimum choice for the effective removal of calculus, for root etching, and for creating a biocompatible surface for cell or tissue reattachment [101, 102]. However, studies on the biocompatibility of CO_2-treated laser surfaces, even when applied at low energy densities, have yielded conflicting results. Some studies [103, 104] reported increased *in vitro* attachment of fibroblasts to laser-treated surfaces compared with controls or chemically treated surfaces. On the other hand, some studies [105, 106] reported a total lack of fibroblast attachment to irradiated surfaces. However, owing to the larger diameter of the hollow delivery tip that is required to transmit CO_2 laser radiation, it has only restricted application in subgingival periodontal therapy. Owing to its high absorption in both water and hydroxyapatite, the bulk of recent research concerning laser-induced root surface modification has involved the Er:YAG laser. The wavelength of this laser has been shown to remove effectively smear layers cementum, and cementum-bound endotoxins [107]. When used at low energy densities with a water spray surface coolant, the majority of studies have reported little or no heat-induced tissue damage and production of smooth root surfaces. In addition, *in vitro* fibroblast adhesion studies have shown that the resultant root surface appears to be at least as biocompatible as that produced by scaling and root planning [108].

72.9 Conclusion

The rapid maturity of laser systems, the availability of improved detection systems and sensitive delivery systems, and high information-processing capabilities of present-day computers are facilitating the use of lasers in noninvasive and sensitive diagnostic and selective therapeutic applications. With the continued developments in the field of lasers and the associated technologies, the application of lasers in dentistry is expected to grow even more rapidly in the coming years.

References

1 Coluzzi, D.J. and Convissar, R.A. (2004) Lasers in clinical dentistry. *Dent. Clin. North Am.*, **48** (4), xi–xii.

2 Miserendino, L. and Robert, P.M. (1995) *Lasers in Dentistry*, Quintessence Publishing, Hanover Park, IL, Q18 3.

3 Brugnera, A. Jr., Garrini dos Santos, A.E.C., Bologna, E.D., and Pinheiro Ladalardo, T.C.C.G. *Atlas of Laser Therapy Applied to Clinical Dentistry*, Quintessence Publishing, Hanover Park, IL.

4 Oho, T. and Morioka, T. (1990) A possible mechanism of acquired acid resistance of human dental enamel by laser irradiation. *Caries Res.*, **24** (2), 86–92.

5 Stern, R.H., Vahl, J., and Sognnaes, R.F. (1972) Lased enamel: ultrastructural observations of pulsed carbon dioxide laser effects. *J. Dent. Res.*, **51** (2), 455–460.

6 Kantola, S. (1973) Laser-induced effects on tooth structure. VII. X-ray diffraction study of dentine exposed to a CO2 laser. *Acta Odontol. Scand.*, **31** (6), 381–386.

7 Nammour, S., Renneboog-Squilbin, C., and Nyssen-Behets, C. (1992) Increased resistance to artificial caries-like lesions in dentin treated with CO2 laser. *Caries Res.*, **26** (3), 170–175.

8 Cooper, L.F., Myers, M.L., Nelson, D.G., and Mowery, A.S. (1988) Shear strength of composite bonded to laser-pretreated dentin. *J. Prosthet. Dent.*, **60** (1), 45–49.

9 Keller, U. and Hibst, R. (1989) Experimental studies of the application of the Er:YAG laser on dental hard substances: II. Light microscopic and SEM investigations. *Lasers Surg. Med.*, **9** (4), 345–351.

10 Anic, I., Pavelic, B., Peric, B., and Matsumoto, K. (1996) In vitro pulp chamber temperature rises associated with the argon laser polymerization of composite resin. *Lasers Surg. Med.*, **19** (4), 438–444.

11 Baik, J.W., Rueggeberg, F.A., and Liewehr, F.R. (2001) Effect of light-enhanced bleaching on in vitro surface and intrapulpal temperature rise. *J. Esthet. Restor. Dent.*, **13** (6), 370–378.

12 Sulieman, M., Addy, M., and Rees, J.S. (2005) Surface and intra-pulpal temperature rises during tooth bleaching: an in vitro study. *Br. Dent. J.*, **199** (1), 37–40.

13 Yazici, A.R., Muftu, A., and Kugel, G. (2007) Temperature rise produced by different light-curing units through dentin. *J. Contemp. Dent. Pract.*, **8** (7), 21–28.

14 Strobl, A., Gutknecht, N., Franzen, R., Hilgers, R.D., Lampert, F., and Meister, J. (2010) Laser-assisted in-office bleaching using a neodymium:yttrium-aluminum garnet laser: an in vivo study. *Lasers Med. Sci.*, **25** (4), 503–509.

15 ADA Council on Scientific Affairs (1998) Laser-assisted bleaching: an update. *J. Am. Dent. Assoc.*, **129** (10), 1484–1487.

16 Moritz, A. (2006) *Oral Laser Application*, Quintessence Publications, Berlin.

17 Wigdor, H.A., Walsh, J.T., Jr. Featherstone, J.D., Visuri, S.R., Fried, D., and Waldvogel, J.L. (1995) Lasers in

dentistry. *Lasers Surg. Med.*, **16** (2), 103–133.
18 Azevedo Rodrigues, L., Nobre dos Santos, M., Pereira, D., Videira Assaf, A., and Pardi, V. (2004) Carbon dioxide laser in dental caries prevention. *J. Dent.*, **32** (7), 531–540.
19 Westerman, G.H., Hicks, M.J., Flaitz, C.M., Blankenau, R.J., Powell, G.L., and Berg, J.H. (1994) Argon laser irradiation in root surface caries: in vitro study examines laserís effects. *J. Am. Dent. Assoc.*, **125** (4), 401–407.
20 Hicks, M.J., Flaitz, C.M., Westerman, G.H., Berg, J.H., Blankenau, R.L., and Powell, G.L. (1993) Caries-like lesion initiation and progression in sound enamel following argon laser irradiation: an in vitro study. *ASDC J. Dent. Child.*, **60** (3), 201–206.
21 Oho, T. and Morioka, T. (1990) A possible mechanism of acquired acid resistance of human dental enamel by laser irradiation. *Caries Res.*, **24** (2), 86–92.
22 Silverstone, L.M., Hicks, M.J., and Featherstone, M.J. (1988) Dynamic factors affecting lesion initiation and progression in human dental enamel. Part I. The dynamic nature of enamel caries. *Quintessence Int.*, **19** (10), 683–711.
23 Silverstone, L.M., Hicks, M.J., and Featherstone, M.J. (1988) Dynamic factors affecting lesion initiation and progression in human dental enamel. II. Surface morphology of sound enamel and caries like lesions of enamel. *Quintessence Int.*, **19** (11), 773–785.
24 Liu, Y. and Hsu, C. (2007) Laser-induced compositional changes on enamel: a FT-Raman study. *J. Dent.*, **35** (3), 226–230.
25 Tagomori, S. and Morioka, T. (1989) Combined effects of laser and fluoride on acid resistance of human dental enamel. *Caries Res.*, **23** (4), 225–231.
26 Walsh, L.J., Abood, D., and Brockhurst, P.J. (1994) Bonding of resin composite to carbon dioxide laser-modified human enamel. *Dent. Mater.*, **10** (3), 162–166.
27 Usumez, A. and Aykent, F. (2003) Bond strengths of porcelain laminate veneers to tooth surfaces prepared with acid and Er, Cr:YSGG laser etching. *J. Prosthet. Dent.*, **90** (1), 24–30.
28 Martınez-Insua, A., Da Silva Dominguez, L., Rivera, F.G., and Santana- Penın, U.A. (2000) Differences in bonding to acid-etched or Er:YAG-laser-treated enamel and dentin surfaces. *J. Prosthet. Dent.*, **84** (3), 280–288.
29 Usumez, A. and Aykent, F. (2003) Bond strengths of porcelain laminate veneers to tooth surfaces prepared with acid and Er,Cr:YSGG laser etching. *J. Prosthet. Dent.*, **90** (1), 24–30.
30 Ramos Lloret, P., Lacalle Turbino, M., Kawano, Y., Sanchez Aguilera, F., Osorio, R., and Toledano, M. (2008) Flexural properties, microleakage, and degree of conversion of a resin polymerized with conventional light and argon laser. *Quintessence Int.*, **39** (7), 581–586.
31 Aguiar, F.H., Barros, G.K., Lima, D.A., Ambrosano, G.M., and Lovadino, J.R. *Biomed. Mater.*, **1** (3), 140–143.
32 Hibst, R. and Keller, U. (1991) Removal of dental filling materials by Er: YAG laser radiation. *Proc. SPIE*, **1424**, 120–126.
33 Takashina, M., Ebihara, A., Sunakawa, M., Anjo, T., Takeda, A., and Suda, H. (2002) The possibility of dowel removal by pulsed Nd:YAG laser irradiation. *Lasers Surg. Med.*, **31** (4), 268–274.
34 Orchardson, R. and Collins, W.J. (1987) Clinical features of hypersensitive teeth. *Br. Dent. J.*, **162** (7), 253–256.
35 Brannstrom, M., Lind_en, L.A., and Astrom, A. (1967) The hydrodynamics of the dental tubule and of pulp fluid. A discussion of its significance in relation to dentinal sensitivity. *Caries Res.*, **1** (4), 310–317.
36 Orchardson, R. and Gillam, D.G. (2006) Managing dentin hypersensitivity. *J. Am. Dent. Assoc.*, **137** (7), 990–998.
37 Kantola, S. (1972) Laser-induced effects on tooth structure. IV. A study of changes in the calcium and phosphorus contents in dentine by electron probe microanalysis. *Acta Odontol. Scand.*, **30** (4), 463–474.
38 Bonin, P., Boivin, R., and Poulard, J. (1991) Dentinal permeability of the dog canine after exposure of a cervical cavity to the beam of a CO_2 laser. *J. Endod.*, **17** (3), 116–118.

39 Liu, H.C., Lin, C.P., and Lan, W.H. (1997) Sealing depth of Nd:YAG laser on human dentinal tubules. *J. Endod.*, **23** (11), 691–693.

40 Renton-Harper, P. and Midda, M. (1992) Nd:YAG laser treatment of dentinal hypersensitivity. *Br. Dent. J.*, **172** (1), 13–16.

41 Cakar, G., Kuru, B., Ipci, S.D., Aksoy, Z.M., Okar, I., and Yilmaz, S. (2008) Effect of Er:YAG and CO_2 lasers with and without sodium fluoride gel on dentinal tubules: a scanning electron microscope examination photomedicine and laser surgery. *Photomed. Laser Surg.*, **26** (6), 565–571.

42 Ipci, S.D., Cakar, G., Kuru, B., and Yilmaz, S. (2009) Clinical evaluation of lasers and sodium fluoride gel in the treatment of dentine hypersensitivity. *Photomed Laser Surg.*, **27** (1), 85–91.

43 Andreasen, J.O., Andreasen, F.M., and Andersson L. (eds) (2007) *Textbook and Color Atlas of Traumatic Injuries of the Teeth*, 4th edn, Blackwell Munksgaard, Copenhagen.

44 Stabholz, A., Sahar-Helft, S., and Moshonov, J. (2004) Lasers in endodontics. *Dent. Clin. North Am.*, **48** (4), 809–832.

45 Matsumoto, K. (2000) Lasers in endodontics. *Dent. Clin. North Am.*, **44** (4), 889–906.

46 Torabinejad, M. and Chivian, N. (1999) Clinical applications of mineral trioxide aggregate. *J. Endod.*, **25** (3), 197–205.

47 Stark, M.M., Myers, H.M., Morris, M., and Gardiner, R. (1964) The localization of radioactive calcium hydroxide Ca45 over exposed pulps in rhesus monkey teeth: a preliminary report. *J. Oral Ther. Pharmacol.*, **54**, 290–297.

48 Paschoud, Y. and Holz, J. (1988) Effect of the soft laser on the neoformation of a dentin bridge following direct pulp capping of human teeth with calcium hydroxide. I. Histological study with the scanning electron microscope. *Schweiz. Monatsschr. Zahnmed.*, **98** (4), 345–356.

49 Melcer, J., Chaumette, M.T., and Melcer, F. (1987) Dental pulp exposed to the CO_2 laser beam. *Lasers Surg. Med.*, **7** (4), 347–352.

50 Santucci, P.J. (1999) Dycal versus Nd: YAG laser and Vitrebond for direct pulp capping in permanent teeth. *J. Clin. Laser Med. Surg.*, **17** (2), 69–75. NdYAG laser treatment of dentinal hypersensitivity.

51 Jukic, S., Anic, I., Koba, K., Najzar- Fleger, D., and Matsumoto, K. (1997) The effect of pulpotomy using CO_2 and Nd: YAG lasers on dental pulp tissue. *Int. Endod. J.*, **30** (3), 175–180.

52 Olivi, G., Genovese, MD., Maturo, P., and Docimo, R. (2007) Pulp capping: advantages of using laser technology. *Eur. J. Paediatr. Dent.*, **8** (2), 89–95.

53 Suzuki, M., Ogisu, T., Kato, C., Shinkai, K., and Katoh, Y. (2011) Effect of CO_2 laser irradiation on wound healing of exposed rat pulp. *Odontology.*, **99** (1), 34–44.

54 Ipci, S.D., Cakar, G., Kuru, B., and Yilmaz, S. (2009) Clinical evaluation of lasers and sodium fluoride gel in the treatment of dentine hypersensitivity. *Photomed Laser Surg.*, **27** (1), 85–91.

55 Berutti, E., Marini, R., and Angeretti, A. (1997) Penetration ability of different irrigants into dentinal tubules. *J. Endod.*, **23** (12), 725–727.

56 Klinke, T., Klimm, W., and Gutknecht, N. (1997) Antibacterial effects of Nd:YAG laser irradiation within root canal dentin. *J. Clin. Laser Med. Surg.*, **15** (1), 29–31.

57 Onal, B., Ertl, T., Siebert, G., and Müller, G. (1993) Preliminary report on the application of pulsed CO_2 laser radiation on root canals with AgCl fibers: a scanning and transmission electron microscopic study. *J. Endod.*, **19** (6), 272–276.

58 Harashima, T., Takeda, F.H., Kimura, Y., and Matsumoto, K. (1997) Effect of Nd: YAG laser irradiation for removal of intracanal debris and smear layer in extracted human teeth. *J. Clin. Laser Med. Surg.*, **15** (3), 131–135.

59 Moshonov, J., Orstavik, D., Yamauchi, S., Pettiette, M., and Trope, M. (1995) Nd: YAG laser irradiation in root canal disinfection. *Endod. Dent. Traumatol.*, **11** (5), 220–224.

60 Harashima, T., Takeda, F.H., Zhang, C., Kimura, Y., and Matsumoto, K. (1998) Effect of argon laser irradiation on

instrumented root canal walls. *Endod Dent Traumatol.*, **14** (1), 26–30.

61 Biedma, B.M., Varela Patino, P., Park, S.A., Barciela Castro, N., Magan Munoz, F., Gonzalez Bahillo, J.D., and Cantatore, G. (2005) Comparative study of root canals instrumented manually and mechanically, with and without Er:YAG laser. *Photomed. Laser Surg.*, **23** (5), 465–469.

62 Kesler, G., Gal, R., Kesler, A., and Koren, R. (2002) Histological and scanning electron microscope examination of root canal after preparation with Er:YAG laser microprobe: a preliminary in vitro study. *J. Clin. Laser Med. Surg.*, **20** (5), 269–277.

63 Stabholz, A., Neev, J., Liaw, L.H., Stabholz, A., Khayat, A., and Torabinejad, M. (1993) Sealing of human dentinal tubules by XeCl 308-nm excimer laser. *J. Endod.*, **19** (6), 267–271.

64 Stabholz, A., Neev, J., Liaw, L.H., Stabholz, A., Khayat, A., and Torabinejad, M. (1993) Effect of ArF-193nm excimer laser on human dentinal tubules. A scanning electron microscopic study. *Oral Surg. Oral Med. Oral Pathol.*, **75** (1), 90–94.

65 Rooney, J., Midda, M., and Leeming, J. (1994) A laboratory investigation of the bactericidal effect of a Nd:YAG laser. *Br. Dent. J.*, **176** (2), 61–64.

66 Bergmans, L., Moisiadis, P., Teughels, W., Van Meerbeek, B., Quirynen, M., and Lambrechts, P. (2006) Bactericidal effect of Nd:YAG laser irradiation on some endodontic pathogens ex vivo. *Int. Endod. J.*, **39** (7), 547–557.

67 Goodis, H.E., Pashley, D., and Stabholz, A. (2002) Pulpal effects of thermal and mechanical irritant, in *Seltzer and Benderís Dental Pulp* (eds K.M. Hargreaves and H.E. Goodis), Quintessence Publishing, Hanover Park, IL, pp. 371–410.

68 Stabholz A., Zeltser, R., Sela, M., Peretz, B., Moshonov, J., Ziskind, D., and Stabholz, A. (2003) The use of lasers in dentistry: principles of operation and clinical applications. *Compend. Contin. Educ. Dent.*, **24** (12), 935–948.

69 Cozean, C., Arcoria, C.J., Pelagalli, J., and Powell, G.L. (1997) Dentistry for the 21st century? Erbium:YAG laser for teeth. *J. Am. Dent. Assoc.*, **128** (8), 1080–1087.

70 Anic, I. and Matsumoto, K. (1995) Dentinal heat transmission induced by a laser-softened gutta-percha obturation technique. *J. Endod.*, **21** (9), 470–474.

71 Potts, T.V. and Petrou, A. (1991) Argon laser initiated resin photopolymerization for the filling of root canals in human teeth. *Lasers Surg. Med.*, **11** (3), 257–262.

72 Pecora, J.D., Cussioli, A.L., Gueri, D.M., Marchesan, M.A., Sousa-Neto, M.D., and Brugnera Junior, A. (2001) Evaluation of Er:YAG laser and EDTACon dentin adhesion of six endodontic sealers. *Braz. Dent. J.*, **12** (1), 27–30.

73 Gekelman, D., Prokopowitsch, I., and Eduardo, C.P. (2002) In vitro study of the effects of Nd:YAG laser irradiation on the apical sealing of endodontic fillings performed with and without dentin plugs. *J. Clin. Laser Med. Surg.*, **20** (3), 117–121.

74 Kimura, Y., Yonaga, K., Yokoyama, K., Matsuoka, E., Sakai, K., and Matsumoto, K. (2001) Apical leakage of obturated canals prepared by Er:YAG laser. *J. Endod.*, **27** (9), 567–570.

75 Maden, M., Gorgul, G., and Tinaz, A.C. (2002) Evaluation of apical leakage of root canals obturated with Nd:YAG laser softened gutta-percha, System-B, and lateral condensation techniques. *J. Contemp. Dent. Pract.*, **3** (1), 16–26.

76 Eriksson, A.R. and Albrektsson, T. (1983) Temperature threshold levels for heat-induced bone tissue injury: a vital-microscopic study in the rabbit. *J. Prosthet. Dent.*, **50** (1), 101–107.

77 Koba, K., Kimura, Y., Matsumoto, K., Takeuchi, T., Ikarugi, T., and Shimizu, T. (1998) A histopathological study of the morphological changes at the apical seat and in the periapical region after irradiation with a pulsed Nd:YAG laser. *Int. Endod. J.*, **31** (6), 415–420.

78 Kimura, Y., Yonaga, K., Yokoyama, K., Matsuoka, E., Sakai, K., and Matsumoto, K. (2001) Apical leakage of obturated canals prepared by Er:YAG laser. *J. Endod.*, **27** (9), 567–570.

79 Blum, J.Y., Peli, J.F., and Abadie, M.J. (2000) Effects of the Nd:YAP laser on

coronal restorative materials: implications for endodontic retreatment. *J Endod.*, **26** (10), 588–592.

80 Yu, D.G., Kimura, Y., Tomita, Y., Nakamura, Y., Watanabe, H., and Matsumoto, K. (2000) Study on removal effects of filling materials and broken files from root canals using pulsed Nd: YAG laser. *J. Clin. Laser Med. Surg.*, **18** (1), 23–28.

81 Miserendino, L.J. (1988) The laser apicoectomy: endodontic application of the CO_2 laser for periapical surgery. *Oral Surg. Oral Med. Oral Pathol.*, **66** (5), 615–619.

82 Bader, G., and Lejeune, S. (1998) Prospective study of two retrograde endodontic apical preparations with and without the use of CO_2 laser. *Endod. Dent. Traumatol.*, **14** (2), 75–78.

83 Stabholz, A., Khayat, A., Ravanshad, S.H., McCarthy, D.W., Neev, J., and Torabinejad, M. (1992) Effects of Nd:YAG laser on apical seal of teeth after apicoectomy and retrofill. *J. Endod.*, **18** (8), 371–375.

84 Arens, D.L., Levy, G.C., and Rizoiu, I.M. (1993) A comparison of dentin permeability after bur and laser apicoectomies. *Compend. Contin. Educ. Dent.*, **14** (10), 1290–1298.

85 Stabholz, A., Khayat, A., Weeks, D.A., Neev, J., and Torabinejad, M. (1992) Scanning electron microscopic study of the apical dentine surfaces lased with Nd: YAG laser following apicectomy and retrofill. *Int. Endod. J.*, **25** (6), 288–291.

86 Ebihara, A., Majaron, B., Liaw, L.H., Krasieva, T.B., and Wilder-Smith, P. (2002) Er:YAG laser modification of root canal dentine: influence of pulse duration, repetitive irradiation and water spray. *Lasers Med. Sci.*, **17** (3), 198–207.

87 Paghdiwala, A.F. (1993) Root resection of endodontically treated teeth by erbium: YAG laser radiation. *J. Endod.*, **19** (2), 91–94.

88 Komori, T., Yokoyama, K., Matsumoto, Y., and Matsumoto, K. (1997) Erbium:YAG and holmium:YAG laser root resection of extracted human teeth. *J. Clin. Laser Med. Surg.*, **15** (1), 9–13.

89 Komori, T., Yokoyama, K., Takato, T., and Matsumoto, K. (1997) Clinical application of the erbium:YAG laser for apicoectomy. *J. Endod.*, **23** (12), 748–750.

90 Gouw-Soares, S., Tanji, E., Haypek, P., Cardoso, W., and Eduardo, C.P. (2001) The use of Er:YAG, Nd:YAG and Ga-Al-As lasers in periapical surgery: a 3-year clinical study. *J. Clin. Laser Med. Surg.*, **19** (4), 193–198.

91 Coleton, S. (2004) Lasers in surgical periodontics and oral medicine. *Dent Clin North Am.*, **48** (4), 937–962 vii. Review.

92 Midda, M. (1992) Lasers in periodontics. *Periodontal Clin Investig.*, (1992) **14** (1), 14–20.

93 Moritz, A., Gutknecht, N., Doertbudak, O., Goharkhay, K., Schoop, U., Schauer, P., and Sperr, W. (1997) Bacterial reduction in periodontal pockets through irradiation with a diode laser: a pilot study. *J. Clin. Laser Med. Surg.*, **15** (1), 33–37.

94 Cobb, C.M. (2006) Lasers in periodontics: a review of the literature. *J. Periodontol.*, **77** (4), 545–564.

95 Aoki, A., Ando, Y., Watanabe, H., and Ishikawa, I. (1994) In vitro studies on laser scaling of subgingival calculus with an erbium:YAG laser. *J. Periodontol.*, **65** (12), 1097–1106.

96 Aoki, A., Ishikawa, I., Yamada, T., Otsuki, M., Watanabe, H., Tagami, J., Ando, Y., and Yamamoto, H. (1998) Comparison between Er:YAG laser and conventional technique for root caries treatment in vitro. *J. Dent. Res.*, **77** (6), 1404–1414.

97 Fontana, C.R., Kurachi, C., Mendonça, C.R., and Bagnato, V.S. (2004) Temperature variation at soft periodontal and rat bone tissues during a medium-power diode laser exposure. *Photomed. Laser Surg.*, **22** (6), 519–522.

98 Spencer, P., Cobb, C.M., Wieliczka, D.M., Glaros, A.G., and Morris, P.J. (1998) Change in temperature of subjacent bone during soft tissue laser ablation. *J. Periodontol.*, **69** (11), 1278–1282.

99 Friesen, L.R., Cobb, C.M., Rapley, J.W., and Forgas-Brockman, L. (1999) *and Spencer P.*, Laser irradiation of bone: II. Healing response following treatment by CO_2 and Nd:YAG lasers. *J. Periodontol.*, **70** (1), 75–83.

100 van As, G. (2004) Erbium lasers in dentistry. *Dent. Clin. North Am.*, **48** (4), 1017–1059.

101 Sasaki, K.M., Aoki, A., Ichinose, S., and Ishikawa, I. (2002) Morphological analysis of cementum and root dentin after Er:YAG laser irradiation. *Lasers Surg. Med.*, **31** (2), 79–85.

102 Chanthaboury, R., and Irinakis, T. (2005) The use of lasers for periodontal debridement: marketing tool or proven therapy? *J. Can. Dent. Assoc.*, **71** (9), 653–658.

103 Pant, V., Dixit, J., Agrawal, A.K., Seth, P.K., and Pant, A.B. (2004) Behavior of human periodontal ligament cells on CO_2 laser irradiated dentinal root surfaces: an in vitro study. *J. Periodontal. Res.*, **39** (6), 373–379.

104 Crespi, R., Barone, A., Covani, U., Ciaglia, R.N., and Romanos, G.E. (2002) Effects of CO_2 laser treatment on fibroblast attachment to root surfaces. A scanning electron microscopy analysis. *J. Periodontol.*, **73** (11), 1308–1312.

105 Belal, M.H., Watanabe, H., Ichinose, S., and Ishikawa, I. (2007) Effect of Er:YAG laser combined with rhPDGF-BB on attachment of cultured fibroblasts to periodontally involved root surfaces. *J. Periodontol.*, **78** (7), 1329–1341.

106 Dilsiz, A., Aydin, T., and Yavuz, M.S. (2010) Root surface biomodification with an Er:YAG laser for the treatment of gingival recession with subepithelial connective tissue grafts. *Photomed Laser Surg.*, **28** (4), 511–517.

107 Liu, C.M., Shyu, Y.C., Pei, S.C., Lan, W.H., and Hou, LT. (2002) In vitro effect of laser irradiation on cementum-bound endotoxin isolated from periodontally diseased roots. *J. Periodontol.*, **73** (11), 1260–1266.

108 Hakki, S.S., Korkusuz, P., Berk, G., Dundar, N., Saglam, M., Bozkurt, B., and Purali, N. (2010) Comparison of Er, Cr: YSGG laser and hand instrumentation on the attachment of periodontal ligament fibroblasts to periodontally diseased root surfaces: an in vitro study. *J. Periodontol.*, **81** (8), 1216–1225.

73
Laser Ablation of Dental Restorative Materials

Ernst Wintner and Verena Wieger

73.1
Introduction

The purpose of the complete study [1] reported in this chapter was to test the applicability of ultra-short pulse laser (USPL) systems for biological hard tissue removal, that is, dental hard tissues including dental restorative materials, and bone structures. The focus of the investigations was restorative or filling materials together with selective ablation in comparison with dentin and enamel. In dental practice, composite filling material often has to be removed to treat secondary caries appearing at the rims of restorations or underneath them. Hence ablation of composites had to be investigated, particularly because hardly any research has been conducted so far on this topic. Therefore, throughout this chapter a comparison between erbium and USPL ablation is made, involving different erbium and USPL systems.

Ablation by erbium lasers has already become a dental treatment standard, despite the fact that only a few percent of the hard tissue treatments involve lasers at all. Employing USPL systems represents a potential future perspective in dentistry, which at present is severely inhibited by the extremely high costs. An estimation by the author yielded a current cost of around €250 000 and more for a USPL system dedicated to dental applications. On the other hand, in materials processing technology, USPL systems are being progressively employed, yielding innovative and superior results. This, together with substantial cost reductions due to series production of such tools, can be expected to lead to applications in dentistry also.

In general, and as an outstanding advantage of USPL ablation, the morphologic characteristics of the cavity boundaries of remaining tissue and/or dental restorative materials are of superior quality. In general, the advantages of scanned [2] USPL ablation are (i) precise cavity preparation resulting in smooth cavity rims; (ii) no molten or resolidified zones; (iii) no carbonization; (iv) no microcracks as there is no collateral damage due to thermal load and shock waves; (v) almost no temperature increase and therefore no heat transport to the adjacent tissue; (vi) gentle tissue removal; and (vii) selective ablation.

Handbook of Biophotonics. Vol.2: Photonics for Health Care, First Edition. Edited by Jürgen Popp, Valery V. Tuchin, Arthur Chiou, and Stefan Heinemann.

73.2 Dental Restorative Materials

Esthetic dental restorative materials generally are composites which initially are pasty to enhance cavity preparations, including plastic shaping. After the restoration, chemical or physical hardening techniques, depending on the specific composite, have to be applied. Thereby a stable polymer network is built. As the term "composites" suggests, they are composed of several chemical substances that determine their characteristics. In the following, a brief overview is provided [3–9].

The main constituents of composites can be arranged in three groups: (i) organic composite matrix; (ii) dispersive phase; and (iii) compound phase. The first group contains monomers, comonomers, initiators, stabilizers, and other additives. The dispersive phase comprises the inorganic filler particles. The compound phase is made of silanes that act as intermediates between the first two phases mentioned.

73.3 Ablation by Erbium Laser

The erbium laser systems used in ablation rate measurements were a Fotona Fidelis Er:YAG laser ($\lambda = 2940$ nm, $\tau \approx 100\,\mu$s) [10] and a Biolase Waterlase Er, Cr:YSGG laser ($\lambda = 2780$ nm, $\tau \approx 50\,\mu$s) [11]. Cavities were generated with front panel power settings ranging from 2 to 6 W. Ablations were always accompanied by an air–water spray (60% water, 65% air, each out of 100% max). With each laser setting, six cavities were prepared for a defined period of time (15 s). The experiments were performed on dentin, enamel, and different composite materials. Concerning teeth, extracted caries-free human permanent third molars were collected and stored in pure water until use. For dentin ablation, the occlusal enamel was removed using a diamond saw under water cooling (Accutom-2, Struers). Before and after laser ablation, the samples were weighed employing a microbalance to determine the total mass loss. The average of all six total mass values was included to calculate the mean total ablated volume according to $V = m/\varrho_{\mathrm{d/e}}$, where the densities are given by $\varrho_{\mathrm{d}} = 2.14\,\mathrm{g\,cm^{-3}}$ for dentin and $\varrho_{\mathrm{e}} = 2.97\,\mathrm{g\,cm^{-3}}$ for enamel [12]. In a final step, the mean ablated volume per pulse was established by dividing the averaged total volumes by the number of applied laser pulses N, which is the product of pulse repetition rate PRR times the duration of ablation D: $N = PRR \times D$.

As the density of the composite samples generally was not known, another method was applied to determine the ablation rates in terms of volume per pulse. For that, imprint material commonly used in dentistry was considered. As this material is capable of reproducing tooth structures exactly, it was assumed that it fits the demands of the experiment, which are to attach closely to the surface of the cavities, to be able to fill even very small holes, and to imprint the cavities accurately without any excess material. Because all of these issues could be confirmed, the laser-ablated cavities were weighed, filled with imprint material, and weighed again. The difference between the mass values gave the mass $m_{\mathrm{i,c}}$ of the imprint model of the cavity.

By producing blocks of imprint material with defined volumes V_i and measuring their masses m_i, the density of the material was determined as $\varrho_i = m_i/V_i$, so that at least the total ablated volume of the cavity could be calculated: $V_c = m_{i,c}/\varrho_i$. This procedure was applied for all cavities per sample. Finally, the mean ablated volumes per pulse were retrieved in a similar way as for dentin and enamel.

73.3.1 Results for Dentin and Enamel

First, results on the basis of the front panel power settings of the lasers were compared. As both erbium systems were in use for dental applications, it was expected that due to regular maintenance, the pre-settings and output parameters would apply. Thereby, a direct comparison of the Fotona Fidelis Er:YAG and the Biolase Er, Cr:YSGG ablation rates was possible by choosing the same powers of 2, 3, 4, 5, and 6 W and a fixed pulse repetition rate of 20 Hz. Table 73.1 (left) gives the results obtained.

In general, the dentin ablation rates obtained with the Fotona system are about 42% lower than those with the Biolase system. Concerning enamel, the situation is similar, as deviations of ~33% can be observed. Because the absorption coefficient of water ($\mu_a = 7000\,\mathrm{cm}^{-1}$) for Er, Cr:YSGG laser radiation at room temperature is only ~55% of that of the Er:YAG laser ($\mu_a = 13\,000\,\mathrm{cm}^{-1}$) [13], the ablation performance of the Er:YAG laser apparently is superior. This discrepancy motivated the measurement of the output parameters of the laser systems. It turned out that relying just on the front panel power settings is insufficient to develop useful data. Actually, the measured average output powers deviate significantly from the front panel settings for each laser system. The output powers of the Biolase system are around 13% higher than the displayed values, whereas the Fotona laser emits on average 31% less power than indicated. Using the measured laser parameters, a second attempt was made to analyze the ablation rates. The basis for the renewed discussion is the radiant exposure or fluence. Table 73.1 (right) reports the ablation rates in this new context to be considered as reliable data.

Owing to the different measured pulse energy values and focal spot diameters of the two erbium laser systems, the single fluence values are not directly comparable. Nevertheless, by drawing regression lines, interpretation of the results is permitted. Obviously, in a wide fluence range the ablation rates of the Er:YAG system are higher than those of the Er,Cr:YSGG laser. This finding is in agreement with the above-mentioned absorption coefficients of the two laser wavelengths. For higher laser fluences the ablation behavior is reversed, with the Er,Cr:YSGG laser performing slightly better. This also corresponds to the results of Vogel and Venugopalan [14], who reported on the changes in the absorption coefficients for both erbium laser wavelengths with rising fluence. The high absorption coefficient of the Er:YAG laser wavelength declines monotonically with increasing radiant exposure and even becomes lower than that of the Er,Cr:YSGG laser. At fluences where laser ablation takes place, the performances of both systems should at least be comparable.

Table 73.1 Mean ablated dentin and enamel volumes per pulse by two different erbium lasers for increasing (imprecise) front panel power settings (left) and for varying laser fluences (right).

Dental tissue	Power (W) (front panel settings)	Fotona Er:YAG	Biolase Er,Cr:YSGG	Fotona Er:YAG		Biolase Er,Cr:YSGG	
		Ablated volume per pulse (mm^3)		Fluence ($J\,cm^{-2}$)	Ablated volume per pulse (mm^3)	Fluence ($J\,cm^{-2}$)	Ablated volume per pulse (mm^3)
Dentine	2	0.0043	0.0062	13.5	0.0043	24.9	0.0062
	3	0.0067	0.0125	16.2	0.0067	38.0	0.0125
	4	0.0101	0.0181	21.7	0.0101	51.4	0.0181
	5	0.0121	0.0234	26.9	0.0121	64.1	0.0234
	6	0.0161	0.0275	32.5	0.0161	77.9	0.0275
Enamel	4	0.0044	0.0063	21.7	0.0044	51.4	0.0063
	5	0.0059	0.0093	26.9	0.0059	64.1	0.0093
	6	0.0079	0.0115	32.5	0.0079	77.9	0.0115

Table 73.2 Ablation rates of dental composite materials with the Biolase Er, Cr:YSGG laser.

Composite	Ablation volume per pulse (mm^3)	
	Fluence 19 J cm^{-2}	Fluence 51 J cm^{-2}
Tetric Ceram	0.0026	0.0161
Tetric Flow	0.0036	0.0187
Heliomar	0.0041	0.0213
Point 4	0.0047	0.0233
Premise	0.0031	0.0176
Z100	0.0021	0.0156
XRV Herculite	0.0031	0.0176

73.3.2 Results for Composites

Composite ablation rates were determined with the Biolase Er,Cr:YSGG laser as it showed the best laser characteristics among Er systems. In Table 73.2, different types of dental restorative materials and their ablation rates for 1.7 and 4.5 W laser ablation, corresponding to fluences of 19 and 51 J cm^{-2}, respectively, are reported. The ablated volumes per pulse were determined with the imprint method.

Although the ablation rates of all composites are on the same scale, deviations among different filling materials are apparent. Ranking the composite samples according to their material removal per laser pulse at 19 J cm^{-2} from the highest to the lowest amount, the Point 4 composite occupies the first position with 4.7×10^{-3} mm^3 per pulse and Z100 occupies the last place with 2.1×10^{-3} mm^3 per pulse. The ranking remains consistent for higher applied laser powers. On average, the ablated volume per pulse is about 5.8 times higher for the 51 J cm^{-2} ablation than the 19 J cm^{-2} ablation.

The effective removal of composite material is determined by its chemical composition and the related absorption of erbium laser wavelengths. On the one hand, there is sufficient water present in all composites for strong absorption around 3 μm, but other components such as quartz and poly(methyl methacrylate) (PMMA) resin also absorb substantially in the mid-infrared region [15]. Kalachandra *et al.* [16] investigated the transmittance of BIS-GMA (bisphenol A- glycidyl methacrylate) depending on the wavenumber and reported a decrease in transmittance at a stretching frequency of 3458.32 cm^{-1} corresponding to a wavelength of $\sim$2.89 μm. This broad absorption band belongs to an OH group of BIS-GMA. As the mentioned components apparently are contained in some of the above-listed composites, although in different concentrations, the observed deviations of the ablation rates can be explained. For example, the concentration of BIS-GMA in Tetric Ceram is 8.3 wt% whereas Tetric Flow contains 13.6 wt% [17]. On this basis, the higher ablation rates of Tetric Flow may be understood.

Comparison of the ablation rates of composites with those of dentin indicates that the selectivity of erbium laser ablation is not very pronounced. A dentin volume of 18.1 $\times 10^{-3}$ mm^3 per pulse ablated with the Er,Cr:YSGG laser at 51 J cm^{-2} fits fairly well into

the range achieved in composites for the same fluence. Whereas for Z100, Tetric Ceram, Premise, and XRV Herculite the tissue removal procedure is slower compared with dentin, Tetric Flow, Heliomar, and Point 4 can be removed faster. A clear tendency concerning selectivity valid for all tested materials could therefore not be found.

Erbium laser ablation thresholds were derived by fitting a regression line (using a plot of ablation rates versus fluence) to measured data and extrapolating it to the abscissa. Dentin threshold values of 5 and 8 J cm^{-2} for Er:YAG and Er, Cr:YSGG lasers, respectively, were obtained. Wannop *et al.* [18] investigated 250 μs Er:YAG laser performance, yielding a threshold value of 10 ± 2 J cm^{-2}, which is somewhat higher than the value we calculated. Several groups have already reported on the erbium laser ablation threshold in enamel: Wannop *et al.* [18] 25 ± 8 J cm^{-2} for Er:YAG (250 μs); Apel *et al.* [19] 9–11 J cm^{-2} for Er:YAG (150 μs) and in identical experiments 10–14 J cm^{-2} for Er,Cr:YSGG; in another report by Apel *et al.* [20] for varying pulse durations of a Fotona Fidelis Er:YAG system, 9–10 J cm^{-2} for 700 μs, 8 J cm^{-2} for 350 μs, and f7 J cm^{-2} or 150 and 100 μs; Fried *et al.* [21] 7–9 J cm^{-2}; Hibst and Keller [22] $\sim$10 J cm^{-2}; and Blinkov *et al.* [23] 8 J cm^{-2}. There are no comparative reports on ablation thresholds of restorative materials.

73.4 Ablation by Ultra-Short Pulse Laser

Ablation rates generated by ultra-short laser pulses were determined using either a High Q [24] IC-10000 REG AMP Microproc 12 ps Nd:vanadate laser ($\lambda = 1064$ nm, $P_{av} = 5$ W) under $r - \varphi$ scanning, or a Spectra-Physics Hurrican-i Ti:sapphire laser with variable pulse duration. The aim was to determine the ablated volume per laser pulse to judge the effectiveness of USPL compared with erbium systems (Tables 72.3 and 72.4). The 12 ps Nd:vanadate laser was operated for a duration of 15 s at a pulse energy of

Table 73.3 Ablation rates (left) and ablated volume per second of dental composite materials obtained with an $r-\varphi$-scanned Nd:vanadate laser (center); $\tau = 12$ ps, $PRR = 50$ kHz, $E_p = 100\,\mu$J, $\Phi = 11.2$ J cm^{-2}; for comparison, corresponding values for an Er,Cr:YSGG laser are given (right).

Composite	Nd:vanadate 5 W	Er,Cr:YSGG 4.5 W	
	Ablation rate (10^{-6} mm^3 per pulse)	Ablated volume (mm^3 s^{-1})	
Tetric Ceram	5.18	0.259	0.322
Tetric Flow	4.15	0.208	0.374
Heliomar	5.53	0.277	0.426
Point 4	5.81	0.291	0.466
Premise	6.08	0.304	0.352
Z100	8.71	0.436	0.312
XRV Herculite	7.88	0.394	0.352
Dentin	0.32	0.016	0.362

Table 73.4 Ti:sapphire laser ablation thresholds of composite materials for 150 fs – 7 ps pulses.

τ (fs)	Ablation threshold (J cm^{-2})								
	Compoglass F	Premise Enamel	Premise Body A2	Heliomar A3	XRV Herculite	XRV Herculite		Point 4	Z100
						Dentin	Enamel		
150	0.27	0.30	0.35	0.24	0.25	0.25	0.30	0.36	0.27
500	0.44	0.38	0.43	0.35	0.39	0.34	0.33	0.48	0.44
2000	0.56	0.58	0.51	0.48	0.57	0.44	0.53	0.51	0.46
7000	0.60	0.63	0.58	0.59	0.64	0.54	0.56	0.56	0.59

100 μJ and a *PRR* of 50 kHz yielding 5 W. As the focal spot diameter was 33.7 μm, this setting corresponds to a fluence of 11.2 J cm^{-2}. Dentin and composite materials were ablated and, again, the imprint method was used to reconstruct the cavity volume from which ablation rates were calculated.

Ablation rates using the Hurrican-i Ti:sapphire via line scans ($\lambda \approx 800$ nm, $\tau = 130$ fs–7 ps, $E_{\text{pulse}} > 1$ mJ, *PRR* 0–10 kHz [25]) have been published [26]. The depths of the grooves were measured by means of digital light microscopy with implemented software. The motivation for these experiments was a comparison with dental tissue ablation rates increasing under rising pulse duration [27].

For sound dentin and enamel and also for carious dentin, ablation thresholds obtained with a Ti:sapphire laser can be derived from the literature. Serbin *et al.* [27] focused on laser ablation with pulse durations from 120 fs to >2 ps. For 120 fs Ti:sapphire pulses, the highest threshold was found for sound enamel at >0.5 J cm^{-2}, followed by sound dentin at >0.3 J cm^{-2}, whereas for carious dentin the threshold was only <0.12 J cm^{-2}. Similar values were found by Lubatschowski *et al.* [28]. For all applied pulse durations, the composite thresholds of this study are lower than the enamel thresholds reported by Serbin *et al.* [27]. Pulse durations of 150 and 500 fs yield comparable values for composite and dentin, whereas for longer pulse widths the dentin thresholds are situated well above composite thresholds (~2 ps corresponding to a threshold of 0.75 J cm^{-2} in dentin). That implies that the selectivity at longer pulse duration is very pronounced for enamel and composite ablation.

73.5 Conclusion

The following conclusions can be drawn:

- The etch depths per pulse achieved by USPL in dental hard tissue and composite restorations are in the micrometer region and therefore much smaller than for erbium ablation rates. The USPL ablation procedure can be enhanced by applying *PRR* of some tens of kiloherz. Ablation rates per second are then comparable to erbium laser ablation rates.

- Selective ablation is very pronounced for USPL as dentin revealed lower ablation rates than composites, which is beneficial for minimum invasive secondary caries treatment. This is not generally so for erbium systems. Depending on the composite, sometimes a controversial effect can be observed, that is, a composite becomes equally or even less ablated than dentin.
- Ablation thresholds in dentin amount to 5 J cm^{-2} for Er:YAG and 8 J cm^{-2} for Er, Cr:YSGG lasers; enamel ablation starts at even higher fluences, whereas femtosecond laser ablation thresholds of these tissues are below 1 J cm^{-2}. USPL thresholds of composites determined in this study are lower than those of dental structures. Again, this fact contributes to selective ablation. With rising pulse duration, thresholds increase and ablation rates decline at constant fluence.
- The remaining dentin surface after erbium laser treatment is fissured and scaly. It depends strongly on the air–water spray, that is, insufficient cooling and hydration, leading to microcracks, melting, or carbonization. The morphology of USPL-processed cavities in dentin involving a scanner shows superior tissue quality. An appropriate set of laser and scanner parameters leads to surfaces with no evidence of melting, carbonization, or microcracks. In contrast to cavities excavated by erbium lasers, the cavity rims after scanned USPL treatment are well defined and smooth.
- Scanned USPL ablation leaves a fine micro-retentive pattern. Although its appearance is distinct from that of an etched surface, this regular structure bears the potential for good adhesion of compound to filling material without additional etching. On the other hand, supplementary etching is recommended after erbium conditioning because of the scaly appearance of the tooth surface.

References

1 Wieger, V. (2006) Ultra-Short Pulse Laser Ablation of Biological Hard Tissue and Dental Restorative Materials, PhD thesis, Vienna University of Technology, Photonics Institute.

2 Strassl, M., Yousif, A., and Wintner, E. (2007) Scanning of ultra-short laser pulses in dental applications. *J. Laser Micro/Nanoeng.*, **2** (3), 206–211.

3 Ivoclar Vivadent (1990) Composite-Füllungsmaterial, Report No. 5, Ivoclar Vivadent, Schaan, Liechtenstein.

4 Ivoclar Vivadent (1992) Der gefüllte Zahn – ein komplexes Verbundsystem, Report No. 7, Ivoclar Vivadent, Schaan, Liechtenstein.

5 Ernst, C.P. and Willsershausen, B. (2000) Quo vadis Komposit? Eine aktuelle Standortbestimmung zahnärztlicher Füllungskomposite. Polyklinik für Zahnerhaltungskunde des Klinikums der Johannes Gutenberg-Universität Mainz, Mainz.

6 Kultermann, G. (2001) Moderne Adhäsivsysteme – Fortschritt oder Marketing?, *Der Freie Zahnarzt*, **5** (1), 36–41.

7 Lonnroth, E. and Shahnavaz, H. (1997) Use of polymer materials in dental clinics, case study. *Swed. Dent. J.*, **21** (4), 149–159.

8 Schärer, P. and Chen, L. (1998) Komposite-Zemente und Dentinhaftmittel. *Philips J.*, **11/12**, 326–334.

9 Ivoclar Vivadent (2004) SR Adoro im Fokus: Indirekte Komposite – Werkstoffkunde und Entwicklung, Report

No. 15, Ivoclar Vivadent, Schaan, Liechtenstein.
10 Fotona (2010) www.fotona.si (last accessed 4 June 2011).
11 Biolase (2010) www.biolase.com (last accessed 4 June 2011).
12 Ciba Found. Symp. (1997) **205**, 54–67; discussion 67–72.
13 Stock, K., Hibst, R., and Keller, U. (1997) Comparison of Er:YAG and Er:YSGG laser ablation of dental hard tissues. *Proc. SPIE*, **3192**, 88–95.
14 Vogel, A. and Venugopalan, V. (2003) Mechanisms of pulsed laser ablation of biological tissues. *Chem. Rev.*, **103**, 577–644.
15 Dumore, T. and Fried, D. (2000) Selective ablation of orthodontic composite by using sub-microsecond IR laser pulses with optical feedback. *Lasers Surg. Med.*, **27**, 103–110.
16 Kalachandra, S., Sankarapandian, M., Shobha, H.K., Taylor, D.F., and McGrath, J.E. (1997) Influence of hydrogen bonding on properties of BIS-GMA analogues. *J. Mater. Sci. Mater. Med.*, **8**, 283–286.
17 *Information sheet of Ivoclar Vivadent*: Tetric Ceram Familie.pdf; www.ivoclarvivadent.com/zoolu-website/media/ (last accessed Aug. 11, 2011).
18 Wannop, N.M., Dickinson, M.R., and King, T.A. (1993) Erbium:YAG laser radiation interaction with dental tissue. *Proc. SPIE*, **2080**, 33–43.
19 Apel, C., Meister, J., Ioana, R.S., Franzen, R., Hering, P., and Gutknecht, N. (2002) The ablation threshold of Er:YAG and Er:YSGG laser radiation in dental enamel. *Lasers Med. Sci.*, **17**, 246–252.
20 Apel, C., Franzen, R., Meister, J., Sarrafzadegan, H., Thelen, S., and Gutknecht, N. (2002) Influence of the pulse duration of an Er:YAG laser system on the ablation threshold of dental enamel. *Lasers Med. Sci.*, **17**, 253–257.
21 Fried, D., Featherstone, J.D.B., Visuri, S.R., Seka, W., and Walsh, J.T. (1997) The caries inhibition potential of Er:YAG and Er:YSGG laser radiation. *Proc. SPIE*, **3593**, 73–78.
22 Hibst, R. and Keller, U. (1989) Experimental studies of the application of the Er:YAG laser on dental hard substances: I. measurement of the ablation rates. *Lasers Surg. Med.*, **9**, 338–344.
23 Belinkov, A.V., Erofeev, A.V., Shumilin, V.V., and Tkachuk, A.M. (1993) Comparative Study of the 3 μm Laser Action on Different Tooth Tissue Samples Using Free-Running Er-Doped YAG, YSGG, YSP and YLF Lasers. *Proc. SPIE*, **2080**, 60–67.
24 High Q Laser (2010) www.highQlaser.com (last accessed 4 June 2011).
25 Spectra-Physics (2003) Manual of the Hurricane-i Laser. Spectra-Physics, Irvine, CA.
26 Strassl, M., Wieger, V., Brodoceanu, D., Beer, F., Moritz, A., and Wintner, E. (2008) Ultra-short pulse laser ablation of biological hard tissue and biocompatibles. *J. Laser Micro/Nanoeng.*, **3** (1), 30–40.
27 Serbin, J., Bauer, T., Fallnich, C., Kasenbacher, A., and Arnold, W.H. (2002) Femtosecond lasers as novel tool in dental surgery. *Appl. Surf. Sci.*, **197–198**, 737–740.
28 Lubatschowski, H., Heisterkamp, A., Will, F., Singh, A.I., Serbin, J., Ostendorf, A., Kermani, O., Heermann, R., Willing, H., and Ertmer, W. (2002) Medical applications of ultrafast laser pulses. *RIKEN Rev.*, **50**, 113–118.

74
Laser Ablation of Hard Tissues

Gregory B. Altshuler, Andrey V. Belikov, and Felix I. Feldchtein

74.1
Introduction

Bone tissue, cartilage, and dental hard tissue (enamel, dentin, cementum) are traditionally classified as hard biological tissues of the human body. This chapter is focused on hard tissues such as enamel and dentin of human teeth. Interest in lasers for the treatment of hard tissues in dentistry has increased because such treatment is localized, comfortable, and less painful (due to the lack of vibration), relatively bloodless, and antiseptic.

74.2
Tooth Structure

A tooth [1] consist of the crown, neck, and root. The root and neck of the tooth are covered with cement. The tooth crown is covered with enamel – the most durable tissue of the human body. The underlying tissue of the tooth is dentin. The pulp chamber is located in the dentin interior. In the root of the tooth, the pulp chamber extends into the root canal. The pulp filling the chamber and the root canal is the only soft and the most sensitive tissue of the tooth, which consists of connective tissue, plexus of nerve fibers, and blood vessels.

Tooth enamel [1] consists of about 96% inorganic material, 1% organic material, and 3% water by weight. The volume water content is about 10%. The inorganic material is mostly a hydroxyapatite (HA), a substance also found in bone and dentin. The basic structural components of enamel are HA-like nanocrystals with the formula $A_{10}(BO_4)_6X_2$, where A is Ca, Cr, Ba, or Cd, B is P, As, or Si, and X is F, OH, or $ClCO_2$. The dominant formula of enamel apatite is an ideal HA $Ca_{10}(PO_4)_6(OH)_2$ with a Ca:P ratio of 1.67. In addition to HA (∼75%), carbide apatite (∼3–20%), chlorine apatite (∼4%), and fluorine apatite (∼0.5%) are also present in enamel. HA nanocrystals form a hexagonal structure with a size of 14–46 × 27–78 nm. These crystals have the typical crystal defects in the lattice

Handbook of Biophotonics. Vol.2: Photonics for Health Care, First Edition. Edited by Jürgen Popp, Valery V. Tuchin, Arthur Chiou, and Stefan Heinemann.

arrangement, including shifted, disrupted, and curved lattice planes. Defective lattices in the boundary between crystals are fused with each other. The crystals in enamel are surrounded by a water shell, with a typical width of about 10 nm. A tightly packed mass of apatite crystals forms the basic structural unit of enamel, called the "enamel rod" or "enamel prism." It is shaped like a keyhole and has an average width of 5 μm. The rod length is determined by the local enamel thickness, with a maximum of ~2.5 mm. Rods run from the dentinoenamel junction perpendicularly to the outer enamel surface and are organized in rows. Neighboring rods are surrounded by 0.1–0.5 μm wide rod sheaths and separated from each other by inter-rod enamel. The enamel rod consists almost entirely of inorganic material, whereas the rod sheaths are made up largely of organic material comprised of amelogenin polypeptide and non-amelogenin proteins impregnated by water.

Dentin comprises [1] the bulk of the tooth crown. The mature dentin consists (by weight) of up to 70% inorganic substances, about 20% organic components (mainly proteins that form collagen fibers), and up to 10% water (about 22% water by volume). The basic inorganic components are HA, calcium carbonate, and a small amount of calcium fluoride. Two main structural units of dentin are ground substance and dentinal tubules. The ground substance of dentin is permeated with numerous dentinal tubules with density ranging from 15 000 to 75 000 per mm^2 of dentin. The diameter of dentinal tubules depends on the location and ranges from 0.5 μm near the dentinoenamel junction to 5 μm near the pulp.

74.3 Laser Ablation

The main application of lasers for hard tissue treatment is laser ablation. The mechanism and parameters of ablation are determined by the optical, thermal, and mechanical properties of treated tissue. The most important characteristic is the coefficient of absorption of a tissue and its components.

Investigation of the absorption spectra of intact tissues allows one to determine wavelength regions with maximum absorption and minimal energy for ablation. Based on this analysis, one can choose a laser with radiation that is best absorbed by tissue and is the most destructive.

Absorption spectra of hard tissues of human teeth have been studied by several groups [2–6]. The spectrum of the transport coefficient for dental enamel and dentin $\mu_{tr} = \mu_a + \mu'_s$ [5], where μ_a is coefficient of absorption and μ'_s is reduced coefficient of scattering, is presented in Figure 74.1a. One can recognize three ranges of strongest absorption of enamel and dentin: in the UV region for $\lambda < 0.3$ μm and in the IR region for 2.7 μm $< \lambda <$ 3.5 μm and 9 μm $< \lambda <$ 11 μm. The UV absorption peak corresponds to electron absorption of all hard tissue components. The 3 μm region is related to free water (2.96 μm peak) and OH group of HA (2.8 μm peak). The 10 μm region mostly corresponds to PO_4 groups of HA (9.6 μm peak) and free water (Figure 74.1b). For these ranges, the absorption is several orders of magnitude higher than the scattering ($\mu_a > \mu'_s$) and penetration in the hard tissue is determined by absorption.

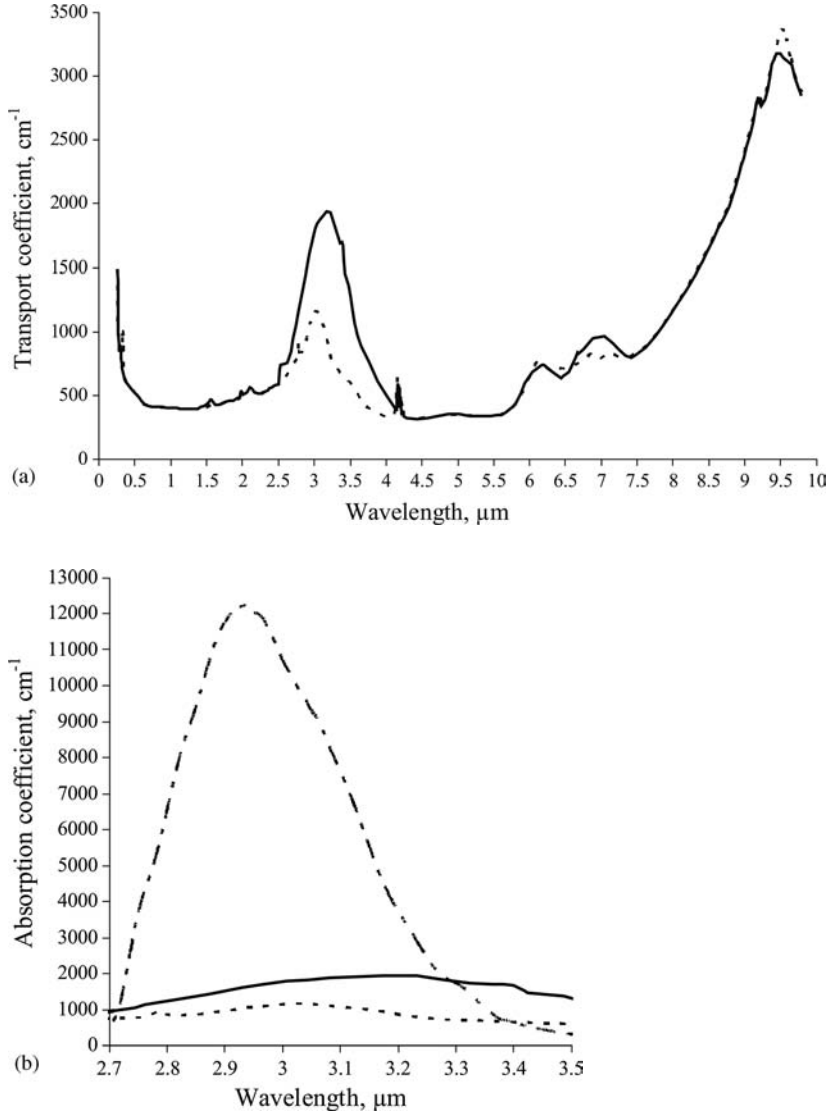

Figure 74.1 Transport coefficient (a) and absorption (b) spectra of intact enamel (dotted line) [5], dentin (solid line) [5], and water (dashed-dotted line) [6].

Due to a very high absorption coefficient in the 3 and 10 μm ranges, the penetration of laser radiation into the tissue is about $1/\mu_a \approx 2$–$20\,\mu m$ for enamel and 1–10 μm for dentin.

The highest absorption in the spectrum is observed for free water in hard tissue at about 2.96 μm. The water absorption at this wavelength is about $12\,000\,cm^{-1}$ [7], whereas the enamel absorption does not exceed $1000\,cm^{-1}$ [5, 8]. Hence the water

absorption is more than an order of magnitude higher (Figure 74.1b). The absorption coefficients of hard dental tissues may change during laser irradiation, for example due to changes in the optical properties of water when it is heated, so although the absorption coefficient at normal body temperature is higher at $\lambda = 2.94\,\mu m$ than at $\lambda = 2.79\,\mu m$, the ratio may change to the opposite with temperature increase because of water absorption changes substantially with temperature. In particular, the absorption coefficient of free water decreases by about an order of magnitude upon heating from room temperature to the critical point of 374 °C [9, 10].

From the analysis of the absorption spectrum, it can be concluded that the most effective and low threshold mechanism of laser ablation can be achieved through selective absorption of free water in the rod sheaths, pores, and surface microcracks for enamel or in free water in dentinal tubules and ground substance of dentin.

The destruction mechanism of dental hard tissues associated with selective absorption was described by Altshuler *et al.* [11]. Selective absorption of laser radiation by water contained in the rod sheaths, pores, and surface microcracks for enamel or in dentinal tubules and ground substance of dentin heats water much faster than HA. As noted by Lee *et al.* [9], at 130 °C the pressure developing in closed pores may reach 1000 bar and, as a consequence, microcracks localized primarily as clusters in inter-rod enamel start to appear and propagate in the material surrounding the pores (Figure 74.2).

Cracks will most likely develop through the inter-rod enamel, where HA crystals are disordered and as a result the inter-rod enamel has a lower mechanical strength. The propagation of cracks through the inter-rod enamel will lead to the separation of individual enamel rods or groups from the ground enamel substance. Such a mechanism of laser ablation will be referred to as "thermomechanical". Thus, radiation with a wavelength of 3 μm does not penetrate deeply into the dental hard tissue owing to the high absorption [12]. Ablation of dental hard tissues occurs in microexplosions, when tissue does not evaporate completely, but breaks into small

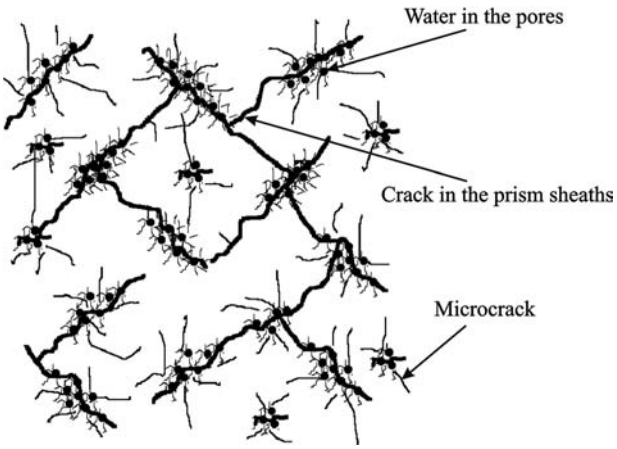

Figure 74.2 Microcrack cluster formation in enamel.

fragments and is ejected from the bulk of the tissue [13]. The role of melting and vaporization of HA and carbonization of organic components is minimal. The rate of tissue removal depends on the amount of water contained in the tissue. Carious dentin contains the largest amount of water among the hard dental tissues [14]. Hence, for this mechanism of laser ablation carious dentin has the highest and sound enamel has the lowest ablation rate.

Selective absorption of the free water content within structural components with size r is possible if the laser pulse duration is shorter than thermal relaxation time (TRT) of these components [15]:

$$TRT = \frac{r^2}{k\alpha} \tag{74.1}$$

where α is the thermal diffusivity of the tissue and k is the form-factor coefficient, equal to 8, 16, and 24 for layer, cylindrical, and spherical structural components, respectively. For enamel $\alpha = 4.7 \times 10^{-7}\,\mathrm{m^2\,s^{-1}}$ and for dentin $\alpha = 1.8 \times 10^{-7}\,\mathrm{m^2\,s^{-1}}$ [16]. A laser pulse duration τ less than the thermal relaxation time TRT is considered optimum for tissue layer destruction because in this case the heat absorbed by the tissue components is not transferred to the surrounding tissues due to the heat conductivity mechanism, providing local and most effective laser action. Thus, in addition to optical and thermophysical properties of tissue, the optimum laser pulse duration is determined by the size of its structural component which is instrumental for ablation. For the thermomechanical mechanism, r is the size of components which contain free water: the rod sheaths ($<0.5\,\mu\mathrm{m}$), pores ($<1\,\mu\mathrm{m}$), and surface microcracks ($<10\,\mu\mathrm{m}$) for enamel and free water in dentinal tubules ($<5\,\mu\mathrm{m}$) and ground substance of dentin. The optimum pulse duration for selective heating of rod sheaths should be shorter than 0.1 μs, for enamel microcracks shorter than 100 μs, and for dentinal tubules shorter than 20 μs. The most effective lasers for thermomechanical ablation are Er:YAG ($\lambda = 2.94\,\mu\mathrm{m}$), Er:YLF ($\lambda = 2.81\,\mu\mathrm{m}$), and Er:YSGG ($\lambda = 2.79\,\mu\mathrm{m}$) lasers.

For the 10 μm wavelength region, the dominant mechanism of laser ablation is melting with subsequent vaporization ("thermal vaporization" mechanism) of HA or removal of the molten phase in the form of individual drops ("hydrodynamic ejection" mechanism) of HA [3]. Both mechanisms require heating of the enamel surface to a temperature higher than melting temperature of HA (about 1280 °C). The optimum pulse duration for both mechanisms should be shorter than the TRT of the hard tissue layer equal to the penetration depth $1/\mu_a$ of the laser radiation. The same basic equation (Eq. 74.1) for the TRT of such a layer for a wavelength of 9.6 μm provides values of about 2 μs for enamel and 4 μs for dentin.

As can be seen for both the thermomechanical and thermal vaporization mechanisms of ablation, a period of nanoseconds provides the most efficient laser ablation. However, the delivery of such pulses to the tissue may be problematic. In addition, plasma formation on the hard tissue surface may be induced by a short pulse with high power density and the laser pulse will be blocked by the plasma due to reflection and absorption. Therefore, the optimum pulse duration for clinical use should be in the submicrosecond or microsecond range.

One known risk of laser dental tissue treatment is overheating of the pulp [17], which results in pulp injury [18]. The temperature on the hard tissue surface during an ablation pulse can be higher than 1300 °C, but the amount of heat left after ablation is very low because of the very small ablation volume per pulse. This amount of heat can be characterized as residual energy factor R, which is the ratio of the energy left in a tissue after ablation to the total energy of the laser pulse. R is critical to parameters of the laser pulse. For optimum conditions of ablation, $R = 0.4$ for the thermomechanical mechanism [19] and 0.25 for the thermal vaporization mechanism [3]. Residual heat from ablation propagates to the pulp and spreads over a large volume. Finally, the temperature rise in the pulp depends on the average laser power and exposure time. The safe temperature limit for pulp is about 42 °C [20]. The temperature rise in the pulp chamber depends on the average laser power and treatment time. Water cooling is used to reduce the likelihood of pulp overheating [18, 21]. Water cooling removes part of the residual heat and allows more laser power to be delivered and the drilling speed to be increased. In the optimum regime, about 50% of residual heat may be removed by water cooling. Heating of the pulp chamber during laser treatment has been simulated and measured *in vitro* in several studies [22–31]. The safety limit for laser ablation with an erbium laser and water cooling is about 6 W, which corresponds to a residual power dissipation of about 1.2 W. The water flow can be pulsed or continuous, in the form of a jet or spray. As a result, a water film is created on the tooth surface. The film absorbs laser light and can decrease the ablation efficiency. However, pulse laser radiation absorption by a water film is normally accompanied by the formation of shock waves. These waves contribute to removing water from the exposure zone on the tissue, if the initial thickness of the water film is small [32], and increase the ablation efficiency [33]. Water can soak (impregnate) a metamorphosed layer formed on the walls of the cavity under laser irradiation, creating additional absorption centers for laser radiation and enhancing the ablation efficiency due to the thermomechanical mechanism.

The efficacy of laser ablation of hard dental tissues by laser irradiation depends on many factors, such as the laser radiation wavelength, laser pulse structure and duration, water cooling, contact or noncontact mode of treatment, laser radiation energy density, distribution of power density in laser beam, repetition rate, and so on. Multimodal free-running erbium lasers with flashlamp pumping at wavelengths of 2.79 and 2.94 μm are the most widely used for hard dental tissue ablation. Pulses of these lasers have durations from 50 to 1000 μs and consist of a set of random spikes with durations from 1 to 10 μs [34].

In experiments on hard tissue laser ablation with an Er:YAG laser [35], the laser damage threshold of hard dental tissues was measured with a photoacoustic method. The threshold value was 4–7 J cm^{-2} for enamel for contact mode irradiation, which is approximately two times lower than for noncontact exposure. The results of measurements of dental hard tissue removal efficiency by the first Er:YAG laser pulse incident on the intact sample surface in contact and noncontact modes are shown in Figures 73.3 and 73.4.

Clearly, the removal efficiency in the contact mode of laser ablation without water cooling for enamel at energy densities up to 100 J cm^{-2} is almost 1.5 times higher

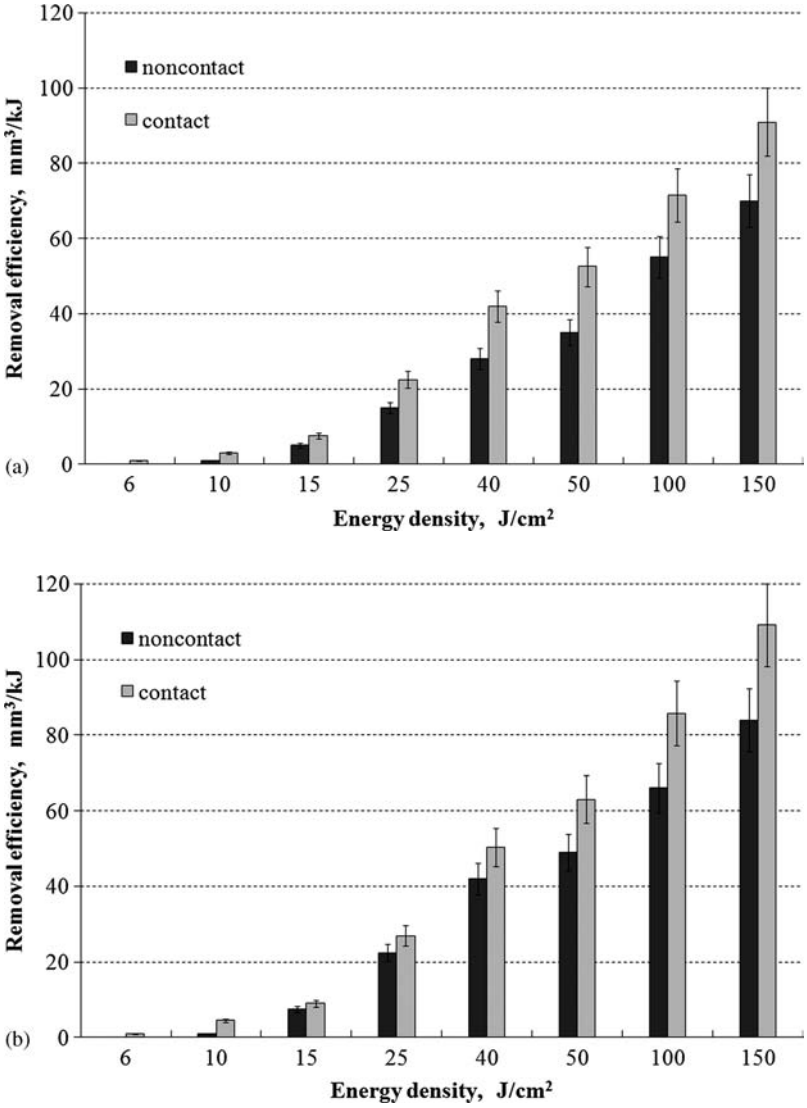

Figure 74.3 Enamel removal efficiency versus energy density of an Er:YAG laser in contact and noncontact modes of treatment, with no water (a) and with water (b) cooling (water flow rate 0.2 ml min^{-1}).

than that in the noncontact mode, and almost 1.3 times higher at energy densities up to 100–150 J cm^{-2}.

The efficiency of dentin removal at energy densities up to 100 J cm^{-2} for laser ablation without water cooling is 1.2 times higher in the contact mode than in the noncontact mode, whereas at energy densities up to 100–150 J cm^{-2} the efficiencies are almost the same in the contact and noncontact modes. In the case of laser

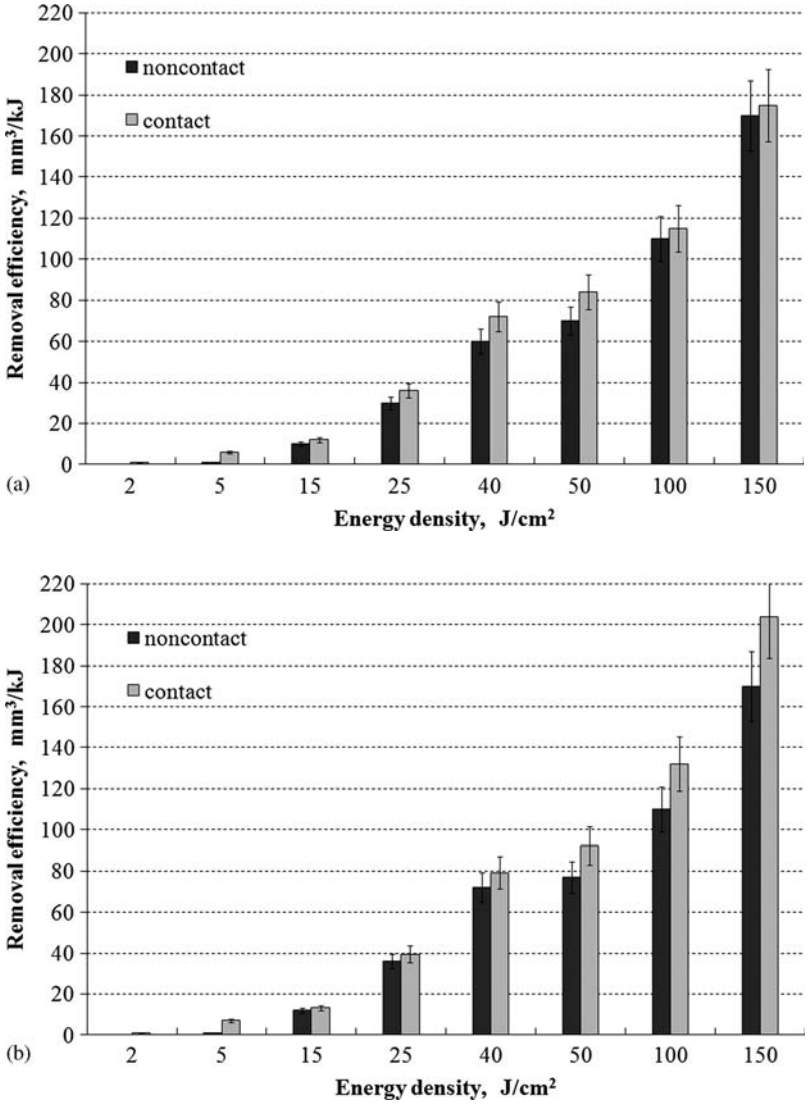

Figure 74.4 Dentin removal efficiency versus energy density of an Er:YAG laser in contact and noncontact modes of treatment, with no water (a) and with water (b) cooling (water flow rate 0.2 ml min^{-1}).

ablation with water cooling, the efficiency of enamel removal at energy densities up to 50 J cm^{-2} is almost 1.2 times higher in the contact mode than the noncontact mode and 1.3 times higher in the contact mode at energy densities of 50–150 J cm^{-2}.

In the contact mode of laser ablation with water cooling (the water flow rate in the experiment was 0.2 ml min^{-1}), the efficiency of dentin removal at energy densities up

to 50 J cm^{-2} was nearly 1.1 times higher in the contact mode, and 1.2 times higher at energy densities of 50–150 J cm^{-2}.

It is worth noting that the presence of water in the noncontact mode enhances the enamel removal efficiency nearly 1.5-fold at energy densities up to 50 J cm^{-2}, and 1.2-fold at energy densities of 50–150 J cm^{-2}. For dentin, the presence of water in the noncontact mode increases the removal efficiency almost 1.2-fold at energy densities up to 50 J cm^{-2} and does not change the removal efficiency at energy densities of 50–150 J cm^{-2}.

Water cooling increases the enamel removal efficiency in the contact mode almost 1.2-fold at energy densities up to 150 J cm^{-2} and does not change the efficiency of dentin removal.

The difference in removal efficiency for the contact and noncontact modes arises from differences in the mechanisms of laser damage. Rapid heating and microexplosions associated with the absorption of light by structural elements containing free water are characteristic for the noncontact mode. The same processes occur in the contact mode, but they are supplemented by a mechanism associated with the motion of particles produced by ablation in a closed space between a laser crater and the distal end of the contact tip (sapphire fiber). Particles of enamel are reflected from the distal end of the tip and produce additional tissue damage due to the high kinetic energy. This effect is similar to hard tissue damage by high-speed sapphire particles (air abrasive). This laser abrasive mechanism is related to the bombardment of the tissue surface by hard particles of the same tissue produced during laser ablation [36].

The efficiency of laser removal of enamel and dentin may be increased by adding hard abrasive particles (sapphire, diamond) to the treatment area [36]. It has been demonstrated [36] that the abrasive particles are accelerated by the laser radiation. The most likely mechanisms of hard particle acceleration by laser irradiation are the reactive mechanism and the mechanism related to microexplosions of particle material. Particles accelerated by laser irradiation reach speeds exceeding 1000 m s^{-1}. The kinetic energy of laser-accelerated particles is sufficient to destroy the hard tooth tissues. When fast abrasive particles collide with the enamel surface, the most likely location of destruction is inter-rod enamel having less mechanical cohesion and hardness than enamel rods. As has been shown [36], delivery of sapphire particles with a diameter of 10–30 μm as a powder or aqueous suspension into the treatment area synchronized with the Er:YAG laser radiation can improve the enamel removal efficiency almost twofold compared with enamel treatment by laser ablation alone.

The impact of erbium and CO_2 laser radiation on hard dental tissues has been investigated [37–41] using multimodal lasers with a 300–1000 μm beam size in the treatment area. In clinical practice, a beam with a diameter of 0.5 – 1 mm is normally used in laser systems for hard tissue drilling. Cavities created by such radiation are characterized by a low aspect ratio and intended for traditional tooth filling. Such a large spot size does not allow the benefits of laser beams with extremely small size, comparable to the wavelength of laser light, to be realized. Apparently, the smaller the beam size, the more local and potentially safe material processing will be. Using smaller beam sizes provides cavity formation with high accuracy, while the lateral size of these cavities may be significantly less than the lateral size of the cavities

formed by mechanical tools. Using microbeams provides cavity formation with a unique profile. Another advantage of microbeams is their ability to form a relief structure on the treated surface with a preset profile and microscopic dimensions comparable to the size of the microbeams, and also extended microchannels. Another characteristic of laser radiation is the ability of lasers to form short solitary spikes and their reproducible sequences – micropulses. These capabilities have not been fully utilized in modern laser dentistry. The process of laser hard tissue removal may be significantly optimized by controlling the spike duration, their duty cycle in a micropulse, and the micropulse repetition rate. Optimization may be achieved by delivering laser energy when it can reach the treated material with minimal loss, and will not be reduced by a water cooling system or by products of laser damage that have not yet left the laser cavity. We call the simultaneous use of micropulses and microbeams "M^2 technology." Single-mode radiation should be used to create optical beams with a small diameter of <0.2 mm [42–44]. Craters formed in human tooth dentin by different modes of YAG:Er laser ablation are shown in Figure 74.5.

The crater depth created by a single-mode laser beam with a diameter of $\sim$0.1 mm greatly exceeds the crater depth created by a traditional multimode laser beam with a large diameter ($\sim$1.0 mm) for the same total laser energy. The crater diameter created by a single-mode laser beam is smaller than the crater diameter created by the traditional multimode laser beam in this case.

The possibility of extended cavity formation with a high aspect ratio [42] in dental hard tissues may create a possibility for new technologies in dentistry, minimally invasive microdrilling for drug delivery to dentin and pulp, dentinal bleaching [45], creating cavities of programmable shape, and so on.

Another possibility is associated with surface texturing to increase the adhesion of filling materials [46]. The M^2 beam can be used to increase the mechanical strength of compounds and reduce microleakage for bonding dental material to hard tissue [46], the essence of which is to increase the contact area of adhesive materials through the creation of textures on the hard material surface by laser radiation. Textures are represented by a sequence of microcraters (Figure 74.6).

In a recent study [47], the composite material Revolution (Kerr, Orange, CA, USA) was placed on a surface containing the texture and polymerized with light radiation produced by a Rembrandt Rembrandt® Allegro™ (Den-Mat® Corporation, Santa Maria, CA, USA) for 30 s. Conventional technology was used as a control, when a smooth enamel surface is first covered with Nano-Bond Self-Etch Primer, then Nano-Bond Adhesive, and after that Revolution, with subsequent polymerization. The shear-bond strength was investigated. It was shown that the bond strength of Revolution with the textured surface was almost three times higher.

In another recent study [48], the adhesion of bonding resin (Tetric EvoCeram; Ivoclar Vivadent, Schaan, Liechtenstein) to dentin of an extracted tooth after texturing was investigated. In control samples, G-Bond (GC America, Alsip, IL, USA) was first applied to the smooth dentin surface, then bonding resin, followed by polymerization. It was shown that the shear-bond strength with the textured dental surface was 24.5 ± 9.6 MPa and for the control surface 14.9 ± 4.4 MPa.

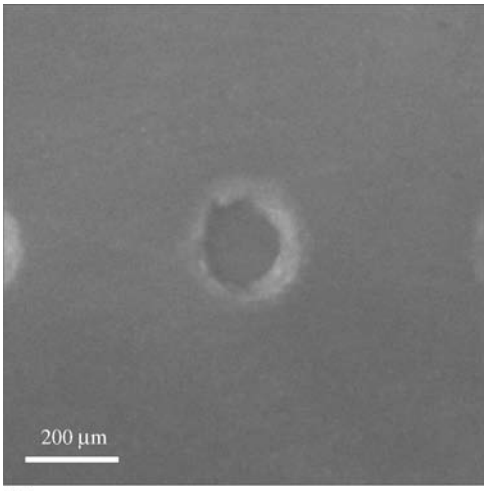

(a)

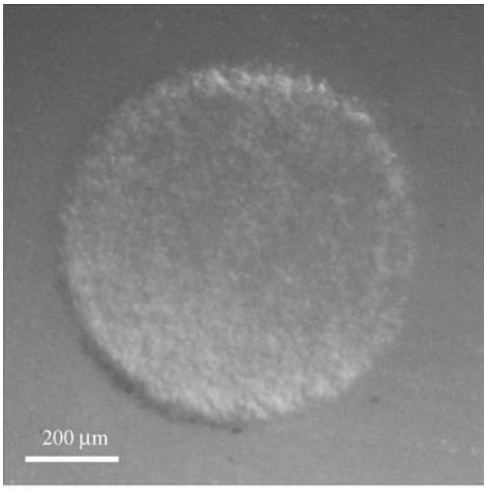

(b)

Figure 74.5 Photographs of craters formed in the dentin by single-mode (a, c) and multimode (b, d) Er:YAG lasers for the same exposure (0.1 J).

74.4 Conclusion

Significant efforts have been made by numerous groups and companies in the period 1985–1995 to understand and optimize laser ablation of dental hard tissue. As a result, in last 15 years the erbium laser for hard tissue was introduced as a commercial instrument for laser drilling. Laser drilling in clinical practice has been proven to be a safe, minimally invasive method for cavity preparation. The speed of

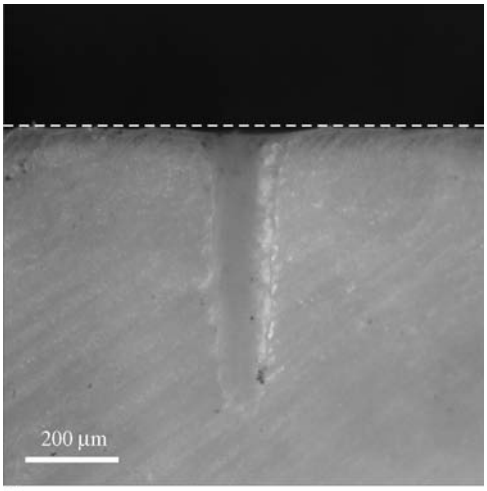

(c)

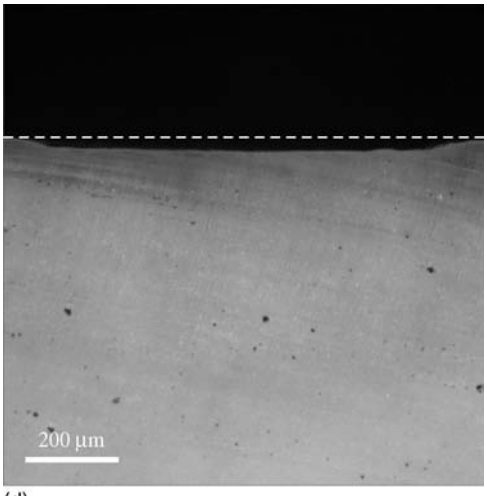

(d)

Figure 74.5 (*Continued*)

laser drilling for the best lasers is comparable to that of mechanical drilling. Laser drilling is less painful than a high-speed turbine but anesthesia is still necessary in about 50% of cases. A laser drill is mostly used for class II and V cavity preparation, selective caries removal, and calculus removal. Future applications may include laser "etching" of hard tissue surfaces before bonding. However, the hard dental tissue laser drill has not yet become a standard instrument in dental practice because of the very high price and complexity of a standard flashlamp-pumped erbium laser and insufficient advantages compared with alternative instruments. Hence further

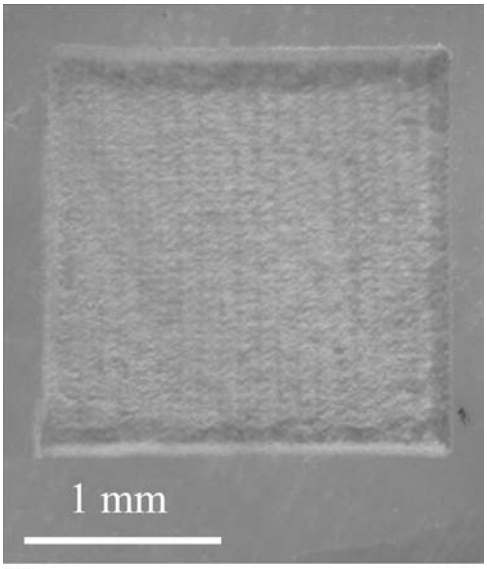

(a)

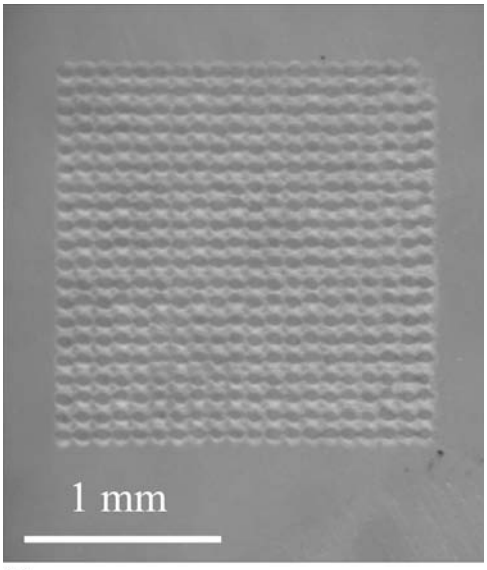

(b)

Figure 74.6 Photograph of human tooth enamel fragment textured by an Er:YAG laser with laser beam diameter $D \approx 100\,\mu m$ and period $dx = 40\,\mu m$ (a) and $D \approx 100\,\mu m$ and $dx = 100\,\mu m$ (b). Scanning electron micrograph of texture with $D \approx 70\,\mu m$ and $dx = 100\,\mu m$ (c).

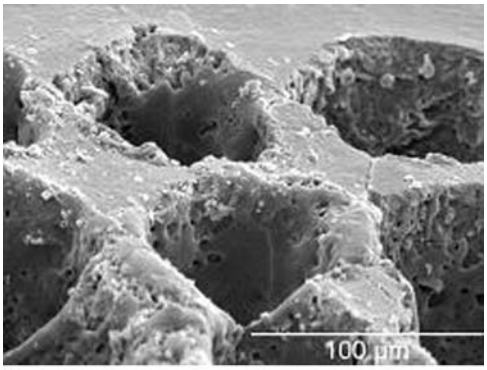

(c)

Figure 74.6 (*Continued*)

improvements in the laser ablation technique, finding more cost-effective lasers and discovering unique and important laser applications in the dental clinic are the new challenges for future research.

References

1 Nanci, A. and Ten Cate, A.R. (2003) *Ten Cate's Oral Histology: Development, Structure, and Function*, Mosby, St. Louis, MO.

2 Tasev, E., Delacretaz, G.P., and Woeste, L.H. (1990) Drilling in human enamel and dentin with lasers: a comparative study. *Proc. SPIE*, **1200**, 437–445.

3 Fried, D. (2000) IR laser ablation of dental enamel. *Proc. SPIE*, **3910**, 136–148.

4 Ragadio, J.N., Lee, C.K., and Fried, D. (2000) Residual energy deposition in dental enamel during IR laser ablation at 2.79, 2.94, 9.6, and 10.6 μm. *Proc. SPIE*, **3910**, 204–209.

5 Belikov, A.V., Skripnik, A.V., and Shatilova, K.V. (2010) Study of the dynamics of the absorption spectra of human tooth enamel and dentine under heating and ablation by submillisecond pulse radiation of an erbium laser with a generation wavelength of 2.79 μm. *Opt. Spectrosc.*, **109** (2), 211–216.

6 Wieliczka, D.M., Weng, S., and Querry, M.R. (1989) Wedge shaped cell for highly absorbent liquids: infrared optical constants of water. *Appl. Opt.*, **28** (9), 1714–1719.

7 Zolotarev, V.M., Mikhailov, B.A., Alperovich, L.I., and Popov, S.I. (1969) Dispersion and absorption of liquid water in the infrared and radio regions of the spectrum. *Opt. Spectrosc.*, **27**, 430–432.

8 Fried, D. (2005) Laser processing of dental hard tissues. *Proc. SPIE*, **5713**, 259–269.

9 Lee, C., Ragadio, J.N., and Fried, D. (2000) Influence of wavelength and pulse duration on peripheral thermal and mechanical damage to dentin and alveolar bone during IR laser ablation. *Proc. SPIE*, **3910**, 193–203.

10 Cummings, J. and Walsh, J. (2009) Erbium laser ablation: the effect of dynamic optical properties. *Appl. Phys. Lett.*, **62** (16), 1988–1990.

11 Altshuler, G.B., Belikov, A.V., Erofeev, A.V., and Egorov, V.I. (1993) Simulation of laser destruction of hard tooth tissues. *Proc. SPIE*, **2080**, 10–19.

12 Majaron, B., Sustercic, D., Lukac, M., Skaleric, U., and Funduk, N. (1998) Heat diffusion and debris screening in Er:YAG

laser ablation of hard biological tissues. *Appl. Phys. B Lasers Opt.*, **66** (4), 479–487.
13 Altshuler, G.B., Belikov, A.V., and Erofeev, A.V. (1994) Laser treatment of enamel and dentine by different Er lasers. *Proc. SPIE*, **2128**, 273–281.
14 Keller, U. and Hibst, R. (1995) Er: YAG laser effects on oral hard and soft tissues in *Lasers in Dentistry* (eds. L.J. Miserendino and R.M. Pick), Quintessence Publishing, Hanover Park, IL, pp. 161–172.
15 Altshuler G.B., Anderson, R.R., Manstein, D., Zenzie, H.H., and Smirnov, M.Z. (2001) Extended theory of selective photothermolysis. *Lasers Surg. Med.*, **29** (5), 416–432.
16 Brown, W.S., Dewey, W.A., and Jacobs, H.R. (1970) Thermal properties of teeth. *J. Dent. Res.*, **49** (4), 752–755.
17 Belikov, A.V., Erofeev, A.V., and Skripnik, A.V. (1995) Thermal response of pulp during laser treatment of enamel and dentine. *Tech. Phys. Lett.*, **21**, 330–331.
18 Visuri, S.R., Walsh, J.T. Jr., and Wigdor, H.A. (1996) Erbium laser ablation of dental hard tissue: effect of water cooling. *Lasers Surg. Med.*, **18** (3), 294–300.
19 Altschuler, G. and Erofeev, A. (1995) New concepts in laser-tissue interaction in *Lasers in Dentistry* (eds. L.J. Miserendino and R.M. Pick), Quintessence Publishing, Hanover Park, IL, pp. 299–315.
20 Zach, L. and Cohen, G. (1965) Pulp response to externally applied heat. *Oral Surg. Oral Med. Oral Pathol.*, **19**, 515–530.
21 Mir, M., Meister, J., Franzen, R., Sabounchi, S.S. *et al.* (2008) Influence of water-layer thickness on Er:YAG laser ablation of enamel of bovine anterior teeth. *Lasers Med. Sci.*, **23** (4), 451–457.
22 White, J.M., Fagan, M.C., and Goodis, H.E. (1994) Intrapulpal temperatures during pulsed Nd:YAG laser treatment of dentin, *in vitro*. *J. Periodontol.*, **65** (3), 255–259.
23 Goodis, H.E., Schein, B., and Stauffer, P. (1988) Temperature changes measured *in vivo* at the dentinoenamel junction and pulpodentin junction during cavity preparation in the *Macaca fascicularis* monkey. *J. Endod.*, **14** (7), 336–339.
24 Mollica, F.B., Camargo, F.P., Zamboni, S.C., Pereira, S.M. *et al.* (2008) Pulpal temperature increase with high-speed handpiece, Er:YAG laser and ultrasound tips. *J. Appl. Oral Sci.*, **16** (3), 209–213.
25 Krmek, S.J., Miletic, I., Simeon, P., Mehicic, G.P. *et al.* (2009) The temperature changes in the pulp chamber during cavity preparation with the Er:YAG laser using a very short pulse. *Photomed. Laser Surg.*, **27** (2), 351–355.
26 Staninec, M., Darling, C.L., Goodis, H.E., Pierre, D. *et al.* (2009) Pulpal effects of enamel ablation with a microsecond pulsed lambda=9.3-microm CO_2 laser. *Lasers Surg. Med.*, **41** (4), 256–263.
27 Glockner, K., Rumpler, J., Ebeleseder, K., and Stadtler, P. (1998) Intrapulpal temperature during preparation with the Er:YAG laser compared to the conventional burr: an *in vitro* study. *J. Clin. Laser Med. Surg.*, **16** (3), 153–157.
28 Attrill, D.C., Davies, R.M., King, T.A., Dickinson, M.R., and Blinkhorn, A.S. (2004) Thermal effects of the Er:YAG laser on a simulated dental pulp: a quantitative evaluation of the effects of a water spray. *J. Dent.*, **32** (1), 35.
29 Park, N.S., Kim, K.S., Kim, M.E., Kim, Y.S., and Ahn, S.W. (2007) Changes in intrapulpal temperature after Er:YAG laser irradiation. *Photomed. Laser Surg.*, **25** (3), 229–232.
30 Geraldo-Martins, V.R., Tanji, E.Y., Wetter, N.U., Nogueira, R.D., and Eduardo, C.P. (2005) Intrapulpal temperature during preparation with the Er:YAG laser: an *in vitro* study. *Photomed. Laser Surg.*, **23** (2), 182–186.
31 Cavalcanti, B.N., Lage-Marques, J.L., and Rode, S.M. (2003) Pulpal temperature increases with Er:YAG laser and high-speed handpieces. *J. Prosthet. Dent.*, **90** (5), 447–451.
32 Hibst, R. and Keller, U. (1993) Mechanism of Er:YAG laser-induced ablation of dental hard substances. *Proc. SPIE*, **1880**, 156–162.
33 Fried F D., Ashouri, N., Breunig, T., and Shori, R. (2002) Mechanism of water augmentation during IR laser ablation of dental enamel. *Lasers Surg. Med.*, **31** (3), 186–193.
34 Altshuler, G.B., Belikov, A.V., Gagarskiy, S.V., Erofeev, A.V., and

Parakhuda, S.E. (1995) Peculiarities of temporal structure of erbium lasers. *Proc. SPIE*, **1984**, 190–200.

35 Belikov, A.V., Erofeev, A.V., Shumilin, V.V., and Tkachuk, A.M. (1993) Comparative study of the 3 μm laser action on different hard tooth tissue samples using free running pulsed Er-doped YAG, YSGG, YAP and YLF lasers. *Proc. SPIE*, **2080**, 60–67.

36 Altshuler, G.B., Belikov, A.V., and Sinelnik, Y.A. (2001) A laser-abrasive method for the cutting of enamel and dentin. *Lasers Surg. Med.*, **28** (5), 435–444.

37 Hibst, R. and Keller, U. (1989) Experimental studies of the application of the Er:YAG laser on dental hard substances: I. Measurement of the ablation rate. *Lasers Surg. Med.*, **9** (4), 338–344.

38 Dostalova, T., Jelinkova, H., Hamal, K., Krejsa, O. *et al.* (1996) Evaluation of depth and profile cavity after laser ablation with different energy of Er:YAG laser radiation. *Proc. SPIE*, **2623**, 88–93.

39 Nishimoto, Y., Otsuki, M., Yamauti, M., Eguchi, T. *et al.* (2008) Effect of pulse duration of Er:YAG laser on dentin ablation. *Dent. Mater. J.*, **27** (3), 433–439.

40 Stock, K., Hibst, R., and Keller, U. (1997) Comparison of Er:YAG and Er:YSGG laser ablation of dental hard tissues. *Proc. SPIE*, **3192**, 88–95.

41 Lizarelli, R., Moriyama, L.T., and Bagnato, V.S. (2002) Ablation rate and micromorphological aspects with Nd:YAG picosecond pulsed laser on primary teeth. *Lasers Surg. Med.*, **31** (3), 177–185.

42 Tokarev, V.N. (2006) Mechanism of laser drilling superhigh-aspect-ratio holes in polymers. *Quantum Electron.*, **36** (7), 624–637.

43 Meister, J., Franzen, R., Apel, C., and Gutknecht, N. (2004) Influence of the spatial beam profile on hard tissue ablation. Part II: pulse energy and energy density distribution in simple beams. *Lasers Med. Sci.*, **19** (2), 112–118.

44 Meister, J., Apel, C., Franzen, R., and Gutknecht, N. (2003) Influence of the spatial beam profile on hard tissue ablation. Part I: multimode emitting Er: YAG lasers. *Lasers Med. Sci.*, **18** (2), 112–118.

45 Belikov, A.V. and Feldchtein, F.I. (2009) New method for intrinsic whitening of vital teeth using Er,Cr:YSGG laser microperforation: first *in vivo* cases. Presented at the Academy of Laser Dentistry 16th Annual Conference, Las Vegas, NV, SA-51.

46 Belikov, A.V., Skrypnik, A.V., and Shatilova, K.V. (2009) YAG:Er laser texturing of human teeth hard tissue surface. *Proc. SPIE*, **7547**, 754705–754706.

47 Belikov, A.V., Pushkareva, A., Skrypnik, A.V., Strunina, T., and Shatilova, K.V. (2009) Laser texturing of material surfaces. *Sci. Instrum.*, **53** (4), 52–56.

48 Samad-Zadeh, A., Kugel, G., Harsono, M., Defuria, C. *et al.* (2009) The influence of laser-textured dentinal surface on the bond strength. Presented at the International Association of Dental Research 87th General Session, Miami, FL.

1
Industrial Perspectives

Andreas Kandelbauer, Manfred Rahe, and Rudolf W. Kessler

1.1
Introduction and Definitions

1.1.1
Introduction

The concept of Quality by Design (QbD) is based on the evident fact that a high level of quality of intermediate or final products cannot be achieved by testing the products but needs to be implemented into the products by intelligently designing the whole manufacturing process. To be able to do so, a comprehensive understanding of the process on a causal basis is required. Only such an understanding ensures reliably defined and consistent quality levels by operating stable and robust processes and, for instance, in the case of pharmaceutical products, allows real-time release of the manufactured goods. The technology that enables translation of the concept QbD into industrial reality is process analytical technology (PAT). PAT is generally considered a science-based and risk-based approach for the analysis and improved control of production processes [1]. Although initially conceived by the FDA for application in the pharmaceutical sector, the PAT initiative continues to grow in importance also for related industries in the applied life sciences, for example, biotechnology, the food industry, as well as the chemical industry [2].

1.1.2
Historical Aspects

In the course of the past decades, the industrial landscape has undergone many changes which were mainly dominated by the shift from a supplier-dominated market to a customer-dominated market (Figure 1.1, [3]). Due to the rebuilding after the Second World War, in the 1950s, the overall product demand exceeded the general capacity supplied by industry. Hence, the quality of a product was mainly defined by the producer's view of what quality was (compare the partial analytical understanding of quality) [4]. This situation has changed dramatically since then. Today the industry faces a market situation that is often characterized by an intense

Handbook of Biophotonics. Vol.3: Photonics in Pharmaceutics, Bioanalysis and Environmental Research, First Edition.
Edited by Jürgen Popp, Valery V. Tuchin, Arthur Chiou, and Stefan Heinemann

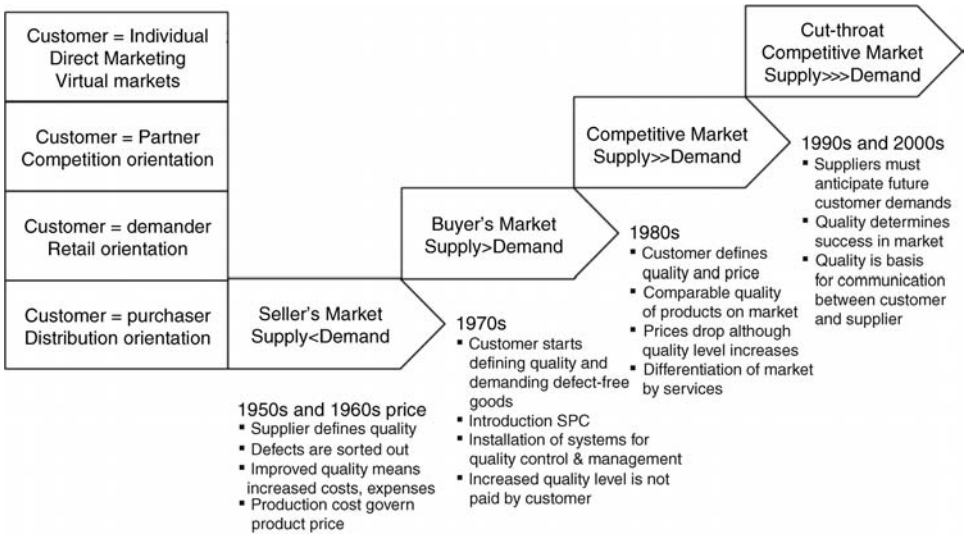

Figure 1.1 Changes in market situation during the past decades and concomitant adaptation of quality concepts (modified after [3]).

cut-throat competition in many branches, by ever increasing product complexity and diversity and by growing customer awareness of high product quality and functionality. In addition, more stringent legislative and regulatory measures imposed by society comprise an increasingly powerful driving force towards comprehensive public health and environmental compatibility of industrial processes. In contrast to the earlier years of industrialization, producing enterprises nowadays can no longer stratify their market position by increasing the mass-per-hour throughput of a certain product. Today, the sustainable success of an industrial company depends more critically than ever on the cost-effective realization of customer-tailored products of high quality that flexibly meet the rapidly changing end-customer's demands.

Reflecting this overall trend towards an increased focus on custom-made quality, increasingly sophisticated and holistic quality management systems have been developed over the years (Figure 1.2), ranging from simple inspection of the finished parts for defects and elimination of inferior ones, over implementing increasingly complex quality systems to avoid the production of any defective parts during manufacturing, to the modern views of process oriented, integrated and comprehensive total quality management systems. It is in this context that the modern concepts of PATs and QbD have to be reviewed. Before this, some general definitions and remarks on quality and process control are given.

1.1.3
Definition of Quality: Product Functionality

Quality may be best defined as product functionality [6]. Several levels of functionality can be identified (see Table 1.1) that are related to the various contexts a product and

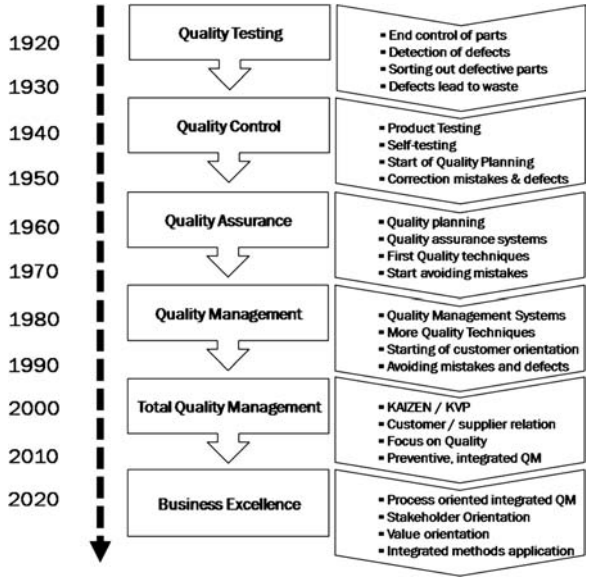

Figure 1.2 Historical development of important quality concepts and their major elements (modified after [5]).

Table 1.1 The various levels of functionality [6].

Functionality level	Description	Examples
Fundamental functionality	Basic properties based on the chemical composition and morphological constitution of the material	Is the material as it should be? Content of ingredients, particle size distribution, distribution of active compounds/traces/ dopants within material, and so on
Technical functionality	Behavior during the production process	Is the product processable? Flow behavior, mixing properties, purification and down-streaming properties, and so on
Technological functionality Value-oriented functionality	Required performance profile for the intended use Cost : benefit ratio	Is the product usable? Hardness, strength, efficacy, durability, Is the tailored quality level appropriate? Displayed product features versus price
Sensory functionality	Appearance and design	Is the product appealing? Haptic behavior, product smell, visual appearance, and so on

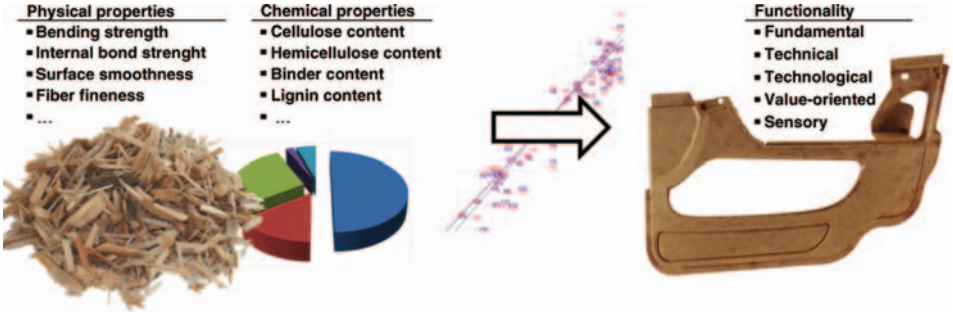

Figure 1.3 Relationship between measurement and product functionality.

its intermediates experience throughout the whole life cycle from manufacturing to the end-use and its disposal. Besides its fundamental functionality, which relates to the basic physical and chemical properties, such as composition and components distribution, surface properties or morphology of a product, the product must also be processable during manufacturing (technical functionality) and must fulfill the customer's requirements during the end-use (technological functionality). Moreover, the extent to which certain quality levels are realized in the product (value-oriented functionality) and its design-related properties (sensory functionality) are also important aspects. In the ideal case, single measured values from various methods are combined and mathematically related to all these different functionality levels (Figure 1.3).

According to the Kano model [7], a product complies with the customer's requirements and expectations when it displays basic, performance and excitement functionalities [8]. All performance characteristics of a group of objects or services intended to successfully populate a certain product niche will steadily have to be improved, expanded and further developed with time, since the customer will get used to the features and functions. This provides the driving force for continuous product development and product innovation. Due to cost issues and a desirably short time-to-market of novel products, only companies that are able to handle very short innovation cycles will sustain economic success. Knowledge-based production, based on a QbD approach and realized by process analytics, is the key element in achieving such short innovation cycles. Furthermore, it allows flexible response to sudden changes in customer's expectations, since the processes to translate the quality characteristics into product features are causally understood.

In this context, two main aspects need to be considered when introducing process analytical tools, for example, on-line spectroscopy, into manufacturing: *quality monitoring* and *product functionality design* [6]. Usually, the identification and quantification of a direct relation between, for instance, the measured spectral information and a target compound like a pharmaceutical ingredient is attempted. In many cases, univariate target responses, such as concentration, purity, or extent of conversion, and so on are determined and compared with standard values. Thereby, deviations of characteristic process parameters may be determined in real-time and the quality of

the manufacturing process may be monitored and controlled. Due to the recent developments of stable on-line and in-line instrumentation, in combination with complex chemometric toolboxes, a robust calibration of such relations is possible and, therefore, applications of process analytics in industry are numerous. In most cases, off-line measurements can be directly substituted by on-line spectroscopy, with the advantage of a possible 100% quality control of a specific response.

However, while process analytics is already widely recognized as a powerful tool to perform such *quality monitoring*, the full potential of this technology is by far not exhausted; process analysis can be exploited to an even much greater extent with economical advantage when it is embedded in a philosophy of continuous process improvement and *product functionality design*. Currently, process analytical data obtained from measurements on intermediate product stages during the running manufacturing process are only very rarely related to the performance of the final product or to the final application properties of the product. However, it is possible to relate process analytical information even to product functionality when a consequent transition from considering univariate data (single parameters and responses) to multivariate data analysis (multiple parameters and responses) is performed. Product functionality may be defined as the fundamental chemical and morphological properties of the material, by its performance through manufacturing, by the technical properties for the final application, and certainly also by its cost/performance ratio. If objectively classifying data for these definitions exist, a direct correlation to, for example, the spectral information in the case of on-line spectroscopy is possible. The exact nature of the individual signature of a spectrum (the "*spectral fingerprint*") is always dominated by the morphology and chemistry of the substrate, due to its substance specific absorbance and scattering behavior. The relative contributions of these two components to the measured spectrum depend on the wavelength of the interaction, on the angle of illumination of the substrate, on the angle of detection, on the difference in refractive indices, and on the particle size and particle distribution. In Figure 1.4 this is illustrated using the example of tablet spectroscopy [9].

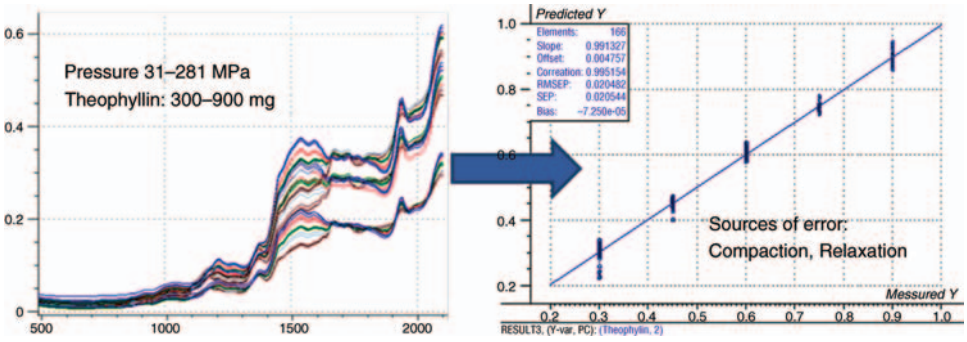

Figure 1.4 The information contained in wavelength-dependent scattering and absorption spectra of tablet samples compacted at different pressures (ranging from 31 to 281 MPa) and containing different amounts of theophyllin can be used to model the theophyllin content [9].

This multivariate information can be used not only to calculate the dependence of a single target (*quality monitoring*), but also allows full and overall classification of the sample quality (*functionality design*). This is especially true for the characterization of solids and surfaces by means of diffuse reflectance spectroscopy. Within the concept of QbD/PAT, a knowledge-based manufacturing is attempted which relies heavily on the combination of various sources of information using chemometric methods like principal component analysis, PLS, multivariate curve resolution, or other multivariate calibration methods.

1.1.4 Quality Control

The term *quality control* may generally be defined as a system that maintains a desired level of quality [10]. In general, this may be accomplished by comparing a specific quality characteristic of some product or service with a reference, and if deviations from the desired state are detected, taking remedial action to reinstate the targeted quality level. Similarly, *process control* may be defined as appropriate measures to readjust the state of a process upon some observed undesired deviation. *Process analytics* provides the required information on the state of the process. While *process analytics* deals with the actual determination of specific data using process analytical devices, like HPLC, optical spectroscopy or other sensors, *process analytical technology* is a system for designing, analyzing and controlling manufacturing by timely measurements [1] (see below), already with quality determination in mind. *Process analysis* is the comprehensive analysis of the industrial process including every single activity involved in the manufacturing of the product. Thereby, all material and virtual flows are considered. Historically, the *PAT initiative* roots in a comprehensive approach to realizing *process analysis* on an instrumental basis. PAT is the essential tool to realize the concept of *Q bD*, which has recently been further developed to the even more comprehensive approach of product quality life-cycle implementation (PQLI) [11, 12].

Essentially, quality control is accomplished by *off-line quality control* procedures, *statistical process control* and, to a lesser degree, by *acceptance sampling plans*. *Off-line quality control* involves selecting and defining controllable product and process parameters in such a way that deviations between process output and a standard will be minimized [10]. A typical tool for such a product or process design is the statistical experimental design approach or design of experiment (DoE). Quality is here basically defined "off-line" before the process has actually been implemented or started. *Statistical process control* (SPC) in contrast compares the results or output of a process with the designated reference states and measures are taken when deviations from a desired condition of a process are statistically significant. When the process is poorly designed (by inappropriate off-line quality control measures, that is, unsuitable or sub-optimal processes) these deviations may be large and cannot be compensated for by statistical process control. Hence, it is obvious that off-line quality control by well-designed processes which are based on a thorough understanding of the effects of the involved process factors on the critical quality features of the product

will govern the achievable product performance, or in other words: quality cannot be tested into products afterwards.

1.1.5
Quality Assurance

Quality assurance relates to a formal system that ensures that all procedures that have been designed and planned to produce quality of a certain level are appropriately followed. Hence, quality assurance acts on a meta-level and continually surveys the effectiveness of the quality philosophy of a company. Internal and external audits, standardized procedures and comprehensive documentation systems (traceability) are important tools to accomplish this "watchdog" function within the company. Strict process descriptions determining every single step required during manufacturing a product, including the required appraisal procedures, may be defined, and deviations from these fixed procedures may be indicative of potential deteriorations in quality; instruments like the Good Manufacturing Practice approach or ISO certifications are typical for quality assurance on a highly sophisticated level. However, defined procedures and certification alone do not necessarily lead to improved performance or functionality of a product; obeying agreed-on procedures merely guarantees conformance within a specifically designed process. Pre-defined and fixed processes that are certified and commissioned by the regulatory authorities, like for instance the manufacturing process of a specific drug by a pharmaceutical company which is accepted and granted by authorities like the Food and Drug Administration (FDA) may even prove to be inflexible, sub-optimal and difficult to develop further. Since every small deviation from the standard routine processing is considered a potential quality risk and, especially in the case of pharmaceuticals or biologicals, may comprise a potential health hazard, all such deviations are required to be communicated to the authorities. Process improvements or further adaptations that usually require significant redefinition of process parameter values need renewed approval by the authorities, which in most cases is time and cost intensive. Thus, in a sense, quality assurance may even be counterproductive to process improvement and impede the establishment of higher quality levels in products. To overcome these limitations of current quality assurance policies, during the past years, the FDA has promoted the PAT initiative which, in a similar form, is also supported by the European Medicine Agency (EMA).

1.2
Management and Strategy

1.2.1
PAT Initiative

The major incentive behind the *PAT initiative* of the FDA is defined in the FDA-Guidance "PAT – a Framework for Innovative Pharmaceutical Development,

Manufacturing and Quality Assurance" [1]: "PAT is a system for designing, analyzing, and controlling manufacturing through timely measurements (i.e., during processing) or critical quality and performance attributes of raw and in-process materials and processes, with the goal of ensuring final product quality. It is important to note that the term *analytical* in PAT is viewed broadly to include chemical, physical, microbiological, mathematical, and risk analysis conducted in an integrated manner." Within the PAT initiative, the manufacturers of pharmaceutical compounds are motivated to undergo a transition from the currently used strategy of testing random samples at the end of the pipeline for their compliance and otherwise strictly sticking to approved routine procedures, towards a causal understanding of the process by means of process-accompanying and process-controlling measurements and tests. This PAT recommendation is valid also for other branches of industry, such as the food industry or biotechnology. By using powerful process analysis in the sense of PAT, manufacturing processes may be controlled and directed towards the desired levels of quality; moreover, PAT also contributes to the resource-efficiency of the production process by, for instance, minimizing the emission of carbon dioxide or reducing the energy consumption. Ideally, a 100% control of the manufactured goods is accomplished by using on-line and in-line sensors. It is anticipated that, by an integrative and system-oriented approach based on process analysis and process control, the industry will experience significant competitive advantages in the manufacturing of high-quality, customized products. Explicitly, the following goals are pursued with employment of process analysis and process control tools (PAT):

- Increase in productivity and product yield
- Minimization of energy and resources consumption
- Minimization of expenses for safety issues in the production facility
- Decreased number of customer complaints
- Increased operational flexibility
- Anticipating maintenance and process-integrated self-diagnosis
- 100% constant and certified quality

PAT will increase the production efficiency by

- Deep understanding of the production process
- Integration of quality into process steps
- Reduction of quality overhead costs
- Higher production quality
- Lower production costs
- Self-adjusting production processes

With the implementation of PAT it will be possible to pursue product-functionality design or a quality by design approach from the very beginning of the product conception. PAT targets a comprehensive feed-forward control approach and adaptive process analysis systems. Implementing PAT consequently requires application of the following modules:

1) Risk analysis of the production process (e.g., by failure mode and effects analysis, FMEA)
2) Process analytics (sensors, spectrometers, etc.)
3) Process control systems (SPC, MSPC)
4) Statistical experimental design (DoE)
5) Multivariate data analysis

This PAT toolbox and its interplay is depicted schematically in Figure 1.5.

1.2.2 PAT Toolbox

Hence, in contrast to a widely anticipated false view, PAT is not restricted to single devices for process analysis; PAT covers numerous tools included multivariate statistical methods for data design, data gathering and data analysis, process analytical sensors, control systems in the manufacturing, testing and admitting of products, as well as measures for continuous process improvement and methods of knowledge management. One of the most important groups of on-line sensors is the *spectroscopic sensors*, using the interaction between electromagnetic radiation and matter for material characterization [6]. Another important group of PAT sensors are based on *chromatographic methods* which employ various types of physical-chemical separation principles to physically de-convolute complex reaction mixtures into single components which may subsequently be identified and quantitatively determined [13]. Yet another and completely different group of sensors is the so-called *soft sensors* [14]. The basic principle behind soft sensors is that some material properties

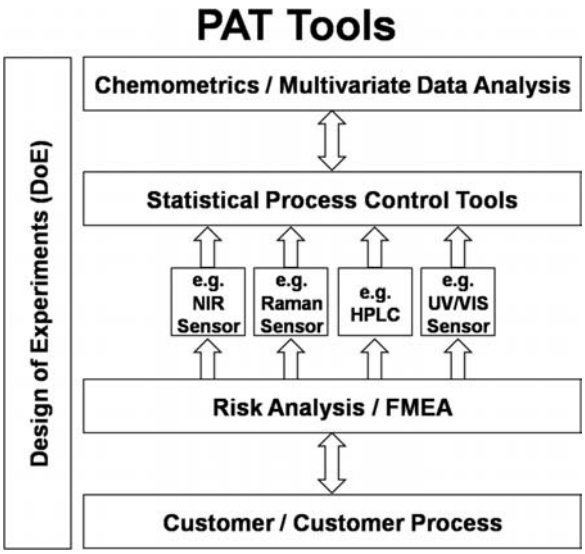

Figure 1.5 The PAT toolbox.

may not be measured directly as physical or chemical material parameters but can only be deduced indirectly by analyzing secondary variables, which in turn can be related to the target property by mathematical models. A very interesting recent account of soft sensors in the PAT context is given in Ref. [14]. With soft sensors, basically two main groups can be distinguished. On the one hand there are purely data driven models which involve no *a priori* knowledge of biological, physical or chemical interrelationships between the various categories of variables. Such models are called *black box models* and have the advantages of requiring no deep process understanding and relative ease of implementation. However, they may over-fit the observed data and be restricted to pure descriptions of the data without yielding true causal relationships which are required for a knowledge-based quality design. Tools often used are artificial neuronal networks, evolutionary algorithms, chemometric models like partial-least squares (PLS), principal component analysis (PCA), principle component regression (PLR), or support vector machines (SVR). *White box models*, in contrast, are based on known physical or chemical relationships based on kinetic or thermodynamic equations. If *a priori* information is integrated into data driven models, so-called *gray box models* are employed [14]. It is evident that numerous mathematical methods and algorithms are also included in PAT and, hence, PAT is not restricted to specific sensors that record specific physical signals. There are numerous requirements from the industrial user for process analytical technologies. The most important ones are summarized in Figure 1.6 [15].

1.2.3 The Concept of Quality by Design (QbD)

The basic concept behind PAT and QbD in the context of regulatory authorities of the pharmaceutical industry has only recently been summarized very concisely by

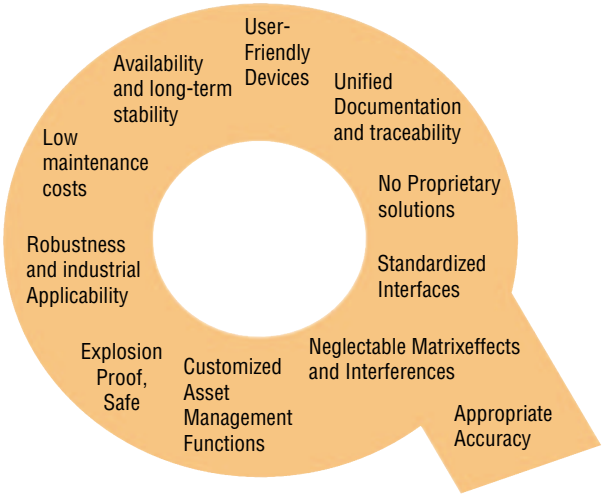

Figure 1.6 User requirements for PAT tools Source: [15].

Schmidt-Bader [16] and in the following paragraphs some of the most relevant aspects from this article will be adapted and summarized. The key aspect with a QbD approach is that quality should not simply be tested at the end after the manufacturing process has finished but should be considered already in the early phase during the conceptual design of the product, and later at all stages of its manufacture. "Quality cannot be tested into products; quality should be built in by design" [1]. In consequence, quality becomes already a matter of product development and, hence, is also strongly dependent on prior research activities into how the desired product features may be realized by industrial processes. The whole processing cycle, ranging from the early developmental stage when the product and its quality features are designed and planned, based on the input from the customers, over the product realization and production phase to its final distribution and end-use is included in such a perspective, and the manufacturer is now in the situation that he needs to demonstrate a causal process understanding throughout the whole cycle, starting from the early phases of product development to the routine production which allows guaranteed compliance with the required critical quality attributes (CQAs) during all steps. This can only be brought about by employing scientific methods. "Using this approach of building quality into products, this guidance highlights the necessity for process understanding and opportunities for improving manufacturing efficiencies through innovation and enhanced scientific communication between manufacturers and the Agency" [1].

All in all, with the PAT initiative the industry faces a shift in paradigm regarding the future of intelligent process and quality control from a *quality by testing* approach towards a *quality by design* approach. This paradigm change offers many opportunities for business excellence. Primary goals in the context of QbD are

- Assurance of a reproducibly high quality of the intermediate and final products
- Reduction of the manufacturing costs
- The promotion and advancement of novel, innovative technologies for quality assurance and process optimization
- The generation of in-depth, causal understanding of manufacturing processes

The transition from QbT to QbD is characterized by numerous significant changes in quality philosophy which are summarized in Figure 1.7 and Table 1.2.

1.2.4 ICH

The concept of QbD as developed by the FDA has been pushed towards realization during the past years mainly by the International Conference on Harmonization of Technical Requirements for Registration of Pharmaceuticals for Human Use (ICH) [18]. The motivation behind ICH was to stimulate world-wide a common and more flexible, science-based approach to the admission of pharmaceuticals. The main focus lies in an international consensus between regulatory authorities and industrial companies regarding the quality of pharmaceutical compounds: "Develop a harmonized pharmaceutical quality system applicable across the life

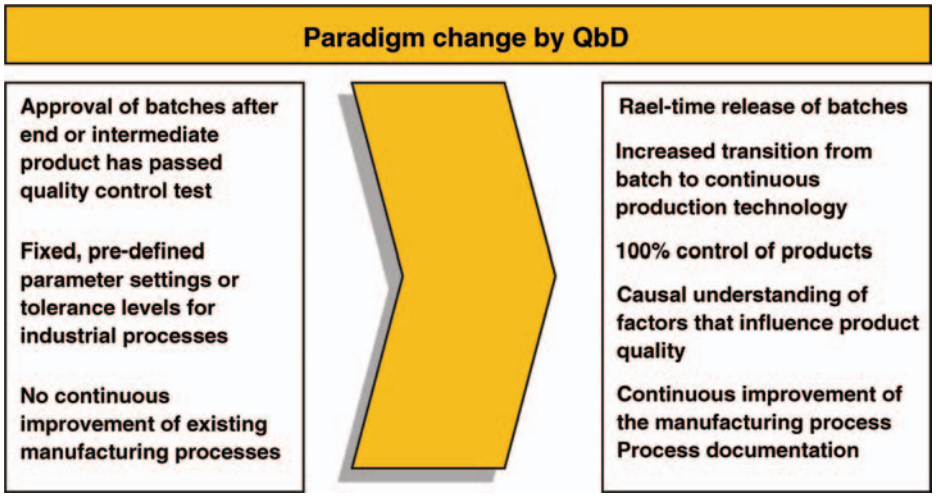

Figure 1.7 Paradigm change by QbD (Courtesy of JH & Partner CATADIA Consulting GmbH, Germany).

cycle of the product emphasizing an integrated approach to risk management and science".

In the ICH Q8 document [19] quality in the context of the QbD concept is defined as follows: "Quality is the suitability of either a drug substance or drug product for its intended use. This term includes such attributes as the identity, strength, and

Table 1.2 Major differences between QbT and QbD (modified after [17]).

	Quality by Testing (QbT)	Quality by Design (QbD)
Development	• Empirical approach • Importance of random findings • Focus on optimization	• Systematic approach • Multivariate strategies • Focus on robustness
Manufacturing	• Fixed • Based on defined specifications	• Variable within design space • Based on knowledge • Supported by robust processes
Process control	• Retrospective analysis • Based on in-process control quality is determined • Data variability is not completely understood • Focus on reproducibility	• Prospective analysis • PAT tools control critical parameters, quality is predicted • Data variability has been subject of research and is completely (causally) understood • Focus on PAT and QbD concepts
Control strategy	• Feed-back control • Control by testing and inspection	• Feed-forward control • Knowledge- and risk-based quality assurance
Product specification	• Acceptance criteria depend on data of specific product charge	• Acceptance criteria depend on end-user benefit

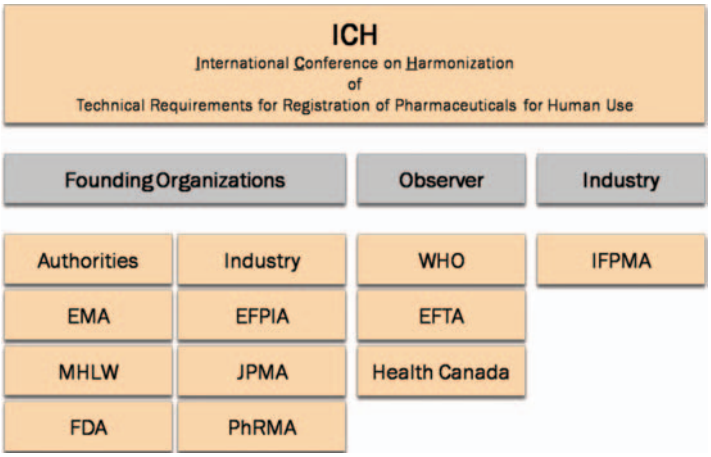

Figure 1.8 The organizational structure of the International Conference of Harmonization of Technical Requirements for Registration of Pharmaceuticals for Human Use (ICH) [18].

purity." [19] Besides considering the traditional definition of drug quality in the sense of the law, the ICH definition also includes all processes and parameters that might have an impact on the quality of the drug and, as documented in the ICH Q6 publication [20], ICH clearly assigns full responsibility to the industrial manufacturers to provide the required level of quality of a drug by appropriate measures: "Specifications are critical quality standards that are proposed and justified by the manufacturer and approved by the authorities" [20].

ICH was founded in 1990 by six independent organizations representing the regulatory authorities as well as the industry involved in pharmaceutical research in USA, Europe and Japan (see Figure 1.8).

The organizations directly involved are

- European Medicines Agency (EMEA)
- European Federation of Pharmaceutical Industries and Associations (EFPIA)
- Food and Drug Administration (FDA)
- Pharmaceutical Research and Manufacturers of America (PhRMA)
- Ministry of Health, Labor and Welfare (MHLW)
- Japan Pharmaceutical Manufacturers Association (JPMA)
- International Federation of Pharmaceutical Manufacturers and Associations (IFPMA)

The European regulatory authorities are represented by the Committee for Medicinal Products for Human Use (CHMP) as a subsection of the EMA. The European pharmaceutical market is represented by EFPIA which represents 29 national pharmaceutical associations in Europe and 45 of the most important industrial companies. For the American authorities, the FDA is involved with the Center for Drug Evaluation and Research (CDER) and the Center for Biologics Evaluation and Research (CBER). The researching American pharmaceutical indus-

try is involved with the PhRMA which represents 67 industrial enterprises and 24 research organizations from the US. The Japanese authorities are represented by the Pharmaceuticals and Medical Devices Agency (PDMA) and the National Institute of Health Sciences (NIHS) while the Japanese industry is represented by the JPMA which heads 75 Japanese pharmaceutical companies and 14 national committees. Pharmaceutical companies and associations situated in other countries all over the world, including threshold and developing countries, are represented by the IFPMA, which is a non-profit, non-governmental organization comprising numerous companies involved in pharmaceutical research, biotechnology and vaccine manufacture.

Additionally, three international organizations of observing status are involved in ICH, whose most important role is to mediate between ICH and non-ICH member countries. These three organizations are

- World Health Organization (WHO)
- European Free Trade Association (EFTA)
- Health Canada

1.2.5 The Concept of a Design Space

For an understanding of the strategy behind PAT/QbD, the concept of a design space is of special importance. The ICH Q8 document [19] defines a design space as a multidimensional correlation, that is, the combination and interaction of numerous production factors governing the built-in quality of a (pharmaceutical) product. Within such a design space, the complex interplay between input variables, like properties of raw materials, process parameters, machine properties or user-effects are completely understood on a causal level (see Figure 1.9).

Causal understanding is achieved by identifying and quantifying the effects of critical factors on product quality at any stage of the process by multivariate mathematical models. A design space can be obtained by applying the design of experiments (DoE) approach which has been established as an important tool in quality management since the 1980s [21, 22], for example, in the Six Sigma concept [10, 23].

As pointed out in the ICH Q8 document [19], from a regulatory point of view, a process would be considered as conforming as long as it is carried out within the predefined design space. Since the exact trace within the design space is of no importance, manufacturing a pharmaceutical or any other product becomes more flexible. Currently, even small deviations from pre-defined values of process parameters need to be addressed with the authorities in a time-consuming and cost-intensive procedure. Such deviations from a specific path within the design space would no longer matter as long as a defined level of final quality can still be guaranteed.

As an example to illustrate this shift in process philosophy in the pharmaceutical industry, an industrial process will be discussed schematically. Consider the chemical synthesis of a given compound X. According to conventional philosophy, the

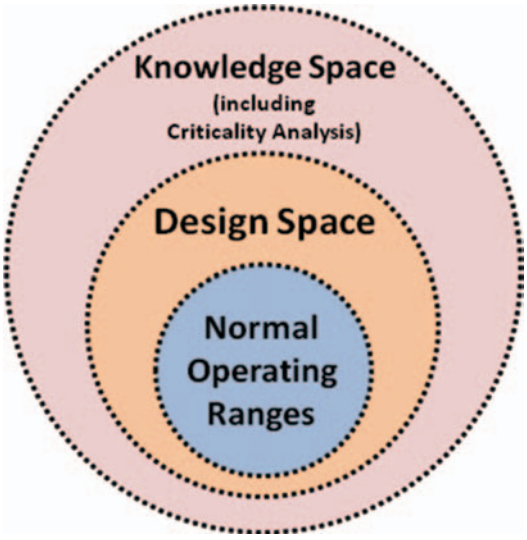

Figure 1.9 Schematic representation of the design space which is based on a knowledge space. The control strategy with a QbD approach is to maintain a process within the design space.

preparation process would have been required to be defined very specifically in terms of production conditions, such as specified reaction temperature, reaction time and, say, catalyst concentration. To conform with the certified procedure all efforts are focused on keeping the process within defined limits. Process analytical technology would be employed to control the parameter settings for temperature and catalyst concentration within agreed narrow boundaries to carry out the process in the predefined way. The target in the traditional philosophy of QbT would be to maintain a process "180 min at 120 °C with 5% of catalyst", all significant deviations therefrom would have to be documented and announced. In a QbD approach, in contrast, the target would be "95% conversion plus defined product specifications" and all feasible combinations of temperature, time and catalyst concentration (= design space) leading to this end would be allowed. Thereby, a quality (and risk) based approach to production is realized and much regulatory effort and certification cost can be avoided.

This offers process analytical technology a decisive role in manufacturing. Process analytical tools would not be used to "measure and control the quality of the product" or intermediate stages thereof, but instead would be employed to determine the current "position of the process in the design space" allowing prediction of the expected degree of quality and adjusting accordingly subsequent process steps to guarantee an agreed final level of quality.

Accordingly, validation of the manufacturing procedure would be focused on the process analytical methods that allow complete control of the design space. Robust process analytical technologies are the key requirement for monitoring and con-

trolling the multivariate design space [16]. Analytically robust methods yield precise and accurate results under modified working conditions. Analytical ruggedness is of importance, too. This means that analytical methods are reproducible under varying analytical circumstances, such as different laboratories, different laboratory personal or different measurement devices. Robustness and reliability of analytical methods as well as their continuous improvement will be of increasing importance for assuring the quality and safety of products. In consequence, industrial processes will become more robust. The robustness of an industrial process may be defined as its tolerance against variability introduced by fluctuations in raw material quality, variations in process and environmental conditions, and variations introduced by equipment (e.g., deterioration with time) and human resources (e.g., habits, moods). With robust processes, companies may be allowed to produce their goods with a higher level of independence at lower cost and still improved guaranteed quality levels.

Currently, manufacturing processes are defined and certified at an early stage when only incomplete information is available on the influence of variations and fluctuations in raw material quality and process parameters. Improvements based on later experience are difficult to implement. Knowledge-based manufacturing allows rapid and continuous adaptation of the process to varying starting conditions and allows cost-effective further development and quality improvement.

A major element within the philosophy of QbD is the exploitation of PAT to accomplish this transition towards a knowledge-based production.

1.2.6 Implications for Other Branches of the Life Sciences

1.2.6.1 General Remarks

Although the basic impetus for pursuing PAT/QbD approaches arises from restrictions imposed by the rigorous legislative and regulatory framework in the context of the good manufacturing policy (GMP) in the pharmaceutical industry, which lead to complicated and cost-intensive approval processes caused by already moderate modifications or even improvements in the production process, the implications of this approach are certainly also of importance for other branches of the life sciences. For example, in biotechnology and the food industry, the total control over the design space in the growth of microorganisms and the harvesting of compounds produced by them has also been targeted recently [24]. Compared to the pharmaceutical industry, however, there are several peculiarities that have to be overcome by these industries, many of which deal with process analytical research questions. Although many of the chemical processes employed in the pharmaceutical industry which are desired to result in well defined compounds of high purity with a very specific biological activity are complex systems governed by numerous factors like concentration, composition, temperature, pH, and so on, in comparison to biotechnological or biosynthetic processes they seem rather simple and well-defined with respect to the possible synthetic pathways encountered.

1.2.6.2 **Biotechnology**

In biotechnology, due to the introduction of living cells or even mixed cultures, another level of complexity is introduced which usually renders classical chemical reaction engineering insufficient to develop a full understanding of the relevant design space. Considering, for instance, recombinant protein expression by genetically modified microorganisms, this typically involves numerous inter- and intracellular interactions, growth and diffusion phenomena, and very complex chemical reaction cascades within the living cells of the microorganisms. Expression of the foreign target compound by the organism has to be balanced with the energy and material demands of the growing microorganism. Intracellular transport phenomena and metabolic processes have to be included in the quantitatively and causally determined design space, as well as external factors like organism selection, fermentation medium development, process parameters, and scale-up effects. Hence, like in conventional chemical or pharmaceutical synthesis, the reactor system may not be treated as a black box; in the case of biotechnology the living microorganism systems need also to be scientifically understood. This imposes great challenges on process analytical technologies and is reflected by numerous recent attempts to monitor in real-time fermentation processes and the cultivation of microorganisms. Although subsequent process steps in biotechnology, such as down-streaming, that is, the purification and enrichment of the desired compounds from the fermentation broth, are also important, the major focus in the application of PAT/QbD concepts in biotechnology clearly lies in the fermentation step. Quality improvement in the course of the down-streaming may be achieved only to a certain degree, and is usually achieved only via a sequence of several process steps and, hence, is rather time-consuming and cost-intensive. Therefore, the development and adaptation of suitable in-line measurement technologies that lead to an improved understanding of microbial fermentation is the most effective and promising way. Again, in comparison to the pharmaceutical industry which was our starting point, specific problem solutions of process analytical tools for biotechnology must, among others, consider that the sterility of the reaction system must be ensured, that many of the targeted analyte species are present only in very small amounts, and that there is usually a large influence of the surrounding medium, which in general is rather complex and not constant with time.

1.2.6.3 **Food Industry**

Another level of complexity is typically added when the food manufacturing industry is considered from a holistic point of view. Here again, purely physical and chemical processes similar to classical chemical and pharmaceutical industries or fermentation processes as in biotechnology may be involved in the manufacturing of food. However, the growth, harvesting and processing of multi-cellular organisms and complex objects has to be taken into consideration, and should actually be included in the causal analysis of the variation pattern observed in food manufacturing. Again, powerful process analytical technologies are required that include measurement and processing of reliable data. However, in the context of

establishing PAT/QbD approaches in the manufacturing industry, the food industry plays a special role, not only because of the complexity of the involved processes but also because it displays a disproportionately low level of automation in comparison to the chemical and pharmaceutical industries or other branches. Hence, the demand for process analytical technologies is especially high. It can be safely assumed that due to the ever increasing cost pressure, to globalization, and to the increasing requirements regarding quality assurance and food safety the food industry will develop to an important emerging market for the automation industry in the coming years. Besides activities directed at the rationalization of not-yet automated processes, two main fields will be of major importance in the food industry, (i) pro-active process and quality management, involving the integration of quality assurance in the production and an improvement in equipment availability; and (ii) the tracking and tracing of goods, that is mainly targeted at an increase in food safety and a reduction in food deterioration caused by microbial decay processes. This implies, in turn, an increasing demand for the engineering and development of appropriate process analytical technologies, suchas, among others, in-line sensors and data extraction tools [25].

1.2.6.4 **Summary and Outlook**

In any industry, process analytical technologies will, hence, gain in importance in the near future. Process analysis as one of the major tools within PAT is concerned with chemical, physical, biological and mathematical techniques and methods for the prompt or real-time acquisition of critical parameters of chemical, physical, biological or environmental processes. The aim of process analysis is to make available relevant information and data required for the optimization and automation of processes (process control) to assure product quality in safe, environmentally compatible and cost-efficient processes [12].

Not only does time-resolved information need to be retrieved and used as a controlling input, but, as becomes most evident from the outlined increase in complexity of the subjects that are dealt with in the life sciences, the retrieved information should also be space-resolved (chemical imaging). While in rather "simple" aqueous reaction systems with quite rapid adjustment of (dynamic) equilibria during chemical synthesis a spatial resolution may not necessarily be required, it is obvious that the distribution of a drug in a pharmaceutical formulation, or the spatial distribution of pathogens on food crops may be of critical importance to the overall quality of the manufactured goods.

The major improvements for industrial processes that are brought about by pursuing a QbD approach with the concomitant rigorous application of PAT tools may be summarized as follows:

- Assurance of reproducibly high quality of intermediates and final products
- Reduction of the manufacturing costs
- Continuous process optimization with respect to an improved exploitation of the employed material and energy resources
- Improved yields of high-quality end-product

- Improved safety and environmental compatibility of the industrial processes
- Stimulation of novel technologies for quality assurance and process optimization
- Generation of a causal understanding of the manufacturing process

1.3
Toolboxes for Process Control and Understanding

1.3.1
Introduction: Causality

Process control and understanding is an important feature for a future knowledge-based manufacturing. Although on-line process control has been well known for the last 20 years, the aspect of PAT in the pharmaceutical industry has become a driving force for recent activities [1]. However, "quality" has different meanings to different companies. For instance, for large companies that produce a standardized material, the major target associated with quality is ensuring close adherence to the defined product specification. In contrast, for smaller companies, "quality" means, in many cases, guaranteeing the flexibility to fit the end-product requirements in relation to rapidly changing market needs. Moreover, nowadays the concept of quality often goes far beyond a specific product but embraces the concepts of plant quality and total quality management (TQM). However, what all views of quality have in common is their dependence on information about the intrinsic properties of a product and knowledge of the relationship between plant parameters and product functionalities.

On-line and inline quality control and process optimization will only be successful when based on appropriate process analysis and process understanding, that is, the analysis of the connection (cause and effect) between process parameters and the quality characteristics of the final product with its specifications. Process analytics in this sense means, therefore, understanding the causal relation between measurement and response. By definition, causality is the strict relationship between an event (the cause) and a second event (the effect), where the second event is a consequence of the first [26]. Very often in chemometrics only descriptive or statistical knowledge is produced which fits the special data set but cannot be used as a general model. Figure 1.10 visualizes the different levels of knowledge for process understanding.

A straightforward "cooking recipe" for knowledge-based production integrates the following procedures (see also Section 1.2.2, Figure 1.5):

Step 1: Detailed analysis of the process and risk assessment
Step 2: Selection of the process analytical toolboxes
Step 3: Define the design space and design the necessary experiments
Step 4: Multivariate data analysis of the data
Step 5: Define the control system and integrate system into production

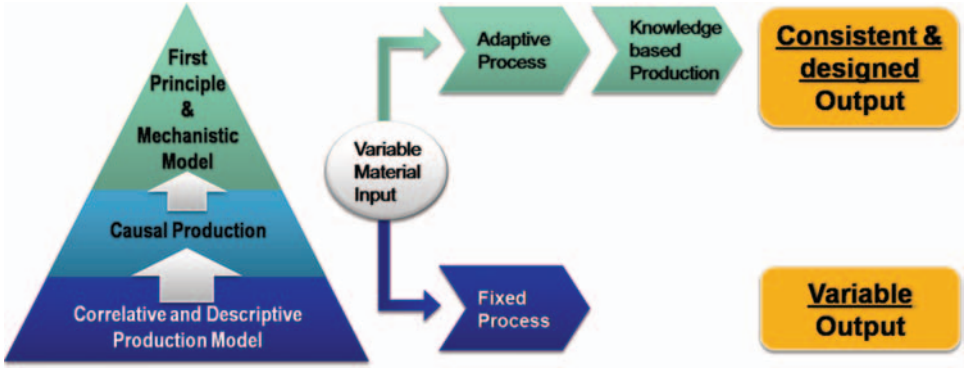

Figure 1.10 Road map for process understanding.

1.3.2 Sampling

In homogeneous systems any sample which is taken will be representative of the whole system. In heterogeneous systems it is difficult to find a way to extract a sample (= fragment) which represents the average of the material. In practice, no sample will be strictly identical to the material as it is a matter of scale [27].

There are four general sampling strategies that are used for process analysis[1)]:

- **Withdrawal**: A portion of the process stream is manually withdrawn and transferred into a suitable container for transport to the analyzer.
- **Extractive sampling**: A portion of the process stream is automatically taken to the analyzer. This may take place either on a continuous basis or at frequent intervals.
- ***In situ* probing**: A probe is inserted into the process stream or vessel and brought into contact with the sample.
- **Non-invasive testing**: Either a "window" into the process stream or another mode of non-contact measurement is used in order to account for interaction of the analysis system with the process material

All four approaches have certain advantages and drawbacks and there is hardly ever a clearly right or wrong approach to sampling.

In *process analytics*, one can distinguish between off-line, at-line, on-line and in-line measurement methods [6]. In the case of *off-line* measurements, samples are withdrawn from the process and analyzed in a laboratory environment which is spatially clearly separated from the industrial equipment. Thus off-line analysis always exerts significant lag times between recognizing and counteracting irregularities. With *at-line* measurements, the sample is withdrawn from the process flow

1) D. Littlejohn, personal communication.

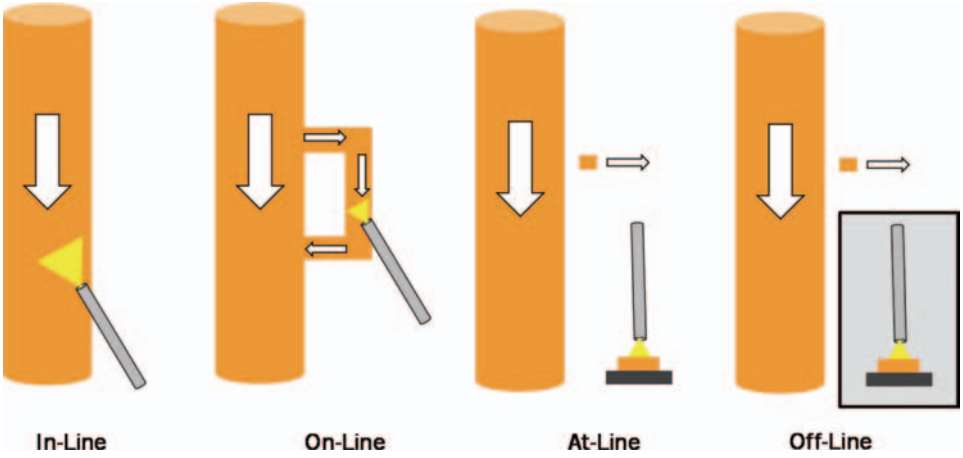

Figure 1.11 Sampling methods.

and analyzed with analytical equipment that is located in the immediate environment of the industrial equipment. Hence, the reaction time for countermeasures is already significantly reduced. Due to the industrial proximity it is often observed that at-line analytical equipment is more robust and insensitive towards process environment but less sensitive or precise than laboratory-only devices. In the case of *on-line* measurements, samples are not completely removed from the process flow but temporarily separated, for example, via a by-pass system which transports the sample directly through the on-line measurement device where the sample is analyzed in immediate proximity to the industrial machining and is afterwards reunited with the process stream. When *in-line* devices are used, the sensor is directly immersed into the process flow and remains in direct contact with the unmodified material flow. Figure 1.11 illustrates various sampling modes realized with in-line, on-line, at-line and off-line sampling. Typical probes for interaction of electromagnetic irradiation with samples are shown schematically in Figure 1.12 for various spectroscopic techniques (transmission, diffuse reflectance, transflection and attenuated total reflectance spectroscopy).

In the ideal case of process control, 100% of the processed elements or products are covered by analytical methods at any time and complete knowledge about the quality of the manufactured goods is obtained throughout the whole process. However, in most cases (when only off-line or at-line devices are used) this is not possible and then *accepted sampling plans* are required which define which and how many samples are inspected at certain intervals [6].

Sampling is always an issue no matter which measurement approach is used, but the nature of the challenge also varies with the approach. For instance, since with on-line analysis a sample may be spatially separated from the main process stream by means of a bypass system, on-line analysis has the advantage over *in situ* or in-line analysis in that the sample can be pre-conditioned (filtrated, extracted, constant

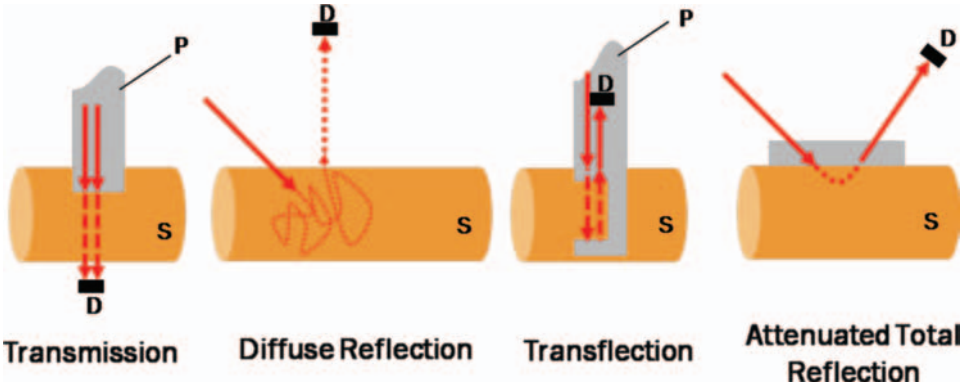

Figure 1.12 Schematic representation of typical spectroscopic probes (D, detector; P, probe; S, sample).

temperature etc.) prior to the analytical procedure. The main concern of sampling is to get access to a representative sample. Besides being representative of the process stream, some additional features need to be considered when selecting a certain sampling approach. Sampling systems must ensure that the sample is[1]:

- obtained and delivered safely,
- conditioned and presented reliably to the analyzer,
- compatible with the analyzer regarding the measurement conditions, such as temperature or pressure,
- obtained in a cost effective way, and
- representative also of the process stage, that is, the lag time from the process to the analyzer must be within an acceptable range

It is generally believed that about 75% of analyzer reliability problems are associated with the sampling system.

Sampling of solids presents the most significant problems. It is clear that finding the key component at low concentrations of a targeted analyte within a complex particulate system with high precision is a real challenge. As a rule of thumb, around 3000 to 10 000 particles are needed to obtain representative values. This can easily be realized when only small particles are present in the medium; however, it is almost impossible to calibrate a system with large particles. In this case, on-line calibration may be the best way to receive representative information over time.

Liquids are considerably easier to sample, unless there are two phases present or the liquids carry high levels of solid compounds.

Gases in general present the least problems, but can still be tricky where there are components close to their dew point. The NESSI consortium has focused on using modular sample system components in building block form that can be linked together to make complete conditioning systems which include pressure regulators, valves, pressure gauges and filters [28].

1.3.3 Process Validation

1.3.3.1 Role of Design of Experiments (DoE)

In January 2011 a new "Guidance for Industry: Process Validation: General Principles and Practices" was introduced by the FDA and will be outlined here [29]. This guidance describes process validation activities in three stages through the whole lifecycle of the product and process, (i) process design, (ii) process qualification, and (iii) continued process verification. These are the basic principles for smart or intelligent manufacturing (see Figure 1.13).

The process should be understood from first principles and from a scientific and engineering point of view. In most cases, the sources of variation during production may already be known by experience; however, only rarely are they really understood or quantified. Thus an important objective of process validation is to attribute all variations in the process and raw materials directly to the product variability. The perfect way to relate product variability to process and raw material changes is to use a DoE strategy [30]. However, it is sometimes difficult to select the appropriate parameters and parameter settings for the design. A parameter is a measurable value which can describe the characteristics of a system, for example, temperature, pressure, and so on. Very often, these parameters may be the factors (= independent variables) which predominantly influence the process and product quality (critical process parameter or factor (CPP)). DoE allows one to identify the relevant factors and to quantify their relative importance. It is logical that the factors which are of importance should be controlled. However, it is sometimes a difficult task to find the correct CPP. Multivariate data analysis (e.g., PCA) of historical data helps to select

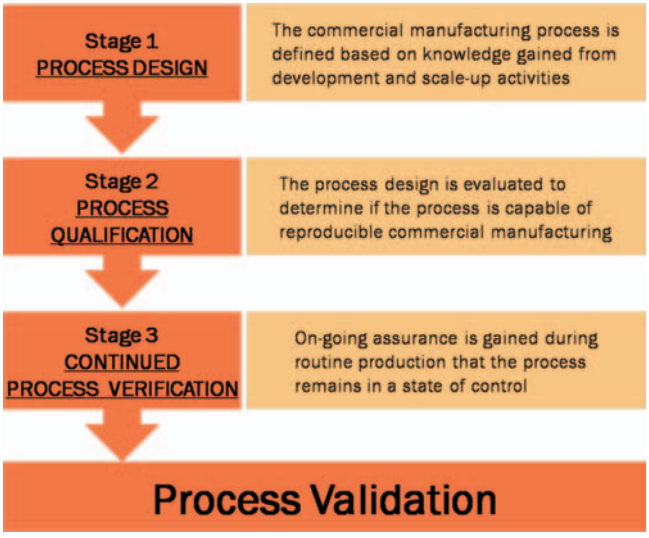

Figure 1.13 Basic principles of smart manufacturing as defined by the FDA [29].

the most important orthogonal parameters [6]. Orthogonality is an important prerequisite in parameter selection for DoE since it is desirable to vary CPPs independently of each other in order to influence the response properties of the product.

Outliers are usually a much better source of information than historical data based on "standard" production, as standard production data only show the variation within the regular production and, therefore, no systematic and significant variation of the factors can be deduced. It is also important to emphasize that a reliable design of the experiments should always include the possibility to evaluate the interaction terms between the factors. When the interaction is more important than the main factors this usually indicates that parameters are used which are not factors and, hence, the DoE has to be modified.

1.3.3.2 Role of Failure Mode and Effects Analysis (FMEA)

Another tool to extract the most important factors is risk assessment such as failure mode and effect analysis (FMEA) or cause and effect matrices [10, 31, 32]. This assists in effectively defining the design space, increases the awareness of the process risks, and yields a better understanding of the relationships between functionality and quality parameters. The critical quality attributes (CQA) are the data that best describe the characteristics that need to be controlled to ensure product quality. Figure 1.14 shows the principal steps involved in FMEA and Figure 1.15 illustrates how FMEA is situated within the production site of a product.

1.3.4 Measurement Technologies (How to Measure)

1.3.4.1 Selection of the Appropriate Technique

One of the key elements for process control is the selection of the best possible technology. Common techniques used in industry measure physical attributes such as conductivity or refractive index. They may be addressed as univariate sensors. Process chromatography can be used to separate the components of complex mixtures, but chromatographic methods are difficult to integrate in *in situ* and

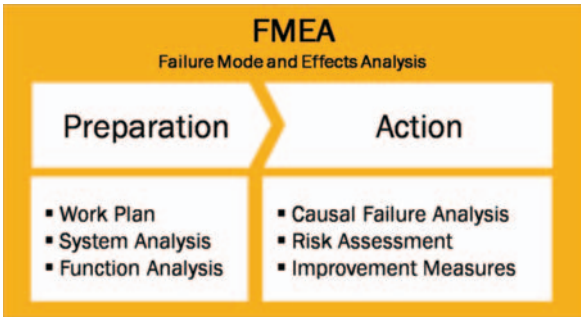

Figure 1.14 Basic approach behind failure modes and effects analysis (FMEA).

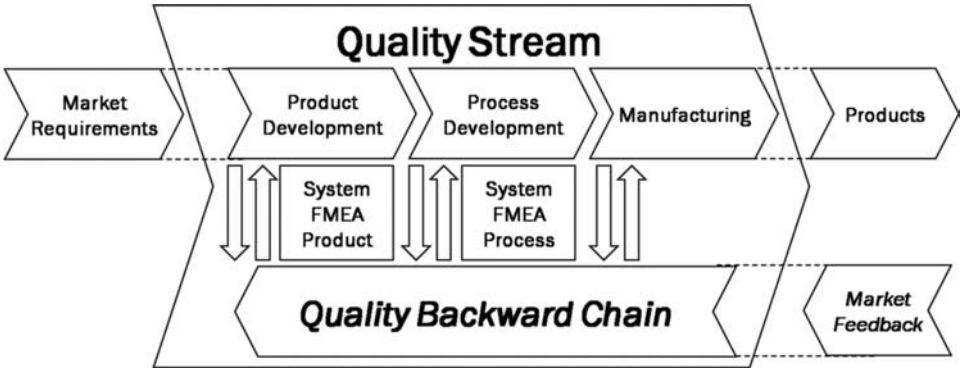

Figure 1.15 Integration of FMEA in the quality stream of a manufacturing facility.

in-line process control set-ups. Unlike optical spectroscopy, new technologies like on-line-NMR or terahertz spectroscopy, as well as mass spectroscopy are not yet standard equipment in in-line process analytics. A detailed overview of the different techniques is given in [6, 33]. Since optical spectroscopy is currently among the most prominent methods used in inline-process analytics, it is discussed in more detail in the following paragraphs.

Optical spectroscopy has developed into a widely used technique in process analytics. Depending on the measurement problem, a broad range of useful wavelength ranges and modes of interaction between electromagnetic radiation and the sample can be used (see Figure 1.16).

Key issues from a practical point of view, besides cost/performance, are the need for high sensitivity and selectivity, as well as the simplicity of application. Although

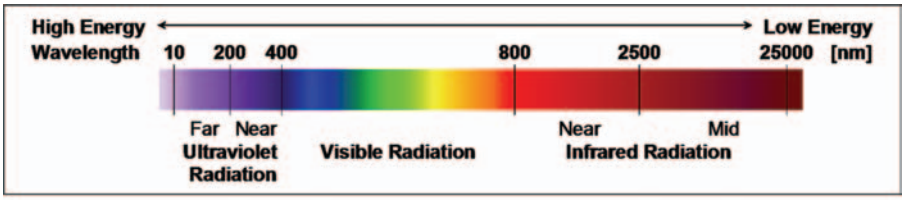

Fluorescence	UV / Vis - sNIR	NIR / MIR	Raman
Excitation / Absorption: $\lambda \approx$ 200 - 600 nm Fluorescence: $\lambda \approx$ 200 - 900 nm	λ = 200 - 400 nm (UV) λ = 400 - 700 nm (Vis) λ = 700 - 1100 nm (NIR)	MIR: λ = 2500 - 25000 nm $\tilde{\nu}$ = 4000 - 400 cm^{-1} NIR: λ = 1000 - 2500 nm $\tilde{\nu}$ = 10000 - 4000 cm^{-1}	λ_0 = 633 nm $\Leftrightarrow \lambda$ = 633 - 813 nm $\Delta\tilde{\nu}$ = 3500 - 0 cm^{-1}
Excitation /Emission of Electrons	Excitation of Electrons (UV / Vis) and Overtones (NIR)	Excitation of Vibrations, Rotations and Overtones	Excitation of Vibrations Complementary to MIR

Figure 1.16 Selection of appropriate wavelength regions depends on the spectroscopic method used and the intended analytical application.

Table 1.3 Selection of the best possible inline technology in optical spectroscopy [6].

	UV/VIS/s-NIR	NIR	MIR	Fluorescence	Raman
Selectivity	+	+ +	+ + +	+ +	+ + +
Sensitivity	+ + +	+(+)	+ + +	+ + + (+)	+(+ +)
Sampling	+ + +	+ + +	+	+ +	+ + +
Working in aqueous media	+ + +	+	+	+ +	+ + +
Applicability	+ + +	+ +	+	+	+
Process analytical tool	+ + +	+ + +	+	+	+ + +
Light guide	+ + +	+ + +	(+)	+ + +	+ + +
Signal	Absorption	Absorption	Absorption	Emission	Scattering
Sampling on-line/in-line	s, l, g	s, l	s, l, g	s, l (g)	s, l, (g)
Techniques	Transmission Reflectance ATR	Transmission Reflectance ATR	ATR (Transmission)	Reflectance Transmission	Reflectance
Relative costs	1	3–5	6–10	4–6	8–12

the basic layout of spectroscopic tools is always very similar (light sensors–sample contact area–detector), the various optical spectroscopic techniques are based on numerous different measurement principles. Ultraviolet- and visible (UV/Vis) spectroscopy is a highly sensitive technique for electronic transitions while mid-infrared (MIR) spectroscopy is specific for vibrational transitions. Since energy transitions between vibrational states of a molecule are highly substance-specific, peaks measured in the MIR region can be directly attributed selectively to fundamental moieties in a molecule. Near-infrared (NIR) spectroscopy is less sensitive due to lower yields of the higher order vibrational transition probabilities. However, although not easily directly interpretable, the major advantage with NIR is that, even at higher concentrations, no sample preparation (e.g., dilution) is needed. It is important to emphasize that both NIR and MIR spectroscopy are highly sensitive to water absorption. Table 1.3 shows a qualitative comparison of the advantages and disadvantages of the different optical spectroscopic tools.

1.3.4.2 **Working in Aqueous Systems**

Figure 1.17 shows the spectra of water in the NIR and MIR wavelength ranges. Due to the different absorption cross sections of the fundamental vibrations (MIR), the combination bands, first second and third overtones in the NIR, different path lengths must be used. The measured MIR spectrum is measured with a diamond ATR system with a mean path length around 5 μm.

The strong water absorption limits a broad application of these techniques in aqueous systems, for example, the study of fermentation processes. Raman spectroscopy may be advantageous over NIR and MIR spectroscopy in aqueous systems. In recent years, Raman spectroscopy has developed into a highly sensitive and versatile technique and, therefore, has proven a very suitable method in biotech-

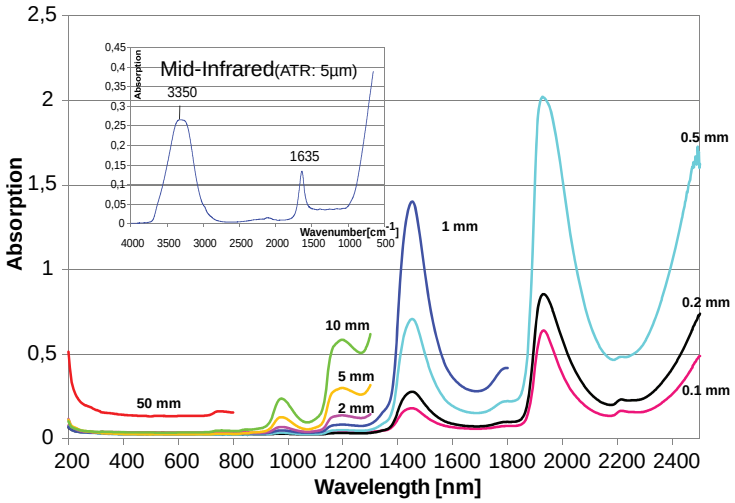

Figure 1.17 Absorption spectra of water in the NIR region with different path lengths and MIR (insert).

nology. For special applications fluorescence spectroscopy is certainly one of the most sensitive techniques in spectroscopic analysis.

1.3.4.3 Trace Analysis

Trace analysis is still a challenge in process analytics. Optical spectroscopy can cover a broad range of sensitivities and selectivities, as described before. One major advantage of NIR is that the absorption cross sections are generally low. Thus the technique can be used even at high concentrations. The typical detection limit for low concentration mixture components lies at around 1%; due to the high absorption coefficient for water as a trace component it is in the range down to 0.1% (or even 0.01%, depending on the system). In contrast, with MIR spectroscopy concentrations as low as 0.01% are easy to measure and standard detection limits can be even as low as 0.001%. Although Raman absorption cross sections lie typically around 10 orders of magnitude lower than in FTIR, due to recent development of extraordinarily sensitive detection systems Raman spectroscopy may approach the performance of FTIR spectrometers in the near future. UV/Vis and fluorescence spectroscopy are very sensitive techniques (in ppm, ppb and even lower), but lack selectivity.

As can be seen, the work horses in PAT are in many cases sufficiently sensitive. However, especially for applications in biotechnology when one is working in an aqueous environment at typically rather low metabolic concentrations, only chromatography in combination with mass spectroscopy may be a reasonable option [6, 33].

1.3.4.4 Qualification of a Spectrometer

Generally the quality of a spectroscopic inline control system can be described in terms of its spectral range, spatial resolution, non-linearity, S/N ratio (stray light),

diffraction efficiency and stability. The parameters needed to characterize the systems are, for example:

- Spectral resolution
- Spectral linearity
- Absolute efficiency of the optics (throughput) and diffraction efficiency of the grating,
- Straylight (S/N), ghost line and ghost image properties.
- Wavelength stability

Spectral axis calibration is done with spectrally well known light sources for example, neon lamps, lasers, fluorescent systems. The background CCD signal (dark current) must be compensated for and – if possible – be minimized by cooling. The detector response to light varies from pixel to pixel and is also strongly wavelength-dependent. Moreover, the energy throughput of lenses and other optical elements also depends on the wavelength. These variations can be calibrated by measuring a white reference surface, storing this image, and then calculating the ratio between a measured sample image and this white image (after dark current subtractions). Light source color temperature drift and lighting spatial non-uniformity are also compensated for, as long as the texture of the reference and the target is similar in terms of specular and diffuse reflectance.

The spectral range defines the wavelength regions covered by the spectrometer. The spectral resolution is related to the monochromator system used and defines the power to resolve the narrowest spectral features in the electromagnetic spectrum. The bandwidth is defined as the full width at half maximum of the spectral line. It is important to notice that the optical resolution is different to the (digital) pixel resolution of, for example, a diode array spectrometer. The pixel resolution describes the number of digital points which are required to represent a peak in the spectrum. Usually the pixel resolution should be about 2 to 3 times higher than the optical resolution. The signal to noise ratio is the ratio of the radiance measured to the noise created by the instrument electronics and the detector.

For on-line process analysis some additional features like the frequency of maintenance and the frequency of recalibration are important and define, among other features, the cost of ownership. Details of the calibration procedures are defined in ASTM standards. The location of the analyzer must be compatible with the safety ratings of the end user area.

1.3.5
Data Analysis and Calibration (How to Process Data and How to Calibrate)

1.3.5.1 Introduction

The basic idea of multivariate data analysis is to extract useful information from data and to transfer this information into knowledge. Figure 1.18 visualizes the methodology of multivariate data analysis to extract useful information from multidimensional data sets.

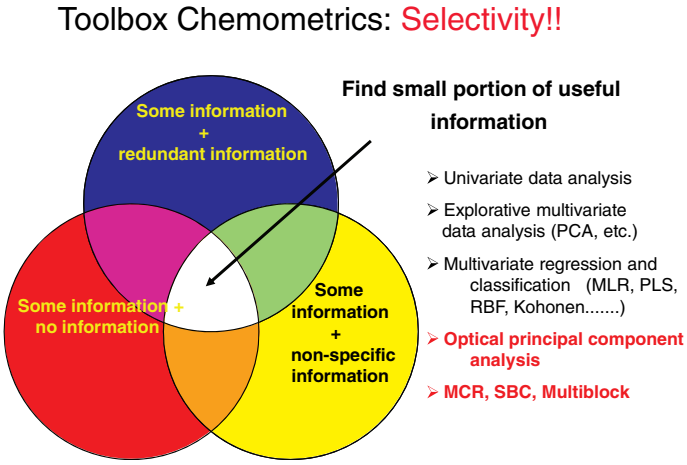

Figure 1.18 Extraction of information from a large data set.

In common data there is high redundancy of the information, overlapping with no-information (white noise) and information which is of no use for the specific problem. Besides univariate data analysis, the chemometric toolbox includes explorative data analysis like principal component analysis (PCA); multivariate regression analysis like partial least square analysis (PLS); and nonlinear approaches like neural networks. It is important to emphasize that the first step for a proper calibration and modeling is always the correct optical set-up of the spectrometer device and the appropriate definition of the measurement procedure. As will be shown later, complex systems are preferably analyzed and described by using multiple spectroscopic methods (multi-modal spectroscopy) which may be addressed as "optical principle component" analysis. Hybrid models like multivariate curve resolution (see below) or science-based calibration (SBC) allow the introduction of knowledge into the modeling.

A standard procedure to extract information and transform this information into knowledge may be:

- Standardization and calibration of the instrument
- Spectral data pretreatment
- Data cleaning
- Principal component analysis
- Regression analysis
- Evaluation and figures of merit

The procedure for standardization and calibration of the instrument was described in the previous section.

1.3.5.2 Spectral Data Pretreatments and Data Cleaning

As common in spectroscopy, the measured dark spectra, reference spectra and sample spectra are used to calculate the corrected sample spectra. Data transformation may

then involve the conversion of the raw data into, for example, absorbance. The measured diffuse reflectance spectra can be transformed to absorbance or Kubelka-Munk units in order to linearize the correlation to chemical constituent concentrations.

Changes in sample surface, sample orientation, particle size distributions, compaction of loose samples like powders and external changes in the illumination or the detector response (for instance by temperature drift) may result in unwanted spectral signals, which are added or subtracted throughout the whole spectral range. To reduce these additive effects a first and second derivative can be carried out. If the spectra are very noisy they have to be smoothed before calculating the derivatives. A detailed overview of standard pretreatment procedures and their effects on the optical spectra is given in [34].

Spectra normalization, either to length one or area one, can be a choice if the interesting information is more related to the shape of the spectral features than to changes in absorbance intensity due to concentration variations of a constituent. In such cases when classification (qualitative information) is aimed at, normalization is a very helpful pretreatment method since the spectra will become independent of their global intensity.

To correct for particle size or other scattering effects a multiplicative signal correction (MSC) can be applied [35, 36]. Several methods have been described in the scientific literature, ranging from simple MSC to more sophisticated methodologies such as extended MSC [37] and stepwise multiplicative scatter correction (PMSC) [38]. Alternatively, the standard normal variate (SNV) correction for scatter effects can be used. SNV is a simpler but purely mathematical-based procedure to correct for scatter.

In order to correct for baseline curvature or other nonlinear effects across the NIR spectral range a de-trending algorithm can be applied subsequently after an SNV transformation. Barnes *et al.* [39] have shown that MSC and SNV give more or less the same results.

1.3.5.3 **Chemometrics**

Chemometrics offers the possibility to extract relevant information from multiple wavelengths and methods instead of using single-wavelength channels only. Additionally, chemometrics reduces this relevant information into one or a few quality defining parameters (underlying entities) by applying either multivariate classification or regression models to the data.

There has been constant development in chemometrics and a number of good reviews and useful tutorials have been published [34, 40–42]. The advent of modern computer systems in the past decades has boosted widespread use of chemometric software packages, and has also had a very positive effect on the broader distribution of mathematics-intensive spectroscopic on-line methods.

Principal component analysis is a chemometric method that decomposes a two-dimensional data Table X into a bilinear model of latent variables, the so-called principal components, according to the following expression:

$$X = TP^T + E \tag{1.1}$$

where T is the scores matrix and P^T the transposed loadings matrix. The matrix E is the residual matrix and accounts for the experimental error (noise), which is not part of the model. The principal components are calculated so that they explain as much variance of the data as possible. The first principal component captures most of the variance in the data set. This information is then removed from the data and the next principal component is calculated, which again captures the major part of the remaining variance; this procedure is continued until a pre-defined stopping criterion is met, which is based on falling below a lower limit of variance explained by an addition of another principal component. All principal components are linearly independent (orthogonal); that means there is no correlation among them and they can, therefore, serve as a new coordinate system with reduced dimensions.

A so-called loading plot shows the relative importance of the individual variables (here: absorbance at different wavelengths). It can be used to assign the spectral classification to molecular structures of the chemical components. The objects can also be represented by their scores in the new principal components space. This allows clustering and structuring the samples quantitatively.

The fact that the principal components have no correlation among each other, as they are calculated to be orthogonal, results in negative scores and loadings. This makes it often difficult to interpret the underlying chemistry. To overcome this deficiency, MCR can be applied instead, where non-negativity is one of the basic prerequisites for calculation. Such MCR methods have been introduced to image analysis only recently, with growing attention and success. More details can be found in [9, 40].

1.3.5.4 Regression Analysis

Regression The target of PCA is more explorative but it is well possible to build regression models with the PCA scores regressed on target values. This is called principal component regression (PCR). However, as in traditional spectroscopy, the most commonly used algorithm for multivariate regression is partial least squares (sometimes also called projection to latent structures). The PLS algorithm builds an inverse calibration model for the spectra X and the target value Y according to the following regression equation:

$$Y = XB \tag{1.2}$$

The matrix X contains the spectra and Y holds the corresponding target values, which are the properties to be predicted. Y can be a matrix, but especially in process control it often has only one y-variable. PLS uses latent variables, similar to the principal components in PCA, to build the calibration model. The latent variables are calculated so that they explain as much as possible of the covariance between X and Y.

The model size (number of latent variables) is determined by the internal validation data set and is checked for correctness with an external data set. The figures of merit are given as bias and root mean square error of prediction as a measure of accuracy and precision. They are calculated separately for the different data sets according to the following formulae:

$$bias = \sum_i (y_i - \hat{y}_i) \tag{1.3}$$

$$RMSEP = \sqrt{\frac{\sum_i (y_i - \hat{y}_i)^2}{n}} \tag{1.4}$$

where y_i is the reference concentration for the ith sample (given by the reference method), $\hat{y}_i$ is the predicted concentration by the calibration model and n the number of samples. When the model has been validated, it can be used to predict y values (e.g., concentration) for measured spectra.

Evaluation of the Calibration The reliability of a method includes accuracy and precision. "*Accuracy*" in testing means "closeness to the true value". Especially in biotechnology, this is hard to define because usually the relevant constituents cannot be prepared in a pure state and their spectral characteristics depend strongly on the interfering matrix material. Within a laboratory, accuracy can be established by repeated analysis. Between laboratories, accuracy can be assessed by using the mean results of collaborative studies (ring tests) among all of the laboratories belonging to the same organization. "*Precision*" in any testing means obtaining the same result every time the measurement is repeated. It includes repeatability and reproducibility. "*Reproducibility*" includes all features of the test, including sub-sampling, sample preparation and presentation to the instrument, and testing by all of the operators that are likely to be involved in the testing. It is determined by repeated analysis of the same sample, including all of the steps involved in the analytical procedure and all of the operators likely to be involved in future testing. "*Repeatability*" includes all features of the test except sub-sampling and sample preparation. It is determined by performing duplicate or replicate tests on the same sample, after sub-sampling and sample preparation, and is a test of the actual method on a single sample after sample preparation. It is important to emphasize that PLS can be misleading if it is not used with care [43, 44]. To select the correct validation technique is the key for causality (see Section 3.1).

1.3.6
Process Control (How to Control a Process)

As described in the "Guidance for Industry: Process Validation: General Principles and Practices" and other papers, process analysis provides quantitative and qualitative information about a chemical process in real time, using on-line and in-line analyzers [29, 45]:

"The information given by these systems is used to control the process. The control strategy is defined as the input material controls, process controls and monitors, and finished product tests, as appropriate, that are proposed and justified in order to ensure product quality. The control strategy will ensure the product is manufactured within the Design Space to meet all Critical Quality

Attributes and other business-driven quality attributes (e.g., that affect cost or manufacturability)".

Process control is important for economic, safety and environmental reasons. Improved process control allows more efficient use of feedstock and energy, giving better product quality and ensuring consistency of quality. It also enables improved treatment of waste products and effluent to meet continually more stringent environmental legislation.

The key to good process control lies in the ability to measure fluctuations in the system behavior (e.g., changes in feedstock composition or temperature build-up). This information is then used to compensate for these changes and to optimize process parameters. How representative measurements are of a system, how long the interpretation of the data takes and how quickly this information can be acted on, are important factors of process control.

In this section, the strategy of a modern manufacturing using feed-back and feed-forward control is described. Figure 1.19 visualizes the strategy for process control and how to manage variability.

Process control summarizes all measures to keep quality within certain limits. *On-line statistical process control* involves actions to monitor deviations from a desired state while the process is actually running and manufacturing takes place. Hence, in order to be able to react promptly in response to observed deviations, real-time monitoring techniques are advantageously employed. Even when a process is well designed, statistical process control measures are always useful, since they allow one to detect and act upon unforeseen effects of immediate or abrupt changes in the process

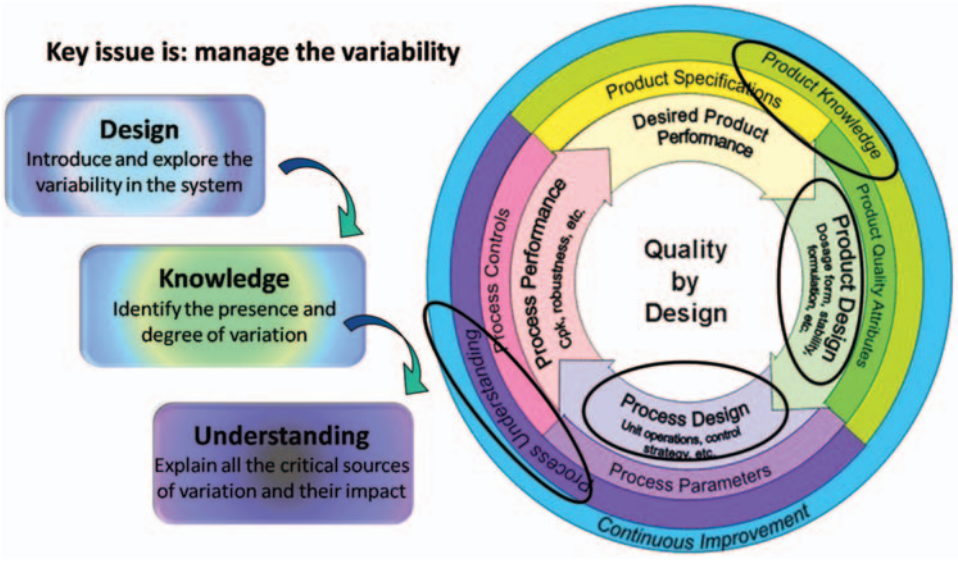

Figure 1.19 Managing variability (modified after FDA).

conditions, and to correct the process for statistical variations that occur, for instance, in the raw material, which is always likely to happen. Moreover, processes when first implemented are usually not yet optimized with regard to the highest possible level of quality they might produce; on-line statistical process control may well assist in such optimization and continuous improvement. Regarding the information that is used for statistical process control, laboratory data or process data may be used. *Laboratory data* typically comprise physical or chemical tests performed on the incoming raw material to control the input quality, or technological tests for the application behavior of the final products to control the output quality. Especially in the early phases of industrial manufacturing, this was the main mode of controlling the overall performance of a process, the major indicator of process quality being the amount of waste production or sorted-out parts (Figure 1.2). Regarding process-related data two different types of *process data* are available: the first includes machine data, which are accessible by recording parameter settings of the machine equipment, or general, unspecific process data, like temperature, pH or conductivity, which may be recorded by various sensors throughout the whole course of the production. The second type includes quality influencing, material specific data which are directly related to and measured on the produced goods by means of process analytical methods which are applied at numerous intermediate product stages. Traditional laboratory data alone, especially when only applied as end-of-pipeline tests of product performance, only allow *feed-back control* loops, that is, after having detected that a fraction of the final

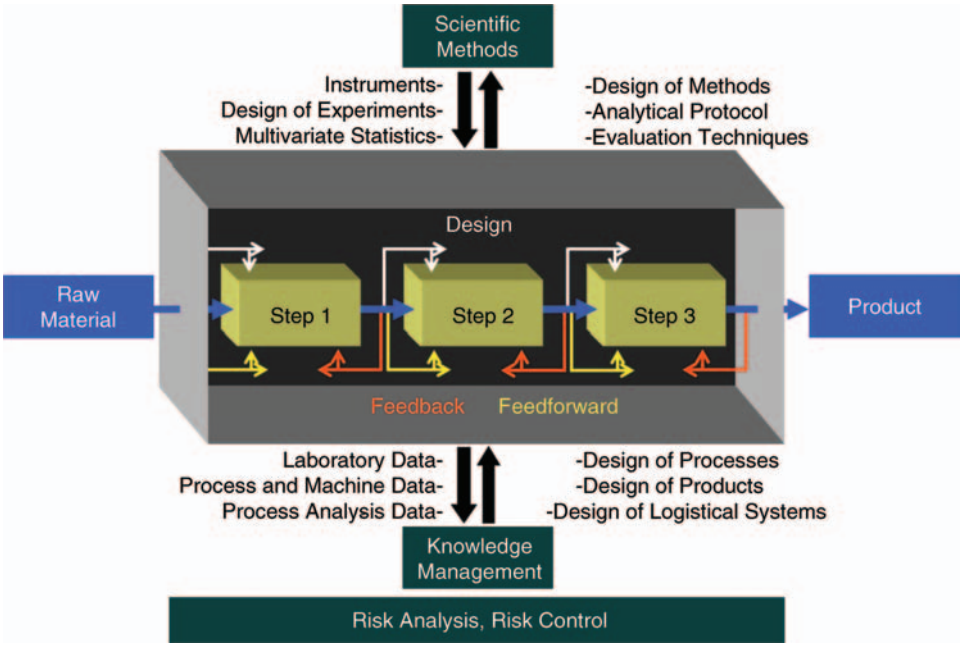

Figure 1.20 Process control by feed-back and feed-forward control requires a holistic view of the process and the trans-disciplinary interplay of numerous techniques and methods [46].

product is unusable and must either be downgraded or even discarded, the process is modified until subsequent batches may again be within specifications. In contrast, process data (in combination with a causal understanding of the overall process) may more intelligently be used in so-called *feed-forward control* loops which allow anticipation of product properties before they have actually manifested. In this way, correcting measures may be undertaken in advance in the case of expected negative deviations and inferior or waste production may be totally avoided. Figure 1.20 (adapted from [46]) summarizes these concepts schematically.

1.4
Specific Problems Encountered in Industrial Process Analytics

In this section, selected process analytical problems that are of crucial importance to many applications throughout various branches of industry are addressed. Since they are often encountered in an industrial environment, this section is dedicated to principle problem solutions that deal with moisture determination, the process analytics of solids and surfaces, strongly scattering systems, and the spatially resolved spectroscopy of samples using spectral imaging.

1.4.1
Moisture Measurements (NIR, MW)

Moisture is an important quantity which influences processability and shelf-life. Moreover, delivering a product of defined moisture content not only saves energy but also increases profit. Off-line moisture measurements are time-consuming and cannot be used for a feed-back or a feed-forward control in manufacturing. Therefore, there is a strong demand in industry for on-line and in-line control of water in a substrate [47].

1.4.1.1 NIR Spectroscopy

As described in the previous chapter, MIR and NIR spectroscopy show strong absorption for water and, therefore, can be used for in-line analysis of moisture content. NIR spectroscopy is based on measurements of light absorbed by the sample when it is exposed to electromagnetic radiation in the range from 780 nm (12 820 cm^{-1}) (short-NIR, s-NIR) to 2500 nm (4000 cm^{-1}) (NIR). As described in the previous chapter, water absorption in the NIR occurs mainly at wavelengths around 1445 and 1900 nm (Figure 1.21).

There are numerous investigations which deal with the determination of surface water and intrinsic water (bulk water). To separate these two kinds of water spectroscopically, it is generally postulated that surface water predominantly absorbs around 1900–1906 nm and intrinsic water, respectively bound water, at 1936 nm. However, bands in the NIR are broad and, in most cases, spectrometers were used which were limited in their optical resolution. Thus care must be taken to interpret spectra obtained from measurements on real life components.

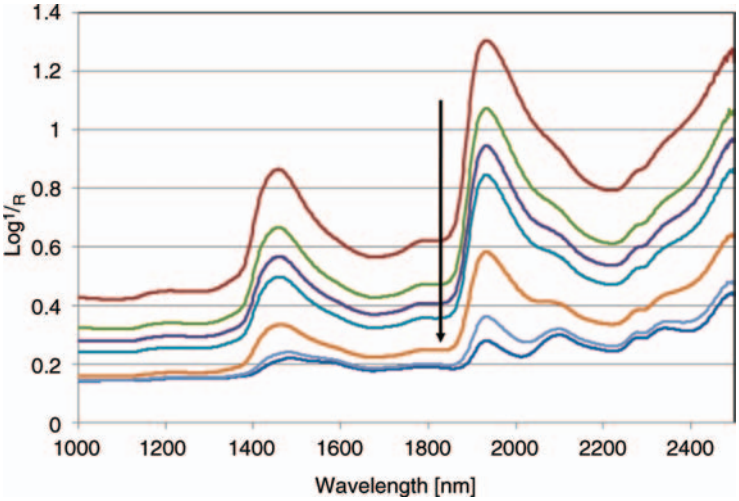

Figure 1.21 NIR spectra showing the typical absorbance pattern of water with maxima at 1450 and 1950 nm. The spectra show the evaporation of water from cellulose-based filter paper during drying. Measurements were performed with a Lambda 1050 NIR spectrometer (Perkin Elmer) in diffuse reflectance using an integrating sphere (150 mm).

Furthermore, as described in the next chapters, the cross sections for absorption, and also for scattering, are usually in a range of low penetration depths of photons. At strong absorptions in the NIR (e.g., combination vibration), penetration and, hence, information depth may, therefore, be only a few hundred microns or even less; in the third overtone of water (s-NIR), penetration into the substrate may go up to several millimeters. Therefore, the measurement of moisture using NIR combination bands is usually restricted to the determination of surface water. The typically used reference measurement techniques for calibration of the spectroscopic signal, such as Karl Fischer titration or gravimetric methods ("loss on drying"), however, determine the overall bulk moisture content, which does not necessarily correlate to the surface moisture that is measured by NIR spectroscopy. Hence, calibration of NIR spectra may be erroneous. Moreover, NIR spectra often also contain spectral contributions from other components which may overlap with water peaks. To make things even more complicated, signals may also be perturbed by scattering due to particles of different (and unknown) size distribution, resulting in nonlinear mean free path length variations of the photons. In multivariate calibrations, SNV, MSC or EMSC have been successfully used to eliminate baseline offsets present in the raw spectra and can compensate for differences in thickness and light scattering of the analyzed samples.

1.4.1.2 **Microwave Resonance Technique (MWR)**

In the case of microwave resonance (MWR) measurements the specific absorption of water in the microwave wavelength range of 2–3 GHz is used. Sensors are designed from cavity resonators or stray field resonators. The penetration depth of the microwaves is in the several-cm range and, therefore, bulk moisture measurements

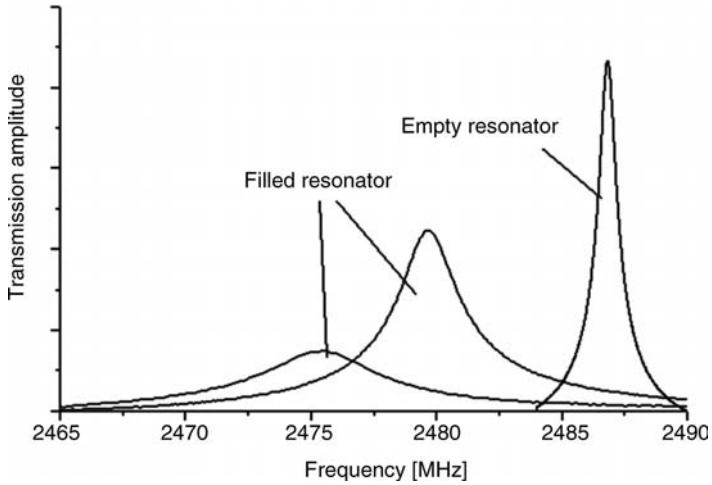

Figure 1.22 Microwave spectra of an empty and filled resonator.

can easily be correlated. Figure 1.22 shows an example of the microwave spectrum of an empty resonator and a resonator filled with a substrate.

Usually, the spectrum of the empty resonator is stable and can be used as an "absolute" reference which is specific for a given system and system set-up under certain temperature-controlled conditions. When a moisture-containing substrate is measured (surface and bulk), the spectrum of the empty resonator changes in two ways: First, the resonance spectrum shifts towards lower frequencies due to the dielectric losses and, secondly the spectral bandwidth increases in response to the density, respectively, the mass of the substrate. This information can be used to compensate for fluctuations of the measured path lengths due to particle size variations or other density changes (like, for instance, compaction) during on-line measurements. Hence, besides being a very precise and reproducible measurement method for moisture content, MWR also allows mass or density determination of the bulk material which is corrected for the moisture content (dry mass determination). Being a very rapid measurement method, the MWR technique allows up to 500 single measurements per second of powders, granules, fibers and even solids. This allows easy averaging of the spectral information. Unlike other dielectric techniques, such as capacitive techniques, conductivity measurements or microwave transmission measurements, unperturbed information is obtained, even in cases where substrates are used that contain high amounts of ionic material. Numerous applications can be found in the literature for food and feed control [48, 49]. Figure 1.23 shows examples for the set-up of on-line measurements in the food industry.

1.4.2
Process Analytics of Solids and Surfaces: Specular and Diffuse Reflectance

In real-life samples of solids or surfaces, reflectance spectra are composed of contributions from specular and diffuse reflected light. Pharmaceutical tablets show

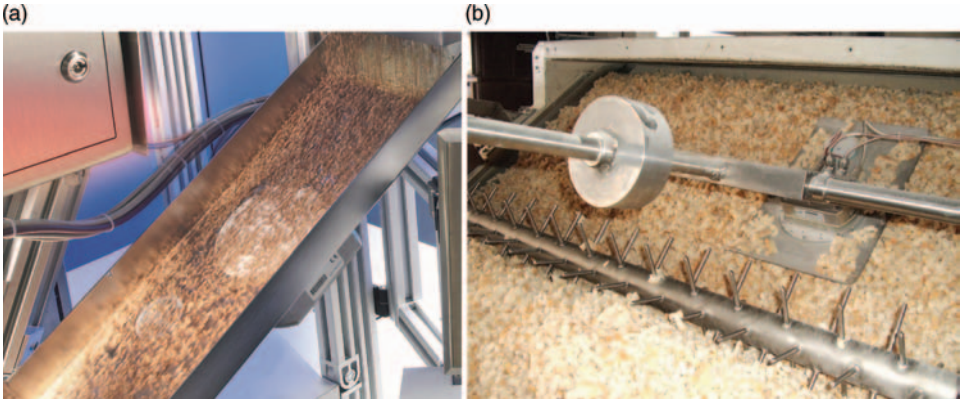

Figure 1.23 On-line control of wheat grains by a microwave stray field sensor (a) and a slide sensor measuring moisture of bread crumbs (b), (courtesy of Sartorius).

primarily diffuse reflectance but, due to different degrees of compaction, specular surface reflectance is also observed. Decisive changes in the scattering coefficient occur during compaction and relaxation and have a great impact on the measured signal. Metal surfaces, on the other hand, exhibit mainly specular reflectance and interference; however, they may also show some diffuse reflectance due to defects within the layer, surface roughness, or contaminants on the surface. In a more complex system like wood chips, on-line control allows correlation of the spectral signature not only to a single target value like lignin, but to a complex quality definition like functionality.

The Fresnel equations are the basis for the calculation and interpretation of the portion of light which is specular reflected from optically smooth surfaces and consists of wavelengths that are comparable to those of the incident light. Diffuse scattering originates from surface irregularities that are of the same order of magnitude (or slightly smaller) as the wavelength of the irradiating light source, as shown schematically in Figure 1.24. Diffuse reflected light is described by the

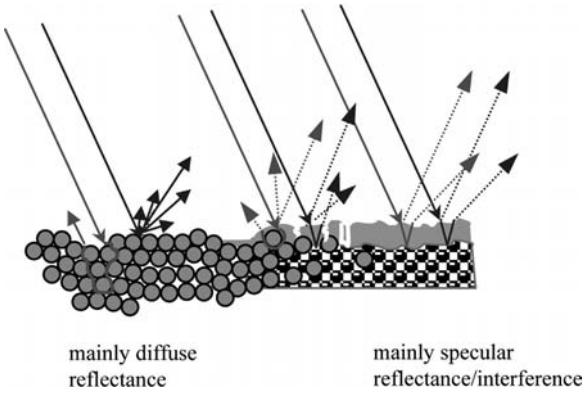

Figure 1.24 Specular and diffuse reflectance of a real-life sample surface [50].

Kubelka Munk function [50]. In this case, diffuse reflectance is influenced by both the absorption and scattering coefficients, which are usually denoted as k and s. In an ideal case, the absorption coefficient k and the scattering coefficient s can be separated by the measurement of a sample with defined thickness in diffuse reflectance on a highly scattering white or black background, or by means of diffuse transmission and reflectance spectroscopy [50].

In real-life samples, specular and diffuse reflectance contribute simultaneously to the overall spectrum, which is then a mixture of both effects. A detailed mathematical description of the resulting solutions of the Fresnel and Kubelka Munk function is given in [51].

The ideal experimental set-up would be to measure the reflectance by means of an integrating sphere. But integrating spheres are not suitable for in-line or on-line control. Moreover, the analytical deconvolution of the spectral information into the contributions of the pure specular and diffuse components is not a simple task. Thus, efforts must be made to focus the measurement on either diffuse reflectance or specular reflectance in order to optimize the response, depending on the required physical or chemical information.

An even stronger discrimination between diffuse and specular reflectance is feasible using polarized light. Polarized light is depolarized by scatter centers and therewith the information on defect sites is emphasized.

A specific target of the PAT initiative of the Food and Drug Administration of the United States of America is to identify and quantify an active pharmaceutical ingredient (API) in a complex formulation. Thus a direct relation between the measured spectrum and the concentration of the API must be established at high precision. The objectives of on-line control are, therefore, a fast and robust noninvasive measurement protocol which is not perturbed by artefacts. Pharmaceutical tablets are made from small particles which can act as ideal scatter centers for diffuse reflectance. Spectra, therefore, simultaneously show (i) wavelength-dependent scattering, and (ii) specific absorption due to their chemical composition. Since the process of tablet formation leads to a smooth surface after compaction, the tablets additionally exhibit specular reflectance which perturbs the diffuse reflectance measurement. For on-line control, the amount of specular reflected light being transmitted to the detector should be minimized. A possible set-up to bring this about is the diffuse illumination of the sample and a detection perpendicular to the illuminated surface. Alternatively, the illumination can be performed at an angle of 45° while the detection of the diffuse reflected light is again done at an angle of 90° to the surface (assignment: 45R0). A detailed description is given in [52].

1.4.3
Working in Multiple Scattering Systems: Separating Scatter from Absorbance

1.4.3.1 Basics in the Measurement of Opaque Systems

In scattering systems, the interaction of light (photons) is complex and includes refraction, specular and diffuse reflectance and/or transmission, as well as absorption and scattering simultaneously. Due to the diffusion of photons, even the spatial

identification and attribution to a defined spatial coordinate in x and y may diminish. Hence, the spectroscopic investigation of samples that contain phase boundaries and, therefore, simultaneously display absorption and scattering effects show several restrictions regarding the experimental procedure (methodological approach) and the substrate:

Methodological influences

- Angle of illumination and detection (specular and diffuse light)
- Wavelength range: for example, UV–VIS–NIR–IR
- Polarization of the light (illumination and detection)
- Illumination and detection area
- Focal planes of illumination and detection

Substrate influences

- Differences in particle and matrix refractive indices
- Particle size
- Particle size distribution
- Volume concentration – compaction
- Scattering and absorption coefficients

Figure 1.25 shows schematically the different effects occurring when photons interact with an opaque substrate.

Particles produce scattered light. The intensity of the scattered light is dependent on the size of the particle and the wavelength of the interacting photons. Smaller particles show higher scatter and light of shorter wavelengths is more strongly scattered than light of longer wavelengths. This results in a difference in mean free path lengths and penetration depths of the photons. In combination with absorption phenomena, the overall spectral response will be significantly different when the same sample is measured in diffuse reflectance or in diffuse transmission. Also, the thickness of the measured sample will have a strong influence on the obtained spectra due to photon loss at the rear side of the sample. These photons cannot be

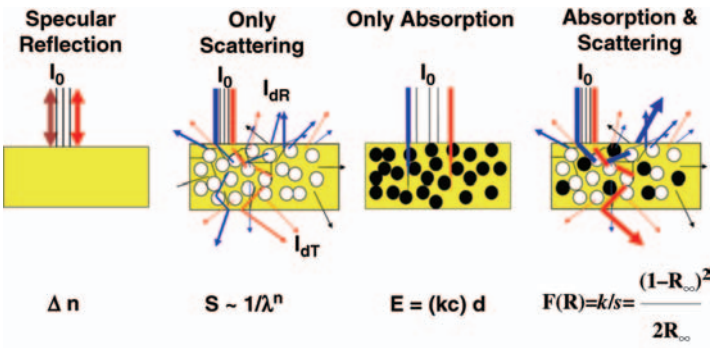

Figure 1.25 Schematic representation of the different possibilities for the interaction of photons with opaque systems.

scattered back again as in the case of infinite sample thickness. Thus, the geometrical set-up of the measurement is an important factor and changes in particle sizes and size distribution must be compensated during calibration.

It is also important to emphasize that scattering also changes the direction of the photons. Theoretical calculations have shown that the travel distance of the photon may even be expressed in millimeters and more. Therefore, in highly scattering systems, information from one spatial region may be influenced by information from another region, resulting in a mixing of the spatially separated spectral information. As a result, there is a trade-off between spatial resolution and chemical (quantitative) information [6].

1.4.3.2 Separation of Scatter from Absorption

In many chemical, pharmaceutical and biotechnological processes not only the chemical changes are of importance but also the morphological variation of the particulates. When spectroscopic in-line control is applied to such complex systems very often the scatter in the spectra is regarded as unwanted and, therefore, eliminated by chemometric methods instead of using it as a supplementary source of information on the morphology of the substrate. One of the most appropriate theories to describe multiple scattering and absorption is the radiative transfer equation (RTE). A summary of RTE is given in [53]. A survey of the different techniques is described in [54].

Using this equation, three separate and independent measurements are necessary to separate scatter from absorption. Kortüm [50] and coworkers have demonstrated extensively the power of diffuse reflectance spectroscopy in quantitative measurements of turbid systems. The simplest approach is to use the Kubelka Munk (KM) function, where $F_{(R\infty)}$ describes the reflectance of an optically infinitely thick sample.

Linearity between the spectral response and concentration is only obtained (i) with a specific optical set-up for diffuse illumination and (ii) when a defined preparation procedure of the samples is used with special consideration for reproducible grinding and dilution of the sample with powders that do not absorb. In practice, the alternative $\log 1/R_\infty$, that is called "absorbance", prevails over $F_{(R\infty)}$ of the KM function in most publications. The KM function is shown in Eq. (1.5). Here K stands for absorption and S for scattering

$$E(R_\infty) = \frac{K}{S} = \frac{(1-R_\infty)^2}{2R_\infty} \tag{1.5}$$

Several models exist to determine the wavelength-dependent scattering and absorption coefficients in diffuse reflectance and diffuse transmission spectroscopy [19]. K and S can be calculated for example, from the simplified solution of the differential equations of the Kubelka Munk function of a light flux into and from the sample. Eqs. (1.6) and (1.7) describe the relation between S and K with the measurements of a sample in diffuse reflectance.

$$S = \frac{2.303}{d} \cdot \frac{R_\infty}{1-R_\infty^2} \cdot \log\left(\frac{R_\infty(1-R_\infty \cdot R_0)}{R_\infty - R_0}\right) \tag{1.6}$$

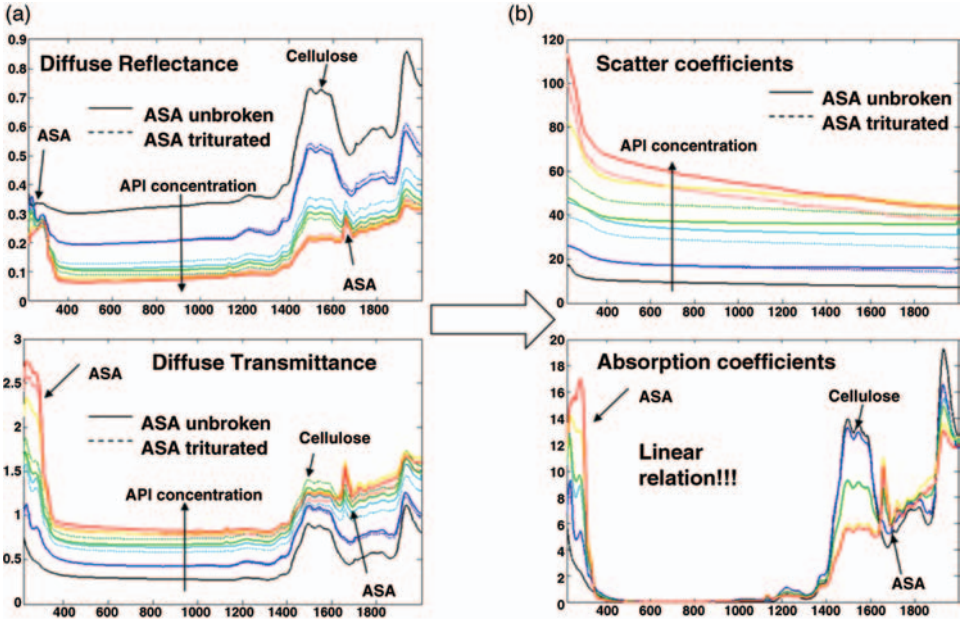

Figure 1.26 Diffuse reflectance and diffuse transmittance spectra of Aspirin in cellulose (a) and calculated wavelength-dependent scatter and "pure" absorption spectra (b) [52].

$$K = \frac{2.303}{2 \cdot d} \cdot \frac{1 - R_\infty}{1 + R_\infty} \cdot \log\left(\frac{R_\infty(1 - R_\infty \cdot R_0)}{R_\infty - R_0}\right) \tag{1.7}$$

Here, R_0 denotes the spectrum measured at a definite sample thickness with a black, strongly absorbing background and R_∞ denotes the measurement of the same sample with an ideal white scatter (= nonabsorbing material for example, barium sulfate) as a background. Other approaches are described by Oelkrug, Dahm and Dahm [55, 56].

Figure 1.26 shows the result of a spectrum where the contributions of scatter and absorption have been separated. For demonstration, an aspirin tablet with cellulose as excipient is measured at different compactions in diffuse reflectance with infinite and definite thickness. For details see [6, 9, 52].

As can be seen clearly, the absorption portion of the spectrum in the longer wavelength region containing chemical information is slightly perturbed by scatter, whereas in the shorter wavelength range, scatter is the dominating information source on the morphology of the sample.

This deconvolution can also be used with advantage in chemical imaging. Figure 1.27 shows the image of an aspirin (ASS) tablet as measured at the specific absorption wavelength of ASS in diffuse transmission and diffuse reflectance. The S and K values were calculated at the specified wavelengths.

The figure shows nicely that the same particle of ASS shows different regions of absorption depending on the geometrical set-up of the measurement and the used

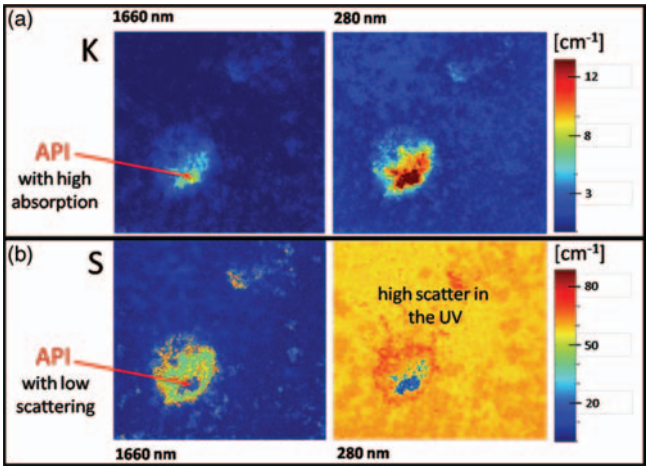

Figure 1.27 Spectral imaging of an aspirin particle in cellulose: (a) "pure" absorption of the aspirin at different wavelengths, (b) "pure" scatter of the particle at different wavelengths (for more details, see [52].

wavelength. UV absorption is significantly stronger than the absorption in the NIR range. This is also true for the scattering, which at lower wavelengths is much stronger than in NIR. It can also be seen that scattering is especially strong at the phase boundaries of the particle.

Figures 1.26 and 1.27 clearly show that the overall spectrum is the superposition of the contributions of absorption and scattering effects. Therefore, the mean free path lengths of a photon into and through a tablet will depend on the number of scattering centers and the scattering characteristics of the particles. The probability of interaction of the photon, and thus the signal intensity, also depends on the portion of photons that is absorbed during their motion through the particulate system. Certainly, the measured intensity also depends on the layer thickness since photons are lost by transmission when the layers are of finite thickness. In theory, if a photon is not absorbed it will travel for an infinite distance within the particulate system.

1.4.3.3 Optical Penetration Depth

The optical penetration can be defined as the depth δ, at which the intensity of the radiation inside the material I falls to 1/e (about 37%) of the value of the incident beam, I_0. For a semi-infinite medium, in the range of validity of the K-M theory, the intensity at a distance z from the surface can be approximated[2)] as:

$$\delta = \frac{1}{\sqrt{K(K+2S)}} \tag{1.8}$$

2) D. Oelkrug, B. Boldrini, and R. W. Kessler, unpublished results.

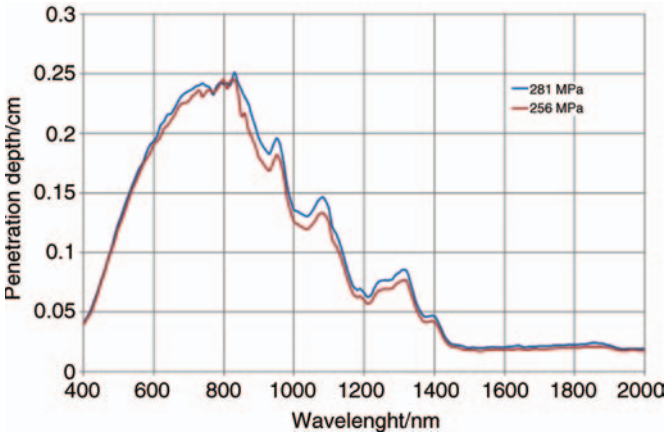

Figure 1.28 Penetration spectrum for the theophyllin tablet in cellactose at different degrees of compaction.

This is a generalized form of the penetration depth integrating absorption and scattering. Details will be described elsewhere.

Figure 1.28 shows the result of a calculated penetration spectrum of the theophyllin tablet example shown in Figure 1.4 at two different compactions. Because of the high absorbance at longer wavelengths the penetration depth is low. On the other hand, due to the strong absorption, the spatial resolution at higher wavelengths may be higher because the number of scattered photons is lower and specular reflectance has a lower probability. In the short NIR range (below 1100 nm), high penetration takes place, mainly due to the low absorption and mean scattering properties of the sample. As demonstrated, the penetration depth and, therefore, the scale of scrutiny can be determined, when the scatter and absorption coefficients are known. Similar approaches with similar results are described in [53, 57].

A much simpler approach is described in [58, 59]. Here the spectral response of an absorber is measured when this absorber is covered with different layers of scattering particles. The description of the determined path length is, however, strongly dependent on the geometrical set-up of the system, the sensitivity of the instrument and the properties of the particulates and, therefore, cannot be generalized.

1.4.4
Spectral Imaging and Multipoint Spectroscopy

Spectral or chemical imaging combines the physical and chemical characterization of samples by spatially resolved spectroscopy. The techniques may either be classified according to the used wavelength ranges or, more generally, into mapping or imaging techniques. *Mapping* usually means to get an image by exploiting the full spectrum (λ) of a local point through point measurements (at spatial x and y coordinates). The term *imaging* is used, when two-dimensional pictures (x, y) are obtained by a camera

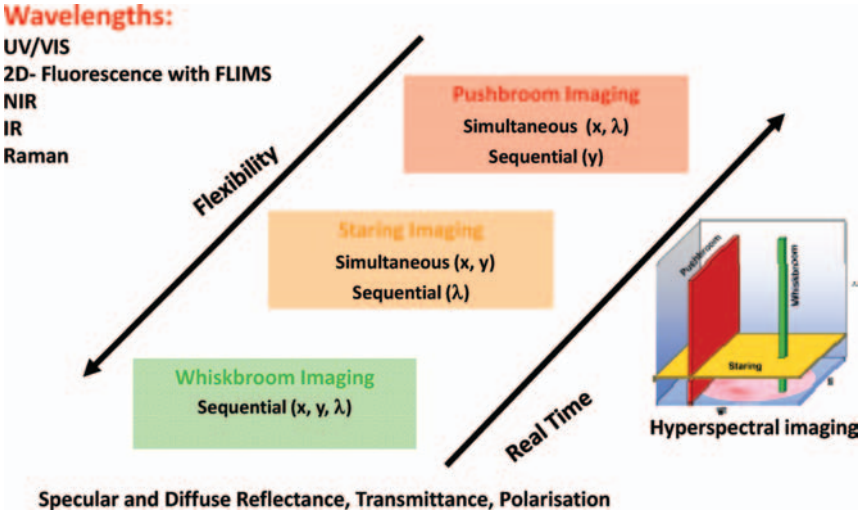

Figure 1.29 Visualization of the different imaging technologies: whiskbroom imaging, staring imaging, pushbroom imaging.

at different wavelengths (λ). In addition, *line scans* are defined as measured spectra along a line [60]. A more straightforward taxonomy is used in remote sensing. The different applied technologies are labeled as:

- Whiskbroom imaging
- Staring ("stardown") imaging
- Pushbroom imaging

Figure 1.29 visualizes the different techniques. All techniques can use the full optical wavelength range from the UV to the IR as well as Raman and fluorescence.

In process control, the spectroscopic method is often applied to moving samples and, therefore, should be as fast as possible. Hence, in this case the pushbroom acquisition mode is usually the best suited technique. Along a line of the sample, which represents the first spatial direction (x-axis), several spectra are measured at the same time. The pixel spatial resolution of this x-axis is determined by the number of pixels used and the distance of the sample from the spectrometer objective lens. The pixel resolution of the spectral λ-direction (z-axis,) is determined by the spectral range of the spectrometer (camera) and the number of pixels that are combined together to yield one spectrum. The second spatial dimension (y-axis) is correlated with time. If the sample is moved before the next line-scan starts, the time and the second spatial dimension on the sample (y-axis) are correlated to the moving speed of the sample. The data cube of the measurement thus represents the two spatial axes and the wavelength axis.

Figure 1.30 shows an example of the data cube of a hyperspectral image of a wood chip on which the letters RRI (Reutlingen Research Institute) are written with a UF (urea formaldehyde) resin binder that is commonly used in the production of

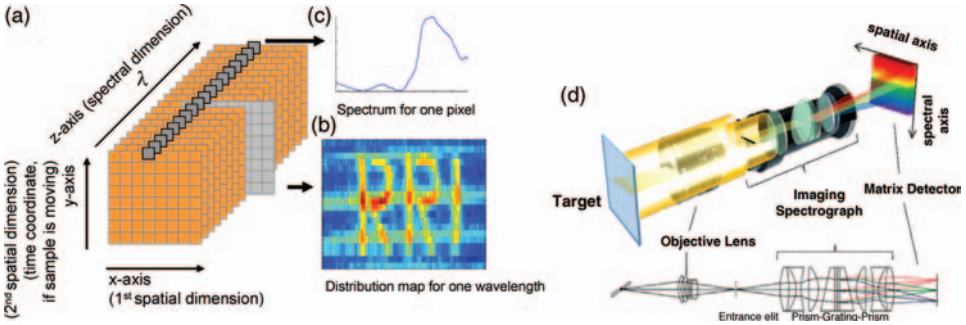

Figure 1.30 left: Sketch of three-dimensional hypercube (a) and distribution map for one selected wavelength $\lambda = 1506$ nm (b) and one spectrum along the spectral direction for one pixel $x = 90$, $y = 10$ (c). (d) Schematic drawing of a pushbroom imager (courtesy of Specim, Finland).

oriented strand boards (OSB). The objective of the chemometric treatment is to separate the information "wood chip" from the information "binder" and is intended finally to determine the thickness of the binder layer. A hyperspectral image was recorded for this sample with a pushbroom imager from Specim Finland. The first spatial resolution (x-axis) contains 180 pixels and each pixel represents 0.1 mm on the sample. For the second spatial direction (y-axis) 20 line-scans were performed after positioning the sample on a conveyer belt another 0.5 mm further in the y-direction from the starting position. This means 20 pixels for this y-direction with a spatial pixel resolution of 0.5 mm. The chemical information for each pixel is contained in 214 NIR absorption values in the wavelength range from 900 to 1700 nm (spectral pixel resolution is 3.7-nm). The resulting three-dimensional data cube ($180 \times 20 \times 214$) is sketched in Figure 1.30 together with a distribution map for one selected wavelength (1506 nm) and one spectrum along the spectral direction for pixel $x = 90$, $y = 10$. The full hyperspectral image has ($180 \times 20 = 3600$) spectra with 214 spectral readings in each spectrum.

To get the full chemical information out of the hyperspectral image it is necessary to look at the full spectral information contained in the image. This can be done by applying multivariate data analysis methodologies to extract the relevant information and at the same time reduce the dimensionality of the data. For images it is called multivariate image analysis (MIA) and for a qualitative analysis it is very often linked to principal component analysis (PCA). If a quantitative value for a quality or process parameter is required it is called multivariate image regression (MIR) and is mostly related to the partial least squares algorithms (PLS) [61].

When an optical fiber bundle is coupled to a pushbroom imager, multi-point spectroscopy at different locations in a reactor will be possible. These fibers can, however, also be coupled to various probes, thereby enabling simultaneous measurements like reflection, transmission or ATR measurements (see Section 6.2).

Pushbroom imaging technology is, for example, used to identify plastics in waste management systems. Figure 1.31 shows an example of a commercial application in separation of the different polymers automatically on a conveyor belt.

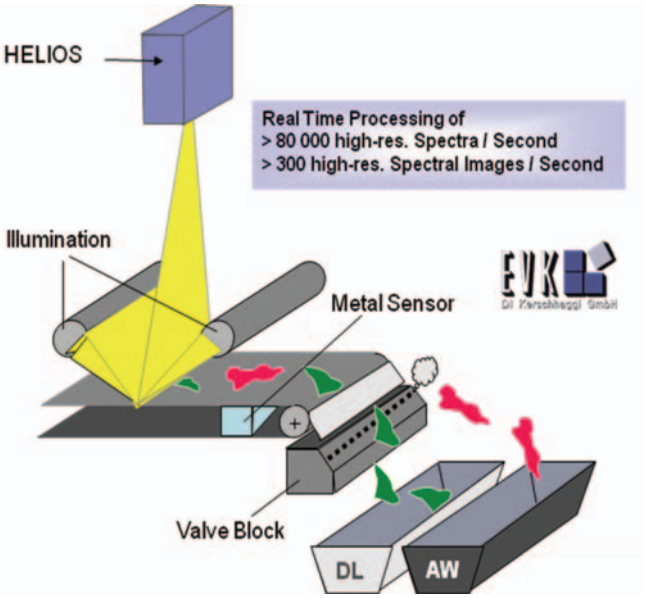

Figure 1.31 Real time characterization of polymers in plastic waste separation (courtesy of EVK company).

1.5
Survey Through Industrial Applications

1.5.1
Selection of Applications

This short survey through selected industrial applications of process analytical technology in the industry should illustrate the potential and widespread use that such methods already experience in the current industrial landscape. It should stimulate interest in potential problem solutions and with several thousand publications on the subject only in the course of the last five years is by far not intended to be comprehensive.

The objective of this section is to give also a short overview of the different applications of hyperspectral imaging in industry and science. It should provide some ideas on the heritage of information which is gained from hyperspectral images. Historically, the pharmaceutical industry uses mainly staring imaging technology, whereas food and agriculture is more focused on pushbroom imaging technology due to its background in remote sensing. Whiskbroom imaging technology will not be included in the selected applications as this technique is more restricted to scientific interests [62].

It is by far beyond the scope of this chapter to mention all relevant techniques and methods in detail, in the following sections only a brief summary of important applications of the various optical spectroscopic techniques is given. For an in-depth

summary of new developments in PAT the reader is referred to the review articles on process analytical chemistry by Workman and coworkers, for instance Refs [2, 63] which are published every couple of years and reflect the most important new developments in the field. Recent accounts of the state of the art of process analytical technology are also to be found, for example, in [6, 33, 64, 65].

1.5.2 Pharmaceutical Industry

The most important applications of process analytical technology in the pharmaceutical industry cover on-line measurements in raw material control, reaction monitoring and control, crystallization monitoring and control, drying, milling, cleaning validation, granulation and blending, drug polymorphism detection, particle size, moisture content determination, and tablet analysis, as well as packaging.

1.5.2.1 UV/Vis Spectroscopy

Spectroscopic analysis in the pharmaceutical industry is very often concerned with the analysis of drug formulations such as tablets. For instance, dissolution testing of tablets is mandatory and there exist guidelines of how to perform these tests. Diode-array spectrometer-based UV/Vis techniques can be employed in this context to monitor the dissolution behavior of tablets [66]. Another important application of UV/Vis spectroscopy is the controlling of cleaning operations. The cleanliness of vessels intended for pharmaceuticals, beverage or food production has to be guaranteed when production shifts from one batch to another with an intermittent cleaning step. Fiber-optic UV/Vis spectrometers have been used for this purpose. UV/Vis spectroscopy has also been used to determine the active ingredients content in tablets, for example paracetamol, ibuprofen, and caffeine [67].

1.5.2.2 NIR Spectroscopy

NIR spectroscopy is an established measurement technology that has been employed for several decades under *in situ* conditions. In comparison to the chemical industry, the diversity of industrial operations is much smaller. Hence, a number of standard applications of NIR spectroscopy have been developed that are established and widely used by numerous pharmaceutical companies. Typical standard applications are, for example, the NIR spectroscopic control of raw material identity by using fingerprint analysis of the incoming substances, the NIR monitoring of mixing processes, the NIR monitoring of granulation, or the NIR analysis of tablet formation and compaction. While raw material control in many cases is accomplished by laboratory equipment, in-process applications are of importance, especially in the control of the granulation process. An important target signal here is the time-dependent moisture content of the aggregate in the course of particle compaction. Besides monitoring the kinetics of the granulate water content, the kinetics of changes in the particle size distribution can be determined [68]. NIR spectroscopy is also used in the characterization of the mixture homogeneity of powder preparations. Here, two major strategies have been followed: (i) on-line NIR monitoring of the mixing process [69–72] by implementing either

stationary or moving NIR-probes directly in the mixing machinery, and (ii) imaging approaches, which will be described below. In the NIR spectroscopic analysis of tablets, the recent development of very rapid measurement devices based on diode array spectrometers allows 100% control of all manufactured tablets [73, 74], which represents an important step forward from random sampling. A typical problem in tablet manufacturing is not only the absolute amount of active ingredient but also its distribution within the particular formulation. While chromatographic analysis upon homogenization of the tablet by dissolution reveals the actual overall content of the drug in the tablet, the information generated by spectroscopic measurements is more complicated to unravel. Since NIR spectroscopy of tablets is typically carried out in diffuse reflectance the simultaneous contributions of scattering and absorption phenomena have to be considered and the arguments presented in Section 4.3 need to taken into account. Besides photon diffusion spectroscopy, here, too, imaging methods will play an increasingly important role in process analysis. Besides the active ingredient content and its distribution, in the automated analysis and quality control of tablets, physical parameters such as mass, diameter, thickness and hardness of the tablets are targeted [75, 76]. More examples on the application of NIR spectroscopy in combination with chemometric techniques can be found in the recently published review by Roggo [77] and in [78].

1.5.2.3 **Raman Spectroscopy**

Since interpretation of Raman bands is much more straightforward than qualitative interpretation of NIR bands and, hence, with Raman less chemometric effort is required, information deduction from Raman spectroscopy provides great potential also for the pharmaceutical industry. Monitoring of pharmaceutical blend homogeneity has been successfully accomplished using Raman based on a calibration-free approach by mean square difference between two sequential spectra; see, for example, [79]. In this study it was demonstrated that particle size and mixing speed significantly influence the time required to obtain homogenous mixing. Raman spectroscopy has also been used to follow the kinetics of polymorph conversion from one form to another [80]. Automated analysis of micro-titer plates can also be performed using Raman spectroscopy. Since it is possible to distinguish between crystal forms Raman spectroscopy has been suggested as a tool for high-throughput screening for different crystal structures [81]. Raman spectroscopy can also be used in combination with NIR data to determine correlations between physical pharmaceutical properties of tablets, such as hardness, porosity, and crushing strength [82]. Among others, the review published by Barnes [83] summarizes more recent examples of the application of Raman spectroscopy in the monitoring of pharmaceutical processes.

1.5.2.4 **Imaging Techniques**

There are still only a limited number of real life on-line applications for chemical imaging in process control in the pharmaceutical industry. Exhaustive reviews of different applications can be found in [33, 84]. Focus is mainly on three different uses: blend uniformity of powders and tablets, composition and morphological features of

coated tablets and granules, spatial changes during hydration, degradation and active release.

Pharmaceutical solid dosage forms are ideally suited for NIR chemical imaging. The systems are chemically complex and the distribution of the components affects dramatically the product quality and performance [85]. Recently, Lewis and coworkers compared wet granulation, direct compression and direct compression together with a micronized API. Besides the evaluation of the homogeneity of the mixing, they could also qualify the appearance and the morphology of API hot spots and agglomeration [86]. It is also possible to relate this information to the performance of the final product [87].

In another work, the utility of NIR chemical imaging in measuring density variations within compacts is demonstrated. The data are also used to relate these variations to tableting forces which are controlled by frictional properties and the quantity of the Mg stearate concentration during production [88]. This is possible as the spectral information also includes the percentage of specular reflected light at the surface of the tablet and the change in penetration depth of the photons which change after compaction.

Counterfeit pharmaceutical products are a real threat to the health of patients. NIR chemical imaging provides a rapid method for detecting and comparing suspected counterfeit products without sample preparation. The advantage of imaging is that the discrimination of the tablets is not only caused by changes in the chemical composition, but also from its spatial distribution. This reflects the use of different raw materials as well as the distribution of the components in the tablet which depends strongly on processing conditions [89]. Thus the combined chemical and morphological information provides an individual measure for the characterization of tablets.

Applications of chemical imaging in the pharmaceutical industry are mainly related to NIR imaging. Some papers describe also the use of terahertz imaging. Terahertz is ideally suited to the identification of chemical components with strong phonon bands, thus components with high crystallinity can easily be distinguished from amorphous systems [90].

1.5.3
Food and Agriculture

Spectroscopic quality monitoring, and especially NIR spectroscopy, has a very long tradition in the food and agricultural industries. The main areas of application here regard the quality control of raw materials, intermediate products and final products. Many different sample types have to be dealt with, as reflected by the vast diversity of possible food stuff, ranging from liquids, powders, slurries to solid materials. One major problem often encountered in the application of NIR in food technology is the preparation of appropriate reference materials – soft matter such as food usually is connected with complex and varying matrix systems. Typical applications include the transmission, transflection and diffuse reflection measurement of crop grains and seeds, fruits and vegetables, livestock products, beverages, marine foods and processed foods.

1.5.3.1 UV/Vis Spectroscopy

UV/Vis spectroscopy is still an under-represented technique in process analysis. The advantages of UV/Vis spectroscopy are the low cost and high reproducibility of the equipment and its precision, especially in quantitative analysis. In recent years, UV/Vis analysis has been successfully implemented in the beverage industry and for wine color analysis [91–93]. The main application is the use of color cameras in food processing, which is also a sort of spectroscopic application.

1.5.3.2 NIR Spectroscopy

Water is an important issue in the food industry and can be measured using NIR spectrometers integrated in the food processing facility [94]. Typically, a rotating filter wheel is used and the characteristic absorbance peak of water at 1940 nm is used for calibration. By this method, water has been determined in a wide variety of dry products, such as instant coffee powder, potato chips, bonbons, tobacco, wheat, noodles, cookies, or dry milk powder [95]. Another important food constituent is fat, which may also be measured using infrared spectroscopy; in aqueous systems, however, it is preferable to use measurements in the mid-infrared range to avoid interfering water bands [96].

Although determination of major components in foodstuff, such as acid or sugar content, is still an important task, increasing attempts are made to determine complex quality parameters governing the expected sensory perception or storage stability of a certain product instead of only measuring one defined component. For comprehensive and recent reviews on the subject, see, for instance [97–101].

Assuring food safety is still a key issue in the food industry. Bacteria usually show broad bands in the NIR region even on taxonomically unrelated bacteria. However, using MVA it is possible to differentiate most of the bacteria [102].

1.5.3.3 Raman Spectroscopy

Raman spectroscopy is also a versatile method in applications related to food and agricultural products [103]. Food components, such as carbohydrates, edible oils, cyanogenic components, or proteins can readily be identified due to their characteristic absorption pattern by means of univariate characterization and peak assignment. For instance, proteins can be studied by comparing changes in the amide I (carbonyl stretch) band, which shifts from 1655 cm^{-1} for the α-helix to 1670 cm^{-1} for the anti-parallel β-sheet structures and, hence, allows detailed studies of food stuff. Cyanides show a very distinctive sharp band for the $C \equiv N$ triple bond at 2242 cm^{-1}. Inorganic food constituents, such as calcium carbonate, can also be identified due to their very sharp spectra. It was, for instance, possible to characterize the pre-freezing treatments of shrimp by studying the relative differences in Raman signals obtained from different crystal structures of calcium carbonate (ratio between calcite and vaterite), respectively, by studying the dehydration of the hexahydrate (ikaite, absorbance at 1070 cm^{-1}) to the anhydrous form (vaterite, 1089 and 1075 cm^{-1}).

Certainly, the potential of Raman spectroscopy can be enhanced by subjecting the spectral information to chemometric post-treatment, opening the field for rather

quantitative applications of Raman methods. For example, alginate powders have been studied quantitatively with respect to their characteristic β-D-mannuronic acid to α-L-guluronic acid (M : G) ratio. It is recognized that Raman spectroscopy must no longer be regarded as an exotic tool for routine analysis of soft matter like food but has its rightful place in the PAT toolbox available for the food and agricultural industries [103].

1.5.3.4 Imaging Techniques

On-line chemical imaging in agriculture is mainly remote sensing. Satellite or aerial remote sensing (RS) technology uses nowadays pushbroom imaging technology in the Vis, s-NIR and NIR-range. Vegetation images show crop growth from planting through to harvest, changes as the season progresses and abnormalities such as weed patches, soil compaction, watering problems, and so on. This information can help the farmer make informed decisions about the most feasible solution.

The differences in leaf colors, textures, shapes, or even how the leaves are attached to plants, determine how much energy will be reflected, absorbed or transmitted. The relationship between reflected, absorbed and transmitted energy is used to determine spectral signatures of individual plants. Spectral signatures are unique to plant species [104].

Remote sensing is used to identify stressed areas in fields by first establishing the spectral signatures of healthy plants. For example, stressed sugar beets have a higher reflectance value in the visible region of the spectrum from 400–700 nm. This pattern is reversed for stressed sugar beets in the non-visible range from about 750–1200 nm. The visible pattern is repeated in the higher reflectance range from about 1300–2400 nm. Interpreting the reflectance values at various wavelengths of energy can be used to assess crop health. The comparison of the reflectance values at different wavelengths, called a vegetative index, is commonly used to determine plant vigor (for details, see [104]).

In the food industry, numerous on-line controls are still made by human vision, especially for sorting bad looking products. Cameras can perform this task more efficiently and, using RGB cameras, a limited certain spectral differentiation is possible in machine vision [105]. However, due to the great variety of states (solid, fragmented, etc.) of the food, shapes, color and chemical composition, as well as seasonal variations it is difficult to monitor and control food in an unbiased manner. The driving force to introduce NIR imaging was to qualify food not only on its appearance but also on its chemical composition, such as water or starch content. An extensive demonstration of different applications is given in [105], which includes on-line characterization of chemical composition, detection of external contamination, surface and subsurface nonconformities and defects in food.

The airborne or on-line information for process control in food qualification can be complemented with a higher resolution by hyperspectral imaging techniques on a laboratory scale. The ripeness of tomatoes was qualified using Vis-spectroscopy [106], moreover, apples were qualified on the quantification of starch and other chemical compounds [107, 108]. Differences in phenol-typing in plant breeding development can also be visualized by NIR imaging as shown in [105].

Chemical imaging in food and agriculture can also be used to identify diseases, rot and contamination by insects, for example, larvae. A method to detect animal proteins in feed is described in [108]. The objective was to determine the limits of detection, specificity and reproducibility.

1.5.4 Polymers

Process analytics is even more widespread in the chemical industry and such diverse processes as polymerization, halogenation, calcination, hydrolysis, oxidation, corrosion, purification, or waste disposal, to name just a few, can be advantageously monitored using PAT tools. As an example for the chemical industry, a few application examples from polymer manufacturing are given.

1.5.4.1 UV/Vis Spectroscopy

Applications of UV/Vis spectroscopy in the polymer industry are numerous; for example it can be successfully used to determine the color of extruded plastics [109]. Color is a key quality criterion for the customer and automated on-line analysis of color is of great importance and relatively easily accomplished, and various experimental set-ups have been described. Another example of the industrial application of UV/Vis spectroscopy is determination of the thickness of polymer films.

1.5.4.2 NIR Spectroscopy

NIR spectroscopy is widely used in laboratory and industrial applications for material classification [65]. One of the most important processes in the industrial synthesis of polymeric materials is polymer extrusion. NIR has been employed to control the extrusion process, for example in terms of characterization of the starting formulation and of the final polymeric product [110–112]. Moreover, the additive content of polymer blends can be determined by using NIR [113, 114]. For that kind of measurement, on-line probes can be installed before or after the actual extrusion unit. More sophisticated application of NIR process analytical technology uses the direct implementation of NIR sensors in the extrusion machinery. Here, a flow cell with an integrated NIR sensor may be located after the mixing unit, directly before the hot polymer melt enters the mold, and spectra may be recorded either in transmission or diffuse reflectance, depending on the transparency of the polymer. Since the absorbance of the glass fiber optics has been shown to be temperature dependent [115], the temperature needs to be carefully controlled in the measurement chamber and the measured spectra have to be baseline corrected. Important requirements for reliable extrusion monitoring are reproducibility, accuracy and long-term stability of the NIR system [116]. For each measurement position (for example, at the end of the extruder, in the transport zone of the extruder, or at the cooling, extruded polymer material) separate calibration has to be performed that, besides polymer composition, also includes parameters like color or particle content and particle size distribution [117].

The moisture content in polymers has also been determined by NIR spectroscopy [116]. Besides composition, physical parameters of polymers such as density [118] and melting flow index [119] have been determined by NIR, and even more complex rheological parameters have been correlated with NIR spectra [120]. When NIR spectroscopy was used in combination with an ultrasonic treatment, even the bubble formation in the transformation of polystyrene was observed, which demonstrated the versatility of the method [121]. A review of process analytical applications in the polymer industry has recently been published by Becker [116]. Siesler also gives a very good overview of the potential of NIR in polymer analysis [122].

1.5.4.3 **Raman Spectroscopy**

Raman spectroscopy has been shown to have great potential in polymer production, for example for monitoring the emulsion polymerization of various polymers [123–126] or polymer curing reactions [127, 128], and also for the determination of the residence time of TiO_2-containing polypropylene in an extruder [129]. Polymer films can also be characterized in real-time during the blown film extrusion process with respect to composition, crystallinity and their microstructure development [130]. Besides polymer bulk and film characterization, application of Raman spectroscopy as a PAT tool may also be very promising in the characterization of synthetic and natural polymer fibers and their composites [131], foams [132], and even liquid crystals [133].

However, so far not so many applications of Raman spectroscopy in industrial polymer processing have been described in comparison to NIR applications. NIR spectroscopy is by far the most commonly employed method here. One major reason for this is the much higher cost of Raman equipment. Recent developments towards lower investment costs will certainly broaden the scope of potential applications.

1.5.4.4 **Imaging Techniques**

While standard spectrometers only allow measurement at one sampling point at a time, NIR spectral imaging techniques can identify, in real-time, both the size and shape of an object, as well as the material it is made from. The robust classification of materials, such as polymers, is based on their characteristic reflectance spectra. Sorting, for example, requires the correct material, size and shape of the entire object to be known for reliable separation [134–136].

1.6 Perspectives

1.6.1 Technology Roadmap 2015 +

Regarding the various PAT, the following trends in future development of process analytical equipment have been identified and summarized in the roadmap 2015 + for process sensors published by NAMUR/GMA [137].

1) It is expected that sensor systems will display much greater robustness and long-time stability, that is, they will be required to depend on much less efforts in maintenance and, hence, will have a significantly lower cost-of-ownership
2) New in-process sensors will not only be incorporated in the design of newly erected industrial plants but they will also be employed in the optimization of existing processes
3) The new requirements for process analysis systems will not be exhausted by the pure collection and storage of process data. Information on the current state of intermediates while production is still operating and predictions on expected end-product properties will be increasingly used for controlling and process management purposes.
4) For specific purposes, an increased accuracy of the gathered process information will be required
5) As a most important trend, spatially resolved information of process and material parameters will become of increasing importance.
6) Since interfaces play an important role for practically all industrial and engineering areas, the localization, identification and characterization of interfaces will play an increasingly important role in process analysis applications
7) There is a growing trend toward manufacturing products in an environmentally compatible way. This means that a growing number of synthetic processes currently performed in a classic chemical pathway will be translated into biotechnological approaches. As a consequence, process monitoring systems suitable for biotechnological applications, and specifically fermentation processes, will gain in importance and will have to be further developed and refined
8) In bioprocess technology, an industrially feasible and robust in-process analysis of specific targeted proteins would be a revolutionary achievement.
9) In order to comply with an ever increasing cost-pressure imposed on industrial processes, the substitution of sophisticated and expensive process analysis methods carrying a significant cost of ownership during maintenance by low-cost, ideally single-use devices that are disposed of after having delivered the required information is an important task for future research and development activities in the field of process analyzers.
10) The growing use of renewable resources or recycled materials as environmentally compatible starting materials for new products imposes novel analytical problems on process analytical devices which will have to be addressed in future development and applications of process analysis
11) The sensitivity of process analysis devices in many cases will have to be significantly increased. For instance, in the analysis of potentially harmful or catalytically effective trace components in gases, continuously lower detection limits will be required
12) In the context of a holistic process management, there is also an increasing demand in developing non-invasive analysis techniques in the field of warehouse logistics and product organization

13) An overall trend towards in-line measurements is evident, which in turn means that intensification of research on the translation from laboratory analytical methods into stable, processable and robust in-line methods that can routinely be applied will be required

Some of the new challenges and developments in PAT are discussed in the following sections.

1.6.2 Medical Applications and Tomographic Imaging

The next step in imaging is to integrate the *z*-spatial axis into the data cube. Especially for medical applications, it is important to feature the spatial distribution in all three directions.

Techniques which are available for 3D-imaging often lack the spectral information or are difficult to introduce into in-line or high throughput applications like optical coherent tomography (OCT) and laser scanning confocal microscopy. As stated in the introduction, medical ultrasonography, magnetic resonance imaging (MRI) and confocal microscopy are not suited to morphological or spectral imaging: the first two have poor resolution; the last lacks millimeter penetration depth and suitable applications in process control. On the other hand, in process analysis, electrical resistance tomography (ERT) is very popular nowadays and involves measurements around the periphery of an object for example, a process vessel or a patient. The instrument operates by taking data from an array of electrodes in contact with the process media. The electrical field lines "communicate" and are, therefore, affected by the presence of conducting and nonconducting regions [138]. However this technique does not provide any information on a molecular basis.

New developments in laser scanning confocal microscopy allow the use of different lasers at selected wavelengths; thus spectral imaging may then be realized. Also, when fluorescence is excited during scanning, for example, acousto-optical tuneable filters can be used to analyze the fluorescence spectrum at each focal point. However, there is still a long way to go for on-line or at-line applications in process control. This is also true for fluorescence imaging techniques, including lifetime imaging systems without using fluorescent markers [139]. On the other hand, multiphoton tomography is now at the edge of a broad "at-line" application in clinical high throughput *in vivo* studies [140].

Diffuse optical imaging (DOI) is a new emerging technique for functional imaging of biological tissues. It involves generating images using measurements in the visible or s-NIR-light scattered across large and thick tissues (about several centimeters) [141, 142]. As shown in Figure 1.7, penetration depth in the s-NIR range is high, therefore the objective of DOI is to provide low cost sensors for *in vivo* applications including imaging for example, of breast and brain cancer. The key issue, however, is the image reconstruction which is difficult due to the scattering of the material and, therefore, low spatial information of the data. Progress has been made on developing

more realistic and efficient models of light transport in tissue and solving the *ill-posed inverse* problem in an increasingly rigorous way [141].

Another way to solve the diffusion of photons problem and to localize spatially resolved features is time-resolved NIR-spectroscopy. This technique enables the separation of the absorption properties of the sample from the scattering properties. This improves the localization of changes in the physical parameters, for example, in a tablet [143].

Until recently, researchers did not extensively explore the material interactions occurring in the terahertz spectral region, the wavelengths that lie between 30 μm and 1 mm. Terahertz spectroscopy can be used to image through materials yielding high spatial resolution in the *x*, *y* and *z* directions. The technique also has the ability to resolve both time and amplitude information. Terahertz has the potential to be applied to many applications, including: on-line non-destructive testing for quality control of products and packaging for industrial markets; weapons and explosives detection for homeland security and defense markets; topical imaging for the medical market; quality control of external skins on space vehicles for the aerospace and military markets and many more. The technique is still quite expensive but will find its way into process control in the future [144].

1.6.3
Multi- Point-Information Systems in Manufacturing

The main objective of any process control is to guarantee a constant and specified product quality. Especially, maximum yield at a minimum of manufacturing costs are more and more important parameters, even in the pharmaceutical industry. Complex manufacturing with many different successive production steps must introduce a feed-back and a feed-forward control in the future. This requires specific efforts to integrate at each step of the production line an appropriate quality control for example, by spectroscopic methods.

Instead of using a single spectrometer at each individual production step, pushbroom imaging systems with numerous attached fiber bundles allow individual control of the quality at each intermediate and the final step. In this context, the pushbroom imager is used as a multipoint information source and can substitute a moving multiplexer. Many fibers per spectrometer can be used for simultaneous measurements. In addition, different spectrometer technologies for UV–Vis–NIR, fluorescence or Raman can also be combined. Thereby the probe becomes a multi-information system, which describes the sample in an ideal and complete way.

Figure 1.32 shows a schematic diagram of some production steps in tablet production with the integration of a multipoint spectroscopic information system using push-broom imaging technology.

In this example the pushbroom technology is able to substitute several single spectrometer systems. For example, at the fluid bed dryer, the moisture or the homogeneity of the blending process is controlled on a molecular level. Combined with multivariate data analysis science-based production can be realized.

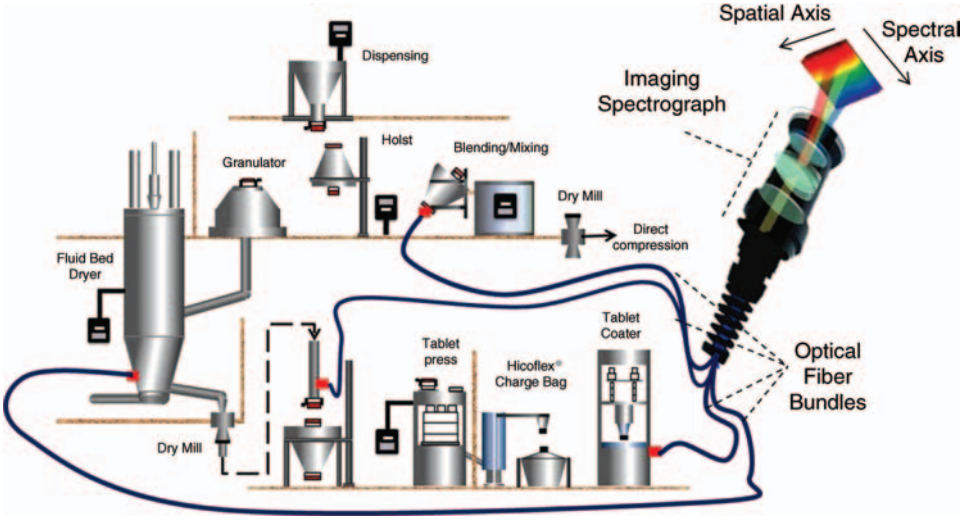

Figure 1.32 Schematic diagram of a tablet production process with different possibilities for pushbroom imaging.

1.6.4 Multimodal Spatially Resolved Spectroscopy

In recent years multimodal methods have matured to an accepted new technology, especially in the field of medicine [145]. The term multimodal relates to the possibility of collecting information on chemical and physical parameters at the same time. Not only chemical changes at the molecular level but also morphological changes in the sample can be detected. Complex interrelations of the system can be reduced and described in an easy and complete way. Several different imaging techniques are frequently used to realize the multimodal concept.

Process control is subject to a continuous change and the approach of multimodal methods will be extended in the future. The increasing complexity of high quality products and the cost pressure demand new strategies. In the future, the focus will not only be on process optimization but also on tailoring property profiles of products according to specifications and individual desires of customers. This will allow the creation of operating instructions, including the choice of materials and process parameters, to design a product with a given preference profile. Multimodal methods will then also enable the realization of multipurpose optimization [146].

Optical molecular spectroscopy, and in particular chemical imaging, will play an important role in implementing these objectives. By combining different wavelength ranges and techniques multimodal spectroscopy synergistically provides much more useful information than each technique on its own. It produces complementary chemical and morphological information about reaction products. Measurements can be carried out quickly, sensitively, selectively and economically at a reasonable

price. In principle, the implementation of the multimodal approach can be achieved in three different ways.

The first implementation strategy uses different wavelength ranges. The UV range is more suitable for scattering effects, while the short near-infrared range has a much higher penetration depth because of the low absorption probability in organic samples. Fluorescence techniques for excitation and emission spectroscopy can be used to separate molecules due to their different spectral signatures. Raman spectroscopy as a light scattering technique can be used as a fingerprint method to identify molecular structures or bonding effects.

The second implementation strategy involves using different technologies within the same wavelength ranges. For example, diffuse reflectance and transmission in the UV or NIR can be used to separate morphological scattering from chemical effects [9]. In addition attenuated total reflection (ATR) spectroscopy can be used to analyze highly concentrated samples without prior dilution and avoiding interference by scatter.

The third implementation strategy deals with laterally resolved measurements to achieve the desired differentiation. Angular resolved spectral measurements or line scans with a pushbroom imaging system lead to different penetration depths, which are highly specific for particulate systems. Besides the chemical information, parameters like homogeneity, particle size, particle distribution and density can also be detected.

1.6.5
Microreactor Control and Reaction Tomography

Microreactor technology is a powerful tool and has become indispensable over a wide application range from organic synthesis to enzymatic controlled reactions [147, 148]. A miniaturization with the possibility of reaction tomography, and thus a significant reduction in costs, will be the next step in the foreseeable future. Many chemical reactions, especially organic and fine chemical synthesis, could already be transferred to continuous microreaction processes [149]. The small geometric dimensions result in an intensified mass and heat transfer which often leads to increased yield and selectivity compared to the classical batch approach. However, microreaction technology today is still at the threshold between academia and industry.

A crucial factor for the successful implementation of microstructured production processes in industry is a suitable process analytical technology. Time and spatially-resolved on-line analysis must be implemented directly in the microfluidic channels. Thus parallel and multiplexed measurement technologies are needed to reduce costs and increase the robustness of information. To date, no commercially available solutions exist.

Typical state of the art procedures to study chemical processes use flow cells positioned after the microstructured environment or off-line methods. However, these approaches have several disadvantages. A critical point is the creation of distorted results due to changed geometrical proportions with measurements

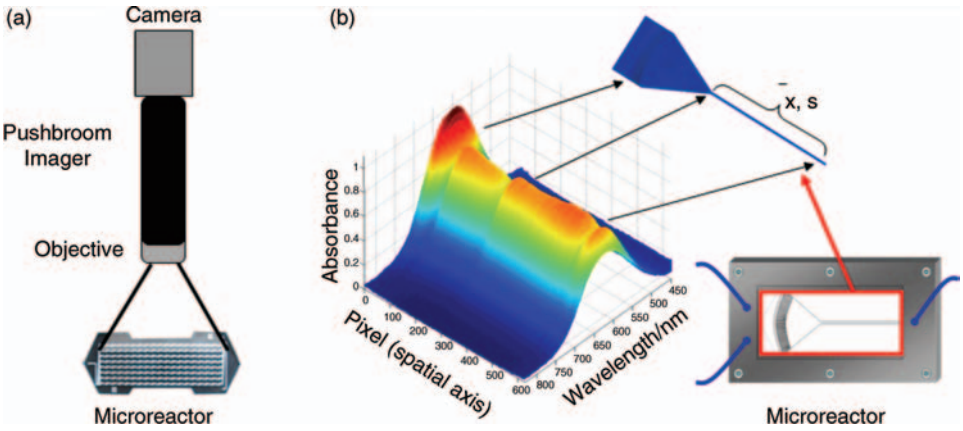

Figure 1.33 (a) Schematic diagram of the experimental set-up for an on-line spectrometer system. (b) Example of reaction monitoring of different concentration levels of an aqueous blue solution flowing through a microreactor system.

downstream of the microstructured environment. Moreover, no information about the actual reaction process inside the microreactor is generated. The major disadvantage, however, especially for industry, is the increasing costs for analytical devices required to assure constant product quality. The production of high added value chemicals by means of a microstructured process requires several hundred microreactors in order to produce sufficiently large amounts of final product. Therefore, large numbers of flow cells, each attached to a separate spectrometer (= pushbroom imager), are needed to meet these unique requirements.

An alternative technology is to analyze several microchannels simultaneously or to analyze a single microchannel spatially resolved along the reaction path using pushbroom imaging technology. This type of optical on-line spectroscopy is an ideal tool to characterize chemical reactions in a fast and reliable way, even on a molecular

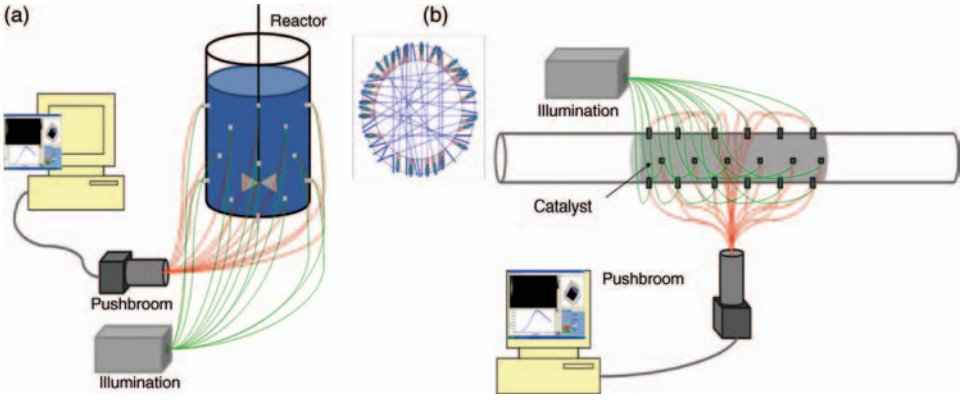

Figure 1.34 Pushbroom imager as a multipoint spectrograph for tomography of a batch reactor (a) and a continuous reactor (b).

level. Transmission or reflectance spectra are registered through a fixed prism–grating–prism optics with a two-dimensional CCD camera attached to it. Thereby, the *x*-axis of the CCD array corresponds to the spatial resolution and the *y*-axis of the camera provides the full spectrum of the sample. Figure 1.33 shows the experimental set-up for an on-line spectrometer system as well as an example for reaction monitoring.

Figure 1.34 shows a sketch of a pushbroom imager connected to a fiber bundle where a batch reactor can be analyzed, and another example is shown where spectroscopy is applied to a continuous reactor.

This multipoint spectroscopy can also be applied to microreaction systems to analyze along a reactor or as a multiplexed microreactor analyzing tool.

References

1 U. S. Department of Health and Human Services, Food and Drug Administration, *Guidance for Industry "PAT – a Framework for Innovative Pharmaceutical Development, Manufacturing and Quality Assurance"*, FDA, Silver Spring (2004) http://www.fda.gov/cvm/guidance/published.html.

2 Workman, J., Koch, M., Lavine, B., and Chrisman, R. (2009) Process analytical technology. *Anal. Chem.*, **81** (12), 4623–4643.

3 Jochem, R. (2010) *Was kostet Qualität? Wirtschaftlichkeit von Qualität ermitteln*, Carl Hanser Verlag, München, Germany ISBN 978-3-446-42182-0.

4 Garwin, D. (1984) What does product quality really mean? *Sloan Manag. Rev.*, **25** (3), 25–43.

5 Zollondz, H.D. (2002) *Grundlagen Qualitätsmanagement. Einführung in Geschichte, Begriffe, Systeme und Konzepte*, 2nd edn, Oldenbourg Verlag, München Wien, Austria, ISBN 978-3-486-57964-2.

6 Kessler, R.W. (ed.) (2006) *Prozessanalytik. Strategien und Fallbeispiele aus der industriellen Praxis*, Wiley–VCH, Weinheim, ISBN 3-527-31196-3.

7 Kano, N., Seraku, N., Takahashi, F., and Tsuji, S. (1984) Attractive quality and must-be quality. *Quality*, **14** (2), 39–48.

8 Cohen, L. (1995) *Quality Function Deployment: How to Make QFD Work for You*, Addison Wesley., Reading, MA.

9 Kessler, W., Oelkrug, D., and Kessler, R.W. (2009) Using scattering and absorption spectra as MCR-hard model constraints for diffuse reflectance measurements of tablets. *Anal. Chim. Acta*, **642**, 127–134.

10 Mitra, A. (2008) *Fundamentals of Quality Control and Improvement*, 3rd edn, John Wiley & Sons, Inc., Hoboken, New Jersey, USA, ISBN 978-0-470-22653-7.

11 ISPE " ISPE Product Quality Lifecycle Implementation (PQLI) Guide: Overview of product design, development and realization: A Science- and risk based approach to implementation" http://www.ispe.org/ispepqliguides/overviewofproductdesign.

12 Woelbeling, C. (2008) Creating Quality by Design/Process Analytical Technology management awareness. *Pharm. Eng.*, **28** (3), 1–9.

13 Rehorek, A. (2006) Prozess-Flüssigchromatographie, in *Prozessanalytik. Strategien und Fallbeispiele aus der Industriellen Praxis* (ed. R.W. Kessler), Wiley-VCH, Weinheim, pp. 429–474.

14 Becker, T. and Krause, D. (2010) Softsensorsysteme-Mathematik als Bindeglied zum Prozessgeschehen. *Chem. Ing. Tech.*, **82** (4), 429–440.

15 BASF Publication.

16 Schmidt-Bader, T. (2010) PAT und QbD im regulatorischen Umfeld der Pharmazeutischen Industrie. *Chem. Ing. Techn.*, **82** (4), 415–428.

17 Maiwald, M. (2010) Prozessanalytik als Instrument des

Informationsmanagements in der Chemischen und Pharmazeutischen Industrie. *Chem. Ing. Tech.*, **82** (4), 383–390.
18 ICH website http://www.ich.org.
19 ICH Guideline Q8 (R2) (August 2009) Pharmaceutical Development, step 4 http://www.ich.org/fileadmin/Public_Web_Site/ICH_Products/Guidelines/Quality/Q8_R1/Step4/Q8_R2_Guideline.pdf.
20 ICH Guideline Q6A (October 1999) Specifications: Test procedures and acceptance criteria for new drug substances and new drug products: Chemical substances (including decision trees), step 5 http://www.ema.europa.eu/docs/en_GB/document_library/Scientific_guideline/2009/09/WC500002823.pdf.
21 Box, G.E.P. and Draper, N.R. (1987) *Empirical Model-Building and Response Surfaces*, John Wiley & Sons, New York, ISBN: 0-471-81033-9.
22 Ghosh, S. (ed.) (1990) *Statistical Design and Analysis of Industrial Experiments*, Marcel Dekker Inc., New York, ISBN: 0-8247-8251-8.
23 Pyzdek, T. (2004) *The Six Sigma Handbook. A Complete Guide for Green Belts, Black Belts and Managers at all Levels*, McGraw-Hill, New York.
24 Herwig, C. (2010) Prozess Analytische Technologie in der Biotechnologie. *Chem. Ing. Tech.*, **82** (4), 405–414.
25 Behrendt, S. (2006) Integrierte Technologie-Roadmap Automation 2015 + http://www.zvei.org/fileadmin/user_upload/Fachverbaende/Automation/Nachrichten/1_Roadmap_Behrendt.PDF.
26 http://en.wikipedia.org/wiki/Causality.
27 Esbensen, K.H. and Paasch-Mortensen, P. (2010) Process sampling: Theory of sampling –the missing link in process analytycal technlogies (PAT), in *Process Analytical Technology*, 2nd edn (ed. K.A. Bakeev), Wiley, UK, pp. 37–79.
28 http://www.cpac.washington.edu/NeSSI/NeSSI.htm.
29 U. S. Department of Health and Human Services, Food and Drug Administration, Guidance for Industry, "Process Validation: General Principles and Practices" (Revision January 2011) http://www.fda.gov/Drugs/GuidanceComplianceRegulatoryInformation/Guidances/default.htm.
30 Myers, R.H. and Montgomery, D.C. (2002) *Response Surface Methodology*, John Wiley and Sons, New York.
31 VDA Band 4: Sicherung der Qualität vor Serieneinsatz, VDA, Frankfurt, Germany (1986)
32 VDA Band 4: Sicherung der Qualität vor Serieneinsatz, Teil 2: System FMEA, VDA, Frankfurt, Germany (1996)
33 Bakeev, K.A. (ed.) (2010) *Process Analytical Technology*, 2nd edn, Wiley, UK.
34 Kessler, W. (2007) *Multivariate Datenanalyse für die Pharma-, Bio- und Prozessanalytik*, Wiley-VCH, Weinheim, ISBN 13: 978-3-527-31262-7.
35 Geladi, P., McDougall, D., and Martens, H. (1985) Linearisation and scatter correction for near infrared reflectance spectra of meat. *Appl. Spectrosc.*, **39**, 491.
36 Burger, J. and Geladi, P. (2005) Hyperspectral NIR Image Regression Part 1: Calibration and Correction. *J. Chemom.*, **19**, 355–363.
37 Martens, H., Nielsen, J.P., and Engelsen, S.B. (2003) Light Scattering and Light Absorbance Separated by Extended Multiplicative Signal Correction. *Anal. Chem.*, **75**, 394–404.
38 Isaksson, T. and Kowalski, B. (1993) Piece-Wise Multiplicative Scatter Correction Applied to Near-Infrared Diffuse Transmittance data from Meat Products. *Appl. Spectrosc.*, **47**, 702–709.
39 Barnes, R., Dhanoa, M., and Sister, S. (1998) Standard Normal Variate Transformation and Detrending fo Near Infrared Diffuse Reflectance. *Appl. Spectrosc.*, **43**, 772–777.
40 Brown, S.D., Tauler, R. and Walczak, B. (eds) (2009) *Comprehensive Chemometrics*, vol. 4, Elsevier, Amsterdam.
41 Jaumot, J., Gargallo, R., de Juan, A., and Tauler, R. (2005) A graphical user-friendly interface for MCR-ALS: a new tool for multivariate curve resolution in MATLAB. *Chemom. Intell. Lab. Sys.*, **76**, 101–110.

42 Ulmschneider, M. and Roggo, Y. (2008) *Pharmaceutical Manufacturing Handbook* (ed. S.C. Gad), John Wiley & Sons, Hoboken NJ, pp. 353–410.

43 Small, G.W. (2006) Chemometrics and near infrared spectroscopy: Avoiding the pitfalls. *Tr. Anal. Chem.*, **25**, 1057–1066.

44 Kjeldahl, K. and Bro, R. (2010) Some common misunderstandings in chemometrics. *J. Chemom.*, **24**, 558–564.

45 Smith, C.L. (2009) *Basic Process Measurements*, John Wiley & Sons, New York.

46 Kandelbauer, A., Gronalt, M., Lammer, H., Penker, A., and Wuzella, G. (2007) Kosteneinsparungen in der Holzindustrie durch Logistikoptimierung, Prozessanalytik und Wissensmanagement, Teil 1: Allgemeine Aspekte und Logistik-Management. *Holztechnol.*, **48** (6), 5–9.

47 Kappes, R. and Grimm, C. (2010) NIR Feuchtemesstechnik mit vereinfachter Kalibrierfunktion. *Techn. Mess.*, **77**, 293–304.

48 Hauschild, T. (2005) Density and moisture measurements using microwave resonators, in *Electromagnetic Aquametry, Electromagnetic Wave Interaction with Water and Moist Substances* (ed. K. Kupfer), Springer Verlag, Heidelberg.

49 Kappes, R., Grimm, C., and Scholz, J. (2010) Feuchtemesstechnik vom Labor bis in den Prozess. *Pharm. Ind.*, **72** (7), 1231–1238.

50 Kortüm, G. (1969) *Reflectance Spectroscopy*, Springer Verlag, New York, USA.

51 Kessler, R.W., Böttcher, E., Füllemann, R., and Oelkrug, D. (1984) *Fresenius Z. Anal. Chem.*, **319**, 695–700.

52 Rebner, K., Kessler, W., and Kessler, R.W. (2010) in *Science Based Spectral Imaging: Combining First Principles with New Technologies, Near Infrared Spectroscopy: Proceedings of the 14th International Conference, 7.-16.11 Bangkok, Thailand* (eds S. Saranwong, S. Kasemsumran, W. Thanapase and P. Williams,), IMPublications, Chichester, UK, pp 919–927, ISBN 978-1-906715-03-8.

53 Bentsson, O., Burger, T., Folestad, S., Danielsson, L.-G., Kuhn, J., and Fricke, J. (1999) Effective sample size in diffuse reflectance Near –IR spectrometry. *Anal. Chem.*, **71**, 617–623.

54 Shi, Z. and Anderson, C.A. (2010) Pharmaceutical Applications of Separation of Absorption and Scattering in Near-Infrared Spectroscopy (NIRS). *J. Pharm. Sc.*, **99**, 4766–4783.

55 Oelkrug, D., Brun, M., Hubner, P., and Egelhaaf, H.-J. (1996) Optical parameters of turbid materials and tissues as determined by laterally resolved reflectance measurements. *SPIE 2445*, **248**.

56 Dahm, D.J. and Dahm, K.D. (2007) *Interpreting Diffuse Reflectance and Transmittance*, NIR Publications, Chichester, UK.

57 Thenadil, S. (2008) Relationship between the Kubelka-Munk scattering and radiative transfer coefficients. *J. Opt. Soc. Am. A*, **25**, 1480–1485.

58 Clarke, F.C., Hammond, S.V., Jee, R.D., and Moffat, A.C. (2002) Determination of the information depth and sample size for the analysis of pharmaceutical materials using reflectance NIR microscopy. *Appl. Spectrosc.*, **56**, 1475–1483.

59 Hudak, S.J., Haber, K., Sando, G., Kidder, L.H., and Lewis, E.N. (2007) Practical limits of spatial resolution in diffuse reflectance NIR chemical imaging. *Nir News*, **18**, 6–8.

60 Griffiths, P.R. (2009) Infrared and Raman Instrumentation for Mapping and Imaging, in *Infrared and Raman Spectroscopic Imaging* (eds R. Salzer and H.W. Siesler), Wiley-VCH, Weinheim, Germany, pp. 3–64, ISBN 978-3-527-31993-0.

61 Lewis, E.N., Schoppelrei, J.W., Makein, L., Kidder, L.H., and Lee, E. (2010) Near infrared chemical imaging for product and process understanding, in *Process Analytical Technology* (ed. K.A. Bakeev), Wiley, pp. 245–278.

62 Kessler, R.W. (2011) *Handbook of Spectroscopy*, 2nd edn (eds G. Gauglitz and T. Vo-Dinh), Wiley-VCH.

63 Workman, J. Jr., Koch, M., and Veltkamp, D. (2007) Process Analytical Chemistry. *Anal. Chem*, **79**, 4345–4364.

64 Chalmers, J.A. (ed.) (2000) *Spectroscopy in Process Analysis*, Sheffield Academic Press, Sheffield, UK.

65 Burns, D.A. and Ciurczak, E.W. (eds.) (2001) *Handbook of Near-Infrared Analysis*, 2nd edn, Marcel Dekker, New York Basel.

66 Lu, X., Lozano, R., and Shah, P.(November (2003)) *In-situ Dissolution Testing Using Different UV Fiber Optic Probes and Instruments*, Dissolution Technologies, pp. 6–15.

67 Khoshayand, M.R., Abdollahi, H., Shariatpnahi, M., Saadatfard, A., and Mohammedi, A. (2008) *Spectrochim. Acta, Part A*, **70A** (3), 491–499.

68 Saal, C. (2006) Prozessanalytik in der pharmazeutischen Industrie, in *Prozessanalytik. Strategien und Fallbeispiele aus der Industriellen Praxis* (ed. R.W. Kessler), Wiley-VCH, Weinheim, pp. 499–512.

69 Ufret, C. and Morris, K. (2001) Modelling of powder blending using on-line near infrared measurements. *Drug Dev. Ind. Pharm.*, **27**, 719.

70 El-Hagrasy, A.S. and Drennen, J.K. (2004) PAT Methods provide process understanding: characterization of intra-shell versus inter-shell mixing kinetics in V-blenders. *NIR News*, **15**, 9–11.

71 Duong, N.-H., Arratia, P., Muzzio, F., Lange, A., Timmermans, J., and Reynolds, S. (2003) A homogeneity study using NIR spectroscopy: tracking Magnesium stearate in Bohle Bin Blender. *Drug Devel. Ind. Pharm.*, **29**, 679.

72 Winskill, N. and Hammond, S.,An industry perspective on the potential for emerhng process analytical technologies, Pfizer Global manufacturing services http://www.fda.gov/ohrms/dockets/ac/ac/02/briefing/3841B1_05_PFIZER.pdf.

73 http://www.uhlmann-visiotec.de/html/dinline-wirkstoffanalyse.html.

74 Herkert, T., Prinz, H., and Kovar, K.A. (2001) One hundred percent on-line identity check of pharmaceutical products by NIR spectroscopy of the packaging line. *Eur. J. Pharm. Biopharm.*, **51**, 9.

75 http://www.brukeroptics.de/ft-nir/tandem.html.

76 http://www.brukeroptics.com/downloads/AF512E_Tablet_Uniformity.pdf.

77 Roggo, Y., Chalus, P., Maurer, L., Lema-Martinez, C., Edmont, A., and Jent, N.J. (2007) *Pharma. Biomed. Anal.*, **44** (3), 683–700.

78 Doherty, S.J. and Kettler, C.N. (2005) On-line applications in the pharmaceutical industry, in *Process Analytical Technology* (ed. K.A. Bakeev), Blackwell Publishing, Oxford, UK, pp. 329–361.

79 Vergote, G.J., De Beer, T.R.M., Vervaet, C., Remon, J.P., Baeyens, W.R.G., Diericx, N., and Verpoort, F. (2004) Inline monitoring of a pharmaceutical blending process using FT Raman spectroscopy. *Eur. J. Pharm. Sci.*, **21**, 479–485.

80 Starbuck, C., Spartalis, A., Wai, L., Wang, J., Fernandez, P., Lindemann, C.M., Zhou, G.X., and Ge, Z. (2002) Process optimization of a complex pharmaceutical polymorphic systemvia in situ Raman spectroscopy. *Cryst. Growth Des.*, **2**, 515–522.

81 Hilfiker, R., Berghausen, J., Blatter, F., DePaul, S.M., Szelagiewicz, M., and Von Raumer, M. (2003) Hiigh throughput screening for polymorphism. *Chem. Today*, **21**, 75.

82 Shah, R.B., Tawakkul, M.A., and Khan, M.A. (2007) *J. Pharm. Sci.*, **96** (5), 1356–1365.

83 Barnes, S., Gillian, J., Diederich, A., Barton, D., and Ertl, D. (2008) *Am. Pharm. Rev.*, **11** (3), 80–85.

84 Reich, G. (2005) Near Infrared spectroscopy and imaging: Basic principles and pharmaceutical applications. *Adv. Drug Delivery Rev.*, **57**, 1109–1143.

85 Fernandez Pierna, J.A., Baeten, V., Dardenne, P., Dubois, J., Lewis, E.N., and Burger, J. (2009) Spectroscopic Imaging, in *Comprehensive Chemometrics*, vol. **4** (eds S.D. Brown, R. Tauler, and B. Walczak), Elsevier, Amsterdam, The Netherlands, pp. 173–197.

86 Makeln, L.J., Kidder, L., Lewis, E.N., and Valleri, M. (2008) Non-destructive evaluation of manufacturing process changes using near infrared chemical imaging. *NIR News*, **19**, 11–15.

87 Clarke, F. (2004) Extracting process related information from pharmaceutical dosage forms using near infrared microscopy. *Vibr. Spectrosc.*, **34**, 25–35.

88 Ellison, C.D., Ennis, B.J., Hamad, M.L., and Lyon, R.C. (2008) Measuring the distribution of density and tabletting force in pharmaceutical tablets by chemical imaging. *J. Pharm. Biomed. Anal.*, **48**, 1–7.

89 Dubois, J., Wolff, J.-C., Warrack, J.K., Schoppelrei, J., and Lewis, E.N. (2007) NIR chemical imaging for counterfeit pharmaceutical product analysis. *Spectrosc.*, **22**, 40–50.

90 Cogdill, R.P., Short, S.M., Forcht, R., Shi, Z., Shen, Y., Taday, P.F., Anderson, C.A., and Drennen, J.K. III (2006) An efficient method-development strategy for quantitative chemical imaging using teraherz pulse spectroscopy. *J. Pharm. Innov.*, **1**, 63–75.

91 Ghosh, P.K. and Jayas, D.S. (2009) Use of spectroscopic data for automation in food processing industry. *Sens. & Instrumen. Food Qual.*, **3**, 3–11.

92 Acevedo, F.J., Jiménez, J., Maldonado, S., Domínguez, E., and Narváez, A. (2007) Classification of Wines Produced in Specific Regions by UV-Visible Spectroscopy Combined with Support Vector Machines. *J. Agric. Food Chem.*, **55**, 6842–6849.

93 Yu, H.Y., Ying, Y.B., Sun, T., Niu, X.Y., and Pan, X.X. (2007) Vintage year determination of bottled rice wine by Vis–NIR spectroscopy. *J. Food Sci.*, **72**, 125–129.

94 Reh, C. (2006) Prozessanalytik in der Lebensmittelindustrie, in *Prozessanalytik. Strategien und Fallbeispiele aus der Industriellen Praxis* (ed. R.W. Kessler), Wiley-VCH, Weinheim, pp. 539–549.

95 Reh, C., Bhat, S.N., and Berrut, S. (2004) Determination of water content in powdered milk. *Food Chem.*, **86**, 457–464.

96 Lanher, B.S. (1996) Evaluation of Aegys MI 600 FTIR milk analyzer for analysis of fat, protein, lactose and solid non-fat: a compilation of eight independent studies. *J. AOAC Int.*, **79** (6), 1388–1399.

97 Kawang, S. (2006) Application of NIR spectroscopy to agricultural products and foodstuffs, in *Near –Infrared Spectroscopy: Principles, Instruments, Applications* (eds H.W. Siesler, Y. Ozaki, S. Kawata, and H.M. Heise), Wiley-VCH, Weinheim, pp. 269–288.

98 Kington, L.R. and Jones, T.M. (2001) Application for NIR analysis of beverages, in *Handbook of Near-Infrared Analysis*, 2nd edn (eds D.A. Burns and E.W. Ciurczak), Marcel Dekker, New York Basel, pp. 535–542.

99 Shenk, J.S., Workman, J.J. Jr., and Westhouse, M.O. (2001) Aplication of NIR spectroscopy to agricultural products, in *Handbook of Near-Infrared Analysis*, 2nd edn (eds D.A. Burns and E.W. Ciurczak), Marcel Dekker, New York Basel, pp. 419–474.

100 Osborne, B.G. (2001) NIR analysis of bakery products, in *Handbook of Near-Infrared Analysis*, 2nd edn (eds D.A. Burns and E.W. Ciurczak), Marcel Dekker, New York Basel, pp. 475–498.

101 Frankhuizen, R. (2001) NIR analysis in dairy products, in *Handbook of Near-Infrared Analysis*, 2nd edn (eds D.A. Burns and E.W. Ciurczak), Marcel Dekker, New York Basel, pp. 499–534.

102 Dubois, J., Lewis, E.N., Fry, F.S., and Calvey, E.M. (2007) Near infrared chemical imaging for high throughput screening of food bacteria. *NIR News*, **18**, 4–6.

103 Viereck, N., Salomonsen, T., van den Berg, F., and Engelsen, S.B. (2009) Raman applications in food analysis, in *Raman Spectroscopy for Soft Matter Applications* (ed. M.S. Amer), John Wiley & Sons, Hoboken NJ, pp. 199–223.

104 Campbell, J.B. (ed.) (2007) *Introduction to Remote Sensing*, 4th edn, Guildford Press, N.Y.

105 Bellon-Maurel, V. and Dubois, J. (2009) Near infrared hyperspectral imaging in food and agriculture science, in *Infrared and Raman Spectroscopic Imaging* (eds R. Salzer and H.W. Siesler), Wiley-VCH, Weinheim, Germany, ISBN: 978-3-527-31993-0, pp. 259–294.

106 Polder, G., Heyden, G.W.A.M.v.d., and Young, I.T. (2003) Tomato sorting using

independent component analysis on spectral images. *Real Time Imaging*, **9**, 253–259.

107 Peirs, A., Scheerlinck, N., de Baerdemaeker, J., and Nicolai, B.M. (2003) Starch index determination of of apple fruit by means of a hyperspectral near infrared hyperspectral imaging system. *J. Near Infrared Spectrosc.*, **11**, 379–389.

108 Fernandez Pierna, J.A., Baeten, V., and Dardenne, P. (2006) Screenig of compound feeds using NIR hyperspectral data. *Chemom. Intell. Lab. Syst.*, **84**, 114–118.

109 Baylor, L.C. and O'Rourke, P.E. (2005) UV-Vis for On-line Analysis, in *Process Analytical Technology* (ed. K.A. Bakeev), Blackwell Publishing, Oxford, UK, pp. 170–186.

110 McPeters, H.L. and Williams, S.O. (1992) 1 In-line monitoring of polymer processes by near-infrared spectroscopy. *Process Contr. Qual.*, **3**, 75–83.

111 Hansen, M.G., and Khettry, A. (1994) In-line monitoring of titanium dioxide content in poly(ethylene terephthalate) extrusion. *Polym. Engin. Sci.*, **34** (23), 1758.

112 Rohe, T., Becker, W., Krey, A., Nägele, H., Kölle, S., and Eisenreich, N. (1998) In-line monitoring of polymer extrusion processes by NIR spectroscopy. *J. Near Infrared Spectrosc.*, **6**, 325–332.

113 Fischer, D., Bayer, T., Eichhorn, K.J., and Otto, M. (1997) In-line process monitoring on polymer melts by NIR-spectroscopy. *Fresen. J. Anal. Chem.*, **359**, 74–77.

114 Rohe, T. and Kölle, S. (2000) *GIT Lab. Fachzeitschr.*, **44**, 1444.

115 Rohe, T. (2001) Inline Nahinfrarot (NIR Spektroskopie bei der Kunststoffextrusion PhD Thesis, University Stuttgart.

116 Becker, W. (2006) Prozessanalytik in der Kunststoffindustrie, in *Prozessanalytik. Strategien und Fallbeispiele aus der Industriellen Praxis* (ed. R.W. Kessler), Wiley-VCH, Weinheim, pp. 551–570.

117 Reshadat, R., Desa, S., Joseph, S., Mehra, M., Stoev, N., and Balke, S.T. (1999) In-line near-infrared monitoring of polymer processing, Part I: Process/monitor interface development. *Appl. Spectrosc.*, **53** (11), 1412.

118 Nagata, T., Oshima, M., and Tanigaki, M. (2000) On-line NIR sensing of CO2 concentration for polymer extrusion foaming processes. *Polym. Eng. Sci.*, **40** (8), 1843–1844

119 Hansen, M.G. and Vedula, S. (1998) In-line fiber-optic near-infrared spectroscopy: Monitoring of rheological properties in an extrusion process. Part I. *J. Appl. Polym. Sci.*, **68** (3), 859–872.

120 Vedula, S. and Hansen, M.G. (1998) In-line fiber-optic near-infrared spectroscopy: Monitoring of rheological properties in an extrusion process. Part II. *J. Appl. Polym. Sci.*, **68** (3), 873–889.

121 Thomas, Y., Cole, K.C., and Daigneault, L.E. (1997) n-line NIR monitoring of composition and bubble formation in polystyrene/blowing agent mixtures. *J. Cell. Plast.*, **33**, 516–527.

122 Siesler, H.W., Ozaki, Y., Kawata, S., and Heise, H.M. (2006) *Near-Infrared Spectroscopy. Principles, Instruments, Applications*, Wiley VCH, Weinheim.

123 van den Brink, M., Pepers, M., and Van Herk, A.M. (2002) Raman spectroscopy of polymer latexes. *J. Raman Spectrosc.*, **33**, 264–272.

124 Bauer, C., Amram, B., Agnely, M., Charmot, D., Sawatzki, J., Dupuy, N., and Huvenne, J.-P. (2000) On-line monitoring of a latex emulsion polymerization by fiber-optic FT Raman spectroscopy, Part 1: Calibration. *Appl. Spectrosc.*, **54**, 528–535.

125 Wenz, E., Buchholz, V., Eichenauer, H., Wolf, U., Born, J.-R., Jansen, U., and Dietz, W. (2001) Process for the production of graft polymers, US Patent Application Publication 2003/0130433 A1, Assigned to Bayer Polymers LLC, Filed in 2002. Priority number DE 10153534.1.

126 Elizalde, O. and Leiza, J.R. (2009) Raman application in emulsion polymerization systems, in *Raman Spectroscopy for Soft Matter Applications* (ed. M.S. Amer), John Wiley & Sons, Hoboken NJ, pp. 95–144.

127 Schrof, W., Horn, D., Schwalm, R., Meisenburg, U., and Pfau, A. (1998) Method for optimizing lacquers, US 6447831 B1, Assigned to BASF

Aktiengesellschaft, filed in 1999, priority number DE 19834184.

128 Van Overbeke, E., Devaux, J., Legras, R., Carter, J.T., McGrail, P.T., and Carlier, V. (2001) Raman spectroscopy and DSC determination of conversion in DDS-cured epoxy resin: application to epoxy copolyethersulfon blend. *Appl. Spectrosc.*, **55**, 540–551.

129 Ward, N.J., Edwards, H.G.M., Johnson, A.F., Fleming, D.J., and Coates, P.D. (1996) *Appl. Spectrosc.*, **50**, 812.

130 Gururajan, G. and Ogale, A.A. (2009) Raman applications in polymer films for real-time characterization, in *Raman Spectroscopy for Soft Matter Applications* (ed. M.S. Amer), John Wiley & Sons, Hoboken NJ, pp. 33–62.

131 Young, R.J. and Eichhorn, S.J. (2009) Raman applications in synthetic and natural polymer fibers and their composites, in *Raman Spectroscopy for Soft Matter Applications* (ed. M.S. Amer), John Wiley & Sons, Hoboken NJ, pp. 63–94.

132 Amer, M.S. (2009) Raman applications in foams, in *Raman Spectroscopy for Soft Matter Applications* (ed. M.S. Amer), John Wiley & Sons, Hoboken NJ, pp. 181–198.

133 Hayashi, N. (2009) Raman applications in liquid crystals, in *Raman Spectroscopy for Soft Matter Applications* (ed. M.S. Amer), John Wiley & Sons, Hoboken NJ, pp. 145–180.

134 Leitner, R., Mairer, H., and Kercek, A. (2003) Real-time classification of polymers with NIR spectral imaging and blob analysis. *Real Time Imaging*, **9**, 245–251, (Special Issue on Spectral Imaging).

135 Kulcke, A., Gurschler, C., Spöck, G., Leitner, R., and Kraft, M. (2003) On-line classification of synthetic polymers using near infrared spectral imaging. *J. Near Infrared Spectrosc.*, **11**, 71–81.

136 Pourdeyhimi, B. (ed.) (1999) *Imaging and Image Analysis Applications for Plastics*, William Andrew Publishing/Plastics Design Library.

137 Maiwald, M., Gerlach, G., and Kuschnerus, N. (2009) Prozess-Sensoren 2015 + . Technologie-Roadmap für Prozess Sensoren in der chemisch-pharmazeutischen Industrie, VDI-VDE – NAMUR, November.

138 Stanley, S.J. and Bolton, G.T. (2008) Review of Recent Electrical Resistance Tomography (ERT) Applications for Wet Particulate Processing. *Particle Particulate Syst. Charact.*, **25**, 207–215.

139 Bearman, G. and Levenson, R. (2003) Chapter 8, *Biological Imaging Spectroscopy, Biomedical Photonics Handbook*, CRC Press, Boca Raton.

140 König, K. (2008) Clinical multiphoton tomography. *J. Biophoton.*, **1**, 13–23.

141 Gibson, A.P., Hebden, J.C., and Arridge, S.R. (2005) Recent advances in diffuse optical imaging. *Phys. Med. Biol.*, **50**, R1–R43.

142 Boas, D.A., Dale, A.M., and Franceschini, M.A. (2004) Diffuse optical imaging of brain activation: approaches to optimizing image sensitivity, resolution and accuracy. *Neuro Image*, **23**, 275–288.

143 Abrahmasson, C., Johansson, J., Anderson-Engels, S., Svanberg, S., and Folestad, S. (2005) Time-resolved NIR spectroscopy for quantitative analysis of intact pharmaceutical tablets. *Anal. Chem.*, **77**, 1055–1059.

144 Dexheimer, S.L. (ed.) (2007) *Terahertz Spectroscopy – Principles and Applications*, CRC Press.

145 Salomatina, E., Muzikansky, A., Neel, V., and Yaroslavsky, A.N. (2009) Multimodal optical imaging and spectroscopy for the intraoperative mapping of nonmelanoma skin cancer. *J. Appl. Phys.*, **105**, 102–110.

146 Merz, T. and Kessler, R.W. (2007) On-line Prozesskontrolle mittels 2D-Fluoreszenzspektroskopie. *Process*, **9**, 44–45.

147 Ahmed-Omer, B., Brandta, J.C., and Wirth, T. (2007) Advanced organic synthesis using microreactor technology. *Org. Biomol. Chem.*, **5**, 733–740.

148 Tisma, M., Zelic, B., Vasic-Racki, D., Znidarsic-Plazl, P., and Plazl, I. (2009) Modelling of laccase-catalyzed l-DOPA oxidation in a microreactor. *Chem. Eng. J.*, **149**, 383–388.

149 Hessel, V. and Löwe, H. (2004) Organische Synthese mit mikrostrukturierten Reaktoren. *Chem. Ing. Tech.*, **76**, 535–554.

2
Applications of Spectroscopy and Chemical Imaging in Pharmaceutics

Aoife A. Gowen and José M. Amigo

2.1
The New Paradigm of Process Control

The US Food and Drug Administration (FDA)-led process analytical technology (PAT) initiative is transforming approaches to quality assurance in the pharmaceutical industry. Core to the PAT initiative is increased process understanding by monitoring of critical performance attributes, leading to better process control and ultimately improved drug quality [1]. Potential advantages of PAT implementation include reduced production cycle times, prevention of rejects, reduction of human error and facilitation of continuous processing to improve efficiency. With adequate knowledge of the ingredient – process relationship, the FDA will allow a pharmaceutical company to adjust their manufacturing process to maintain a consistent output without notification to the FDA [2]. The real-time release paradigm assures that when the last manufacturing step is passed, all final release criteria are met [3]. Adoption of such a quality by design approach would allow significant benefits to be gained by pharmaceutical companies: labor- and time-intensive finished product testing would be avoided if the product could be released based on in-process data.

This possibility is driving pharmaceutical companies to gain a more complete understanding of their processes and input variable relationships to realize the benefits of PAT registrations. Summarizing, pharmaceutical companies are encouraged to:

1) Implement real-time process analyzers and control tools
2) Develop new multivariate tools for design, data acquisition and analysis
3) Utilize (1) and (2) for continuous improvement and knowledge of the process.

Process monitoring and control are necessary at all stages of pharmaceutical processing, from raw material to packaged product characterization (Figure 2.1).

Traditional quality control methods (e.g., high performance liquid chromatography (HPLC) or mass spectroscopy (MS)) are time consuming, destructive, expensive, require lengthy sample preparation and give no information about the distribution of components within a sample. Due to the destructive and time-consuming nature of these methods, only small samples of drugs may be tested from given production

Handbook of Biophotonics. Vol.3: Photonics in Pharmaceutics, Bioanalysis and Environmental Research, First Edition.
Edited by Jürgen Popp, Valery V. Tuchin, Arthur Chiou, and Stefan Heinemann

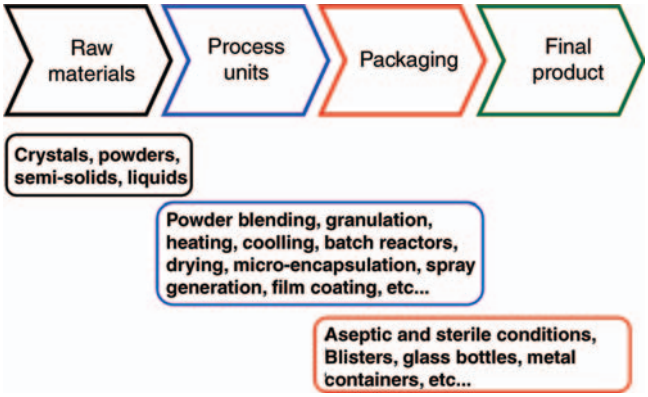

Figure 2.1 Flow-chart of the main steps in the production of pharmaceutical products.

batches [4]. Motivated by the PAT initiative, numerous techniques have been developed to provide real-time process control in order to improve understanding of the chemical and physical processes that occur during pharmaceutical unit operations. This chapter will focus on the major spectroscopic and chemical imaging techniques that have been applied in this context.

2.2 Overview of Spectroscopic Techniques Commonly Used

Spectroscopy concerns the scattering, absorption and emission of light originating from various regions of the electromagnetic spectrum. The ultraviolet (UV), visible (Vis), near-infrared (NIR) and mid-infrared (MIR) wavelength regions have been demonstrated as the most important areas of the electromagnetic spectrum for the collection of information about pharmaceutical processes. UV–Vis light is energetic enough to cause electronic transitions in molecules, while light in the NIR and MIR wavelength ranges results in molecular vibrations. A summary of the key features of various spectroscopic techniques employed in pharmaceutical analysis is presented in Table 2.1.

UV–Vis spectroscopy has a long history of use in pharmaceutical quality control, and is regarded as one of the most important techniques in analytical chemistry due to its low cost, ruggedness of spectrometers, rapidity and lower sensitivity to environmental factors (e.g., temperature) than the vibrational spectroscopies. This method is usually applied to samples in the liquid state; chromophore-containing materials require dilution by factors of 10^3–10^5 in a nonabsorbing solvent prior to spectral acquisition. In order to overcome this limitation, attenuated total reflectance (ATR), a technique more commonly associated with MIR spectroscopy, has been coupled with UV–Vis spectroscopy. ATR-UV–Vis spectroscopy is suitable for monitoring crystallization and for quantitative analysis of solid dosage forms containing chromophores [5, 6].

Table 2.1 Summary of main features of UV–Vis, NIR, MIR and Raman (RS) spectroscopies.

	UV–Vis	NIR	MIR	RS
Electromagnetic region	190–700 nm.	2500–7500 nm.	10000–2500 nm.	LASER radiation in UV–Vis or NIR
Low cost[a)]	X	x		
High speed	X	XX	x	X
Rugged instrumentation	X	X		X
Selective spectra			x	X
Portability	x	XX (probes)		
Possibility of plugging into a reactor[b)]	x	XX		
Nondestructive		x		X

a) The cross denotes the degree of the property in relationship to their implementation in PAT methodologies. For instance, in "low cost" property, the X denotes that there are devices affordable at a reasonable price. The x denotes that there are devices, but with higher cost.

b) The availability of portable probes makes it possible to plug them into reactors, blenders, or any device for real-time acquisition of spectra.

NIR spectroscopy (NIRS) is well recognized as a nondestructive tool in pharmaceutical analysis for raw material testing, quality control and process monitoring, mainly due the advantages it allows over traditional methods, for example, speed, little/no sample preparation, capacity for remote measurements (using fiber optic probes), prediction of chemical and physical properties from a single spectrum. Räsänen and Sandler [7] provide a comprehensive review of the applications of NIRS in the solid dosage form development, documenting the usefulness of this technique for each of the manufacturing steps, from raw material screening to assessment of the final dosage form. Absorption bands in the NIR are overtones and combinations of bands originating in the MIR region. As a consequence, they are relatively weak and overlapped, making molecular structural elucidation difficult. Nevertheless, multivariate data analysis has facilitated the development of robust calibration models from NIRS data.

MIR light excites fundamental molecular vibrations; therefore, MIR spectra are more selective than NIR, facilitating the extraction of information on the structure of molecules. Fourier transform infrared (FT-IR) spectroscopy is the standard spectroscopic method currently used for acquisition of MIR spectra. However, the high absorption of water in the MIR range means that, in order to measure aqueous samples, very thin samples are required. About 10–100 μm path length is necessary to avoid signal saturation, and at the same time to provide a sufficiently strong signal. Such thin samples are difficult to prepare, however, attenuated total reflection (ATR) - FTIR, also known as evanescent wave spectroscopy (EWS) provides a solution to this problem.

Raman spectra are more distinct and less overlapped than NIR spectra. Low signal to noise ratio is, however, a problem for RS, which arises due to the very small proportion of scattered photons that make up the Raman signal, and the need to use

filters to remove the excitation line from the collected radiation. Rantanen [8] recently published a review documenting the process analytical applications of RS in the area of pharmaceutical dosage forms. Its potential application in dosage formulation, from chemical synthesis to tablet coating was described, along with a discussion of the main challenges facing its implementation in process analysis, which include: interfacing with the process environment, sample heating during measurement and small sampling area. Šašić provides a good introduction to Raman spectroscopy and applications in pharmaceutical process monitoring in his recent book [9].

Some spectrometers integrate spatial information to give an average spectrum for each sample studied. The inability of NIR and Raman spectrometers to capture internal constituent gradients within samples may lead to discrepancies between predicted and measured composition. Furthermore, point-source spectroscopic assessments do not provide information on spatial distribution of different constituents, which is important in many pharmaceutical applications such as blending. Chemical imaging (CI) integrates conventional imaging and spectroscopy to attain both spatial and spectral information from an object (Figure 2.2). The terms *spectral*

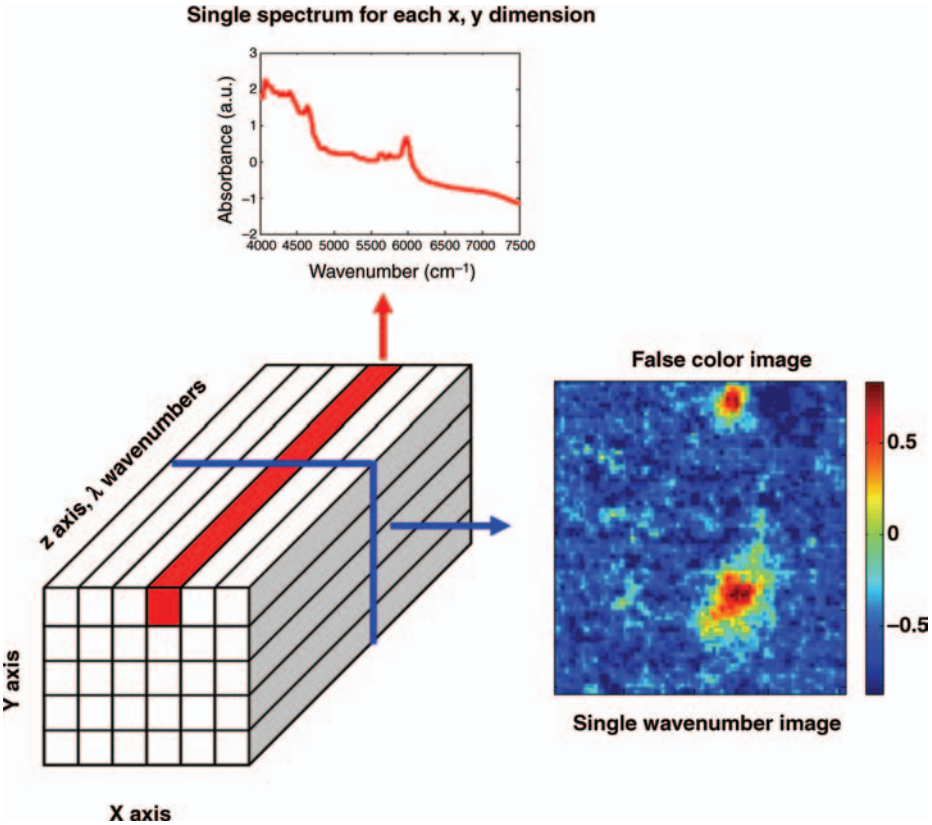

Figure 2.2 Hyperspectral data cube obtained with a chemical imaging device. In this case, the device is a NIR system.

and *chemical* are often interchanged to describe this type of imaging: Spectral imaging is an umbrella term that can be applied to almost any optical spectroscopic technique (e.g., IR, Raman, fluorescence, UV), while chemical imaging generally refers to the vibrational spectroscopies (IR, NIR, Raman). By combining the chemical selectivity of vibrational spectroscopy with the power of image visualization, CI enables a more complete description of ingredient concentration and distribution in inhomogeneous solids, semi-solids, powders, suspensions and liquids.

What basically is obtained by using chemical imaging devices is a hyperspectral data cube of information. That is, for each pixel of the surface scanned (*X* and *Y*-axes in Figure 2.2) a spectrum is recorded.

The attractiveness of surface information provided by, mainly MIR, NIR and Raman imaging devices, together with proper data analysis methods, has opened new research pathways in pharmaceutics, providing excellent possibilities toward obtaining reliable and accurate information in different stages of the process (e.g., correct distribution of components in tablets and powdered mixtures, monitoring mixtures being blended, studies of segregation in granulated preparations, study of the interface between the coating and the core of the tablet, detection of minor compounds, counterfeits, contaminants, etc.). This is confirmed by the high quality publications and book chapters, generated in a few years, encompassing the fundamentals of the new technology and its applications in pharmaceutical research and development [10–18]. Moreover, advances in the production of low cost array detectors have resulted in faster data collection and cheaper chemical imaging systems [19]. Recently, a novel chemical imaging instrument has been developed [48], in which the broadband light source has been replaced by a tunable laser source. The laser source (based on optical parametric oscillator, OPO technology) generates a single wavelength light source at a time. The wavelength can be varied on demand over the wavelength range of interest. This eliminates the need for filters, since only one wavelength is generated at a time. Moreover, this technology reduces the time required for chemical image acquisition to a few seconds.

2.3 The Need for Multivariate Data Analysis

As in classical spectroscopy, the use of multivariate data analysis techniques is becoming a crucial part of the data analysis in CI. The basic steps of the data analysis are summarized in Figure 2.3.

2.3.1 Pre-Processing

The spectral patterns collected are usually affected by noise or by instrumental variations that may alter the analysis and conclusions that may be drawn with further data processing [10, 20]. The most common de-noising techniques are based on the

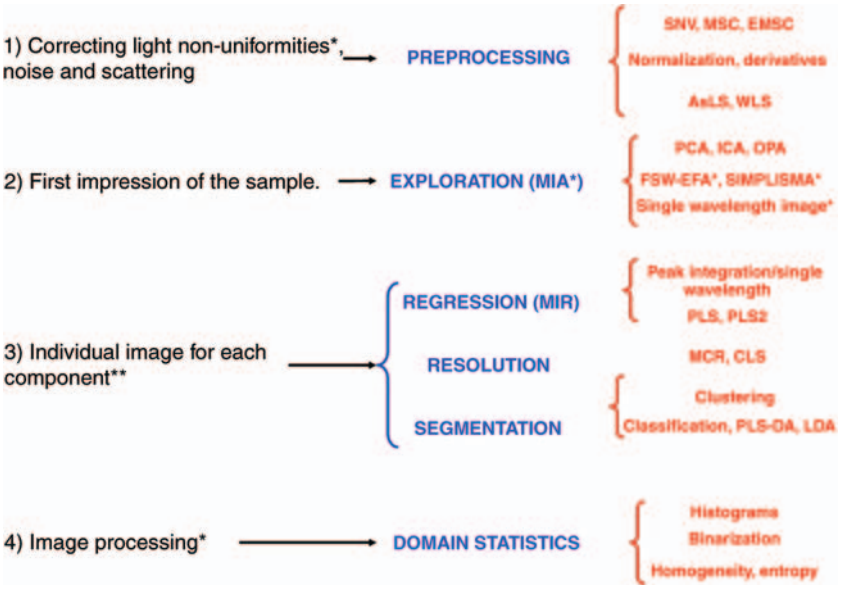

Figure 2.3 Data processing steps. The steps marked with (*) are exclusively applied on hyperspectral image data cubes.(**) The third step is also applied in classical spectroscopy (single measurement/sample). SNV standard normal variate, MSC multiplicative scatter correction, EMSC extended multiplicative scatter correction, AsLS asymmetric least squares, WLS weighted least squares, PCA principal component analysis, ICA independent component analysis, OPA orthogonal projection approach, FSW fixed-size windows, EFA evolving factor analysis, SIMPLISMA simple-to-use interactive self-modeling mixture analysis, PLS partial least squares, PLS2 partial least squares 2, MCR multivariate curve resolution, CLS classical least squares, DA discriminant analysis, LDA linear discriminant analysis.

Savitzky–Golay approach, which fits the spectral pattern to a polynomial function (second-order polynomial) in a step-wise manner [10]. Less used is wavelet-based filtering or principal component analysis. Pre-processing is a convenient and often necessary step. Nevertheless, it can introduce data artifacts or generate the loss of significant spectral information if the method is not properly selected. Consequently, minimal and careful data pre-processing is usually preferred.

2.3.2 Exploration Techniques

Principal components analysis (PCA) (also called multivariate image analysis MIA) is arguably the most useful exploratory technique in spectroscopy. This technique was designed with the aim of explaining the main sources of variability in bi-dimensional experimental datasets (e.g., classical spectroscopy). That is, PCA gives information about the main compounds (chemical compounds and physical

artifacts) and their distribution on the measured surface. This has generated the adaptation of the general PCA method to methods more focused on considering the spatial information gathered, by incorporating the spatial information in the analysis. For instance, methods like fixed-size windows-evolving factor analysis (FSW-EFA) or enhancing contrast methods try to explore the analyzed surface, merging surface and spectral information [21–24].

2.3.3
Regression, Resolution and Classification Techniques

Regression, resolution and classification techniques are demanded when more precise information is required from the samples (e.g., active pharmaceutical ingredient (API) concentration or micro-domain segmentation), Regression methods aim to extract quantitative information from spectroscopic data. The setting-up of calibration models is usually performed by laboratory-made tablets that cover the whole concentration range of the components. In chemical imaging datasets, owing to pixel-to-pixel heterogeneity the quantitative model is usually built using the average spectrum of the regions of interest (ROI) in the surface [25, 26] and the bulk concentration.

On the contrary, resolution techniques (e.g., multivariate curve resolution (MCR) [22, 27–29]) do not usually require a complete calibration set. The feasibility of MCR models relies on the assumption that the spectral information in each sample is the weighted sum of the spectral influence of each component in the mixture. Therefore, the concentration values obtained are fractions or percentages of the pure component sample.

Classification techniques are very useful when the target is to find groups with similar chemical composition, as a function of their similarity in the spectral profiles. They are especially useful in CI to locate and identify impurities or physical defects, coating thickness, or counterfeit detection.

2.3.4
Image Processing Techniques

Up to now, the abovementioned methods have been adapted from classical multivariate analysis to the study of three-way arrays found in CI experiments. Image processing techniques, though, answer the need to extract additional information from the images derived from resolution/regression/classification techniques. That is, study of the distribution (surface distribution) of elements in an image, texture, histogram statistics, and particle domain statistics. These tools are especially useful in the monitoring of blending and granulation processes (Figure 2.4).

Binarization plays a major role in the calculation of domain size statistics. The binary images are created by setting a threshold value, and converting the resulting image into a mixture of two colors denoting the presence or absence of the component of interest. Selection of the proper threshold is critical, since this selection

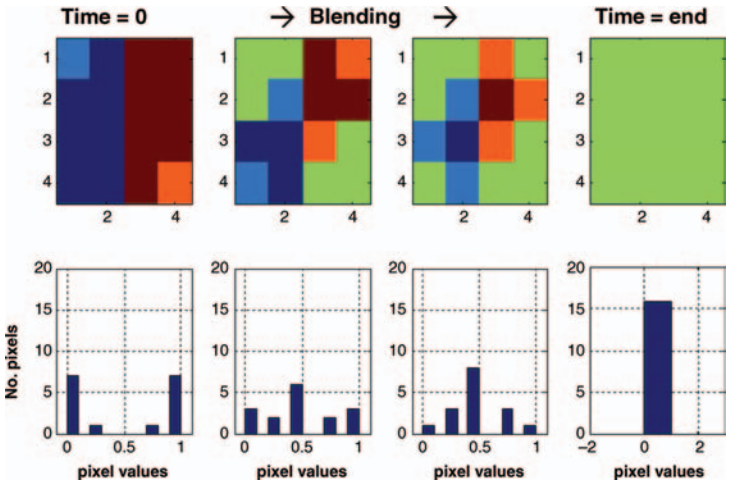

Figure 2.4 Simulation of a blending process monitored by looking at the histograms.

is subjective and will always depend on the final spatial resolution, the correct performance of the data analysis and the criteria of the operator (Figure 2.5).

2.4 Applications in Pharmaceutical Process Monitoring and Quality Control

Rising awareness of spectroscopic techniques and their potential role in the realization of PAT has promoted an increase in the number and diversity of research carried out on their application in manufacturing, development and real implementation of pharmaceutical products. New perspectives and challenges emerge to deeply understand the process or to control the final quality of the preparation. A selection of important applications is discussed below.

2.4.1 Spray Formulations

Doub *et al.* [30] reported the application of Raman-CI for particle size characterization of nasal spray formulations. In order to analyze the formulations, it was necessary to spray aqueous suspensions onto inverted aluminum-coated glass microscope slides which were dried before imaging. A Raman imaging particle size distribution (PSD) protocol was developed and validated using polystyrene (PS) microsphere size standards. Good statistical agreement was obtained between reported PS particle sizes and those estimated using Raman-CI. Moreover, Raman-CI was demonstrated as being suitable for distinguishing between active samples and placebos. It was noted, however, that vigorous validation of Raman-CI for PSD is required, due to the high variability associated with replicate measurements.

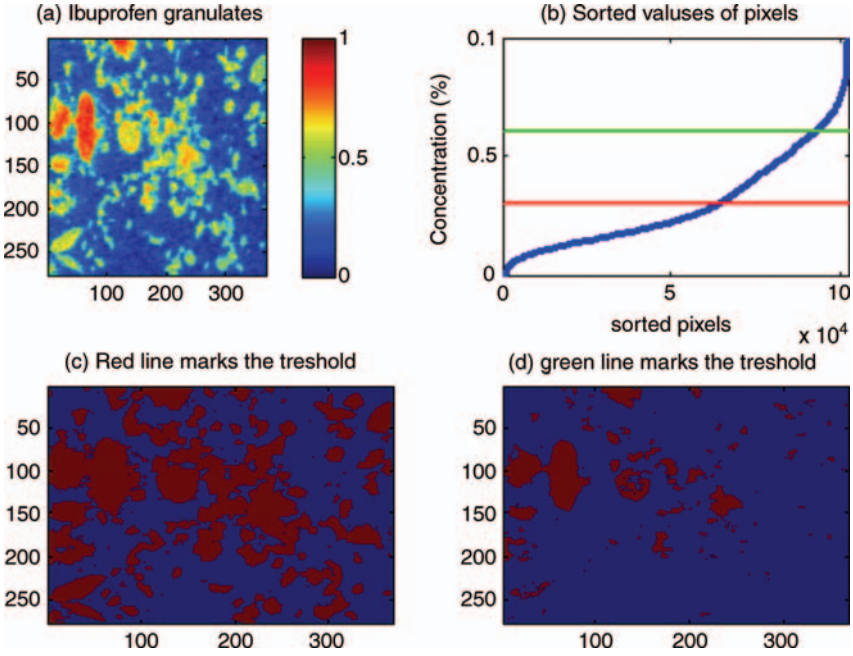

Figure 2.5 (a) Concentration surface obtained for an ibuprofen granulate. (b) Sorted values of the pixels to select a threshold. (c) and (d) Binary images obtained with different thresholds (red and blue denote presence and absence, respectively).

2.4.2
Powders

Powder blend homogeneity in final dosage product poses a significant problem in pharmaceutical quality assurance; poor blending tends to adversely affect tablet hardness, appearance and dissolution kinetics. Lyon *et al.* in 2002 [31] compared the ability of NIR-CI and NIRS in distinguishing blending grade for a selection of final dosage forms. While NIRS was limited in its ability to evaluate drug product homogeneity, NIR-CI provided the opportunity to investigate localized microdomains of ingredients within a drug. It was noted that physical and chemical abnormalities that made minimal contribution to the bulk tablet would be undetected by traditional NIRS but detected by NIR-CI. Compared to conventional "thief" sampling, traditionally used in UV analysis of powder samples, imaging multiple sections of a powder blend offers improved blend characterization [32].

2.4.3
Polymorphism

Characterization of identical chemicals of different crystalline form (polymorphs) is important for quality control in drug development, since polymorphs have different

physical properties such as solubility. Current methods for polymorph screening, such as X-ray diffraction, are time consuming and expensive. Raman spectroscopy coupled with hot-stage microscopy has been demonstrated for rapid screening of polymorphism [33]. More recently, transmission RS has been applied to quantify the polymorphic content of pharmaceutical formulations [34]. This method has the advantage of bulk measurement as compared with backscattering RS methods.

2.4.4
Solid Dosage Forms

Many new drug release systems require complex tablet architecture. In 2001, Lewis *et al*. [35] showed how NIR-CI could be employed for the qualitative description of composition and architecture of a solid dosage form. Bell *et al*. [36–39] published findings on the development of quantitative analytical methods for Raman analysis of solid dosage forms using point mapping. Another more recent article discusses the impact of spatial sampling density in Raman imaging [40]. It was demonstrated that the coarse measurement could be useful for selection of regions which required further fine measurement. Although the fine grid method is time consuming, it would allow visualization of the chemical distribution of the sample, showing greater details of crystal morphology. Li *et al*. [42] applied NIR-CI for characterization of swellable matrix tablets. Tablets were immersed in water for various periods of time and dissected along the radial direction prior to image acquisition. Single wavelength images were used for estimation of the thickness of the gel layer, while PCA images were interpreted in terms of the glass–rubber phase transition.

2.4.5
Root Cause Analysis

Pharmaceutical products undergo various chemical and physical changes during processing. Characterizing the nature and sources of these changes is a major challenge for PAT. Clarke [43] reported the utilization of NIR-CI microscopy for identification of tablets which experienced problems during processing, and for investigation of pre-tabletting blends with dissolution issues. The cluster size of ingredients was measured from chemical images to investigate the effect of compaction force on dissolution properties. In another study, the potential of NIR-CI for investigating the effects of processing on tablet dissolution was examined [44]. It was shown that NIR-CI could be used for the prediction of coating time and to understand batch differences due to different processing conditions.

2.4.6
API Distribution

Henson and Zhang [45] published an article on drug characterization of low dosage pharmaceutical tablets using Raman microscopic mapping. Raman images were obtained using a Raman line-mapping instrument. Domain size and spatial

distribution of the API and major excipients were estimated from Raman maps of the tablets. It was demonstrated that the domain size of the API was dependent upon the particle size distribution of the ingoing API material; therefore, the Raman maps could be used to indicate the source of API used in tablet manufacturing. The potential utility of Raman microscopic mapping in manufacturing process optimization or predictive stability assessments was also outlined.

2.4.7
Coatings

Lewis *et al.* [46] applied NIR-CI for quantification of coating thickness in a single time release microsphere. NIR chemical images demonstrated the differences in chemical structure of the tablet core and coating, enabling quantitative information on coating thickness and homogeneity to be determined. Uneven coating could be clearly identified by visualization of the total intensity image at 2080 nm. A group of 135 microspheres containing two different microsphere types was also imaged in this study. Discrimination of microsphere type was visualized using a spectral difference image.

2.4.8
Counterfeit Identification

Rodionova *et al.* [48] reported advances in the feasibility of detecting counterfeit drugs using both NIRS and NIR-CI. The authors remarked that NIR-CI is useful for identifying small differences in ingredient distributions, which is important for identification of so-called "high quality" counterfeit samples. Westenberger *et al.* [49] compared quality assessment of pharmaceutical products purchased via the internet using a variety of traditional (HPLC-based) and non-traditional (NIR, NIR-CI) techniques. The NIR-CI technique had an added advantage over traditional techniques in its ability to detect suspect manufacturing issues, such as blending and density pattern distribution of components within a drug product, allowing direct qualitative comparison with control products. Lopes *et al.* have developed novel multivariate data analysis techniques for detection and classification of counterfeit drugs using NIR-CI [50–52].

2.4.9
High Throughput Analysis

The huge volume of production encountered in the pharmaceutical industry necessitates high throughput quality analysis techniques. NIR-CI may be adapted to perform analysis on multiple samples in a single field of view by increasing the distance between the camera and target. Fast and nondestructive identification of active ingredients and excipients in whole tablets can be achieved, even through packaging. Hamilton and Lodder [53] reported that a typical NIR chemical imaging

system could simultaneously analyze around 1300 tablets in blister packaging. In another, more recent, paper [54] high throughput analysis of pharmaceutical tablet content uniformity was reported using NIR-CI. A large field of view NIR-CI device was used to take simultaneous chemical images of 20 tablet samples at 61 wavelengths. The total time for image acquisition was less than 2 min, while the conventional UV method took approximately half a working day for sample analysis. It was observed that the mean intensity of images at 1600 nm was proportional to API concentration; the authors suggested that a multispectral instrument based on a small number of wavelengths around 1600 nm could be built to rapidly identify API concentration of these tablets in packaged form.

2.5 Issues Facing the Implementation of Spectroscopic Techniques in the Pharmaceutical Industry

A wealth of evidence suggests that advances in the control of pharmaceutical processes are possible through the on-line implementation of PATs, such as the spectroscopic techniques described in the previous section. These advances would include decreased batch variability, fewer rejects, faster response, lower costs, improved productivity and better process understanding. However, many emerging PAT methods have not yet been implemented in routine process control. The hesitancy to implement PATs in industry may be due in part to resistance to change in some processes and also, as has been suggested by Winskill and Hammond [55], due to concerns over delays in regulatory approval. Reich [37] reviewed the regulatory status of NIR analysis in the pharmaceutical industry, noting that although many pharmaceutical companies have successfully implemented NIR systems in QC labs for raw material identification and qualification, only a few quantitative NIR methods have yet gained regulatory approval.

Apart from regulatory issues, despite the benefits associated with chemical imaging, measurements and subsequent data analysis are not exempt from issues and drawbacks that should be considered to extract accurate and meaningful information and to relate the results obtained to the objective pursued. Key issues and limitations associated with the quality and interpretation of chemical imaging data are discussed below.

2.5.1 Sampling

Nondestructive techniques, such as NIR, RS and their imaging counterparts, offer the possibility of sampling each tablet in a manufacturing process. However, consideration of within-object sampling is an important, if often overlooked, issue. The most common way of measuring NIR and mid-IR radiation in pharmaceutical research is diffuse reflectance. When the incident radiation, composed of millions of photons, reaches the sample surface, it may be immediately reflected (specular

reflectance) or enter the sample, depending on the radiation wavelength and the nature of the sample [16, 35–37]. Some of the photons will be absorbed by the material, whereas others will pass through the entire sample or be scattered/reflected to such a degree that they will not be captured and detected by the instrument. Thus, the photons that ultimately arrive at the detector (the diffusely reflected ones) will contain mixed information about the sample components at various depths and locations in the sample (Figure 2.6a). The final result is a spectral pattern influenced not only by the components of the measured pixel, but also by neighboring pixels and by the depth of penetration. Raman scattering measurements, in contrast, are less affected by this last parameter since the laser beam source, with which the sample is irradiated, penetrates only a few micrometers into the sample.

2.5.2 Spatial Resolution

An important consideration in chemical imaging experiments of pharmaceutical experiments is the domain size of components (e.g., APIs) in comparison to the spatial resolution of the system. Spatial resolution is typically calculated by dividing

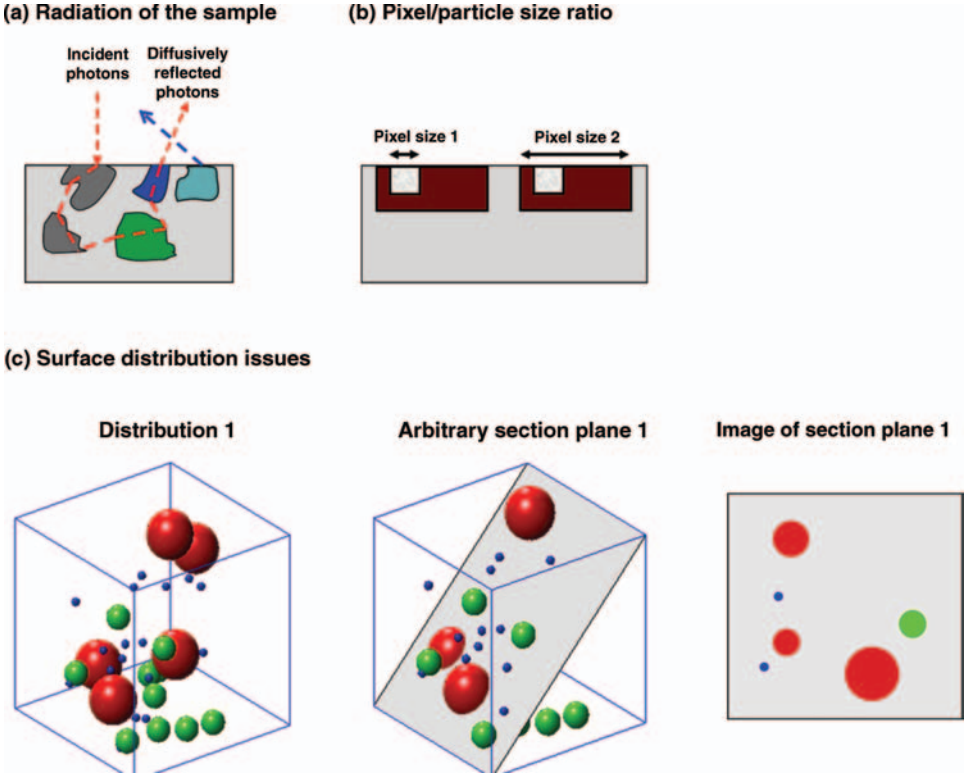

Figure 2.6 Some spatial issues in the analysis of pharmaceutical surfaces [18].

the width and length of the field of view by the number of pixels in the *x*- and *y*- dimensions of the detector. Should the domain size be smaller than the nominal spatial resolution, it is necessary to apply spectral unmixing algorithms (e.g., MCR) to estimate the relative abundance of a species in a given pixel. This kind of situation, where pixels contain contributions from numerous sources, is endemic in remote-sensing hyperspectral imaging where spatial resolution can range from meters to kilometers. The particle sizes of pharmaceutical products vary in nature, depending on the formulation and the product itself, but it is common to find particles with an effective diameter less than 10 μm. This plays a fundamental role in hyperspectral measurements, since the pixel size can usually vary from 10 to 100 μm, depending on the configuration. Figure 2.6b illustrates a schematic model of a pharmaceutical sample where a small particle (gray) is embedded in a larger one (red). The sample is analyzed using two different pixel sizes. In the first case, the pixel size is small enough to obtain selective information about the gray particle. The second case represents a pixel size much bigger than the smallest particle. Thus, depending on the absorptivity of the red particle, the gray one will be difficult to detect because it may be overwhelmed by the signal of the former.

Moreover, spatial resolution obtainable by a given CI system is not just a function of the size of the detector and image magnification but fundamentally limited by photon diffusion through the sample. Sub-surface scattering often distorts the image obtained and thus limits the spatial resolution that can be obtained. In order to address this issue, special spatial resolution targets have been developed that mimic pharmaceutical materials [57].

2.5.3
Representativeness of the Measured Surface

Another concept to bear in mind is that chemical imaging techniques are surface-based techniques. This is especially relevant in tablets, which are usually presented as homogeneous volumetric samples. However, tablets are usually formed from components with different physical and chemical properties, as well as diverse particle sizes, promoting nonhomogeneous distributions of the components in the tablet. Figure 2.6c presents one "volumetric" tablet with the same quantitative composition (equal amount, size, and shape of red, green, and blue spheres) [38–41]. If a section is cut through the tablet (arbitrary section plane) intersecting the components, then an image of that section plane will show two important aspects:

1) The concentration of the components obtained in the surface plane is not representative of their bulk concentration in the tablet.
2) The sizes of the particles in section plane 1 in Figure 2.6c do not correspond to the real sizes of the components in the tablet (clearly visible in the red component). This may lead to the conclusion that the sample is composed of differently sized particles of the same component.

Therefore, special care must be taken in the interpretation of a chemical image obtained from a cross-section of one tablet. A possible solution is to measure several

samples of a product (different tablets of the same batch) or to measure a number of cross-sections of each sample, to guarantee the representativeness of the cross-section with respect to the bulk content of the components.

2.5.4
Irregularities in the Measured Surface

One of the advantages of chemical imaging devices is that almost no sample preparation is needed prior to data acquisition. However, flat-surface samples are preferable owing to the focusing nature of the devices. Moreover, the surface must be parallel to the image plane. Since tablets often have a convex shape, the use of a bevel-blade is necessary to mill flat samples after fixing the tablet to a crystal slide with acrylonitrile adhesive [58]. The microtoming milling technique may present some problems as some component materials may smear or be displaced during sample preparation [59]. It is also convenient to attain a surface as plane as possible when powders or mixtures being blended are measured, to avoid the scattering of the light source owing to the roughness of the surfaces.

The intensity of the light source is one of the key points to consider when obtaining spectral patterns of high quality. Powerful light sources are usually needed in mid-IR and NIR devices to irradiate polychromatic light in the spectral range selected. Laser beam radiation devices working at high resolution are also needed in Raman measurements. These illumination sources generate high levels of energy that induce strong heating of the samples. This may reveal several problems in samples, such as structural changes in granulates and effervescent tablets, and melting or even burning of some organic dyes used in coatings. To overcome this difficulty, cooling systems (e.g., using liquid nitrogen) are usually added to the device. Still, new advances in detectors and dispersive systems are continuously occurring, mainly intended to avoid cooling needs [60].

2.6
Conclusions

Attempts to apply spectroscopy and chemical imaging to real processes have demonstrated high potential to provide useful information in routine pharmaceutical tasks. However, further development in instrumentation technology, speed, and data processing is needed to fully employ chemical imaging in manufacturing process environments. The cost of equipment is commonly stated as a barrier to the implementation of chemical imaging in routine process monitoring. However, the non-destructive, rugged and flexible nature of chemical imaging makes it an attractive PAT for identification of critical control parameters that impact on finished product quality, and time savings associated with its implementation would result in lower production costs over the long term. Judging by the continuing emphasis on process analytical technologies to provide accurate, rapid, nondestructive analysis of pharmaceutical processes, it is likely that CI will be increasingly

adopted for process monitoring and quality control in the pharmaceutical industry, as has been the case with NIR spectroscopy. Future innovations in CI equipment manufacture are likely to depress purchase costs and encourage more widespread utilization of this emerging technology in the pharmaceutical sector.

Acknowledgements

A.A. Gowen acknowledges funding from the EU FP7 under the Marie Curie Outgoing International Fellowship.

References

1 www.fda.gov/cder/OPS/PAT.htm.
2 http://www.emea.europa.eu/Inspections/PAThome.html.
3 Schoneker, D. (2006) Impact of Excipient Variability on PAT Applications: The Need for Good Qualification Processes, AAPS Annual Meeting and Exposition, October 28 - November 3, San Antonio, TX.
4 Skibsted, E.T., Westerhuis, J.A., Smilde, A.K., and Witte, D.T. (2007) Examples of NIR based real time release in tablet manufacturing. *J. Pharm. Biomed. Anal.*, **43**, 1297–1305.
5 Florence, A.J. and Johnston, A. (2011) Applications of ATR UV/vis spectroscopy in physical form characterisation of pharmaceuticals, *Spectrosc. Eur.*, 24–27.
6 Doyle, W.M. and Tran, L. (1999) Analysis of strongly absorbing chromophores by UV-visible ATR spectroscopy. *Spectroscopy*, **14** (4), 46–54.
7 Räsänen, E. and Sandler, N. (2007) Near infrared spectroscopy in the development of solid dosage forms. *J. Pharm. Pharmacol.*, **59**, 147–155.
8 Rantanen, J. (2007) Process analytical applications of Raman spectroscopy. *J. Pharm. Pharmacol.*, **59**, 171–177.
9 Šašić, S. (2007) *Pharmaceutical Applications of Raman Spectroscopy*, Wiley.
10 Amigo, J.M., Cruz, J., Bautista, M., Maspoch, S., Coello, J., and Blanco, M. (2008) *Trends Anal. Chem.*, **27**, 696–713.
11 Gendrin, C., Roggo, Y., and Collet, C. (2008) *J. Pharm. Biomed. Anal.*, **48**, 533–553.
12 Clark, D., Henson, M.J., LaPlant, F., Sasic, S., and Zhang, L. (2007) *The Handbook of Vibrational Spectroscopy, Applications in life, Pharmaceutical and Natural Sciences, Pharmaceutical Applications* (eds D.E. Pivonka, J.M. Chalmers, and P.R. Griffiths), Wiley, Hoboken, pp. 1–27.
13 Gowen, A.A., O'Donnell, C.P., Cullen, P.J., and Bell, S.E.J. (2008) *Eur. J. Pharm. Biopharm.*, **69**, 10–22.
14 Hammond, S.V. and Clarke, F.C. (2002) *The Handbook of Vibrational Spectroscopy, Sampling Techniques, Microscopy* (eds J.M. Chalmers and P.R. Griffiths), Wiley, Hoboken, pp. 1405–1431.
15 Lewis, E.N., Dubois, J., Kidder, L.H., and Haber, K.S. (2007) *Techniques and Applications of Hyperspectral Image Analysis* (eds H. Grahn and P. Geladi), Wiley, Hoboken, pp. 335–361.
16 Lewis, E.N., Schoppelrei, J., Lee, E., and Kidder, L.H. (2005) *Process Analytical Technology*, Blackwell, Cambridge.
17 Reich, G. (2005) *Adv. Drug. Delivery Rev.*, **57**, 1109–1143.
18 Amigo, J.M. (2010) Practical issues of hyperspectral imaging analysis of solid dosage forms. *Anal. Bioanal. Chem.*, **398** (1), 93–109.
19 Kim, M.S., Chao, K., Chan, D., and Lefcourt, A. (2009) Line-scan imaging for high-speed food safety inspection. *SPIE Newsroom*. doi: 10.1117/2.1200903.1564
20 Levin, I.W. and Bhargava, R. (2005) *Annu. Rev. Phys. Chem.*, **56**, 429–474.

21 Cairós, C., Amigo, J.M., Watt, R., Coello, J., and Maspoch, S. (2009) *Talanta*, **79**, 657–664.

22 de Juan, A., Tauler, R., Dyson, R., Marcolli, C., Rault, M., and Maeder, M. (2004) *Trends Anal. Chem.*, **23**, 70–79.

23 de Juan, A., Maeder, M., Hancewicz, T., and Tauler, R. (2005) *Chemom. Intell. Lab. Syst.*, **77**, 64–74.

24 de Juan, A., Maeder, M., Hancewicz, T., and Tauler, R. (2008) *J. Chemom.*, **22**, 291–298.

25 Burger, J. and Geladi, P. (2006) *Analyst*, **131**, 1152–1160.

26 Kolomiets, O., Hoffmann, U., Geladi, P., and Siesler, H.W. (2008) *Appl. Spectrosc.*, **62**, 1200–1208.

27 Amigo, J.M. and Ravn, C. (2009) *Eur. J. Pharm. Sci.*, **37**, 76–82.

28 Awa, K., Okumura, T., Shinzawa, H., Otsuka, M., and Ozaki, Y. (2008) *Anal. Chim. Acta*, **619**, 81–86.

29 Cruz, J., Bautista, M., Amigo, J.M., and Blanco, M. (2009) *Talanta*, **80**, 473–478.

30 Doub, W.H., Adams, W.P., Spencer, J.A., Buhse, L.F., Nelson, M.P., and Treado, P.J. (2007) Raman chemical imaging for ingredient-specific particle size characterization of aqueous suspension nasal spray formulations: a progress report. *Pharm. Res.*, **24**, 934–945.

31 Lyon, R.C., Lester, D.S., Lewis, E.N., Lee, E., Yu, L.X., Jefferson, E.H., and Hussain, A.S. (2002) Near-infrared spectral imaging for quality assurance of pharmaceutical products: analysis of tablets to assess powder blend homogeneity. *AAPS PharmSciTech.*, **3**, 17.

32 Ma, H. and Anderson, C.A. (2008) Characterization of pharmaceutical powder blends by NIR chemical imaging. *J. Pharm. Sci.*, **97**, 3305–3320.

33 Al-Dulaimi, S., Aina, A., and Burley, J. (2009) Rapid polymorph screening on milligram quantities of pharmaceutical material using phonon-mode Raman spectroscopy. *CrystEngComm*, **12**, 1038–1040.

34 Aina, A., Hargreaves, M.D., Matousek, P.A.U., and Burley, J.C. (2010) Transmission Raman spectroscopy as a tool for quantifying polymorphic content of pharmaceutical formulations. *Analyst*, **135**, 2328–2333

35 Lewis, E.N., Carroll, J.E., and Clarke, F.M. (2001) A near-infrared view of pharmaceutical formulation analysis. *NIR News*, **12**, 16–18.

36 Bell, S.E.J., Beattie, J.R., McGarvey, J.J., Peters, K.L., Sirimuthu, N.M.S., and Speers, S.J. (2004) Development of sampling methods for Raman analysis of solid dosage forms of therapeutic and illicit drugs. *J. Raman Spectrosc.*, **35**, 409–417.

37 Bell, S.E.J., Barrett, L.J., Burns, D.T., Dennis, A.C., and Speers, S.J. (2003) Tracking the distribution of "ecstasy" tablets by Raman composition profiling: a large scale feasibility study. *Analyst*, **128**, 1331–1335.

38 Bell, S.E.J., Burns, D.T., Dennis, A.C., and Speers, J.S. (2000) Rapid analysis of ecstasy and related phenethylamines in seized tablets by Raman spectroscopy. *Analyst*, **125**, 541–544.

39 Bell, S.E.J., Burns, D.T., Dennis, A.C., Matchett, L.J., and Speers, J.S. (2000) Composition profiling of seized ecstasy tablets by Raman spectroscopy. *Analyst*, **125**, 1811–1815.

40 Lee, E., Adar, F., and Whitley, A. (2006) The impact of spatial sampling density in Raman imaging. *Spectrosc.*, **21S**, 21.

41 Lee, E., Adar, F., and Whitley, A. (2006) The impact of spatial sampling density in Raman imaging. *Spectrosc*, **21**, 21.

42 Li, W., Woldu, A., Araba, L., and Winstead, D. (2010) Determination of Water Penetration and Drug Concentration. Profiles in HPMC-Based Matrix Tablets by Near Infrared. Chemical Imaging. *J. Pharm. Sci*, **99** (7), 3081–3088.

43 Clarke, F. (2004) Extracting process-related information from pharmaceutical dosage forms using near infrared microscopy. *Vib. Spectrosc.*, **34**, 25–35.

44 Roggo, Y., Jent, N., Edmond, A., Chalus, P., and Ulmschneider, M. (2005) Characterizing process effects on pharmaceutical solid forms using near-infrared spectroscopy and infrared imaging. *Eur. J. Pharm. Biopharm.*, **61**, 100–110.

45 Henson, M. and Zhang, L. (2006) Drug Characterization in Low Dosage Pharmaceutical Tablets Using Raman Microscopic Mapping. *Appl. Spectrosc.*, **60**, 1247–1255.

46 Lewis, E.N., Kidder, L., and Lee, E. (2005) NIR Chemical Imaging as a Process Analytical Tool. *Innov. Pharm. Tech.*, **17**, 107–111.

47 Spectral imaging device with tunable light source (2007) US patent 7,233,392.

48 Rodionova, O., Houmøller, L., Pomerantsev, A., Geladi, P., Burger, J., Dorofeyev, V., and Arzamastsev, A. (2005) NIR spectrometry for counterfeit drug detection: A feasibility study. *Anal. Chim. Acta*, **549**, 151–158.

49 Westenberger, B.J., Ellison, C.D., Fussner, A.S., Jenney, S., Kolinski, R.E., Lipe, T.G., Lyon, R.C., Moore, T.W., Revelle, L.K., Smith, A.P., Spencer, J.A., Story, K.D., Toler, D.Y., Wokovich, A.M., and Buhse, L.F. (2005) Quality assessment of internet pharmaceutical products using traditional and non-traditional analytical techniques. *Int. J. Pharm.*, **306**, 56–70.

50 Lopes, M.B., Wolff, J.-C., Bioucas-Dias, J.M., and Figueiredo, M.A.T. (2010) Near-infrared hyperspectral unmixing based on a minimum volume criterion for fast and accurate chemometric characterization of counterfeit tablets. *Anal. Chem.*, **82**, 1462–1469.

51 Lopes, M.B., Wolff, J.-C., Bioucas-Dias, J.M., and Figueiredo, M.A.T. (2009) Determination of the composition of counterfeit HeptodinTM tablets by near-infrared chemical imaging and least squares estimation. *Anal. Chim. Acta*, **641**, 46–51.

52 Lopes, M.B. and Wolff, J.-C. (2009) Investigation into classification/sourcing of suspect counterfeit HeptodinTM tablets by near infrared chemical imaging. *Anal. Chim. Acta*, **633**, 149–155.

53 Hamilton, S.J. and Lodder, R.A. (2002) Hyperspectral imaging technology for pharmaceutical analysis. *Proc. SPIE*, **4626**, 136–147.

54 Malik, I., Poonacha, M., Moses, J., and Lodder, R.A. (2001) Multispectral imaging of tablets in blister packaging. *AAPS PharmSciTech*, **2**, 9.

55 Winskill, N. and Hammond, S., An industry perspective on the potential for emerging process analytical technologies http://www.fda.gov/ohrms/dockets/ac/02/briefing/3841B1_05_PFIZER/sld001.htm.

56 Reich, G. (2005) Near-infrared spectroscopy and imaging: Basic principles and pharmaceutical applications. *Adv. Drug Deliv. Rev.*, **57**, 1109–1143.

57 Kauffman, J.F., Gilliam, S.J., and Martin, R.S. (2008) Chemical imaging of pharmaceutical materials: fabrication of micropatterned resolution targets. *Anal. Chem.*, **80** (15), 5706–5712.

58 Sasic, S. (2008) *Anal. Chim. Acta*, **611**, 73–79.

59 LaPlant, F. (2004) *Am. Pharm. Rev.*, **7**, 16–24.

60 Onat, B.M., Carver, G., and Itzler, M. (2008) *Proc. of SPIE*, **7310**, 731004-1/11.

3
Quality Control in Food Processing

Colette C. Fagan

3.1
Introduction

Food processors have come under increased pressure to ensure the large-scale production of consistently high quality food products with specific functional properties. This has been driven by the requirement for consumer acceptability of products as either food ingredients or consumer products, as well as increased concerns over the safety and, to some degree, authenticity of food products. If food processors are to meet these demands, they must implement and maintain procedures which will ensure this outcome. However, there are a number of challenges which the food industry must overcome to achieve this, for example most unit operations are batch or semi-continuous operations, there is often a large inherent variation in the raw material used, and food products and processes are complex, heterogeneous and involve the interaction of a number of factors. Therefore, the food industry has looked towards strategies, for example process analytical technology (PAT), to achieve consistently high quality products. PAT is a systems for designing, analyzing and controlling manufacturing through timely measurements of critical quality and performance attributes of raw and in-process materials and processes [1]. However, this requires the control of the manufacturing process through real-time analysis of critical quality parameters. Therefore, techniques and technologies, that is, PAT tools, which can rapidly, accurately and preferably nondestructively, assess the quality, and functional properties of food products, are essential for the modern food processing industry. These tools should also facilitate increased process understanding, development of risk-mitigation strategies, and continuous improvement. Optical and imaging technologies have been developed which have the potential to be ideal PAT tools. These have primarily been applied to quality and safety assessment, authenticity determination, and process control applications. These include near-infrared (NIR) spectroscopy, mid-infrared (MIR) spectroscopy, fluorescence spectroscopy, hyperspectral imaging (HSI), and Raman spectroscopy (Table 3.1).

Handbook of Biophotonics. Vol.3: Photonics in Pharmaceutics, Bioanalysis and Environmental Research, First Edition.
Edited by Jürgen Popp, Valery V. Tuchin, Arthur Chiou, and Stefan Heinemann

Table 3.1 Examples of the application of optical and imaging technologies to food quality and processing.

Principle	Application	Product	Reference
NIR	Sensory quality	Cheese	[111]
FTIR, FT-NIR and FT-Raman	Authenticity	Oils and fats	[59]
FTIR	Geographic origin	Honey	[112]
NIR	Process monitoring	Hamburger meat	[113]
Fluorescence and MIR	Geographic origin	Cheese	[114]
Spectral imaging	Defect detection	Fruit	[115]
Hyperspectral imaging	Contaminant detection	Poultry	[116]

Integration of such strategies and technologies results in the generation of large amounts of diverse data. Therefore, appropriate data management and processing approaches are critical if such data rich technologies are to be employed in the food processing sector.

Advances in chemometrics, which applies optimal mathematical and statistical methods to process data, has been key to the adoption of PAT tools. Chemometric approaches are vital in understanding, diagnosing real-time processes, and keeping them under multivariate statistical control. Multivariate calibration and multivariate classification are two of the most common chemometric methodologies. Chemometric approaches can be used to overcome problems in spectroscopy such as collinearity that is, where variables in the calibration have high correlations between them, or where it is difficult to select a specific wavelength for calibration as infrared spectra frequently contain data points carrying overlapping information [2]. Calibration approaches such as principal components analysis (PCA) and partial least squares regression (PLSR), and classification approaches such as cluster analysis or discriminant analysis (DA) are commonly used and have been explained in detail elsewhere [3, 4].

Recent advances in instruments have widened the potential applications of photonics in the food industry. Developments in fiber optics have assisted the expansion of NIR reflectance and transmission sensors for online analysis, while the move towards miniaturization of spectrometers has opened up new opportunities for food processors to monitor critical control point. The development and improvement in MIR instrumentation, in particular Fourier transform infrared (FTIR) spectrometers, has increased the feasibility of applying MIR spectroscopy to the precise control and monitoring of a manufacturing process. Emerging platform technologies such as hyperspectral imaging (HSI), which integrates conventional imaging and spectroscopy to attain both spatial and spectral information from an object, have also shown potential for widespread adoption in the areas of food quality, safety, and product development. Table 3.2 outlines the advantages and disadvantages of some of technologies most commonly applied to food products.

Table 3.2 Advantages and disadvantages of the near infrared (NIR), Fourier transform infrared (FTIR) and fluorescence spectroscopy from [117].

Techniques	Sensitivity	Information content	Absence of interferences	Repeatability	Absence of light scatter
NIR	**	**	*	**	**
FTIR	***	***	*	***	**
Fluorescence	***	*	***	**	*

Sensitivity and information content: *, low; ***, high; Absence of interferences: *, many interferences; ***, few interferences; Repeatability: *, poor; ***, good; Absence of light scatter: *, severe light scatter; ***, no light scatter.

3.2 Quality Applications

Food quality cannot be considered as a single, well-defined attribute. In fact it encompasses a number of properties or characteristics, which are often referred to as the quality indices of the product under test [5]. Examples of such indices may be chemical composition, sensorial and textural attributes, aroma, and appearance. While the use of photonics offers a solution to the challenge of determining such complex attributes, one must ensure that the basis for the prediction of quality is fully understood, as well as its inherent limitations.

The advantages of employing FTIR spectroscopy in conjunction with attenuated total reflectance (ATR) as a quantitative quality control tool for the food industry have been previously outlined [6]. Villé *et al.* [7] developed a method for the determination of total fat and phospholipid content in intramuscular pig meat using FTIR spectroscopy. Meat samples were extracted with chloroform and methanol and FTIR spectra were recorded in transmission mode. They developed a linear regression equation to predict total fat using the spectral region associated with the C=O band (1785–1697 cm^{-1}). The resulting model had a determination coefficient of 99%. FTIR spectroscopy has also been employed to predict the fatty acid content in fat extracts of pork meat [8]. Samples were again extracted using chloroform and methanol and the sample accessory was an ATR cell. Models were developed which predicted four fatty acids with R^2 values between 0.91 and 0.98.

Lefier *et al.* [9] employed FTIR spectroscopy to predict milk fat, crude protein, true protein and lactose content. Due to the success of the FTIR measuring principle for the analysis of milk this technology has been successfully commercialized with products such as the MilkoScan™ FT 120 (Foss, Denmark), which employs this principle in compliance with IDF and AOAC standards.

The quality of any given type of cheese is related to a large extent to its texture, which in turn is influenced by moisture and other composition components, and processing conditions. Therefore MIR spectroscopy has been investigated as a tool for predicting not only compositional parameters but also textural attributes.

The organoleptic quality of cheese is determined by complex changes that occur during ripening [10, 11]. The three reactions, which are primarily responsible for the development of texture and flavor, are proteolysis, glycolysis and lipolysis. Irudayaraj *et al.* (1999) investigated the use of FTIR spectroscopy to follow texture development in Cheddar cheese during ripening. They demonstrated that springiness could be successfully correlated with a number of bands in mid-infrared spectra. The development of cheese microflora during ripening is extremely important in the development of flavor and texture. Leifer *et al.* [12] demonstrated that FTIR spectroscopy could be used as a rapid and robust method for the qualitative analysis of cheese flora. They developed a model for the identification of *Lactococcus* sp. using a number of strains of *Lactcoccus lactis* ssp. *lactis* and *cermoris*. FTIR spectroscopy has also been used to evaluate the shelf-life period in which "freshness" is maintained in Crescenza cheese [13]. PCA was found to detect the decrease of Crescenza "freshness" and to define the critical day during shelf-life. Fagan *et al.* [14] determined the potential of FTIR spectroscopy coupled with PLS regression for the prediction of processed cheese instrumental texture and meltability attributes. The strongest models developed predicted hardness ($R^2 = 0.77$), springiness ($R^2 = 0.77$), cohesiveness ($R^2 = 0.81$) and Olson and Price meltability ($R^2 = 0.88$).

Fruit quality indices consist of internal quality, such as soluble solids content (SSC) and total acidity (TA), and external quality, such as size and weight [15]. Bureau *et al.* [16] studied the potential of FTIR spectroscopy to simultaneously determine the sugar and organic acid content of apricot fruit slurries. They identified the most suitable spectral region as 1500 to 900 cm^{-1} for model development ($R^2 \geq 0.74$ and root mean square error of prediction (RMSEP) $\leq$18%).

NIR spectroscopy has been widely employed for the prediction of the chemical composition of numerous products including, milk [17, 18], cheese [19–22], butter [23], meat [24–26], wheat [27, 28], and fruit [29].

For compositional analysis of products such as cheese NIR reflection has primarily been used. As early as 1982 NIR spectroscopy was applied to the determination of the fat, protein and moisture content of cheese [19]. More recently, NIR spectroscopy has also been applied to the prediction of the composition of processed cheese with much success (root mean square error of cross validation (RMSECV) = 0.45, 0.50, and 0.26% for fat, moisture and salt, respectively) [21]. Downey *et al.* [30] subsequently examined the potential of NIR spectroscopy to predict the sensory attributes and maturity of Cheddar cheese. The most successfully predicted parameters were maturity, crumbliness, rubberiness, chewiness, mouth-coating and massforming. A similar study on processed cheese in general found that it was possible to predict processed cheese sensory and instrumental texture parameters using NIR spectroscopy [31].

The texture of fruit is also a critical quality parameter. Valente *et al.* [32] employed a combination of visible and NIR spectroscopy and a nondestructive acoustic technique to estimate mango fruit firmness. The best calibration result was obtained using the second derivative spectra for two genetic algorithm selected spectral ranges (736–878 and 955–1022 nm) and had an associated RMSEP value of 3.28 ($R^2 = 0.82$), however, they were deemed not to be sufficiently good to allow automated fruit sorting.

Cayuela and Weiland [33] compared two commercial portable spectrometers for prediction of orange quality. The first spectrometer (Vis–NIR) used fiber optics to collect the reflected radiation and transmit it to three detectors (350–2500 nm). The second instrument (AOTF-NIR) had a reflectance post-dispersive optical configuration and InGaAs detector (1100–2300 nm). They predicted 11 parameters, that is, soluble solids content, acidity, titratable acidity, maturity index, flesh firmness, juice volume, fruit weight, rind weight, juice volume to fruit weight ratio, fruit color index and juice color index. They found the results were particularly good for the direct NIR prediction of soluble solids content, and maturity index (Vis–NIR spectrometer: RPD = 1.67–2.21 and AOTF-NIR spectrometer: 1.03 to 2.33).

A limited number of studies have employed Raman spectroscopy to characterize cheese during ripening. Some of the most common excitation wavelengths used today for Raman spectroscopy are 532, 633, 785 and 1064 nm. While the Raman scattering effect is more efficient at short wavelengths, the use of short wavelength lasers can induce fluorescence in the sample under test, which is stronger than the Raman scattering. NIR excitation does not give rise to such an effect and one of the most common NIR laser sources for Raman spectroscopy of foodstuffs has been the Nd: YAG (neodymium-doped yttrium aluminum garnet) solid state laser (1064 nm). However, when this laser is used water-based samples suffer from self-absorption of Raman scatter, as well as significant laser absorption [34]. Additional information on lasers used for Raman spectroscopy can be found elsewhere [34–36].

Rudzik *et al.* [37] have stated that Raman spectroscopy is an excellent tool for protein secondary structure determination. Fontecha *et al.* [38] used Raman spectroscopy with a 514.5 nm excitation laser to study the secondary structure of caseins from various sources, including ewes cheese. They assigned bands at 1609 and 1616 cm^{-1} to ring vibrations of aromatic amino acid side-chains, a band at 1655 cm^{-1} to the α-helix segments, and bands in the region of 1665 cm^{-1} to disordered and turn structures. They also stated that bands corresponding to the β-strand structures of casein were located in the region of 1680 cm^{-1} with β-sheet structures appearing at 1630 cm^{-1}. An increase in intensity at 1630 cm^{-1} occurred during cheese ripening as a result of increased β-sheet structures.

Raman spectroscopy has also been employed to understand how protein structure changes with processing to elucidate the impact on thermal processing on the functional properties of food [39].

Asfseth *et al.* [25] evaluated Raman spectroscopy for determining fatty acid composition and contents of the main constituents in a complex food model system. They developed a model system consisting of 70 different mixtures of protein, water, and oil blends. The PLS regression models predicted the total level of unsaturation in the form of the iodine value with an error of 2.8% of the total iodine value range. The same authors went on to apply Raman spectroscopy to the assessment of real food systems (salmon) [40]. The Raman spectra of intact salmon muscle, ground salmon and oil extracts were used to predict the degree of fatty acid unsaturation (iodine value) of the salmon ($n = 50$). The best model was developed using the oil extract spectra ($R = 0.87$, RMSECV = 2.5 g I_2/100 g fat) using only one latent variable.

3.3 Safety Applications

The area of photonics and food safety has grown over the last decade or so. Technologies have been developed which could be used to detect contaminants such as foreign objects, fecal matter, or microbial contamination. The potential to identify microbial populations and validate cleaning protocols has also been investigated.

The contamination of carcasses by fecal matter is the primary pathway for pathogens to contaminate such products. Fluorescence spectroscopy has been employed to determine excitation and emission characteristics of fecal matter derived from cows, deer, swine, chickens, and turkeys [41]. Spectra were recorded of fecal matter, animal meats, and swine, chickens', and turkeys' feedstuff. Excitation at approximately 410 to 420 nm yielded the highest level of fluorescence for both feces and feedstuffs. The emission maxima for feces were at 675 nm with the exception of chicken feces which occurred at 632 nm.

A number of studies have examined the potential of HSI to detect fecal contamination [42–46]. Park *et al.* [42] studied the performance of supervised classification algorithms and HSI to identify fecal and ingesta contaminants. The six different supervised classification algorithms examined were parallelepiped, minimum distance, Mahalanobis distance, maximum likelihood, spectral angle mapper and binary coding. The classification accuracies varied from 62.9 to 92.3%, depending on the classification method. The highest classification accuracy for identifying contaminants from corn-fed carcasses was 92.3% with a spectral angle mapper classifier. The overall mean classification accuracy for classifying fecal and ingesta contaminants was 90.3%. The same group also utilized a band-ratio image processing algorithm using 2-wavelengths (I_{565}/I_{517}) and 3-wavelength ($I_{576} - I_{616}$)/($I_{529} - I_{616}$) models [43]. Figure 3.1 describes the hyperspectral image processing procedure and shows the results of the 3-wavelength models. The 2-wavelength model had a correct classification rate of 96.4% and 147 false positives, while the 3-wavelength models had a correct classification rate of 98.6% but 388 false positives. A similar approach was employed by Liu *et al.* [45] to detect fecal contamination on apples. They recorded hyperspectral images of two apple cultivars, and they used 2- (I_{725}/I_{811}) and 3-wavelength ($I_{811} - I_{557}$)/($I_{725} - I_{557}$) band ratio equations to identify fecal contaminated skins, with the dual band ratio giving the best results.

Fourier transform Raman spectroscopy has been studied for the characterization and differentiation of six different microorganisms, including the pathogen *Escherichia coli* O157: H7 on whole apples [47]. They stated that the technology successfully discriminated between *E. coli* strains as well as accurately differentiating pathogens from non-pathogens. Sivakesava *et al.* [48] also attempted to identify and classify various species of microorganisms, in this case using FTIR and NIR spectroscopy. Using canonical variate analysis (CVA) and NIR spectra they achieved a 95.6% correct classification rate, while FTIR spectra achieved a lower correct classification rate of 93%, however, FTIR required a lower number of principal components. Harz *et al.* [49] employed micro-Raman spectroscopy to identify bacterial bulk material

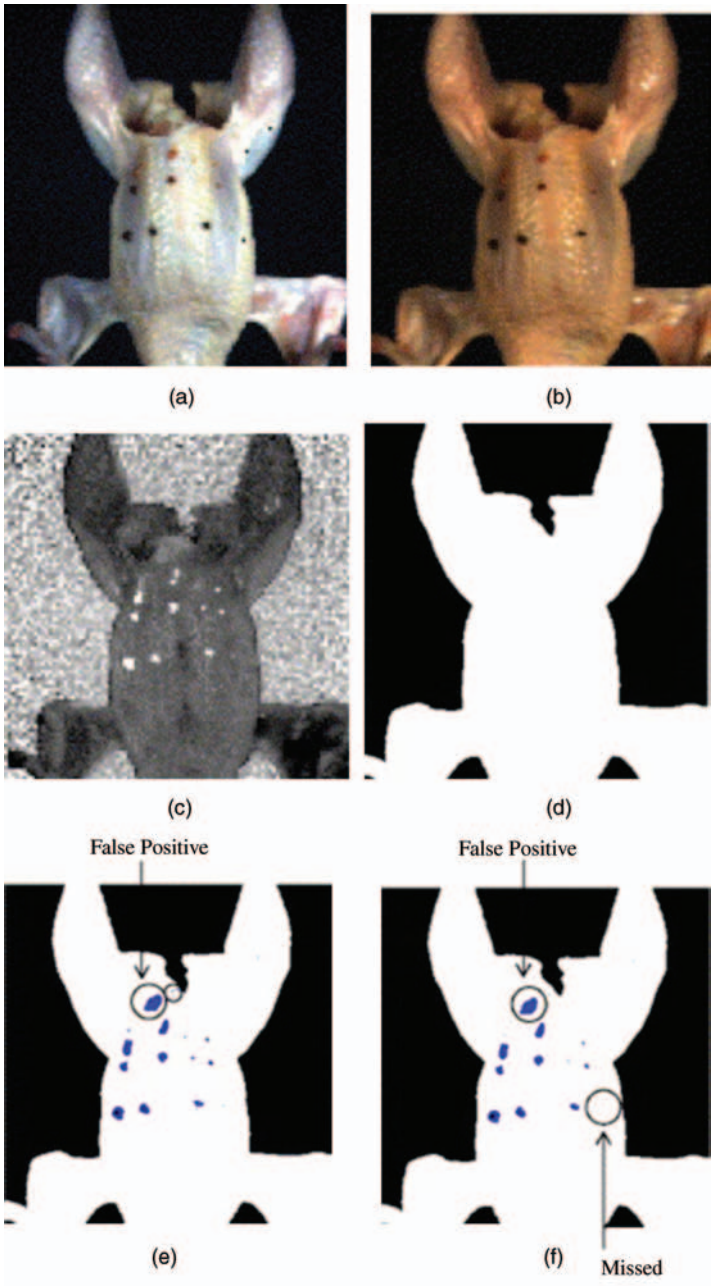

Figure 3.1 Procedure of hyperspectral image processing of a poultry carcass: (a) color composite; (b) calibrated color image; (c) ratio image (calibrated and smoothed); (d) background mask and band ratio results of three wavelengths (529, 576, and 616 nm) selected by single term regression model using the region of interest of the hyperspectral images at (e) threshold = 1.05; (f) threshold = 1.05 with filter. From [43].

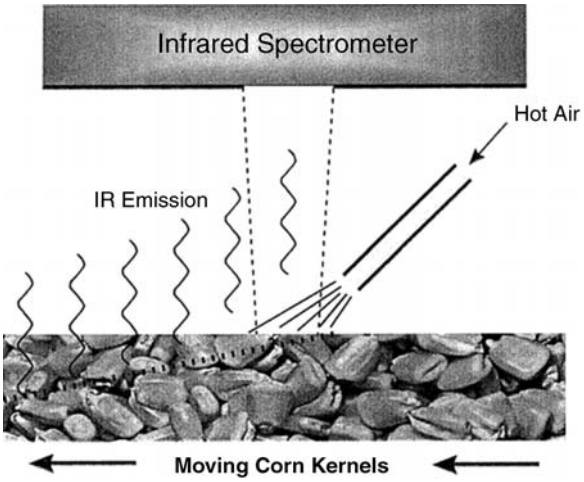

Figure 3.2 Schematic illustration of corn kernels moving past the detector in TIRS. [50].

and single cells of different species within the genus *Staphylococcus*. They found it was possible to make a distinction between strains in the bulk material when a support vector machine and hierarchical cluster analysis were employed. For single bacterial spectra they achieved an average recognition rate of 94.1% on the strain level and 97.6% on the species level.

Mycotoxins can pose a significant health risk to humans. Transient infrared (TIR) spectroscopy and FTIR photoacoustic spectroscopy have been employed to detect toxigenic fungi (*Aspergillus flavus*) in corn [50] (Figure 3.2). It was found that TIR spectroscopy effectively distinguished healthy corn from corn infected with *Aspergillus flavus* with a 85 or 95% success rate. Berardo *et al.* [51] challenged NIR spectroscopy to identify toxigenic fungi and their toxic metabolites produced in naturally and artificially contaminated products. They indicated that NIR could accurately predict the incidence of kernels infected by fungi, and by *Fusarium verticillioides* in particular. They were also able to predict the quantity of ergosterol and fumonisin B_1 in the meal. The best model predicted the percentage of global fungal infection and *Fusarium verticillioides* when data from the maize kernels ($R^2 = 0.75$ and standard error of cross validation (SECV) = 7.43) and maize meals ($R^2 = 0.79$ and SECV = 10.95).

3.4 Authenticity Application

Food manufacturers are required to demonstrate the authenticity of their products [2]. The European Union set out the rights of consumers and genuine food processors in terms of food adulteration and fraudulent or deceptive practices in food processing [52]. There are three EU schemes which are used to promote and protect the

Table 3.3 Examples of product names registered under protected designation of origin (PDO), protected geographical indication (PGI) and traditional specialty guaranteed (TSG) schemes.

Designation	Country	Type	Product Categrory
Scotch Lamb	United Kingdom	PGI	Class 1.1
Prosciutto di Parma	Italy	PDO	Class 1.2
Timoleague Brown Pudding	Ireland	PGI	Class 1.2
Edam Holland	Netherlands	PGI	Class 1.3
Mozzarella	Italy	TSG	Class 1.3
Emmental de Savoie	France	PGI	Class 1.3
Huile d'olive de Corse; Huile d'olive de Corse-Oliu di Corsica	France	PDO	Class 1.5
灊县麻山药 (Lixian Ma Shan Yao)	China	PGI	Class 1.6
Yorkshire Forced Rhubarb	United Kingdom	PDO	Class 1.6
Brussels grondwitloof	Belgium	PGI	Class 1.6
Herefordshire cider/perry	United Kingdom	PGI	Class 1.8
Dortmunder Bier	Germany	PGI	Class 2.1
Pierekaczewnik	Poland	TSG	Class 2.3
Kalakukko	Finland	TSG	Class 2.3

Class 1.1 Fresh meat (and offal), Class 1.2 Meat products (cooked, salted, smoked), Class 1.3 Cheeses, Class 1.5 Oils and fats (butter, margarine, oil, etc.), Class 1.6 Fruit, vegetables and cereals fresh or processed, Class 1.8 other products of Annex I of the Treaty (spices etc.), Class 2.1 Beers, Class 2.3 Confectionery, bread, pastry, cakes, biscuits and other baker's wares.

names of quality agricultural products and foodstuffs. These are protected designation of origin (PDO), protected geographical indication (PGI) and traditional specialty guaranteed (TSG). Examples of products protected under these schemes are shown in Table 3.3. The authenticity of incoming raw materials is also of concern to food processors.

Detection of adulterated oils, for example, olive oil is critical both in terms of economic and health aspects [53]. A number of studies have been undertaken to examine the potential of a range of technologies to detect adulterated oils [53–57].

Lai [54] employed FTIR spectroscopy in conjunction with PCA and linear DA to determine the authenticity of vegetable oils. They found that samples clustered according to their origin (plant species) and it was also possible to discriminate between extra virgin and refined olive oils (correct classification rate: 93% calibration and 100% validation). Lai *et al.* [55] also examined the potential of FTIR spectroscopy to quantify the level of adulterants (refined olive oil and walnut oil) in extra virgin olive oil with some success (standard error of prediction (SEP) = 0.68–0.92 g $(100\,g)^{-1}$). The potential of Fourier transform Raman spectroscopy in such an application has also been reported [56]. They adulterated virgin olive oil with soybean, corn, and raw olive residue (olive pomace) oils at 1, 5, and 10%, respectively and also collected six genuine virgin olive oil samples. They achieved a 100% correct discrimination between genuine and adulterated samples and 91.3% correct classifications at different adulteration levels using principal component regression. Marigheto

et al. [58] went on to compare the potential of FTIR and Raman spectroscopies to discriminate between oils of differing botanical origin, and for their ability to detect added adulterants. Ultimately they found that MIR, in combination with linear discriminant analysis, gave the best classification rates and adulteration detection levels were comparable with Raman spectroscopy. Determination of olive oil geographic origin using visible and NIR spectroscopy was also examined by Downey *et al.* [57]. They collected samples from three regions that is, Crete ($n = 18$), the Peloponese ($n = 28$), and other parts of Greece ($n = 19$), and spectral analysis was carried out in transflectance mode using a gold-plated accessory. The results indicated that the highest classification rate was achieved using raw spectra (400–2498 nm) and factorial DA, although it was noted that the samples were from a single harvest. A comparison between FTIR (MIR), FT-NIR, and FT-Raman spectroscopy for discrimination among 10 different edible oils and fats has also been carried out [59]. In agreement with other studies they found that FTIR spectroscopy was the most successful in discriminating between oils and fats (98%), followed by Fourier transform Raman spectroscopy (94%) and Fourier transform NIR spectroscopy (93%).

Cheese authenticity is an emerging research area, which is becoming increasingly important to the dairy sector [60]. Pillonel *et al.* [61] employed a small data set of Emmental cheeses from different regions, that is, Switzerland ($n = 6$), Allgau (Germany) ($n = 3$), Bretagne (France) ($n = 3$), Savoie (France) ($n = 3$), Vorarlberg (Austria) ($n = 3$) and Finland ($n = 2$) to compare NIR and FTIR spectroscopy for their potential to discriminate samples on the basis of geographic origins. They found that FTIR transmission spectra achieved 100% correct classification in conjunction with LDA when differentiating Swiss Emmental from the other samples pooled as one group, while NIR diffuse reflection spectroscopy allowed a classification by the six regions of cheese origin (100% correct classification). Karoui *et al.* [62] went on to combine FTIR and front-face fluorescence spectroscopy to discriminate between Emmental cheeses originating from different European countries: Austria ($n = 12$), Finland ($n = 10$), Germany ($n = 19$), France ($n = 57$), and Switzerland ($n = 65$). By pooling the first 20 principal components from both the FTIR and fluorescence spectral datasets, and subjecting them to factorial DA they achieved correct classifications of 76.7% of the validation spectra.

Aulrich and Molkentin [63] investigated the potential of NIR spectroscopy to discriminate between organically and conventionally produced milk on the basis of ω3-fatty acids predictions. They found it was possible to predict ω3-FA content and that, with due consideration to seasonal variations in the contents of the ω3-FA C18 : 3ω3 and C20 : 5ω3 in milk, that NIR spectroscopy could be used as screening tool in discriminating between organically and conventionally produced milk. The potential of FTIR spectroscopy to discriminate between milk samples on the basis of origin that is, cow, goat, or sheep has been investigated [64]. Blends of sheep and cow milk, goat and cow milk, and sheep and goat milk were prepared which contained between 0 and 100% of each milk in increments of 5%. A second set of samples was prepared containing a blend of sheep, cow, and goat milk, also in increments of 5%. The best result was achieved using kernel PLS regression for the

first data set (error = 4 to 6%) while errors of 3.9 to 6.4% were achieved for the second dataset.

Over the last decade there has been a drive towards rapid nondestructive techniques for determining honey authenticity and geographic origin.

Goodacre *et al.* [65] employed Raman spectroscopy to discriminate between honey samples from different floral and geographical origins. Analysis was carried out on 51 samples, from 5 countries and from a number of botanical sources: acacia (7), chestnut (9), eucalyptus (4), heather (10), lime (4), rape (5), sunflower (4), citrus (2), lavender (2), rosemary (1), *Echium plantagineum* (1), orange (1), and fior di sulla (1). They stated that cluster analysis indicated that differences between the honeys were due to their botanical origin rather than their country of origin.

Sivakesava and Irudayaraj [66] employed FTIR spectroscopy as a screening tool for the determination of beet medium invert sugar adulteration in three different varieties of honey. They developed PLS regression models using first derivative spectra (1500–950 cm^{-1}) for determination of beet invert sugar in honey samples. The most successful model for discriminating adulterated honey samples was achieved with canonical variate analysis (classification rate 88–94%). However, care should be taken to ensure the experimental design does not facilitate classification on the basis of alteration of the solids content of the honey [67]. Therefore, honey samples and the adulterant solutions are usually adjusted to a standard solids (°Brix) level.

Detection of honey adulteration using FTIR spectroscopy has been examined [67]. Irish honey samples ($n = 221$) were adulterated using D-fructose and D-glucose solutions, while authentic samples ($n = 99$) were also collected. Samples and adulterant solutions were adjusted to 70°Brix. The classification model developed using PLS regression of first derivative spectra gave the best classification rate (93 or 99% if greater than 14% w/w adulterant). Kelly *et al.* [68] went on to examine the potential of FTIR spectroscopy to detect adulteration of Irish honeys by five adulterants. Authentic Irish honeys ($n = 580$) and honeys adulterated by fully inverted beet syrup ($n = 280$), high-fructose corn syrup ($n = 160$), partial invert cane syrup ($n = 120$), dextrose syrup ($n = 160$), and beet sucrose ($n = 120$) were adjusted to 70°Brix and analyzed. They were able to classify authentic honey and honey adulterated by beet sucrose, dextrose syrups, and partial invert corn syrup (correct classification rates: 96.2, 97.5, 95.8, 91.7% respectively). However, they were not able to clearly detect high-fructose corn syrup or fully inverted beet syrup adulteration. This group also examined the potential of NIR transflectance spectroscopy in such an application [69]. They used authentic honey ($n = 83$) and honeys adulterated with beet invert syrup ($n = 56$) and high fructose corn syrup ($n = 40$). In this scenario they found that NIR spectroscopy could be used as a rapid screening tool for detection of Irish honey adulterated with these compounds.

The work of Ruoff *et al.* [70, 71] investigated the potential of fluorescence and FTIR spectroscopy to classify honey according to its botanical and geographical origin. The samples analyzed were 11 unifloral (acacia, alpine rose, chestnut, dandelion, heather, lime, rape, fir honeydew, metcalfa honeydew, oak honeydew) and polyfloral honey types (fluorescence: $n = 371$; FTIR: $n = 411$).

Using fluorescence spectroscopy the discriminant models had error rates of less than 0.1% for polyfloral and chestnut honeys to 9.9% for fir honeydew honey, by using single spectral data sets. If two data sets were combined the error rates were from <0.1% (metcalfa honeydew, polyfloral, and chestnut honeys) to 7.5% (lime honey). For FTIR spectroscopy the error rates ranged from <0.1% (polyfloral, heather honeys, honeydew honeys from metcalfa, oak, and fir) to 8.3% (alpine rose honey). Fluorescence spectroscopy could only classify samples according to geographical origin within a group of honeys of the same botanical origin, however, linear DA of FTIR spectra of acacia, lime, dandelion, and honeydew honey samples from Germany and Switzerland resulted in an average correct classification rate of 85%. However, botanical origin had a more significant effect than geographical origin, hence, the results may in fact be due to the indirect effects of the botanical origin.

They have also tried to create a specific NIR spectral fingerprint for Corsican honey [60]. They collected NIR spectra from authentic Corsican samples, and mathematically processed them so as to develop a univariate specification based on fingerprint spectroscopy. The specification was then challenged by spectra of separate Corsican and non-Corsican honey samples over two production seasons. The best PLS discriminant models produced correct classification rates of 90.0% (Corsican), 90.3% (non-Corsican) and 90.4% (Corsican) and 86.3% (non-Corsican) for models validated via cross-validation and an independent test set, respectively.

Al-Jowder *et al.* [72] applied FTIR spectroscopy to the authenticity of fresh meats. Using PCA they were able to discriminate between chicken, pork and turkey meats. The basis for this discrimination was found to be the lipid (1740 cm^{-1}) and protein (1650 and 1550 cm^{-1}) bands with protein bands increasing in intensity for chicken, turkey and pork consecutively. They also differentiated between fresh samples and the frozen samples that had been thawed. McElhinney *et al.* [73] also investigated the potential of FTIR spectroscopy for quantitative analysis of meat mixtures. A PLS regression model was able to predict the lamb content of minced beef and lamb mixtures with an R value of 0.97, however, the study also developed models using NIR spectra, which were found to have an R value of 0.99. Al-Jowder *et al.* [74] went on to employ FTIR spectroscopy to discriminate between pure beef and beef containing 20% offal (heart, kidney, liver and tripe) in both raw and cooked samples. Ding and Xu [75] found that NIR spectroscopy could be used to discriminate between authentic beef hamburgers and those adulterated with 5–25% mutton, pork, skim milk powder, or wheat flour with an accuracy up to 92.7%. A comparative study has also been carried out to compare the potential of FTIR, NIR and visible spectroscopy to discriminate samples on the basis of origin (i.e., chicken, turkey, pork, beef, lamb) [76]. Difficulties arose when trying to discriminate between chicken and turkey. Therefore the authors developed models with both five meat classes and also with four, where chicken and turkey samples were combined as one group. For the five class model, incorporating FTIR spectra with visible and NIR spectra did not improve model accuracy. However, in the case of the four class model it did by improving the discrimination between chicken and turkey.

The use of fruit purees rather than whole fruits as a raw material is advantageous from an economic perspective, and in the case of some soft fruits a requirement [77]. However, determining the authenticity of fruit purees can be a challenge. FTIR spectroscopy has been used to discriminate between fruit purees using DA [77]. They could classify purees according to a number of factors that is, strawberry, raspberry, or apple (100% success); fresh or freeze-thawed (98.3% for strawberry, 75% for raspberry); sulfur dioxide addition (90% for apple); and Bramley versus non-Bramley apples (86%). Contal *et al.* [78] went on to examine if visible and NIR spectroscopy could be used for detecting strawberry and raspberry purees adulterated with apple. They prepared authentic strawberry ($n = 32$) and raspberry ($n = 32$) purees as well as strawberry and raspberry purees adulterated with 10, 20, 30, 50 and 75% apple ($n = 28$). Ultimately the developed model could detect apple adulteration at levels above 20% in strawberry and between 10 and 20% in raspberry. More recently, FT-NIR spectroscopy of cell wall components has been evaluated for determining the authenticity of fruit and the fruit content of products [79]. They collected NIR spectra of the alcohol-insoluble residues ($n = 92$) and hemicellulose ($n = 109$) fractions obtained from the samples. They found that the calibration models developed to predict alcohol-insoluble residues and hemicellulose correlated very well with the reference data ($R^2 = 0.98$).

A robust, rapid, and inexpensive method for quality assurance purposes is needed in the wine industry to monitor that wine parameters conform to specification, in order to ensure the quality of the final product delivered to the consumer [80]. FTIR spectroscopy has been used to classify 165 wines from three different geographical origins (Gaillac, Beaujolais and Touraine) which were made from the same grape variety, that is, Gamay. The spectra of dried samples were recorded in transmission mode. By employing factorial DA they were able to classify the samples according to geographic origin with a correct classification rate of 97% [81]. Bevin *et al.* [80] also employed FTIR spectroscopy for wine assessment. They analyzed three Australian wine varieties, Shiraz, Cabernet Sauvignon, and Merlot ($n = 161$). Spectra, which excluded the regions 1543 to 1717 cm^{-1}, 2971 to 3627 cm^{-1} and 2276–2431 cm^{-1}, were recorded in transmission mode. They found that for five of the six wineries they obtained a correct classification rate of 98%. Acevedo *et al.* [82] went on to examine if classification of wines according to their origin could be improved by using UV–Vis spectroscopy and support vector machines (SVM). They stated that SIMCA, k-neural network, and PLSR DA seemed to require more selective techniques/variables than SVM if a large variety of wines was to be discriminated according to the specific region in which they are produced. In terms of its simplicity the SVM was preferred over NN-MPL. Finally, Cozzolino *et al.* [83] compared and combined UV–Vis, NIR and FTIR spectroscopy to determine their efficacy as tools for the classification of commercial Sauvignon Blanc from Australia (seven regions) and New Zealand (four regions). Spectral analysis was carried out in transmission mode. The best results employed a model developed using PLS DA. Concatenation of the NIR and MIR data resulted in the highest overall correct classification rate (93%). While MIR was the next strongest (90%) followed by NIR (76%) and UV–Vis (67%).

3.5 Process Control

Development of technologies which facilitate the control and monitoring of critical control points during food processing is essential. This includes the monitoring and detection of microbial populations, which is critical not only from a food safety but also from a process monitoring perspective. Microbial populations are critical to flavor and texture development in products such as cheese. Oberreuter *et al.* [84] employed FTIR spectroscopy to rapidly monitor the population dynamics of bacteria in cheese during ripening. They found that only 1% of the coryneform bacteria could not be identified by FTIR spectroscopy. Gaus *et al.* [85] successfully employed UV-resonance Raman spectroscopy for the classification of lactic acid bacteria on a strain level; the observed clusters corresponding to the different strains when PCA and hierachical cluster analysis were used.

NIR technology has been successfully applied at laboratory and commercial scale for monitoring processes during dairy processing. In particular, the milk coagulation process during cheese production has received a great deal of attention. Cutting the coagulum either before or after the optimum point results in losses of curd and fat. An increase in cheese moisture also occurs if the gel is too firm when cut. Originally, the determination of the cutting time was established by the cheese maker. Although accurate this method is not feasible in closed commercial vats and, together with an increased desire for automation in the cheese industry, has led to the need for an on-line objective method for the monitoring of milk coagulation. Early methods, which utilized the changes in the optical properties of the milk, were reflection photometry [86] and absorbance [87]. Although the reflection photometry and absorbance methods were found to monitor coagulation they were rarely used. However, developments in fiber optics have overcome many of the problems associated with these techniques. Light in the NIR region can be transmitted through a fiber optic bundle and diffuse reflectance or transmission monitored. As the gel is formed the reflectance will increase while transmission will decrease. Payne *et al.* [88] developed a method based on changes in diffuse reflectance during milk coagulation. Reflectance was measured using a fiber optic probe, utilizing a photodiode light source at a wavelength of 940 nm. The time to the inflection point (t_{max}) was determined from the first derivative and was found to correlate well with Formograph cutting times. Linear prediction equations, which were considered to be of the form required for predicting cutting time, were also developed using t_{max}. This technology has been commercialized as the CoAguLite sensor (Reflectronics Inc, Lexington, KY). It could also be used in conjunction with other sensors, for example the FiberView dairy waste sensor system, which could be used to monitor waste streams in dairy facilities. This enables the location, occurrence or concentration of the discharge to be determined. It monitors solids concentration in dairy plant effluents in the range of 0 to 1% solids (or higher), and, due to its quick response to loss events, it allows operators to take corrective actions.

Syneresis is a critical phase in cheese manufacture, with the rate and extent of syneresis playing a fundamental role in determining the moisture, mineral and

lactose content of drained curd, and hence that of the final cheese [89, 90]. Therefore, research is ongoing into the development of a syneresis control technology. A number of potentially noninvasive technologies have been investigated for such an application, including ultrasound and computer vision [91–94] and NIR sensing [95–97]. Initial studies focused on off-line optical sensing of whey samples [98]. An adaption of this technology led to the development of a sensor which could be installed in the wall of a cheese vat for on-line continuous monitoring of both coagulation and syneresis [99]. The sensor operated at 980 nm and was sensitive to casein micelle aggregation and curd firming during coagulation, and to changes in curd moisture and whey fat contents during syneresis. This sensor was also used to predict whey fat content (i.e., fat losses), curd yield and curd moisture content with SEPs of 2.37 g, 0.91 and 1.28%, respectively [100]. Further work used a wider spectral range (300–1100 nm) in conjunction with PLS regression to predict whey fat and curd moisture with RMSECV values of 0.094 and 4.066%, respectively [101]. Mateo *et al.* [102] developed another set of models which predicted the yield of whey ($R^2 = 0.83$, error = 6.13 g/100 g) using three terms, namely light backscatter, milk fat content and cutting intensity. These studies were carried out in laboratory scale cheese vats (7–11 l), therefore, further scaling up and development under commercial conditions of the technology will be required if it is to become viable at a commercial scale. Fluorescence spectroscopy has also been studied for its potential as a syneresis control tool [103]. In this preliminary evaluation it was found that tryptophan and riboflavin fluorescence had strong relationships with curd moisture and whey total solids content during syneresis, and that it was possible to develop simple one- and two-parameter models to predict curd moisture content, curd yield and whey total solids using parameters derived from the sensor profiles (error = 0.0005 to 0.394%; $R^2 = 0.963$ to 0.999).

NIR spectroscopy has also been investigated as a process control tool in yoghurt production. Cimander *et al.* [104] studied the potential of NIR spectroscopy to monitor yogurt fermentation in a 4.2-l laboratory scale vat. A sensor signal fusion approach was adopted with NIR (400 to 2500 nm), electronic nose, and standard bioreactor sensors installed as part of a multi-analyzer set-up. While the electronic nose followed changes in galactose, lactic acid, lactose and pH, the NIR sensor signal correlated well with the changes in the physical properties during fermentation. Therefore, the signals from the sensors were fused using a cascade artificial neural network (ANN). Results suggested that the accuracy of the neural network prediction was acceptable. This approach was further investigated by Navrátil *et al.* [105] under industrial conditions in a 1000-l vat. Signal responses from NIR and electronic nose sensors were subjected to PCA separately. The scores of the first principal component from each PCA were then used to make a trajectory plot for each fermentation batch. PLS regression of the NIR spectra was also used to predict pH and titratable acidity (expressed as Thorner degrees, °Th) during fermentation with reasonable success (SEPs of 0.17 and 6.6 °Th, respectively). MIR spectroscopy has also been employed to monitor the sorghum fermentation process [106]. FTIR spectroscopy was used to detect differences due to the effect of lactic bacteria on sorghum fermentation. It was found possible to differentiate between samples

which used natural yogurt and *Lactobacillus fermentum* as inocula due to variations in protein and starch structures.

Optical sensors have also been developed to monitor meat emulsion stability [107–110]. Initial work focused on prediction of meat emulsion stability using reflection photometry [107]. The authors found that L^* values increased at the beginning of chopping, associated with reduced cooking losses, following 8 min of chopping there was a reduction in L^* and b^* values and an associated increase in cooking losses, which suggested the feasibility of an on-line optical sensor technology to predict the optimum endpoint of emulsification in the manufacture of finely comminuted meat products. These authors then recorded light backscatter intensity from beef emulsions manufactured with different fat/lean ratio and chopping duration using a dedicated fiber optic prototype [108]. They found several optically derived parameters to be significantly correlated with fat loss during cooking. In subsequent work they found normalized intensity decreased with increased chopping time as a result of emulsion homogenization, and with increased distance and that chopping time had a positive correlation with fat losses during cooking, which in turn had a negative correlation with normalized light intensity and loss of intensity. They suggest therefore that light extinction spectroscopy could provide information about emulsion stability [109].

3.6 Conclusions

NIR, MIR, fluorescence and Raman spectroscopic techniques are ideal PAT tools which could be implemented in a variety of quality, safety, authenticity and process control applications. Advances in equipment design, such as the move toward micro and miniature spectrometers will assist in the deployment of such technologies in the food industry. However, where studies have primarily been at laboratory scale further research is required to ensure appropriate scaling up and transfer of the technology to industry. The combination of spectroscopic and imaging technologies in emerging platforms may also allow enhanced identification of quality problems during food processing.

3.7 Glossary

Artificial neural network (ANN)
Attenuated total reflectance (ATR)
Canonical variate analysis (CVA)
Discriminant analysis (DA)
Fourier transform infrared (FTIR)
Hyperspectral imaging (HSI)
Mid-infrared (MIR)

Near-infrared (NIR)
Neodymium-doped yttrium aluminum garnet (Nd:YAG)
Partial least squares regression (PLSR)
Process analytical technology (PAT)
Protected designation of origin (PDO)
Protected geographical indication (PGI)
Principal components analysis (PCA)
Root mean square error of cross validation (RMSECV)
Root mean square error of prediction (RMSEP)
Soft independent modeling of class analogy (SIMCA)
Soluble solids content (SSC)
Standard error of prediction (SEP)
Traditional specialty guaranteed (TSG)
Transient infrared (TIR)
Total acidity (TA)

References

1 Balboni, M.L.(October 2003) Process analytical technology concepts and principles, *Pharm. Technol.*, 54–66.
2 Woodcock, T. *et al.* (2008) Application of Near and Mid-Infrared Spectroscopy to Determine Cheese Quality and Authenticity, *Food Bioproc. Technol.*, **1** (2), 117–129.
3 Martens, H. and Næs, T. (1989) *Multivariate Calibration*, Wiley, Chichester.
4 Martens, H. and Martens, M. (2001) *Multivariate Analysis of Quality: An Introduction*, John Wiley & Sons., Chichester.
5 Abbott, J.A. (1999) Quality measurement of fruits and vegetables, *Postharvest Biol. Technol.*, **15** (3), 207–225.
6 Vandevoort, F.R. (1992) Fourier-transform infrared-spectroscopy applied to food analysis, *Food Res. Int.*, **25** (5), 397–403.
7 Villé, H. *et al.* (1995) Determination of phospholipid content of intramuscular fat by Fourier Transform Infrared spectroscopy. *J. Meat Sci.*, **41**, 283–291.
8 Ripoche, A. and Guillard, A.S. (2001) Determination of fatty acid composition of pork fat by Fourier transform infrared spectroscopy. *Meat Sci.*, **58** (3), 299–304.
9 Lefier, D., Grappin, R., and Pochet, S. (1996) Determination of fat, protein, and lactose in raw milk by Fourier transform infrared spectroscopy and by analysis with a conventional filter-based milk analyzer. *J. AOAC Int.*, **79** (3), 711–717.
10 McSweeney, P.L.H. and Fox, P.F. (1993) Cheese: Methods of Chemical Analysis, In Cheese: Chemistry, Physics and microbiology, Vol 1, 2nd Ed (ed. P.F. Fox). Chapman & Hall, London, pp. 341–388.
11 Irudayaraj, J., Chen, M., and McMahon, D.J. (1999) Texture Development in Cheddar Cheese During Ripening, *Can. Agr. Eng.*, **41** (4), 253–258.
12 Lefier, D., Lamprell, H., and Mazerolles, G. (2000) Evolution of lactococcus strains during ripening in brie cheese using fourier transform infrared spectroscopy. *Lait*, **80** (2), 247–254.
13 Cattaneo, T.M.P. *et al.* (2005) Application of FT-NIR and FT-IR spectroscopy to study the shelf-life of Crescenza cheese. *Int. Dairy J.*, **15** (6–9), 693–700.
14 Fagan, C.C. *et al.* (2007) Evaluating mid-infrared spectroscopy as a new technique for predicting sensory texture attributes of processed cheese. *J. Dairy Sci.*, **90** (3), 1122–1132.
15 Liu, Y. *et al.* (2010) Nondestructive measurement of internal quality of

Nanfeng mandarin fruit by charge coupled device near infrared spectroscopy. *Comput. Electron. Agr.*, **71** (Supplement 1), S10–S14.

16 Bureau, S. *et al.* (2009) Application of ATR-FTIR for a rapid and simultaneous determination of sugars and organic acids in apricot fruit. *Food Chem.*, **115** (3), 1133–1140.

17 Carl, R.T. (1991) Quantification of the Fat-Content of Milk Using a Partial-Least-Squares Method of Data-Analysis in the near-Infrared. *Fresen. J. Anal. Chem.*, **339** (2), 70–71.

18 Kawamura, S. *et al.* (2007) Near-infrared spectroscopic sensing system for online monitoring of milk quality during milking. *Sens. Instrum. Food Qual. Safety*, **1** (1), 37–43.

19 Frank, J.F. and Birth, G.S. (1982) Application of near infrared reflectance spectroscopy to cheese analysis. *J. Dairy Sci.*, **65** (7), 1110–1116.

20 Molt, K. and Kohn, S. (1993) Near-IR spectroscopy. Chemometry for processed cheese products in quality control and process analysis. *Dtsch. Milchw.*, **44** (22), p. 1102, 1104–1107.

21 Blazquez, C. *et al.* (2004) Prediction of moisture, fat and inorganic salts in processed cheese by near infrared reflectance spectroscopy and multivariate data analysis. *JNIRS*, **12** (3), 149–157.

22 Rodriguezotero, J.L., Hermida, M., and Cepeda, A. (1995) Determination of fat, protein, and total solids in cheese by near-Infrared reflectance spectroscopy. *J. AOAC Int.*, **78** (3), 802–806.

23 Meagher, L.P. *et al.* (2007) At-line near-infrared spectroscopy for prediction of the solid fat content of milk fat from New Zealand butter. *J. Agr. Food Chem.*, **55** (8), 2791–2796.

24 Mlcek, J., Sustova, K., and Simeonovova, J. (2006) Application of FT NIR spectroscopy in the determination of basic chemical composition of pork and beef. *Czech J. Anim. Sci.*, **51** (8), 361–368.

25 Afseth, N.K. *et al.* (2005) Raman and near-infrared spectroscopy for quantification of fat composition in a complex food model system. *Appl. Spectrosc.*, **59** (11), 1324–1332.

26 Kim, Y.B. and Lee, M. (1997) Utilization on the near-infrared (NIR) for the chemical composition analysis of raw meat. *Korean J. Anim. Sci.*, **39** (1), 77–92.

27 Owens, B. *et al.* (2009) Prediction of wheat chemical and physical characteristics and nutritive value by near-infrared reflectance spectroscopy. *Br. Poult. Sci.*, **50** (1), 103–122.

28 Miralbes, C. (2003) Prediction chemical composition and alveograph parameters on wheat by near-infrared transmittance spectroscopy. *J. Agr. Food Chem.*, **51** (21), 6335–6339.

29 Peirs, A. *et al.* (2002) Comparison of Fourier transform and dispersive near-infrared reflectance spectroscopy for apple quality measurements. *Biosystems Eng.*, **81** (3), 305–311.

30 Downey, G. *et al.* (2005) Prediction of maturity and sensory attributes of Cheddar cheese using near-infrared spectroscopy. *Int. Dairy J.*, **15** (6–9), 701–709.

31 Blazquez, C. *et al.* (2006) Modelling of sensory and instrumental texture parameters in processed cheese by near infrared reflectance spectroscopy. *J. Dairy Res.*, **73** (1), 58–69.

32 Valente, M. *et al.* (2009) Multivariate calibration of mango firmness using vis/NIR spectroscopy and acoustic impulse method. *J. Food Eng.*, **94** (1), 7–13.

33 Cayuela, J.A. and Weiland, C. (2010) Intact orange quality prediction with two portable NIR spectrometers. *Postharvest Biol. Technol.*, **58** (2), 113–120.

34 Wilson, H.M.M. *et al.* (1996) Fourier transform Raman spectroscopy: A comparison of Nd:YAG and lower-frequency sources. *Vib. Spectrosc.*, **10** (2), 89–104.

35 Pan, M.-W., Benner, R.E., and Smith, L.M. (2002) Continuous lasers for raman spectrometry, in *Handbook of Vibrational Spectroscopy* (eds J. Chalmers and P. Griffiths), John Wiley & Sons Ltd., Chichester, pp. 490–506.

36 Saleh, B.E.A. and Teich, M.C. (2007) *Fundamentals of Photonics*, John Wiley & Sons Ltd., Hoboken.

37 Rudzik, L. *et al.* (2007) Raman spectroscopic investigations on the

secondary structure of proteins in cheese. *Dtsch. Milchw.*, **58** (6), 196–198.

38 Fontecha, J., Bellanato, J., and Juarez, M. (1993) Infrared and Raman-Spectroscopic Study of Casein in Cheese - Effect of Freezing and Frozen Storage. *J. Dairy Sci.*, **76** (11), 3303–3309.

39 Kilil, R. and Irudayaraj, J. (2007) Applications of Raman spectroscopy for food quality measurement, in *Nondestructive Testing of Food Quality* (eds J. Irudayaraj and C. Reh), Blackwell Publishing, Oxford, pp. 143–163.

40 Afseth, N.K., Wold, J.P., and Segtnan, V.H. (2006) The potential of Raman spectroscopy for characterisation of the fatty acid unsaturation of salmon. *Anal. Chim. Acta*, **572** (1), 85–92.

41 Kim, M.S., Lefcourt, A.M., and Chen, Y.R. (2003) Optimal fluorescence excitation and emission bands for detection of fecal contamination. *J. Food Prot.*, **66** (7), 1198–1207.

42 Park, B. *et al.* (2006) Performance of supervised classification algorithms of hyperspectral imagery for identifying fecal and ingesta contaminants. *Trans. ASABE*, **49** (6), 2017–2024.

43 Park, B. *et al.* (2006) Performance of hyperspectral imaging system for poultry surface fecal contaminant detection. *J. Food Eng.*, **75** (3), 340–348.

44 Heitschmidt, G.W. *et al.* (2007) Improved hyperspectral imaging system for fecal detection on poultry carcasses. *Trans. ASABE*, **50** (4), 1427–1432.

45 Liu, Y.L. *et al.* (2007) Development of simple algorithms for the detection of fecal contaminants on apples from visible/near infrared hyperspectral reflectance imaging. *J. Food Eng.*, **81** (2), 412–418.

46 Park, B. *et al.* (2007) Fisher linear discriminant analysis for improving fecal detection accuracy with hyperspectral images. *Trans. ASABE*, **50** (6), 2275–2283.

47 Yang, H. and Irudayaraj, J. (2003) Rapid detection of foodborne microorganisms on food surface using Fourier transform Raman spectroscopy. *J. Mol. Struct.*, **646** (1–3), 35–43.

48 Sivakesava, S., Irudayaraj, J., and DebRoy, C. (2004) Differentiation of microorganisms by FTIR-ATR and NIR spectroscopy. *Trans. ASABE*, **47** (3), 951–957.

49 Harz, M. *et al.* (2005) Micro-Raman spectroscopic identification of bacterial cells of the genus Staphylococcus and dependence on their cultivation conditions. *Analyst*, **130** (11), 1543–1550.

50 Gordon, S.H. *et al.* (1999) Transient infrared spectroscopy for detection of toxigenic fungus in corn: Potential for on-line evaluation. *J. Agr. Food Chem.*, **47** (12), 5267–5272.

51 Berardo, N. *et al.* (2005) Rapid detection of kernel rots and mycotoxins in maize by near-infrared reflectance spectroscopy. *J. Agr. Food Chem.*, **53** (21), 8128–8134.

52 European Commission (2002) Article 8, Regulation (EC) No. 178/2002D. Laying down the general principles and requirements of food law, establishing the European Food Safety Authority and laying down procedures in matters of food safety.

53 Lichan, E. (1994) Developments in the Detection of Adulteration of Olive Oil. *Trends Food Sci. Tech.*, **5** (1), 3–11.

54 Lai, Y.W., Kemsley, E.K., and Wilson, R.H. (1994) Potential of Fourier Transform-Infrared Spectroscopy for the Authentication of Vegetable-Oils. *J. Agr. Food Chem.*, **42** (5), 1154–1159.

55 Lai, Y.W., Kemsley, E.K., and Wilson, R.H. (1995) Quantitative-Analysis of Potential Adulterants of Extra Virgin Olive Oil Using Infrared-Spectroscopy. *Food Chem.*, **53** (1), 95–98.

56 Baeten, V. *et al.* (1996) Detection of virgin olive oil adulteration by Fourier transform Raman spectroscopy. *J. Agr. Food Chem.*, **44** (8), 2225–2230.

57 Downey, G., McIntyre, P., and Davies, A.N. (2003) Geographic classification of extra virgin olive oils from the eastern Mediterranean by chemometric analysis of visible and near-infrared spectroscopic data. *Appl. Spectrosc.*, **57** (2), 158–163.

58 Marigheto, N.A. *et al.* (1998) A comparison of mid-infrared and Raman spectroscopies for the authentication of edible oils. *J. Am. Oil Chem. Soc.*, **75** (8), 987–992.

59 Yang, H., Irudayaraj, J., and Paradkar, M.M. (2005) Discriminant analysis of edible oils and fats by FTIR, FT-NIR and

FT-Raman spectroscopy. *Food Chem.*, **93** (1), 25–32.

60 Woodcock, T., Downey, G., and O'Donnell, C.P. (2009) Near infrared spectral fingerprinting for confirmation of claimed PDO provenance of honey. *Food Chem.*, **114** (2), 742–746.

61 Pillonel, L. *et al.* (2003) Analytical methods for the determination of the geographic origin of Emmental cheese: mid- and near-infrared spectroscopy. *Eur. Food Res. Technol.*, **216** (2), 174–178.

62 Karoui, R. *et al.* (2004) Determining the geographic origin of Emmental cheeses produced during winter and summer using a technique based on the concatenation of MIR and fluorescence spectroscopic data. *Eur. Food Res. Technol.*, **219** (2), 184–189.

63 Aulrich, K. and Molkentin, J. (2009) Potential of Near infrared Spectroscopy for differentiation of organically and conventionally produced milk. *Landbauforsch. Volk.*, **59** (4), 301–307.

64 Nicolaou, N., Xu, Y., and Goodacre, R. (2010) Fourier transform infrared spectroscopy and multivariate analysis for the detection and quantification of different milk species. *J. Dairy Sci.*, **93** (12), 5651–5660.

65 Goodacre, R., Radovic, B.S., and Anklam, E. (2002) Progress toward the rapid nondestructive assessment of the floral origin of European honey using dispersive Raman spectroscopy. *Appl. Spectrosc.*, **56** (4), 521–527.

66 Sivakesava, S. and Irudayaraj, J. (2001) Detection of inverted beet sugar adulteration of honey by FTIR spectroscopy. *J. Sci. Food Agr.*, **81** (8), 683–690.

67 Kelly, J.F.D., Downey, G., and Fouratier, V. (2004) Initial study of honey adulteration by sugar solutions using midinfrared (MIR) spectroscopy and chemometrics. *J. Agr. Food Chem.*, **52** (1), 33–39.

68 Kelly, J.D., Petisco, C., and Downey, G. (2006) Application of Fourier transform midinfrared spectroscopy to the discrimination between Irish artisanal honey and such honey adulterated with various sugar syrups. *J. Agr. Food Chem.*, **54** (17), 6166–6171.

69 Kelly, J.D., Petisco, C., and Downey, G. (2006) Potential of near infrared transflectance spectroscopy to detect adulteration of Irish honey by beet invert syrup and high fructose corn syrup. *JNIRS*, **14** (2), 139–146.

70 Ruoff, K. *et al.* (2006) Authentication of the botanical and geographical origin of honey by front-face fluorescence spectroscopy. *J. Agr. Food Chem.*, **54** (18), 6858–6866.

71 Ruoff, K. *et al.* (2006) Authentication of the botanical and geographical origin of honey by mid-infrared spectroscopy. *J. Agr. Food Chem.*, **54** (18), 6873–6880.

72 Al-Jowder, O., Kemsley, E.K., and Wilson, R.H. (1997) Mid-infrared spectroscopy and authenticity problems in selected meats: A feasibility study. *Food Chem.*, **59** (2), 195–201.

73 McElhinney, J., Downey, G., and O'Donnell, C. (1999) Quantitation of lamb content in mixtures with raw minced beef using visible, near and mid-infrared spectroscopy. *J. Food Sci.*, **64** (4), 587–591.

74 Al-Jowder, O., Kemsley, E.K., and Wilson, R.H. (2002) Detection of adulteration in cooked meat products by mid-infrared spectroscopy. *J. Agr. Food Chem.*, **50** (6), 1325–1329.

75 Ding, H.B. and Xu, R.J. (2000) Near-infrared spectroscopic technique for detection of beef hamburger adulteration. *J. Agr. Food Chem.*, **48** (6), 2193–2198.

76 Downey, G., McElhinney, J., and Fearn, T. (2000) Species identification in selected raw homogenized meats by reflectance spectroscopy in the mid-infrared, near-infrared, and visible ranges. *Appl. Spectrosc.*, **54** (6), 894–899.

77 Defernez, M., Kemsley, E.K., and Wilson, R.H. (1995) Use of Infrared-Spectroscopy and Chemometrics for the Authentication of Fruit Purees. *J. Agr. Food Chem.*, **43** (1), 109–113.

78 Contal, L., Leon, V., and Downey, G. (2002) Detection and quantification of apple adulteration in strawberry and raspberry purees using visible and near infrared spectroscopy. *JNIRS*, **10** (4), 289–299.

79 Kurz, C. *et al.* (2010) Evaluation of fruit authenticity and determination of the fruit content of fruit products using FT-NIR spectroscopy of cell wall components. *Food Chem.*, **119** (2), 806–812.

80 Bevin, C.J. *et al.* (2006) Development of a rapid "fingerprinting" system for wine authenticity by mid-infrared spectroscopy. *J. Agr. Food Chem.*, **54** (26), 9713–9718.

81 Picque, D., Cattenoz, T., and Corrieu, G. (2001) Classification of red wines analysed by middle infrared spectroscopy of dry extract according to their geographical origin. *J. Int. Sci. Vigne Vin*, **35** (3), 165–170.

82 Acevedo, F.J. *et al.* (2007) Classification of wines produced in specific regions by UV-Visible spectroscopy combined with support vector machines. *J. Agr. Food Chem.*, **55** (17), 6842–6849.

83 Cozzolino, D. *et al.* (2011) Can spectroscopy geographically classify Sauvignon Blanc wines from Australia and New Zealand? *Food Chem.*, **126** (2), 673–678.

84 Oberreuter, H. *et al.* (2003) Fourier-transform infrared (FT-IR) spectroscopy is a promising tool for monitoring the population dynamics of microorganisms in food stuff. *Eur. Food Res. Technol.*, **216** (5), 434–439.

85 Gaus, K. *et al.* (2006) Classification of lactic acid bacteria with UV-resonance Raman spectroscopy. *Biopolymers*, **82** (4), 286–290.

86 Hardy, J. and Fanni, J. (1981) Application of Reflection Photometry to the Measurement of Milk Coagulation. *J. Food Sci.*, **46** (6), 1956–1957.

87 McMahon, D.J., Brown, R.J., and Ernstrom, C.A. (1984) Enzymic coagulation of milk casein micelles. *J. Dairy Sci.*, **67** (4), 745–748.

88 Payne, F.A., Hicks, C.L., and Shen, P.S. (1993) Predicting optimal cutting time of coagulating milk using diffuse reflectance. *J. Dairy Sci.*, **76** (1), 48–61.

89 Pearse, M.J. and Mackinlay, A.G. (1989) Biochemical aspects of syneresis: A review. *J. Dairy Sci.*, **72** (6), 1401–1407.

90 Lawrence, R.C. and Gilles, J. (1980) The assessment of the potential quality of young Cheddar cheese. *New Zeal. J. Dairy Sci. Technol.*, **15** (1), 1–12.

91 Taifi, N. *et al.* (2006) Characterization of the syneresis and the firmness of the milk gel using an ultrasonic technique. *Meas. Sci. Technol.*, **17** (2), 281–287.

92 Tellier, C. *et al.* (1993) Evolution of water proton muclear magnetic relaxation during milk coagulation and syneresis: structural implications. *J. Agr. Food Chem.*, **41** (12), 2259–2266.

93 Everard, C.D. *et al.* (2007) Computer vision and color measurement techniques for inline monitoring of cheese curd syneresis. *J. Dairy Sci.*, **90** (7), 3162–3170.

94 Fagan, C.C. *et al.* (2008) Application of image texture analysis for online determination of curd moisture and whey solids in a laboratory-scale stirred cheese vat. *J. Food Sci.*, **73** (6), E250–E258.

95 Fagan, C.C. *et al.* (2009) Visible-near infrared spectroscopy sensor for predicting curd and whey composition during cheese processing. *Sens.Instrum. Food Qual. Safety*, **3**, 62–69.

96 Fagan, C.C. *et al.* (2007) Novel online sensor technology for continuous monitoring of milk coagulation and whey separation in cheesernaking. *J. Agr. Food Chem.*, **55**, 8836–8844.

97 Castillo, M., Payne, F., and Shea, A. (2005) Development of a combined sensor technology for monitoring coagulation and syneresis operations in cheese making. *J. Dairy Sci.*, **88**, 142–142.

98 Castillo, M. *et al.* (2005) Optical sensor technology for measuring whey fat concentration in cheese making. *J. Food Eng.*, **71** (4), 354–360.

99 Fagan, C.C. *et al.* (2007) Novel online sensor technology for continuous monitoring of milk coagulation and whey separation in cheese making. *J. Agr. Food Chem.*, **22**, 8836–8844.

100 Fagan, C.C. *et al.* (2008) On-line prediction of cheese making indices using backscatter of near infrared light. *Int. Dairy J.*, **18** (2), 120–128.

101 Fagan, C. *et al.* (2009) Visible-near infrared spectroscopy sensor for predicting curd and whey composition during cheese processing. *Sens. Instrum.Food Qual. Safety*, **3** (1), 62–69.

102 Mateo, M.J. *et al.* (2009) Influence of curd cutting programme and stirring speed on the prediction of syneresis indices in cheese-making using NIR light backscatter. *Lwt-Food Sci. Technol.*, **42** (5), 950–955.

103 Fagan, C.C. *et al.* (2011) Preliminary Evaluation of Endogenous Milk Fluorophores as Tracer Molecules for Curd Syneresis. *J. Dairy Sci.*, **94** (11), 5350–5358.

104 Cimander, C., Carlsson, M., and Mandenius, C.-F. (2002) Sensor fusion for on-line monitoring of yoghurt fermentation. *J. Biotechnol.*, **99** (3), 237–248.

105 Navratil, M., Cimander, C., and Mandenius, C.F. (2004) On-line multisensor monitoring of yogurt and Filmjolk fermentations on production scale. *J. Agr. Food Chem.*, **52** (3), 415–420.

106 Correia, I. *et al.* (2005) Sorghum fermentation followed by spectroscopic techniques. *Food Chem.*, **90** (4), 853–859.

107 Alvarez, D. *et al.* (2007) Prediction of meat emulsion stability using reflection photometry. *J. Food Eng.*, **82** (3), 310–315.

108 Alvarez, D. *et al.* (2009) A novel fiber optic sensor to monitor beef meat emulsion stability using visible light scattering. *Meat Sci.*, **81** (3), 456–466.

109 Alvarez, D. *et al.* (2010) Application of light extinction to determine stability of beef emulsions. *J. Food Eng.*, **96** (2), 309–315.

110 Alvarez, D. *et al.* (2010) Prediction of beef meat emulsion quality with apparent light backscatter extinction. *Food Res. Int.*, **43** (5), 1260–1266.

111 Gonzalez-Martin, M.I. *et al.* (2011) Prediction of sensory attributes of cheese by near-infrared spectroscopy. *Food Chem.*, **127** (1), 256–263.

112 Hennessy, S., Downey, G., and O'Donnell, C. (2008) Multivariate Analysis of Attenuated Total Reflection-Fourier Transform Infrared Spectroscopic Data to Confirm the Origin of Honeys. *Appl. Spectrosc.*, **62** (10), 1115–1123.

113 Tgersen, G. *et al.* (1999) On-line NIR analysis of fat, water and protein in industrial scale ground meat batches. *Meat Sci.*, **51** (1), 97–102.

114 Karoui, R. *et al.* (2004) Fluorescence and infrared spectroscopies: a tool for the determination of the geographic origin of Emmental cheeses manufactured during summer. *Lait*, **84** (4), 359–374.

115 Blasco, J. *et al.* (2007) Citrus sorting by identification of the most common defects using multispectral computer vision. *J. Food Eng.*, **83** (3), 384–393.

116 Nakariyakul, S. and Casasent, D.P. (2008) Hyperspectral waveband selection for contaminant detection on poultry carcasses. *Opt. Eng.*, **47** (8).

117 Karoui, R. and De Baerdemaeker, J. (2007) A review of the analytical methods coupled with chemometric tools for the determination of the quality and identity of dairy products. *Food Chem.*, **102** (3), 621–640.

4
Application of Optical Methods for Quality and Process Control of Topically Applied Actives in Cosmetics and Dermatology

Juergen Lademann, Martina C. Meinke, Maxim E. Darvin, and Joachim W. Fluhr

4.1
Introduction

The skin is not only the largest organ of the human body, but also its barrier to the sometimes harsh environment. It provides protection against dehydration and penetration of pollutants and microorganisms. The skin barrier is mainly formed by the uppermost skin layer, the stratum corneum. It consists of dead cornified cells, which are surrounded by bilamellar lipid layers and is easily accessible for non-invasive assessment [1–3]. The skin is composed of the epidermis and the dermis. The stratum corneum is the uppermost part of the epidermis.

In dermatology and cosmetics a multitude of active substances are topically applied. These substances are intended to target the epidermis and eventually the dermis. To exert their effect they have to penetrate through the stratum corneum. As healthy skin has a strong barrier, only very small amounts of topically applied substances reach the living cells [4]. Maibach and Feldmann [5] demonstrated that, in the case of steroids, only approximately 0.1% of the topically applied substances reach the target structures in the living tissue. In contrast, an impaired epidermal barrier allows the penetration of larger amounts of drugs, thus reaching their target structures in deeper parts of the skin.

To develop and optimize cosmetic products and drugs the penetration of topically applied substances into and through the skin barrier must be analyzed. Diffusion cell experiments are among the most important *in vitro* techniques employed in such cases [6]. During these experiments, membrane samples of artificial or excised human and animal skin are placed into a diffusion cell. In most cases the tissue membranes are in contact with a receptor fluid so that the topically applied substances which penetrate the skin can be detected in the receptor fluid. A general drawback of the *in vitro* techniques is that they reflect the *in vivo* conditions only to a limited extent. Penetration investigations require measurements over an extended period of time. For ethical reasons it is not possible to take large numbers of biopsies from volunteers or patients for penetration studies.

Handbook of Biophotonics. Vol.3: Photonics in Pharmaceutics, Bioanalysis and Environmental Research, First Edition.
Edited by Jürgen Popp, Valery V. Tuchin, Arthur Chiou, and Stefan Heinemann

In recent years, optical methods have been widely established for analyzing the penetration of topically applied substances *in vivo*, and investigating structural tissue changes during the application of medicinal and cosmetic products [7]. In contrast to the internal organs, the skin is easily accessible to optical investigation methods.

The optical and spectroscopic analytical methods that are currently used in dermatology and cosmetic testing can be divided into two major groups: The first group comprises microscopic techniques suited to investigation of cellular structures noninvasively up to a depth of approximately 150 μm; this is limited by the light penetration into the skin and the scattering properties of the skin [8, 9]. This allows one to analyze the effect of topically applied substances and their action at the cellular level. The second group comprises spectroscopic methods, which are mainly based on the detection of topically applied substances in the skin. Again, microscopic techniques are used, for example Raman microscopy, which is capable of analyzing at an axial resolution of approximately 5 μm the distribution of specific substances in various layers of the human skin, and specifically in the epidermis [10]. Furthermore, this group includes remission measurements, which are widely employed for the noninvasive detection of topically applied substances in human skin over an extended period of time. In this chapter, both groups of analytical methods are discussed and explained, based on practical examples.

4.2
Laser Scanning Microscopy

4.2.1
Fluorescence Measurements

Three main laser scanning microscopy techniques are currently used for analyzing the cellular structures on human skin [11]. The first technique is based on fluorescence measurements with fluorescent dyes, for example fluorescein, being injected into the skin as a contrast medium [12]. By means of UV excitation, for example, at 488 nm (the wavelength of an argon laser system), cellular structures can be visualized as the dye accumulates in the lipid layers surrounding the cellular structures. In Figure 4.1 various cellular structures which were analyzed by fluorescence measurements are shown. Figure 4.1a shows the corneocytes of the stratum corneum. Distinct differences in the structures of the living cells of the stratum basale are visible in Figure 4.1b. In deeper skin layers even the papillary structure can be visualized (Figure 4.1c). This method is suited to detection of changes in the cellular structure. Figure 4.2a, for example, shows the stratum corneum of dry skin. Dry skin loses its regular honeycomb-like arrangement of corneocytes [13]. The skin surface exhibits a relief-like structure. Following the application of a moisturizing cream, the barrier characteristics of the concerned skin area were improved. Figure 4.2b shows that the regular corneocyte arrangement has regenerated.

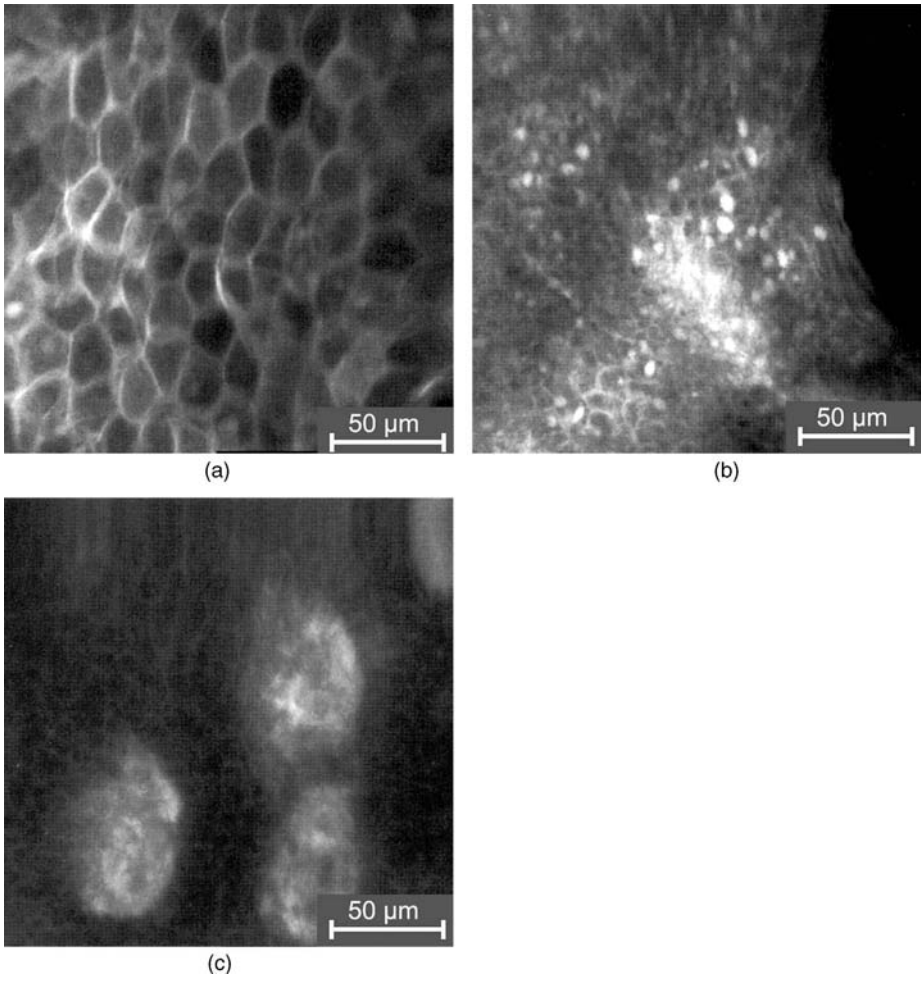

Figure 4.1 Cellular structure analyzed by fluorescence measurements. Corneocytes of the stratum (a), stratum basale (b) and papillary structure (c).

The latest studies have demonstrated that investigations to determine the barrier properties by *in vivo* laser scanning microscopy are a convenient alternative for analysis of the state of the skin compared to transepidermal water loss (TEWL) measurements, which have been the gold standard, so far [14]. This is because TEWL measurements are strongly influenced by external factors, such as ambient temperature and air humidity. In addition, these measurements are disturbed by topically applied substances themselves. To what extent topically applied substances, like steroids or ointments, accelerate wound healing can be analyzed by *in vivo* laser scanning microscopy while the epidermal barrier (stratum corneum) is regenerating [15]. Figure 4.3 represents the histological section of the stratum corneum,

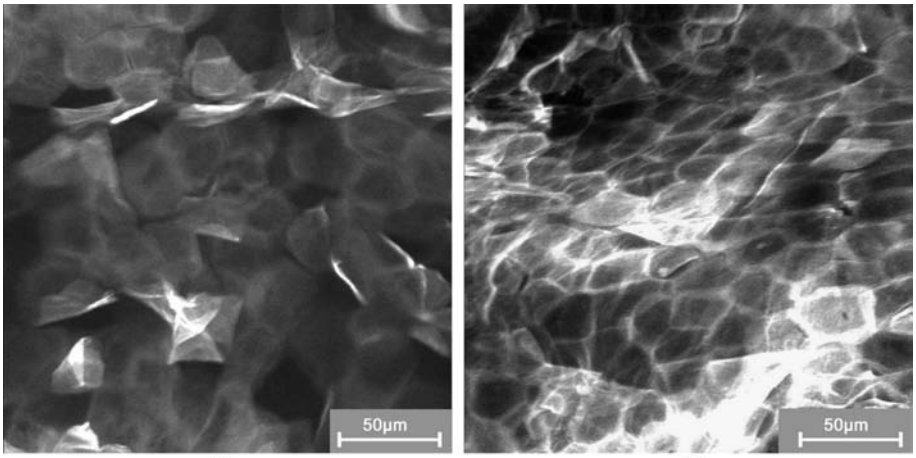

Figure 4.2 Stratum corneum of dry skin (a) and regular corneocyte arrangement after regeneration (b).

the epidermis and the dermis. The thickness of the barrier can be determined by focusing the laser upon the skin surface and adjusting it into the skin until the boundary between the stratum corneum and the stratum granulosum becomes visible [16]. This situation is illustrated in Figure 4.4. Figure 4.4a shows the skin surface with the characteristic structures of the corneocytes of the stratum corneum, whereas Figure 4.4b depicts the boundary between the stratum corneum and the stratum granulosum. Thus the transition allows the differentiation of cellular structures. The laser focus adjustment between the skin surface and the transition from the stratum corneum to the stratum granulosum corresponds to the thickness of the stratum corneum. This *in vivo* technique permits noninvasive detection of the time-dependent regeneration of an impaired epidermal barrier [17].

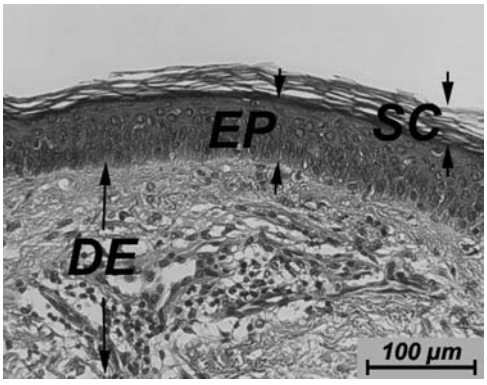

Figure 4.3 Histological section of the stratum corneum, the epidermis and the dermis.

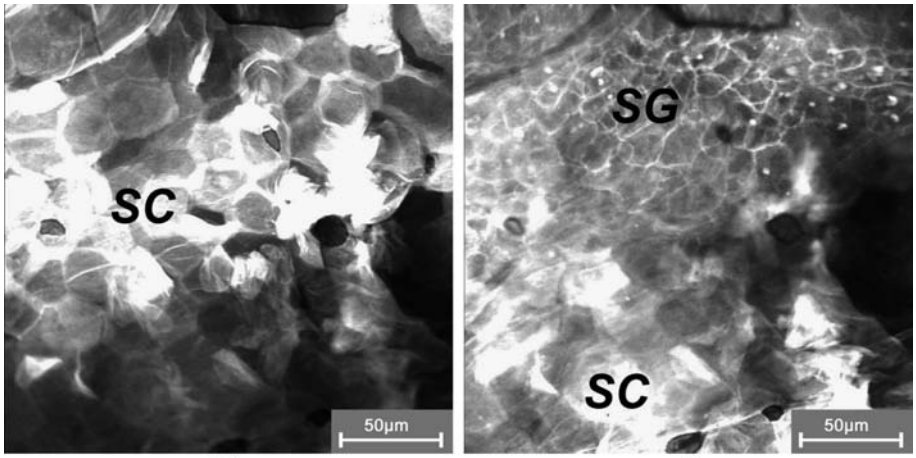

Figure 4.4 Differentiation in the cellular structures: corneocytes of the stratum corneum (a) and the boundary between the stratum corneum and the stratum granulosum (b).

Comparing the wound healing process of untreated skin with that of skin treated with ointments or steroids allows quantification of the repair capacity of topically applied products [18, 19].

If the *in vivo* laser scanning microscopy is used in fluorescence mode it is possible not only to evaluate topically applied substances in cosmetics and dermatology for their effects on cellular structures, but also to directly detect the penetration of these substances, provided these have been labeled with a fluorescent dye [20, 21]. Figure 4.5 illustrates the distribution of pigments used in sunscreens on the skin surface in a furrow. The pigments were labeled with a fluorescent dye which made them detectable when located in different skin structures. In Figure 4.5a the pigments are homogeneously distributed on the skin surface. The skin surface without pigments would appear black. If the laser focus is adjusted only a few microns deeper into the stratum corneum, a thin pigment film becomes visible, which covers the wall of the skin furrow homogeneously (Figure 4.5b). Furthermore, Figure 4.5b shows that the pigments are exclusively located on the skin surface. At the sites where the pigments were visible in Figure 4.5a, the fluorescence signal is no longer detectable in Figure 4.5b because the focus is located below the first layers of corneocytes. Moving the focus on the bottom of the furrow (Figure 4.5c), the bottom is covered by a pigment film. Using this investigation method one can test whether substances, such as pigments in sunscreens, are homogeneously distributed on the skin and form a homogeneous protective layer on structured skin areas.

The penetration kinetics of substances for topical application, as used in drugs and cosmetics, can be visualized by *in vivo* laser scanning microscopy in the fluorescence mode. A schematic drawing of this penetration pathway is shown in Figure 4.6. According to the bricks and mortar model [22] the stratum corneum is represented here as a wall consisting of bricks (corneocytes) and mortar (lipids).

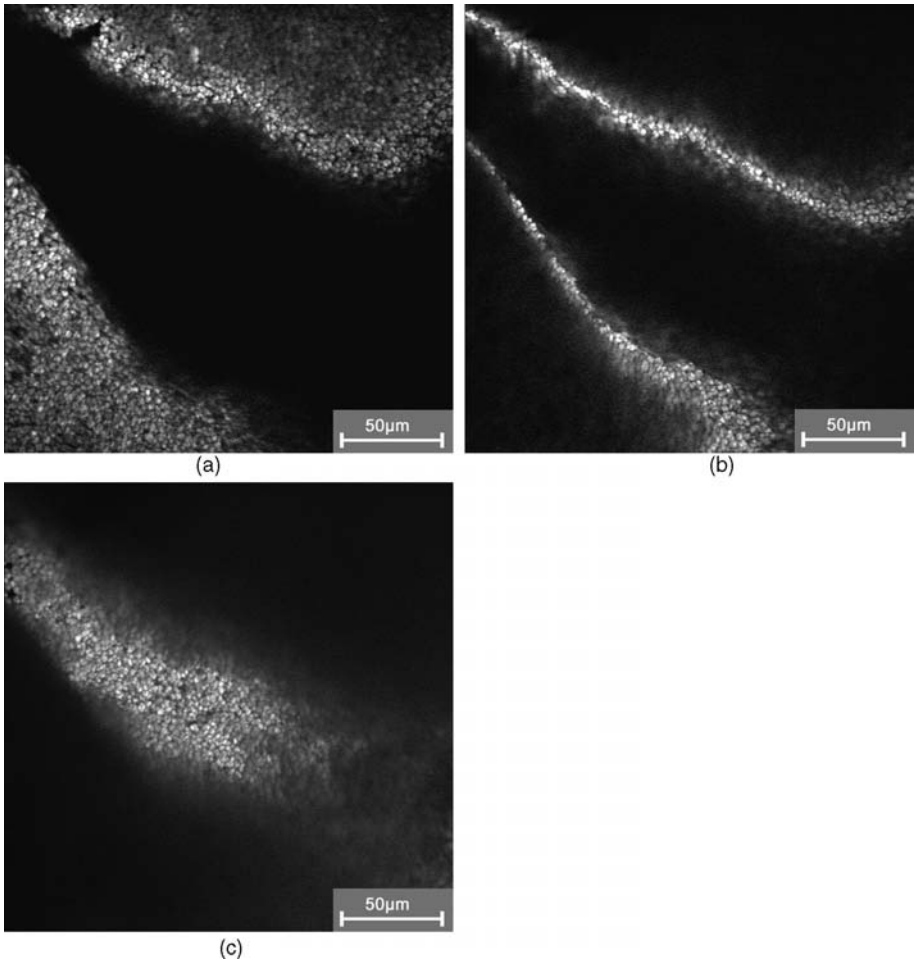

Figure 4.5 Penetration of fluorescein-labeled substance (white spots on the figure) into the skin measured with laser scanning microscopy on the skin surface near the furrow at 5 µm depth (a), 15 µm depth (b) and 25 µm depth (c).

Under real conditions, the corneocytes (black in this figure) are surrounded by lipid layers (white structures). If a substance is applied topically and penetrates into the stratum corneum, it reaches increasingly deeper corneocyte cell layers with time (Figure 4.6a–c). As the corneocytes are very thin structures, permeable to laser light, the various cell layers of the corneocytes can be detected if they are reached by fluorescence labeled substances. This situation is depicted in Figure 4.7 under *in vivo* conditions. Figure 4.7a shows the distribution of the substance 5 min after topical application. The fluorescence is detectable only within the first layer of corneocytes. After 20 min a fluorescence signal is also visible in the spaces of deeper cell layers (Figure 4.7b). This means that the topically applied substance has penetrated into

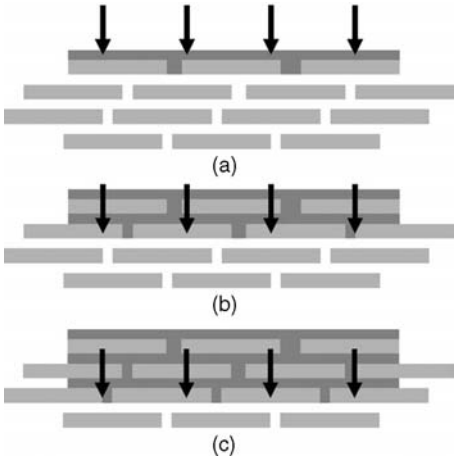

Figure 4.6 Schematic penetration pathway based on the classical bricks and mortar model.

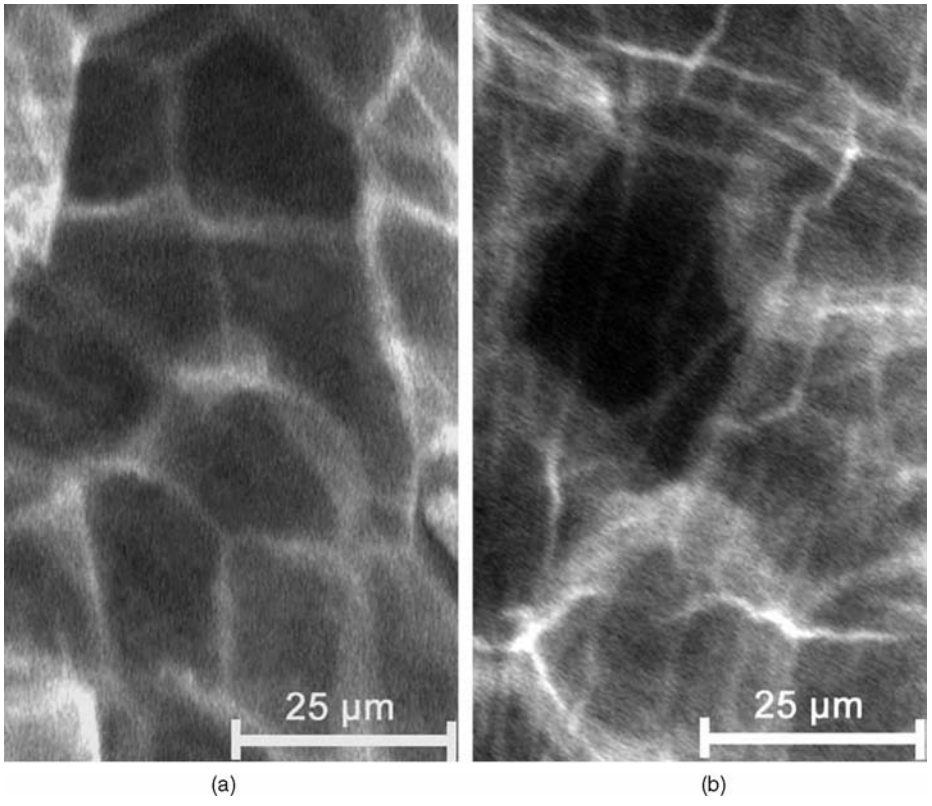

Figure 4.7 Distribution of fluorescein 5 min (a) and 20 min (b) after its topical application.

deeper skin layers within 20 min. In general, the intercellular penetration, that is, the penetration within the lipid layers around the corneocytes, can be distinguished from follicular penetration inside the hair follicles [23, 24]. While the intercellular penetration had long been supposed to be the only penetration pathway, it is now known that follicular penetration is also an important pathway, allowing topically applied substances to pass the skin barrier [25–27].

The hair follicles represent an interesting target structure [28, 29]. Surrounded by a dense network of blood capillaries, they also accommodate dendritic and stem cells [30]. The penetration of a fluorescence-labeled substance into the hair follicles is shown in Figure 4.8. The substance is located in the orifice of the follicle, before it penetrates deeper into the hair follicle, as seen in Figure 4.8a–c.

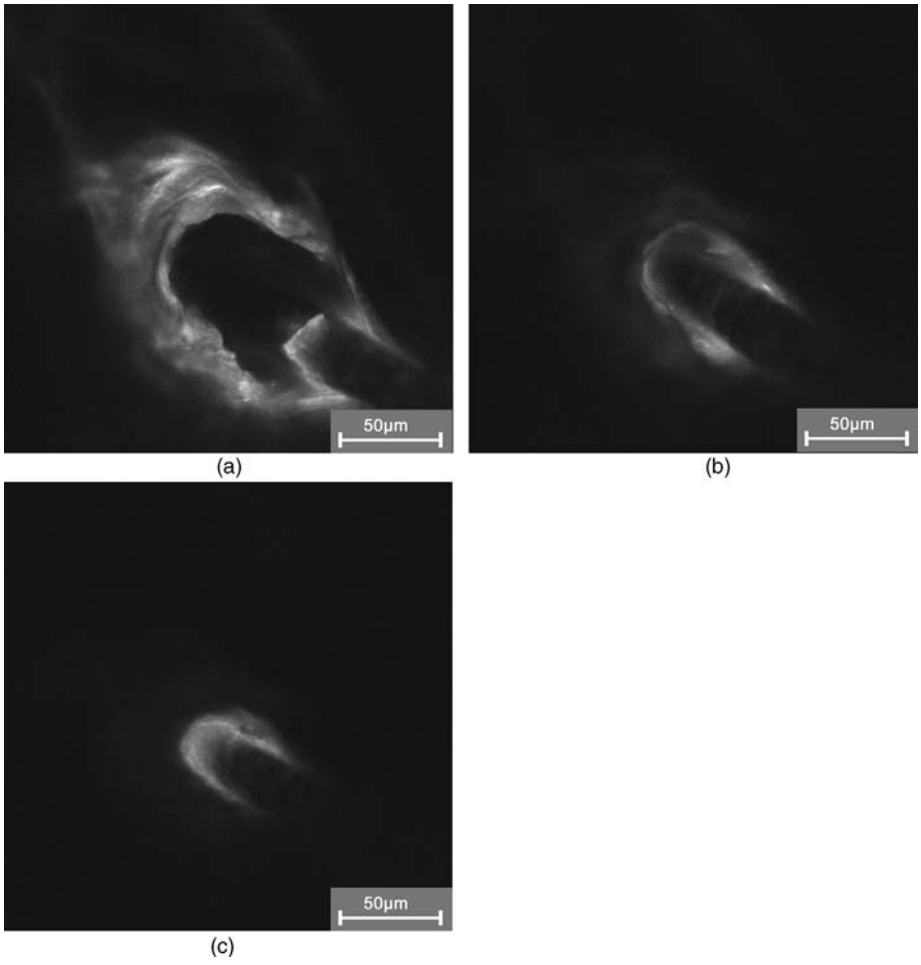

Figure 4.8 The penetration of a fluorescence-labeled substance into the hair follicle.

4.2.2
Remission Measurements

The presented examples demonstrate that investigations using *in vivo* laser scanning microscopy in the fluorescence mode are suitable to analyze changes in cellular structures and the kinetics of fluorescence-labeled topically applied substances at the same time. The disadvantage of this technique is that it requires a fluorescence marker. As long as this fluorescence marker is applied topically, which is necessary to differentiate between dry and "normal" healthy skin, the use of such markers does not entail any limitations. Most topically applied cosmetic products and drugs do not exhibit an auto-fluorescence signal, thus impeding direct detection of their penetration and distribution in fluorescence mode. The analysis of cellular changes in the epidermis and in the dermis is limited, because this analysis requires the injection or topical application of a fluorescence dye. Whereas this method can be used on healthy skin, its application is strongly restricted in the case of skin lesions or skin cancer to dyes approved for *in vivo* application in humans. These cases require analytic methods which are not based on fluorescence markers. To overcome the above-mentioned disadvantages of laser scanning microscopy using the fluorescence mode, reflectance measurements can be performed to visualize the morphology due to differences in the optical properties of the cellular structures [31]. As the optical properties of these skin layers show only slight differences, the contrast is less than that obtained by fluorescence measurements. Nevertheless, using this technique permits verification of the hypothesis about cellular changes during cosmetic or dermatological therapy [32, 33]. The reflectance measurements are performed at higher wavelengths, above 700 nm, leading to a higher penetration depth of the light. Therefore, visualization up to the dermis becomes feasible. Modern instruments offer a dermatoscopic overview of the skin allowing selection of the optimal skin area.

4.2.3
Multiphoton Measurements

In recent years two-photon microscopy has gained considerable importance [34, 35]. This technique uses ultrashort femtosecond pulses to excite by two-photon processes the autofluorescence of tissue. This makes it possible to analyze structures without any dyes. The results obtained by this method are at least similar to *in vivo* laser scanning microscopy, with fluorescence markers being unnecessary. Typical images obtained by *in vivo* two-photon microscopy are shown in Figure 4.9. Due to the initial wavelength being above 700 nm, the penetration depth of the light reaches the dermis discussed for single photon LSM in reflectance mode using red light. With multiphoton irradiation collagen structures can produce second harmonic generation (SHG) signals and can be visualized with an enhanced contrast [36].

Moreover, the short pulses used in two-photon microscopy lend themselves to the measurement of fluorescence life time generation. Some topically applied substances exhibit life time fluorescences which are distinctly different from those of the

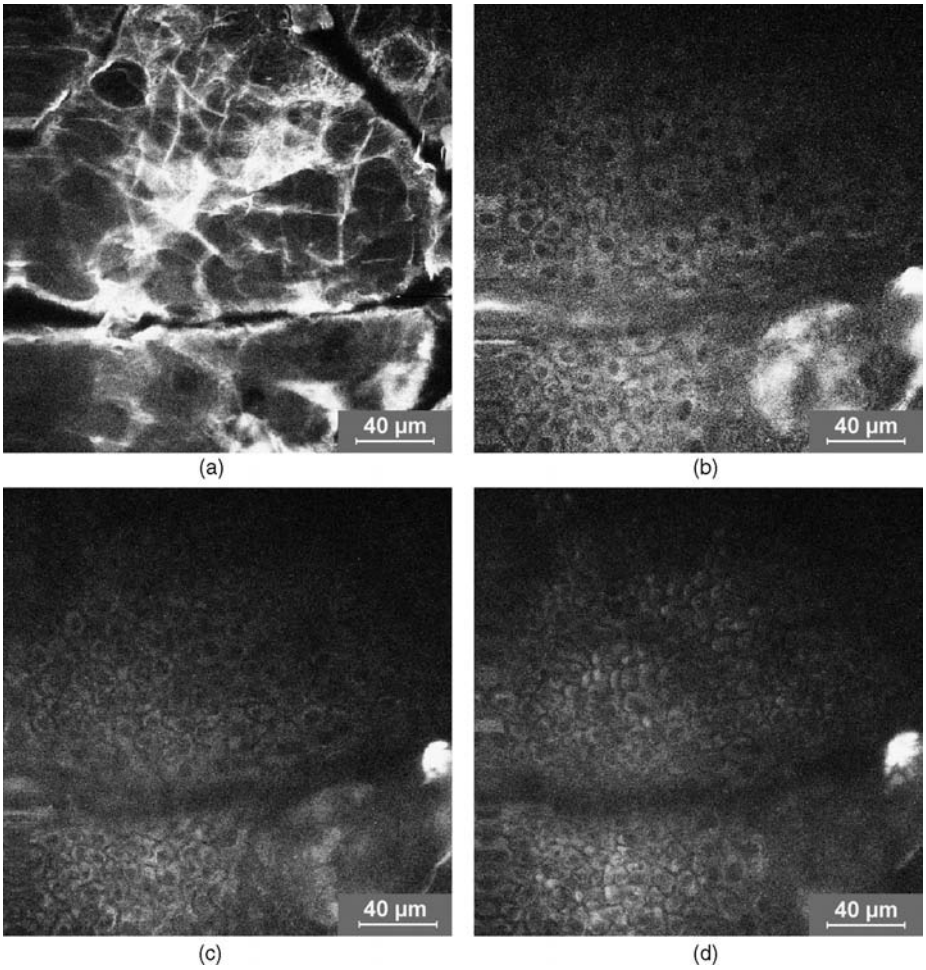

Figure 4.9 Typical images of human skin obtained by *in vivo* two-photon microscopy. Stratum corneum (a), stratum granulosum (b), stratum spinosum (c), stratum basale (d).

autofluorescence of the tissue. In such cases, the penetration of these substances into human skin can also be investigated *in vivo* using fluorescence life time imaging (FLIM) [37].

The first experiments to set up a system, which combines two-photon microscopy imaging of cellular structures with CARS (coherent anti-Stokes Raman scattering) microscopy [38] for the detection of substances in the tissue, have been performed. This opens new possibilities for analyzing the penetration of topically applied substances and their effects on the cellular structures of the skin. Using such a system, the therapeutic effect on the structure of the skin lipids and the distribution of the inflammatory cells in psoriasis patients could be successfully analyzed. This development is still at an early stage, but will become increasingly important in future

dermatological and cosmetic research. The drawback of this system is its high cost. However, for many investigations it is not necessary to image cellular structures at different depths of the skin, at the same time detecting in these skin layers the topically applied substances.

4.3
Raman Spectroscopic Measurements

Microscopic methods like Raman microscopy, permitting substances to be detected in the skin at high spatial resolution, are well suited to analysis of penetration processes [39]. Raman microscopes can be used to detect the distribution of moisture in the different cell layers of human skin [10, 40]. These investigations are suitable for both characterizing wound healing in dermatology and evaluating cosmetic products, such as moisturizing creams. Various other substances can also be detected in skin by laser scanning Raman microscopy. These substances include carotenoids, which are the main constituents of the antioxidants in human skin, but other topically applied substances also show clearly detectable Raman bands [41]. Figure 4.10 represents a typical example of the carotenoid distribution within the stratum corneum after disinfectant application. These studies were performed with an *in vivo* Raman micro-spectroscope (River Diagnostics Ltd., Rotterdam). Figure 4.10 shows the natural stratum corneum distribution of carotenoids prior to

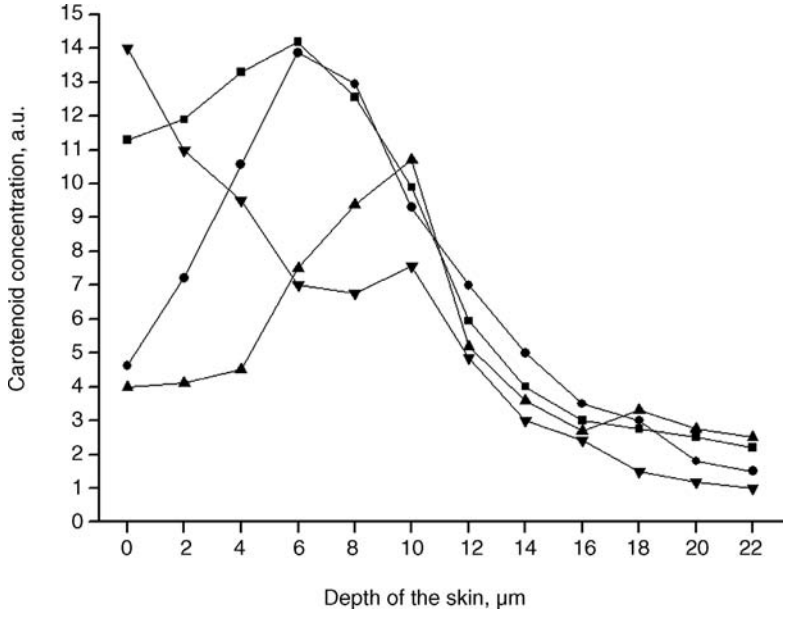

Figure 4.10 Distribution of carotenoids within the stratum corneum after disinfectant application measured with confocal Raman microscopy at different time points.

contact with the disinfectant (baseline; $t = 0$ min). After disinfectant application the carotenoid concentration declines specifically in the upper cell layers of the stratum corneum, whereas deeper layers remain unaffected ($t = 20$ min). At later time points, the penetrating disinfectant leads also to a reduction in the carotenoid concentration in deeper stratum corneum layers ($t = 40$ min). After 60 min a regeneration process is initiated showing increasing carotenoid concentrations in the upper cell layers. This is because the carotenoids are delivered continuously with the sweat and sebaceous lipids onto the skin surface, where they spread and penetrate into the skin like topically applied substances [42]. Consequently, the carotenoids re-penetrate into the upper cell layers after 60 min, while the carotenoid concentration in the deeper layers of the stratum corneum still remains unchanged. By carotenoid delivery with sweat and sebaceous lipids onto the skin surface and repenetration into the skin, the original profile of the carotenoid distribution in the stratum corneum is gradually restored (data almost similar to the $t = 0$ value; not shown in the present figure). In this case the penetration of the disinfectant could be indirectly detected through the decreased carotenoid concentration. In many cases it is also possible to detect substances directly by Raman spectroscopy and analyze their distribution at different depths of the skin. Figure 4.11 represents a typical distribution of the water concentration in the stratum corneum. This distribution can be changed by a disturbed skin barrier or by topically applied drugs and cosmetic products.

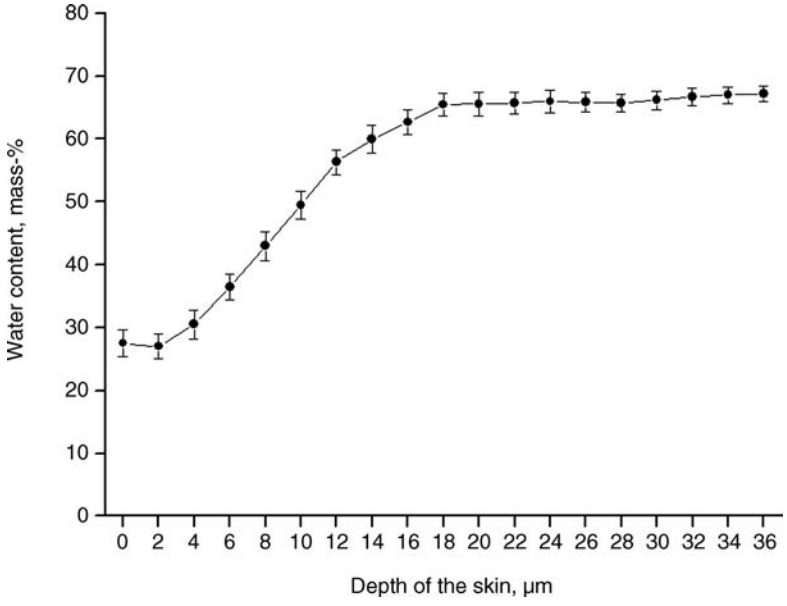

Figure 4.11 A typical distribution of water concentration in the stratum corneum measured with confocal Raman microscopy.

Using Raman microscopy it is possible to investigate the distribution of specific substances, either topically applied or constituents of our body, at different depths of the skin.

4.4 Resonance Raman Spectroscopy

There are also techniques which can detect substances in human skin without spatial resolution exclusively by remission methods. This was demonstrated by a measuring system for the *in vivo* detection of carotenoids in human skin. Carotenoids absorb in the blue–green range of the spectrum [43, 44]. Thus, due to their resonant excitation, an argon laser operated at 488 and 514.5 nm is well suited. Based on the differences in absorption spectra for beta-carotene and lycopene under excitation at 488 and 514.5 nm, and, as a result, on the differences in Raman scattering efficiencies, the measuring system is capable of detecting the carotenoid concentration in human skin selectively and sensitively [45]. The resonance Raman signal of the carotenoids measured at 1525 cm^{-1} is acquired through a detection channel and delivered to a spectrometer attached to an evaluation unit. The measuring skin volume is determined by the penetration depth of the laser radiation at 488 and 514 nm into the skin, which is approximately 150 μm, and the laser spot diameter on the skin surface. To avoid any disturbances due to inhomogeneities and the microstructure of the skin surface, the laser beam diameter upon the skin surface was approximately 6.5 mm. To reduce the dermal fluorescence background, which could influence the accuracy of Raman measurements, the photo-bleaching effect is used [46]. With the help of this system the storage of carotenoids contained in cosmetic products, such as anti-aging creams, can be followed for an extended period of time [47] without the use of expensive laser scanning microscopy.

4.5 Conclusions

The skin is the organ of our body ideally suited to noninvasive analysis by laser scanning microscopy for quality and process control of topically applied drugs and cosmetic products, as well as for diagnostic and therapy control. For this purpose a wide range of optical methods is available, extending from simple remission measurements to sophisticated combined investigations by two-photon CARS microscopy. Which method is best suited for specific investigations depends decisively on the research objective. In any case, *in vivo* investigations have already contributed to considerably deepening our knowledge of penetration and storage of topically applied substances in human skin. As a result, follicular penetration was recognized and verified as a new penetration pathway besides intercellular penetration. The use of optical techniques in the development and optimization of drugs and cosmetic products for topical application is likely to improve their efficacy.

With the ongoing miniaturization of the optical systems, and the related price reduction, these techniques will become increasingly established in clinical research, routine diagnostics and therapy control of topically applied substances.

References

1 Elias, P.M. and Steinhoff, M. (2008) Outside-to-inside (and now back to outside) pathogenic mechanisms in atopic dermatitis. *J. Invest. Dermatol.*, **128**, 1067–1070.

2 Darlenski, R., Sassning, S., Tsankov, N., and Fluhr, J.W. (2009) Non-invasive in vivo methods for investigation of the skin barrier physical properties. *Eur. J. Pharm. Biopharm.*, **72**, 295–303.

3 Elias, P.M. (1983) Epidermal lipids, barrier function, and desquamation. *J. Invest. Dermatol.*, **80** (Suppl), 44s–49s.

4 Rougier, A., Rallis, M., Krien, P., and Lotte, C. (1990) In vivo percutaneous absorption: a key role for stratum corneum/vehicle partitioning. *Arch. Dermatol. Res.*, **282**, 498–505.

5 Feldmann, R.J. and Maibach, H.I. (1967) Regional variation in percutaneous penetration of 14C cortisol in man. *J. Invest. Dermatol.*, **48**, 181–183.

6 Trauer, S., Lademann, J., Knorr, F., Richter, H., Liebsch, M., Rozycki, C., Balizs, G., Buttemeyer, R., Linscheid, M., and Patzelt, A. (2010) Development of an in vitro modified skin absorption test for the investigation of the follicular penetration pathway of caffeine. *Skin Pharmacol. Physiol.*, **23**, 320–327.

7 Ansari, R.R., Gonchukov, S.A., and Lademann, J. (2003) Laser methods in medicine and biology. *Laser Phys.*, **13**.

8 Gotter, B., Faubel, W., and Neubert, R.H. (2008) Optical methods for measurements of skin penetration. *Skin Pharmacol. Physiol.*, **21**, 156–165.

9 Bashkatov, A.N., Genina, E.A., Kochubey, V.I., and Tuchin, V.V. (2005) Optical properties of human skin, subcutaneous and mucous tissues in the wavelength range from 400 to 2000nm. *J. Phys. D. Appl. Phys.*, **38**, 2543–2555.

10 Caspers, P.J., Lucassen, G.W., Carter, E.A., Bruining, H.A., and Puppels, G.J. (2001) In vivo confocal Raman microspectroscopy of the skin: noninvasive determination of molecular concentration profiles. *J. Invest. Dermatol.*, **116**, 434–442.

11 Meyer, L., Otberg, N., Richter, H., Sterry, W., and Lademann, J. (2006) New prospects in dermatology: fiber-based confocal scanning laser microscopy. *Laser Phys.*, **16**, 758–764.

12 Jacobi, U., Toll, R., Audring, H., Sterry, W., and Lademann, J. (2005) The porcine snout--an in vitro model for human lips? *Exp. Dermatol.*, **14**, 96–102.

13 Byrne, A.J. (2010) Bioengineering and subjective approaches to the clinical evaluation of dry skin. *Int. J. Cosmet. Sci.*, **32**, 410–421.

14 Patzelt, A., Sterry, W., and Lademann, J. (2010) In vivo measurements of skin barrier: comparison of different methods and advantages of laser scanning microscopy. *Laser Phys. Lett.*, **7**, 843–852.

15 Lange-Asschenfeldt, B., Alborova, A., Kruger-Corcoran, D., Patzelt, A., Richter, H., Sterry, W., Kramer, A., Stockfleth, E., and Lademann, J. (2009) Effects of a topically applied wound ointment on epidermal wound healing studied by in vivo fluorescence laser scanning microscopy analysis. *J. Biomed. Opt.*, **14**.

16 Lademann, J., Richter, H., Astner, S., Patzelt, A., Knorr, F., Sterry, W., and Antoniou, C. (2008) Determination of the thickness and structure of the skin barrier by in vivo laser scanning microscopy. *Laser Phys. Lett.*, **5**, 311–315.

17 Rieger, T., Teichmann, A., Richter, H., Sterry, W., and Lademann, J. (2007) Application of in-vivo laser scanning microscopy for evaluation of barrier creams. *Laser Phys. Lett.*, **4**, 72–76.

18 Schatzlein, A. and Cevc, G. (1998) Non-uniform cellular packing of the stratum corneum and permeability barrier function of intact skin: a high-resolution

confocal laser scanning microscopy study using highly deformable vesicles (Transfersomes). *Br. J. Dermatol.*, **138**, 583–592.

19 Teichmann, A., Sadeyh Pour Soleh, H., Schanzer, S., Richter, H., Schwarz, A., and Lademann, J. (2006) Evaluation of the efficacy of skin care products by laser scanning microscopy. *Laser Phys. Lett.*, **3** (10), 507–509.

20 Alvarez-Roman, R., Naik, A., Kalia, Y.N., Fessi, H., and Guy, R.H. (2004) Visualization of skin penetration using confocal laser scanning microscopy. *Eur. J. Pharm. Biopharm.*, **58**, 301–316.

21 Martschick, A., Teichmann, A., Richter, H., Schanzer, S., Antoniou, C., Sterry, W., and Lademann, J. (2007) Analysis of the penetration profiles of topically applied substances by laser scanning microscopy. *Laser Phys. Lett.*, **4**, 395–398.

22 Elias, P.M. (2005) Stratum corneum defensive functions: an integrated view. *J. Invest. Dermatol.*, **125**, 183–200.

23 Otberg, N., Richter, H., Schaefer, H., Blume-Peytavi, U., Sterry, W., and Lademann, J. (2004) Variations of hair follicle size and distribution in different body sites. *J. Invest. Dermatol.*, **122**, 14–19.

24 Teichmann, A., Jacobi, U., Ossadnik, M., Richter, H., Koch, S., Sterry, W., and Lademann, J. (2005) Differential stripping: determination of the amount of topically applied substances penetrated into the hair follicles. *J. Invest. Dermatol.*, **125**, 264–269.

25 Otberg, N., Richter, H., Knuttel, A., Schaefer, H., Sterry, W., and Lademann, J. (2004) Laser spectroscopic methods for the characterization of open and closed follicles. *Laser Phys. Lett.*, **1**, 46–49.

26 Otberg, N., Richter, H., Schaefer, H., Blume-Peytavi, U., Sterry, W., and Lademann, J. (2003) Visualization of topically applied fluorescent dyes in hair follicles by laser scanning microscopy. *Laser Phys.*, **13**, 761–764.

27 Jung, S., Otberg, N., Thiede, G., Richter, H., Sterry, W., Panzner, S., and Lademann, J. (2006) Innovative liposomes as a transfollicular drug delivery system: penetration into porcine hair follicles. *J. Invest. Dermatol.*, **126**, 1728–1732.

28 Vogt, A., Hadam, S., Heiderhoff, M., Audring, H., Lademann, J., Sterry, W., and Blume-Peytavi, U. (2007) Morphometry of human terminal and vellus hair follicles. *Exp. Dermatol.*, **16**, 946–950.

29 Krause, K. and Foitzik, K. (2006) Biology of the hair follicle: the basics. *Semin. Cutan. Med. Surg.*, **25**, 2–10.

30 Oshima, H., Rochat, A., Kedzia, C., Kobayashi, K., and Barrandon, Y. (2001) Morphogenesis and renewal of hair follicles from adult multipotent stem cells. *Cell*, **104**, 233–245.

31 Meyer, L.E., Otberg, N., Sterry, W., and Lademann, J. (2006) In vivo confocal scanning laser microscopy: comparison of the reflectance and fluorescence mode by imaging human skin. *J. Biomed. Opt.*, **11**, 044012-.

32 Dietterle, S., Lademann, J., Rowert-Huber, H.J., Stockfleth, E., Antoniou, C., Sterry, W., and Astner, S. (2008) In-vivo diagnosis and non-inasive monitoring of imiquimod 5% cream for non-melanoma skin cancer using confocal laser scanning microscopy. *Laser Phys. Lett.*, **5**, 752–759.

33 Ulrich, M., Roewert-Huber, J., Gonzalez, S., Rius-Diaz, F., Stockfleth, E., and Kanitakis, J. (2011) Peritumoral clefting in basal cell carcinoma: correlation of in vivo reflectance confocal microscopy and routine histology. *J. Cutan. Pathol.*, **38**, 190–195.

34 Koehler, M.J., Vogel, T., Elsner, P., Konig, K., Buckle, R., and Kaatz, M. (2010) In vivo measurement of the human epidermal thickness in different localizations by multiphoton laser tomography. *Skin Res. Technol.*, **16**, 259–264.

35 Konig, K. (2008) Clinical multiphoton tomography. *J. Biophoton.*, **1**, 13–23.

36 Koehler, M.J., Hahn, S., Preller, A., Elsner, P., Ziemer, M., Bauer, A., Konig, K., Buckle, R., Fluhr, J.W., and Kaatz, M. (2008) Morphological skin ageing criteria by multiphoton laser scanning tomography: non-invasive in vivo scoring of the dermal fibre network. *Exp. Dermatol.*, **17**, 519–523.

37 Sanchez, W.Y., Prow, T.W., Sanchez, W.H., Grice, J.E., and Roberts, M.S. (2010) Analysis of the metabolic deterioration of ex vivo skin from ischemic necrosis

through the imaging of intracellular NAD (P)H by multiphoton tomography and fluorescence lifetime imaging microscopy. *J. Biomed. Opt.*, **15**, 046008-.

38 Evans, C.L. and Xie, X.S. (2008) Coherent anti-stokes Raman scattering microscopy: chemical imaging for biology and medicine. *Annu. Rev. Anal. Chem. (Palo Alto CA.)*, **1**, 883–909.

39 Caspers, P.J., Williams, A.C., Carter, E.A., Edwards, H.G., Barry, B.W., Bruining, H.A., and Puppels, G.J. (2002) Monitoring the penetration enhancer dimethyl sulfoxide in human stratum corneum in vivo by confocal Raman spectroscopy. *Pharm. Res.*, **19**, 1577–1580.

40 Caspers, P.J., Lucassen, G.W., and Puppels, G.J. (2003) Combined in vivo confocal Raman spectroscopy and confocal microscopy of human skin. *Biophys. J.*, **85**, 572–580.

41 Darvin, M.E., Fluhr, J.W., Caspers, P., van der, P.A., Richter, H., Patzelt, A., Sterry, W., and Lademann, J. (2009) In vivo distribution of carotenoids in different anatomical locations of human skin: comparative assessment with two different Raman spectroscopy methods. *Exp. Dermatol.*, **18**, 1060–1063.

42 Lademann, J., Caspers, P.J., van der Pol, A., Richter, H., Patzelt, A., Zastrow, L., Darvin, M., Sterry, W., and Fluhr, J.W. (2009) In vivo Raman spectroscopy detects increased epidermal antioxidative potential with topically applied carotenoids. *Laser Phys. Lett.*, **6**, 76–79.

43 Darvin, M.E., Gersonde, I., Albrecht, H., Meinke, M., Sterry, W., and Lademann, J. (2006) Non-invasive in vivo detection of the carotenoid antioxidant substance lycopene in the human skin using the resonance Raman spectroscopy. *Laser Phys. Lett.*, **3**, 460–463.

44 Darvin, M.E., Gersonde, I., Ey, S., Brandt, N.N., Albrecht, H., Gonchukov, S.A., Sterry, W., and Lademann, J. (2004) Noninvasive detection of beta-carotene and lycopene in human skin using Raman spectroscopy. *Laser Phys.*, **14**, 231–233.

45 Darvin, M.E., Gersonde, I., Meinke, M., Sterry, W., and Lademann, J. (2005) Non-invasive in vivo determination of the carotenoids beta-carotene and lycopene concentrations in the human skin using the Raman spectroscopic method. *J. Phys. D Appl. Phys.*, **38**, 2696–2700.

46 Darvin, M.E., Brandt, N.N., and Lademann, J. (2010) Photobleaching as a method of increasing the accuracy in measuring carotenoid concentration in human skin by Raman spectroscopy. *Opt. Spectrosc.*, **109**, 205–210.

47 Darvin, M.E., Sterry, W., and Lademann, J. (2010) Resonance Raman spectroscopy as an effective tool for the determination of antioxidative stability of cosmetic formulations. *J. Biophotonics*, **3**, 82–88.

5
Agricultural Applications: Animal Epidemics and Plant Pathogen Detection

Robert Möller

5.1
Introduction

Livestock and field crops are always threatened by various natural threats. While farmers always had to accept and adapt to bad weather conditions, like freezing temperatures, hail, drought and others, threatening especially their crops, they can actively fight other threats like pests and pathogens. However, a timely implementation of eradication and containment strategies to limit the effects and spread of pest and pathogens requires a clear detection and identification of the biological threat. While most pests can more or less easily be identified, because most of them can be seen by the naked eye or with a low magnification, the identification of pathogens is much harder. As pathogens are microorganisms, a conventional direct identification is only possible using the classical basic steps of isolation, cultivation and optical detection. These identification strategies are basically the same for all microorganisms and are based on the principles of microbial detection established by Louis Pasteur and Robert Koch. Especially for bacterial or fungal pathogens, the cultivation steps are comparably simple; a big drawback of this strategy is the time that is needed. Often many days or even weeks are lost till a clear identification of a pathogen can be achieved and defined countermeasures can be taken. So a rapid detection and identification of the pathogen would also be of high relevance for agricultural applications.

As agriculture is an important infrastructure the fast and accurate detection and identification of pathogens should be of the highest interest. A natural, accidental or deliberate introduction of pathogens into the farming industry in the western world could have devastating economic, social and environmental effects. This was demonstrated in 2001 by the reappearance of foot-and-mouth disease (FMD) in the UK. The outbreak resulted in multi-billion dollar losses associated not only with agriculture, but also a wide range of activities including the pharmaceutical and tourist industries [1]. The outbreak could only be controlled by slaughtering millions of animals, most of which were not infected, to quickly achieve eradication of the virus and to achieve the FMD-free status of the UK [2]. The main problem during this FMD outbreak was that the clinical screening was time-consuming and

Handbook of Biophotonics. Vol.3: Photonics in Pharmaceutics, Bioanalysis and Environmental Research, First Edition.
Edited by Jürgen Popp, Valery V. Tuchin, Arthur Chiou, and Stefan Heinemann

labor-intensive. Because of the scale of the outbreak national reference laboratories using the standardized testing procedures were unable to test the hundreds and thousands of individual animals on suspected infected premises. During a large scale outbreak of a highly infectious disease the system of national reference laboratories quickly reaches its capacity limits. After the 2001 FMD outbreak the use of rapid diagnostic assays was recommended by two major reports [3, 4]. The driving force for the establishment of novel testing devices for on-site diagnosis has been largely influenced by the desire to reduce the time to perform diagnostic tests, so that objective data can be used to support the decision-making process during the outbreak [5].

The development of on-site diagnostics will be discussed in the following, mostly using the example of FMD and *Phytophthora* detection. FMD is one of the most significant animal diseases affecting trade. Although rarely fatal in adult animals, the appearance of FMD in a disease-free country results in severe trade restrictions and agricultural losses [6]. The disease is caused by the foot-and-mouth disease virus (FMDV), leading to vesicles on the foot, mouth, tongue, and teats of cloven-hooved animals, and is one of the most contagious disease agents known. FMD is classified as a reportable disease by the Office International des Epizooties (OIE) [6].

As a second example, the detection of the notifiable plant pathogen *Phytophthora* is chosen. We have chosen to focus on two specific examples because there are over 500 plant pathogens alone that can cause major disease losses [7]. *Phytophthora* is a genus of plant-damaging oomycetes. Certain species can cause enormous economic losses on crops worldwide, as well as environmental damage in natural ecosystems. The most prominent *Phytophthora* species is probably *P. infestans* the infective agent of late blight or potato blight. The most famous occurrence of *P. infestans* was in the middle of the 19th century, when it caused the Great Irish Famine, but it is still a problem today, causing estimated damage worth 6 billion $ a year worldwide. As the spread and large scale outbreak of *Phytophthora infestans* can be at least partially controlled by fungicides, recently, other members of the genus have raised interest in fast diagnostic devices. *Phytophthora ramorum*, the causal agent of the sudden oak death [8], and the more recently described pathogen *P. kernoviae*, the cause of dieback and leaf blight on a broad range of plant species [9], are two species of the genus that are under surveillance. To prevent the introduction and spread of the pathogens emergency phytosanitary measures were enforced in the EU in 2002 [5]. Specific and sensitive detection devices are necessary to avoid the planting of contaminated material, as it is difficult to control diseases caused by the two *Phytophthora* species, because of the lack of efficient products for chemical treatment under field conditions [10].

5.2
Diagnosis Under Field Conditions

As already described, the effective disease management and implementation of plant and animal health legislation is reliant upon rapid and accurate disease

diagnosis, based upon recognition of symptoms in the field and identification of the causal agent [11]. For important notifiable diseases, samples from suspected cases are normally sent to regional or national reference laboratories, where validated assays are deployed and results can be reported to national competent authorities [5]. However, as time is a critical factor during a disease outbreak, valuable time is lost by transporting the samples. Furthermore, during a large scale outbreak these laboratories using routine diagnostic procedures have only a limited capacity to handle a large number of samples in a short amount of time. Fast on-site testing might be the solution to these problems, but specific requirements have to be fulfilled to allow testing away from dedicated laboratory facilities. These assays are commonly referred to as "point-of-care tests" (POCT), "pen-side", "portable", "on-site", "field tests" or "point of decision" tests [5]. To allow the detection and identification of pathogens away from a centralized laboratory infrastructure under field conditions the applied assays and the devices used have to be easy to handle and robust.

The diagnosis of a plant or animal disease can be relative simple when typical, definitive symptoms are evident. However, symptoms are not always unique and can be confused with other diseases [7]. Especially important for the detection of a pathogen is the taking of the sample. This should be normally be done by trained personnel (farmers, veterinarians, or inspectors) who can recognize the signs of a disease.

The first tests that would allow detection of plant viruses on site were introduced 30 years ago. These tests were based on chloroplast agglutination [12] and latex agglutination [13, 14]. Both tests relied on an immunological reaction that leads to the agglutination of chloroplasts or latex after a short period. Although extremely simple, these tests were never widely accepted, being not sufficiently robust for routine use in the field. It was also difficult to distinguish a positive agglutination from a false-positive clumping [15]. By replacing the latex with sensitized *Staphylococcus aureas* agglutination tests were improved and are still in use for the detection of bacterial pathogens, especially in laboratories, but they can also be used in the field. The problems with the agglutination test illustrate the problems and requirements for on-site testing. As already mentioned, ease of handling, a good discrimination of positive and negative results, a high sensitivity and specificity, and a robustness of the test are the main requirements for field tests.

5.3
Immunological Based-Techniques

All immunological tests use the specific antigen/antibody interaction for the detection of pathogens or substances. The underlying principle is basically an adaptation of the enzyme linked immunoabsorbent assay (ELISA). The interaction of antibody and antigen is visualized by an enzyme-mediated color change reaction. This method has been adapted also for on-site diagnostics.

5.3.1 Flow Through Format

In this format the capture antibodies for the detection are either bound to a membrane or to modified filter plugs. The so-called Alert test (Neogen Corporation) used a membrane with three spots (Figure 5.1a). The modified membrane is housed in a plastic container on a hydroscopic "cork". When the extracted sample is added to the membrane it flows over the membrane and the antigen can bind to the antibody. An enzyme-tagged antibody is then added, which binds to the captured antigen. Finally a substrate (4 chloronaphthol) for the enzyme is flowed over the disc. In the presence of the captured enzyme a blue precipitate is formed. If no antigen is present no enzyme is bound and no color change detected. In a final step the membrane is rinsed to stabilize the color reaction. The test has three spots or discs, the smallest disc is loaded with the antigen, serving as positive control. One of the larger discs carries no antibody (negative control) while the final disc is pre-treated with a specific antibody [15]. Alert kits are available for several plant pathogens including *Phytophthora* and have been demonstrated for monitoring diseases and as a valuable tool for the management of fungicide applications [16, 17]. Even so, these tests are relatively sophisticated and are quite laborious to perform. Because of these constraints the test has been applied only in high value applications.

By assembling three specifically modified filter plugs in the tip of a syringe the so-called AffiniTip (Hydros Inc.) is formed (Figure 5.1b). One filter plug holds the antigen (positive control), one contains no antibody, and the third is modified with a target specific antibody. The test is performed by attaching the tip to a syringe and all the necessary solutions are drawn over the filters. All necessary chemicals are packed in a small disposable container. A drawback of the system is the relatively long test time and some skill is also needed in handling the syringe accurately [15].

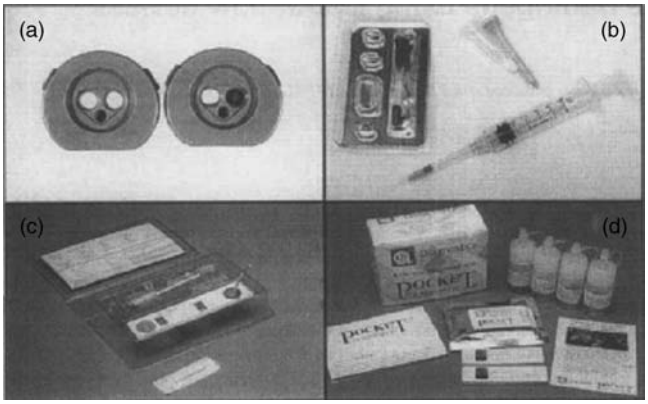

Figure 5.1 Four methods of immunological testing, flow through format Alert (a) and AffiniTip (b) and two lateral flow assays from DeTechtor (c) and Pocket Diagnostic (d) [15].

5.3.2 Lateral Flow Assays

The previously described test schemes still rely on the use of an enzyme for the detection of the antigen; this makes the assay time consuming and complicates the assay. The enzyme can be replaced by modified colloidal gold, latex or silica particles. These particles are sensitized by modification with a specific antibody. If these labels accumulate they can be easily visualized.

A typical lateral flow assay or lateral flow device (LFD) (Figure 5.1c and d) consists of a membrane on which a specific capture antibody is immobilized on a line. On a second line an antibody is immobilized that directly binds the sensitized particle label, thus serving as a positive control. As the sample is loaded to the release pad the antigen binds to the antibodies on the labeled particles and the fluid is drawn over the membrane. In the presence of the antigen the labels accumulate on both lines and become visible (Figure 5.2). If no antigen is present the particles only bind on the second line.

LFDs were initially developed during the mid 1980s for clinical applications and were first commercialized for home pregnancy testing. The test was first introduced by Unipath in 1988. Since then the test scheme has been adapted to a variety of clinical and nonclinical applications. The devices are rapid, inexpensive, disposable, and easy to use, and test results can easily be interpreted by a nonspecialist. Ferris and coworkers have developed and validated LFDs (Figure 5.3) for the detection of all seven serotypes of FMDV [18].

Even though the analytical sensitivity appeared to be lower than RT-PCR, the ability to sample multiple animals within a herd, with this simple and cost-efficient on-site detection, increases the confidence in the results (at herd level) [5]. Field trials with LFDs were taken during the FMD outbreak in Southern England in 2007. These tests showed that results could be achieved in as little as 10 min [19].

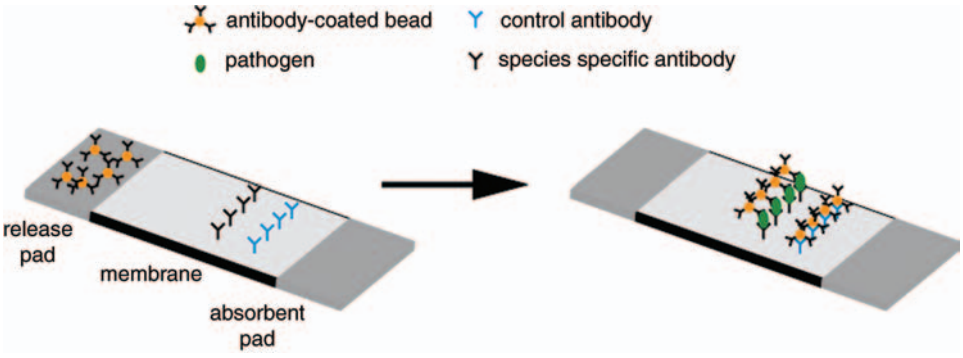

Figure 5.2 Scheme of a one-step lateral flow assay. If the sample is loaded onto the release pad the fluid flows over the membrane releasing the modified beads. If the specific pathogen is present the beads bind to the pathogen and are accumulated at the specific lines.

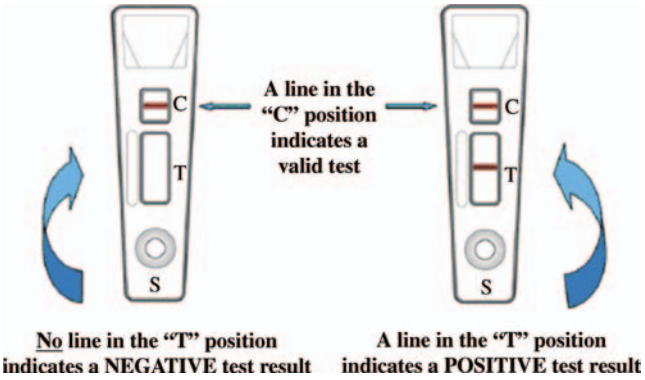

Figure 5.3 Depiction of negative and positive results on a lateral flow assay [18].

By using LFDs the presence of *Phytophthora* can also be detected in symptomatic plant material [11]. However, the detection was not species specific, so positive samples had to be sent to a laboratory for specific molecular testing for *P. ramorum* and *P. kernoviae*. When compared to species-specific methods (both PCR-based and cultural methods) the LFDs showed a high diagnostic sensitivity, indicating their suitability as a pre-screening method in the field [20]. LFDs have also been used for the rapid detection of DNA for the identification of pathogens. Tomlinson and coworkers combined an isothermal amplification of extracted DNA with detection on an LFD to identify *P. ramorum* and *P. kernoviae* [21].

5.4 Nucleic Acid-Based Testing

Although the previously described method of lateral flow assay seems well suited for on-site application, its application is limited. Especially when relying on the immunological reaction, low concentrations of pathogens are often not detectable. Furthermore, specific and stable antibodies are needed and are not always easily available for all pathogens. To enable a more sensitive and more specific, down to the strain level, detection and identification of pathogens, nucleic acid-based methods are used. The most common method is probably PCR. However, it seems technologically quite challenging to develop portable devices for this highly sensitive and specific testing method.

The major bottleneck for the establishment of on-site PCR systems seems to be the extensive sample preparation that is often necessary to isolate DNA out of a complex sample [22]. Nevertheless, there have already been successful on-site PCR tests using existing equipment. This has been done for the FMDV [23–25] as well as for *Phytophthora* [26] detection, and for *P. ramorum* assays have been successfully used in the field [27]. For these tests Cepheid SmartCyclers (Cepheid, Sunnyvale, CA, USA) have been used. Other portable devices that enable pathogen detection via real time PCR are the Enigma FL (Enigma Dagnostics, Port Down, GB) and the Bioseeq

Vet (Smith Detection, Watford, GB). These systems are automated, starting with sample preparation, followed by the PCR and then the readout of the results. Despite the fact, that the systems allow a fast and specific detection, their broad application is mainly limited by their high equipment and per assay costs.

The use of highly precise optical components for the detection and instrumentation for precise temperature control are probably the two expensive components in portable real-time PCR devices. In order to reduce equipment costs isothermal amplification methods have been investigated for their possible use in on-site applications. Especially, loop-mediated isothermal amplification (LAMP) [28] and nucleic acid sequence-based amplification (NASBA) [29, 30] have been of high interest. These isothermal amplification strategies seem to be well suited for field settings as only a stable reaction temperature is needed, instead of a cycling of different reaction temperatures. RT-LAMP and LAMP assays have been developed for the detection of FMDV [31] and *P. ramorum* [32]. Isothermal amplification strategies can also be combined with a simple detection of the PCR product on a simple lateral flow device [21]. This also eliminates costly optical components for the detection, enabling the development of simple, robust and cost-efficient devices for on-site testing.

5.5 Emerging Technologies

Compared to medical applications, the development of systems suitable for on-site diagnosis for agricultural applications is just at the beginning. This is probably due to an uncertainty over whether a viable market exists for the on-site detection of plant and livestock diseases. However, the requirements for on-site diagnostics are very similar to those for medical applications, surprisingly, many detection platforms have only been developed for medical applications. In order to identify possible developments, it is necessary to search for the latest developments in the medical point-of-care field.

One of the biggest trends in recent years in the field of pathogen diagnostics for point-of-care applications is the development of so-called lab-on-a-chip (LOC) or micro total analysis systems (μTAS). The objective of these devices is to integrate as many as possible, or even all, steps necessary for the analysis on a small device. The main steps that can be identified for these systems are sampling, sample preparation, isolation of the compound of interest, amplification, detection, and readout [33]. Different concepts for these devices and the surrounding technologies are reviewed elsewhere [34–37].

Although the main goal is the integration of the entire analysis process in one small device, extensive work has been done on integrated preanalytics, as sample preparation is still the key bottleneck for on-site analytics. By using a laser irradiation magnetic bead system (LIMBS) Lee and coworkers have realized a portable sample preparation system [38]. Instead of magnetic particles, Au nanorods can be used to employ an optothermal effect for the lysis of bacteria cells. The sample can then be

used for a real-time PCR without removing the nanorods [39]. The LIMBS principle has been transferred to a polymer-based CD, with preloaded reagents, employing microchannels and centrifugal forces to guide the fluids [40]. Using this system an analysis of viral or bacterial pathogens was demonstrated in 12 min.

There have also been a couple of successful demonstrations of true sample-to-answer systems integrating all necessary steps in one small device. For the analysis of whole blood a chip has been realized by Easley and colleagues that purifies DNA by a solid phase extraction, followed by a PCR amplification, and detection by microchip electrophoresis [41]. Another system used real-time PCR for the detection of the avian flu virus H5N1 [42]. Sample preparation, RT-PCR and fluorescence detection were done in droplets on a Teflon-coated chip (Figure 5.4). The droplet itself functions as a solid phase extractor and real-time thermocycler. Using superparamagnetic beads, viral RNA is isolated, purified and concentrated. The droplet is then moved clockwise over the chip for thermocycling. The real-time detection is achieved by using SYBR Green and placing the chip on an integrated optical detection system [43]. Interestingly, the authors have also developed a pocket-size real-time PCR system [44]. By doing so, they have created a true point-of-care system, which could serve as a platform for a variety of applications.

Besides the analysis of genetic material, other sample-to-answer systems rely on immunological detection schemes. By combining open channel electrophoresis and laser induced fluorescence detection the identification of swine influenza virus has been shown [45]. By using antibody-coated microbeads and a microfluidic device marine fish iridovirus has been detected. When the virus is present in the sample the particles conjugate and are trapped in a filter, followed by washing and fluorescence detection [46]. This relatively simple approach shortened the analysis time to 30 min from over 3 h for the conventional ELISA, and also showed improved sensitivity. By using a micr flow cytometer and antibody-coated magnetic beads Yang and coworkers have relized a complete analysis system with multiplexing potential [47].

Even though these LOC and μTAS approaches are all quite interesting, it is still uncertain if they can be used in routine diagnostic applications. Many of the described systems are highly sophisticated and expensive. In order to be used as

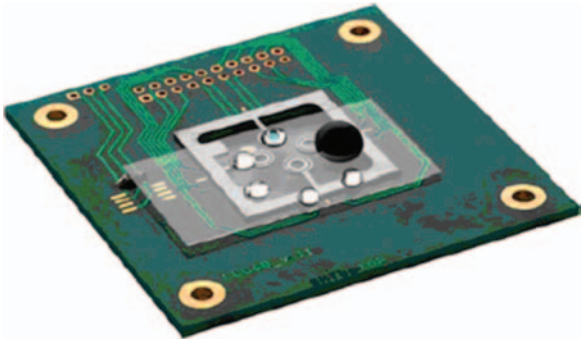

Figure 5.4 Example of a sample-to-answer system for the detection of avian flu virus H5N1 [42].

standard analytical tools these devices have to be produced reproducibly at low cost for the consumables (chips, reagents, etc.) and the detection units.

A totally different approach for the fast on-site diagnosis of foot-and-mouth disease has been demonstrated by using infrared thermography (Figure 5.5)[6]. Using this technique it was possible to rapidly identify infected cattle before vesicular lesion could be observed. Even though the systems allow fast diagnosis of whether the cattle have fever or not, and allow the fast screening of large numbers of animals, the method relies only on relatively unspecific symptoms but could be used as a pre-screening method during a FMD outbreak.

5.6 Conclusion

The developments of recent years, from LFDs to portable PCR platforms and isothermal amplification techniques, leave no doubt that an on-site diagnosis of livestock or plant disease is possible and will probably revolutionize pathogen diagnostics. However, many of these developments still lack proper sample preparation, making the entire diagnostic process still quite laborious. The advances in the development of true integrated devices and sample-to-answer systems over the last decade show the possibilities of this technology. So far these systems have not been developed for agricultural application, but an adaption will come as these devices are established first as routine diagnostic tools in medical applications.

The use of on-site analytics in agriculture will have significant impact, not only on the detection of pathogens, but also on other sectors of agriculture and horticulture. Faster decision making will allow the reduced and targeted use of pesticides, better risk prediction, and reduced waste in supply chains, benefiting both farmers and consumers alike [5]. Furthermore, the implementation of decentralized diagnostics will probably be most beneficial to developing countries, as they lack established

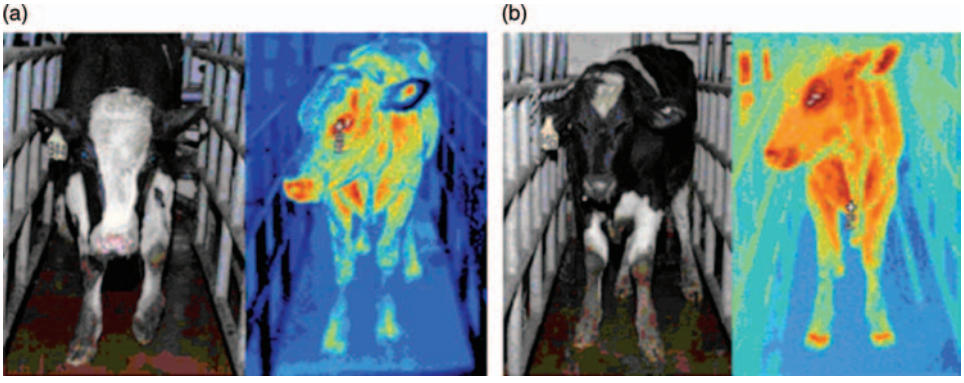

Figure 5.5 Using infrared thermography for the detection of FMD. Digital and infrared images of cattle without (a) or with (b) fever and viremia at 24 h post challenge, before vesicular lesions were observed. [6]

structures for centralized testing. Comparable to the mobile phone industry, this might lead to a development where these countries leapfrog the installation of costly centralized laboratory structures, enforcing the decentralized and mobile detection technology.

Even though the principal strategies have been successfully demonstrated and the advantages of on-site testing are clear, much work has to been done to transfer the described results into routine diagnostics.

References

1 Thompson, D. *et al.* (2002) Economic costs of the foot-and-mouth disease outbreak in the United Kingdom in 2001. *Rev. Sci. Tech.*, **21**, 675–687.

2 Davies, G. (2002) The foot-and-mouth disease (FMD) epidemic in the United Kingdom 2001. *Comp. Immunol. Microbiol. Infect. Dis.*, **25**, 331–343.

3 Anderson, I. (2002) Foot and Mouth Disease 2001: Lessons to be Learned, Inquiry Report, The Stationary Office: London.

4 Society, R. (2002) *Infectious Diseases in Livestock*, Royal Society, London.

5 King, D.P. *et al.* (2010) Plant and veterinary disease diagnosis: a generic approach to the development of field tools for rapid decision making? *Bull. OEPP/EPPO Bull.*, **40** (40), 34–39.

6 Rainwater-Lovett, K. *et al.* (2009) Detection of foot-and-mouth disease virus infected cattle using infrared thermography. *Vet. J.*, **180** (3), 317–324.

7 Schaad, N.W. *et al.* (2003) Advances in molecular-based diagnostics in meeting crop biosecurity and phytosanitary issues. *Annu. Rev. Phytopathol.*, **41**, 305–324.

8 Werres, S. *et al.* (2001) Phytophthora ramorum sp. nov. a new pathogen on Rhododendron and Viburnum. *Mycol. Res.*, **105**, 1155–1165.

9 Brasier, C.M. *et al.* (2005) Phytophthora kernoviae sp. nov., an invasive pathogen causing bleeding stem lesions on forest trees and foliar necrosis of ornamentals in the UK. *Mycol. Res.*, **109** (Pt 8), 853–859.

10 Lopez, M.M. *et al.* (2003) Innovative tools for detection of plant pathogenic viruses and bacteria. *Int. Microbiol.*, **6** (4), 233–243.

11 Lane, C.R. *et al.* (2007) Evaluation of rapid diagnostic field test kit for the identification of Phytophthora species, including P. ramorum and P. kernoviae at the point of inspection. *Plant Pathology*, **56**, 828–835.

12 Seaby, D.A. and Caughey, C. (1977) Mechanization of the slide agglutination test. *Potato Res.*, **20**, 343–344.

13 Talley, J. *et al.* (1980) A simple kit for detection of plant viruses by latex serological tests. *Plant Pathol.*, **29**, 77–79.

14 Torrance, L. and Jones, R.A.C. (1981) Recent development in serological methods suited for the use in routine testing for plant viruses. *Plant Pathol.*, **30**, 1–24.

15 Danks, C. and Barker, I. (2000) On-site detection of plant pathogens using lateral-flow devices. *Bull. OEPP/EPPO Bull.*, **30**, 421–426.

16 Miller, S.A. *et al.* (1988) Application of rapid, field-useable immunoassays for the diagnosis and monitoringof fungal pathogens in plants. *Proc. Br. Crop. Protect. Conf.*, **2**, 795–803.

17 Holmes, S.J. (1996) The validation and commercial development of immunological diagnostic technology for non-medical applications. *Proc. BCPC Symp.: Diagn. Crop. Prod*, **1**, 333–342.

18 Ferris, N.P. *et al.* (2009) Development and laboratory validation of a lateral flow device for the detection of foot-and-mouth disease virus in clinical samples. *J. Virol. Methods*, **155** (1), 10–17.

19 Ryan, E. *et al.* (2008) Clinical and laboratory investigations of the outbreaks of foot-and-mouth disease in southern

England in 2007. *Vet. Rec.*, **163** (5), 139–147.

20 Kox, L.F. *et al.* (2007) Diagnostic values and utility of immunological, morphological, and molecular Methods for in planta detection of Phytophthora ramorum. *Phytopathology*, **97** (9), 1119–1129.

21 Tomlinson, J.A., Dickinson, M.J., and Boonham, N., (2010) Rapid detection of Phytophthora ramorum and P. kernoviae by two-minute DNA extraction followed by isothermal amplification and amplicon detection by generic lateral flow device. *Phytopathology.*, **100** (2), 143–149.

22 King, D.P. *et al.* (2008) Prospects for rapid diagnosis of foot-and-mouth disease in the field using reverse transcriptase-PCR. *Vet. Rec.*, **162** (10), 315–316.

23 Callahan, J.D. *et al.* (2002) Use of a portable real-time reverse transcriptase-polymerase chain reaction assay for rapid detection of foot-and-mouth disease virus. *J. Am. Vet. Med. Assoc.*, **220** (11), 1636–1642.

24 Donaldson, A.I., Hearps, A., and Alexandersen, S. (2001) Evaluation of a portable, "real-time" PCR machine for FMD diagnosis. *Vet. Rec.*, **149** (14), 430.

25 Hearps, A., Zhang, Z., and Alexandersen, S. (2002) Evaluation of the portable Cepheid SmartCycler real-time PCR machine for the rapid diagnosis of foot-and-mouth disease. *Vet. Rec.*, **150** (20), 625–628.

26 Tomlinson, J.A. *et al.* (2005) On-site DNA extraction and real-time PCR for detection of Phytophthora ramorum in the field. *Appl. Environ. Microbiol.*, **71** (11), 6702–6710.

27 Hughes, K.J.D. *et al.* (2006) On-site real time PCR detection of Phytophthora ramorum causing dieback of Parrotia persica in the UK. *Plant Pathol.*, **55**, 813.

28 Notomi, T. *et al.* (2000) Loop-mediated isothermal amplification of DNA. *Nucleic Acids Res.*, **28** (12), E63.

29 Compton, J. (1991) Nucleic acid sequence-based amplification. *Nature*, **350** (6313), 91–92.

30 Lau, L.T. *et al.* (2008) Detection of foot-and-mouth disease virus by nucleic acid sequence-based amplification (NASBA). *Vet. Microbiol.*, **126** (1–3), 101–110.

31 Dukes, J.P., King, D.P., and Alexandersen, S. (2006) Novel reverse transcription Loop-Mediated Isothermal Amplification (RT-Lamp) for rapid detection of Foot-and-Mouth disease virus. *Arch. Virol.*, **151** (6), 1093–1106.

32 Tomlinson, J.A., Barker, I., and Boonham, N. (2007) Faster, simpler, more-specific methods for improved molecular detection of Phytophthora ramorum in the field. *Appl. Environ. Microbiol.*, **73** (12), 4040–4047.

33 Schulze, H. *et al.* (2009) Multiplexed optical pathogen detection with lab-on-a-chip devices. *J. Biophoton.*, **2** (4), 199–211.

34 Liu, W.T. and Zhu, L. (2005) Environmental microbiology-on-a-chip and its future impacts. *Trends Biotechnol.*, **23** (4), 174–179.

35 Ligler, F.S. (2009) Perspective on optical biosensors and integrated sensor systems. *Anal. Chem.*, **81** (2), 519–526.

36 Auroux, P.A. *et al.* (2004) Miniaturised nucleic acid analysis. *Lab. Chip.*, **4** (6), 534–546.

37 Myers, F.B. and Lee, L.P. (2008) Innovations in optical microfluidic technologies for point-of-care diagnostics. *Lab. Chip.*, **8** (12), 2015–2031.

38 Lee, J.G. *et al.* (2006) Microchip-based one step DNA extraction and real-time PCR in one chamber for rapid pathogen identification. *Lab. Chip.*, **6** (7), 886–895.

39 Cheong, K.H. *et al.* (2008) Gold nanoparticles for one step DNA extraction and real-time PCR of pathogens in a single chamber. *Lab Chip*, **8** (5), 810–813.

40 Cho, Y.K. *et al.* (2007.) One-step pathogen specific DNA extraction from whole blood on a centrifugal microfluidic device. *Lab Chip*, **7** (5), 565–573.

41 Easley, C.J. *et al.* (2006) A fully integrated microfluidic genetic analysis system with sample-in-answer-out capability. *Proc. Natl. Acad. Sci. USA*, **103** (51), 19272–19277.

42 Pipper, J. *et al.* (2007) Catching bird flu in a droplet. *Nat. Med.*, **13** (10), 1259–1263.

43 Pipper, J. *et al.* (2008) Clockwork PCR including sample preparation. *Angew. Chem. Int. Ed. Engl.*, **47** (21), 3900–3904.

44 Neuzil, P. *et al.* (2010) Rapid detection of viral RNA by a pocket-size real-time PCR system. *Lab Chip*, **10** (19), 2632–2634.
45 Reichmuth, D.S. *et al.* (2008) Rapid microchip-based electrophoretic immunoassays for the detection of swine influenza virus. *Lab Chip*, **8** (8), 1319–1324.
46 Liu, W.T. *et al.* (2005) Microfluidic device as a new platform for immunofluorescent detection of viruses. *Lab Chip*, **5** (11), 1327–1330.
47 Yang, S.Y. *et al.* (2008) Micro flow cytometry utilizing a magnetic bead-based immunoassay for rapid virus detection. *Biosens. Bioelectron.*, **24** (4), 861–868.

6
On-Site Analysis

Günther Proll and Günter Gauglitz

6.1
Introduction

Chemical contamination, allergens, and pathogenic compounds are ubiquitous in the environment. They can be found in contaminated ground water, in sediments, and in soil. Accordingly, this contamination can be absorbed by plants and transferred through the food chain to animals and humans. Furthermore, contact between humans is also responsible for inter-human transfer of such toxic substances. In the last decade, nanoparticles have come increasingly into focus regarding their influence on environmental and health problems. Because of their ability to act as carriers for any pathogenic compounds, due to their adsorptive effects, their influence on health care (in addition to their own potential toxicity) is now also considered.

State-of-the-art monitoring of environmental conditions and pollution in the food chain makes use of a large variety of classical analytical instruments [1]. Hyphenated techniques allow detection and identification of such molecules as allergens or pathogens and, in principal, of all chemical contaminants, even in complex matrices, in mixtures, sometimes at low concentrations (especially after enrichment procedures), and with necessary specificity [2–4]. Sampling, sample preparation and analysis are time-consuming and usually require a well equipped laboratory and qualified personnel. These facts cause problems for monitoring with respect to time, expenditure, and costs [5]. On the other hand, in the past decade the EU Commission has published quite a few directives which expect Communities and companies producing food to permanently monitor water quality [6–8] and/or foodstuff purity [9, 10]. Also, the US Environmental Protection Agency (EPA) enforces analytical monitoring of water to reduce cases of illnesses and deaths due to potential fecal contamination and waterborne pathogen exposure [11]. A similar requirement is enforced in many European member states, for example, Germany [12]. Recent trends in new developments of sensors for measuring priority pollutants are discussed using a list of these substances and comparing some methods [13]. Sensors and biosensors can be applied to support the EU Water Framework Directives and the related Marine Strategy Framework Directives [14].

Handbook of Biophotonics. Vol.3: Photonics in Pharmaceutics, Bioanalysis and Environmental Research, First Edition.
Edited by Jürgen Popp, Valery V. Tuchin, Arthur Chiou, and Stefan Heinemann

For this reason, new possibilities of fast, cost-effective and reliable analyses have been considered and developed within recent years. Photonics provides perfect tools for these upcoming tasks. Presently, a large variety of optical detection methods are being applied in bio- and chemo-sensors, some are even at a high level of development. Further improvement and production strategies are expected as photonics is increasingly used to provide miniaturized improved instrumentation for analytical purposes. These optical methods are especially suitable for miniaturization and parallelized detection of multi-analyte samples in cost-effective and fast monitoring of contaminants in water, food, and the environment. Miniaturization allows reduction of the sample volume and the number of agents. Thus, these improvements in instrumentation reduce cost and waste, and support portability.

Presently, the urgent problem is the requirement that, especially when looking for bacteria in many applications, just a few molecules have to be detected in small sample volumes. Instrumentation has not yet overcome the limitations of LODs (limits of detection) in such application areas, although quite a few approaches to enrichment strategies have been published and applied down to 10^{-19} mol l^{-1}. To give an idea of the problem, drinking water regulations require the verification of the absence of *E. coli* and coliforms in a 100 mL water sample. Thus, 1 cfu (colony forming unit) has to be detected. Accordingly, the EPA defined standard methods for enrichment of salmonella in biosolids [15] many years ago. Best results of "enrichment" have been achieved using PCR (polymerase chain reaction). However, this approach is time-consuming and regarded as unsuitable for on-site analysis. Therefore, in recent years some techniques of enrichment have been developed, allowing automated pre-concentration and combination with detection platforms. However, most of them are not fully automated and cannot always achieve high recovery rates, but at least they avoid cultivation steps. Thus, different concentration–elution methods using filtration, membranes or liquid–liquid extraction [16, 17] have been compared. Other concepts of enrichment use cross-flow microfiltration [18], by which a hollow fiber membrane module allows enrichment factors of more than 100. Another approach is immunomagnetic separation (IMS) [19] which takes advantage of coupling nanoparticles to antibodies or affinity ligands and by these means isolating bacterial cells, even in complex samples. Epoxy-based monoliths used for the affinity capturing of bacteria have also been reported [20].

In recent publications, such techniques are discussed for various applications [21]. In many papers enrichment using PCR is proposed. Combined enrichment and real-time PCR is described to obtain quantitative data for salmonellae [22]. Sandwich ELISA (enzyme-linked immunosorbent assay) in combination with PCR amplification has been developed for enrichment and detection of *legionella pneumophila* [23].

However, such approaches can amplify not only the bacteria that are being looked for, but also other components in the sample. Therefore, cross-flow microfiltration combined with immunomagnetic separation as pre-concentration steps and subsequent PCR amplification with DNA microarray detection are considered to come close to the required limits of detection [24]. Thereby, the stipulated limit of 0 bacteria is rather problematic from an analytical point of view. Regulation defining a limit of 1 cell in 100 ml is preferable as a LOD.

The concentration requirements are rather restrictive. However, there are quite a few areas in which monitoring, quantification and identification of contaminants in various samples, such as soil, water and food, are of high interest, even at higher concentrations. A rather expensive market research study covering advantages in label-free detection technologies gives a technical insight into developments at different companies, a description of platform technologies, patents and key application areas [25]. New methods to identify trace amounts of infectious pathogens rapidly, accurately and with high sensitivity are in constant demand in order to prevent epidemics and loss of lives, and have been reviewed recently [26]. This publication states that there is an urgent need for sensitive, specific, accurate, user-friendly diagnostic tests. Photonics shows promising perspectives for future development and application.

6.2
Substances to be Monitored

Contaminants of the emerging compound classes (listed in Table 6.1) are suspected to cause adverse effects in humans and wildlife. For instance, pentabromobiphenylether, 4-nonylphenol, C10-C13 chloroalkanes and the di(2-ethylhexyl)phthalate (DEHP) have been listed as priority hazardous substances in the field of water policy by EC Water Directive 2000/60/EC [7] and the final EU decision No. 2455/2001/EC. Active hormonal substances (natural hormones are active at levels of ng l^{-1}) such as estrogens, anti-inflammatory cortico-steroids and anabolic androgens are being widely used in human and veterinary medicine [27].

Table 6.1 List of emerging compound classes.

Emerging Compound Classes	Examples
biocides and plant protection products (e.g., pesticides)	atrazine, chlorpyrifos, diuron, endosulfan, isoproturon, simazin, trifluralin
pharmaceuticals	
veterinary and human antibiotics	sulfonamides, tetracyclines
analgesics, anti-inflammatory drugs	codeine, ibuprofen, diclofenac
psychiatric drugs and so on	diazepam
β-blockers	metoprolol, propanolol, timolol
X-ray contrasts	iopromide, iopamidol, diatrizoate
Surfactants and surfactant metabolites	nonylphenol, octylphenol, alkylphenol carboxylates
flame retardants	polybrominated diphenyl ethers (PBDEs), tetrabromo bisphenol A,
industrial additives and agents	chelating agents (EDTA), aromatic sulfonates
gasoline additives	dialkyl ethers, methyl-*t*-butyl ether (MTBE)
hormones and EDCs	estradiol, estrone, ethinylestradiol, bisphenol A, phthalic acid, nonylphenol, atrazine
natural toxins	saxitoxin, zearalenone, microcystins

It is important to notice that the mentioned emerging compounds can accumulate in different matrices in the environment (e.g., water, sediment, soil, etc.) with varying persistence and bioaccumulation. For many of these emerging contaminants, there are no data for eco-toxicological potential and risk assessments available. Therefore, it is difficult to predict what health effects they may have on humans, terrestrial and aquatic organisms, and ecosystems.

6.3 Optical Methods for Monitoring

There are a large number of different detection methods. These can be classified according to, for example, electrochemical, mass-sensitive, thermal, or optical methods. In this chapter, especially optical methods will be considered. There are quite a few recent review articles and book chapters which cover trends in optical detection techniques, considering various aspects. Present optical biosensors and perspective developments are presented and discussed in some chapters of a book by Ligler [28]. Beginning with fiber optic-based biosensors, a large number of evanescent field-based set-ups are discussed. The special principle of surface plasmon resonance (SPR), which is also commercialized, is described in detail. A special chapter covers plasmonic amplification, as has been realized in SERS (surface enhanced Raman spectroscopy) arrangements. In addition, the principle of fluorescence life time measurements and the use of planar wave guides for fluorescence sensors are covered. Electrochemiluminescence as a sensitive tool is reviewed. Cavity ring-down, cantilever, nanoparticles and fluorescence-based intracellular biosensing are handled, demonstrating future trends.

Fluorescence is the main approach for detecting biomolecular interactions. Presently, most assays are based on this method. Therefore many review articles have been published, and books or book chapters have been written [29]. The field of chemical and biochemical sensors based on fluorescence detection techniques has been classified, former development and present status as well as trends are given [30]. Optical chemical sensors (OCS) have experienced increasing interest: Their advantages of being non-invasive and allowing on-line detection are presented in a review article on multiple fluorescent sensing and imaging [31]. The state of the art in terms of spectroscopic methods, materials, and selected examples for dual and triple sensors is discussed, together with a look into the future. The different methods using direct optical detection have been reviewed [32, 33], and commercially available instrumentation as well as typical applications are presented [34].

It is possible to distinguish between direct measurements of pollutants without reagents, which can be the case for bacteria, virus, or self-fluorescent poly-aromatic hydrocarbons, and monitoring contamination by interaction between a reagent and a pollutant. These methods can be further divided into experiments based on interaction partners where at least one of the partners is labeled, and other methods using non-labeled partners. In addition, different techniques provide optimum approaches if the interaction between analyte and reagent takes place in the homogeneous phase

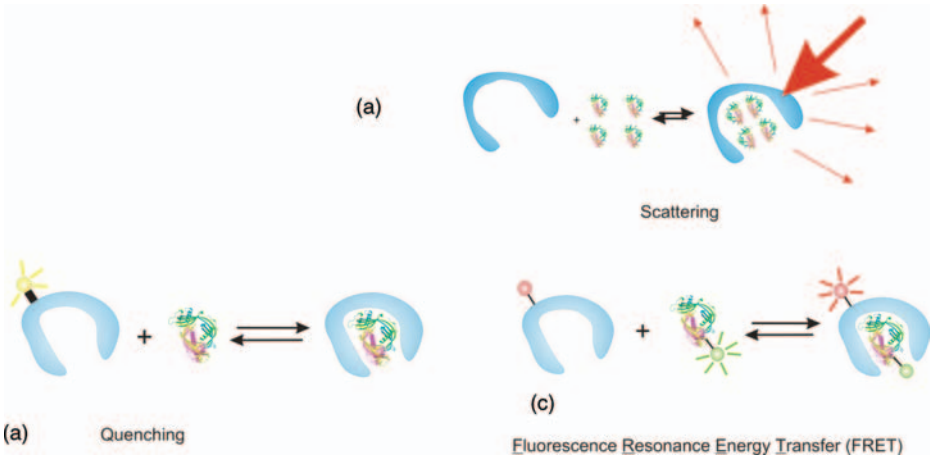

Figure 6.1 Interaction processes between analyte and receptor. (a) Interaction results in modified structure or increased size, allows measurement with scattering methods, (b) interaction can cause quenching, (c) fluorescence resonance energy transfer (FRET), fluorescence emission wavelength is different.

or in the heterogeneous phase of a transduction element, as used in bio- or chemosensors. These different principle experimental set-ups are surveyed in Figures 6.1 and 6.2.

With regard to the homogeneous phase, it is possible to distinguish between interactions between non-labeled compounds and those between partners where one or both are labeled. Accordingly, in Figure 6.1 different detection methods of these interactions are used. In the case of (a), methods of light scattering can quantify the amount of interaction of non-labeled partners. For (b), quenching effects of the labeled molecule during interaction can be considered, but indirect detection using the transduction element is preferable. Fluorescence resonance energy transfer (FRET) is state of the art in many applications (c). Diffusion to the transducer has always to be taken into account in all the other possibilities of monitoring interaction, as is demonstrated in Figure 6.2, where detection at the interface to the transduction element (heterogeneous phase detection) presents a variety of principles. Even the simplest and most preferred approach of direct measurements (a), with the "analyte" as a ligand to a receptor being immobilized on the transducer surface (also considering additional biopolymer layers against non-specificity) is influenced by this diffusion process. The signal is usually only high enough for the quantification of such an interaction if the measured partner is large or heavy enough (b) or the analyte is self-fluorescent (for case (a)). If the receptor is labeled in assay (b), the measurement is also successful. This indirect measurement is more frequently applied in competitive or binding inhibition tests (c), where the receptor in the homogeneous phase is not necessarily labeled by a fluorophore (e). For this approach, a derivative of the analyte has to be immobilized at the transducer as a recognition element. Case (d) demonstrates the same assay for a system where the receptor is labeled and

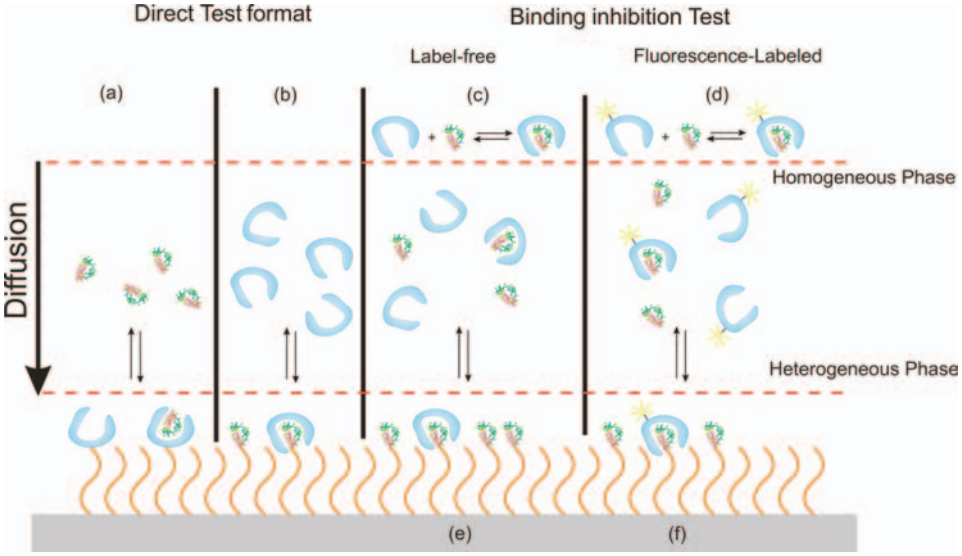

Figure 6.2 Interface with biomolecular layer and nonspecific binding and diffusion layer responsible for mass transport limitation (a) direct assay with immobiliised receptors attracting small analytes, (b) rather large analytes interacting with small receptors immobilized at the transducer, (c) derivative of analyte immobilized to biopolymer layer, in the equilibrium of the homogeneous phase non-blocked receptors can be detected in a second equilibrium in the heterogeneous phase (e), this type of interaction can also be monitored if the receptor is labeled ((d) and (f)).

interaction is monitored at the transducer interface (f). For these different approaches a variety of optical detection principles are suitable, either based on fluorescence detection or using direct optical detection principles. New methods based on Raman enhanced spectroscopy provide, in most of these approaches, not only quantitative information about the amount of interaction but also allow characterization of the interacting specimen.

For monitoring in the homogeneous phase, typically at least one of the partners requires a label, such as a fluorophore. However, if the pollutant can cause light scattering or if the interaction-complex between contaminant and reagent molecules causes drastic changes in either size or form, changes in scattering properties can be used for detection. Accordingly, light scattering [35, 36] is a typical detection principle used in flow cytometry, which allows detection and characterization of cells or other particles suspended in a stream of fluid. This method is frequently used in environmental microbiology and biotechnology [37], or even in the food industry, as reviewed recently [38]. In the latter case, mostly labeled particles are measured, also taking advantage of fluorescence-activated cell-sorting (FACS). A modification of the light scatter-based method was introduced at Purdue university with BARDOT (bacteria rapid detection using optical scattering technology) [39] as a label-free system looking at unique patterns found by laser light scattering from bacteria colonies. Pathogens can be detected and classified. An instrument to measure

nanoparticles with respect to size, concentration, zeta potential, and aggregation, as well as population in liquids in a multi-parameter approach is provided by Nanosight [40]. The real-time measurement provides information about the kinetics of protein aggregation, the development of viral vaccines, nano-toxicology and biomarker detection, and is also useful for pollutant detection. Applied to pathogens, light scattering is reported as a fast and sensitive detection tool [41].

In environmental control, electrochemical and optical detection methods are currently popular. Recent application of flow-based methods competes with chromatographic methods. They have been compared recently [42]. Flow methodology has been modified and multiparameter flow-through optosensors are reviewed and current trends of such detection techniques are critically discussed.

Fluorescence intensity or quenching effects of an analyte detecting reagents such as labeled antibodies can be determined in dependence on analyte concentration. If the diffusion property of the labeled reagent is changed significantly through interaction with a large analyte, fluorescence correlation spectroscopy becomes measurable. Also, detection in the homogeneous phase is possible if both partners of the interaction process are labeled and fluorescence resonance energy transfer takes place. FRET requires a labeled molecule as donor and another labeled molecule as acceptor, that is, the fluorescence of the donor must be within the wavelength range of the absorption of the acceptor molecule. As soon as these partners become very close, that is, if the distance between them is less than approximately 10 nm, energy from the donor is transferred to the acceptor which starts to fluoresce at the long wavelength side [43, 44]. In general, Förster resonance energy transfer-based analytical techniques have found great interest in bioanalysis because they allow detection of protein–protein interactions and conformational changes of biomolecules. This can be done at the nanometer scale, both *in vitro* and *in vivo* in cells, tissues, and organisms. FRET measurement principles and procedures have been continuously improved in recent years. Nevertheless, in some cases only qualitative or semi-quantitative information can be obtained. Recent applications are given and their advantages and limitations are discussed in[45]. Special applications allow the monitoring of intra- and intermolecular reactions occurring in microfluidic reactors performing highly efficient and miniaturized biological assays for the analysis of biological entities such as cells, proteins and nucleic acids [46]. Even multiplexed analytics using quantum dots are used to improve signals [47]. A review of bioluminescence resonance energy transfer in bioanalysis is found in [48].

Measurements in the heterogeneous phase provide an even larger number of methods for detection of the final interaction state, and even the kinetics of the interaction process. Some of these methods even allow the characterization of bacteria. An ELISA providing colorimetric read-out is one of the basic methods to detect pathogens. Immunographic assay strips supply a simple method of multiplex detection on a somewhat semi-quantitative basis [49].

For many years chemiluminescence or bioluminescence have been used as methods to detect low amounts of molecules [50]. A chemical or biochemical reaction leads to electronically excited products which decay, emit photons, or pass their energy to other species which will emit light. Some advantages in comparison to

normal fluorescence can be discussed [51]. In principle, all the chemiluminescence-based techniques are fundamentally limited by system properties, such as reaction yield and quantum yield. However, new technology has emerged which uses metal surface plasmons to amplify chemiluminescence signals. A tutorial review gives a survey on the next-generation of chemiluminescent-based technologies [52]. In the detection of salmonella, legionella and other pathogenic bacteria such detection principles, in combination with flow-through techniques have been successfully applied [53, 54].

A large number of different fluorescence methods exist. They can be used in different types of assays for detection, including heterogeneous phase assays. They demonstrate low limits of detection. However, labeling can influence the interaction process and reduce bioactivity. For this reason, in recent years, direct optical detection techniques have gained increasing interest. Therefore, methods like Raman measurements and reflectance-based monitoring will be discussed next. Figure 6.3 shows reflectance at a thin layer. Radiation is reflected at each interface between media of different refractive index [55]. Using a thin layer the reflected beams at the two interfaces can superimpose (grey lines, Figure 6.3a). This can be considered as micro-reflectometry [56]. If radiation is coupled into such a thin layer then total reflection occurs beyond a certain critical angle of incidence and radiation is guided (see Figure 6.3b) within the fiber or the waveguide. In addition, the guided radiation's electrical field vector couples to the outside of the waveguide creating an exponential decay field vector which is influenced by the refractive index next to this interface. Accordingly, as demonstrated in Figure 6.4, this so-called evanescent field can either excite fluorophores close to the interface or read-out changes in refractive indices close to this grating. A simple application of this effect has been demonstrated using long waveguides with long interaction lengths and measuring finally the reduction of

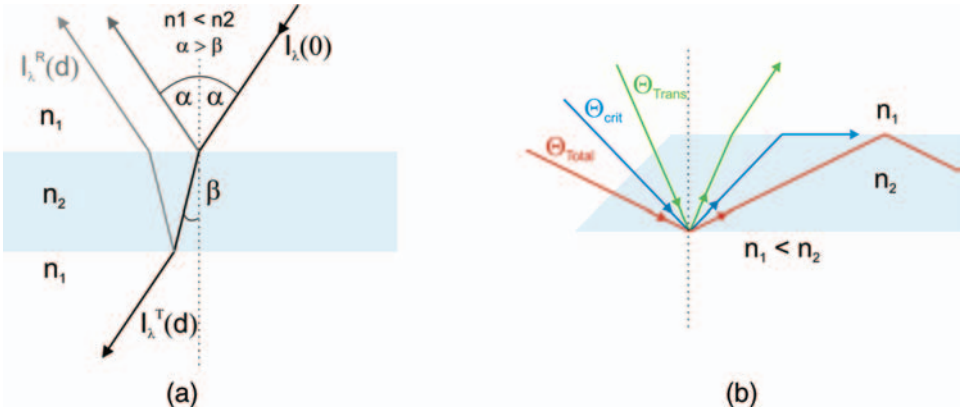

Figure 6.3 (a) Reflectance at a thin layer, refraction into layer at smaller angle to optical axis for incidence from medium at lower optical density to one at higher optical density. Multiple reflections at interfaces (grey lines) forming superimposed reflected partial beams. (b) reflectance at interface between medium of higher optical density and one with lower optical density can result in total reflectance and guided waves.

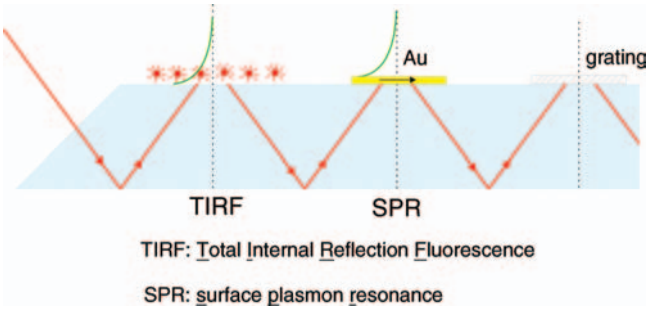

Figure 6.4 A guided wave couples to an evanescent field at the outside of the waveguide which decays exponentially. This can be absorbed in part and excite fluorophores in close contact to the waveguide or excite surface plasmons in a metal coated on the waveguide (SPR) or couple out at a grating in the interface of the waveguide in dependence on changes at this grating.

guided radiation intensity [57], or using integrated optics to improve stability [58]. Modern waveguide based set-ups use a variety of read-outs, such as surface plasmon resonance (SPR), grating coupler, resonant mirror, Young interferometers, and Mach-Zehnder chips. They and some more can be summarized as micro-refractive principles and are discussed in [59].

In the heterogeneous phase chemical modification of the surface is essential. This layer has to reduce (better suppress) non-specific binding, allow high loading (as many recognition sites as possible) and to be very stable (for potential regeneration steps). A recent review covers the surface functionalization methods regarding the recognition elements, the immobilization techniques, self-assembled monolayers and covalent coupling [60]. In addition, microfluidic devices are presented for different materials and various optical detection techniques for label-free assays are discussed; evanescent field devices are listed, resonant cavities and especially surface plasmon devices discussed. The special polyethylene glycol layer, a well established biopolymer coating of transducer surfaces against non-specific binding, was characterized and discussed with respect to its feasibility [61]. The new approach to biosensing, using scaffolds in complex matrices has been recently presented [62]. An essential part of any device for monitoring pathogenic compounds is the quality of the flow cell. Nowadays, these devices are miniaturized to fit to many detection principles, to reduce the amount of reagent, and to optimize flow conditions combined with defined diffusion processes to the transducer surface. Such miniaturized tools have been reviewed recently [63].

Many approaches to the monitoring of pollutants in the environment are based on microarray technology. Even protein microarrays are suggested, which have been reviewed some years ago [64]. These arrays can use direct optical detection techniques [65], which is becoming of increasing interest. Interferometric reflectance imaging sensors allow sensitive protein and DNA detection in real time and even on a high through-put basis [66]. However, as mentioned, most approaches are based on fluorescence detection [67]. In principle, DNA sequences supply good chances for

selective detection of pollutants with such read-out techniques [68]. Such DNA microarray technology is especially considered for microbial pathogen detection [69]. Some of these different detection platforms [70] are named, a large number of references are given, and the applicability to detection of pathogenic bacteria is discussed [71].

Fluorescence is one of the most used methods in analytics. Because of the capability to measure low concentrations, fluorescence is the basis of many microarrays. In the general review on DNA and protein mircroarrays [67] fluorescent labeling of nucleic acids and protein strains is discussed. Fluorescence labeling of nanoparticles is classified according to polymeric nanoparticles, silica particles, and quantum dots. The latter have a semiconductor core of different particle sizes (CdSe, CdTe e.g., 1–10 nm in diameter). The core is covered by a transparent layer, for example, ZnS, to increase quantum effects and stability. The surface is functionalized with biocompatible material which can be used for proteins and makes them water soluble. The advantage is that a single wavelength of excitation can be used to offer various emission wavelengths, just dependent on the particle size [72]. Optical, magnetic and electrochemical methods of nanoparticle-based biosensors are compared in an overview of the progress, the limitations and future challenges of such devices for detection of pathogenic bacteria [73]. The synthesis of various types of nanoparticles supplies a large variety of properties with gold magnetic or quantum dot nanoparticles. A review gives a large number of recent applications in environmental analysis, it discusses different detection principles and mentions key trends as well as future perspectives [74]. The use of such nanoparticles, even in combination with new recognition elements like scaffolds, results in interesting advantages for nano-structured biosensors [75]. Crystalline europium-doped gadolinium oxide nanoparticles also offer a large Stokes shift and long fluorescence lifetime (1 ms) [76].

The read-out of microarrays can consist of either a scanner or an imaging system. Commercially available readers are compared on the internet [77].

Excitation of fluorescence close to a waveguide's interface is considered as total internal fluorescence reflectance (TIRF) [78]. This method is frequently used to excite fluorescence of appropriate arrays. Another approach is to measure fluorescence anisotropy, time resolved fluorescence, or fluorescence lifetime imaging (FLIM) [79]. FRET is also used [45].

Using interaction at a heterogeneous interface, or at the interface between a surface with recognition elements and the analyte in solution, direct optical detection becomes possible in addition to the detection of fluorophores. This can be done either in a single-channel system or in an array of detection elements, called a micro-array, with a corresponding parallel read-out of all interaction spots. Under these conditions, all read-out methods for microarrays can usually also be used for single-channel readout. For the read-out of fluorescence, a large variety of fluorophores labels is available commercially. The excitation even ranges up to the far-red wavelength range, which improves the quality of the fluorescence signal with respect to noisy scattering. Besides the measurement of fluorescence intensity, especially time-resolved fluorescence is preferable and also the increase in sensitivity by nanoparticle-enhanced signals using the effect of plasmons. In all cases, the

photo-stability of the label and quenching effects can reduce the efficiency of excitation and signal-to-noise ratio. The gain using such plasmon enhancing effects can be demonstrated in antigen–antibody interaction studies [80]. It even allows measurements using microscopy and multispot approaches [81]. The urgent need to determine infectious pathogens rapidly, accurately, and at low concentration is argued in detail using modern approaches in surface modification and fluorescent nanoparticles in a general review [82].

It had been mentioned that labeling can reduce bioactivity. Therefore, in recent years direct optical detection methods have gained increasing interest, keeping in mind the problems with matrices and the greater influence of non-specific binding and limitations of limits of detection. Nevertheless, quite a few good arguments exist for these direct methods. They have been classified above as either micro-refractometric or micro-reflectometric. Figure 6.4 demonstrated the existence of an evanescent field which is dependent on the refractive index of a solution or a layer close to the interface of the transducer. Binding of analytes or receptor molecules to the recognition elements in this layer causes changes in the refractive index. The monitoring evanescent field couples to the field of the guided wave within the waveguide or fiber. There exist a large number of optical principles to read-out changes of the propagating wave, thus allowing calibration of a pollutant's concentration with changes in the effective refractive index [83–85]. A huge number of publications deal with such evanescent field-based biosensors. The most discussed methods are grating couplers [86–88], resonant mirrors [89–91] and SPR [84, 92–94]. The effect of refractometric measurement can be combined with interference. Such is the case in Mach–Zehnder chips and in its modified form, the Young interferometer. Both split the waveguide into two arms, one of which is undisturbed (reference arm) and the other is in contact with the analytical process. Thus, a phase shift between these two arms takes place and can be very sensitively observed. Calculations prove that limits of detection far beyond the normal could be expected. However, even in Mach–Zehnder rearrangements measurable concentrations are less limited by the optics than by microfluidics and the biomolecular interaction process. Measurements of pesticides have been published [95, 96]. If the arms are not re-unified, but a free radiation optical arrangement is chosen without rejoining the waveguide arms then this is called a Young interferometer [97]. Such set-ups are rather costly at present and lack mechanical stability.

SPR was commercialized many years ago [98]. Therefore, it is the most commonly used evanescent field technique. Normally, a 50 nm thick gold layer is coated on a prism (half-cylinder); radiation is incident on the gold film via this prism. Electron density fluctuations can be excited at total internal reflection conditions at a suitable angle and/or wavelength of incident radiation. Then, reflected radiation is reduced in intensity at the resonance condition. This resonance condition depends on the refractive index close to the gold film in the solution inside the sample cell. Resonance is either observed at a shifting angle of reflection or wavelength. Applications to bio- and chemo-sensing were reviewed many years ago [99]. The analytical approach using SPR to measure contaminants like pesticides, mycotoxins, or surfactants in food is discussed with respect to immobilization strategies (avoiding

non-specific binding) and assay formats [100]. At present, an urgent aim is to multiplex SPR [101]. To advance food-safety towards high-throughput control, development of SPR is pushed forward in the areas of medical, pharmaceutical, biotechnological, and agri-food industries [102].

Recently, some applications of SPR in simultaneous multianalyte antibiotic detection in milk samples have been published for three important antibiotic families (fluoroquinolones, sulfonamides and phenicols) with LODs below $1\,\mu g\,l^{-1}$ [103]. To avoid contamination of food the rapid detection of foodborne pathogens is of vital importance. The developed biosensor array chip is able to specifically detect the presence of two known pathogens. This biosensor array is integrated into a self-contained PDMS microfluidic chip [104]. The detection of microcystins (MCs) in drinking water has also been developed. Among several, the selected assay format is based on a competitive inhibition assay, in which microcystin-LR (MCLR) is covalently immobilized onto the surface of a SPR chip functionalized with a self-assembled monolayer [105]. By these means SPR is even combined with fluorescence [106, 107] which improves detection.

In all the discussed optical detection techniques the product of refractive index and the physical thickness of the considered interaction layer ("optical thickness") is measured. In the case of evanescent field techniques the change in refractive index has the dominant influence on the signal. Unfortunately, this refractive index is rather dependent on temperature. For this reason temperature control is essential and requires well referenced measurements together with thermostating. This fact is also valid, in part, for reflectometric methods. Thus, ellipsometry is also temperature dependent. Multiple reflections at interfaces of a layer system cause superpositions of the partial radiation beams resulting in an interference pattern. Both polarization states of the electromagnetic radiation are used. The two modes (two states of polarization) are differently influenced by the effective refractive index. Thus, in spectral ellipsometry, the phase shift and change in amplitude of the two modes allow information about physical thickness and refractive index [108, 109]. Such instrumentation has been very expensive, however, process control of wafers has widened the applications and reduced instrument prices.

Ellipsometry can be further simplified just by using non-polarized light. This method is called reflectometric interference spectroscopy (RIfS) [110, 111]. The principle is demonstrated in Figure 6.5. Changes in optical thickness shift the interference spectrum. Since time-resolved measurements are no problem, binding processes can be observed. Glass or transparent polymer layers can be used, even ITO-coated glass plates are suitable. Thus, the material is cheap. Even measurement at one wavelength (or better at four) is possible [112, 113]. Temperature dependence is negligible in contrast to evanescent field techniques. Increase in temperature will reduce the refractive index, in contrast to the increasing physical thickness. Thus, both effects nearly compensate and allow measurements without thermostating. The optical robustness and simple set-up allow easy parallelization, 700 spots per square centimeter have been achieved [114]. The principle has been used to measure pesticides [115] and endocrine disruptors [116] in food.

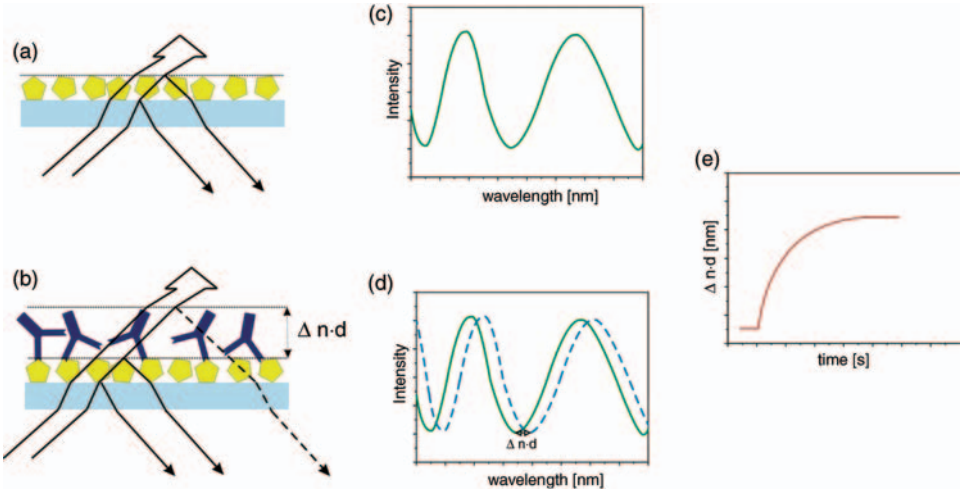

Figure 6.5 Multiple reflection takes place at interfaces of layers in dependence on physical thickness, wavelength, refractive index and angle of incidence. The result is an interference pattern (c). Changes in either refractive index or physical thickness cause a shift in interference pattern. Time-resolved measurement can be correlated to a binding process (e).

Since Raman spectroscopy has drastically developed towards simple and robust instrumentation, it is considered to be suitable for on-line analysis [117]. Metallic surfaces or even metallic nanoparticles can increase the signal, resulting in surface enhanced Raman scattering/spectroscopy (SERS) [118]. In Raman spectroscopy vibrational and rotational excitations of molecules are studied. It is an inelastic scattering process. The Raman scattering is excited by a laser in the visible or near-infrared range. It is complementary to infrared spectroscopy. Spontaneous Raman scattering is typically very weak. Accordingly, the main difficulty of Raman spectroscopy is in separation of the weak inelastically scattered light from the intense Rayleigh scattered light. Use of lasers has overcome some of the problems. A number of advanced types of Raman spectroscopy, including surface-enhanced Raman (SERS), resonance Raman, tip-enhanced Raman (TERS), polarized Raman, and hyper Raman have advanced Raman to a powerful analytical tool. Modern instrumentation even offers hand-held devices, or at least systems usable out of lab [119, 120]. A recent special issue in the *Journal of Analytical and Bioanalytical Chemistry* lists in the editorial the advantages, developments and possibilities [121]. Within this volume some applications are given.

The capabilities of SERS as a technique for applications related to environmental analysis and monitoring are presented in a recent review [122]. This method has proven to give good results in the structural characterization of soils, ultrasensitive detection of pollutants and heavy metal ions, and the analysis of plants, tissues and microorganisms. In addition, a critical approach with respect to the drawbacks and difficulties associated with the various experimental configurations and enhancing substrates is introduced. Raman spectroscopy is a direct technique to detect

pathogenic bacteria in food without prior enrichment. This is demonstrated for three different milk-contaminating bacteria; *Escherichia coli*, *Brucella melitensis*, and *Bacillus thuringensis* [123]. Vibrational spectroscopy is feasible for the validation of bacteria in microfluidic devices, as demonstrated by the use of SERS [124].

Recent biosensor developments use photonic crystals. These optical components are formed by structured transparent semiconductors, glasses, or polymers with dielectric structures with a periodicity of refractive index which influence refraction and interference of photons. The dimensions of these structures have the dimensions of wavelengths and are three-dimensional. This is in contrast to interference filters or gratings [125, 126]. They also can be used for Bragg reflection [127]. A review of the recent progress and novel applications of photonic fibers is given for photonic crystal fibers [128]. Different types are discussed and even the terahertz guidance is discussed. An overview of such systems can also be found for various applications to sensing [129]. Even though cantilevers are easily damaged and difficult to set up for field applications, recently, an online portable micro-cantilever biosensor for salmonella has been described [130].

6.4 Assays

For specificity, an analytical method can either use an intrinsic property of the analyte (e.g., IR fingerprint) or specific recognition elements capable of discriminating between the analyte molecule and other compounds In the latter, the specific interaction of a recognition element with an analyte is then transferred into a detectable physical signal change by the transducer element. Together with the developments in the area of biophotonics for on-site environmental analysis, the need for automated assays has lead to the development of new test formats. Usually, these methods combine the principles of various immunoassays or chemical sensing approaches performed on sensor surfaces, taking advantage of microfluidics and different fluorescence or label-free transduction technologies. Current developments in microfluidics and microarray technology are the basis for multiplexed quantitative measurements in the area of environmental on-site analysis [67, 133, 134].

Each assay type or test format, together with the applied detection principle, provides individual properties suited for various applications, as indicated in Section 6.5. The predominant test formats used for environmental analysis are enzyme linked immunosorbent assay (ELISA, see Figure 6.6), replacement assay, sandwich assay, binding inhibition assay, and the direct test format. The selection of the test format, in combination with the transduction principle, has to be driven by the analytical needs of each individual application. In addition, the properties of the recognition element (e.g., antibody, aptamer, scaffold, molecular imprinted polymer, etc.) have to meet the requirements for a given test format. This is not only for the affinity/avidity or selectivity, but is also a question of chemical stability and the diffusion relations in flow injection analysis (FIA) systems [135].

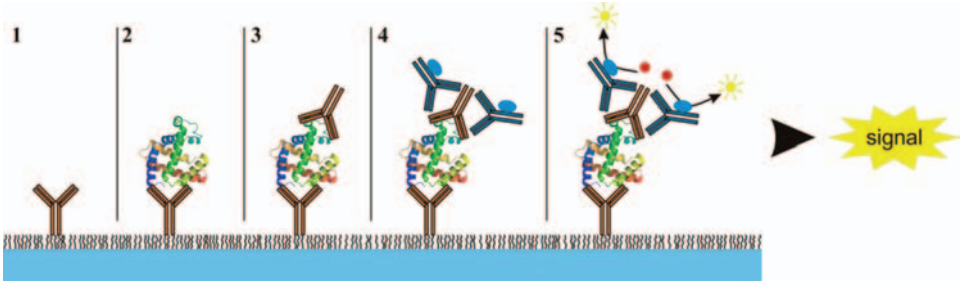

Figure 6.6 ELISA (enzyme linked immunosorbent assay).

The ELISA was developed more than 40 years ago and is one of the best known test formats with a wide range of applications and variations [136]. Because of the stop-flow conditions, an ELISA needs washing steps between the incubation phases. As shown in Figure 6.6 for the most common type of ELISA assay, the first incubation phase starts with a capture antibody-coated surface, which is incubated with the sample. After washing, a detection antibody is applied, followed by an incubation phase and further washing. The next steps produce the read-out signal via a secondary antibody directed towards the detection antibody, and linked with an enzyme as a chromogenic reporter system. There are many commercially available ELISA tests available for a wide range of analytes. However, their usability as on-site tests is limited due to the washing steps, which have to be performed manually or via complex automated liquid handling. Therefore, the developments in the area of optical (bio)sensors included flow injection analysis (FIA) [137–140] systems or microfluidics.

One of the test formats used for environmental immunoassays is the replacement assay (Figure 6.7a). For this testformat the sensor surface is modified with an antibody carrying a labeled analyte analog. During the incubation step the analyte in the sample replaces the bound labeled analog. Replacement assays can handle large and small analytes and should be carried out with an antibody offering a not too high dissociation rate constant for the analyte analog. Usually the replacement assay is combined with fluorescence read out. Limitations of this test format are the stability of the immobilized antibodies during regeneration procedures, which is necessary for a quasi-continuous monitoring.

For the sandwich assay (Figure 6.7b) a capture antibody (or other recognition element) is immobilized onto a sensor surface (heterogeneous phase). The sample can be either incubated with this surface, followed by subsequent incubation with a detection antibody (2 steps), or the surface can be incubated with the mixture of sample and detection antibody (1 step). In the latter case, the detection antibody needs to bind to a different epitope of the analyte than the capture antibody. In general, it is advantageous to select antibodies with low dissociation rates because it is a non-competitive test format. The read-out can be either label-free, for example, SPR (3a in Figure 6.7b) or fluorescence-based (3b in Figure 6.7b) for example, scanning or TIRF. The combination with fluorescence-based detection allows a very low limit of

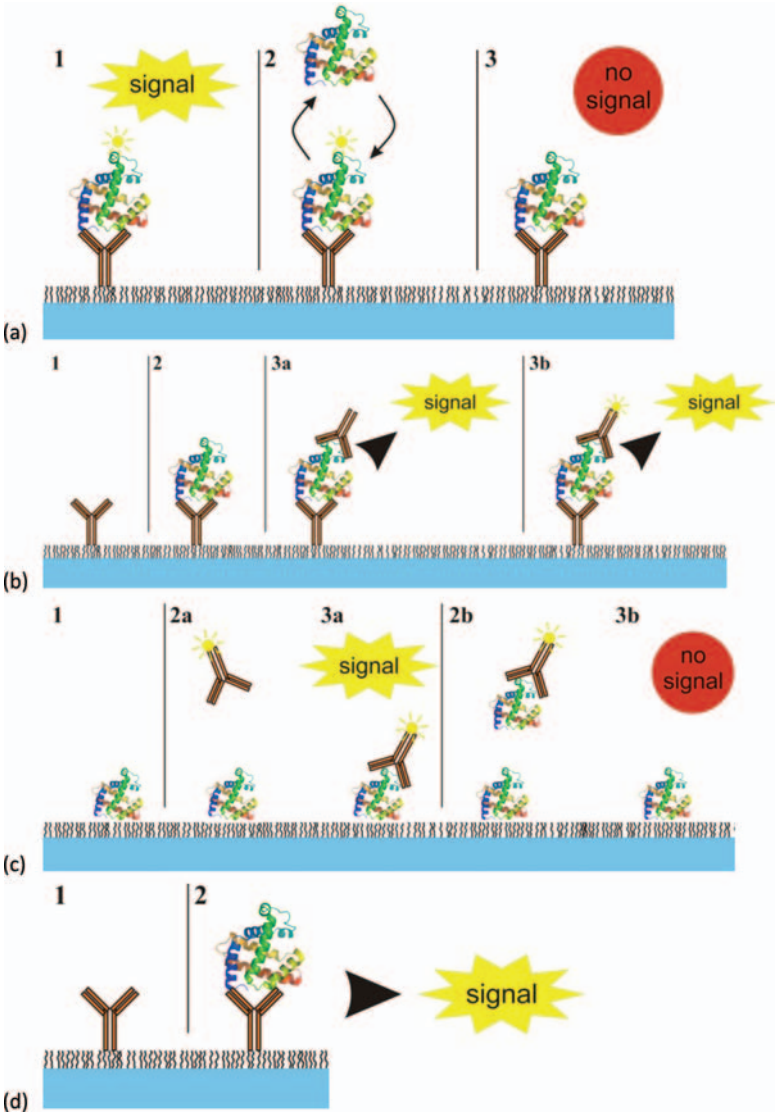

Figure 6.7 (a) Replacement assay, (b) sandwich assay (c) binding inhibition assay (d) direct test format.

detection. Especially for the sandwich assay, there is the additional advantage of very high selectivity because of the involved detection- and secondary antibody. Furthermore, this test format in the labeled mode is preferable when resistance against matrix compounds (e.g., dissolved organic carbon) of environmental samples is important. The only relevant limitation of this test format exists for small molecules which do not offer two epitopes that can be bound by two antibody molecules

simultaneously, for example, because of steric hindrance. This is often the case for small chemical compounds, like pesticides or endocrine-disrupting chemicals. Furthermore, the regeneration of the sensor surface is problematic, as mentioned for the replacement assay, because of the low chemical stability of the capture antibody. This might be overcome in the future by using more stable recognition elements (e.g., scaffolds).

A test format which overcomes the limitations described for the sandwich assay in terms of small molecule detection, and to some extent the stability of the sensor surfaces, is the binding inhibition test (Figure 6.7c). A drawback is the complexity of the necessary automation. This is due to the step-wise assay procedure which starts with a pre-incubation step of the antibody with the sample. According to the law of mass action, the paratops can bind to their epitopes. In the subsequent incubation phase each antibody molecule with at least one free binding site can bind to an immobilized antigen derivative at the sensor surface. This test format is non-competitive, because the incubation step with the modified surface is mass transport controlled (due to flow conditions the equilibrium in the bulk solution is not changed) due to a very high surface loading with antigen derivative molecules. If this test format is performed with high affinity antibodies (low-off rates) together with a TIRF set-up for read out, extremely low limits of detection can be achieved. Label-free detection is also applicable and offers the advantage to use recognition elements, which cannot easily be labeled with a fluorescence dye. A further big advantage is the easy adaption towards multianalyte immunoassays for small molecules, when the surface modification is based on a spatially resolved chemistry protocol of antigen derivatives (e.g., derivatives of pesticides or pharmaceuticals). Many of these antigen derivatives are robust towards the chemical conditions of regeneration procedures, which allows several hundreds of measurement cycles with the same sensor surface.

Restricted only to label-free transduction principles, but superior in simplicity, is the direct test format (Figure 6.7d). This non-competitive testformat employs a sensor surface with immobilized recognition elements. In a one-step procedure the sample incubated with this surface and the binding can be directly recorded, for example, with SPR or RIFS. However, there are many critical conditions to be aware of. The antibody, or any other recognition element, should provide very low off-rates (high affinity constants) to the analyte (antigen), and during the immobilization process it is necessary to bind many recognition elements (high surface loading) in such a way that the binding sites are intact and accessible for the analyte. A limitation for any label-free transduction technology is the rather high limit of detection due to the mass sensitivity, which correlates with the molecular weight of the analyte. Furthermore, non-specific binding of matrix compounds to the sensor surface can disturb the measurement, which is the main source of artefacts. However, the direct test format is a very good choice for fast and reliable detection of particles, for example, pathogens and bigger molecules such as allergens even in complex matrices, if combined with sophisticated surface-shielding polymers.

6.5 Applications

6.5.1 Chemical Contaminants, EDCs, Pharmaceuticals and Toxins

Environmental monitoring of chemical contaminants covers a wide field of chemical species and sample matrices, such as air, water or soil. Furthermore, there is a requirement to analyze directly the immissions of industrial processes or effluents from wastewater treatment plants. The focus of this section will be on technologies for on-site analytics of chemical contaminants in ground water and surface water bodies. In general, there are different approaches for the quantification of individual compounds up to effect-directed analytics. Besides the introduced optical detection technologies and assays, the recognition elements play an essential role in the performance of the monitoring system.

Because drinking water, as one of our most important resources, depends on the quality of the above-mentioned water bodies, it is necessary to take into account the European Water Framework Directive (WFD) and the related Marine Strategy Framework Directive which give maximum values for allowed concentrations of a set of chemical contaminants. Furthermore, the list of priority substances (EU decision No. 2455/2001/EC) lists numerous very important chemical contaminants with thresholds. These values are important for water analytical methods, because the method applied has to meet, at least, these standards. For example, the threshold for a single pesticide is at 0.1 ppb (equivalent to $0.1\,\mu g\,l^{-1}$) and for the sum-concentration of pesticides in water samples the threshold is 0.5 ppb. A recently published study clearly indicates the need for long-term monitoring data as one of the future challenges of the WFD implementation [141].

The analytical requirements can become much more ambitious when taking into account some endocrine disrupting chemicals (EDC) – EDCs act like hormones in the endocrine system and disrupt the physiological function of endogenous hormones – the no-effect level in living animals or humans can be much lower. Different studies have linked endocrine disruptors to adverse biological effects in animals [142]. This has led to increasing concerns that low-level exposure might cause similar effects in human beings [143]. Furthermore, the quantification of single compounds does not give an answer to the much more complex situation when mixtures of compounds like EDCs act in a cumulative or amplified way. Aside from synthetic EDCs, naturally occurring toxins, such as the resorcyclic acid lactones (RALs) are also known to have endocrine-disrupting potential. The most prevalent compound of the RALs is the mycotoxin zearalenone (ZON), which is orders of magnitude more potent than notorious synthetic EDCs such as DDT, BPA or atrazine. In addition to the above-described compounds, natural toxins, like saxitoxin from bluegreen algae, are of great importance. Although not official, a threshold concentration for saxitoxin of $3\,\mu g\,l^{-1}$ is under discussion.

Another class of emerging chemical contaminants are pharmaceutical residues, which can be found in drinking water and represent an up-to-date topic in water

quality [144]. The human body excretes applied medication in the original or metabolized form. Although wastewater is treated before it is discharged into reservoirs, rivers or lakes, these measures do not remove all drug residues. Even if the concentrations of these pharmaceuticals are of the order of parts per billion or trillion, the presence of many pharmaceuticals causes worries among scientists about long-term consequences to human health. As with EDCs, residues of pharmaceuticals have been proven to cause major ecological damage [145]. Beside antibiotics or ethinylestradiol from the contraceptive pill, there is a long list of pharmaceuticals which can be found in water bodies, including radio-opaque substances, analgesics (e.g., diclophenac) or anti-epileptic and anti-anxiety medications.

Fully automated immunoassays based on the described test formats and hyphenated to optical transduction provide an interesting analytical strategy for on-site quasi-continuous quantification of chemical contaminants [13, 67, 146–148]. These systems should be designed for quick analysis without the need for labor-intensive sample pretreatments or enrichment steps, as is necessary for classical analytical methods. Monitoring systems offering such capabilities are useful additions to classical analytical methods. The development of multi-analyte immunoassays for water monitoring has not only to meet the above-mentioned threshold but also specific requirements related to practicability. For example, a quasi-continuous measurement mode will only be possible with a regeneration of the sensitive surface after each single measurement, combined with resistance toward bio-fouling and degradation. Therefore, it is necessary to create a specific surface coating including the recognition element, which is chemically stable during repeated complete measurement cycles. Especially, the research efforts in developing new robust and chemically stable recognition elements with tunable affinity show very promising results [149].

The replacement assay can look back on a long success story for environmental applications. It allows the quantification of small organic molecules but is limited in its regeneration capabilities for quasi-continuous measurements because the capture antibodies are not chemically stable. Furthermore, the antibodies have to be designed with reasonable dissociation rates to allow the replacement step during the incubation with the analyte-containing sample. On the other hand a too high off-rate will lead to a high degree of dissociation of the labeled analyte derivative. If set up in a proper way, including a flow injection analysis system and fluorescence transduction, it has been demonstrated that the replacement assay works with adequate LODs for pesticides [150, 151]. Variations of the competitive test format with fluorescence can also be found in the literature [152].

It was shown that the PASA system can handle the different test formats. For the detection of pesticides an indirect competitive immunoassay was combined with chemiluminescence detection. This test format is related to the binding inhibition assay performed under competitive conditions and allows multi-analyte detection with regeneration capabilities for monitoring applications [153]. The same system was used to quantify antibiotics [154].

The binding inhibition test performed under non-competitive conditions was used by the systems RIANA [155] and AWACSS [156]. This test format meets the analytical

and performance requirements described above. The sensor surface is modified with an analyte derivative or with the hapten-carrier protein-complex used during antibody production. The advantage is the chemical stability of these molecules compared to antibodies. To achieve chemically stable sensitive layers it is advantageous to covalently attach these molecules to the transducer surface in combination with a biopolymer and standard microarray printing procedures for multi-analyte capability. The incubation phase can be performed, even with a mixture of specific antibodies, in one step, as for the indirect competitive assay. Although cross reactivity of the antibodies has to be taken into account it has been shown, that it is possible to use this test format in a fully automated TIRF biosensor for the parallel quantification of six analytes from different chemical classes (pesticides, pharmaceuticals and EDCs) [157]. For the AWACSS biosensor fully automated and unattended monitoring has been realized for in-field testing [158]. Together with the implemented intelligent communication to a data base, the system is able to monitor thresholds recommended by the EU legislation.

The binding inhibition test can also be combined with label-free read-out. For example Ref. [159] showed a SPR-based biosensor for the detection of bisphenol A in water samples. Reference [160] reports the detection of atrazine with a similar approach. The advantage compared to fluorescence-based technologies is obviously the prevention of the antibody labeling step. However, the achievable limit of detection is above labeled systems. The simpler direct test format, in combination with label-free read-out, is not a preferable choice due to the necessary low LODs and the low molecular weights of many analytes such as pesticides. Furthermore, antibody surfaces are not stable during the regeneration procedures. The same applies for the sandwich assay, which fails for these applications because of the small target molecules, offering in many cases only one accessible epitope. A completely different situation applies for several toxins, such as microcystin LR. This relatively large molecule is rather unstable when immobilized to a sensor surface. Therefore, the direct test format has been successfully used in combination with SPR transduction to quantify this toxin [105, 161]. Other toxins, such as botulinum, ricin or cholera toxin are especially interesting for security reasons. These molecules can be quantified in a multi-analyte approach using the sandwich immunoassay in combination with a TIRF-based detection [162].

Employing nuclear receptors as the analytical tool enables a new analytical strategy called effect-based analytics. Compared to conventional immunoassay-based biosensor technology the advantage is that the total effect on the nuclear receptor can be measured, instead of concentrations of single compounds, and that even currently unknown ligands are also found. Usually, the measured concentrations are given as hormone-equivalents, for example, as estrogen-equivalents in the case of the estrogen receptor. TIRF read-out, combined with the binding inhibition assay [163] employing the ERα-LBD as the analytical tool, is a promising approach for a next generation biosensor technology to be used in environmental monitoring. The recognition structure is derived from a natural nuclear receptor, which mediates the effects of estrogenic EDCs *in vivo*. Therefore, the assay gives a measure of the exogeneous influences on the hormone system, expressed in estrogen equivalents.

For the future it is important to develop ERα-LBD based assays which are able to distinguish between estrogenic and anti-estrogenic effects. A first step in this direction was reported in [164]. The developed label-free assay can quantify these different effects. The application of this knowledge for the development of a new set of TIRF assays can lead to high-sensitivity effect-based environmental assays for EDCs with estrogenic effects for the first time.

This problem can be overcome by introducing cell-based assays for effect-based analytics. However, the practicality differs extremely with the used cell-lines/bacteria [165]. Mammalian cell lines can report effects with a very high sensitivity, as is known from toxicity studies, for example, in pharma screening. However, the stability of these cells in monitoring systems is low and the handling needs special and expensive cultivation environments. Bacteria with reporter systems, such as the green fluorescence protein, are more robust and easy to use. Although there are commercial products already on the market [166], the comparability to quantifying analytical methods is still an ongoing discussion.

6.5.2 Pathogens

The detection of pathogens in water samples is a very challenging analytical problem. Following the Drinking Water Directive it is necessary to detect one single colony-forming unit (cfu) in 100 ml (the directive threshold value e.g., for *E. coli* is 0 per 100 ml). The classical test for bacteria is based on filtration and cultivation, as has been state-of-the-art for more than 100 years. This time- and labor-intensive method has the advantage that it is very reliable in detecting only viable bacteria. For virus particles the situation is even more complicated, because the virus particles cannot replicate autonomously.

One of the most promising strategies is nucleic acid-based analytical methods, which make use of the polymerase chain reaction (PCR) to amplify genomic DNA or RNA molecules. This technology offers the advantage that quantification of very low copy numbers is possible in a multi-analyte approach. However, the usability is also limited when the extremely low thresholds of the drinking water directive have to be applied. Furthermore, the technology can lead to false positive results if nucleic acid of dead pathogens is amplified. In practice, the analytical procedure is complex and time consuming and starts with cell lysis followed by nucleic acid extraction and PCR amplification. The detection is usually based on fluorescence measurements and can be performed in, for example, a sandwich hybridization format on microarrays, as a real-time PCR experiment, flow cytometry-based or as a fiber sensor array [24, 167–170].

Another strategy makes use of mammalian cell lines, which are sensitive to the presence of pathogens. In [171] it has been shown that several bacterial pathogens can be detected at very low cfu concentrations. A big advantage of this method is that only living pathogens are detected. However, the analytical procedure is very complicated and time-consuming. The introduction of immunoassays to pathogen detection in water samples is linked to some fundamental challenges: the need for extremely low

LODs, and the very low diffusion rate of these pathogens/particles during the incubation phase of an assay. Therefore, it is mandatory to include sample preconcentration steps prior to the analytical procedure. Recently it has been shown that special filtration procedures can help to overcome these problems by a quick preconcentration of the sample by a factor of 200 [172]. A further problem is the availability of antibodies or other recognition elements which allow species-specific detection, because of the high cross-reactivity between the groups or families of pathogens. Typically the applied test format is the sandwich immunoassay. This test format is especially helpful in increasing the specificity by the detection antibody. In a multi-analyte approach it is possible to detect several pathogens in parallel in microarray- or bead-based approaches [53, 54, 173–178]. It has also been shown that with a stopped-flow immunoassay it is possible to detect viable *E. coli* more effectively, because of the reduction of the above-mentioned hydrodynamic restrictions [179], or to combine detection and quantification by a nanoparticle-based sandwich ELISA [19].

Recently many strategies have been developed to enhance the performance of immunoassays for pathogen detection in water samples. One example is the liposome-based colorimetric sensor using a novel immobilization procedure [180] which allows the multiplexed detection of six pathogens. An overview of nanomaterial-enabled biosensors for pathogen detection employing different recognition elements, such as antibodies, aptamer carbohydrates, or even antimicrobial peptides can be found in [181]. Instrumental techniques for direct and indirect identification of bacteria, such as IR, flow cytometry, chromatography, and others have also been used to address this analytical task [182].

Label-free transduction can also be successfully used for pathogen detection in water samples. Different test formats have been described so far, but the most interesting is of course the direct test format. Here the detection of the pathogens is performed by a one step assay via a capture antibody, which is immobilized on the transducer surface [183]. The relatively low LOD of label-free methods is partially compensated by the enormous size of the pathogens compared to small molecules like pesticides [184, 185]. However, the limited specificity of the direct test format allows a quick first screening rather than a precise identification. This limitation can be overcome by methods which combine an immunoassay with the advantages of SERS. This detetction principle gives added value to the pathogen detection due to the species-specific SERS spectra as a whole-organism fingerprint [186–189]. A further elegant method for the identification of bacteria is provided by a detection principle that makes use of the different scattering properties of the pathogens. This sensor technology also enables the label-free detection of multiple bacterial pathogens [190].

6.6 Perspectives and Visions

Normally, just a specific interaction is used to monitor pollutants. However, some years ago so-called Quorum sensing [192] was introduced to environmental analysis

to direct conventional analytics away from measuring the concentration of specific compounds to an effect-based "quantification", as in a dose measurement known in radioactivity control [131, 132]. The influence of some pollutants on health does not depend on concentration but rather on, for example, endocrine activity. Thus, this new approach of effect-based "quantification" opens some perspectives for better analysis. Another approach is to use spores in genetically engineered bacteria-based sensing systems [191] using their biospecific recognition capability. Recent activities in photonics will also lead to new instrumentation [193].

References

1 Skoog, D.A., Holler, F.J., and Crouch, S.R. (2007) *Principles of Instrumental Analysis*, 6th edn, Brooks/Cole Publishing Company, Pacific Grove.

2 Radojević, M. and Bashkin, V.N. (2009) *Practical Environmental Analysis*, Royal Society of Chemistry, Cambridge.

3 Alloway, B.J. and Ayres, D.C. (1993) *Chemical Principles of Environmental Pollution*, Blackie Academic & Professional, London.

4 Fifield, F.W. and Haines, P.J. (2000) *Environmental Analytical Chemistry*, John Wiley & Sons.

5 Capdeville, M.J. and Budzinski:, H. (2011) Trace-level analysis of organic contaminants in drinking waters and groundwaters. *TrAc, Trends Anal. Chem.*, **30**, 586–606.

6 Urban Waste Water Treatment Directive (91/271/EEC).

7 Water Framework Directive (2000/60/EC).

8 Community Strategy for Endocrine Disrupters COM (99)706, COM (2001) 262.

9 Regulation (EC) No 178/2002 of the European Parliament and of the Council of 28 January 2002 laying down the general principles and requirements of food law, establishing the European Food Safety Authority and laying down procedures in matters of food safety, OJ L 31, 1.2.2002, p. 1–24.

10 Commission Regulation (EC) No 1881/2006 of 19 December 2006 setting maximum levels for certain contaminants in foodstuffs, OJ L 364, 20.12.2006, p. 5.

11 http://water.epa.gov/scitech/methods/cwa/bioindicators/biological_index.cfm, http://water.epa.gov/scitech/drinkingwater/labcert/analyticalmethods.cfm#approved.

12 http://www.dvgw.de/fileadmin/dvgw/wasser/recht/1104gerhardy.pdf.

13 Namour, P., Lepot, M., and Jaffrezic-Renault, N. (2010) Recent trends in monitoring of European Water Framework Directive priority substances using micro-sensors: A 2007–2009 review. *SENSORS*, **10**, 7947–7978.

14 Farre, M., Kantiani, L., Perez, S., and Barcelo, D. (2009) Sensors and biosensors in support of EU directives. *TrAC, Trends Anal. Chem.*, **28**, 170–185.

15 EPA Method 1682: Salmonella spp. in Biosolids by Enrichment, Selection, and Biochemical Characterization http://water.epa.gov/scitech/methods/cwa/bioindicators/upload/2008_11_25_methods_method_biological_1682-bio.pdf.

16 Ferguson, C., Kaucner, C., Krogh, M., Deere, D., and Warnecke, M. (2004) Comparison of methods for the concentration of Cryptosporidium oocysts and Giardia cysts from raw waters. *Can. J. Microbiol.*, **50**, 675–682.

17 Morales-Morales, H.A., Smith, G.B., Vidal-Martinez, G. *et al.* (2003) Optimization of a reusable hollow-fiber ultrafilter for simultaneous concentration of enteric bacteria, protozoa, and viruses from water. *Appl. Environ. Microbiol.*, **69**, 4098–4102.

18 Peskoller, C., Niessner, R., and Seidel, M. (2009) Cross-flow microfiltration

system for rapid enrichment of bacteria in water. *Anal. Bioanal. Chem.*, **393**, 399–404.

19 Pappert, G., Rieger, M., Niessner, R., and Seidel, M. (2010) Immunomagnetic nanoparticle-based sandwich chemiluminescence-ELISA for enrichment and quantification of *E. coli*. *Microchem. Acta*, **168**, 1–8.

20 Peskoller, C., Niessner, R., and Seidel, M. (2009) Development of an epoxy-based monolith used for the affinity capturing of *Eschericha coli* bacteria. *J. Chromatogr. A*, **1216**, 3794–3801.

21 Aprodu, I., Walcher, G., and Schelin, J. (2011) Advanced sample preparation for the molecular quantification of Staphylococcus aureus in artificially and naturally contaminated milk. *Int. J. Food Microbial.*, **145**, S61–S65.

22 Krämer, N., Löfström, Ch., Vigre, H., Hoorfar, J., Bunge, C., and Mlorny, B. (2011) A novel strategy to obtain quantitative data for modelling: Combined enrichment and real-time PCR for enumeration of salmonellae from pig carcasses. *Int. J. Food Microbiol.*, **145**, S86–S95.

23 Reidt, U., Geisberger, B., Heller, C., and Friedberger, A. (2011) Automated immunomagnetic processing and separation of *Legionella pneumophila* with manual detection by sandwich ELISA and PCR amplification of the ompS Gene. *J. Lab. Automation*, **16**, 157–164.

24 Donhauser, S., Niessner, R., and Seidel, M. (2011) Sensitive quantification of Escherichia coli O157:H7, salmonella enterica, and campylobacter jejuni by combining stopped polymerase chain reaction with chemiluminescence flow-through DNA microarray analysis. *Anal. Chem.*, **83**, 3153–3160.

25 Advances in label-Free Detection Technologies, Frost&Sullivan, June30, 2008 – Pub ID: MC2018124 (www.marketresearch.com/product/display.asp).

26 Tallury, P., Malhotra, A., Byrne, L.M., and Santra, S. (2010) Nanobioimaging and sensing of infectious diseases. *Adv. Drug Deliv. Rev.*, **62**, 424–437.

27 [http://www.eugris.info/FurtherDescription.asp?Ca=2&Cy=0&T=Emerging%20Pollutants&e=95].

28 Ligler, F. and Taitt, Ch.R. (eds) (2008) *Optical Biosensors: Today and Tomorrow*, Elsevier, Amsterdam.

29 Borisov, S.M. and Wolfbeis, O.S. (2008) Optical biosensors. *Chem. Rev.*, **108**, 423–461.

30 Nagl, S., Wolfbeis, O.S., and Otto, S. (2008) Classification of chemical sensors and biosensors based on fluorescence and phosphorescence. in Springer Series on Fluorescence, Vol. **5** *Standardization and Quality Assurance in Fluorescence Measurements I*, 325–346, Springer.

31 Stich, M.I.J., Fischer, L.H., and Wolfbeis, O.S. (2010) Multiple fluorescent chemical sensing and imaging. *Chem. Soc. Rev.*, **39**, 3102–3114.

32 Gauglitz, G. (2005) Direct optical sensors: principles and selected applications. *Anal. Bioanal. Chem.*, **381**, 141–155.

33 Fan, X.-D., White, I.M., Shopova, S.I., Zhu, H.-Y., Suter, J.D., and Sun, Y.-Z. (2009) Sensitive optical biosensors for unlabeled targets: A review. *Anal. Chim. Acta*, **620**, 8–26.

34 Gauglitz, G. (2010) Direct optical detection in bioanalysis: an update. *Anal. Bioanal. Chem.*, **398**, 2363–2372.

35 van de Hulst, H.C. (1957) *Light Scattering by Small Particles*, DoverPublications, New York.

36 Nobbmann, U. (2003) Characterization down to nanometers: Light scattering from proteins and micelles in Mesoscale phenomena in fluid systems. *ACS Symp. Ser.*, **861**, 44–59.

37 Bergquist, P.L., Hardiman, E.M., Ferrari, B.C., and Winsley, T. (2009) Applications of flow cytometry in environmental microbiology and biotechnology. *Extremophiles*, **13**, 389–401.

38 Comas-Riu, J. and Rius, N. (2009) Flow cytometry applications in the food industry. *J. Ind. Microbiol. Biotechnol.*, **36**, 999–1011.

39 Rajwa, B., Dundar, M.M., Akova, F., Bettasso, A., Patsekin, v., Hirleman, E.D., Bhunia, A.K., and Robinson, J.P. (2010) Discovering the unknown: detection of emergin pathogens using a label-free light-scattering system. *Cytometry, Part A*, **77**, 1103–1112.

40 http://www.nanosight.com/technology/nanosights-technology.

41 Bhunia, A.K., Banada, P., Banerjee, P., Valadez, A., and Hirleman, E.D. (2007) Light scattering fiber optic- and cell-based sensors for sensitive detection of foodborne pathogens. *J. Rapid Methods Autom. Microbiol.*, **15**, 121–145.

42 Llorent-Martínez, E.J., Ortega-Barrales, P., Fernández-de Córdova, M.L., and Ruiz-Medina, A. (2011) Trends in flow-based analytical methods applied to pesticide detection: A review. *Anal. Chim. Acta*, **684**, 30–39.

43 Förster, Th. (1948) Zwischenmolekulare Energiewanderung und Fluoreszenz. *Ann. Physik*, **2**, 55–75.

44 Van der Meer, B.W., Coker, G. III, and Chen, S. (eds) (1994) *Resonance Energy Transfer – Theory and Data*, VCH Publishers Inc., Weinheim.

45 Roda, A., Guardigli, M., Michelini, E., and Mirasoli, M. (2007) Nanobioanalytical luminescence: Förster-type energy transfer methods. *Anal. Bioanal. Chem.*, **393**, 109–123.

46 Varghese, S., Zhu, Y., Davis, T.J., and Trowell, S.C. (2010) FRET for lab-on-a-chip devices — current trends and future prospects. *Lab Chip*, **10**, 1355–1364.

47 Algar, W.R. and Krull, U.J. (2010) New opportunities in multiplexed optical bioanalyses using quantum dots and donor-accceptor interactions. *Anal. Bioanal. Chem.*, **398**, 2439–2449.

48 Daunert, S. and Deo, S.K. (eds) (2006) *Photoproteins in Bioanalysis, Chapter 6: Bioluminescence Resonance Energy Transfer in Bioanalysis*, Wiley-VCH GmbH, Weinheim.

49 Park, J., Park, S., and Kim, Y.-K. (2010) Multiplex detection of pathogens using an immunochromatographic assay strip. *BioChip J.*, **4**, 305–312.

50 Chouhan, R.S., Vivek Babu, K., Kumar, M.A., Neeta, N.S., Thakur, M.S., Amitha, B.E., Pasha, A., Karanth, N.G.K., and Karanth, N.G. (2006) Detection of methyl parathion using immuno-chemiluminescence based image analysis using charge coupled device. *Biosens. Bioelectron.*, **21**, 1264–1271.

51 Roda, A., Guardigli, M., Michelini, E., Mirasoli, M., and Pasini, P. (2003) The possibility of detecting a few molecules using bioluminescence and chemiluminescence is exciting, especially in the context of miniaturized analytical devices. *Anal. Chem.*, **75**, 462A–470A.

52 Aslan, K. and Geddes, Ch.D. (2009) Metal-enhanced chemiluminescence: advanced chemiluminescence concepts for the 21st century. *Chem. Soc. Rev.*, **38**, 2556–2564.

53 Karsunke, X.Y.Z., Niessner, R., and Seidel, M. (2009) Development of a multichannel flow-through chemiluniescence microarray chip for parallel calibration and detection of pathogenic bacteria. *Anal. Bioanal. Chem.*, **395**, 1623–1630.

54 Wolter, A., Niessner, R., and Seidel, M. (2008) Detection of *Escherichia coli* O157: H7, *Salmonella typhimurium,* and *Legionella pneumophila* in water using a flow-through chemiluminescence microarray read-outsystem. *Anal. Chem.*, **80**, 5854–5863.

55 Hecht, E. (2001) *Optics*, Pearson Addison Wesley, München.

56 Gauglitz, G. and Nahm, W. (1991) Observation of spectral interferences for the determination of volume and surface effects of thin polymer films. *Fresenius' J. Anal. Chem.*, **341**, 279–283.

57 Bürk, J., Conzen, J.P., and Ache, H.J. (1992) A fiber optic evanescent field absorption sensor for monitoring contaminants in water. *Fresenius' J. Anal. Chem.*, **342**, 421–430.

58 Bürk, J., Zimmermann, B., Mayer, J., and Ache, H.J. (1996) Integrated optical NIR-evanescent wave absorbance sensor for chemical analysis. *Fresenius' J. Anal. Chem.*, **354**, 284–329.

59 Gauglitz, G. (2010) Direct optical detection in bioanalysis: an update. *Anal. Bioanal. Chem.*, **398**, 2363–2372.

60 Hunt, H.K. and Armani, A.M. (2010) Label-free biological and chemical sensors. *Nanoscale*, **2**, 1544–1559.

61 Mehne, J., Markovic, G., Pröll, F., Schweizer, N., Zorn, S., Schreiber, F., and Gauglitz, G. (2008) Characterisation of morphology of self-assembled PEG monolayers: a comparison of mixed and pure coatings for biosensor

applications. *Anal. Bioanal. Chem.*, **391**, 1783–1791.

62 Albrecht, C., Fechner, P., Honcharenko, D., Baltzer, L., and Gauglitz, G. (2010) A new assay design for clinical diagnostics based on alternative recognition element. *Biosens. Bioelectron.*, **25**, 2302–2308.

63 Chudy, M., Grabowska, I., Ciosek, P., Filipowicz-Szymanska, A., Stadnik, D., Wyzkiewicz, I., Jedrych, E., Juchniewicz, M., Skolimowski, M., Ziolkowska, K., and Kwapiszewski, R. (2009) Miniaturized tools and devices for bioanalytical applications: an overview. *Anal. Bioanal. Chem.*, **395**, 647–668.

64 Bally, M., Halter, M., Vörös, J., and Grandin, H.M. (2006) Optical microarray biosensing techniques. *Surf. Interface Anal.*, **38**, 1442–1458.

65 Yu, X.-B., Xu, D.-K., and Cheng, Q. (2006) Label-free detection methods for protein microarrays. *Proteomics*, **6**, 5493–5503.

66 Lopez, C.A., Daaboul, G.G., Vedula, R.S., Özkumur, E., Bergstein, D.A., Geisbert, T.W., Fawcett, H.E., Goldberg, B.B., Connor, J.H., and Ünlü, M.S. (2011) Label-free multiplexed virus detection using spectral reflectance imaging. *Biosens. Bioelectron.*, **26**, 3432–3437.

67 Seidel, M. and Niessner, R. (2008) Automated analytical microarrays: a critical review. *Anal. Bioanal. Chem.*, **391**, 1521–1544.

68 Schäferling, M. and Nagl, S. (2006) Optical technologies for the read-outand quality control of DNA and protein mircoarrays. *Anal. Bioanal. Chem.*, **385**, 500–517.

69 Rasooly, A. (2008) Food microbial pathogen detection and analysis using DANN microarray technologies. *Foodborne Pathog. Dis.*, **5**, 531–550.

70 Chandra, H., Reddy, P.J., and Srivastava, S. (2011) Protein microarrays and novel detection platforms. *Expert Rev. Proteomics*, **8**, 61–79.

71 Ivnitski, D., Abdel-Hamid, I., Atanasov, P., and Wilkins, E. (1999) Biosensors for detection of pathogenic bacteria. *Biosens. Bioelectron.*, **14**, 599–624.

72 Medintz, I.L., Uyeda, H.T., Goldman, E.R., and Mattoussi, H. (2005) Quantum dot bioconjugates for imaging, labelling and sensing. *Nature Materials*, **4**, 435–446.

73 Sanvicens, N., Pastells, C., Pascual, N., and Marco, M.-P. (2009) Nanoparticle-based biosensors for detection of pathogenic bacteria. *TrAC, Trends Anal. Chem.*, **28**, 1243–1252.

74 Wang, L.-B., Ma, W., Xu, L.-G., Chen, W., and Zhu, Y.-Y. (2010) Nanoparticle-based environmental sensors. *Mater. Sci. Eng., R*, **70**, 265–274.

75 Asefa, T., Duncan, C.T., and Sharma, K.K. (2009) Recent advances in nanostructured chemosensors and biosensors. *Analyst*, **134**, 1980–1990.

76 Nichkova, M., Dosev, D., Gee, S.J., Hammock, B.D., and Kennedy, M. (2005) Microarray immunoassay for phenoxybenzoic acid using polymer encapsulated Eu: Gd2O3 nanoparticles as fluorescent labels. *Anal. Chem.*, **77**, 6864–6873.

77 http://www.biocompare.com/ProductCategories/192/Microarrays.html.

78 Sapsford, K.E. and Ligler, F.S. (2004) TIRF array biosensors for environmental monitoring. in Springer Series on Chemical Sensors and Biosensors, Vol. **1** *Optical Sensors* 359–439, Springer.

79 Nagl, S., Schaeferling, M., and Wolfbeis, O.S. (2005) Fluorescence analysis in microarray technology. *Microchim. Acta*, **151**, 1–21.

80 Yu, F., Yao, D.F., and Knoll, W. (2003) Surface plasmon field-enhanced fluorescence spectroscopy studies of the interaction between an antibody and its surface-coupled antigen. *Anal. Chem.*, **75**, 2610–2617.

81 Liebermann, T. and Knoll, W. (2003) Parallel multispot detection of target hybridization to surface-bound probe oligonucleotides of different base mismatch by surface-plasmon field-enhanced fluorescence microscopy. *Langmuir*, **19**, 1567–1572.

82 Tallury, P., Malhotra, A., Byrne, L.M., and Santra, S. (2010) Nanobioimaging and sensing of infectious diseases. *Adv. Drug Deliv. Rev.*, **62**, 424–437.

83 Hecht, E. (1997) *Optics*, 3rd edn, Addison Wesley, London.

84 Vo-Dinh, T. and Allain, L. (2003) Biosensors for medical applications, in *Biomedical Photonics* (ed. V.-D. Tuan), CRC Press, Boca Raton, 20/1-20/40.

85 Cooper, M.A. (2002) Optical biosensors in drug discovery. *Nat. Rev. Dru. Disc.*, **1**, 515–528.

86 Clerc, D. and Lukosz, W. (1994) Integrated optical output grating couper as biochemical sensor. *Sens. Actuator, B*, **19**, 581.

87 Dubendorfer, J. and Kunz, R.E. (1998) Compact integrated optical immunosensor using replicated chirped grating coupler sensor chips. *Appl. Opt.*, **37**, 1890.

88 Grego, S., McDaniel, J.R., and Stoner, B.R. (2008) Wavelength interrogation of grating-based optical biosensors in the input coupler configuration. *Sensor Actuator B*, **131**, 347–355.

89 Cush, R., Cronin, J.M., Stewart, W.J. *et al.* (1993) The resonant mirror – a novel optical biosensor for sensing of biomolecular interaction. 1. Principle of operation and associated instrumentation. *Biosens. Bioelectron.*, **8**, 347–353.

90 Goddard, N.J., Pollard-Knight, D., and Maule, C.H. (1994) Real-time biomolecular interaction analysis using the resonant mirror sensor. *Analyst*, **119**, 583–588.

91 de Tommasi, E., De Stefano, L., Rea, I., Di Sarno, V., Rotiroti, L., Arcari, P., Lamberti, A., Sanges, C., and Rendina, I. (2008) Porous silicon based resonant mirrors for biochemical sensing. *Sensors*, **8**, 6549–6556.

92 Kretschmann, E. and Raether, H. (1968) Radiative decay of non radiative surface plasmons excited by light. *Z. Naturforsch. A*, **23**, 2135–2136.

93 Liedberg, B., Nylander, C., and Lundström, I. (1983) Surface plasmon resonance for gas detection and biosensing. *Sens. Actuators*, **4**, 299–304.

94 Liedberg, B., Nylander, C., and Lundstrom, I. (1995) Biosensing with surface plasmon resonance–how it all started. *Biosens. Bioelectron.*, **10**, i–ix.

95 Frank, R. (2005) *Reflektometrische und integriert optische Sensoren für die Bioanalytik*, Dissertation Eberhard-Karls-Universität Tübingen, http://tobias-lib.uni-tuebingen.de/volltexte/2005/2095/pdf/Diss_Ruediger_Frank.pdf.

96 Laib, Th. (2008) Anwendung moderner Auswerteverfahren in der Chemometrie und Geostatistik, Definition von Kenngrößen von Bioanalytsystemen und Charakterisierung eines Mach-Zehnder-Interferometers für die Bioanalytik, Dissertation, Eberhard-Karls-Universität Tübingen, http://tobias-lib.uni-tuebingen.de/volltexte/2008/3471/pdf/Anwendung_ moderner_Verfahren_in_der_Chemometrie_und_ Geostati.pdf.

97 Washburn, A.L. and Bailey, R.C. (2011) Photonics-on-a-chip: recent advances in integrated waveguides as enabling detection elements for real-world, lab-on-a-chip biosensing applications. *Analyst*, **136**, 227–236.

98 http://www.biacore.com/lifesciences/company/index.html.

99 Homola, J., Yee, S.S., and Gauglitz, G. (1999) Surface plasmon resonance sensors. *Sens. Actuators, B*, **54**, 3–15.

100 Petz, M. (2009) Recent Applications of surface plasmon resonance biosensors for analyzing residues and contaminants in food. *Monatsh. Chem.*, **140**, 953–964.

101 Dostalek, J., Pribyl, J., Homola, J., and Skladal, P. (2007) Multichannel SPR biosensor for detection of endocrine-disrupting compounds. *Anal. Bioanal. Chem.*, **389**, 1841–1847.

102 Situ, C., Buijs, J., Mooney, M.H., and Elliott, C.T. (2010) Advances in Surface Plasmon resonance biosensor technology towards high-throughput, food-safety analysis. *TrAC, Trends Anal. Chem.*, **29**, 1305–1315.

103 Fernandez, F., Hegnerova, K., Piliarik, M., Sanchez-Baeza, F., Homola, J., and Marco, M. (2011) A label-free and portable multichannel surface plasmon resonance immunosensor for on site analysis of antibiotics in milk samples. *Biosens. Bioelectron.*, **26**, 1231–1238.

104 Zordan, M.D., Grafton, M.M.G., and Leary, J.F. (2011) An integrated microfluidic biosensor for the rapid screening of foodborne pathogens by

surface plasmon resonance imaging. *Proc. SPIE*, **7888** (Frontiers of Biological Detection) 1–10.

105 Herranz, S., Bockova, M., Marazuela, M.D., Homola, J., and Moreno-Bondi, M.C. (2010) An SPR biosensor for the detection of microcystins in drinking water. *Anal. Bioanal. Chem.*, **398**, 2625–2634.

106 Huang, Ch.-J., Dostalek, J., Sessitsch, A., and Knoll, W. (2011) Long-range surface plasmon-enhanced fluorescence spectroscopy biosensor for ultrasensitive detection of E. coli O157:H7. *Anal. Chem.*, **83**, 674–677.

107 Liebermann, T. and Knoll, W. (2003) Parallel multispot detection of target hybridization to surface-bound probe oligonucleotides of different base mismatch by surface-plasmon field-enhanced fluorescence microscopy. *Langmuir*, **19**, 1567–1572.

108 Azzam, R.M.A. and Bashara, N.M. (1989) *Ellipsometry and Polarised Light*, North Holland, Amsterdam.

109 Jin, G., Tengvall, P., Lundstrom, I., and Arwin, H. (1995) A biosensor concept based on imaging ellipsometry for visualization of biomolecular interactions. *Anal. Biochem.*, **232**, 69–72.

110 Gauglitz, G. and Nahm, W. (1991) Observation of spectral interferences for the determination of volume and surface effects of thin polymer films. *Fresenius' J. Anal. Chem.*, **341**, 279–283.

111 Brecht, A., Gauglitz, G., and Nahm, W. (1992) Interferometric measurements used in chemical and biochemical sensors. *Analusis*, **20**, 135–140.

112 Frank, R., Möhrle, B., Fröhlich, D., and Gauglitz, G. (2005) A transducer-independent optical sensor system for the detection of biochemical binding reactions. *Proc. SPIE*, **5993**, 49–59.

113 Gauglitz, G., Brecht, A., Reichl, D., and Seemann, J. (1999) Apparatus and methods for detection using physical or chemical effects. Ger. Offen., DE 19830727 A1 19990114.

114 Pröll, F., Markovic, G., Schweizer, N., and Gauglitz, G. (2008) Imaging reflectometric interference spectroscopy (iRIfS): a versatile tool for high throughput biomolecular interaction analysis. Proceedings of The TenthWorld Congress on Biosensors, Shanghai, China.

115 Brecht, A. and Gauglitz, G. (1997) Label free optical immunoprobes for pesticide detection. *Anal. Chim. Acta*, **347**, 219–233.

116 Fechner, P., Pröll, F., Albrecht, C., and Gauglitz, G. (2011) Kinetic analysis of the estrogen receptor alpha using RIfS. *Anal. Bioanal. Chem.*, **400**, 729–735.

117 Schluecker, S. (ed) (2011) *Surface Enhanced Raman Spectroscopy: Analytical, Bioanalytical and Life Science Applications*, Wiley VCH Verlag, Weinheim, p. 331.

118 Vo-Dinh, T. (1995) Surface-enhanced raman scattering, in *Photonic Probes of Surfaces* (ed. P. Halevi), Elesevier Scince.

119 http://www.enwaveopt.com/EZRaman-MSeries.htm?gclid=CKPA4t_6nqkCFUqIzAodDTyZuA.

120 http://www.ramansystems.com/?gclid=CPvNwbX7nqkCFUe_zAodmWactw.

121 Popp, J. and Mayerhöfer, Th. (2010) Surface-enhanced Raman spectroscopy. (*Anal. Bioanal. Chem.* **394**, 1717–1718.

122 Álvarez-Puebla, R.A. and Liz-Marzán, L.M. (2010) Environmental applications of plasmon assisted Raman scattering. *Energy Environ. Sci.*, **3**, 1011–1017.

123 Bossecker, A., Popp, J., Meisel, S., Roeschl, P., and Stoeckel, St. (2010) Tracing of pathogenic bacteria by light. Raman spectroscopic detection of bacteria in complex matrices. *Bioforum*, **33**, 22–24.

124 Angela, W., Maerz, A., Schumacher, W., Roesch, P., and Popp, J. (2011) Towards a fast, high specific and reliable discrimination of bacteria on strain level by means of SERS in a microfluidic device. *Lab on a Chip*, **11**, 1013–1021.

125 Zengerle, R. (1987) Light propagation in singly and doubly periodic planar waveguides. *J. Mod. Opt.*, **34**, 1589–1617.

126 Sakoda, K. (2005) *Optical Properties of Photonic Crystals, Springer Series in Optical Sciences*, 2nd edn, vol. **80**, Springer-Verlag GmbH, Heidelberg, XIV, p. 253.

127 Kashyap, R. (1999) *Fiber Bragg Gratings*, Academic Press, San Diego.

128 Cerqueira S. Jr., A. (2010) Recent progress and novel applications of photonic crystal

fibers. *Rep. Prog. Phys.*, **73**, 1–21. doi: 10.1088/0034-4885/73/2/024401

129 Nair, R.V. and Vijaya, R. (2010) Photonic crystal sensors: an overview. *Prog. Quantum Electron.*, **34**, 89–134.

130 Ricciardi, C., Canavese, G., Castagna, R., Digregorio, G., Ferrante, I., Marasso, S.L., Ricci, A., Alessandria, V., Rantsiou, K., and Cocolin, L.S. (2010) Online portable microcantilever biosensors for *Salmonella enteric* serotype *Enteritidis* detection. *Food Bioprocess. Technol.* doi: 10.1007/s11947-010-0362-0

131 Fechner, P., Gauglitz, G., and Gustafsson, J.A. (2010) Nuclear receptors in analytics - a fruitful joint venture or a wasteful futility? *TrAC*, **29**, 297–305.

132 Fechner, P., Pröll, F., and Carlquist, M. (2009) An advanced biosensor for the prediction of estrogenic effects of endocrine-disrupting chemicals on the estrogen receptor alpha. *Anal. Bioanal. Chem.*, **393**, 1579–1585.

133 Henares, T.G., Mizutani, F., and Hisamoto, H. (2008) Current development in microfluidic immunosensing chip. *Anal. Chim. Acta*, **611**, 17–30.

134 Borrebaeck, C.A.K. (2000) Antibodies in diagnostics – from immunoassays to protein chips. *Immunol. Today*, **21**, 379–382.

135 Ruzicka, J. and Hansen, E.H. (1975) Flow injection analysis. Part I. A new concept of fast continuous flow analysis. *Anal. Chim. Acta*, **78**, 145–152.

136 Price, C.P. and Newman, D.J. (1997) *Principles and Practice of Immunoassay*, Stockton Press, New York.

137 Fintschenko, Y. and Wilson, G.S. (1998) Flow injection immunoassay: a review. *Mikrochim. Acta*, **129**, 7–18.

138 Hansen, E.H. (1996) Principles and applications of flow injection analysis in biosensors. *J. Mol. Recognit.*, **9**, 316–325.

139 Cerda, V., Estela, J.M., Forteza, R., Cladera, A., Becerra, E., Altimira, P., and Sitjar, P. (1999) Flow techniques in water analysis. *Talanta*, **50**, 695–705.

140 Krämer, P. and Schmid, R. (1991) Flow Injection Immunoanalysis (FIIA) - a new immunoassay format for the determination of pesticides in water. *Biosens. Bioelectron.*, **6**, 239–243.

141 Hering, D., Borja, A., Carstensen, J., Carvalho, L., Elliott, M., Feld, C.K., Heiskanen, A.S., Johnson, R.K., Moe, J., Pont, D., Solheim, A.L., and de Bund, W. (2010) The european water framework directive at the age of 10: a critical review of the achievements with recommendations for the future. *Sci. Total Environ.*, **409**, 4007–4019.

142 Thorpe, K.L., Maack, G., Benstead, R., and Tyler, C.R. (2009) Estrogenic wastewater treatment works effluents reduce egg production in fish. *Environ. Sci. Technol.*, **43**, 2976–2982.

143 Schell, L.M. and Gallo, M.V. (2010) Relationships of putative endocrine disruptors to human sexual maturation and thyroid activity in youth. *Physiol. Behav.*, **9**, 246–253.

144 Oetken, M., Nentwig, G., Löffler, D., Ternes, T., and Oehlmann, J. (2005) Effects of Pharmaceuticals on Aquatic Invertebrates. *Arch. Environ. Contam. Toxicol.*, **49**, 353–361.

145 Cunningham, V.L., Binks, S.P., and Olson, M.J. (2009) Human health risk assessment from the presence of human pharmaceuticals in the aquatic environment. *Regul. Toxicol. Pharmacol.*, **53**, 39–45.

146 Rodriguez-Mozaz, S., Lopez de Alda, M.J., and Barceló, D. (2006) Biosensors as useful tools for environmental analysis and monitoring. *Anal. Bioanal. Chem.*, **386**, 1025–1041.

147 Farréa, M., Péreza, S., Gon¸8calves, C., Alpenduradab, M.F., and Barceló, D. (2010) Green analytical chemistry in the determination of organic pollutants in the aquatic environment. *TrAC, Trends Anal. Chem.*, **29**, 1347–1362.

148 Farréa, M., Kantiania, L., Péreza, S., and Barceló, D. (2009) Sensors and biosensors in support of EU Directives. *TrAC, Trends Anal. Chem.*, **28**, 170–185.

149 Van Dorst, B., Mehta, J., Bekaert, K., Rouah-Martin, E., De Coen, W., Dubruel, P., Blust, R., and Robbens, J. (2010) Recent advances in recognition elements of food and environmental biosensors:

a review. *Biosens. Bioelectron.*, **26**, 1178–1194.

150 Krämer, P.M. and Schmid, R.D. (1991) Automated quasi-continuous immunoanalysis of pesticides with a flow injection system. *Pestic. Sci.*, **32**, 451–462.

151 Kusterbeck, A.W. and Blake, D.A. (2008) Flow Immunosensors, in *Optical Biosensors: Today and Tomorrow,* 2nd edn (eds F.S. Ligler and C.R. Taitt), Elsevier, Washington.

152 González-Martíneza, M.A., Puchadesa, R., Maquieiraa, A., Ferrerc, I., Marcob, M.P., and Barceló, D. (1999) Reversible immunosensor for the automatic determination of atrazine. Selection and performance of three polyclonal antisera. *Anal. Chim. Acta*, **286**, 201–210.

153 Weller, M.G., Schuetz, A.J., Winklmair, M., and Niessner, R. (1999) Highly parallel affinity sensor for the detection of environmental contaminants in water. *Anal. Chim. Acta*, **393**, 29–41.

154 Knecht, B.G., Strasser, A., Dietrich, R., Märtlbauer, E., Niessner, R., and Weller, M.G. (2004) Automated microarray system for the simultaneous detection of antibiotics in milk. *Anal. Chem.*, **76**, 646–654.

155 Tschmelak, J., Proll, G., and Gauglitz, G. (2004) Verification of performance with the automated direct optical TIRF immunosensor (River Analyser) in single and multi-analyte assays with real water samples. *Biosens. Bioelectron.*, **20**, 743–752.

156 Tschmelak, J., Proll, G., Riedt, J., Kaiser, J., Kraemmer, P., Bárzaga, L., Wilkinson, J.S., Hua, P., Hole, J.P., Nudd, R., Jackson, M., Abuknesha, R., Barceló, D., Rodriguez-Mozaz, S., López de Alda, M.J., Sacher, F., Stien, J., Slobodník, J., Oswald, P., Kozmenko, H., Korenková, E., Tóthová, L., Krascsenits, Z., and Gauglitz, G. (2005) Automated water analyser computer supported system (AWACSS) - Part I: project objectives, basic technology, immunoassay development, software design & networking. *Biosens. Bioelectron.*, **20**, 1499–1508.

157 Tschmelak, J., Proll, G., Riedt, J., Kaiser, J., Kraemmer, P., Bárzaga, L., Wilkinson, J.S., Hua, P., Hole, J.P., Nudd, R., Jackson, M., Abuknesha, R., Barceló, D., Rodriguez-Mozaz, S., López de Alda, M.J., Sacher, F., Stien, J., Slobodník, J., Oswald, P., Kozmenko, H., Korenková, E., Tóthová, L., Krascsenits, Z., and Gauglitz, G. (2005) Automated water analyser computer supported system (AWACSS) - Part II: intelligent, remote-controlled, cost-effective, on-line, water-monitoring measure-ment system. *Biosens. Bioelectron.*, **20**, 1509–1519.

158 Proll, G., Tschmelak, J., Kaiser, J., Kraemmer, P., Sacher, F., Stien, J., and Gauglitz, G. (2006) Advanced environmental biochemical sensor for water monitoring: automated water analyser computer supported system (AWACSS), in *Soil and Water Pollution Monitoring, Protection and Remediation, IV, Earth and Environmental Sciences NATO Science Series*, Vol. **69** (eds I. Twardowska, H.E. Allen, and M.M. Häggblom), Springer, pp. 131–145.

159 Hegnerováa, K. and Homola, J. (2010) Surface plasmon resonance sensor for detection of bisphenol A in drinking water. *Sens. Actuator B-Chem.*, **151** (1), 177–179.

160 Farré, M., Martínez, E., Ramón, J., Navarro, A., Radjenovic, J., Mauriz, E., Lechuga, L., Marco, M.P., and Barceló, D. (2010) Part per trillion determination of atrazine in natural water samples by a surface plasmon resonance immunosensor. *Anal. Bioanal. Chem.*, **388** (1), 207–214.

161 Vinogradova, T., Danaher, M., Baxter, A., Moloney, M., Victory, D., and Haughey, S.A. (2011) Rapid surface plasmon resonance immunobiosensor assay for microcystin toxins in blue-green algae food supplements. *Talanta*, **84** (3), 638–643.

162 Taitt, C.R., Shriver-Lake, L.C., Ngundi, M.M., and Ligler, F.S. (2008) Array biosensor for toxin detection: continued advances. *Sensors*, **8**, 8361–8377.

163 Le Blanc, A., Albrecht, C., Bonn, T., Fechner, P., Proll, G., Pröll, F., Carlquist, M., and Gauglitz, G. (2009) A novel analytical tool for quantification of estrogenicity in river water based on fluorescence labeled estrogen receptor α. *Anal. Bioanal. Chem.*, **395** (6), 1769–1776.

164 Fechner, P., Pröll, F., and Carlquist, M. (2009) An advanced biosensor for the prediction of estrogenic effects of endocrine-disrupting chemicals on the estrogen receptor alpha. *Anal. Bioanal. Chem.*, **393** (6–7), 1579–1585.

165 Eltzov, E. and Marks, R.S. (2011) Whole-cell aquatic biosensors. *Anal. Bioanal. Chem.*, **400** (4), 895–913.

166 van der Linden, S.C., Heringa, M., Puijker, L., Van der Burg, B., and Brouwer, A. (2007) Application of a steroid receptor-based battery of CALUX bioassays for water quality control analysis. *Organohalogen Compounds*, **69**, 1908–1911.

167 Donhauser, S.C., Niessner, R., and Seidel, M. (2009) Quantification of *E. coli* DNA on a flow-through chemiluminescence microarray read-out system after PCR amplification. *Anal. Sci.*, **25**, 669–674.

168 Corrie, R., Lawrie, G.A., Battersby, B.J., Ford, K., Rühmann, A., Koehler, K., Sabath, D.E., and Trau, M. (2008) Quantitative data analysis methods for bead-based DNA hybridization assays using generic flow cytometry platforms. *Cytometry A*, **73A** (5), 467–476.

169 Song, L., Ahn, S., and Walt, D.R. (2006) Fiber-optic microsphere-based arrays for multiplexed biological warfare agent detection. *Anal. Chem.*, **78** (4), 1023–1033.

170 Elsholz, B., Wörl, R., Blohm, L., Albers, J., Feucht, H., Grunwald, T., Jürgen, B., Schweder, T., and Hintsche, R. (2006) Automated detection and quantitation of bacterial RNA by using electrical microarrays. *Anal. Chem.*, **78** (14), 4794–4802.

171 Banerjee, P. and Bhunia, A.K. (2010) Cell-based biosensor for rapid screening of pathogens and toxins. *Biosens. Bioelectron.*, **26** (1), 99–106.

172 Peskoller, C., Niessner, R., and Seidel, M. (2009) Cross-flow microfiltration system for rapid enrichment of bacteria in water. *Anal. Bioanal. Chem.*, **393**, 399–404.

173 Pappert, G., Rieger, M., Niessner, R., and Seidel, M. (2010) Immunomagnetic nanoparticle-based sandwich chemiluminescence-ELISA for the enrichment and quantification of *E. coli*. *Microchim. Acta*, **168**, 1–8.

174 Sapsford, K.E., Rasooly, A., Taitt, C.R., and Ligler, F.S. (2004) Detection of campylobacter and Shigella species in food samples using an array biosensor. *Anal. Chem.*, **76** (2), 433–440.

175 Taitt, C.R., Shubin, Y.S., Angel, R., and Ligler, F.S. (2004) Detection of Salmonella enterica serovar typhimurium by using a rapid, array-based immunosensor. *Appl. Environ. Microbiol.*, **70** (1), 152–158.

176 Dunbar, S.A., Vander Zee, C.A., Oliver, K.G., Karem, K.L., and Jacobson, J.W.J. (2003) Quantitative, multiplexed detection of bacterial pathogens: DNA and protein applications of the Luminex LabMAP system. *J. Microbiol. Methods.*, **53** (2), 245–252.

177 Jing, W., Ya, C., Yuanyuan, X., and Li, G. (2009) Colorimetric multiplexed immunoassay for sequential detection of tumor markers. *Biosens. Bioelectron.*, **25** (2), 532–536.

178 Huelseweh, B., Ehricht, R., and Marschall, H.-J. (2006) A simple and rapid protein array based method for the simultaneous detection of biowarfare agents. *Proteomics*, **6** (10), 2972–2981.

179 Langer, V., Niessner, R., and Seidel, M. (2011) Stopped-flow microarray immunoassay for the detection of viable *E. coli* by use of chemiluminescence flow-through microarrays. *Anal. Bioanal. Chem.*, **399**, 1041–1050.

180 Park, C.H., Kim, J.P., Lee, S.W., Jeon, N.L., Yoo, P.J., and Sim, S.J. (2009) A direct, multiplex biosensor platform for pathogen detection based on cross-linked polydiacetylene (PDA) supramolecules. *Adv. Funct. Mat.*, **19** (23), 3703–3710.

181 Vikesland, P.J. and Wigginton, K.R. (2010) Nanomaterial enabled biosensors for pathogen monitoring - a review. *Environ. Sci. Technol.*, **44** (10), 3656–3669.

182 Ivnitski, D., Abdel-Hamid, I., Atanasov, P., and Wilkins, E. (1999) Biosensors for detection of pathogenic bacteria. *Biosens. Bioelectron.*, **14** (7), 599–624.

183 Bergwerff, A.A. and van Knapen, F. (2006) Surface plasmon resonance biosensors for detection of pathogenic microorganisms: strategies to secure

food and environmental safety. *J. AOAC Int.*, **89** (3), 826–831.

184 Dudak, F.C. and Boyaci, I.H. (2009) Rapid and label-free bacteria detection by surface plasmon resonance (SPR) biosensors. *Biotechnol. J.*, **4** (7), 1003–1011.

185 Leonarda, P., Heartya, S., Brennana, J., Dunnea, L., Quinna, J., Chakrabortyc, T., and O'Kennedy, R. (2003) Advances in biosensors for detection of pathogens in food and water. *Enz. Microb. Tech.*, **32** (1), 3–13.

186 Knauer, M., Ivleva, N., Liu, X., Niessner, R., and Haisch, C. (2010) Surface-enhanced Raman scattering-based label-free microarray read-outfor the detection of micro-organism. *Anal. Chem.*, **82**, 2766–2772.

187 Ivleva, N., Wagner, M., Horn, H., Niessner, R., and Haisch, C. (2010) Raman microscopy and SERS for in situ analysis of biofilms. *J. Biophotonics*, **3**, 548–556.

188 Sengupta, A., Mujacic, M., and Davis, E.J. (2006) Detection of bacteria by surface-enhanced Raman spectroscopy. *Anal. Bioanal. Chem.*, **386** (5), 1379–1386.

189 Jarvis, R.M. and Goodacre, R. (2008) Characterisation and identification of bacteria using SERS. *Chem. Soc. Rev.*, **37**, 931–936.

190 Banada, P.P., Huff, K., Rajwa, B., Aroonnual, A., Bayraktar, B., Adil, A., Robinson, J.P., Hirleman, E.D., and Bhunia, A.K. (2010) Label-free detection of multiple bacterial pathogens using light-scattering sensor. *Biosens. Bioelectron.*, **24**, 1685–1692.

191 Knecht, L.D., Pasini, P., and Daunert, S. (2011) Bacterial spores as platforms for bioanalytical and biomedical applications. *Anal. Bioanal. Chem.*, **400**, 977–989.

192 Kumari, A., Pasini, P., and Daunert, S. (2008) Detection of bacterial quorum sensing N-acyl homoserine lactones in clinical samples. *Anal. Bioanal. Chem.*, **391**, 1619–1627.

193 http://www.optischetechnologien.de/forschung.

7
Body Scanner

Torsten May and Hans-Georg Meyer

7.1
Introduction

Many recent terrorist assaults on public places – such as airports or train stations – would have been prevented if a bomb hidden by the attacker underneath his clothing could have been detected. It is obvious that current security technologies, like walk-through metal detectors, are not adequate for such scenarios; as a matter of principle they can only detect electric conductors, for example, firearms or metallic knifes. Therefore, the idea of "body scanning", meaning the electromagnetic visualization of hidden threats against the human body, became the concept of choice for future security screening aimed at prevention of terrorist attacks.

Reviewing suggested or realized body scanner technologies shows that all of them have a common approach: the object to be detected has electromagnetic properties (absorption, reflection, transmission) which differ from those of the human body. In an electromagnetic image, they become visible if the clothing above them is at least partly transparent in the used spectrum. Both preconditions limit the usable bands for imaging. Basically, appropriate technologies can be divided into two major categories: high photon energy bands above the visible part of the electromagnetic spectrum, and at the opposite extreme, low energy bands below the visible spectrum. The first category is addressed by X-ray technology, which relies on longstanding developments for medical application. The latter – low photon energy methods – include a variety of different methods, ranging from RADAR techniques to thermal far-infrared imaging. A categorization is difficult, since many of the suggested approaches overlap in terms of operation bands and components used. Therefore, the classification chosen in this review is somewhat arbitrary. The frequency band of operation covers the section between approx. 30 GHz ($\lambda = 1$ cm) and 1 THz ($\lambda = 300\,\mu$m). Hence, it ranges from bands used for microwave techniques to optical bands in the far-infrared region. Although a synergy between these two traditional technology areas is observable, for competitiveness a fuzzy line can be drawn at a wavelength of about 1 mm. Longer waves (millimeter waves) are mostly used by body scanners based on electronic technologies. At shorter wavelength (sub-millimeter

Handbook of Biophotonics. Vol.3: Photonics in Pharmaceutics, Bioanalysis and Environmental Research, First Edition.
Edited by Jürgen Popp, Valery V. Tuchin, Arthur Chiou, and Stefan Heinemann

waves) electronic technologies become less competitive in technical terms, and at the same time they become costly. Consequently, body scanners for sub-millimeter waves make use of emerging photonic technologies.

7.2 X-Ray Techniques

7.2.1 Overview

The concept of creating an image of a human body (or at least of parts of it) using X-rays is as old as the discovery of these rays by Wilhelm Conrad Roentgen in 1895, who soon thereafter published the first X-ray image of his wife's left hand. Ever since, this technique has evolved into a unique tool for medical imaging, with a remarkable impact on medical sciences [1]. It was obvious to implement these developed technologies also in other fields of social life, like security technologies. However, although X-ray imaging is in use for security screening of inanimate objects (e.g., baggage at an airport check-in), for a long time the screening of humans was excluded because of the radiation exposure and the implied health risk.

Within the last decades, increasing attention has been paid to the minimization of radiation exposure during medical examination. Partly because of emerging semiconductor X-ray detector technologies – which nowadays have almost completely replaced the traditional photosensitive film – it became possible to create X-ray images using only a fraction of the previous radiation dose.

Moreover, sophisticated detectors have been proven to be sensitive enough to record not only transmitted radiation but also the weak backscattered response from an illuminated human body. The backscatter technique became the concept of choice for security body scanning, because the required radiation dose is very low, allowing several hundred exposures per year within the legal limits of radiation safety. With it, on the other hand, one loses the unique feature of X-ray imaging of being the only technique able to reveal objects *inside* a human body. Although the transmission technique is in use in some security-sensitive places, the considerable radiation exposure justifies its employment only under extreme circumstances.

7.2.2 Physical and Technical Background

X-rays have been defined as electromagnetic waves having wavelength from 10^{-8} m (photon energy 100 eV) up to 10^{-12} m (1 MeV). The spectrum is strongly overlapping with gamma rays, which are differentiated from X-rays not by band definition but by their origin (electron vs. nuclear processes). In imaging, several interaction processes between X-rays and matter (soft tissue of the human body, the material of the object to be detected) are exploited. Relevant for security imaging are the photoelectric effect and the *Compton* scattering process [2].

The photoelectric effect is the absorption of an X-ray photon by electrons from the inner shells of an atom. In consequence, this electron is knocked out, having energy of the original photon energy minus its original binding energy. The cross section of this process is proportional to Z^5 (where Z is the atomic number). In contrast, in *Compton* scattering the X-ray photon elastically impacts free or weakly bound electrons of the illuminated matter. In this process, the X-ray photon loses energy and is reflected into all solid angles. The amount of backscattered radiation is a function of the photon energy and the matter composition, mostly the electron density; it is linearly dependent Z.

For security, as for medical imaging, typical operating bands are between 50 and 150 keV. Here, *Compton* scattering is dominant for the soft tissue of the human body, resulting in a high backscatter response. In contrast, for example, metal objects (high Z) absorb strongly because of the dominating photoelectric effect, consequently showing only a weak response, and hence a high contrast to the human body. For explosives, which are often based on organic compounds chemically similar to biological matter, the contrast is rather low, which makes their detection difficult.

For illumination, as in almost all medical devices, X-ray sources based on a metallic cathode in a vacuum tube are used [3], with varying materials and configurations depending on the intended energy range, output power and beam size. Recently published measurement techniques (see below) use a scanning configuration, with the source shuttered into a line or needle beam.

The detection of X-rays can be accomplished with a variety of different methods. As state of the art, solid state detectors have replaced established photosensitive film technologies, which are still competitive in terms of resolution. However, for technical reasons, especially the speed of image construction, electronic technologies have been favored. In general, these detectors can be divided into two major groups: direct and indirect [4]. An indirect detector uses a scintillating material to convert the incoming X-ray photon into visible light, which is detected by a charge coupled device (CCD) camera or by an array of photodiodes whose electrical charge response is read by thin film transistors (TFT) [5]. In contrast, an X-ray photoconductor (e.g., amorphous selenium) can directly convert the radiation into electrical charges, again read by a TFT.

The achievable spatial resolution is defined not by the diffraction limit of X-rays but by the digital resolution of the scanning technique. A reasonable goal, and hence the design rule for X-ray security imaging devices, is a spatial resolution of about 1 mm. An even better spatial resolution of below 0.1 mm would require an extremely high sampling of the image ($20\,000 \times 10\,000$ pixels for a full body scan), rendering the system unnecessarily complex, and thus costly.

In the following, two system approaches are briefly introduced, both relying on the X-ray technologies described above.

7.2.3
Backscatter Imaging

A recent implementation of the X-ray backscatter technique is the *Smartcheck*™ by the US American company American Science and Engineering Incorporation [6].

It is based on scientific work from the 1990s, patented by ASEs predecessor, the IRT Corporation. The current realization is already in use by the Transportation Security Agency (TSA, Department of Homeland Security), which has installed at least 94 machines at various airports in the United States. The worldwide dissemination is slow, because of European objections to the use of X-rays for non-medical applications [7]. However, machines can be found at least in the United Kingdom (London and Manchester airports), since currently they are still the most effective security solution.

The manufacturer specifies his machine as operating at photon energies of about 50 keV, creating a backscatter image of one side of a human body in approx. 3 s. The scan is performed using a mechanically steered needle beam in the center of the set-up, whilst two large-volume scintillator detectors at each side of the device integrate the backscattered response over a notable solid angle. For security purposes, a subsequent second image is required from the opposite side, although some installations use a master-slave set-up with a second device for parallel recording. The radiation exposure during the scan is specified by the manufacturer as 0.1 μSv per single-side scan, compared to the typical 5 μSv for dental radiography [8].

The machine is shown in Figure 7.1, alongside a typical X-ray backscatter image. The example demonstrates the suitability for security applications: the clothing of the subject is almost invisible, and hidden objects become apparent with high resolution, allowing object identification by shape. This answers one of the crucial problems of body scanner technologies: because it is almost impossible to determine the actual material of a detected object, only a telling shape would allow its identification. The displayed X-ray image has sufficient spatial resolution to detect for example, the belt buckle as a non-dangerous object, where the longwave technologies described later, due to their restricted spatial resolution, would probably create a false alarm with the same object.

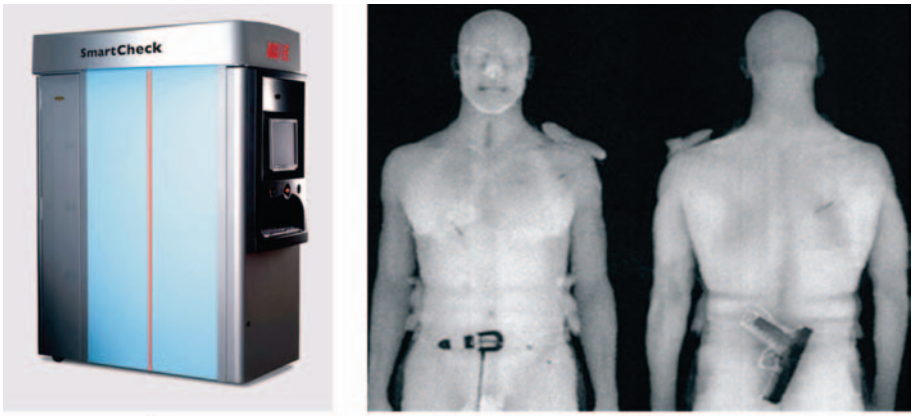

Figure 7.1 American Science and Engineering Inc, System *Smartcheck*™ at a US airport (a), X-ray backscatter image recorded by the device (b). William J. Baukus. X-ray Imaging for On-The-Body Contraband Detection Presented to 16th Annual Security Technology Symposium & Exhibition Session V: Technology Forum Focus Group II Transportation Security Technologies and Tools June 28, 2000.

7.2.4 Transmission Imaging

The transmission technique goes one step further in making use of X-rays. Recent implementations are for example, the *CONPASS* by Braun and Company Limited, the *Soter RS* by OD security, the *BS16HR* by Smith Detection and the *Scannex* by DebTech (De Beers).

As an example, the *CONPASS* device uses a narrow monochromatic X-ray beam and utilizes a linear array of semiconductor scintillation detectors for image scanning. Choosing between two different modes (LD and HR, corresponding to 0.25 μSv and 3 μSv per scan, respectively) images can be recorded [9]. Thereby, radiation passing through the inspected person is recorded, thus revealing – as the only body scanning technique – objects hidden inside the body or even behind the back, which would make a second scan from the opposite direction unnecessary (see Figure 7.2). During a scan, which takes about 8 s, the person is moved by a platform whilst the X-ray beam scans vertically. The reconstructed image with 2688×1000 pixels allows a spatial resolution of better than 2 mm (better than 0.2 mm for high contrast objects such as metals, according to the manufacturer's information).

Despite the undeniable security value of detecting objects inside the human body, the use of this technology did not become common in public places, mostly due to the obvious ethical issues involved. However, the manufacturer's literature reveals that in locations with restricted personal rights (e.g., prisons, diamond mines) its use is valid. Moreover, under the precondition of reasonable suspicion for example, of smuggling, even European border control officials are using this technology.

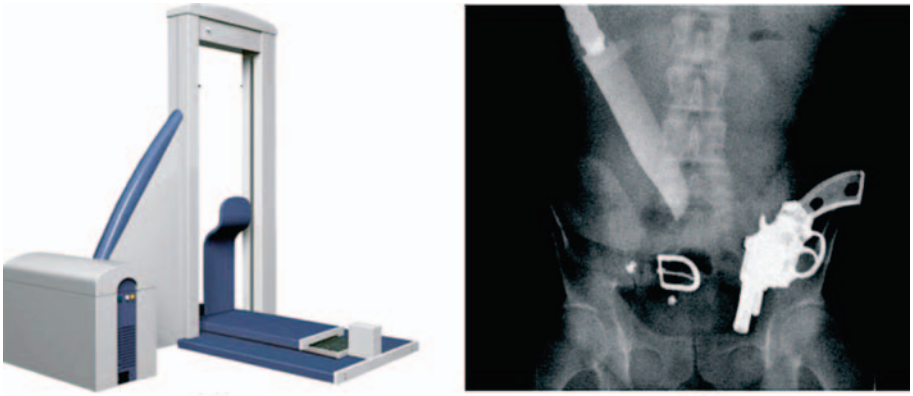

Figure 7.2 Braun and Company Limited, System "*CONPASS*" (a), X-ray transmission image revealing a Teflon knife behind the person (b) [10].

7.3
Millimeter Wave Electronic Techniques

7.3.1
Overview

In general, the basic idea of millimeter wave body scanning is the same as for X-ray imaging: the recorded electromagnetic image reveals objects because they differ in reflectivity and/or emissivity, whilst the covering cloth is at least partly transparent. The most crucial difference is the by 6 orders of magnitude larger wavelength compared to X-rays, making almost every system approach diffraction limited. Moreover, the maximum useful wavelength is limited. Although one could easily conceive a centimeter wave body scanner (the physics would be almost identical), in practice the achievable spatial resolution would be too low for security applications.

The term millimeter wave refers to electromagnetic waves in the range between 1 mm and 1 cm, corresponding to the definition for "extremely high frequency, EHF" (30 GHz to 300 GHz) for radio waves. Although it is strongly overlapping with the so-called sub-millimeter or terahertz waves in terms of physical properties, it is described separately because of the different technologies used for building body scanners in the respective wavelength band. For millimeter wave bands, technical components evolving from microwave technologies are in use.

7.3.2
Physical and Technical Background

The human body thermally generates millimeter wave photons according to Planck's equation; however, in the long wave Rayleigh limit its spectral emission is very low. Consequently, thermal imaging, as established in infrared bands, is technically ambitious. Hence, for visualization, in most cases a secondary photon source is required. Fittingly, here the human skin acts as an adequate reflector [11], whilst for the shorter sub-millimeter waves the reflectivity drops substantially [12] (see Figure 7.3). In conclusion, at millimeter wavelength it is reasonable to create a radiometric image using reflected secondary photons as contrast amplification.

At the same time, waves longer than 1 mm can easily penetrate clothes [13], so an object with different reflectivity becomes visible in contrast to the skin. Likewise, the atmospheric attenuation of millimeter waves is also acceptable for security screening [14], which is typically performed from distances not longer than a few meters. However, simply because many of the technical components used (emitters and receivers) have been developed for parallel use in other applications such as telecommunications, all recent body scanners still favor operation in atmospheric windows, such as the K_a band (27–40 GHz) or the W band (75–110 GHz) [15].

One of the first approaches to realizing millimeter wave imaging was to use the help of a cold background in order to increase the natural radiometric contrast between the warm human body and its surroundings. That can be accomplished because the atmosphere features an equivalent noise temperature well below

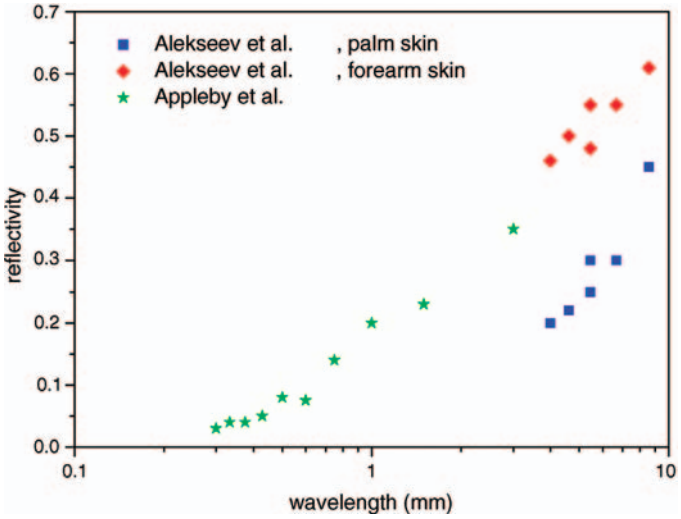

Figure 7.3 Reflectivity of human skin, according to Alekseev *et al.*: and Appleby *et al.*

100 K [16], increasing the indoor contrast of typically 15 K (35 °C skin temperature of human body vs. 20 °C room temperature) by about one order of magnitude. Consequently, many of the systems described later can operate without a technical source in outdoor operation, and are therefore described – somehow misleadingly – as passive, although they are not sensitive enough to effectively resolve the weak thermal millimeter wave radiation.

Applications which require indoor operation (e.g., security scanning at airports) are dependent on technical sources. As a result of the long heritage of microwave technology, there exists a variety of different emitter concepts, among them for example, varactor/varistor-mode frequency multipliers [17], backward-wave oscillators [18], Gunn oscillators [19], and more. Microwave sources in general share some physical similarities, allowing general statements on millimeter wave sources: typically they feature a relatively narrow output band, not larger than ±10% full-width-half-maximum (FWHM) of the center wavelength. Some concepts allow tuning the center emission to various bands. State of the art for the achievable output power is of the order of several watts at 10 mm wavelength; exponentially decaying to hundreds of milliwatts at 1 mm. Recently, the concepts of millimeter wave sources have been extended to sub-millimeter wavelength, and in the extreme to beyond 1 THz frequency (< 0.3 mm wavelength). However, the output power becomes increasingly small [20], making their use reasonable only for scientific experiments.

Similar performance trends are observable for millimeter wave detectors. They can be categorized into coherent and incoherent, the latter sensing only the power (or amplitude) of the incoming signal instead of the full wave information. Basically, millimeter wave detectors utilize an electronic device with a highly nonlinear characteristic, allowing for rectification (i.e., conversion of a high frequency signal

into a dc voltage response) or mixing with a known source (i.e., heterodyne principle) [21]. One of the most widespread devices is the *Schottky* diode [22], which has been in use for radio frequency applications for almost half a century. A major leap was the development of thin-film semiconducting *Schottky* diodes, which made them suitable for direct detectors as well as for mixers. Even today there is still notable research activity [23] on the *Schottky* effect. One of the reasons for its success is the compatibility with the so-called monolithic microwave integrated circuit (MMIC) technology [24], which allows cost-effective manufacturing of microwave devices in an integrated semiconductor fabrication technology. Please note, that the technical term MMIC is misleadingly used without suffix in different contexts, since there exist MMIC microwave sources as well as MMIC direct (incoherent) detectors and MMIC (coherent) mixers.

7.3.3
Active Imaging

The most mature system is the *ProVision* portal (see Figure 7.4), patented by the US American company Safeview (now L3 Communications) [25]. The device uses two columns with linear arrays of millimeter wave transmitters and receivers operating in the K_a band (with an actual bandwidth of 27–33 GHz) to scan a person by moving the columns around the subject. The procedure takes about 2 s. A frequency modulated continuous wave technique (FMCW) [26] is used to measure delays, in order to reconstruct a three-dimensional image of a human body from the reflected millimeter waves.

Figure 7.4 *L3 Communication Provision ATD* portal [27].

L3 devices were among the first body scanners deployed in real application. TSA has been using them since 2007 at various US airports. Since 2009, European airports have followed, favoring the millimeter wave technology over the much disputed X-ray scanners. They are now in test use in many European countries. A still existing obstacle is caused not by technical problems but by the political constraint to use the devices in a fully automated mode without raw data display. Thus the challenge to implement an algorithm for automated threat detection arises. Taking into account typical features of millimeter wave images (artifacts from clothing due to partial absorption, limited spatial resolution), a separation between potential threats and non-dangerous objects is ambitious. To date, some countries (e.g., Italy and Germany) are still working on this software problem, delaying the routine use of the device.

A newer system, the *eqo* by Smith Detection, favors a scan procedure with a stationary receiver. In the set-up shown in Figure 7.5, the emitters and receivers (ISM band 24–24.25 GHz) are installed in the column of the walk-through portal, whereas the panel behind contains an array of steerable patch antennae [28] which are used to scan a 3D volume in between. *eqo* delivers an output video stream with 10 to 25 Hz frame rate, with an image quality comparable to the *Provision ATD*. The specified spatial resolution is of the order of 1 cm and below for high contrast objects.

The current state of the art in active millimeter wave imaging is represented by the ongoing German research project *QPASS*, using a multistatic sparse array of transmitters and receivers for 77 GHz [30]. The modular system allows a full 3D image reconstruction with about 2 mm spatial resolution, gaining from the three

Figure 7.5 Smith Detection *eqo* [29] (a), and recorded millimeter wave image taken from a video stream with 10 Hz frame rate (b) courtesy of Smith Detection.

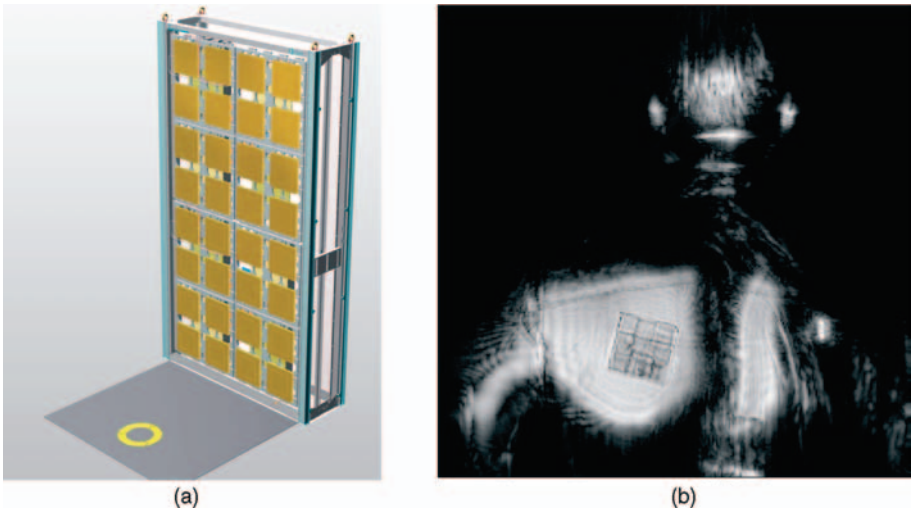

Figure 7.6 *Andromeda* flat-panel detector under construction (courtesy by Rohde & Schwarz Germany) (a), and millimeter wave image [31] recorded in a scanning test set-up(b).

times smaller wavelength compared to the L3 system, Figure 7.6. In this way the problem of automated threat detection could be answered, since the achievable spatial resolution approaches the reference of X-ray imagery, allowing classification of detected objects by their shape. Moreover, the relatively high bandwidth of the system allows direct determination of the dielectric constant of the detected object, potentially enabling a material identification.

7.3.4 Passive Imaging

As mentioned above, the available energy of thermal millimeter wave radiation from a human body is weak. However, some systems address a passive operation, especially in the case of intended stand-off operation. That is mainly because it becomes increasingly difficult to effectively illuminate subjects from a distance. A directed radiation from a point source will be reflected back in a relatively small solid angle; whereas a distributed illumination is elaborate and would result in a small reflected energy per area.

Obviously, an intended passive operation requires highly sensitive detectors. Flat panel architectures with a large number of state-of-the-art receivers are still too expensive; consequently, all systems described below are based on reasonably small arrays (10 to 100 pixels) in combination with an opto-mechanical scanner. However, even with the most sophisticated detectors one still has to trade-off a passive operation for less frame rate or less resolution.

Recent implementations have demonstrated different approaches to solve this compromise. The most elaborate system has been developed by the UK's QinetiQ, who have been building millimeter wave imagers for military application for the past

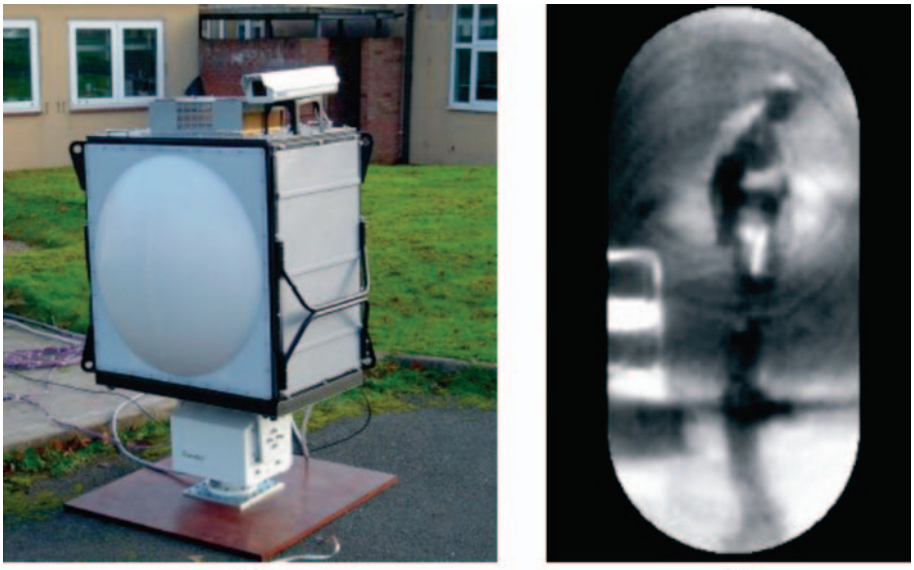

Figure 7.7 QinetiQ *SPO 30* stand-off imager for outdoor screening (a), passive millimeter wave video (b) [33].

20 years. The highlight is a 3 mm (94 GHz) helicopter-borne imager [32] with 150 MMIC receivers, achieving a 25 Hz video frame rate.

Modified implementations of this system's technology have been used to demonstrate the usability for body scanning; however, for effectual indoor operation the sensitivity of the receivers is too low. Therefore, devices such as the *SPO 20* (see Figure 7.7) are in use for stand-off explosive detection in outdoor operation, where they are still subjected to extensive trials by the US and British armies.

In order to achieve a passive operation indoors, the US Company Millivision has followed an unconventional approach. In their *Portal 350* [34] (see Figure 7.8), they

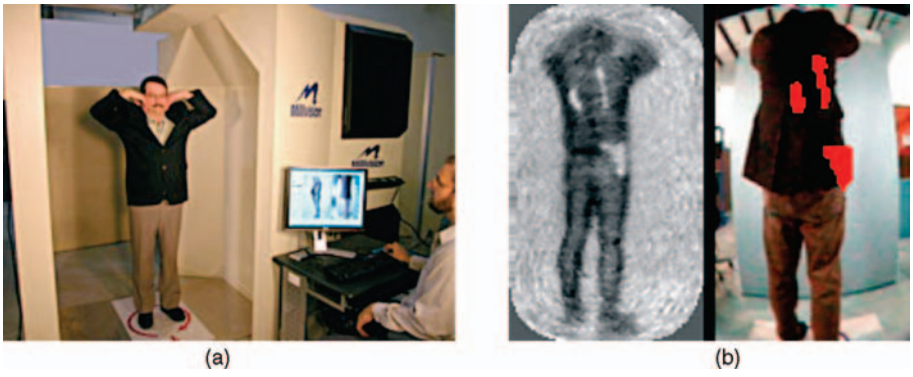

Figure 7.8 Millivision *Portal 350* (a), and recorded still image from a 10 Hz video stream (b).

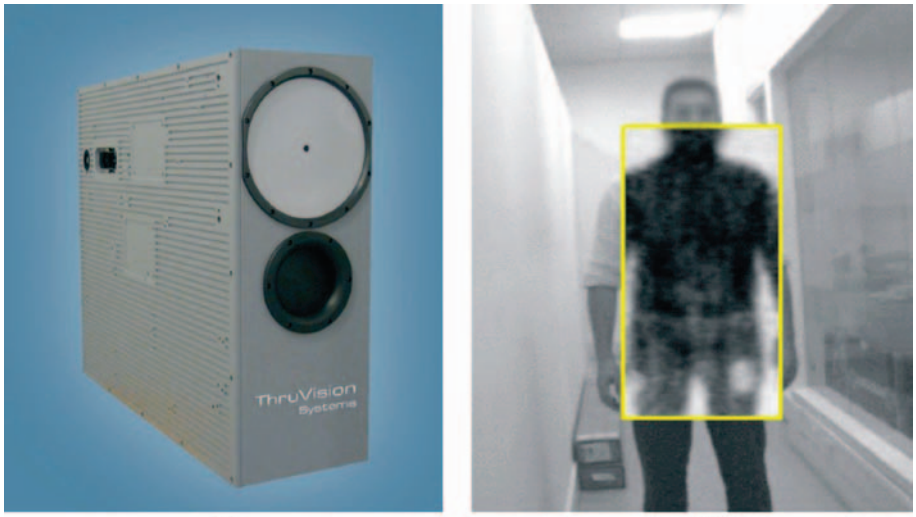

Figure 7.9 Thruvision *TS4* (a), passive millimeter wave image recorded from 5 m distance (b) [35].

achieve a reasonable spatial resolution and a high frame rate (10 Hz) by increasing the radiometric contrast with a cooled wall inside the inspection cabin. In that way, there is no obstacle of artificial illumination by a technical source, whilst the cooled wall allows the system to operate in the same environmental conditions as in outdoor operation.

Another approach is followed by the British company Thruvision: their systems are based on technology developed in the ESA Startiger program. Stretching the millimeter wave technology to the limit, namely to a wavelength of about 1.2 mm (220 GHz), the useable thermal energy is already by a factor of 5 higher compared to the QinetiQ system at 3 mm (94 GHz). In combination with a sophisticated heterodyne detection it allows for reasonable spatial resolution at frame rates of about 6 Hz in indoor operation (see Figure 7.9).

7.4 Sub-Millimeter Wave (Terahertz) Photonic Techniques

7.4.1 Overview

Security scanning at sub-millimeter bands extends the general idea of using low-energy photons for imaging. The physical reason to enhance the millimeter wave technique to shorter wavelengths is the diffraction effect, which limits the achievable spatial resolution of security relevant images. However, despite the strong connection between millimeter and sub-millimeter bands, crucial parameters are different, consequently changing the design constraints.

In general, sub-millimeter wave systems are investigated because of the intended capability to perform a body scan from a certain distance of a few meters up to 100 m. This is motivated by the wish to free the person under test from inspection cabins. At the same time, it would allow a security check to be carried out from a safe distance, preventing, for example, a suicide bomber from approaching the site to be protected.

In such application scenarios, millimeter wave systems could achieve a reasonable spatial resolution only by using oversized optics. On the other hand, simply scaling the millimeter wave technology to shorter wavelength would result in a disproportional increase in system complexity and costs because of the technical constraints of the electronic devices used. Therefore, the sub-millimeter band is dominated by emerging photonic technologies which are more closely related to infrared technologies.

7.4.2
Physical and Technical Background

Compared to millimeter wave bands, the issue of atmospheric and clothing attenuation becomes much more pronounced. In general, every sub-millimeter wave system is a compromise between spatial resolution and transparency, which narrows the band of suitable wavelengths to a range between 1 mm and a minimum of 0.3 mm. Even in this restricted band, the trend for worsening transparencies of atmosphere and clothing (see Figure 7.10) strongly influences the performance, so prototypes have been demonstrated only in atmospheric windows at 0.9 mm (350 GHz), 0.45 mm (660 GHz) and 0.35 mm (850 GHz). Although even shorter wavelengths would be very attractive, especially for explosive detection (see Chapter 8), the inadequate clothing transparency makes a "real" terahertz system ($f > 1$ THz, $\lambda < 0.3$ mm) almost useless for security applications.

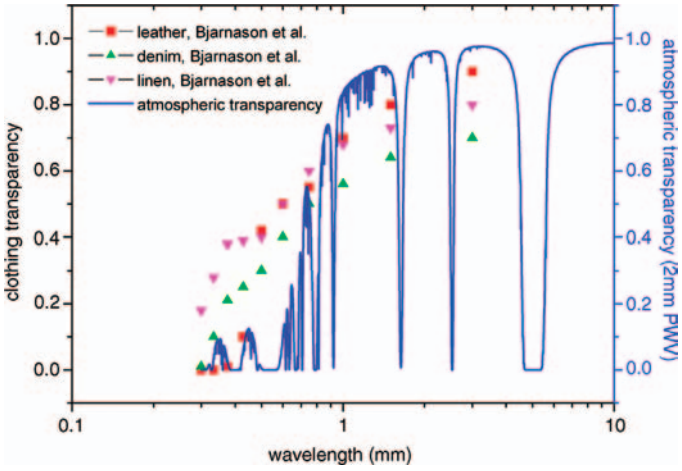

Figure 7.10 Comparison of clothing transparencies (Bjarnason *et al.* [13]) with a calculated atmospheric spectrum using the APEX transmission calculator [36].

The question whether to build an active or passive system is also answered differently compared to millimeter wave bands. The thermal radiation of a human body is notably stronger, so a passive operation is feasible with an acceptable technical effort. At the same time, the reflectivity of a human body is small (compare Figure 7.3). This brings up a problem for an active system, since for example, direct reflections from metallic objects would result in a – by orders of magnitude – larger signal compared to the weak response from the human body. Consequently, any detector for an active sub-millimeter body scanner is required to achieve a high dynamic range ($>10^3$), which constitutes a technical challenge.

Eligible technical sources for sub-millimeter radiation can be categorized into derivations of the already described microwave technologies, and photonic sources, for example, lasers. As mentioned above, electronic sources suffer from an inevitable loss in performance with decreasing wavelength, although substantial progress has been achieved by recent research [37]. From the opposite side of the sub-millimeter spectrum, sources based on photonic infrared concepts are extended to longer waves, facing the inverse problem of decreasing efficiency with increasing wavelength. Among these are quantum cascade lasers (QCL) [38], terahertz pulse lasers pumped by femtosecond infrared lasers [39], photomixers [40], and more. Up to now, the use of sub-millimeter sources for active imaging has been demonstrated only in research projects; there is no commercial system based on this technology. The development is driven mainly by the intended use for terahertz spectroscopy, which, in a security context, could be used to identify explosives.

The field of detector technologies for sub-millimeter waves is quite heterogenic. First, concepts for millimeter wave detectors have been enhanced by modern research to stay competitive. A completely different branch is occupied by broadband incoherent (power or energy) detectors based on bolometric principles, typically cooled to low temperatures for high sensitivity [41]. They have been shown to achieve unprecedented performance, making them the first choice for passive sub-millimeter wave imaging, but at the same time raising the constraint to implement cooling technologies in the system. In the case of active methods, detectors of choice are coherent, in order to gain full wave information for spectroscopy or 3D image reconstruction. Here, two major categories are available: heterodyne mixer technologies, for quantum-limited performance based on superconducting elements [42], and electro-optical concepts which are directly adapted to time domain spectroscopy with femtosecond lasers [43].

7.4.3
Active Imaging

An example of the further enhancement of millimeter wave technologies is a US project (lead by the Pacific Northwest National Laboratory for the Department of Energy) aiming for an active 350 GHz system [44]. This system uses planar GaAs *Schottky* diodes in a MMIC multiplier set-up. To date it has been demonstrated that a 3D image can be reconstructed at distances up to 10 m, at a frame rate of 10 s.

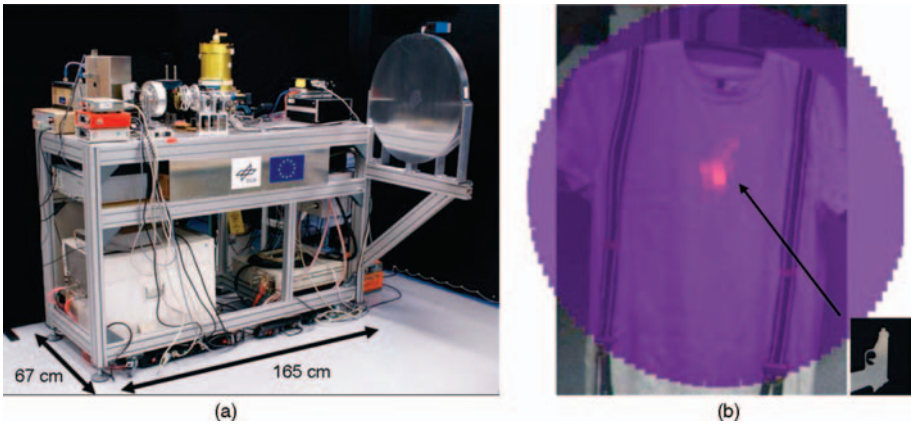

Figure 7.11 *TERASEC* system demonstrator (a) and detected handgun mock-up from 18 m distance, recorded within 0.5 ms (b).

In Europe, the project *TERASEC* has been accomplished in frame of the Preparatory Action for Security Research (PASR) program, started in 2004. Here, at the German Aerospace Centre (DLR) a real-time scanner (see Figure 7.11) has been demonstrated, which is able to detect objects from distances up to 20 m [45]. An optically pumped THz gas laser was used as transmitter, combined with a single superconducting hot-electron bolometric mixer as detector. To date, this is still the largest stand-off distance demonstrated.

These two projects are only two of a lively research field. They demonstrate the trend to use continuous wave sources combined with heterodyne detection for 3D imaging. The acclaimed time-domain spectroscopy method has not made it into security imaging, mainly because of the issue of diverging pulses over a stand-off distance. It is still the method of choice for nondestructive testing or spectroscopy, for a review see [46].

7.4.4
Passive Imaging

As mentioned above, building a passive system for sub-millimeter wave bands is much more promising compared to the millimeter wave spectrum: thermal radiation is notably stronger, so it is possible to conceive a passive imager whose designed spatial and thermal resolution is not limited by technical constraints but by physical limits.

As for infrared thermal imagers, the figure of merit is the background limit of inevitable signal noise (Poisson-distributed fluctuations in received photon number) [47]. Recent research has demonstrated that, using cryogenic incoherent detectors, it is possible to achieve this ideal mode of operation (background limited photometry, BLIP). Two groups have followed this approach; a European

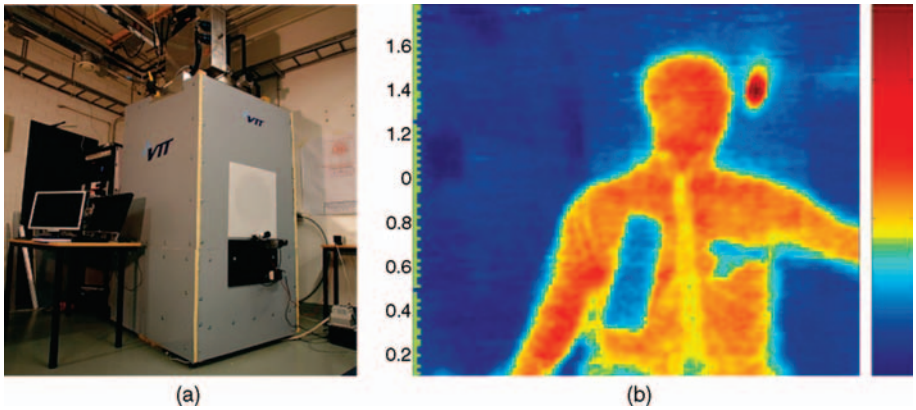

Figure 7.12 Current realization of a passive terahertz imager at VTT Finland (a), and typical image recorded at 8 m distance (b).

and US consortium led by the Technical Research Centre of Finland (VTT) in Helsinki, and a German consortium lead by the Institute of Photonic Technologies (IPHT) in Jena.

The Helsinki team has chosen antenna-coupled micro-bolometers, cooled to about 4 K by a commercial pulse tube cooler (PTC). The PTC technology is based on a *Stirling* process utilizing pressure impulses. Cryogenic temperatures well below 4 K are achievable by emerging two-stage devices, rather than single-stage implementations which have been in routine use for many years, for example, for cooling infrared focal plane arrays [48].

The current VTT system (see Figure 7.12) uses a linear array of 64 bolometers, in combination with a conical scanner as part of a folded Schmidt optics [49]. In contrast to almost all body scanners described in this chapter, the system features a notably large optical bandwidth between 1 and 0.3 mm (300 GHz up to 1 THz). Consequently, it integrates over the corresponding atmospheric windows, which in some sense constitutes an inherent fusion of bands with high clothing transparency and bands with higher spatial resolution. At the same time it eases the demands on the detectors, because the available energy from different bands is notably larger than for single-band operation.

At the same time, the Jena group has independently followed a parallel path [50] by using a smaller number of detectors which feature a higher sensitivity beause they are cooled to even lower temperatures of 0.3 K. This allows the system to be operated in a single atmospheric window, in this case 0.9 mm (350 GHz).

Again, the operation temperature is achieved by a two-stage PTC, featuring an additional closed-cycle ^{3}He evaporation cooler for thermal stability. The built system (see Figure 7.13) uses a receiver with 20 transition-edge bolometers, which to date is the limit for an economically priced scanning system. The scanning is accomplished on a spiral trace by simultaneously tilting and rotating the secondary mirror of the Cassegrain optics, allowing for video frame rates up to 10 Hz.

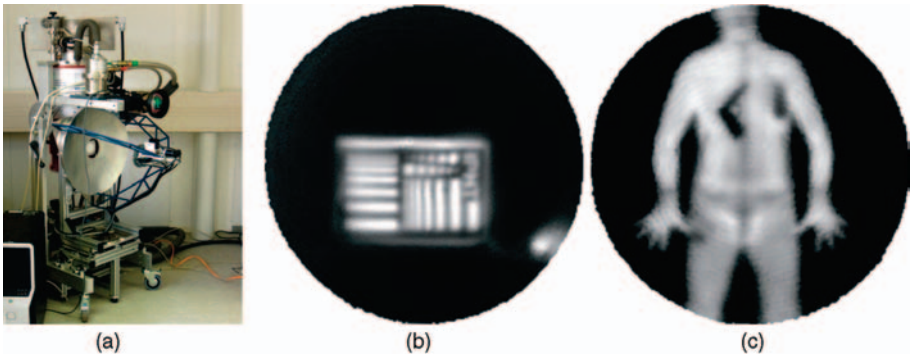

Figure 7.13 System demonstrator built at IPHT Jena (a) and images recorded from 8 m distance (resolution test (b) person with handgun and explosive mock-ups (c)).

7.5 Conclusion and Outlook

Body scanning for security applications has evolved into a highly dynamic market with enormous growth potential, driven by the permanent threat of terrorist attacks. The first systems made use of X-ray technologies, relying on the heritage of medical imaging. However, because of ethical issues and health effects, X-ray imaging did not become widely accepted, at least in the presence of an existing alternative.

The gap is being filled by emerging millimeter wave technologies. The enhancement of traditional microwave techniques into the millimeter wave band has reached a high state of maturity, enabling the production of the first commercial systems which can compete with X-ray imaging at an almost negligible exposure level to harmless millimeter wave radiation. Moreover, by using techniques related to the RADAR approach, the unique feature of 3D image reconstruction of the person under test allows an improved detection capability, overcoming the obstacle of fully automated object recognition, as required by security officials.

Thinking beyond established security concepts, the further enhancement of security technologies could, by using camera-like sub-millimeter wave systems able to perform security checks *en passant*, remove the need for the people under test to be examined in inspection cabins. This is the subject of recent research, which is additionally driven by the vision of material identification, for example, explosives, by means of terahertz spectroscopy.

References

1 Bushburg, J., Seibert, A., Leidholdt, E., and Boone, J. (2002) *The Essential Physics of Medical Imaging*, Lippincott, Williams & Wilkins, USA.

2 Towe, B.C. and Jacobs, A.M. (1981) X-Ray Compton Scatter Imaging Using a High Speed Flying Spot X-Ray Tube. *IEEE Trans. Bio.-Med. Eng.*, **28** (10), 717–721.

3 Huda, W. and Slone, R.M. (2003) *Review of Radiological Physics*, Lippincott, Williams & Wilkins, USA.

4 Chotas, H.G., Dobbins, J.T., and Ravin, C.E. (1999) Principles of digital radiography with large-area, electronically readable detectors: a review of the basics. *Radiology*, **210**, 595–599.

5 Kotter, E. and Langer, M. (2002) Digital radiography with large-area flat-panel detectors. *Eur. Radiol.*, **12**, 2562–2570.

6 http://www.as-e.com/products_solutions/smart_check.asp.

7 council directive 96/29/EURATOM of the European Atomic Energy Community (1996).

8 Brenner, D.J. and Hall, E.J. (2007) Computed tomography—an increasing source of radiation exposure. *N. Engl. J. Med.*, **357** (22), 2277–2284.

9 http://www.brauninternational.com/conpass-body-scanner-2-37-217.php.

10 Company Presentation of the Braun Full-body scanner Part No BRAU1950, company website, http://www.brauninternational.com.

11 Alekseev, S.I. and Ziskin, M.C. (2007) Human Skin Permittivity Determined by Millimeter Wave Reflection Measurements. *Bioelectromagnetics*, **28**, 331–339.

12 Appleby, R. and Wallace, H.B. (2007) Standoff Detection of Weapons and Contraband in the 100GHz to 1 THz Region. *IEEE Trans. Antenn. Propag.*, **55** (11), 2944–2956.

13 Bjarnason, J.E., Chan, T.L.J., Lee, A.W.M., Celis, M.A., and Brown, E.R. (2004) Millimeter-wave, terahertz, and mid-infrared transmission through common clothing. *Appl. Phys. Lett.*, **85** (4), 519–521.

14 Liebe, H.J. and Layton, D.H. (1987) *Millimeter-Wave Properties of the Atmosphere Laboratory Studies and Propagation Modelling*, U.S. Dept. of Commerce, National Telecommunications and Information Administration, Washington.

15 Whitaker, J.C. (2005) *Standard Handbook of Broadcast Engineering*, McGraw-Hill Professional, USA.

16 Shambayati, S. (2008) Atmosphere attenuation and noise temperature at microwave frequencies, in *Low-Noise Systems in the Deep Space Network* (ed. M.S. Reid), Wiley.

17 Faber, M.T., Chramiec, J., and Adamski, M.E. (1995) *Microwave and Millimeter-Wave Diode Frequency Multipliers*, Artech House Microwave Library.

18 Kantorowicz, G. and Palluel, P. (1979) Backward wave oscillators, in *Infrared and Millimeter Waves* (ed. K. Button), Academic Press.

19 Chen, J.C., Pao, C.K., and Wong, D.W. (1987) Millimeter-wave monolithic gunn oscillators. *Microwave and Millimeter-Wave Monolithic Circuits*, **87** (1), 11–13.

20 http://vadiodes.com/index.php.

21 Hagen, J.B. (1996) *Radio-Frequency Electronics: Circuits and Applications*, Cambridge University Press, Technology & Engineering.

22 Pozar, D.M. (1993) *Microwave Engineering*, Addison-Wesley Publishing Company.

23 Pardo, D., Grajal, J., Pérez, S., Mencía, B., Mateos, J., and González, T. (2011) Analysis of noise spectra in GaAs and GaN Schottky barrier diodes. *Semicond. Sci. Tech.*, **26** (5), 55023–55033.

24 Siweris, H.J., Werthof, A., Tischer, H., Schaper, U., Schafer, A., Verweyen, L., Grave, T., Bock, G., Schlechtweg, M., and Kellner, W. (1998) Low-cost GaAs pHEMT MMIC's for millimeter-wave sensor applications. *IEEE Trans. Microw. Theory*, **46** (12), 2560–2567.

25 Grudkowski, T.W., Rowe, R.L., Blasing, R.R., Trosper, S.T., Trawick, T.W., Meyer, K.A., Genske, D.J., Van Eyck, G.J., and Brinkerhoff, M.D. (2006) Millimeter-wave active imaging system, US patent application 6992616.

26 Federici, J.F., Schulkin, B., Huang, F., Gary, D., Barat, R., Oliveira, F., and Zimdars, D. (2005) THz imaging and sensing for security applications and explosives, weapons and drugs. *Semicond. Sci. Tech.*, **20** (7), 266–280.

27 http://www.sds.l-3com.com/advancedimaging/provision-at.htm.

28 Sugiura, S. (2009) A Review of Recent Patents on Reactance-Loaded Reconfigurable Antennas. *Recent Patents Electr. Eng.*, **2**, 200–206.

29 http://www.smithsdetection.com/eqo.php.

30 Ahmed, S.S., Schiessl, A., and Schmidt, L.P. (2009) Near field mm-wave imaging

with multistatic sparse 2D-arrays. Proceedings of the 6th European Radar Conference 2009, Rome.
31 Ahmed, S.S., Ostwald, O., and Schmidt, L.P. (2009) Automatic detection of concealed dielectric objects for personnel imaging. Proceedings of the IEEE MTT-S International Microwave Workshop on Wireless Sensing, Local Positioning, and RFID.
32 Appleby, R., Anderton, R.N., Thomson, N.H., and Jack, J.W. (2004) The design of a real-time 94-GHz passive millimetre-wave imager for helicopter operations. *Proc. SPIE*, **5619**, 38–46.
33 Appleby, R. (2006) Passive Millimetre Wave Imaging what it can and cannot do, presentation at International Forum on Terahertz Spectroscopy and Imaging, March 2 2006.
34 http://www.millivision.com/.
35 http://www.thruvision.com.
36 http://www.apex-telescope.org/sites/chajnantor/atmosphere/transpwv/.
37 Siegel, P.H. (2002) Terahertz technology. *IEEE Trans. Microw. Theory*, **50** (3), 910–928.
38 Williams, B.S. (2007) Terahertz quantum-cascade lasers. *Nat. Photon.*, **1**, 517–525.
39 Hu, B.B., Zhang, X.-C., and Auston, D.H. (1991) Terahertz radiation induced by subband-gap femtosecond optical excitation of GaAs. *Phys. Rev. Lett.*, **67**, 2709–2712.
40 Vergheses, S., McIntosch, K.A., Calawa, S., Dinatale, W.F., Duerr, E.K., and Molvar, K.A. (1998) Generation and detection of coherent terahertz waves using two photomixers. *Appl. Phys. Lett.*, **73** (26), 3824–3826.
41 Walcott, T.M. (ed.) (2011) *Bolometers: Theory, Types and Applications*, Nova Science.
42 Zmuidzinas, J. and Richards, P.L. (2004) Superconducting Detectors and Mixers for Millimeter and Submillimeter Astrophysics. *Proc. IEEE*, **92** (10), 1597–1616.
43 Wu, Q. and Zhang, X.C. (1996) Ultrafast electro-optic field sensors. *Appl. Phys. Lett.*, **68** (12), 1604–1606.
44 Sheen, D.M., Hall, T.E., Severtsen, R.H., McMakin, D.L., Hatchell, B.K., and Valdez, P.L.J. (2009) Active wideband 350 GHz imaging system for concealed-weapon detection. *Proc. SPIE*, **7309**, 73090I-1.
45 Hübers, H.W., Semenov, A.D., Richter, H., and Böttger, U. (2007) Terahertz imaging system for stand-off detection of threats. *Proc. SPIE*, **6549**, 65490A.
46 Chan, W.L., Deibel, J., and Mittleman, D.M. (2007) Imaging with terahertz radiation. *Rep. Prog. Phys.*, **70** (8), 1325–1379.
47 Benford, D.J., Hunter, T.R., and Phillips, T.G. (1998) Noise Equivalent Power of Background Limited Thermal Detectors at Submillimeter Wavelengths. *Int. J. Infrared Millim.*, **19** (7), 931–938.
48 Radebaugh, R. (2000) Pulse Tube Cryocoolers for Cooling Infrared Sensors. *Proc. SPIE*, **4130**, 363–379.
49 Grossman, E., Dietlein, C., Ala-Laurinaho, J., Leivo, M., Gronberg, L., Gronholm, M., Lappalainen, P., Rautiainen, A., Tamminen, A., and Luukanen, A. (2010) Passive terahertz camera for standoff security screening. *Appl. Opt.*, **49** (19), 245–259.
50 Heinz, E., May, T., Zieger, G., Born, D., Anders, S., Thorwirth, G., Zakosarenko, V., Schubert, M., Krause, T., Starkloff, M., Krueger, A., Schulz, M., Bauer, F., and Meyer, H.G. (2010) Passive Submillimeter-wave Stand-off Video Camera for Security Applications. *J. Infrared Millim. Terahertz W.*, **31** (11), 1355–1369.

8
Detection of Explosives

Wolfgang Schade, Rozalia Orghici, Mario Mordmüller, and Ulrike Willer

8.1
Introduction

Nowadays, much attention is given to the detection of explosives in order to prevent terrorist activities and assure security at airports, aviation, public transportation, convention halls, concerts, and so on. The location of undetonated and buried landmines is also a matter of great importance that could help to minimize fatalities and injuries among civilians caused by mines detonating. Another problem related to the use of explosives is the fact that nitrogen-based explosives, such as trinitrotoluene (TNT), are toxic and able to rapidly penetrate the skin, leading to significant health problems [1, 2]. For this reason, the sensing of hazardous substances may be of great interest at many facilities, where explosive materials were/are still manufactured and deposited, in order to avoid contamination of the soil or groundwater with the toxic compounds that can result from improper waste disposal, and to ensure the safety of both workers and nearby residents.

As can be seen, the detection of explosives is a significant task in the field of security and environmental analysis. Over the last several years major efforts have been focused on developing innovative sensing devices, capable of detecting hazardous species. In contrast to commonly used methods, such as ion mobility spectrometry (IMS), gas chromatography, or mass spectrometry, that require sampling for performing analysis and are relatively cost-intensive, optical methods are ideally suited for a fast online and *in situ* detection of hazardous substances due to their contact-free and nondestructive operation.

However, at the present time, there is no sensing system available which can identify all explosive compounds, promising high sensitivity, selectivity, and low false-alarm rate, simultaneously. Depending on the nature of the applications, sensing devices based on different laser spectroscopic methods have been developed, each of them offering high efficiency for a specific type of explosive material. A reliable detection of explosive traces in the vapor phase or in the form of particles, essential for security applications, can only be achieved by combining the sensing methods and their respective features. In the following, an overview of several laser-

Handbook of Biophotonics. Vol.3: Photonics in Pharmaceutics, Bioanalysis and Environmental Research, First Edition.
Edited by Jürgen Popp, Valery V. Tuchin, Arthur Chiou, and Stefan Heinemann

based detection techniques will be given, including examples of the first photonic devices and their practical application for the detection of explosives.

8.2
Optical Methods for the Detection of Explosives – Overview

Common optical stand-off, remote detection methods of trace amounts of samples have been shown to provide detection of explosives and their stimulants under specific conditions. These include laser-induced breakdown spectroscopy (LIBS), fragmentation via laser photolysis (LP) combined with fragment detection via laser-induced fluorescence (LIF), laser ionization in combination with mass spectroscopy (MS), mid-infrared (MIR) spectroscopy and spontaneous Raman scattering [3–7]. These methods suffer, at least to some extent, from one (or both) of the two following major drawbacks: false alarms and low sensitivity, since they do not efficiently discriminate between the "real" and the background signals, and since they rely on noncoherent emissions. At the present time, several approaches are being discussed and investigated but a suitably reliable, highly sensitive optical stand-off, remote detection method is not available. For point detection the situation is different, here several techniques do exist. However, a multi-species analysis is still problematic. In the following, existing laser-based methods will be discussed and evaluated with respect to the detection of explosives in near- and far-field applications.

Vibrational spectroscopy is well suited for identification of molecular species, providing spectral signatures and recognition of specific compounds. However, vibrational spectroscopy based on near- infrared (NIR) and MIR absorption is often barely applicable, due to weak overtone absorption bands and/or the possible interference of strong NIR/MIR absorbers, for example, water on a surface, which can obscure significant portions of the spectrum.

Spontaneous Raman spectroscopy has been more successful, despite the relatively low Raman scattering cross sections that lead to weak signals. Indeed, portable chemical sensors, combining nanosecond (ns) pulses in the ultraviolet (UV) or visible laser excitation for light detection and ranging (LIDAR) have been developed and evaluated [7–10]. These sensors were applied for remote sensing to identify the vibrational "fingerprints" of substances on surfaces. In principle, these systems have the potential for stand-off detection of contaminant films several micrometers thick at distances of up to ten meters, and bulk quantities of substances at distances of hundreds of meters. Nevertheless, detection sensitivity is still of major concern.

One way to enhance the sensitivity is by replacing spontaneous Raman with a two- or four- wave coherent, parametric process, namely, stimulated Raman scattering (SRS) [11, 12] and coherent anti-Stokes Raman spectroscopy (CARS) [11–13]. Both SRS and CARS are powerful nonlinear scattering processes, providing unique spectroscopic tools promising high sensitivity, molecular specificity, and detailed structural information based on Raman signatures of materials. In spontaneous Raman scattering, a laser "pump" beam at a frequency ω_p illuminates the sample, and, due to inelastic scattering, a signal is generated at the Stokes and anti-Stokes

frequencies, ω_S and ω_{AS}, respectively. In conventional SRS and CARS, however, two laser beams at ω_p and ω_S coincide on the sample. For SRS, when the difference frequency, $\Delta\omega = \omega_p - \omega_S$, matches a particular molecular vibrational frequency, efficient vibrational excitation is induced. In the CARS process, a particular Raman transition is coherently driven by the ω_p and ω_S incident laser beams, and subsequently the vibrational coherence is probed by a third laser beam (usually ω_p), giving rise to the (anti-Stokes) CARS signal, designated as ω_{CARS}. Due to their nonlinear nature, SRS and CARS share the benefits of multiphoton processes, including significant signal enhancement over spontaneous Raman, as well as enhanced depth penetration. One very significant advantage of SRS over other excitation processes is its extremely high efficiency: as an example, 18–28% of the population of the vibrational ground state was transferred to the $v'' = 1$ stretch of C–D in $CDCl_3$ [14] and up to 60% to the C–H stretch in the ring of 2-phenylethylamine. For CARS, the ratio between the intensity of its signal and that of spontaneous Raman under comparable conditions is typically several orders of magnitude, depending on the molecules at hand [12, 13]. Moreover, the Raman signal is red-shifted relative to the exciting frequency, whereas CARS is blue-shifted, therefore, when applying CARS, scattering and fluorescence produced by the exciting light can easily be filtered and false alarms minimized. A scheme of SRS and CARS is presented in Figure 8.1.

Indeed, due to these benefits there has been extensive use of SRS [15–18] and CARS [19–21] in spectroscopic studies and in a variety of applications, including the use of the latter for bacterial spores [22] and for stand-off detection of various species [23]. Very recently, coherent control techniques, applying single beam, shaped femtosecond (fs) pulses [24], as well as narrowband nanosecond excitation [25], were employed for obtaining backscattered-CARS (B-CARS) (resulting from diffuse reflections of the forward-generated CARS, occurring in the sample itself) to detect solid particles of explosives and explosive-related compounds. It has been shown that the positions of the major spectral features of spontaneous Raman scattering of each compound remain essentially the same in B-CARS, but the latter allows much higher detection sensitivity [25].

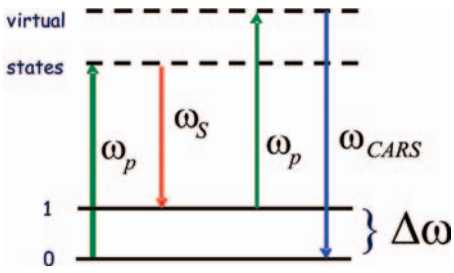

Figure 8.1 SRS and CARS schemes, where two lasers of frequencies ω_p and ω_S are used; $\Delta\omega$ is the frequency by which the vibrational state is excited by the SRS process induced by the ω_p and ω_S beams represented by the two arrows on the left. ω_p also induces the CARS transition shown on the right.

In principle, SRS and CARS spectroscopy can be implemented by applying pulses ranging from femtoseconds to nanoseconds. Whereas for fs excitation a broadband single beam was applied [24], for narrowband ns excitation [25] the spectra was produced by the time-consuming process of tuning ω_S over the excitation frequencies. However, it is anticipated that applying an ultrabroadband ns laser source for the ω_S beam will enable simultaneous excitation in a wide vibrational range, and hence capturing of multiplex SRS and CARS spectra in a short time, using a relatively simple and robust device.

Another recent development relevant to the sensitive and selective detection of explosives in the gas phase is the quartz-enhanced photoacoustic spectroscopy (QEPAS), a modification of conventional photoacoustic spectroscopy (PAS) [26]. PAS is well known as a very selective and sensitive detection technique for measuring gas concentrations down to the ppt (parts per trillion) level for specific species. However, in the past this technique required a bypass through a cell where the spectroscopic analysis has to be performed. In standard linear PAS, the gas in the cell is selectively excited by laser radiation tuned in resonance to a molecular vibrational or rotational absorption line. This is followed by vibrational–translational or rotational–translational energy transfer and generation of an acoustic wave that is detected by a microphone mounted on the cell walls. One significant disadvantage of conventional PAS is the background acoustic signals generated by the environment. Using a piezoelectric quartz tuning fork as detector, the exciting laser beam is focused between the two prongs of the tuning fork. Tuning the laser radiation on resonance with a vibrational line of a species to be investigated induces an acoustic wave which drives the tuning fork, and in the case of piezoelectric materials induces a piezo voltage in the tuning fork.

QEPAS has very recently been applied to explosive detection [27], allowing the development of an extremely compact and ultra-sensitive laser sensor. This technique is not limited to piezoelectric materials for the tuning fork since optical readout of a QEPAS device was demonstrated very recently. This allows, for the first time, fabrication of a QEPAS sensor device on a silicon chip applying well known techniques from integrated optics [28].

For gas phase detection, the combination of SRS and QEPAS, via single beam fs laser or broadband ns excitation, offers a novel approach and, up to now, nearly unexplored possibilities for engineering a new generation of multi-compound gas sensor devices that have high potential to find interesting applications in civil security. An additional advantage of these devices is the potential to combine them to build a system capable of detecting explosives in both the condensed and gas phases. Since the lasers for detecting explosives in both types of phases can be the same, it is feasible that just one system can be devised for their detection. This will have important consequences for the following reasons: it is well known that, on the one hand, some explosives have very low vapor pressure and environmental conditions (e.g., wind) make their detection very difficult, but, on the other hand, the vapor may form a thin film or particle layer on the surface of its container and, moreover, particles often adhere to the container or to the clothes of the person preparing, delivering or carrying the explosives [4]. In addition, the approach of laser

hole drilling in sealed samples followed by spectroscopic analysis will also offer new possibilities for *in situ* explosive detection. Highly sensitive, multi-compound stand-off detection systems in both the condensed and gas phases will be an important step forward in the means for defense against terrorism.

8.2.1 State of the Art Spectroscopic Methods

Laser spectroscopic methods all rely on the interaction of light and matter. One of the great advantages, in contrast to, for example, chemical analysis, is the fact that no sample preparation is necessary. Therefore, the performance of measurements online and *in situ*, and often in a stand-off configuration is possible. The methods are based on the different light–matter interactions and are highlighted in the following, together with some examples with respect to the application for the detection of explosives.

8.2.1.1 Absorption Spectroscopy

Conventional laser absorption spectroscopy is a method that allows the *in situ*, contact-free and nondestructive detection of gaseous substances. Especially in the MIR spectral region, selective and sensitive detection is possible, because nearly all molecules possess distinctive absorption lines there, that can be addressed with narrowband laser sources.

The major difficulty for the detection of explosives, however, is their low vapor pressure. For nitro-aromatic explosives, it ranges between 10^{-6} and 10^{-9} mbar, leading to a concentration at ambient conditions in the ppb to ppt range. In contrast, peroxide-based explosives, for example, triacetone triperoxide (TATP), which is an explosive favored by terrorists because of its high explosive force and relative simplicity in production, have much higher vapor pressures ($p = 7$ Pa for TATP [29] at ambient conditions), leading to concentrations in the range of tens of ppm (parts per million). The equilibrium concentrations for different explosives extracted from [30, 31] are given in Figure 8.2. It can clearly be seen, that the equilibrium concentrations for different explosives vary dramatically. So, not only the different optical properties, but also the different vapor pressures call for distinctive methods for single classes of explosives.

In the case of TATP direct absorption spectroscopy is possible in the MIR spectral region. Calculation of vibrational spectra has been performed by Oxley *et al.* [32] and Brauer *et al.* [33]. First results for a differential absorption LIDAR system for the stand-off detection of TATP by Pal *et al.* are very promising, and yield a sensing limit of 52 ppm for an absorption path of 30 cm [34].

However, for nitro-aromatics, methods have to be used to enable detection even with the much lower equilibrium concentrations at ambient conditions. This can be done using a pre-concentration set-up: the gas containing the explosive is led over a trap that consists of a cooled surface or a filter on which the molecules are adsorbed. Subsequently, the trap is heated; the molecules desorb and are present in a much higher concentration within the gas that is used to flush the trap. With this kind of

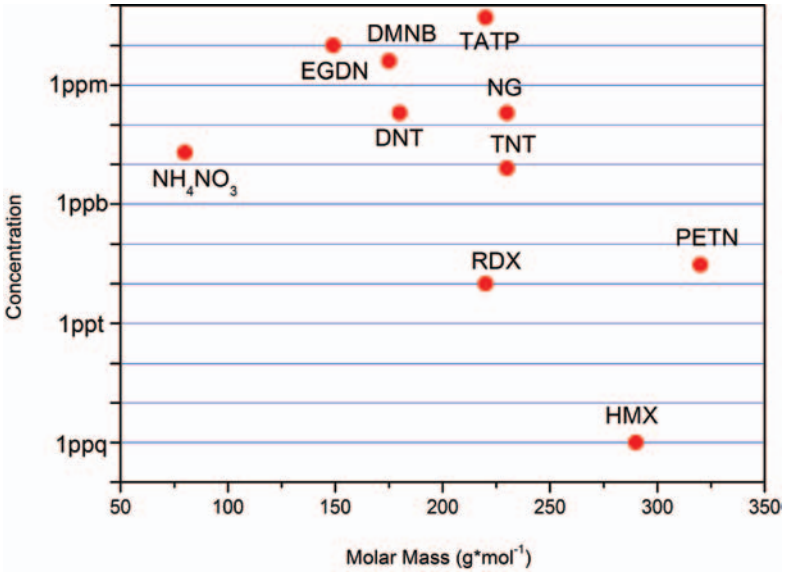

Figure 8.2 Equilibrium concentrations for different explosives as extracted from [29–31].

pre-concentration used for cavity ring down spectroscopy, detection of TNT in the ppt concentration range is expected [35].

8.2.1.2 Detection of Decomposition Products and Fragments

A different approach is to detect decomposition products rather than the explosive itself. The vapor phase concentration of the natural decay products can be several orders of magnitude higher than that of their parent explosive and the special composition of the vapors of the explosive and its decomposition products might be the key for the amazing sensitivity of canines for the detection of traces of explosives [36]. The concentrations of the decay products are dependent on the ambient temperature and pressure. Nadezhdinski *et al.* evaluated the possibility of detecting explosives by their natural decomposition products with tunable diode laser spectroscopy (TDLS) [37]. The decay products are smaller molecules which are easier to address with narrow line width tunable diode lasers than the explosives themselves, which are mostly broad-band absorbers.

Another possibility is the active production of fragments of the explosive, for example, by the use of photofragmentation. This technique is used in different spectral regions and the decomposition products can be detected with different techniques: laser induced fluorescence spectroscopy (LIF) [38], resonance enhanced multiphoton ionization (REMPI) [39–41], chemiluminescence [42] or absorption spectroscopy of the photofragments [6] (see Figure 8.3). Investigations have shown that a different ratio of NO/NO_2 production is present for explosives and non-energetic material, for example, plastics. Therefore, the possibility of the discrimination of

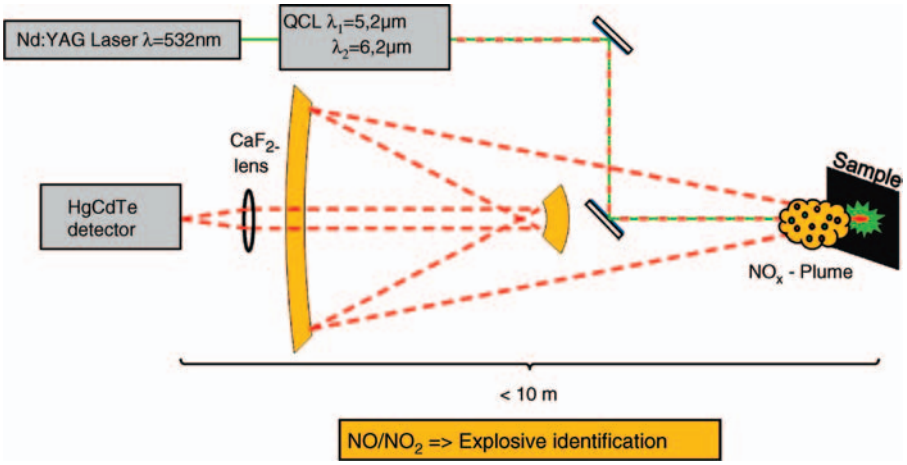

Figure 8.3 Stand-off configuration by photofragmentation followed by mid-infrared QCL detection of NOx fragments in the plume.

explosives and harmless materials is investigated by simultaneous absorption spectroscopy of the NO and NO_2 concentration after photofragmentation (Figure 8.4).

8.2.1.3 Laser Induced Breakdown Spectroscopy (LIBS)

Laser induced breakdown spectroscopy is an established method for surface investigation of bulk materials, for example, different kinds of metals and alloys [43]. With

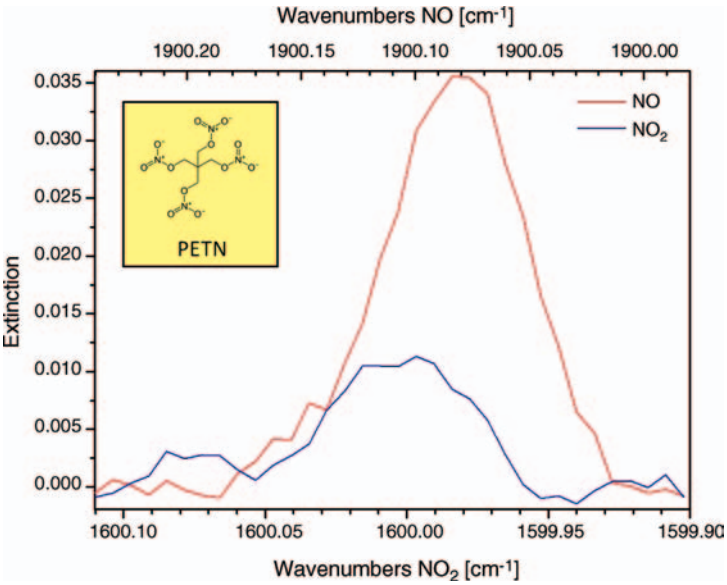

Figure 8.4 Mid-infrared QCL stand-off detection of NO and NO_2 after photofragmentation of the explosive PETN.

an intense laser pulse, a plasma is generated on the surface of a sample. This leads to different subsequent or simultaneous processes: plasma expansion, build-up of a shock wave, continuum emission (Bremsstrahlung), de-excitation of the ions, atoms and molecules through optical emission. These emission lines are detected for LIBS. Collisions represent a competing de-excitation process, inverse Bremsstrahlung and reabsorption alter the photon field. The spectral position of the emission lines, their intensity ratio and, for time-resolved LIBS, their decay rates, are parameters that are used for the identification of the substance.

LIBS is also discussed for the identification of landmines, explosives and biological warfare agents. Especially, the army research lab (ARL, USA) investigated the applicability of LIBS for the detection of bulk explosives and trace amounts on different surfaces [44–46]. The detection of trace amounts of explosives with LIBS is difficult because of matrix effects. These manifest not only in the simultaneous measurement of emission lines of the background material; as a consequence of different absorption behavior of the explosive and the matrix, different trace amounts of explosives lead to different plasma temperatures and, therefore, the intensities of lines associated with the explosive and their ratios are altered.

The surrounding atmosphere (gas composition and the pressure) and the efficiency of the collecting optics also have great influence on the signal. Therefore, data analysis is of great importance. Principal component analysis (PCA) [47] as well as partial least squares discriminant analysis (PLS-DA) [48] has proven to be powerful for the identification of explosives, even in the presence of matrix effects.

Effects of the surrounding gas atmosphere can be reduced by use of double-pulse excitation [49, 50]. With a first laser pulse, a plasma is generated which expands and locally reduces the air pressure. The plasma generated by a second, timely synchronized laser pulse then expands in a more rarefied gas atmosphere, thus the influence of the atmosphere on this plasma is reduced. Based on this technique, portable systems have been developed, for example, "TeleLis" by the Fraunhofer Institut für Lasertechnik (Germany) and "MP-LIBS" and "ST-LIBS" in the collaboration of the ARL and Ocean Optics. LIBS was also used to upgrade the function of a conventional mine prodder for the humanitarian search for anti-personnel mines. For this purpose fiber optics have been integrated into the prodder and the combination of LIBS with a miniaturized microchip laser and neural network for data analysis enables reliable identification of different mine casings [51, 52]. The concept for the fiber-based LIBS prodder system and experimental results from a field campaign for the identification of different casing materials in soil are shown in Figure 8.5.

8.2.1.4 **Raman Spectroscopy**

Raman spectroscopy relies on the inelastic scattering of photons. During this instantaneous process some energy is lost to the target molecule. Therefore, the scattered light possesses a different wavelength with respect to the incident. The change in wavelength corresponds to the differences in the vibrational energy levels of the target molecule, thus providing a means to identify it by its characteristic vibrational modes. A drawback of the method is the weak signal intensity since spontaneous Raman scattering has a very low cross section.

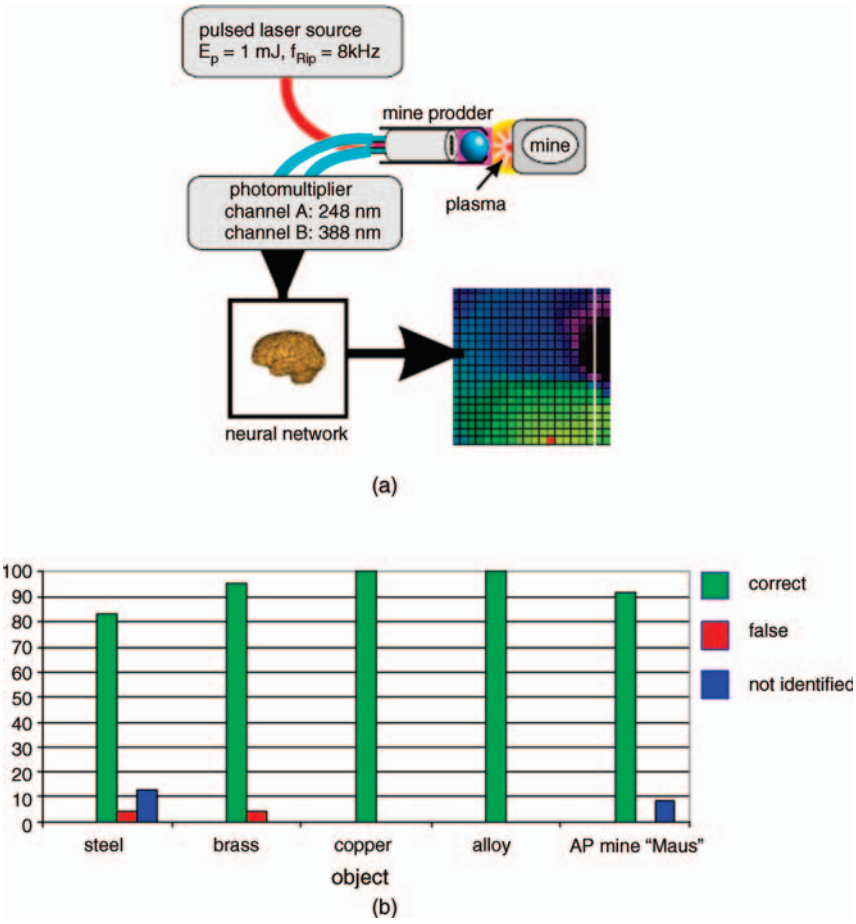

Figure 8.5 (a) Concept of a fiber coupled LIBS set-up for mine detection. (b) Results from field measurements for identification of different materials in soil by the LIBS prodder [52].

Lewis *et al.* investigated the Raman spectra of 32 different nitro-containing explosives and were able to group them into three classes with respect to their spectra: nitrates esters, nitro-aromatics and nitramines [53].

An advantage of the method is that it can be applied to small sample amounts and, in principle, through glass vials, transparent plastic bags and thin translucent materials. A limiting factor is the luminescence of background materials that might mask the weak Raman signals. Eliasson *et al.* demonstrated the noninvasive detection of hydrogen peroxide within plastic and glass containers [54]. Nagli *et al.* [55, 56] investigated the feasibility of different excitation wavelengths with respect to the strength of the Raman signal and suppression of luminescence. They found that with an excitation wavelength of $\lambda = 248\,\text{nm}$ it is possible to identify even Semtex, which was impossible with excitation at $\lambda = 532\,\text{nm}$ due to fluorescence [56].

Extensive work for the application of Raman spectroscopy to the detection of explosives has been done by FOI of Sweden [57]. Carter *et al.* demonstrated the detection of RDX, TNT, PETN and nitrate- and chlorate-containing materials in a stand-off configuration using CARS [58]. KNO_3, urea-nitrate and RDX were detected by Portnov *et al.* with backward coherent anti-Stokes Raman spectroscopy [25]. A mobile Raman stand-off system has been demonstrated by Wu *et al.* for the detection of chemicals [59]. Miniaturization enabled the set up of even portable stand-off systems, as described by Carter *et al.* [60], Ray *et al.* [8], and Sharma *et al.* [9].

There are some commercially available portable and hand-held devices relying on Raman spectroscopy. They were recently reviewed by Moore and Scharff with respect to their applicability for the detection of explosives [7]. They conclude that good Raman spectra are obtainable for white powder explosives. For colored explosives there are two issues to be noted: (i) the signal acquisition is more difficult because of fluorescence (thus demanding at least longer acquisition times) and (ii) materials that are highly absorbent for the excitation laser might pose a safety risk [7, 61].

Surface enhanced Raman spectroscopy (SERS) overcomes the low intensity levels of the signal by substantial enhancement of the effective Raman cross section of spatially confined molecules within high electromagnetic fields. Such fields are present at nanostructured noble metal surfaces. Practical application of this method is hampered by the fact that the analyte must be close to the metal surface. However, Stuart *et al.* have demonstrated the detection of a vapor phase chemical warfare agent simulant which might lead the way towards real-time detection [62]. Zhang *et al.* showed the detection of an Anthrax biomarker with SERS within the same time frame as with immunoassays [63].

8.2.1.5 **Photoacoustic Spectroscopy of Explosives**

Photoacoustic spectroscopy (PAS) is a very sensitive method for the measurement of gaseous species. Due to the modulated irradiation of the sample molecules with laser radiation, periodic absorption occurs, leading to the build-up of a sound wave which can be detected with a microphone. The signal depends mainly on the absorption coefficient of the molecule under investigation and on the incident laser power.

Patel recently summarized different gases for which photoacoustic sensing at ppb/sub-ppb level was achieved [64]. Investigation of the photoacoustic spectra of TNT and RDX have been performed by Prasad *et al.* [65]. The practical applicability of the method might be impaired by interferences with surrounding gases. Webber *et al.* analyze the problem of identifying explosives and warfare agents under real-world conditions [66] and Patel *et al.* report detection of TNT at a level of 0.1 ppb and TATP at $\sim$1 ppb by use of multiple wavelengths and reduced pressure [64, 67].

A very important step for the set-up of a miniaturized and rugged sensor was the invention of quartz-enhanced photoacoustic spectroscopy (QEPAS) [26]. For QEPAS, the conventional microphone is replaced by a commercially available quartz tuning fork and the excitation laser is focused between its prongs while modulated at the resonance frequency of the tuning fork (Figure 8.6). Upon absorption, a sound wave is formed which can be sensitively measured by the piezo current that is produced by the tuning fork.

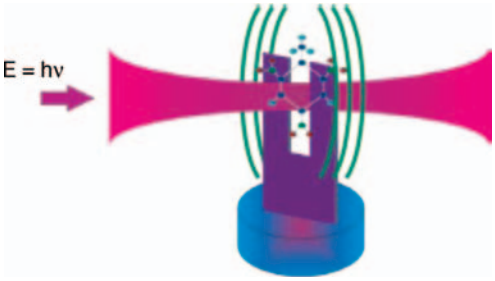

Figure 8.6 Concept of QEPAS.

As an example, the QEPAS method is demonstrated for detection of the explosive triacetone triperoxide (TATP). Figure 8.7a shows a FTIR spectrum of atmospheric water and for TATP under room temperature conditions. For the QEPAS measurements a pulsed external cavity quantum cascade laser operating between 1155 and 1220 cm^{-1} was used. The tuning position of the laser is marked within Figure 8.7b, here "water-free" detection of TATP is possible. The laser was amplitude modulated at a repetition rate of $f = 32.756$ kHz and a duty cycle of 5%, which results in an output power of $P = 5$ mW. The TATP was synthesized as described by Wolfenstein [68]. A small amount of TATP (<500 µg) was placed inside the cell and after a few seconds it could be detected via QEPAS. Figure 8.8a shows the response time for acetone detection while Figure 8.8b shows the recorded TATP spectrum. The two C−O stretch bands near $\tilde{\nu} = 1200\ cm^{-1}$ can clearly be seen. Assuming the equilibrium concentration of ~65 ppm for TATP in ambient air, a theoretical detection limit of 1 ppm TATP can be estimated with this set-up at ambient pressure and temperature conditions [69].

Based on this technique, a portable sensor with hand-held sensor head was designed, as shown in Figure 8.9. The QCL, together with all the electronics and coupling optics, is enclosed in a 19 inch box. The laser radiation is coupled into a hollow core fiber which is connected to the sensor head. There the light is focused

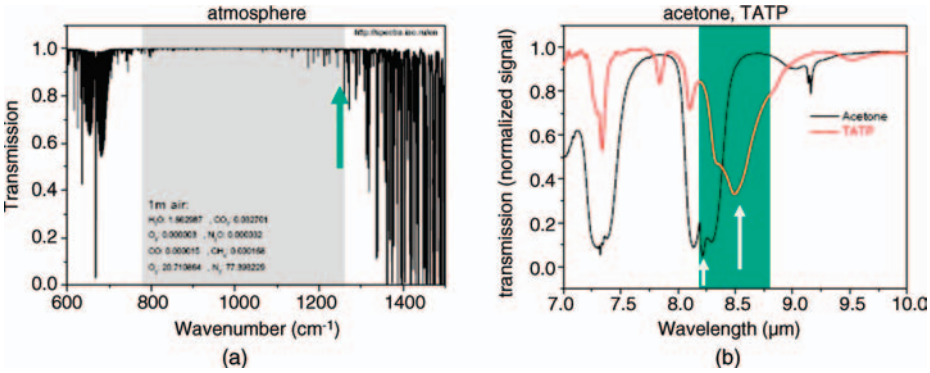

Figure 8.7 Calculated MIR spectra of the atmosphere including water vapor from Hitran database (a) and FTIR spectra for the explosive TATP and its precursor acetone (b). The arrow indicates the spectral position for "water free" detection of TATP.

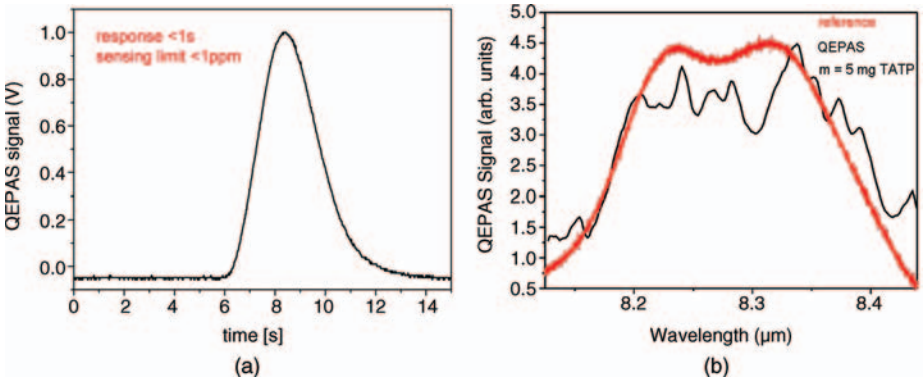

Figure 8.8 (a) Response time for acetone detection [69]. (b) Mid-infrared QEPAS recording of TATP [100].

between the prongs of the tuning fork. With a pump it is possible to generate a gas flow through the sensor head. First measurements with acetone (whose absorption can also be addressed with the QCL) are promising. The timely behavior of the QEPAS signal is shown in Figure 8.8a where the sensor head was positioned over a cloth moist with acetone and air was sucked through the sensor head.

Very recently, the optical readout of QEPAS was successfully demonstrated [28]. Thus, the design of the tuning forks is not restricted only to piezo-electric materials. In particular, this allows chip sensors for gas detection to be manufactured from silicon, making them extremely compact and ultra-sensitive. A design example is shown in Figure 8.10. Furthermore, this silicon technology allows mass production of a QEPAS chip.

8.2.1.6 **Cavity Ring Down Spectroscopy**

Cavity ring down spectroscopy (CRDS) is a very sensitive method for the determination of gas concentrations. For this method, the temporal behavior rather than the intensity of light that couples out of an optical cavity is measured. Therefore, fluctuations in laser intensity do not influence the accuracy of the measurement. For explosives, sub-ppb detection limits have been reported [70] using CRDS in the

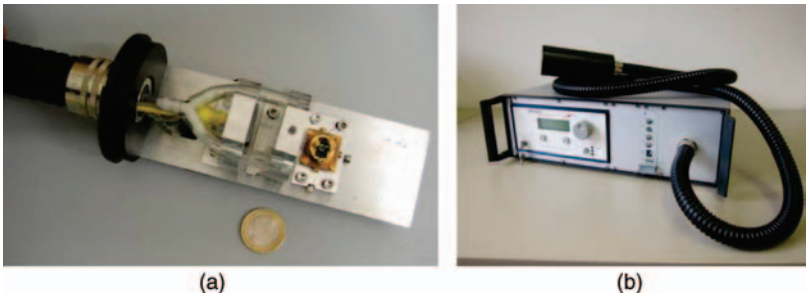

Figure 8.9 (a) QEPAS sensor head. (b) QEPAS hand-held system for explosive detection [100].

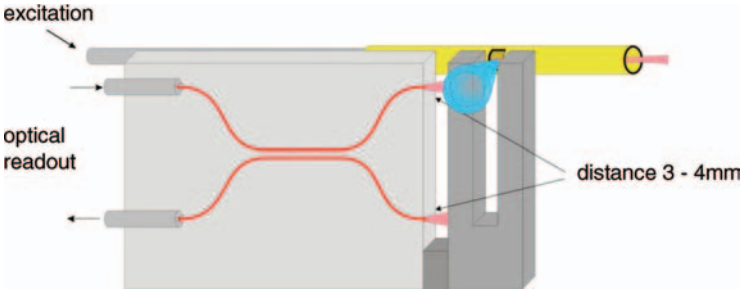

Figure 8.10 Chip-design of an optically integrated QEPAS sensor in silicon.

UV spectral range. Despite the high sensitivity they discuss the disadvantage of comparing poor selectivity in the UV range and possible interference with ozone, and propose the combination of their sensor with a second, less sensitive but more selective one [70]. Todd *et al.* use CRDS in the MIR spectral region with an optical parametric oscillator as laser source and report ppb level detection for TNT, TATP, RDX, PETN, and Tetryl, and anticipate the possibility of detecting 75 ppt TNT with pre-concentration [35]. Since the high reflectivity of the cavity mirrors is of the utmost importance, the adsorption of explosives on them has to be prevented. Therefore, heating of the optical cavity is needed.

8.2.2 Novel Approaches

Current optical stand-off and remote detection methods of trace amounts of samples suffer from several drawbacks. Especially, novel methods and recent developments from some research facilities in Israel and Europe have tried to overcome these drawbacks. Major novel development concentrates on miniaturization, simple laser excitation sources and multi-species analysis.

8.2.2.1 Femtosecond Coherent Control

The Weizmann Institute in Israel has pioneered the field of femtosecond coherent control of Raman scattering processes, in particular with connection to CARS [24, 71–76]. By using pulses shorter than the molecular vibration period, it is possible to coherently excite molecular vibrations with a single pulse. The main advantage of this approach is the simplicity of the source (a single, fixed frequency ultrashort laser oscillator), and the inherent spatial overlap of the different excitation wavelengths of the single beam, as necessary in conventional CARS schemes. Single-pulse excitation with broadband pulses by itself is unsuitable for spectroscopy, as it suffers from poor spectral resolution. Nonetheless, by controlling the phase and polarization of the single broadband pulse, it is possible both to restore the spectral resolution and to selectively excite a specific vibrational level of interest. Vibrational spectroscopy by a shaped femtosecond pulse was experimentally demonstrated for both microscopic [71] and stand-off remote detection application [24, 76], and, in particular, selective excitation of a given Raman level out

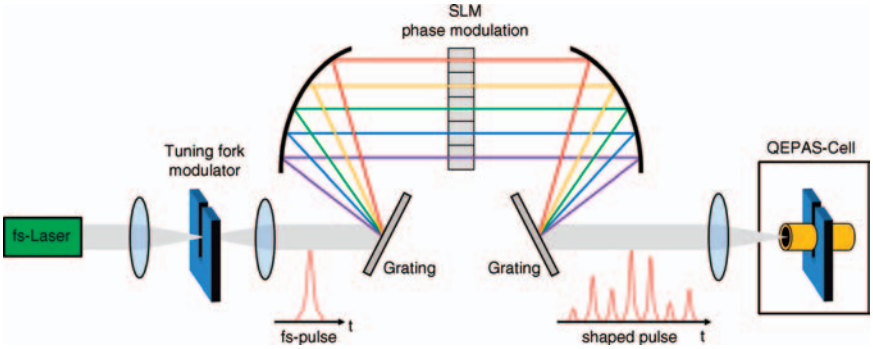

Figure 8.11 Femtosecond pulse shaping and QEPAS signal detection.

of the several vibrational levels that lie within the excitation pulse bandwidth [71]. In the work reported in Refs. [24, 76] a single-beam, stand-off (>10 m) detection and identification of various materials including minute amounts of explosives under ambient light conditions was demonstrated. It was obtained by multiplex CARS using a single femtosecond phase-shaped laser pulse. The strong nonresonant background was exploited for amplification of the backscattered resonant CARS signals by employing a homodyne detection scheme. It is thus demonstrated that this simple and highly sensitive spectroscopic technique has a potential for detection applications of hazardous materials, especially when QEPAS is used for signal detection [77]. The basic concept for such an experiment is shown in Figure 8.11. Here, the first tuning fork is used for the intensity modulation of the laser beam while the QEPAS signal detection is performed by the second tuning fork in the cell.

In addition, the Ben-Gurion University in Israel has pioneered the application of several methods for remote detection of various compounds. These methods include blue shifted LP/LIF [78–81], LIBS [82, 83] and the method of detection of particles of explosives via B-CARS, applying relatively narrowband nanosecond laser pulses [25], that has been extended to remote detection applying femtosecond pulses [24, 76]. It has been demonstrated that visible CARS in the nanosecond time domain allows favorable detection compared to spontaneous Raman spectroscopy, which has been applied for stand-off detection but with limited success due to the inherently weak Raman scattering. These first measurements were conducted at short distances, but the observed enhancement of several orders of magnitude of CARS versus spontaneous Raman indicate that the distance can be scaled to stand-off detection, in particular by applying higher power lasers. It was estimated that even by using energies of 10 mJ of the narrowband nanosecond pump and Stokes beams, detection of samples from distances of meters to hundreds of meters will be possible, depending on the specific compound.

8.2.2.2 THz-Spectroscopy

The terahertz spectral region is of great interest for the detection of drugs, hazardous materials and weapons since the radiation can penetrate easily through many nonmetallic, nonpolar materials. Explosives, pharmaceuticals and drugs show

characteristic spectra and can selectively be detected with THz radiation. Shen *et al.* show the detection of explosives via THz imaging [84] and Federici *et al.* give an excellent overview of THz imaging and sensing for security applications [85]. With increasing availability of powerful sources and detectors for the THz spectral region, scanning velocities reach practical values. The energy level of the radiation is harmless for people; however, broad application for passenger screening is hindered by ethical concerns. Despite this limitation, wide fields of application, for example, postal screening, are open for this promising technique.

8.2.2.3 **Photonic Ring Resonator Sensors**

The detection of various species in the gaseous or fluid phases by using silicon photonic microring resonators is an emerging sensing technology increasingly gaining recognition due to the high sensitivity, mechanical stability, robustness and cost efficiency of these sensors. Their miniaturized design and compatibility with fiber networks or other photonic devices makes them suitable for field operation, which is an important feature for real-world applicability.

Microring resonator based sensors are commonly used for different biological and chemical applications [86–91]. Combining this sensing technology with specifically synthesized receptors, the molecular identification of hazardous substances like nitroaromatic explosives becomes possible. Trinitrotoluene (TNT), for example, belongs to this class of explosives and is the most commonly used compound for military and industrial purposes. It possesses a good thermal and chemical stability, enabling safe handling, and, due to its widespread availability, has been used in several terrorist incidents. Due to its very low vapor pressure in the gas phase, ($\sim$5 ppb [29, 92] at ambient conditions), the detection of TNT still remains one of the challenging tasks.

A new sensor concept consisting of a photonic silicon microring resonator sensitized with receptor molecules based on triphenylene-ketals, which enables the detection of TNT in the low parts per billion range, has been recently developed by the Fraunhofer Heinrich Hertz Institute, Goslar, in collaboration with the Johannes Gutenberg-University Mainz, both in Germany [93]. Figure 8.12 shows a scanning electron microscope (SEM) image of the silicon nitride microring resonator. The ring resonator designed in the form of a race track is positioned close to a straight waveguide that couples light in and out of the resonator via evanescent tunneling, since both waveguides are only 1 μm apart.

The resonance condition of the ring resonator is given by $m\lambda = n_{\text{eff}} 2\pi r$ where m is an integer, n_{eff} is the effective refractive index, and r is the microring radius. As can be seen, the resonant wavelength of the ring resonator is directly proportional to the effective index of refraction and to the circumference of the ring. The light evanescing into the ring returns to the straight waveguide and exhibits a phase shift (which is exactly π at resonance) relative to the light propagating down the waveguide. Due to the destructive interference caused by the phase shift, the resonance is measured as a dip in the transmitted light intensity. Highly sensitive detection of molecular species using this photonic device is achieved by monitoring the resonance shift of the ring resonator, induced by changes in the local refractive index at the microring surface

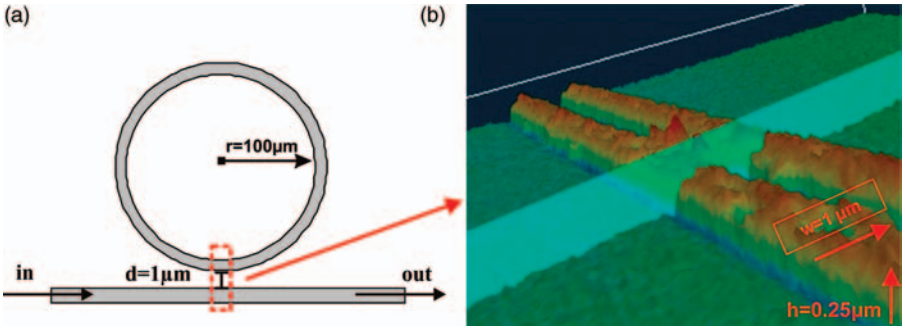

Figure 8.12 (a) Concept of a photonic microring resonator. (b) SEM image of the silicon nitride microring resonator and the coupling area between the ring and the straight waveguide [93].

that lead to changes in the effective refractive index of the guided mode inside the waveguides [94]. An increase in effective index causes a shift of the resonance towards a longer wavelength, whereas a decrease in effective index causes a shift towards a shorter wavelength.

However, this detection modality is not selective for a special species. Selectivity is gained only by functionalizing the sensor surface with specially developed coatings or receptor molecules. Therefore, the surface of the microring, that is, the sensor chip, was coated with a receptor film based on triphenylene-ketals that enables selective binding of TNT molecules in a reversible manner and via a key–lock-principle. The general synthesis of these molecules is described in detail by Schopohl *et al.* [95]. When TNT molecules are adsorbed onto the receptor layer an intensively colored intercalation complex is formed, exhibiting a charge-transfer band in the spectral region between 420 and 650 nm. In addition to the specific color change, the refractive index within the layer is changed, influencing the propagation of the light within the microring and leading to resonance shifts that can be measured by scanning the wavelength.

First investigations regarding the optical detection of the intercalation between receptor and TNT were performed via evanescent field spectroscopy by using a bare silica multimode fiber coated with the synthesized receptor molecules [96]. The sensing of species using this spectroscopic method is based on the interaction between the light guided within an optical waveguide, for example, fiber, and the surrounding medium, which occurs upon total internal reflection at the interface between two media with different index of refraction. For this purpose, a frequency doubled passively Q-switched $Cr^{4+}:Nd^{3+}:YAG$ microchip laser (emission wavelength $\lambda_1 = 1064$ nm and frequency doubled to $\lambda_2 = 532$ nm) was used as light source, enabling the simultaneous measurement at both wavelengths and showing the wavelength sensitivity and selectivity of this sensor concept, since changes in the signal intensity were measured only by the interaction of the green light with TNT, whereas the intensity of the infrared light remained constant. The registered changes in the signal can be attributed to the formation of the colored charge-transfer complex between the receptor and TNT molecules that has its absorption

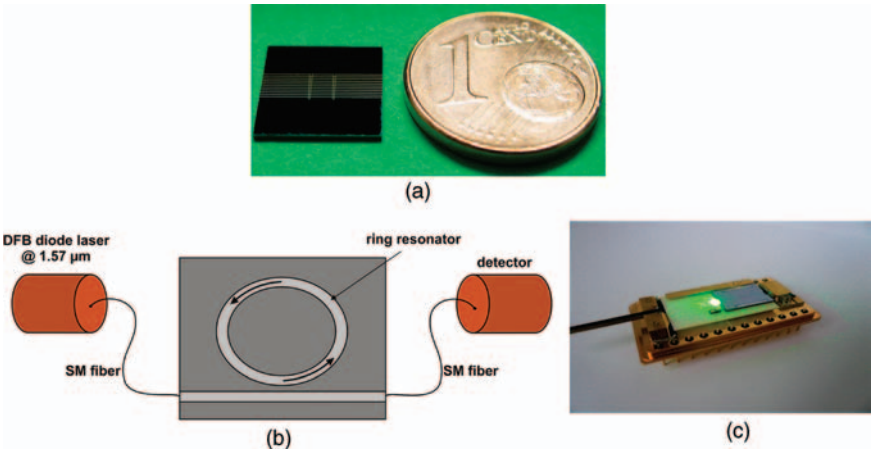

Figure 8.13 (a) Silicon ring resonator chip. (b) Schematic of the photonic ring resonator sensor. (c) Optically-integrated sensor chip.

peak around 532 nm [96]. However, even though this sensor concept allows the identification of TNT, the implementation of optical fibers as detection devices is not very convenient for field applications, because their sensitivity depends on the penetration depth of the evanescent field, which is connected to the acceptance and additionally the coupling angle of the fiber. Furthermore, due to the unknown modal distribution of the light within the fiber, changes in the transmitted intensity can occur when the fiber is bent or moved from its initial position, so that the determination of the concentration of absorbed molecules requires subsequent calibration measurements.

The situation is different for ring resonators where the whole assembly is fiber coupled and the concentration of species is determined by measuring the shift in the resonance dip. Figure 8.13b shows the experimental set-up which includes a standard telecommunication fiber coupled DFB laser diode with central wavelength at $\lambda = 1.57\,\mu m$, the microring resonator sensor and a detector for measuring the transmitted intensity through the sensor. The linear waveguide is coupled to the laser source and detector, respectively, via two single mode fibers.

The sensor surface is coated with the specially designed receptor molecules using the electrospray technique [97, 98]. By the incorporation of TNT into the receptor molecules, changes in the effective refractive index occur, inducing a shift of the microring resonant wavelength. The resultant shift can be accurately measured by scanning the wavelength around 1.57 µm, allowing in this way the estimation of the TNT concentration in the gaseous medium surrounding the sensor. Figure 8.14 shows typical resonance spectra of the microring resonator sensor measured at different concentrations of TNT under ambient conditions. As can be seen, the curves are consistently shifted with larger TNT concentrations. The limit of detection for TNT is in the range of 0.5 ppb and can be further enhanced by increasing the Q factor of the ring resonator.

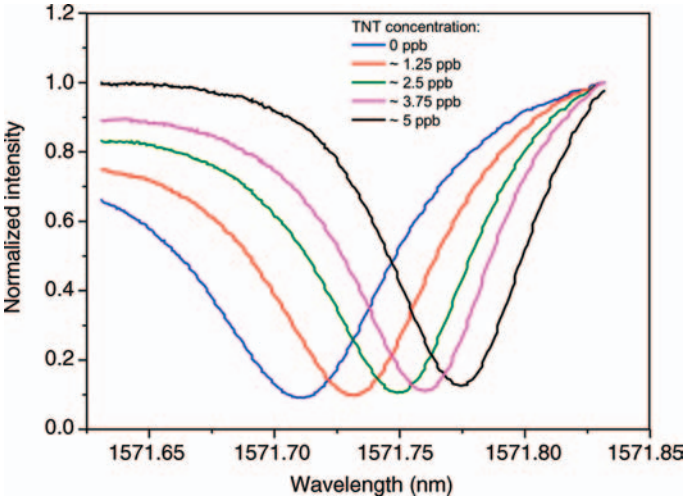

Figure 8.14 Shift of the resonance wavelength for different concentrations of the explosive TNT.

The adsorption of the TNT molecules onto the receptor layer is a reversible process, so that real time measurements can be performed. After contamination with the analyte, the sensor has to be flushed with air for desorption and can be reused within a few seconds, since the dip returns to its original position [93].

Since this sensor device is fiber coupled, it can easily be used as a hand-held device or adapted to a security gate for TNT detection in the gas phase, see Figure 8.15. The graph in Figure 8.15 shows the shift of the resonant wavelength when a person is passing the air lock security gate with and without TNT [101]. In addition, the multiplexing of several ring resonators coated with different kinds of receptors allows multi-species detection to be simplified [99]. Mass production of the sensor chips is feasible by applying standard silicon processing technology for manufacturing the sensor chips.

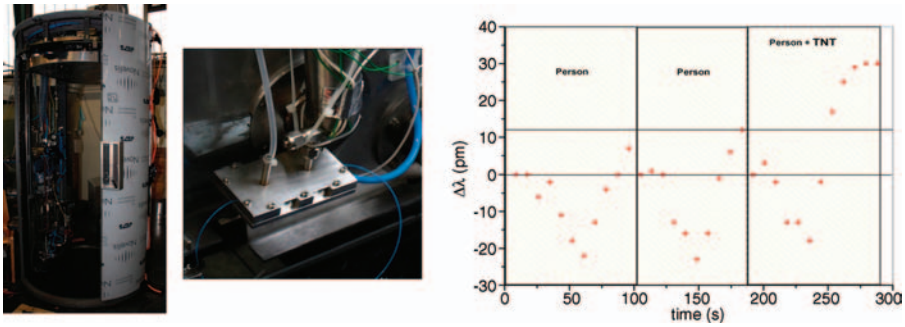

Figure 8.15 Detection of the explosive TNT in a security gate by the ring resonator sensor device [101].

8.3 Summary

Different spectroscopic methods that can be applied for the detection of explosives have been described, taking into account their specific advantages for the identification of special classes of hazardous materials. Some first generation sensing devices that are currently applied to sense explosives have been highlighted. The discussion shows that one method will not cover the identification of several explosives at the same time. Sensor fusion will be the next step to develop a spectroscopic system that allows multi-component analysis. The most important further steps besides this will be the development of novel laser sources that allow selective excitation over a wide range of molecules. In this context, shaped femtosecond laser excitation will provide a new and very interesting tool because broadband excitation in combination with pulse phase modulation will allow selective molecular excitation. On the other hand miniaturization will drive spectroscopic techniques towards applications. In particular, silicon photonics will offer new and very interesting possibilities in this field. In this context photoacoustics with microtuning forks and microring resonators will have a high potential for optically-integrated and sensitive photonic sensor devices of the next generation.

References

1 Rahal, A.Gh. and Moussa, L.A. (2011) Degradation of 2,4,6-trinitrotoluene (TNT) by soil bacteria isolated from TNT contaminated soil. *Aust. J. Basic Appl. Sci*, **5** (2), 8–17.

2 Neumann, H.-G., van Dorp, C., and Zwirner-Baier, I. (1995) The implications for risk assessment of measuring the relative contribution to exposure from occupation, environment and lifestyle: hemoglobin adducts from amino- and nitro-arenes. *Toxicol. Lett.*, **82/83**, 771–778.

3 Moore, D.S. (2004) Instrumentation for trace detection of high explosives. *Rev. Sci. Instrum.*, **75**, 2499–2512.

4 Napadensky, H.S. (ed.) (2004) *Existing and Potential Standoff Explosives Detection Techniques*, The National Academies Press, Washington, D.C.

5 Petryk, M.W.P. (2007) Promising spectroscopic techniques for the portable detection of condensed-phase contaminants on surfaces. *Appl. Spectrosc. Rev.*, **42**, 287–353.

6 Bauer, C., Sharma, A.K., Willer, U., Burgmeier, J., Braunschweig, B., Schade, W., Blaser, S., Hvozdara, L., Müller, A., and Holl, G. (2008) Potentials and limits of mid-infrared laser spectroscopy for the detection of explosives. *Appl. Phys. B*, **92**, 327–333.

7 Moore, D.S. and Scharff, R.J. (2009) Portable Raman explosives detection. *Anal. Bioanal. Chem.*, **393**, 1571–1578.

8 Ray, M.D., Sedlacek, A.J., and Wu, M. (2000) Ultraviolet mini-Raman lidar for stand-off, in situ identification of chemical surface contaminants. *Rev. Sci. Instrum.*, **71**, 3485–3489.

9 Sharma, S.K., Misra, A.K., Lucey, P.G., Angel, S.M., and Mckay, C.P. (2006) Pulsed Raman spectroscopy of inorganic and organic materials to a radial distance of 100 meters. *Appl. Spectrosc.*, **60**, 871–876.

10 Gaft, M. and Nagli, L. (2007) Standoff laser-based spectroscopy for explosives detection. *Proc. SPIE*, **6739**, 673903.

11 Bloembergen, N. (1967) The stimulated Raman effect. *Am. J. Phys.*, **35**, 989.

12 Valentini, J.J. (1987) *Laser Spectroscopy and its Applications*, vol. 11 (eds L.J. Radziemski, R.W. Solarz, and J.A.

Paisner), Optical Science and Engineering Series, Marcel Dekker, New York, pp. 507–564.
13 Nibler, J.W. and Knighten, G.V. (1979) *Raman Spectroscopy of Gases and Liquids* (ed. A. Weber), Springer, Berlin, pp. 253.
14 Lanzisera, D.V. and Valentini, J.J. (1997) State-to-state dynamics of the $H + CDCl_3(v1''=1) \rightarrow HD(v',j') + CCl_3$ reaction. *J. Phys. Chem. A*, **101**, 6496–9503.
15 Owyoung, A. (1977) Sensitivity limitations for CW stimulated Raman spectroscopy. *Opt. Commun.*, **22**, 323–328.
16 Levine, B.F., Shank, C.V., and Heritage, J.P. (1979) Surface vibrational spectroscopy using stimulated Raman scattering. *IEEE J. Quantum. Electron.*, **15**, 1418–1432.
17 Kukura, P., McCamant, D.W., and Mathies, R.A. (2007) Femtosecond stimulated raman spectroscopy. *Annu. Rev. Phys. Chem.*, **58**, 461–488.
18 Freudiger, C.W., Min, W., Saar, B.G., Lu, S., Holtom, G.R., He, C., Tsai, J.C., Kang, J.X., and Xie, X.S. (2008) Label-free biomedical imaging with high sensitivity by stimulated raman scattering microscopy. *Science*, **322**, 1857–1861.
19 Grisch, F., Pealat, M., Bouchardy, P., Taran, J.P., Bar, I., Heflinger, D., and Rosenwaks, S. (1991) Real time diagnostics of detonation products from lead azide using coherent anti-stokes Raman scattering. *Appl. Phys. Lett.*, **59**, 3516–3518.
20 Zumbusch, A., Holton, G.R., and Xie, X.S. (1999) Three-dimensional vibrational imaging by coherent anti-stokes raman scattering. *Phys. Rev. Lett.*, **82**, 4142–4145.
21 Hashimoto, M. and Araki, T. (2000) Molecular vibration imaging in the fingerprint region by use of coherent anti-Stokes Raman scattering microscopy with a collinear configuration. *Opt. Lett.*, **25**, 1768–1770.
22 Petrov, G.I., Yakovlev, V.V., Sokolov, A.V., and Scully, M.O. (2005) Detection of Bacillus subtilis spores in water by means of broadband coherent anti-stokes Raman spectroscopy. *Opt. Expr.*, **13**, 9537–9542.
23 Li, H., Harris, D.A., Xu, B., Wrzesinski, P.J., Lozovoy, V.V., and Dantus, M. (2008) Coherent mode-selective Raman excitation towards standoff detection. *Opt. Expr.*, **16**, 5499–5504.
24 Katz, O., Natan, A., Silberberg, Y., and Rosenwaks, S. (2008) Standoff detection of trace amounts of solids by nonlinear Raman spectroscopy using shaped femtosecond pulses. *Appl. Phys. Lett.*, **92**, 171116.
25 Portnov, A., Rosenwaks, S., and Bar, I. (2008) Detection of particles of explosives via backward coherent anti-Stokes Raman spectroscopy. *Appl. Phys. Lett.*, **93**, 041115.
26 Kosterev, A.A., Bakhirkin, Y.A., Curl, R.F., and Tittel, F.K. (2002) Quartz-enhanced photoacoustic spectroscopy. *Opt. Lett.*, **27**, 1902–1904.
27 Bauer, C., Willer, U., Lewicki, R., Pohlkötter, A., Kosterev, A., Kosynkin, D., Tittel, F.K., and Schade, W. (2009) A Mid-infrared QEPAS sensor device for TATP detection. *J. Phys. Conf. Ser.*, **157**, 012002.
28 Köhring, M., Pohlkötter, A., Willer, U., Angelmahr, M., and Schade, W. (2010) Tuning fork enhanced interferometric photoacoustic spectroscopy: a new method for trace gas analysis. *Appl. Phys. B-Lasers O.*, **102**, 133–139.
29 Oxley, J.C., Smith, J.L., Shinde, K., and Moran, J. (2005) Determination of the vapor density of triacetone triperoxide (TATP) using a gas chromatography headspace technique. *Propell. Explos. Pyrot.*, **30**, 127–130.
30 Moore, D. (2007) Recent advances in trace explosives detection instrumentation. *Sens Imaging*, **8**, 9–38.
31 Thiesan, L., Hannum, D., Murray, D.W., and Parmeter, J.E. (2005) Survey of Commercially Available Explosives Detection Technologies and Equipment 2004, http://www.ncjrs.gov/App/Publications/abstract.aspx?ID=208861.
32 Oxley, J., Smith, J., Brady, J., Dubnikova, F., Kosloff, R., Zeiri, L., and Zeiri, Y. (2008) Raman and infrared fingerprint spectroscopy of peroxide-based explosives. *Appl. Spectrosc.*, **62**, 906–915.

33 Brauer, B., Dubnikova, F., Zeiri, Y., Kosloff, R., and Gerber, R.B. (2008) Vibrational spectroscopy of triacetone triperoxide (TATP): Anharmonic fundamentals, overtones and combination bands. *Spectrochim. Acta A*, **71**, 1438–1445.

34 Pal, A., Clark, C.D., Sigman, M., and Killinger, D.K. (2009) Differential absorption lidar CO2 laser system for remote sensing of TATP related gases. *Appl. Opt.*, **48**, B145–B150

35 Todd, M.W., Provencal, R.A., Owano, T.G., Paldus, B.A., Kachanov, A., Vodopyanov, K.L., Hunter, M., Coy, S.L., Steinfeld, J.I., and Arnold, J.T. (2002) Application of mid-infrared cavity-ringdown spectroscopy to trace explosives vapor detection using a broadly tunable (6–8 μm) optical parametric oscillator. *Appl. Phys. B-Lasers O.*, **75**, 367–376.

36 Furton, K.G. and Myers, L.J. (2001) The scientific foundation and efficacy of the use of canines as chemical detectors for explosives. *Talanta*, **54**, 487–500.

37 Nadezhdinskii, A.I., Ponurovskii, Y.Y., and Stavrovskii, D.B. (2008) Non-contact detection of explosives by means of a tunable diode laser spectroscopy. *Appl. Phys. B-Lasers O.*, **90**, 361–364.

38 Wu, D., Singh, J.P., Yueh, F.Y., and Monts, D.L. (1996) 2,4,6-Trinitrotoluene detection by laser-photofragmentation-laser-induced fluorescence. *Appl. Opt.*, **35**, 3998–4003.

39 Cabalo, J. and Sausa, R. (2005) Trace detection of explosives with low vapor emissions by laser surface photofragmentation-fragment detection spectroscopy with an improved ionization probe. *Appl. Opt.*, **44**, 1084–1091.

40 Heflinger, D., Arusi-Parpar, T., Ron, Y., and Lavi, R. (2002) Application of a unique scheme for remote detection of explosives. *Opt. Commun.*, **204**, 327–331.

41 Swayambunathan, V., Singh, G., and Sausa, R.C. (1999) Laser photofragmentation-fragment detection and pyrolysis-laser-induced fluorescence studies on energetic materials. *Appl. Opt.*, **38**, 6447–6454.

42 Monterola, M., Smith, B., Omenetto, N., and Winefordner, J. (2008) Photofragmentation of nitro-based explosives with chemiluminescence detection. *Anal. Bioanal. Chem.*, **391**, 2617–2626.

43 Vadillo, J.M. and Laserna, J.J. (2004) Laser-induced plasma spectrometry: truly a surface analytical tool. *Spectrochim. Acta B*, **59**, 147–161.

44 Gottfried, J.L., De Lucia, F.C. Jr., Munson, C.A., and Miziolek, A.W. (2008) Strategies for residue explosives detection using laser-induced breakdown spectroscopy. *J. Anal. Atom. Spectrom.*, **23**, 205–216.

45 Lopez-Moreno, C., Palanco, S., Laserna, J.J., De Lucia, F.C. Jr., Miziolek, A.W., Rose, J., Walters, R.A., and Whitehouse, A.I. (2006) Test of a stand-off laser-induced breakdown spectroscopy sensor for the detection of explosive residues on solid surfaces. *J. Anal. Atom. Spectrom.*, **21**, 55–60.

46 De Lucia, F.C. Jr., Samuels, A.C., Harmon, R.S., Walters, R.A., McNesby, K.L., LaPointe, A., Winkel, R.J. Jr., and Miziolek, A.W. (2005) Laser-induced breakdown spectroscopy (LIBS): a promising versatile chemical sensor technology for hazardous material detection. *Sensor J. IEEE*, **5**, 681–689.

47 De Lucia, F.C. Jr., Gottfried, J.L., Munson, C.A., and Miziolek, A.W. (2007) Double pulse laser-induced breakdown spectroscopy of explosives: Initial study towards improved discrimination. *Spectrochim. Acta B*, **62**, 1399–1404.

48 De Lucia, F.C. Jr., Gottfried, J.L., Munson, C.A., and Miziolek, A.W. (2008) Multivariate analysis of standoff laser-induced breakdown spectroscopy spectra for classification of explosive-containing residues. *Appl. Opt.*, **47**, G112–G121

49 Gottfried, J.L., De Lucia, F.C. Jr., Munson, C.A., and Miziolek, A.W. (2007) Double-pulse standoff laser-induced breakdown spectroscopy for versatile hazardous materials detection. *Spectrochim. Acta B*, **62**, 1405–1411.

50 Colao, F., Lazic, V., Fantoni, R., and Pershin, S. (2002) A comparison of single and double pulse laser-induced

breakdown spectroscopy of aluminum samples. *Spectrochim. Acta B*, **57**, 1167–1179.

51 Schade, W., Bauer, C., Orghici, R., Waldvogel, S., and Börner, S. (2008) Miniaturized photonic sensor devices for real time explosive detection, in *Detection of Liquid Explosives and Flammable Agents in Connection with Terrorism* (eds A. Kuznetsov, O.I. Osetrov, and H. Östmark), Springer Science + Business Media B.V., Dordrecht, pp. 215–227.

52 Bohling, C., Scheel, D., Hohmann, K., Schade, W., Reuter, M., and Holl, G. (2006) Fiber-optic laser sensor for mine detection and verification. *Appl. Opt.*, **45**, 3817–3825.

53 Lewis, I.R., Daniel, N.W., and Griffiths, P.R. (1997) Interpretation of Raman spectra of nitro-containing explosive materials. Part I: group frequency and structural class membership. *Appl. Spectrosc.*, **51**, 1854–1867.

54 Eliasson, C., Macleod, N.A., and Matousec, P. (2007) Noninvasive detection of concealed liquid explosives using Raman spectroscopy. *Anal. Chem.*, **79**, 8185–8189.

55 Nagli, L., Gaft, M., Fleger, Y., and Rosenbluh, M. (2008) Absolute Raman cross-sections of some explosives: Trend to UV. *Opt. Mater.*, **30**, 1747–1754.

56 Gaft, M. and Nagli, L. (2008) UV gated Raman spectroscopy for standoff detection of explosives. *Opt. Mater.*, **30**, 1739–1746.

57 Johansson, I., Norrefeldt, M., Pettersson, A., Wallin, S., and Östmark, H. (2008) Close-range and standoff detection and identification of liquid explosives by means of raman spectroscopy, in *Detection of Liquid Explosives and Flammable Agents in Connection with Terrorism* (eds A. Kuznetsov, O.I. Osetrov, and H. Östmark), Springer Science + Business Media B.V., Dordrecht, pp. 143–153.

58 Carter, J.C., Angel, S.M., Lawrence-Snyder, M., Scaffidi, J., Whipple, R.E., and Reynolds, J.G. (2005) Standoff detection of high explosive materials at 50 meters in ambient light conditions using a small raman instrument. *Appl. Spectrosc.*, **59**, 769–775.

59 Wu, M., Ray, M., Fung, K.H., Ruckman, M.W., Harder, D., and Sedlacek, A.J. (2000) Stand-off detection of chemicals by UV Raman spectroscopy. *Appl. Spectrosc.*, **54**, 800–806.

60 Carter, J.C., Scaffidi, J., Burnett, S., Vasser, B., Sharma, S.K., and Angel, S.M. (2005) Stand-off Raman detection using dispersive and tunable filter based systems. *Spectrochim. Acta A*, **61**, 2288–2298.

61 Harvey, S.D., Peters, T.J., and Wright, B.W. (2003) Safety considerations for sample analysis using a near-infrared (785nm) raman laser source. *Appl. Spectrosc.*, **57**, 580–587.

62 Stuart, D.A., Biggs, K.B., and Van Duyne, R.P. (2006) Surface-enhanced Raman spectroscopy of half-mustard agent. *Analyst*, **131**, 568–572.

63 Zhang, X., Young, M.A., Lyandres, O., and van Duyne, R.P. (2005) Rapid detection of an anthrax biomarker by surface-enhanced Raman spectroscopy. *J. Am. Chem. Soc.*, **127**, 4484–4489.

64 Patel, C.K.N. (2008) Laser photoacoustic spectroscopy helps fight terrorism: High sensitivity detection of chemical Warfare Agent and explosives. *Eur. Phys. J. - Spec. Top.*, **153**, 1–18.

65 Prasad, R.L., Prasad, R., Bhar, G.C., and Thakur, S.N. (2002) Photoacoustic spectra and modes of vibration of TNT and RDX at CO_2 laser wavelengths. *Spectrochim. Acta A*, **58**, 3093–3102.

66 Webber, M.E., Pushkarsky, M., Patel, C., and Kumar, N. (2005) Optical detection of chemical warfare agents and toxic industrial chemicals: Simulation. *J. Appl. Phys.*, **97**, 113101.

67 Dunayevskiy, I., Tsekoun, A., Prasanna, M., Go, R., and Patel, C.K.N. (2007) High-sensitivity detection of triacetone triperoxide (TATP) and its precursor acetone. *Appl. Opt.*, **46**, 6397–6404.

68 Wolfenstein, R. (1895) Über die einwirkung von wasserstoff superoxyd auf aceton und mesityloxyd. *Chem. Ber.*, **28**, 2265–2269.

69 Willer, U. and Schade, W. (2009) Photonic sensor devices for explosive detection. *Anal. Bioanal. Chem.*, **395**, 275–282.

70 Ramos, C. and Dagdigian, P.J. (2007) Detection of vapors of explosives and

explosive-related compounds by ultraviolet cavity ringdown spectroscopy. *Appl. Opt.*, **46**, 620–627.

71 Dudovich, N., Oron, D., and Silberberg, Y. (2002) Single-pulse coherently controlled nonlinear Raman spectroscopy and microscopy. *Nature*, **418**, 512–514.

72 Oron, D., Dudovich, N., Yelin, D., and Silberberg, Y. (2002) Quantum control of coherent anti-Stokes Raman processes. *Phys. Rev. A*, **65**, 043408.

73 Dudovich, N., Oron, D., and Silberberg, Y. (2002) Single-pulse phase-contrast nonlinear raman spectroscopy. *Phys. Rev. Lett.*, **89**, 273001.

74 Dudovich, N., Oron, D., and Silberberg, Y. (2003) Femtosecond phase-and-polarization control for background-free coherent anti-stokes raman spectroscopy. *Phys. Rev. Lett.*, **90**, 213902.

75 Dudovich, N., Oron, D., and Silberberg, Y. (2003) Single-pulse coherent anti-Stokes Raman spectroscopy in the fingerprint spectral region. *J. Chem. Phys.*, **118**, 9208.

76 Katz, O., Natan, A., Rosenwaks, S., and Silberberg, Y. (2008) Shaped femtosecond pulses for remote chemical detection. *Opt. Photonics News*, **19**, 47.

77 Schippers, W., Gershnabel, E., Burgmeier, J., Katz, O., Willer, U., Averbukh, I.Sh., Silberberg, Y., and Schade, W. (2011) Stimulated Raman rotational photoacoustic spectroscopy using a quartz tuning fork and femtosecond excitation. *Appl. Phys. B*, **105**, 203–211.

78 Daugey, N., Shu, J., Bar, I., and Rosenwaks, S. (1999) Nitrobenzene detection by one-color laser-photolysis/laser-induced fluorescence of NO (v'=0–3). *Appl. Spectrosc.*, **53**, 57–64.

79 Shu, J., Bar, I., and Rosenwaks, S. (1999) Dinitrobenzene detection by use of one-color laser photolysis and laser-induced fluorescence of vibrationally excited NO. *Appl. Opt.*, **38**, 4705–4710.

80 Shu, J., Bar, I., and Rosenwaks, S. (2000) The use of rovibrationally excited NO photofragments as trace nitrocompounds indicators. *Appl. Phys. B*, **70**, 621–625.

81 Shu, J., Bar, I., and Rosenwaks, S. (2000) NO and PO photofragments as trace analyte indicators of nitrocompounds and organophosphonates. *Appl. Phys. B*, **71**, 665–672.

82 Portnov, A., Rosenwaks, S., and Bar, I. (2003) Identification of organic compounds in ambient air via characteristic emission following laser ablation. *J. Lumin.*, **102–103**, 408–413.

83 Portnov, A., Rosenwaks, S., and Bar, I. (2003) Emission following laser-induced breakdown spectroscopy of organic compounds in ambient air. *Appl. Opt.*, **42**, 2835–2842.

84 Shen, Y.C., Lo, T., Taday, P.F., Cole, B.E., Tribe, W.R., and Kemp, M.C. (2005) Detection and identification of explosives using terahertz pulsed spectroscopic imaging. *Appl. Phys. Lett.*, **86**, 241116-241116-3.

85 Federici, J.F., Schulkin, B., Huang, F., Gary, D., Barat, R., Oliveira, F., and Zimdars, D. (2005) THz imaging and sensing for security applications—explosives, weapons and drugs. *Semicond. Sci. Tech.*, **20**, S266–S280

86 Passaro, V.M.N., Dell'Olio, F., and De Leonardis, F. (2007) Ammonia optical sensing by microring resonators. *Sensors*, **7**, 2741–2749.

87 Chao, C.-Y. and Guo, L.J. (2003) Biochemical sensors based on polymer microrings with sharp asymmetrical resonance. *Appl. Phys. Lett.*, **83**, 1527–1529.

88 De Vos, K., Bartolozzi, I., Schacht, E., Bienstman, P., and Baets, R. (2007) Silicon-on-Insulator microring resonator and label-free biosensing. *Opt. Expr.*, **12**, 7610–7615.

89 Kim, G.-D., Son, G.-S., Lee, H.-S., Kim, K.-D., and Lee, S.-S. (2008) Integrated photonic glucose biosensor using a vertically coupled microring resonator in polymers. *Opt. Commun.*, **281**, 4644–4647.

90 Kwon, M.-S. and Steier, W.H. (2008) Microring-resonator-based sensor measuring both the concentration and temperature of a solution. *Opt. Expr.*, **16**, 9372–9377.

91 Luchansky, M.S. and Bailey, R.C. (2010) Silicon photonic microring resonators

for quantitative cytokine detection and T-cell secretion analysis. *Anal. Chem.*, **82**, 1975–1981.

92 Dionne, B.C., Rounbehler, D.P., Achter, E.K., Hobbs, J.R., and Fine, D.H. (1986) Vapor pressure of explosives. *J. Energ. Mater.*, **4**, 447–472.

93 Orghici, R., Lützow, P., Burgmeier, J., Koch, J., Heidrich, H., Schade, W., Welschoff, N., and Waldvogel, S.R. (2010) A microring resonator sensor for sensitive detection of 1,3,5-trinitrotoluene (TNT). *Sensors*, **10**, 6788–6795.

94 Rabus, D.G. (2007) *Integrated Ring Resonators*, Springer-Verlag, Berlin Heidelberg.

95 Schopohl, M.C., Faust, A., Mirk, D., Fröhlich, R., Kataeva, O., and Waldvogel, S.R. (2005) Synthesis of rigid receptors based on triphenylene ketals. *Eur. J. Org. Chem*, **14**, 2987–2999.

96 Orghici, R., Willer, U., Gierszewska, M., Waldvogel, S.R., and Schade, W. (2008) Fiber optic evanescent field sensor for detection of explosives and CO_2 dissolved in water. *Appl. Phys.*, **B90**, 355–360.

97 Rapp, M., Bender, F., Lubert, K.-H., Voigt, A., Bargon, J., Wächter, L., Klesper, G., Klesper, H., and Fusshöller, G. (2005) Vorrichtung zum Aufbringen von Electrospraybeschichtungen auf elektrisch nicht leitfähigen Oberflächen. German Patent No. DE 10,344,135.

98 Lubczyk, D., Siering, C., Lörgen, J., Shifrina, Z.B., Müllen, K., and Waldvogel, S.R. (2010) Simple and sensitive online detection of triacetone triperoxide explosive. *Sensor Actuat. B*, **143**, 561–566.

99 Lützow, P., Pergande, D., and Heidrich, H. (2011) Integrated optical sensor platform for multiparameter biochemical analysis. *Opt. Expr.*, **19** (14), 13277–13284.

100 Bauer, C., Willer, U., and Schade, W. (2010) Use of quantum cascade lasers for detection of explosives: progress and challenges. *Opt. Eng.* **49** (11), 1111261–1111267.

101 Orghici, R., Spad, C., Lützow, P., and Schade, W. (accepted for submission 2012) Microring resonators for optical sensing of hazardous materials. *Appl. Phys. B.*

9
High-Throughput and -Content Screening/Screening for New Pharmaceutics

Astrid Tannert and Michael Schaefer

Abbreviations

ADP	adenosine diphosphate
ALPHA	amplified luminescence homogeneous assay
AM	acetoxymethyl ester
ATP	adenosine triphosphate
cAMP	cyclic adenosine monophosphate
BRET	bioluminescence resonance energy transfer
cGMP	cyclic guanosine monophosphate
cpFP	circular permuted FP
CRE	cAMP response element
CREB	CRE binding protein
DELFIA	dissociation-enhanced lanthanide fluorescent immunoassay
DTT	dithio-treitole
ER	endoplasmic reticulum
FCS	fluorescence correlation spectroscopy
FIDA	fluorescence intensity distribution analysis
FLT	fluorescence lifetime technology
FP	fluorescent protein
FRET	fluorescence resonance energy transfer
GPCR	G-protein-coupled receptor
HCS	high-content screening
HTS	high-throughput screening
LSC	laser scanning cytometry
NMR	nuclear magnetic resonance
TR-FRET	time-resolved FRET

Handbook of Biophotonics. Vol.3: Photonics in Pharmaceutics, Bioanalysis and Environmental Research, First Edition.
Edited by Jürgen Popp, Valery V. Tuchin, Arthur Chiou, and Stefan Heinemann

9.1 Introduction

The need for new pharmaceutics is underlined by the fact that about 90% of human diseases are not sufficiently controlled, let alone cured, by currently available drugs.

Screening approaches are consistently among the primary tools for developing new pharmaceutics. In contrast to so-called rational approaches, screening utilizes large collections of chemical compounds (libraries) to be tested on biological targets. Compounds identified in a primary screen to bind to the target or to modify its biological activity are designated as hits. The primary hit list might be long and most of the hits might not be relevant for further development. Therefore, known or non-relevant compounds have to be identified, a procedure called dereplication. Confirmed hits might become lead molecules for further optimization. Starting from the lead molecules, other compounds are developed with better physico-chemical or biological properties, which might eventually lead to potential new drugs in clinical testing. Optimizing lead molecules for drug candidates includes improving their binding properties, specificity and tissue distribution, decreasing their toxicity, and characterization and optimization of their metabolic profile and elimination pathway.

Compound libraries can be tested for their ability to modify a biological target in many different ways. The simplest form to identify potential interacting molecules is to test for binding of compounds to isolated targets, or to prevent binding of an established ligand by compound competition. More relevant information may be obtained by testing compounds for their biological activity in functional assays. Assay formats that detect photons as readout (i.e., most commonly fluorescence or bioluminescence) are currently the most widely applied methods in screening campaigns. Optical assays generally are cheap, simple and fast to perform, and inherently amendable to miniaturization. They are characterized by a high sensitivity and selectivity combined with a large dynamic range. For cell-based studies, using photonics is non-invasive, at least if no exposure to excitation light of high intensity and short wavelength is necessary. Imaging at a nanometer scale provides resolution almost unmatched. Other techniques applied for affinity-based screening approaches include mass spectrometry, NMR and X-ray crystallography, which have a decreased throughput rate and often require more material than optical techniques [1]. Alternative functional assays include automated patch clamp approaches in the field of ion channel studies, which again yield much lower throughput than optical methods. In former screening approaches, the use of radioactive tracers was very popular. Environmental and safety concerns have led to an extensive replacement of radioactive techniques by fluorescent or bioluminescent methods.

To enable high-throughput screening (HTS), an assay should be as easy as possible while being robust in the generation of the required readout. To achieve this, the number of handling steps has to be reduced, for instance by avoiding separation steps in signal generation. Screening approaches should be feasible to miniaturization to reduce consumption of reagents and, thus, to save money and time.

The logical course of events in most screening campaigns is to identify a target related to disease, and then screen for compounds that alter the target's biological

activity. Alternatively, one can apply models of certain diseases and screen for compounds that improve the disease-related parameters, a process known as phenotypic screening. In this case, the underlying molecular processes of the compound's action have to be identified thereafter.

HTS is mostly achieved by assay designs that yield one simple readout, such as fluorescence intensity, bioluminescence, or fluorescence polarization. With today's increased computational power, it is now possible to acquire and analyze multiple parameters from a single assay, thus gaining additional information, which can help to further characterize the effects of the tested compound on a biological system. Simple HTS assays are nowadays often substituted or complemented by multi-parametric screening approaches like automated image acquisition both in academic and in industrial screening campaigns. Because of the high content of information deduced from such approaches, they are summarized under the term high-content screening (HCS).

The aim of industrial screening is to develop pharmaceutics that have fewer side effects than current drugs or that target diseases where no adequate treatment is available. Consequently, industrial screening campaigns are influenced by the potential market and have to apply economic considerations for drug development. Even though the number of identified targets is increasing rapidly, the number of new chemical entities developed into approved drugs is not growing in a similar manner. One reason for this is that industrial drug development is focussed on a few highly relevant drug targets. Academic screening can potentially address the gaps in industrial screening by enabling a characterization of new drug targets and present hits, addressing those targets currently under-represented in industrial screening campaigns. Academic screening, therefore, often addresses broader questions, including targets where the market is not big enough for industry to set up screening campaigns [2]. The basic aim in academic screening is to develop new probes for the investigation of biological processes, which might in some cases finally also lead to the development of new drugs.

In this chapter, we briefly summarize the general considerations for screening. These considerations include target classes, compound libraries and data analysis aspects. We will focus on biophotonic assays applied in screening campaigns, starting from simple assays that achieve very high-throughput to complex screening formats that acquire multiple parameters.

9.2 Targets

Screening for new pharmaceutics primarily means testing libraries of molecules for their ability to act on a preselected biological target. A good target in a medical sense is a biological pathway which is associated with disease and whose modification is likely to provide a therapeutic option. In a chemical sense, a good target can be easily addressed by a small molecule, meaning the target is "druggable".

About half of the current pharmaceutics target only a few protein families, namely G-protein-coupled receptors (GPCRs), enzymes (especially protein kinases and phosphodiesterases), nuclear hormone receptors, or voltage-gated and ligand-gated ion channels [3, 4]. Other targets are severely under-represented by current drugs, mainly because they do not provide binding sites for small molecules from available libraries. The need to develop pharmaceutics that address such target classes is underlined by the lack of suitable therapies for many diseases in which interactions of proteins with other intracellular proteins or nucleic acids play essential roles.

Target selection for screening approaches might be influenced by previously successful targets. Receptors or other proteins that belong to an established target class, but currently lack suitable drugs that modify their activity are addressed in this case. The advantage of this approach is that screening assays for these classes are established and specialized compound libraries can be generated by similarity to known modulators of the target family [3, 5].

To develop screening strategies for targets which are less frequently modulated by existing drugs, greater efforts in assay development and library configuration are necessary. By expanding the range of possible drugs from small molecules to nucleic acids, proteins and peptides (so called biologicals), targets that were previously defined as "undruggable" can now be addressed [3].

Whereas industrial screening mainly aims for drug or lead discovery, academic screening rather covers the area of target validation, that is, investigators search for molecules that can be utilized to analyze signaling pathways or protein activities, to more precisely understand physiological and pathophysiological roles of these targets [2]. For these tool-like compounds less chemical criteria have to be fulfilled, that is, oral bioavailability or possible covalent target modification is not a major concern for research targets [6]. Target identification and validation can also be achieved by gene knock down or silencing. The number of published siRNA screens is growing rapidly, and knockout mice have also been applied for target identification, suggesting that about 10% of human genes are disease-associated [7]. Nonetheless, the acute modulation of protein functions by biologically active small molecules will always remain an important source for understanding the role of a protein within its signaling network. Since most drugs act by competing with naturally occurring molecules for binding sites on proteins, new targets might also be identified by metabolic profiling [8].

The use of optical methods is well established in screening for most common drug targets like G-protein-coupled receptors (GPCRs) and many enzymes. They have been less frequently applied in screening of ion channel function, which is classically studied by electrophysiology (though with low-throughput), but fluorescence-based functional screening assays are now also becoming common for this target class.

9.3 Substance Libraries

Classical libraries applied in drug screening consist of small molecules, mostly of less than 500 Da, which share building blocks with basic structural features of

existing drugs. Lipinski introduced the so-called "rule of five", which suggests whether a compound is drug-like with respect to hydrogen-bond donors, molecular mass, lipophilicity, and the sum of nitrogen and oxygen atoms [9]. This rule has strongly influenced the selection of compounds included in small molecule libraries. There are a number of commercially available small molecule libraries, ranging from small collections containing about 1000 approved drugs and natural compounds (e.g., LOPAC1280™ or Spectrum Collection™) to huge libraries containing several 100 000 compounds. In addition, libraries exist that are enriched for compounds expected to bind to a specific target class. Industrial companies host their own preferred huge libraries (in the range of one million compounds). The arrangement of these libraries is governed by the company's intellectual property, as resulting hits are more easily developable into patented drugs.

The existing small molecule libraries are frequently not successful in identifying modulators of less common targets. Since a considerable part of natural products and metabolite scaffolds are not included in current libraries, a new trend emerges to incorporate compounds based on structures that are biologically validated but less represented in current libraries (e.g., less hydrophobic compounds and natural products or metabolite-like compounds) [10–12]. Extending the chemical space covered by screening libraries, using combinatorial chemistry or diversity-oriented synthesis, may also lead to drug developments for targets that were difficult to address previously [13].

Fragment-based libraries have been developed recently and provide an alternative lead discovery approach. These libraries are usually relatively small (1000–10 000 compounds), containing considerably smaller molecules of less than 300 Da. These so-called fragments will mostly bind target proteins with lower potency (K_D between 100 μM and 10 mM). However, they possess a high ligand efficiency, meaning that they are extremely potent with regard to their size. Fragment hits have to be further developed to yield leads, for example, by fragment linking, self-assembly or fragment optimization [14]. Starting from fragment-based libraries, drug development might succeed where classical small molecule libraries have failed [15].

Peptides are important modulators of signaling pathways, and can, thus, represent suitable pharmaceutics to address disease-relevant targets, both in basic research and in drug formulations. To identify peptides that modulate biological targets, peptide libraries are available. They can either be biologically encoded, for example, using the phage display technique, or produced by synthetic approaches. Peptide microarrays generated by SPOT-synthesis [16] can be screened by positional scanning using fluorescent readouts. Random or combinatorial peptide libraries can be used to identify biologically active substances, like kinase substrates or inhibitors [17], or GPCR modulators [18]. Moreover, libraries derived from protein-sequences are applied to characterize protein–protein interaction sites by scanning the binding of a target protein to small linearized epitopes of its interaction partner.

To increase throughput and multiplexing in affinity assays, DNA-encoded libraries were developed where each small molecule compound is tagged by a specific DNA

sequence, enabling identification of binding molecules by subsequent sequencing of their DNA barcode [19, 20].

For target identification and validation, RNA interference (RNAi) libraries, relying on double-stranded short RNAs or short-hairpin RNA can be used (see [21] for a detailed discussion on strategies in RNAi library design and application).

9.4 Biomarkers and Labels

Nowadays, the most widely applied detection techniques in screening approaches include fluorescence or chemiluminescence. Label-free optical techniques like surface plasmon resonance or Raman scattering are applied in some screening approaches, but often suffer from a decreased sensitivity or limited throughput [1]. Utilizing absorbance limits assay miniaturization for HTS as absorption depends on the optical pathlength [22]. In contrast, assays that are based on photon emission are very sensitive, easily adaptable to biological targets and feasible for automation methods and miniaturization [23]. The fundamental difference between fluorescence and chemiluminescence assays is that the former requires excitation light to induce photon emission from a chromophore, while the latter converts chemical energy to light emission. An enzyme and its substrate must be available to induce a signal in bioluminescence, a special case of chemiluminescence. Emission is usually much brighter in fluorescence than in bioluminescence assays, because the excited state can be induced quickly by a high rate of excitation photons. In contrast, bioluminescence assays generally exhibit much lower background signals than fluorescence assays, since no external light has to be introduced. For the same reason, bioluminescence assays are less influenced by absorbing or fluorescent library compounds. For assays based on the detection of subcellular structures using microscopy, fluorescent probes are preferred, to allow the collection of a sufficient number of photons. The same is true for fast dynamic processes where short detection times are required. For macroscopic measurements where background signal interference is more severe, bioluminescence assays may be preferable over fluorescence [23]. Most bioluminescence assays are based on firefly or *Renilla* luciferases. The former emits light at 560 nm utilizing D-luciferin and ATP, while the latter catalyses the oxidation of coelentrazine, yielding light at 480 nm. Moreover, aequorin, a luminescent sensor which, upon calcium binding, emits blue light, is frequently applied. While fluorescence assays may be more prone to interference from colored compounds, there are a substantial number of compounds in common libraries that inhibit luciferase activity, making counterscreening utilizing a different assay format indispensable [24].

Quantum dots feature increased brightness, uniform emission profiles and resistance to photobleaching while excited at a single wavelength. Their application in screening approaches is still scarce, mainly because of difficulties in associating them with cells, though they have been used as indicators for cell position in cell microarrays [25].

9.4.1 Labels for Cell-Free Assays

A number of bioluminescence assays are applied for the detection of enzyme activity or in affinity assays. Since the intensity of bioluminescence is correlated to the concentration of reaction components, variation of one component can be translated into a signal, while holding the other reagents constant. Bioluminescence assays are well-known for the detection of ATP, but also substrate (using specifically developed "pro-luciferins" that become cleaved during the assay) or the enzyme itself may be the variable assay component. Because of their low background, bioluminescence assays yield a linear range over several orders of magnitude [23].

Fluorescence readouts include labeled antibodies detecting products from enzyme activity, labeled ligands for affinity assays, or labeled substrates for enzyme reactions. Specifically designed fluorophores may be used to sense chemical modifications. A classical example is the detection of phosphorylation by Lewis metal chelates, which is now frequently used in ALPHA assays to replace phosphorylation-specific labeled antibodies. Using fluorescent readouts, to circumvent compound interference, lanthanides may be applied, either for fluorescence intensity measurement or as FRET donors. Because of their extremely long fluorescence lifetime, gate detection can be applied. In this so-called "time-resolved" fluorescence detection method, molecules are excited with a short light pulse and fluorescence detection is delayed by about 100 μs. During this time, fluorescence of most fluorophores that may occur in compound libraries has decayed and only lanthanide fluorescence is detected. When using lanthanides in FRET assays it might be counterproductive to decrease the distance between donor and acceptor below a certain value, since this will also dramatically decrease the donor fluorescence lifetime and, thus, interfere with gated detection [26]. Using classical fluorophores, interference from fluorescent compounds can be reduced by applying red-shifted dyes [27]. Moreover, ideal fluorophores should exhibit a high quantum yield, high photostability, a large Stokes shift, and insensitivity to environmental factors like pH.

9.4.2 Labeling of Cells

In cell-based assays, fluorophores have to be introduced externally or cells have to be modified genetically to express auto-fluorescent proteins or luciferases to yield a photon emission signal. To ensure stability in screening assays, labeling procedures have to be specific, quantitative and feature high reproducibility. Moreover, interference with biological processes, other than the one they have been designed for, has to be minimized [28].

9.4.2.1 Synthetic Fluorophores

A huge number of chemical probes has been designed and is commercially available, partitioning into subcellular structures (like mitochondria, nucleus, Golgi apparatus, plasma membrane). These probes can, therefore, serve as compartment markers.

The visualization of specific proteins within the cell is usually achieved by labeled antibodies, which requires fixation and permeabilization of cells if the epitope is not exposed at the cell surface. Unfortunately, this kind of labeling typically restricts cellular imaging to endpoint measurements [29].

Other probes may indicate cellular parameters like ion concentration. Most widely applied indicators of cellular parameters are calcium indicators and probes for changes in membrane potential.

For toxicity screening a number of fluorescent or fluorogenic indicators are available (reviewed in [30]), indicating either membrane integrity, metabolic cell activity, or cellular respiration.

9.4.2.2 **Genetically-Encoded Marker Proteins**

Modern biology was greatly influenced by the possibility to introduce genes that produce a photonic signal into cells. Genetically encoded fluorescent proteins (FPs) as well as luciferases can be utilized as genetic reporters under the transcriptional control of a target molecule (see Section 9.6.7) [31].

FPs are also frequently applied to monitor the influence of compound libraries on protein activity or signaling pathways. Activation of signaling pathways or protein function can be monitored in three ways using FPs: by altered optical properties (fluorescence intensities or spectra) of the FP, by an altered FRET ratio between two FPs (or one FP and one small fluorophore), or by changes in subcellular localization of the reporter protein within the cell [32]. While the first two mechanisms can be followed in bulk measurements, the latter usually requires automated microscopy (see Section 9.6.11). Since immunostaining of cells is labor- and cost-intensive, FP fusion proteins may be preferred in localization studies over immunoassays. Moreover, once stably transfected, FP-expressing cells can be readily and repetitively monitored using microscopy, enabling the detection of dynamic processes. One limitation may arise from the size of the FP, which can alter the function of the protein it is fused to.

FPs are nowadays available in a variety of colors, which enables the use of the red and far-red spectral range, where phototoxicity of the excitation light is reduced, and less interference from cellular and compound autofluorescence is expected [33].

To probe for protein–protein interaction, protein cleavage, or protein phosphorylation, a variety of FRET probes have been designed. The dynamic range, which is defined as the difference between the minimum and maximum signal, is frequently low in FRET-based sensors, making these probes less suited for a robust HTS assay format. To overcome these drawbacks, either the linker between FPs and the sensor sequence can be altered, or circularly permuted FPs (cpFPs) can be introduced, increasing the dynamic range of the FRET-based sensors [32]. cpFPs are usually more sensitive to their physicochemical environment and are, therefore, highly suitable as sensors, for example, for pH changes. Insertion of a sensor domain of a protein within a cpFP can yield highly sensitive biosensors, for instance for calcium or hydrogen peroxide [34].

Specialized FPs have been engineered, for example, with the property of induced-color switching (Kaede, EosFP, Dendra), or that change color while aging (fluorescent

timers). Moreover, FP that release reactive oxygen species upon illumination (KillerRed) can be used to degrade proteins in their proximity [29]. For investigation of chloride-conductive ion channels, halide-sensitive FP variants have been developed, which sense chloride influx by decreased fluorescence intensity [35]. These applications, though not widely used for HTS today, might enable the design of new HTS and HCS assay formats.

Using FPs in screening approaches requires transfection of DNA into cells which can be difficult for some cell types. Moreover, timing and level of expression are difficult to control [36]. If cell lines stably express the protein of interest, however, screening is straightforward since it does not require dye-loading steps.

9.5 Instrumentation

For detection of optical readouts a number of different devices can be applied. Nowadays, the standard format for many HTS applications is a 384-well or a 1536-well plate. Due to limitations that arise from capillary forces, current miniaturization attempts translate into the development of microarrays and microfluidic devices for screening applications. Here, the spatial resolution has to be maintained by patterning the stationary phase, for example, with printing techniques.

Averaged readouts of entire wells are the simplest form to obtain signals from a multi-well plate. They can be collected either in a well-by-well mode or by simultaneous assessing of the signals from all wells. For averaged well-by-well measurements, a number of commercially available plate readers can be used. Typical readouts from plate readers include absorbance, fluorescence intensity, fluorescence polarization, and luminescence. Some plate readers may also be used for time-resolved gated fluorescence measurements, or for fluorescence lifetime analysis. Standard plate readers generally apply photomultiplier tubes to detect light while scanning the plate well by well. The excitation and emission wavelengths can be selected either by the use of monochromators or filters, the former improving flexibility and offering spectrometry, the latter bearing the potential of higher sensitivity and facilitating multi-channel readouts. For simultaneous whole plate readouts, CCD-based fluorometric imaging plate readers have been developed, enabling faster data acquisition and multiplexing.

Spatially resolved readouts from microplates, enabling single cell observation, can be obtained by using laser scanning cytometry or high resolution automated microscopy (see Section 9.6.11).

Flow cytometry allows the detection of cells or particles according to their spectral properties in a homogeneous assay format where different reactions are identified by optical rather than spatial addressing [37]. When using inhomogeneous cell populations, where the target-relevant cell type represents only a minor fraction of all cells, biological signals from these cells are frequently missed in averaged measurements. Especially in these cases, flow cytometry is an important tool that easily allows the

analysis and quantification of signals from cell sub-populations by means of gated detection.

The development of microfluidic techniques has made tremendous progress in the past decade. It has the potential to increase throughput dramatically while decreasing reaction size and, thus, required biological material and cost [38]. Microfluidic platforms, commercially available from Caliper, have already been successfully applied in screening for kinase inhibitors [39, 40].

In order to miniaturize cell-based screening approaches, methods to attach live cells to microarrays are being developed [41, 42]. In a non-compartmentalized cell culture approach, a continuous cell layer was exposed to spots containing different substances, using a sophisticated microdelivery system [43]. Another recent approach is the delivery of substances to cells using sandwiched microarrays, one containing cells seeded in microwells onto which a compound-loaded array is sealed [44]. Reverse transfection on microarrays [45] can be used to screen for RNA interference in a miniaturized way [41].

In addition to optical detection systems, the integration of automated liquid handling and compound transfer systems is essential for HTS, but will not be further discussed here.

9.6 Assays

There is a huge variety of assays to screen for new pharmaceutics. Historically, assays that utilized radioactive tracers were very popular. Nowadays, they are more and more replaced by optical methods. Screening assays can be classified into binding studies and functional assays. Simple binding assays, which achieve a very high throughput, detect the binding of compounds to purified target proteins. In contrast, functional assays measure the compound-induced modification of a biological function, either by detecting products from biochemical pathways or by phenotypic alterations. Functional assays may either detect accumulated metabolic products and second messengers or phenotypes in end-point measurements, or monitor compound-induced changes in a kinetic way.

One disadvantage of binding studies using isolated protein targets is that they do not allow conclusions about the kind of modification the binding molecule might induce in the protein of interest. For this reason, one cannot predict if a hit from an affinity assay might prove as a full or partial agonist, neutral or inverse antagonist. Therefore, intensive secondary characterization of primary hits becomes essential. Moreover, allosteric modulators of protein function might be missed in binding studies.

Classical binding assays require a separation step to remove unbound molecules either by filtration, centrifugation or dialysis. To minimize working steps “mix and run assays” that require no washing step are now widely applied [46]. These include non-separation assays (containing a solid and a liquid phase) or homogeneous phase assays. Nowadays, available homogeneous assay formats allow detection of binding

of compounds to isolated targets by competition with labeled ligands, or by directly coupling screening compounds to fluorophores. Ligand binding can also be detected in a label-free manner using surface plasmon resonance. In addition to the application of fluorescence or luminescence-based binding assays to detect target-compound interaction, these assay formats can also be used in functional approaches. Here, metabolic products are detected by binding to specific antibodies. The principle of some widely applied competition immunoassays to detect metabolic analytes is illustrated in Figure 9.1.

Functional assays can be classified as cell-free (i.e., measuring the activity of an isolated enzyme) or cell-based assays, assessing the activity of a protein by monitoring the biological response of a cell that expresses the target protein. The latter has the advantage of simultaneously providing information about off-target effects of compounds on living cells, for example, allowing the detection of toxic compounds, but requires extensive cell culture work. Using cell-based assays in signal transduction, one might detect early (e.g., second messenger production) or later (e.g., gene expression) events, regarding modulation of the protein/receptor of interest. Distal readouts, like expression of reporter genes, might increase signal strength due to cellular amplification steps, but will also increase the number of false positive hits due to additional effects of the investigated compounds on downstream processes. Therefore, screening for a gain of function rather than a suppression in downstream signals is considered to yield more robust results with respect to possible off-target or toxic effects of compounds.

In order to increase throughput, multiplexing approaches, that is, the simultaneous acquisition of multiple data sets (each representing one analyte), are becoming more and more popular. One possibility for easy implementation of multiplexing is the application of flow cytometric approaches [47].

Another current trend in screening approaches is the application of multiparametric analysis. The simultaneous measurement of several different characteristics of live cells can be achieved by flow cytometric approaches or by using automated imaging techniques.

9.6.1 Fluorescence Polarization

Fluorescence polarization measurements provide a cheap and easy method to detect a variety of molecular interactions and enzyme activities in a homogeneous assay format. In fluorescence polarization assays, a small molecule of interest is coupled to a fluorophore (e.g., fluorescein) and excited with polarized light. Fluorescence intensity is detected with polarization filters, measuring the polarization of the emission light parallel ($I_{||}$) and perpendicular ($I_{\perp}$) to that of the excitation. Fluorescence polarization is calculated according to:

$$FPol = \frac{I_{||} - I_{\perp}}{I_{||} + I_{\perp}}$$

(a) Fluorescence polarization

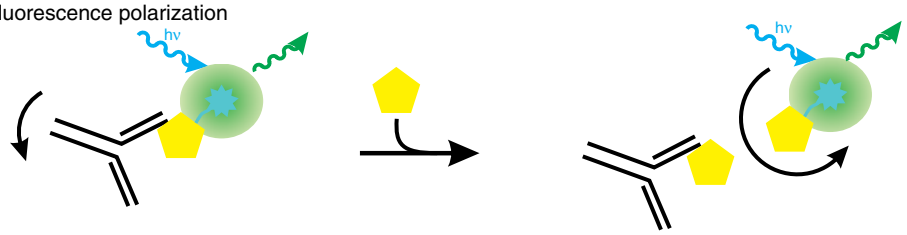

(b) TR-FRET

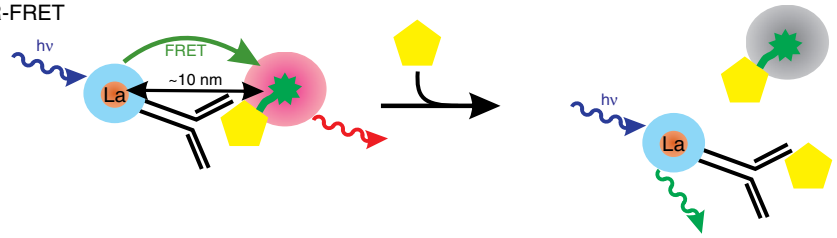

(c) ALPHA

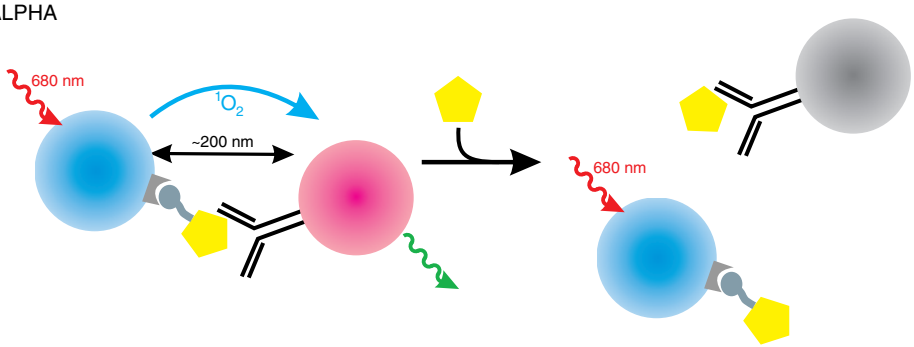

(d) Enzyme complementation

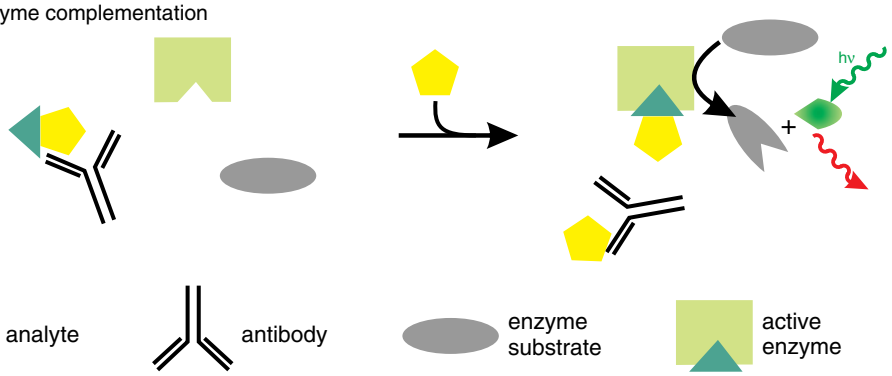

If rotation of the fluorophore is fast with respect to its fluorescence lifetime, its emission is strongly depolarized, and both detection channels record nearly the same intensity. Binding of a larger structure (e.g., an antibody) to the fluorophore analyte complex slows down the rotation of the fluorophore. The more slowly the fluorophore rotates, the more photons will be detected in the parallel detection channel compared to the perpendicular channel, resulting in an increased fluorescence polarization value. In order to reach a sufficiently small fluorescence polarization value for the unbound analyte fluorophore complex, the analyte size has to be small and the fluorescence lifetime of the fluorophore should be relatively long [48].

Fluorescence polarization differs from other affinity detection methods in that bound and unbound molecules are measured simultaneously [49]. This may lead to low signal-to-noise ratios and only minor total shifts in fluorescence polarization values. Nevertheless, since the fluorescence polarization measurements are very precise and steady, high *Z*-factors (see Section 9.6.1) may be achieved with this technique. Fluorescence polarization assays can be applied in competition assays for antibody-based second messenger detection, to analyze displacement of labeled ligand from their receptors, or for direct assessment of binding of a small labeled ligand to a larger structure. Utilizing labeled substrates, enzyme activity can be assessed by fluorescence polarization upon binding of the converted substrate to specific antibodies, or in the case of phosphorylation to immobilized metal affinity nanoparticles (IMAP™), resulting in an increased fluorescence polarization value. Fluorescence polarization assays are simple and cost-efficient, however fluorescent compounds may interfere with the assay signal. Such cases might be detected by their unusually high total fluorescence intensity, or by spectroscopically detecting an overlapping fluorochrome. A number of commercially available plate readers include the option to measure fluorescence polarization.

Figure 9.1 Schematic representation of some competition affinity assays. (a) A labeled analyte competes with the free analyte for binding to a bulky antibody. If the labeled analyte is displaced from the binding site, it rotates faster, leading to a decrease in detected fluorescence polarization. (b) Molecules labeled with a resonance energy transfer acceptor for lanthanide fluorescence compete with unlabeled molecules of interest for binding sites at a lanthanide-coupled antibody. The FRET signal is measured in a time-gated fashion, to minimize unspecific signal. Displacement of labeled molecules leads to a decreased FRET signal. (c) Biotinylated analyte binds to donor beads coated with streptavidine. Free analyte competes for antibody coupled to acceptor beads. Upon excitation at 680 nm, singlet oxygen is produced which diffuses about 200 nm before decaying. If singlet oxygen reaches a closely positioned acceptor bead, it produces a fluorescence at about 520–600 nm, this signal decreases with the amount of competing non-biotinylated molecules. (d) Analytes of interest are bound to a peptide, which will complement a mutated enzyme to restore its activity. Antibodies against the molecule of interest prevent enzyme complementation, free analytes displace peptide-bound molecules from the antibody leading to a restoration of enzyme activity and the production of fluorescent or luminescent products from nonfluorescent substrates.

9.6.2 Time-Resolved Fluorescence

To circumvent interferences from fluorescent compounds, gated detection can be applied (see Section 9.4.1). This is most frequently done in time-resolved FRET (TR-FRET) assays like LANCE®, homogeneous time-resolved fluorescence (HTRF®) or LanthaScreen™. In TR-FRET, lanthanides that exhibit a very long fluorescence lifetime act as donor molecules. Acceptor molecules are classically red fluorescent, but can also be green fluorescent molecules when utilizing a terbium instead of a europium donor, which has an additional emission band in the green spectrum. This extends the spectrum of possible acceptor fluorophores to genetically encoded autofluorescent proteins like GFP, which simplifies assay development and allows, for example, a kinase substrate to be expressed in a cell [50]. Rare earth ions alone are not absorbing and, therefore, require light-collection assisted by chelates or cryptates to be excited. Cryptates are more stable under certain chemical conditions [51]. The assay principle is similar for various applications. An antibody recognizing the analyte under investigation is coupled to the lanthanide donor. The acceptor is either coupled to the molecules that will be detected directly or binds the molecule of interest via streptavidin-biotin or immunological interaction. When the acceptor comes close to the donor (usually in the range of 10 nm), energy transfer occurs and acceptor fluorescence is detectable. TR-FRET assays generally detect fluorescence at both the donor and the acceptor emission wavelength, allowing for some compensation of compound interference. Additionally, fluorescence is detected after a time-window of about 50–100 μs after excitation, when interfering fluorescence from compounds has already decayed. In kinase assays, the donor is a lanthanide-coupled antibody recognizing the phosphorylated substrate. The substrate is labeled with the acceptor, leading to increased acceptor fluorescence upon kinase activity. In contrast, in competition assays (i.e., to detect second messengers) acceptor-labeled molecules compete with cellular produced molecules for antibody binding, leading to a decrease in acceptor fluorescence with increasing second messenger concentrations.

Ready-to-use TR-FRET assay systems are available to detect a variety of second messengers like cAMP [52] or inositol 1,4,5-trisphosphate (IP_3), for monitoring kinase activity [53] by utilizing labeled kinase substrates or by detecting ADP generation, for a variety of other enzyme reactions, or for the analysis of protein–protein interactions.

In contrast to TR-FRET assays, dissociation-enhanced lanthanide fluorescent immunoassay (DELFIA®) is a heterogeneous time-resolved assay based on fluorescence enhancement of lanthanides after dissociation. Its principle is similar to that of an ELISA assay. In competition assays, antibodies specific for the analyte of interest are immobilized at the plate surface, for example, via biotin–streptavidin interaction. The plates are incubated with a mixture of lanthanide-labeled and competing analytes. Unbound molecules are washed away, the lanthanides are dissociated into solution, and incubated with an enhancement solution, leading to the formation of highly fluorescent chelates. Competing molecules are detected by a decreased

fluorescence, since less labeled molecules remain bound to the surface. For enzyme assays the substrate is immobilized and incubated with the enzyme. After washing, the plates are incubated with lanthanide-coupled antibodies specifically recognizing the modulated substrate. Unbound antibodies are washed away, and detection occurs as in competition assays. Here, a high fluorescence intensity indicates high enzyme activity. As in TR-FRET, emission is detected delayed after excitation, allowing interfering compounds to decay within the delay window.

DELFIA® can be multiplexed by using lanthanide probes with different emission characteristics. It shows superior sensitivity and dynamic range in kinase assays and for detection of cAMP [52], which is achieved by the enhancement step. However, due to the heterogeneous nature of the assay, it requires a number of washing steps, making it less suited for HTS and placing its application rather in secondary hit confirmation.

A number of state-of-the-art plate readers are compatible with time-resolved fluorescence measurements.

9.6.3 Proximity Assay

Amplified luminescent proximity homogeneous assay (ALPHAScreen®) is a homogeneous immunoassay that utilizes donor and acceptor beads of about 200 nm size. Donor beads contain phtalocyanine that, upon excitation at 680 nm, produces singlet oxygen (about 200 molecules per excited donor bead). Singlet oxygen has a half-life of about 4 μs in which it can diffuse about 200 nm. Acceptor beads are coupled to three dyes (thioxene, anthracene and rubrene), of which thioxene, when reacting with singlet oxygen, produces a UV luminescence, which is transferred by energy transfer to the other dyes, eventually leading to emission at 520–620 nm. Emission occurs only when donor and acceptor beads are at a distance of less than 200 nm. This distance is about one order of magnitude longer than that feasible for resonance energy transfer. Therefore, larger binding partners, like large proteins or even phages, which cannot be analyzed by the TR-FRET method, can be studied using ALPHA technology. The surface of the beads is coated with latex-based hydrogels and reactive aldehydes, reducing unspecific binding and providing a surface to covalently attach various binding partners. Often, the donor bead is coated with streptavidin to bind a biotinylated small molecule, protein or an antibody against the molecule of interest, while the acceptor bead is coupled to an antibody detecting a different binding site of the analyte [54].

AlphaLISA™ is a variation of the ALPHAScreen® technology, utilizing europium as acceptor fluorophore, which provides a high intensity emission at 615 nm, enabling a narrow detection band. AlphaLISA™ can also be more easily adapted to smaller sample volumes required for higher throughput.

The ALPHA technology can be used to detect second messengers like cAMP after cell lysis [52], to monitor enzyme activity from both purified enzymes and cell lysates, and to analyze protein–protein interaction. The method is characterized by a high sensitivity with low background signal but is also prone to temperature-induced

signal variabilities, sensitive to light and interference of compounds with antioxidant properties. Owing to the longer excitation compared to the emission wavelength, ALPHAScreen®-based technologies require specialized plate readers.

9.6.4 Protein Complementation Assays

In protein complementation assays (PCA) a reporter protein is split into two fragments that cannot fold when separated. Each protein fragment is fused to one of two interacting partners. Once interaction occurs, the two fragments are able to form a functional protein [55]. Since protein complementation relies on protein folding rather than assembly of folded subunits, it cannot be applied for measurements of fast kinetics. Moreover, some split proteins, including FP variants, form quite stable proteins after interaction, making them unsuitable for the investigation of dynamic processes. Irreversible association might also lead to higher background signals due to spontaneous interaction, especially if the expression level is high. A luciferase-based assay has overcome these problems and was shown to efficiently report the disruption of protein–protein interaction [56].

DiscoveRx offers a huge variety of assay systems based on complementation of β-galactosidase fragments to generate a fluorescence or luminescence signal. Besides cell-based complementation assays that report on protein–protein interaction [57], there is a panel of assays to detect the production of signaling molecules or enzyme activity compatible with standard plate readers. The principle is similar for a variety of target assays: a β-galactosidase missing certain amino acids for functionality (enzyme acceptor) is complemented with a small fragment peptide that binds to the acceptor with high affinity, enabling substrate hydrolysis, and thus generating the signal. This complementation can only occur when the fragment binding site for the acceptor is not covered by a bulky structure. The signal can, therefore, be produced by cleavage processes or by competition of fragment-bound small molecules with molecules of interest for antibody binding sites, enabling the detection of a variety of processes [58]. Available assays include detection of cAMP, activation of nuclear hormone receptors, protein kinase assays, and protease assays that are either cell-based or biochemical.

9.6.5 Resonance Energy Transfer

Fluorescence or Förster resonance energy transfer (FRET) can be used to detect binding of a ligand to its receptor in a homogeneous assay format. FRET occurs when the emission spectrum of the donor overlaps significantly with the excitation spectrum of a closely positioned acceptor fluorophore. FRET efficiency declines with the 6th power of the distance between donor and acceptor, giving efficient energy transfer when the distance between donor and acceptor is in the lower nanometer range for most fluorophores. One disadvantage of FRET is that it requires labeling of ligand and receptor. Since spectral separation of FRET-based indicators may be low,

even weak background fluorescence and absorbance of screening compounds might considerably interfere with the assay. By using lanthanides with long excited state lifetimes as donor molecules, and measuring FRET in a time-resolved manner, the latter problem might be solved [46].

A number of FRET sensors based on genetically encoded FPs have been designed. The most commonly applied FRET systems apply variants of cyan FP as donor and yellow FP or its improved variants as acceptor molecules. When donor and acceptor are fused to different proteins, interaction of these proteins is sensed by an increased FRET ratio. In other FRET sensors, donor and acceptor chromophores are intramolecularly fused to two different positions within a target molecule, detecting conformational changes by an altered FRET ratio. Such intelligent designed FRET sensors are applied for the detection of a huge variety of cellular signaling events, including protease, kinase, and GTPase activity. The susceptibility to interfering background signals might be overcome in cell-based assays by a higher expression rate of fluorescent proteins. Bioluminescence resonance energy transfer (BRET) utilizes a luminescent donor and a fluorescent acceptor protein, meaning that no external excitation is required and reducing the influence of background interference.

In cell-based resonance energy transfer assays, a spatially resolved readout, applying imaging techniques, is often used. This allows analysis of subcellular localization of the signaling molecules and reduces the influence of background signals. Technically, FRET can be detected by analyzing the changes in donor fluorescence lifetime, by using spectral readouts like sensitized acceptor emission, or by detecting donor quenching/unquenching.

9.6.6
Fluorescence Fluctuation Approaches

In fluorescence fluctuation techniques, samples diffuse through a diffraction-limited focus of a laser beam, and variations in fluorescence intensity are monitored. Fluorescence correlation spectroscopy (FCS) is based on autocorrelation curves, from which the diffusion time of molecules can be calculated. Since small fluorescent molecules diffuse significantly faster than molecules attached to a larger structure, this technique can be applied to the detection of binding reactions. The concentration of labeled molecules has to be relatively low to ensure single molecule detection. As a consequence, longer measuring times are required for robust statistics, making this technique less suitable for HTS [59]. A complementary approach is fluorescence intensity distribution analysis (FIDA) based on the statistics of fluorescence fluctuations, where slightly higher concentrations of labeled molecules and much shorter detection times are applied. In FIDA, the molecular species in the sample are quantified according to their molecular brightness, using frequency histograms of signal amplitudes. Compared to fluorescence polarization measurements, FIDA is less sensitive to compound autofluorescence and light scattering [60]. In 2D-FIDA, signals from two detection channels (either based on polarization or emission bands) are analyzed, resulting in improved performance [61].

9.6.7
Reporter Gene Expression

The activation of signaling cascades can be monitored by observing the expression of reporter genes, whose transcription is controlled by specific promoters. These promoters contain binding sites for transcription factors produced downstream of the investigated receptor or regulatory protein [62]. A common example for the detection of cAMP production is the CRE sequence, which is activated by CREB. Widely applied reporter gene products include fluorescent proteins, luciferases, β-galactosidase and β-lactamase. A variety of detection methods exists for β-galactosidase, enabling cheap assays with fluorescent, luminescent or colorimetric readouts. FPs have the advantage that they are autofluorescent and do not require co-factors, so they can be measured in live cells. FPs and β-galactosidase possess relatively long lifetimes, which might lead to higher background signals. To overcome this limitation, genetically modified FPs with decreased stability have been constructed. In contrast, luciferase and β-lactamase have shorter half-lives per se. For firefly luciferase detection, various reagents are commercially available. For the detection of β-lactamase activity, a cell permeable FRET sensor (CCF2/AM) has been developed, which is cleaved by the enzyme, resulting in reduced FRET efficiency. This non-toxic sensor enables ratiometric measurements in live cells [63].

Since protein synthesis has to occur for the signal to develop, these assays require longer incubation times. Moreover, since the expression level may depend on certain factors not influenced by the test compound, results deviate with uneven cell seeding or metabolic integrity. Expression of a second reporter gene, which is constitutively active, enables correction for these fluctuations but requires either another colored variant or sequential reading of both products, which may prolong assay time considerably. A typical reporter gene assay, correlating reporter gene expression to constitutive expression is shown schematically in Figure 9.2. Dual reporter gene assays may also be used to simultaneously assess the activation of two different signaling pathways by monitoring the expression of two different reporter genes [64]. Luciferase isoforms emitting at different wavelengths but using the same substrate have been developed, enabling parallel measurement of different gene products [65].

9.6.8
Measurement of Intracellular Calcium

Changes in the intracellular calcium concentration can arise from the activation of GPCRs coupled to $G\alpha_q$, which, via the activation of PLC β and production of IP_3, leads to a calcium release from the ER. With several hundred members in the human genome, non-olfactory GPCRs form a large druggable family. Note that activation of other GPCR family members that couple to $G\alpha_s$ or $G\alpha_i$ leads to changes in cellular cAMP rather than calcium due to the activation or inhibition of adenylyl cyclase, respectively. However, these pathways can be switched to result in

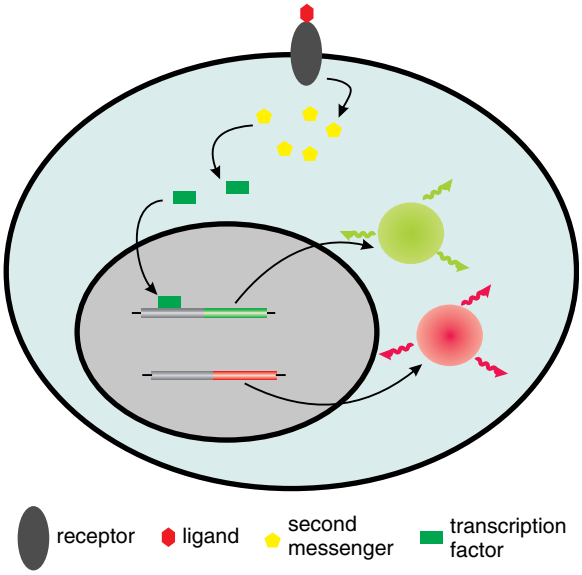

Figure 9.2 Schematic drawing of a dual reporter gene expression assay: After ligand binding to a receptor, second messengers are produced, which then control the activation of transcription factors. Binding of these transcription factors to the promoter of the reporter gene induces protein expression, and a detectable fluorescence or luminescence signal is established. A protein of different spectral properties, which is constitutively expressed, serves as an internal control for differences in cell viability, metabolic fidelity, or uneven seeding.

a calcium increase by using chimeric or promiscuous Gα subunits [66, 67]. Coexpression of these subunits is frequently applied, since calcium measurements are most easily incorporated in many HTS platforms. In addition, this technique is widely used for de-orphaning GPCRs with as yet unknown physiological activators. Intracellular cAMP or cGMP production can also be detected indirectly by coexpressing variants of cyclic nucleotide-gated cation channels (CNGs) that translate cyclic nucleotide accumulation into a calcium signal [68, 69], enabling high-throughput kinetic measurements of these messengers [70–72]. Other important pharmacological targets that causes changes in intracellular calcium levels, are calcium-permeable ion channels, like voltage-, ligand-, or second messenger-gated calcium channels.

There is a huge variety of small chemical calcium indicators available (for a comprehensive review of their properties see [73]). For easy loading of cells, these dyes can be used in the acetoxymethyl ester (AM) form, which facilitates membrane crossing and, when hydrolyzed by cellular esterases, the anionic dyes remain trapped within the cells. In addition to various calcium affinities, chemical calcium sensors can be classified according to their spectral properties as single wavelength indicators and ratiometric dyes. The former change their fluorescence intensity upon calcium binding, while the latter undergo a shift in either their excitation or emission spectra.

While single wavelength dyes like Calcium Green-1, Fluo-3, Fluo-4, and Oregon Green 488 BAPTA have a low spectral bandwidth and, thus, can be easily combined with other fluorophores, they are more prone to photobleaching, uneven dye loading or interferences from compound fluorescence. The most widely applied ratiometric calcium sensor is Fura-2, which emits above 510 nm and shifts its absorption maximum from 380 nm in the calcium-free to 340 nm in the calcium-bound state. The ratiometric approach enables calibration as well as corrections for certain assay interferences due to the added compound. However, it requires a device with dual UV channel excitation.

When choosing the right calcium sensor for a screening approach, the spectral properties, as well as the calcium affinity of the dyes must be considered. Generally, the K_D of the dye should be in the same range as the measured calcium concentration. While high affinity sensors have a higher sensitivity, they will also buffer a greater amount of calcium and might, thus, affect physiological signaling. Another consideration for choosing the sensor for HTS might be the minimization of working steps. Loading cells with the classical calcium sensors requires removal of the dye that has not been internalized. When using cell suspensions, this can easily be achieved by loading and washing the cells before dispensing into a microplate. For adherent cells that are cultured within a multiwell plate, the newly developed no wash dyes [74], which use nonmembrane-permeable quenchers to suppress extracellular reporter fluorescence, might be advantageous.

In addition, genetically encodable calcium sensors, like variants of the luminescent aequorin [75], and fluorescent proteins that either change their fluorescence intensity (like camgaroos or pericams) or FRET-ratio (cameleon) may be used [76]. These proteins have the advantage of being targetable to specific subcellular environments or fusable to proteins of interest. Their disadvantages include a lower sensitivity and slower response rates, and they are more difficult to introduce into some cells or tissues [76].

Due to the easy application of calcium measurements, they are widely applied in HTS, especially when screening for GPCR or calcium channel modulators. Since the increase in intracellular calcium is rapid and transient in most cases, calcium measurements do not represent equilibrium conditions for receptor–ligand interaction, and pharmacological parameters obtained under these conditions are indirect. This may cause different conclusions about agonist/antagonist potency, or even reversal in agonist potency orders when different assay systems are used (see [77] for a detailed discussion).

Calcium measurements can be easily performed using plate imagers, plate readers, or microchip approaches. When subcellular localization or intracellular spreading of the calcium signals is of interest, automated microscopy may be applied. Most physiological calcium signals are rapid and transient (i.e., in the range of seconds after agonist addition). Thus, systems are required that measure with a high temporal resolution [78]. The fastest kinetic acquisitions are achieved with imaging plate readers, enabling parallel measurement of an entire multiwell plate. State-of-the-art plate readers nowadays achieve a temporal resolution that is sufficient for most applications in calcium signaling by measuring all wells of one plate before

proceeding to the next time point of the kinetics. However, when cellular imaging is required, a kinetic measurement has to be completed within one well before moving to the next, decreasing the throughput considerably.

9.6.9 Indicators for Ion Channel Activity

Ion channel activity of calcium-permeable channels can be easily detected by measuring changes in the intracellular Ca^{2+} (see above). Other ion channels have been a difficult target class for drug development, partly because some functional assays do not fulfill the demands of HTS [79]. Functional screening for ion channel modulators can be performed using ion flux measurements but these suffer from poor detection specificity. Recently, platforms for automated patch clamp measurements (like IonWorks® Quattro platform, QPatch™ 16 or PatchLiner® 8) have been introduced, however, the throughput of these devices is still considerably slower than that of optical methods. They are, therefore, rather suited for confirmation of primary hits acquired from a fluorescence-based screening assay [80], and are applied in testing drug candidates for unwanted effects (e.g., long-QT syndrome) to meet safety regulations.

Methods based on fluorescent indicators remain the only assays that allow real high-throughput. Indicators for ion channel activity can be classified into those sensing changes in the membrane potential and dyes detecting ions that pass through the channel.

Sensors for ions other than calcium are not that well established for HTS. A Tl^+ uptake assay to monitor opening of K^+ channels has been developed. Loading cells with Tl^+-detecting fluorophores leads to an increase in fluorescence intensity upon uptake of Tl^+ through open K^+ channels [81, 82]. Other available ion indicators include sodium green for the detection of sodium, and several indicators that detect halide ions via diffusion-limited collisional quenching. Chloride or iodide fluxes can be also detected by variants of FPs, which have been applied in screening for cystic fibrosis transmembrane conductance regulator modulators [35, 83].

Voltage-sensing probes are organic fluorophores that bind to the plasma membrane. According to their mechanism of action, these dyes can be subdivided into probes that, upon changes in membrane potential, rearrange their transmembrane distribution, and probes that change their electronic structure, resulting in altered fluorescence properties. The latter exhibit a fast response to voltage changes, which is especially required for fast transient processes. However, the potential-dependent changes in fluorescence signals are tiny, resulting in low signal-to-noise ratios, which make these dyes unfavorable for HTS. In contrast, dyes that cross the membrane, like cationic rhodamines or anionic oxonols, have been successfully applied in HTS. Redistribution of dyes across the membrane is rather slow (equilibrium is reached in seconds to minutes) [84]. Negatively charged oxonols are probably the most commonly applied voltage sensors for screening. Upon hyperpolarization, they leave the cells and are quenched in the extracellular environment, leading to a decrease in fluorescence signal, whereas depolarization

results in increased fluorescence intensity [79]. Fluorescence changes can be increased by adding quenching dyes to the extracellular compartment and no-wash kits with improved fluorescence properties and kinetics are commercially available [85, 86].

Moreover, ratiometric approaches have been developed to sense membrane potential changes, relying on FRET, for example, between a coumarin-linked phospholipid at the outer leaflet of the plasma membrane as donor and a negatively charged oxonol as acceptor. Upon depolarization, the acceptor accumulates at the inner plasma membrane leaflet, leading to a decrease in FRET efficiency [80, 87]. As explained above, ratiometric approaches are less prone to artefacts from unequal dye loading and cell density as well as autofluorescence of compounds, but require dual excitation or emission and occupy a broader spectral range.

Since, in most cases, the number of ion channels that have to open to induce changes in membrane potential is small compared to the total number of channels of the investigated type, assays that rely on membrane potential changes may yield low EC_{50} values in agonist screening but higher IC_{50} values and, thus, reduced sensitivity in antagonist screenings [87].

Potentiometric indicators and ion-sensitive probes are compatible with imaging plate readers [88].

9.6.10 Flow Cytometry

Flow cytometry, originally developed to characterize and sort cells based on their fluorometric properties, can also be extended to the analysis of other fluorescent particles of similar size, like synthetic microspheres. Microspheres may serve as solid supports for antibodies in immunoassays or molecular assemblies of drug targets. Flow cytometric applications in drug screening include competition assays where compounds are identified that block the binding of fluorescent ligands to their receptor expressed on cells. Also, protease activity can be monitored using a fluorescent substrate attached to a microsphere [89]. Flow cytometry is capable of detecting bound molecules in the presence of about 100 nM of free label in a homogeneous assay format.

Modern flow cytometers are capable of acquiring multiple parameters, ranging from fluorescence intensities at different wavelengths to light scattering which reports on the size of the analyzed particle. Multiparametric analysis or multiplexing by color coding different microspheres is thus supported [37]. In the Luminex® approach, a reporter molecule is labeled with one fluorophore and the interaction with the microsphere surface containing possible binding partners is analyzed. These microspheres contain two fluorophores of varying concentration allowing multiplexing of up to 100 different binding partners by spectral addressing of their microspheres [47].

Fluorescent cell barcoding with different fluorophores in varying concentrations is another possibility to achieve multiplexing using live cell samples [90].

Flow cytometers adapted for the demands of HTS applying microfluidic dimensions are now commercially available.

9.6.11 Automated Microscopy

Biochemical assays and measurements of bulk cell responses provide the basis for high-throughput screening approaches. Although information on target-specific compound activity can be gained rapidly by these assays, certain important information on phenotypic changes on a cellular level might be missed. The development of automated microscopic workstations has greatly facilitated the application of image-based assays in screening approaches. Because of the high amount of information gained using imaging of cells and subcellular structures, the term high-content screening was coined. Image-based screening has been primarily applied for secondary screening or target identification and validation, as evident by the huge number of published high-content siRNA screens. With the sophisticated hardware and software solutions for HCS now available, there is a trend in academia, as well as in industry, to apply HCS also in primary compound screening campaigns. The advantage of using multiplexed imaging approaches in primary screening is gaining the additional information on solubility, permeability and stability of compounds in a cellular context, which has to be obtained in secondary screening for hits when using classical biochemical approaches [91].

Automated microscopy, when applied at low resolution, can serve to analyze phenotypic changes of larger cell populations at a single cell level, while high resolution microscopy enables the detection of subcellular effects [92]. HCS permits the use of assays that do not rely on changes in the overall fluorescence or luminescence intensity of a cell mixture. Information on single cells and subcellular structures can be gained, for example, changes in subcellular location of fluorescent biomarkers can be assessed [33].

For HCS, a number of specialized instrumental solutions are required (see [93] for a detailed review). To achieve reasonable throughput, all steps in HCS have to be automated, starting from sample preparation via image acquisition and analysis to data storage and handling [94]. The amount of data generated by HCS experiments is enormous compared to classical biochemical assays, requiring a high degree of bioinformatic processing.

Since HCS is a young and upcoming technique, we will briefly discuss some aspects of image acquisition in this section. When choosing an automated microscopy platform, speed and flexibility, sample positioning, available excitation sources and detection methods (confocal versus wide-field), as well as the possibility to add substances before or during measurement have to be considered [93, 95]. Microscopes should provide different objectives to allow imaging at various magnifications. As a rule of thumb, the objective with the lowest magnification that is still capable of resolving the structures of interest should be used to increase the size of the field of view. By this scheme, more cells can be measured per image acquisition, decreasing the required number of fields to be imaged per well [93]. When live cell imaging is intended, exposure times with excitation light have to be minimized to reduce phototoxicity. Consequently, a very sensitive detection system is required, and the objectives should feature a high numerical aperture [96]. Moreover, automated

microscopes may be equipped with an incubation chamber which allows control of the temperature, humidity and CO_2 level to enable prolonged live cell imaging.

Choosing a confocal detection system will usually provide sharper images with improved resolution and lower background, since out-of-focus light is eliminated. Image acquisition in confocal systems is, however, restricted to certain excitation laser lines and, generally, much slower than wide-field detection since scanning is required. Faster throughput is achieved with confocal systems by applying line scanning instead of point scanning or Nipkow spinning disc systems. By contrast, wide-field microscopes provide fast image acquisition, and their excitation source is usually a cheaper metal halide lamp or long-life light-emitting diodes. When using metal halide lamps, excitation wavelengths are selected using appropriate filters or a monochromator device. When LEDs are used as the excitation source, several LEDs of different colors are usually collimated and then combined by dichroic mirrors to offer various excitation wavelengths, with fast interchange and almost unlimited lifetime of the light source.

Automated microscopy requires focus control, which can be achieved by two different methods. For software-based autofocus an image stack in the *z*-direction is rapidly acquired, and online image analysis identifies the correct focal plane. Hardware-based autofocus implementations use optical methods (mostly an additional laser in the IR spectral range) to locate the bottom of the substrate and acquire images at a user-defined offset. While software-based methods are generally slow and might induce photobleaching or phototoxicity due to the additional excitation, they provide superior focus quality for culture plates with irregularities at the bottom or variations in cell size [94]. To minimize photo-induced damage, digital focus control using DIC images has been developed [97, 98]. Hardware-based autofocus may operate faster and still achieve good quality images with standard 384-well culture plates. Several imaging systems also use combinations of hardware and software-based autofocus, identifying the coarse focus optically and then using software autofocus for fine adjustment.

There are a number of commercially available fully automated imaging platforms. Laser scanning cytometers (LSC) have been developed, in analogy to flow cytometers, and are now offered by a couple of companies. They usually scan a whole multi-well plate with low magnification, enabling the identification of individual cells. In contrast to the flow cytometer, LSC uses spatial information of cell location and can thus repetitively scan the same cells, thereby enabling kinetic measurements. LSC use certain integrated laser lines as the excitation source. Higher resolution and often broader excitation spectra can be achieved with automated microscopes.

Microscopy-based screening approaches can either be adopted for endpoint measurements, or to analyze the dynamic behavior of cells. For endpoint measurements, cells are usually fixed using automated preparation protocols. Subcellular localization of proteins or compartments can be visualized by labeling with small molecules, expression of genetically encoded FPs, or immunostaining. Endpoint measurements feature high reproducibility and relatively high throughput, while not requiring specialized incubation procedures during imaging. However, fixation might induce artefacts. In the case of immunofluorescence, labeling protocols might

be labor-intensive, require expensive reagents, and only static information can be gained [95]. In contrast, dynamic processes can be followed in live cells by time-lapse microscopy, yielding even more information. Consequently, for live cell kinetic measurements, data evaluation is considerably more complex [94]. Most HCS assays apply cell lines, often stably expressing fluorescent marker proteins. Primary cells, though better representing the physiological conditions of the target in the human body, are often difficult to obtain in sufficient quantity and with reproducible quality. Embryonic, adult, or reprogrammed stem cells may be used as an alternative [92].

The big advantage of HCS over classical biochemical assays is that library compounds are not only tested for their influence on a specific target, but also for their effects on other related or unrelated processes. This includes information on cytotoxicity and cellular morphology. Multiplexing can principally be achieved in two different ways. One is to use a single staining and to analyze various cellular objects by supervised machine learning to classify multiple phenotypes. This approach requires considerable input from the field of bioinformatics. The other is to employ different fluorescent reporters for distinct signaling processes. If spectra of different fluorophores overlap, spectral unmixing may be applied prior to a morphological image analysis. The number of channels that can be simultaneously acquired is limited due to the spectral properties of the available fluorophores [94].

Currently, time resolution of automated microscopy seriously lowers throughput, especially when live cell kinetic measurements are performed. Since many signal transduction pathways give signals that last for seconds to minutes only, parallelization of image acquisition from all wells of one plate is difficult. Mostly, image acquisition has to be completed in one well before proceeding to the next when fast dynamic processes are investigated.

HCS has great potential, but also requires very careful assay design and optimization, especially when no commercially pre-optimized assays are being used [92].

9.6.11.1 **Image Analysis**

With modern HCS platforms, images are now captured much faster than is analyzable by human observation. Visual inspection and manual scoring, though still frequently used, are slow and prone to biasing by the experimenter. Fortunately, in recent years, the progress in developing computer-assisted analysis methods has been significant. The simplest goal of automated image analysis is, therefore, to reduce time-consuming labor, requiring human researchers to visually inspect single images [99]. In providing objective and quantitative measurements, automated image analysis extracts information that can be fed into statistical analysis algorithms. In some cases, computer-assisted analysis may even detect phenotypic changes (e.g., by analyzing changes in intensity distribution) that are difficult to annotate by visual inspection. Modern software can be trained by supervised machine learning, for example, to classify subcellular structures. However, there are still applications, where computer vision performs much worse than human examination [100]. It is, therefore, important to develop simple assay readouts that fit to a subsequent computer-assisted automated image analysis.

Image processing steps in automated analysis include correction for uneven illumination, background correction, segmentation, and identification of subcellular compartments. Simple outputs from automated analysis can be count, size, shape, and mean intensity of objects. Moreover, information about texture and localization can be extracted and statistically analyzed [99]. Image analysis on a single cell level generally provides a number of advantages compared to averaging over cells. These include subpopulation analysis, cellular statistics and cell filtering [91].

HCS is characterized by the acquisition of multiple parameters. According to the values of these parameters, cells are classified into distinct categories. For robust statistical analysis, one should choose the minimal parameter set that enables discrimination between different categories [100].

A number of software solutions are available for HCS image analysis. Specialized automated imaging platforms usually come with their own data analysis software which is tightly adjusted to the assay format provided with this system. Online image analysis during the screening procedure is often available with these commercial systems. Some third-party commercial software packages offer processing and statistical analysis of image data from screens. In addition, there are a number of open source software packages, comprising flexible analysis tools that can be adapted for specific tasks by a skilled user. These open source packages include CellProfiler [101, 102] and CellClassifier [103, 104], CellCognition [105], packages of the Open Microscopy Environment (OME), and CellHTS, which is part of the Bioconductor/R project.

9.7 Data Mining and Quality Control

Screening campaigns produce large data sets that must be statistically analyzed and evaluated to identify those compounds that possess a desirable biological activity. In this process, quality control and identification of possible errors is essential to reduce the number of false-positive hits or false-negative results. False-positive hits will increase the secondary screens work burden, false-negatives may cause hits to be missed or falsely dropped in secondary screens. In this section we briefly summarize some methods to inspect the quality of screening data and to identify active compounds. For a more detailed discussion on this topic, the reader is referred to some excellent recent reviews [106–108]. Appropriate statistical data analysis procedures are provided by commercially available software packages or by open source software like web cellHTS2 [109].

9.7.1 Quality Control

To increase the quality of a screening campaign, certain measures have to be applied before starting the actual screen. These assay validation procedures include pilot tests to identify the appropriate assay format, to maximize the signal window, to minimize

variabilities and screening with a subset of the compound library. From this test screen, statistical variability and suitable parameters for hit identification (see Section 9.7.2) can be deduced. Moreover, each screen should contain an appropriate amount of control samples where either no compounds are added or (if available) compounds with known biological activity are included.

Typical parameters to evaluate data quality are signal-to-noise or signal-to-background ratios. Variability of the observed parameter and signal strength together determine the sensitivity and robustness of an assay. To obtain a quantitative measure of assay reliability, the dimensionless Z factor [110] has been introduced to assess the quality of screening data:

$$Z = 1 - \frac{3\ \text{SD of sample} + 3\ \text{SD of control}}{|\text{mean of sample-mean of control}|}$$

where the control in an activation assay is a positive control and in an inhibition assay it is a negative control. Alternatively for assay validation, Z' can be calculated, including only positive and negative control samples to test the suitability of a chosen assay for screening. In the case of an ideal assay, Z would reach its maximal value, which is one. Generally, in good screening assays Z is higher than 0.5. When Z becomes negative, the separation of samples showing activity from inactive samples is impossible.

Several sources of error might interfere with the assay quality. These include random and systematic errors, as well as interferences from the tested compounds with the assay signal.

9.7.1.1 Random and Systematic Errors

Random errors, often referred to as noise, arise from technical failures like pipetting errors, robotic failures, and unequal compound concentration due to solvent evaporation or solubility issues. Realtime quality control procedures during the screen may help to identify and deal with these problems promptly. Moreover, the influence of random errors is easily recognized, and strongly diminished, if screens are run in duplicate.

Systematic errors may arise from temporal and spatial effects using multi-well plates, where inaccuracies are caused by location on the plate (e.g., edge effects) and time of measurement [106]. There are a number of statistical methods attempting to deal with these systematic errors. Most of them assume random distribution of compounds on the plates and identify segments of the plate that deviate significantly from the random activity. These algorithms have to be used with care when structurally similar compounds are places in adjacent wells.

Spatial systematic errors may impact significantly on assay quality if hit identification is based on activity in control samples (see Section 9.6.2), which are often placed in border columns, where edge effects can severely alter readout values [107]. Therefore, when possible, control samples should be placed randomly across a multi-well plate.

9.7.1.2 Compound Interferences

In HTS assays, it may be challenging to discriminate between hits that represent compound activity against the investigated biological target and off-target assay interferences [111]. A very common assay interference is due to the spectroscopic properties of the tested compounds, especially when the concentration of the read-out substance is low and compounds are tested in the micromolar range. Assay interference is more common in gain-of-function assays (i.e., expecting an increase in the fluorescence signal) where it is caused by compound fluorescence or light scattering. However, interference may also occur in loss-of-function assays due to quenching and absorbance [22]. Pretesting of the compound library before assay initiation is one possibility to identify these false positive hits. Fluorescence properties of certain libraries are also available from the literature [112]. Since the number of molecules that are fluorescent using UV or blue excitation is generally much higher than by exciting with longer wavelengths, the use of red-shifted dyes as assay readout can reduce interference [27]. Ratiometric approaches are generally less prone to interferences, however, shifts in fluorophore quantum yield due to compound binding or formation of scattering aggregates might constrict such assays, necessitating the definition of appropriate cut-off criteria [22]. Applying gated detection using lanthanides with extremely long fluorescence lifetimes generally reduces interference from fluorescent compounds considerably. Another possibility is to apply fluorescence lifetime technology (FLT) to discriminate between interfering compounds and the detection signal [113]. Since fluorescence lifetimes are largely dependent on the physicochemical environment of a fluorophore, they can also be utilized as readout for physiological processes, for example, the detection of phosphorylation events in an antibody-independent manner. FLT requires longer measurement times per well and specialized plate-readers which are now becoming commercially available.

Certain compounds tend to aggregate under specific conditions leading to particles of 50–400 nm in size that may interfere with the assay by sequestering enzymes on the particle surface. In cell-free assays, using low concentrations of nonionic detergents, like Triton X-100, effectively prevents enzyme inhibition by this process [114]. Further assay interferences may arise from redox-active compounds if DTT is used in the assay, which is commonly done to keep enzymes in a reduced state. In this case counterscreens to identify these compounds, for example, by the detection of the produced H_2O_2, are needed [115]. Again, for some substance libraries, redox cycling compounds are already identified and published [116]. In the case of target oxidation by the compound, the addition of DTT to the assay solution may prevent this effect. Furthermore, counterscreens for cytotoxicity using standard assays should be performed.

A number of assays utilize enzymes like firefly luciferase, phosphatase or peroxidase activities, which might be inhibited by the screened compound, producing false-positive results. In such cases, orthogonal assays utilizing another reporter are necessary to identify the hits corresponding to the biological target during secondary screening.

9.7.2 Identification of Hits

There are numbers of approaches to the identification of hits from screening campaigns. The best suited available method for a given assay must be identified in advance, preferably by conducting pretests [117].

Most hit annotation approaches use some kind of data normalization. In principle, sample values can be compared with values of negative control wells, or with the mean of all sample values, assuming that most compounds have no biological activity. If samples are compared to controls, the number of control wells must be sufficiently high to enable robust statistics. Using mean sample values for normalization may be error-prone when a higher number of compounds per plate induces increased signal activity.

For hit identification one can define signal thresholds above which compounds are regarded to be active. Sometimes a certain percentage of compounds, showing the highest activity is chosen. The *Z*-score is a simple measure for rescaling screening values based on within-plate variations:

$$Z = \frac{X_i - \bar{X}}{S_x}$$

where X_i is the signal produced by compound i, $\bar{X}$ is the mean value of all signals per plate and S_x is the mean standard deviation of all signals. To correct for systematic errors associated with the plate layout, the *B*-score has been introduced [118], which requires more sophisticated statistical analysis. Since mean and standard deviation are strongly influenced by statistical outliers, more resistant scale estimations, such as the median absolute deviation (MAD), can be used.

For further developmental steps, compounds have to be scored according to their potential to have biological activity and to be developable into drugs. Sometimes this scoring is not only based on the activity of the tested compound, but also on the activity that chemically related compounds have shown in the screen. The rationale behind this process, also referred to as "hit-clustering", is that certain scaffolds produce biological activity and a compound is more likely to be truly active when compounds sharing the same or similar scaffolds also show some kind of activity [106].

9.8 Conclusions

Photonics approaches are, and will presumably remain, the most widely applied techniques in industrial and academic screening campaigns for drug development. The trend to miniaturize screening formats is compatible with photonic detection methods. Especially, the ability to excite sub-picoliter volumes with a diffraction-limited light focus and to detect fluorescence at the single molecule level renders this technique most relevant today and in future.

Owing to the increasing complexity and availability of compound libraries, fueled by a variety of chemical approaches and an increasing number of biological targets that are identified by genetic screens, the need for fast and reliable screening methods with ultra-high throughput increases. Further developments in optical assays and miniaturization approaches applying new microfluidic and chip technologies will certainly help to meet these demands.

In spite of the request for methods to achieve even higher throughput, we notice a trend to deduce more information from the primary screen, which is achieved by multiparametric and high content rather than simple assay readouts. The reason for this development is that unsuitable compounds are pinpointed early in the screen, saving material and reducing the load of follow-up studies. Multiparametric assays require careful statistical analysis and data mining procedures, which represents another rapidly developing field.

Acknowledgment

We thank Christian Hellwig, Anke Klein, and Sebastian Tannert for critically reading the manuscript.

References

1 Zhu, Z. and Cuozzo, J. (2009) Review article: high-throughput affinity-based technologies for small-molecule drug discovery. *J. Biomol. Screen.*, **14** (10), 1157–1164.
2 Baker, M. (2010) Academic screening goes high-throughput. *Nat. Methods*, **7**, 787–792.
3 Betz, U.A.K. (2005) How many genomics targets can a portfolio afford? *Drug Discov. Today*, **10** (15), 1057–1063.
4 Overington, J.P., Al-Lazikani, B., and Hopkins, A.L. (2006) How many drug targets are there? *Nat. Rev. Drug Discov.*, **5** (12), 993–996.
5 Heilker, R., Wolff, M., Tautermann, C.S., and Bieler, M. (2009) G-protein-coupled receptor-focused drug discovery using a target class platform approach. *Drug Discov. Today*, **14** (5–6), 231–240.
6 Lipinski, C. and Hopkins, A. (2004) Navigating chemical space for biology and medicine. *Nature*, **432** (7019), 855–861.
7 Walke, D.W., Han, C., Shaw, J., Wann, E., Zambrowicz, B., and Sands, A. (2001) In vivo drug target discovery: identifying the best targets from the genome. *Curr. Opin. Biotechnol.*, **12** (6), 626–631.
8 Hopkins, A.L. and Groom, C.R. (2002) The druggable genome. *Nat. Rev. Drug Discov.*, **1** (9), 727–730.
9 Lipinski, C.A., Lombardo, F., Dominy, B.W., and Feeney, P.J. (2001) Experimental and computational approaches to estimate solubility and permeability in drug discovery and development settings. *Adv. Drug Deliv. Rev.*, **46** (1–3), 3–26.
10 Dobson, P.D., Patel, Y., and Kell, D.B. (2009) "Metabolite-likeness" as a criterion in the design and selection of pharmaceutical drug libraries. *Drug Discov. Today*, **14** (1–2), 31–40.
11 Bauer, R.A., Wurst, J.M., and Tan, D.S. (2010) Expanding the range of "druggable" targets with natural product-based libraries: an academic perspective. *Curr. Opin. Chem. Biol.*, **14** (3), 308–314.
12 Drewry, D.H. and Macarron, R. (2010) Enhancements of screening collections to address areas of unmet medical need:

an industry perspective. *Curr. Opin. Chem. Biol.*, **14** (3), 289–298.
13 Spandl, R.J., Bender, A., and Spring, D.R. (2008) Diversity-oriented synthesis; a spectrum of approaches and results. *Org. Biomol. Chem*, **6** (7), 1149–1158.
14 Rees, D.C., Congreve, M., Murray, C.W., and Carr, R. (2004) Fragment-based lead discovery. *Nat. Rev. Drug Discov.*, **3** (8), 660–672.
15 Carr, R.A.E., Congreve, M., Murray, C.W., and Rees, D.C. (2005) Fragment-based lead discovery: leads by design. *Drug Discov. Today*, **10** (14), 987–992.
16 Volkmer, R. (2009) Synthesis and application of peptide arrays: quo vadis SPOT technology. *Chembiochem*, **10** (9), 1431–1442.
17 Kim, M., Shin, D.S., Kim, J., and Lee, Y.S. (2010) Substrate screening of protein kinases: detection methods and combinatorial peptide libraries. *Biopolymers*, **94** (6), 753–762.
18 Gruber, C.W., Muttenthaler, M., and Freissmuth, M. (2010) Ligand-based peptide design and combinatorial peptide libraries to target G protein-coupled receptors. *Curr. Pharm. Des.*, **16** (28), 3071–3088.
19 Scheuermann, J. and Neri, D. (2010) DNA-encoded chemical libraries: a tool for drug discovery and for chemical biology. *Chembiochem*, **11** (7), 931–937.
20 Buller, F., Mannocci, L., Scheuermann, J., and Neri, D. (2010) Drug discovery with DNA-encoded chemical libraries. *Bioconjug. Chem.*, **21** (9), 1571–1580.
21 Fuchs, F. and Boutros, M. (2006) Cellular phenotyping by RNAi. *Brief Funct. Genomic Proteomic*, **5** (1), 52–56.
22 Gribbon, P. and Sewing, A. (2003) Fluorescence readouts in HTS: no gain without pain? *Drug Discov. Today*, **8** (22), 1035–1043.
23 Fan, F. and Wood, K.V. (2007) Bioluminescent assays for high-throughput screening. *Assay Drug. Dev. Technol.*, **5** (1), 127–136.
24 Thorne, N., Inglese, J., and Auld, D.S. (2010) Illuminating insights into firefly luciferase and other bioluminescent reporters used in chemical biology. *Chem. Biol.*, **17** (6), 646–657.
25 Walling, M.A., Wang, S., Shi, H., and Shepard, J.R.E. (2010) Quantum dots for positional registration in live cell-based arrays. *Anal. Bioanal. Chem.*, **398** (3), 1263–1271.
26 Vogel, K.W. and Vedvik, K.L. (2006) Improving lanthanide-based resonance energy transfer detection by increasing donor-acceptor distances. *J. Biomol. Screen.*, **11** (4), 439–443.
27 Vedvik, K.L., Eliason, H.C., Hoffman, R.L., Gibson, J.R., Kupcho, K.R., Somberg, R.L., and Vogel, K.W. (2004) Overcoming compound interference in fluorescence polarization-based kinase assays using far-red tracers. *Assay Drug. Dev. Technol.*, **2** (2), 193–203.
28 Pepperkok, R. and Ellenberg, J. (2006) High-throughput fluorescence microscopy for systems biology. *Nat. Rev. Mol. Cell Biol.*, **7** (9), 690–696.
29 Wolff, M., Kredel, S., Wiedenmann, J., Nienhaus, G.U., and Heilker, R. (2008) Cell-based assays in practice: cell markers from autofluorescent proteins of the GFP-family. *Comb. Chem. High Throughput Screen.*, **11** (8), 602–609.
30 Fritzsche, M. and Mandenius, C.F. (2010) Fluorescent cell-based sensing approaches for toxicity testing. *Anal. Bioanal. Chem.*, **398** (1), 181–191.
31 Roda, A., Pasini, P., Mirasoli, M., Michelini, E., and Guardigli, M. (2004) Biotechnological applications of bioluminescence and chemiluminescence. *Trends Biotechnol.*, **22** (6), 295–303.
32 VanEngelenburg, S.B. and Palmer, A.E. (2008) Fluorescent biosensors of protein function. *Curr. Opin. Chem. Biol.*, **12** (1), 60–65.
33 Wolff, M., Wiedenmann, J., Nienhaus, G.U., Valler, M., and Heilker, R. (2006) Novel fluorescent proteins for high-content screening. *Drug Discov. Today*, **11** (23–24), 1054–1060.
34 Chudakov, D.M., Matz, M.V., Lukyanov, S., and Lukyanov, K.A. (2010) Fluorescent proteins and their applications in imaging living cells and tissues. *Physiol. Rev.*, **90** (3), 1103–1163.
35 Verkman, A.S., Lukacs, G.L., and Galietta, L.J.V. (2006) CFTR chloride channel drug discovery-inhibitors as

antidiarrheals and activators for therapy of cystic fibrosis. *Curr. Pharm. Des.*, **12** (18), 2235–2247.
36 Morris, M.C. (2010) Fluorescent biosensors of intracellular targets from genetically encoded reporters to modular polypeptide probes. *Cell Biochem. Biophys.*, **56** (1), 19–37.
37 Sklar, L.A., Carter, M.B., and Edwards, B.S. (2007) Flow cytometry for drug discovery, receptor pharmacology and high-throughput screening. *Curr. Opin. Pharmacol.*, **7** (5), 527–534.
38 Kintses, B., van Vliet, L.D., Devenish, S.R.A., and Hollfelder, F. (2010) Microfluidic droplets: new integrated workflows for biological experiments. *Curr. Opin. Chem. Biol.*, **14** (5), 548–555.
39 Perrin, D., Frémaux, C., and Scheer, A. (2006) Assay development and screening of a serine/threonine kinase in an on-chip mode using caliper nanofluidics technology. *J. Biomol. Screen.*, **11** (4), 359–368.
40 Blackwell, L.J., Birkos, S., Hallam, R., Carr, G.V.D., Arroway, J., Suto, C.M., and Janzen, W.P. (2009) High-throughput screening of the cyclic AMP-dependent protein kinase (PKA) using the caliper microfluidic platform. *Methods Mol. Biol.*, **565**, 225–237.
41 Castel, D., Pitaval, A., Debily, M.A., and Gidrol, X. (2006) Cell microarrays in drug discovery. *Drug Discov. Today*, **11** (13–14), 616–622.
42 Zawko, S.A. and Schmidt, C.E. (2010) Simple benchtop patterning of hydrogel grids for living cell microarrays. *Lab Chip*, **10** (3), 379–383.
43 Upadhyaya, S. and Selvaganapathy, P.R. (2010) Microfluidic devices for cell based high throughput screening. *Lab Chip*, **10** (3), 341–348.
44 Wu, J., Wheeldon, I., Guo, Y., Lu, T., Du, Y., Wang, B., He, J., Hu, Y., and Khademhosseini, A. (2011) A sandwiched microarray platform for benchtop cell-based high throughput screening. *Biomaterials*, **32** (3), 841–848.
45 Ziauddin, J. and Sabatini, D.M. (2001) Microarrays of cells expressing defined cDNAs. *Nature*, **411** (6833), 107–110.
46 de Jong, L.A.A., Uges, D.R.A., Franke, J.P., and Bischoff, R. (2005) Receptor-ligand binding assays: technologies and applications. *J. Chromatogr. B Analyt. Technol. Biomed. Life Sci.*, **829** (1–2), 1–25.
47 Krishhan, V.V., Khan, I.H., and Luciw, P.A. (2009) Multiplexed microbead immunoassays by flow cytometry for molecular profiling: Basic concepts and proteomics applications. *Crit. Rev. Biotechnol.*, **29** (1), 29–43.
48 Burke, T.J., Loniello, K.R., Beebe, J.A., and Ervin, K.M. (2003) Development and application of fluorescence polarization assays in drug discovery. *Comb. Chem. High Throughput Screen.*, **6** (3), 183–194.
49 Banks, P. and Harvey, M. (2002) Considerations for using fluorescence polarization in the screening of G protein-coupled receptors. *J. Biomol. Screen.*, **7** (2), 111–117.
50 Vogel, K.W., Zhong, Z., Bi, K., and Pollok, B.A. (2008) Developing assays for kinase drug discovery - where have the advances come from? *Exp. Opin. Drug Discov.*, **3** (1), 115–129.
51 Degorce, F., Card, A., Soh, S., Trinquet, E., Knapik, G.P., and Xie, B. (2009) HTRF: A technology tailored for drug discovery - a review of theoretical aspects and recent applications. *Curr. Chem. Genomics*, **3**, 22–32.
52 Gabriel, D., Vernier, M., Pfeifer, M.J., Dasen, B., Tenaillon, L., and Bouhelal, R. (2003) High throughput screening technologies for direct cyclic AMP measurement. *Assay Drug. Dev. Technol.*, **1** (2), 291–303.
53 Jia, Y. (2008) Current status of HTRF technology in kinase assays. *Exp. Opin. Drug Discov.*, **3** (12), 1461–1474.
54 Eglen, R.M., Reisine, T., Roby, P., Rouleau, N., Illy, C., Bossé, R., and Bielefeld, M. (2008) The use of AlphaScreen technology in HTS: current status. *Curr. Chem. Genomics*, **1**, 2–10.
55 Michnick, S.W., Ear, P.H., Manderson, E.N., Remy, I., and Stefan, E. (2007) Universal strategies in research and drug discovery based on protein-fragment complementation assays. *Nat. Rev. Drug Discov.*, **6** (7), 569–582.
56 Remy, I. and Michnick, S.W. (2006) A highly sensitive protein-protein interaction assay based on gaussia luciferase. *Nat. Methods*, **3** (12), 977–979.

57 Olson, K.R. and Eglen, R.M. (2007) Beta galactosidase complementation: a cell-based luminescent assay platform for drug discovery. *Assay Drug. Dev. Technol.*, **5** (1), 137–144.

58 Eglen, R.M. (2002) Enzyme fragment complementation: a flexible high throughput screening assay technology. *Assay Drug. Dev. Technol.*, **1** (1 Pt 1), 97–104.

59 Eggeling, C., Brand, L., Ullmann, D., and Jäger, S. (2003) Highly sensitive fluorescence detection technology currently available for HTS. *Drug Discov. Today*, **8** (14), 632–641.

60 Rüdiger, M., Haupts, U., Moore, K.J., and Pope, A.J. (2001) Single-molecule detection technologies in miniaturized high throughput screening: binding assays for g protein-coupled receptors using fluorescence intensity distribution analysis and fluorescence anisotropy. *J. Biomol. Screen.*, **6** (1), 29–37.

61 Kask, P., Palo, K., Fay, N., Brand, L., Mets, U., Ullmann, D., Jungmann, J., Pschorr, J., and Gall, K. (2000) Two-dimensional fluorescence intensity distribution analysis: theory and applications. *Biophys. J.*, **78** (4), 1703–1713.

62 Michelini, E., Cevenini, L., Mezzanotte, L., Coppa, A., and Roda, A. (2010) Cell-based assays: fuelling drug discovery. *Anal. Bioanal. Chem.*, **398** (1), 227–238.

63 Williams, C. (2004) cAMP detection methods in HTS: selecting the best from the rest. *Nat. Rev. Drug Discov.*, **3** (2), 125–135.

64 Hill, S.J., Baker, J.G., and Rees, S. (2001) Reporter-gene systems for the study of G-protein-coupled receptors. *Curr. Opin. Pharmacol.*, **1** (5), 526–532.

65 Nakajima, Y., Kimura, T., Sugata, K., Enomoto, T., Asakawa, A., Kubota, H., Ikeda, M., and Ohmiya, Y. (2005) Multicolor luciferase assay system: one-step monitoring of multiple gene expressions with a single substrate. *Biotechniques*, **38** (6), 891–894.

66 Conklin, B.R., Farfel, Z., Lustig, K.D., Julius, D., and Bourne, H.R. (1993) Substitution of three amino acids switches receptor specificity of Gq alpha to that of Gi alpha. *Nature*, **363** (6426), 274–276.

67 Kostenis, E., Waelbroeck, M., and Milligan, G. (2005) Techniques: promiscuous Galpha proteins in basic research and drug discovery. *Trends Pharmacol. Sci.*, **26** (11), 595–602.

68 Rich, T.C., Tse, T.E., Rohan, J.G., Schaack, J., and Karpen, J.W. (2001) In vivo assessment of local phosphodiesterase activity using tailored cyclic nucleotide-gated channels as cAMP sensors. *J. Gen. Physiol.*, **118** (1), 63–78.

69 Wunder, F., Stasch, J.P., Hütter, J., Alonso-Alija, C., Hüser, J., and Lohrmann, E. (2005) A cell-based cGMP assay useful for ultra-high-throughput screening and identification of modulators of the nitric oxide/cGMP pathway. *Anal. Biochem.*, **339** (1), 104–112.

70 Reinscheid, R.K., Kim, J., Zeng, J., and Civelli, O. (2003) High-throughput real-time monitoring of Gs-coupled receptor activation in intact cells using cyclic nucleotide-gated channels. *Eur. J. Pharmacol.*, **478** (1), 27–34.

71 Wunder, F., Kalthof, B., Müller, T., and Hüser, J. (2008) Functional cell-based assays in microliter volumes for ultra-high throughput screening. *Comb. Chem. High Throughput Screen.*, **11** (7), 495–504.

72 Titus, S., Neumann, S., Zheng, W., Southall, N., Michael, S., Klumpp, C., Yasgar, A., Shinn, P., Thomas, C.J., Inglese, J., Gershengorn, M.C., and Austin, C.P. (2008) Quantitative high-throughput screening using a live-cell cAMP assay identifies small-molecule agonists of the TSH receptor. *J. Biomol. Screen.*, **13** (2), 120–127.

73 Paredes, R.M., Etzler, J.C., Watts, L.T., Zheng, W., and Lechleiter, J.D. (2008) Chemical calcium indicators. *Methods*, **46** (3), 143–151.

74 Zhang, Y., Kowal, D., Kramer, A., and Dunlop, J. (2003) Evaluation of FLIPR calcium 3 assay kit-a new no-wash fluorescence calcium indicator reagent. *J. Biomol. Screen.*, **8** (5), 571–577.

75 Brini, M. (2008) Calcium-sensitive photoproteins. *Methods*, **46** (3), 160–166.

76 McCombs, J.E. and Palmer, A.E. (2008) Measuring calcium dynamics in living cells with genetically encodable calcium indicators. *Methods*, **46** (3), 152–159.

77 Charlton, S.J. and Vauquelin, G. (2010) Elusive equilibrium: the challenge of interpreting receptor pharmacology using calcium assays. *Br. J. Pharmacol.*, **161** (6), 1250–1265.

78 Liu, K., Southall, N., Titus, S.A., Inglese, J., Eskay, R.L., Shinn, P., Austin, C.P., Heilig, M.A., and Zheng, W. (2010) A multiplex calcium assay for identification of GPCR agonists and antagonists. *Assay Drug. Dev. Technol.*, **8** (3), 367–379.

79 Lü, Q. and An, W.F. (2008) Impact of novel screening technologies on ion channel drug discovery. *Comb. Chem. High Throughput Screen.*, **11** (3), 185–194.

80 Zheng, W., Spencer, R.H., and Kiss, L. (2004) High throughput assay technologies for ion channel drug discovery. *Assay Drug. Dev. Technol.*, **2** (5), 543–552.

81 Weaver, C.D., Harden, D., Dworetzky, S.I., Robertson, B., and Knox, R.J. (2004) A thallium-sensitive, fluorescence-based assay for detecting and characterizing potassium channel modulators in mammalian cells. *J. Biomol. Screen.*, **9** (8), 671–677.

82 Beacham, D.W., Blackmer, T., Grady, M.O., and Hanson, G.T. (2010) Cell-based potassium ion channel screening using the fluxOR™ assay. *J. Biomol. Screen.*, **15** (4), 441–446.

83 Sui, J., Cotard, S., Andersen, J., Zhu, P., Staunton, J., Lee, M., and Lin, S. (2010) Optimization of a Yellow fluorescent protein-based iodide influx high-throughput screening assay for cystic fibrosis transmembrane conductance regulator (CFTR) modulators. *Assay Drug. Dev. Technol.*, **8** (6), 656–668.

84 Przybylo, M., Borowik, T., and Langner, M. (2010) Fluorescence techniques for determination of the membrane potentials in high throughput screening. *J. Fluoresc.*, **20** (6), 1139–1157.

85 Molokanova, E. and Savchenko, A. (2008) Bright future of optical assays for ion channel drug discovery. *Drug Discov. Today*, **13** (1–2), 14–22.

86 Baxter, D.F., Kirk, M., Garcia, A.F., Raimondi, A., Holmqvist, M.H., Flint, K.K., Bojanic, D., Distefano, P.S., Curtis, R., and Xie, Y. (2002) A novel membrane potential-sensitive fluorescent dye improves cell-based assays for ion channels. *J. Biomol. Screen.*, **7** (1), 79–85.

87 González, J.E. and Maher, M.P. (2002) Cellular fluorescent indicators and voltage/ion probe reader (VIPR™) tools for ion channel and receptor drug discovery. *Receptors Channels*, **8** (5–6), 283–295.

88 Dabrowski, M.A., Dekermendjian, K., Lund, P.E., Krupp, J.J., Sinclair, J., and Larsson, O. (2008) Ion channel screening technology. *CNS Neurol. Disord. Drug Targets*, **7** (2), 122–128.

89 Edwards, B.S., Young, S.M., Saunders, M.J., Bologa, C., Oprea, T.I., Ye, R.D., Prossnitz, E.R., Graves, S.W., and Sklar, L.A. (2007) High-throughput flow cytometry for drug discovery. *Exp. Opin. Drug Discov.*, **2** (5), 685–696.

90 Krutzik, P.O. and Nolan, G.P. (2006) Fluorescent cell barcoding in flow cytometry allows high-throughput drug screening and signaling profiling. *Nat. Methods*, **3** (5), 361–368.

91 Zanella, F., Lorens, J.B., and Link, W. (2010) High content screening: seeing is believing. *Trends Biotechnol.*, **28** (5), 237–245.

92 Lang, P., Yeow, K., Nichols, A., and Scheer, A. (2006) Cellular imaging in drug discovery. *Nat. Rev. Drug Discov.*, **5** (4), 343–356.

93 Vaisberg, E.A., Lenzi, D., Hansen, R.L., Keon, B.H., and Finer, J.T. (2006) An infrastructure for high-throughput microscopy: instrumentation, informatics, and integration. *Methods Enzymol.*, **414**, 484–512.

94 Starkuviene, V. and Pepperkok, R. (2007) The potential of high-content high-throughput microscopy in drug discovery. *Br. J. Pharmacol.*, **152** (1), 62–71.

95 Lee, S. and Howell, B.J. (2006) High-content screening: emerging hardware and software technologies. *Methods Enzymol.*, **414**, 468–483.

96 Bickle, M. (2010) The beautiful cell: high-content screening in drug discovery. *Anal. Bioanal. Chem.*, **398** (1), 219–226.

97 Shen, F., Hodgson, L., and Hahn, K. (2006) Digital autofocus methods for

automated microscopy. *Methods Enzymol.*, **414**, 620–632.

98 Shen, F., Hodgson, L., Price, J.H., and Hahn, K.M. (2008) Digital differential interference contrast autofocus for high-resolution oil-immersion microscopy. *Cytometry A*, **73** (7), 658–666.

99 Ljosa, V. and Carpenter, A.E. (2009) Introduction to the quantitative analysis of two-dimensional fluorescence microscopy images for cell-based screening. *PLoS Comput. Biol.*, **5** (12), e1000603.

100 Wollman, R. and Stuurman, N. (2007) High throughput microscopy: from raw images to discoveries. *J. Cell Sci.*, **120**Pt (21), 3715–3722.

101 Carpenter, A., Jones, T., Lamprecht, M., Clarke, C., Kang, I., Friman, O., Guertin, D., Chang, J., Lindquist, R., Moffat, J., Golland, P., and Sabatini, D. (2006) CellProfiler: image analysis software for identifying and quantifying cell phenotypes. *Genome Biol.*, **7** (10).

102 Jones, T., Kang, I., Wheeler, D., Lindquist, R., Papallo, A., Sabatini, D., Golland, P., and Carpenter, A. (2008) CellProfiler Analyst: data exploration and analysis software for complex image-based screens. *BMC Bioinformatics*, **9**, 482.

103 Rämö, P., Sacher, R., Snijder, B., Begemann, B., and Pelkmans, L. (2009) CellClassifier: supervised learning of cellular phenotypes. *Bioinformatics*, **25** (22), 3028–3030.

104 Misselwitz, B., Strittmatter, G., Periaswamy, B., Schlumberger, M.C., Rout, S., Horvath, P., Kozak, K., and Hardt, W.D. (2010) Enhanced CellClassifier: a multi-class classification tool for microscopy images. *BMC Bioinformatics*, **11**, 30.

105 Held, M., Schmitz, M.H.A., Fischer, B., Walter, T., Neumann, B., Olma, M.H., Peter, M., Ellenberg, J., and Gerlich, D.W. (2010) CellCognition: time-resolved phenotype annotation in high-throughput live cell imaging. *Nat. Methods*, **7** (9), 747–754.

106 Harper, G. and Pickett, S.D. (2006) Methods for mining HTS data. *Drug Discov. Today*, **11** (15–16), 694–699.

107 Malo, N., Hanley, J.A., Cerquozzi, S., Pelletier, J., and Nadon, R. (2006) Statistical practice in high-throughput screening data analysis. *Nat. Biotechnol.*, **24** (2), 167–175.

108 Birmingham, A., Selfors, L.M., Forster, T., Wrobel, D., Kennedy, C.J., Shanks, E., Santoyo-Lopez, J., Dunican, D.J., Long, A., Kelleher, D., Smith, Q., Beijersbergen, R.L., Ghazal, P., and Shamu, C.E. (2009) Statistical methods for analysis of high-throughput RNA interference screens. *Nat. Methods*, **6** (8), 569–575.

109 Pelz, O., Gilsdorf, M., and Boutros, M. (2010) web cellHTS2: a web-application for the analysis of high-throughput screening data. *BMC Bioinformatics*, **11**, 185.

110 Zhang, J., Chung, T., and Oldenburg, K. (1999) A simple statistical parameter for use in evaluation and validation of high throughput screening assays. *J. Biomol. Screen.*, **4** (2), 67–73.

111 Thorne, N., Auld, D.S., and Inglese, J. (2010) Apparent activity in high-throughput screening: origins of compound-dependent assay interference. *Curr. Opin. Chem. Biol.*, **14** (3), 315–324.

112 Simeonov, A., Jadhav, A., Thomas, C.J., Wang, Y., Huang, R., Southall, N.T., Shinn, P., Smith, J., Austin, C.P., Auld, D.S., and Inglese, J. (2008) Fluorescence spectroscopic profiling of compound libraries. *J. Med. Chem.*, **51** (8), 2363–2371.

113 Gakamsky, D.M., Dennis, R.B., and Smith, S.D. (2011) Use of fluorescence lifetime technology to provide efficient protection from false hits in screening applications. *Anal. Biochem.*, **409** (1), 89–97.

114 McGovern, S.L., Helfand, B.T., Feng, B., and Shoichet, B.K. (2003) A specific mechanism of nonspecific inhibition. *J. Med. Chem.*, **46** (20), 4265–4272.

115 Johnston, P.A., Soares, K.M., Shinde, S.N., Foster, C.A., Shun, T.Y., Takyi, H.K., Wipf, P., and Lazo, J.S. (2008) Development of a 384-well colorimetric assay to quantify hydrogen peroxide generated by the redox cycling of compounds in the presence of reducing agents. *Assay Drug. Dev. Technol.*, **6** (4), 505–518.

116 Soares, K.M., Blackmon, N., Shun, T.Y., Shinde, S.N., Takyi, H.K., Wipf, P., Lazo,

J.S., and Johnston, P.A. (2010) Profiling the NIH small molecule repository for compounds that generate H_2O_2 by redox cycling in reducing environments. *Assay Drug. Dev. Technol.*, **8** (2), 152–174.

117 Shun, T.Y., Lazo, J.S., Sharlow, E.R., and Johnston, P.A. (2011) Identifying actives from HTS data sets: practical approaches for the selection of an appropriate HTS data-processing method and quality control review. *J. Biomol. Screen.*, **16** (1), 1–14.

118 Brideau, C., Gunter, B., Pikounis, B., and Liaw, A. (2003) Improved statistical methods for hit selection in high-throughput screening. *J. Biomol. Screen.*, **8** (6), 634–647.

10
Optical Measurements for the Rational Screening of Protein Crystallization Conditions

Christoph Janzen and Kurt Hoffmann

10.1
Introduction

The determination of protein structures by X-ray diffraction is a complex process because optimal solution parameters must be found for the growth of single crystals, and these are usually defined empirically. In this chapter we describe a rational crystallization process, combining automated sample preparation with the objective evaluation of crystallization trials based on optical measurements. The computerized analysis of such measurements allows the optimum crystallization conditions to be deduced rationally. We developed three new optical measurement techniques for the characterization of small protein droplets. First, static laser light scattering (SLS) allows thermodynamic interaction parameters (e.g., osmotic virial coefficients) to be determined, indicating the attractive and repulsive forces between solute particles. Second, dynamic laser light scattering (DLS) allows the determination of particle radius distributions and the detection of aggregation. Finally, quantitative polarization light microscopy generates a set of three images for transmission, the amplitude of birefringence, and the orientation of the axis of the sample's indicatrix, allowing the detection and quantitative analysis of birefringent structures (e.g., protein crystals or crystalline precipitates). By combining SLS, DLS and quantitative polarization microscopy, it is possible to carry out a rational optical analysis of the pre-crystallization, crystallization and post-crystallization phases. All three methods were developed in combination with a novel crystallization protocol that can be applied to droplets with a volume $<1\,\mu l$. A demonstrator was built that contains an optical measurement unit for light scattering and microscopy, and a liquid-handling unit for sample preparation. This demonstrator provides a unique and novel platform for the development of rational crystallization strategies.

Handbook of Biophotonics. Vol.3: Photonics in Pharmaceutics, Bioanalysis and Environmental Research, First Edition.
Edited by Jürgen Popp, Valery V. Tuchin, Arthur Chiou, and Stefan Heinemann

10.2
State of the Art of Protein Crystallization Techniques

The three-dimensional structures of macromolecules such as proteins provide useful reference data and facilitate downstream biotechnology applications, such as drug development, because they allow drug–target interactions to be modeled accurately. The three-dimensional structures of biological macromolecules are usually determined by X-ray diffraction analysis, which requires the preparation of macromolecules and their complexes as individual monocrystals.

Protein crystals are usually obtained from highly-purified protein solutions in the presence of salts or polymers (such as polyethylene glycol) that act as precipitation reagents. Water is extracted slowly and in a controlled manner so that the protein solution becomes oversaturated. Local fluctuations in protein concentration can then lead to the formation of aggregates that nucleate to seed crystals. Although nucleation is a prerequisite for the formation of crystals, the more nucleation seeds that are formed simultaneously, the more likely that polycrystalline precipitates will form, and these cannot be used for X-ray diffraction. Optimal crystallization conditions are achieved when very few nucleation seeds are formed, and these grow into large single crystals. The protein solution is said to exist in a metastable state when the solid phase of the protein is thermodynamically favored over the solute form, yet the appearance of seed crystals is hindered due to the large free surface enthalpy that must be overcome. All crystallization experiments try to achieve this metastable state because this favors individual nucleation events that can grow to form large single crystals. The crystallization conditions are usually tested empirically by selecting different protein concentrations, different salts at varying ionic strengths, and different solution parameters (e.g., pH, buffers, polymers, organic solvents and temperatures). However, this results in a vast matrix of distinct multi-parameter conditions [1].

There are many crystallization methods. In a batch process, the target protein is added to an aqueous solution containing buffer, salts and other crystallizing reagents (the so-called crystallization solution) or vice versa [2]. The two solutions are combined in a closed sample compartment, such as a microtiter plate with a closure head or layer of paraffin oil to inhibit evaporation. In these closed systems, there is no enrichment of the precipitation reagents or proteins over a prolonged period and all concentrations can be adjusted directly by applying the protein and crystallization solutions in different relative proportions (Figure 10.1). However, the batch process does not support the slow and continuous change of conditions that allow entry into the metastable region of the protein phase diagram, so the great merit of classical crystallization processes is lost (kinetic and dynamic properties of the end point, see Figure 10.2).

A modified batch process method replaces the pure paraffin oil with paraffin oil containing dimethylsiloxane (DMS), which allows the continuous diffusion (evaporation) of water from the covered solution. This gradually increases the protein and salt concentrations, and the metastable region can thus be reached (Figure 10.2). However, since this is an open system, an end point cannot be set. The main

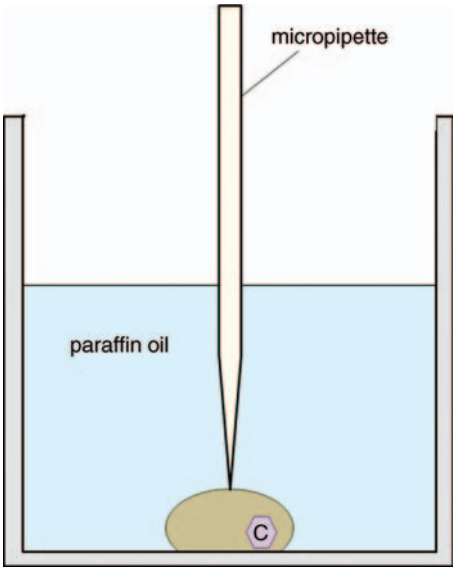

Figure 10.1 Schematic illustration of a micro-batch experiment. A drop is covered with immersion oil, and liquids can be added under the oil with a micropipette. If pure paraffin oil is used, no water loss is expected (batch experiment), but where an open diffusion oil is used (such as paraffin with dimethylsiloxane) the water can evaporate and the protein concentration increases.

disadvantage is that the protein solution will dry out completely over a period time and this approach is therefore only of limited use (see "diffusion oil" path, Figure 10.2).

The traditional and most widely used protein crystallization techniques are hanging and sitting droplets. Here a drop of protein solution (mixed with reservoir solution) is incubated in a closed vessel with a reservoir of aqueous solution containing higher concentrations of salt (Figure 10.3). Over time, water evaporates from the droplet and is transported to the reservoir solution so that the concentration of the protein and the precipitant increases continuously. An end point is reached when the droplet is in equilibrium with the reservoir (identical chemical potential) (see "h/s-drop" path, Figure 10.2). The salt concentration in the reservoir solution determines the end point of the diffusion process.

Crystals suitable for structure determination by X-ray diffraction are very difficult to prepare using the above conventional methods, and it is often not possible to grow crystals of a suitable size and quality. Crystallization often fails for unknown reasons. The interplay between physical and chemical processes during the formation of crystals is complex and still not completely understood.

Over the last few years, we have witnessed rapid progress in the automated determination of gene and protein sequences, and it would be advantageous to apply the same high-throughput paradigm to protein structure determination. This has become possible, in theory, because of recent advances in X-ray crystallography, such

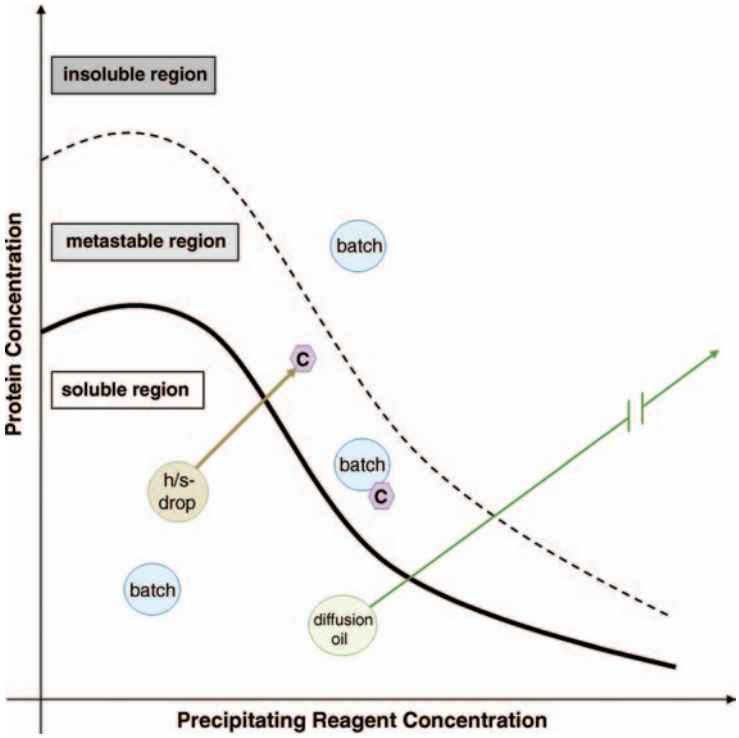

Figure 10.2 Simplified phase diagram summarizing typical crystallization techniques. The soluble, metastable and insoluble regions for the protein are shown. The encircled "batch" indicates crystallization trials performed under paraffin oil, where the initial concentrations do not change, whereas "diffusion oil" indicates a modified batch experiment with oil that allows diffusion covering the protein solution. No endpoint for water loss is determined. Finally, "h/s-drop" shows the classical approach to crystallization (hanging/sitting drop) with a defined end point for the diffusion process.

as the availability of high-brilliance X-ray sources (synchrotrons), improved hardware, and software that allows rapid data interpretation and structure calculations. Unfortunately, conventional methods for protein crystallization have not evolved in the same manner and, despite there being numerous automated, high-throughput approaches, no process exists that easily yields protein crystals of sufficient size and quality for X-ray diffraction [3]. The achievement of optimal conditions for the formation of single crystals is still a labor-intensive empirical process that depends mainly on the intuition of the crystallographer. Protein crystallography is therefore the bottleneck in the structural determination of biological macromolecules and there is a great demand for novel protein crystallization methods that can be automated and evaluated objectively, thus enabling the systematic production of crystals.

Automated diffusion experiments based on the hanging-drop or sitting-drop methods are performed in systems that are closed with siliconized glass lids or

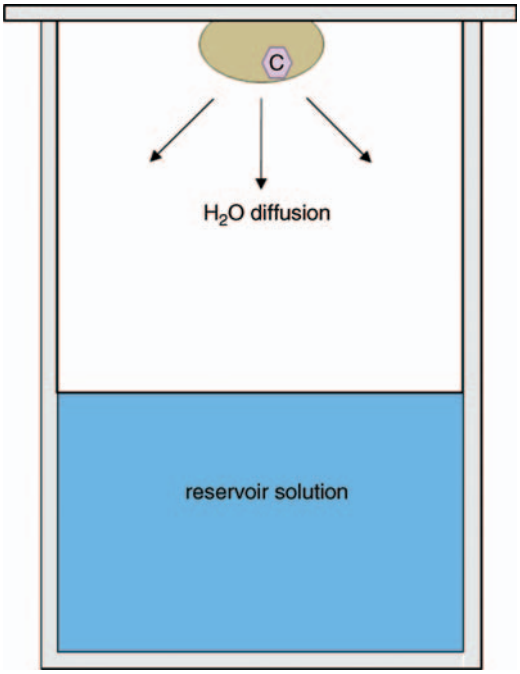

Figure 10.3 Schematic illustration of a hanging drop crystallization experiment. The liquid in the hanging drop is in diffusion contact with the reservoir solution, which has a higher salt concentration. Water evaporates from the drop and is deposited in the reservoir, the protein concentration in the drop rises. When the concentrations are equilibrated, the net transport process stops (defined end point).

self-adhesive transparent films. The automation of liquid handling systems requires many complex steps (e.g., closing the lid) and current systems tend to be expensive, slow, irreproducible and incompatible with the smallest sample volumes (in the microliter to nanoliter range). Protection against evaporation is required for these small sample volumes as long as the systems are not closed by the application of self-adhesive foils or glass lids, because water losses can vary considerably and thus affect the delicately balanced concentrations of proteins and precipitation reagents.

In automated batch processes, robots are used to deposit protein and crystallization solutions directly under paraffin oil to prevent evaporation. Such automated methods are associated with the usual disadvantages of batch processes (i.e., no change in concentration under pure oil, and no end to the diffusion process under open diffusion oil). Nevertheless, most automated high-throughput crystallization systems in use today are based on batch processes. Large numbers of crystallization trials are necessary to test different combinations of conditions empirically, with automated camera systems used to identify amorphous precipitates, microcrystalline precipitates or large single crystals. The parameter field under investigation is based upon the experience and intuition of the crystallographer. With the exception of the

post-crystallization phase, no optical analysis of these experiments is possible, therefore the outcome depends on trial and error and thousands of experiments may be required to produce adequate crystals, if this is possible at all.

In order to improve the process of crystallization significantly, we have developed a combination of novel rational methods for protein crystallization based on optical measurement techniques, and these are discussed in more detail below.

10.3
A New Crystallization Method that Enables the Use of Optical Measurement Technologies

We have developed a new crystallization method to integrate light scattering measurements within a screening process using only small amounts of protein [4]. The method uses two oils and combines the advantages of vapor diffusion methods with the automation capability of micro-batch methods. As in the micro-batch method, the total system is protected from evaporation, for example, by paraffin oil (first phase). However, the protein/precipitant mixture (fourth phase) can equilibrate with a reservoir solution (third phase) via a second layer of oil (second phase) that is placed under the paraffin oil. The second oil is immiscible with the paraffin oil, and does not interact with or influence the properties of phases three and four. The system is summarized in Figure 10.4.

The system can be set up in several ways, using different plate geometries. In one approach, the protein/precipitant and the reservoir can be applied under the paraffin oil, resulting in a classic micro-batch experiment. When the second oil is added, water begins to diffuse from the protein droplet to the reservoir solution. The removal of phase II allows dynamic control of water diffusion and, because the system is protected from evaporation by the paraffin oil, small volumes of protein solution can

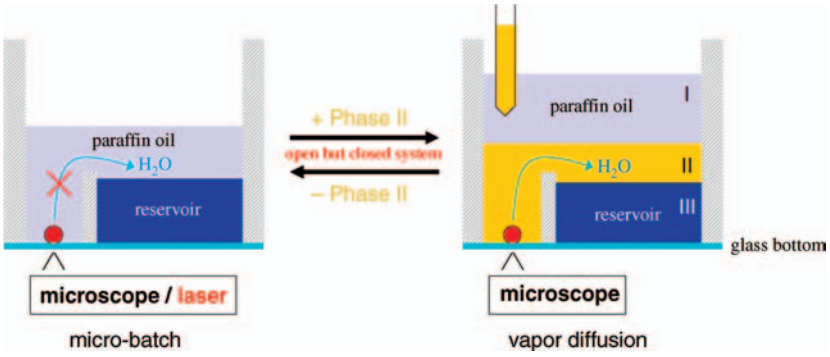

Figure 10.4 A new crystallization method based on a specially-designed oil phase that allows controlled water diffusion from the protein sample to the reservoir phase. The paraffin oil protects the system from evaporation and the glass bottoms of the plates enable optical measurements for the characterization of the protein samples.

Figure 10.5 A novel microplate was developed for the new crystallization system. This figure shows how the protein solution is applied under paraffin oil. A series of six droplets of various protein concentration are applied for the determination of the second virial coefficient. 96 virial coefficients can be determined within a single microplate.

be applied using a conventional liquid-handling system. The microtiter plates are equipped with a glass bottom that allows optical analysis of the protein sample without distortions from curved meniscus surfaces (Figure 10.5). The droplets of protein solution sit on the glass surface and adopt a hemispherical form. This can be supported by structuring the glass surface with a polar and nonpolar surface pattern. The light scattering optics can then be placed under the microtiter plate and the laser beam does not need to pass through curved surfaces on its way to the sample, so the laser beam can be focused precisely inside the sample even in small sample droplets.

10.4 Optical Measurements for a Rational Crystallization Process

Optical measurements can be used to characterize all three phases of the crystallization process, which avoids the need for trial and error strategies to find optimal solution conditions. Before nucleation takes place (pre-nucleation phase) the solute protein molecules interact with each other and with the solvent molecules, and this interaction potential can be measured by static light scattering. The formation of seed crystals begins with the aggregation of proteins (nucleation phase) which can be detected by dynamic light scattering. After the nucleation and growth phase (post-nucleation phase), the resulting single crystals, microcrystalline, or amorphous precipitates can be detected and characterized by quantitative polarization microscopy, which is better suited than standard microscopy for the detection and evaluation of crystalline features.

10.4.1 Static Light Scattering for the Analysis of the Pre-Nucleation Phase

Crystals form when attractive interactions between protein molecules are sufficient to drive them from the solute state to a thermodynamically more stable ordered solid state. If protein molecules repel each other, crystals do not form and the protein remains in solution. However, if the attractive interactions are too strong, massive precipitation may occur, yielding polycrystalline or even amorphous precipitates, because in this case even a disordered solid state is thermodynamically favored over the solute state. Therefore, conditions must be selected to favor slightly attractive interactions that achieve the necessary delicate balance between the absence of nucleation processes and the presence of too many nucleation processes. Only under these conditions is it possible to grow large single crystals.

In the pre-nucleation phase, static light scattering can be used to analyze the interaction potential between dissolved protein molecules. Static light scattering is a technique that measures the absolute intensity of the scattered light as a function of the scattering angle or the sample concentration. For static light scattering experiments, a high intensity monochromatic laser is focused on a protein solution, and one or more detectors are used to measure the scattering intensity at one or more angles. The average molecular weight M_w of a macromolecule, such as a protein, can be calculated from the angular dependence. The scattering intensity of different samples with identical crystallization conditions (salt concentrations, pH-value etc.) but different protein concentrations allows the second osmotic virial coefficient A_2 to be calculated. This empirical parameter can be used to describe the behavior of the osmotic pressure in a real sample, in contrast to an ideal sample. The deviation in osmotic pressure from the ideal behavior is expressed using A_2. To describe the osmotic pressure Π of a solution containing proteins of concentration c_P and molecular weight M_W, the osmotic virial expansion is set up as follows, where R is the universal gas constant and T is temperature:

$$\Pi = RTc_P\left(\frac{1}{M_W} + A_2c_p + \ldots\right)$$

The virial expansion is usually aborted after the second term [5].

If $A_2 = 0$, the virial expansion describes ideal behavior (compare with the corresponding formula for ideal gases). This means that the interaction between protein molecules in solution is neither attractive nor repulsive and they interact with each other as they interact with the solvent. If $A_2 > 0$, the osmotic pressure rises above ideal behavior, indicating repulsion between protein molecules. For negative A_2 values, the osmotic pressure is lower than under ideal conditions, and in this case the protein molecules attract each other more than they attract the solvent molecules. From a series of static light scattering measurements taken from solutions containing different protein concentrations c_P, the osmotic second virial coefficient A_2 and the molecular weight M_W can be deduced from the slope and the intercept of the so-called

Zimm plot based on the following equation:

$$\frac{Kc_P}{R} = \frac{1}{M_W} + 2A_2c_P$$

Here, K is an optical constant, representing the laser wavelength, the refractive index of the solvent and the refractive index increment of the sample. R is the so-called Rayleigh ratio, representing the normalized scattering intensity of the protein sample divided by the scattering intensity of toluene (the reference scattering compound). With the help of the reference substance, instrument-specific parameters (e.g., light collection efficiency, detector sensitivity) are regarded. The necessary calculations are explained in more detail by Wyatt [6].

The usefulness of the osmotic virial coefficient for the prediction of protein crystallization parameters was first described in 1994 by George and Wilson [7]. They showed for the first time that protein crystals often form when the precipitant induces a slight attraction between protein molecules in solution, which was a sound perception. Several other studies have demonstrated the importance of the second osmotic virial coefficient for the crystallization behavior of various proteins [8–10]. The point at which the virial coefficient becomes slightly negative, indicating slight but not excessive attraction between dissolved protein molecules, was therefore named the "*crystallization window*". The second virial coefficient can be determined by static light scattering (SLS), but alternative methods have been developed [11]. However, these are not easily combined within a screening process. Figure 10.6 shows several Zimm plots for the protein lysozyme with different salt concentrations.

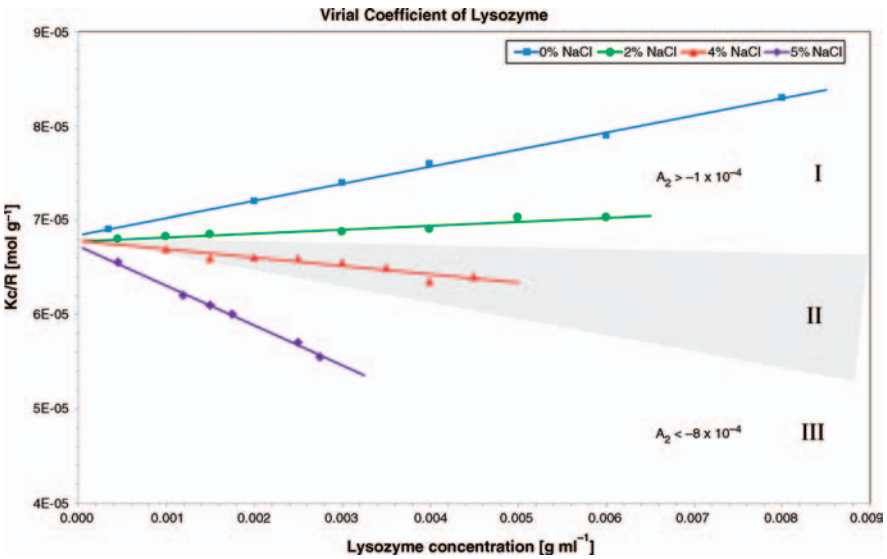

Figure 10.6 Measurement of the virial coefficient in the form of a Zimm plot. The crystallization window (area II) is highlighted in gray. This figure is based on the review by George and Wilson [7].

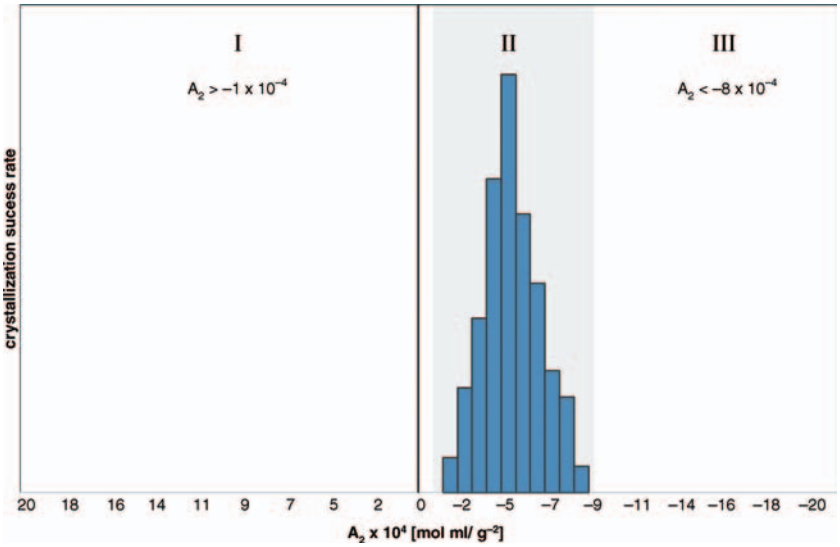

Figure 10.7 Success rate for different crystallization trials as a function of A_2. This figure is based on the review by George and Wilson [7].

Higher NaCl concentrations induce attractive forces between the protein molecules (negative slope in the Zimm plot). Crystals are only formed in area II (highlighted in gray), which has moderately negative A_2 values.

In order to verify the general utility of the crystallization window concept, many different proteins have been analyzed and the crystallization success rate was found to correlate with the second virial coefficient. Figure 10.7 shows that successful crystallization trials are concentrated in the crystallization window.

10.4.2 Dynamic Light Scattering for the Analysis of the Nucleation Phase

Quasielastic light scattering (QLS), also known as dynamic light scattering (DLS), is an optical method well-suited to determination of the diffusion coefficients of particles undergoing Brownian motion in solution. Diffusion coefficients are determined by particle size, shape and flexibility, as well as by inter-particle interactions. The dependence between the diffusion constant D_0 and the hydrodynamic radius R_h is described by the Stokes–Einstein equation:

$$D_0 = \frac{k_B T}{6\pi\eta R_h}$$

Here k_B is the Boltzmann constant, T the temperature and η the viscosity. Once the diffusion constant is known, it is possible to calculate particle sizes and to evaluate the distribution of heterogeneous particle mixtures.

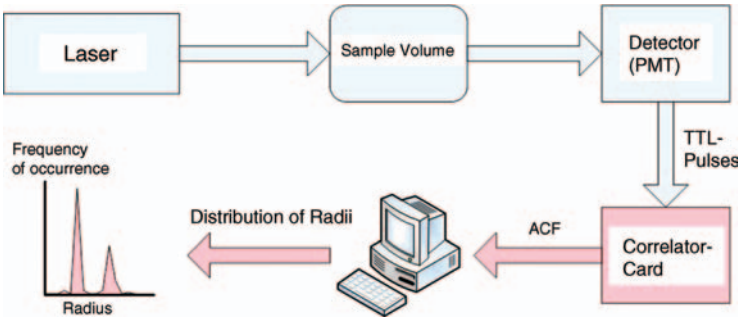

Figure 10.8 Concept of the dynamic light scattering process. The detector is a photon counting photomultiplier, and single photons are converted to electrical TTL-pulses. A correlator card calculates the autocorrelation function (ACF). With a computer, the distribution function of the radii can be calculated from the ACF.

Although the experimental set-ups used to measure DLS and SLS can be comparable, data processing and interpretation differ significantly (see Figure 10.8). A collimated or partially-focused laser beam is directed through the sample and scattered light reaching the detector at a defined collection angle is recorded as a function of time. Because the incident light is coherent, the scattered light forms an interference pattern. The pattern changes with the movement of the sample (e.g., Brownian motion), leading to intensity fluctuations that are related directly to the diffusion of the scattering particles.

Autocorrelation analysis can then be used to extract the diffusion coefficient from the temporal fluctuations in scattering intensity, and by inserting the diffusion coefficient into the Stokes–Einstein equation, it becomes possible to calculate the hydrodynamic radius of the moving particle. The autocorrelation function does not usually fit to a single particle size but to a distribution of hydrodynamic radii. The calculation of the size distribution is carried out with iterative fit-analysis containing inverse Laplace transformations. Specialized software packages such as CONTIN [12] are frequently used for this purpose following DLS experiments.

Figures 10.9 and 10.10 show the autocorrelation function and the calculated radius distribution for a lysozyme sample with a concentration of 50 mg ml^{-1}. The measurements were collected using a commercial light scattering instrument [13].

The polydispersity of the proteins in the size distribution is closely correlated to the success of protein crystallization. The presence of non-specific aggregates, various oligiomeric states and impurities widens the size distribution and, at the same time, reduces the likelihood that high-quality crystals will be generated. In this manner, DLS can be used to characterize the quality of a protein sample. With time-resolved measurements, it is also possible to monitor the process of aggregation. Aggregates can be seen as a pre-form to seed crystals, so the initial phase of nucleation can be directly observed with dynamic light scattering [14–16].

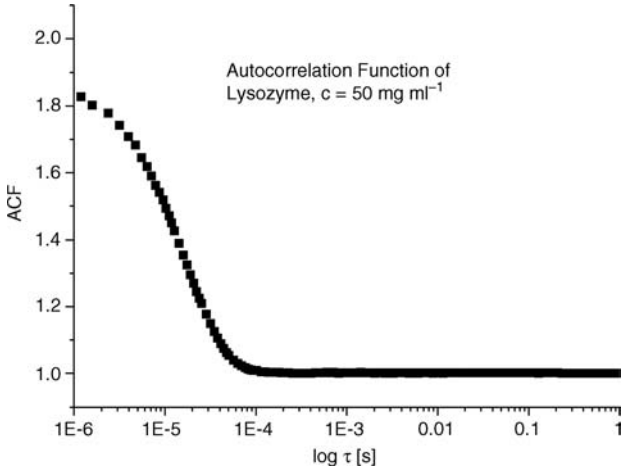

Figure 10.9 Autocorrelation function for lysozyme, recorded with a commercial light scattering instrument.

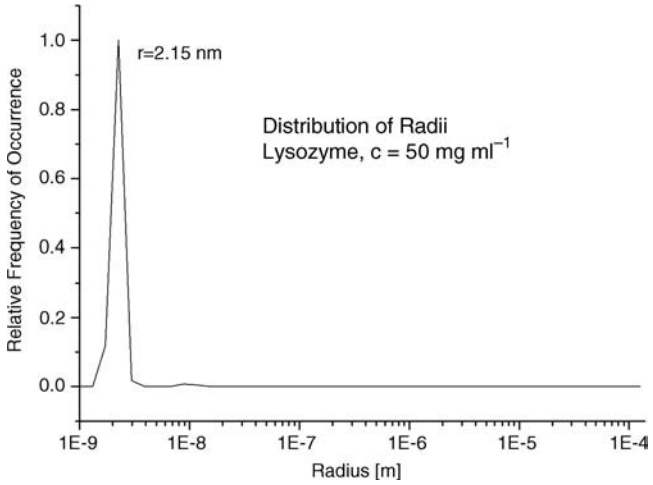

Figure 10.10 Calculation of the lysozyme radius from the ACF calculated in Figure 10.9.

10.4.3
Quantitative Polarization Microscopy for the Analysis of the Post-Nucleation Phase

Quantitative polarization microscopy is a robust and nondestructive method to analyze anisotropic properties of materials. Optical anisotropy of crystals leads to birefringence. The variation of the refractive index is dependent on the orientation of the incident light with respect to the crystal. It can be visualized by a mathematical

representation the so-called indicatrix. Light passing such anisotropic material undergoes birefringence corresponding to the ellipse axes length difference (Δn) of the indicatrix cross-section ellipse orthogonal to the propagation direction of the light. In the case of crystals, the shape of the indicatrix is defined by the symmetry of the crystal. In this respect, cubic crystal systems present a spherical indicatrix and shown birefringence. In order to detect birefringence, light with defined polarization states is used to probe the sample and the resulting properties of the light after transmittance through the sample are analyzed.

The technique we use to analyze anisotropic properties of protein crystals is based on the so-called rotating polarizer method [17], as implemented in the Taorad MP-1 microscope. This method allows the birefringence of precipitates and crystals to be determined quantitatively [18], and the diffraction quality of crystals to be predicted accurately [19]. Knowledge of the optical properties of a protein crystal allows the nondestructive determination of crystal diffraction quality before any X-ray data collection is attempted. This enables the pre-selection of high-quality crystals and provides a ranking system for crystallization experiments producing many crystals.

The optical train of a quantitative polarization microscope typically consists of a light source, a bandpass-filter, a (motorized) linear polarizer, a sample/microplate holder, a microscope objective, a circular analyzer and a camera (see Figure 10.11). The light intensity, which is recorded by each pixel (i,j) of the camera is described by:

$$I_{i,j} = I_{0_{ij}}[1-\sin 2(\alpha-\varphi)\sin\delta]$$

where $I_{0_{ij}}$ is the absorption affected incident light intensity (transmittance), α describes the relative orientation of the transmission axis of the rotating polarizer, $|\sin\delta|$ the relative optical anisotropy and φ the optical orientation of the indicatrix.

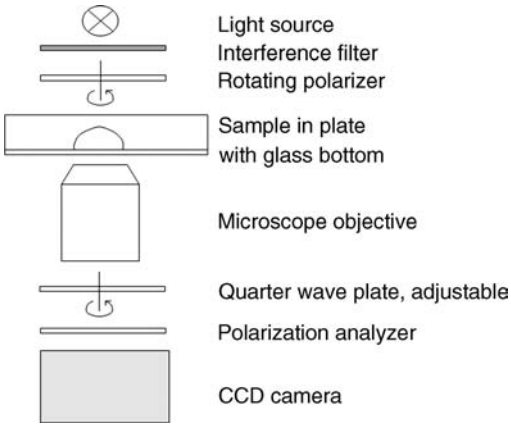

Figure 10.11 Concept of quantitative polarization microscopy. A series of images is recorded using different angular positions (α) of the rotating analyzer.

δ is the phase shift of the light:

$$\delta = \frac{2\pi}{\lambda}\Delta nL$$

where λ is the wavelength of the light, L the thickness of the sample, and $\Delta n = n_1 - n_2$; ΔnL represents the optical retardation.

In order to determine $I_{0_{ij}}$, $|\sin\delta|$ and φ, several images at different linear polarizer orientations (α) are recorded, the data processed pixelwise and represented as grayscale image ($I_{0_{ij}}$) or as false-colored images ($|\sin\delta|$ and φ). $|\sin\delta|$ is related to the thickness of the crystals and φ represents the orientation of the observed slow axis of the elliptical cross-section through the indicatrix on each image pixel of the crystal and can be correlated with the internal order of the crystal.

Quantitative polarization microscopy is not only suitable for analysis of the properties of larger monocrystals, but is also extremely useful to detect anisotropic properties of precipitates (Figure 10.12), and to discriminate between amorphous and microcrystalline precipitates.

Echalier *et al.* showed [18], that the application of quantitative polarization microscopy allowed a much earlier detection of microcrystals as compared to classical microscopic observations (see Figure 10.13).

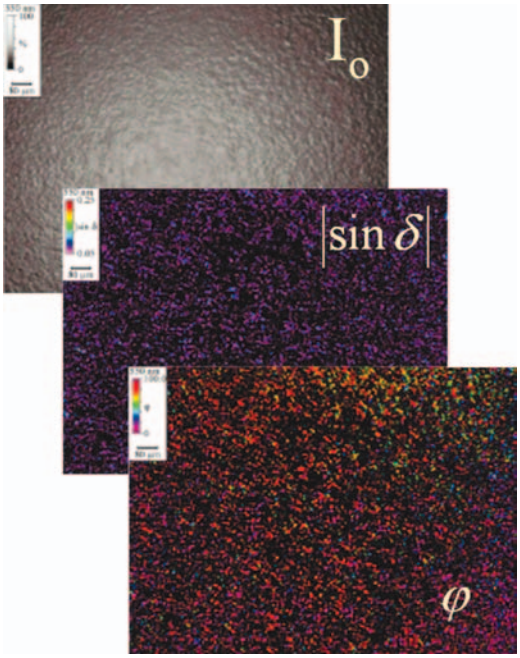

Figure 10.12 Three images for transmission (I_0), birefringence amplitude $|\sin\delta|$ and orientation φ of a microcrystalline sample. This figure is taken from the review by Echalier *et al.* [18].

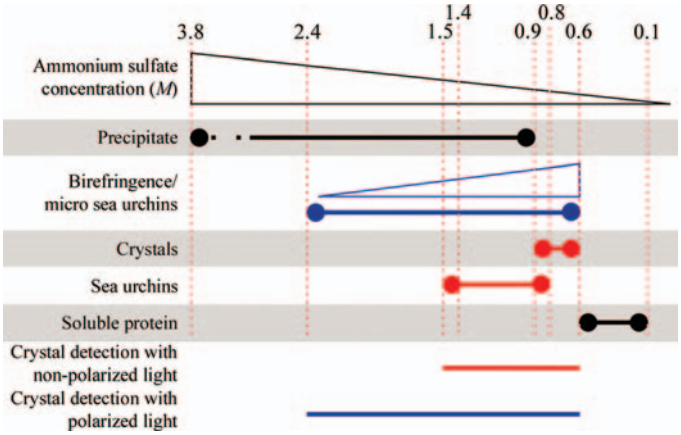

Figure 10.13 Early detection of crystals with the help of quantitative polarization microscopy. Crystallization of glucose isomerase using ammonium sulfate as precipitant was detectable at concentrations between 1.5 and 0.6 M using classical microscopic inspection and from 2.4 to 0.6 M using quantitative polarization microscopy. The crystallization space is more efficiently screened and the risk of missing productive crystallization conditions reduced. This figure is sourced from the review by Echalier *et al.* [18].

10.5
Development of a New Optical Instrument

10.5.1
Measurement of Static and Dynamic Light Scattering in Small Volumes

The new crystallization process is based on the automated optical measurement of crystallization solutions. Because target proteins for crystallization experiments are often expensive and strictly limited in availability, crystallization experiments are usually set up using small sample volumes. Ideally, measurements should be possible in droplets $<1\,\mu l$ in volume. Commercial light scattering instruments for the measurement of virial coefficients use expensive glass cuvettes with volumes typically in the10 µl to 1 ml range. Static measurements in microtiter plates are not possible using commercial instruments because of the suboptimal measurement geometry. Automated sample preparation with liquid-handling robotics can only be achieved using microtiter plates, whereas single glass cuvettes must be cleaned and refilled manually. Plastic cuvettes cannot be used because the optical quality is insufficient.

Our novel crystallization concept, therefore, required the design and development of a new optical instrument allowing precise static and dynamic light scattering measurements to be obtained from small droplets less than 1 µl in volume in microtiter plates [20]. The measurement of dynamic light scattering is based on the evaluation of signal fluctuations caused by particle movement, therefore a background caused by reflections from interfaces that is constant over time does not significantly influence the readings. Static light scattering measurements are

more demanding because the absolute scattered light intensity must be measured in a small droplet volume in close proximity to several interfaces (glass/oil, oil/water). The curved surfaces of the droplet create reflections of the incident laser beam that are difficult to control, which is why precise measurements of static light scattering inside small droplets have appeared impossible to achieve. Unlike confocal laser scanning microscopy the static light scattering experiment does not include a frequency shift resulting from the fluorescence phenomenon that can be used to effectively suppress the excitation light with the help of interference filters. The detected scattered light has more or less the same frequency as the excitation laser, so only geometrical approaches can be used to separate scattered light from the unwanted background. The suppression of undesirable reflections and scattering from interfaces is, therefore, the key for successful static light scattering measurements in small volumes. The closer the interfaces are, the more difficult effective suppression becomes.

The solution to this technical challenge is to use an optical device that combines confocal microscopy optics with dark-field illumination. The confocal concept allows three-dimensional limitation of the probed sample volume, but unlike conventional confocal microscopy the illumination has a separate optical path to that used for light collection. An annular parabolic mirror is used to focus a laser beam with the same profile into the sample, and data are collected from the middle of this mirror by the light-detection optics. The system is summarized in Figure 10.14 and the following numbers refer to those in the figure. The laser beam (single mode fiber-coupled diode laser, 658 nm) (1) passes through a beam-shaping optical system (2) to form an

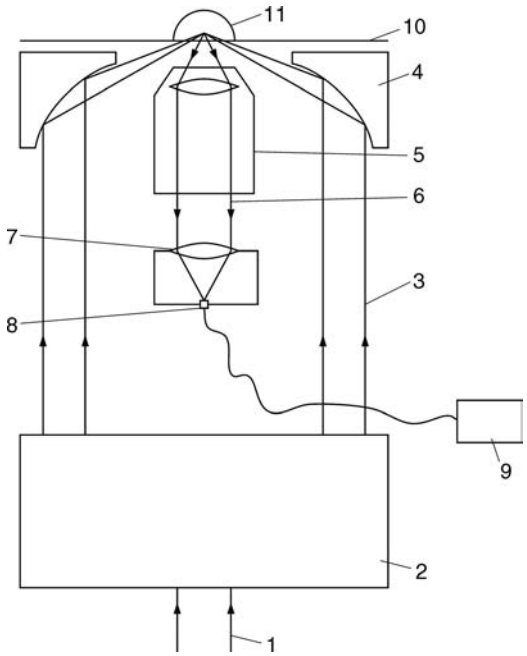

Figure 10.14 Schematic drawing of the confocal dark-field optics used for static and dynamic light scattering measurements in small sample droplets (see text for full explanation).

annular beam (3). The easiest way to generate an annular beam is to enlarge the beam diameter with a telescope and then to use an annular aperture that removes unwanted parts of the beam. The overall transmission of this concept is poor, and if maximum laser intensity is needed for the measurement, special ring-shaping optics can be used with more than 80% transmission. This can be achieved with two glass axicons or with two metallic mirrors in the form of inner and outer cones. The annular beam is then focused by the parabolic mirror (4) into the sample droplet (11), which is placed on a microtiter plate with a glass bottom (10). To prevent the small droplet from evaporating, it is protected under oil. This dark-field illumination strongly suppresses direct reflections from the air/glass and glass/water interfaces because the acceptance angle of the detection optics (microscope objective 5) is much smaller than the illumination angle. From the laser focus inside the sample droplet, light is scattered in all directions and reaches the detection optics (5). Because the focal planes of the parabolic mirror and microscope objective are precisely aligned, light from the focus forms a collimated beam (6). Reflections coming from the curved surface of the sample droplet or from scratches and impurities on the glass surface can also reach the microscope objective, but will form converging or diverging beams as their origin lies outside the objective focal plane. To form a confocal microscope, the scattered light is focused with an achromatic lens (7) onto a small confocal aperture, the front surface of a single mode fiber (8). All unwanted unfocused light collected by the microscope objective is strongly suppressed here and cannot enter the waveguide fiber, which directs the detected photons to a sensitive single-photon counting detector, for example, a photomultiplier (9). Here the integral intensity and the temporal fluctuations of the scattered light are detected and evaluated for static and dynamic measurements. We used a Hamamatsu R2949 photomultiplier with photon-counting ability for this purpose.

The twofold suppression of light reflected from the interfaces (confocal principle and dark-field illumination) generates an excellent signal-to-background ratio and enables static and dynamic light scattering measurements to be collected from

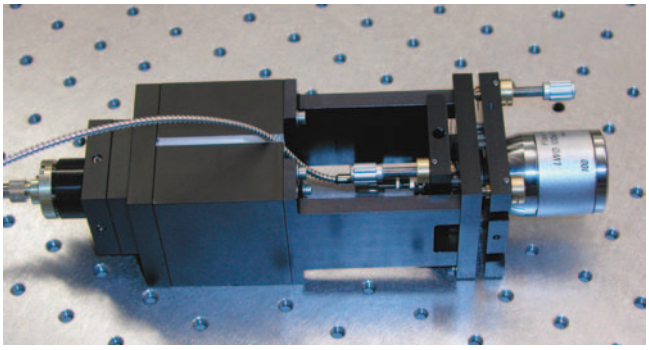

Figure 10.15 Optical apparatus for the measurement of static and dynamic light scattering in small droplets. The dark-field microscope objective with a parabolic mirror can be seen on the right, and the beam-shaping optics for the formation of the annular excitation beam is inside the housing on the left. Two single-mode fibers connect the optics to the excitation laser and detector.

proteins in droplets with a volume as low as 200 nl. The concept of this new optics was patented by the authors [20].

The compact optical apparatus used to achieve the above measurements is shown in Figure 10.15. Both the parabolic mirror and the single-mode fiber-coupling optics must be aligned accurately. Tilting the parabolic mirror with respect to the axis of the annular excitation beam distorts the focus, and maladjustment of the fiber-coupling optics results in a sharp drop-off in signal intensity because the focused scattered light must be aligned precisely onto the single-mode fiber, which has a diameter of just a few micrometers.

10.5.2
Quantitative Polarization Microscopy

The quantitative polarization microscopy module was designed similarly to the system already described by Glazer and colleagues [17], that is, an inverted, infinity-corrected microscope with a motorized rotating polarizer. A fixed offset was introduced between the optical modules for light scattering and polarization microscopy along the *x*-axis. Both optics are used by the automation module of the demonstrator (see below) to measure laser-light scattering and microscopic data in the same droplets (see Figure 10.16).

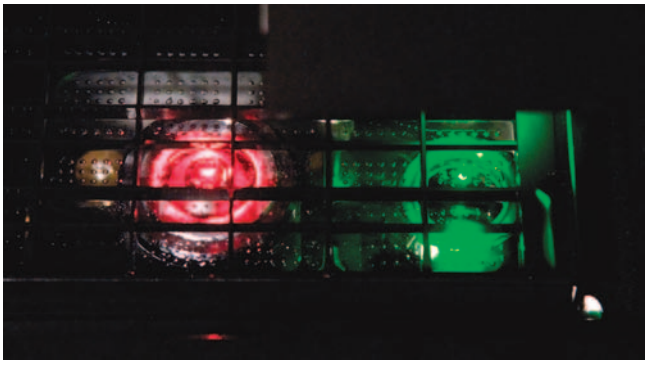

Figure 10.16 The two optical modules for the light scattering (left) and quantitative polarization microscopy (right) are shown within the demonstrator. A crystallization plate containing small droplets of protein solution is placed on top of the modules as shown.

10.5.3
System Integration, Automation and Data Processing

To evaluate the new crystallization procedure, we built a demonstrator containing a liquid-handling system for sample preparation, a light scattering and microscopy module, an *x*/*y* translational stage to position microtiter plates, a *z* translational stage to focus the light scattering and microscopy module, and a rotational stage for the

Figure 10.17 Demonstrator for the new crystallization system. A liquid-handling system for sample preparation is positioned above the optical modules inside the housing.

polarization microscopy (Figure 10.17). The system was fully automated and connected to a database application to manage the acquisition, archiving, retrieval and analysis of experimental data.

10.6 Optical Measurements

The demonstrator was used to obtain measurements from small droplets (typically 1 μl volume) in microtiter plates with a glass base. The demonstrator was set up in a temperature-controlled laboratory with 1 °C temperature stability over 24 h. In this section we report the first performance measurements for the light scattering optics, then virial coefficient determinations for different proteins with different solvent conditions. Examples are also provided for measurements recorded by dynamic light scattering and quantitative polarization microscopy.

10.6.1 Static Light Scattering

10.6.1.1 Instrument Performance

The performance of the light scattering optics was tested using solutions containing reference particles, that is, stable latex beads with a uniform diameter of 20 nm. The concentration of the particles was adjusted so that the light scattering signal from the highest bead concentration was comparable to the scattering intensity of a 50 mg ml^{-1} solution of lysozyme.

The most important feature of the light scattering optics is the signal-to-background ratio. The background comprises all the signal components from interfaces in the sample and from the instrument itself. We measured this background using a droplet of filtered water, assuming that the water itself gives no significant scattering signal. The water droplet was then replaced with droplets containing latex bead suspensions of different concentrations. The recorded scattering intensity is shown in Figure 10.18, presented as photon counts per second as a function of the relative bead concentration. The minimal signal generated by the pure water droplet confirms the effective suppression of unwanted reflections and scattering from the interfaces achieved by combining confocal optics and dark-field illumination. The signal is also near linear, allowing the calculation of a regression coefficient of $R = 0.99974$.

The measurement volume of the light scattering optics is much smaller than the diameter of the sample droplet. The size of 1 μl droplets is typically 700 μm, the focus of the detection optics is less than 5 μm in diameter. In order to determine the influence of the droplet walls on the scattering intensity, we scanned the microtiter plate moving the laser focus, and recorded the signal along a trace through the

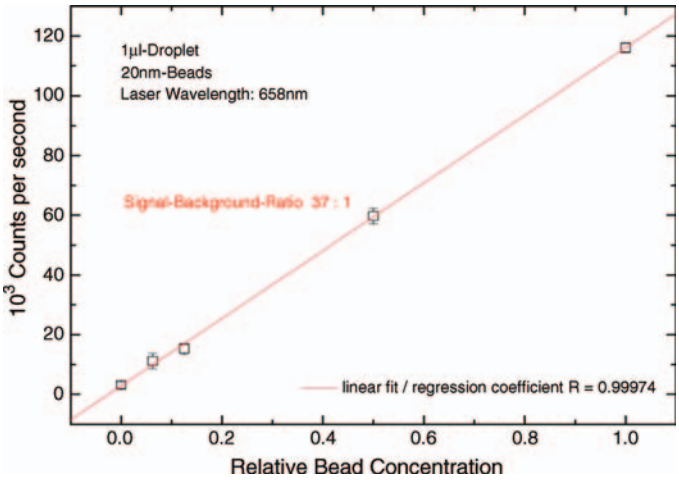

Figure 10.18 Signal-to-background ratio for measurements taken from 1-μl droplets containing latex beads (20 nm diameter). Only minor components of the signal originate from the interfaces, generating an excellent signal-to-background ratio of 37 for the highest bead concentration. The signal also remains linear over a range of relative bead concentrations.

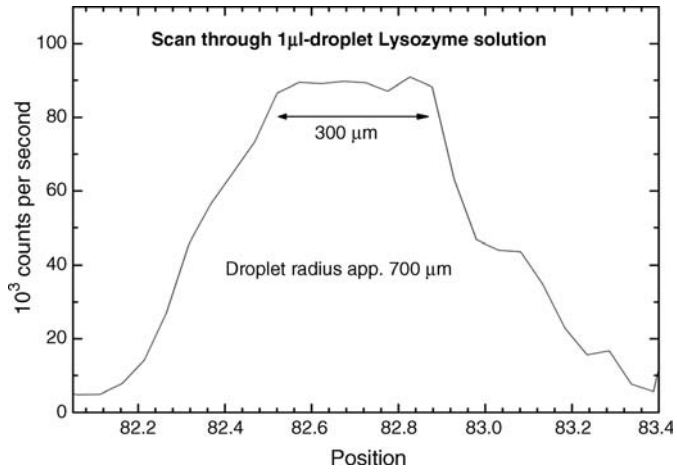

Figure 10.19 Scan through a droplet containing 1 µl of a lysozyme solution. The middle of the droplet is characterized by a constant scattering intensity which decreases as the laser focus moves closer to the wall of the droplet.

droplet. As shown in Figure 10.19 a plateau of relatively stable signal intensity forms in the center of the droplet, and the intensity only decreases when the focus approaches the droplet walls, due to shadowing effects. This behavior confirms that unwanted reflections and scattering signals from the interfaces are strongly and efficiently suppressed by our new optics.

10.6.1.2 **Measuring the Virial Coefficient of Proteins**

Two model proteins were used to test our new system, as this allowed our data to be compared to virial coefficients that have already been published. Lysozyme is a relatively small, compact protein whose crystallization behavior is well known, and it has been extensively studied with various light scattering methods. The second model, glucose isomerase, is a much larger protein than lysozyme, and belongs to a different protein family. In the case of lysozyme, we added NaCl to modify the interaction forces between dissolved molecules, changing them from repulsive to weakly attractive, as previously described [21].

Figure 10.20 shows the scattering intensity measured for the lysozyme solution, and the insert shows a three-dimensional model of lysozyme. Figure 10.21 shows the Zimm plot for the corresponding measurements. Only relative virial coefficients are plotted because no toluene reference measurements were collected. The optical constant K is defined to be one and the protein concentration is divided by the recorded scattering intensity (measured in counts per second, cps) minus the background intensity (the signal that is recorded with crystallization solution without protein, cps[0]). For automated crystallography, it is crucial to observe trends in the relative virial coefficient that correspond to changes in solution conditions. Positive and negative values can be clearly distinguished, and relative virial coefficients differ only by a multiplication factor from absolute virial coefficients.

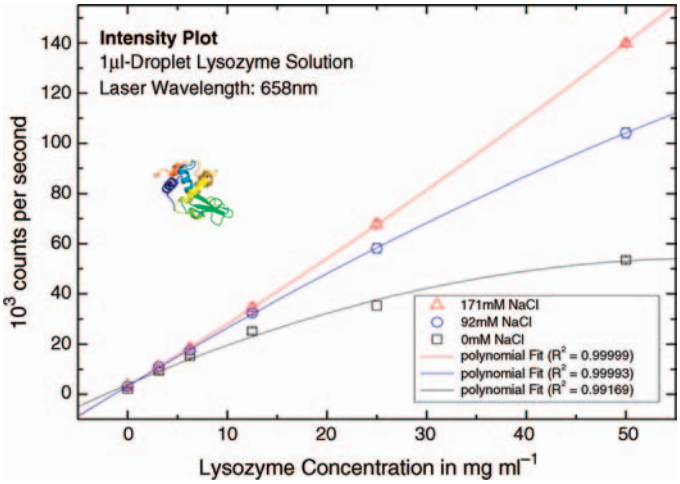

Figure 10.20 Scattering intensities observed in lysozyme solutions with three different sodium chloride concentrations. Measurements were recorded using 1-µl droplets.

The Zimm plot clearly shows the change in the interaction potential between protein molecules. The higher salt concentrations strongly reduce intermolecular repulsive forces and promote intermolecular attraction. As the solutions are clear, microscopic analysis does not yield any information about the status of the crystallization experiment.

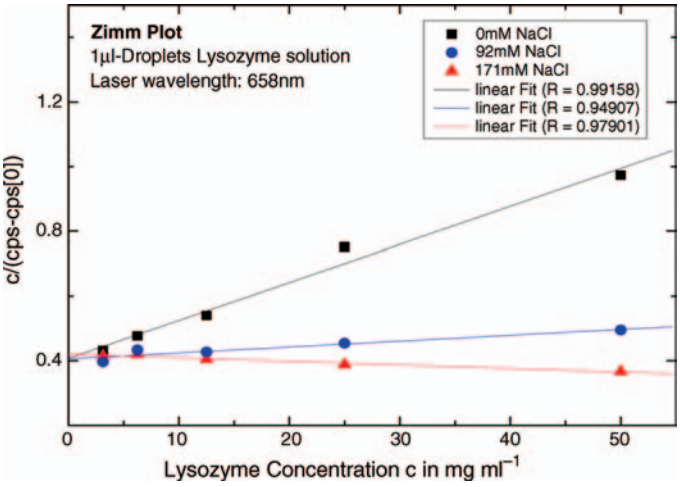

Figure 10.21 Zimm plot for lysozyme solutions under different conditions. The gradient indicates the molecular interaction potential. Positive gradients indicate repulsive forces between molecules, and negative gradients indicate attractive forces. Proteins that interact to the same degree with protein and solvent molecules (ideal solution) generate a horizontal line in the Zimm plot.

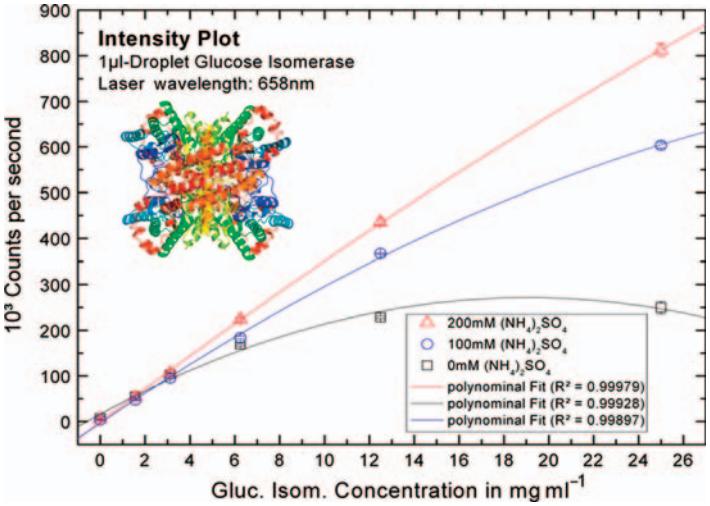

Figure 10.22 Scattering intensities observed in glucose isomerase solutions with three different ammonium sulfate concentrations. Measurements were recorded using 1-µl droplets.

Figure 10.22 shows the scattering intensity measured for the glucose isomerase solution and the corresponding Zimm plot is shown in Figure 10.23. These reveal that interactions between protein molecules are influenced by the addition of ammonium sulfate, changing repulsive forces in water to weakly attractive forces

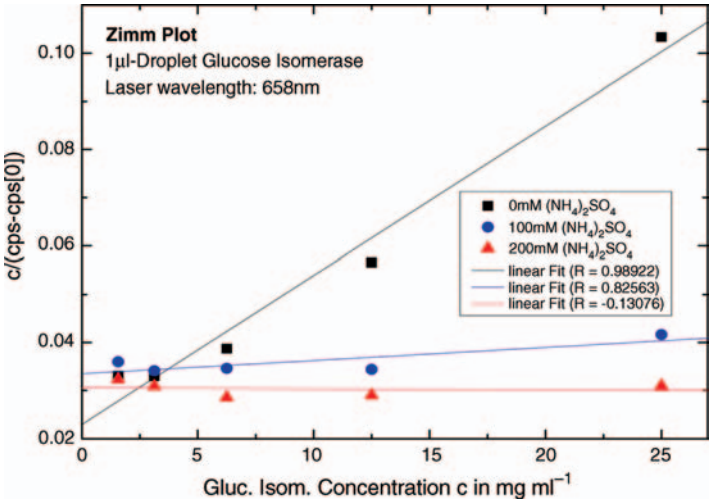

Figure 10.23 Zimm plot for glucose isomerase under different conditions. The gradient indicates the molecular interaction potential. Positive gradients indicate repulsive forces between molecules, and negative gradients indicate attractive forces. Proteins that interact to the same degree with protein and solvent molecules (ideal solution) generate a horizontal line in the Zimm plot.

in 200 mM ammonium sulfate. Glucose isomerase is larger than lysozyme, so the incident light is scattered much more strongly and the scattered light intensities are correspondingly higher.

10.6.1.3 Development of the Virial Coefficient with Different Solvent Parameters

We next set out to determine the robustness of the crystallization window as a requirement to obtain protein crystals (not to be confused with assuming the crystallization window in any way guarantees the formation of protein crystals). For this purpose, we used *Tritirachium album* proteinase K as a model because it forms crystals in the presence of many different precipitant formulations, hence the sparse matrix reagent kits that can be purchased from different providers. The virial coefficients resulting from such productive crystallization conditions should indicate small negative values for the second virial coefficient. The outcome of this experiment clearly validated the hypothesis, since all crystallization conditions yielded a negative virial coefficient even though some precipitants with negative virial coefficients were unable to generate protein crystals (Figure 10.24).

In order to test the validity of our approach in a screening process, we constructed a two-dimensional grid screen and used glucose isomerase as a reference protein. We screened the pH of the solution and the ammonium sulfate concentration, producing

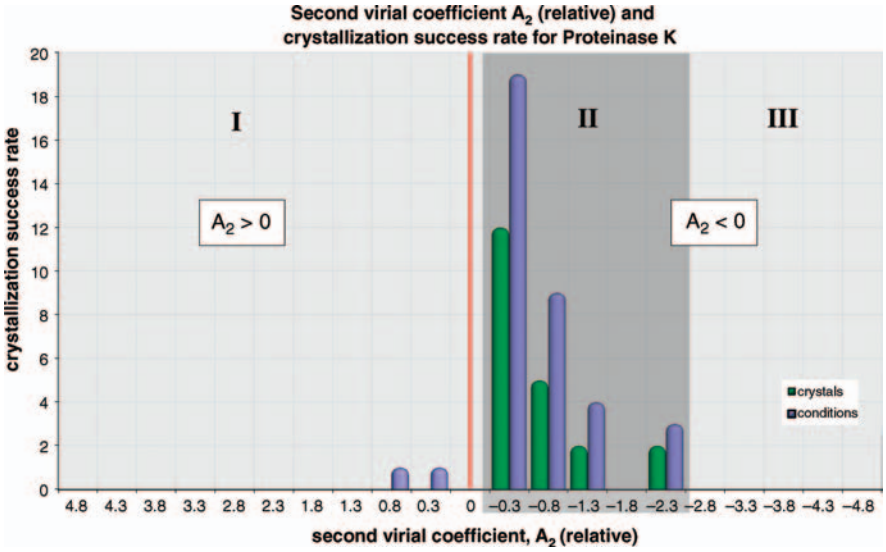

Figure 10.24 Crystallization success rate for *Tritirachium album* proteinase K as a function of the relative second virial coefficient (A_2). We tested 42 different crystallization conditions (Hampton Research, Crystal Screen I). In 37 cases, A_2 was determined via SLS. Each of the 21 experiments that produced crystals had a negative A_2 value. Furthermore, 14 experiments yielded a negative virial coefficient without forming any crystals or precipitates. In 8 of these 14 experiments, crystals were obtained by increasing the precipitant concentration. Two conditions yielded a positive virial coefficient and neither crystals nor a precipitate were formed.

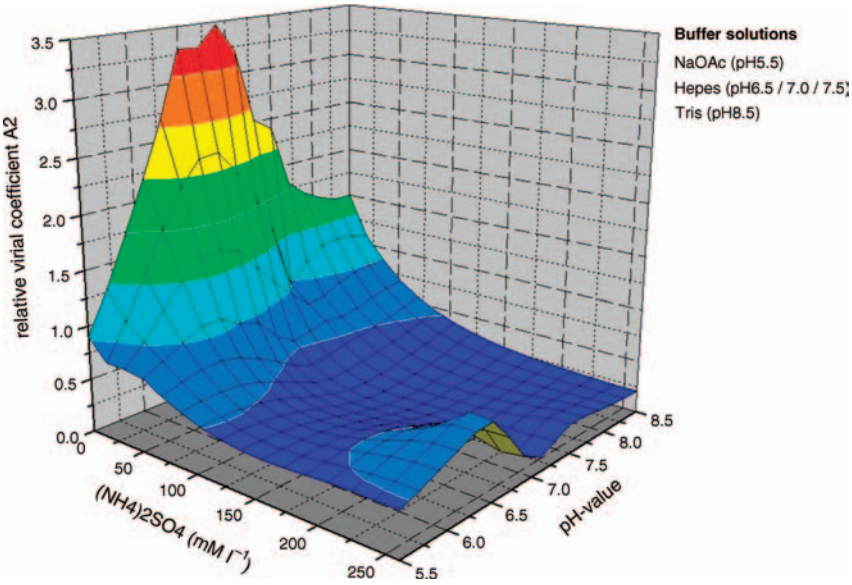

Figure 10.25 Evaluation of the second virial coefficient A_2 as a function of the ammonium sulfate concentration and pH of the precipitant solution.

a three-dimensional representation of the virial coefficients as a function of both parameters. On this surface, we observed a clear tendency towards a productive crystallization solution, as represented by the valley toward a negative virial coefficient (neutral pH at higher ammonium sulfate concentrations) (Figure 10.25). This indicates that a systematic characterization of solution parameters using the second virial coefficient to optimize molecular interactions can help to identify the most productive crystallization conditions objectively. Furthermore, this method can also be used to optimize solution parameters that favor repulsion between protein molecules, for example, in applications such as the formulation of biopharmaceuticals to prevent aggregation/precipitation and increase shelf-life.

10.6.2
Dynamic Light Scattering

We used the demonstrator to carry out a proof-of-concept analysis on the size distributions of bead particles, proteins and protein aggregates. To cover the typical size range for proteins, we measured the light scattered from a small protein (lysozyme) and from 20-nm latex beads. Figures 10.26 and 10.27 show the autocorrelation function and the size distribution for beads with a nominal diameter of 20 nm, and these match the expected values. Figures 10.28 and 10.29 show the autocorrelation function and the corresponding size distribution for lysozyme, and this indicates a hydrodynamic radius of 1.3 nm. A commercial instrument using a

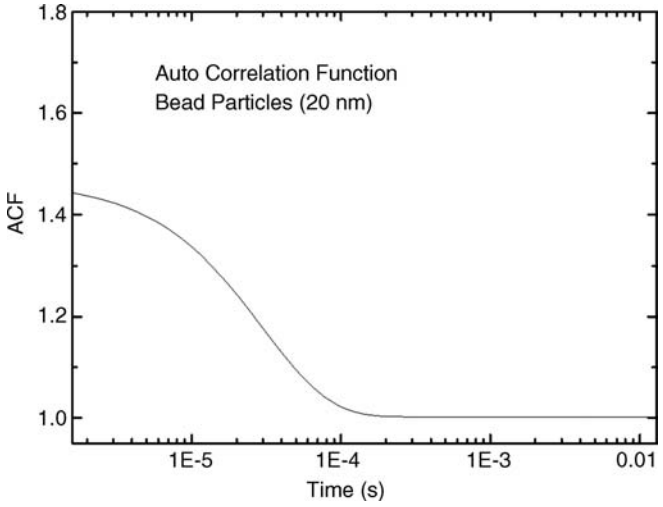

Figure 10.26 Autocorrelation function for bead particles 20 nm in diameter, measured in a 1-μl droplet with the new confocal dark-field optics.

fixed back-scattering angle of 173° indicates a hydrodynamic radius of approximately 1.89 nm [22]. The deviation between these measurements reflects the different light collection geometries of the instruments.

In crystallization experiments, it is particularly important to detect changes in particle size distributions. We used bovine serum albumin (BSA) to verify the ability

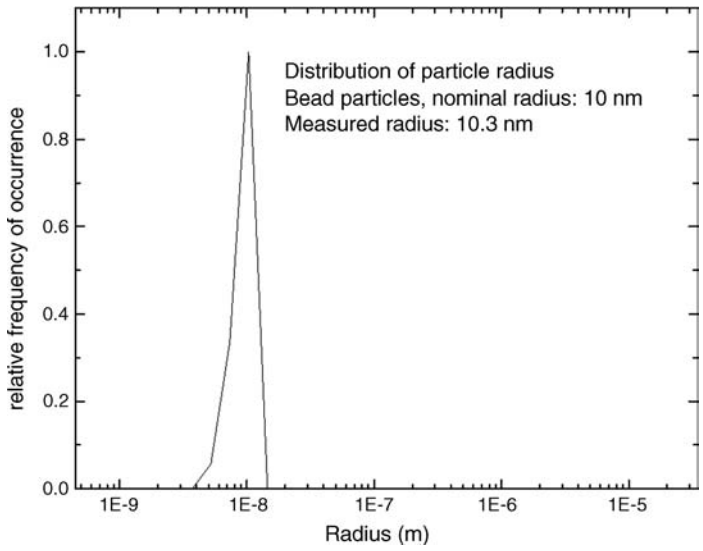

Figure 10.27 Size distribution for bead particles 20 nm in diameter calculated from the autocorrelation function in Figure 10.26, indicating a good agreement between nominal and measured size.

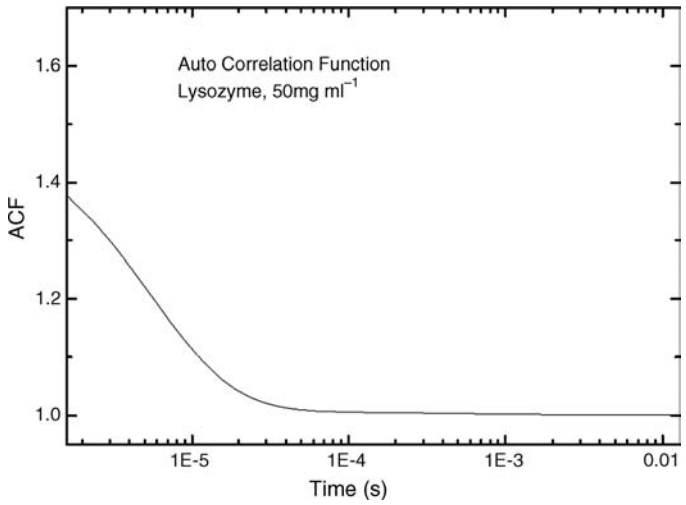

Figure 10.28 Autocorrelation function for lysozyme, measured in a 1-µl droplet with the new confocal dark-field optics.

of our new system to detect such changes because this protein undergoes a conformational change when heated to 70 °C. Heat-denatured BSA molecules aggregate to form larger units, and can therefore be used as a model for aggregation processes in protein solutions. Dynamic light scattering measurements were therefore carried out using a BSA sample before and after heating to 70 °C (Figure 10.30).

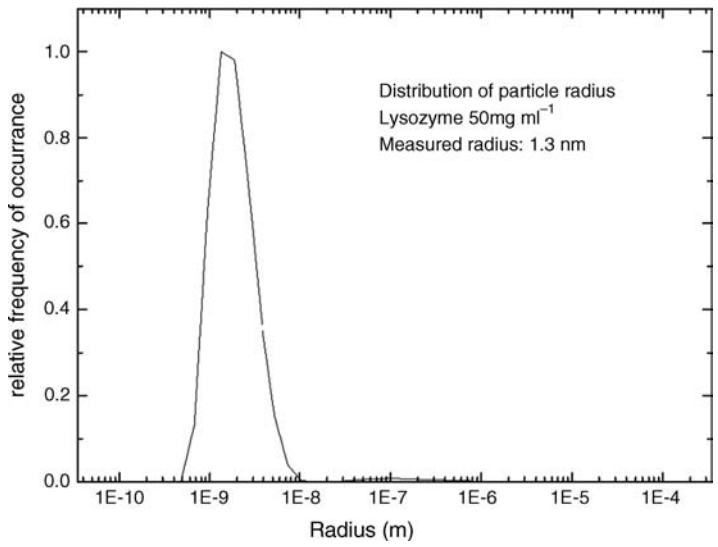

Figure 10.29 Size distribution for lysozyme calculated from the autocorrelation function in Figure 10.28, indicating a good agreement between nominal and measured size.

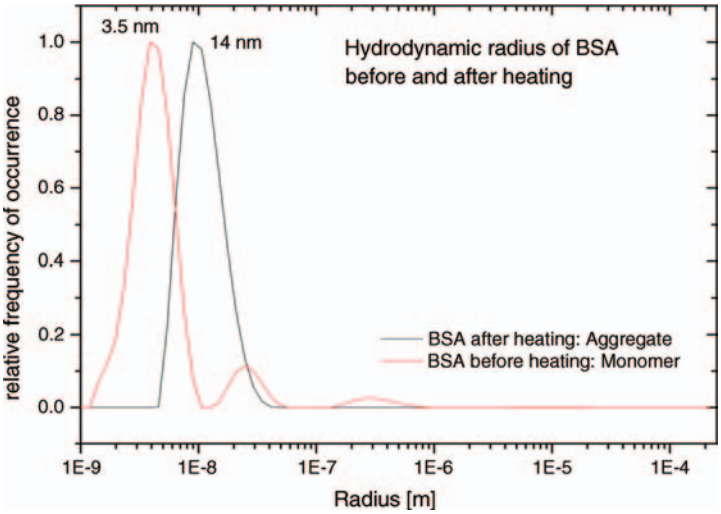

Figure 10.30 Size distribution of a BSA sample before and after heating to 70 °C. The shift in size distribution due to aggregation can be detected clearly.

The aggregation process can be followed clearly using DLS measurements and our results agree well with those already published [23].

10.6.3 Quantitative Polarization Microscopy

The optical properties of the novel crystallization plate provide the means to analyze crystallization experiments by quantitative polarization microscopy. As shown by Echalier *et al.* [18], microcrystals can be identified earlier under more productive crystallization conditions, allowing the efficient screening of crystallization environments to identify productive conditions rapidly. Furthermore, the ability of quantitative polarization microscopy to discriminate between amorphous and microcrystalline precipitates can, for the first time, be introduced into an automated crystallization screening platform.

Quantitative polarization microscopy data are presented as a series of three images, representing the birefringence properties of the precipitates or crystals within the crystallization droplet, namely the transmittance I_0, and the amplitude $|\sin \delta|$ and the orientation of the birefringence φ (Figure 10.31). The orientation of the birefringence, in particular, allows the identification of microcrystals in situations where all known classical methods would fail and even experienced crystallographers would not be able to identify suitable crystals.

Figure 10.32 shows a variety of possible outcomes often observed in classic protein crystallization experiments. The first series of images shows situations that can be difficult to interpret. Phase separation might be suspected in Figure 10.32a because of the droplet-like appearance of a second phase within the crystallization droplet, as seen in the transmittance image. However, the orientation image clearly indicates

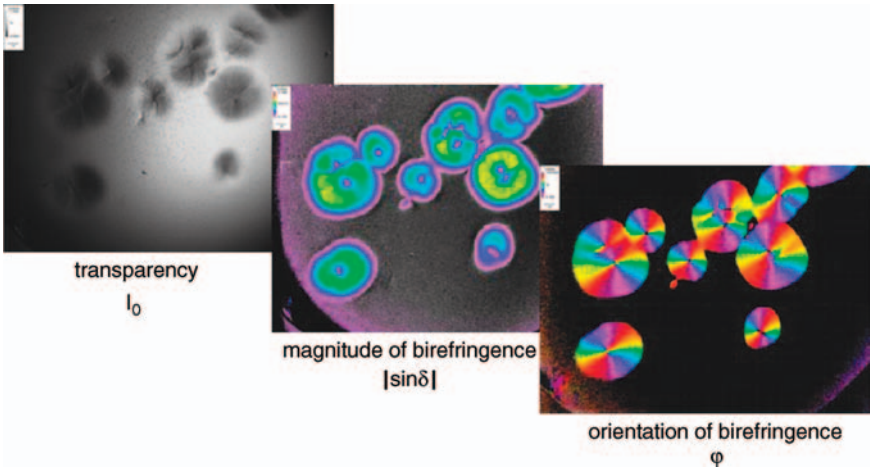

Figure 10.31 Analysis of a classical crystallization experiment, yielding so-called "sea-urchins" (thin needles clustered around a single nucleation site). The results are presented as a calculated transmission image (I_0), an amplitude image ($|\sin\delta|$) of the birefringence, and an orientation image (φ) of the birefringence. Sea-urchins are obtained when a central nucleation event is followed by the growth of a multitude of crystal-needles in all directions in space, as deduced by the centrosymmetric orientation of the microcrystals in the orientation image (φ) of the birefringence.

the presence of microcrystals, even identifiable as "sea-urchins", as already shown in Figure 10.31.

Quantitative polarization microscopy can also be used to identify well-ordered crystals, and to evaluate the impact of potential heterogeneity on crystal diffraction qualities. Figure 10.33 shows how the orientation image (φ) can be used to identify disordered regions of larger monocrystals that might interfere with diffraction analysis. In both panels, the transmission image highlights a potential region of disorder. In panel (a) the disordered region is also revealed in the orientation image, and several crystal lattices are thus shown in the diffraction image. In contrast, the potentially disordered region in panel (b) is not shown in the orientation image (φ). This indicates there is no disturbance of the anisotropic properties of the crystal and the diffraction image clearly shows the presence of a unique crystal lattice.

10.7
Outlook – An Iterative Optimization Process Based on Optical Measurements

To rationally determine crystallization conditions in the future, we developed an integrated and automated crystallization environment, based on a new crystallization method, a new crystallization plate, and new detection systems, allowing for the first time the application of objective measurements like static and dynamic light

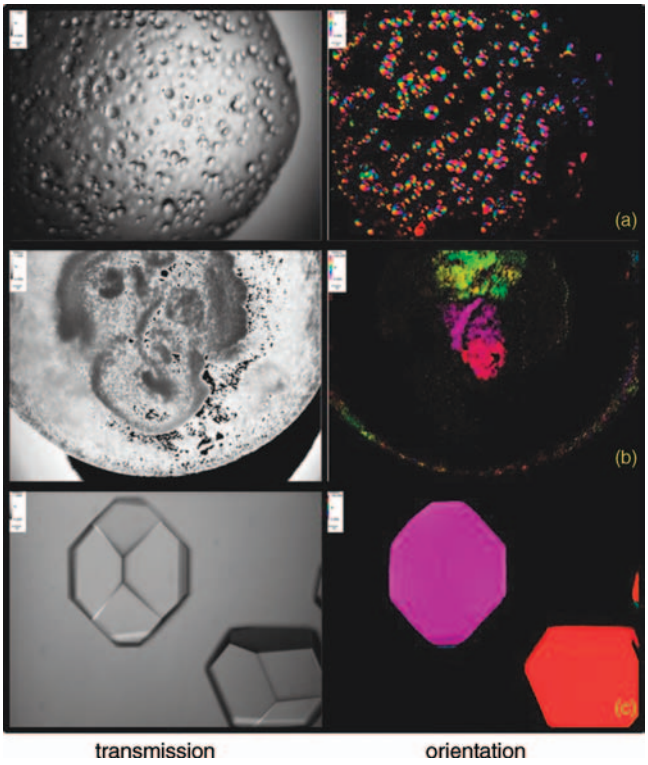

Figure 10.32 Quantitative polarization microscopy data from different crystallization experiments. Each row shows a different case (a, b, c), left side the transmittance image (I_0), right side the orientation image (φ):
(a) discriminating between sea-urchins and phase separation becomes possible, since phase separation would show no birefringence; (b) discriminating between amorphous precipitate (dark region in orientation image) and microcrystals (colored regions in orientation image); here both within the same drop, resulting from fast and slow mixing zones; (c) large and well-ordered monocrystals.

scattering, as well as quantitative polarization microscopy within each single crystallization droplet. The optical properties of our crystallization plate and the triple-phase system will allow us to further integrate valuable techniques, like the autofluorescence-based discrimination between protein and salt crystals using UV-light [24].

The implementation of sound, well-documented and unbiased information derived from thermodynamic solution parameters, such as the second virial coefficient, the detection of aggregates and nucleation sites using dynamic light scattering, the early and objective identification of microcrystalline precipitates, and the qualitative analysis of protein crystals using quantitative polarization microscopy, together with the potential to dynamically intervene within the crystallization process

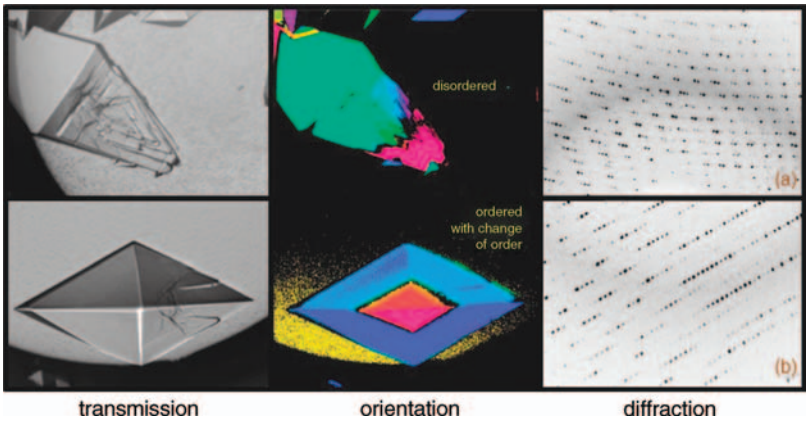

Figure 10.33 (a) transmission and orientation image of a disordered crystal, as predicted by the orientation image and confirmed by the diffraction data on the right side; (b) transmission and orientation image of an ordered crystal as predicted by the orientation image (despite apparent defects in the transmission image) and confirmed by the diffraction data. The two colors in the orientation image reflect a change in order due to the thickness of the crystal, resulting in a change of $\pi/2$ in the value of the orientation.

using classic liquid handling systems will cause a paradigm shift in the way protein crystallization is approached.

In the future, a fully automated crystallization system might become reality, which has the following unique features:

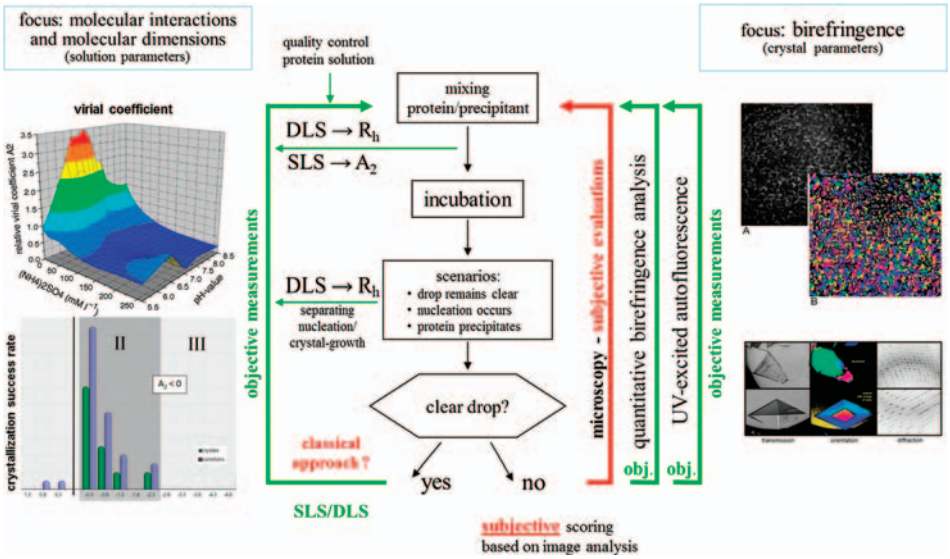

Figure 10.34 The concept for an iterative approach to the optimization of crystallization conditions based upon objective optical measurements.

- An automated iterative process based on cycles of static light scattering experiments to iteratively and automatically prepare precipitant conditions, placing all crystallization experiments within the necessary "*crystallization window*", avoiding non-productive crystallization conditions with positive virial coefficients.
- Quantitative polarization microscopy is used for early detection of microcrystals from unproductive amorphous precipitates.
- Dynamic laser light scattering is used to detect polydisperse protein solutions in order to optimize their monodispersity.
- Nucleation is uncoupled from crystal growth to produce larger crystals [14] by the control of vapor diffusion within the triple-phase system.
- Large single crystals are directly analyzed regarding their diffraction quality using quantitative polarization microscopy.

Figure 10.34 summarizes this new rational approach for a crystallization procedure based on objective optical measurements. The newly developed optical light scattering and polarization microscopy techniques described in this chapter form the basis of such an approach.

The research presented here was sponsored by the German Ministry of Economic Affairs and Employment.

References

1 McPherson, A. (1999) *Crystallization of Biological Macromolecules*, Cold Spring Harbor Press, New York.

2 Chayen, N.E. (1999) Crystallization with oils: a new dimension in macromolecular crystal growth. *J. Cryst. Growth*, **196** (2–4), 434–441.

3 Chayen, N.E. and Saridakis, E. (2002) Protein crystallization for genomics: towards high-throughput optimization techniques. *Acta Crystallogr. D*, **58** (2), 921–927.

4 Hoffmann, K. (2002) Protein crystallization method, patents WO2004012841, AU2003266957, CA2493335, EP2003747867, JP2005506071, KR1020057001501, US10522690.

5 Neal, B.L., Asthagiri, D., Velev, O.D., Lenho, A.M., and Kaler, E.W. (1999) Why is the osmotic second virial coefficient related to protein crystallization? *J. Cryst. Growth*, **196** (2–4), 377–387.

6 Wyatt, P.J. (1993) Light scattering and the absolute characterization of macromolecules. *Anal. Chim. Acta*, **272** (1), 1–40.

7 George, A. and Wilson, W.W. (1994) Predicting protein crystallization from a dilute-solution property. *Acta Crystallogr. D*, **50** (4), 361–365.

8 Neal, B.L., Asthagiri, O.D., Velev, O.D., Lenhoff, A.M., and Kaler, E.W. (1999) Why is the osmotic second virial coefficient related to protein crystallization? *J. Cryst. Growth*, **196** (2–4), 377–387.

9 Liu, T. and Chu, B. (2002) Light scattering by proteins. in *Encyclopedia of Surface and Colloid Science*, (ed. Arthur Hubbard, Marcel Dekker, New York), 3023–3043.

10 Ruppert, S., Sandler, S.I., and Lenhoff, A.M. (2001) Correlation of the osmotic second virial coefficient and the solubility of proteins. *Biotechnol. Prog.*, **17** (1), 182–187.

11 Tessier, P.M. and Lenhoff, A.M. (2003) Measurements of protein self-association as a guide to crystallization. *Curr. Opin. Biotech.*, **14** (5), 512–516.

12 CONTIN is a general-purpose constrained regularization method for continuous

distributions, such as inverse Laplace transforms in relaxation studies and in dynamic light scattering. The program can be downloaded from this site http://s-provencher.com/index.shtml.

13 Spectroscatter 201, RiNA GmbH.

14 Saridakis, E. and Chayen, N.E. (2000) Improving protein crystal quality by decoupling nucleation and growth in vapor diffusion. *Protein Sci.*, **9** (4), 755–757.

15 Chayen, N., Dieckmann, M., Dierks, K., and Fromme, P. (2004) Size and Shape determination of Proteins in Solution by a noninvasive depolarized dynamic light scattering instrument. *Ann. N.Y. Acad. Sci.*, **1027**, 20–27.

16 Lomakin, A., Teplow, D.B., and Benedek, G.B. (2005) Quasielastic light scattering for protein assembly studies, methods in molecular biology, in *Amyloid Proteins: Methods and Protocols*, vol. **299** (ed. E.M. Sigurdsson), Humana Press Inc., Totowa, NJ, pp. 153–174.

17 Geday, M.A., Kaminsky, W., Lewis, J.G., and Glazer, A.M. (2000) I mages of absolute retardance L. Deltan, using the rotating polariser method. *J. Microsc.*, **198** (1), 1–9.

18 Echalier, A., Glazer, R.L., Fulop, V., and Geday, M.A. (2004) Assessing crystallization droplets using birefringence. *Acta. Crystallogr.D*, **60** (4), 696–702.

19 Owen, R.L. and Garman, E. (2005) A new method for predetermining the diffraction quality of protein crystals: using SOAP as a selection tool. *Acta Crystallogr.D*, **61** (2), 130–140.

20 Hoffmann, K., Janzen, C., Noll, R., and Uhl, W. (2007) Device and method for measuring static and dynamic scattered light in small volumes. patents WO2009003714, EP 2008784613, JP2010513791, US12667601, DE 102007031244B3.

21 Muschol, M. and Rosenberger, F. (1995) Interactions in undersaturated and supersaturated lysozyme solutions: Static and dynamic light scattering results. *J. Chem. Phys.*, **103** (24), 10424–10432.

22 Parmar, A.S. and Muschol, M. (2009) Hydration and hydrodynamic interactions of lysozyme: effects of chaotropic versus kosmotropic ions. *Biophys. J.*, **97** (2), 590–598.

23 Bulone, D., Martonaraa, V., and San Biagio, P.L. (2001) Effects of intermediates on aggregation of native bovine serum albumine. *Biophys. Chem.*, **91** (1), 61–69.

24 Judge, R.A., Swift, K., and Gonzalez, C. (2005) An ultraviolet fluorescence-based method for identifying and distinguishing protein crystals. *Acta Crystallogr.D*, **61** (Pt 1), 60–66.